

# HIGH PRESSURE SCIENCE AND TECHNOLOGY

---

Proceedings of the Joint XV AIRAPT and  
XXXIII EHPRG International Conference

EXERCISES IN SCIENCE

Approved for public release  
Distribution Unlimited

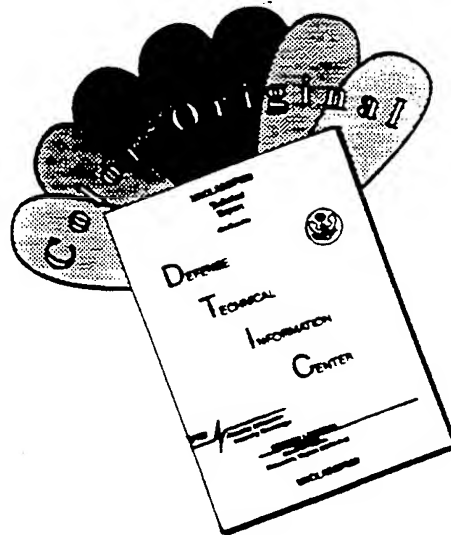
edited by

W A Trzeciakowski

19970516 057

World Scientific

# DISCLAIMER NOTICE



THIS DOCUMENT IS BEST QUALITY AVAILABLE. THE COPY FURNISHED TO DTIC CONTAINED A SIGNIFICANT NUMBER OF COLOR PAGES WHICH DO NOT REPRODUCE LEGIBLY ON BLACK AND WHITE MICROFICHE.



# **HIGH PRESSURE SCIENCE AND TECHNOLOGY**

---

**Proceedings of the Joint XV AIRAPT and  
XXXIII EHPAG International Conference**

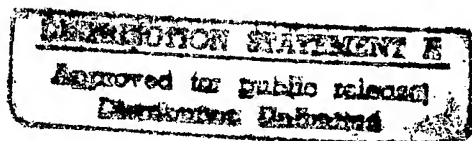
# High Pressure Science & Technology

Proceedings of the  
Joint XV AIRAPT&XXXIII EHPRG  
International Conference  
Warsaw, Poland, September 11-15, 1995

organized by

**High Pressure Research Center (UNIPRESS)**  
**Polish Academy of Sciences**  
and  
**Institute of Experimental Physics**  
**Warsaw University**

Editor:  
**Witold A. Trzeciakowski**



AIRAPT - International Association for the Advancement of High Pressure Science  
and Technology

EHPRG - European High Pressure Research Group.

DTIC QUALITY INSPECTED 1

---

*Published by*

World Scientific Publishing Co. Pte. Ltd.

P O Box 128, Farrer Road, Singapore 912805

*USA office:* Suite 1B, 1060 Main Street, River Edge, NJ 07661

*UK office:* 57 Shelton Street, Covent Garden, London WC2H 9HE

## **HIGH PRESSURE SCIENCE AND TECHNOLOGY**

Copyright © 1996 by World Scientific Publishing Co. Pte. Ltd.

*All rights reserved. This book, or parts thereof, may not be reproduced in any form or by any means, electronic or mechanical, including photocopying, recording or any information storage and retrieval system now known or to be invented, without written permission from the Publisher.*

For photocopying of material in this volume, please pay a copying fee through the Copyright Clearance Center, Inc., 222 Rosewood Drive, Danvers, MA 01923, USA.

ISBN 981-02-2547-4

Printed in Singapore.

## **CONFERENCE SPONSORS**

State Committee for Scientific Research (KBN)  
Polish Academy of Sciences (PAN)  
Ministry of Education (MEN)  
European Commission  
Siemens AG  
Gordon and Breach Publishers  
European Research Office, USARDSG-UK  
IRIS - Central Europe  
WACER Ceramics Ltd

## COMMITTEES

### ORGANIZING COMMITTEE

S. Porowski	<i>Chairman</i>
M. Baj	<i>Program Committee Chairman</i>
M. Siudecka	<i>Conference Secretary</i>
B. Pałosz	<i>Finances and Local Arrangements</i>
W. Trzeciakowski	<i>Publications</i>
J. Arabas	<i>Exhibition</i>
S. Szpakowski	<i>Local Arrangements</i>

### INTERNATIONAL PROGRAM COMMITTEE

B.A. Austin	<i>UK</i>	G.A. Samara	<i>USA</i>
M. Baj (Chairman)	<i>Poland</i>	A.B. Sawaoka	<i>Japan</i>
N.B. Brandt	<i>Russia</i>	S. Stishov	<i>Russia</i>
M. Chmielewski	<i>Poland</i>	K. Syassen	<i>Germany</i>
W. Łojkowski	<i>Poland</i>	M. Tkacz	<i>Poland</i>
A. Polian	<i>France</i>	B.A. Weinstein	<i>USA</i>
J-L. Robert	<i>France</i>	E. Włodarczyk	<i>Poland</i>

### NATIONAL ADVISORY COMMITTEE

M. Baj	J. Leliwa Kopystyński
B. Baranowski	J. Langer
J. M. Baranowski	W. Łojkowski
W. Bujnowski	K. Łukaszewicz
M. Falkowska	B. Pałosz
Z. Galus	J. Stankowski
J. Gustkiewicz	T. Suski
M. Grabski	W. Trzeciakowski
M. Grynberg	R. Wiśniewski
J. Jurczak	

## INTERNATIONAL ADVISORY COMMITTEE

A.R. Adams	<i>UK</i>	G. Molinar	<i>Italy</i>
K. Allakhverdiev	<i>Azerbaijan</i>	Y. Miyamoto,	<i>Japan</i>
B.A. Austin	<i>UK</i>	A. Niedbalska	<i>Poland</i>
V.D. Blank	<i>Russia</i>	W. Paul	<i>USA</i>
R. Boehler	<i>Germany</i>	A. Polian	<i>France</i>
J.B. Clark	<i>UK</i>	P. Pruzan	<i>France</i>
G. Demazeau	<i>France</i>	R. Pucci	<i>Italy</i>
S. Ellialtioglu	<i>Turkey</i>	J-L. Robert	<i>France</i>
O. Fukunaga	<i>Japan</i>	R.G. Ross	<i>Sweden</i>
V.E. Fortov	<i>Russia</i>	A.L. Ruoff	<i>USA</i>
P.D. Hatton	<i>UK</i>	P. Salański	<i>Poland</i>
D. Hausermann	<i>France</i>	E. Salje	<i>UK</i>
L. Helm	<i>Switzerland</i>	H. Schulz	<i>Germany</i>
K. Heremans	<i>Belgium</i>	J. Shaner	<i>USA</i>
W.B. Holzapfel	<i>Germany</i>	A. Sharp	<i>UK</i>
J. Jonas	<i>USA</i>	O. Shimomura	<i>Japan</i>
E. Kaldis	<i>Switzerland</i>	A.K. Singh	<i>India</i>
J. Kamarad	<i>Czech Republic</i>	V.T. Solozhenko	<i>Ukraine</i>
A. Laisaar	<i>Estonia</i>	R.A. Stradling	<i>UK</i>
V.I. Levitas	<i>Ukraine</i>	B. Sundqvist	<i>Sweden</i>
H. Lorenz	<i>Germany</i>	Y. Taniguchi	<i>Japan</i>
H.D. Lüdemann	<i>Germany</i>	H. Vollstadt	<i>Germany</i>
H. Ludwig	<i>Germany</i>	P. Wyder	<i>France</i>

## From the Editor

AIRAPT/EHPRG conferences are very broad in scope. They cover various aspects of high-pressure physics, chemistry, biology, geology, mechanical and material engineering etc. It is not easy to deal with papers (and authors) from all these different areas. First of all it is necessary to set some common scientific standards to all submitted papers. These standards are not the same in different communities. For example, some authors from engineering areas were reluctant to include a list of references as if they were the first to work on certain subjects. In several cases when the scientific content seemed valuable I did not reject such papers although I was not satisfied with the presentation. I also have to excuse myself for being very tolerant as far as the English of some presentations was concerned. I realise that some authors have a very poor command of English and that their papers have been translated by non-specialists in the area. This often leads to very awkward styling or to expressions that are hardly understandable.. My policy was not to reject such papers if it seemed that the scientific content was not totally obscured by the language mistakes.

All papers went through a two-stage refereeing process i.e. in case when the paper required corrections, the authors had the chance to introduce them and to resubmit the paper again. In all dubious cases I looked for a second referee. In particular, all rejected papers have been evaluated by two referees.

The papers have been divided into eleven chapters and chapters into sections. This division was somewhat arbitrary because the categories overlap. I believe that it would make sense to create the list of subjects for the AIRAPT/EHPRG conferences so that in the future the authors submitting their paper could choose the most appropriate category. Also a set of keywords picked up by the authors from some complete list would help create a useful subject index.

I would like to thank my colleagues, Prof. M. Baj, Drs. M. Tkacz, W. Łojkowski and Z. Witczak, for their help in the evaluation of the papers and Dr. P. Wiśniowski and Mr. P. Stępiński for their help in the editorial job.

The organisers tried their best to have a truly international meeting. I hope that these proceedings will serve as a thorough review of high-pressure research all over the world.

**Witold A. Trzeciakowski**

*Warsaw*

*November 1995*

## WELCOME ADDRESS

You will probably agree that during the last years high pressure research developed fast and it was very successful in many areas of sciences like physics, chemistry, geology, material sciences and lately in the newest extremely quickly developing field of biological sciences and high pressure food processing. In Poland high pressure research has been growing rapidly since 1960 and now there are more than 20 laboratories which are devoted to this kind of research. The successful development of this domain was very much helped by broad international collaboration which still happily continues. As the chairman of this Conference I am glad to have an opportunity to express my appreciation of this continuing collaboration.

This Conference has been organised with a lot of international help and I am very happy to observe that it brings together participants from all important centers of high pressure research.

During the Conference you can visit a small exhibition of various types of equipment which we have prepared for you. Among this equipment you will find one piece which is very special and I am very happy that it will remain permanently in Warsaw. It is a gift from Professor William Paul and Harvard University to us. It is a 30 kilobar apparatus which was actually constructed and used by Percy W. Bridgman. By careful examination of this equipment one can learn a lot about ingenious experimental methods of developing and containing high pressure.

Finally, let me wish you all the most productive collaboration during the days of formal Conference and informal discussions.

Sylwester Porowski  
Conference Chairman



## **Recent history of AIRAPT**

(outlined by its president, Prof. A.L. Ruoff)

I have been asked to write a brief history of how AIRAPT came to be formed. The period from 1965 to 1979 is discussed in the Preface of the Proceeding of the 1979 Conference in Le Creusot entitled High Pressure Science and Technology, ed. by B. Vodar and Ph. Marteau.

Perhaps, the first international conference on high pressure was the one with the modest title: "First International Conference on the Physics of Solids at High Pressure." The proceedings were published as *Physics of Solids at High Pressure*, ed. by C. T. Tomizuka and R. M. Emrick, Academic Press, N.Y. (1965). This conference in Tucson, Arizona, was attended by 17 foreign delegates from France, USSR, Japan, England and Italy and about 160 from America. It was a conference which originated as the result of a collaborative effort of Harry Drickamer, Andrew Lawson and William Paul. While this conference in 1965 claimed to be the first international conference, such a claim could equally well be made by the Gordon Conference on Research at High Pressure. It was here in 1964 that Professor Ulrich Franck (an attendee from Germany) along with many other attendees from foreign countries and from the USA saw Orson Anderson jump to the platform and remark (and here I paraphrase), "we should have an international high pressure conference with changes in venue." This challenge was met by L. Deffet, U. Franck, J. Osugi, H. Li. Pugh, C. J. M. Rooymans, L. F. Verschagen and B. Vodar. The organization was named by Deffet with a French title and the acronym AIRAPT which over time has evolved into the title, "International Association for the Advancement of High Pressure Science and Technology."

Boris Vodar was the first president and chaired the first conference in Le Creusot, France in 1966. The second conference, in 1968, was at Schloss Elman, Germany. These first two conferences were similar to Gordon conferences with no publications (regrettably, I think). The proceedings of the third AIRAPT conference and of all those that followed have been published. Succeeding presidents were Ulrich Franck, Nestor Trappeniers, Boris Keeler, Bogdan Baranowski, John Shaner and our current president, Arthur Ruoff.

At the AIRAPT meeting in Moscow in 1985, Vodar suggested the idea of the Bridgman Award to recognise outstanding contributors to High Pressure Science. The Bridgman Award winners are as follows: Harry Drickamer (1979, Boulder), Boris Vodar (1979, Le Creusot), Ulrich Franck (1981, Uppsala), Francis Birch (1983, Albany), Nestor Trappeniers (1985, Amsterdam), Francis Bundy (1987, Kiev), H.-K. David Mao (1989, Paderborn), Shigeru Minomura (1991, Bangalore), Arthur Ruoff (1993, Colorado Springs), Bogdan Baranowski (1995, Warsaw). Nominations are by members. An international committee, headed by the previous winner, selects a few candidates from this list of nominees and the AIRAPT Executive Committee elects.

AIRAPT holds an international meeting every two years, the next being outside Kyoto in 1997. Since our founding in 1965, when the pressure limit was 20GPa, we have progressed to making x-ray measurements at 560GPa and optical studies at 420GPa. We owe a great deal to those who have been officers and who have organised conferences, but our

real debt is to those who do the outstanding research and technology and who educate and encourage the next generation of high pressure experts. They will insure our continued success.

Arthur L. Ruoff,  
Cornell University, USA

## **History of EHPRG**

(outlined by its president, Prof. K. Heremans)

The origin of the group goes back to the initiative of the High Pressure Section of the Standard Telecommunication Laboratories, Harlow (UK) in 1963 to bring scientists together active in the field of high pressure for informal discussion of common problems. The success of the first meeting led to the organisation of High Pressure Meetings with C. Goodman as secretary. In 1966, the meeting moved to Eindhoven, The Netherlands and the following year the European High Pressure Research Group (EHPRG) was formally organised. As stated in his rules, EHPRG has as its main task to promote research at high pressure and to hold annual meetings of scientists, engineers and others interested in high pressure. The Committee consists of the Chairman, a Secretary, a Treasurer and members who reflect the various research areas in representative European countries. EHPRG has close connections with AIRAPT and the Condensed Matter Division of the European Physical Society. The 25th Annual meeting was held in the former East Germany with a celebration of the 20th birthday of the Group. It was also the first meeting of EHPRG in what was then called "an Eastern European country". In 1988, during the meeting in Mragowo, Poland, it was decided to create the EHPRG Award. The Award is given every year to a young scientist to promote high pressure science and to help him/her to attend the meetings. The 1996 EHPRG Meeting will be held in Leuven, Belgium, and will focus on High Pressure Bioscience and Biotechnology. The 1997 Meeting will be held at Reading, UK. This meeting will be of a wider scope and includes Physics, Chemistry, and Food Science. Italy is on our list for 1998 with as tentative topic: Molecular crystals. In 1999 we will have a joint meeting with AIRAPT, possibly in St. Petersburg. In the year 2000 we hope to in Erlangen, Germany. Finally, EHPRG has its own home page on INTERNET at <http://www.kuleuven.ac.be/~EHPRG>. On that page we present not only the purpose of EHPRG, the rules for the EHPRG Award, and the names and addresses of the Committee members, but also future conferences in the field, both our own and those organised by other societies. In many cases we have also made links to the home pages of these conferences/organisers. Since one important task for EHPRG is to create international cooperation by bringing people into contact, we invite any one of you who has your own Department, University, or Company Home Page to communicate this as indicated in our home page. We will then insert a link, such that anyone browsing the EHPRG home page can immediately jump to any department/university/company of interest.

K. Heremans,  
Katholieke Universiteit Leuven, Belgium

# CONTENTS

Conference Sponsors	v
Committees	vii
From the Editor	ix
Welcome Address	xi
Recent History of AIRAPT	xiii
History of EHPRG	xv
<b>I Award Lectures</b>	<b>1</b>
1. My Adventure with Hydrogen (Bridgman Lecture) B. BARANOWSKI	3
2. Thermodynamics and Crystal Growth of III-N Compounds at N <sub>2</sub> Pressure up to 2 GPa (Jamieson Award) I. GRZEGORY	14
<b>II Instrumentation and Experimental Techniques</b>	<b>23</b>
1. Optimal Design of Diamond Culet Profiles A.L. RUOFF, H. POON, S. MUKHERJEE	25
2. Apparatus with Punches Made of Cubic Boron Nitride to Provide the Highest Pressure A.V. GERASIMOVICH, N.V. NOVIKOV, N.M. GRIGORIEV	29
3. Magnetization Measurement under High Pressure and Pulsed High Magnetic Field by a Diamond Anvil Cell S. ENDO, S. IMADA, K. KINDO, S. MIYAMOTO, H. HORI, F. ONO, T. TAKEUCHI, M. HONDA	32
4. Garnet Anvil Cell (GAC) for Hydrothermal Studies to 6.0 GPa and 1200°C M.R. RIEDEL, S.G. BUGA, A.-H. SHEN	35
5. Strength of the High Pressure Chamber Made from Paramagnetic Materials S.V. MIROSHNICHENKO, V.G. SYNKOV	38
6. Calorimetric System for Evaluation of Enthalpy of Liquid-to-Solid Transition and Heat Capacity of Liquids and Solids at High Pressures I. CZARNOTA-KUBASZEWSKA	41
7. Acoustic Emission Sensors for In-Situ Measurements under Pressure Z. WITCZAK, R. JEMIELNIAK, P. WITCZAK	45
8. Registration of Phase Transitions in Materials at High Pressures up to 30 GPa V.V. SHCHENNIKOV, A.YU. DEREVSKOV, V.A. SMIRNOV	48
9. Strain Gage Method of Volume Measurements under Hydrostatic Pressure J. KAMARAD, K.V. KAMENEV, Z. ARNOLD	51

10. A New Device for High Temperature and High Pressure: A Heating Gasket in a Ceramic DAC 54  
R. LETOULLEC, F. DATCHI, P. LOUBEYRE, N. RAMBERT, B. SITAUD, TH. THEVENIN
11. High Pressure System for EPR Measurements 57  
J. SZCZEPEK, A. SIENKIEWICZ
12. Increasing in Limit Load of Thick-Wall Chambers by Designing Plugs — Particularly Optical Plugs 60  
J. ARABAS, J. ZWOLINSKI
13. Miniature Universal High Pressure Clamp Cell 63  
A.V. KORNILOV, V.A. SUKHOPAROV, V.M. PUDALOV

### III Pressure Metrology

1. Limits in Present Static Pressure Metrology (*Invited*) 69  
W.B. HOLZAPFEL
2. Optical Pressure Calibration by Quantum-Well Spectra 75  
T.P. SOSIN, W. TRZECIAKOWSKI, P. STEPINSKI, M. HOPKINSON
3. High Hydrostatic Pressure Effects in Liquid Crystalline Optical Fibers 78  
T.R. WOLINSKI, W.J. BOCK, A. ZACKIEWICZ
4. Piston Gauges for Pressure Measurements in Liquids up to 3 GPa 81  
G.F. MOLINAR
5. Effects of a Pressure Dependent Viscosity Fluid in a Pressure Balance 84  
R.J. LAZOS-MARTINEZ, E. PINA
6. A Capacitive Free Element Bulk-Modulus Pressure Transducer 87  
R. WISNIEWSKI, A.J. ROSTOCKI
7. New Version of Bulk-Modulus High Pressure Transducers 90  
G.F. MOLINAR, R. WISNIEWSKI, R. MAGHENZANI, A. MAGIERA

### IV Material Engineering

#### IVA. Material Preparation Using Static Pressure: SHS, HIP, CIP, etc.

1. Creation of Hyperfunctional Materials with Graded Structures by SHS/HIP (*Invited*) 99  
Y. MIYAMOTO, K. TANIHATA, Z.-S. LI, Y.-S. KANG, H. MORIGUCHI, A. IKEGAYA, T. NOMURA
2. High Pressure Self Propagating High Temperature Synthesis of Nickel Aluminides 104  
M.C. DUMEZ, R.M. MARIN-AYRAL, J.C. TEDENAC
3. The Interaction Between WO<sub>3</sub> and Carbon under High Pressure 107  
V.P. FILONENKO, I.P. ZIBROV

		xix
4.	The System W-O under High Pressure (the Region $WO_2$ - $WO_{2.8}$ ) V.P. FILONENKO, I.P. ZIBROV, M. SUNDBERG	110
5.	Sintering at High Pressures and Properties of Aluminum Nitride Ceramics V.S. URBANOVICH	112
6.	Simultaneous Synthesis and Sintering of Silicon Carbide under High Pressure and Temperature S.K. BHAUMIK, C. DIVAKAR, M. MOHAN, S. USHA DEVI, P.M. JAMAN, A.K. SINGH	115
7.	Hydrostatic Compaction Pressure Influence on Sintered Spodumene Pyroceramics Properties T.E. KONSTANTINOVA, E.I. LYAFER	118
8.	The Effect of Desorbed Gases on Sintering Diamond Powders at High Pressures and Temperatures A.A. BOCHECHKA, S.F. KORABLEV, A.A. SHULHZENKO, I.A. PETRUSHA	121
9.	Metastable Phases Formation in Zr-Zn Alloys during Mechanical Alloying under Pressure N.I. TALUTS, A.V. DOBROMYSLOV, R.V. TCHURBAEV	124
10.	X-Ray Structure Studies of Aluminum Nitride in cBN-AlN Composites Produced by High Pressure Sintering N.P. BEZHENAR, S.A. BOZHKO, N.N. BELYAVINA, V.YA MARKIV	127
11.	Quenched High Density $ZrO_2$ and $HfO_2$ S. DESGRENIERS, K. LAGAREC	130
	<b>IVB. Mechanical Properties: Plasticity, Hydroextrusion, etc.</b>	133
1.	Efficient Implementation of Associative Flow Equations in Continuum Mechanics Codes E.C. FLOWER, L.G. MARGOLIN, R.R. VERDERBER	135
2.	An Application of Multisurface Plasticity Theory: Yield Surfaces of Textured Materials P.J. MAUDLIN, S.I. WRIGHT, U.F. KOCKS, M.S. SAHOTA	138
3.	Mathematical Simulation of Stability and Viscous Fracture of Materials Deformed under Pressure YA.E. BEIGELZIMER, B.M. EFROS, V.N. VARYUKHIN, A.V. SPUSKANYUK	141
4.	Investigation of Plastic Properties under High Pressures S.B. POLOTNYAK, A.V. IDESMAN, L.K. SHVEDOV	144
5.	Phase Transitions under Compression and Shear of Materials in Bridgman Anvils: Theory and Interpretation of Experiments V.I. LEVITAS	147
6.	Calculation of the Hydroextrusion Formed Billet Quality Properties A.V. SPUSKANYUK, YA.E. BEIGELZIMER	150
7.	The Structure and Properties of Polymers Produced by Extrusion of Powder Semi-Products V.A. BELOSHENKO, V.N. VARYUKHIN, G.V. KOZLOV, V.G. SLOBODINA	153

8. Metal Microfibres Obtained by Packet Hydroextrusion 156  
V.G. SYNKOV, L.D. TRANKOVSKAYA, S.G. SYNKOV
9. The Effect of Deformation under High Hydrostatic Pressure on the Structure and Properties of High Strength Metallic Materials 159  
B.M. EFROS, N. SHISHKOVA, I. KONAKOVA, L. LOLADZE
10. Specific Features of Behaviour of Heterophase Metallic Materials under Pressure at Deformation in Diamond Anvils 162  
B.M. EFROS, N.V. SHISHKOVA, YA.E. BEIGELZIMER, L.V. LOLADZE, S.V. GLADKOVSKII
11. Effect of Hot Hydrostatic Extrusion on Grain Size and Shape in Brass 165  
M.S. KOZLOWSKI, J.J. BUCKI, A. MAZUR
12. Acoustic Emission Investigations of the Plasticity of L1<sub>2</sub> Mn-Modified Al<sub>3</sub>Ti under Pressure 168  
Z. WITCZAK

#### **IVC. Microstructure of Materials: Grain Boundaries, Diffusion, etc.** 171

1. Effect of Hydrostatic Pressure on the Solid State Diffusional Reactions in Multilayers *(Invited)* 173  
D.L. BEKE
2. Pressure Dependence of Diffusion in Metal-Metalloid Glasses *(Invited)* 178  
K. RATZKE, A. HEESEMANN, F. FAUPEL
3. Differential Stress of MgO and Mg<sub>2</sub>SiO<sub>4</sub> under Uniaxial Stress Field: Variation with Pressure, Temperature and Phase Transition 183  
T. UCHIDA, N. FUNAMORI, T. OHTANI, T. YAGI
4. The Compensation Pressure for Thermally Activated Processes 186  
W. LOJKOWSKI, D.A. MOLODOV, L.S. SHVINDLERMAN
5. High Pressure Investigations of Grain Boundary Migration Mechanism in Aluminium 189  
W. LOJKOWSKI, Y. MINAMINO, S. HOZUMI, J. WYRZYKOWSKI
6. Features of Plastic Deformation of FCC Metals Having Different Stacking Faults Energy under High Pressure 192  
A.A. DOBRIKOV, A.S. DOMAREVA
7. The Study of Plastic Deformation Mechanisms of High-Nitrogen Steels under Pressure 195  
A.S. DOMAREVA, V.M. BLINOV, A.A. DOBRIKOV, V.N. VARYUKHIN
8. Compression and Thermal Expansion of Splat-Quenched Ni<sub>3</sub>Al to 5 GPa and 900°C 198  
J.W. OTTO, J.K. VASSILIOU, T. PEUN, G. FROMMEYER, E. HINZE

#### **IVD. Nanocrystalline Materials** 201

1. High Pressure Research on Nanocrystalline Solid Materials *(Invited)* 203  
W. SU, YU SUI, D. XU, F. ZHENG

2. Physics of Aging of Nanophase Alloys: Mossbauer Investigation of Nanocrystalline Iron-Copper Pseudo-Alloy 208  
V.G. GRYAZNOV, A.G. GAVRILIUK, V.P. FILONENKO, G.N. STEPANOV
3. Influence of Physico-Chemical Treatment on the Surface Composition of Nanometric Diamond 211  
A. SMEKHNOV, V. DANILENKO, S. KUZENKOV, B. PALOSZ, S. GIERLOTKA, O. BUGAETZ

## V Crystal Growth and Processing

### VA. Diamond

1. Numerical Simulation of the Growth Process of Diamond in the Temperature Gradient Method 219  
M. WAKATSUKI, W. LI, X. JIA
2. Formation of Diamond by Decomposition of SiC 222  
W. LI, T. KODAMA, M. WAKATSUKI
3. Thermomechanical State of a HPA Reaction Cell at the Graphite-to-Diamond Phase Transition 225  
A.A. LESHCHUK, N.V. NOVIKOV, A.P. MAYDANYUK
4. Nucleation and Growth of Diamond in Fe-Co Solvent at High Pressure and High Temperature 228  
T. SUGANO, N. OHASHI, T. TSURUMI, O. FUKUNAGA
5. High Pressure High Temperature Nucleation of Diamond 231  
E.A. EKIMOV, H.F. BOROVNIKOV, B. PALOSZ, M. LESZCZYNSKI, G.V. SAPARIN, S.K. OBYDEN, S.A. KLIMIN
6. The Stability of the Regrowth-treated Carbon Source in the Excess Pressure Method of Growing Diamonds 235  
Y. WANG, R. TAKANABE, M. WAKATSUKI
7. The Influence of Temperature Gradients on the Kinetics of Seed Growing of Diamond Single Crystals 238  
S.A. IVAKHNENKO, S.A. TEREITYEV, I.S. BELOUSOV, O.A. ZANEVSKY
8. Diamond Synthesis in a Laser-Heated Diamond Anvil Cell 241  
H. YUSA, K. TAKEMURA, Y. MATSUI, H. YAMAWAKI, K. AOKI
9. Effect of Interfacial Energy Anisotropy on the Diamond Crystal Habit 244  
V.M. PEREVERTAILO, L.YU. OSTROVSKAYA, S.M. IVAKHNENKO, O.B. LOGINOVA, A.A. SMEKHNOV
10. LP/LT Diamond Hydrosynthesis 247  
E. ABGAROWICZ, A. BAKON, S. MACIEJOWSKA, R. SALACINSKI, A. NIEDEBALSKA, A. SZYMANSKI
11. Structural Variations in Diamond due to Extreme External Effects 250  
N.V. NOVIKOV, G.P. BOGATYREVA, A.B. ROITSIN



<b>VB. Boron Nitride and Gallium Nitride</b>	253
1. New Route for Preparing c-BN at Medium Pressure and Temperature G. DEMAZEAU, V. GONNET, H. MONTIGAUD, B. TANGUY, V.L. SOLOZHENKO	255
2. B-C-N Graphitic Material and its Transient Heating Products at 15 GPa H. KAGI, I. TSUCHIDA, Y. MASUDA, M. OKUDA, K. KATSURA, M. WAKATSUKI	258
3. The Research of Influence of Preliminary Heat Treatment in Fluorine of gBN on cBN Synthesis A.A. SHULZHENKO, A.N. SOKOLOV, A.A. SMEHKNOV	261
4. Nitrogen High Pressure Influence on GaN Crystal Growth Conditions — A Computational Analysis S. KRUKOWSKI, I. GRZEGORY, M. BOCKOWSKI, J. JUN, B. LUCZNIK, A. WITEK, M. WROBLEWSKI, J.M. BARANOWSKI, S. POROWSKI, J. ADAMCZYK	264
<b>VC. Other Materials</b>	267
1. High Oxygen Pressures: A Route to the Stabilization of the Highest Oxidation States of Transition Metals in Oxygen Lattices G. DEMAZEAU, D.Y. JUNG, L. FOURNES, A. LARGETEAU, J.P. SANCHEZ	269
2. A New Route for the Synthesis of Boron-rich Rare-earth Borides B <sub>6</sub> R (R=La, Nd, Eu) under High Pressure and High Temperature X. LIU, X. ZHAO, F. LIN, W. LIU, W. SU	272
3. Development of New Solvents for the Hydrothermal Crystal Growth of $\alpha$ -Quartz F. LAFON, G. DEMAZEAU, Y. PEYTAVIN, P. CHVANSKI, A. LARGETEAU, C. QUETEL	275
4. The Solvothermal Synthesis of a New Class of Materials: The Phyllosiloxides P. REIG, G. DEMAZEAU, R. NASLAIN	278
<b>VI Phase Transitions and Phase Diagrams of Inorganic Materials</b>	281
<b>VIA. Theoretical and General Aspects</b>	283
1. Kinetics and Mechanism of Amorphous-to-Amorphous and Crystal-to-Amorphous Transitions under High Pressure ( <i>Invited</i> ) V.V. BRAZHKIN, A.G. LYAPIN, O.V. STALGOROVA, E.L. GROMNITSKAYA, S.V. POPOVA, O.B. TSIOK	285
2. XAFS Study of Pressure Induced Amorphization F. WANG, R. INGALLS	289

	xxiii
3. Peculiarities of Phase Transition Thermodynamics at Lability Boundaries under High Pressure E.A. ZAVADSKII, B.YA SUHAREVSKII	292
<b>VIB. Phase Diagrams</b>	295
1. Binary Phase Diagrams under High Pressure ( <i>Invited</i> ) T. YAMANE	297
2. Agreement Between Static and Shock Melting Measurements R. BOEHLER	302
3. Phase Equilibria in the Mixture He-CO <sub>2</sub> M.E. KOOI, J.A. SCHOUTEN	305
4. Regularities of Variations in Phase Diagram Construction of Carbon-3d Transition Metals Systems at High Pressure V.Z. TURKEVICH, O.G. KULIK	308
5. Thermodynamics of Phase Equilibria in the Mn-Ni-C System at High Pressures and Temperatures V.Z. TURKEVICH	311
6. Melting Curve of the Fe-36at.% Ni Alloy up to 49 GPa R. COUTY, B. SITAUD, J. PERE, TH. THEVENIN, J.L. TRUFFIER	314
7. Influence of the Pressure on the Phase Diagram and the Percolation Line of a Ternary Microemulsion Z. SAIDI, J.L. DARIDON, C. BONED, P. XANS	317
<b>VIC. Structural Phase Transitions</b>	321
<b>VIC.1 Diamond, Graphite, Iondaleite</b>	323
1. Graphite-Lonsdaleite Transformation under Static Pressure in Combination with Temperature and Shear V.D. BLANK, G.A. DUBITSKY, S.A. PLOTYANSKAYA	325
2. The Effect of Graphite Structure Ordering on the Parameters of HP-HT Graphite-to-Diamond Transition G.P. BOGATYREVA, G.F. NEVSTRUYEV, P.A. NAGORNY, G.D. ILNITSKAYA, G.A. BAZALIY, N.A. OLEINIK, V.L. GVMYAZDOVSKAYA	328
<b>VIC.2 Boron Nitride</b>	331
1. The Metastable Behaviour of Boron Nitride in Phase Transformations ( <i>Invited</i> ) I. PETRUSHA, A. SVIRID, B. SHARUPIN	333
2. Equilibrium Phase Diagram of Boron Nitride: Recent Results V.L. SOLOZHENKO	338

3. The Equation of State of Hexagonal Graphite-like Boron Nitride to 12 GPa and Phase Transformation HBN-WBN 343  
V.L. SOLOZHENKO, G. WILL, F. ELF
4. Behaviour of Less Ordered Boron Nitride under High Pressure and Temperature in the Presence of a Catalyst-Solvent 346  
M.M. BINDAL, B.P. SINGH, S.K. SINGHAL, R.K. NAYAR, R. CHOPRA, E.S.R. GOPAL, G. WILL

### **VIC.3 Molecular Solids** 349

1. Phase P-T Diagrams, Structural Disorder and Internal Motion at  $\text{MSiF}_6 \cdot 6\text{H}_2\text{O}$  (M=Mg, Mn, Fe, Co, Ni, Zn) under Pressure 351  
S.K. ASADOV, E.A. ZAVADSKII, V.I. KAMENEV, K.V. KAMENEV, B.M. TODRIS
2. Phase Transition of Hydrogen Cyanide under Pressure 354  
H. YAMAWAKI, M. SAKASHITA, K. AOKI
3. Pressure-induced Transformations in  $\text{A}_2\text{BX}_4$  Molecular Ionic Solids 357  
G. SERGHIOU, H.J. REICHMANN, R. BOEHLER
4. New Structural Transition of Oxygen at 96 GPa 360  
Y. AKAHAMA, H. KAWAMURA, D. HAUSERMANN, M. HANFLAND, O. SHIMOMURA
5. Crystalline Structure of the High Density  $\epsilon$  Phase of Solid  $\text{O}_2$  363  
S. DESGRENIERS, K.E. BRISTER
6. High Pressure Study of Ices VII and VIII using Synchrotron X-Ray Diffraction 366  
E. WOLANIN, PH. PRUZAN, J.C. CHERVIN, B. CANNY, M. GAUTHIER, D. HAUSERMANN, M. HANFLAND
7. Neutron Spectroscopy of Ice III 369  
I. NATKANIEC, L.S. SMIRNOV, A.I. KOLESNIKOV, A.N. IVANOV
8. Conical Geometry for Energy Dispersive X-Ray Diffraction. High Pressure Investigation of  $\text{NH}_3$  372  
M. GAUTHIER, J.P. ITIE, A. POLIAN, M. HAUSERMANN, M. HANFLAND
9. Methane High Pressure Crystal Structure Studied by FTIR Spectroscopy 375  
L. ULIVI, R. BINI, H.J. JODL, P.R. SALVI

### **VIC.4 Metals** 379

1. Electrical Conductivity and X-Ray Measurements of hcp-fcc Transition in Iron to 40 GPa 381  
T. YAGI, T. UCHIDA, N. FUNAMORI
2. Structure Systematic and Equations of States for the Alkaline Earth Metals under Pressure 384  
M. WINZENICK, W.B. HOLZAPFEL
3. Ultra-High Pressures Structural Changes Study in Dysprosium, Holmium and Erbium 387  
J. AKELLA, G.S. SMITH, S.T. WEIR, CH. RUDDLE

4. Kinetics of the Pressure-induced HCP→FCC Transformation in Thallium under Isobaric-Isothermal Conditions 390  
M. MOHAN, A.K. SINGH
5. A Pressure Induced  $\alpha'' \rightarrow \omega$  Transition in Ti-Nb Alloys 393  
A.V. DOBROMYSLOV, G.V. DOLGIKH, A.N. MARTEM'YANOV
6. Acoustic Emission from Cerium under High Pressure Isomorphic  $\gamma \leftrightarrow \alpha$  Phase Transitions 396  
Z. WITCZAK, V.A. GONCHAROVA
7. The Softening of the Shear Moduli of the  $\text{Ti}_{50}\text{Ni}_{48}\text{Fe}_2$  Shape Memory Single Crystal under Hydrostatic Pressures 399  
V.A. GONCHAROVA, E.V. CHERNYSHEVA, D.R. DMITRIEV, A.I. LOTKOV, V.P. LAPSHIN, V.N. GRISHKOV

## **VIC.5 Other Solids** 403

1. Structural Systematics of the  $\text{AX}_2$  Compounds with Coordination Numbers from 6 to 11 at High Pressures 405  
J. HAINES, J.M. LEGER, O. SCHULTE, A. ATOUF
2. A Topological Phase Transition of AgCl under High Pressure 408  
K. KUSABA, Y. SYONO, T. KIKEGAWA, O. SHIMOMURA
3. Influence of Pressure and Temperature on the EPR Spectrum of  $\text{Gd}^{3+}$  in  $\text{CsCaCl}_3$  411  
M. KRUPSKI, P. MORAWSKI, T. REWAJ, J.Y. BUZARE, Y. VAILLS
4. X-Ray Diffraction Study of the Critical Behaviour of  $\text{KMnF}_3$  Close to the Pressure Induced Phase Transition 414  
S. ASBRINK, A. WASKOWSKA
5. High Pressure Phase Transitions of Sodium Niobate ( $\text{NaNbO}_3$ ) by Raman Spectroscopy 417  
Z.X. SHEN, X.B. WANG, Z.P. HU, L. QIN, S.H. TANG, M.H. KUOK
6. High Pressure Raman Scattering Study of Lead Molybdate 420  
Z.X. SHEN, X.B. WANG, T.C. CHONG, Y.T. TAN, Z.P. HU, M.H. KUOK, S.H. TANG
7. Phase Transitions of  $\text{CuGeO}_3$  at High Pressures 423  
T. ZHOU, A.R. GONI, S. VES, R. KREMER, K. SYASSEN
8. Structural Phase Transformation of InS at High Pressures 427  
U. SCHWARZ, A. GONCHAROV, K. SYASSEN, N.M. GASANLY
9. Tetragonal Modification of CuI with Octahedral Coordination of Cu-Atoms under Shear Deformation and High Pressure up to 38 GPa 430  
N.R. SEREBRYANAYA, S.S. BATSANOV, V.D. BLANK, V.A. IVDENKO
10. XAFS Study of the B1-B2 Transition in RbCl 432  
R. INGALLS, S. JONES, F. WANG
11. Structural Phase Transition of  $\text{TmGa}_2$  at High Pressure 435  
S. BRAUNINGER, U. SCHWARZ, YU. GRIN, K. SYASSEN

12. HgO under High Pressure: A Combined X-Ray Absorption and X-Ray Diffraction Study 438  
A. SAN MIGUEL, A. GONZALEZ PENEDO, J.P. ITIE, A. POLIAN,  
P. BORDET
13. Recent Results of High Pressure Structural Studies on the Alkaline-Earth Chalcogenides 441  
H. LUO, K. GHANDEHARI, T. LI, R.G. GREENE, A.L. RUOFF
14. Structural Studies on CuFeS<sub>2</sub> (eskebornite) under High Pressure 445  
T. TINOCO, A. POLIAN, J.P. ITIE, P. GRIMA, E. MOYA, A. SAN MIGUEL,  
J. GONZALEZ, F. GONZALEZ-JIMENEZ

## VID. Magnetism and Ferroelectrics 449

1. Pressure Dependence of Magnetic Ordering in Ce-Pd-Al Intermetallic Compounds 451  
J. TANG, A. MATSUSHITA, H. KITAZAWA, T. MATSUMOTO
2. Magnetite (Fe<sub>3</sub>O<sub>4</sub>) at High Pressure and Low Temperatures 454  
G.KH. ROZENBERG, G.R. HEARNE, M.P. PASTERNAK, P.A. METCALF,  
J.M. HONIG
3. Magnetic Phase Transition of Ce<sub>2</sub>Fe<sub>17</sub>H<sub>0.8</sub> under Pressure 457  
S. NIZIOL, R. ZACH, T. KANIOWSKI, O. ISNARD, M. BACMANN,  
S. MIRAGLIA, J.L. SOUBEYROUX, D. FRUCHART
4. Pressure Magnetisation Measurements of MnRhAs<sub>1-x</sub>P<sub>x</sub> 460  
R. ZACH, M. GUILLOT, S. NIZIOL, R. FRUCHART
5. Pressure Study of UCu<sub>2</sub>Si<sub>2</sub>, UCu<sub>2</sub>Ge<sub>2</sub>, UMn<sub>2</sub>Si<sub>2</sub> and UMn<sub>2</sub>Ge<sub>2</sub> Compounds 463  
R. DURAJ, A. SZYTULA
6. Electronic and Magnetic Properties of USb under High Pressure 466  
H. TAKAHASHI, N. MORI, A. OCHIAI, E. HOTTA, T. SUZUKI
7. p-T Phase Diagrams of Sn<sub>2</sub>P<sub>6</sub>S<sub>6</sub> and Sn<sub>2</sub>P<sub>6</sub>Se<sub>6</sub> 469  
YU.I.L. TYAGUR, J. JUN
8. Structural Origin of Tricritical Point in KDP-type Ferroelectrics 472  
A. KATRUSIAK
9. X-Ray Diffraction and Dielectric Constant Measurement of KH<sub>2</sub>PO<sub>4</sub> under High Pressure 475  
Y. KOBAYASHI, S. ENDO, K. KOTO, K. DEGUCHI
10. Raman Spectroscopic Study of Giant Mode-Coupling and Phase Transitions in KNbO<sub>3</sub> under High Pressure 478  
Z.X. SHEN, Z.P. HU, T.C. CHONG, C.Y. BEH, S.H. TANG, M.H. KUOK
11. Effect of Pressure on Ferroelectric Transition in Pb(Fe<sub>1/2</sub>Nb<sub>1/2</sub>)O<sub>3</sub> 481  
S.K. RAMASESHA, M.V. RADHIKA RAO, A.K. SINGH, A.M. UMARJI

## VIE. Electronic Phase Transitions 485

1. The Metal-Insulator Transition in Thiospinel CuIr<sub>2</sub>S<sub>4</sub> 487  
T. KAGAYAMA, G. OOMI, I. YOSHIDA, Y. SAKURAI, T. HAGINO,  
S. NAGATA

	xxvii
2. Magnetoresistance of High Pressure Phases V.V. SHCHENNIKOV	490
3. Pressure-induced Phase Transitions in HgTeS and HgSeS Crystals V.V. SHCHENNIKOV, V.I. OSOTOV, N.P. GAVALESHKO, V.M. FRASUNYAK	493
4. Pressure-driven Metal-Insulator Transition in La-doped SmS by Excitonic Condensation A. JUNG, P. WACHTER	496
5. Electrical Resistance Measurements of Solid Bromine at High Pressures and Low Temperatures K. SHIMIZU, K. AMAYA, S. ENDO	498

## VII Physical Properties of Matter Under Static Pressures 501

### VIIA. Hydrogen and Hydrides 503

1. Solid Hydrogen at Ultrahigh Pressures ( <i>Invited</i> ) H.-K. MAO, R.J. HEMLEY	505
2. Hydrogen at Multimegabar Pressures ( <i>Invited</i> ) A.L. RUOFF	511
3. Pressing for Metallic Hydrogen ( <i>Invited</i> ) I.F. SILVERA, N.H. CHEN, E. STERER	517
4. Electrical Conductivities and Shock Temperatures of Fluid Hydrogen up to 200 GPa (2 Mbar) ( <i>Invited</i> ) W.J. NELLIS, N.C. HOLMES, M. ROSS, S.T. WEIR, A.C. MITCHELL	521
5. Chemical Approach to the Possibility of Hydrogen-Hydride Formation B. BARANOWSKI	524
6. Calculation of the Raman and Infrared Frequencies of Solid Hydrogen at High Pressures J.A. SCHOUTEN, M.I.M. SCHEERBOOM	527
7. The Structure and Dynamics of High Pressure Phases of Hydrogen J.S. TSE, D.D. KLUG	530
8. Orientational Order, Disorder, and Possible Glassy Behavior in Dense Deuterium A.F. GONCHAROV, I.I. MAZIN, J.H. EGGERT, R.J. HEMLEY, H.-K. MAO	533
9. Penetration Depth of Nickel Hydride Into Bulk Nickel at Different Activities of Gaseous Hydrogen A. STROKA, B. BARANOWSKI	536
10. New High Pressure Crystal Structure, Equation of State, and Phonon Reflectivity of CsH to 2.5 MBar and CsD to 1.37 Mbar A.L. RUOFF, K. GHANDEHARI	539
11. Synthesis of Rhenium and Molybdenum Hydrides in DAC M. TKACZ	543

12. Correlation Between Pressure Dependence of Electrical Resistance and Phase Diagram of the Metal-Hydrogen Systems 546  
A.W. SZAFRANSKI
13. High Pressure Studies of YbH<sub>2</sub> and YbD<sub>2</sub> 549  
J. S. OLSEN, S. STEENSTRUP, L. GERWARD
14. Generation and Accumulation of Tritium in Metal Surface Layer Melted and Quick Quenched by Treatment with Dense Deuterium Plasma Streams 552  
V.A. ALEKSEEV, V.A. ROMODANOV, S.V. RYLOV, YU.F. RYZHKOV,  
V.I. SAVIN, YA.B. SCURATNIK, V.M. STRUNNIKOV, V.I. VASILIEV

## **VIIB. Diamond and Insulators** 557

1. A Study of Diamond Lattice Deformations Occurring in Uniaxial Compression by Changes in Kossel's Line Intensity Profile 559  
V.N. TKACH, A.G. GONTAR
2. Mechanisms of Internal Stresses Formation in Superhard Materials under High Pressure 562  
G.A. VORONIN, I.A. PETRUSHA
3. Cobalt and Manganese as Impurities in Synthetic Diamonds 565  
X. JIA, H. KAGI, W. LI, M. WAKATSUKI, S. HAYAKAWA, Y. GOHSHI
4. The Effect of Isotopic Composition on Diamond Thermal Conductivity 568  
A. WITEK, A.P. PODOBA, S.V. SHMEGERA
5. High Pressure and Fluorescence Lifetime of R Line in MgO:Cr<sup>3+</sup> 571  
B.R. JOVANIC, R. RADENKOVIC, LJ.D. ZEKOVIC
6. Mixing of Electronic States of KZnF<sub>3</sub>:Cr<sup>3+</sup> 573  
V. LEMOS, P.T.C. FREIRE, O. PILLA
7. Studies on Local Distortions Around Sm<sup>2+</sup> in MFCl Host Lattice by High Pressure Fluorescence 576  
Y.R. SHEN, W.B. HOLZAPFEL
8. Luminescence Studies on Sm<sup>2+</sup> and Eu<sup>3+</sup> in Different Host Materials under Pressure — Nephelauxetic Effects 579  
Y.R. SHEN, W.B. HOLZAPFEL

## **VIIC. Semiconductors** 583

### **VIIC.1 Bulk Materials** 583

1. The Use of High Pressures in the Investigation of the Electronic Properties of Semiconductors (*Plenary*) 585  
W. PAUL
2. Is Light Coming Out of Silicon in Porous Silicon? (*Invited*) 591  
J. ZEMAN, M. ZIGONE, G.L.J.A. RIKKEN, G. MARTINEZ

3. Structural and Optical Properties of GaN Single Crystals (*Invited*) 596  
T. SUSKI, P. PERLIN, H. TEISSEYRE, M. LESZCZYNSKI, I. GRZEGORY,  
J. JUN, M. BOCKOWSKI, S. POROWSKI
4. Carrier-induced Strain in Silicon Nanocrystals 600  
X.-S. ZHAO, P.D. PERSANS, J. SCHROEDER
5. Resonant Raman Scattering and Photoluminescence in II-VI Semiconductor Nanocrystals:  
Enhanced High Pressure Phase Stability 603  
J. SCHROEDER, M.R. SILVESTRI, L.-W. HWANG, P.D. PERSANS
6. Electrical Conductivity and Thermo-EMF of the High Pressure Phase of CdX and ZnX (X=0,  
S, Se, Te) 606  
A.N. BABUSHKIN, O.A. IGNATCHENKO
7. High Pressure Study of Impurity States in Cubic GaN and AlN Crystals 609  
I. GORCZYCA, A. SVANE, N.E. CHRISTENSEN
8. Effect of Pressure on Direct Optical Transitions in InSe from Photoreflectance Spectroscopy 612  
C. ULRICH, A.R. GONI, K. SYASSEN, O. JEPSEN, A. CANTARERO,  
V. MUNOZ
9. The U-Parameter and Optical Properties under Pressure on AgGaS<sub>2</sub> 615  
Y. MORI, K. TAKARABE, Y. KANDA, S. MINOMURA, E. NIWA,  
K. MASUMOTO
10. Observation of Resonant Defect States in Heavily Carbon-doped GaAs under Hydrostatic  
Pressure 618  
U.D. VENKATESWARAN, J. BAK, R. SOORYAKUMAR,  
S. SUBRAMANIAN
11. Shallow and Deep States of Group VI Donors in GaAs and Al<sub>x</sub>Ga<sub>1-x</sub>As at High Pressures 621  
J.E. DMOCHOWSKI, M.A. SADLO, R.S. JAKIELA, R.A. STRADLING,  
A.D. PRINS, J.L. SLY, D.J. DUNSTAN, K.E. SINGER
12. Electron Emissions from Si-DX and Te-DX under Pressure 624  
K. TAKARABE, N. SHIRASE, S. MINOMURA

## VIIC.2 Heterostructures

627

1. High Pressure Studies of Resonant Tunneling in Semiconductor Heterostructures (*Invited*) 629  
P.C. KLIPSTEIN
2. High Pressure Study of Electron-Electron Interactions in Double-Layer 2D Electron Gases  
(*Invited*) 634  
A.R. GONI, S. ERNST, K. SYASSEN, K. EBERL
3. Quantum Hall Effect in Be-doped GaAs/AlGaAs Heterostructure under Uniaxial  
Compression 641  
O.P. HANSEN, W. KRAAK, N. MININA, J.S. OLSEN, A. SAVIN, B. SAFFIAN
4. Absorption of ZnSe/ZnSSe and ZnCdSe/ZnSe Superlattices under High Hydrostatic Pressure 644  
E. GRIEBL, G.F. SCHOTZ, W. KERNER, CH. BIRZER, T. REISINGER, B. HAHN,  
W. GEBHARDT



5. Photoreflectance Spectroscopy of GaAs/Al<sub>x</sub>Ga<sub>1-x</sub>As SQW Structures under Pressure  
C. ULRICH, A.R. GONI, K. EBERL, K. SYASSEN 647
6. Pressure Tuning of Semiconductor Laser Diodes  
P. STEPINSKI, Y. TYAGUR, T.P. SOSIN, W. TRZECIAKOWSKI 651
7. Spatial Correlations of Donor-Charges in  $\delta$ -doped AlGaAs/InGaAs/GaAs Structures  
E. LITWIN-STASZEWSKA, T. SUSKI, P. WISNIEWSKI, F. KOBBI,  
S. CONTRERAS, J.L. ROBERT, V. MOSSER 654
8. Study of Classical and Quantum Scattering Times in Pseudomorphic AlGaAs/InGaAs/GaAs  
Heterostructures by Means of Pressure  
L.H. DMOWSKI, A. ZDUNIAK, E. LITWIN-STASZEWSKA, S. CONTRERAS,  
W. KNAP, J.L. ROBERT, V. MOSSER 657
9. High Temperature Electrical Properties of Si-Planar Doped GaAs-AlAs Superlattices under  
Hydrostatic Pressure  
F. BOSC, J. SICART, J.L. ROBERT 660
10. Effect of "Memory" in P-type GaAs/AlGaAs Heterostructure Piezoresistivity  
O.P. HANSEN, V. KRAVCHENKO, N.YA. MININA, J.S. OLSEN, A. SAVIN 664
11. Potential Barrier at a Grain Boundary in p-Hg<sub>1-x</sub>Cd<sub>x</sub>Te ( $x=0.23$ ) under Uniaxial Compression  
N.B. BUTKO, W. KRAAK, N.YA. MININA, A. SAVIN 667

## VIID. Superconductors

1. Pressure-induced Oxygen Ordering Effects in High-T<sub>c</sub> Superconductors (*Invited*)  
J.S. SCHILLING, A.K. KLEHE, C. LOONEY 671
2. A Model for Short-Range Oxygen-Ordering Effects in High-T<sub>c</sub> Superconductors  
A.K. KLEHE, J.S. SCHILLING 673
3. T<sub>c</sub>(P) from Magnetic Susceptibility Measurements in High Temperature Superconductors:  
YBa<sub>2</sub>Cu<sub>3</sub>O<sub>7-x</sub> and HgBa<sub>2</sub>Ca<sub>2</sub>Cu<sub>3</sub>O<sub>8+x</sub>  
V.V. STRUZHNIKIN, YU.A. TIMOFEEV, R.T. DOWNS, R.J. HEMLEY,  
H.-K. MAO 679
4. On the Dependence of the Critical Temperature on Pressure in the Bipolaron Model of High  
T<sub>c</sub> Superconductors  
G.G.N. ANGILELLA, R. PUCCI, F. SIRINGO 682
5. Peculiarities of Crystal Lattice Dynamics for HT<sub>c</sub>SC Ceramics YBa<sub>2</sub>Cu<sub>3</sub>O<sub>7.8</sub> Obtained under  
High Pressure  
A.D. SHEVCHENKO 685
6. Strontium-based Mercury Cuprates with Perovskite-like Structure  
E.P. KHLIVBOV, G.M. KUZMICHEVA, V.N. KOCHETKOV, T. PALEWSKI,  
J. WARCHULSKA, I.N. AFANAS'IEVA 688
7. Superconductivity and Magnetism in Gd<sub>1+x</sub>Ba<sub>2-x</sub>Cu<sub>3</sub>O<sub>7-y</sub> System. Influence of Pressure and  
Gd, Occupying Ba- Site  
V.N. NAROVZHNYJ, V.I. NIZHANKOVSKII, E.P. KHLIVBOV, A.V. GUSEV,  
G.G. DEVIATYKH, A.V. KABANOV, Z. BUKOWSKI 690

**VIII. Fullerenes**

695

1. Fullerenes under Pressure: Structure, Order and Disorder *(Invited)* 697  
B. SUNDQUIST, O. ANDERSSON, A. LUNDIN, P-A. PERSSON,  
A. SOLDATOV
2. Fullerenes Transition to Diamond under High Pressure and High Temperature *(Invited)* 702  
Y. MA, G. ZOU
3. Experimental Study of the Hardness and Electric Conductivity of Superhard Bulk Samples  
Created from Solid C<sub>60</sub> under Pressure up to 13 GPa and Temperature up to 1830 K 707  
V.D. BLANK, S.G. BUGA, G.A. DUBITSKIY, M.YU. POPOV,  
N.R. SEREBRYANAYA
4. The Structural Peculiarities of C<sub>60</sub> after High Pressure and High Temperature Treatment 710  
V.D. BLANK, B.A. KULNITSKIY, YE.V. TATYANIN
5. Raman Study of Ultra- and Superhard Phases of C<sub>60</sub> 713  
V.D. BLANK, S.G. BUGA, G.A. DUBITSKY, V.N. DENISOV, A.N. IVLEV,  
B.N. MAVRIN, M.YU. POPOV
6. Physical Properties of Pressure Polymerized C<sub>60</sub> 716  
P-A. PERSSON, U. EDLUND, A. FRANSSON, A. INABA, P. JACOBSSON,  
D. JOHNELS, C. MEINGAST, A. SOLDATOV, B. SUNDQVIST
7. C<sub>60</sub>-Polymorphous Transformations at 300–1800 K up to 13 GPa 719  
N.R. SEREBRYANAYA, V.D. BLANK, G.A. DUBITSKIY, S.G. BUGA,  
V.V. AKSENENKOV, M.YU. POPOV

**VIIIF. Metals and Intermetallics**

723

1. Electronic Properties of Solids under Pressure *(Invited)* 725  
N.E. CHRISTENSEN
2. Pressure Derivative of Bulk Modulus of Metals from a Uniform Interstitial Electron Gas  
Model 730  
N. SURESH, S.C. GUPTA, S.K. SIKKA
3. Compressibility and Magnetovolume Effects in Novel R-Fe Intermetallics 733  
J. KAMARAD, Z. ARNOLD, K.V. KAMENEV, M.R. IBARRA
4. Influence of High Pressure Hydrogenation on Electrical Resistance, Magnetoresistance and  
Magnetic Susceptibility of Disordered Ni-Mn Alloys 736  
D.K. SCHWARZ, I. DUGANDZIC, S.M. FILIPEK, H.J. BAUER
5. Hyperfine Magnetic Fields at <sup>119</sup>Sn Nuclei and Curie Temperature in Heusler Alloy Ni<sub>2</sub>MnSn  
under High Pressure 739  
A.G. GAVRILIUK, G.N. STEPANOV, V.A. SIDOROV, S.M. IRKAEV
6. Mossbauer Study of High Pressure Influence on Hyperfine Fields at Tin and Compressibility  
Measurements in Co<sub>2</sub>MnSn up to 12 GPa 742  
G.N. STEPANOV, A.G. GAVRILIUK, O.B. TSIOK, S.M. IRKAEV

7. Pressure Dependence of the Debye Temperature in Aluminium, Copper and Brass at High Pressure up to 6 GPa 745  
K. SUIITO, T. SASAKURA, J. HAMA, H. FUJISAWA
8. High Pressure X-Ray Study of Zn 748  
K. TAKEMURA

## **VIIG Magnetic- and Heavy-Fermion compounds** 751

1. Pressure-induced Instability of Heavy Fermion State in Ce Compounds (*Invited*) 753  
G. OOMI, T. KAGAYAMA
2. Pressure Studies of Electronic Instabilities in Heavy-Fermion Compounds (*Invited*) 758  
A. DE VISSER, K. BAKKER, N.H. VAN DIJK, J.J.M. FRANSE
3. High Pressure Study of CeTX Compounds 764  
T. ISHII, G. OOMI, Y. UWATOKO, T. TAKABATAKE, S.K. MALIK
4. Pressure-induced Valence Changes in  $\text{Yb}_4\text{As}_3$  767  
N. MORI, H. TAKAHASHI, Y. OKUNUKI, S. NAKAI, T. KASHIWAKURA,  
A. KAMATA, H. TEDUKA, Y. KOZUKA, Y. YOKOHAMA, Y. HAGA,  
A. OCHIAI, T. SUZUKI, M. NOMURA

## **VIIH. Other Solids** 771

1. Mossbauer and XPS Studies on  $\text{Sr}_{1-x}\text{Eu}_x\text{TiO}_{3+y}$  Synthesized by High Pressure and Temperature 773  
L. LI, Q. WEI, W. SU
2. High Pressure Resistivity Studies on Cu-Ge-Te Glasses 776  
K. RAMESH, S. ASOKAN, K.S. SANGUNNI, E.S.R. GOPAL
3. Refractive Index of Solid Argon up to 45 GPa at 298 K 779  
N. RAMBERT, B. SITAUD, TH. THEVENIN

## **VIII. Liquids and Gases** 783

1. Absorption Coefficient in Liquid Iodine under High Pressure 785  
U. BUONTEMPO, P. POSTORINO, M. NARDONE
2. Characterization of Thermodynamic Properties of Aqueous Saline Solutions at High Pressures. A New Approach using Ultrasound Velocity Data 788  
S. YE, H. CARRIER, P. XANS
3. Measurement and Prediction of Ultrasound Velocity under High Pressure in a Condensate Gas 791  
J.L. DARIDON, B. LAGOURETTE, P. LABES, H. SAINT-GUIRONS
4. Computer Simulations of the Raman Q-Branch in Fluid Nitrogen 794  
J.P.J. MICHELS, M.I.M. SCHEERBOOM, J.A. SCHOUTEN

## VIII Chemistry and Physics of Organic Materials

797

1. The Effects of Pressure and of Radiation on the Phosphorescence of a Series of Nitriles, Aldehydes and Ketones Dissolved in Solid Polymers (*Invited*) 799  
H.G. DRICKAMER, Z.A. DREGER, J.-M. LANG
2. Recent Advances in High Pressure Organic Synthesis: High Pressure-mediated Macrocyclization Processes (*Invited*) 804  
J. JURCZAK, K. CHMURSKI, D.T. GRYKO, P. LIPKOWSKI, R. OSTASZEWSKI, P. SALANSKI
3. High Pressure Hydrothermal Combustion (*Invited*) 809  
E.U. FRANCK, G. WIEGAND
4. High Pressure Kinetics of Z/E Isomerization at Highly Viscous Conditions. Further Evidence for Solvent Rearrangement prior to the Rate-determining Step 815  
T. ASANO, H. FURUTA, H. SUMI
5. High Pressure Studies of Dynamic Solvent Effects on the Intramolecular Charge Transfer (ICT) in the Excited State 818  
K. HARA, D.S. BULGAREVICH, N. KOMETANI
6. Pressure Studies in Two-Dimensional Organic Superconductors 821  
YU.V. SUSHKO
7. Pressure Dependence of Primary Charge Separation in a Photosynthetic Reaction Center 824  
H.-C. CHANG, R. JANKOWIAK, N.R.S. REDDY, G.J. SMALL
8. Conformational Changes of Poly(3-alkylthiophene)s with Pressure 828  
P. BARTA, T. KANIOWSKI, W. LUZNY, S. NIZIOL, J. SANETRA, M. ZAGORSKA
9. Viscosity as a Function of Pressure and Temperature of Three Contrasted Binaries: A Representation with a Self-Referencing Method 831  
A. ET-TAHIR, C. BONED, B. LAGOURETTE, J. ALLIEZ
10. Light Scattering of Linolenic Acid and Triolein Liquids under High Pressure 834  
R.M. SIEGOCZYNSKI, R. WISNIEWSKI, W. EJCHART
11. The Relative Permittivity and Dielectric Loss of BIS(2-ethylhexyl)sebacate under Pressure up to 1.5 GPa at Room Temperature 837  
R. WISNIEWSKI, T. BUCHNER, A. JAROSZEWICZ, T. KUCINSKI
12. State Equation of BIS(2-ethylhexyl)sebacate for Pressure Range 0-1 GPa at Room Temperature 840  
R. WISNIEWSKI, P. KOMOROWSKI, P. MACHOWSKI
13. The Spontaneous High Pressure Generation and Stability of Hydrocarbons: The Generation of n-Alkanes, Benzene, Toluene and Xylene at Multi-Kilobar Pressures 843  
J.F. KENNEY
14. Hydrogenated Amorphous Carbon from Compression of Acetylene and Polyacetylene 846  
M. BERNASCONI, M. PARRINELLO, G.L. CHIAROTTI, P. FOCHER, E. TOSATTI
15. X-Ray Diffraction Study of Solid Acetylene under Pressure 849  
M. SAKASHITA, H. YAMAWAKI, K. AOKI

<b>IX Biology and Food Processing</b>	<b>853</b>
1. High Pressure Effects on Structure and Function of Nucleic Acids ( <i>Invited</i> ) A. KRZYZANIAK, P. SALANSKI, J. JURCZAK, J. BARCISZEWSKI	855
2. NMR Studies of Pressure-induced Reversible Unfolding of Proteins J. JONAS	860
3. High Pressure FT-IR Studies on Hemoproteins L. SMELLER, K. GOOSSENS, K. HEREMANS	863
4. High Pressure Effects on the Secondary Structure of Bovine Pancreatic Trypsin Inhibitor Studied by FT-IR Spectroscopy N. TAKEDA, M. KATO, Y. TANIGUCHI	866
5. Gene Expression of Aspartate $\beta$ -D-Semialdehyde Dehydrogenase at Elevated Hydrostatic Pressure in Deep-Sea Barophilic and Barotolerant Bacteria C. KATO, M. SMORAWINSKA, K. HORIKOSHI	869
6. Pressure Effects on Protein Structure-Function C. BALNY, R. LANGE	872
7. Effect of Hydrostatic Pressure on the Yeast Vacuoles F. ABE, K. HORIKOSHI	875
8. High Pressure Studies of Excitonically Coupled Photosynthetic Antenna Complexes N.R.S. REDDY, H.-M. WU, R. JANKOWIAK, G.J. SMALL	878
9. Effect of Dynamic High Pressure on Fish Bacteria: A Case Study K.D. JOSHI, G. JYOTI, S.C. GUPTA, S.K. SIKKA, R. CHIDAMBARAM, A.S. KAMAT, V. VENUGOPAL, P. THOMAS, P.C. KESAVAN	882
10. Employment of High Pressure for Keeping Biological Materials V.L. SEREBRENNIKOV, YU.A. KUDRENKO	885
11. High Pressure Technique for Sterilization of Mandarin Orange Juice T. YAMAMOTO, Y. IFUKU	889
12. The Effect of High Hydrostatic Pressure on Vegetative Bacteria and Spores of <i>Aspergillus Flavus</i> and <i>Bacillus Cereus</i> M. FONBERG-BROCZEK, B. WINDYGA, H. SCIEZYNSKA, K. GORECKA, A. GROCHOWSKA, B. NAPIORKOWSKA, K. KARLOWSKI, J. ARABAS, J. JURCZAK, S. PODLASIN, S. POROWSKI, P. SALANSKI, J. SZCZEPEK	892
13. FTIR Studies on Food Components in Diamond Anvil Cell L. SMELLER, K. GOOSSENS, P. RUBENS, K. HEREMANS	895
14. Influence of High Pressure on Changes of Cheese Characteristics P. KOLAKOWSKI, A. REPS, A. BABUCHOWSKI, L. ZMUJDZIAN, S. PODLASIN, S. POROWSKI	898
15. Effect of Dynamic High Pressure on Model Bacterial Cultures M. RADOMSKI, M. FONBERG-BROCZEK, H. SCIEZYNSKA, B. WINDYGA	902

**X Geophysical and Planetary Sciences**

905

1. Magnetic Parameters of Rocks under Stress Conditions of the KTB Main Drill and Investigation of Anisotropy Carriers 907  
A. KAPICKA, E. PETROVSKY, J. POHL
2. Permanent Changes in Deformations and Strengths of Rocks Due to Hydrostatic Pressure 909  
J. GUSTKIEWICZ
3. Planetary Phase Equilibria and Constitution of the Terrestrial Planets 913  
O.L. KUSKOV
4. Crystallization of "Shungite" at High Pressure and High Temperature 916  
K. SUTO, H. SHINN, S. OHBAYASHI
5. Properties of MgO-SiO<sub>2</sub> Phases: Lattice and Molecular Dynamics Study 918  
A.B. BELONOSHKO, L.S. DUBROVINSKY
6. New High Pressure Silica Phases Obtained by Computer Simulation 921  
L.S. DUBROVINSKY, A.B. BELONOSHKO, N.A. DUBROVINSKY, S.K. SAXENA
7. Phase and Glass Transitions in Crude Oils and their Fractions at High Pressure 924  
V. KUTCHEROV, R. ROSS, A. CHERNOUITSAN

**XI Shock Waves**

927

**XIA. Material Treatment Using Shock Waves, Explosives**

929

1. The Role of Dynamic Shock Compaction in the Development of Dense, Sintered Ceramic Microstructures 931  
J. FREIM, J. MCKITTRICK, W.J. NELLIS
2. Differentiation of Transition Pathway — Diamond Transition and Graphitization — under Shock Compression 934  
H. HIRAI, K-I KONDO
3. Compaction of Ultradisperse Diamonds by Weak Shock Loading 937  
E.E. LIN, V.A. MEDVEDKIN, S.A. NOVIKOV
4. Baushinger Effect in Steel under Dynamic Loading 939  
V.A. PUSHKOV, P.A. TSOI, S.A. NOVIKOV
5. Spall Behavior and Damage Evolution in Tantalum 941  
A.K. ZUREK, W.R. THISSELL, D.L. TONKS
6. Cavitation Erosion as a Process of Fatigue Spallation 944  
S. BURAVOVA
7. Nonlocal Effects in the High Strain-Rate Processes in Solids 947  
T.A. KHANTULEVA, YU.I. MESCHERYAKOV

8.	Structural and Phase Transitions of Zirconium and its Alloys with Niobium in Spherical Stress Waves	950
	E.A. KOZLOV, B.V. LITVINOV, E.V. ABAKSHIN, G.V. KOVALENKO, V.K. ORLOV, V.M. TEPLINSKAYA, S.S. KISLYAKOV, A.A. KRFUGLOV, A.V. DOBROMYSLOV, N.I. TALUTS, N.V. KAZANTSEVA, G.G. TALUTS	
9.	The Behaviour of $\alpha$ -Quartz under High Dynamic and Static Pressures: New Results and Views	953
	YU.N. ZHUGIN	
9.	Comparison of the Effects of Loading Alumina in Shock and Detonation Waves	957
	R. TREBINSKI, E. WLODARCZYK, S. CUDZILO, A. MARANDA, J. NOWACZEWSKI, W. TRZCINSKI	
10.	Physical and Chemical Transformations of Serpentine in Spherical Stress Waves	960
	E.A. KOZLOV, YU.N. ZHUGIN, B.V. LITVINOV, V.N. KOZLOVSKY, E.V. ABAKSHIN, D.D. BADJUKOV, L.A. IVANOVA, F.A. LETNIKOV, V.N. ANFILOGOV, E.V. BELOGUB, V.A. KOTLIJAROV	
11.	Freeze-Out of Carbon Monoxide in Calorimetry Tests	963
	F.H. REE, W.J. PITZ, M. VAN THIEL, P.C. SOUERS	
<b>XIB. Ultrahigh Dynamic Pressures, Equation of State</b>		967
1.	The Pressure Regime 10–750 Mbar: Use of Lasers in EOS Measurements ( <i>Invited</i> )	969
	R. CAUBLE, L.B. DA SILVA, B.A. HAMMEL, N.C. HOLMES, R.-W. LEE, T.S. PERRY, D.W. PHILLION	
2.	Plasma Physics Research with Shock Waves ( <i>Invited</i> )	974
	A. NG	
3.	Shock Wave Measurements ( <i>Invited</i> )	979
	N.C. HOLMES	
4.	Wide-Range Equation of State	983
	N.N. KALITKIN	
5.	Microfield Modelling in Nonideal Multicomponent Plasmas	986
	I.O. GOLOSNOY	
6.	Measurement of Near-Mbar Shock Fronts in Crystals by X-ray Diffraction	989
	N.C. WOOLSEY, A. ASFAW, R.W. LEE, J.S. WARK, R. CAUBLE	
7.	Quasi-Isentropic Compression of Liquid Argon at Pressure up to 500 GPa	992
	V.D. URLIN, M.A. MOCHALOV, O.L. MIKHAILOVA	
8.	Strong Shock Wave Excitation by Z-Pinch Generated Soft X-Rays	994
	M. LEBEDEV, K. DYABILIN, V. FORTOV, V. SMIRNOV, E. GRABOVSKIJ, K. DANILENKO, I. PERSIANTZEV, A. ZAKHAROV	
Index		997

## **I Award Lectures**



# MY ADVENTURE WITH HYDROGEN

B. BARANOWSKI

*Institute of Physical Chemistry, Polish Academy of Sciences, 01-224 Warsaw, Poland*

The development of the high pressure technique with gaseous hydrogen up to 30 kbar, opening a new area of activity in Me-H systems, will be shortly characterized. The discovery of nickel hydride and investigations with different Me-H<sub>2</sub>D systems are presented. The leading idea was to solve consecutive problems whereby the requirement of high hydrogen pressures was unavoidable. Some problems, related to high thermodynamic activity of hydrogen, like non-local diffusion of hydrogen in elastic metallic lattice, hysteresis in metallic hydrides and the hypothesis of hydrogen-hydride existence will be discussed.

**Introduction:** Serious high pressure research is not an easy job. In my opinion two different reasons exist here for being involved: Either there is no escape from high pressure technique if one wants to solve the problem considered or one is falling in love with this technique. Being honest, I belong to the first category of people: I was feeling pressed into the high pressure methods by the problem chosen and it took a long time before I was falling in love with this technique. In my scientific activity I preferred the hunting and explaining anomalies - of course apparent anomalies as Nature is normal by definition. She is the only femal being who cannot be violated.

**The entrance:** When I finished in 1956 my career as theoretical chemist at the Jagiellonian University in the sleepy Cracow and went over to the dynamic Warsaw, I met in Prof. Śmiałowski's group research on electrolytic charging of nickel wires by hydrogen. Trying to evaluate the diffusion coefficient of hydrogen from the desorption kinetics, I faced the anomaly presented on Fig. 1. Assuming a uniform absorption, the hydrogen content for a given weight unit of Ni should be constant, that is radius independent. The above curve suggests a high hydrogen concentrated layer near the surface of the wire [1].

In order to determine the thickness of this layer and its hydrogen content, controlled nickel layers were deposited on copper [2,3]. The result is shown on Fig. 2: As can be seen up to about 30  $\mu$  ( $10^{-6}$  m) nearly 0.7 atom of hydrogen accompanies 1 atom of nickel in the metallic lattice. This high hydrogen content in nickel was a surprise: At the same temperature the hydrogen content in nickel being in equilibrium with gaseous hydrogen of 1 atm pressure is by five orders of magnitude lower. The hydrogen concentration, expressed in atomic ratio, is comparable with the well known, since 100 years, palladium hydride. In fact the high concentrated nickel/hydrogen layers

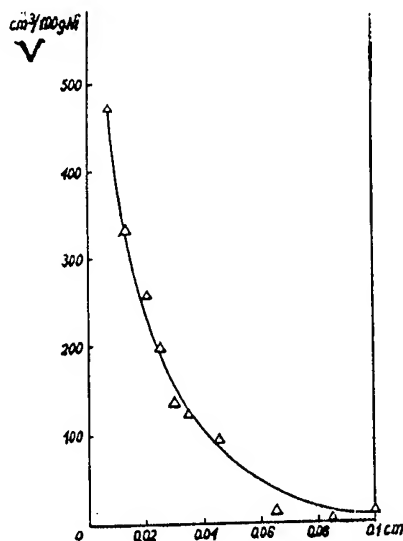


Fig. 1. Stationary volume of absorbed hydrogen ( $\text{cm}^3/100 \text{ g Ni}$ ) at  $25^\circ \text{C}$  and 760 Torr) as a function of the Ni wire radius.

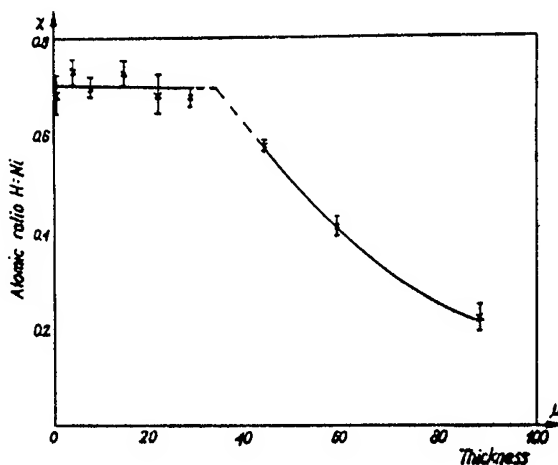


Fig. 2. Stationary hydrogen content in atomic ratio of hydrogen to nickel in nickel layers deposited on copper. Electrolytic charging of hydrogen like in Fig. 1

exhibited all physico - chemical characteristics of a hydride phase [4,5]. Thus the so far unknown nickel hydride was discovered and one could now play an infinite game with electrochemical methods[6]. Electrochemistry is a technique of unlimited possibilities, like US in respect to people.

**The step too far:** But I was unsatisfied with the electrochemical offer and put a trivial question whose answer could put the problem on a solid ground of thermodynamics: Namely I asked the question: What is the pressure which is developed when nickel hydride decomposes up to the equilibrium state with the gaseous phase? In other words, what is the maximal hydrogen pressure we can achieve when nickel hydride returns to nickel [7]? Of course, the next question was: Can nickel hydride be obtained from metallic nickel and gaseous hydrogen, without any electrochemistry involved? The answer of these two simple thermodynamic questions pressed me in fact into the high pressure technique.

**The challenge:** The simplest method for determination of the equilibrium pressure above nickel hydride was to close a sufficient amount of this phase in a compact volume and to measure the pressure developed. Well, we tried it many times using small bronze cylinders and traditional Bourdon manometers but above two kilobars of gaseous hydrogen the simple sealings did not work anymore - and first of all - the experiments became more and more dangerous [7]. We became familiar with many noisy explosions and the number of people ready to cooperate with me became less and less numerous. The problem was, that besides some discouraging remarks about high pressure hydrogen in Bridgman's book, nothing was in fact available in the literature. My contacts with two high pressure groups in Warsaw were not encouraging. Nobody was interested to commit with me the hydrogen suicide. Forgetting dramatic incidents, I found in Mr Rohn from our workshop a person who realized my simple ideas and Fig. 3 presents the scheme of the device which allowed to measure the equilibrium hydrogen pressure above nickel hydride [8,9]. The Bridgman sealing applied allowed to keep a constant hydrogen pressure for weeks. The obtained pressure plateau for nickel hydride decomposition is presented on Fig. 4. As can be seen the maximal pressure developed by nickel hydride at 25° C equals  $3400 \pm 70$  atm. From this value the free energy of formation could be calculated [9]. Previous calorimetric determination

of the decomposition enthalpy [10] allowed the calculation of the entropy of formation - thus a complete thermodynamic characterization of nickel hydride was realized.

**The break-through:** The equilibrium pressure achieved was the starting point for the decisive step: The direct synthesis of nickel hydride from metallic nickel and gaseous hydrogen. Here we

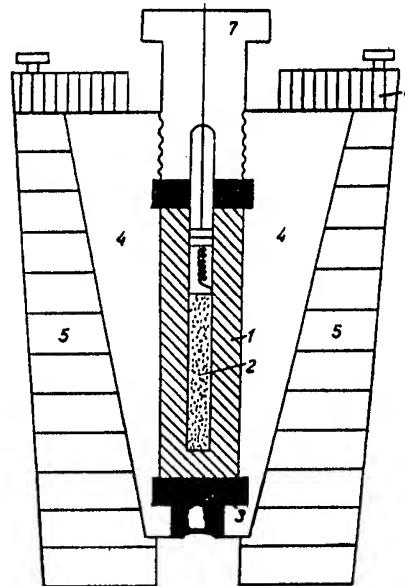


Fig. 3. Scheme of the high pressure device for measuring the equilibrium pressure above nickel hydride: 1- copper cylinder, 2 - hydride sample, 3,6,7 - closings, 4,5 - steel supports

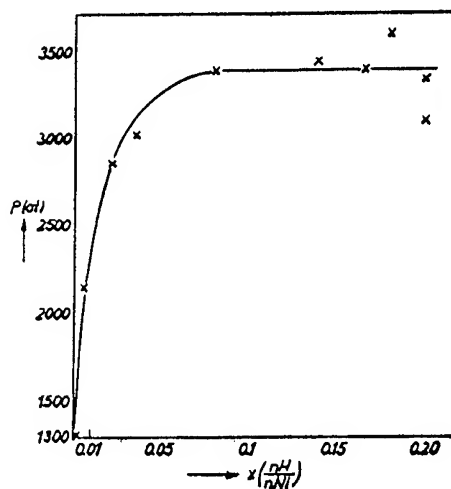


Fig. 4. The stationary hydrogen pressure as a function of mean hydrogen content (in atomic ratio H/Ni) at 25° C.

needed a new high pressure device where high pressure of hydrogen was created mechanically. Basing on the experience of the device presented on Fig. 3 and forgetting again intermediate steps, let me present on the next two figures high pressure devices developed with Mr Bujnowski from Unipress.

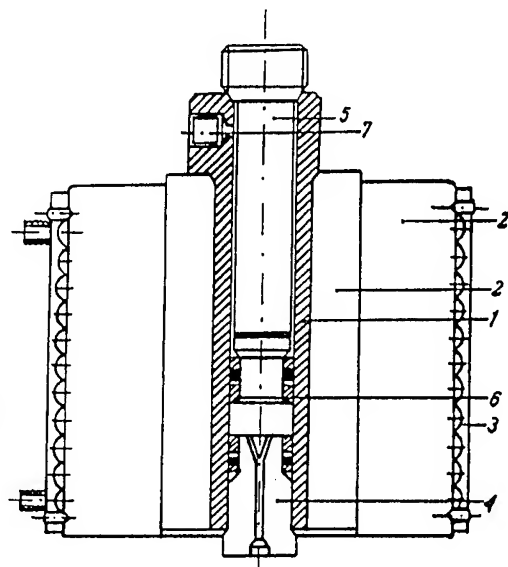


Fig. 5. Piston-cylinder device for hydrogen pressures up to 15 kbar: 1 - beryllium bronze cylinder, 2-5 - steel elements 6 - working volume, 7 - inlet capillary

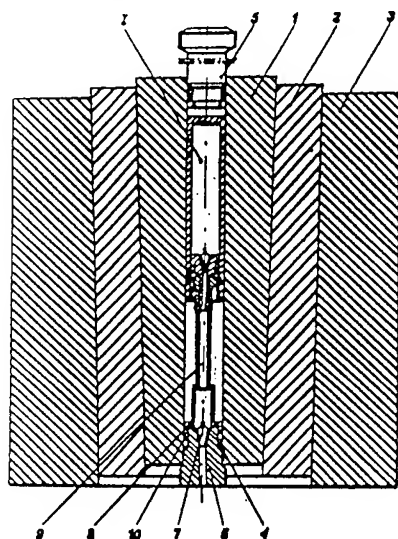


Fig. 6. Piston-cylinder device for hydrogen pressures up to 30 kbar: 1 - beryllium vessel with hydrogen, 2-6 - steel elements, 7 - sealing conus with electrical leads, 8, 10 - Bridgman sealing.

Figure 5 presents the so called „dry” device [12,13] - this means that no pressure transmitting liquid is used. These devices are used permanently in our group up to now. Hydrogen is purified before use and does not come into contact with any organic medium. Fig. 6 presents a device in which the hydrogen working volume is separated from the pressure transmitting liquid by a mobile piston [14-16]. The devices presented on Fig. 5 and 6 were the breakthrough results which opened a wide field of activity. These devices allowed to overcome the traditional hydrogen fears. For me it was the time where I fall in love with high pressure technique. In fact the high pressure device with maximal hydrogen pressure of 30 kbar is equivalent to an upper limit of hydrogen fugacity of  $10^{11}$ . Thus we enlarged the available range of hydrogen fugacity by 9 orders of magnitude. So far Me-H systems were investigated up to  $10^2$  fugacity only. The synthesis of nickel hydride was performed even earlier in cooperation with Prof. Wiśniewski [17], using a device, which was very expensive because of hydrogen explosions, caused by a direct contact of gaseous hydrogen with the pressure transmitting liquid. We reached here the economic limit, what means that further Me-H research became too expensive for a continuation.

**March forward:** The final victory in the Ni-H system was the measurement of the absorption and desorption isotherms [18] presented as an example on Fig. 7

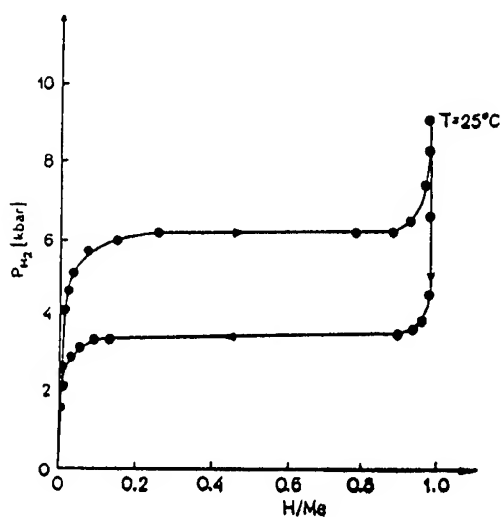


Fig. 7 The ab- and desorption isotherm of nickel hydride at 25° C

As can be seen, up to 6 kbar of gaseous hydrogen practically no considerable absorption of hydrogen takes place. Above this pressure we face a critical hydrogen pressure at which a radical increase of the hydrogen content is observed. This is the transition from the low content hydrogen solution in the nickel lattice to the formation of the hydride phase with a nearly 1:1 atomic ratio content. When decreasing the hydrogen pressure, we do not trace the same course. The decomposition of the hydride phase occurs at about 3,4 kbar of hydrogen. Thus a very large hysteresis is found. Comparing Fig. 7 with previous Fig. 4 we see the advantage of the high pressure vessel presented on Fig. 5 as compared with the device presented on Fig. 3: What initially had to be achieved by tedious separate measurements (with large amounts of electrolytically prepared nickel hydride samples) can now be obtained in a continuous procedure with one loading of nickel powder. The same device can be used for the investigation of the kinetics of hydride formation and decomposition [19,20] by a relaxation procedure presented on Fig. 8

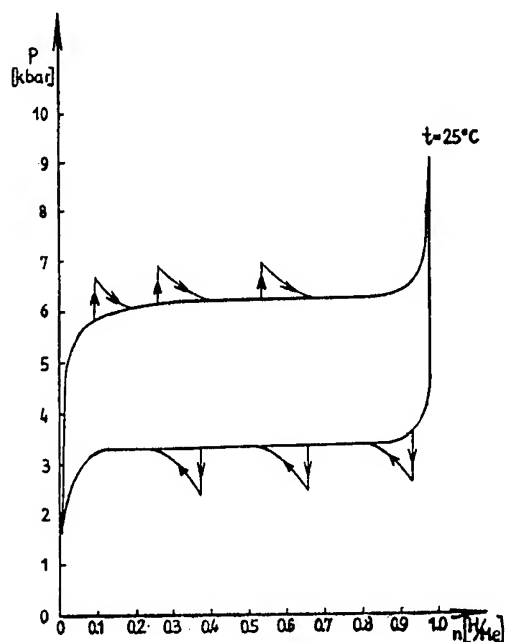


Fig. 8. The schema of the relaxation technique for the kinetics of formation and decomposition of nickel hydride

After reaching the beginning of the formation plateau, we increase the pressure above the plateau value - thus disturbing the previous equilibrium. The system relaxes back to the plateau whereby the pressure as function of time can be recorded. The same procedure with an inverse course of the pressure can be applied for the investigation of the decomposition kinetics of nickel hydride. In both cases - that is as well the formation as the decomposition - the simplest analytical description of both kinetics is given by

$$\Delta P / \Delta P_{\max} = \alpha = a + b \ln t \quad (1)$$

where  $\Delta P$  denotes the pressure difference between the hydrogen pressure at time  $t$  and the plateau value and  $\Delta P_{\max}$  is the maximal (initial) pressure difference of the relaxation step. (1) represents the so called logarithmic law in solid state kinetics. For nickel hydride the corresponding kinetics exhibits a negligible activation energy. Most probably the chemisorption of the hydrogen on the nickel surface forms the rate determining step. Complete different is the desorption kinetics if we are far from the decomposition plateau. The simplest procedure is the decomposition kinetics of nickel hydride at ambient hydrogen pressure. In such case a first order kinetics is observed. Thus instead of (1) we observe

$$\ln P - \ln P_0 = kt \quad (2)$$

This process is clearly thermal activated with an activation energy of 35 kJ/mol  $H_2$ , being in agreement with previous kinetic measurements of nickel hydride prepared electrolytically [21]. A logarithmic law of kinetics was also previously observed in decomposition of aluminium hydride [22]. Comparing (1) with (2) we meet here a process where the kinetics is clearly dependent on the distance between the starting hydrogen activity (characteristic for the sample considered) and the hydrogen activity in the accompanying gaseous phase.

It is clear that high pressure devices, presented on Fig. 5 and 6 opened an extensive field of activity in Me-H systems. First of all the so far inert, in respect to hydride formation, transition metals could be attacked. Table 1 below summarizes the formation and decomposition pressures of four metallic hydrides treated by our high pressure technique [22]:

Table I

System	Formation pressure (kbar)	Temp. (°C)	Decomposition pressure (kbar)	Temp. (°C)
NiH <sub>2</sub>	6,0±0,2	25	3,4±0,1	25
CrH <sub>2</sub>	17,8±0,4	150	3,2±0,2	150
MnH <sub>2</sub>	5,6±0,3	450		
AlH <sub>3</sub>	28±1	300	7,1±0,2	140

Formation and decomposition pressures of new hydrides

In the case of aluminium hydride we reach practically the limit of our high pressure device. Experiments carried out with alloys of nickel with cobalt and iron, as well as alloys of palladium with platinum proved that much higher hydrogen pressure are required to reach the minimal activity of gaseous hydrogen for forcing the formation of the hydride phases [22]. In this direction worked later the Russian group in Chernogolovka [23].

But our high pressure devices could lead to new results in already well known Me-H systems. The classical palladium - hydrogen system is here a good example. Fig. 9 presents the relative electrical resistance of palladium sample as a function of the chemical potential of gaseous hydrogen.

In the known book on the palladium - hydrogen system from 1967 [24] even the maximum of the electrical resistance in Fig. 9 was not sure. As we see in pressures above 20 kbar of gaseous hydrogen, the electrical resistance of palladium hydride is more than 15% lower than that of metallic palladium. In other words palladium hydride is in these conditions more metallic than pure palladium. Electrical resistance is an easy property measurable in situ conditions in high hydrogen pressures. It often serves as an indication for the hydride formation, as shown on Fig. 10 for chromium hydride [25].

The rapid increase of the electrical resistance was an indication for the formation of the hydride phase. A similar role could be played by the in situ measurement of the thermopower [22]. Normally the course of both properties went quite parallel whereby the thermopower was sometimes more sensitive. Much more involved are the in - situ measurements of lattice constants [26,27] and magnetic moment [28,29,30]. Fig. 11 presents a simplified scheme of the in situ magnetic moment of the device developed by Dr. Bauer from Munich.

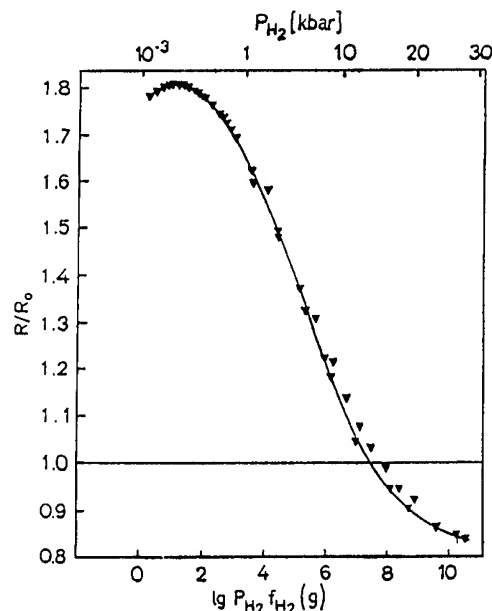


Fig. 9. Relative electrical resistance of palladium as a function of logarithm of hydrogen fugacity.

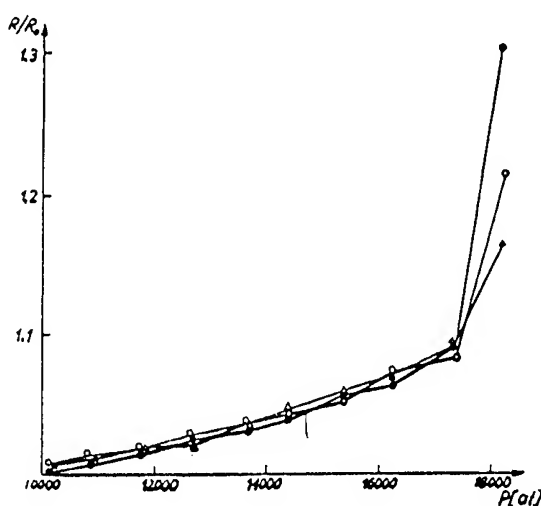


Fig.10. The relative electrical resistance of a chromium sample at 150° C as a function of hydrogen pressure - taking after 30 min time of the given pressure.

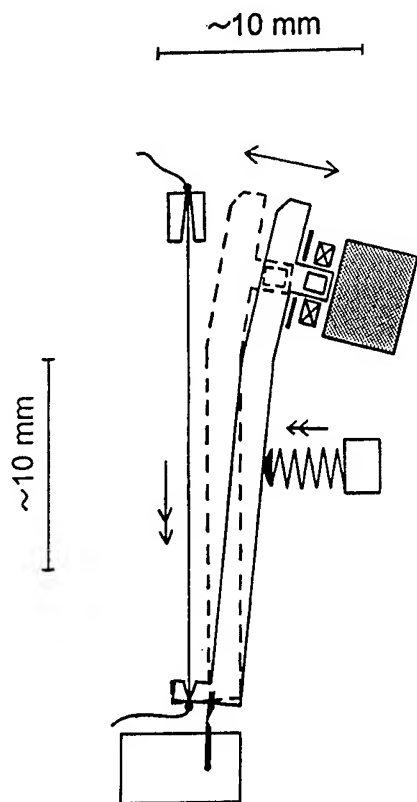


Fig. 11. Scheme of a „pull - out” device for magnetic moment measurements in gaseous hydrogen.

The method is based on the movement of the sample in the magnetic field of a permanent magnet. This movement is caused by the release of the mechanic energy stored by a spring through an expanding heated wire. Fig. 12 presents the changes of the magnetic moment of a  $\text{Ni}_{84}\text{Fe}_{16}$  alloy sample as a function of the hydrogen pressure. The reduction of the initial magnetic moment above 16 kbar of gaseous hydrogen is caused by the hydride formation which in nickel as well as in its ferromagnetic alloys reduces the initial high ferromagnetic moment to the paramagnetic region.

When going back with hydrogen pressure we face the recover of the ferromagnetic behavior. In situ measurements were also performed for thermal conductivity [22,23] and diffusion of hydrogen [32-36]. Especially interesting was the evaluation of the volume of activation for the diffusion of hydrogen in the palladium lattice [36,37]. It equals to  $1.2 \pm 0.2 \text{ cm}^3 \text{ mol}^{-1}$  [37] that is below  $1.9 \text{ cm}^3 \text{ mol}^{-1}$ , the partial molar volume of hydrogen in the same metal. This

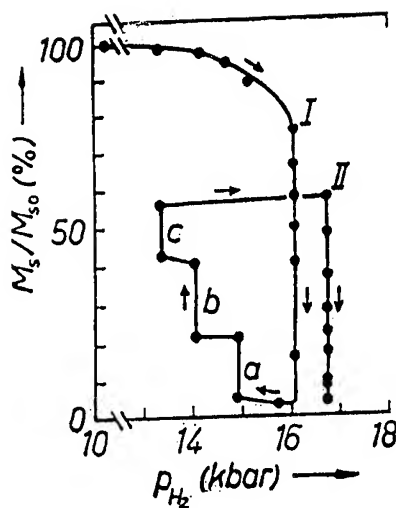
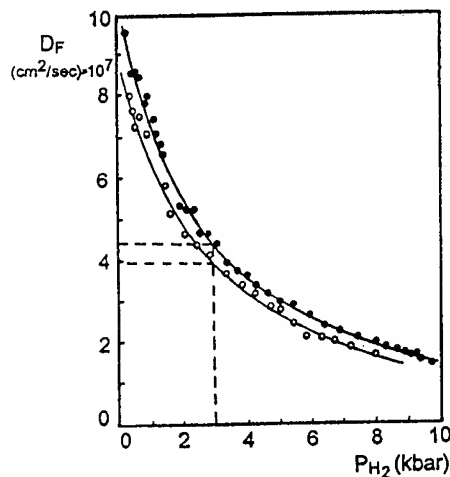


Fig. 12. The relative magnetic moment of a  $\text{Ni}_{84}\text{Fe}_{16}$  alloy as a function of hydrogen pressure at ambient temperature.

inequality is typical for the interstitial mechanism as the elementary diffusion step. Fig. 13 presents the course of the Fick's diffusion coefficients measured in pure gaseous hydrogen and in a gaseous mixture of



$$D_1 = D_0 \exp\left(-\frac{\Delta V^*}{RT} P_1\right)$$

$$\ln D_1 - \ln D_2 = -\frac{\Delta V^*}{RT} (P_1 - P_2)$$

$$\Delta V^* = 1.2 \pm 0.2 \text{ cm}^3 \text{ mol}^{-1}$$

Fig.13. Fick's diffusion coefficient of hydrogen in the metal as a function of the hydrogen pressure at  $25^\circ\text{C}$ : o - measured in pure hydrogen o - measured in the mixture of hydrogen and helium. Below the figure the scheme of calculation is given.

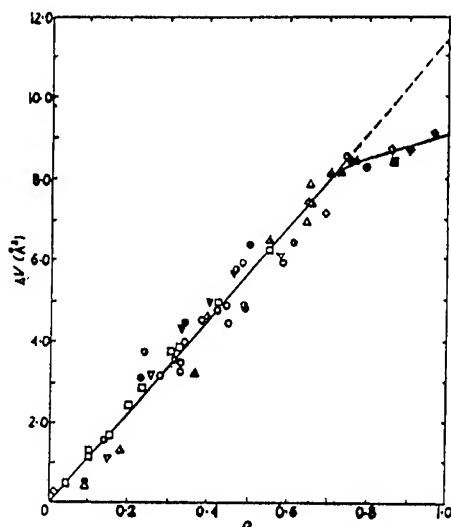


Fig. 14 Volume change of the unit cell of different Ni and Pd alloys of  $f_{cc}$  lattice as a function of atomic ratio  $H/Me = n$  at  $25^\circ \text{C}$ .

hydrogen and helium but at the same hydrogen activity. This equality was proved by the measurement of the relative electrical resistance of palladium in both media. As it is seen, the diffusion coefficient in the mixture is lower than in pure hydrogen what is evidently caused by the hydrostatic pressure. The synthesis of different hydride phases of the systems Pd-H and Ni-H as well as their alloys [22,38] led to an unexpected discovery of the universal volume of the hydrogen particle in these systems [39], presented on Fig. 14. The conclusion from Fig. 14 is very simple in its simple physical meaning: Each hydrogen particle occupying the octahedral vacancies in the  $f_{cc}$  lattice requires the same volume increase. This is independent of the different mechanical and electronic properties of the metal bulk phases considered. In a trivial statement the hydrogen particle behaves like a hard sphere penetrating a soft continuum which has no influence on the final volume relations. The universal hydrogen volume was later extended to other systems, besides the alloys on Pd and Ni basis [40]. With the introduction of diamond anvil technique the pressure dependence of this hydrogen volume in metallic hydrides could be investigated in a wide pressure range. Figures 15 and 16 present the pressure dependence of molar volumes of palladium and chromium with the corresponding volumes of the deuteride and hydride [41,42].

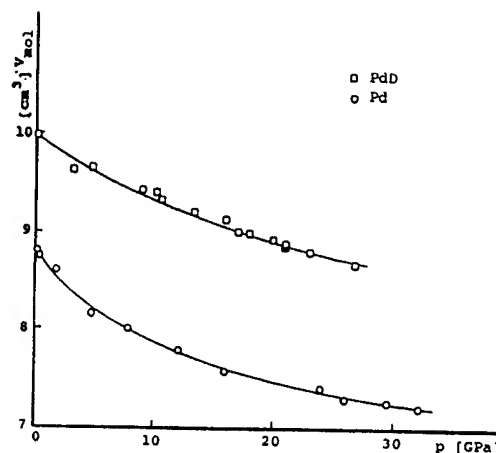


Fig. 15 Molar volumes of Pd and PdD as a function of pressure

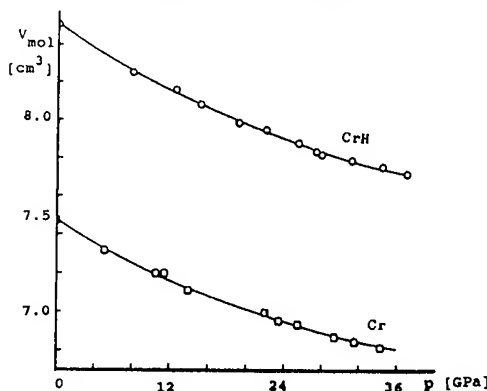


Fig. 16. Molar volumes of Cr and CrH as a function of pressure

Inside the experimental error range the curves for the pure metals are parallel to that corresponding to the deuteride and hydride. This means that the compressibility is identical for the pure metals and their hydrides. In other words the hydrogen involved is much less compressible than the pure metals. Such a behavior is characteristic for transition metals.

A quite different course is observed by intermediate hydrides, like aluminum hydride [43] and copper hydride [44]. Here the hydrogen volume is clearly compressible, approaching at higher pressures the value characteristic for transition metal hydrides. The logical conclusion could be that these hydrides, clear isolators at ambient pressure, approach a similar metallic behavior known for transition metal hydrides. More involved is the pressure dependence of the alkaline metal hydrides [45,46]. Here the extraction of the hydrogen volume is not as unique as in previous metals, but the pressure dependence of the anionic hydrogen particle exhibits a clear

tendency for a decrease at high pressures [41]. Values corresponding to that characteristic for transition metal hydrides can be expected in pressures of  $10^2$  GPa [41]. This is an interesting result for the later discussion of the possible existence of hydrogen hydride.

Let me at this point close the short overview of results achieved due to the break - through in our high pressure technique years ago. I even did not mention the superconductivity of palladium hydride, a hot subject in the seventeenth in Me-H systems [47,49] and discovered in consequent investigations of high concentrated palladium hydride at low temperatures [50]. If we would go below the temperature of liquid helium in 1968, the superconductivity of palladium hydride could be discovered 4 years earlier. But this required the availability of larger amounts of liquid helium. This was only possible if modern helium liquifiers could be bought in the West. But helium liquifiers were classified at that time as strategic material - thus not allowed for an export to so called socialistic countries. Here we meet an example how cold war could retard the scientific progress. (In fact on Fig. 1 in [50]) in sample 1 ( $H/Pd = 0.89$ ) a small decrease of the electrical resistance is noticed at temperatures below 10 K. This sample should exhibit the critical temperature around 3 K [52], thus about 1 degree below the liquid helium temperature available in these measurements).

### Side effects:

#### a.) Non-local hydrogen diffusion:

The experience gathered in the investigations characterized above allowed recently to participate in solutions of some new anomalies. One of them is presented on Fig. 17

The hydrogen pressure in the tube without initial hydrogen content behaves classically, that is in accord with the diffusion kinetics foreseen by Fick's law: Thus increasing the hydrogen pressure at the entrance wall of the tube, one observes in a certain time interval no changes of the internal pressure. The diffusion wave requires a certain characteristic break - through time to change the pressure inside the tube. This break - through time allows the evaluation of the diffusion coefficient if the wall thickness is known. A curious behavior is observed if initially some uniform hydrogen content is inside the metallic wall of the tube: Namely immediately when the

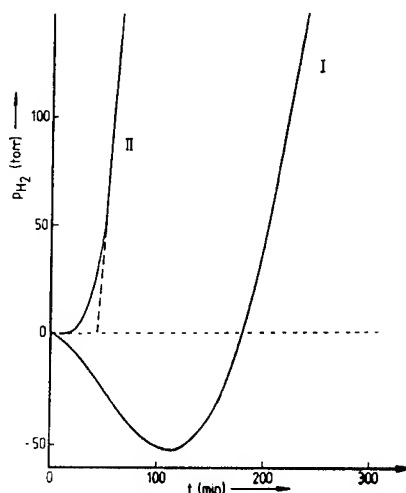


Fig. 17. Time course of hydrogen pressure in a  $Pd_{81}Pt_{19}$  alloy tube during hydrogen penetration: I - the alloy with an initial hydrogen content, II - the alloy without initial hydrogen content [52].

hydrogen pressure is increased at the outside wall, a certain amount of hydrogen is sucked into the wall of the tube from inside causing a reduction of the hydrogen pressure inside the tube and, after tracing a minimal pressure, the normal trend is restored. What happened that: 1.) The time course of the internal pressure exhibits an abnormal initial tendency. 2.) This abnormal course of the pressure is observed without any time lag. Well, one can even ask what has this behavior common with high pressures of hydrogen? Perhaps I am selling you here a complete different stuff? No - what happens is the following sequence of events: The entrance of hydrogen particles into the metallic lattice - supposing that it behaves as an elastic medium - causes the creation of slight displacements of the lattice elements what is the origin of stresses. In terms of high pressure language - this means that high pressure regions are created. The hydrostatic part of the stress tensor involved acts as a high pressure region created by the mobile diffusing component - the hydrogen particles. This hydrostatic part of the stress tensor gives a new contribution to the chemical potential of the mobile component. The very property of the self-stresses created is that they extend further than the diffusion wave with velocity of sound. This means that the thermodynamic consequences of the entrance of hydrogen particles at the outer wall are felt immediately (as compared with the long relaxation of diffusion at the inner wall of the tube. Thus we face here a simple non-local diffusion



phenomenon which causes the unexpected behavior presented by curve I of Fig. 17. This non - locality has an interesting mathematical consequence. The local time derivative of the concentration is given by [52]:

$$\begin{aligned} \partial C_H / \partial t = & D_H \{ (1 + \partial \ln f_H / \partial \ln C_H) + \\ & 2/3 V_H^2 C_H Y / RT \} \partial^2 C_H / \partial z^2 + \\ & 2 D_H V_H^2 / 3 RT (\partial C_H / \partial z)^2 - \\ & \{ 8 V_H^2 D_H Y / L^3 RT \} \Delta C_H (z - L/2) dz \} \partial C_H / \partial z \end{aligned}$$

where  $C_H$ ,  $D_H$  and  $V_H$  mean the concentration, Fick's diffusion coefficient and the molar volume of hydrogen,  $L$  - denotes the thickness of the tube wall,  $Y$  is the abbreviation  $E/(1-\nu)$ , where  $E$  is Young modulus,  $\nu$  the Poisson ratio of the alloy considered,  $z$  is the coordinate of the wall,  $R, T$  have the usual meaning. Thus we derived a non - linear partial differential - integral equation, whereby the classical Fick's law is really a trivial part:

$$D_H (1 + \partial \ln f_H / \partial \ln C_H) \partial^2 C_H / \partial z^2$$

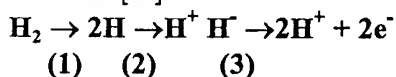
The above integro - differential equation exhibits feed - back character: The entrance of hydrogen particles into the metallic lattice creates a stress field which modifies the field of the chemical potential and thus changes the next diffusion step. We hope that a suitable change of boundary conditions into a forced periodic course will lead to interesting interactions between the diffusion and stress waves, including a possible chaotic behavior. This would be the first example of diffusional chaos in isothermic conditions without chemical reactions and hydrodynamics. But this is still an expectation only.

#### b.) Hysteresis in metallic hydrides:

The positive result of the quantitative explanation of the non - local diffusion presented on Fig. 17 and discovered by Lewis in 1983 [53], suggested me a quantitative approach to the hysteresis in metallic hydrides. As presented previously on Fig. 7 for nickel hydride, the formation plateau of this phase does not coincide with the decomposition plateau which lies below by nearly three kilobars of gaseous hydrogen. This is not - as sometimes suggested - a kinetic effect. For well trained samples (that means that the formation and decomposition processes are repeated many time), it is a quite reproducible phenomenon in terms of the pressure values, independent are the pressure changes slow or quick. The higher formation pressure can be explained by the additional work which has to be performed by hydrogen due to the necessity of the overcome of the stress field created during the hydride formation.

The larger volume of the new phase created guarantees the coherence between the starting nickel lattice and the expanding hydride lattice. This coherency rises the „prize“ of the hydride formation and remains an unavoidable condition for the hydride building. On the other hand the decomposition of the hydride phase, creating a less voluminous nickel lattice, cannot maintain the previous coherency. This means that the decomposition process takes place without any influence of a stress field - therefore the decomposition pressure is lower by the part of the free energy due to the stress created by the volume expansion during the formation process. A quantitative approach for the palladium and nickel hydrides gave good agreement with experimental data [54]. In this case my previous high pressure experience with hydrogen allowed an explanation of hydride behavior both in low as in high pressure region. Of course, this approach is limited to the elastic range of the metallic lattice.

**c.) Hydrogen joke:** The discovery of a vibron discontinuity in dense hydrogen at about 150 GPa by Mao and coworkers in 1988[55] raised the hope that the metallization pressure of this element was reached. This explanation was not confirmed by reflection and refraction measurements. Instead a large absorption was found in the infrared region confirming a radical change of the electronic structure of the previous covalent hydrogen molecule [56]. Comparing the details of this phase transition in dense hydrogen with the known behavior of metallic hydrides, I came in 1992 to the conclusion that one possibility of the phase transition mentioned could be a radical reconstruction of the hydrogen molecule from the previous covalent structure into ionic molecule [57]. This means the creation of hydrogen - hydride, that is a combination of cationic (protonic) and anionic (negatively charged) hydrogen species. Let me remember that in the metallic lattices hydrogen can appear as an anionic - in hydrides of alkaline metals - or as cationic - in hydrides of transition metals. I shall speak this afternoon about some more details of such approach [58]. But let me mention the energetics of the following sequence of transitions [59]:



Step (1), that is dissociation of hydrogen molecule

into atoms requires 432 kJ/mol. Step (2), that is the formation of hydrogen hydride from the atoms, needs 1240 kJ/mol, whereby the conversion of two hydrogen atoms into two protons and two electrons, what can be termed as a simplified metallization, requires 2624 kJ/mol. Thus from pure energetic point of view, the ionic combination of hydrogen - that is hydrogen - hydride - is placed between hydrogen atoms and their full metallization. But let me finish the detailed explanation of my hydrogen joke. It requires a radical change of the chemical bond in the hydrogen molecule, but should we be not prepared for surprises in dense hydrogen?

Finishing my hydrogen story, which led me from electrolytic charging of nickel wires over high pressure techniques, including the modern diamond anvil device, and the final hydrogen - hydride joke, let me mention some, not all, of my Polish coworkers and my friends from abroad, who participated in the activities described previously:

From Poland: K. Bocheńska, R. Rohn, R. Wiśniewski, W. Bujnowski, K. Bojarski, A.W. Szafranski, S. Majchrzak, S. Filipek, M. Tkacz,

From abroad:

T.B. Flanagan (USA), F.A. Lewis (Northern Ireland), H.J. Bauer (FRG), H.D. Hochheimer (FRG).

Without some of them my results could not be achieved, and therefore to all, and all others not mentioned above, I would like to express my deep gratitude.

#### References:

1. B. Baranowski, Z. Szklarska-Śmiałowska and M. Śmiałowski, Bull. Polon Acad. Sci., Ser. Chim., 6 (1958)179.
2. B. Baranowski and M. Śmiałowski, Bull. Acad. Polon. Sci. Ser. Chim., 7(1959)663.
3. B. Baranowski and M. Śmiałowski, J. Phys. Chem. Solids 12 (1959)206.
- 4.) B. Baranowski, Bull. Acad. Polon. Sci. Ser. Chim. 7(1959)897
- 5.) B. Baranowski, Naturwiss. 47(1960) 225
- 6.) B. Baranowski, and Z. Szklarska-Śmiałowska, Electrochim. Acta, 9(1964)1497.
- 7.) B. Baranowski, Bull. Acad. Polon. Sci., Ser. Chim., 10(1962)451.
8. B. Baranowski and K. Bocheńska, Roczn. Chemii, 38(1964)1419.
- 9.) B. Baranowski and K. Bocheńska, Z. Phys. Chem. (N.F.) 45(1965)140.
- 10.) B. Baranowski and I. Czarnota, Naturwiss., 51(1964)262
- 11.) B. Baranowski and I. Czarnota: Bull. Acad. Polon. Sci. Ser. Chim., 14(1966)191.
12. B. Baranowski, M. Tkacz and W. Bujnowski: High Temp.- High Pressure, 8(1976), 656.
13. M. Tkacz and B. Baranowski: Roczn. Chemii, 50(1976)2159.
- 14.) B. Baranowski and W. Bujnowski, Roczn. Chemii, 44(1970)2271
- 15.) B. Baranowski, Platinum Met. Rev., 16(1972)10.
- 16.) B. Baranowski, Ber. Bunsen Ges. Phys. Chemie, 76(1972)714.
- 17.) B. Baranowski and R. Wiśniewski, Bull. Acad. Polon. Sci., Ser. Chim., 14(1966)273.
- 18.) B. Baranowski and M. Tkacz, Roczn. Chemii, 49437(1975)
- 19.) B. Baranowski and M. Tkacz, Physica, 139&140B(1986)688
- 20.) B. Baranowski and M. Tkacz, Z. Phys. Chem. (N.F.), 163(1989)457.
- 21.) B. Baranowski, Bull. Polon. Acad. Sci., Ser. Chim., 7(1959)887.
- 22.) B. Baranowski, Metal - Hydrogen Systems at High Pressures, in Hydrogen in Metals II, eds.: G. Alefeld and J. Völkl, Topics in Applied Physics, 29(1978)157. Springer Verlag.
- 23.) E. G. Ponyatovski, V.E. Antonov, and T. Belask, High Hydrogen Pressures, Synthesis and Properties of New Hydrides in Problems in Solid - State. Physics, eds. A.M. Prokhorov and A.S. Prokhorov, Mir Publ, Moscow 1984 p. 109
24. F.A. Levis, The palladium Hydrogen System. (Academic Press, 1967).
- 25.) B. Baranowski, K. Bojarski: Roczn. Chemii, 46 (1972)525.
26. S. Majchrzak, B. Baranowski, W. Bujnowski and M. Krukowski, Roczn. Chemii, 46(1972)1173.
27. B. Baranowski, Ber. Bunsenges. Phys. Chem., 76(1972)714.
28. H.J. Bauer and B. Baranowski, Phys. Stat. Sol. (a) 40(1977)35
29. H.J. Bauer, J. Phys. E10(1977)332.
- 30.) H.J. Bauer, J. Magn. & Magn. Mat. 15-18(1980)1267.
- 31.) A.W. Szafranski and B. Baranowski, J. Phys., E8(1975)823.

- 32.) B. Baranowski and K. Bocheńska, Penetration of High Pressure Hydrogen into Nickel, in Atomic Transport in Solids and Liquids, eds.: A. Loadding and T. Lagerwall (Verlag der Z. Naturf., Tübingen, 1971)p.360
- 33.) M. Kuballa and B. Baranowski, Ber. Bunsenges. Phys. Chem., 78(1974)335.
- 34.) B. Baranowski, Z. Phys. Chem. (NF)114(1979)59.
35. B. Baranowski, J. Less-Comm. Met., 101(1984)115.
36. S. Majorowski and B. Baranowski, J. Phys. Chem. Solids, 43(1982)1119.
- 37.) B. Baranowski and S. Majorowski, J. Less-Comm. Met., 98(1984)L27.
- 38.) B. Baranowski and S.M. Filipek, Synthesis of Metal Hydrides, in High Pressure Chemical Synthesis, eds.: J. Jurczak and B. Baranowski (Elsevier, 1989)p.55.
- 39.)B. Baranowski, S. Majchrzak and T.B. Flanagan, J. Phys. F 1(1971)258.
- 40.) H. Peisl, Lattice Strain due to Hydrogen in Metals, in Hydrogen in Metals I, eds.: G. Alefeld and J. Völkl, Topics in Applied Physics, 28(1978), 53.
- 41.) B. Baranowski, M. Tkacz and S. Majchrzak, Pressure Dependence of Hydrogen Volume in Some Metallic Hydrides, in Molecular Systems under High Pressure, eds.: R. Pucci and G. Piccito (North Holland, 1991) p. 139.
- 42.) M. Tkacz and B. Baranowski, Polish J. Chem., 66(1992)1301.
- 43.) B. Baranowski, H. D. Hochheimer, K. Stroessner and W. Hoenle, J. Less-Comm. Met., 133(1985)341.
- 44.) M. Tkacz, S. Majchrzak and B. Baranowski, Z. Phys. Chem. (N.F.), 163(1989)467.
- 45.) H.D. Hochheimer, K. Stroessner, W. Hoenle, B. Baranowski and S. Filipek, Z. Phys. Chem.(N.F.), 143(1985)139.
- 46.) J. Duclos, V.K. Vohra, A.L. Ruoff, S. Filipek and B. Baranowski, Phys. Rev., B36(1987)7664.
- 47.) T. Skośkiewicz, Phys. Stat. Sol., (a)11(1972)K123.
- 48.) B. Baranowski and T. Skośkiewicz, High Hydrogen Pressures in Super Conductivity, in High - Pressure and Low Temperature, eds.: C.W. Chu and J.A. Wollam (Plenum Press N.Y, 1978)p.43.
49. B. Stritzker and H Vühl, Superconductivity in Metal - Hydrogen Systems, in Hydrogen in Metals II, eds.: G. Alefeld and J. Voelkl, Topics in Applied Physics, 29(1978)243.
- 50.) T. Skośkiewicz and B. Baranowski, Phys. Stat. Sol., 30(1968), K33.
- 51.) T. Skośkiewicz, A.W. Szafrński, W. Bujnowski and B. Baranowski, J. Phys., C7(1974)2670.
- 52.) B. Baranowski, J. Less-Comm. Met., 154(1989) 329.
- 53.) F.A. Levis, J.P. Magemius, S.G. Mc Kee and Ssebuwufu, Nature, 306(1983)673.
- 54.)B. Baranowski, J. Alloys & Comp., 200(1993)87.
- 55.) R.J. Hemley and H.K. Mao, Phys. Rev. Lett., 61(1988)857.
- 56.) M. Hanfland, R.J. Hemley and H.K. Mao, Phys. Rev. Lett., 70(1993)3760.
57. B. Baranowski, Polish J. Chem., 66(1992)1737.
- 58.) B. Baranowski: Chemical Approach to the Possibility of Hydrogen - Hydride Formation (Proceedings of this Conference).
- 59.) B. Baranowski, Polish J. Chem., 69(1995)981.

# THERMODYNAMICS AND CRYSTAL GROWTH OF III-N COMPOUNDS AT N<sub>2</sub> PRESSURE UP TO 2 GPa

I. GRZEGORY

*High Pressure Research Center Polish Academy of Sciences  
ul. Sokolowska 29/37, 01-142 Warsaw, Poland*

In this paper, the gas pressure - high temperature experimental set up with precise pressure and temperature control is presented. It is shown, that the application of programmable multi-zone furnaces at hydrostatic gas pressure allows to obtain useful information concerning phase diagrams of materials in large pressure (up to 2 GPa) and temperature (up to 2000K) range. The presented system can be used for the growth of high quality crystals even by the methods where relatively large working volumes and long time processes are required, such as crystallization from diluted solutions. It is demonstrated for important class of semiconducting compounds III-V nitrides, which are currently considered as the most promising materials for optoelectronics, in particular for blue and ultraviolet lasers.

From the analysis of thermodynamical properties of AlN, GaN and InN, which is shortly summarized in the paper follows, that the best conditions for crystal growth at available pressure and temperature conditions can be achieved for GaN. The crystallization of AlN is less efficient due to relatively low solubility of AlN in liquid Al. Possibility for the growth of InN crystals is strongly limited since this compound loses its stability at  $T > 600^{\circ}\text{C}$ , even at 2 GPa N<sub>2</sub> pressure.

The crystals of GaN grown at high nitrogen pressure are first crystals of this material successfully used for homoepitaxial layer deposition by MOCVD and MBE. It opens new prospects for GaN based laser. The mechanisms of nucleation and growth of GaN crystals is discussed on the basis of the experimental results.

## 1 Introduction

One of the challenges in present day electronics is the fabrication of semiconductor laser emitting light in blue and UV spectral range.

The material for such a device should have wide direct energy gap necessary for efficient radiative recombination. There are two groups of semiconductors having this property: II-VI compounds (i.e. ZnSe, ZnS) and III-V nitrides (AlN, GaN and InN). Additionally, the material for laser should have stable structure and low concentration of defects. From technological point of view, it means that both substrate crystals and epitaxial layers of high quality should be available.

The technology for II-VI compounds is well developed and high quality laser structures have been grown<sup>1</sup>. Unfortunately, these weakly bonded compounds are structurally unstable and the lasers degrade after several minutes of work. Therefore the only technically viable solution is the use of III-V nitrides.

Currently, thin layers of these compounds are grown on foreign substrates<sup>2,3</sup> by Molecular Beam Epitaxy and Metal Organic Chemical Vapor Deposition. Both n- and p-type layers can be

crystallized and the commercial blue diode based on InGaN/GaN is now available.

However it was shown that the layers grow on SiC or sapphire substrates as columns of perfect crystallites separated by dislocations to compensate for lattice mismatch. The lowest dislocation density for heteroepitaxial layers of GaN is as high as  $10^8/\text{cm}^2$ . This is 5 orders of magnitude higher than the dislocation defect density required for laser.

Moreover no reliable, continuously operating laser have been made successfully by heteroepitaxy in any semiconductor material system. Therefore, it seems that the growth of layers on nitride single crystal substrate is the only solution of the blue - UV laser.

Unfortunately, bulk crystals of nitrides cannot be obtained by known methods such as Czochralski or Bridgman growth from stoichiometric melts. This is due to extremely high melting temperatures and very high decomposition pressures at melting. The conditions of melting have not been determined experimentally. In Table 1, the estimations for melting temperatures and nitrogen pressures are shown.

Table 1 Melting conditions for III-N compounds

nitride	$T^M$ , K	$P_{N_2}$ ** kbar	$P_{N_2 \text{ exp}}$ *** kbar
AlN	$\sim 3500^4$	$0.2^6$	$> 0.1^6$
GaN	$\sim 2800^4$	$45^{7,8}$	$> 40^{7,8}$
InN	$\sim 2200^{4,5}$	$60^5$	$> 35^5$

\* calculated by VanVechten

\*\*extrapolation of the experimental equilibrium data,

\*\*\*the highest pressure at which the decomposition has been observed.

They are extremely difficult to be applied in technology and therefore the crystals have to be grown by methods requiring lower temperatures and corresponding pressures.

We have analysed the possibility of growing crystals from high temperature solutions in liquid Ga, Al and In and the results of this analysis is shown in the paper.

## 2 Experimental

For successful growth of large single crystals the conditions of the process that is pressure, temperature and temperature gradients have to be carefully controlled during many hours in crucibles of the volume of at least few cubic cm. Moreover in many cases these parameters should be changed during the process in programmable way.

In this work, the nitrides have been studied with the system allowing experiments at gas pressure up to 20 kbar in smaller volumes (internal diameter of the chamber - 30mm) and 15 kbar in larger ones (internal diameter of the chamber - 40mm). Before filling with nitrogen, the chamber can be evacuated and the system annealed in vacuum.

For crystal growth experiments two or three zone furnaces, with graphite or tungsten heating elements, have been used. The thermocouples, usually four, were arranged along the crucible. Two or three of them were coupled to the corresponding heating zones by standart input power control electronics. Therefore the temperature profile was controlled in few points with the precision better than  $1^\circ\text{C}$ . The cross-section of the high pressure chamber with the furnace and crucible is schematically shown in Fig. 1.

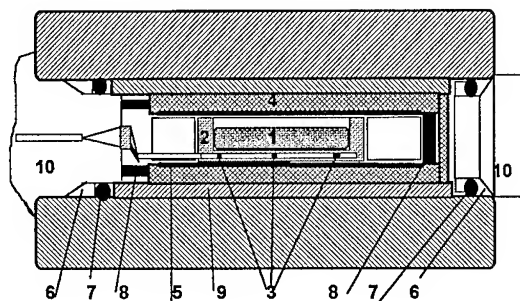


Fig. 1 Cross - section of the high pressure chamber for crystal growth experiments: 1 - sample, 2 - crucible, 3 - thermocouples, 4 - thermal insulation, 5 - heater, 6 - metal gasket, 7 - o-ring, 8 - electrical lead, 9 - steel tube, 10 - steel plug.

## 3 Thermal stability of III-V nitrides

### 3.1 Experimental data

What pressures of nitrogen are necessary for nitrides to be in equilibrium with their constituents at high temperatures?

We have quite clear information for GaN and AlN.

On Fig.2, we have shown the equilibrium  $P_{N_2}$ - $T$  curve for AlN-Al-N<sub>2</sub> system calculated by Slack and McNelly<sup>9</sup>. It follows from the diagram that even for very high temperatures, the pressures necessary for thermodynamical stability of the nitride are not too elevated.

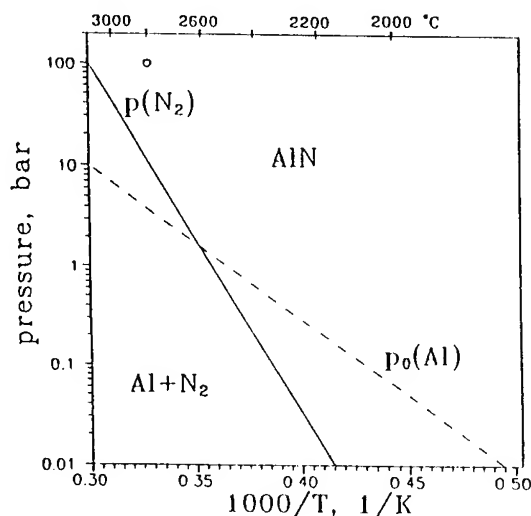


Fig.2 Equilibrium curve for AlN.

For GaN the equilibrium pressure of  $N_2$  over GaN-Ga system has been experimentally determined by Karpinski, Jun and Porowski<sup>7</sup> (Fig.3). From their data we can conclude that equilibrium pressures of nitrogen are much higher than in previous case and for temperature 1100 - 1690K they are between 100bar and 20 kbar.

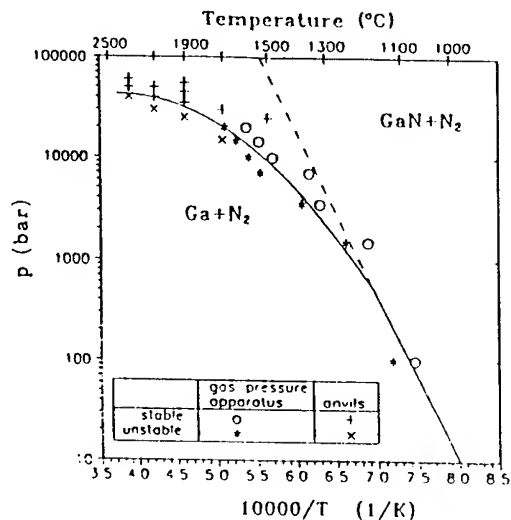


Fig.3 Equilibrium curve for GaN.

For InN the situation was much more complicated since the published data scattered many orders of magnitude. If we compare the proposed values of the equilibrium nitrogen pressures for, let's say 600°C, we can see that they are between  $10^{-5}$  bar to 1 kbar - Fig.4.

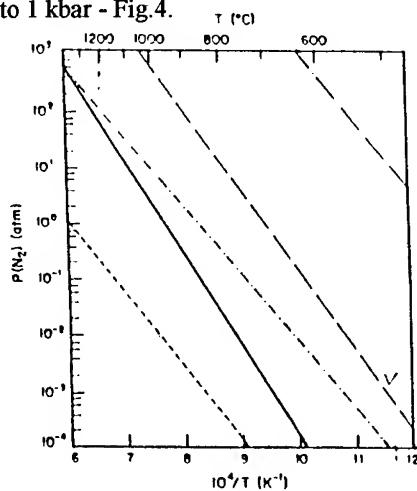


Fig.4 Equilibrium curve for InN: — - Ref.<sup>10</sup>, --- Ref.<sup>11</sup>, -.-.- Ref.<sup>12</sup>, .....Ref.<sup>13</sup>, .....Ref.<sup>14</sup>

In that situation experimental verification of the data was necessary to estimate crystal growth conditions for this difficult compound.

The experiments of Differential Thermal Analysis of decomposition of InN powder have shown that the nitride dissociates at 720+20°C independently on nitrogen pressure lying between 100bar and 18.5 kbar. this suggested that observed decomposition was related rather with overcoming of the kinetic barrier than the equilibrium temperature.

Indeed the long time annealing experiments confirmed this conclusion. For example after 10 hours at 600°C InN decomposed completely at 10 kbar  $N_2$  pressure.

It is much higher pressure than it follows from the highest curve of Fig.4, according to which for 600°C InN should be stable already at 1 kbar.

Full decomposition at 18.5 kbar was observed at 620 C.

The annealing of the compound in temperature gradient leads to the large zone of partial decomposition which indicates that at the equilibrium temperatures corresponding to nitrogen pressure up to 20 kbar the slow kinetics unables exact determination of equilibrium conditions at available pressure range.

Therefore, the problem of of the equilibrium curve of InN is still open, although as we will see later on, the obtained data are sufficient to estimate the possibilities of growing InN crystals from the solution in liquid In.

### 3.2 Discussion

Assumming that at 10 kbar and at 600°C (870K) InN is in equilibrium with its constituents (in fact it is already unstable), we can demonstrate what will happen with this temperature for nitrogen pressure of 1 bar. For that, we will show the Gibbs free energy  $G$  of InN and of the system of its constituents as a function of temperature and nitrogen pressure.

Taking into account that for  $N_2$  and In the enthalpy and entropy data are tabulated<sup>15,16</sup> and assumming that for InN the entropy  $S$  determining the slope of the curve  $G(T)$  is equal to the entropy of GaN, which is known<sup>17</sup> (in fact it is bigger but unknown), we can construct diagram showing the relation of  $G(T)$  for InN and its constituents. It is shown in Fig.5.

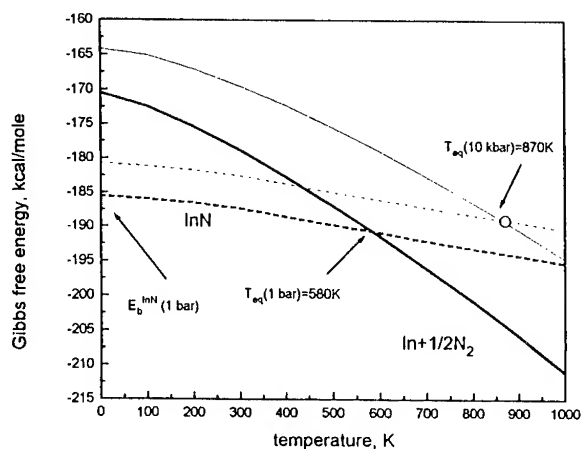


Fig.5 Gibbs free energy  $G(p, T)$  for InN and its constituents.

Therefore, lowering the pressure down to 1 bar we note the shift of the equilibrium temperature to the temperature as low as 580 K. In fact, at 1 bar pressure, InN loses its stability at temperature even lower than this 580K.

Using temperature dependences of the free energy we can illustrate the analogies and differences in the properties of Al, Ga and InN. At first, all of them are crystals of high bonding energies (AlN-11.52eV/atom, GaN- 8.92eV/atom, InN-7.72eV/atom)<sup>18</sup> comparing to the classic III-V semiconductors (i.e. GaAs - 6.52eV/atom). The consequences of this are high melting temperatures and good thermal stability especially for AlN and GaN.

On the other hand the strong bond in nitrogen molecule (4.78eV/at.) lowers the free energy of the constituents approaching its position to that of the nitride. Especially close for InN.

Since the free energy of the constituent system, containing gaseous nitrogen, decreases faster, due to the higher entropy, than the free energy of the crystal, the nitride loses its stability at high temperatures.

The lost of thermodynamical stability of each of considered compounds, at 1 bar nitrogen pressure occurs at very different temperatures, which is caused mainly by the differences in bonding energy in the crystals.

This is shown in Fig.6 where we have the averaged free energy curves for constituents and the curves for crystals. It is also shown that the application of high nitrogen pressure allows the extension of the stability range of nitrides in relation to their

constituents since with increasing pressure the free energy of nitrogen increases significantly faster than the free energy of condensed phases in the system. The degree of that extension is the smallest for InN and the biggest for AlN.

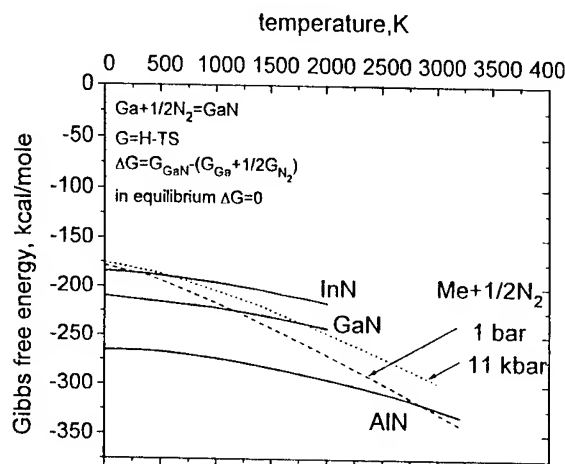


Fig.6  $G(p, T)$  for III-V nitrides and their constituents.

For crystallization experiment it is important that for each of the nitride there is a temperature limit following from its thermodynamical properties and technical possibilities of the experimental system.

- For AlN, we have only the technical limit related to temperature of about 2000K available in our gas pressure system. The available pressures are sufficient even for melting.

- For InN, we have the pressure limit - 20kbar which determines the maximum temperature of InN stability. This is lower than 900K which is very far from the expected melting point.

For GaN, the maximum equilibrium temperature determined by nitrogen pressure of 20 kbar is 1960K which comes closest to melting and suggests the best conditions for crystallization.

In the next section it is estimated what concentrations of nitrogen in Al, Ga and In can be expected at temperatures where corresponding nitrides are stable and could be crystallized.

#### 4 Solutions

Fig. 7a shows the liquidus lines for the systems of nitrides and corresponding liquid metals, calculated in ideal solution approximation.

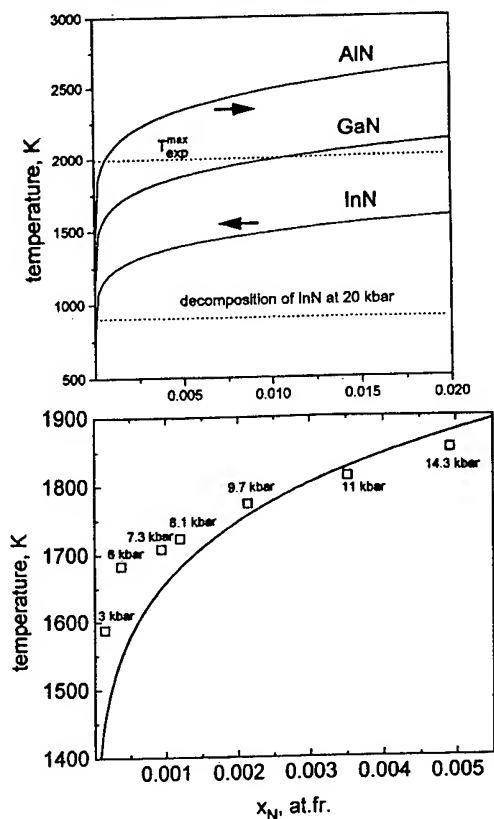


Fig. 7 a- Liquidus lines for AlN, GaN and InN calculated in ideal solution approximation. The arrows indicate the influence of non ideality of the solution, horizontal lines show the max. concentrations in Al, Ga, and In available in high pressure experimental system, b - the same line for GaN with the experimental points.

The data of the figure suggest that the highest solubilities at temperatures and pressures available in our experimental system can be expected for GaN and the lowest for InN.

The curve in Fig. 7b is the same line for GaN with the experimental points determined at the conditions close to the three phase equilibrium. The data indicate that the nitrogen content in gallium can be increased up to the values higher than 0.1% for temperatures exceeding 1700K and corresponding pressures higher than 8kbar.

From the solubility data we can estimate the heat of nitride dissolution which is useful for

description of crystallization process since it expresses bonding energy in the crystal in relation to its mother phase that is the solution.

Assuming ideal behavior of the solution and melting parameters of GaN proposed by Van Vechten one can express the heat of GaN dissolution as:

$$\Delta H_{\text{sol}} = \Delta H^M = \Delta S^M T^M = 44.6 \text{ kcal/mole} \quad 3.1$$

where  $\Delta H^M$ ,  $\Delta S^M$  and  $T^M$  are enthalpy, entropy and temperature of GaN melting.

#### 5 Crystal growth

In this section some typical results of GaN crystallization from the solution in the liquid gallium at high nitrogen pressure will be shown.

Supersaturation, that is the driving force for the crystallization process has been created by the application of temperature gradient of order of 30 - 100°C/cm along the axis of the crucible. An alternative method could be the slow cooling of the solution. But since the solubilities are rather low, we had to use temperature gradient to achieve continuous transport of nitrogen into the growth zone during many hours.

Typical arrangements of the crucibles and temperature profiles are shown in Fig. 8.

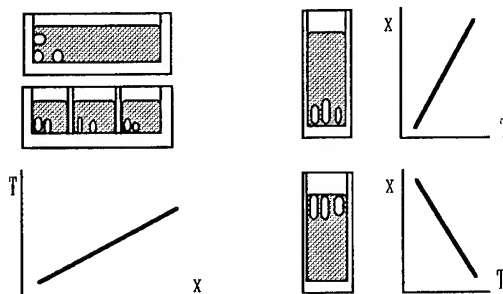


Fig. 8 Typical arrangements of crucibles and temperature profiles used in high pressure crystal growth experiments.

Usually the pressure of the experiment, 10 to 20 kbar, was higher than the equilibrium one for high temperature end of the solution. Therefore the



pressure and temperature in whole the crucible corresponded to GaN stability range.

The final conditions of the experiment were reached by the compression of the gas followed by heating of the system at high pressure or the system was heated at low pressure and then gas was compressed up to the required pressure. The sequence of these operations influences the creation of the GaN polycrystalline layer on gallium surface which is the first step GaN synthesis in considered process.

The surface layer consists of GaN single crystals the size of which depends upon the sequence of compression and heating. If the compression is performed after heating, the crystals are bigger since they are growing at low supersaturation, if the system is heated at high pressure the crystals in the layer are significantly smaller.

The surface layer inhibits further synthesis and then the long time crystallization in temperature gradient become possible.

On the other hand the surface layer is the source of numerous growth centers which leads to the growth many GaN crystals in the cooler zone of the growth solution. This complicates the control of growth conditions of particular crystals.

Significant limitation of the number of the growth centers is achieved if grains creating the surface layer are big.

Obviously the optimum way of decreasing the influence of the layer on further crystallization is the introduction of single crystalline GaN seed into the cold part of the solution.

For the processes without an intentional seeding we could make some conclusions. It is observed that the crystals growing slowly with average growth rate into the fastest growth direction of 0.1 - 0.2mm/h are single crystalline platelets or hexagonal prisms with stable morphology.

This means that they have sharp edges and plane, smooth faces perpendicular to main crystallographic directions of the wurtzite structure. The best quality crystals grown without an intentional seeding were hexagonal plates with smooth plane faces, reaching dimensions 2-3mm. Some of such crystals are shown in Fig.9

The observation of the crystal morphology allows to conclude about dominating growth mechanisms. It seems that dominating mechanism especially for higher rates is two dimensional layer

growth with nucleation at the edges exposed to the growth solution. Such a mechanism suggests relatively high local supersaturations and express a tendency to loose a stability of the growing face with further increase of the growth rate.

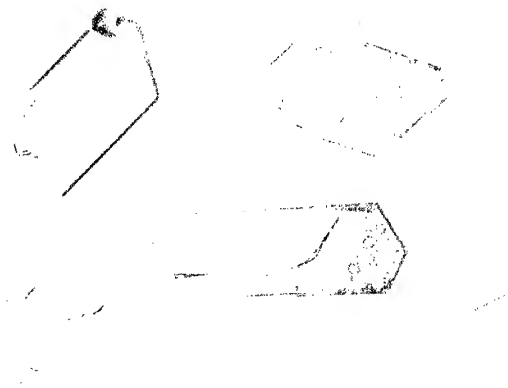


Fig.9 GaN crystals grown without intentional seeding.  
— 1mm

On the hexagonal surface of some GaN platelets, after its etching in liquid gallium at high temperature, we have observed patterns indicating the presence of screw dislocations which are active centers for two dimensional growth (Fig.10)

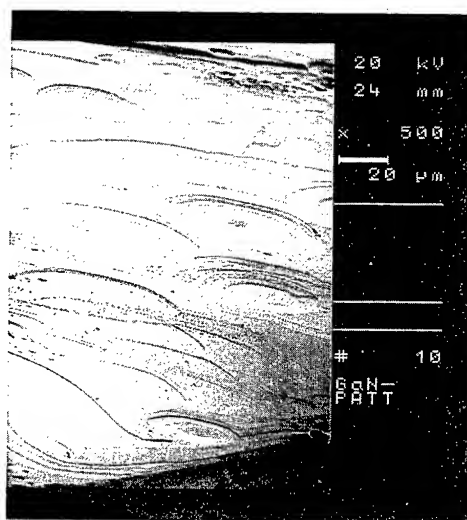


Fig.10 screw dislocations on(0001) face of GaN crystal.

The quality of GaN crystals was estimated by X-ray rocking curves. Full Width at Half Maximum

Maximum of the curves for crystals of stable morphology was 23-32 arcsec which indicates high quality of the structure of the pressure grown GaN crystals. The curves are significantly narrower than the curves of heteroepitaxial GaN layers grown by MBE or MOCVD.

GaN platelets can be cleaved along the plane perpendicular to the 1010 direction.

The quality of the crystals deteriorates with increasing growth rate and size. This is related to the non-uniform distribution of nitrogen in the solution across the growing face, especially if this face reaches a size comparable with the size of the crucible. In this case the layer-by-layer growth mechanism is strongly disturbed which leads to the formation of macrosteps on the crystal surfaces and acceleration of the growth near edges and corners of the crystals. For the growth above 1mm/h the formation of unstable hollow, skeletal or dendritic crystals is observed.

The deterioration of the quality of the fast growing crystals is reflected by the broadening of the rocking curve (Fig. 11). In some cases the splitting of the reflection curve into two or three peaks is observed indicating the presence of low angle grain boundaries in the cm size GaN crystals.

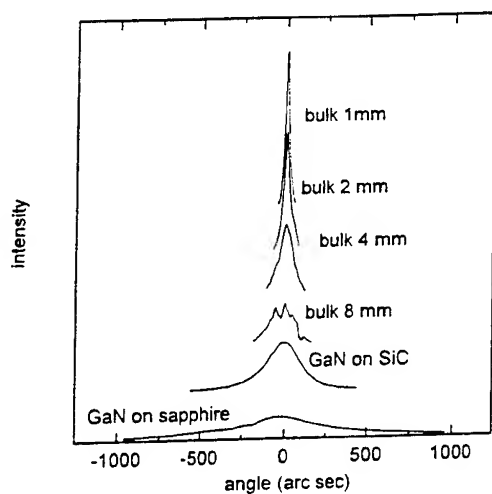


Fig. 11 Rocking curves of GaN plates with increasing size.

The attempts of seeding of the growth with GaN crystal introduced into the cooler zone of the solution have been performed in order to establish wetting conditions and to suppress the spontaneous nucleation on the surface layer. Wetting of GaN with

the liquid Ga is difficult to achieve especially if the system is heated at high  $N_2$  pressure. The formation of the surface layer on the Ga surface adjacent to the seed eliminates the introduced crystal as a seed for further growth. The wetting has been achieved by partial dissolution of the crystal at low  $N_2$  pressure.

Layer growth on the seed faces have been observed, however, patterns characteristic for unstable growth like edge nucleation and macrosteps are also visible (Fig. 12). As in the previous case this is due to the too high and non-uniform supersaturation.

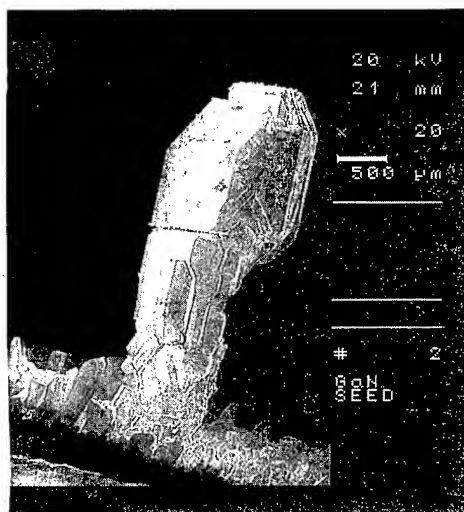


Fig. 12 Growth of GaN on GaN seed crystal.

For typical supercooling that is the temperature difference between the hot and cold end of the crucible, used in our experiments 100 - 150°C, the maximum supersaturation possible in the solution is very high. For indicated conditions this is about 300%.

Since in our process, the number of crystals grow at the same time with various rates, the growth conditions of particular crystal is strongly modified by surrounding neighbors. Therefore, the local supersaturations can be significantly lower than in the volume of the solution.

Indeed if we evaluate the supersaturation<sup>20</sup> for GaN crystal growing at a rate 0.1 mm/h, by two dimensional layer by layer mechanism, at 1400°C, we obtain  $\sigma$  of the order of 50% which corresponds to the supercooling of 30 - 50°C.

It follows from above that we have to work with smaller temperature differences to increase the size of GaN crystal without deterioration of its quality.

Since the dislocation density in pressure grown GaN crystals is usually of the order of  $10^4 - 10^5 \text{ cm}^{-2}$ , we believe that after additional optimization of both substrate and layer growth, it will be possible to demonstrate the laser action in GaN homoepitaxial structure.

The rate of AlN synthesis at high nitrogen pressure is so high that a thermal explosion is observed during heating of a bulk Al sample<sup>21</sup> at pressures of 0.1 to 6.5 kbar. The combustion product is AlN powder or ceramics. At pressures higher than 6.5 kbar, a tight AlN layer on the surface of liquid Al inhibits further reaction, and the metal can be heated up to the temperature of crystallization. Due to low solubility, the crystallization rate of AlN, at 1600-1800°C, is rather low ( $< 0.02 \text{ mm/h}$ ).

For InN, due to kinetic (low temperature) and thermodynamical (low solubility) barriers crystal growth experiments resulted in very small crystallites (5-50  $\mu\text{m}$ ) grown by slow cooling of the system from the temperatures exceeding the stability limit for InN.

## 6 Conclusions

High quality crystals of III-N compounds can be grown at nitrogen pressure up to 20 kbar. At this pressure range, the best results have been obtained for GaN. AlN requires higher temperatures to increase the solubility of N in the liquid Al. For InN, the pressure of 20 kbar is not sufficient for effective crystallization.

The main obstacle in growing large substrate quality GaN crystals in the crystallization processes described in this work, is instability of the growth related to the supersaturation which is too high for growing crystals exceeding 2-3 mm in size. Stable growth can be achieved by decreasing supersaturation during growth.

Nonuniform distribution of nitrogen in the solution caused by the spontaneous nucleation of GaN crystals on the surface layer and the small volume of the crucible are also the reasons for deterioration in crystal quality during growth. The spontaneous nucleation on the surface layer can be suppressed by the introduction of single crystalline GaN seed into the growth solution.

## References

1. H. Morkoc, S. Strite, G.B. Gao, M.E. Lin, B. Sverdlov and M. Burns, *J. Appl. Phys.* 76(3), 1994, 1363
2. Amano H, Kito M, Hiramatsu K and Akasaki I *Jpn. J. Appl. Phys.* 28, 2112, (1989).
3. Nakamura S., Mukai T., Senoh M. and Iwasa N., *Jpn. J. Appl. Phys.* 31,, 139 (1992).
4. Van Vechten J.A., *Phys. Rev.* B7, 1479 (1973)
5. Grzegory I, Krukowski S, Jun J, Bockowski M, Wroblewski M. and Porowski S., *Proceedings of XX AIRAPT Conference*, Colorado Springs (1993)
6. Class W, *Contract Rep.*, NASA-Cr-1171 (1968)
7. Karpinski J., Jun J. and Porowski S., *J. Cryst. Growth*, 66, 1, (1984)
8. Karpinski J., and Porowski S. *J. Cryst. Growth*, 66, 11 (1984)
9. Slack G.A. and Mac Nelly T.F., *J. Cryst. Growth*, 34, 276 (1976).
10. R.D. Jones and K. Rose, *CALPHAD* 8, (1984) 343
11. J.B. Mac Chesney, P.M. Bridenbaugh and P.B. O'Connor, *Mater. Res. Bull.* 5, (1970) 783
12. A.M. Vorob'ev, G.V. Evseeva and L.V. Zenkevich, *Russ. J. Phys. Chem.* 45, 1971, 1501
13. A.M. Vorob'ev, G.V. Evseeva and L.V. Zenkevich, *Russ. J. Phys. Chem.* 47, (1973), 1616
14. S. P. Gordienko, *Russ. J. phys. Chem.* 51, (1977), 315
15. Glushko W. P. et al. in *Termodinamitscheskije svoystva individualnykh veshtchestv*, (Nauka, Moscow, 1979)
16. A. A. Antanovitsch and M. A. Plotnikov, *Inzhen-Fiz. Zh.* 2, 1977, 280
17. A. N. Sinkariev, N. J. Andreeva and J. Ch. Saulov, *Chimia i Chim. Techn.* 10, nr9 (1973), 1451
18. Harrison W. A. 1980, *Electronic Structure and Properties of Solids* Freeman, San Francisco, (1980).
19. M. Leszczynski, I. Grzegory and M. Bockowski, *J. Cryst. Growth* 126, 1993, 601.
20. I. Grzegory and S. Porowski, to be published
21. I. Grzegory, M. Bockowski, J. Jun, *High Press. Res.*, vol 10, (1992), 288

---

## **II Instrumentation and Experimental Techniques**

# OPTIMAL DESIGN OF DIAMOND CULET PROFILES

Arthur L. Ruoff

*Department of Material Science and Engineering, Cornell University  
Ithaca, NY 14853-3801, U.S.A.*

Harrison Poon and Subrata Mukherjee

*Department of Theoretical and Applied Mechanics, Cornell University  
Ithaca, NY 14853-3801, U.S.A.*

## ABSTRACT

We describe an iterative method for obtaining the optimal profile of a diamond culet for use in the diamond anvil cell. In the present paper, as an example, we determined the initial shape which a diamond culet should have such that it would be flat when the molybdenum gasket reaches a uniform thickness of 4.63  $\mu\text{m}$ . We note that this involves a maximum pressure of 5.14 Mbar (514 Gpa). The analysis accounts for the cubic elastic anisotropy of the diamond and for the pressure dependence of the elastic coefficients. The plasticity model includes the effect of pressure on the yield strength, using the Chua-Ruoff scaling relation, and elastic constants computed as a function of volume (and pressure) by others.

## Introduction

The diamond anvil cell (DAC) makes it possible to study material behavior under pressures in the multi-megabar regime and has made it possible to achieve a pressure of 5.6 Mbar [1].

For the purpose of the present paper, the optimal shape design of diamond amounts to choosing values for the parameters  $\alpha$ ,  $\beta$ ,  $a$ ,  $b$ ,  $c$ , (see Figure 1) so as to maximize the final pressure achieved before structural failure of the DAC. Currently, these values are chosen based on empirical experience, rather than using a theoretical or computational approach. An attempt at taking a rational approach to this design process, through the use of numerical modelling in an iterative fashion, is the central theme of this paper.

The optimization problem presented here is further limited in scope. Only two parameters are allowed to change, namely, the tip radius  $a$ , and the inner bevel angle  $\alpha$ .

## Constitutive model for the diamond

The diamond crystal exhibits cubic symmetry. The stress-strain relation can be written in the form:

$$\begin{Bmatrix} \sigma_1 \\ \sigma_2 \\ \sigma_3 \\ \sigma_4 \\ \sigma_5 \\ \sigma_6 \end{Bmatrix} = \begin{bmatrix} C_{11} & C_{12} & C_{12} & & & \\ & C_{12} & C_{11} & C_{12} & & \\ & C_{12} & C_{12} & C_{11} & & \\ & & & C_{44} & & \\ & & & & C_{44} & \\ & & & & & C_{44} \end{bmatrix} \begin{Bmatrix} \epsilon_1 \\ \epsilon_2 \\ \epsilon_3 \\ \epsilon_4 \\ \epsilon_5 \\ \epsilon_6 \end{Bmatrix} \quad (1)$$

with the usual convention that subscripts 1 to 3 are associated with direct components while

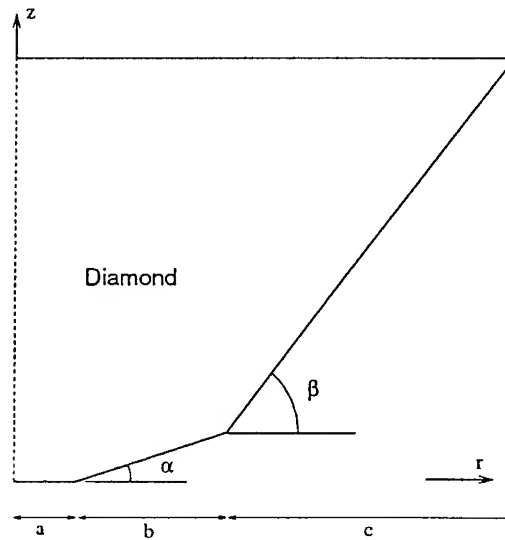


Figure 1. Diamond anvil shape parameters

subscripts 4 to 6 are associated with shear components. The coefficients  $C_{11}$ ,  $C_{12}$ ,  $C_{44}$  are themselves functions of pressure. At low pressures ultrasonic measurements lead to Eqn (2)[2], where we extrapolate to high pressures.

$$\begin{aligned} C_{11}(P) &= C_{11}^0 + C'_{11} P \\ C_{12}(P) &= C_{12}^0 + C'_{12} P \\ C_{44}(P) &= C_{44}^0 + C'_{44} P \end{aligned} \quad (2)$$

with the following numerical values

$$\begin{aligned} C_{11}^0 &= 1079 \text{ GPa} \\ C_{12}^0 &= 124 \text{ GPa} \\ C_{44}^0 &= 578 \text{ GPa} \\ C'_{11} &= 5.98 \\ C'_{12} &= 3.06 \\ C'_{44} &= 2.98 \end{aligned}$$

### Constitutive model for the gasket

Since the gasket undergoes extremely large plastic deformations, elasticity can be ignored in our simplified analysis. The simplified equilibrium equation for a fully yielded, axisymmetric state (including sufficient friction between the diamond and anvil that sticking occurs) takes the form [3,4]

$$\frac{dP}{dr} = -\frac{\sigma_0}{h} \quad (3)$$

where  $\sigma_0$  is the (pressure dependent) Mises yield stress,  $P$  is the pressure,  $r$  the distance from the symmetry axis, and  $h$  the gasket thickness.

Eqn (3) allows the pressure distribution to be computed easily by numerical integration given the geometry of the gasket. The Chua-Ruoff scaling law for the yield stress gives [5]

$$\sigma_0 = \sigma_{00} \frac{G/(1-\nu)}{G_0/(1-\nu_0)} = \sigma_{00} F \quad (4)$$

where  $\sigma_0$  is the yield stress,  $G$  the shear modulus,  $\nu$  the Poisson's ratio at a given pressure, and  $F$  is the pressure strengthening factor. The added zero subscripts refer to zero pressure values. The complete set of elastic constants for molybdenum

were obtained as a function of pressure from first-principle all-electron calculations [6]. The shear constant  $G$  was evaluated from

$$G = [C_{44}(C_{11} - C_{12})/2]^{1/2} \quad (5)$$

and  $\nu$  from the bulk modulus,  $B$ , and  $G$  according to

$$\nu = (3B - 2G)/2(3B + G) \quad (6)$$

Hence  $F(P)$  is obtained. Give  $\sigma_{00} = 6 \text{ GPa}$  for heavily strain-hardened molybdenum and using for the tip radius,  $a = 150 \mu\text{m}$ , we obtain from (3) for a maximum pressure of 514 GPa,  $h = 4.63 \mu\text{m}$ . Then

$$\int_0^P dP/F = \frac{\sigma_{00} a}{h} \left(1 - \frac{r}{a}\right) \quad (7)$$

enables us to plot  $P$  vs  $r$  as shown in Figure 2.

### Computational model

Implicit, geometrically nonlinear finite element analysis (FEM) (using ABAQUS Version 5.3) is performed for the diamond anvil. The pressure dependent constitutive relation (Eqns(1) and (2)) is implemented by writing a "user material" subroutine. The cubic anisotropy necessitates a three-dimensional analysis. For simplicity in meshing, the real 16-sided diamond is approximated by a solid of revolution, generated by a cross section schematically shown in Figure 1. Furthermore, cubic symmetry implies that only a 45° sector needs to be modelled. The loading is a pressure distribution  $P(r)$  acting in the  $z$ -direction on the culet.

It is observed that the computed displacement does not vary much in the circumferential  $\theta$  direction. The deformed shape remains almost axisymmetric. In what follows, the deformed shapes shown are all averaged along  $\theta$ . An axisymmetric analysis is carried out for the gasket according to Eqn (3).

It must be emphasized that the current model captures some of the most salient aspects of the DAC operation. These include the pressure dependence of diamond elastic moduli and gasket yield strength, the cubic nature of diamond, and geometrically nonlinear finite element analysis.

### Iterative design procedure

The current design procedure is based on the conjecture that failure of the DAC may be delayed by not allowing the diamonds to approach each other closely (resulting in contact). Figure 3 shows an example where the deformed diamond "cups," resulting in close contact at the culet edge.

A reasonable objective is to design a diamond whose deformed shape is flat, thereby avoiding diamond contact and delaying failure. The procedure is as follows:

**Step 1.** Take a deformed gasket with a specified uniform thickness. Integrate the plasticity Eqn (3) to get the pressure profile  $P(r)$ . As an example, a uniform molybdenum gasket  $4.63 \mu\text{m}$  thick results in the pressure profile shown in Figure 2, with a peak pressure of 514 GPa.

**Step 2.** Load the diamond with the above pressure profile. Obtain its deformed shape using a finite element calculation. An example is shown in Figure 3.

**Step 3.** The crux of the whole design technique lies in the following idea. Take the deformed shape of the diamond shown schematically in Figure 4. Draw a horizontal mean line (representing the ideal deformed shape). Measure the deviation between the two. Then apply the same deviation to the undeformed diamond shape. The modified undeformed shape for our example is shown by the solid line in Figure 5.

**Step 4.** Examine the modified undeformed shape to fit an approximate tip radius  $a$  and a bevel angle  $\alpha$ . In our example,  $a = 10 \mu\text{m}$  and  $\alpha = 14.4^\circ$ . This shape is the guess for the undeformed diamond anvil for the next iteration.

**Step 5.** Repeat steps 2 to 4 above using the modified diamond, until convergence. In our example, near-convergence is observed immediately, as shown in Figure 6.

Thus the pair of diamonds with the initial shape shown by the solid line (and to a fair approximation by the dashed line) would, if supporting the pressure profile of Figure 2, be deformed to planar parallel surfaces.

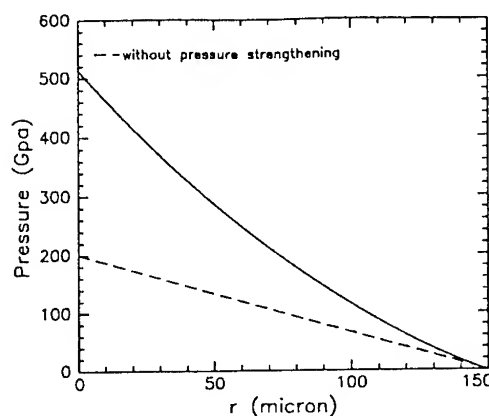


Figure 2. Pressure profile of gasket

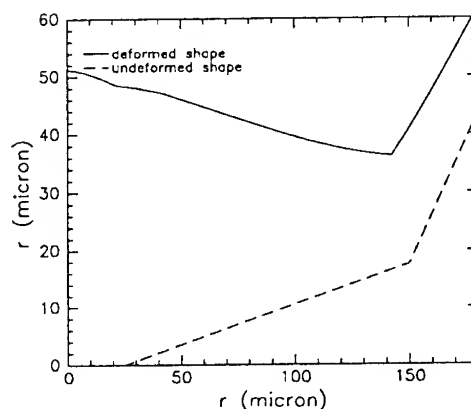
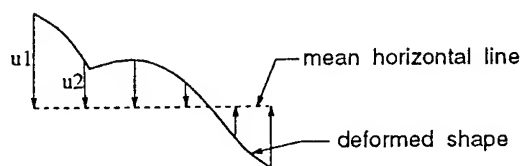


Figure 3. Example of diamond deformation



Idea: apply the same  $u$ 's to the undeformed shape

Figure 4. Key iterative design idea

## Conclusion

An iterative technique for designing the optimal shape of the diamond in a diamond anvil cell is presented. The diamond is modelled using finite elements with exact implementation of its cubic, pressure dependent constitutive response. The gasket behavior is approximated by a simplified equilibrium equation based on the assumption of a fully yielded state and sticking conditions. By coupling the two models in a meaningful, fruitful manner, an iterative scheme results which turns out to be very effective (rapid convergence) and computationally inexpensive (FEM computations for the diamond alone requires few increments, thanks to the relatively small overall deformation). A sample optimization problem involving molybdenum as a gasket material demonstrates the rapid convergence of the method, resulting in a design which showed promise in a preliminary experiment.

## Acknowledgements

This work was funded by NSF grant number MSS-9301443 at Cornell University. The computing for this project was supported by the Cornell National Supercomputer facility, which receives major funding from the NSF and IBM Corporation, with additional support from New York State.

## References

1. A.L. Ruoff, H. Xia and Q. Xia, *Rev. Sci. Instrum.* **63** 4342.
2. H.J. McSkimmin and P. Andreach, Jr., *J. Appl. Phys.* **43** 2944. (1972).
3. E. Siebel, *Stahl und Eisen* **43** 1295 (1923).
4. W.F. Hosford and R.M. Caddell, *Metal Forming Mechanics and Metallurgy*, Prentice Hall, Englewood Cliffs, New Jersey. (1983).
5. J.O. Chua and A.L. Ruoff, *J. Appl. Phys.* **46** 4659. (1975).
6. N.E. Christensen, A.L. Ruoff, and C.O. Rodriguez, *Phys. Rev B* **52** Oct(1995).

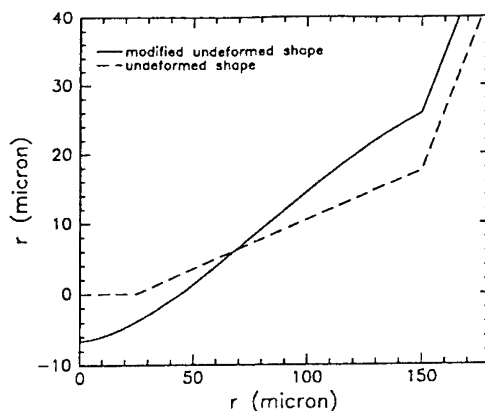


Figure 5. Modification of undeformed shape

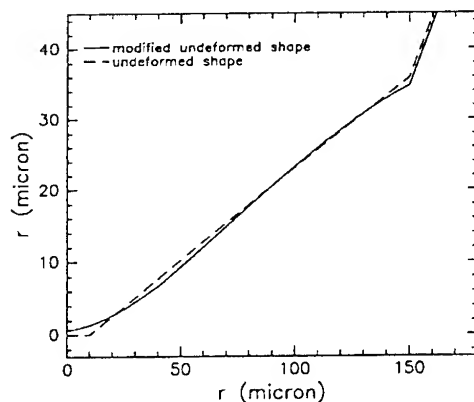


Figure 6. Convergence of design



# APPARATUS WITH PUNCHES MADE OF CUBIC BORON NITRIDE TO PROVIDE THE HIGHEST PRESSURE

A.V. GERASIMOVICH, N.V. NOVIKOV, N.M. GRIGORIEV  
*V.N. Bakul Institute of Superhard Materials, Ukrainian National Academy of Sciences  
 2 Avtozavodskaya St., 254074 Kiev, Ukraine*

## ABSTRACT

The high pressure apparatus with cubic boron nitride polycrystal punches have been designed. The diameter of the punch working end is equal to 1 mm. The optimum punch and gasket unit geometry allows to produce the pressure up to 40 GPa.

At the present to ensure pressures exceeding 15 GPa, Dricamer's anvil-type apparatuses and multiple anvils are used. The pressure attained in them is conditioned by mechanical properties of a punch material. Dricamer's anvil-type apparatus

with diamond-tipped carbide punches allowed Bundy to produce pressure up to 60 GPa. However, difficulties in processing of diamond polycrystals restrict the application of such an apparatus.

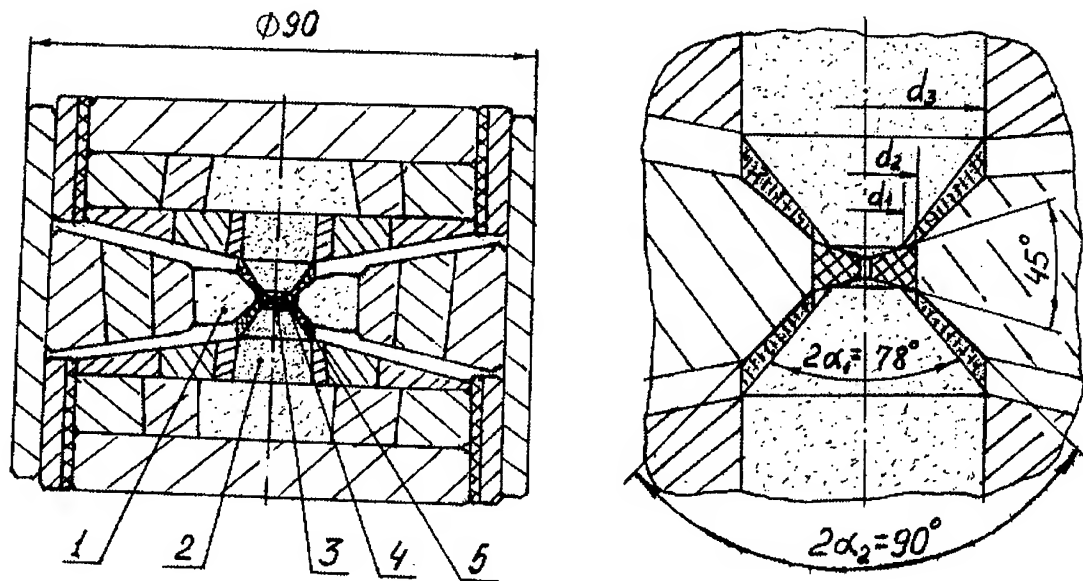


Fig.1. Schematic diagram of the apparatus high pressure unit.: 1— die (VK8); 2 — punch; 3 — pressure sensor; 4 — disc; 5 — gasket.  $d_1=5.3$  mm;  $d_2=6.0$  mm;  $d_3=13.5$  mm.

In this connection, easily processed cubic boron nitride polycrystals are of great interest. The apparatus designed by the authors has a matrix unit and two punch units. Out-to-outs of the completed apparatus, including supporting plates, guide and insulating bushes and yoke are 74 mm in height and 90 mm in diameter. The insert of the matrix unit has been made of the VK8 cemented carbide. It has the shape similar to that of the insert of a girdle-

type apparatus with a hole 6 mm in diameter and 90° angle of a cone. In their tapered part, the punches form regions corresponding to Dricamer's anvils, but unlike the latter, the punch lateral faces are conical with a 78° angle. This ensures a smooth application of a supporting pressure caused by a deformable gasket throughout the height of the punch. The diameter of the working end is 1 mm. Pyrophyllite and talc have been used as gasket

materials. A disc placed into the insert hole has been made of lithographic stone, pyrophyllite or magnesium oxide. The pressure sensors (GaAs, GaP, S,  $\text{Fe}_2\text{O}_3$ ; Si) have been located in the hole 0.3 mm in diameter along the disc axis. Pressure has been evaluated by measuring the electrical resistance of the above mentioned reference materials. When using cBN polycrystal punches, terminals have been made of foil strips.

Figure 1 shows a schematic diagram of the apparatus high pressure unit.

Figure 2 shows a calibration curve for an apparatus with cBN polycrystal punches based on the use of known reference points both for the lithographic stone discs 0.7 mm thick in the center and for pyrophyllite gaskets.

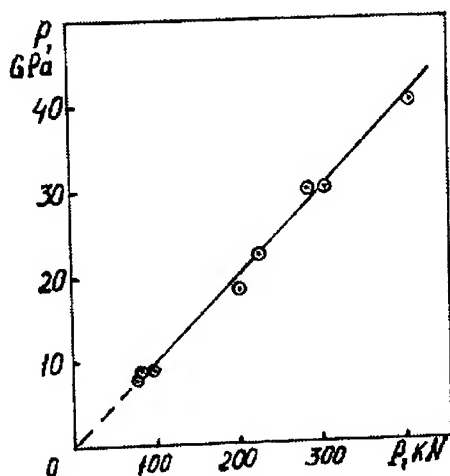


Fig.2. Calibration curve for an apparatus with cubic boron nitride polycrystal punches.

Figure 3 shows the graphs of electrical resistance changes depending on force for some sensor materials. The highest pressure achieved is estimated 44 GPa.

It is interesting to find a relationship between the value of the pressure provided and punch material (cBN polycrystal) mechanical properties. Assuming that stress distribution over the radius  $r$  of the spherical segment marked in a punch is uniform [1], we can formulate the equivalent stress in the considered section (see Fig. 4) by the following:

$$\sigma_e = q_0 \cdot \frac{a^2}{r^2} + \frac{2}{r^2} \int_a^r q r dr - q, \quad (1)$$

where  $q_0$  is the pressure on the radius  $r = a$  of the punch working end;  $q$  is the pressure on the punch lateral conic surface.

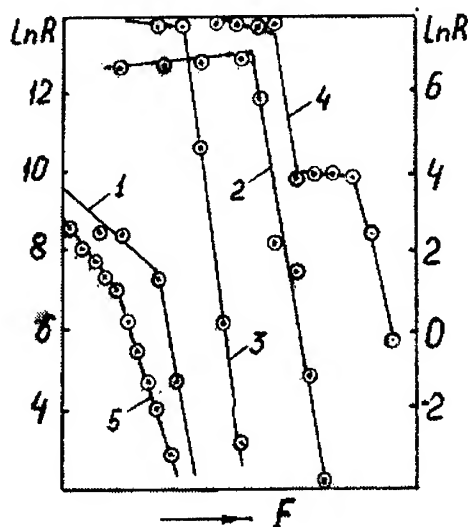


Fig.3. Variations of reference materials electrical resistance. 1 — GaAs; 2 — S; 3 — GaP; 4 —  $\text{Fe}_2\text{O}_3$ ; 5 — Si; lines 1, 2 correspond to the  $\ln R$  right scale and 3-5 — to the left one.

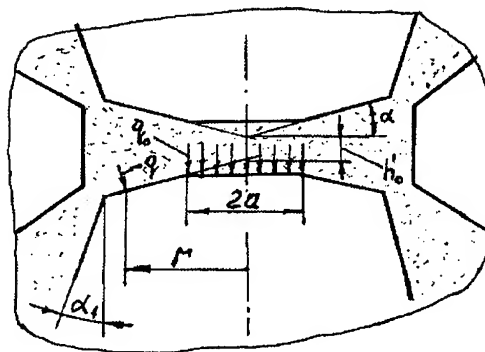


Fig.4. Scheme of the punch loading.

After integration of Eq. (1) we obtain

$$\sigma_e = -\frac{1}{r^2} \int_a^r r^2 \cdot q' dr. \quad (2)$$

To find the maximum, we equate to zero the first derivative of Eq. (2):  $d\sigma_e/dr = 0$ . It gives

$$(q')_m = \frac{2}{r_m^3} \cdot \int_a^{r_m} r^2 \cdot q' dr, \text{ where } r_m \text{ is the section}$$

radius, in which maximum equivalent stresses act, and  $(q')_m$  is the pressure derivative on the radius  $r_m$ .

Equation for  $\sigma_e$  can be written in a very simple form:

$$\sigma_e = -\frac{r_m}{2} \cdot (q')_m. \quad (3)$$

It follows from Eq. (3), that the less equivalent stresses, the less  $(q')_m$ .

Punch conic surfaces support is provided by the stresses acting in the compressed disc and in the gasket. Analyzing the stress distribution in a disc portion adjacent to the working end, one can write:

$$\frac{dq}{dr} + \frac{q}{h} \frac{dh}{dr} = -\frac{2\tau_s}{h}, \quad (4)$$

where  $\tau_s$  is the disc material shear stress. In studying properties of gasket materials using Bridgman anvils, we came to conclusion that a good agreement with experimental results is when the pressure dependence of shear stresses is represented in the form of two ranges. In the low-pressure range, shear stresses increase with pressure (a power dependence is used), while in the high pressure range, shear stresses attain the highest values (each material exhibits its own value)  $\tau_m$  and with the further pressure increase remain unchanged.

In the case under consideration the stresses have achieved the maximum value, and Eq. (4) gives the following distribution (when  $h_0 = 0$ ):

$$q = (q_0 + \frac{\tau_m}{tg\alpha}) \cdot \frac{a}{r} - \frac{\tau_m}{tg\alpha}, \quad (5)$$

which leads to  $r_m = 2a$  and  $\sigma_e = \frac{q_0 + \frac{\tau_m}{tg\alpha}}{4}$ . If

$q_0 = 40$  GPa,  $\alpha = 22.5^\circ$ , then  $\sigma_e = 10.6$  GPa.

We have studied mechanical properties of cBN polycrystals by the high pressure technique [2,3]. The essence of the method lies in the fact that a cylindrical specimen with flat ends made of the above material is used as one of the anvils of the Bridgman anvil-type apparatus. The second anvil is a usual Bridgman anvil made of cemented tungsten carbide. In compressing a talc (or pyrophyllite) disc, a residual deflection appears in the disc center. Its value was recalculated in the value of a relative strain according to the Dunn and

Bundy method [4] and then the stresses in the specimen were calculated from the known mechanical properties of the disc material. Our findings have shown that a cBN polycrystal with the density of  $3.35 \text{ g/cm}^3$  and Knoop hardness of 29 GPa (under the 9.8 N load) exhibits:

- Elastic limit  $\sigma_1 = 5.5 - 6$  GPa;
- Yield strength based on 0.1% offset  $\sigma_{0.1} = 6.76$  GPa.

Comparing the values presented with the pressures achieved, we see that the maximum pressure of 40 GPa corresponds to the equivalent stress of 10.6 GPa exceeding  $\sigma_{0.1}$ . The residual deflection at the punch body leads to generation of the tensile stresses in its external layers and, hence, to crack initiation and growth. According to our observations, radial cracks have appeared on the cone lateral surface ( $\alpha_1 = 39^\circ$ ) after the loading up to  $\sim 38$  GPa. With these cracks, the apparatus was still able to operate.

Thus, it has been proved that an efficient lateral support of the punches due to the optimum gasket unit geometry and the right choice of deformable gasket material allows the pressure of up to 40 GPa to be produced in the described apparatus.

## References

1. F.P. Bundy, *Rev. Sci. Instrum.* **6** (1977) 3.
2. A.V. Gerasimovich and N.M. Grigoriev, in *High Pressure in Material Science and Geoscience*, (abstracts of XXXII Annual Meeting of the European High Pressure Research Group, Brno, 1994).
3. N.V. Novikov, A.V. Gerasimovich, N.M. Grigoriev, *J. of Superhard Mater.* **1** (1993) 3.
4. K.J. Dunn, F.P. Bundy, *J. Appl. Phys.* **49** (1978) 12.

# MAGNETIZATION MEASUREMENT UNDER HIGH PRESSURE AND PULSED HIGH MAGNETIC FIELD BY A DIAMOND ANVIL CELL

S. ENDO,<sup>1</sup> S. IMADA,<sup>1</sup> K. KINDO,<sup>1</sup> S. MIYAMOTO,<sup>1</sup> H. HORI,<sup>2</sup>  
F. ONO,<sup>3</sup> T. TAKEUCHI,<sup>4</sup> and M. HONDA<sup>5</sup>

<sup>1</sup>Research Center for Extreme Materials, Osaka University, 1-3 Machikaneyama-cho, Toyonaka, Osaka 560, Japan

<sup>2</sup>School of Materials Science, Japan Advanced Institute of Science and Technology, Tatsunokuchi, Nomi-gun, Ishikawa 923-12, Japan

<sup>3</sup>Faculty of Science, Okayama University, 3-1-1 Tsushima-Naka, Okayama 700, Japan

<sup>4</sup>Low Temperature Center, Osaka University, 1-1 Machikaneyama-cho, Toyonaka, Osaka 560, Japan

<sup>5</sup>Department of Physics, Naruto University of Education, Naruto, Tokushima 772, Japan

## ABSTRACT

By combining a diamond anvil cell and a pulse magnet, we have developed the system which enabled the magnetization measurement under the complex extreme conditions of high pressure and high magnetic field. In order to avoid the electromagnetic interaction between metal and pulsed field, which would be fatal for the measurement, all parts of the diamond cell including a gasket were made of insulators. A pick-up coil method demonstrated successfully the magnetization curve for a ferromagnetic invar alloy of  $\text{Fe}_{0.7}\text{Ni}_{0.3}$  under pressure.

## Introduction

Pressure, temperature, and magnetic field are the most fundamental parameters in science. The realization of complex extreme conditions of high pressure and high magnetic field has been a long-standing wish. One of the most typical methods adopted hitherto has been the use of a pressure-clamp cell set in a superconducting magnet.<sup>(1)</sup> But, the clamp cell must be made of nonmagnetic alloy, which limits the pressure up to, at most, 2 GPa. On the other hand, the superconducting magnet limits the magnetic field up to, for example, 10 T (tesla) although stronger magnets are recently developed. In the present paper we report briefly the first attempt to measure the magnetization under high pressure and high magnetic field simultaneously generated by combination of a diamond anvil cell

and a pulse magnet.

In order to extend a magnetic field largely, the use of a pulse magnet is indispensable. But, many troubles occur when it is coupled with high-pressure cells, because all types of cells including a diamond anvil cell (DAC) have been, at least partly, made of metals; when a metallic body is placed in a pulsed magnetic field, various electromagnetic interactions undesirable for the measurement arise between the metal and the pulsed field. An induction current is induced in the metal, which heats the cell and the field induced by the current itself strongly disturbs the magnetic signal from the sample, and so on.

Therefore, we have made a ceramic diamond cell by modifying a previous one which we used for an optical measurement under high pressure and pulsed high magnetic field.<sup>(2,3)</sup>

### Pressure generation

In order to avoid the use of a metallic gasket, which made it impossible to measure the magnetization under pulsed field by the same reason described above, we have adopted a so-called Drickamer cell; a sample can be enclosed within an insulator gasket sandwiched between a pair of diamond anvils. Almost all parts of the cell was made of partially-stabilized zirconia because of its toughness. The outside diameter of the cell was 38 mm.

Pressure was determined by a ruby fluorescent method using a fiber technique.

### Pulse magnet

A pulse magnet used in the present study was a solenoid made of maraging steel with the inside and outside diameters of 80 and 150 mm, respectively. It can generate 40 T for a pulse width of 400  $\mu$ sec from a capacitor bank of 1.25 MJ (20 kV). The DAC was set in the magnet as shown in Fig. 1.

### Magnetization measurement

There are many methods to measure the magnetization of materials. In pulsed field, the time change of magnetic field,  $dH/dt$ , is very large, which produces the large time change of the magnetization induced in the sample,  $dM/dt$ . Therefore, the pick-up method is very effective in the present case.

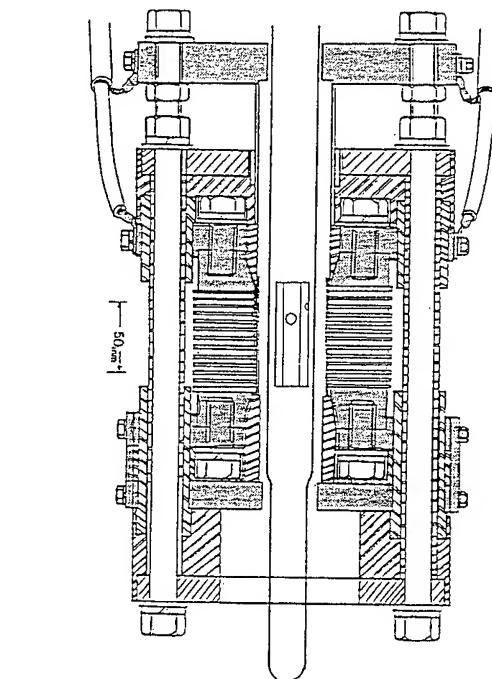


Fig. 1 The cross section of a ceramic diamond cell (DAC) set in a pulse magnet.

In this attempt, a pick-up coil was wound around the sample and a compensation coil to cancel the component of the magnetic field was set in the cell. The block diagram of the measuring system for the magnetization of the sample under high pressure and pulsed high magnetic field is shown in Fig. 2. The output

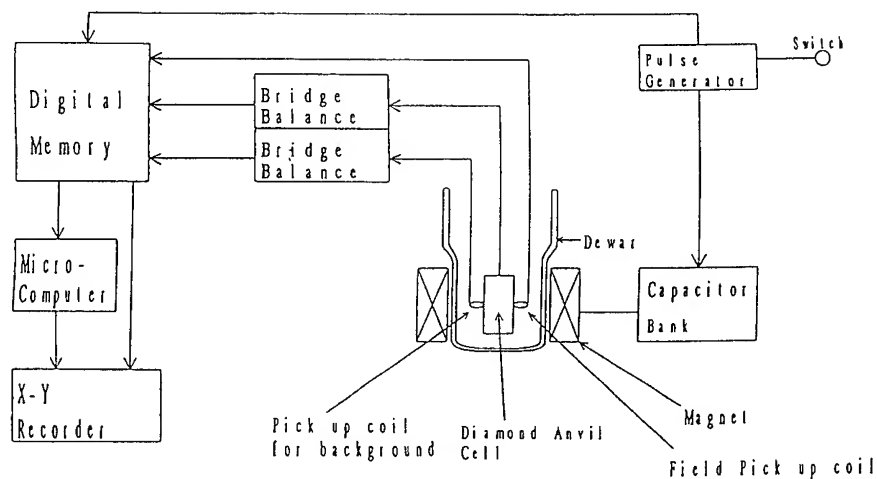


Fig. 2 A diagram used for measuring the magnetization of samples under high pressure and pulsed high magnetic field.

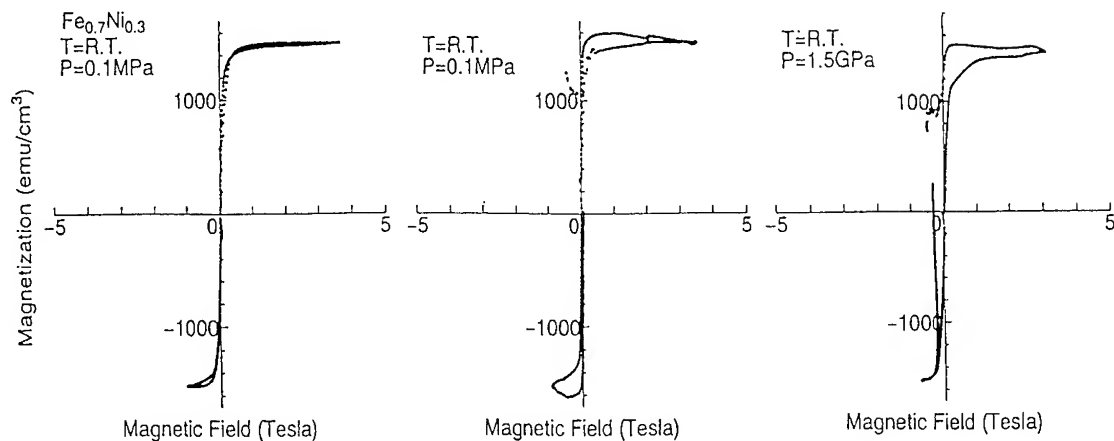


Fig.3 The magnetization curves for  $\alpha'$ (bcc)- $\text{Fe}_{0.7}\text{Ni}_{0.3}$ . (a) The curve measured by a standard system at ambient pressure; (b) the curve for a sample in DAC at ambient pressure, and (c) the curve for a sample in DAC at 1.5 GPa.

voltage in proportion to  $dM/dt$  was stored in a digital memory, from which the magnetization curve was drawn by numerical operation using a micro computer.

The magnetic field of the magnet was calibrated by detecting the spin-flop transition in antiferromagnetic  $\text{MnF}_2$  at 9.2 T and 4.2 K under ambient pressure. This measurement was made for the sample set in the DAC by the present system to examine the performance of it.

#### On an Fe-Ni alloy

As the test sample under pressure for the present system,  $\text{Fe}_{0.7}\text{Ni}_{0.3}$  alloy was selected. It belongs to the so-called ferromagnetic invar alloys. The fcc austenitic  $\gamma$  phase transforms to the bcc martensitic  $\alpha'$  phase below  $-50^\circ\text{C}$  at ambient pressure. The reverse transition from  $\alpha'$  to  $\gamma$  phase takes place at about  $350^\circ\text{C}$ . Our previous study using x-ray diffraction and electrical resistance measurement showed that this reverse transition point decreases with increasing pressure down to room temperature at around 8 GPa.<sup>(4)</sup> The magnetization of this alloy substantially decreases at the  $\alpha'$ - $\gamma$  transition. The objective of the present measurement is the pressure effect on the magnetization of  $\alpha'$  phase in pulsed high magnetic field.

#### Preliminary results

We have tried to obtain the magnetization curves for a  $\text{Fe}_{0.7}\text{Ni}_{0.3}$  sample with 0.6 mm in diameter and 0.6 mm in thickness. First, the results at ambient conditions are shown in Fig. 3; (a) is by a standard system not used for high pressure and (b) is by the present system for the sample set in the DAC. Finally, the example of the curve at 1.5 GPa is shown in Fig. 3(c). No substantial change in magnetization occurs up to 1.5 GPa for  $\alpha'$  phase.

We have established the method to measure the magnetization under high pressure and pulsed high magnetic field. Now we are detecting the pressure-induced transition from  $\alpha'$  to  $\gamma$  phase of  $\text{Fe}_{0.7}\text{Ni}_{0.3}$  at around 8 GPa.

#### References

1. F. Ono, S. Endo, and M. Asano, *Proc. 2nd Int. Symp. Physics of Magnetic Materials, Beijing, 1992 (Int. Acad. Publ. 1992)*, Vol. 2, p. 840.
2. K. Yamamoto, S. Endo, A. Yamagishi, H. Mikami, H. Hori, and M. Date, *Rev. Sci. Instrum.* 62 (1991) 2988.
3. H. Hori, S. Endo, K. Yamamoto, H. Mikami, A. Yamagishi, and M. Date, *Physica B*, 177 (1992) 71.
4. K. Yamamoto, M. Asano, S. Endo, and G. Oomi, *Mat. Trans. JIM*, 32 (1991) 305.

# GARNET ANVIL CELL (GAC) FOR HYDROTHERMAL STUDIES TO 6.0 GPa AND 1200 °C

MICHAEL R. RIEDEL

*Universität Potsdam, Telegrafenberg C7, D-14473 Potsdam, Germany*

SERGEJ G. BUGA

*Institute of Spectroscopy, Russian Academy of Sciences, Troizk, Russia*

ANDY H. SHEN

*Bayerisches Geoinstitut, Universität Bayreuth, D-95440 Bayreuth, Germany*

We have set up a high pressure cell with transparent garnet anvils for the study of hydrothermal mineral reactions and the deformation of rocks/minerals under visual observation in the pressure range up to 6.0 GPa and to temperatures of 1200 °C. Its main advantages are the higher temperature that can be achieved under nearly isothermal conditions and the much easier handling of garnet anvils in comparison with a diamond anvil cell. The new cell has been used for optical microscope observations and for deformation experiments in a special shear cell with one rotatable anvil.

## 1 Introduction

Diamond anvil cells (DAC) have been used in a wide variety of high-pressure studies both at room and high temperature. Under external heating, oxidation of diamonds and the metal heaters require protection of the inner cell assembly by an inert or reducing gas atmosphere. Graphitization of diamond sets in above 900 - 1000 °C with increasing intensity. Furthermore, the strength of necessary supporting material (e.g. tungsten carbide) is considerably reduced at temperatures above 800 °C, thus limiting the reachable pressure in an externally heated DAC at very high temperatures to at least 2.5 GPa<sup>1</sup>. Instead of diamond, we used cubic garnet single crystals (YAG) as transparent anvils in a high-pressure cell. Among the various materials of the garnet structure, Y<sub>3</sub>Al<sub>5</sub>O<sub>12</sub> (YAG) has the highest melting point ( $T_m = 2273$  K) and hence is likely to be the most resistant to plastic deformation at high temperatures. Garnets in general appear to have a creep strength higher by a factor of 3-10 than other oxides, compared at the same homologous temperatures  $T/T_m$ <sup>2</sup>. From these findings, we expect that a garnet anvil cell (GAC) can operate even up to 1500 °C under external heating, i.e. under nearly hydrothermal conditions compared to laser-heated cells. We have performed experi-

ments with a garnet anvil cell up to 800 °C without any special precautions, and up to 1200 °C under protection gas. The reachable pressure depends on the size and shape of the active anvil face, with coned (diamond-like) garnet cylinders with 5 mm outer diameter and a 500 mm anvil face we were able to get 6.0 GPa without any problems. With a gasket-free preparation, we used a special cell with shear mechanism to study the brittle-ductile transition in calcite by deforming small calcite cylinders (2 mm diameter and 30 mm thickness) in the GAC under visual control.<sup>3</sup>

## 2 The Garnet Anvil Cell (GAC)

The cell body was designed for the study of high pressure phase transitions under shear deformation up to 100 GPa confining pressure at ambient temperatures and is described in detail in the literature<sup>4</sup>. In short, it consists of a lever-arm pressure loading mechanism pressing two opposing anvils together, where the lower anvil can be rotated using a suitable external lever rod, see Figure 1. With diamond anvils, the setup was successfully used to determine the equilibrium phase boundary of a range of solid-solid phase transitions at low or room temperatures<sup>5</sup>.

For present purposes, the inner part of the cell consisting of the two anvils combined with a re-

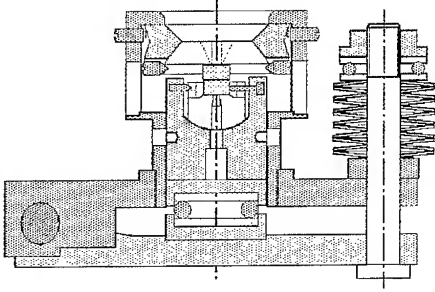


Figure 1: Side view of the shear cell with garnet anvils. The inner assembly is shown schematically only.

sistance heating, was completely re-designed: Instead of diamonds with tungsten carbide support, we use temperature resistive garnet single crystals machined to small cylinders of 5 mm in diameter and with a spherical upper surface to build the anvils.

A small compression face up to 2.5 mm in diameter is formed by creating a polished face on top of the upper surface. The smaller the diameter  $d_{cf}$  of the compression face, the more effectively it is supported by the mass around it. The back side of the anvils is a plane circle with slightly bevelled edges. The maximum pressure that can be reached in the central part of the sample is given with <sup>3,6</sup>

$$p_{max}(\text{in GPa}) = \frac{12.5}{[d_{cf}(\text{in mm})]^2} \quad (1)$$

We estimate that a pressure of up to 2 GPa can be reached for  $d_{cf} \cong 2.5$  mm. Using garnet anvils with smaller upper face (0.5 mm diameter), we were able to reach 6.0 GPa at room temperature without any problems.

Commercially available mantled heater wires (0.5 mm in diameter) wound around the anvils deliver heat mainly by direct thermal conduction. This geometry requires the least input of power and the lowest heater temperature in order to

achieve a desired sample temperature <sup>1</sup>. The parallel alignment of both garnet anvils must be guaranteed in order to prevent their destruction during shearing under an external axial load. Under applied torque during the deformation experiments, the cubic symmetry of the garnet anvils is slightly disturbed, and a weak cross shadow appears under crossed nicols superimposed to the sample image. Taking a time series of digitized snapshot images, it is possible to compensate this effect using suitable numerical routines.

### 3 Temperature and pressure distribution

As a consequence of the inner geometry of the cell, the temperature gradients over a sample sandwiched between the anvils remain negligibly small. This was checked by heating homogeneous discs of metals with a low melting point. This reveals no significant spatial dependency of melting onset under visual detection up to 330 °C and atmospheric pressure (melt transitions of Sn, Bi and Pb at 231, 9 °C, 271, 4 °C and 327, 5 °C, respectively).

Under uniaxial loading, the stresses generated between the two Bridgman anvils obey the general relationship

$$\frac{d\sigma_r}{dr} + \frac{\sigma_r - \sigma_\theta}{r} + \frac{2f\sigma_z}{h} = 0, \quad (2)$$

with the radial stress  $\sigma_r$ , tangential stress  $\sigma_\theta$ , and axial stress component  $\sigma_z$  depending on radius  $r$ .  $h$  is the thickness of the sample disc and  $f$  is the coefficient of friction between the sapphire anvil and the sample surfaces <sup>7</sup>. Its solution for a cylinder with radius  $R$  under the external loading force  $F$  is given either by

$$\sigma_r(r) = 2f\sigma_z(R - r)/3h, \quad (3a)$$

$$\sigma_\theta(r) = 2f\sigma_z(R + r)/3h, \quad (3b)$$

$$\sigma_z = F/\pi R^2, \quad (3c)$$

for completely elastic deformations, or alternatively by

$$\begin{aligned} \sigma_r(r) &= \sigma_\theta(r) = \sigma_z(r) - \sigma_0 \\ &= \sigma_0[\exp(2f(R - r)/h) - 1] \end{aligned} \quad (4)$$



for a cylinder deformed in the fully plastic regime, where  $\sigma_0$  is the yield stress according to the Tresca yield criterion<sup>7</sup>. The radial pressure distribution inside the sample chamber is given by

$$p(r) = \frac{1}{3} [\sigma_r(r) + \sigma_\theta(r) + \sigma_z] \quad (5)$$

and is either independent on radius  $r$  in the elastic limit according to eq. (3), or decreases exponentially with  $r$  in the flow region, in dependence of the friction coefficient  $f$  and the aspect ratio  $R/h$ , as shown in eq. (4).

It can be shown, that, for uniaxial loading, the central part of a sample between rigid cylindrical anvils remains at nearly hydrostatic conditions, separated from a surrounding ring showing plastic flow<sup>8</sup>. In this sense, the outer plastic ring of the sample acts as a gasket for its inner parts.

In addition to uniaxial loading, we are able to apply independent shear forces by rotating the lower anvil. The shear stresses produced in the sample disc are, under boundary conditions of no-slip, a linearly increasing function of  $r$  in the central (nearly elastic) region. The total shear stress experienced by the sample is therefore gradually increasing from zero at the centre and reaches its maximum near to yield stress at the periphery ring. The displacement field at the surface of the sample may be reconstructed either by image processing (subtraction of subsequent digitized images), or by means of strain markers distributed over the sample. In both cases, the accuracy is mainly limited by the spatial resolution of the digitizing device (video camera or scanner).

#### 4 Discussion

Using a standard gasket preparation, the GAC cell operates like a regular diamond anvil cell. It can therefore be used for in situ x-ray diffraction experiments as well as for optical spectroscopy, since garnet is transparent for the respective wavelength spectra.

However, the garnet structure gives rise to many Raman- and IR-active lattice modes, which is clearly disadvantageous for optical in situ studies and a drawback of the cell in comparison to a diamond anvil cell. On the other hand, deformation experiments using this technique are relatively simple and inexpensive. Furthermore, combining

deformation experiments with ultrasonic measurements using a recently developed technique<sup>9</sup> seems to be a particularly interesting application of this cell. In-situ information on the time dependency of specific subprocesses could lead to a better understanding of the underlying kinetic mechanisms at the microscopic scale. The work on this topic is in current progress.

#### Acknowledgments

The authors gratefully acknowledge the helpful assistance of Hans Richter during his stay at the University of Potsdam in 1994. In addition, we would like to thank Christoph Janssen and Richard Wirth for their interest and support of the present work.

The usage of garnets instead of diamonds in a high pressure cell is a suggestion of Shun Karato.

#### References

1. W. A. Bassett, A. H. Shen, M. Bucknum and I-M. Chou, *Rev. Sci. Instrum.* **64**, 2340 (1993).
2. S. Karato, Z. Wang and K. Fujino, *J. Mater. Sci.* **29**, 6458 (1994).
3. M. R. Riedel and C. Janssen, *J. Structural Geol.* **17**, 455 (1995).
4. I. A. Barabanov, V. D. Blank and Yu. S. Konyaev, *Prib. Tech. Eksper.* **2**, 176 (1987).
5. V. D. Blank and A. Yu. Zerr, *High Press. Res.* **8**, 567 (1992).
6. D. J. Dunstain and I. L. Spain, *J. Phys. E: Sci. Instrum.* **22**, 913 (1989).
7. J. W. Jackson and M. Waxman in *High Pressure Measurements*, eds. A. M. Giardini and E. C. Lloyd, p. 39 (Butterworth, Sevenoaks, Kent, 1963).
8. J. F. Prins, *High Pressures - High Temperatures* **16**, 657 (1984).
9. H. Spetzler, G. Chen, A. H. Shen, R. Weigel and K. Müller, American Geophysical Union, 1995 spring meeting, Baltimore, EOS suppl. (abstract only), p.277 (1995).

## STRENGTH OF THE HIGH PRESSURE CHAMBER MADE FROM PARAMAGNETIC MATERIALS

S.V.MIROSHNICHENKO, V.G.SYNKOV

*High Pressure Aparatus Laboratory, Donetsk Physico-Technical Institute of National Academy of sciences, 72, R. Luxemburg str., 340114, Donetsk, Ukraine*

### ABSTRACT

We present the strength analysis of the bilayer high-pressure chamber (HPC) operating in the 3 GPa range with the diameter ratio  $D/d \leq 5$ . The methods of chamber strengthening are based on numerical analysis.

### Preface

For several decades the high pressure chambers (HPC) were used with mechanical fixation of piston before cooling of the chamber for magnetic investigations at low temperatures. These chamber had monolayer body made of diamagnetic materials [1]. Further development of the HPC was performed with the help of more strong paramagnetic materials [2], multilayer design [3], autofretting [4], hydrostatic support [5].

An experiment puts on additional limitations on the mass of materials of the HPC, maintenance work, intensity and uniformity of magnetic field etc.

It is possible to ascertain that strength and the mass of materials of the HPC are determined at least by its three basic assemblies: a body, a piston and an obturator as well as properties of materials from which these assemblies were made.

### Construction materials

Depending on heat-mechanical treatment paramagnetic material that is Ni-Cr alloy (Ni - 55%, Cr - 40%, Al - 4%) used here has the following characteristics:

Treatment I. Hardening at 1150 °C, hydroextrusion - 50 %, ageing at 700 °C during 5 hours;  $t_s = 2,2$  GPa,  $UTS = 2,1$  GPa,  $UCS = 2,8$  GPa;  $EL=6\%$ ; magnetic permeability,  $\mu = 5,2$ .

Field of application: external layer of the body, the obturator, the screws.

Treatment II. Hardening at 1200 °C, hydroextrusion - 50 %, ageing at 500 °C during 5 hours;  $t_s = 2,5$  GPa;  $UTS = 2,45$  GPa;  $UCS = 3,4$  GPa;  $EL=0,5\%$ ; magnetic permeability,  $\mu = 16,5$ ;

Field of application: internal layer of the body, the piston, the obturator.

Application of deformation stimulation of dispersive hardening at the hydroextrusion treatment allowed to obtain rather high complex of mechanical properties at the high magnetic permeability. At the same time it is necessary to note that after Treatment II the material became mechanically unstable, sensitive to concentration of stresses and to shock unloadings. Its mechanical characteristics approach to WC90 - Co10 alloy, but it has better magnetic permeability.

### Chamber's body.

As it was determined before [6], the bilayer construction having autofretting external layer and internal layer pressed in it with great tensions and adapted mainly to the conditions of compression occurs to be an optimal construction of the body. Such body provides operation pressure  $P = (1,6 - 1,8) \sigma_s$ .

While making of the HPC body we use two technologies:

- autofretting of an external layer before its pressing on internal one;

- autofretting of an external layer in the process of layers' pressing.

In the first variant the autofretting is made by pressing the cone mandrel in a space of the external layer. To exclude secondary plasticity in the hardening layer while its pressing with internal one and during following loadings, the autofretting is realized in cyclic regime "loading - absolute unloading" and is finished at the stabilization of contactive stresses level on the mating surfaces (as a rule after 4 - 5 "loading - unloading" cycles). As a result of plastic sign alternate deformation the level of contactive stresses ( $P_C$ ) at which the linear-elastic cycling is realised corresponds to value  $P_C \approx \sigma_{s,2}$ , i.e. by 20 - 30 % lower than  $P_C$  in the first loading cycle. Therefore maximum operation pressure ( $P_m$ ) in body made on the scheme I corresponds to  $P_m \leq 1,6\sigma_{s1}$  ( at diameter ratio  $D/d \leq 5$ ,  $P_m = 3,4 - 3,9$  GPa).

On the scheme 2 the hardening of the external layer is realized by pressing the internal one to reach absolute plasticity in the external layer and then by partial unpressing of the internal layer. It excludes secondary plasticity in the external layer and provides later on the linear-elastic character of loading both layers by operation pressure  $P_m \approx 1,8\sigma_{s1}$  at the same wall-thickness of the body ( $P_m = 3,8-4,4$  GPa).

#### Piston.

Strength of the piston at compression is determined by its shape and conditions of loading. That's why the maximum loading can differ greatly from estimate value calculated according to uniform distribution of compressive stresses along the dangerous cross-section [7]. It requires the usage of additional piston strength methods because with regard to friction losses the nominal axial stresses can attain 3,4-3,6 GPa at  $P_m = 3$  GPa. Besides it is necessary to remember that eccentricity of load application as a result of error while making of mating parts and the chamber mounting on the press decreases the ranges of possible pressures up to  $P_m = 2,2-2,3$  GPa.

The hydrostatic support of the piston together with the internal layer of the body increases mass of materials of the HPC greatly and complicates the

work with it. But the possibility of the mechanical support influence of a back part of the piston on concentration of axial and equivalent stresses at various geometrical conditions of support realization were analysed by us with the help of FEM [7].

Analysis shows that failure zone can occur lower than the upper end face of the chamber body where there is no radial support. Even at the initial zero split between the body and the piston the length of unsupported section of the piston grows in the process of the pressure increase. It decreases efficiency of use of a washer from KBr having phase transition at 18 kbar for back end face support.

We propose to execute the sequence of annular round off lugs. So that their external diameter could provide tension on the surface of the piston at its mating with the body of the HPC. At short distances between annular section (0,2 d) the effect of the hardening can double. Alternative way to escape limitations is to remove the piston from the structure. It can be attained by the usage of the obturator containing a valve instead of a piston. The HPC made of paramagnetic materials is joined through this valve to any booster and can be disconnected from it to fulfill measurements.

#### Obturator.

The pressure transmitting medium is used as hydrostatic support for obturator hardening. Cases of failure of the obturator both in the process of loading and at the rapid unloading are known. In the latter case it is the result, apparently, of a delay (or absolute lack) of reverse displacement of electric leads of the case.

If a condition of friction in mating provides self-braking of electric leads case after decrease operation pressure then maximum pressure in the chamber must not exceed value ( $P_m$ ):

$$P_m \leq \frac{k\sigma_s(R-1)(\operatorname{tg} \alpha + f)}{R \operatorname{tg} \alpha}$$

where  $k = 0,35 - 0,45$  - obturator body stiffness, coefficient calculated by the finite elements method;

$R = D^2 / d^2 \leq 7$  - hydroextrusion factor;

$D, d$  - big and short diameter of funnel of obturator accordingly;

$\alpha$  - pitch of an electric leads case cone;

$f$  - friction coefficient in the mating.

Because of the epoxy resin usage to cover wires put into the chamber the friction coefficient is  $f = 0,2 - 0,3$ , i.e. at values  $\alpha < 17^\circ$  because of the self-braking of the electric leads case the failure of the obturator takes place after unloading of the HPC at values  $P_m = 1,3 - 1,5$  GPa.

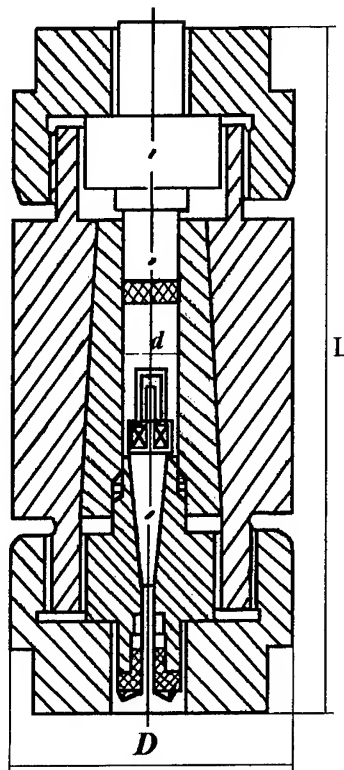
On the other hand at  $\alpha > 10^\circ$  the cases of damage of the wires or insulation fault become more frequent because of high local loads on the wires in the upper part of the obturator and the decrease of section length.

We use electric leads with angle  $\alpha = 5^\circ$ ; in this case at  $f = 0,2 - 0,3$  calculated value of breaking pressure corresponds  $P_m = 2,1 - 2,8$  GPa (2,4 - 3,2 GPa, Treatment II) at the considerable lower probability of wires break down.

If it is necessary to work at higher operation pressures, then it is necessary to use constant or alternating mechanical support.

It should be mentioned that all these evaluations are made for uniform distribution of contact stress over the surface of mating.

The figure shows the typical structure of the generally used chamber.



**Technical Data:**

inside diameter, $d$ :	5 - 15 mm
external diameter, $D$ :	25 - 75 mm
length, $L$ :	90 - 250 mm
working volume:	0,3 - 10 cm <sup>3</sup>
numbers of electric leads:	6 - 20
temperature variation:	1 - 700 K

**References**

1. C. A. Swenson, *Physics at high pressure* (Academic press, 1960 ).
2. A.V Alymov ect. *Istr. and Tech Exp.* 1 (1972) 37.
3. E.S. Itskevich ect. *Istr. and Tech Exp.* 6 (1966) 64.
4. P.I. Polyakov ect. *Istr. and Tech Exp.* 1 (1977) 15.
5. E.S. Itskevich ect. *Istr. and Tech Exp.* 1 (1979) 17.
6. V.G. Synkov ect. *Problems of strength* 11 (1976) 80.
7. M.V.Astrahan ect. *FTHP.* 4 (1994) 81.

# CALORIMETRIC SYSTEM FOR EVALUATION OF ENTHALPY OF LIQUID-TO-SOLID TRANSITION AND HEAT CAPACITY OF LIQUIDS AND SOLIDS AT HIGH PRESSURES

I. CZARNOTA

Institute of Physical Chemistry, Polish Academy of Sciences, 01-224 Warsaw,  
Kasprzaka 44/52

The construction and operation of a high-pressure calorimeter for the evaluation of the enthalpy of liquid-solid transition in a temperature range 288 K to 308 K and pressure range 0.1 MPa to 400 MPa are described. The calibration, measurement and calculation procedures are outlined.

## 1. Introduction

The design and operation of a high-pressure calorimetric system for the evaluation of the heat capacity of liquids at high pressures up to 1200 MPa were described elsewhere [1]. In this calorimeter specific heats  $c_p(p)$  for several liquids were measured [2-8].

During the calorimetric measurements of  $c_p(p)$  of liquid benzene [6] a test of the use of the same high-pressure calorimeter for the evaluation of  $c_p(p)$  of solid benzene and for the evaluation of its enthalpy of liquid-solid transition at high pressures was undertaken. Benzene was chosen due to its very low pressure of solidification, which is about 70 MPa at ambient temperature. However, the calorimetric measurements of  $c_p(p)$  for solid benzene in this calorimeter presented many difficulties owing to the possibility of fusion of the layer of the solid sample in connection with the heater. Also, the measurement of the enthalpy of the liquid-solid transition (LST) was not successful because of the high changes of pressure in this calorimeter during the phase transition of the sample.

To sum up the results of these preliminary measurements it could be said that evaluation of the enthalpy of LST is not possible in this high-pressure calorimetric system and a new one must be constructed.

## 2. Construction and operation

### 2.1. High-pressure calorimeter

This high-pressure calorimeter, as well as the high-pressure calorimeter up to 1200 MPa constructed before, differs fundamentally from conventional calorimeters based on transmission of pressure to massive calorimetric vessels. Until the end of the 1960s, flow calor-

imetry has been the main experimental technique used at high pressures and temperatures and the upper bound of pressure for this method was only about 60 MPa. Recently developed pressure-scanning calorimeters [9-14] have mainly been used for high-pressure calorimetric measurements and none have been extended to pressures beyond 400 MPa. Exceptionally high pressures up to 1000 MPa were applied to the high-pressure calorimeter constructed by Pruzan and Ter Minassian [15]. The reported accuracy of measurements in these calorimeters is about 2% and it decreases with increasing pressure due to the increase of heat capacities of the calorimeters used in high-pressure experiments. Therefore, the main idea of the construction of the calorimeter was to minimize its heat capacity. A low heat capacity of the calorimetric vessel allowed us to carry out a calorimetric measurement with high precision in the whole range of pressures. In this calorimeter (shown in figure 1) an open-sided steel calorimetric vessel with thin walls is situated in a high-pressure chamber, whose body is a constant-temperature environment of the calorimetric vessel. The sample in the calorimetric vessel and in the overflow reservoir is separated from the chamber liquid by a mercury seal at the bottom of the overflow reservoir. An increase of chamber pressure gives rise to a new pressure equilibrium state of the calorimetric vessel; the chamber liquid applies increased pressure to the mercury seal, which forces the investigated substance from the overflow reservoir into the calorimetric vessel up to the moment when temperature and pressure equilibria are attained within the calorimeter.

### 2.2. High-pressure supply system

The supply system of constant high pressure up to 400 MPa to the calorimeter is schematically shown in

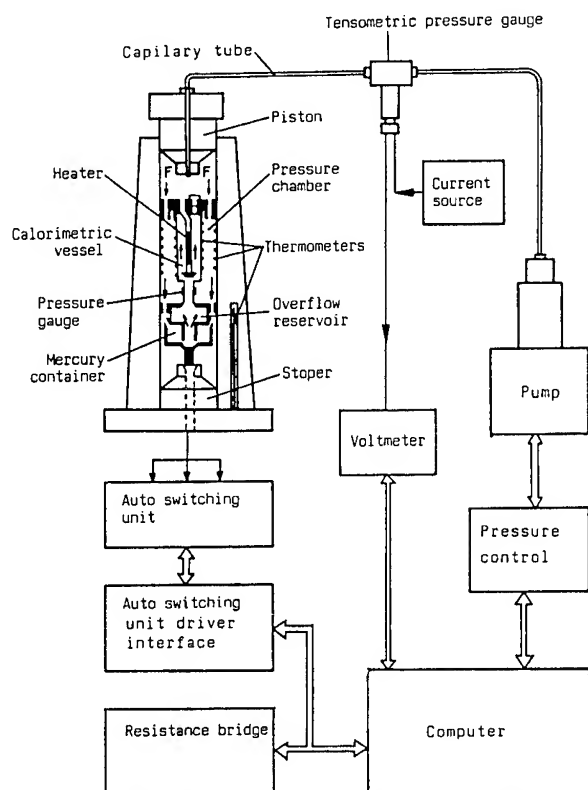


Figure 1. Calorimetric system for evaluation of enthalpy of liquid-to-solid transition at high pressures.

figure 1. The tensometric pressure gauge and the high-pressure plunger pump are connected to the high-pressure chamber of the calorimeter, filled with the chamber liquid, by the capillary tube. The pressure signal from the pressure gauge goes to the pressure control system. If the pressure in the calorimeter is beyond the pressure range  $p \pm \Delta p$ , which is fixed in the control system, the signal from the control system automatically switches the step motor on, which starts the pump. The direction of the motion of the motor depends on the pressure in the calorimeter. If this pressure is higher or lower than the fixed pressure in the control system the pressure transmitting liquid is pumped from or to the high-pressure chamber of the calorimeter respectively, up to the moment when these pressures are identical. The volume of the chamber of the pump is equal  $9 \text{ cm}^3$ . The productivity of the pump, at full speed of the motor, is equal to  $400 \mu\text{l}$  per minute. The speed of pressure change in the calorimeter, connected with the work of the pump, depends on the value of the fixed pressure in the control system. In the fixed pressure range  $0.1 \text{ MPa}$  to  $400 \text{ MPa}$  the pump can compensate the differences between the fixed pressure and the pressure in the calorimeter at the rate of  $0.5 \text{ MPa}$  a minute to  $5 \text{ MPa}$  a minute respectively. This supply system of constant high pressure to the calorimeter is operated automatically by a PC AT computer connected with an 8255 interface.

### 2.3. Measurement system

The temperature and pressure signals from the resistance thermometers and pressure gauge of the calorimeter are measured by an ASL† resistance measurement system, which is also shown in figure 1. This system consists of three parts: the F17A resistance bridge, the 158 auto switching unit driver interface and 148 auto switching unit. This system is operated automatically by the PC AT computer connected with an IEEE488 interface, which enables communication between the measurement system and computer. The temperature and pressure signals from the calorimeter are measured alternately in the programmed order and time. A minimum time between consecutive readings is  $10 \text{ s}$ . A high precision of these measurements results from the parameters of the F17A resistance bridge. The measured resistance  $R_m$  from  $0$  to  $4 \times 10^3 \Omega$  is evaluated as a ratio of  $R_m$  to  $R_s$  standard in the range  $0$  to  $3.999999$ . The resistance  $R_m^T$  of the thermometers and  $R_m^p$  of the pressure gauge, where  $R_m^T \approx R_m^p \approx 100 \Omega$ , with  $100 \Omega R_s$ , are measured with a resolution of  $10^{-4} \Omega$ . This means that, at the ratios  $\Delta R_m^T / \Delta T \approx 0.4 \Omega \text{ K}^{-1}$  for the resistance thermometers and  $\Delta R_m^p / \Delta p \approx 2 \times 10^{-3} \Omega \text{ MPa}^{-1}$  for the pressure gauge, the temperature and pressure signals from the calorimeter are measured with resolutions  $2.5 \times 10^{-4} \text{ K}$  and  $5 \times 10^{-2} \text{ MPa}$  respectively.

## 3. Calorimetric experiment

### 3.1. Heat capacity

All calorimetric measurements of the total heat capacity  $C_{\text{tot}}$  of the calorimetric vessel filled with the examined substance start when temperature and pressure equilibria are attained within the calorimeter. Each calorimetric experiment involves the measurement of: power input  $P(t)$  to the calorimetric vessel; temperature response  $T_1(t)$  of the calorimetric vessel; temperature response  $T_2(t)$  of the outer shield of the calorimeter; temperature response  $T_3(t)$  of the body of the high-pressure chamber; and pressure response  $p(t)$  of the high-pressure chamber, during the heating to equilibrium and during the cooling to the final condition. It is assumed that the sample is in a uniform temperature  $T_1(t)$  region, because the steel thermal conductors are situated in the calorimetric vessel. Because the temperature responses  $T_1(t)$  and  $T_2(t)$  are measured at high pressure by the specially constructed thermometers their readings are verified by the measurement of the temperature response  $T_3(t)$ , which is measured at normal pressure by the standard thermometer during the initial and final conditions, when  $T_1(t) \equiv T_2(t) \equiv T_3(t) = \text{constant}$ .

Owing to the presence of the chamber liquid, convection took place between the calorimetric vessel and the constant-temperature outer shield. Thus the calorimeter

† Automatic Systems Laboratories.

exhibited a dependence of the heat transfer coefficient  $h$  on the temperature difference  $(T_1 - T_2) = \theta$ . The heat transfer coefficient  $h$  was evaluated during the calorimetric measurements of the heat capacity of the sample from the heat transfer in the steady state as the ratio of the known heat power input  $P = P(t) = \text{constant}$  to the developed temperature differences  $\theta = \theta(t) = \text{constant}$ . To evaluate the dependence  $h = h(\theta)$  a series of  $N$  calorimetric runs at the same constant pressure had to be performed with different but constant powers:  $P_1 \neq P_2 \neq \dots \neq P_N$ .

To evaluate the specific heat  $c_p(p)$  of the sample as a function of pressure,  $X$  series of the runs had to be performed with different but constant pressures:  $p_1 \neq p_2 \neq \dots \neq p_X$ .

### 3.2. Enthalpy of phase transition

The calorimetric measurement of the enthalpy of LST is carried out at constant pressure  $p_s^{\text{tr}}$  and in the temperature interval from  $T_0^{\text{sol}}$  to  $T_n^{\text{liq}}$ , where  $p_s^{\text{tr}}$  is the pressure of the solidification of the sample at the temperature  $T_s^{\text{tr}}$ ,  $T_0^{\text{sol}} < T_s^{\text{tr}} < T_n^{\text{liq}}$  and  $T_n^{\text{liq}} - T_0^{\text{sol}} \approx 2$  K, in order that fusion and solidification of the sample could take place during the heating and the cooling processes respectively.

The total heat capacity  $C_{\text{tot}}$  of the calorimetric vessel filled with sample is measured twice:  $C_{\text{tot}}^{\text{liq}}$  for liquid sample and  $C_{\text{tot}}^{\text{sol}}$  for solid sample. The measurements of  $C_{\text{tot}}^{\text{liq}}$  and  $C_{\text{tot}}^{\text{sol}}$  are carried out at the same constant pressure  $p_s^{\text{tr}}$ , but in the different temperature intervals from  $T_0^{\text{liq}}$  to  $T_n^{\text{liq}}$  and from  $T_0^{\text{sol}}$  to  $T_n^{\text{sol}}$  respectively, where  $T_s^{\text{tr}} < T_0^{\text{liq}} < T_n^{\text{liq}}$ ,  $T_s^{\text{tr}} > T_n^{\text{sol}} > T_0^{\text{sol}}$ ,  $T_n^{\text{liq}} - T_0^{\text{liq}} = T_n^{\text{sol}} - T_0^{\text{sol}} \approx 1$  K and  $T_0^{\text{liq}} - T_s^{\text{tr}} = T_n^{\text{sol}} - T_s^{\text{tr}} \approx 2$  K. The dependence  $h = h(\theta)$  is also evaluated during these calorimetric measurements from the steady state heat transfer.

## 4. Calculation

### 4.1. Heat capacity

The evaluated dependence  $h = h(\theta)$  is approximated by the least-squares regression:

$$h = h(\theta) = A_0 + A_1 \theta^{1/4}. \quad (1)$$

The dependence  $h = h(\theta)$  implies that the operation of this calorimeter is described by the nonlinear differential equation:

$$C_{\text{tot}} d\theta(t)/dt + h(\theta)\theta(t) = P(t). \quad (2)$$

Three methods of using the nonlinear differential equation (2) for evaluation of the total heat capacity  $C_{\text{tot}}$  were proposed earlier [16]. The first uses the transformed form of the differential equation (2), the second uses its integral form, and the third, used in this work, is based on its analytical solution expressed by the relation:

$$H[\theta(t)] = -\beta t + D. \quad (3)$$

The term  $H[\theta(t)]$  corresponding to respective polynomials  $h = h(\theta)$  for the case  $P \equiv 0$ ,  $\theta_0 = \theta(t_0) > 0$  and for the case  $P \equiv W = \text{constant}$ ,  $\theta_0 = \theta(t_0) = 0$ , is a linear combination of logarithms of the temperature response  $\theta(t)$  and was given earlier [9]. For the regression (1) used in this work and  $P \equiv 0$ , the term  $H[\theta(t)]$  in relation (3) is equal to

$$H[\theta(t)] = \ln |\theta/(A_0 + A_1 \theta^{1/4})|.$$

The case  $h = A_0 + A_1 \theta^{1/4}$ ,  $P \equiv W$  is not an analytical solution. In relation (3)  $\beta = A_0/C_{\text{tot}}$  and the constant of integration  $D$  includes the initial condition  $\theta_0 = \theta(t_0)$ . It is sufficient to consider the initial condition implicit in the constant  $D$ , because evaluation of  $C_{\text{tot}}$  can be grounded on the slope of the regression line.

The values of  $C_{\text{tot}}(p, T)$  evaluated from equation (3) are used for calculations of the corresponding specific heat capacities  $c_p(p, T)$  of the sample from the relation:

$$c_p(p, T) = C_s(p, T)/m_s(p, T) = (C_{\text{tot}} - C_e)/\rho_s(p, T)V(4)$$

where  $C_s$  is the heat capacity of the sample in the calorimetric vessel,  $m_s$  is the mass of the sample in the calorimetric vessel,  $C_e$  is the heat capacity of the empty calorimetric vessel,  $\rho_s$  is the density of the sample and  $V$  is the volume of the calorimetric vessel. In equation (4) a value of  $m_s(p, T)$  is calculated as a product of  $\rho_s(p, T)$  and  $V$ , because the change in pressure of the calorimeter during the succeeding experiments is accompanied by a change of the mass of the sample in the calorimetric vessel. The values of  $V$  and  $C_e$  were evaluated during the calibration runs and the results are given below.

### 4.2. Enthalpy of phase transition

The total heat  $Q_{\text{tot}}^{\text{tr}}|_{t_0}^t$  evolved in the calorimetric vessel during the phase transition at  $p_s^{\text{tr}}$  and in the temperature interval from  $T_0^{\text{sol}}$  to  $T_n^{\text{liq}}$  is calculated from the integral form of the equation (2) expressed by the relation:

$$Q_{\text{tot}}^{\text{tr}}|_{t_0}^t = \sum_{i=1}^n [\bar{C}_{\text{tot}}(\theta_i - \theta_{i-1}) + \bar{\theta}_i(A_0 + A_1 \bar{\theta}_i^{1/4})(t_i - t_{i-1})] \quad (5)$$

where

$$\bar{C}_{\text{tot}} = (C_{\text{tot}}^{\text{liq}} + C_{\text{tot}}^{\text{sol}})/2$$

and

$$\bar{\theta}_i = (\theta_{i-1} + \theta_i)/2.$$

In equation (5)

$$Q_{\text{tot}}^{\text{tr}}|_{t_0}^t = Q_j|_{t_0}^t + Q_s^{\text{tr}}|_{t_0}^t$$

for the heating process and

$$Q_{\text{tot}}^{\text{tr}}|_{t_0}^t = Q_s^{\text{tr}}|_{t_0}^t$$

for the cooling process.

$Q_j$  is the known, constant Joule effect, and  $Q_s^{\text{tr}}$  is the heat of the phase transition of the sample.

The change of enthalpy  $\Delta H_s^{\text{tr}}$  of the LST of the examined substance is calculated from the equation:

$$\Delta H_{\text{tr}}^{\text{tr}} = Q_{\text{tr}}^{\text{tr}} M_{\text{s}} / \bar{m}_{\text{s}} = Q_{\text{tr}}^{\text{tr}} M_{\text{s}} / \bar{\rho}_{\text{s}} V \quad (6)$$

where  $M_{\text{s}}$  is the molecular weight of the examined substance and  $\bar{m}_{\text{s}}$  is the average mass of the sample, which is calculated from the average density  $\bar{\rho}_{\text{s}}$  of the sample.  $\bar{\rho}_{\text{s}} = (\rho_{\text{s}}^{\text{liq}} + \rho_{\text{s}}^{\text{sol}})/2$ , where  $\rho_{\text{s}}^{\text{liq}}$  and  $\rho_{\text{s}}^{\text{sol}}$  are the densities of the liquid and solid sample at the same constant pressure  $p_{\text{s}}^{\text{tr}}$  but in different, average temperatures  $\bar{T}^{\text{liq}} = (T_0^{\text{liq}} + T_n^{\text{liq}})/2$  and  $\bar{T}^{\text{sol}} = (T_0^{\text{sol}} + T_n^{\text{sol}})/2$  respectively.

## 5. Results of calibration

During the calibration runs two parameters of the calorimeter—the heat capacity  $C_{\text{e}}$  of the empty calorimetric vessel and the volume  $V$  of the calorimetric vessel—were evaluated. The heat capacity  $C_{\text{e}} = 8.68 \text{ J K}^{-1}$  was measured as the total heat capacity of the calorimetric vessel filled with air at normal pressure and room temperature. The volume  $V$  was also evaluated in the calorimetric way, because the calorimetric vessel is opened and connected to the overflow reservoir by the capillary tube. The volume  $V = 5.20 \text{ cm}^3$  was evaluated from the measured values of  $C_{\text{tot}}$  for the calorimetric vessel filled with water and its values of  $c_{\text{p}}$  and  $\rho$  at normal pressure and room temperature, from equation (4). These values of  $C_{\text{e}}$  and  $V$  were assumed to be constant and independent of the substance measured over the range of temperature and pressure employed and they are used in all calculations.

**Table 1.** Comparison of evolved  $Q_{\text{tr}}^{\text{tr}}(t)$  and measured  $Q_{\text{tr}}^{\text{m}}(t)$  values of Joule effect.

$t_{\text{e}}$ (min)	$Q_{\text{tr}}^{\text{e}}$ (J)	$Q_{\text{tr}}^{\text{m}}$ (J)	$Q_{\text{tr}}^{\text{e}} - Q_{\text{tr}}^{\text{m}}$ (J)	$t_{\text{e}} - t_{\text{m}}$ (min)	$Q_{\text{tr}}^{\text{e}}$ (J)	$Q_{\text{tr}}^{\text{m}}$ (J)	$Q_{\text{tr}}^{\text{e}} - Q_{\text{tr}}^{\text{m}}$ (J)
1	6.75	5.85	0.90	1	6.75	6.73	0.02
2	13.49	12.58	0.91	2	13.49	13.44	0.05
3	20.24	19.29	0.95	3	20.24	20.16	0.08
4	26.98	26.01	0.97	4	26.98	26.89	0.09
5	33.73	32.74	0.99	5	33.73	33.62	0.11
6	40.47	39.47	1.00	6	40.47	40.35	0.12
7	47.22	46.21	1.01	7	47.22	47.09	0.13
8	53.96	52.94	1.02	8	53.96	53.83	0.13
9	60.71	59.69	1.02	9	60.71	60.58	0.13
10	67.46	66.43	1.03	10	67.46	67.32	0.14
11	74.20	73.18	1.02	11	74.20	74.08	0.12
12	80.95	79.93	1.02	12	80.95	80.84	0.11
13	87.69	86.69	1.00	13	87.69	87.60	0.09
14	94.44	93.45	0.99	14	94.44	94.36	0.08
15	101.19	100.21	0.98				

To evaluate the precision of the calorimetric measurement in this calorimeter the known, constant Joule effect  $Q_{\text{tr}}^{\text{tr}}(t)$  was measured. A series of calibration runs was

performed with different but constant powers and with different but constant pressures. The results showed that the precision of all these calibration runs was the same. The exemplary results of the calorimetric measurement of the known, constant Joule effect  $Q_{\text{tr}}^{\text{tr}}(t)$  evolved in the calorimetric vessel filled with benzene at  $p = 65 \text{ MPa}$  and  $T = 25^\circ \text{C}$  are summarized in table 1. These results show that the largest difference between evolved and measured values of the Joule effect is observed in the first minutes of the measurement (columns 1 and 4 of table 1), and if the calorimetric measurement starts one minute after switching on the electric heater in the calorimetric vessel the difference between  $Q_{\text{tr}}^{\text{e}}$  and  $Q_{\text{tr}}^{\text{m}}$  is smaller than 0.4% of  $Q_{\text{tr}}^{\text{e}}$  (columns 5 and 8 of table 1).

## References

- [1] Czarnota I 1979 Calorimetric system for measurement of specific heat capacity of liquids,  $c_{\text{p}}$ , at high pressures *Bull. Acad. Polon. Sci. Ser. Sci. Chim.* **27** 763–72
- [2] Czarnota I 1982 Heat capacity of 3-methylpentane at high pressures *Bull. Acad. Polon. Sci. Ser. Sci. Chim.* **28** 651–59
- [3] Czarnota I 1984 Heat capacity of water at high pressure *High Temp. High Pressures* **16** 295–302
- [4] Czarnota I 1985 Heat capacity of n-pentane, n-hexane, and n-heptane at high pressure *High Temp. High Pressures* **17** 543–46
- [5] Czarnota I 1988 Heat capacity of 2-methylbutane at high pressures *J. Chem. Thermodynamics* **20** 457–62
- [6] Czarnota I 1991 Heat capacity of benzene at high pressures *J. Chem. Thermodyn.* **23** 25–30
- [7] Czarnota I 1993 Heat capacity of octane at high pressures *J. Chem. Thermodyn.* **25** 355–59
- [8] Czarnota I 1993 Heat capacity of decane at high pressures *J. Chem. Thermodyn.* **25** 639–42
- [9] Ter Minassian L and Pruzan P 1977 High-pressure expansivity of materials determined by piezo-thermal analysis *J. Chem. Thermodyn.* **9** 375–90
- [10] Randzio S L 1983 A pressure-scanning calorimeter *J. Phys. E: Sci. Instrum.* **16** 691–4
- [11] Ter Minassian L and Milliou F 1983 An isothermal calorimeter with pneumatic compensation—principles and application *J. Phys. E: Sci. Instrum.* **16** 450–5
- [12] Randzio S L 1984 The analysis of a pressure-controlled differential scanning calorimeter *J. Phys. E: Sci. Instrum.* **17** 1058–61
- [13] Randzio S L 1988 An automated calorimeter for the measurement of isobaric expansivities and of isothermal compressibilities of liquids by scanning pressure from 0.1 to 400 MPa at temperatures between 303 and 503 K *J. Chem. Thermodyn.* **20** 937–48
- [14] Randzio S L 1991 Scanning calorimetry with various inducing variables and multi-output signals *Pure Appl. Chem.* **63** 1409–14
- [15] Pruzan P and Ter Minassian L 1976 High pressure calorimetry as applied to piezothermal analysis *Rev. Sci. Instrum.* **47** 66–71
- [16] Czarnota I and Tabaka A 1979 Evaluation of the total heat capacity of a constant temperature environment calorimeter with nonlinear heat transfer *Bull. Acad. Polon. Sci. Ser. Sci. Chim.* **27** 489–99



## ACOUSTIC EMISSION SENSORS FOR IN-SITU MEASUREMENTS UNDER PRESSURE

Z. WITCZAK, R. JEMIELNIAK, P. WITCZAK

*High Pressure Research Center, Polish Academy of Sciences, Sokolowska 29, 01-142 Warszawa, Poland*

The effect of hydrostatic pressure on the sensitivity of acoustic emission (AE) sensors for in-situ measurements under pressure was investigated. The sensors were made of monocrystalline  $\text{LiNbO}_3$  plates of the Y-35° orientation. They were designed in the form of 3 MHz resonant frequency discs of various diameters. For all tested sensors the dependence of their sensitivity on pressure in the pressure range up to 1 GPa can be described with the polynomial of not more than the second power. The results allow to design AE sensors nearly insensitive to pressure.

### Introduction

Two experimental techniques can be applied for acoustic emission (AE) investigations of materials under high hydrostatic pressures.

The first technique requires a special high pressure equipment in which AE sensors are placed outside the pressure vessel. In this case the tested sample needs a special acoustic bonding to some parts of the pressure vessel working as a waveguide. The bonding should be insensitive to pressure, which is difficult to achieve.

The second technique, in which the AE sensors are placed directly on the sample, requires sensors possibly insensitive to pressure. The material for such sensors cannot be a commercial piezoelectric ceramics because of its polycrystalline, non-homogeneous structure that itself generates AE signals under pressure and changes irreversibly its properties. Besides the piezoelectric material should possess good piezoelectric properties, temperature stability and chemical resistance to the pressure medium. From this point of view the monocrystalline lithium niobate is an excellent material. Its properties are affected by pressure reversibly<sup>1</sup>. This work is aimed at investigating the sensitivity of various sensors made of lithium niobate in order to design a sensor insensitive to pressure.

### Experimental Procedure

The measurement set is presented in Fig. 1. A piezoelectric transducer working as a standard source of AE signals was placed on the outer face of the high pressure vessel plug while investigated sensors were bonded to its inner

(reference) face. A nonaqueous stopcock grease insoluble in the pressure medium (extraction naphtha) was used for bonding. The sensors were cut off from a lithium niobate single crystal plate of the Y-35° orientation. The plate was ground to the thickness of 1.23 mm which was giving 3 MHz resonant frequency of piston vibrations in it.

Two different sensors were investigated in the beginning, a resonant one in the form of a disc ( $\phi 12$  mm) — R12 and a broadband one in the form of a spherical segment with a circular flat contact area ( $\phi 2$  mm)<sup>2</sup> — B2. Then two intermediate sensors of a cylindrical shape were tested — R4 and R2 ( $\phi 4$  and  $\phi 2$  mm). All of them were acoustically damped at their back faces with brass dampers.

Standard AE signals were generated by RITEC equipment. The signals detected by investigated sensors were recorded by TEKTRONIX oscilloscope. The form of the standard AE signal at the reference face was determined with a broadband capacitive sensor<sup>3</sup>. It was a single sinusoid of 3 MHz frequency (Fig. 2).

### Results and Discussion

An example of the signal that was measured in this experiment is presented in Fig. 3. The signal is well damped although it is generated by a resonant sensor (R12). To avoid the influence of pressure variations in acoustic impedance of naphtha on the accuracy of measurements the first peak of the signal (A) was taken as a measure of detected AE signal, although the results obtained for the second (higher) peak were the same. The dependence of this value on pressure is presented in Fig. 4 in relation to its value at atmospheric

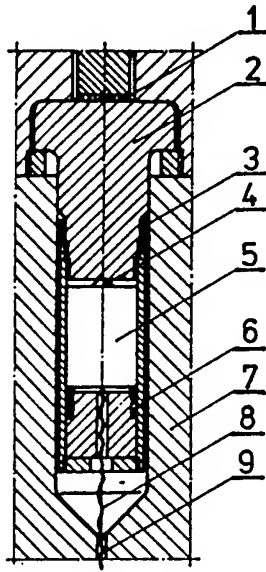


Figure 1: Setup for testing AE sensors under pressure: 1) standard transducer, 2) plug, 3) seals, 4) tested sensor, 5) damper, 6) spring, 7) pressure vessel, 8) lead, 9) capillary.

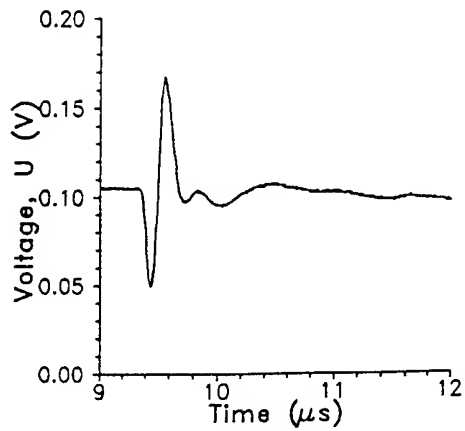


Figure 2: Standard ultrasonic pulse measured with a broad-band capacitive sensor.

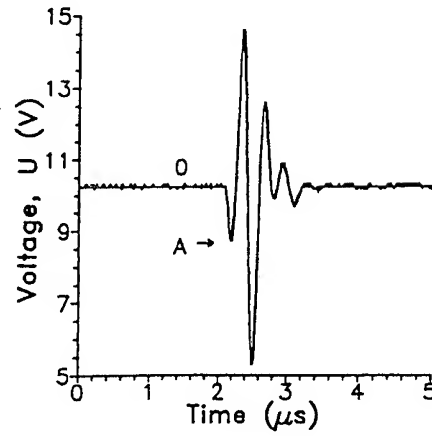


Figure 3: Signal generated by the resonant sensor R12.

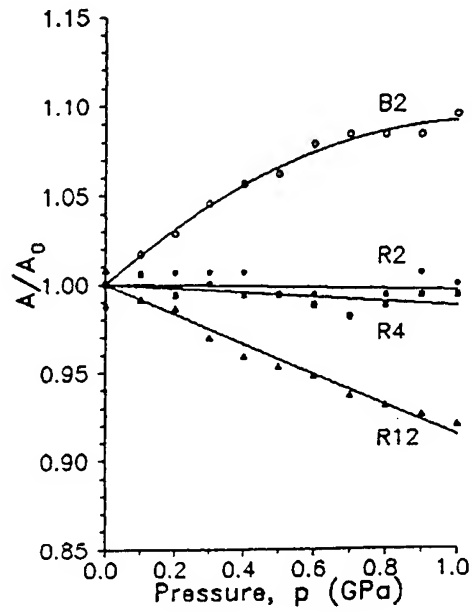


Figure 4: Relative sensitivity of various AE sensors vs pressure.

pressure (R12). It fits well to the straight line of a negative slope. The results for the broadband sensor (B2) presented in the same figure can be well described by a polynomial of a second power with a positive linear and a negative parabolic components.

Various pressure media (kerosine, oil) were tested in order to determine the effect of changes in acoustic impedance of pressure medium on the results and no significant effect was noticed. This indicates that the sensitivity of AE sensors depends only on their shape and variation in their properties. The only reasonable explanation for that were the changes of vibration modes of sensors under pressure. This was partially verified by Fourier analysis made according to the procedure presented elsewhere<sup>3</sup> for the signals generated by the R12 sensor. A drift of frequency of this sensor towards lower values was observed.

Although the problem needs further investigations the present results allowed to predict which shape of the sensors is least sensitive to pressure. Two cylindrical sensors of smaller diameters — R4 and R2 (4 and 2 mm) were tested. The results are presented in Fig. 4. It is seen that the characteristics of the R2 sensor is almost pressure independent.

The sensor R2 is practically insensitive to pressure but similarly to the broadband B2, it is the least sensitive of all (by several times than R12). That is due to the small area of its measuring surfaces (small capacitance). It is obvious that to cope with this problem a mosaic sensor made from several small elements (e.g. R2) can be applied.

## Conclusions

1. Hydrostatic pressure affects the sensitivity of AE sensors made of monocrystalline lithium niobate according to their shape. The sensitivity of the resonant sensors decreases with pressure whereas it increases for the broadband ones. The changes are in the order of 10% per 1 GPa.

2. It is possible to design the mosaic sensor nearly insensitive to pressure made from small cylindrical elements.

## Acknowledgements

The authors thank the State Committee for Scientific Research in Poland for support of this work (grant 3-P407-071-04).

## References

1. Y.Cho and K. Yamanouchi, *J. Appl. Phys.*, 61 (1987) 875.
2. T.M. Proctor, *JASA*, 71 (1982) 1163.
3. R. Jemielniak, J. Krolkowski, P. Witczak and Z. Witczak, in *Optoelectronic and Electronic Sensors COE'92*, Zegrze 26-28 May 1992, conf. proceedings, p. 86. (in Polish)

# REGISTRATION OF PHASE TRANSITIONS IN MATERIALS AT HIGH PRESSURES UP TO 30 GPa

V. V. Shchennikov, A. Yu. Derevskov

*Institute of Metals Physics Ural Branch RAS, 620219 Ekaterinburg GSP-170, Russia*

V. A. Smirnov

*Ecological Centre of National Academy of Sciences of Ukraine 314000 Poltava, Ukraine*

The pressure apparatus, allowing to perform simultaneous measurements of several parameters of sample under high pressure is described. The apparatus contains the microcontroller for the operation by measurements and keeping the experimental data. The examples, comprised the volume, resistance and thermoelectric power jumps recording in HgSeS crystal during the pressure-induced phase transition, are represented.

Properties of substances, suffering structural phase transitions under pressure  $P$ , as a rule, are a complex functions of the extent of transformation, so the abrupt changes of it, for example, volume  $V$ , resistance  $R$  and thermoelectric power  $S$ , sometimes occur at various values of pressure<sup>1,2</sup>. So, for the rising of the accuracy of the phase transition investigations the measurements of several properties of sample have to be performed simultaneously. Use of various type high pressure cells also allows to improve accuracy of research.

## Experimental results

The appropriate equipment, satisfied the above intention, was constructed by the authors of present paper. It includes the high pressure apparatus (fig.1) and recording block (fig.2). Apparatus contains the pressure chamber 1, lever mechanism 2 with the reduction gear and electromotor drive 3, and sensors of pressure  $P$  (stress), displacement of plunger  $X$  and temperature  $T$ . The removable high pressure cell, inserting in the pressure chamber 1,

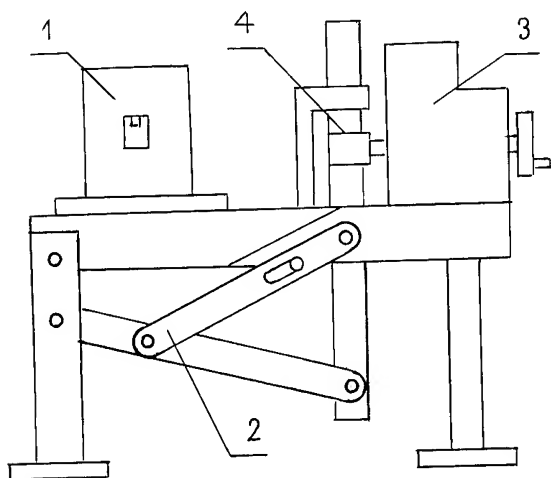


Figure 1: High pressure apparatus 1 – pressure chamber, 2 – lever mechanism, 3 – reduction gear and electromotor drive, 4 – worm-gear

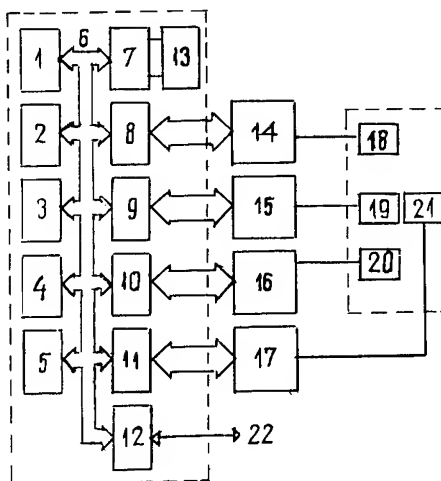


Figure 2: Functional scheme of recording block (microcontroller) 1 – CPU, 2 – ROM, 3 – RAM, 4 – timer, 5 – power supply, 6 – bus, 7–11 – PIA, 12 – serial interface, 13 – keyboard/display, 14–17 – voltmeter, 18 – P sensor, 19 – T sensor, 20 – V sensor, 21 – sample, 22 – port RS-232S (communication with computer).

consists of the metal, tungsten carbide or sintered diamond anvils<sup>3</sup>. The various kinds of sintered diamond materials were trialed for generation the pressures up to 30 GPa. For this purpose the modified apparatuses of Bridgman anvils type<sup>1,4</sup>, were developed using a tungsten carbide plungers with the tied diamond (or BN) tips. The rest elements of apparatus were made of titanium alloys. The value of pressure was estimated from the value of acting stress  $F$  and tabulated dependence  $P(F)$ , recording in the apparatus<sup>1</sup>.

The recording block (microcontroller) contains the microprocessor 1, interfaces 8–11 for the connection an outputs of standart digital voltmeters 14–17 and interface 12 for the transfer data of measurements to IBM-PC. Sensors 18–20 and electical outputs from sample 21 are connected with digital voltmeters 14–17. Recording block allows to perform simultaneos measurements of four parameters of sample during the phase transition. Operation by measurements and choice a step of ruling parameter ( $P$ ,  $T$ ,  $X$ ) may be done by keyboard 13, the results being read off from 4-digit indicator 13. The program of operation and testing is stored in ROM. Experimental data are stored in the energy supply independent RAM and may be transferred to IBM-PC.

The following examples of investigation of phase transition  $B3 \rightarrow B9$  in  $HgSe^3$  and  $HgSeS$  crystals demonstrated the potentialities of the discussed equipment. In fig.3 there is the measured jumps of thermoelectric power  $S$  at  $B3 \rightarrow B9$  phase transition in  $HgSe^3$ , received in the Gexanit (BN) anvils. The platinum-silver ribbons made the electrical contact with a sample. The lithographic stone was used as the pressure-transmitting medium. The method of the research was described in<sup>3,5</sup>. The measurements were performed at the constant gradient of  $T$ , and also at the progressive reducing of one, when the heat supply was cut off ("regular" thermal regime). As can be seen, the results of relative investigation of  $S$  in the both cases are approximately the same; it agree well with the data published formerly<sup>3,6</sup>.

The results of investigation of analogous phase transition in  $HgSe_{0.4}S_{0.6}$  crystal are shown at Fig.4. The measurements were performed in the tungsten carbide anvils, the lithographic stone was the pressure-transmitting medium. There are two observed jumps of  $R$  and  $X$  within the width of transition. One can see, that the sufficient jump of

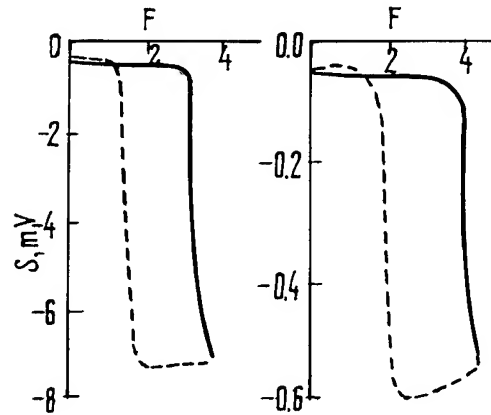


Figure 3: The dependence of thermoelectric voltage of  $HgSe$  sample vs the increasing (solid line) and decreasing (dashed line) stress  $F$ ; left curve received at the constant gradient of  $T$ ; right curve received at the progressive reduce of one in the "regular" thermal regime when the heat supply was cut off.

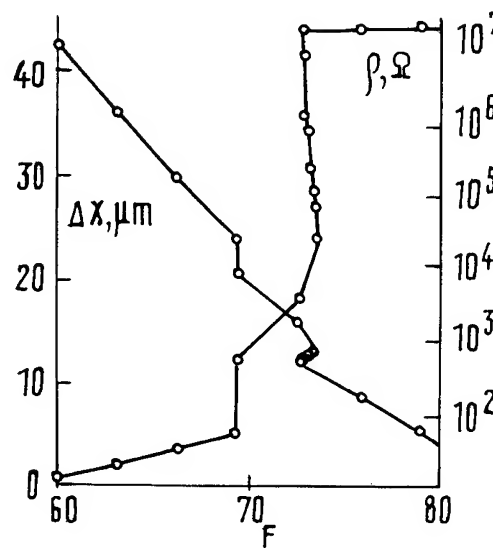


Figure 4: The data of synchronous measurements of plunger displacement and resistance of  $HgSe_{0.4}S_{0.6}$  sample versus the stress  $F$  (arbitrary units), driving by the pressure apparatus,  $T = 296$  K. The  $B3 \rightarrow B9$  phase transition, beginning at  $P = 0.4$  GPa, can be seen.

plunger displacement X occurs before the appropriate jump of resistance, as was mentioned above. The used equipment allows also to observe the small effect of pressure drop, resulting from the volume contraction of sample, suffering B3→B9 structural transition. The resemble effect of P reducing by 0.02–0.03 GPa we observed at purely hydrostatic conditions in the piston-cylinder chamber at similar samples.

### Acknowledgments

This work was supported by Russian Fundamental Research Foundation through Grant N 93-02-2832.

### References

1. C. C. Bradley, *High Pressure Methods in Solid State Research* (London, Butterworths, 1969.)
2. V. V. Shchennikov, *The Physics of Metals and Metallography* **67**, 93 (1989).
3. I. M. Tsidil'kovskii, V. V. Shchennikov, N. G. Gluzman, *Sov. Phys. Semiconductors* **17**, 604 (1983).
4. F. P. Bundy, *Rev. Sci. Instruments* **46**, 1318 (1975).
5. V. V. Shchennikov, *Rasplavy* **2**, 33 (1988).
6. S. K. Ramasesha, A. K. Singh, *Rev. Sci. Instruments* **5**, 1372 (1991).

# STRAIN GAGE METHOD OF VOLUME MEASUREMENTS UNDER HYDROSTATIC PRESSURE

J. Kamarád, K.V. Kamenev\*, Z. Arnold

*Institute of Physics, AV CR, Cukrovarnická 10, 162 00 Praha 6, Czech Republic*

## ABSTRACT

The modern foil micro-strain gages have been successfully used to the magnetovolume measurements under high hydrostatic pressures up to 1.4 GPa in the temperature range from 20 to 450 K. The strain gages were calibrated under normal and high pressure conditions with the use of Cu, Fe, and Titanium Silicate as reference materials. The accuracy of measurements of thermal expansion and volume changes under pressure is better than 10% in low temperature range. The temperature correction of the pressure coefficient of the Manganin pressure sensor was also determined.

## Introduction

The results of precise volume measurements under pressure always belong to a basic and very useful information of studied materials. Very sophisticated apparatuses were designed for the direct measurements of volume changes under static pressures in the past. *p-V* curves have been determined for many materials up to hundreds of GPa using DAC and synchrotron radiation [1]. Nevertheless, all these experiments have been performed in a relatively narrow temperature range near room temperature. Recently, we have used calibrated strain gages to measurements of large magneto-volume effects in novel R-Fe intermetallics at low temperatures [2]. The calibration procedure of the micro-strain gages in the temperature range 20 - 450 K under pressures up to 1.4 GPa is described in this contribution.

## Calibration procedure

We have used micro-strain gages (Series SK and WK, Micro-Measurements Group, Inc.) which are fully encapsulated in high temperature epoxy resin with glass fibres. The grid dimensions are

0.8x0.8 mm<sup>2</sup>, operating temperatures lie in the range from 4 to 500 K and strain limit is ~1.5%. All the pressure measurements were performed in a clamp CuBe hydrostatic cell that was cooled down to 10 K in a closed cycle He-refrigerator. Temperature and pressure were measured by a Si-diode outside and by a Manganin sensor inside the pressure cell, respectively.

## Temperature corrections

As the first step of the calibration, we have measured the linear thermal expansion of pure Cu, Fe and Titanium Silicate (material TSB-1, Measurements Group, Inc.) under normal pressure. According the producer, the thermal expansion coefficient of the TSB-1 is less than  $6 \cdot 10^{-8} \text{ K}^{-1}$  at temperatures from 150 to 450 K. The reference data of thermal expansion of Cu and Fe were obtained from [3].

The basic linear relation between the measured relative resistance of the gage  $r_m = \Delta R/R$  and strain  $\varepsilon = \Delta l/l$  is characterized by a gage factor  $G$ :

$$r_m = G \cdot \varepsilon \quad (1)$$

At temperature  $T \neq T_0 = 293 \text{ K}$ , the magnitude of  $r_m(T) = [R(T)/R(T_0) - 1]$  is given not only by the thermal expansion of the specimen,  $\varepsilon_s(T)$ , but also by the thermal expansion of the gage and by

\* on the leave from the Donetsk Physico-Technical Institute of the Ukrainian Academy of Sciences

thermal changes of electrical conductivity of the grid alloy. So, we have to correct the measured  $r_m(T)$  by a correction function  $F(T)$  to obtain  $\varepsilon_s(T)$  :

$$\varepsilon_s(T) = 1/G(T) * [r_m(T) + F(T)] \quad (2)$$

Using the reference data  $\varepsilon_{c1}(T)$ ,  $\varepsilon_{c2}(T)$  of two reference materials and the relevant measured values  $r_{m1}(T)$ ,  $r_{m2}(T)$ , we can calculate  $G(T)$  and  $F(T)$  as :

$$G(T) = \frac{[r_{m1}(T) - r_{m2}(T)]}{[\varepsilon_{c1}(T) - \varepsilon_{c2}(T)]} \quad (3)$$

$$F(T) = G(T) * \varepsilon_{c1}(T) - r_{m1}(T) \quad (4)$$

We have tested an accuracy of the calibration by permutation of the couples of the reference materials.

#### Pressure corrections

Neglecting the higher powers of small magnitudes, the isothermal volume changes of isotropic materials can be expressed as:

$$\Delta V/V = 3 * \varepsilon \text{ or } \varepsilon = 1/3 * \kappa * p \quad (5)$$

where  $\kappa$  is the isothermal compressibility. In addition to the effect of temperature, we have to correct the measured relative resistance of the strain gage  $r_m(T, p) = [R(T, p)/R(T_o, 0) - 1]$  with respect to the pressure response of the grid alloy. A careful analysis shows that we can include the effect of pressure on the electrical conductivity of the grid alloy into the  $F$ -function and the compressibility of the grid makes an additional contribution to the strain in the form of the relation (5). The gage factor  $G$  seems to be pressure independent. The relation (2) can then be written as:

$$\varepsilon_s(T, p) = 1/G(T) * [r_m(T, p) + F(T, p)] + 1/3 \kappa_g * p \quad (6)$$

where  $F(T, p) = F(T) + C_g * p$ ;  $C_g$  and  $\kappa_g$  can be determined from relevant calibration measurements under pressure.

## Results and Discussion

Fig.1 shows the temperature dependence of the gage factor  $G(T)$  and the curve of its linear regression. The linear dependence  $G$  on  $T$  is presented by the manufacturer in range 200 - 450 K but its slope is slightly higher than the slope of our linear regression in this temperature range. The correction function  $F(T)$  is displayed on Fig.2. Based on the data of the electrical conductivity and compressibility of the grid alloy given in [4], we have used  $C_g = 2 * 10^{-3} \text{ GPa}^{-1}$  and  $\kappa_g = 6 * 10^{-3} \text{ GPa}^{-1}$  in relation (6).

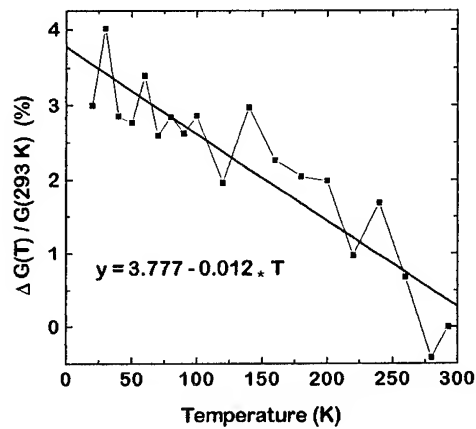


Fig.1 The gage factor  $G(T)$  and the curve for its linear regressions.

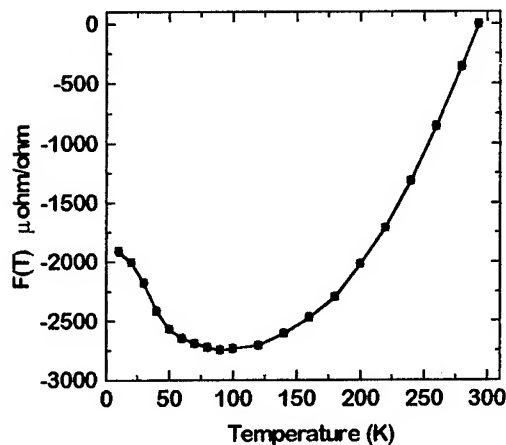


Fig. 2 The correction function  $F(T)$ .



To avoid the inherent thermal output of the strain gages under normal pressure, it is common to use the second strain gage bonded to a reference material and to keep both at the same temperature. Unfortunately, we met two serious obstacles to use this technique under high pressure. One is a difficulty to keep the referential gage placed out of the pressure cell at the same temperature as the sample inside the cell. Otherwise, we need to know the temperature dependence of the compressibility of the reference material in a wide range of temperatures and such data seem to be very rare. We have used for this purpose a rough linear approximation of the temperature dependence of the compressibility of Cu based on data in [5]:

$$\kappa_{Cu}(T) = \kappa_{Cu}(300\text{ K})[1 + A(T - 300\text{ K})] \quad (7)$$

where  $A = 0.00016\text{ K}^{-1}$ .

The modern foil strain gages are fabricated as temperature-compensated with respect to the material of a specimen under the test. That effects all the corrections. The strain gages with the thermal compensation for steel have been calibrated in this work. A possibility of voids and bubbles existing in the adhesive layer or in the encapsulation of the gage must be excluded in the high pressure measurements. Local deformations in a portion of the grid generate unreproducible error signal.

To take into consideration the largest sources of possible errors, i.e. the accuracy of the determination of  $G(T, p)$ , the approximation of  $\kappa_{Cu}(T)$  and its pressure dependence and the accuracy of the pressure and temperature determinations, we can conclude that the reached precision of this strain gage method is better than 5% in strain determination and better than 10% in the compressibility calculation in the low temperature range and more than two times better in the vicinity of room temperature.

Using the strain gage placed on the outer surface of the pressure cell, we have measured its elastic deformation and calculated the relevant pressure variations with temperature. We verified a necessity to take into account the temperature

dependence of the pressure coefficient of the Manganin pressure sensors when they are used to determine pressure at low temperature.

This strain gage method of volume measurements under hydrostatic pressure was successfully used to measure the thermal expansion  $\delta l/l$  (see Fig.3) and compressibility anomalies on  $R_2\text{Fe}_{17}$  and  $R_3(\text{FeTi})_{29}$  [6] intermetallic compounds.

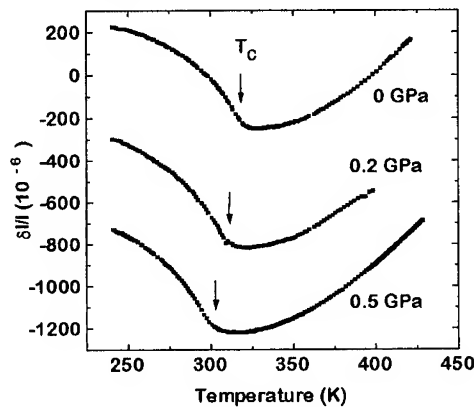


Fig.3 Linear thermal expansion of  $\text{Ce}_3(\text{FeTi})_{29}$  under different pressures near  $T_c$ .

#### Acknowledgement

We acknowledge the financial support from Project of the Grant agency of AV CR No. 110117.

#### References

- [1] S.N.Vaidya, G.C.Kennedy, *J.Phys.Chem. Solids* **31** (1970) 2329 ; D.Hausermann in this Proc.
- [2] J.Kamarád, Z.Arnold, K.V.Kamenev, M.R.Ibarra in this Proceedings.
- [3] R.J.Corrucini, J.J.Gniewek, *NBS Monograph* **29** (NBS Washington, 1961) ; F.R.Kroeger, C.A.Swenson, *J.Appl.Phys.* **48** (1977) 853.
- [4] Measurements Group Inc., Catalog 500 and Tech Note TN-513-1 (1986).
- [5] C.A.Swenson, *Solid State Physics, Vol. 11* (Academic Press, 1960), p. 58.
- [6] Z.Arnold et al., *J.Appl.Phys.*, - in press.

# A NEW DEVICE FOR HIGH TEMPERATURE AND HIGH PRESSURE: A HEATING GASKET IN A CERAMIC DAC

†R. LeToullec, †F. Datchi, †P. Loubeyre, †N. Rambert, ‡B. Sitaud and ‡Th. Thevenin.

†*Physique des Milieux Condensés, Université Paris 6, 4 place Jussieu  
75252 Paris Cedex 05, France.*

‡*Commissariat à l'Energie Atomique, centre d'étude de Bruyères-le-Chatel, BP12  
91680 Bruyères-le-Chatel, France.*

## ABSTRACT

This paper describes a new design of diamond anvil cell (DAC) for high pressure and high temperature measurements. This DAC presents two main innovations with respect to other DACs designed for high temperature: the ceramic body and the heating gasket. It offers the same optical access as the classical DACs for room temperature use, and presents a good mechanical stability and a very fast temperature stabilization. As a preliminary study, we measured the melting curve of argon up to 620 K, using a new high pressure-high temperature metrology.

## 1 Introduction

Diamond anvil cell is now a widely used tool to study materials under high static pressure. Combining high temperature with high pressure studies in DAC offers new and very attractive possibilities but is unfortunately not straightforward. Various difficulties arise, depending on the method used to generate high temperatures. In the case where the cell, or a large part of it, is directly heated [1, 2, 3], special care has to be granted to the choice of the materials used for the different parts of the cell. Specifically, they must fit mechanical constraints in order to obtain a good mechanical stability at high temperature and high pressure. Also, designs with external heating cause limitations on the use of the cell, like for example a reduced optical access to the sample, which is a critical parameter in X-ray diffraction experiments.

The diamond anvil cell that we present in this paper was designed to overcome the difficulties mentioned above. It is based on two new technological developments: the use of ceramic for the body of the cell and the heating gasket. Its principle is simple: the low thermal conductivity of the ceramic confine the high temperature to the system diamonds + gasket. In that manner, heat losses are minimized and the external parts of the cell are moderately heated. Heating directly the metallic gasket also implies that the

heat is mainly transferred by conduction to the sample, which makes the heating process much faster. This cell is thus characterized by:

- *Fast and homogeneous temperature stabilization of the sample,*
- *The same optical access and mechanical stability of the cell as at room temperature.*

We performed a preliminary study to test the working order of this cell by measuring the melting curve of argon at high pressure. The results shown in this paper, though limited to moderately high temperatures, are very promising.

## 2 Description of the ceramic DAC

### 2.1 The ceramic body

The body of the cell (Figure 1) is built out of alumina. It is inserted inside a steel jacket which allows the use of a membrane to generate the force on the piston. The cell can support a force of at least 15 kN which should be sufficient to obtain pressures up to 100 GPa. The diamond seats, on which the diamonds are fixed with high temperature cement, are made of zirconia.

In order to prevent diamonds from graphitization at temperatures above 600°C, the cell must be placed in a vacuum chamber. If one wishes to work at high temperature for a long

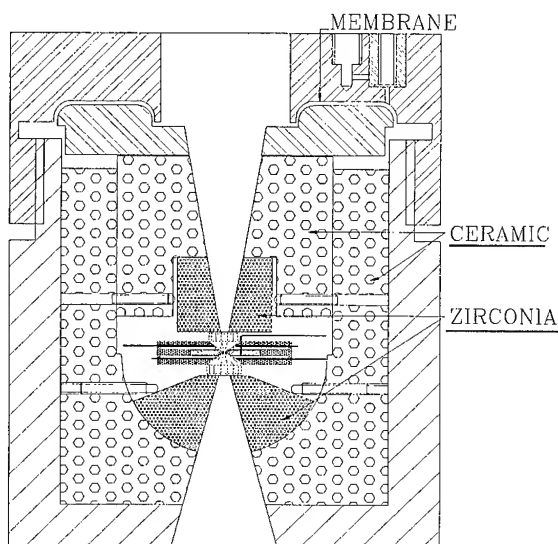


Figure 1: Cross-section of the ceramic diamond anvil press.

time, it is also necessary to cool the cell body so that the membrane is kept at low temperature.

## 2.2 The heating gasket

The gasket is made of rhenium which was pointed out as the best material for high temperature works [2]. Two resistances made of kanthal (Fe-CrAl alloy) are connected in series by soldering them on each side of the metallic gasket. The spiral shape of the resistances was computed so as to obtain a good temperature homogeneity in the central part of the gasket. Electrical insulation is guaranteed by a thin alumina layer deposited on the resistances by plasma projection. In order to limit the heating by radiation of the surrounding pieces, mica screens are mounted on each side of the gasket. The resulting pile of these different elements has a thickness of 2.6 mm, which is

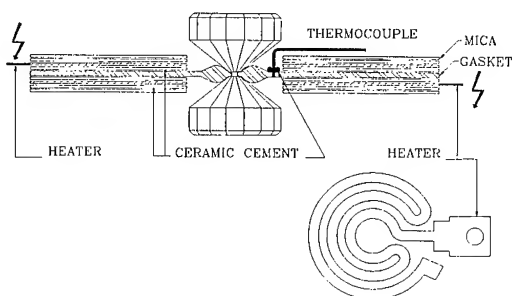


Figure 2: Cross-section of the heating gasket.

sensibly lower than the 5 mm distance separating the two diamond seats.

Figure 3 shows the temperature measured by a thermocouple placed at the center of the gasket as a function of the input power when no force is applied. It can be seen that a rather small power is needed to achieve high temperature, e.g. 15 W is enough to reach 1000 K.

Finally, a K-type thermocouple is inserted in a hole drilled at 1 mm away from the sample chamber and kept in position by high temperature ceramic cement.

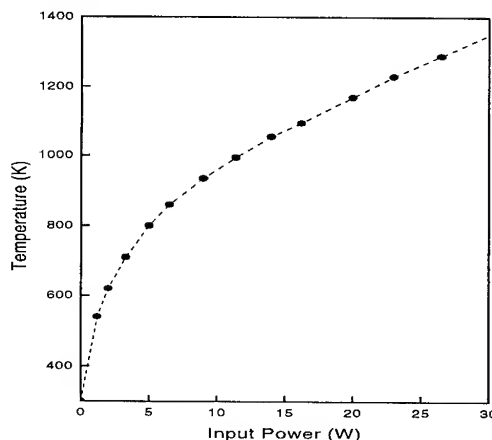


Figure 3: Temperature at the center of the gasket as a function of the input power in the resistances.

## 3 Application: melting curve measurements at high pressure

The ceramic DAC was loaded with argon at 50 MPa. We obtained a sample of 150  $\mu\text{m}$  diameter. Both pressure and temperature of the sample were measured by the means of two luminescence gauges<sup>1</sup>, ruby and  $\text{SrB}_4\text{O}_7:\text{Sm}^{2+}$ , which were placed in the sample chamber and excited with the 488nm line of an  $\text{Ar}^+$  laser.

<sup>1</sup>In order to perform accurate measurements of melting curves of simple molecular systems at high pressure, we developed a new high pressure-high temperature metrology based on two luminescence gauges: ruby and  $\text{SrB}_4\text{O}_7:\text{Sm}^{2+}$ . It is derived from the simple observation that, whereas the shift of the  $R_1$  line of the ruby depends on both pressure and temperature, the shift of the  ${}^5D_0 - {}^7F_0$  line of  $\text{SrB}_4\text{O}_7:\text{Sm}^{2+}$  with temperature is very small (less than  $10^{-4}$  Å/K) and can be considered with an excellent estimate only dependent on pressure, with a slope of 2.55 Å/GPa [4]. Hence, from the position of both lines, it is possible to compute simultaneously the pressure and the temperature of the sample.

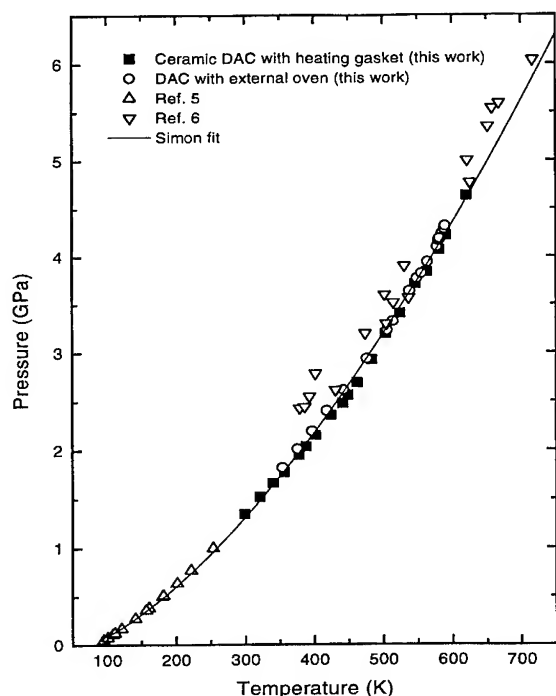


Figure 4: Argon melting curve.

By decreasing the force on the piston, we obtained a solid germ in equilibrium with the liquid at room temperature. We then slowly increased the temperature and the pressure in order to continuously observe the solid/liquid equilibrium. Unfortunately, a cut-off of the resistance at  $T = 620$  K, due to a bad soldering on the gasket, prematurely stopped the experiment. Figure 4 shows the results of this run and of another experiment in which a classical DAC heated with an external oven was used. Comparison can be made with previous measurements of the argon melting curve [5, 6]. The very good agreement between our two sets of data and the continuous aspect of the resulting melting curve are proofs of the ability of the cell for this kind of measurements. A new Simon curve has been fitted on the basis of this work and ref. 5:

$$P_m[\text{GPa}] = 1.4336 \cdot 10^{-4} T_m^{1.6187}[\text{K}] - 0.1544$$

An excellent agreement between the Simon law and the experimental data can also be noted from figure 4.

## 4 Conclusion

The diamond anvil cell for high pressure-high temperature studies presented in this paper differs mainly from previous designs by the use of ceramic for the cell body and by the heating device composed of the metallic gasket and the two resistances. We showed that this system is mechanically stable at high temperature, which is an important constraint in measurements like melting of materials at high pressure. Actually, no pressure drop occurred in our experiment during heating, in contrast to reported studies made with DACs built out of high temperature steel like Inconel [1]. However, this cell has not been yet fully characterized and further work is in progress to fix the temperature and pressure limits of this system.

## References

- [1] M.H. MANGHNANI and Y. SYONO, editors. *High pressure Research in Mineral Physics*. American Geophysical Union, Washington DC, 1987.
- [2] D. SHIEFERL. *Rev. Sci. Instrum.*, **58**, 1987.
- [3] Y. FEI and H.K. MAO. *Science*, **266**:1678, 1994.
- [4] A. LACAM and C. CHATEAU. *J. Appl. Phys.*, **66**:366, 1989.
- [5] V.N. CHENG, W.B. DANIELS, and R.K. CRAWFORD. *Phys. Lett.*, **43 A**:109, 1973.
- [6] C. ZHA, R. BOEHLER, D.A. YOUNG, and M. ROSS. *J. Chem. Phys.*, **85**:1034, 1986.

# HIGH PRESSURE SYSTEM FOR EPR MEASUREMENTS

J. SZCZEPEK\*, A. SIENKIEWICZ\*\*

\* *High Pressure Research Center, Polish Academy of Sciences,  
Sokołowska 29/37, 01-142 Warszawa, Poland*

\*\* *Institute of Physics, Polish Academy of Sciences,  
Al. Lotników 32/46, 02-668 Warsaw, Poland*

## ABSTRACT

The technical aspects of the system design for performing X-band EPR measurements at high hydrostatic pressures are presented. This design is notable in that it operates with regular high-frequency magnetic field modulation (100 kHz) and enables one to change hydrostatic pressure up to 0.8 GPa in the temperature range 4.2 to 400 K. In particular, technical problems of the adaptation of the system to the commercially available top-loaded Helium gas-flow cryostat are discussed.

## Introduction

Combination of Electron Paramagnetic Resonance (EPR) with high hydrostatic pressure was first introduced by Walsh and Blombergen [1]. Techniques to make EPR measurements at moderately high hydrostatic pressure have been described [3,4]. This experimental method, which takes advantages of the overall high sensitivity of EPR and of its high resolution, can offer the unique information when studying pressure- and temperature-dependent phenomena, phase transition or transport and magnetic properties. In spite of these advantages, EPR at high hydrostatic pressure has not become a well-established spectroscopic technique, mainly because of technical problems encountered while combining the microwave part of the typical EPR spectrometer with the otherwise seal pressure chambers. Furthermore, the EPR measurements at variable hydrostatic pressures, in conjunction with the temperature variations, impose additional technical difficulties.

Generally, the topology of the high pressure EPR system requires to attach the microwave pathway from the spectrometer bridge (usually a rectangular waveguide) to the upper part of the pressure cell. For a typical, X-Band operating device, the diameter of the microwave matching element (rectangular-to-cylindrical waveguide adapter) is comparable to the diameter of the pressure cell.

In such case, the pressure capillary has to be fastened either to the bottom plug of the pressure cell, or can be attached laterally to the cell body.

While adapting our high pressure EPR system for operation at low (cryogenic) temperatures with the use of the Oxford Instruments gas-flow top-loaded Helium cryostat, the solution with the CuBe capillary attached askew to the cell wall seemed to fulfil the topology requirements (Fig. 1). However, this type of capillary attachment revealed considerable technological problems. Significant disadvantages in operation, especially while assembling the system, have also been found.

## Technical problems and solution

As mentioned above, for the reported EPR pressure cell assembly, there are two possibilities of mounting the capillary: (i) directly to the cell body (laterally or straight) or (ii) to the bottom plug of the cell. Both solutions have some advantages and shortcomings.

(i). Mounting the capillary tube to the cell body encounters significant technical problems. When mounted, the capillary is screwed into a threaded bore and tightened with a solder which requires that the cell body has to be heated up and kept within a rather narrow temperature range. Temperatures from beyond this range can either make the connection untight or influence

mechanical properties of the cell body material.

(ii). Mounting the capillary to the plug has been widely applied in high pressure cells. However, if only the bottom plug is available, a special solution is necessary: the capillary, mounted to the bottom plug, must form a  $180^\circ$  bend below the cell in order to get out from the cryostat through the cap (Fig. 1).

This configuration reveals another shortcoming: when working at cryogenic (liquid Helium) temperatures, the capillary bend may hinder pressure transmission to the cell. An electric heater seems to be a good solution in this case.

In the first stage of the system design, the capillary tube was mounted askew to the cell body. (This askew location of the capillary attachment to the cell body is depicted by dotted lines in Fig. 1.) When tested, the cell assembly worked properly to the maximum pressure of 500-600 MPa only. For higher pressures leaks occurred. Furthermore, the cell with the askew assembly of the capillary, appeared to be inconvenient when assembling with the cryostat insert.

In the further development of the EPR pressure system, the capillary was attached straight to the top of the cell body. This time the capillary was screwed into a straight machined threaded bore at the top of the cell body. An additional skew bore was machined for connecting to the central "main" hole of the cell.

With this capillary attachment the cell worked properly up to 0.4-0.5 GPa but when pressurised up to about 0.6 GPa, a break occurred.

When analysed the case, two main reasons of the break were found. Firstly, the two additional bores, rather long and exposed to the full pressure, significantly decreased the strength of the cell. Secondly, there appeared to be a local material weakening due to technological defect.

For the final version of the system, we adopted the solution with the capillary attached to the bottom plug of the cell. As mentioned, for this case a  $180^\circ$  capillary bend was necessary for connecting the cell to the gas compressor. To prevent the difficulties of pressure transmission through the

capillary bend at low temperatures, an electric heater attached to the capillary bend, was provided.

For manufacturing the capillary bend, a non-hardened capillary tube OD/ID 3/0.3 mm was used. After machining and shaping, the capillary bend was hardened and then attached to the bottom plug of the cell.

This solution appeared to be successful. In the pressure tests, the cell assembly worked properly without any leakage up to 900 MPa, *i.e.* more than 110% of the assumed maximum pressure.

After the pressure tests, the cell was equipped with the elements of the microwave structure, as described previously [2,4], as well as with the semiconductor pressure gauge - InSb crystal, and then successfully passed a new series of pressure tests up to 900 MPa.

For adapting the cell to the Oxford Instruments gas-flow top-loaded Helium cryostat, a complete gas-flow insert was designed and manufactured, incorporating cryostat cap equipped with several feed-throughs for the X-Band wave guide, pressure capillary, 4 mm quartz rod for cavity coupling and tuning, as well as several feed-throughs for electric wires (for the modulation loop, semiconductor pressure gauge, and thermocouples).

The capillary was equipped with the electric resistance heater, wound around the bend. Outside the cryostat, ca. 10 cm above the cap, the coupling element was attached to the pressure capillary for connecting to the gas compressor.

Unipress Gas Compressor U11 1500 MPa was used for pressurising the EPR cell through a 3 m long, OD/ID 3/0.3 mm flexible CuBe capillary tube.

The entire measuring system worked properly at room and Nitrogen temperatures. However at liquid Helium temperatures, even with the heater, some problems of pressure transmission through the capillary bend occurred.

Recently, the whole assembly has been successfully used for studying the spin dynamics under high hydrostatic pressure in disordered conducting polymers [5].

### Acknowledgements

The development of the system resulted from the order from the Swiss Federal Institute of Technology Lausanne

### References

1. W. M. Walsh and W. Blombergen, *Phys. Rev.* 107, 904 (1957).
2. M. Jaworski, K. Chęciński, W. Bujnowski, *Rev. Sci. Instr.* (1978) 49, 383.
3. J. Stankowski, A. Galazewski, M. Krupski, S. Waplak, *Rev. Sci. Instr.* (1976) 47, 255
4. A. Sienkiewicz, M. Jaworski, *High Pressure Research* (1990) 5, 877.
5. O. Chauvet, A. Sienkiewicz, L. Forro and L. Zuppiroli: High Pressure Electron Spin Dynamics in Disordered Conducting Polymers; to be published in *Phys. Rev. B* (1995).

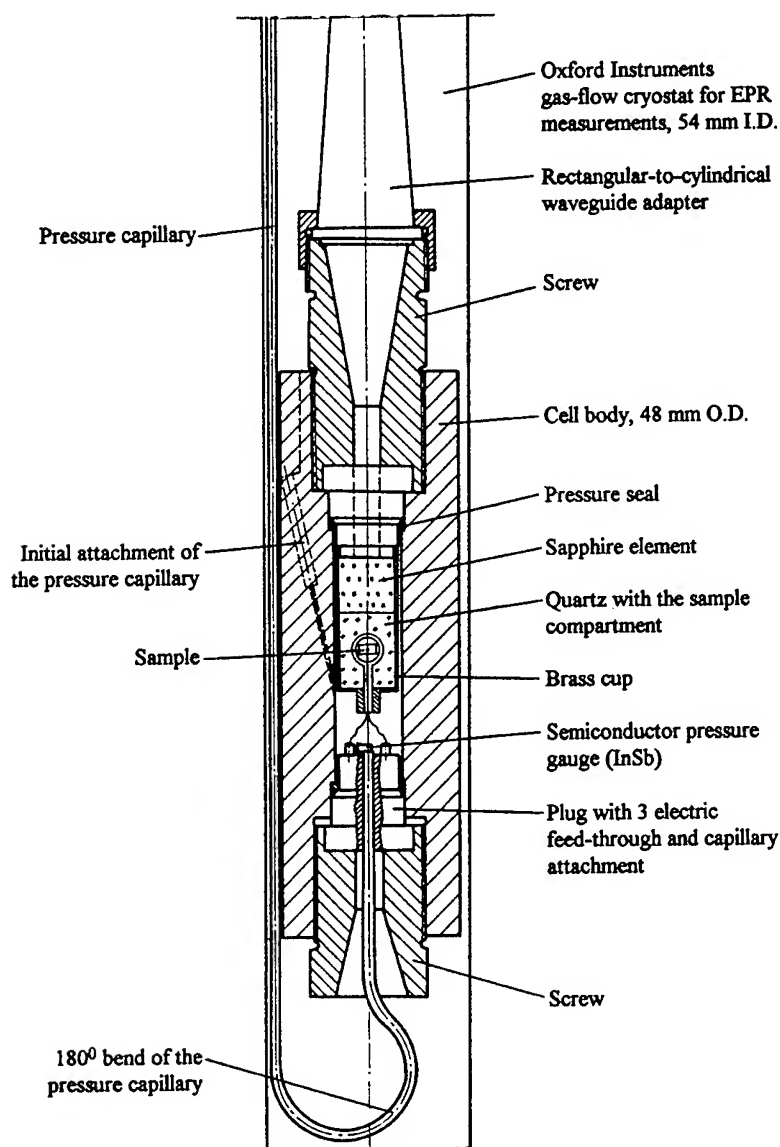


Fig. 1. Assembly for the EPR measurements at high pressure and low temperature

# INCREASING IN LIMIT LOAD OF THICK-WALL CHAMBERS BY DESIGNING PLUGS - PARTICULARLY OPTICAL PLUGS

JACEK ARABAS\*, JANISŁAW ZWOLIŃSKI\*\*

\*High Pressure Research Center

Polish Academy of Sciences

01-142 Warszawa, Sokołowska 29/37, Poland

\*\*Institute of Aeronautics and Applied Mechanics

Warsaw University of Technology

00-665 Warszawa, Nowowiejska 22/24, Poland

## ABSTRACT

High pressure chambers usually have one or more entrance holes closed with plugs, such as optical windows, plugs with electrical lead-throughs, plugs with tubing and others. Such chambers have enormously reduced limit load. The main purpose of these investigations was to increase limit load of the thick-wall pressure chamber by protecting edge of the entrance hole against plastic flow of the wall material in the hole. For this effect it is assumed that the chamber is a sphere with two coaxial holes closed with conical plugs - spherical sector. The plugs are fixed to the appropriate fasteners. We have shown that supporting the edge of a hole with a plug allows enormous increasing of bursting pressure even up to many times the elastic limits of the chamber material. We are going to consider the use of our "supporting plugs" particularly for optical chambers. The appropriate prototype has been tested. All equations indicated in this paper have been confirmed by finite element analysis.

To support maximum pressure, a thick-wall chamber should take the shape of the sphere. Limit load of so designed chamber is twice the limit load of the typical cylindrical thick-wall chamber and is given by

$$\bar{p}_L = 2\ln k \quad (1)$$

where  $\bar{p}_L = p_L/\sigma_Y$  is pressure normalised to the yield stress  $\sigma_Y$  and  $k$  is the ratio of outside to inside diameter.

High pressure chambers usually have one or more holes closed with plugs, such as optical windows, plugs with electrical lead-throughs, plugs with tubing and others. Such chambers have enormously reduced limit load.

We have derived equations that describe the variations of the principal stresses throughout the wall of spherical chamber with a free conical hole. Applying these equations we have defined the highest pressure  $p_L$ :

$$\bar{p}_L = k - 1 \quad \text{for } 1 < k \leq 2 \quad (2)$$

$$\bar{p}_L = 1 \quad \text{for } k > 2 \quad (3)$$

The main purpose of these investigations was to increase the limit load of the thick-wall chamber with holes by protecting edge of hole against plastic flow of the wall material. For this effect it is assumed that the chamber is a sphere with two coaxial holes closed with conical plugs - spherical sector. The plugs are fixed to the appropriate fasteners. Limit load of the chamber designed in such a way is given by

$$\bar{p}_L = 2\ln k - (2\ln 2 - 1) \quad \text{for } k \geq 2 \quad (4)$$

## Limit load of spherical thick-wall chamber with conical holes - analytical solution.

Figure 1 shows a schematic diagram of a spherical high pressure chamber with two coaxial holes. Inside radius of the chamber is  $a$ , and outside radius is  $c$ . Inner surface of the chamber is loaded with pressure  $p_a$ , outer surface is unloaded. Conical holes are closed with fitted, non-deforming, conical plugs - spherical sectors. Each plug closes the hole from the inner surface of the chamber to the spherical surface with radius  $b$ . Figure 2 shows a spherical co-ordinate system and stresses in this system.



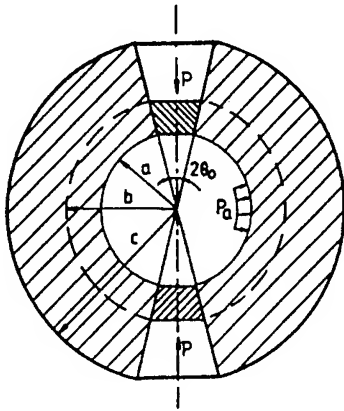


Figure 1: Schematic diagram of the spherical high pressure chamber

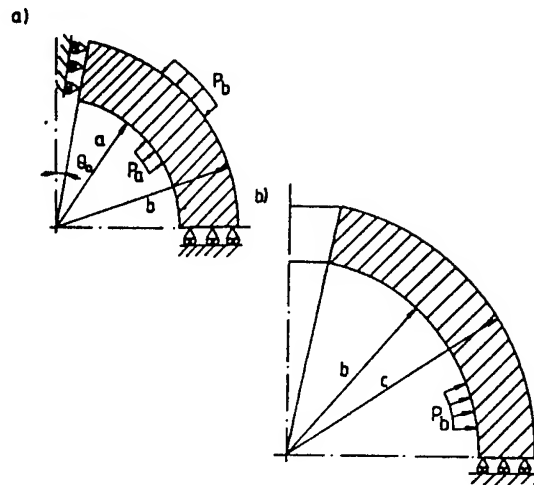


Figure 3: Schematic diagram of the division of the chamber in two shells: a) internal and b) external

So, we have an additional boundary condition for both shells. Finally, using Tresca yield conditions we can find static admissible stress state in the external and internal shells. Applying these equations and the boundary condition we have defined the highest pressure of spherical chamber with conical free hole and with holes closed with conical supporting plugs.

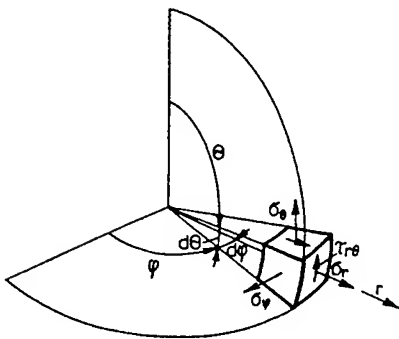


Figure 2: Spherical co-ordinate system and stresses in this system

The stresses must satisfy a static equations and boundary conditions. Taking into account the boundary conditions we can divide the chamber along the radial coordinate  $r = b$  in two thick-wall shells in figure 3:

- internal, loaded by internal pressure  $p_a$  and external pressure  $p_b$ ,
- external, loaded by pressure between the shells  $p_b$ .

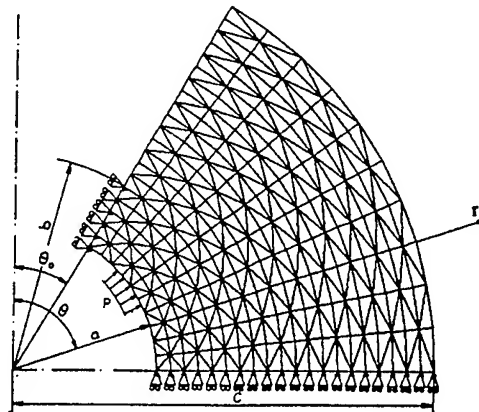


Figure 4: FEM mesh used in calculations

### Limit load of spherical thick-wall chamber with conical holes - finite element method analysis.

All equations indicated in this paper have been confirmed by finite element analysis. An IBM PC program MINIRES was applied [2], [3]. Figure 4 shows FEM mesh used in calculations. Figures 5,6 show stress distribution respectively for elastic and plastic limit state, and figure 7 shows plastic area at pressure close to the limit load.

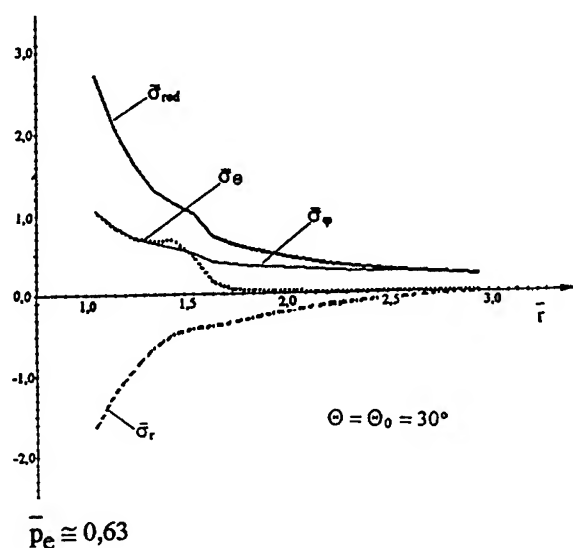


Figure 5: Stress distribution for elastic state (edge of the hole)

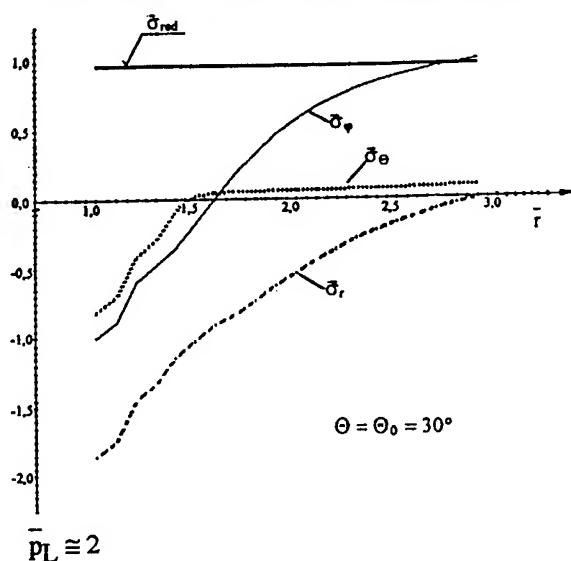


Figure 6: Stress distribution for plastic limit state (edge of the hole)

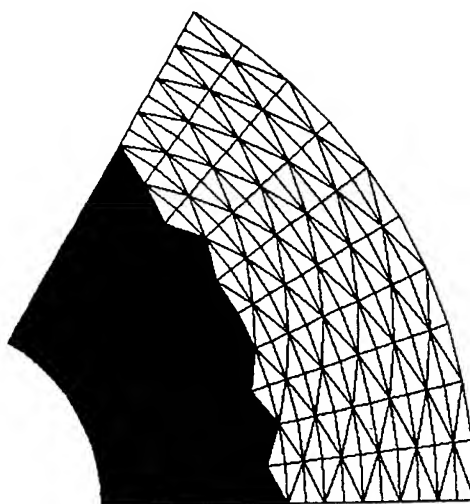


Figure 7: Plastic area at pressure close to the limit load

### Conclusions

We have shown that supporting the edge of a hole with a plug allows us to increase the bursting pressure to a surprising degree - many times the elastic limits of the chamber material. Also limit load does not depend on the quantity of the holes. We are going to consider the use of our "supporting plugs" particularly for optical chambers. The appropriate prototype has been tested.

### References

1. W. F. Sherman and A. A. Stadtmuller, *Experimental Techniques in High-Pressure Research*, John Wiley & Sons Ltd, Chichester, New York, Brisbane, Toronto, Singapore, 1987.
2. J. Zwoliński, G. Bielawski, *Optimizational approach to the elasto-plastic analysis*, Euromech 1st European Solid. Mech. Conf., Munchen, 1991.
3. J. Zwoliński, *Min-Max approach to shakedown and limit load analysis for elastic perfectly plastic and kinematic hardening materials* in Z. Mróz et al. (eds.), *Inelastic Behaviour of Structures under Variable Loads*, Kluwer Academic Publishers, Dordrecht, Boston, London, 1995.
4. J. Arabas, J. Zwoliński, Patent Application P307489, filled 1995.
5. M. Dudziak, A. Seweryn, M. Siemieniuk, J. Zwoliński, *Analiza elementów konstrukcyjnych metodami nośności granicznej*, Wydawnictwo Politechniki Poznańskiej, Poznań, 1995.

## MINIATURE UNIVERSAL HIGH PRESSURE CLAMP CELL

A. V. Kornilov, V. A. Sukhoparov, and V. M. Pudalov  
*Institute for High Pressure Physics, Troitsk, Moscow District, 142092, Russia*

### Abstract

We describe a miniature non-magnetic low-temperature hydrostatic pressure cell for transport and optical measurements at pressure up to 3 GPa. Combination of new strong non-magnetic materials and a new approach to constructing the optical inputs allowed us to minimise the dimensions, to expand the wavelength range, and to enhance the optical signal more than by a factor of 10. The ratio of the optical input diameter to that of the sample space approaches the maximal value 1. The sample space diameter is 3.2 mm, the outer diameter of the cell is 18 mm, and its overall length is 44 to 55 mm.

### Introduction

There are few specific requirements for high pressure cells operating at low temperatures and in the presence of magnetic field. They have to be made of non-magnetic materials, to be rather compact (in order to fit the small bore of magnets and that of dilution refrigerators), and to provide electrical and optical access to the sample space. In this paper we present the new design of the universal piston-cylinder type pressure cell. At an outer diameter of 18 mm, it operates up to 3 GPa and is suitable for both transport and optical measurements in the wide wavelength range, from 140 nm to 7 mm.

### New approach to the optical input design: Piston-plug pressure cell.

The main feature of the described pressure cell is the new design of the optical inputs. In order to provide optical access into a piston-cylinder type cell, the Poulter window [1,2] and its modifications [3] are commonly used. This type of the window is shown schematically in Fig. 1,a. The thick transparent plug shuts the optical hole, and no additional sealing is necessary since the contact pressure is greater than the hydrostatic pressure. This is in accord with the unsupported area principle. The hole diameter,  $w$ , depends on the

maximal pressure in the cell. For 3 GPa and a sapphire window, the ratio of  $w/d$  must be less than

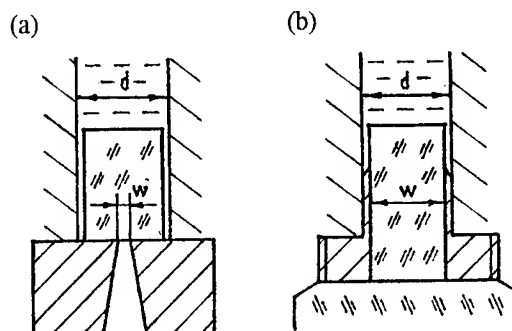


Fig. 1. Schematic view of the optical inputs: (a) "Poulter window",  $w/d \ll 1$ ; (b) "Piston-plug",  $w/d \approx 1$ .

1/6 [4]. In our design, the sapphire piston plays the role of the window, as shown in Fig. 1,b.

This new approach provides two important advantages of the "piston-plug" cell over the regular "Poulter window":

- (1) As  $w/d \rightarrow 1$ , the optical signal enhances. The enhancement factor in the novel design is about  $(w/d)^{-2} \sim 36$  for a typical ratio  $w/d = 1/6$ , optimised at  $P = 3$  GPa for the Poulter window.
- (2) The transparent pistons, in contrast to the regular window, can be plugged in from both sides of the cell.

The above advantages make it possible to use the cell of the outer diameter 18 mm in a wide wavelength range, from 140 nm to 7 mm. Thus,

both transmission and reflection measurements can be done, that allows one to derive all parameters of the sample using the Kramers-Kronig relation. One of the sapphire pistons covered with high-conducting metal film can serve as a resonant cavity in the mm-wavelength band. At a given optical input diameter,  $w$ , the volume of the pressure transmitting medium may be reduced with increasing  $w/d$ -ratio. This becomes especially important for measurements in the far-infrared and sub-mm ranges, where transmitting media are usually strongly absorbing. The transparent pressure cell allows one to use signal detectors outside the high pressure volume, providing their better performance. This is important for detecting small signals in a wide wavelength range.

### Construction of the pressure cell

Schematic cross-section of the optical version of the piston-plug pressure cell is presented in Fig. 2. It

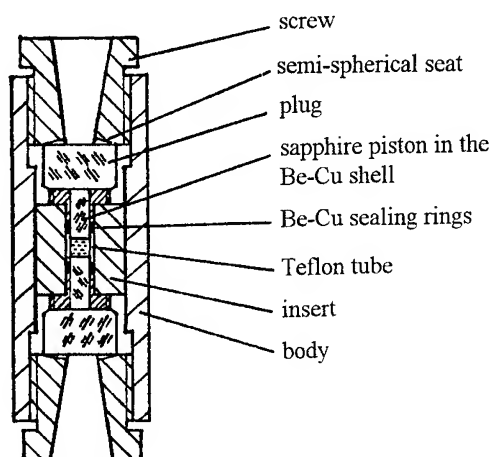


Fig. 2. Schematic cross-section of the pressure cell.

contains two sapphire pistons, two sapphire plugs with semi-spherical adjusting seats, and two fixing screws. The insert with 3.7-mm channel diameter is pressed into the body of 18 mm outer diameter.

For transport measurements one, (or both) of the sapphire pistons with corresponding sapphire plugs are replaced by a regular metal plug with electrical leads [5]. As far as we know, this cell has the smallest dimensions at the given sample space and

the maximal pressure of 3 GPa. The miniature cell design is provided by a number of factors:

- (1) Strong non-magnetic alloys were used instead of the usual Be-Cu bronze. The body was made of Ti-alloy ( $HR_c = 42$ ), and the insert of NiCrAl alloy ( $HR_c = 52$ ).
- (2) The "short piston" approach was used. Since the high pressure is obtained in a very small volume, this small region of the channel is well supported by the insert material.
- (3) A Teflon cell-sealing system was used. As a result, the pressure cell of the outer diameter 18 mm and the inner diameter 3.7 mm operates up to 3 GPa. This is illustrated in Fig. 3 by the loading

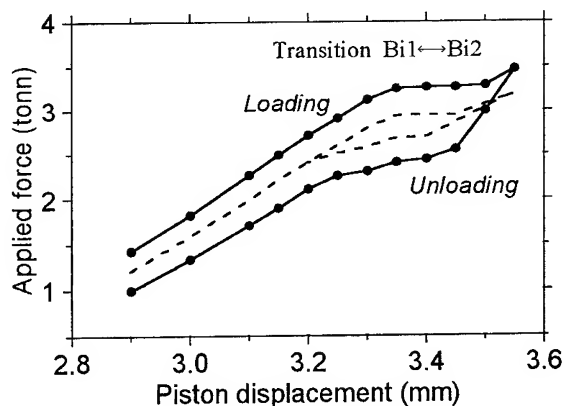


Fig. 3. Loading curve of the cell. Bismuth sample exhibits the phase transition at 2.55 GPa.

curve of bismuth showing the transition  $Bi1 \leftrightarrow Bi2$ . The latter is known [6] to occur at 2.55 GPa. Such a miniature cell can be placed in a magnet not only along the bore axis, but also perpendicular to it. The cell is even suitable for studying angular dependencies in magnetic field by tilting it with respect to the magnetic field direction. Due to the miniature design and small heat capacity, the cell requires small amount of liquid helium for cooling and can be used in a dilution refrigerator or other small cooling power systems.

This work was supported in part by the Russian Foundation for Fundamental Research (grant #94-02-04941), by Nederlandse Organisatie voor Wetenschappelijk Onderzoek (grant #07-13-217), by the International Science Foundation (grant MUG300), and by the Russian Ministry for Science and Technical Policy.

## References

1. T. C. Poulter, *Phys.Rev.* **40** (1932) 860.
2. E. Walley, A. Lavergne and P. T. T. Wong, *Rew.Sci.Instrum.* **47** (1976) 845..
3. M. I. Eremets and A. N. Utjuzh, *Bull.Am.Phys.Sos.*, Ser. I, **38** (6) (1993) 1531.
4. see: H. C. Alt and J. Kalus, *Rew.Sci.Instrum.* **53** (8) (1982) 1235, and the references therein.
5. E. S. Itskevich, A. N. Voronovskii, A. F. Gavrilov and V. A. Sukhoparov, *Pribori i Tekhn.Exper.* **7** (1966) 161; [*Instrum.and Exper. Techn.* **7** (1966)].
6. *Progress in Very High Pressure Research* (New York, 1961).

### **III Pressure Metrology**

# LIMITS IN PRESENT STATIC PRESSURE METROLOGY

W.B. HOLZAPFEL

Fachbereich Physik, Universität-GH Paderborn  
D-33095 Paderborn, Germany

Various new luminescence sensors are compared with the wellknown ruby luminescence pressure sensor to give recommendations for the use of specialized sensor materials for special applications and for further developments on more precise and more versatile new sensor materials. These sensors may reach a precision or resolution in pressure measurements of better than 5 MPa corresponding to 500 ppm at 10 GPa. The problem of their absolute calibration is discussed with respect to present accuracies in the determination of equation of state data by X-ray diffraction on reasonable standard materials like Al, Cu, Ag, Au, Pt, Mo, or W.

## The problem

While accurate pressure determinations with an (absolute) accuracy of better than 160 ppm can be performed by force per area measurements to 500 MPa for instance[1], at higher pressures only high precision and high resolution but not the same high accuracy can be maintained at present times with different secondary gauges or sensors[2], whereby new luminescence sensors offer much higher precision than the most commonly used ruby sensor[3] not only at ambient temperature but especially at higher temperatures[4-13], and progress towards better (absolute) accuracies in the extended static pressure range to 100 GPa and above can be obtained from a better understanding of the physical properties used for the realization of the pressure scale as for instance by the comparison of the "real" behavior of simple solids with some "ideal" behavior[14], as it was used long ago for the realization of the absolute temperature scale by measurements of equations of states (EOS) on "real" gases and comparison with the "ideal" gas behavior.

## EOS for ideal and real solids

Besides pressure  $p$ , volume  $V$ , and temperature  $T$ , the EOS for the ideal gas contains also the

universal gas constant  $R$  and the mole number  $n$  as free parameters. Similarly, the EOS for ideal solids includes the mole number  $n$ , the atomic number  $Z$  (or an appropriate average value for alloys and compounds[15]) and three universal constants: Avogadro's number  $N_A$ , the Fermi gas constant  $a_{FG}=23.36905(2) \text{ nm}^5 \text{ MPa}$  to evaluate the Fermi gas pressure at ambient condition,  $p_{FG0}=a_{FG} \cdot (Z \cdot N_A \cdot n/V_0)^{5/3}$ , and an average electron screening parameter[14]  $\beta=5.76 \text{ nm}^{-1}$ .

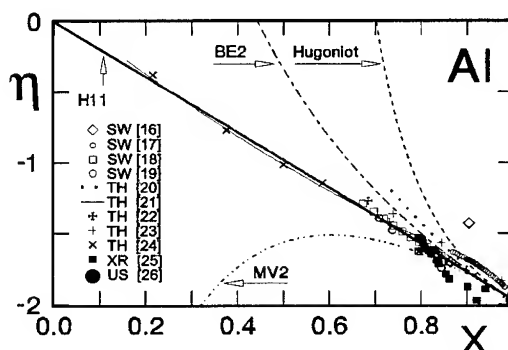


Fig.1 EOS data for Al at room temperature in  $\eta$ - $x$  scaling explained in the text with theoretical (TH), shock wave (SW), X-ray (XR), and ultrasonic (US) data from different sources [16-26-].

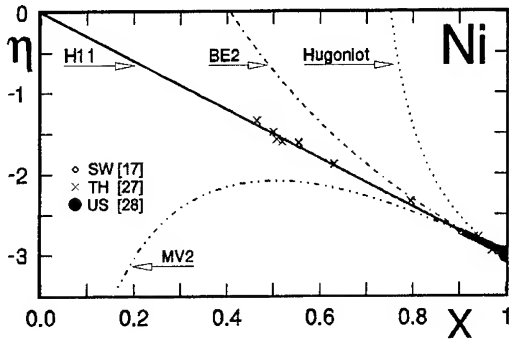


Fig.:2 EOS data for Ni at room temperature in  $\eta$ - $x$  scaling explained in the text with theoretical (TH), shock wave (SW), and ultrasonic (US) data from different sources [17,27,28].

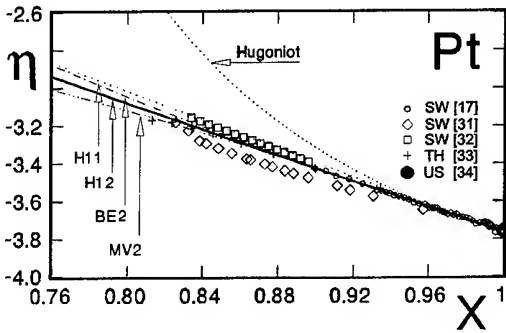


Fig.: 3 EOS data for Pt at room temperature in  $\eta$ - $x$  scaling explained in the text with theoretical (TH), shock wave (SW), and ultrasonic (US) data from different sources [17, 31-34].

With these parameters together with the relations  $v_0 = V_0/(N_A \cdot n)$ ,  $c_0 = \beta(Zv_0 \cdot 3/(4\pi))^{1/3}$ ,  $K_0 = p_{FG0}/(3 \cdot \exp c_0)$ , and  $x = (V/V_0)^{1/3}$  the EOS for ideal solids is then given by [14]:

$$p = 3 K_0(1-x)/x^5 \cdot \exp(c_0(1-x)) \quad (1).$$

Since only a few solids come close to this average behavior, one can take in a first step just  $\beta$  or  $c_0$  as the next free parameter (in addition to  $Z$ ,  $V_0$ , and  $n$ ) to take into account the exact

experimental value for the bulk modulus at ambient condition  $K_0$ . Its pressure derivative  $K_0' = 3 + (2/3) \cdot c_0$  is thereby still fixed (or correlated) to the value of  $K_0$ . This first order EOS form (labeled H11) describes already perfectly the data for many "simple" solids as shown in fig. 1 and 2 for Al and Ni at ambient temperature, where the data are scaled [14] according to  $\eta = \ln(p/p_{FG0}) + 5 \ln x - \ln(1-x)$  which leads to the linear relation

$$\eta = c_0 \cdot x \quad (2)$$

for the form H11.

Especially for Ni, where theoretical data extend into the multi-TPa region, strong deviations can be noticed in fig. 2 for the common second order Birch (BE2) and Vinet et al. (MV2) forms as previously discussed [29,30]. Other solids, like for instance Pt, Cu, Ag, Au, Mo and W, with their reduced initial slopes as represented in fig. 3 and 4 just for Pt and Au, are not quite that "simple" but require one more free parameter to represent independently the value for  $K_0'$ . By replacing  $c_0$  in (1) and (2) by  $c_0 + x \cdot c_2$  with  $c_2 = (3/2)(K_0' - 3) + \ln(3K_0/p_{FG0})$  one obtains [14] a second order form (labeled H12 in fig. 3 and 4) which describes perfectly also these data and shows in contrast to the forms BE2 and MV2 the correct asymptotic behavior for  $x \rightarrow 0$ .

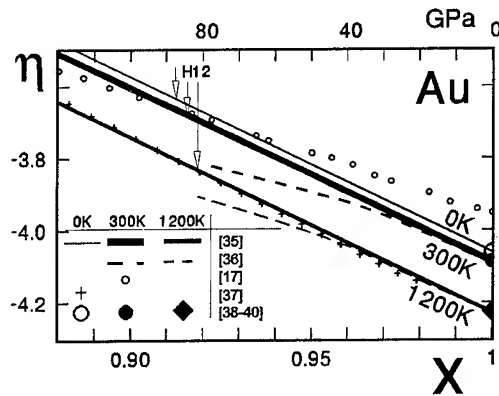


Fig.: 4 EOS data for Au with three isotherms in  $\eta$ - $x$  scaling explained in the text with theoretical (TH), shock wave (SW), and ultrasonic (US) data from different sources [16-26].



**Table 1:** Parameters for pressure determination by EOS measurements using various fcc and bcc metals as calibrants with the EOS form H12 and the reference temperature  $T_R = 300\text{K}$ . Numbers in brackets represent the uncertainties of the last significant digit substantiated by inspection of the respective literature[28,34-45].

Material	$a_{0R}/\text{pm}$	$K_{0R}/\text{GPa}$	$K'_{0R}$	$\alpha_{0R} \times 10^6 \text{K}$	$\delta_{\alpha R}$
Al	404.98(1)	72.5(4)	4.3(5)	23.0(4)	5.5(11)
Cu	361.55(1)	133.2(2)	5.4(2)	16.6(3)	6.1(6)
Ag	408.62(1)	101.0(2)	6.2(2)	19.2(4)	7.1(6)
Au	407.84(1)	166.7(2)	6.3(2)	14.2(2)	7.2(6)
Pd	388.99(1)	189(3)	5.3(2)	11.6(4)	6.0(11)
Pt	392.32(1)	277(5)	5.2(2)	8.9(4)	5.9(11)
Mo	314.73(1)	261(5)	4.5(5)	5.0(4)	5.2(14)
W	316.47(1)	308(2)	4.0(2)	4.5(4)	4.7(11)

Since only minor oscillations around the simple straight line interpolation of  $\eta$  between  $\eta(0) = 0$  and  $\eta_0 = \eta(1) = -c_0$  are possible for "regular" solids, where band structure calculations can also produce the same smooth variation [21,24,27,33,37], the form H12 incorporates more information on the behavior of solids under pressure than the other second order EOS forms (BE2 or MV2) and guarantees therefore minor deviations in extrapolations of experimental data into the TPa region than any other form[29,30].

With these consideration in mind table 1 presents now the "best" values for the free parameters of the form H12 to be used in pressure determinations by lattice parameter measurements. In fact, comparative lattice parameter measurements on various couples of these proposed calibrants under pressure could well reduce the uncertainties given for the values of  $K'_0$ , however, almost hydrostatic conditions and much higher precision compared to one such attempt[46] are necessary to result in significant progress with the potential[2] to improve the accuracy of the pressure scale to better than 3% if lattice parameters of these reference substances are measured (with synchrotron radiation) with an accuracy of better than 10ppm obtainable only

with well annealed samples[47]. One should note also that the estimate[48] of a possible accuracy of  $\Delta p/p = 20$  ppm at 1 GPa for an absolute pressure scale to be established by correlated measurements of ultrasonic travel times and X-ray densities was obviously base on a logical error, assuming a possible accuracy of 100 ppm not only for the density  $\rho$  but also for its change  $\Delta\rho$  under pressure which would require in that case an accuracy of  $\Delta\rho/\rho < 7$  ppm in contrast to their statements and difficult to achieve[2].

### Thermal effects

As illustrated in fig. 4, thermal effects are well represented also by the form H12 with temperature dependent values for  $V_0$  and  $K_0$  (with minor corrections for  $K'_0$ ). At elevated temperatures ( $T > 300$  K), where the thermal volume expansion coefficient  $\alpha$  and its logarithmic volume dependence  $\delta_\alpha = \partial \ln \alpha / \partial \ln V|_T$  are almost independent of  $T$ , the parameters given in table 1 can be useful to derive the complete (temperature dependent) EOS forms[35] also for pressure determinations at elevated temperatures.

Table 2: Parameters for pressure determinations by luminescence measurements using different sensor materials. Numbers in brackets represent the accuracy for ruby and the precision with respect to the ruby scale in all other cases.

Material	$\lambda$ (nm)	$\frac{d\lambda}{dp}$ $\left(\frac{\text{nm}}{\text{GPa}}\right)$	$\frac{d\lambda}{dT}$ $\left(\frac{\text{pm}}{\text{K}}\right)$	$\frac{dp}{dT}$ $\left(\frac{\text{MPa}}{\text{K}}\right)$	$\frac{\Gamma/10}{d\lambda/dp}$ (MPa)	Transition	Ref.
Cr <sup>3+</sup> :Al <sub>2</sub> O <sub>3</sub>	694.2	365(9)	6.2(3)	18.6	204	<sup>2</sup> E → <sup>4</sup> A <sub>2</sub>	doubl. 3
Eu <sup>3+</sup> :YAG	590.6	.197	-.54	-2.7	140	<sup>5</sup> D <sub>0</sub> → <sup>7</sup> F <sub>1</sub>	doubl. 4
Eu <sup>3+</sup> :LaOCl	578.7	.25	-.5	-2	100	<sup>5</sup> D <sub>0</sub> → <sup>7</sup> F <sub>0</sub>	singl. 5
Sm <sup>2+</sup> :SrB <sub>4</sub> O <sub>7</sub>	685.4	.255	-.1	-.4	59	<sup>5</sup> D <sub>0</sub> → <sup>7</sup> F <sub>0</sub>	singl. 7
Sm <sup>2+</sup> :SrFCl	690.3	1.106(5)	-2.36(3)	-2.1	17	<sup>5</sup> D <sub>0</sub> → <sup>7</sup> F <sub>0</sub>	singl. 10
Sm <sup>3+</sup> :YAG	617.8	.308(2)	.2	.7	440	Y1	mult. 6
	616.1	.248(2)	.1	.4	500	Y2	6
	612.3	.283(3)	-	-	3000	Y3	11
	603.1	.175	-	-	-	Y4	doubl. 13
Pr <sup>3+</sup> :LaOCl	660.9	.87	1.2	1.3	86	<sup>3</sup> P <sub>0</sub> → <sup>3</sup> F <sub>0</sub> (A <sub>1</sub> )	singl. 49

### Luminescence sensors

Usually luminescence measurements under pressure are much more convenient than lattice parameter determinations, and therefore possible improvements with respect to the ruby luminescence sensor[3] stimulate still present research activities[10-13,49]. Interesting parameters are thereby not only absolute pressure and temperature shifts of the luminescence wave length, table 2, but also their ratio  $dp/dT$  and an estimate of the precision in the pressure measurements characterized by the pressure  $\Delta p = (\Gamma/10)/(d\lambda/dp)$  corresponding to a shift of 10% of the line width  $\Gamma$ , which is easily measurable for single lines (and computer fits may result even in 10 times better resolution). However, for strongly overlapping double or multiple lines, larger uncertainties may be encountered. Inspection of table 2 illustrates that some of the sensors show much weaker temperature sensitivities than ruby (and weaker intensity decrease with temperature not quantified in this table). The excellent resolution of 17MPa for the single line of Sm<sup>2+</sup>:SrFCl is largely maintained under pressures up to 30 GPa

due to the partial compensation of the line broadening by the nonlinear increase in the shift[10]. However, quenching of the intensity limits the application of this sensor to  $p \leq 30$  GPa and  $T \leq 600$  K but this type of limitations can be avoided by the Sm<sup>3+</sup>:YAG sensors which shows on the other hand much lower sensitivity.

Thus the search is still going on for a sensor with a resolution of possibly 10MPa, small temperature effects, and no quenching or structural instabilities to pressures in excess of 200GPa and temperatures between 0 - 1000 K. Some sharp line luminescence of Pr<sup>3+</sup> in stable host materials may ultimately satisfy these demands[49].

### Conclusion

There are good physical arguments to expect still much progress in accuracy and precision of pressure measurements in the 1 - 500 GPa region.

## References

- [ 1 ] V.E. Bean and G.F. Molinar, *High Pressure Research* **5** (1990) 804
- [ 2 ] W.B. Holzapfel, in *Landolt-Börnstein "Units and Fundamental Constants in Physics and Chemistry"*, ed. J. Bortfeldt and B. Kramer (Springer, 1991) p. 2.177
- [ 3 ] J.D. Barnett, S. Block, G.J. Piermarini, *Rev. Sci. Instrum.* **40** (1973) 1
- [ 4 ] H. Arashi and M. Ishigame, *Jpn. J. Appl. Phys.* **21** (1982) 1647
- [ 5 ] Y. Chi, S. Liu, Q. Wang, L. Wang, and G. Zou *High Pressure Research* **3** (1990) 150
- [ 6 ] N.J. Hess and G.J. Exarhos, *High Pressure Research* **2** (1989) 57
- [ 7 ] A. Lacam and C. Chateau, *J. Appl. Phys.* **66** (1989) 366
- [ 8 ] Y. Chi, S. Liu, W. Shen, L. Wang, and G. Zou, *Physica* **139 & 140B** (1986) 555
- [ 9 ] Y.R. Shen, T. Gregorian, and W.B. Holzapfel, *High Press. Res.* **7** (1991) 73
- [ 10 ] B. Lorenz, A.R. Shen, and W.B. Holzapfel, *High Pressure Res.* **12** (1994) 91
- [ 11 ] H. Yusa, T. Yagi and H. Arashi, *J. Appl. Phys.* **75** (1994) 1463
- [ 12 ] J. Liu and Y.K. Vohra, in *High Pressure Science and Technology*, eds. S.C. Schmidt, J.W. Shaner, G.A. Samara, M. Ross (Am. Inst. Phys., 1993) p. 1681
- [ 13 ] J. Liu and Y.K. Vohra, *Appl. Phys. Lett.* **64** (1994) 3386
- [ 14 ] W.B. Holzapfel, *Europhys. Lett.* **16** (1991) 67
- [ 15 ] L. Knopoff, *Phys. Rev. A* **138** (1965) 1445
- [ 16 ] R.G. McQueen, S. P. Marsh, W.J. Taylor, J.N. Fritz, W.J. Carter, in *High Velocity Impact Phenomenon*, ed. R. Kinslow (Academic Press, New York, 1970) p. 293
- [ 17 ] R.N. Keeler, G.C. Kennedy in *American Institute of Physics Handbook*, ed. D.E. Gray (McGraw Hill, 1972) p. 4938
- [ 18 ] W.J. Nellis, J.A. Moriarty, A.C. Mitchell, M. Ross, R.G. Dandrea, N.W. Ashcroft, N.C. Holmes, R.G. Gathers, *Phys. Rev. Lett* **60** (1988) 1414
- [ 19 ] A.C. Mitchell, W.J. Nellis, J.A. Moriarty, R.A. Heinle, N.C. Holmes, R.E. Tipton, J. *Appl. Phys.* **69** (1991) 2981
- [ 20 ] C. Friedli, N.W. Ashcroft, *Phys. Rev. B* **12** (1975) 5552
- [ 21 ] A.K. McMahan, M. Ross, in *High-Pressure Science and Technology*, ed. K.D. Timmerhaus, M.S. Barber (Plenum, 1979) p. 920
- [ 22 ] B.K. Godwal, S.K. Sikka, R. Chidambaram *Phys. Rev. Lett.* **47** (1981) 1144
- [ 23 ] J.C. Boettger, S.B. Rickey, *Phys. Rev B* **29** (1984) 6434
- [ 24 ] J. Meyer-ter-Vehn, W. Zittel, *Phys. Rev. B* **37** (1988) 8647
- [ 25 ] R.G. Greene, H. Luo, A.L. Ruoff, *Phys. Rev. B* **51** (1995) 597
- [ 26 ] R.C. Lincoln, A.L. Ruoff, *Phys. Rev.* **44** (1973) 1239
- [ 27 ] A.K. McMahan, R.C. Albers, *Phys. Rev. Lett.* **49** (1982) 1198
- [ 28 ] M.W. Guinan, D.J. Steinberg, *J. Phys. Chem. Solids* **35** (1974) 1501
- [ 29 ] W.B. Holzapfel, *High Press. Res.* **7** (1991) 290
- [ 30 ] W.B. Holzapfel, *Physica B* **190** (1993) 21
- [ 31 ] J.A. Morgan, *High Temp.-High Press.* **6** (1974) 195
- [ 32 ] N.C. Holmes, J.A. Moriarty, G.R. Gathers, W.J. Nellis, *J. Appl. Phys.* **66** (1989) 2966
- [ 33 ] AS94 R. Ahuja, P. Söderling, O. Eriksson, J.M. Willis, B. Johansson, *High Press. Res.* **12** (1994) 161
- [ 34 ] G. Simmon, H. Wang, ed. in *Single Crystal Elastic Constants and Calculated Aggregate Properties: A Handbook* (MIT, 1971) p.234
- [ 35 ] W.B. Holzapfel, *J. Phys. Chem. Solids* **55** (1994) 711
- [ 36 ] J.C. Jamieson, J.N. Fritz, M.H. Manghnani, in *High Pressure Research in Geophysics*, ed. S. Akimoto, M.H. Manghnani (Center for Acad. Public, Tokyo 1982) p. 234
- [ 37 ] B.K. Godwal, A. Ng, R. Jeanloz, *High Press. Res.* **10** (1992) 687
- [ 38 ] J.R. Neighbours, G.A. Alers, *Phys. Rev.* **III** (1958) 707
- [ 39 ] Y.A. Chang, L. Himmel, *J. Appl. Phys.* **37** (1966) 3567
- [ 40 ] S.N. Biswas, P. Van't Klooster, N., Trappeniers, *Physica B* **103** (1981) 235

- [41] D.E. Gray ed., *American Institute of Physics, Handbook*, (McGraw Hill, New York (1972)
- [42] R.W.G. Wyckoff, *Crystal Structures* (Interscience, 1963)
- [43] K.A. Gschneidner, Jr., *Solid State Phys.* **16** (1964) 275
- [44] R.C. Weast, M.J. Astle in *CRC Handbook of Chemistry and Physics, 59th edition* (CRC Press, West Palm Beach, 1979) p. D-225
- [45] Yo91 D.A. Young ed., in *Phase Diagrams of the Elements* (University of California Press, Berkeley, 1991)
- [46] L.G. Liu, H. Liu, H. Verbeek, Ch. Höffner, G. Will, *J. Phys. Chem. Solids* **5** (1990) 435
- [47] D.J. Weidner, Y.Wang, Y. Ming, M.T. Vaughan in *High-Pressure Science and Technology*, eds. S.C. Schmidt, J.W. Shaner, G.A. Samara, M. Ross (Am. Inst. Phys., 1994) p. 1025
- [48] A. Yoneda. H. Spetzler, I. Getting in *High Pressure Science and Technology*, eds. S.C. Schmidt, J.W. Shaner, G.A. Samara, M. Ross (Am. Inst. Phys., 1994) p. 1609
- [49] C. Bungenstock, *private communication Paderborn* (1995)

## OPTICAL PRESSURE CALIBRATION BY QUANTUM-WELL SPECTRA

T.P. SOSIN<sup>a,b</sup>, W. TRZECIAKOWSKI<sup>a</sup>, P. STĘPIŃSKI<sup>a,b</sup>, and M. HOPKINSON<sup>c</sup>

*a) High Pressure Research Center "Unipress", Polish Academy of Sciences, 01-142 Warsaw, Poland*

*b) Institute of Physics, Warsaw University of Technology, 00-662 Warszawa, Poland*

*c) SERC Central Facility, University of Sheffield, Mappin Street, Sheffield S1 3JD, UK*

Photoluminescence, absorption, and laser emission from different quantum wells have been studied with the purpose of pressure calibration in the 10 GPa range. We demonstrate that in this range the quantum-well calibration is superior to the commonly used ruby calibration. InGaAs/GaAs strained wells work up to 5 GPa but only in absorption. The InAsP/InP structures work in the 10 GPa range. In all cases we found the same pressure coefficient of the lines at 300 K and at 80 K. We discuss the possibility of using InGaAsP/InP laser diodes as pressure calibrants up to 2 GPa.

### Introduction

Most research in the diamond anvils is performed in the 10 GPa range. The pressure is typically determined from the shift of the R1-R2 doublet in the ruby fluorescence. This method is very accurate at low temperatures but at 300 K the accuracy is around 1 kbar (0.1 GPa) which in some cases may be insufficient. Moreover, the ruby lines are narrow and they shift very little so that high quality spectrometers have to be used and stable temperature conditions have to be maintained. Semiconductor quantum wells (QW) yield very bright photoluminescence (PL) lines at room temperature (and above) and their pressure shift is about two orders of magnitude higher than that of the ruby doublet [1]. The linewidth of the quantum-well PL is about one order of magnitude larger than that of the ruby so that one order of magnitude in the accuracy of the pressure calibration can be gained with the help of less precise spectrometers. The pressure shift of the QW lines is temperature independent. The pressure range for the QW calibration is determined by the phase-transition pressure or by the pressure of the direct-indirect transition in the conduction band, whichever is lower.

In the most studied case of GaAs/AlGaAs wells the pressure coefficient depends slightly on the parameters of the well (thickness and depth) [1-3]. This implies different calibration for different QW samples. There has been very little effort to determine precisely the pressure shift of the lines and to calibrate it against some accurate gauge (ruby is obviously insufficient). Thus we can only demonstrate the potential of the QW calibration in the 10 GPa range but much work is required to make this method practical and widely applicable.

The ideal QW pressure sensor should have the following features: (i) wide pressure range, (ii) narrow and strong line at 300 K, (iii) large pressure

coefficient of the line, (iv) convenient spectral range. The first requirement favours InP-based structures as compared to GaAs-based structures because of the  $\Gamma$ -X crossover in GaAs around 4 GPa. Room-temperature linewidths in good samples are about 15 meV for the wells 5-8 nm wide. The strongest signal in PL is for a multiple QW with 10-20 repetitions while the absorption requires 30-50 wells. The pressure coefficient of the direct gap is in the 70-120 meV/GPa range for most III-V and II-VI semiconductors.

### Experimental

The InGaAs/GaAs sample was grown by MBE on (100) GaAs substrate. It consisted of 50  $\text{In}_{0.14}\text{Ga}_{0.86}\text{As}$  wells (104 Å wide) with 200 Å GaAs barriers. The results for this sample were already presented in [4]. The InAsP/InP sample was grown by MBE and contained three wells of 10 nm width (50 nm barriers) and various InAs content in each well (36%, 40%, and 45%). For the Diamond Anvil Cell (DAC) experiments the samples were etched down to 30  $\mu\text{m}$  thickness. For the experiments with laser emission we used the commercial 1.3  $\mu\text{m}$  diodes by Siemens (SFH4410) - we only cut the window of the package and put it in our optical clamp cell.

Our DAC was filled with argon gas and the pressure was varied in situ both at 300 K and at 80 K. For the studies of laser diodes we used a special Unipress optical clamp cell which works up to 2 GPa.

### Pressure calibration by the absorption lines in InGaAs wells

For the samples with QW lines lying below the bandgap of the substrate (like InGaAs/GaAs, InGaAs/InP, InAsP/InP etc.) it is possible to observe the QW absorption lines on thick samples. In Fig.1 we show (after [4]) the absorption from the

$\text{In}_{0.14}\text{Ga}_{0.86}\text{As}/\text{GaAs}$  sample at 300 K and we compare it with the ruby R1 fluorescence for the same values of the pressure. The ratio of the pressure shift of the line to its width is about 15 times greater

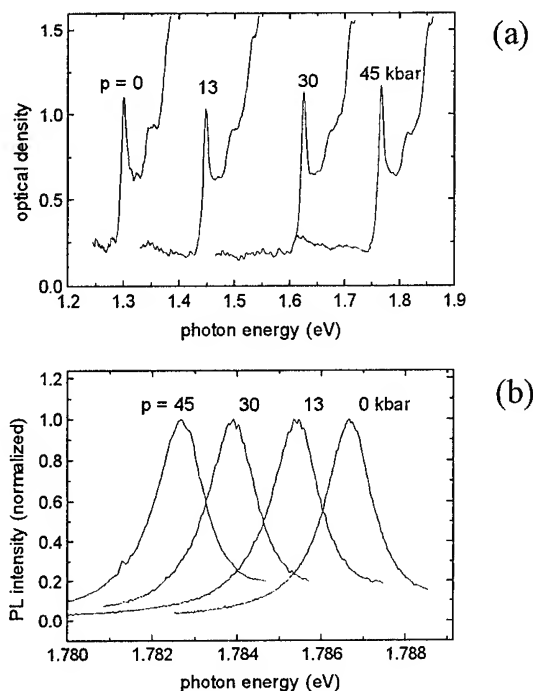


Fig.1 (a) Absorption line at 300 K in  $\text{InGaAs}/\text{GaAs}$  (b) ruby R1 fluorescence line for the same pressures.

for the QW. The pressure limit for this sample was 5 GPa when the direct/indirect transition took place. We observed the same pressure shift of the QW line at 300 K and at 20 K [4]. No PL could be seen at room temperature [5]. Absorption is usually less convenient than PL but the power on the sample is low and there are no heating effects. For metrological purposes it could be of interest. Another interesting optical quantity is the photorefectance which yields narrower lines than absorption but is more difficult to measure in the DAC [6].

### Photoluminescence in $\text{InAsP}/\text{InP}$ wells

Very deep wells can be obtained in case of the strained  $\text{InAsP}$  grown on  $\text{InP}$ . The PL spectra of the sample described above (three 10 nm wells) were measured up to 10 GPa at 300 K and at 80 K (Fig.2). At 300 K the spectrum improves with pressure while at 80 K it deteriorates at pressures above 8 GPa. This is probably due to nonhydrostaticity in the DAC at low temperature. The QW spectra are more sensitive

to nonhydrostatic conditions than the ruby. From the side of the substrate we observed a broad PL line at the  $\text{InP}$  bandgap energy. The room-temperature results are summarized in Fig.3. For this sample, within the experimental accuracy, we observed no difference between the pressure shift of different lines. Both the QW lines and the substrate line (Fig.3) could be fitted with the quadratic expression

$$\Delta E(p) = 83p - 2p^2, \quad (1)$$

where the energy is in meV, pressure in GPa. This is

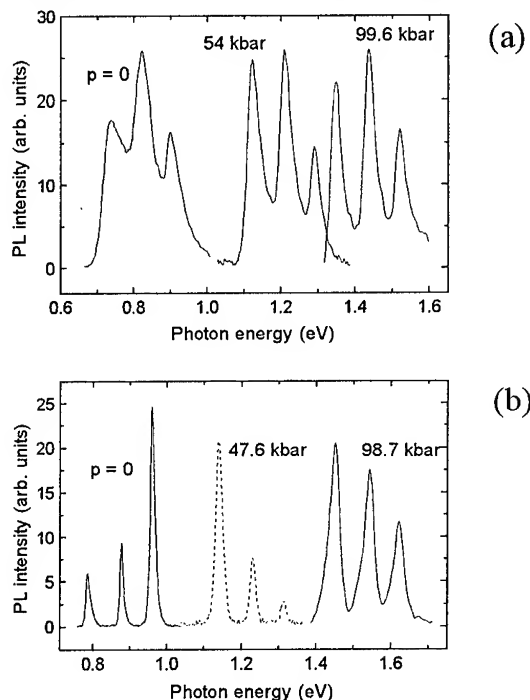


Fig.2 PL spectra of three  $\text{InAsP}/\text{InP}$  wells: (a) at 300 K, (b) at 80 K

in agreement with the bulk  $\text{InP}$  results of [7]. In Fig.4 we compare the pressure evolution of the middle line (two others subtracted from the spectra) with the pressure evolution of the lorentzian fit of the R1 ruby line. It should be stressed that our QW sample was not optimised as a pressure calibrant (a multiple QW would yield a much stronger signal, smaller linewidths can be obtained etc.). Yet the superiority of the QW calibration is visible. Around 10.5 GPa the structural phase transition occurs in  $\text{InP}$  and the QW lines disappear.

### Calibration by the shift of the laser-diode emission

Single-mode laser diodes have extremely narrow and strong emission lines which shift with pressure

similarly to the PL lines. More details on our studies of different types of laser diodes under pressure are given in a separate paper at this conference [8]. For the purpose of pressure calibration the laser diode

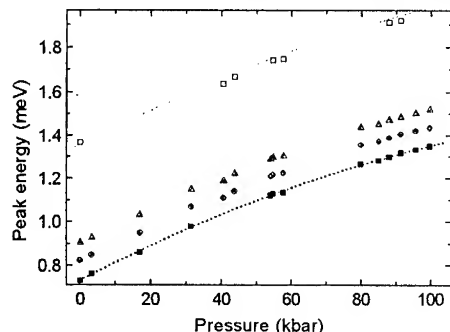


Fig.3 Position of the 3 peaks shown in Fig.2a vs pressure. For some pressures the position of the InP substrate line is also shown. Lines correspond to Eq.(1).

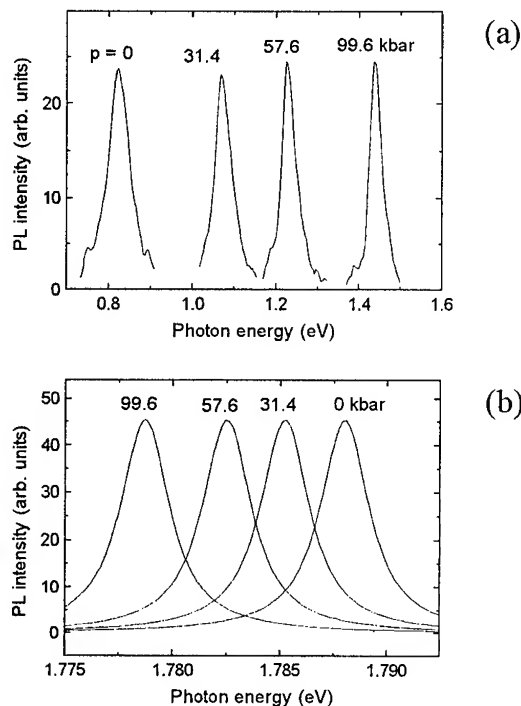


Fig.4 Comparison of the pressure shift of the InAsP/InP line (a) with the shift of the fit to the R1 line of the ruby (b) in the 10 GPa range.

emission has several drawbacks. First of all, the current has to be supplied and this is very difficult in the diamond-anvil cell [9]. Secondly, the emission spectrum is sensitive to the current and very often the threshold current increases with pressure. However, for the InGaAsP/InP laser diode we found very nice performance up to 2 GPa (which was the limit of our

optical cell) for the fixed value of the current. In [8] we show the emission spectrum at different pressures and the position of the emission line versus pressure. The shift was linear with pressure with the coefficient 87 meV/GPa (in good agreement with our PL results). In this experiment the pressure was determined by the piezoresistive InSb gauge [10]. The laser is a very bright source so that the detection is easy. The major problem we encountered was the mode hopping and small hysteresis of the pressure-induced mode hops. Our InSb pressure calibration was not precise enough to study these effects in detail. In spite of these problems, the 1.3  $\mu\text{m}$  and 1.5  $\mu\text{m}$  InGaAsP/InP laser diodes seem quite interesting as pressure calibrants in the 2 GPa range (and possibly higher).

#### Acknowledgements

This work was supported by the Polish Committee for Scientific Research (KBN) through grant nr 2 P03B 138 08.

#### References

1. W. Trzeciakowski, P. Perlin, H. Teisseyre, C.A. Mendonca, M. Micovic, P. Ciepielewski, and E. Kamińska, *Sensors and Actuators A* **32**, 632 (1992)
2. U. Venkateswaran, M. Chandrasekhar, H.R. Chandrasekhar, B.A. Vojak, F.A. Chambers, and J.M. Meese, *Phys.Rev.B* **33**, 8416 (1986)
3. P. Perlin, W. Trzeciakowski, E. Litwin-Staszewska, J. Muszalski, and M. Micovic, *Semicon. Science and Technology* **9**, 2239 (1994)
4. T.P. Sosin, P. Perlin, W. Trzeciakowski, and R. Tober, *J.Phys.Chem.Sol.* **56**, 419 (1994)
5. J.D. Lambkin, D.J. Dunstan, K.P. Homewood, L.K. Howard, and M.T. Emeny, *Appl.Phys.Lett.* **57**, 1986 (1990)
6. A. Kangarlu, H.R. Chandrasekhar, M. Chandrasekhar, Y.M. Kapoor, F.A. Chambers, B.A. Vojak, and J.M. Meese, *Phys.Rev.B* **38**, 9790 (1988)
7. H. Muller, R. Trommer, M. Cardona, P. Vogl, *Phys.Rev.B* **21**, 4879 (1980)
8. P. Stępiński, Y. Tyagur, T. Sosin, and W. Trzeciakowski, this conference
9. D. Patel, C. Menoni, H. Temkin, C. Tome, R.A. Logan, D. Coblenz, *J.Appl.Phys.* **74**, 737 (1993)
10. M. Kończykowski, M.Baj, E. Szafarkiewicz, L. Kończewicz, and S. Porowski, "High Pressure and Low-Temperature Physics", eds. C.V. Chu and J.A. Woolam, (Plenum, New York 1978) p.523

# HIGH HYDROSTATIC PRESSURE EFFECTS IN LIQUID CRYSTALLINE OPTICAL FIBERS

TOMASZ R. WOLIŃSKI, WOJTEK J. BOCK\*, and ANDRZEJ ZACKIEWICZ

*Institute of Physics, Warsaw University of Technology, Koszykowa 75, 00-662 Warszawa, Poland*

*\*University of Québec at Hull, Hull, Québec, J8X 3X7 Canada*

## ABSTRACT

Initial results of experimental studies of light propagation by optical fibers with liquid crystalline cores under high hydrostatic pressure conditions have been reported. Specially drawn hollow-core fibers (capillary tubes of radii 10 to 130  $\mu\text{m}$ ) were filled with a chiral nematic mixture. The whole system composed of the fiber and the liquid crystal has been placed in a high pressure chamber designed to sustain pressures up to 200 MPa. The paper presents preliminary characteristics of the all-fiber liquid crystalline pressure sensor utilizing hollow-core fibers. Envisaged areas of applications include pipe-lines, mining instrumentation, process-control technologies, and environmental protection.

## Introduction

High hydrostatic pressure effects in liquid crystals have been intensively studied over the past years giving new insights into the nature of molecular interactions responsible for liquid crystalline ordering [1] and also still holding great potential for applications to high pressure metrology utilizing fiber optic sensing techniques [2-5]. Since any prospective liquid crystal pressure sensing device should be coupled to optical fibers that deliver optical signals to an elevated-pressure region, a special attention is paid to liquid crystalline configuration inside capillaries with few micrometers diameters [6-8]. This case is also especially important from integrated optics point of view since liquid crystalline waveguides could be used in modulators, couplers and switches.

It is well known that chiral forms of nematic liquid crystals possess unique optical properties associated with a special helical arrangement of two dimensional nematic layers as selective (Bragg) reflection and high rotatory power. Since the chiral phase optical parameters such as helicoidal pitch  $L$  and birefringence  $\Delta n = n_e - n_o$ , strongly depend on temperature, pressure, or strain liquid crystals can be applied in fiber optic metrology. In chiral nematic mixtures, the optical parameters can be appropriately modified due to elaborate synthesis procedures to achieve high sensitivity for pressure with reduced thermal response. Recently, we have developed novel and cost-effective methods for measurement of low (of the order 1 MPa) and high (up to 100 MPa) hydrostatic pressure applied to a sensing element comprising a chiral nematic liquid crystal coupled to optical fibers [4,9].

Since in the functional fiber optics there is a general tendency to replace all the optical bulk elements by the equivalent fiber-optic realizations, in this paper initial results of experimental studies of light propagation by optical fibers with liquid crystalline cores under high hydrostatic pressure conditions have been reported. Specially drawn hollow-core fibers (capillary tubes of radii 15 and 30  $\mu\text{m}$ ) were filled with a chiral nematic mixture. The whole system composed of the fiber and the liquid crystal has been placed in a high pressure chamber designed to sustain pressures up to 200 MPa. The liquid crystalline-core optical fiber acts as an optically anisotropic medium characterized by an index ellipsoid. Since stress effects occurring in the system due to external perturbations generate additionally induced birefringence, a new class of fiber-optic hydrostatic pressure sensors can be introduced. The paper presents preliminary characteristics of the all-fiber liquid crystalline pressure sensor utilizing hollow-core fibers.

## Liquid crystal molecular ordering in a hollow-core fiber structure

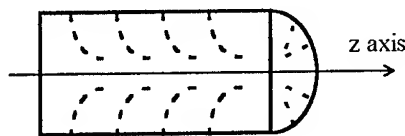


Fig. 1. Director field for axial structure.

To describe the sensing element i.e. a hollow-core fiber filled up with nematic liquid crystal, molecular ordering inside the core should be well defined. It has been shown [6] that for capillaries



with radius  $R \geq 0.5 \mu\text{m}$  for typical materials an axial configuration (Fig. 1) is energetically favorable.

For that situation the director is perpendicular to the cylinder axis  $z$  at the surface and parallel to it at the center of the core. In cylindrical co-ordinates, the director field (describing local molecular ordering) is given by:

$$n = n(\sin\theta, 0, \cos\theta)$$

where  $\theta$  is an angle between the director  $n$  and the symmetry axis  $z$ . From the expression for  $n$  the dielectric tensor  $\epsilon$  has the form:

$$\epsilon = \begin{bmatrix} \epsilon_{rr} & 0 & \epsilon_{rz} \\ 0 & \epsilon_{\phi\phi} & 0 \\ \epsilon_{zr} & 0 & \epsilon_{zz} \end{bmatrix}$$

where:

$$\epsilon_{rr} = \epsilon_{\perp} + \Delta\epsilon \sin^2 \theta, \quad \epsilon_{zz} = \epsilon_{\parallel} = \Delta\epsilon \sin^2 \theta \cos \theta,$$

$$\epsilon_{\phi\phi} = \epsilon_{\perp}, \quad \epsilon_{zz} = \epsilon_{\perp} + \Delta\epsilon \cos^2 \theta, \quad \text{and} \quad \Delta\epsilon = \epsilon_{\parallel} - \epsilon_{\perp}$$

refer to the dielectric constant for polarizations perpendicular and parallel to the director, respectively

Since a very low energy is required to induce a helical twist within a mesophase, the molecular arrangement of a cholesteric liquid crystal is expected to be affected by external pressure. We expect, a decrease of a pitch  $Z$  since the centers of mass of the molecules come closer together as a result of the compressibility of liquid crystals. On the other hand, there may be an additional structural change with pressure due to variation of the relative arrangement of the molecules [9].

### Experimental procedure and instrumentation

A hollow-core fiber filled up with special mixtures of liquid crystals described elsewhere was spliced to lead-in and lead-out multimode fibers. The sensor was placed inside a standard thermally stabilized high pressure chamber (Fig. 2.). High pressure generation and calibration up to 105 MPa was performed using a Harwood DWT-35 dead-weight tester (reading accuracy of 0.01%). The light source were He-Ne laser (633 nm) and laser diode (787 nm) modulated by chopper or external frequency generator respectively. Detection was proceed using lock-in voltmeter connected by

analog/digital converter to computer's interface card. Temperature was controlled and stabilized by Haake F3 thermostatic device (stabilization accuracy of 0.1K).

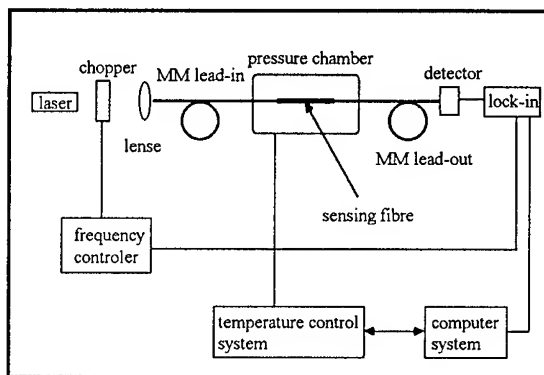


Fig. 2. Experimental set-up of the all-fiber liquid crystalline pressure sensor.

Second configuration was prepared to observe polarization effects. The state of polarization is maintained if incident linearly polarized beam is introduced parallel to one of fiber's axes. Then state of polarization on the entrance of the sensing fiber can be determined.

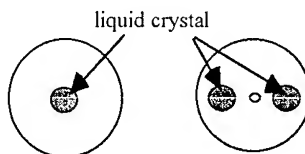


Fig. 3. Cross section of hollow-core (at the left) and side-hole (at the right) fiber.

Since long-term temperature stabilization inside the pressure chamber was required all measurement had to be done very slowly. Overall length of hollow-core sensing fibers was within a range of 14 up to 48 mm. Almost all sensors were straight. The liquid crystalline material was a special mixture of a nematic liquid crystal characterized by refractive indices  $n_o = 1.517$ ,  $n_e = 1.732$  doped with an optically active chiral compound and was introduced to the holes by capillary action (Fig. 3).

### Results

The hollow-core liquid crystalline fibers with diameters 10, 15, 30 and 130  $\mu\text{m}$  have been investigated. Fig. 4-6 present, for the first time to

our best knowledge, pressure characteristics of highly birefringent fibers with liquid crystalline cores, obtained for two laser sources. It is evident that hydrostatic pressure significantly influences the level of the optical signal propagating along the elongated hollow-core fiber (30  $\mu\text{m}$ ) in comparison to the capillary (130  $\mu\text{m}$ ) and a pressure hysteresis was observed in lower temperatures, for hollow cores. However, when a 15  $\mu\text{m}$  hollow-core fiber had been initially bent (Fig. 6.), the pressure characteristics revealed a residual hysteresis and the effect was nearly temperature independent. This is particularly interested from the pressure sensing applications point of view. Further experiments are still in progress.

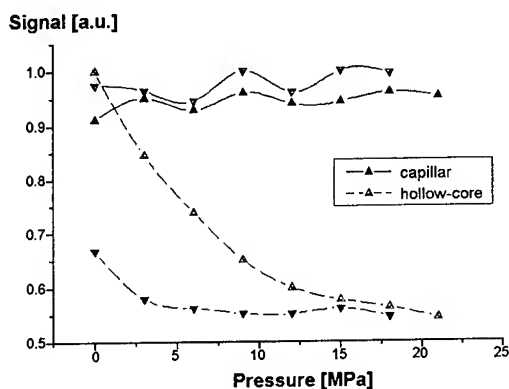


Fig. 4. Pressure characteristics of a 30- $\mu\text{m}$  hollow-core fiber (787 nm) compared with a 130- $\mu\text{m}$  capillary (633 nm) filled up with 6CHBT, at  $T = 15^\circ\text{C}$  (full hysteresis runs,  $\blacktriangle$ : increasing pressure).

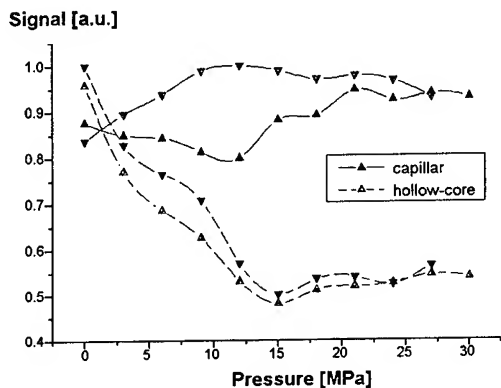


Fig. 5. Pressure characteristics of a 30- $\mu\text{m}$  hollow-core fiber (787 nm) compared with a 130- $\mu\text{m}$  capillary (633 nm) filled up with 6CHBT, at  $T = 25^\circ\text{C}$  (full hysteresis runs,  $\blacktriangle$ : increasing pressure).

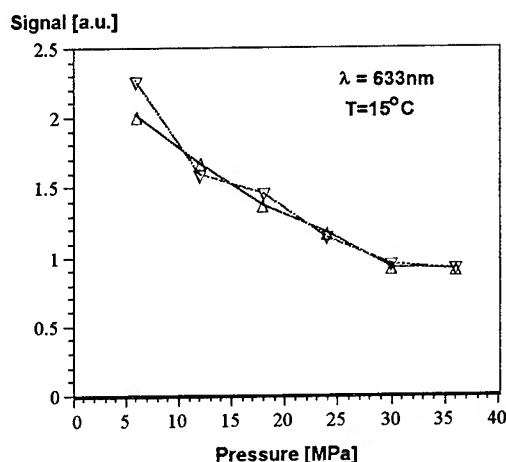


Fig. 6. Long-term pressure characteristics of a 15- $\mu\text{m}$  bent hollow-core fiber filled up 60% mixture (20 minutes between single points, full hysteresis run).

## Acknowledgments

The work was supported by the Warsaw University of Technology and by the University of Québec at Hull, Canada.

## References

1. P. Pollmann, "Eine Apparatur zur Messung der Lichtreflektion cholesterischer Mesophasen bei hohen Drücken" *J. Phys. E Sci. Instrum.*, Vol 7, 490-492 (1974).
2. T. R. Woliński, W. J. Bock, "Cholesteric Liquid Crystal Sensing of High Hydrostatic Pressure Utilizing Optical Fibers", *Mol. Cryst. Liq. Cryst.*, Vol. 199, 7-17 (1991).
3. T. R. Woliński, W. J. Bock, "Fiber-Optic Liquid Crystal High Pressure Sensor", in "Fiber-Optic Sensors: Engineering and Applications", 14-15 March, The Hague, The Netherlands, *Proc. SPIE (USA)*, vol. 1511, 281-288 (1991).
4. W. J. Bock, T. R. Woliński, "Method for Measurement of Pressure Applied to a Sensing Element Comprising a Cholesteric Liquid Crystal", *US Patent No. 5 128 535*, issued on July 7, 1992.
5. T. R. Woliński, W. J. Bock, R. Dąbrowski, "Fiber-Optic Measurement of High Hydrostatic Pressure with Cholesteric Liquid Crystals," *SPIE Vol. 1845 Liquid and Solid State Crystals*, 558-562 (1992).
6. G.P. Crawford, A. Scharowski, R.D. Polak, *Mol. Cryst. Liq. Cryst.* vol. 251, 265-269 (1994).
7. H. Lin, P. Palffy-Muhoray, Michael A. Lee; *Mol. Cryst. Liq. Cryst.* vol. 204, 189-200 (1991).
8. H. Lin, P. Palffy-Muhoray; *Optics Letters* vol. 17, No. 10 (May 15, 1992).
9. T. R. Woliński, R. Dąbrowski, W. J. Bock, A. Bogumił, S. Kłosowicz, "Liquid Crystalline Films for Fiber Optic Sensing of High Hydrostatic Pressure", *Thin Solid Films*, Vol. 247, 252-257 (1994).

# PISTON GAUGES FOR PRESSURE MEASUREMENTS IN LIQUIDS UP TO 3 GPa

GIANFRANCO MOLINAR  
C.N.R. – Istituto di Metrologia "G. Colonnetti"  
Strada delle Cacce 73, 10135 Torino, Italy

## ABSTRACT

An analysis is made of the main current research problems associated with piston gauges. Attention is particularly focused on the few existing piston gauges, constructed in past years, for pressure measurements from 1,4 GPa to about 3 GPa; a few of them are still in continual operation. The need of having piston gauges to be used routinely to perform pressure measurement calibrations from 1,4 GPa to 3 GPa is considered in particular.

## 1. Introduction

A brief hystorical review and a summary of the different kinds of piston gauges used for measurements in liquids up to 1 GPa is given in [1].

It is somewhat strange that in spite of the manifold pressure-metrology research, not much work has been undertaken to extend the routine use of piston gauges above 1,4 GPa.

Let us observe that

- few liquids are purely hydrostatic at pressures close to 3 GPa under room temperature conditions;
- the size of the tubing transmitting the pressure becomes a serious problem at very high pressures;
- control systems, valves, fittings, intensifiers for pressures close to 3 GPa are complex devices;
- a piston gauge is essentially a small-diameter piston to be in a state of balance between the applied pressure and the counterbalancing force by weight pieces and this requires very careful application of the balancing force.

The possibility of using some selected pressure fixed points below 3 GPa is also considered.

The need of having more easily available piston gauges to be used routinely

- to perform pressure measurements from 1,4 to 3 GPa for fixed-point determination;
- to connect the pressure scale defined by means of piston gauges with that realized by application of the NaCl equation of state;
- to better express the uncertainty of the pressure scale based on optical phenomena

is discussed.

Pressure measurement uncertainty, (at  $1\sigma$  level),

with the present-day piston gauges varies from 10 ppm (from 0,1 MPa to 100 MPa) to well within 100 ppm at 1 GPa and close to 0,1 % at 3 GPa.

## 2. Piston gauges operating above 1,4 GPa

Table 1 gives some metrological characteristics of different-type piston gauges, operating in liquid media with pressures higher than 1 GPa and extending their pressure range at least up to 2,6 GPa.

All the piston gauges given in Table 1 are of the controlled-clearance type and are listed according to the date of their presumable installation or the date of the paper presenting the design and their metrological characteristics.

The Harwood piston gauge [2], designed to operate up to 1,4 GPa, was the first that gained wide diffusion among national standards laboratories and industries and is still widely used for calibration of secondary standard devices.

This piston gauge, which is a relatively compact system, has been since the 60's produced industrially; its measurement uncertainty is from 100 ppm to 300 ppm at 1 GPa (the uncertainty estimate depends to a great extent on the relation between the operative values of the jacket pressures  $p_j$  vs. the measurement pressure  $p_m$ , selected in order to keep a constant piston fall rate).

If this system is used with large inner-diameter tubes it can be used satisfactorily up to 1,4 GPa.

The NBS (now NIST) piston gauge, designed to operate up to 2,6 GPa [3], was essentially meant for use for phase transition determinations (particularly the  $\text{Bi}_{I-II}$  phase transition at 25 °C).

Table 1

Lab./Experts	Year installat. result publ.	Max. p range /GPa	Piston/Cylinder Materials	Nominal eff. area/mm <sup>2</sup>	Masses at full scale/kg	Fluids	Main paper
Harwood- USA D.H.Newhall	1953	1,4	Tung.carb./hard steel	3,225	500	a) 1:10 oil and gasoline mixture b) pentane/isopentane mixture	[2]
NBS, now NIST - USA D.P. Johnson P.L.M.Heydemann	1967	2,6	Tung.carb./ special hard steel	3,14 pist.diam. 2 mm	840	a) oil and i-pentane mixture b) i-amyl alcohol c) pure i-pentane	[3]
VNIIFTRI-Russia A.E. Bremeiev S.S. Sekoyan	1974	2,6	Hard VK-8 alloy /hard EP592 steel	7,1 pist.diam 3 mm	Force of 18 kN at f.s. measured by hyd.multiplier Unc. 20 ppm	Glycerine and ethylene-glycol mixture	[4]
NRLM - Japan S. Yamamoto	1980	2	Tung. carb. / maraging steel	5	1000	a) white gasoline b) di-hethyl-hexyl sebacate	[5]
Shanghai Institute of Metrology and Technology/China Wang-Ting-He	1981	2,6	Tung. carb./hard steel	4 pist.diam. 2,25 mm	1040	//	[6]

This piston gauge was not intended to carry high-pressure fluids into long tubes, but the general philosophy was that of compressing the liquid just below the rotating piston and obtain a fluid volume of about 1 cm<sup>3</sup>, large enough to be used for phase transition. In this system the liquid is compressed using a specially designed movable seal, whose movement is actuated by a hydraulic ram. A careful analysis of all the contributions to the uncertainty of the measurement pressure by this system was made, mainly aimed at finding the most efficient way of evaluating the uncertainty of the transition pressure for Bi<sub>I-II</sub> at 25 °C based on volume changes. The uncertainty of the Bi<sub>I-II</sub> phase transition at 25 °C was evaluated to be 6 MPa (equivalent to 0,23 % at 2,6 GPa); this uncertainty was mainly due to the uncertainty of the effective-area value which was stated to be accurate inside 0,2 %, account being taken also of the relatively high leakage during the Bi<sub>I-II</sub> phase transition experiment.

This pioneer result, achieved in 1967, also stimulated the design and construction of other systems and the execution of similar measurements; in spite of the very high leakage at high pressures, the NBS(NIST) 2,6 GPa piston gauge could operate very satisfactorily.

An interesting system was also developed in 1974 at VNIIFTRI in Soviet Union [4]. This controlled-clearance system was extensively studied in order to find the best way of adjusting the jacket pressure around the cylinder; the designers of this

instrument found that the best results were obtained with a linearly varying jacket pressure able to produce a quasi-linear pressure distribution in the piston-cylinder gap. The uncertainty of this piston gauge, which was quoted 0,1 % in the pressure range from 1,5 GPa to 2,6 GPa, was checked in comparison with other piston gauges covering narrower pressure ranges and with the use of the mercury melting line and manganin gauge transducers. This system was also subsequently used for the redetermination of the Bi<sub>I-II</sub> phase transition at 25 °C by means of electrical resistance changes.

Another interesting device, influenced by the Harwood design but extending its maximum pressure range up to 2 GPa, was designed and constructed in Japan at the NRLM [5].

The overall uncertainty of pressure measurements was evaluated to be 0,37 MPa or 0,023 % at 1,6 GPa and the sensitivity was 0,01 MPa up to 800 MPa and 0,02 MPa at higher pressures. This piston gauge operates safely but at 2 GPa different problems in sealing, giving rise to consistent leaks, have been reported.

Another interesting system, about which no written papers unfortunately are available [6], was that in Shanghai in The People's Republic of China. This huge system uses a 3-stage intensifier system (60 MPa- 1 GPa- 2,6 GPa) and a very large set of weights (automatically loaded on the piston); the estimated uncertainty of pressure measurements with this system was 0,15 %.

Another interesting system, not appearing in Table 1, is a recent development of a gas(argon)-charged piston-cylinder device capable of operating up to 4 GPa [7].

This system use a 3 cm<sup>3</sup> volume, can be pre-charged with argon at 0,5 GPa, then the tungsten carbide piston is advanced into the cylinder chamber to generate a pressure estimated to be as high as 4 GPa. In this device the force applied on the piston is measured by load cells; friction is a big problem and carefully evaluated corrections must be applied, amounting to about 2,5 % of the applied force.

The paper in [7] mention a 0,2 % pressure measurement uncertainty only at the pressure of 1,3 GPa. The system in question is of interest especially for its potential use for accurate ultrasonic measurements under pressure and for the determination of the equation of state of substances of interest in pressure metrology (e.g., NaCl), and can be adapted for use at high temperatures up to 1200 K.

There exist different compression devices, to be used for equation of state determination, for a typical maximum pressure of 1,5 GPa; with such devices the isothermal bulk modulus and the thermal expansivity of materials can be measured with estimated uncertainties from 0,4 % to 1 %.

As an alternative to piston gauges, phase transitions can be used as transfer standards in pressure ranges compatible with the temperature values of the phase transitions.

The mercury melting line, for example, can be used up to 1,2 GPa (uncertainty of 325 ppm at 1,2 GPa) and extended to 4 GPa (uncertainty of 1 % at 4 GPa). As regards the Bi<sub>I-II</sub> phase transition at 25 °C, the present AIRAPT recommended value is 2,5499 GPa with an estimated uncertainty of 6 MPa. A more recent determination of the Bi<sub>I-II</sub> phase transition gave a value of 2,534 GPa with an estimated uncertainty of 3 MPa.

The latter uncertainty is half that of the recommended value and was achieved with the use of a special piston gauge [4]. The discrepancy between the two phase transition values for Bi<sub>I-II</sub> indicates the need, in this pressure range, for a calibration setup allowing certified uncertainties as low as 0,1 % to be achieved.

Other calibration means and methods, such as the laser-induced fluorescent shift of ruby (uncertainty of 1,1 % for pressures from 2,5 GPa to 5 GPa), and the laser-induced fluorescent shifts of

Sm:YAG, Sm<sup>2+</sup>:BaFCl or Sm<sup>2+</sup>:SrFCl and the luminescence of semiconductor quantum wells can also be used above 2,5 GPa. These luminescence gauges have, in comparison with ruby, a higher ratio of the line width to the line shift and reduced temperature sensitivity. Sm<sup>2+</sup>:SrFCl was tested successfully up to 20 GPa and 650 K, with an estimated uncertainty close to 0,1%.

### 3. Conclusions

Few piston gauges are really fully operative and routinely used for pressure measurements above 1,4 GPa. All the piston gauges operating with pressures higher than 1,4 GPa, generally limited to below 2,6 GPa, were in fact intended for use only to dedicated experiments for phase transition determination.

It is necessary to develop new kinds of piston gauges able to be used routinely for pressures up to 3 GPa; such piston gauges must have a volume of compressed fluid large enough to allow them to be used for phase transition determination.

Largely disseminated piston gauges of an extended pressure range must be made available mainly for

- improvement of the pressure uncertainty value in phase transitions at high pressure;
- their use to test the metrological characteristics of secondary standard transducers;
- improvement of the pressure uncertainty for pressures below 5 GPa when the scale starts from the NaCl equation of state and reduction of the uncertainty value of the pressure scale based on the ruby fluorescent shift or other calibrants.

### References

1. G.F. Molinar, *Metrologia* **30**(6), 1994, 615.
2. D.P. Johnson and D.H. Newhall, *Trans. ASME*, 1953, 301.
3. D.P. Johnson and P.L.M. Heydemann, *Rev. Sci. Instrum.* **38**(6), 1967, 1294.
4. A.E. Eremeev, Translated from *Izmeritel'naya Tekhnika* **7**, 1974, 19.
5. K. Nishibata, S. Yamamoto and R. Kaneda, *Jap. Journ. Appl. Phys.* **19-11**, 1980, 2245.
6. Personal communications of Mr. Wang Ting-He and his co-workers (1983, 1995).
7. I.C. Getting and H.A. Spetzler, In *Proc. AIRAPT Conference 1993*, Boulder, CO, USA, Amer. Inst. of Phys., 1994, 1581.

# EFFECTS OF A PRESSURE DEPENDENT VISCOSITY FLUID IN A PRESSURE BALANCE.

R. J. Lazos-Martínez, Centro Nacional de Metrología, km 4.5 Carr. Los Cués Querétaro,  
México. C. P. 76900

and

E. Piña, Universidad Autónoma Metropolitana - Azcapotzalco. Ap. Postal 16 - 306  
México, D.F. C. P. 02200.

The dynamics of the fluid in the clearance between the piston and cylinder in a pressure balance is modeled starting from the fundamental fluid dynamics equations including a pressure effect on the viscosity. The viscosity dependence on pressure is according to experimental data. The solution of such equations and the impact on the effective area are displayed under a number of assumptions. The results are discussed comparing to the experimental pressure profile, and other methods calculations.

## Introduction

The oil-operated pressure balance is nowadays the primary standard for pressure in a wide range.

It is built by a piston carefully fitted in a cylinder in such a way that the oil contained in a pressure chamber is able to flow through the clearance between them. A force is applied on the piston by placing weights on its upper end, so the pressure generated at a reference level is given, corrections due, by [1]

$$p = \frac{Mg}{A_p} \quad (1)$$

where  $M$  means the mass of the weights,  $g$  the intensity of the local gravitational field, and  $A_p$  the effective area of the assembly at pressure  $p$ .

One of the most important source of uncertainty is that associated to the effective area  $A_p$ , since it is not a well defined quantity yet. It depends on both the area of the piston and that of the cylinder, the location along the axis of the ensemble, which in turn is dependent on the pressure profile and, therefore, on the fluid dynamics in the gap [2,3,4,5] so a better understanding of the flow of a pressure dependent viscosity fluid becomes important.

There have been a number of attempts to characterize the distortion which take into account the elastic-hydrodynamic interaction [4,5,6,7,8]. Generally speaking, to determine the pressure profile, they assume an approximate equation for the flowrate strictly valid when the viscosity and the pressure gradient are constant [9], apply it to a narrow slide and sum over the entire length. Then, the elastic distortion is calculated in different ways, and finally some of them use an iterative scheme to

calculate new pressure profiles and new shapes for the assembly.

The aim of this paper is to try another approach by developing a model where account of a pressure dependent viscosity is taken since the basic equations, and solve them for the pressure profile.

## The model equations

The governing equations for the flow of fluids at uniform temperature are the law of conservation of mass,

$$\frac{\partial \rho}{\partial t} + \nabla \cdot (\rho \underline{v}) = 0, \quad (2)$$

where  $\rho$  is the fluid density and  $\underline{v}$  is the velocity vector of the fluid, and the law of balance of linear momentum,

$$\rho \frac{d\underline{v}}{dt} = \rho \underline{f} + \nabla \cdot \underline{T} \quad (3)$$

with  $\underline{f}$  the body force and  $\underline{T}$  the stress tensor.

When the flow is stationary,  $\underline{f} = 0$  and the fluid incompressible, eq. (3) goes to

$$\rho (\underline{v} \cdot \nabla) \underline{v} = -\nabla p + \mu \nabla^2 \underline{v} + \nabla \mu \cdot [\nabla \underline{v} + \nabla \underline{v}^T] \quad (4).$$

In circular cylindrical coordinates, where  $r$  is the radial coordinate and  $z$  the axial one, and assuming an axisymmetric geometry,  $v_\phi = 0$  (meaning no

rotations in the fluid),  $\frac{\partial}{\partial \phi} = 0$ , and  $v_r = 0$ , eq.

(2) leads to

$$\frac{\partial v_z}{\partial z} = 0 \quad (5).$$

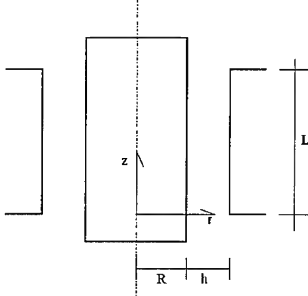


Fig. 1. Diagram of the piston and the cylinder of a pressure balance, with the coordinates used.

We denote the derivative of a function respect to the variable  $r$  with a prime, e. g.  $\frac{\partial v_z}{\partial r} = v'$ . Thus, the  $r$  and  $z$  components of (4) are

$$-\frac{\partial p}{\partial r} + \frac{\partial \mu}{\partial z} v' = 0 \quad (6)$$

and

$$-\frac{\partial p}{\partial z} + \mu \left( \frac{v'}{r} + v'' \right) + \frac{\partial \mu}{\partial r} v' = 0 \quad (7)$$

respectively. Note that the assumption of  $p$  independent on  $r$  implies either  $v' = 0$  or the viscosity independent on  $z$ , and so the pressure.. Inversely, a pressure dependence on  $z$  implies a pressure dependence on  $r$ .

When a pressure viscosity law [10] is included,

$$\mu = \mu_o e^{\alpha p} \quad (8)$$

where  $\alpha$  is constant, (6) y (7) can be written as

$$-\frac{\partial p}{\partial r} + \alpha \mu_o \frac{\partial p}{\partial z} v' = 0 \quad (9)$$

and

$$-\frac{\partial p}{\partial z} + \mu_o e^{\alpha p} \left( \frac{v'}{r} + v'' \right) + \alpha \mu_o e^{\alpha p} \frac{\partial p}{\partial r} v' = 0 \quad (10).$$

It is noteworthy that assuming a constant pressure gradient does not mean a constant viscosity gradient and that  $\alpha = 0$  reduces the equations to those for constant viscosity properly.

The exact solution for both of the equations is

$$z = -\frac{1}{2} \alpha \mu_o e^{\alpha p} B r^2 - \frac{1}{2 \alpha \mu_o B} e^{-\alpha p} + C \quad (11)$$

where  $B$  and  $C$  are constant.

Regarding the boundary conditions

$$p(z = L) = 0$$

$$p(z = 0) = P_M,$$

i. e.  $P_M$  means the pressure at the bottom or the nominal operation pressure, eq. (11) becomes

$$z = \frac{1}{2} \frac{e^{\alpha P_M} - e^{\alpha p}}{e^{\alpha P_M} - 1} (L + b) + \frac{1}{2} \frac{r^2}{L + b} \left( 1 + e^{-\alpha p} - e^{\alpha(P_M - p)} - e^{-\alpha P_M} \right) \quad (12).$$

where

$$b = \sqrt{L^2 - r^2 (2 - e^{\alpha P_M} - e^{-\alpha P_M})} \quad (13).$$

It gives the pressure profile as a function of the geometry and the pressure at the bottom, and shows a pressure dependent on the coordinate  $r$ , which does not appear in models dealing with uniform viscosity [9]. However, the numerical contribution of this term is not significant for typical pressure balances.

Once the pressure profile is given, the elastic distortions of the piston  $u$  and that of the cylinder  $U$ , are calculated using some of the methods already developed, e. g. by entering the results of the same eq. (12) into a finite element method code, and then calculate the contribution to the effective area due to the distortion of the ensemble through the Dadson equation [11]

$$A_u = -\frac{\pi R}{P_M} \int_0^L (u + U) \frac{dp}{dz} dz \quad (14).$$

where the derivative is taken from (12) in this work.

## Results and discussion

A pressure profile between piston and cylinder is calculated using some typical values found in pressure balances,  $\alpha = 0,002 \text{ MPa}^{-1}$ ,  $L = 0,02 \text{ m}$ ,

The pressure profile predicted by this model shows a trend departing from linearity as pressure increases that agrees with results derived using iterative techniques [4,5,6,7] with narrow gaps ( $h < 1 \text{ } \mu\text{m}$ ) and with experimental data [12]. However the profile curvature seems too low compared to those. On the other hand, the pressure profile does not depend on the gap  $h$ .

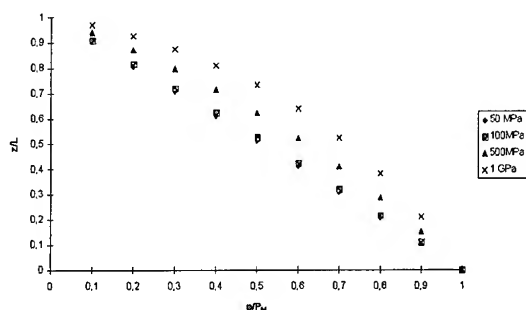


Fig. 2 The normalized z-coordinate as a function of the normalized pressure for  $\alpha = 0,002 \text{ MPa}^{-1}$  calculated with Eq.12.

As an example, the contribution to the effective area  $A_u$  is calculated as eq. (14) for tungsten carbide. The value obtained for  $A_u$  is  $9,62 \times 10^{-12} \text{ m}^2$ , equivalent to a contribution of

$\lambda_u = A_u / (p A_0) = 3,062 \times 10^{-8} \text{ MPa}^{-1}$ . The uncertainty of these results has not been evaluated yet.

Summarizing, this model: a) includes an experimental law for pressure dependent viscosity; b) accepts an exact analytical solution; c) provides a formula for the slope of the pressure profile to be used in the equation for the effective area; d) predicts a velocity profile quite sensitive to the choice of boundary conditions, which is a process not fully understood yet [13]; e) may provide values for the velocity inconsistent with typical data for pressure balances; and, f) it may provide an initial proposal for iterative purposes.

## Conclusions

This paper provides an exact and analytical solution for the pressure profile in a pressure balance, with a pressure dependent viscosity, under assumptions of flow incompressibility, axial symmetry and velocity parallel to the axis.

The results display a number of features in agreement with results that came from the experiment and from calculations started from approximate equations, but its numerical values are not accurate enough yet to be used as final results. Furthermore, the velocity and thus the flowrate predicted values are far from expected due to the choice of the boundary conditions and the assumption  $v_r=0$ , which requires further exploration. However, the resulting equations may provide an initial solution for iterative schemes and

a basis for a better understanding of pressure balances.

## Acknowledgments

We are indebted to Alfredo Esparza to have run the finite element code for this paper.

## References

- [1] P. L. M. Heydemann, B. E. Welch, in *Experimental Thermodynamics. Volume II. Experimental Thermodynamics of Non-reacting Fluids*. Ed. B. Le Neindre and B. Vodar. Butterworths, London, (1975), p. 153.
- [2] R. S. Dadson, R. G. P. Greig and A. Horner, *Metrologia*, 1-2, (Apr. 1965), pp. 55.
- [3] G. Klingenberg, *High Pressure Metrology*, Monographie 89/1, BIPM, (1989) pp. 1.
- [4] M. P. Fitzgerald and A. H. McIlraith, *Metrologia*, 30-6 (Apr 94) pp 631.
- [5] G. F. Molinar, *Metrologia*, 30-6, (Apr. 94) pp.615
- [6] G. Molinar, *High Pressure Metrology*, Monographie 89/1, BIPM, (1989) pp. 13.
- [7] N. D. Samaan, *Proceed. XIII IMEKO World Congress*, 3, (Torino, Italy, 1994) pp. 1963.
- [8] P. R. Stuart, *High Pressure Metrology*, Monographie 89/1, BIPM, (1989) pp. 31.
- [9] M. K. Zhokhovskiy, *Theory and Design of Instruments with Packing-Free Pistons*. English translation from the Russian. (Moscow, 1959) p. 39
- [10.] J. K. N. Sharma, K. K. Jain, V. E. Bean, B. E. Welch and R. J. Lazos, *Rev. Sci. Instr.* (Apr. 1984) pp. 563.
- [11] R. S. Dadson, S. L. Lewis and G. N. Peggs, *The Pressure Balance. Theory and Practice*. NPL, (United Kingdom, 1982) p. 30.
- [12] B. E. Welch and V. E. Bean, *Rev. Sci. Instrum.* 55-12 (Dec. 1984) pp. 1901.
- [13]. P. M. Gresho, *Annu. Rev. Fluid. Mech.* 23 (1991) pp 413



# A CAPACITIVE FREE ELEMENT BULK-MODULUS PRESSURE TRANSDUCER

R. WIŚNIEWSKI AND A. J. ROSTOCKI

*Institute of Physics, Warsaw University of Technology, ul. Koszykowa 75, 00-662 Warszawa, Poland*

## ABSTRACT

New idea of the high pressure measurement on the base of a free active element bulk modulus determination has been developed. Contrary to the previous methods based on the strain measurement of the active element of the transducer measured by the strain gauges inside of it or on the constrain measurement of the active element measured by the LVDT transducers, the method presented here is based on the precise measurement of the change of the inside diameter of the active element of the transducer. The capacitive method using the free cylinder as the outer electrode of the concentric capacitor has been applied with very good results. The measurement made within the pressure range up to 1 GPa have shown excellent performance of the applied method with the repeatability better than 0.2% of the full scale.

## Introduction

The bulk-modulus pressure transducers are convenient for the applications in chemically aggressive or electrically conducting fluids when an electrical resistance (e.g. manganin) pressure transducer cannot be used and the pressure is too high to use separating membranes.

The idea of the bulk-modulus pressure transducer was developed in 1882 by P.G. Tait [1] and adopted by Newhall and Abbot [2], for the measurements of pressure measurements up to 1.4 GPa.

The principle of operation of this type of transducer is based on the contraction of tube proportional to the external pressure. This contraction can be detected by different methods. In case of Tait it was the level of the mercury pushed out of the tube due to its contraction whereas in case of Newhall and Abbot [2] the longitudinal contraction was measured by the motion of a stem all time in contact with the active-element closed end. Linear motion of the stem (relative to the outer end of the tube) was measured using pneumatic transmitter and electrical resistance strain gauges as well.

The moderate accuracy of bulk-modulus transducers described in [1] or [2] (mainly high hysteresis, high temperature sensitivity) were due to unsatisfactory design. Significant progress in accuracy of the bulk modulus transducers has been

made by the application of the idea of "free element" [3] [4] and improvement of the tube design.

The authors of those papers were detecting longitudinal strain of the modified bulk modulus tube using strain gauges or the LVDT detector. Contrary to those methods, the method presented here is based on the precise measurement of the change of the inside diameter of the active element of the transducer. The capacitive method using the free cylinder as the outer electrode of the concentric capacitor has been applied for the detection of the internal radial deformation. For the comparison the measurements of the conventional bulk modulus transducer with a tube of the same diameter have been done using the same capacitance arrangement.

## Description of Transducers

The main advantage of the "free element" concept is that the transducers made on the base of this principle are calculable in terms of deformation, since they work in the well defined state of stress. It is especially important in cases of new designs of the transducer since it allows to compare the experimentally obtained metrological properties with the theoretical expectations. In some cases [7] it is possible even to calculate expected metrological properties with an accuracy better than 3%. For this

reason two versions of the capacitive bulk modulus transducer have been design , built and tested. Both versions of the capacitive transducer are shown in fig. 1. It shows the cross-section of the transducer and the high pressure arrangement. For the experiments the authors have used the same high pressure chamber and active parts which have been used for the LVDT measurements [6]. The "classic" version designed by the modification of Newhall and Abbot arrangement [2] is shown in upper part of figure 1 whereas the lower part shows the new version described in [3].

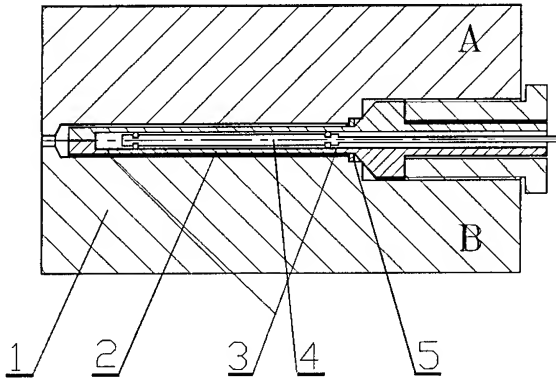


Fig.1. Capacitive Bulk-Modulus high pressure transducer  
a) version of transducer design by the modification of Newhall and Abbot arrangement [2]  
b) "free element" version of the transducer  
1-high pressure chamber; 2-free-active element (heat-treated maraging steel); 3-Bridgman plastic sealing rings; 4-capacitor inner electrode (maraging steel) 5-high pressure sealing (Viton O-ring and anti-extrusion steel ring)

From the figure 1. one can see that the "free element" version was arranged by the design of the transducer tube in form of 3 sections, where the central one is separated from the undefined stress due to the effects of the "dead end" (first section) and the sealing system (last section) . In both versions the inner electrode of the transducer (4) in form of cylindrical rod was placed in the central part of the tube. To obtain the proper axially of that electrode two small o-rings were placed at the ends of the rod.

At low pressures, the sections were sealed by the plastic Bridgman rings (3). The active cylinder (2) and the inner electrode (4) were made of the same material i.e. maraging steel.

In the "classic version" the high pressure sealings (5) were placed as far as possible from fixed end of the active element.

### Metrological properties

According to the simple elastic theory, connected with Lamé's equations, the deformations of the central part of the "free element" transducer due to the pressure  $p$ , considered at the internal surface of the cylinder can be described by the following equations:

$$\varepsilon_l = -p\{W^2(1-2\mu)/E(W^2-1)\} \quad (1)$$

$$\varepsilon_r = -p\{W^2(2-\mu)/E(W^2-1)\} \quad (2)$$

where:  $\varepsilon_r$  and  $\varepsilon_l$  are the circumferential and the longitudinal strains,  $W$  is the wall ratio i.e. ratio of the outer to inner diameter of the active element.  $E$  is the Young's modulus and  $\mu$  the Poisson's ratio of the active element.. For the investigated transducers they were:

$$W=2\pm0,005, \mu=0,295\pm0,002, E=(186\pm2) \text{ GPa}$$

The length of the inner electrode was smaller than the length of the active part of the tube and it was equal to:  $l=(75 \pm 0,05) \text{ mm}$ .

Since the principle of operation of the transducers described in the papers [3],[4],[5] was based mainly on the equation (1) , for the capacitive transducer the equation (2) is essential.

The capacity of the transducer can be calculated from the formula:

$$C(p) = 2\pi\varepsilon_0\varepsilon_r \frac{l}{\ln \frac{R_2(p)}{R_1}} \quad (3)$$

where:  $R_2(p)$  - inside radius of the tube,  $R_1$  - radius of inner electrode of the capacitive transducer,  $C$  - capacity of transducer,  $\varepsilon_0 = 88,85 \cdot 10^{-12} \text{ F/m}$ ,  $l = 75 \text{ mm}$ .

The measurement have been done using Hewlett-Packard HP 4270A digital capacitance meter with the resolution 0,01 pF. The initial capacitance for different versions was varying from 60 pF (0,3 mm - gap) up to 800 pF (for  $\sim 0,1 \text{ mm}$  gap). An example of the experimental pressure dependence is shown in fig. 2.

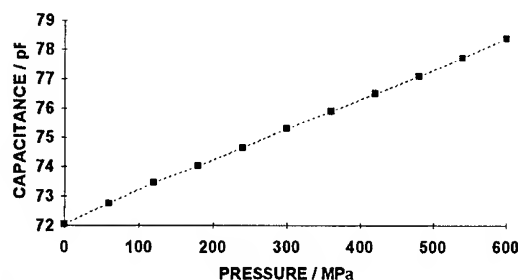


Fig. 2. Pressure dependence of the capacitance of the transducer obtained during calibration

The pressure was generated by the 0,6 GPa piston-gauge of 0,05 % accuracy. The measurements have shown good agreement of the pressure dependence  $C(p)$  with theoretical results obtained by the calculation of the pressure change of the inside diameter using equations (2) and (3). However the temperature sensitivity of the transducer was much bigger than in the versions described in [3], [4], [5], thus requiring the thermal stabilisation with accuracy better than  $\pm 0,2^\circ\text{C}$ .

## References

1. P. G. Tait, *Voyage of HMS Challenger*, Vol. II-Appendix A, (London-UK, 1882)
2. D. Newhall and L. Abbot, Bulk-Modulus Cell, *Measurement and Data*, (1969)
3. R. Wiśniewski and GF. Molinar, Free-Active Element Bulk-Modulus High Pressure Transducer, submitted for publication to *Rev. of Sci. Instruments*.
4. GF. Molinar and R. Wisniewski, Strain-Gauge Free-Active Element Bulk Modulus High Pressure Transducer, submitted for publication to *Sensors and Actuators-A Physical*.
5. R. Wisniewski and GF. Molinar, *Metrologia* 30 (6), (1994), p. 683.
6. GF. Molinar, R. Wisniewski, R. Maghenyani, and A. Magiera, New Version of Bulk Modulus High Pressure Transducer, prepared for publication.
7. A. J. Rostocki, G. F. Molinar, R. Wiśniewski, R. Maghenzani, and F. Trevissoi; "Testing of Metrological Properties of Free Dilating Cylinder Strain Gauge Pressure transducer Using the Pressure and Force Standards". Proceedings of the XXXII. Annual Meeting of the EHPRG, Brno 1994, pp. 37 - 40.

## NEW VERSION OF BULK-MODULUS HIGH PRESSURE TRANSDUCERS

G.F. MOLINAR<sup>(\*)</sup>, R. WIŚNIEWSKI<sup>(\*\*)</sup>, R. MAGHENZANI<sup>(\*)</sup>  
AND A. MAGIERA<sup>(\*\*)</sup>

<sup>(\*)</sup> *Istituto di Metrologia "G. Colonnetti"-CNR, Strada delle Cacce 73, 10135 Torino, Italy*  
<sup>(\*\*)</sup> *Institute of Physics, Warsaw University of Technology, ul. Koszykowa 75, 00-662 Warszawa, Poland*

### ABSTRACT

Bulk modulus type high pressure transducers with active element being in "free condition" are described. An electronic length measuring gauge with uncertainty of  $\pm 0,1 \mu\text{m}$  as active element for longitudinal deformation detection and strain gauges measuring longitudinal and circumferential strains of the active element were used. A maximum pressure of about 2 GPa can be measured with accuracy better than 0,2 % electrically conducting fluids can be used.

### Introduction

The bulk-modulus pressure transducer was developed in 1882 by P.G. Tait when studying the pressure effect on his deep-sea thermometer [1].

In his device an externally pressurised (up to 50 MPa) steel tube, closed at one end and sealed on the other, was filled up with mercury. The contraction of tube was proportional to the external pressure and was measured by displacements of the free surface of mercury in the capillary mounted in the open end of the steel tube.

The same principle of operation has been adopted by Newhall and Abbot [2], extending the pressures measurements up to 1,4 GPa.

The active element-tube was similar to that used by Tait, but its axis (longitudinal) contraction was measured by the motion of a stem all time in contact with the active-elements closed end. Linear motion of the stem (relative to the outer end of the tube) was measured using a pneumatic transmitter and electrical resistance strain gauges as well.

The most important applications of the bulk-modulus pressure transducers are found when an electrical resistance (e.g. manganin) pressure transducer cannot be used because of rapid pressure change in high viscosity media, or when electrically conducting fluids are used. The moderate accuracy of bulk-modulus transducers described in [1] or [2] (mainly high hysteresis, high temperature sensitivity) are due to unsatisfactory design. In the present paper new ways of operation for bulk-modulus high pressure transducer are

described. They allow to reduce and avoid some sources of systematic and random errors and consequently to improve the transducer uncertainty. Another shape of the transducer body is given in order to be used in higher pressure investigations.

### Description of Transducers

Fig. 1 shows the cross-section of the transducer as developed by Newhall and Abbot (top part) and its new version described in [3] (bottom part).

In the active element of original version we can imagine three sections. The first being in a well-defined stress (strain) states, in the second under undefined stress and in the third it is free on any stresses (see fig.1).

The stem used as a detector of the axis constrains on the active element is as long as all the three parts together. The second section of the active element is the source of many errors, connected with friction forces acting in the high pressure seals.

In the version presented here, the active element (2) is in a well-defined stress state, is separated from parts (4) and (7) and it is in fact a free active element of the transducer.

At low pressures, elements (4 and 5) and (5 and 7) are sealed by the Bridgman plastic rings (3). The active cylinder (2) and the cylinder (4) must be made with the same material and should have the same diameters.

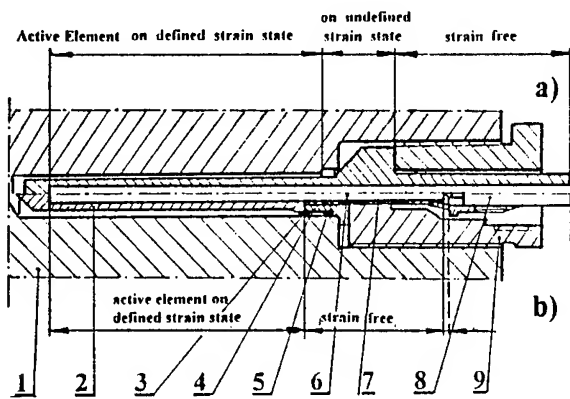


Fig. 1. The Bulk-Modulus high pressure transducer  
 a) scheme of transducer as designed by Newhall and Abbot [2]  
 b) scheme of the transducer after modification by the present authors  
 1-high pressure chamber; 2-free-active element (heat-treated maraging steel); 3-Bridgman plastic sealing rings; 4-sealed cylinder (heat-treated maraging steel) 5-high pressure sealing (Viton O-ring and anti-extrusion steel ring); 6-stem (maraging steel); 7-spacer and holder; 8-probe of 1  $\mu$ m accuracy length electronic gauge; 9-tightening screw (heat-treated)

The high pressure sealing (5) should be placed as far as possible from the fixed end of the active element. Part (7) is permanently in contact with the flat surfaces of the active element (quasi fixed end) because it is pressed by a constant force generated by a spring; this element is also the base surface for a high resolution electronic length gauge (8) which measures length changes in the active element due to applied pressure, independently of stress generated in part (4) and of reacting forces due to high pressure seals (5) and of the stress in screw tightening (9).

Fig. 2a shows the transducer design adopted to use strain gauges for measuring the deformation of the active element [4].

In this solution, the active element is a thick-walled cylinder of small height with strain gauges bonded axially and circumferentially on its inner cylindrical surface.

In this design the active element (5) is under well defined stress state and separated from other elements (1) and (7), in order to be a free active element of the transducer.

The parts (1), (5) and (7), made from the same material, are accurately fitted one to the others by means of flat (carefully lapped) surfaces. At low pressure these elements are sealed by plastic

Bridgman rings (6). Fig. 2b. shows a cross-section of a simple high pressure apparatus in which a strain-gauge bulk-modulus pressure transducer is mounted together with an electric leadthrough pressure transducer system.

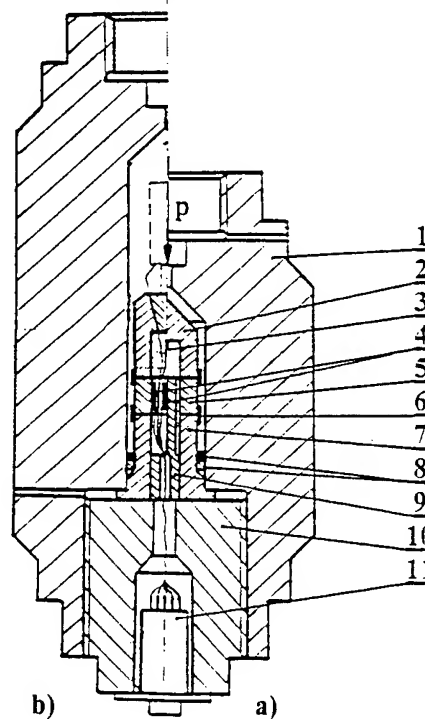


Fig. 2. Strain-gauge bulk-modulus pressure transducer  
 1-pressure vessel; 2-closing cylinder; 3-thermocouple 4-strain gauges, (Micro-Measurement N2A-06-TO35R-35B type); 5-active element; 6-plastic Bridgman sealing rings; 7-bottom cylinder; 8-high pressure seals (Viton O-ring, antiextrusion steel ring); 9-closing element; 11-leads connector

### Metrological properties

According to the simple elastic theory, connected with Lamé's equations, the changes of the length of the active element- $\Delta l$  due to pressure  $p$ , can be described by the following equation:

$$\Delta l = p \{ l / (1 - 2\mu) W^2 / E (W^2 - 1) \} \quad (1)$$

where:  $l$  is a length of the active element,  $W$  is the wall ratio i.e. ratio of the outer to inner diameter of the active element,  $E$  is the Young's modulus and  $\mu$  the Poisson ratio of the active element..

The data of the present realisation are:

$$l = (100 \pm 0,05) \text{ mm}, W = 2 \pm 0,005,$$

$$\mu = 0,295 \pm 0,002, E = (186 \pm 2) \text{ GPa}$$

and one obtains the following relation:

$$\Delta l = \{(0,294 \pm 0,007) \mu\text{m/MPa}\} p \quad (2)$$

Using an electronic length gauge as a position detector with average resolution of  $\pm 0,05 \mu\text{m/digit}$  of reading, we have obtained a resolution of this transducer of about 0,1 MPa. As can be seen from the above calculation this transducer can measure pressure (without calibration procedure) to an accuracy of some percents.

By Lamé's theory, for infinite thick-walled cylinder one can easily derive the expressions for circumferential ( $\epsilon_r$ ) and longitudinal ( $\epsilon_l$ ) strains of the inside surface of the second type active element as a function of pressure:

$$\epsilon_r = -p \{ W^2(2-\mu) / E(W^2-1) \} \text{ and}$$

$$\epsilon_l = -p \{ W^2(1-2\mu) / E(W^2-1) \} \quad (3)$$

Using a full Wheatstone bridge, created by four active strain gauges, in which two longitudinal gauges also serve for temperature compensation, one obtains the following expression for the relative output voltage  $\Delta V/V$  as a function of pressure  $p$ :

$$\Delta V/V = p \{ kW^2(1+\mu) / 2E(W^2-1) \} \quad (4)$$

where  $V$  is the supply voltage of the bridge and  $k$  the gauge factor of the strain gauges.

Fig. 3 and fig. 4 show the pressure dependence of calibration factors (output of measuring signal-divided by the standard pressure) for the case of bulk-length and strain-gauge transducers.

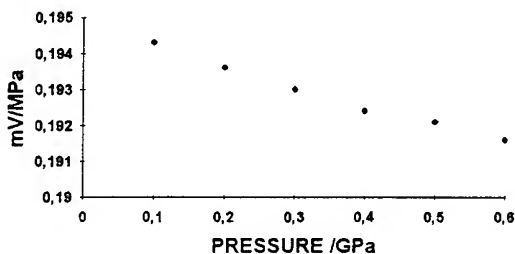


Fig. 3. Calibration factor of bulk-modulus transducer vs. pressure

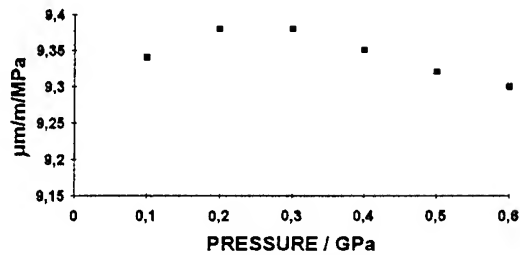


Fig. 4. Calibration factor of strain-gauge bulk-modulus transducer vs. pressure

Fig. 5 and fig. 6 show the pressure dependence of hysteresis of the transducers. The hysteresis behaviour shows different character; in the case of transducer with electronic length measuring gauge there is a random scattering.

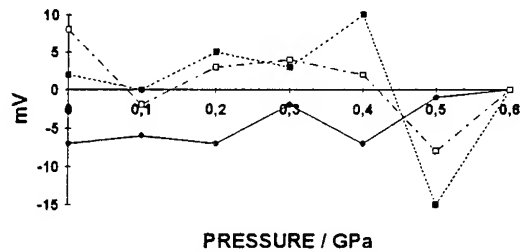


Fig. 5. Hysteresis of bulk-modulus pressure transducer vs. pressure for three cycles

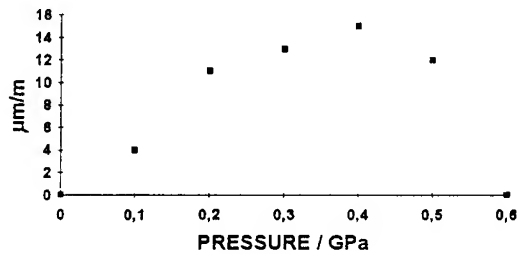


Fig. 6. Hysteresis of strain-gauge bulk-modulus pressure transducer vs. pressure

Preliminary tests, with the strain gauge bulk-modulus transducer, having a resolution of, at least,  $1 \mu\text{m/m}$  and piston gauge with pressure measurement uncertainty (at the  $2\sigma$  level) of 0,01% and pressure capacity of 0,6 GPa in room temperature conditions, gave the following results:

- very good reproductibility of zero reading,
- no zero drift even for period of months,

- repeatability of readings always within 0,04% of transducer full scale,
- hysteresis always better than 0,23 % of the full scale,
- the linearity of the calibration factor typically inside 0,5 % of the full scale.

### Closing remarks

A simple and accurate expression for relative voltage output allow to calculate  $p$  versus  $\Delta V/V$  dependence with some % accuracy if the parameters:  $k$ ,  $W$ ,  $V$ ,  $\mu$  and  $E$  are known. Testing of pressure transducers using high pressure standards with maximum pressure higher than 1 GPa is not easy, because a limited number of this standard piston-gauges are really operatives.

Using pressure transducers in the pressure range from 1 to 2 GPa with an estimated accuracy of 2,3 % for many purposes (especially technological) satisfy the large majority of calibration needs.

Noting that equation (4) is identical to the one of a rod type transducer (for example the case described in [5]) whose active element is a cylinder on which pressure acts on the closed ends only; the transducer here described can be as well calibrated using force standards with capacity up to approximatively 0,5 MN as it was previously done in the case of other transducers.

### References

1. P. G. Tait, *Voyage of HMS Challenger*, Vol. II-Appendix A, (London-UK, 1882)
2. D. Newhall and L. Abbot, Bulk-Modulus Cell, *Measurement and Data*, (1969)
3. R. Wiśniewski and GF. Molinar, Free-Active Element Bulk-Modulus High Pressure Transducer, submitted for publication to *Rev. of Sci. Instruments*.
4. GF. Molinar and R. Wisniewski, Strain-Gauge Free-Active Element Bulk Modulus High Pressure Transducer, submitted for publication to *Sensors and Actuators-A Physical*.
5. R. Wisniewski and GF. Molinar, *Metrologia* 30 (6), (1994), p. 683.

---

## **IV Material Engineering**



---

**IV(A) Material Preparation Using Static Pressure: SHS, HIP, CIP, etc.**

# CREATION OF HYPERFUNCTIONAL MATERIALS WITH GRADED STRUCTURES BY SHS/HIP

YOSHINARI MIYAMOTO, KIMIAKI TANIHATA, ZHENSI LI, YAN-SHENG KANG,  
The Institute of Scientific and Industrial Research, Osaka University, Ibaraki, Osaka 567, Japan

HIDEKI MORIGUCHI, AKIHIKO IKEGAYA AND TOSHIO NOMURA  
Sumitomo Electric Industries, Ltd. Itami Works, Koya kita, Itami Hyogo 664, Japan

## ABSTRACT

SHS/HIP is a combined process that uses a chemical oven containing low cost silicon as a fuel and a hot isostatic press. This process is suited for the consolidation of compositionally graded materials like  $\text{Al}_2\text{O}_3/\text{TiC}/\text{Ni}/\text{TiC}/\text{Al}_2\text{O}_3$  and  $\text{Al}_2\text{O}_3/\text{Cr}_3\text{C}_2/\text{Ni}/\text{Cr}_3\text{C}_2/\text{Al}_2\text{O}_3$ . These dense graded materials can exhibit outstanding functions beyond conventional alumina ceramics, such as a potential ability of sensing surface damages as well as simultaneous improvements in toughness, hardness and strength. These hyperfunctions are created due to the internal stress balance of compression/tension/compression with symmetrically graded structures.

## 1. Introduction

Numerous refractory and intermetallic compounds can be formed rapidly by self-propagating high temperature synthesis (SHS)<sup>(1)</sup>. The SHS is regarded as an exothermic synthesis process of compounds with high formation enthalpy. When pressure is applied during or just after the SHS, dense compounds can be obtained in a short time<sup>(2)</sup>.

The exothermic heat exceeds over 2000°C, that can be used as an instantaneous heat source for rapid consolidation of ceramic and metal powders under pressure. The SHS/HIP compaction uses such a chemical heat of SHS for the material consolidation under isostatic gas pressure<sup>(3)</sup>. It is useful to consolidate functionally graded materials because the graded compositions are quickly consolidated before the long range phase migrations occur<sup>(4)</sup>.

Various graded compositions can be tailored in

the ceramic/metal system by SHS/HIP, that can induce unique stress states of compression and tension due to their thermal expansion mismatches, resulting in enhancement of physical and mechanical properties. The concept of so-called hyperfunctional materials with graded compositions is demonstrated as well as their fabrication and properties in this paper.

## 2. SHS/HIP: A rapid high pressure-temperature compaction

SHS/HIP is a combined process that uses a chemical oven containing silicon as a fuel and a hot isostatic press as shown in Fig.1. The silicon can react with pressurized nitrogen over 3 MPa and release high heat following the reaction.



The ideal reaction temperature can reach to

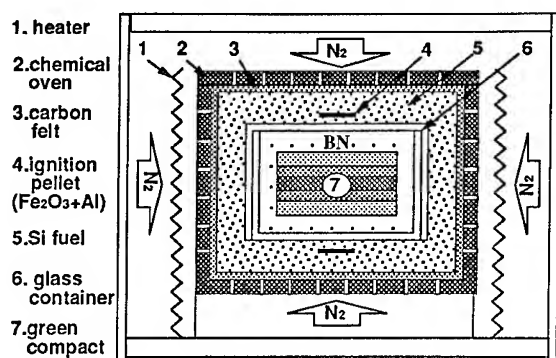


Fig.1. A schematic of SHS/HIP device.

4100 °C, however, the real temperature is limited below the decomposition temperature of  $\text{Si}_3\text{N}_4$ , that depends on nitrogen pressure. Figure 2 shows the decomposition temperature of  $\text{Si}_3\text{N}_4$  calculated as a function of nitrogen pressure. Therefore, the maximum combustion temperature of Si at any nitrogen pressure can be estimated from this curve. For instance, the maximum temperatures at 10 and 100 MPa nitrogen pressure are about 2300 °C and 2500 °C, respectively. However, the duration of the maximum temperature is usually limited within several ten seconds. Figure 3 shows a temperature profile when 30 g silicon is burned under 10 MPa.

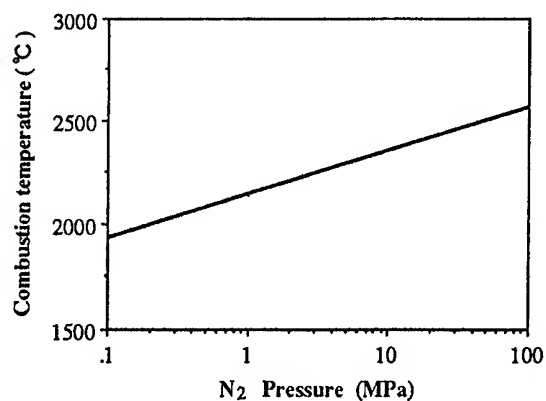


Fig.2. Decomposition temperature of  $\text{Si}_3\text{N}_4$  as a function of nitrogen pressure.

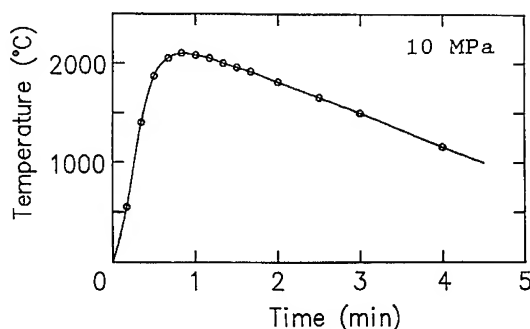


Fig.3. A temperature profile measured for the nitriding reaction of Si under 10 MPa nitrogen pressure.

The green compacts with graded compositions are vacuum sealed with BN powder bed into a borosilicate glass container and then subjected to SHS/HIP. When the glass container is heated up to 980 °C with a HIP heater, thermit pellets in a chemical oven react and ignite silicon fuel. The silicon volume is several tens gram for laboratory scale samples and the nitrogen pressure 100 MPa. Usually the material temperature is 200 °C or 300 °C below the maximum combustion temperature.

This process is suited for the rapid densification of a variety of ceramics and metals, as well as the preparation of functionally gradient materials because the graded compositions are half-melted and consolidated simultaneously and rapidly before long range phase migrations occur. The silicon used is a byproduct of zinc smelting. After it is burned up, it converts to silicon nitride. Therefore, the silicon fuel makes the SHS/HIP a recycling and energy saving process.

### 3. Creation of hyperfunctional materials with graded structures and stresses

Material functions or performances depend on its

inherent material properties, and material properties vary with temperature and pressure. However, material functions are usually limited with material properties at normal pressure. If the stress can be built in materials effectively, a variety of modified functions are expected to be created. An example of such stress-inspired materials is ion exchanged or tempered glass, which can induce the compressive stress at the surface and reinforce their mechanical properties. Prestressed concrete is also reinforced by compression of high tension steel embedded. The brittle nature of these materials can be modified by such stable built-in stress.

It is possible to design the internal stress distribution by integrating dissimilar compositions and optimizing the structure with a gradual change in a single body. Axial graded compositions from a ceramic to metal can relax the internal thermal stress caused from their thermal expansion mismatches and integrate different functions of dissimilar materials<sup>(5)</sup>.

The symmetric configuration of the axial graded compositions like the ceramic/metal/ceramic can induce the stress distribution of compression/tension/compression, that results in reinforcing physical and mechanical properties of the outer ceramic layers by a self-induced compressive stress. The middle layer of the ceramic-metal composite has high toughness over  $15 \text{ MPa}\cdot\text{m}^{1/2}$ , which can keep strength against tensile stress. It is possible to control the tensile stress in the middle layer by reducing the thickness of the outer layers or increasing that of the inner layer.

Figure 4 shows a composition profile distributed symmetrically in the  $\text{Al}_2\text{O}_3/\text{TiC}/\text{Ni}/\text{TiC}/\text{Al}_2\text{O}_3$  system. Figure 5 compares some physical and mechanical properties such as the compressive

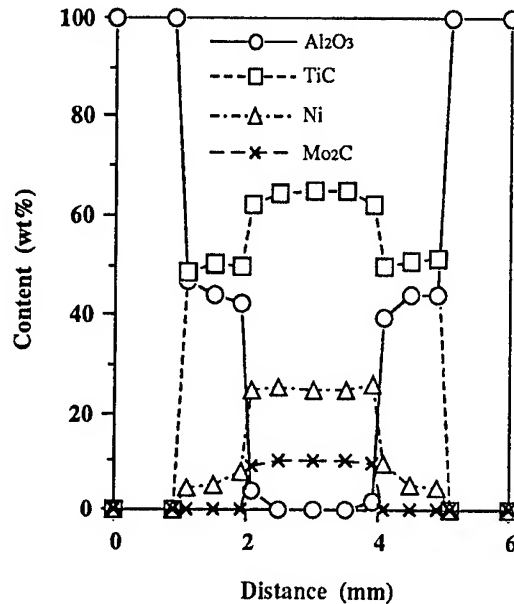


Fig.4. Composition profile of the  $\text{Al}_2\text{O}_3/\text{TiC}/\text{Ni}$  symmetrically graded material.

residual stress at the surface  $\text{Al}_2\text{O}_3$ , hardness, toughness, and strength with those of a monolithic  $\text{Al}_2\text{O}_3$  ceramic. The toughness, hardness and strength are improved remarkably and simultaneously. It is known as a general trend that the material hardness decreases when the toughness increases. The obtained results show, however, that the material functions can be inspired and preceded beyond the original material properties with the design of built-in stress.

Moreover, the stress balance state such as the compression/tension/compression produced can create an intelligent function to detect surface damages. Because the local stress balance is lost, when some surface damages like cracks or abrasions occur at some parts. This stress change at the surface damage is transmitted to the opposite side surface with a strain change. When a fine cut line

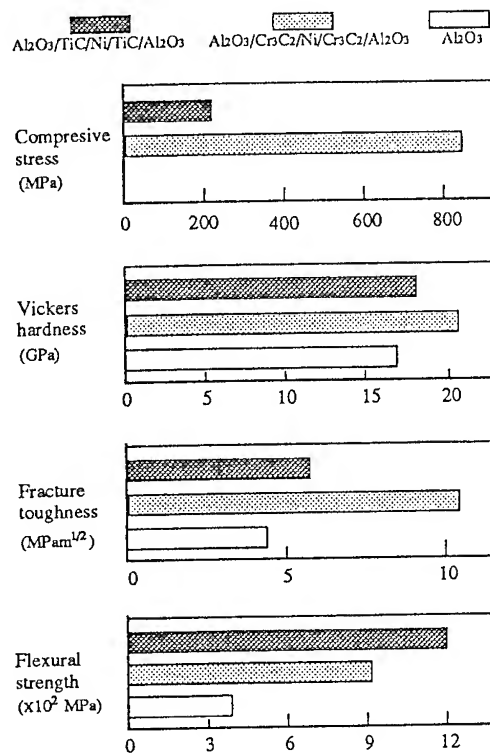


Fig.5. Physical and mechanical properties of the graded Al<sub>2</sub>O<sub>3</sub>/TiC/Ni, Al<sub>2</sub>O<sub>3</sub>/Cr<sub>3</sub>C<sub>2</sub>/Ni and a monolithic Al<sub>2</sub>O<sub>3</sub>.

was introduced along the surface of Al<sub>2</sub>O<sub>3</sub>/TiC/Ni/TiC/Al<sub>2</sub>O<sub>3</sub>, a stress change at the back surface was detected as much as 10 to 20 % along the line direction by X-ray stress analysis as shown in Fig.6. If some strain sensors are attached on the opposite side, some surface damages or displacements with wear would be detected.

When the radial graded structure is designed as schematically illustrated in Fig.7, the radial stress distribution can be obtained. Figure 8 shows the stress distributions of the symmetrically axial and radial graded structures in the system of Al<sub>2</sub>O<sub>3</sub>/TiC/Ni, that was analyzed with finite

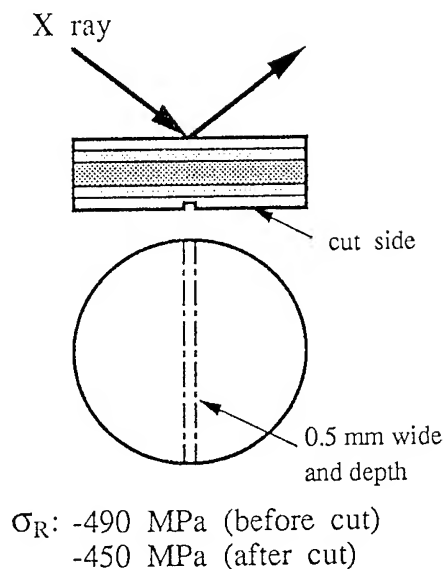


Fig.6. A schematic illustration of X-ray stress measurement for a cut line introduced at the back side of the symmetrically graded materials.

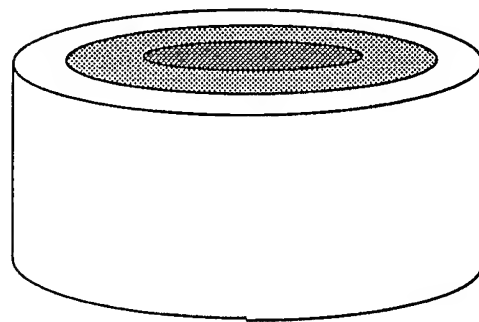


Fig.7. A schematic of the radial graded structure.

element method. In the case of the symmetrically axial graded structures, the residual compressive stress is released at side edges, but strong compressions can remain at the cylindrical edges in the radial graded structure. It is expected, therefore, to apply the radial graded structure for cutting tools. Figure 9 shows the wear rate as a function of wet cutting duration. It is observed that the

homogeneous and axial graded test samples were chipped at around 30 to 40 seconds, while the radial graded ones could withstand over 120 seconds.

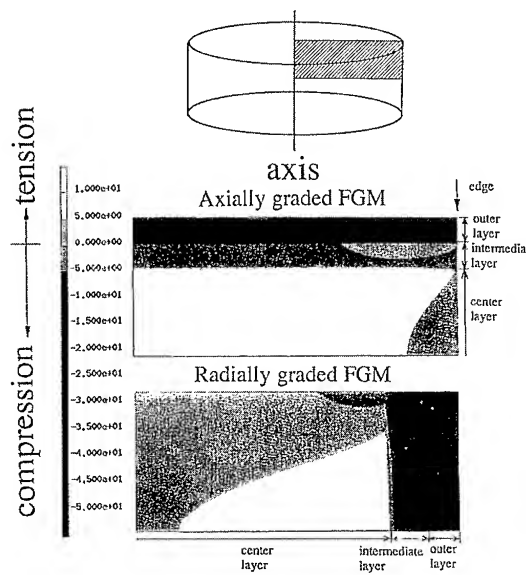


Fig.8. Stress distributions of symmetrically axial and radial graded ceramic/metal materials.

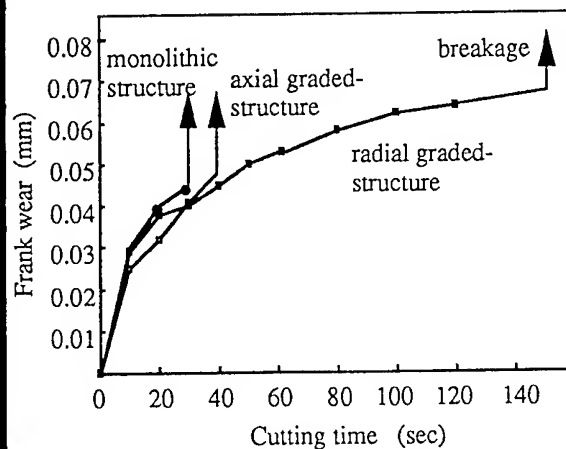


Fig.9. Wear rate vs cutting time for damage resistant test.

#### 4. Summary

It was demonstrated that material properties can be modified and integrated by designing internal stress with graded compositions and structures. Incorporation of well balanced stress distribution of compression and tension into materials can extend their applications. The SHS/HIP is suited to produce such graded materials in the ceramic/metal systems.

#### References

1. A.G.Merzhanov and I.P.Borovinskaya, Dokl. chem.(Engl. Trans.), 204, 429-32(1972)
2. "Combustion and Plasma Synthesis of High-Temperature Materials", edited by Z.A.Munir and J. B.Holt, ( VCH Publishers Inc., 1990).
3. Y.Miyamoto, K.Tanihata, Z.Li, Y.Kang, K.Nishida and T.Kawai, Proc. 8th CIMTEC Conf. "New Horizons for Materials" ed. P. Vincenzini (TECHNA, 1995) p. 387
4. Y.Miyamoto, K.Tanihata, Z.Li, Y.Kang and H. Murakawa, Proc. 8th CIMTEC Conf. "Intelligent Materials and Systems", (TECNA, 1995) p. 87
5. "Functionally Graded Materials", Ceramic Transaction, 34, (Am, Cram, Soc. 1993).

# HIGH PRESSURE SELF PROPAGATING HIGH TEMPERATURE SYNTHESIS OF NICKEL ALUMINIDES

M.C. DUMEZ, R.M. MARIN-AYRAL, J.C. TEDENAC,

Laboratoire de Physicochimie des Matériaux Solides, U.M. II, c.c 003, Pl. E. Bataillon,  
34095 Montpellier Cedex FRANCE

## ABSTRACT

Intermetallic NiAl compound was prepared by combustion synthesis under high hydrostatic pressure. The materials obtained were characterized by X-ray analysis, SEM, Vickers hardness. Finally, a kinetic approach of the synthesis was proposed and discussed.

## Introduction

Intermetallic compounds based on aluminium have the attractive combinations of low density, high strength, good corrosion and oxidation resistance.

The application of pressure in high pressure vessel has impacts on the products: a structural one with changes in porosity, and other one on the mechanical properties of the materials (1). The SHS process (Self propagating High temperature Synthesis) is based on an exothermic chemical reaction occurring between constituent of mixtures, which is ignited at one point and propagates through the sample in the form of a combustion wave (2,3).

This paper describes high hydrostatic pressure combustion synthesis interest for elaboration of materials.

In our studies (1,4), combustion synthesis and high pressure are associated in order to ensure a good control of the exothermicity of reaction and to realize a densification in situ for the materials.

The aim of this presentation is to evaluate the mode of combustion under high pressure and its evolution in function of pressure.

## Experimental procedure

Combustion experiments were carried out in a high pressure-high temperature equipment which can be divided in three parts (5):

- a gas compressor which allows to reach pressures up to 1.5 GPa
- a high pressure chamber

- a high temperature furnace (temperatures up to 1600°C) which consists of a heating graphite spiral.

Temperature is controlled by means of three PtRh 6%- PtRh 30% thermocouples. The signals from the thermocouples and manganine gauge for the pressure are stored and processed by a data acquisition system (40 points per second).

The combustion reactions involved aluminium and nickel powders in stoichiometric ratio, which were pressed into pellets. These compacts were then ignited in various argon pressures with heating rates varying from 2 to 90°/mn.

In our first experiments (1), the pellets were pressed uniaxially at a pressure of 370 MPa; two heating rates (20 and 50 °/mn) were used and argon gas pressure in the high pressure vessel ranged from 50 to 300 MPa. After that, to obtain greater densities of the products by lowering the closed porosity, the powders were pressed at pressures just lower than 40 MPa, yield strength value of the aluminium. In this case, argon pressure was taken as 60, 100, 320 et 500 MPa. For each pressure, heating rate is varying from 10 to 90°/mn by step of 10°. For 100 MPa, two other experiments were made at 2 and 5 °/mn.

The products obtained are characterized by X-ray diffraction, MEB, porosity measurements and Vickers microhardness.

## Results

Temperature-time history obtained for the synthesis of NiAl during heating and ignition is registered for each experiment. The ignition

temperature is found to be typically about 900K. Moreover, the signal shows the low exothermicity of this reaction. We will show that we obtain by this method pure NiAl compound.

For powders compacted under isostatic pressure of 370 MPa, porosity was determined with variation of gas pressure in the chamber. As can be seen on figure 1, when the pressure in the reaction vessel increases, the porosity of products decreases.

With powders compacted under 40 MPa, the heating rate has a tremendous influence on the macroscopic aspect of the samples. At a pressure of 100 MPa, under low heating rates ( $2^\circ/\text{mn}$ ), the samples keep their initial shape with the morphology of the compact. As the heating rate increases to  $10^\circ/\text{mn}$ , NiAl product presents a dense region with a large central void, whereas where the reaction starts, it remains porous. Then, at  $80^\circ/\text{mn}$ , the whole product seems densified with large central voids. For another value of argon pressure, the same phenomenon is observed but the transition between the two aspects of the material is situated at a different heating rate. The X-ray diffractograms registered for the products obtained for low heating rates, 2 and  $5^\circ/\text{mn}$  at 100 MPa, 10 and  $20^\circ/\text{mn}$  at 320 MPa, and 10 and  $20^\circ/\text{mn}$  at 500 MPa, reveal that these samples contain several phases. In each other case, we always obtain pure stoichiometric NiAl phase. These results are confirmed very well by scanning electronic microscopy study.

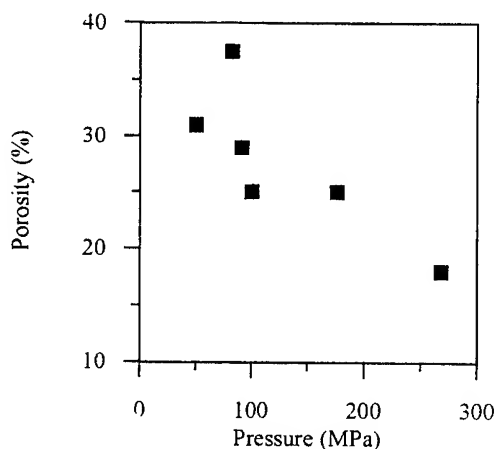


Figure 1: NiAl porosity as a function of pressure

The microhardness results obtained for samples synthesised at 500 MPa and with different heating

rates are shown on figure 2, which confirm the existence of two domains.

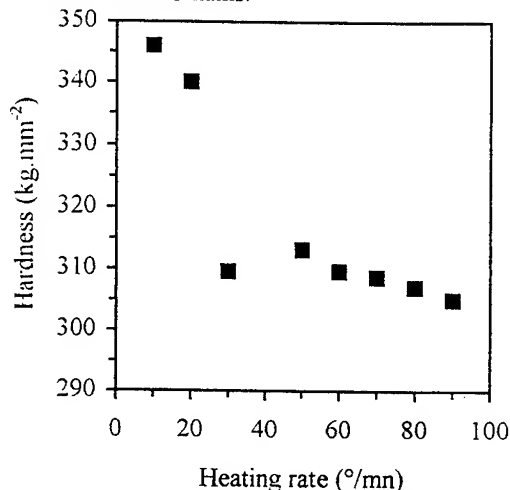


Figure 2: Vickers microhardness as a function of heating rate

### Kinetic analysis

We got information about the combustion mode by using a simplified kinetic model, established by Boddington (6,7). This model is based on a general equation of heat released during the SHS process and gives several thermodynamic and kinetic parameters through the analysis of the temperature profile obtained during combustion synthesis. These parameters are rate of combustion, adiabatic temperature and activation energy of the reaction.

The temperature profiles associated with the passing of a self propagating wave in the combustion synthesis of NiAl were investigated for four pressures: 60, 100, 320 and 500 MPa.

From profile analysis of 100MPa, two activation energies of  $47 \text{ kJ.mol}^{-1}$  and  $525 \text{ kJ.mol}^{-1}$  were calculated (figure 3), according to the Arrhenius

$$\text{law } \frac{\partial \eta}{\partial t} = K_0 f(\eta) \exp\left(-\frac{E_a}{RT}\right), \quad (\eta \text{ is the degree}$$

of conversion,  $t$  the time,  $\frac{\partial \eta}{\partial t}$  the reaction rate,  $T$

the temperature,  $E_a$  the activation energy,  $R$  the gas constant,  $K_0$  a constant, and  $f(\eta)$  a kinetic function) and were found to agree very well with different aspects of the obtained products. From profile analysis of 500 MPa, one activation energy of  $117.1 \text{ kJ.mol}^{-1}$  was calculated (figure 4).

This study shows that different combustion modes exist for this solid-solid reaction. We assume that they correspond to:



- at lower heating rates, a diffusion process in the solid state, with a diffusion barrier (I)
- for intermediate rates, non stable SHS (II)
- at higher heating rates, stable SHS, with approaching adiabatic conditions (III).

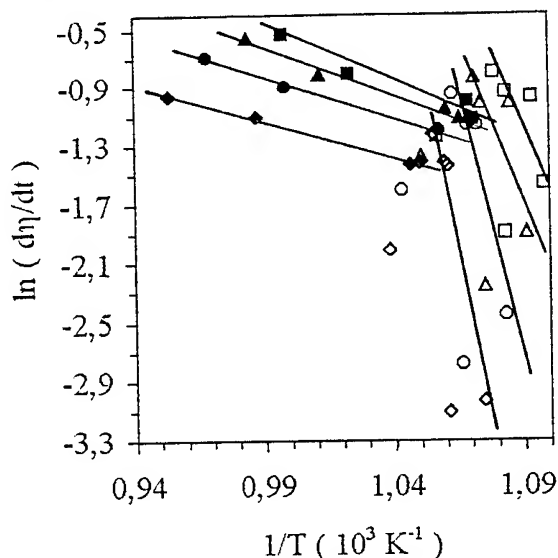


Figure 3: Activation energies determination for SHS process at a pressure of 100 MPa

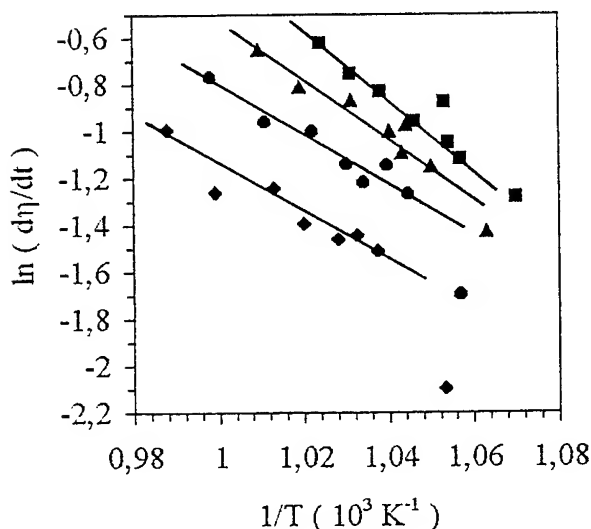


Figure 4: Activation energies determination for SHS process at a pressure of 500 MPa

Moreover, we show that the limits between these modes are varying with pressure. Thus, a pressure-heating rate diagram can be established (figure 5), which gives the reaction type occurring, depending on the experimental conditions.

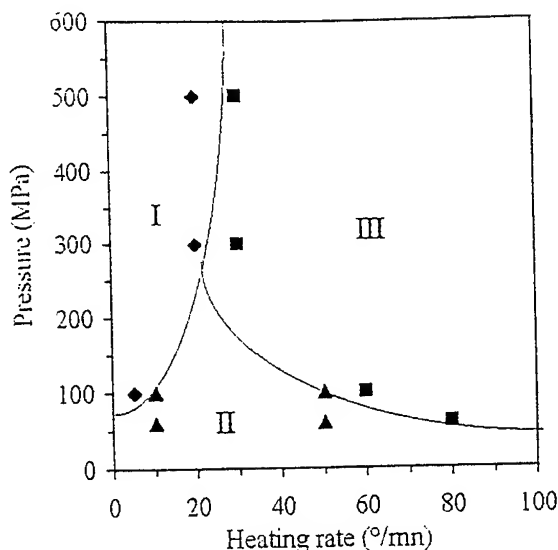


Figure 5: SHS diagram for NiAl

## Conclusion

Possible reaction mechanisms of the SHS reaction between nickel and aluminium powders under high hydrostatic pressure have been proposed. This was possible through the analysis of variation of reactant heating rate at different gas pressures. Then this study leads to the establishment of a diagram which will permit to choose the conditions of synthesis for NiAl. At the same time, characterization of the obtained materials was made. As can be seen, we are able to prepare NiAl intermetallics with excellent purity, known porosity, and relatively high hardness.

## References

1. M.C. Dumez, R.M. Marin-Ayral and J.C. Tédénac, *Mat. Res. Bull.* 29, 6 (1994) 611
2. A.G. Merzhanov, *Combust. Flame* 13 (1969) 143
3. Z.A. Munir, *Ceram. Bull.* 67, 2 (1988) 342
4. M. Bockowski, J. Jun, I. Grzegory, R.M. Marin-Ayral and J.C. Tédénac, *Cer. Acta* 6, 4 (1994) 43
5. M. Porowski, J. Jun and I. Grzegory, in *High Pressure Chemical Synthesis*, ed. Jurczak and Baranowski (1989) p.21
6. T. Boddington, P.G. Laye, J.R.G. Pude and J. Tipping, *Combust. Flame*, 47 (1982) 235
7. T. Boddington, P.G. Laye and J. Tipping, *Combust. Flame*, 63 (1986) 359

## THE INTERACTION BETWEEN $\text{WO}_3$ AND CARBON UNDER HIGH PRESSURE.

FILONENKO V.P.

Institute for High Pressure Physics, Russian Academy of Sciences, Troitsk, Moscow Region, 142092, Russia.

ZIBROV I.P.

Institute of Crystallography, Russian Academy of Sciences, Leninsky pr.59, Moscow 117333, Russia.

### ABSTRACT

The interaction between  $\text{WO}_3$  and carbon was investigated under pressure 3-8 GPa and temperature 1000-1500° C. It was shown that the reduction of  $\text{WO}_3$  with carbon occurs with the help of the gas phase. The two new high pressure phases  $\text{W}_3\text{O}_8$ (I and II) were obtained as a result of the reduction. The crystal growth problems are discussed.

There are very many papers devoted to the reduction problems of  $\text{WO}_3$  by carbon and  $\text{H}_2$  so as these reactions are used widely to obtain of the metallic W and the hard alloys based on WC. The interaction of  $\text{WO}_3$  with carbon occurs with the help of the gas phase (reactions (1)-(3)). In this work we tried to estimate the conditions when  $\text{WO}_3$  reduction occurs under high pressure.

The interaction between  $\text{WO}_3$  and carbon was investigated by using both "lentic" and toroid type of the high pressure chambers. These chambers consist of the two hard metal anvils with a special profile. The pressure is generated in the

lithographic limestone cell placed between the anvils. The cell insertion contains the graphitic tube-type heater and the sample (pressed from  $\text{WO}_3$  pellet) put into the heater and closed with the two graphitic covers (Fig.1). The required pressure was achieved for the period 15-20 minutes. After that the sample was heated by the electric current. The applied pressure and the temperature were calibrated in previous experiments. The pressure 3-8 GPa, the heater temperature 1000-1500°C and the reaction time 3-5 min. was used in experiments.

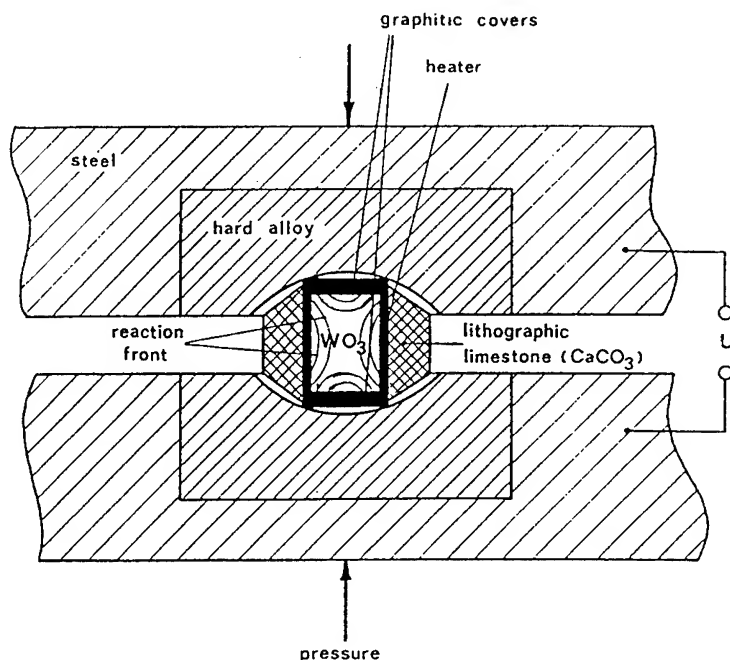
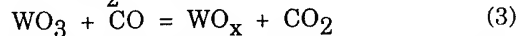
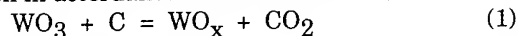
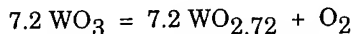


Fig.1. The "lentic" type high pressure chamber.

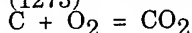
In order that the reduction of  $\text{WO}_3$  by CO might be started (reaction (3)),  $\text{CO}_2$  has to be appeared in the closed system due to the direct interaction of  $\text{WO}_3$  with carbon in accordance with the reaction (1).



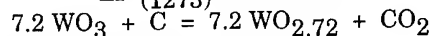
The thermodynamical calculations show that all three reactions occur in this system. The pressure of  $\text{CO}_2$  in equilibrium at  $T=1000^\circ\text{C}$  for the reaction (1) is 4.8 GPa and increases sharply with the temperature increasing.



$$\Delta F^\circ_{(1273)} = +66.92 \text{ kcal}$$



$$\Delta F^\circ_{(1273)} = -94.2 \text{ kcal}$$



$$\Delta F^\circ_{(1273)} = -RT \ln P_{\text{CO}_2} = -27283 \text{ cal}$$

$$P_{\text{CO}_2} = 4.8 \text{ GPa}$$

The constant of equilibrium for the reaction (2) is more then 1 at  $T > 1000^\circ\text{C}$ . The interaction would lead to the pressure increasing in the chamber and the reaction has to be stopped. But this process does not take place in our case because the new synthesizing phases ( $\text{W}_3\text{O}_8$ ) are more dense in compare with  $\text{WO}_3$ , and so the appearing gases (CO,  $\text{CO}_2$ ) can fill the empty volume. Really, there is one spherical cavity 1-2 mm in diameter in the centre (or near centre) of the each sample. Very many channels go away from this cavity in all directions and have size from tens till hundreds micrometers in diameter. Along these channels  $\text{CO}_2$  moves from the reaction front to the carbon heater and CO - in the back direction. The reaction front moves from the heater to the sample centre with the speed  $\sim 1 \text{ mm/min}$  due to the fast gas transport.

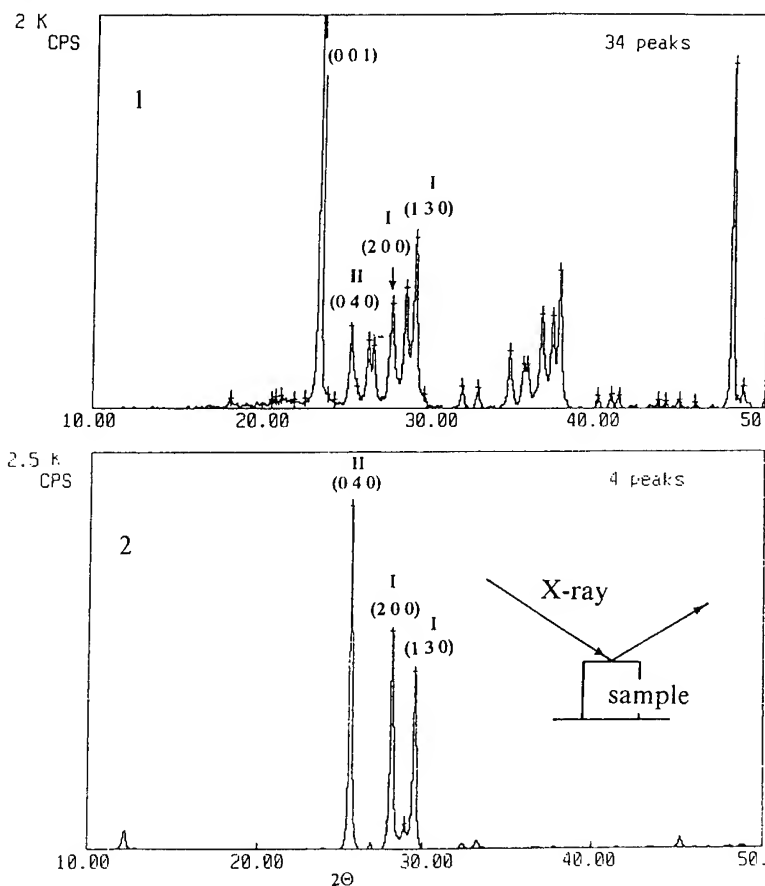


Fig. 2. 1-XRD pattern, taken from the powder material; 2- XRD pattern, taken from the compact sample in the geometry shown in the picture.

As a result of the reduction process the samples which consist of the mixture of the two modifications of  $W_3O_8$  (I and II) [1] were obtained. After synthesis the samples had the form of the cylinder with the almost plane bases. The X-ray patterns taken from these bases show that only reflections (200) and (130) from  $W_3O_8$ (I) and (040) from  $W_3O_8$ (II) are present in the region  $10^\circ$ - $50^\circ$  ( $2\theta$ )(fig 2). It means that the crystals of  $W_3O_8$ (I and II) grow along the planes with the maximum density -"ab". The axis "c" and the intergrowth planes (the planes in which these two modifications can be connected without distortions:(h00) and (130) for  $W_3O_8$ (I) and (0k0) for  $W_3O_8$ (II) [1] ) lay in the plane of the reaction

front. The main directions of the crystal growth in the plane "ab" are [100] and [110] for  $W_3O_8$ (I) and [010] for  $W_3O_8$ (II).

ACKNOWLEDGMENT: The research described in this publication was made possible in part by Grant N NFP000 from the International Science Foundation.

#### REFERENCES

1. M.Sundberg et al. Acta Cryst. (1993). B49, 951-958.

## THE SYSTEM W-O UNDER HIGH PRESSURE (THE REGION $\text{WO}_2$ - $\text{WO}_{2.8}$ ).

FILONENKO V.P.

Institute for High Pressure Physics Russian Academy of Sciences, c.Troitsk, Moscow Region  
142092, Russia.

ZIBROV I.P.

Institute of Crystallography Russian Academy of Sciences, Leninsky pr.59, Moscow 117333, Russia.

SUNDBERG M.

Arrhenius Laboratory University of Stockholm, S-106 91 Stockholm, Sweden.

### ABSTRACT

The phase diagram W-O (the range  $\text{WO}_2$ - $\text{WO}_{2.8}$ ) was investigated by using the solid state reaction between  $\text{WO}_3$  and W powders in the toroid-type high pressure chamber. The temperature regions of the stability for the five new tungsten oxides ( $\text{WO}_2$ -hp,  $\text{W}_{32}\text{O}_{84}$  ( $\text{WO}_{2.625}$ ),  $\text{W}_3\text{O}_8$ (I) and  $\text{W}_3\text{O}_8$ (II) ( $\text{WO}_{2.667}$ ),  $\text{W}_2\text{O}_5$ ) are defined at the pressures 6.0 and 8.0 GPa.

The phase diagram W-O is investigated very carefully at the ambient pressure. The main method used in these studies was the solid state sintering of the mixtures W+ $\text{WO}_3$  at sealed tubes. It allows to keep the constant composition during the annealing.

The solid state reaction between W(99.9%) and  $\text{WO}_3$ (99.95%) powders (3-10  $\mu\text{m}$ ) was used for the synthesis of the tungsten oxides under high pressure. The mixtures with the composition  $\text{WO}_2$ - $\text{WO}_{2.8}$  were prepared by using the both dry and wet (in acetone) mixing. Then the pellets 12 mm in diameter and 6 mm height for the pressure 6.0 GPa and 6 mm in diameter and 3 mm height for the pressure 8.0 GPa were pressed. The high pressure toroid-type chamber was used for synthesis. This chamber consists of the two hard metal anvils with a special profile. The pressure generated in the lithographic limestone cell placed between the anvils. The cell insertion contains the graphitic tube-type heater and the sample, wrapped into the protecting foil (fig 1). The required pressure was achieved for the period 15-20 minutes. After that the sample was heated by the electric current. The samples were annealed at temperature and pressure from 20 till 30 minutes at 6.0 GPa and from 10 till 15 minutes at 8.0 GPa. After training the samples were cooled under pressure with the average speed 10 C/sec., then the pressure was decreased and the samples were taken for analysis. The

"Rigaku" powder diffractometer (Cu  $K\alpha$  irradiation, Ni filter) was used for the X-ray phase analysis. The electronmicroscopic investigations were carried out at the microscope JEOL 200CX.

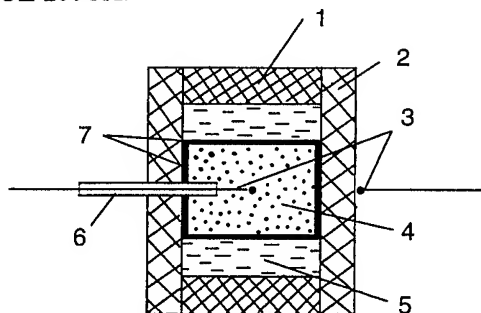


Fig.1. The cell insertion.

- 1) graphitic covers; 2) graphitic heater;
- 3) thermocouples; 4) sample; 5) BN covers;
- 6)  $\text{Al}_2\text{O}_3$  tube; 7) W foil.

The temperature and the pressure were calibrated in previous experiments. The temperature was measured by the thermocouples placed in the different parts of the sample and near the heater. It was established that the temperature gradient along the sample height is less than 50 C. The pressure was calibrated by measurement of the electric conductivity of Bi (it has phase transformations at 2.55 and 7.7 GPa) and Ba (5.5 GPa).

Phase formation in the system was investigated in the temperature region 700-1250 C. At the temperatures below 700 C the

interaction between W and  $\text{WO}_3$  was practically absent. At the temperatures higher than 1250 C the protecting foil interacted strongly with the heater and the sample.

At 6.0 GPa the four new high pressure phases were obtained:  $\text{WO}_2\text{-hp}$ ,  $\text{W}_{32}\text{O}_{84}(\text{WO}_{2.625})$ ,  $\text{W}_3\text{O}_8(\text{I})$  and  $\text{W}_3\text{O}_8(\text{II})$  ( $\text{WO}_{2.667}$ ). The structure of these phases are described in [1,2,3] and the temperature regions of stability is shown in Fig.2. One can see that  $\text{WO}_2\text{-hp}$  is stable in the very narrow interval - 900-1000 C. At higher temperature the ambient pressure modification is stable. The compound  $\text{WO}_{2.625}$  is the most stable at the pressure 6.0 GPa - it is synthesized in the temperature interval 900-1250 C.  $\text{W}_3\text{O}_8(\text{I})$  appears in the reaction products at 800 C and exists until 1150 C. It was impossible to obtain  $\text{W}_3\text{O}_8(\text{II})$  at high pressure as a single phase - only in the mixture with  $\text{W}_3\text{O}_8(\text{I})$ .

The investigations under the pressure 8.0 GPa show that the W-O phase diagram changes strongly in compare with the pressure 6.0 GPa. At first it was established that the pressure increasing leads to the increasing of the temperature at which the starting components begin to interact - from 800 till 950 C. The temperature region of the stability of  $\text{WO}_2\text{-hp}$  is more wider - 950-1200 C.  $\text{W}_3\text{O}_8$  modifications are stable until 1250 C.  $\text{WO}_{2.625}$  disappears from the phase diagram and instead it the new phase with the close composition  $\text{WO}_{2.5}$  appears. The X-ray and electronmicroscopic investigations show that this phase is isotypical with  $\text{L-Ta}_2\text{O}_5$ , has the very disordered structure (probably oxygen sublattice) and the unit cell parameters  $a=6.124$ ,  $b=39.901$  and  $c=3.789$  Å.

**ACKNOWLEDGMENT:** The research described in this publication was made possible in part by Grant N NFP000 from the International Science Foundation.

## REFERENCES

1. P.-E. Werner et al. Zeitschrift für Kristallographie 209,662-666,(1994).
2. Yu.A. Barabanenkov et al. Acta Cryst.(1993), B49, 169-171.
3. M. Sundberg et al. Acta Cryst.(1993), B49, 951-958,

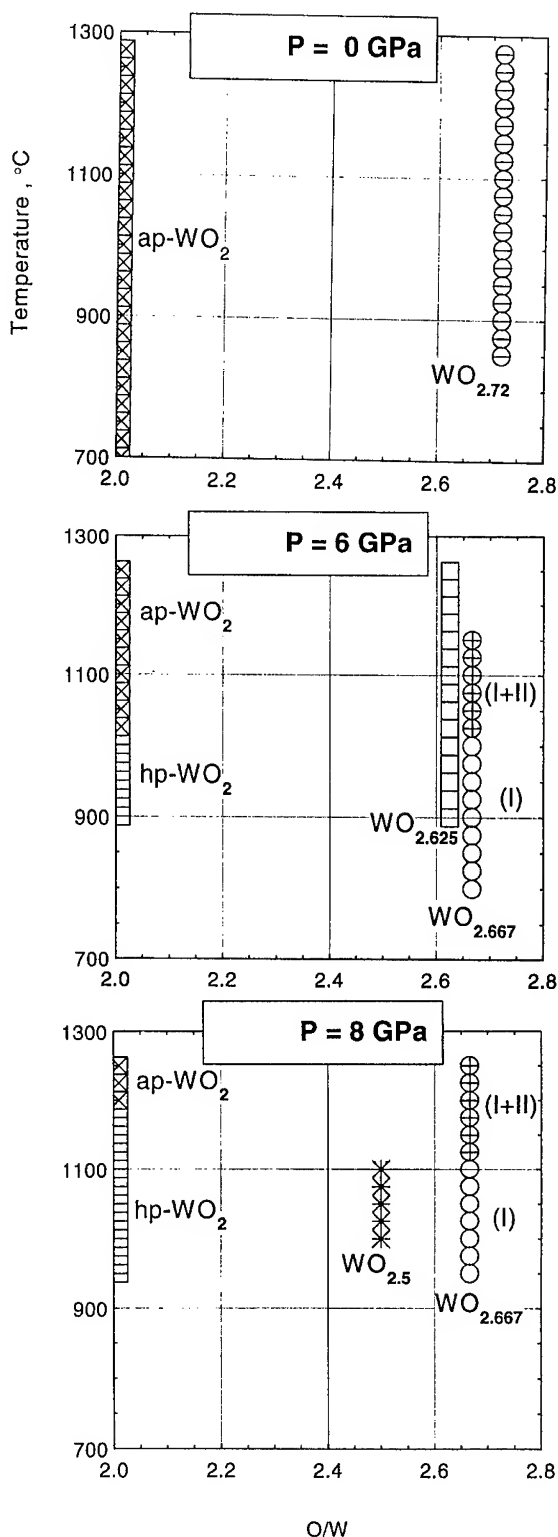


Fig. 2. The stability ranges of the tungsten oxides.

# SINTERING AT HIGH PRESSURES AND PROPERTIES OF ALUMINUM NITRIDE CERAMICS

V. S. URBANOVICH

*Institute of Solid State and Semiconductor Physics, Belarussian  
Academy of Sciences,  
17 P. Brovka str, Minsk, 220072, Belarus*

## ABSTRACT

Single-phase ceramic samples of AlN with density of  $3.25 \text{ g/cm}^3$  and thermal conductivity of  $185 \text{ W/(m} \cdot \text{K)}$  without use of any activating additions have been produced by sintering under high pressures. Density, thermal conductivity and lattice strains of aluminum nitride have been investigated depending upon regimes of thermal pressure treatment at pressures up to 4 GPa and at temperatures (0.64 - 1.0) of a decomposition temperature ( $T_m$ ). An increase of a microstrain level and generation of deformation defects and oriented microstrains is also observed under temperature and pressure treatment up to temperatures (0.64-0.72)  $T_m$ .

## Introduction

Aluminum nitride complies most fully with the current requirements for the IC substrates and electronic instrumentations (1). It belongs among the compounds with the highest thermal conductivity (2,3). However, its realization in ceramic materials presents difficulty (4). The known methods of production of aluminum nitride-based ceramics require protracted in time high-temperature sintering and use of the activating additions, that leads to a more complicated sintering process and results in lowering the properties of the material (5).

High pressure technology allows to significantly intensify the sintering process and without use of activating additions to produce single-phase high density ceramics with reduced sintering time. The properties of such single-phase materials are close to the properties of substances on the basis of which they are formed (6). However, the literature provides scarce data on sintering of the aluminum nitride powder under superhigh pressures, as well as on properties of the sample produced (7-10).

The paper (7) describes that under impact-loading of aluminum nitride crystallites grinding and increase of the lattice strains, following the growth of compression rate, take place. It is noted there with that lattice strains are higher under

dynamic compression compared to the static one. The value of the compression rate for the static regime is not provided. Shimada et al. (8) were the first to produce ceramic samples of aluminum nitride with 100% density under pressure of 5 GPa and temperatures (0.4-0.6)  $T_m$ . However, information on the properties of these samples has not been provided.

Investigating the structure of AlN samples by electron diffraction method sintered under pressure 7-10 GPa the authors (9) found out the availability of the second phase of  $\alpha - \text{Al}_2\text{O}_3$ . They showed that solubility of oxygen in AlN decreased under high pressure.

The paper (10) describes that AlN samples were produced under pressure of 5 GPa having 100% density and thermal conductivity up to  $170 \text{ W/(m} \cdot \text{K)}$  and the value of the sintering activation energy was determined under pressure of 5 GPa and temperatures (0.88-1.0)  $T_m$ . The value of activation energy of 34 kJ/mol evidences that mass transfer takes place on the basis of boundary sliding. The authors (10) are of the opinion that the mechanism of plastic deformation followed by post-deformation annealing forms the basis for the process of AlN sintering under high pressures.

## The experimental procedure

Aluminum nitride powder with particle size

0.5-6.5  $\mu\text{m}$  and oxygen content up to 1% produced by furnace synthesis was used for investigation. The blanks 11 mm in diameter and 5 mm in height were formed from it under pressure 1 GPa which then were subjected to pressure of 2.5 and 4 GPa in the high pressure anvil-type device with a hollow (11). A container made of lithographic stone has been used as a pressure transferring environment for the sample. The sample heating was effected by a graphite tubular heater. The sample contacted with the graphite-like boron nitride on both ends. Device pressure calibration has been done at a room temperature by phase transitions in Bi, Tl and Yb taking place under pressures 2.55, 7.7, 3.67 and 4 GPa respectively, and temperature calibration has been effected by using chromel-alumel thermocouple and by melting points of reference-metals, namely: nickel, rhodium, molybdenum and platinum. The accuracy of temperature determination was in the average 3.8%.

The density of the ceramic samples has been determined by the hydrostatic weighing in a carbon tetrachloride and the value of the thermal conductivity coefficient by a comparative stationary method. X-ray diffraction meter DRON-3 was used for X-ray structural investigation in  $\text{Cu-K}_2$  radiation. Accuracy in determining the lattice parameters was  $\pm 0.0001$  nm.

## Results and discussions

The results of the investigation of aluminum nitride-based ceramic samples produced by sintering under pressures 2.5-4 GPa are shown in Figs.1-2. The Fig.1 shows changes of sample density as a function of sintering temperature. It is evident that as sintering temperature increases the sample density is growing and it reaches the level of saturation, and this is attained at a lower temperature with a lower pressure. A higher density of aluminum nitride samples sintered at low temperature and pressure of 2.5 GPa is probably conditioned by the fact that under the given pressure the powder particle hardening in the process of reduction takes place at a lesser extent than under pressure of 4 GPa. That is why transition of the material to the plastic state, when heated further, takes place at a lower temperature. However, at higher sintering temperatures the

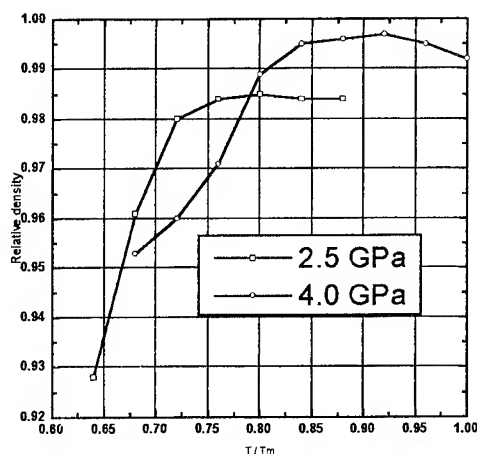


Figure 1. Relative density of AlN samples vs sintering temperature at pressures of 2.5 and 4 GPa.

density of sintered samples increases with pressure build-up.

Thermal conductivity coefficient of aluminum nitride samples - sintering temperature under 4 GPa pressure relationship is provided in Fig.2 which shows that, as temperature increases, its value grows reaching the maximum of 185  $\text{W}/(\text{m}\cdot\text{K})$ , and then it decreases. Sample thermal conductivity increase, with sintering temperature increasing, is related to reduction of their porosity and higher grain sizes, as well as to reduction of lattice microdeformations. It is likely, that thermal conductivity reduction with further increase of sintering temperature is conditioned by aluminum nitride dissociation at higher

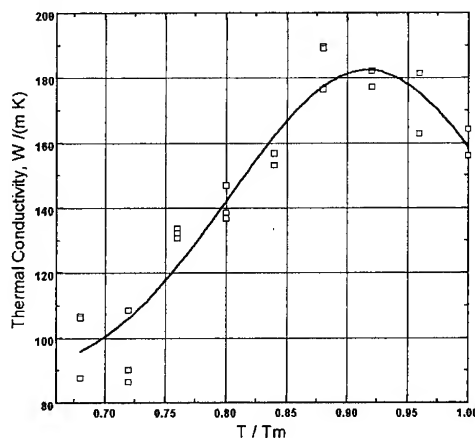


Figure 2. Thermal conductivity of AlN samples sintered at pressure 4 GPa vs sintering temperature.



temperatures and by a higher porosity.

Lattice parameter values obtained by us are provided in table. In the process of thermal and

Table : Lattice parameter of aluminum nitride.

Sintering regime	a · 10, nm	c · 10, nm	c/a
Lit. data (5)	3.113	4.982	1.600
Initial powder	3.113	4.979	1.559
P=2.5 GPa, 60s			
room temp.	3.115	4.968	1.595
T=0.72 T <sub>m</sub>	3.116	4.980	1.598
T=0.88 T <sub>m</sub>	3.113	4.974	1.598
P= 4 GPa, 60 s			
room temp.	3.115	4.983	1.599
T=0.72 T <sub>m</sub>	3.116	4.978	1.597
T=0.88 T <sub>m</sub>	3.117	4.979	1.597
T=0.96 T <sub>m</sub>	3.114	4.977	1.598
P= 4 GPa			
T=0.88 T <sub>m</sub>			
20 s	3.115	4.978	1.598
180 s	3.115	4.971	1.596

pressure treatment of aluminum nitride, alongside with widening of X-ray lines, a shift of specific reflexes is observed that may be related to packing defects and, probably, to oriented microstrains.

Formation of the packing defects under the given regimes of thermal and pressure treatment is also supported by the dependence of the half-width of the line upon the scattering angle. It is actually linear for the initial powder, while a significant deviation of specific reflexes from such a dependence is observed for aluminum nitride-based ceramic samples. As line widening is of a symmetric character we have assumed that these are deformation-related defects.

## Conclusion

1. Increase of the level of microstrains and formation of deformation defects and oriented microstrains is observed in the process of thermal and pressure treatment up to temperatures (0.64-0.72) T<sub>m</sub>. With pressure increase from 2.5 to

4 GPa presence of defects in sintered samples increase. However with sintering temperature increasing, due to recrystallization the lowering of the level of the presence of defects up to that of the level of the initial powder and increase of the thermal conductivity of the sintered samples up to the maximum value are taking place.

2. The conducted investigations have enabled to improve the technology for producing high density ceramics from aluminum nitride for substrates of the hybride IC with the diameter up to 50 mm.

3. Application of AlN powder of the higher purity as an initial material will enable to increase thermal conductivity of ceramics.

## Acknowledgements

I would like to thank Dr. A.I.Olekhovich for the X-ray diffraction analysis and A.V.Chuevski for his help in the thermal conductivity measurements.

## References

1. W. Werdecker and F. Aldinger, *IEEE Trans. CHMT-7*, 4 (1984), 399.
2. G. A. Slack, *J. Phys. Chem. Sol.* 34 (1973), 321.
3. G. A. Slack, et al., *J. Phys. Chem. Sol.*, 48 (1987), 641.
4. M. P. Borom, et al., *Bull. Am. Ceram. Soc.* 51 (1972), 852.
5. T. Y. Kosolapova, et al. *Nonmetallic high-melting compounds* (Metallurgiya, Moscow, 1985) (in Russ.).
6. M. Shimada, et al., in *Ceramic Powders* (Elsevier, Amsterdam, 1983), p. 871.
7. M. Akaishi, et al., in *High Press. Sci. Technol.* (New York e.a., 1984), p. 159.
8. M. Shimada, et al., *J. Jap Soc. Powd. Met.* 25 (1978), 275.
9. A. N. Pilyankevich, et al., *Powd. Met. Kiev*, (in Russ.), 3 (1991), 38.
10. V. B. Shipilo, et al., in *Wide Band Gap Electronic Materials*, ed. M. A. Prelas et al. (Kluwer Academic Publishers, 1995), p. 421.
11. A. M. Mazurenko, et al., *Vestsi of Belarus. Acad Sci., ser.phys.-tech. sci.* (in Russ.), 1 (1994), 42.

# SIMULTANEOUS SYNTHESIS AND SINTERING OF SILICON CARBIDE UNDER HIGH PRESSURE AND TEMPERATURE

S.K.BHAUMIK, C.DIVAKAR, MURALI MOHAN, S.USHA DEVI,  
P.M.JAMAN and A.K.SINGH

*Materials Science Division, National Aerospace Laboratories,  
Bangalore 560 017, India*

## ABSTRACT

The microstructures of the SiC compacts synthesized and sintered from elemental Si and C at 3 GPa and temperatures below and in excess of 2500°C are discussed. The formation of SiC is enhanced by (a) the reduction in the particle size and (b) degassing of the starting powder mixture. In the temperature range 2100-2500°C,  $\beta$ -SiC is formed, and exhibits an equiaxed grain morphology with hardness values 22-25 GPa. Around 2700°C, the  $\beta$ -SiC formed initially undergoes transformation to the  $\alpha$ -phase exhibiting the characteristic plate-like morphology with a hardness of 30 GPa. At still higher temperatures ( $\approx$  2900°C), decomposition of  $\alpha$ -SiC into Si and C is observed.

## Introduction

The self-propagating high temperature synthesis (SHS) has been used to synthesize a number of ceramic materials [1-4]. The products of SHS are porous because the high temperature in the combustion zone is not maintained long enough to cause sintering. Further, the volatile impurities and the released gases hinder sintering. Miyamoto *et al* [5] suggested that the synthesis and compaction can be achieved in a single step by carrying out the SHS under high pressure. This process is commonly referred to as the high pressure self-combustion sintering (HPCS). The HPCS of SiC by Yamada *et al* [6] resulted in compacts of 90% theoretical density and hardness of 21 GPa. Our earlier study [7] on the HPCS of SiC has shown that SHS does not go to completion and thermal energy has to be supplied from an external source for the completion of the reaction.

## Experimental Details

Silicon powder > 99.999 % pure (Koch-Light Ltd., UK) and amorphous carbon powders were used as the starting materials. Three different sources of carbon were used in the study: (a) Philips carbon black, (b) soot collected by burn-

ing camphor, and (c) activated charcoal (GR grade, Sarabhai Chemicals, India). The carbon powder (b) was heated to 1000°C under vacuum ( $\approx 10^{-4}$  Torr) for 15 minutes to remove the volatile matter. The carbon powders (a) and (c) were reported to be almost free from volatile impurities (< 0.2%). The Si + C mixtures, in the molar ratio 1:1, were prepared by both dry (Spex mill-8000, USA, 40 min) and wet (Fritsch pulverisette-5, 24 h in hexane) milling. The mixtures with carbon powders (a), (b) and (c) are referred to as specimens A, B and C respectively. Degassing of the mixture was carried out at 400°C in vacuum ( $\approx 10^{-4}$  Torr) for 2 hours.

The synthesis and sintering experiments at high pressures and high temperatures were carried out using a 200-ton cubic anvil apparatus (anvil face - 10 mm square) capable of generating pressures up to 6.5 GPa and temperatures in excess of 2500°C [7]. The powder-mixture of Si and C was packed in a graphite tube fitted in a pyrophyllite cube; the graphite tube was used to heat the specimen. The oil pressure-specimen pressure relation was obtained using the Bi I  $\rightarrow$  II (2.55 GPa) and Yb fcc  $\rightarrow$  bcc (4.0 GPa) transformations. A power-temperature plot was established up to 1700°C using a Pt-Pt10%Rh

thermocouple and higher temperatures were estimated by extrapolation of the plot. The sample was first pressurized to 3 GPa, heated to the required temperature at  $\approx 60^\circ\text{C/s}$  and cooled after a waiting period ranging from 30 s to 5 min. The recovered specimens ( $\approx 3.5$  mm in diameter and 4 mm in thickness) were characterized by X-ray, optical metallography (Neophot-2) and hardness (Shimadzu HSV-20, load-1.96 N) measurements.

## Results

The wet milled powder had an average particle size of  $3.2\ \mu\text{m}$  with 80 wt% in the range  $1.5\text{--}3.8\ \mu\text{m}$  and the remaining above  $3.8\ \mu\text{m}$ . In contrast, the dry milled powder had an average particle size of  $8.6\ \mu\text{m}$  with 30 wt% in the range  $1.5\text{--}3.8\ \mu\text{m}$  and 70 wt% above  $3.8\ \mu\text{m}$ .

The optical micrographs of specimen B after 30 s of sintering are shown in Fig. 1a (dry milled) and Fig. 1b (wet milled). Fig. 1a reveals three distinct phases which appear as white, grey and black regions. The grey regions had very high microhardness ( $\approx 22$  GPa) and were identified as  $\beta$ -SiC. The white regions had a lower hardness ( $\approx 11$  GPa) than the grey regions, and were identified as unreacted free Si; this was also confirmed by Si-etchant. Further, the microstructure shows the clustering of carbon (black regions) due to poor mixing. The microstructure of the specimen prepared from the wet milled powder (Fig. 1b) shows predominantly the SiC phase; unreacted Si and C are barely seen. This

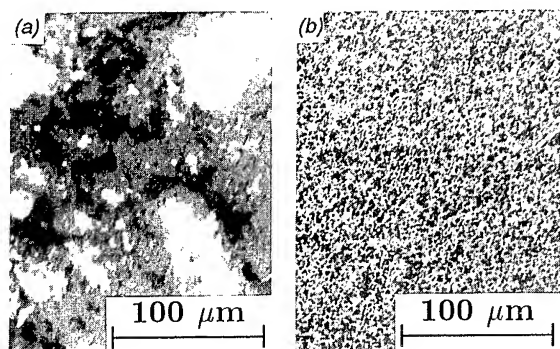


Figure 1. Optical micrographs of the specimen B sintered at  $2500^\circ\text{C}$  for 30 s: (a) dry milled and (b) wet milled. The SiC (grey), Si (white) and C (black) phases are seen.

shows that the formation of SiC is facilitated by fine particle size and narrow size distribution in the powder mixture. In view of this, further experiments were carried out with the starting powder mixture having a finer particle size only.

Figs. 2a and 2b show the microstructures of sintered specimen B before and after degassing of the reactant mixture. The sintering was carried out for 5 minutes to complete the reaction. A careful examination of the microstructure (Fig. 2a) shows the presence of pores in the sintered compacts. These pores appear to arise mainly due to the adsorbed gases in the starting powder mixture. The porosity is significantly reduced (Fig. 2b) when the starting powder mixture was degassed. Similar results were obtained for specimens A and C.

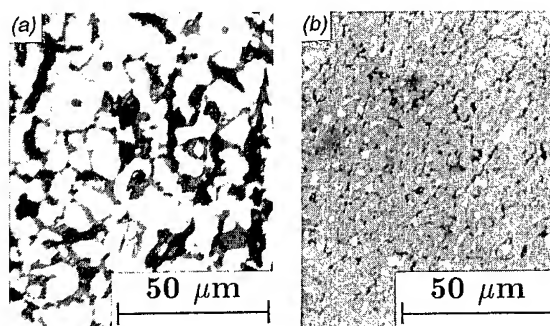


Figure 2. Optical micrographs of the specimen B sintered at  $2500^\circ\text{C}$  for 5 min: (a) before degassing and (b) after degassing. The dark regions are pores. The equiaxed grains of  $\beta$ -SiC are seen.

The hardness values on pore-free regions of sintered compacts with  $\beta$ -SiC were in the range 22–25 GPa. The compacts prepared from the powder mixtures without degassing had low hardness values (14–16 GPa).

The X-ray diffractogram of the specimens sintered in the temperature range  $2100\text{--}2500^\circ\text{C}$  showed highly crystalline  $\beta$ -SiC, whereas those sintered in the temperature range  $2500\text{--}2700^\circ\text{C}$  showed the presence of  $\alpha$ -phase in addition to the  $\beta$ -phase. The hardness value in the  $\alpha$ -SiC regions was  $\approx 30$  GPa. The typical microstructure of such a specimen is shown in Fig. 3a. The specimens sintered around  $2900^\circ\text{C}$  consisted of  $\alpha$ -SiC, Si and C (Fig. 3b).

## Discussion

It has been shown earlier [7] that the SHS in Si + C system does not go to completion due to the weak exothermic nature of Si-C reaction, and thermal energy has to be supplied from an external source for the completion of the reaction. Further, the SiC precipitates out at the Si-C interface forming a solid shell around the molten Si-pool (Fig.1a). The solid rim physically separates C and molten Si. The reaction proceeds further by the C atoms diffusing through the SiC shell and reacting with molten Si. As the reaction progresses, the SiC shell thickens, and the average distance through which C atoms have to diffuse in SiC to reach molten Si increases.

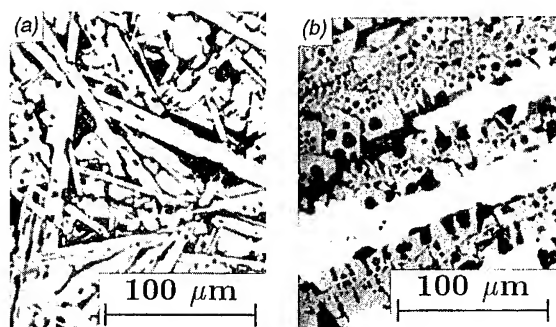


Figure 3. Optical micrographs of the specimen B showing (a) the  $\beta \rightarrow \alpha$  transformation and (b) the decomposition of  $\alpha$ -SiC. The  $\alpha$ -phase has a plate-like morphology.

The exothermicity of the Si + C reaction and the self-diffusivity of SiC being low, it is important that the reactants are in a finely divided form and intimately mixed. This reduces the diffusion distances for C to reach Si, and also increases the specific contact area between the reactants. In turn, this provides a large number of nucleation sites for the reaction (Fig.1b). The agglomerating tendency of carbon during dry milling prevents the intimate mixing of Si and C resulting in segregation (Fig.1a). This segregation was avoided by wet milling (Fig.1b).

Powders are generally observed to contain a substantial amount of adsorbed gases in them due to high specific surface area. During sintering, these gases are released and develop a pos-

itive pressure inside the pores and hinder densification. In pressureless sintering, most of the released gases come out of the sample. However, in high pressure sintering, no gaseous product can escape and hence results in the formation of pores (Fig.2a). Degassing of the reactant mixtures reduces the porosity in the sintered compacts markedly (Fig.2b).

In the reaction synthesis of SiC, C reacts with molten Si and generally forms  $\beta$ -SiC (Fig.2a). Typically, the microstructure exhibits equiaxed grains of the  $\beta$ -phase. The presence of the  $\alpha$ -phase in addition to the  $\beta$ -phase (Fig.3a) at temperatures  $> 2500^\circ\text{C}$  is due to the  $\beta \rightarrow \alpha$  transformation. The microstructure exhibits the grains having the plate like morphology, known to develop [8] when  $\beta$ -SiC transforms to  $\alpha$ -SiC. The grains with high aspect ratios (Fig.3a) are identified as the  $\alpha$ -phase. The fraction of the transformed  $\alpha$ -phase was observed to increase with increase in sintering temperature ( $> 2500^\circ\text{C}$ ) and holding time. It was observed that  $\beta \rightarrow \alpha$  transformation was complete at a sintering temperature of  $2700^\circ\text{C}$  in about 5 min. Around  $2900^\circ\text{C}$ , onset of the decomposition of  $\alpha$ -SiC to Si and C was observed (Fig.3b).

## References

- 1 A.G.Merzhanov and I.P.Borovinskaya, *Dokl. Chem (Eng. Trans.)* **204** (1972) 429.
- 2 Z.A.Munir, *Am. Ceram. Soc. Bull.* **67** (1988) 354.
- 3 J.F.Crider, *Ceram. Eng. Sci. Proc.* **3** (1982) 519.
- 4 J.Subrahmanyam and M.Vijayakumar, *J. Mat. Sci.* **27** (1992) 6249.
- 5 Y.Miyamoto, M.Koizumi and O.Yamada, *Commun. Am. Ceram. Soc., C* - 224 (Nov. 1984).
- 6 O.Yamada, Y.Miyamoto and M.Koizumi, *Am. Ceram. Soc. Bull.* **64** (1985) 319.
- 7 S.K.Bhaumik, C.Divakar, Murali Mohan, P. M. Jaman, S. Usha Devi and A.K.Singh, in *Adv. in High Press. Sci. & Tech.*, ed. A.K.Singh (Tata McGraw-Hill, New Delhi, 1995) p.225.
- 8 M.Lancin, F.Anxionnaz, J.Thibault - Desseaux, D.Stutz and P.Griel, *J. of Mat.Sci.* **22** (1987) 1150.

# HYDROSTATIC COMPACTION PRESSURE INFLUENCE ON SINTERED SPODUMENE PYROCERAMICS PROPERTIES

T.E. KONSTANTINOVA, E.I. LYAFER

*Donetsk Physico-Technical Institute, Ukrainian Academy of Sciences, Luxemburg str.72, Donetsk, Ukraine*

In the present work the influence of hydrostatic compaction pressure on the properties of compacts from glass powders and sintered pyroceramics of spodumene composition  $LiAlSi_2O_6$  has been studied. It has been shown that the density and the strength increase with pressure. After pressure treatment of 1500 MPa the relative density of compacts was 0.8 and the bending strength was 1 MPa. After sintering at 1000°C during 30 minutes the bending strength of sintered spodumene pyroceramics was 110 MPa, being 2 times higher as compared with the strength of specimens obtained with application of the dry glass powder compaction in press mold under pressure of 20 MPa.

## 1 Introduction

The compaction pressure influences noticeably on properties of sintered materials made from crystalline powders<sup>1,2,3,4,5</sup>. The base of the influence is a change of powder particle size under pressure treatment, a change of structure of powders and a porosity decrease of compacts. A particle size decrease as result of compaction has been established for various powder materials: chamotte<sup>1</sup>, glass<sup>6</sup>, oxides<sup>2</sup>. A structure change has been observed on powders of iron<sup>3</sup>, magnesium oxide<sup>4</sup>, high temperature superconductor<sup>5</sup>. A porosity decrease of compacts with compaction pressure is well known. These effects are peeped out under following sintering. The particle size decrease provokes the acceleration of sintering of metallic powders<sup>7,8</sup>. The change of structure of initial powders brings to the change of structure of sintered crystalline materials, for example iron<sup>3</sup> and magnesium oxide<sup>4</sup>. The porosity of sintered metallic materials decreases proportionally to porosity of compacts<sup>9</sup>.

Relatively recently one has started to use the powder technology for making articles from pyroceramics<sup>10</sup> which are made usually by glass technology<sup>11</sup>. The base of obtaining the pyroceramics is a crystallization which takes place in glass castings under heating to certain temperature. The process of sintering of glass powders of pyroceramics is accompanied by crystallization and it distinguishes the process as compared to sintering of crystalline powders.

The most widespread way of compaction - compaction in press mold - has restriction of upper pressure value. It is due to nonuniformity of

compactness of article bulk the cause of which is friction between a punch and a mold. As result, a fracture of compacts after unloading takes place because of elastic aftereffect. A hydrostatic compaction has no such a restriction and allows to apply very high pressures. Works in the field of hydrostatic compaction use for powder systems especially for pyroceramics are not numerous yet.

We have studied earlier the hydrostatic compaction pressure influence on properties of compacts and sintered articles on base of cordierite and aluminium tetraborate<sup>12</sup>. It has been shown that the density and the strength of compacts and sintered materials increases with pressure. So far as the magnitude of pressure effects varies for various powders and may not be calculated a priori the object of present work is investigation of hydrostatic compaction pressure influence on properties of compacts from glass powder and sintered pyroceramics of spodumene composition.

## 2 Technique

Compacts from glass powder and sintered specimens have been investigated. The powder has been made by melting of glass from oxides  $SiO_2$ ,  $Al_2O_3$ ,  $Li_2O$ ,  $TiO_2$ ,  $BaO$ ,  $ZnO$ ,  $As_2O_3$  and  $CeO_2$ , by grinding of the glass in a ball mill and by screening through the sieve of 63  $\mu m$ . The material crystallizes with formation of spodumene  $LiAlSi_2O_6$ . Compacts with dimensions of 6x6x55 mm were made by method of quasihydrostatic compaction of dry powder using paper molds and thin wall latex covers<sup>13</sup> under pressure up to 2000 MPa and for comparing - by method of press mold

compaction. The sintering has been performed in laboratory resistor furnace at temperature of 1000°C during 30 min, a charging of compacts for sintering being made to furnace heated to designed temperature, with air cooling. We have measured the apparent density  $\rho_a$  by method<sup>14</sup>, the bending strength with base of 20 and 45 mm by method<sup>15</sup>, the shrinkage under sintering, the pycnometric density  $\rho_t$  and have calculated the relative density  $\rho = \rho_a / \rho_t$  and total porosity  $\Theta = 1 - \rho_a / \rho_t$ .

### 3 Results and Discussion

The hydrostatic compaction pressure increase causes the increase of density and strength of compacts from dry powder of composition under study (fig.1). The strength increases linearly in whole interval of pressure under study though the density does not change above 1000 MPa. It witnesses that in addition to more dense packing of powder particles under pressure treatment also a change of state of boundaries between particles takes place. After hydrostatic compaction by pressure of 1500 MPa the relative density is 0,8 and the bending strength is 1 MPa. The strength of compacts from dry powder treated by pressure of 500 MPa and more appears to be sufficient for performing of further operations of powder technology - transporting, charging into a furnace *etc.* It has to be emphasized that closed mold compaction does not allow to obtain compacts with sufficient strength from dry powder under study. Though the strength of compacts increases with pressure of press mold compaction it takes place in narrow pressure interval because the upper pressure value is restricted by phenomenon of fracture of compacts under elastic aftereffect, apparently because of compaction nonuniformity. Usually one overcomes this shortcoming thanks to using of binders but such a way in one's turn reduces properties of sintered materials and deteriorates noticeably atmosphere under sintering because of burning down of binders.

The density and the strength of sintered spodumene pyroceramics increase with hydrostatic compaction pressure (fig.2). The most intensive growth of characteristics takes place in pressure field up to 500-600 MPa. Like for compacts, the change of density of sintered material ceases at 1000 MPa as the strength goes on to increase. Apparently the change of boundary state in com-

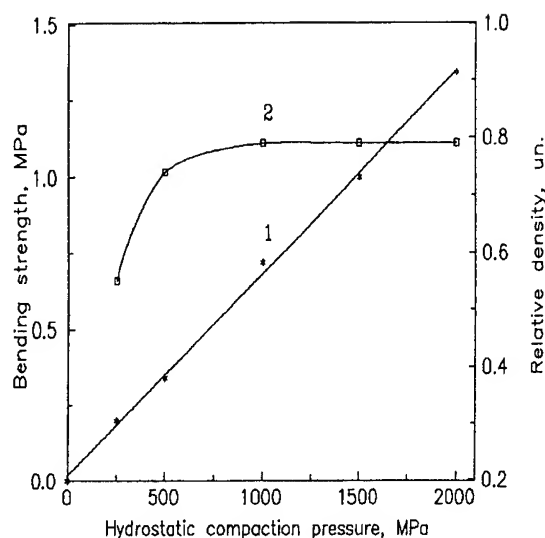


Figure 1: Dry powder compacts bending strength (1) and relative density (2) dependence on the hydrostatic compaction pressure value.

pacts influences on processes which take place in the boundaries under sintering. After treatment by pressure of 1500 MPa the sintered spodumene pyroceramics strength is 110 MPa. That is 2 times higher as compared with maximal strength by compaction in press mold which is obtained with pressure of 20 MPa.

One more positive effect of hydrostatic compaction application is a low shrinkage under sintering. The shrinkage decreases with pressure and reaches rather low values (fig.2).

The application of hydrostatic compaction of articles of various shapes instead of press mold compaction has allowed to obtain compacts with sufficient strength from dry glass powder of spodumene composition without of binders. The cut of unsintered compacts has appeared to be possible. Together with the low shrinkage under sintering it reduces noticeably the volume of finishing operations after the sintering. The sintering process becomes clean ecologically. The density of articles increases. It has been established that the application of the hydrostatic compaction of the glass powder without binders instead of the press mold compaction decreases 2 times sintered article rejects bounded up with cracks.

The glass powder of spodumene composition has been used for making of articles like drawing

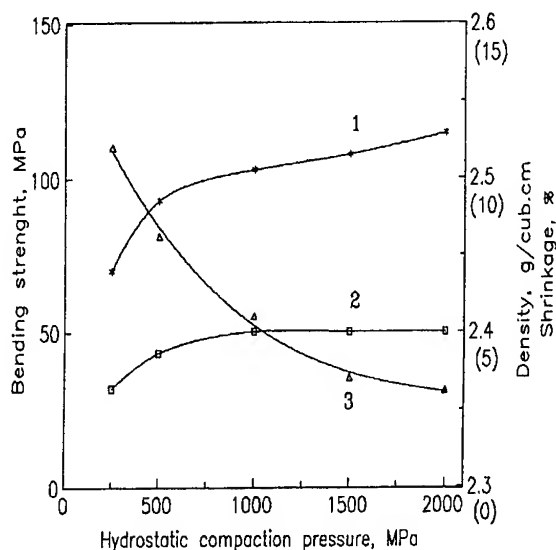


Figure 2: Bending strength (1), density (2) and shrinkage (3) of sintered spodumene pyroceramics depending on the hydrostatic compaction pressure value.

die. The dies being pressurized into steel bandage have been tested in laboratory conditions by drawing of wire from technical copper with reduction of 10% per die. The durability of dies is satisfactory. Taking into account the low cost of the material and the low volume of finishing operation the technology may be recommended for using in industries, especially in chemical industry, for composites manufacturing etc.

## References

1. *Pressovanie keramicheskikh poroshkov*, ed. R.Ja. Popilskii and F.V. Kondrashov (Metallurgia, Moscow, 1968).
2. K.K. Artemova, L.A. Rudenko and G.Ja. Maslova, *Ogneupory* **10**, 56(1981).
3. W.Ja. Bulanov and W.N. Nebolcinov in *Prognozirovanie svoistw spechennykh materialov*, ed. W.Ja. Bulanov and W.N. Nebolcinov (Nauka, Moscow, 1981).
4. *Dislocation activated sintering mechanisms for the ultrafine MgO treated with the hydrostatic pressure*, ed. V.V. Storog, G.Ya. Akimov, G.K. Volkova et al (DFTI, Donetsk, 1989).
5. A.J. Akimov, W.B. Bojko, A.L. Karpej et al in *26 Vsesoyuznoe soveshanie po fizike nizkikh temperatur* (DFTI, Donetsk, 1989).
6. W.J. Zaitsev, E.J. Lyafer and A.A. Raskov in *Problemy tonkogo ismelchenia, klassifikatsii i dozirovania* (Ivanovo, 1982).
7. *Osnovi poroshkovoi metallurgii*, ed. M.Yu. Balshin and S.S. Kiparisov (Metallurgia, Moscow, 1978).
8. *Poroshkovoye materialovedenie*, ed. R.A. Andrievskii (Metallurgia, Moscow, 1991).
9. *Rheologicheskie osnovi teorii spekania*, ed. W.W. Skorohod (Naukova dumka, Kiev, 1972).
10. T.J. Fedoseeva, Ye.W. Sobolev and Ye.A. Takher, *Steklo i keramika* **4**, 29(1972).
11. *Osnovi technologii sitallov*, ed. N.M. Pawlushkin (Stroiizdat, Moscow, 1979).
12. T.E. Konstantinova, I.B. Kurits, E.I. Lyafer et al, *Fizika i tehnika visokih davlenii* **2**, 23(1992).
13. V.V. Storog, G.Ya. Akimov, Yu.J. Yurkowsky et al, *Awtorskoe swidetelstwo SSSR N 1433804* (1988).
14. State USSR Standart N 473.4-81
15. State USSR Standart N 473.8-81

## THE EFFECT OF DESORBED GASES ON SINTERING DIAMOND POWDERS AT HIGH PRESSURES AND TEMPERATURES

A.A. BOCHECHKA, S.F. KORABLEV, A.A. SHULZHENKO AND I.A. PETRUSHA,  
*V.N. Bakul Institute for Superhard Materials of the Ukrainian  
National Academy of Sciences, Kiev 254074, Ukraine*

### ABSTRACT

The quantity has been defined of gases, which are desorbed from the surface of diamond particles in heating up to 1000 °C in a vacuum. The limiting values of density of as-sintered diamond powders and counterpressure of gases were calculated depending on the amount of desorbed gases, the size of particles being sintered, pressure and temperature. They are in good agreement with experimental results on sintering diamond powders at 1600 °C and initial pressure of 8 GPa.

### Introduction

The desorption of gases from the surface of particles being sintered occurs in high pressure-high temperature sintering of superhard material powders. In sintering powder of wurtzitic boron nitride, the pressure of gases being desorbed in pores of a polycrystal being sintered can be considerable [1]. This reduces the density of sinters obtained.

The mass variations have been found of diamond powders due to the gas desorption from the particle surfaces in heating up to 1000°C in a vacuum.

Plastic flow induced by external pressure [2] is the basic mechanism of sintering diamond powder. Mackenzie-Shuttleworth model [3] with McClelland's amendment for pressure variations [4] is used to describe the compaction of such a system. We have used the above model to calculate the limiting density values of as-sintered diamond polycrystals. The calculation was made based on our results on gas desorption and the data on the temperature dependence of the critical shear stress in diamond, available in the literature [5]. The values calculated are in good agreement with experimental results on sintering diamond powders at 1600°C and initial pressure of 8 GPa.

### Calculation of limiting density values of as-sintered diamond polycrystals

The effective pressure  $p$  that causes compaction equals the difference between the external pressure  $p_{ex}$  affecting the object being sintered and that of gases  $p_g$  in the object pores [1]:

$$p = p_{ex} - p_g. \quad (1)$$

As  $p_g$  depends on the pore volume, then  $p$  is also a function of the relative density value. From the differential equation for kinetics of pressure-induced compaction of a porous body [3] and a correction for the pressure decrease due to a compaction [4], we obtain the relative density limiting value  $r_l$  of a polycrystal being sintered:

$$[1 - (1 - r_l)]^{2/3} \ln[1/(1 - r_l)] = (\sqrt{2}/2)(p/\sigma_s), \quad (2)$$

where  $\sigma_s$  is the critical shear stress.

We assume that the pores are interconnected and the gas volume equals that of pores. Let the mass of powder be  $m_d$  and the mass of a gas with a molecular weight of  $\mu$  be  $m_g$ . With the relative density  $r_l$ , the volume of pores  $V_p$  is  $(1 - r_l)m_d/(\rho r_l)$ , where  $\rho$  is the density of a diamond single crystal. Then the reduced mole volume of the gas is

$$V_m = V_p(\mu/m_g) = [(1 - r_l)/r_l][(m_d\mu)/(m_g\rho)]. \quad (3)$$

At high pressures, the process is described by an equation that differs from the equation of state of the ideal gas. Therefore as in [1], for finding  $p_g$



we used the empirical equation of state of powder gases at high pressures .

In the framework of the model under consideration, the compaction of diamond powder according to formula (2) is defined by both the pressure  $p$  and the effective critical shear stress  $\sigma_s$  in diamond. Substituting eqs. from [5] for  $\sigma_s$ , (1) for  $p$  into eq. (2), we obtain the equation for  $r_l$ , the right-hand side of which  $F$  is the function of  $r_l$ ,  $m_g/m_d$ , and  $\mu$  values that are determined from gas desorption experiments and sintering parameters ( $p_{ex}$ ,  $T$ ). Even in case, when  $F$  is constant, to solve this eq. in the analytical form seems impossible. Therefore, the  $r_l$  value can be determined numerically, calculating step by step the left-hand side of the equation and  $F$ -function and comparing the results. To execute the procedure, a program on the Turbo Basic language has been developed and verified. The calculations were made using an ASI PC.

## Experimental procedure

28-40  $\mu\text{m}$  grain-sized ACM diamond powders (D1) produced by the Pilot Plant of the Institute for Superhard Materials were used for experiments. As-heated in a vacuum they were treated in mineral acids to remove metal impurities. Then one part of the powder was heated in a hydrogen atmosphere (D2 powder) and the other was treated in the fatty acids (D3 powder).

Gas desorption from the above powders was found from a variation of sample masses using a Setaram MTB-10-8 microthermoanalyzer in a vacuum. The heating temperature was 1000 °N, residual gas pressure being  $10^{-4}$  mm Hg. The results are given in Table 1, where  $m_0$  is the initial mass of a diamond powder sample,  $\Delta m_1$  is the decrease of the sample mass on attaining working vacuum at room temperature,  $T_{des}$  is the temperature, at which the desorption occurs,  $\Delta m_2$  is the mass decrease during desorption, and

Table 1

Variations of sample masses of diamond powders found in studying the gas desorption on a microthermoanalyzer

Sample	$m_0$ , mg	$\Delta m_1$ , mg	$T_{des}$ , °C	$m_0$ , mg	$m_0$ , mg
D1	261,1	0,52	220	0,20	0
D2	249,2	0,48	160	0,24	0
D3	262,55	0,30	40	1,0	0,3
			210	0,8	

$\Delta m_0$  is the decrease in sample mass after the system regained its original state.

The sintering was performed in a toroid-type high pressure apparatus with the recess diameter of 20 mm [6]. The procedure involved creating the pressure of 8.0 GPa, heating up to the needed temperature, holding for 1.5 min, cooling down to room temperature and removing the pressure.

As-sintered samples were cleaned of graphite, covered with paraffin to keep pores free of liquid and then their density was defined by hydrostatic weighing in water [7].

## Results and discussion

The results of desorption experiments show

that gas, which desorbs from the D1 and D2 powders is air because on cooling the chamber down to room temperature and filling it with air, the initial mass of the sample recovers. In this case, the sample mass of the D3 powder does not recover. The fact suggests that in heating, along with the air desorption a decomposition of organic compounds deposited on diamond particles occurs. In this case, the formation of CO and  $C_nH_m$  gases is most probable. As the molecular weight of CO is much lower than that of  $C_nH_m$ , the carbon monoxide makes the greatest contribution to the

pressure of gases that are desorbing in pores in a polycrystal being sintered. Therefore, it is assumed in calculations that from powder D3, air and carbon monoxide desorb. The air that is in pores in a diamond sample prior to sintering is also allowed for in calculations. It takes about 45 vol % [8]. Limiting density values of sinters calculated using the developed program are given in Table 2.

Table 2  
Calculated ( $r_c$ ) and experimental ( $r_{ex}$ ) densities of diamond polycrystals

Sample	$m_g/m_d, \%$	$r_c, g/cm^3$	$r_{ex}, g/cm^3$
D1	0,310	3,358	$3,36 \pm 0,01$
D2	0,324	3,358	$3,36 \pm 0,01$
D3	$0,840_{air} + 0,115_{CO}$	3,329	$3,32 \pm 0,01$

It is seen that they are in good agreement with experimental results on diamond powder sintering at 1600 °C and the initial pressure of 8.0 GPa.

The counterpressure of desorbed air becomes essential ( $> 0.5$  GPa) when air mass versus diamond powder mass relation exceeds 0.5 %. When the latter is 12 %, the counterpressure attains the value, at which the resulting pressure is lower than the critical shear stress, and compaction due to the plastic strain does not occur. The decrease in the grit size of the powder being sintered causes its specific area  $S_s$  and, consequently, the amount of gases desorbed in sintering to increase. Let us assume that the desorbed gas amount is proportional to the whole surface  $S$ :  $m_g = kS$ , where  $k$  is the proportionality coefficient independent of particle sizes. Then  $m_g = kS_s m_d$  or

$$(m_g/m_d) = kS_s. \quad (4)$$

The specific surface areas of variously sized ACM diamond powders produced by the Pilot Plant of the Institute for Superhard Materials are given in [9]. For the D1 powder,  $S_s = 180 \text{ m}^2/\text{kg}$  [9], and according to Table 2,  $(m_g/m_d) = 2.765 \cdot 10^{-3}$ , whence  $k = 1.536 \cdot 10^{-5} \text{ kg/m}^2$ . The polycrystal limiting density vs mean size of particles being sintered has been calculated. The  $m_g/m_d$  value

was allowed for according to expression (4) and the data [9] for variously.

The decrease in size of the powder being sintered results in both the increase of the counterpressure and the decrease of the polycrystal density. The gas counterpressure affects greatly the results of sintering of powders with grit sizes of 10/7 and below and makes impossible the sintering of powders with particles less than 0.9  $\mu\text{m}$  at 1600 °C.

## References

1. M.S. Kovalchenko and S.S. Dzhamarov, *Poroshkovaya Metallurgiya*, **2** (1984) 31.
2. V. F. Britun, G.S.Oleinik, and N.P.Semenenko, *Soviet J. of Superhard Materials*, **13**, 3 (1991), 3.
3. J.K.Mackenzie, R.Shuttleworth, *Proc. Phys. Soc.*, **62**, 12B (1949), 833.
4. J.D.McClelland, *J. Amer. Ceram. Soc.*, **44**, 10 (1961), 526.
5. A.A.Aptekman, O.V.Bakun, O.N.Grigoriev, and V.I.Trefilov, *Doklady AN SSSR*, **290**, 4 (1986) 845.
6. A.A.Shulzhenko, V.G.Gargin, V.A.Shishkin, and A.A.Bochechka, *Diamond-Base Polycrystalline Materials* (Naukova Dumka, 1989)
7. S.S.Kivilis, *Densimeters* (Energiya, 1980).
8. W.D.Jones, *Fundamental Principles of Powder Metallurgy* (Edward Arnold LTD, 1960)
9. Yu.I.Nikitin, *Manufacturing Technology and Quality Control of Diamond Powders* (Naukova Dumka, 1984)

# METASTABLE PHASES FORMATION IN Zr-Zn ALLOYS DURING MECHANICAL ALLOYING UNDER PRESSURE

N.I.TALUTS, A.V.DOBROMYSLOV, and R.V.TCHURBAEV

*Institute of Metal Physics, Ural Division of Russian Academy of Science, 18 Kovalevskaya Street, Ekaterinburg, 620219, RUSSIA*

The series of Zr-Zn alloys with the content of Zn up to 20 at.% were prepared by mechanical alloying under pressure. The structure of these alloys was studied by X-ray diffraction analysis and transmission electron microscopy. It was established that the high pressure  $\omega$ -phase is formed and zinc atoms are dissolved in zirconium crystal lattice. At temperatures above 500°C, the  $\omega$ -phase decomposes into the  $\alpha$ -phase and intermetallic compound ZrZn.

## 1 Introduction

Until recently, the phase transformations in Zr-Zn alloys were not experimentally studied because of technological difficulties associated with the preparation of these alloys. Zinc burns away on melting because of the considerable difference in the melting temperatures of Zr and Zn. The method of mechanical alloying under pressure has an advantage for preparing these alloys. However in this case the high pressure phases among stable products can be formed in synthesised alloys and these phases can be retained in metastable state after removal of pressure. The aim of the present investigation is to study the structure of Zr-Zn alloys after mechanical alloying under pressure.

## 2 Experimental

The alloys containing 5; 10 and 20 at.% Zn were prepared from the mixture of powders of the constituent elements at ambient temperature using a high pressure apparatus. The powders were pressed between Bridgman anvils and then deformed by rotating one anvil about the other. The maximum value of pressure was 10 GPa. The effect of pressure and deformation on the phase constitution and compositional homogeneity of the synthesised alloys was studied. Diffractometer DRON-3 with single crystal graphite monochromator and Cu  $K_\alpha$  radiation was used for the X-ray diffraction studies and JEM-100C microscope was used for the transmission electron microscopy (TEM). The foils were prepared by chemical polishing in the solution of HF and HNO<sub>3</sub> acids.

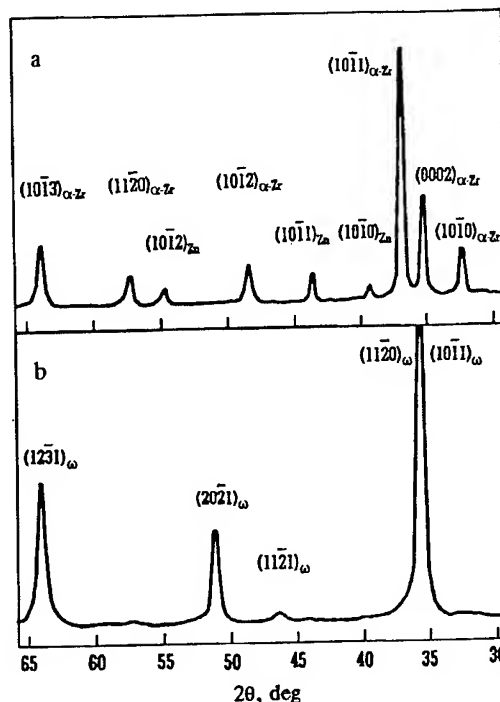


Figure 1: X-ray diffraction patterns of (a) mixed Zr -10 at.% Zn powders and (b) the Zr -10 at.% Zn alloy obtained by mechanical alloying under pressure.

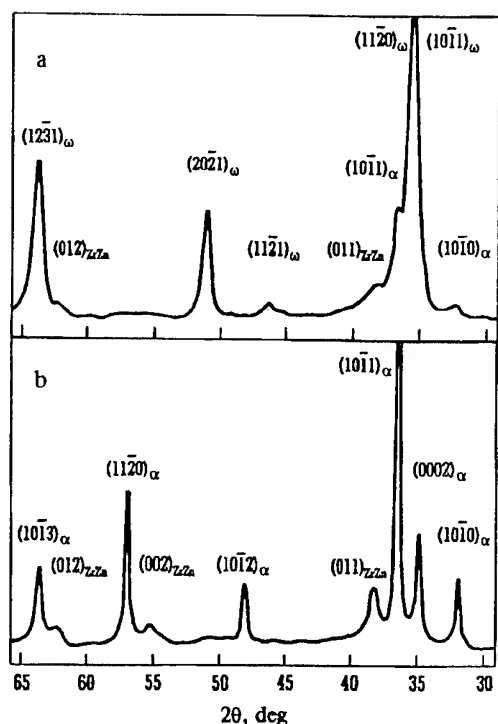


Figure 2: X-ray diffraction patterns of the Zr -20 at.% Zn alloy (a) obtained by mechanical alloying under pressure and (b) annealed at 500°C for 15 min.

### 3 Results and Discussion

The formation of the alloys was verified by the fact that zinc lines on the diffractograms disappeared after the mechanical alloying. The alloys with the content of 5 and 10 at.% Zn synthesised under pressure contain the high pressure  $\omega$ -phase and small amount of the hexagonal  $\alpha$ -phase (Fig.1). In addition to the  $\omega$ -phase and the  $\alpha$ -phase, the stable ZrZn intermetallic compound with the B2 type crystal structure is formed in the alloy with 20 at.% Zn (Fig.2a). There are no signs of the formation of the other intermetallic compounds in these alloys.

The high pressure  $\omega$ -phase is identical with the  $\omega$ -phase in the titanium-base and zirconium-base alloys with  $\beta$ -stabilizing elements. The disappearance of the zinc diffraction lines was accompanied by a little shift of the  $\alpha$ -phase lines to the higher diffraction angles  $\Theta$ . This fact shows clearly that the zinc atoms are dissolved in the lattice of the  $\alpha$ -phase of zirconium. The high pressure phase forms most probably from pure zirconium,

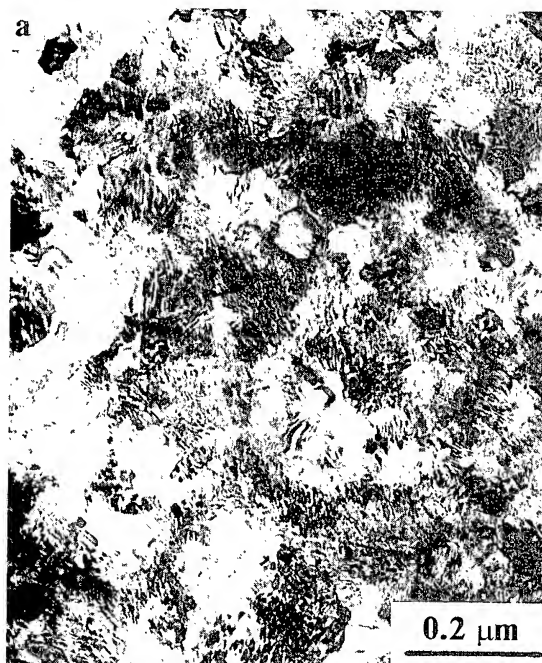


Figure 3: Microstructure of the Zr -20 at.% Zn alloy obtained by mechanical alloying under pressure: (a) TEM bright-field image; (b) selected area diffraction pattern corresponding to (a).

and then it is enriched by the zinc atoms. The present results show that mechanical alloying under pressure can extend the solid solubility of zinc in the  $\alpha$ -phase of zirconium in comparison with the solid solubility value at equilibrium phase diagram.

The morphology and crystallography of  $\omega$ -phase of the Zr-Zn alloys were investigated. It was found that the microstructure of the alloys depends mostly on deformation rather than on the zinc content. Figure 3 shows the typical structure of the Zr-Zn alloys after mechanical alloying under pressure. The main feature of the structure is the small grains size (nanocrystal structure) and the blurred boundary between them. The grain size of the  $\omega$ -phase varies with degree of the shear deformation.

The annealing of the Zr-Zn alloys has shown that the high pressure  $\omega$ -phase is stable up to 500°C. At temperatures above 500°C (Fig.2b), the decomposition in the Zr-Zn alloys can be described as

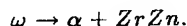


Figure 4 shows the microstructure of the Zr -20 at.% Zn alloy after annealing at 500°C for 15 min. The grain size increases strongly in comparison with the initial state and the grains have clearly defined boundaries.

It is to be noted that the morphology of the  $\omega$ -phase, formed during mechanical alloying under pressure, differs essentially from the morphology of the  $\omega$ -phase, formed after static <sup>1</sup> or shock <sup>2</sup> pressure action.

## References

1. A.V. Dobromyslov *et al*, *Fiz.Met.Metalloved.* **57**(1), 90 (1984).
2. E.A. Kozlov *et al*, *Fiz.Met.Metalloved.* **79**(6), 113 (1995).

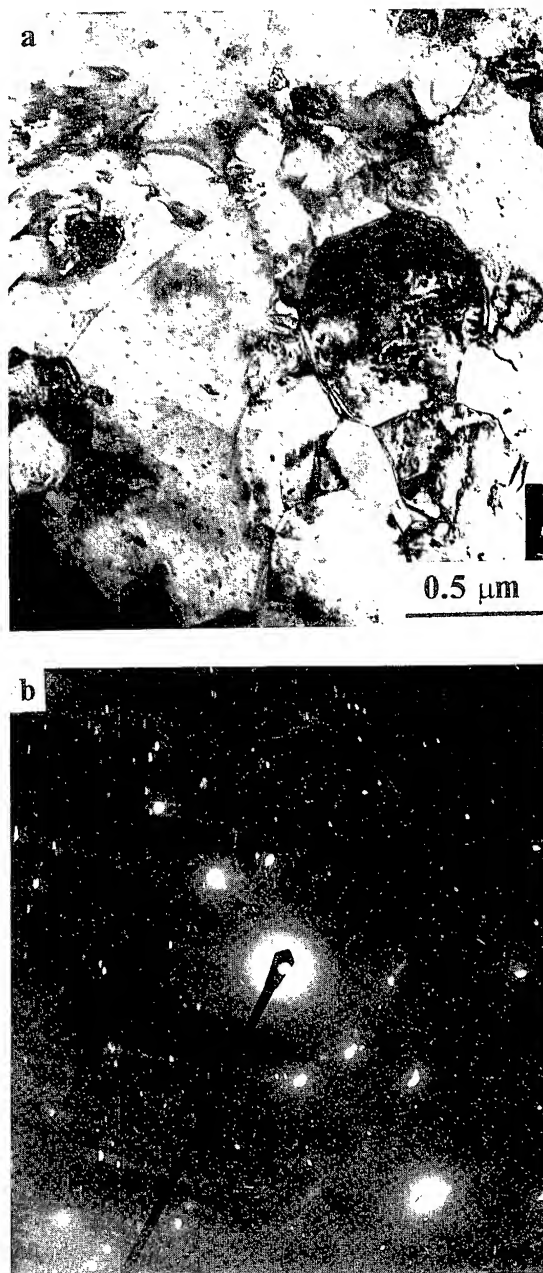


Figure 4: Microstructure of the Zr -20 at.% Zn alloy annealed at 500°C for 15 min: (a) TEM bright-field image; (b) selected area diffraction pattern corresponding to (a).

# X-RAY STRUCTURE STUDIES OF ALUMINUM NITRIDE IN cBN-AIN COMPOSITES PRODUCED BY HIGH PRESSURE SINTERING

N.P.BEZHENAR, S.A.BOZHKO

*V.N.Bakul Institute for Superhard Materials of the Ukrainian  
National Academy of Sciences,*

N.N.BELYAVINA, V.YA.MARKIV

*T.G.Shevchenko Kiev University, Kiev, Ukraine*

## ABSTRACT

A mixture containing AlN and cBN powders was subjected to barothermal treatment in a toroid-type high pressure apparatus. X-ray diffraction spectra of AlN were studied after both cold pressing (7.7 GPa, 300 K) and sintering (8 GPa, 1000, 1600 and 2300 K). With increasing sintering temperature, the  $c/a$  ratio and the unit cell volume of the AlN crystal lattice decreased. Residual thermal stresses in cBN-AlN two-phase composite have been calculated. A stabilization of the AlN lattice state was concluded to be a result of both diffusion processes in the sintering of an AlN+cBN charge and residual thermal compression stresses in the AlN lattice.

## Introduction

High pressure and high temperature effects on the aluminum nitride crystal structure have been studied in a number of papers. At atmospheric pressure no phase transformations have been found in AlN (P6<sub>3</sub>mc, wurtzitic type). The  $c/a$  ratio of the lattice constants is close to 1.599, which is somewhat lower than in a close-packed structure (1.633). X-ray diffraction analysis of AlN at pressures from atmospheric up to 30 GPa was made in a diamond-anvil cell [1]. It has been shown in the above paper that with increasing pressure, the  $c/a$  ratio of the AlN crystal lattice decreases, and at the pressure of 22.9 GPa, a transformation from wurtzite to NaCl structure occurs.

The pressure-induced decrease of the  $c/a$  ratio is reversible. No stabilization of the high pressure state upon thermobaric treatment could be observed. Thus, X-ray analysis of AlN ceramics sintered for 90 s at 5 GPa and 2120 K showed [2], that the  $a$  and  $c$  lattice constants returned to the initial values after pressure release.

## Experimental Results

We have studied by X-ray diffraction pure AlN powder as well as mixtures after the

following barothermal treatment: AlN+cBN compressed in a toroid-type high pressure apparatus to 7.7 GPa at room temperature; sintering under the same pressure for 90 s at 1000, 1600 and 2300 K.

The initial AlN powder consisted of particles with grain size of 7-10  $\mu\text{m}$ . Oxygen was the basic impurity in the AlN powder (up to 3.3 mass %). Other impurities (Fe, Si, Ni, Cr, Ti, Ca) added up to 0.3 mass % in total. cBN powder contained 0.3 % carbon, 0.2% oxygen and other impurities (Si, Al, Mg, Ca, Fe, Ni) up to 0.4 % in total.

X-ray analysis was performed using a DRON-3M diffractometer. To measure  $2\theta$  accurate to 0,001-0,005°, a thin layer of semiconductor-purity Si was applied to the surface of the sample under study. The correction of gravity centers of X-ray peaks and determination of the lattice constants accurate to  $10^{-5}$ - $10^{-4}$  nm were made using a PC software package.

Table 1 shows the  $c/a$  ratio (column 7) and variation of the unit cell volume of the AlN lattice after cold pressing and sintering under the above conditions as compared with the unit cell volume of the initial powder (column 4). The  $V_{p,T}$  and  $V_0$  volumes were calculated based on experimental values of the AlN lattice constants.

**Table 1.**  
Characteristics of the AlN crystal lattices after p,T-treatment.

Conditions of sample preparation			$[(V_{p,T} - V_0)/V_0] \cdot 10^3$			c/a
cBN, vol. %	p, GPa	T <sub>sint</sub> , K	Measurement	Calculation thermoelastic strains	Physico-chemical processes	
0	10 <sup>-5</sup>	300	0	0	0	1.59955(9)*
50	7.7	300	-0.47 ± 0.55	0	0	1.6000(5)
50	8.0	1000	1.45 ± 0.37	-0.13	1.58	1.5980(3)
50	8.0	1600	0.61 ± 0.33	-0.23	0.84	1.5978(2)
50	8.0	2300	-1.23 ± 0.35	-0.36	-0.87	1.5973(3)
90	8.0	1000	3.02 ± 1.09	-0.28	3.30	1.5988(10)
90	8.0	1600	0.88 ± 0.53	-0.52	1.40	1.5979(5)
90	8.0	2300	-1.01 ± 0.45	-0.81	-0.20	1.5949(4)

\*)Errors in the last figure are indicated in parentheses.

It can be seen from the Table, that after compression at room temperature the c/a ratio of the AlN crystal lattice changes only slightly. No variations of the AlN unit cell volume within the experimental error have been observed either. With the increase in the barothermal effect temperature, the c/a ratio decreased. The lowest c/a value 1.5949(4) has been found in samples of a composite sintered at 2300 K with a high second phase content (90 vol. % cBN). Irrespective of cBN content of the charge, the AlN unit cell volume increased in sintering at low temperatures (1000 K) and decreased in sintering at high temperatures (2300 K).

#### Interpretation of the data

In general, the unit cell volumes of the AlN crystal lattice in the initial powder and in samples of an as-sintered composite can differ due to physico-chemical processes occurring in sintering, such as formation or decomposition of solid solutions, as well as due to physico-mechanical interaction between phases of a composite. The latter is expressed by elastic strains in the phases of the composite, their value being associated with the difference between elastic moduli and thermal expansion

coefficients of the phases that constitute the composite.

The values of elastic strains were calculated by the procedure developed for a two-phase macroscopically isotropic composite [3]. Values for bulk moduli of AlN and cBN at 8 GPa and the thermal expansion coefficients at 0.1 MPa were used for the calculation. The results show that in the AlN phase of an as-sintered composite, the compression strains increase with the cBN content, for a given sintering temperature (see Table 1, column 5).

A comparison between experimental and calculated data  $(V_{p,T} - V_0)/V_0$  shows no agreement. This indicates that the volume variations of the AlN crystal lattice unit cell, we observed in the experiment after sintering, are caused also by other factors which are evidently associated with physico-chemical interaction between the charge components.

The values of the volume variations that might be associated with the physico-chemical processes occurring in sintering of composites are listed in column 6 of the Table. These values are defined as the difference between experimental data of the volume variations of the AlN unit cell and calculated values of thermoelastic strains.

The possibility of diffusion of light elements (boron, oxygen) into the AlN lattice to form a solid solution should be considered first in explaining the above volume variations.

Boron can isomorphically substitute for aluminum in the AlN lattice. Despite the fact that the ion and covalence radii of aluminum are well in excess of those of boron, boron dissolution in AlN and a subsequent thermobaric treatment resulted in the increase of the AlN lattice constants ( $a$  and  $c$ ) [4]. Therefore, one can assume, that in our experiments, the increase in the AlN unit cell volume after sintering at 1000 K is attributed to a formation of a boron solid solution in the AlN lattice. The fact that after sintering at all temperatures, the volume of an AlN unit cell was larger in samples with the higher cBN content also supports this assumption.

At higher sintering temperatures, the AlN unit cell volume decreased and after sintering at 2300 K became smaller than that in the initial powder. This can be attributed to the interaction between aluminum nitride and oxygen. Oxygen dissolution up to 1.1 % was accompanied by the reduction of the AlN unit cell volume (down to  $1.2 \cdot 10^{-3}$ ), and with the further increase of the oxygen content, the volume recovered [5]. Electron microscopic studies [6] have shown that oxygen facilitates the decrease of the stacking fault energy in the AlN structure, a formation and stabilization of its multilayer polytypes. High pressures slow down such processes and cause a decomposition of a solid solution with precipitation of aluminum oxide or oxinitride.

The initial AlN powder in our experiments contained 3.3 mass % oxygen. With the data given in [5], one can suggest that the decrease in the AlN unit cell volume after sintering at 2300 K is associated with the decrease of the

oxygen content of the AlN lattice, i.e. with the decomposition of a solid solution.

In samples of cBN-AlN composites sintered under pressure (8 GPa, 2300 K), we find a wurtzitic-type structure of the AlN lattice, with  $c/a$  ratio between 1.595 and 1.597 depending on the second phase content (see the Table).

Based on the suggestion [2], the deviation of the  $c/a$  value from that inherent in a close packing (1.633), points to the increase of a portion of the ion-type bond in the AlN lattice as compared to the covalent one. In our experiments, it started already at the earliest stages of high pressure sintering. It may be suggested, that the formation of boron solid solution and decomposition of oxygen solid solution in aluminum nitride result in the increase of a portion of ion bonds in the lattice. This stabilizes the high pressure state of AlN after pressure release.

## References

1. M.Ueno, A.Onodera, O.Shimomura and K.Takemura, *Phys.Rev.B*, **45**, no.17 (1992) 10123.
2. V.B.Shipilo, T.V.Rapinchuk, N.S.Orlova and O.E.Kochkarik, in *Novelty Materials and Technologies*, (Homatex, 1994), p.87.
3. N.V.Novikov, A.L.Maistrenko and V.N.Kulakovsky, *Fracture Resistance of Superhard Composite Materials*, (Naukova Dumka, 1993).
4. T.S.Bartnitskaya, A.K.Butylenko, E.S.Lugovskaya and I.I.Timofeyeva, in *High Pressures and Properties of Materials* (Ed.I.N.Frantsevich, Naukova Dumka, 1980) p. 90.
5. R.A.Youngman and J.H.Harris, *J.Am.Ceram.Soc.*, **73**, no.11 (1990) 3238.
6. A.N.Pilyankevich, V.F.Britun, G.S.Oleinik and M.A.Kuzenkova, *J.Powder Metall.*, **3**, (1991) 38.



# Quenched High Density $\text{ZrO}_2$ and $\text{HfO}_2$

Serge DESGRENIERS and Ken LAGAREC

*Département de physique, Université d'Ottawa et Institut de physique Ottawa-Carleton,  
150 Louis Pasteur, Ottawa, Ontario, CANADA. K1N 6N5*

Numerous reports have shown the existence of high density quenched phases of  $\text{ZrO}_2$  and  $\text{HfO}_2$  from high pressure at room temperature. On the basis of Raman spectra and energy-dispersive X-ray diffraction patterns of samples of  $\text{ZrO}_2$  and  $\text{HfO}_2$  decompressed from 70 GPa and 72 GPa, respectively, we argue that the quenched phases are equivalent for the two oxides. Furthermore, it is demonstrated that the high pressure quenching process produces materials shown to be in a pure high density phase, stable at room conditions. From energy-dispersive and angle-dispersive X-ray diffraction using synchrotron radiation, the structure of the quenched phase is confirmed to be of the cotunnite ( $\text{PbCl}_2$ ) type, space group  $Pnma$  ( $Z = 4$ ), as proposed earlier. Rietveld refinements of angle-dispersive diffraction patterns provide atomic positions for the quenched  $\text{ZrO}_2$ . Finally, Raman spectra and X-diffraction patterns indicate stress broadened lines. It is shown that the volume-pressure relationship for the quenched phase cannot be modelled by an usual equation of state based on finite strain, as the room conditions bulk moduli are very high and the first derivative of the bulk moduli approaches zero for both oxides.

## 1 Introduction

At room conditions, zirconium and hafnium form with oxygen isostructural phases in the form of  $\text{MO}_2$ , in which the metal M is 7-coordinated. Similarity between  $\text{ZrO}_2$  and  $\text{HfO}_2$  is often attributed to the lanthanide contraction which explains the equivalent size of Hf and Zr. Several authors have also noted the similarity among the dense phases of the two compounds, obtained at high pressures. In this paper, we report the study of  $\text{ZrO}_2$  and  $\text{HfO}_2$  at pressures in excess of 70 GPa using Raman spectroscopy and synchrotron X-ray diffraction at near room temperature. We show that both compounds adopt the same structural phases, in similar pressure ranges, and that both dioxides may be quenched at room conditions from high pressure to give polycrystalline solids which present optical transparency and relatively low volume compressibility. Furthermore, refinement of angle-dispersive patterns for the quenched materials gives a 9-coordinate structure of the cotunnite type. Equations of state of the three different phases encountered in the pressure range investigated are also given.

## 2 Experimental

The polycrystalline dioxides were obtained from AESAR (Johnson Matthey), with nominal purities of 99.99%. Several samples of both compounds were studied in gasketed diamond anvil cells with different anvil configurations to gener-

ate pressures ranging from 0.1 MPa to 70 GPa. In order to compare our results with those already published, different pressure media were used, namely methanol-ethanol (4:1 in volume), silicone oil (Dow Corning) and no pressure medium. Pressures were estimated from the spectral shift of the  $R_1$  luminescence of  $\text{Al}_2\text{O}_3\cdot\text{Cr}^{3+}$  and/or from the lattice parameter of bcc Mo using a fit to the second-order Birch-Murnaghan function of the 293 K isothermal equation of state data<sup>1</sup> (with  $B_0 = 266.8$  GPa and  $B_0' = 3.867$ ). Micro-Raman spectroscopy (RS), energy-dispersive (EDXD) and angle-dispersive (ADX) X-ray diffraction using synchrotron radiation were combined to assess the structural properties of our samples. Micro-Raman spectra were recorded on an S3000 Jobin-Yvon subtractive triple monochromator equipped with a liquid nitrogen cooled CCD detector. EDXD experiments were performed at the National High Pressure Facility of CHESS<sup>2</sup>. Diffraction spectra were analysed using XRDA<sup>3</sup>. ADXD was performed at CHESS (D1 line), with synchrotron radiation at  $\lambda = 0.4079$  Å from a double-bounced Ge(111) monochromator. Full powder diffraction images were recorded on FUJI imaging plates digitized by a FUJI BAS2000 scanner. Further analysis of all images, i.e., visualization, scanner field correction, calibration, and  $2\theta$  profile generation, were carried out using IPA<sup>4</sup>. Finally, Rietveld analysis of  $2\theta$  diffraction patterns were performed using DBWS9411<sup>5</sup>.

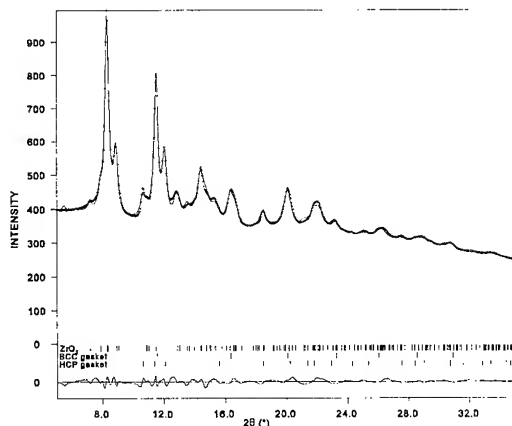


Figure 1: Rietveld analysis results of an angle-dispersive X-ray diffraction pattern of a sample of  $\text{ZrO}_2$  quenched at room conditions from 70 GPa. Crosses indicate the observed data and the continuous line the calculated pattern, according to the parameters of Table . The fit also contains diffraction lines of bcc and hcp phases of stainless steel from the gasket. Analysis results on given in Table 1.

### 3 Results and Discussion

#### 3.1 Low pressure transitions

The stability range of the monoclinic baddeleyite phase (MI) extends, at room temperature, from 0.1 MPa to fairly high pressure, as indicated the strong  $11\bar{1}$  and  $111$  reflections still present at 25 GPa . Transitions to a new phase are observed at  $10 \pm 1$  GPa and  $10.0 \pm 0.2$  GPa for  $\text{ZrO}_2$  and  $\text{HfO}_2$ , respectively. Both compounds are found to transform to an orthorhombic structure with space group  $Pbca$  ( $Z=8$ ) (OI). Our results are in agreement with those already reported.

#### 3.2 Structure of the quenched dense materials

Both compounds transform to another, definite, structural phase above 25 and 30 GPa, for  $\text{ZrO}_2$  and  $\text{HfO}_2$ , respectively. As noted earlier by Arashi<sup>6</sup>, the quenched phase of  $\text{HfO}_2$  resembles that of  $\text{ZrO}_2$  obtained under identical experimental circumstances. Our results (RS and EDXD) provide strong indications from which we conclude that both  $\text{ZrO}_2$  and  $\text{HfO}_2$  adopt the same structure above 30 GPa, which structure is retained upon decompression to atmospheric conditions. The quenchable phase in question has been assigned numerous structures, as surveyed from the literature: tetragonal<sup>7</sup> and orthorhombic<sup>9,10</sup> for  $\text{ZrO}_2$ , and tetragonal<sup>11,6</sup> and for  $\text{HfO}_2$  . Analysis of our ADXD patterns of  $\text{ZrO}_2$  samples

Table 1: Results of the Rietveld refinement of the X-ray diffraction pattern of Figure 1. The refinement includes the bcc and hcp phases of stainless steel in massic proportions of 0.07% and 0.67%, respectively.

	a	$5.620 \pm 0.004 \text{ \AA}$
	b	$3.347 \pm 0.002 \text{ \AA}$
	c	$6.503 \pm 0.004 \text{ \AA}$
	V	$122.32 \pm 0.14 \text{ \AA}^3$
Zr	x	$0.2622 \pm 0.0009$
	y	0.2500 fixed
	z	$0.1094 \pm 0.0005$
O1	x	$0.4589 \pm 0.0035$
	y	0.2500 fixed
	z	$0.4523 \pm 0.0034$
O2	x	$0.1065 \pm 0.0058$
	y	0.7500 fixed
	z	$0.3243 \pm 0.3243$
	$R_{wp}$	1.37
	$R_p$	1.11
	$R_{Bragg}$	2.30

quenched from 70 GPa to room pressure indicate a structure of the cotunnite type (OII), space group  $Pnma$  with  $Z=4$ <sup>8</sup>. Figure 1 shows the result of a Rietveld refinement and Table 1 gives the refined parameters which, incidentally, are in very good agreement with those proposed by Haines *et al.*<sup>10</sup>. It should be emphasized however that, apart from reflections of the bcc and hcp phases of stainless steel (gasket), the spectrum of Figure 1 is that of a pure phase of  $\text{ZrO}_2$ , namely, cotunnite. Our results are similar to those obtained by Haines *et al.*<sup>10</sup>, although a phase mixture of MI, OI, OII and fcc-Ni(gasket) was necessary to completely explain their recorded pattern. It should be mentioned that the appearance of the baddeleyite phase MI was also noticed in our quenched samples, but only after heating the recovered sample in an Ar atmosphere at 600 °C for 8 hours, for instance.

#### 3.3 Isothermal Equations of State

Figures 2 and 3 show the pressure dependence of the relative volumes of  $\text{ZrO}_2$  and  $\text{HfO}_2$  at room temperature. Results of fits to the Birch-Murnaghan equation of state for each phase are also plotted according to the parameters listed in Table 2. It should be noticed that the OII

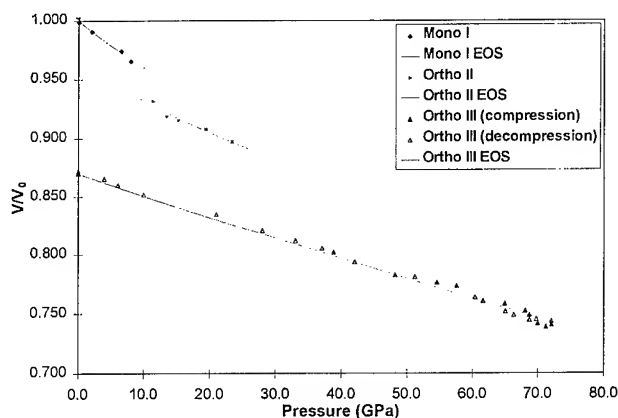


Figure 2: Pressure dependence of the volume of the high pressure phases of  $\text{ZrO}_2$ , with Birch-Murnaghan equations of state plotted according to parameters given in Table 2.

Table 2: Parameters of the Birch-Murnaghan equations of state for the observed dense phases of  $\text{ZrO}_2$  and  $\text{HfO}_2$ .

		MI	OI	OII
$\text{HfO}_2$	$B_0$	$284 \pm 30$	$281 \pm 10$	$340 \pm 10$
	$B'_0$	$4.6 \pm 2.0$	$4.2 \pm 1.0$	$2.6 \pm 0.3$
	$V/V_0$	1.000	0.955	0.876
$\text{ZrO}_2$	$B_0$	$212 \pm 24$	$243 \pm 10$	$444 \pm 15$
	$B'_0$	$8.0 \pm 4.0$	$6.7 \pm 1.7$	1.0 (fixed)
	$V/V_0$	1.000	0.981	0.870

phase (cotunnite) of both compounds, quenched at room pressure, present unusual volume changes as a function of pressure, namely that  $V(P)/V_0$  is described to some extent with a near-linear relationship above the transition pressure and over a wide range of decreasing pressure. Consequently, the pressure derivatives of the bulk moduli are smaller than 4, the nominal value normally encountered for other solids. Undoubtedly, the validity of finite strain theory is in question and fit parameters obtained using the Birch-Murnaghan EoS are given here only as an indication of the solid's behaviour.

X-ray diffraction patterns indicate that the quenched materials are highly polycrystalline (with very small grain sizes). Furthermore, line broadening is observed in both the Raman spectra and the X-ray diffraction patterns of the OII phase, indicative of residual stresses. This most likely relates to the relatively small change of the bulk moduli with pressure.

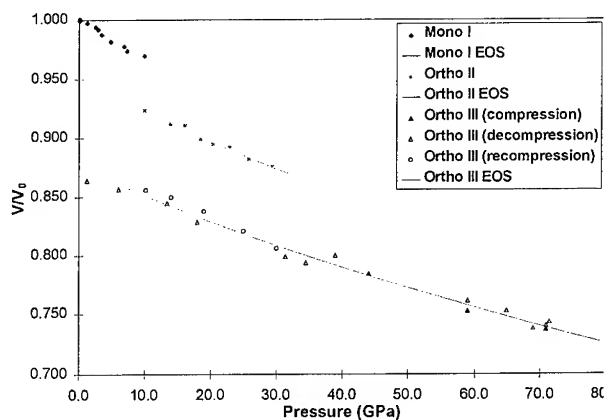


Figure 3: Pressure dependence of the volume of the high pressure phases of  $\text{HfO}_2$ , with Birch-Murnaghan equations of state plotted according to parameters given in Table 2.

### Acknowledgements

It is a pleasure to acknowledge the help of the CHESS staff and Dr. K. Brister. K. L. acknowledges the financial support of NSERC. This work was conducted under the auspices of NSERC.

### References

1. R. S. Hixson and J. N. Fritz. *J. Appl. Phys.* **71**, 1721 (1992).
2. K. E. Brister, Y. K. Vohra, and A. L. Ruoff. *Rev. Sci. Instrum.* **57**, 2560 (1986).
3. S. Desgreniers and K. Lagarec. *J. Appl. Cryst.* **27**, 432 (1994).
4. K. Lagarec and S. Desgreniers. 1995 CHESS Users' Meeting, CHESS, Cornell University.
5. A. Sakthivel and R. A. Young. DBWS9411 User's Guide. Georgia Inst. of Tech., 1994.
6. A. Jayaraman, S. Y. Yang, S. K. Sharma, and L. C. Ming. *Phys. Rev. B* **47**, 9205 (1993).
7. H. Arashi, T. Yagi, S. Akimoto and Y. Kudo. *Phys. Rev. B* **41**, 7 (1990).
8. L.-G. Liu. *J. Phys. Chem. Sol.* **41**, 331 (1979).
9. J. M. Léger, P. E. Tomaszewski, A. Atouf, and A. S. Pereira. *Phys. Rev. B* **47**, 14075 (1993).
10. J. Haines, J. M. Léger and A. Atouf. *J. Am. Ceram. Soc.* **78**, 445 (1995).
11. J. M. Léger, A. Atouf, P. E. Tomaszewski, and A. S. Pereira. *Phys. Rev. B* **48**, 93 (1993).

#### **IV(B) Mechanical Properties: Plasticity, Hydroextrusion, etc.**

# EFFICIENT IMPLEMENTATION OF ASSOCIATIVE FLOW EQUATIONS IN CONTINUUM MECHANICS CODES

Elane C. Flower<sup>a</sup>, Len G. Margolin<sup>a</sup> and Rudy R. Verderber<sup>b</sup>

<sup>a</sup> Los Alamos National Laboratory, Los Alamos, New Mexico 87545, USA

<sup>b</sup> Livermore Software Technology Corporation, Livermore, California 94550, USA

## ABSTRACT

The usual numerical procedure for integrating the elastoplastic stress-strain relations is a geometric construction due to Wilkins, called the method of Radial Return. The virtue of this construction is its simplicity and numerical robustness. Under some circumstances, this procedure is inaccurate, and leads to errors in the predictions of the final stress state and plastic strain rate. Here we propose an alternative, an exact closed-form integration of the Associative Flow equations assuming that the strain rate is constant over a time step. This technique was implemented in the Lagrangian finite-element codes, DYNA and EPIC, and is evaluated with a simple rectangular shear metal plasticity test problem.

## I. Introduction

In explicit numerical solutions of solid dynamics problems, the total strain rates  $\dot{\epsilon}_{ij}$  (rate of deformation tensor) are calculated from velocity gradient fields and become input to constitutive models. For elastic-plastic material elements, this strain rate, integrated over a computational (time step) cycle  $\Delta t$  and assumed to be elastic, may be large enough to cause the stress state to exceed the specified yield function  $f$  (not physically allowed in a rate-independent theory). Instead, the actual stress path must move along the yield surface, implying that part of  $\dot{\epsilon}_{ij}$  is realized as plastic (irreversible) strain.

The commonly used numerical approach for integrating the elastoplastic stress-strain relations is a geometric construction due to Wilkins(1), called the method of Radial Return. The virtue of this construction is its simplicity and numerical robustness. Under some circumstances, this procedure is inaccurate and leads to errors in the predictions of the final stress state and plastic strain rate. Instead of Radial Return we propose analytically solving a scalar form(2) of the associative flow equations that facilitates a complete closed form solution for the final stress state. In principle this analytic solution is more accurate and avoids the numerical stiffness problems(3) inherent

in numerically integrating the classical associative flow differential equations.

In the work described here we assume that  $\dot{\epsilon}_{ij}$  is a known constant over  $\Delta t$ , and that hardening in the constitutive model is explicitly time dependent. We implemented the proposed technique in the Lagrangian finite-element codes, DYNA and EPIC. In order to validate this implementation and investigate its accuracy relative to the method of Radial Return, we compare the results from a simple rectangular shear metal plasticity problem using data for isotropic copper and the Mechanical Threshold Stress (MTS) model(4) to describe hardening.

## II. Classical Associative Flow Equations

Most explicit continuum mechanics codes use Radial Return, that can be shown to be a first order accurate approximation for associative flow. A computed trial stress is determined following Hooke's Law in deviatoric rate form, assuming that  $\dot{\epsilon}_{ij}$  is elastic ( $\mu$  is the shear modulus):

$$\dot{s}_{ij} = 2\mu\dot{\epsilon}_{ij} \quad (1)$$

When this trial stress state is outside the yield surface, the final state is determined by scaling the trial state by the ratio of the flow stress  $\sigma$  to the square root of the trial stress invariant, and the amount of plasticity is

determined by the difference between this final stress state and the trial stress(1).

Classical associative flow equations based upon physical laws also start with Hooke's law Eq. (1), and proceed by partitioning the total strain rate into elastic and plastic portions:

$$\dot{\epsilon}_{ij} = \dot{\epsilon}_{ij}^e + \dot{\epsilon}_{ij}^p \quad (2)$$

The associative plastic flow law(5) written for a von Mises yield function is:

$$\dot{\epsilon}_{ij}^p = \dot{\lambda} \frac{\partial f}{\partial s_{ij}} = \dot{\lambda} s_{ij} \quad (3)$$

where the unknown  $\dot{\lambda}$  is a time-dependent proportionality scalar between the plastic strain rate and the stress state. Combining Eqs. (1) through (3) we have for the stress rate:

$$\dot{s}_{ij} = 2\mu(\dot{\epsilon}_{ij} - \dot{\lambda} s_{ij}) \quad (4)$$

The von Mises yield function can be expressed as:

$$f = \frac{1}{2} s_{ij} s_{ij} - \frac{1}{3} \sigma^2(c^p, \dot{\epsilon}^p, T) = 0 \quad (5)$$

where the flow stress  $\sigma$  is a function of strain, strain-rate and temperature invariants. The scalar  $\dot{\lambda}$  is obtained by enforcing yield surface consistency(5):

$$\dot{\lambda} = \frac{3/4}{\mu\sigma^2} \left( 2\mu\dot{\epsilon}_{ij}s_{ij} + \frac{\partial f}{\partial c^p} \dot{c}^p + \frac{\partial f}{\partial \dot{\epsilon}^p} \ddot{\epsilon}^p + \frac{\partial f}{\partial T} \dot{T} \right) \quad (6a)$$

Here, the strain, strain-rate and temperature dependence in Eq. (6a) are assumed to be expressed as explicit functions of time, i. e.,

$$\dot{\lambda} = \frac{3/4}{\mu\sigma^2} \left( 2\mu\dot{\epsilon}_{ij}s_{ij} + \frac{\partial f}{\partial \sigma} \frac{\partial \sigma}{\partial t} \right) \quad (6b)$$

After substituting Eq. (6a) into Eq. (4), the resulting stress ordinary differential equations can be solved numerically in an explicit fashion in the codes; however, stiffness problems arise that can result in explicit oscillation of the solutions(3), requiring  $\Delta t$  to be 10 to 100 times smaller than the Courant-Friedrichs-Levy (CFL)  $\Delta t$  to dampen these oscillations. To avoid this problem, we propose solving Eq. (4) analytically.

### III. An Associative Flow Scalar Solution

The analytical solution to Eq. (4) requires two integration steps: following Margolin and Flower(2), a work rate scalar  $w$  is defined:

$$w = s_{ij}\dot{\epsilon}_{ij} \quad (7)$$

Equation (6b) is now used to substitute for  $\dot{\lambda}$  in Eq. (4), and the result is contracted with  $\dot{\epsilon}_{ij}$  and simplified with Eq. (7) to obtain

$$\dot{w} = 2\mu I^2 - \frac{\mu 3w^2}{\sigma^2} + \frac{\dot{\sigma}}{\sigma} w \quad (8)$$

where  $I \equiv \sqrt{\dot{\epsilon}_{ij}\dot{\epsilon}_{ij}}$ .

It is then easy to integrate Eq. (8) for  $w$ :

$$w = \sqrt{\frac{2}{3}} I \sigma(t) \frac{A_o \chi - 1}{A_o \chi + 1} \quad (9)$$

where the constant  $A_o$  is:

$$A_o = \frac{\sqrt{2} I \sigma(t_o) + \sqrt{3} s_{ij}^e \dot{\epsilon}_{ij}}{\sqrt{2} I \sigma(t_o) - \sqrt{3} s_{ij}^e \dot{\epsilon}_{ij}} \quad (10)$$

and, for an arbitrary flow stress function, the quantity  $\chi$  is:

$$\chi = \exp \left\{ \sqrt{6} I \mu \int_{t_o}^{t_o + \delta t} \frac{dt}{\sigma(t)} \right\} \quad (11)$$

The initial time  $t_o$  in the above equations corresponds to the beginning of the time step, and the increment  $\delta t$  (where  $\delta t \leq \Delta t$ ) is the plastic flow time step(2).

Again following Margolin and Flower, Eqs. (6b) and (9) are inserted into Eq. (4), and the result integrated using an integrating factor. This gives the final stress state at the end of the time step in analytical form:

$$s_{ij} = \frac{\sqrt{2}\sigma(t)\dot{\epsilon}_{ij}}{A_o\chi^2 - 1} \left[ \frac{s_{ij}^e \chi (A_o + 1)}{\sqrt{2}\sigma(t_o)\dot{\epsilon}_{ij}} + \frac{A_o\chi^2 - A_o\chi + \chi - 1}{\sqrt{3} I} \right] \quad (12)$$

where the exact form of  $\chi$  depends upon the choice of flow stress function.

### IV. Incorporation of a Flow Stress Model

The MTS model(4) is used here in a specific form for copper. Under the assumptions of constant strain rate and temperature, the thermal activation  $s_{th}$ , saturation threshold stress  $\hat{\sigma}_s$  and dislocation generation  $\Theta_o$ .

functions are all constant, and in conjunction with a Voce law gives a closed-form relationship for the flow stress as a function of plastic strain:

$$\sigma = \hat{\sigma}_a + s_{th} \hat{\sigma} \quad (13a)$$

where  $\hat{\sigma}_a$  is a material constant and the mechanical threshold stress  $\hat{\sigma}$  is

$$\chi_{MTS} = \exp \left\{ \frac{\sqrt{6} \hat{\sigma}_s I \mu}{(\hat{\sigma}_a + s_{th} \hat{\sigma}_s) \Theta_0 \dot{e}^p} \left[ \frac{\Theta_0 \dot{e}^p}{\hat{\sigma}_s} \delta t + \ln \left( \frac{\hat{\sigma}_a + s_{th} \hat{\sigma}_s - s_{th} \hat{\sigma}_s \left( 1 - \frac{\hat{\sigma}(t_0)}{\hat{\sigma}_s} \right) e^{-\frac{\Theta_0 \dot{e}^p}{\hat{\sigma}_s} (t_0 + \delta t)}}{\hat{\sigma}_a + s_{th} \hat{\sigma}_s - s_{th} \hat{\sigma}_s \left( 1 - \frac{\hat{\sigma}(t_0)}{\hat{\sigma}_s} \right) e^{-\frac{\Theta_0 \dot{e}^p}{\hat{\sigma}_s} t_0}} \right) \right] \right\} \quad (14)$$

## V. Results

A 1-cm square quadrilateral plane-strain element was modeled with the EPIC code using for boundary conditions the prescribed kinematics for the simple rectangular shear problem, where the nonzero total strain-rate and strain are  $\dot{e}_{12} = k/2$  and  $e_{12} = kt/2$ . The corresponding strain invariants are  $\dot{e}^p = k/\sqrt{3}$  and  $e^p = kt/\sqrt{3}$ ;  $k$  is a kinematic constant.

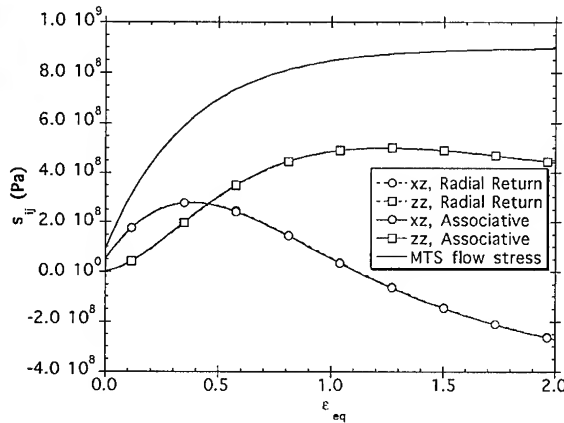


Figure 1: Material frame(3) deviatoric stress components versus equivalent strain for the simple rectangular shear problem where the MTS flow stress model is used.

Figure 1 shows results from an EPIC simulation, running at the CFL time step, for the simple rectangular problem shown over 200% strain for a shearing velocity of 1000 m/s ( $k=10^5 \text{ s}^{-1}$ ). These stress results compare Radial Return with the analytical solution from Eq. (12) using MTS copper (i.e.,  $\chi$  from

$$\hat{\sigma} = \hat{\sigma}_s \left[ 1 - \left( 1 - \frac{\hat{\sigma}(t_0)}{\hat{\sigma}_s} \right) e^{-\frac{\Theta_0}{\hat{\sigma}_s} e^p} \right] \quad (13b)$$

Substitution of Eqs. (13) into Eq. (11) and carrying out the indicated integration gives the MTS form for  $\chi$  as:

Eq. (14)) and indicate insignificant differences.

The results lead to two conclusions:

- 1) The closed-form associative flow solution, Eq. (13), gives a stable result for a CFL time step, as opposed to previously experienced(3) unstable numerical solutions for Eq. (4) when integrated explicitly with the same step size;
- 2) In metal plasticity, insignificant accuracy differences between the two methods are observed, whereas, for other materials that exhibit stronger hardening, e.g., soils, the difference can be very significant(2).

## References

1. M. L. Wilkins, Chap. VI in Theoretical Foundation for Large-Scale Computations of Nonlinear Material Behavior, S. Nemat-Nasser, R. J. Asaro and G. A. Hegemeir, Eds., (Martinus Nijhoff Publishers, 1984), 147-156.
2. L. G. Margolin and E. C. Flower, *High-Temperature Constitutive Modeling*, 1991, ASME Winter Annual Meeting, Atlanta, Georgia, December 1-6, 1991.
3. P. J. Maudlin and S. K. Schiferl, *Comp. Meth. in Appl. Mech. and Engr.* (accepted for publication, June, 1995).
4. P. S. Follansbee and U. F. Kocks, *Acta Metall.*, 36, No. 1, 81-93 (1988).
5. A. Mendelson, Plasticity: Theory and Application, Krieger Publishing Company, Malabar, Florida, 1968.

# AN APPLICATION OF MULTISURFACE PLASTICITY THEORY: YIELD SURFACES OF TEXTURED MATERIALS

P. J. Maudlin, S. I. Wright, U. F. Kocks and M. S. Sahota

*Los Alamos National Laboratory  
Los Alamos, New Mexico 87545, USA*

## ABSTRACT

Directionally dependent descriptions of the yield behavior of metals as determined by polycrystal plasticity computations are discrete in nature and, in principle, are available for use in large-scale application calculations employing multi-dimensional continuum mechanics codes. However, the practical side of using such detailed yield surfaces in application calculations contains some challenges in terms of algorithm development and computational efficiency. Discrete representations of yield as determined from Taylor-Bishop-Hill polycrystal calculations can be fitted or tessellated into a multi-dimensional piece-wise linear yield surface for subsequent use in constitutive algorithms for codes. Such an algorithm that utilizes an associative flow based multisurface plasticity theory has been implemented in the three dimensional EPIC code and is described in this effort.

## I. Introduction

X-ray diffraction techniques can be used to measure the distribution of crystallographic orientations in a polycrystalline material(1). The resultant orientation distribution (OD) can then be used to weight a set of discrete orientations to generate a representation of the material texture(2). This discrete representation of the measured texture can be probed in the context of a Taylor-Bishop-Hill polycrystal calculation with a set of incremental strain probes in order to form a set of deviatoric stress points that map out the material's yield surface(3). These stress points can be fitted or tessellated(4) into a multi-dimensional piece-wise linear yield surface for subsequent use in a continuum code constitutive algorithm. Koiter(5) and later Simo(6) developed an associative flow based theory (multisurface plasticity) that can accept a piece-wise linear description of the yield envelope. A constitutive algorithm that utilizes this theory has been implemented in the explicit three dimensional (3D) EPIC code and is described and illustrated below.

## II. Tessellation of Polycrystal Information

In general, yield functions are five dimensional (5D) in terms of the deviatoric stress components  $s_{ij}$ , i.e.,

$$[s_{ij}] = \begin{bmatrix} s_{11} & s_{12} & s_{13} \\ & s_{22} & s_{23} \\ & & s_{33} \end{bmatrix} \quad (1)$$

where this tensor has five independent components (recall  $s_{kk} = 0$ ). Therefore the stress components ( $s_{11}, s_{22}, s_{12}, s_{13}, s_{23}$ ) define the general 5D space that needs to be spanned by some convex yield function, constraining the magnitude of the stress state during plastic flow. For the sample yield surface presented in Fig. 1, a 3D stress space ( $s_{11}, s_{22}, s_{12}$ ) is assumed, although the algorithm discussed in Sec. III is appropriate for the 5D problem.

Now consider the 3D case where a set of stress points are generated by repetitive polycrystal probes of a measured material OD. This set of points is tessellated (a linear fitting complete with associated connectivity) into a piece-wise surface in three space using a tessellation algorithm(4). An example of such a tessellation is shown in Fig. 1, which is a tantalum (BCC) yield surface corresponding to a rolling texture and thus closely approximates an orthotropic mechanical response. This surface is basically a linear interpolation of 647 stress points with  $m = 1226$  linear functions or planes (in 5D say *hyperplanes*), the whole of which can be



mathematically expressed (using indicial notation) as the set:

$$\{f^\beta \equiv \alpha_{ij}^\beta s_{ij} - \sigma^\beta = 0, \beta = 1, 2, \dots, m\} \quad (2)$$

The linear functions appearing in Eq. (2) are expressed in normal form that defines the  $\alpha_{ij}^\beta$  as coefficients of a vector normal to the hyperplane and  $\sigma^\beta$  as the closest distance between the origin and the  $\beta$  hyperplane.

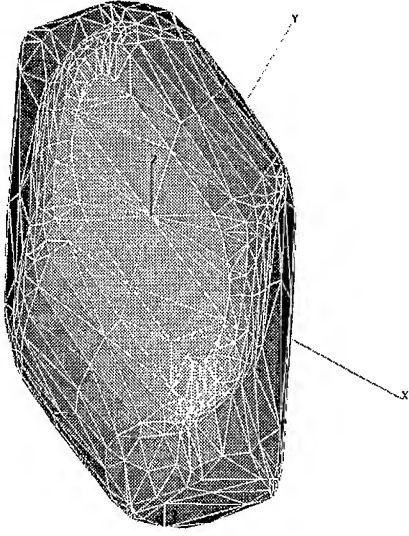


Figure 1: Perspective view of a piece-wise linear representation of a tantalum yield surface constructed from polycrystal calculations that use experimental measurements of the material texture as the initial grain orientation basis. The  $x, y, z$  axes shown are stress axes corresponding to  $S_{11}, S_{22}, S_{12}$ .

The yield function shown in Fig. 1 is actually only a normalized yield shape and thus needs to be scaled with some flow stress function  $\sigma$  (in equivalent stress units) to obtain the absolute surface in deviatoric stress space, i.e.,

$$s_{ij} = \tilde{s}_{ij} \sigma \frac{1}{\bar{M}}, \quad \sigma^\beta = \tilde{\sigma}^\beta \sigma \frac{1}{\bar{M}} \quad (3, 4)$$

where the quantities over scored with a tilde represent normalized variables: the results of tessellated polycrystal calculations. The average Taylor factor  $\bar{M}$  appearing in Eqs. (3) and (4) corresponds in direction to that of the uniaxial stress data obtained to characterize the flow stress function  $\sigma$ ; normalization of the polycrystal stress  $\tilde{s}_{ij}$  is such that the

uniaxial stress relationship between deviatoric stress and  $\sigma$  can be recovered from Eq. (3).

### III. Multisurface Plasticity Algorithm

If we now assume that the set of discontinuous piece-wise linear functions as represented by Eq. (2) is given, this yield surface can be utilized in an elastoplastic constitutive algorithm based on the multisurface plasticity theory of Koiter(5) and later Simo(6). This algorithm is modified here to facilitate its use in the framework of an explicit continuum code whose purpose is high-rate applications. The approach follows classical associative flow theory starting with a general anisotropic form of Hooke's law written in terms of a deviatoric stress rate and strain rate  $\dot{e}_{ij}$  (deviatoric portion of the symmetrical part of the velocity gradient tensor):

$$\dot{s}_{ij} = E_{ijkl} \dot{e}_{kl} \quad (5)$$

where  $E_{ijkl}$  is a symmetric elastic constant (stiffness) tensor. Assuming the standard practice of partitioning the strain-rate  $\dot{e}_{ij}$  into elastic and plastic parts, we can rewrite Eq. (5) as

$$\dot{s}_{ij} = E_{ijkl} (\dot{e}_{kl} - \dot{e}_{kl}^p) \quad (6)$$

with a flow rule for the plastic part expressed as a summation of contributions from those linear functions which are *active*:

$$\dot{e}_{ij}^p = \sum_{\beta=1}^{m_{act}} \dot{\lambda}^\beta \frac{\partial f^\beta}{\partial s_{ij}} \quad (7)$$

Here  $\dot{\lambda}^\beta$  is a time dependent proportionality scalar. Note that the stress gradients in Eq. (7) are just the constants  $\alpha_{ij}^\beta$  since the individual  $f^\beta(s_{ij})$  functions are linear; thus we have for our particular choice of Eq. (2)

$$\dot{e}_{ij}^p = \sum_{\beta=1}^{m_{act}} \dot{\lambda}^\beta \alpha_{ij}^\beta \quad (8)$$

The next step is to enforce yield surface consistency by taking the time derivative of Eq. (2), assuming that the flow stress is constant over the explicit time step  $\Delta t$  (this is good assumption as discussed in (7)), and

substitute for the stress rate and the plastic strain rate via Eqs. (6) and (8):

$$\dot{f}^\beta = \frac{\partial f^\beta}{\partial s_{ij}} \dot{s}_{ij} = \alpha_{ij}^\beta E_{ijkl} \left( \dot{e}_{kl} - \sum_{\zeta=1}^{m_{act}} \dot{\lambda}^\zeta \alpha_{ij}^\zeta \right) = 0 \quad (9)$$

Now if the total strain rate  $\dot{e}_{ij}$  is assumed to be a given (and constant over the time step), then yield surface consistency as represented by the right-hand portion of Eq. (9) is applied to each of the  $m_{act}$  active hyperplanes, resulting in a system of  $m_{act}$  equations to be solved for the  $m_{act}$  unknowns  $\dot{\lambda}^\zeta$ .

Most of the work associated with the use of this theory involves identifying the active hyperplanes out of a total population of candidate hyperplanes that can be arbitrarily large. From the mathematical concept of linear independence, the number of active linear functions can't be any larger than the dimension of our stress solution domain, i.e.,  $m_{act} \leq \dim\{f^\beta(s_{ij})\}$ , which is 5D for the general case of Eq. (1) and 3D for the simpler case illustrated by Fig. 1. For the Fig. 1 case the stress state during plastic flow can reside on a vertex (intersection of three planes, thus three linear functions are active), on an edge (intersection of two planes, thus two linear functions are active) or anywhere on a single plane (one linear function active); the analogy for the general 5D case is also valid.

Therefore the algorithm proceeds by identifying the active linear functions with a final step to correct for numerical error, as discussed in more detail in (8).

#### IV. A Simple Rectangular Shear Test Problem

A useful problem for checking the continuum code implementation of any constitutive algorithm is simple rectangular shear. A 1-cm-square quadrilateral plane-strain element was modeled with the EPIC code using the Fig. 1 yield surface, a set of  $E_{ijkl}$  for orthotropic rolled tantalum, and the multisurface plasticity algorithm presented above. Figure 2 shows stress history results from the EPIC simulation over 200% strain or 40  $\mu$ s of time for a shearing velocity of 1000

m/s. The non-smooth nature of this stress solution as the material flows plastically from a state of pure shear to one dominated by the normal components is a direct result of the discontinuous piece-wise nature of the yield surface; in contrast, if the surface were represented by single analytic function, then the stress solution would be smooth.

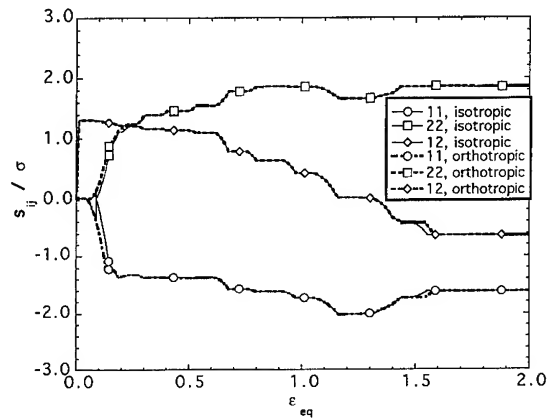


Figure 2: Material frame deviatoric stress components versus equivalent strain for the simple rectangular shear problem where a constant value for the flow stress  $\sigma$  has been assumed for convenience. Results using both isotropic and orthotropic elasticity are shown.

#### References

1. J. S. Kallend, U. F. Kocks, A. D. Rollett and H.-R. Wenk, *Mat. Sci. and Engr.*, **A132** 1-11 (1991).
2. U. F. Kocks, J. S. Kallend and A. C. Biondo, *Textures and Microstructures*, **14-18** 199-204 (1991).
3. G. R. Canova, U. F. Kocks, C. N. Tomé and J. J. Jonas, *J. Mech. Phys. Solids*, **33** 371-397 (1985).
4. M. S. Sahota, *Proceed. Next Free-Lagrange Conf.*, Moran, Wyoming, 3-7 June, 1990.
5. W. T. Koiter, *Quart. Appl. Math.*, **11**, 350-354 (1953).
6. J. C. Simo, J. G. Kennedy and S. Govindjee, *Int. J. Num. Meth. Engr.*, **26**, 2161-2185 (1988).
7. P. J. Maudlin and S. K. Schiferl, *Comp. Meth. in Appl. Mech. and Engr.* (accepted for publication, June, 1995).
8. P. J. Maudlin, S. I. Wright, U. F. Kocks and M. S. Sahota, *Acta Metall.* (submitted for publication, March 1995).

# MATHEMATICAL SIMULATION OF STABILITY AND VISCOUS FRACTURE OF MATERIALS DEFORMED UNDER PRESSURE

YA.E.BEIGELZIMER, B.M.EFROS, V.N.VARYUKHIN, A.V.SPUSKANYUK

*Donetsk Physics & Technical Institute of the Ukrainian Academy of Sciences,  
72 R. Luxembourg St., Donetsk, 340114, Ukraine*

## ABSTRACT

The mathematical model of plastic deformation of structurally inhomogeneous material with defects of inhomogeneity-type has been developed. The principal relationships have been obtained which are based on the results of the physical investigations. The proposed model has been used as a basis for the investigation of viscous fracture and deformation localization at pressure treatment of compact and noncompact materials. The model has been compared with the experiment both qualitatively and quantitatively.

The development of the hydrostatic treatment technologies should be based on the mathematical models describing microfracture of solids at deformation and taking into account the pressure effect on this process.

An adequate description of the microfracture is possible in the framework of the continuum concepts. In this case the consideration involves the magnitude of porosity that is the total relative volume of microdefects.

Thus, the present option is embodied in defining of physical relations of the continuum theory, comprising material porosity in terms of inner variable.

The further reduction of the problem can be fulfilled with the help of assumption of the flow theory in terms of which physical relations are defined by loading function.

The principal relationships of the flow theory have the form [1]

$$\dot{\epsilon}_{ij} = \lambda \frac{\partial f}{\partial \sigma_{ij}}; \quad (1)$$

here the following conditions are fulfilled:

$$\text{at } f = 0, \frac{df}{dt} = 0, \frac{\partial f}{\partial \sigma_{ij}} d\sigma_{ij} \neq 0, \quad \lambda > 0 \quad (2)$$

$$\text{at } f = 0, \frac{df}{dt} = 0, \frac{\partial f}{\partial \sigma_{ij}} d\sigma_{ij} = 0, \quad \lambda = 0 \quad (3)$$

$$\text{at } f = 0, \frac{df}{dt} < 0, \quad \lambda = 0 \quad (4)$$

$$\text{at } f < 0, \quad \lambda = 0. \quad (5)$$

where  $\sigma_{ij}$  and  $\dot{\epsilon}_{ij}$  are the tensor components of

stresses and rates of plastic deformation, respectively;  $f$  is the loading function;  $\lambda$  is the Lagrange factor.

Relationship (1) is the mathematical expression of the gradient condition.

Conditions (2)-(5) show that the plastic deformation takes place only when the stresses satisfy the condition of yielding  $f = 0$  at the time moment under consideration and the closest one to it and, the stress increment vector does not lie on the loading surface.

Condition (2) is assumed by us in an extended form to take into account the possible loss of the material stability (for stable materials in condition (2)  $(\partial f / \partial \sigma_{ik}) d\sigma_{ik} > 0$ , [1]).

The expression for loading function can be designed on the basis of the physical model reflecting the main features of the deformation mechanisms and fracture of material.

The following physical model is suggested by us in the article [2]:

- the material consists of interconnected structural elements;
- plastic deformation of material can be realized by means of joint coordinated deformation of its structural elements, more over its behavior is defined by the ability of elements to accommodate to each other;
- the ability to be accommodated is determined by the plastic deformation mechanisms acting at this or that moment. If they provide arbitrary deformation of the structural elements (e.g., five slip systems work), complete accommodation is possible. Otherwise ac-

commodation is only partial. As a result, gaps (or microinhomogeneities) appear between the elements (if at the beginning the elements were closely adjusted to each other), which results in loosening of the material. If, on the other hand, microinhomogeneities were present before the deformation, they may disappear at certain conditions since the structural elements are able to adjust to each other.

On the basis of analysis of the suggested physical model the following results are achieved by us: expression for loading function and physical equations of plasticity theory of structurally inhomogeneous materials.

Those equations are located in the table below where for comparison Mises' plasticity theory equations, describing the plastic deformation of unstructured material are also enlisted.

Notations:  $\psi(\theta) = \frac{(1-\theta)^{2n-1}}{6a\theta^m}$ ,

$\varphi(\theta) = (1-\theta)^{2n-1}$ ,  $\theta$  - porosity,

$$\sigma = \frac{1}{3} \sigma_{ik} \delta_{ik}, \quad \dot{\epsilon} = \dot{\epsilon}_{ik} \delta_{ik},$$

$$\tau = \sqrt{\left( \left( \sigma_{ik} - \frac{1}{3} \sigma \delta_{ik} \right) \left( \sigma_{ik} - \frac{1}{3} \sigma \delta_{ik} \right) \right)},$$

$$\dot{\gamma} = \sqrt{\left( \left( \dot{\epsilon}_{ik} - \frac{1}{3} \dot{\epsilon} \delta_{ik} \right) \left( \dot{\epsilon}_{ik} - \frac{1}{3} \dot{\epsilon} \delta_{ik} \right) \right)},$$

$k_0, \alpha, a, m, n$  -- material parameters.

In physical equations of structurally inhomogeneous material the parameter  $\alpha$  -- coefficient of inner friction is inherent. According to [2] it is quantitative measure of separate structural elements' ability to accommodate to each other.

In the case when complete adaptation of the elements to each other is possible  $\alpha = 0$ . The value of  $\alpha$  grows with the increase of a number of restrictions to the joint plastic deformation. That is, the less efficient are the mechanisms of plastic deformation of the structural elements, the higher is  $\alpha$ .

Table. Physical equations of plasticity theory of structurally inhomogeneous materials.

Physical equations for structurally inhomogeneous material	Physical equations for unstructured material (according to Mises)	Comments
$f = \frac{\sigma^2}{\psi(\theta)} + \frac{\tau^2}{\varphi(\theta)} - (1-\theta)(k_0 - \alpha\sigma)^2$	$f = \tau - k_0$	loading function
$\frac{\sigma^2}{\psi(\theta)} + \frac{\tau^2}{\varphi(\theta)} = (1-\theta)(k_0 - \alpha\sigma)^2$	$\tau = k_0$	condition of yielding
$\frac{\dot{\epsilon}\tau}{\varphi(\theta)} = \dot{\gamma} \left( \frac{\sigma}{\psi(\theta)} + \alpha(1-\theta)(k_0 - \alpha\sigma) \right)$	$\dot{\epsilon} = 0$	gradient condition
$\dot{\epsilon}_{ij} - \frac{1}{3} \dot{\epsilon} \delta_{ij} = \frac{\dot{\gamma}}{\tau} (\sigma_{ij} - \sigma \delta_{ij})$	$i \neq j$	
$\theta = \theta_c$	--	criteria of microfracture of the material
$\frac{d\tau}{d\gamma} \leq 0$	--	criteria of instability of the material and localization of plastic deformation

The physical investigations show that the growth of hydrostatic pressure gives rise to inclusion of few channels of plastic deformation. And there is the number of critical pressures which, being exceeded, activate new deformation mechanisms. Thus it follows that the value of  $\alpha$  should decrease with the increase in pressure  $p$ . And it should be noted that at intermediate pressures (i.e., those between the critical ones)  $\alpha$  does not depend on  $p$ .

In order to simulate the process of fracture and localization of deformation physical equations of structurally inhomogeneous materials are supplemented by the criteria of macrofracture and stability of the material (see the table above).

Physical equation system of Mises' plasticity theory increased by the equilibrium of continuous body equations permits to investigate plastic deformation liberal processes to define the strength-stress parameters of material. The equal abilities are provided by the physical equation system of the structurally inhomogeneous material. Nevertheless in addition to the above mentioned the stated system permits to analyze the changes of porosity (defectiveness) of material, to define the areas of macroscopic fracture and localization of deformation, to investigate hydrostatic pressure influence upon the behavior of material under the deformation.

Let us illustrate the functioning of the suggested model on the example of proportional loading of material under pressure. This type of loading is being realized, for example, during the cylindrical sample extension up to the moment of appearance of the neck or during the settling till the moment of creation of the barrel. The picture shows how the microporosity of the sample changes with the growth of the deformation under the constant value of the rigidity index of the stressed state  $\eta = \sigma / \tau$ .

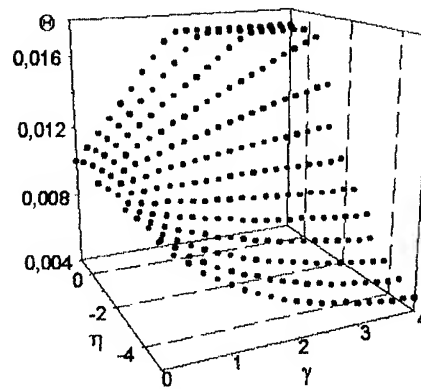


Figure. The calculated dependence of porosity  $\theta$  on the deformation value  $\gamma$  and stressed state rigidity index  $\eta$  (in the calculations:  $\theta_0=0.01$ ;  $\alpha=0.01$ ).

As it is seen, the increase of the hydrostatic pressure enlarges the plasticity; but under the pressures excelling some critical value the deformation leads to the diminishing of the defectiveness of the material.

The suggested model of deformation of structurally inhomogeneous material was applied by us while investigating of such processes as hydroextrusion [3], hydromechanical pressure, hydromechanical squeezing, uniaxial extension with the appearance of the neck, shift under pressure.

On the basis of this concept the continuum model of contact friction during the treatment of metals under pressure is being elaborated.

## References

1. D.D.Ivlev and G.I.Bykovtsev, *Theory of Hardening Plastic Body* (Nauka, 1971).
2. Ya.E.Beigelzimer et al., *Engineering. Fracture Mech.* 48 (1994) 629-640.
3. Ya.E.Beigelzimer et al., *Engineering. Mech.* 2 (1995) 17-26.

# INVESTIGATION OF PLASTIC PROPERTIES UNDER HIGH PRESSURES

S.B. POLOTNYAK, A.V. IDESMAN and L.K. SHVEDOV

*V.N.Bakul Institute for Superhard Materials of the National Academy of Sciences of Ukraine,  
2 Avtozavodskaya St., Kiev, 254074, Ukraine*

## ABSTRACT

A theoretico-experimental procedure for the measurement of material plastic properties when compressed in a diamond anvil cell (DAC) is developed. The principle of the procedure is as follows. A thin film sample is compressed between diamond anvils. Then, the pressure distribution vs. the sample radius is determined by the ruby fluorescence technique. Using the calculated model of plastic straining of a thin layer in compression, the pressure dependence of the shear strength of the sample has been determined from the as-measured pressure distribution. Using the procedure developed, the plastic properties of samples of KCl, NaCl (granular media) and stainless steel were studied under high pressures.

## Introduction

At present many technological processes are associated with plastic deformation of materials at high pressures. Therefore, the study of the material plastic behaviour at high pressures is an urgent problem. Thus, the influence of high pressure on shear strength of more than 300 materials was studied experimentally by Bridgman, Vereshchagin and other researchers. These results promote the understanding of the plastic deformation and failure mechanism as well as of phase transformations in materials.

Practically all methods for determination of the pressure dependence of the material shear strength  $\tau_s(\sigma_0)$  are based on compression of a thin disc of a material between two opposed anvils. Both traditional anvils and rotating anvils (during the compression one of the anvils rotates around the axis) are used in experiments. As a rule, the highest pressure for these investigations does not exceed 15 GPa. It is stipulated by the use of cemented tungsten carbide or hardened steels as materials for anvils.

Now, the highest static pressure can be attained in DAC. The combination of unique properties of diamond, the ruby fluorescence technique for pressure calibration and laser heating of the sample have turned the DAC into a fine quantitative tool for modern physical researches

at pressures up to 500 GPa and temperatures up to 3000°C. However, investigations aimed at measurement of material plastic properties at ultrahigh pressures using DAC have not been reported yet.

## Theory

A theoretico-experimental procedure for determination of the pressure dependence of the material shear strength at compression in DAC has been developed [1]. The principle of the procedure is as follows. A thin disc of a material

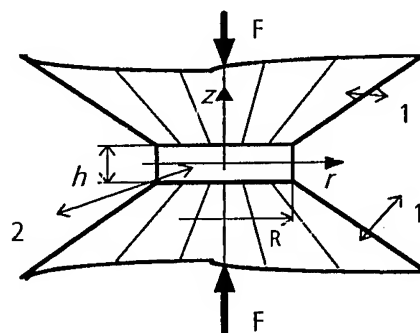


Fig. 1. Material disc compressed in DAC :  
1 — diamond anvils, 2 — sample.

is compressed between the flat parallel faces of two opposed diamond anvils (see Fig. 1).

Then the pressure over the sample contact area on the face of the diamond anvil is

determined by the ruby fluorescence technique. When the thin sample is compressed, a considerable material flow to the periphery of the disc (except a small region near the center of the sample) occurs. In the plastic flow region, the pressure gradient  $d\sigma_0/dr$  along the radius is just balanced by the shear stress of the material  $\tau_s(\sigma_0)$  that leads to the equation

$$\frac{d\sigma_0}{dr} = -\frac{2\tau_s(\sigma_0)}{h(r)}, \quad (1)$$

where  $h(r)$  is the sample thickness. Differentiating (numerically or graphically) the as-measured pressure and executing the necessary transformation we obtain the pressure dependence of the sample material shear strength. As a result of received dependence processing, the material plastic constants are determined. To verify the result obtained we have to integrate equation (1) and by the substitution the  $\tau_s(\sigma_0)$  values we obtain the calculated pressure distribution, which can be compared with the experimental one.

It is necessary to note, that the part of "the pressure-anvil radius" curve near the anvil center should be excluded from consideration at the material plastic properties determination. In this region, the considerable plastic flow of the sample material from the center to periphery of the disc does not occur, and, therefore, the equation of force balance (1) is not executed. Let's assume that the pressure dependence of the material shear strength is not decreasing, then in the first approximation the part of curve  $\sigma_0(r)$  from the center of the sample to the inflection point may be excluded from consideration (see Fig. 2).

The suggested procedure is realized as a software for a personal computer. The procedure has been tested with satisfactory results.

Thus, as compared to known procedures, the given method is more simple and allows us to find the nonlinear pressure dependence of the shear strength by the deformation of the material in a DAC.

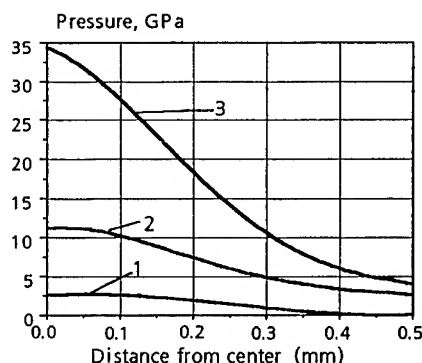


Fig. 2. Pressure distribution as a function of distance from the anvil center for: 1 — KCl sample, 2 — NaCl sample, 3 — stainless steel sample.

## Experiment

For investigation of substances under conditions of uniaxial stress and shear deformation in a plane perpendicular to the stress axis, the installation consisting of a DAC (a similar DAC has been described in [2]) and a set of measuring equipment was developed. The anvils were made from natural brilliant-cut diamonds. The anvil flat has a diagonal distance of 0.5 - 0.8 mm, the anvil height is 2 mm, the surface opposite to the anvil flat has a diagonal distance about 3 mm. The vertical axis of anvils coincides with direction  $\langle 100 \rangle$  of the diamond. The pressure over the sample surface is determined by the pressure shift of the ruby fluorescence wavelength emitted from the ruby particles dusted on the sample before pressurization.

As an application of the procedure developed, plastic properties of KCl, NaCl (both granular media) and hardened stainless steel X18H10T (18% Cr, 10 % Ni) were studied under high pressures. For powdered samples, a mixture of a substance and fine ruby crystals in proportion 100:1 was placed on the diamond anvil without a gasket. For the third material, the sample was a gasket from the hardened stainless steel, upon which a layer of finely powdered ruby crystals was placed. (The gasket, which had an initial thickness of 300  $\mu\text{m}$ , was preindented in the diamond cell to a thickness of about 70  $\mu\text{m}$ ,

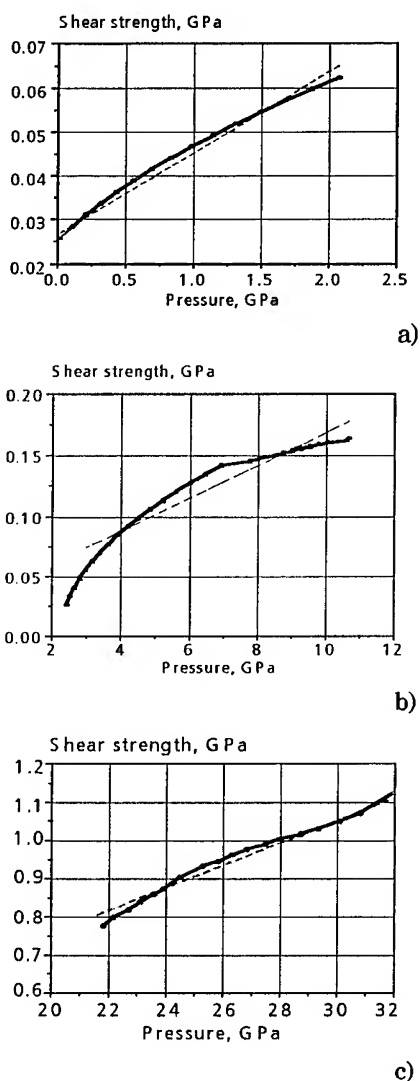


Fig. 3. Pressure dependencies of the shear strength for: a — KCl sample, b — NaCl sample, c — stainless steel sample. The dotted lines are a linear approximation.

unloaded to 0.1 MPa, and then covered with a ruby powder). Data acquired during these experiments consisted of visual observations of the ruby plus sample in reflected light and measurements of pressures at a total of more than 1000 points during the experiments. Pressure was measured in two-dimensional grids with the automated system to find the radial pressure profiles on each step of loading. Figure

2 shows the averaged pressure distributions as a function of the distance from the anvil center for the samples of NaCl, KCl and hardened stainless steel at the maximum pressures achieved.

It should be noted, that the average size of ruby grains was 3 micron, that was considerably less than the final thickness of the composite sample, substance plus ruby, at the highest pressure (10, 15, 20  $\mu\text{m}$  for KCl, NaCl and stainless steel, respectively).

## Results

Fig. 3 shows the obtained pressure dependencies of shear strength for materials under study. Assuming, that the shear strength pressure dependence has a linear form (the dotted lines in Fig. 3):

$$\tau_s = K + \sigma_0 \tan(\rho),$$

where  $K$  is the shear strength at  $\sigma_0 = 0$ ,  $\rho$  is the angle of internal friction, we obtain for:

$$\text{KCl} — K = 0,0263 \text{ GPa}, \rho = 0,0192;$$

$$\text{NaCl} — K = 0,0344 \text{ GPa}, \rho = 0,0135;$$

$$\text{steel} — K = 0,5412 \text{ GPa}, \rho = 0,0141.$$

Thus, the use of high pressure apparatus with diamond anvils allows the extension of the pressure range when studying plastic properties of materials.

## Acknowledgments

The authors are grateful to Prof. V.I. Levitas and Prof. N.V. Novikov for helpful discussions in doing this work.

## References

1. N.V. Novikov, V.I. Levitas, S.B. Polotnyak and M.M. Potyomkin, *Strength of Materials*, **26**(1994), N 4, p. 64.
2. I.A. Barabanov, V.D. Blank and Yu.S. Konyaev, *Pribory i Tekhnika Experimenta*, **2** (1987), p.176.



# PHASE TRANSITIONS UNDER COMPRESSION AND SHEAR OF MATERIALS IN BRIDGMAN ANVILS: THEORY AND INTERPRETATION OF EXPERIMENTS

VALERY I. LEVITAS

*Institut für Baumechanik und Numerische Mechanik, Universität Hannover, Appelstraße 9A,  
30167 Hannover, Germany;*

*Institute for Superhard Materials, Avtozavodskaya 2, 254074 Kiev, Ukraine*

## ABSTRACT

A simple analytical description of PT under compression and shear of materials in Bridgman anvils is developed. It is found that an improvement of PT conditions due to a rotation of an anvil is attributed not to the plastic strain, but to a possibility of an additional displacement, compensating a volume decrease because of PT. It is connected with a reduction of frictional shear stress in a radial direction due to the rotation of an anvil. New explanation of the pressure self-multiplication effect is obtained based on the higher yield stress of the new phase.

## Introduction

After compression of materials in Bridgman anvils, especially in diamond anvils, a very high pressure in the center can be reached. A number of PT can occur under such conditions. Additional rotation of an anvil and consequently plastic strain lead to significant reduction of PT pressure and to fundamentally new materials, which can not be produced without additional plastic strains. Volume fraction of the new phase is an increasing function of the rotation angle and consequently plastic shear strain. That is why plastic strain is considered as a factor, producing new physical mechanisms of PT. It seems to us a little bit unrealistic. At the compression of materials in Bridgman non-rotating anvils, the mean value of plastic strain reaches 1000 %, additional plastic shear strains near surfaces of anvils due to a contact friction exceed several thousand percents and have completely the same character, as a shear strain in rotating Bridgman anvils. Why no one of physical mechanisms of effect of plastic strains on PT manifests itself at such large plastic shear strain, but appears at rotation of an anvil, giving additional 10 – 100 % plastic strain only?

In the paper, a simple theory is developed, which gives a new look on the above phenomena.

## Phase transition criterion

The PT criterion for nucleation in elastoplastic materials was derived [1, 2] in the form

$$\int_{\epsilon_1}^{\epsilon_2} \int \sigma : d(\epsilon^e + \epsilon^f) dV - \int \Delta\psi dV = \int k dV, \quad (1)$$

where  $\sigma$  is the stress tensor,  $\epsilon^e$  and  $\epsilon^f$  are elastic and transformation strains,  $V$  is the volume of nucleus,  $\psi$  is the Helmholtz free energy per unit volume,  $k$  is the dissipation increment due to phase transition in a unit volume, related e.g. to the emission of acoustic waves and lattice friction,  $\Delta\psi = \psi_2 - \psi_1$  (subscripts 1 and 2 denote the phase before and after PT). Formally Eq. (1) has the same form as for PT in elastic materials; plasticity affects implicitly a variation of  $\sigma$  in the course of PT and the  $k$  value. At equal elastic properties of phases we have [1, 2]

$$\int_{\epsilon_1^f}^{\epsilon_2^f} \int \sigma : d\epsilon^f dV - \int \Delta\psi^\theta dV = \int k dV, \quad (2)$$

where  $\psi^\theta$  is the thermal part of the free energy, i.e. the elastic strains also disappear. Here we consider pure dilatational transformation strain  $\epsilon^f = 1/3 \epsilon_o^f I$ , where  $I$  is the unit tensor,  $\epsilon_o^f$  is the volumetric transformation strain. In this case,  $\sigma : d\epsilon^f = p d\epsilon_o^f$ , where  $p$  is the hydrostatic pres-

sure. As the volumetric transformation strain and  $k$  are distributed homogeneously in the nucleus, Eq. (2) can be transformed into the form

$$\int_{\epsilon_{01}^f}^{\epsilon_{02}^f} \bar{p} d\epsilon_o^f - \Delta\psi^\theta = k, \quad \bar{p} = \frac{1}{V} \int p dV, \quad (3)$$

where  $\bar{p}$  is the averaged over the nucleus pressure. Eq. (3) is a final form of the phase transformation criterion which is used in the present paper.

### Stress state of a thin cylindrical disk under compression and shear in anvils

We shall neglect the elastic deformations of anvils and deformed disk and use the well-known simplified equilibrium equation

$$\frac{\partial p}{\partial r} = -\frac{2\tau_r}{h}, \quad (4)$$

where  $r$  is the radial coordinate,  $h$  is the current thickness of the disk,  $\tau_r$  is the radial component of the shear frictional stress  $\tau$  on the boundary  $S$  between anvils and a disk. Shear frictional stresses  $\tau$  directed opposite to the velocity  $\mathbf{v}$  of relative sliding of a compressed material on the boundary  $S$ . For a thin disk, the modulus  $\tau$  reaches usually its possible maximum value equal to the half of yield limit  $\sigma_y$ . In the case without rotation of the anvil  $\tau_r = 0.5\sigma_y$  and Eq. (4) yields

$$\frac{\partial p}{\partial r} = -\frac{\sigma_y}{h}; \quad p = \sigma_o + \sigma_y \left(1 + \frac{R-r}{h}\right), \quad (5)$$

where boundary condition  $p = \sigma_o + \sigma_y$  at the external radius of anvil  $r = R$  is taken into account,  $\sigma_o$  is the pressure at  $r = R$  due to external support of material being outside the working region of anvils  $r > R$ . Applied load is determined by integration of  $p(r)$  over  $S$

$$Q = \pi R^2 \left( \sigma_o + \sigma_y \left(1 + \frac{R}{3h}\right) \right). \quad (6)$$

Radial velocity  $u$  is defined from the incompressibility condition and condition  $u = 0$  at  $r = 0$  by the equation

$$u = -\frac{\dot{h}r}{h}. \quad (7)$$

During rotation of one of the anvils with an angular velocity  $\omega$  Eq. (7) is still valid, but the circumferential velocity  $v = \omega r$  appears. In this case, velocity vector  $\mathbf{v}$  and shear frictional stresses  $\tau = 0.5\sigma_y \mathbf{v}/|\mathbf{v}|$  are inclined at an angle  $\alpha$  to the radius with

$$\cos \alpha = \frac{u}{\sqrt{u^2 + v^2}} = \frac{1}{\sqrt{1 + (\omega h/\dot{h})^2}} \quad (8)$$

and consequently

$$\tau_r = 0.5\sigma_y \cos \alpha. \quad (9)$$

Application of Eq. (4) with account for Eq. (9) leads to

$$p = \sigma_o + \sigma_y \left(1 - \frac{R-r}{H}\right); \quad (10)$$

$$Q = \pi R^2 \left( \sigma_o + \sigma_y \left(1 + \frac{R}{3H}\right) \right); \quad (11)$$

$$H = \frac{h}{\cos \alpha} = h \sqrt{1 + (\omega h/\dot{h})^2}, \quad (12)$$

i.e. it is equivalent to the substitution of  $H$  for  $h$ . Let rotation occur at the fixed axial load  $Q$ . Then condition  $Q = \text{const}$  with assumption  $\sigma_o = \text{const}$  results in  $H = \text{const} = h_o$ , where  $h_o$  is the thickness of the disk at the beginning of rotation, and in differential equation of reduction of thickness

$$d\varphi := \omega dt = \frac{dh}{h} \sqrt{\left(\frac{h_o}{h}\right)^2 - 1}. \quad (13)$$

Eq. (12) shows that at  $Q = \text{const}$  due to  $H = \text{const}$ , pressure distribution is independent of rotation, which corresponds to known experiments [3].

Consequently, rotation is equivalent to *reduction of friction* in the radial direction and results in a *decrease* of the *disk thickness* and this decrease is uniquely related to the rotation angle  $\varphi$ .

Let us consider PT in the central part of the disk and assume that transformation strain is pure volumetric compression (Fig.1). We adopt that the volume fraction of the new phase in transforming region  $A$  is  $c$ . In the case without rotation of the anvil one part of the disk material moves to the center of the anvil. A neutral circle  $EF$  with zero velocity of relative sliding can be easily found using

a volume balance. Eq. (4) is valid, but shear stress in the region  $EF$  changes sign and in the region  $A$  the yield stress  $\sigma_{y2}$  of a new material, which depends on  $c$ , should be used. We assume that the pressure is continuous across the interface. Results of an analytical solution are shown schematically in Fig. 1. It is important, that under a fixed axial force  $Q$ , pressure in the transforming region and the work integral in Eq. (3) decrease significantly, which makes PT condition worse. The higher  $\sigma_{y2}$ , the bigger pressure reduction in the transforming region.

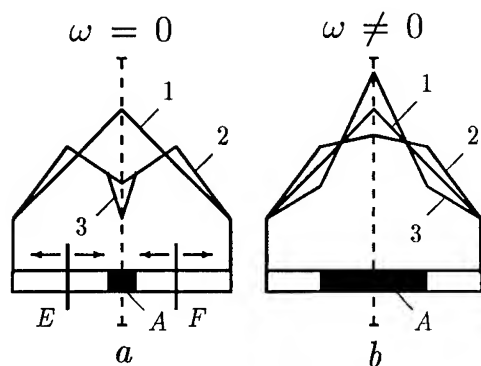


Fig. 1. Pressure distribution

- a. 1 - before PT; 2 - after PT at  $\sigma_{y1} = \sigma_{y2}$ ;  
 3 - after PT at  $\sigma_{y1} < \sigma_{y2}$ ;  
 b. 1 -  $\sigma_{y1} = \sigma_{y2}$ ; 2 -  $\sigma_{y1} > \sigma_{y2}$ ; 3 -  $\sigma_{y1} < \sigma_{y2}$ ;

Rotation, decreasing the thickness, reduces a negative pressure variation in the transforming particle. Optimal pressure variation (in a sense of the postulate of realizability [1, 2]) will be, when infinitesimal radial flow from the disk center occurs. In this case, shear stress does not change the sign, pressure monotonically grows with decreasing radius and volume decrease due to PT is completely compensated by the thickness reduction. The last condition together with Eq. (13) results in differential equation

$$dc\epsilon_o = \frac{dh}{h} = d\varphi \left( \left( \frac{H}{h} \right)^2 - 1 \right)^{-0.5}, \quad (14)$$

which relates uniquely variation of volume fraction of new phase in transformed region and rotation angle, as is observed in experiments [4]. According to Eq. (4) if both phases have the same yield limit, pressure distribution after PT is the same as before

PT (Fig. 1,b). If the new phase is weaker, pressure decreases in the center, if new phase is harder, pressure increases in the center. Consequently, despite the volume decrease due to PT, pressure increases due to appearance of the harder phase and additional plastic flow, which agrees with experiments (effect of pressure self-multiplication [3]).

Note that explanation of pressure self-multiplication effect based on increasing of elastic moduli after PT [3] is not correct, because it does not take into account the plasticity. Even at infinite moduli (as in our model), the pressure is limited by solution of the problem of plastic equilibrium, e.g. presented here. If  $\sigma_{y1} > \sigma_{y2}$  or material flows to the center of the disk, the pressure in the new phase can not be increased irrespective of the increase in elastic moduli.

Let us summarize the results. Improvement of PT conditions due to rotation of the anvil is related to the possibility of additional displacement, compensating a volume decrease. It is connected with a decrease of friction stress in a radial direction. But when we understand that the reason lies in additional displacement (and not in a plastic straining), it is possible to find another ways to obtain additional displacement without rotation.

Account for the deviatoric part of transformation strain tensor, pressure dependence of the yield stress and elastic strain will be considered elsewhere.

## Acknowledgments

The financial support of Volkswagen Foundation, as well as discussions with Prof. E. Stein and N. Novikov are gratefully acknowledged.

## References

1. V.I. Levitas, *Mech. Res. Commun.* **22** (1995) 87.
2. V.I. Levitas, *Journal de Physique IV, Colloque C2 5* (1995) 41.
3. V.D. Blank et al., *Sov. Phys. JETP* **87** (1984) 922.
4. M.M. Alexandrova et al., *Sov. Phys. Solid State* **30** (1988) 577.

# CALCULATION OF THE HYDROEXTRUSION FORMED BILLET QUALITY PROPERTIES

A.V.SPUSKANYUK, Y.YE.BEIGELZIMER

Donetsk Phys.&Tech. Institute of the National Academy of Sciences of Ukraine,  
72 R. Luxembourg St., Donetsk, 340114, Ukraine

## ABSTRACT

Attempt of calculation of the technological plasticity and mechanical properties of hydroextrusion processed billets basing on the physically grounded model of structurally-inhomogeneous body has been performed.

Hydroextrusion is known as one of the most effective methods of the material structure and properties modification. The high level of hydrostatic pressure provided in process allows one to reach significant deformation without the billet fracture. Material undergoing hydroextrusion makes the proper structure that provides increased level of strength and notably high level of residual plasticity which in some cases may even exceed the initial one [1].

The experimental study of the structure and mechanical properties of billets after hydroextrusion is described in many publications. At the same time theoretical works are rare and mostly having phenomenological character (see, e.g. [2]).

In the present paper the attempt of calculation of the technological plasticity and mechanical properties of hydroextrusion processed billets based on the physically grounded model of structurally-inhomogeneous body that is given in our paper [3] has been performed. This model is based on the plasticity condition that takes into account influence of hydrostatic pressure on the mechanisms of plastic relaxation of inner stress that is read

$$6\alpha\Theta\sigma^2 + \tau^2 = (k_0 - \alpha\sigma)^2, \quad (1)$$

where  $\Theta$  -- porosity of material that shows loosening of its structure ( $\Theta < 10^{-2}$ );  $\sigma$  -- hydrostatic component of the stress tensor;  $a$  -- parameter describing morphology of mesoinhomogeneity;  $\tau$  -- stress deviator intensity;  $k_0$  -- shear adhesion coefficient;  $\alpha$  -- internal friction coefficient that is a

quantitative measure of the acting plastic deformation channels' efficiency.

Using condition (1) in [3] the following kinetic equation for the porosity  $\Theta$  has been obtained:

$$\frac{d\Theta}{d\gamma} = \alpha + 6\alpha\Theta\eta, \quad (2)$$

where  $\eta = \sigma/k_0$  -- rigidity index of the stressed state;  $\gamma$  -- strain deviator intensity. According to [3] the calculation of material structure loosening caused by hydroextrusion is reduced to the full system of the plasticity mechanics that has to be solved together with equation (2). The  $\eta = \eta(\gamma)$  dependence must be obtained to integrate relationship (2). In [3] it is shown that the following relationship is valid near the billet axis:

$$\eta(\gamma) = -\left(1 + \frac{\mu_r}{2\sqrt{3}\tan(\beta/2)}\right)\gamma - \sqrt{\frac{2}{3}}\left(1 + \frac{3P_{CP}}{2\sigma_T}\right), \quad (3)$$

where  $2\beta$  -- die cone angle;  $\mu_r$  -- plastic friction coefficient;  $P_{CP}$  -- counter pressure value;  $\sigma_T$  -- yield limit of material being deformed.

Integration of the equation (2) considering (3) allowed to study transformation of structure loosening level during hydroextrusion [3].

In order to predict mechanical properties of billets let us do the following:

1. We will take into account deformational hardening of material in the relationships (1) and (3). Plasticity condition (1) is reduced to the Mises condition if  $\sigma = 0$ , where parameter  $k_0$  is the deforma-

tion resistance value ( $k_0 = \sqrt{2/3}\sigma_s$ ). Therefore, let  $k_0 = \sqrt{2/3}\sigma_s(\gamma)$ , where  $\sigma_s(\gamma)$  — curve of deformation hardening of material that is usually approximated by the power function.

In [4] the relationship between deformation hardening curve and diagram of structural states of material as well as multistage character of this curve have been shown. Each stage corresponds to the certain type of dislocational structure and, therefore, certain deformation mechanism. Parameters of approximation power function are firm within a stage and change with the change of stage.

Since the internal friction coefficient  $\alpha$  characterizes acting deformation mechanisms [3] it is evident to suppose multistage behavior of  $\alpha$  vs  $\gamma$  dependence while  $\alpha = \text{const}$  within each stage.

2. Let us investigate uniaxial tension process using model described by (1) and (2). Also we will find out moment of billet fracture according to the concentrational criteria [3]. It will allow us to calculate relative reduction in neck  $\Psi$  at the moment of destruction and ultimate strength of material  $\sigma_B$ .

It is easy to show that for the tension without forming a neck  $\eta = 1/\sqrt{3}$ , for the tension that forms a neck in its minimal section

$$\eta = \frac{1}{\sqrt{3}} \left( 1 + \frac{3}{2} \sqrt{\frac{2}{3}\gamma - 0.1} \right). \quad (4)$$

The last relationship is taken from the Bridgman's formula considering relationship  $\gamma = \sqrt{2/3}\epsilon$  where  $\epsilon$  is the logarithmic deformation.

Integrating kinetic equation (2) considering relationships for  $\eta$  we have relationship for the material loosening level  $\Theta$  vs  $\alpha$ . Defining fracture moment by condition  $\Theta = \Theta_{CR}$  (where  $\Theta_{CR} = 0.01$  — critical porosity) and considering connection between relative reduction and  $\gamma$  we have

$$\Psi = 1 - \exp\left(-\sqrt{\frac{2}{3}}\gamma_{CR}\right), \quad (5)$$

where  $\gamma_{CR}$  is the value of  $\gamma$  of when  $\Theta = \Theta_{CR}$ .

Value of  $\sigma_B$  is calculated using

$$\sigma_B = \sigma_s(\ln R + 0.1), \quad (6)$$

taken from [5]. Here  $R$  is the billet elongation coefficient during hydroextrusion.

In order to conduct computer experiments basing upon the model described above the computer program has been designed. It solves differential equations using numerous Runge-Kutta's methods, approximation of the hardening curve is read according to Hollomon's model as  $\sigma_s = Ke^n$ . Having been given parameters of material  $K, n, \alpha, a$  this program may be used to identify parameters of model according to the results of experiments including hydroextrusion and uniaxial tension. In this case hydroextrusion and tension of billets until their fracture may be seen as a new method of mechanical testing of materials that allows one to find out their parameters ( $K, n, \alpha, a$ ).

As an example we show data obtained for the high-nitrogen steel (wt. %: Cr 22.3; Mn 15.2; Ni 8.4; Mo 1.2; V 0.9; N 0.67). This is an austenitic steel with the average initial grain size about 40  $\mu\text{m}$ . Theoretical curves  $\Psi(\alpha, P_{CP}, R)$  for different values of counter pressure and experimentally obtained data are shown at the Fig. 1. Dependencies  $\sigma_B(\alpha, P_{CP}, R)$ ,  $\sigma_{0.2}(\alpha, P_{CP}, R)$  and experimentally obtained data are found at the Fig. 2. The calculations were conducted using the following values of parameters of model:  $\alpha = 0.0074$ ;  $a = 0.04$ ;  $K = 2200$  MPa;  $n = 0.323$ .

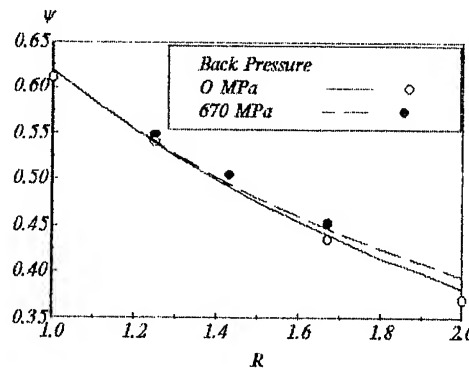


Figure 1. Dependencies  $\Psi(\alpha, P_{CP}, R)$  at various levels of counter pressure.

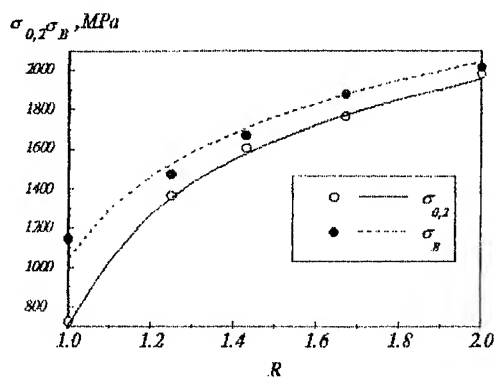


Figure 2. Dependencies  $\sigma_B(\alpha, P_{CP}, R)$ ,  $\sigma_{0,2}(\alpha, P_{CP}, R)$ .

Good correspondence of the theoretical calculations and experimental results using these values of  $\alpha$  and  $a$  obtained according to described method as well as with ones described in [3] proves good accuracy and adequacy of model.

## References

1. K.V.Volkov et.al., *Hardening of materials by means of hydroextrusion* (Naukova Dumka, Kiev, 1991).
2. G.L.Kolmogorov et.al., *Hydroextrusion of hard metals and alloys* (Metallurgia, Moscow, 1991).
3. Ya.Ye.Beigelzimer et.al., *Continuum model of the structural-inhomogeneous porous body and its application for the study of stability and viscous fracture of material deformed under pressure* (Preprint of the Donetsk Phys.&Tech. Institute of the National Academy of Sciences of Ukraine, 1994).
4. V.I.Trefilov, *Deformational hardening and fracture of polycrystalline materials* (Naukova Dumka, Kiev, 1987).
5. P.V.Bridgeman, *Big plastic deformation and fracture research. Influence of the high hydrostatic pressure on mechanical properties of materials*. (Moscow, Izdatelstvo inostrannoy literatury, 1955).

## THE STRUCTURE AND PROPERTIES OF POLYMERS PRODUCED BY EXTRUSION OF POWDER SEMI-PRODUCTS

V.A. BELOSHENKO, V.N. VARYUKHIN, G.V. KOZLOV, V.G. SLOBODINA

*Donetsk Physico-Technical Institute of the Ukrainian National Academy of Sciences, R. Luxemburg-str.  
72, Donetsk, 340114, Ukraine*

### ABSTRACT

Specific features of the structural modification of polymers and polymer composites produced by the plunger extrusion method from powder semi-products are studied. It is shown that the character of observed changes in properties of extrudates is determined by the structure of polymers.

### Introduction

The solid-phase extrusion is a promising method to improve deformational and strength characteristics of block polymers. As a rule, monolith polymer rods are used for extrusion. This complicates the fabrication process and makes it energy-consuming. Formerly a new method has been proposed for treating of raw polymers, namely, the plunger extrusion of powder semi-products [1]. The method comprises compacting of powder semi-product, heating of it up to the temperature values approaching the melting point and extrusion of the heated semi-product. Application of this method is mostly effective for polymers with high viscosity of melt, for treating of which the common high-productive methods of treatment are not feasible. In the present paper the structure and properties of extrudates of such materials with different structure - amorphous and semi-crystalline polymers and filled composites - are studied.

### Experimental results and discussion

#### *Amorphous polymers*

The study was carried out for polyarylene on the basis of a diene and the mixture of dichloranhydride of iso- and terephthalic acids (1:1), namely, polyarylene A and polyarylene B, which is a composite on the basis of polyarylene A and co-

polysulfoneformal (9:1), where co-polysulfoneformal is a product on the basis of a diene with 4,4'-dichlorodiphenylsulfon and chloric methylene (1:1).

In Table the test results of compression of polyarylene A control samples, produced by hot pressing ( $\lambda = 1$ ) and of extrudates are given. It is seen that at increase of values of extrusion ratio  $\lambda$  values of elasticity module  $E$  remain practically constant, and values of breaking stress  $\sigma_b$  and breaking strain  $\epsilon_b$  are increased. Extruded polymer products possess better characteristics in comparison with those produced by pressing methods. Similar improvements are observed for polyarylene A.

To explain the stated relationships we propose a model of deformation of the macromolecular interlace. According to this model, at extrusion stresses are applied to this interlace. They compress it longitudinally and make it loose transversely relative to the extrusion axis. As a result, a certain degree of anisotropy of polymers takes place. The consequence of it is the observed changes in mechanical properties.

#### *Semi-crystalline polymers*

The study was carried out for superhigh molecular polyethylene (SHMPE) as polymer with flexible chains and polyetherketone as a co-polymer on the basis of dipheniloxide and chloranhydrides of iso- and terephthalic acids of the class of polymers with semihard chains.

### The effect of extrusion on mechanical properties of polymer samples

POLYMER	$\lambda$	$E \cdot 10^{-3}$ , MPa	$\sigma_b$ , MPa	$\epsilon_b$ , %	POLYMER	$\lambda$	$E \cdot 10^{-3}$ , MPa	$\sigma_b$ , MPa	$\epsilon_b$ , %
Polyarylene B	1	1.5	81	37	SHMPE - 54 % Al	1	0.7	(26)	(8.1)
	3	1.4	130	44		3	0.8	37	7.4
	4	1.5	120	40		5	1.2	41	5.3
	5	1.5	140	40		6	1.1	40	5.4
	6	1.5	175	58		7	1.1	38	4.8
	7	1.6	180	50		9	0.9	34	6.1
SHMPE - 45 % caolin	1	0.8	(33)	(15)	SHMPE - 51 % Al(OH) <sub>3</sub>	1	0.7	(14)	(4.5)
	3	0.9	38	6.7		3	0.8	19	3
	5	1.1	44	6.2		4	0.9	22	3.5
	6	1.3	49	6.0		5	0.8	17	3
	7	1.2	45	5.5		6	0.8	16	2.5
	9	1.2	47	5.2		9	0.4	13	4.9

( ) -- instead of  $\sigma_b$  and  $\epsilon_b$  a conventional field point and its respective relative deformation are taken

Unlike amorphous polymers crystalline polymers show most variations produced by extrusion for  $E$ -values. In comparison with control samples for SHMPE extrudates  $E$ -values at compression are increased nearly two times ( $\lambda = 6$ ), and for polyetherketone 1.3 times ( $\lambda = 2.8$ ). The strength values are either slightly higher (SHMPE), or constant (polyetherketone). According to X-ray data the degree of crystallinity of SHMPE samples is increased from 55 % at  $\lambda = 1$  up to 75 % at  $\lambda = 7$ . For polyetherketone samples it varies but slightly equaling 40 % and the crystalline phase of extrudates is the mixture of two crystalline modifications. The extreme values of  $\lambda$ , at which extrudates show no visible damage, are  $\lambda = 6$  (SHMPE) and  $\lambda = 2.8$  (polyetherketone).

The quantitative variations in behavior and properties of polymers under study are associated with specific features of their structure. It is evident that in the case of polymer with flexible chains as effective materials one has good chances to form orientated states and obtain the maximum increase of useful properties.

Comparison of values of mechanical characteristics of SHMPE samples with X-ray, the degree of volume crystallization data and values of thermal shrinkage made it possible to determine the character of the evolutions of different structure components at solid-phase extrusion. These processes are well described in the framework of the three-component model of the structure of semi-crystalline polymers [2].

#### Filled polymer composites

The study was carried out for composite samples on the basis of SHMPE polymers produced by the technique of the polymer filling. As filling materials caolin (28 and 45 mass. %), Al (54 and 70 %), bauxite (45 %), Al(OH)<sub>3</sub> (51 %) were used.

Addition of filling materials changes the character of  $E$  and  $\sigma_b(\lambda)$  relationships, stated for SHMPE samples. For all composite samples, except SHMPE - 28 % of caolin samples the extreme behavior of these characteristics with the maximum point near  $\lambda = 4...6$  ([1], Table) is observed. SHMPE - caolin



composite samples show the most inclination for strengthening, SHMPE -  $\text{Al}(\text{OH})_3$  samples show the least inclination for strengthening.

It is known that for filled polymer materials  $E$  values are closely associated with the degree of adhesion at the polymer-filler interface [3]. Therefore decrease of  $E$  values at high  $\lambda$  might mean decrease of the adhesion-interaction degree at the interphase boundary. The form of  $\sigma_b(\lambda)$  relationships also is a proof in the favor of it. From the filling materials under choice only caolin represents anisodiametrical particles in the form of platelets, the particles of other materials are spheres in shape. According to [3] particles anisotropic in shape promote the high interphase interaction and thus SHMPE - caolin samples partly show the cohesion mechanism of destruction. And SHMPE -  $\text{Al}(\text{OH})_3$  samples show the adhesion mechanism of destruction at a full scale.

## Conclusions

Thus, the method of plunger extrusion can be effectively applied for structural modifying of polymers and polymer composites of different structure. If it is applied for crystalline polymers the most impact is on the value of the elasticity modules, and in case of amorphous polymers the impact is on the breaking stress.

## References

1. V.A. Beloshenko, V.G. Slobodina, V.G. Grin'ov and E.V. Prut, in *Proceedings Joint AIRAPT/APS. Conference on High Pressure Science and Technology. Colorado Springs, USA, 1993 (American Institute of Physics, 1994), p. 1029.*
2. L. Mandelkern, *Polymer J.* **17** (1985) 337.
3. I.L. Dubnikova, Yu.M. Tovmasyan, I.N. Meshkova and F.S. Dyachkovskii, *Vysokomol. sojed.* **A30** (1988) 2345

## METAL MICROFIBRES OBTAINED BY PACKET HYDROEXTRUSION

V.G. SYNKOV, L.D. TRANKOVSKAYA, S.G. SYNKOV

*High pressure apparatus laboratory, Donetsk Physico-Technical Institute of the National Academy of Science, Donetsk, 340114, str. R. Luxemburg, 72., Ukraine.*

### ABSTRACT

The four stages of billet compaction during hydroextrusion are noted with the help of the following characteristics: the billet mezostructure, porosity, the fibre mean diameter. The first stage is the most important because the imperfections formed during it corrected hardly on the following stages.

Metallic fibres with typical dimension of 1...10  $\mu\text{m}$  can be obtained by the method of deformation of a pack of wire elements at the considerably less technological expenses and the higher productivity than with the traditional methods of obtaining microfibrs, e.g. by drawing. Diamond dies are not necessary. The developed surface of the fibres promotes their application as composite materials, as additions to woven materials for removal of electrostatic charge, in working clothes for radiation protection and mechanical protection, for production of porous mats with high filterability on their basis [1].

Different requirements to surface quality and shape, homogeneity of dimensions and mechanical characteristics are presented to fibres depending on the purpose.

Apparently, that is possibly to control these parameters by changing of preparation regimes of starting packing billet deformation, by varying quantity and properties of separating substance.

The quality of fibres in a considerable degree formed on the stage of the packet billet preparation when wire of 0,1...2,0 mm diameter, is cut into gauge lengths and covered with separating substance, assembled into packet, placed into the enclosure and pressed with preliminary compaction by application of radial loads. Deviation from linearity of individual wire pieces, burrs and ovality lead to the decrease of starting packing billet density. While making billet with 40-50 mm inner diameter shell the packet porosity after assembly varies from 25 to 50%. It was found experimentally that hydroextrusion of packing billet can be made at porosity not more than 20%, therefore after

assembly it is necessary to perform an additional compaction of the packet, e.g. by method of reduction.

In the reduction process the decrease of voids between separate wires and the partial removal of separating substance takes place through faces of the billet.

On the different stages of deformation of the billet the considerable shape deviation of separate wire cross-section from circle is observed because of irregularity of initial distribution of porosity within the cross-section of the packet. This leads to irregular decrease of plasticity resource of separate wires, their failure, and causes process instability of hydroextrusion of the packet as a whole.

Value of such deviation was determined experimentally on the different stages of deformation with the help of observation of cross microsection metallographic specimens of the packing billets and their separate fragments by determination of interfibrs streaks area (porosity,  $P$ ) and estimation of dimensions of separate fibres ( $d$ ), their ovality ( $N$ ) [2].

Cross microsection metallographic specimens were cut out of packing billets of 24; 16; 10; 5mm diameter for which the mean calculation of accumulated stretching (ignoring porosity) made up accordingly  $\mu_A = 2,8; 6,3; 16; 64$ .

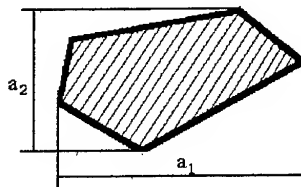


Fig. The scheme to determine the size of the fibres.

The mean fibres diameter

$$d = \frac{\sum_{i=1}^n (a_1 + a_2) \times i}{n}, \text{ where}$$

$n$  is the number of fibres which was measured  
 $i$  is the number measuring fibres.

The ovality:  $N = \frac{\alpha_1}{\alpha_2}$ .

Determination of interfibres streaks area (porosity, P)

is  $P = \frac{S_s}{S_p}$ , where  $S_s = S_p - S_f$ ,

$$S_f = \frac{\pi d^2 n}{4} M, \text{ where}$$

$n = n + 0,5n_2 - 1$

$S_s$  is the area of second phase,

$S_f$  is the photo area,

$M$  is the scale of the photo.

Dependences of mean fibre diameter ( $d$ ), ovality ( $N$ ) and porosity ( $P$ ) on logarithm of stretching ( $\ln \mu_A$ ) of the packing billet are represented in fig. 1.

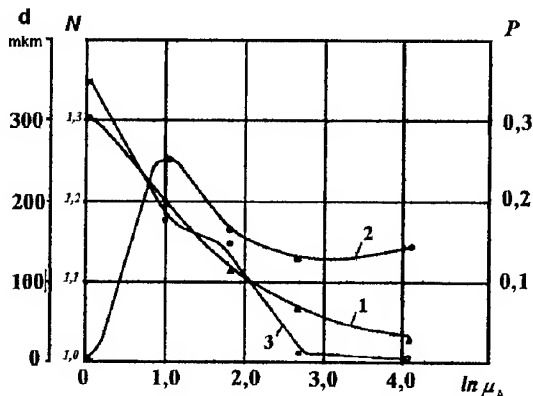


Fig. 1. The dependence of the mean diameter of fibres (1), of ovality (2) and porosity (3) on the logarithm of the inclined stretching.

The wire made of corrosion-resistant steel 30Cr13 ( $d = 300 \mu\text{m}$ ,  $N = 1$ ,  $P = 0,35$ ) was used for the initial packing billet. The mean fibre diameters ( $d$ ) and porosity ( $P$ ) decrease monotonically with the increase of accumulated stretching ( $\mu_A$ ). On the primary deformation

stage (the decrease of the packing billet diameter by 15-20 %) the mean diameter of fibres changes little; the decrease of the billet diameter takes place at the expense of abrupt decrease of porosity (from 35 to 20 %, I section). On the same stage the ovality of the fibres practically does not change, as the compaction of the packet takes place, mainly, at the expense of the decrease of distance between the fibres, their compact packing occurs without bearing strain of contacting surfaces.

Technologically this stage usually is realized by multitransitional (3...5 transitions) reduction of the billet or its treatment in the hydrostat.

After realization of the first transition of hydroextrusion ( $\mu_A = 2,8$ ) the fibre ovality reaches maximum value ( $N = 1,25$ ), but the rate of porosity decrease stays at a level  $\Delta P / \Delta \ln \mu_A = 0,035$  up to value of accumulated stretching  $\mu_A = 6,3$  (II section). Then the rate of the porosity decrease increases again (III section;  $\Delta P / \Delta \ln \mu_A = 0,13$ ). As we decided to name the space between metallic fibres filled with separating substance and voids (gaseous atmosphere) as porosity, then it is necessary to mention that section II corresponds, apparently, to absolute removal of voids and section III corresponds to redistribution of separator all over volume of the billet and removal of its surpluses. Section IV (at  $\mu_A \geq 16$ ) corresponds to little change of porosity (1,5-1,0 %,  $\Delta P / \Delta \ln \mu_A = 0,007$ ).

Ovality of the fibres ( $N$ ) decreases monotonically at the change of result stretching in the range  $\mu_A = 2,8 \dots 16$  ( $N_{\min} = 1,14$ ). At the following increase of stretching up to  $\mu_A = 64$  the ovality is slightly increased ( $N = 1,16$ ) which probably is associated with the increase of inclosure of periphery fibres, the scheme of stressed-deformed state (SDS) of which differs from SDS of fibres positioned in layers on distance of at least 3...5 diameters of the fibre from outward ones.

The most dangerous stage of packing deformation is the first technological transition of hydroextrusion; it takes place at high irregularity of the porosity in the billet cross-section. Broad fields (5...8 fibre diameters) with great quantity of separating substance are stay after this transition. Such sections are present up to the stretching  $\mu_A = 16$ , however their number

and dimensions decrease with the increase of the stretching.

Value of the porosity of rarefied sections decreases with the increase of stretching approximately with the same regularity that the mean porosity of the packet (26% - at  $\mu_A = 2,8$ ; 23% - at  $\mu_A = 6,3$ ; 10% - at  $\mu_A = 16$ ). Cracks of 0,5...2,0mm length, 0,01...0,1 mm width, appearance of which, may be, is connected with elastic post-effect of packet after hydroextrusion are exposed on surface of the cross microsection metallographic specimen at the stretching  $\mu_A = 64$ .

The cracks have a radial orientation and extend only along fibre boundaries.

Under such conditions the value of plastic deformation in direction of billet axis for its different zones is different along radius. It is confirmed by the comparison of average grain diameters of local sections with surplus of the separating substance and other fields.

The divergence makes up 6...15,5 %. This can lead to local stresses inner breakage of the fibres

the packet and instability of process of billet outflow.

Thus, the four stages of the packing billet compaction are choosen in dependence on accumulated stretching, the constant rate of porosity change being kept on each of them. At the accumulated stretching  $\mu_A = 16$  the porosity of the packet makes up 1,5% ; at the following accumulation of stretching it decreases insignificantly. The most dangerous stage of deformation is the first technological transition of hydroextrusion ( $\mu_A = 2,8$ ), which corresponds to the increase of fibres difference.

#### References

1. V.G.Synkov, S.G.Synkov, L.D.Trankovskaya, A.N.Sapronov, *EHPRG XXXIII st Annual Meeting*, (Brno, 1994), p. 251.
2. V.G.Synkov, L.D.Trankovskaya, S.G.Synkov, N.I.Matrosov, *FTHP* 1 (1991)56.

## THE EFFECT OF DEFORMATION UNDER HIGH HYDROSTATIC PRESSURE ON THE STRUCTURE AND PROPERTIES OF HIGH-STRENGTH METALLIC MATERIALS

B.M. EFROS, N. SHISHKOVA, I. KONAKOVA, L.V. LOLADZE

*Donetsk Physico-Technical Institute, National Ukrainian Academy of Sciences, 72 R. Luxemburg str.,  
Donetsk, 340114, Ukraine*

### ABSTRACT

The effect of conditions of temperature and deformation treatment of high-strength steels under high pressure has been studied using stainless maraging steel as an example. The study has been aimed to find the possibility of considerable reduction of forces at forming and obtain the improved mechanical properties. The deformation under pressure has been performed at temperatures  $T_{he} = 30... 800^{\circ}\text{C}$  with percent reduction  $\epsilon_{he} = 0...50\%$  using hydropressing.

### Introduction

The optimum combination of plastic deformation with thermal treatment allows one to increase the strength characteristics of maraging steels still preserving and, in some cases, even improving their plasticity and fracture toughness. The application of thermomechanical treatment in combination with plastic deformation under pressure using various schemes and operating conditions in the case of maraging steels usually results in the increase in both strength and plasticity [1,2].

### Experimental results and discussion

This paper studies the effect of thermomechanical treatment of high-strength steels using stainless maraging steel as an example in order to find a possibility to obtain high level strength and plasticity.

Prior to being subjected to thermomechanical treatment the maraging steel ingots of vacuum-induction melting (chemical composition, wt.% : 0.03 C, 11.13 Cr, 9.48 Ni, 1.96 Mo, 0.88 Ti, Fe-base) were homogenised at  $1150...1200^{\circ}\text{C}$  during 12 hours and forged into bars. Before hydroextrusion the bars were quenched from austenization temperature ( $950^{\circ}\text{C}$ ). The critical points of the  $\alpha/\gamma$ -transformation of this steel were  $A_{c1}=590^{\circ}\text{C}$ ,  $A_{c3}=680^{\circ}\text{C}$ ,  $M_s=140^{\circ}\text{C}$ ,  $M_f=30^{\circ}\text{C}$ . Hydroextrusion of maraging steel was carried out at  $20...800^{\circ}\text{C}$  with percent reduction  $\epsilon_{he}=0...50\%$ . The deformed specimens were subjected to ageing at  $500^{\circ}\text{C}$  during 2 hours [3].

Usually after the quenching from the temperature higher than the austenization temperature the structure contains 5...10% of residual austenite  $\gamma$ , distributed uniformly throughout the martensite matrix which cannot be detected by any

metallographic technique. This uniform martensite structure in its initial state has properties: ultimate strength  $\sigma_b=950\text{MPa}$ , yield strength  $\sigma_{0.2}=920\text{MPa}$ , relative elongation  $\delta=12\%$  and percentage reduction of area  $\psi=43\%$ .

Heating of this maraging steel results in a number of complex processes due to the phase and structural transitions. The investigations performed at heating in the temperature range of  $20... 800^{\circ}\text{C}$  revealed the following processes: delamination in chromium ( $200...450^{\circ}\text{C}$ ), formation of metastable f.c.c.-  $\text{Ni}_3\text{Ti}$ - phase ( $400...480^{\circ}\text{C}$ ), formation of stable hcp-  $\text{Ni}_3\text{Ti}$ - phase ( $480...560^{\circ}\text{C}$ ), inversed  $\alpha\rightarrow\gamma$ - transformation ( $590...680^{\circ}\text{C}$ ) (the temperature range of  $\beta$ - $\text{Ni}_3\text{Ti}$ - solution and formation of  $\eta$ - $\text{Ni}_3\text{Ti}$ - phase is superimposed on the  $\alpha\rightarrow\gamma$ -transformation), formation of the Laves phase of the  $\lambda\text{-Fe}_2(\text{Ti},\text{Mo})$  ( $650...850^{\circ}\text{C}$ ), solution of the secondary phases ( $\geq 850^{\circ}\text{C}$ ), recrystallization processes in austenite ( $\approx 850^{\circ}\text{C}... \geq 1050^{\circ}\text{C}$ ) ( the heating temperatures  $850^{\circ}\text{C}$  and  $1050^{\circ}\text{C}$  are the temperatures at which recrystallization and collective recrystallization, respectively, start).

The study of the evolution of the defect structure of maraging steel formed at different  $\epsilon_{he}$  and  $T_{he}$  showed that at deformation under pressure the structure evolution has rather a regular character. The main structural changes which take place with the growth of  $\epsilon_{he}$  are the destruction of the structure of massive martensite and fragmentation of the substructure at the mesoscopic level. In addition to the structural changes the deformation of maraging steel under high pressure may produce effects of thermodynamic and kinetic character at the phase and structural transformations. For designing the operating conditions of thermomechanical treatment using hydroextrusion of primary importance is the

temperature dependence of the hydroextrusion pressure (Fig. 1).

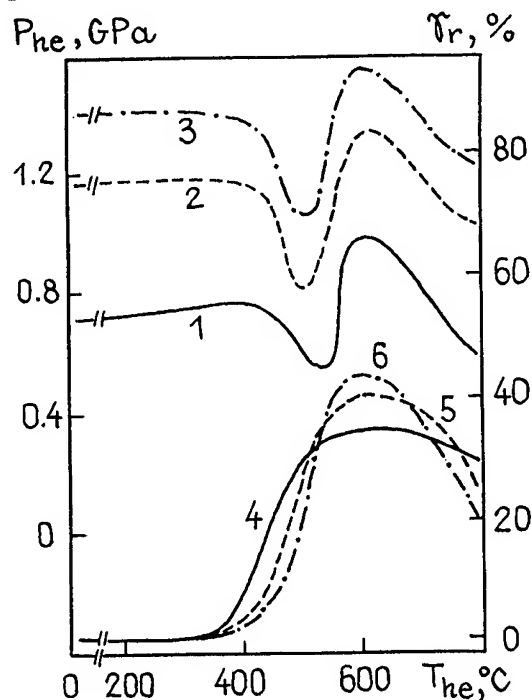


Figure 1. Hydropressing pressure  $P_{he}$  (1-3) and residual austenite amount (4-6) as a function of hydropressing temperature  $T_{he}$  of the tested maraging steel: 1,4-  $\epsilon_{he}=10\%$ ; 2,5-  $\epsilon_{he}=30\%$ ; 3,6-  $\epsilon_{he}=50\%$

The change in the hydroextrusion pressure  $P_{he}$  and, consequently, in resistance to deformation under pressure in the temperature range under study is essentially connected with the beginning and development of the inverse  $\alpha \rightarrow \gamma$ -transformation. The experimental nature of the "P-T" dependence on the investigated steel is due to the fact that the temperature at which the phase  $\alpha \rightarrow \gamma$ -rearrangement starts is close to the temperature of delamination, precipitation of intermetallic compounds and destruction of metastable products of decay [4,5].

The character of the change in the mechanical properties of maraging steel as a function of  $\epsilon_{he}$  and hydroextrusion temperature  $T$  as well as the following ageing is shown in Fig. 2. The analysis of the modified specimens showed the following operating conditions providing a higher level of properties:  $T_{he}=20^\circ\text{C}$ ,  $\epsilon_{he}=50\%$ ,  $T_{ag}=500^\circ\text{C}$  ( $\sigma_{0.2}=1820$  MPa,  $\sigma_b=1850$  MPa,  $\delta=9.9\%$  and  $\psi=29\%$ );  $T_{he}=550^\circ\text{C}$ ,  $\epsilon_{he}=50\%$ ,  $T_{ag}=500^\circ\text{C}$  ( $\sigma_{0.2}=1550$  MPa,  $\sigma_b=1670$  MPa,  $\delta=7\%$ ,  $\psi=28\%$ );  $T_{he}=800^\circ\text{C}$ ,  $\epsilon_{he}=50\%$ ,  $T_{ag}=500^\circ\text{C}$  ( $\sigma_{0.2}=1620$  MPa,  $\sigma_b=1720$  MPa,  $\delta=8.5\%$ ,

$\psi=36\%$ ). The most efficient treatment operating conditions is hydroextrusion of maraging steels in the  $\alpha$ -region with the following ageing. The efficiency of this treatment grows with the decrease of  $T_{he}$  and increase of  $\epsilon_{he}$ . As to the magnitude of resistance to deformation in the process of hydroextrusion more efficient is the treatment in the temperature range  $T=480\ldots 560^\circ\text{C}$  where extrusion force ( $P$ ) is minimum.

The obtained results show that the peculiarities of phase and structure forming of maraging steels at different kinds of thermomechanical treatment (maroforming, aus-forming, deformation in the intercritical ( $\alpha+\gamma$ )-range) using hydroextrusion essentially determine the strength and plastic properties of these steels, their resistance to deformation and hardening and, finally, fracture of extruded products. At hydroextrusion of maraging steels in the  $\alpha$ -range (maroforming) the considerable growth of strength (up to two times) at adequate plasticity is connected with the specific character of texture and defect structure forming at  $\epsilon_{he} > 30\%$  followed by ageing. The increase in the dislocation density of the supersaturated solid solution at deformation under high hydrostatic pressures promotes the increase in density and uniformity of precipitation which is one the main factors of the positive role of thermomechanical treatment at maroforming operating conditions. The thermomechanical treatment of stainless maraging steels at ausforming conditions in the test range of  $T_{he}$  and deformation in the intercritical ( $\alpha+\gamma$ )-range do not result in considerable increase in the level of mechanical properties.

## Conclusion

In this paper, the peculiarities of phase and structure formation when the steel has been treated under different modes of thermomechanical influences largely define the properties of extruded products. A more substantial increase of the strength properties with satisfactory plasticity has been found at hydroextrusion of stainless maraging steels in  $\alpha$ -region due to peculiarities of texture and defect structure formation at  $\epsilon_{he} > 30\%$  with subsequent ageing.

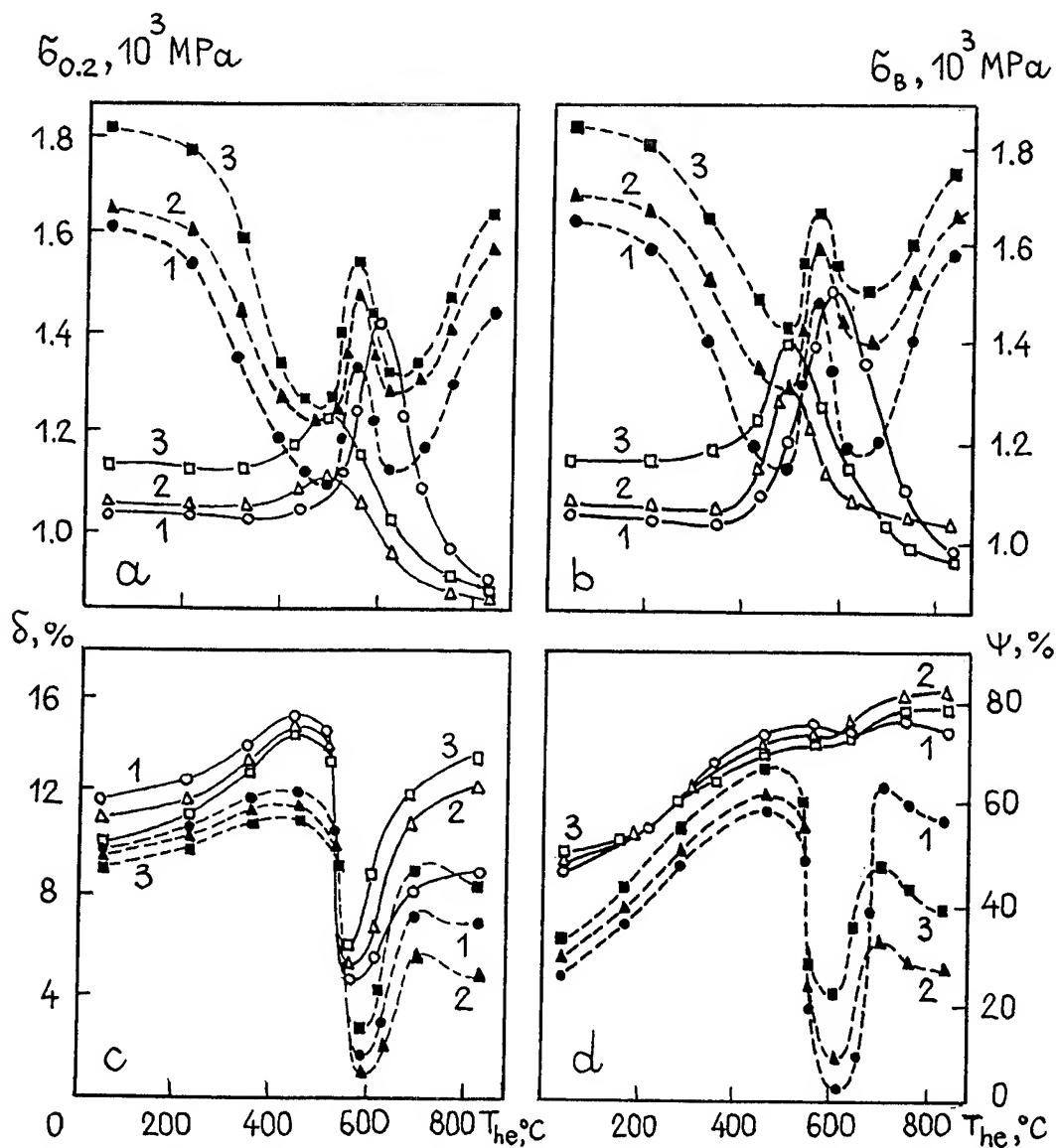


Figure 2. Change in the mechanical properties  $\sigma_{0.2}$  (a),  $\sigma_b$  (b),  $\delta$  (c) and  $\psi$  (d) of the tested maraging steel as a function of the thermomechanical treatment parameters: 1- $\epsilon_{he}=10\%$ ; 2- $\epsilon_{he}=30\%$ ; 3- $\epsilon_{he}=50\%$  (solid lines-quenching+hydroextrusion at the given  $T_{he}$ , dashed lines- quenching+hydroextrusion at given  $T_{he}$  + ageing (500°C, 2 h))

## References

1. B.I.Beresnev, K.I.Ezerskii, E.V.Trushin et al., High pressure in modern technologies of metal forming, Moscow: Nauka, 1988, 245p.
2. V.Uralskii, V.Plakhotin, N.Sheftel et al., Deformation of metals by high pressure fluid, Moscow: Metallurgija, 424p.
3. N.V.Zvigintsev, B.M.Efros, I.P.Konakova et al., Fizika i tekhnika vysokikh davlenii, 2,N1, 70 (1992).
4. N.Zvigintsev, B.Mogutnov, M.S. Khadnev et al., Fizika metallov i metallovedeniye, 59,N1, 130 (1990).
5. M.D.Perkas, V.M. Kadonskii, High-strength maraging steels, Moscow: Metallurgija, 1971, 224p.

# SPECIFIC FEATURES OF BEHAVIOUR OF HETEROPHASE METALLIC MATERIALS UNDER PRESSURE AT DEFORMATION IN DIAMOND ANVILS

B.M.EFROS, N.V.SHISHKOVA, Ja.E. BEIGELZIMER, L.V. LOLADZE, S.V.GLADKOVSKII

*Donetsk Physico-Technical Institute of the Ukrainian Academy of Sciences*

*72 R.Luxemburg str., 340114, Donetsk, Ukraine*

## ABSTRACT

The method of diamond anvils has been used to study the influence of deformation on phase and structure formation, hardening and plasticity of metastable heterophase materials with the example of  $(\gamma+\varepsilon)$ -steel Fe-20Mn-2Si.

## Introduction

One of the promising directions of modern metal sciences at designing of new structural materials with high physico-mechanical and service properties is systematic and purposeful usage of effects which accompany austenite-martensite transition at deformation of metastable steels [1,2]. In general case the intensity of appearance of deformational martensite phases is determined by internal (chemical composition and structure) and external (conditions of deformation) factors.

## Experimental results and discussion

In the paper studies are described of specific features of phase and structure formation as well as of strengthening and plasticity of metastable Fe-20Mn-2Si steel (wt. %: Fe; 19.9 Mn; 1.9Si; 0.05 C) at deformation under pressure. In the initial (quenched) state the structure of this steel consists of the plates of  $\varepsilon$ -martensite ( $\sim 45\%$ ) with the habitus  $\{111\}_\gamma$  and the residual austenite ( $\sim 55\%$ ). The characteristic feature of studied steel which determines its capability of plastic deformation is the development of plastic deformation martensite transformations  $(\gamma+\varepsilon) \rightarrow \varepsilon', \alpha'$ . They are accompanied by negative at  $(\gamma+\varepsilon) \rightarrow \varepsilon'$  and positive at  $(\gamma+\varepsilon) \rightarrow \alpha'$  bulk variations [1]. Therefore the phase composition of metastable Fe-20Mn-2Si steel depends both on the amount of accumulated shearing strain  $\Lambda$  ( $\Lambda = \sqrt{3} \ln(1-e)^{-1}$ ), where  $e$  is degree of

deformation) and on the character of the stressed state at which this treatment was carried out. With increase of the value of  $\Lambda$  the amount of produced b.c.c. of  $\alpha'$  - phase is permanently increased, however, the application of external pressure resulting in variation of the stressed state affects the formation of  $\alpha'$ -phase as a whole: at first the amount of  $\alpha'$ -phase is increased but then passing over the maximum point it is decreased at increasing  $\Lambda$  (Fig.1).

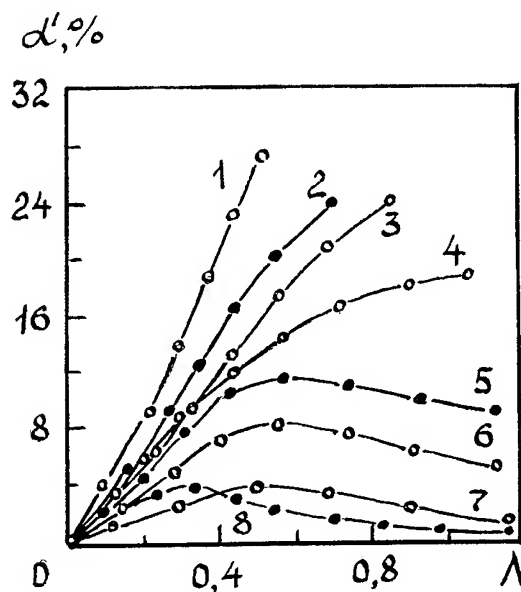


Fig.1. Dependence of the amount of bcc  $\alpha'$ -deformation martensite on  $\Lambda$  value at different modes of steel Fe-20Mn-2Si loading: 1-torsion; 2-tension; 3-upsetting; 4-rolling; 5-hydroextrusion; 6 nonstationary hydroextrusion; 7- hydroextrusion with back pressure ( $P_{bp}=600$  MPa); 8- the diamond anvil technique



At investigation of the structure of the region of compression for Fe-20Mn-2Si steel depending on the value of the accumulated shearing strain  $\Lambda$  one can differ two types of the substructure. The first (I) is characterized by thin plates of  $\epsilon$ -phase in austenite along two or three intersection planes  $\{111\}_\gamma$ . The second (II) is characterized by availability of large plates of  $\epsilon$ -phase usually along one plane from the system  $\{111\}_\epsilon$  in which  $\alpha'$ -crystals of lath shape are arranged, having alike orientation or forming structural complex "frame"-type. At this the intensity of deformation  $(\gamma+\epsilon) \rightarrow \epsilon$ -transformation, twinning in density packed phases, as well as the density of stacking faults in  $\gamma$  and  $\epsilon$  phases are increased (intensity of  $(\gamma+\epsilon) \rightarrow \alpha'$  transformation is decreased) with increase of the value of  $\Lambda$  as well as from the periphery to the center of the compression region of studied steel at given  $\Lambda$ . The considered features of phase and structure formation at deformation of Fe-20Mn-2Si steel by the diamond anvil method determine the character of the value of deformation hardening  $H_\mu$  as well as the baric contribution in  $H_\mu - \Delta H_\mu^P$  ( $\Delta H_\mu^P = H_\mu(r=0) - H_\mu(r=b)$ , where  $b$ -radius diamond anvil, at given  $\Lambda$ ) (Fig.2).

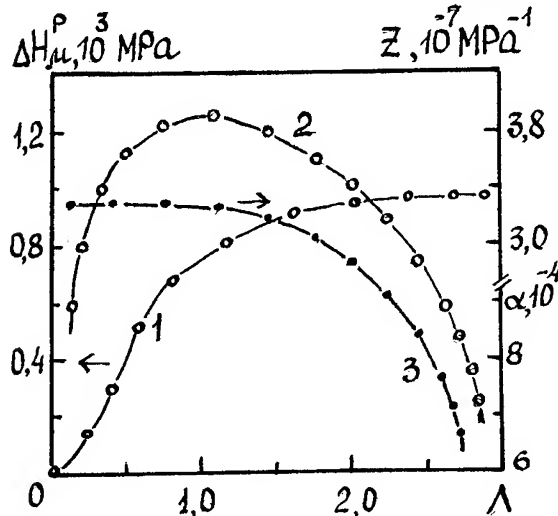


Fig.2. Influence of  $\Lambda$  on baric contribution of deformation hardening  $\Delta H_\mu^P$  (1), rate of plastic loosening  $\alpha$  (2) and its baric component  $Z$  (3) of steel Fe-20Mn-2Si samples at deformation by the diamond anvil technique

Calculated  $\sigma/T$  ( $\sigma/T$  characterizing "hardness" of the stressed state, where  $\sigma$ - is the mean of normal stress,  $T$ - is the intensity of tangential stresses values [3]) were used to estimate the intensity of plastic loosening  $\alpha$  and its baric component  $Z$  in the compression region of Fe-20Mn-2Si steel by the diamond- anvil method [4] (see Fig.2). With increase of accumulated shearing strain  $\Lambda$  the rate of plastic loosening  $\alpha$  is increased up to maximum values at ( $\Lambda \approx 1.2$ ), and at ( $\Lambda > 1.2$ )  $\alpha$  values are decreased due to generation of the higher level of pressure in the compressed region which is reflected by reduction of  $Z$ - value ( $Z = \alpha(P)$ - baric contribution in  $\alpha$  in the given range  $\Lambda$ . The observed character of  $\alpha(\Lambda, P)$  variation corresponds qualitatively to specific features of spread of the macrocrack [5].

The considered dependencies for the factor of the stressed state  $\sigma/T(\Lambda)$  at deformation under pressure of Fe-20Mn-2Si steel by the diamond anvil method makes it possible to consider that the intensity of martensitic  $(\gamma+\epsilon) \rightarrow \alpha'$ - transformation at deformation is determined by two competing processes : increase of  $\Lambda((\gamma+\epsilon) \rightarrow \alpha'$ -transformation) and "softness" of the stressed state, i.e. decrease of the factor  $\sigma/T(\sigma/T < 0)$  resulting in the non-monotonous character of the dependence " $\alpha$ - $\Lambda$ " in experiment (see Fig.1).

To divide contributions of  $\sigma/T$  and  $\mu_\sigma$  factors (Lode-Nadai factor  $\mu_\sigma$  which characterizes the view of the stressed state scheme [3]) the intensity of phase transformations and to plasticity of studied steel special experiments were carried out with deformation of samples by tension, torsion and compression in the chamber with regulated pressure [5].

The calculated dependence of the relative intensity of  $\alpha'$ - martensite formation under conditions of plane deformation of torsion of cylinder-shaped samples ( $\mu_\sigma = 0$ ) is higher, than at axisymmetrical deformation by tension ( $\mu_\sigma = -1$ ) and compression ( $\mu_\sigma = 1$ ). At  $\sigma/T \leq -2.5$  generation of  $\alpha'$ - martensite, which is practically completely blocked by increase of compression stresses and practically slightly depends on the scheme of applying them, determined by the Lode-Nadai factor. The plasticity diagram at deformation under pressure of this steel

shows a clear pronounced minimum never before observed in experiment (Fig.3). One can, it seems, explain this minimum by competing influence on the plasticity under pressure: by intensifying of the process of formation of less plastic h.p.  $\epsilon$ - phase and by plastification of the material with increase of compressing stresses. The down-going part of curve at the plasticity diagram is the result of the first and the upgoing branch is second of these factors. The analysis of the obtained data shows that at the choice of the method of deformation or deformation hardening of metastable Fe-20Mn-2Si steel, e.g., at the condition of conservation of its nonmagnetic state and satisfactory technological plasticity it is to be restricted by such methods of plastic deformation, at which the stressed state satisfied the following conditions :  $\sigma/T < -2.5$  and  $\mu_s = 1$  or  $\mu_s = 1$ .

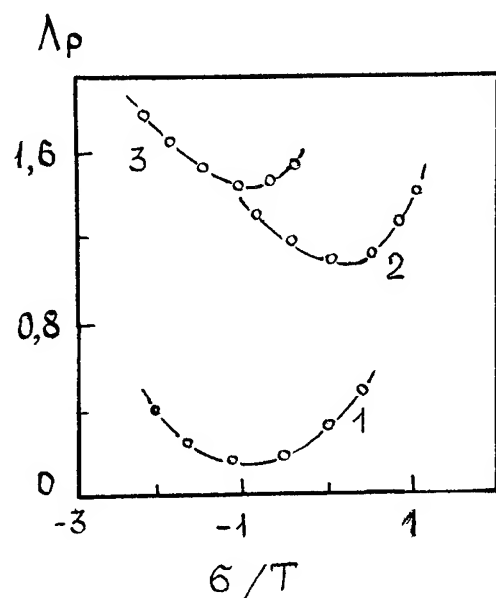


Fig.3. Diagram of plasticity  $\Delta p(\sigma/T, \mu_s)$  of steel Fe-20Mn-2Si at deformation under pressure: 1-  $\mu_s=0$ ; 2-  $\mu_s=1$ ; 3-  $\mu_s=1$

## Conclusion

Finally it is to note that the diamond-anvil technique combines two methods of affecting the structure and the phase composition of metastable

materials: due to generating of pressures and applying of high plastic deformations, which are mutually - dependent processes. Therefore this technique can be used both as the method of bulk deformation under "soft" scheme condition of the stressed state and as the effective method of regulation of the phase compositions and deformation substructure and thus variation of the properties of given materials in the optimal direction in the wide range under the conditions of activation of plastification under pressure.

## References

1. I.N Bogachov., V.F.Egolaev, *Structure and properties of Fe-Mn-alloys*.-M.: Metallurgia, 1973.-295p.
2. M.A.Filippov, V.S.Litvinov, Yu.R. Nemirovskii, *Steels with metastable austenite*.-M.: Metallurgia, 1988.-256p.
3. A.A.Bogatov, O.I.Mizhritskii, C.V Smirnov, *Plasticity resource at metal treatment under pressure*.-M.: Metallurgia,1983.-144p.
4. B.I.Beresnev, B.M.Efros, Ya.E.Beigelzimer et al. *Superhard materials*, -4,(1990) 38.
5. B.M.Efros, N.V.Shishkova, S.V.Gladkovskii et al. *Fizika i tehnika vysokikh davlenii*, V.5, N1, (1995) 26.

# EFFECT OF HOT HYDROSTATIC EXTRUSION ON GRAIN SIZE AND SHAPE IN BRASS

Marek S. KOZŁOWSKI, Janusz J. BUCKI\*, Andrzej MAZUR  
High Pressure Research Center - Unipress, Polish Academy of Sciences,  
Sokolowska 29/37, 01-142 Warsaw, Poland

\* Department of Materials Science and Engineering, Warsaw University of Technology,  
Narbutta 85, 02-524 Warsaw, Poland

## ABSTRACT

Samples of commercial brass type 65/35 (polish mark M63) have been extruded by means of hot hydrostatic extrusion. Different reduction ratios varying from 40 to 225 have been obtained. Studies of microstructure have been carried out on sections parallel and perpendicular to the axis of extrusion by means of automatic image analyzer connected to light microscope. It has been found that the average grain size decreases with increasing reduction ratio. Shape of grain depends on both reduction ratio and distance from the surface. Distance from the surface has been found to influence the shape factor of grains stronger than reduction ratio applied.

## Introduction

Extrusion is widely used as a forming process of copper and brass. Constant and consistent development of this technology has led to a considerable increase of extrusion plant efficiency (see for example 1,2). On the other hand the technology is still mainly experience-driven and the microstructure changes occurring during process are not yet completely known.

The grain size and shape in a polycrystal are well-known to influence the mechanical properties of polycrystalline materials (see for example 3-6). On the other hand grain size and shape are strongly effected by materials processing technology.

## Material and methods

The specimens were prepared from commercial 65/35 brass of chemical composition given in Tbl. 1.

Table 1. Chemical composition of the material.

Element	Cu	Pb	Fe	Sn	Zn
weight %	64.4	0.02	0.01	0.006	balance

Samples were extruded on UNIPRESS 3.2MN hydrostatic extrusion press. One end of each billet

had a conical nose with an angle of 88°. The billets before extrusion were lubricated with BN and heated to 850°C. Rape oil has been used as a medium. The pressure dependence on the reduction ratio follows a linear equation of the form

$$p = -260.6 + 181.71 \ln R \quad (1)$$

where  $p$  is the extrusion pressure expressed in MPa and reduction ratio,  $R$ , is defined as

$$R = A_0/A \quad (2)$$

where  $A_0$  is billet cross section area and  $A$  is produced wire cross section area.

All samples were extruded from the same type of cylindrical billet (of 50 mm diameter), so different reductions were obtained by means of different diameter of die and resulting wire. Detailed information on reduction ratios used in the present study is given in Tbl. 2.

Table 2. Diameter  $d$  of resulting wire and reduction ratio  $R$  for samples studied.

$d$ mm	7.91	6.80	5.81	4.81	3.82	3.33
$R$	40	54	74	108	171	225

Examples of microstructures after extrusion on sections parallel an perpendicular to extrusion axis are shown on Fig.1.and 2. The size and shape of grains were measured using an automatic image

analysis system connected to a light microscope. Parallel sections were located as close as possible to the axis of the produced wire. The measured parameters included the equivalent diameter  $d_{eq}$  and maximum diameter  $d_{max}$  of each grain. It has been found earlier (7-9) that  $d_{max}/d_{eq}$  ratio is a valuable measure of grain elongation and can be used as an effective shape factor.

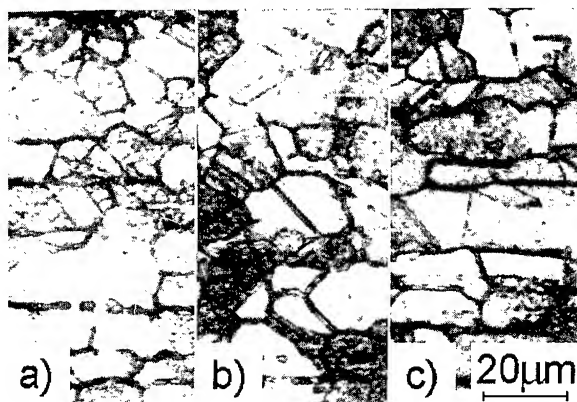


Fig. 1. Microstructures after 225 reduction on section parallel to axis of extrusion. Distance from surface: a) 0.15 mm, b) 0.6 mm, c) 1.2 mm.

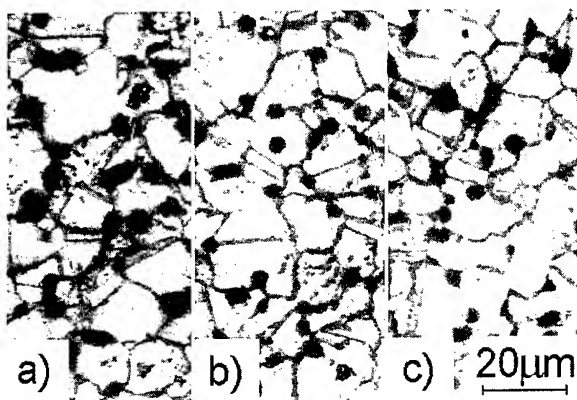


Fig. 2. Microstructures after 225 reduction on section perpendicular to axis of extrusion. Distance from surface: a) 0.15 mm, b) 0.6 mm, c) 1.2 mm.

## Results

The influence of the reduction ratio on the size of grains is shown in Fig.3. and 4. The results of equivalent diameter measurements are shown for two locations of the testing area - one just under, and the other 1 mm from the surface of the sample.

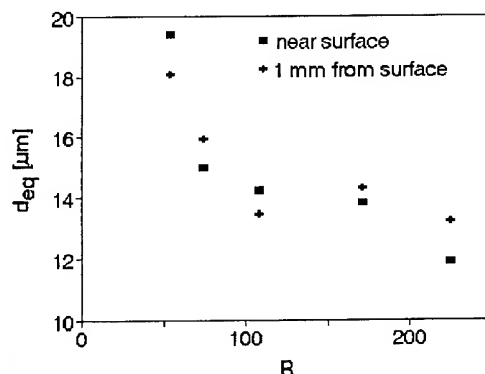


Fig. 3. Influence of reduction ratio on the grain size measured on section parallel to extrusion axis.

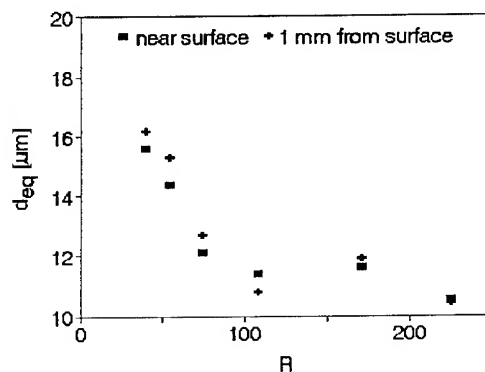


Fig. 4. Influence of reduction ratio on the grain size measured on section perpendicular to extrusion axis.

Fig.5. and 6. show the influence of measurement field distance from the surface on the  $d_{max}/d_{eq}$  shape factor for different values of the reduction ratio.

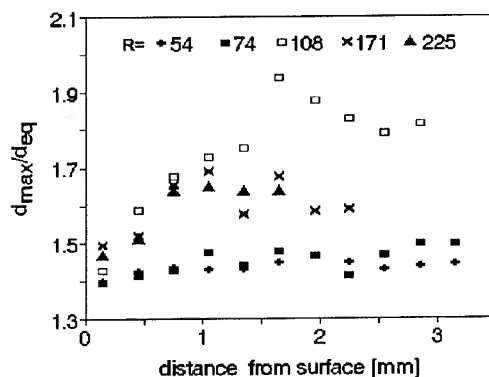


Fig. 5. Influence of distance from surface on grain shape on section parallel to extrusion axis.

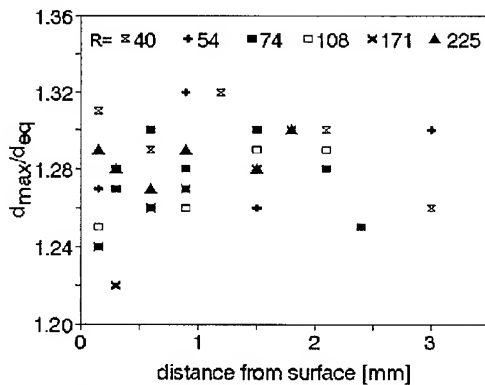


Fig. 6. Influence of distance from surface on grain shape on section perpendicular to extrusion axis.

### Discussion

On both sections one can easily observe strong influence of reduction ratio on grain size (Fig. 3. and 4.). This follows general expectations for the influence of extrusion process on grain size (see for example 10,11). the distance of measurement field from the surface of the sample do not affect significantly grain size. It can be noticed, that there are two areas of this influence. For reduction ratios lower than c.a. 100 the influence is very strong. For higher reductions is much weaker, but still keeps general tendency.

Changes of grain shape are of more complex nature. Results of measurements on section perpendicular to extrusion direction (Fig. 6.) show that grains on this section are of rather equiaxed shape and there is no significant influence of distance from the surface and reduction ratio on grain shape. For the parallel section (Fig. 5.), the general tendency can be observed, that for a thin, ca. 1 mm., layer near the surface the shape factor value increases with increasing distance from the surface. In the core of the samples the shape factor has been found to vary irregularly and no clear tendency could be observed. There is also effect of reduction ratio on the value of shape factor. As one could expect, the grain shape factor increases with increasing reduction ratio, but this influence is not as strong as distance from the surface effect. In the outer area one can observe very weak influence of reduction ratio on the shape factor of grains, while

this influence seems to be much bigger in the core area. This could be probably interpreted as the influence of different extrusion conditions (stress and yield distribution) and different cooling conditions in outer and inner (core) part of samples. Also free surface influence on equilibrium of grain boundaries can cause such an effect.

### Acknowledgments

Valuable discussions with Professor K.J. Kurzydłowski are appreciated.

### References

1. A. Steinmetz, W. Staschull, *Metall* **45** (1991) 1104.
2. A. G. Ovchinnikov, K. K. Volchaninov, A. V. Khabarov, *Kuznechno-Shtampovochnoe Proizvodstvo* **7** (1991) 6.
3. C. P. Brittain, R. W. Armstrong, G. C. Smith, *Scripta Metallurgica* **19** (1985) 89.
4. R. W. Armstrong, *Transactions of the Indian Institute of Metals* **39** (1986) 85.
5. J. J. Bucki, K. J. Kurzydłowski, *Materials Characterization* **29** (1992) 375.
6. K. J. Kurzydłowski, J. J. Bucki, *Acta Metallurgica et Materialia* **41** (1993) 3141.
7. J. J. Bucki, M. S. Kozłowski, A. Mazur, *On the influence of reduction on grain geometry in hot hydrostatic extruded brass samples* (Proceedings of IVth Int. Conf. Stereology and Image Analysis in Materials Science 1994) 291.
8. K. J. Kurzydłowski, K. J. McTaggart, K. Tangri, *Philosophical Magazine A* **61** (1990) 61.
9. K. J. Kurzydłowski, J. J. Bucki, *Bulletin of the Polish Academy of Sciences, Technical Sciences* **39** (1991) 463.
10. R. G. Arkhipov, E. S. Itskevich, E. V. Polyakov, E. N. Yakovlev, *Soviet Journal of Superhard Materials* **9** (1987) 4.
11. A. P. Bashenko, V. E. Vaganov, A. V. Omelchenko, V. D. Berbentsev, V. V. Solovov, Y. S. Konyaev, *Russian Metallurgy (Metally)* **3** (1987) 109.

# ACOUSTIC EMISSION INVESTIGATIONS OF THE PLASTICITY OF L1<sub>2</sub> Mn-MODIFIED Al<sub>3</sub>Ti UNDER PRESSURE

Z. WITCZAK

*High Pressure Research Center, Polish Academy of Sciences, Sokolowska 29, 01-142 Warszawa, Poland*

The compression tests of the L1<sub>2</sub> Mn-modified titanium trialuminide samples were carried out under various hydrostatic pressures with the in-situ monitoring of the deformation process by the acoustic emission (AE) method. An application of hydrostatic pressure enabled large deformation of this brittle material without fracture. However an increase of AE activity was observed at the early stage of deformation. Microscopic investigations revealed that it was caused by the change of the plastic deformation into cataclastic one. All of that allowed to separate both regions of deformation and to determine the effect of pressure on them.

## Introduction

The results of the high pressure compression tests of L1<sub>2</sub> Mn-modified Al<sub>3</sub>Ti were presented elsewhere<sup>1</sup>. It was shown there that the pressure caused a dramatic increase in the permanent deformation at fracture and simultaneously, a significant increase in the work-hardening rate of the material. The latter suggested the action of cataclastic mechanism of deformation similar to that in ceramics and rocks<sup>2,3</sup>. Besides an unusual development of microcracks far from fracture confirmed this assumption. The purpose of this work was investigation the process of deformation in-situ under pressure with an acoustic emission (AE) method in order to determine the real effect of pressure on ductility of this intermetallic.

## Experimental Procedure

The setup for the compression testing with the in-situ monitoring of AE activity was presented elsewhere<sup>4</sup>. The chemical composition and microstructure of the material tested here were presented in the previous paper<sup>1</sup>. The samples of the material ( $\phi 3$  mm,  $h/d=1.7$ ) were prepared according to the procedure described there too. They were tested under pressures up to 500 MPa. AE signals were detected by the AE sensor made of LiNbO<sub>3</sub> and recorded with GACEK AE signals analyzer working in the bandpass of 50 kHz – 1.5 MHz.

Several specimens were deformed at 500 MPa, then cut across in the centre with a wire saw, polished and etched. They were observed with a microscope in order to study the process of microcracking in the material.

## Results and Discussion

The compression curves ( $\sigma$ - $\epsilon$ ) for some samples are presented in Fig. 1. They are rather smooth and no dramatic change is visible on them till fracture. Simultaneously a cumulative number of AE events recorded versus true strain of the sample (e.g. Fig. 2) shows a quite different behaviour. Two sharp changes in the AE activity are observed at the strains of  $\sim 0.1$  (C) and  $\sim 0.6$  (D). The increase in the AE rate at the point D can be easily

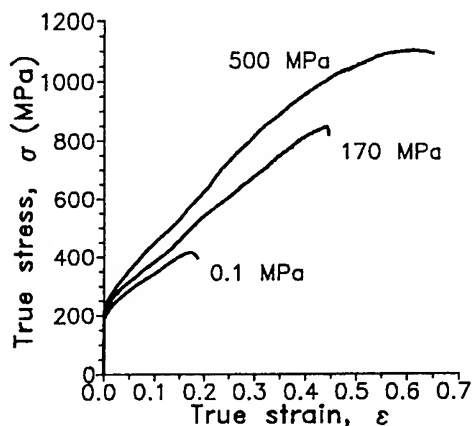


Figure 1: Compression curves of the material under some hydrostatic pressures.

explained in accordance with the  $\sigma$ - $\epsilon$  dependence as a beginning of the catastrophic damage process. However there is no noticeable change on the  $\sigma$ - $\epsilon$  curve which corresponds to the point C. It is reasonable to suppose that this point is just the

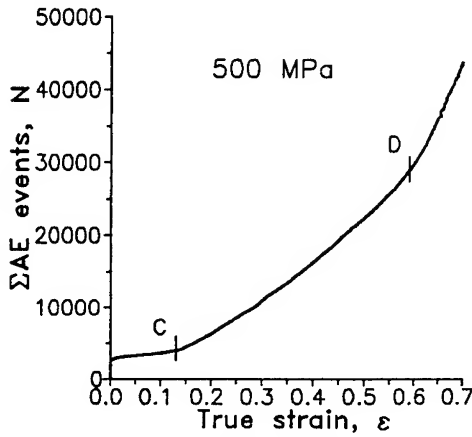


Figure 2: Cumulative number of AE events versus true strain for the material tested under 500 MPa.

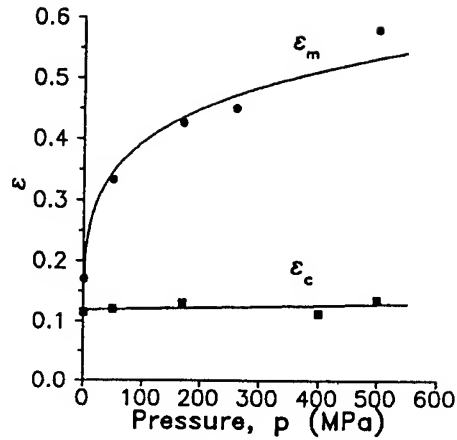


Figure 4: Critical strain,  $\epsilon_c$ , and strain at fracture,  $\epsilon_m$  versus pressure.

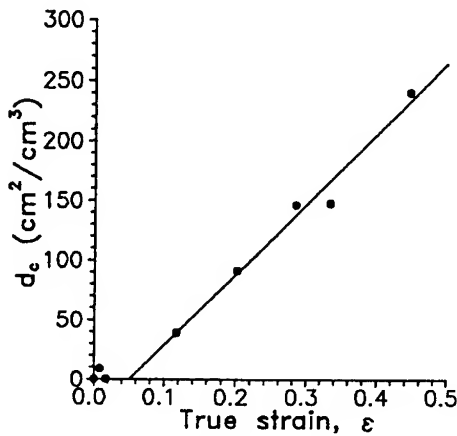


Figure 3: Microcracks density versus true strain for the material tested under 500 MPa.

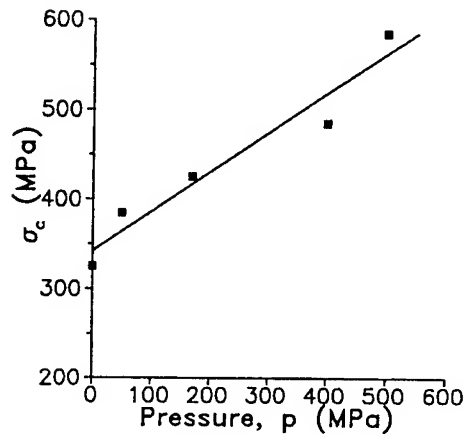


Figure 5: Stress at the transition point from plastic to cataclastic deformation versus pressure.

beginning of the cataclastic deformation. To settle the problem the density of microcracks in the material versus its true strain was measured (Fig. 3). It is seen that the process of cracking in the material really begins at the strains close to the point C.

The critical point of the transition from plastic to cataclastic deformations was observed for all curves of the cumulative number of AE events versus true strain. The dependence of the critical strain,  $\epsilon_c$ , on pressure is shown in Fig. 4. For the comparison the true strains at fracture,  $\epsilon_m$ , are presented too. A great difference between both strains is visible. The increase in the critical strain,  $\epsilon_c$ , can be estimated only at  $\sim 0.02$

per 1 GPa whereas the strain at fracture increases by  $\sim 0.4$ . This indicates that the pressure has only small effect on the nucleation of microcracks, which is consistent with the theory<sup>5</sup>.

The dependence of the true stress at the beginning of cataclastic deformation,  $\sigma_c$ , on pressure,  $p$ , presented in Fig. 5 is linear and can be expressed as:

$$\sigma_c = \sigma_o + p \tan \psi \quad (1)$$

where:  $\sigma_o$  and  $\tan \psi$  are the constants. When new constants,  $\tau_o$  and  $\tan \phi$ , are introduced in such a way that:

$$\tau_o = \sigma_o / 2(1 + \tan \phi)^{1/2} \quad (2)$$

and

$$\tan \phi = \tan \psi / 2 (1 + \tan \psi)^{1/2} \quad (3)$$

the Eq. 1 can be expressed as:

$$\tau = \tau_o + \sigma_n \tan \phi \quad (4)$$

where:  $\tau$  and  $\sigma_n$  are the shear and normal stresses in the Mohr's coordinates on the plane creating the  $\pi/4 - \phi/2$  angle with the compression axis of the sample<sup>6</sup>. The Eq. 4 presents the Coulomb's equation describing the friction mechanism of deformation which is used in mechanics of rocks. The deformation of rocks is generally of a cataclastic type due to their brittleness so, in the sense of mechanics, they are similar to the intermetallics.

### Conclusions

1. The deformation of the intermetallics by compression under pressure consist of two stages: the plastic and cataclastic ones. The acoustic emission monitoring of the deformation process allows to separate these stages.

2. The process of deformation of the intermetallics at its cataclastic stage can be expressed by the Coulomb's equation (Eq. 4) similarly to other brittle materials.

### Acknowledgements

The author thanks the State Committee for Scientific Research in Poland for support of this work (grant 3-P407-071-04).

### References

1. M.B. Winnicka, Z. Witczak, R.A. Varin, *Metall. Mater. Trans. A*, 25A (1994) 1703.
2. M.S. Paterson, C.W. Weaver, *J. Am Ceram Soc.*, 53 (1970) 463.
3. J.T. Fredrich, B. Evans, Teng-Fong Wong, *J. Geophys. Res.*, 94, B4 (1989) 4129.
4. Z. Witczak, R. Jemielniak, J. Szczepek, in *Proc. of the 1993 Joint AIRAPT/APS Topical Conference on High Pressure Science and Technology*, Colorado Springs, 28 June – 2 July, 1993.
5. D. Francois, T.R. Wilshaw, *J. Appl. Phys.*, 39 (1968) 4170.
6. M.S. Paterson, *Experimental rock deformation — the brittle field*, Springer-Verlag, Berlin, NY, 1978.



---

**IV(C) Microstructure of Materials: Grain Boundaries, Diffusion, etc.**

# EFFECT OF HYDROSTATIC PRESSURE ON THE SOLID STATE DIFFUSIONAL REACTIONS IN MULTILAYERS

D.L. BEKE

*Department of Solid State Physics, L. Kossuth University  
H-4010 Debrecen, P.O.Box 2. Hungary*

## ABSTRACT

Effect of low hydrostatic pressures (up to 200 bar) on solid state reactions in crystalline Ni-Zr and Co-Sn systems was investigated. In crystalline Ni-Zr multilayers a small enhancement of the growth of amorphous layer was observed at 200 bar and 502 K as compared to the case of normal pressure. This effect can be interpreted by the increase of the cross section of the reaction across the suppression of the porosity formation in samples under small hydrostatic pressure. In the crystalline Co-Sn system the kinetics of electrical resistivity,  $\rho$ , at 298 K showed a characteristic cross-over, as the pressure increased up to 200 bar, from the regime of increasing resistivity to the decrease of  $\rho$ . One of the possible interpretation of this phenomenon is the effect of the hydrostatic pressure on the diffusional growth of the reaction products: the pressure favours the formation of the crystalline phase(s) instead of the amorphous one.

## Introduction

If we would like to describe the possible effects of hydrostatic pressure on solid state diffusional reactions we have to consider the effect of pressure both on the nucleation and growth of the reaction products as well as the effect of pressure on the structural defects (e.g. pores, internal surfaces and their role in annihilation or production of vacancies and in the effective diffusivity). The problem of prediction of the sequence of appearance of different equilibrium or not equilibrium phases in diffusion couples is a very classical problem, which - due to the development of atomic resolution techniques such as RBS, SIMS, HRTEM - nowadays has a renaissance [1]. This fact is also related to the complication that the condition for the appearance of a phase depends not only on the growth kinetics but also on the conditions of the nucleation [2].

Even if we neglect the role of the interface reactions the nucleation problem in the diffusion zone will be different from the classical nucleation process. This is because in this case the formation of the new phase takes place along a plane interface and - in order to nucleate - the critical size of a nucleus of the new phase should be larger than the thickness of the diffusion zone.

### *a) Growth kinetics*

If the diffusion zone is wide enough to fulfill the condition for nucleation of all possible phases, then - because the pressure dependence of the diffusion coefficient (which is proportional to the growth rate constant) is expressed by a factor of  $\exp(-p\Omega/kT)$  - phases which smaller (or negative) activation volume will grow faster. In case  $\Omega \geq 0$  for all phases, growth rates will be *lower* as compared to the growth at normal pressure and only their relative magnitude can be different i.e. a shift in the phase sequence is possible because of this kinetic reason [2]. If the role of interface reaction is also important than the thickness of a growing phase can be given as

$$X = \sqrt{Kt} + At \quad (1)$$

where  $K$  and  $A$  are the growth rate constant and a factor characterizing the interface velocity. In this case the effect of pressure on  $A$  can be also important.

### *b) Nucleation*

The effect of the hydrostatic pressure on the nucleation can be estimated from the classical nucleation theory [3]. Let us consider

the case of the competition of growth of an amorphous and crystalline phase and suppose that the amorphous phase appears first in the diffusion zone at normal pressure and - after a critical thickness - the new crystalline phase appears and grows consuming the amorphous phase as well. The critical nucleus of a new phase can be simply given as:

$$r^* = -2\sigma/(\Delta f + p\Delta V/V), \quad (2)$$

where  $\sigma$  is the surface energy term,  $\Delta f$  is the free energy change per atom, containing the elastic strain energy as well, and  $\Delta V/V$  is the relative change of the atomic volume ( $V$  is the average atomic volume in the molecule of the new phase). (2) is analogous to (10a) in [3]; the difference is only the meaning of the surface term (here it is the difference of the interfacial energies per unit area of the initial interface and of the two interfaces created by the layer [2]) and the second term in the brackets. This is what was neglected in [3], and interesting here.

Now for the formation of an amorphous phase  $\Delta V/V > 0$ , while for a crystalline phase usually  $\Delta V/V < 0$  and the pressure dependence of  $r^*$  for both phases is shown schematically in Fig.1. Thus the critical pressure, where the

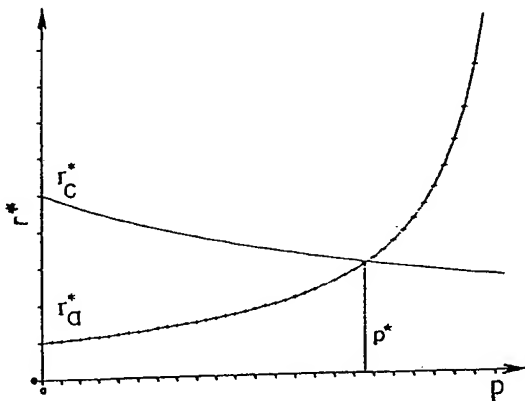


Fig.1. Critical size versus pressure for an amorphous and crystalline phases.

critical sizes of the two phases are equal can be given as

$$p^* = (\Delta f_c/\sigma_c - \Delta f_a/\sigma_a) / [(\Delta V/V)_a - (\Delta V/V)_c] \quad (3)$$

Since at  $p \approx 0$   $\Delta f_c < \Delta f_a$  the critical pressure is positive and its magnitude will be determined by the  $\Delta f$ ,  $\sigma$  and  $\Delta V/V$  terms of the two phases in question. According to Fig.1 a crossover from the initial nucleation of the amorphous phase to the first nucleation of the crystalline one is expected.

#### c) Structural defects

Regarding the role of structural defects the formation of Kirkendall-porosities will be considered here in details. It is well-known that in diffusion controlled solid state reactions the inequality of the atomic currents usually leads to a volume transport, which can result in porosity formation [4,5]. These Kirkendall porosities are usually present e.g. in solid state amorphization reactions as well [6,7]. On the another hand it is also well-known [4,5,8] that small external hydrostatic pressures can suppress the porosity formation. This offers a possible way of the production of porosity free massive amorphous samples and it is expected that the kinetics of the growth of the amorphous layer will not be considerably different.

There are only very restricted number of publications on the role of the hydrostatic pressures on the solid state diffusional reactions. Investigations on the pressure dependence would bring essential contribution to the understanding of these processes, which are very important in many applications (coatings, high temperature corrosion, diffusion welding, microelectronics etc.).

The application of multilayers in these investigations has some advantages. Changing the modulation length we can scan a wide range of the diffusion distances and can reach in short length limit ( $\lambda < 10-20$  nm) the regime where stress gradients developed by the diffusion process itself can play decisive role [9]. Furthermore these samples can be routinely produced and investigated by different high resolution techniques (RBS, HRTEM) or by classical methods (electrical resistivity).

In this paper results on the effect of low hydrostatic pressures (up to 200 bar) on solid state reactions in amorphous Si-Ge as well as in crystalline Ni-Zr and Co-Sn systems are presented and discussed. Preliminary short

report on the experimental results can be found in [10].

### Experimental

The amorphous Si3nm/Ge3nm and the crystalline Ni60nm/Zr60nm multilayers were prepared by dc magnetron sputtering onto oxidized Si substrate (kept at room temperature). The base pressure was  $10^{-7}$  mbar and the argon pressure was  $4 \cdot 10^{-3}$  mbar. The crystalline Sn100nm/Co100nm bilayers were fabricated by conventional evaporation onto Pyrex glass substrate (kept at 298 K) under a base pressure better than  $10^{-5}$  mbar. The bilayers were covered by a silicon monoxide film to avoid the oxidation. Good modulation profiles (as checked by TEM) were obtained in both multilayers (Si-Ge and Ni-Zr). In the as-deposited Ni-Zr films no amorphous layer formation was observed (i.e. its thickness should be less than 2 nm).

The porosity formation and the growth of the amorphous phase were followed by transmission electron microscopy (TEM), selected area electron diffraction and by the four probe method for the electrical resistivity.

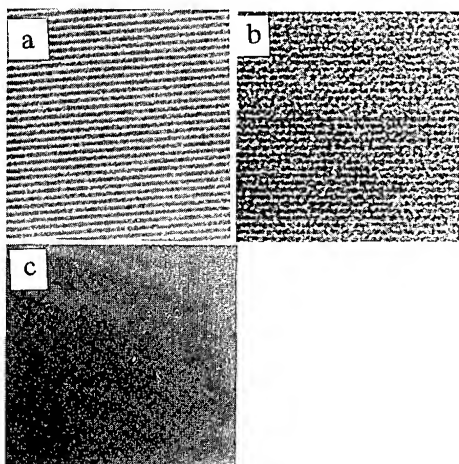


Fig.2. TEM micrographs of as-deposited (a) and heat treated amorphous Si-Ge multilayers at 858 K for 10 min. at 1 and 180 kbar (b and c), respectively. In order to make the lines of spots due to the Kirkendall voids visible figures b) and c) were taken with negative defocus.

Heat treatments were carried out in purified argon atmosphere using a IF-012A type high pressure equipment.

Fig. 2 shows the results of TEM for amorphous Si-Ge samples after a heat treatment at 858 K for 10 min. at 1 and 180 bar. It can be clearly seen that in sample heat treated at 1 bar pores parallel to the original interface are formed in the place of the Si indicating that the silicon is the fast diffusing component. On the other hand for sample heat treated at 180 bar there are no visible pores (even at higher magnification) and a homogeneous amorphous layer was formed.

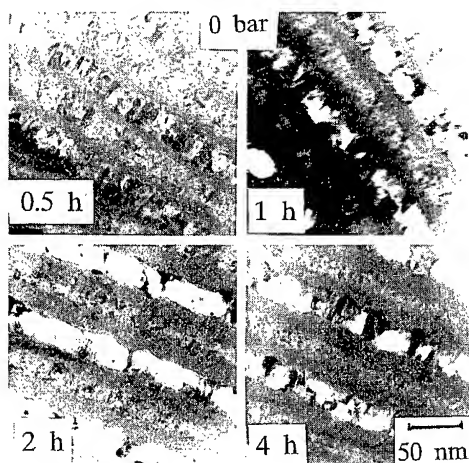


Fig.3. TEM micrographs of Ni-Zr multilayers heat treated at 502 K under vacuum ( $10^{-5}$  mbar).

Fig. 3 shows TEM micrographs of the crystalline Zr-Ni multilayers heat treated at 502 K under vacuum ( $10^{-5}$  mbar) at different annealing times. Fig. 4 illustrates the time dependence of the reciprocal values of the resistance ratio ( $R_0/R$ ) versus the square root of the annealing time. It is expected that the conductivity ( $R_0/R$ ) is the measure of the residual conductivity of the crystalline layers because the conductivity of the amorphous layer is negligibly small [11]. Thus the  $R_0/R$  vs.  $t^{1/2}$  function can be approximated by straight line, if there is a diffusion control (see eq. (1)). The deviation from the linearity at long annealing times in Fig. 4 can be attributed to the overlapping of the diffusion

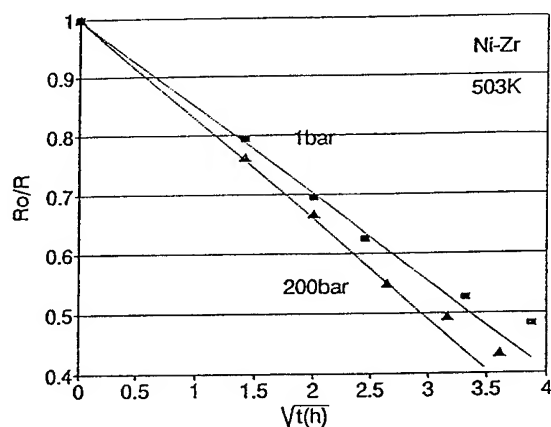


Fig. 4. Time dependence of the thickness of the amorphous layer measured by the conductivity for Ni-Zr multilayers at 502 K at two different pressures.

fields. It was hard to get a definite conclusion about the quantity of the porosity from the TEM pictures (because of the different brightness caused by the polycrystallinity).

The effect of small hydrostatic pressures on the amorphization process in the Sn-Co system is shown on Fig. 5. The reaction rate decreases

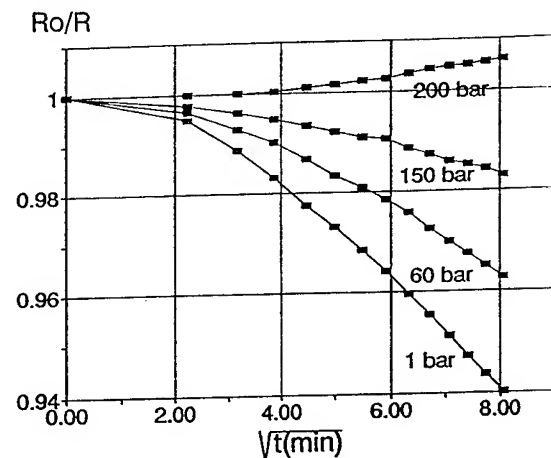


Fig. 5. Time dependence of the reduced electrical conductivity at different pressures at 298 K in Co-Sn bilayers.

with increasing pressure and at 200 bar a slight increase of the conductivity can be observed instead of the decrease measured at lower pressures.

## Discussion and conclusions

In case of amorphous Si-Ge system the disappearance of the Kirkendall porosity under 180 bar at 858 K has been illustrated. This is in accordance with results in crystalline systems with vacancy mechanism: the application of small pressures suppress the porosity formation by shifting the relative role of the different type of vacancy sinks. The efficiency of annihilation at dislocations (and thus the Kirkendall shift) is enhanced and the nucleation and growth of pores is suppressed [5]. Although the same effect is observed in amorphous system the analogy is not complete: here the mechanism of diffusion is probably a "dangling bond" mechanism [12] (the absence of periodicity leads to formation unfilled bonds by the removal of an atom and these dangling bonds can migrate), which result in a negative activation volume. Nevertheless the formation of porosity is a strong evidence of the fast diffusion of Si as compared to Ge (see also [13]). The suppression of the porosity formation by pressure can be due to the increasing critical radius of clusters of these bonds (free volumes) and/or due to the increased role of other "sinks".

Our results in crystalline Ni-Zr multilayers again are in accordance with the physical picture described above. Although we were not able to measure the decrease of porosity, if we suppose that their number and sizes were reduced by the small pressure applied then a 10% increase of the rate constant can be explained by the increase of the diffusional cross-section.

In the case of Co-Sn system two phenomena deserve attention. First the conductivity, which measures the residual thickness of the crystalline phases, shows deviations from the parabolic law: the first linear part at 1 bar (Fig. 6) indicate an interface controlled process, similarly as it was observed in the Co-Zr system [11]. The second is the crossover in the character of the reaction as the function of the pressure. The possible interpretation of this phenomenon is the pressure dependence of the critical radius of the amorphous and crystalline phases as it is indicated in Fig. 1.

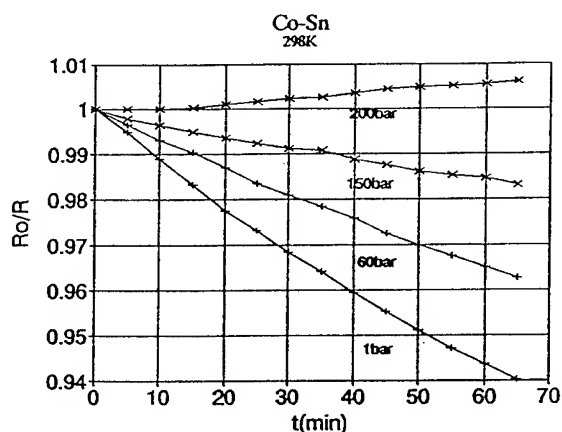


Fig.6. Time dependence of the conductivity vs. annealing time (linear plot), it can be seen that the first part of the curve can be approximated by a straight line indicating an interface limited process.

#### Acknowledgment

This work was financially supported by the OTKA Board of Hungary through grants No 1735, T-014283 and T-013954. The author is indebted to colleagues taking part in experiments: G. Radnóczy and Zs. Czígány from Res. Inst. for Techn. Phys., Budapest and G. Langer and L. Daróczy from our Department.

#### References

1. J. Philibert, "Reactive Phase Formation at Interfaces and Diffusion Processes" (Eds. Y. Limoge and J.L. Bocqueto, *Materials Science Forum* 155-156 (1994) 15.
2. J. Philibert: Atom Movements, Diffusion and Mass Transport in Solids, *Les Editions de physique*, 1991, p. 428.
3. R.D. Doherty in "Physical Metallurgy" (ed. J.W. Cahn) p. 943.
4. D.L. Beke, *Defect and Diffusion Forum* 95-98 (1993) 537.

5. Yu.E. Geguzin, *Dokl. Akad. Nauk. SSSR*, 5 (1956) 839.
6. H. Schröder, K. Samwer, U. Köster, *Phys. Rev. Lett.* 54 (1994) 197.
7. L. Schultz, Proc. of MRS Meeting: "Amorphous Metals and Non-Equilibrium Processing" Strasbourg (ed. M.V. Alluden) 1984, p. 135.
8. R.S. Barnes, D.J. Mazey, *Acta Met.* 6 (1958) 1.
9. L.A. Greer, Proc. of Int. Workshop "Diffusion and Stresses" (eds. D.L. Beke, I.A. Szabó) Trans Tech Publ. 1995.
10. L. Daróczy, D.L. Beke, G. Langer, G. Radnóczy, Zs. Czígány, *J. Magn. Magn. Mater.*, submitted
11. U. Herr, H. Geisler, K. Samwer, *Materials Science Forum* 155-56 (1994) 447.
12. S.D. Theiss, S. Mitha, F. Shaepen, M.J. Aziz, *Mat. Res. Soc. Symp. Proc.* Vol. 321 (1994) 59.
13. Zs. Czígány, G. Radnóczy, K. Järendall, J.E. Sundgren, to be published

# PRESSURE DEPENDENCE OF DIFFUSION IN METAL-METALLOID GLASSES

K. RÄTZKE, A. HEESEMANN, F. FAUPEL

*Lehrstuhl für Materialverbunde, Technische Fakultät der Christian-Albrechts Universität zu Kiel,  
Kaiserstr. 2, 24143 Kiel, Germany*

## ABSTRACT

The main question in diffusion in metallic glasses is, whether it is, as in crystals, mediated by thermally generated defects, or occurs by a direct cooperative rearrangement process of many atoms. Vital information has been obtained from investigations of pressure and mass dependence of diffusion in fully relaxed metallic glasses, which are reviewed here with emphasis on pressure dependence. The vanishing pressure dependence of Co diffusion in metal-metalloid glasses together with the absence of a significant isotope effect are interpreted in terms of a highly cooperative diffusion mechanism. Results of other experiments and recent theoretical models will be alluded to. Additionally, the effect of excess volume on the diffusion process will be discussed.

## Introduction

Metallic glasses, also termed amorphous alloys, have no long range order and consist of at least two elements, e.g., an early and a late transition metal or a metal and a metalloid. Typical examples are  $\text{Co}_{50}\text{Zr}_{50}$  and  $\text{Fe}_{40}\text{Ni}_{40}\text{B}_{20}$  alloys. Some are extremely soft-magnetic, mechanically hard and highly corrosion resistant. Hence, they are used in various technical applications, e.g. transformer cores, flexible shieldings and surface coatings. For basic research metallic glasses serve as a paradigm of dense, randomly packed structures and of metastable systems. Therefore, they are widely investigated [1-4].

During moderate heat treatment, metallic glasses undergo various rearrangement processes, such as structural relaxation, where the density increases and the diffusivity  $D$  drops up to one order of magnitude until it reaches, within experimental accuracy, a time independent plateau value. Finally, they crystallize and drastically change most of their interesting properties. All these processes involve diffusion. Due to the onset of crystallization at relatively low temperatures the average diffusion length  $\bar{x} = 2\sqrt{Dt}$  is mostly restricted to some tens of nm.

It is still discussed controversially whether diffusion in metallic glasses is mediated by vehicles similar to vacancies in crystals or whether the amorphous structure gives rise to a cooperative rearrangement of several atoms [4-6]. Various ex-

perimental results have been interpreted within a quasivacancy model, e.g. the linear Arrhenius plots and radiation-enhanced diffusion [5]. On the other hand, there are findings which are not compatible with a quasivacancy mechanism, e.g. the large variation of the prefactor over more than 14 orders of magnitude and of the activation energy in different alloys and the correlation between these two quantities [7,8]. The latter results are rather indicative of a collective mechanism involving several atoms [9], which has also been predicted by recent theoretical models [10] addressed below.

## Pressure dependence of diffusion

A key experiment to elucidate the diffusion mechanism is to measure the pressure dependence of diffusion at constant temperature. From this quantity one can, under the assumption of thermal activation, derive the activation volume of diffusion,

$$V_{act} \cong -kT \left. \frac{\partial \ln D}{\partial p} \right|_T, \quad (1)$$

which is nearly vanishing for direct interstitial diffusion and only slightly smaller than one atomic volume for a single-vacancy mechanism in densely-packed metals [11] (see below).

The first indirect experiments on the pressure dependence of diffusion in a metallic glass have been performed by Limoge and co-workers [12] in

(FeNi)<sub>8</sub>(PB)<sub>2</sub>. From the change in the crystallization kinetics with pressure, they calculated an activation volume of about one atomic volume. These results have frequently been criticized [13], and reliable results are only expected from direct radiotracer measurements.

Here a thin layer of radioactive material - in isotope-effect studies one uses a mixture of two isotopes (e.g. <sup>57</sup>Co and <sup>60</sup>Co) - is deposited onto the cleaned surface of the sample. Afterwards the sample is annealed in high vacuum or under hydrostatic pressure in purified argon to avoid contamination of the surface, which could lead to severe artifacts.

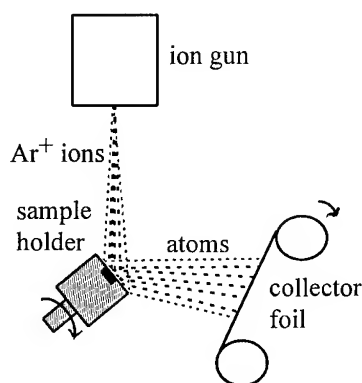


Fig. 1. Schematic sketch of a typical set-up used for microsectioning of diffusion samples by means of a dc ion gun. The whole arrangement is placed in a high-vacuum chamber.

Subsequently, the sample is cut into pieces parallel to the surface. Due to the low penetration depths this microsectioning is usually performed with a specially designed ion-beam sputtering apparatus with an intense, electronically controlled Ar<sup>+</sup>-beam (see Fig. 1) [15]. The material sputtered off is collected on a foil, which is advanced like a film in a camera after each section.

After sputtering the activity of each section is counted in a well-type NaI or a high-resolution Ge detector which allows separation of the  $\gamma$  radiation of different isotopes. According to the thin-film solution of Fick's second law [14],

$$c(x) = \text{const} \exp\left(-\frac{x^2}{4Dt}\right), \quad (2)$$

the activity, which is proportional to the concentration  $c$  of the tracer, is plotted against the square of the penetration depth  $x$ .

The first direct radiotracer studies of the pressure dependence of diffusion in metallic glasses have been performed in  $\text{Co}_{76.7}\text{Fe}_2\text{Nb}_{14.3}\text{B}_7$ , a material which allowed large penetration depths and proved not to be much prone to surface crystallization and oxidation [16, 17]. All samples were preannealed in order to reach the structurally relaxed metastable state.

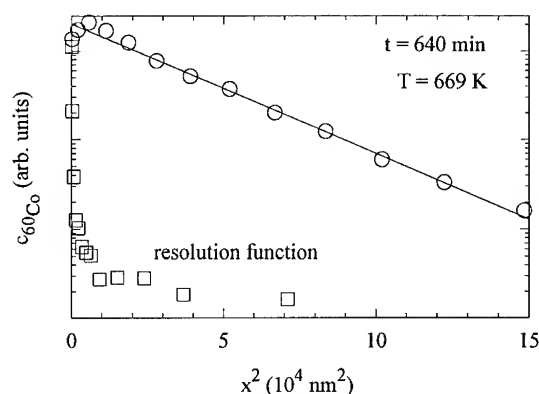


Fig. 2. Typical penetration profile for <sup>60</sup>Co diffusion into amorphous  $\text{Co}_{76.7}\text{Fe}_2\text{Nb}_{14.3}\text{B}_7$  at 669 K. The tracer activity is plotted versus the square of the penetration depth. The resolution function of the ion-beam microsectioning technique is depicted for comparison.

Fig. 2 shows a typical penetration profile of <sup>60</sup>Co in  $\text{Co}_{76.7}\text{Fe}_2\text{Nb}_{14.3}\text{B}_7$  and the corresponding resolution function, i.e the "penetration profile" of a non-annealed specimen [16]. Obviously, artifacts from the sectioning process can be neglected in the evaluation. Therefore, the diffusivity can be directly calculated via eq. 2 from the straight line fitted to the data, if the annealing time  $t$  is known.

Fig. 3 shows typical penetration profiles for different pressures. Only the very first few points are affected by surface artifacts and deviate from the straight lines fitted to the data. In Fig. 4 the corresponding <sup>60</sup>Co diffusivities are depicted as function of pressure, together with data from corresponding measurements in fcc cobalt, which were carried out for comparison [19]. In order to test the general validity of these results, we have recently performed further measurements in amorphous  $\text{Fe}_{39}\text{Ni}_{40}\text{B}_{21}$ , a well known and well characterized



material [18]. The diffusivities are also displayed as function of pressure in Fig. 4.

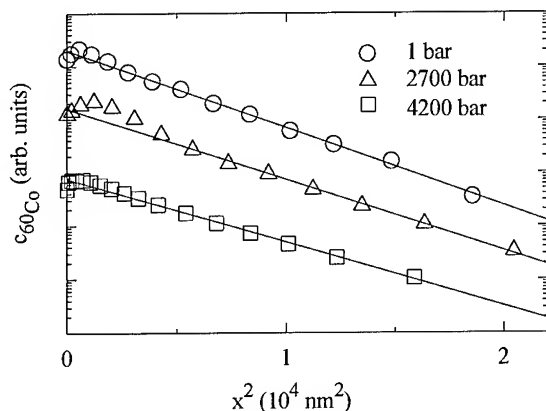


Fig. 3. Penetration profiles for diffusion of  $^{60}\text{Co}$  into amorphous  $\text{Co}_{76.7}\text{Fe}_2\text{Nb}_{14.3}\text{B}_7$  at 669 K for 640 min and different pressures.

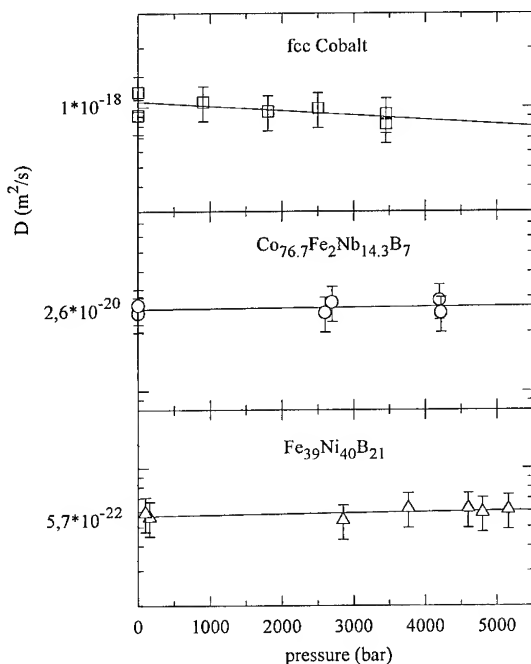


Fig. 4.  $^{60}\text{Co}$  diffusivity on a semilogarithmic scale, in fcc Co and two metal-metalloid glasses vs. hydrostatic pressure. The absolute values of the diffusivities at zero pressure are given as numbers.

From the slope of these plots the activation volume of diffusion can be calculated via eq. 1. For fcc cobalt one obtains  $V_{\text{act}} = (0.71 \pm 0.2) \Omega$ , where  $\Omega$  is the atomic volume. This is a typical value for diffusion via monovacancies in dense packed

crystals [11]. Here the activation volume is essentially given by the volume of a relaxed vacancy and a usually small contribution from the displacement of the atoms surrounding the tracer in the saddle point configuration. These contributions are called formation volume and migration volume, respectively.

For the amorphous alloys no significant activation volume is observed.  $V_{\text{act}} = -(0.06 \pm 0.1) \Omega$  for  $\text{Co}_{76.7}\text{Fe}_2\text{Nb}_{14.3}\text{B}_7$  and  $V_{\text{act}} = -(0.1 \pm 0.1) \Omega$  for  $\text{Fe}_{39}\text{Ni}_{40}\text{B}_{21}$ , where  $\Omega$  is the average atomic volume of the alloy. Measurements by Rummel and Mehrer [20] in the latter alloy corroborate the extremely small  $V_{\text{act}}$  value.

So far very small, sometimes even negative activation volumes have only been observed for direct interstitial diffusion of small atoms, e.g. C in Fe [11], and for self-diffusion in some open bcc lattices [21]. In the present metal-metalloid glasses the diffusor has the size of matrix atoms, and the structure is densely packed in contrast to the open bcc lattices. The absence of a significant activation volume clearly shows that diffusion does not involve thermal formation of vacancy-like defects. Moreover, we conclude that diffusion without defects in a dense structure requires the cooperative rearrangement of several atoms. This view has been confirmed by isotope-effect measurements (see below).

Recently, Höfler et. al. [22] obtained activation volumes between one and two atomic volumes for Co diffusion in different  $\text{Ni}_x\text{Zr}_{1-x}$  ( $42 < x < 62$ ) alloys. The high activation volumes were interpreted as being indicative of a substitutional-interstitial mechanism similar to the diffusion of Co and Fe in  $\alpha\text{-Zr}$ . This is not inconsistent with the results for the metal-metalloid alloys discussed above because Ni-Zr is a typical metal-metal glass, and pronounced differences with respect to the nature of bonding, short-range order and structure have been observed between metal-metal and metal metalloid glasses. Therefore different mechanisms may apply.

Similar arguments might be valid for experiments on the pressure dependence of Au diffusion in  $\text{Pd}_{40}\text{Ni}_{40}\text{P}_{20}$  performed by Duine and co-workers, who measured an activation volume of about one atomic volume [23]. Furthermore, it cannot be

excluded that Au, being a much larger diffusor than Co, exhibits a different diffusion behavior. Obviously, the determination of the pressure dependence of diffusion is a key experiment to obtain information on the diffusion mechanism in different amorphous alloys. This information is complemented by measurements of the mass dependence.

### Isotope Effect of Diffusion

For thermally activated single-jump diffusion the attack frequency of a tracer atom with mass  $m$  is proportional to  $1/\sqrt{m}$  in the harmonic approximation of the interatomic potential. Therefore, the mass dependence of diffusion is usually expressed in terms of the isotope-effect parameter  $E$  defined as

$$E = \frac{D_\alpha}{D_\beta} - 1 \bigg/ \sqrt{\frac{m_\beta}{m_\alpha}} - 1, \quad (3)$$

with  $m_i$  and  $D_i$  being the mass and diffusivity of the isotopes  $\alpha$  and  $\beta$ , respectively [14]. An isotope-effect parameter near unity is indicative of a single-jump mechanism [11], whereas many atoms participating in the elementary jump process lower this value drastically. Therefore one can infer further information on the basic diffusion mechanism from this isotope-effect parameter.

Due to the relatively large error concomitant with the determination of absolute diffusivities in comparison to the expected isotope effect, one measures the simultaneous diffusion of two radioactive isotopes of the same element and discriminates both isotopes from each other by their radiation [14, 15].

For fcc Co, an isotope effect of  $E = 0.74$  was obtained [24]. This value - like the above-mentioned activation volume of  $0.71 \Omega$  - is typical of single-jump diffusion via vacancies.

We also performed several investigations in different fully relaxed amorphous alloys including metal-metal and metal-metalloid glasses. The results are summarized in Fig. 5 [17, 24-26]. The data do neither indicate any temperature-dependence nor significant differences between the different alloys. It is obvious that the isotope-effect of diffusion is extremely small for all investigated metallic glasses.

In fact,  $E$  is below the very low experimental detection limit, except for  $\text{Co}_{76.7}\text{Fe}_2\text{Nb}_{14.3}\text{B}_7$ .

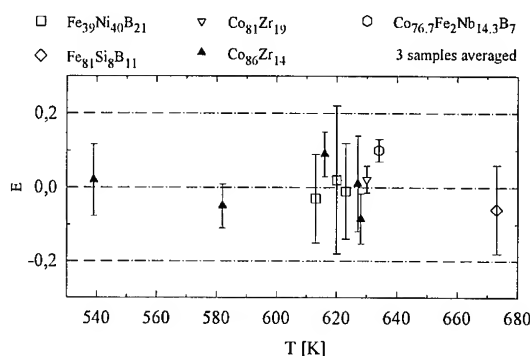


Fig. 5. Isotope effect of Co diffusion in different amorphous metal-metal and metal-metalloid alloys.

This absence of a significant isotope effect is not compatible with a single-jump diffusion mechanism (see [25] for a detailed discussion), but rather indicates that the mass effect is strongly diluted through the participation of many atoms in the elementary jump process. A rough estimate [25] suggests an effective mass of the order of 50 atomic masses.

Strongly collective diffusion is also expected from theoretical models. The extended mode coupling theory [10] predicts a dynamical phase transition at a critical temperature  $T_c$  somewhere above the experimental glass transition. Below  $T_c$  liquid-like diffusion should freeze in, and long-range atomic transport is envisioned as a medium-assisted highly cooperative hopping process, where whole clusters of atoms perform thermally activated transitions into new configurations.

Very large effective masses between 20 and 100 atomic masses have recently been found for localized low-frequency relaxations in molecular dynamics simulations of glasses. The simulations were performed with soft-sphere potentials, which are a good first approximation for metals [27, 28]. Based on these simulations and experimental evidence, e.g. from neutron scattering, the localized low-frequency relaxations were regarded as a universal phenomenon in glasses, which appears to develop from localized, highly collective vibrational low-frequency excitations. The jump lengths of the individual atoms participating in the relaxations and the number of atoms were shown to increase at elevated temperatures, and it was suggested that the

relaxations may lead to long-range diffusion with effective masses being in excellent agreement with the values evaluated from our isotope-effect data.

So far, we have only discussed diffusion in metallic glasses that were in a well-defined structurally relaxed state. Unrelaxed glasses usually contain excess volume, quenched in from the liquid state. This excess volume is very beneficial in most technological applications and leads to a marked increase in ductility and an enhancement of diffusion. Recently, we have demonstrated by isochronic isotope-effect measurements in as-quenched  $\text{Co}_{76.7}\text{Fe}_2\text{Nb}_{14.3}\text{B}_7$  glasses at different temperatures, corresponding to different stages of structural relaxation, that excess volume may give rise to single-jump diffusion similar to a vacancy mechanism in crystals [29]. At low temperatures, where diffusion essentially takes place in the as-quenched state, a marked isotope effect of  $E \approx 0.5$  was observed, which points to the prevalence of single-atom jumps. At higher temperatures the quenched-in volume anneals out during diffusion, and  $E$  was found to decrease and finally to approach the very low  $E$ -value of the fully relaxed state, where diffusion is highly collective (see above). These experiments show that excess volume may coalesce in the form of vacancy-like entities and may thus drastically change the diffusion mechanism.

### Acknowledgments

Financial support by Deutsche Forschungsgemeinschaft is gratefully acknowledged.

### References

- [1] Amorphous Metallic Alloys, ed. F. E. Luborsky, (Butterworth, 1983)
- [2] Rapidly Quenched Metals 5, eds. S. Steeb, H. Warlimont, (North Holland, 1985).
- [3] Proc. LAM 8, published in: *Mat. Sci. Eng. A* **179/180** (1994).
- [4] F. Faupel, *phys. stat. sol. (a)* **134** (1992) 9.
- [5] R. S. Averbach, *MRS Bulletin XVI* (1991) 47.
- [6] H. Kronmüller, to be published in: *Lecture Notes on Physics* (Springer Verlag, 1995).
- [7] S. K. Sharma, S. Banerjee, Kuldeep and Animesh K. Jain, *J. Mater. Res.* **4** (1989) 603.
- [8] H. Kronmüller, W. Frank, and A. Hörner, *Mater. Sci. Eng. A*, **133** (1991) 410.
- [9] W. Frank, J. Horváth, and H. Kronmüller, *Mater. Sci. Eng.* **97** (1988) 415.
- [10] Sjögren L 1990 *Z. Phys. B.: Cond. Matter* **79** 5
- [11] Landolt Börnstein, Neue Serie III/26 ed. H. Mehrer (Springer Verlag, 1991).
- [12] Y. Limoge, *Mat. Sci. For.* **15 - 18** (1987) 517.
- [13] F. Spaepen and D. Turnbull, *Scripta Metall.* **25** (1991) 1563.
- [14] Y. Adda and J. Philibert, *La Diffusion dans les Solides* (Press Universitaires de France, 1966).
- [15] F. Faupel, P. W. Hüppe, K. Rätzke, R. Willecke, and Th. Hehenkamp, *J. Vac. Sci. Technol. A* **10** (1992) 92.
- [16] K. Rätzke and F. Faupel, *Phys. Rev. B* **45** (1992) 7459.
- [17] F. Faupel, P. W. Hüppe, and K. Rätzke, *Phys. Rev. Lett.* **65** (1990) 1219.
- [18] K. Rätzke, and F. Faupel, *J. Non-Cryst. Sol.* **181** (1995) 261.
- [19] K. Rätzke, and F. Faupel, *Scripta Met.* **25** (1991) 2233.
- [20] G. Rummel, and H. Mehrer *phys. stat. sol. (a)* **185** (1994) 327.
- [21] J. A. Cornet, *Phys. Chem. Sol.* **32** (1971) 1489.
- [22] H. J. Höfler, R. S. Averbach, G. Rummel, and H. Mehrer, *Phil. Mag. Lett.* **66** (1992) 301.
- [23] P.A. Duine, S.K. Wonnell, and J. Sietsma, *Mat. Sci. Eng. A* **179/180** (1994) 270.
- [24] P. W. Hüppe and F. Faupel, *Phys. Rev. B* **46** (1992) 120.
- [25] A. Heesemann, K. Rätzke, F. Faupel, J. Hoffmann J, and K. Heinemann, *Europhys. Lett.* **29** (1995) 221.
- [26] K. Rätzke, A. Heesemann, F. Faupel *J. Phys.: Cond. Matt.* **7** (1995) 7663.
- [27] H. R. Schober, C. Oligschleger, and B. B. Laird, *J. Non-Cryst. Sol.* **156-158** (1993) 965.
- [28] C. Oligschlaeger, H. Schober, *Solid State Communications* **93** (1995) 1031.
- [29] K. Rätzke, P. W. Hüppe, and F. Faupel, *Phys. Rev. Lett.* **68** (1992) 2347.

# DIFFERENTIAL STRESS OF MgO AND Mg<sub>2</sub>SiO<sub>4</sub> UNDER UNIAXIAL STRESS FIELD: VARIATION WITH PRESSURE, TEMPERATURE, AND PHASE TRANSITION

Takeyuki Uchida, Nobumasa Funamori, Teruyuki Ohtani, and Takehiko Yagi  
*Institute for Solid State Physics, University of Tokyo*  
*Roppongi, Minato-ku, Tokyo 106, Japan*

## ABSTRACT

Differential stress  $t$  and the parameter  $\alpha$ , which describes the stress and strain state across the grain boundaries of the specimen, have been determined by high pressure *in situ* X-ray diffraction study. Measurements were made for MgO and Mg<sub>2</sub>SiO<sub>4</sub> (forsterite) up to 20GPa at 300K and up to 35GPa and 1200K, respectively. The results show that for MgO, inversion of the sign of elastic anisotropy factor occurs at around 3GPa. For Mg<sub>2</sub>SiO<sub>4</sub>, the differential stress  $t$  increased with increasing pressure, decreased slightly with heating, and decreased to zero at the phase transitions.

## INTRODUCTION

Recently, Singh<sup>(1)</sup>, and Singh and Balasingh<sup>(2)</sup> used the anisotropic elasticity theory and derived the expressions for the lattice strains of cubic and hexagonal crystals under uniaxial stress field, respectively. Funamori *et al.*<sup>(3)</sup> have shown experimentally the differential stress and the dependence of the lattice strains on the Miller indices for NaCl using an opposed-anvil type high pressure apparatus (modified Drickamer-type apparatus), which generates the uniaxial stress field. Duffy *et al.*<sup>(4)</sup> compressed MgO at room temperature up to 227GPa using diamond anvil cell and found that the sign of elastic anisotropy factor is reversed under pressure. Uchida *et al.*<sup>(5)</sup> extended the expressions of lattice strains derived by Singh for all the crystal symmetry. In the present study, differential stress  $t$  and the parameter  $\alpha$ , which describes the stress and strain state across the grain boundaries of the specimen, have been determined by high pressure *in situ* X-ray diffraction study. Measurements were made for MgO and Mg<sub>2</sub>SiO<sub>4</sub> up to 20GPa at 300K and up to 35GPa and 1200K, respectively.

## EXPERIMENTAL

Figure 1 shows the schematic illustration of high pressure apparatus and X-ray diffraction geometry used in the present study. Diffracted X-rays were observed in two different directions: One is in a vertical plane containing the loading

axis and the other is in a horizontal plane perpendicular to it. Subscripts V and H are attached for the quantities derived from the observations in vertical and horizontal planes, respectively. Synchrotron radiation is employed as

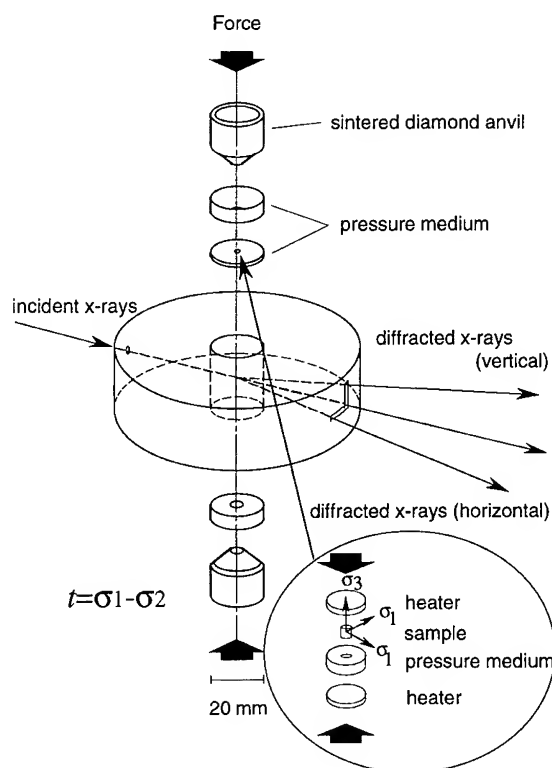


Fig.1. Schematic illustration of modified Drickamer-type apparatus and X-ray geometry. The differential stress  $t$  is represented as the difference of  $\sigma_3$  and  $\sigma_1$ .

X-ray source. Diffracted X-rays are detected simultaneously in the two directions using two sets of solid state detectors by energy dispersive method. The diffraction angle  $2\theta$  was fixed at  $9^\circ$  in both directions. The sample can be heated by the internal heaters made of the mixture of titanium carbide and diamond. The temperatures were estimated from the power-temperature relation calibrated by other runs using thermocouple. Hydrostatic stress component  $P$ , differential stress  $t$ , and parameter  $\alpha$  are calculated from the detected X-rays in the two directions. Two materials MgO or  $\text{Mg}_2\text{SiO}_4$  (forsterite) are employed as starting materials.

## RESULTS AND DISCUSSIONS

### MgO

The apparent pressures  $P_v$  and  $P_H$  were calculated from the lattice strains  $\epsilon_v(hkl)$  and  $\epsilon_H(hkl)$  using the third-order Birch-Murnaghan equation of state at each pressures. Hydrostatic stress component  $P$  is calculated in the same way from the hydrostatic strain component  $\epsilon_p$ ,

$$\epsilon_p = (\epsilon_v(hkl) + 2\epsilon_H(hkl))/3.$$

In Fig. 2, the differences of the apparent pressures  $P_v - P_H$  were plotted for hydrostatic stress component  $P$ . In the uniaxial stress field, it

increases systematically with pressure, depending on the Miller indices. Of course, all of them remain zero under the hydrostatic compression. In the pressure region above 3GPa, the differences obtained from the 200 diffraction line are the smallest. In contrast with it, the differences calculated from the 111 diffraction line are the largest. However, in the pressure region below 3GPa, the relation is reversed. Recently, Duffy *et al.*<sup>(4)</sup> reported that the sign of the elastic anisotropy factor of MgO has reversed at high pressure based on the systematic difference of the lattice parameters determined from the two diffraction lines of 220 and 200. As is evident in Fig. 2, present result clearly shows that the reversal occurs at around 3GPa. The differential stress  $t$  increased monotonously with the increasing pressure (Fig. 3). At about 20GPa, the value of  $t$  was about 5GPa. This value is quite large compared with that of NaCl (about 0.4GPa)<sup>(3)</sup>. This result reflects the fact that the strength of MgO is larger than that of NaCl.

### $\text{Mg}_2\text{SiO}_4$

The variation of the differential stress  $t$  in  $\text{Mg}_2\text{SiO}_4$  is shown in Fig. 4. For forsterite ( $\alpha$  phase),  $t$  increased rapidly at room temperature

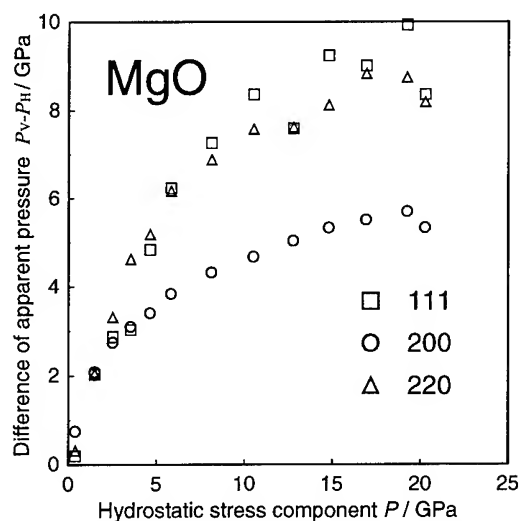


Fig. 2. Plot of the difference of the apparent pressure  $P_v - P_H$  vs. hydrostatic stress component  $P$ . The sign of the elastic anisotropy factor changes at about 3GPa.

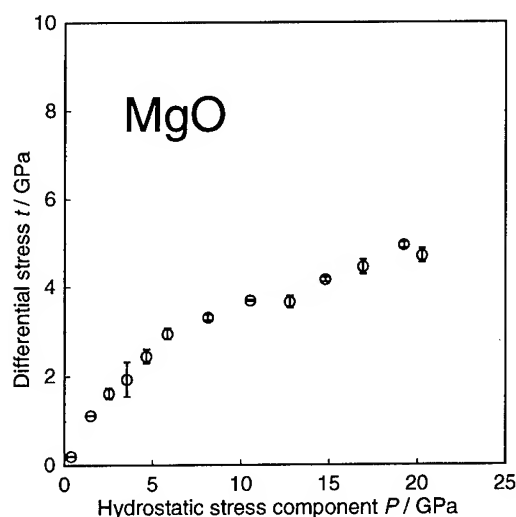


Fig. 3. Differential stress  $t$  vs. hydrostatic stress component  $P$  plot for MgO. Differential stress  $t$  increases monotonously with increasing pressure.

with increasing pressure and decreased slightly with heating at about 15GPa. Further heating to 1100K resulted in the phase transition into  $\gamma$  phase. At that time,  $t$  becomes about 0GPa. For spinel ( $\gamma$  phase),  $t$  increased monotonously with increasing pressure at constant temperature of 1100K, decreased slightly with further heating at about 28GPa, and then dropped to almost 0GPa when phase transition was occurred at 1200K. Spinel ( $\gamma$  phase) decomposed to perovskite ( $\text{MgSiO}_3$ ) and periclase ( $\text{MgO}$ ) at that temperature. After the decomposition, in contrast to former two phases, the differential stress  $t$  of the decomposed phase did not increase so much with further compression at 1200K. The compression was carried out to about 35GPa.

Differential stress  $t$  accumulated in the mixture of  $\text{MgSiO}_3$  and  $\text{MgO}$  was much less than that of  $\gamma$  phase, although the difference of temperature was only 100K. It is known that the seismic activity disappears below the depth of 670km. Therefore, there was an argument that slab does not penetrate below this depth. From the present study, it can be argued that no earthquake will occur because the differential stress accumulated in the decomposed phase of  $\text{Mg}_2\text{SiO}_4$  is not high enough, even if the slab subduct into the lower mantle. The reason why the mixture of  $\text{MgSiO}_3$  and  $\text{MgO}$  accumulate less differential stress could be explained either by the superplasticity of the very fine grain mixture or by the viscoelastic properties of perovskite and periclase. The true reason has, however, not been clarified yet. Another interesting point in the present study is that the differential stress becomes almost 0GPa when the phase transition occurred. This result implies that, if the deep-focus earthquake is triggered by the phase transition, the energy of released differential stress should be taken into account, in addition to the energy caused by the volumetric change, as the released energy associated with the transition.

#### Parameter $\alpha$

The differential stress  $t$  and the parameter  $\alpha$  are calculated at the same time from the observed X-

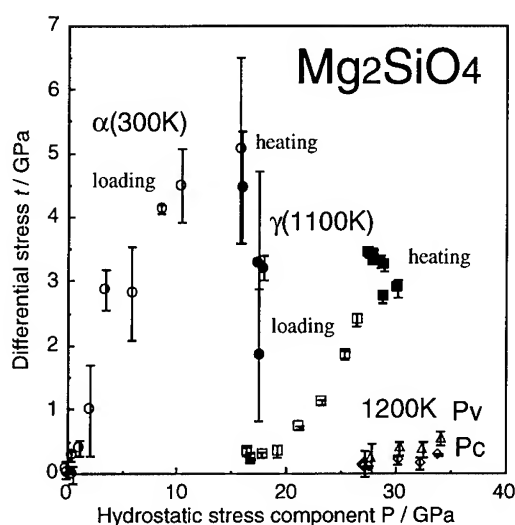


Fig. 4. Differential stress  $t$  for  $\text{Mg}_2\text{SiO}_4$ . For  $\alpha$  and  $\gamma$  phases, it increases monotonously with increasing pressure, but for decomposed phase (Pv+Pc), it increases only little.

rays in two directions. However, the error of the parameter  $\alpha$  becomes much larger than that of the differential stress  $t$  for  $\text{MgO}$  and forsterite, because of the effect of anisotropy factor or orthorhombic symmetry<sup>(5)</sup>. Therefore, no meaningful variation of the parameter  $\alpha$  was observed in the present study.

#### ACKNOWLEDGMENTS

Authors are grateful to O. Shimomura and T. Kikegawa for their support for the experiment. Thanks are also due to T. Kondo, Y. Ida and Y. Sato-Sorensen for their helpful comments and discussions. The X-ray experiment was carried out at KEK using the MAX80 system.

#### REFERENCES

1. A. K. Singh, *J. Appl. Phys.* **73** (1993) 4278.
2. A. K. Singh and C. Balasingh, *J. Appl. Phys.* **75**, (1994) 4956.
3. N. Funamori, T. Yagi, and T. Uchida, *J. Appl. Phys.* **75** (1994) 4327.
4. T. S. Duffy, R. J. Hemley, and H. K. Mao, *Phys. Rev.* **74** (1995) 1371.
5. T. Uchida, N. Funamori, and T. Yagi, in preparation.

# THE COMPENSATION PRESSURE FOR THERMALLY ACTIVATED PROCESSES

W.LOJKOWSKI

*High Pressure Research Centre, Polish Academy of Sciences, Sokolowska 29,  
01-142 Warsaw, Poland.*

D.A.MOLODOV, L.S.SHVINDLERMAN

*Institute für Metallkunde und Metallphysik  
RWTH Aachen, Kopernikusstr. 14, D-52056 Aachen, Germany  
and*

*Institute of Solid State Physics, Russian Academy of Sciences, Chernogolovka,  
Moscow 142432 Russia*

## ABSTRACT

In a recent study the effect of high pressures on the migration rate of grain boundaries (GBs) in aluminum bicrystals was studied. It was found that for the  $\langle 110 \rangle$  boundaries the activation volume  $V^*$  was proportional to the activation energy. The proportionality constant has a dimension of pressure and was in the range 4-5 GPa. For the  $\langle 111 \rangle$  and  $\langle 100 \rangle$  boundaries the activation volumes ( $V^*$ ) for migration was independent on the activation energy. It seems that the pressure 4-5 GPa is the pressure level inside the activated cluster formed during the transfer of atoms across the boundary. The above results speak for the idea of compensation pressure, as a characteristic property of the activated cluster formed during atomic jumps.

## 1. Introduction

The well known correlation between the logarithm of the pre-exponential factor for diffusion and the activation enthalpy is frequently called compensation relationship [1]:

$$\ln(D_0) = \text{const} \cdot H^* \quad (1)$$

Here  $D_0$  is the pre-exponential factor, called hereafter pre-factor and  $H^*$  is the activation enthalpy. The variable is the matrix or the diffusing atom for constant matrix [cf. 1]. In the case of grain boundary diffusion or migration, the variable is the grain boundary misorientation [3-5].

In a number of papers [3-5] the term "compensation temperature"  $T_c$  was introduced, defined as follows:

$$S^* = \frac{H^*}{T_c} \quad (2)$$

For  $T=T_c$  all boundaries have the same diffusion coefficient or migration rate (4). It was proposed that formation of the activated cluster is equivalent to a local phase transformation [cf. ref. 3-5] and  $T_c$  is the temperature of the cluster. The purpose of the present paper is to study the pressure inside the activated cluster.

If the pressure inside the activated cluster is constant ( $P_c$ ) there must be a linear relationship

between pressure and activation energy. This follows from the fact that  $H^* = Q^* + P_c V^*$ . Further, from eq. 1 it follows that:

$$S^* = \frac{H^*}{T_c} = \frac{Q^*}{T_c} + \frac{P_c V^*}{T_c} \quad (3)$$

Hence there must be a linear relationship between  $S^*$  and  $V^*$ , where the proportionality constant is  $P_c/T_c$ .

## 2. Comparison with experiment

Figs. 1 and 2 show the recently observed correlation between pre-factor and activation volume (fig. 1) as well as between the activation volume and activation energy (fig. 2). The experiment concerns grain boundary migration in aluminium bicrystals under pressure. The variable is the misorientation of the crystals. It can be seen that the activation volume and energy are proportional to each other. The proportionality factor is  $P_c = 3.9$  GPa for  $\langle 110 \rangle$  boundaries. For  $\langle 100 \rangle$  and  $\langle 111 \rangle$  boundaries  $P_c$  is not known since  $V^*$  is const (1.2 at.vol.). From fig. 2 it can be deduced that for  $\langle 110 \rangle$  boundaries  $H^* = P V^*$ , where  $P = 5.0(\pm 1.0)$  GPa.

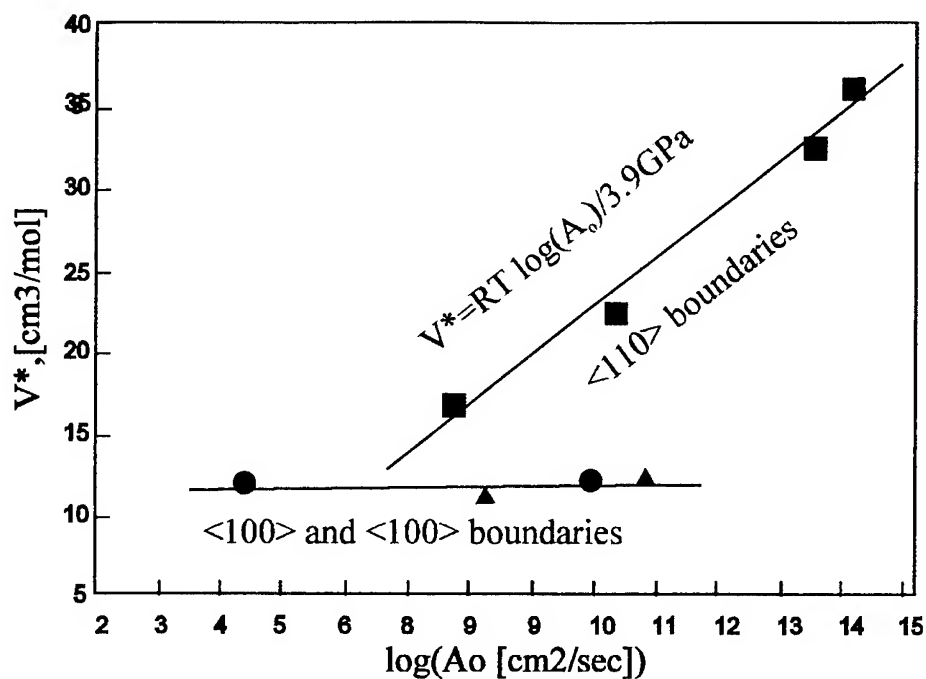


Fig.1. Correlation between pre-factor and activation volume for grain boundary migration in Al bicrystals.

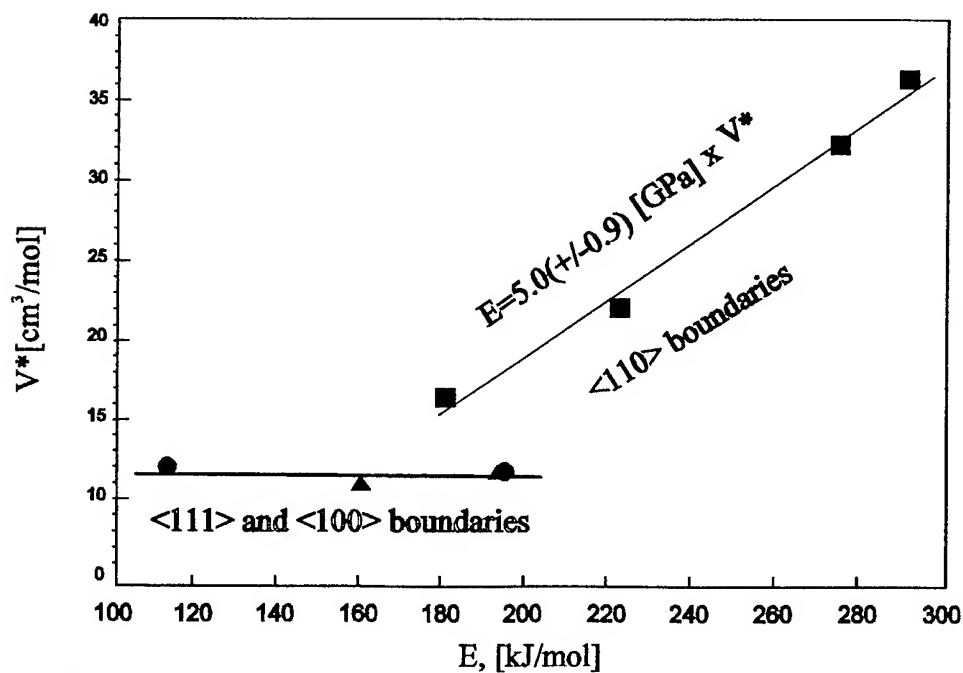


Fig.2. Correlation between activation energy and activation volume for grain boundary migration in Al bicrystals.



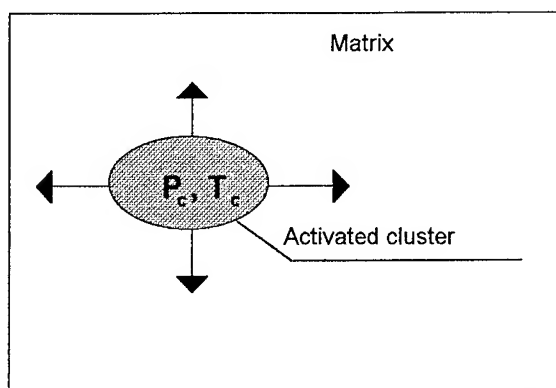


Fig.3. Schematic representation of the activated cluster characterized by local temperature  $T_c$  and pressure  $P_c$ .

### 3. The compensation pressure

According to the heterophase fluctuation theory [3-5], the activated cluster formed in the saddle point configuration is equivalent to a small nuclei of another phase corresponding to the locally disordered structure.  $T_c$  and  $P_c$  correspond therefore to the local temperature and pressure in the cluster (fig.3). The assumption of a phase transformation is crucial, because it permits to understand why all clusters have the same temperature and pressure.

### 4. Conclusions for the grain boundary migration mechanism

The pressure inside the activated cluster for  $\langle 110 \rangle$  boundaries is of the order of 3-4 GPa. This is the order of magnitude of the pressure close to a dislocations' core. At the same time, the  $\langle 110 \rangle$  direction is a close packed direction in the fcc lattice. The high pressure inside the activated cluster could be understood in terms of whole segments of close packed rows of atoms in one grain jumping across the boundary into the other grain. On the other hand, for  $\langle 100 \rangle$  and  $\langle 111 \rangle$  boundaries, it is apparently possible that atoms jump from one crystal to the other taking the opportunity of a "hole" in the grain boundary structure.

### 5. Conclusions

The compensation pressure is the pressure inside the activated clusters formed during thermally activated processes. For migration of  $\langle 110 \rangle$  tilt grain boundaries in Al the activated cluster is under a pressure reaching 5 GPa.

### Acknowledgment

W.L is grateful to the Polish Committee for Scientific Research for financial support under contract 3P407 008 04.

### References

1. C.Zener, in "Imperfections in Nearly Perfect Crystals", ed. by W.Shockley, J.H.Hollomon, R.Maurer and F.Seitz, J.Wiley&Sons, NY, p.289 (1952)
2. Ye.L.Maksimova, B.B.Straumal, V.Ye.Fradkov, L.S.Shvindlerman, *Phys.Met.Metall*, **56**, 133 (1983)
3. B.B.Straumal, L.M.Klinger, L.S.Shvindlerman, *Scripta Met.*, **17**, 275 (1983)
4. B.S.Bokstein, Ch.V.Kopetzky, L.S.Shvindlerman, "Grain Boundary Thermodynamics and Kinetics in Metals", (in russian), Moscow, *Metallurgia*, (1986)
5. B.S.Bokstein, in "Diffusion in Metals and Alloys" (DIMETA-88), J.F.Kedves, D.Beke editors, *Trans.Tech.Publ.*, p.631 (1988)
6. D.A.Molodov, J.Swidorski, G.Gottstein, W.Lojkowski, L.S.Shvindlerman, *Acta Metall&Mater.***42**, 3397 (1994)

# HIGH PRESSURE INVESTIGATIONS OF GRAIN BOUNDARY MIGRATION MECHANISM IN ALUMINIUM

W.LOJKOWSKI

*High Pressure Research Centre, Polish Academy of Sciences, Sokolowska 29,  
01-142 Warsaw, Poland.*

Y.MINAMINO, S.HOZUMI

*Department of Materials Science and Engineering, Faculty of Engineering, 2-1, Yamadaoka, Suita, Osaka 565,  
Japan*

J.WYRZYKOWSKI

*Department of Materials Science and Engineering, Warsaw University of Technology, Narbutta 85, Warsaw,  
Poland*

## ABSTRACT

The effect of pressure on the rate of grain growth in aluminum polycrystals was measured as a function of temperature. The pressure range was 0-2.5 GPa. The initial grain size was 4.2  $\mu\text{m}$ . The final grain size was in the range 25-30  $\mu\text{m}$ . The activation volume was  $0.7\Omega$  in the temperature range 400K-500K, where  $\Omega$  is the atomic volume. It abruptly decreases to  $0.3\Omega$  at 700K. The transition temperature is 600K. This result speaks for a change of grain boundaries structure at 600K. Presumably at this temperature the grain boundary migration mechanism changes from one where vacancies play a major role to one where atoms in the grain boundary change positions without cooperation of vacancies.

## 1. Introduction.

Grain boundary migration (GBM) plays an important role during materials recovery, sintering, superplasticity, segregation, diffusion etc. However, despite its technological importance, the GBM mechanism is not fully understood yet. It is well known, that impurities in materials strongly influence the GBM rate [1]. At high temperatures, when impurities desegregate, GBs become more mobile. The same holds for very high purity materials. Measurements of the activation volume for GBM as a function of temperature may help to understand the effect of impurities on the GBM mechanism.

Experimental investigations of the pressure effect on GBM carried out till now have lead to activation volumes in the range 0.6-1.2  $\Omega$  ( $\Omega$ -atomic volume) (cf.2,3). These values are close to the activation volume for vacancy diffusion and indicate that participation of vacancies is necessary for GB migration. However, to the authors knowledge, no measurements of the temperature effect on the activation volume have been carried out till now. The purpose of the present work is to measure the temperature effect on the activation volume for GB migration.

## 2. Experimental methods

The pressure effect on the GB migration rate was assessed indirectly, based on the kinetics of grain growth. For a material with uniform grain size distribution, the grain growth kinetics is described by the equation:

$$DdD = Mdt \quad (1)$$

where  $D$  is the average grain size,  $M$  is the GB mobility,  $t$  is the grain growth time. It follows, that for isochronal annealing:

$$M = \frac{D^2 - D_0^2}{t} \quad (2)$$

Since: 
$$V^* = -RT \frac{\partial \ln M}{\partial p} \quad (3)$$

the activation volume is:

$$V^* = -RT \frac{\partial \ln(D^2 - D_0^2)}{\partial p} \quad (4)$$

where  $D_0$  is the initial grain size.

The high pressure anneals were carried out in the high pressure anvil apparatus of the Osaka University. The pressure range was 1.5-2.5 GPa. The annealing time was 1 hour. The grain size after the experiments was measured by standard metallographic methods: the grain size distribution was determined and the average grain size was calculated. The material used was aluminum of 99.99% purity with initial grain size 4.2  $\mu\text{m}$ . One experiment was carried out with Al99.999% purity.

### 3. Results

Under high pressure the rate of grain growth decreased. At low pressures, the final average grain size was 25-30  $\mu\text{m}$ . The pressure effect decreases as the temperature is increased or the purity of the material increases. Fig.1 shows the activation volume for grain growth in the temperature range 570K-700K. It can be seen that the activation volume is about  $0.7\Omega$  at low temperatures but abruptly decreases to  $0.3\Omega$  at 700K. The transition temperature is 600K. Therefore, the activation volume is a function of temperature.

### 4. Discussion

The present result indicates a structural change in grain boundaries at 600K. This change must be

caused by impurity desegregation. At high temperatures the activation volume becomes equal to the activation volume for GB migration in Al5N. It might be concluded that at low temperatures the GB structure is "compact" owing to the segregated impurities. As a consequence, no jumps of atoms from one grain to the other across the boundary are possible without a cooperation of a vacancy (Fig.2a,b). On the other hand, at high temperatures, owing to impurity de-segregation, the grain boundary structure becomes open (Fig.2c). As a consequence, the atoms can move from one grain to the other by a shuffling mechanism [4], where the bonds between atoms move rather than the atoms themselves.

### 5. Conclusions

The activation volume for grain growth in aluminum decreases from the value 0.7 at.vol. to 0.3 at.vol. when the temperature is raised above 600K. This speaks for a transformation of the grain boundaries structure when the impurities desegregate from grain boundaries. 600K seems to be the desegregation temperature. Below this temperature grain boundaries move by a vacancy assisted mechanism. Above that temperature a vacancy less mechanism is operative.

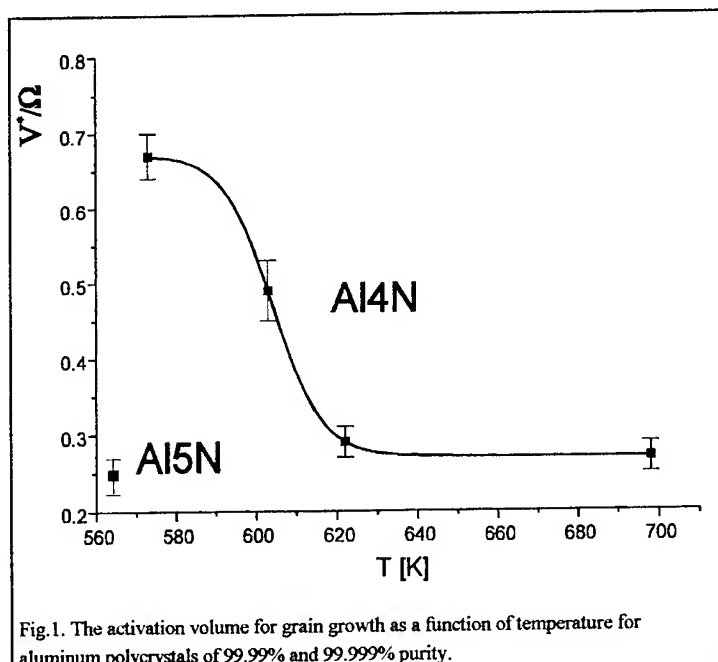
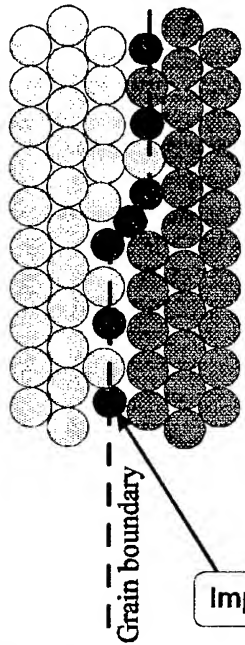
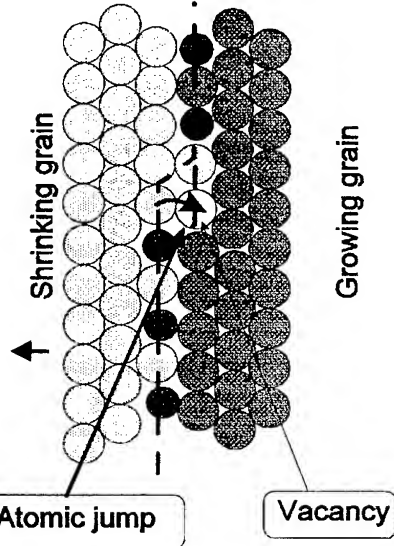


Fig.1. The activation volume for grain growth as a function of temperature for aluminum polycrystals of 99.99% and 99.999% purity.

Immobile grain boundary  
owing to the impurities



Mobile grain boundary  
owing to the vacancy



Mobile grain boundary  
No impurities

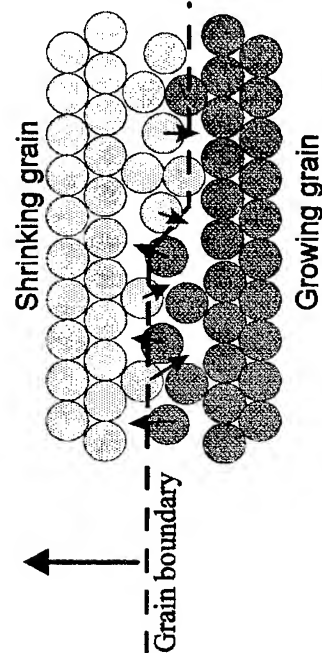


Fig.2 a and b  
Fig.2. Grain boundary migration mechanism for: low temperature and or strong segregation compared to high temperature and/or low segregation

Fig.2.c

## Acknowledgments

W.L. Is grateful to the Polish Committee for Scientific Research for support of part of the present work under contract 3P407 008 04. The authors are grateful to prof.Y.Miyamoto for access to the high pressure anvil apparatus.

## References

1. R.Smoluchowski, in "Imperfections in nearly perfect crystals", W.Shockley, J.H.Hollomon, R.Maurer, F.Seitz, eds., p.451, J.Wiley&Sons, NY, (1952)
2. H.Hahn, H.Gleiter, *Scripta Metall.* **13**, 3 (1979)
3. D.Molodov, J.Swidorski, G.Gottstein, W.Lojkowski, L.S.Shvindlerman, *Acta metall.&mater.*, **42**, 3397 (1994)
4. H.Gleiter, A.Lissowski, *Zeitschr. f. Metallk.*, **62**, 237 (1971)

# FEATURES OF PLASTIC DEFORMATION OF FCC METALS HAVING DIFFERENT STACKING FAULTS ENERGY UNDER HIGH PRESSURE

A.A.DOBRIKOV, A.S.DOMAREVA

*Donetsk Physiko-Technical Institute of the Ukrainian Academy of Science, 72,R.Luxemburg str.  
Donetsk, 340114 Ukraine*

## ABSTRACT

The transmission electron microscopy method has been used to investigate the processes of dislocation structure formation for a number of austenite alloys at deformation under high hydrostatic pressure(HHP). It has been shown that upon decreasing the stacking fault energy(SFE) of materials the mechanism of plastic deformation changes from slipping to twinning. Transformation of the cellular dislocation structure to the disperse twin one is accompanied by an abrupt increase of the strength with good plasticity being conserved.

## Introduction

It is known [1] that in metals the formation of ordered dislocation structure provides good combination of strength and plasticity. One of the examples of such an ordering is the formation of cellular structure the perfection of which at atmospheric pressure depends on deformation degree, temperature of deformation and stacking fault energy of a material. It is also known that high hydrostatic pressure makes formation of the cellular structure in metals with BCC lattice easier [2].

The present paper studies the influence of HHP on ordering of dislocation ensemble in FCC metals of different SFE.

## Experimental details

The investigated materials were polycrystalline copper of 99,99% purity, austenite steels 2 (0.12 % C; 18 % Cr; 10 % Ni; 1 % Ti) and 4 (0.38 % C; 12 % Cr; 8 % Mn; 8 % Ni; 1.5 % V) and model alloys 1 (Fe - 28 % Ni - 2.7 % Ti) and 3 (0.5 % C; 4 % Cr; 12 % Mn; 6 % Ni; 1.5 % V; 1 % Si). The SFE ( $\gamma$ ) values for the above materials are given in Table 1:

Material	Cu	Alloy			
		1	2	3	4
$\gamma$ , MJ/m <sup>2</sup>	60	30	18	13	10
Number of deformation twins,% $\epsilon=50\%$	-	-	33	41	45

The SFE of austenite alloys were determined by triple extended dislocation nodes using transmission electron microscopy according to [3]. The dislocation structure has been investigated at electron microscope JEM 200A. Deformation of these materials were carried out by two methods: uniaxial compression with deformation degrees  $\epsilon = 0...5\%$  at atmospheric and high (P to 1.2 GPa) pressures and hydroextrusion at pressures up to 2.5 GPa with deformation degrees  $\epsilon = 0...50\%$ .

## Results and discussion

The electron microscopic studies of dislocation structure evolution in polycrystalline copper under high pressure provides a more complete formation of cellular structure with other conditions being the same (Fig.1a,b).

Method of statistic analysis of function of frequency dislocation distribution allows [4] us to observe for evolution of dislocation assembly according to change of its main parameters (see Table 2):

P, MPa	$\rho$ , $10^9$ cm <sup>-2</sup>	$r_p$ , nm	$r_m$ , $10^3$ nm	$V_p$ , nm
0.1	2.3	120	38	36
800	3.1	90	40	30
1200	3.6	73	46	21

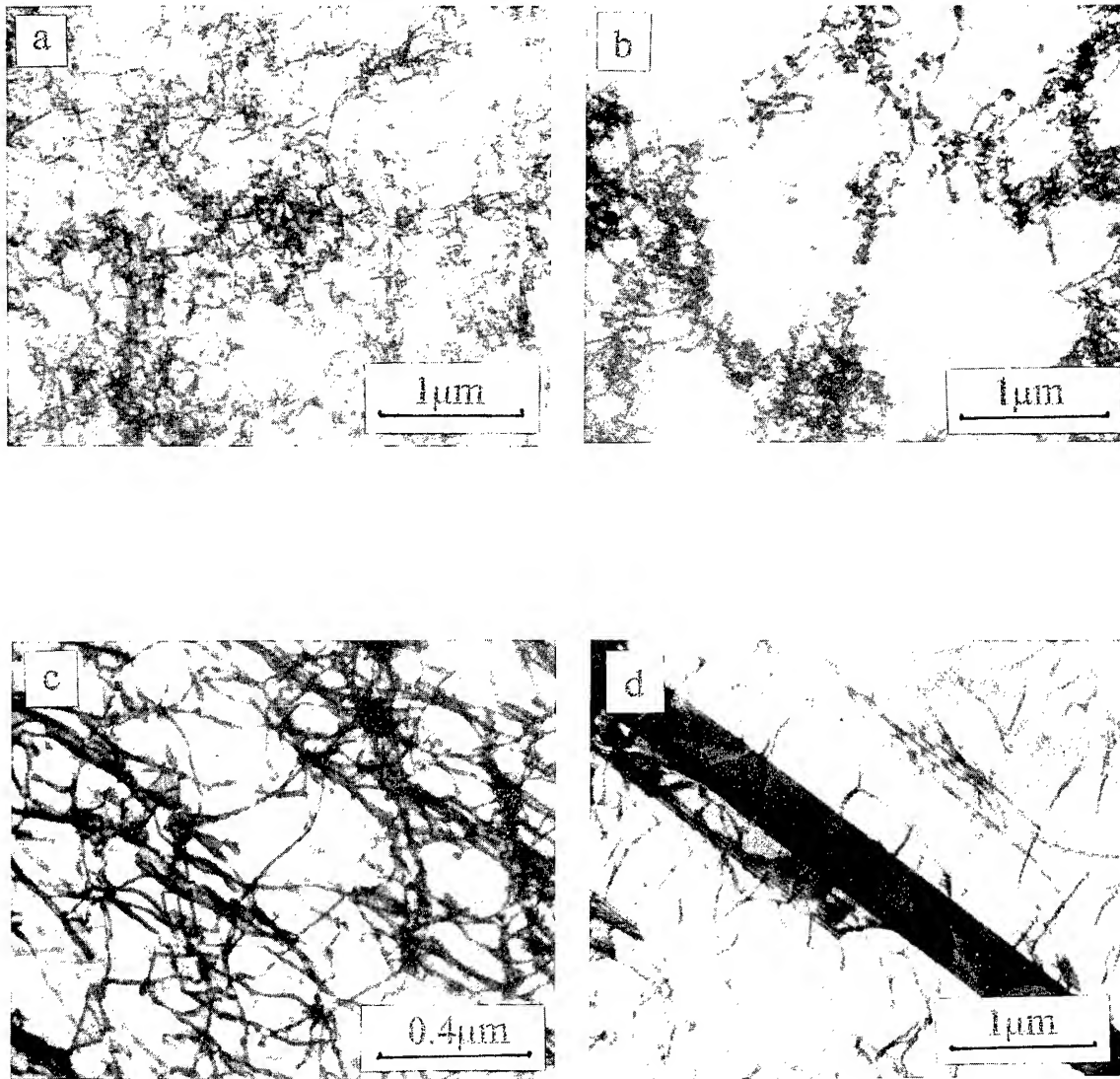


Fig.1 Structure of deformed copper (a,b) and austenite alloy 2 (c,d): a -  $\varepsilon = 4\%$ ,  $P = 0.1$  MPa; b -  $\varepsilon = 4\%$ ,  $P = 1.2$  GPa; c -  $\varepsilon = 4\%$ ,  $P = 0.1$  MPa, d -  $\varepsilon = 4\%$ ,  $P = 0.5$  GPa,

Despite small deformation value ( $\varepsilon = 4\%$ ), pressure results in essential ordering of dislocations  $\rho$ , namely general density of dislocations grows and a number of free dislocations inside the cells

decreases, the length of free moving of dislocation inside the cells  $r_m$  increases. The boundary itself between cells changes, the length of free portion of dislocations  $r_p$  there becomes less, the width of bo-

undary decreases  $V_p$ . Pressure results in cells freeing from dislocations with their departure to the boundaries.

In alloy 1 at deformation under HHP a quasi-cellular dislocation structure with high dislocation density at the cell walls is formed.

At 4% deformation of alloy 2 under atmospheric pressure and room temperature conditions, the general dislocation density increases from  $2 \cdot 10^7$  to  $7 \cdot 10^9 \text{ cm}^{-2}$ . The dislocation networks as well as an aggregate of dislocations are formed (Fig. 1c). At 4% deformation under high pressure (250 MPa), at the background of high dislocation density the deformation stacking faults (DSF) are seen which are formed at density packed planes  $\{111\}$ . Pressure increase to 500 MPa results in the formation of deformation twins (Fig. 1d).

Increase of deformation degree (and thus the increase of pressure under hydroextrusion) initiates new systems of slipping and twinning. The dislocation density at 20% deformation reaches  $10^{11} \text{ cm}^{-2}$ , there is also an increase in the volume fraction of deformation twins. The twin colonies are seen. The 50% deformation under HHP results in further increase of the density of twins and their dispersivity.

So, in the result of deformation under high pressure an ordered structure is formed in the studied materials. In materials with the SFE equal to 60 and 30  $\text{MJ/m}^2$  a cellular structure is formed. In alloys with a lower SFE value the processes of deformation twinning take place alongside with slipping. With the SFE decrease the role of twinning being the mechanism of plastic deformation under HHP increases. As a result, the share of twins increases (Table). Volume fraction of twins and the twin dispersivity grow also with pressure and deformation rate increase. This is because of the fact that HHP results, in such materials, in the increase of the equilibrium width of dislocation splitting, i.e. in the SFE lowering [5]. Lowering of the SFE, in its turn, decreases the critical stress of twinning onset [6].

Different structures formed at deformation under HHP give different level of mechanical properties of the studied alloys. With one and the

same degree of deformation ( $\epsilon = 50\%$ ) the strength properties of alloys with low SFE are essentially higher (Fig. 2). Formation of finely dispersed twin structure provides not only increase of the strength but it conserves rather good level of plastic characteristics.

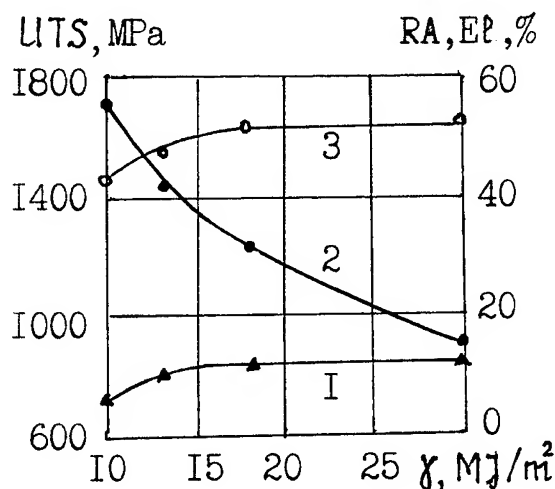


Fig. 2. Mechanical properties depending on the stacking fault energy of austenite alloys. 1 - the percent total elongation (El), 2 - ultimate tensile strength (UTS), 3 - the percent reduction of area (RA);  $\epsilon = 50\%$ .

## References

1. Trefilov V.I., Milman Ju.V., Firstov S.A. Physical bases of the refractory metal strength.- Kiev: Naukova Dumka, 1975, 325 pp.
2. Martynov E.D., Trefilov V.I., Firstov S.A. et. al. Dokl.Acad.Nauk SSSR, 1967,176, N6, p.1276-1277.
3. Ruff A.W.- Metall.Trans. 1970,1,p.2391-2413.
4. Brandon D.J., Komem J. Metallography. - 1970, v.3, №1, p.111-126.
5. Dulin M.A., Tokii V.V. Zaitsev V.I.- Metallophysica, 1975, iss.62, p.99-101.
6. Vishnyakov Ja.D. Stacking faults in a crystal structure. M., Metallurgiya, 1970, 480pp.

## THE STUDY OF PLASTIC DEFORMATION MECHANISMS OF HIGH-NITROGEN STEELS UNDER PRESSURE

A.S. DOMAREVA<sup>1</sup>, V.M. BLINOV<sup>2</sup>, A.A. DOBRIKOV<sup>1</sup>, V.N. VARJUKHIN<sup>1</sup>

<sup>1</sup> *Donetsk Physico-Technical Institute of Ukrainian National Academy of Sciences, 72,*

*R. Luxemburg-str, Donetsk, 340114, Ukraine*

<sup>2</sup> *Institut of Metallurgy of Russian Academy of Sciences, 49, Leninskii ov., Moscow, Russia*

### ABSTRACT

The microstructure and mechanical properties of austenite steels with above equilibrium nitrogen content after deformation under high hydrostatic pressure (HHP) were investigated. It has been shown that deformation under high pressure conditions of the studied steels is carried out by two mechanisms: slip and twinning. Twinning intensity increases with growth of pressure and deformation degree.

### Introduction

Nitrogen is the austenite - forming element, its addition to steel effects in a saving of nickel which is scarce. This also results in hardening of the solid solution. Steels containing nitrogen above the normal limit of solubility are principally new ones and possess some peculiarities.

The typical feature of high-nitrogen steels (HNS) is their high hardening ability under cold strain due to the low level of the stacking fault energy (SFE) [1]. Such steels, after the cold rolling or drawing, when total reduction is higher than 50 %, can obtain high strength (> 1800 MPa) with the value of single reduction not higher than 10...20 %. Use of high pressure liquid as a deforming tool makes it possible to realize high one-stage deformations without material failure to obtain articles in the nonmagnetic state of better quality of the surface [2]. In its turn, deformation under HHP is an effective way for the austenite steels defect structure formation providing an increased level of mechanical characteristics [3]. These features are extremely suitable for treatment of steels with high nitrogen content.

### Experimental details

This paper studies the influence of strain under high pressure on hardening and structure peculiarities of austenite steels, consisting (wt. %)

0.67 N and the following chemical compositions: 19 Cr - 10 Mn - 1.7 Si (steel 1) and 22 Cr - 15 Mn - 8 Ni - 1.3 Mo - 1 V (steel 2). Deformation of these steels were carried out by two methods: uniaxial compression with deformation degrees  $\varepsilon = 0...50$  % at atmospheric and high (P to 2.1 GPa) pressures and hydroextrusion at pressures up to 2.5 GPa with deformation degrees  $\varepsilon = 0...60$  %.

### Results and discussion

At plastic deformation under HHP of the studied steels high deformation hardening of austenite is observed. Change of the mechanical characteristics of the steel 1, depending on the degree of reduction under hydroextrusion, is shown in Fig 1. As is seen in Fig 1, the yield strength ( $Y_{So,z}$ ) of investigated steel at nonmagnetic state increases up to three times, ultimate tensile strength (UTS) increases for two times and attains values 2000 MPa, the percent total elongation (El) decreases up to 9%, the percent reduction of area (RA) decrease up to 53%. Value of diamond (pyramid) hardening (HV) is 4900 MPa (Fig.2).

The peculiarities of plastic deformation and strain hardening of HNS depending on scheme of strain-stress state were studied. It has been shown that deformation under HHP results in a more intensive hardening of nitrogen steels than at atmospheric pressure (compare curves 1 and 2 in



Fig 2). At hydrostatic extrusion the hardening effect is larger as compared with the case of the uniaxial compression under the high pressure conditions

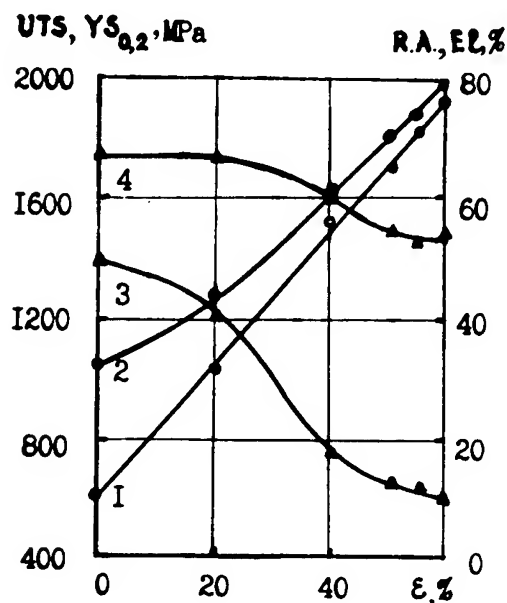


Fig 1. Dependence of the mechanical properties of steel 1 on the degree of reduction  $\varepsilon$  after hydroextrusion. 1 -  $YS_{0.2}$ ; 2 - UTS; 3 - EI; 4 - R.A.

(compare curves 2 and 3 in Fig 2). This is evidently explained by a favourable scheme of the stressed state at hydrostatic extrusion which becomes close to the scheme of the uniform compression. The bulk compression hardens the material, decreases the effect of the embrittling action of tension stresses occurring under non-uniform deformation, prevents the intercrystallite deformation which results in quick failure of metal.

High deformation hardening of HNS is connected with the change of their structure in result of deformation. Deformation of HNS under high pressure conditions is carried out by two mechanisms, they are slip and twinning. Twinning intensity increases with growth of deformation degree. HHP favours a more earlier and intense twinning as compared with deformation at atmospheric pressure (Fig 3). This can be explained as follows, HHP decreases the SFE in such materials [4], which makes the processes of the deformation

twinning formation easier. As a result, a disperse twinning structure is formed which gives the combination of the high level of strength and plasticity.

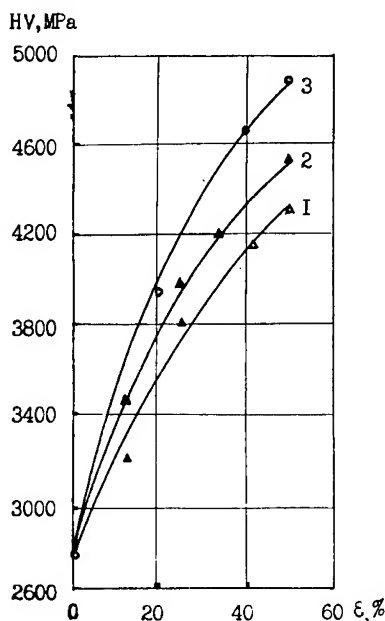


Fig 2. Dependence of the diamond (pyramid) hardening (HV) of steel 1 on the degree of reduction under various types of deformation. 1 - uniaxial compression at atmospheric pressure; 2 - uniaxial compression at high pressure (P up to 2.1 GPa); 3 - hydroextrusion (P up to 2.3 GPa).

## References

1. O.A. Bannykh, V.M. Blinov. *Dispersion hardening nonmagnetic vanadium containing steels*. - M.: Nauka, 1980. - 190 p.
2. B.I. Beresnev, K.I. Yezerskii, E.V. Trushin et al. *High pressures in modern techniques of material treatment*. - M.: Nauka, 1988. - 145 p.
3. A.A. Galkin, V.I. Zaitsev, A.A. Dobrikov, A.S. Domareva. *Dokl. AN SSSR*, 253, 92 (1980).
4. M.A. Dulin, V.V. Tokii, V.I. Zaitsev. *Metallofizika*. 62, p. 99 (1975).

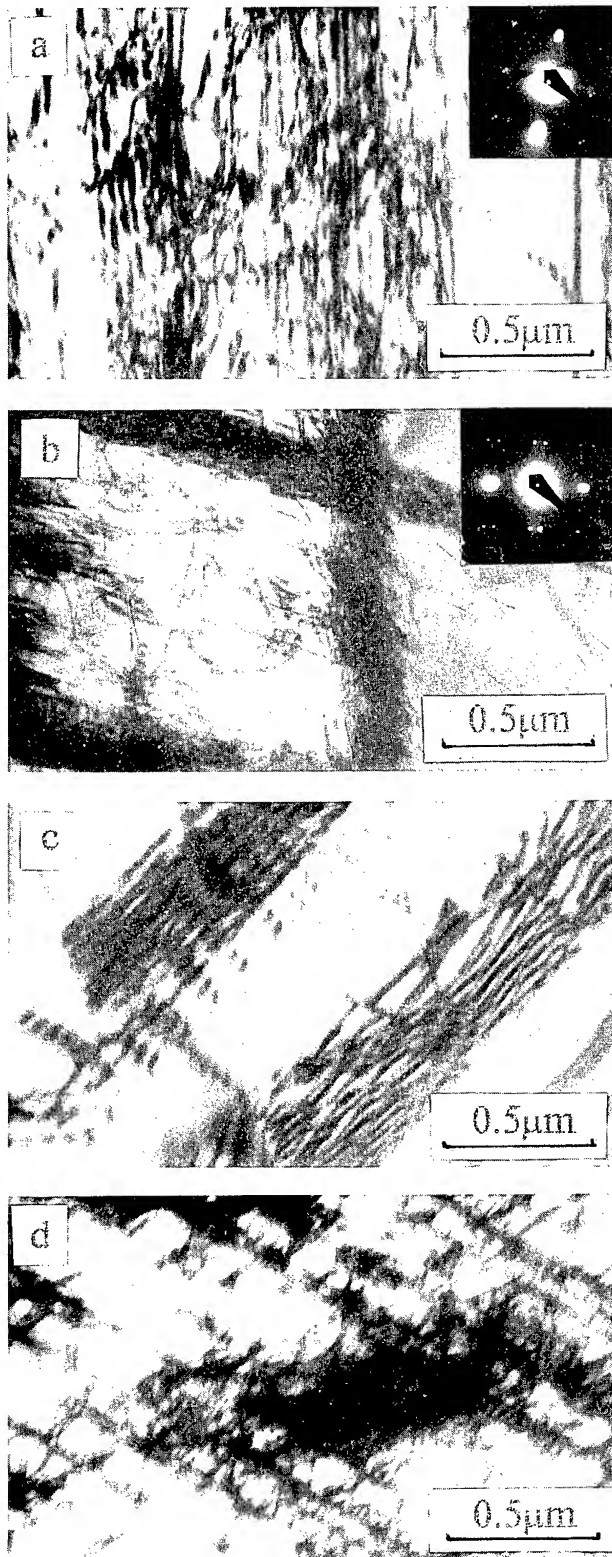


Fig 3. Structure of steel 1 after deformation (uniaux compression). a -  $\epsilon = 5\%$ ,  $P = 0.1$  MPa; b -  $\epsilon = 5\%$ ,  $P = 1.7$  GPa; c -  $\epsilon = 10\%$ ,  $P = 1$  MPa; d -  $\epsilon = 10\%$ ,  $P = 2.0$  GPa.

# COMPRESSION AND THERMAL EXPANSION OF SPLAT-QUENCHED $\text{Ni}_3\text{Al}$ TO 5 GPa AND 900°C

J.W.OTTO<sup>#</sup>, J.K.VASSILIOU<sup>†</sup>, T.PEUN<sup>‡</sup>, G.FROMMEYER<sup>¶</sup>, and E.HINZE<sup>§</sup>,

<sup>#</sup>*FB Physik, Uni-GH-Paderborn, D-33095 Paderborn*, <sup>†</sup>*Dept. Physics, Villanova University, Villanova, PA 19085, USA*, <sup>‡</sup>*Geoforschungszentrum Potsdam, D-14473 Potsdam*, <sup>¶</sup>*MPI Eisenforschung, D-40237 Düsseldorf*, <sup>§</sup>*Inst. Lithosphärenforschung, Uni Giessen, D-35390 Giessen*

## ABSTRACT

Splat-quenched  $\text{Ni}_3\text{Al}$  was studied under elevated pressures and temperatures in a multi-anvil device using energy-dispersive x-ray diffraction with synchrotron radiation. No evidence was found for a phase transition. The bulk modulus ( $B_0 = 164.5 \pm 4.5$  GPa) and the thermal expansion coefficients at 1.8 GPa ( $\alpha = 1.8 \cdot 10^{-5} \pm 0.1$  °C<sup>-1</sup>) and 3.3 GPa ( $1.9 \cdot 10^{-5} \pm 0.1$  °C<sup>-1</sup>) were determined.

## INTRODUCTION

$\text{Ni}_3\text{Al}$  belongs to a class of intermetallic compounds which shares properties with both ceramics and metals. Among its industrially useful properties are the high melting point and low weight, improved oxidation resistance at high temperatures, increasing strength with increasing temperature and ductility in single crystals [1]. Many experimental and theoretical studies of its mechanical and elastic properties have been performed in order to improve its ductility in polycrystalline form. Since this requires retaining the high cubic  $L1_2$  symmetry, the stability of this phase is of particular interest. While shock-wave studies [2] and plastic deformation experiments [3] (both at elevated temperatures) have suggested the possibility of a structural instability to other close-packed superlattices, theory [4] and static compression experiments to 12 GPa at room temperature [5] have shown it to be very stable. However, the bulk moduli determined by theory and experiment do not agree closely and the static compression experiments carried out so far suffer from a large scatter in the data. For this reason, we have started a series of experiments to investigate the elastic properties and stability of  $\text{Ni}_3\text{Al}$  at high pressure and temperature.

## EXPERIMENTAL TECHNIQUES

The special experimental difficulties in x-ray

studies of  $\text{Ni}_3\text{Al}$  are its low scattering power (the lattice constant is only slightly larger than that of Ni (fcc)) and its high elastic stiffness. The former requires a large amount of very small crystallites, the latter the dilution of the sample in a hydrostatic pressure medium. We have started our experiments with a splat-quenched sample prepared at the Max-Planck-Institut für Eisenforschung. The splat was a 40-50  $\mu\text{m}$  thick foil of very small crystallites (resulting in good scattered intensity and statistics even in the volume of  $(40 \mu\text{m})^3$  of a diamond anvil cell). No evidence for disorder was found in the as-quenched material.

The foil was embedded between two pre-compressed discs of NaCl and placed flat in an assembly [6] for a MAX80 multi-anvil press [7]. The white x-ray beam from the synchrotron at HASYLAB (4.5 GeV, 120-60 mA positron current, station F2) collimated to 160  $\mu\text{m}$  H by 40  $\mu\text{m}$  V was parallel to the plane of the foil and perpendicular to the movement of the anvil. Scattering was observed at approx. 4.5° in the vertical direction with two slits of 80  $\mu\text{m}$  between sample and detector at a distance of 45 cm.

Temperature was measured with a Ni-Cr thermocouple with its bead 300-400  $\mu\text{m}$  vertically below the foil. This was done to avoid contamination and to minimize the effect of thermal gradients. No correction was made for the effect of pressure on thermocouple emf. The temperature

was controlled to within  $\pm 2^\circ\text{C}$  at low temperatures and to within  $\pm 4^\circ\text{C}$  at the highest temperatures. Pressure was determined from the lattice parameter of NaCl using the equation of state parameters of a second-order Birch-Murnaghan fit [8] to the data of [9]. We measured the pressure (at room temperature) under compression at different locations in the sample, and found a maximum difference of 1 kbar between pure NaCl and NaCl in contact with the foil. This is within the estimated experimental uncertainty in the determination of the relative volume ( $\pm 4 \times 10^{-3}$ ). Lattice parameters were determined by a least-squares refinement to 7 or 8 lines of both  $\text{Ni}_3\text{Al}$  and NaCl.

## RESULTS

The weak superlattice reflections (110), (210) and (211) of  $\text{Ni}_3\text{Al}$  were observed under all conditions indicating that no disordering took place (Fig.1). No evidence for a phase transition was

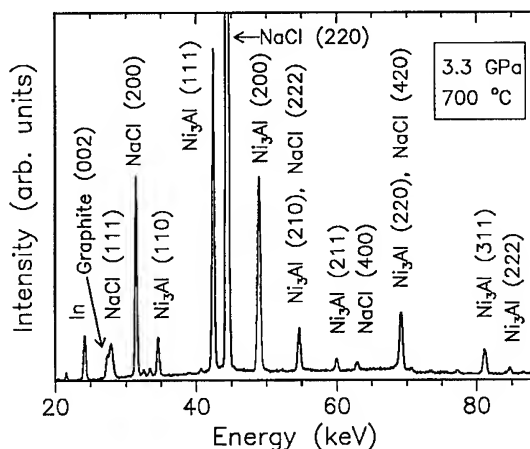


**Fig.1** Energy-dispersive x-ray diffraction spectrum of splat-quenched  $\text{Ni}_3\text{Al}$  embedded in NaCl (conditions: 3.3 GPa,  $700^\circ\text{C}$ , diffraction angle of  $4.5^\circ$ ). The relative intensities of the NaCl peaks are evidence of recrystallization. The graphite (002) reflection is caused by the heater surrounding the sample. The peak labelled "In" is indium fluorescence from the seal of the germanium detector crystal.

found. Preliminary results from diamond-anvil cell work at CHESS indicate that the  $\text{L1}_2$  struc-

ture is stable to at least 50 GPa. While the scatter of the pressure-volume data at room temperature is reduced in comparison with a previous study [5] (which employed a rotating anode, powdered  $\text{Ni}_3\text{Al}$  in a methanol-ethanol pressure medium in a diamond anvil cell, and determined pressure from ruby fluorescence), it still corresponds to roughly 1 GPa in pressure (Fig.2). This is due partly to the effects of the limited

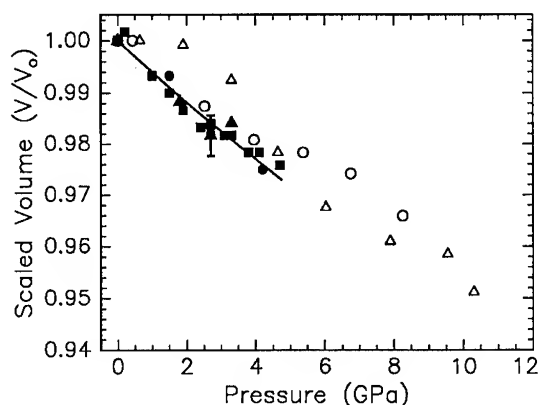


**Fig.2** Pressure dependence of the volume of splat-quenched  $\text{Ni}_3\text{Al}$ . The open symbols represent two runs of [5] on powder and the full symbols the experiments reported here (the full triangles represent each a different run). The solid line is a first-order Birch-Murnaghan equation of state fit to the present data yielding a bulk modulus of  $B_0 = 164.0 \pm 4.5$  GPa. The error bars represent an estimated absolute uncertainty in the scaled volume of  $\pm 4 \times 10^{-3}$ .

resolution of energy-dispersive diffraction when used with an incompressible material over a small pressure range, and partly to the presence of weak uniaxial stresses. A first-order Birch-Murnaghan equation of state fit to the present data yields a bulk modulus of  $B_0 = 164.5 \pm 4.5$  GPa compared with 185 GPa estimated from a straight-line fit in the previous study.[5] Previous ultrasonic measurements up to 1.4 GPa on oriented single crystals yielded the values  $B_0 = 169$  GPa and  $B'_0 = 4.88$  [10], whereas theoretical calculations give values around 210 GPa. [4] It should be noted that this is close to the value of the  $c_{11}$  elastic constant (223 GPa), while  $c_{12}$

(150 GPa) and  $c_{44}$  (123 GPa) are significantly lower. [10]

The thermal expansion of the splat-quenched  $\text{Ni}_3\text{Al}$  was determined at pressures of 1.8 and 3.3 GPa (Fig. 3). While the data show a fair amount of scatter, the thermal expansion at 1.8 GPa seems to be below the experimental resolution to 100 °C. This is currently being investigated at higher pressures. For temperatures above the Debye Temperatures (177 °C for Ni, 155 °C for Al [11] and 48 °C for NaCl [12]), the coefficient of thermal expansion is expected to be linear. Using a linear fit, the values obtained

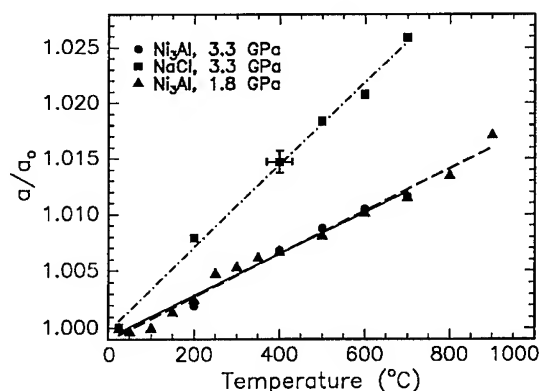


**Fig.3** Thermal expansion of splat-quenched  $\text{Ni}_3\text{Al}$  at pressures of 1.8 (circles) and 3.3 GPa (triangles), and of NaCl at 3.3 GPa (squares). Linear fits to the data yield the values  $\alpha = 1.8 \times 10^{-5} \pm 0.1 \text{ } ^\circ\text{C}^{-1}$  at 1.8 GPa and  $1.9 \times 10^{-5} \pm 0.1 \text{ } ^\circ\text{C}^{-1}$  at 3.3 GPa for  $\text{Ni}_3\text{Al}$  and  $3.7 \times 10^{-5} \pm 0.1 \text{ } ^\circ\text{C}^{-1}$  at 3.3 GPa for NaCl.

( $\alpha = 1.8 \times 10^{-5} \pm 0.1 \text{ } ^\circ\text{C}^{-1}$  and  $1.9 \times 10^{-5} \pm 0.1 \text{ } ^\circ\text{C}^{-1}$  at 1.8 and 3.3 GPa, respectively) are indistinguishable within experimental error. These values are in between those for Al ( $\alpha = 2.5 \times 10^{-5} \text{ } ^\circ\text{C}^{-1}$ ) and Ni ( $\alpha = 1.3 \times 10^{-5} \text{ } ^\circ\text{C}^{-1}$ ) at atmospheric pressure.[13] As a check, the thermal expansion coefficient of NaCl was determined at 3.3 GPa. The value obtained ( $\alpha = 3.7 \times 10^{-5} \pm 0.1 \text{ } ^\circ\text{C}^{-1}$ ) compares well with that at atmospheric pressure ( $\alpha = 4.0 \times 10^{-5} \text{ } ^\circ\text{C}^{-1}$ ) [14], but is larger than that obtained by [15] from a fit to their P-V-T data. A more complete analysis of the data extended to higher pressures will be presented elsewhere.

## References

- [1] J.H. Westbrook and R. L. Fleischer, *Intermetallic Compounds* (Wiley 1994).
- [2] D. P. Dandekar and A. G. Martin, in *Shock Waves and High-Strain Rate Phenomena in Metals*, ed. M. A. Meyers and L. E. Murr (Plenum 1981) p.573.
- [3] T. Suzuki, Y. Oya, and D. M. Wee, *Acta Metall.* **28** (1980) 301.
- [4] J. -h. Xu, B. I. Min, A. J. Freeman, and T. Oguchi, *Phys. Rev. B* **41** (1990) 5010.
- [5] F. A. Mauer, R. G. Munro, G. J. Piermarini, and S. Block, *J. Appl. Phys.* **58**, (1985) 3727.
- [6] Y. Kawashima and T. Yagi, *Rev.Sci-Instrum.* **59** (1988) 1186.
- [7] O. Shimomura, S. Yamaoka, T. Yagi, M. Wakatsuki, K. Tsuji, H. Kawamura, N. Hamaya, O. Fukunaga, K. Aoki and S. Akimoto in *Solid State Physics under Pressure* ed. S. Minomura (Terra 1985) p. 351.
- [8] F. Birch, *J.Geophys.Research* **83** (1978) 1257.
- [9] D. L. Decker, *J.Appl.Phys.* **42** (1971) 3239.
- [10] J. Frankel, J. K. Vassiliou, J. C. Jamieson, D. P. Dandekar and W. Scholz, *Physica B* **139 & 140**, 1986 198.
- [11] J. T. Lewis et al., *Phys. Rev.* **161** (1967) 877.
- [12] J. de Launay, in *Solid State Physics*, vol.2, ed. F. Seitz and D. Turnbull, (Academic Press 1956).
- [13] W. B. Pearson, *A Handbook of Lattice Spacings and Structures of Metals and Alloys* (Pergamon 1958).
- [14] G. K. White, *Proc.Roy.Soc.London* **A286** (1965) 204.
- [15] R. Böhler and G. C. Kennedy, *J. Phys. Chem. Solids* **41** (1980) 517.

#### **IV(D) Nanocrystalline Materials**

# HIGH PRESSURE RESEARCH ON NANOCRYSTALLINE SOLID MATERIALS \*

Wenhui SU <sup>a,b,c</sup>, Yu SUI <sup>a</sup>, Dapeng XU <sup>a</sup>, Fanlei ZHENG <sup>a</sup>,

*a. Group of Rare Earth Solid State Physics and Physics Department,  
Jilin Univ., Changchun 130023 P.R.China*

*b. International Center for Materials Physics, Academia Sinica, Shenyang 110015, P.R.China*

*c. Center for Condensed Matter and Radiation Physics, CCAST (World Lab.),  
P.O.Box 8730, Beijing 100080, P.R.China*

## ABSTRACT

In this paper, high pressure research results of recent years on nanocrystalline materials have been introduced. The preparation methods of the bulk nanocrystalline solid material(nanosolid), the transformation from free surface into interface among the nanoparticles, and the variations of microstructure as well as physical properties of nanosolid during the forming process under high pressure have been covered.

## I. Introduction

When particle size is reduced into nanometer scale (1~100nm), the particle is usually called nanoparticle and has many specific physical effects and properties because of its very large volume fraction of surface atoms[1~3]. Nanoparticle with many novel properties has become a new type of material having a wide application prospect. In order to use nanoparticle wider and better, the nanoparticles are usually compacted or sintered to form nanocrystalline solid material (nanosolid) that has a regular shape and a certain mechanical strength, but their nanoproperties are still preserved. While nanoparticles are compacted into nanosolid, their surfaces transform gradually into the interfaces of nanosolid, so the atoms in the nanosolid can be divided into two parts. One is those atoms locating in the nearly perfect lattice of nanocrystallites; the other is those atoms locating in the surface layer and interface region of nanosolid. It is not yet confirmed that whether the atomic arrangement in the interface region of nanosolid is in a completely disorder "gas-like" structure[4], or in a short-range order structure [5~7], or in a changeable structure mixed by order and disorder structure[8]. A lot of experimental results indicate that the interface atoms of nanosolid are in a unstable state with lower atomic density, higher atomic energy and wider distribution of interatomic distance than that of atoms in core of nano-crystallites[9]. Therefore, the external condition, especially pressure and temperature, can affect strongly the structure and state of interface atoms, and so that of nanosolid because of the very large volume fraction of interface atom in it.

In the compacting procedure under high pressure, nanoparticles undergo the transformation of nanometer material (microscopic dimension)→micro meter material

(mesoscopic dimension)→bulk material (macroscopic dimension), followed by a series of changes of micro-structure and physical phenomena. Therefore, it will be very important both for the basic research and practical application to study the regularity and microscopic mechanism of the effect of pressure on nanosolid.

In this paper, we introduce the recent progress in studying the effects of pressure on the structure and properties of nanosolid, including the work of our group.

## II. The preparation of bulk nanosolid material under high pressure

Several high pressure methods have been used to prepare bulk nanosolid material, such as: (1). compact immediately the nanoparticles obtained by other methods into nanosolid in high vacuum[10] or in atmosphere[11, 12]; (2). anneal the amorphous nanoparticles under high pressure to obtain bulk nanosolid by controlling the annealing temperature and rate[13, 14]; (3). prepare bulk nanosolid immediately by quenching the melting metal or alloy under high pressure[15]; (4). for some brittle matter that has obvious phenomenon of pressure-induced breaking of crystallites, prepare bulk nanosolid by compacting their bulk or micrometer materials immediately[16]; (5) prepare nanosolid or nanoparticle by the method of shock wave compression[17]. Though all these methods can be used to prepare the bulk nanosolid which people need in the study and application of nanosolid, the interface of nanosolid prepared by different methods will have different structure and state and will be polluted to various extent.

## III. The variations of nanosolid under high pressure

\* This project was supported by the National Natural Science Foundation of China, and the Science Foundation of the National education Commission of China.

### 1. The effect of pressure on the core structure in nanocrystallites of nanosolid

The bulk nanosolid material is usually prepared by compacting nanoparticles under cold or hot-pressing conditions, which the pressure ranges from 0 to 10GPa and the temperature is far below the melting point of conventional bulk material.

If materials have pressure-induced structural transformation in conventional bulk state, their nanosolids will undergo same structural transformation form under high pressure. However, the transformation pressure will increase notably with the reduction of crystallite size due to their increment of surface energy, such as the wurtzite to rock salt structural transformation in CdSe nanosolid (3.5→7.5GPa with size<2.2nm)[18] and monoclinic to orthorhombic transformation in ZrO<sub>2</sub> nanosolid (3.4→6.1GPa with size<30nm)[19].

For  $\beta$ -FeOOH nanosolids prepared by compacting nanoparticles(the average size is 12nm) in atmosphere under pressure up to 4.5GPa, the temperature of their heat-induced structural transformation ( $\beta$ -FeOOH→ $\alpha$ -Fe<sub>2</sub>O<sub>3</sub>) increases gradually with increasing pressure, from 203.8℃ at atmosphere to 274.0℃ under 4.5GPa, which approaches to that of bulk material (290.0℃)[20].

When  $\beta$ -FeOOH nanoparticles have been compacted under hot press, the form of their structural transformation are changed because high pressure suppresses the escape of OH<sup>-</sup> group in  $\beta$ -FeOOH nanosolids[20]. Under the condition of hot press(3.0GPa, 210℃ and 4.5GPa, 350℃), a new structural transformation from the  $\beta$ -FeOOH phase to the  $\alpha$ -FeOOH phase is observed; under 4.5GPa and 210℃, a new intermediate metastable phase in the above transformation can be obtained, which structure belongs to the tetragonal system ( $a=0.9953$ nm,  $c=1.0243$ nm). Therefore, high pressure can affect strongly the kinetics and dynamics of the heat-induced structural transformation nanosolid, and the instability of structure and state of interface atoms in nanosolid can also promote the occurrence of new phase and metastable phase under high pressure.

### 2. The effect of pressure-induced crystallite breaking on the microstructure and properties of nanosolid material

For some brittle matter binding with ionic bond mainly, it is easy to observe the pressure-induced crystallite breaking(PICB) phenomena in them. We have found that the crystallites of SrB<sub>2</sub>O<sub>4</sub>·Eu<sup>2+</sup> material were broken from micrometer to nanometer under high pressure[21]. It has been also observed that there are anomalous changes of magnetic and optical properties of CdS nanosolid caused by PICB[22,23]. Recently, we have also observed the PICB phenomenon in the

La<sub>0.7</sub>Sr<sub>0.3</sub>Mn<sub>1-x</sub>Fe<sub>x</sub>O<sub>3</sub> ( $x=0, 0.1$ ) nanosolids and the effect of breaking on the microstructure and properties of nanosolid[16].

The La<sub>0.7</sub>Sr<sub>0.3</sub>Mn<sub>1-x</sub>Fe<sub>x</sub>O<sub>3</sub> ( $x=0, 0.1$ ) nanosolids were prepared by compacting the nanoparticles synthesized by sol-gel method under 0.0~4.5GPa. The detailed analysis of the X-ray Diffraction(XRD) results shows that the core structure of nanoparticles does not change under high pressure, which are rhombic and cubic perovskite structure for  $x=0$  and 0.1 respectively, but the PICB in nanosolid has been observed obviously after the effect of microscopic strain has been deducted. For example, in the sample of  $x=0.1$ , the average crystallite sizes of nanoparticles along [110] and [111] direction decrease from 30nm of 0.0GPa to 18nm of 4.5GPa, and that along [100] and [211] direction decrease from 24nm and 20nm to 10nm under the same pressure. In their Transmission Electron Microscopy(TEM) micrographs, there are two breaking situations observed in nanosolid, in which a larger particle breaks into many smaller particles separately or many subcrystallites occur in a small particle, just as that found in literature[21]. Their Positron Annihilation(PAS) results also provide a strong evidence for the PICB of nanoparticles(see next section). The reason that La<sub>0.7</sub>Sr<sub>0.3</sub>Mn<sub>1-x</sub>Fe<sub>x</sub>O<sub>3</sub> ( $x=0, 0.1$ ) nanosolids can be broken easily under high pressure is mainly due to the strong ionic binding characteristics of this matter. Meanwhile, a large amount of oxygen ion vacancy caused by the partly substitution of Sr<sup>2+</sup> for La<sup>3+</sup> can also promote the occurrence of PICB.

In the PICB process of La<sub>0.7</sub>Sr<sub>0.3</sub>Mn<sub>1-x</sub>Fe<sub>x</sub>O<sub>3</sub> ( $x=0, 0.1$ ) nanosolids, the occurrence of a lot of new interface and the enhancement of disorder degree of interface atoms make the microstructure of nanosolid become more complicated, and this will affect strongly their properties. The Mossbauer spectra of these nanosolids show that the surface and interface component of nanosolids increase from 31.0% to 42.2% with increasing pressure from 0.0GPa to 4.5GPa, and the crystal environment of this part of Fe atoms become more and more asymmetrical. Correspondingly, the  $g$ -factor of the Electron Spin Resonance(ESR) spectral lines of nanosolids increases from 2.048(0.0GPa) to 2.092 (4.5GPa) because of the reduction of crystal symmetry of interface atoms. On the other hand, the decrease of crystallite size caused by PICB made the specific saturation magnetization of nanosolid decrease from 13.8e.m.u/g(0.0GPa) to 4.4e.m.u/g (4.5GPa), and made the resonance linewidth of ESR spectra decrease from 589Gs(0.0GPa) to 370Gs(4.5GPa) due to the reduction of magnetic dipole interaction. In a word, the PICB has increased greatly the number of interface of La<sub>0.7</sub>Sr<sub>0.3</sub> Mn<sub>1-x</sub>Fe<sub>x</sub>O<sub>3</sub> ( $x=0, 0.1$ ) nanosolids and then influenced seriously their microstructure and physical properties, though the crystal structure inside nanoparticles has not been changed.



### 3. The effects of pressure on the pore and defect in nanosolid material

In the compacting procedure of nanosolid under high pressure, the surface of nanoparticles changes gradually into the interface of nanosolid because of the contact among nanoparticles. At the same time, the pores and defects will form on the interface and vary obviously with increasing pressure, and then this must affect the structure and properties of nanosolid. The PAS measurements on nanosolids Pd and Fe have indicated that there are three kinds of defects on the interface of nanosolid, including the interface free volume, the microvoid and the large void with size of monovacancy, several vacancies and tens of vacancies respectively, and these defects have different compressibility under high pressure[24,25].

The PAS measurements of  $\text{La}_{0.7}\text{Sr}_{0.3}\text{MnO}_3$  nanosolids[16] show that there are also three types of defects in nanosolids which are consistent with the result of their TEM micrographs, as well as that in metal nanosolids observed by other people. Their lifetimes are  $\tau_1=151\rightarrow 171\text{ps}$  for the interface free volume and oxygen vacancy inside crystallites,  $\tau_2=301\rightarrow 340\text{ps}$  for the interface microvoid and  $\tau_3=662\rightarrow 2600\text{ps}$  for the larger void respectively with pressure of  $0.0\rightarrow 4.5\text{GPa}$ . The relative intensities of these defects, notated by  $I_1$ ,  $I_2$  and  $I_3$  respectively, indicate that  $I_2$  increases but  $I_3$  decreases rapidly under pressure below  $1.0\text{GPa}$ , and they all have no obvious change under higher pressure. These results mean that a large number of three-branch crystal boundary occurs through the collapse of larger voids and the contact among nanoparticles under low pressure. It is worth pointing out specially that  $\tau_1$  and  $\tau_2$  all increase with increasing pressure up to  $4.5\text{GPa}$ . This interesting phenomenon just indicates that interface free volume and microvoid are replenished continuously with larger defects because of the PICB in these nanosolids.

The PAS measurements of  $\text{NiFe}_2\text{O}_4$  nanosolids[16] show that there are only two types of defects, interface free volume and microvoid in three-branch crystal boundary, in nanosolid. With increasing pressure, the sizes of these defects all decrease, in contrast to the variations in nanosolids that have PICB effect[16].

### 4. The effect of pressure on the interface state in the nanosolid materials

In previous literature about the study of interface state in nanosolid, people's attention is usually focused on comparing the difference between nanosolid and uncompact nanoparticles by means of many methods [9,26~28]. However, to our knowledge, there is not yet detailed investigation so far about the pressure effect on the interface state of nanosolid. For those nanosolids in

which the core crystal structures do not change under high pressure, their interface structure and state and their properties as well can be changed strongly by pressure. Some examples have been observed in the studies of  $\text{NiFe}_2\text{O}_4$  and  $\beta\text{-FeOOH}$  nanosolids under cold pressure.

The structural studies of  $\beta\text{-FeOOH}$  nanosolids, which was obtained by compacting nanoparticles ( $3\sim 24\text{nm}$ ) under cold pressure below  $6.0\text{GPa}$ , have been reported in literature[29]. No obvious changes in the size distribution and structure of crystallites have been observed by TEM and XRD methods. However, the intensities of diffraction patterns in XRD spectrum of nanosolid compacted under  $6.0\text{GPa}$  are stronger than that of  $0.0\text{GPa}$ . Meanwhile, in the far-IR spectrum of the nanoparticles, many fine absorption structures with different intensities appeared near the four main absorption peaks corresponding to the lattice vibration of  $\beta\text{-FeOOH}$ . These fine absorption structures can be attributed to the vibration of surface atoms in nano-particles that have unsaturated atomic coordination. With increasing pressure, the intensities of these fine absorption structures will be reduced gradually but the intensities and frequencies of the four main peaks have no change. Under  $6.0\text{GPa}$ , nearly only the four main peaks are left in the spectrum. The results of XRD and IR spectra indicate that the structure in crystallites of  $\beta\text{-FeOOH}$  nanosolids does not change but the order degree of atomic arrangement on interface enhances and their coordination states tend to saturated state with increasing pressure. Therefore, the atomic structure in  $\beta\text{-FeOOH}$  nanosolids will undergo an evolution process with increasing pressure, from the surface of nanoparticle to the interface of nanosolid and then to the grain boundary of conventional bulk polycrystalline at last.

Other measuring methods, such as ESR, Mossbauer spectroscopy and Extended X-ray Absorption Fine Structure(EXAFS), have also been used to investigate the changes of interface structure and state of nanosolid caused by high pressure. In the ESR study of  $\text{NiFe}_2\text{O}_4$  nanosolids[30], it can be found that the resonance linewidth  $\Delta H$  and g-factor all increase gradually with increasing pressure at first and reach their maximum values under  $4.5\text{GPa}$ (from  $727\text{Gs}$  and  $2.30$  under  $0.0\text{GPa}$  to  $1031\text{Gs}$  and  $2.82$  under  $4.5\text{GPa}$ ), then turn to decrease slightly under higher pressure( $973\text{Gs}$  and  $2.78$  under  $6.0\text{GPa}$ ). These phenomena can be interpreted by the different variation laws of interparticle magnetic dipole interaction and the superexchange interaction between interface ions in nanosolids under high pressure. The magnetic dipole interaction can make  $\Delta H$  and g-factor increase and its magnitude is inversely proportional to the interparticle distance, but the superexchange interaction will reduce them and its magnitude is related to the order degree of arrangement of interface ions. Under lower pressure, nanoparticles are compacted to be in contact with each other to make the interparticle distance

decrease rapidly, and this results in the enhancement of magnetic dipole interaction. Under higher pressure, the interface ions are forced to arrange more order. At the same time, the reduction of interparticle distance becomes fewer and fewer because of the support among nanoparticles. Therefore, the superposition of these two interactions can lead to the above regular changes of  $\Delta H$  and  $g$ -factor. According to these variations, it can be concluded that interface atoms undergo a transition from nearly disorder state to order state to a certain extent with increasing pressure. This interpretation is also supported by the results of Mossbauer spectra of  $\text{NiFe}_2\text{O}_4$  nanosolids[16].

The superparamagnetic critical size of  $\text{NiFe}_2\text{O}_4$  at room temperature determined by Mossbauer spectroscopy is  $D_c=14.3\text{nm}$ . Therefore, the Mossbauer spectra of nanoparticles with average size  $D=8\text{nm}$  and  $12\text{nm}$  exhibit a single superparamagnetic quadrupole doublet and a complicated spectrum respectively, the latter superposed by a strong quadrupole doublet and a weak six-line magnetic hyperfine pattern because of the inevitable particle size distribution.

The Mossbauer spectra of  $\text{NiFe}_2\text{O}_4$  nanosolids with  $D=12\text{nm}$  show the pronounced pressure effect on their interface state. With increasing pressure, the magnetic hyperfine component enhances obviously while the doublet component is suppressed strongly. Under  $4.5\text{GPa}$ , the relative spectral area of magnetic hyperfine component has increased by 170% over that of uncompacted nanoparticles, and a pronounced asymmetrically broadening has appeared in this spectrum at lower field. The fitting parameters of these spectra are listed in table 1.

Under atmosphere pressure, the magnetic hyperfine component in the Mossbauer spectrum of uncompacted nanoparticles can be attributed to those particles whose sizes are larger than  $D_c$ . In the lattice inside these particles, iron atoms occupy in octahedral and tetrahedral sites in the same ratio, so the six-line part of spectrum is symmetrical and the hyperfine magnetic field of the two sites are lower than that of bulk material by 6~8% because of the collective magnetic excitation effect[31].

When nanoparticles are compacted under high pressure, the interparticle distance decreases rapidly and this leads to the enhancement of interparticle magnetic dipole interaction. This interaction energy adds to the magnetic anisotropic energy and this raises the potential barrier, which must be climbed over by the magnetization vector of particle in superparamagnetic state. This is equivalent to that  $D_c$  is reduced and the number of superparamagnetic particles in nanosolids decreases. Therefore, the superparamagnetic relaxation (SPMR) of  $\text{NiFe}_2\text{O}_4$  nanosolids would be suppressed under high pressure. Similarly, some one has found that the SPMR of ferrimagnetic  $\gamma\text{-Fe}_2\text{O}_3$  nanosolid was suppressed strongly

under  $1.3\text{GPa}$ , but no detailed explanation had been given[32]. However, other authors have observed pronounced suppression of the SPMR in antiferromagnetic  $\alpha\text{-Fe}_2\text{O}_3$  nanosolid but no change on that of  $\gamma\text{-Fe}_2\text{O}_3$  nanosolid under pressure of  $5.0\text{GPa}$ [33]. Consequently, the effect of pressure on the SPMR of nanosolid needs to be studied further.

Table 1 The fitting parameters of the Mossbauer spectra of  $\text{NiFe}_2\text{O}_4$  nanosolids

P (GPa)	0.0	2.0	4.5
QS(O)(mm/s)	0.06	0.12	0.14
QS(T)(mm/s)	0.31	0.23	0.10
QS(I)(mm/s)			0.73
H(O)(KOe)	483	482	481
H(T)(KOe)	462	453	452
H(I)(KOe)			377
W(O)(mm/s)	0.16	0.23	0.24
W(T)(mm/s)	0.33	0.34	0.55
W(I)(mm/s)			0.76
DA (%)	81.92	68.92	51.5
HA (%)	18.0	31.1	48.5

O: octahedral site T: tetrahedral I: interface  
W: linewidth H: internal magnetic field  
QS: quadrupole splitting  
DA: doublet spectral area  
HA: six-line spectral area

With increasing pressure, the magnetic hyperfine component becomes stronger and stronger because of the further enhancement of interparticle magnetic dipole interaction. At the same time, the relative position of interface ions are forced to adjust under high pressure and this leads to formation of superexchange coupling pairs of  $\text{Fe}^{3+}\text{-O-Fe}^{3+}$  and  $\text{Fe}^{3+}\text{-O-Ni}^{2+}$ . With the increase of number of the coupling pairs, the magnetic structure of interface ions becomes more and more order, so the asymmetrically broadening of the six-line spectrum in low field becomes more and more seriously. Under pressure of  $4.5\text{GPa}$ , a subspectrum can be clearly resolved with lower hyperfine magnetic field, larger linewidth and larger quadrupole splitting than that of Fe atoms inside lattice because interface atoms have a wider distribution of interatomic distance and atomic state, lower atomic density and weaker crystalline symmetry. The variations of interface atomic state under high pressure can be proved by the appearance of satellite peak with high binding energy in the  $\text{Fe}_{2p}$  photoelectron spectra of  $\text{NiFe}_2\text{O}_4$  nanosolids[16]. These results indicate that the order degree of interface atomic arrangement is improved and the number of stable superexchange coupling pairs among interface ions increases with increasing pressure, so the interface atomic structure and state will begin to transform into the grain boundary of

bulk polycrystalline material to a certain extent under high pressure.

The Mossbauer spectra at low temperature (220K and 110K) of  $\text{NiFe}_2\text{O}_4$  nanosolids compacted under 0.0GPa and 4.5GPa respectively show similar phenomenon[16] that the SPMR of nanosolid is suppressed strongly by high pressure at 220K, just as it at room temperature. Though the SPMR of nanosolids have disappeared completely at 110K, the asymmetrically broadening in low field still exists obviously, corresponding to the contribution of interface atoms.

The EXAFS measurements of  $\text{NiFe}_2\text{O}_4$  nanosolids[16] indicate that, under high pressure of 5.0GPa, the average coordination number and average bond length of all coordination shell of Fe atom increase relative to that of uncompact nanoparticles and tend to that of conventional bulk polycrystalline. However, there exists an obvious effect of high pressure on the parameter and shape only in the second and third coordination shells of Fe atom for the Fourier transform amplitude curve.

To sum up, there exists a nearly perfect atomic structure only in the first coordination shell for the interface metallic atoms in nanosolid. In higher coordination shells of interface atoms, there are wider interatomic distance distribution, weaker order degree of atomic arrangement, much more atomic state and poorer atomic structural stability than that in bulk material. With increasing pressure, the surface of nanoparticles transforms gradually into the interface of nanosolid and the order degree of interface rises and tend to the grain boundary of bulk polycrystalline. However, in those nanosolids that have remarkable PICB phenomena, the occurrence of a large number of new interfaces because of breaking will change the microstructure of nanosolid and lead to many abnormal properties. Therefore, the interface structure and state will play a decisive role in effect of the properties of nanosolids.

## Reference

1. R. E. Cavicchi et al., *Phys. Rev. Lett.* **52** (1984) 1453.
2. R. Kubo, *J. Phys. Soc. Jpn.* **17** (1962) 975.
3. P. Ball et al., *Nature* **355** (1992) 761.
4. X. Zhu et al., *Phys. Rev.* **B 35** (1987) 9085.
5. J. A. Eastman et al., *Nanostructured Materials* **1** (1992) 47.
6. M. R. Fitzsimmons et al., *Phys. Rev.* **B44**(6) (1991) 2452.
7. W. Wunderlich et al., *Script. Met. Mat.* **24** (1990) 403.
8. D. X. Li et al., *Mat. Lett.* **18**(1-2) (1993) 29.
9. H. Gleiter, *Prog. Mat. Sci.* **33** (1989) 223.
10. R. Birringer et al., *Phys. Lett.* **A102**(8) (1984) 365.
11. M. D. Matthews et al., *J. Am. Ceram. Soc.* **74**(7) (1991) 1547.
12. W. Wagner et al., *J. Mat. Res.* **6**(10) (1991) 2193.
13. C. Rachman *Nanostructured Materials* **1**(6) (1992) 479.
14. B. Yao et al., *Mat. Lett.* **22**(1-2) (1995) 81.
15. D. J. Li et al., *Nanostructured Materials* **4** (1994) 545.
16. The results of the present group, to be published.
17. Kondo Kenichi et al., *J. Am. Ceram. Soc.* **73**(7) (1990) 1983.
18. S. H. Tolbert et al., *Science* **265** (1994).
19. S. Kawasaki et al., *Solid State Comm.* **76**(4) (1990) 527.
20. Y. Sui et al., *Mat. Res. Bull.* (1995) in press.
21. W. N. Liu et al., (a) in *High-Pressure Science and Technology—1993. AIP Conference Proceedings* **309** Edited by S. C. Schmidt et al., (AIP Press, 1994), Pt 1, p437.  
(b) *Chin. J. High Pressure Phys.* **7**(3) (1993) 168.
22. D. P. Xu et al., *ibid* **21**(a) Pt 2 (1994) 1267.
23. X. Tong et al., *ibid* **21**(a) Pt 2 (1994) 1271.
24. H. E. Schaefer et al., *Phys. Rev.* **B38**(14) (1988) 9545.
25. R. Wurschum et al., *Nanostructured Materials* **2** (1993) 55.
26. T. Haubold et al., *J. Less-Comm. Met.*, **45** (1988) 557.
27. U. Herr et al., *Appl. Phys. Lett.* **50**(8) (1987) 472.
28. P. Ayyub et al., *J. Phys.* **C21** (1988) 2229.
29. Y. Sui et al., *Chinese Science Bulletin* (1995) in press.
30. Y. Sui et al., *J. Appl. Phys.* (1995) in press.
31. S. Morup, *Appl. Phys.* **11** (1976) 63.
32. P. V. Hendriksen et al., *Nuclear Instrument and Methods in Physics Research* **B76** (1993) 138.
33. J. Jing et al., *Hyperfine Interactions* **54** (1990) 571.

# PHYSICS OF AGING OF NANOPHASE ALLOYS: MÖSSBAUER INVESTIGATION OF NANOCRYSTALLINE IRON-COPPER PSEUDO - ALLOY

V.G.Gryaznov, A.G. Gavriluk, V.P.Filonenko and G.N. Stepanov  
*Institute for High Pressure Physics, Russian Academy of Science, Troitsk, Moscow  
Region, 142092, Russia*

## ABSTRACT

This communication considers structural features of nanocrystals synthesized on the base of high- pressure- consolidated mixed nanopowders. This system presents a mixture of mutually insoluble elements Fe and Cu (and pores amounting to several volume percents). The study aims to demonstrate quasi-stable state of nanocrystals and factors preventing their aging. Mössbauer and X-ray analyses show a strong dependence of phase composition of the Fe-Cu nanocrystalline pseudo-alloy on pressure and time duration. It is found that pressure coarsens phase inhomogeneities which existed previously in the as-synthesized Fe- Cu pseudo-alloy. Time duration is shown to affect the nanophase state in the same manner. It is argued that aside with typical parameters as the grain size, density, phase content of nanocrystalline substances, one should take into account prehistory of every sample: time duration, temperature conditions, pressure which has a marked influence on physical properties of nanophase compacts. It is observed that the Mössbauer - disorder in Fe- complexes, existing in the Cu- lattice, substantially depends on a magnitude of the pressure of compacting.

## I. HISTORY AND SAMPLE PREPARATION

Nanocrystalline materials, materials of the XXI century, show both unique physical properties and rather unstable internal structure [1]. This investigation considers aging phenomena in nanocrystals using a model system of mutually insoluble elements Fe- Cu. Nanopowders of Fe- Cu have been produced by the Evaporation- Condensation Technique [2]. Nanopowders of Fe-Cu have been mixed and compacted under a high pressure technique [3].

Two types of samples have been investigated.

Sample (I) - a mixture  $\text{Fe}_{0.15}\text{Cu}_{0.85}$ : which has been oxidized in air at normal conditions after synthesis and compacted afterwards.

Sample (II) -  $\text{Fe}_{0.19}\text{Cu}_{0.81}$ : has been placed into a rubber shell and then treated at hydrostatic pressure up to 2 GPa in a piston- cylinder high pressure camera [3].

Normally some methods for synthesis of Fe- Cu nanocrystalline pseudo- alloys are used: the Mechanical Alloying (MA) by ball-milling or rolling [4,5]; the Sol-Gel Route (SGR) [6]; the Evaporation - Condensation in an Inert gas Atmosphere (ECIA) [7]. The Fe- Cu pseudo-alloys produced by these methods revealed similar structure properties and, particularly, shapes of the Mössbauer absorption spectra [4,5,6,7]. However, this study shows unusual spectral parameters of as-treated pseudo-alloys.

## II. EXPERIMENTS

It has been found that behavior of the Fe-Cu pseudo-alloy sample (I) depends both on aging and high pressure treatments.

The aging of sample (I) results in appearing weak copper- oxide- reflexes on X-ray patterns. The main oxidation process was over in some minutes after

placing the sample from an inert gas atmosphere into air. The following oxidation seems to be a result of forming oxide phases from an oxygen solution in the copper nanograins.

Magnetic states of iron in the copper nanograins change with time. The spectrum of sample (I), aged during 8 months, is shown in Fig. 1(b). Fitting this spectrum was done for a sextet and two doublets. It is clearly seen from the figure that the paramagnetic subspectrum has strongly changed (compare with Fig. 1(a)). The relative content of single iron atoms in copper has decreased approximately by 10%. The relative contributions of dimers, atomic complexes and bulk clusters have markedly increased. A number of atoms in the complexes and bulk clusters has enhanced during aging due to diffusion.

Mössbauer spectra of sample (I) have been measured at helium temperatures after 4 - month aging (Fig. 1(c)) in order to demonstrate that the paramagnetic subspectrum was not caused by the superparamagnetism. The fitting of the experimental spectrum has been done for a sextet and doublet, since it was difficult to distinguish single and doublet lines for Mössbauer spectra measured at  $T=10\text{K}$ .

### Annealing

The Mössbauer spectra of the annealed sample (II) shows unusual features (Fig. 2). The spectrum is strongly broadened and asymmetrical. This fact is wonderful if one takes into account that there are no any visible changes in the X-ray pattern. The Mössbauer spectrum presented in Fig. 2 has been fitted by two subspectra: a sextet with small quadrupole interaction and a sextet with a large contribution of the quadrupole interaction  $\sim 5\text{mm/s}$ ! However, this fitting, perhaps, does not reflect adequately a real situation.

### Pressure influence on Fe-Cu pseudo-alloy

Treatment of the sample (I) at high pressure has given the same result like the aging. Mössbauer spectra have transformed in the same manner like in the case of the long- period aging. Mössbauer spectra of sample (I) treated with high pressures up to 4 GPa and 8 GPa are shown in Figs 3(a) and 3(b), respectively.

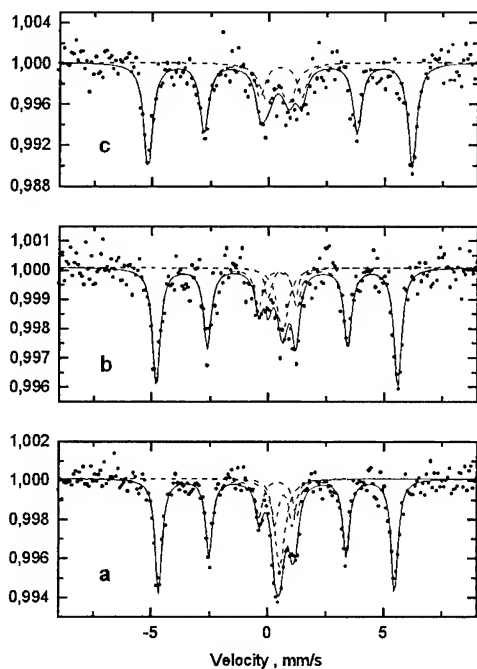


FIG. 1. Mössbauer spectrum of the sample (I). (a): just after production; (b): aging during 8 months; (c): at  $T=10$  K, aging four months.

From this spectra one can conclude that as in the case of a long- period aging the density of single iron atoms in the copper lattice depleted, the contribution of dimers, small- atomic complexes and bulk clusters increased; sizes of new nucleated clusters and bulk clusters increased also.

Hydrostatic high pressure prevented oxidation of the sample and stabilized pseudo- alloy nanostructure.

### III. RESULTS AND DISCUSSION

The results of experiments with sample (I) that has been aged during 8 months can be summarized as follows:

1) The amount of atoms in bulk iron clusters increases with aging. This conclusion follows from the

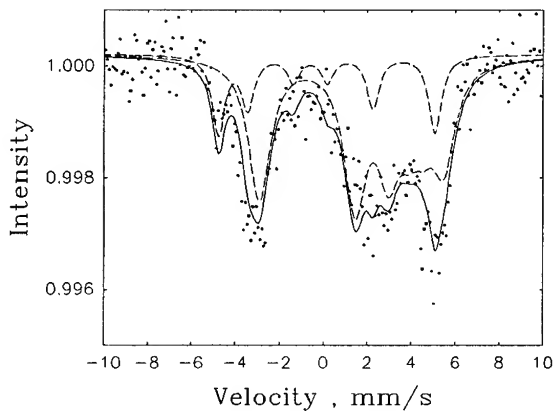


FIG. 2. Mössbauer spectrum for annealed sample (II). Annealing at 150 C during 1 hours.

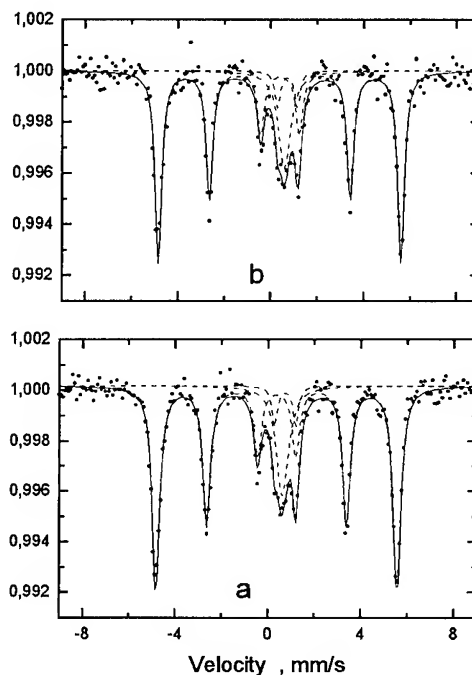


FIG. 3. Mössbauer spectra of the sample (I) treated with high pressures. (a): 4 GPa; (b): 8 GPa.

increase in the relative area under Fe sextet in Mössbauer spectra.

2) The size of the bulk iron clusters increases as it follows from a mathematical analysis of spectra in Figs. 1(a), 1(b) that show the enhancing of the magnetic field in the bulk clusters of the annealed sample (see [10]).

3) One can conclude that density of the small clusters increases contrary to decreasing the density of single iron atoms in the copper matrix with time.

The similar results have been obtained after the high pressure treatment up to 4 and 8 GPa.

Annealing of the sample type (I) during 1 hour at 150 C has resulted in full oxidizing Fe-Cu particles. Iron clusters have oxidized to the paramagnetic  $x\text{-Fe}_2\text{O}_3$  phase with an average size of clusters 50 Å [9].

The results of experiments with sample (II) can be summarized as follows:

1) High pressure treatment up to 2 GPa prevents oxidation of the sample and fixes the pseudo- alloy structure. High pressure and time aging influence the chemical structure of the Fe - Cu pseudo - alloy similarly: the density of single iron atoms in copper matrix decreases.

2) The X-ray data looks ideal which contradicts Mössbauer spectra showing the marked asymmetry. We believe that annealing provides relaxation of internal stresses in the sample resulting from compacting Fe-Cu nanopowder under high pressure. Relaxation gives rise to opening of free surface: voids and gaps, having dimensions comparable with initial size of the

consolidated nanoparticles of Fe and Cu. Presence of Fe atomic complexes in the these interfaces and nanopores causes the asymmetry of Mössbauer spectra (Fig. 4).

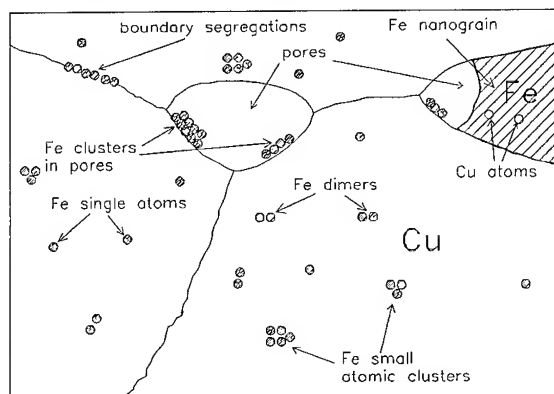


FIG. 4. Schematic structure of Fe-Cu pseudo- alloy.

ACKNOWLEDGMENTS. This investigation has been supported by the ICF grant No R51000.

## REFERENCES

1. V.G.Gryaznov and L.I.Trusov, Prog.Mater.Sci. **37**, 289 (1993)
2. M.Gen, and A. Miller, Surface (USSR) **2**, 150(1983).
3. V.P.Filonenko, private communication, (1995).
4. S. Nasu, S. Imaoka, S. Marimoto, H. Tahimoto, B. Huang, T. Tanaka, J.Kuyama, K.N. Ishihara, and P.N. Shingu, Mater. Sci. Forum **88-90**, 569(1992).
5. J.Kuyama, K.N.Ishihara and P.H.Shingu, Mater. Sci. Forum **88-90**, 521(1992).
6. A.Chatterjee, A.Datta, Anit K.Giri, D.Das, and D.Chakravorty, J. Appl. Phys. **72**, 3832(1992).
7. U. Herr, J. Jing, U. Gonser, and H. Gleiter, Solid State Commun. **76**, 197(1990).
8. Kundig W., Nucl. Instr. Methods **48**, 219(1967).
9. Yu. F. Krupyansky, and I.P. Suzdalev, JETP **65**, 1715(1973).
10. J. Eckert, J.C. Holzer, and W.L. Johnson, J. Appl. Phys. **73**, 131(1993).

## INFLUENCE OF PHYSICO-CHEMICAL TREATMENT ON THE SURFACE COMPOSITION OF NANOMETRIC DIAMOND

A. SMEKHNOV<sup>1</sup>, V. DANILENKO<sup>2</sup>, S. KUZENKOV<sup>1</sup>,  
B. PALOSZ<sup>3</sup>, S. GIERLOTKA<sup>3</sup> AND O. BUGAETZ<sup>1</sup>

<sup>1</sup>*Institute for Superhard Materials, National Academy of Sciences of Ukraine,  
2 Avtozavodskaya St., Kyiv, 252074 Ukraine*

<sup>2</sup>*Institute of Material Problems, National Academy of Sciences of Ukraine,  
3 Krzhizhanovsky St., Kyiv, 252142 Ukraine*

<sup>3</sup>*High Pressure Research Centre, Polish Academy of Sciences,  
29 Sokolowska St., Warsaw, PL-01-142 Poland*

### ABSTRACT

Thermochemical analysis, electron Auger spectroscopy and secondary ion mass spectrometry were used to study surface of powders of nanometric diamond produced by explosive decomposition of trotyl and hexagen. It was found that: (i) chemical processing in liquid oxidisers cleaned the surface of the explosion product from the silicon oxide and reduced the oxygen concentration, (ii) bombardment of the nanometric materials with argon ions graphitized the surface of the explosion product, (iii) oxidation of nanometric powders in air occurred at temperatures lower than oxidation of micron powders and the incombustible remainder appears to be a silicon oxide.

### Introduction.

It was indicated before [1, 2] that the formation of finely dispersed particles is possible during detonation of condensed explosive substances with a negative oxygen balance, i. e., of those which are decomposed with the release of free carbon. The pressure of hundred thousands atmospheres and the temperature of thousands degrees which characterise the detonation process correspond the area of thermodynamic stability of diamond phase on the P-T diagram of carbon.

The existing equipment allows to produce tens of kgs of nanometric diamond per one cycle. In order to define the scope of application of this unique material it is necessary to carry out the comprehensive research of its properties including its surface characteristics.

### Sample preparation and research methods.

The nanometric diamonds we studied were produced by explosive decomposition of trotyl and hexagen mixture. The explosions were set off in a closed volume and in an inert environment without any oxygen in the chamber to prevent burning of nanometric diamonds. The maximum speed of cooling of the explosion products was

provided. The pressure at the detonation front exceeded 20 GPa.

The nanometric diamonds produced were of grey colour with the particles density of 3,4 g/cm defined by gas pycnometry and 5 + 50 nm in size. The peak of the size-distribution curve of the particles is located in the area of 10 - 15 nm. The shape of the particles is close to sphere. The specific surface as defined by B.E.T. equals 200 m<sup>2</sup>/g.

The impurities composition of the initial samples was determined by emission spectroscopy (Fe, Si, Ti, Cu, Al, Mg, Mn), restoring extraction (O, N) and X-ray diffraction analysis (graphite). The samples contain Fe (0,3-0,7 %), Si (0,2-0,8 %), Ti, Cu, Al (in the amount of < 0,5 %), O (9-10 %), N (1-2%) and graphite (less than 0,5 %) as impurities.

During the research process the methods of X-ray diffraction analysis, Auger electron spectroscopy (AES), secondary ion mass spectrometry (SIMS) and thermochemical analysis were used. When using SIMS the primary ion beam was formed of argon (Ar). The analysis of the particles surface was conducted on LAS-3000. The complex thermal analysis was executed on Q-1500 D derivatograph

of MOM system when heating the surface with the speed of 10 degrees/min. The weighted amount made 20 mg.

### Results.

The X-ray diffractogram of nanometric diamonds contain the lines (111), (220), (311) which are typical of diamond cubic phase.

AES and SIMS methods were used for investigating the composition of the initial explosion product and the nanometric diamonds extracted after chemical processing, heating in hydrogen environment at the temperature of 850 °C and cleaning with a beam of argon ions. Table 1 displays the surface composition of the investigated samples which was determined using AES.

Table 1. Surface composition of the explosion product and the nanometric diamonds.

Processing	Concentration, at%			
	C	O	Si	Ar
explosion product	80	14	6	-
chem. processing 1	95,4	4,6	-	-
chem. processing 2	96,0	4,0	-	-
chem. processing 3	97,0	3,0	-	-
heating in H <sub>2</sub>	100,0	-	-	-
Ar <sup>+</sup> , 3 keV	97,6	-	-	2,4

Chemical processing 1 consisted of treating of the explosion product with hydrofluoric acid (HF). Chemical processing 2 was the processing of nanometric materials obtained after chemical processing 1 in the 3:1 mixture of muriatic (HCl) and nitric (HNO<sub>3</sub>) acids. Chemical processing 3 was the processing of nanometric materials after chemical processing 2 in the 1:1 mixture of chromic (H<sub>2</sub>CrO<sub>4</sub>) and concentrated sulphuric (H<sub>2</sub>SO<sub>4</sub>) acids.

As follows from Table 1., chemical processing 1 eliminates the silicon oxide from the particles' surface. Chemical processings 1 and 2 reduce the oxygen concentration. Heating in hydrogen removes oxygen from the surface of diamond. In the process of cleaning the surface with a beam of argon ions, the surface purification takes place and

the argon penetrates into the near-surface area. The spectra of the positive and the negative secondary ions of the samples after chemical processing 3 and heating them in hydrogen environment have the lines which correspond H<sup>±</sup>, Li<sup>+</sup>, <sup>10</sup>B<sup>+</sup>, <sup>11</sup>B<sup>+</sup>, C<sup>±</sup>, CH<sup>±</sup>, CH<sub>2</sub><sup>±</sup>(N<sup>+</sup>), CH<sub>3</sub><sup>+</sup>, O<sup>±</sup>, H<sub>2</sub>O<sup>+</sup>, Na<sup>+</sup>, C<sup>±</sup>(Mg<sup>+</sup>), C<sub>2</sub>H<sup>-</sup>, C<sub>2</sub>H<sub>2</sub><sup>-</sup>, C<sub>2</sub>H<sub>3</sub><sup>+</sup>, Al<sup>+</sup>, Si<sup>+</sup>, Cl<sup>-</sup>, C<sub>3</sub><sup>±</sup>, K<sup>+</sup>, Ca<sup>+</sup>, Cr<sup>+</sup>, Fe<sup>+</sup>. The line intensity corresponding to H<sup>±</sup> is decreasing after the annealing in hydrogen that can be explained by the elimination of the moisture from the surface as well as the groups having hydrogen which are absorbed by the surface of the nanometric material during its chemical processing. The annealing in hydrogen promotes the cleaning of the surface from metallic impurities which is testified by the weakening of the respective lines in the spectra of the positive secondary ions. The saturation degree of free (broken) links on the surface of the particles with hydrogen allows to conclude on the basis of the spectrum of the negative secondary ions that the intensity of the lines corresponding to C<sub>2</sub>H<sub>2</sub><sup>-</sup> considerably increased after heating in hydrogen.

The effect of the beam of argon ions on the surface of nanometric diamonds was studied in an ultrahigh vacuum chamber of analysis in LAS-3000. The radiation of Ar<sup>+</sup> ion energy was 3 keV. The spectra of Auger electrons were registered both for the initial sample and the sample after the next radiation stage. The argon concentration was determined by using the method of the coefficients of element sensitivity. It is stated that the argon content in the near-surface area of nanometric diamonds is nearly two times less than in a monocrystal of a synthetic diamond produced by spontaneous crystallization at the same radiation doses. [3]

The carbon KLL Auger spectra illustrate the state of the surface of the initial sample before and after the effect of the ion beam. The change in the fine structure of the spectrum in the low-energy area after irradiation testifies to the change in the surface structure. The spectrum of Auger electrons of the initial surface is close to the diamond spectrum. After the effect of the argon beam, the changes in the fine structure of the spectrum take place in the low-energy area and the Auger



spectrum takes the form typical of graphite[4,5]. Thus, the bombardment of the surface of nanometric diamond with an argon beam leads to the surface grafitization.

The effect of heating on the behaviour of diamond powders was studied in air when they were heated from room temperature to 650 °C. Both the initial samples and the samples heated in hydrogen were studied. The results of the complex thermal analysis of the samples under research allow to state that the temperature of the beginning of the oxidation process for the nanometric diamonds is lower than for the micropowders that can be explained by their higher specific surface. The specific features of the curves obtained from the differential thermal analysis and certain increase of mass on the TG curve in the range of 400-475 °C are explained by the reaction  $2C + O_2 = 2CO$  going on the surface and the formation of the sorbed CO layer. The oxidation start of the nanometric diamond heated in hydrogen is shifted to the area of lower temperatures (460 °C) as compared to the initial sample that can be explained by the absence of other impurities on the surface besides the hydrogen atoms, their desorption from the surface and the start of the oxidation process at reduced temperatures. The speed of the diamond oxidation after heating in hydrogen is increasing as well that is illustrated by the DTG curve. The oxidation of these samples is happening more intensively in narrower range of temperatures (460-610 °C) that comes from the DTG results. The oxidation process is accompanied by more intensive exothermal effect as compared to the initial sample.

The Auger spectra were obtained for the surface of the initial sample and the incombustible remainder after the thermochemical research. As the AES spectra illustrate, there is some oxygen on the surface of the initial sample in the amount of 4 at%, and the incombustible remainder contains carbon (29 at%) and silicon (51 at%). The position of the silicon energy peak corresponds to that of silicon oxide.

#### Acknowledgements.

The authors appreciate the help rendered by their colleagues from the Institute for Superhard Materials, L.Lavrinenko and Professor H. Bohatyreva in carrying out the research.

#### References

1. A.M. Staver, N.V. Chubarev et al., *FGV*, **3** (1984), 79.
2. G.I. Savvakín, V.L. Trefilov, *DAN SSSR*, **282** (1985), 67.
3. A.A. Smekhnov, S.P. Kuzenkov and S.N. Savchenko, *Electron Technology*, **27** (1994) 3.
4. O.P. Bugaetz, A.A. Smekhnov, S.P. Kuzenkov, *J. Elect. Spect.*, **68** (1994) 3.
5. V.G. Alyoshin, A.A. Smekhnov, H.P. Bohatyreva, V.B. Kruk. *Chemistry of Diamond Surface*, Kiev, Naukova dumka, (1990).

## **V Crystal Growth and Processing**

**V(A) Diamond**

# Numerical Simulation of The Growth Process of Diamond in The Temperature Gradient Method

Masao Wakatsuki, Wei Li and Xiaopeng Jia

Institute of Materials Science, University of Tsukuba, Tsukuba, Ibaraki 305, Japan

## ABSTRACT

Simulation for the temperature-gradient growth of diamond at high pressure and high temperature is tried on the basis of the growth rate which is limited by the diffusional transportation of carbon from the source to the growing diamond, through the molten metallic solvent. Characters of the growth processes are successfully reproduced qualitatively. Quantitative agreement is also excellent if each parameter of the growth process is properly selected. The calculated diffusion field can predict some phenomena which are accompanied with the growth process and actually observed in experiments. The simulation has further revealed an important character of the process, such as a growth rate peak which occurs in the early stage of the growth of the seed and is related to formation of inclusions.

## Introduction

Large single crystals of diamond are grown in molten metallic solvents for carbon at high pressure and high temperature, by the temperature gradient method[1]. It is believed that the growth rate of diamond in the metallic solvent is controlled by the transportation of the dissolved carbon through the solvent[2]. Getting sound crystals without containing the solvent material as inclusions, growing them in a reasonable period, having their shape as required, and any other problems to control the characters of grown diamonds are all dependent on proper control of the diffusion field surrounding the growing crystal. Its characterization by experiment is, however, very difficult because of the extreme conditions, and calculation will be helpful to make clear the detailed features of the diffusion field.

## Method of Calculation

The basic concept for the growth system is a disc-like metallic solvent contacted on its top surface to a carbon source (a lump of small diamond particles) having the same sectional area as that of the solvent. At the center of its bottom surface (the seed-bed surface), is located a small diamond seed crystal to be grown. In the present study, the growing crystal, which is surrounded mainly by the prevailing {100}-facets, is modeled

as a circular disk having the same surface area as that of the actual square seed, and the growth geometry has an axial symmetry.

Concentration distribution of the dissolved carbon is calculated on the basis of the diffusion equation,

$$D\nabla^2 c = \left(\frac{\partial c}{\partial t}\right), \quad (1)$$

where  $c$  is the carbon concentration,  $D$  is the diffusion constant and  $t$  stands for time. Temperatures at the source and the seed-bed surfaces of the solvent are fixed at given values, and the temperature distribution within the solvent is assumed to be kept unchanged during the growth period. As the initial condition, carbon concentration is zero at every point within the solvent, except for at the source surface, where it is kept at the solubility of diamond for the temperature there throughout during the growth period. The boundary condition at the wall surface is given so as to have no net flow of dissolved carbon, or  $(\partial c / \partial n) = 0$ ,  $n$  being a coordinate in the normal direction. While, on the growing crystal surface, the concentration is assumed to be equal to the solubility of diamond for the temperature at the concerned position. The normal growth rate,  $R$ , for a growing facet is deduced by the normal gradient,  $(\partial c / \partial n)$ , which is averaged over the concerned facet. That is,  $R = D \langle \partial c / \partial n \rangle / \rho_d$ , where  $\rho_d$  is the density

of diamond. The facet is displaced in a time interval  $DT$  by  $R \cdot (DT)$ , and gives a new boundary condition for the next step of calculating the field. The diffusion constant,  $D = 3.9 \times 10^{-5} \text{ cm}^2/\text{s}$  at 5.8 GPa and 1330-1400 °C, and the solubility of diamond,  $X_d[\text{wt \%}] = 4.2 + 0.00957(T[^\circ\text{C}] - 1270)$  at 5.8 GPa and 1300-1500 °C, were evaluated by our own experiments for an alloy solvent of Fe-Ni-Co (55:29:16 by wt).

### Application to Some Actual Cases

#### A Simple Case

The calculated results can reproduce some features of actual growth processes very well. In a simple case where a seed of 0.5 mm square was grown in a solvent of 2 mm $\phi$   $\times$  2 mm thick with temperature gradients of 36, 29 and 19 °C/mm, the crystal weight increased at an almost constant rate of 1.0, 0.87 and 0.52 mg/h, respectively. In the simulation, values of the diameter and the thickness of the solvent during the growth were adopted as those evaluated for the solvent recovered from the growth experiment (1.85 mm and 2.34 mm, respectively). The seed was assumed to be a disc of 0.6 mm $\phi$ . The simulated growth curves are almost linear with the weight increase rates of 1.06, 0.87 and 0.57 mg/h for the three temperature gradients, respectively. The excellent agreement shows the usefulness of the simulation in understanding the essential features of the growing processes.

#### Diffusion Field in Details and Growth Curves

Fig.1 shows the concentration distribution in a solvent of 6.4 mm $\phi$   $\times$  2mm, together with the size

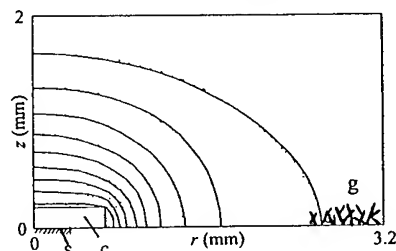


Fig.1 Calculated concentration distribution of carbon and the size of the growing crystal  
s: seed, c: growing crystal, g: graphite precipitation

of the growing crystal, at a growth time of 60 min. Based on the calculated diffusion field, some growth features can be deduced: ① The seed grows preferentially in the radial direction, resulting in a flat shape. ② The crystal weight vs time relation is curved with its slope increasing with the growing time, if the seed is small (0.6 mm $\phi$ ). However, the relation becomes linear with use of a large seed. ③ A region with high carbon concentration and low temperature appears in the peripheral zone of the seed-bed surface, which often drives metastable precipitation of graphite. All of these features correspond to observed facts in actual cases[3,4].

#### Appearance of A Peak in The Growth Rate

It has also been revealed by the simulation that there appears a large peak of a growth rate at an early stage of the growth process (Fig.2, curve (a)). The cause of this peak is now understood as a concentration of diffusional carbon flux onto a small area of the seed surface, followed by a rapid expansion (growth) of the crystal surface area.

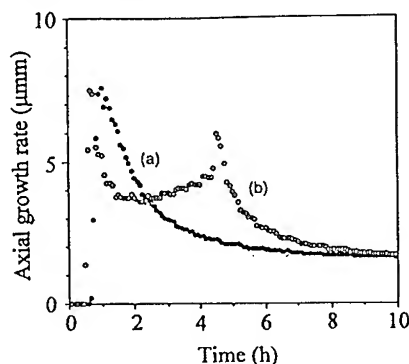


Fig.2 Peaks in the growth rate of the top facet.  
(a) conventional geometry, (b) two-stage geometry

Important features of the growth process can be deduced clearly by the present simulation even for some complicated systems, though quantitative agreement with experimental results are not always attained. Knowledge deduced from the simulation can lead us to be aware of unexpected facts related to the natures of the temperature-gradient process in some case, and it suggests improvements of the growth process as well. As for the growth rate peak mentioned above, it seems that the peak relates to formation of inclusions of the metallic solvent. That

is, suppression of the peak is an effective guiding principle for realizing a growth process that can give a crystal containing few metallic inclusions. The two-stage method[5], for growing large single crystals with an improved growth rate, is a successful example. Locating the seed in a recess, as illustrated in Fig. 3, the initial peak in the growth rate can be made narrow even with use of a small

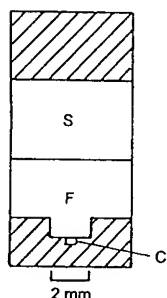


Fig.3 Sample geometry for the two-stage growth  
S: carbon source, F: solvent, C: seed crystal

seed. However, such a geometry induces another (second) peak at a time when the crystal comes out of the recess (Fig.2, curve (b)). For the best geometry determined as growing a crystal free from inclusions, the simulation gave the initial and the second peaks which are both small. The details will be reported elsewhere[6]. The two-stage method

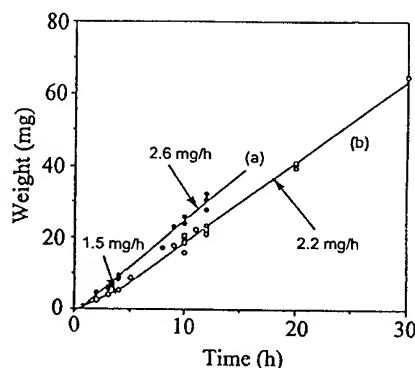


Fig.4 Growth curves for the conventional growth geometry (a) and the two-stage geometry (b)

gives a slope of the growth curve that is nearly the same as that for the conventional method, if the temperature-gradient is the same for the both method (Fig.4). The two-stage growth gives sound crystals, while in the conventional geometry, crystals contain a lot of inclusions if they are grown with a rate shown in Fig.4.

## Conclusions

Simulation was tried for studying detailed features of the temperature-gradient growth process at high pressure and high temperature. It can qualitatively reproduce very well the features of the process, such as the growth curve, the growth rate and the crystal shape. Quantitative agreement with results of experiments were excellent in some simple cases. The mechanism of the metastable precipitation of graphite, occurring together with the growth of diamond can also be explained on the basis of the calculated diffusion field of carbon in the solvent. Furthermore, the simulation made us be aware of an important character of the process, the peak of the growth rate, which was revealed to be related to formation of metallic inclusions in the growing crystal. Further improved calculation will reproduce, or predict, more detailed characters of the growing process. It is expected that the simulation can be applied for realizing an optimized process for growing crystals.

## Acknowledgments

The present study was supported by Grant-in-Aid for Scientific Research, The Ministry of Education, Science and Culture (02204002, 03204003 and 04204002).

## References

- [1] R.H.Wentorf, Jr: *Advances in High Pressure Research* Vol.4, ed. by R.H.Wentorf, Jr., Academic Press, London, 1974, pp. 249-281
- [2] H.M.Strong and R.E.Hanneman: *J. Chem. Phys.*, **46**(1967)3668
- [3] S.Vagarali, M.Lee and R.C.DeVries: *J. Hard Materials*, **1**(1990)233
- [4] M.Wakatsuki: in *Recent Trends in High Pressure Research*, ed. by A.K.Singh, Oxford & IBH Publishing Co., Ltd., New Delhi, 1992, 671-675
- [5] W.Li, H.Kagi and M.Wakatsuki: *Trans. MRS of Japan*, Vol.14B (Proc. IUMRS-ICAM93), Elsevier, Amsterdam, 1994, 1451-1454
- [6] W.Li, H.Kagi and M.Wakatsuki: *J. Cryst. Growth*, accepted for publication

# FORMATION OF DIAMOND BY DECOMPOSITION OF SiC

W. Li, T. Kodama and M. Wakatsuki

Inst. of Mater. Science, Univ. of Tsukuba, Tsukuba, Ibaraki 305, Japan

## ABSTRACT

Silicon carbide decomposes to form free carbon as diamond or graphite at the existence of diamond-forming solvent at high pressure and high temperature. When silicon is added to the solvent, the amount of free carbon decreases as the added silicon increases. The critical percentage of Si is determined as about 20 wt% at 1300 °C and 5.5 GPa for an alloy of Fe-Ni-Co. The solubility difference between Si and carbon into the solvent should be considered as the driving force for the formation of free carbon.

## Introduction

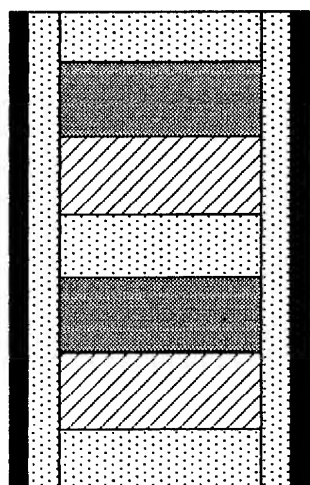
It is reported that diamond was formed from a system of silicon carbide (SiC) and Co metal at high pressure and high temperature [1]. We also confirmed that Fe-Ni-Co alloy gave the same reaction. It was also found that Ni-Mn-Co alloy was more effective in forming diamond [2, 3]. The mechanism of this kind of new reaction is unknown. Our aim is to make clear the mechanism, and to find the possibility for other carbides to form diamond.

It is expected that the driving force for the formation of free carbon is originated from the solubility difference between silicon and carbon into the solvent. Thus, we can expect that addition of Si to the solvent will influence the decomposition of SiC.

## Experimental procedures

Fig. 1 shows the sample assembly. Two kinds of experiments were carried out for characterizing SiC decomposition in the solvent. In the first, the amount of the

starting material SiC was kept constant (47.0 mg). Si powder was uniformly added to the solvent which was also a powder mixture of Ni, Mn and Co in a ratio of 70 : 25 : 5 wt%. The weight ratios of Si to the solvent was varied as 0, 5, 10, 15, 18, 20 and 30 wt%. The total weight of the solvent including Si was fixed at 235.0 mg, for every run of experiments.



2 mm  
Carbon heater Insulator  
SiC Solvent

Fig. 1 Sample assembly

In the second kind of experiments, the weight of SiC was changed while the amount of the solvent was kept constant. No Si was added to the solvent in this case. The weight ratios of SiC to the solvent were varied as 1 : 2, 1 : 3 and 1 : 4.

The samples were heated to 1300 °C at 5.5 GPa for one hour. The recovered samples were examined by SEM and x-ray diffraction. Then, they were treated in aqua regia to remove the metallic substances. The products were identified by powder x-ray diffraction. Finally, they were treated by HF acid, and all products except for carbon and SiC were excluded, and the residues were weighted.

Carbides of transition metals such as TiC, VC, Cr<sub>3</sub>C<sub>2</sub>, WC, Mo<sub>2</sub>C, TaC and NbC were treated with the above mentioned solvent and at the same P-T condition as in the case of SiC. The methods of processing and examination were the same, as well.

## Results and discussion

The results of the first experiments are summarized in Table I. By powder X-ray diffraction, it was found that, when Si percentage in the solvent was below 18 wt%, diamond or graphite was detected. However, when Si percentage was larger than 20 wt%, neither diamond nor graphite could be detected. By SEM and diffraction observation, it was found that, at 20 wt% Si, graphite particles became very limited in number or could not be found in some runs. When the content of the added Si was 30 wt%, neither diamond nor graphite could be observed. Therefore, there should exist a critical Si percentage for the formation of free carbon, and it is most probably around 20 wt%.

It was also found that, as the Si percentage increased, both the size and the number of diamond or graphite particles decreased. Measurement of the weight of the residues coincided with this result. This suggests a decrease in the driving force for the formation of free carbon as the amount of Si in the solvent increases.

Table I Results of the first kind of experiments.

Si wt%	SEM	x-ray diff.		SiC
	free carbon	diamond	graphite	
0	○	○	○	×
5	○	○	○	×
10	○	○	○	×
15	○	×	○	○
18	○	×	○	○
20	○	×	×	○
30	×	×	×	○



Another experimental fact is as follows. When Si added was less than 10 wt%, all of the starting material SiC was decomposed. Both diamond and graphite were detected in this case. However, when Si added was between 15 wt% and 18 wt%, part of SiC remained unchanged, and only graphite was detected. This phenomenon can be understood as supersaturation required for nucleation of diamond may be larger than that for graphite. The second kind of experiments showed that, all of SiC was decomposed in the case of SiC : solvent = 1 : 3, whereas part of SiC remained unchanged in the case of SiC : solvent = 1 : 2. Therefore, the critical condition for the free carbon to be formed should exist between these two cases. Because the ratios of 1 : 2 and 1 : 3 correspond to Si contents of 23 and 18 wt%, respectively, this result is consistent with the critical value of 20 wt%, obtained in the first kind of experiment.

Although there are no published data about the solubility of Si and carbon in the above described solvent, the present results show that the solubility of Si should be at least 20 wt%. On the other hand, it can be accepted that the solubility of carbon in the solvent does not exceed 10 wt% in this solvent. Difference between these solubilities drives the formation of the free carbon.

Carbides of the transition metals such as TiC, VC, Cr<sub>3</sub>C<sub>2</sub>, WC, Mo<sub>2</sub>C, TaC and NbC were not decomposed by the same solvent, nor did they give formation of diamond or graphite. Although the solubility of the transition metals in the solvent should be quite larger than that of carbon, addition of the transition metals

may also increase the solubility of carbon, making carbon difficult to be separated.

## Conclusions

1. In the reaction of forming diamond from the decomposition of SiC, the weight of free carbon decreased as the amount of Si added to the solvent increased. The critical percentage which gives no free carbon was determined as about 20 wt%.
2. The solubility of Si is larger than that of carbon in the solvent, and this solubility difference provides the driving force for free carbon separation.
3. There has been found no transition metal carbides which can separate free carbon at the same condition as in the case of SiC.

## Acknowledgment

The present study was supported by Grant-in-Aid for Scientific Research, The Ministry of Education, Science and Culture (04044033, 06919017 and 07044119).

## References

- 1 S-M Hong and M. Wakatsuki: *J. Mater. Sci. Lett.*, **12** (1993) 283
- 2 S-M Hong, W. Li, X-P Jia and M. Wakatsuki: *Diamond and Related Materials*, **2** (1993) 508
- 3 L. Guo, S-M Hong and Q-Q Guo: in *Advances in New Diamond Science and Technology*, ed. by S. Saito, et al., MYU, Tokyo (Proc. 4th ICNDST, Kobe, 1994), (1994) 513

## THERMOMECHANICAL STATE OF A HPA REACTION CELL AT THE GRAPHITE-TO-DIAMOND PHASE TRANSITION

A. A. LESHCHUK, N. V. NOVIKOV and A. P. MAYDANYUK

*V. N. Bakul Institute for Superhard Materials of the National Academy of Sciences of Ukraine  
2 Avtozavodskaya St., 254074 Kiev, Ukraine*

### ABSTRACT

A thermomechanical model of the graphite-to-diamond phase transition has been developed, taking into account thermodynamic criterion of phase transition. The problem on determination of temperature, stress and concentration fields in the reaction cell of the high pressure apparatus (HPA) and in the local diamond-melt-graphite system under diamond synthesis conditions is solved. The results demonstrate a interrelation of the solutions for the reaction mixture and for the local diamond-melt-graphite system.

### Introduction

Let us briefly consider the processes, which occur in a HPA reaction cell at the stage of heating and synthesis.

Before heating, the reaction cell is a compressed mixture (up to 4 – 5 GPa) of graphite and a metal-solvent. The cell is heated by passing electric current and, as a result, by evolving Joule heat [1]. In heating, there occurs the redistribution of the HPA stress state. With distinct parameters on pressure and temperature attained in the reaction cell, there initiate graphite-to-diamond phase transitions [2]. The zone of possible transformations should be determined on the graphite-diamond phase equilibrium diagram with account for hysteresis, i.e. the area around the equilibrium line, in which the phase transformations do not occur. Thus, there exists the interrelation between the processes of electrical conduction, nonstationary heat conduction, thermoelastoplastic straining and phase transitions in HPA in material synthesis.

### Numerical technique

The listed processes were considered for the whole HPA (first level) and for an individual diamond crystal growing in the liquid metal (second level). To describe the above processes on first level, a complete set of equations of a coupled problem on nonlinear nonstationary electrical and

heat conduction and thermoplasticity with due account of material phase transitions has been formulated. Each point of the volume is considered as an  $N$ -component mixture of different materials. All equations are written for effective values of physico-mechanical constants.

The above set includes:

- Equation of quasi-stationary electrical conduction.
- Equation of nonlinear nonstationary heat conduction.
- Equations of plastic flow rule for a model of an isotropic thermoelastoplastic material with account of finite elastic, plastic and phase deformations.
- Equations of phase transition, which include a kinetic equation for the rate of changes in diamond mass concentration, which is valid in the region of a possible diamond synthesis, i.e. in the region where the condition of pressure excess over transition pressure and the condition of metal-solvent melting are satisfied.

The coupling of the above equations is caused by the following dependences: of physico-mechanical characteristics on pressure, temperature and phase concentration; of field of Joule heat sources on temperature; of concentration fields on temperature and stress distributions. In addition, the following physical and geometric nonlinearities are taken into account: temperature

dependence of thermophysical properties; pressure dependence of elastic and plastic properties; the presence of finite strains caused by phase transitions.

The reaction mixture is considered as a stochastically inhomogeneous composite material, efficient characteristics of which are defined from the model of a generalized singular approach of the random function theory.

For the second level, we take the following calculation scheme: a spherical diamond crystal surrounded by spherical layers of metal-solvent melt and graphite. The pressure at any point of reaction mixture determined from solving the problem for the first level is applied to outer surface of graphite. Then, the thermodynamic criterion of phase transition is entered, which takes into account inhomogeneity and nonhydrostatic character of the stress-strain state in the diamond-melt-graphite system and describes the hysteresis area of transformations.

To solve the problem stated, an appropriate algorithm has been devised. The principle of the algorithm is the successive solution of the following interrelated problems at each time step: first, the problem on electrical conduction is solved and the field of the electric potential is defined. Then, the field of density of Joule heat sources is defined from the electric potential field after which we solve the problem on heat conduction and define the temperature increment; knowing the temperature increment, we solve the thermoelastoplastic problem and define the distribution of components of stress tensor and pressure; knowing temperature and pressure fields, we calculate the region of the possible diamond synthesis, and in each element of the region we integrate the equation for the rate of diamond mass concentration changes and define its increment.

## Results

Let us turn to the consideration of the problem on the modelling of the diamond synthesis process. The data on a compressed state of the reaction cell have been taken as initial ones. From the solution,

we have obtained the fields of temperature, pressure and diamond concentration with synthesis time. The temperature field features a pronounced nonuniformity: temperature gradient along the vertical axis of the reaction zone is  $150^{\circ}\text{C}$ , and along the horizontal axis is  $50^{\circ}\text{C}$ . At the initial instant of synthesis time, the pressure field shows a lower nonuniformity. With diamond growing, however, the pressure drops and nonuniformity of its distribution increases. Diamond growth initiates from the center of HPA in the direction to the reaction zone periphery, which agrees with the experiment. At first the transition pressure is assumed to be equal to the equilibrium one, i.e. hysteresis of transformation is not taken into account (Fig. 1, line 1). At some instant of time the diamond growth is terminated. This corresponds to

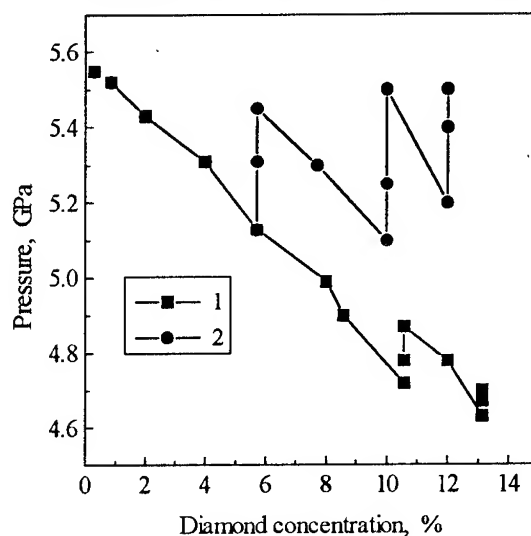


Fig. 1. Pressure changes in the center of the reaction mixture during diamond synthesis with (2) and without (1) regard to hysteresis of the graphite-to-diamond phase transformation.

the pressure drop below the graphite-diamond equilibrium line. Next, an interesting thing is observed: at a constant concentration of diamond the pressure at the point under consideration increases. This is attributed to the rise in temperature and the increase in the system rigidity, but what is more important — to the phase transitions at the points of the reaction zone which are adjacent to the one under consideration, on condition that the force in a horizontal section of HPA is constant. Then the

point appears in the diamond stability region, the diamond growth is recommenced, the pressure drops and so on. In this manner the phenomenon of pressure self-regulation in proximity to the graphite-diamond equilibrium line is simulated.

The pressure change during diamond synthesis with regard to hysteresis of transformation is given by line 2 in Fig. 1. The considerable differences of these results in comparison with the first variant of phase transition conditions are obtained. These differences attain the pressure of 0.2 to 1.0 GPa.

The kinetics of pressure change in the center of the reaction mixture and in the diamond crystal is shown in Fig. 2. The pressure in diamond crystal practically always increases that can be explained by the increase in the rigidity of the diamond-melt-graphite system and by the stress concentration near the melt-graphite phase boundary. The obtained results point to significant differences between the effective pressure in the reaction mixture and the pressure in the diamond crystal.

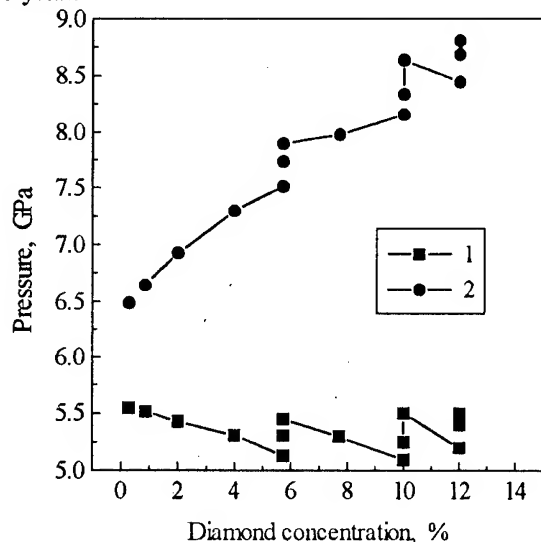


Fig. 2. Pressure changes in the center of the reaction mixture (1) and in the diamond crystal (2) with regard to hysteresis of the graphite-to-diamond phase transformation.

The stress distributions in a local diamond-melt-graphite system (Fig. 3) indicate the presence of inhomogeneity of the internal stress energy. These data are used for determination of

hysteresis area of the graphite-to-diamond transformation, when simulating the process of diamond synthesis in the reaction mixture. In such a way, the relation between the solutions for a reaction mixture and local diamond-melt-graphite system is realized.

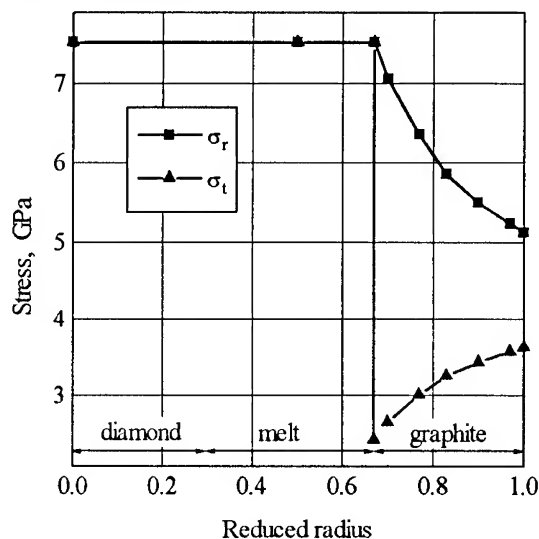


Fig. 3. Distribution of radial  $\sigma_r$  and hoop  $\sigma_t$  stresses in the diamond-melt-graphite system at the pressure of 5.13 GPa and diamond concentration of 5.7%.

To clarify the influence of phase transitions on thermostressed state of HPA, a similar problem has been solved but without regard for phase transitions. The following discrepancies between the results have been obtained: in volume of the zone of a possible diamond synthesis — about 20%, and in pressure — about 1 GPa.

Thus, the solution of the problems considered supports the need for an obligatory allowing for the coupling of the processes and the hysteresis of the phase transformations, when simulating physico-mechanical state of the HPA reaction cell.

## References

1. N. V. Novikov, V. I. Levitas, and A. A. Leshchuk, *Soviet J. of Superhard Materials* 6, No. 4 (1984) 1.
2. N. V. Novikov, V. I. Levitas, A. A. Leshchuk, and A. V. Idesman, *High Pressure Research* 7 (1991) 195.

# NUCLEATION AND GROWTH OF DIAMOND IN Fe-Co SOLVENT AT HIGH PRESSURE AND HIGH TEMPERATURE

T.SUGANO, N.OHASHI, T.TSURUMI AND O.FUKUNAGA  
Department of Inorganic Materials, Tokyo Institute of Technology  
Ookayama, Meguro-ku, Tokyo 152, Japan

## ABSTRACT

Nucleation and growth stage of diamond in the Fe-Co alloy solvent was examined by observing grown diamond crystals treated at 6.2 GPa and between 1150 °C and 1440 °C. It was found that below 1310 °C, dissolution and precipitation of diamond was observed and growth rate was very low, while between 1320 °C and 1400 °C stable diamond growth on the seed was observed. At 1420 °C, unstable dissolution and precipitation was observed. These data suggested that optimum growth condition of diamond crystal was limited in narrow temperature range in this system.

## INTRODUCTION

Although diamond crystal grow in an alloy solvents at HP/HT, nucleation and growth stage of diamond has not been observed extensively. In this report, we present an experimental result of nucleation and growth process of diamond on the seed crystal. We used Fe-Co solvent which is a typical alloy to grow diamond. It was found that small crystalline diamonds of about 20  $\mu\text{m}$  in size were precipitated on the (100) face of the seed crystal when temperature was below 1310 °C at about 6 GPa, whereas layer growth on the seed crystal was observed above 1310 °C. The boundary temperature 1310 °C corresponds to the decomposition of metastable cementite.

## EXPERIMENTS

Cell assembly[1] for the temperature gradient growth of diamond was adopted in this experiment using FB25 type belt apparatus. Temperature and pressure was estimated based on the diamond forming region of Ni-C system.[2] The Fe-Co solvent was prepared by sintering a mixed powder in a vacuum at about 1100 °C.

## RESULTS AND DISCUSSION

### (1) Morphology of the Seed Crystal Recovered from HP/HT Run

The (100) surfaces of the seed crystal contacted to

the solvent showed dissolution and precipitation patterns. As shown in Fig. 1(a), the (100) surface dissolved into the Fe-Co solvent at 1312 °C at 6.2 GPa but small precipitated new diamond hills are observed on a higher magnified surface shown in Fig. 1(b). When growth temperature was increased, the seed crystal dissolves but new diamond layer was grown by the carbon supply from the source zone. The surface of the seed crystal was more smooth. These morphological observations of the seed crystals suggested that dissolution of the seed is preferential at temperature region below 1310 °C and the size of the precipitated diamonds are ranging 5-10  $\mu\text{m}$  in size. The surface of the seed crystals are smooth in the temperature range between 1310 and 1350 °C, but seed crystal dissolve much at about 1400 °C.

### (2) Observation of the Grown Diamond

The grown diamond part was observed with seed crystal and solvent zone as shown in Fig. 2(a) and (b). As the seed crystal was embedded in the salt plate, the molten solvent was penetrated into the seed crystal with dissolving the seed thus the shape of the solvent is similar to the shape of the seed. New diamond zone was grown on the residual seed. The interface between the seed and the grown diamond was very smooth. When temperature was increased, residual amount of the seed was

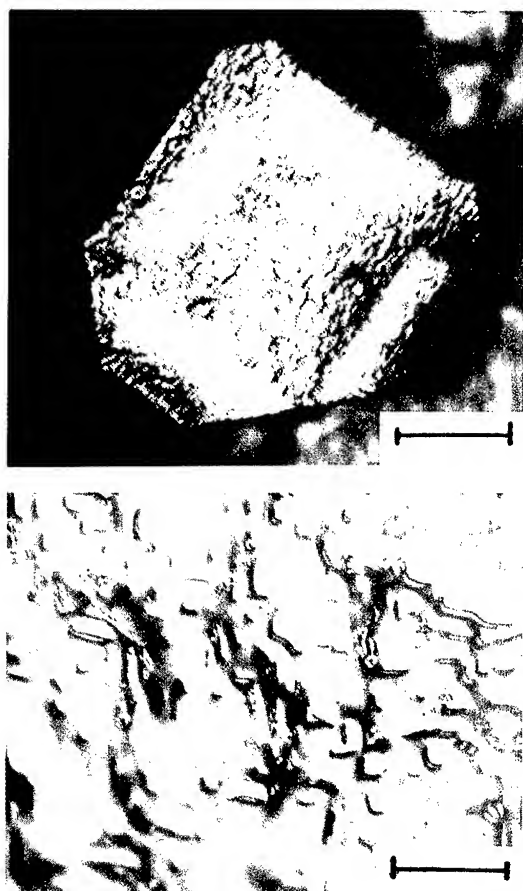


Fig. 1 (a) A (100) surface contacted to the solvent at 6.2 GPa and 1315 °C. Bar = 200  $\mu\text{m}$  (b) Higher magnification of the (100) surface which can be seen growth step on the dissolved rough surface. Bar = 20  $\mu\text{m}$

decreased reflecting the increase of carbon solubility. When temperature was about 1420 °C, a large part of the seed crystal was dissolved and complex shaped grown diamond was observed.

### (3) Instability of the Interface

As described previous section, no dissolution of the seed crystal was found in the sample treated below 1190 °C. Temperature between 1190 °C and 1310 °C, the seed was dissolved slightly and showed rough dissolved and precipitated surface. It was believed that liquid formation starts from 1190 °C. Above 1310 °C, grown diamond zone was



Fig.2 (a) (100) surfaces of the seed and grown crystal. Bar = 100  $\mu\text{m}$  (b) (111) surface of the seed and grown crystal showing smooth connection of seed, grown crystal and solvent. Solvent is attached at the top. Bar = 100  $\mu\text{m}$

observed with seed and solvent.

Stability of the interface between the seed and solvent was observed at the narrow temperature range such as between 1320 °C and 1400 °C. When we intend to obtain better quality crystal, it is very important to conduct the diamond growth at this temperature range. If we select higher temperature, dissolution of the seed and precipitation of the new diamond zone competed and instability of the interface will be increased. Fig.3 shows complex shaped grown crystal and solvent which treated at 1420 °C.

#### (4) Discussion on the Seeded Growth of Diamond by the Temperature Gradient Method

On the seeded growth process of diamond, anti-dissolving zone such as thin Pt foil was normally used between the seed and solvent lump. [3] Even if we place Pt foil as an anti-dissolving zone, partial dissolution of the seed crystal will occur. If temperature was high enough to dissolve the seed, interface between the seed and solvent will be rough because of instability of seed dissolution.

As a result, interface stability must be kept through the growth stage of the diamond. As indicated in this result, optimum temperature condition of the smooth connection of the seed and growing crystal is limited. It is generally observed various imperfections such as pore, inclusion, mismatch in the grown crystal near the seed. [4] But these imperfections will be decreased by growing in the stable interface condition.

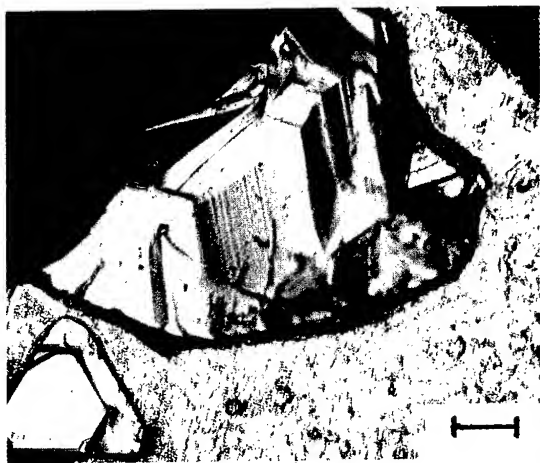


Fig.3 An example of unstable dissolution and precipitation of diamond. The sample was treated at 6.2 GPa and 1420°C for 3 h. Bar = 200  $\mu\text{m}$

#### REFERENCES

- [1] H.Kanda et al. J.Cryst. Growth, 60(1982) 441-444
- [2] H.M.Strong and R.E.Hanneman, J. Chem. Phys., 46(1967)3668-3676

#### (5) As Grown Surface of the Diamond

The diamond layer grown on the partially dissolved seed crystal was connected smoothly to the seed. The seed crystal used in this experiment (SDA grade of DeBeers) was possibly grown in the Ni containing solvent, but grown diamond in this experiment was grown in the Fe-Co melt. Cathode luminescence at 480 nm (2.56 eV Ni luminescence) was detected only on the (111) face of the seed crystal, whereas luminescence at about 500 nm (H3 center of N-N-V pair) was detected on the (100) face of both seed and grown crystal. But laminar structure of the H3 luminescence was observed on the grown diamond.

The surfaces of the grown diamond in this experiment were all contacted to the molten salt without one (100) face interfaced to the molten solvent. These surfaces showed as-grown patterns. It must be noted that surface of growing crystal was covered by the secondary precipitation of the diamond during the cooling when growth process is carried out in the solvent bath. [5] As shown in Fig.4, as-grown surface showed typical two-dimensional growth steps along (111) surface.

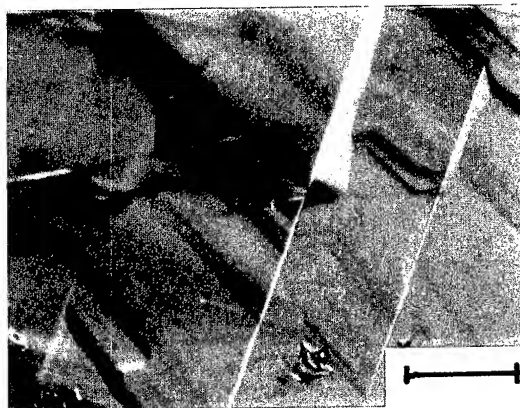


Fig.4. Two-dimensional growth layer on the (111) surface of grown diamond. Bar = 20  $\mu\text{m}$

- [3] H.M.Strong et al., Japanese Pat. S-52-88289, July 23, 1977
- [4] H.Kanda and O.Fukunaga, Advance in Earth and Planetary Sci. vol. 12 pp525-53
- [5] H.Kanda et al., J. Mat. Sci., 15(1980) 2743-2748

# HIGH PRESSURE HIGH TEMPERATURE NUCLEATION OF DIAMOND

Ekimov E.A., Borovikov H.F.

*Institute for High Pressure Physics of the Russian Academy of Sciences, Troitsk, Moscow Region, Russia*

Palosz B., Leszczynski M.

*High Pressure Research Centre Polish Academy of Science, Warsaw, Poland*

Saparin G.V., Obyden S.K.

*Department of Physics, Moscow State University, Moscow, Russia*

Klimin S.A.

*Institute of Spectroscopy of Russian Academy of Science, Troitsk, Moscow region, Russia*

## ABSTRACT

Diamonds were grown in the vicinity of the "diamond-graphite" equilibrium state by the method of spontaneous crystallization in order to study creating defects and crystallinity imperfections. The yellow crystals revealed the infra-red (IR) absorption spectra within the range  $800-4000\text{ cm}^{-1}$  being peculiar for diamonds of the 1a group. IR spectra displayed a number of additional absorption peaks for black semi-transparent crystals. A marked peak at  $2835\text{ cm}^{-1}$  and a less pronounced at  $2919\text{ cm}^{-1}$  unambiguously demonstrate the presence of hydrogen. Presence of the peaks with maximum at  $2919, 1252, 1332\text{ cm}^{-1}$  in the IR spectra of the black diamonds and FL-CVD diamond films indicated a certain similarity of diamond formation for high pressure and vapor deposition techniques and an important role of hydrogen in the high pressure diamond growth.

## Introduction

The studying of influence of absorbed gases on the graphite - diamond conversion at the presence of the metal melt at high pressures and temperatures indicated the most harmful role of hydrogen among the possible gaseous impurities [1]. Modern methods of diamond growth at the high pressure always provide the hydrogen presence in the growth system. This occurs either as impurity in the graphite or as the element in the absorbed gases. It is necessary to note the presence of hydrogen in the natural crystals was detected both in the composition of fluid inclusions and in the chemisorbed phase which is observed by the vibrational spectroscopy methods [2]. It was indicated by infra-red spectroscopy that the  $1100, 1010, 1180$  and  $1132\text{ cm}^{-1}$  lines in natural diamond are accompanied as a rule by the absorption line on  $3107\text{ cm}^{-1}$  which corresponds to C-H stretching mode [3].

As concerns the diamonds synthesized at high pressures and temperatures with participation of the metal - solvent, no features connected with the hydrogen presence in the crystals were found by infra-red absorption spectroscopy [4]. However, C-H lines were found both in the diamond and in the diamond like films obtained by CVD methods [5]. The correlation of the  $2918$  and  $2849\text{ cm}^{-1}$  peaks attributed to the  $\text{CH}_2$  group vibration with  $1332,$

$1252$  and  $2695\text{ cm}^{-1}$  peaks of infra-red absorption spectra; This is not typical for both natural and synthetic diamonds obtained by classical methods.

The subject of this work is the role of hydrogen in the formation of diamond at high pressures and temperatures.

## Conditions of Growth of Diamond Crystals

Some features of diamond crystal growth at the spontaneous nucleation in the Ni-Mn-C system were studied at the pressure of  $42-46\text{ kbar}$  and the temperature of  $1100-1350^\circ\text{C}$  for  $30\text{ min}$ . The crystal growth was realized at minimum supersaturation (pressure) for every temperature from this interval.

## Results

The first diamond crystal group is a combined curved faces type. The development of flat habitus (100) faces and a small display of smooth taking the edges off (111) faces are typical. Crystal growth was carried out at the minimum probable temperature of diamond synthesis in the presence of Ni-Mn-C melt. Heterogeneous carbon distribution in the solvent around the crystal causes the combination of flat and curved crystal surface areas. The crystals are black, non-transparent in visible light.

The second type of crystals is a cubic-octahedral combination form with predominant role



of cube faces. In the transmitted light the samples have green - brown color which is condensed in the growth pyramid of the cube. Examination of the fracture surface testify the heterogeneous color of the crystal, bonding of the color condensing with the growth pyramid of cube and absence of large solvent inclusions and pores. More uniform growth conditions at the temperature 1250°C cause relatively isometric form and absence of the rounded faces.

Crystals of the third type having cubic - octahedral habit reflect the favorable growth conditions at the temperature 1300-1350°C.

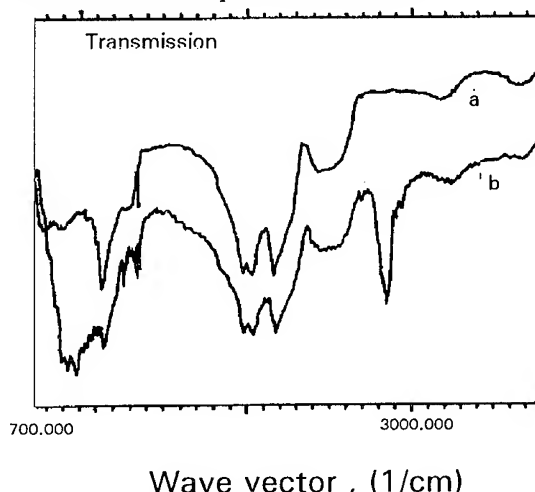


Fig.1. IR transmission spectrum of synthetic diamond: a) yellow crystal of 1b type; b) black crystal.

IR absorption spectra analysis of selected for testing yellow diamond crystal in the one-phonon range has shown (Fig.1) that this crystal group is classified as "clear" 1b type. The band on 1135  $\text{cm}^{-1}$  is regarded as display of resonance absorption, connected with nitrogen atoms in paramagnetic state. The other spectral peculiarities are interpreted as follows: sharp band on 1335  $\text{cm}^{-1}$  corresponds to local self-induced vibration of nitrogen atom; band at 850-880  $\text{cm}^{-1}$ , weak small peaks on 1065 and 1100  $\text{cm}^{-1}$ , shoulder on 1290  $\text{cm}^{-1}$  correspond to display of the normal mode in definite critical points of the Brillouin zone [6].

The absorption spectra of black semi-transparent diamond crystals did not allow us to attribute this group of samples to any known type. Besides the lines which are typical for IR absorption spectra of 1b type crystals the additional absorption line on 850-920, 960-970, 1060, 1165, 1250, 1335, 2688, 2835, 2920  $\text{cm}^{-1}$  of various intensity are

present. Intensive absorption on 2835  $\text{cm}^{-1}$  have some features as small peaks or bends on 2780, 2815, 2845, 2890  $\text{cm}^{-1}$ . On the base of previous reports [5,7] on research on hydrogen in epitaxial films grown on the natural diamonds by CVD methods, we may attribute the wide and intensive band on 2835  $\text{cm}^{-1}$  to the symmetrical stretch mode of  $\text{sp}^3$  - hybridized  $\text{CH}_3$  bonds, absorbed by the (111) faces. Shoulder of line with maximum on 2890  $\text{cm}^{-1}$  is caused by  $\text{CH}_3$  asymmetrical stretching mode. Absorption on 2919  $\text{cm}^{-1}$  is due to  $\text{sp}^3$ -hybridized C-H stretching mode of monohydride absorbed on the (100) faces. Absorption on 1080 and 1252  $\text{cm}^{-1}$  is due to C-H bending mode of  $\text{sp}^3$  - hybridized  $\text{CH}_3$  group, absorbed on (111) faces. Absorption on 1164  $\text{cm}^{-1}$  is due to C-H bond bending modes of monohydride, absorbed on (111) diamond faces. Absorption presence on the Raman frequency is caused by the structural defects of diamond lattice. Defects which give the additional absorption in the range of 700-1080  $\text{cm}^{-1}$  with two peaks on 920 and 980  $\text{cm}^{-1}$  may be different. For example, it may be due to the presence of metal atoms in the diamond lattice [8] and hydrocarbon fragments on the surfaces of crystal micropores (C-C stretching modes, C-H bending modes). The curved flat-faced type of the black non-transparent crystals in this frequency interval absorbed the radiation completely.

The Raman spectra of the yellow crystal in the frequency range of 500-3800  $\text{cm}^{-1}$  are displayed by one characteristic line at 1332  $\text{cm}^{-1}$ . On Raman spectra of semi- and non-transparent diamond crystal types (besides the 1332  $\text{cm}^{-1}$  line corresponding to self-induced vibration of diamond crystal lattice) the weak lines at 3650, 2919, 2835, 1580, 1470, 1141, 964  $\text{cm}^{-1}$  are present. Presence of weak line at 2835 and 2919  $\text{cm}^{-1}$  in Raman spectrum is probably connected with diamond surface hydrogenation. Band with the center at 3650  $\text{cm}^{-1}$  is the most probably due to O-H stretching mode. The weak, but the wide band of Raman spectrum with maximum at 1580  $\text{cm}^{-1}$  is induced by the O-H group bending mode. Presence of the lines at 1147 and 1470  $\text{cm}^{-1}$  in the spectrum is connected with the existence of amorphous diamond like carbon and explained by vibrations of diamond atoms which are not fitting in the diamond lattice but have four bonds (placed on tetrahedral form) with heavy fragments. As concerns 964  $\text{cm}^{-1}$  line it might be classified as C-H bending modes and C-C stretch modes. It is necessary to note that intensity of lines at 2919, 2835, 1470, 1141, 964  $\text{cm}^{-1}$  remained the same

at the changing of testing spot position. It is impossible to say anything about intensity of line on 1580 and 3650  $\text{cm}^{-1}$  which in some cases decreased down to the background level. This intensity changes may origin from the water presence in the heterogeneously distributed fluid inclusions because no additional absorption at 3650 and 1580  $\text{cm}^{-1}$  in the IR spectrum of all crystals was observed.

Surface study of (111) and (100) crystal faces and the study of cathodoluminescence topographs corresponding to these faces and inside zones which are placed under the face, allowed us to determine: i) the relation between the temperature conditions of crystal growth and face relief, ii) luminescence spectrum of growth pyramid. It was found, that if the growth pyramid of the yellow crystal is yellow (in the central part) and the blue (near of crystal surface) luminescence colors are typical, then the yellow-green colors are typical for the semi- and non-transparent black crystals. The layers and structureless forms in the growth pyramid of black crystals are formed due to refaceting of the central face parts at the intrinsic block and step structure. They show blue and rosy luminescence. Appearance of surface faceting by (110) and (111) faces is noted on the step butt-end and the face hollow. For the semi-transparent black crystals the blue luminescence is not typical. It is necessary to note that the curved faced crystal part does not have luminescence as distinct as it is from the flat faced part. Octahedral growth pyramid structure and color (red-brown) do not significantly change when the diamond growth temperature decreases. Investigation of the yellow and black crystals cathodoluminescence spectra showed the black crystals unlike the yellow ones, as they do not contain centers responsible for the luminescence at the 484 and 575 nm. The absence of luminescence line in the spectra of black crystals (maybe connected with the hydrogen centers) do not exclude the definite connection between the yellow-green luminescence of the cube growth pyramid and the additional absorption in IR frequency range.

## Discussion

The question about the form of hydrogen incorporation in the diamond lattice obtained at high pressure - high temperature from solution in metal melts is still open. However, our investigations showed for the first time that the hydrogen presence inside the crystal volume is probably in the

chemisorbed form as established by the vibrational spectroscopy methods. Taking into account the known research data on structure of the CVD-diamond film surfaces it may be supposed the hydrogen absorption in diamond crystal takes place on the inside micropore surfaces having primary facet by the (111) and (110) planes. The participation of (100) planes in micropore faceting is restricted. Apart from the absorbed hydrogen the presence of the hydroxyl group on the micropore surfaces is probable, but according to our results the water presence in the separate heterogeneously distributed inclusions is the most probable. The hydroxyl group was not established by IR absorption spectroscopy for all the crystal. Discovery of the chemisorbed hydrogen in the inside layers of semi-transparent black crystals is rather due to the carbon complex stabilization in the synthesis at the 42 kbar (at room temperature) and temperatures less than 1250 °C (or at the sufficient supersaturation). The additional absorption bands for the synthetic diamonds, which was observed before in the IR range 700-1400  $\text{cm}^{-1}$  at 870-920, 1065, 1290 and 1332  $\text{cm}^{-1}$ , do not have any rational interpretation [9] (their existence is not explained by the nitrogen presence). It is necessary to note the micropore size is rather such that the incorporation of another gaseous impurities is impossible. The synthesis temperature increase (supersaturation decrease) results in a reduction of the absorbed hydrogen capture probability. The hydrogen presence depends on both the impurity composition of parent materials and the absorbed gases, and at the significant hydrogen concentration no diamond lattice formation can occur.

## Conclusions

The absorption lines connected with the  $\text{sp}^3$ -hybridized C-H bonds were found for the first time by the IR absorption spectroscopy methods in the diamond crystals grown at high pressure and temperature in the presence of metals. Hydrogen discovery in the semi-transparent black crystals is caused by its presence inside the part of crystals of this group. For the Ni-Mn-graphite growth system the hydrogen defect formation takes place at temperature less than 1200 °C and at pressure 42 kbar.

## References

1. Tsuzuki A., Hirano Sh., Naka Sh.: Influence factors for diamond formation from several starting carbon. *Journal of Materials Science* 20, 2260-2264 (1985).
2. Davies G., Collins A.T., Spear P.: Sharp infra-red absorption lines in diamond. *Solid State Communications* 49(5), 433-436 (1984).
3. Orlov Yu. A.: Mineralogiya almaza, Nauka, Moscow (1984) 263 (in Russian).
4. Field J.E.: The properties of natural and synthetic diamond, Academic Press, New York (1992), 707.
5. Janssen G., van Enckelvort W.J.P., Vollenberg W. and Giling L.J.: Characterization of single-crystal diamond grown by chemical vapor deposition process. *Diamond and Related Materials* 1, 789-790 (1992).
6. Vavilov V.S., Gippius A.A., Konorova E.A.: *Elektronniye i opticheskiye processy v almaze*. Nauka, Moscow (1985) 118 (in Russian).
7. Aizawa T., Ando T., Kamo M. and Sato Y. : High-resolution electron-energy-loss spectroscopic study of epitaxially grown diamond (111) and (100) surfaces. *Physical Review B* 48(24), 18 348-18 351 (1993).
8. Malogolovets V.G., Vishnevskiy A.S., Povarennih A.S.: O vliyaniy primesei pechodnih metallov na i.-k. pogloshcheniye sinteticheskikh almazov. *Doklady Akademii Nauk* 243(1), 111-113 (1978) (in Russian).
9. Vishnevskiy A.S., Malogolovets V.G., Nikityuk A.F., Posunko L.S.: O nekotorykh osobennostyuh katodoluminescencii sinteticheskikh almazov. *Sinteticheskiye almazi*, Naukova Dymka, Kiev, 7-11 (1975) (in Russian).

# THE STABILITY OF THE REGROWTH-TREATED CARBON SOURCE IN THE EXCESS PRESSURE METHOD OF GROWING DIAMONDS

Y. WANG, R. TAKANABE AND M. WAKATSUKI  
*Institute of Materials Science, University of Tsukuba,  
Tsukuba, Ibaraki 305, Japan*

## ABSTRACT

The size of diamonds grown by the film growth method or the excess pressure method is limited within 1 or 2 mm. The cease of the growth has so far been explained by pressure drop caused volume contraction accompanied by the conversion of graphite to diamond. This study presents another reason for the cease of the growth. The mechanism for the suppression of diamond nucleation from the regrowth-treated graphite can also be explained by the same reason.

## 1. Introduction

In the excess pressure method of growing diamonds at high pressure and high temperature[1], it is difficult to continue the growth over a period of about two hours[2]. Conversion of graphite to diamond causes a volume contraction and results in a decrease in pressure. This inherent pressure decrease has been considered as the reason for the stop of the diamond growth. Recent experiments have, however, suggested another reason.

Synthetic graphite with low crystallinity is usually used as the carbon source for growing diamonds in the excess pressure method. SEM observation on the surface of the carbon source recovered from the regrowth-treated sample revealed that well-grown graphite particles were formed on the surface, and among these particles the original graphite remained unchanged even after the regrowth-treatment for 10 minutes. In this paper we call the regrown graphite as r-graphite, and the unchanged synthetic graphite as s-graphite, for simplicity.

The thermodynamic stability of r-graphite should be superior to that of s-graphite since the former grows from the latter. It is most probably that the s-graphite is the effective carbon supply for the growth of diamond. However, if the difference of the stability is very small, then the r-graphite can also act as the carbon supply. The purpose of this study is to compare the stability of the two graphites quantitatively, and further, to make clear the detailed process of change of carbon from the source to diamond.

## 2. Experiments

Experiments were conducted in a cubic anvil apparatus. The pressures were calibrated against the press load at room temperature using the pressure reference of Bi, Tl and Ba. The effect of heating on the generated pressure was not corrected. The relative pressure values in the experiments are considered as

meaningful, though the absolute values may contain some errors. The temperatures were evaluated by thermocouples (Pt30%Rh/Pt6%Rh) of a diameter of 0.2 mm, the hot junction being set at the center of the reaction cell. The pressure effect on the emf was not correct.

### *The diamond nucleating pressures*

The higher stability of a graphite means that it equilibrates with diamond at a higher pressure. Thus, it is expected that we can evaluate the relative stability of graphites by difference in their critical pressures for diamond nucleation.

The reaction cell for determining the nucleation pressure is illustrated in Fig. 1. The starting graphite and the solvent (Fe:Ni:Co=55:29:16, by weight) were the same as what used in our earlier

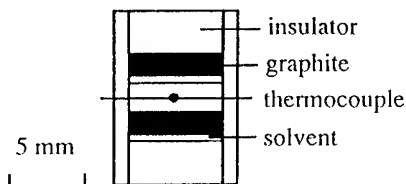


Fig.1 The reaction cell for observation of the diamond nucleation.

study[1,2]. The sample assembly was exposed to a pressure  $P_1$  and a temperature  $T$  for a duration  $t$  for the regrowth-treatment. The pressure  $P_1$  (4.9 GPa) was apparently lower than a critical pressure that can nucleate diamond from the untreated starting graphite. Then the pressure was raised to a higher level  $P_2$ , while the temperature was unchanged. Recovered reactants were acid-treated and examined on whether diamonds nucleated or not.  $T$  was always 1290 °C but  $P_2$  and  $t$  was changed from experiment to experiment.

The result is summarized in Fig. 2. The nucleating pressure  $P_n$  increases with the treatment

duration  $t$ , from 5.10 GPa for  $t=0$ , and approaches slowly to a constant value of 5.65 GPa ( $P_n^*$ ).

Particles of r-graphite grow during the regrowth-treatment, and covers the s-graphite completely after a long treatment duration. The r-graphite should be transformed to diamond at a pressure higher than  $P_n^*$ . However, at a pressure lower than  $P_n^*$ , the crystals of the r-graphite are stable and absorb the carbon atoms dissolved in the molten metallic solution, and mask the starting graphite from the solution. Both of these effects suppress the carbon concentration in the solution. Consequently, a higher pressure is needed for forming the critical supersaturation necessary for the diamond nucleation. In other words, the width of pressure range available for growing a seed diamond is possibly expanded up to 0.55 GPa by the regrowth-treatment.

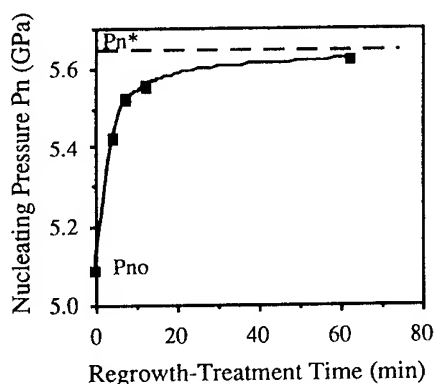


Fig.2 The dependence of the nucleating pressure  $P_n$  on the regrowth-treatment time.

The result shows that the r-graphite is more stable than the s-graphite. It also implies that the real carbon supply for the growth of diamond is the s-graphite remaining among the particles of the r-graphite, as far as the reaction pressure  $P_2$  is lower than  $P_n^*$ .

#### *The melting temperatures of the graphite/cobalt systems*

It is believed that the higher stability of the r-graphite arises from its sound crystallinity. If this is correct, then the stability of natural graphite with perfect crystallinity should be close to what of the r-graphite. In order to confirm this expectation, we measured and compared the eutectic melting temperatures for the s-graphite/Co and natural graphite/Co systems by the differential thermal analysis(DTA) method.

The sample assembly is illustrated in Fig. 3. The experiments were performed at a pressure of 4.9 GPa, which is close to, but certainly lower than, the equilibrium pressures between diamond and these

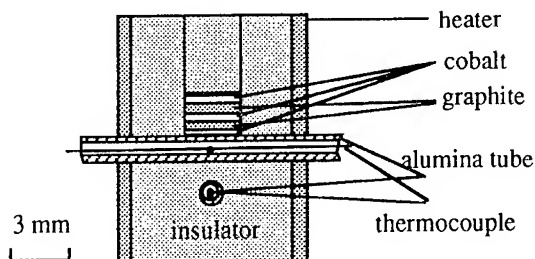


Fig.3 Experimental cell for the differential thermal analysis.

graphites. The heating power was so operated that the temperature of the sample was increased and decreased slowly and repeatedly around the melting temperature. The period of the repetition was 12 min. The latent heat signals were clearly detected both in the heating and cooling cycles. The sensitivity of the method was 0.1 °C of the temperature difference.

The results are shown in Fig. 4. The observed melting temperature of cobalt contacted with natural

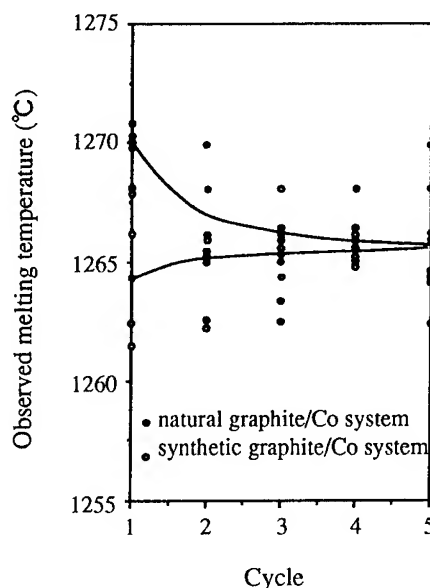


Fig.4 The variations of the observed melting temperatures of the natural graphite/cobalt system and of the synthetic graphite/cobalt system at a pressure of 4.9 GPa.

graphite was 1270 °C in the first cycle, but it decreased along with the cycle to a stable value of 1266 °C. At first the metal and the graphite existed as large lumps in contact to each other through a small interface, which should have caused the thermal arrest be detected at a temperature a little higher than the correct eutectic melting point. However, the texture became finer in the later cycles, resulting in the decrease of the observed temperature. The final stable value is most possibly considered as the correct eutectic melting temperature of the system. While, for the s-graphite/Co system which showed the initial temperature of 1264 °C, the observed increase in the temperature should be a composed result of the effect of the growth of the r-graphite from the s-graphite (increased crystallinity) and the texture effect mentioned above. It is very likely that the texture effect was canceled by the regrowth effect. To have the same final value, 1266 °C, for the both systems is reasonable. Thus, the difference of the temperatures observed in the first cycle, 6 °C, corresponds to the difference in the stability of the two graphites.

### 3. Discussion

The difference ( $\Delta P$ ) between the equilibrium pressure of diamond/r-graphite ( $P_{e^*}$ ) and that of diamond/s-graphite ( $P_e$ ) was evaluated from the solubility difference for the two graphites, which was estimated on the basis of the observed difference in the eutectic temperatures with a supposed binary phase diagram for the present metallic solvent and graphite. The phase diagram is unknown and we referred to those for the Ni-C system instead, and a value of about 0.3 GPa were deduced for  $\Delta P$ , with the molar volumes of the two graphites assumed to be the same.

On the other hand, it is expected that  $\Delta P$  is approximately equal to the difference in their diamond-nucleating pressures, or

$$P_{e^*} - P_e = P_{n^*} - P_{n0} = 0.55 \text{ GPa} \quad (1)$$

The results are quite reasonable. The numerical discrepancy should be explained on the basis of the assumptions placed in the discussion, but the following factor also be considered. The crystal lattice of the natural graphite should have suffered from a plastic deformation at the compression before heating. This degradation in crystallinity may lead to an under-estimation of the stability difference of the two graphites.

In the excess pressure method, the r-graphite grows both in the regrowth-treatment stage and in the diamond growth stage. The role of the r-graphite

is to suppress the carbon concentration in the solution by covering the s-graphite as well as by absorbing the carbon atoms dissolved from the s-graphite. When the s-graphite exposed to the solvent is consumed out, or when the whole surface of the s-graphite is covered perfectly by the regrown particles, both diamond and the r-graphite stop their growth. The r-graphite itself can not act as the carbon supply due to its higher stability, as far as the pressure  $P_2$  is below  $P_{n^*}$ .

### 4. Conclusions

(1) The diamond nucleation pressure,  $P_n$ , showed a further increase by the extended period of the regrowth-treatment, approaching to a pressure  $P_{n^*}$ , which is higher by 0.55 GPa than that for a typical untreated synthetic graphite.

(2) The first cycle melting temperature of a well-crystallized graphite/cobalt system was about 6 °C higher than that of a typical synthetic graphite/cobalt system. The difference of 6 °C corresponds to an increase of about 0.3 GPa in the diamond/graphite equilibrium pressure, due to the crystallinity difference of the graphites.

(3) The regrown graphite can not act as the effective carbon source for the diamond growth, because of its higher stability. The existence of the regrown graphite results in an expanded pressure range available for the seeded diamond growth. It gives, at the same time, a negative effect of stopping the growth of diamond after a long period (a few hours) of the growth stage.

### References

- [1] M.Wakatsuki and K.J.Takano, High Pressure Research in Mineral Physics, ed. by M.H. Manghanani and Y.Shono, Terra Scientific Publishing Co.,Tokyo, 203-207(1987).
- [2] Y.Wang, R.Takanabe, H.Kagi, K.J.Takano and M.Wakatuki, Advances in New Diamond Science and Technology, ed. by S.Saito, N.Fukunaga, M.Kamo, K.Kobashi and M.Yoshkawa, MYU, Tokyo, 521- 524(1994).

# THE INFLUENCE OF TEMPERATURE GRADIENTS ON THE KINETICS OF SEED GROWING OF DIAMOND SINGLE CRYSTALS

S.A. IVAKHNENKO, S.A. TERENTYEV, I.S. BELOUSOV, O.A. ZANEVSKY  
V.N. Bakul Institute for Superhard Materials of the Ukrainian  
National Academy of Sciences, Kiev, Ukraine.

## ABSTRACT

To choose optimum parameters of synthesis of crystals having predetermined mass and quality, the kinetic dependence of diamond single crystals growing using the temperature gradient method were experimentally studied. The growth experiments were carried out in growing systems, where alloys based on iron with nickel and cobalt were used as solvents, under  $\sim 5.5$  GPa and  $\sim 1673$  K. The analysis of the obtained time dependencies shows that the temperature drop between the carbon source and a seed system greatly affects a crystal mass. In this case, the kind of dependencies for different heating outlines varies.

## Introduction

The essence of the temperature gradient method is that the reactive volume, containing carbon source, metal solvent and seed system is located in temperature field, which provides higher temperature in the area of carbon source. The driving force to carry atoms of carbon in this case is the difference between solubilities of carbon at carbon source and at growing crystal. The above-stated effect is determined by difference of temperatures on the interfaces: the source - metal and metal - crystal (1). The significance of the temperature

gradient renders the considerable influence on the diamond crystal growth rate. Therefore the problem of controlling of the temperature gradient during growth of single diamond crystals is of special importance.

## Experiment

The growth experiments were carried out in toroid type high pressure apparatus with cavity diameter of 40 mm in growth systems, where alloys based on iron with nickel and cobalt were used as solvents.

The typical outline of assembly growth cell is shown on Fig.1.

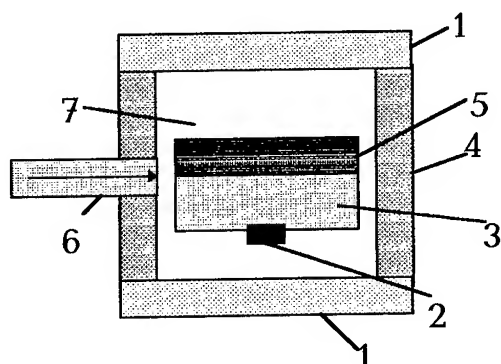


Fig.1. The outline growth cell: 1 - heating disks, 2 - seed system, 3 - alloy solvent, 4 - graphite heater, 5 - carbon source, 6 - thermocouple block, 7 - isolation of growth system.

The study of seed growth kinetics of single diamond crystals was carried out at pressures of 5.0 - 5.5 GPa and temperatures 1250 - 1400 °C. The temperature of growth was

continuously and kept constant during all time of synthesis with help of thermocouple PR 30/ 6.

The selection of heating device configuration and geometry of the growth cell was done both by experimental way, and with use of mathematical simulation methods of potential and thermal fields using the specially developed set of applied programs. To check the correctness of calculations the comparison of theory and experiment results was carried out.

### Experimental results

In the result of the influence of heating device configuration and growth cell geometry study, the optimum method of temperature fields control in reaction volume for growing of single diamond crystals was found.

If the heating device is in shape of tubular graphite heater 4 (Fig. 1), axial gradient of temperature on sample of alloy-solvent is of 8 K. The radial temperature gradient on bottom surface of sample 4 K.

Using the described above design of heating device the change of the temperature gradient in the sample of alloy-solvent can be achieved by displacement of the sample along at cell axis. For example, displacement of the cell downwards by 0.5 mm from symmetry planes results in increase of axial temperature gradient from 8 to 12 K, radial temperature gradient is then increased from 4 to 6 K.

The shortcoming of given design of heating device is the complexity in radial gradient control.

The insertion into the reaction volume of additional heating elements in forms of disks 1 (Fig. 1) permits to change axial as well as radial temperature differences in sufficiently wide interval, depending of their thickness.

The experimental kinetic dependencies of weight of diamond crystals, obtained by the method of temperature gradients are shown on Fig. 2.

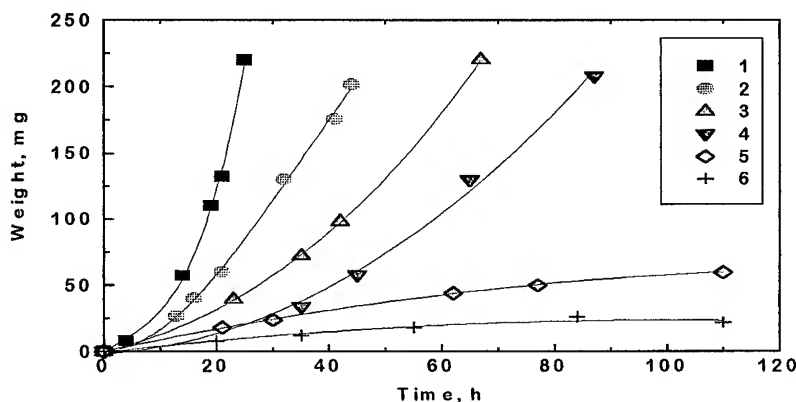


Fig. 2. The experimental kinetic dependencies of seed growing of diamond crystals for various significance's of temperature gradient: 1 - average temperature difference 20 K; 2 - 15 K; 3 - 10 K; 4 - 8 K; 5 - initial temperature gradient 15 K; 6 - 10 K

Curves 1-4 correspond to the heating, where the tubular graphite heater together with additional heating elements in forms of disks. Curve 5 - 6 corresponds to the outline without additional heating disks.

### Discussion of results

The analysis of grown single crystals quality permits to make the following conclusions. Perfect and well-faced single



crystals are obtained at growth rates, corresponding to curves 4 and 6. The slight defects in form of crystals were observed at rates, corresponding to curve 3, 5.

For curve 1 the grab of plenty of alloy-solvent inclusions by growing crystal, occurrence of doubles and joints is typical.

For curve 2 the occurrence of deflections above centers of sides and availability of small quantity of alloy-solvent inclusions is significant.

The analysis of given dependencies shows, that the weight of crystals of diamond largely depends on the temperature difference (curve 1 - 4, Fig. 2), and kind of dependencies for various outlines of heating strongly differs.

It is possible to demonstrate the reasons of given distinctions by the following example.

In this work the outline of heating with one tubular heater and initial temperature gradient in axial direction between source of carbon and seed crystal of diamond  $\sim 15$  K was used. It was found in the process of single diamond crystals growing, that at increase of crystal weight up to 50 mg the temperature gradient between source and top surface of growing crystal drops to 4 K, that corresponds practically to zero speeds of growth. The growth of crystal in this case can happen only in radial direction. However, sharp decrease of growth rate at increase of the weight crystal of 40 - 50 mg (curve 5, Fig. 2), makes the growth process of crystals at times longer than 50 - 60 hours not effective.

The introduction in given outline of heat or local seekers allows to increase the effective time of growing.

So, using of growth design, for which the dependence of diamond crystal weight on time has the kind, appropriate to curve 1 - 4 on Fig. 2, temperature difference in axial direction between source carbon and seed crystal makes 12 K. At increase of weight of crystal to 50 mg the given difference is reduced to 8 K, that provides the speeds of growth of about 0.8 mm/day.

The effect of axial and radial temperature gradient variations on the kinetic of diamond crystal growth has been studied. When the axial gradient value is 10 - 12 K/mm, a formation of spontaneous crystals along a cylindrical genetrix is observed. The temperature gradient exceeding 12 K/mm, results in formation of aggregates and spontaneous crystals over the whole surface of the substrate.

It has been found that if the axial gradient value is more than 1.5 times less of the radial temperature gradient value, the skeleton crystal growth is observed. To produce single diamond crystals with no inclusions, the mass growth rate should not exceed 3.5 mg/hour.

#### Reference

1. H.H. Strong and R.W. Wentorf, *J. Naturwissenschaften*, **59** (1972) 1.

## DIAMOND SYNTHESIS IN A LASER-HEATED DIAMOND ANVIL CELL

Hitoshi Yusa, K. Takemura, Yoshio Matsui  
*National Institute for Research in Inorganic Materials,  
1-1 Namiki, Tsukuba, Ibaraki 305, Japan*

Hiroshi Yamawaki, Katsutoshi Aoki  
*National Institute of Materials and Chemical Research,  
1-1 Higashi, Tsukuba, Ibaraki 305, Japan*

### ABSTRACT

Cubic diamond is synthesized with a diamond anvil cell and a CO<sub>2</sub> laser above 11 GPa. The bonding nature and the fine structure of the diamond was elucidated by Raman scattering and high resolution transmission electron microscopy. The Raman spectrum shows the  $sp^3$  bonding. Images by the high resolution transmission electron microscope indicate that the diamond has twins of {111} plane in nanometer size.

### Introduction

Diamond synthesis from graphite without catalyst needs very high temperatures (above 3000 K) as well as high pressures. In general, it is difficult to hold such high temperatures under high pressure for a long time. Therefore, under static pressures, experiments have been carried out by a flash heating method (1). Owing to short time for the reaction (less than 10 ms), however, most of graphite remained untransformed in such experiments. Laser heating using a diamond anvil cell (DAC) (2) is an alternative way for generating high temperatures under high pressures.

We carried out laser heating experiments of graphite for the purpose of the direct conversion to diamond above 11 GPa. Special efforts have been made to clarify the fine structure and the bonding characteristics of synthesized diamond with the use of high resolution transmission electron microscopy (HRTEM) and micro Raman spectroscopy.

### Experimental and results

#### *Laser heating*

A single crystal of kish graphite was used as a starting material. The sample was sliced thin along with a cleavage of the (002) plane (1~2  $\mu\text{m}$  thickness).

A U-700 gasket was prepared for a sample chamber. Dried KBr was used for a pressure transmitting medium. The KBr worked as a thermal insulator as well as a window for the incident laser beam. A few grains of small ruby chips were also placed in the sample chamber as a marker to measure pressures before and after heating. The sample was compressed to 14.4 GPa at room temperature (Fig. 1A). Single crystal graphite was broken into a few parts during compression in the solid pressure medium.



Fig. 1 (A)  
Photomicrograph  
of graphite  
sample at 14.4  
GPa in a DAC  
with a transmitted  
light before laser  
heating.  
Scale bar is  
0.1mm.



(B) The sample  
after laser  
heating. The  
graphite  
drastically  
changes into a  
transparent phase.

A continuous CO<sub>2</sub> laser with a single mode was focused to the sample in the DAC with 100  $\mu\text{m}$  in diameter for about 10 minutes. The laser power irradiated to the sample was 160 W at maximum. Type IIA diamond was used as an upper anvil for its low absorbance of the laser wavelength (10.6  $\mu\text{m}$ ). In comparison with the laser heating methods using a pulsed YAG laser (3, 4), an extensive area can be heated simultaneously with the CO<sub>2</sub> laser for a long time. The maximum temperature was estimated to be higher than 3000 K, on the basis of the visual observation of the thermal radiation from the sample. After 10 minutes heating, the laser was quickly turned off, and the sample was quenched. After heating, the sample color drastically changed from black to transparent (Fig. 1B). The products remained transparent on release of pressure to 1 atm. No damage on the surface of the diamond anvil was confirmed after the experiments.

We repeated the experiments by varying the pressure conditions. Below about 10 GPa, no transparent phase appeared after heating. Only observed was melted graphite, which percolated through KBr grains. The transparent phase emerged on heating at pressures higher than 11.7 GPa. Therefore the transition pressure to the transparent phase can be estimated to be 11 ~ 12 GPa at high temperatures.

#### Characterization

The sample embedded in KBr was removed from the gasket and placed on a stainless steel mesh with 5  $\mu\text{m}$ -diam holes. KBr was washed away by water, and the sample remained on the mesh. We analyzed the sample on the mesh by using Raman spectroscopy and transmission electron microscopy. Before starting the analysis, we checked the possibility of the chemical reaction of graphite with the KBr pressure medium by using a transmission electron (TEM) microscope equipped with an energy dispersive x-ray spectrometer. Both K and Br were not detected in the samples.

Raman spectra were taken at room temperature by using an argon ion laser (488 nm), a triple polychromator and a CCD detector. The Raman

spectrum of the recovered sample is shown in Fig. 2. The  $F_{2g}$  mode of cubic diamond is clearly observed at 1324  $\text{cm}^{-1}$ . The peak slightly shifts to lower wave number in comparison with the value of 1332  $\text{cm}^{-1}$ , which is commonly observed for cubic diamond. In addition, the peak width is larger. These features can be explained by the effect of strain or small grain size (5).

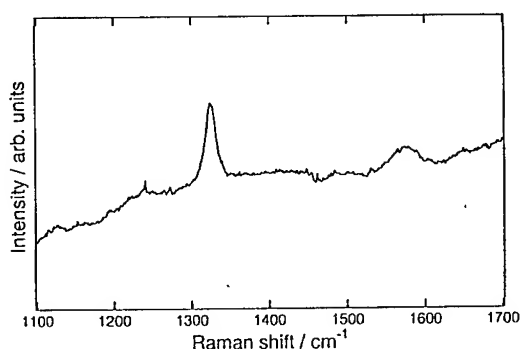


Fig. 2 The Raman spectrum of the recovered sample.

We analyzed the sample by using a TEM (200 kV) and a HRTEM (1500 kV). Most area of the recovered sample was thin enough for the TEM observations. The TEM image shows that an angular particle consists of small grains of about 100 nm. The electron diffraction patterns (EDP) of the small grains yield  $d$ -values consistent with cubic diamond. The orientation of the grains was mostly perpendicular to the cubic [111] direction. Some grains were oriented to other directions. The fine structure of the grains was further studied by using a HRTEM. The HRTEM image of a grain viewed along the [110] direction is shown in Fig. 3. A number of twin boundaries exist on the {111} plane at about 10 nm intervals.

It is worth noting the mechanism of the transformation on the basis of the fine structure. According to the orientation relationship, it can be thought that the {111} twins have its origin in the hexagonal diamond. We think that the transformation proceeded as follows.

At the beginning of heating, the hexagonal diamond was formed from the graphite by a martensitic transformation (6). Afterwards, the hexagonal diamond gradually changed to the cubic diamond with rearranging atoms in a short range, and most of the twins disappeared. Such a mechanism should be characteristic of the direct transformation without solvent. In other words, the fine structure is one of the evidences that the transformation occurred without passing through a solution state.

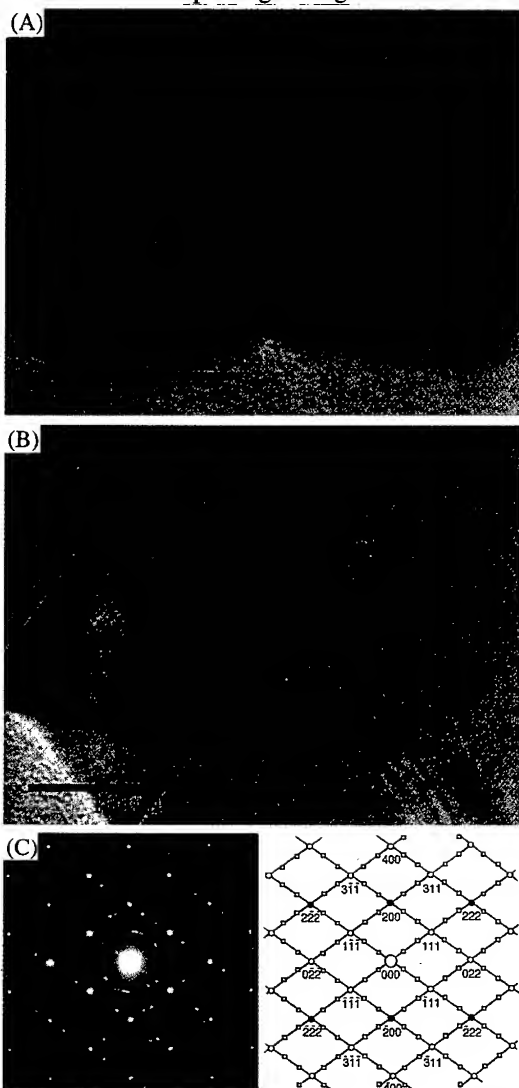


Fig. 3 (A), (B) High resolution transmission micrograph of a diamond grain viewed from the  $[110]$  direction.  $\{111\}$  twins in nanometer size are observed. (C) The electron diffraction pattern of (B) (left) and its indices

## Conclusion

Direct conversion of graphite to cubic diamond was achieved using a laser-heated DAC. A high-power  $\text{CO}_2$  laser with a continuous wave made it possible to heat the sample at high pressures for a long time. The reaction product consists of angular and round particles. The angular particles are made up of tiny grains, which have many twins and stacking faults. This fine structure would be characteristic of the cubic diamond directly transformed from graphite without catalyst.

## Acknowledgment

We thank Dr. W. Utsumi and Dr. P. Schields for valuable discussions about the relationship between cubic and hexagonal diamond.

## References

1. F. P. Bundy, *J. Chem. Phys.* **38**, 618 (1963).
2. Q. Williams, R. Jeanloz, J. Bass, B. Svendsen, and T. J. Ahrens, *Science* **236**, 181 (1987).
3. J. S. Gold, W. A. Bassett, M. S. Weather, and J. M. Bird, *Science* **225**, 921 (1984).
4. M. S. Weathers and W. A. Bassett, *Phys. Chem. Minerals* **15**, 105 (1987).
5. M. Yoshikawa, Y. Mori, M. Maegawa, G. Katagiri, H. Ishida, and A. Ishitani, *Appl. Phys. Lett.* **62**, 3114 (1993).
6. W. Utsumi, M. Yamakata, T. Yagi, and O. Shimomura, in *High-Pressure Science and Technology, Proceeding of the XIVth AIRAPT International Conference, Colorado, USA, 1993*, pp. 535-538.

## EFFECT OF INTERFACIAL ENERGY ANISOTROPY ON THE DIAMOND CRYSTAL HABIT

V.M.PEREVERTAILO, L.YU.OSTROVSKAYA, S.M.IVAKHNENKO, O.B.LOGINOVA,  
A.A.SMEKHNOV

*Bakul Institute for Superhard Materials of the Ukrainian  
National Academy of Sciences, 2, Avtozavodskaya St., 254074, Kiev, Ukraine*

### ABSTRACT

For the first time, at pressures up to 7.0 GPa, the wettability of diamond different crystallographic faces {hkl} with metal melts suitable for diamond growth has been studied. Based on findings on wettability as well as on analysis of diamond crystal forms grown in melts by the T-gradient method, the correlation between the diamond crystal habit and capillary properties of the mother melt has been found. It is shown that an interface-active impurity added to the growth medium changes the ratio of interfacial energies  $\sigma_{sl}^{hkl}$  of different faces, which changes the habit of diamond crystals being grown (all other factors: temperature, pressure, oversaturation being equal). Criteria for the selection of an impurity are suggested, which enables one to produce diamond single crystals of the wanted habit (octahedron, cubooctahedron, cube). The mechanism of the impurity effect is analyzed.

### Introduction

The making of synthetic diamond crystals of different habits is of great practical and scientific interest. It is known that to the best use of diamond cutting properties in diamond tools, crystals of octahedron habit are needed; diamond crystals which feature a predominant development of cube faces are used as dies and heat sinks; those of complex habit with high-index {113}, {115} faces are used for superprecision machining of a variety of materials.

On the other hand, as, by Wulff, for diamond structure crystals, the octahedron formed by highly stable {111} faces, is a dynamically stable habit [1], the problem of making diamond crystals of other habits (cube, cubooctahedron) presents severe difficulties.

Pressure and temperature dependence of diamond crystal habit being grown from a metal-carbon melt has been adequately studied. Analysis of the relationship between the crystal form when crystallized from a solution-melt and the interfacial energy of the crystal-melt system was not a subject of a single work. Meanwhile, just in the solution there is a possibility of changing interfacial properties by the change of its composition, and it is likely that this may entail a crystal habit change. This is the subject of the present investigation.

The present work gives experimental results on growing single crystals of Ge and diamond of cubic and cubooctahedron habits from growth media of different compositions for model and real growth systems.

### Experimental

Experiments were performed under identical conditions (P,T parameters) for a number of growth media (Ni-base metal melts) on growing synthetic diamond single crystals as well as on wetting diamond cube and octahedron faces with melts. Crystals were grown onto seeds by the temperature gradient method at pressure of 5.5 - 6.5 GPa and temperature of 1300-1700° C, holding time being up to 100 hours and above. The maintenance of pressure and temperature was accurate to within  $\pm 0.1$  GPa and  $\pm 2^\circ$  C, respectively. The wetting of diamond different faces was studied for the first time following a specially developed procedure under high pressures (up to 7 GPa) and temperatures (up to 2000 K) in the diamond stability region. Natural planes (111) of natural diamonds as well as substrates of (100) orientation cut out from large natural diamond crystals (deviation from a crystallographic plane is no more than  $0.5^\circ$ ) were used. The wetting angles of diamond were measured from solidified drops of the melt after the samples

were removed from HPA. The growth medium composition was varied by the addition of impurities of different interfacial activity (Ge, Sn, Cr, Mn, B, Cu) at the diamond-melt interface.

## Results and Discussion

The forms of the as-grown diamond crystals were compared with data on wetting. The results are summarized in Table 1.

The interface-inactive impurity (Cu) does not cause the inversion of diamond different faces wettability, no changes in diamond crystal habit occur as well.

The interfacial energy anisotropy for the crystal-melt system can be evaluated for different crystallographic planes from Young-Neuman equation known in the capillarity theory [2]:

$$\sigma_{sl} = \sigma_{sv} - \sigma_{lv} \cdot \cos \theta \quad (1)$$

Table 1. Wetting anisotropy of natural diamond octahedral and cube faces with metal melts and forms of growing diamond crystals

Growth system		Test conditions		Wetting angles, deg.		Diamond crystal form
Solvent	Impurity	P, GPa	T, °C	(111) face	(100) face	
Ni	-	6,7	1750	73	68	octahedron
Ni	Ge	6,7	1750	91	117	cube
Ni-Cr	-	6,7	1500	73	59	cubooctahedron
Ni-Cr	Sn	6,7	1500	69	86	cube
Ni-Mn	-	$2 \cdot 10^{-6}$	1200	42	22	cubooctahedron
Ni-Mn	B	$2 \cdot 10^{-6}$	1200	60	68	cube
Ni-Mn	Cu	6,7	1200	120	108	cubooctahedron

A correlation between diamond crystal habit and capillary properties of a mother solution is found: a face which is more developed in habit is worse wetted with a mother solution as compared with other faces.

The addition of an interface-active element to the melt (Ge, Sn, B) causes the inversion of wettability (Table 1). The crystal habit changes accordingly, as shown by SEM micrographs of diamond single crystals (Fig. 1).

here  $\sigma_{sl}$ ,  $\sigma_{sv}$ ,  $\sigma_{lv}$  are the solid-liquid, solid-vapour and liquid-vapour surface energies, respectively,  $\theta$  - experimental wetting angle.

In view of the fact that the evaluation of  $\sigma_{sl}$  by Eq.(1) for real growth media is impracticable (experimental values of  $\sigma_{sv}$  for diamond and  $\sigma_{lv}$  for metal melts at high pressures are unknown), we have performed [3] a series of model experiments on

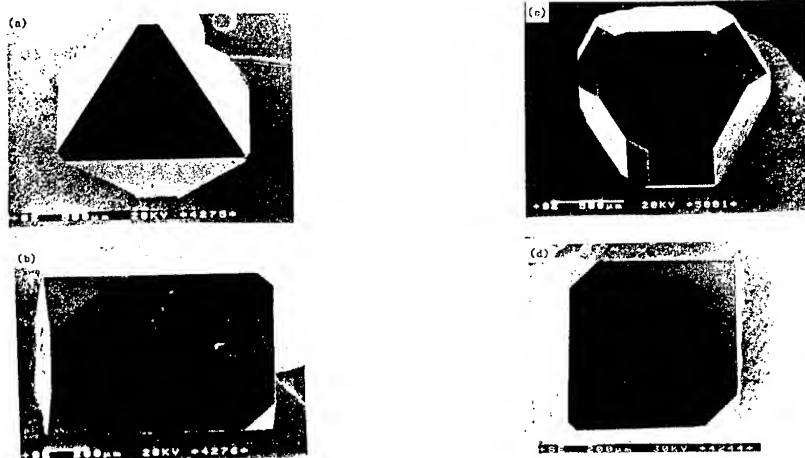


Fig. 1. Habits of diamond crystals grown in different growth media: (a) Ni-C; (b) Ni-Ge-C; (c) Ni-Cr-C; (d) Ni-Cr-Sn-C

growing germanium single crystals in the Me-Ge systems (Ge is an analog of diamond in structure), which showed the same correlation between the form of the as-grown Ge crystals and the properties of the crystal-melt interface (Table 2)

The impurity, which meets the above requirements and added into the main solvent, changes the ratio of interfacial energies for different faces of a crystal being grown. This causes the crystal habit to change. Following the criteria

Table 2. Anisotropy of capillary characteristics of the Ge crystal - Sn-Ge melt system

Structural and energy characteristics of Ge single crystal faces [2]					T, °C	Composition of a growth medium, at. %	Capillary characteristics of the contact system					Ge crystal form
Face index {hkl}	$\rho_{hkl} \cdot 10^{14} \text{ cm}^{-2}$	m	$m \cdot 10^{14} \text{ cm}^{-2}$	$\sigma_{sv} \frac{\text{mJ}}{\text{m}^2}$			$\sigma_{lv} \frac{\text{mJ}}{\text{m}^2}$	$\theta \text{ deg}$	$\sigma_{lv} \cos \theta$	$\sigma_{sl} \frac{\text{mJ}}{\text{m}^2}$	$\frac{\sigma_{sl}^{(100)}}{\sigma_{sl}^{(111)}}$	
100	6,24	2	12,48	1903	937	Ge-melt	666	9	658	1245	2,38	oct
					800	Sn+62 Ge	522	33	438	1465	2,24	oct
					600	Sn+18 Ge	433	48	290	1613	2,14	cubooct
					400	Sn+4,6 Ge	489	63	222	1681	2,12	cubooct
111	7,21	1	7,21	1100	937	Ge-melt	666	30	577	523	2,38	oct
					800	Sn+62 Ge	522	31	446	655	2,24	oct
					600	Sn+18 Ge	433	37	390	710	2,14	cubooct
					400	Sn+4,6 Ge	489	51	308	792	2,12	cubooct

Note.  $\rho_{hkl}$  is the reticular density of atoms; m is the number of dangling bonds per atom on a face;

Our calculations have allowed the following mechanism of an impurity effect to be suggested: an interface-active impurity (Sn for Ge and Ge, Sn, B for C) is selectively adsorbed by faces {100} having a higher surface energy (Table 2); this is supported by variation of wetting angles, which are very sensitive to adsorption processes at the solid-liquid interface, owing to which the interfacial energy anisotropy of cube and octahedron faces of germanium (diamond) alters essentially. As a result, at the interface there develop energy prerequisites for the appearance of usually unstable cube faces.

Based on the findings of the investigations, criteria were suggested for selection of additives for growth media which permit changing the proportion of the development of cube and octahedron faces in diamond. The impurity added to the mother melt should be:

(a) interface-active one with respect to the solvent; (b) an electronic analog of carbon (for impurities which do not enter into structure); (c) inactive with respect to carbon to lower the melt-carbon bonding energy.

suggested, it has been possible, in a number of growth systems, to increase essentially (from 10 to 70 %) a portion of cube planes in a diamond crystal being grown.

Thus, by varying interfacial and capillary properties in the diamond crystal-growth medium system, one can purposefully change diamond crystal habit in the process of growing it. The crystal habit is precisely predicted by measuring wetting angles for different diamond faces under P,T-conditions fully identical to those of growing. In this case, faces of the worst wettability will be the most developed crystallographic planes, while those of the best wettability will be either nonexistent at all or poorly developed.

## References

1. I. Sunagava, *J. of Cryst. Growth* **99** (1990) 1156.
2. Yu. V. Naidich, V. M. Perevertailo, N. F. Grigorenko, *Kapillarnie Javlenia v Processah Rosta i Plavlenia. Kristallov* (Kiev: Naukova dumka, 1983).
3. V. M. Perevertailo, L. Yu. Ostrovskaya, O. B. Loginova, *Sverkhtrudye materialy*, **2** (1995) 52.

## LP/LT DIAMOND HYDROSYNTHESIS

E. ABGAROWICZ<sup>1</sup>, A. BAKOŃ<sup>1</sup>, S. MACIEJOWSKA<sup>1</sup>, R. SAŁACIŃSKI<sup>1,2</sup>,  
A. NIEDBALSKA<sup>1</sup>, A. SZYMAŃSKI<sup>1,3</sup>

<sup>1</sup> A.Szymański & CO-DiaTech LTD., 15, Skrzetuskiego St.,  
05-092 Łomianki, Poland

<sup>2</sup> Warsaw University, Faculty of Geology, 93, Żwirki i Wigury St.,  
02-089 Warszawa, Poland

<sup>3</sup> Warsaw University of Technology, Faculty of Chemistry,  
75, Koszykowa St., 00-622 Warszawa, Poland

### ABSTRACT

In the paper future development of static diamond coarsening and bonding processes through low-pressure and low temperature liquid phase epitaxy (LP/LTLPE) is discussed. Natural and synthetic seeds crystal were located in especially prepared environment and subjected to pressure of 170 MPa and temperature of about 400°C. As result the seeds crystal were coated with the multicrystalline irregular layer of homoepitaxially grown colourless diamonds or connected with diamond phase interlayer.

### Introduction

*Nature Is The Best Teacher* - that is essential establishment taken by us in development of the bulk diamond overgrowth. Many processes occurred in near-superficial Earth's mantle zones are inscrutable in technological utilise respect.

Sol-gel colloidal processes are an example as capable to form stable crystals in thermodynamically unstable conditions.

In the Polish mineralogical circle opinion about the occurrence of the diamond hydrothermal genesis in the Nature was formulated by Thugutt thirty years before the first positive high pressure/high temperature (HP/HT) diamond synthesis realised by ASEA and GE researches.

From a few years authors demonstrated theoretical views on pneumatolytic-hydrothermal environment as potential source of diamonds in the Earth mantle as well as possibility of diamond hydrosynthesis.

### Experimental and Results

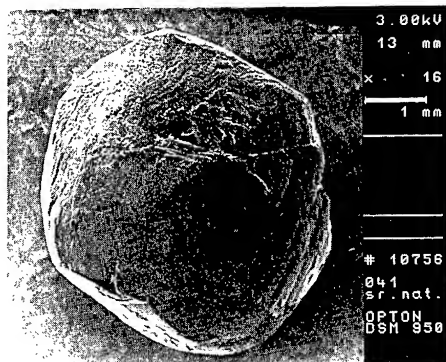
The diamond hydrothermal synthesis process was carried out at typical pressure autoclave filled with colloidal especially prepared carbon enriched water solution and subjected to pressure of 170 MPa and temperature of about 400 °C. As the seeds were used:

1. natural diamond with weight 1,1ct (Fig.1a) and
2. five grams of MDA type synthetic diamonds with size about 0.4 mm (Fig.2a).

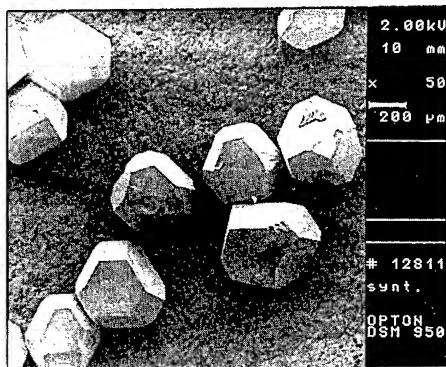
A 21 days process cycle was allowed. After process seeds were acid cleaned and analysed by optical microscopy, SEM and Raman spectroscopy.

As result seed crystal of natural diamond was coated with the multicrystalline irregular layer of homoepitaxially grown up second generation of colourless diamonds with octahedral habit and size up to 10 µm (Fig. 1b and 1c). The synthetic diamond grains were connected with diamond phase interlayer (Fig. 2b and 2c).

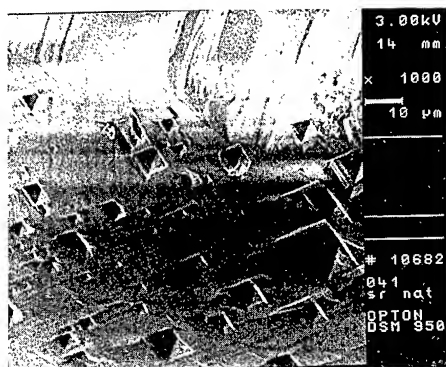




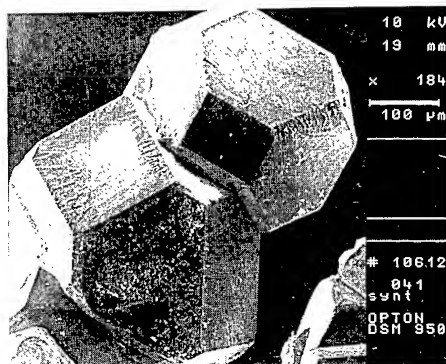
a)



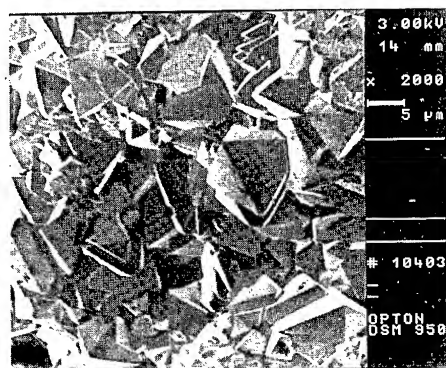
a)



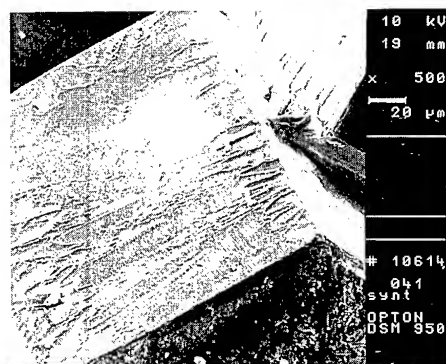
b)



b)



c)



c)

Fig.1. The sample of natural seed diamond:

- a) before experiments,
- b) and c) the multicrystalline layer colourless diamond as the homoepitaxially grown up second generation.

Fig.2. Samples of synthetic seeds diamond:

- a) before experiments,
- b) and c) the synthetic diamond grains connected with diamond phase interlayer.

## Conclusion

Growth of the stable monocrystalline diamonds, in the pseudo-metastable condition for diamond plot, may be realised with processes going at colloidal environment by the long time and with participation of free radicals catalysts. Bulk diamond coarsening and close-structure

multigrain diamond composites production is possible using the hydrothermal processes.

At this moment there are two possible ways of crystallization through liquid phase: the first way is a traditional high pressure high temperature system and the second way connected with hydrothermal homogenic nucleation (Fig.3).

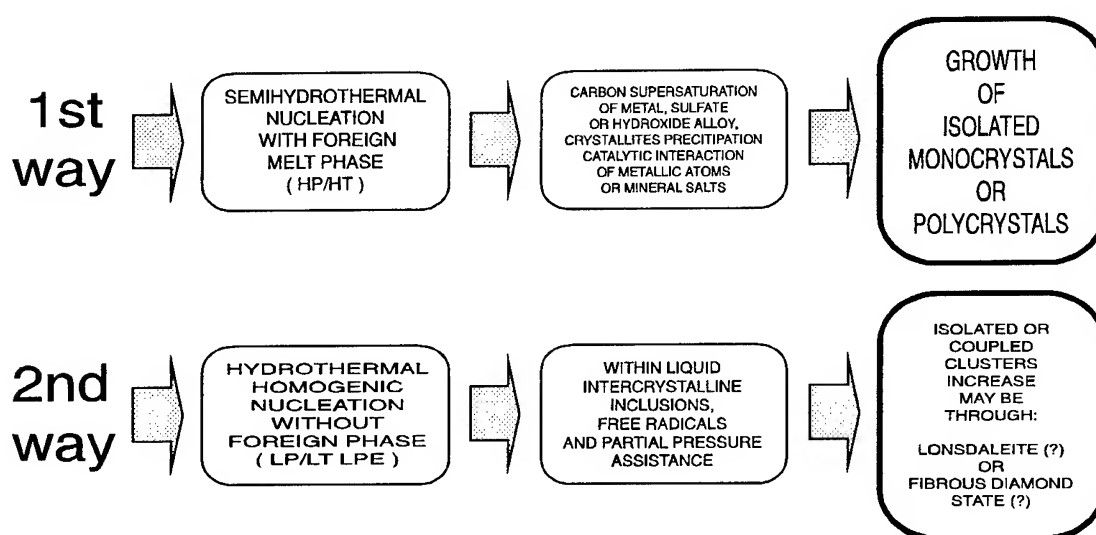


Fig. 3. Two ways of diamond crystallization through liquid phase.

## References:

1. St. Thugutt, Rev.Sci. 61 (4), 1923, 97-102
2. A. Szymański, L.Hozer and A.Niedbalska: Proc.Second Int.Conf. on New Diamond and Technol., Washington, MRS Pub.,Pittsburg (1991)
3. A.Niedbalska, A.Szymański: Proc.ICAM'91, Int.Congress on Applied Mineralogy, Pretoria, Sept. 2-4,1991, paper 56.
4. A.Niedbalska, R.Sałaciński, J.Sentek, A.Szymański: Proc. 4<sup>th</sup> Int.Conf. on New Diamond and Technol., Kobe , July 18-22, 1994, Sci.Pub.Div.MYU, Japan,1994,
5. Szymański: Arch.Min., 50, (2), 1994, 11-28
6. A.Szymański, E.Abgarowicz, A.Bakoń, A.Niedbalska, R.Sałaciński, J.Sentek: Diamond and Related Mater., Letter, 4 ,1995, 234-235.
7. A.Szymański,: Proc.2<sup>nd</sup> Int.Conf. on C-BN and Diamond, Jabłonna, Jun 27-29 (1995), in press.
8. A.Szymański: 6<sup>th</sup> European Conf. on Diamond, Diamond-like and Related Materials, Barcelona, Spain 10-15 Sept.,1995

# STRUCTURAL VARIATIONS IN DIAMOND DUE TO EXTREME EXTERNAL EFFECTS

N.V. NOVIKOV, G.P. BOGATYREVA and A.B. ROITSIN\*

*V.N. Bakul Institute for Superhard Materials of the Ukrainian  
National Academy of Sciences, Kiev, Ukraine*

*\* Institute of Semiconductors of the Ukrainian National Academy  
of Sciences, Kiev, Ukraine*

## ABSTRACT

Powder diamond samples were acted upon by gaseous chlorine, hydrogen and nitrogen at 1000 °C and laser-irradiated in the IR wavelength range. Studied were EPR spectra, magnetic susceptibility, dielectric losses, physico-mechanical properties, hydrophilic nature as well as qualitative and quantitative composition of impurities.

## INTRODUCTION

It has been shown that due to extreme external effects, essential structural variations occur both in the bulk and on the surface of diamond.

Interest in studying and ever-improving diamond synthesis technology is dictated by the fact that being a typical covalent crystal it has a number of unique properties. It is commonly supposed that diamond is resistant to aggressive media. The data we obtained recently, however, gives grounds to consider a synthetic diamond (SD) surface as the one with a hypomolecular structure that originates due to a chemical interaction of the diamond carbon and metal inclusions with reagents during diamond recovery and treatment [1].

The above interaction is accompanied by a change in physico-chemical and chemical properties, which suggests the possibility of both bulky and surface structural variations.

## PROCEDURE

In the present paper, an attempt is made to define the effect of a high-temperature chemical treatment and laser irradiation on structural variations in diamond. The EPR method was taken as a structure-sensitive one [2]. Subjects of investigations were diamond powders synthesized in the (Ni-Mn-C) system. The powder characteristics are given in Tables 1 and 2.

A 5/3 grit-sized micron powder was treated for 15 - 25 min at 1000 °C in various gas media: reducing (hydrogenation), oxidizing (chlorination) and neutral (nitrogen) ones [3]. 400/315 grit-sized grinding powders with the lowest (sample 1) and enhanced

(sample 2) amounts of metal inclusions were laser-irradiated. The degree of structure perfection was assessed from dielectric loss tangent ( $\text{tg } \delta$ ).

Table 1 Main Characteristics of 5/3 Grit-Sized Synthetic Diamond Micron Powders in the Initial State and after Thermochemical Treatment

State of the sample	$\chi$ , $10^{-8} \text{ m}^3/\text{kg}$	$\text{tg } \delta$ , 10-3	$\Delta C_s$ mJ/(mole.g)
Initial	1,19	14,6	-227,1
Chlorinated	-0,48	21,9	-973,2
Hydrogenated	1,10	23,8	-36,5
Nitrided	24,8	-	-

Table 2 Characteristics of 400/315 Grit-Sized Synthetic Diamond Grinding Powders

Sample number	$\chi$ , $10^{-8} \text{ m}^3/\text{kg}$	$\text{tg } \delta$ , 10-3	$K_a$ , %	D.L., N.	
				init	as-laser treated
1	2,7	14,1	0,37	129	198
2	27,0	33,4	1,27	73	64

The value of specific magnetic susceptibility ( $\chi$ ) has been used to characterize the amount of metal inclusions. For grinding powders, the surface roughness degree was evaluated from the surface roughness coefficient ( $K_a$ ) and for micron powders, from the value of water saturation free energy ( $\Delta C_s$ ) [1]. The samples were laser-treated under similar conditions: IR wavelength range (1 - 10.6 nm) the density of irradiation energy being (5-6).103 Jcm<sup>-2</sup>. EPR spectra were taken using a RE-1306 3-cm range spectrometer at room temperature. The EPR spectra from nitrogen and metal inclusions are shown in Figs. 1, 2, 3, and 4.

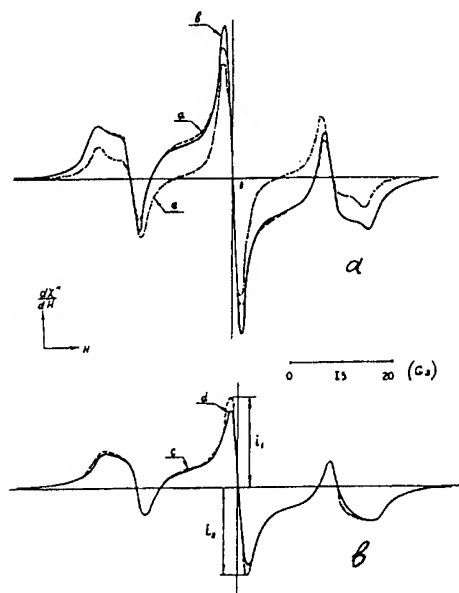


Fig.1 EPR spectra from nitrogen in initial (a) and as-laser treated (b) grinding powders.

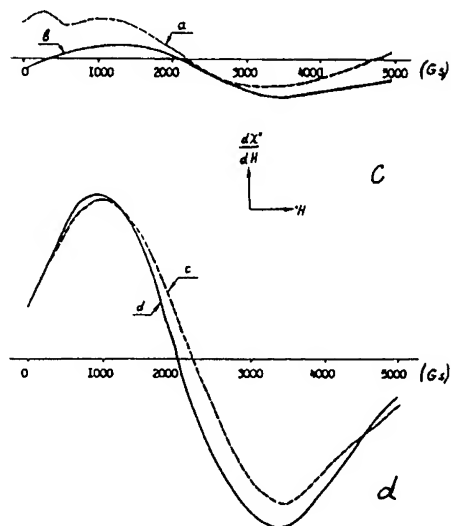


Fig.2 EPR spectra from metal inclusions in initial (c) and as-laser treated (d) grinding powders.

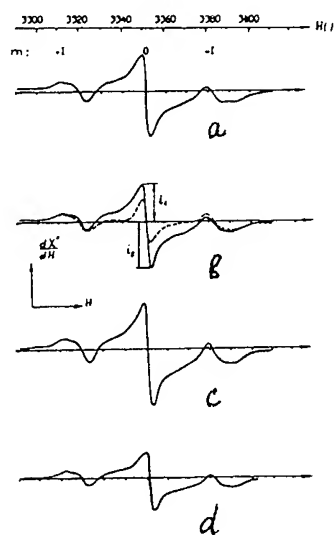


Fig.3 EPR spectra from nitrogen in 5/3 grit-sizes micron powders initial (a) and after treatment with gaseous hydrogen (b), chlorine (c) and nitrogen (d) at 1000 °C.

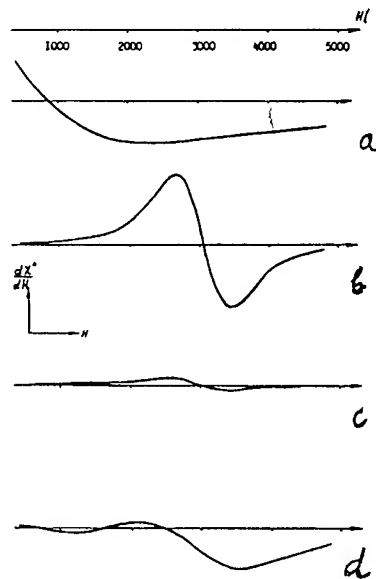


Fig.4 EPR spectra from metal inclusions in 5/3 grid-sized micron powders initial (a) and after treatment with gaseous hydrogen (b) chlorine (c) and nitrogen (d) at 1000 °C.

## DISCUSSION

Our findings suggest that ferromagnetic impurities are mainly on the surface of samples and due to thermochemical effect, they undergo various structural transformations (phase transitions), partially intersecting the diamond surface. The most radical changes occur under the effect of chlorine. The comparison of the results obtained shows that the EPR data correlate with those of physico-chemical measurements (see Table 1) and indicate that along with the variation in the number of broken bonds due to the heat treatment in the atmosphere of hydrogen, chlorine and nitrogen, the variation in the resonating nitrogen concentration owing to its migration in the sample, clustering and heavy dependence of the processes on the condition and dimensions of diamond surface is possible as well.

Analysis of as-IR laser-irradiated diamond grinding powders has shown that their main characteristics ( $\chi$ ,  $\tan \delta$ , D.L. etc.) as well as EPR spectra depend on the sample type and state. High- and lower-strength synthetic diamond (SD) powders have different  $c$ ,  $\tan \delta$  and roughness coefficient values, which suggests the different degree of the sample imperfection. As-laser treated high-strength powder exhibit further strengthening, while the lower-strength ones lose their strength. These data correlate with the EPR results. Analysis of the above spectra points to the relationship between the strength of SD and the state and amount of ferromagnetic inclusions. It is suggested that in higher-strength SD, inclusions are distributed uniformly over the bulk, while in the lower-strength ones they are in the form of clusters, inducing high inner stresses. An intensive exchange interaction of atoms within a cluster facilitates a formation of the ferromagnetic resonance. In this case, the laser irradiation acts as a "distributor" of metal inclusions over the crystal.

## CONCLUSIONS

EPR and FMR studies have shown that the laser treatment of SD results in elimination of different type structural imperfections of the crystal lattice, including those caused by metal inclusions. Laser treatment was found to exert a selective effect on the strength of different type diamond. An imperfect structure of was shown to be one of the main factors responsible for the SD strength, which in its turn is affected by the laser treatment.

Thus, structural variations in SD caused by extreme external effects have been established using the FMR and EPR methods.

## References

1. V.G. Aleshin, A.A. Smekhnov, G.P. Bogatyreva, and V.B. Kruk, *Chemistry of Diamond Surface*, ed. N.V. Novikov, (Naukova Dumka, 1990) [in Russian].
2. A.B. Roitsin and V.M. Mayevsky, *Surface Radioscopy of Solids* (Naukova Dumka, 1992) [in Russian].
3. G.P. Bogatyreva, L. Yu. Vladimirova, E.P. Zusmanov, V.M. Mayevsky, and A.B. Roitsin, *Poverkhnost*, 1 (1995) 95.
4. G.P. Bogatyreva, G.A. Bazaly, E.P. Zusmanov, V.M. Mayevsky, and A.B. Roitsin, *Zhurnal Teoreticheskoi Fiziki*, vol. 65, 2 (1995) 55.

**V(B) Boron Nitride and Gallium Nitride**

## NEW ROUTE FOR PREPARING c-BN AT MEDIUM PRESSURE AND TEMPERATURE

G. DEMAZEAU, V. GONNET, H. MONTIGAUD and B. TANGUY  
Institut de Chimie de la Matière Condensée de Bordeaux - Avenue du Dr. A. Schweitzer  
33608 PESSAC Cedex (France)

V.L. SOLOZHENKO  
Institut des Matériaux Ultra-Durs de l'Académie des Sciences d'Ukraine - Kiev 254-253 (Ukraine)

### ABSTRACT

Cubic boron nitride appears to be a material with exceptional physico-chemical properties.

Prepared for the first time in 1967, all the processes developed involve high pressure ( $P > 5$  GPa) and high temperatures ( $T > 1100^\circ\text{C}$ ) conditions.

On the basis of recent thermodynamical calculations claiming that c-BN could be the stable form at normal pressure, a new process has been set-up. The objective was to reduce the kinetic effects governing the h-BN  $\rightarrow$  c-BN conversion. Consequently, we have developed nitriding solvents as  $\text{NH}_2\text{NH}_2$  in supercritical conditions due to the physico-chemical properties of such specific state (high thermal diffusivity, high diffusion of the chemical species...).

Starting from the graphitic form h-BN and using some additives as  $\text{Li}_3\text{N}$  in order to improve the ionicity of the solvent, it has been possible to prepare c-BN in reduced P,T conditions ( $1.8 < P < 2.5$  GPa ;  $500 < T < 700^\circ\text{C}$ ).

### 1. Introduction

Due to the position of boron and nitrogen in the Periodic Table, BN is isoelectronic of two carbons. Few years after the synthesis of diamond [1,2], the zinc-blende form of Boron nitride was prepared by Wentorf [3].

The principle of the c-BN synthesis is mainly based on the difference of solubility of the starting graphitic form (h-BN) and the resulting cubic form (c-BN). The fluxes generally developed are derived from nitrides, fluoronitrides [4] (Table I). An equilibrium-line between c-BN and h-BN was proposed on the basis of thermodynamical calculations at high temperatures and through extrapolations at low temperatures by comparison with the equilibrium line between the corresponding structures of carbon [5,6]. Recent thermodynamical calculations by Solozhenko [7-10] and then confirmed by Maki et al. [11] claimed that c-BN could be the stable form of boron-nitride at normal pressure (Fig. 1). Nevertheless, no synthesis of c-BN crystallites at normal or medium pressures have been described up to now in the literature.

The difficulties for preparing the cubic form at low or medium pressures could be attributed to kinetic effects. On the basis of recent physico-chemical characterizations the domain of composition of the cubic form (c-BN) seems to be very narrow [12,13]. Such a condition implies that, during the crystal growth process, B and N species must be deposit on the nucleus at the same concentration.

Table I - Different flux precursors previously used for the flux-assisted h-BN  $\rightarrow$  c-BN conversion

Group	Material
a1	Li, Mg, Ca
a2	$\text{Li}_3\text{N}$ , $\text{Mg}_3\text{N}_2$ , $\text{Ca}_3\text{N}_2$
a3	$\text{Li}_3\text{BN}_2$ , $\text{Mg}_3\text{B}_2\text{N}_4$ , $\text{Ca}_3\text{B}_2\text{N}_4$ , $\text{Sr}_3\text{B}_2\text{N}_4$ , $\text{Ba}_3\text{B}_2\text{N}_4$
a4	$\text{Mg}_2\text{NF}$ , $\text{Mg}_3\text{NF}_3$ , $\text{Ca}_2\text{NF}$ , $\text{Ca}_3\text{B}_2\text{N}_4 + x\text{LiF}$ , $\text{Mg}_3\text{B}_2\text{N}_4 + x\text{LiF}$
b1	$\text{H}_2\text{O}$
b2	$(\text{NH}_2)_2\text{CO}$ , $\text{NH}_4\text{NO}_3$ , $\text{H}_3\text{BO}_3$ , $\text{NH}_4\text{B}_5\text{O}_8$
c	$\text{NaF}$ , $\text{LiBF}_4$ , $\text{MgF}_2$ , $\text{NH}_4\text{F}$ , $\text{Na}_2\text{SiF}_6$ , $(\text{NH}_4)_2\text{SiF}_6$
d1	Si, $\text{Si}_3\text{N}_4$ , Si alloys
d2	AlN
d2	Sn, Sn, Pb, various alloys

In order to reduce such kinetic effects, and the difference of diffusion rates between boron and nitrogen species into the selected flux, nitriding solvents in supercritical conditions have been investigated due to their specific physico-chemical properties (thermal diffusivity and high chemical diffusion).

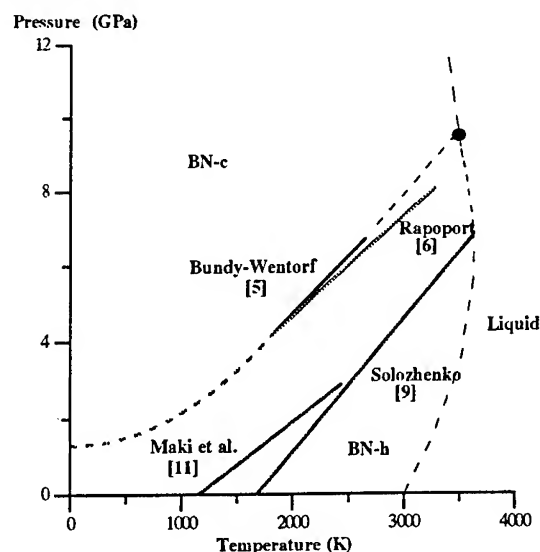


Figure 1 - Stability diagram (P,T) for boron nitride versus different authors

## 2. c-BN synthesis with $\text{NH}_2\text{NH}_2$ in supercritical conditions

$\text{NH}_2\text{NH}_2$  has been preferred to  $\text{NH}_3$ , this solvent being a liquid phase in normal pressure and temperature conditions.

Using a belt-type equipment a specific cooper capsule is used as container in the high pressure reaction cell. The graphitic modification was selected as starting material. In order to improve its solubility in the solvent, ionic nitride  $\text{Li}_3\text{N}$  was used as additive (8 mg for  $0.2 \text{ cm}^3$  of  $\text{NH}_2\text{NH}_2$ ).

The P,T domain of formation of the cubic form is given on Figure 2. Single crystals with a size close to  $100 \mu\text{m}$  can be obtained after few minutes. The Raman spectrum of the resulting material given on figure 3 indicates on the formation of the cubic form. The optimization of such a new process is now in progress in order to investigate the pressure-limit of the c-BN nucleation [14].

## 3. Conclusion

Due to its physico-chemical properties, nitriding solvent as  $\text{NH}_2\text{NH}_2$  in supercritical conditions can be used for preparing c-BN in medium pressure and temperature conditions ( $2,3 < P < 1,7 \text{ GPa}$ ,  $500 < T < 650^\circ\text{C}$ ) [15].

Solvothermal synthesis of c-BN through the reduction of the kinetic effects appears to be a promising route for reducing the experimental conditions. In addition, the investigation of such new processes is important for evaluating the recent thermodynamical calculations [16].

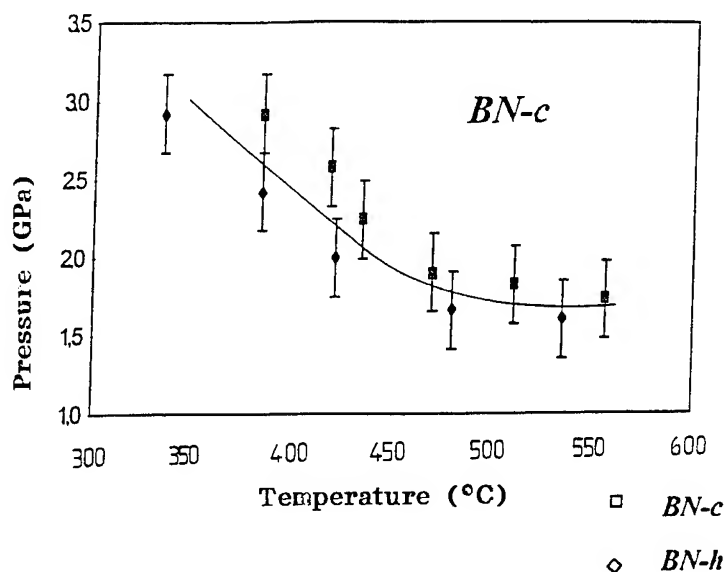


Figure 2 - (P,T) domain of synthesis for cubic BN using  $\text{NH}_2\text{NH}_2$  in supercritical state and  $\text{Li}_3\text{N}$  as additive



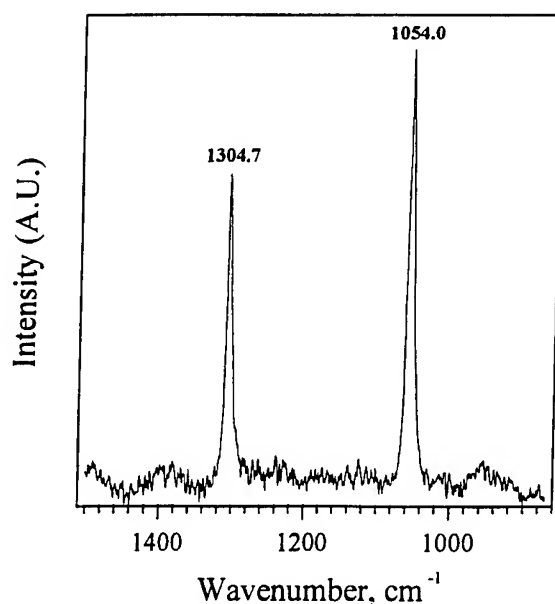


Figure 3 - Raman spectrum of the resulting c-BN crystallites

## References

- 1 H. Liander, *A.S.E.A. J.*, **28** (1995) 97
- 2 F.P. Bundy, H.T. Hall, H.M. Strong and R.H. Wentorf Jr., *Nature*, **176** (1955) 51
- 3 R.H. Wentorf Jr., *J. Chem Phys.*, **26** (1957) 956.
- 4 L. Vel, G. Demazeau and J. Etourneau, *Materials Science and Engineering*, **B10** (1991), 149.
- 5 F.P. Bundy and R.H. Wentorf Jr., *J. Chem. Phys.*, **28** (1963), 1144.
- 6 E. Rapoport, *Ann. Chim. Fr.*, **10** (1985) 607.
- 7 V.L. Solozhenko, *Dok. Phys. Chem.*, **301** (1988) 592.
- 8 V.L. Solozhenko, *High Pressure Res.*, **7** (1991) 201.
- 9 V.L. Solozhenko, *Thermochim. Acta*, **218** (1993) 221.
- 10 V.L. Solozhenko, *Diamond and Related Materials*, **4** (1994) 1.
- 11 J. Maki, H. Ikawa and O. Fukunaga, *New Diamond Science and Technology*, Ed. R. Messier, J.T. Glass, J.E. Butler, R. Roy, M.R.S. (1991) 1051.
- 12 G. Demazeau, L. Vel-Boutinaud, V. Gonnet, M. Jaouen, T. Cabioch, G. Hug, *Advances in New Diamond Science and Technology*, Proceedings of the fourth International Conference on the New Diamond Science and Technology - ICNDST-4, Kobe, Japan, July 18-22, 1994, S. Saito, N. Fujimori, O. Fukunaga, M. Kamo, K. Kobashi and M. Yoshikawa (Editors), Myu, Tokyo (1994) 545-549.
- 13 M. Jaouen, G. Hug, V. Gonnet, G. Demazeau and G. Tourillon, *Micros. Microanal. Microstruct.*, **6** (1995) 127.
- 14 G. Demazeau, V. Gonnet, V. Solozhenko, B. Tanguy and H. Montigaud, *C.R.Acad. Sc. Paris*, **321 Série IIb** (1995) 419.
- 15 G. Demazeau, V. Gonnet, V. Solozhenko, B. Tanguy and H. Montigaud, CNRS Fr. Patent, demand n° 94.11132, 19/09/1994.
- 16 V.L. Solozhenko, Phase Diagram of BN in *Properties of Group III nitrides*, Ed. J.H. Edgar (IEE-INSPEC) (1995) 43.

# B-C-N GRAPHITIC MATERIAL AND ITS TRANSIENT HEATING PRODUCTS AT 15 GPa

HIROYUKI KAGI, IKARI TSUCHIDA, YOSHITAKE MASUDA,  
MASAFUMI OKUDA, KAZUMASA KATSURA and MASAO WAKATSUKI  
*Institute of Materials Science, University of Tsukuba, Ibaraki 305, Japan*

## ABSTRACT

We have shown that a new type of carbonaceous material denoted as  $B_xC_{2(1-x)}N_x$  ( $x = 0.34$ ) obtained by thermal CVD method have several properties indicating semiconducting behavior, and its high pressure phase is a single phase of cubic form lying between cBN and diamond. Band gap of the B-C-N graphite proved by STS plot was approximately 1 eV and the electric conductivity increased with temperature. Flash heating experiment at 15 GPa generating transient melt of sample resulted in the formation of the cubic form. The lattice parameter was  $3.580 \pm 0.013$  Å and followed Vegard's law taking into account the chemical composition. Flash heating experiment at the same condition for the mixture of hBN and graphite resulted in the formation of wBN and diamond.

## Introduction

Mixed crystals of diamond and cubic BN (cBN) were first obtained by the direct phase transformation<sup>(1)</sup> by the method of flash heating via transient melt<sup>(2)</sup>. In his paper<sup>(1)</sup>, the starting material was deposited on a graphite rod heated at 2200 °C in mixed gases of  $BCl_3$ ,  $CCl_4$ ,  $N_2$  and  $H_2$ . However, it was not clear whether the starting hexagonal graphitic crystals were single phase or mixture of several phases. Recently, stoichiometric graphitic compound described as  $BC_2N$  was synthesized by vapor phase interaction between  $CH_3CN$  and  $BCl_3$ <sup>(3)</sup>, and its high pressure phase has been investigated by several groups. Shock compression of  $BC_2N$  resulted in the formation of cubic  $BC_2N$  and the lattice constant was larger than that expected from Vegard's law<sup>(4)</sup>. Static high pressure of 7.7 GPa and high temperature of 2150-2300 °C resulted in the formation of the cubic  $BC_2N$ <sup>(5)</sup>, and they showed that the product was thermodynamically unstable compared to cBN and diamond. These two results concerning to the high pressure phase suggest that the formation of cubic  $BC_2N$  is strongly dependent on the reaction time at high pressure and high temperature. In flash heating method<sup>(1)</sup>, duration of the transient current is in order of millisecond, its time scale in occurring physical and chemical changes lies in the

intermediate between those of shock compression and static high pressure experiment. Therefore, flash heating technique is also expected to quench metastable phases efficiently and stably, and it is worthwhile to consider the relationship between the lattice constant and chemical composition for the obtained materials. In this study, our attention was directed to the physical properties of the graphitic  $BC_2N$  and of products after rapid melting (flash heating) experiment at a high pressure of 15 GPa.

## Experimental Procedure

### *Preparation of $BC_2N$ graphitic matter*

Graphitic  $BC_2N$  was synthesized by the thermal CVD method<sup>(3)</sup>. The Ar-diluted vapors of  $BCl_3$  and  $CH_3CN$  were introduced into a quartz tube heated at 950 °C with a total flow rate around 40 cc/min. Black deposits with a thickness of several hundreds' micrometers were obtained by 8 hour reaction on a nickel substrate put in the reaction tube. In this paper, we denote the  $BC_2N$  compound as "B-C-N" for convenience, because its chemical composition deviated from B : C : N = 1 : 2 : 1 as described later. To characterize obtained graphitic B-C-N as a starting material of flash heating experiments at high pressure, we

investigated powder X-ray diffraction (XRD), scanning tunneling microscopy (STM), electric conductivity and chemical composition provided by X-ray photoelectron spectroscopy (XPS).

#### *Flash heating experiment at 15 GPa*

High pressure experiments were carried out with a Bridgeman anvil apparatus. Diameter of a flat face of the tungsten carbide core was 20 mm. Pyrophyllite discs baked at 650 °C for 1 h with 2.2 mm thick and 20 mm in diameter were used for gasket.  $\text{BC}_2\text{N}$  specimens were embedded in the central part of the disc as a fine tip of 0.5 mm diameter. Transient current enough to melt the starting material was put into the sample at a pressure of 15 GPa. Pulse current was discharged from a 24.6 mF capacitor, life time of the current was of the order of 10 milliseconds. Occurrence of melting was confirmed both from the discharging current curve and from the texture of the recovered specimens. Well-crystallized texture characterizes a crystal growth from liquid phase. X-ray diffraction patterns were collected with Debye-Scherrer camera of 57.6 mm radii.

## Results and Discussion

#### *Properties of B-C-N graphite*

Powder XRD pattern of the graphitic B-C-N material obtained by the thermal CVD method showed several broad diffractions (Fig. 1). These lines correspond to (002), (101), (004) and (110) diffractions of graphite. This suggests that the crystal structure of the obtained B-C-N material is basically same as that of graphite. Atomic configuration of B, C and N atoms on the honeycomb plane of  $\text{BC}_2\text{N}$  has been of interest. Not only the crystal form of  $\text{BC}_2\text{N}$ , but also theoretical calculation<sup>(6)</sup> revealed that possible several atomic configurations assuming periodic geometry in the honeycomb plane resulted in different electronic properties. Choosing well-grown smooth surface, we tried to observe STM image of graphitic B-C-N in order to clarify the atomic arrangement of B, C and N on honeycomb lattice of  $\text{BC}_2\text{N}$ , but we cannot encounter surface enough flat to provide atomic images of the B-C-N graphitic material. STS (scanning tunneling spectroscopy) plot being an indicator of density of states showed that the obtained B-C-N material

was semiconductor with a band gap of 1 eV approximately. This energy gap is consistent with theoretical prediction for  $\text{BC}_2\text{N}$  monolayer<sup>(6)</sup>. Furthermore, to ensure the semiconducting behavior, temperature dependence of electric conductivity for the B-C-N graphitic matter was obtained ranging from room temperature to 300 °C. The conductivity was confirmed to increase with temperature.

XPS measurement showed that chemical composition of the surface of the deposit was  $\text{B}_{0.33}\text{CN}_{0.26}$ , but Ar sputtering resulted in the decrease of B and O, and the amounts of B and N balanced. Boron oxide as a surface contamination was removed by the sputtering process. This phenomenon has been confirmed for another B-C material,  $\text{BC}_3$  recently<sup>(8)</sup>. Therefore, we assume that the composition of B-C-N graphitic matter as  $\text{B}_{0.26}\text{CN}_{0.26}$ . Anyway, this result shows that the obtained B-C-N material contain a considerable excess of carbon over that expected from the chemical formula of  $\text{BC}_2\text{N}$ . At present, it was not clear but it is possible to consume that our B-C-N deposit have some bearings to  $\text{BC}_3\text{N}$  similarly grown by thermal CVD deposit starting from  $\text{C}_2\text{H}_5\text{OH}$  and  $\text{BCl}_3$ .

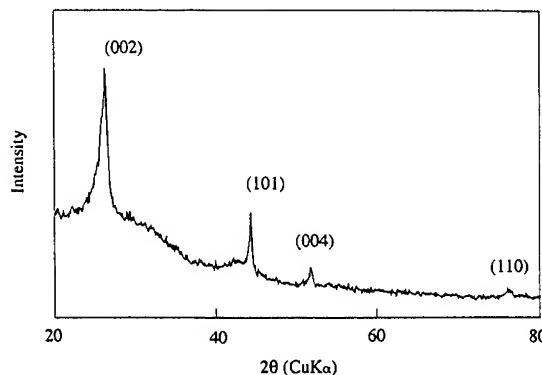


Fig. 1. Powder X-ray diffraction pattern for the B-C-N graphitic matter as a starting material of the flash heating experiment.

### High pressure phase of B-C-N graphitic matter

Recovered specimen after the flash heating experiment on the B-C-N graphitic matter at high pressure of 15 GPa showed X-ray diffractions indicating single phase of cubic form. (111), (220) and (311) diffraction lines were observed and consistent lattice parameter was  $3.580 \pm 0.013$  Å. In Fig. 2, lattice parameter is plotted against its chemical composition ( $B_{0.26}CN_{0.26}$ ;  $B_xC_{2(1-x)}N_x$ ,  $x = 0.34$ ), the obtained point in this study lie on the straight line connecting cBN and diamond. This result implies that high pressure phase of B-C-N material obtained by the flash heating experiment at high pressure follows Vegard's law. It is consistent with the first report by Badzian<sup>(1)</sup> showing lattice parameter of mixed crystal of cBN and diamond following Vegard's law. In contrast with our results, Kakudate *et al.*<sup>(4)</sup> reported that cubic phase of  $BC_2N$  obtained by shock compression showed apparent deviation from Vegard's law. Although it is not unambiguous at present, the difference in reaction time between flash heating and shock compression could attribute to the difference in the relationship between the lattice parameter and chemical composition.

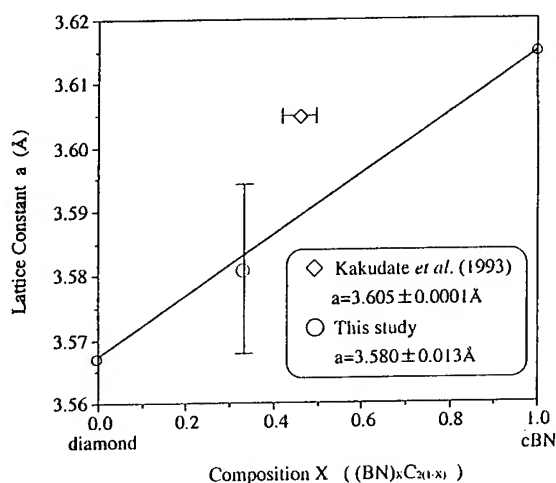


Fig.2. Composition dependence of lattice constant for cubic B-C-N. Straight line shows Vegard's law between diamond and cBN.

For comparison, flash heating experiment at 15 GPa was carried out for 1:1 mixture of hBN and graphite. X-ray diffraction pattern showed the formation of diamond and wBN (wurtzitic boron nitride). No apparent reaction between BN and diamond such as the formation of solid solution between cBN and diamond cannot be confirmed. The difference in the starting material strongly attributed to the product.

### Conclusions

1. Graphite-like material denoted as  $B_xC_{2(1-x)}N_x$  ( $x = 0.34$ ) was synthesized by thermal CVD method. X-ray diffraction pattern of the obtained material showed graphite-like structure, STS plot indicated that band gap of the material was approximately 1 eV and its electric conductivity was characterized to increase with temperature. These results suggest that the obtained material was semiconductor.

2. Product of flash heating experiment at 15 GPa starting from B-C-N graphite was cubic phase with the lattice parameter of  $3.580 \pm 0.013$  Å. This parameter follows Vegard's law. Flash heating at the same condition for the mixture of hBN and graphite resulted in the formation of mixture of wBN and diamond.

### Acknowledgments

The authors are grateful to Dr. T. Sasaki for his kind discussion and advise on the synthesis of B-C-N graphitic material. XPS measurements were debt to Ms. A. Nakao of RIKEN. We also thank Mr. K. Miyake and Prof. H. Shigekawa for STM measurement. This research was supported by Iketani Science and Technology Foundation.

### References

1. Bundy, F. P. (1963) *J. Chem. Phys.*, **38**, 618.
2. Badzian, A. R. (1981) *Mat. Res. Bull.*, **16**, 1385.
3. Sasaki, T. *et al.* (1993) *Chem. Mater.* **5**, 695.
4. Kakudate, Y. *et al.* (1994) *Proc. 3rd Int. Conf. Advanced Materials*, Tokyo, 1447.
5. Nakano, S. *et al.* (1994) *Chem. Mater.* **6**, 2246.
6. Liu, A. Y. *et al.* (1989) *Phys. Rev. B* **39**, 1760.
7. Kouvetakis, J. *et al.* (1986) *J. Chem. Soc., Chem. Commun.*, 1758.
8. Kagi, H. *et al.* to be published

## THE RESEARCH OF INFLUENCE OF PRELIMINARY HEAT TREATMENT IN FLUORINE OF gBN ON cBN SYNTHESIS

A.A.SHULZHENKO, A.N.SOKOLOV AND A.A.SMEHKNOV

*V.N.Bakul Institute for Superhard Materials of the Ukrainian National Academy of Sciences,  
2, Avtozavodskaya St., Kiev, 254074*

### ABSTRACT

The method of secondary ion mass spectrometry (SIMS) conducts the research of the influence of preliminary heat treatment in fluorine environment of initial powders gBN on the impurity composition of cubic boron nitride crystals.

### 1. Introduction

As it is known, synthesis of cBN is executed under severe barothermal conditions ( $p > 6,5$  GPa,  $T > 2000$  K]. To reduce the  $p,T$ -value, specific substances (sometimes called solvent-catalysts by analogy with diamond synthesis). Thus, more exactly, according to the nature of the processes induced by the substances being entered along with BN into the initial charge for synthesis should be defined as initiators of transformation.

In practice, nitrides of alkaline-earth metals (for instance,  $Li_3N$ ) or magnesium are most widely used as initiators of transformation.

In parallel with the entry of modification into a reaction charge there also is another tendency for reduced pressure synthesis of cBN it is an activation of the initial gBN structure a thermochemical one, in particular [1].

Certain experimental experience concerning to direct (without initiators of conversion)  $gBN \rightarrow cBN$  phase transformations, has been present accumulated which indicates that the structural condition gBN (crystal perfection and degree of presence of defects) and impurity composition considerably influence on the  $p-T$  conditions and the speed of this transformation.

Previously [2, 3] in reasonable detail the interrelation of the structure and properties of the near-surface layers cBN monocrystals, in different crystallization mediums growth, were investigated. It as shown, that the monocrystal surface is very sensitive to chemical structure of

the crystallization mediums and their growth conditions and also the interrelation of their chemical structure with impurities structure of the initial charge components takes place.

The present work displays the results of the research by method SIMS and the influence of the preliminary heat treatment in fluorine environment of the surface of the initial powders gBN on the impurity composition and the properties of cubic boron nitride crystals.

### 2. Experimental procedure

#### 2.1. Starting materials and instruments

For experimental studies of synthesis, high pressure apparatus (HPA) of different designs were used: of the type of anvils with a hole in the form of a cone conjugated with a sphere. The reaction cell volume varied from 1.2 to 20 cm<sup>3</sup>.

A ZAK (Zaporozhie) -produced graphite-like BN powder was used as an initial material for cBN synthesis.

The powders of graphite-like and cubic modifications BN were investigated by SIMS. The spectra of secondary ions of BN powders were obtained on the installation for complex research of the surface of solids LAS-3000. The spectra of secondary ions in SIMS chamber were received with the help duoplasmatron with a cold cathode. The oxygen with high degree of cleanliness (99,999) served as a working gas. The analysis of the spectra both positive and negative ions was by quadrupole analyzer.

### 3. Results and discussion

#### 3.1. Structure and impurity composition of gBN powders heat treatment in fluorine

The comparison of gBN powders processed in fluorine with the initial ones has shown, that the latter actively influences the structure, impurity composition and properties of powders (Tab. 1).

Table 1

Crystallographic characteristic of gBN samples, subjected to thermo-chemical activation in fluorine environment

Sample	Crystal lattice parameter		Size of coherent scattering regions, $\text{\AA}$
	a (nm)	c (nm)	
initial gBN	0,25066(7)	0,6666(3)	$\approx 1500$
gBN after heat treatment in $\text{F}_2$	0,25068(6)	0,66663(20)	$\approx 1500$

As results from table 1 the processing in fluorine results in some change of lattice parameters, that, can, by connected with the formation of the intermediate compounds of  $\text{B}_x\text{N}_y\text{F}_z$  type.

It has been found that astreated gBN powder is characterized by a higher degree of the crystal structure and much lower level of impurities and inclusions. For example the EPR spectrum intensity increases by a factor of 2 - 2,5, the

resolution of individual lines also increases. These data testify that the heat treatment in fluorine promotes the elimination of imperfect structures and, probably, some activation of centres, causing the occurrence of the EPR spectrum.

Tables 2 and 3 reflect the data on the chemical structure of the surface of gBN powders, obtained SIMS.

Table 2

The impurity composition of gBN surface as to SIMS data

Sample	The contents of impurity, $I/I(^{11}\text{B})$					
	$\text{C}^+$	$\text{CH}^+$	$\text{CH}_3^+$	$\text{O}^+$	$\text{Na}^+$	$\text{Mg}^+$
	$4,7 \cdot 10^{-2}$	$8,9 \cdot 10^{-3}$	$8,9 \cdot 10^{-3}$	$8,9 \cdot 10^{-3}$	$5,4 \cdot 10^{-2}$	$6,7 \cdot 10^{-3}$
gBN processed $\text{F}_2$	$7,8 \cdot 10^{-2}$	$6,5 \cdot 10^{-2}$	$1,6 \cdot 10^{-2}$	$1,9 \cdot 10^{-2}$	$5,7 \cdot 10^{-1}$	-

Table 3

Fluorine contents in the near-surface layers of gBN powders

The studied materials	The contents of impurity, $I/I(^{11}\text{B})$
gBN initial	$1,0 \cdot 10^{-1}$
gBN processed $\text{F}_2$	$1,3 \cdot 10^{-1}$

As it goes from table 3, the thermo-chemical activation has resulted in the 30 % increase of

fluorine contents in the near-surface layers of gBN.

### 3.2. Influence of heat treatment in fluorine on cBN synthesis and its properties

The study of the effect of the thermo-chemical pretreatment in fluorine on the  $\text{gBN} \rightarrow \text{cBN}$  transformation also points to the high efficiency of the latter.

The obtained result is the consequence of the formation of the definite surface structure and its condition that is by the reduction of impurities and inclusions and especially by the reduction of oxygen contents, as well as the increase in the degree of perfection of gBN crystal structure and more uniform size fractional composition of the initial gBN

particles, majority the of which have high isometric degree.

As a result, during the synthesis the process of solving and crystallization goes regularly enough without sharp fluctuations in oversaturation.

Table 4 submits the data on impurity composition cBN grinding powder surface, obtained from gBN.activated in fluorine and the initial gBN.

The submitted data testify that the content of the impurities in the near-surface layers of cBN, obtained from activated gBN, is 1,5-2 times lower, than in the initial cBN.

Table 4

The impurity composition of surface cBN on data SIMS

Sample	Impurity content, $I/I(^{11}\text{B})$					
	$\text{C}^+$	$\text{CH}^+$	$\text{CH}_3^+$	$\text{O}^+$	$\text{Na}^+$	$\text{Mg}^+$
cBN, obtained from the initial gBN	$6,0 \cdot 10^{-4}$	$6,0 \cdot 10^{-4}$	-	$6,0 \cdot 10^{-4}$	$7,3 \cdot 10^{-2}$	$1,0 \cdot 10^{-2}$
cBN, obtained from gBN activated in fluorine	$3,0 \cdot 10^{-4}$	$3,0 \cdot 10^{-4}$	-	$3,0 \cdot 10^{-4}$	$6,3 \cdot 10^{-2}$	$1,0 \cdot 10^{-2}$

## 4. Conclusion

At should, that a preliminary activation of the initial gBN together with the introduction of modifiers of transformation into the crystallization medium permits a substantial reduction of the synthesis pressure and simultaneous control of quantity, granulometric composition and quality of cBN powders being synthesized.

## Acknowledgements

Authors express their thanks to Dr. V.Ya.Markiv and Dr. N.N.Belyavina (T.G. Shevchenko Kiev University) for the X-ray studies.

## REFERENCES

1. L.E.Pechentkovsky and T.N.Nazarchuk, *Poroshkovaya Metallurgia* [in Russian]. 7 (1981) 83.
2. V.G.Aleshin and et. al., *Dokl. AN UkrSSR* [in Russian]. 12 (1984) 71.
3. V.G.Aleshin and et. al., *Poroshkovaya Metallurgia* [in Russian]. 12 (1986) 76.

# NITROGEN HIGH PRESSURE INFLUENCE ON GaN CRYSTAL GROWTH CONDITIONS — A COMPUTATIONAL ANALYSIS

S. KRUKOWSKI, I. GRZEGORY, M. BOCKOWSKI, J. JUN, B. LUCZNIK, A. WITEK,  
M. WROBLEWSKI, J. M. BARANOWSKI, S. POROWSKI

*High Pressure Research Center, Sokolowska 29/37, 01-142 Warsaw, Poland*

J. ADAMCZYK

*Crystal Growth Physics Laboratory, Physics Department, Warsaw University, Poland*

An influence of high pressure on the equilibrium and transport properties of nitrogen was estimated by the use of scaling assumption. These transport properties were used in the computational analysis of the growth process in one zone furnace in nitrogen pressure equal to 15 kbar. The vertical high pressure growth configuration was analyzed using finite element code FIDAP. The temperature field in the high pressure chamber and the velocity in liquid Ga were obtained.

## 1 Introduction

Recent development of growth and doping methods of nitride semiconductors located GaN in the position of the most promising material for optoelectronic devices: blue diodes and lasers<sup>1</sup>. Heteroepitaxially grown GaN layers are used in a fabrication of commercially available blue diodes<sup>2</sup>. However, at present there are no substrates with close matching of lattice constants which hampers the progress in the fabrication of lasers. Thus, methods of growth of high quality single GaN crystals which will be used as substrates for GaN homoepitaxy are of general interest.

Growth of GaN crystals of the required size (of order of 25 mm) is difficult because of formidable thermodynamic and kinetic obstacles. The liquid phase methods are limited by a low solubility of nitrogen in liquid Ga<sup>3,4</sup>. To overcome this barrier, the temperatures higher than 1500°C have to be used. Since ammonia undergoes decay above 1200°C, nitrogen under pressures close to 15 kbar is used to assure GaN stability<sup>3</sup>. An alternative way is to grow GaN single crystals from the vapor. However no reports of the growth of large GaN single crystals from the vapor phase have been published.

At present high pressure methods are the only viable way to obtain large size GaN single crystals<sup>4</sup>. Good quality GaN crystals grown by this technique have 3 mm in diameter. Further progress requires better control of the growth that can be achieved by numerical analysis of the growth system and verification of the numerical results in the experiment. Therefore one need to know transport and

equilibrium properties of nitrogen and solid materials under pressure of 15 kbar and in the temperatures from 300K to 1800K. At present such data are not known from the experiment. Therefore one has to resort to extrapolation of the existing data to higher temperatures and pressures.

In this paper we scaling hypothesis to estimate physical properties of N<sub>2</sub>. Subsequently we use them in numerical analysis of the growth system by use of finite element based code FIDAP. The results include the temperature inside high pressure chamber and the velocity field in the liquid gallium in pressure equal to 5 kbar, 10 kbar and 15 kbar .

## 2 Nitrogen properties under pressure

High pressure of nitrogen changes drastically nitrogen transport properties like thermal conductivity and viscosity. On the other hand its equilibrium properties such as specific heat at constant pressure or thermal expansion coefficient change less dramatically.

The experimentally covered range of viscosity and thermal conductivity extends for pressure up to 1 kbar and temperatures up to 1200K<sup>5,6</sup>. For temperatures above 1200 K these properties were measured only for low pressures. A most successfully applied scaling law for these properties relates them to logarithm of the density<sup>7</sup>. Since our extrapolation covers the gas states that are within the same density range but for higher temperatures one can expect that the series expansion is valid for the range under consideration.



The dependence of thermal conductivity of nitrogen on temperature for several pressures is presented in Fig. 1. For low temperatures the

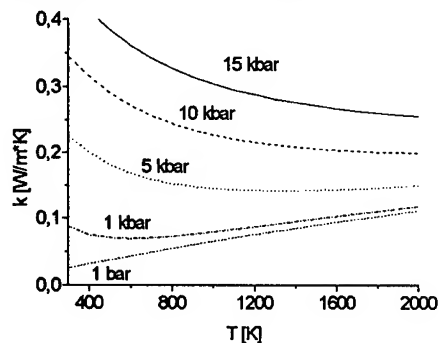


Figure 1 Thermal conductivity of  $N_2$

dominant mode of heat transfer is via collisions and vibrational motion of the molecules and for high temperatures the free flight motion dominates. In the intermediate region we observe a minimum of thermal conductivity known as Enskog minimum<sup>8</sup>. It is shifted towards higher temperatures for higher pressures. The conductivity increases sharply with the pressure, it is at least 100 % higher for 15 kbar than for 5 kbar at the same temperatures.

Nitrogen viscosity is presented in Fig. 2. The temperature dependence of nitrogen viscosity is similar, but the decrease with the temperature is much steeper and the pressure influence is stronger, especially at lower temperatures. The Enskog minimum is shifted towards higher temperatures.

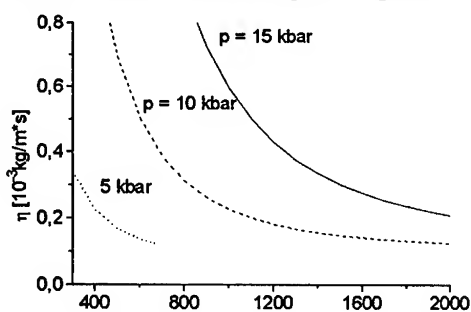


Figure 2 Shear viscosity of  $N_2$

The most important equilibrium properties, i.e. coefficient of thermal expansion and heat capacity are plotted in Fig. 3 and Fig. 4 respectively. The thermal expansion coefficient decreases monotonically with temperature and pressure, the highest values are obtained for lowest pressures. Thus high pressure reduces the effects of the buoyancy forces.

Heat capacity change is relatively small, the increase at high temperature is due to excitation of internal degrees of freedom of  $N_2$  molecule.

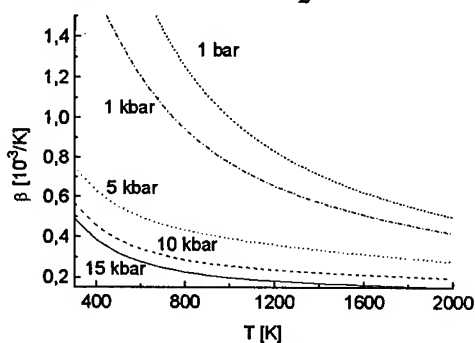


Figure 3 Thermal expansion coefficient of  $N_2$

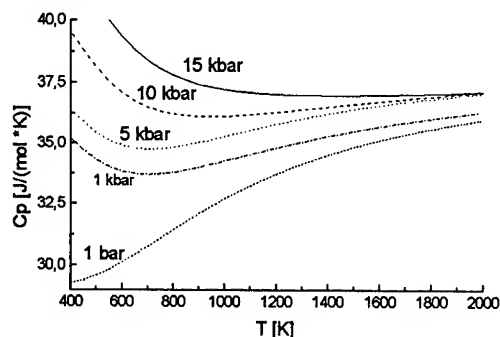


Figure 4 Heat capacity at constant pressure of  $N_2$

### 3 Experimental set-up

The experiments, compared with calculations were conducted in the vertically arranged high pressure chamber of the internal diameter of 30 mm<sup>4</sup>. In the growth experiments the graphite heater is used. The details of the growth set up are presented in Fig. 5.

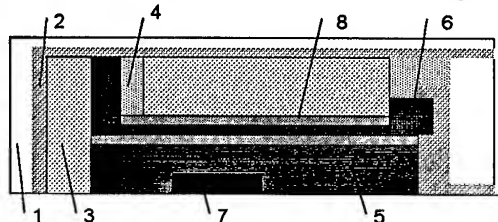


Fig. 5 Design of the one-zone furnace used in high pressure crystal growth of GaN; 1 -  $N_2$ , 2 - steel, 3 - graphite fiber, 4 - pyrophyllite, 5 - BN, 6 - graphite, 7 - Ga (l), 8 -  $Al_2O_3$

### 4 The calculation procedure

The nitrogen properties are strongly affected by pressures used in our experiments. On the contrary, molten metals do not change their transport properties

drastically with pressures up to 15 kbar<sup>5</sup>. The temperature varies from 100°C at the outside of the chamber to about of 1500°C in the growth zone. This caused considerable change of thermal conductivity of materials e.g. for BN it decreases from 30 W m<sup>-1</sup>K<sup>-1</sup> at 100°C to about 7 W m<sup>-1</sup>K<sup>-1</sup> at 1500°C. e to extrapolate these data to higher temperatures. The temperature change of the properties of these materials has been accounted for. Similarly the black body radiation model has been used for radiation heat exchange.

We have solved the equation of the conservation of the energy for the entire internal part of the chamber. The equation is reduced to heat conductivity equation for the solid part of the apparatus. For the fluid part we have solved the entire set of Navier-Stokes, i.e. density, energy and momentum equations.

In our calculation we have used finite element code FIDAP (Fluid Dynamics Analysis Package) distributed commercially by FDI. The package is capable to handle complicated geometries with the account of the radiation heat exchange and temperature dependent material properties.

We have set constant temperature,  $T = 373$  K at the internal surface of high pressure chamber. No slip conditions has been adopted for all solid surfaces. The heat source intensity was calculated from the measured heat power used in the growth experiments. The graphite spiral has been substituted by the tube heater with the uniform heat generation.

## 5 The calculation results

The results obtained in the calculations are: the temperature distribution inside the high pressure chamber and the velocity in the nitrogen gas and the liquid gallium

The temperature distributions were obtained for 5 kbar, 10 kbar and 15 kbar. The maximal temperatures were 1845 K, 1718 K and 1500 K, respectively. This variation indicate on the dominant role of nitrogen conductivity, especially affecting the thermal resistance of graphite fiber isolation. The calculation results differ by about 10% from the temperatures measured in our high pressure crystal growth experiments. In light of a large uncertainty of the estimation of the thermal properties of the materials used in the experiments, especially in high temperatures we feel that this agreement is reasonable.

The radial temperature difference in the liquid Ga is affected by its high thermal conductivity. In the

high temperature end the radial temperature difference is dominated by heat flow from the heater to the center i.e. higher temperature is at the circumference of liquid Ga. In the cold end we observe "rejection" of the isotherms from the liquid Ga. In the result, the temperature difference has the opposite sign: higher temperature is at the center.

The velocity of the liquid in molten Ga is characterized by two convection rolls.. The direction of the rolls is controlled by the horizontal, i.e. radial temperature difference. Therefore we observe one roll in the hotter part of gallium. It extends over the dominant part of the liquid. The second roll is caused by the radial temperature at the cold end. That roll has the opposite velocity direction as indicated by the temperature distribution.

## 6 Conclusions

- density based scaling is capable to recover transport properties of nitrogen in pressures up to 15 kbar and temperatures up to 2000 K
- equation of state approach can be applied to the determination of the thermal equilibrium properties of nitrogen in pressures up to 15 kbar and temperatures up to 2000 K
- finite element code is capable to give the thermal distribution in high pressure gas apparatus in pressures up to 15 kbar

## References

- 1 I. Akasaki and H. Amano, *Optoelectronics* 7, 49 (1992).
- 2 S. Nakamura, T. Mukai and M. Senoh, *Jpn. J. Appl. Phys.* 30, L1998 (1991).
- 3 S. Porowski and I. Grzegory, in: *Properties of Group III Nitrides*, ed. J. H. Edgar, (British Institution of Electrical Engineers Publ., London 1994).
- 4 S. Porowski, I. Grzegory and J. Jun, in *High Pressure Chemical Synthesis* ed. J. Jurczak and B. Baranowski (Elsevier Amsterdam, 1989).
- 5 W. B. Streett, in: *High Pressure Technology*, ed I. L. Spain and J. Paauwe (Dekker, N. York 1977).
- 6 B. Le Neindre, *Int. J. Heat Mass Transfer* 15, 1 (1971)
- 7 K. Stephen and R. Krauss, A. Lausecke, *J. Phys. Chem. Ref. Data* 16, 993 (1987).
- 8 E. McLaughlin, in *Thermal Conductivity* ed. R. P. Tye (Academic, London 1969)

**V(C) Other Materials**

# HIGH OXYGEN PRESSURES : A ROUTE TO THE STABILIZATION OF THE HIGHEST OXIDATION STATES OF TRANSITION METALS IN OXYGEN LATTICES

G. DEMAZEAU, D.Y. JUNG, L. FOURNES, A. LARGETEAU  
Institut de Chimie de la Matière Condensée de Bordeaux - Avenue du Dr. A. Schweitzer  
33608 PESSAC Cedex (France)

J.P. SANCHEZ

Centre d'Etudes Nucléaires de Grenoble - DRFMC/SPSMS/LIH - 85X - 38041 GRENOBLE Cedex (France)

## ABSTRACT

During these last twenty years numerous new oxides containing 3d elements with a high valency have been prepared [1]. This paper presents the main results concerning the synthesis, the structural determination, Mössbauer characterization and the physical properties of a new series of oxides  $A_2M\text{Ir(VI)}O_6$  ( $A = \text{Sr, Ba}$ ;  $M = \text{Mg, Ca, Sr, Zn}$ ) with Ir(VI). The influence of the oxygen pressure on the stabilization of Ir(VI) is emphasized.

## 1. Introduction

Through the optimization of different parameters controlling the stabilization of specific oxidation state: (i) local structure and chemical bonding characterizing the first cationic neighbours, (ii) the thermodynamical parameters governing the building of the lattice (in particular oxygen pressure), the highest valencies of the first row of transition metals have been obtained and characterized during these last twenty years: Fe(IV), Fe(V), Co(III), Co(IV), Ni(III), Cu(III) [1].

The objective of such a study was to correlate the strength of the  $M^{n+}\text{-O}$  bond and consequently the evolution of the resulting physico-chemical properties of the corresponding oxides with the increase of the  $n$  value.

Due to the improvement of the local crystal field energy from the first to the third row of transition metal, the Ir(VI)-O bond appeared as one of the strongest bond in an oxygen lattice.

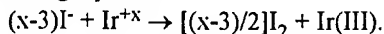
## 2. Stabilization of Ir(VI) in the oxygen lattices $A_2M\text{Ir(VI)}O_6$ ( $A = \text{Sr, Ba}$ ; $M = \text{Mg, Ca, Sr, Zn}$ ).

Iridium (VI) due to its isotropic electronic configuration ( $d^3$ ) fits very well with a Oh site. Consequently, the selected host structure was the perovskite one  $\text{ABO}_3$ .

In order to improve the local crystal field energy at the iridium site, able to help the stabilization of the VI+ valency, weak competing M(II)-O bonds have been chosen.

All the oxides  $A_2M\text{IrO}_6$  have been prepared through a conventional Solid State Chemistry process combined with oxygen pressure [2-4]. The first step consists on the calcination at 850°C, for 24h, of starting carbonates, hydroxides or oxides ( $\text{BaCO}_3$ ,  $\text{SrCO}_3$ ,  $\text{CaCO}_3$ ,  $\text{MgCO}_3$ ,  $\text{Mg(OH)}_2$ ,  $5\text{H}_2\text{O}$ ,  $\text{ZnO}$  and  $\text{IrO}_2$ ). The second step was a high oxygen pressure treatment using compressed gas (pressure value being limited by the external heating of the reaction vessel [5]). The third step was an oxygen pressure treatment using the "in situ" thermal decomposition of  $\text{KClO}_3$  into the reaction cell of a belt-type apparatus [5].

Table I gives the different oxygen pressure values required for the stabilization of Ir(VI). The value of the iridium oxidation state has been obtained from iodometric chemical titration according to the following equation:



From the values of iridium oxidation state given in Table I, it appears that oxygen pressures are required for stabilizing Ir(VI). The maximum content of Ir(VI) (close to 100 %) is observed for  $\text{Ba}_2\text{M}\text{IrO}_6$  ( $M = \text{Ca, Sr, Zn}$ ) and  $\text{Sr}_2\text{CaIrO}_6$ .

Table I - Iridium oxidation state determined by iodometric titration and the oxygen stoichiometries for  $A_2M\text{IrO}_6$  oxides (A=Ba,Sr : M=Sr,Ca,Mg,Zn) prepared under various oxygen pressure conditions.

Normal Composition	Experimental conditions Temp.(°C), PO <sub>2</sub> , time	Average Ir oxidation state	Experimental formula
Ba <sub>2</sub> CaIrO <sub>6</sub>	→ 880°C, 60 MPa, 48 hrs	5.99	Ba <sub>2</sub> CaIrO <sub>6.00</sub> *
	→ 900°C, 6 GPa, 10 mins	6.00	Ba <sub>2</sub> CaIrO <sub>6.00</sub>
Ba <sub>2</sub> SrIrO <sub>6</sub>	→ 880°C, 60 MPa, 48 hrs	5.88	Ba <sub>2</sub> SrIrO <sub>5.94</sub> *
Ba <sub>2</sub> ZnIrO <sub>6</sub>	→ 1000°C, 7 GPa, 15 mins	5.96	Ba <sub>2</sub> ZnIrO <sub>5.98</sub> *
Sr <sub>2</sub> CaIrO <sub>6</sub>	→ 880°C, 60 MPa, 48 hrs	5.98	Sr <sub>2</sub> CaIrO <sub>5.99</sub> *
Sr <sub>2</sub> MgIrO <sub>6</sub>	→ 880°C, 60 MPa, 48 hrs	5.75	Sr <sub>2</sub> MgIrO <sub>5.88</sub> *
Sr <sub>2</sub> ZnIrO <sub>6</sub>	→ 1000°C, 7 GPa, 15 mins	5.72	Sr <sub>2</sub> ZnIrO <sub>5.86</sub> *

\* Samples characterized by X-ray powder diffraction and other physico-chemical characterizations.

### 2.1 Structural study of the $A_2M\text{IrO}_6$ phases

The chemical titration results and crystallographic data for the prepared iridium perovskite oxides after high oxygen pressure treatment are given on Table II. All these oxides are characterized by an 1/1 cationic M/Ir ordering.

From Rietveld X-ray diffraction refinement, the average value of the Ir-O bond is close to 1.92 Å. Such a value corresponds to a Ir(VI) ionic radius of 0.52 Å (considering the ionic radius of six-coordinated oxygen close to 1.40 Å [6])

Table II - The chemical titration results and crystallographic data for the prepared iridium perovskite oxides after high oxygen pressure treatments.

Compound	n (Ir <sup>III+</sup> )	crystal structure	Space group	unit cell parameters (Å)
Ba <sub>2</sub> SrIrO <sub>5.94</sub> *	5.88	Rhombohedral	R $\bar{3}$ m	a = 6.0250(1), α = 60.48(5)°
Ba <sub>2</sub> CaIrO <sub>6.00</sub> *	5.99	Cubic	Fm3m	a = 8.3639(6)
Ba <sub>2</sub> ZnIrO <sub>5.98</sub>	5.96	Cubic	Fm3m	a = 8.103(2)
Sr <sub>2</sub> CaIrO <sub>5.99</sub> **	5.98	Monoclinic	P2 <sub>1</sub> /n	a=5.7830(2), b=5.8283(2), c=8.1997(1), β=90.26(50)°
Sr <sub>2</sub> ZnIrO <sub>5.86</sub>	5.72	Cubic	Fm3m	a = 7.932(2)
Sr <sub>2</sub> MgIrO <sub>5.88</sub> **	5.75	Cubic	Fm3m	a = 7.8914(2)

### 2.2 Magnetic study for the $A_2M\text{IrO}_6$ perovskites

Due to its d<sup>3</sup> electronic configuration and the 1/1 cationic ordering into the perovskite lattice only antiferromagnetic interactions through super-superoxchange mechanism can be expected [3].

The T<sub>N</sub> value seems correlated to the Ir(VI)-O distance into the perovskite lattice (Table III), a small value increasing the antiferromagnetic exchange. The very high observed T<sub>N</sub> values for super-superoxchange interactions can be attributed to the strong covalency of the Ir(VI)-O bond.

Table III - Magnetic data and distances between iridium ions for the perovskite  $A(II)_2M(II)Ir(VI)O_6$  prepared under high oxygen pressure.

Compound	Structure	d(Ir-Ir) <sup>a</sup>	T <sub>N</sub> (K)
Ba <sub>2</sub> SrIrO <sub>5.94</sub>	Rhombohedral	6.025	45
Ba <sub>2</sub> CaIrO <sub>6.00</sub>	Cubic	5.914	55
Ba <sub>2</sub> ZnIrO <sub>5.98</sub>	Cubic	5.730	55
Sr <sub>2</sub> CaIrO <sub>5.99</sub>	Monoclinic	5.798	55
Sr <sub>2</sub> ZnIrO <sub>5.86</sub>	Cubic	5.609	45
Sr <sub>2</sub> MgIrO <sub>5.88</sub>	Cubic	5.580	80

<sup>a</sup> Ir-Ir distances (Å) between the nearest Ir in the ordered perovskite structure.

### 2.3 <sup>193</sup>Ir Mössbauer spectroscopy for the $A_2M(II)Ir(VI)O_6$ perovskites

A three dimensional ordering is observed in the Mössbauer spectra at 4.2 K in agreement with the magnetic measurements (T<sub>N</sub> ≈ 50 K).

The values of the isomer shift and hyperfine field denote a strong covalency of the Ir(VI)-O bond (Table IV) [7].

Table IV - Mössbauer parameter for Ir(VI) oxides.

Compound	δ <sub>IS</sub> (mm/s)
IrF <sub>6</sub>	+1.45(2) +1.44(2)
Ba <sub>2</sub> CaIrO <sub>6</sub>	+1.36(2)
Ba <sub>2</sub> SrIrO <sub>6</sub>	+1.33(1)
Sr <sub>2</sub> CaIrO <sub>6</sub>	+1.32(1)
Ba <sub>2</sub> ZnIrO <sub>6</sub>	+1.33

### 3. Conclusion

The stabilization of Ir(VI) seems dependent on the distortion of the lattice (for example Ba<sub>2</sub>SrIrO<sub>6</sub> and Ba<sub>2</sub>CaIrO<sub>6</sub>) and on the ionicity of the competing M(II)-O bond (for example Sr<sub>2</sub>CaIrO<sub>6</sub> and Sr<sub>2</sub>MgIrO<sub>6</sub>) [7].

The development of high oxygen pressures appears to be a powerful tool for stabilizing the highest oxidation states of transition metals and consequently to investigate the influence of the strength of the chemical bond on the resulting physical properties of the corresponding host-oxides.

### References

- 1 G. Demazeau, *Synthesis under high oxygen pressure of oxides with unusual oxidation state or electronic configuration of transition elements*. Chap. 5, High Pressure Chemical Synthesis, Ed. J. Jurczak and B. Baranowski, Elsevier 1989.
- 2 G. Demazeau, D.Y. Jung, J.P. Sanchez, E. Colineau, A. Blaise and L. Fournes *Solid State Comm.*, **85**(6), 1993, 479.
- 3 D.Y. Jung, P. Gravereau and G. Demazeau *Eur. J. Solid State Inorg. Chem.*, **30**, 1993, 1025.
- 4 D. Y. Jung and G. Demazeau *J. Solid State Chem.*, **115**, 1995, 447.
- 5 G. Demazeau, Thesis of Doctorat ès Sciences, University of Bordeaux I, 1973.
- 6 R.D. Shannon, *Acta Crystallogr. Sect. A.*, **32**, 1976, 751.
- 7 D.Y. Jung, Thesis University Bordeaux I, n° 1313, 1995.

# A NEW ROUTE FOR THE SYNTHESIS OF BORON-RICH RARE-EARTH BORIDES $B_6R$ ( $R=La, Nd, Eu$ ) UNDER HIGH PRESSURE AND HIGH TEMPERATURE

XIAOYANG LIU<sup>a</sup>, XUDONG ZHAO<sup>a</sup>, FENG LIN<sup>a</sup>, WEINA LIU<sup>d</sup>, WENHUI SU<sup>a,b,c</sup>

*a. Group of Rare Earth Solid State Physics, Jilin University, Changchun 130023, P.R.China*

*b. International Center for Materials Physics, Academia Sinica, Shenyang 110015, P.R.China*

*c. Center for Condensed Matter and Radiation Physics, CCAST(World Lab.), P.O.Box 8730,*

*Beijing 100080, P.R.China*

*d. Changchun Institute of Physics, Academia Sinica, Changchun 130023, P.R.China*

## ABSTRACT

The boron-rich rare-earth borides,  $RB_6$  ( $R=La, Nd, Eu$ ), which are all pure phases without the intergrowth of other phases, have been obtained for the first time by the reduction of rare-earth oxides with elemental boron under the extreme conditions of high pressure and high temperature. The above experiments can be carried out in air from the beginning to the end without the protection of inert gas, and the synthetic reactions can be completed in a shorter time. The residual rare-earth oxides and the elemental rare-earth metals produced in the process of synthesis can be easily removed by leaching them in HCl.

## Introduction

Borides emerge many curious physical and chemical properties because of the electron deficiency of boron, in which the boron-rich rare-earth borides have more abundant physical properties. They show different properties such as superconductivity, high efficiency thermoionic emission and narrow-band semiconductivity etc. for different rare earth elements. Therefore, boron-rich rare-earth borides have much more uses in many fields, and their synthesis are paid wide attention.

By now there is much work on the synthesis of boron-rich rare-earth borides. Because the synthesis of boron-rich rare earth borides are very difficult and complicated, many synthetic methods had been developed. For example, the sintering at high temperature, the solution and the molten salt electrolysis method etc.. The sintering method at high temperature is to synthesize them in the high temperature furnace with the mixture of elemental boron and rare-earth or rare-earth hydride mixed by stoichiometric composition as raw materials[1]. The temperature for the reaction is usually above 1500°C, and the reaction time is usually more than ten hours or even more than several days. Because the oxidation of the elemental rare-earths is very easy in air, the reaction must be carried out in high vacuum. Meantime, the reaction requires high-quality crucible because of high reaction temperature. The molten salt electrolysis method is to electrodeposit the molten salts of boron oxide (or borax) and rare-earth oxide[2]. This

method has three shortcomings: inefficient electric power, several borides intergrowth and difficult to separate the product from the molten salt. The reduction method is reducing the mixture of boron oxide and rare-earth oxide with carbon at high temperature[3], which can produce large amount of rare-earth boride, but the stoichiometric composition can be changed because the different volatilization of several oxides and the product can be contaminated by boron, carbon or carbonates. The solution method make elemental rare-earth metal and boron fusing into melting aluminum after heating to about 1300°C [4], then lower the temperature slowly to crystallize the rare-earth boride from molten aluminum. This method needs protecting by inert gas and the product contains impurities of aluminum and boron-aluminum compounds. Floating zone melting method is the best one to prepare the rare-earth boride and allows to obtain single crystal[5], but it needs the precursor of powder boride. This method is very expensive because it needs complex equipment.

From the above discussions, it can be seen that each method mentioned above has its own advantages and disadvantages. Therefore, it is necessary to find a new route to synthesize the boron-rich rare-earth borides, which is rapid and easy to obtain a single phase product. We report here the synthesis of the boron-rich rare-earth borides,  $RB_6$  ( $R=La, Nd, Eu$ ) by the reduction of rare-earth oxides with elemental boron under the extreme conditions of high pressure and high temperature for the first time. Since the rare-earth oxides are chosen as the source of rare-earth elements, the above experiments can

be carried out in air from the beginning to the end without the protection of inert gas.

### Experimental

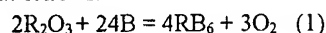
The amorphous boron (with purity of 99.99%) was mixed with rare-earth oxide  $R_2O_3$  ( $R=La, Nd, Eu$ ) (with purity of 99.9%) separately (which was weighed according to the stoichiometric composition), and ground uniformly, then they were placed in hexagonal boron nitride (h-BN) surrounded by a graphite cylindrical heater[6].

High pressure experiment was carried out using  $4.903 \times 10^6$  N Bridgman apparatus. The magnitude of pressure generated inside the cell was calibrated by the electrical changes on the basis of the phase transformations of Bi (2.55, 2.69 and 7.7 GPa). The temperature of the sample was controlled by the electric power supplied through the carbon heater, and calibrated by inserting a Pt30%Rh-Pt6%Rh thermocouple in the cell. When the high pressure synthesis are followed, the pressure increases up to expected value, the temperature then increases to expected value, too. After maintaining the desired high pressure and high temperature conditions for 15 mins, the sample was quenched to room temperature prior to the release of the applied pressure.

X-ray powder diffraction studies are performed using a Rigaku 12kW D/max copper rotating-anode X-ray diffractometer with a graphite monochromator. Silica was used as an internal standard, and cell parameters are refined by least squares.

### Results and Discussion

Under the extreme conditions of high pressure and high temperature, the boron-rich rare-earth borides  $RB_6$  ( $R=La, Nd, Eu$ ) are prepared by the reduction of rare-earth oxides with elemental boron. The synthesis reaction is as follows:



After the reaction, there are still some excess rare-earth oxides and the elemental rare-earth metals produced in the process of synthesis, and they can be removed by leaching them in HCl.

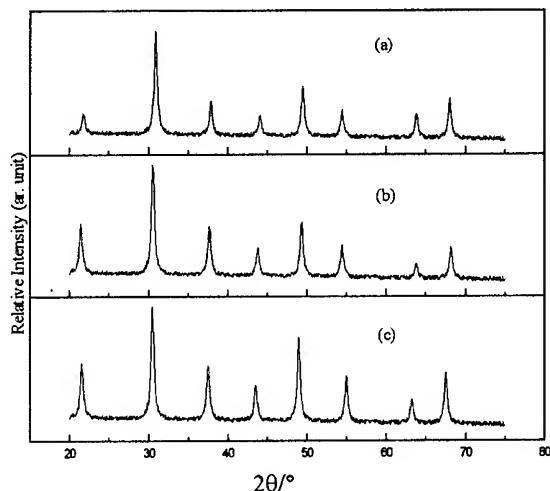


Fig.1 XRD pattern of boron-rich rare-earth boride  $LaB_6$ (a),  $NdB_6$ (b),  $EuB_6$ (c)

The conditions for the synthesis of boron-rich rare-earth boride  $RB_6$  ( $R=La, Nd, Eu$ ) are at the pressure of 4.0 GPa and at the temperature of 1600°C for 15 min. The X-ray powder diffraction patterns of boron-rich rare-earth boride  $RB_6$  ( $R=La, Nd, Eu$ ) synthesized in this paper are shown in Fig.1(a), (b), (c), respectively. Corresponding XRD data are listed in Tab.1.  $RB_6$  ( $R=La, Nd, Eu$ ) crystallizes in the cubic system with lattice constants  $a=0.4098, 0.4125, 0.4150$  nm for  $R=La, Nd, Eu$  respectively (average values derived from a least squares fitting of X-ray powder diffraction data). Comparison with the XRD data of [7], [8], [9], shows that boron-rich rare-earth borides  $RB_6$  ( $R=La, Nd, Eu$ ) synthesized in this work are not contaminated by boron and they are pure phases.

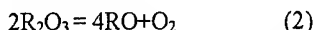
The chemical reaction (1) is not a simple one but a complex one which can be divided into several steps of

Tab.1 XRD data of boron-rich rare-earth boride  $RB_6$  ( $R=La, Nd, Eu$ )

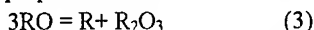
$2\theta(^{\circ})$			$d_o(\text{nm})$			$d_e(\text{nm})$			h k l
$LaB_6$	$NdB_6$	$EuB_6$	$LaB_6$	$NdB_6$	$EuB_6$	$LaB_6$	$NdB_6$	$EuB_6$	
21.74	21.40	21.50	0.4089	0.4152	0.4133	0.4098	0.4148	0.4150	1 0 0
30.88	30.52	30.46	0.2895	0.2928	0.2935	0.2897	0.2933	0.2934	1 0 1
37.84	37.64	37.48	0.2377	0.2389	0.2399	0.2366	0.2395	0.2396	1 1 1
44.06	43.78	43.50	0.2055	0.2067	0.2080	0.2049	0.2074	0.2075	2 0 0
49.44	49.30	48.92	0.1843	0.1848	0.1862	0.1832	0.1855	0.1856	2 1 0
54.38	54.38	54.92	0.1687	0.1687	0.1700	0.1673	0.1693	0.1694	2 1 1
63.78	63.74	63.16	0.1459	0.1460	0.1472	0.1449	0.1466	0.1467	2 2 0
67.98	68.14	67.48	0.1379	0.1376	0.1388	0.1366	0.1383	0.1383	3 0 0



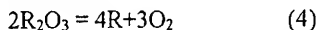
reactions. In the previous experiments[10], we had confirmed the reduction of transition metal oxides and rare-earth metal oxides under high pressure and high temperature, i.e. a pure oxide will change to elemental metal and  $O_2$  under high pressure and high temperature. Different from the transition metal oxides, the rare-earth oxides  $R_2O_3$  decomposes into RO and  $O_2$  firstly, under high pressure and high temperature, and the valence of R decreases from 3+ to 2+:



then, RO disproportionates into R and  $R_2O_3$ :



Above two reactions can be considered a total decomposition reaction:



The elemental R produced in the process of above reactions reacts with boron immediately, and combine with boron into  $RB_6$ :



The method for the synthesis of boron-rich rare-earth borides by the reduction of rare-earth oxides with elemental boron under high pressure and high temperature has many obvious advantages than the previous ones.

(a)The synthetic reaction can be completed in a shorter time. Because the starting materials is all powder, they can be mixed homogeneously and once the reaction is carried out, the elemental rare-earth which has higher reactivity than that of bulk rare-earth elements will produce and it will greatly accelerate the completion of synthetic reaction.

(b)It is easy to obtain the single phase product of boron-rich rare-earth borides  $RB_6$  ( $R=La, Nd, Eu$ ). In the past, the most frequently used synthesis of boron-rich rare-earth boride  $RB_6$  ( $R=La, Nd, Eu$ ) was to mix boron with rare-earth elements according to the atomic ratio which leads to the formation of boron-rich rare-earth boride  $RB_6$  ( $R=La, Nd, Eu$ ), and the reaction was carried out. Because of the oxidation of rare-earth elements in air, an inaccuracy in weighing would occur, so it was very difficult to obtain a pure product. Most products were mixtures of boron-rich rare-earth boride  $RB_6$  ( $R=La, Nd, Eu$ ) with either boron or rare-earth oxides. These problems can be avoided by the reduction of rare-earth oxides with elemental boron under high pressure and high temperature, and the final product can be formed repeatedly. It is easy to remove the residual rare-earth oxide and elemental rare-earth produced in the process of synthesis by leaching the product with hydrochloric (HCl).

(c)High pressure can decrease the reaction activation energy, because it accelerates the diffusion between the reaction material powder.

(d)High pressure can increase the coordination numbers of atoms, and it is of benefit to the synthesis of boron-rich rare-earth boride. Boron-rich rare-earth borides  $RB_6$  has the symmetry of b.c.c., which have six boron octahedron locating at the eight vertexes and a rare-earth atom locating at the center of the cubic. So the R atom has the circumstance of octahedral coordination which is in high coordinated state. If the usual synthetic methods are used, it is very easy to product many borides, such as  $RB_2$ ,  $RB_4$ ,  $RB_6$  etc.. If high pressure is used, the high-coordination borides  $RB_6$  can be synthesized directly and the impurities of  $RB_2$ ,  $RB_4$  can be transformed into  $RB_6$ , too.

(e) High pressure can provide a reduction circumstance, and it is equivalent to the use of the inert gas. This will accelerate the reduction of rare-earth oxides.

In conclusion, a new route for the synthesis of boron-rich rare-earth borides  $RB_6$  ( $R=La, Nd, Eu$ ) that yields a pure and well-crystallized product is reported here.

#### Acknowledgment

The authors wish to thank the National Natural Science Foundation of China for their financial supports.

#### Reference

1. J. M. Laffery, *J. Appl. Phys.* **22**(3) (1951), 299.
2. P. W. Shen *et al.*, *Wuji Huaxue Xuebao* **7** (1991) 306.
3. T. Tanaka *et al.*, *J. Less-Common Met.* **67** (1979) 167.
4. V. N. Gurin *et al.*, *J. Less-common Met.*, **67** (1979) 115.
5. T. Tanaka *et al.*, *J. Cryst. Growth*, **30** (1975) 193.
6. X. Liu *et al.*, *Science in China(Ser. B)*, **37** (1994) 1054.
7. *Nat. Bur. Stand. (U. S.) Monogr.* **20** (1983) 62.
8. J. Perri *et al.*, *Div. Appl. Phys.*, Polytechnic Inst. of Brooklyn, New York, (1957).
9. Samsonov *et al.*, *Proc. Acad. Sci. USSR (Chem. Sect.)*, **119** (1958) 237.
10. X. Liu *et al.*, *J. Alloy and Compnd.*, **223** (1995) L7.

## DEVELOPMENT OF NEW SOLVENTS FOR THE HYDROTHERMAL CRYSTAL GROWTH OF $\alpha$ -QUARTZ

F. LAFON, G. DEMAZEAU, Y. PEYTAVIN, P. CHVANSKI, A. LARGETEAU  
Institut de Chimie de la Matière Condensée de Bordeaux - Avenue du Dr. A. Schweitzer  
33608 PESSAC Cedex (France)

Interface Hautes Pressions - E.N.S.C.P.B. - Avenue Pey Berland - BP 108 - 33402 TALENCE Cedex

C. QUETEL

L.P.P.M. - Université BORDEAUX I - 351 Cours de la Libération - 33405 TALENCE Cedex (France)

### ABSTRACT

The performances of  $\alpha$ -quartz for high frequencies applications are limited by the density of physical and chemical defects. Chemical defects are mainly inclusions or ionic substitutions. Physical defects are represented by dislocations and etch-channels. To reduce the anionic ( $O^{2-} \rightarrow OH^-$ ) and cationic ( $Si^{4+} \rightarrow M^{3+}$ ) substitutions with  $M^{3+} = Al^{3+}$  or  $Fe^{3+}$ , it is necessary to decrease the concentration of hydroxyl groups. Two different routes have been set up: (i) the use of high pressures in order to decrease the molar concentration of NaOH used as conventional solvent, (ii) the development of non-conventional solvent as NaF, less basic than NaOH. This contribution describes some results concerning these researches.

### 1. Introduction

Acoustic-wave resonators are now conventionally developed in RF circuits for numerous industrial and military equipments. The value of so-called "quality factor"  $Q$  defined as the ratio of the resonant frequency to the full width in frequency at half the maximum of the conductance [1] must be very high.

Among the piezoelectric materials able to be used for resonators, in particular  $\alpha$ -quartz appears to be a good one due to its ability to be industrially synthesized. The increase of the working-frequency leads to a strong decrease of the thickness for piezoelectric-sheet, reaching the average size of the intrinsic defects into the material.

### 2. Main defects observed in $\alpha$ -quartz single crystals

The defects in  $\alpha$ -quartz lattice can be roughly described as chemical and physical nature.

The chemical defects can be divided in two categories: those corresponding to a foreign chemical phase inserted into the  $\alpha$ -quartz lattice and called "inclusions", those induced by chemical substitutions ( $O^{2-} \rightarrow OH^-$  associated to  $Si^{4+} \rightarrow M^{3+}$ ) on atomic positions of the  $\alpha$ -quartz lattice. These defects, in particular the presence of hydroxyl groups play an important role on the decrease of the  $Q$  quality factor [2].

The structural defects are mainly represented by dislocations.

The chemical defects are induced by chemical contamination during the crystal growth process induced either by the solvent, the nutrient or the metallic-walls of the reaction vessel. Consequently the growth of high purity crystals is a prerequisite for obtaining both high  $Q$  piezoelectric  $\alpha$ -quartz and the development of devices.

### 3. Main factors involved in the synthesis of $\alpha$ -quartz single crystals

Due to the low temperature transition  $\alpha \rightarrow \beta$  quartz (573°C) at normal pressure (0,1 MPa) the conventional crystal growth processes cannot be used. Thus the hydrothermal process has been developed [3-5]. This crystal growth method is based on the use of pressure for improving, at low temperature, the solubility of the corresponding material. Conventionally the pressure-temperature domain developed for the crystal growth of  $\alpha$ -quartz is:

$$500 \leq P \leq 2000 \text{ bar (50 - 200 MPa)}$$

$$350 \leq T \leq 400^\circ\text{C.}$$

Pressure-parameter being constant inside the reaction-vessel containing a liquid-like phase as solvent. The transport phenomena from the nutrient to the seeds is governed by a temperature gradient ( $5 \leq \Delta T \leq 30^\circ\text{C}$ ), the  $\alpha$ -quartz solubility increases differently with pressure and temperature.

The objective of our study was to reduce highly the density of chemical defects- in particular hydroxyl groups concentration- through two different routes :

(i) the reduction of the concentration of a conventional basic solvent as NaOH or  $\text{Na}_2\text{CO}_3$  using pressure-parameter for controlling the solubility of the nutrient,

(ii) the development of new solvents free of OH-groups in order to reduce the anionic substitution ( $\text{O}^{2-} \rightarrow \text{OH}^-$ ) into the  $\alpha$ -quartz lattice.

The comparison of the solubility-limit values in the same experimental conditions ( $P=300 \text{ MPa}$ ,  $T=400^\circ\text{C}$ ,  $t=192\text{h}$ ) is given on Table I for two solvents : aqueous solutions of NaOH(1M) and NaF(1M).

The modification of the solubility versus pressure for NaF(1M) could be explained by the mobility of the silicon-complexes near the  $\text{SiO}_2$  cristallites.

Using a non-basic solvent as NaF with corresponding experimental conditions the solubility limit is greatly increased.

Table I - Comparison of solubility-limit at (P, T) fixed in NaOH(1M) and NaF(1M)

Solvent : aqueous solution	Solubility-limit of $\alpha$ -quartz at 400°C - 200MPa - 192h
NaOH (1M)	47 g/l
NaF (1M)	70 g/l

#### 4. Tentative of $\alpha$ -quartz crystal-growth using different solvent-conditions

The equipment used for such crystal-growth experiments is given on figure 1.

Table II shows a comparison of the crystal-growth rate on a (0001) face from the seeds for two solvents [aqueous solutions of NaOH(1M) and NaF(0,5M)] and two pressures (180 and 265 MPa), using the same experimental conditions (growth temperature =  $365^\circ\text{C}$ ,  $\Delta T = 35^\circ\text{C}$ ).

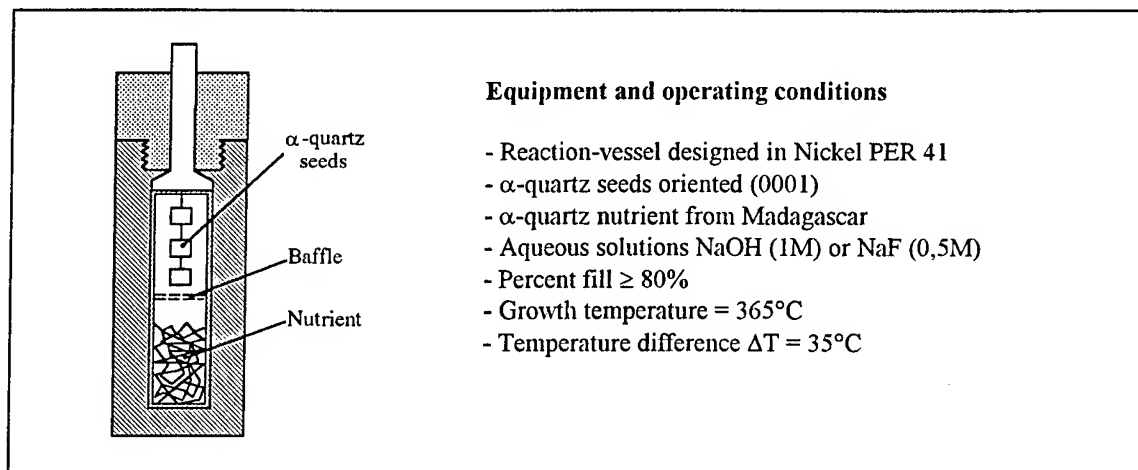


Figure 1 - High Pressure equipment for hydrothermal  $\alpha$ -quartz growth

Table II - Comparison of  $\alpha$ -quartz crystal-growth rate in NaOH(1m) and NaF(0.5M)

Growth rate on (0001) mm/d	NaOH(1M)	NaF(0,5M)
P = 180 MPa	0,185	0,260
P = 265 MPa	0,21	0,38

The kinetics of the crystal growth seems enhanced with an aqueous solution of NaF (0,5M). The corresponding I.R. spectra for both  $\alpha$ -quartz single crystals are given on figure 2. The calculated extinction coefficients  $a_{3585}$  at the maximum of the I.R. absorption [ $a_{3585} = (\text{I.R. Absorbance at } 3585 \text{ cm}^{-1}) / (\text{thickness of the prepared sample})$ ] for both resulting  $\alpha$ -quartz single crystals are compared on Table III.

The development of a non-basic solvent as NaF confirms the reduction of hydroxyl groups concentration into the resulting  $\alpha$ -quartz single crystal.

Table III - Extinction coefficients ( $a_{3585}$ ) for both samples designed in the same experimental (P, T,  $\Delta T$ ) conditions, only aqueous solution is different

SAMPLES	$a_{3585} \text{ (mm}^{-1}\text{)}$
$\alpha$ -quartz grown in NaF(0,5M)	3
$\alpha$ -quartz grown in NaOH(1M)	14,6

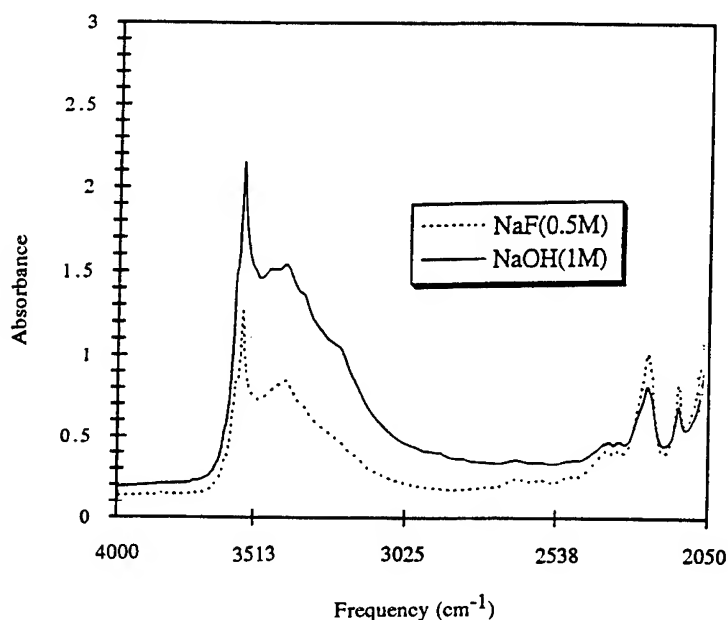


Figure 2 - I.R. spectra comparison at 25°C for synthetic  $\alpha$ -quartz prepared in NaF(0,5M) and NaOH(1M)

## 5. Conclusion

These preliminary results concerning the  $\alpha$ -quartz crystal-growth have underlined both the role of pressure-parameter using a conventional solvent as NaOH (1M) and the role of the basicity of the solvent on the OH-groups-concentration into the resulting single-crystal. These results open new researches in order to improve the quality factor Q.

## Acknowledgements

This work is supported by DRET.

## References

- 1 A. Ballato, J.G. Gualtieri, *IEEE Trans. on Ultrasonics, Ferroelectrics, and Freq. Cont.* 41(6), 834-844, (1994).
- 2 J.F. Balascio, N.C. Lias, *Proceedings of the 37th Annual Freq. Cont. Symp.*, 157-163, (1983).
- 3 R.A. Laudise, J.W. Nielsen, *Hydrothermal Crystals Growth in Solid State Physics*, Academic Press N.Y. 12, (1961).
- 4 A.F. Armington, J.F. Balascio, *Proceedings of the 38th Annual Freq. Cont. Symp.*, 3-6, (1984).
- 5 R.A. Laudise, R.L. Barns, *IEEE Trans. on Ultrasonics, Ferroelectrics, and Freq. Cont.* 35(3), 277-287, (1988).

# THE SOLVOTHERMAL SYNTHESIS OF A NEW CLASS OF MATERIALS : THE PHYLLOSILOXIDES

P. REIG, G. DEMAZEAU

Institut de Chimie de la Matière Condensée de Bordeaux - Avenue du Dr. A. Schweitzer  
33608 PESSAC Cedex (France)

R. NASLAIN

Laboratoire des Composites ThermoStructuraux - Avenue de la Boétie - 33600 PESSAC (France)

## ABSTRACT

The thermal stability of natural phyllosilicates is strongly limited by the presence of hydroxyl groups (OH) in the lattice ( $2\text{OH}^- \rightarrow \text{O}^{2-} + \square$ ). On the basis of the structure of mica-phlogopite  $[\text{KMg}_3(\text{Si}_3\text{Al})\text{O}_{10}(\text{OH})_2]$  and using cationic substitutions on both Oh and Td sites a new composition can be set up :  $\text{K}(\text{Mg}_2\text{Al})\text{Si}_4\text{O}_{12}$ .

Using combined two steps-process - (i) an all alkoxide sol-gel conversion and (ii) a solvothermal treatment (in supercritical conditions of the residual solvent  $50 \leq P \leq 100 \text{ MPa}$  ;  $700 \leq T \leq 800^\circ\text{C}$  ;  $48 \leq t \leq 72 \text{ h}$ ) - this new layered oxide was prepared and characterized.

This axis of research open a route to a new class of layered oxides isostructural of phyllosilicates and called : PHYLLOSILOXIDES.

## 1. Introduction

In a composite material with a ceramic (or a vitreous) matrix (CMC or CMV), an interphase is used for controlling the fiber-matrix bonding. The role of such an interphase is : (i) to act as a fuse in order to deflect the propagation of the microcracks in the matrix from perpendicularly to the fibers (mode I) to parallelly to the fibers (mode II) when the composite is loaded along the fiber axis, (ii) to allow enough load transfer from the matrix to the fiber, (iii) to release part of the residual stresses due to processing and (iv) to act as a diffusion barrier.

From the present state of knowledge, compliant materials with a layered crystal structure or a layered microstructure have been shown to be the best interphase materials [1].

The choice of the interphase material depends on three main criteria :

- the first is structural, a layered structure or microstructure being perforated,

- a good resistance to oxidation in particular for composites used in oxidizing atmospheres,

- a high thermal stability.

Through the first criteria, three types of materials can be selected : pyracarbon (PyC), boron nitride with turbostratic structures (hex-BN) and phyllosilicates. Table I gives a comparison of the main properties of these three materials with a view to their use as interphase in CMC's.

It appears that none of these materials fulfilled perfectly all the required properties.

The resistance to oxidation cannot be improved very significantly for graphite and BN. Consequently the objective of our research-work was to improve the thermal stability of phyllosilicates. Such a challenge required to eliminate the hydroxyl groups [2].

The substitution of  $\text{F}^-$  for  $\text{OH}^-$  has been tested and fluoro-micas (which exist in nature) have been tentatively used as interphase in CMV [3].

TABLE I - Some properties required for interphase use in CMCs.

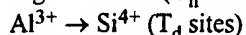
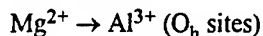
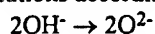
Material	PyC	hex-BN	Phyllosilicates
Criteria			
Cleavage (fuse function)	Yes	Yes	Yes
Resistance to oxidation	No	limited	Yes
High thermal stability	Yes	Yes	No

We have developed another route involving the anionic substitution  $\text{OH}^- \rightarrow \text{O}^{2-}$  in order to prepare new layered oxides. Such a route required in parallel cationic substitutions, e.g.  $\text{M}^{2+} \rightarrow \text{M}^{3+}$  into the (T) or (O) layers of the phyllosilicate lattice. The corresponding oxides, free of hydroxyl groups, has been called the "phyllosiloxides".

## 2. Preparation of the "phyllosiloxide" derived from mica-phlogopite

Mica-phlogopite has been selected as starting model. With a general formula  $[\text{KMg}_3(\text{Si}_3\text{Al})\text{O}_{10}(\text{OH})_2]$ , where  $\text{Mg}^{2+}$  are located in octahedral sites ( $\text{O}_h$ ),  $\text{Al}^{3+}$  and  $\text{Si}^{4+}$  being in the tetrahedral ones ( $\text{T}_d$ ).

The selected compensated ionic and cationic substitutions according to the following equations :



lead to the theoretical formula :  $\text{KMg}_2\text{AlSi}_4\text{O}_{12}$ .

The first step was an all alkoxide sol-gel process in order to achieve a great homogeneity of the final product. The starting compounds were  $\text{Si}(\text{OC}_2\text{H}_5)_4$ ,  $\text{Al}(\text{OC}_2\text{H}_5)_3$ ,  $\text{Mg}(\text{OC}_2\text{H}_5)_2$  and  $\text{KOCH}_3$ . The sol-gel transformation was induced by a thermal treatment at  $150^\circ\text{C}$  during 1 hour.

All the conventional thermal treatment tested as second step for transforming the resulting gel to a layered oxide have led to three dimensional materials as  $\text{MgSiO}_3$ ,  $\text{Mg}_2\text{SiO}_4$  and  $\text{Al}_2\text{SiO}_5$  [4]. Consequently, we have developed a solvothermal treatment of the

gel issued from the first step. A solvothermal treatment can be described as a chemical reaction into a solvent in supercritical conditions using high temperatures and high pressures condition [5]. This type of process, using the specific physico-chemical properties of the solvents in supercritical conditions can help the synthesis of materials [6].

In our case, the solvent was the glycol monoethyl ether used in the first step and adsorbed on the resulting gel. The experimental conditions were  $50 \leq P \leq 100 \text{ MPa}$ ,  $700 \leq T \leq 800^\circ\text{C}$ ,  $48 \leq t \leq 72 \text{ h}$ .

## 3. Physico-chemical characterizations of the phyllosiloxide $\text{K}(\text{Mg}_2\text{Al})\text{Si}_4\text{O}_{12}$

### 3.1 X-ray diffraction

The X-ray pattern is isotypic of the mica-phlogopite used as starting model. A HR-TEM image starting underlines the layered structure of this new oxide.

### 3.2 SEM characterization of the microcrystallites

SEM images were used to determine the average size (close to  $1 \mu\text{m}$ ) and the morphology (hexagonal platelets) of the phyllosiloxide microcrystallites.

### 3.3 I.R. spectroscopy

The domain of investigation was limited to  $400\text{--}3800 \text{ cm}^{-1}$ . The powder samples were in suspension in nujol or mixed with KBr. The observed IR-spectrum is given on the figure.

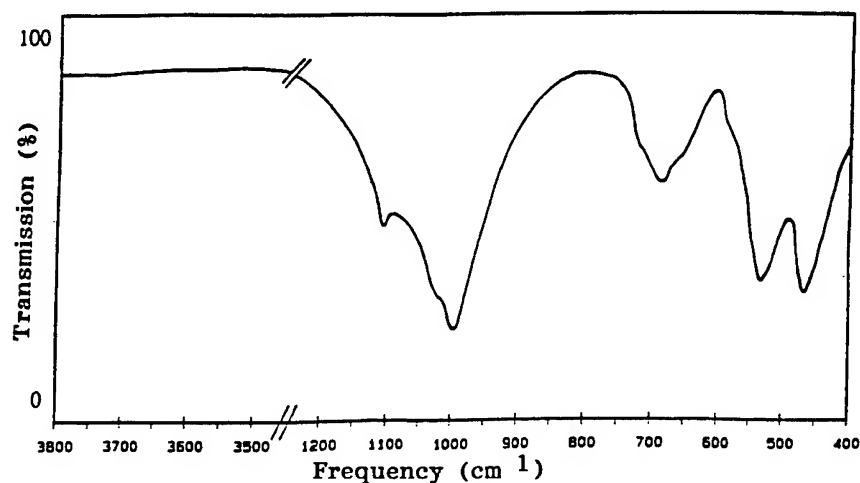


Figure - IR spectrum of the  $\text{KMg}_2\text{AlSi}_4\text{O}_{12}$  "phyllosiloxide".

The absence of adsorption bands in the 3500-3800  $\text{cm}^{-1}$  domain corresponding to the vibration of elongation  $\nu(\text{OH}^+)$  or in that attributed to the  $\text{OH}^-$  deformation  $\delta(\text{OH}^-)$ ,  $\gamma(\text{OH}^-)$  (600-900  $\text{cm}^{-1}$ ) [7] confirms clearly the absence of hydroxyl groups in the mica-phlogopite lattice and thus the preparation of a new layered oxide : the phyllosiloxide.

#### 3.4 Thermal stability of the $\text{KMg}_2\text{AlSi}_4\text{O}_{12}$ phyllosiloxide

XRD experiments have been performed between 25 and 1000°C. No change (after an isothermal-plateau of 1 hour) is observed between 25 and 800°C. Beyond 900°C, the intensity of the (002) diffraction line decreases. The phyllosiloxide tends to become amorphous at a temperature close to 950°C. At 1000°C tridimensional structures (i.e.  $\text{SiO}_2$ ,  $\text{Mg}_2\text{SiO}_4$ ...) resulting from a thermal decomposition are observed. Consequently, it appears clearly that the  $\text{KMg}_2\text{AlSi}_4\text{O}_{12}$  phyllosiloxide is thermally more stable ( $T \approx 950^\circ\text{C}$ ) than the corresponding mica-phlogopite (500-700°C).

#### 4. Conclusions

On the basis of the phyllosilicate lattices, in particular the mica-phlogopite ones, and using associated anionic and cationic substitutions, the preparation of a new class of layered oxides : the phyllosiloxides can be possible through a high pressure solvothermal process [6].

#### Acknowledgements

This work has been supported by the French Ministry of Research and Universities (M.R.E.S.) (through a grant to P.R.) and by S.E.P.. The authors are undebted to A. Guette from L.C.T.S. for his assistance in HT-XRD and M. Chambon, from CUMEMSE, for his assistance in the HR-TEM analysis.

#### References

- [1] R. Naslain, Composite Interfaces, 1, 253 (1993).
- [2] P. Pascal, "Nouveau Traité de Chimie Minérale : le silicium", Tome VIII, Ed. Masson et Cie (1965).
- [3] G.H. Beall, S.B. Dawes and K. Chyung, US Patent n° 366,234 (1990).
- [4] P. Reig, Thesis University Bordeaux I n° 1226 (1995).
- [5] Th Dubois and G. Demazeau, Materials Letters, 19, 38 (1994).
- [6] G. Demazeau, Proceedings of the First International Conference on Solvothermal Reactions, Takamatsu (Japan), Ed. High Pressure Technology Research Committee of Shikoku, 52, 1 (1994).
- [7] V.C. Farmer, J.D. Russel, J.L. Ahlrichs and B. Velde, Bull. Gp. Fr. Argiles, 19, 5 (1967).

## **VI Phase Transitions and Phase Diagrams of Inorganic Materials**



---

## **VI(A) Theoretical and General Aspects**

# KINETICS AND MECHANISM OF AMORPHOUS-TO-AMORPHOUS AND CRYSTAL-TO-AMORPHOUS TRANSITIONS UNDER HIGH PRESSURE.

V.V. BRAZHNIKIN, A.G. LYAPIN, O.V. STALGOROVA,  
E.L. GROMNITSKAYA, S.V. POPOVA, and O.B. TSIOK

*Institute of High Pressure Physics, Troitsk,  
Moscow Reg, 142092, Russia*

## ABSTRACT

In the paper we concern the questions of high-pressure solid state amorphization (SSA) and amorphous-to-amorphous transformations (AAT). We have shown that the kinetic lines of amorphization on  $P,T$ -plane smoothly convert to the ordinary crystal-to-crystal hysteresis lines at high temperatures. The SSA occurs with small activation energy (in comparison with that of diffusion). For the first time the experimental evidence for the elastic softening in a vicinity of the SSA region is presented. Using high-pressure SSA it is possible to obtain the amorphous tetrahedral semiconductors in the bulk form: Si, Ge, III-V compounds - by decompression of high pressure phases and carbon - by compression of  $C_{60}$ -crystals. We have studied the mechanical properties of the "amorphous diamond" and intermediate phases of carbon. For the first time the pressure and time dependence of the volume of amorphous  $GeO_2$  were measured during the AAT process. The AAT occurs in wide pressure region and is accompanied by the volume anomaly as well in  $\alpha$ -GaSb. The volume has logarithmic time dependence. The softening of the shear modulus has been found near the pressure of the AAT. The comparison of the SSA and the AAT is made.

Recently a lot of substances are found to undergo a crystal-to-amorphous transition during pressure change [1]. In experimental observations usually only a fact of disordering at certain  $P,T$ -parameters (point on  $P,T$ -plane) was registered. The temperature dependence of the SSA process and a correspondence between the SSA and the usual polymorphic transition occurring at high temperatures were not clear. The "cold melting" mechanism was the most popular still recently for the explanation of the SSA phenomenon [2]. However this model can not correctly predict the sign of the heat effect during the SSA and the short range order structure (SROS) of the amorphous phases obtained. The "mechanical instability" model is more adequate for the explanation of SSA, but up to date there were no experimental confirmations of phonon softening or decrease of elastic constants in a vicinity of the SSA process.

The nature of the AAT at high pressure is also under discussion. There are a few experimental observations of the SROS reconstruction in  $SiO_2$ ,

$GeO_2$ ,  $H_2O$  amorphous solids under pressure using x-ray, Raman and EXAFS measurements. It is unclear up to date whether AAT is similar to ordinary thermodynamic first order phase transition and what are the driven forces of the AAT.

We have established by the volume, by the resistivity measurements and by the quenching experiments the positions of the kinetic lines of the SSA for several substances (see Fig. 1). It was found that all SSA lines are the low-temperature continuations of usual hysteresis lines for crystal-crystal transitions. The positions of the SSA lines are not in an accordance with "cold melting" model.

We have studied the kinetics of the amorphization of the high pressure phases of  $SiO_2$  (Stishovite) and found that the corresponding activation energy of the SSA process ( $\sim 2$  eV/atom) is significantly less than the activation energy of diffusion in  $SiO_2$  ( $\sim 5$  eV/atom). It means that the SSA are diffusionless martensitic-like processes, but with a large

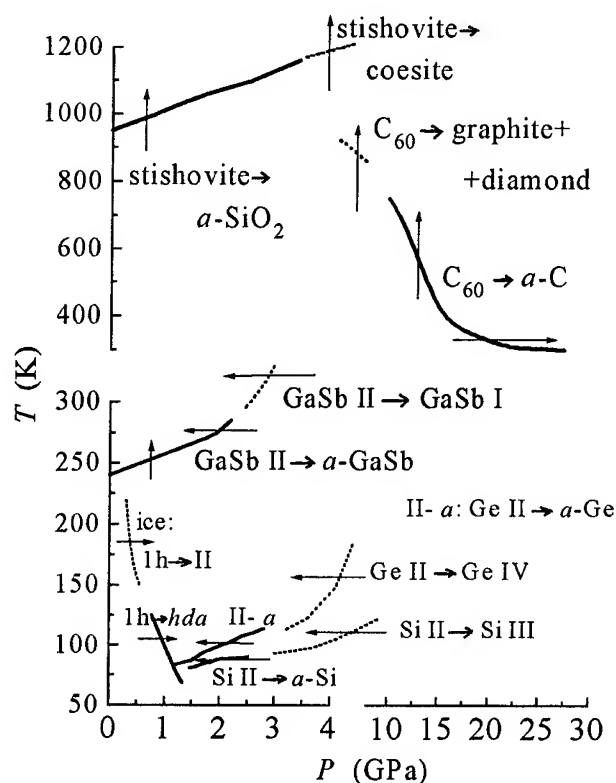


Fig. 1. The  $P,T$ -diagram with transition lines of some crystal-amorphous transformations and corresponding crystal-crystal transitions. Some data for  $\text{C}_{60}$  and for  $\text{H}_2\text{O 1h} \rightarrow \text{H}_2\text{O II}$  transition are used from Refs. [3, 4].

volume change. The decrease of the activation energy may be connected with the phonon softening. To prove "mechanical instability" model we have executed the ultrasonic measurements of the shear constants for the different phases of ice in the vicinity of the SSA.

The results are presented in Fig 2. We found 10÷12% decrease of shear modulus of ice I before the SSA. It means at least 20÷25% softening of  $(1/2)(C_{11}-C_{12})$  or  $C_{44}$  elastic constant. It can be mentioned in this respect that the more drastic softening should be observed for the phonons on the Brillouin zone boundary, as in ultrasonic measurements we observed a behavior of long-wave phonons.

The SSA process enables to prepare the amorphous tetrahedral semiconductors in the bulk form:  $a\text{-Si}$ ,  $a\text{-Ge}$ ,  $a\text{-A III B V}$  compounds - by

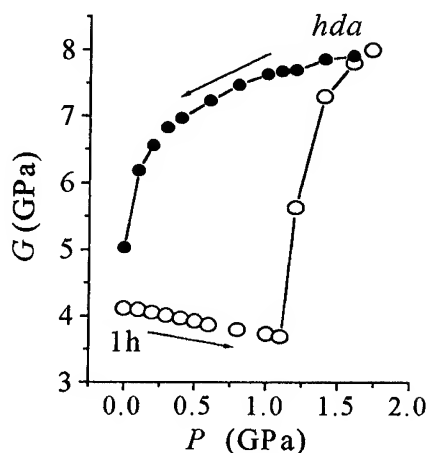


Fig. 2. The pressure dependence of shear modulus during transformation: crystalline hexagonal ice 1h  $\rightarrow$  amorphous high-density (hda) ice.

decompression of the  $\beta$ -tin high pressure phases and  $\alpha$ -C - by compression and subsequent heating of  $C_{60}$  crystals. The amorphization of  $C_{60}$  during compression occurs in wide  $P,T$ -region through intermediate phases  $i$ -C (see Fig 3). The  $i$ -C phases consist of  $C_{60}$  molecules connected by covalent bonds (three-dimensional polymer). The properties of the several amorphous semiconductors prepared by the SSA are summarized in Table I. The unique mechanical characteristics of "amorphous diamond" ( $a$ -C) and intermediate carbon phases ( $i$ -C) should be mentioned,  $a$ -C phase has the hardness and Young modulus slightly less than those of diamond, as the fracture toughness coefficient of  $a$ -C ( $10\text{--}15 \text{ MNm}^{-3/2}$ ) is two times higher that of the diamond ( $5\text{--}12 \text{ MNm}^{-3/2}$ ). The intermediate phases of  $C_{60}$  have the hardness and Young modulus by 2-3 times less the corresponding values for diamond, but they have totally plastic regime of indentation similar to metals. These data refute sensational claims about possibility of preparation of the  $C_{60}$  phases with larger modulus and larger hardness than those of the diamond. Nevertheless the unique mechanical

characteristics and large plasticity of  $i$ -C and  $a$ -C states enable to hope these phases to have great prospects as superhard materials.

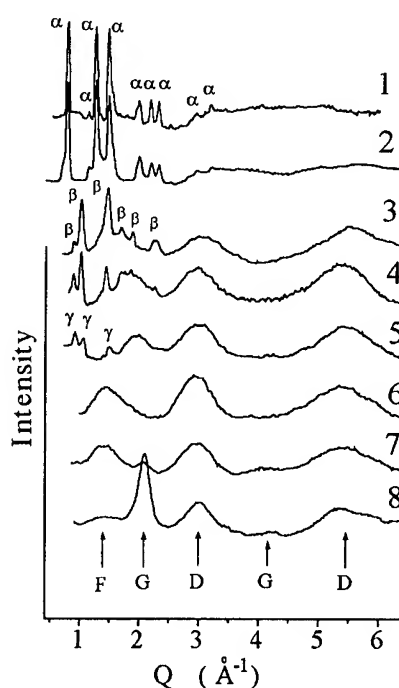


Fig 3. X-ray diffraction data for the samples of  $C_{60}$  after heating under high pressure ( $P=12.5 \text{ GPa}$ ). The numbers of curves correspond to different temperatures: 1 - initial  $C_{60}$ ; 2 -  $T=20^\circ\text{C}$ ; 3 -  $300^\circ\text{C}$ ; 4 -  $400^\circ\text{C}$ ; 5 -  $450^\circ\text{C}$ ; 6 -  $500^\circ\text{C}$ ; 7 -  $600^\circ\text{C}$ ; and 8 -  $700^\circ\text{C}$ . The crystalline reflexes of  $\alpha$  (initial  $C_{60}$ ),  $\beta$  and  $\gamma$  phases are marked by letters. The amorphous peaks of  $C_{60}$  (F), "amorphous diamond" (D) and graphite (G) are indicated by arrows.

Table I. The structural (density  $\rho$  and amorphous correlation length  $L$ ) and mechanical (Young modulus  $E$  and hardness  $H_V$ ) properties of the bulk amorphous tetrahedral semiconductors in comparison with their crystalline counterparts.

Substance	$\rho$ , $\text{g cm}^{-3}$	$L$ , $\text{\AA}$	$E$ , $\text{GPa}$	$H_V$ , $\text{GPa}$
$\alpha\text{-Si}_{0.9}\text{GaAs}_{0.1}$	2.2	9	-	$8 \pm 2$
$c\text{-Si}$	2.33	-	165	10
$\alpha\text{-GaSb}$	5.6	14-25	60	$5 \pm 1$
$c\text{-GaSb}$	5.6	-	90	7
$\alpha\text{-Ge}_{0.4}\text{GaSb}_{0.6}$	5.5	10	70	$5 \pm 1$
$c\text{-Ge}_{0.4}\text{GaSb}_{0.6}$	5.5	-	100	7
$a\text{-C}$	3.15	12.5	800	70-80
$i\text{-C}$	2.6	11.5	400	25-50
diamond	3.5	-	1100	70-140

One can suppose, that the AAT are also connected with a "mechanical" instability of an amorphous network. The main distinction of the AAT from the SSA should consist in a large dispersion of local elastic constants of the amorphous network and consequently a wide  $P,T$ -interval of the AAT should be observed.

We have fulfilled for the first time the volume measurements of AAT for  $a\text{-GaSb}$  and  $a\text{-GeO}_2$  (see Fig. 4 a,b).

In these substances the AAT is accompanied by the large volume anomalies like the ordinary

polymorphic transition, but in more wide pressure interval ( $P \sim 4-8$  GPa instead 0.1-1 GPa for polymorphic transitions). For the first time the relaxation processes (time dependencies of the volume of the amorphous phases) were studied into the region of the AAT (fig 4 c). The logarithmic dependence obtained for various pressures means the wide range of the activation energies of the relaxation.

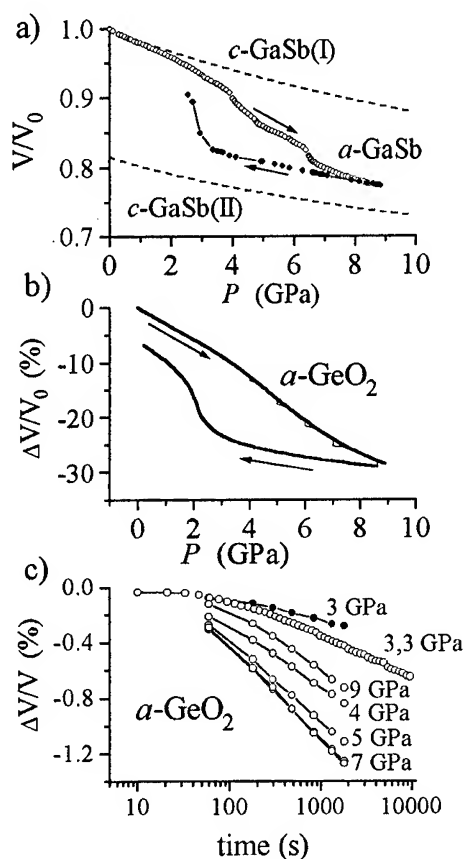


Fig. 4. The pressure dependence of relative volume for  $\alpha$ -GaSb and for  $\alpha$ -GeO<sub>2</sub> and time dependence of  $\Delta V/V$  for  $\alpha$ -GeO<sub>2</sub> at fixed pressures. The  $\Delta V/V(P)$  dependence for revaxation experiment in  $\alpha$ -GeO<sub>2</sub> is also presented (small steps).

We have made the ultrasonic measurements of the shear modulus during the AAT in ice,  $hda \rightarrow lda$  (Fig 5). The decrease of the shear modulus before the transition has been found for  $hda$  phase.

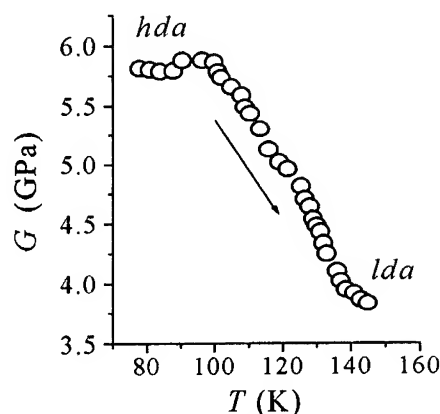


Fig. 5. The temperature dependence of shear modulus during transformation  $hda - lda$ .

In summary, we conclude that the high-pressure SSA and the AAT are governed by the phonon softening and the "mechanical instability" of the crystalline lattices or amorphous networks. In the case of the AAT there is a wide dispersion of the local elastic constants in the amorphous network, that leads to the wide  $P, T$ -interval of the transition and to the logarithmic relaxation behavior.

#### Acknowledgments

We are grateful to Dr. Yu.A. Kluev, Dr. A.M. Naletov, and Dr. N.N. Melnic for the experimental measurement assistance.

The work was financially supported by ISF (Soros Foundation) (Grant No. MTK 300) and Russian Science Foundation (Grant No. 05-02-03677).

#### References

1. E.G. Ponyatovsky and O.I. Barcalov, Mat. Sci. Rep. **8**, 147 (1992).
2. O. Mishima, L.D. Calvert, and E. Whalley, Nature **314**, 76 (1985).
3. M.N.Regueiro, P.Monceau, A.Rassat, P. Bernier, and A. Zahab, Nature **354**, 289 (1991).
4. O. Mishima, J. Chem. Phys. **100**, 5910 (1994)

# XAFS STUDY of PRESSURE INDUCED AMORPHIZATION

F. Wang and R. Ingalls

Department of Physics, University of Washington  
Seattle, WA 98105, USA

## ABSTRACT

Tin tetraiodide ( $\text{SnI}_4$ ) undergoes a phase transition between 9 GPa and 18 GPa. The transformation is simultaneously from crystalline to amorphous and from insulating to metallic. Here we report the results of XAFS (x-ray absorption fine structure) spectroscopy at the K-edges of tin and iodine, measured to pressures above 20 GPa. We observe a detailed evolution of the Sn-I bond, and also the I-I bond, which becomes observable in the amorphous phase.

## Introduction

Most amorphous materials have been prepared by rapid cooling of the liquid phase. Recent work has also shown that the amorphous state can also be obtained by hydrostatic pressurization of certain crystals. Many compounds exhibit this kind of transition.<sup>1,2</sup> Pressure induced amorphous states, like conventionally prepared amorphous materials, have broad halo like x-ray diffraction patterns. However these pressure induced amorphous states seems to have some memory of their original crystallographic orientation. In many cases, the crystalline state is recovered upon decompression; in some cases, a single crystal recovers it's original orientational property;<sup>3</sup> in some cases, the amorphous state shows anisotropy along it's original crystallographic axes.<sup>4</sup> How the translational structural information hides in apparently disorderd configurations is a very interesting question. Study of the local structure of this new kind of disorder is essential in understanding the mechanism of pressure induced amorphization. Here we report an XAFS spectroscopy study of molecular crystal tin tetraiodide ( $\text{SnI}_4$ ) at pressures up to 22 GPa.  $\text{SnI}_4$  molecules have tetrahedral symmetry, forming a cubic lattice ( $T_h^6 - Pa3$ ,  $a = 12.273\text{\AA}$ ) with eight molecules in a unit cell. Earlier work has shown that  $\text{SnI}_4$  undergoes a phase transition between 9 GPa and 18 GPa. The transformation is simultaneously from crystalline to amorphous and from insulating to metallic.<sup>2</sup> XAFS spectra at the K-edges of tin and iodine have been measured and analyzed. A possible structural model is proposed.

## Experimental

The  $\text{SnI}_4$  sample was obtained commercially from Alfa Aesar Company. A Bridgman anvil cell with sintered boron carbide anvils was used to generate pressure.<sup>5</sup> Inconel 601 was used to make 0.2 mm thick gaskets with 0.5 mm diameter holes. The samples were ground and loaded into the pressure cell under argon environment. No pressure medium was used because of the solubility of  $\text{SnI}_4$  in most organic solvents. The sample pressure was obtained from the applied force. The XAFS spectra were obtained at a wiggler side-station at the Stanford Synchrotron Radiation Laboratory (SSRL) using silicon (220) monochromator crystals. The XAFS data were analyzed using FEFF6 program.<sup>6</sup>

## Results and Discussion

Sn K-edge spectra at different pressures are shown in Fig. 1. We observe that the amplitude of the oscillations in the high  $k$  range ( $8\text{\AA}^{-1} - 16\text{\AA}^{-1}$ ) drops considerably above 9 GPa, and then gradually decreases until it totally disappears at 19 GPa, only returning to its original value after release of pressure. We interpret this as a distortion of the  $\text{SnI}_4$  molecule due to pressurization, and then a restoration after pressure release. The Sn-I bond lengths for undistorted and distorted  $\text{SnI}_4$  molecules are shown in Fig. 2. We notice that the Sn-I bond length of the distorted  $\text{SnI}_4$  molecule is longer when distorted. The electronic structure of  $\text{SnI}_4$  has changed to give a longer bond upon pressurization. This agrees with the conclusion drawn by Pasternak

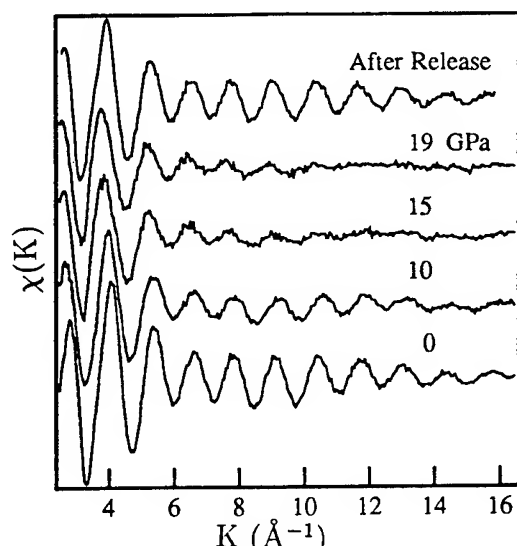


Fig. 1. Sn K-edge XAFS in  $\text{SnI}_4$  at several pressures.

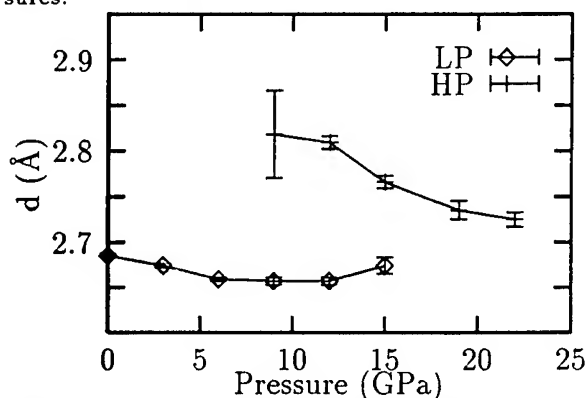


Fig. 2. Sn-I bond length in undistorted ( $\diamond$ ) and distorted (+)  $\text{SnI}_4$ .

et. al. from their Mössbauer measurement<sup>7</sup>.

Comparing the bond length of distorted  $\text{SnI}_4$  molecules (2.75 Å) with that of  $\text{I}_2$  (2.70 Å) and that of the I-I (3.45 Å) (see Fig. 6), we conclude that the Sn-I distance is still very short and that the tin and iodine atoms should still be strongly bonded. Our analysis indicates that the coordination number for Sn remains four within experimental error during the whole process, supporting our conclusion that the  $\text{SnI}_4$  molecules stay intact. The mean-square deviation in the Sn-I bond in the high pressure phase is quite large compared to that in the low pressure phase (see Fig. 3), suggesting that the  $\text{SnI}_4$  molecules in the high pressure phase are distorted. We use the amplitude of undistorted  $\text{SnI}_4$  to calculate

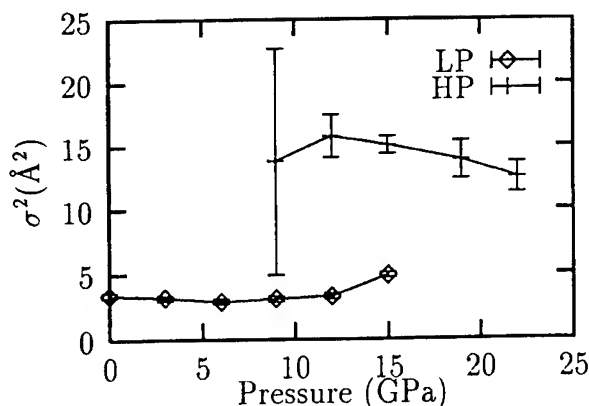


Fig. 3. Mean-square deviation in the Sn-I bond length in undistorted ( $\diamond$ ) and distorted (+)  $\text{SnI}_4$ .

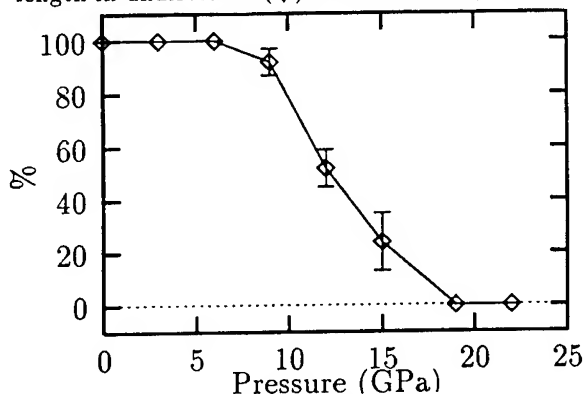


Fig. 4. Percentage of crystalline  $\text{SnI}_4$  versus pressure.

the relative percentage of the crystalline phase, as shown in Fig. 4. It agrees with previous results.<sup>7</sup>

Because the iodine atoms in crystalline  $\text{SnI}_4$  interact very weakly with their iodine neighbors, the amplitude of the associated spectra is very small. At high pressure, the iodine atoms form stronger bonds among themselves and the amplitude of the XAFS spectra increases (see Fig. 5). In Fig. 6 we see that the distance between I atoms decreases dramatically with pressure. For comparison, in metallic iodine<sup>8</sup> at 22 GPa, each I atom has 4 neighbouring atoms at a distance of 3.0 Å, and has 8 neighbouring atoms at a distance of 3.5 Å. So the bond lengths are quite similar, suggesting that the I-I bonds in  $\text{SnI}_4$  could be metallic bonds. The number of I-I bonds each I atom has is shown in Fig. 7. This is quite different from results of Pasternak et. al.<sup>7</sup>

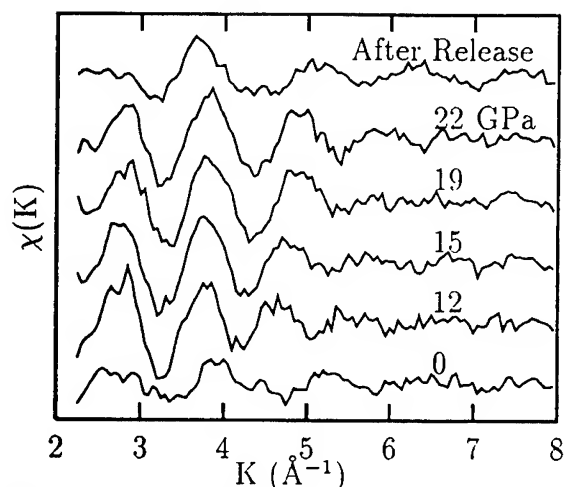


Fig. 5. I K-edge XAFS in  $\text{SnI}_4$  at several pressures.

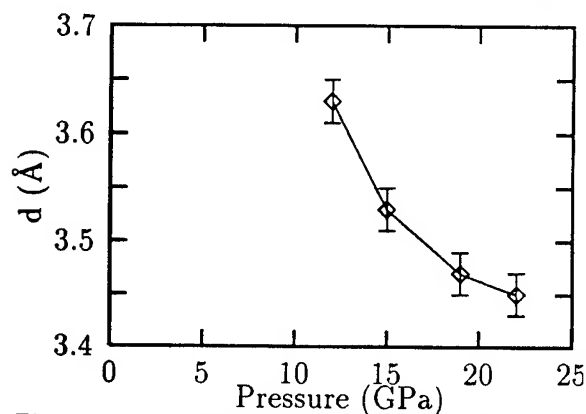


Fig. 6. I-I bond distances as a function of pressure.

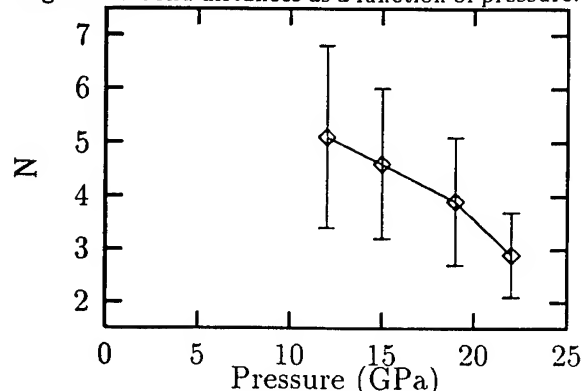


Fig. 7. Number of I-I bonds per iodine atom.

They reported an average 0.5 I-I bond for each I atom. We have good reason to believe that the distorted  $\text{SnI}_4$  molecules in the amorphous phase are pretty close to an ideal tetrahedron. From the Sn-I bond length we then determine

the distance between I atoms within a  $\text{SnI}_4$  unit to be about 4.44 Å. Comparing this with the I-I bond length (3.45 Å), we can conclude that only I atoms from different molecules effectively form bonds. Our fitting results (see Fig. 7) suggest that each I atom only bonds with 3 other neighboring I atoms. Our model is that when pressurized,  $\text{SnI}_4$  molecules are distorted and rotated to join neighbouring  $\text{SnI}_4$  molecules so that new smaller tetrahedral units (without the central tin atom) also form among I atoms. This is quite different from the model of randomly oriented  $\text{SnI}_4$  chains proposed by Pasternak et. al.<sup>7</sup> Further investigation is needed to answer this point.

#### Acknowledgements

The authors are pleased to thank S. Jones for assistance with various aspects of this work. This research was supported by the US Department of Energy Grant No. DE-FG-06-84ER-45163, while SSRL is supported by the US Department of Energy and the National Institutes of Health.

#### References

1. O. Mishima, L. D. Calvert, and E. Whalley, *Nature* **310**, 393(1984).
2. M.P. Pasternak, R. D. Taylor, M. B. Kruger, R. Jeanloz, Jean-Paul Itie, and A. Polian, *Phys.Rev.Lett.* **72**, 2733 (1994), and references therein.
3. M. B. Kruger and R. Jeanloz, *Science* **249**, 647 (1990).
4. L. E. McNeil and M. Grimsditch, *Phys. Rev. Lett.* **68**, 83 (1992).
5. R. Ingalls, E. D. Crozier, J. E. Whitmore, A. J. Seary and J. M. Tranquada, *J.Appl.Phys.* **51**, 3158 (1980).
6. J. Mustre de Leon, J.J. Rehr, S.I. Zabin-sky and R.C. Albers, *Phys.Rev.* **B44**, 4146 (1991).
7. M. Pasternack and R. D. Taylor, *Phys.Rev.* **37**, 8130 (1988).
8. Takemura, S. Minomura, O. Shimomura, Y. Fujii and J. D. Axe, *Phys. Rev. B* **26** 998 (1982).



# PERCULIARITIES OF PHASE TRANSITION THERMODYNAMICS AT LABILITY BOUNDARIES UNDER HIGH PRESSURE

E.A. ZAVADSKII, B.Ya. SUKHAREVSKII

*Donetsk Physico-Technical Institute, Ukrainian Academy of Sciences, Luxemburg str. 72, Donetsk, Ukraine*

A phenomenological Landau-type model with two bonded order parameters, structural  $\eta$  and nonstructural  $\xi$  ones, has been proposed. The model makes it possible to describe the main peculiarities of the experimental diagrams, in particular, the appearance of a closed region of ordered-phase existence, "the anisotropy" of phase transitions in the low-pressure range - two at cooling and one at heating, the signs of volume change under transitions. The theoretical results agree well with the experimental P-T diagram of potassium nitrate.

## 1 Introduction

Usage of high pressure has made it possible to study both the stable and metastable states. It has been found experimentally that (i) the number of phase transitions (PhT) on cooling and heating may differ <sup>1,2</sup>; (ii) in the P-T diagram the region of ordered phase existence can be the closed one <sup>2</sup> even at not high pressure  $dT/dP > 0$ , and at high pressure  $dT/dP < 0$ ; (iii) at low temperatures the area of the metastable (with respect to pressure) region grows beyond all bounds <sup>4</sup> and the anomalous changes of volume and thermal effects at phase transitions are possible <sup>3</sup>. Some of the peculiarities are explained in this paper. The object of experimental data and theoretical results is potassium nitrate in which at pressure to 200 MPa the three phases have been found: I -  $D_{3d}$ , II -  $D_{2h}$ , III -  $C_{3v}$ . Phases I and II are paraelectric ones and III is ferroelectric phase.

## 2 The Landau model potential

The symmetry group of II is not a subgroup of I. Usage of the Landau theory tool needs the introduction of a hypothetical phase 0 with the point symmetry group  $O_h$  and the three order parameters (OP):  $\eta = (\eta_1; \eta_2)$  characterising PhT 0-II;  $\varphi = (\varphi_1; \varphi_2; \varphi_3)$  determining the deformation of structure at PhT 0-I ( $\varphi_1 = \varphi_2 = \varphi_3 \neq 0$ ) and I-III ( $\varphi_1 \neq 0; \varphi_2 = \varphi_3 = 0$ ) and  $\xi$  - ferroelectric ordering.

The Landau potential including the invariants of the above OP is rather awkward. Therefore instead of a real crystal with a real PhT we consider a hypothetical crystal with a more higher symmetry of phases: I -  $O_h$ , II -  $D_{4h}$ , III -  $O_h$ , the

ferroelectric one. Such a simplification is permissible at a strong bond of OP  $\eta$  and  $\xi$ . We suppose also that the PhT I-III is the second order PhT.

So the problem reduces to the analysis of the model potential

$$\phi = \phi(\eta) + \phi(\xi) + q\eta^2\phi(\xi) \quad (1)$$

In Eq. 1  $\phi(\eta) = a\eta^2 + b\eta^4 + c\eta^6$ ;  $\phi(\xi) = d\xi^2 + f\xi^4$ ;  $q = \text{const} > 0$  is the coupling coefficient. II is the paraelectric one ( $\eta \neq 0, \xi = 0$ ) at strong coupling of  $\eta$  and  $\xi$ :  $q\eta^2 > 1$  <sup>3</sup>.

## 3 Analysis of the model potential and results

By analogy with <sup>4</sup> we write:

$$a_{a,d} = \alpha_{a,d}[\lambda_{a,d}(P - P_0) + (T - T_0) + \delta_{a,d}(T - T_0)^2] \quad (2)$$

where  $a_a = a$ ;  $a_d = d$ ;  $P_0$ ;  $T_0$  are the coordinates of point  $M_1$  where curves  $a = 0$  and  $d = 0$  intersect.

Conditions of phase stability

$$\frac{\partial^2 \phi}{\partial \eta^2} \geq 0 \text{ and } \frac{\partial^2 \phi}{\partial \xi^2} \geq 0 \quad (3)$$

with  $\eta$  and  $\xi$  conforming to

$$\frac{\partial \phi}{\partial \eta} = \frac{\partial \phi}{\partial \xi} = 0 \quad (4)$$

From Eq. 3 and Eq. 4 the conditions are determined for the stability of phases:

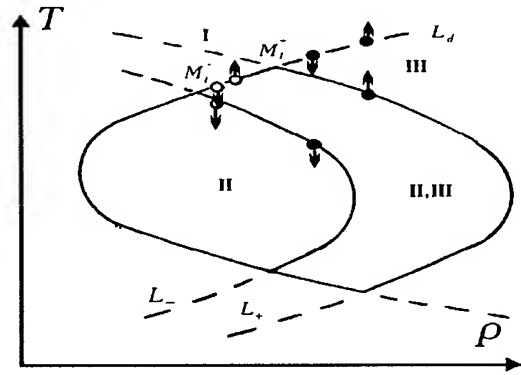


Figure 1: I,II,III-stable phases, I,II-metastable states;  $L_- (a=0)$ , boundary lability, transitions III $\rightarrow$ II;  $L_+ (b^2-3ac=0)$ , boundary lability, transitions II $\rightarrow$ III;  $L_d (d=0)$ , PhT I $\rightarrow$ III and III $\rightarrow$ I at  $P > P_1^\dagger$ ; PhT II $\rightarrow$ I at  $P < P_1^\dagger$ ,  $M_1^\dagger (T_1, P_1^\dagger)$ ;  $M_2^\dagger (T_0, P_0)$ ,  $\uparrow, \downarrow$  - PhT at  $P > P_1^\dagger$ ,  $\uparrow, \downarrow$  - PhT at  $P < P_1^\dagger$ .

At  $P > P_1^\dagger$  the situation is more "symmetrical": I  $\rightarrow$  III (on  $d=0$ )  $\rightarrow$  II (on  $a=0$ ) and II  $\rightarrow$  III (on  $b^2-3ac=0$ )  $\rightarrow$  I (on  $d=0$ ).

So the strong coupling between the order parameters results in the following:

1. Parameter  $\xi$  is "forced out" of the region of II existence. This phase is ordered only with respect to  $\eta$ .
2. Curve  $d=0$  closed the region of II existence. On this curve  $dT/dP > 0$ , so  $\Delta V > 0$ . The right hand segments of lability boundaries are the curves  $a=0$  and  $b^2-3ac=0$  on which  $dT/dP < 0$  and  $\Delta V < 0$ .

In spite of considerable simplifications of the model potential, this model well demonstrates the main peculiarities of PhT in  $KNO_3$  which have been mentioned in the quoted papers.

## References

1. U. Kawabe, T. Uanagi and S. Sawada, *Journal of Physical Society of Japan* **20**, 2059 (1965).
2. S.K. Asadov, I.P. Vasilenko, E.A. Zavadskii et al, *Fiz. Tverd. Tela* (to be published).
3. E.A. Zavadskii, B.Ya. Sukharevskii, *Fiz. Nizkikh. Temp.* **8**(1995)(to be published)
4. B.Ya. Sukharevskii, E.A. Zavadskii, *Fiz. Nizkikh. Temp.* **8**(1995)(to be published)

$$I: \quad \eta = 0; \xi = 0; a \geq 0; d \geq 0 \quad (5)$$

$$III: \quad \eta = 0; \xi = -d/2f; f = \text{const} > 0; \quad (6) \\ a \geq 0; d \leq 0$$

$$II: \quad \eta = (-b + \sqrt{b^2 - 3ac})/3c; \xi = 0; \quad (7) \\ b^2 - 3ac \geq 0; b = \text{const} < 0; \\ c = \text{const} > 0$$

$$d(1 - q\eta^2) \geq 0; q = \text{const} > 0 \quad (8)$$

In the limit of strong coupling in the whole region  $\eta \neq 0$ ,  $1 - q\eta^2 < 0$  the II exists only at  $d < 0$ . At  $d > 0$  condition Eq. 8 is satisfied at  $\eta = 0$ .

Assuming in Eq. 2

$$\alpha_{a,d} > 0; \delta_{a,d} > 0; \lambda_a > 0; \lambda_d < 0 \quad (9)$$

we obtain the closed region of II existence.

Fig.1 shows the diagram of states constructed basing on the analysis of potential Eq. 1.

The lability boundaries for II are determined by parabolas  $b^2 - 3ac = 0$  and  $d = 0$ . As it is seen from fig.1, at  $P < P_1^\dagger$  the II is formed as the result of two transitions: I $\rightarrow$ III on the curve  $d=0$  and III $\rightarrow$ II on the curve  $a=0$ .

As it follows from Eq. 2 and Eq. 3, on the curve  $d=0$   $dT/dP > 0$  so that  $V_I - V_{III} > 0$ ; on the curve  $a=0$   $dT/dP < 0$ , and  $V_{III} - V_{II} > 0$ .

Phase I is realized in the result of PhT III $\rightarrow$ I on the curve  $d=0$   $dT/dP > 0$  so that  $V_I - V_{III} > 0$ .

## **VI(B) Phase Diagrams**

# BINARY PHASE DIAGRAMS UNDER HIGH PRESSURE

Toshimi YAMANE

*Department of Mechanical Engineering, Hiroshima Institute of Technology  
2-1-1 Miyaka, Saeki-ku, Hiroshima 731-51, Japan*

## ABSTRACT

This is a review of the author's research works on binary phase diagrams at high pressure for past fourteen years long. Six iron, nine aluminum and ten titanium base binary phase diagrams at high pressure have been constructed, and these experimental phase diagrams agree with those theoretically calculated using Gibbs free energies.

## Introduction

Monocomponent matters such as pure elements and compounds at high pressure, change sometimes their crystal structures with their properties when pressure increases. Famous examples are the formations of diamond and cubic boron nitride at high pressures and temperatures. At present time, High pressure is available cold isostatic pressing, hot isostatic pressing, self-heating synthesis, solid bonding, explosion forming, hydrostatic extrusion and so on. But binary phase diagrams at high pressure are not so many comparing with those of one components (1,2). Here, iron, aluminum and titanium base binary phase diagrams at high pressure, which I have investigated are mentioned.

## Investigation Methods on Experimental Binary Phase Diagrams at High Pressure

Experiments at high pressure take plenty time. It is favorable to get many data from one experiment. The utilization of reaction diffusion is one of methods. In Fig.1, a reaction diffusion couple of pure  $\alpha$  and  $\beta$  is heated at  $T_0$  at high pressure. Interface concentrations between  $\alpha/\alpha+\beta$  and  $\beta/\alpha+\beta$  can be obtained from the diffusion profile.

Fig.2 shows the reaction diffusion profile of Al-Ag couples plotted as a function of Boltzmann parameter  $x/t^{1/2}$ , where  $x$  is the

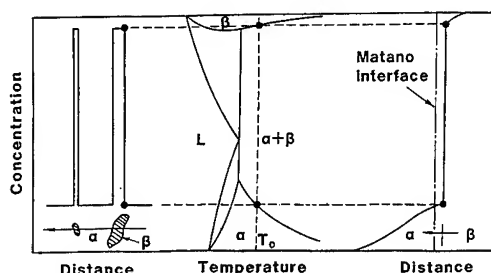


Fig.1 Establishing method of a binary phase diagram by interface concentrations in a reaction diffusion couple at high pressure and temperature  $T_0$  (right figure) and by alloy method (left one).

diffusion distance from Matano interface,  $t$  the diffusion time. All diffusion profiles are on the same curve. This means that the partial equilibrium is kept.

After long time annealing of alloys, concentrations of a matrix and second phase are plotted as shown the left figure in Fig.1.

A 12 MN compressive press machine is a generator of high pressure and temperature. Fig.3 shows a vertical section figure of a high pressure cubic capsule which is pressed by six anvils from top and bottom, left and right, front and rear. The reaction specimen are 4 mm in diameter and 2.5 mm in height. Two specimens which have different composi-

ions are connected together, and its total height is 5 mm.

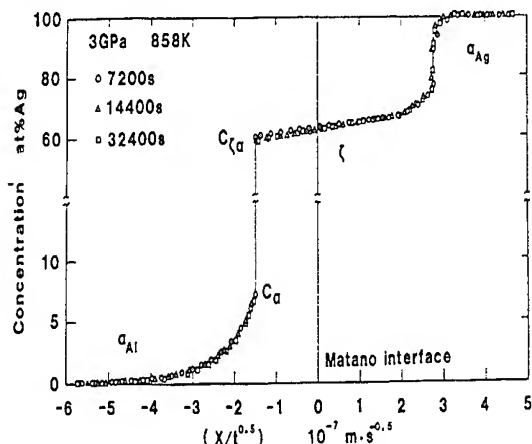


Fig. 2 Diffusion profile of Boltzmann parameter in Al/Ag diffusion couples annealed at 3 GPa and 858 K for 7.2, 14.4 and 32.4 ksec(3).

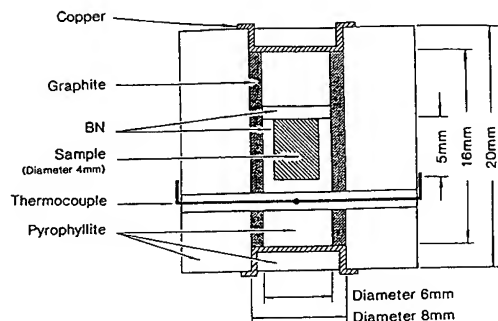


Fig. 3 Section figure of heating cell at high pressure. Electricity passes through graphite heater connected with top and bottom anvils, and temperature measurements are made by thermocouple connected with right and left anvils.

## Experimental Binary Phase Diagrams at High Pressure

### Iron Base Binary Phase Diagrams

Fe-Al(4), Fe-Cr(5), Fe-Mo(6), Fe-Ti(7), Fe-V(8), Fe-W(9) and Fe-Al-Mn(10) systems are investigated. These all systems belong to

the  $\gamma$  loop forming group. Figs. 4- 8 show these phase diagrams at high pressure. In these phase diagrams, the  $\gamma$  field expands at high pressure, but the boundaries between  $\alpha$  and  $\alpha$ +intermetallic compounds do not move by high pressure.  $A_3$  point moves to lower temperatures at high pressure for the decrease in the molar volume of  $\alpha$  to  $\gamma$  transformation. Contradictory,  $A_4$  point moves to higher temperatures. As a result of the expansion of the  $\gamma$  field, an eutectoid reaction is formed and a peritectoid reaction is done at a lower temperature. Fe-Mo, Fe-Ti and Fe-W systems belong to this type.

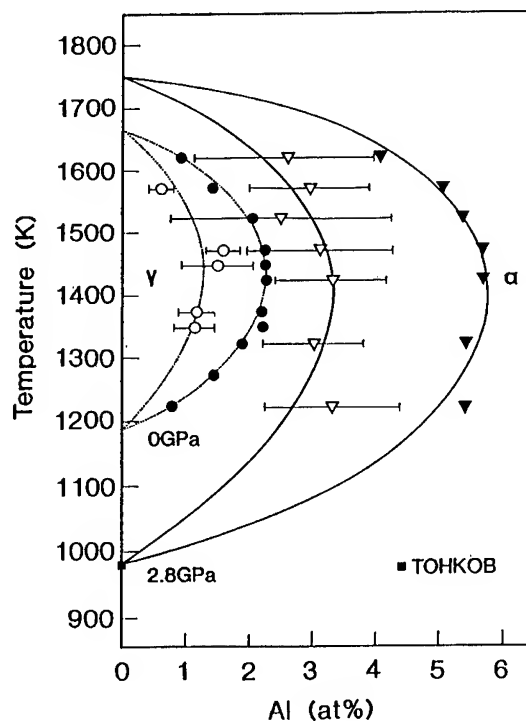


Fig. 4 Fe-Al phase diagram at high pressure (4).

If higher pressure is applied, even in Fe-Al, Fe-Cr and Fe-V systems, similar changes might occur.

### Aluminum Base Binary Phase Diagrams

Al-Ag(3), Al-Cr(11), Al-Cu(12), Al-Ge(13)

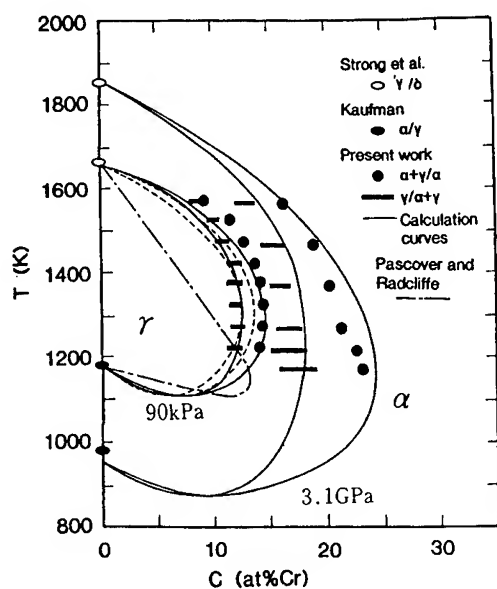


Fig. 5 Fe-Cr phase diagram at high pressure (5).

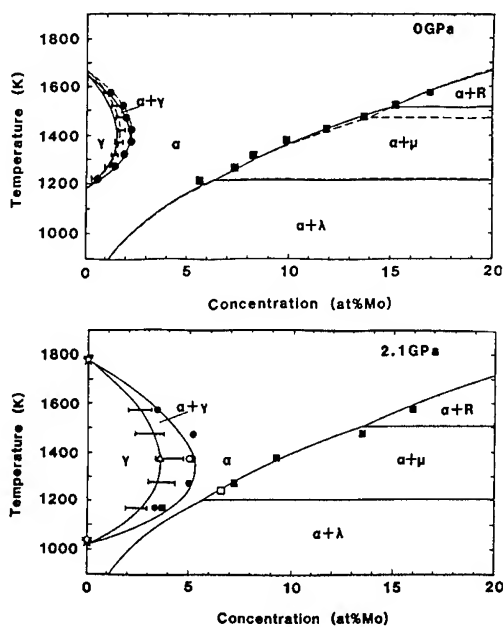


Fig. 6 Fe-Mo phase diagrams at 0, 2.1, 3.2 GPa(6).

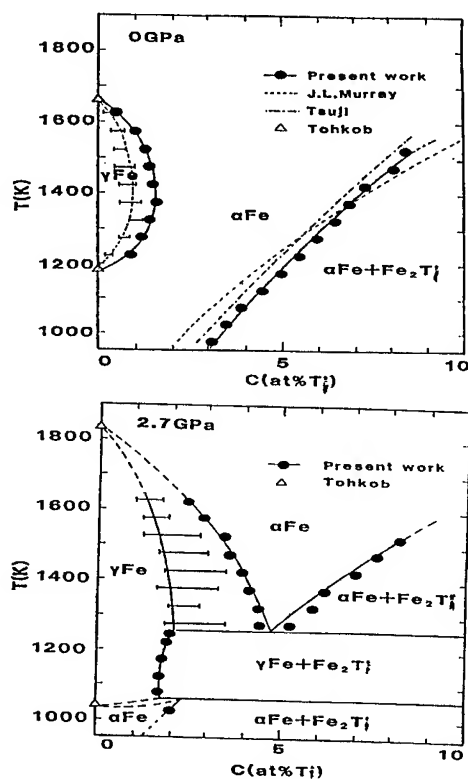


Fig. 7 Fe-Ti phase diagrams at 0 and 2.7 GPa (7).

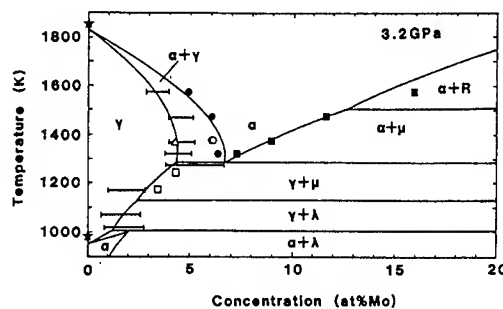


Fig. 8 Fe-Al-Mn phase diagram at 1373K(10).  
○● : 0 GPa, △▲ : 2.3 GPa

Al-Mg(14), Al-Mn(15), Al-Si(16), Al-Ti((15) and Al-Zn(17,18) systems are investigated. Aluminum alloys are usually age-hardened, so

that, solid solubilities in aluminum alloys are very important. The dependence of pressure on the solid solubility in an A phase  $x^A$  is expressed by a following equation(19),

$$dx^A/dP = -x^A [dV^A/dx^A - (V^B - V^A)/(x^B - x^A)] / RT \quad (1)$$

where,  $V^A$  and  $V^B$  are the molar volumes of A and B phases,  $x^A$  and  $x^B$  the equilibrium solid solubilities in A and B phases, and  $x^A$  is less than  $x^B$ , R is the gas constant, P the pressure and T the temperature. From Eq (1), 1. When  $dV^A/dx^A > 0$  and  $V^B < V^A$ , then the solid solubility in the A phase decreases at high pressure. The Al-Ag (Fig. 9), Al-Mn, Al-Ti and Al-Zn (Fig. 10) systems belong to this category. 2. When  $dV^A/dx^A < 0$ , and  $V^B > V^A$ , then the solubility in the A phase increases at high pressure. Al-Cr, Al-Ge (Fig. 11), Al-Mg (Fig. 12) and Al-Si systems belong to this category. 3. If the difference between  $dV^A/dx^A$  and  $(V^B - V^A)/(x^B - x^A)$  is small, the change in the solid solubility in the A phase at high pressure is small. The Al-Cu system belongs to this category.

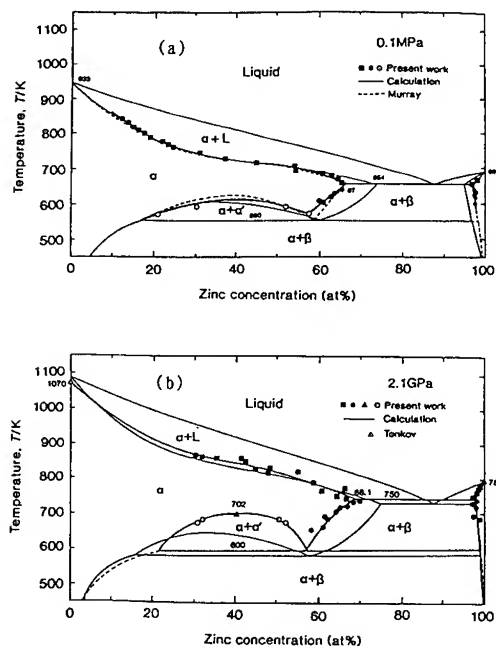


Fig. 10 Al-Zn phase diagrams at 0.1 MPa and 2.1 GPa (18).

#### Titanium Base Binary Phase Diagrams

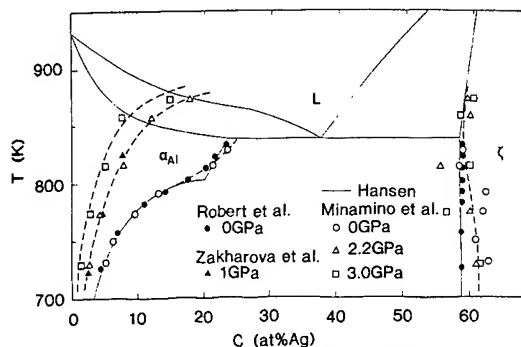


Fig. 9 Al-Ag phase diagram at 0.1 MPa and high pressures (3).

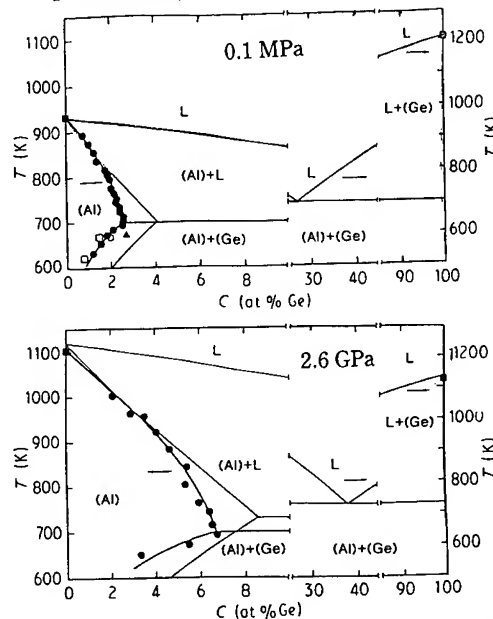


Fig. 11 Al-Ge phase diagrams at 0.1 and 2.6 GPa (13).

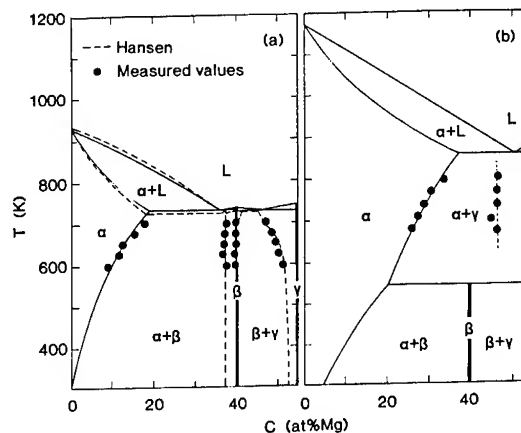


Fig. 12 Al-Mg phase diagrams (14). (a) at 0 GPa, (b) at 2.2 GPa.

Ti-Al(20), Ti-Co(21), Ti-Cr(22), Ti-Cu(23), Ti-Fe(7), Ti-Ni(24), Ti-O(25), Ti-Mn(26), Ti-Si(27) and Ti-Sn(20) systems are investigated. Fig.13 shows the Ti-Fe phase diagram. The  $\beta$  region expands to  $\alpha$ . This owes to the molar volume of  $\beta$  is smaller than that of  $\alpha$  taken by extrapolation of that of  $\alpha$  to higher temperatures. In other titanium alloys, the same phenomenon is observed.

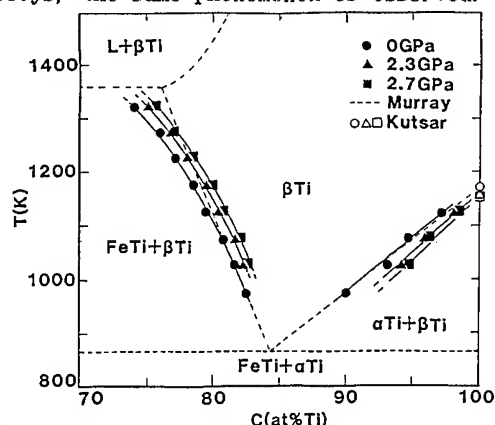


Fig.13 Ti-Fe phase diagram(7).

#### Calculation of Binary High Pressure Phase Diagram

Lattice stabilities, interaction parameters, and compound parameters for free energies of regular solutions of phases in main binary alloys at atmospheric pressure are reported. These free energies increase as  $PxV$  terms at high pressure, where  $P$  is high pressure and  $V$  the molar volume of a phase.  $V$  changes with pressures, temperatures and solute concentrations, so that  $V$  contains a compressibility, a thermal expansion coefficient and solute concentration dependence. This  $V$  is integrated by pressure. Coexisting two phases have the same chemical potential. Details of the high pressure binary phase diagram calculation are mentioned in Refs. (5, 6, 9, 13, 14, 16, 18).

#### References

1. E. Yu. Tonkov, *Fazovye Diagrammy Elementov Pri Bysokom Davlenii*, (Nauka, 1979)
2. E. Yu. Tonkov, *Fazovye Prevrashcheniya Soedinienii Pri Bysokom Davlenii*, (Metallurgiya, 1988)
3. Y. Minamino, T. Yamane et al., *J. Jpn Inst. Met.*, 48(1984)No. 8, 478
4. T. Yamane, M. Kubo et al., Unpublished Data
5. Y. Minamino, H. Araki, T. Yamane et al., *J. High Temp. Soc.*, 18(1992)No. 6, 356
6. Y. Minamino, T. Yamane et al., *J. Iron Steel Jpn.*, 74(1988)No. 4, 733
7. Y. Minamino, T. Yamane et al., *Fall Meet. Abstracts*, Jpn. Inst. Met., 1989, p. 574
8. Y. Minamino, T. Yamane et al., *Spring Meet. Abstracts*, Jpn. Inst. Met., 1986, p. 244
9. T. Yamane, Y. S. Kang et al., *Z. Metallkd.*, 86(1995)No. 7, 453
10. T. Yamane, H. Araki, M. Kubo et al., Unpublished Data
11. T. Yamane, Y. S. Kang et al., *J. Mat. Sci. Lett.*, 13(1994)No. 21, 1528
12. T. Yamane, Y. Minamino et al., *Defects and Diffusion Forum*, 66-69(1989) 1269
13. Y. Minamino, T. Yamane et al., *J. Mat. Sci.*, 26(1991)No. 20, 5623
14. Y. Minamino, T. Yamane et al., *Mat. Sci. & Tech.*, 2(1986)No. 8, 777
15. Y. Minamino, T. Yamane et al., *Met. Trans.*, 22A(1991)No. 3, 783
16. Y. Minamino, T. Yamane et al. *J. Jpn Inst. Light Met.*, 38(1988)No. 12, 800
17. H. Araki, Y. Minamino, T. Yamane et al., *J. Mat. Sci. Lett.*, 11(1992)No. 1, 181
18. Y. S. Kang, T. Yamane et al., *J. Jpn. Inst. Met.*, 57(1993)No. 9, 990
19. L. Kaufman, *Solid under High Pressure*, ed W. Paul, (McGraw Hill, 1963, p. 302)
20. T. Yamane, T. Tei, Unpublished Data
21. H. Araki, T. Yamane et al., *J. Mat. Sci. Lett.*, 13(1993)No. 2, 355
22. H. Araki, T. Yamane et al., *Fall Meet. Abstracts*, Jpn. Inst. Met., 1989, p. 574
23. T. Yamane, S. Nakajima et al., *J. Mat. Sci. Lett.*, 13(1994)No. 2, 162
24. H. Araki, T. Yamane et al., *Spring Meet. Abstracts*, Jpn. Inst. Met., 1990, p. 66
25. H. Araki, T. Yamane et al., *Spring Meet. Abstracts*, Jpn. Inst. Met., 1991, p. 99
26. T. Yamane, *Korean J. Mat. Research*, 3(1993)No. 4, 424
27. T. Yamane, Y. Fujiishi et al., *J. Mat. Sci. Lett.*, 13(1994)No. 2, 200



# AGREEMENT BETWEEN STATIC AND SHOCK MELTING MEASUREMENTS

R. BOEHLER

*Max-Planck-Institut für Chemie, 55020 Mainz, Germany*

## ABSTRACT

Melting measurements on iron in laser-heated diamond anvil cells to 2 Mbar and shock temperature measurements showed large differences in the melting temperatures (1-4). However, the phase diagram of iron, measured in a diamond cell can be reconciled with Brown and McQueen's 1986 (5) shock sound velocity measurements. Recent measurements of the thermal conductivity of corundum, the window material used in some shock experiments (6), resulted in a reduction of shock temperatures by 1000 K. If, additionally, overshoot is considered in shock melting experiments, as has been measured on KBr and SiO<sub>2</sub>, shock data are found to be in very good agreement with static diamond cell results. This results in a melting temperature of iron at the pressure of the inner core boundary (3.3 Mbar) of slightly less than 5000 K. New data on the Fe-FeS eutectic to over 600 kbar are also presented.

## Introduction

Melting temperatures of iron, measured under static pressure conditions by four groups (Canberra, Livermore, Uppsala, and Mainz) (1,7-9) are in excellent agreement with each other, and fall within the experimental uncertainty of order 100 degrees. Boehler (1) and Saxena et al (10) independently found evidence of a possible new high pressure phase which could replace the hcp phase predicted for the inner core and which could also explain the solid-solid transition found by Brown & McQueen (5) in their shock experiment. This phase diagram, obtained from diamond - cell experiments is shown in Figure 1.

The temperature gap between the solid-solid transition and the melting curve of about 1000 K in the shock experiment by Brown and McQueen is the same as that observed between the  $\epsilon$ - $\theta$  boundary and the melting curve in the phase diagram obtained in the diamond-cell (1). It is therefore quite likely that Brown & McQueen measured these two transitions in their shock experiment.

Direct shock temperature measurements (3,4) are also shown in Figure 1. In order to

reconcile static and shock data, Anderson (11) placed a further triple point at 1.9 Mbar near 4100 K. This would deflect the melting curve sharply upwards to satisfy the lower bounds of some of the data points of the Livermore and Caltech shock measurements. Such a large increase in the melting gradient, however, is difficult to explain thermodynamically.

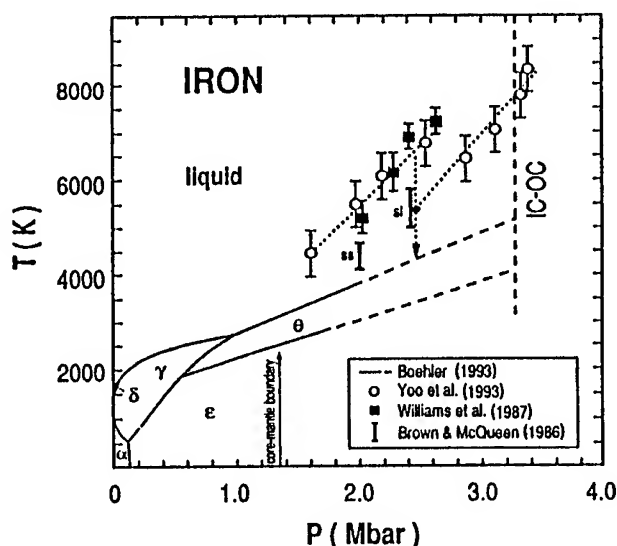


Figure 1. Phase diagram of iron (1) and shock temperature measurements (3,4).

### Comparison to shock experiments

Recent measurements on the thermal conductivity of window materials used in shock experiments (6) have lead to a reduction of the temperatures reported earlier by about 1000 degrees. In addition, there are strong indications that equilibrium conditions may have been overshoot in shock experiments due to the extremely rapid temperature rise. For quartz and silica glass (12) and for KBr (13), the solid Hugoniot overshoots the melting curve by about 1000 degrees and the P-T curves of the solid and the liquid shock states are much steeper than the melting curve. In both cases the melting temperature is below the lowest temperature measured in the liquid state. This may be applied to iron: there is general agreement, that in shock experiments, iron melts at about 2.5 Mbar. Back-extrapolation of the lower bounds of the liquid Hugoniot data of Yoo et al (3) to this pressure yields good agreements with the upper bounds of Boehler's extrapolated melting curve. The presently best estimate of the melting temperature of pure iron at the inner-core boundary pressure (3.3 Mbar) is therefore about 5000 K.

### Fe-FeS eutectic to 600 kbar

Eutectic melting temperatures for the system Fe-FeS have been measured for the first time in the diamond anvil cell, using improved techniques to identify the solidus temperatures. Precompressed, dried, homogeneous mixtures of fine grained FeS and iron in a KBr pressure medium were used. In the present study the beginning of melting was observed by monitoring discontinuous changes of the surface texture of the sample during heating. For this purpose the surface of the sample, which was heated with a strongly defocused Yttrium-Lithium-Fluoride (YLF)-laser, was illuminated with a defocused (blue) argon laser beam and observed via a CCD

camera. The argon laser light produced a random interference pattern due to small irregularities on the solid sample surface. Changes to the sample surface, even on submicron scales, caused significant modification of this interference pattern and allowed the direct observation of the first occurrence of melting. The results are shown in figure 2.

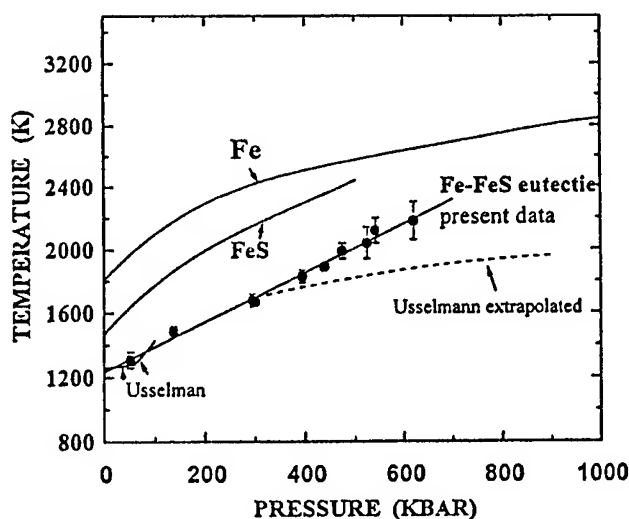


Figure 2. Eutectic melting temperatures of Fe-FeS.

Eutectic temperatures rise linearly with pressure and the difference between the melting curves of FeS and Fe suggest that the Fe-FeS system exhibits eutectic behavior over this entire pressure range. Extrapolation of the data, however, indicates a decrease of the eutectic melting depression at higher pressure, and possible closure of the temperature gap near 1 Mbar. This is in contrast to the extrapolation by Usselman (14).

### References

1. R. Boehler, *Nature* 363 (1993)534.
2. S.K. Saxena, G. Shen, and P. Lazor, *Science* 264 (1994)405.

3. C.S. Yoo, N.C. Holmes, M. Ross, D.J. Webb, and C. Pike, *Phys. Rev. Lett.*, **70** (1993) 3931.
4. Q. Williams and R. Jeanloz, *J. Geophys. Res.* **95** (1990) 19299.
5. J.M. Brown and R.G. McQueen, *J. Geophys. Res.*, **91** (1986) 7485.
6. K.G. Gallagher and T.G. Ahrens, *EOS Trans. Am. Geophys. U.* (1994) 75.
7. G. Shen, P. Lazor, and S.K. Saxena, *Phys. Chem. Miner.* **20** (1993) 91.
8. C.S. Yoo, J. Akella, and C. Ruddle, *EOS Trans. Am. Geophys. U.* **73** (1992) 64.
9. A.E. Ringwood and W. Hibberson, *Phys. Chem. Miner.* **17** (1990) 313.
10. S.K. Saxena, G. Shen, and P. Lazor, *Science* **260** (1993) 1312.
11. O.L. Anderson, in *High Pressure Research Science and Technology - 1993*, ed. SC Schmidt, JW Shaner, GA Samara, M Ross. Woodbury/NY: American Institute of Physics (1994) p.907.
12. G.A. Lyzenga, T.J. Ahrens, and A.C. Mitchell, *J. Geophys. Res.* **88** (1983) 2431.
13. D.A. Boness and J.M. Brown, *Phys. Rev. Lett.*, **71** (1993) 2931.
14. T.M. Usselman, *Am. J. Sci.* **275** (1975) 291.

## PHASE EQUILIBRIA IN THE MIXTURE He-CO<sub>2</sub>

M. Eline Kooi and Jan A. Schouten

Van der Waals - Zeeman Institute, University of Amsterdam, Valckenierstraat 65,  
1018 XE Amsterdam, The Netherlands

### ABSTRACT

Phase equilibria in the mixture He-CO<sub>2</sub> have been studied in a DAC by p-T scans and visual observations at pressures up to 3 GPa and at temperatures from 200 K to 450 K. The fluid-fluid equilibrium and the three phase line solid-fluid-fluid have been investigated. A phase diagram is proposed. The results are in reasonable agreement with those of Ciklis, although the fluid-fluid coexistence curves have a greater width than suggested by Ciklis. The three phase line solid-fluid-fluid is remarkably close to the melting line of pure carbon dioxide in temperature and pressure.

### Experimental procedure and results

Ciklis [1] had studied the system helium - carbon dioxide in a temperature range from 295 till 375 K and at pressures up to 0.8 GPa. He found a fluid-fluid equilibrium of the first kind with a critical composition of about 70 vol.-% helium at the highest pressure. Phase equilibria including one or more solid phases have not been investigated. This seems to be the only study of the system at high pressures.

In this work we have used a diamond-anvil cell (DAC) connected to a temperature control system to study the phase behaviour of the mixture helium - carbon dioxide at temperatures from 200 to 450 K and pressures from .1 to 3 GPa as described by Schouten et al. [2]. A mixture of a known composition is prepared in a gas compressor. The gas compressor is connected to the DAC. To make sure the mixture is in the homogeneous phase during the loading procedure, the DAC and the gas compressor were kept above 113 K and the loading pressure did not exceed 20 MPa.

Five experiments have been performed on mixtures with respectively 15.8, 23.3, 38.8, 39.5 and 60.5 mole% helium. In case of the mixtures with 38.8, 39.5 and 60.5 mole% helium a solid-fluid equilibrium is observed at low temperatures. By increasing the temperature the three-phase line solid-fluid-fluid is reached. The three-phase line has been measured by p-T scans and visual observations. A change of the slope in the p-T

scan clearly indicates the three-phase line as shown in fig. 1a and 1b.

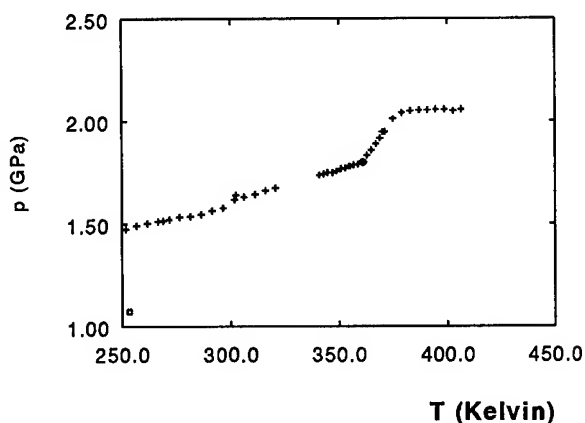


Fig. 1a. p-T scan with a 39 mole% He mixture;  
• = visual observation of the three-phase line.

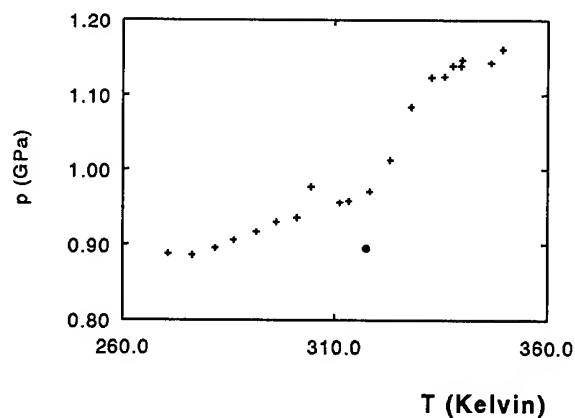


Fig. 1b. p-T scan with a 61 mole% He mixture;  
• = visual observation of the three-phase line.

At still higher temperatures we find the fluid-fluid two-phase region. When the temperature is further increased the bubble disappears and the mixture becomes homogeneous. The fact that the bubble disappears in these mixtures implies that the critical composition must be higher than 60.5 mole% helium as the bubble is assumed to be the helium-rich phase. The temperature at which the bubble disappears is referred to as the fluid-fluid transition point. The fluid-fluid transitions are measured by visual observation. The results are shown in fig. 2.

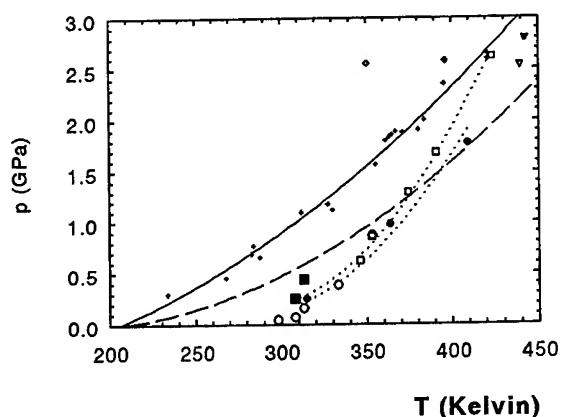


Fig. 2. An overview of the measurements. This work: + = S-F<sub>1</sub>-F<sub>2</sub> three-phase line;  $\diamond$  = F<sub>1</sub>-F<sub>2</sub> transition point (16 mole% He);  $\blacklozenge$  = F<sub>1</sub>-F<sub>2</sub> transition point (23 mole% He);  $\blacksquare$  = F<sub>1</sub>-F<sub>2</sub> transition point (40 mole% He);  $\bullet$  = F<sub>1</sub>-F<sub>2</sub> transition point (61 mole% He);  $\nabla$  = solidification point (16 mole % He);  $\blacktriangledown$  solidification point (23 mole% He); — = melting line CO<sub>2</sub> [3]; Ciklis [1];  $\blacksquare$  = F<sub>1</sub>-F<sub>2</sub> transition point (40 mole% He);  $\circ$  = F<sub>1</sub>-F<sub>2</sub> transition point (61 mole% He).

The mixtures of 15.8 and 23.3 mole% helium show a solid-fluid equilibrium at low temperatures. By increasing the temperature the solid will melt until the sample space contains a homogeneous fluid phase. We will refer to this point as the solidification temperature. The solidification temperatures have been measured by visual observations and have been plotted in fig. 2. The undercooling of the fluid phase can be more than 90 Kelvin. Metastable fluid-fluid equilibria have been found in the phase region

where the solid phase is stable. The metastable fluid-fluid transitions are shown in fig. 2 as well. Even the turbulent appearance of a metastable fluid-fluid equilibrium at about 90 Kelvin below the solidification point does not necessarily trigger the solid phase.

## Discussion

The proposed phase diagram at 2.55 GPa is given in fig. 3.

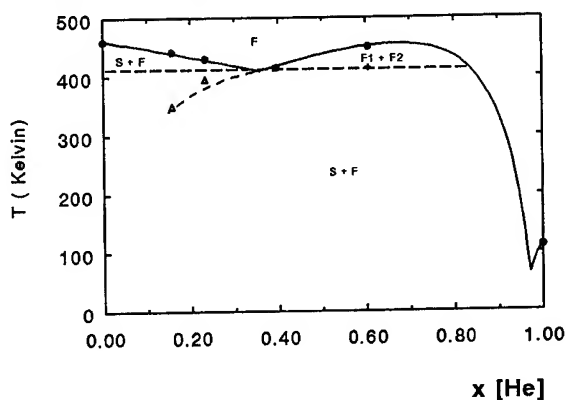


Fig. 3. Proposed phase diagram at 2.55 GPa.

As the fluid-fluid transition of the 38.8 mole% mixture at this pressure is only a few Kelvin above the three-phase line the composition at which the solidification curve crosses the fluid-fluid coexistence curve is expected to lie just below 38.3 mole%. At lower pressures this point is supposed to move to lower helium compositions as the temperature range, in which a fluid-fluid equilibrium exists in the 38.8 mole% mixture at constant pressure, is greater at these pressures. The solidification temperatures are very close to the melting temperature of pure carbon dioxide. The helium lowers the solidification temperature less than expected considering the melting temperature of pure helium.

In a diamond-anvil cell the effect of adsorption of carbon dioxide on the gasket can be important due to the small size of the sample space. In this work adsorption is even more important since the sample space has to

be reduced enormously after closing the cell to reach high pressures, as the loading pressure is quite low. Adsorption might influence the composition of the mixture as the adsorption of carbon dioxide is expected to be higher than that of helium. Note that the three-phase line is independent of the composition.

There seems to be a small discrepancy between the fluid-fluid transitions measured by Ciklis and those measured in this work. This could be caused by adsorption of carbon dioxide. At low pressures a small change in the composition has an enormous effect on the fluid-fluid transition.

The width of the coexistence curve is much greater than suggested by Ciklis. Ciklis suggests that above 350 Kelvin no fluid-fluid equilibrium exists in mixtures with a composition less than 40 vol.-% helium. In this work even in the 15.8 mole% helium mixture a metastable fluid-fluid equilibrium has been found at 350 Kelvin.

As the critical composition is higher than 60.5 mole% helium the temperature of the fluid-fluid transition of the 38.8 mole% mixture must always be lower than that of the 60.5 mole% helium mixture at the same pressure. Therefore the curves through the fluid-fluid transitions of the 38.8 and 60.5 mole% helium can not cross.

## References

1. Ciklis, *Phasen trennung in Gas gemischen* (VEB Deutscher Verlag für Grundstoffindustrie, 1972).
2. Schouten, N.J. Trappeniers and L.C. van den Bergh, *Rev. Sci. Instrum.* **54** (1983) 1209.
3. Grace and G.C. Kennedy, *J. Phys. Chem. Solids* **28** (1967) 977.

## REGULARITIES OF VARIATIONS IN PHASE DIAGRAM CONSTRUCTION OF CARBON - 3D TRANSITION METALS SYSTEMS AT HIGH PRESSURE

V.Z. TURKEVICH, O.G. KULIK

*V.N.Bakul Institute for Superhard Materials of the Ukr. Nat'l Acad. of Sci.;  
2, Avtozavodskaya, Kiev, 254074, Ukraine*

### ABSTRACT

The paper reviews and summarizes data available on phase equilibria with a melt contribution in the Fe-Ni-C, Fe-Co-C, Mn-Ni-C, Fe-Mn-C, Co-Mn-C, and Co-Ni-C ternary systems as well as in the binary ones that are involved in the above ternary systems. A classification of carbides of 3-d transition metals is suggested based on a criterion, which is the ratio of the Gibbs thermodynamic potential of carbide formation to its mole volume. An interrelation is found between a criterion value and the topology of the melting diagram of the system at high pressures. Melting diagrams of the Fe-Mn-C, Co-Mn-C, and Co-Ni-C ternary systems at 6 GPa are predicted.

### Introduction

The papers on construction of carbon-transition metals phase diagrams at high pressures are few in number (they are reviewed in [1]) and a very small amount of them deals with high pressure melting diagrams of ternary systems with carbon. Among them are Fe-Ni-C [2, 3], Mn-Ni-C [4], Fe-Al-C and Fe-Si-C [2, 5]. The attention is drawn to the discrepancy between the results given in [2] and [3] as well as the practice of diamond manufacture in the Fe-Ni-C system.

Since the publication of the Reference Book [1], a series of works aimed at the construction of unknown before phase diagrams of ternary systems of 3-d transition metals with carbon (Fe-Co-C) and refinement of some known ones (Fe-Ni-C and Mn-Ni-C) has been carried out at the V. N. Bakul Institute for Superhard Materials of the Ukrainian National Academy of Sciences [6-10]. At the first stage, experimental studies were conducted to determine a relative position of primary crystallization fields of the phases as well as temperatures of non- and univariant reactions at atmospheric and high pressures. Then the data obtained on phase equilibria together with

thermodynamic ones known from literature were used to find unknown parameters of models of competing phases and a thermodynamic calculation of melting diagrams of the systems under study was made.

Experimental study of phase equilibria at high pressure is an extremely labor-consuming process. The use of thermodynamic calculations without invoking the data on phase equilibria as the reference can result in inaccuracy not only of qualitative indices of the phase diagram (pressure, temperature, composition) but of its topology as well. This is associated with both the absence of the equation of state reliably established for many phases and the low accuracy of experimental determination of excessive values responsible for deviation of concentrational dependence of thermodynamic characteristics from the additive behavior. Not infrequently different authors report excessive parameters that vary not only in value but in sign also. In this connection, a generalization of available thermodynamic information and data on phase equilibria in the carbon - 3-d transition metal systems and the development of a method on their basis to predict the topology of high pressure melting diagrams is an urgent problem.

## Results and discussion

Stabilization of carbides is the main factor responsible for topology variations of melting diagrams of the carbon - 3d transition metal systems under pressure. The stability of a carbide at atmospheric pressure is defined by the Gibbs thermodynamic potential (GTP) of the carbide formation  $\Delta G_{car}^f$ . Carbides having the lowest GTP of their formation are the most stable ones. The carbides with the lowest mole volume  $V_{car}$  are stabilized by high pressure. Therefore the present paper uses the  $\Delta G_{car}^f / V_{car}$  ratio as a classification criterion. The GTP of carbide formation are available in literature for a small number of compounds only. For the rest of carbides the  $\Delta G_{car}^f / V_{car}$  - value was assessed by solving the inverse problem using the information on phase equilibria with carbide as the initial one. The mole volume is calculated from X-ray data on the structure and parameters of a unit cell.

The  $Mn_7C_3$  carbide possesses one of the lowest both GTP of formation and  $\Delta G_{car}^f / V_{car}$  ( $-1655 \cdot 10^6 \text{ J/m}^3$ ) criterion. It is in equilibrium with a liquid; at high pressures (4 GPa) in the Mn-C binary system, it melts congruently; and in ternary systems, the field of primary  $Mn_7C_3$  crystallization extends and the carbide enters necessarily into the composition of a ternary eutectic.

The  $Mn_5C_2$  carbide has a somewhat higher ( $\Delta G_{car}^f / V_{car} = -1349 \cdot 10^6 \text{ J/m}^3$ ). The carbon content of this carbide, however, is 28.6 at %, which is very close to that of the  $Mn_7C_3$  carbide (30 at %). As a result, the liquidus of the  $Mn_5C_2$  carbide turns out to be below that of  $Mn_7C_3$ , and  $Mn_5C_2$  has no equilibrium with a melt both at atmospheric and high pressures. In the C-Mn-Fe (Co, Ni) ternary systems, a considerable solubility of Fe, Co, Ni in the  $Mn_5C_2$  carbide can result in the carbide equilibrium with a liquid phase inside a concentrational triangle. However, the solubility of these metals in  $Mn_7C_3$  is also considerable, and experimentally constructed melting diagrams of the Mn-Ni-C and Fe-Mn-C systems at atmospheric pressure indicate that the liquidus of the  $Mn_5C_2$

carbide remains metastable in ternary systems as well.

The  $\Delta G_{car}^f / V_{car}$  classification criterion for  $\epsilon$ -carbide of the Mn-C system is essentially higher ( $-451 \cdot 10^6 \text{ J/m}^3$ ). The carbon content of it, however, is much lower than that of  $Mn_7C_3$  (13-25 at %). The  $\epsilon$ -carbide is in equilibrium with a liquid phase at atmospheric pressure and keeps it at high pressures.

The  $Fe_3C$  carbide ( $\Delta G_{car}^f / V_{car} = -214 \cdot 10^6 \text{ J/m}^3$ ), that is metastable at 0.1 MPa, stabilizes under 0.1 GPa and enters into ternary eutectic of the Fe-Ni-C, Fe-Co-C and Fe-Mn-C systems.

The  $Fe_7C_3$  carbide ( $\Delta G_{car}^f / V_{car} = 45 \cdot 10^6 \text{ J/m}^3$ ) stabilizes at 6 GPa and participates in nonvariant peritectic, but not in nonvariant eutectic reactions in the Fe-Mn-C, Fe-Ni-C and Fe-Co-C systems.

At 6 GPa, the  $Co_3C$  carbide ( $\Delta G_{car}^f / V_{car} = 128 \cdot 10^6 \text{ J/m}^3$ ) is still not stable. The pressure of its stabilization is 6.5 GPa and it forms by the  $L + C \leftrightarrow Co_3C$  peritectic reaction.

The stabilization pressure of the  $Ni_3C$  carbide ( $\Delta G_{car}^f / V_{car} = 870 \cdot 10^6 \text{ J/m}^3$ ) exceeds 12 GPa. Both the  $Co_3C$  and  $Ni_3C$  carbides are very sensitive to impurities. In the case of a low impurity content, they can be obtained at lower pressures too.

Experimental studies of phase equilibria in the Co-Mn-C system at atmospheric pressure have shown that the  $Co_2Mn_2C$  double carbide, along with  $Mn_7C_3$ ,  $\gamma$ -solid solution and a liquid, participates in the nonvariant eutectic reaction. As the value of the  $\Delta G_{car}^f / V_{car}$  classification criterion of this carbide ( $-2205 \cdot 10^6 \text{ J/m}^3$ ) is very low (even lower than that of  $Mn_7C_3$ ),  $Co_2Mn_2C$  has a stable equilibrium with the liquid phase and contributes to the invariant eutectic reaction at high pressures.

In the case of existence of the four-phase nonvariant eutectic type equilibrium, in which liquid, carbon, metal-base solid solution and carbide participate (the Fe-Ni-C, Fe-Co-C or Mn-Ni-C systems), it is possible to satisfy the diamond synthesis requirement for the emergence of a melt in ternary systems at high pressures and a relatively low temperature. If there are no carbides, the



ternary eutectic does not form, and the liquid phase emerges due to a melting of a univariant eutectic with contribution of a melt, solid solution and carbon. The temperature of this univariant eutectic can go through a minimum, but often it varies smoothly between the temperatures of binary eutectics in the boundary Me-C systems. Such a case is observed in the Co-Ni-C system, in which  $\text{Co}_3\text{C}$  and  $\text{Ni}_3\text{C}$  carbides do not stabilize up to 6 GPa. Experiments on growing diamond in the Co-Ni-C system show that p,T-parameters of synthesis in this system are close to those in the Co-C and Ni-C binary systems.

In the Fe-Mn-C and Co-Mn-C systems a few carbides form already at atmospheric pressure. The ternary eutectic involves these carbides and no carbon. At high pressures, the fields of carbide primary crystallization extend and the melt is in equilibrium with carbon at temperatures exceeding that of a peritectic reaction of carbide melting and much higher than that of ternary eutectic (fig.1). This restricts the possibility of using the Fe-Mn-C and Co-Mn-C systems for making diamond on an industrial scale.

The Fe-Ni-C, Fe-Co-C and Mn-Ni-C ternary systems are most completely adequate for the requirements to diamond growth systems in terms of phase equilibria. The intersection of the curves of the graphite-diamond equilibrium and the pressure dependence of a melting temperature of a carbon-containing ternary eutectic in the p,T-coordinates provides the lowest possible parameters of diamond crystallization. Thus, they are 1380 K and 4.4 GPa for the Mn-Ni-C system and 1400 K and 4.5 GPa for the Fe-Ni-C and Fe-Co-C systems. In practice of diamond industrial production, however, essentially higher parameters are used. Firstly, the temperature of the graphite-diamond equilibrium should exceed that of melting of ternary eutectic by the value, within which the maintenance of the temperature distribution in a high pressure apparatus is possible. Secondly, the temperature increase within the diamond thermodynamic stability region results in the decrease of metal inclusions into the diamond crystal.

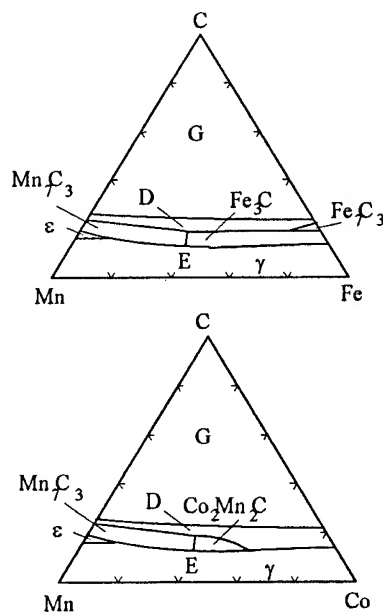


Fig.1 Melting diagrams topology of the Fe-Mn-C and Co-Mn-C systems at 6 GPa.

## References

1. Yu.A.Kocherzhinsky, in *Physical Properties of Diamond* (Naukova Dumka, 1987) p. 8.
2. H. M. Strong and R. M. Chrenko, *J. Phys. Chem.* **75** (1971) 1838.
3. G. Muncke, in *The Properties of Diamond* ed. J. F. Field (Academic Press, 1979) p. 473.
4. I. Yu. Ignat'eva and A. K. Butylenko, *High Temp. - High Pres.* **9** (1977) 677.
5. D. S. Kamenetskaya, I. A. Korsunskaya, and Yu. A. Litvin, *FMM*, **45** (1978) 569.
6. V. Z. Turkevich, in *New Developments in Superhard Materials* (Inst. for Superhard Materials of Ukr. Ac. Sci., 1992) p. 4.
7. Yu. A. Kocherzhinsky et al., *Sverkhтвердые Materialy*, **6** (1992) 3.
8. Yu. A. Kocherzhinsky, O. G. Kulik and V. Z. Turkevich, *High Temp. - High Pres.* **25** (1993) 113.
9. S. A. Ivakhnenko et al., in *Diamond Interaction with Transition Metals* (Inst. of Geophysics and Geology of Siberian Branch USSR Ac. Sci., 1989) p. 60.
10. V. Z. Turkevich, *Fizika i Tekhnika Vysokikh Davlenii* **4** (1994) 17.

# THERMODYNAMICS OF PHASE EQUILIBRIA IN THE Mn-Ni-C SYSTEM AT HIGH PRESSURES AND TEMPERATURES

V. Z. TURKEVICH

*V.N. Bakul Institute for Superhard Materials of the Ukr. Nat'l Acad. of Sci.;  
2, Avtozavodskaya, Kiev, 254074, Ukraine,*

## ABSTRACT

The experimental data on the solid-liquid phase equilibria in the Mn-Ni-C system was analyzed in thermodynamic terms. Gibbs free energy of liquid phase and substitute solutions was described by a regular solution model, and the energy of interstitial solutions by model with two sublattices. The models have been extended in the high pressure region and the numerical values of their parameters were determined. An expression was suggested to describe the dependence molar volume of interstitial solutions on composition. The results were used to calculate the isobaric sections of the Mn-Ni-C system melting diagram at 0.1 MPa, 4.7 GPa, and 6 GPa. The calculations are in a reasonable agreement with the experimental data on diamond crystallization. It was shown that at 4.7 GPa, a wide diamond crystallization field exists in the concentration triangle and it does not intersect to the Mn-C, Ni-C binary systems.

## Introduction

Melting diagram of the Mn-Ni-C system at ambient pressure has been experimentally constructed by Butylenko and Ignat'eva [1]. Later the same authors have constructed the melting diagram of the Mn-Ni-C system at 6 GPa. They published, however, two different variants of the diagram, in one of them the ternary eutectic consists of the  $\epsilon$ -phase,  $\gamma$ -solid solution, and carbon [2], while in the other variant of  $\text{Mn}_7\text{C}_3$ ,  $\gamma$ -solid solution, and carbon [3]. Experimental studies [4] have verified the results [3] and discrepancies between the invariant equilibria temperatures do not exceed experimental errors.

In the present paper the experimental data on the solid-liquid phase equilibria in the Mn-Ni-C system was analyzed in thermodynamic terms.

## Thermodynamic models

Gibbs free energy of liquid phase and substitute solutions was described by a regular solution model:

$$\begin{aligned} G_m^l = & x_{\text{Ni}}^l G_{\text{Ni}}^l + x_{\text{Mn}}^l G_{\text{Mn}}^l + x_{\text{C}}^l G_{\text{C}}^l \\ & + RT(x_{\text{Ni}}^l \ln x_{\text{Ni}}^l + x_{\text{Mn}}^l \ln x_{\text{Mn}}^l + x_{\text{C}}^l \ln x_{\text{C}}^l) \\ & + x_{\text{Mn}}^l x_{\text{C}}^l L_{\text{MnC}}^l + x_{\text{Ni}}^l x_{\text{Mn}}^l L_{\text{NiMn}}^l + x_{\text{Ni}}^l x_{\text{C}}^l L_{\text{NiC}}^l \\ & + x_{\text{Mn}}^l x_{\text{Ni}}^l x_{\text{C}}^l L_{\text{MnNiC}}^l + \int_0^p V_m^l dp, \end{aligned} \quad (1)$$

where composition dependence of the molar volume was presented by following expression:

$$\begin{aligned} V_m^l = & x_{\text{Ni}}^l V_{\text{Ni}}^l + x_{\text{Mn}}^l V_{\text{Mn}}^l + x_{\text{C}}^l V_{\text{C}}^l \\ & + x_{\text{Mn}}^l x_{\text{C}}^l V_{\text{MnC}}^l + x_{\text{Ni}}^l x_{\text{Mn}}^l V_{\text{NiMn}}^l \\ & + x_{\text{Mn}}^l x_{\text{C}}^l V_{\text{MnNiC}}^l + x_{\text{Ni}}^l x_{\text{Mn}}^l x_{\text{C}}^l V_{\text{MnNiC}}^l. \end{aligned} \quad (2)$$

Model with two sublattices was used to describe Gibbs free energy of interstitial solutions [5]:

$$\begin{aligned} G_m = & y_{\text{Ni}} G_{\text{Ni}} + y_{\text{Mn}} G_{\text{Mn}} + y_{\text{C}} (G_{\text{NiC}} - G_{\text{Ni}}) \\ & + RT[(y_{\text{Ni}} \ln y_{\text{Ni}} + y_{\text{Mn}} \ln y_{\text{Mn}} \\ & + c(1 - y_{\text{C}}) \ln(1 - y_{\text{C}})] + y_{\text{Mn}} y_{\text{C}} \Delta G \\ & + y_{\text{Ni}} y_{\text{Mn}} [y_{\text{C}} L_{\text{NiMn}}^{\text{C}} + (1 - y_{\text{C}}) L_{\text{NiMn}}^{\text{Ni}}] \\ & + y_{\text{C}} (1 - y_{\text{C}}) [y_{\text{Ni}} L_{\text{NiC}}^{\text{Ni}} + y_{\text{Mn}} L_{\text{NiC}}^{\text{Mn}}] + \int_0^p V_m dp, \end{aligned} \quad (3)$$

where

$$\Delta G = {}^{\circ}G_{Ni} + {}^{\circ}G_{MnCe} - {}^{\circ}G_{Mn} - {}^{\circ}G_{NiCe}, \quad (4)$$

$$y_{Ni} = 1 - y_{Mn} = x_{Ni} / (1 - x_C), \quad (5)$$

$$y_C = x_C / [c(1 - x_C)].$$

In equations (3)-(5)  $c = 1$  for  $\gamma$ -solid solution and  $c = 0.5$  for  $\epsilon$ -phase.

An expression was suggested to describe the dependence molar volume of interstitial solutions on composition [6]:

$$V_m = x_{Ni} V_{Ni}^v + x_C x_{Ni} / (1 - x_C) V_{Ni}^C + x_{Mn} V_{Mn}^v + x_C x_{Mn} / (1 - x_C) V_{Mn}^C + x_{Ni} x_{Mn} V_{NiMn}^v + x_{Ni} x_{Mn} x_C V_{NiMn}^C. \quad (6)$$

Free energy of  $Mn_7C_3$  carbide was described by following expression:

$$G_m = y_{Ni} {}^{\circ}G_{Ni_7C_3} + y_{Mn} {}^{\circ}G_{Mn_7C_3} + RT(y_{Ni} \ln_{Ni} + y_{Mn} \ln_{Mn}) + y_{Ni} y_{Mn} L_0 + \int_0^p V_m dp, \quad (7)$$

where

$$V_m = y_{Ni} V_{Ni_7C_3} + y_{Mn} V_{Mn_7C_3} + y_{Ni} y_{Mn} V_{(MnNi)_7C_3}. \quad (8)$$

The Murnaghan approximation (a linear dependence of the bulk modulus vs. pressure) was used to describe the pressure dependence of Gibbs free energy [7]:

$$\int_0^p V dp = V_0 \frac{\exp(A_0 T + 0.5 A_1 T^2)}{k(n-1)} \left[ (1 + nkp)^{\frac{1-n}{n}} - 1 \right]. \quad (9)$$

The numerical values of models parameters were taken from the literature and determined on the base of phase equilibria data. They are listed below and in the table 1.

Liquid (J/mole)

$${}^{\circ}G_{Ni}^L = 11235.527 + 108.457 T - 22.096 T \ln T - 4.8407 \cdot 10^{-3} T^2 - 3.82318 \cdot 10^{-21} T^7$$

$${}^{\circ}G_{Mn}^L = 4.1968 (-3109 + 67.733 T - 11.0 T \ln T)$$

$${}^{\circ}G_C^L = 100000 + 146.1 T - 24.3 T \ln T - 2562600 T^{-1} - 2.643 \cdot 10^8 T^{-2} + 1.2 \cdot 10^{10} T^{-3}$$

$${}^{\circ}G_{Ni}^L = 11235.527 + 108.457 T - 22.096 T \ln T - 4.8407 \cdot 10^{-3} T^2 - 3.82318 \cdot 10^{-21} T^7$$

$$L_{Mn}^L = -111684$$

$$L_{NiMn}^L = (-64434 + 10.878 T) x_{Mn}^L + (-76986 + 10.878 T) x_{Ni}^L$$

$$L_{NiC}^L = -110160 + 34.6 T$$

$$L_{MnNiC}^L = -40000.$$

$\gamma$ -solid solution (J/mole of metal atoms)

$${}^{\circ}G_{Ni}^{\gamma} = -5179.159 + 117.854 T - 22.096 T \ln T - 4.8407 \cdot 10^{-3} T^2$$

$${}^{\circ}G_{Mn}^{\gamma} = 4.1968 (-3109 + 67.733 T - 11.0 T \ln T) - (16450 - 10.931 T)$$

$${}^{\circ}G_{NiCe}^{\gamma} = {}^{\circ}G_{Ni}^{\gamma} + {}^{\circ}G_g + 45000 + 1.88 T$$

$${}^{\circ}G_{MnCe}^{\gamma} = {}^{\circ}G_{Mn}^{\gamma} + {}^{\circ}G_g + 16000$$

$$L_{NiMn}^{\gamma} = -35000$$

$$L_{NiMn}^{\gamma} = (-51882 + 10.878 T) x_{Mn} + (-64434 + 10.878 T) x_{Ni}$$

$$L_{NiC}^{\gamma} = 0$$

$$L_{MnCe}^{\gamma} = -52000 + 8 T.$$

$\epsilon$ -phase (J/mole of metal atoms)

$${}^{\circ}G_{Ni}^{\epsilon} = -5179.159 + 117.854 T - 22.096 T \ln T - 4.8407 \cdot 10^{-3} T^2$$

$${}^{\circ}G_{Mn}^{\epsilon} = 4.1968 (-3109 + 67.733 T - 11.0 T \ln T) - (16450 - 10.931 T)$$

$${}^{\circ}G_{NiCe}^{\epsilon} = {}^{\circ}G_{Ni}^{\epsilon} + 0.5 {}^{\circ}G_g + 13000$$

$${}^{\circ}G_{MnCe}^{\epsilon} = {}^{\circ}G_{Mn}^{\epsilon} + 0.5 {}^{\circ}G_g - 12100$$

$$L_{NiMn}^{\epsilon} = -130714 + 71.43 T$$

$$L_{NiMn}^{\epsilon} = 0$$

$$L_{NiC}^{\epsilon} = 0$$

$$L_{MnCe}^{\epsilon} = -1000.$$

Carbide  $Mn_7C_3$  (J/mole of metal atoms)

$${}^{\circ}G_{Ni_7C_3} = 7 {}^{\circ}G_{Ni}^{\gamma} + 3 {}^{\circ}G_g + 30000$$

$${}^{\circ}G_{Mn_7C_3} = 7 {}^{\circ}G_{Mn}^{\gamma} + 3 {}^{\circ}G_g - 94700$$

$$L_0 = -80000$$

Graphite (J/mole)

$${}^{\circ}G_g = -17369 + 170.73 T - 24.3 T \ln T - 4.723 \cdot 10^{-4} T^2 + 2562600 T^{-1} - 2.643 \cdot 10^8 T^{-2} + 1.2 \cdot 10^{10} T^{-3}$$

Diamond (J/mole)

$${}^{\circ}G_d = -16360 + 175.61 T - 24.31 T \ln T - 4.723 \cdot 10^{-4} T^2 + 2698000 T^{-1} - 2.61 \cdot 10^8 T^{-2} + 1.11 \cdot 10^{10} T^{-3}$$

Table 1. Coefficients of pressure dependences (eq. 9)

$\int V_m dp$	$V_0 10^6$	$A_0 10^5$	$A_1 10^9$	$k 10^{12}$	$n$
$\int V_{Ni}^I dp$	6.465	10.12	-8.3	5.07	4.593
$\int V_{Mn}^I dp$	5.959	28.7	0	7.32	5.488
$\int V_C^I dp$	7.626	2.32	5.7	160	2
$\int V_{Ni}^{II} dp$	6.753	3.207	5.868	6.91	4.007
$\int V_{Ni}^{III} dp$	4.092	3.207	5.868	6.91	4.007
$\int V_{Mn}^{IV} dp$	7.459	6	80	7.319	5.488
$\int V_{Mn}^{V} dp$	4.751	6	80	7.319	5.488
$\int V_{Ni}^{VI} dp$	7.73	10.1	0	7.319	5.488
$\int V_{Ni}^{VII} dp$	3.13	10.1	0	7.319	5.488
$\int V_{Mn}^{VIII} dp$	7.73	10.1	0	7.319	5.488
$\int V_{Mn}^{IX} dp$	3.13	10.1	0	7.319	5.488
$\int V_{Mn_7C_3} dp$	5.72	15	0	3	5.488
$\int V_{Mn_7C_3} dp$	5.72	15	0	3	5.488

The next values of mixture volumes ( $m^3/mole$ ) were adopted in the calculation:

$$V_{Mn}^I = 3.85 \cdot 10^{-6}, V_{Ni}^I = 2.8 \cdot 10^{-6}, V_{NiMn}^I = 0; V_{MnNiC}^I = 0; V_{NiMn}^{II} = -0.55 \cdot 10^{-6}; V_{NiMn}^{III} = -1.8 \cdot 10^{-6}; V_{NiMn}^{IV} = -6.5 \cdot 10^{-6}; V_{NiMn}^{V} = 0; V_{(MnNi)7C_3} = 1.23 \cdot 10^{-15} p - 10.392 \cdot 10^{-6}.$$

## Results and discussion

The results were used to calculate the isobaric sections of the Mn-Ni-C system melting diagram at 0.1 MPa, 4.7 GPa, and 6 GPa. The calculations are in a reasonable agreement with the experimental data on diamond crystallization [8]. It was shown that at 4.7 GPa, a wide diamond crystallization field exists in the concentration triangle and it does not intersect to the Mn-C, Ni-C binary systems.

High pressure leads to the increase of Ni solubility in the manganese carbide  $Mn_7C_3$ , and a primary crystallization field of  $Mn_7C_3$  extends. The temperatures of four-phase invariant equilibria of eutectic  $L \leftrightarrow \gamma + Mn_7C_3 + C$ , and peritectic  $L + \epsilon \leftrightarrow Mn_7C_3 + \gamma$  types are 1390 and 1590 K, respectively (fig. 1). With the pressure rise up to 6 GPa, the eutectic equilibrium temperature increases

up to 1410 K and the peritectic equilibria one up to 1620 K.

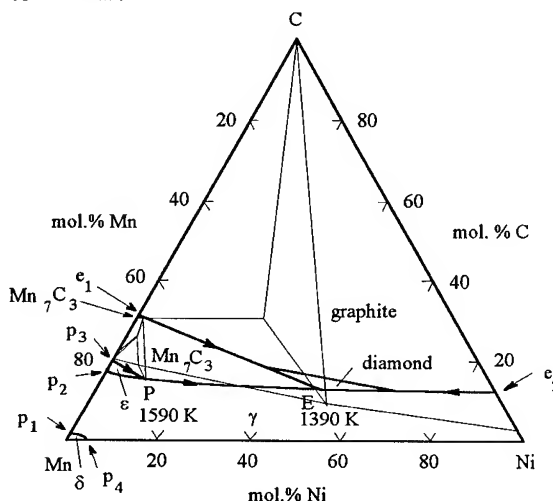


Fig. 1. Melting diagram of the Mn-Ni-C system at 4.7 GPa.

In general, high pressure causes the shift of univariant eutectic and peritectic lines towards carbon side as compared with their position at atmospheric pressure. The shape of the Mn-Ni-C melting diagram is unchanged up to 6 GPa.

## References

1. A.K. Butylenko and I.Yu. Ignat'eva, *Doklady AN SSSR* **1** (1976) 79.
2. I.Yu. Ignat'eva and A.K. Butylenko, *High Temp. - High Pres.* **9** (1977) 677.
3. A.K. Butylenko, I.Yu. Ignat'eva, *Doklady AN SSSR* **2** (1977) 161.
4. S.A. Ivakhnenko et al., in *Diamond and Transition Metals Interaction* (Inst. of Geophysics and Geology of Siberian Branch USSR Ac.Sci., 1989), p.60.
5. M. Hillert and L.-I. Steffansson, *Acta Chem. Scand.* **24** (1970) 3618.
6. V.Z. Turkevich, O.G. Kulik, *Dopovidi AN Ukrainy* **7** (1993) 75.
7. A. Fernandez Guillermet, *Inter. J. of Thermodynamics* **8** (1987) 481.
8. M. Ya. Katsay, Yu.N. Sakovich, *J. of Superhard Materials* **1** (1989) 15.

## MELTING CURVE OF THE Fe-36at.%Ni ALLOY UP TO 49 GPa

R. COUTY \*, B. SITAUD, J. PERE, Th. THEVENIN  
and J. L. TRUFFIER

*\* Laboratoire de Physique Thermique (URA-CNRS 857) ESPCI  
10 rue Vauquelin, F-75231 Paris Cedex 05, France  
Commissariat à l'Energie Atomique, Centre d'Etudes de Bruyères-le-Châtel,  
BP 12, F-91680 Bruyères-le-Châtel, France*

The melting temperatures of the Fe-36at.%Ni alloy corresponding to a taenite meteorite have been determined under high static pressure up to 49 GPa using pulse laser heating in diamond anvil cell. The Fe-Ni system has been selected since his interest in geophysics, metallurgy of meteorites and the scarcity of data on melting of binary alloys under pressure. The samples are loaded under argon in diamond anvil cell and heated during very short times by Nd:YAG laser. Solid to liquid phase transition and melting temperature are evidenced on both radiance and reflectivity curves. Results are compared with those on pure iron and nickel and suggest a Ni effect under pressure.

### Introduction

The Earth core is supposed to consist of metallic iron, Fe(Ni) alloys, and light alloying elements (1-3). The real composition is in fact dependent on mechanisms of the accretion of the Earth from primitive cosmic dust which is also generally presumed to be the origin of meteorites and asteroids (4,5). Hence, from the observed compositions of such meteorites (2,3) and shock wave experiments on selected alloys (6), the relative concentration of nickel has been estimated at 2.4wt.% in the Earth (1) and about 6wt.% in the core (2), making nickel the second or the third most abundant element (7). However, controversies have arisen regarding other rich-iron meteorites thought to be also formed in planetary cores and containing more nickel, i.e., from 6 to 14wt.% for octahedrite and until 67wt.% in taenite. Differences could be also found from models considered in describing the mechanism of accretion and for which the knowledge of behaviors of different components and alloys under high pressure and high temperature take a great importance (8). Work on pure iron has continued for decade leading now to a well defined phase diagram in a large pressure-temperature domain (9,10). During the same time, the solubility of candidate elements in iron and their effects on the properties under pressure have been analyzed, particularly with regard to light alloying components (11,12).

Due to the similarity between iron and nickel, the role of this latter element has been seldom

studied and its effect on the melting of iron has been still limited to low pressures (13). In the present work, we extend the pressure range up to 49 GPa of the melting curve determination for the Fe-36at.%Ni (37.2wt.%) alloy by using the laser-heating technique combined with pressure generation in diamond anvil cell (DAC).

We have selected this alloy because of its high nickel concentration (> 27wt.%Ni) corresponding to the  $\gamma$  phase called taenite in meteorites. This phase is often observed as an intimate lamellar mixture with the low-nickel or  $\alpha$  phase kamacite (6wt.%Ni). This structure was suggested as a result of a miscibility gap induced by pressure exceeding 6 GPa (14). Our purpose is to study the effect of pressure and temperature on Fe-Ni alloy stability and to describe the physico-thermal process involved in the evolution of this binary system during accretion and formation of planetary cores.

### Experimental technique

The experimental technique considered here is approximately the same as that described in detail previously (15). Only the special arrangements and the improvements are mentioned in this paper.

The samples, roughly square-shaped with an approximate side of 80  $\mu\text{m}$ , were cut out of a 15 - 20  $\mu\text{m}$  thick polished foil of high purity Fe-36at.%Ni alloy supplied by Goodfellow Metal Ltd. The experimental cavity was formed from a 270  $\mu\text{m}$  diameter hole electroerosion drilled at the center of

preindented rhenium gasket. Argon was used as pressure transmitting medium and several ruby chips were inserted between the lower diamond flat and the sample reducing the thermal losses of sample heating treatments. Pressures were measured using the calibrated pressure shift of ruby R1 fluorescent line in the case of hydrostatic conditions (16) at room temperature before and after each melting experiment.

The sample was heated by a multimode Nd:YAG pulse laser power output of up to 5 kW at 1.064  $\mu\text{m}$ . The pulses are typically of the order of 0.5 ms. The temperature variations of the opposite face of the laser interaction were determined by measuring the intensity of the thermal radiation emitted in the near infrared range and detected, through bandpass filter, by a Ge photodiode. Melting was defined in situ by correlation between plateaux or changes of slope on the radiance curves and sudden variations in intensity of reflected 0.514  $\mu\text{m}$  Ar laser light from the hot spot. Reflectivity measurements are collected through a photomultiplier. An analyzed area of 10  $\mu\text{m}$  x 10  $\mu\text{m}$  viewed by the different detectors was kept constant for all Fe(Ni) experiments. Melting temperatures were calculated by assuming a constant value for the emissivity factor at the end of solid to liquid transition over the pressure range investigated. A sample shot under a low argon pressure (0.05 GPa) was included in each run making the melting reference at 1730 K.

## Results and discussion

Figure 1 shows typical time-radiance and time-reflectivity profiles measured during heating of Fe-36at.%Ni samples under pressure. The sudden variations of radiance associated with the great reflection changes at around 0.4 ms have been explained by melting of the analyzed area relating to the detection threshold of the system. The decreasing part of the radiance curve shows a comparable evolution explained by the reversible reaction (freezing) which was recorded until 20 GPa. Above this pressure, the cooling rates increased of several orders of magnitude and no significant slope changes were observed. So, only the increasing parts of the radiance curve have been considered to estimate the

melting temperature.

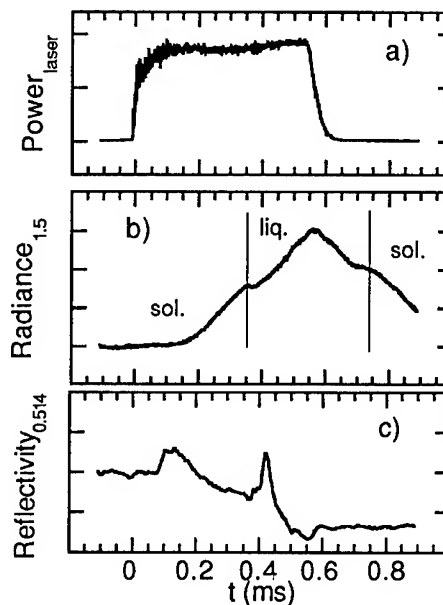


Figure 1 : Experimental measurements (b, c) on Fe-36at.%Ni at 6.4 GPa during pulse laser heating (a).

The experimental results on melting of the Fe(Ni) alloy at pressures up to 49 GPa are shown in Figure 2 with the pure nickel (17) and pure iron (18,19) data. In the pressure range 0 to 20 GPa, our values are closed to the melting of pure nickel (17). The iron-nickel phase diagram at atmospheric pressure indicates that an addition of 36at.%Ni to iron shifts the melting temperature of alloy to nickel melting value. Our results suggest that no major changes in the liquidus arise with pressure up to 20 GPa. At higher pressure the temperature rises and deviates gradually from nickel curve. In the pressure range of 35 to 49 GPa, the melting curve of alloy does match the iron results (19). This deviation could be explained from two plausible assumptions :

a) A change in the solid state when the pressure is increased. While below 30 GPa the  $\gamma$  phase melts, we could expect above 30 GPa melting from another high pressure phase as mentioned for pure iron around 100 GPa (10). A room temperature compression study on Fe-20at.%Ni (20) has indicated a stability of the  $\epsilon$  phase with a hcp

structure up to 255 GPa, but experiments are still lacking to determine its stability at high temperature;

b) A nickel differentiation under pressure. This idea is supported by calculations (14) on the phase diagram of iron-nickel system at high pressure from microstructure observations of metallic meteorites. The qualitative features of this analysis indicate a miscibility gap formation at 5 GPa and an eutectoid decomposition starting above 6 GPa. Therefore, at higher pressure, the metastable alloy could be transformed in a mixture of kamacite (6wt.%Ni) and taenite (> 27wt.%Ni) phases with a respective ratio depending on pressure. This interpretation is coherent with Uhlig (8) hypothesis assuming the final taenite composition as a direct function of the maximum pressure viewing by the alloy. The higher is the pressure, the lower is the corresponding nickel concentration of taenite and according to the iron-nickel alloy diagram, the higher is melting temperature. In fact the melting temperature of the sample is associated to the ratio of kamacite/taenite which is dependent on pressure.

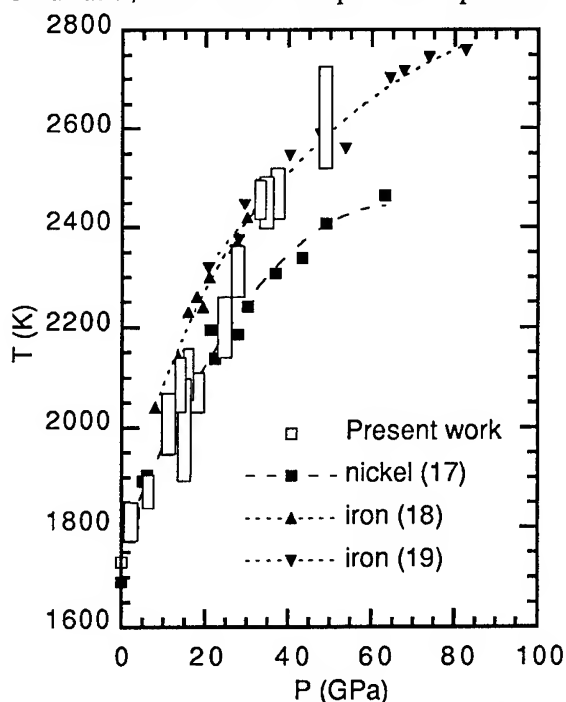


Figure 2 : Melting temperatures of Fe-36at.%Ni as function of pressure. Literature values for iron and nickel are shown for comparison.

In order to test these solutions, we have planned to correlate the melting temperature and the nickel-iron distribution using electron beam spectroscopy on samples after pressure release.

## References

1. E. Anders, *Philos. Trans. R. Soc.* **285** A (1977) 23
2. A. E. Ringwood, *Geochim. Cosmochim. Acta* **30** (1966) 41 and *Geochim. J.* **11** (1977) 111
3. R. Brett, *Rev. Geophys. Space Phys.* **14** (1976) 375
4. S. R. Taylor, *Origin of the Earth*, ed. H. E. Newsom and J. H. Jones (Oxford University Press, 1990), p. 277
5. M. J. Gaffet, *Origin of the Earth*, ed. H. E. Newsom and J. H. Jones (Oxford University Press, 1990), p. 18
6. R. G. McQueen and S. P. Marsh, *J. Geophys. Res.* **71** (1966) 1751
7. L. Liu, *Geochim. J.* **16** (1982) 179
8. H. H. Uhlig, *Geochim. Cosmochim. Acta* **6** (1954) 282
9. G. Shen, P. Lazor and S. K. Saxena, *Phys. Chem. Minerals* **20** (1993) 91
10. R. Boehler, *Nature* **363** (1993) 534
11. S. Urukawa, M. Kato and M. Kumazawa, *High Pressure Research in Mineral Physics*, ed. M. H. Manghani and Y. Syono (Terrabub, Tokyo/Amer. Geophys. Union Washington, 1987) 95
12. A. Zerr and R. Boehler, *Science* **262** (1993) 553
13. T. M. Usselman, *Am. J. Sci.* **275** (1975) 278
14. L. Kaufman and A. E. Ringwood, *Acta Met.* **9** (1961) 941
15. B. Sitaud, J. Péré and Th. Thévenin, *High Pressure Research* **12** (1994) 175
16. H. K. Mao, J. Xu and P. M. Bell, *J. of Geophysical Research* **91** (1986) 4673
17. P. Lazor, G. Shen and Saxena, *Phys. Chem. Minerals* **20** (1993) 86
18. R. Boehler, *Geophys. Res. Lett.* **13** (1986) 1153
19. R. Boehler, N. von Bagen and A. Chopelas, *J. of Geophysical Research* **95** (1990) 21731
20. H. K. Mao, Y. Wu, L. C. Chen and J. F. Shu, *J. of Geophysical Research* **95** (1990) 21737

# INFLUENCE OF THE PRESSURE ON THE PHASE DIAGRAM AND THE PERCOLATION LINE OF A TERNARY MICROEMULSION

Z. SAIDI, J.L. DARIDON, C. BONED, P. XANS

*Laboratoire Haute Pression, Centre Universitaire de Recherche Scientifique  
Avenue de l'Université, 64000, PAU, (France)*

## ABSTRACT

The phase diagram of the water-AOT-undecane system (AOT : sodium bis [2-ethylhexyl] sulfosuccinate) which is a ternary microemulsion, was determined in the  $P - \phi$  plane ( $P$  : pressure,  $\phi$  : volume fraction of dispersed matter). The microemulsions were observed at  $T = 20^\circ\text{C}$  with the molar ratio  $n = [\text{water}]/[\text{AOT}] = 30$ , in the pressure interval 1-40MPa. The electrical conductivity  $\sigma$  was used to trace the percolation threshold line in the single-phase zone of the  $P - \phi$  plane. It has been possible to evaluate quantitatively the variations of interactions with pressure and to adjust very satisfactorily both the percolation threshold line and the cloud-points curve in the  $P - \phi$  plane.

## Introduction

For the water-AOT-undecane system (AOT : sodium bis [2-ethylhexyl] sulfosuccinate) it was observed (1,2) that the percolation threshold falls when pressure increases, which indicates in this case an increase in interactions. It has also been verified that the scaling exponents characteristic of percolation are independent of pressure and are the same (to within uncertainties) that those already determined at 0.1MPa, which reflects a universality of behavior. To describe completely the percolating behavior as a function of pressure it remains to describe quantitatively the percolation threshold line  $\phi_c(P)$ . In this article we present the transposition to pressure of a method already successfully used (3,4,5) to describe quantitatively the threshold line  $\phi_c(T)$  as a function of temperature at atmospheric pressure. In this case it was possible to calculate variations  $\phi_c(T)$  on the basis of knowledge of variations of interactions versus temperature  $T$ , the latter being deduced indirectly from the phase diagram in the  $T - \phi$  plane ( $\phi$  : volume fraction of dispersed matter). As for pressure  $P$ , it is above all diagrams in the  $P - T$  plane at constant  $\phi$  which have been established (see for example references (6) and (1)). It is clear that these diagrams are much easier to establish than the corresponding diagrams in the  $P - \phi$  plane at constant  $T$ .

## Experimental results

The system selected is water-AOT-undecane because it has already been studied elsewhere as regards its percolating behavior as a function of pressure (1,2). In particular the threshold line has already been determined and as far as this aspect is concerned we refer the reader to the original articles. The substances used are distilled water, AOT supplied by Sigma (purity > 99%) and undecane supplied by Fluka (purity > 99%). Samples at given  $P$  and  $T$  are characterised by volume fraction  $\phi$  of dispersed matter (water + AOT) and by the molar ratio  $n = [\text{water}]/[\text{AOT}]$ . The measurements were made at  $T = 20^\circ\text{C}$  and  $n = 30$ , taking account of the previous studies. In order to determine  $\phi$  at each pressure  $P$ , the densities of the sample, of the water and of the undecane have to be measured (that of AOT is assumed to be constant). The density  $\rho$  is measured by means of a semi-automatic DMA 45 ANTON PAAR KG densitometer to which the additional DMA 512 cell has been added, enabling measurements to be made up to 40MPa. The  $P - \phi$  phase diagram is determined by means of a full-visibility sapphire ROP cell. The apparatus operates up to 50MPa. The sample is subjected to isothermal pressure variation and the liquid-liquid transition is identifiable because the liquid becomes opaque and scatters light. The pressures are measured with a H.B.M. - P3M probe with a measurement uncertainty of 0.05MPa within the 0-50MPa interval. The results concerning the phase



diagram and the percolation line are indicated in Figure 1.

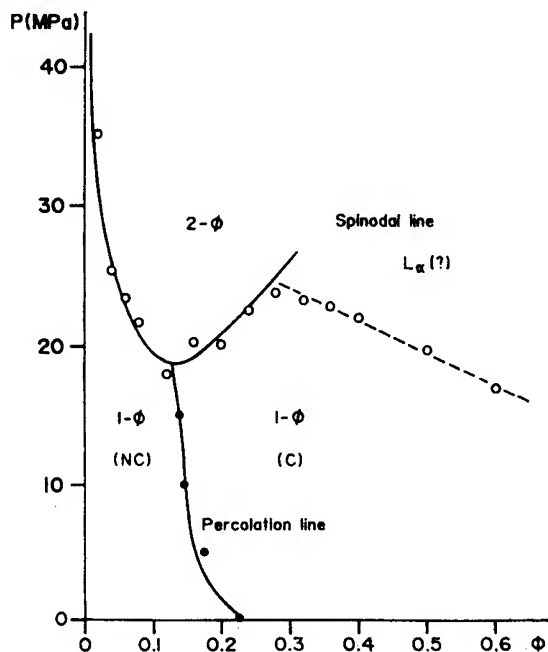


Fig.1: Water-AOT-undecane system ( $n = 30$   $T = 20^\circ\text{C}$ )  $P$ - $\phi$  plane;  $\bullet$ : threshold line;  $\circ$ : cloud-point curve; —: calculated curves; C: conducting area; N-C: non conducting area.

It is interesting to compare it with the phase diagram obtained (3) in the  $T$ - $\phi$  plane at  $P = 0.1\text{MPa}$  for the water-AOT-decane system (with  $n = 40.8$ ). The similarity of shape between the diagram in the  $P$ - $\phi$  plane (Figure 1) and the diagram in the  $T$ - $\phi$  plane (Figure 2) will be observed.

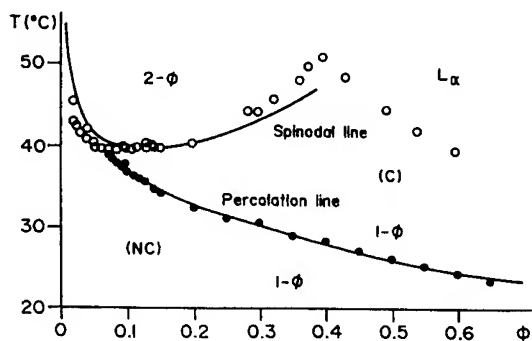


Fig.2: Water-AOT-decane system ( $n = 40.8$   $P = 0.1\text{MPa}$ )  $T$ - $\phi$  plane (from ref.3). Same symbols as in Figure 1.

In the second case the existence of a lamellar water-oil phase was demonstrated (phase  $L_\alpha$ ). Because of the similarity between the two figures it is reasonable to suggest that the increase in pressure at high values of  $\phi$  also causes the existence of such a phase.

### Determination of interactions

The ternary microemulsions studied here represent real systems which correspond to a dispersion of spheres in a continuum, in which the spheres interact. It has been verified (3,4,5) that the Yukawa fluid model provides a realistic representation of this real fluid, which moreover presents the advantage of being suitable for analytical calculations. Generally, the interaction potential is defined as follows:

$$\beta U(r) = - \sum_{i=1}^N k_i \exp[-z_i(x-1)]/x \quad \text{for } x \geq 1$$

and  $\beta U(r) = \infty$  for  $x < 1$ ; in which  $\beta = \frac{1}{k_B T}$

( $k_B$ : Boltzmann constant,  $T$ : temperature),  $x = r/d$ , and where  $r$  is the distance between two particles and  $d$  the diameter of the hard-sphere. The quantities  $k_i$  and  $z_i$  correspond to the intensity and range of the interaction respectively. The greater the number of terms introduced into the interaction model, the closer the model fits to reality. However, only considering the case  $N = 1$  provides results which can be interesting. Thus it is within the framework of the quantitative determination of the position of percolation thresholds that the percolation model developed by Xu and Stell (7) with  $N = 1$  has already been applied to the case of water-AOT-decane microemulsions (3,5) and waterless glycerol-AOT-isooctane (4) systems with varying temperature. It has also been shown that one could solve the thermal problem in this way, in other words determine the liquid-liquid coexistence curve (or at least the separation curve  $1$ - $\phi$ ,  $2$ - $\phi$  from the diagram  $T$ - $\phi$ , fig. 2). For the thermal problem, Xu and Stell used the Mean Spherical Approximation (MSA) with  $N = 1$ . All previous

studies show that the Yukawa fluid presents a gas-liquid type transition. The solution of the thermal problem provides, among other features, the points at which the compressibility becomes infinite, and thus the coexistence curve (or spinodal curve) can be obtained. Assuming that the range of interaction  $z$  is independent of  $T$  (and  $P$ ) the calculation provides, for the values of  $\phi$  of the spinodal, the following expression :

$$k\phi = \frac{z^2}{6(z+2)^2} \left[ \frac{w - \gamma y}{(w - \gamma)y} \right]^2 U_o = C(z, \phi) \quad (\text{eq.1})$$

$$w = \frac{1}{2z} \left[ \frac{z-2}{z+2} + e^{-z} \right] ; \quad y = \frac{4+2z-z^2}{2(2+z)} \frac{U_o}{U_1}$$

$$\gamma = \frac{1}{2z} \left[ \frac{z^2 + 2z - 4}{4 + 2z - z^2} + e^{-z} \right]$$

$$U_o = \frac{1}{2} \left[ p + \sqrt{p^2 + z^2 p} \right] ; \quad U_1 = (2 - \sqrt{p}) U_o - \Gamma$$

$$p = \left( \frac{1+2\phi}{1-\phi} \right)^2 ; \quad \Gamma = \frac{1}{4} z^2 \sqrt{p}$$

As regards the percolation threshold lines Xu and Stell [7] obtained  $k\phi = C(z, 0) / \lambda$  in which the function  $C(z, 0)$  is defined on the basis of equation 1 and in which  $\lambda$  is an adjustable parameter. We determined variations of the intensity of interactions with pressure  $k(P)$  by using the above theory and by simultaneously adjusting the cloud-points curve and the percolation threshold line. As in the  $T - \phi$  plane it was assumed (3) that  $k(T)$  is a polynomial of the third order on  $T$ , we assumed here that  $k(P)$  is a polynomial of the third order on  $P$ , i.e.  $k(P) = A_0 + A_1P + A_2P^2 + A_3P^3$ . The least square adjustment program gave  $A_0 = 4.6045 \cdot 10^{-2}$ ,  $A_1 = 6.1521 \cdot 10^{-3}$ ,  $A_2 = -5.1973 \cdot 10^{-4}$  and  $A_3 = 1.6454 \cdot 10^{-5}$  when  $P$  is expressed in MPa (the adjustment is made on the part of the curve  $\phi \leq 0.30$ ). We also obtained  $z = 0.369$  and  $\lambda = 0.386$ . It will first be observed that the function  $k(P)$  increases with  $P$ , consistent with the reduction in the threshold when pressure increases (which means that here, for a given value of  $\phi$ , conductivity increases with pressure). In fact it is because for these systems the intensity of the interactions  $k$  increases with  $T$  and  $P$  that the shape

of the phase diagram is similar in the  $T - \phi$  and  $P - \phi$  planes. Thus it is that in equation 1, the parameters  $T$  and  $P$  only intervene through  $k$  and do not appear explicitly. In Figure 1 the curves drawn in full lines correspond to the calculated curves. It will be seen that the fit is very satisfactory, quite comparable to that obtained in the  $T - \phi$  plane (Figure 2).

## Conclusion

It is very satisfying to note that despite the approximation used the quantitative results obtained are coherent with the experimental observations and that it is thus possible to evaluate the order of magnitude of interactions with  $P$  as well as of the interaction parameter  $z$ . Thus the percolation model adopted, called "percolation probability" by Xu and Stell, allows interpretation of experimental curves in the  $T - \phi$  and  $P - \phi$  planes both with respect to the percolation threshold line and also part of the cloud-points curve.

## Bibliography

1. Z. Saïdi , C. Boned , P. Xans and J. Peyrelasse, *Progress Colloid Polymer Sci.* **97** (1994) 247.
2. C. Boned , Z. Saïdi , P. Xans and J. Peyrelasse, *Physical Review E* **49** (1994) 5295.
3. C. Cametti , P. Codastefano , P. Tartaglia , S.H. Chen and J. Rouch, *Physical Review A* **45** (1991) R 5358.
4. J. Peyrelasse , C. Boned and Z. Saïdi, *Physical Review E* **47** (1993) 3412.
5. C. Cametti , P. Codastefano , P. Tartaglia , J. Rouch and S.H. Chen, *Physical Review Letters* **64** (1990) 1461.
6. J. Eastoe , B.H. Robinson and D.C. Steytler, *J. Chem. Soc. Faraday Trans.* **86** (1990) 511.
7. J. Xu and G. Stell, *J. Chem. Phys.* **89** (1988) 1101.

## **VI(C) Structural Phase Transitions**

## **VI(C.1) Diamond, Graphite, Lonsdaleite**

# GRAPHITE-LONSDALEITE TRANSFORMATION UNDER STATIC PRESSURE IN COMBINATION WITH TEMPERATURE AND SHEAR

V.D. BLANK, G.A. DUBITSKY, S.A. PLOTYANSKAYA

*Scientific and Technical Center "Superhard materials"  
Troitsk, Moscow Region, 142092 Russia*

## ABSTRACT

The irreversible graphite - lonsdaleite transition have been realized in the pressure interval 5.5 - 12 GPa and the temperature interval 1070 - 1600 K. The yield increase of lonsdaleite correlates with the increase of the hysteresis electrical resistance of specimens. The shear deformation makes possible graphite - lonsdaleite transition at the room temperature and high pressure.

## Introduction

In 1962, Ergun and Alexander[1] have predicted a possibility of existence of new tetrahedral carbon form with wurzite structure and proposed some calculated parameters of this structure. Experimentally this form was obtained at non-hydrostatic pressure and high temperature [2,3], shock compression [4] and was subsequently found in meteorites and another natural sources [5,6]. Nowadays, two names: "hexagonal diamond" [2] and "lonsdaleite" [5,6] are being used for this form of carbon. As a rule the specimens contain lonsdaleite (hexagonal diamond) together with diamond.

This combination makes an identification of lonsdaleite difficult since all the peaks of it occur at the same place in x-ray diffraction patterns. The lonsdaleite structure was investigated as the quenched specimens as well as *in situ* [7].

In general, it have been estimated that quantity of lonsdaleite in specimens, the relation between lonsdaleite and diamond and also the perfection of its structure depend on experimental and natural conditions of its production. But, a lot of details of the lonsdaleite production are not clear and its properties are not study carefully.

We propose the results of the electrical resistance measurements for three kinds of graphite under high pressure and temperature also the dependence of the lonsdaleite yield

versus P,T-condition and the features of the lonsdaleite structure .

## Experiment

Our experiments were carried out by means of different high pressure apparatus: 1) toroid-type chamber for the synthesis of bulk samples [8]; 2) shear Bridgman-type tungsten carbide and diamond "carbonado" anvils [9]. Prior to the experiments, the apparatus (1,2) were pressure-calibrated according to polymorphic transitions in Bi(2.5GPa), Ba(5.3, 12GPa), Fe(11.2GPa), Pb (13 GPa), ZnS (14.5 GPa), GaP (22 GPa).

Three kinds of graphite were used: 1) the natural cleansed well-crystallized graphite (from Zavalye deposit); 2) the graphite single crystals; 3) the polycrystalline graphite that is used usually for manufacture of synthetic diamond.

In the shear anvils the experiments have been performed at room temperature. In toroid-type chamber the direct resistance heating of graphites was employed by passing an alternating current through a bulk sample. Temperature in a reaction volume was measured by Pt-Pt10Rh and W5Re-W20Re thermocouples. The electric resistance dependence of bulk samples have been estimated on heating as well as on cooling under  $P = 5 - 12$  GPa and  $T = 320 - 1500$  K.

Lonsdaleite was separated from specimens by dissolving of unconverted graphite in acids and it was investigated.

We have used Debye camera with 114mm, x-ray diffractometer HZG-4a with  $\text{CuK}\alpha$ -monochromated radiation and transmission electron microscope JEM-100C.

## Results

For the natural graphite the resistance increase took place under pressure over 5.5 GPa. The resistance raises with the pressure increase on heating as well on cooling [Fig.1].

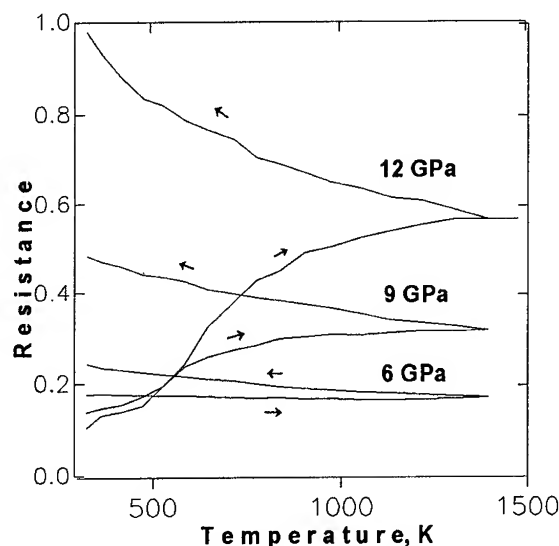


Fig.1. Resistance vs. temperature for natural graphite.

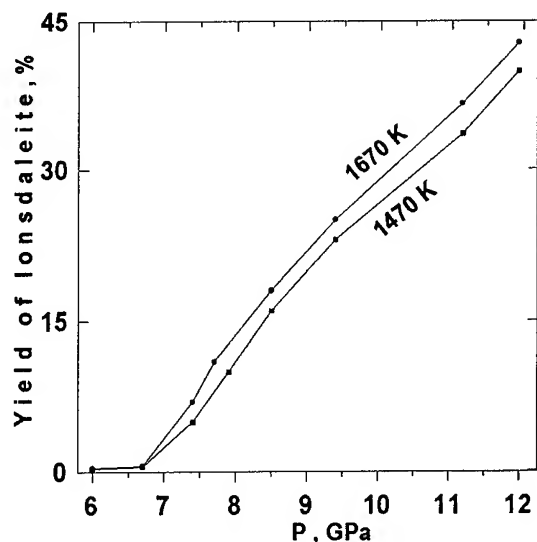


Fig.2. The lonsdaleite yield vs. the pressures.

Under more high pressure Bundy and Kasper [2] observed the similar variation and anticipated that the new semiconductor carbon phase was formed.

The resistance of polycrystalline graphite almost coincide on heating as well on cooling cycles and lonsdaleite was not separated from these specimens.

We separated the lonsdaleite from quenched specimens (diameter=4mm, h=3mm) obtained from the natural graphite by means a chemical treatment. In Fig.2 two plots illustrate the increase of the lonsdaleite yield versus the pressure increase.

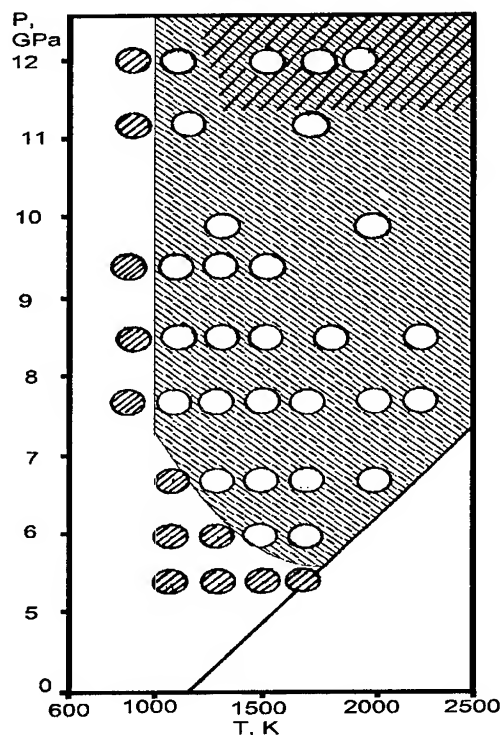


Fig.3. P,T-region of the production of lonsdaleite.

Under  $P < 5.5 \text{ GPa}$  the resistance variations were not observed really and lonsdaleite was not separated from such specimens. The variations of the x-ray diffraction profiles of lonsdaleite take place versus pressure from 6 to 12 GPa ( $T = 1670 \text{ K}$ ). X-ray patterns contain broad and diffuse peaks especially for lonsdaleite obtained at minimal pressure. The peak intensity raised

with the pressure increasing, therewith the (002) peak became stronger of the (001) peak, probably because of an overlap with the (111) diamond peak. Parameters of a structure of the obtained lonsdaleite are:  $a = 2.52\text{\AA}$ ,  $c = 4.17\text{\AA}$ .

In Fig.3 the P,T-region of the lonsdaleite production is exhibited on the base of experimental data. Minimal pressure and temperature are correspondingly about 5,5 GPa and 1070K.

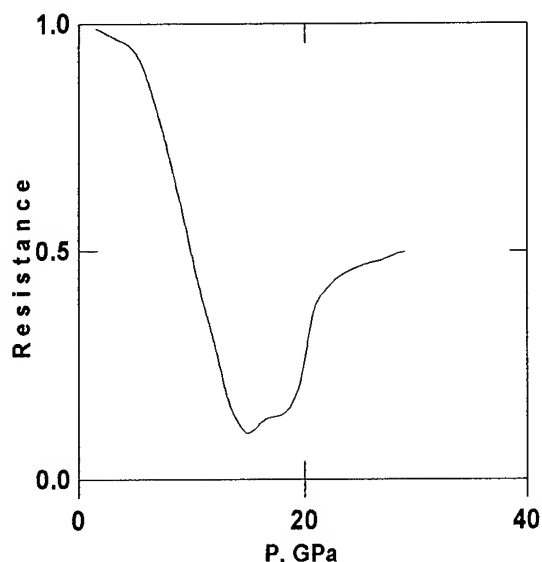


Fig.4. Resistance vs. pressure in the shear anvils.

The diamond type "carbonado" anvils were used in the measurements of the resistance variation of polycrystalline graphite and the graphite single crystals at room temperature ( $\gamma=0$ ). The resistance increase was observed only for the graphite single crystals under  $P=16-30\text{ GPa}$  (Fig.4). According to [2,7] the resistance increase caused by the reversible graphite transition to dense form. This transition was reversible, it was proved by subsequent x-ray analysis of specimens isolated from anvils. The resistance variation of polycrystalline graphite did not take place under these pressures.

A disordered structure of initial graphites were produced by high pressure up to 8 GPa and shear stress ( $\gamma = 2.5$ ). The irreversible graphite-lonsdaleite transition was realized in the specimens of single-crystal graphite using the shear deformation ( $\gamma = 0.25$ ) at fixed pressures 17.9 GPa. The specimens treated at 17 GPa contained graphite

and lonsdaleite, whereas specimens treated  $P = 19\text{ GPa}$  contained also diamond. Almost complete conversion graphite-diamond have been obtained in pressure interval 21-25 GPa at  $\gamma = 0.25$ . Unconverted carbon had amorphous form.

To conclude, the irreversible graphite-lonsdaleite transition have been realized in the pressure interval 5.5-12 GPa and the temperature interval 1070 - 1600 K. The yield increase of lonsdaleite correlates with the increase of the hysteresis electrical resistance of specimens.

Using of shear deformation makes possible the irreversible graphite-lonsdaleite transition at the room temperature under 17 and 19 GPa, where the reversible transition takes place without the shear deformation.

Distinctions ( $\Delta P \approx 5\text{ GPa}$ ) between the minimal pressure of the graphite-lonsdaleite transition obtained by us and the result obtained by Bundy and Kasper [2], probably may be explained by the more intensive shear deformation in the bulk apparatus of toroid-type than in the apparatus of belt-type.

## References

1. S.Ergun and L.E.Alexander, *Nature*, **195** (1962) 765.
2. F.P.Bundy and J.S.Kasper, *J.Chem.Phys.*, **46** (1967) 3437.
3. A.V.Kurdyumov, V.N.Slesarev et al., *Dokl. Akad. Nauk USSR* (in Russian), **255** (1980) 1381.
4. L.F.Trueb, *J.Appl.Phys.*, **39** (1968) 4707.
5. R.E.Hanneman, H.M.Strong and F.P.Bundy, *Science*, **155** (1967) 995.
6. C.Frondel and U.B.Marvin, *Nature*, **214** (1967) 587.
7. T.Yagi, W.Utsumi et al., *Phys.Rev.* **B46** (1992) 6031.
8. N.N.Kuzin et al., *Dokl.Akad.Nauk USSR* (in Russian), **286** (1986) 1391.
9. V.V.Aksenkov, V.D.Blank et al., *Fiz.Metalloved.* (in Russian) **57** (1993) 394.

## THE EFFECT OF GRAPHITE STRUCTURE ORDERING ON THE PARAMETERS OF HP-HT GRAPHITE-TO-DIAMOND TRANSITION

G.P.Bogatyreva, G.F.Nevstruyev, P.A.Nagorny, G.D.Ilnitskaya,  
G.A.Bazaliy, N.A.Oleinik, and V.L.Gvyazdovskaya  
*V.N.Bakul Institute for Superhard Materials of the National  
Academy of Sciences of Ukraine, Kiev, 254074, Ukraine*

### ABSTRACT

The structure of an initial carbon-containing material influences to a certain extent quantitative and qualitative characteristics of the graphite-to-diamond transition in diamond synthesis. Graphites are judged by structural ordering, graphitization degree and porosity. Graphites of a lower structural ordering are found to be more suitable for synthesizing stronger diamonds because of a lower rate of diamond crystal growth, whereas perfectly structured graphites are mainly used to synthesize brittle and fine diamonds due to a large number of crystallization centers [1].

Almost all natural and artificial graphites can be used to synthesize one or other types of diamond [1,2].

The object of the present investigation was the thermally expanded graphite (TEG), which has not been previously used as a G is produced from natural graphite following a specially devised procedure, which gives rise to the formation of specific graphite lattice defects. A comparison between the initial natural graphite and TEG based on it shows [3] that the latter exhibits larger interlayer spacings and decreased sizes of the crystallites mainly along the C-axis.

X-ray diffraction observations of TEG and GMZ OSCh-grade graphite [4] allow the suggestion that the use of the TEG-type material in diamond synthesis will give rise to a greater number of crystallization centers and cause the graphite-to-diamond transition rate to increase.

The authors give the results of absorption-structure studies of two samples (TEG and GMZ OSCh-grade graphite) by the nitrogen low-temperature adsorption method on an Acousorb-2100 device [5]. The obtained adsorption isotherms allowed the specific surface ( $S_{sp}$ ) and porosity ( $V_p$ ) of the samples to be calculated.

It is found the specific surface and porosity of the GMZ OSCh-grade graphite (-500 +250 particle size) is an order of magnitude lower than those of TEG (1.9 m<sup>2</sup>/g and 0.0006 ml/g against 15.1 m<sup>2</sup>/g and 0.084 ml/g). The quality characteristics of the materials' porosity is given in Fig. 1 by the pore-size distribution (R) curves, which evidence that the total amount of pores in TEG is two orders of magnitude greater than in GMZ OSCh-grade graphite.

For comparison, an experiment was conducted on diamond synthesis under pressure of 5.0 GPa,

temperature of 1250 °C and holding time 10 min. The mixture of the Ni-Mn alloy and graphites (TEG and GMZ OSCh in 1:3 ratio (in mass)) was used. A reference synthesis was carried out with the use of GMZ OSCh-grade graphite.

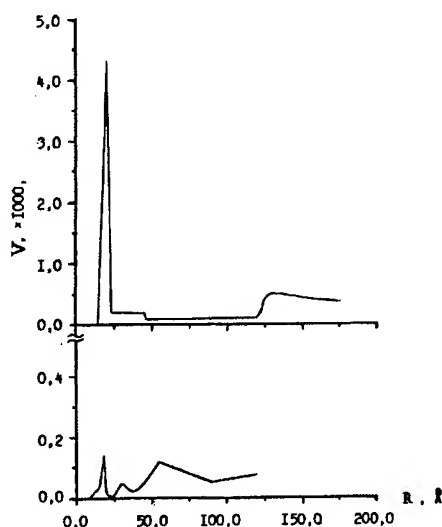


Fig. 1. Pore-size distribution in thermally expanded graphite (TEG) and GMZ OSCh-grade graphite.

It is found that the degree of the graphite component-to-diamond transition in the test sample is 19.8 % greater than in the GMZ OSCh-grade graphite. Diamond products recovered from the test batch show a higher by (6.2 %) yield of fine diamond fractions (below 160/125) as compared with the reference batch.

Qualitative characteristics were studied on 400/315 and 250/200 diamond grits from the two



batches under consideration. Diamond grits on hard carriers were separated in magnetic field to yield five products, each being tested for strength, intracrystalline inclusion content ( $\beta$ ) and diamond surface imperfection in terms of surface activity factor  $K_a$ . The findings of investigations have shown that the initial diamond powders contain particles whose strength varies by a factor of 2.5 - 3. On the average, the strength of diamond particles synthesized with the use of GMZ OSCh-grade graphite is somewhat higher than for TEG.

Figure 2 shows variation of  $\beta$ -content by classification products (N) in 400/315 diamond. It is seen that the  $\beta$ -content of the test batch diamonds (curve 1) and that in the reference batch diamonds (curve 2) varies within 0.4 to 3.0 %. The arrangement of curves 1 and 2 evidences that the  $\beta$ -content of diamond synthesized using GMZ OSCh-grade graphite exceeds that of TEG-base diamond. This is an indirect support of the fact that in the case of TEG, the diamond growth rate is lower than that in the case of GMZ OSCh-grade graphite.

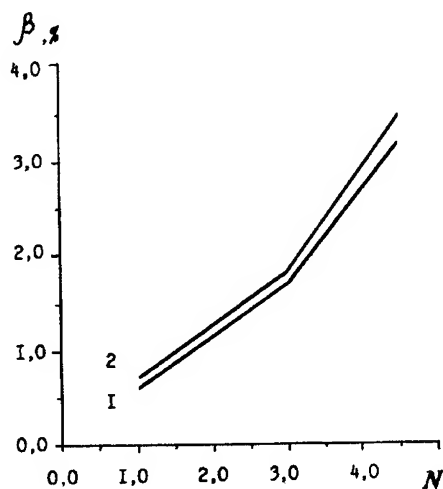


Fig. 2. Distribution of diamonds by the intracrystalline metal inclusion content ( $\beta$ ): 1 - test batch, 2 - reference batch.

Curves in Fig. 3 show the trend of  $K_a$  variation in diamond of the test (curve 1) and reference (curve 2) batches. The arrangement of the curves allows the conclusion that the use of TEG gives rise to the yield of diamond particle having more imperfect rough surface.

The studies have shown that the use of TEG as a constituent of graphite component of the reaction mixture causes the degree of the graphite-

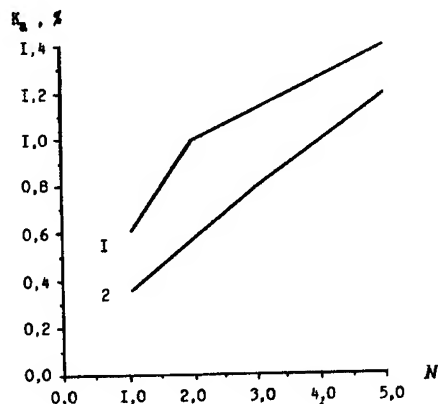


Fig. 3. Distribution of diamonds by the surface imperfection degree ( $K_a$ ): 1 - test batch, 2 - reference batch.

to-diamond transition to increase, the amount of intracrystalline inclusions to decrease, a grit surface roughness to be higher and diamond particle strength to be lower. The results agree well with known concepts that the state of carbon-containing materials affects qualitative and quantitative characteristics of diamond being synthesized.

#### References

1. N.V.Novikov, D.V.Fedoseyev, A.A.Shulzhenko, and G.P.Bogatyreva, *Diamond Synthesis* (Naukova Dumka, 1987).
2. Ya.A.Kalashnikov, *Priroda*, no. 5 (1980) 34.
3. I.G.Chernysh, I.I.Korkov, G.P.Prikhodko, and V.M.Shay, *Physico-Chemical Properties of Graphite and its Compounds* (Naukova Dumka, 1990).
4. G.P.Bogatyreva, V.L.Gvyazdovskaya, and G.A.Bazaliy, in *Physico-Chemical Properties of Superhard Materials and Methods to Evaluate Them* (ISM Ac.Sci.of UkrSSR, 1987), p. 4.
5. G.P.Bogatyreva and V.L.Gvyazdovskaya, *Sverkhtverdye Materialy*, no. 2 (1986) 25.

## **VI(C.2) Boron Nitride**

# THE METASTABLE BEHAVIOUR OF BORON NITRIDE IN PHASE TRANSFORMATIONS

I. PETRUSHA<sup>1</sup>, A. SVIRID<sup>1</sup> AND B. SHARUPIN<sup>2</sup>

<sup>1</sup>*Institute for Superhard Materials of the National Academy of Sciences of Ukraine, 2, Avtozavodskaya St., 254074, Kiev, Ukraine* <sup>2</sup>*Russian Scientific Center Applied Chemistry, 9, Dobrolyubova St., St.-Petersburg, 197198, Russia*

## ABSTRACT

Possible variant of an alternative metastable behaviour of BN in phase transformations have been analyzed in terms of thermodynamics of activation state (quasi-equilibrium approach) with regard to thermodynamic parameters of phases. Structure and phase variations in superheated materials were investigated at 2 GPa up to 3300 K. Undercooled states of phases and their behaviour in freezing out were studied at 8 GPa between 300 and 2870 K. CVD materials and polycrystals of BN dense phases of different origin were the subjects for study. Analysis of X-ray data has shown that the formation of metastable phases is associated with low-activation transformations of hexagon layer splitting by puckering or buckling.

## Introduction

Boron nitride (BN) is a high-temperature compound. The diffusion activity is dictated by the necessity of breaking strong  $sp^2$ -bonds in graphite-like structures of hexagonal (hBN) and rhombohedral (rBN) boron nitride or  $sp^3$ -bonds in tetrahedral structures of cubic (cBN) and wurtzitic (wBN) modifications. There are several variants of BN transformations with low activation barriers that define the possibility of alternative metastable behaviour (AMB). As applied to graphite-like structures, this mechanism is based on a deformation resulting in splitting of basic layers via puckering or buckling [1]. One of the main features of martensite transformation is a high degree of structure imperfection of finite phases in their regular orientation with respect to the parent phase. In highly-defective structures, the activation barrier of a rearrangement transformation becomes lower due to a high energy of elastic distortion of the crystal lattice near defects. The active role of boron oxide, moisture and oxygen in BN recrystallization is suggested in [2]. A relatively high degree of perfection of a BN structure being formed indicates that rearrangement transformation occurs with a contribution of fluid phases. Our experimental results will be discussed in the context of the above notions. The main subject of investigations were CVD materials of different

originated BN, whose behaviour under p,T-conditions is poorly known [3-7]. The AMB has been studied both under the conditions of phase superheating at 2 GPa and phase cooling at 8 GPa.

## Experimental procedure

### *High-pressure experiments.*

The experiments were carried out in a toroid-type high pressure apparatus. The pressure of 8 GPa and temperatures up to 2870 K were created in a cell made of block lithographic stone. At 2 GPa and temperatures up to 3300 K, a special refractory cell made of boron carbide was employed. High temperatures were achieved by passing an alternating current through the graphite tube, in the middle part of which a 9-mm diameter sample was placed. The sample chamber volume did not exceed  $0.2 \text{ cm}^3$ . The apparatus was pressure- and temperature calibrated from a compression force and current power in the heater, respectively, both for a cell of litho-graphic stone and a cell of boron carbide. Bi and PbSe were used as reference materials. At room temperature, the pressure was created accurate to about 0.3 GPa. The temperature calibration curves for both the cells were obtained employing a Pt10 %Rh-Pt thermocouple. For temperatures above 2000 K, the as-found dependences were extrapolated. In most

cases the holding time at high temperature was 90 s. The cell cooling rate after the experiment was about 500 K/s.

#### *X-ray diffractometry.*

The phase composition of samples and the degree of three-dimensional ordering structure ( $P_3$ ) of BN graphite modifications were determined by the X-ray method following the procedure suggested by A. Kurdyumov [8]. For limiting cases of a three-dimensional and a fully one-dimensional disordered (turbostratic) structures,  $P_3 = 1$  and  $P_3 = 0$ , respectively. In studying the behaviour of highly-textured BN materials, X-ray photographing of as-recovered samples before they are powdered for X-ray phase analysis is very important. The orientational relations of structures of BN layered and dense modifications were traced from the sample texture peculiarities before and after the thermobaric treatment. With a weak absorption of X-ray radiation by boron nitride, the sample texture was found easier to study by a comparison between sample diffraction patterns taken by reflection and by transmission. In this case, the X-ray incident beam was directed on a sample CVD surface. Photograph taken by transmission corresponded to that taken by reflection from a surface in the sample section parallel to the texture axis. The studies were carried out using a DRON-2.0 diffractometer (CuK  $\alpha$ -radiation).

#### *Initial materials.*

Four different CVD BN samples [9] were studied: 1) tBN - a bulk material with a turbostratic structure ( $P_3=0$ ) and a density  $d = 2.01 \text{ g/cm}^3$ ; 2) LO-hBN - a low degree of three-dimensional structure ordering hBN material with  $P_3 = 0.22$  and  $d = 2.02 \text{ g/cm}^3$ ; 3) MO-hBN - a medium structure ordered material ( $P_3 = 0.62$ ,  $d = 2.12 \text{ g/cm}^3$ ) with a bimodal structure [9]; 4) HO-rBN - a highly-ordered ( $P_3=0.77$ ) rBN-base di-phasic material with about 20 mass % hBN, the material density is close to the theoretical one

( $2.27 \text{ g/cm}^3$ ). Besides, the behaviour was studied of a fully ordered ( $P_3=1$ ) hBN material (FO-hBN), produced in a way as will be shown below. The tBN, LO-hBN and MO-hBN are low-textured materials, whose structure is characterized by a quasi-crystalline state with the size ( $d$ ) of disoriented elements in the basal plane being 10 nm and less. HO-rBN and FO-hBN are highly-textured coarse-grained materials with  $d$  up to hundreds micrometers in size. All the materials are high-purity pyrolytic residues with a total amount of microimpurities of metals, C, O, F, and Si lower than 0.05 mass %, as mass-spectral analysis shows.

In addition to CVD BN, two polycrystalline cBN materials that differ in degree of structure perfection were also studied. Highly-defective isotropic material (HD-cBN) was produced by high pressure sintering of cBN powders. The highest level of elastic distortions of the material structure corresponds to the lattice imperfection density  $\rho > 10^{11} \text{ cm}^{-2}$ . Besides, HD-cBN differs by the higher total oxygen, carbon and metal microimpurities content (the basic phase content is up to 98.8 mass %) from other materials. Low-defective isotropic material (LD-cBN) was produced as a result of hBN complete phase transformation using LO-hBN as the initial material. The substructure of it was characterized by the presence of individual dislocations and microtwins in grains of size up to 10 micrometres, that corresponds to the density of defects of about  $10^6\text{-}10^7 \text{ cm}^{-2}$ , which is typical of single crystals.

## **Results and discussions**

### *BN phase relations.*

Rhombohedral and wurtzitic BN have no thermodynamic stability regions, at least up to 10 GPa [10]. Cubic BN is stable at low and hexagonal at high temperatures. Of a great number of suggested variants of the equilibrium line position, the results [3] for a high-temperature region and extrapolation of the data [11] for a low-temperature one are a good compromise.

According to the above, the cBN-hBN equilibrium at 2 and 8 GPa correspond to the temperatures of about 1100 and 2800 K.

A relative variation of Gibbs free energy of BN polymorphs with temperature in general terms shows that at 2 GPa in the high temperature range, the  $w\text{BN} \rightarrow c\text{BN} \rightarrow r\text{BN} \rightarrow h\text{BN}$  sequence of the transitions corresponds to the reduction of  $G$ -values. At 8 GPa in the undercooling state, the transitions in the  $r\text{BN} \rightarrow h\text{BN} \rightarrow w\text{BN} \rightarrow c\text{BN}$  direction are possible. Thus, thermodynamically possible AMB transformations are  $w\text{BN} \rightarrow c\text{BN}$ ,  $w\text{BN} \rightarrow r\text{BN}$  and  $c\text{BN} \rightarrow r\text{BN}$  in the first case, while  $r\text{BN} \rightarrow h\text{BN}$ ,  $r\text{BN} \rightarrow w\text{BN}$  and  $h\text{BN} \rightarrow w\text{BN}$  in the second. AMB transformations from diamond-like into graphite-like phases and their converse (two transformations into the basic state among them) have the highest driving force and can occur by low-activated martensite mechanisms. Other interphase transformations do not occur by simple shear operations that include puckering or buckling. They need more complicated ones, including rearrangement transformations with a high energy of activation.

#### *Experiments at 2 GPa (superheated specimen)*

**HD-cBN behaviour.** Phase transitions in the material occur with no AMB. A highly-ordered ( $P_3 = 0.88$ ) stable hBN phase forms in it for 90 s already at 1870 K, which suggests a diffusion nature of the transformation activated by impurities and structure defects. At the same time, a high level of defects of HD-cBN renders impossible a cooperative rearrangement of the structure resulting in the formation of an intermediate metastable rBN.

**LD-cBN behaviour.** It has been found that at superheating up to temperatures above 1870 K, the transformations occur to form mainly rBN and small quantities of stable hBN. In samples with complete cBN transformation ( $T > 2170$  K,  $t = 60$  s), quantities of rBN and hBN are in the ratio of about 3:1. The most probable mechanism of cBN-to-rBN transformation is shear transformation: a repuckering of double close-packed planes and

extending of the lattice along the normal to this planes. The hBN formation occurs with a contribution of diffusion processes at the intergranular boundaries and triple joints of grains, where these processes are most active. The structure perfection of graphite-like modifications increases with temperature of di-phasic samples production. In particular,  $P_3$  grows from 0.45 to 0.78 when transformation temperature varies between 1870 and 2670 K. In all cases, rBN had more defects as compared to hBN. This fact is an additional evidence of the rBN martensite nature and the hBN formation by diffusion mechanisms that are made easier by the presence of impurities and structure defects. rBN that forms due to an AMB process resists to transformation into a stable hBN up to 2770 K. A rearrangement highly-energetic transition, that is evidently controlled by a volume self-diffusion and resulting in the complete transformation into hBN, is observed beginning with 2770 K.

**tBN behaviour.** Pure turbostratic CVD BN material, the structure nonequilibrium state of which is a relatively weak driving force for structure transformations, exhibits an extremely high thermal stability. Thus, after 60-s effect of 2770 K, no essential structural changes were found in the material. At temperatures close to 3300 K on the background of the general low ordering, the appearance of bimodality is observed. Thus, the structure ordering of tBN has been found to show indications of the type 1 phase transition and to be under the effect of a recrystallization of the two-dimensionally ordered component into a three-dimensional hBN one, which is accompanied by an abrupt change of a (002) interplanar spacing.

**HO-rBN behaviour.** rBN involved in this material also exhibits stability up to 2770 K. After 210-s holding time no more than 5 % rBN remains in the sample and  $P_3$  in this case increases up to 0.91. The complete transformation into the stable hBN occurs above 2870 K and results in the formation of a highly-textured FO-hBN material ( $P_3 = 1$ ). Samples of this material have been used in our subsequent experiments. The texture relation observed corresponds to the parallelism of

basal planes of the parent and finite phases. This fact indicates that a rearrangement process that results in the formation of a completely ordered stable hBN structure is a process of active diffusion inside of the networks of hexagons.

#### *Experiments at 8 GPa (undercooled specimen)*

**tBN, LO-hBN and MO-hBN behaviour.** In all the materials at sufficiently high temperatures, only a stable cBN formation is observed. The difference in the behaviour lies in the different stability of materials with regard to a phase transformation and the lowest ordered forms exhibit higher stability. A pure tBN bulk material, whose two-dimensional ordering prevents from the development of martensite transformations, remains stable up to 2670 K. At exceeding temperatures it transforms into a stable cBN by the diffusion mechanism. In bimodal MO-hBN ( $P_3 = 0.2$ ) the onset of transformation is observed at about 2150 K. At 2270-2370 K the transformation completes in 60 s. At temperatures above 2670 K due to a cBN accumulative recrystallization, the obtaining of coarse-grained structures with a low level of grain imperfection is possible (LD-cBN).

**HO-rBN behaviour.** With the temperature increase starting with the room one, a complex cascade of AMB transformations occurs in HO-rBN. The main stage of the transformation is the formation of wBN from the ADAD intermediate structure by the "basis-prism" shear mechanism [9]. The process occurs at a high speed between 470 and 670 K. Electron-microscopic data [11] show that above 1770 K, a 4H polytype appears together with wBN. A stable cBN appears at higher temperatures and the formation of a single phase material completes above 2270 K. The 4H polytype that has 50 % degree of hexagonality is considered as an intermediate structure on the way of the wBN (2H) hexagonal structure transformation into the cBN (3C) cubic structure. The basal plane parallelism is kept at all stages of polytype rearrangement.

**FO-hBN behaviour.** A cBN formation in FO-hBN is recorded as from 1570 K and at lower

temperatures AMB is not observed. A distinct texture relation of phases  $(111)_c // (001)_h$ , the high level of cBN imperfection and relatively low temperatures of the process point to a cooperative nature of the transformation, a crystallographic mechanism of which remains unclarified. The kinetic differences in behaviour between tBN and FO-hBN, in which the starting temperatures of cBN formation differ by almost 1000 K, formally can be described in the framework of Kolmogorov-type crystallization models. The temperature dependence of the process rate constant is defined by the Arrhenius equation. In optimization of the model parameters, it has been shown that a best fit of the model to the experimental data on the degree of a phase transformation is attained when the value of the transformation enthalpy is 580 kJ/mole.

Under a pulse pressure above 12 GPa, the hBN highly-ordered structure is known [8] to undergo a martensite transformation into the wurtziticone by puckering mechanism. Our experiments show that a static compression at 8 GPa is insufficient for realization of puckering in FO-hBN. Under similar conditions this mechanism is not observed in the case of HO-rBN too, since in this case rBN should directly transform into a stable cBN with the bases-bases type of mutual orientation. As is shown above the rBN-to-cBN transformation at 8 GPa involves the AMB stages that result in other orientation: the  $(111)_c$  is normal to the rBN basal plane. The shock-induced rBN-to-cBN phase transformation in HO-rBN [12], unlike the one occurring under the static pressure of 8 GPa, takes place by the puckering mechanism, as it follows from the observed  $(111)_c // (001)_r$  texture relation. The degree of transformation did not, however, exceed 40 %, which is evidently defined by a certain disordering of the HO-rBN structure at shock compression and up to 20 % hBN impurity content of the initial sample. Up to 60 GPa in MO-hBN, no formation of BN dense phases have been observed, which is associated with an insufficiently high  $P_3$  value of the initial material, that prevent from the development of martensite transformation. The absence of cBN

in products of shock compression suggests that pulse-induced temperature in a material is not high enough as cBN appears in a low-ordered structure only due to a rearrangement process. Since HO-rBN was exposed to a similar action, this fact is an additional evidence for the martensite nature of cBN being formed and not a result of a rearrangement transformation of rBN structure.

### Conclusions

The variety of modes and mechanisms of BN structure and phase transformations in bulk CVD materials is associated primarily with the parent structure perfection and purity. Under the conditions of both superheating and undercooling, the transformation into a basic state might be accompanied by AMB that convert the system into the state of a relative minimum of the Gibbs free energy. AMB transformations are characterized by low-activation barriers and go by diffusionless mechanisms that can be defined by direct and inverse simple deformations by puckering or buckling. The crystallographic mechanism of hBN-to-cBN transition in the HO-hBN can not be explained in terms of the simple shear deformations of a lattice. On the other hand, a break of bonds, which is needed due to the different periodicity of atomic packing in the two forms, would seem to be difficult to achieve, since the transition occurs in the temperature range, where self-diffusion processes are hindered. This aspect of the problem calls for further investigations.

### Acknowledgment

The authors express their sincere gratitude to Dr. G.S.Oleinik for her help in TEM studying of BN sample structure.

### References

1. A.V. Kurdyumov and N.F.Ostrovskaya, *Fizika i Tekhnika Vysokih Davlenii*, **2**, No 3 (1992) 5.
2. Jr.J.Thomas, N.E.Weston and T.E.O'Connor, *J. Amer. Chem. Soc.*, **84** (1963) 4619.
3. F.R.Corrigan and F.P.Bundy, *J. Chem. Phys.*, **63** (1975) 3812.
4. A.Onodera, K.Inoue, H.Joshihara, H.Nakae, T.Matsuda and T.Hirai, *J. Mater. Sci.*, **25** (1990) 4279.
5. I.A.Petrusha and A.A.Svirid, *High Press.Res.*, **9** (1992) 136.
6. M.Ueno, K.Hasegawa, R.Oshima, A.Onodera, O.Shimomura, K.Takemura, H.Nakae, T.Matsuda and T.Hirai, *Phys. Rev., B*, **45** (1992) 10226.
7. V.F.Britun, A.V.Kurdyumov and I.A.Petrusha, *J. Mater. Sci.* **28** (1993) 6575.
8. A.V.Kurdyumov, V.G.Malogolovets, N.V.Novikov, A.N.Pilyankevich and L.A.Shulman, *Polymorphic Modifications of Carbon and Boron Nitride* (Metallurgiya, 1994), in Russian.
9. B.N.Sharupin, A.E.Kravchik, M.M.Efremenko, R.U.Mametyev, E.V.Tupitsina and A.S.Osmakov, *Zh. Prikl. Khim.*, **63** (1990) 1698.
10. V.L.Solozhenko, in *Properties of Group III Nitrides*, ed. J.H.Edgar (1994), p. 43.
11. F.P.Bundy and R.H.Wentorf, Jr, *J. Chem. Phys.*, **38** (1963) 1144.
12. I.Petrusha, A.Svirid, A.Markov and B.Sharupin (XXXII Annual meeting of EHPRG; Abstr.- Brno: Technical University, 1994), p. 42.

# EQUILIBRIUM PHASE DIAGRAM OF BORON NITRIDE: RECENT RESULTS

V.L. SOLOZHENKO

*Institute for Superhard Materials of the Ukrainian National Academy of Sciences  
Kiev 254074, Ukraine*

## ABSTRACT

On the basis of new experimental data on thermodynamic properties and equations of state of BN modifications, coordinates of triple points (including metastable ones) have been calculated, and thermodynamic stability regions of crystalline phases, liquid and vapour on the equilibrium phase p,T-diagram of boron nitride have been refined. Rhombohedral and wurtzitic modifications of BN have been found to be metastable. New experimental data on phase thermal stability of the dense modifications of BN at high pressure, BN solubility in supercritical ammonia and low-pressure synthesis of cBN are discussed.

## Introduction

The concept of an equilibrium phase diagram of boron nitride I suggested in 1988 [1], and developed in succeeding years [2-6], is most completely represented in the latest reviews [7,8]. The main distinction of this diagram from the generally accepted BN phase diagram of Corrigan and Bundy [9] is the position of the hBN  $\rightleftharpoons$  cBN equilibrium line. According to the Corrigan-Bundy diagram, the hBN  $\rightleftharpoons$  cBN equilibrium line is parallel to the graphite  $\rightleftharpoons$  diamond equilibrium curve and intersects the pressure axis at 1.3 GPa, suggesting metastability of cubic boron nitride at lower pressures over the whole temperature range. However, we have shown that this curve intersects the temperature axis at 1590 K (Fig. 1). Hence, it follows that at normal pressure cubic boron nitride is the thermodynamically stable modification of BN up to temperatures of the order of 1600 K.

The present paper briefly reviews new experimental results on stable and metastable modifications of BN, and the p,T-boundaries of the regions in which they may exist.

## Recent Investigation

New experimental data on thermodynamic properties of graphite-like modifications of BN [10-13] and wBN [10,12,14] as well as on equations of state of rBN [15,16], wBN [17] and

hBN [18] obtained during last two years have made it possible to refine the coordinates of all triple points, including metastable ones, and to consider the problem of the existence of thermodynamic stability regions for rhombohedral and wurtzitic modifications on the phase diagram of boron nitride.

### *The hBN-L-V triple point*

As there are no literature data on thermodynamic and thermophysical properties of

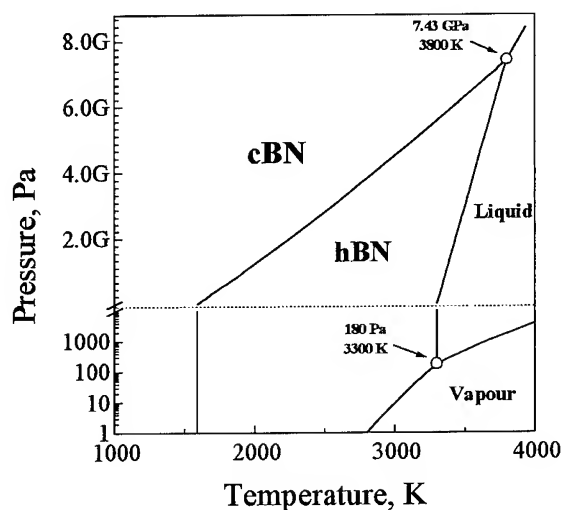


Fig. 1 Equilibrium phase p,T-diagram of boron nitride



liquid BN, the melting enthalpy of hBN was evaluated from Wentorf's data [19] on hBN melting between 3.0 and 7.1 GPa using the melting entropy value of 25 J/(K · mol) given in [20]. Considering the slope of the melting curve, the standard value of molar volume of liquid BN was assumed to be 12.4 cm<sup>3</sup>/mol.

To calculate the equilibria with contribution of vapour, thermodynamic data for gaseous boron nitride given in [20] were used. Dissociation in the vapour phase as well as formation of gaseous species that differ from monomeric BN molecules have not been accounted.

The calculations of the curves of hBN  $\rightleftharpoons$  liquid, hBN  $\rightleftharpoons$  vapour and liquid  $\rightleftharpoons$  vapour equilibria have shown that the hBN-L-V triple point has the following coordinates:  $p=180$  Pa and  $T=3300$  K (Fig. 1). Because of this the thermodynamic stability region of vapour on the BN phase diagram is extremely small (for comparison: the coordinates of the graphite-liquid-vapour triple point are 10.3 MPa and 4766 K [21]).

#### *The hBN-cBN-L triple point*

Using new data on the hBN compressibility [18], the hBN  $\rightleftharpoons$  cBN and hBN  $\rightleftharpoons$  liquid equilibrium curves have been calculated, which allowed the coordinates of the hBN-cBN-L triple point to be defined as 7.43 GPa and 3800 K (Fig. 1) instead of 6.9 GPa and 3700 K (as calculated earlier [5] using equation-of-state data for hBN determined by Lynch and Drickamer [22]).

#### *The rBN-cBN-L triple point*

On the basis of the experimental data on thermodynamic properties [10-13], thermal expansion [7] and compressibility [15] of rBN, the lines have been calculated for rhombohedral boron nitride phase equilibria with other BN crystalline modifications, as well as with vapour and liquid from 0 to 14 GPa and from 0 to 4000 K. The triple point rBN-cBN-L was found to have coordinates of 7.27 GPa and 3780 K, i.e. it lies in the hBN

thermodynamic stability region (Fig. 2). Our findings permit an unambiguous conclusion that there is no rBN thermodynamic stability region on the phase  $p,T$ -diagram of boron nitride over the whole range of pressures and temperatures.

#### *The wBN-hBN-L triple point*

From new experimental data on wBN [17] and hBN [18] equations of state, the lines have been calculated for phase equilibria between wurtzitic and other crystalline BN modifications and with liquid over a wide range of pressure and temperature. The wBN-hBN-L triple point was found to have the coordinates of 7.82 GPa and 3830 K and to lie in the thermodynamic stability region of cBN (Fig. 2). Since the curve of the

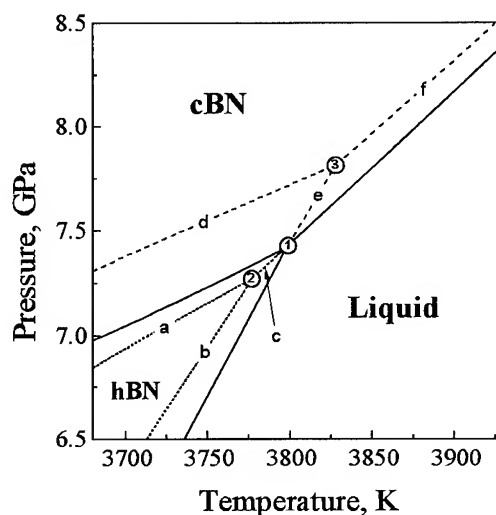


Fig. 2 Fragment of BN equilibrium phase diagram in vicinity of hBN-cBN-liquid triple point

- 1 - hBN-cBN-liquid triple point
- 2 - metastable rBN-cBN-liquid triple point
- 3 - metastable hBN-wBN-liquid triple point
- a - line of rBN  $\rightleftharpoons$  cBN metastable equilibrium
- b - line of rBN metastable melting
- c - metastable beam of cBN melting curve
- d - line of hBN  $\rightleftharpoons$  wBN metastable equilibrium
- e - metastable beam of hBN melting curve
- f - line of wBN metastable melting

metastable equilibrium  $wBN \rightleftharpoons$  liquid is virtually parallel to cBN melting curve it follows that wurtzitic BN (as well as rhombohedral modification) has no thermodynamic stability region on the phase diagram of boron nitride.

#### *cBN-to-hBN phase transformation*

Analysis of publications dealing with the studying of the cBN  $\rightarrow$  hBN transformation points to a considerable diversity of data obtained by different researchers (see, for instance, a review [7]), which is defined by the difference in the experimental conditions as well as in structural state, impurity content and dispersity of the samples used.

Recently we have studied this phase transformation in 0-1.4 GPa range using perfect single crystals of cBN in a medium with a very low partial pressure of oxygen. The onset temperature of the cBN-to-hBN transformation at normal pressure was found to be  $1555 \pm 15$  K and to increase with pressure ( $dT/dp = 300$  K/GPa). The results obtained are in good agreement with the calculated line of cBN  $\rightleftharpoons$  hBN equilibrium (Fig. 3).

#### *wBN-to-hBN phase transformation*

Recently the wBN-to-hBN phase transformation has been studied *in situ* in the 0-6 GPa pressure range using powder diffraction of synchrotron radiation. It was shown that phase stability of wBN is strongly defined by the degree of imperfection of the material. For the most perfect sample produced by the thermal phase stabilisation of wBN, synthesised by shock-wave compression, pressure dependence of the onset temperature for this transformation virtually coincides with the calculated curve of wBN  $\rightleftharpoons$  hBN metastable equilibrium.

#### *rBN phase stability*

Recent studies of thermal phase stability of rhombohedral boron nitride between 0 and 9 GPa

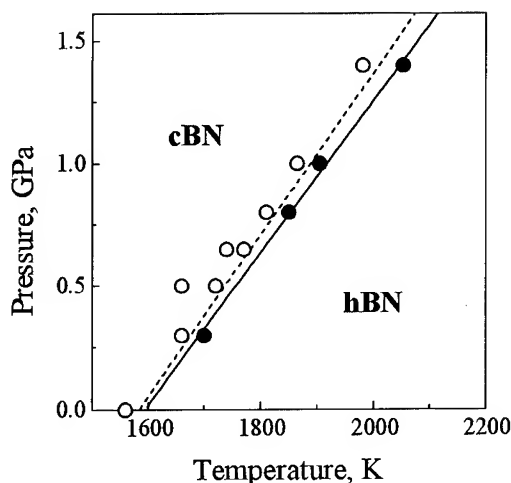


Fig. 3 Experimental results on cBN-hBN phase transformation. Open circles show untransformed cBN, solid ones indicate hBN. Dash line shows experimental cBN-hBN boundary, while solid curve corresponds to hBN  $\rightleftharpoons$  cBN equilibrium

up to 2700 K indicate the decisive role of kinetic factors in rBN phase transformations. In this case, structural state and dispersity of the samples under study are also very important. Phase transformations of rBN in the region of thermodynamic stability of cBN on the equilibrium phase diagram of boron nitride occur in accordance with the Ostwald stepwise principle by the rBN  $\rightarrow$  hBN  $\rightarrow$  (wBN)  $\rightarrow$  cBN scheme (Fig. 4) which provides another example of the metastable behaviour in the B-N system.

#### *BN solubility in supercritical ammonia*

Recently we have experimentally studied the solubility of hBN and cBN in supercritical ammonia at pressures of 65.0 to 95.0 MPa in the 750-1050 K temperature range [23]. Based on the values of ultimate solubility obtained, the standard value of Gibbs energy for the hBN  $\rightarrow$  cBN transition has been calculated to be  $\Delta G_{tr} = -13.5 \pm 2.5$  kJ/mol, this agrees well with the value of  $\Delta G_{tr} = -13.7 \pm 3.0$  kJ/mol calculated from the calorimetric data

(see review [7]). Thus, the reliability of the thermodynamic data that were used in calculation of the equilibrium phase diagram of BN has been supported once more.

#### Low-pressure synthesis of cBN

Earlier we have shown [6,24-26] that in the presence of  $\text{Li}_3\text{N}$ ,  $\text{Mg}_3\text{N}_2$ ,  $\text{AlN}$  and  $\text{MgB}_2$  the threshold pressure of spontaneous crystallization of cBN from solutions of boron nitride in supercritical ammonia can be reduced down to 2 GPa (Fig. 5).

Recently similar results have been obtained by Demazeau et al. [27] when studying spontaneous crystallization of cubic boron nitride in the hBN- $\text{Li}_3\text{N-N}_2\text{H}_4$  system.

Very recently Singh et al. [28] have shown that in the amorphous boron nitride -  $\text{Mg}_3\text{B}_2\text{N}_4$  system, the minimum pressure of cBN formation is 2.5 GPa at 2100 K (Fig. 5), which is the lowest value for the process of cBN crystallization when traditional "solvent-catalysts" are used.

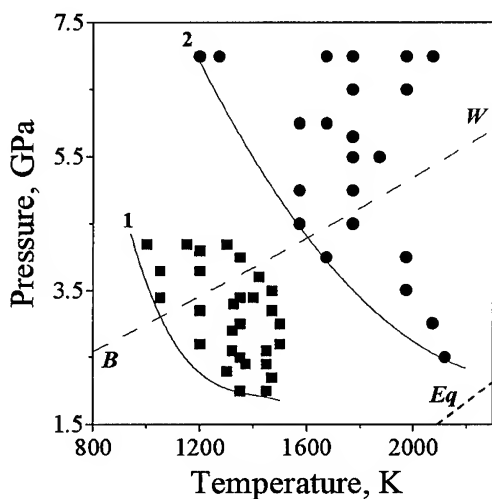


Fig. 5 p,T-regions of cBN crystallization in non-traditional growth systems

1 - Solozhenko et al. [6,24-26]

2 - Singh et al. [28]

BW is experimental hBN = cBN boundary [29]

Eq is the hBN = cBN equilibrium line.

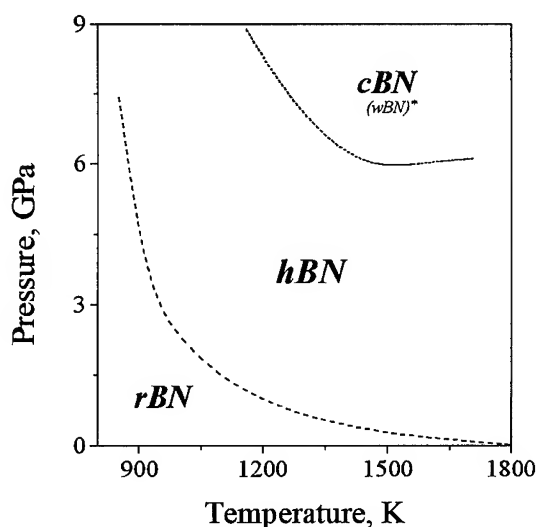


Fig. 4 Kinetic phase stability regions of BN graphite-like modifications (\* indicates the formation of wBN in small quantities)

Thus, according to the equilibrium phase diagram of BN, the synthesis of cubic modification in non-conventional growth systems expands the p,T-region of cBN formation (Fig. 5), opening wide prospects for the development of new technologies of cubic boron nitride production at reduced pressures.

#### Conclusions

On the basis of new experimental data on thermodynamic properties and equations of state of boron nitride polymorphs, thermodynamic stability regions of crystalline (cBN and hBN), liquid and vapor phases on the equilibrium phase p,T-diagram of BN have been refined.

Rhombohedral and wurtzitic modifications of BN have been found to be metastable and their phase transformations in the region of thermodynamic stability of cBN occur via formation of more stable hBN phase according to the Ostwald stepwise principle, which is another example of the metastable behaviour in the B-N system.

From the experimental data on the ultimate solubility of hBN and cBN in supercritical ammonia, a standard value of Gibbs energy of the hBN-to-cBN transformation has been determined, which is in good agreement with the corresponding value calculated from calorimetric data, that were used for calculation of BN equilibrium phase diagram.

New data on cBN synthesis at reduced pressure suggest the possibility of further decreasing the p,T-parameters of spontaneous crystallization of cubic boron nitride by using non-conventional growth systems.

## References

1. V.L. Solozhenko, *Doklady Phys. Chem.* **301** (1988) 592.
2. V.L. Solozhenko, *High Press. Res.* **7-8** (1991) 201.
3. V.L. Solozhenko, *High Press. Res.* **9** (1992) 140.
4. V.L. Solozhenko and V.Ya. Leonidov, *J. Superhard Mater.* **15** (1993) 62.
5. V.L. Solozhenko, *Thermochim. Acta* **218** (1993) 221.
6. V.L. Solozhenko, *Diamond & Rel. Mat.* **4** (1994) 1.
7. V.L. Solozhenko, in *Properties of Group III Nitrides*, ed. J.H. Edgar (INSPEC, 1994), p. 43.
8. V.L. Solozhenko, *High Press. Res.* **13** (1995) 199.
9. F.R. Corrigan and F.P. Bundy, *J. Chem. Phys.* **63** (1975) 3812.
10. K.S. Gavrichev, V.L. Solozhenko, V.E. Gorbunov et al., *Thermochim. Acta* **217** (1993) 77.
11. V.L. Solozhenko, *Zh. Fiz. Khim.* **67** (1993) 1580.
12. K.S. Gavrichev, V.L. Solozhenko and V.B. Lazarev, *Inorgan. Mater.* **30** (1994) 1025.
13. V.L. Solozhenko, *J. Thermal Anal.* **44** (1995) 97.
14. V.L. Solozhenko, *Thermochim. Acta* **218** (1993) 395.
15. V.L. Solozhenko, G. Will, H. Hüpen and F. Elf, *Solid State Comm.* **90** (1994) 65.
16. V.L. Solozhenko and G. Will, in *Proc. XXXII EHPRG Annual Meeting* (1994), p. 57.
17. M. Ueno, M. Yoshida and A. Onodera, *Jpn. J. Appl. Phys. (Suppl.)* **32** (1993) 42.
18. V.L. Solozhenko, G. Will and F. Elf, *Solid State Comm.* **96** (1995) 1.
19. R.H. Wentorf, *J. Phys. Chem.* **63** (1959) 1934.
20. *Thermodynamic properties of individual substances*, ed. V.P. Glushko et al. (Nauka, 1981).
21. P. Gustafson, *Carbon* **24** (1986) 169.
22. R.W. Lynch and H.G. Drickamer, *J. Chem. Phys.* **44** (1966) 181.
23. V.L. Solozhenko, V. Gonnet and G. Demazeau, *Materials Letters* (in press).
24. V.L. Solozhenko, V.A. Mukhanov and N.V. Novikov, *Doklady Phys. Chem.* **308** (1989) 728.
25. V.L. Solozhenko, V.A. Mukhanov and N.V. Novikov, *Doklady Chem.* **312** (1990) 125.
26. V.L. Solozhenko, A.B. Slutsky and Yu.A. Ignatiev, *J. Superhard Mater.* **14** (1992) 61.
27. G. Demazeau, V. Gonnet, V.L. Solozhenko et al., *C. R. Acad. Sci. Ser. II* **320** (1995) 419.
28. B.P. Singh, G. Nover and G. Will, *J. Crystal Growth* **152** (1995) 143.
29. F.P. Bundy and R.H. Wentorf, *J. Chem. Phys.* **38** (1963) 1144.

# THE EQUATION OF STATE OF HEXAGONAL GRAPHITE-LIKE BORON NITRIDE TO 12 GPa AND PHASE TRANSFORMATION HBN→WBN

V.L. SOLOZHENKO,\* G. WILL, F. ELF

*Mineralogical Institute, University of Bonn, D-53115 Bonn, Germany*

## ABSTRACT

The compressibility of hexagonal graphite-like boron nitride has been measured at room temperature up to 12 GPa, using a diamond anvil cell and energy-dispersive X-ray diffraction with synchrotron radiation. From the obtained pressure-volume relation for hBN the isothermal bulk modulus of  $36.7 \pm 0.5$  GPa and its first pressure derivative of  $5.6 \pm 0.2$  have been calculated. High-pressure *in situ* X-ray diffraction studies of hBN-to-wBN phase transition has been carried out at room temperature. It was found that the transition starts at about 8 GPa and occurs in a wide range of pressures.

## Introduction

Graphite-like hexagonal boron nitride (hBN) is the best studied polymorphous modification of BN. Nevertheless from the literature on the hBN compression [1-4], one cannot make an unambiguous conclusion about the equation of state of this phase. While the data obtained by different researchers between 0-2 GPa are in good agreement with each other, at higher pressures a considerable disagreement is found for static [3] and shock [4] compression data. Moreover, in all these publications the degree of three-dimensional ordering of the hBN samples have not been considered resulting very likely in uncertainties of the data obtained.

In the present study we wish to report on measurements of the isothermal compression of a highly ordered hBN at static pressures up to 12 GPa at room temperature using energy-dispersive X-ray diffraction with synchrotron radiation.

## Experimental Procedure

### *Sample preparation and characterisation*

In this study we used commercial hBN from Fluka. To remove impurities, the powder was

annealed at 2100 K for 5 hours in nitrogen atmosphere with an oxygen content less than 0.003 vol. %.

The grit size of the hBN sample used for the experiments has been estimated by granulometry and transmission electron microscopy (JEM 100C Jeol). It was in the range of  $0.3 \div 10 \mu\text{m}$  with an average particle size of  $3.1 \mu\text{m}$  corresponding to the maximum in the mass distribution curve. The specific surface value was  $2.6 \text{ m}^2/\text{g}$  estimated from the absorption isotherm of nitrogen at 77 K by the BET-method.

The impurity contents of the hBN sample under study according to the data of mass-spectrometry, spectral analysis and X-ray microanalysis did not exceed 0.2 mass. % in total.

Using conventional X-ray powder diffraction the lattice parameters of hBN were determined to  $a = 2.504(2) \text{ \AA}$  and  $c = 6.660(8) \text{ \AA}$ . The degree of three-dimensional ordering of the sample studied has been calculated by the method described in [5] to  $P_3 = 0.98 \pm 0.02$ .

### *High-pressure X-ray diffraction*

The experiments have been done at room temperature in a Mao-Bell-type diamond anvil cell with anvil tips of  $400 \mu\text{m}$  in diameter. The sample

\* On leave from the Institute for Superhard Materials of the Ukrainian National Academy of Sciences, Kiev 254074, Ukraine

chamber was a 150  $\mu\text{m}$  diameter hole drilled in a T301 stainless steel gasket of thickness 300  $\mu\text{m}$  preindented to about 20 GPa.

The diffraction measurements were performed in energy-dispersive mode at the HASYLAB-DESY (Hamburg) at the electron-positron storage ring DORIS III. Conditions were 4.455 GeV and 80 mA to 20 mA.

The experimental set-up has been described elsewhere [6]. The primary beam was collimated along the axis of force of the diamond anvil cell to a 80  $\mu\text{m}$  spot at the geometric centre of the pressurised sample. Exposure times were between 1 h and 3 h depending on the electron current. In total 33 diffraction diagrams were collected at increasing pressure in two runs up to a maximum pressure of 12 GPa. The diffracted X-rays were collected using an intrinsic Ge solid-state detector and a Canberra S100 multichannel analyser. The Canberra System S100 software installed on an IBM Personal Computer 486/25 was used for collection and preliminary on-site analysis of the data.

A radioactive  $^{241}\text{Am}$ -source provided X-ray

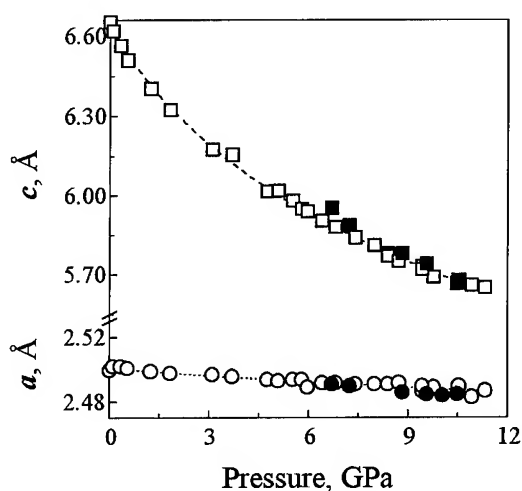


Fig. 1  $a$  and  $c$  vs pressure for hBN (open and solid symbols represent data from the first and from the second run, respectively).

fluorescence  $K_{\alpha}$  and  $K_{\beta}$  lines from Rb, Mo, Ag, Ba and Tb targets for energy calibration of the detector. The angle calibration was done with Ag powder (EC120, Johnson Matthey GmbH Alpha Products), yielding a diffraction angle of  $2\theta = 11.191 \pm 0.001^{\circ}$ .

The pressure was determined by measuring the lattice constant of NaCl contained in the chamber and the Decker's data of the equation of state for sodium chloride [7].

#### Data analysis

A typical X-ray diffraction pattern shows the diffraction lines (002), (100), (101), (102) and (110) of hBN. Occasionally also (004) and (112) could be observed. They were used to calculate the lattice parameters and the molar volume of hexagonal graphite-like boron nitride under pressure. The lines (111), (200), (220), (222) and (422) of NaCl were used for the pressure determination.

The uncertainty in pressure and also in the lattice parameters of hBN is determined by the uncertainty of the positions of the reflections. We estimate the uncertainty in pressure to less than 4 kbar, and of the lattice parameters of hBN to about 1 % in  $c$  and 3 % in  $a$ .

#### Results and Discussion

The experimental values of hBN lattice parameters are plotted in Fig. 1, and  $V/V_0$  data in Fig. 2. A first-order Murnaghan equation of state [8] was used to represent the above data. A non-linear two-parameter least squares fit of the experimental data gave  $B_0 = 36.7 \pm 0.5$  GPa and  $B'_0 = 5.6 \pm 0.2$  ( $V_0 = 10.892$  cm<sup>3</sup>/mol).

As can be seen from Fig. 1 the lattice constant  $a$  is only insignificantly influenced by pressure, while  $c$  is compressed to about 85 % of its original value at 12 GPa. The ratio between linear coefficients of hBN compressibility towards the  $c$  and  $a$  axes is  $k_c/k_a = 60 \pm 8$ , which is indicative of a strong anisotropy of bond forces in the hBN

lattice in agreement with the crystal structure, which consists of hexagonal arranged B-N sheets with covalent bonding between B and N, stacked on top of each other in a sequence  $AA'AA'$  with weak Van der Waals bonding between the layers.

The final data, shown in Fig. 2, are in reasonable agreement with the results on hBN from dynamic compression [4], however in serious disagreement with the data by Lynch and Drickamer [3] from static compression, especially at pressures above 2 GPa.

The comparison of our p-V data obtained for hBN with those for rBN [9] shown as a dashed curve in Fig. 2, is indicative of a slightly higher compressibility of the rhombohedral phase, which is evidently due to the higher energy of interaction between layers in hBN [10].

Above 8 GPa the polymorphic transformation of hBN into wurtzitic phase was observed. The value of the threshold pressure for the hBN→wBN transformation observed by us *in situ* ( $8.1 \pm 0.1$  GPa) is lower than the corresponding value obtained earlier in quenching experiments ( $\sim 10$  GPa [11]). By increasing pressure, the intensity of wBN peaks increased, but even at the high pressure achieved in our experiments (25.0 GPa), the hBN peaks were still observed. Equation-of-state data obtained for wBN in range of 10–25 GPa have yielded the bulk modulus and its pressure derivative to be  $230 \pm 20$  GPa and  $4.1 \pm 0.9$ , respectively. A large discrepancy by a factor of about 2 exists in the bulk modulus of wBN between our experiment and previous data ( $390 \pm 3$  GPa [12]).

**Acknowledgements** - One of us (VLS) is grateful to the Alexander von Humboldt-Stiftung for assistance and financial support. We are indebted to Dr. Jens W. Otto of the HASYLAB-DESY for his valuable help during the high-pressure experiment. We are also grateful to Prof. A. V. Kurdyumov for fruitful discussion.

## References

1. S.S. Kabalkina and L.F. Vereshchagin, *Sov. Phys. - Doklady* **5** (1960) 1065.
2. Yu.S. Genshaft, L.D. Livshits and Yu.N. Ryabinin, *Zh. Prikl. Mekhan. i Tekhn. Fiz.* **5** (1962) 107.
3. R.W. Lynch and H.G. Drickamer, *J. Chem. Phys.* **44** (1966) 181.
4. N.L. Coleburn and J.W. Forbes, *J. Chem. Phys.* **48** (1968) 555.
5. A.V. Kurdyumov, *Sov. Phys. Crystallogr.* **17** (1972) 534.
6. J.W. Otto, HASYLAB Jahresbericht 1993 (1994) 931.
7. D.L. Decker, *J. Appl. Phys.* **37** (1966) 5012.
8. F.D. Murnaghan, *Proc. Nat. Acad. Sci.* **30** (1944) 244.
9. V.L. Solozhenko, G. Will, H. Hüpen and F. Elf, *Solid State Comm.* **90** (1994) 65.
10. V.M. Danilenko, A.V. Kurdyumov and A.V. Meike, *Sov. Phys. Crystallogr.* **26** (1981) 191.
11. A. Onodera, H. Sumiya, K. Higashi et al., *High Temp.-High Press.* **24** (1992) 45.
12. M. Ueno, M. Yoshida, A. Onodera et al., *Phys. Rev. B* **49** (1994) 14.

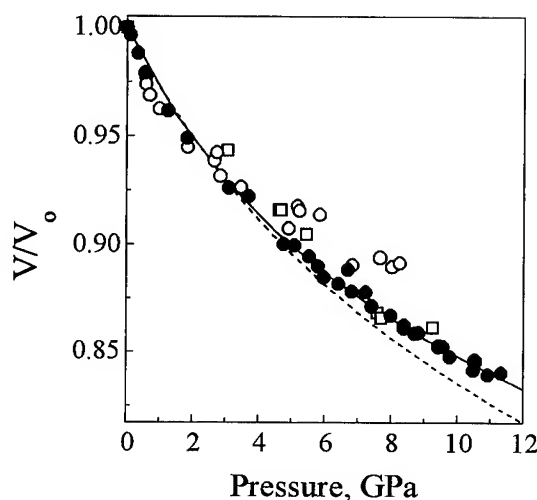


Fig. 2  $V/V_0$  vs pressure for hBN (● - present work; ○ - Lynch and Drickamer [3]; □ - Coleburn and Forbes [4]). The solid line gives the fit of our data to the Murnaghan equation. The dashed line shows for comparison compression vs pressure for rBN [9].

# BEHAVIOUR OF LESS ORDERED BORON NITRIDE UNDER HIGH PRESSURE AND TEMPERATURE IN THE PRESENCE OF A CATALYST-SOLVENT

M.M. BINDAL, B.P. SINGH, S.K. SINGHAL, R.K. NAYAR, R. CHOPRA AND  
E.S.R. GOPAL

*National Physical Laboratory, New Delhi - 110 012, India*

G.WILL

*Mineralogical Institute, Univ. Bonn, Bonn, Germany*

## ABSTRACT

The present paper describes the results of a series of investigations on the behaviour of turbostratic boron nitride (tBN) and amorphous boron nitride (aBN) under high P - T conditions using magnesium boron nitride ( $\text{Mg}_3\text{B}_2\text{N}_4$ ) as the catalyst - solvent. It has been shown that the conversion to harder phases takes place at much lower pressures if we use the least ordered form of boron nitride i.e. aBN. The study reveals that whereas hexagonal form changes to the cubic boron nitride (cBN) at  $P > 4$  GPa the amorphous form changes to the cubic form at pressures as low as 2.5 GPa.

## Introduction

The study of behaviour of well crystallized form of boron nitride (hBN) under high P-T conditions both directly and in the presence of a catalyst-solvent have led to the synthesis of denser forms of boron nitride [1, 2]. In recent years some studies have been made to synthesize cubic form of boron nitride (cBN) from less ordered (amorphous/turbostratic) boron nitride under high P-T conditions [3, 4, 5]. We have undertaken a detailed study of behaviour of less ordered boron nitride under high P-T conditions in the presence of  $\text{Mg}_3\text{B}_2\text{N}_4$  as the catalyst solvent. It was observed that tBN undergoes various structural changes accompanied with the formation of hexagonal boron nitride (hBN), cBN and wBN modifications of boron nitride with the minimum pressure of cBN formation at 4 GPa [6] while for aBN the minimum pressure for cBN formation was found to be 2.5 GPa [7]. In the present we report the details of these investigations and discuss the results in the light of existing phase diagram of boron nitride with a com-

parative analysis of results of cBN synthesis using, tBN and aBN as the starting materials.

## Experimental Details

High pressure-high temperature experiments were carried out on a 200-tonne cubic press and a belt apparatus. The pressure calibration was carried out by using standard pressure fixed points of phase transitions in Bi(I-II) at 2.54 GPa, Yb(fcc  $\rightarrow$  bcc) at 3.9 GPa and Ba(I-II) at 5.5 GPa. The temperature was calibrated in terms of electric power input in watts using Pt/Pt-Rh 10% and chromel-alumel thermocouple placed at the centre of the reaction cell. The tBN and aBN used in this work were prepared chemically by heating a mixture of  $\text{KBH}_4$  and  $\text{NH}_4\text{Cl}$  in about 1 : 1 mass ratio in  $\text{N}_2$  atmosphere at 900°C for about two hours followed by quenching the products. The XRD studies of the product confirm the turbostratic and amorphous characteristic.



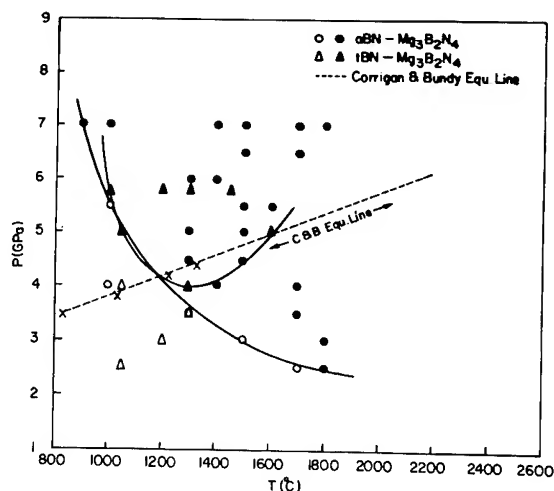


Figure 1: P-T diagram of aBN/tBN  $\rightarrow$  cBN transformation.

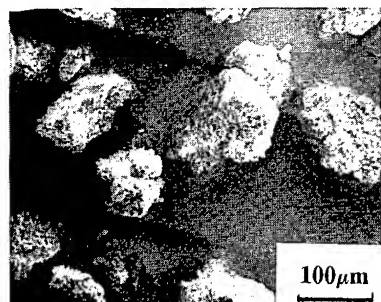
## Results and Discussion

Fig. 1 shows the P-T diagram obtained from different high P-T experiments. The cBN formation has been observed at pressures and temperatures higher than the solid curves shown in Fig. 1. The open triangles represent regions where no conversion was observed from tBN whereas filled triangles represent P-T regions where cBN formation took place. The open circles represent regions where no cBN was obtained from aBN. The filled circles represent P-T regions where aBN  $\rightarrow$  cBN transformation was observed. The minimum pressure for tBN  $\rightarrow$  cBN transformation was found to be 4 GPa at 1300°C, whereas the minimum temperature was found to be 1000°C at 5.8 GPa. The minimum pressure for aBN  $\rightarrow$  cBN transformation was found to be 2.5 GPa at 1800°C, whereas the minimum temperature was found to be 900°C at 7 GPa.

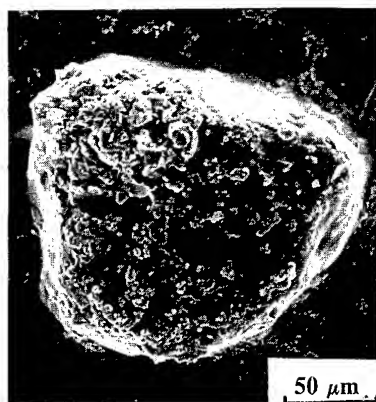
The cBN crystals synthesized were brown-black in colour with their sizes in the 10–100  $\mu\text{m}$  range for high pressures experiments conducted at 4–6 GPa and 1000–1600°C when tBN was used as the starting material. In case of aBN  $\rightarrow$  cBN transformation the cBN crystals were

again brown-black but with their sizes in the 10–200  $\mu\text{m}$  range for the experiments performed in 2.5–7 GPa and 900–1800°C region. Fig. 2(a) shows a typical SEM micrograph of cBN crystals synthesized from tBN at 5.8 GPa and 1000°C and Fig. 2(b) shows some of the well formed cBN crystals grown at 7 GPa and 1500°C from aBN.

The XRD studies confirmed the formation of cBN both from tBN and aBN at the threshold P-T conditions and the tBN  $\rightarrow$  cBN or aBN  $\rightarrow$  cBN transformation was found to increase at higher pressures and temperatures as evidenced by the increase in (111) diffraction peak height of cBN and disappearance of amorphous character. It may be mentioned that the formation of cBN at such low pressures from tBN as well as from aBN has been reported for the first time by us employing the catalyst-solvent process [6, 7]. The general features of the reaction products synthesized at high pressures ( $P > 5$  GPa) and low temp. ( $T \leq 1200^\circ\text{C}$ ) and at high pressures ( $P > 5$  GPa) and high temp. ( $T > 1300^\circ\text{C}$ ) from tBN and aBN were more or less the same except for the quality of the cBN crystals. The cBN crystals were generally better with the formation of well developed faces in case of crystals synthe-



(a)



(b)

Figure 2: SEM micrographs of cBN crystals synthesized from (a) tBN and (b) from aBN.

sized at higher P-T conditions. The most important result of the present investigation is the low pressure (2.5 GPa) synthesis of cBN from aBN. The crystallization of cBN at such low pressures can not be understood on the basis of present knowledge of cBN conversion and available equilibrium data in the various polymorphs of boron nitride. Uptil now even with the use of catalyst-solvents the minimum pressure for cBN formation was reported to be higher than 4 GPa. It may be mentioned that the synthesis of cBN at pressures as low as 2 GPa has also been reported by Solozhenko [8, 9] in presence of some supercritical fluids and obtained a new equilibrium phase diagram of BN which is able to ex-

plain the present low pressure synthesis of cBN from aBN. The growth of harder phases of BN from tBN/aBN in the present work may be explained on the basis of dissolution and precipitation process in analogy to graphite  $\rightarrow$  diamond conversion in molten metal. The driving force appears to be the solubility difference of tBN/aBN, hBN and cBN in the eutectic liquid. The formation of cBN at temperatures as low as 900°C under high pressures is presumably due to direct transformation of tBN/aBN which is also operative in the present system.

### Acknowledgements

One of us (BPS) is thankful to CSIR-DAAD for providing financial assistance for a two months' stay at Bonn during which part of the work was carried out.

### References

- [1] F.P. Bundy and R.H. Wentorf Jr., *J. Chem. Phys.* **38** (1963) 1144.
- [2] R.C. DeVries and J.F. Fleischer, *J. Cryst. Growth* **13/14** (1982) 88.
- [3] H. Sumiya, T. Iseki and A. Onodera, *Mat. Res. Bull* **18** (1983) 1203.
- [4] I.S. Gladkaya, G.N. Kremkova and V. Slesarev, *J. Less-Common Metals* **117** (1986) 241.
- [5] L. Vel and G. Demazeau, *Solid State Commun.* **79** (1991) 1.
- [6] M.M. Bindal, B.P. Singh, S.K. Singhal, R.K. Nayar, R. Chopra, *J. Cryst. Growth* **114** (1994) 97.
- [7] B.P. Singh, G. Nover and G. Will, *J. Cryst. Growth* (in press).
- [8] V.L. Solozhenko, *Diamond and Related Materials* **4** (1994) 1.
- [9] V.L. Solozhenko, *Thermochim. Acta.* **218** (1993) 221.

### **VI(C.3) Molecular Solids**

**PHASE P-T-DIAGRAMS, STRUCTURAL DISORDER AND  
INTERNAL MOTION AT  $\text{MSiF}_6 \cdot 6\text{H}_2\text{O}$  ( $\text{M} = \text{Mg}, \text{Mn}, \text{Fe}, \text{Co}, \text{Ni}, \text{Zn}$ )  
UNDER PRESSURE**

S.K.Asadov<sup>1</sup>, E.A.Zavadskii<sup>1</sup>, V.I.Kamenev<sup>1</sup>, K.V.Kamenev<sup>2</sup>, B.M.Todris<sup>1</sup>

<sup>1</sup> *Donetsk Physico-Technical Institute of the Ukrainian Academy of Sciences,  
Donetsk, Ukraine*

<sup>2</sup> *Institute of Physics of the Academy of Sciences of the Czech Republic,  
Prague, Czech Republic*

ABSTRACT

The fluorsilicate hexahydrates of some bivalent metals were experimentally investigated in the temperature region from 15K to 300K under pressure up to 200 MPa and a variety of physical phenomena was found. The realisation of a homological rule for the series has been established which allowed to construct the generalized P-T-diagram for the series. Basic rules for the behaviour of the compounds are derived considering both weak hydrogen bonds between octahedral ions forming the structure and structural disorder of these ions in the crystal lattice.

**Introduction**

The fluorsilicate hexahydrates of some bivalent metals (M-HFS) with general formula  $\text{MSiF}_6 \cdot 6\text{H}_2\text{O}$  ( $\text{M} = \text{Mg}, \text{Mn}, \text{Fe}, \text{Co}, \text{Ni}, \text{Zn}$ ) have similar structures in which two complex ions  $\text{M}(\text{H}_2\text{O})_6$  and  $\text{SiF}_6$  form a slightly distorted CsCl-type lattice. Each of the ions has a shape close to octahedral. Weak hydrogen bonds between the ions make them sensitive to their mutual orientation and to forming a number of phase modifications (characterized by different kinds of ionic disorder) under insignificant change of external conditions. In this article we have generalised the results of the influence of the hydrostatic pressure on the structural phase transitions between such phase modifications.

**Experiment**

For our study we have used two independent methods: X-ray and Differential Thermal Analysis (DTA).

The X-ray diffraction technique was used to determine the temperature and pressure dependencies of the position and the intensity of the diffraction lines corresponding to different phases. A sample of M-HFS with crystallographic

planes (440) in the reflection position (the indices refer to the hexagonal basis of the crystal lattice) was placed into the low-temperature high-pressure X-ray chamber made in the form of a beryllium container reinforced by beryllium-bronze banding. Pressure was generated by a gas compressor and applied to the container via a steel capillary. Gaseous helium was used as transmitting medium. The temperature of the sample under study was controlled by blowing He-vapour from liquid helium onto the body of the chamber.

The DTA method was used for determining thermal anomalies accompanying the phase transitions in sample. The high-pressure chamber was the same for both methods in order to unify experimental conditions. The experimental equipment using gaseous helium as transmitting medium allowed us to vary independently the pressure from 0 to 200 MPa and the temperature from 15 to 300 K.

We have used single crystals grown from saturated aqueous solutions as samples.

**Results and Discussion**

We have summarized the experimental results in the form of P-T-phase diagrams and published

them earlier: [1] - for Mn-HFS, [2] - for Fe-, Co-, Ni-HFS, and [3] - for Zn-HFS. A detailed study of Mg-HFS was made by authors of [4,5]. These diagrams reveal the unique combination of structural phases, triple points, critical pressure, and wide ranges of metastable states. In spite of essential differences between the compounds, there are several elements presented on almost each diagram. This allows to represent a P-T-diagram of each M-HFS as a part of the generalized P-T-diagram (fig.1) to the right side of the vertical line corresponding to a given M-HFS. Going from M-HFS of one metal to that of another, from left to right, the lines are arranged to the extent of decrease in triple point pressure and critical pressure values (Table 1).

Table 1

$\text{MSiF}_6 \cdot 6\text{H}_2\text{O}$	$T_t$ , K	$P_t$ , MPa	$P_k$ , MPa	$T_{\alpha-\beta}$ , K
$\text{MgSiF}_6 \cdot 6\text{H}_2\text{O}$	307.5*	217*	350**	?
$\text{MnSiF}_6 \cdot 6\text{H}_2\text{O}$	230	90	125	180
$\text{FeSiF}_6 \cdot 6\text{H}_2\text{O}$	240	7.5	63	70
$\text{CoSiF}_6 \cdot 6\text{H}_2\text{O}$	-	-	50	150
$\text{NiSiF}_6 \cdot 6\text{H}_2\text{O}$	-	-	-	220
$\text{ZnSiF}_6 \cdot 6\text{H}_2\text{O}$	-	-	-	200

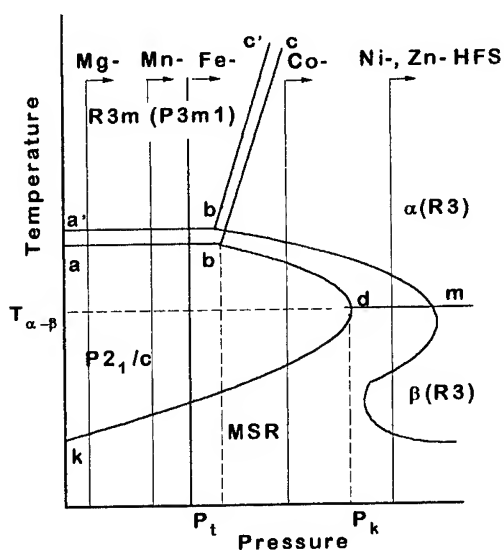


Fig.1

The series of compounds formed in the result of such an arrangement repeats the location of their corresponding bivalent metals M in the Periodic Chart of Elements. This means that there exists the relation between the shape of the diagram for each M-HFS and the ordinal number N of incoming metal M, according to which the increase of N in M-HFS is equivalent to the displacement of the origin of its diagram in the generalized diagram towards higher pressures. Thus, a homological rule is fulfilled in this case but the whole picture of behaviour is rather complicated and can be seen only if pressure is applied.

In order to explain the distinction in crystal structure between the M-HFS with different values of N we have gathered the results of X-ray and neutron diffraction [6-8] (fig.2). This figure shows that in the high-temperature (HT) region Mg-HFS (N=12), Mn-HFS (N=25), and Fe-HFS (N=26) possess structures having elements of 3m symmetry and Co-HFS (N=27), Ni-HFS (N=28), and Zn-HFS (N=30) have crystal lattices of space group symmetry R3. In the low temperature (LT) region the symmetry of M-HFS of light 3d-metals M is changed to monoclinic  $P2_1/c$ , while the compounds with heavier metals remain trigonal. Co-HFS shows features typical for both groups since it is located on the border between them.

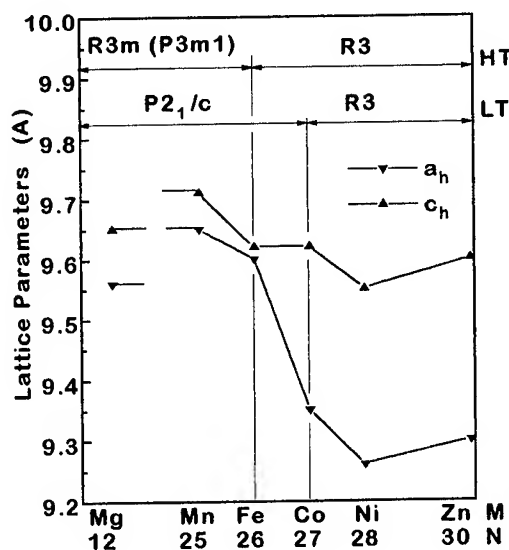


Fig.2

It was natural to assume that substitution of light 3d-metals by heavier M works like increase of pressure applied to the sample. To get better insight into the role of such a substitution we have collected the NMR results [9-10] and compared the temperatures of the structural phase transitions with the temperature dependencies of fluorine and hydrogen linewidths (fig.3). The range below the fluorine line stands for stop turning of both water and fluorine octahedrons. Above this line, motion of the fluorine ions begins, but ions of water are still unmovable. Only in the range above the hydrogen line motion of both types of ions is allowed. The temperatures  $T_s$  and  $T_d$  of phase transitions  $R3m(P3m1)$ - $P2_1/c$  and  $\alpha(R3)$ - $\beta(R3)$ , respectively, are marked by dashed lines. The correspondence is clear between the transition to the monoclinic state and stoppage of internal motion in light 3d-metal-HFS. The  $\alpha$ - $\beta$  transition is connected with slowing down of fluorine ions while the static order of water ions already exists.

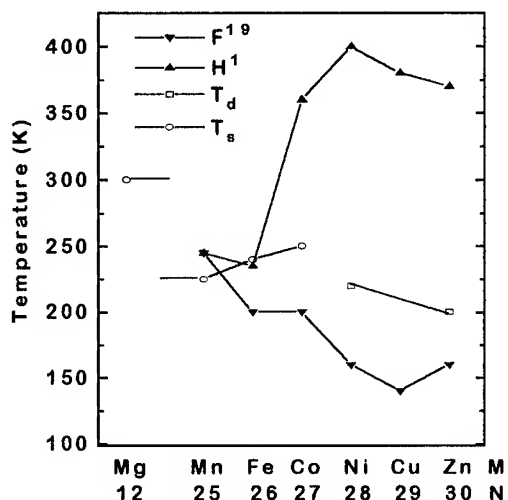


Fig.3

This correspondence between phase transitions and internal motion has allowed us to establish that the four types of structural modifications at the M-HFS presented on the generalized diagram (fig.1) are characterised by different types of orientational disorder: dynamically disordered structure  $R3m(P3m1)$  (both  $SiF_6$  and  $M(H_2O)_6$  ions participate in

the internal motion); "partly" dynamically disordered structure  $\alpha(R3)$  (only  $SiF_6$  octahedrons participate in the motion); static disorder  $\beta(R3)$  ( $SiF_6$  octahedrons are distributed between the two disordered positions and internal motion is absent). The only ordered phase is  $P2_1/c$ .

All the variety of properties of M-HFS can be easily explained by taking into account an assumption about strengthening of hydrogen bonds between the octahedrons under two circumstances: increase of the ordinal number N of incoming metal M (because of the shielding of the core of 3d-metal by additional electron) and decrease of the inter-ionic distances by compression of the sample. Thus the pressure is an analog of the metal change. That is the reason for fulfilling of the homological rule. Increase of the both pressure and number of metal makes more difficult internal motion and of octahedrons and leads to the phase transitions from dynamical disorder  $R3m(P3m1)$  to partly dynamical disorder  $\alpha(R3)$ . The peculiar shape of the metastable states' region (MSR) (Fig.1) is the result of barothermal "freezing" in the state of dynamical disorder of the crystals with the light metal M ( $M = Mg, Mn, Fe, Co$ ).

## References

1. S.K. Asadov et al., *XXIX Meeting on Low Temperature Physics, Booklet of Abstracts*, (Kazan, 1992), T28.
2. S.K. Asadov. et al., *Physica B* **182** (1992) 167.
3. S.K. Asadov et al, *Sov. Solid State Physics* **33**, 2 (1991) 631.
4. M.V. Gorev et al., *Sov. Solid State Physics* **33** (1991) 2210.
5. I.M. Krygin et al., *FTVD* **4**, 1 (1994) 12.
6. V.C.Hamilton, *Acta Cryst.* **15** (1962) 353.
7. S. Ray et al., *Acta Cryst.* **B29**, 12 (1973) 2741.
8. P.G. Jehanno *Acta Cryst.* **A31**, 6 (1975) 857.
9. G.Rangarajan, J.Ramakrishna, *J.Chem.Phys.* **59**, 10 (1973) 5571.
10. S.M.Skjæveland, I.Svare, *Physica Scripta.* **10** (1974) 273.

# PHASE TRANSITION OF HYDROGEN CYANIDE UNDER PRESSURE

H. YAMAWAKI, M. SAKASHITA, K. AOKI

*National Institute of Materials and Chemical Research (JAPAN)  
Tsukuba, Ibaraki 305, Japan*

Raman spectra of hydrogen cyanide (HCN) were measured under high pressure at 90 K. HCN molecules form linear molecular chains by hydrogen bonds  $N\cdots H-C$  in an orthorhombic phase (space group  $Im\bar{m}2$ ,  $z=2$ ) at 90 K and ambient pressure. Raman bands of C-H stretching mode,  $C\equiv N$  stretching mode, H-C-N bending mode (two bands) and librational mode (TO and LO bands) were observed. The splitting of librational TO bands above 2 GPa showed a transition to a new crystalline phase with lowering of symmetry of the crystal structure. HCN molecules polymerized above 4 GPa.

## Introduction

Hydrogen cyanide (HCN) is a polar molecule with a  $C\equiv N$  triple bond. Two crystalline phase are known under low temperature: a phase I (tetragonal,  $I4mm$ ) below 257 K and phase II (orthorhombic,  $Im\bar{m}2$ ) below 170 K [1]. In both phases, HCN molecules are aligned in a head-to-tail configuration along molecular axis by hydrogen bonds, forming linear chains oriented parallel to crystallographic  $c$ -axes. Both structures are body-centered ones with two molecules per unit cell as shown in Figure 1. Their structures differ only by a distortion in the  $ab$  base plane; the  $ab$  plane is a square ( $b/a = 1$ ) for the phase I and a rectangle ( $b/a > 1$ ) for the phase II.

In low-temperature Raman spectra of HCN solids, only one libration was observed in the range of lattice mode for the phase I and II [2], although correlation diagram predicts two bands for the librational mode of the phase II. On the other hand, high-pressure Raman measurements showed that phase I transformed to phase II at 0.8 GPa with a peak splitting of the librational mode [3]. Appearance of a shoulder at the low frequency side of the librational TO band was clearly observed in a spectrum measured at 1.3 GPa, corresponding to a symmetry-allowed splitting predicted for the  $Im\bar{m}2$  structure. Further compression of phase II caused polymerization of HCN molecules above 1.3 GPa.

Purpose of the present study is to clarify phase transition in solid HCN by Raman measurements at low temperature.

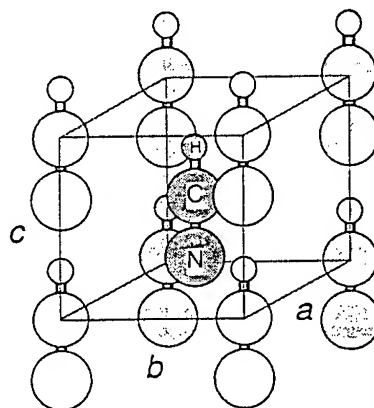


Figure 1 Crystal structure of HCN phase I or II: the  $ab$  base plane is a square for the phase I and a rectangle for the phase II.

## Experimental

Liquid HCN was prepared by reaction of NaCN with  $H_2SO_4$ . No peak from impurities was observed in its Raman and infrared spectra.

High pressure was generated with a gasketed diamond-anvil cell [4]. The cell was cooled with liquid nitrogen, and subsequently a drop of liquid HCN was fallen on the metal gasket. The liquid froze in the hole was quickly packed. Raman measurements was performed in a cryostat with optical windows by monitoring the cell temperature with chromel-alumel thermocouples. The pressure was determined from shift of ruby fluorescence lines.

Raman spectra were measured with a triple polychromator (SPEX 1877 Triplemate) with a CCD

detector. The 514.5 nm line of an argon-ion laser was used for excitation. The beam was focused to a spot of approximately 100  $\mu\text{m}$  on the sample. The spectral resolution was 1  $\text{cm}^{-1}$ . All measurements were made at  $90 \pm 1$  K.

## Results and Discussion

Raman spectra of HCN were taken up to 5 GPa at 90 K. All fundamental modes of phase II were observed: a C-H stretching, C $\equiv$ N stretching, H-C-N bending, and librational modes. Two bands, a longitudinal-optical (LO) and transverse-optical (TO) bands, were observed for H-C-N bending and librational modes. Librational bands measured at 0.1 GPa are shown in the bottom spectrum of Figure 2. According with a correlation diagram, the librational mode is expected to split into two components except TO-LO splitting in the phase II (*I*mm2 structure). However, no splitting of the librational mode by crystal field was observed as the previous Raman study[2].

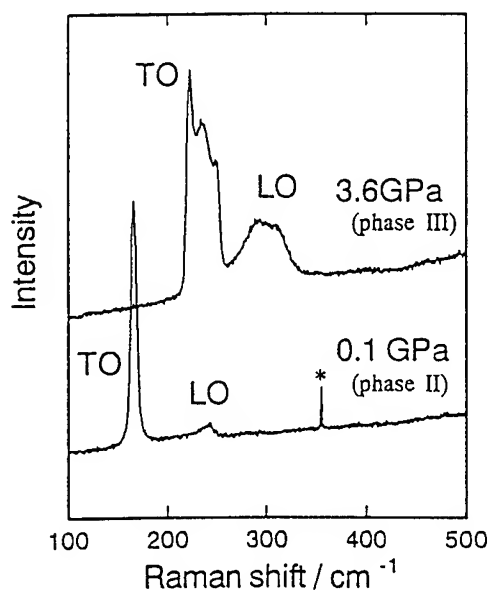


Figure 2 Raman spectra of HCN in the librational range for phase III at 3.6 GPa (top) and for phase II at 0.1 GPa (bottom). In the top spectrum, the librational TO mode splits into at least three peaks. A cosmic-ray line is marked with an asterisk(\*).

The librational TO mode showed gradual peak-splitting with increasing pressure; two peaks at 0.6 GPa and at least three peaks above about 2 GPa. Since the libration is expected to split into two components as a result of the crystal field in *I*mm2 structure, the observed splitting indicates appearance of a new crystalline phase (phase III).

The top spectrum in Figure 2 shows a typical spectrum in the librational region for the phase III measured at 3.6 GPa. Three peaks can be seen in the librational TO peak. The II-III transition is very sluggish, showing only gradual shift and splitting of the original TO peak. Other changes were not observed in association with the transition. These results suggest that the II-III phase transition is accompanied by very slight rearrangement of HCN molecules and characterized as a second order (like) transition.

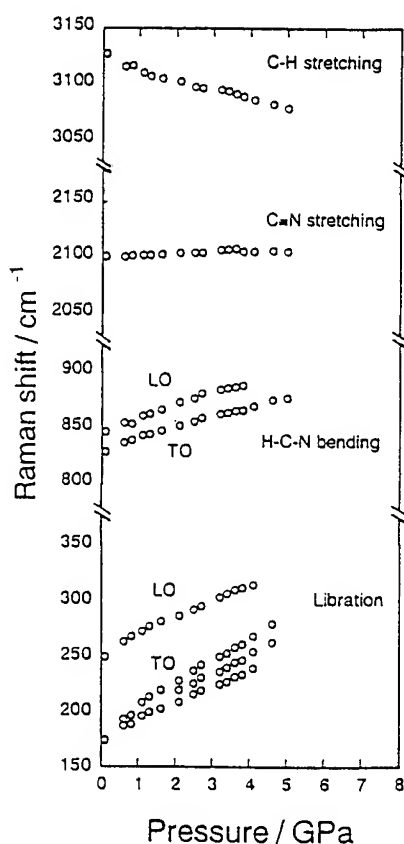


Figure 3 Pressure-dependence of Raman shifts of HCN. No discontinuous change of the frequency is found up to 5 GPa.



The pressure-dependence of Raman shifts is shown in Figure 3. The frequency of the C-H stretching band shifts to the lower frequency with pressure, in contrast to the other vibrational modes which show increase in frequency, indicating strengthening of the intrachain hydrogen bond. The rate of decrease about  $8 \text{ cm}^{-1}/\text{GPa}$  is close to that observed for the phase I at room temperature [3]. No discontinuous change of the frequency is found up to 5 GPa in the CH stretching vibration as well as in the other bands. Thus the linear chains formed by hydrogen bonded HCN molecules are maintained through the transition.

We consider the structural change associated with the II-III transition. The transition in HCN crystal can be described in terms of rearrangement of the linear molecular chains. In the I-II transition at 170 K and ambient pressure, for instance, the packing of molecular chains changes from a square to rectangle[1]. Hence it is naturally expected that the  $b/a$  ratio deviates from unity and increases to  $\sqrt{3}$  to form a close packing of linear chains as the pressure is increased in the phase II. However, such a deformation of the base plane does not cause lowering in the space group and hence gives rise to no peak splitting for the librational mode.

The translational sliding of molecular chain along  $c$ -axis is a likely candidate for the structural transition. In the unit cell of phase II, two HCN molecules are located at equivalent body center and corner positions as shown in Figure 1. If the central molecule was pushed up slightly parallel to the  $c$ -axis, the space group of the orthorhombic lattice lowers from  $Imm2$  to  $Pmm2$ . Two molecular positions become unequivalent to make the librational peak split into four bands by crystal field effects. This seems to be consistent with the observed splitting of the librational TO band. The spectrum at 3.6 GPa shows three peaks for the libration. One peak is missing probably due to its weak Raman intensity or still overlapping with the other peaks.

There has been argued for a long time about the molecular orientation in HCN crystals, that is, parallel or antiparallel configuration. The above discussion was based on the parallel configuration

of molecules in the adjacent chains (Figure.1). Several theoretical studies have revealed that there is some possibility for formation of antiparallel configuration, in which molecular chains arrange antiparallel to closest chains. If we assume such an antiparallel configuration for the phase II, the space group is assigned to  $Pmnn$  and the sliding displacement of centered molecules along the  $c$ -axis causes no change in the space group.  $Pmnn$  symmetry is maintained for such a speculated rearrangement of molecules, and consequently no splitting is expected for the libration. The present Raman results exclude the antiparallel configuration model, supporting the parallel orientation proposed by X-ray measurements[1] and some other calculation studies[5].

HCN molecules polymerized above 4 GPa at 90 K. The sample turned dark gradually and Raman intensities of all bands decreased. The infrared spectrum of the recovered sample well agreed with that of polymers prepared at high pressure and at room temperature, showing formation of cyclized polymers.

## Reference

- [1] W.J.Dulmage and W.N.Lipscomb, *Acta crystallogr.* **4**, (1951) 330.
- [2] B.Müller, H.D.Lutz, J.Hermeling, and E.Knözinger, *Spectrochim. Acta* **49** (1993) 191.
- [3] K.Aoki, B.J.Baer, H.C.Cynn, and M.Nicol, *Phys. Rev.* **B42**, (1990) 4298.
- [4] K. Aoki, Y. Kakudate, M. Yoshida, S. Usuba, K. Tanaka, and S. Fujiwara, *Jpn. J. Appl. Phys.* **26**, (1987) 2107.
- [5] (a)I. Panas, *Chem. Phys. Lett.* **194**, (1992) 239. (b)I. Panas, *Chem. Phys. Lett.* **201**, (1993) 255.

# PRESSURE-INDUCED TRANSFORMATIONS IN $A_2BX_4$ MOLECULAR IONIC SOLIDS

G. Serghiou, H. J. Reichmann and R. Boehler

*Max-Planck Institut f. Chemie, PF 3060, 55020 Mainz, Germany*

## ABSTRACT

High-pressure X-ray diffraction measurements show that  $Rb_2ZnCl_4$  and  $K_2ZnCl_4$  become amorphous in the 200-400 kbar regime, whereas isomorphous  $Cs_2ZnCl_4$  and  $K_2SeO_4$  remain crystalline to the highest pressures measured. This indicates that the tendency of  $A_2BX_4$  molecular ionic solids to amorphize depends predominantly on the ratio of the size of the anionic tetrahedral  $BX_4$  units to that of the interstitial  $A^+$  cations.

## Introduction

Pressure-amorphized solids offer the possibility of "ideal" amorphous solids since their structure is bounded by that of the ambient pressure crystal. A central question in the study of these crystalline to non-crystalline transitions is: "What basic structural feature of a crystal dictates its tendency to amorphize upon compression?" We address this question here for the case of  $A_2BX_4$  molecular ionic solids (fig. 1) through a comparative examination of the pressure-induced transformations of four isomorphs within this family, namely  $K_2ZnCl_4$ ,  $Rb_2ZnCl_4$ ,  $Cs_2ZnCl_4$  and  $K_2SeO_4$ . These systems essentially differ from each other via the ratios of the sizes of their  $BX_4$  units to that of their interstitial  $A^+$  cations; ( $ZnCl_4/K^+ = 1.70$ ,  $ZnCl_4/Rb^+ = 1.55$ ,  $ZnCl_4/Cs^+ = 1.35$ ,  $SeO_4/K^+ = 1.22$ ) (1,2,3).

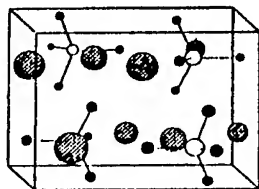


(Figure 1. A schematic of the structure of

$A_2BX_4$  molecular ionic crystals ( $A=K,Rb,Cs$ ;  $B=Zn,Se$ ;  $X=Cl,O$ ). The interstitial sites between the isolated tetrahedral units are filled with A cations (grey balls). The white balls represent B cations and the black balls designate X anions.)

## Experimental Procedures

The X-ray diffraction patterns were measured by Energy dispersive X-ray diffraction at the Hamburg Synchrotron source (HASYLAB) using a Germanium solid state detector.  $E_d$  was determined using a gold foil and ranged from 60 to 80 keV-Å. The amorphizations of  $K_2ZnCl_4$  and  $Rb_2ZnCl_4$  were observed using both (a) no medium (those shown here), and (b) in an argon medium. Pressure was applied using a diamond cell of our own design and was measured using the ruby calibration method, the diffraction lines of gold, or those of argon.

## Results and discussion

Our high pressure x-ray diffraction results (see fig. 2a,b) show that the x-ray patterns of  $\text{K}_2\text{ZnCl}_4$  and  $\text{Rb}_2\text{ZnCl}_4$  collapse at approximately 200 kbar and become completely x-ray amorphous in the 250-400 kbar regime. In contrast to this (see fig. 2c)  $\text{Cs}_2\text{ZnCl}_4$ , despite its intimate structural and chemical similarity to its two isomorphs, remains strongly crystalline to 570 kbar, the highest pressures measured. This behavior is also exhibited by  $\text{K}_2\text{SeO}_4$  which as seen in figure 2d remains crystalline to 580 kbar, the highest pressures attained. Moreover a more detailed examination of the pressure response of the four isomorphs shows the emergence of new peaks and the development of a halo-like feature caused by peak clustering, at pressures ranging from 33 kbar for  $\text{K}_2\text{ZnCl}_4$  to 139 kbar for  $\text{Cs}_2\text{ZnCl}_4$ . This is demonstrated here by the diffraction pattern of  $\text{Rb}_2\text{ZnCl}_4$  (fig. 2b) and the evolving halo-like feature at 102 kbar at  $\sim 27.5$  keV. For the case of the  $\text{Cs}_2\text{ZnCl}_4$  and  $\text{K}_2\text{SeO}_4$  structures this is a precursor pattern to that of a new phase since the high pressure patterns cannot be indexed in terms of the ambient pressure structure, whereas for  $\text{K}_2\text{ZnCl}_4$  and  $\text{Rb}_2\text{ZnCl}_4$  the high pressure phase is impeded resulting in intermediate amorphous phases. The transformations were hysteretically reversible.

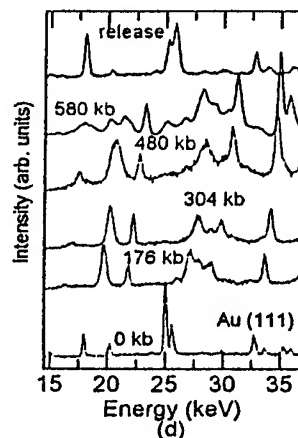
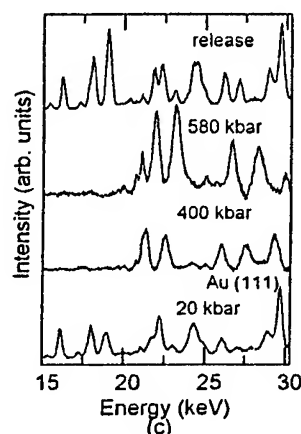
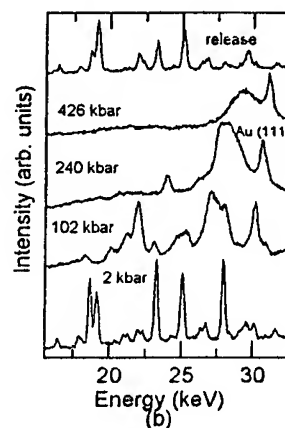
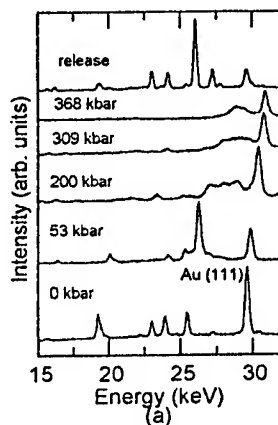


Figure 2. Energy dispersive x-ray diffraction measurements of  $\text{K}_2\text{ZnCl}_4$  (a),  $\text{Rb}_2\text{ZnCl}_4$  (b),  $\text{Cs}_2\text{ZnCl}_4$  (c) and  $\text{K}_2\text{SeO}_4$  (d), at various pressures. Pressure was measured using the equation of state of gold (shown), or Argon (not shown).

These results indicate that order-disorder transitions upon compression may not occur when crystals within this family have  $BX_4/A^+$  ratios below a certain value. These results are compatible with the already observed pressure-induced amorphizations of simpler " $BX_4$ " molecular solids (where  $B=Ge, Sn$  and  $X=I, Cl, Br$ ) where the interstitial sites between the  $BX_4$  units are empty (4). This in light of the present viewpoint implies a small or "0" value for the size of the  $A^+$  cation and hence a high tendency as observed experimentally to amorphize upon compression.

**Acknowledgements.** We thank J. Otto for invaluable assistance and G.S. also thanks A. Zerr for advice.

## References

1. I. Etxebarria, J. M. Perez-Mato and A. Criado, *Phys. Rev. B* **42** (1990) 8482.
2. A. Kalman, J. S. Stephens and D. W. J. Cruickshank, *Acta Cryst.* **B26** (1970) 1451.
3. M. Quilchini and J. Pannetier, *Acta Cryst.* **B39** (1983) 657.
4. Y. Fujii, M. Kowaka and A. Onodera, *J. Phys. C* **18** (1985) 789; A. L. Chen, P. Y. Yu and M. P. Pasternak, *Phys. Rev B* **44**, (1991) 2883.

## New Structural Transition of Oxygen at 96 GPa

Y. AKAHAMA and H. KAWAMURA

*Faculty of Science, Himeji Institute of Technology, Kamigohri, Hyogo, 678-12 Japan*

D. HÄUSERMANN and M. HANFLAND

*European Synchrotron Radiation Facility, B.P. 220, F-38043, Grenoble, France*

O. SHIMOMURA

*Photon Factory, National Laboratory for High Energy Physics, Tsukuba, Ibaraki, 305 Japan*

### ABSTRACT

By using a high-energy and high-brilliance synchrotron radiation source in ESRF and PF, an angle-dispersive powder x-ray diffraction study of solid oxygen has been carried out up to 116 GPa at room temperature. A new high-pressure structural transition was observed at 96 GPa. Metallization of oxygen reported by S. Desgreniers, Y. K. Vohra, and A. L. Ruoff is ascribed to the transition.

### Introduction

Metallization and molecular dissociation of homonuclear molecular solids of light elements,  $H_2$ ,  $N_2$  and  $O_2$  have attracted special interest of high-pressure scientists. Recently, for solid  $O_2$  Drude type metallic behavior has been observed in reflectivity spectra above 95 GPa by S. Desgreniers, Y. K. Vohra and A. L. Ruoff<sup>1</sup>. They have concluded that a transformation to a nearly free electron state takes place in solid oxygen.

Since the first observation of dramatic color changes at pressures on the order of 10 GPa in solid oxygen<sup>2</sup>, a great deal of structural and optical studies concerned with the high-pressure phases have been reported. The structures of three high-pressure phases at room temperature have been determined by single crystal x-ray diffraction experiments to be  $R\bar{3}m$  for  $\beta$ - $O_2$  at 5.5 GPa<sup>3,4</sup>,  $Fmmm$  for  $\delta$ - $O_2$  at 9.6 GPa<sup>4</sup> and monoclinic for  $\epsilon$ - $O_2$  at 19.7 GPa<sup>5,6</sup>. The stability of the  $\epsilon$ - $O_2$  phase up to 61 GPa at room temperature has been observed in an energy-dispersive x-ray diffraction experiment<sup>7</sup>. Optical studies of absorption spectra<sup>8</sup> and infrared and Raman spectra<sup>9,10</sup> have suggested the presence of a strong intermolecular force between  $O_2$  molecules in the  $\epsilon$ - $O_2$  phase.

The aim of this study is to research pressure-induced metallization and molecular dissociation of solid  $O_2$  from a structural aspect. We have performed high-pressure powder x-ray diffraction experiments up to 116 GPa.

### Experimental

A DAC was used for high-pressure generation. Diamond anvils had a top surface diameter of 300  $\mu m$ , a bevel angle of 7 deg. and a culet diameter of 400  $\mu m$ . Liquid oxygen was loaded into a 150  $\mu m$  diameter hole of a metal gasket(U-700) in the DAC at a low temperature of 77 K. Pressure was increased at room temperature and measured by the quasihydrostatic ruby scale<sup>11</sup>.

X-ray diffraction experiments were carried out by an angle-dispersive method using an image-plate detector up to 116 GPa. High-brilliance synchrotron radiation(SR) from BL3 in the European Synchrotron Radiation Facility(ESRF) and from BL16A and BL6-B in the Photon Factory(PF), National Laboratory for High Energy Physics, which was monochromated to a wavelength, was used with remarkable success to obtain high-quality powder patterns of oxygen at megabar pressure region. Detailed descriptions of SR experimental system and image integration software in ESRF<sup>12</sup> and PF<sup>13</sup> have been given elsewhere.

### Results and Discussion

Figure 1 illustrates the pressure variation in the powder diffraction patterns of oxygen at room temperature. Patterns at pressures lower than 88 GPa, which come from the  $\epsilon$ - $O_2$  phase and have six reflections, exhibit a monotonic high-angle shift with in-

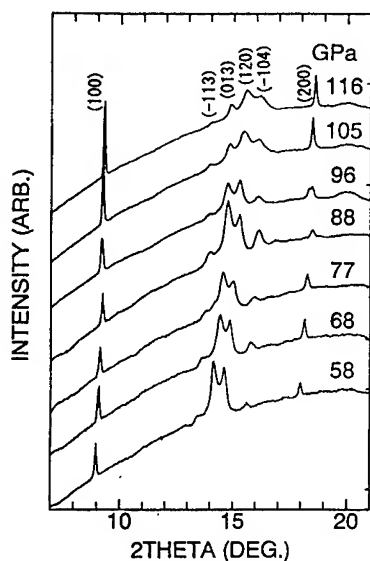


Fig.1 Pressure variation in x-ray diffraction profiles for solid oxygen at room temperature up to 116 GPa. This was obtained with a monochromated beam of  $\lambda=0.4817$  Å in ESRF. Lines of a new high-pressure phase were assigned to the same unit cell as  $\epsilon$ -O<sub>2</sub>.

creasing pressure up to 88 GPa. Though the diffraction images indicated a strong preferred orientation, the reflections were well assigned to a monoclinic lattice reported by D. Schiferl et al.<sup>5</sup>

A structural transition was observed around 96 GPa. A new reflection occurs at close quarters to the (200) reflection of the  $\epsilon$ -O<sub>2</sub> phase around  $2\theta=18.5^\circ$ . In Fig.2, the pressure dependence of the d-value for each line is shown up to 116 GPa. It is clear from the dependence that the structural phase transition occurs around 96 GPa. The number of observed diffraction lines in the new high-pressure phase is the same as those for  $\epsilon$ -O<sub>2</sub>, and the change in the d-value for each line at the transition is very slight.

The observed diffraction lines of the  $\epsilon$ -O<sub>2</sub> phase were well interpreted by assuming a monoclinic unit cell as reported by D. Schiferl et al.<sup>5</sup>, and the lattice constants were obtained at each pressure. The index of each line was also satisfied by an extinction rule for the base-centered lattice(A2/m) proposed by W. Johnson et al.<sup>6</sup>. On the other hand, the lines were not assigned to an orthorhombic unit cell proposed previously<sup>7,14</sup> within our experimental accuracy (typical value is  $\pm 0.003$  Å).

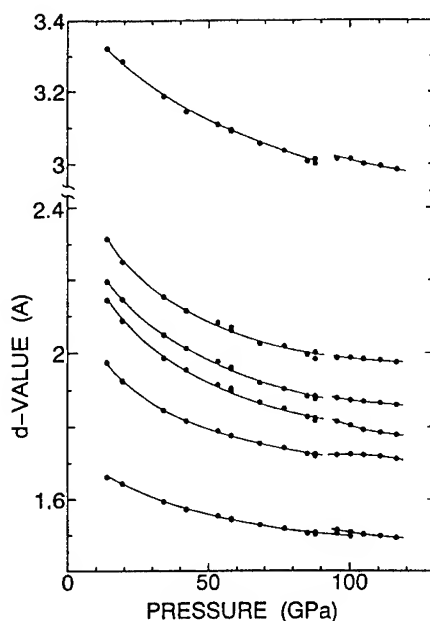


Fig.2 Pressure dependence of d-values for solid oxygen up to 116 GPa. This indicates a new structural phase transition at 96 GPa.

Six diffraction lines in the new high-pressure phase( $\zeta$ -O<sub>2</sub>) were also explained as the same monoclinic lattice as the  $\epsilon$ -O<sub>2</sub> phase although the patterns at 96 and 101 GPa could not be assigned due to coexistence of the  $\epsilon$ -O<sub>2</sub> and  $\zeta$ -O<sub>2</sub> phases.

Figure 3 represents the pressure dependence of the lattice constants in the  $\epsilon$ -O<sub>2</sub> and the  $\zeta$ -O<sub>2</sub> phases normalized by the values ( $a_0=3.699$  Å,  $b_0=5.617$  Å and  $c_0=7.953$  Å) at 13.7 GPa. Lattice constants in the  $\epsilon$ -O<sub>2</sub> phase exhibit monotonic pressure dependence, while the monoclinic angle,  $\beta$ , was almost constant at  $116^\circ$  within  $\pm 0.5^\circ$ . The dependence indicates a strong anisotropy of compressibility. The lattice constant,  $b$ , contracts twice as much as the lattice constant,  $a$ . Discontinuity of lattice constants is found in Fig.3 corresponding to the structural transition at 96 GPa. Lattice constants,  $a$  and  $c$ , elongate by about 0.7% of the values at 96 GPa and  $b$  contracts by about 1.4%.

The molar volume was calculated by assuming that the monoclinic unit cell contains 8 oxygen molecules. The volume reduction of the  $\delta$ - $\epsilon$  phase transition was estimated to be 0.6–0.8 cm<sup>3</sup>/mole by extrapolating the smooth fitted data to the phase

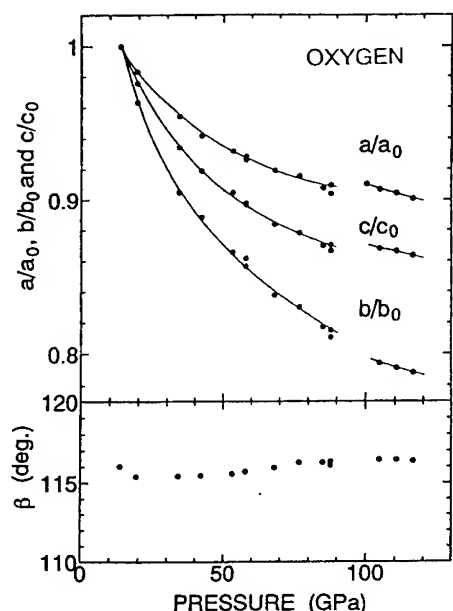


Fig.3 Pressure dependence of lattice constants,  $a$ ,  $b$ ,  $c$  and  $\beta$ , of a monoclinic unit cell for the  $\epsilon$ - and  $\zeta$ - $O_2$  phases. Values are normalized by those of  $\epsilon$ - $O_2$  at 13.7 GPa.

boundary. The value corresponds to 5–6% of the volume of the  $\delta$ - $O_2$  phase just before the transition ( $-\Delta V/V_B$ ). The volume reduction of the new high-pressure phase transition from  $\epsilon$ - to  $\zeta$ - $O_2$  was smaller than 0.1 cm<sup>3</sup>/mole ( $-\Delta V/V_B < 1.4\%$ ) and was difficult to estimate by extrapolation. It seems that the volume reduction is too small compared with that expected in molecular dissociation. The molar volume at the highest pressure of 116 GPa in this study was 6.83 cm<sup>3</sup>/mole, which corresponds to 0.47 of 14.44 cm<sup>3</sup>/mole of the  $\beta$ - $O_2$  phase at 5.9 GPa<sup>3</sup>.

From visual observation under a metallurgical microscope, we saw that the appearance of the oxygen sample has become as shinier as the metal gasket after the structural transition at 96 GPa. This behavior has also been observed by Desgreniers *et al.*<sup>1</sup>. They have reported that at an approximate pressure of 95 GPa, an increase in the near-infrared reflectivity is observed. This was attributed to the onset of creation of a nearly free electron by a pressure-induced band overlap. Because the metallization is accompanied by the structural transition, the band gap may close discontinuously.

## Conclusion

Powder x-ray diffraction experiments with oxygen were performed up to 116 GPa at room temperature, and a structural transition was observed at 96 GPa. The structural change was slight and not drastic as expected in molecular dissociation. The results suggested that in the newly observed high-pressure phase ( $\zeta$ - $O_2$ ), oxygen molecules do not dissociate; that is, the phase is in a molecular metallic state.

## Acknowledgements

This work was financially supported by a Grant-in-Aid for Scientific Research (07454069), (07454154) from the Ministry of Education Science and Culture, Japan.

## References

1. S. Desgreniers, Y. K. Vohra and A. L. Ruoff, *J. Phys. Chem.* **94**(1990)1118.
2. M. Nicol, K. R. Hirsch and W. B. Holzapfel, *Chem. Phys. Lett.* **68**(1979)49.
3. H. d'Amour, W. B. Holzapfel and M. Nicol, *J. Phys. Chem.* **85**(1981)130.
4. D. Schiferl *et al.*, *Acta Cryst.* **B39**(1983)153.
5. D. Schiferl, S. W. Johnson, and A. S. Zinn, *High Pressure Research* **4**(1990)293.
6. S. W. Johnson *et al.*, *J. Appl. Cryst.* **26**(1993)320.
7. A. L. Ruoff and S. Desgreniers, in *Molecular Systems under High Pressure*, ed. R. Pucci and G. Piccitto (Elsevier, Amsterdam, 1991), pp. 123.
8. M. Nicol and K. Syassen, *Phys. Rev.* **B28** (1983)1201.
9. K. Syassen and M. Nicol, in *Physics of Solids under Pressure*, ed. J. S. Schilling and R. N. Shelton (North-Holland, 1981), pp. 33.
10. S. F. Agnew *et al.*, *J. Chem. Phys.* **86**(1987) 5239.
11. H. K. Mao, J. Xu and P. M. Bell, *J. Geophys. Research* **91**(1986)4673.
12. R. O. Piltz *et al.*, *Rev. Sci. Instrum.* **63**(1992)700.
13. O. Shimomura *et al.*, *Rev. Sci. Instrum.* **63** (1992)967.
14. B. Olinger *et al.*, *J. Chem. Phys.* **81**(1984)5068.

# CRYSTALLINE STRUCTURE of the HIGH DENSITY $\epsilon$ PHASE of SOLID O<sub>2</sub>

Serge DESGRENIERS

*Institut de Physique Ottawa-Carleton, Université d'Ottawa, Ottawa, Canada.*

Keith E. BRISTER

*CHESS, Wilson Laboratory, Cornell University, Ithaca NY, USA.*

At room temperature, solid oxygen is known to undergo a pressure-induced phase transition from  $\delta$ -O<sub>2</sub> to  $\epsilon$ -O<sub>2</sub> at around 10 GPa. Although the structure of  $\delta$ -O<sub>2</sub> has been well characterized ( $Fmmm$ ,  $Z=4$ ), the proposal for the structure of  $\epsilon$ -O<sub>2</sub> has yet to be confirmed and refined. This paper presents the results of angle-dispersive X-ray diffraction experiments using synchrotron radiation on polycrystalline  $\epsilon$ -O<sub>2</sub> samples. As suggested earlier by Johnson *et al.*, the structure is well described by the  $A/2m$  monoclinic space group with the following measured lattice parameters at  $12.5 \pm 0.1$  GPa and  $297 \pm 3$  K:  $a = 3.688$  Å,  $b = 5.621$  Å,  $c = 7.944$  Å and  $\beta = 116.7^\circ$ . From various X-ray diffraction measurements, we calculate an equation of state for  $\epsilon$ -O<sub>2</sub> to high pressures. Samples grown in a diamond anvil cell show inevitably strong preferred orientations, making difficult a complete Rietveld analysis of their diffraction patterns.

## 1 Introduction

At room temperature, oxygen solidifies at 5.5 GPa in a phase,  $\beta$ -O<sub>2</sub> ( $R\bar{3}m$ ), stable to 9.6 GPa, at which pressure a transition takes place to a phase labelled as  $\delta$ -O<sub>2</sub> ( $Fmmm$ ). A third phase has also been observed beyond 10 GPa:  $\epsilon$ -O<sub>2</sub>. Recent experiments have established the stability of the  $\epsilon$ -O<sub>2</sub> phase to high pressures, first to 62 GPa<sup>1</sup> and then up to 96 GPa<sup>2</sup>, where noticeable changes in the diffraction pattern were recorded. Incidentally, these changes, indicative of a different phase, occur in the pressure range where indications of metallization has been previously reported<sup>3</sup>. In spite of several attempts<sup>4,1,5</sup>, the definite structure of  $\epsilon$ -O<sub>2</sub> has yet to be determined. In this paper, we present a preliminary analysis of angle-dispersive X-ray diffraction of an  $\epsilon$ -O<sub>2</sub> sample, recorded using high flux monochromated synchrotron radiation.

## 2 Experimental

The solid oxygen sample was obtained in a modified Merrill-Bassett diamond anvil cell (DAC) starting from 99.99% pure O<sub>2</sub> in the liquid phase. The  $\epsilon$ -O<sub>2</sub> phase was grown in the required pressure field according to the phase diagram<sup>3</sup>. The purity of the  $\epsilon$ -O<sub>2</sub> sample was ascertained from the X-ray diffraction pattern as well as the frequency of the Raman-active molecular stretching mode<sup>6</sup>.

Angle dispersive X-ray diffraction (ADX) was performed at the F2 station (24-pole wiggler) of the Cornell High Energy Synchrotron Source, with sagittally and vertically focussed radiation at 0.4908 Å from a Si(111) monochromator. ADX images were recorded at room temperature on FUJI image plates, digitized by a FUJI BAS2000 scanner and later analyzed by IPA<sup>7</sup> (i.e., visualization, calibration, plate orientational correction, scanner file correction, and  $2\theta$ -profile generation). XRDA<sup>8</sup> was used for peak profile and structure fittings. Rietveld refinements were those of DBWS9411<sup>9</sup>.

## 3 Results and Discussion

At  $12.5 \pm 0.1$  GPa, measured by the pressure-shifted R<sub>1</sub>-line of Al<sub>2</sub>O<sub>3</sub>:Cr<sup>3+</sup> fluorescence, the entire sample was in the  $\epsilon$ -O<sub>2</sub> phase and showed the usual reddish color and high polycrystallinity. As mentioned before by other authors<sup>4,3,1</sup> but never well documented, polycrystalline  $\epsilon$ -O<sub>2</sub> sample show inevitably strong preferred orientation. As seen in Figure 1, the recorded Debye rings of our  $\epsilon$ -O<sub>2</sub> sample show strong azimuthal (i.e. along the ring) intensity variations, indicating sample texture. Rietveld refinements of the structure have been so far inconclusively conducted using only one preferred orientation. In fact, it is believed that crystallites in the sample are oriented on average along at least two preferred directions. Optical



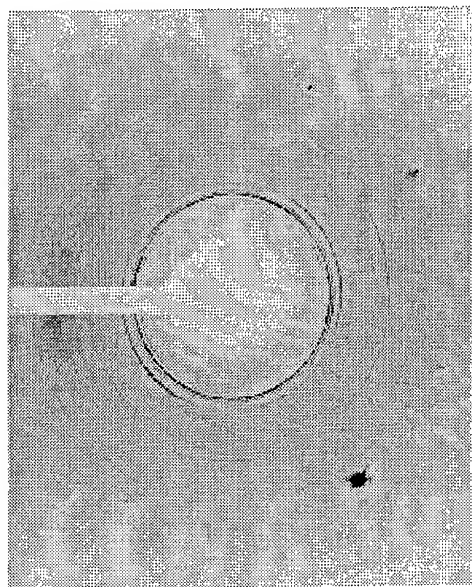


Figure 1: Debye rings of  $\epsilon$ -O<sub>2</sub> at 12.5 GPa recorded on an image plate. Although the background is high, the image clearly indicates preferred orientation, as discussed in the text.

studies<sup>6,3</sup> have shown the anisotropy of  $\epsilon$ -O<sub>2</sub> and a stacking of planes in which oxygen molecules are in parallel alignment has been proposed<sup>10</sup>. Consequently, one has to expect  $\epsilon$ -O<sub>2</sub> to present texture effects.

The  $2\theta$  profile at  $12.5 \pm 0.1$  GPa, derived from the ADXD image recorded and shown in Figure 2, comprises many reflections found to fit very well a monoclinic structure with the lattice parameters given in Table 1. Our results for the lattice parameters are in very good agreement with those reported by Johnson *et al.*<sup>5</sup> for a sample at 19.7 GPa and 297 K. Table 2 lists the observed d-spacings along with the calculated differences according to the lattice parameters of Table 1. Based on absent reflections, the space group proposed by Johnson *et al.*<sup>5</sup>, namely the base-centered  $A2/m$  with  $Z=8$ , is likely the right one.

Finally, based on the present result, data points obtained by Ruoff and Desgreniers<sup>1</sup>, Johnson *et al.*<sup>5</sup>, and Akahama *et al.*<sup>2</sup>, the pressure dependence of the molar volume of  $\epsilon$ -O<sub>2</sub> is fitted to a third-order equation of state with  $B_0 = 31.1$  GPa,  $B'_0 = 4.3$  and an extrapolated  $V_{0GPa} = 14.8$  cm<sup>3</sup>/mole. It should be noted that this equation of state is in agreement with that proposed by Ruoff and Desgreniers<sup>1</sup>.

Table 1: Lattice parameters of  $\epsilon$ -O<sub>2</sub> at  $12.5 \pm 0.1$  GPa.

a	$3.688 \pm 0.012$ Å
b	$5.621 \pm 0.011$ Å
c	$7.944 \pm 0.011$ Å
$\beta$	$116.7 \pm 0.1^\circ$

Table 2: Observed reflections and observed d-spacings and calculated d-spacing differences of monoclinic  $\epsilon$ -O<sub>2</sub> at  $12.5 \pm 0.1$  GPa.

(hkl)	$2\theta_{obs}$ (°)	$d_{obs}$	$d_{obs}-d_{calc}$
011	6.390	4.4033	-0.0026
002	9.951	3.5397	-0.0074
100	8.550	3.2925	-0.0010
$10\bar{2}$	8.644	3.2565	0.0059
$11\bar{1}$	9.131	3.0829	-0.0003
020	10.082	2.7927	-0.0180
022	12.800	2.2015	-0.0015
013	12.874	2.1889	0.0092
$12\bar{2}$	13.248	2.1274	0.0013
102	13.987	2.0155	0.0103
$10\bar{4}$	14.269	1.9758	-0.0004
$12\bar{3}$	15.004	1.8796	-0.0033
$11\bar{4}$	15.159	1.8605	-0.0039
031	15.571	1.8116	-0.0001
004	15.906	1.7736	0.0000
$13\bar{1}$	16.900	1.6700	-0.0005
200	17.135	1.6473	0.0006
$12\bar{4}$	17.457	1.6171	0.0004
103	17.575	1.6053	-0.0021
113	18.299	1.5433	-0.0033
131	18.562	1.5165	0.0010
024	18.781	1.5041	0.0042
033	19.232	1.4691	0.0005
$22\bar{4}$	20.108	1.4057	-0.0013
$23\bar{2}$	21.445	1.3190	0.0048
140	21.885	1.2928	0.0002
222	24.153	1.1729	0.0016
$14\bar{4}$	24.731	1.1459	0.0006
203	25.005	1.1336	0.0003

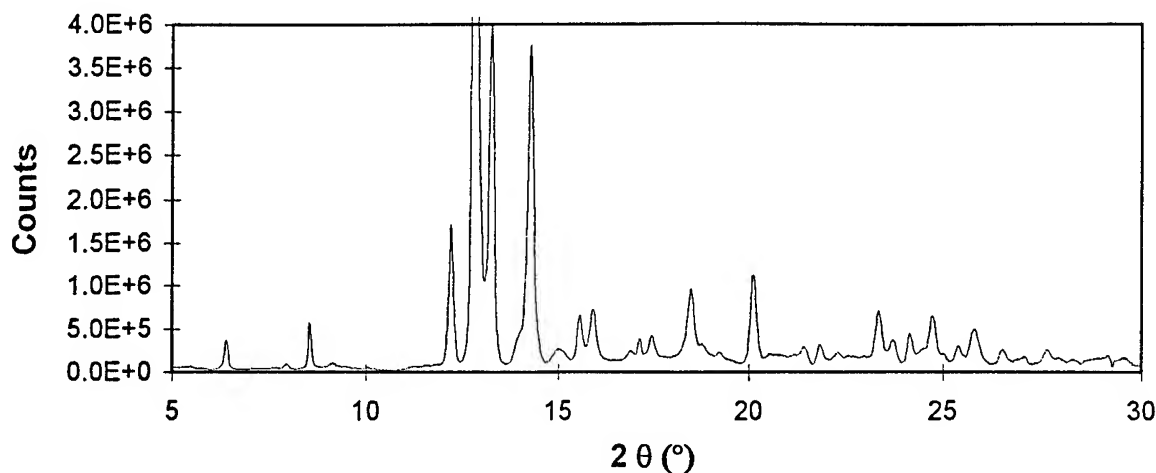


Figure 2: ADXD pattern of  $\epsilon$ -O<sub>2</sub> recorded at  $12.5 \pm 0.5$  GPa. This pattern has been obtained from the integration of nearly complete Debye rings recorded on an image plate and an appropriate background subtraction.

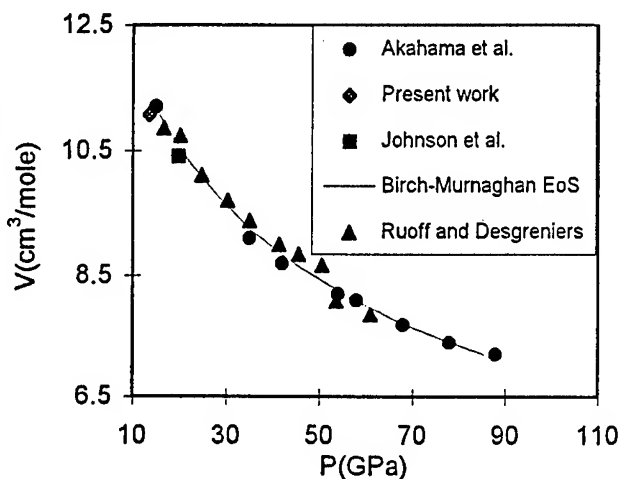


Figure 3: Room temperature equation of state of  $\epsilon$ -O<sub>2</sub>. The solid line represents a fit to the Birch-Murnaghan equation of state with  $B_0 = 31.1$  GPa,  $B'_0 = 4.3$  and  $(V/V_0)_{0\text{GPa}} = 0.61$ , where  $24.21\text{cm}^3/\text{mole}$ , the molar volume at the gas-liquid-solid triple point, was used as  $V_0$ .

#### 4 Summary

From X-ray diffraction images recorded on image plates using synchrotron radiation, solid oxygen is found to present pronounced texture in the  $\epsilon$ -O<sub>2</sub> phase, at 12.5 GPa and room temperature. The X-ray diffraction pattern is that of a monoclinic structure of space group  $A2/m$  with  $Z=8$ . An equation of state is reported using all high pressure data reported so far for monoclinic  $\epsilon$ -O<sub>2</sub>.

#### Acknowledgments

We acknowledge the help of the entire CHESS Staff. This work was financially supported by NSERC of Canada.

#### References

1. A. L. Ruoff and S. Desgreniers. In *Molecular Systems at High Pressure*, R. Pucci and G. Picitto, editors, Elsevier Science Publishers, 1991.
2. Y. Akahama, H. Kawamura, D. Hausermann, M. Hanfland, and O. Shimomura. *Phys. Rev. Lett.*, **74**, 4690 (1995).
3. Serge Desgreniers, Yogesh K. Vohra, and Arthur L. Ruoff. *J. Phys. Chem.*, **94**, 1117 (1990).
4. Bart Olinger, R. L. Mills, and R. B. Roof Jr. *J. Chem. Phys.*, **81**, 5068 (1984).
5. S. Johnson, M. Nicol, and D. Schiferl. *J. Appl. Cryst.*, **26**, 320 (1993).
6. Malcolm Nicol and Karl Syassen. *Phys. Rev. B*, **28**, 120 (1983).
7. K. Lagarec and S. Desgreniers. In *CHESS Users's Meeting 1995*, CHESS, Cornell University, 1995.
8. Serge Desgreniers and Ken Lagarec. *J. Appl. Cryst.*, **27**, 432 (1994).
9. A. Sakthivel and R. A. Young. User's Guide to DBWS9411. School of Physics, Georgia Institute of Technology, 1994.
10. S. F. Agnew, B. I. Swanson, and L. H. Jones. *J. Chem. Phys.*, **86**, 5239 (1987).

# HIGH PRESSURE STUDY OF ICES VII AND VIII USING SYNCHROTRON X-RAY DIFFRACTION

E. WOLANIN, Ph. PRUZAN, J.C. CHERVIN, B. CANNY and M. GAUTHIER

*Physique des Milieux Condensés  
Université P. et M. Curie, B 77,  
4, place Jussieu, F-75252 Paris, Cedex 05, France*

D. HÄUSERMANN, M. HANFLAND

*ESRF  
BP 220, F-38043 Grenoble Cedex, France*

## ABSTRACT

Using a powder x-ray diffraction technique the equation of state of ice VII corrected from uniaxial stress component was determined up to 102 GPa. Preliminary results were obtained on ice VIII at 180 K up to 24 GPa. Data on ice VII are discussed using the universal equation of state of Vinet.

## Introduction

Above 2.1 GPa only two solid forms are known for ice ; - ice VII, which is cubic and proton disordered, is stable above 270 K at 2.1 GPa - ice VIII, which is tetragonal and proton ordered, is stable below this temperature.<sup>(1)</sup> Recently the VII-VIII transition line was determined by Raman scattering ; the pressure dependence of the transition temperature  $T_c$  has strong similarities with what is observed in ferroelectric H-bonded compounds of the  $\text{KH}_2\text{PO}_4$  type.<sup>(2)</sup> For data treatment and understanding of the physical behavior of ice at very high pressure, specifically the search of a symmetrical H-bonded solid, structural and volume data are of fundamental importance. Till now only the equation of state (EOS) of ice VII has been determined at 300 K<sup>(3)</sup> and, apart recent measurement in the 2-10 GPa range obtained with neutron

diffraction,<sup>(4)</sup> the EOS of ice VIII is not known.

This work is part of a systematic x-ray study of ice undertaken at 300 K and at low temperature. The aim concerning the reinvestigation of ice VII was to obtain various x-ray peaks in order to estimate the uniaxial stress component and consequently improve the EOS accuracy. A very good accuracy is required at very high pressure (above 100 GPa) but also in the 10-70 GPa pressure range where higher-order phase transitions are expected.<sup>(5,6)</sup>

## Experimental

The high pressure cells used were a membrane diamond anvil cell (DAC) with a 2 x 28° x-ray aperture<sup>(7)</sup> and a Diacell (DXR-5) with a 2 x 45° x-ray aperture. For low temperature measurements the membrane DAC was placed in a cryostat<sup>(8)</sup> equipped with

mylar and capton windows. High-pressure powder-diffraction was performed with an angle-dispersive technique on station BL3 ID9 at ESRF (Grenoble, F) with an imaging plate detector. Close to the DAC the beam was collimated to  $50 \times 50 \mu\text{m}$  by appropriate slits.

Runs were performed with tridistilled  $\text{H}_2\text{O}$  and 99.80 % isotopic purity  $\text{D}_2\text{O}$  (from Euriso-top, CEA). The pressure was determined from the shift of the ruby luminescence R1 line, corrected from the temperature dependence of the zero pressure R1 wave number.<sup>(8)</sup>

## Results and data treatment

At room temperature (293 K) three runs were performed on  $\text{H}_2\text{O}$ , the upper pressure reached was 102 GPa, and two runs on  $\text{D}_2\text{O}$  up to 58 GPa. At 176 K preliminary results on  $\text{H}_2\text{O}$  VIII were obtained up to 24 GPa.

Depending on the x-ray aperture of the DAC, several peaks were observed in ice VII among which 110, 111, 200 and 211. Above 18 GPa, the 111 diffraction peak, assigned to the hydrogen atoms, became too faint to be observed. At each experimental pressure point data, the cell parameter computed from these various diffraction lines exhibits systematic differences. This effect is due to the presence of a uniaxial stress component (USC) involved by the compression system. In order to estimate the USC and to propose a corrected EOS, we used the formula of Singh and Balasingh<sup>(9)</sup> applying for the diffraction geometry of a cubic system compressed in a DAC (parallel geometry).

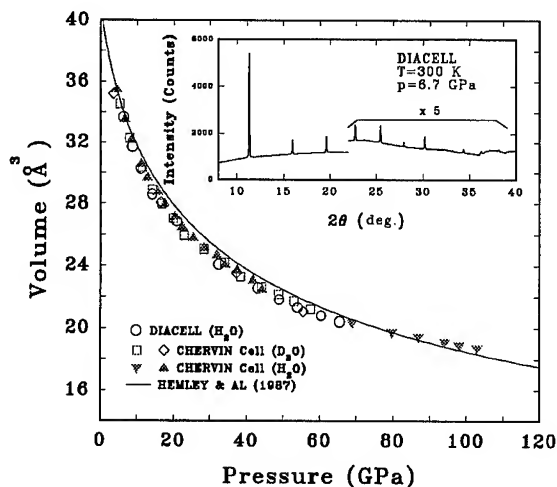


fig. 1 : corrected unit cell volume vs corrected (hydrostatic) pressure

The knowledge of the  $c_{ij}$  elastic coefficients vs pressure and the room pressure lattice parameter  $a_0$  are required. The former information up to  $\sim 7$  GPa is now available from Shimizu *et al.*<sup>(10)</sup> We have assumed that the  $c_{ij}$  coefficients vary linearly with pressure up to 100 GPa. The room pressure lattice parameter  $a_0$  was taken to be  $3.44 \text{ \AA}$  as indicated by the low pressure extrapolation of the Hemley *et al* EOS. At each pressure the hydrostatic cell parameter and the USC were obtained. The USC was found around 10 % of the measured pressure. The correction applied to the measured pressure was one third of USC. The computed cell volume, as a function of corrected pressure from the USC, is plotted in Fig. 1. Within the experimental errors, the corrected data for  $\text{D}_2\text{O}$  VII exhibit no difference with  $\text{H}_2\text{O}$  VII at least up to 58 GPa, the upper pressure for  $\text{D}_2\text{O}$  runs. Presently the relationships for the USC corrections are only available for cubic systems.

For tetragonal ice VIII we assumed to have the same pressure correction as for ice VII. Compared to ice VII, ice VIII results, at 176 K and up to 24 GPa, show a slightly stiffer behavior.

A least square fit to a Birch-Murnaghan equation of state of our ice VII corrected data gives  $B_1 = 5.42$  and  $a_0 = 3.45 \text{ \AA}$ , with  $B_0 = 14.9 \text{ GPa}$  from Shimizu *et al.*<sup>(10)</sup>

## Discussion

Our data show some differences with the EOS of Hemley *et al* : ice VII appears softer in the 10-40 GPa pressure range and stiffer above 80 GPa. From the pressure dependence of the VII-VIII transition temperature, higher-order transitions are expected around 18 and 60 GPa respectively.<sup>(5,6)</sup> One of the goals of the present work was to check this assumption. Actually our data (Fig. 1) exhibit a smooth behavior with no indication of regime change of the compressibility pressure dependence in narrow pressure ranges. To proceed further in the search of phase changes in our ice VII data, we used a method based on the universal EOS of Vinet *et al*<sup>(11)</sup> : for a solid with no phase transition, the quantity  $\ln H(x)$  is a linear function of  $1-x$ , where  $x = a/a_0$  and  $H(x) = p(x)x^2 / 3(1-x)$ , where  $a$  is the cell parameter at the pressure  $p$ . This method was previously used by Hama for the treatment of the Hemley *et al* data.<sup>(12)</sup> Results of our analysis are plotted in Fig. 2. They suggest two phase changes at respectively  $\sim 15$  and  $66 \text{ GPa}$ . This finding supports the conclusions obtained from the analysis of the VII-VIII transition line : three pressure

domains are expected for the proton disordering in ice VII.

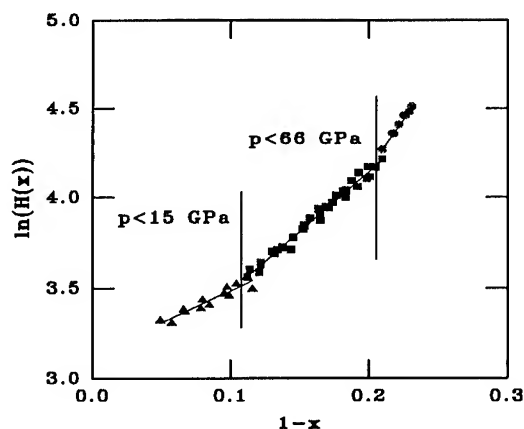


fig.2 : Treatment of our ice VII data;  
 $\ln(H(x))$  vs  $(1-x)$

## References

1. W.F. Kuhs, J.L. Finney, C. Vettier, and D.V. Bliss, J. Chem. Phys. **81** (1984) 3612.
2. Ph. Pruzan, J.C. Chervin, and B. Canny, J. Chem. Phys. **99** (1993) 9842.
3. R.J. Hemley, A.P. Jephcoat, H.K. Mao, C.S. Zha, L.W. Finger, and D.E. Cox, Nature **330** (1987) 737.
4. J.M. Besson, Ph. Pruzan, S. Klotz, G. Hamel, B. Silvi, R.J. Nelmes, J.S. Loveday, R.M. Wilson, and S. Hull, Phys. Rev.B **49** (1994) 12540.
5. Ph. Pruzan, J. Mol. Struct. **322** (1994) 279.
6. Ph. Pruzan, J.C. Chervin, and B. Canny. Proceedings of the XIVth Int. Conf. on Raman Spectroscopy. N.T. Yu and X.Y. Li Ed. John Wiley (1994) 1048.
7. J.C. Chervin, B. Canny, J.M. Besson, and Ph. Pruzan, Rev. Sci. Instrum. **66** (1995) 2595.
8. J.C. Chervin, B. Canny, M. Gauthier, and Ph. Pruzan, Rev. Sci. Instrum. **64** (1993) 203.
9. A.K. Singh and C. Balasingh, J. Appl. Phys. **48** (1977) 5338.
10. H. Shimizu, M. Ohnishi, S. Sasaki, and Y. Ishibashi, Phys. Rev. Lett. **74** (1995) 2820.
11. H. Schlosser and J. Ferrante, J. Phys. Chem. Solids **52** (1991) 635.
12. J. Hama, and K. Suito, Physics Letters A **187** (1994) 346.

## NEUTRON SPECTROSCOPY OF ICE III

I.NATKANIEC<sup>#@</sup>, L.S.SMIRNOV<sup>#</sup>, A.I.KOLESNIKOV<sup>&</sup>, A.N.IVANOV<sup>\*</sup>

<sup>#</sup>-Frank Laboratory of Neutron Physics, JINR, 141980 Dubna, RUSSIA,

<sup>@</sup>-on leave from: H. Niewodniczanski Institute of Nuclear Physics, 31-342 Krakow, Poland,

<sup>&</sup>-Institute of Solid State Physics RAS, 142432 Chernogolovka, RUSSIA,

<sup>\*</sup>-Vereshchagin Institute for High Pressure Physics RAS, 142902 Troitsk, RUSSIA

### ABSTRACT

The amplitude-weighted phonon density of states  $G(E)$  of ice III, measured *in situ* by inelastic incoherent neutron scattering is presented. The obtained  $G(E)$  of ice III matches the general behaviour of the Ih and II ice phases: with increasing density, the first maximum of the translational band shifts to higher energies, and the low energy cutoff of the librational band shifts to lower energies.

### Introduction

The region where ice III exists on the p-T equilibrium phase diagram of water is confined to a small range of pressures (approximately from 220 up to 360 MPa) and temperatures (from about 245 up to 255 K at  $P=300$  MPa) [1].

The inelastic incoherent neutron scattering (IINS) method has been applied to study the dynamics of various phases of ice [2 and ref. therein]. Most of these phases were investigated in a recovered metastable state. Ice III upon quenching transforms to ice IX and cannot be recovered [3].

Here, the results of an IINS experiment on ice III, carried out *in situ* under high pressure conditions, are reported.

### Experiment

A titanium-zirconium clamped high pressure cell (HPC) was used for the *in situ* measurements (Fig. 1) [4]. The HPC, filled with distilled water, was pressurized to an initial pressure of  $P_{in}=300$  MPa at room temperature. The sample was a hollow cylinder with a 10 mm external diameter, thickness of 1 mm (to eliminate multiple neutron scattering), a height of 20 mm and a volume of about  $0.5 \text{ cm}^3$ . A platinum resistor thermometer was installed on the external surface of the HPC. The temperature of the HPC was changed with the help of a flow cryostat.

Measurements of the IINS spectra were carried out with the NERA-PR inverted geometry neutron spectrometer of the IBR-2 high flux pulsed neutron source of FLNP JINR. The IINS spectra were obtained at 249-250 K for ice III and at 200-201 K and 80 K for ice II (ice

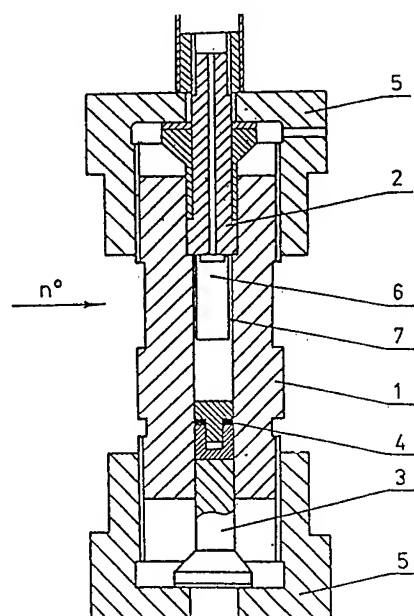


Fig. 1. The high pressure clamped cell: 1- cylinder of the high pressure cell produced from a titanium-zirconium doped alloy with a 'hull' matrix, 2- obturator, 3- piston, 4- Bridgman's gasket, 5- nut, 6- aluminium cylinder, 7- hollow cylinder of the ice sample.

II was formed because cooling rate of the HPC was significantly less than 10 K/s to prevent transformation to ice-IX [5]). It should be noted that the process of cooling and the subsequent transformations from liquid to ice III and then to ice II in the clamped HPC are quasi-isobaric. The IINS spectrum of ice Ih was measured in the same HPC at  $P_{in}=1$  MPa and 80 K.

## Discussion

The obtained amplitude-weighted phonon density of states  $G(E)$  are presented in Fig. 2.

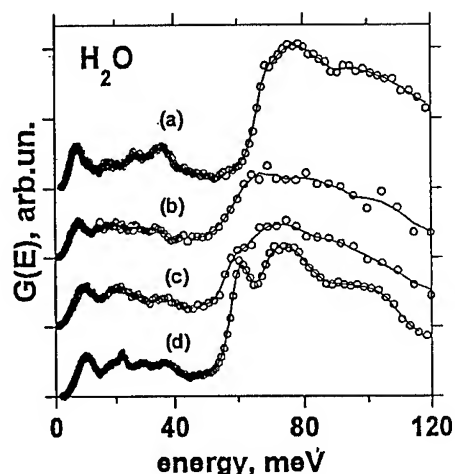


Fig. 2. The measured amplitude-weighted phonon density of states  $G(E)$  of ice phases: (a)-Ih (80 K,  $P=1$  MPa), (b)-ice III (250 K,  $P=300$  MPa), (c) and (d) - ice II (200 and 80 K,  $P=300$  MPa, respectively).

The  $G(E)$  for different ice phases allowed us to analyse changes in the vibrational spectra accompanying the crystal transformations. The vibrational spectra of ice show a gap between the bands of the translational and librational modes. The librational band has a sharp low-energy cutoff ( $E_c^L$ ). The high-energy side of the librational band has no such sharp boundary, apparently due to the contribution of multiphonon neutron scattering from the translational and librational modes. A comparison of the  $E_c^L$  values of the librational bands for ice phases Ih, III and II (66.5, 58.5 and 56.0 meV, respectively) shows a shift to lower energies. The observed dependence correlates with the changes in the crystal structures of these ice phases. The increasing distance between nearest

neighbour oxygen atoms leads to a decrease in the interaction between neighbouring water molecules and the energy of the librational modes.

Figure 3 shows the translational part of the  $G(E)$  for different ice phases.

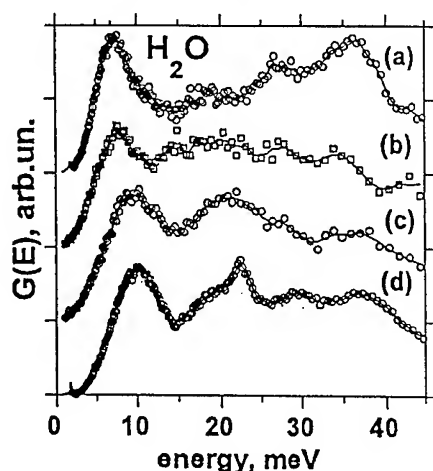


Fig. 3 The translational bands at  $G(E)$  of the ice phases: (a)-Ih (80 K,  $P=1$  MPa), (b)-ice III (250 K,  $P=300$  MPa), (c) and (d) - ice II (200 and 80 K,  $P=300$  Mpa, respectively)

The position of the first maximum in the acoustic band ( $E_1^T$ ) of the spectrum correlates with ice density [2,6]: the higher the density, the greater the shift of  $E_1^T$  to higher energy. It is obvious that the  $E_1^T$  of ice II at 200 K ( $E_1^T = 9.5$  meV) shifts to a higher energy in comparison with the position of  $E_1^T$  of ice III at 250 K ( $E_1^T = 7.8$  meV). The  $E_1^T$  shift of ice III in comparison with ice Ih is only approximately 0.5 meV. However, one should take into account the large temperature difference of the corresponding measurements. The position of  $E_1^T$  increases with decreasing

temperature as can be seen from the spectra of ice II at 200 and 80 K, respectively, where the  $E_1^T$  increases at about 0.5 meV.

## Conclusion

The IINS spectra of Ih, III and II ice phases were obtained *in situ* under quasi-isobaric conditions. The softening of the librational modes in the Ih-III-II ice sequence correlates with an increase in the distance between nearest neighbour oxygen atoms in the crystal structures of these ice phases. The observed shift of the first maximum of the  $G(E)$  of the translational band to higher energies correlates with the increase in the density of ice in subsequent phases.

## References:

1. G.Tammann, *Ann.Phys.*, **2** (1900) 1.
2. J.-C.Li, J.D.Londono, D.K.Ross, J.L.Finney, J.Tomkinson, and W.F.Sherman, *J.Chem.Phys.*, **94** (1991) 6770. J.C.Li, J.D.Londono, D.K.Ross, J.L.Finney, S.Bennington, and A.D.Taylor, *J.Phys.: Condens. Matter*, **4** (1992) 2109.
3. B.Minceva-Sukarova, W.F.Sherman and G.R.Wilkinson, *J.Phys. C: Solid State Phys.*, **17** (1984) 5833.
4. A.N.Ivanov, D.F.Litvin, B.N.Savenko, L.S.Smironov, V.I.Voronoi, A.E.Teplykh, *High Pressure Research*, **14** (1995) 209.
5. J.D.Londono, W.F.Kuhs, J.L.Finney, *J.Chem.Phys.*, **98** (1993) 4878.
6. A.I.Kolesnikov, V.V.Sinitsyn, E.G.Ponyatovsky, I.Natkaniec, L.S.Smironov, *J.Phys.: Condens. Matter*, **6** (1994) 375.



# Conical geometry for energy dispersive x-ray diffraction

## High pressure investigation of $\text{NH}_3$

M. Gauthier, J.P. Itié, A. Polian

*Physique des Milieux Condensés., Université P.&M. Curie, B77, 4 place Jussieu, F-75252 Paris cedex 05*

D. Häusermann and M. Hanfland

*ESRF, rue des Martyrs, BP 220, F-38043 Grenoble cedex*

The equation of state of ammonia has been studied up to 43 GPa at room temperature. The symmetry of phase IV is shown not to be hexagonal as previously reported. A particular attention has been paid to the spectrum and sample quality. This enables us to detect a subtle phase transformation which has been already seen by Raman scattering but never by x-ray diffraction. It has been possible by the achievement of a new energy dispersive x-rays diffraction technique. The association of a conical collimator and a large area detector has been used to recorded the full diffracted beam. Acquisition time has been reduced by 1-2 orders of magnitude and the problem of statistics due to the powder quality was partly resolved.

Ammonia belongs to the very fundamental simple molecular systems like  $\text{H}_2\text{O}$ ,  $\text{CH}_4$ ,  $\text{H}_2$  and He. The knowledge of the interatomic interactions in these simple molecular systems has been central to theoretical physical-chemistry. With the advent of modern computational methods in quantum chemistry, quasi-exact calculations can be performed and have to be compared with experimental data<sup>(1,2)</sup>. Among the most attractive model systems is the isoelectronic family of simple H-bonded crystals  $\text{CH}_4$ ,  $\text{NH}_3$ ,  $\text{H}_2\text{O}$ , HF and Ne.

For ammonia, the main experimental problem is due to the fact that the crystals are grown in the cell from the gas phase. Monocrystal can be grown from the liquid only in phase I below 220 K, phase II between 220 and 270 K and phase

III above 270 K. Due to phase transformations, monocrystal diffraction technics are then possible only up to 3.6 GPa for these well known phases. For phases which are obtained at higher pressure, a very good powder quality is required. With energy dispersive x-ray diffraction up to  $10^4$  grains are needed to collect reliable data. Rotating  $\chi$  and tilting  $\omega$  of the cell are then useful to decrease this number to a small value and to avoid the preferential growing axis observed for molecular solids. Unfortunately this is very time consuming with large background.

New diffraction technics have been developed to solve these problems<sup>(3,4)</sup>. A classical energy dispersive x-ray setup (EDX) is used with a large area detector (800 mm<sup>2</sup>) and a conical

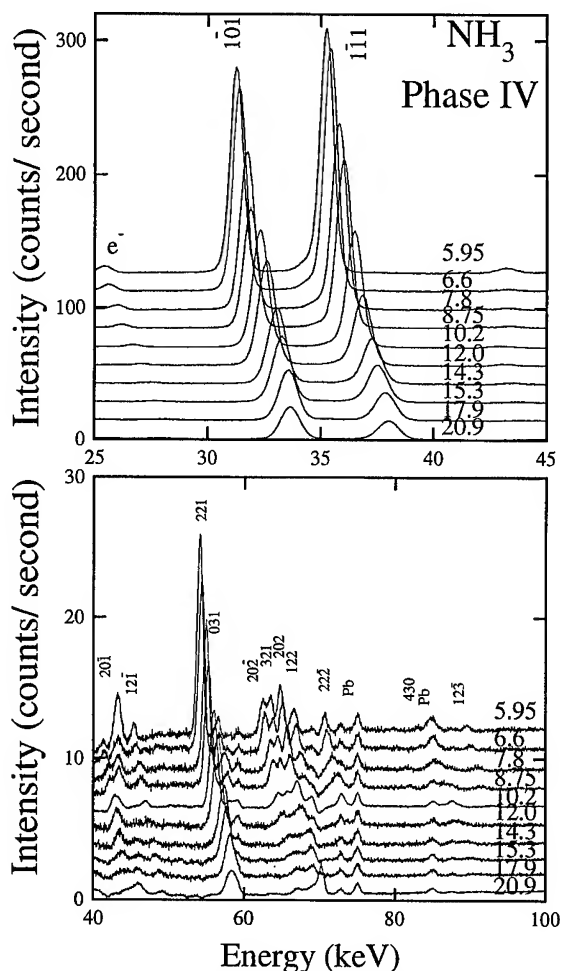


Fig.1 Normalized x-ray diffraction spectrum obtained in a single pressure increased run. (Monoclinic indexation).

collimator. The cone length is 28 mm with  $4\theta = 16.24^\circ$ . The incident beam spot dimensions were  $10 \times 10 \mu\text{m}$  and the adjustable width of the conical slits has been reduced down to  $10 \mu\text{m}$ . This leads to a maximum beam divergence of 0.7 mrad. The maximum length of the lozenge of diffraction determined by the intersection of the incident and diffracted beams is less than  $150 \mu\text{m}$  so that the ratio of the active volume of diamond of the membrane diamond anvil cell used as pressure generator to sample is roughly 2 orders of magnitude less than the ratio obtained in angular dispersive x-ray diffraction (ADX): the Compton

background is weak. With this setup, the full diffracted beam hits the detector. The problem of the low statistics due to the low number of crystallites in the beam spot is partly resolved since all the reflections arising at  $2\theta$  from a particular crystallite are detected. The total intensity of the reflections is obtained without any search in the full  $\chi \propto \theta$  space and then acquisition time is reduced to few minutes. This improves by 1 to 2 orders of magnitude the classical collection time used in EDX<sup>(5)</sup>, ADX<sup>(6)</sup> or time of flight neutron powder diffraction in large volume cell<sup>(7,8)</sup>.

Fig. 1. summarizes the results obtained in a single pressure run. Compton background has been used to calibrate the intensities and subtracted for clarity. Peak intensity changes were observed around 12 GPa. This is correlated with the spreading of the  $dhkl$  data versus pressure (Fig. 2) and may be linked to the phase V transformation observed by Raman scattering<sup>(9)</sup> at 14 GPa.

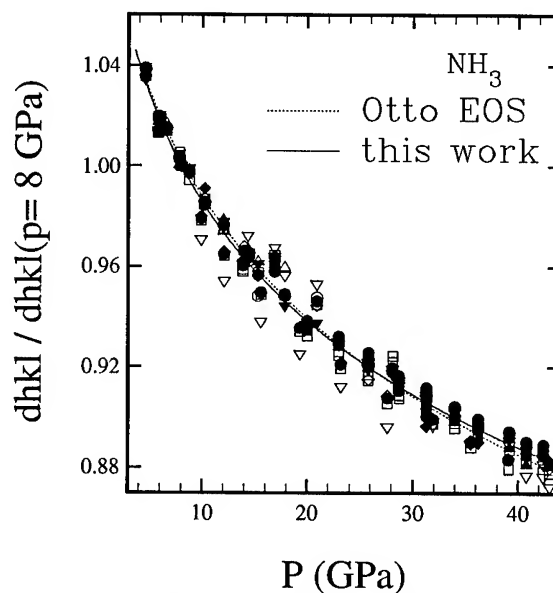


Fig.2 Equation of state of  $\text{NH}_3$  phase IV. Dispersion of data above 12 GPa is due to a phase transformation. The symbols correspond to the different  $hkl$  lines.

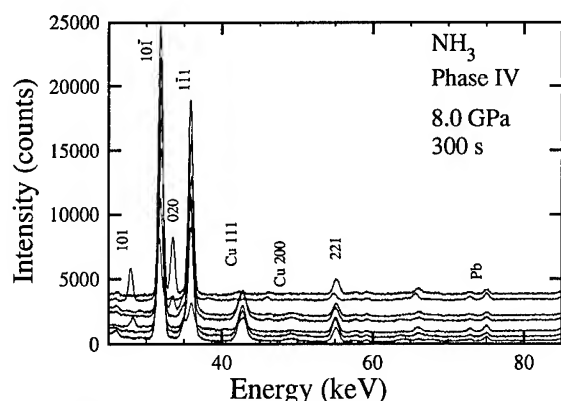


Fig.3 Diffraction spectrum collected at constant pressure on a single crystallite at various  $\omega$  orientations of the sample.

Systematic searches for diffraction peaks have been done on large crystallites (Fig. 3). Two extra peaks not observed in fig2. have been obtained. The lowest energy peak (29 keV) has been recorded for only two  $\omega$  values at 8 GPa. It should be emphasized that this line was not seen from  $\text{ND}_3$  neutron scattering<sup>(8)</sup> but can not be due either to diamond or to the ruby chips or the gasket. Indexation of all the 14 lines observed in phase IV, including the low energy one, leads to a monoclinic structure with 4 molecules per cell  $a=5.396$  Å,  $b=5.224$  Å,  $c=3.121$  Å and  $\beta=92.36^\circ$  at 8 GPa. If this first line is taken away an orthorhombic structure compatible with the neutron determination ( $z=4$ ,  $a=5.517$  Å,  $b=5.232$  Å and  $c=3.175$  Å) is found. These two structures are very close and differ only by the beta angle. They are related to the hexagonal structure since we have the transformations  $c \rightarrow a_{\text{hcp}}=c$ ,  $b \rightarrow c_{\text{hcp}}$   $a \rightarrow a_{\text{hcp}}=a^*(z_{\text{hcp}}/z)/\sin(60)$ , with  $z_{\text{hcp}}=2$  molecules per cell for the hcp structure. The phase transformation at 12 GPa has been neglected in the equation of state (EOS) calculation and we have found  $B_0=9.4$  GPa and  $B'=5.4$  with the Vinet EOS. This is in good agreement with Otto results ( $B_0=7.56$  GPa and  $B'=5.29$  obtained using the second order Birch Murnaghan EOS).

## Conclusion

The phase diagram of  $\text{NH}_3$  has been studied up to 43 GPa by energy dispersive x-rays diffraction using conical slits and synchrotron radiation. This technique is shown to be well adapted to high pressure experiments. The equation of state of  $\text{NH}_3$  solid phase IV has been determined and it is shown that the diffraction pattern of this phase can not be indexed in an hexagonal lattice as it was previously reported.

## References

- 1 B. Silvi, *Phys. Rev. Lett.* **73** (1994) 842
- 2 J.M. Besson, Ph. Pruzan, S. Klotz, G. Hamel, B. Silvi, R.J. Nelmes, J.S. Loveday, R.M. Wilson and S. Hull, *Phys. Rev. B* **47** (1994) 12540
- 3 D. Häusermann and J.P. Itié, *Rev. Sci. Instrum.* **63** (1992) 1080
- 4 H.W. Neuling, O. Schulte, T. Krüger and W.B. Holzapfel, *Meas. Sci. Technol.* **3** (1992) 170
- 5 J.W. Otto, R.F. Porter and A. Ruoff, *J. Phys. Chem. Solids* **50** (1989) 171
- 6 E. Wolanin, Ph. Pruzan, J.C. Chervin, B. Canny, M. Gauthier, D. Häusermann and M. Hanfland, *Proceedings of the XV AIRAPT & XXXIII EHPRG conference, Warsaw Poland* (1995)
- 7 S. Klotz, J.M. Besson, G. Hamel, R.J. Nelmes, J.S. Loveday, W.G. Marshall and R.M. Wilson, *Appl. Phys. Lett.* **66** (1995) 1735
- 8 S. Klotz, M. Gauthier, J.M. Besson, G. Hamel, R.J. Nelmes, J.S. Loveday, R.M. Wilson and W.G. Marshall, *Appl. Phys. Lett.* **67** (1995)
- 9 M. Gauthier, Ph. Pruzan, J.C. Chervin and J.M. Besson, *Phys. Rev. B* **37** (1988) 2102

# METHANE HIGH PRESSURE CRYSTAL STRUCTURE STUDIED BY FTIR SPECTROSCOPY

LORENZO ULIVI<sup>+</sup>, ROBERTO BINI\*, HANS J. JODL<sup>⊕</sup>, PIER R. SALVI\*

*European Laboratory for Nonlinear Spectroscopy Largo E. Fermi 2, 50124 Firenze, Italy  
and*

<sup>+</sup> *Istituto di Elettronica Quantistica, CNR, via Panciatichi 56/30, 50127 Firenze, Italy*

<sup>\*</sup> *Laboratorio di Spettroscopia Molecolare, Dipartimento di Chimica, Università di Firenze, via  
Gino Capponi 9, 50121 Firenze, Italy*

<sup>⊕</sup> *Fachbereich Physik, Universität Kaiserslautern, E. Schrödinger Straße, 6750 Kaiserslautern,  
Germany*

## ABSTRACT

Infrared absorption and Raman spectra of solid CH<sub>4</sub>, measured at room temperature in the pressure range 0.8-30 GPa, are reported and discussed in this paper. The IR experiment has been performed coupling a Diamond Anvil Cell to a FTIR spectrometer by means of a high efficiency beam condensing system. Two solid-solid phase transitions (phase I-phase A, at 5.1 GPa, and phase A-phase B, between 7 and 9 GPa) have been evidenced and studied. In particular, the kinetics of the A-B phase transition has been studied at constant pressure, measuring infrared absorption spectra as a function of time. From the analysis of the infrared and Raman spectra, structural properties of both A and B phases are derived.

## Introduction

In the solid state methane exhibits several crystal phases, that differ mainly for the orientation of the molecules in the unit cell. At low temperature and pressure (T<80 K, P<1.3 GPa), the solid phase diagram has been studied in the past with different experimental techniques, and it has been demonstrated the existence, in this P-T region, of six different crystal phases only two of which have been characterized from the structural point of view.

At room temperature three different solid phases have been found, but only phase I, which is stable in the pressure range 1.3-5.1 GPa has been characterized as a fcc plastic phase, with one freely rotating molecule per unit cell.

In contrast with the abundance of experimental and theoretical data at low temperatures and pressures, there are much fewer experimental reports at room temperature and high pressure.

We have measured infrared and Raman spectra of solid methane at room temperature in the pressure range 0.8-30 GPa (1).

## Experiment

For this experiment we have used a membrane Diamond Anvil Cell (DAC) (2), equipped with type IIa diamonds and a stainless steel gasket. The DAC is filled with high purity CH<sub>4</sub>, by means of a high pressure gas loading system, at 0.1 GPa. Due to the small sample size, the infrared absorption measurements must be performed with the help of a beam-condensing system, whose optical scheme is shown in fig. 1. This is constituted of four gold-coated plane mirrors (M1-M4) and of two Cassegrain-type microscope objectives. Using this systems, it is possible to demagnify, of a factor close to 8, the linear dimensions that the lamp image normally possess in the center of the sample compartment. The DAC and the optics are mounted on a independent metal base, that can be easily positioned in the sample compartment of the instrument (Bruker 120 HR), under vacuum. The sample pressure can be varied remotely controlling the pressure of the helium gas in the membrane, through a capillary pipe entering the vacuum chamber. An aluminium-coated mirror can be positioned on the IR beam path, between the cell and the detector, for visual observation of the

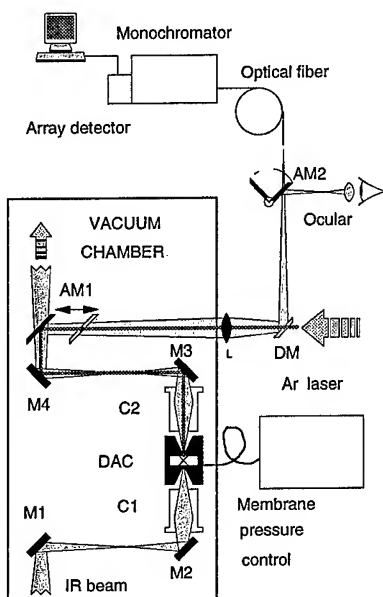


Fig 1. Experimental apparatus for high pressure infrared experiments. Labels have the following meaning: DAC, diamond anvil cell; M1, M2, M3, M4, gold-coated plane mirror; C1 and C2, Cassegrain-type microscope objectives; AM1, AM2, aluminium-coated plane mirrors, DM, dichroic mirror.

sample and for pressure measurement, by the ruby fluorescence technique. Few milliwatts of an Ar ion laser are focused on a small ruby crystal, immersed in the sample. Ruby fluorescence is collected backward, along the same optical path, and after a reflection on a dichroic mirror is focused on an optical fiber coupled to a dedicated fixed-grating spectrometer equipped with a cooled array detector.

The Raman measurements were carried out by using the 514.5 nm line of an Ar<sup>+</sup> laser with incident power of 100 mW. The scattered radiation is dispersed through a Jobin-Yvon U-1000 double monochromator and a CCD detection system, coupled to a PC, is used for spectral detection.

## Results

The CH<sub>4</sub> molecule has four internal modes, all of which Raman active, while only two ( $\omega_3$  and  $\omega_4$ ) infrared active. In the present study we have measured the vibrational spectrum in the  $\omega_1$  and  $\omega_3$  region (3000–3200 cm<sup>-1</sup>) as a function of pressure up to 30 GPa at room temperature by means of infrared and Raman spectroscopy.

The presence of a solid-solid phase transition at 5.1 GPa, evidenced in Ref. 3, is confirmed in this

study by the sudden change of slope of the peak position of the  $\omega_3$  IR band when reported versus pressure. The new phase, which will be referred to as phase A, since no conclusive evidence relates it to some specific low temperature phase, is stable up to about 9–10 GPa. Increasing the pressure above this value, a further transition to a second high pressure phase occurs. This transition is affected by a large hysteresis: changes in both the Raman and the IR spectrum start to appear, during compression, above 7.6 GPa, but when the pressure is increased rapidly, phase A can be frozen up to 17 GPa. On the other hand, during expansion from phase B, the transition to phase A occurs only when the pressure is lowered to 6.4 GPa. This phase transition has been studied by monitoring the IR spectrum as a function of time, and it has been demonstrated to follow a first order kinetics, with a rate constant increasing with pressure (1).

## Phase A

The Raman spectrum of the  $\omega_1$  mode in phase A show a maximum in very good agreement with values from previous studies (3). The band is asymmetric, and the spectral deconvolution shows that a weak second component on the high frequency side contributes to the actual band profile. In the infrared a very weak single absorption band is observed for this transition, which is not infrared active in the isolated molecule. It is important to note that the  $\omega_1$  infrared component is red shifted with respect to the lowest Raman one by  $\approx 2$  cm<sup>-1</sup>. Given the frequency accuracy of our FTIR and Raman spectrometers, the infrared band may be confidently considered not coincident with the Raman peak. In the  $\omega_3$  region ( $\approx 3080$ – $3090$  cm<sup>-1</sup>) one infrared and one Raman band are found, separated by  $\approx 7$  cm<sup>-1</sup>. These broad bands may be easily formed by more than one component.

The low temperature phases of solid methane has been discussed in the past on the basis of a crystal model consisting of three different types of sites (4). Two factor groups, D<sub>4h</sub> (5,6) and D<sub>2d</sub> (7) were proposed. Using the three site model to discuss also the structure of the room temperature phase A, we can draw some conclusions about the site symmetry and the crystal structure on the basis of the measured infrared and Raman activity. Taking into account the

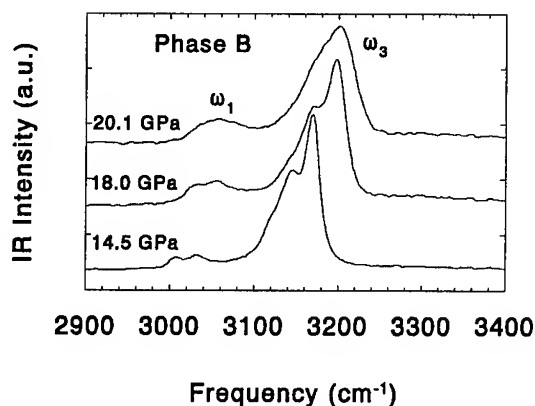


Fig. 2. Infrared spectra of solid  $\text{CH}_4$  (B phase) in the  $\omega_1$  and  $\omega_3$  regions at different pressures (as shown) and at room temperature.

two proposed factor groups  $D_{4h}$  and  $D_{2d}$ , we have calculated all the expected Raman and IR components for the  $\omega_1$  vibration, considering as site groups all possible subgroups of both the molecular and the factor group. With the further assumption that molecules on different sites give rise to almost degenerate frequencies, we prove that, for phase A, only a tetragonal structure ( $D_{4h}$ ) is possible, with molecules arranged on sites of three different symmetries, which are  $C_{2v}$ , and two other among  $D_2$ ,  $D_{2d}$ , and  $S_4$ . Unfortunately, our spectroscopic results do not allow an unambiguous choice among the last three possible site symmetries.

#### Phase B

Infrared spectra of solid  $\text{CH}_4$  at pressure  $\geq 14.5$  GPa are shown in fig. 2. The  $\omega_1$  and  $\omega_3$  modes have two and three components, respectively. Their infrared frequencies have been measured in the range 8-25 GPa and are plotted as a function of pressure in fig. 3. Raman spectra of phase B, measured between 13.8 and 22 GPa, show three components for the  $\omega_1$  mode, whose dependence on pressure matches perfectly that reported in ref. 3. In the case of the  $\omega_3$  multiplet, it is more difficult to deconvolute the components, due to band weakness. At least three peaks may be distinguished, as suggested by ref. 3. Finally, it should be stressed that for both the  $\omega_1$  and the  $\omega_3$  modes the infrared components have, at a given pressure, different frequencies from the Raman values. This point is fundamental for structural predictions on phase B.

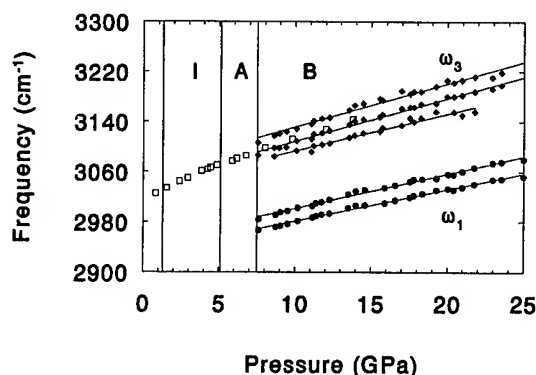


Fig. 3. Pressure dependence of the  $\omega_1$  and  $\omega_3$  infrared frequencies. The vertical lines indicate the pressure of fluid  $\rightarrow$  I,  $I \rightarrow$  A, and  $A \rightarrow$  B phase transitions at room temperature. The full lines represent the best linear fit to the experimental data.

Since phase B is stable at least to 30 GPa, a fully ordered, single site, crystal structure has probably been reached. A detailed analysis of the correlations diagram from the molecular ( $T_d$ ) to all possible factor groups compatible with the same site symmetry has been carried out, considering as site all  $T_d$  subgroups (1). The results is that there is only one site symmetry,  $C_s$ , and four factor groups,  $D_{4h}$ ,  $D_{6h}$ ,  $T_h$ , and  $O_h$ , consistent with our spectroscopic findings. Assuming as the most favorable for phase B a close-packed structure, the  $D_{4h}$  symmetry is excluded. Taking advantage of the analogy with the noble gases and ammonia, where the hcp structure is stabilized at high pressure, phase B may be described as a  $D_{6h}$  structure with 12 molecules on  $C_s$  sites in the unit cell.

#### References

1. R. Bini, L. Ulivi, H. J. Jodl, and P. R. Salvi, *J. Chem. Phys.* **103**, 1353 (1995).
2. R. Le Toullec, J.P. Pinceaux, and P. Loubeyre, *High Press. Res.* **1**, 77 (1988).
3. P. Hebert, A. Polian, P. Loubeyre, and R. Le Toullec, *Phys. Rev.* **B36**, 9196 (1987).
4. D. Fabre, M. M. Thiery, H. Vu, and K. Kobashi, *J. Chem. Phys.* **71**, 3081 (1989).
5. F.D. Medina, and W. B. Daniels, *J. Chem. Phys.* **70**, 2688 (1979).
6. B. W. Baran and F. D. Medina, *Chem. Phys. Lett.* **176**, 509 (1991).
7. A. I. Prokhorov, and a. P. Isakina, *Acta Cryst.* **B 36**, 1576 (1980).

#### **VI(C.4) Metals**

# ELECTRICAL CONDUCTIVITY AND X-RAY MEASUREMENTS OF hcp-fcc TRANSITION IN IRON TO 40 GPa

Takehiko Yagi, Takeyuki Uchida, and Nobumasa Funamori  
*Institute for Solid State Physics, University of Tokyo*  
*Roppongi, Minato-ku, Tokyo 106, Japan*

## ABSTRACT

Simultaneous observations of electrical conductivity and X-ray diffraction were made on iron up to 40 GPa and 1800K. Discontinuous change of the electrical conductivity associated with the  $\epsilon$ - $\gamma$  transition was observed clearly. The axial ratio,  $c/a$ , of  $\epsilon$  phase remains practically unchanged with pressure while it increases with temperature. There was no indication of the existence of a new phase proposed recently.

## INTRODUCTION

Iron is one of the most intensively studied material under pressure because of its importance for understanding the Earth's core. In spite of the intensive works, however, there are still many controversies on its phase relation. Recently, existence of a new high pressure-temperature phase was proposed based on experiments using laser heated diamond anvil cell (Boehler, 1993; Saxena *et al.*, 1993, 1994). They observed a change in slope in plot of laser power against the corresponding sample temperature and claimed that a new phase exist above about 30 GPa between  $\epsilon$ -phase (hcp) and  $\gamma$ -phase (fcc). In order to clarify the existence and the structure of this new phase, we have carried out high pressure and temperature *in situ* electrical conductivity and/or X-ray observations up to about 40 GPa and 1800 K.

## EXPERIMENTAL

Experiments were made using two different types of high pressure apparatus; an opposed-anvil type sintered diamond apparatus which is a modification of Drickamer cell (Yagi, 1994; Uchida *et al.*, 1994) and a MA8-type double stage multi anvil apparatus (Kondo *et al.*, 1993; Funamori *et al.*, 1995). Simultaneous observations of electrical conductivity and X-ray measurement were made using the former apparatus while high quality X-ray observations under well defined temperature were made using the latter. X-ray measurements were made using synchrotron radiation at the Photon Factory in National

Laboratory for High Energy Physics (KEK). Sample assembly used for the opposed anvil apparatus is shown in Fig. 1. The sample is a thin iron foil of 99.998% purity, which was sandwiched between two MgO disks. The sample was heated by directly running regulated DC power through the sample, and the resistance was measured from the voltage drop observed at the both ends of the sample. Temperature was estimated from the input

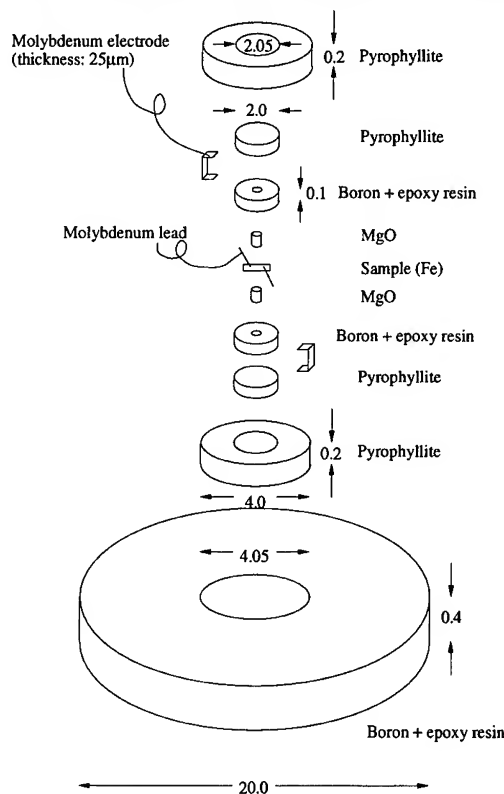


Figure 1. Sample assembly used in the opposed anvil apparatus.



power vs. temperature relation, assuming that temperature increases linearly with power. Temperature calibration was made using the  $\epsilon$ - $\gamma$  transition temperature of iron at around 11 GPa. Pressure was determined from the diffraction lines of MgO using third order Birch-Murnaghan equation of state. In this experiment, we had to use very thin foil of iron because it was necessary to make the resistance of the sample higher compared with the other portion of the electric circuit. As a result, the quality of the observed X-ray diffraction profile becomes low. In order to improve this problem, another X-ray experiments were made using double stage multi-anvil apparatus. Sample assembly for this experiment is very similar to that used for studying  $\text{MgSiO}_3$  perovskite (Funamori *et al.*, 1995). In this case powdered sample was mixed with MgO powder to avoid the grain growth and heated by two disk heaters which are made of the mixture of TiC and diamond. Sample temperature was measured by a tungsten-rhenium thermocouple.

## RESULTS AND DISCUSSIONS

An example of the electrical conductivity measurements is shown in Fig. 2. The resistance change associated with the transition is clearly

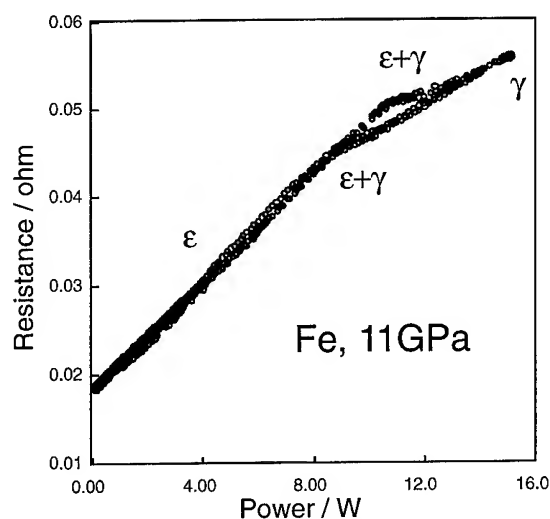


Figure 2. Electrical conductivity of iron observed at about 11 GPa. The discontinuous change of the resistance associated with the  $\epsilon$ - $\gamma$  iron transition is clearly observed.

observed. The variation was reversible with a small hysteresis. Simultaneous X-ray observations made at several points in temperature increasing cycle clarified that although there is an intermediate region between  $\epsilon$ - and  $\gamma$ -iron, this is ascribed to the coexistence of two phases, rather than the existence of a new phase. The electric power at the onset of the transition increases with increasing pressure and the estimated transition temperature is in harmony with the previous results (Boehler *et al.*, 1987).

An example of the X-ray observations obtained by multi-anvil apparatus is shown in Fig. 3. Diffractions from  $\gamma$ -iron are clearly observed together with those of MgO and a trace of  $\epsilon$ -iron. Very recently, Saxena *et al.* (1995) reported that they have observed a small change of the X-ray diffraction pattern of iron during and after the heating at pressures between 35 and 40 GPa and temperatures below 1500K. Observed diffraction patterns were explained by a mixture of hcp phase and a new phase. They modeled the new phase as a 4-layer closed pack hcp phase (dhcp phase). If this new dhcp phase was formed, we could expect the growth of several new diffraction lines, together with the discontinuous shift of the peaks observed in hcp phase. Actually, such a change was clearly

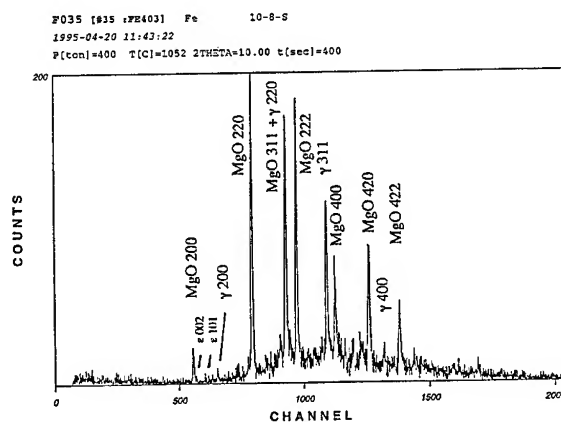


Figure 3. X-ray diffraction pattern of the sample and MgO at about 32 GPa and 1325K. Exposure time is 400 sec.

observed in hcp-dhcp transition of iron hydride (Yamakata *et al.*, 1992). In the present observation, however there was no indication of the formation of such diffraction lines, although both  $\epsilon$ - and  $\gamma$ -phases were observed clearly. The transition temperature at 32 GPa was between 1300K and 1325K, which is in good agreement with the boundary reported by Boehler *et al.* (1987).

Axial ratio,  $c/a$ , of the hcp phase is plotted in Fig. 4. Open and solid symbols represent the data at room temperature and at elevated temperature, respectively. An open circle is a ratio,  $c/2a$ , of the dhcp phase reported by Saxena *et al.* (1995) and a solid line represents the variation of  $c/a$  with pressure at room temperature determined by Jephcoat *et al.* (1986) in the pressure range up to 80 GPa. As is clear from this figure, the axial ratio observed in this study at room temperature is in good agreement with that reported by Jephcoat *et al.*, although the experimental technique is quite different. At elevated temperature, the ratio increases and comes close to the ideal close packing, which is in accordance with the result reported by Huang *et al.* (1987). On the other hand, the modeled dhcp phase proposed by Saxena *et al.* (1995) has smaller axial ratio ( $c/2a=1.58$ ). They reported that the new phase was observed even at room temperature, once it was formed at elevated temperature. Many of the room temperature data plotted in Fig. 4 were obtained after the heating. However, we did not find any evidence of the smaller  $c/a$  ratio in the present study.

As discussed above, the present experimental result is negative to the existence of the new phase of iron. The pressure range of the present study is, however, still closed to the lower limit of the proposed stability field and further study will be required to clarify the phase diagram of iron in this region.

#### ACKNOWLEDGMENTS

Authors are grateful to Y. Nakamura, O. Shimomura, and T. Kikegawa for their support for the experiment. The X-ray experiment was carried

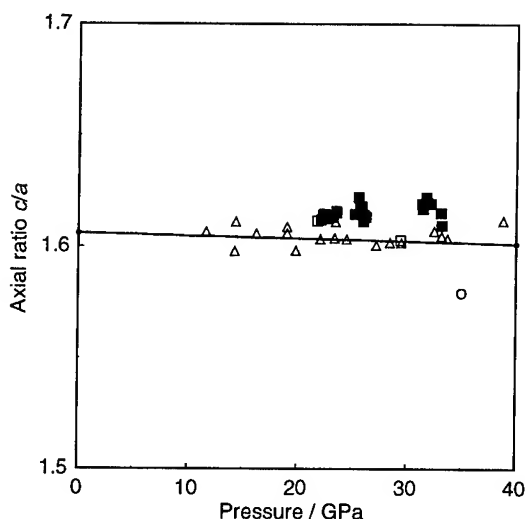


Figure 4. The axial ratio,  $c/a$ , of the  $\epsilon$ -iron observed at room temperature (open symbols) and at high temperatures (solid symbols). Triangles and squares represent the results obtained by opposed anvil and by multi anvil, respectively. An open circle represents  $c/2a$  of the dhcp phase proposed by Saxena *et al.* (1995) and a solid line represents the variation of  $c/a$  of  $\epsilon$ -phase at room temperature reported by Jephcoat *et al.* (1986).

out at KEK using the MAX80 system.

#### REFERENCES

- R. Boehler *et al.*, in *High Pressure Research in Mineral Physics*, M. H. Manghnani and Y. Syono, Eds. (American Geophysical Union, Washington, DC) 173, 1987.
- R. Boehler, *Nature*, **363**, 534, 1993.
- N. Funamori *et al.*, *J. Geophys. Res.*, in press, 1995.
- A. P. Jephcoat *et al.*, *J. Geophys. Res.*, **91**, 4677, 1986.
- E. Huang *et al.*, *J. Geophys. Res.*, **92**, 8129, 1987.
- T. Kondo *et al.*, *High Temp. High Press.* **25**, 105, 1993.
- S. K. Saxena *et al.*, *Science*, **260**, 1312, 1993.
- S. K. Saxena *et al.*, *Science*, **264**, 405, 1994.
- S. K. Saxena *et al.*, preprint, 1995.
- T. Uchida *et al.*, *J. High Pressure Inst. Jpn.*, **32**, 66, 1994 (in Japanese).
- T. Yagi, *AIP Conference Proceedings*, **309**, 1621, 1994.
- M. Yamakata *et al.*, *Proc. Japan Acad.*, **68**, 172, 1992.

# STRUCTURE SYSTEMATIC AND EQUATIONS OF STATES FOR THE ALKALINE EARTH METALS UNDER PRESSURE

M. WINZENICK and W.B. HOLZAPFEL

*Fb6-Physik, Universität GH Paderborn*

*Warburger Str. 100, 33095 Paderborn, Germany*

Recent results on structural systematic of the alkaline earth metals Magnesium, Calcium, Strontium and Barium are compared with anomalies in the equations of states under pressures up to 100 GPa at room temperature. The observed complex structures for the heavy alkaline earth metals are discussed with the model of  $s \rightarrow d$  transfer.

## Introduction

In recent years the different high pressure phases of the alkaline earth metals were investigated in many theoretical and experimental studies [1-3]. Theoretical calculations reproduced at first the systematic structural changes from the cubic face centered (cF4) to the cubic body centered (cl2) structure around 20 GPa for Ca, at 3.5 GPa for Sr and (theoretically) at small negative pressures for Ba [4-6]. The calculations for these elements show an increase of the d-band occupation under pressure [7]. This phenomenon is known as  $s \rightarrow d$  transfer. At higher pressures the heavy alkaline earth metals crystallize in complex structures associated with this  $s \rightarrow d$  transfer. Only the open cP1 structure for Ca III above 32 GPa [8] was confirmed by theoretical calculations [9]. Band structure calculations indicate that simple structures should be realized after completion of the  $s \rightarrow d$  transfer. These theoretical results are only confirmed for Ba which crystallize in the hexagonal-close-packed structure (hP2) above 42 GPa [10]. Thereby Ba shows the interesting phenomenon that the hcp phases Ba-II and -V are separated by a complex intermediate Ba IV phase.

## Experimental and Results

The high pressure structures of the alkaline earth metals Mg, Ca, Sr and Ba were investigated with energy dispersive x-ray diffraction (EDXD) at HASYLAB using a

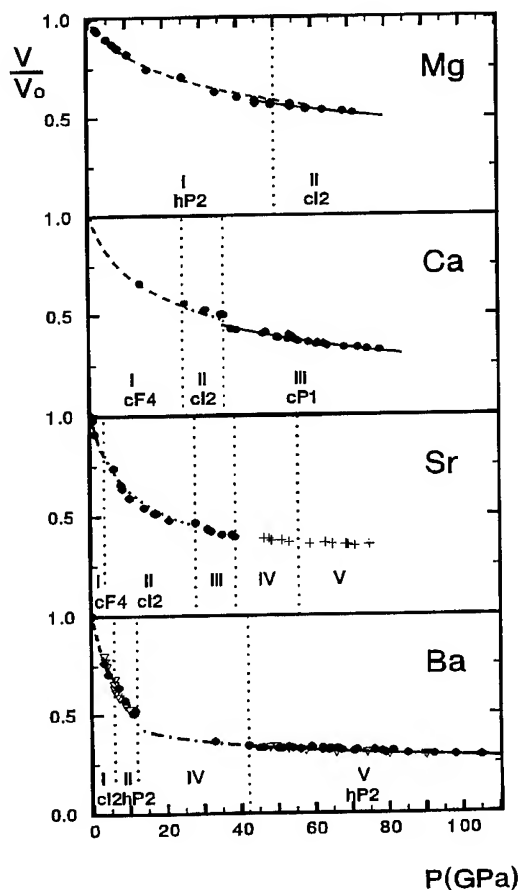


Fig. 1: Atomic volume of Mg, Ca, Sr and Ba at ambient temperature.

- present data with best fit —
- - - extrapolation of Ba IV
- ..... previous data of refs. 2, 13, 14, 16
- ..... previous data of refs. 2, 16; ▽ ref. 3

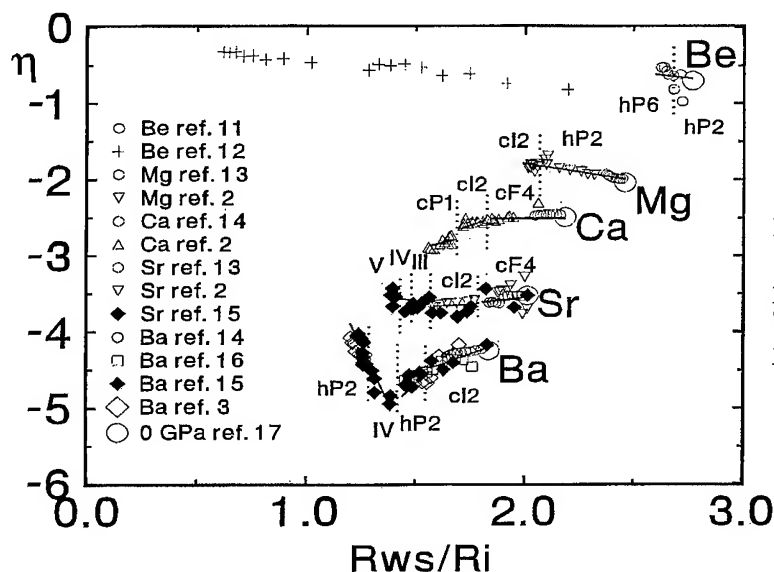


Fig. 2: The EOS-data for the alkaline earth metals in scaled form with  $\eta = \ln(p/p_{FG}) - \ln[1 - (V/V_0)^{1/3}]$  using the Fermi-gas pressure  $p_{FG}$ .  $R_w/R_i$  is the scaled Wigner-Seitz radius. Different phases are separated by vertical lines. The large open circles are the zero pressure values of Refs. 17 and 18.

diamond anvil cell DAC in the pressure range up to 100 GPa. The corresponding  $p$ - $V$  relation are presented in fig. 1. The high pressure structures cl2 and cP1 for Mg and Ca are observed up to 70 and 80 GPa, respectively. In the case of Sr the volumes for the unknown phases are calculated from the shifts of the  $d$ -values and marked by (+) in fig.1 and no further phase transition was observed in these experiments up to 150 GPa.

The present data for Ba up to 105 GPa confirm the previous observations [3, 10] of the hP2 structure for Ba-V. The structure of Ba-IV between these two hP2 phases II and V is complex with no resemblance to hP2 so that the phase transitions II→IV and IV→V are probably first order.

### Equation of State Data

For a more detailed discussion the EOS-data for the alkaline earth metals were presented in fig. 2 with a useful "linearisation", whereby the scaled stress variable [19]

$$\eta = \ln \frac{p}{p_{FG}} - \ln \left( 1 - \left( \frac{V}{V_0} \right)^{1/3} \right) \quad (1)$$

is plotted versus the radius ratio of the pressure dependent Wigner-Seitz-Radius  $R_w$  with respect to the pressure independent ionic radius  $R_i$ . Thereby

$$p_{FG} = a_{FG} \cdot \left( \frac{Z}{V} \right)^{5/3} \quad (2)$$

represents the pressure of a Fermi gas with  $Z$  electrons in the atomic volume  $V$  and

$$a_{FG} = \frac{(3\pi^2)^{2/3}}{5} \cdot \frac{\hbar^2}{m_0} = 23.369 \text{ MPa nm}^5 \quad (3)$$

is a universal constant. As discussed previously in more detail [20] the EOS-data are represented thereby in such a way that the limiting behavior at very strong compression, given by the Thomas-Fermi-Gas, and at small compression, given by Hook's Law, is interpolated by a straight line in the case of "simple" solids. A linear interpolation is therefore considered as the "regular" behavior. In contrast to this "regular" behavior the heavier alkaline earth metals are characterized by a special softness at intermediate pressures. The almost flat curves for Ca, Sr and Ba with partly negative slopes are typical for continuous electronic changes referred to the  $s \rightarrow d$  transfer [21]. Different strength in the anomalies are

due to the fact that these anomalies occur in the lighter elements at higher pressures but still at the same radius ratio  $R_w/R_i$ . The curve for Ba shows a minimum with a sharp break near  $R_w/R_i = 1.4$ . At higher pressures the curve is linear and has an unusually steep slope which indicates the approach towards normal behavior and the end of the  $s \rightarrow d$  transfer. This conclusion is supported by the observed phase transition from the complex Ba-IV phase to the much simpler hP2 phase Ba-V and it is expected that after completion of the  $s \rightarrow d$

transfer simple structures are energetically favorable. On the other hand the lighter elements Be and Mg show their own systematic. These elements have no empty d-band near the Fermi-level and therefore only minor electronic changes. The curves of both elements show nearly regular behavior with normal slopes. The  $\eta$ -representation is therefore very suitable to quantify the anomalies in the EOS-data of alkaline earth metals.

## References:

- [1] D.A. Young *Phase Diagrams of the Element* (University of California Press Berkley and Los Angeles, California 1991).
- [2] H. Olijnyk, PhD. thesis, Universität GH Paderborn, (1985).
- [3] K. Takemura, *Phys. Rev. B* **50**, 16239 (1994).
- [4] H.L. Skriver, *Phys. Rev. B* **31**, 1909 (1985).
- [5] J.A. Moriarty, *Phys. Rev. B* **8**, 1338 (1973).
- [6] J.A. Moriarty, *Phys. Rev. B* **34**, 6738 (1986).
- [7] J.C. Duthie and D.G. Pettifor, *Phys. Rev. Lett.* **38**, 564 (1977).
- [8] H. Olijnyk and W.B. Holzapfel, *Phys. Lett.* **100A**, 191 (1984).
- [9] R. Ahuja, O.Eriksson, J.M. Wills, B. Johansson, (unpublished).
- [10] H. Olijnyk, W.B. Holzapfel, *High Pressure Geosciences and Material Synthesis*, Academie Verlag, Berlin, p.75-79 (1988).
- [11] L.C. Ming, M.H. Manghnani, *J.Phys.F:Met.Phys.* **14** (1984) L1-L8.
- [12] J. Meyer-ter-Vehn, W. Zittel, *Phys. Rev. B* **37** 8674 (1988).
- [13] S.N. Vaidya, G.C. Kennedy, *J. Phys. Chem. Solids*, **33** 1377 (1972).
- [14] S.N. Vaidya, G.C. Kennedy, *J. Phys. Chem. Solids*, **31** 2329 (1970).
- [15] M. Winzenick Diplomarbeit Universität GH Paderborn (1992).
- [16] S. Akimoto, T. Yagi, Y. Ida, K. Inoue, *High Temp-High Press.* **7**, 287 (1975).
- [17] M.S. Anderson, C.A. Swenson, *Phys. Rev. B* **41**, 3329 (1990).
- [18] M.S. Anderson, C.A. Swenson, *Phys. Rev. B* **28**, 5395 (1983).
- [19] W.B. Holzapfel, *Europhys. Lett.* **16**, 67 (1991).
- [20] W.B. Holzapfel, *High Pressure Res.* **7**, 290 (1991).
- [21] M. Winzenick, V. Vijayakumar, W.B. Holzapfel *Phys. Rev. B* **50** 12381 (1994).

# ULTRA-HIGH PRESSURE STRUCTURAL CHANGES STUDY IN DYSPROSIUM, HOLMIUM AND ERBIUM

JAGANNADHAM AKELLA, GORDON S. SMITH,  
SAMUEL T. WEIR, AND CHANTEL RUDDLE  
*Lawrence Livermore National Laboratory, Livermore, CA 94550, USA*

## ABSTRACT

Crystal structural changes in Dy, Ho and Er were studied under pressure in a diamond-anvil cell. We found remnant lines from the ambient hcp phase being present in Sm-type stability field suggesting the sluggishness of this transformation. We tend to regard the fcc and "six-layered hexagonal" stability fields to be one mixed phases region.

## Introduction

A study of the systematics in the high pressure behavior of the rare-earth elements is of theoretical and experimental importance. Jayaraman and Sherwood proposed structural sequence as a function of pressure for lanthanides, and it is hcp-Sm-type-dhcp-fcc.<sup>1</sup> With further increase in pressure, new structures were discovered: a "six-layered hexagonal" phase (Grosshans et al.<sup>2</sup> and Smith and Akella<sup>3</sup>); in Pr, an orthorhombic ( $\alpha$  U type) phase (Smith and Akella<sup>4</sup>, and Grosshans, et al.<sup>5</sup>), and recently a body-centered tetragonal phase (bct) for Sm at about 90 GPa (Vohra et al.<sup>6</sup>) which is similar to that in Ce (Endo et al.<sup>7</sup> and Olsen et al.<sup>8</sup>).

In this report we present the high pressure structures in Dy, Ho and Er and newer relevant observations about their stability. Details about the experimental gear and procedures are presented elsewhere (Akella, et al.<sup>9</sup>). X-ray data were collected at the National Synchrotron Light Source, beam line x-17C using an energy dispersive system.

## Results

Under ambient conditions dysprosium, holmium and erbium have the hcp structure and retain that structure even at 3.6 GPa for Dy; 10.0 GPa in Ho; and 10.8 GPa for Er.

We observed diffraction lines that are characteristic for Sm-type structure at pressures 8.9 GPa, 11.0 GPa, and 12.04 GPa for Dy, Ho, and Er, respectively. However, remnant lines of hcp still remain at these pressures for all the three elements. In fact, in the case of Er, we observed the hcp reflections to persist throughout the Sm-type structure region and seem to be a major component.

The sluggishness of the hcp-Sm-type transformation seems to increase with the increasing atomic number for these three elements.

Diffraction lines characteristic of the dhcp structure first appear for Dy above 12 GPa but definitely lower than 17.5 GPa. For Ho at 18.9 GPa the structure is Sm-type, however the next run we made at 24.6 GPa showed possible dhcp reflections. The run at 40.0 GPa was completely dhcp. For Er we saw dhcp characteristics at 24.17 GPa. The transformation from Sm-type to dhcp appears to be sharp for all three elements. Our study revealed some interesting feature in the "fcc region." Although the most prominent diffraction lines in the spectra do indeed index quite satisfactorily as fcc, all the spectra across this field also contain a number of weak lines. The onset pressure for this transformation in Dy is 42.7 GPa and continues to the highest pressure of this study, 57.0 GPa. For Ho at 45 GPa it is still dhcp, however at 70.4 GPa we saw definite change. The same structural pattern continues up to 156 GPa, beyond which the sample lines are overlapped by the Pt marker lines. Even at 186 GPa we failed to see any new reflections emerging out of Pt lines. For Er this phase appeared at 67.4 GPa.

Full diffraction pattern for each run in this region, however, can be indexed on the basis of a "6-layered hexagonal" cell with  $c/a \approx 3 \times (c/a)_{\text{hcp}}$ . Two different atomic arrangements have been proposed (Vohra, et al.<sup>10</sup>; McMahan and Young<sup>11</sup>; and Smith and Akella<sup>3</sup>). *Each model has some difficulties in explaining the observed intensities and hence the issue is not yet resolved.*

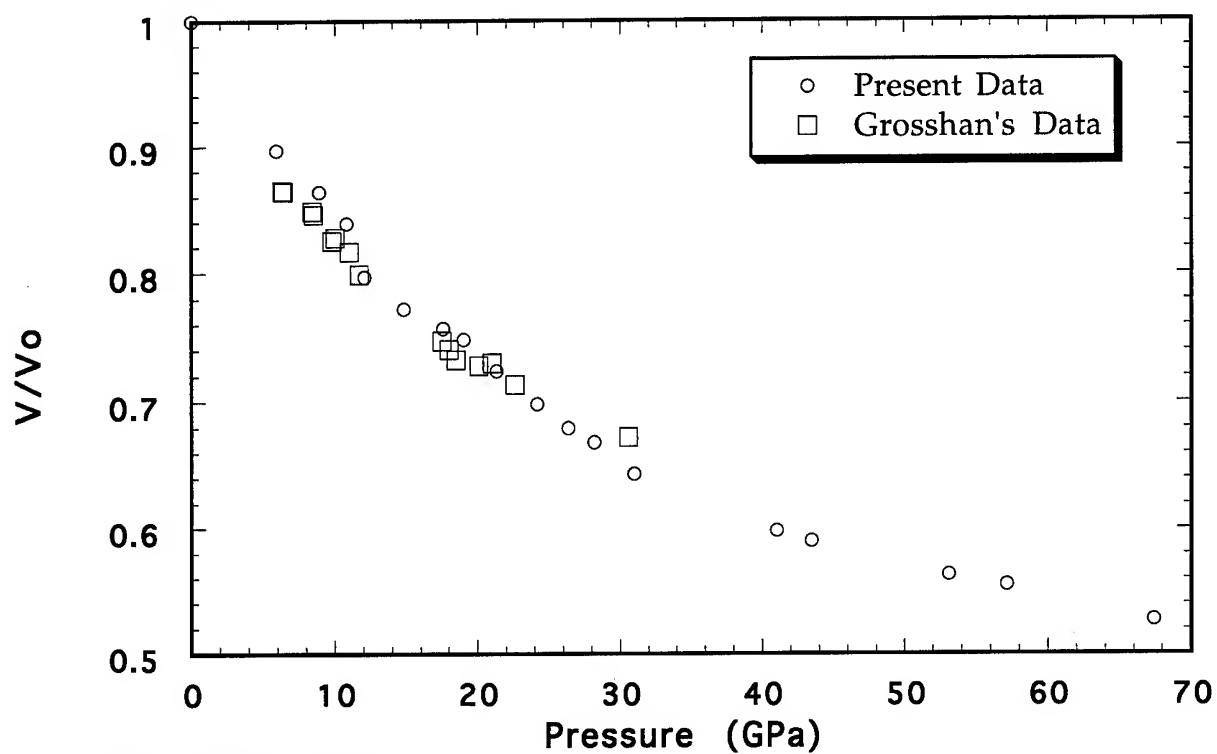
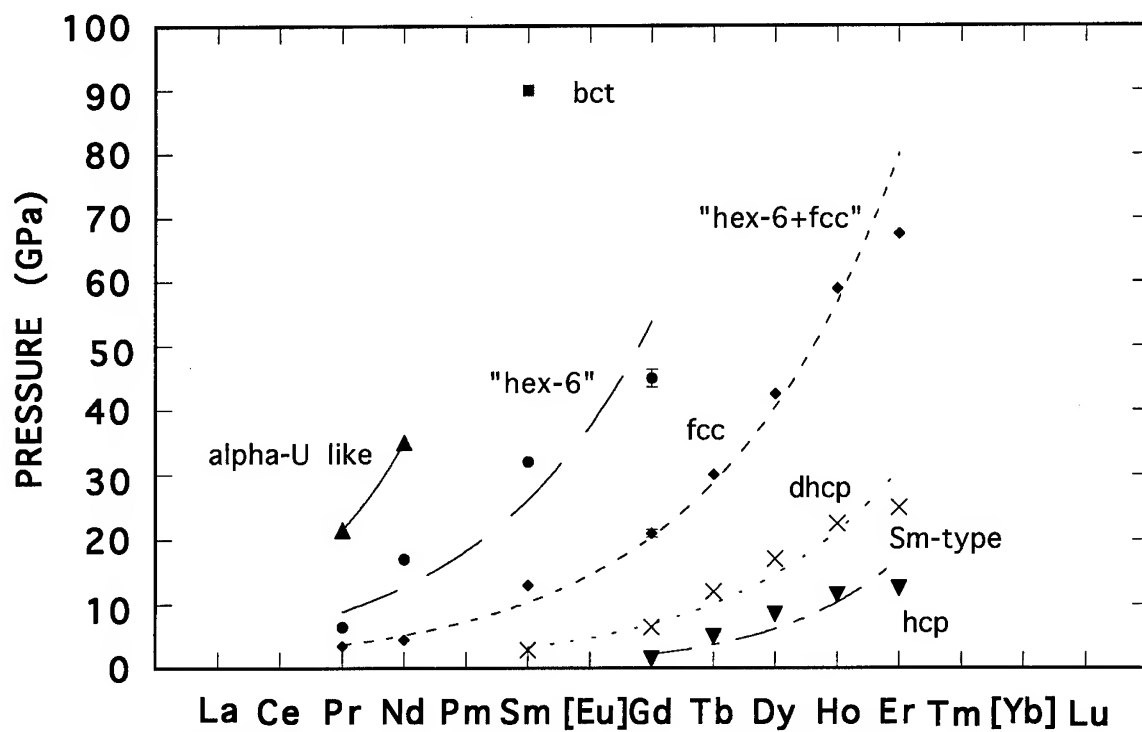
FIG. 1  $P$ - $V/V_0$  for erbium

FIG. 2 Rare-earth phase diagram

This stability region could represent a single-phase 6-layered structure or an admixture of fcc plus 6-layered structure. As we did not notice the splitting of the pseudo fcc lines, which is permitted if it were a "6-layered hexagonal" structure, we tend to regard this region, for all the three elements studied, as a mixed phase region of fcc plus "6-layered hexagonal" structure. We failed to encounter a pure fcc region for Dy, Ho, and Er. Also, no discernible discontinuities in  $V/V_0$  were noted over the various phase regions. (See Fig. 1 for erbium.) Our up-to-date phase diagram for the rare-earth elements is presented in Figure 2 and is similar to that of Krüger. Further work is underway to locate the bct structures in the other elements similar to that reported in Ce and Sm.

### Discussions

Our results are generally in good agreement with the results of Grosshans, et al.<sup>12</sup> with the exception that we find persistence of the hcp phase into the Sm-type stability field. The maximum pressure of Grosshans' study was 50 GPa and thus an exact comparison of the data cannot be easily made between these two studies. In a paper published by Krüger, et al.<sup>13</sup>, they modified Grosshans' rare-earth phase diagram by replacing the fcc and dfcc phase stability region with a "fcc" field. This is remarkably close to the phase diagram we proposed.

It is also interesting to note that Grosshans, et al.<sup>14</sup> reported seeing this same type of "6-layered hexagonal" structure in Y, La and Pr. They contend that this is a post-fcc structure type and that this "fcc region" is in fact a mixed phase region with the pure fcc phase being a remnant phase.

In our previous study of gadolinium (Akella, et al.<sup>15</sup>) we reported a fcc stability field for Gd from 44 to 55 GPa and beyond that till 106 GPa, Gd has a "6-layered" structure. In view of the new fcc plus "6-layered" mixed phase region postulated in this study, it will be of utmost importance to reinvestigate the structural changes in Gd.

### Acknowledgments

We are thankful to Dr. Jing Zhu Hu at the National Synchrotron Light Source (NSLS) Hutch X-17C for technical help. We acknowledge the financial support from the B-Division at LLNL and

thank Drs. Bruce Goodwin and Mike Anastasio for their encouragement. Chantel Ruddle helped us prepare the cells. This work was performed under the auspices of the U. S. Department of Energy by Lawrence Livermore National Laboratory under Contract W-7405-ENG-48.

### References

1. A. Jayaraman and R.C. Sherwood, *Phys. Rev. Lett.* **112**, 22 (1964)
2. W.A. Grosshans, Y.K. Vohra, and W.B. Holzapfel, *Phys. Rev. Lett.* **49**, 1572 (1982).
3. G.S. Smith and J. Akella, *Phys. Lett.* **105A**, 132 (1984).
4. G.S. Smith and J. Akella, *J. Appl. Phys.* **53**, 9212 (1982).
5. W.A. Grosshans, Y.K. Vohra, and W.B. Holzapfel, *J. Phys. F: Met. Phys.* **13**, L-147 (1983).
6. Y.K. Vohra, J. Akella, S. Weir, and G.S. Smith, *Phys. Lett. A* **158**, 89 (1991).
7. S. Endo, N. Fujioka, and H. Sasaki, *High Pressure Science and Technology Vol. 1*, K.D. Timmerhaus and M.S. Barber, eds., Plenum Press, New York, 219 (1979).
8. J.S. Olsen, L. Gerward, V. Benedict, and J.P. Itie, *Physica* **113B**, 139 (1985).
9. J. Akella, G.S. Smith, J.Z. Hu, and S. Weir, *XIII AIRAPT High Pressure Science and Technology Vol. 1*, 134 (1991).
10. Y.K. Vohra, V. Vijayakumar, B.K. Godwal, and S.K. Sikka, *Phys. Rev B* **30**, 6205 (1984).
11. A.K. McMahan and D.A. Young, *Phys. Lett.*, **105A**, 129 (1984).
12. W.A. Grosshans, Röntgengengung on linigen Seltenen Erden unter Druck, Ph.D. Thesis, University of Paderborn, Germany, 1987.
13. T. Krüger, B. Merkau, W.A. Grosshans, and W.B. Holzapfel, *High Press. Res.* **2**, 193 (1990).
14. W.A. Grosshans, Y.K. Vohra, and W.B. Holzapfel, *Phys. Rev. Lett.* **149**, 1572 (1982).
15. J. Akella, G.S. Smith, and A.P. Jephcoat, *J. Phys. Chem. Solids*, **49**, 573 (1988).



# KINETICS OF THE PRESSURE-INDUCED HCP $\rightarrow$ FCC TRANSFORMATION IN THALLIUM UNDER ISOBARIC-ISOTHERMAL CONDITIONS

MURALI MOHAN and ANIL K.SINGH

*Materials Science Division, National Aerospace Laboratories,  
Bangalore 560 017, India*

## ABSTRACT

The kinetics of hcp  $\rightarrow$  fcc transformation in thallium have been measured under isobaric conditions at 300 K at different pressures in the range 3.4-4.1 GPa. The kinetics data at 3.5 GPa under isobaric-isothermal conditions have been also measured at different temperatures in the range 300-365 K. The transformed fractions at different intervals of time have been obtained by monitoring the time-dependence of the electrical resistance change associated with the transformation. The analysis of the kinetics data suggests that the transformation proceeds without a measurable incubation period. The activation volume  $\Delta V^*$  and activation free enthalpy  $\Delta H^*$  for the total process decrease as the transformation progresses. For 20% transformation,  $\Delta V^* = -37 \text{ cm}^3 \text{ mol}^{-1}$  and  $\Delta H^* = 30.3 \text{ kcal mol}^{-1}$  and for 90% transformation,  $\Delta V^* = -30.5 \text{ cm}^3 \text{ mol}^{-1}$  and  $\Delta H^* = 22.6 \text{ kcal mol}^{-1}$ . The occurrence of the transformation at pressures below the accepted thermodynamic equilibrium pressure (3.68 GPa at 300 K) is discussed.

## Introduction

The phase boundaries and the triple point between the hcp, bcc and fcc modifications of thallium in the pressure-temperature plane have been investigated in detail in the past [1-5]. The pressure-induced hcp  $\rightleftharpoons$  fcc transformation in Tl occurring at 3.68 GPa at 300 K [2,4-8] has been widely used as a fixed point for the measurement of static pressure which lies between 2.55 GPa (Bi I  $\rightarrow$  II) and 5.5 GPa (Ba I  $\rightarrow$  II). In this paper, we report the pressure and temperature dependences of the kinetics of the hcp  $\rightarrow$  fcc transformation in Tl. The activation volume and the activation free enthalpy obtained from the analysis of these data are compared with the corresponding values obtained earlier for the  $\alpha \rightarrow \omega$  transformation in Ti [9-10] and the fcc  $\rightarrow$  bcc transformation in Yb [11-12].

## Experimental Details

The specimens measuring  $5 \times 0.5 \times 0.05 \text{ mm}^3$ , used in the present studies, were obtained from Tl-shots (99.999% pure from Atomergic Chemetals Corporation, USA) by the method discussed earlier [13]. The details of the tungsten carbide opposed anvil set up, the high pressure electrical

resistivity cell with pyrophyllite gasket and talc pressure transmitter, the pressure calibration at 300 K [9-11], the step-loading arrangement [14] for rapid pressurization ( $\sim 10 \text{ GPa s}^{-1}$ ) of the specimen and the data recording procedure [13] employed in the present study have been discussed earlier.

The following points about the experimental procedure are noteworthy: (1) the pressure difference between the center of the specimen and the voltage leads (in a four-probe resistivity measurement) was  $\sim 0.05 \text{ GPa}$  [13] (2) the uniaxial stress component was  $\sim 0.05 \text{ GPa}$  at a specimen pressure of  $\sim 4 \text{ GPa}$  [13] (3) isobaric conditions were established before appreciable transformation took place (4) the applied load was held constant (1 part in 200) during the transformation using a gas accumulator (5) the accuracy in the measurement of specimen resistance was 1 part in  $10^3$  (6) the uncertainty in the specimen pressure was  $\pm 0.05 \text{ GPa}$  at 300 K (7) during isobaric holding, the changes in the specimen pressure, if any, arising from the gasket relaxation effects over a period of 24 h was  $\sim 0.03 \text{ GPa}$  [13] (8) in the high temperature experiments, the temperatures were maintained within  $\pm 1 \text{ K}$ .

The specimen was initially pressurized at a rate  $\sim 0.1 \text{ GPa min}^{-1}$  to 2.5 GPa, and then step loaded to desired pressures in the range 3.4–4.1 GPa. The transformation progressed with time under isobaric-isothermal conditions as indicated by a time dependent resistance decrease. The transformed fraction,  $\zeta$ , at various time intervals were calculated from the resistance versus time data by the method suggested earlier [9–11,13]. The least value of  $\zeta$  that could be detected was  $\sim 0.005$ .

## Results and Discussion

The hcp  $\rightarrow$  fcc transformation ran to completion at all pressures in the range 3.4–4.1 GPa. The time for the completion of the transformation at 3.4 GPa was  $> 30 \text{ h}$ . At 3.2 GPa, the transformation did not start even after 240 h. At 4.2 GPa, the transformation was complete in  $< 10 \text{ s}$ . The pressurization rates were not fast enough to reach a desired pressure  $> 4.2 \text{ GPa}$  before appreciable transformation took place. The fractional resistance change associated with the transformation was found to be independent of pressure with a value of  $0.218 \pm 0.01$ .

The transformation began on pressurization without exhibiting an incubation period. This feature is in sharp contrast to that of the Ti [9] and Yb [11] transformations which were preceded by a strongly pressure dependent incubation period.

The  $\zeta - t$  data at 300 K were found to be sigmoidal in nature. This feature is qualitatively similar to that of the transformations in Ti and Yb. However, the  $\ln \ln (1 - \zeta)^{-1}$  versus  $\ln t$  data for the Tl-transformation do not fall on a single straight line implying that  $\zeta - t$  data do not satisfy the standard form of Avrami equation [10]. This feature is also in sharp contrast to that obtained for the Ti- and the Yb- transformations. However, the time dependent nature of the Tl-transformation suggests a thermally activated nucleation and growth mechanism.

The time,  $t_\zeta$ , for a given fraction of transformation,  $\zeta$ , decreased rapidly with increasing pressure indicating that the kinetics of the transformation becomes faster with increasing over pressure. On fitting an equation of the form

$$\ln t_\zeta = a_0(\zeta) + a_1(\zeta) p \quad (1)$$

where  $t_\zeta$  is in s and  $p$  in GPa,  $a_0 = 60.9$ ,  $a_1 = -14.8 \text{ GPa}^{-1}$  for  $\zeta = 0.2$  and  $a_0 = 52.7$ ,  $a_1 = -12.2 \text{ GPa}^{-1}$  for  $\zeta = 0.9$  were obtained. The activation volumes  $\Delta V^*(\zeta) (= a_1(\zeta)RT)$  were  $-37 \text{ cm}^3 \text{ mol}^{-1}$  for  $\zeta = 0.2$  and  $-30.5 \text{ cm}^3 \text{ mol}^{-1}$  for  $\zeta = 0.9$ . These values may be compared with the values of  $\Delta V^* = -22 \text{ cm}^3 \text{ mol}^{-1}$  for  $\zeta = 0.1$  and  $-15 \text{ cm}^3 \text{ mol}^{-1}$  for  $\zeta = 0.9$  for the fcc  $\rightarrow$  bcc transformation in Yb [11]. It is seen that  $\Delta V^*$  for the Tl-transformation is nearly double that of the Yb-transformation;  $\Delta V^*$  for the  $\alpha \rightarrow \omega$  transformation in Ti [9] is much smaller, being  $-4.3 \text{ cm}^3 \text{ mol}^{-1}$ .

In terms of the activation free energy,  $\Delta G^*$ ,  $t_\zeta$  is given by [10]

$$\ln t_\zeta = b + (\Delta G^*/RT) \quad (2)$$

and may be rewritten as

$$\ln t_\zeta = b_0 + (\Delta H^*/RT) \quad (3)$$

where  $b_0 = b - (\Delta S^*/R)$ , and  $\Delta S^*$  and  $\Delta H^*$  are respectively the activation entropy and activation enthalpy. Eq.(3) suggests that  $\Delta H^*$  can be determined if  $t_\zeta$  is measured at different  $T$ . At 3.5 GPa, experiments were carried out at different temperatures over the range 300–365 K and  $t_\zeta$  values were determined.  $t_\zeta$  decreased rapidly with increasing temperature indicating that the kinetics of the Tl-transformation is enhanced at higher temperatures. This suggests that the transformation is thermally activated.

On fitting Eq.(3) to the  $t_\zeta - T$  data,  $b_0 = -42.4$  and  $\Delta H^* = 30.3 \text{ kcal mol}^{-1}$  for  $\zeta = 0.2$  and  $b_0 = -28$  and  $\Delta H^* = 22.6 \text{ kcal mol}^{-1}$  for  $\zeta = 0.9$  are obtained. Both  $b_0$  and  $\Delta H^*$  depend on  $\zeta$  at a given  $p$ -value. Thus, the activation energy barrier for the Tl-transformation at a given  $p$ -value does not remain constant but decreases as the transformation progresses. For the Ti- [9] and Yb- [11] transformations,  $\Delta H^*$  for  $\zeta = 0.6$  was in the range  $10\text{--}20 \text{ kcal mol}^{-1}$ .

Combining Eqs.(1) and (3) and rearranging the various terms leads to

$$\Delta H_\zeta^* = RT [c_0(\zeta) + a_1(\zeta) p] \quad (4)$$

where  $c_0(\zeta) = a_0(\zeta) - b_0(\zeta)$ . Since  $a_1(\zeta)$  is negative,  $\Delta H_\zeta^*$  decreases with increasing pressures. Consequently, the kinetics of the transformation is enhanced at higher pressures.

The values of  $\Delta H_\zeta^*$  calculated using Eq.(4) with experimental values of  $c_0(\zeta)$  and  $a_1(\zeta)$  at  $p = 3.5$  GPa are  $30.6 \text{ kcal mol}^{-1}$  for  $\zeta = 0.2$  and  $22.6 \text{ kcal mol}^{-1}$  for  $\zeta = 0.9$ . These values are in excellent agreement with  $\Delta H_\zeta^*$  values of  $30.3$  and  $22.6 \text{ kcal mol}^{-1}$  respectively for  $\zeta = 0.2$  and  $0.9$  obtained from the temperature dependence of  $\ln t_\zeta$  at  $3.5$  GPa. The calculation of  $\Delta H_\zeta^*$  from Eq.(4) uses the information on the pressure dependence of the kinetics at  $300$  K and  $b_0(\zeta)$  obtained from the temperature dependence of the kinetics; information on the second term in Eq.(3) which contains  $\Delta H_\zeta^*$  is not used. A good agreement between the  $\Delta H_\zeta^*$  values obtained from the temperature dependence of the kinetics ( $\ln t_\zeta$  versus  $1/T$  data) only and the corresponding values obtained from Eq.(4) provides the justification for the use of Eq.(3) in the analysis of the present kinetics data.

The average of the reported values [2,4-8] of the equilibrium pressure,  $p(0)$ , for the hcp  $\rightleftharpoons$  fcc transformation in Ti at  $300$  K is  $3.68 \pm 0.03$  GPa. Typically, Kennedy and LaMori [7] obtained the start pressure of the forward transformation ( $p_f^s$ ) as  $3.682$  GPa and that of the reverse transformation ( $p_r^s$ ) as  $3.656$  GPa and a  $p(0) = 3.669$  GPa. In the present studies, the kinetics of the forward transformation could be measured down to  $3.4$  GPa. Since, a pressure-induced transformation can, in principle, occur at any pressure above  $p(0)$ , the present data suggests that  $p(0)$  for the Ti-transformation is  $< 3.4$  GPa. If  $p(0) < 3.4$  GPa, then the occurrence of the reverse transformation at  $3.656$  GPa observed in ref.[7] is puzzling. This will mean that on decreasing the pressure from a region where high-pressure phase is stable, the low-pressure phase appears above  $p(0)$ , i.e., in the pressure region where the high-pressure phase is stable. The bcc  $\rightleftharpoons$  hcp transformation in Fe exhibits similar behaviour [15]. Bridgman [1] observed the Ti-transformation at  $2.5$  GPa in shearing experiments. While shear stresses affect both  $p_f^s$  and  $p_r^s$ , it is not clear whether  $p(0)$  is also affected. The earlier work on the  $\alpha \rightarrow \omega$  transformation

in Ti [10] and on some reconstructive type transformations [16] suggest that  $p(0)$  is not altered by the shear stresses. What is altered is the hysteresis-width of the transformation. Following this view, Bridgman's data suggest that  $p(0)$  is  $\sim 2.5$  GPa. In such a case, the occurrence of the transformation at pressures as low as  $3.4$  GPa stands explained.

## References

- 1 P.W.Bridgman, *Phys.Rev.* **48** (1935) 893.
- 2 F.R.Boyd and J.L.England, *J.Geophys.Res.* **65** (1960) 741.
- 3 A.Jayaraman, W.Klement Jr., R.C.Newton and G.C.Kennedy, *J.Phys.Chem. Solids* **24** (1963) 7.
- 4 P.N.Adler and H.Margolin, *Trans. Metall. Soc. AIME*, **230** (1964) 1048.
- 5 P.N.LaMori, in *Accurate Characterization of the High Pressure Environment*, ed. E. C. Lloyd, (NBS-Special Publication **326**, 1971) p.279.
- 6 G. C. Kennedy and P. N. LaMori, in *Progress in Very High Pressure Research*, eds. F. P. Bundy, W. R. Hibbard and H. M. Strong, (John Wiley, 1961) p.304.
- 7 G. C. Kennedy and P. N. LaMori, *J. Geophys. Res.* **67** (1962) 851.
- 8 R.J.Zeto and H.B.Vanfleet, *J.Appl.Phys.* **40** (1969) 2227.
- 9 A.K.Singh, Murali Mohan and Divakar. C, *J. Appl. Phys.* **53** (1982) 1221; **54** (1983) 5721.
- 10 A.K.Singh, *Bull. Mater. Sci (India)*. **5** (1983) 219; *Mater. Sci. For. (Trans Tech-Switzerland)* **3** (1985) 291.
- 11 C.Divakar, Murali Mohan and A.K.Singh, *J. Appl. Phys.* **56** (1984) 2337.
- 12 M.Mohan, C.Divakar and A.K.Singh, *Physica*, **139 & 140B** (1986) 253.
- 13 Murali Mohan and A.K.Singh, in *Adv. in High Press. Sci. & Tech.* ed. A.K.Singh (Tata McGraw-Hill, 1995) p.121.
- 14 A.K.Singh, C.Divakar and Murali Mohan, *Rev. Sci. Instrum.* **54** (1983) 1407.
- 15 E.Huang, W.A.Bassett and P.Tao, in *High-Press. Res. in Min.Phys.*,ed.M.H.Manghnani and Y.Syono, (Terra Scientific, 1987) p.165.
- 16 F. Dachille and R. Roy, in *Reactivity of Solids*, ed. J.de Boer, (Elsevier - Amsterdam, 1961) p.502.

# A PRESSURE INDUCED $\alpha'' \rightarrow \omega$ TRANSITION IN Ti-Nb ALLOYS

A.V.DOBROMYSLOV, G.V.DOLGIKH, and A.N.MARTEM'YANOV

*Institute of Metal Physics, Ural Division of Russian Academy of Science, 18 Kovalevskaya Street, Ekaterinburg, 620219, RUSSIA*

The structure of five binary Ti-Nb alloys with composition between 7 and 15 at.% Nb exposed to a quasi-hydrostatic pressure of 8 GPa has been studied by X-ray diffraction, optical microscopy, and transmission electron microscopy. It has been found that the pressure-induced  $\omega$ -phase retains upon pressure removal. This phase forms large massive regions and in part inherits the morphology of the original  $\alpha''$ -phase. As a result of accommodation processes, a large number of stacking faults have been observed to arise in the high-pressure phase. From an analysis of diffuse scattering, it is concluded that the structure of the  $\omega$ -phase contains line defects.

## 1 Introduction

A number of investigations have been devoted to the study of the effect of pressure on the structure of various titanium alloys. The  $\alpha' \rightarrow \omega$  phase transition has been studied most fully. The effect of pressure on the  $\alpha'' \rightarrow \omega$  transformation in titanium alloys has virtually not been studied. However, the study of this question is important not only for the purpose of determination of mechanism of emergence of the orthorhombic  $\alpha''$ -phase, but also for the understanding of the nature of formation of this phase in titanium and zirconium alloys.

Hence, in this investigation the task was set to realize  $\alpha'' \rightarrow \omega$  phase transformation in Ti-Nb alloys under pressure and to study the specific features of the emerging  $\omega$ -phase over a wide niobium concentration range.

## 2 Experimental

The Ti-Nb alloys containing 7; 9; 11; 13 and 15 at.% Nb were melted from iodide titanium and 99.98% niobium in a helium-filled arc furnace. The ingots were refined by triply remelting, deformed by rolling to 50% strain, homogenized in a vacuum of  $1 \times 10^{-3}$  Pa at 1000°C for 3h, and quenched in icy water. From the quenched specimens, disks 3 and 5 mm in diameter and 0.1 mm thick were cut. Disks of the same diameter were assembled into a stack, subjected to compression by a quasi-hydrostatic pressure of 8 GPa in a toroid-type high-pressure unit. The pressure-transmitting medium was sodium chloride. The pressure was calibrated on the basis of phase transformation in bismuth. The X-ray diffraction anal-

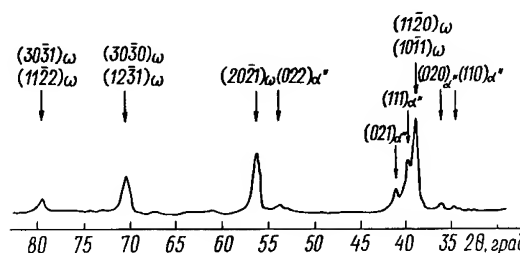


Figure 1: X-ray diffraction pattern of Ti-13 at.% Nb alloy,  $\beta$ -quenched and pressurized at 8 GPa.

ysis was carried out on a diffractometer DRON-3, using  $\text{Cu } K_\alpha$  radiation. The metallographic examination was performed with an Epityp light microscope, and the transmission electron microscopic (TEM) study on a JEM-100C microscope.

## 3 Results and Discussion

According to X-ray analysis the orthorhombic  $\alpha''$ -phase is observed in Ti-Nb alloys starting from niobium concentrations of 9 at.%. No presence of  $\omega$ -phase was revealed after quenching in any of the investigated alloys.

Metallographic analysis of the quenched Ti-7 at.% Nb alloy has revealed a typical martensitic structure with fairly extensive and thick primary martensitic plates of the  $\alpha'$ -phase. The plates size in this alloys is significantly less than that of the initial  $\beta$ -grains. In the Ti-9 at.% Nb alloy the thickness of martensitic plates is reduced of the overage an order of magnitude. Such a structure is virtually retained in the quenched Ti-11 at.%

Nb alloy. However, in some places of the structure of this alloy there appear small regions in which thin martensitic plates of  $\alpha''$ -phase start to arrange themselves in parallel rows. These structural features are revealed more clearly in the Ti-13 at.% Nb alloy, whereas in the quenched Ti-15 at.% Nb alloy thin extensive plates of the  $\alpha''$ -phase already fill up uniformly the entire bulk of the initial  $\beta$ -phase grain forming a typical Widmanstatten structure.

Thus, transition from the  $\alpha'$ -phase to the  $\alpha''$ -phase is characterized by a substantial change in the morphology of martensite plates, an increase in their length and a more uniform distribution of the martensitic plates in the bulk of the initial  $\beta$ -grains.

In contrast to metallographic structure analysis, TEM study does not reveal any substantial difference in the structure of quenched alloys with varying niobium contents. In all the alloys, whatever the niobium contents, the structures are relatively similar: a large number of martensite plates is mainly observed, including within themselves numerous dislocations and irregularly arranged twins.

As a result of application of 8 GPa pressure a high-pressure phase ( $\omega$ -phase) is formed in all the alloys, whatever the type of the initial phase crystal lattice (Figure 1). This phase, the prototype of  $\omega$ -phase forming in the titanium-base and zirconium-base alloys with  $\beta$ -stabilizing elements, is retained in the alloy in the metastable state after the pressure is removed. A certain amount of  $\alpha'$ -phase or  $\alpha''$ -phase is retained, depending of the niobium contents, in all the alloys together with the high-pressure phase. In contrast to  $\omega$ -phase, emerging in these alloys in the process of tempering or quenching, the high-pressure phase is formed in the shape of massive regions. The initial morphology of the quenched structure in alloys with a lower niobium content is in the main retained after the pressure is removed. However, metallographic structural analysis shows that in titanium alloys containing from 13 to 15 at.% of niobium the initial structural pattern is replaced with a Widmanstatten pattern similar to that found in a number of zirconium and titanium alloys after quenching when an  $\omega$ -phase is formed. Electromicroscopy examination of structure of alloys subjected to pressure also reveals that the application of pressure does not lead to changes

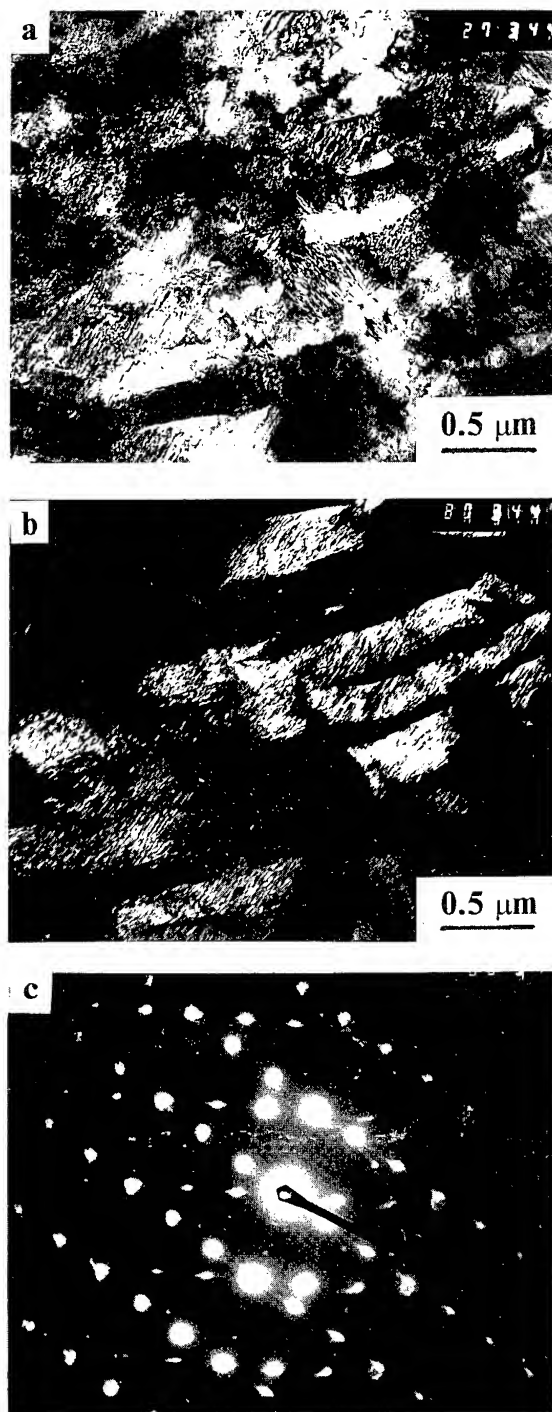


Figure 2: Structure of Ti-13 at.% Nb alloy,  $\beta$ -quenched and pressurized at 8 GPa. Bright-field image (a); dark-field image (b); selected area diffraction pattern corresponding to (a,b), zone axis [011]  $\omega$ -phase (c).

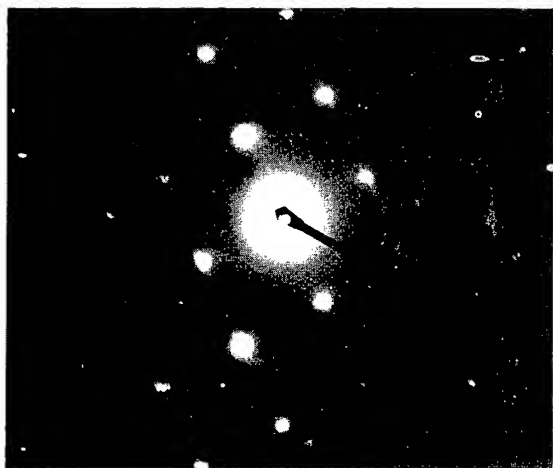


Figure 3: Diffuse effects associated with  $\alpha'' \rightarrow \omega$  transformation, zone axis  $[122]$   $\omega$ -phase.

in morphology of initial martensite plates (Figure 2). However, inside martensite plates characteristic stripes appear. Such a structural defects were observed earlier inside martensite plates in various zirconium alloys<sup>1</sup> and in Ti-V alloy<sup>2</sup> after they were subjected to pressure. Electron micrographs taken from such plates reveal a diffraction pattern corresponding to the  $\omega$ -phase. In the dark-field image the entire plate "shines" in the  $\omega$ -phase reflex. Some micrographs show a diffuse scattering in the shape of streaks corresponding to planes of diffuse scattering over (001) in the  $\omega$ -phase reciprocal lattice (Figure 3).

A characteristic feature of the pressure-induced  $\alpha' \rightarrow \omega$  transformation is the retaining of morphological shapes of the initial martensitic structure. A similar type of transformation has been revealed by us also in Ti-Nb alloys regardless of the structural state of the initial quenched alloy ( $\alpha'$ - or  $\alpha''$ -phase). In all cases the emergence of the  $\omega$ -phase takes place with the retaining of all the transformation special features which accompany this process in other investigated alloys, both zirconium and titanium based, namely: massive character of transformation, presence of stripes, observed both in the bright-field and dark-field images, emergence of diffuse scattering. The stripes observed in bright-field images are associated with these defects. In this investigation no attempt was made to carry out a special analysis of the structural defect type. However, according<sup>1</sup>,

the emergence of stripes is linked to the formation of stacking faults in the structure of the alloys following application of pressure. These defects are arranged in  $\{\bar{2}110\}$  planes of the  $\omega$ -phase. The process of the stacking faults formation is an accommodation mechanism for the reduction of elastic energy of  $\alpha'' \rightarrow \omega$  transformation.

The emergence of diffuse scattering effects is connected with the presence of linear defects due to the displacement of atom rows along the  $[001]$  directions of the  $\omega$ -phase lattice. All these special structure features were earlier accounted for with the help of the model of  $\alpha \rightarrow \omega$  transformation<sup>3</sup>. The similarity in the transformation peculiarities observed in alloys having  $\alpha'$ -phase structure, as well as in alloys with orthorhombic  $\alpha''$ -phase, testify to that the restructuring of the orthorhombic  $\alpha''$ -phase lattice into that of the  $\alpha''$ -phase proceeds by displacements of closely packed atomic rows of the  $\alpha''$ -phase corresponding to the  $\omega$ -phase  $[001]$  rows.

#### References

1. A.V. Dobromyslov *et al*, *Fiz.Met.Metalloved.* 59(1), 111 (1985).
2. A.V. Dobromyslov *et al*, *Fiz.Met.Metalloved.* 74(4), 130 (1992).
3. A.V. Dobromyslov *et al*, *Fiz.Met.Metalloved.* 69(5), 108 (1990).

# ACOUSTIC EMISSION FROM CERIUM UNDER HIGH PRESSURE ISOMORPHIC $\gamma \leftrightarrow \alpha$ PHASE TRANSITIONS

Z. WITCZAK, V.A. GONCHAROVA

*High Pressure Research Center, Polish Academy of Sciences, Sokolowska 29, 01-142 Warszawa, Poland*

Acoustic emission (AE) from cerium under multiple high pressure isomorphic  $\gamma \leftrightarrow \alpha$  phase transitions (PT) at room temperature has been studied. The dependences of the cumulative number of AE events on the number of  $\gamma \leftrightarrow \alpha$  PT were distinctly different for the  $\gamma \rightarrow \alpha$  and  $\alpha \rightarrow \gamma$  ones. The AE event rates for both  $\gamma \rightarrow \alpha$  and  $\alpha \rightarrow \gamma$  PT were also significantly different, in that the AE rate versus pressure had nearly symmetrical feature for the  $\gamma \rightarrow \alpha$  PT and plainly asymmetrical one for the  $\alpha \rightarrow \gamma$  PT. The observed phenomena were qualitatively explained on the basis of the simple micromechanical model of the PT with a volume change.

## Introduction

An acoustic emission method (AE) is very useful for the in-situ investigations of dynamic processes in materials under pressure. The good examples for that are isomorphic  $\gamma \rightarrow \alpha$  or  $\alpha \rightarrow \gamma$  phase transitions (PT) in cerium at room temperature which practically occur by non-diffusional process of plastic deformation due to the large volume changes ( $\sim 13.5\%$ ) at these PT<sup>1</sup>. This process can be well detected and recorded<sup>2</sup>. That makes possible investigations the kinetics of the  $\gamma \leftrightarrow \alpha$  PT in cerium and effects of the real structure of the material. In this work we try to determine experimental requirements that should be met for such investigations.

## Experimental Procedure

A cylindrical sample ( $d=15\text{mm}$ ,  $h=10\text{mm}$ ) was prepared from the material of a 99.7% purity according to the procedure presented elsewhere<sup>2</sup>. The structural and mechanical properties of the material are also described there. In the centre of the flat face of the sample a broadband piezoelectric sensor of AE made of monocrystalline  $\text{LiNbO}_3$  was placed and this set was applied to hydrostatic pressurization in a medium of extraction naphtha. The  $\gamma \leftrightarrow \alpha$  PT were investigated under pressure rate of 2 MPa/s. Ten minute stops were made at 0.4 GPa and 1 GPa pressures between pressurizations. The AE signals detected by the sensor were recorded with GACEK AE signals analyzer working within a 100 kHz – 2 MHz bandpass. The sensitivity of the AE sensor in the applied pressure range is not affected very much by pressure<sup>3</sup>.

## Results and Discussion

Cumulative numbers of AE events recorded at several consecutive  $\gamma \rightarrow \alpha$  and  $\alpha \rightarrow \gamma$  PT are presented in Fig. 1 and Fig. 2, respectively. It is seen that both dependences are asymptotic curves. The decline of AE activity at  $\gamma \rightarrow \alpha$  PT is a result of work hardening of the material while its increase at  $\alpha \rightarrow \gamma$  PT seems to result from other phenomena<sup>2</sup>. In particular, a dramatic decrease of AE activity follows the first  $\gamma \rightarrow \alpha$  PT. This is even more visible in Fig. 3 where the AE events rate for this PT is shown. The dependence of AE events rate on pressure for  $\alpha \rightarrow \gamma$  PT distinctly differs from that during  $\gamma \rightarrow \alpha$  PT. Except for the first  $\gamma \rightarrow \alpha$  PT the AE events rate during the process of this PT has a symmetric character against the mean transition pressure while it varies completely asymmetrically at  $\alpha \rightarrow \gamma$  PT (Fig. 4).

The results can be explained qualitatively with a simple micromechanical model of this isomorphic transition when a spheric shape of the sample is assumed. In such a case the movement of the spheric interphase boundary under pressure can be expressed for both  $\gamma \leftrightarrow \alpha$  PT as follows:

$$r/R = \exp(-\Delta p/2\sigma_0) \quad (1)$$

where:  $r$  is the radius of the interphase boundary,  $R$  is the radius of the sample,  $\Delta p = p - p_i$  is the difference between the applied pressure  $p$ , and the pressure in the initial phase (inner)  $p_i$ ,  $\sigma_0$  is the yield strength of the new phase (outer). This expression is derived from the theory of plasticity<sup>4</sup> and based on the reasonable assumption that the PT process begins at the surface of the sample and spreads to its centre. To finish the

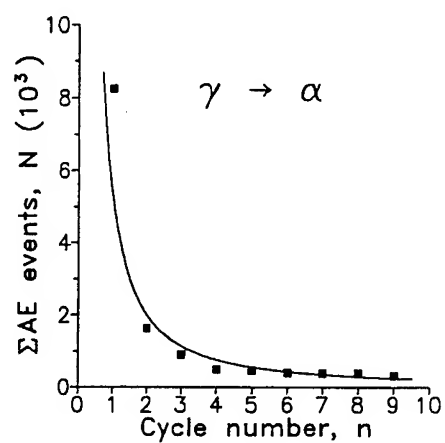


Figure 1: Cumulative number of AE events *versus* pressure cycle number for  $\gamma \rightarrow \alpha$  PT.

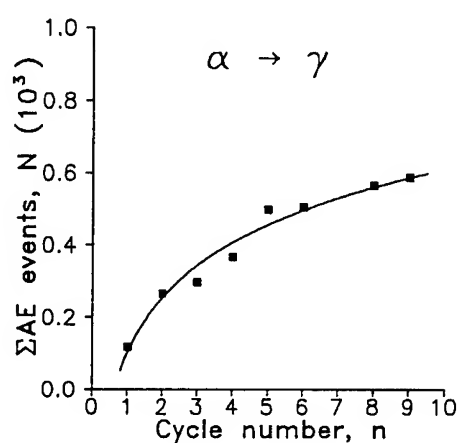


Figure 2: Cumulative number of AE events *versus* pressure cycle number for  $\alpha \rightarrow \gamma$  PT.

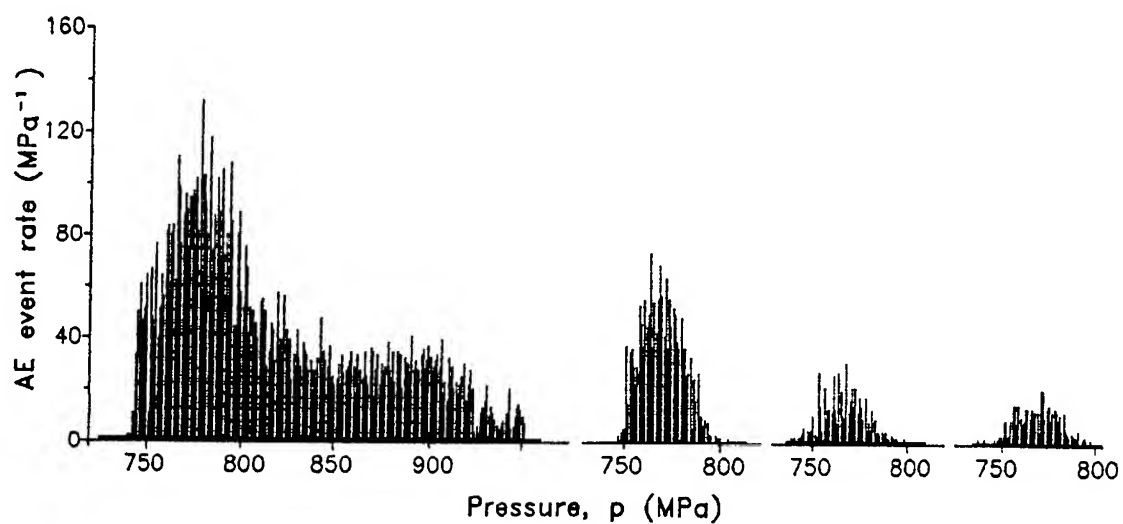


Figure 3: AE event rate during  $\gamma \rightarrow \alpha$  PT for the 1-st, 2-nd, 4-th and 6-th pressure cycle, respectively.



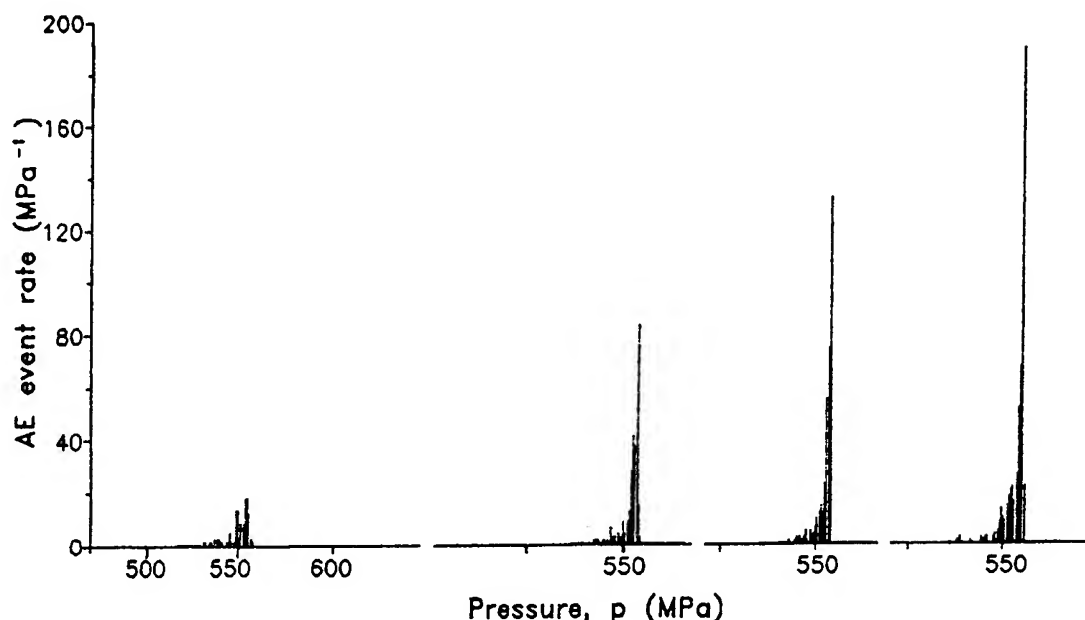


Figure 4: AE event rate during  $\alpha \rightarrow \gamma$  PT for the 1-st, 2-nd, 4-th and 6-th pressure cycle, respectively.

process of transformation of the material the second phase should be fully plasticized in the sense of this theory. This needs infinitely high value of  $\Delta p$ , which is not quite true for the material of a real structure, however this definitely indicates the existence of residual stresses in the material after PT as a result of plastic deformations. Unrelaxed at high pressure such stresses accelerate the action of the positive value of  $\Delta p$ , when the pressure is decreasing. That makes the  $\alpha \rightarrow \gamma$  PT of a burst type. This is clearly seen for the further pressure cycles when the material becomes more homogeneous due to cumulated deformation in it. Irregularity of the PT process is especially visible at the first  $\gamma \rightarrow \alpha$  PT (Fig. 3) when the interphase boundary had to be very complicated, may be not single. To avoid the asymmetry of this PT process it should be used the sample of the shape that secure only one plane interphase boundary. In such a case the  $\gamma \rightarrow \alpha$  PT would not create any significant residual stresses in the material and the initial states of both phases would be similar.

## Conclusions

1. Investigations the kinetics of  $\gamma \leftrightarrow \alpha$  isomorphic PT in cerium require the previous high pressure cycling of the material to stabilize its real structure.

2. The shape of the sample for such investigations should secure only one plane interphase boundary during these transitions.

## References

1. E.Yu. Tonkov, High Pressure Phase Transitions, Philadelphia, Reading, Paris, Montreaux, Tokyo, Melbourne, Gordon and Breach Sci. Pub., 1992.
2. Z. Wiczak and V.A. Goncharova, Scripta Metall. Mater. 33 (1995) 195.
3. Z. Wiczak, R. Jemielniak and P. Wiczak, Acoustic emission sensors for in-situ measurements under pressure, in this conference proceedings.
4. R. Hill, Mathematical Theory of Plasticity, Clarendon Press, Oxford (1950) p. 97.

# THE SOFTENING OF THE SHEAR MODULI OF THE $\text{Ti}_{50}\text{Ni}_{48}\text{Fe}_2$ SHAPE MEMORY SINGLE CRYSTAL UNDER HYDROSTATIC PRESSURES

V.A. GONCHAROVA, E.V. CHERNYSHEVA, D.R. DMITRIEV

*Institute of High Pressure Physics, Russian Academy of Sciences, Troitsk, Moscow Region, Russia*

A.I. LOTKOV, V.P. LAPSHIN, V.N. GRISHKOV

*Institute of Physics of Strength and Materials Engineering, Russian Academy of Sciences, Tomsk, Russia*

Ultrasonic pulse echo overlap method was used for determining the transit times of one longitudinal and two transverse elastic waves of the 3–5 MHz frequency in the single crystal of  $\text{Ti}_{50}\text{Ni}_{48}\text{Fe}_2$  cut out in the [110] direction. The study was carried out under hydrostatic pressures up to 6 GPa at room temperature. The pressure dependences of the density, velocities of sound, effective elastic moduli, Debye temperature, microscopic Gruneisen parameters and equation of state were calculated. Alternating softening and stiffening of shear elastic moduli is supposed to result from a transformation of the parent B2 phase to incommensurate (IC) phase at  $\sim 4$  GPa and further at  $\sim 5.4$  GPa to rhombohedral R phase.

## Introduction

Among transition metal alloys the TiNi-based ones are widely known as the shape memory materials which undergo at cooling series of phase transitions (PT) of the first and second order. These PT are accompanied by anomalous behaviour of many physical properties. The factors influencing the martensitic PT and shape memory phenomenon in these alloys (composition, transition metals doping, thermomechanical treatment) are extensively investigated. However examinations of high pressure effects are still in the beginning. Determined at various pressures up to 6 GPa temperature dependences of electrical resistance of  $\text{Ti}_{50}\text{Ni}_{47}\text{Fe}_3$ <sup>1</sup> showed that the high pressure slightly stabilizes a high temperature B2 phase and essentially widens the p-T boundaries of intermediate rhombohedral R phase. Recently we reveal the softening of the  $(C_{11} - C_{12})/2$  shear modulus of  $\text{Ti}_{50}\text{Ni}_{48}\text{Fe}_2$  single crystal under pressures up to 0.6 GPa at room temperature<sup>2</sup>.

In this article we present a thorough study of all elastic moduli of the  $\text{Ti}_{50}\text{Ni}_{48}\text{Fe}_2$  single crystal under high hydrostatic pressures up to 6 GPa at room temperature.

## Experimental Procedure

A truncated cone of 3.2 mm height and  $\sim 13$  mm mean diameter was cut out from a large single

crystal ingot by spark erosion. The specimen faces were perpendicular to a [110] direction and parallel to each other within 1  $\mu\text{m}$  accuracy.

Ultrasonic transit time measurements were performed by pulse echo overlap method. The transducers of the 3 and 5 MHz frequency made of the X or Y cut quartz plates were bonded to the specimen with honey. The accuracy of the single transit time reading was equal to 1–2 ns.

To generate high hydrostatic pressure the apparatus of piston–cylinder and toroidal types were used. The pressure medium was extraction naphtha. The uncertainty in the pressure value determination was equal to  $\sim 2\%$  at the highest pressures.

Some details of experimental procedure and physical properties of  $\text{Ti}_{50}\text{Ni}_{48}\text{Fe}_2$  at ambient conditions are given elsewhere<sup>2</sup>.

## Results and Discussion

Fig. 1 shows pressure dependences for three independently measured elastic constants of  $\text{Ti}_{50}\text{Ni}_{48}\text{Fe}_2$  at the pressure rising up to 6 GPa at room temperature. Alternating softening and stiffening of the shear elastic moduli  $(C_{11} - C_{12})/2$  and  $C_{44}$  indicates the series of some PT. Because of the lack of the X-ray data under pressure for this material it is difficult to assign the observed anomalies of shear elastic moduli to expected type of PT unambiguously. However it is

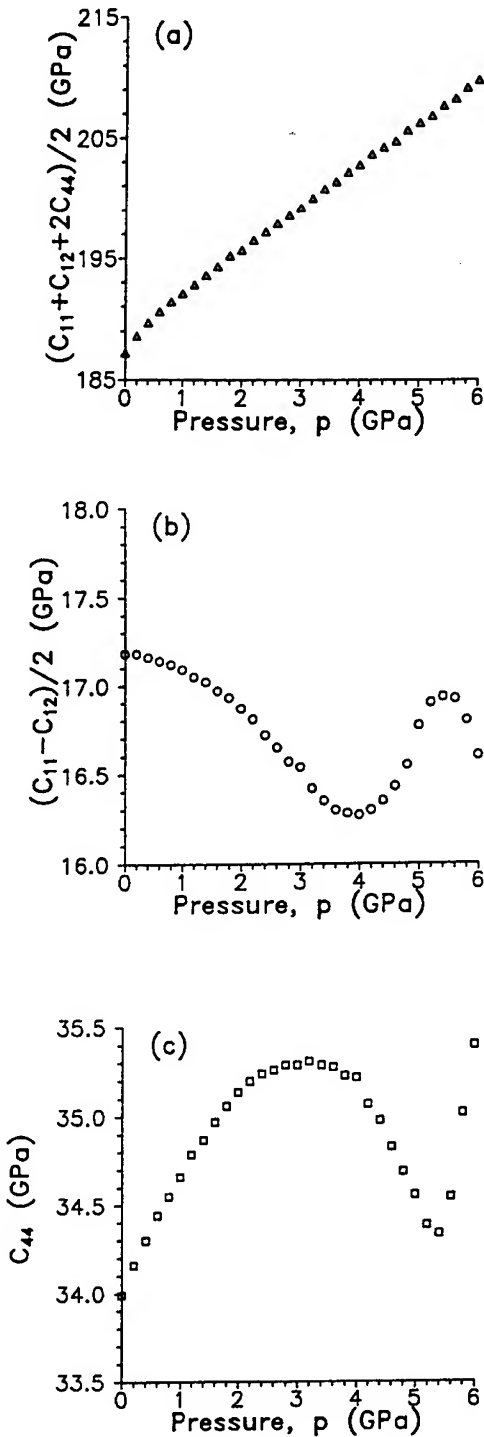


Figure 1: Pressure dependence of the elastic moduli of  $\text{Ti}_{50}\text{Ni}_{48}\text{Fe}_2$ : (a) longitudinal mode  $(C_{11} + C_{12} + 2C_{44})/2$ ; (b) transverse mode  $(C_{11} - C_{12})/2$ ; and (c) transverse mode  $C_{44}$ .

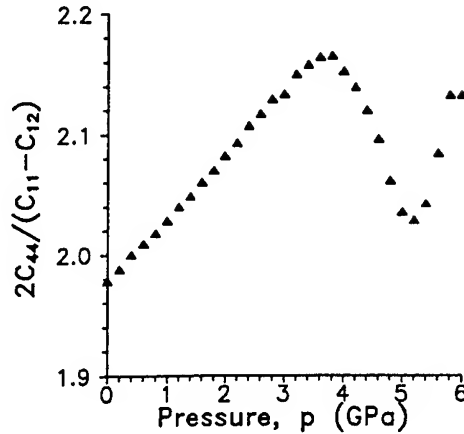


Figure 2: Pressure dependence of the elastic anisotropy  $2C_{44}/(C_{11} - C_{12})$  of  $\text{Ti}_{50}\text{Ni}_{48}\text{Fe}_2$ .

known<sup>1</sup> that  $\text{Ti}_{50}\text{Ni}_{47}\text{Fe}_3$  is subjected under pressure to the same consequence of PT as  $\text{Ti}_{50}\text{Ni}_{48}\text{Fe}_2$  does at cooling, i.e.  $B2 \rightarrow IC \rightarrow R \rightarrow B19'$ . Besides we can compare our results with the temperature dependences of elastic moduli of TiNi-based alloys undergoing at cooling the same series of PT.

The smaller of two shear elastic moduli of  $\text{Ti}_{50}\text{Ni}_{48}\text{Fe}_2$   $(C_{11} - C_{12})/2$  softens at the very beginning of a pressure rise. This indicates the initial instability of the parent B2 phase. Approaching the  $B2 \rightarrow IC$  PT at  $\sim 4$  GPa was accompanied by the softening only this shear modulus of  $\sim 5.2\%$ . At cooling under ambient pressure towards the  $B2 \rightarrow IC$  PT all elastic constants (even the longitudinal  $(C_{11} + C_{12} + 2C_{44})/2$  one) of  $\text{Ni}_{50.5}\text{Ti}_{49.5}$ <sup>3</sup> exhibited an increasing softening. At the occurrence of R phase there was a minimum on the temperature dependence of the elastic anisotropy. This minimum is a consequence of the sharp decrease ( $\sim 50\%$ ) of the  $C_{44}$  shear modulus and increase of the  $(C_{11} - C_{12})/2$  one. The pressure dependence of elastic anisotropy of  $\text{Ti}_{50}\text{Ni}_{48}\text{Fe}_2$  (Fig. 2) has a minimum at  $\sim 5.4$  GPa as a result of the  $C_{44}$  softening ( $\sim 2.6\%$ ) and  $(C_{11} - C_{12})/2$  stiffening ( $\sim 3.8\%$ ) in the interval 4–5.4 GPa. At pressures higher than  $\sim 5.2$  GPa we observed a dramatic attenuation of ultrasonic signal which generally accompanies PT.

Comparison between our data and those of Brill *et al.*<sup>3</sup> shows both the qualitative and quantitative difference in the elastic behaviour of TiNi-based alloys near the same PT taking place under pressure and at cooling. For example it was seen no softening of the longitudinal

$(C_{11} + C_{12} + 2C_{44})/2$  modulus (Fig. 1a) unlike at cooling<sup>3</sup>.

### Conclusions

The softening of the  $(C_{11} - C_{12})/2$  shear modulus under pressure precedes the B2-IC phase transition whereas the occurrence of R phase of  $\text{Ti}_{50}\text{Ni}_{48}\text{Fe}_2$  is accompanied by the softening of the  $C_{44}$  shear modulus. This gives rise to the dramatic change of anisotropy factor. However the effects of softening are very weak if compared with that at cooling<sup>3</sup>.

### References

1. I.G. Zakrevskii, V.V. Kokorin, V.A. Chernenko and V.M. Kachalov, *Metallofizika* (Kiev) 9 (1987) 107.
2. A.I. Lotkov, V.A. Goncharova, V.P. Lapshin, V.N. Grishkov and M.N. Podlevskich, *Phys. Solid State (Russia)* 35 (1993) 1415.
3. T.M. Brill, S. Mittelbach, W. Assmus, M. Mullner and B. Luthi, *J.Phys.: Condens. Matter* 3 (1991) 9621.

## **VI(C.5) Other Solids**

# STRUCTURAL SYSTEMATICS OF THE $AX_2$ COMPOUNDS WITH COORDINATION NUMBERS FROM 6 TO 11 AT HIGH PRESSURES

J. HAINES, J. M. LÉGER, O. SCHULTE and A. ATOUF

*C.N.R.S., Laboratoire de Physico-Chimie des Matériaux,*

*1, Place Aristide Briand, 92190 Meudon, France*

## ABSTRACT

An extensive investigation of the structural phase transitions in the  $AX_2$  compounds, in particular, transitions occurring in the metal dioxides and dihalides, has been performed by *in-situ*, angle-dispersive, x-ray powder diffraction using an imaging plate and time-of-flight, neutron powder diffraction. The recent advances in these techniques allow for the refinement of structures obtained at high pressure by the Rietveld method. The present results require significant changes to be made to the structural systematics of the  $AX_2$  compounds. There are two principal pathways between the rutile and cotunnite structures, neither of which pass by the fluorite structure. Two additional steps beyond the cotunnite structure have been added to the phase transition sequence of these materials.

## Introduction

There has been considerable interest in the high pressure behavior of rutile-structured compounds due to the existence of a polymorph of silica, stishovite, which adopts this structure. It has long been proposed that rutile-type structures, in which the cation coordination number (CN) is 6, transform to the fluorite-type (CN=8) and then to the cotunnite-type (CN=9) structures (1). These proposals were based primarily on unit cell constants obtained from *in situ* powder diffraction experiments or from experiments on quenched samples. More recent results indicate that the high-pressure structural systematics of rutile-structured materials are more complex. Stishovite itself has been found to undergo a second-order transition to a  $CaCl_2$ -type structure (2,3) in agreement with *ab initio* calculations (4), which indicate a further transition to a cubic  $Pa\bar{3}$  structure, rather than the fluorite structure. Rutile ( $TiO_2$ ), on the other hand, has been found to transform to the baddeleyite structure (CN=7) (5). The present series of experiments on the  $AX_2$  compounds were intended to investigate the various pathways between the rutile and cotunnite structures and to determine the next step in the phase transition sequence, possibly to a structure in which the CN is greater than 9.

## Experimental

High pressure diffraction experiments were performed on the following  $AX_2$  compounds,  $MO_2$  ( $M=Ti, Zr, Hf, Nb, Mn, Ru, Sn, Pb$ ) and  $BaX_2$  ( $X=F, Cl, Br, I$ ) and  $SnCl_2$  and  $PbCl_2$  by *in-situ*, angle-dispersive, x-ray powder diffraction up to 60 GPa in diamond anvil cells and by time-of-flight, neutron powder diffraction on  $RuO_2$  and  $BaF_2$  up to 7 GPa in the Paris-Edinburgh cell. High-pressure x-ray data were acquired initially on film, which has subsequently been replaced by an imaging plate. Full experimental details have been published elsewhere (6-16).

## Results and Discussion

Two distinct transformation pathways are observed in the metal dioxides (figure 1). The high pressure behavior of the group IVa ( $Ti, Zr, Hf$ ) dioxides has been the subject of much controversy; however, recent experiments present a clearer picture. Rutile ( $TiO_2$ ),  $P4_2/mnm$ ,  $Z=2$ , transforms to the baddeleyite structure (5). Baddeleyite-structured  $ZrO_2$  and  $HfO_2$ ,  $P2_1/c$ ,  $Z=4$ , both transform to an orthorhombic  $Pbca$  structure,  $Z=8$ , (CN=7) as determined by neutron and x-ray diffraction, respectively (17,18).  $ZrO_2$  and  $HfO_2$  undergo a further transition to the cotunnite structure,  $Pnam$ ,  $Z=4$  (19), which has been refined recently in the

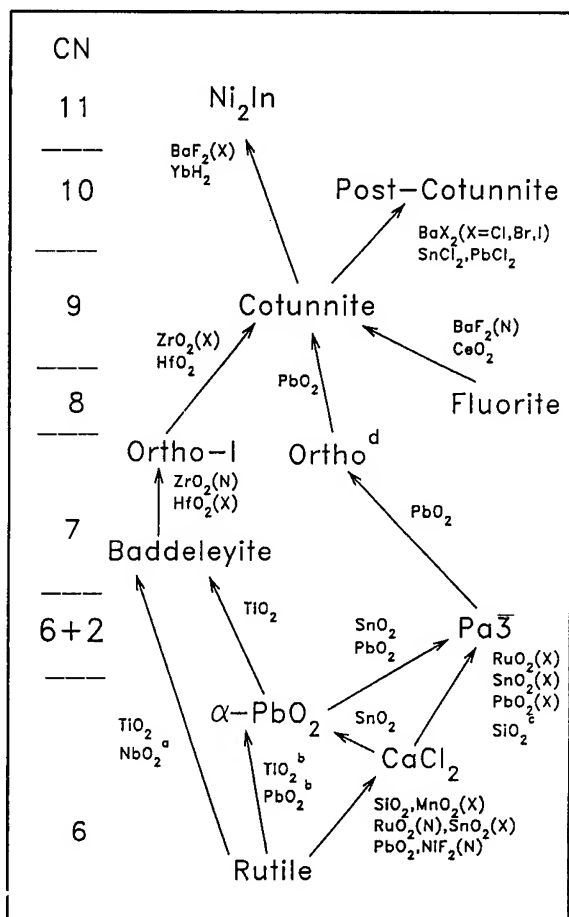


Figure 1: Structure map of the AX<sub>2</sub> compounds as a function of coordination number. Arrows indicate high pressure phase transformations. Selected examples (2-23) are given and are labelled X or N where the structure has been refined from x-ray or neutron diffraction data, respectively. <sup>a</sup>: distorted rutile → distorted baddeleyite, <sup>b</sup>: high pressure, high temperature conditions, <sup>c</sup>: calculated, <sup>d</sup>: this phase and ortho I could be isostructural.

case of ZrO<sub>2</sub> (7). To summarize, these dioxides exhibit transitions along the following pathway: rutile → baddeleyite → orthorhombic I → cotunnite. The group Va dioxide NbO<sub>2</sub> has a distorted rutile structure, *I*4<sub>1</sub>/*a*, *Z*=32, under ambient conditions and adopts a monoclinic, baddeleyite-related structure, *P*2<sub>1</sub>/*c*, *Z*=4, at high pressure. The group IVb dioxides, SnO<sub>2</sub> and PbO<sub>2</sub> (8-10), along with MnO<sub>2</sub> (group VIIa) (11) and RuO<sub>2</sub> (group VIII) (8, 12) exhibit one or more steps along a different pathway: rutile → CaCl<sub>2</sub> →

*Pa* $\bar{3}$  modified fluorite → orthorhombic → cotunnite. The structures of the high-pressure CaCl<sub>2</sub>-type phases, *Pnnm*, *Z*=2, of MnO<sub>2</sub> (11) and SnO<sub>2</sub> (9) were refined by the Rietveld method from x-ray data and from neutron data in the case of CaCl<sub>2</sub>-type RuO<sub>2</sub>. This pathway is of particular interest for SiO<sub>2</sub>, as both calculations and experimental results indicate that stishovite transforms to a CaCl<sub>2</sub>-structured phase at high pressure (2, 3). Refinements of the cubic phases of RuO<sub>2</sub>, SnO<sub>2</sub> and PbO<sub>2</sub> (8) indicate that these phases have a modified fluorite structure, *Pa* $\bar{3}$ , *Z*=4, instead of the fluorite structure, *Fm* $\bar{3}m$ , *Z*=4. This is consistent with the results of *ab initio* calculations for SiO<sub>2</sub> (4). The present results indicate the absence of the fluorite structure at high-pressure in the rutile-type dioxides. The coordination number is 6+2 in the *Pa* $\bar{3}$  structure as opposed to 8 in the fluorite structure. The fluorite structure is not a good candidate for a high pressure structure due to the empty cubic site at the center of the unit cell. Compounds that are fluorite structured under ambient conditions transform to the cotunnite structure at high pressure. PbO<sub>2</sub> was found to undergo further transformations to two orthorhombic phases. The first phase has similar cell constants to the orthorhombic *Pbca* phases of ZrO<sub>2</sub> and HfO<sub>2</sub>, and could in fact be isostructural. The second orthorhombic phase has the cotunnite structure. An additional phase is found in the transition sequence of the compounds with larger cations. This phase,  $\alpha$ -PbO<sub>2</sub>, *Pbcn*, *Z*=4, is stabilized relative to rutile under certain conditions due to cation-cation repulsions.

Until recently, the cotunnite structure was the example of the highest CN among the AX<sub>2</sub> compounds. Transitions are observed in cotunnite-structured BaX<sub>2</sub> (X=Cl, Br, I), PbCl<sub>2</sub>, and SnCl<sub>2</sub> (13-15) under high pressure to the same monoclinic, post-cotunnite phase, *P*112<sub>1</sub>/*a*, *Z*=8, with a CN of 10, which is a distortion of the orthorhombic Co<sub>2</sub>Si structure adopted by many intermetallic compounds, in which the coordination number is also 10. BaF<sub>2</sub> (16), which transforms from a fluorite-type to a cotunnite-type structure below 3 GPa, undergoes a second transition to a hexagonal Ni<sub>2</sub>In structure, *P*6<sub>3</sub>/*mmc*, *Z*=2, in which the barium

ion is in eleven-fold coordination. The structures of the cotunnite-type and  $\text{Ni}_2\text{In}$ -type phases have been refined from neutron and x-ray data, respectively. This  $\text{Ni}_2\text{In}$ -structured  $\text{BaF}_2$  is the first example of a coordination number of 11 in the  $\text{AX}_2$  compounds. The difference in behavior between  $\text{BaF}_2$  and the other cotunnite structured compounds can be understood in terms of ionic radius ratios.

### Conclusion

There are two distinct pathways for the series of transitions between the rutile and cotunnite structures at high pressure. The first, which concerns the group IVa and Va dioxides, passes via a baddeleyite-type structure, whereas the group VIIa, VIII and IVb dioxides pass by a  $\text{Pa}\bar{3}$  structure. Phase transitions beyond the cotunnite structure have been observed in the metal dihalides to two previously unencountered structures, in which the CN is 10 and 11, respectively.

### References

1. K. F. Seifert, *Fortschr. Miner.* **45** (1968) 214.
2. Y. Tsuchida and T. Yagi, *Nature* **340** (1989) 217.
3. K. J. Kingma, R. E. Cohen, R. J. Hemley and H. K. Mao, *Nature* **374** (1995) 243.
4. R. E. Cohen, in: *High-Pressure Research: Application to Earth and Planetary Sciences*, ed. M. H. Manghnani and Y. Syono (Terra Scientific and Am. Geophys. Union, 1992), p. 425.
5. H. Sato, S. Endo, M. Sugiyama, T. Kikegawa, O. Shimomura and K. Kusaba, *Science* **251** (1991) 786.
6. J. Haines and J. M. Léger, *Physica B* **192** (1993) 233.
7. J. Haines, J. M. Léger and A. Atouf, *J. Am. Ceram. Soc.* **78** (1995) 445.
8. J. Haines, J. M. Léger and O. Schulte, to be published.
9. J. Haines and J. M. Léger, to be published.
10. J. Haines, J. M. Léger and O. Schulte, to be published.
11. J. Haines, J. M. Léger and S. Hoyau, *J. Phys. Chem. Solids* **56** (1995) 965.
12. J. Haines and J. M. Léger, *Phys. Rev. B* **48** (1993) 13344.
13. J. M. Léger, J. Haines, A. Atouf, *Phys. Rev. B* **51** (1995) 3902.
14. J. M. Léger, J. Haines and A. Atouf, *J. Appl. Cryst.* **28** (1995) 416.
15. J. M. Léger, J. Haines and A. Atouf, *J. Phys. Chem. Solids*, in press.
16. J. M. Léger, J. Haines, A. Atouf, O. Schulte and S. Hull, *Phys. Rev. B*, in press.
17. O. Ohtaka, T. Yamanaka, S. Kume, N. Hara, H. Asano and F. Izumi, *Proc. Japan Acad.* **66(B)** (1990) 193.
18. O. Ohtaka, T. Yamanaka and S. Kume, *Nippon Seramikkusu Kyokai Gakujutsu Ronbunshi* **99** (1991) 826.
19. L.-G. Liu, *J. Phys. Chem. Solids* **41** (1980) 331.
20. J. D. Jorgensen, T. G. Worlton and J. C. Jamieson, *Phys. Rev. B* **17** (1978) 2212.
21. L. Liu and W. A. Bassett, *Elements, Oxides and Silicates* (Oxford University Press, 1986).
22. S. J. Duclos, Y. K. Vohra, A. L. Ruoff, A. Jayaraman and G. P. Espinosa, *Phys. Rev. B* **38** (1988) 7755.
23. J. Staun-Olsen, B. Buras, L. Gerward, B. Johansson, B. Lebech, H. L. Skriver and S. Steenstrup, *Physica Scripta* **29** (1984) 503.



# A TOPOLOGICAL PHASE TRANSITION OF AgCl UNDER HIGH PRESSURE

Keiji Kusaba<sup>1</sup>, Yasuhiko Syono<sup>1</sup>, Takumi Kikegawa<sup>2</sup> and Osamu Shimomura<sup>2</sup>

<sup>1</sup>; Institute for Materials Research, Tohoku University, Sendai 980-77, Japan

<sup>2</sup>; National Laboratory for High Energy Physics, Tsukuba 305, Japan

## Abstract

High pressure phase transitions of AgCl were investigated by *in-situ* X-ray diffraction method using the MAX80 system. A new B1-B2 transition with two intermediate phases (the KOH and TII type phases) was observed in the pressure and temperature range up to 18GPa and 500°C. We demonstrate that these four structures can be described systematically using a common monoclinic cell. A topological mechanism by a simple deformation is proposed to explain these transformations, in which the [100] and [011] directions exchange each other between the B1 and B2 structures.

## Introduction

Many MX type compounds with the NaCl (B1) structure are known to transform to the CsCl (B2) structure under high pressure. The phase transition has been discussed in terms of both reconstructive and displacive mechanisms.

For the displacive one, there were many studies and controversies, which were summarized in Onodera et al. [1]. The studies and controversies about the pressure-induced B1-B2 transitions were based on a diffraction method using a single crystal. It is difficult to discuss the displacive mechanism of the phase transition under high pressure only from the preferred orientation relationship of the broken grains. If an intermediate structure can be identified in the midway of the B1-B2 transition induced by pressure, we may obtain a hint to discuss the B1-B2 phase transition mechanism.

The aim of the present work is to reconsider the displacive mechanism of the B1-B2 transition on the basis of the pressure behavior of AgCl.

## Experiments

High pressure experiments of AgCl were carried out using a DIA type cubic anvil apparatus "MAX80" installed at AR-NE5 beam line in National Laboratory for High Energy Physics, Tsukuba, Japan [2]. By using sintered diamond

anvils with 3mm truncations, the MAX80 system can generate high pressure conditions up to 18GPa [3]. Chemical reagent of dry AgCl (5N) and a mixture of NaCl (5N) and BN (4N) were separately encased in a boron-epoxy cubic pressure medium, in which an internal carbon disk heater system was also encased. Between AgCl and the mixture, a BN disk was inserted in order to prevent chemical reaction between AgCl and NaCl under high temperature.

## Results

Typical energy dispersive type X-ray diffraction patterns of AgCl are shown in Fig. 1a. The low pressure phase (LPP) with the B1 structure was stable up to about 7.5GPa at room temperature. Above 7.5GPa X-ray diffraction patterns became complicated, as shown in Fig. 1b. By applying an automatic indexing computer code "DICVOL" [4] to twenty-five *d*-value data of the high pressure phase I (HPPI) at 9.0GPa, the HPPI is suggested to have the KOH structure (space group;  $P2_1$ ), as shown in Fig. 2b. The KOH structure is a kind of distorted NaCl structures, in which coordination numbers of both  $\text{Ag}^+$  and  $\text{Cl}^-$  are 6+1. The phase boundary of the transition has a positive slope, as shown in Fig. 3. It is consistent with the behavior of real KOH, which has the B1 type phase as a high temperature form.

The HPPI transformed to another high pressure phase II (HPPII) around 11.5GPa, as shown in Fig. 1c. The phase transition pressure is independent from temperature within a pressure determination error, as shown in Fig. 3. Major observed diffraction data were consistent with previous reports [5,6]. Probably previous reporters were in confusion by taking the HPPI as a mixture of the B1 phase and HPPII. From twenty-four diffraction line data at 13.5GPa, the computer code showed that the HPPII is suggested to have the TII

structure (space group;  $Cmcm$ ), as shown in Fig. 2c. The TII structure can also be explained as an intermediate structure between the B1 and B2 structures. Coordination numbers are 7 for both  $Ag^+$  and  $Cl^-$ .

The high pressure phase III (HPPIII) with the B2 type structure was found at 17.5GPa and 500°C, as shown in Figs. 1d and 2d. The slope of the phase boundary with the HPPII is negative, as shown in Fig. 3. It is consistent with the fact that real TII has the B2 type structure as a high temperature form. From extrapolation of the phase boundary to room temperature, the B2 type phase is suggested to be stable at room temperature above about 20GPa.

The HPPIII completely converted to the HPPII in the cooling process, and HPPII finally reverted to the LPP with the NaCl (B1) structure by way of the HPPI in the decompression process. No chemical reactions of AgCl was detected after the high pressure experiment.

### Discussion

We consider the mechanism for the B1-B2 transition of AgCl on the basis of a topological relationship among the B1, B2 and the intermediate structures. The NaCl, KOH, TII and CsCl structures can be represented by a common monoclinic cell, which is just the cell of the KOH structure itself, as shown in Fig. 2. From changes of the cell dimensions versus pressure, the B1-KOH-TII-B2 transitions can be considered to be consecutive phenomena: The cell parameter of  $b$  elongates, the parameter of  $a$  shortens and the angle value of  $\beta$  opens with increasing pressure. The value of  $c \sin \beta$  also decreases, but there is no general relationship between the parameter  $c$  and pressure. Figure 2 from the top to the bottom illustrates a simple mechanism for the B1-B2 transition under high pressure: In the B1-B2 transition, the [100] and [011] directions of the B1 and B2 structures exchange each other.

It is clear that the crystal orientation relationship is just the same as that found in the single crystal -

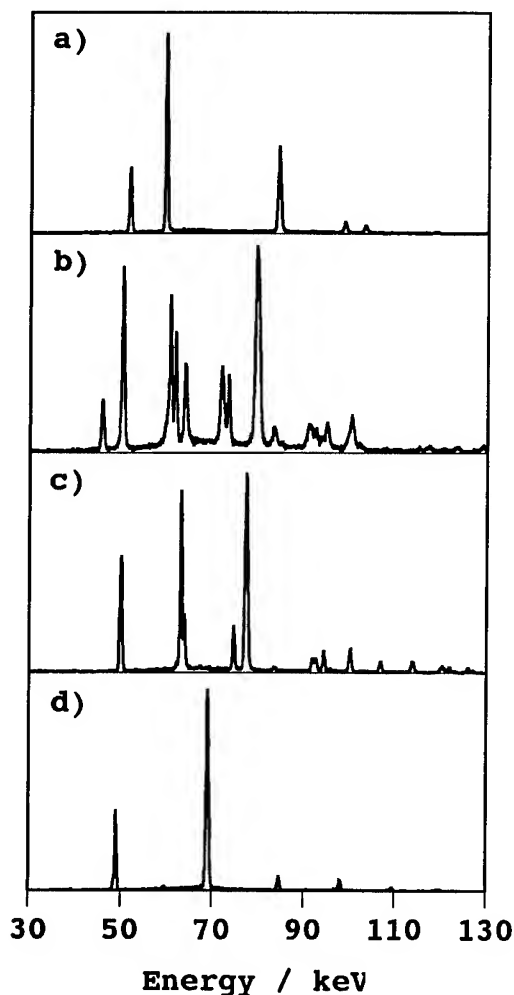


Fig. 1 Energy dispersive X-ray diffraction patterns of AgCl, taken at  $2\theta=4.5^\circ$ ; a) the NaCl structure at 7.5GPa and 27°C, b) the KOH structure at 9.0GPa and 27°C, c) the TII structure at 13.5GPa and 27°C and d) the CsCl structure at 17.5GPa and 500°C.

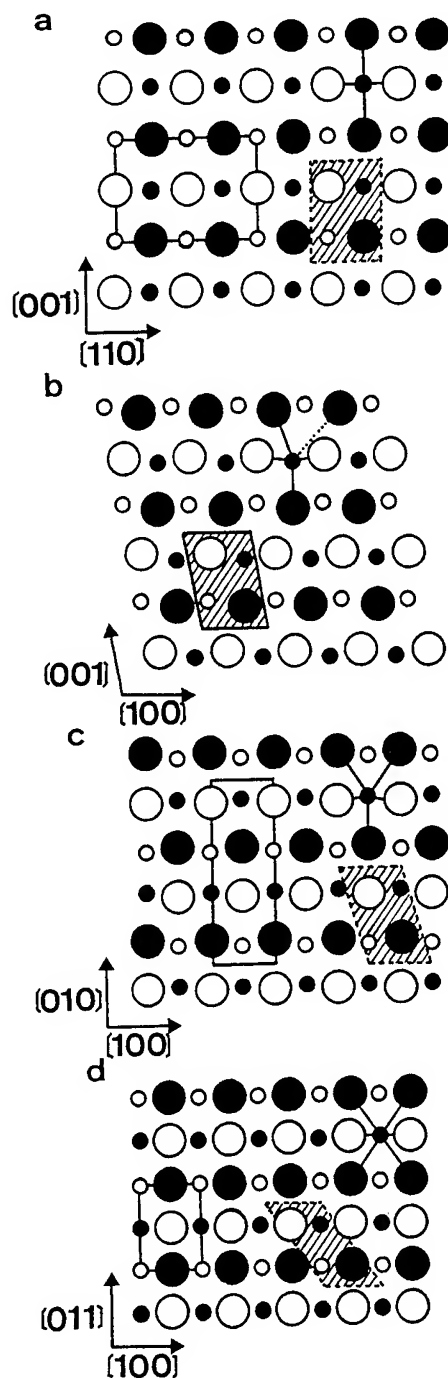


Fig. 2 Crystal structures of the (a) LPP, (b) HPPI, (c) HPPII and (d) HPPIII. Small and large circles show  $\text{Ag}^+$  and  $\text{Cl}^-$ , respectively. Open and solid marks show different layers. Solid lines show unit cells, and hatched parallelograms indicate the virtual monoclinic unit cell for the KOH structure.

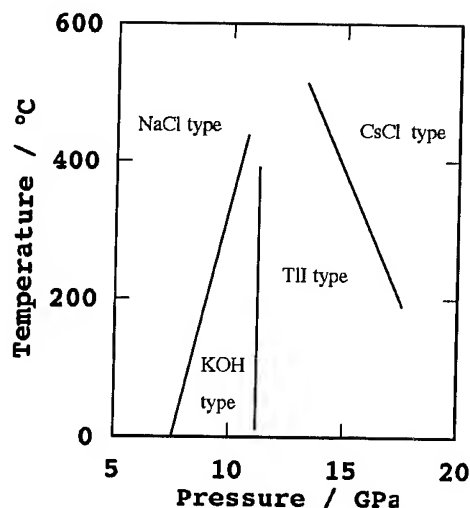


Fig. 3. A tentative phase diagram of AgCl.

single crystal transition in CsCl induced by temperature, in which the [100] and [011] directions exchange each other between the B1 and B2 structures [7].

#### Acknowledgments

This work has been performed under the approval of the Photon Factory Program Advisory Committee (Proposal No. 94G152).

#### References

- [1] Onodera A., Nakai Y., Kawano S., Achiwa N., *High Temp. High Press.* **24**, 55 (1992).
- [2] Shimomura O., Yamaoka S., Yagi T., Wakatsuki M., Tsuji K., Fukunaga O., Kawamura H., Aoki K. and Akimoto S., *Solid State Physics Under Pressure in Recent Advance with Anvil Devices* (Edited by S. Minomura), p. 351. KTK/Reidel, Tokyo/ Dordrecht (1985).
- [3] Shimomura O., Utsumi W., Taniguchi T., Kikegawa T. and Nagashima T., *High-Pressure Research: Application to Earth and Planetary Sciences* (Edited by Y. Syono and M. H. Manghnani), p. 3. Terra/AGU, Tokyo/Washington D.C. (1992).
- [4] Louer D. and Louer M., *J. Appl. Cryst.* **5**, 27 (1972).
- [5] Schock R. N. and Jamieson J. C., *J. Phys. Chem. Solids* **30**, 1527 (1969).
- [6] Kabalkina S. S., Shcherbakov M. O. and Vereshchagin A. L. F., *Sov. Phys. Doklady* **15**, 751 (1971).
- [7] Watanabe M., Tokonami M. and Morimoto N., *Acta Cryst.* **A33**, 294 (1977).

# INFLUENCE OF PRESSURE AND TEMPERATURE ON THE EPR SPECTRUM OF $\text{Gd}^{3+}$ IN $\text{CsCaCl}_3$

M. KRUPSKI, P. MORAWSKI

*Institute of Molecular Physics, Polish Academy of Sciences, Smoluchowskiego 17/19  
60-179 Poznań, Poland*

T. REWAJ

*Institute of Physics, Technical University of Szczecin, Al. Piastów 17  
70-310 Szczecin, Poland*

J. Y. BUZARÉ

*Laboratoire de Physique de l'Etat Condensé, Unité de Recherche associée au CNRS  
807 Av. Olivier Messiaen, 72017 Le Mans Cédex, France*

Y. VAILLS

*Centre de Recherche sur la Physique des Hautes Températures, CNRS  
Université d'Orléans, France*

## ABSTRACT

The effect of temperature and hydrostatic pressure on the  $b_4^o$  spin-Hamiltonian parameters for  $\text{Gd}^{3+}$  in  $\text{CsCaCl}_3$  is studied up to 800 MPa over the temperature range 80 - 400 K. It was found that the temperature dependence of  $b_4^o$  is predominantly caused by spin-phonon interactions (66.5% of the total temperature dependence). The phase transition temperature ( $T_c = 95$  K) from a cubic to a tetragonal phase is a linear function of pressure with the pressure coefficient  $dT_c/dp = (46 \pm 1)$  K/GPa, and the deviation of  $b_4^o(T)$  from the linear dependence near  $T_c$ , caused by the local rotational fluctuations, is larger under pressure.

## Introduction

Comprehensive electron paramagnetic resonance studies of the temperature and pressure dependences of the parameter  $b_4^o$  for the fluoroperovskite crystals doped with  $\text{Gd}^{3+}$  ions revealed that the temperature dependence of  $b_4^o(T)$  is predominantly caused by spin-phonon interactions [1]. The effect of hydrostatic pressure on the critical phenomena at the vicinity of the phase transition in  $\text{RbCaF}_3$  ( $T_c = 195$  K) was observed by the EPR method [2]. The transition remains of first order up to 800 MPa and the discontinuity of the order parameter  $\phi$  at  $T_c$  increases slightly with increasing pressure.

Our aim was to continue these studies on  $\text{CsCaCl}_3:\text{Gd}^{3+}$  single crystals for which the transition from a cubic phase to a tetragonal phase is observed at  $T_c = 95$  K [3].

## Experimental

A single crystal of  $\text{CsCaCl}_3$  doped with  $\text{Gd}^{3+}$  was grown by the Bridgman-Stockbarger technique in the Equipe de Physique de l'Etat Condensé, Le Mans.

EPR measurements under high hydrostatic pressure were performed in the Institute of Molecular Physics (Poznań) applying a special appliance which is a modified version of the apparatus used previously [4]. Now, it is used up to 800 MPa over the temperature range 80 - 400 K. Pressure and temperature are regulated simultaneously with the high accuracy needed to study the vicinity of the phase transition.

The sample of  $\text{CsCaCl}_3:\text{Gd}^{3+}$  was cut along [001] axis into 5 mm rods of 1.5 mm diameter and placed in the centre of the corundum resonator with the cylindrical axis perpendicular to the direction of the static magnetic field.

## Results

The temperature dependences of the absolute value of the  $b_4^0$  spin-Hamiltonian parameter for  $\text{CsCaCl}_3:\text{Gd}^{3+}$  in the cubic phase are shown in Fig. 1 at atmospheric pressure and at 600 MPa. The linear parts of these dependences, 80 K above  $T_c$ , have the same temperature coefficient:

$$(\partial b_4^0 / \partial T)_p = -(51 \pm 1) \cdot 10^{-8} \text{ cm}^{-1}/\text{K}.$$

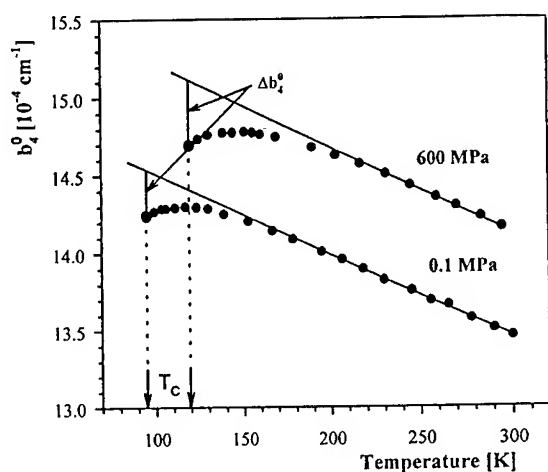


Fig. 1. The temperature dependence of the zero-field parameter  $b_4^0$  at atmospheric pressure and at 600 MPa for  $\text{CsCaCl}_3:\text{Gd}^{3+}$  in the cubic phase.

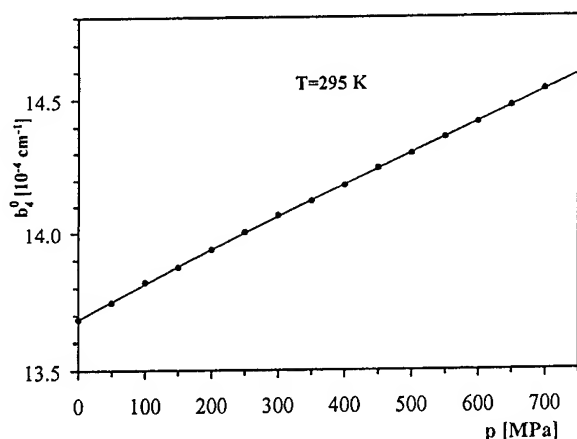


Fig. 2. Hydrostatic pressure dependence of the  $b_4^0$  spin-Hamiltonian parameter for  $\text{CsCaCl}_3:\text{Gd}^{3+}$  at room temperature.

From pressure measurements performed at room temperature (Fig. 2) the following pressure dependence of  $b_4^0$  is found:

$$b_4^0 = 13.68 + 12.9 \cdot 10^{-4} p - 12 \cdot 10^{-8} p^2$$

where  $b_4^0$  is in  $10^{-4} \text{ cm}^{-1}$  and  $p$  in MPa.

This temperature dependence contains thermal expansion and spin-phonon contributions which may be separated using the following thermodynamic relation

$$\left( \frac{\partial b_4^0}{\partial T} \right)_V = \left( \frac{\partial b_4^0}{\partial T} \right)_p - \frac{\beta}{\kappa} \left( \frac{\partial b_4^0}{\partial p} \right)_T \quad (1)$$

where  $\beta$  is the volume thermal expansion coefficient and  $\kappa$  is the volume compressibility coefficient.

The values of  $\beta$  and  $\kappa$  are not known for  $\text{CsCaCl}_3$ . Because  $\beta$  for various perovskite crystals has approximately the same value, we assume that  $\beta = 53 \cdot 10^{-6} \text{ K}^{-1}$ , the same value as for  $\text{CsCaF}_3$ . From the elastic constants, known for some perovskites, the values of  $\kappa$  for chloroperovskites are known to be two times larger than for fluoroperovskites. Therefore, for  $\text{CsCaCl}_3$  we assume

$$\kappa = 40 \cdot 10^{-6} \text{ MPa}^{-1}.$$

From these values and according to the relation (1) the contribution to the  $b_4^0(T)$  resulting from lattice vibrations is estimated to be

$$(\partial b_4^0 / \partial T)_V = -34 \cdot 10^{-8} \text{ cm}^{-1}/\text{K}.$$

It is 67 % of the total temperature change in  $b_4^0$  and only 33 % can be related to the thermal expansion of the crystal, similarly as for  $\text{Gd}^{3+}$  ions in fluoroperovskites [1].

The empirical dependence of  $b_4^0$  parameter upon the metal-ligand distance is of the form:

$$b_4^0 \propto r^k$$

Hence, by differentiation the exponent  $k$  may be determined from the expression:

$$k = - \frac{3}{b_4^0 \kappa} \left( \frac{\partial b_4^0}{\partial p} \right)_T$$

From the experimental data we obtain for  $\text{CsCaCl}_3$   $k = -7.1$ . This value is approximately equal to the

value obtained previously for the simple fluorides  $\text{MF}_2\text{:Gd}^{3+}$  [5], but it is considerable less than the value of  $k$  for fluoroperovskites [1].

The influence of hydrostatic pressure on the phase transition was studied in detail up to 800 MPa.  $T_c$  is defined as temperature at which the cubic spectrum vanishes. The phase coexistence is equal to 0.3 K and may be seen as evidence for a first order transition [6].

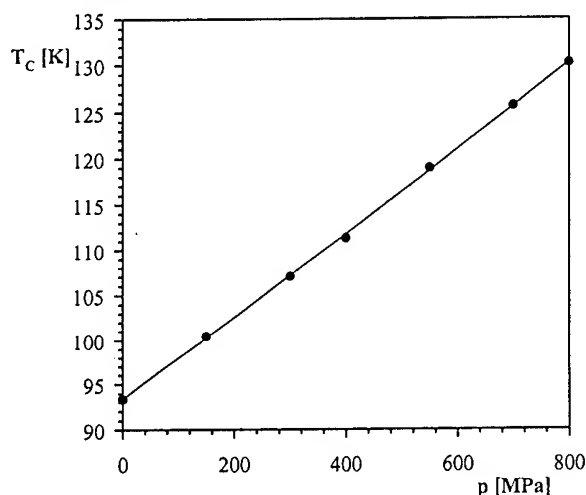


Fig. 3. Variation of the transition temperature with pressure in  $\text{CsCaCl}_3$ .

Two results are the most important.

(i) The hydrostatic pressure dependence of the phase transition temperature  $T_c$  up to 800 MPa in  $\text{CsCaCl}_3$  is a linear function (Fig. 3) with the pressure coefficient  $dT_c/dp = (46 \pm 1)$  K/GPa and this value is less than for other compounds of the family  $\text{CsMCl}_3$  with  $M = \text{Pb}$  and  $\text{Sr}$  [7]. It is in accordance with the calculations of  $T_c$  and  $dT_c/dp$  on the basis of the „rigid sphere model” [8].

(ii) The deviation of  $b_i^\circ$  from the linear dependence near  $T_c$ , caused by the rotational fluctuations, is larger under pressure. The deviation of  $\Delta b_i^\circ$  at  $T_c$  equal  $0.27 \cdot 10^{-4} \text{ cm}^{-1}$  at normal pressure and  $0.355 \cdot 10^{-4} \text{ cm}^{-1}$  at 600 MPa. Similar behaviour in the vicinity of  $T_c$  was observed in  $\text{RbCaF}_3$  [2].

## References

1. Rewaj, M. Krupski, J. Kuriata and J. Y. Buzaré, *J. Phys.: Condens. Matter* **4** (1992) 9909.
2. M. Krupski and J. Y. Buzaré, *J. Phys.: Condens. Matter* **6** (1994) 9429.
3. Y. Vaills, J. Y. Buzaré, A. Gibaud and Ch. Launay, *Solid State Commun.* **60** (1986) 139.
4. J. Stankowski, A. Gałęzewski, M. Krupski, S. Waplak and H. Gierszal, *Rev. Sci. Instrum.* **47** (1976) 128.
5. T. Rewaj and M. Krupski, *phys. stat. sol. (b)* **99** (1980) 285.
6. Y. Vaills and J. Y. Buzaré, *J. Phys. C.: Solid State Phys.* **20** (1987) 2149.
7. M. Midorikawa, Y. Ishibashi and Y. Takagi, *J. Phys. Soc. Japan* **41** (1976) 2001.
8. M. Krupski, *phys. stat. sol. (a)* **78** (1983) 751; **116** (1989) 657.

# X-RAY DIFFRACTION STUDY OF THE CRITICAL BEHAVIOUR OF $\text{KMnF}_3$ CLOSE TO THE PRESSURE INDUCED PHASE TRANSITION

S. ÅSBRINK

*Department of Inorganic Chemistry, Arrhenius Laboratory, University of Stockholm,  
106 91 Stockholm, Sweden*

A. WAŚKOWSKA

*Institute of Low Temperature and Structure Research, Polish Academy of Sciences,  
50 950 Wrocław, Poland*

## ABSTRACT

The nature of the pressure induced structural phase transition at  $P_c = 3.1$  GPa in the perovskite  $\text{KMnF}_3$  has been studied by a single-crystal X-ray diffraction. The transition showing departures from the classical second - order behaviour was accompanied with several effects pointing to the weak, first - order character. These were: i) non-vanishing intensity of superlattice reflections considered as the primary order parameter  $Q$ ; ii) small discontinuity of the intensities close to  $P_c$ ; iii) low value of the critical exponent  $\beta$  of the power law:  $Q = A(P - P_c)^\beta$ ; iv) domain structure and hysteresis ( $\Delta P_c = 0.15 \pm 0.04$  GPa).

## Introduction

Perovskite  $\text{KMnF}_3$  crystals undergo temperature dependent structural and magnetic phase transitions transforming from the cubic ( $Pm3m$ ) into the tetragonal or orthorhombic phases as the temperature is reduced [e.g. 1 - 3]. Since it is known that hydrostatic pressure may modify the character of some transitions, we have performed a single crystal diffraction study of the pressure dependent characteristics of this material.

Unit cell parameters measured up to 10 GPa have shown discontinuity at 3.1 GPa (Fig. 1), connected with a transition to the tetragonal phase [4]. From a detailed single crystal structure analysis below and above the transition it was found that the structure compression was related to antiphase rotations of  $\text{MnF}_6$  octahedra around the [001] axis in adjacent unit cells [5]. Attempting to describe the nature of the transition, we have used the Landau thermodynamical approach to observe the critical behaviour of  $\text{KMnF}_3$ . According to [6] in the  $Pm3m \rightarrow I4/mcm$  transition a role of the order parameter  $Q$  can play superlattice Bragg intensities, which are entirely caused by  $F_1$  - atoms displacements from the high symmetry positions (Fig. 2).

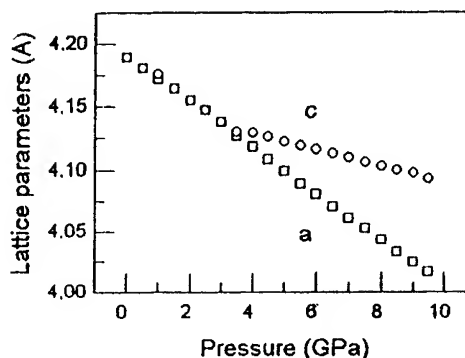


Figure 1 Unit cell parameters versus pressure [4].

Being aware of the generally lower precision of the high pressure experiments we have extended our earlier investigations by measuring: (1) integrated intensity variation of the superlattice reflections  $(211)_t$  and  $(123)_t$  as a function of pressure and (2) full width at the half maximum (FWHM) of the main Bragg reflections  $(400)_c$  and  $(004)_c$  in connection with the appearance of a domain structure due to the tetragonal deformation.

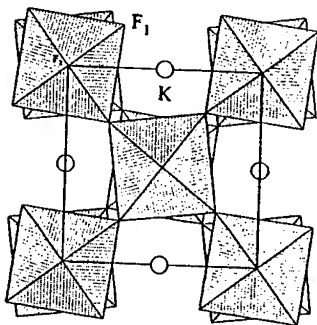


Figure 2 Crystal structure in the tetragonal phase ( $a_t = a_c\sqrt{2}$ ;  $c_t = 2c_c$ ;  $Z = 4$ ).

### Experimental procedure

In the present study the pressure range has been confined up to 4.1 GPa, which allowed the use of a relatively large sample,  $\sim(150 \times 160 \times 50) \mu\text{m}$  ensuring better counting statistics. A high quality monodomain crystal was mounted in a diamond-anvil cell (Diacell products, DXR-4 UK) together with a crystal of fluorite for pressure calibration. A 4 : 1 mixture of methanol : ethanol was used as the pressure transmitting medium. The Inconel X-750 gasket had at the start a hole of the diameter  $d = 0.25 \text{ mm}$ . This gasket permits the pressure to be increased and decreased with small increments (of  $\leq 0.1 \text{ GPa}$ ). The X-ray diffraction experiment was carried out on a STOE 4-circle diffractometer with graphite monochromated  $\text{MoK}\alpha$  radiation (60 kV, 40 mA). Before and after each pressure point the  $2\theta$  angles of two  $\{111\}$  fluorite reflections were measured and used to determine the pressure from the equation of state for  $\text{CaF}_2$  [7] with a precision of 0.04 GPa. Crystal offset-errors and instrumental systematic errors were controlled by using a procedure of Hamilton, modified by King and Finger. The orientation of the sample was controlled at each pressure from setting angles of  $12$  to  $14$  strong reflections ( $9^\circ < 2\theta < 19^\circ$ ) using the standard centering and double scan procedure ( $\omega_- \theta_-$ ,  $\omega_+ \theta_+$ ) of the STOE software. The intensities and profiles of superlattice reflections together with their Friedel pairs were measured with counting time 100sec/step, using  $\omega$ -scan technique. Normal Bragg reflections were measured with time 10sec/step. The intensities were corrected for background, and Lorentz and polarization effects. A special care had been taken to slowly compress the sample in order to perform

the measurements with as small pressure intervals as possible.

### Results and Discussion

Above  $P_c$  new Bragg superlattice reflections appear, and evolution of the  $(211)_t$  peak profile as a function of pressure is shown in Fig. 3. The profile at  $P = 3.03 \text{ GPa}$  has been obtained after decreasing the pressure below  $P_c$ , but all the others were measured with the increasing pressure. The non-vanishing intensity below  $P_c$  can be attributed either to diffuse scattering or to a hysteresis of about 0.15 GPa.

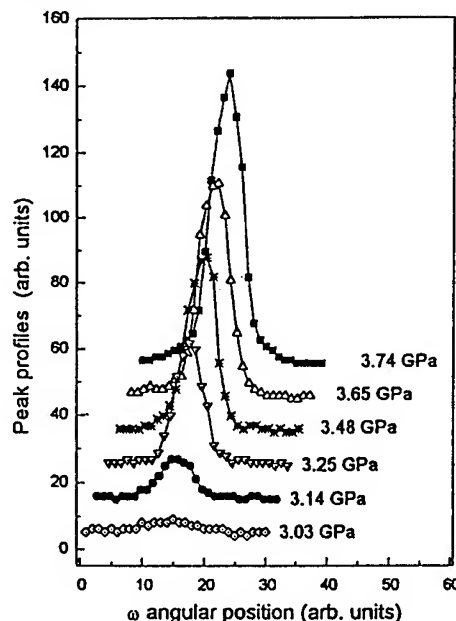


Figure 3 The evolution of the peak profiles ( $\omega$  scan) of superlattice reflection  $(211)_t$  with pressure. Solid lines are eye-guides.

It was observed that intensities corresponding to increased and decreased pressures were different within this pressure range. If we relate this effect to the pressure hysteresis, its magnitude appears slightly higher than three standard deviations of the pressure determination (0.04 GPa).

The integrated intensities of the  $(211)_t$  and  $(123)_t$  reflections between 2.5 and 4.1 GPa across  $P_c$  are shown in Fig. 4. These dependencies were individually fitted by the least-squares method to the experimental power law:  $I = A(P - P_c)^{2\beta}$  with  $A$ ,  $\beta$  and  $P_c$  as the refined parameters (Fig. 4).



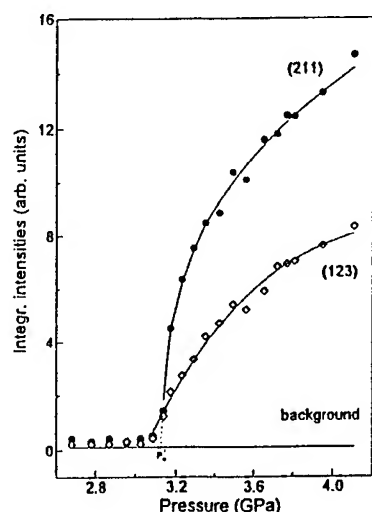


Figure 4 Integrated intensities of the  $(211)_t$  and  $(123)_t$  reflections as a function of pressure. The solid lines are the least squares fit to the power law,  $P_c$  shows the transition pressure from  $(211)_t$ , mean  $\beta=0.23(7)$ .

It is seen that the two reflections differ in character: the strong  $(211)_t$  shows the features corresponding to a first order transition, while the weak  $(123)_t$  - due to the poorer counting statistics - changes less rapidly above  $P_c$ . For  $(211)_t$  also the squared integrated intensity shows departure from the classical second order behaviour (Fig. 5).

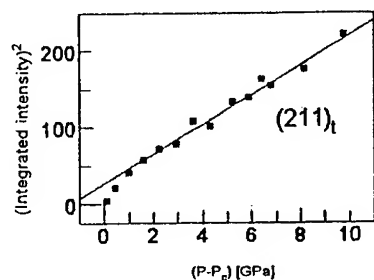


Figure 5 Squared integrated intensity of the  $(211)_t$  reflection versus  $(P - P_c)$ .

Considering the effects influencing the transition character we have measured a full width at the half maximum (FWHM) of  $(400)_c$  and  $(004)_c$  reflections as a functions of pressure. Appearance of the domain structure resulted in a rapid broadening of both reflections in the vicinity of  $P_c$  (Fig. 6). Apart from the transition pressure the FWHM did not change significantly, as long as the sample was not decompressed below  $P_c$ . The hydrostatic pressure suppresses the creation of large clusters

with definite orientation. Numerous, narrow domains could be a reason for the intensity tail below  $P_c$  in Fig. 3.

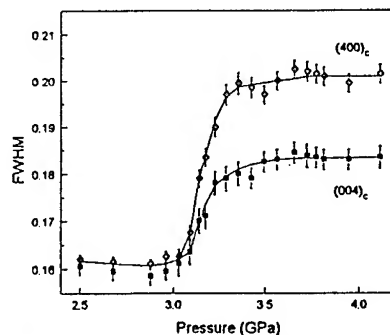


Figure 6 Full width at the half maximum of the Gaussian fit to the peak profiles, FWHM, (arc deg in  $\omega$ ) of the reflections  $(400)_c$  and  $(004)_c$ .

The conclusions are the following: our observations of: i) non-vanishing intensity of the superlattice reflections below  $P_c$ ; ii) discontinuity of the intensity of superlattice reflections above  $P_c$ ; iii) low value of the critical exponent  $\beta$ ; iv) domain structure and hysteresis, all these phenomena allow the transition character to be considered the first order type.

## References

1. V. J. Minkiewicz, Y. Fujii and Y. Yamada, X-ray scattering and the phase transitions of  $\text{KMnF}_3$  at 184 K. *J. Phys. Soc. Japan*, **28** (1970) 443.
2. G. Shirane, V. J. Minkiewicz and A. Linz, Neutron scattering study of the lattice dynamical phase transitions in  $\text{KMnF}_3$ . *Solid State Commun.* **8** (1970) 1941.
3. A. Gibaud, S. M. Shapiro, J. Nouet and H. You, Phase diagram of  $\text{KMn}_{1-x}\text{Ca}_x\text{F}_3$  determined by high-resolution X-ray scattering. *Phys. Rev. B* **14** (1991) 2437.
4. S. Åsbrink, A. Waśkowska, and A. Ratuszna, A high-pressure X-ray diffraction study of a phase transition in  $\text{KMnF}_3$ . *J. Phys. Chem. Solids*, **54** (1993) 507.
5. S. Åsbrink and A. Waśkowska, High-pressure crystal structures of  $\text{KMnF}_3$  below and above the phase transition at  $P_c = 3.1$  GPa. *Eur. J. Solid State Inorg. Chem.* **31** (1994) 747.
6. U. J. Nicholls and R. A. Cowley, Determination of the critical exponents at the R-point instability in  $\text{KMnF}_3$ . *J. Phys. C: Solid State Phys.* **20**, (1987) 3417.

## HIGH PRESSURE PHASE TRANSITIONS OF SODIUM NIOBATE ( $\text{NaNbO}_3$ ) BY RAMAN SPECTROSCOPY

Z. X. Shen, X. B. Wang, Z. P. Hu, L. Qin, S. H. Tang, and M. H. Kuok

*Dept. of Physics, National University of Singapore, Lower Kent Ridge Road, Singapore 0511.*

### ABSTRACT

Sodium niobate ( $\text{NaNbO}_3$ ) has been studied under high pressure up to 220 kbar using Raman spectroscopy. A rich pressure-induced changes have been observed and at least one phase transition involving major structural changes occurs between 63 and 75 kbar, and it is a two-step process. Similarities exist between  $\text{NaNbO}_3$  and  $\text{KNbO}_3$ . The paraelectric cubic phase is not observed under pressure at room temperature.

### Introduction

The  $\text{ABO}_3$  family perovskite materials show a rich variety of phase transitions with pressure and temperature, which provide good examples for the study of phase transition mechanisms [1-6].  $\text{NaNbO}_3$  displays an unusually large number of phase transitions with temperature and unlike most other perovskites, it exhibits typical antiferroelectric (AF) properties at room temperature and transforms to a ferroelectric phase (FE) at low temperature. Above the critical temperature  $T_c=914$  K, it belongs to the cubic paraelectric phase (PE). On cooling, the following transitions to the AF phases have been observed:  $T<914$  K, tetragonal  $T_2$  phase;  $T<848$  K, orthorhombic  $T_1$  phase;  $T<793$  K, orthorhombic S phase;  $T<753$  K, orthorhombic R phase;  $T<646$  K, orthorhombic P phase. Below 170 K, it becomes FE rhombohedral N phase [1-5].

The motivation for this study is threefold: (i). as the AF-FE phase transition is accompanied by a significant reduction in unit cell volume, it would be interesting to see if this transition can also be induced by pressure. (ii) a number of the barium titanate family ferroelectrics have been studied under high pressure [6-10], and a variety of changes have been observed. For example, pressure-induced FE-PE phase transitions have been reported at

room temperature for  $\text{PbTiO}_3$  and  $\text{BaTiO}_3$ , indicating a significant decrease of  $T_c$  under pressure. (iii) soft modes have been the benchmark for the PE-FE transitions, and they are also present with pressure variations. In literature, the only high pressure work on  $\text{NaNbO}_3$  seems to be the electrical measurements up to 10 kbar [5].

### Experimental

The powder form of  $\text{NaNbO}_3$  used was of Puratronic grade purchased from Johnson Matthey without further treatment. High pressure was generated by a gasketed diamond anvil cell with predeformed stainless steel gaskets and 4:1 mixture of methanol-ethanol as pressure medium. The pressure was calibrated by ruby fluorescence. Raman spectra were recorded in the backscattering geometry using a Spex double grating monochromator coupled to a photon counting system. The 488 nm line of an  $\text{Ar}^+$  ion laser was used as the excitation source. All spectra were recorded at room temperature.

### Results and discussion

A total of 19 Raman peaks were observed under ambient pressure and listed in Table 1. Some bands in the high frequency region above  $300\text{ cm}^{-1}$  are very weak and quite broad. They

show up more distinctively at low temperature. The typical high pressure Raman spectra are shown in Fig. 1. It can be seen that there are a variety of spectral changes with pressure. In general, the spectrum is simpler at higher pressure, indicative of higher symmetry.

**Table 1** The observed Raman bands in the ambient condition phase

Freq/cm <sup>-1</sup>	Intensity	$\frac{d\omega}{dp}$ cm <sup>-1</sup> /kbar
64.3	vs, sp	0.038
76.9	vs, sp	0.0
94.0	w, sh	0.144
125.1	w	0.018
145.7	m	0.144
157.1	w	0.157
179.9	w, sh	0.11
187.5	m	0.419
202.8	w, sh	
223.2	s	0.206
258.7	s	0.255
280.2	vs	0.331
294.2	w, sh	0.454
374.8	vw	0.588
438.3	w	0.310
563.3	sh	0.393
607.1	vs	-0.090
644	w, sh, br	0.107
868	w, br	0.380

v - very s - strong sp - sharp w - weak  
sh - shoulder m - medium br - broad

Figure 2 shows representative spectra below 300 cm<sup>-1</sup> between 0-60 kbar. Many Raman bands show continuous changes. The intensity of the strong peak at 280 cm<sup>-1</sup> decreases with pressure and becomes very weak at 70 kbar. Another strong peak at 223 cm<sup>-1</sup> weakens very fast and has almost disappeared by 18 kbar. The weak band at 203 cm<sup>-1</sup> disappears at 8 kbar, and is replaced by a peak of medium intensity at 215 cm<sup>-1</sup>. The peak at 188 cm<sup>-1</sup> gains strength at higher pressure until 54 kbar thereafter it becomes a soft mode and its

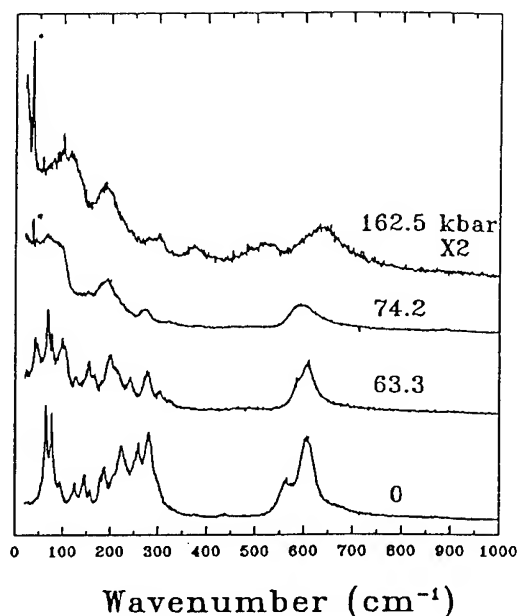


**Fig.1** High pressure Raman spectra of KNbO<sub>3</sub>. The asterisk denotes a plasma line.

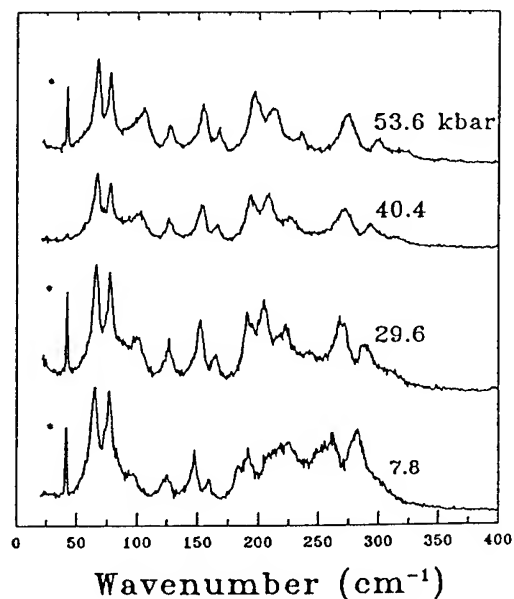


**Fig. 2** Raman spectra showing changes in the low frequency region.

intensity starts to drop dramatically. The weak band at 180 cm<sup>-1</sup> also grows stronger under compression and becomes the strongest peak of the 100-300 cm<sup>-1</sup> region at 45 kbar. The intensities of the peaks at 145, 125 and 77 cm<sup>-1</sup>

remain roughly constant until 63 kbar above which pressure they start to weaken drastically at higher pressure, while the shoulder peak at  $94\text{ cm}^{-1}$  gains prominence until 63 kbar. The two peaks at  $563$  and  $607\text{ cm}^{-1}$  move towards each other and the latter is a soft mode.

Major spectral changes occur at about 63 kbar, in addition to what has been discussed above, a new low frequency mode appears at  $46\text{ cm}^{-1}$ . At higher pressure, the spectral change accelerates, most noticeable is the drastic increase in the background in the low frequency region and the disappearance of most of the peaks below  $300\text{ cm}^{-1}$ . Above 75 kbar, the spectra look much simpler and the new low frequency band has vanished into the increasing background. The two peaks at around  $600\text{ cm}^{-1}$  merges into one. At higher pressure, the low frequency background decreases and all the peaks become broader. The band frequency against pressure plot is shown in Fig. 3.

It is apparent that at least one major structural change occurs between 63 and 75 kbar. The structures before and after the transition are so different that it is necessary that the transition is a two-step process, indicated by the abrupt spectral changes at 63 and 75 kbar respectively. The high pressure phase has a higher symmetry since it has fewer Raman peaks and the two bands at around  $600\text{ cm}^{-1}$  merges into one.

In comparison with the  $\text{FE KNbO}_3$  [6], they both show phase transitions characterized by the rising low-frequency background (ca 60 kbar for  $\text{KNbO}_3$ ); the softening of the lowest Raman band; the quite strong Raman bands at the highest pressure implying that the PE cubic phase can not be achieved at room temperature by compression; and the softening of a major high frequency peak near  $600\text{ cm}^{-1}$ .

1. C. N. W. Darlington and H. D. Megaw, *Acta Cryst. B* 29, 2171 (1973).
2. C N W Darlington, *Solid State Commun.* 29, 307 (1979).

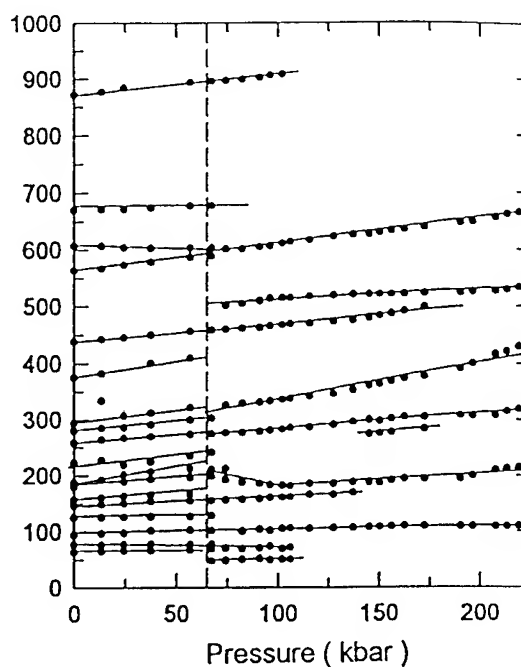


Fig. 3 P- $\omega$  plot. The dashed line indicates phase transition.

3. F. Gervais, J. L. Servoin, J. F. Baumard and F. Denoyer, *Solid State Commun.* 41 345 (1982).
4. A. M. Glazer and H. D. Megaw, *Acta Cryst. A* 29, 489 (1973).
5. M. Pisarski, *Phys. Stat. Sol. (b)* 101, 635 (1980).
6. Z. X. Shen, Z. P. Hu, T. C. Chong, C. Y. Beh, S. H. Tang, and M. H. Kuok, *Phys. Rev. B* (1995) in press.
7. Y. Akishige, H. Takahashi, N. Mori and E. Sawaguchi, *J. Phys. Soc. Jpn.* 63, 1590 (1994).
8. F. Cerdeira, W. B. Holzapfel and D. Bauerle, *Phys. Rev. B* 11, 1188 (1975).
9. J. A. Sanjurjo, E. Lopez-Cruz and G. Burns, *Solid State Commun.* 48, 221 (1983).
10. A. Jayaraman, J. P. Remeika and R. S. Katiyar, *Materials Research Society Symposia Proc., Vol. 22; High Pressure in Science and Technology. Part I* (North-Holland, New York, 1984), pp165-168.

## HIGH PRESSURE RAMAN SCATTERING STUDY OF LEAD MOLYBDATE

Z X Shen<sup>1</sup>, X B Wang<sup>1</sup>, T C Chong<sup>2</sup>, Y T Tan<sup>1</sup>, Z P Hu<sup>1</sup>, M H Kuok<sup>1</sup> and S H Tang<sup>1</sup>

<sup>1</sup> *Department of Physics, National University of Singapore,  
Lower Kent Ridge Road, Singapore 0511.*

<sup>2</sup> *Department of Electrical Engineering, National University  
of Singapore, 10 Kent Ridge Crescent, Singapore 0511.*

### ABSTRACT

Lead molybdate ( $\text{PbMoO}_4$ ) single crystals have been studied up to 170 kbar by Raman spectroscopy. Our result confirms the first order phase transition observed at about 90 kbar. Our Raman spectra also reveal spectral changes which may be indicative of phase transition at 22 and 44 kbar. The transition at 22 kbar involves the relative movement of the Pb ions along the  $z$  direction. The crystal has either lost its centre of inversion or has doubled its unit cell size after the second transition. Both the lowest and the highest frequency bands are soft modes above 44 kbar, and the softening of the latter may imply the instability of the  $\text{MoO}_4$  tetrahedra at high pressure.

### Introduction

Lead molybdate ( $\text{PbMoO}_4$ ) has been widely used in applications because of its outstanding acousto-optical properties. The structure of lead molybdate belongs to space group  $I4_1/a$  ( $C_{4h}^6$ ), with two formula groups in the unit cell. The point group symmetry for the tetragonal unit cell is  $4/m$  ( $C_{4h}$ ). Based on factor group analysis, 13 Raman active bands are expected. Of which, seven belongs to the internal vibrational modes of the  $\text{MoO}_4$  tetrahedra and six are the external modes.

Raman studies of the single crystal samples of  $\text{PbMoO}_4$  at ambient and elevated temperature have been reported in the literature [1,2]. High pressure study up to 120 kbar have also been performed by Jayaraman *et al* [3], and a first order phase transition at around 90 kbar was observed. They reported a contraction of the  $\text{MoO}_4$

tetrahedra and a reduction in the Mo–O distance in the high pressure phase based on the jump to higher frequency of the highest frequency peak, which is associated with the  $A_g$ -type symmetrical vibrational mode of the  $\text{MoO}_4$  tetrahedra, whereas expansion of the  $\text{WO}_4$  tetrahedra was found in  $\text{PbWO}_4$  in the high pressure phase above 45 kbar.

### Experimental

$\text{PbMoO}_4$  were grown as large single crystal samples by the Czochralski technique [4,5]. The samples used in the high pressure experiments are small fragments about 50  $\mu\text{m}$  in thickness and 100  $\mu\text{m}$  in other dimensions. High pressure was generated with a gasketed diamond anvil cell with 4:1 methanol-ethanol mixture as the quasi-hydrostatic pressure medium. The pressure was calibrated using

the ruby fluorescence technique [6]. Raman spectra were recorded using a Spex double grating monochromator coupled to a photon counting system. The 514.5 or 488 nm line of an Ar<sup>+</sup> laser was used as the excitation source. No special care was taken to align the samples in any particular direction, so that the spectra consist of bands of all symmetries.

## Results and Discussion

Of the 13 Raman active bands predicted by group theory, 11 were observed in our experiment at ambient pressure and they are listed in Table 1 together with their assignment. The  $\nu_1$ ,  $\nu_2$ ,  $\nu_3$  and  $\nu_4$  are the internal vibrational modes of the molybdate ions, and others are external modes. Figure 1 shows the pressure dependence of the Raman bands up to 170 kbar. The phase transition at 90 kbar is clearly indicated.

At the low pressure range, there are a lot of changes involving the low frequency

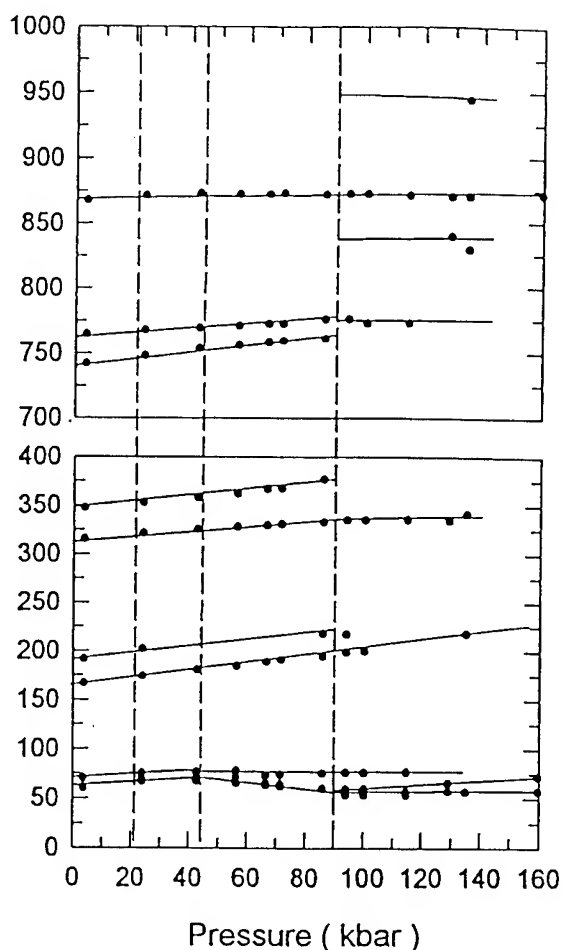


Fig.1 The Raman frequency shifts with pressure for PMoO<sub>4</sub>. The dashed vertical lines donate the proposed phase transition pressures.

**Table 1 The ambient condition Raman bands and their assignments**

Freq/cm <sup>-1</sup>	symmetry	assignment*
63	B <sub>g</sub>	MoO <sub>4</sub> (z)
69	E <sub>g</sub>	Pb-Pb(xy)
74	B <sub>g</sub>	Pb-Pb (z)
104	E <sub>g</sub>	MoO <sub>4</sub> -MoO <sub>4</sub> (xy)
169	A <sub>g</sub>	MoO <sub>4</sub> R(z)
194	E <sub>g</sub>	MoO <sub>4</sub> R(xy)
320	B <sub>g</sub>	$\nu_2$
351	B <sub>g</sub>	$\nu_4$
745	E <sub>g</sub>	$\nu_3$
767	B <sub>g</sub>	$\nu_3$
870	A <sub>g</sub>	$\nu_1$

\* The assignment follows that in ref 2.

external Raman modes. Figure 2 illustrates the pressure dependence of the Raman bands in this region together with the band at 870 cm<sup>-1</sup> for a single crystal sample oriented to enhance the weak bands. From this figure, it is very tempting to consider the band at 74 cm<sup>-1</sup> as a soft mode which extends beyond 100 kbar, i.e. it becomes the lowest frequency mode above 44 kbar. The dramatic intensity change occurs for this mode, however, leads us to interpret

the data differently. For this orientation, the band at  $74\text{ cm}^{-1}$  is stronger than that at  $63\text{ cm}^{-1}$  with the band at  $69\text{ cm}^{-1}$  being by far the weakest at 0 kbar. The intensity of the  $74\text{ cm}^{-1}$  band decreases drastically with pressure and its frequency remains constant, while the other two bands show the expected frequency increase under compression. At around 20 kbar, the  $74\text{ cm}^{-1}$ -band disappears and the gradient of the frequency-pressure plot for the  $63\text{ cm}^{-1}$ -band changes. As the band at  $74\text{ cm}^{-1}$  is associated with the Pb-Pb vibration along the  $z$  axis, we suggest a phase transition at 22 kbar involving the movement of the Pb ions in the  $z$  direction.

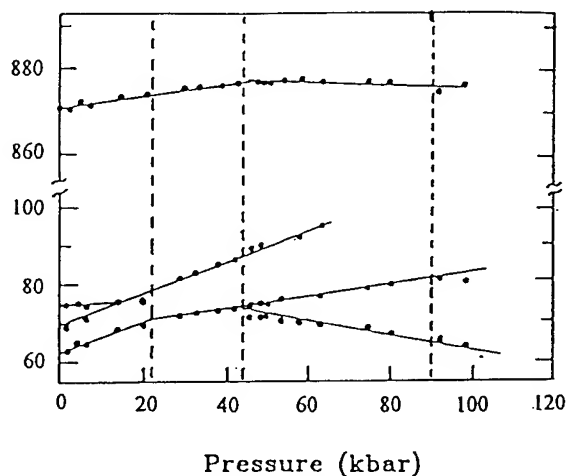


Fig. 2 The pressure dependence of the highest frequency peak and some Raman bands in the low frequency region for a sample specially oriented. The soft modes above 44 kbar are clearly demonstrated.

Another phase transition occurs at 44 kbar. At this pressure, the  $63\text{ cm}^{-1}$ -band splits into two components, of which the lower one behaves as a soft mode and the other has the same pressure dependence as

its parent band. Also at the same pressure, the highest frequency band at  $870\text{ cm}^{-1}$  starts to soften slightly with compression, which implies the instability of the  $\text{MoO}_4$  tetrahedra. Note that the  $63\text{ cm}^{-1}$ -band is a non-degenerate mode. Its splitting indicates either the crystal has lost its symmetry of centre of inversion or the size of its unit cell has doubled.

At 90 kbar, we observed a first order phase transition as has been reported previously [3]. This transition is marked by the merging of the two bands around  $760\text{ cm}^{-1}$  and the splitting of the highest frequency component. The lowest frequency band starts to strengthen after the transition. Since it involves changes of high frequency bands associated with the molybdate ions, the tetrahedral  $\text{MoO}_4$  ions, which have behaved more or less as rigid elements during the transitions at lower pressures, have been involved. As Jayaraman *et al* [3] have pointed out that because the highest frequency band jumps to higher frequency, the tetrahedra should have shorter Mo-O distance suggesting a contraction of the tetrahedra.

1. R. K. Khanna, W. S. Rrower, B. R. Guscott and E. R. Lippincott. *J. Res. Nat. Bur. Standards A72*, 81 (1968).
2. H. S. Lee, S. D. Lee, J. H. Lee and M. S. Jang, *Ferroelectrics* **107**, 151 (1990).
3. A. Jayaraman, B. Batlogg and L. G. van Uiter, *Phys. Rev. B* **31**, 5423 (1985).
4. H. C. Zeng, T. C. Chong, L. C. Lim, H. Kumagai and M. Hirano, *J. Crystal Growth* **140**, 148 (1994).
5. E. Pfeifer and P. Rudolph, *Cryst. Res. Technol.* **25**, 3 (1990).
6. G.J. Piermarini and S. Block, *Rev. Sci. Instrum.* **46**, 973 (1975).

# PHASE TRANSITIONS OF $\text{CuGeO}_3$ AT HIGH PRESSURES

T. ZHOU, A.R. GOÑI, S. VES, R. KREMER, K. SYASSEN

*Max-Planck-Institut für Festkörperforschung, Heisenbergstrasse 1, D-70569 Stuttgart, Germany*

We have measured Raman and optical absorption spectra of  $\text{CuGeO}_3$  under hydrostatic pressures at room temperature as well as at low temperature. Raman spectra at 300 K indicate a reversible structural phase transition at 6.3 GPa and an irreversible crystalline to amorphous transition starting near 14 GPa. Raman spectra at low temperatures show that the critical temperature of the spin-Peierls transition at 14 K increases linearly with pressure at the rate of 3.9 K/GPa. Furthermore, a new low-temperature phase is discovered and its stability range is mapped out using Raman spectroscopy. Optical absorption in the visible range is found to be weak for the crystalline phases, indicating that the onset of charge transfer excitations lies in the UV spectral range. A broad absorption band centered near 1.8 eV is attributed to three overlapping ligand field excitations of the  $\text{Cu}^{2+}$  ions.

## 1 Introduction

$\text{CuGeO}_3$  is an insulating compound crystallizing in a unique orthorhombic structure<sup>1</sup> where edge-sharing chains of planar  $\text{CuO}_2$  groups as well as tetrahedral  $\text{GeO}_4$  groups run along the *c*-axis (see Fig. 1). Recent interest in  $\text{CuGeO}_3$  results from the observation of the rapid drop of the magnetic susceptibility below  $T = 14$  K in all three crystal axis directions.<sup>2</sup> This indicates that  $\text{CuGeO}_3$  may be the first observed inorganic compound which undergoes a spin-Peierls transition with dimerization taking place along the chain direction. Among other evidence,<sup>3</sup> Raman observations support the picture of a spin-Peierls transition occurring in  $\text{CuGeO}_3$ .<sup>4,5</sup>

As for the high pressure behavior of  $\text{CuGeO}_3$ ,

x-ray powder diffraction and infrared absorption measurements have revealed a structural phase transition occurring at 6.6-7.3 GPa.<sup>6</sup> The high pressure phase was tentatively assigned as monoclinic. Between 11 to 22 GPa, due to the disappearance of some X-ray diffraction peaks, a further very sluggish transition to a higher symmetry phase was proposed.

We report results of high pressure Raman and optical absorption measurements of  $\text{CuGeO}_3$  at room and low temperature. The motivation was (i) to use information about the *P*-dependence of the Raman modes of the ambient pressure phase for an unambiguous mode assignment, (ii) to characterize high pressure phases by Raman spectroscopy, (iii) to study in particular the effect of hydrostatic pressure on the spin-Peierls transition of  $\text{CuGeO}_3$ , and (iv) to demonstrate that the optical response in the visible spectral range is governed by weak ligand-field (intraionic  $d-d$ ) transitions of  $\text{Cu}^{2+}$  and not by strong charge transfer transitions, as was proposed recently.<sup>7</sup>

## 2 Experiment

Well crystallized needle-shaped single crystals of  $\text{CuGeO}_3$  were grown from a 1:1.2 mixture of  $\text{GeO}_2$  and  $\text{CuO}$  according to a procedure described elsewhere.<sup>8</sup> The samples were cleaved to a thickness of about 30  $\mu\text{m}$ , cut into pieces about  $100 \times 100 \mu\text{m}^2$  in size and then loaded into a diamond-anvil cell. Alcohol and condensed helium were used as pressure-transmitting media for room and low temperature measurements, respectively. Pressure was measured *in situ* using the ruby lu-

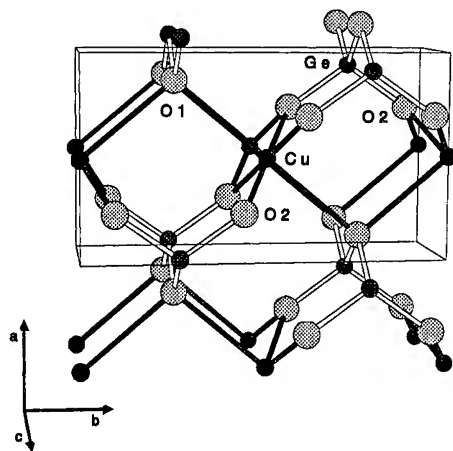


Figure 1: The crystal structure of  $\text{CuGeO}_3$  at ambient conditions.



minescence method with appropriate temperature correction of the ruby calibration.<sup>9</sup> Raman spectra in near back-scattering geometry were excited with the 5145 Å line of an Ar<sup>+</sup> ion laser and recorded employing a triple spectrograph coupled with a multichannel detector. Optical absorption spectra were measured using a microoptical system with a focal spot on the sample of about 30 μm diameter.

### 3 Results and Discussion

Figure 2 shows unpolarized Raman spectra of CuGeO<sub>3</sub> measured at different pressures up to 20 GPa ( $T = 295$  K). At zero pressure we observe eight Raman-active modes. The intensities of two lines at 388 cm<sup>-1</sup> and 712 cm<sup>-1</sup> are weak, and they disappear rapidly under pressure. Frequencies of the other six modes increase with increasing pressure. Pressure coefficients are listed in Table I. Of the six modes, the phonons at 113, 183 and 859 cm<sup>-1</sup> have been assigned previously.<sup>10</sup> For the other modes we propose the assignment and corresponding normal coordinates given in Table I. For this assignment we take into account that (i) the bond lengths of Ge-O1 and Cu-O1 are larger

than those of Ge-O2 and Cu-O2, (ii) the Ge-O1 bonding strength along the *a* direction is likely to be stronger than that along the *b* direction, and (iii) the pressure coefficients of the two medium-energy modes are significantly larger than those of the two highest-energy modes.

At 6.3 GPa, all of the six modes of the orthorhombic phase disappear. Instead, twelve new modes are observed. This indicates a first-order structural phase transition at this pressure. The transition pressure is roughly in agreement with previous x-ray diffraction results.<sup>6</sup> With increasing pressure, the frequencies of all the twelve phonons of the new phase (phase II) increase linearly up to 14 GPa.

Above 14 GPa, CuGeO<sub>3</sub> samples start to turn opaque, and Raman spectra degrade, until at 20 GPa spectra become almost featureless. These changes are irreversible after releasing the pressure to zero. Optical reflectivity measurements above 14 GPa show no major change of oscillator strength in the infrared regime. This excludes the possibility of an insulator-metal transition. Therefore we conclude that an irreversible crystalline-amorphous transition occurs in CuGeO<sub>3</sub> starting at about 14 GPa. The similar coordination of Ge

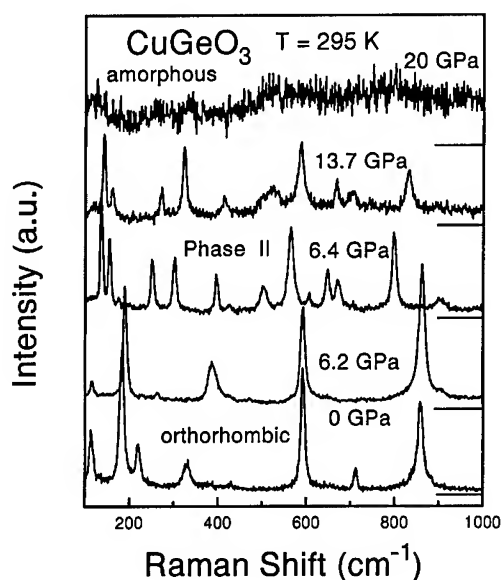


Figure 2: Room temperature Raman spectra of CuGeO<sub>3</sub> at different pressures. For clarity, the spectra are displaced vertically with baselines indicated for each spectrum.

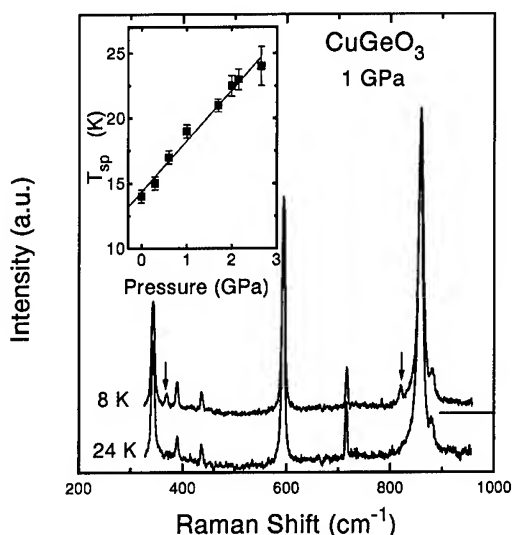


Figure 3: Raman spectra of CuGeO<sub>3</sub> at 1 GPa for temperatures below and above the spin-Peierls transition. Arrows point to additional Raman lines appearing in the spin-Peierls phase. The inset shows transition temperature versus pressure.

Table 1: The frequencies, linear pressure coefficients and the normal coordinates of six Raman modes in the low pressure phase of  $\text{CuGeO}_3$ . The atom displacements along the  $a$ ,  $b$  and  $c$  directions are denoted by  $x$ ,  $y$  and  $z$ , respectively. For atomic positions and labeling see Devic *et al.*<sup>10</sup>

$\omega_0$ ( $\text{cm}^{-1}$ )	$d\omega/dP$ ( $\text{cm}^{-1}/\text{GPa}$ )	$d^2\omega/dP^2$ ( $\text{cm}^{-1}/\text{GPa}^2$ )	Mode Symmetry	Atom	Position	Normal Coordinate
113.4	$3.41 \pm 0.42$	$-0.4 \pm 0.1$	$B_{2g}$	Ge	(2e)	$y_1 - y_2$
183.3	$4.66 \pm 0.52$	$-0.5 \pm 0.1$	$A_g$	Ge	(2e)	$x_1 - x_2$
220	$8.16 \pm 1.22$	0	$B_{2g}$	O1	(2f)	$y_1 - y_2$
330	$14.22 \pm 0.93$	$-0.8 \pm 0.1$	$A_g$	O1	(2f)	$x_1 - x_2$
593.2	$2.47 \pm 0.48$	$-0.3 \pm 0.1$	$A_g$	O2	(4e)	$x_1 + x_2 - x_3 - x_4$
859	$3.61 \pm 0.65$	$-0.3 \pm 0.1$	$A_g$	O2	(4e)	$y_1 - y_2 - y_3 + y_4$

atoms in  $\text{CuGeO}_3$  and  $\alpha$ -quartz  $\text{GeO}_2$ <sup>11</sup> suggests that the crystalline-amorphous transition mechanism may be closely related in these two materials.

Polarized Raman spectra of single crystal  $\text{CuGeO}_3$  measured at temperatures below 14 K ( $P = 0$ ) show altogether five new peaks.<sup>4,5</sup> Figure 3 shows Raman spectra of  $\text{CuGeO}_3$  measured at 1 GPa for temperatures just above and below the spin-Peierls transition. The arrows point to new modes which appear in the spin-Peierls phase for the given sample orientation.<sup>4,5</sup> Using the appearance of these new modes to discriminate between the normal and spin-Peierls phases, we obtain the phase transition temperature  $T_{sp}$  versus pressure relation shown in the inset to Fig. 3. The solid line corresponds to a pressure coefficient of 3.9 K/GPa.

Crystals with Peierls-like distortions occurring at ambient pressure often show a negative slope for the transition pressure versus temperature curve. In the case of  $\text{CuGeO}_3$ , however, we have the opposite trend. The free energy changes due to magnetic interactions and elastic deformation are likely to be two competing factors in driving the phase transition. Since  $T_{sp}$  increases with pressure, we argue that when  $\text{CuGeO}_3$  undergoes the spin-Peierls transition, the decrease of the free energy due to magnetic interactions is larger than the cost in free energy related to the lattice distortion. We note that the pressure coefficient for  $T_{sp}$  predicted on the basis of ambient pressure thermal expansion experiments<sup>3</sup> is in good agreement with the present experimental result.

The modes used to monitor the spin-Peierls transition are not observed any more at pressures above 2.8 GPa. Instead, other additional modes appear in the Raman spectra. This indicates the

transition to a new low-temperature phase. Without going into details here, we just note that the corresponding PT phase boundary increases with pressure and reaches a temperature of about 150 K at 5.5 GPa.

Figure 4 shows room temperature optical absorption spectra of  $\text{CuGeO}_3$  for different pressures up to 12.7 GPa. The most prominent feature at ambient pressure is a broad and asymmetric band centered at about 1.75 eV. The first moment of this band shows a small blue shift with increasing pressure and its pressure coefficient increases above the phase transition at 6.3 GPa. The weak pressure dependence of the transition energy as well as the low absorption strength are typical for ligand field excitations of transition metal ions. Moreover, crystal field transitions in the range 1.3 to 1.8 eV are characteristic for  $\text{Cu(II)}$  compounds with similar  $\text{Cu}^{2+}$  coordination.<sup>12</sup> The corresponding energy level scheme for a  $d^9$  configuration in  $D_{4h}$  symmetry is indicated schematically in the inset of Fig. 4. We thus ascribe the 1.75 eV absorption band seen at room temperature to three unresolved ligand field excitations of  $\text{Cu}^{2+}$ . The low-temperature absorption spectrum ( $P = 0$ ) also shown in Fig. 4 indeed reveals three components centered at 1.57, 1.73 and 1.91 eV.

The high pressure phase clearly shows a second absorption band centered at about 3 eV. This band may originate from defect states created at the first-order phase transition. However, a corresponding but somewhat weaker band is also observed in the ambient pressure phase. Thus, another assignment to be considered would be  $d-d$  double excitations, which have been discussed in detail for bridged Cu dimers.<sup>12</sup> The mechanism responsible

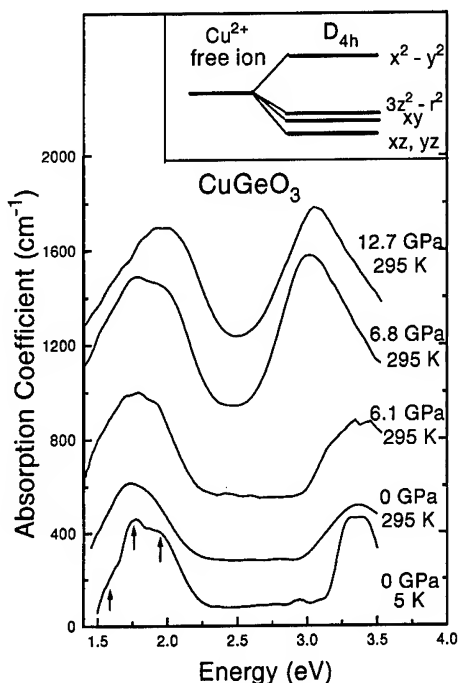


Figure 4: Optical absorption spectra of  $\text{CuGeO}_3$  at different pressures ( $T=295$  K). Also shown is a low temperature absorption spectrum at ambient pressure. For the sake of clarity spectra are displaced vertically in steps of  $200 \text{ cm}^{-1}$ . Arrows point to the energies of overlapping peaks.

for double excitations may be related to the magnetic interaction between neighboring Cu ions.

At pressures above 14 GPa the overall absorption increases considerably and samples become opaque. This means that new absorption mechanisms dominate in the proposed amorphous phase.

Recently, the optical reflectivity of  $\text{CuGeO}_3$  was investigated at ambient pressure.<sup>7</sup> The reported spectra showed pronounced features at 1.8 eV, which were interpreted in terms of charge transfer transitions. This result obviously is inconsistent with the weak oscillator strength found in the present work. Our explanation is that the reflectivity spectra were corrupted by intensity reflected at the back surface of the thin samples. Thus, the analysis and interpretation of the optical reflectivity data<sup>7</sup> is considered to yield misleading information about the electronic structure of  $\text{CuGeO}_3$ .

In conclusion, we have investigated the high pressure behavior of  $\text{CuGeO}_3$  by Raman and opti-

cal absorption spectroscopy at room temperature as well as low temperatures. New results include a crystalline to amorphous transition above 14 GPa, the pressure dependence of the spin-Peierls transition temperature, the discovery of a new low-temperature phase at high pressures, and the interpretation of the visible optical response in terms of ligand-field transitions. Further Raman studies are in progress, and preliminary results indicate that magnetic interactions in the high pressure phases of  $\text{CuGeO}_3$  differ substantially from those observed near ambient pressure.

#### 4 Acknowledgement

We thank U. Oelke, U. Engelhardt and W. Dietrich for technical assistance. One of the authors (T. Z.) would also like to thank the Volkswagen-Stiftung for financial support.

#### References

1. H. Völlenkle, A. Wittmann and H. Nowotny, *Monatsh. Chem.* **98**, 1352 (1967).
2. M. Hase, I. Terasaki and K. Uchinokura, *Phys. Rev. Lett.* **70**, 3651 (1993).
3. H. Winkelmann *et al.*, *Phys. Rev. B* **51**, 12884 (1995), and references therein.
4. H. Kuroe *et al.*, *Phys. Rev. B* **50**, 16468 (1994).
5. M. Udagawa *et al.*, *J. Phys. Soc. Japan* **63**, 4060 (1994).
6. D. M. Adams, J. Haines and S. Leonard, *J. Phys. Condens. Matter* **3**, 5183 (1991).
7. I. Terasaki *et al.*, *Phys. Rev. B* **52**, 295 (1995).
8. G. A. Petrakovskii *et al.*, *Sov. Phys. JETP* **71**(4), 772 (1990).
9. S. Buchsbaum, R.L. Mills, and D. Schiferl, *J. Phys. Chem.* **88**, 2522 (1984); R. A. Noack and W. B. Holzapfel, in *High Pressure Science and Technology*, edited by K.D. Timmerhaus and M.S. Barber (Plenum, New York, 1979), Vol.1, p.748.
10. S. D. Devic *et al.*, *J. Phys. Condens. Matter* **6**, L745 (1994).
11. J. P. Itie *et al.*, *Phys. Rev. Lett.* **63**, 398 (1989).
12. F. Tuscek and E.I. Solomon, *Inorg. Chem.* **32**, 2850 (1993) and references therein.

# STRUCTURAL PHASE TRANSFORMATION OF InS AT HIGH PRESSURES

U. SCHWARZ<sup>1</sup>, A. GONCHAROV<sup>1</sup>, K. SYASSEN<sup>1</sup>, and N.M. GASANLY<sup>2</sup>

<sup>1</sup> Max-Planck-Institut für Festkörperforschung, Heisenbergstr. 1, D-70569 Stuttgart,

<sup>2</sup> Middle East University, Ankara, Turkey

We have measured Raman spectra and angle-dispersive x-ray diffraction diagrams of InS up to 30 GPa. Anomalies in the pressure dependence of Raman frequencies clearly indicate a phase transition at 5.0(3) GPa. The continuous structural changes of the low-pressure modification as well as the crystal structure of the monoclinic high-pressure polymorph have been investigated by full profile refinements.

## 1 Introduction

The ambient pressure polymorph of InS is a pure In(II) compound with semiconducting properties. Fig. 1 shows a view of the crystal structure (*Pmnn*, no. 58, non-standard setting,  $Z = 4$ ) along the  $[100]$  direction<sup>1</sup>. Anions and cations together form a distorted cubic primitive lattice. Short contacts of the In-atoms to one indium and three sulfur atoms and two longer distances  $d(\text{In-S})$  form a distorted coordination octahedron. The covalent In-In bonds are tilted with respect to the crystallographic  $c$ -axis. A pressure-induced structural phase transition was predicted on the basis of decreasing mode frequencies observed in Raman measurements at pressures up to 1.2 GPa<sup>2</sup>. Subsequent measurements of the electrical resistance<sup>3</sup>, Raman spectra, optical properties and lattice parameters<sup>4</sup> show anomalies between 2.5 GPa and 5 GPa. In an earlier x-ray powder diffraction investigation of InS<sup>5</sup> a pressure-induced structural phase transition into a high-pressure polymorph with  $\text{Hg}_2\text{Cl}_2$  structure was claimed to occur at 7.5(5) GPa.

Despite the previous investigations the structural behaviour of InS at high pressures appears to be not well characterized. Thus, we have studied the properties of InS by means of Raman spectroscopy and powder x-ray diffraction experiments at pressures up to 30 GPa and 16 GPa, respectively.

## 2 Experiment

InS single crystals were grown by a modified Bridgman technique<sup>6</sup>. All measurements were performed at room temperature using the ruby luminescence method<sup>7</sup> for pressure calibration. Condensed helium or alcohol mixtures were used

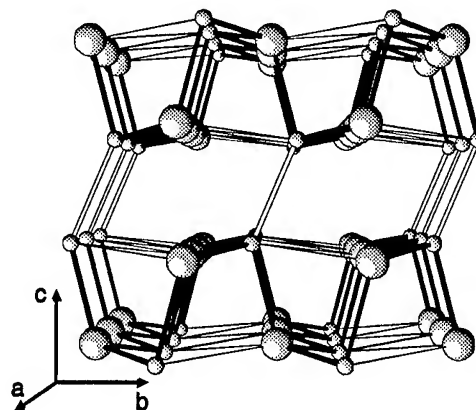


Figure 1: Crystal structure of the orthorhombic low-pressure modification of InS viewed along the  $[100]$  direction. In: o, S: O.

as pressure transmitting media. Raman spectra in near back-scattering geometry were measured employing a triple monochromator equipped with a multichannel detector.

Angle dispersive powder patterns up to  $2\theta = 30^\circ$  were collected with a two circle diffractometer using  $\text{MoK}\alpha$  radiation and a position-sensitive proportional counter. Diffraction data used for the full profile refinements were collected on station 9.1 at the Synchrotron Radiation Source, Daresbury, using an angle dispersive setup and an image-plate area detector. The incident wavelength was 0.4654 Å. Details of the experimental setup and the program to generate conventional 1-d profiles from the 2-d data have been described elsewhere<sup>8</sup>. Peak fitting, indexing, and finally full-profile refinements were performed using the program system CSD<sup>9</sup>.

### 3 Results and Discussion

Raman spectra were measured at various pressures up to 30 GPa. Fig. 2 shows the pressure dependence of mode frequencies and the mode assignment obtained from group theoretical analysis and polarisation dependent Raman measurements<sup>10</sup>. The behaviour of phonon frequencies and intensities is completely reversible within the limits of experimental accuracy. For the stability range of the low-pressure modification our measurements confirm the finding of decreasing mode frequencies with increasing pressure<sup>2</sup>. At 5.0(3) GPa an abrupt jump in frequency of two  $A_g$  modes at 150 and 200  $\text{cm}^{-1}$  and the disappearance of two other modes is observed, clearly demonstrating a phase transformation at this pressure. Around 9 GPa we find pronounced relative intensity changes of the modes near 170  $\text{cm}^{-1}$  and 200  $\text{cm}^{-1}$ . Above 10 GPa only three strong modes can be observed. The disappearance of weak modes above 10 GPa is not considered as sufficient evidence for a second structural phase transformation near 10 GPa, although the pressure dependence of electrical resistance reveals an anomaly at 10.8 GPa<sup>3</sup>.

X-ray diffraction experiments were carried out

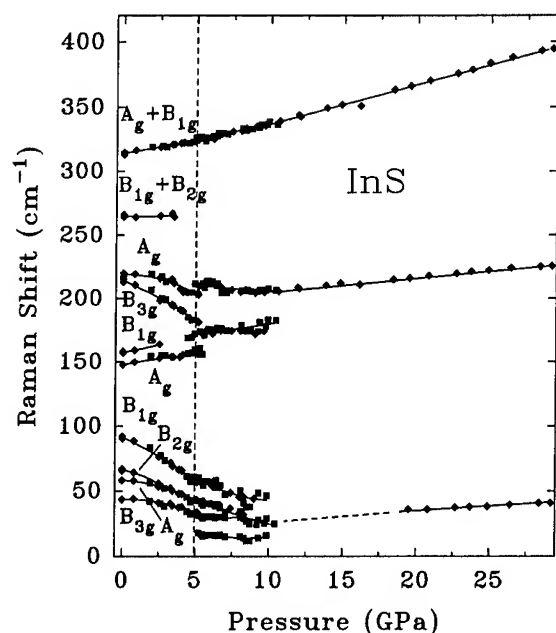


Figure 2: Pressure dependence of Raman shifts of InS. Discontinuous changes at 5 GPa indicate the phase transition which is marked by a dashed line at 5 GPa.

at pressures up to 16 GPa. A least squares fit of a Murnaghan type function to the experimental pressure-volume data up to 5 GPa results in  $V_0=186.7(4) \text{ \AA}^3$ ,  $B_0=29(2) \text{ GPa}$ , and  $B'_0=6(1)$ . Fig. 3 shows the pressure dependence of lattice parameters as a function of pressure. Up to 5 GPa we observe a slight linear increase of  $c$  with pressure and a strong nonlinear decrease of  $b$ . The positional parameter  $y(\text{In})$  shifts towards smaller values with increasing pressures. Thus, the tilting of the In-In dumbbells is reduced by the pronounced compressibility of the  $b$  axis and the change of the positional parameter  $y(\text{In})$ <sup>11</sup>, but the parameter change is much smaller than expected on the basis of the accompanying metrical changes.

Above the phase transition at 5.0(3) GPa the high pseudosymmetry ( $a\sqrt{2} \approx b\sqrt{2}$ ) causes overlap of reflections like (101) and (011), and indexing of powder diagrams measured with conventional x-ray sources becomes impossible. Intensities of reflections with  $h+k+l \neq 2n$  decrease strongly above 5 GPa but do not disappear, indicating that the lattice does not become body centered up to 16 GPa. Thus, the tilt of the In-In dumbbell with respect to the  $c$ -axis is further reduced with pressure, but does not disappear completely.

Data from full profile refinements of powder diagrams measured with synchrotron radiation at 7.9 GPa are shown in Tab. 1. In agreement with re-

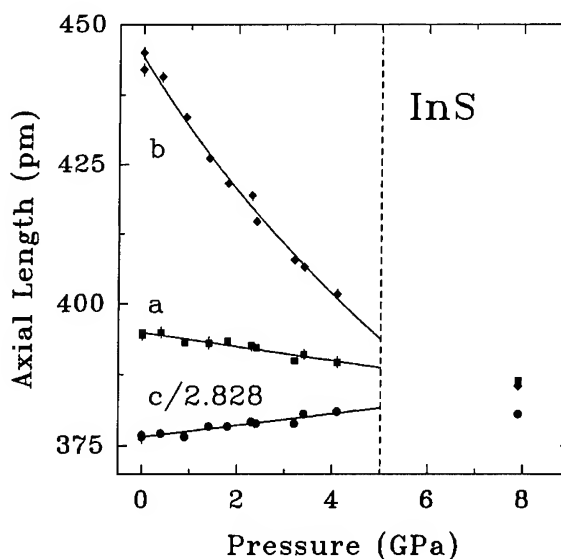


Figure 3: Lattice constants of InS at pressures up to 7.9 GPa. The pronounced difference in compressibility indicates a strong anisotropy of the low-pressure modification.

sults of a single crystal unit cell determination<sup>11</sup> the diffraction diagram of the high-pressure polymorph can be indexed using a monoclinic unit cell. The crystal structure of the high-pressure phase can be refined in space group  $P112_1/n$  (sg no. 14,  $P2_1/c$ , unique axis  $c$ , cell choice 2) using full-profile powder-diffraction data. Comparison of the R-values shows that those of the high-pressure modification are almost identical with those of the known low-pressure polymorph (see Tab. 1). With the monoclinic angle between the two short axes  $a$  and  $b$  being only slightly different from  $90^\circ$ , both modifications exhibit a close structural relationship. The alterations associated with the structural phase transformation induce a decrease of the In-In dumbbell tilt and a significant reduction of the differences between short and long In-S distances. Both changes reduce the deviation of the atomic arrangement from a cubic primitive lattice. On the basis of the data presented here we can definitively rule out a  $\text{Hg}_2\text{Cl}_2$  type crystal structure of InS at pressures up to 16 GPa.

Optical reflectivity and absorption data indicate that InS remains semiconducting up to 40 GPa. On the contrary, in the homologous compounds GaTe and InSe structural phase transitions at 10 GPa are associated with a breaking of the metal-metal bonds and semiconductor-to-metal transitions. Thus, we conclude that the In-In dumbbells in InS remain stable up to the highest investigated pressure.

Table 1: Results of full-profile powder refinements for the low- and high-pressure modification of InS.

space group	$Pmnn$	$P112_1/n$
$p$ (GPa)	3.2	7.9
$2\Theta_{max}$	27	25
$a$ (pm)	389.9(1)	386.3(1)
$b$ (pm)	407.8(1)	385.4(1)
$c$ (pm)	1071.4(1)	1076.2(1)
$\gamma$ (degree)	90	90.88(1)
$x$	0	-.0568(9)
In $y$	.1019(4)	.037(1)
$z$	.1199(3)	.1202(3)
$x$	0	-.017(2)
S $y$	.011(1)	.001(2)
$z$	.3510(7)	.3567(9)
$R_I$	.0562	.0501
$R_{PR}$	.1027	.1086

#### 4 ACKNOWLEDGEMENT

We are indebted to R.J. Nelmes, M.I. McMahon, and the group at Daresbury for using the synchrotron facilities. We gratefully acknowledge their support with imaging plate software.

#### References

1. K. Schubert, E. Dörre, E. Günzel, *Naturwissenschaften* **41**, 448 (1954); W.J. Duffin, J.H.C. Hogg, *Acta Cryst.* **20**, 566 (1966); W.J. Duffin, J.H.C. Hogg, *Phys. Stat. Sol.* **18**, 755 (1966); H.-J. Deiseroth, R. Walter, *Z. Kristallogr.* **210**, 360 (1995).
2. F.E. Faradzhev, N.M. Gasanly, A.S. Ragimov, A.F. Goncharov, S.I. Subbotin, *Solid State Commun.* **39**, 587 (1981); E.A. Vinogradov, N.M. Gasanly, A.F. Goncharov, G.N. Zhizhin, N.N. Melnik, V.V. Panfilov, A.S. Ragimov, S.I. Subbotin, *Fiz. Tverd. Tela.* **24**, 139 (1982), Engl. transl.: *Sov. Phys. Solid State* **24**, 77 (1982).
3. K. Takarabe, K. Wakamura, E. Ito, *Solid State Commun.* **46**, 215 (1983).
4. K. Takarabe, *Phys. Stat. Sol. (b)* **143**, K67 (1987); K. Takarabe, *Phys. Stat. Sol. (b)* **145**, 219 (1988).
5. S.S. Kabalkina, V.G. Losev, N.M. Gasanly, *Solid State Commun.* **44**, 1383 (1982).
6. A.F. Goncharov, I.N. Makarenko, N.M. Gasanly, *Phys. Stat. Sol. (b)* **129**, K79 (1985).
7. H.K. Mao, P.M. Bell, J.W. Shaner, D.J. Steinberg, *J. Appl. Phys.* **49**, 3276 (1978).
8. R.J. Nelmes, P.D. Hatton, M.I. McMahon, R.O. Piltz, J. Crain, R.J. Cernik, G. Bushnell-Wye, *Rev. Sci. Instrum.* **63**, 1039 (1992); R.O. Piltz, M.I. McMahon, J. Crain, P.D. Hatton, R.J. Nelmes, R.J. Cernik, G. Bushnell-Wye, *Rev. Sci. Instrum.* **63**, 700 (1992).
9. L.G. Akselrud, Yu. Grin, V.K. Pecharsky, program package *CSD: Crystal Structure Determination* version 4.10, STOE & Cie., Darmstadt (1992).
10. F.E. Faradev, N.M. Gasanly, B.N. Mavrin, N.N. Melnik, *Phys. Stat. Sol. (b)* **85**, 381 (1978).
11. U. Schwarz, H. Hillebrecht, K. Syassen, *Z. Kristallogr.* **210**, 495 (1995).

# TETRAGONAL MODIFICATION OF CuI WITH OCTAHEDRAL COORDINATION OF Cu-ATOMS UNDER SHEAR DEFORMATION AND HIGH PRESSURE UP TO 38 GPa

N.R. SEREBRYANAYA, S.S. BATANOV, V.D. BLANK, V.A. IVDENKO  
*Institute of Spectroscopy of RAS, 142092 Troitsk, Moscow region, Russia*

## ABSTRACT

The new reversible CuI-phase transition was found at 17 GPa and the shear deformation by using a diamond anvil cell with one rotating anvil. This apparatus is designed for creating shear deformation. The crystal structure of new pressure-induced phase (CuI-VIII') is a tetragonal-distorted of the rocksalt type, the volume change is equal to 17%. The pressure transition into a cubic structure is calculated by a/c linear extrapolation to 1 and it is equal to 113 GPa.

Copper(I) halides crystallize in the zinc-blende structure at ambient conditions. The available experimental evidence suggests that all three Cu(I) halides adopt the rocksalt structure at pressures up to 10-12 GPa. However this transition into NaCl-type was observed only for two halides: CuCl and CuBr by the "in situ" X-ray diffraction study [1-3]. It was found that CuCl and CuBr - transformations from fourfold to sixfold coordination occur via several intermediate phases of apparently lower symmetry, despite the simple geometric relationship between the zinc-blende and rocksalt structures. Considering the ionicity of CuI ( $f=0.692$ ), which is less than the ionicity of CuBr ( $f=0.735$ ) [4], we proposed that the rocksalt phase of CuI - CuI-VIII will be obtained at higher pressure than for CuBr. Earlier [1] NaCl-structure was obtained for CuI by preheating up to 100°C at 8 GPa and the NaCl-pattern was produced at room temperature and 12 GPa. Attempts to obtain the rock-salt-phase for CuI up to 12 GPa without previously heating was unsuccessful [1,3].

It well known that the application of shear deformation decreases the transition pressure and the hysteresis of the phase transition. The phase transitions, which are unreal in hydrostatics, are getting more possible under non-hydrostatic pressures with shear deformation.

Taking into account these facts, we decided to obtain the densest CuI-phases by applying shear deformation under high pressure. Earlier we designed an X-ray diamond anvil cell with

one rotating anvil opposite another for creating shear deformations [5].

The size of the diamond culet is equal to 400  $\mu\text{m}$ . Mo-radiation is used with photo-registration of the diffraction patterns. The sample-film-distance is equal to 25 mm. The exposures usually lasted about 48 h. A steel-gasket compressed beforehand is used. The hole diameter of the gasket is equal to 0.25 mm. The pressure distribution is determined by the ruby-luminescence method. The transitions are fixed by the anomalous steps at the pressure-distribution-curve (Fig.1).

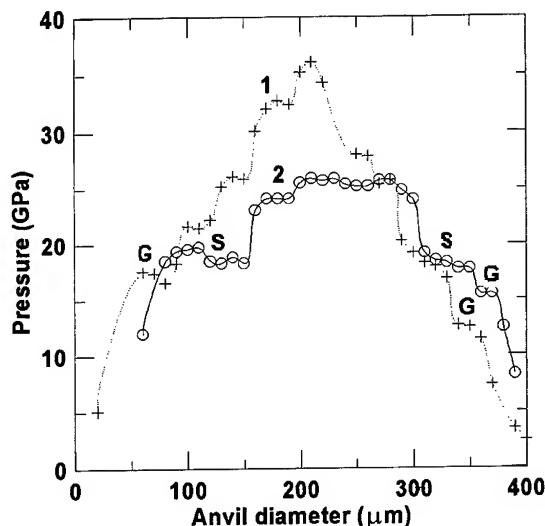


Fig.1. Pressure distribution in CuI specimens before(1) and after(2) shear deformation. S - are anomalies such as steps corresponding to the two-phase regions. G - is gasket.

The effect of the shear deformation on the crystal structure of CuI was studied in the following way. First, the diffraction patterns were obtained at the definite pressure, then the shear deformation is applied by a smooth rotation of the movable support of the anvil through an angle =  $30^\circ$  and the movable assembly is rotated back to the initial position. The pressure distribution is recorded and the pattern is produced once again.

Since already [1,3] the phase diagram has been investigated up to 12 GPa, we began to carry out the experiments from 11 GPa. Two pressure-induced phases of CuI: CuI-IV and CuI-V were known up to 12 GPa [1,3]. The fourfold coordination is still retained in these phases: CuI-IV is a rhombohedral-distorted structure of zinc-blende type, CuI-V has an antilitharge (anti-PbO) type of structure.

The new reversible CuI-phase transition was found at 17 GPa with shear deformation [6]. The long two-phase-region (17-22GPa) was observed in the diffraction patterns and the pressure-distribution curves. All lines of the new phase, named by CuI-VIII', were indexed in a tetragonal system. The most strong reflexes have either even or odd indexes as well as in the rocksalt-type. Unit-cell parameters are refined by least-squares method (Table):  $a=5.068(5)$  Å,  $c=4.846(5)$  Å,  $Z=4$ ,  $a/c=1.046$  at 38 GPa and shear deformation. Volume change is equal to 17% (in the two-phase region).

Table. Interplanar spacing of CuI-VIII' at 38 GPa with a shear deformation.

I/I max %	$d_{\text{obs.}}$ , Å	hkl	$d_{\text{calc.}}$ , Å
40	2.886	111	2.881
100	2.531	200	2.534
50	2.422	002	2.423
30	2.265	120	2.266
10	2.060	121	2.053
30	1.790	220	1.792
20	1.667	221	1.680
20	1.440	222	1.441

Crystal structure is proposed to be a tetragonal-distortion of NaCl-type. We found the oriented relationship between CuI-VIII' and CuI-III (initial zinc-blende-type of structure):

$[100]_{\text{tetr.}}/[112]_{\text{cub.}}$ ,  $[001]_{\text{tetr.}}/[111]_{\text{cub.}}$ . The (110) - projection of CuI-VIII'-structure may be placed in the (101) - projection of CuI-V (antilitharge) [6]. We proposed that the angle between two [112] cubic directions, which is no  $90^\circ$ , is getting rectangular under high pressure and shear deformation, therefore CuI-VIII'-structure is getting tetragonal. Considering the Cu - coordination polyhedrons of CuI-phases, we traced the change of it: from tetrahedrons of CuI-III, CuI-IV, CuI-V-phases to distorted octahedron of CuI-VIII' and octahedron of CuI-VIII.

The  $a/c$ -ratio of unit-cell of CuI-VIII' - structure is equal to 1.054 at 17 GPa. It is a tetragonal distortion. When the pressure increases this value decreases. We calculated the transition-pressure into a cubic structure by  $a/c$  linear extrapolation to 1. This pressure is occurred to be equal to 113.5 GPa.

The main result of the present report is a detection of CuI-VIII' - phase with a tetragonal-distorted rocksalt structure. Shear deformation relieves the transition pressure from 23 GPa to 17 GPa. Now all copper(I) halides CuCl, CuBr, CuI have pressure-induced phases with the octahedral coordination of Cu-atoms.

## References

1. V.Meisalo, M.Kalliomaki, *High Temp.-High Press.*, **5** (1973) 663.
2. N.Serebryanaya, S.Popova, A.Rusakov, *Fizika Tverdogo Tela (in Russian)*, **17** (1975) 2772
3. S.Hull, D.Keen, *Phys. Rev.*, **B50** (1994) 5868
4. J.C.Phillips, *Rev.Mod. Phys.*, **42** (1970) 317.
5. V.D.Blank, N.R.Serebryanaya, A.Vorontsov, A.Yu.Zerr, *Fizika i Tehnika Vys. Davl (in Russian)*, **3** (1993) 36.
6. S.S.Batsanov, N.R.Serebryanaya, V.D.Blank, V.A.Ivdenko, *Crystallogr. Rep.*, **40** (1995) 598.



# XAFS STUDY of the B1-B2 TRANSITION in RbCl

R. Ingalls, S. Jones and F. Wang

Department of Physics, University of Washington  
Seattle, WA 98105, USA

## ABSTRACT

An XAFS (x-ray absorption fine structure) study of RbCl at room and liquid nitrogen temperatures (LNT) to pressures over 10 GPa is reported. We find the pressure-induced NaCl- to CsCl-type transition at 0.5 GPa to exhibit a mixed phase region which is relatively broad at LNT. We give the results of an analysis of the resulting spectra that includes a full multiple-scattering, curved-wave treatment, and yields the associated crystal structure fractions and bond lengths as a function of pressure.

## Introduction

The pressure-induced B1-B2 transition (NaCl to CsCl structure) has been extensively studied at room temperature (RT) in a number of the alkali metal halides. Here we report further results on RbCl for which the transformation occurs at approximately 0.5 GPa. Of particular interest is the large volume decrease of approximately 14%, and the steric relationship between the crystal axes in the two phases.<sup>1</sup>

In contrast to the above volumetric and diffraction measurements, XAFS (x-ray absorption fine structure) spectroscopy gives site-specific local information about the rubidium atoms. In particular the method yields bond lengths, and their mean-square deviations. Such earlier experimental RT work on this system by our group has been reported.<sup>2</sup> More recently a theoretical explanation has been given of the striking change in the XANES (x-ray absorption near edge structure) observed in the spectra near the Rb K-edge.<sup>3</sup>

Here we report preliminary liquid nitrogen temperature (LNT) XAFS measurement of this transition as well as a state-of-the-art analysis of both the LNT and the previous RT data using the FEFF curved-wave, multiple scattering program.<sup>4</sup>

## Experimental

The experimental XAFS spectra reported here were obtained from a wiggler side-station at the Stanford Synchrotron Radiation Laboratory using silicon (111) monochromator crystals. High pressure at room temperature was generated as described previously.<sup>5</sup> The method was modified for a liquid nitrogen cryostat using a washer-shaped diaphragm pressurized by helium gas, as described by Daniels and Ryschkewitsch.<sup>6</sup> Anvils of boron carbide with tip diameters of 2.0 mm were used. Pressure was obtained by comparing the XAFS determined structural information with the known equation of state (EOS) of RbCl.<sup>7</sup>

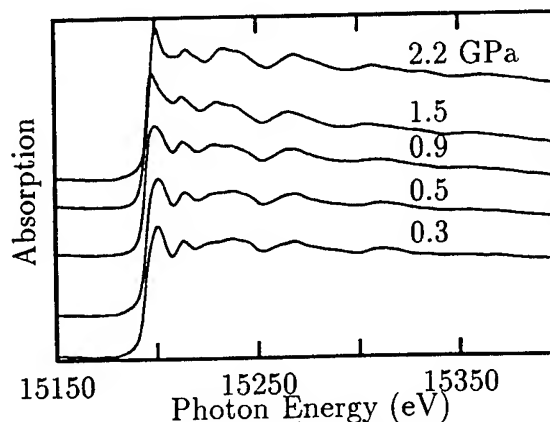


Fig. 1. LNT XANES spectra of the Rb K-edge in RbCl at several pressures.

## Results

In Fig. 1 we show representative XANES spectra at LNT at several pressures associated with the Rb K-edge in RbCl. In the  $\sim 1$  GPa region above the B1-B2 phase transition at 0.5 GPa there is a gradual change in the character of the spectra. The RT results (not shown) are rather similar except the transition is sharper. In Fig. 2 are shown the XAFS oscillations of the full XAFS spectra associated with Fig. 1 versus wave number,  $k$ , rather than energy,  $E$ , where

$$E = (\hbar k)^2 / 2m + \text{const.} \quad (1)$$

The change in character due to the phase transition is more apparent in such a plot. Also shown for comparison is the RT result at atmospheric pressure. High pressure and, especially, low temperature enhances the amplitude of these oscillations by reducing the mean-square deviations in the bond-lengths, that is, the atom-pair Debye-Waller type factors. The radial distribution about the x-ray absorbing atom is readily obtained from the magnitude of the Fourier transform of the type of data of Figure 2. This is shown for the LNT data in Figure 3, where the gradual change in structure due to the phase transition is evident.

The state-of-the-art analysis program, FEFF,<sup>4</sup> referred to earlier, has been perfected to extract structural parameters from XAFS spectra. It is especially accurate when the actual crystal structures are already known. Because of the evolving nature of the spectra above the phase transition the best fits to the data are obtained assuming both B1 and B2 phases are present in this region. Proceeding in this way we obtain the nearest neighbor bond lengths,  $d$ , for the two phases as shown in Fig. 4. The relative amounts of the two phases are shown in Fig. 5. for both RT and LNT. A plot of the type shown in Fig. 4 for the RT results is quite similar to that shown LNT results, except, because of the sharper transition, the B1 phase disappears before it can reach as great a compression.

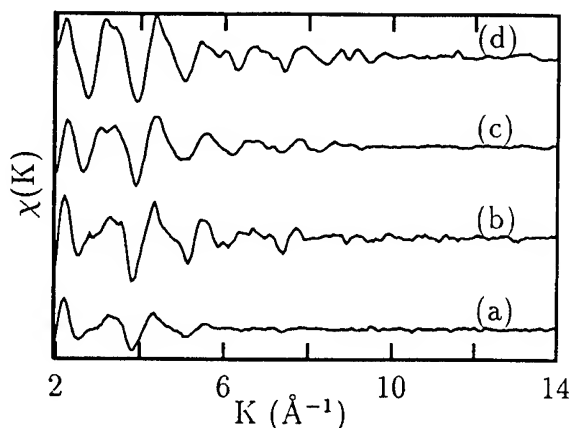


Fig. 2. EXAFS oscillations at the Rb K-edge in RbCl at several temperature and pressures: (a) RT and 0.1 MPa; (b)-(d) LNT and 0.1 MPa, 0.3, and 0.7 GPa, respectively.

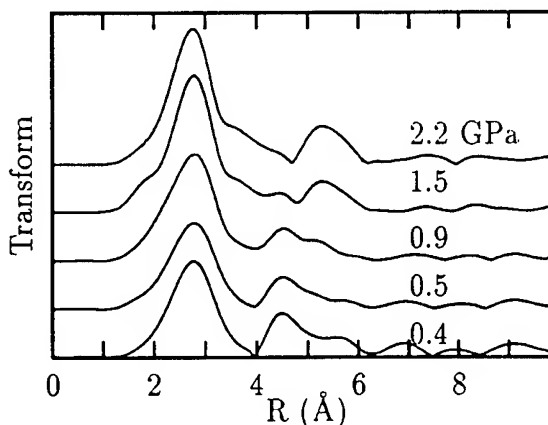


Fig. 3. XAFS determined radial distribution functions about the Rb atom in RbCl at LNT at several pressures.

## Discussion

From the measured EOS of RbCl,<sup>7</sup> the nearest neighbor distance,  $d$ , would be expected to follow the dashed curve in Fig. 4 if the transition were infinitely sharp. That is, although there is a large decrease in volume, because the number of nearest neighbors increases from six to eight,  $d$  is expected to actually increase. We have on occasion used RbCl as an XAFS pressure calibrant for RT experiments. However, when only the B2 phase was assumed to be present immediately above the transition, a fit to the data failed

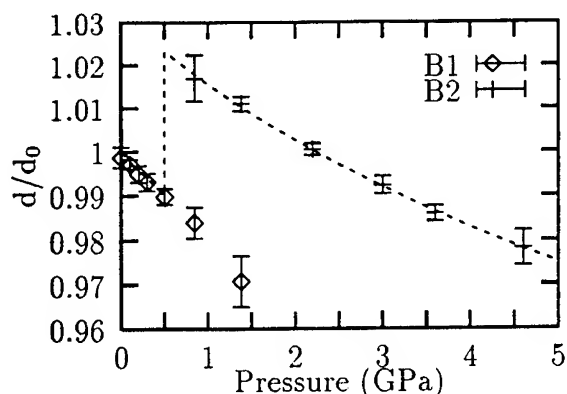


Fig. 4. Nearest neighbor distance at LNT in the B1 and B2 phases of RbCl as determined from XAFS.

to yield such an increase in  $d$ . A similar treatment of the LNT data yielded even poorer fits to the data. Clearly the assumption of two phases present *at the same pressure* above the transition yields result consistent with the expected EOS if the behavior for the B1 phase is extended to higher pressures. If instead, sizeable pressure gradients are used to explain the presence of both phases, one would expect to extract different pressures for each phase, with the B1 phase yielding the lower pressure. This is not observed. In fact, it is common for Martensitic phase transitions to exhibit mixed phase regions that decrease as the temperature is raised. The bcc-hcp transition in metallic iron is another such example.<sup>8</sup> It is expected that local strains, possible epitaxy between the phases present and the transition mechanism itself, such as suggested by Onodera, et. al.<sup>1</sup> must be treated in detail to completely explain the data.

## Conclusions

We have shown the strength of the XAFS technique for observing the local behavior of pressure-induced crystallographic phase transitions. Accurate analysis methods now permit the decomposition of the data associated with more than one phase. In addition the data is of sufficient quality to be of use in theoretical models of such transitions. Moreover, we now believe that this treatment of the results for RbCl greatly enhances its use as an XAFS pressure calibrant.

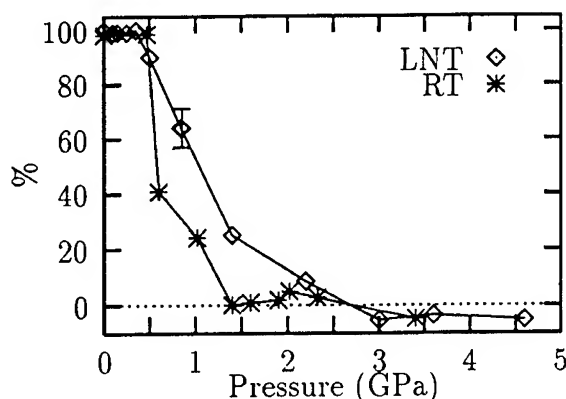


Fig. 5. Percentage of the B1 phase of RbCl at RT and LNT as a function of pressure.

## Acknowledgements

The authors are pleased to thank E.D. Crozier and B. Houser for help with various aspects of this work. This research was supported by the US Department of Energy Grant No. DE-FG-06-84ER-45163, while SSRL is supported by the US Department of Energy and the National Institutes of Health.

## References

1. A. Onodera, Y. Nakai, S. Kawano and N. Achiwa, *HighTemp. - HighPress.* **24**, 55 (1992).
2. J. Freund, R. Ingalls and E. D. Crozier, *Phys. Rev.* **B43**, 9894 (1991).
3. A.V. Soldatov, T.S. Ivanchenko, I.E. Stekhin, A. Bianconi and R. Ingalls, *Phys.Stat. Sol. (b)* **184**, 237 (1994).
4. J. Mustre de Leon, J.J. Rehr, S.I. Zabin-sky and R.C. Albers, *Phys.Rev.* **B44**, 4146 (1991).
5. R. Ingalls, E. D. Crozier, J. E. Whitmore, A. J. Seary and J. M. Tranquada, *J.Appl.Phys.* **51**, 3158 (1980).
6. W.B. Daniels and M.G. Ryschkewitsch, *Rev. Sci.Instrum.* **83**, 115 (1983).
7. S.N.Vaidya and G.C. Kennedy, *J.Phys. Chem.Solids* **32**, 951 (1971).
8. F. Wang, R. Ingalls and E.D. Crozier, *Jpn.J. Appl.Phys.* **32**, Suppl. 32-2, 749 (1992), and references therein.

# STRUCTURAL PHASE TRANSITION OF $\text{TmGa}_2$ AT HIGH PRESSURE

S. BRÄUNINGER, U. SCHWARZ, Yu. GRIN and K. SYASSEN

*Max-Planck-Institut für Festkörperforschung, Heisenbergstrasse 1, D-70569 Stuttgart, Germany*

We have investigated pressure-induced structural changes of  $\text{TmGa}_2$  by means of x-ray powder diffraction using diamond anvil cell techniques in combination with an imaging plate system for data collection. The ambient pressure modification of  $\text{TmGa}_2$  (orthorhombic  $\text{KHg}_2$ -type structure) undergoes a reversible structural phase transition to the hexagonal  $\text{AlB}_2$ -type structure at  $36 \pm 2$  GPa. Within experimental uncertainty there is no discontinuous change of volume at the phase transition. The associated breaking of the interlayer Ga-Ga bonds could be reproduced by LMTO calculations of the electron density and localization. Optical reflectivity spectra indicate that both polymorphs are metallic.

## 1 Introduction

Rare-earth intermetallics have attracted broad interest in recent years because they exhibit a large variety of unusual magnetic properties and/or mixed valence phenomena<sup>1</sup>. In the case of  $\text{TmGa}_2$  the electropositive rare-earth metal can formally supply up to 1.5 electrons to each gallium atom for the formation of covalent bonds. According to the Zintl-Klemm-Busmann formalism gallium gaining one electron should form a diamond-like partial structure.

All compounds  $\text{REGa}_2$  (RE=rare-earth element) crystallize either in the  $\text{KHg}_2$ - or the  $\text{AlB}_2$ -type structure, except for  $\text{YbGa}_2$  ( $\text{CaIn}_2$ -type).  $\text{TmGa}_2$  crystallizes in the  $\text{KHg}_2$ -type structure ( $\text{Imma}$ ,  $\text{CeCu}_2$ -type)<sup>2,3,4</sup>, and the Ga atoms form a framework of six membered rings in chair conformation with puckered Ga layers oriented perpendicular to the crystallographic a-axis (Fig. 1). The layers are connected by Ga-Ga bonds (3) thus forming cavities occupied by Tm atoms. The structure can be described as a three-dimensional network of distorted gallium tetrahedra with Tm (CN=4+4+2+2) in its cavities. In the  $\text{AlB}_2$ -type structure ( $\text{P6}/\text{mmm}$ ) the six membered rings are planar forming hexagonal prisms centered by the RE atom (CN=12).

X-ray powder diffraction experiments were carried out to investigate structural changes. Our primary motivation was to examine the influence of hydrostatic pressure on the 3D covalent gallium network. In order to monitor electronic structure changes caused by the application of pressure we measured the optical reflectivity in the energy range 0.5 to 4 eV.

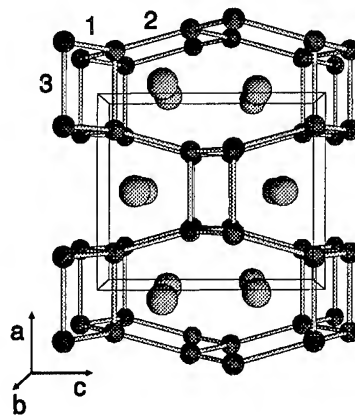


Figure 1: View of the orthorhombic low pressure modification of  $\text{TmGa}_2$  along the  $[010]$  direction. Tm:○, Ga:●.

## 2 Experimental details

The compound was prepared from high purity elements in 1:2 atomic ratio by arc-melting under helium atmosphere. The sample was annealed in a sealed silica tube at  $873^\circ\text{C}$  for 350 hours to ensure homogeneity. After quenching in water the reaction product was brittle with metallic lustre.

The thoroughly ground sample was loaded into a gasketed diamond anvil cell, with a 4:1 methanol-ethanol mixture as pressure-transmitting medium. The pressure was measured by the ruby luminescence method. Below 25 GPa the x-ray powder diffraction data were measured using an imaging plate setup and  $\text{AgK}\alpha$ -radiation. A modified Weissenberg camera serving as a cell holder allowed oscillation of the sample to improve the powder statistics. Integration of the two-dimensional powder image<sup>5</sup> and distance calibration results in one-dimensional intensity data.

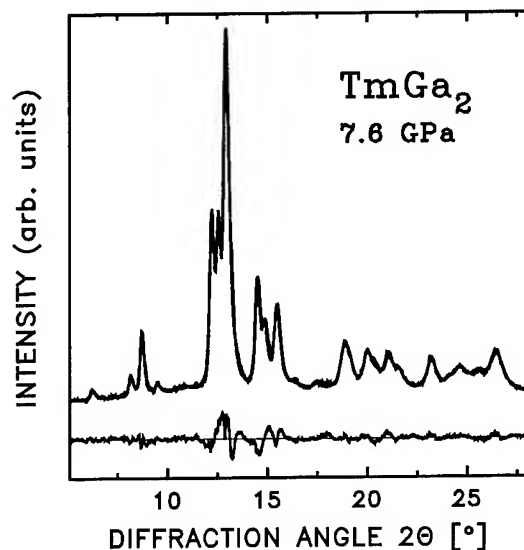


Figure 2: Refined powder diffraction diagram of the low pressure modification (KHg<sub>2</sub>-type).

Full-profile refinements of the structural parameters were performed with the program CSD<sup>6</sup>. Diffraction patterns above 25 GPa were measured in Debye-Scherrer geometry using a slit-type cell, MoK $\alpha$  radiation, and a position sensitive proportional counter. The observation angle in both cases is limited by the high pressure cell to  $2\theta \leq 30^\circ$ .

### 3 Results and Discussion

X-ray investigations starting from the ambient pressure orthorhombic modification of TmGa<sub>2</sub> were performed up to a maximum pressure of 46 GPa. Full-profile refinements below 8 GPa (Fig. 2) indicate that the initial step of the structural change is the decrease of the longest Ga-Ga distance (2) within the six membered rings of the low pressure phase. Up to 10 GPa the Ga-Ga bond lengths along the crystallographic *a*-axis (3) remain almost constant. Above 10 GPa they increase significantly and the reflection intensities deviate considerably from those calculated for the ideal KHg<sub>2</sub>-type structure. Between 10 and 26 GPa the *c/b* axial ratio approaches  $\sqrt{3}$  indicating an approximation towards a hexagonal metric. Above 26 GPa it is not possible anymore to resolve the individual reflections. However, we monitored the merging by determining the width of the reflection group (112), (202), (211), (103) (Fig. 3). The

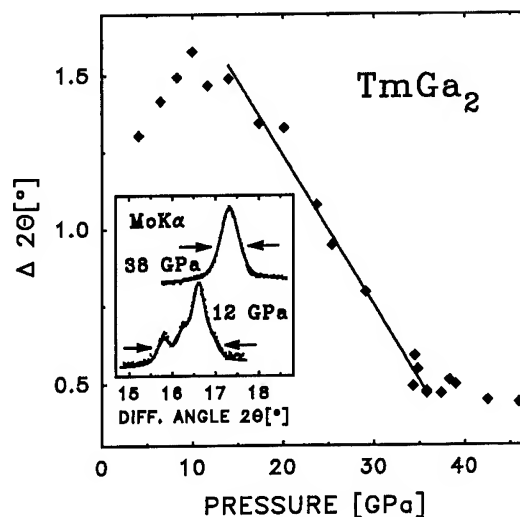


Figure 3: Width of the reflection group 112, 202, 211, 103.

width increases slightly up to 10 GPa and then decreases significantly for pressures up to 36 GPa. Above this pressure the peak shape becomes symmetric and the width remains constant. We conclude that TmGa<sub>2</sub> is hexagonal above  $36 \pm 2$  GPa (Fig. 4). The high pressure polymorph can be identified as AlB<sub>2</sub>-type structure (P6/*mmm*).

Structural parameters of both polymorphs are listed in Table 1. Obviously, the phase transition is

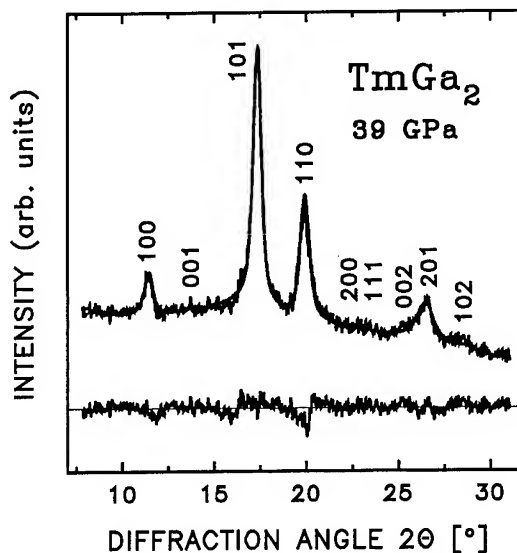


Figure 4: Refined powder diffraction diagram of the high pressure modification (AlB<sub>2</sub>-type).

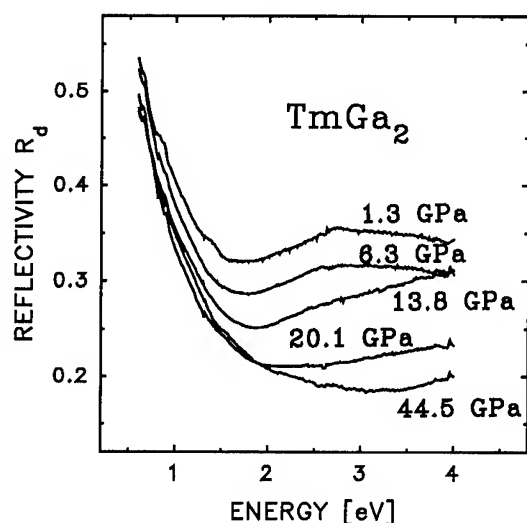


Figure 5: Optical reflectivity spectra of  $\text{TmGa}_2$  at the sample-diamond interface.

associated with a breaking of the interlayer Ga-Ga bonds (3). Therefore the pressure-induced change of hybridization results in a transformation of a three-dimensional covalent network to a layered gallium partial structure. This result can be reproduced by electron density maps obtained from LMTO calculations which will be reported elsewhere.

Experimental pressure-volume data were fitted by a Murnaghan-type equation of state<sup>7</sup> with the bulk modulus  $B_0=96(4)$  GPa, and its pressure derivative  $B'_0=4(1)$ , both at atmospheric pressure. Thus  $\text{TmGa}_2$  is a comparably incompressible solid with a bulk modulus similar to that of silicon ( $B_0=97.7$  GPa). Within experimental uncertainty there is no discontinuous change in volume associated with the transformation.

Apart from the changes in volume compounds containing rare-earth elements often show anomalies in various physical properties when changing their valency state. Optical reflectivity spectra of  $\text{TmGa}_2$  are shown in Fig. 5. The Drude-like edge below 1.5 eV indicates that  $\text{TmGa}_2$  is metallic in both modifications. With increasing pressure loss of interband oscillator strength for energies above 2 eV is observed. In view of the continuous changes in the optical reflectivity spectra and the continuous pressure-volume behavior we conclude that there is no major valency change of Tm involved in driving the structural changes. This is consistent with magnetic measurements at am-

Table 1: Results of the full-profile powder refinements for the low- and high-pressure modification of  $\text{TmGa}_2$ .  $B_{iso}$ =isotropic temperature factor;  $R_I$ =intensity R-value.

	<i>Imma</i>	<i>P6/mmm</i>
<i>p</i> (GPa)	7.6	39
<i>a</i> (Å)	6.725(2)	4.090(3)
<i>b</i> (Å)	4.146(1)	
<i>c</i> (Å)	7.835(2)	3.130(4)
<i>Ga-Ga</i> (1) (Å)	2.489(2)	2.361(3)
<i>Ga-Ga</i> (2) (Å)	2.616(4)	
<i>Ga-Ga</i> (3) (Å)	2.739(1)	3.130(4)
<i>B<sub>iso</sub></i> (Å <sup>2</sup> )	1.31	1.62
<i>R<sub>I</sub></i>	0.069	0.092

bient conditions indicating that  $\text{TmGa}_2$  is paramagnetic with an effective moment  $\mu_{eff}=7.3\mu_B$  in good agreement with compounds containing  $\text{Tm}^{III}$ .

## References

1. K. Buschow, Rep. Prog. Phys. **42**, 1374 (1979).
2. E.I. Gladyshevskij, Yu. Grin, S.P. Jacenko, J.P. Jarmoljuk, K.A. Chuntunov, Dopovidi Akademii Nauk Ukrain'skoi RSR, Seriya A: Fiyiko-Matematichni Ta Tekhnichni Nauki **42**(6), 82 (1980).
3. H. Lüscher, K. Girgis, P. Fischer, J. Less Comm. Met. **83**, L23-L25 (1982).
4. Yu. Grin, Y.P. Yarmolyuk, Russian Metallurgy, Translated From Izvestiya Akademii Nauk SSSR, Metally, **1**, 161 (1983).
5. R.J. Nelmes, P.D. Hatton, M.I. McMahon, R.O.Piltz, J. Crain, R.J. Cernik, G. Bushnell-Wye, Rev. Sci. Instrum. **63**, 1039 (1992); R.O. Piltz, M.I. McMahon, J. Crain, P.D. Hatton, R.J. Nelmes, R.J. Cernik, G. Bushnell-Wye, Rev. Sci. Instrum. **63**, 700 (1992).
6. L.G. Akselrud, Yu. Grin, V.K. Pecharsky, program package *CSD: Crystal Structure Determination* version 4.10 STOE & Cie., Darmstadt (1992).
7. F.D. Murnaghan, Proc. Natl. Acad. Sci. U.S. **30**, 244 (1944).

# HgO UNDER HIGH PRESSURE: A COMBINED X-RAY ABSORPTION AND X-RAY DIFFRACTION STUDY.

A. SAN MIGUEL<sup>1</sup>, A. GONZALEZ PENEDO<sup>1,\*</sup>  
J.P. ITIE<sup>2</sup>, A. POLIAN<sup>2</sup>  
P. BORDET<sup>3</sup>

(1) *European Synchrotron Radiation Facility, BP 220, 38043 Grenoble, France.*

(2) *Physique des Milieux Condensés, Centre National de la Recherche Scientifique  
Université Pierre et Marie Curie, B 77, 4 Place Jussieu, F-75252 Paris CEDEX 05*

(3) *Laboratoire de Cristallographie BP 166 38042 Grenoble, France.*

(\*) *Present address: Dpto. de Química Física, Facultade de Química, Universidade de Santiago,  
15706 Santiago de Compostela, Spain.*

## ABSTRACT

We have studied the high pressure behaviour of monrodyt HgO by x-ray absorption at the Hg LIII-edge and energy dispersive x-ray diffraction experiments using synchrotron radiation. Three phase transformations at 2, 5 and 13±1 GPa have been unambiguously identified. Chain structures persist up to 13±1 GPa, from where a new form with higher coordination appears. Quenched samples from the higher coordination phase recover a chained structure but they do not show a reversible transformation to the monrodyt structure. A first order Murnaghan equation of state fitted to the observed volume compressibility in the monrodyt phase gives a bulk modulus of 30-45 GPa.

## Introduction

It has been observed that for the heaviest II-VI semiconductor-semimetals (HgS, HgSe, HgTe, CdTe and ZnTe) the formation of chained structures (cinnabar type) precedes the transition to phases with coordination higher than 4<sup>1,2,3</sup>. HgO is known to present at ambient conditions a chained structure but the very few studies realised on its high pressure behaviour does not let know its structural evolution.

The most common phase of HgO is a large gap semiconductor material (2.19 eV) with the monrodyt structure type, an orthorhombic form constituted of flat zigzag chains of alternated atoms<sup>4</sup>. There has been reported up to four other different polytypes of HgO at ambient pressure, the cinnabar one (with spiral chains) being one of this forms<sup>4</sup>.

Even if the geometry of the chains is different between the cinnabar and the monrodyt structures, the interatomic distances and angles in the chains are markedly similar in both structures. It has been also observed that single crystals of these two modifications show very often an epitaxial growth which could be interpreted as being due to a transition of the infinite spiral chain (cinnabar) into the infinite planar zigzag chain (monrodyt). This

structural resemblance suggests that physical properties as the local structure evolution with high pressure could be equivalent for both starting structures.

## Results and discussion

We have investigated the high pressure behaviour of monrodyt yellow powdered samples by means of energy dispersive x-ray diffraction up to 27 GPa and by means of energy dispersive x-ray absorption spectroscopy at the Hg LIII-edge up to 15 GPa. In both cases fine grained powders were loaded in membrane-type diamond cells<sup>5</sup> using silicon oil as pressure transmitting medium and the pressure was measured using the linear ruby fluorescence scale<sup>6</sup>. All experiments were done using the DCI storage ring of L.U.R.E. (Orsay, France).

Fig 1 shows the observed  $d_{hkl}$  evolution with pressure for two different experiments. Because of preferential orientation effects some of the peaks were better observed in one or other of the experiments. At 2 GPa, the apparition of two new strong diffraction peaks in the 2.2 Å region evidence the transformation to a new phase. This observation is corroborated by the discontinuity in the evolution of the distances in the first and second neighbour

shells observed by EXAFS (extended x-ray absorption fine structure) (fig 2).

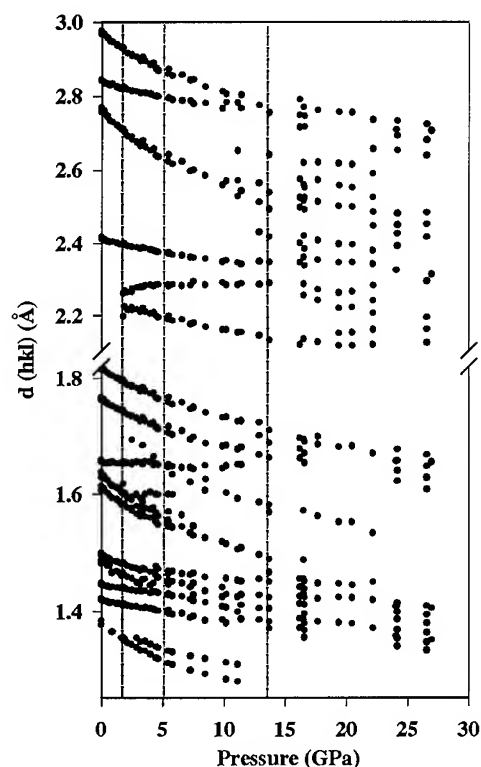


Fig 1. HgO  $d$  spacing evolution with pressure obtained in two different diffraction experiments. Vertical lines represent the unambiguously determined phase transitions

We have fitted the volume evolution in the montrodyt structure with a first order Murnaghan equation of state<sup>7</sup> (fig 3). The relative scattering of the volume values does not let to obtain a very precise value for the bulk modulus. Fixing its pressure derivative value between 3 and 4.5, we obtain a bulk modulus ranging from 30 to 45 GPa.

In a similar way to the first transition (figs 1 and 2), other transitions are observed at about 5 and 11 GPa. We do not discard other phase transformations, but the accuracy of our results do not let to identify them unambiguously. Trials to determine the structure of the high pressure phases by indexing the observed  $d_{hkl}$  in the different regions gave very poor values for our confidence parameters. Unless strong phase mixture is present, structures with a symmetry lower than orthorhombic should be discarded. Nevertheless the possibility of phase mixing should be considered

in particular because of the progressive enlargement of some of the diffraction peaks with increasing pressure. From about 11 GPa the diffraction peaks enlarge very much making the interpretation of our diffraction data very difficult (only for some of the pressures the data has quality enough to separate the contributions of different picks). Up to about 13 GPa all the diffraction peaks of the montrodyt structure are kept (the doublet at about 1.3 Å is also present but the intensities are very weak), and the effects of pressure are of changes in the slope of the  $d_{hkl}$  and the apparition of new peaks. This lets suppose that the phase transitions up to 13 GPa correspond to the formation of superstructures in agreement with the observed phases synthesised at high pressure<sup>4</sup>.

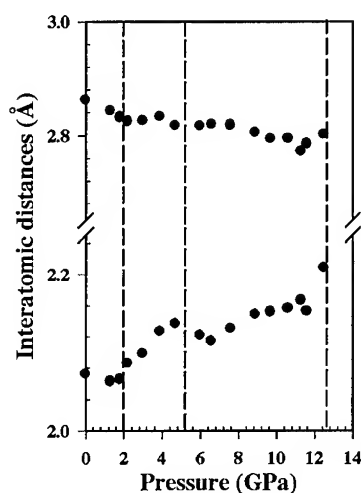


Fig 2. Hg-O interatomic distances obtained by EXAFS analysis as a function of pressure. The vertical lines point to the structural transformations

The pseudo radial distribution functions obtained from the observed EXAFS signal, show two clear peaks corresponding to the average distance in the chains and in between the chains. The signal corresponding to these peaks were filtered and fitted with a spherical-wave EXAFS model using theoretical phases and amplitudes. Fits with an structure corresponding to the montrodyt one consisting in three shells of two atoms each one gave, with our resolution, the same distances for the second and the third shell. Good fits were obtained with two shells of atoms consisting in two oxygen atoms at the same average distance at around 2.1 Å and four oxygen atoms at an average distance of



about 2.8 Å. The distance evolution with pressure is represented in Fig 2. It is observed that up to the pressure value where the model could be fitted (12.5 GPa) the in-chain distance increases for all phases except for the montrodyt one.

The average interatomic distance in between the chains shows a relatively small compressibility when compared with the augmentation of the in-chain bond distance. This indicates that the better packing of the infinite chains has an important role in the compression of HgO up to about 11-13 GPa. A full structure determination will be needed to quantify the packing evolution.

The peak in the EXAFS pseudo radial distribution function corresponding to the chain distances persists up to 12.5 GPa from where it suddenly disappears (next spectrum at 14 GPa). EXAFS fits show an important increment in the pseudo Debye-Waller factors from 12 GPa.

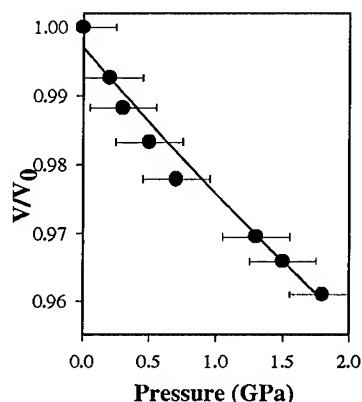


Fig 3. Relative volume variation in the montrodyt structure (dots) and first order Murnaghan fit with  $B'_0$  fixed to 4

This evidence shows that up to about that pressure the different structures are chain based and that from that pressure the chain structure is destroyed. This should be correlated with the observed non reversibility of samples pressurised at pressures  $\approx 10$  GPa<sup>8</sup> and the indications of metallization from this pressure<sup>9</sup>.

A comparative study of the form of the Hg LIII-edge XANES (x-ray absorption near edge structure) of the low and high pressure structures both of HgO and HgS, indicates that the high pressure phases of both compounds should share the same general local structure. The high pressure phase of HgS being the rocksalt structure, this indicates that from  $13 \pm 1$  GPa the local structure of HgO must have an octahedral

based coordination. This fact is corroborated by the observed augmentation of the integrated area of the pseudo radial distribution function peak of the last spectra taken at 14.9 GPa.

Both diffraction and x-ray absorption experiments show that samples quenched from the high coordination phase do not come back to the original montrodyt structure. Nevertheless the diffraction pattern of the recovered samples show peaks at essentially the same positions that the ones of the montrodyt structure but much larger. This together with the lack of some of the peaks is in agreement with what has been observed for samples quenched from 35 GPa<sup>8</sup> and that were identified as belonging to a tetragonal modification. We were also able to index the recovered samples with a tetragonal structure, but again our confidence values are not good enough to ensure a structure determination. The XANES of the recovered samples show only slightly differences with the XANES of montrodyt samples, and the pseudo radial distribution function shows both peaks at the in-chain and inter-chain distances, indicating that HgO recovers a chain-based structure.

## References

- <sup>1</sup> T.L. Huang and A.L. Ruoff, Phys. Rev. B **31**, 5976 (1985); A. Onoreda, A. Ohtani, M. Motobayashi, T. Seide, O. Shimomura, O. Fukunaga, in Proceedings of the 8th AIRAPT Conference, Uppsala, Sweden, 1981, edited by C. M. Backman, T. Johannisson, and L. Tegner (Arkitektopia, Uppsala, 1982), Vol.1, p.321; A. San Miguel, A. Polian and J.P. Itié, J. Phys. Chem. Solids **56**, 555 (1995).
- <sup>2</sup> A. San Miguel, A. Polian, M. Gauthier and J.P. Itié, Phys. Rev. B, **48**, 8683 (1993).
- <sup>3</sup> R.J. Nelmes, M. I. McMahon, N.G. Wright and D. R. Allan, Phys. Rev. B, **48**, 1314 (1993).
- <sup>4</sup> K. Aurivillius, Arkiv för Kemi, **24**, 151 (1965) and references herein.
- <sup>5</sup> R. Le Toullec, J. P. Pinceaux, and P. Loubeyre, High Pressure Res. **1**, 77 (1988).
- <sup>6</sup> G. J. Piermarini and S. Block, Rev. Sci. Instrum. **46**, 973 (1975).
- <sup>7</sup> F. D. Murnaghan, Proc. Natl. Acad. Sci. U.S.A **30**, 244 (1944).
- <sup>8</sup> V.I. Voronin and V.V. Shchennikov, Sov. Phys. Crystallogr. **34**, 293 (1989).
- <sup>9</sup> I.M. Tsidil'kovskii, V.V. Shchennikov and N. G. Gluzman, Sov. Phys. Semicond., **19**, 901 (1985).

# RECENT RESULTS OF HIGH PRESSURE STRUCTURAL STUDIES ON THE ALKALINE-EARTH CHALCOGENIDES

H. LUO, K. GHANDEHARI, T. LI, R. G. GREENE, AND A. L. RUOFF

*Department of Materials Science and Engineering, Cornell University*

*Ithaca, New York 14853, USA*

## ABSTRACT

Recent studies of pressure-induced phase transition of eight chalcogenides of Group IIA elements SrSe, CaS, CaSe, CaTe, MgSe, MgTe, BeSe and BeTe are summarized. Of the five octahedrally coordinated compounds, SrSe, CaS, CaSe, and CaTe undergo a first-order phase transition from the NaCl (B1) to the CsCl (B2) structure, while MgSe transforms to a proposed FeSi (B28) structure at  $107 \pm 8$  GPa, the highest transition pressure found so far in this series. Of the three tetrahedrally coordinated compounds, MgTe transforms from the wurtzite (B4) to the NiAs (B8) structure, while BeSe and BeTe transform from the zincblende (B3) to the B8 structure.

## 1. Introduction

The alkaline-earth chalcogenides (AEC) (AB: A = Be, Mg, Ca, Sr, Ba; B = O, S, Se, Te) form a very important closed-shell system crystallized in either tetrahedrally coordinated or octahedrally coordinated structures under normal conditions. Most of the AEC are ionic except for the Be compounds which are primarily covalently bonded. Because of their low coordination numbers (CN = 4, 6), simple structures, and moderate bulk moduli except for BeO and MgO, the AEC are suitable for a systematic study of pressure-induced phase transition.

The high-pressure structural studies of the AEC started over two decades ago on some heavy compounds such as Ba, Sr and Ca oxides [1-3]. Basically, a first-order phase transition from the NaCl (B1) to the CsCl (B2) phase was observed in each of the Ba, Sr, and Ca compounds at elevated pressures. A summary was provided by Syassen [4] which covered most of the early results.

Among the AEC, the oxides form a special group of materials that has been of great experimental and theoretical interest

in both solid-state physics and geological science, and is one of the most extensively investigated system under high pressure. The most recent work on the oxides was made on MgO by Duffy *et al* [5].

Over the past two years, we have studied eight AEC compounds of different crystal structures and chemical bonds. For each of the eight compounds studied, at least one phase transition was found with the new structure determined. Thus, pressure-induced phase transition, i.e. from 4-fold to 6-fold or from 6-fold to 8-fold, has been observed in most of the AEC except for MgO, MgS, BeO, and BeS, where no phase transition has been confirmed experimentally. In this paper, we briefly review our recent studies of AEC.

## 2. Experimental techniques

A combined technique involving the diamond anvil cell and synchrotron energy-dispersive x-ray diffraction was primarily used to generate static compressions on the sample and to obtain crystallographic data from the sample. Other methods, such as

angular-dispersive x-ray diffraction and Raman scattering, were also involved in the study. All the transition pressures given below are based on the uploading data.

### 3. Results

#### A. B1 $\rightarrow$ B2 transition

SrSe [6], CaS, CaSe and CaTe [7] were each found to transform from their original B1 phase to the B2 phase at 14, 40, 38, and 33 GPa, respectively. The B1-B2 transition in each sample is of a first-order change accompanied by a volume decrease ranging from 4.6 % in CaTe to 10.7 % in SrSe. Only CaTe experiences an intermediate state before it reaches the B2 phase. This intermediate state is determined to be a mixture of B1 and MnP phases. The latter has an orthorhombic unit cell containing four pairs of ions with their atomic sites determined for CaTe [7].

Figures 1 and 2 show diffraction spectra of SrSe and CaTe, respectively.

#### B. B1 $\rightarrow$ B28 transition

MgSe undergoes a phase transition from the B1 to the B28 (FeSi) at  $107 \pm 8$  GPa [8] without measurable volume collapse at the transition. The B28 structure comes from a simple cubic distorted rocksalt structure and fits the best to the diffraction data of the transformed MgSe. However, it is not conclusive to choose the B28 structure here because our diffraction data are not good enough, especially in regard to the peak intensities, to pin down one from several possible candidates. Figure 3 shows diffraction patterns of MgSe at three selected pressures.

The results of MgSe provide a clue for the phase transition sequences of MgS and MgO. Apparently, all three cubic Mg compounds including MgSe would need much higher pressures than 107 GPa to transform to 8-fold coordinated structures.

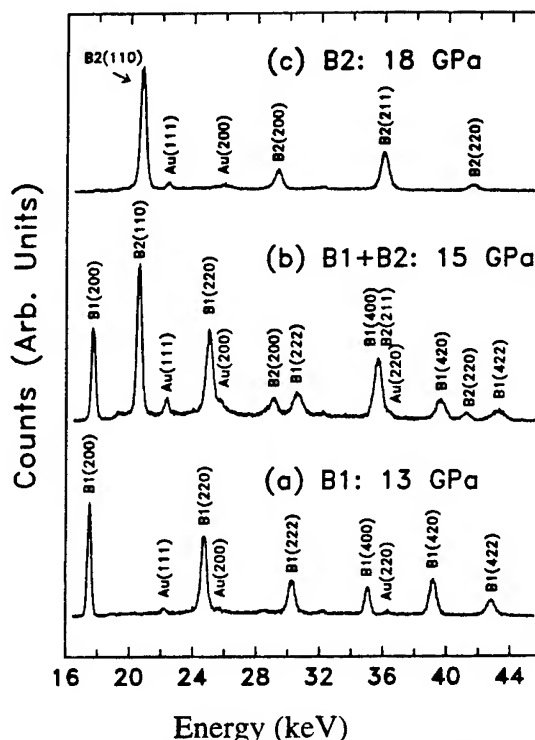


FIG. 1. X-ray diffraction patterns of SrSe

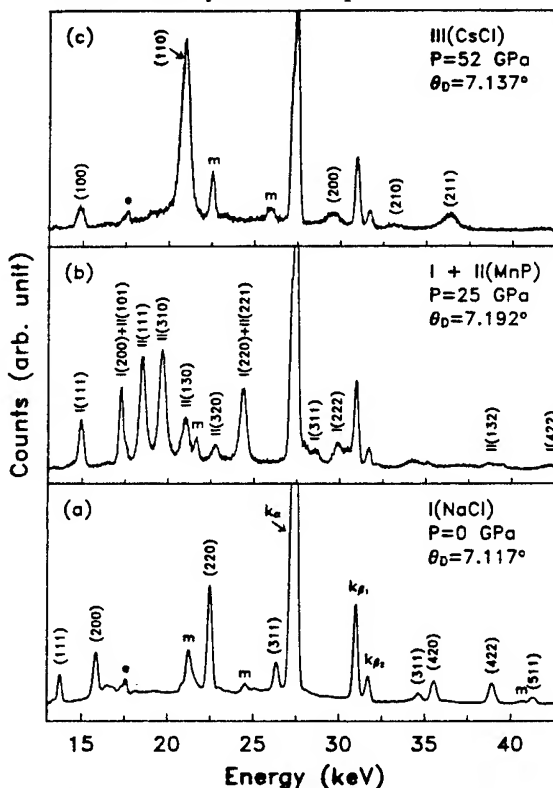


FIG. 2. X-ray diffraction spectra of CaTe

### C. B3 $\rightarrow$ B8 transition

In the entire AEC series, only three Be compounds, BeS, BeSe and BeTe, adopt the cubic 4-fold coordinated zincblende (B3) structure at normal conditions.

A first-order phase transition from the B3 to the hexagonal 6-fold coordinated NiAs (B8) structure takes place in BeSe at 61.3 and BeTe at 39.3 GPa [9]. The B3-B8 transition is accompanied by a volume decrease of 11.8 % in BeSe and 11.3 % in BeTe. The  $c/a$  ratio in the B8 structure remains unchanged with pressure at a value of 1.587 in BeSe and 1.615 in BeTe.

Figure 4 shows three selected spectra of BeTe corresponding to B3, B3 + B8, and B8 phases during uploading.

Based on the results of BeSe and BeTe, we expect BeS, also in the B3 phase initially, to transform to the B8 phase at a pressure of 69 GPa. For BeO, in a wurtzite phase initially, our estimated transition pressure is around 139 GPa.

### D. B4 $\rightarrow$ B8 transition

MgTe undergoes a first-order structural transition from the wurtzite (B4) to the NiAs (B8) at a very low pressure between 1-3.5 GPa [10]. This B4-B8 transition is the first experimental observation in the whole binary compounds. The diffraction patterns involving this transition are shown in Figure 5. The B8 phase is stable with further increasing pressure to at least 60 GPa. Interestingly, the B8 phase in MgTe *persists* during downloading to at least 0.2 GPa and even after annealing for 10 hours at 100 °C (Because this sample is highly sensitive to air, we had to keep a minimum pressure of  $\sim 0.2$  GPa). Thus, one may ask what the stable phase is in MgTe, is it wurtzite or NiAs ?. Our results provide the supporting evidence to theoretical predictions [11, 12] that at low temperatures the ground state of MgTe has the NiAs instead of the wurtzite structure.

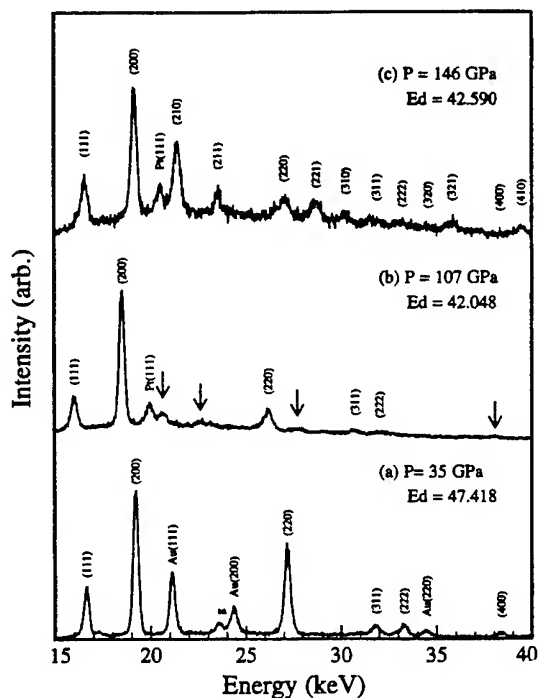


FIG. 3. X-ray diffraction spectra of MgSe

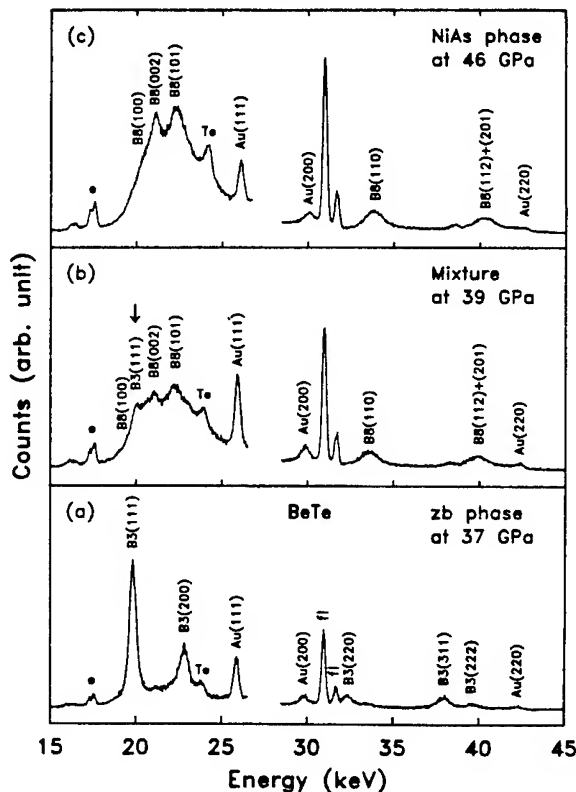
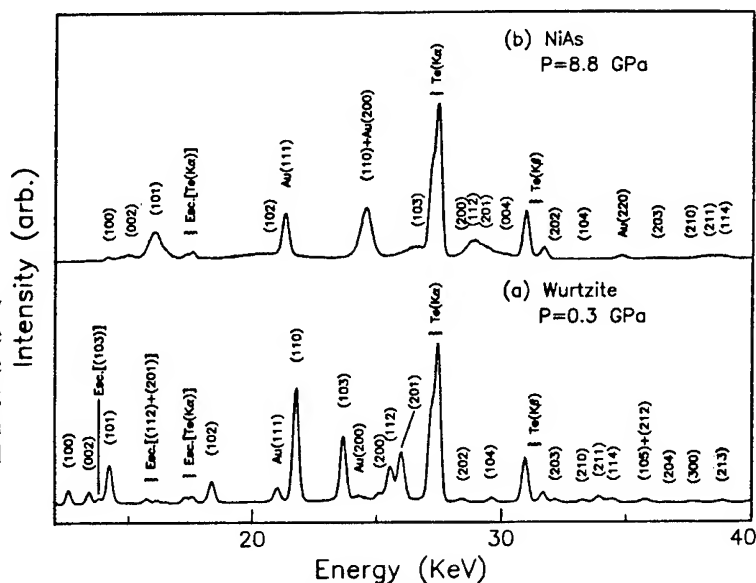


FIG. 4. X-ray diffraction spectra of BeTe



**FIG. 5.** Energy-dispersive x-ray diffraction spectra of MgTe in (a) the wurtzite phase at 0.3 GPa and (b) the NiAs phase at 8.8 GPa. Au is gold; Esc. stands for the escape peak from the Ge detector; all other labeled peaks are from the sample.

#### 4. Concluding remarks

Among four untransformed AEC, BeS and BeO will be seen to transform to either NiAs or NaCl structure at any time, while MgS and MgO may require extension of our present techniques to achieve the transition pressure and to perform *in situ* physical measurements.

The two major structures, NiAs (B8) and CsCl (B2), observed in the AEC at high pressures are expected to remain stable in a large pressure range. Pursuing further transitions of these structures can be a big challenge but still within the capability of today's high pressure techniques.

#### 5. Acknowledgments

We acknowledge the continuous support from the National Science Foundation, the Department of Energy, the Cornell Materials Science Center, the staff of Cornell High Energy Synchrotron Source, and Drs. S. S. Trail and F. J. DiSalvo who provided us with samples.

#### 6. References

1. L. G. Liu and W. A. Bassett, *J. Geophys. Res.* **77**, 4934 (1972).
2. Y. Sato and R. Jeanloz, *J. Geophys. Res.* **86**, 11773 (1981).
3. R. Jeanloz, T. Ahrens, H. K. Mao, and P. M. Bell, *Science* **206**, 829 (1979).
4. K. Syassen, *Physica* **139&140B**, 277 (1986).
5. T. S. Duffy, R. J. Hemley, and H. K. Mao, *Phys. Rev. Lett.* **74**, 1371 (1995).
6. H. Luo, R. G. Greene, A. L. Ruoff, *Phys. Rev. B* **49**, 15341 (1994).
7. H. Luo, R. G. Greene, K. Ghandehari, T. Li, and A. L. Ruoff, *Phys. Rev. B* **50**, 16232 (1994).
8. T. Li, R. G. Greene, H. Luo, A. L. Ruoff, S. S. Trail, and F. J. DiSalvo, submitted for publication.
9. H. Luo, K. Ghandehari, R. G. Greene, A. L. Ruoff, S. S. Trail, F. J. DiSalvo, *Phys. Rev. B*, to be pub. Sept. 1, 1995.
10. T. Li, H. Luo, R. G. Greene, A. L. Ruoff, S. S. Trail, and F. J. DiSalvo, *Phys. Rev. Lett.* **74**, 5232 (1995).
11. C. Y. Yeh, Z. W. Lu, S. Froyen, and A. Zunger, *PRB* **46**, 10086 (1992).
12. P. E. Van Camp and V. E. Van Doren, *Int. J. Quant. Chem.*, to be published.

# Structural Studies on CuFeSe<sub>2</sub> (eskebornite) under high pressure

T. Tinoco\*, A. Polian\*, J. P. Itié\*, P. Grima\*, E. Moya\*, A. San Miguel\*, J. González†  
and F. González-Jiménez‡

\* *Physique des Milieux Condensés, CNRS, Université P. & M. Curie, B 77, 4 Place Jussieu, F-75252 Paris CEDEX 05.*

† *Centro de Semiconductores, Facultad de Ciencias, ULA, Mérida 5101 Venezuela.*

‡ *Dpto. de Física, UCV, Ap 47586, Caracas 1041A, Venezuela.*

## ABSTRACT

Pressure-induced phase transitions of CuFeSe<sub>2</sub> have been investigated by energy dispersive x-ray diffraction (EDX) and x-ray absorption (EXAFS) up to 23 GPa. EDX measurements show two phase transitions. The first one at 2 GPa from the tetragonal eskebornite structure, to another tetragonal structure, which indexes in the space group I42m. The second one at 9 GPa is a transition to a cubic structure. The volume variations associated with the two transitions are 4% and 6%, respectively. Fits with a first order Murnaghan equation of state give bulk moduli of  $B_0 = 33$  GPa and  $B_0 = 37$  GPa for the tetragonal phases and  $B_0 = 200$  GPa for the cubic high pressure phase, with  $B_0' = 4$ . EXAFS measurements were performed at the Cu K-edge and confirm the presence of the first phase transition (2 GPa).

**keywords:** eskebornite, x-ray diffraction, x-ray absorption, phase transition.

## Introduction

The CuFeVI<sub>2</sub> (VI: S, Se, Te) semimagnetic compounds form a very interesting and curious family of materials. Interchange of the anion atom produces very different crystallographic structures.

CuFeSe<sub>2</sub> is the natural eskebornite. This structure has a tetragonal symmetry<sup>1</sup>, but is not related to that of chalcopyrite type. The space group<sup>2</sup> is  $P\bar{4}2c$ , with  $a = 5.530\text{\AA}$  and  $c = 11.049\text{\AA}$ ,  $Z = 4$  and  $\rho_{\text{calc}} = 5.44\text{ g cm}^{-3}$ . Eskebornite is a superstructure of a cubic closed packed array of anions with the cations occupying a fraction of the available tetrahedral sites. X ray diffraction<sup>2</sup> and Mössbauer<sup>3</sup> data show that the Cu atoms are in 4m positions, and the Fe in 2a and 2c (Fig. 1).

Recent studies<sup>4</sup> on CuFeSe<sub>2</sub> have shown that this compound has a metallic character and the magnetic parameters are weaker than in CuFeS<sub>2</sub>.

In the present work, using energy dispersive x-ray diffraction (EDX) and x-ray absorption (EXAFS) with synchrotron radiation, we have determined the crystallographic structure of CuFeSe<sub>2</sub> as a function of pressure. From the analysis of the data, pressure transition values and bulk modulus have been determined.

## Experimental Procedure

Samples were prepared by the usual melt and anneal technique. Membrane diamond anvil cell<sup>5</sup> (DAC) have been used as high pressure generator. The pressure medium was silicon oil and the pressure was measured using the linear ruby

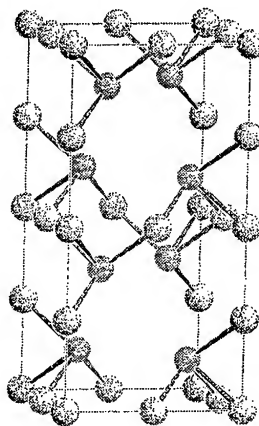


Fig. 1 Unit cell model showing the eskebornite structure and bond lengths.

fluorescence scale.

EDX experiments were performed at DCI (LURE synchrotron radiation facility, Orsay-France) at the DW11 station, on the wiggler line. The white beam was collimated down to  $50 \times 50\text{ }\mu\text{m}$ . The diffracted beam was detected by a Ge solid state detector. In this experiment the diffraction angle was  $\theta = 6.35^\circ$ . The  $a$  and  $c$  parameters have been calculated from the experimental spectra using

EDX<sup>6</sup> and PDP11<sup>7</sup> softwares.

EXAFS measurements were performed at the energy dispersive X9 station of LURE, at the Cu K edge (8.979 keV). The experimental set-up has been described elsewhere<sup>8</sup>. For each pressure, the transmission is measured through the DAC and the incident beam  $I_0$  without the cell. Moreover, in order to take into account possible beam displacement, reference samples at room pressure are measured at the sample position for each pressure point. The spectra were analyzed using the CDXAS software<sup>9</sup>. It should be emphasized that

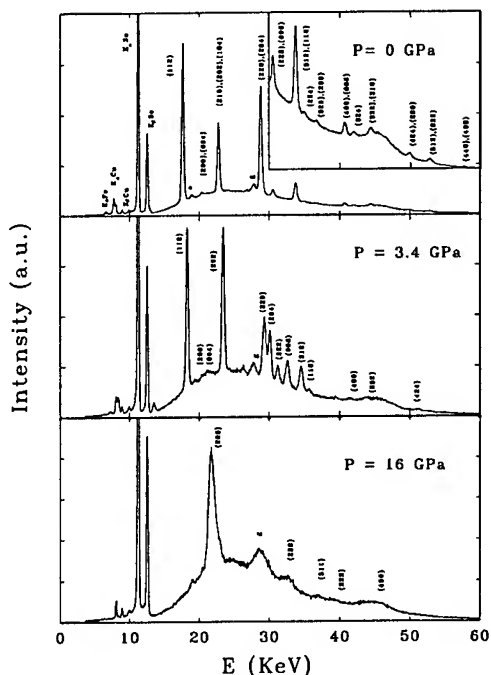


Fig. 2. Diffraction spectra in three different phases for  $\text{CuFeSe}_2$ .  $K_\alpha$  and  $K_\beta$  are the fluorescence peaks for each atom. The peaks labeled  $g$  originate from the gasket and  $e$  are escape peaks.

with this experiment only the relative values of the structural parameters can be determined with a high precision.

## Results and Discussion

Two different phase transitions at 2 and 9 GPa are observed with EDX. The spectra obtained in different phases are shown in Fig. 2. Indexation of the ambient condition spectrum using the eskebornite structure gives  $a = (5.5049 \pm 0.0011)$

$\text{\AA}$ ,  $c = (11.012 \pm 0.003) \text{\AA}$ . These values are in reasonable agreement with those recently reported<sup>2</sup>.

The eskebornite lines have been observed up to about 2 GPa and no splitting of the lines has been found, indicating that  $c/a = 2$ . Above 2 GPa splitting of the 220/204, 222/006, and 316/116

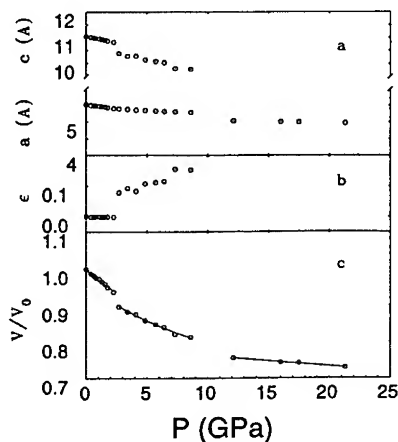


Fig. 3 Pressure volume and lattice parameters data. The solid line connecting the data points of the structure is from the Murnaghan equation of state.

diffraction lines (Fig. 2), indicates a phase transition to another structure. In the new phase, the lattice parameter  $c$  decreases faster than the  $a$  parameter inducing a tetragonal distortion along the  $c$  direction and hence  $c/a < 2$ . This is shown in Fig. 3.a and 3.b where  $a$ ,  $c$  and  $\epsilon$  ( $\epsilon = 2 - c/a$ ) are shown as a function of pressure. This new structure can be viewed as a denser cation-disordered eskebornite-type. This supposition is based on the fact that a cation disorder could be present in  $\text{CuFeSe}_2$  at normal pressure<sup>2</sup>, so, it is expected that such disorder tends to increase with pressure. The systematic absences enable the determination of the crystallographic space group I42m.

Above 9 GPa the eskebornite-type peaks disappear. New peaks, which may be indexed in a cubic structure, are observed in the diffraction spectra (Fig. 2). The relative volume variation with pressure up to 22 GPa is shown in Fig. 3.c. In the stability range of the eskebornite and intermediate disordered phase, the volume evolution has been fitted with a first-order Murnaghan equation of state:

$$\frac{V}{V_0} = \left( 1 + \frac{B'_0 P}{B_0} \right)^{-\frac{1}{B_0}}$$

where  $B_0$  is the bulk modulus at ambient conditions,  $B'_0$  its pressure derivative and  $V_0$  the volume per unit formula.

$B_0$  has been calculated as  $(33 \pm 6)$  GPa and  $(37 \pm 6)$  GPa for the low and intermediate pressure phases respectively, using  $B'_0 = 4$ .

The volume discontinuities at the phase transitions have been determined to be 4% and 6% respectively for the first and second transition.

In the high-pressure phase, the value of  $B_0$

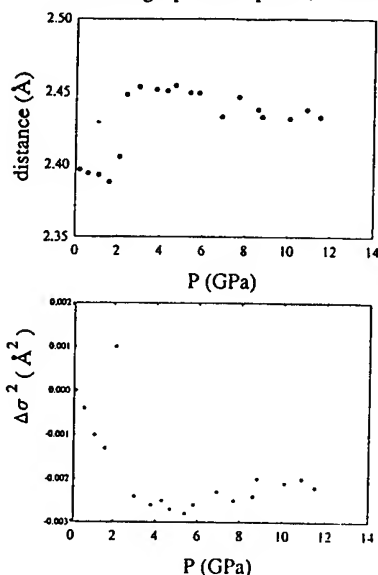


Fig. 4 Evolution of the first-neighbours mean distance and of the pseudo-Debye-Waller as a function pressure

is  $B_0 = (200 \pm 15)$  GPa, using  $B'_0 = 4$ .

There are two remarkable differences in the evolution under high pressure of the eskebornite phase and of the neighbour chalcopyrite ( $\text{CuFeS}_2$ ): i) the bulk modulus is three times smaller in eskebornite,  $B_0 = 91$  GPa in  $\text{CuFeS}_2$  ( $B'_0 = 4$ ) and ii) there are two transitions in  $\text{CuFeS}_2$  for only one in  $\text{CuFeS}_2$ , although the total volume change at the two transitions is equal to that at the only phase transition of  $\text{CuFeS}_2$  (10%)<sup>10</sup>. The difference on the bulk modulus is essentially due to the fact that the chalcopyrite structure is more compact than the eskebornite one.

One phase transition has been observed on EXAFS measurements, around 2 GPa. Between 0-2 GPa an isotropic compression of the mean Cu-Se distance was observed. The first neighbours of the Cu are two Se at 2.36 Å and two Se at 2.43 Å. Fits using one shell of neighbours at the mean distance or two shells at the actual distances are equivalents, so the first procedure was chosen. Fig. 4 shows the pressure dependence of the mean Cu-Se distance and of the pseudo Debye-Waller factor. In

the 0-2 GPa range the pseudo Debye-Waller decreases gradually. At 2 GPa a large increase shows the disorder at the transition. Between 4 and 12 GPa the  $\Delta\sigma^2$  is approximately constant, which indicates that there is no local disorder around the Cu atoms, even at the second transition, which is not observed around 9 GPa.

## Conclusion

$\text{CuFeSe}_2$  shows two phase transitions at 2 and 9 GPa associated with volume variations of 4 and 6% respectively. EXAFS measurements at the Cu K-edge indicate that the Cu-Se mean distance decreases up to 2 GPa. For a complete determination of the interatomic distances with pressure, EXAFS measurements at the Fe and Se K-edges are planned.

## Acknowledgements

Two of the authors (TT and PG) wish to thank the Universidad de Los Andes, Mérida-Venezuela, and the BID-CONICIT for financial support.

## References

1. Z. Johan, N. Jb. Miner. Mh. 8, 337 (1988)
2. J. M. Delgado, G. Díaz de Delgado, M. Quintero and J. C. Woolley, Mat. Res. Bull. 27, 367 (1992)
3. J. Lamazares, F. Gonzalez-Jimenez, E. Jaimes, L. D'Onofrio, R. Iraldi, G. Sanchez-Porras, M. Quintero, J. Gonzalez, J. C. Woolley and G. Lamarche, J. of Mag. and Mag. Materials 104-107, 997 (1992)
4. J. Lamazares, E. Jaimes, L. D'Onofrio, F. Gonzalez-Jimenez, G. Sanchez-Porras, R. Tovar, M. Quintero, J. Gonzalez, J. C. Woolley and G. Lamarche, Hyperfine Interactions 67, 567 (1991)
5. R. Le Toullec, J. P. Pinceaux and P. Loubeyre, High Pressure Research 1, 77 (1988)
6. A. Polian, M. Gauthier and A. San Miguel, unpublished
7. M. Calligaris, unpublished
8. E. Dartyge, C. Depaulex, J. M. Dubuisson, A. Fontaine, A. Jucha and G. Tourillon, Nucl. Instrum. Methods A 246, 452 (1986)
9. A. San Miguel, Physica B 208, 177 (1995)
10. T. Tinoco, J. P. Itié, A. Polian, A. San Miguel, E. Moya, P. Grima, J. Gonzalez and F. Gonzalez, J. Physique, 4, C9-151 (1994)



## **VI(D) Magnetics and Ferroelectrics**

# PRESSURE DEPENDENCE OF MAGNETIC ORDERING IN Ce-Pd-Al INTERMETALLIC COMPOUNDS

JIE TANG, A. MATSUSHITA, H. KITAZAWA and T. MATSUMOTO  
National Research Institute for Metals, Tsukuba, Ibaraki 305, Japan

## ABSTRACT

The pressure effect on the antiferromagnetic ordering for CePd<sub>2</sub>Al<sub>3</sub> and CePdAl has been studied. From the specific heat measurement it is shown that the pressure dependence of these compounds is different, although their transition temperatures are almost equal at the ambient pressure.  $T_N$  of CePd<sub>2</sub>Al<sub>3</sub> initially increases, then passes through a maximum near 0.8GPa and falls at higher pressures, while  $T_N$  of CePdAl is almost constant for  $P \leq 0.3$ GPa and decreases rapidly for  $P > 0.3$ GPa. The results are discussed in terms of the competition between the Kondo effect and the RKKY interaction and they can be understood effectively with the Doniach phase diagram.

## Introduction

Since the discovery of the heavy fermion (HF) superconductors UPd<sub>2</sub>Al<sub>3</sub> and UNi<sub>2</sub>Al<sub>3</sub> with  $T_C$  above 1 K, similar compounds of the rare earth series have been studied extensively for both theoretical and experimental interests. Structural, transport, thermodynamic, and magnetic properties have already been reported for CePd<sub>2</sub>Al<sub>3</sub><sup>[1]</sup> and CePdAl<sup>[2]</sup>. Both were characterized as HF compounds with electronic specific heat coefficients  $\gamma$  of 380 mJ/molK<sup>2</sup> and 270 mJ/molK<sup>2</sup>, respectively. CePd<sub>2</sub>Al<sub>3</sub> crystallizes in a PrNi<sub>2</sub>Al<sub>3</sub>-type structure (similar to UM<sub>2</sub>Al<sub>3</sub>, M=Ni, Pd) and CePdAl crystallizes in a ZrNiAl-type structure (a high temperature phase)<sup>[3]</sup>. Antiferromagnetic ordering temperatures of Ce spins have been reported to be  $T_N = 2.8$ K and 2.7K, respectively, in annealed polycrystals of CePd<sub>2</sub>Al<sub>3</sub> and as-cast CePdAl, whereas single crystals remain paramagnetic down to 0.4K for CePd<sub>2</sub>Al<sub>3</sub>. The magnetic moments of CePd<sub>2</sub>Al<sub>3</sub> align ferromagnetically in basal planes and couple with an antiferromagnetic stacking along the c-axis<sup>[4,5]</sup>. Because the magnetic properties of these compounds are determined by a competition between the RKKY interaction and the Kondo effect, pressure is believed to be an effective parameter for understanding magnetism in these compounds.

In the present work we investigated the pressure dependence of the magnetic order in CePd<sub>2</sub>Al<sub>3</sub> and CePdAl in order to learn how the competition changes under high pressures, which make the exchange coupling strength ( $J_{cf}$ ) increase.

## Experimental

Polycrystalline samples were prepared by arc-melting pure elements in their stoichiometric ratio using a pure argon atmosphere. CePd<sub>2</sub>Al<sub>3</sub> samples

were annealed at 900°C for one week in sealed quartz ampules. The reported structures were confirmed at room temperature by X-ray diffraction patterns for both the annealed CePd<sub>2</sub>Al<sub>3</sub> and the as-cast CePdAl.

The specific heat for both compounds was measured with a quasiadiabatic method under pressures up to 1.2GPa between 0.9K and 6K. AgCl was used as the pressure transmitting medium. A Be-Cu piston and a cylinder clamp were used to generate and retain the hydrostatic pressure which was applied at room temperature.

The pressure dependence of lattice parameters of the two compounds was measured by the *in-situ* X-ray experiment under high pressures at room temperature. The pressure was generated up to 10GPa by a cubic-anvil type apparatus, which was connected to an X-ray diffraction system with a rotary target type X-ray source and an energy dispersive detector. The pressure dependence of  $J_{cf}$  was estimated from the obtained changes of lattice constants.

## Results and Discussions

Both CePd<sub>2</sub>Al<sub>3</sub> and CePdAl samples exhibited antiferromagnetic ordering which has features of a strongly f-correlated 4f-electron Ce<sup>3+</sup>(4f<sup>1</sup>) system. Figure 1 shows the results of the specific heat measurements under various pressures for CePd<sub>2</sub>Al<sub>3</sub>. The specific heat has a peak at about 2.9K, which we define as the antiferromagnetic transition temperature  $T_N$ . The absolute values of our result at ambient pressure are in agreement with those from the usual specific heat measurements. The pressure dependence of  $T_N$  is plotted in the inset of Fig.1. It can be seen that  $T_N$  increases initially with the rate of 0.22K/GPa, which almost equals the rate obtained by Nolting *et al.*, 0.2K/GPa<sup>[6]</sup>. However, above 0.8GPa,  $T_N$  starts to decrease gradually with

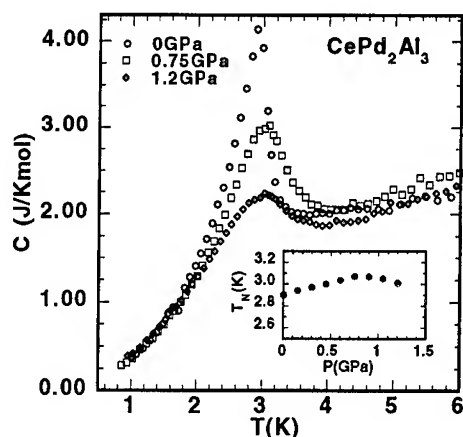


Fig. 1 Specific heat of  $\text{CePd}_2\text{Al}_3$  at various pressures. The inset shows the pressure dependence of magnetic transition temperature  $T_N$ .

the rate which is much smaller than the rate reported previously. As shown in Fig. 1, the peak of specific heat becomes broad and decreases, especially, after  $T_N$  starts to fall down. This fact indicates that there is a dramatic suppression of the specific heat anomaly at  $T_N$  under higher pressures.

By extrapolating  $C/T$  vs.  $T^2$  below  $T_N$  to 0K, we can estimate the electronic specific heat coefficient  $\gamma_0$ . For  $0.9 < T < 2\text{K}$ , the specific heat is well represented by  $C = \gamma_0 T + \beta T^3$ . For  $T < 1.5\text{K}$ ,  $C/T$  at 1.2GPa is significantly greater than that at 0GPa, as shown in Fig. 2. This increase in  $\gamma_0$  was obtained as  $\Delta\gamma_0 = \gamma_0(1.2\text{GPa}) - \gamma_0(P=0\text{GPa}) = 100\text{mJ/K}^2\text{mole}$ . Such a change of  $\Delta\gamma_0$  has been also observed in  $\text{UPd}_2\text{Al}_3$ <sup>[7]</sup>, which is very different from other magnetic and nonmagnetic Ce- and U-based HF com-

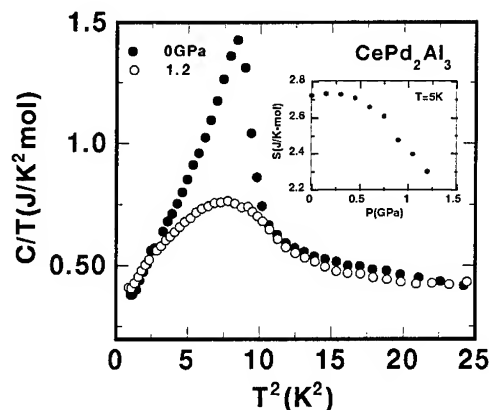


Fig. 2 Specific heat of  $\text{CePd}_2\text{Al}_3$  at 0GPa and 1.2GPa as  $C/T$  vs  $T^2$ . The inset shows the pressure dependence of entropy at 5K.

pounds in which  $\gamma_0$  decreases with increasing pressures. By integrating  $C/T$  over  $T$ , the entropy can be obtained. It can be shown that there is a negative entropy difference between 0GPa and 1.2GPa, which changes its sign near 1.6K. This fact is reflected by the anomalous positive  $\Delta\gamma_0(P)$ . The pressure dependence of entropy obtained at  $T=5\text{K}$  ( $T > T_N$ ) for  $\text{CePd}_2\text{Al}_3$  is shown in the inset of Fig. 2. The entropy rapidly decreases under higher pressures. These facts imply that the Kondo effect overcomes the RKKY interaction as pressure increases.

In contrast to  $\text{CePd}_2\text{Al}_3$ , as shown in Fig. 3, the specific heat of  $\text{CePdAl}$  under pressure monotonically

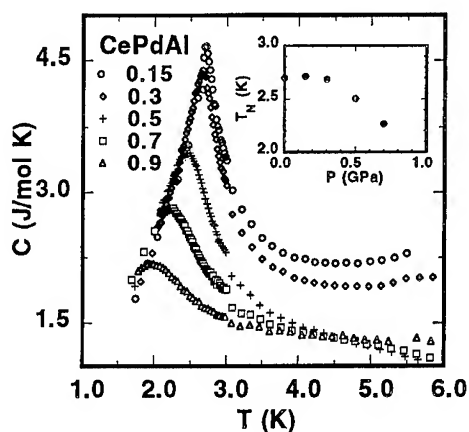


Fig. 3 Specific heat measurement of  $\text{CePdAl}$ . The inset shows the pressure dependence of the magnetic transition temperature  $T_N$ .

cally decreases and the peak falls down more quickly than that of  $\text{CePd}_2\text{Al}_3$ .  $T_N$  for  $\text{CePdAl}$  is insensitive to pressure in the low pressure region but it decreases rapidly in the high pressure region. Although the transition temperatures of  $\text{CePd}_2\text{Al}_3$  and  $\text{CePdAl}$  are almost equal at the ambient pressure, the behaviors of  $T_N$  are different under pressure. In the specific heat measurement for  $\text{CePdAl}$ , we used Fluorinert as the pressure transmitting medium. The large error is caused by using Fluorinert because of its large specific heat and strong pressure dependence.

Doniach<sup>[8]</sup> established theoretically a magnetic phase diagram of the one-dimensional system with the competition between the Kondo singlet and an RKKY-type antiferromagnetic state. According to his theory, the RKKY interaction dominates and ordering temperature increases proportionally with  $|J_{cf}|^2$  for small values of  $|J_{cf}|N(E_F)$ , where  $N(E_F)$  is the density of conduction electron states at the Fermi energy  $E_F$  and  $J_{cf}$  is the exchange coupling

strength. For a large value of  $|J_{cf}|N(E_F)$ , the magnetic ordering is suppressed due to the Kondo effect. As a result, the maximum of  $T_N$  appears at a certain value of  $|J_{cf}|N(E_F)$ .

According to the Anderson model, the parameter  $J_{cf}$  can be expressed as follows<sup>[9]</sup>:

$$J_{cf} \propto V_{cf}^2/(E_F - E_f),$$

where  $V_{cf}$  is the matrix element for the conduction-electron hybridization,  $E_f$  the location of the f level and  $E_F$  the Fermi energy. The variation of  $E_F - E_f$  can be regarded as constant comparing with that of  $V_{cf}$  in our pressure range. Since the value  $V_{cf}$  depends strongly on the interatomic distance, a strong pressure dependence of  $V_{cf}$  is expected. Therefore, the pressure dependence of  $J_{cf}$  for  $\text{CePd}_2\text{Al}_3$  and  $\text{CePdAl}$  can be estimated from the measurements of lattice parameters as a function of pressure. Combined with the results of specific heat measurements, we can analyze the competition between the RKKY interaction and the Kondo effect for  $\text{CePd}_2\text{Al}_3$  and  $\text{CePdAl}$ . Details are described elsewhere<sup>[10]</sup>. Having the result of the pressure dependence of  $J_{cf}$  and  $T_N$ , the relationship between  $J_{cf}$  and  $T_N$  is plotted by open circles and open squares in Fig. 4, where both quantities have been normalized to their maximum values. It can be seen

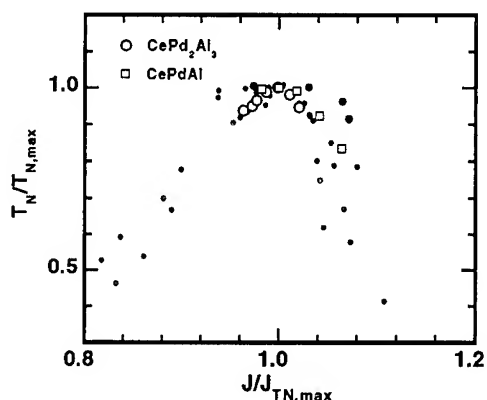


Fig. 4 The magnetic transition temperature  $T_N$  versus the coupling strength  $J_{cf}$  for  $\text{CePd}_2\text{Al}_3$  and  $\text{CePdAl}$  shown by the open marks. Both quantities have been normalized to their values where  $T_N$  exhibits a maximum value.  $T_N$  versus  $J_{cf}$  for other compounds are also represented with solid circles (c.f. Ref. 11).

that the value of  $J_{cf}$  increases with pressure for both  $\text{CePd}_2\text{Al}_3$  and  $\text{CePdAl}$ , and all data points can be mapped onto the universal curve which was predicted by Doniach<sup>[8]</sup> for the one-dimensional Kondo

necklace, like those of some other Ce compounds (solid circles in Fig. 4)<sup>[11]</sup>. This  $J_{cf}$  dependence on  $T_N$  suggests that  $\text{CePdAl}$  is located in the right side of  $\text{CePd}_2\text{Al}_3$  and is close to the maximum of  $T_N$  in the Doniach phase diagram. In fact, this is consistent with the fact that the  $\gamma$  value of  $\text{CePdAl}$  is smaller than that of  $\text{CePd}_2\text{Al}_3$  at ambient pressure<sup>[1,2]</sup>, indicating the value of  $T_K$  in  $\text{CePdAl}$  is higher than that of  $\text{CePd}_2\text{Al}_3$ .

## Conclusions

We have studied the pressure response of HF compounds  $\text{CePd}_2\text{Al}_3$  and  $\text{CePdAl}$ . For  $\text{CePd}_2\text{Al}_3$ , the results suggest that the enhancement of the Kondo effect results from an increase of the hybridization between the conduction and the 4f electronic states with increasing pressures. The effect of pressure on the antiferromagnetic ordering in these two materials can be understood from the enhancement of the Kondo effect with the Doniach magnetic phase diagram in spite of their different structures.

## References

- [1] H. Kitazawa, C. Schank, S. Thies, B. Seidel, C. Geibel and F. Steglich, *J. Phys. Soc. Jpn.* **61** (1992) 1461.
- [2] H. Kitazawa, A. Matsushita, T. Matsumoto and T. Suzuki, *Phys. B* **199&200** (1994) 28.
- [3] C. Schank, F. Jahliag, L. Lou, A. Grauel, C. Wassilew, R. Borth, G. Olesch, C.D. Bredl, C. Geibel and F. Steglich, *J. Alloys Compounds* **207-208** (1994) 329.
- [4] S. Mitsuda, T. Wada, K. Hosoya, H. Yoshizawa and H. Kitazawa, *J. Phys. Soc. Jpn.* **61** (1992) 4667.
- [5] A. Dönni, P. Fischer, B. Roessli and H. Kitazawa, *Z. Phys. B* **93** (1994) 449.
- [6] F. Nolting, A. Eichler, S.A.M. Mentink and J.A. Mydosh, *Physica B* **199&200** (1994) 614.
- [7] R. Caspary, P. Hellmann, M. Keller, G. Sparr, C. Wassilew, R. Köhler, C. Geibel, C. Schank, F. Steglich and N.E. Phillips, *Phys. Rev. Lett.* **71** (1993) 2146.
- [8] S. Doniach, in *Valence Instability and Related Narrow Band Phenomena*, ed. R.D. Parks (Plenum, 1977).
- [9] J.R. Schrieffer and P.A. Wolff, *Phys. Rev.* **149** (1966) 491.
- [10] J. Tang, A. Matsushita, H. Kitazawa and T. Matsumoto, to be published.
- [11] A.L. Cornelius and J.S. Schilling, *Phys. Rev. B* **49** (1994) 3955.

## MAGNETITE ( $\text{Fe}_3\text{O}_4$ ) AT HIGH PRESSURE AND LOW TEMPERATURES \*

G. Kh. Rozenberg<sup>a</sup>, G. R. Hearne<sup>b</sup>, M. P. Pasternak<sup>a</sup>, P. A. Metcalf<sup>c</sup> and J. M. Honig<sup>c</sup>

<sup>a</sup>*School of Physics and Astronomy, Tel-Aviv University, 69978 Tel-Aviv, Israel;* <sup>b</sup>*Department of Physics, University of the Witwatersrand, Private Bag 3, Wits 2050, Johannesburg-Gauteng, South Africa;*

<sup>c</sup>*Department of Chemistry, Purdue University 1393 Brown Building, West Lafayette, IN 47907-1393, USA.*

The resistivity of  $\text{Fe}_3\text{O}_4$  single crystals very close to ideal stoichiometry has been measured between 4.2 and 300 K up to  $P = 158$  kbar. The Verwey transition temperature decreased with rising  $P$ , in close analogy to prior studies on  $\text{Fe}_{3(1-\delta)}\text{O}_4$ ,  $\text{Fe}_{3-x}\text{Zn}_x\text{O}_4$ , and  $\text{Fe}_{3-y}\text{Ti}_y\text{O}_4$  at ambient pressure with rising  $\delta$ ,  $x$ ,  $y$ . One observes three regimes: between 0 and 60 kbar the transition is first order; between 60 and 125 kbar it is second or higher order and above 125 kbar no transition is observed. This information is rationalized in terms of partial electron ordering involving  $\text{Fe}^{2+}$  and  $\text{Fe}^{3+}$  in octahedrally coordinated B sites of the inverted spinel structure.

### Introduction

The Verwey transition in magnetite ( $\text{Fe}_3\text{O}_4$ ) [1] has been the subject of numerous studies over many years. Many mechanisms have been proposed to account for the experimental data; this includes partial ordering under the influence of Coulomb interactions among electrons which transfer between iron atoms in octahedrally coordinated interstices. Experimentally, the transition is manifested as a discontinuity in the resistivity  $\rho$  at a fixed temperature  $T = T_v \approx 121$  K in stoichiometric magnetite [1]. It was demonstrated [2] that the Verwey temperature  $T_v$  in  $\text{Fe}_{3(1-\delta)}\text{O}_4$  diminishes with increasing deviations  $\delta$  from the ideal composition. Moreover, beyond a critical value  $\delta > \delta_c$  one encounters a discontinuity in  $d\rho/dT$  rather than in  $\rho$ . This reflects a change-over from a first order to a second or higher order phase transformation. Heat capacity studies have confirmed that the latent heat of the transition is suddenly lost [3] in the switch from the first order to a second or higher order transition at  $\delta_c = 0.0039$ .  $T_v$  diminishes with increasing  $\delta$  linearly up to a critical composition  $\delta_c$ ; there is a discontinuous drop at  $\delta = \delta_c$  of roughly 8 K, beyond which  $T_v$  again falls linearly with rising  $\delta$  (see Fig. 3(b)). Near  $\delta = 3\delta_c$  the transition is lost.

In this paper we report detailed investigations of changes in the Verwey transition when the sample is subjected to hydrostatic pressure. This avoids the problem engendered by the disorder generated in the cation sublattice in nonstoichiometric magnetite or when  $\text{Zn}^{2+}$  or  $\text{Ti}^{4+}$  is introduced to achieve variations in  $T_v$  [4]. High-pressure studies have previously been reported by several authors, but only in the range below 60 kbar and

for temperatures between 77 and 300 K. All authors [5-8] report that  $T_v$  drops linearly with increasing pressure  $P$ ; however, the reported slope fell into two categories, namely  $dT_v/dP \approx -2.5$  K/GPa or  $\approx -4.5$  K/GPa. This may reflect the difficulties of achieving hydrostatic conditions, the taking of measurements without allowing sufficient time for relaxation, and/or the use of samples of uncontrolled stoichiometry. In the present publication the range of applied pressure and of the temperature region has been greatly extended. Great care has been taken to work with samples of uniform and essentially stoichiometric  $\text{Fe}_3\text{O}_4$ .

### Experimental

Resistance vs. pressure studies have been performed on crystals of pure (99.999%)  $\text{Fe}_{3(1-\delta)}\text{O}_4$  ( $\delta = 0.0006$ ;  $T_v = 121(1)$  K) grown by the skull-melter technique and annealed accordingly [9]. The sample with small ruby chips as a pressure marker was loaded into a cavity drilled in a  $\text{Ta}_{90}\text{W}_{10}$  gasket for studies in a miniature Merrill-Basset type diamond-anvil cell. The area surrounding the cavity was coated with epoxy and with an insulating mixture of  $\text{Al}_2\text{O}_3$  and  $\text{NaCl}$ . Some  $\text{CaSO}_4$  was prepressed into the cavity to help ensure a quasi-hydrostatic environment at pressure. Contacts were fabricated onto the culet flat and pavilion facets of one of the anvils to permit four-probe resistance measurements. The pressure gradient in the regions between contacts overlapping the sample area during resistance studies was typically 5-10% of the average pressure. Four-probe  $dc$  resistivities were measured between 4.2 and 300 K on both cooling and heating. The cooling and heating rate was  $\sim 0.3$  K/min. with a measurement interval of 0.1 K.

## Results

Below 16 GPa and at  $30\text{ K} < T < T_v$  the conductance  $\sigma$  is typical of *variable-range hopping* [10],  $\sigma = \sigma_0 \exp(T_0/T)^{1/4}$  with  $T_0$  decreasing with increasing pressure (Fig. 1). Below 30 K  $\sigma(T)$  deviates from the  $T^{1/4}$  law at all pressures.

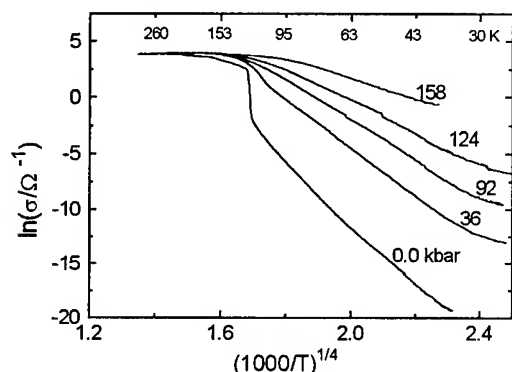


Fig. 1. Temperature dependence of the conductance of magnetite under pressure. The data for different samples are normalized to room temperature.

At temperatures  $T > T_v$  the conductance tends to rise slightly with increasing pressure. The same observation was reported in prior work [5-7] over the pressure range 0-60 kbar. By contrast, at  $T \approx T_v$  three different effects were noted based on the different behaviour of the derivative,  $D$ , of conductance-temperature curves [11]:

- 1) In the range 0-60 kbar the transition temperature  $T_v$  is detected by the pronounced minimum in a plot of  $D$  vs.  $1/T^{1/4}$  (Fig. 2).
- 2) On increasing the pressure beyond 60 kbar the Verwey transition changes significantly in that it becomes quite diffuse and can be detected only by examining the  $D$  vs.  $1/T^{1/4}$  plots in Fig. 2.
- 3) Beyond 125 kbar no unusual features are seen in the derivative plot. This indicates that the transition is completely eliminated at pressures  $P > 125$  kbar.

The above results are summarized in Fig. 3(a) as a plot of  $T_v$  vs. applied pressure  $P$ . This graph bears a remarkable resemblance to the variations in  $T_v$  encountered by increasing  $\delta$  in  $\text{Fe}_{3(1-\delta)}\text{O}_4$  or by lightly doping the magnetite with Ti to form  $\text{Fe}_{3-y}\text{Ti}_y\text{O}_4$  or with Zn to form  $\text{Fe}_{3-x}\text{Zn}_x\text{O}_4$  [4] (Fig. 3(b))

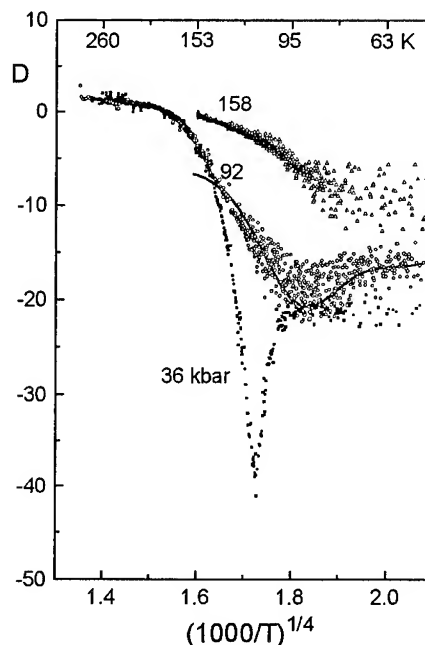


Fig. 2. Temperature dependence of the derivative  $D = d(\ln\sigma)/d(1/T^{1/4})$  under pressure. The solid line is a Gaussian fit to the data at  $P = 92$  kbar.

In Fig. 3(a) one clearly discerns two regions: the first spans the temperature range 122 - 107 K in which  $T_v$  decreases linearly with rising pressure. The data by Kakudate et al., obtained at pressure below 20 kbar [6], are in excellent agreement with our own observations; the slope of the line in fig. 3 is  $-0.25\text{ K/kbar}$ . As has been established by earlier work on magnetite under ambient conditions [4] (see also Fig. 3b) this region corresponds to the range of first order transitions. At the critical value  $P = P_c = 60$  kbar there is a discontinuous shift to the temperature range 100 - 82 K, in which  $T_v$  again drops with rising pressure. Earlier experiments under ambient conditions [4] indicate that this region falls in the regime of a second or higher order transition.

## Discussion

The Verwey transition temperature decreases with rising  $P$ , in close analogy to prior studies on  $\text{Fe}_{3(1-\delta)}\text{O}_4$ ,  $\text{Fe}_{3-x}\text{Zn}_x\text{O}_4$ , and  $\text{Fe}_{3-y}\text{Ti}_y\text{O}_4$  at ambient

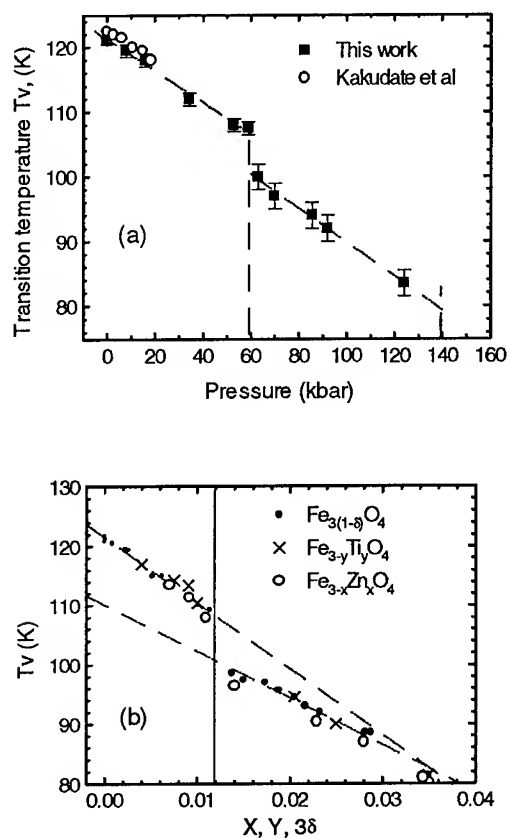


Fig. 3. (a) Pressure variation of  $T_v$ . (b) Composition variation of  $T_v$  at ambient pressure [4].

pressure with rising  $\delta$ ,  $x$ ,  $y$ . Irrespective of whether the experiments are carried out at ambient pressure via changes in sample composition or, on stoichiometric  $\text{Fe}_3\text{O}_4$  by altering the pressure, the two  $T_v$  ranges for the first and second order regimes are exactly the same.

The alterations induced by doping all produce quite similar effects and can be correlated with a local loss of charge, electrons through addition of oxygen and zinc, and holes through doping with titanium, on octahedrally coordinated iron. However, such a mechanism does not explain the results obtained on application of pressure. We therefore rationalize the coincidence of results by focusing on the on-site repulsion between electrons. This is characterized by a Coulomb "gap"  $V \sim e^2/ka$ , where  $k$  is the dielectric constant;  $a$  is the distance between nearest-neighbour cation sites. According to the Cullen-Callen condition [12] an ordered insulator is encountered for  $V/B \geq 2.2$ , where  $B$  is

the polaron bandwidth. If the system is near the critical condition  $V/B \approx 2.2$  a small change of the Coulomb "gap" energy  $V$  or of the bandwidth  $B$  can lead to a loss of the ordered state, thereby eliminating the Verwey transition. Such a change can be achieved either by diminishing  $V$  via a decrease in the average charge per unit cell, through doping, or by broadening the polaron bandwidth on application of pressure. The latter process also increases  $V$  via the decrease of  $a$ , but this effect is anticipated to be small (at  $P=70$  kbar  $\Delta a/a \sim 0.013$  [13]).

## References

\* Work partially supported by BSF grant 92-0008 and Israel Ministry of Science grant 6326-1-94.

1. E.J. Verwey and P.W. Haayman, *Physica* **8** (1941) 979.
2. R. Aragón, R.J. Rasmussen, J.P. Shepherd, J.W. Konitzer and J.M. Honig, *J. Magn. Magn. Mater.*, **54-57** (1986) 1335.
3. J.P. Shepherd, J.W. Konitzer, R. Aragón, J. Spalek, and J.M. Honig, *Phys. Rev. B* **43** (1991) 8461, and references therein.
4. Z. Kakol, J. Sabol, J. Stickler, and J.M. Honig, *Phys. Rev. B* **46** (1992) 1975, and references therein.
5. G.A. Samara, *Phys. Rev. Lett.*, **21**, (1968) 795.
6. Y. Kakudate, N. Mori, Y. Kino, *J. Magn. Magn. Mater.* **12** (1979) 22.
7. S. K. Ramasesha, M. Mohan, A.K. Singh, J.M. Honig, C.N.R. Rao, *Phys. Rev. B* **50**, (1994) 13789, and references therein.
8. S. Tamura, *J. Phys. Soc. Jpn.* **59** (1990) 4462.
9. R. Aragón, D.J. Buttrey, J.P. Shepherd, and J.M. Honig, *Phys. Rev. B* **31** (1985) 430.
10. H. Graener, M. Rosenberg, T.E. Whall, M.R. Jones, *Phil. Mag. B* **40** (1979) 389, and references therein.
11. An unavoidable pressure gradient in the cell broadens the transition width and  $T_v$  may be located more accurately by examining the derivative plots
12. J.R. Cullen and E.R. Callen, *Phys. Rev. B* **7** (1973) 397.
13. D.R. Wilburn, W.A. Basset, *High Temperature- High Pressures* **9** (1977) 35.

## MAGNETIC PHASE TRANSITION OF $\text{Ce}_2\text{Fe}_{17}\text{H}_{0.8}$ UNDER PRESSURE

S.NIZIOL

*University of Mining and Metallurgy, Mickiewicza 30, Cracow, Poland*

R.ZACH

*Institute of Physics, Technical University, 1 St. Podchorążych, Cracow, Poland*

T.KANIOWSKI

*University of Mining and Metallurgy, Mickiewicza 30, Cracow, Poland*

O.ISNARD, M.BACMANN, S.MIRAGLIA, J.L.SOUBEYROUX and D.FRUCHART

*Laboratoire de Crystallographie, CNRS, BP-166X, 38-042 Grenoble, France*

### ABSTRACT

In the case of  $\text{Ce}_2\text{Fe}_{17}\text{H}_x$  (control of hydrogen insertion is possible up to 5 H/f.u.) some correlations between the magneto-volume effects and external hydrostatic pressure have been recently observed. The intermediate valence state of cerium atoms and the changes of the critically short Fe-Fe distances modify the magnetic phase diagram

### Introduction

Recently, the alloys of  $\text{R}_2\text{Fe}_{17}$  series, where R denotes a rare earth element, have been investigated extensively. These materials are very interesting from either fundamental or application point of view. The physical properties of  $\text{R}_2\text{Fe}_{17}$  compounds are, however, not appropriate enough for permanent magnet application (that is, they have too low Curie temperature and magneto-crystalline anisotropy). That can be significantly changed when H, C or N elements are introduced into corresponding sublattices [1,2].  $\text{Ce}_2\text{Fe}_{17}$  as a basic material is a one of the ground examples of such behaviour. In that case it is very interesting to study the dependence of the physical properties of the mentioned material upon the hydrogen insertion. The crystal structure and magnetic properties of such compound have been already presented by several authors [3,4,5,6]. The neutron diffraction studies, reported by Givord, show that in the magnetic ordering state a non-collinear magnetic structure exists with the Néel temperature above  $T_N$  of about 225 K. Moreover, at the 'Curie temperature' of 90 K the transition to 'fun' structure can also be observed. Such properties depend on the competition between the positive and negative magnetic exchange interactions, corresponding to different Fe sublattices, especially Fe-Fe of the

dumb. In the case of  $\text{Ce}_2\text{Fe}_{17}$  the hydrogen insertion can be controlled up to 5H/f.u. Some correlations between the magnetovolume effect along with the changes of intermediate valence state of Ce as well as a short distance of Fe-Fe dumb were observed. The insertion of hydrogen results in so called "negative chemical pressure". The cell volume as well as the Curie temperature increase with concentration of inserted H atoms. Above the concentration of 2H/f.u., only transition from para to ferromagnetic state can be observed. Therefore, it is of significant interest to study how the hydrostatic pressure affects the mentioned phenomena. Some preliminary results were presented on the ICM'95 conference [7]. In this paper more detailed results for  $\text{Ce}_2\text{Fe}_{17}\text{H}_{0.8}$  are reported.

### Experimental results

Details on the preparation of the pristine alloy and its hydrides have been presented elsewhere [4]. The measurements of the magnetic phase transition temperature under pressure up to 1.2 GPa have been performed by means of a.c. susceptibility technique. Hydrostatic pressure have been obtained by CGA compressor, made by UNI-PRESS, Warsaw, Poland. Moreover, the isothermal magnetisation curves in pulsed high magnetic field have been obtained.



## Results and discussion

At atmospheric pressure the pure  $\text{Ce}_2\text{Fe}_{17}$  compound exhibits an antiferromagnetic properties with the Néel temperature of about 225 K. The pressure measurements of the pristine sample showed the evidence that the Néel temperature decreases versus external applied pressure. In the Fig. 1 the selected a.c. susceptibility runs for selected pressure values are presented. At atmospheric pressure, the appropriate maximum observed at  $T_1=225$  K is associated with the magnetic phase transition from the paramagnetic state to an intermediate ordered state. One can suppose that at lower temperature range the phase transition (at  $T_2$ ) to ferromagnetic state is observed.

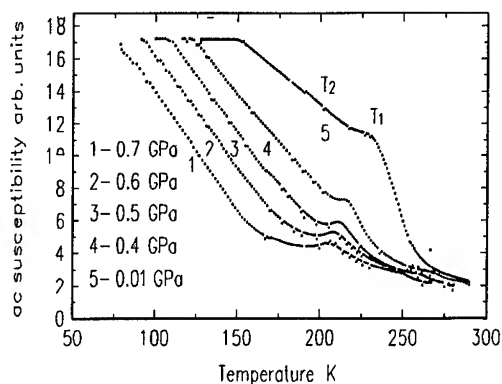


Fig. 1. a.c. susceptibility temperatures runs for different pressure values.

The isothermal magnetisation curves (Fig.2), measured in magnetic field range up 4 T, confirm the existence of the intermediate magnetic state exists at atmospheric pressure. At

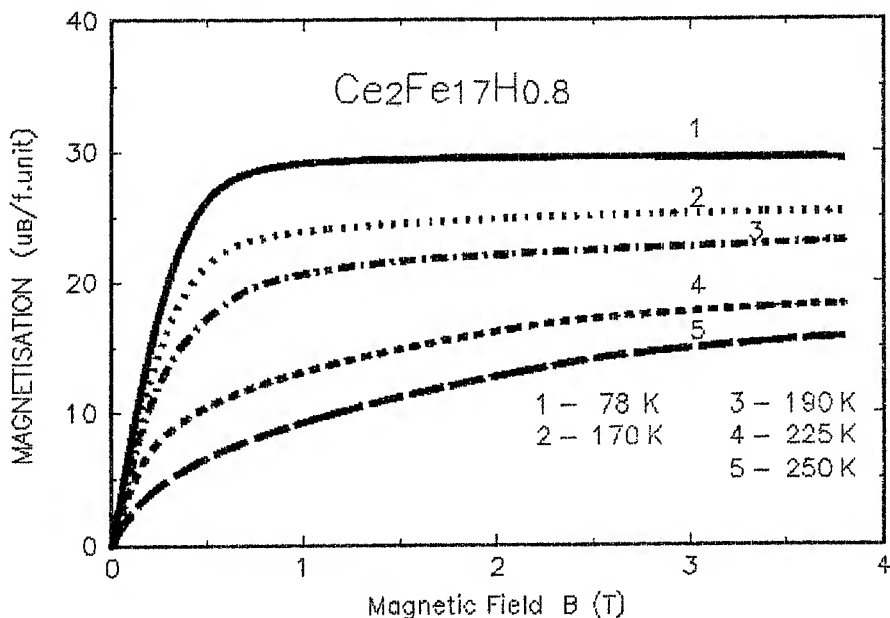


Fig. 2. Magnetisation curves of  $\text{Ce}_2\text{Fe}_{17}\text{H}_{0.8}$  sample for different temperatures.

temperatures below 150 K, a saturation of magnetisation is observed at magnetic field of about 0.7 T. The spontaneous magnetisation  $\sigma_0$  was estimated as equal to  $29.8 \mu_B/\text{mol}$  remains in agreements with results reported in the papers [5,6]. for  $\text{Re}_2\text{Fe}_{17}$  systems. Within the temperature region, between  $T_1$  and  $T_2$ , no saturation on magnetisation curves was found in the magnetic field range up to 4 T. Thus this fact supports the supposition that the non-collinear magnetic structure exists. When an external pressure is applied, new magnetic state arises at pressure  $P > 0.7$  GPa. In fact the drop of the magnetic susceptibility is observed for higher pressures, as it was shown in the Fig. 3. This pressure induced state exhibits an incommensurate long period antiferromagnetic properties. Note, that such behaviour was previously reported for pristine  $\text{Ce}_2\text{Fe}_{17}$  compound. Full compensation of the internal "chemical" pressure created by the hydrogen atoms may be obtained for pressures greater than 1.5 GPa. Therefore, having in mind the values of the derivatives  $dT_1/dP$  and  $dT_2/dP$  and also the Néel and the Curie-like dependencies versus the insertion level one can suppose that for the concentration of 1.5H/f.u. a tricritical

point can be supposed. Such a magnetic phase diagram, including external pressure, for pure  $\text{Y}_2\text{Fe}_{17}$  compound was experimentally and theoretically obtained by Nikitin [8].

#### Acknowledgements

We have to thank the French-Polish "Action Intégrée" that founded several exchanges between our Institutes. Part of this work was undertaken under the auspices of the "Concerted European Action on Magnets" as well as partly supported by KBN Polish Scientific Project.

#### References

1. H.Sun, J.M.D. Coey, Y.Otani, D.P.F.Hurley *J. Phys.: Condens.Matter* 2 6465 (1990)
2. X.C.Kon, R.Grössinger, T.H.Jacobs, K.H.J. Buschow *J.Magn.Magn.Mat.* 88 (1990) 1
3. D.Givord, R.Lemaire C.R. *Acad.Sci.Paris* 274 (1972) 1166
4. D.Givord *Thesis, University of Grenoble* (1973)
5. O.Isnard, S.Miraglia, D.Fruchart *J.Magn.Magn.Mat* 103 (1992) 157
6. O.Isnard, *Thesis, University of Grenoble* (1993)
7. O.Isnard, R.Zach, S.Niziol, M.Bacmann, S.Miraglia, J.L.Soubeyroux, D.Fruchart *J.Magn.Magn.Mat* 140- 144 (1995) 1073
8. S.A.Nikitin, A..M.Tishin, M.D.Kuzmin, Yu.I. Spichkin *Phys.Letters A* 153 (1991) 155

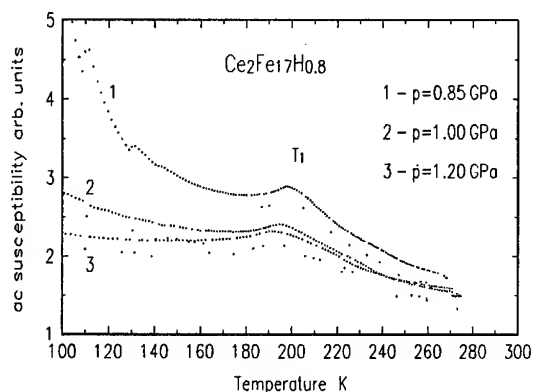


Fig. 3. a.c. susceptibility curves in the vicinity of  $T_1$  for higher pressure values.

## PRESSURE MAGNETISATION MEASUREMENTS OF $\text{MnRhAs}_{1-x}\text{P}_x$

R.ZACH

*Institute of Physics, Technical University, 1 St. Podchorazych 30084 Cracow, Poland*

M.GUILLOT

*SNCI - MPI, CNRS, BP 166X, 38-042 Grenoble, France*

S.NIZIOL

*University of Mining and Metallurgy, Mickiewicza 30, 30-059 Cracow, Poland*

R.FRUCHART

*ENSPG, CNRS, BP-46, 38-402 St. Martin d'Heres, France*

### ABSTRACT

A new d.c. magnetic field pressure set-up for magnetisation measurements is briefly described. The magnetisation under pressure of the samples with  $x=0.0$ ,  $x=0.4$ ,  $x=0.5$  and  $x=0.6$  for  $\text{MnRhAs}_{1-x}\text{P}_x$  solid solutions is measured. Several pressure and/or magnetic field induced phase transitions are presented.

### Introduction

$\text{MnRhAs}_{1-x}\text{P}_x$  system presents various types of magnetic order. For  $x < 0.5$  antiferromagnetic (AF) or ferrimagnetic (Ferri) order, depending on the temperature, was found. While  $x > 0.5$  only ferromagnetic (F) order was present [1].

Magnetic behaviour of these compounds is strongly pressure influenced, how it was revealed by the a.c. susceptibility pressure measurements [2]. On the basis of high d.c. field magnetisation measurements ( $x=0.33$ ,  $x=0.4$ ,  $x=0.5$ ) carried on atmospheric pressure several magnetic field induced phase transitions between the AF state and another ordered ones were found previously [3].

The aim of this work was to study pressure behaviour of the field induced magnetic phase transitions. Four samples:  $x=0$ ,  $x=0.4$ ,  $x=0.5$  and  $x=0.6$  have been chosen for this purpose.

### Experiment

Pulsed and d.c. magnetic field magnetisation experiments under pressure were performed. The pulsed magnetic field pressure set-up for magnetisation measurements up to 16 T (77 K - 400 K) was used [4].

A new pressure facility for magnetisation measurements in d.c. magnetic field under hydrostatic pressure was developed at MPI-SNCI, Grenoble (magnetic field up to 24 T, pressure up to 0.35 GPa, temperature range 50 K - 300 K). The high d.c. magnetic field magnetisation set-up (described elsewhere [5,6]) was enriched with the set-up for pressure experiments.

The set-up for pressure measurements (Fig.1) consists of a very small pressure vessel /outer diameter of 6.9 mm/, made of non-magnetic beryllium-copper. A flexible capillary tube joins the pressure vessel and the pressure generator via the intermediate pressure chamber. The aim of the pressure chamber is to make sample replacement easier.

The pressure vessel, with a teflon sample holder inside, can be easily mounted into the calorimeter and altogether into the cryostat and in the Bitter magnet [6]. The calorimeter enables good temperature control and regulation.

The temperature is measured by a platinum resistor placed outside of the pressure vessel but having metallic contact with it. High purity gaseous helium was used as a pressure transmitting medium.

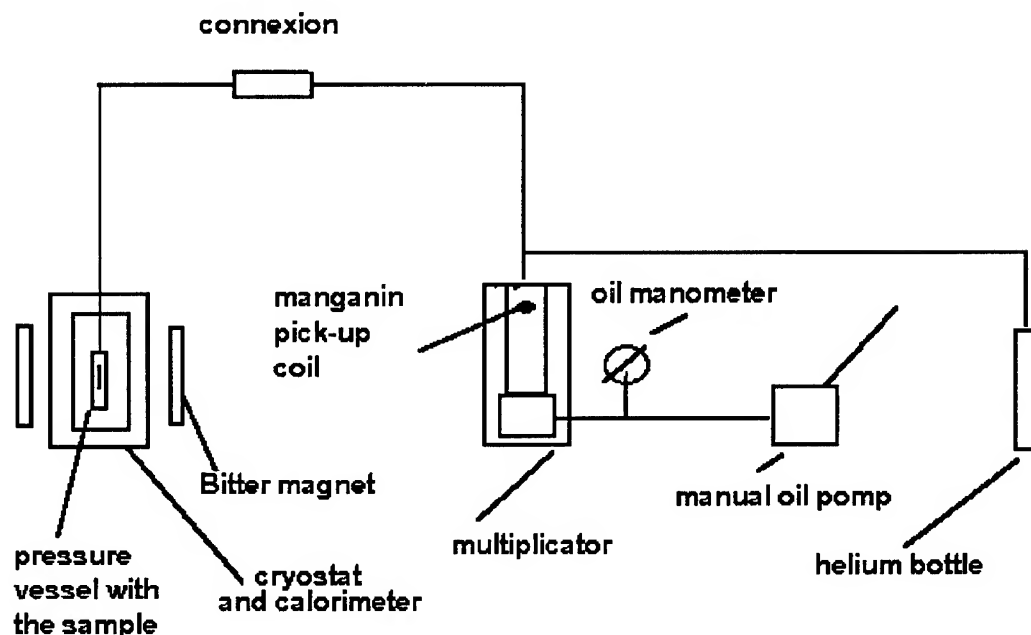


Fig. 1. Pressure facility for magnetisation measurements in continuous d.c magnetic field up to 24 T in hydrostatic pressure up to 0.35 GPa.

The manganin pick-up coil, placed inside of the pressure generator, as a pressure detector was used.

The new facility gives good sensitivity and a good accuracy in determining of magnetic moment value under pressure.

### Results and discussion

In the case of  $\text{MnRhAs}_{0.6}\text{P}_{0.4}$  sample the isothermal  $M_T(B)$  magnetisation curves collected at 80 K confirm the existence of the field induced phase transitions [3]. The critical field  $B_c^+$  ( $B_c^+$ ,  $B_c^-$  are defined as the abscissa corresponding to the maximum and minimum on the  $dM/dB$  curve, respectively) slightly increases versus pressure (up to 0.4 GPa) (Fig. 2). The critical field  $B_c^-$  of the second phase transition, observed only for the decreasing field, also increases with increasing pressure.

The similar behaviour was also found for  $\text{MnRhAs}$  compound in d.c. magnetic field (Fig. 3).

On the other hand, for the  $\text{MnRhAs}_{0.4}\text{P}_{0.6}$  sample the ferromagnetic phase was proposed only. Within the experimental error, no change in the critical field versus pressure, is found on the basis of our pressure measurements ( $B_c^+=0.2$  T, 80 K). Moreover, the magnetic moment value in the ferromagnetic state slightly increase versus pressure.

In the case of  $\text{MnRhAs}_{0.5}\text{P}_{0.5}$  content a sharp field induced transformation between the AF phase and another ordered one was previously found ( $B_c^+(0.01 \text{ GPa}) = 3.1$  T, 80 K). External pressure applied at 80 K leads to a decrease in the critical field as a function of pressure for  $P < 0.3$  GPa while for  $P \geq 0.3$  GPa no critical

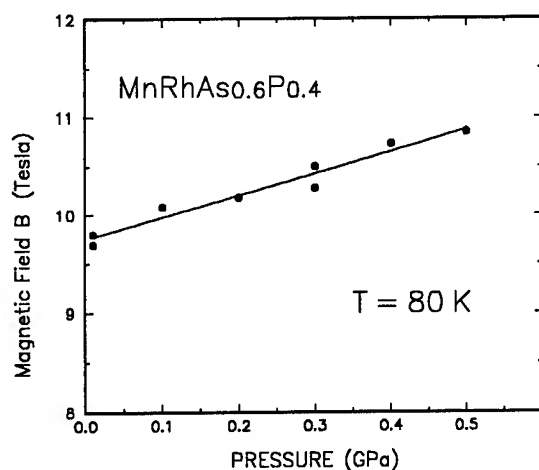


Fig. 2. Critical field  $B_c^+$  pressure behaviour for  $\text{MnRhAs}_{0.6}\text{P}_{0.4}$  sample.

field variation versus pressure, within the experimental error, is observed ( $B_c^+(0.3 \text{ GPa}) = 0.2 \text{ T}$ ) and the latter  $B_c^+$  value is equal to the appropriate value found for the ferromagnetic  $\text{MnRhAs}_{0.4}\text{P}_{0.6}$  sample. These allows to assume, that this pressure induced magnetic phase exhibits ferromagnetic properties.

Electronic band structure calculations for the ground (0 K) state for  $\text{MnRhAs}$  and  $\text{MnRhP}$  compounds show that magnetic moments are well localised only on the manganese atoms [2]. In the case of rhodium atoms high density of states near the Fermi level is found however the Stoner condition of ferromagnetism is not fulfilled. For the solid solutions with  $x = 0.8$  and  $x = 0.6$  similar behaviour was also found recently [9]. This suggests that magnetic moments carried by rhodium atoms exhibit fluctuating character [7,8].

One may conclude, that the increase of the ferromagnetic interactions in  $\text{MnRhAs}_{1-x}\text{P}_x$  system of solid solutions provoked by an external applied pressure and/or by the anion substitution have the electronic band structure origin.

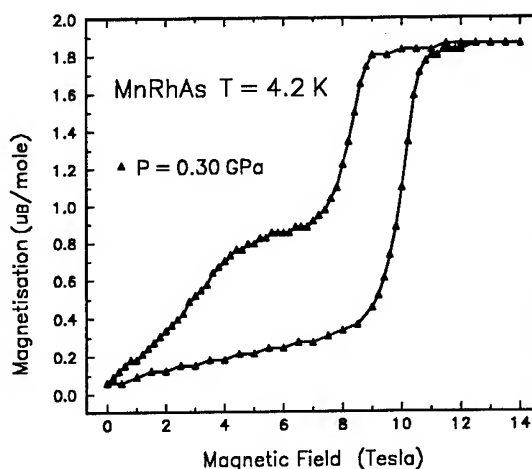


Fig. 3. Magnetisation of  $\text{MnRhAs}$  compound in d.c. magnetic field under pressure.

#### Acknowledgements

We would like to acknowledge for the financial support obtained from the French-Polish cooperation project "Action Intégrée ATP S-15". This job was also partly supported by Polish Scientific Committee (KBN) and by Technical University of Cracow, Poland.

#### References

1. P. Chaudouet *Thesis, Grenoble* (1983)
2. R. Zach, R. Fruchart, D. Fruchart, S. Kaprzyk and S. Niziol *J. Magn. Magn. Mat.* 104-107 (1992) 1929
3. R. Zach, M. Guillot, J.C. Picoche, R. Fruchart *J. Magn. Magn. Mat.* 140-144 (1995) 143
4. A. Zieba, M. Ladecka and R. Zach *Physica B* 177 (1992) 51
5. J.C. Picoche, P. Rub and H.J. Schneider-Muntau *J. Magn. Magn. Mat.* 11 (1979) 308
6. J.C. Picoche, M. Guillot and A. Marchand *Physica B* 155 (1989) 407
7. T. Kaneko, H. Yasui, K. Nakagawa, T. Kanomata *J. Magn. Magn. Mat.* 104-107 (1992) 1949
8. B. Chenevier, M. Anne, M. Bacmann, D. Fruchart, P. Chaudouet *VIII SCTE, Vienna* (1985)
9. J. Tobola *Private communication*

## PRESSURE STUDY OF $\text{UCu}_2\text{Si}_2$ , $\text{UCu}_2\text{Ge}_2$ , $\text{UMn}_2\text{Si}_2$ AND $\text{UMn}_2\text{Ge}_2$ COMPOUNDS

R. DURAJ

*Institute of Physics, Technical University of Cracow, ul.Podchorążych 1,30-084 Cracow, Poland*

A. SZYTUŁA

*Institute of Physics, Jagellonian University, ul.Reymonta 4,30-059 Cracow, Poland*

### ABSTRACT

The effect of hydrostatic pressure on the Curie temperature of polycrystalline  $\text{UCu}_2\text{Si}_2$ ,  $\text{UCu}_2\text{Ge}_2$ ,  $\text{UMn}_2\text{Si}_2$  and  $\text{UMn}_2\text{Ge}_2$  compounds was measured up to 1.4 GPa by means of a.c. magnetic susceptibility. The obtained data indicate a localized magnetism in  $\text{UCu}_2\text{X}_2$  compounds and itinerant magnetism in  $\text{UMn}_2\text{X}_2$  compounds.

### Introduction

The ternary compounds  $\text{RT}_2\text{X}_2$ , where R is a rare earth or an actinide element, T is a transition metal and X is silicon or germanium, are a subject of intensive studies in the last few years. These compounds crystallize, predominantly, in the body centered  $\text{ThCr}_2\text{Si}_2$  structure and exhibit a variety of properties, including different types of magnetic order.

In the paper results of the pressure effect on the Curie temperature measured for four ternary compounds  $\text{UCu}_2\text{Si}_2$ ,  $\text{UCu}_2\text{Ge}_2$ ,  $\text{UMn}_2\text{Si}_2$  and  $\text{UMn}_2\text{Ge}_2$  are reported. These compounds were previously studied by means of the magnetization and neutron diffraction measurements [1-6]. Chełmicki et al. concluded that  $\text{UCu}_2\text{Si}_2$  was a simple collinear ferromagnet with  $T_C \approx 105(2)$  K [1]. The new magnetization data give a second transition at  $T_N = 107$  K [2]. The  $\text{UCu}_2\text{Ge}_2$ , studied by the neutron diffraction [3,4] was reported to order ferromagnetically below  $T_C = 100$  K, transforming at  $T_0 = 25-40$  K to an antiferromagnetic phase. In both compounds a magnetic moment is localized only on uranium atoms. Neutron diffraction and magnetization measurements of  $\text{UMn}_2\text{Si}_2$  and  $\text{UMn}_2\text{Ge}_2$  indicates a ferromagnetic ordering below the Curie points of 377 K and 388 K, respectively [5,6]. Both uranium and manganese moments are ordered ferromagnetically and are parallel to the c-axis.

### Experiment

Experiments were carried out on polycrystalline samples as reported in previous papers [1,5]. X-ray diffractograms show that all samples have the  $\text{ThCr}_2\text{Si}_2$  type structure.

The changes in magnetic transition temperatures under external pressure were determined by using the a.c. susceptibility ( $\chi_{ac}$ ) method. The measurements of  $\chi_{ac}$  were performed over the temperature range 80-300 K applying a weak magnetic field with a frequency of several hundreds Hz and a maximum induction of  $10^{-3}$  T. The voltage induced in the pick-up coils was measured by a selective nanovoltmeter. The temperature was determined by use of a copper-constantan thermocouple placed in direct contact with the sample. The Curie temperature was defined as the temperature at which  $d\chi_{ac}/dT$  has its minimum.

The generating magnetic field coil as well as the pick-up coils, with the sample inside, were placed in a Be-Cu pressure vessel. High purity gaseous helium was used as a pressure transmitting medium. A gas compressor of the IF-012A type, produced by UNIPRESS (Warsaw, Poland) was employed. The pressure was determined by a manganin pick-up coil placed in the compressor. The measurements were carried out under isobaric conditions.

## Results and Discussion

The temperature dependence of  $\chi_{ac}$  for  $UCu_2Si_2$  compound, measured in the vicinity of its critical temperature for different values of the external pressure is shown in Fig. 1.

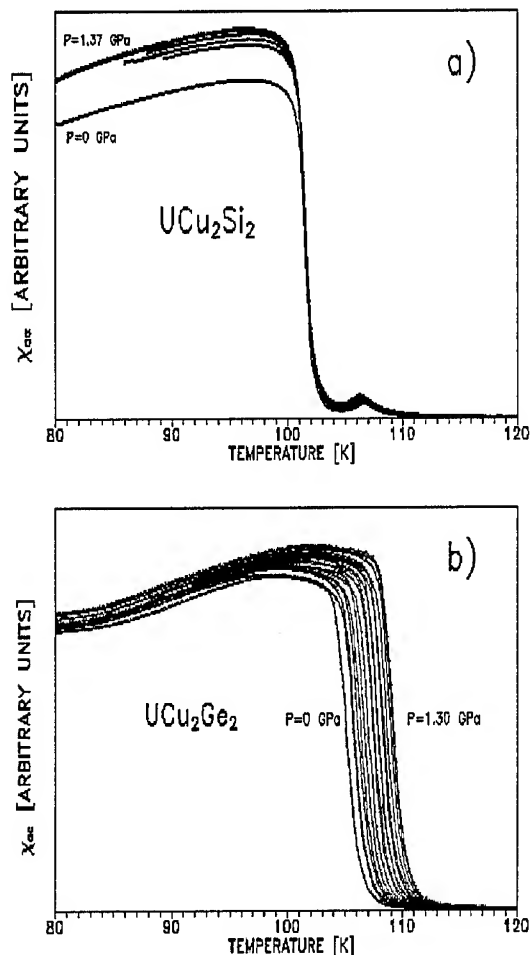


Fig.1. The a.c. susceptibility of (a)  $UCu_2Si_2$  and (b)  $UCu_2Ge_2$  as a function of temperature and pressure.

The  $\chi_{ac}$  versus  $T$  curve shows a small peak at  $T_N=108$  K and a large increase at  $T_C \gg 100$  K.

The  $T_C$  values do not change with pressure (Fig. 2) while the  $T_N$  values give the  $dT_N/dP$  equal  $-0.24(5)$  K/GPa. Fig. 1 shows also the  $\chi_{ac}$  curves versus temperature ( $T$ ) under various pressures for  $UCu_2Ge_2$ , whereas Fig.2 displays the determined values of the Curie temperature  $T_C$  versus pressure.

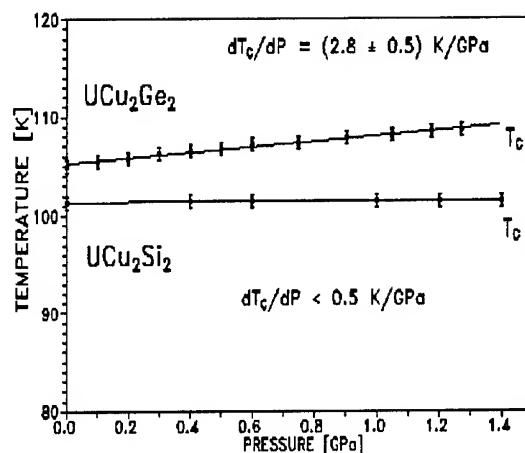


Fig. 2. Pressure dependence of the Curie temperatures of  $UCu_2Si_2$  and  $UCu_2Ge_2$ .

The  $T_C$  of  $UCu_2Ge_2$  increases linearly with pressure and the  $dT_C/dP$ , is  $+2.8(5)$  K/GPa. For both compounds the values of the a.c. susceptibility in ferromagnetic phase increases with an increasing pressure.

Fig. 3 presents the results for the  $UMn_2Si_2$  compound. The determined values of the Curie temperatures decreases linearly with increasing pressure (see Fig. 4). The  $dT_C/dP$ , equals  $-12(1)$  K/GPa. The dependence of the a.c. susceptibility of  $UMn_2Si_2$  is anomalous at low temperatures. The  $T_C$  values for the isostructural  $UMn_2Ge_2$  - practically do not depend of pressure and  $dT_C/dP < 1$  K/GPa. The magnetic moments of  $UCu_2Si_2$  and  $UCu_2Ge_2$  are localized only on the uranium atoms. The U-U distances in these compounds are 0.3985 and 0.4058 nm, respectively and they are much bigger that the so-called Hill limit for the uranium compounds. The magnetic properties in the ordered region can be described by a localized magnetism. The observed in  $UCu_2Ge_2$  effect of pressure on  $T_C$  supports the localized nature of 5f-state magnetism in this compound. A small decrease of  $T_N$  the insensitivity of  $T_C$  to pressure found for  $UCu_2Si_2$  can also indicate a fairly high stability of the uranium moments [7].

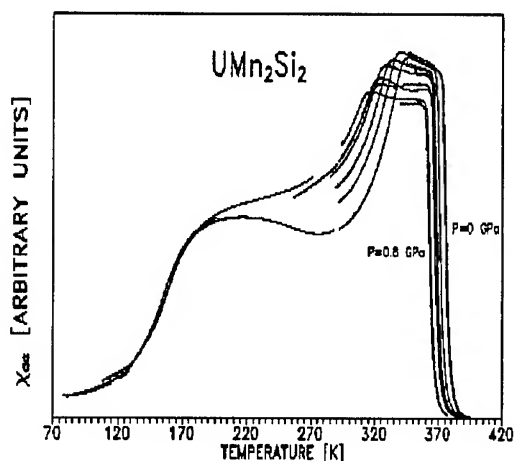


Fig. 3. The a.c. susceptibility  $\chi_{ac}$  vs. temperature for  $UMn_2Si_2$  under various pressures.

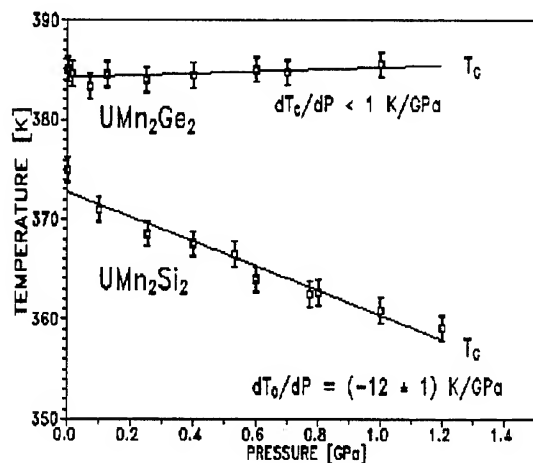


Fig. 4. Pressure dependence of the Curie temperatures of  $UMn_2Si_2$  and  $UMn_2Ge_2$ .

The  $UMn_2X_2$  compounds have different magnetic properties. In this case the neutron diffraction measurements detect that the magnetic moments are localized on U and Mn atoms at low temperatures and on Mn atoms only in high temperatures. In both phases the magnetic moments order ferromagnetically and are aligned along c-axis[5]. The observed anomaly at  $T \approx 150$  K (see Fig.3) is connected with the change of magnetic structure. The observed decrease at the  $T_C$  temperature with increasing pressure for  $UMn_2Si_2$  is  $-12(1)$  K/GPa

and is similar to that observed for the isostructural rare earth  $RMn_2X_2$  compounds, for example:  $LaMn_2Si_2$  ( $-16.6(5)$  K/GPa),  $LaMn_2Ge_2$  ( $-11.0(5)$  K/GPa) [8],  $SmMn_2Ge_2$  ( $-11(1)$  K/GPa) [9],  $NdMn_2Ge_2$  ( $-6$  K/GPa),  $PrMn_2Ge_2$  ( $-2$  K/GPa) [10]. The case of  $UMn_2Ge_2$  where  $dT_C/dP \approx 0$  is anomalous.

The calculations of the electronic energy band of the rare earth  $RMn_2X_2$  compounds suggest an itinerant behaviour of the manganese magnetic moments [11]. The pressure dependence of the Curie temperatures of  $UMn_2X_2$  compounds confirms the theoretical prediction.

#### Acknowledgements

The authors thank Doc.Dr.hab. A. Zygmunt for the samples for the experiments.

#### References

1. L. Chełmicki, J. Leciejewicz and A. Zygmunt, *J. Phys. Chem. Solids* 46 (1985) 529.
2. M.S. Torikachvili, R.F. Jardim, C.C. Beccera, C.H. Westphal, A. Padnan-Filho, V.M. Lopez and L. Rebelsky, *J. Magn. Magn. Mater.* 104-107 (1992) 69.
3. J. Leciejewicz, L. Chełmicki and A. Zygmunt, *Solid State Commun.* 41 (1982) 167.
4. M. Kuznietz, H. Pinto, H. Ettegnig and M. Melamud, *Phys. Rev.* B48 (1993) 318.
5. A. Szytuła, S. Siek, J. Leciejewicz, A. Zygmunt and Z. Ban, *J. Phys. Chem. Solids* 49 (1988) 1113.
6. A.J. Dirkmaat, *Ph.D. Thesis*, (University of Leiden, 1989).
7. J.M. Fournier, *Physica* 130 B (1985) 268.
8. R. Duraj and A. Szytuła, private information.
9. M. Duraj, R. Duraj, A. Szytuła and Z. Tomkowicz, *J. Magn. Magn. Mater.* 73 (1988) 240.
10. T. Kawashima, T. Kanomata, H. Yoshida and T. Kaneko, *J. Magn. Magn. Mater.* 90-91 (1990) 721.
11. S. Ishida, S. Asano and J. Ishida, *J. Phys. Soc. Japan* 55 (1986) 936.



# ELECTRONIC AND MAGNETIC PROPERTIES OF USb UNDER HIGH PRESSURE

H. Takahashi, N. Mōri, A. Ochiai,<sup>a</sup> E. Hotta<sup>b</sup> and T. Suzuki<sup>b</sup>

Institute for Solid State Physics, The University of Tokyo, Roppongi, Minato-ku, Tokyo 106, Japan

<sup>a</sup>The Oarai Branch, Institute for Materials Research, Tohoku University, Oarai, Ibaraki 311-13, Japan

<sup>b</sup>Department of Physics, Tohoku University, Sendai 980, Japan

## ABSTRACT

The electrical resistivity of single crystalline USb with high quality has been measured up to 8.5 GPa. It is observed that the Néel temperature ( $T_N$ ) decreases with increasing pressure at a rate of 18 K/GPa, and a peak-shape anomaly of the electrical resistivity appears at 77 K at 2 GPa, which is considered to correspond to a new phase transition. A large decrease of the electrical resistivity at room temperature was observed at pressure around 7 GPa and it can be ascribed to the structural phase transition from NaCl-type to CsCl-type structure.

## Introduction

Uranium monopnictides and monochalcogenide with the NaCl-type crystal structure show ferromagnetic and antiferromagnetic behaviors and have been investigated intensively. There has been considerable interest in these properties related to the localized or itinerant behavior of the 5f electrons. Hill [1] pointed out that the distance between the metal atoms in the actinide compounds is very important parameter to determine their physical properties through 5f-5f overlapping and/or 5f-7s6d hybridization. According to his scheme, the compounds are not magnetic below a critical interatomic distance and they are magnetic above it. This critical distance is 3.5 Å for uranium compounds. Hybridization of 5f electrons with the d or p orbital of the ligand can also occur. In addition the degree of localization of the 5f electrons depends on the pnictogen and the actinide element besides the interatomic distance. It seems that the localization of 5f electrons is higher in the heavier pnictides [2] and it increases with the atomic number of the actinide element, from uranium to plutonium. Thus a lot of alloying works have been performed to elucidate the characters of the materials including f electrons. From this point of view, high pressure works would allow us to separate the influence of the character of both actinide and pnictogen atoms themselves.

USb undergoes a magnetic phase transition from paramagnetism to the type-I fcc antiferromagnet with a triple-k structure at 215K [3] and well-defined magnetic excitation of spin wave is found below  $T_N$  [4]. The Hall coefficients at 4.2 K was reported -0.2 cm<sup>3</sup>/C which corresponds to carrier number of 1.8% per uranium ion [5,6]. However, the Hall coefficients at room temperature depend on investigators. USb seems to be subject to sample dependence because of its semimetallic character having large electrical resistivity.

Recent de Haas-van Alphen effect study for USb suggests that the valence of the uranium is not 4+ but 3+ [7]. However, the analysis of lattice constants of the uranium monopnictides suggests that the valence of uranium is near to 4+ [8]. Therefore the valence of uranium in USb can not be simply determined and this is one of the interesting problems.

In this work single crystalline USb with good quality could be grown and the electrical resistivity measurements under high pressure up to 8.5 GPa were performed.

## Experimental

Single crystalline USb was grown by Bridgman technique and characterized as described elsewhere [5]. The electrical resistivity was measured with dc four-terminal method. The

pressure was generated using a cubic anvil cell up to 8.5 GPa [9]. The nearly hydrostatic pressure was retained in a Teflon cell filled with a fluid pressure transmitting medium, a mixture of Fluorinert FC 70 and FC 77. The pressure below room temperature was estimated to be controlled within 3%. The force applied to the high pressure apparatus was controlled not to change the pressure during the measurements on cooling and heating, that is, these measurements were performed always at constant pressure.

## Results and discussion

Figure 1 shows the electrical resistivity of USb as a function of temperature for each pressure. The Néel temperatures were determined from the kink of the  $\rho$ - $T$  curve, which are indicated by arrows in Fig. 1. It is observed that  $T_N$  decreases with pressure. Above 3.5 GPa the kink of the  $\rho$ - $T$  curve corresponding to  $T_N$  becomes ambiguous. However, it is still observed at around 90 K at 6.5 GPa. The pressure dependence of  $T_N$  is shown in Fig. 2. The solid line is drawn for guides to the eye in Fig. 2

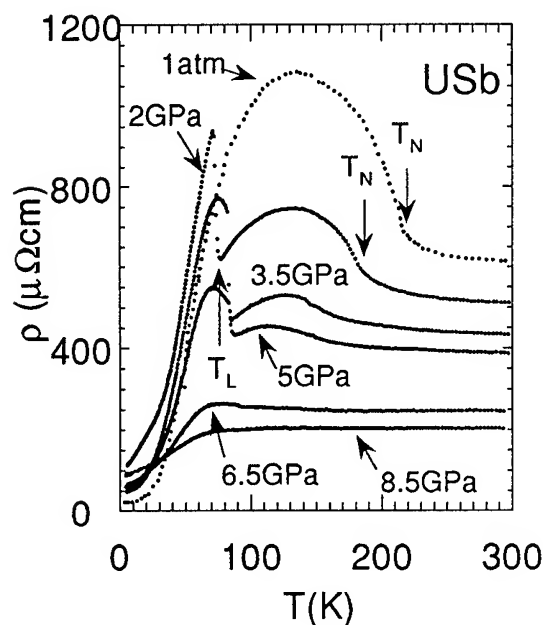


Fig.1 Electrical resistivity as a function of temperature for each pressure.  $T_N$  and  $T_L$  denote Néel temperature and the temperature at which the electrical resistivity changes abruptly, respectively.

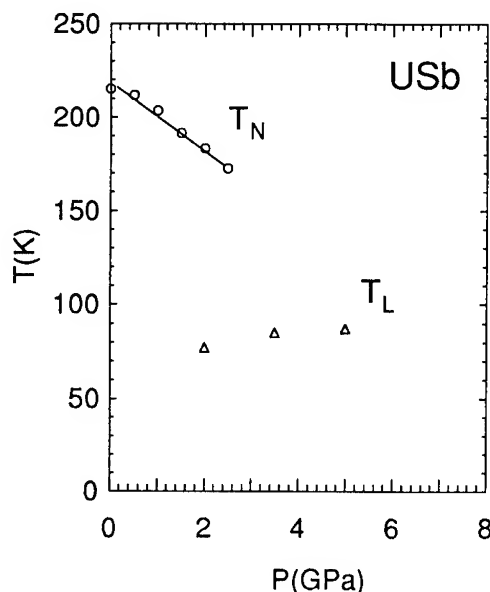


Fig.2 Pressure dependence of  $T_N$  and  $T_L$ . The solid line is drawn for guides to the eye.

and  $T_N$  decreases with pressure at a rate of 18 K/GPa. The  $T_N$  could not be determined definitely at more than 3.5 GPa. Large decrease of electrical resistivity at room temperature is observed between 5 and 6.5 GPa in Fig.1. This is due to the NaCl-type to CsCl-type structural phase transition, since it is reported that the volume discontinuity in  $\Delta V/V_0$  (P) curve is observed at 8 GPa and assigned to the NaCl-type to CsCl-type structural phase transition from the x-ray diffraction measurements under high pressure[10]. The discrepancy of the transition pressure may be due to the difference of the sample.

Another interesting result from the electrical resistivity data is the appearance of an anomalous behavior at 77 K at 2 GPa, whose temperature is indicated by an arrow and denoted by  $T_L$  in Fig. 1. It is considered that this anomaly corresponds to a new phase transition. At this transition temperature a sharp jump of the electrical resistivity was observed and disappears in the CsCl-type structure phase. The pressure dependence of  $T_L$  is shown in Fig. 2. It is observed that  $T_L$  appears at 77 K at 2 GPa and increases a little up to 5 GPa.

Recently Braithwaite et al. [11] measured the electrical resistivity of USb using a Bridgman anvil device and reported that  $T_N$  decreases with increasing pressure and the new phase appears above 2 GPa. Although they reported the relative resistance normalized to that obtained at 273 K, their results are basically consistent with the present ones. Moreover they carried out neutron diffraction measurements under high pressure and proposed that the new phase under high pressure is single-k antiferromagnetic structure from a careful analysis[12]. It is natural that single-k structure occurs at high pressure, since UAs having shorter U-U distance shows single-k and double-k structure at atmospheric pressure.

In summary, we carried out electrical resistivity measurements of single crystalline with high quality USb under nearly hydrostatic pressure up to 8.5 GPa. It was observed that  $T_N$  decreases at a rate of 18 K/GPa. The large decrease of electrical resistivity at room temperature between 5 and 6.5 GPa was observed and it is due to the structural phase transition. The new phase transition was observed at 77 K at 2 GPa. Braithwaite et al. pointed out that from neutron diffraction measurement under high pressure the new phase could be single-k antiferromagnetic structure[12]. However the origin of the new phase is not clear. Further investigations of USb under high pressure are ongoing.

### Acknowledgments

The authors would like to acknowledge Dr. J. -M. Mignot of Laboratoire Léon Brillouin at CE-Saclay for sending them valuable high-pressure data of USb. A part of this work is supported by a Grant-in Aid of the Ministry of Education, Science and Culture in Japan.

### References

- [1] H.H. Hill, The early actinides: the periodic system's f electron transition metal series. In W.M. Miner (ed.), Plutonium, Met. Soc., AIME, New York, 1970, pp2-19.
- [2] D.Damien and C.H.de Novion, J.Nucl. Mater., **100** (1981) 167.
- [3] G.H.Lander, M.H.Mueller, D.M.Sparlin, and O.Vogt, Phys. Rev. **B14** (1976) 5035, J. Rossat-Mignod, P. Burlet, S.Quezel, and O.Vogt, Physica **102B** (1980) 237.
- [4] G.H.Lander and W.G.Stirling, Phys. Rev. **B21**, (1980) 436.
- [5] A.Ochiai, Y.Suzuki, T.Shikama, K.Suzuki, E.Hotta, Y.Haga, and T.Suzuki, Proc. of SCES '93 at Sendai.
- [6] J. Schoenes, B.Frick, and O.Vogt, Phys. Rev. **B30** (1984) 6578.
- [7] A.Ochiai, E.Hotta, Y.Haga, T.Suzuki, Y.Suzuki, and T.Shikama, preprint.
- [8] G.Buch, F.Hulliger, and O.Vogt, J. de Phys. **C4** (1979) 62.
- [9] N.Môri and H.Takahashi, Pressure Engineering **28** (1990) 124.
- [10] L.M.Leger, K.Oki, A.M.Redon, I.Vedel, J.Rossat-Mignod, and O.Vogt, Phys. Rev. **B33** (1986) 7205.
- [11] The results were presented at the Journées des Actinides in l'Aquila in 1995.
- [12] D.Braithwaite, I.N.Goncharenko, J.-M.Mignot, O.Vogt, and A.Ochiai, to be published.

# p-T PHASE DIAGRAMS OF $\text{Sn}_2\text{P}_6\text{S}_6$ AND $\text{Sn}_2\text{P}_6\text{Se}_6$

Yu. II. TYAGUR

*Uzhorod State University, 13 Kapitulna St. Uzhorod 24900, Ukraine*

J. JUN

*High Pressure Research Center, Sokolowska 29/37, 01-142 Warsaw, Poland*

High hydrostatic pressure influence on the temperature of ferroelectric phase transition (FEPT) and melting transition of  $\text{Sn}_2\text{P}_2\text{S}_6$  and  $\text{Sn}_2\text{P}_2\text{Se}_6$  is measured. The p-T phase diagrams have been determined. The line of the solid-solid and solid-liquid phase transitions and the triple point have been found. The analysis of p-T phase diagram of  $\text{Sn}_2\text{P}_2\text{S}$  and  $\text{Sn}_2\text{P}_2\text{Se}$  indicates that there exists the incommensurate phase transition, new solid phase transition, the Lifshitz points (LP) and the triple points.

## 1 Introduction

At atmospheric pressure the Curie temperature of the second order ferroelectric phase transition (FEPT) for  $\text{Sn}_2\text{P}_2\text{S}_6$  crystals is equal to  $T_0 = 336.0 \text{ K}$  [1-3]. The maximum value of dielectric constant for the Curie temperature and  $p = 0$  is  $\epsilon_{\text{max}} = 1.14 \cdot 10^5$ . The  $k$  - parameter determined from the "law of two" is in the interval between 3.35 and 3.80. The phase transition is of a displacive type (in Fedorov notation)  $P_C \approx P_{21/C}$  [4].

High hydrostatic pressure decreases the temperature of FEPT in  $\text{Sn}_2\text{P}_2\text{S}_6$ . For the pressure  $p_{L0} = 0.20 \pm 0.03 \text{ GPa}$  the order of FEPT is changed, the FEPT line splits and an interval of the incommensurate phase (ICP) appears [5] and most likely the Lifshitz point (LP) occurs. It follows from the previously published results [6] that either the Lifshitz point is close to the tricritical Lifshitz point (TCLP) or for pressures around  $p_{L0}$ , the tricritical point (TCP) and the triple point (tp) are close to each other.

The group of similar compounds such as  $\text{Sn}_2\text{P}_2\text{S}_6$ ,  $\text{Sn}_2\text{P}_2\text{Se}_6$ ,  $\text{Pb}_2\text{P}_2\text{S}_6$  and  $\text{Pb}_2\text{P}_2\text{Se}_6$ , melt at 1048K (1051K); 943K (947K); 1187K (1198K); 1048K (1057K) respectively [4,1]. All  $\text{M}_2\text{P}_2\text{X}_6$  compounds crystallize in Fedorov group of  $P_{21/C}$  and form continuous series of solid solutions. For Pb-P-S system, the  $\text{Pb}_3\text{P}_2\text{S}_8$  compound of Fedorov group of  $P_{213}$  and cubic primitive cell with lattice constant  $a = 10.927 \text{ \AA}$  is formed in peritectic reaction at 928 K [1].

The equation describing the temperatures of FEPT in  $\text{Sn}_2\text{P}_2(\text{Se}_x\text{S}_{1-x})_6$ ,  $(\text{Pb}_y\text{Sn}_{1-y})_2\text{P}_2\text{S}_6$ ,  $(\text{Pb}_y\text{Sn}_{1-y})_2\text{P}_2\text{Se}_6$ ,  $(\text{Pb}_y\text{Sn}_{1-y})_2\text{P}_2(\text{Se}_x\text{S}_{1-x})_6$ , and

the equation of hypersurface of the Lifshitz points in  $(\text{Pb}, \text{Sn})_2\text{P}_2(\text{Se}, \text{S})_6$  are given in Ref. 5 and 7.

The dependence of FEPT temperature  $T_0(p)$  on hydrostatic pressure is described by the following equation [5]:

$$T_0(p) = A \left( 1 - \frac{p}{p_A} \right)^y \quad (1)$$

where;  $A = 336.1 \pm 0.5$ ,  $p_A = 1.25 \text{ GPa}$  and  $y = 0.82 \pm 0.06$ . This equation is analogous to the Simon's empirical equation for melting transition

$$T = \frac{(b + p)^c}{a} \quad (2)$$

where  $a$  and  $c$  are constants.

It is known that the pressure dependence of the temperature of  $T_i(p)$  of ICPT (incommensurate phase transition) fulfils the relation

$$T_i = T_0 + T_{tp} \left( \frac{p - p_{L0}}{p_{tp} - p_L} \right)^n \quad (3)$$

where  $T_{tp}$  - is the temperature of "low temperature" triple point,  $p_{tp}$  - pressure of "low temperature" triple point,  $p_{L0}$  - the pressure at which the line 1 of FEPT splits and  $n$  - exponent which, according to the theoretical prediction, in the vicinity of Lifshitz point ( $p_{L0}, T_{L0}$ ) should be equal to 2.

According to the obtained results, the above listed parameters for the transition labelled 2 are in the

following intervals:  $30 \text{ K} \leq T_{tp} \leq 600 \text{ K}$ ,  $1.35 \text{ GPa} \leq p_{tp} \leq 1.66 \text{ GPa}$  and  $1 \leq n \leq 2$ .

## 2 Experimental

The pressure dependence of melting temperature (Fig. 1 - line 4) has been determined by the use of high pressure Differential Thermal Analysis (DTA).

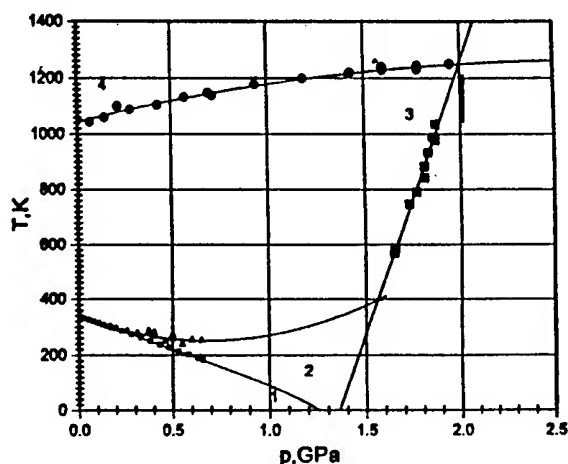


Fig. 1 p-T phase diagram of  $\text{Sn}_2\text{P}_2\text{S}_6$  1 - FEPT line  $T_0(p)$ , 2 - ICPT line  $T_i(p)$ , 3 - melting line  $T_m(p)$ , 4 - new phase transition line  $T_n(p)$ .

The example of DTA profile measured during thermal cycle is presented in Fig. 2.

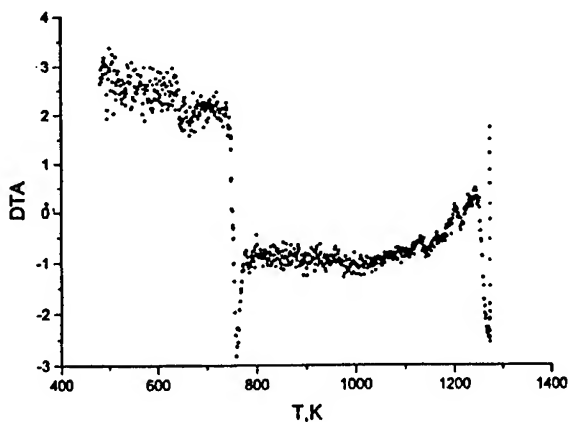


Fig. 2. DTA signal for  $\text{Sn}_2\text{P}_2\text{S}_6$  crystal at high hydrostatic pressures.  $T_n = 745 \text{ K}$ ,  $p_n = 1.7298 \text{ GPa}$ ;  $T_m = 1249 \text{ K}$ ,  $p_m = 1.9474 \text{ GPa}$ .

The heating part has two peaks. The first peak denotes solid-solid phase transition (line 3 in Fig. 1). The second peak is due to melting transition. More details about the high pressure DTA technique can be found in Ref. 8.

## 3 Results

The melting temperature of  $\text{Sn}_2\text{P}_2\text{S}_6$  increases with pressure. The dependence can be approximated by linear relation:

$$T_m = 1050 + 110 p \quad (4)$$

or more precisely by

$$T_m = 1044 + 167 p - 32 p^2 \quad (5)$$

Using phenomenological Lindemann theory of melting, C. L. Reynolds derived the equation describing the effect of pressure on the melting temperature  $T_m$  that includes the effects of anharmonicity [9]:

$$\frac{T_m - T_m(0)}{T_m(0)\beta p} = \frac{2\left(\gamma - \frac{1}{3}\right)}{(1 + C_2\beta p)} \quad (6)$$

where  $T_m(0)$  - melting temperature at zero pressure,  $\beta$  - the isothermal compressibility  $(1/V)(dV/dp)$ ,  $\gamma$  - Gruneisen constant at the melting point and  $C_2$  - the constant describing anharmonic properties of the solids, for alkaline halides  $C_2$  is approximately equal to 2.4.

The melting temperature  $T_m$  dependence on  $p$  for  $\text{Sn}_2\text{P}_2\text{S}_6$  (Eq. 5) can be transformed to

$$\frac{T_m - 1044}{1044 \beta p} = \frac{167}{1044 \beta} \left(1 - \frac{32 \beta p}{167 \beta}\right) \quad (7)$$

The comparison of the Eqs. (6) and (7) indicates that  $\gamma$ ,  $\beta$  and  $C_2$  are related as follows

$$\gamma = \frac{167}{2088 \beta} + \frac{1}{3} \quad (8a)$$

$$C_2 = -\frac{32}{167 \beta} \quad (8b)$$

Thus in order to obtain  $\gamma$ , it is necessary to determine the value of  $\beta$ . Let us assume that  $\beta$  is close to pressure coefficient of the energy bandgap which is equal [2] to  $-0.034 \text{ GPa}^{-1}$  at  $T = 363 \text{ K}$ . Using this assumption,  $\gamma$  and  $C_2$  have been calculated from (8 a and b) and are equal to 2.69 and  $-5.64$  respectively. The parameter  $\gamma$  for  $\text{Sn}_2\text{P}_2\text{S}_6$  agrees with  $\gamma$  for  $\text{NaBr}$  [9] and  $C_2$  for  $\text{Sn}_2\text{P}_2\text{S}_6$  is approximately twice larger than  $C_2$  for alkaline halides.

On the  $p$ - $T$  diagram of  $\text{Sn}_2\text{P}_2\text{S}_6$  at high pressures a new solid phase transitions line (labelled 3)  $T_n(p)$  has been found. The dependence of  $T_n$  temperature on pressure is described by the linear relation

$$T_n(p) = -2650 + 1952p \quad (9)$$

The point of intersection of the lines  $T_m(p)$  (5) and  $T_n(p)$  (9) on Fig. 1 gives "high temperature" triple point coordinates:  $p_{tp} = 2.0 \text{ GPa}$ ,  $T_{tp} = 1250 \text{ K}$ . For pressures higher than  $1.36 \text{ GPa}$  to the right of the line 3 it is supposed the existence of a "new" previously unknown solid phase in  $\text{Sn}_2\text{P}_2\text{S}_6$ .

For pure  $\text{Sn}_2\text{P}_2\text{S}_6$ , at atmospheric pressure, apart from the melting temperature DTA peak of  $T_m(p) = 1048 \text{ K}$  Carpentier and Nitsche [4] observed a small but significant reversible endothermic reaction at  $903 \text{ K}$ . For mixed compounds  $\text{Sn}_2\text{P}_2\text{S}_6 - \text{Sn}_2\text{P}_2\text{Se}_6$  this small DTA peak can be observed up to about 60 at %Se. We measured the dependence of this temperature  $T_{um}$  on pressure, up to  $0.6 \text{ GPa}$ . The  $T_{um}$  temperature increases linearly with pressure:

$$T_{um} = 901 + 112p \quad (10)$$

The relation (10) agrees well with previously reported  $T_{um} = 903 \text{ K}$  for  $p = 0$ . From relation (5) and (10) the coordinates of the point of intersection of lines 3 and 4 are:  $p = 3.132 \text{ GPa}$ ,  $T = 1252.4 \text{ K}$ .

Phase diagram of  $\text{Sn}_2\text{P}_2\text{Se}_6$  (Fig. 3) is similar to phase diagram of  $\text{Sn}_2\text{P}_2\text{S}_6$ . The melting temperature of  $\text{Sn}_2\text{P}_2\text{Se}_6$  is quadratic function of pressure:

$$T_m(p) = 945 + 80p - 17p^2 \quad (11)$$

The temperature of solid-solid phase transition is given by the relation

$$T_n(p) = -2744 + 1989p \quad (12)$$

The triple point coordinates are:  $T = 1037 \text{ K}$  and  $p = 1.9 \text{ GPa}$ .

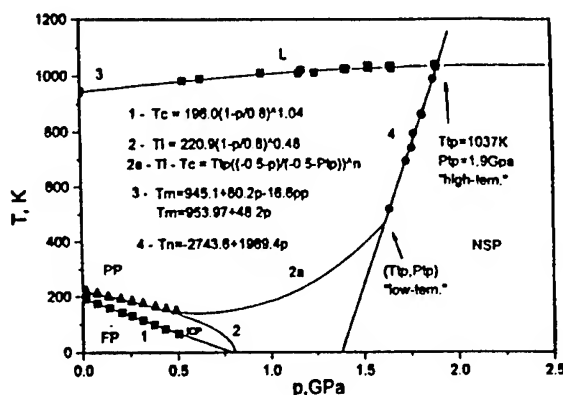


Fig. 3.  $p$ - $T$  phase diagram of  $\text{Sn}_2\text{P}_2\text{Se}_6$  crystal.

## References

- 1 Yu. Il. Tyagur, Yu. Yu. Firtsak and L. V. Lada, *Informal abstract review on materials on  $A_2^{IV}B_2^{VI}C_6^{VI}$* , (Ukraine Patent, Uzhorod, 1992).
- 2 Yu. Il. Tyagur, PhD Thesis, Uzhorod State University, Ukraine 1985
- 3 Yu. Il. Tyagur and E. I. Gerzanicn, *Kristallografiya* 29, 957 (1984) in Russian
- 4 C. D. Carpentier and R. Nitsche, *Mat. Res. Bull.* 9, 401 (1974)
- 5 Yu. Il. Tyagur, *Izvestiya Ruskoi Akademii Nauk, Seriya Fizicheskaya* 3, 171 (1993) in Russian
- 6 Yu. M. Vysochanskij and V. Yu. Slivka, *Uspehy Fiz. Nauk* 162, 139 (1992) in Russian
- 7 Yu. Il. Tyagur, *Kristallografiya* 40, 322 (1995) in Russian
- 8 S. Porowski et al., 1994 *American Institute of Physics* p. 485
- 9 C. L. Reynolds et al, *Phys. stat. sol. (a)* 42, K151 (1977)

# STRUCTURAL ORIGIN OF TRICRITICAL POINT IN KDP-TYPE FERROELECTRICS

ANDRZEJ KATRUSIAK

*Department of Crystallography, Adam Mickiewicz University  
Grunwaldzka 6, 60-780 Poznań, Poland*

## Abstract

First order contribution to the phase transitions in KDP-type ferroelectrics (KDP stands for  $\text{KH}_2\text{PO}_4$ ) is attributed to molecular or ionic displacements, induced into the structures by hydrogen bonds. These displacements are reduced or eliminated at elevated pressures. The tricritical point ( $P^*$ ,  $T^*$ ), at which the first-order contribution disappears, can be assessed from structural data.

## Introduction

At atmospheric pressure the phase transitions in ferroelectric crystals are continuous with some contribution of the first-order character. The first-order contribution is reduced at higher pressures, and above a tricritical point ( $P^*$ ,  $T^*$ ) the phase transitions become purely continuous [1–3]. Several experimental studies of the character of the phase transitions were carried out for the  $\text{KH}_2\text{PO}_4$  (KDP) crystals [4–9], the latest results indicate that the tricritical point in this prototypic substance occurs at 0.28 GPa and 108.6 K. Although described phenomenologically and measured experimentally, no theory relating the critical point with structural transformations has been presented. In this report the occurrence of tricritical point is explained by the pressure-induced changes in the molecular/ionic arrangement in the crystal structure.

## Discussion

In the atomic scale the phase transitions in KDP-type ferroelectrics have a mixed order-disorder and displacive character [10]. The order-disorder structural transformations are associated with the disordering of protons in the  $-\text{OH}-\text{O}'=$  hydrogen bonds at  $T_c$  [11]. Most recently the structural displacements in the KDP-type ferroelectrics

have been associated with the tilts of molecules or ions [12, 13]. These molecular tilts result from the different electronic structure of the oxygen atoms involved in the hydrogen bond: the proton-donor oxygen is close to the  $sp^3$  hybridization, and the acceptor oxygen is close to the  $sp^2$  hybridization. Consequently, the  $\text{R}-\text{O}\cdots\text{O}'$  angle is smaller than angle  $\text{O}\cdots\text{O}'=\text{R}'$  [14] ( $R$  and  $R'$  denote atoms to which O and  $\text{O}'$  are chemically bonded, respectively). In Figure 1 angle  $\text{R}-\text{O}\cdots\text{O}'$  is denoted as  $\eta'_d$  and angle  $\text{O}\cdots\text{O}'=\text{R}'$  as  $\eta'_a$ . To accommodate the difference between  $\eta'_d$  and  $\eta'_a$  the molecules are tilted with respect to their neighbours. When such a structure is heated above  $T_c$ , the protons become disordered and the two hydrogen-bonded groups symmetry-related. Thus, the two  $\eta'$  angles become equal. In this way tilts of the molecules or ions disappear in the paraelectric structure. The angular displacements of the molecules result in a compression of the  $\text{O}\cdots\text{O}'$  distance and cause a volume change, which can be associated with the first-order contribution to the phase transition [12, 15]. On the other hand, the tilts of the molecules can be removed by increasing the pressure. At high pressures the intermolecular voids are squeezed and the molecules or ions adjust their orientations to their symmetrical surrounding in crystal lattice. In result the  $\eta'$

angles become equal in such more densely packed structures, while the protons may still remain ordered (Figure 1). When such a structure is then heated above  $T_c(P)$ , the disordering of protons will not be coupled with molecular tilts and will cause no changes in the O...O distance. Thus, no anomalous volume change will occur and the phase transitions will have a purely continuous character. The relation combining the sequence of structural changes with the occurrence of the tricritical point can be straightforwardly applied for calculating the magnitudes of the tricritical-point pressure from structural data. The pressure of the tricritical point, at which the phase transition becomes a continuous one, can be assessed by comparing the contraction of the O...O distance, induced by disordering of the protons at atmospheric pressure [12], with the compressibility of the hydrogen bond [16].

## References

1. L. D. Landau and E. M. Lifshitz, *Statisticheskaya Fizika*, (Izdatelstvo Nauka, Moscow 1976).
2. J. Klamut, K. Durczewski and J. Sznajd, *Wstęp do fizyki przejść fazowych* (Ossolineum, 1979).
3. K. Gesi, *Phase Transitions* 40 (1992) 187.
4. J. Kobayashi, Y. Uesu, I. Mizutani and Y. Enomoto, *Phys. Stat. Sol. (a)* 3 (1970) 63.
5. V. H. Schmidt, A. B. Western and A. G. Baker, *Phys. Rev. Lett.* 37 (1976) 839.
6. A. B. Western, A. G. Baker, C. R. Bacon and V. H. Schmidt, *Phys. Rev. B* 17 (1978) 4461.
7. P. Bastie, M. Vallade, C. Vettur, C. M. E. Zeyen and H. Meister, *J. Physique* 42 (1981) 445.
8. A. N. Zisman, Y. N. Kachinski and S. M. Stishov, *J.E.T.P. Lett.* 31 (1980) 172.
9. F. Troussaut & M. Vallade, *J. Physique* 46 (1985) 1173.
10. R. A. Cowley, *Advances in Physics*, 29 (1980) 1.
11. J. C. Slater, *J. Chem. Phys.* 9 (1941) 16.
12. A. Katrusiak, *Phys. Rev. B* 48 (1993) 2992.
13. A. Katrusiak, *Phys. Rev. B* 51 (1995) 589.
14. A. Katrusiak, *J. Mol. Struct.* 269 (1992) 329.
15. A. Katrusiak, *Crystallogr. Rev.* — in press.
16. A. Katrusiak, *Solid. State Commun.* — submitted.



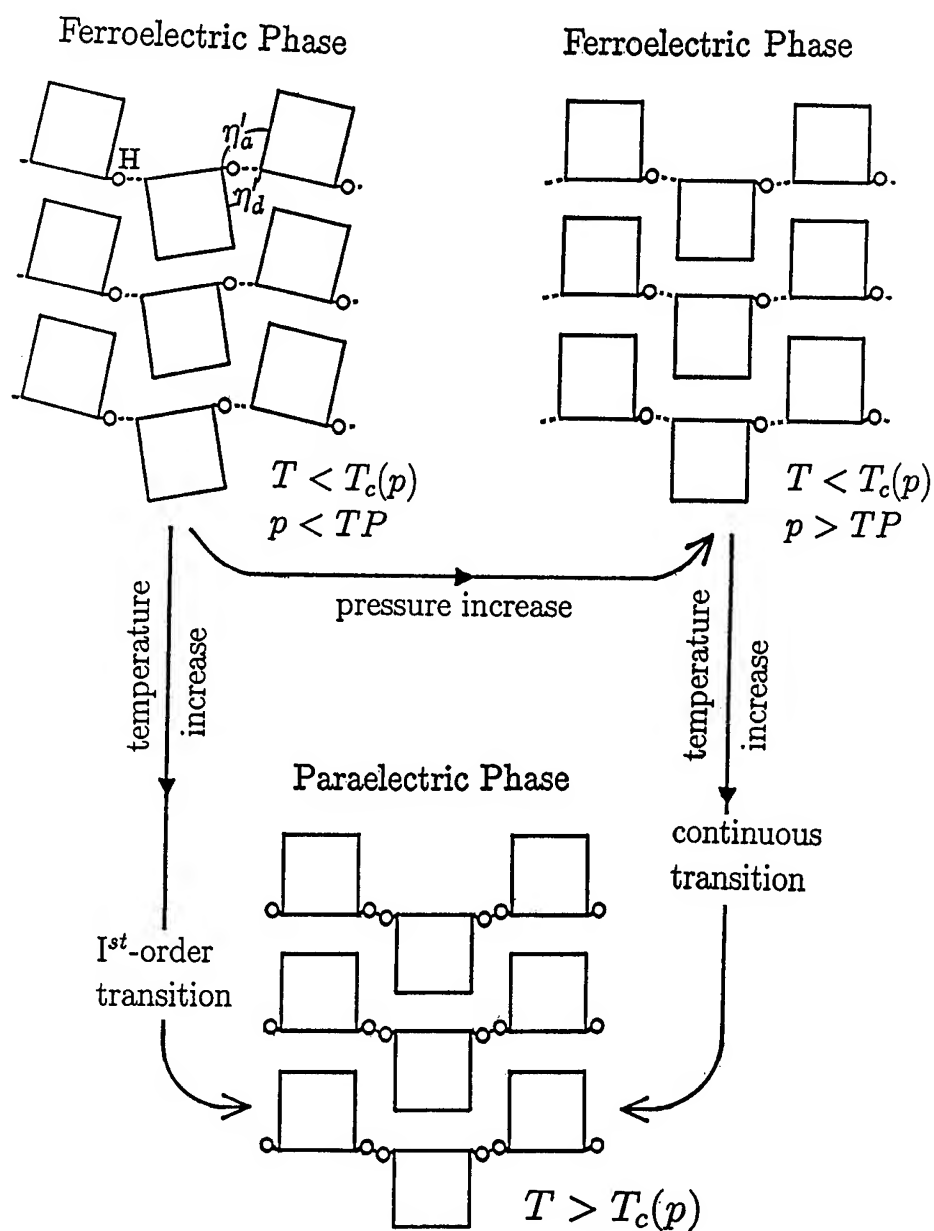


Fig. 1. Schematic representation of the KDP-type ferroelectric structure at various thermodynamic conditions. A rigid-box model is applied, the molecules are shown as square boxes, hydrogen atoms as small circles, and the hydrogen bonds as dashed lines. Arrows indicate changes in temperature or pressure (see the text).

# X-RAY DIFFRACTION AND DIELECTRIC CONSTANT MEASUREMENT OF $\text{KH}_2\text{PO}_4$ UNDER HIGH PRESSURE.

Y. KOBAYASHI,<sup>1</sup> S. ENDO,<sup>1</sup> K. KOTO,<sup>2</sup> and K. DEGUCHI<sup>3</sup>

<sup>1</sup>Research Center for Extreme Materials, Osaka University, 1-3 Machikaneyama-cho, Toyonaka, Osaka 560, Japan

<sup>2</sup>Faculty of Integrated Arts and Sciences, Tokushima University, Tokushima 770, Japan

<sup>3</sup>Shizuoka Institute of Science and Technology, Fukuroi, Shizuoka 437, Japan

## ABSTRACT

X-ray diffraction and dielectric constant measurements were carried out for a hydrogen-bonded ferroelectrics  $\text{KH}_2\text{PO}_4$  under high pressure. In addition to the confirmation of phase V previously proposed by Rapoport, a new high pressure phase VI was observed to exist above 7.5 GPa at room temperature, and the P-T phase diagram, in which the triple point of phases IV, V and VI exists at 7.5 GPa and 140°C, was determined. Phase V quenched to room temperature became amorphous at 30 GPa. Anomalies in dielectric constant were observed at the IV-VI and IV-V phase transitions.

## Introduction

Potassium dihydrogen phosphate,  $\text{KH}_2\text{PO}_4$  (abbreviated as KDP) is the most typical hydrogen-bonded ferroelectrics, and many studies have been accumulated to clarify the mechanism of paraelectric-ferroelectric transition at  $T_C=123\text{K}$  at ambient pressure. Rapoport<sup>1</sup> proposed the appearances of two high pressure phases named IV and V by a differential thermal analysis, and determined the P-T diagram up to 4 GPa and 450°C. Recently we have confirmed phase V, and observed a new phase VI by *in situ* x-ray diffraction at higher pressure. In this paper we report the stable P-T regions of these two high pressure phases,

On the other hand, Bao et al.<sup>2</sup> carried out the capacitance measurements of KDP using a diamond anvil cell at room temperature and reported the anomalies at 2.5 and 7.0 GPa. We have also performed the dielectric constant measurements to clarify the nature of the three phase transitions, II-IV, IV-VI and IV-V.

## Experimental

Two types of high pressure apparatus were used in the present study: a diamond anvil cell (DAC) and a "6-8 type" double-stage multianvil. Both of them were used for x-ray diffraction and the multianvil only was used for the dielectric

constant measurements. The details of x-ray diffraction is described in Ref.<sup>3</sup>

Dielectric constant measurements were made with a YHP-4194A impedance analyser operated at 0.4k - 1MHz. Single crystal disks, the axes of which are parallel to the a- and c- axis of the tetragonal lattice were prepared. They were set in the hole of a boron-epoxy octahedral cell and compressed under a quasihydrostatic condition. Copper foil electrodes were introduced to contact the gold-plated upper and lower surfaces of the disk.

## Results and discussion

### 1. X-ray diffraction

X-ray diffraction experiments were carried out along various routes in the P-T diagram. In a heating process at 2 GPa, the diffraction pattern of phase II, which is stable at ambient conditions, existed up to 250°C and then its peaks began to disappear. A remarkable change was not observed when it entered into the region of phase IV proposed by Rapoport.<sup>1</sup> However, Endo et al.<sup>4</sup> made a single crystal x-ray analysis of KDP under pressure and detected a characteristic change such as a drastic elongation of the length of the hydrogen bond, O-H...O, connecting  $\text{PO}_4$  tetrahedra at 2.7 GPa. Since the II-IV boundary proposed by Rapoport is extrapolated so as to pass through the point around 2.7 GPa

at room temperature, the previous result is understood in correlation with the II-IV phase transition. No crystal symmetry change at 2.7 GPa observed by the single crystal x-ray analysis does not contradict with no appreciable change in the powder x-ray pattern.

Once the diffraction peaks of phase II disappeared in the region of phase I, other peaks never appeared to the highest temperature 550°C in the run. There was no apparent distinction between the hallow pattern of phase I and that of liquid at high pressure and temperature. But, a clear difference was seen between the patterns of the samples recovered to ambient conditions; the diffraction lines of phase II was again seen for the sample recovered from phase I, while no line from liquid. The present study indicates the possibility that phase I is amorphous.

As to phase V named by Rapoport, we have confirmed it by x-ray diffraction in a heating process at 5 GPa. The interplaner  $d$  values determined from the x-ray patterns at 5 GPa are plotted as a function of temperature in Fig. 1(a). At 250°C phase IV transformed to phase V completely, and the main peak corresponding to that of phase IV, seems to remain still, which indicates that the same atomic plane is conserved in phase V. Phase V was retained by cooling to room temperature, but was converted to phase II when decompressed to ambient pressure.

The  $d$  values obtained in a compression proc-

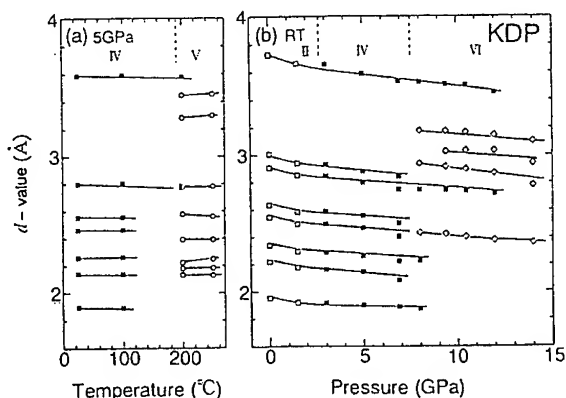


Fig.1.(a)The  $d$  values of the x-ray diffraction lines of phase IV(■) and V(O) plotted as a function of temperature at 5 GPa. (b)The  $d$  values of phases II(□), IV(■), and VI(O) as a function of pressure at room temperature.

ess at room temperature are plotted as a function of pressure in Fig. 1(b), which indicates that a new high pressure phase VI appeared at 7.5 GPa. This phase was converted to phase II when decompressed to ambient pressure, too.

In order to clarify the mutual relations of phases IV, V and VI in the  $P$ - $T$  diagram, a heating experiment was carried out at 10 GPa. Phase VI formed at room temperature grew up with increasing temperature, but at 203°C began to transform to phase V, indicating that phase V is stable at higher temperature.

All the results by *in situ* X-ray diffraction experiments are summarized in Fig. 2, where the identified phases are marked by different symbols. The following conclusions are obtained; (i) the triple point of phases IV, V and VI locates at about 7.5 GPa and 140°C, (ii) phase V is the high temperature phase of phases IV and VI, and (iii) the stable region of phase I and the melting curves of phases I and V, both of which proposed by Rapoport,<sup>1)</sup> are in almost agreement with the present results. Finally, we refer to the remarkable fact that amorphous

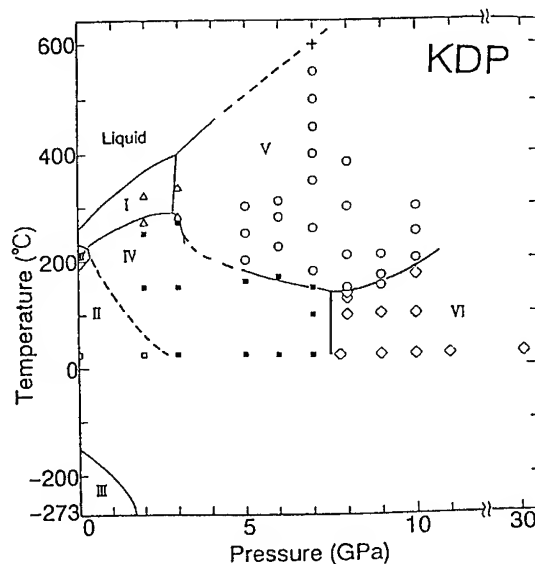


Fig.2. The  $P$ - $T$  phase diagram of KDP determined by the present x-ray diffraction study (thick line) combined with that of Rapoport<sup>1)</sup> (thin line). The phase boundary between phases II and IV is tentatively drawn based on the previous studies.<sup>2,4</sup> The cross (+) represents the melting point.

state was realized in KDP by compressing phase V metastably up to about 30 GPa in the stable region of phase VI.

We are now trying to determine the crystal structures of high pressure phases V and VI.

## 2. Dielectric constants

First, the dielectric constants were measured with increasing pressure at room temperature. The results along the a-axis are shown in Fig. 3. Anomalies were clearly observed at about 7 GPa; the dielectric constants began to decrease abruptly, which is certainly associated with the IV-VI transition clarified by the x-ray diffraction. Bao et al.<sup>2</sup> also detected the sudden increase in the slope of the capacitance-pressure curve at 7.0 GPa in their experiments using a powdered KDP sample. As to the anomaly expected for the II-IV transition, the relatively gradual changes of the slopes were seen at around 3 GPa for the curves in Fig. 3, although Bao et al. observed a broad peak at about 2.5 GPa.

The measurements were made for the c-axis, too. But, the obtained results depended strongly on the frequency and gave no definite tendency indicating the IV-VI transition at 7 GPa. An anomaly suggesting the II-IV transition was not observed, too.

We measured the dielectric constants of phase

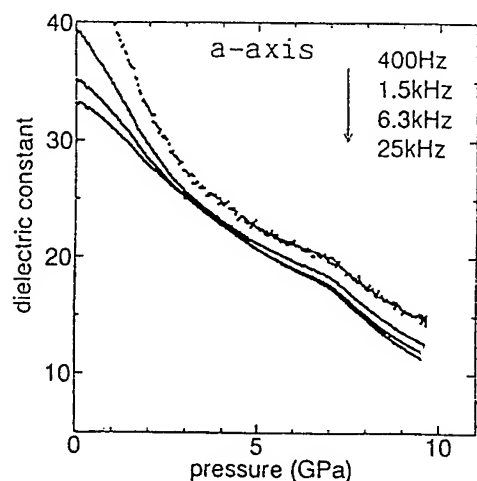


Fig. 3. The pressure dependence of the dielectric constants of phase II, IV and VI measured along the a-axis of original phase II.

V formed by heating and quenched to room temperature at 5 GPa. As to the a-axis, the dielectric constant of phase V was smaller than that of phase IV before heating, but, as to the c-axis the larger constant was obtained as shown in Fig. 4. On the further compression of phase V at room temperature no anomaly was obtained, which is in agreement with the result by X-ray diffraction, that is, phase V quenched to room temperature does not transform to phase VI at 7 GPa.

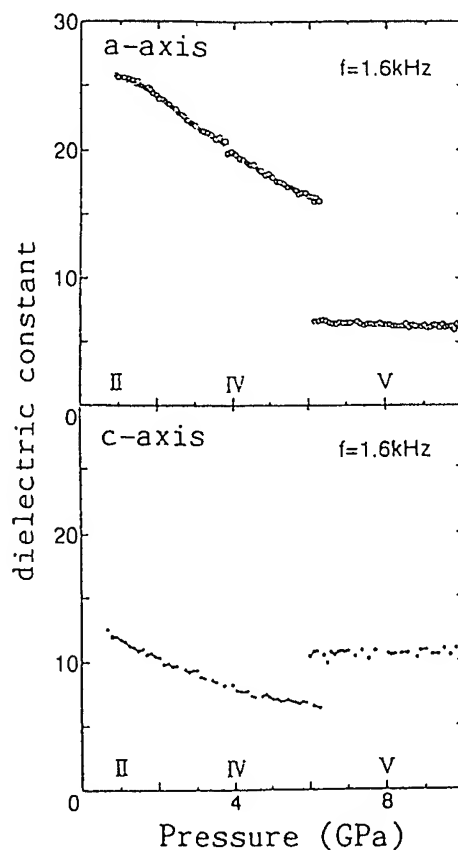


Fig. 4. The dielectric constants of phases II, IV and those of phase V after heating along the a- and c- axis of the original phase II.

## References

- 1) E. Rapoport, J. Chem. Phys. 53, 311 (1970).
- 2) Z. X. Bao et al., J. Appl. Phys. 70, 6840 (1991).
- 3) Y. Kobayashi et al., Phys. Rev. B 51, 9302 (1995).
- 4) S. Endo et al., Nature (London) 340, 452 (1989).

# RAMAN SPECTROSCOPIC STUDY OF GIANT MODE-COUPPLING AND PHASE TRANSITIONS IN $\text{KNbO}_3$ UNDER HIGH PRESSURE

Z X. Shen<sup>1</sup>, Z P. Hu<sup>1</sup>, T C. Chong<sup>2</sup>, C Y. Beh<sup>2</sup>, S H. Tang<sup>1</sup> and M H. Kuok<sup>1</sup>

<sup>1</sup> *Department of Physics, National University of Singapore,  
Lower Kent Ridge Road, Singapore 0511.*

<sup>2</sup> *Department of Electrical Engineering, National University  
of Singapore, 10 Kent Ridge Crescent, Singapore 0511.*

## ABSTRACT

$\text{KNbO}_3$  has been studied by Raman scattering up to 200 kbar, and the effect of pressure is extremely large. Mode softening occurs for many characteristic Raman bands. Intensity transfer and frequency repelling have been observed in the  $200\text{ cm}^{-1}$  region as a result of strong coupling between two  $B_1(\text{TO})$  modes, whose frequencies have been brought closer under pressure. Three new crystalline phases and an amorphous phase were observed, and two of the phase transitions are thought to be displacive type. The samples do not transform back to the ambient pressure phase on decompression.

## Introduction

The barium titanate family ferroelectrics have outstanding electro-optical, nonlinear optical, photorefractive properties, and have found widespread applications in nonlinear optics and electro-optics. They are also the prototype perovskite ferroelectrics and their successive phase transformations provide the typical examples for the study of paraelectric (PE)-ferroelectric (FE) transitions [1,2]. It is therefore not surprising that they have been among the most intensively studied materials. The properties of potassium niobate are similar to that of barium titanate and has been studied by many techniques. Much work on  $\text{KNbO}_3$  have been done to study the mechanisms of these transitions, as to whether they are displacive type characterized by a soft mode, or order-disorder type indicated by a central peak [3, 4]. While the softening of a transverse optical mode above each

transition favors a displacive model for the transitions, disorder-order type transitions for the C-T and T-O phase transitions have also been proposed.

## Experimental

The  $\text{KNbO}_3$  single crystal samples were grown from melt comprised of a mixture of  $\text{K}_2\text{CO}_3$  and  $\text{Nb}_2\text{O}_5$  using the top-seeded solution growth (TSSG) technique. The samples used in the high pressure experiments are small fragments about  $50\text{ }\mu\text{m}$  in thickness and  $100\text{ }\mu\text{m}$  in other dimensions. High pressure was generated with a gasketed diamond anvil cell with 4:1 methanol-ethanol mixture as the quasi-hydrostatic pressure medium. The pressure was calibrated using the ruby fluorescence technique. Raman spectra were recorded using a Spex double monochromator coupled to a photon counting system. The 488 nm line of an  $\text{Ar}^+$  laser was used as the excitation source. No special care was

taken to align the samples in any particular direction, so that the spectra recorded consist of bands of all allowed symmetries.

**Table 1. The ambient pressure Raman bands and assignments<sup>a</sup>**

Freq/cm <sup>-1</sup> [3]	Freq/cm <sup>-1</sup>	Assignment <sup>a</sup>
40(27×2) <sup>b</sup>	51	B <sub>2</sub> (TO)
192(2)		
193(2)	196	mixed
194.5(3)		
196.5		
249(25)		
270	266(s, br)	B <sub>1</sub> (TO)
281.5(33)	280(s, br)	A <sub>1</sub> (TO)
282(6)	283(sp)	A <sub>2</sub>
295(5)		
297(5)	298(sp)	A <sub>1</sub> (LO+TO)
434.5(10)	435(vw, br)	A <sub>1</sub> (LO)
513(20)		
534(20)	535(m, br)	B <sub>1</sub> (TO)
606.5(33)	597(s, br)	A <sub>1</sub> (TO)
834(27)	836(m, br)	A <sub>1</sub> (LO)

a: The assignments follows ref. 3.

b: The figure in parentheses is the FWHM.

## Results and Discussion

Under ambient conditions, KNbO<sub>3</sub> belongs to space group  $C_{2v}^{14}$  (Amm2), Z=1. Point group analysis predicts 12 optical modes (4A<sub>1</sub>+4B<sub>1</sub>+3B<sub>2</sub>+A<sub>2</sub>) and all are Raman active. All the expected Raman modes have been observed by polarized Raman spectra including the bands due to TO-LO splitting [3]. Fewer bands were observed in our high pressure experiment due to overlapping and mixing of modes with different symmetries. Table 1 lists the observed Raman bands together with the polarized Raman results of ref. 3. Figure 1 shows representative spectra at various

pressure. There is a strong continuous background and it interferes with the very sharp band at 196 cm<sup>-1</sup> and makes the latter very asymmetrical. The effect of pressure is extremely large and there exists a rich variety of pressure-induced changes [5].

(1) Intensity transfer and frequency repelling have been observed between a very sharp B<sub>1</sub> band at 196 cm<sup>-1</sup> and a very broad B<sub>1</sub> band at 265 cm<sup>-1</sup>, as a result of strong coupling between two modes of the same symmetry. The frequency of the sharp band increases with pressure while the high frequency broad band softens drastically with pressure. Hence the two bands are brought closer under compression. At about 50 kbar, where the cross-over of the bands occurs and the interaction is the strongest, the two bands completely lose their original characteristics and the two bands look very similar (Fig. 1). The bands gradually resume their respective shapes at higher pressures when they move away from each other after the crossing.

(2) More than half of all the Raman bands show typical soft mode behaviour, including the strongest Raman bands in the 260 and 600 cm<sup>-1</sup> regions. Under compression, the frequency of the 50 cm<sup>-1</sup>-band decreases and the band disappears into the increasing background at about 20 kbar. The 280 cm<sup>-1</sup>-band diminishes drastically with pressure whereas the shoulder band at 266 cm<sup>-1</sup> gains strength while its frequency softens. As a result the 266 cm<sup>-1</sup>-band is almost symmetrical at 13 kbar. The broad band at 435 cm<sup>-1</sup> is barely seen below 80 kbar, but above which pressure its intensity increases steadily.

(3) On decompression, the samples do not go back to the ambient phase, instead it stays at the phase stable above 20 kbar.

(4) The pressure dependence of the Raman bands is plotted in Fig. 2. Based on our results, we propose the following phase transitions: (i) a displacive type phase transition (to phase HPI) at 20 kbar characterized by the low frequency soft mode. (ii) another phase transition (HPI/HPII) at 60 kbar indicated by the new broad band at  $150\text{ cm}^{-1}$ , whose frequency is nearly independent of pressure. (iii) a displacive phase transition at 90 kbar induced by the soft mode at  $266\text{ cm}^{-1}$ . The symmetry of this phase (HPIII) should be higher than the other phases since it has fewer Raman bands. (iv) the phase above 150 kbar may be amorphous (AM) as all the bands are broad.

(5) In the case of  $\text{PbTiO}_3$  and  $\text{BaTiO}_3$ , the FE-PE transition has been found at 100 and 19 kbar respectively, where the cubic PE phases do not have Raman active modes [6,7]. However the PE phase can not be obtained solely by compression at room temperature for  $\text{KNbO}_3$ . This difference is explained by the different behavior of the lattice constants in the various phases for these materials [5].

1. W. Cochran, *Adv. Phys.* 9 387 (1960).
2. A. F. Devonshire, *Adv. Phys.* 3, 85 (1954)
3. M D Fontana, A Ridah, G E. Kugel and C Carabatos-Nedelec, *J. Phys. C: Solid State Phys.* 21, 5853 (1988).
4. T P Dougherty, G P Wiederrecht, K A Nelson, M H Garrett, H P Jensen and C Warde, *Science* 258, 770 (1992).
5. Z X. Shen, Z. P. Hu, T. C. Chong, C. Y. Beh, S. H. Tang and M. H. Kuok, *Phys. Rev. B* in press
6. J. A. Sanjurjo, E. Lopez and G. Burns, *Solid State Commun.* 48, 221 (1983).
7. A. Jayaraman, J. P. Remeika and R. S. Katiyar, *Materials Research Society Symposia Proceedings*, 22; High Pressure

in *Science and Technology*. Part I (North-Holland), 165 (1984).

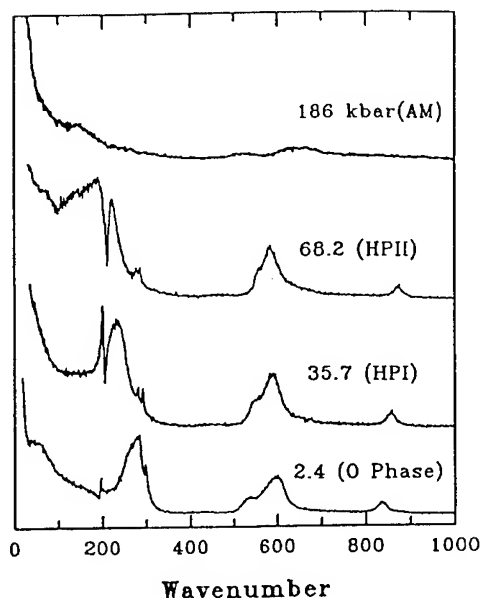


Fig. 1 Typical high pressure Raman spectra in different phase.

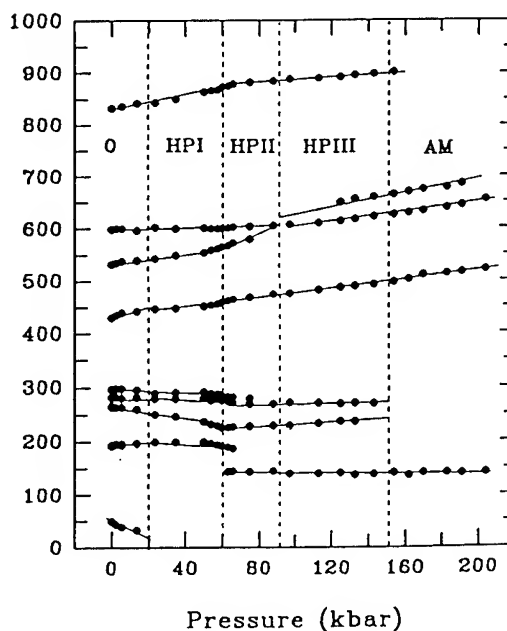


Fig. 2 Pressure dependence of the Raman bands. Dashed lines indicate phase transition pressures.

# EFFECT OF PRESSURE ON FERROELECTRIC TRANSITION IN $\text{Pb}(\text{Fe}_{1/2}\text{Nb}_{1/2})\text{O}_3$

SHEELA K. RAMASESHA<sup>1</sup>, M.V. RADHIKA RAO<sup>2</sup>,  
A.K. SINGH<sup>1</sup> and A.M. UMARJI<sup>2</sup>

<sup>1</sup>Materials Science Division, National Aerospace Laboratories,  
Bangalore 560017, INDIA

<sup>2</sup>Materials Research Centre, Indian Institute of Science,  
Bangalore 560012, INDIA

## ABSTRACT

The dielectric constant of lead iron niobate has been measured as a function of pressure up to 6 GPa and under isothermal conditions between room temperature and 348 K. The relaxor transition temperature measured with 1 kHz excitation varies at a rate -24.5 K/GPa.

## Introduction

Lead Iron Niobate (PFN) belongs to the Pb-based relaxor ferroelectrics having complex perovskite structure with a general formula  $\text{Pb}(\text{B}'\text{B}'')\text{O}_3$  where B' and B'' are different valent cations. PFN is attractive for the multilayer ceramic capacitor applications. At room temperature and pressure, PFN has a rhombohedral structure ( $a=4.014$  Å,  $\alpha = 89.92^\circ$ , space group  $R_{3m}$ ) and undergoes a diffuse phase transition at 385 K to cubic  $P_{m3m}$  structure (1). PFN is different from the other relaxors in that its  $T_c$ , the temperature at which the dielectric constant is maximum, is independent of the frequency of measurement.

Some high pressure studies are reported in the literature on such dielectric perovskites. The  $T_c$  in  $\text{BaTiO}_3$  decreased linearly with increase in pressure with a slope of -46.0 to -59.0 K/GPa (2). The induced (under applied field of 4.1 kV/cm) ferroelectric type transition temperature of  $\text{SrTiO}_3$  also shows a pressure dependence of -160 K/GPa (3). In PZN ( $\text{Pb}(\text{Zn}_{1/3}\text{Nb}_{2/3})\text{O}_3$ ), which is closely related to PFN, the  $T_c$  was found to decrease at a rate of 55.0 K/GPa with increasing pressure up to 2.5 GPa (4). Variation of  $T_c$  of PFN with pressure was studied only up to 0.6 GPa in a hydrostatic medium and  $T_c$  was found to decrease at

a rate of 37.0 K/GPa (5). The decrease of ferroelectric  $T_c$  upon the application of pressure has been attributed to the tendency of the structure to become more symmetric under pressure (6). In this paper we report the effect of quasihydrostatic pressure up to 6 GPa on the capacitance and the ferroelectric transition temperature of PFN.

## Experimental

PFN was prepared by two step calcination method using high purity oxides, the details of which are published elsewhere (7). Briefly, the first calcination was carried out at 1273 K for 4 hours between  $\text{Fe}_2\text{O}_3$  and  $\text{Nb}_2\text{O}_5$  to produce intermediate phase  $\text{FeNbO}_4$ . This was calcined with 1% excess PbO at 1173 K for 1 hour in a closed crucible. After checking for phase purity, the powder was pelletized using 2% PVA binder solution, which was burnt off. The pellets were sintered at 1273 K for 1 hour in lead rich atmosphere. The quality of sample was checked by powder x-ray diffraction and dielectric measurements at room pressure.

A pair of tungsten carbide opposed anvils (12.5 mm dia. anvil face) was used in these high pressure experiments. The cell assembly consisted of two pyrophyllite gaskets (12.5 mm o.d., 5 mm i.d. and 0.42 mm thick) and a stack of three



talc epoxy disc. The two gaskets contained the flattened copper leads. 0.3 mm thick and 1.5x1.5 mm<sup>2</sup> face sample was set in a 0.3 mm thick metal gasket (5 mm i.d.) with talc and epoxy mixture. After allowing the epoxy to set, the talc epoxy disc with the sample was separated from the metal gasket and polished on both sides on a 600 grade emery paper down to 0.22 mm thick. The talc epoxy disc with the sample formed the central disc with one talc epoxy disc on top and the other (both 0.28 mm thick) below insulating the sample from the anvils. Aluminium foils cut exactly to the size of the sample were inserted between the copper leads and the sample. Bismuth was placed in the lower gasket along with two copper leads for in situ pressure calibration. The capacitance was measured at 1 kHz using a GR 1656 bridge. The temperature of the sample was varied with the help of a tubular furnace around the anvils. A chromel-alumel thermocouple placed next to sample was used to measure and control the temperature.

## Results and Discussion

The x-ray diffraction pattern showed 100% perovskite phase formation, which could be indexed based on a pseudocubic unit cell of 4.013 Å. The ambient pressure dielectric constant measurements showed broad ferroelectric transition with a  $T_c$  of 385 K which was frequency independent. The dielectric constant at  $T_c$  was 12800. A  $\tan\delta$  value of 0.044 showed the good quality of the sample.

The variation of the capacitance with pressure at ambient temperature is shown in fig. 1. Since unelectroded samples were used, the initial large change in capacitance is attributed to the process of formation of proper contact electrode. The ferroelectric to paraelectric phase transition is marked by a maximum in the capacitance around 3.2 GPa. Similar isothermic experiments were carried out at different temperatures and the variation of transition pressure with temperature is given in fig. 2. In this figure, the data point at zero pressure is from the capacitance measurements at ambient pressure. The experiment could be done only up to 348 K as the dielectric

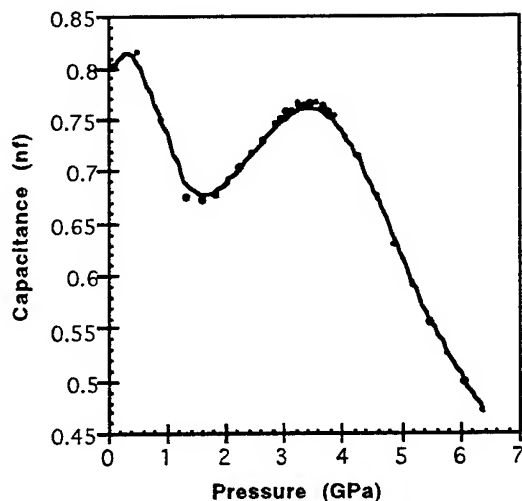


Figure 1. Variation of capacitance of PFN with pressure at room temperature.

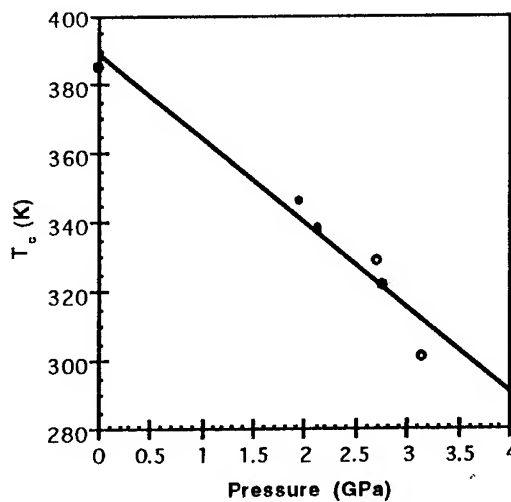


Figure 2. Plot of  $T_c$  vs pressure for PFN.

maximum due to transition started merging with initial peak at higher temperatures. The transition temperature decreases linearly with increase in pressure. A straight line fit indicates that the slope is -24.5 K/GPa and the intercept is 388 K. The value of pressure coefficient of  $T_c$  is lower

than the reported value of -37 K/GPa (5). This difference can either be due to the small pressure range investigated in the earlier studies or due to quasi hydrostatic nature of the pressure in this study.

## References

- 1 M. Yokosuka, *Jap. J. Appl. Phys.*, **32**, 1142 (1993)
- 2 G. A. Samara, *Phys. Rev.*, **151**, 378 (1966)
- 3 E. Hegenbarth and C. Frenzel, *Cryogenics*, **7**, 331 (1967)
- 4 J. Yoshimoto, B. Okai and S. Nomura, *J. Phys. Soc. Jap.*, **31**, 307 (1971)
- 5 N. Yasuda and Y Ueda, *Ferroelectrics*, **95**, 147 (1989)
- 6 G.A. Samara, *Advances in High Pressure Research*, ed. R.S. Bradley, Vol. 3, 1969, P 155.
- 7 M.V. Radhika Rao, A. Halliyal and A.M. Umarji, *J. Amer. Ceram. Soc.* (1995).

## **VI(E) Electronic Phase Transitions**

## THE METAL-INSULATOR TRANSITION IN THIOSPINEL $\text{CuIr}_2\text{S}_4$

TOMOKO KAGAYAMA, GENDO OOMI, IKUE YOSHIDA AND YASUHIRO SAKURAI

*Department of Physics, Faculty of General Education, Kumamoto University, 2-40-1 Kurokami,  
Kumamoto 860, Japan*

TAKATSUGU HAGINO AND SHOICHI NAGATA

*Department of Materials Science and Engineering, Muroran Institute of Technology, 27-1 Mizumoto-cho,  
Muroran, Hokkaido 050, Japan*

### ABSTRACT

Thermal expansion of  $\text{CuIr}_2\text{S}_4$  has been measured at high pressure in order to clarify the origin of metal-insulator phase transition. X-ray diffraction study at high pressure was also carried out at room temperature. It is found that the transition temperature  $T_{\text{M-I}}$  increases with pressure having the rate  $dT_{\text{M-I}}/dP = 2.7$  K/kbar and the discontinuity in volume at the transition is less than 1%.

The ternary spinel  $\text{CuIr}_2\text{S}_4$  has the cubic spinel structure at room temperature with lattice constant  $a=9.847$  Å and has the normal spinel structure where the Cu ion occupy the tetrahedral *A* site and the Ir ion occupy the octahedral *B* site. Recently it has been discovered for  $\text{CuIr}_2\text{S}_4$  to show a metal-insulator transition at  $T_{\text{M-I}} \sim 230$  K. The conductivity drops by three orders of magnitude on cooling through the transition[1]. According to the X-ray diffraction study, the transition is a first order structural phase transition from cubic to tetragonal with volume discontinuity of 0.7%[2].

In order to clarify the origins of the transition, we have made an attempt to study the physical properties of  $\text{CuIr}_2\text{S}_4$  under high pressure. We reported that the  $T_{\text{M-I}}$  increases rapidly with increasing pressure with a rate of 2.8 K/kbar by the electrical resistance measurement under hydrostatic pressure up to 20 kbar[3]. From this result, it is expected that the  $T_{\text{M-I}}$  becomes room temperature around 30 kbar.

In this paper we report the results of the thermal expansion measurement at high pressure to show accurately the volume discontinuity at the transition and the result of X-ray diffraction at high pressure to obtain the compressibility at room temperature.

The specimen was prepared by sintering in

pressed parallelepiped form at 850°C for 48 hours after regrinding the calcined mixture of Cu, Ir and S powder.

The thermal expansion was measured by strain gauge glued on the face of the sintered sample. The hydrostatic pressure was generated by using tungsten-carbide (WC) piston and copper-beryllium cylinder having 8 mm in diameter. Pressure transmitting medium was a 1:1 mixture of Fluorinert, FC70 and 77.

In the X-ray diffraction measurement the pressure was generated by means of a WC Bridgman-anvil having a face 3 mm $\phi$ . The powdered sample and NaCl as a standard were placed in a 0.3 mm $\phi$ -hole at the center of a beryllium disk gasket having 0.5 mm thickness. A 4:1 methanol/ethanol mixture was used as a pressure transmitting medium. The pressure was determined by using Decker's equation of state of NaCl [4]. A Guinier type focusing camera and highly sensitive film were used to get a good diffraction pattern at high pressure.

Figure 1 shows the relative change in length,  $(\Delta l/l)(T)$ , of  $\text{CuIr}_2\text{S}_4$  at ambient pressure. It is clearly observed a steep variation of  $(\Delta l/l)(T)$  on cooling and heating process around 223 K and 232 K, respectively, which corresponds to the  $T_{\text{M-I}}$  transition with a hysteresis of about 10 K. The

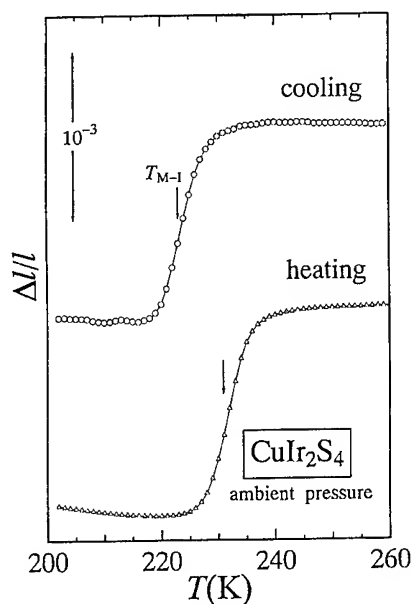


Fig. 1 The thermal expansion of  $\text{CuIr}_2\text{S}_4$  at ambient pressure.

magnitude of the length change at  $T_{M-I}$  is nearly 0.1%, which is smaller than the previous one obtained by X-ray diffraction study[2] since present work deals whole length change of the sintered specimen in which the packing is not complete.

To make clear the transition, the thermal expansion coefficient  $\alpha$  is obtained by differentiating  $(\Delta l/l)(T)$ . Figure 2 indicates the  $\alpha(T)$  on heating under high pressure. The  $\alpha$  has a peak corresponding to the abrupt change in the length in Fig. 1. The

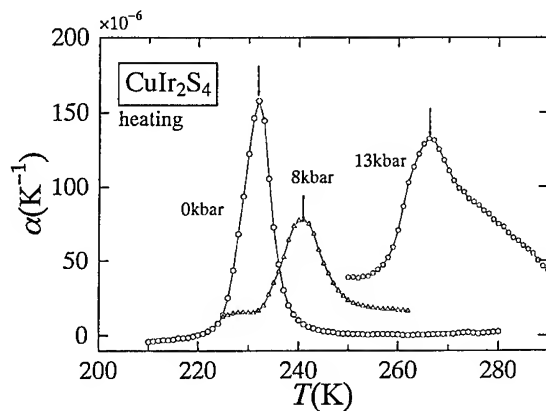


Fig. 2 The thermal expansion coefficient  $\alpha$  at various pressures on heating. The  $\alpha$ -maximum temperature is shown by an arrow.

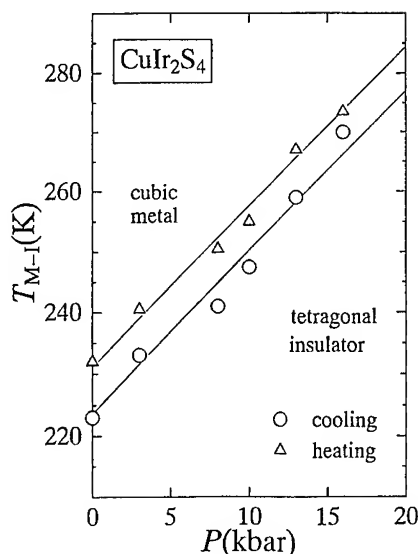


Fig. 3 The phase diagram of  $\text{CuIr}_2\text{S}_4$ .

peak shifts toward higher temperature as pressure increases. We determined the transition temperature  $T_{M-I}$  as a temperature at which the  $\alpha$  has a maximum as shown by arrows in Fig. 2.

Figure 3 shows the  $T_{M-I}$  both on heating and cooling as a function of pressure. The  $T_{M-I}$  is linearly increased by applying pressure having hysteresis of about 10 K between heating and cooling process. The value of the pressure coefficient  $dT_{M-I}/dP$  is 2.7 K/kbar, which is in good agreement with the previous one[3]. This value is also nearly the same as 3 K/kbar expected from the Clausius-Clapeyron relation, using published data,  $\Delta V/V = 5.0 \times 10^{-7} \text{ m}^3/\text{mol}$ [2] and  $\Delta S = 15.9 \text{ J/Kmol}$ [5].

Next we mention the results of X-ray diffraction study under high pressure at room temperature. Figure 4 shows the spacing of lattice planes,  $d(\text{\AA})$ , for the most intense reflection as a function of pressure. The  $d$ -values decrease with pressure smoothly up to 25 kbar. Above 25 kbar the X-ray diffraction pattern shows the change of crystal structure. Mixed phase is observed in the pressure range between 25 kbar and 30 kbar. The diffraction pattern at higher pressure than 30 kbar corresponds to that at low temperature tetragonal phase.

According to the previous work in the X-ray

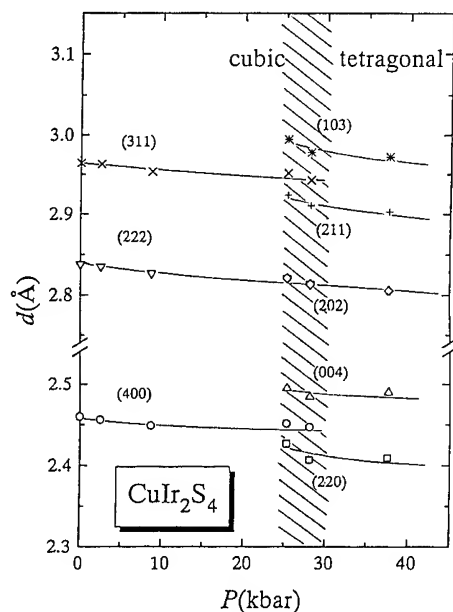


Fig. 4 The  $d$ -values for most intense reflection as a function of pressure.

diffraction at low temperature, the tetragonal structure is derived by expanding along [001] and shortening along [100] and [010] of the cubic unit cell of spinel[2]. The  $a$ -axes of the tetragonal structure are along [110] and  $[1\bar{1}0]$  and the  $c$ -axis is [001] of the cubic. In Fig. 3 the reflection (222) in the cubic structure corresponds to that of (202) in the tetragonal structure. It is expected that the unit cell volume changes discontinuously at structural phase transition, since the transition is the first order. Because the (222) line of cubic and the (202) line of the tetragonal structure are not observed separately in the transition region between 25 kbar and 30 kbar, the volume change at transition is considered to be small.

The lattice constants are illustrated in Fig. 5 as a function of pressure. The  $a$ -value of tetragonal structure is shown as  $\sqrt{2}a_t$ . The axial ratio  $c_t/\sqrt{2}a_t$  is about 1.03 which is almost the same with that of low temperature tetragonal phase. The cubic root of the modified volume of the tetragonal phase,  $(2V_t)^{1/3} = ((\sqrt{2}a_t)^2 c_t)^{1/3}$ , is shown in Fig. 5 to examine the volume discontinuity at transition, which is estimated to be between 0.5% and 1%.

The volume compression in the cubic phase is

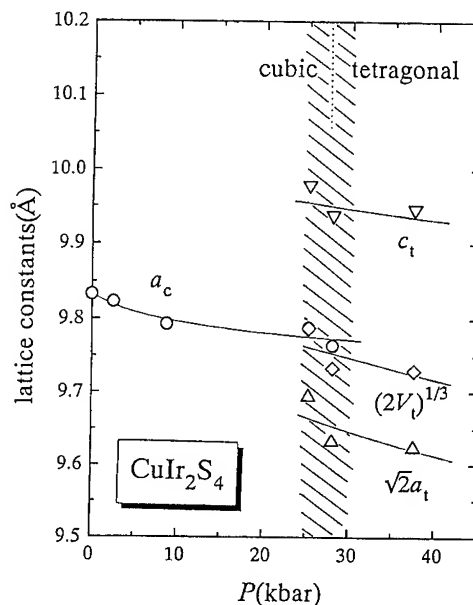


Fig. 5 Pressure dependence of the lattice constants.

$\sim 1.6\%$  at 20 kbar, which corresponds to the compressibility of  $\sim 0.8 \times 10^{-3} \text{ kbar}^{-1}$ . From this value and  $(1/T_{M-I})dT_{M-I}/dP = 0.012 \text{ kbar}^{-1}$ , the Grüneisen parameter of the  $T_{M-I}$ ,  $-\partial \ln T_{M-I} / \partial \ln V$ , is calculated to be about 16.

To conclude, we observed the pressure dependence of the metal-insulator transition temperature  $T_{M-I}$  up to 20 kbar by measuring thermal expansion. The result shows that  $T_{M-I}$  increases with pressure. The X-ray diffraction at high pressure confirmed the first order cubic-tetragonal transition near 25 kbar.

## References

1. S. Nagata, T. Hagino, T. Seki and T. Bitoh, *Physica B* **194-196** (1994) 1077.
2. T. Furubayashi, T. Matsumoto, T. Hagino and S. Nagata, *J. Phys. Soc. Jpn.* **63** (1994) 3333.
3. G. Oomi, T. Kagayama, I. Yoshida, T. Hagino and S. Nagata, *J. Magn. Magn. Mater.* **140-144** (1995) 157.
4. D. L. Decker, *J. Appl. Phys.* **42** (1971) 3239.
5. T. Hagino, T. Tojo, T. Atake and S. Nagata, *Philos. Mag. B* **71** (1995) 881.

# MAGNETORESISTANCE OF HIGH PRESSURE PHASES

V. V. Shchennikov

*Institute of Metals Physics Ural Branch of RAS 620219 Ekaterinburg GSP-170, Russia*

The transverse magnetoresistance of semiconductor materials  $\text{Hg}_{1-x}\text{Cd}_x\text{Se}$ ,  $\text{ZnSe}$ ,  $\text{ZnS}$ ,  $\text{GaP}$ ,  $\text{Se}$  was investigated at high pressures up to 25 GPa. Based on the obtained results the electron structure of high pressure phases is discussed.

An investigation of the high pressure phase electron structure of solids needs the data of some kinetic coefficients. Resistivity ( $R$ ) and thermoelectric power ( $S$ ) characterize a type and concentration of charge carriers. The magnetoresistance effect (MR) contains the information of the conduction mechanism and mobilities of charge carriers<sup>1</sup>, so the high pressure data of MR may be to complete  $R$  and  $S$  for suggesting the electron structure model. The aim of this paper is to investigate the MR of high pressure phases of different type semiconductors  $\text{Hg}_{1-x}\text{Cd}_x\text{Se}$ ,  $\text{ZnSe}$ ,  $\text{ZnS}$ ,  $\text{GaP}$ ,  $\text{Se}$ , at pressure-induced phase transitions<sup>2-9</sup>.

## 1 Experimental Procedure

The piston-cylinder chambers were used for the generation of hydrostatic pressures up to 2 GPa. For the generation of quasihydrostatic pressure up to 30 GPa we used the sintered diamond anvils, the values of  $P$  being measured by calibration graphs<sup>6</sup>. Diameters of the working areas of the diamond anvils were 0.6 – 1.0 mm. Samples were placed in a container, made of lithographic stone, which acted as a pressure-transmitting medium.

The dimensions of samples in the chambers of the first and the second types were  $0.5 \times 0.5 \times 5$  and  $0.2 \times 0.2 \times 0.1$  mm, respectively. In hydrostatic pressure,  $R$  and MR were measured by the four-probe method. In diamond chambers the plungers played a role of current contacts and platinum-silver ribbons 5  $\mu\text{m}$  thick were the potential probes<sup>6</sup>. The transverse MR effect was investigated, the measurements of MR being performed using different polarities of the field and current<sup>7</sup>. The voltage developed across the potential contacts was compensated, amplified, and delivered to the input potentiometer with a X-Y plotter<sup>7</sup>. The pressure dependence of  $R$  and thermoelectric power  $S$  of the selenium samples were also investigated in

the same pressure region. In the other substances, the  $S$  data of high pressure phases have been investigated formerly<sup>8</sup>.

## 2 Results

The obtained dependences of MR on magnetic field in all the materials may be described by the following equation

$$\frac{\Delta\rho}{\rho} = D \frac{(\mu B)^2}{1 + (\mu B)^2}, \quad (1)$$

where  $B$  is the magnetic field,  $\mu$  the parameter characterized by the rate of resistivity change in magnetic field, coefficient  $D$  determines the sign and value of MR. We found as positive effect ( $D > 0$ ) and negative one ( $D < 0$ ). Eq. 1 accords with the theoretical dependences of the positive and negative magnetoresistance (NMR) in the most significant cases<sup>1,10</sup>.

### 2.1 $\text{Hg}_{1-x}\text{Cd}_x\text{Se}$ crystals.

Mercury selenide has undergone the pressure-induced phase transition from a semimetal phase to semiconductor one, the start of transition being at pressure  $P = 0.8$  GPa, and the finish – at pressure higher, than 1.2 GPa<sup>2</sup>. The temporal rising of  $R$  suggested, that the sample of  $\text{HgSe}$  consisted of both phases in the intermediate region of pressure, and the content of semiconductor phase increased<sup>2</sup>. We obtained a stable state of  $\text{HgSe}$  in the two-fold phase region and investigated its electrical properties. The same results were obtained for the  $\text{Hg}_{1-x}\text{Cd}_x\text{Se}$  alloys, the pressure of the transition start rose when the fraction of  $\text{Cd}$  increased<sup>6</sup>.

The  $R$  of samples in the new state rose by 3–4 orders in the comparison with the semimetal phase, but it conserved the positive sign of a

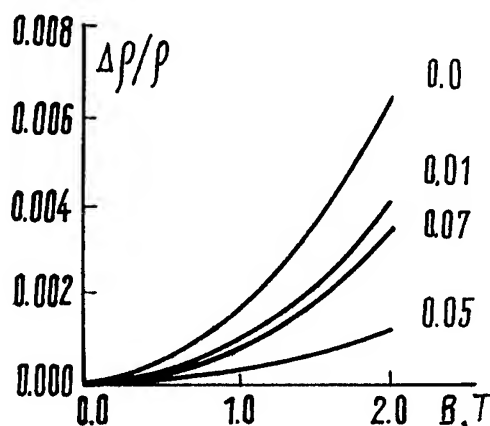


Figure 1: Magneto-resistance of  $\text{Hg}_{1-x}\text{Cd}_x\text{Se}$  crystals at metastable state in the vicinity of  $B_3 \rightarrow B_9$  phase transition at  $T=296$  K. The portion of Cd atoms is written near the curves. The values of resistivities of the metastable state and the initial semimetal phase were as follows:  $x = 0.0 - 0.18$  and  $0.00015 \Omega\text{-cm}$ ;  $x = 0.01 - 0.16$  and  $0.00063 \Omega\text{-cm}$ ;  $x = 0.05 - 0.99$  and  $0.00018 \Omega\text{-cm}$ ;  $x = 0.07 - 0.11$  and  $0.00029 \Omega\text{-cm}$ .

temperature coefficient. Magneto-resistance of new state was positive and had a parabolic dependence on  $B$  (fig.1). Using Eq. 1 for the MR of electron gas with the standart electron band in a weak magnetic field ( $D = 1$ ,  $\mu B \ll 1$ ), we had calculated the mobilities of electrons:  $\mu = 200\text{--}400 \text{ cm}^2/\text{Vc}$ . The values of mobilities were smaller for the samples with the higher values of  $R$  and, consequently, the extent of phase transformation.

The resistivity of semiconductor high pressure phase is about 3 order higher, than in two-fold phase state, and its temperature dependences has the activation nature<sup>2,6</sup>. In  $\text{HgSe}$  and  $\text{HgTe}$  it was found the reversal change of MR sign from positive to NMR at the phase transitions semimetal  $\leftrightarrow$  semiconductor<sup>7</sup>. So, it seems, that electrical properties of  $\text{Hg}_{1-x}\text{Cd}_x\text{Se}$  alloys in the new state are defined mainly by the inclusions of semimetal phases. In comparison with semimetal phase, the  $B$  dependences of  $R$  in new state are weaker because of decreasing of the electron mobilities.

## 2.2 GaP.

Semiconductor-metal phase transition occurred at  $P = 22 \text{ GPa}$ <sup>5</sup>, the resistivity drops about 6 orders. The magneto-resistance was found to be negative with the parabolic dependence on  $B$  (fig.2). The value of thermoelectric power  $S < 10 \mu\text{V/K}$ <sup>8</sup> indicated, that the concentration of conduction holes

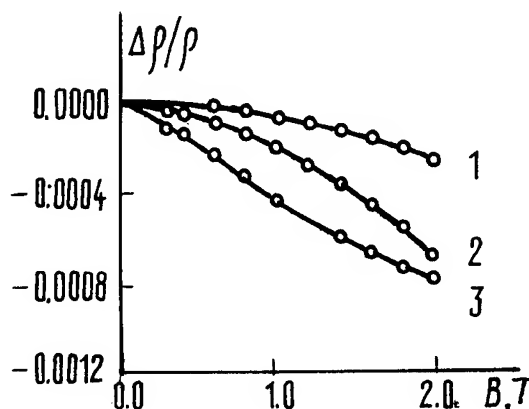


Figure 2: The magneto-resistance versus magnetic field dependence for the high pressure "metallic" phases of GaP at  $P = 22 \text{ GPa}$  (1), ZnS at  $P = 15.5 \text{ GPa}$  (2) and ZnSe at  $P = 15 \text{ GPa}$  (3) at  $T = 77 \text{ K}$ .

in the metal phase is high, and the hole gas is degenerated (chemical potential  $\eta \gg k_0 T$ <sup>1</sup>, where  $k_0$  is Boltzman constant). The classical positive MR must be small in this case because the factor  $D = (k_0 T / \eta)^2 \ll 1$ <sup>1</sup>, so the NMR prevailed. The dependence of NMR-effect on magnetic field and its rise with the lowering of the temperature suggest, that it may be due to the interference quantum additions to conductivity<sup>10</sup>. It's interesting to compare the MR of high pressure metal phases of GaP and mercury chalcogenides, having approximately the same values of  $S$ <sup>7,8</sup>. In  $\text{HgSe}$  the MR remained negative after the transition to the metal phase, and in  $\text{HgTe}$  near the phase transition at  $P = 12 \text{ GPa}$  NMR changed the sign for the appearance of mobile holes in the metal phase<sup>7</sup>.

## 2.3 ZnSe, ZnS.

The measurements of MR were performed just after the phase transition points, the resistance drop under the transition was about 7 orders of magnitude (fig.2). The effect MR was also negative, as in case of GaP. The same NMR effects were observed formerly in the high pressure "metallic" phases of Cd chalcogenides<sup>6</sup>. The values of  $S$  in the high pressure phases are rather significant:  $S = -0.1 \text{ mV/K}$ , as in the heavy doped electron semiconductors, not metals<sup>8</sup>. The theoretical calculations, indeed, gave the energy gap about 1 eV in electron structure of high pressure phase of ZnS<sup>11</sup>. The rising of NMR with lowering of  $T$ , and depen-



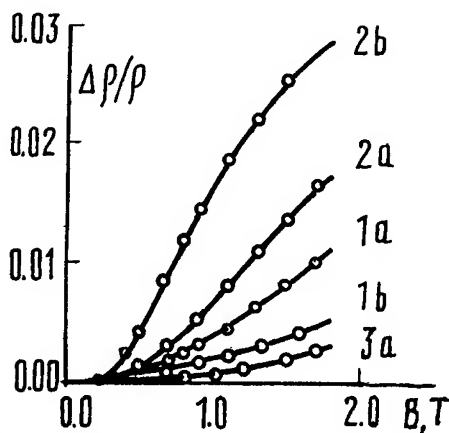


Figure 3: Magnetoresistance of Selenium at  $T = 296$  K (a) and  $T = 77$  K (b) at high pressures: 1 – 18.6 GPa, 2 – 23 GPa, 3 – 12 GPa.

dence on  $B$  are consistent with the suggestion, that NMR is caused by interference quantum addition to conductivity<sup>10</sup> or by the impurity levels splitting in magnetic field<sup>12</sup>. We observed the change of field dependence of NMR from pure parabolic type (curve 2) to slower form (curve 3) by changing the pressure.

#### 2.4 Se.

Selenium under high pressure  $P > 5$  GPa transforms to trigonal lattice, and at higher  $P = 10$ –14 GPa undergoing the phase transition to a new low resistance phase<sup>4,9</sup>. Our measurements of thermoelectric power of Se during this transition gave the drop of  $S$  to the value equal 0.03 mV/K (0.01 mV/K – when the rate of pressure change was high).

The NMR effect was observed in amorphous Se under pressure below 7 GPa. Increase of  $P$  makes the transition from NMR to positive MR, the last rising with the pressure (fig.3).

The dependence of MR on  $B$  was satisfactorily described by Eq. 1. Using the model of semiconductor with standart hole band, we have estimated the value of hole mobilities at pressures up to 25 GPa. The mobilities were so high, that at  $B > 1$  T the behaviour of MR showed the deviation from the pure parabolic low, which is correct in a weak magnetic field conditions ( $\mu B < 1$ )<sup>1</sup>. Our estimates of  $\mu$  from MR data gave the values approximately equal to 2000 cm<sup>2</sup>/Vc, which are much greater, than the hole mobility in semiconductor trigonal phase  $\mu = 50$  cm<sup>2</sup>/Vc<sup>13</sup>.

Reviewing the main peculiarities of MR in high pressure phase of Se one can see some similarities with MR behaviour of trigonal Se, for example, identical temperature and magnetic field dependences in both phases<sup>13</sup>. The main difference of high pressure phase consists in the independence of its properties  $R(T)$ ,  $S$  on pressure. It allows to suggest, that there is a small energy gap in high pressure phase electron structure, caused by instabilities of p-bonded systems due to lattice distortions<sup>14</sup>. Authors of<sup>9</sup> supposed, based on X-ray data, that high pressure phase of Se had the distorted lattice of trigonal Se. This opinion gave support to our suggestion.

#### References

1. K. Seeger, *Semiconductor Physics*, (Springer Verlag, Berlin, 1984).
2. A. Kafalas, H. C. Gatos, M. C. Lavine, and M. D. Banus, *J. Phys. Chem. Solids* **23**, 1541 (1962).
3. S. Minomura, G. A. Samara, H. G. Drickamer, *J. Appl. Phys.* **33**, 3196 (1962).
4. W. Fuhs, P. Schlotter, J. Stuke, *Phys. Stat. Solidi* **57**, 587 (1973).
5. G. J. Piermarini, S. Block, *Rev. Sci. Instruments* **46**, 973 (1975).
6. I. M. Tsivil'kovskii, V. V. Shchennikov, N. G. Gluzman, *Sov. Phys. Solid. State* **27**, 269 (1985).
7. V. V. Shchennikov, *Sov. Phys. Solid. State* **35**, 401 (1993).
8. V. V. Shchennikov, *The Physics of Metals and Metallography* **67**, 93 (1989).
9. D. R. McCann, L. Carts, *J. Chem. Physics* **56**, 2552 (1972).
10. V. L. Al'tshuler, A. G. Aronov, A. I. Larkin, and D. E. Khmel'nitskii, *Sov. Phys. JETP* **54**, 411 (1981).
11. J. E. Jaffe, R. Pandey and M. J. Seel, *Phys. Review B* **47**, 6299 (1993).
12. S. A. Obukhov, *Preprint N 1459* (A.F.Ioffe Physico-technical Institute, Academy of Sciences of the USSR, Leningrad, 1991).
13. H. Mell, J. Stuke, *Phys. Stat. Solidi* **24**, 183 (1967).
14. J. P. Gaspard, F. Marinelly, A. Pellegatti, *Europhys. Letters* **3**, 1095 (1987).

# PRESSURE-INDUCED PHASE TRANSITIONS IN HgTeS AND HgSeS CRYSTALS

V. V. Shchennikov, V. I. Osotov

*Institute of Metals Physics Ural Branch RAS, 620219 Ekaterinburg, GSP-170, Russia*

N. P. Gavaleshko, V. M. Frasunyak

*Chernovtsy State University, Chernovtsy 274012, Ukraine*

In HgTe<sub>1-x</sub>S<sub>x</sub> and HgSe<sub>1-x</sub>S<sub>x</sub> crystals semimetal (SM) → semiconductor (SC) → metal (M) phase transitions were investigated at high pressures up to 25 GPa. The decreasing of SM→SC phase transition pressure, and increasing of SC→M transition pressure was found for higher contents of sulfur. The pressure dependences of resistance R and thermoelectric power S received in the work allowed to estimate the widening of energy gap in the electron structure of high pressure SC phases as a function of x.

## Introduction

HgTe and HgSe undergo the structural phase transitions from zinc blend to cinnabar lattice at high pressures 0.8 and 1.4 GPa respectively<sup>1-9</sup>. At pressures up to 25 GPa the transitions into rock salt and white tin type phases were found<sup>10,11</sup>. The first structural phase transformation corresponds semimetal (SM) → semiconductor (SC) electronic transition<sup>2-6</sup>, and the subsequent ones – to semiconductor → metal (M) transition<sup>9-11</sup>. Replacement of cation or anion atoms is known to influence the electron structure of mercury chalcogenides and the transition pressure<sup>7,8</sup>. The aim of this paper was to investigate the influence of sulfur replacing atoms on phase transitions pressure and on the electron structure of high pressure phases.

## 1 Experimental procedure

Experiments were performed in piston-cylinder chambers up to 1.2 GPa, in steel Toroid chambers up to 3 GPa, and in sintered diamond anvils up to 25 GPa<sup>6,12</sup>. The pressure-transmitting media were, respectively, transformer oil-kerosene mixture, pyrophyllite and catlinite. The value of hydrostatic pressure P was measured by means of a manganin manometer with an error 0.02 GPa. In solid media P was estimated within the accuracy of ± 10 % using calibration graphs<sup>12</sup>. Electrical measurements in hydrostatic conditions were performed by four-point probe methods<sup>6</sup>. In solid medium plungers were used as current contacts, and platinum-silver ribbons 5 μm thick were the potential probes in the diamond anvils cell<sup>12</sup>.

At hydrostatic conditions a measurements of resistivity and magnetoresistance were performed; in addition to it, in solid media a thermoelectric power S was investigated using the method, described formerly<sup>12</sup>. In fact, values of S of high pressure phases were estimated relatively to ones of initial SM phases. Accuracy of S measurements ~ 20 %. We also used apparatus with the diamond anvils for the phase transition observations. An ethanol-methanol mixture was the pressure medium. Pressure up to 2 GPa was determined from the shift of R1 ruby luminescence line with error 0.2 GPa<sup>13</sup>. After the high pressure treatment samples were investigated by using an optical microscope "Neofot".

Crystals of substances under consideration were sintered by melting high-purity components (99.9999 %). The chemical composition of samples was established using X-ray spectrum analysis by means of "Superprobe - JCXA".

## 2 Results

### 2.1 SM→SC transitions

#### HgSeS crystals

The data of measurements in solid medium were consistent with ones, obtained in hydrostatic conditions (Fig. 1). The result is that the transition pressure is reduced as the portion of submitting sulfur atoms x rises. Pressure dependences of resistivity were detected by keeping HgSe<sub>1-x</sub>S<sub>x</sub> samples at every value of hydrostatic pressure in an hour. At the beginning of phase transition from

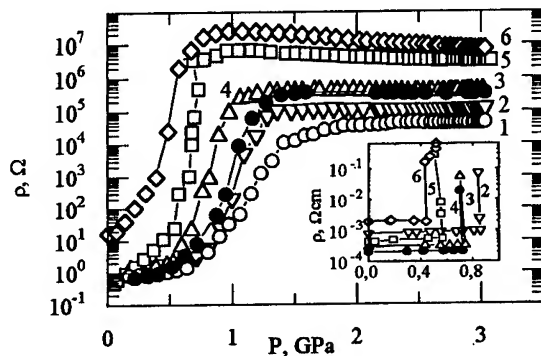


Figure 1: Pressure dependences of resistance of  $\text{HgSe}_{1-x}\text{S}_x$  samples at  $T=296$  K, obtained in Toroid chamber, the portion of sulfur atoms  $x$  being: 1 – 0.050; 2 – 0.104; 3 – 0.202; 4 – 0.302; 5 – 0.508; 6 – 0.601. The insert shows data of resistivity vs hydrostatic pressure.

zinc blend to cinnabar lattice a temporal change of  $R$  was observed<sup>3</sup>. In hydrostatic medium we have got stable intermediate states of samples before the end of phase transition (insert of Fig. 1), and have investigated their properties. The data of magnetoresistance, Hall effect and temperature dependence of  $R$  showed the similarity of new state with the initial SM phase, and a large difference from the final SC phase. It seems, that properties of samples in the intermediate state are determined by inclusions of SM phase. Preliminary calculations using ellipsoidal heterophase model gave a reasonable agreement with the experimental data. The observations of samples, going into the intermediate state during high pressure treatment and after it, showed the obvious signs of structural transformation; it gave a support to the proposed heterophase model.

The value of resistance of high pressure phases enlarged approximately by exponential law, when  $x$  increased (Fig.1). Using the usual expression for a resistivity  $R = R_0 \exp(E_g/2k_0T)$ , where  $k_0$  – is Boltzmann constant, and  $E_g$  – is an energy gap of semiconductor, and supposing that change of  $R$  is due to  $E_g$  change only, one can estimate the enlarging rate of  $E_g$  with  $x$ :  $\Delta E_g/\Delta x = 0.5\text{--}1$  eV, that is in rough agreement with the values of energy gaps of cinnabar  $\text{HgS}$  ( $\sim 2$  eV<sup>14</sup>) and SC phase of  $\text{HgSe}$  ( $\sim 0.7\text{--}1.0$  eV<sup>6</sup>). Data of thermoelectric power  $S$  also showed a shift of transition pressure to zero and rising  $S$  (and, hence,  $E_g$ <sup>14</sup>) when portion of sulfur atoms increased, that is

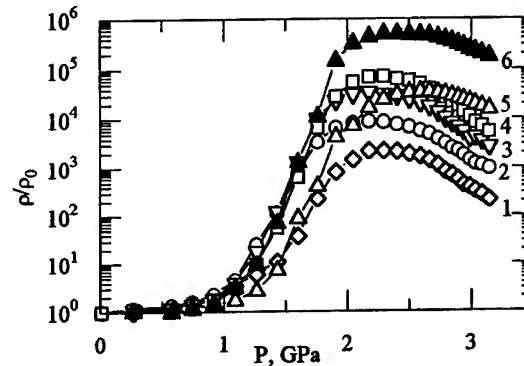


Figure 2: Pressure dependences of relative resistance of  $\text{HgTe}_{1-x}\text{S}_x$  crystals at  $T=296$  K; the portions of sulfur atoms are follows: 1 – 0.0; 2 – 0.042; 3 – 0.094; 4 – 0.139; 5 – 0.203; 6 – 0.271.

consistent with the  $R$  data.

### HgTeS crystals

In  $\text{HgTe}_{1-x}\text{S}_x$  crystals a shift of phase transition pressure and variation of SC phase resistance value on  $x$  were in outline similar to ones in  $\text{HgSe}_{1-x}\text{S}_x$  system (Fig.2). Dependence of  $R$  of SC phase on  $x$  was roughly exponential. The estimation of the energy gap enlarging in SC phase as function of  $x$  gave  $\Delta E_g/\Delta x \sim 1$  eV, that is consistent with the value of energy gaps of cinnabar  $\text{HgS}$ <sup>14</sup> and SC phase of  $\text{HgTe}$  ( $\sim 0.6$  eV<sup>9</sup>). The behaviour of  $S$  is rather complex: introducing of sulfur atoms gave the complementary effect of the charge carriers type change in the high pressure SC phase (Fig.3). For example, in a sample with  $x=0.271$  the pressure dependence of  $S$  became similar to the analogous dependence for  $\text{HgSe}$ . The observed decreasing of  $\text{SM} \rightarrow \text{SC}$  transition pressure in both compounds  $\text{HgSeS}$  and  $\text{HgTeS}$  is due to the instability of zinc blend crystal structure of initial phase when the ratio of cation to anion radii enlarged<sup>6,7</sup>, owing to replacing Se and Te atoms by sulfur. Substituting Te and Se by sulfur atoms in anion sublattice enhanced the semimetallic properties of the initial phase<sup>15</sup>, but enlarged the energy gap of the high pressure semiconductor phase.

### 2.2 SC $\rightarrow$ M transitions

At pressure 10–25 GPa the  $\text{SC} \rightarrow \text{M}$  phase transitions were observed in the both compounds. The point of  $\text{SC} \rightarrow \text{M}$  transition corresponds to the es-

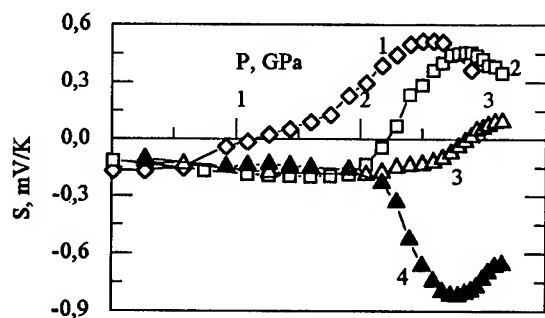


Figure 3: Pressure dependences of thermoelectric power  $S$  for  $\text{HgTe}_{1-x}\text{S}_x$  crystals at  $T=296$  K; portion of sulfur atoms were: 1 – 0.042; 2 – 0.139; 3 – 0.203; 4 – 0.271.

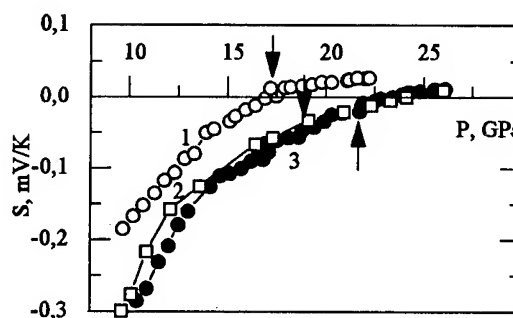


Figure 4: Pressure dependence of thermoelectric power  $S$  of  $\text{HgSe}_{1-x}\text{S}_x$  samples, the portion of sulfur atoms  $x$  being: 1 – 0.15; 2 – 0.302; 3 – 0.601. Proposal  $\text{SC} \rightarrow \text{M}$  transition is marked by arrows.

sential change of pressure dependence of  $R$  and  $S$ . In metal phases thermopower of samples became nearly independent of  $P$ , the value of  $S$  being less, than  $10 \mu\text{V/K}$  (Fig.4). Transition pressure had tendency to increase when portion of sulfur atoms  $x$  was rising. Pressure of  $\text{SC} \rightarrow \text{M}$  transition in cinnabar  $\text{HgS}$  formerly was found to be 28 GPa<sup>12</sup>. It seems, that dependence  $P(x)$  was approximately linear (Fig.4). Enlarging of  $\text{SC} \rightarrow \text{M}$  transition pressure agrees with the determined broadening of energy gap of  $\text{SC}$  phase. We suppose, that  $\text{SC} \rightarrow \text{M}$  transition is related to phase transition into the tetragonal lattice [11]. The curves of  $R(P)$  had also a peculiarities at smaller  $P < 20$  GPa, which may be attributed to a structural transition from cinnabar to rock salt lattice<sup>10,11</sup>.

## Aknowlegment

This work was supported by Russian Fundamental Research Foundation and, in part, by a Soros Foundation Grant awarded by the American Physical Society.

## References

1. P. W. Bridgman, *Proc. Amer. Acad. Arts. Sciences* **74**, 24 (1940).
2. J. Blair, A. L. Smith, *Phys. Rev. Letters* **7**, 124 (1961).
3. J. A. Kafalas, H. G. Gatos, M. C. Lavine, M. D. Banus, *J. Phys. Chem. Solids* **23**, 1541 (1962).

4. A. Jayaraman, W. Jr. Klement, G. C. Kennedy, *Phys. Review* **130**, 2277 (1963).
5. S. Porowski, R. R. Galazka, *Phys. Stat. Solidi* **5**, K71 (1964).
6. N. G. Gluzman, V. V. Shchennikov, *Sov. Phys. Solid. State* **21**, 1844 (1979).
7. A. Lacam, J. Peyronneau, L. J. Engel, B. A. Lombos, *Chem. Phys. Lett.* **18**, 129 (1973).
8. B. A. Lombos, B. Chicopoulos, S. Bhattacharya, B. C. Pant, *Can. J. Physics* **54**, 48 (1976).
9. V. V. Shchennikov, N. G. Gluzman, *Sov. Phys. Solid. State* **23**, 1800 (1981).
10. A. Ohtani, T. Seike, M. Motobayashi, A. Onodera, *J. Phys. Chem. Solids* **43**, 827 (1982).
11. T. L. Huang, A. L. Ruoff, *Phys. Review B* **31**, 5976 (1985).
12. V. V. Shchennikov, N. P. Gavaleshko, V. M. Frasunyak, *Sov. Phys. Solid. State* **35**, 199 (1993).
13. G. J. Piermarini, S. Block, *Rev. Sci. Instruments* **46**, 973 (1975).
14. M. Pai, D. Buttrey, J. M. Joshi, J. M. Honig, *Phys. Review* **24B**, 1087 (1981).
15. N. N. Berchenko, V. Krevs, V. G. Sredin, *Semiconductor solid solution and their applications* [in Russian], Moscow (1982).

# Pressure-driven Metal-Insulator Transition in La-doped SmS by Excitonic Condensation

A.Jung and P.Wachter

*Laboratorium für Festkörperphysik, Eidgenössische Technische Hochschule, C.H. - 8093 Zürich*

Once more, the existence of an excitonic condensed phase could be verified. Similar to some Tm-Te-Se alloys, another intermediate-valent rare earth system, La-doped SmS, has been found to be an excitonic insulator under pressure at low temperatures. Certain experimental conditions favour that insulating effect: Intermediate valence and pressure raise the Coulomb interaction between valence band holes and conducting electrons, while low temperature and high effective mass of the holes suppress thermal agitation and prevent the excitons from ionization.

The theory of excitonic insulation was developed by Mott [1]. It could be proven by experiments on Tm-Se-Te alloys [2]. Now La-doped SmS, another system of rare earth chalcogenides, has turned out as well to become insulating under pressure at low temperature [3].

The parent compound, SmS, is a divalent semiconductor, which exhibits under increasing pressure at first intermediate valence, before reaching the final integer-valent metallic state.

The pseudo-binary  $\text{Sm}_{1-x}\text{La}_x\text{S}$  with  $x = 0.1, 0.25$  and  $0.35$ , however, is intermediate-valent already in the ground-state at ambient conditions - displaying a metallic temperature dependence of the electrical resistivity. Being pressurized at low temperature, it does not turn directly into an integer-valent metal. Instead a condensation of excitons takes place. The loss of free carriers causes a significant resistivity increase, which Fig.1 shows for  $\text{Sm}_{0.90}\text{La}_{0.10}\text{S}$  in an exemplary way.

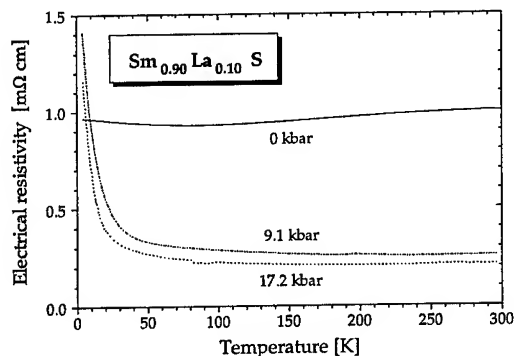


Fig.1. Temperature dependence of the electrical resistivity of  $\text{Sm}_{0.90}\text{La}_{0.10}\text{S}$  for selected initial pressures (measured at room temperature)

As Fig. 2 points out for all three treated Sm-La-S compounds, a band gap of meV magnitude opens, which is evaluated from the Arrhenius representation of their resistivity vs. temperature relations at varied pressure. It corresponds to the activation energy necessary for breaking the excitons and restoring metallic conductivity.

The more external pressure is applied now, the more the binding energy of the excitons diminishes and the more electrons are driven into the conduction band. Sufficient additional

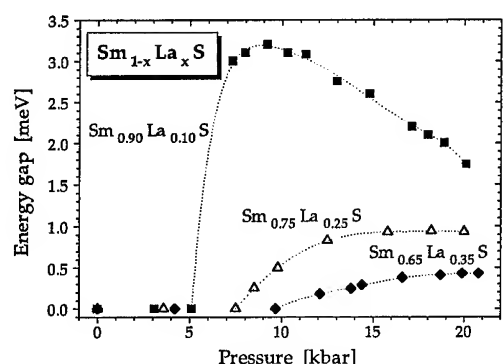


Fig.2. Pressure dependence of the activation energy of  $\text{Sm}_{1-x}\text{La}_x\text{S}$  with  $x = 0.10, 0.25$  and  $0.35$ : A band gap opens between 5 and 10 kbar (measured at room temperature), indicating the onset of the excitonic phase

free charge screens the Coulomb attraction to such an extent, that the excitons hold no longer together. So the extraordinary excitonic phase is always followed and ended up by a very common semiconductor-metal transition.

Particular boundary conditions must be met in order to trigger and to stabilize the excitonic phase. They influence the main antagonists of the process: the *kinetic energy* of the conducting electrons and their *Coulomb interaction* with the 4f holes, which are left after electronic 4f-5d transitions due to intermediate valence. The extreme narrowness of the hybridized 4f band - making rare earth solids so distinctive - leads to heavy valence electrons and holes. The inertia and strong localization of a hole, when coupling with a conducting electron, lend the formed excitonic quasi-particle a *high effective mass*. Thereby thermal agitation remains suppressed, and all the more it is the case at *low temperature*, being another

prerequisite to insulation. The probability of the excitons to be scattered at the lattice or to collide with neighbouring atomic trunks is considerably reduced.

The application of *pressure* principally promotes holes and free electrons to approach each other, resulting in a certain amount of the Coulomb interaction. *Intermediate valence* widens the originally undispersed 4f states and reduces the band gap. That might be decisive to settle the excitonic phase in an accessible pressure range. SmS becomes intermediate-valent not only by pressure, but also by donor doping - independently of the substituents to be smaller (like  $\text{Y}^{3+}$ ) or bigger (like  $\text{La}^{3+}$ ) than the  $\text{Sm}^{2+}$  atoms replaced. So the electronic nature of the effect is evident, based on a screening-induced shift of the 4f levels towards the conduction band. It disproves the established opinion, which primarily holds lattice or external pressure responsible for such a valence transition. On the other hand, doping works only, if at the same time the *charge screening* keeps within limits. In Fig. 2, the tendency of the  $\text{La}^{3+}$  donors to screen is obvious - the higher their share, the smaller the energy gap in the excitonic phase. Beyond a critical concentration of free carriers, electrons and holes cannot take up a bound state any more.

#### References :

- [1] N.F. Mott, Phil. Mag. 6, 287, 1961
- [2] J. Neuenchwander and P. Wachter, Phys. Rev. B 41, 12693, 1990
- [3] P. Wachter, A. Jung and P. Steiner, Phys. Rev. B 51, 5543, 1995

# ELECTRICAL RESISTANCE MEASUREMENTS OF SOLID BROMINE AT HIGH PRESSURES AND LOW TEMPERATURES

Katsuya Shimizu and Kiichi Amaya

*Department of Material Physics, Faculty of Engineering Science,  
Osaka University, Toyonaka, Osaka 560, Japan*

and

Shoichi Endo

*Research Center for Extreme Materials, Osaka University,  
Toyonaka, Osaka 560, Japan*

## ABSTRACT

Electrical resistance of bromine is measured at temperatures down to 50mK and at several pressures up to 150GPa using a diamond-anvil cell. The electrical resistance at room temperature decreases as a function of pressure and the reached resistivity at 100GPa is estimated as  $1 \times 10^{-4} \Omega \cdot \text{cm}$ . Analogous to iodine, bromine also undergoes the metallization under pressures before the molecular dissociation and becomes the monatomic metal above 80GPa. Small drops in electrical resistance are observed below 1.5K at pressures higher than 90GPa, which show the onset of superconductivity.

## Introduction

A diatomic molecular solid is expected to show a molecular-to-monatomic and an insulator-to-metal transition at an extremely condensed state. In the case of iodine, the pressure-induced metallization<sup>1</sup> and molecular dissociation<sup>2</sup> are already reported. The electrical resistance measurements reveal the existence of a metallic state even at the molecular phase. The molecular-to-monatomic phase transition called 'molecular dissociation' at 21GPa and the successive structural phase transitions are reported in the monatomic metallic state. The carrier of iodine<sup>3</sup> is confirmed to be a hole in agreement with the theoretical prediction. At low temperatures, the pressure-induced superconductivity of iodine<sup>4</sup> is observed at all monatomic high pressure phases. In the case of bromine, the molecular-to-monatomic phase transition is reported to take place at 80GPa.<sup>5</sup> The crystal structure at the monatomic phase is found to be body-centered orthorhombic, as previously observed in monatomic iodine (phase-II). There is no report on the electrical properties of bromine. Therefore, we performed measurements of the pressure and temperature dependence of electrical resistance up to 150GPa and down to 50mK, expecting the

pressure-induced metallization and/or superconductivity analogous to the case of iodine.

## Experimental Results

A diamond anvil cell(DAC)<sup>5</sup> with beveled 1/3 carat anvils is used to generate high pressures up to 150GPa. The cell is made of nonmagnetic Be-Cu alloy for magnetic and cryogenic experiments. Bromine sample with purity of 99% obtained from Wako Chemical Industries, Ltd., is frozen and cut into a suitable piece in nitrogen gas chamber, and

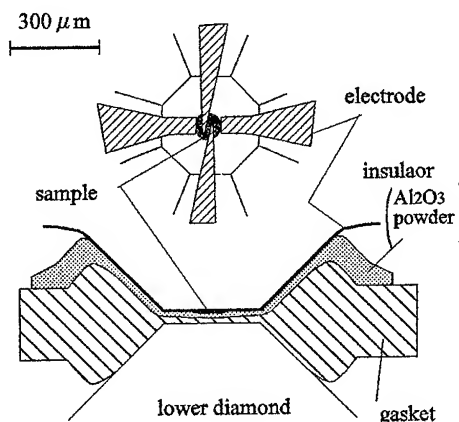


Fig.1 The arrangement of the sample and electrodes in DAC.

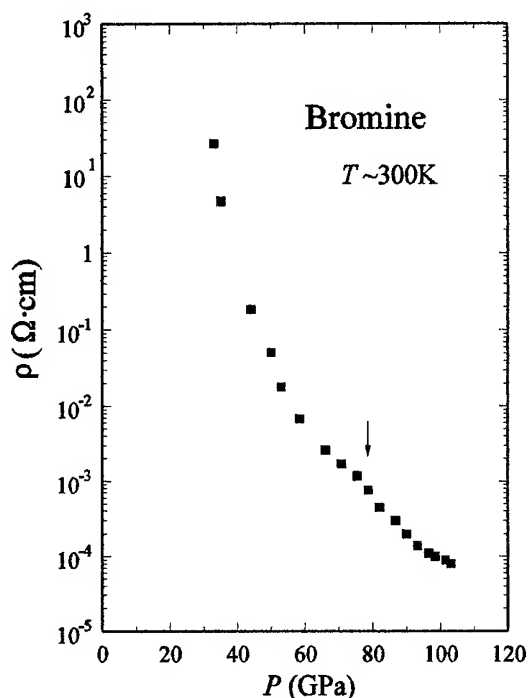


Fig.2 Electrical resistivity of bromine as a function of pressure. A small hump can be seen at around 80GPa.

placed on the electrodes in DAC. The electrical resistance measurements are performed by ac 4-terminal method with excitation current of  $10\mu\text{A}$  and measuring frequency of 800Hz. The arrangement of the sample and electrodes is shown in Fig.1. The pressure is determined by the wavelength of the fluorescence from ruby chips placed close to the sample, however, is not expected to be hydrostatic. We can estimate the pressure at low temperatures below 77K from the value measured at 77K.

The electrical resistivity is estimated from the shape of the sample of  $1\mu\text{m} \times 20\mu\text{m} \times 20\mu\text{m}$  after deformation by compression. Figure 2 shows the pressure dependence of the resistivity of bromine measured at room temperature up to 105GPa. The resistivity decreases logarithmically with increasing pressure and reaches  $8 \times 10^{-5} \Omega \cdot \text{cm}$  at 105GPa. The resistivity is still larger by several orders of magnitude than those of typical metals like Ag and Au., however, not only the value of

resistivity but also the behavior under pressure are very similar to those of iodine already reported. A small hump observed at around 80GPa is considered to be related with the molecular-to-monatomic transition just like the case of iodine.<sup>6</sup> Analogous to iodine, bromine is also considered to undergo the metallization at the molecular state under pressure and become the monatomic metal above 80GPa. With cooling down by the  $^3\text{He}/^4\text{He}$  dilution refrigerator, the temperature dependence of electrical resistance of bromine is measured down to 50mK at several pressures from 75GPa to 150GPa. The resistance of bromine decreases almost linearly at temperatures above 50K as shown in Fig.3. Decreasing the temperature further, we found slight but abrupt resistance drop at 1.5K for pressures above 90GPa. The reduced resistance ( $R/R_{5K}$ ) versus temperature curves for lower temperatures are shown in Fig.4. Further, the resistance drop is found to shift to lower temperature with the applied magnetic field as shown in the inset.

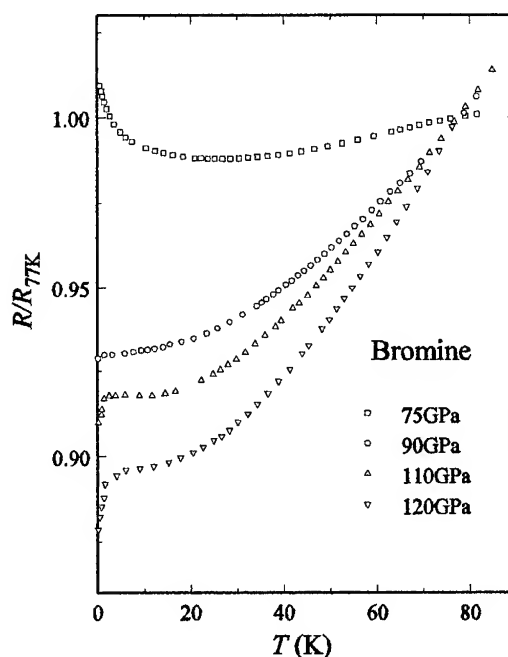


Fig.3 Temperature dependence of reduced resistance for bromine at several pressures.



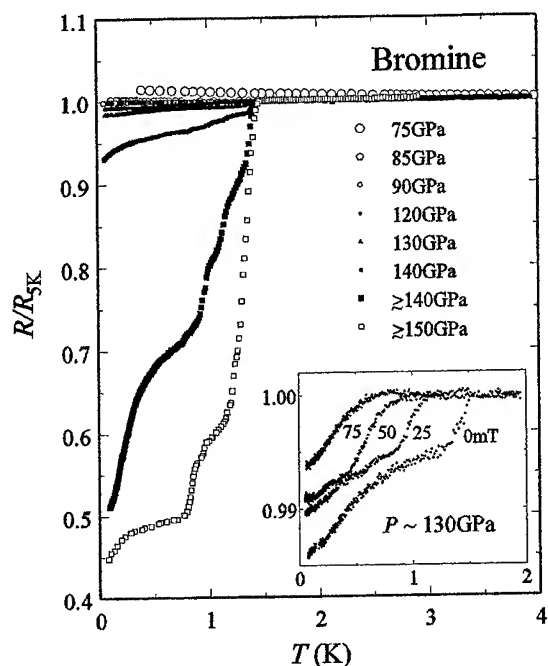


Fig.4 Temperature dependence of reduced resistance ( $R/R_{5K}$ ) of bromine at several pressures. Inset shows magnetic field dependence of  $R/R_{5K}$  at 130 GPa.

The residual resistance at the lowest measured temperature decreases with increasing pressure. For pressures lower than 90 GPa, resistance increases below 5 K and no transition is observed down to 50 mK. These are quite the same behavior as the case of iodine<sup>4</sup> and we attribute the resistance drop as due to the onset of superconductivity. Figure 5 shows the temperature dependence of the critical magnetic field of bromine at 150 GPa. The transition temperatures are determined in the onset.

We conclude that the pressure-induced metallization of bromine is observed, and that the abrupt decrease of resistance at 1.5 K observed in the monatomic state above 90 GPa is attributed to the onset of superconductivity.

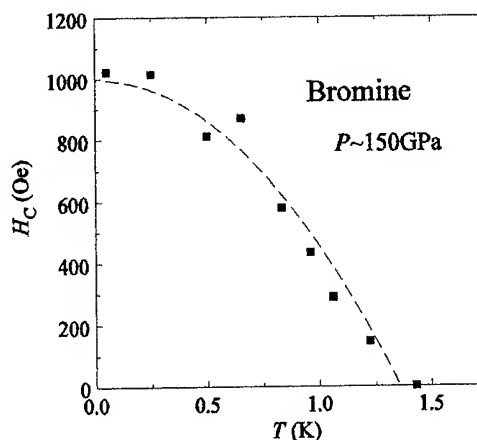


Fig.5 Temperature dependence of the magnetic field of bromine at 150 GPa.

This work was supported by a Grant-in Aid for Scientific Research(A) from the Ministry of Education, Science and Culture of Japan, and also partly by Research Fellowship of the Japan Society for the Promotion of Science for Young Scientists.

## REFERENCES

1. A.S.Balchan and H.G.Drickamer, *J. Chem. Phys.* **34**,1948(1961).
2. Y.Fujii, K.Hase, N.Hamaya, Y.Ohishi, A.Onodera, O.Shimonura and K.Takemura, *Phys. Rev. Lett.* **58**,796(1987).
3. T.Yamauchi, K.Shimizu, N.Takeshita, M.Ishizuka, K.Amaya and S.Endo, *J. Phys. Soc. Jpn.* **63**,3207(1994).
4. K.Shimizu, T.Yamauchi, N.Tamitani, N.Takeshita, M.Ishizuka, K.Amaya and S.Endo, *Journal of Superconductivity* **7**,921(1994).
5. Y.Fujii, K.Hase, Y.Ohishi, H.Fujihisa, N.Hamaya, K.Takemura, O.Shimomura, T.Kikegawa, Y.Amemiya and T.Matsushita, *Phys. Rev. Lett.* **63**,536(1989).
6. N.Sakai, K.Takemura and K.Tsuji, *J. Phys. Soc. Jpn.* **51**,1811(1982).

## **VII Physical Properties of Matter under Static Pressures**

## **VII(A) Hydrogen and Hydrides**

## SOLID HYDROGEN AT ULTRAHIGH PRESSURES

HO-KWANG MAO and RUSSELL J. HEMLEY

*Geophysical Laboratory and Center for High Pressure Research,, Carnegie Institution of Washington,  
5251 Broad Branch Road, N. W., Washington, DC 20015-1305, U. S. A.*

### ABSTRACT

During the past decade, great progress has been made in the experimental study of solid hydrogen at ultrahigh pressures as a result of developments in diamond-cell technology. Pressures at which metallization has been predicted to occur have been reached (250-300 GPa). A wide range of techniques, including visible-to-infrared transmission and reflectance, and Raman spectroscopy, is applied for *in-situ* determination of hydrogen properties at megabar pressures. With the development of microsampling technology, particularly by employing laser and synchrotron radiation, the accuracy and resolution of *in-situ* measurements have been improved steadily to approach the quality of measurements at ambient conditions. The newly acquired capabilities enable us to perform detailed studies of the dynamic, structural, and electronic properties of dense hydrogen. The results reveal a system unexpectedly rich in physical phenomena, exhibiting a variety of transitions at ultrahigh pressures.

### Introduction

The present paper reviews the progress in static ultrahigh-pressure research of hydrogen since 1988. During this period, a series of structural, vibrational and electronic transitions has been discovered in dense hydrogen. Meanwhile, the initial simple goal of searching for metallic hydrogen has matured to a comprehensive study of a system extremely rich in physical phenomena. This progress is the result of, as well as the driving force for, advances in three fronts of high-pressure technology, namely: the extension of maximum attainable pressure, the development of multiple analytical techniques for *in-situ* characterization, and the orders-of-magnitude improvements in accuracy and sensitivity of measurements at megabar pressures.

In 1985 [1], the megabar barrier for hydrogen study was first exceeded and a maximum pressure of 147 GPa was achieved. The real excitement marking a new era of hydrogen research came later in 1988 when a new phase was discovered above 150 GPa [2], and in 1989 when pressures above 250 GPa were reached [3]. Mao and Hemley [3] reported hydrogen studies with pressure measurements up to 230 GPa above which the pressure could not be measured with ruby fluorescence calibration in the presence of an intense pressure-induced

diamond luminescence background [4]. Nevertheless, in several of these experiments, the hydrogen sample survived the increase in load to double the load at 230 GPa. Based on x-ray diffraction pressure calibration of the load-pressure relation of other hydrogen-free experiments, a conservative estimate yielded maximum pressures above 300 GPa.

While these early experiments [3] were encouraging because they demonstrated that pressures far beyond 230 GPa could be achieved in hydrogen, they were unsatisfying because quantitative measurements of hydrogen properties or pressure were absent. Subsequently, developments have focused on analytical techniques including Raman spectroscopy, and IR-VIS reflectivity and absorption spectroscopy of hydrogen in megabar pressures. Most importantly, the accuracy and sensitivity have been improved steadily. For example, comparing the high-pressure Raman vibron of deuterium reported in 1985 [1] and 1995 [5], the peak resolution has improved from  $5\text{ cm}^{-1}$  to  $0.5\text{ cm}^{-1}$ , and the signal/noise ratio from 20 to 20,000. These improvements have led to the observation of 10 additional vibron peaks, which reveal two low-temperature phases and constrain the symmetry and size of their unit cells [5].

During the past seven years, such improvements have been typical in the

TABLE 1. HIGH-PRESSURE PHASE DIAGRAM OF HYDROGEN

1988	Hemley, Mao [2]	Discovery of 150-GPa transition in H <sub>2</sub> at 77K
1989	Hemley, Mao [6]	Discovery of 150-GPa transition in D <sub>2</sub> at 77K
1989	Lorenzana, Silvera, Goettel [7]	Confirmation of phase-A (150-GPa trans.) in H <sub>2</sub> at 4-150K
1990	Hemley, Mao [8]	Discovery of critical behavior in 150-GPa trans. of H <sub>2</sub>
1990	Lorenzana, Silvera, Goettel [9]	Confirmation of the critical point
1992	Hanfland, Hemley, Mao [10]	Observation of 110-GPa transition in H <sub>2</sub> at 85 K
1994	Mao, Hemley [11]	Triple point of D <sub>2</sub> phases I-II-III
1994	Cui et al. [12]	Triple point of D <sub>2</sub> I-II-III; refuting critical point
1995	Goncharov et al. [13]	Phase diagram with triple and (tri)critical points

hydrogen research. Breakthroughs resulted from sustained experimental progress. This development of our empirical understanding of the phase transitions and physical properties of dense hydrogen is narrated as follows.

#### Megabar Phase Diagram

Publications that shaped our knowledge of the hydrogen  $P$ - $T$  phase diagram above 100 GPa are summarized chronologically in Table 1. In 1988, Hemley and Mao [2] discovered a major pressure-induced phase transition in solid hydrogen at 150 GPa and 77 K. The transition is evidenced by a large discontinuity ( $100 \text{ cm}^{-1}$ ) in the intramolecular vibron frequency as a function of pressure. The high-pressure phase displays several intriguing properties and has been a focus of numerous experimental and theoretical investigations ever since. In 1989, Hemley and Mao [6] discovered the same transition in the deuterium isotope. The transition in hydrogen was confirmed by Lorenzana, Silvera, and Goettel in 1989 [7]. They extended the temperature range to cover 4.3 to 150 K, and found the transition pressure is independent of temperature below 80 K but increases mildly with temperature above 80 K.

In early 1990, Hemley and Mao [8] further extended the study of the phase boundary from 77 to 295 K, and discovered interesting behavior: the magnitude of the hydrogen vibron discontinuity decreased with increasing temperature, and became immeasurable above

150 K and 170 GPa. Termination of the first-order phase boundary was interpreted as evidence for a critical point if the boundary simply terminated [8], or a tricritical point if the transition changed from first- to second-order [14]. The precise  $P$ - $T$  position of the point, however, was not given [8, 14] because it required knowledge of where the discontinuity vanished. With a resolution of  $10 \text{ cm}^{-1}$ , a small discontinuity extending above 150 K and 170 GPa could not be ruled out [8]. In late 1990, Lorenzana, Silvera, and Goettel [9] confirmed the critical point in hydrogen and gave its  $P$ - $T$  position at 173(4) GPa and 151(15) K. Critical behavior was also observed in deuterium [15].

In a study of infrared vibron absorption of hydrogen, Hanfland, Hemley, and Mao [16] observed another phase at 110 GPa and 85 K as indicated by the sudden appearance of an additional sharp vibron  $45 \text{ cm}^{-1}$  below the principal vibron. This phase boundary had a small positive  $dT/dP$  slope. Its extrapolation to higher pressures would intercept the nearly vertical phase boundary at 150 GPa, thus forming a triple point below the (tri)critical point. The  $P$ - $T$  phase diagram of deuterium with three divariant phases and three univariant phase boundaries meeting at an invariant triple point was mapped out and summarized in a review article [11].

Mao and Hemley [11] named the three phases as I for the low-pressure phase, II for the low-temperature phase, and III for the phase above 150 GPa. Since the discoveries of the phase III in hydrogen [2] and deuterium

[6], the group had referred it by a descriptive name of "150-GPa phase," which was cumbersome and inexact because of the variability of transition pressures with temperatures and isotopes and the possibility of additional transition(s) near 150 GPa. The Harvard group [7] had named it the H-A phase by analogy to the A phase of helium at low temperature. However, when multiple high-pressure phases are present, the crystallographic convention is I-II-III..., so that this simple scheme was adapted. After the I-II-III nomenclature was proposed [11, 17, 18], it was later adopted by the Harvard group [12].

The deuterium phase diagram presented by Cui et al. [12] also showed a triple point as did that of Mao and Hemley [11], but with the following significant differences. Cui et al. observed two clear phase lines (I-II and I-III) but failed to detect the discontinuity along the third (I-III) in either Raman or IR vibron. Without considering tricritical behavior, they concluded that previous reports of a critical point in hydrogen were erroneous. Moreover, their II-III boundary was  $\sim 10$  GPa lower than that in Ref. [11]. The lower value could be explained by their use of IR spectroscopy for

determination of the II-III boundary coupled with a large pressure variation across the sample. Because of the strength of the IR vibron of phase III [16], this technique is highly sensitive to the presence of trace amounts of phase III. Cui et al. would have identified the II-III boundary in the region of maximum pressure, whereas their pressure determined from Raman scattering would correspond to the average pressure; this results in a mismatch equivalent to half of the pressure variation across the sample. Such problems are not encountered if Raman spectrum is used for identifying II-III boundary in a sample with small pressure variation [11, 13].

Goncharov et al. presented an extensive and detailed Raman study [13] of deuterium to 200 GPa and 20-300 K. The highly concentrated, high-resolution data reconfirmed the existence of a (tri)critical point and the phase diagram in ref. [11]. The discontinuity at I-III phase boundary was well defined and tracked from the I-II-III triple point at 167 GPa and 130 K to the (tri)critical point at 182(3) GPa and 235(15) K. The phase diagrams of deuterium and hydrogen [19] are now summarized in Fig. 1.

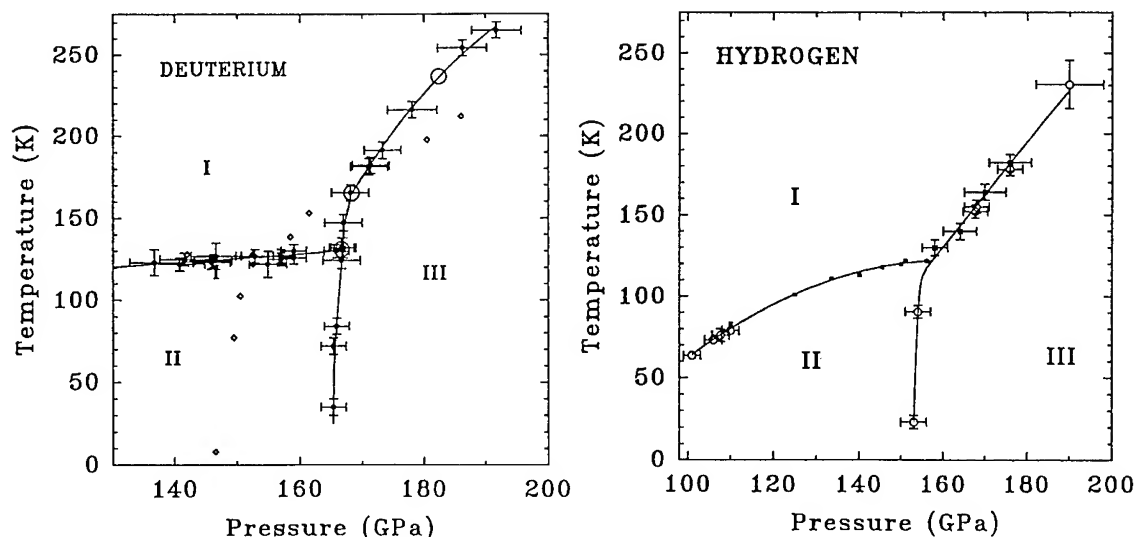


Fig. 1. Megabar phase diagrams. Phases I, II and III meet at the triple point. For deuterium, the upper circle is a (tri)critical point; lower circle, another possible invariant point [13]. Open diamond symbols are data of Cui et al. [12]. All other symbols are IR or Raman data from our group.

TABLE 2. ELECTRONIC AND VIBRATIONAL PROPERTIES OF HYDROGEN ABOVE 150 GPa

1989	Mao, Hemley [3]	H <sub>2</sub> above 250 GPa; evidence for band-overlap mechanism
1990	Eggert, Goettel, Silvera [24]	Dielectric catastrophe (metallization) at 148 GPa
1990	Eggert, Goettel, Silvera [25]	Dielectric catastrophe (metallization) at 205 GPa
1990	Mao, Hemley, Hanfland [26]	Reflectivity down to 0.5 eV; Drude edge, metallization
1991	Hemley, Hanfland, Mao [27]	No dielectric catastrophe to at least 300 GPa
1991	Eggert et al. [28]	Absorption and reflectance down to 0.8 eV; hypotheses: metallic with low $\omega_p$ or non-metallic
1991	Hanfland, Hemley, Mao [29]	Absorption and reflectance down to 0.5 eV; hypotheses: metallic with low $\omega_p$ ; anisotropic metal with high $\omega_p$ ; or non-metallic with interband or vibrational absorption
1992	Hanfland et al. [10]	Dramatic increase in intermolecular coupling ( $\times 10^2$ )
1993	Hanfland, Hemley, Mao [16]	Dramatic increase in IR vibron absorption ( $\times 10^3$ ) in phase III
1994	Hemley et al. [30]	Charge-transfer states in dense hydrogen
1995	Cui, Chen, Silvera [31]	Transmission to 0.37 eV, no clear evidence of metallization but Drude model with $\omega_p < 0.95$ eV possible
1995	Mao, Hemley (this report)	Transmission to 0.15 eV; $\omega_p < 0.4$ eV

### Electronic and Vibrational Transitions

Major publications on experimental studies of electronic and vibrational properties of hydrogen above 150 GPa are summarized chronologically in Table 2. Shortly after the discovery of the 150-GPa phase transition [2], theoretical calculations suggested that the new phase could be metallic [20]. Indeed, a large number of subsequent calculations at that time predicted significant changes in electronic properties at these pressures, and one of the major theoretical problems was how to preserve the band gap to these pressures [21-23]. The spectroscopic features indicated that the transition involved orientational and structural changes. In addition, the sample remained transparent in the high-pressure phase to at least 250 GPa [3, 14]. To test the theoretical prediction of metallization, optical experiments were designed and conducted.

Eggert, Goettel, and Silvera [24] measured the index of refraction to 70 GPa and on the basis of an extrapolation of a single-oscillator model for the index predicted band-overlap metallization at 148 GPa from an apparent dielectric catastrophe (corrected to 205 GPa in an addendum [25]). Direct measurements of the index of refraction at these pressures revealed

no dielectric catastrophe [27] but instead revealed a pressure variation of the electronic transitions associated with the direct gap consistent direct observations approaching 300 GPa [3]. However, closure of the indirect gap was still possible, as predicted by numerous theoretical calculations [20, 23, 32-34].

Searching for a Drude feature as direct evidence of metallization started in 1990 [26] when IR reflectivity of hydrogen at 177 GPa measured down to 0.5 eV showed a systematic and reproducible increase at the low energy range of the spectrum. Mao, Hemley, and Hanfland [26] demonstrated that the reflectance could be modeled as Drude edge with a plasma frequency  $\omega_p$  as high as 2.42 eV, suggesting metallization. However, when both absorption and reflectance over a limited energy range ( $>0.8$  eV) were measured later [28], the low absorbance contradicted the Drude model of high  $\omega_p$ . Eggert et al. [28] concluded that either the hydrogen above 150 GPa might not be metallic or it was metallic with a small  $\omega_p$  which could be tested at lower photon energy (further into the infrared). Hanfland, Hemley, and Mao [29] presented IR absorption measurements down to 0.5 eV, and showed a systematic rise with increasing

pressure; but the strength of the absorption was weaker than that predicted by the reflectivity with a large  $\omega_p$ . It was pointed out that if sample texture due to the anisotropy of the material, thin film effects, and diffraction were significant, the reflectance (which measures interface property) and the absorption (which measures a bulk property) might be uncoupled [29]. Alternative hypotheses [29] proposed to explain the observations included Drude absorption with a small  $\omega_p$ , vibron excitation, and electronic interband transitions. This year (1995) Cui, Chen, and Silvera [31] presented absorption data down to 0.37 eV showing a tantalizing rising absorption that they interpreted as supporting the possibility that phase III is metallic. They showed that Drude models with  $\omega_p$  as high as 0.95 eV in phase III (D<sub>2</sub> at 194 GPa) were still consistent with the data. Due to the limited frequency range, however, they concluded that all existing data were inadequate to determine whether the phase III is metallic; it would be necessary to extend measurements to still lower energy. With type II diamonds which is transparent at low energy, we measured absorption spectra down to 0.15 eV (1200  $\text{cm}^{-1}$ ) to compare with Drude model calculations. As shown in Fig. 2, our data rule out Drude models with  $\omega_p > 0.4$  eV. If the phase III is metallic, it must have a lower  $\omega_p$ .

To test the hypotheses of small  $\omega_p$  or interband transitions requires measurement capabilities to unprecedented low energy and high resolution. The synchrotron IR high-pressure technique was in fact developed for this reason, and since 1992 has provided a wealth of new information on the nature of dense hydrogen [10, 16]. Unlike the Raman vibron, which reaches a maximum at 30 GPa and decreases at higher pressures, the IR vibron, which occurs near the band origin, rises continuously without turnover up to 140 GPa [10]. At 150 GPa and 85 K, the IR vibron shows an identical discontinuous drop in frequency as the Raman vibron, and decreases continuously at higher pressures, indicating weakening of the molecular bond. Meanwhile, the intermolecular coupling measured by the frequency difference of the IR and Raman

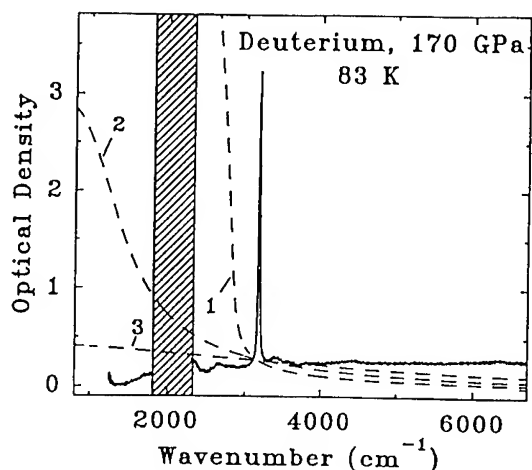


Fig. 2. IR absorption spectrum of D<sub>2</sub> (to be published by Hemley, Goncharov, Hanfland, Li, Mao). The sharp peak is vibron. The shaded region is blocked by diamond absorption. 1, 2, 3 are Cui, Chen, and Silvera's [31] calculated Drude curves which could fit their data but not the present data extending to lower energy.

vibron shows a dramatic increase from 3  $\text{cm}^{-1}$  to 500  $\text{cm}^{-1}$  in this pressure range.

The most striking feature observed in high-pressure hydrogen is the enhancement of IR vibron absorption in phase III [16]. IR intensity measures the change in electric dipole moment. Being a homonuclear molecule without a dipole, hydrogen normally only has a very weak collision-induced IR vibron. Above the transition to phase III, however, the absorption suddenly increases by three orders of magnitude. This has potential implications ranging from crystallographic and orientational symmetry breaking to electronic transitions. Hemley et al. [30] explored the role of charge transfer in affecting the dramatic enhancement of infrared vibron absorption in phase III, and focused the relevance of mechanisms used to understand similar behavior in charge-transfer salts and conducting polymers upon chemical doping. They developed a dimer model to explain the extraordinary infrared response of hydrogen; the model also predicts the existence of new excited intermolecular charge transfer states in the dense solid as the band gap closes. The dimer model was extended to examine charge transfer and vibronic coupling in dense, crystalline hydrogen [35].



Alternatively to molecular hydrogen dissociation to neutral atoms, Baranowski [36] proposed a hypothesis of transition of  $H_2$  to  $H^+H^-$ . Such transition would have a dynamic charge of 100%, while the measured dynamic charge in the intense IR vibron of the phase III is only 4%. The IR data are thus consistent with a partial intramolecular charge transfer of 4% at the maximum pressure (216 GPa).

### Acknowledgment

This work is supported by NSF and NASA.

### References

1. H. K. Mao, P. M. Bell and R. J. Hemley, *Phys. Rev. Lett.* **55** (1985) 99.
2. R. J. Hemley and H. K. Mao, *Phys. Rev. Lett.* **61** (1988) 857.
3. H. K. Mao and R. J. Hemley, *Science* **244** (1989) 1462.
4. H. K. Mao and R. J. Hemley, *Nature* **351** (1991) 721.
5. A. F. Goncharov, I. I. Mazin, J. H. Eggert, R. J. Hemley and H. K. Mao, this proceedings.
6. R. J. Hemley and H. K. Mao, *Phys. Rev. Lett.* **63** (1989) 1393.
7. H. E. Lorenzana, I. F. Silvera and K. A. Goettel, *Phys. Rev. Lett.* **63** (1989) 2080.
8. R. J. Hemley and H. K. Mao, *Science* **249** (1990) 391.
9. H. E. Lorenzana, I. F. Silvera and K. A. Goettel, *Phys. Rev. Lett.* **65** (1990) 1901.
10. M. Hanfland, R. J. Hemley, H. K. Mao and G. P. Williams, *Phys. Rev. Lett.* **69** (1992) 1129.
11. H. K. Mao and R. J. Hemley, *Rev. Mod. Phys.* **66** (1994) 671.
12. L. Cui, N. H. Chen, S. J. Jeon and I. Silvera, *Phys. Rev. Lett.* **72** (1994) 3048.
13. A. F. Goncharov, I. I. Mazin, J. H. Eggert, R. J. Hemley and H. K. Mao, *Phys. Rev. Lett.* **75** (1995) 2514.
14. R. J. Hemley, H. K. Mao and M. Hanfland, in *Molecular Systems under High Pressure, Proceeding of the II Archimedes Workshop "Molecular solid under pressure"*, Catania, May 21-31, 1990, ed. R. Pucci and G. Piccitto (Elsevier, 1991), p. 223.
15. R. J. Hemley, H. K. Mao and M. Hanfland, *Bull. Am. Phys. Soc.* **36** (1991) 529.
16. M. Hanfland, R. J. Hemley and H. K. Mao, *Phys. Rev. Lett.* **70** (1993) 3760.
17. R. J. Hemley, H. K. Mao and M. Hanfland, *Bull. Am. Phys. Soc.* **39** (1994) 336.
18. M. Li, M. Hanfland, R. J. Hemley and H. K. Mao, *Bull. Am. Phys. Soc.* **39** (1994) 336.
19. R. J. Hemley and H.-k. Mao, in *Oji Seminar Volume: Elementary Processes in Dense Plasmas*, ed. S. Ichimaru and S. Ogata (Addison-Wesley Pub. Co., 1995), p. 271.
20. T. W. Barbee, A. Garcia, M. L. Cohen and J. L. Martins, *Phys. Rev. Lett.* **62** (1989) 1150.
21. N. W. Ashcroft, in *Molecular Solids under High Pressure*, ed. R. Pucci and G. Piccitto (Elsevier, 1991), p. 201.
22. H. Chacham and S. G. Louie, *Phys. Rev. Lett.* **66** (1991) 64.
23. A. Garcia, T. W. Barbee, M. L. Cohen and I. F. Silvera, *Europhys. Lett.* **13** (1990) 355.
24. J. H. Eggert, K. A. Geottel and I. F. Silvera, *Europhys. Lett.* **11** (1990) 775.
25. J. H. Eggert, K. A. Geottel and I. F. Silvera, *Europhys. Lett.* **12** (1990) 381.
26. H. K. Mao, R. J. Hemley and M. Hanfland, *Phys. Rev. Lett.* **65** (1990) 484.
27. R. J. Hemley, M. Hanfland and H. K. Mao, *Nature* **350** (1991) 488.
28. J. H. Eggert, F. Moshary, W. J. Evans, H. E. Lorenzana, K. A. Goettel, I. F. Silvera and W. C. Moss, *Phys. Rev. Lett.* **66** (1991) 193.
29. M. Hanfland, R. J. Hemley and H. K. Mao, *Phys. Rev. B, Rapid Communication* **43** (1991) 8767.
30. R. J. Hemley, Z. G. Soos, M. Hanfland and H. K. Mao, *Nature* **369** (1994) 384.
31. L. Cui, N. H. Chen and I. F. Silvera, *Phys. Rev. Lett.* **74** (1995) 4011.
32. E. Kaxiras, J. Broughton and R. J. Hemley, *Phys. Rev. Lett.* **67** (1991) 1138.
33. C. Friedli and N. W. Ashcroft, *Phys. Rev. B* **16** (1977) 662.
34. H. Chacham, X. Zhu and S. G. Louie, *Phys. Rev. B* **46** (1992) 6688.
35. Z. G. Soos, J. H. Eggert, R. J. Hemley, M. Hanfland and H. K. Mao, *Chem. Phys.* (1995) in press.
36. B. Baranowski, *Polish J. Chem.* **66** (1992) 1637.

## HYDROGEN AT MULTIMEGABAR PRESSURES

ARTHUR L. RUOFF

*Department of Materials Science and Engineering  
Cornell University, Ithaca, NY 14853, U.S.A.*

### ABSTRACT

Previous workers have reached 230 GPa on hydrogen (without filling the sample hole with ruby). The vibron has been studied to 170 GPa at room temperature. In order to increase this pressure range, three important technological developments were made. A cell with a gasket with a 15  $\mu\text{m}$  diameter sample hole was loaded with hydrogen at high pressure in the gas phase. The diamond tips were 35  $\mu\text{m}$  in diameter. As the pressure was increased, the sample hole remained closely circular while its diameter decreased to 6  $\mu\text{m}$  at 240 GPa at which time the diameter was stable under further loading. Pressure was measured using the x-ray marker method. Results on the vibron frequency versus pressure will be presented. The possibility that an analog of LiH, i.e., proton hydride, HH will be formed and will greatly delay metallization in diamond is discussed.

In September of 1992, I submitted a three year proposal to the National Science Foundation which included extensive high pressure structural and optical studies on the alkali hydrides. These are not potential materials for making practical devices and so this proposal ran counter to the trend toward applied research in the U.S.A. One may wonder: Why alkali hydrides? In the previous spring I had thought considerably about hydrogen and it was evident that hydrogen was every bit as much a halogen as an alkali. In fact its behavior as an  $\text{H}^+$  ion in solution was greatly exaggerated since it was really present as an  $\text{H}_3^+\text{O}$  ion where it is tightly bonded to the water molecule. Table I compares some properties of the alkalis and the halogens (1). The typical alkali metals have ionization potentials of about 5 eV. It will be difficult to make hydrogen, with its huge ionization potential, into an alkali metal. If we look at the binding energies in the halogen molecules, we see hydrogen as the most strongly bonded halogen.

Next I scanned the electron affinities. Here again, hydrogen stood out, the isolated hydride ion being stable by only 0.75 eV. Thus in

making LiH, we can think of starting with the  $\text{Li}^+$  ion for which it takes 75.64 eV to remove an electron and the  $\text{H}^-$  ion which requires only 0.75 eV to remove an electron. In  $\text{Li}^+$ , on the one hand, the electrons are truly tightly bonded and the ion can be thought of as nearly incompressible. However in  $\text{H}^-$ , on the other hand, the outer electron is so loosely bound that it can be considered to behave almost as a free electron gas (confined to the ion, however).

Table I

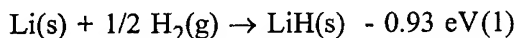
Element	IP* (eV)	MD* energy	Element	DE* (eV)	EA (eV)
H	13.60	4.52	$\text{H}_2$	4.52	0.754
Li	5.39	1.14	$\text{F}_2$	1.64	3.40
Na	5.14	0.76	$\text{Cl}_2$	2.48	3.61
K	4.34	0.52	$\text{Br}_2$	2.00	3.36
Rb	4.18	0.50	$\text{I}_2$	1.58	3.06
Cs	3.89	0.40			

\* IP=Ionization Potential; MD=Molecular Dissociation;  
DE=Dissociation Energy; EA=Electron Affinity.

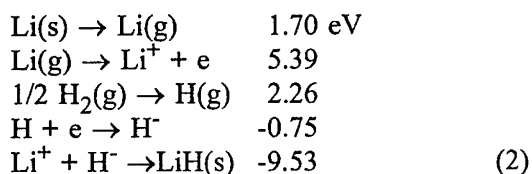
I must stop here to reminisce on a conversation with Peter Debye in 1963 when I was a

young Associate Professor. One of his post-doctoral associates had applied for a faculty position in our department and we were discussing his abilities and potential. Debye made the point that these young people are so much more sophisticated mathematically than he was (this from the person who had developed the method of steepest descents for working with asymptotic expansions) but they often lacked intuitive feeling for chemistry and physics. The discussion which follows relies heavily on this intuitive approach. It began in the spring of 1992 with the question: If LiH forms [primarily but not exactly an ionic solid (2)] why not proton hydride  $H^+H^-$ ?

We consider the reaction



We can visualize this as



Next I considered the ions in the LiH crystal (NaCl type, B1) whose lattice parameter is 4.072 Å. The distance from the center of the  $H^-$  ion to the center of the rigid  $Li^+$  ion is 2.036 Å [Pauling (3)]. Also,  $r_{Li^+} = 2.036$ . Hence

$$r_{H^-} = 2.036 - 0.59 = 1.446 \text{ Å} \quad (3)$$

Along the [110] direction we have

$$r_{H^-} \sqrt{3} a/4 = 1.44 \text{ Å} \quad (4)$$

That these two distances were equal (essentially) struck me as interesting. A hydride ion has been compressed equally by 12 nearest neighbor rigid hydride ions and by 6 nearest neighbor lithium ions in the crystal. Thus the crystal potential could be written

$$U = - \frac{Ae^2}{4\pi\epsilon_0} + \frac{Zb}{r^n} \quad (5)$$

with  $Z = 18$  at  $r = r_0$ . The equilibrium distance is

$$r_0^{n-1} = Z(b4\pi\epsilon_0/Ae^2) \quad (6)$$

Because the outer electron of the hydrogen ion was nearly free electron-like I expected  $n \approx 2$ . In checking the literature on LiH I found the paper of Gerlick and Smith (4) which gave the bulk modulus,  $B^s$ , and  $(\delta B^s/\delta P)_T$  at zero pressure. The latter was 3.7 and converted to 3.2 for  $(\delta B^T/\delta P)_T = B_0'$ . For a central force model, as in Eq. (2),

$$B_0' = (n+7)/3, \quad (7)$$

and a value of  $n = 2$  gives  $B_0' = 3$ . I proceeded with this assumption. It is worthy of note that the results of Besson et al. (5) which came out in 1992 showed  $B_0' = 3.05$  justifying the assumption that  $n = 2$  and so equation (6) becomes

$$r_0 = Zb4\pi\epsilon_0/Ae^2. \quad (8)$$

[For comparison for KCl,  $B_0' = 5.44$  (6) and for CsI,  $B_0' = 5.93$  (7) and these lead to values of  $n = 9.3$  and  $n = 10.8$  respectively, drastically different from that of LiH.]

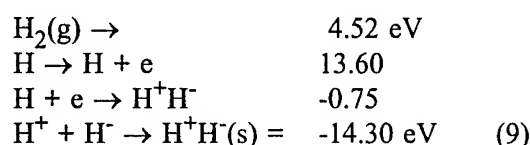
Proton hydride differs from lithium hydride in that there is no repulsion between the proton and the hydride ion, i.e.  $Z = 12$  and so from (4) and (8) it follows that

$$r_{oH^+H^-} = (2/3) r_{oLiH}$$

so

$$V_{oH^+H^-} = (8/27) V_{oLiH}$$

Since  $V_{\text{LiH}} = 10.16 \text{ cm}^3/\text{mole}$ ,  $V_{\text{H}^+\text{H}^-} = 3.01 \text{ cm}^3/\text{mole}$ . From (6) it follows that  $U_0 \propto 1/r_0$  and since  $U_0 = -9.53 \text{ eV}$  for LiH (experimental from the Born-Haber cycle) we have  $U_0 = -14.30 \text{ eV}$  for  $\text{H}^+\text{H}^-(\text{s})$ . Likewise it follows from (5) that  $B_0 \propto 1/r_0^4$ . Since for LiH  $B_0 = 32.1 \text{ GPa}$  we have  $B_0 = 162.5 \text{ GPa}$  for proton hydride. For the formation of proton hydride we have



While proton hydride is stable relative to the isolated atoms by  $-1.45 \text{ eV}$ , the molecule is much more stable. The question a high pressure scientist asks next is obvious. Can pressure change this? The Gibbs free energy of reaction (9) is changed by

$$\int_0^P V_{\text{H}^+\text{H}^-} dP - \int_0^P V_{\text{H}_2} dP \quad (10)$$

and, if this difference becomes  $-3.07 \text{ eV}$ , the two phases  $\text{H}_2(\text{s})$  and  $\text{H}^+\text{H}^-$  have the same Gibbs free energy. For  $\text{H}_2(\text{s})$  the integral had already been evaluated to  $200 \text{ GPa}$  (8) using for  $P > 26.5 \text{ GPa}$

$$V = 4.791 \times 10^{-6} \text{ m}^3 (26.5/P)^{1/2.9} \quad (11)$$

For  $\text{H}^+\text{H}^-$  the Murnaghan equation was used with  $V_0 = 3.01 \times 10^{-6} \text{ cm}^3$ ,  $B_0 = 162.5 \text{ GPa}$  and  $B'_0 = 3$ . Here

$$\Delta G_{\text{H}^+\text{H}^-} = B_0 V_0 \quad (12)$$

$$\left\{ \left( 1 + B'_0 P / B_0 \right)^{1-1/B'_0} - 1 \right\} / \left( B'_0 - 1 \right)$$

This gives  $-3.07 \text{ eV}$  for the difference in (1) when  $P = 191 \text{ GPa}$ .

Do I believe the result? It has been said that action speaks louder than words. While I take this number with reservations, I felt the possible stabilization of the ionic phase  $\text{H}^+\text{H}^-$  was sufficiently likely that we began an extensive research program on the alkali hydrides and some of our results on CsH are given later. I should note that Baranowski has speculated on the formation of proton hydride (9) and that more recently Ashcroft has looked at it more quantitatively [10]. An important aside: The Monte Carlo calculations (11) did not contain the possibility of  $\text{H}^+\text{H}^-(\text{s})$ , i.e., an asymmetry for the hydrogen species (12). This could be placed in the program in the future.

Of the alkali hydrides from CsH to HH (I drop the + and - signs), surely CsH would metallize at the lowest pressure. The approach here was the same which led to our metallization of BaTe (13). It had the smallest band gap and the highest compressibility of the alkaline chalcogenides and was therefore chosen. Although the band gap of the hydrides was not known when we began this study (except for that of LiH) it was assumed to be the lowest for CsH, and we knew from previous equation of state studies that CsH had the smallest  $B_0$  (2,14). Before discussing our results on CsH, it is useful to discuss the only theoretical work on the EOS electronic band structure of these materials, which is on LiH. Baroni et al. (15) carried out exhaustive studies of the band structure of LiH at atmospheric pressure. Their calculated band gap (direct  $X_1^+ - X_2^-$ ) at  $P = 0$  is  $5.24 \text{ eV}$  in close agreement with the experimental value of  $5.25 \text{ eV}$ . Regrettably these studies were not carried to high pressure. In 1988, Hama and Kawakami (16) made studies to high pressure. Their results are shown in Figure 1. Note that their gap at zero pressure is only  $2.6 \text{ eV}$  and they state  $E_g = 4.99 \text{ eV}$  at  $P = 0$ . Their  $E_g$  (change in fractional density) was fitted to a quadratic. ( $E_g = 0$  corresponded to  $\Delta\rho/\rho_0 = 2$  and  $P = 226 \text{ GPa}$ . If it is assumed that the rate of

4.99 describes the situation ( $E_g = 0$  corresponds to  $\Delta\rho/\rho_0 = 4.28$  and  $P = 816$  GPa, the latter computed from Murnaghan's equation with  $B_0 = 3$  and  $B_0' = 32.1$ . The gap does not change rapidly. (While the indirect gap of  $H_2(s)$  has been estimated to go to zero in the neighborhood of 200 GPa, the direct gap is 6.8 eV (17).)

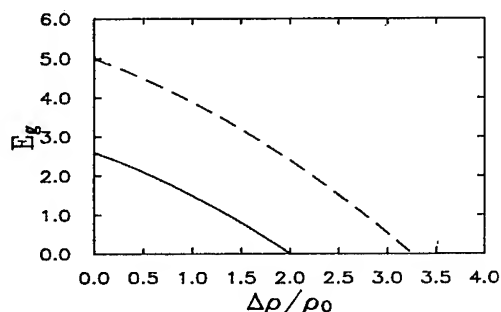


Figure 1. Lower curves show the computed  $E_g$  vs  $\Delta\rho/\rho_0$  curve which can be fitted by  $E_g = 2.6 - 0.915 \Delta\rho/\rho_0 - 0.190 (\Delta\rho/\rho_0)^2$ . The upper curve is scaled upward to  $E_g = 4.99 - 0.915 \Delta\rho/\rho_0 - 0.190 (\Delta\rho/\rho_0)^2$ .

We have made structural studies on CsH to 253 GPa (18), and the structure and EOS is determined to this pressure. Figure 2 shows the band gap of CsH to 251 GPa (19). At this pressure,  $E_g = 1.9$  eV, and the gap is closing slowly so that in the absence of a phase transition metallization may well be above 400 GPa. The picture that emerges is that it is very difficult to close the gap in the hydrides, that the metallization pressure will increase from CsH to HH, that it is already very high for CsH, and that it may be very high, indeed, for HH.

It should be noted that if  $H_2(s)$  transforms to HH(s), the vibron will disappear. The new lattice phonons in the multimegabar range should be observable in the near infrared with the upper edge of the phonon peak at about 1.4 eV (the reduced mass will be 1/2 and the bulk modulus will be very high [much higher than diamond at room pressure] as are those in CsH at high pressure which will be described in a later paper at this meeting (20).

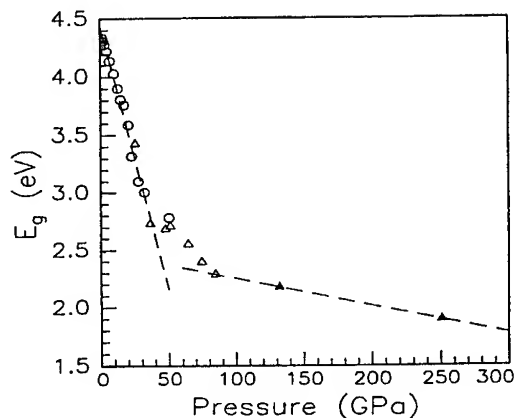


Figure 2. The band gap of CsH versus pressure.

So we turn now to the vibron in  $H_2$ . I want to clarify the experimental situation with which we are faced. This is shown in Figure 3. The top line is the fit to data for transmission through a diamond anvil pair with OD = 0.3 (21). Too much absorption at high intensity causes fracture of the diamond. The bottom line is probably the safe operation limit for diamond with extremely low fluorescence. When studying ruby fluorescence or the vibron of hydrogen we have to have intensity of sufficient strength to induce excitation and to provide an observable signal. (When studying absorption in the diamond anvils we can work at very low intensities.) Thus the 488 nm argon line (2.54 eV) can usually be used at reasonably high intensity (100 mW) on a 5  $\mu$ m spot) to 210 GPa and the 514.5 nm argon line (2.41 eV) to 230 GPa. Clearly, absorption in the diamonds using the 514.5 nm line typically limits ruby measurements to below 230 GPa. "We have found that the  $R_1$  ruby peak above 230 GPa are generally very weak and difficult to measure, even when light-chopping techniques are used to remove background diamond fluorescence" (22) and regarding vibron measurements to 230 GPa "The disappearance [of the Raman vibron signal] could also have been caused by the pressure-induced absorption of the exciting laser photons . . ." (23). I recall

the nervous 4 AM call from Steven Duclos in a study on Mo in which attempts to measure the pressure at about 230 GPa led to failure of the diamonds. One doesn't get the signal, so one increases the excitation intensity and--fracture ensues.

In our first hydrogen experiment we started with one slightly cracked diamond but were able to study the vibron to 190 GPa. In the second experiment we reached 210 GPa when the sample hole moved to the side and blew out.

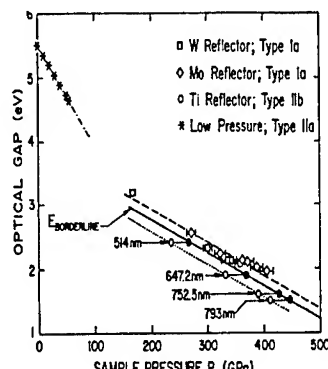


Figure 3. Absorption edge of diamond. The dashed line is a fit of the data for OD = 0.3 which corresponds to a loss of 50% in transmission through two diamond lengths. The dotted line is usually a safe limit (below which absorption does not appear to cause fracture at 300 mW on 5  $\mu$ m diameter).

In our third experiment we had reached 220 GPa (x-ray marker). We had just enough time left at CHESS so that if we increased the pressure we could get one more pressure measurement at CHESS and then return to study the vibron. I had a cold (perhaps this is why I forgot Figure 3) and said "let's go for 300+ GPa." We tightened the nut and waited. We tightened again and waited. We tightened again and waited. We observed the cell in transmission each time and white light was still transmitting. We tightened once more and waited. I had one hand on the cell and Huan was two steps away when a unique (to us) fracture occurred. Unlike the usual click (often nearly inaudible), there was a deafening noise similar to the report of a heavy duty rifle. We

had close to 5000 lbs of force on the tips. In our fourth experiment with diamonds of unusually low fluorescence we obtained the results shown in Figure 4. Somehow we were able to reach 260 GPa without destroying the diamonds with the laser beam. The vibron is present so we still do not have HH. The pressure was increased and measured to be 290 GPa.

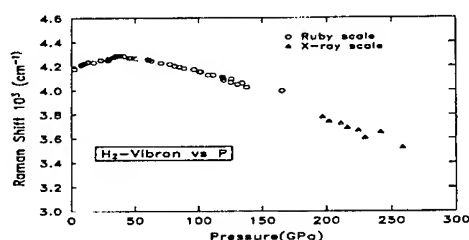


Figure 4. The Raman shift for the vibron of  $H_2$ .

Using the previous 50 mW of 514 nm we could not get a signal and increasing this in steps led to failure at 300 mW. So all we know at 290 GPa is that the specimen still transmits visible light. It is not H metal. It could be  $H_2$  metal although no studies were made in the IR on this sample. It could be HH. It could be just  $H_2$ . We note that the initial sample diameter had decreased from 15 to 6  $\mu$ m and stabilized there, nicely located at the center of the two 35  $\mu$ m diameter tips at 290 GPa. (The colored version is shown on the table of contents page of *Physics World* in which Ashcroft (24) discusses possible reasons why experimentalists have not seen metallic forms of hydrogen.) We suspect that substantially higher pressure would have been reached if laser-induced failure were avoided. We now have a krypton laser so vibron excitation can be carried out at lower energies (see Figure 3), so that, with a new CCD IR detector, we are in a position to carry these experiments further. CHESS has been down since April but comes up again in November [with more than double the previous beam flux] so we look forward to

further experiments (we need synchrotron radiation to measure the pressure).

We are traversing uncharted territory. Transitions in the molecular structure could

substantially reduce the  $\int_0^P V_{H_2} dP$  term in

Equation (10) for a given pressure so that higher pressure than so far calculated would be needed to make metallic  $H_2(s)$  (17), metallic  $H(s)$  (11,25,26) or to make  $HH(s)$  metallic. If  $HH$  is found first, then we can probably forget about achieving metallic  $H_2(s)$ , and we can then reasonably expect that the pressure to achieve metallic  $H(s)$  will be near to 1 TPa or so.

When David Young asked me in 1993 to co-edit High Pressure Research I told him that I had made a full-commitment to reach 450 GPa in molecular solids in the next five years and had to decline. That may not be sufficient to metallize hydrogen.

## References

1. D.R. Lide, Ed., *Handbook of Chemistry and Physics*, CRC Press, Ann Arbor (1993).
2. S.J. Duclos, Y.K. Vohra, A.L. Ruoff, S. Filipek and B. Baranowski, *Phys. Rev. B* **36**, 2664 (1987).
3. L. Pauling, *Nature of the Chemical Bond*, Cornell U. Press, Ithaca, NY (1948).
4. D. Gerlick and C.S. Smith, *J. Phys. Chem. Solids* **35**, 1587 (1974).
5. J.M. Besson, G. Weill, R.J. Nelmea, J.S. Loveday and S. Hull, *Phys. Rev. B* **45**, 2613 (1992).
6. A.L. Ruoff, *J. Appl. Phys.* **38**, 4976 (1967); P.J. Reddy and A.L. Ruoff in *Physics of Solids at High Pressure*, ed. by C.T. Tomizuka and R.M. Emrick, Academic Press Inc., New York (1965), p. 516.
7. G.R. Barsch and Z.P. Chang, in *Accurate Characterization of the High-Pressure Environment*, ed. by E.C. Lloyd, NBS Special Publication 326, Washington, D.C. (1971), p. 173.
8. A.L. Ruoff and C.A. Vanderborgh, *Phys. Rev. Lett.* **66**, 754 (1991).
9. B. Baranowski, *Polish J. Chem.* **66**, 1737 (1992). *Ibid.*, **69**, 981 (1995).
10. N.W. Ashcroft, in *Elementary Processes in Dense Plasmas*, ed. by S. Ichimaru and S. Ogata, Addison-Wesley Publishing Co., New York (1995), p. 251.
11. V. Natoli, R.M. Martin and D.M. Ceperly, *Phys. Rev. Lett.* **70**, 1952 (1993).
12. R. Martin, Private Communication.
13. T.A. Gryzbowski and A.L. Ruoff, *Phys. Rev. Lett.*, **53**, 489 (1984).
14. H.D. Hochheimer, K. Strossner, V. Honle, B. Baranowski and F. Filepek, *Z. Phys. Chem.* **143**, 139 (1985).
15. S. Baroni, G.P. Parravicini and G. Dezzica, *Phys. Rev. B* **32**, 4077 (1985).
16. J. Hama and N. Kawakami, *Phys. Lett. A* **126**, 348 (1988).
17. C. Friedli and N.W. Ashcroft, *Phys. Rev. B* **16**, 662 (1977).
18. K. Ghandehari, H. Luo, A.L. Ruoff, S.S. Trail and F.J. Di Salvo, *Phys. Rev. Lett.* **74**, 2264 (1995).
19. K. Ghandehari, H. Luo, A.L. Ruoff, S.S. Trail and F.J. Di Salvo, *Solid State Commun.* **95**, 385 (1995).
20. A.L. Ruoff and K. Ghandehari (CsH and CsD paper at this conference).
21. A.L. Ruoff, H. Luo and Y.K. Vohra, *J. Appl. Phys.* **69**, 643 (1991).
22. H.K. Mao and R.J. Hemley, *Science* **244**, 1462 (1989).
23. H.-K. Mao and R.J. Hemley, *Rev. Mod. Phys.* **66**, 671 (1994).
24. N.W. Ashcroft, *Physics World*, July 1955, p. 43. The photo is on page 1.
25. E.G. Brofman, Yu Kagan and A. Kholas, *Zh. Eksp. Teos. Fiz.* **61**, 2429 (1971) [*Sov. Phys.-JETP* **34**, 1300 (1972)].
26. J. Hammerberg and N.W. Ashcroft, *Phys. Rev. B* **9**, 409 (1974).

## PRESSING FOR METALLIC HYDROGEN

ISAAC F. SILVERA, NANCY H. CHEN, AND ERAN STERER

Lyman Laboratory of Physics, Harvard University  
Cambridge MA, 02138, U.S.A.

At sufficiently high pressures believed to be in the 150-400 GPa range, hydrogen and its isotopes are predicted to become metallic. The hydrogens have rich and unusual phase diagrams at high pressure. In the megabar range they are predicted to have a band overlap insulator-metal transition within the molecular phases. At still higher pressure, molecules should dissociate to form the atomic metallic state, also predicted to be a high temperature superconductor. At about 150 GPa both hydrogen and deuterium have transitions to a new phase called the A phase. Although the A phase has been suspected to be the molecular metallic phase, our infrared measurements find no evidence of metallic behavior. We provide an explanation for earlier reports that hydrogen was metallic.

### Introduction

One of the great modern challenges of condensed matter and high pressure physics is to produce metallic hydrogen in the laboratory. Since the original estimate of Wigner and Huntington [1] over 60 years ago of 25 GPa for the transition pressure to the atomic metallic state, modern estimates have been in the region of 300-500 GPa. Later calculations, starting with Ramaker, Kumar, and Harris [2] have predicted that before the Wigner-Huntington transition, hydrogen would become a metal in the molecular phase by band overlap. In the late 60's interest in trying to produce metallic hydrogen in the laboratory was stimulated by the prediction of Ashcroft [3] that metallic hydrogen might be a high temperature superconductor. In the last decade, static pressures achievable in a diamond anvil cell (DAC) have pushed into the megabar range and for hydrogen are currently on the fringe of 300 GPa. Thus, the first searches for metallic hydrogen have been for the molecular metallic phase. Surprising results have been found as both the theoretical and experimental tools for finding this complex simple metal have been honed.

### The A Phase

In 1988 Hemley and Mao [4] observed a discontinuity in the frequency of the Raman active vibron at about 150 GPa and 77 K. They interpreted this as a phase transition and thought that it was an extension of the well-known low pressure phase of orientational order due to electric quadrupole-quadrupole anisotropic interactions. Subsequently, Lorenzana, Silvera, and Goettel [5] showed that this was a unique new high pressure phase; they determined the phase line (see Fig. 1) and showed that this phase only existed for pressures above approximately 150 GPa.

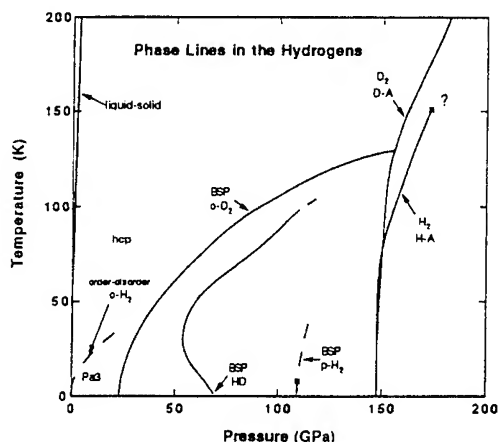


Fig. 1 Phase lines as a function of temperature and pressure for the solid hydrogens.

This high pressure phase was named the hydrogen-A phase (H-A) and was immediately suspected of being the metallic molecular phase of hydrogen. Lorenzana et al [6] also showed that the H-A phase was a structure with orientational order of the molecules. Hemley and Mao [7] also found a discontinuity in the vibron frequency in deuterium and recently Cui, Chen, and Silvera [8] have determined the phase line for the deuterium-A (D-A) phase.

### Metallic Molecular Hydrogen

The first attempt to establish the metallic properties of the A phase was a dielectric study by Eggert, Goettel, and Silvera [9] to determine the pressure at which the conduction-valence band closes. They measured the pressure dependence of the real part of the dielectric constant up to 73 GPa and extrapolated from their pressures to predict closure at pressures in the region of the A



phase. They soon after revised this result to much higher pressures with an improved extrapolation [10], realizing that the dielectric studies correspond to closure of the direct gap, whereas metallization was expected to occur by closure of an indirect gap at much lower pressures. Thus, if an indirect gap closes, this technique would not reveal the closure pressure. This picture was confirmed by Hemley, Mao, and Hanfland [11] who improved the pressure range of this study to 170 GPa.

A more direct method of determining the metallization pressure is to search for free electron behavior. According to the Drude model which is characterized by the plasma frequency (proportional to the square root of the electron carrier density) and the scattering rate, for a metal the optical reflectance and absorption increase rapidly as frequencies are decreased below the plasma frequency. Mao, Hemley, and Hanfland [12] observed a rising edge in reflectivity, within their spectral range limited to  $\sim 4000 \text{ cm}^{-1}$  in the IR and interpreted this as a Drude edge and reported direct evidence of metallization by band overlap. Eggert et al [13] studying hydrogen to much higher pressures, 230 GPa, found no evidence of metallization. Although their frequency range was not as low they could show that Mao et al's analysis was inconsistent with causality or the Kramers-Kronig relation of reflectivity and absorption. Hanfland et al [14] then reported a Drude edge in absorption to support their report of metallization, but had to revise their Drude parameters, including the index of refraction of hydrogen and diamond which enter into the analysis, in order to make the reflection and absorption compatible. Silvera [15] showed that the index of hydrogen used in this analysis was unphysical and therefore the Drude analysis was not a reliable interpretation. In spite of these results belief was retained by Mao and coworkers that hydrogen was metallic.

In order to understand the Drude behavior it was necessary to extend the spectral range of study to lower frequencies. This is difficult for two reasons. In general the available radiation from a black body source is falling rapidly at lower energies, and due to the small size of the sample in the DAC (diameter of order 10-30 microns) diffraction losses from the gasket increase rapidly as the wavelength becomes comparable with the hole radius. Hanfland et al [16] utilized a powerful synchrotron source of radiation and later developed their own synchrotron IR station [17]. Evidently, until very recently [18] they were unable to sort out the Drude problem. They did, however, extend their

range of frequencies and found that in the A phase a vibron mode was IR active and had an absorption strength that could grow to be orders of magnitude stronger than IR active vibrons in lower pressure phases. (We shall remark on the relationship between the IR vibron and the reported Drude edge later in this article). A similar behavior has been found by Cui, Chen, and Silvera in the D-A phase [8], [19]. This strong absorption strength cannot be understood in terms of the normal mechanism of dipole moments induced by fields from neighboring molecules and is believed to be an important, but as yet not understood key to the structure of the A phase.

Cui, Chen, and Silvera [20] developed a tunable color center laser for broad band IR studies and extended the spectral limit down to  $3000 \text{ cm}^{-1}$ . In a study of deuterium they found no strong evidence of Drude behavior. Since the density (pressure) for the A phase line is almost identical in hydrogen and deuterium one might expect the onset of the Drude edge to be at roughly the same frequency for the two isotopes if they are metallic. Although they saw a slowly rising absorption with decreasing energy, especially for pure ortho deuterium, the range of study was insufficient to identify metallic behavior and suggested that still lower frequencies were required.

We report here studies of hydrogen with a new spectroscopic system optimized for "Drude spectroscopy", i.e. broad band low resolution spectroscopy, which operates to  $1000 \text{ cm}^{-1}$ , extending our useful range of studies for this type of search by a factor of three. This system, which uses a very hot graphite IR source and reflective optics, will be described elsewhere [21]. A low resolution spectrum is shown in Fig. 2 for pure para hydrogen at 9 K in a DAC at a pressure of 191 GPa, well into the A phase. We also compare to the absorption spectra of Hanfland et al. There is clearly no Drude edge in the region reported earlier and there is no evidence of Drude behavior throughout the range that has been studied. This now represents the most exhaustive reported study for metallization in hydrogen at the combined highest pressure and lowest frequency yet. Moreover, the sample is in the low temperature limit at  $T=9 \text{ K}$  and is completely converted to equilibrium para-hydrogen, with a purity probably better than a part in  $10^4$ . This is [20] important as it has been suggested by Ashcroft [22] that ortho-para mixtures might suppress metallization due to Anderson localization. Based on this study we can state that there exists no experimental

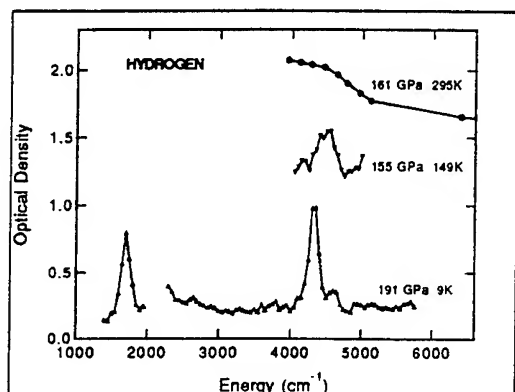


Fig. 2 Infrared absorption spectra for hydrogen. The lowest curve is our recent measurement on para hydrogen to be compared to the upper curve of Mao et al. The middle curve shows vibron absorption in the LP phase. The curves are displaced for clarity. The missing segment of data in the region near  $2000\text{ cm}^{-1}$  is due to strong IR absorption by the diamond anvils.

evidence for metallic behavior in hydrogen in the A phase. We note that this does not exclude metallic behavior in the A phase as it is possible that a Drude edge lies at still lower frequencies than have been studied. We think that it will be difficult to push this experimental technique much further as higher pressures will require smaller gasket holes and thus increased attenuation at long wavelength due to diffractive scattering, and the signal-to-noise is already becoming poor. The most attractive and rigorous method of establishing the conductive properties of the A phase would be to measure the static electrical conductivity at low temperature.

## Explanation of Reports of Metallization

We are now left with the question of what did Mao, Hemley, and Hanfland observe in their spectroscopic studies of 1990 in which metallic hydrogen was claimed. Ruoff and Vanderborgh [23] suggested that the copious amounts of ruby in their samples may have been reduced by the hydrogen to elemental aluminum; however, their original estimates of the pressure for this to occur were in error [24]. It has also been suggested that the reflectivity could have been affected by gradients in the index of refraction due to the ruby powder mixed in with the sample of hydrogen

[25], but it has been argued that this explanation is inadequate [26]. From Fig. 2 an obvious explanation which has been proposed earlier [20] is that the observed optical edge was actually the leading edge of the high pressure IR active vibron in the vicinity  $4100\text{ cm}^{-1}$ . For a sample of pure para hydrogen at room temperature, studied by Mao et al this absorption would not be present. At this temperature the sample is not in the A phase, but rather the LP (low pressure) phase which is known to have the hcp structure in which the vibron is infrared inactive. However, a sample which has been prepared at room temperature from normal hydrogen will remain equilibrium hydrogen with a mixture of 0.75 ortho/0.25 para, (based on low temperature rotational properties of hydrogen). In this case the lattice no longer has translational symmetry and the vibron might be active for all values of lattice  $\mathbf{k}$ -vector. To test this hypothesis we studied a hydrogen sample at 155 GPa at temperatures above the transition temperature to the LP phase ( $104 \pm 8\text{ K}$ ) several hours after it had been at temperatures above 77 K (so that the ortho concentration was 0.5 or greater) and indeed observed strong absorption, shown in Fig. 2, in the region where the  $\mathbf{k}=0$  vibron is observed for para hydrogen. Thus, we believe that at room temperature what was observed was the leading edge of the vibron absorption in a translationally disordered ortho-para mixture of hydrogen. An earlier claim of metallic hydrogen in 1989 by Mao and Hemley [27] at pressures above 200 GPa still remains. We believe that this claim was adequately refuted by Silvera [28] already in 1990.

## Future Prospects

What are the current prospects for metallization in the hydrogens. It may be that the molecular phase will not exhibit metallic behavior and will be unstable to distortions to states such as antiferromagnetic ones, with finite band gaps. We compare to molecular iodine which indeed has been observed to have a transition to a molecular metallic state. The difference may be that the molecules of iodine are sterically hindered from rotating, whereas at a pressure of a few hundred GPa, even though the single molecule states of hydrogen are no longer free rotor states they are still characterized by broad orientational distributions and this in itself might be enough to suppress metallization [22]. The argument here is that the electron motions are much faster than the reorientational motions of the molecules, so the

electrons sample a disordered lattice of atoms. An interesting possibility for the A phase is the proposal by Klug and Tse (in this conference proceedings) that the molecules partition into two groups with short bonds and long bonds at high pressure to form a rhombic lattice with a non zero band gap. Another is proposal by Baronowski [29] that molecular hydrogen polarizes to form permanent molecular dipole moments in analogy with LiH. For both of these proposals it is difficult to understand the rather strong absorption that we have observed at 155 GPa in the LP phase. The future challenges for hydrogen research are to understand the A phase and to push to yet higher pressures.

### Acknowledgements

We thank the U.S. Air Force Phillips Laboratory for support of this research.

### References

1. E. Wigner and H.B. Huntington, J. Chem. Phys. **3**, 764 (1935).
2. D.E. Ramaker, L. Kumar, and F.E. Harris, Phys. Rev. Lett. **34**, 812 (1975).
3. N.W. Ashcroft, Phys. Rev. Lett. **21**, 1748 (1968).
4. R.J. Hemley and H.K. Mao, Phys. Rev. Lett. **61**, 857 (1988).
5. H.E. Lorenzana, I.F. Silvera, and K.A. Goettel, Phys. Rev. Lett. **63**, 2080 (1989).
6. H.E. Lorenzana, I.F. Silvera, and K.A. Goettel, Phys. Rev. Lett. **64**, 1939 (1990).
7. R.J. Hemley and H.K. Mao, Phys. Rev. Lett. **63**, 1393 (1989).
8. L. Cui, N.H. Chen, S.J. Jeon, and I.F. Silvera, Phys. Rev. Lett. **72**, 3048 (1994).
9. J.H. Eggert, K.A. Goettel, and I.F. Silvera, Europhys. Lett. **11**, 775 (1990).
10. J.H. Eggert, K.A. Goettel, and I.F. Silvera, Europhys. Lett. **12**, 381 (1990).
11. R.J. Hemley, M. Hanfland, and H.K. Mao, Nature **350**, 488 (1991).
12. H.K. Mao, R.J. Hemley, and M. Hanfland, Phys. Rev. Lett. **65**, 484 (1990).
13. J.H. Eggert, F. Moshary, W.J. Evans, H.E. Lorenzana, K.A. Goettel, and I.F. Silvera, Phys. Rev. Lett. **66**, 193 (1991).
14. M. Hanfland, R.J. Hemley, and H.K. Mao, Phys. Rev. B **43**, 8767 (1991).
15. I.F. Silvera, *NATO ARW on Frontiers of High Pressure Research*. 1991, Plenum Press, New York.
16. M. Hanfland, R.J. Hemley, H.K. Mao, and G.P. Williams, Phys. Rev. Lett. **69**, 1129 (1992).
17. M. Hanfland, R.J. Hemley, and H.K. Mao, Phys. Rev. Lett. **70**, 3760 (1993).
18. H.K. Mao has shown extended IR data in this conference which do not support the earlier report of band closure metallization.
19. L. Cui, N.H. Chen, and I.F. Silvera, Phys. Rev. B **51**, 14987 (1995).
20. L. Cui, N.H. Chen, and I.F. Silvera, Phys. Rev. Lett. **74**, 4011 (1995).
21. N.H. Chen, E. Sterer, and I.F. Silvera, submitted for publication (1995).
22. N.W. Ashcroft, Journal of Non-crystalline Solids **156**, 621 (1993).
23. A.L. Ruoff and C.A. Vanderborgh, Phys. Rev. Lett. **66**, 754 (1991).
24. R.G. Greene, H. Luo, and R.L. Ruoff, , *High Pressure Science and Technology-1993*, J.W.S. S.C. Schmidt G.A. Samara, M. Ross, Editor. 1994, AIP Conf. Proc.: Colorado Springs, CO.
25. R.G. Greene and A.L. Ruoff, , *High Pressure Science and Technology-1993*, S.C. Schmidt, et al., Editor. 1994, AIP: Colorado Springs, CO. p. 1515.
26. H.K. Mao, J.H. Eggert, and R.J. Hemley, Mod. Phys. Lett. B **9**, 201 (1995).
27. H.K. Mao and R.J. Hemley, Science **244**, 1462 (1989).
28. I.F. Silvera, Science **247**, 863 (1990).
29. B. Baranowski, Polish J. Chem. **66**, 1737 (1992).

# ELECTRICAL CONDUCTIVITIES AND SHOCK TEMPERATURES OF FLUID HYDROGEN UP TO 200 GPa (2 Mbar)

W. J. NELLIS, N. C. HOLMES, M. ROSS, S. T. WEIR, AND A. C. MITCHELL

*Lawrence Livermore National Laboratory, Livermore, CA 94550, USA*

Electrical conductivities and shock temperatures were measured for shock-compressed liquid H<sub>2</sub> and D<sub>2</sub>. Conductivities were measured at pressures of 93–180 GPa (0.93–1.8 Mbar). Calculated densities and temperatures were in the range 0.28–0.36 mol/cm<sup>3</sup> and 2200–4400 K. The resistivity data are interpreted in terms of a continuous transition from a semiconducting to metallic diatomic fluid at 140 GPa and 3000 K. Shock temperatures up to 5200 K were measured at pressures up to 83 GPa. These data are interpreted in terms of a continuous dissociative phase transition above 20 GPa. This dissociation model indicates a dissociation fraction of  $\approx 5\%$  at 140 GPa and 3000 K. Metallization is occurring in the molecular phase.

## Introduction

The properties of hydrogen at high pressures and temperatures are of interest to understand the nature of metallization,<sup>1</sup> the isentropes of Jupiter and Saturn,<sup>2,3,4</sup> and the equation of state of hydrogen in laser fusion experiments. For these reasons we have measured electrical conductivities and temperatures of hydrogen and deuterium shock compressed to pressures up to 200 GPa. The conductivity experiments were performed with a reverberating shock wave to minimize the temperature and maximize pressure. The temperature measurements were performed to investigate effects of molecular dissociation. The theoretical model for dissociation derived from the temperature measurements was used to show that the conductivity experiments probed hydrogen primarily in the molecular phase.

## Experiments

High shock pressures were generated by impact of a hypervelocity impactor onto the front surface of a sample holder containing liquid hydrogen.<sup>5</sup> The impactors were accelerated to velocities up to 7 km/s with a two-stage light-gas gun. Both hydrogen and deuterium were used to obtain different densities and temperatures. In the conductivity experiments hydrogen was contained between Al<sub>2</sub>O<sub>3</sub> anvils which in turn were contained between Al disks. Hydrogen shock pressure was determined by shock impedance matching the measured impactor velocity and known Hugoniot equations of state of the impactor, Al, and Al<sub>2</sub>O<sub>3</sub>. The pressure in hydrogen reverberates up to the

first shock pressure in the Al<sub>2</sub>O<sub>3</sub>, independent of the equation of state of hydrogen.<sup>6</sup> The electrical resistance was measured and electrical resistivity was obtained by calibration. Due to the large density mismatch between hydrogen and Al<sub>2</sub>O<sub>3</sub> the first-shock pressure in hydrogen is a factor of  $\approx 25$  lower than the first shock in Al<sub>2</sub>O<sub>3</sub>. The reverberation of the shock in hydrogen between the Al<sub>2</sub>O<sub>3</sub> anvils further compresses the hydrogen to the first shock pressure of Al<sub>2</sub>O<sub>3</sub> while maintaining a relatively low final hydrogen temperature. The configuration was illustrated previously.<sup>7</sup> In the temperature experiments hydrogen was contained between an Al disk and an Al<sub>2</sub>O<sub>3</sub> or LiF window. Pressure and density were obtained by shock impedance matching. The temperatures of the first shock and of this shock reflected off the window were determined by fitting the spectrum of the emitted radiation to a greybody spectrum.

## Results

Although condensed molecular hydrogen is a wide band gap insulator at ambient pressure ( $E_g = 15$  eV), at sufficiently high pressure the energy gap is expected to close to zero. Previous experiments have measured the electrical conductivity of hydrogen in the fluid phase at single-shock pressures up to 20 GPa and 4600 K.<sup>8</sup> In the present conductivity experiments pressures of 93–180 GPa were achieved. Hydrogen is in the fluid phase because the calculated temperatures are well above the calculated melting temperatures of  $\approx 1000$  K at 100 GPa pressures.<sup>9</sup> The shock-compression technique is very well suited for measuring the electrical conductivity of hydrogen because: i) the

high pressure reduces the energy gap, ii) the reverberating shock maintains temperatures at a few 0.1 eV,  $\approx 10$  times lower than the temperature which would be achieved by a single shock to the same pressure, iii) the relatively low shock temperatures activate sufficient conduction electrons to produce measurable conductivities, and iv) electrode dimensions and separations are of order mm's, which are straightforward to assemble. In these experiments the thickness of the hydrogen layer decreases from the initial value of 500  $\mu\text{m}$  down to the compressed value of  $\approx 60 \mu\text{m}$ . Although the  $\text{Al}_2\text{O}_3$  disks become somewhat conducting at Mbar shock pressures, supplemental experiments examining the electrical conductivity of shock-compressed  $\text{Al}_2\text{O}_3$ <sup>10</sup> show that the conductivity of hydrogen is 2–4 orders of magnitude greater than that of  $\text{Al}_2\text{O}_3$ , which causes a small to negligible correction to the hydrogen data.

The electrical resistivities decrease from about 1  $\Omega\text{-cm}$  at 93 GPa to  $5 \times 10^{-4} \Omega\text{-cm}$  at 140 GPa and are constant at  $5 \times 10^{-4} \Omega\text{-cm}$  at 155 and 180 GPa. Since our previous data<sup>8</sup> show that the electrical conductivity of hydrogen is thermally activated, we analyzed these results in the range 93–135 GPa using our previous dependence for a fluid semiconductor:

$$\sigma = \sigma_0 \exp(-E_g/2k_B T) \quad (1)$$

where  $\sigma$  is electrical conductivity,  $\sigma_0$  depends on density  $\rho$ ,  $E_g(\rho)$  is the density-dependent energy gap in the electronic density of states of the fluid,  $k_B$  is Boltzmann's constant, and  $T$  is temperature.

The density and temperature were calculated by computationally simulating each experiment using a standard equation of state of hydrogen.<sup>11</sup> This equation of state is for the molecular fluid phase. Although a computational model for hydrogen introduces systematic uncertainties in the calculated densities and temperatures, the results are useful for understanding the slope change at 140 GPa. Our least-squares fit of Eq. 1 to data gives  $E_g(\rho) = 0.905 - 67.7(\rho - 0.3)$  where  $E_g$  is in eV,  $\rho$  is in moles/cm<sup>3</sup>, and  $\sigma_0 = 140 (\Omega\text{-cm})^{-1}$ . A value of  $\sigma_0 \approx 10^3 (\Omega\text{-cm})^{-1}$  is typical of liquid semiconductors.<sup>12</sup>  $E_g(\rho)$  derived from this fitting procedure and  $k_B T$  are equal at a temperature of 0.3 eV and a density of 0.31 mol/cm<sup>3</sup>. In this region of density and temperature the energy gap is smeared out thermally, activation of electronic carriers is complete, disorder is already saturated

in the fluid, and conductivity is expected to be weakly sensitive to further increases in pressure and temperature. At 0.31 mol/cm<sup>3</sup> the pressure is 120 GPa, which is close to the pressure at which the slope change in the electrical resistivity occurs at 140 GPa. At higher pressures of 155 and 180 GPa the resistivity is essentially constant at  $5 \times 10^{-4} \Omega\text{-cm}$ , a value typical for liquid metals.<sup>13</sup> Thus, fluid hydrogen becomes metallic at about 140 GPa and 3000 K via a continuous transition from a semiconducting to metallic fluid.<sup>14</sup>

Because molecular dissociation of hydrogen has been observed in optical shock temperature measurements, the theoretical model derived from those data<sup>15,16</sup> was used to calculate the dissociation fraction in these conductivity experiments. At 140 GPa and 3000 K the dissociation fraction is calculated to be about 5%. Metallization is occurring within the diatomic molecular phase.

We have also measured temperatures of liquid deuterium and hydrogen shocked at pressures up to 83 GPa and 5200 K.<sup>15,16</sup> Previously we measured the Hugoniot pressure-density curves of deuterium and hydrogen up to 80 GPa.<sup>5</sup> Temperatures were measured by fitting the optical radiation emitted from the shock front to a greybody spectrum. The first-shock temperatures up to 20 GPa are in excellent agreement with predictions based on molecular hydrogen.<sup>17</sup> The second-shock temperatures up to 83 GPa, obtained by reflection of the first shock off a window, are lower than predicted for the molecular phase. The lower measured temperatures are caused by a continuous dissociative phase transition above 20 GPa. This partial dissociation from the molecular to the atomic phase absorbs energy, which causes lower temperatures than were thought previously. These data are for hydrogen in thermal equilibrium because all the relaxation times are small compared to the time resolution of the experiments. Thus, these results are generally important for understanding the condensed matter physics of metallization of hydrogen and for understanding isentropes of the interiors of Jupiter and Saturn. These giant planets are essentially fluid hydrogen at high pressures and high temperatures. Calculations based on these data indicate that the interior of Jupiter is cooler and has much less temperature variation than believed previously. The continuous dissociative phase transition means that there is no sharp boundary between the molecular layer and

the metallic-H core of Jupiter.<sup>16</sup> A possible maximum in temperature versus pressure might induce an additional layer in the molecular region, as has been predicted by Zharkov *et al.*<sup>4</sup>

### Acknowledgments

We thank M. Ross, D. A. Young, G. Chabrier, and N. W. Ashcroft for discussions. We acknowledge P. C. McCandless, E. See, J. Crawford, S. Weaver, K. Stickle, and R. Silva for technical assistance. We thank R. Kays of Lockheed-Martin for providing a storage dewar for liquid-H<sub>2</sub> coolant. This work was performed with support from the Lawrence Livermore National Laboratory's Directed Research and Development Program under the auspices of the U. S. Department of Energy under Contract No. W-7405-ENG-48 and with support from NASA under grant W16.180.

### References

1. E. Wigner and H. B. Huntington, *J. Chem. Phys.* **3** (1935) 764.
2. W. B. Hubbard, *Science* **214** (1980) 145.
3. D. J. Stevenson, *Annu. Rev. Earth Planet. Sci.* **10** (1982) 257.
4. V. N. Zharkov and T. V. Gudkova, in *High-Pressure Research: Application to Earth and Planetary Sciences*, ed. Y. Syono and M. H. Manghnani (Terra Scientific Publishing, 1992), pp. 393-401.
5. W. J. Nellis, A. C. Mitchell, M. van Thiel, G. J. Devine, R. J. Trainor, and N. Brown, *J. Chem. Phys.* **79** (1983) 1480.
6. K. M. Ogilvie and G. E. Duvall, *J. Chem. Phys.* **78** (1983) 1077; C. S. Yoo, G. E. Duvall, J. Furrer, and R. Granholm, *J. Phys. Chem.* **93** (1989) 3012.
7. S. T. Weir, A. C. Mitchell and W. J. Nellis, in *High-Pressure Science and Technology—1993*, ed. S. C. Schmidt, J. W. Shaner, G. A. Samara, and M. Ross (American Institute of Physics, 1994), p. 881-883.
8. W. J. Nellis, A. C. Mitchell, P. C. McCandless, D. J. Erskine, and S. T. Weir, *Phys. Rev. Lett* **68**, (1992) 2937.
9. M. Ross, H. C. Graboske, and W. J. Nellis, *Phil. Trans. R. Soc. Lond.* **A303** (1981) 303.
10. S. T. Weir, A. C. Mitchell and W. J. Nellis, submitted (1995).
11. G. I. Kerley, in *Molecular-Based Study of Fluids*, ed. J. M. Haile and G. A. Mansoori (American Chemical Society, 1983), pp. 107-138.
12. N. F. Mott, *Phil. Mag.* **24** (1971) 1.
13. M. Shimoji, *Liquid Metals* (Academic Press, 1977), p. 381.
14. S. T. Weir, A. C. Mitchell, and W. J. Nellis, submitted (1995).
15. N. C. Holmes, M. Ross, and W. J. Nellis, *Phys. Rev. B* (in press).
16. W. J. Nellis, M. Ross, and N. C. Holmes, *Science* (in press).
17. M. Ross, F. H. Ree, and D. A. Young, *J. Chem. Phys.* **79** (1983) 1487.

# CHEMICAL APPROACH TO THE POSSIBILITY OF HYDROGEN - HYDRIDE FORMATION

B. BARANOWSKI

*Institute of Physical Chemistry, Polish Academy  
of Sciences, 01-224 Warsaw Poland*

Metallization of hydrogen is normally treated by collective physical methods. As the phase transition at 150 GPa seems not to be connected with metallization, an individual chemical approach seems valuable. The unique position of hydrogen in the periodic table is first presented, giving arguments for both metallic and halogen like behaviour. Furtheron the energetic sequence of events is presented when going over from covalent to the metallic state of hydrogen. Later some calculation of the energy - distance curves are presented and historical considerations of the  $H^+$  appearance in the early quantum chemistry are mentioned.

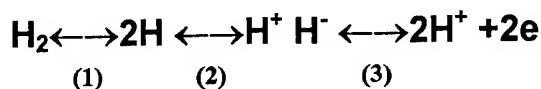
Hydrogen occupies a unique position in the periodic table of the elements: Placed mostly together with alkali metals suggests a close similarity with them including the possibility of metallization. A rich theoretical literature about this possibility is a clear confirmation of such expectation [1]. The similarity of hydrogen to alkali metals is manifested by the large affinity to halogens and comparable electron affinities: 0.75 eV for H and 0.62 and 0.47 for Li and Cs respectively. Furthermore in the alkali metals and hydrogen one electron occupies the external shell.

But on the other hand some properties make hydrogen related to halogens: 1.) The ionization energies are comparable - 13.6 eV for hydrogen and 17.4 eV for F to 10.5 eV for I. Let us remark at this place the comparable ionization energy of hydrogen atom (13.6 eV) and the valence - conduction bond gap (16 eV) in the solid hydrogen [1]. 2.) At ambient conditions halogens and hydrogen form stable two - atomic covalent molecules as well in gaseous as in the liquid and solid states. 3.) All these elements form stable noble gases structures after addition of one electron (but -as mentioned above with different electronic affinities). 3.) In organic compounds the substitution of hydrogen by halogens does not cause radical changes. 4.) Halogens exhibit, like hydrogen, low melting temperatures.

These similarities are the reason for which in some periodic tables of the elements hydrogen is placed in the group of halogens. Perhaps as most reasonable seems the intermediate (non fixed in a certain sense) position of hydrogen in the periodic table, what can be found in the literature [2]. This intermediate, unique position of hydrogen in the

periodic table suggests the possibility that hydrogen could play in respect to himself the simultaneous role of an alkali metal and a halogen. Then the existence of hydrogen - hydride seems probable. Such a structure means the realization of both extreme behaviours of hydrogen in the same ionic molecule [3]. These two extreme roles - as an anion or cation - plays hydrogen in hydrides of alkali metals (as anion) or hydrides of transition metals, where its behaviour can be simplified to a screened proton (cation).

Let us consider pure energetic aspects of hydrogen - hydride formation in comparison with the metalization of hydrogen [4]. The following sequence of transformations has to be discussed:



Step (1) describes the dissociation of hydrogen molecule into two hydrogen atoms. It requires 432 kJ/mol  $H_2$ . Step (2) corresponds to the transformation of two hydrogen atoms into the cation and anion of hydrogen - what is identical with the formation of hydrogen - hydride. Step (2) requires 1240 kcal/mol, thus it is a quite expensive transformation. But step (3) that is the transformation of hydrogen - hydride into full ionized protons and electrons - thus a metallization of hydrogen requires again 1384 kcal/mol. This is more than the transition from hydrogen atoms to the hydride form. In other words the metallization of hydrogen atoms is twice as expensive as the transition to the hydrogen- hydride. The last mentioned form appears really as an energetic

intermediate step between the covalent and metallic form of hydrogen. In other words if the increase of hydrostatic pressure in solid hydrogen is equivalent with a continuous increase of the chemical potential of hydrogen, the hydride (ionic or salt) form of hydrogen seems as a logic preform of the metallization. In fact hydrogen - hydride represents a partial metallization as already one proton is present in the ionic bond assumed.

For the ionic pair  $H^+$  and  $H^-$  it is easy to perform calculations of the energy - distance potential curves, basing on similar principles as realized for alkaline metal - hydrogen ionic bonds [5]. Separating the total interaction into three parts:

$$V = V_1 + V_2 + V_3 \quad (1)$$

In (1)  $V_1$  means:

$$V_1 = V_j(H) + V_{aH}(H) \quad (2)$$

where  $V_j(H)$  is the ionization energy of the hydrogen atom and  $V_{aH}(H)$  the electronic affinity of hydrogen.

$$V_2 = -(q_H^+ q_H^-)/r \quad (3)$$

is the coulombic attractive energy,  $q_H^+$  and  $q_H^-$  are the charges of both ions and  $r$  the distance between  $H^+$  and  $H^-$ .

$$V_3 = be^{-r/\rho} \quad (4)$$

denotes the repulsive energy, where  $b$  and  $\rho$  are constants. The  $b$  constant can be evaluated if a given equilibrium distance (the energy minimum) is assumed. Thus as the only arbitrary constant remains  $\rho$ .

In Fig.1 one has to remark that smaller  $r_0$  values correspond to deeper potential wells. Thus with increasing pressure a situation can be realized where a transition from the potential curve characteristic for the covalent  $H_2$  molecule to the potential curve of the hydrogen - hydride ionic pair may be energetically favorable. This transition is not necessary accompanied by a large energy jump, as was sometimes suggested [6]. From quantum mechanical point of view a continuous transition from the covalent to ionic bond is not excluded. Such a point of view was represented in the early

quantum chemistry [7]. Being more specific let us present shortly the molecular orbital (MO) approach for the hydrogen molecule. Terming by  $A$  and  $B$  hydrogen nuclei and by 1 and 2 the electrons, we have four wave functions

$$\Psi_A(1), \Psi_A(2), \Psi_B(1) \text{ and } \Psi_B(2) \quad (5)$$

In terms of the MO the wave function of the hydrogen molecule  $AB$  equals:

$$\Psi_{AB} = N^2[\Psi_A(1)\Psi_A(2) + \Psi_B(1)\Psi_B(2) + \Psi_A(1)\Psi_B(2) + \Psi_A(2)\Psi_B(1)].$$

It is a clear that  $\Psi_A(1)\Psi_A(2)$  and  $\Psi_B(1)\Psi_B(2)$  correspond to  $[H^+H^-]$ . In fact the MO approach overestimates the ionic (heterogenic) combinations of wave functions. This is not the case in the Heitler - London method [8]. Now we know that the complete disregard of the ionic combinations leads to an excellent agreement with the properties of the hydrogen molecule at ambient conditions [9]. But this must not be continued in the extremal conditions of dense hydrogen. The question to be put is the following: Does dense hydrogen with increasing pressure present the tendency to transition to ionic bond? This question is interesting both for theoreticians and experimentalists.

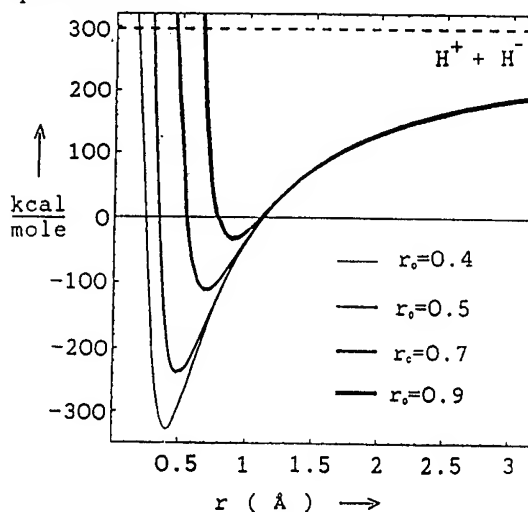


Fig. 1. The energy - distance curves for the ionic pair  $H^+H^-$  at different (supposed) minimum energy distances ( $r_0$ ) if for  $\rho$  the value 0.1 was taken.



References:

1. N.W. Ashcroft, in *Frontiers of High Pressure Research* ed. H.D. Hochheimer and R.D. Elters (Plenum Press, 1992) p.115.
2. F. Sherwood Taylor: *Inorganic and Theoretical Chemistry*, 8. Ed. 1948, W. Heinemann LTD, Melbourne
- 3.) B. Baranowski, *Polish J. Chem.* 66(1992)1737.
- 4.) B. Baranowski, *Polish J. Chem.* 69(1995)981.
- 5.) W.W. Porterfield: *Inorganic Chemistry*, 1984, Addison - Wesley Publ. Comp.
6. ) R.J. Hemley, Z.G. Soos, M. Hanfland and H.K. Mao, *Nature* 369 (1994) 384.
- 7.) L. Pauling, *The Nature of Chemical Bond*. III. ed., 1960, Cornell Univ. Press.
- 8.) J.H. Van Vleck, A. Sherman, *Rev. Mod. Phys.*, 7(1935)167.
- 9.) W. Kołos, *Polish J. Chem.* 67(1993)553.

# CALCULATION OF THE RAMAN AND INFRARED FREQUENCIES OF SOLID HYDROGEN AT HIGH PRESSURES

Jan A. Schouten and Marcel I.M. Scheerboom

Van der Waals-Zeeman Institute, University of Amsterdam, Valckenierstraat 65,  
1018 XE Amsterdam, The Netherlands.

## ABSTRACT

The vibrational frequencies of solid hydrogen have been calculated for pressures up to 2 Mbar. It will be shown that the turn-over in both the Raman and infrared frequency can be explained in the molecular approach, without the assumption of charge transfer or bond-weakening.

## Introduction

The vibrational spectra of solid hydrogen have attracted a great deal of interest since both frequencies show a maximum as a function of pressure. It was suggested that this maximum in the Raman frequency was due to a weakening of the bond between the hydrogen atoms [1], finally leading to metallization. Later it was shown [2] that the turn-over of the Raman-active vibron at about 30 GPa is primarily due to intermolecular interactions. The abnormal behaviour of the infrared frequency, which was measured later, was attributed to charge transfer or bond weakening [3].

Several investigators have calculated the Raman frequency as a function of pressure with limited success. The results are given in fig. 1. Wijngaarden et al. [4] presented a semi-empirical model which is in reasonable agreement with experiment up to 20 GPa but is invalid at higher pressures. In particular, it is unable to describe the decrease in frequency above 30 GPa. Chakravarty et al. [5] used a density-functional method. The pressure dependence is very large and there is no frequency maximum. From ab initio data Raynor [6] predicted the observed reversal in the pressure shift of the frequency. However, the initial very sharp rise leads to a shift which is too high by a factor of 3 at the maximum and the decrease beyond this maximum is too slow so that above 1 Mbar the calculated shift is large and positive while the experimental shift is negative. Resonance

coupling was not addressed in these investigations.

We have performed calculations of the infrared as well as the Raman frequencies based on potential data obtained from literature. In particular, the spherical averaged derivatives of the two-body intermolecular potential energy with respect to the bond length have been taken into account.

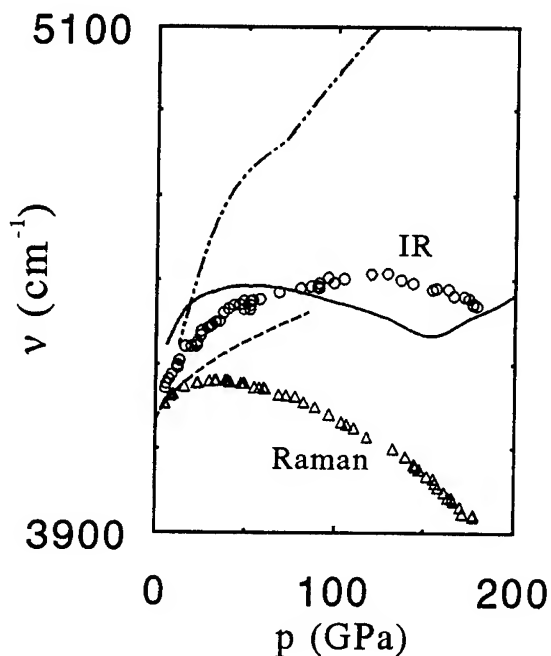


fig. 1. Comparison between experimental and calculated Raman and IR frequencies of solid  $H_2$ . O,  $\Delta$  experimental. --- Wijngaarden et al. [4]. — — — Chakravarty et al. [5]. — Raynor [6].

## Procedure and results

For an isolated molecule the intra-molecular potential can be expanded around the equilibrium bond length  $r_e$ :

$$V_{\text{intra}} = 1/2fx^2 + 1/6gx^3 + 1/24hx^4 \quad (1)$$

where  $x = r - r_e$ ,  $r$  is the bond length, and  $f$ ,  $g$ , and  $h$  are the force constants. This leads to the well known value of the harmonic vibrational frequency  $\omega_e = (f/\mu)^{1/2}$ , with  $\mu$  the reduced mass. There might also be a contribution to the frequency due to the vibration-rotation coupling.

To calculate the frequencies in the solid we need an expression for the forces acting on a molecule. The intermolecular potential energy between two molecules  $i$  and  $j$  at fixed orientation and with a fixed distance between their centres of mass can also be expanded around  $r_e$ :

$$\begin{aligned} \phi(ij) = & \phi(ij)_{r_e} + F_{ij}x_i + F_{ji}x_j + \\ & 1/2G_{ij}x_i^2 + 1/2G_{ji}x_j^2 + C_{ij}x_ix_j + \dots \end{aligned} \quad (2)$$

where the derivatives with respect to the bond length  $F_{ij}$ , etc. are evaluated at  $r = r_e$ . The mixing term with coefficient  $C_{ij}$  represents the vibrational coupling between two molecules. In special cases the vibrational excitation can be transferred during the process, such that molecule  $i$  and its nearest neighbours vibrate in phase (resonance coupling).

For the total potential of  $N$  molecules the sum has to be taken over all pairs in eq.(2) and over all molecules in eq.(1). In the case of Raman spectroscopy (resonance coupling!) the total potential can be written in the same form as eq.(1) with a small, but important, change in the equilibrium bond length and adjusted force constants. In the case of IR spectroscopy no coupling occurs [7] and all the non-mixing terms can also be written in the form of eq. (1); the vibrational average of the mixing terms gives only a small correction to the IR frequency.

The calculation procedure is as follows. The intermolecular potential of Duffy et al. [8] has

been rewritten in the form of the Silvera-Goldman potential [9].

$$\phi(R_{ij}) = \phi_{\text{scf}}(R_{ij}) - f_{\text{at}}(R_{ij}) \sum C_k R_{ij}^{-k} \quad (3)$$

where  $f_{\text{at}}$  is an damping function, related to  $\phi_{\text{scf}}$ , and  $R_{ij}$  is the distance between the centres of mass of the molecules. The SCF part has been improved by including the SCF calculations of Ree and Bender [10] for small values of  $R_{ij}$ . The multipole coefficients were taken from Meyer [11] as in the Silvera Goldman potential. By comparing the right hand side of eq.3 with the empirical potential the damping function can be calculated as a function of  $\phi$ . We assume that the relation between  $f_{\text{at}}$  and  $\phi$  holds for all values of the bond length.

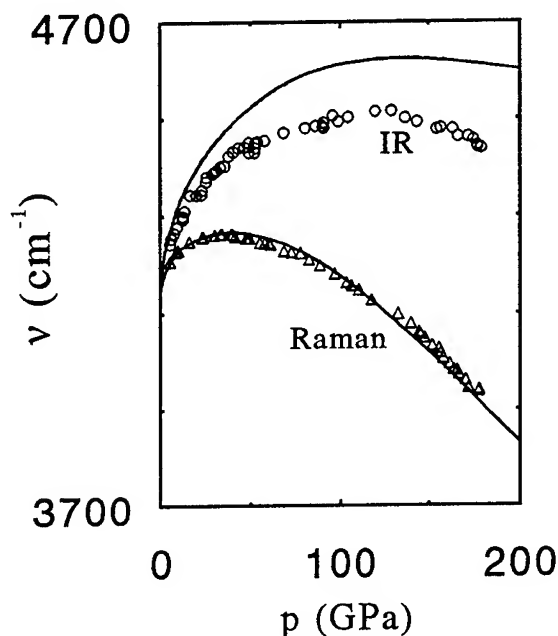


fig. 2. Comparison between experimental and calculated Raman and IR frequencies of solid  $H_2$ . O,  $\Delta$  experiment — calculated, this work.

Since Ree and Bender calculated  $\phi_{\text{scf}}$  for five values of  $r$  and four standard orientations, and Meyer determined the multipole coefficients for various values of  $r$ , the bond length dependence of the total potential can be calculated. Therefore, the bond length derivatives in eq.(2) can be obtained for the four orientations. It should be noted that  $G_{ij}$

and  $C_{ij}$  can not be determined independently from the  $\phi_{scf}$  data, but only the sum. A theory is available to obtain independent values for  $G_{ij}$  and  $C_{ij}$  from the multipole data. The same holds for the higher order contributions.

We have performed the calculations for an ideal hcp lattice. As shown in fig.2, the theoretical Raman frequencies show very good agreement with experiment, in particular the position of the turn-over is well represented. The calculations show that the dispersive contributions become dominant at high pressures and that the contribution of the damping term to the dispersive effect is about 15% (positive). The derivatives of  $\phi_{scf}$  with respect to the bond length could not be calculated for values of  $R_{ij}$  larger than 0.26 nm due to lack of data. Therefore, we have made an extrapolation of the value of  $F_{ij}/\phi_{scf}$  such that agreement with experiment is obtained at  $p=0$ . If we do not use any experimental data and take a linear extrapolation the calculated value will be somewhat lower in particular at the highest pressures.

## References

1. Mao, P.M. Bell, and R.J. Hemley, *Phys. Rev. Lett.* **55** (1985) 99.
2. Silvera, S.J. Leon, and H.E. Lorenzana, *Phys. Rev. B* **46** (1992) 5791.
3. Hemley, Z.G. Soos, M. Hanfland, and H.K. Mao, *Nature* **369** (1994) 384.
4. Wijngaarden, A. Lagendijk, and I.F. Silvera, *Phys. Rev. B* **26** (1982) 4957.
5. Chrakravarty, J.H. Rose, D. Wood, and N.W. Ascroft, *Phys. Rev. B* **24** (1981) 1624.
6. Raynor, *J. Chem. Phys.* **87** (1987) 2795.
7. Mao and R.J. Hemley, *Rev. Mod. Phys.* **66** (1994) 671.
8. Duffy, W.L. Vos, C.S. Zha, R.J. Hemley, and H.K. Mao, *Science* **263** (1994) 1590.
9. Silvera and V.V. Goldman, *J. Chem. Phys.* **69** (1978) 4209.
10. Ree and C.F. Bender, *J. Chem. Phys.* **71** (1979) 5362.
11. Meyer, *Chem. Phys.* **17** (1976) 27.

# THE STRUCTURE AND DYNAMICS OF HIGH PRESSURE PHASES OF HYDROGEN

J.S. TSE AND D.D. KLUG  
Steacie Institute for Molecular Sciences  
National Research Council of Canada  
Ottawa, Canada K1A 0R6

## ABSTRACT

The phase transitions of solid hydrogen up to 270 GPa at 77 K have been investigated using an *ab initio* molecular dynamics method which has the ability to sample many possible structures without restriction on the space group symmetry. The theoretical results reproduce the experimentally observed intramolecular H-H vibrational results in this pressure range. At low pressures, solid hydrogen exists as a rotor phase stable up to 60 GPa, and then transforms to an orientationally ordered structure. When the pressure is raised to 160 GPa, a novel orthorhombic structure with space group *Pnma* is obtained. The unit cell is constructed of three strongly interacting hydrogen molecules with two different H-H bond lengths with the population ratio of the short and long bond lengths in an exact ratio of 2 to 1. This new structure is shown to be possibly responsible for the charge transfer interactions suggested for the explanation of the peculiar features reported in the experimental infrared and Raman spectra of solid hydrogen at high pressure.

## INTRODUCTION

The condensed phases of molecular hydrogen have been of special interest to condensed matter researchers for many decades<sup>(1)</sup>. In recent years, the reports of the possible metalization of hydrogen in the laboratory<sup>(2)</sup> have stimulated a large effort of both experimental and theoretical research. In spite of the great amount of work in this area, little is yet known about the exact nature of the high pressure phases. A number of phase transitions have been documented through the use of spectroscopic methods used for samples contained in high pressure diamond anvil cells<sup>(3,4)</sup>. These methods include both Raman scattering and infrared absorption. It is now reasonably certain that there are at least three solid phases in solid hydrogen at low temperatures that are molecular solids. The exact structures of the two phases that are found at high pressures are unknown.

Theoretical studies have yielded a number of suggested structures for the high pressure molecular phases as well as the metallic phases. The basic approach has been to deduce a reasonable structure from what is known about the low pressure solid phase and then to carry out complete quantum calculations on the possible systems for

their total energies and the pressure dependence of the band-gap behavior as a function of density. In this paper we report on the use of first principles molecular dynamics to obtain the structures and the dynamical properties of the high pressure phases of solid hydrogen.

## Computational Methods

The first-principles method for molecular dynamics (FPMD) developed by R. Car and M. Parrinello<sup>(5)</sup> was employed. The method uses density functional theory along with a pseudopotential plane wave approximation. The method of Perdew-Zunger for parametrization<sup>(6)</sup> of the Ceperly-Alder results for the exchange-correlation potential in a homogeneous electron gas were employed for nonlocal contributions<sup>(7,8)</sup>. A Vanderbilt ultrasoft pseudopotential<sup>(9)</sup> was employed which allowed a energy cutoff of 20 Ryd to be used. Brillouin zone sampling was restricted to the  $\Gamma$  ( $k=0$ ). The pseudopotential gave a bond length of 1.427 a.u. for the gas phase molecule and a vibrational frequency as obtained from a molecular dynamics calculation of 4034  $\text{cm}^{-1}$  compared with the experimental values of 1.400 a.u. and 4161  $\text{cm}^{-1}$ .

A simulation cell of 96 atoms was required for adequate convergence of the properties of the solid. Calculations were started with the hydro-

gen molecules located at hexagonal close packed lattice sites. The  $c/a$  ratio was maintained at the value of 1.633 for most calculations while the atomic positions were relaxed. After annealing the sample at 77 K for 2000 time steps (one time step = 3 a.u.), molecular dynamics runs of 20000 time steps were used dynamical data. For structural data 5000 time steps were used. The vibrational density of states was obtained from the Fourier transform of the single particle velocity autocorrelation function.

### Results and Discussion

The calculated equation of states as determined from the derivative of the total energy versus data is in good agreement with extrapolated data. Three distinct phases were found in the pressure range 15 to 260 GPa. At low pressures the hydrogen molecules rotate almost freely at the hexagonal lattice sites as in a plastic crystalline phase. The rotational motion stops at about 60 GPa and this phase is an orientationally ordered phase where the hydrogen molecules are aligned in layers parallel to the  $ab$  plane. Another phase transformation begins at about 160 GPa and is completed by 260 GPa. The sluggish nature of this transition is most likely an artifact associated with the simulation of solid state phase transitions in small cells and short annealing times. Several views of the phases are depicted in Fig. 1. Zero-point motion is not included in the calculations but it is not yet certain how the structures or transition pressures will be affected. For example, the transition pressures for  $D_2$  and  $H_2$  between the last two molecular phases are very close<sup>(1)</sup>.

The distribution of the hydrogen bond lengths is shown in Fig. 2. In the low pressure range the intramolecular bond length is shorter than the gas phase value by  $0.005 a_0$ . At 150 GPa, the hydrogen bond length is reduced to  $1.37 a_0$ . As the pressure is increased the bond length distribution broadens to cover the range from 1.35 to  $1.37 a_0$  and then goes to a sharp distribution with two bond lengths with a population ratio of exactly 2:1 of short to long bonds.

The vibrational density of states for the intramolecular stretching vibrations consists of a band at about  $4000 \text{ cm}^{-1}$  at low pressures. As

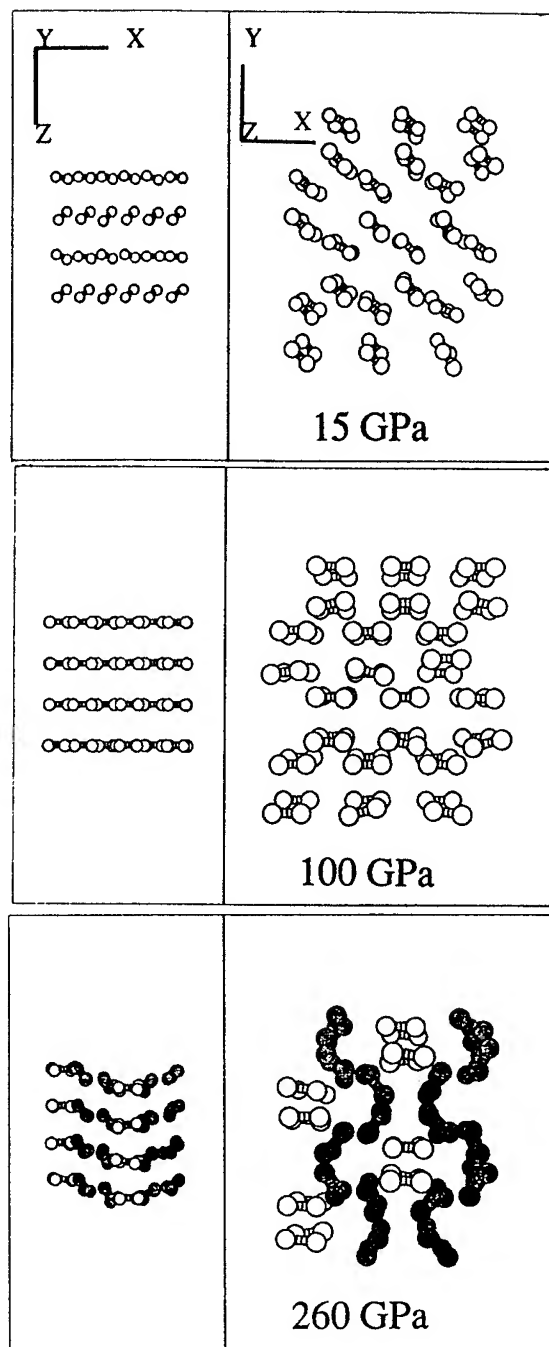


Figure 1. Views of the calculated structures of the phases of hydrogen as seen down the crystallographic directions indicated. The molecules with shorter bonds in the lower frames are shaded.

the pressure is raised the stretching band splits into two bands and the frequency rises to about

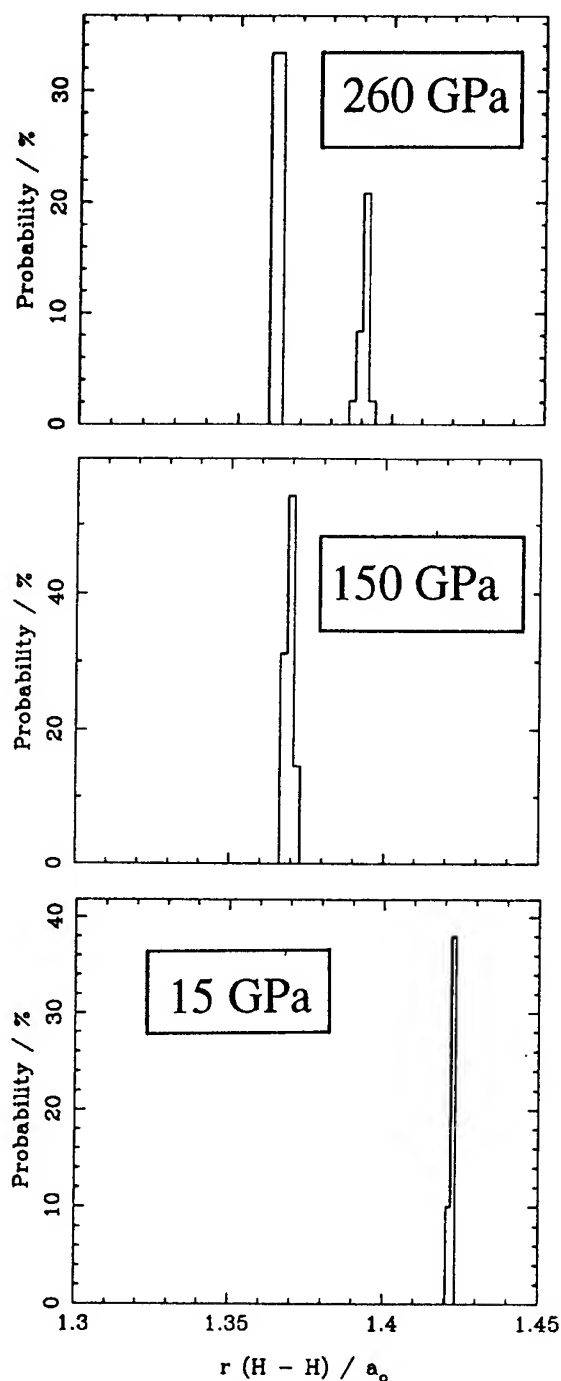


Figure 2. The distribution of intramolecular H-H bond lengths in the three calculated phases of solid hydrogen at 77 K.

$4400\text{ cm}^{-1}$ . The band then consists of three distinct peaks at pressures greater than 150 GPa. Each component decreases in frequency as the

pressure is raised further which is in qualitative agreement with the Raman and infrared spectroscopic data<sup>(1)</sup>.

The infrared spectra of the intramolecular vibrations shows a significant increase in the absorptivity in the phase above 150 GPa. A charge transfer mechanism has been proposed to explain this<sup>(1)</sup>. The main advantage of the FPMD method is that the details of the structure are obtainable. The calculated structure is depicted in the lower frame of Figure 1. It is orthorhombic *Pnma* with  $a = 2.767\text{ \AA}$ ,  $b = 4.971\text{ \AA}$ , and  $c = 2.87\text{ \AA}$ , and consists of grouping of three molecules with two equivalent short bonds and one long bond. In this structure, a simple molecular orbital argument can be applied to show that there is a donation of charge density from the two peripheral hydrogen molecules to the central molecule thus forming a weak charge-transfer complex. This charge transfer yields a strong enhancement of the infrared absorptivity which is observed experimentally. As a result of the crystal symmetry, the central molecule does not have a permanent dipole moment and the stretching vibration is at lower frequency and is Raman active as observed in the experimental spectrum.

In summary, the phase transitions of solid hydrogen have been studied with a method which allows the calculation of the structure, dynamics and electronic effects. No structures are required to be *a priori* suggested.

## References

- [1] H.K. Mao and R.J. Hemley, *Rev. Mod. Phys.* **66** (1994) 671.
- [2] H.K. Mao and R.J. Hemley, *Science* (1989) 1462.
- [3] M. Hanfland, R.J. Hemley, and H.K. Mao, *Phys. Rev. Lett.* **70** (1993) 3760.
- [4] R.J. Hemley, and H.K. Mao, *Phys. Rev. Lett.* **61** (1988) 857.
- [5] R. Car and M. Parrinello, *Phys. Rev. Lett.* **55** (1985) 2471.
- [6] J.P. Perdew and A. Zunger *Phys. Rev.*, **B23** (1981) 5048.
- [7] J.P. Perdew, *Phys. Rev.* **B33** (1986) 8822.
- [8] A.D. Becke *Phys. Rev.* **B38** (1988) 3098.
- [9] D. Vanderbilt, *Phys. Rev.* **B41** (1990) 7892.

# ORIENTATIONAL ORDER, DISORDER, AND POSSIBLE GLASSY BEHAVIOR IN DENSE DEUTERIUM

A. F. Goncharov, I. I. Mazin, Jon H. Eggert\*, Russell J. Hemley, and Ho-kwang Mao  
*Geophysical Laboratory and Center for High-Pressure Research,  
Carnegie Institution of Washington, 5251 Broad Branch Rd. N.W., Washington, D.C. 20005-1305*

## ABSTRACT

The transition to the orientationally ordered phase of deuterium was studied using Raman spectroscopy to temperatures of 4 K and pressures to 40 GPa. Samples of normal deuterium exhibit a large enhancement of high-frequency vibron sidebands and significant changes in the low-frequency rotational excitations upon passage into the low-temperature ordered phase (phase II). The spectra also reveal a transition to an intermediate phase (II'). We suggest that this phase may be an orientational glass associated with the mixture of  $J=0$  and  $J=1$  molecules.

\*Present Address: *Department of Physics, Pomona College, Claremont, CA 91711*

## Introduction

At all pressures  $H_2$  and  $D_2$  freeze in a hexagonal-close-packed (hcp) orientationally-disordered structure (phase I). Above 30 GPa for  $D_2$ , 60 GPa for  $HD$ , and 100 GPa for  $H_2$  a phase transition is observed in both Raman and infrared absorption studies (phase II) [1-6]. The I-II transition pressure is affected by the rotational state of the molecules, indicating that the ordering objects are angular momenta. However, the structure of the phase is the subject of continuing debate, and a detailed picture of the transition is not known [7]. Here we present detailed Raman measurements of ortho-para mixtures of deuterium down to 4 K to study the nature of the I-II phase transition.

## Experiment and Results

High-purity normal deuterium was loaded at room temperature using techniques described elsewhere (Ref. [7]). The evolution of the Raman spectrum of normal deuterium with temperature at 37.5 GPa is shown in Fig. 1. At 44 K significant changes are observed in all three frequency ranges. The main vibron at  $3084\text{ cm}^{-1}$  shows a shift to lower frequency of about  $2\text{ cm}^{-1}$ . We are able to clearly resolve peaks corresponding to each phase in the

transition-temperature region so that the frequency shift is truly discontinuous. As the temperature is reduced further, the main vibron continuously shifts to lower frequency. We also observed a dramatic intensity increase and narrowing of the high-frequency vibron sidebands (right panel), which are very weak and broad in the high-temperature phase, and approximately 200 times weaker than the principal vibron in the low-temperature phase. In previous work, two sidebands were evident [5]; we now observe a total of eleven vibrons in the low temperature phase. The low-frequency roton band, contiguous with the ambient pressure  $J=0 \rightarrow 2$  transition (left panel) splits at the transition temperature and develops into a triplet, and a weak feature appears below the triplet. All the changes reported above are reversible, and within the precision of our temperature determination ( $\sim 0.5\text{ K}$ ) we did not observe any hysteresis at the transition. A second major change in the spectra occurs between 37 and 38 K. Although the vibron frequency has no discontinuity, its temperature derivative changes. The high-frequency vibron sideband structure changes much more dramatically. Three of the lower frequency sidebands show a discontinuity, and a very weak new lines appear at 37 K in the frequency range between the main vibron and sidebands [8]. A new low-frequency line appears at  $100\text{ cm}^{-1}$  and each component of the



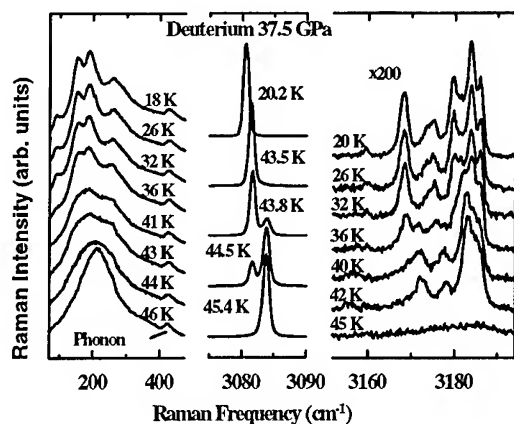


Fig. 1. Raman spectra of deuterium at 37.5 GPa at various temperatures.

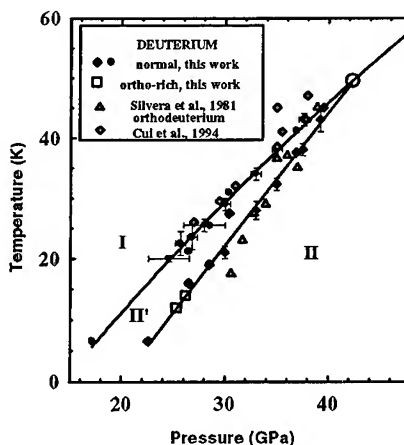


Fig. 2. Phase diagram of deuterium at low temperatures.

broad triplet narrows and becomes more distinct.

We were able to detect both transitions for normal deuterium throughout our measured P-T range (Fig. 2) and the phase lines appear to merge near 42 GPa and 50 K. We shall refer to the narrow phase between the two phase lines as phase II' and the lowest-temperature phase as phase II. For comparison we studied sample of ortho-rich deuterium. We estimated the ortho-fraction of the sample (approximately 80%) by measuring the ratio of intensities of the  $J=0 \rightarrow 2$  and  $J=1 \rightarrow 3$  Raman roton transitions. We found that transition associated with vibron discontinuity shifts to higher pressures in

this case (Fig. 2). Raman spectra of the corresponding low-temperature phase differ from that of normal deuterium (Fig. 3) [8]. We note that the II-II' line for the normal sample is close to the I-II line measured for ortho-rich deuterium. In addition, this line also agrees with that determined by Silvera and Wijngaarden [1] for the ortho solid. The I-II' phase line is close to that determined by Cui et al. [9] who studied a sample loaded as normal  $D_2$ . This indicates that their sample did not fully convert to pure ortho- $D_2$ .

### Discussion

The lack of hysteresis rules out a reconstructive transformation for both I-II' and II'-II transitions. The I-II' phase transition, which manifests itself as the shift in the vibron frequency, the appearance of vibron sidebands, and the roton-like band splitting, can be interpreted as orientational ordering of the freely rotating molecules of phase I to a phase with preferred orientation of angular momenta. The spherical symmetry of the  $J=0$  molecules is broken in this phase by admixing of the  $J=2$  states [1]. Orientational ordering leads to a lowering of the crystal symmetry and an increase of the number of molecules in the unit cell. The finite discontinuity implies that the I-II' transition is first order. Large changes at the transition [8] occur in the roton spectra for the normal solid. In contrast, only small changes are observed in the roton spectra of the ortho-rich sample (Fig. 3). In addition, there are fewer vibron sidebands in the ortho-rich solid in

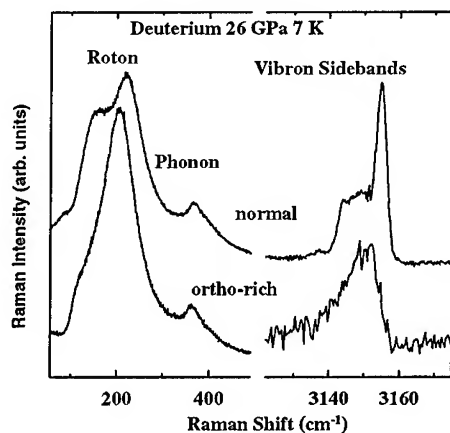


Fig. 3. Comparison of the Raman spectra of normal and ortho-rich deuterium in phase II.

phase II. At a critical concentration  $c_1$  between 0.2 and 0.33 of  $J=1$  molecules, an orientational superstructure forms in phase II [8].

The existence of two, apparently related, phase transitions in such solids having a critical concentration of  $J=1$  molecules poses an interesting theoretical question and experimental challenge. The proximity of the II'-II phase line discovered in this work to the that of ortho-rich  $D_2$  (as well as the phase line reported by Silvera and Wijngaarden for pure ortho- $D_2$  [1]) is striking. The result suggests that one in fact observes an ordering of the para- $D_2$ -molecules with odd  $J$  at a higher temperature and ordering of the ortho- $D_2$ -molecules (even  $J$ ) at lower temperature.

The microscopic physics for this process probably depends on quadrupolar interaction between the nearest-neighbor molecules, random occupation of the hcp lattice sites by the two types of molecules, and explicit dependence of the quadrupole moments of the ortho-molecules on the local crystal field at a given site. We are not aware of any theoretical work dealing with such a problem. However, we can suggest the following qualitative picture. The concentration of the  $J=1$  in our experiment was 30%; this means that each  $J=1$  molecule has an average of 4 nearest-neighbor  $J=1$  molecules, and the molecules form clusters of  $\approx 10^1$  sites. On the other hand,  $c_1=0.3$  is above the percolation threshold, so these clusters are connected by narrow "bridges" of a few lattice parameter lengths. A possible scenario is that upon cooling first the strongly bound clusters order internally (this order may be similar, but not identical to that assumed by the regular lattice of pure para- $D_2$ ); the relative orientation of clusters with respect to each other is random, and is defined by the bridge passes that connect them. The situation is similar to that found in hydrogen at ambient pressure where a glassy phase was detected by NMR at low temperatures [10]. In our case, however, the situation differs quantitatively because the interactions are stronger. In addition, instead of a passive background of  $J=0$  molecules, these molecules at high pressure have a high quadrupole polarizability, and can undergo a transition into a fully ordered phase with an induced quadrupole moment at all  $J=0$  sites just a few Kelvins lower). If the ortho- $D_2$  molecules have

substantial admixture of the  $J=2$  state already in the phase I, there would be no source for frustration and apparently only one phase transition, which is presumably what happens at higher pressure, with ultimate disappearance of phase II' at 42 GPa and 50 K. Further understanding of phase II' requires detailed theoretical studies and numerical simulation of the key features of the system: the anisotropy and short range portion of the intermolecular interaction, the presence of the two species, and the "soft" (polarizable) character of one of them.

## References

- [1] I. F. Silvera and R. J. Wijngaarden, *Phys. Rev. Lett.* **47**, 39 (1981).
- [2] H. E. Lorenzana, I. F. Silvera and K. A. Goettel, *Phys. Rev. Lett.* **64**, (1990) 1939.
- [3] M. Hanfland, R. J. Hemley and H. K. Mao, *Phys. Rev. Lett.* **70**, (1993) 3760.
- [4] R. J. Hemley, J. H. Eggert and H. K. Mao, *Phys. Rev. B* **48**, (1993) 5779.
- [5] J. H. Eggert, R. J. Hemley and H. K. Mao, in *Proceedings of the XIV International Conference on Raman Spectroscopy*, edited by N. Yu and X. Li (Wiley, New York, 1994) p. 1008.
- [6] F. Moshary, N. H. Chen and I. F. Silvera, *Phys. Rev. Lett.* **71**, (1993) 3814.
- [7] H. K. Mao and R. J. Hemley, *Rev. Mod. Phys.* **66**, (1994) 671.
- [8] A. F. Goncharov, J. H. Eggert, I. I. Mazin, R. J. Hemley and H. K. Mao, submitted.
- [9] L. Cui, N. H. Chen, S. J. Jeon and I. F. Silvera, *Phys. Rev. Lett.* **72**, (1994) 3048.
- [10] N. S. Sullivan, M. Devoret, B. P. Cowan and C. Urbina, *Phys. Rev. B* **17**, (1978) 5016.

# PENETRATION DEPTH OF NICKEL HYDRIDE INTO BULK NICKEL AT DIFFERENT ACTIVITIES OF GASEOUS HYDROGEN

A. STROKA and B. BARANOWSKI

*Institute of Physical Chemistry, Polish Academy of Sciences  
Warsaw, Poland*

## ABSTRACT

Systematic measurements of the penetration depth of nickel hydride into nickel layers were carried out at hydrogen pressures from 6.5 to 13.0 kbar at 25 °C. The penetration depth of nickel hydride is a linear function of the chemical potential of the hydrogen being in equilibrium with nickel. For example, at 12360 bars hydrogen pressure the penetration depth of nickel hydride equals 59.5  $\mu\text{m}$ , compared to 30.0  $\mu\text{m}$  observed for nickel hydride formed electrochemically

The penetration depth of nickel hydride formed electrochemically does not exceed about 30 microns at room temperature [1], whereas nickel deuteride prepared in similar conditions exhibits a penetration of about 25  $\mu\text{m}$  [2]. This behavior may be due to kinetic or thermodynamic reasons, but so far no convincing explanation has been offered. To fix clear thermodynamic conditions for the evaluation of the penetration depth of nickel hydride, experiments were carried out at different fugacities of gaseous hydrogen (for hydrogen pressures from 6.5 to 13 kbar, at  $25.0 \pm 0.2$  °C).

## Experimental

Nickel foils of purity 99.98 % Ni were used. The surfaces were purified by several hours extraction in Soxhlet with benzene and alcohol. The high pressure device used [3,4], allowed us to maintain a constant hydrogen pressure in the range 5 to 13 kbar for several months. The nickel foils were double side charged by hydrogen under constant pressure chosen. Nickel foils of 15 different thicknesses in the range from 2.2 to 300  $\mu\text{m}$  were exposed simultaneously to gaseous hydrogen in each experiment. The hydride formation process was followed by electrical resistance measurements of the charged samples. Four probe technique of the electrical resistance measurements was used for this purpose. The charging was continued until the electrical resistance of all probes did not change. From each sample 3-7 independent analyses of the hydrogen content were performed mass spectrometrically. In terms of the atomic ratio H/Ni the error was 0.015. The samples were later analyzed, being taken out from the high pressure vessel after previous cooling to -45 - -55 °C and reduction of the pressure to ambient condition.

## Results and discussion

The stationary hydrogen absorption in the nickel foils of different thicknesses at constant hydrogen pressure for  $7650 \pm 50$ ,  $10260 \pm 80$  and  $12360 \pm 80$  bars was measured. For the pressures quoted above the foils were exposed to hydrogen for 5400, 4130 and 2510 hours. In fig. 1, 2 and 3 are presented the final average H/Ni ratios as a function of the charged nickel layers thicknesses at the above hydrogen pressures.

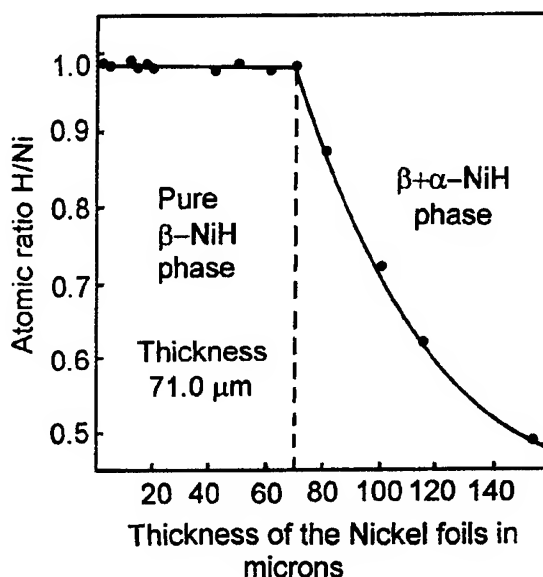


Fig. 1. Ni foil double side charged at constant  $\text{H}_2$  pressure of  $7650 \pm 50$  bars at 25.0 °C. Charging time 5400 hours. The penetration depth of  $\beta$ -NiH phase in the Ni foil in above conditions equals 35.5  $\mu\text{m}$ .

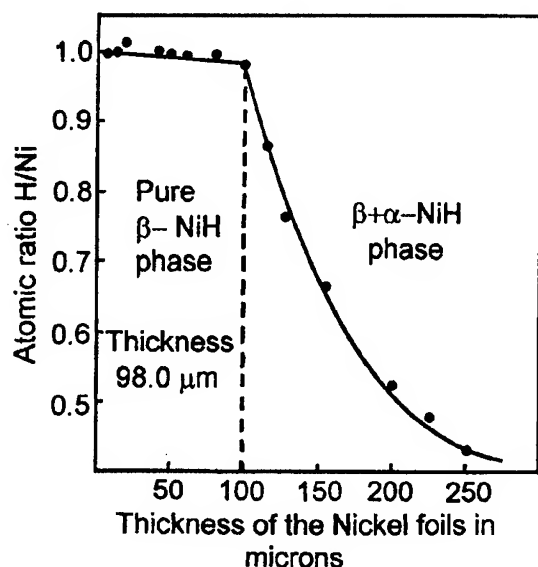


Fig. 2. Ni foil double side charged at constant  $H_2$  pressure of  $10260 \pm 80$  bars at  $25.0^\circ C$ . Charging time 4130 hours. The penetration depth of  $\beta$ -NiH phase in the Ni foil in above conditions equals  $49.0 \mu m$ .

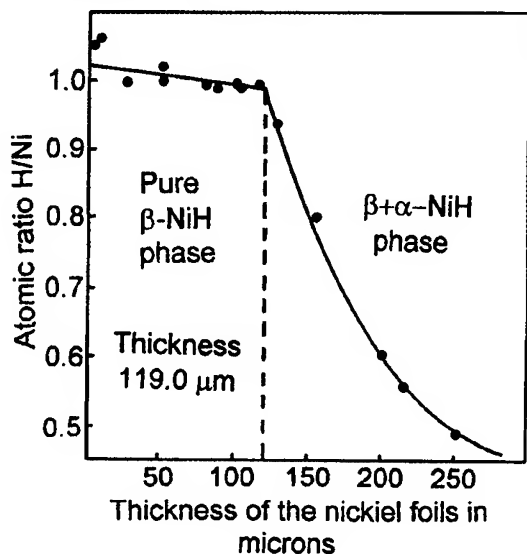


Fig. 3. Ni foil double side charged at constant  $H_2$  pressure of  $12360 \pm 80$  bars at  $25.0^\circ C$ . Charging time 2510 hours. The penetration depth of  $\beta$ -NiH phase in the Ni foils in above conditions equals  $59.5 \mu m$ .

phase). The charged probes on the right side of the curves are ferromagnetic (the descending part of the curves). This is due to unconverted nickel in the hydride phase. The penetration depths of the nickel hydride phase into the nickel layers were determined by graphical interpolations from the experimental curves, presenting H/Ni as a function of the nickel foils thicknesses. (fig1, 2, 3). The following maximal penetration depths of the nickel hydride (beta phase) were obtained:  $35.5 \mu m$  for a pressure 7650 bars,  $49 \mu m$  for 10360 bars and  $59.5 \mu m$  for 12360 bars, which means that the penetration depth depends on the hydrogen fugacity. Thus the increase of penetration depth from  $35.5$  to  $59.5 \mu m$  requires an increase of the hydrogen fugacity from  $6.69 \times 10^5$  to  $1.11 \times 10^7$  bars. Fig.4 presents the penetration depth of NiH as a function of the natural logarithm of hydrogen fugacity, kept in equilibrium with the nickel foils. As can be seen, the above dependence is linear in the investigated hydrogen pressure range. The extrapolation of the hydrogen fugacity necessary for the formation of  $30 \mu m$  NiH thick nickel hydride layer (this thickness was obtained at electrochemical charging) gives a value of  $3.11 \times 10^5$  bars. This corresponds to an external pressure of 6520 bars, which is not far above the observed minimal hydride formation pressure[4].

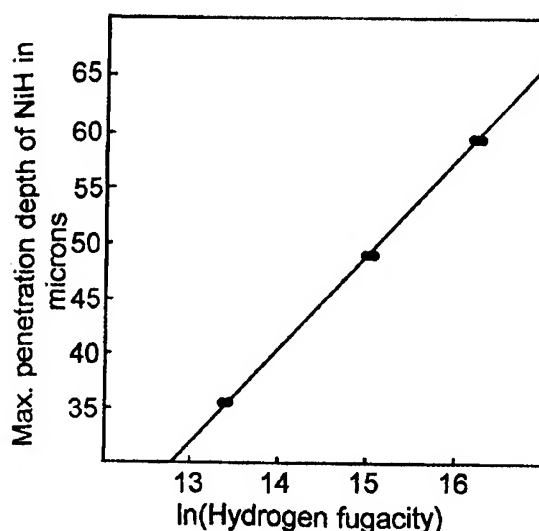


Fig. 4 Maximal penetration depth of NiH into Ni foils as a function of the natural logarithm of the hydrogen fugacity.

The charged nickel foils on the horizontal part of the curve on fig. 1,2 and 3 correspond to pure NiH (beta

In conclusion, we have proved that the penetration depth of the nickel hydride is a linear function of the

chemical potential of hydrogen used for charging the nickel layers(fig.4). Stresses at the interphase layer of nickel-nickel hydride seem to be responsible for the limited penetration depth. At the same time we have confirmed that the formation kinetics of the nickel hydride is strongly dependent on the mechanical and thermal pretreatments and on contaminations in the nickel foils.

#### References

1. B.Baranowski and M.Smialowski, *Bull.Acad.Sci., ser. sci. chim. geol. et geogr* **7** (1959) 663  
*J. Phys. Chem. Solids* **12** (1959) 206.
2. A.Stroka and B.Baranowski, *Bull.Acad.Polon.Sci., ser.sci. chim. geol. et. geogr* **10** (1962) 147.
3. B.Baranowski and W.Bujnowski, *Roczn.Chemii*, **44** (1970) 224.
4. M.Tkacz and B.Baranowski, *Roczn.Chemii*, **50** (1976) 2159.

# NEW HIGH PRESSURE CRYSTAL STRUCTURE, EQUATION OF STATE, AND PHONON REFLECTIVITY OF CSH TO 2.5 MBAR AND CsD TO 1.37 MBAR

ARTHUR L. RUOFF AND KOUROS GHANDEHARI

*Department of Materials Science and Engineering  
Cornell University, Ithaca, New York 14853, U.S.A.*

## ABSTRACT

A new orthorhombic high pressure phase was observed in CsH at approximately 17.5 GPa and  $V/V_0 = 0.53$ . This high pressure phase was assigned to the CrB structure with the Cmcm space group based upon 19 x-ray diffraction peaks. It was studied to  $V/V_0 = 0.260$  at 253 GPa. This is the highest compression measured in the ionic alkali hydrides to date. Reflectivity studies were made on CsH from 0 to 251 GPa. The high energy side of the reflection peak was found to be in the near infrared (1 eV) at the higher pressure and is due to phonons. (The corresponding value for CsI at atmospheric pressure is only 0.01 eV.) The exceptionally high energy of the phonon peak in CsH at 251 GPa is due to: (1) Its bulk modulus is enormous (nearly twice that of diamond at atmospheric pressure). (2) Its reduced mass is tiny. The expected isotope effect for phonons was found in studies of CsD. This was measured at atmospheric pressure and as a function of pressure for CsH to 251 GPa. These are the first studies of phonon reflectivity in the diamond anvil cell to 2.5 Mbar and are the first high pressure phonon studies at pressure in any of the alkali hydrides.

## Introduction

While we commonly think of the alkali hydrides as ranging from LiH to CsH, there is the interesting possibility that hydrogen may, at high pressure, form proton hydride (1). At atmospheric pressure, hydrogen forms a molecular solid with covalent bonding. The sum of the ionic radii for the proton and the hydride anion are much greater than the radius of the covalent molecule. However, it has been shown that the ionic radius of the hydride ion is pressure dependent (2) so that it may be possible to form a stable ionic-bonded solid if the sum of the ionic radii becomes less than the bond length of the covalent molecule. The formation of proton hydride by ionic bonding could be a precursor to metallic hydrogen and may substantially increase the insulator-metal transition pressure currently computed to be 300 to 350 GPa (3,4).

The alkali halides have been studied extensively by x-ray diffraction and transitions to

lower symmetry structures have been observed in several instances (5). The alkali hydrides are also highly ionic and we expect the possibility of a transition to a low symmetry structure at high pressure. Here, we report a phase transition from the B2 structure to the low symmetry orthorhombic CrB structure with the Cmcm space group.

The insulator-metal transition was studied in CsH to 2.5 Mbar. A rise in reflectivity was observed in the near infrared for pressures above 100 GPa in CsH. This is attributed to phonon reflectivity, not to the plasma edge of a metal formed by band gap closure. Phonon reflectivity can be shown to be dependent upon the bulk modulus and the reduced mass of the ion pair so that for the alkali hydrides we expect the edge of the phonon reflectivity to be in the near infrared at elevated pressures since the reduced mass of the ion pair, MH, in the alkali hydrides is nearly equal to the mass of the hydrogen atom and the bulk modulus increases dramatically with pressure. In order to

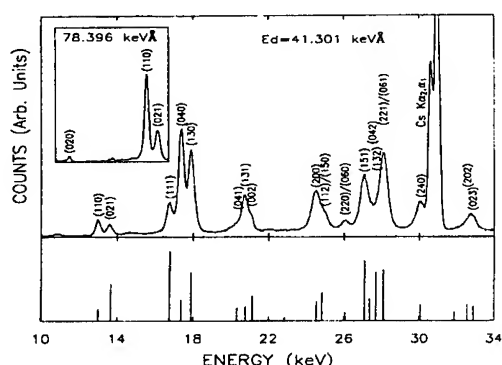


Fig. 1: Main figure shows EDXD spectrum for CsH at 25.1 GPa and ED = 41.301 keV. Inset shows a portion of spectrum taken at Ed = 78.396 keV. Note appearance of higher d-spacing line (020). This was the highest d-spacing line detected. Bottom graph shows expected relative intensities for CrB structure as a comparison to the data at Ed = 41.301 keV.

corroborate that the reflectivity observed is due to phonon reflectivity, a phenomenological model is employed along with the reflectivity in the infrared of CsH at atmospheric pressure to observe the shift with pressure and the reflectivity of CsD at 137 GPa to observe the isotopic shift.

### X-ray Diffraction Studies

CsH was studied using energy dispersive x-ray diffraction (EDXD) to 253 GPa (5) using platinum (6) and molybdenum (7) markers and ruby fluorescence (8) to measure pressure. CsH was observed to transform from the B1 to B2 phases at 0.8 GPa and to a new phase at an average pressure of 17.5 GPa. The new phase was determined to be an orthorhombic structure with four atom pairs per unit cell and the average relative volume change upon transition to the orthorhombic phase was 6.3%.

To closely examine this high pressure phase, a sample was annealed at 75 C for three hours to relieve texturing due to internal strain. The pressure was measured to be 25.1 GPa by ruby fluorescence. Figure 1 shows the EDXD spectrum taken of CsH in the new high pressure phase at Ed = 41.301 keV. The inset shows a

portion of an EDXD spectrum taken at Ed = 78.396 keV which shows the (020) peak which is the highest lattice spacing observed for this phase. The bar graph shown below the main graph of Figure 1 shows the predicted intensities for the CrB structure which were computed as per Reference 9. A complete tabulation of the observed and expected intensities for this spectrum can be found in Table 1 of Reference 5.

The diffraction peaks for the new high pressure phase shown in Figure 1 had systematic absences consistent with those of the Cmc<sub>2</sub>m space group. Further, the indexing shown gives axial ratios similar to the CrB lattice (10) which has the Cmc<sub>2</sub>m space group. The coordination for the B1 phase is 6 and for the B2 phase is 8. For the CrB structure, with the Cs atom at the Cr position and the H atom at the B position (10), the coordination of either the alkali atom or the hydrogen atom is higher than in the B2 phase. This is consistent with the general trend for equal or higher coordination with succeeding phases.

Each EDXD spectrum was fitted to the CrB structure for pressures above approximately 17 GPa and a plot of relative volume versus pressure was made. Figure 2 shows the data for relative volume versus pressure in the CrB phase and a portion of the data in the B2 phase taken using three separate means to measure pressure. The solid lines are fits to the first order Birch equation of state (EOS) (11) given by the following:

$$P = \frac{3}{2} B_0 \left[ \left( V/V_0 \right)^{-7/3} - \left( V/V_0 \right)^{-5/3} \right] \left[ 1 + \frac{3}{4} \left( B_0' - 4 \right) \left( \left( V/V_0 \right)^{-2/3} - 1 \right) \right]$$

$B_0$  and  $B_0'$  are the zero pressure bulk modulus and bulk modulus derivative respectively.  $V_n/V_0$  is the relative volume of the high pressure phase when extrapolated to zero pres-

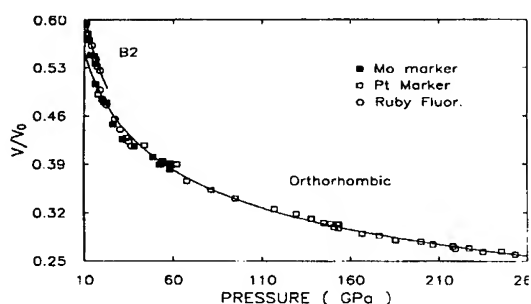


Fig. 2: Data from three separate experiments are plotted for  $V/V_0$  vs pressure in the B2 and orthorhombic phases between 10 and 260 GPa. The solid lines are first order Birch equation of state fits to the data for both phases.

sure. For the B1 phase,  $B_0 = 8.0$  GPa and  $B_0' = 4.0$ . For B2,  $B_0 = 14.2$  GPa,  $B_0' = 4.0$  and  $V_n/V_0 = 0.858$ . For the CrB phase, the fit to the first order Birch EOS yields  $B_0 = 21.6 \pm 0.1$  GPa,  $B_0' = 4.7 \pm 0.1$ , and  $V_n/V_0 = 0.711 \pm 0.004$ .

The EOS for CsH in the CrB phase was measured to 253 GPa and  $V/V_0 = 0.260$ . This is a significantly high compression rivaled only by x-ray diffraction work on the rare gases, CsI, and the alkali metals.

### High Pressure Optical Studies

The insulator-metal transition has been studied in CsH to pressures of 251 GPa (12) and data for the band gap suggests a zero pressure band gap of 4.44 eV. This band gap closes rapidly with pressure initially with a slope of  $-46 \pm 2$  meV/GPa. This initial slope predicts metallization due to band gap closure at a pressure of 97 GPa. However, the magnitude of the slope changes dramatically so that between the pressures of 85 GPa and 251 GPa the slope is decreased to  $-2.37 \pm 0.1$  meV/GPa. With this final decrease in slope, the band gap of CsH at 251 GPa closes only to the measured value of 1.89 eV. Thus at the final pressure measured, 251 GPa, CsH is still an insulator.

To complement the transmission studies presented in Reference 12, reflectivity studies were made on CsH to 251 GPa on the energy

range of 0.5 eV to 3.0 eV. At pressures above 100 GPa, a sharp rise in the reflectivity in the near infrared between 0.5 eV and 1.0 eV was observed. The high pressure reflectivity curves of CsH can be found in Figure 3. Also found on the main graph is the reflectivity of CsD at 137 GPa and in the inset is the reflectivity of CsH at zero pressure.

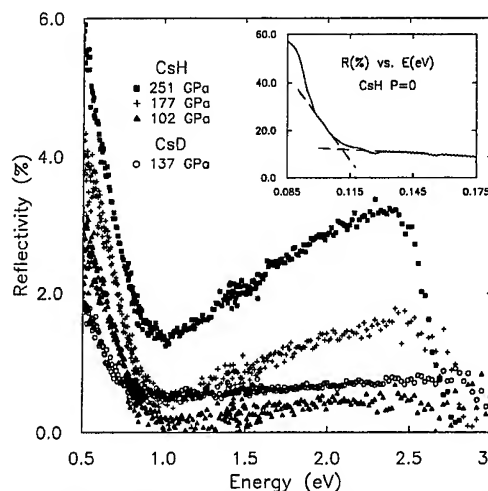


Fig. 3: Inset: reflectivity at the sample-diamond interface for CsH at atmospheric pressure. The value of  $E_{PRE}$  in this case is estimated from the intersection of the two dashed lines. The main figure shows reflectivity at the sample-diamond interface for CsH and CsD at various pressures.

As can be seen in the inset, the reflectivity of CsH is nearly level and rises dramatically at lower energies in the infrared. The region of high reflectivity is termed the reststrahlen band and is referred to here as phonon reflectivity since it is due to resonance with the lattice phonons in reflection. The energy at the high energy side of the reflection peak = 0.11 eV at zero pressure.

It was shown previously for the alkali halides, that the frequency of the maximum reflectivity for a transverse optical wave is well represented by  $(2Ba/\mu)^{1/2}$  where  $B$  is the bulk modulus,  $a$  is the lattice parameter and  $\mu$  is the reduced mass of the ion pair (13). It was also shown that the frequency of the upper edge of the phonon reflectivity peak is reasonably well described by  $[5.5 B_0 a/\mu]^{1/2}$ . The latter yields



for CsH 0.09 eV at  $P = 0$ , in the neighborhood of the observed value of 0.11 eV. See the inset of Figure 3. The previous relation can be used to develop a scaling law

$$\omega = \omega_0 \left[ (B/B_0)(\rho_0/\rho) \right]^{1/3}.$$

Here  $\omega_0$  is the value of the appropriate frequency at  $P = 0$ .

The reflectivity curves in Figure 3 have two distinct regions. At energies below the minimum the curves are determined primarily by phonon behavior while above the minimum electron polarization dominates. Both effects increase with pressure. To compare the phonon portion of the curves we consider the results at 2% reflectivity in the energy region below the minimum. We find the results in Table I. The fact that we get approximate agreement is taken as evidence that we are dealing with phonons. The description used is to be considered only as an approximate representation. The fact that the isotope effect is very close to the expected ratio is taken as confirmation that we are dealing with phonons.

Table I. Experimental  $E_c$  ( $R = 2\%$ ) and calculated  $E_c$  ( $R = 2\%$ ), based on  $E_0 = 0.1$  eV.  $P$  and  $K$  have units of GPa. Here  $K_0 = 8.0$  GPa\*

	$P$	$K$	$\rho/\rho_0$	$E_e$	$E_c$
CsH	102	385	3.01	0.62	0.58
CsH	177	634	3.49	0.73	0.73
CsH	251	864	3.86	0.80	0.83
CsD	137	502	3.25	0.46	0.47**
CsH <sup>#</sup>	137	502	3.25	0.66	0.66

\*  $K$  and  $\rho/\rho_0$  values are from Reference 5.

\*\* The  $E_0$  for CsD used is 0.7097 times the  $E_0$  for CsH due to the reduced mass effect.

<sup>#</sup> By interpolation from data at 102 and 177 GPa.

## References

1. B. Baranowski, Polish J. Chem. **66**, 1737 (1992).
2. B. Baranowski, M. Tkacz, and S. Marjchrzak, in *Molecular Systems Under High Pressure*, edited by R. Pucci and G. Piccitto (North-Holland, Amsterdam, 1991), p. 139.
3. H. Nagara and T. Nakamura, Phys. Rev. Lett. **68**, 2468 (1992).
4. V. Natoli, R.M. Martin, and D.M. Ceperly, Phys. Rev. Lett. **70**, 1952 (1993).
5. K. Ghandehari, H. Luo, A.L. Ruoff, S.S. Trail, and F.J. DiSalvo, Phys. Rev. Lett. **74**, 2264 (1995).
6. N.C. Holmes, J.A. Moriarty, G.R. Gathers, and W.J. Nellis, J. Appl. Phys. **66**, 2962 (1989).
7. W.J. Nellis, J.A. Moriarty, A.C. Mitchell, M. Ross, R.G. Dandrea, N.W. Ashcroft, N.C. Holmes, and G.R. Gathers, Phys. Rev. Lett. **60**, 1414 (1988).
8. P.M. Bell, J.A. Xu, and H.K. Mao, in *Shock Waves in Condensed Matter*, edited by Y.M. Gupta (Plenum, New York, 1986), p. 125.
9. M. Baublitz, Jr., V. Arnold, and A.L. Ruoff, Rev. Sci. Instrum. **52**, 1616 (1981).
10. J.L.C. Daams, P.H. Villars, and J.H.N. van Vucht, *Atlas of Crystal Structure Types* (ASM International, Materials Park, 1991), Vol. 2, p. 2522.
11. F. Birch, J. Geophys. Res. **83**, 1257 (1978).
12. K. Ghandehari, H. Luo, A.L. Ruoff, S.S. Trail, and F.J. DiSalvo, Sol. State Comm. **95**, 385 (1995).
13. A.L. Ruoff, K. Ghandehari, H. Luo, S.S. Trail, F.J. DiSalvo, and G.L. Bucher, submitted for publication.

# SYNTHESIS OF RHENIUM AND MOLYBDENUM HYDRIDES IN DAC

MAREK TKACZ

*Institute of Physical Chemistry, Polish Academy of Sciences, Kasprzaka 44/52, 01-224 Warsaw*

## ABSTRACT

This paper will present the x-ray investigations of the rhenium and molybdenum under high pressure of hydrogen in DAC. Formation and decomposition of the hydride phases have been directly observed in DAC using the energy dispersive x-ray diffraction method. Structural transformation from bcc to hcp was detected during the synthesis of molybdenum hydride while the only small lattice expansion of the original hcp structure of the rhenium metal was observed.

## Introduction

The first high pressure synthesis of metal hydrides were carried out in our laboratory in the middle 1960 s with the help of special design in which hydrogen was isolated from the steel high pressure chamber by copper or beryllium bronze container. The significant increase in the pressure up to 3.0 GPa and temperature up to 400° C range has permitted synthesizing nickel, chromium aluminum and manganese hydrides. An extensive review of research conducted during this period of time has been given by Baranowski [1]. The capabilities of the piston-cylinder apparatus have been exhausted by pressure of the order of 3 GPa . After that a Russian group came up with the new idea which allowed them to increase the pressure range up to 9 GPa and synthesize quite impressive number of the metal hydrides [2]. Recently the diamond anvil cell, commonly abbreviated as DAC, has become the most widely known type of high pressure research equipment and the first successful applications for the investigations of iron and rhenium under high pressure of gaseous hydrogen were already reported [3,4]. It has been also shown that the thermodynamic conditions reported by the Russian group concerning formation of the iron hydride were significantly overestimated. We have also proved by employing the new technique for the loading DAC with gaseous hydrogen up to 1GPa as a starting pressure [5] that the rhodium hydride can be formed at room temperature and under pressure as high as 3.8 GPa. According to the data published in [2] , below 200 ° C even at

pressure about 9 GPa formation of the rhodium hydride failed. These facts have encouraged us to take a look on behavior of the other metal-hydrogen systems, studied already at high hydrogen pressure [2], by the „*in situ*” x-ray investigations in DAC. We have chosen the rhenium and molybdenum metals from two different reasons. Rhenium is the only known hcp metal which forms the hydride phase without structural changes (only small lattice expansion is observed) and yet the hydrogen content in this phase is uniquely small as estimated based by employing the idea of universal value of the hydrogen atomic volume in metal lattice. On the other hand more accurate data of the formation of molybdenum hydride are needed to estimate possibility of the tungsten hydride formation as tungsten is the only metal from chromium family which has not been converted to the hydride at any hydrogen pressure attainable so far.

Another purpose of these studies was determination of the pressure-volume relationships, which allow for the hysteresis observations and deriving the pressure of decomposition of the corresponding hydrides. These information are necessary for the calculations of the thermodynamic functions of formation of the hydrides since the only pressure of decomposition describes the true equilibrium of the metal hydrogen reaction. So far such a calculations are limited for the Ni-H, Cr-H, Al-H, and Mn-H only.

## Experimental

Novel high pressure technique for loading DAC with hydrogen has been recently published [5]. The main part of this apparatus is presented in Figure 1.

The originality of this technique rely on an idea of transformation of the piston movement, during pressure increase, into rotation of the supporting screw which closes gasket cavity.

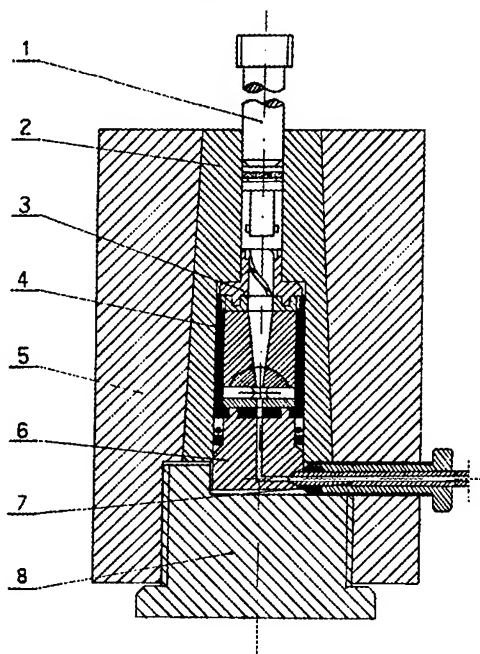


Fig1. High pressure chamber (1-piston, 2-beryllium bronze insert, 3-worm wheel device, 4-DAC, 5-steel high pressure cylinder, 6-stopper, 7-supporting screw),

In the high pressure x-ray measurements the energy dispersive x-ray diffraction method has been employed for the taking diffraction patterns as a function of pressure. The white beam of x-ray coming out from the conventional tungsten target tube, has been collimated down to 0.1 mm while the gasket hole had diameter of 0.2 mm. Pressure has determined by ruby fluorescence method. The samples were compacted from a powder into layers of a few microns thick to make load into the DAC easier. The volume of the samples was much smaller than a gasket cavity to keep molar ratio hydrogen to metal possibly high as the total amount of  $H_2$  has to be divided

on two parts: hydride formation and maintaining the hydrogen pressure inside DAC.

## Results

### Rhenium- hydrogen system

As an example of experimentally recorded x-ray diffraction patterns, the results for rhenium-hydrogen system at pressure 3.5 GPa (darkened spectrum) and 8.1 GPa (dotted spectrum) are presented in Fig.2. ( $E_d=45.66$ )

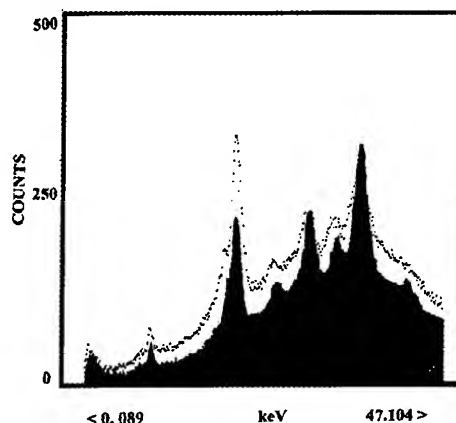


Fig.2. Energy dispersive x-ray diffraction patterns for the rhenium at hydrogen pressure of 3.5 GPa (darkened spectrum) and 8.1 GPa (dotted spectrum).

The calculated and observed values of the interplanar spacings are presented in Table 1.

Table 1

hkl	$d_{calc}$ Re -H [Å]	$d_{obs.}$ Re-H [Å]
100	2.370	-
102	2.216	2.24
101	2.090	2.11
102	1.619	1.64
110	1.368	1.39
103	1.254	1.27
200	1.185	1.20

Pressure-volume relationship determined from the *in situ* x-ray investigations is presented in Fig.3.

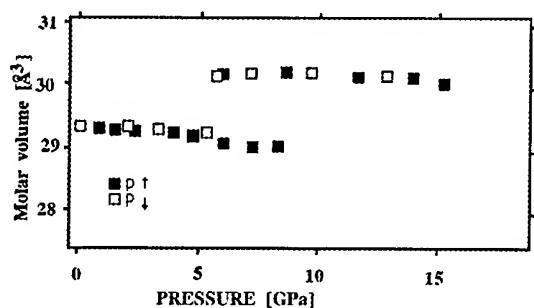


Fig.3. Molar volume of rhenium metal as a function of the hydrogen pressure,  $T=298$  K.

Pressure of formation has been determined as 8.1 GPa while pressure of decomposition was around 5.2 GPa. Starting value of rhenium molar volume has been determined as  $28.8 \text{ \AA}^3$  and extrapolated value to zero pressure of the rhenium hydride was  $30.4 \text{ \AA}^3$ . Assuming  $2.9 \text{ \AA}$  on the hydrogen atom in hcp rhenium lattice one can estimate H/Re content as about 0.27 in atomic ratio.

Similar results were obtained by the Badding's group [4] but pressure of decomposition was not determined there.

#### Molybdenum-hydrogen system

The phase transformation from the original bcc molybdenum metal structure to hcp is observed during hydride formation. This transformation is reversible when going down with pressure. The pressure-volume relationship for the molybdenum-hydrogen system is presented in Fig.4. As can be seen, a clear hysteresis gap is equal about 1.5 GPa. Initial value of molybdenum molar volume was  $31.13 \text{ \AA}^3$  in comparison with that for MoH equal  $35.0 \text{ \AA}^3$  extrapolated to zero pressure. Estimated hydrogen concentration as described above was about 0.7 H/Mo in an atomic ratio.

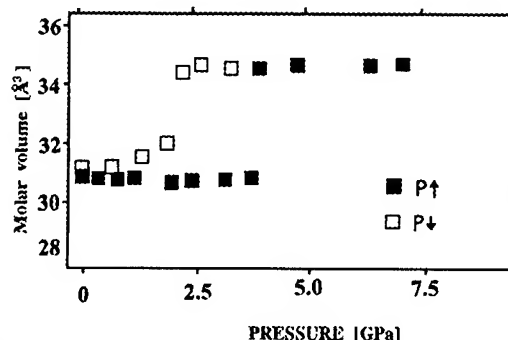


Fig.4. Molar volume of molybdenum metal as a function of hydrogen pressure.  $T=298$  K.

#### Discussion

These results confirm the Russian data [2] concerning formation and phase determination but there are significant differences in pressures and temperatures required for the corresponding hydride formations. Very probable reason for these discrepancies could come from the difficulties in determination true hydrogen activity in the apparatus they used.

The thermodynamic calculation based on the data presented will be published elsewhere.

#### References

1. B. Baranowski, *Metal Hydrogen System at High Pressure*, in G. Alefeld and J. Voelkl, (eds) *Hydrogen in Metals*, Top. Appl. Phys. **29** (1978) 157
2. E. G. Ponyatovsky, V. E. Antonov, I. T. Belash, *High Hydrogen Pressures, Synthesis and Properties of New Hydrides*, in „Problems in Solid-State Physics”, A. M. Prokhorov and A. S. Prokhorov (eds), Mir Publ., Moscow, 1984, pp 109-171
3. J. V. Badding, R. J. Hemly and H. K. Mao *Science*, **253** (1991) 421
4. J. V. Badding, D. C. Nesting and R. B. Baron, *Proc. of joint Intr. Assoc. for Res. and Adv. of High Pressure Science and Technology and APS Top. Group on Shock Compr. of Condensed Matter held at Colorado Springs*, p. 1317.
5. M. Tkacz, *Pol. J. Chem.*, **69** (1995) 1205

# CORRELATION BETWEEN PRESSURE DEPENDENCE OF ELECTRICAL RESISTANCE AND PHASE DIAGRAM OF THE METAL-HYDROGEN SYSTEMS

A.W. SZAFRAŃSKI

*Institute of Physical Chemistry, Polish Academy of Sciences,  
Kasprzaka 44/52, 01-224 Warsaw*

## ABSTRACT

A simple model is proposed which correlates typical pressure-composition isotherms known for transition metal - monohydride systems with simplified resistance-composition relationships of the Nordheim type. The calculated  $r(p_{H_2})$  relationships are compared with the available experimental high pressure results and the origin of the observed  $\Lambda$  and M-type anomalies is explained.

## Introduction

During the hydrogen absorption by fcc alloys the hydrogens enter the interstitial (octahedral) positions of the host lattice forming a disordered hydrogen sublattice. The random distribution of the screened protons among the available sites results in an increase of the electrical resistance. On the other hand, if hydrogen content approaches stoichiometry,  $c \rightarrow 1$ , where all octahedral interstitial sites are occupied, that part of resistivity, which is due to H-sublattice disorder should vanish. In the case of a continuous transition from the hydrogen-free alloy to the stoichiometric hydride (such a behavior occurs at and above the critical temperature) the electrical resistance of the metal/hydrogen system plotted as a function of hydrogen content should pass a maximum.

The experimental studies indicated that in many cases the hydride phase,  $MH_c$ , is formed with a non-stoichiometric composition,  $c < 1$ . An abrupt change of the hydrogen content from the value characteristic for the saturated  $\alpha$  phase to the value characteristic for the  $\beta$  phase takes place at a threshold pressure  $p_{form}$  if the temperature is lower than the critical temperature,  $T_{cr}$ . With the increase of the temperature this pressure increases and the range of hydrogen contents where the two phases coexist decreases. At and above the critical temperature a monotonic  $p$ - $c$  dependence can be observed only. During the phase transition the resistance changes accordingly. Further increase of the hydrogen

pressure in equilibrium with non-stoichiometric hydride leads to further increase of hydrogen content, towards  $c=1$ , and either to further increase or decrease of the resistance.

A characteristic feature of the metal-hydrogen systems is the difference of the value of the formation and decomposition pressures. It results in a hysteresis loop observed in the resistance vs. hydrogen pressure relationship,  $r(p_{H_2})$ , for increasing and decreasing pressure. When hydrogen pressure decreases, after the  $p_{form}$ -value was overpassed, the electrical resistance continues its course till it reaches the decomposition pressure. At this point an abrupt transition of electrical resistance to the value characteristic for the  $\alpha$  phase takes place.

An anomalous  $r(p)$ -relationships, of a  $\Lambda$ -type (a sharp maximum with a discontinuity of the  $dr/dp$ -derivative) were observed in the case of Ni/Si (8-10 at% Si[1]) and Ni/Al (10 at% Al[2]) alloys. The peaked structure suggested the existence of a phase transition but the absence of any hysteresis indicated that it could not be the typical  $\alpha$ - $\beta$  phase transition. The nature of the phenomenon remained unclear.

Another anomaly of a M-type was observed in Ni[1] and in the above mentioned alloys but with lower content of the second element — Ni/Al (2-5 at% Al[2]), Ni/Si (2 at% Si[3]) and in Ni/Cr (0.5 at% Cr[4]). Two peaks on the  $r(p)$ -curves, one corresponding to the absorption and the other to the desorption, were completely separated.

## Model

The theoretical expression for the  $p$ - $c$  isotherm for the metal-monohydride system is a rather complicated function of the hydrogen content. Thus for the purpose of this work the isotherms were taken in a simple form of a polynomial  $p^{1/2} = Ac^3 + Bc^2 + Cc$ . (1)

where the  $C$ -parameter simulates the temperature. With  $A=10$ ,  $B=-12$  and  $3.5 < C < 5.5$  they exhibit properties mentioned above.

The relationship between the electrical resistance of the  $MH_c$  alloy and the hydrogen content was assumed to be a modification of the Nordheim rule known for a simple substitutional alloy and adapted to the case of the interstitial alloy,  $MH_c\vartheta_{1-c}$ , where  $\vartheta$  denotes the vacancy in the interstitial position:

$$r = 1 + a_1c(1-c) + a_2c, \quad (2)$$

The second term represents the *structural resistivity* of the hydrogen sublattice and the last term takes into account the possible difference of resistivities of the H-free alloy and its stoichiometric hydride.

## Results and Discussion

A simple combination of the model isotherms  $p$ - $c$  with the model relationship  $r(c)$  gives relationships between the electrical resistance and the hydrogen pressure,  $r(p)$ . Typical results for four selected temperatures (much lower (I), slightly lower (II), equal (III) and higher (IV) than  $T_{cr}$ ) and several sets of the  $a_1, a_2$  parameters are presented on Fig. 1. The parts of the model  $r(p)$  curves that correspond to the portions of the absorption and desorption isotherms not realized in nature are given by dot lines.

If we compare the experimental data obtained for room temperature (some of them are shown on Fig. 2-4) with the present calculations, the following conclusions can be drawn.

- S-type  $r(p)$ -relationship occurs (compare Figs. 1a and 2) if the resistivity of the stoichiometric hydride is much higher than that of the H-free alloy and the *structural resistivity* of the hydrogen sublattice is small,

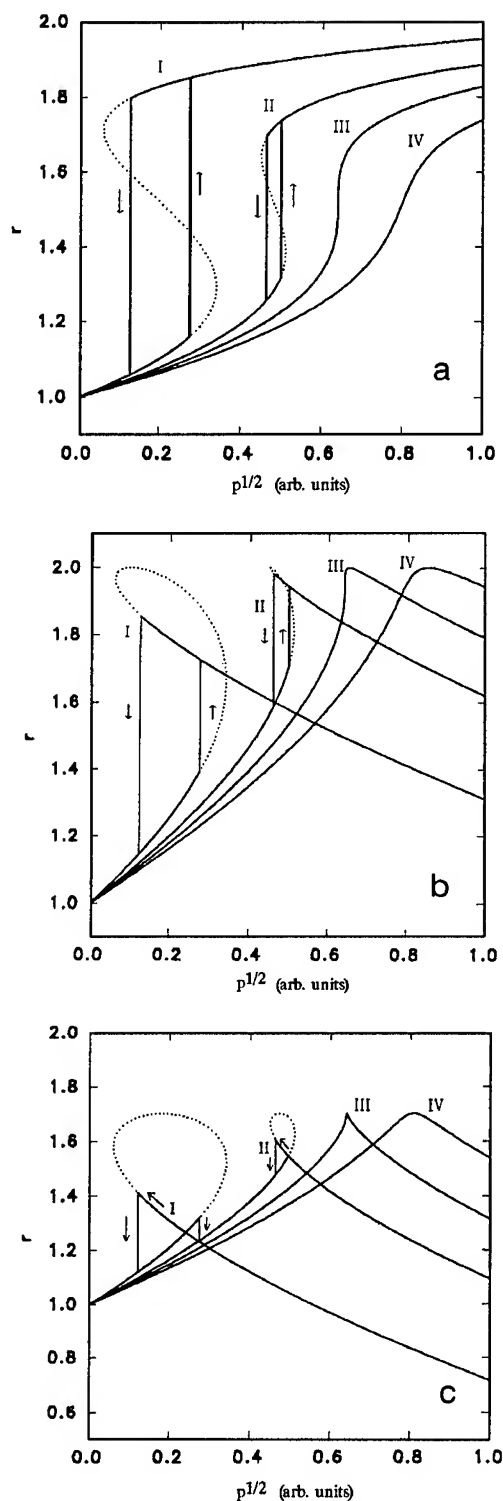


Fig. 1.  $r(p)$  relationships resulting from combinations of  $p(c)$  isotherms I-IV given by eq. 1 and the Nordheim-type  $r(c)$  relationships given by eq. 2: (a) -  $a_2=1$ ,  $a_1=0.5$ ; (b) -  $a_1=4$ ,  $a_2=0$ ; (c) -  $a_1=4$ ,  $a_2=-0.65$ .

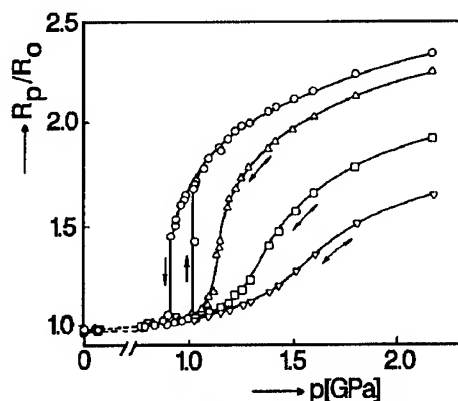


Fig. 2. Pressure dependence of electrical resistance of the Ni/V alloys in deuterium; circles - 6 at%, triangles up - 9 at%, squares - 12 at% and triangles down - 15 at% V[1].

- $\Lambda$ -type relationships with hysteresis (compare Figs. 1b and 3) occur if the resistivities of the stoichiometric hydride and the H-free metal do not differ much.
- $\Lambda$ -type anomaly is not the manifestation of any phase transition. It can be observed if

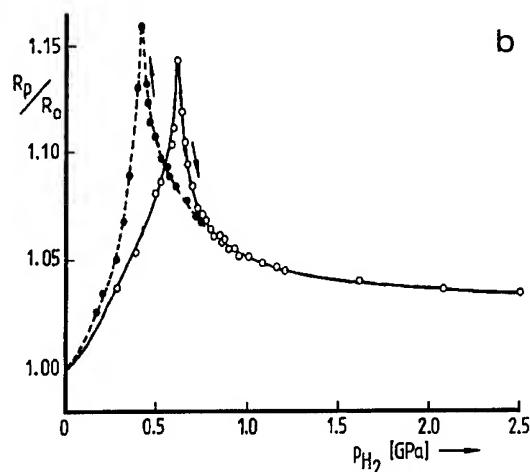
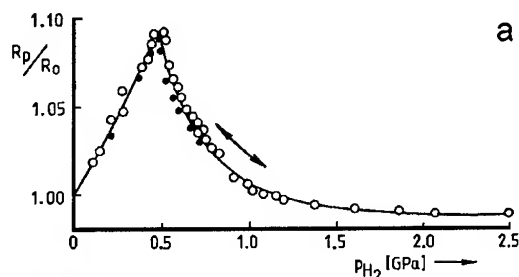


Fig. 4. Pressure dependence of electrical resistance of Ni/Al alloys in hydrogen; (a) -  $\Lambda$ -type anomaly in the 10 at% Al alloy; (b) - M-type anomaly in the 5 at% alloy[2].

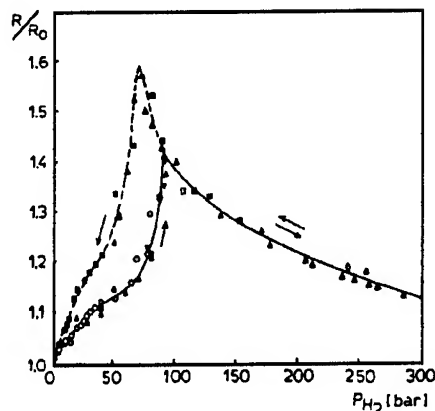


Fig. 3. Pressure dependence of electrical resistance of the Pd/Ni alloy (25 at% Ni) in hydrogen [5].

- the temperature of the measurement is close to  $T_{cr}$  and the hydrogen content corresponding to the maximum of the  $r(c)$ -relationship is close to the composition of the critical point (compare the experimental data shown on Fig. 4a with the curve labeled III on Fig. 1c).
- M-type anomaly corresponds to the case of large *structural resistivity* of the hydrogen sublattice and much lower resistivity of the stoichiometric hydride as compared to the H-free alloy (compare Fig. 4b with the curve labeled I on Fig. 1c).

For more details see [6].

#### References

- 1 S.M. Filipek, A.W. Szafranski, M. Warsza and S. Majchrzak, *J. Less-Common Met.* **158** (1990) 177.
- 2 S.M. Filipek and A.W. Szafranski, *Polish J. Chem.* **65** (1991) 493.
- 3 B. Baranowski and S.M. Filipek, in *High Pressure Chemical Synthesis*, eds. J. Jurczak and B. Baranowski (Elsevier, 1989), p. 81.
- 4 S. Filipek, H.J. Bauer, S. Majchrzak and H. Yamamoto, *Z. phys. Chem. N.F.* **163** (1989) 485.
- 5 A.N. Niemirow, A.W. Szafranski and T. Skośkiewicz, *J. Less-Common Met.* **101**, (1984) 305.
- 6 A.W. Szafranski, *Polish J. Chem.* **69**, (1995) 1340.

## HIGH PRESSURE STUDIES OF $\text{YbH}_2$ AND $\text{YbD}_2$

J. Staun Olsen and S. Steenstrup

Niels Bohr Institute, Ørsted Laboratory, Universitetsparken 5,  
DK-2100, Copenhagen, Denmark  
and

L. Gerward

Physics Department, Technical University of Denmark  
DK-2800, Lyngby, Denmark

### ABSTRACT

High-pressure x-ray diffraction was performed on  $\text{YbH}_2$  and  $\text{YbD}_2$  up to 61 GPa. A first order transition from an orthorhombic structure to a hexagonal structure has been found at about 16 GPa. Bulk modulus  $B_0$  and its pressure derivative  $B_0'$  in the orthorhombic phase were found to be:  $\text{YbH}_2$ , 36 GPa and 6.7,  $\text{YbD}_2$ , 55 GPa and 3.7. In the hexagonal phase:  $\text{YbH}_2$ , 132 GPa and 0.4,  $\text{YbD}_2$ , 154 GPa and 0.4.

A valence change seems to start in the hexagonal phase.

### Introduction

The structure of ytterbium dihydride has been studied by x-ray diffraction and neutron diffraction at ambient pressure and temperature in both the deuterated (1), (2) and the hydrogenated forms (3), (4). The stable structure of  $\text{YbD}_2$  and  $\text{YbH}_2$ , at ambient pressure and temperature is orthorhombic  $D_{2h}^{16}$  ( $P_{nma}$ ), but cubic phases formed at elevated temperatures can exist at room temperature.  $\text{YbH}_2$  was studied by x-ray scattering (5) at ambient temperature, and high pressure up to 27 GPa. It was found that at  $\sim 15$  GPa the orthorhombic structure of  $\text{YbH}_2$  transforms to a hexagonal structure.

In the rare-earth compounds, the valence state of the rare-earth ion may be changed between the  $4f^{n+1}(5d6s)^2$  and  $4f^n(5d6s)^3$  configuration by application of pressure. At zero pressure  $\text{YbH}_2$  and  $\text{YbD}_2$  share the ground state configuration  $4f^{n+1}(5d6s)^2$ . In contrast the ground state configuration of the other rare-earth dihydrides are  $4f^n(5d6s)^3$ , and they all crystallize in the fcc fluorite structure. If the valence state is changed, one would expect  $\text{YbH}_2$  and  $\text{YbD}_2$  to transform into a fcc structure. The present report describes x-ray diffraction studies on both  $\text{YbH}_2$  and  $\text{YbD}_2$  at ambient temperature and high pressure up to 61 GPa.

### Experimental

Yb powder of purity 99.9% was supplied by Rare Earth Products Ltd. England. The powder was hydrogenated in a high pressure microbalance, and the sample was heated at 5K/min. in hydrogen and deuterium at a pressure of 0.2 MPa to 575 K. The formed  $\text{YbH}_2$  and  $\text{YbD}_2$  powders have the composition  $\text{YbH}_{1.92}$  and  $\text{YbD}_{1.92}$ . In the report the samples will be referred to as  $\text{YbH}_2$  and  $\text{YbD}_2$ . A diamond anvil cell was used for the high pressure studies. The crushed powder was enclosed in an inconel gasket (hole diameter 200  $\mu\text{m}$ ), together with a 4:1 methanol-ethanol mixture. The pressure was measured by the ruby method. The Bragg angle was determined from a diffraction spectrum of NaCl in the diamond cell. The experiments were performed using synchrotron radiation and energy dispersive powder diffraction at Hasylab in Germany and Daresbury in England.

### Results

Figure 1 and 2 show diffraction spectra of  $\text{YbD}_2$  at zero pressure and at the maximum used pressure 61 GPa. Peak positions E have been obtained from the energy-dispersive x-ray spectra by processing using the maximum-entropy method (6), and the



measured lattice constants were refined using the program PURUM (7).

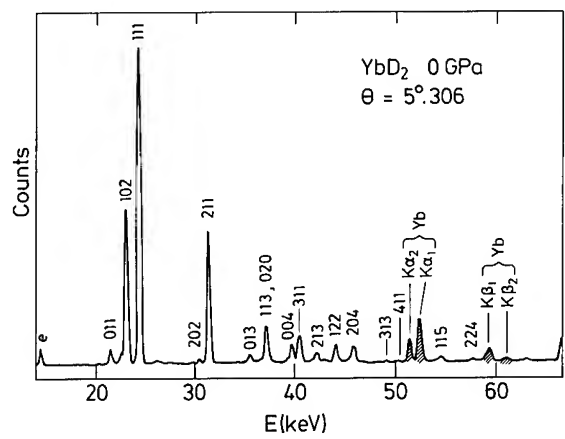


Figure 1  
X-ray energy-dispersive diffraction spectrum of orthorhombic YbD<sub>2</sub> at atmospheric pressure, e escape peak.

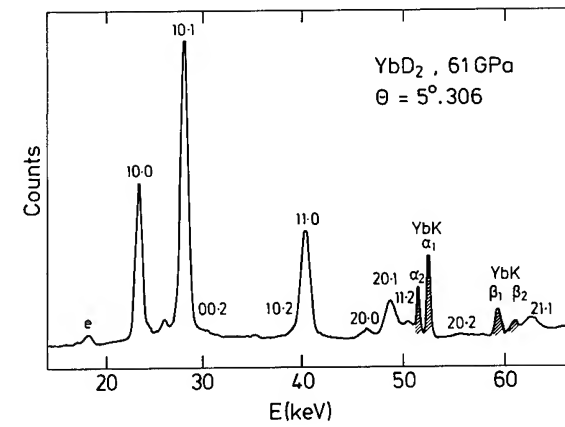


Figure 2  
X-ray diffraction spectrum of hexagonal YbD<sub>2</sub> at 61 GPa.

The goodness of the fit is characterized by a reliability factor

$$R = \sum |d_{obs.} - d_{calc.}| / \sum d_{obs.} \quad (1)$$
  
where  $d_{obs.}$  and  $d_{calc.}$  are observed and calculated lattice-plane spacings, respectively. At ambient pressure 13 lines could be fitted with a reliability factor  $R = 0.05\%$  and at 61 GPa with 9 lines  $R = 0.2\%$ .

In table 1 the unit cell parameters of orthorhombic YbH<sub>2</sub> and YbD<sub>2</sub> are compared with published values.

Table 1

Unit cell parameters of orthorhombic YbH<sub>2</sub> and YbD<sub>2</sub> at ambient pressure

Author	Sample	a(Å)	b(Å)	c(Å)
Korst and Warf	YbD <sub>2</sub>	5.871	3.561	6.763
Warf and Hardcastle	YbH <sub>2</sub>	5.905	3.570	6.792
Messer and Gianoukos	YbH <sub>1.78</sub>	5.895	3.574	6.801
Lebech et al.	YbD <sub>2</sub>	5.875	3.565	6.781
	YbH <sub>2</sub>	5.900	3.576	6.776
This work	YbD <sub>2</sub>	5.887	3.565	6.765
accuracy ± 0.08%	YbH <sub>2</sub>	5.890	3.573	6.773

The volume per Yb atom is calculated from the refined unit cell parameters and shown for YbD<sub>2</sub> in figure 3.

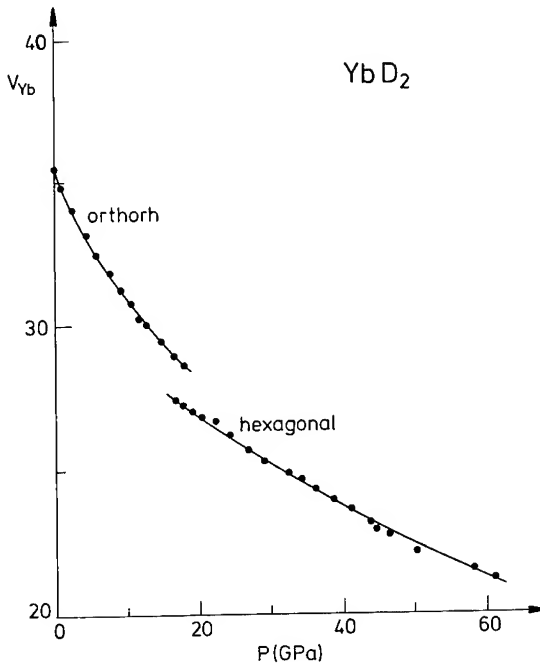


Figure 3  
Equation of state for YbD<sub>2</sub>,  $V_{Yb}$  means volume in (Å<sup>3</sup>) per Yb atom in the unit cell.

As found before there is a 5-6% change of the volume at the 1.order transition at about 16 GPa, and the structure changes to hexagonal. No further change in structure is found in the used pressure range.

The compressibility of the two phases are calculated by a fit to a modified Murnaghan's equation of state

$$P = \left( \frac{B_0}{B_0'} \right) \left[ \left( \frac{V_1}{V} \right)^{B_0'} - 1 \right] + \left( \frac{V_1}{V} \right)^{B_0'} P_1 \quad (2)$$

where  $V_1$  and  $P_1$  are the unit-cell volume and pressure respectively at the start of a new phase.  $B_0$  is the bulk modulus,  $B'_0$  is the derivative of the bulk modulus at ambient pressure and  $V$  the unit-cell volume at pressure  $P$ . Table 2 shows the calculated bulk modulus  $B_0$  and its pressure derivative  $B'_0$  for  $\text{YbH}_2$  and  $\text{YbD}_2$  in the orthorhombic phase and the hexagonal phase.

Table 2

Sample	$B_0$ (GPa)	$B'_0$
$\text{YbD}_2$ ort.	$55 \pm 3$	$3.7 \pm 0.7$
$\text{YbH}_2$ ort.	$36 \pm 3$	$6.7 \pm 0.7$
$\text{YbD}_2$ hex.	$154 \pm 10$	$0.4 \pm 0.3$
$\text{YbH}_2$ hex.	$132 \pm 19$	$0.9 \pm 0.6$

The values for  $\text{YbH}_2$  is in agreement with the value found before (5). The equation of state for the high pressure phase is very close to be a straight line in the shown pressure range. Using absorption edge measurements, a pressure induced shift of the  $L_{III}$  absorption edge of Yb metal was measured (8). At 33 GPa the shift is 6.6 eV to a higher binding energy as compared to the value at ambient pressure. This corresponds to a pressure induced valence transition from divalent to trivalent. We have performed some preliminary  $L_{III}$  absorption edge measurements of  $\text{YbH}_2$  up to 31 GPa. The position of the 'white line' at the absorption edge of Yb (at 8.938 KeV at ambient pressure) was compared with the position of the absorption edge of Cu at 8.9795 KeV at ambient pressure.

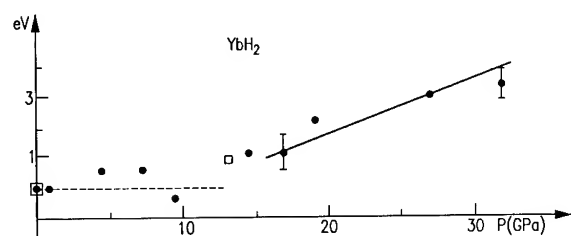


Figure 4  
Pressure induced shift of the  $L_{III}$  absorption edge of Yb in  $\text{YbH}_2$  compared with the absorption edge of Cu (8.9795 KeV) at ambient pressure.  $\square$  means decreasing pressure.

Figure 4 shows a pressure induced shift of the Yb edge, which starts at the phase transition. We find that the shift indicates a change in valence of the divalent  $\text{YbH}_2$  at 16 GPa, towards the trivalent rare-earth ions. Further absorption studies must be performed to clarify the pressure necessary to change the valence to trivalent.

## Conclusion

It has been shown that the equation of state can be described by Murnaghan's equation and that bulk modulus  $B_0$  and its pressure derivative  $B'_0$  can be obtained for both the orthorhombic phase and the hexagonal phase. The unexpected hexagonal structure can be related to the non-integral valence as the valence first starts to change after the transition.

## Acknowledgements

We thank HASYLAB-DESY and DARESBUURY Laboratory for the use of the synchrotron radiation facility. We thank G. Harrison for linguistic correction of this article. Financial support from the Danish Natural Science Research Council is gratefully acknowledged.

## References

1. W.L. Korst and J.C. Warf, *Acta Cryst.* 9 (1956) 452.
2. B. Lebech, H.L. Skriver and S. Steenstrup, *Physica Scripta* 29 (1984) 503.
3. J.C. Warf and K.I. Hardcastle, *Inorg. Chem.* 5 (1966) 1736.
4. C.E. Messer, P.C. Gianoukos, J. Less. *Com. Met.* 15 (1968) 377.
5. J.S. Olsen, B. Buras, L. Gerward, B. Johanson, B. Lebech, H.C. Skriver and S. Steenstrup, *Physica Scripta* 29 (1984) 503.
6. S. Steenstrup, *Aust. J. Phys.* 38 (1985) 319.
7. F.E. Werner, *Ark. Kemi* 31 (1969) 513.
8. K. Syassen, G. Wortman, J. Feldhaus, H.K. Frank and G. Kaindl, in *Physics of Solids under High Pressure* ed. J.S. Shilling and R.N. Shelton (North-Holland 1981) 319.

# GENERATION AND ACCUMULATION OF TRITIUM IN METAL SURFACE LAYER MELTED AND QUICK QUENCHED BY TREATMENT WITH DENSE DEUTERIUM PLASMA STREAMS

V.A. ALEKSEEV, V.A. ROMODANOV\*, S.V. RYLOV, YU.F. RYZHKOV, V.I. SAVIN\*, YA.B. SCURATNIK\*\*, V.M. STRUNNIKOV, V.I. VASILIEV

*TRINITI, 142092, Troitsk, Moscow reg., Shkol'naya 1, RUSSIA*

*\*SSRI SPA LUTCH, 142100, Podol'sk, Moscow reg., Zheleznodorozhnaya 24*

*\*\* Karpov SRPCI, Moscow, Vorontsovo pole 10, RUSSIA*

## ABSTRACT

In this work we have presented results of research on the intensity of nuclear reactions in condensed media (NRCM) and determined tritium output as result of plasma-surface interaction in a Z-pinch device, primary intended for thermonuclear research. The high intensity of the NRCM has allowed to receive a tritium generation rate of  $10^{15} \text{ s}^{-1}$  at a pressure about 1 kbar in deuterium plasma. We discuss the effectiveness of different targets and the development of NRCM in the hot plasma - target systems.

## Introduction

The processes of superfast destruction of a crystal lattice and following very rapid quenching of metal surface with a rate of  $10^7 - 10^8 \text{ K s}^{-1}$  (V.A. Alekseev et al. [1]) during pulse powerful plasma-solid interaction open up new possibilities in the studies of NRCM. As a result of the quenching, a metastable state of dissolved gases in metals can exist and the quantity of the dissolved gases can exceed the equilibrium values by more than one order of magnitude [2]. The second important fact is in that hydrogen penetration in metals increases exponentially with increasing of temperature [3]. These conditions can be realized with using Z-pinch and one might expect products of cold fusion reactions.. Recent experiments (Romodanov V.A. et al. [4,5], Shrinivasan M.H. et al. [6], Alekseev V.A. et al. [7]) showed, that the cold fusion reactions can go at comparatively low ion energies at interaction of deuterium plasma with a solid surface. In this case, the efficiency of the tritium channel exceeds that of the neutron channel by some orders of magnitude and depends on the density of ions, falling on the surface. Due to these facts, the studies of low-energy fusion reactions may be perspective with using devices, generating dense streams of deuterium plasma.

## Methods

The experiments were carried out on a device of TRINITI (Fig. 1). The device is a system for formation of Z-pinch discharge. The discharge develops between electrodes 1 and 2 within a volume, limited by the electrodes and ceramic insulator 3., when high voltage from high-voltage capacity bank 8 is applied to the electrodes through vacuum switch 7. The discharge starts on the inner surface of the insulator tube, and then the plasma of the discharge is compressed to axis of the vacuum chamber due to interaction between a discharge current and its own magnetic field. The cylindrical sample 4 is mounted on the upper electrode 1, which had a negative electrical potential. The accelerated plasma impinges on the sample surface. The sample is of 150 mm long and 8-12 mm in diameter. As a plasma-forming gas, the deuterium with initial pressure about 30 Pa is used. The treatment of the metal samples with plasma pulses was carried out at voltage of 12,5 kV and energy of 22,5 kJ. The quantity of plasma pulses acting on the sample was changed from 20 to 100, at a pulse duration 5-10 microsecond with interval between the shots of the device about 1 min. The plasma-forming gas and the metal samples were

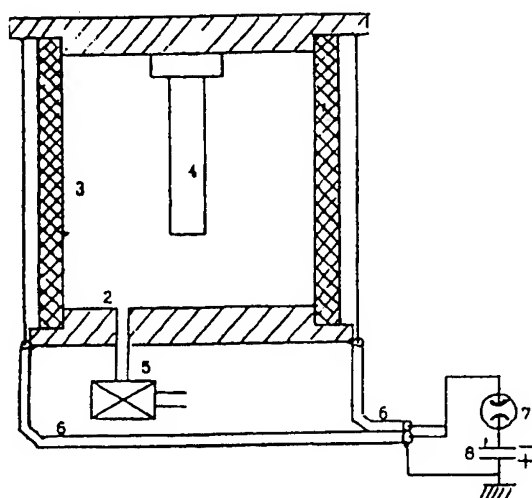


Fig.1. The sheme of the experimental device:

1 -upper current electrode; 2 - lower current electrode;  
3 - ceramic insulator; 4 - cylindrical metal sample; 5 -  
vacuum system; 6 - set of conductors; 7 - vacuum  
switch; 8 - pulse high-voltage capacity bank

analysed for tritium in the same day. The samples of  
different metals were examined but the most full  
cycle of the investigations, to the present time, was  
carried out on the samples of titanium, vanadium,  
zirconium and niobium. The analysis of deuterium for

tritium was performed by measuring beta-activity by  
the liquid scintillation method with using Beta-2  
device. The absolute error of the tritium content  
measurement in the specimens did not exceed 50%  
and relative one did not exceed 10%. To increase the  
measurement accuracy, the every cycle of measuring  
of plasma-forming gas specimens was accompanied  
by checking of initial deuterium gas. The  
measurements of tritium content in the metal  
specimens was carried out by the similar method, in  
which specimens of water to analysis were got by  
etching of the metal specimens in acid.

### Results and discussion

The main results are given in table 1. In this table one  
can see, that the summary quantity of tritium in gas  
specimens, taking after the plasma treatment, was  
achieved value of  $10^9$  to  $10^{11}$  atoms. Tritium had  
been found in the gas specimens in cases of all metal  
samples except for niobium sample. The exceeding of  
specimen activity over background values was of 8%  
to 320%. The quantity of tritium in a sample material  
may exceed 100 times that of the gas specimen and  
for the studied metal samples was  
from  $10^{11}$  to  $10^{12}$  atoms. Tritium was not detected in  
samples of vanadium and tantalum. The abnormally

Table 1 The tritium generation on Z-pinch for different materials of target

Material	Number of cycles	Gas specimen		Metal specimen		Summary quantity of tritium Atom	Specific tritium generation rate At/(s × cm <sup>2</sup> )
		Specific activ.	Quantity of tritium	Specific activ.	Quantity of tritium		
		Bc/ml	Atom	Bc/ml	Atom		
Without samles	40	-	-	-	-	-	-
	100	-	-	-	-	-	-
Ti	100	28	$6.0 \times 10^{10}$	19	$1.2 \times 10^{12}$	$1.2 \times 10^{12}$	$2.7 \times 10^{13}$
V	38	5	$1.1 \times 10^{10}$	166	-	$1.1 \times 10^{10}$	$5.5 \times 10^{11}$
SS steel	100	9	$2.0 \times 10^{10}$	-	-	-	-
Zr	20	4.7	$1.0 \times 10^{10}$	-	-	-	-
	40	8.5	$1.8 \times 10^{10}$	261	$2.1 \times 10^{12}$	$2.1 \times 10^{12}$	$1.5 \times 10^{14}$
	100	2.4	$5.2 \times 10^9$	-	-	-	-
Nb	100	-15	-	25	$4.0 \times 10^{11}$	$4.0 \times 10^{11}$	$9.1 \times 10^{12}$
Mo	92	3.2	$6.8 \times 10^9$	-	-	-	-
Er	75	79.2	$1.7 \times 10^{11}$	48.8	$2.6 \times 10^{12}$	$2.8 \times 10^{12}$	$7.1 \times 10^{13}$
Ta	100	25.5	$5.6 \times 10^{10}$	70	-	-	-
W	20	2.1	$4.8 \times 10^9$	-	-	-	-

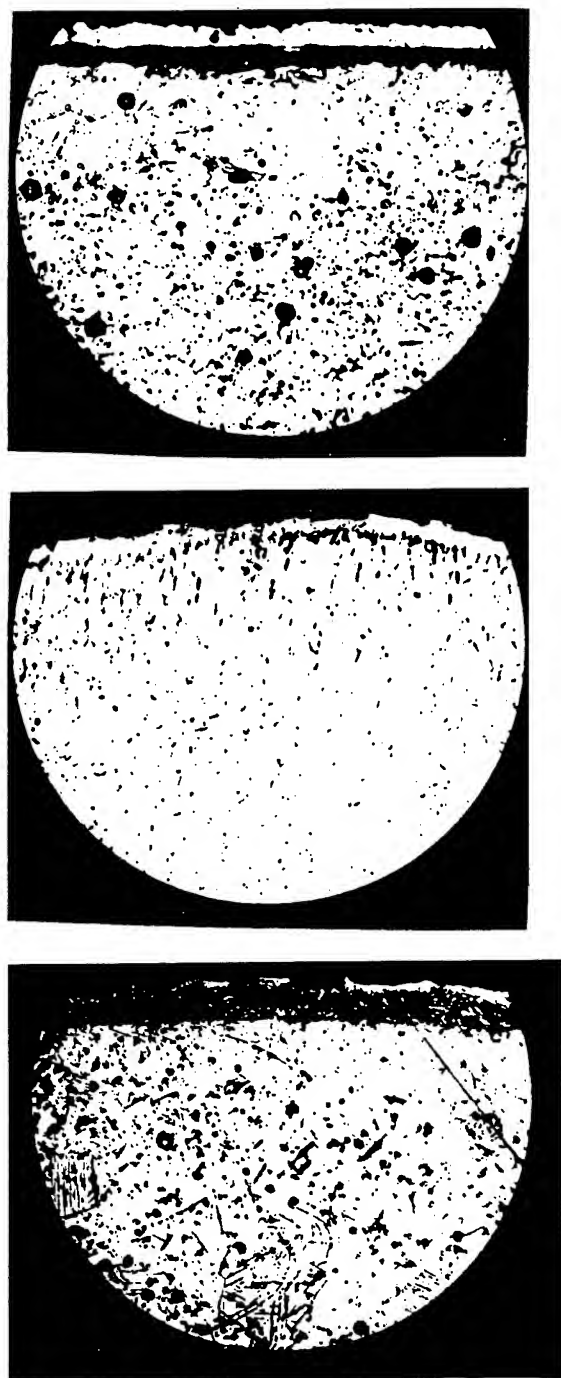


Fig.2. The structures of the samples cross-sections after the treatment by Z-pinch plasma,  $\times 200$ :  
a - titanium, 100; b - zirconium, 40; c - niobium, 100 cycles

high value of tritium in the metal samples is connected with a peculiarity of the experimental method: during the plasma pulse the sample surface is heated to a temperature near melting point and than is

cooled very rapidly due to thermoconductivity of the metal. Durations of these processes are about few microseconds. Such thermocycling changes periodically the solubility of hydrogen in the sample and lead to periodical absorption of hydrogen and its desorption. The straight isotope effect assistes an accumulation in metal of more heavy isotopes. Especially strongly this effect is observed in niobium, (Romodanov V.A. et al., [4]). High tritium generation rates were found in samples of titanium, zirconium, erbium and were  $(1-5) \times 10^{15}$  at/s. The specific tritium generation rate, relative to area of surface, was higher by more than one order of magnitude in titanium, as compared with vanadium and in zirconium as compared with niobium. It seems reasonable to say, that this is connected with more high solubility of hydrogen in metals of fourth group. The specific tritium generation rate in the zirconium sample is approximately one order of magnitude more than that is in the titanium sample, and the rate in the niobium sample is approximately one order of magnitude more than that is in vanadium sample. The analysis of distribution of tritium concentration along length of titanium sample shows, that the quantity of tritium is almost a two times more at upper part of the sample than that is in lower part of the sample. Reasons of this phenomenon need further investigations. It should be noted, that tritium in the gas specimens was not found in experiments without metal sample. Obviously, the lack of tritium in experiments without a sample may be explain by more low tritium generation rate in compressed deuterium plasma than at interaction of this plasma with a solid. The structures of some samples after plasma treatment are shown in Fig.2. On surfaces of all samples one can see the external layer of melted metal 0.005-0.020 mm thick. In titanium the melted layer is the most thick, in zirconium it is thinner and the most thin one is in niobium. A great quantity of small gas bubbles is observed in volume of subsurface layer in all the samples. In the titanium sample, a size of the bubbles is about 0.015 mm. It is believed, the bubbles move during the plasma treatment cycles (and their stretching in radius direction form in zirconium sample (Fig. 2b) gives an indication of it) and are accumulated under surface melted layer. If a number of plasma treatment cycles is increased the accumulated bubbles can form then unbroken cavity and tear off the surface layer from base as in titanium (Fig. 2a). The accumulation of the bubbles under surface melting layer of niobium sample was not

observed but there is a layer of deuterated phase 0.03 mm thick (Fig. 2c). Nevertheless, the regions with inclusion of deuterated phase were observed in subsurface layers of all the samples. On the whole, the concentration of deuterium in the samples was not high and the samples were kept their initial plasticity of high orders. Possibly, this behaviour of bubbles with deuterium is conditioned by the plasma treatment by which the gas of superfluous concentration had no time to dissolve because of very rapid cooling. These results are while still preliminary, but even so they show, that the stability of materials to prolonged influence of powerful plasma streams present the serious problem due to gas bubbles formation. Obviously, one may be noted, that the refractory metals of niobium type are more steadfast to influence of powerful plasma streams.

## Conclusions

The presented results show, that at interaction of dense deuterium plasma with metal samples the intensive tritium generation may be observed with rate about  $10^{15}$  at/s, that is six order of magnitude more than that in method in which a plasma of a glow discharge is used. It is suggested that this tritium is a product of nuclear reaction



It is shown, that the intensity of tritium generation might be increased with increasing a solubility of hydrogen in metal and with increasing atomic number of metals.

## References

1. V.A. Alekseev, I.K. Konkashbaev, Ye.A. Kiselev, T.D. Kiseleva, V.N. Lyashenko, B.E. Matveev, Yu. V. Scvortzov, V.M. Strunnikov, S.S. Tzerevitinov, V.M. Chistyakov, *Pis'ma v JTPh*, t. 9, n. 1 (1983) 42.
2. T.P. Shmyryeva, V.A. Alekseev, A.P. Babichev, G.M. Vorob'yev, *Pis'ma v JTPh*, t.8 (1982) 109.
3. A.P. Kanaev, V.M. Sharapov, A.P. Zakharov, A.M. Naidenov, V.A. Alekseev, *JPhCh*, t. 62, (1988) 803.
4. V.A. Romodanov, V. I. Savin, M.V. Shakhurin et al. "Nuclear Fusion in a Solid". *International conference on Radiative Material Science*. Alushta, May 22-25, 1990. Poster report t-100.
5. V.A. Romodanov, V. I. Savin, M.V. Shakhurin et al. "Nuclear Fusion in a Solid". *Zhurnal Tekhnicheskoy Fiziki*, 1991, v.81, is.5, p. 122 (In Russian).
6. M. S. Srinivasan et al. "Observation of Tritium in Gas/Plasma Loaded Tritium Samples". *Proceedings of the conference on Anomalous Nuclear Effects in Deuterium/Solid Systems*. Provo, Utah, October 22-24, 1990, AIP, 1991, p.514.
7. V.A. Alekseev, V.A. Romodanov, S.V. Rylov, Yu.F. Ryzhkov, V. I. Savin, Ya.V. Skuratnik, V.M. Strunnikov, V.I. Vasiliev, *Pis'ma v JTPh*, tom 21, n. 6 (1995) 64.

## **VII(B) Diamond and Insulators**

# A STUDY OF DIAMOND LATTICE DEFORMATIONS OCCURING IN UNIAXIAL COMPRESSION BY CHANGES IN KOSSEL'S LINE INTENSITY PROFILE

V.N.TKACH AND A.G.GONTAR

*V.N.Bakul Institute for Superhard Materials  
of the Ukrainian National Academy of Sciences,  
Kiev, Ukraine*

## ABSTRACT

Based on the results of precision measurements of interplanar spacings in 8 crystallographic directions, the components of a strain tensor as well as their variations were determined in a uniaxial compression of synthetic diamond single crystals up to 2.5 GPa. Values of principal deformations of growth pyramids of cubic and octahedral faces as well as a lattice stored elastic energy have been found to vary nonmonotonically, which is defined by the differences in stressed-strained states of growth pyramids of real crystals.

In compressing diamond up to 1.3 - 1.5 GPa, the intensity profile of  $K_{\alpha}$ -lines widens considerably and can transform into a smeared band. With the further increase of loading above 2.0 GPa, the profiles of  $K_{\alpha_{1,2}}$ -lines become distinct again, which points to a relaxation of elastic stresses in diamond during loading of crystals at room temperature.

## Introduction

The study of a stressed-strained state of diamond single crystals is rather difficult due to extremely high mechanical characteristics of the material. At the same time the influence of the initial state on the mode and intensity of the crystal deformation and the loading-induced variations of a lattice imperfect structure are of great scientific and practical interest.

In the present work, variations of stressed-strained states have been studied of 1 mm-sized diamond single crystals grown in the Ni-Mn-C system. The crystal lattice strain was studied both from the analysis of Kossel's lines mutual arrangements on a diffraction pattern [1-3] and from variations of their intensity profiles [4]. Based on the results of precision measurements ( $\Delta d_{\{hkl\}} = 2 \times 10^{-6} \text{ nm}$ ) of interplanar spacings in 8 crystallographic directions using Kossel's method, the components of strain tensor and their variations in uniaxial compression of synthetic diamond single crystals up to 2.5 GPa were determined.

## Experimental results

The crystals under study were characterized by strains in crystal lattices with the highest value of 0.08 %. In this case, the orientation of the

strain tensor did not coincide with the fourfold axis, the direction that best fit for mechanical loading of crystals.

Variations of the stressed-strained state at the uniaxial compression of a diamond single crystal synthesized in the Ni-Mn-C system are given in Table. These data show that under mechanical loading, values of the principal strain of growth pyramids of cubic and octahedron faces change differently. This suggests different elastic characteristics of  $\langle 111 \rangle$  and  $\langle 100 \rangle$  growth pyramids of diamond single crystals. A nonmonotonic increase in both a stored elastic energy ( $W_s$ ) and lattice deformation intensity observed with the increase in external loading is defined by the differences in the initial stressed-strained states of growth pyramids of simple habits of real crystals.

Intensity profiles of Kossel's lines were studied using a densitometer as described in [4]. Figure displays the variations in intensity profiles of Kossel's lines in the uniaxial compression of a crystal at room temperature. It has been found that in the uniaxial compression of crystals up to 1.3 - 1.5 GPa, the intensity profiles of  $K_{\alpha_{1,2}}$ -lines (curve a) widen drastically and can transform into a smeared band (curve b), which takes distinct forms of  $K_{\alpha_{1,2}}$ -lines again when the loading increases above 2.0 GPa (curve c). The



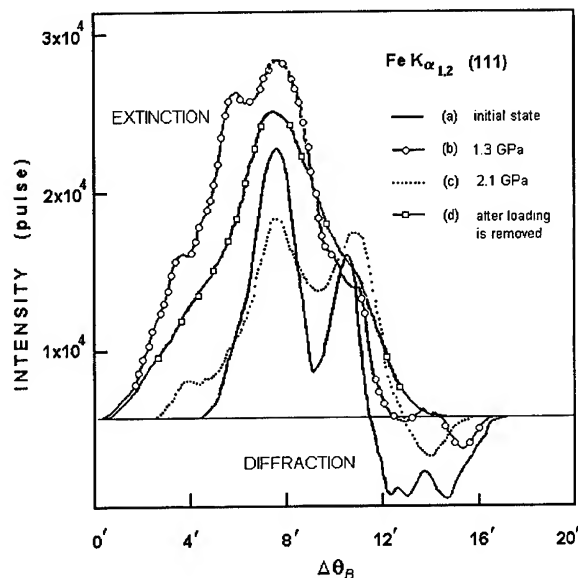
The stressed-strained state at the uniaxial compression of a diamond single crystal synthesized in the Ni-Mn-C system

$\sigma_{[100]}$ ( GPa )	Growth pyramid	Principal strains $\varepsilon$ , ( % )				Energy $W_s \times 10^{-5}$ ( Jm <sup>-3</sup> )
		$\varepsilon_1$	$\varepsilon_2$	$\varepsilon_3$	$\sqrt{\varepsilon_i^2}$	
0.00	- - -	0.022	-0.008	-0.010	0.025	
0.48	<111>	0.057	-0.083	-0.092	0.136	5.5
	<100>	0.049	-0.024	-0.077	0.094	3.9
0.94	<111>	0.061	-0.067	-0.036	0.097	9.6
	<100>	0.058	-0.054	-0.120	0.144	7.6
1.05	- - -	0.051	-0.023	-0.043	0.071	2.2
1.24	<111>	0.066	0.038	-0.189	0.204	17.9
	<100>	0.104	0.033	-0.154	0.189	18.3
1.44	<111>	0.100	0.140	-0.228	0.286	26.2
	<100>	0.093	0.031	-0.248	0.267	28.2
1.55	<111>	0.105	0.041	-0.224	0.251	30.3
	<100>	0.099	0.031	-0.238	0.260	31.9

fact points to the relaxation of elastic stresses in the lattice at the loading of crystals. The redistribution of  $K_{\alpha_1}$  and  $K_{\alpha_2}$  - line intensities, that takes place in this case, is defined by the interaction between a diffraction constituent and an extinction component of the black-white structure of Kossel's lines and characterizes the effect of the real structure of diamond on the lattice dynamics in compression. After the external load is removed, irreversible changes of the diamond structure (plastic deformation) are observed. They manifest themselves both in a considerable smearing of Kossel's  $K_{\alpha_{1,2}}$  - lines (curve d) and in variations of strain tensor components.

### Discussion

The data of the Table show that the increase in external load up to 1 GPa results not only in variations of deformation absolute values, but of deformation tensor orientation in a space associated with crystallographic axes and the angle between directions of the maximum deformations in growth pyramids of a cube and octahedron faces. When the load attains 0.9-1.2 GPa, the absolute values of deformations and stored elastic energy of the lattice decrease



Variations in intensity profiles of Kossel's lines in the uniaxial compression of a crystal at room temperature.

abruptly, which is indicative of a stress relaxation in crystals. The further increase of external load causes, as a rule, a change in characteristic surface of the strain tensor due to a plastic deformation of diamond at room temperature. Thus, the deformation tensor of the crystal

described in Table transforms from a two-sheeted hyperboloid into a one-sheeted one.

In uniaxial compression of diamond, stresses in the lattice relax due to both a microtwinning in the (211) and shear into the (110) direction on the (111) plane [ 3 ]. The ratio between these two processes is 96:86, i. e., both mechanism of the inner stress relaxation in diamond crystal loading are equally probable. Based on the energy of the C-C bond in diamond [5], that is equal to  $5.8 \times 10^{17}$  J, and the variation of the shear stored elastic energy in relaxation of inner stresses, the number of broken bonds in a real crystal can be calculated. For the crystal shown in Table, this value is of the order of  $10^{18}$  cm<sup>-3</sup> that corresponds to 10-3 % of the total amount of atoms in the crystal under study.

The fact has engaged our attention that the loading ranges, in which the relaxation is observed of inner stresses defined from variations of the stored elastic energy and from variations of Kossel's line intensity profiles, do not coincide (0.9-1.2 and about 2 GPa, respectively). As relaxation on the octahedral plane in the (110) direction is inherent in the rearrangement of a dislocation structure of the lattice of crystals with a cubic system [6], the change of Kossel's line profile is likely to characterize mainly this process. For diamond, the above shear elements are typical of a screw dislocation. In studying by direct methods of diamond ceramics produced at 1400 °C and 6 GPa, the formation of dislocation interlayers and twinned lamellas on the (111) plane has been observed in the (110) and (211) directions, respectively [7]. Unlike the above researchers, that compressed diamond

hydrostatically at high temperature, we have established the microtwinning (from variations of the lattice stored energy) and a rearrangement of the dislocation structure in diamond (from variations of Kossel's line intensity profile) at room temperature and uniaxial compression.

These investigations have allowed us to study the effect of the initial stressed state of diamonds on the mode and intensity of the lattice deformation, to establish the mechanisms of inner stresses relaxation (the microtwinning and variations of the dislocation structure) during the uniaxial compression at room temperature.

#### Acknowledgements

The authors express their thanks to Dr. A.S.Vishnevsky for a useful discussion of our findings.

#### References

1. A.S.Vishnevsky, N.V.Novikov, V.N.Tkach, *Dokl. Akad. Nauk UkrSSR, ser."A"* 5 (1984), 55.
2. N.V.Novikov, V.N.Tkach, A.S.Vishnevsky, *Dokl.Akad.NaukSSSR*, **302**(6) (1988) 1368
3. V.N.Tkach, *Diamond and Related Materials*, **3** (1993) 112.
4. V.N.Tkach, A.S.Vishnevsky, *Soviet Journal of Superhard Materials*, **13** (3) (1992) 10.
5. J.E.Field, *Properties of Diamond* (London, Acad. Press, 1979).
6. M.P.Shaskolskaya, *Crystallography* (Vysshaya Shkola, 1979).
7. J.C.Walmsley, A.R.Lang, *J. Mater. Sci. Lett.*, **2** (1983) 785

## MECHANISMS OF INTERNAL STRESSES FORMATION IN SUPERHARD MATERIALS UNDER HIGH PRESSURE

G.A.VORONIN, I.A.PETRUSHA  
*V.N.Bacul Institute for Superhard Materials,  
2, Avtozavodskaya St., Kiev, 254074, Ukraine*

### ABSTRACT

Mechanisms of formation of internal stresses in synthetic diamond crystals and diamond-based composites, sintered at high pressures, have been studied. The method of birefringence between crossed Polaroids was used to study the internal stresses in diamond single crystals. Calculations have been made of internal stresses in synthetic diamond crystals, determined by inclusions of solvent-metal, in the processes of cooling, pressure removal and the subsequent heating under the normal pressure. Two mechanisms of inclusion capturing were studied.

Internal stresses in diamond crystals were studied by the method of birefringence between crossed Polaroids. It was shown, that the main causes of birefringence in natural diamonds are plastic deformation, inclusions, impurity zoning and sectorial structure. Internal stresses in synthetic diamond crystals are caused mainly by the last two reasons. This statement is proved by the coincidence of the elements of symmetry of crystal's birefringence image with the projections of cube-growth-sectors and octahedron-growth-sectors on the plane of polarization. The centre of symmetry of the image coincides with the point of crystal nucleation. It is well known, that the concentration of structural impurities ( N, B, etc.) in cube- and octahedron-growth-sectors vary considerably. As a result of it, the correspondent lattice parameter variations cause significant internal stresses. The zonal birefringence ( especially in cube-growth-sectors ) is also characteristic of synthetic diamonds. It is caused by internal stresses, arising from varying concentration of impurities in growth layers.

In contradiction to natural diamonds, there are no birefringence effects around inclusions in synthetic diamond crystals, as a rule. It proves the statement, that inclusions are capturing by growing crystals in the liquid

state and crystallize at the following cooling without generation of internal stresses in diamond matrix. The birefringence picture was observed only around some small inclusions, that may be ascribed to other mechanism of capturing. Most often such inclusions were noticed in crystals, synthesized in Fe-containing growth systems, and presumably are carbides.

The thermal stability of synthetic diamonds depends mainly on the sizes, concentration and phase constitution of inclusions, which are almost in all crystals. Metal and carbide inclusions also significantly effect the strength and thermal stability of diamond-based composites.

The calculation of stresses in diamond crystal around inclusion, captured at the process of synthesis, was made. The model of spherical inclusion in the infinite matrix was chosen, so as it became possible to obtain the closed analytical solution of the corresponding thermoelasticity problem. In this problem the starting parameters are the synthesis temperature  $T_c$  and pressure  $P_c$ . At these parameters the system is in the state of hydrostatic compression:

$$\sigma_r^{(1)} = \sigma_\theta^{(1)} = \sigma_r^{(2)} = \sigma_\theta^{(2)} = -P_c \quad (1)$$

where  $\sigma_r^{(1)}, \sigma_\theta^{(1)}, \sigma_r^{(2)}, \sigma_\theta^{(2)}$  are the radial and tangential stresses in the inclusion (1) and diamond matrix (2) respectively.

Let us suppose, that the inclusion was captured in solid state. The solution of the problem in this case is following:

$$\begin{aligned}\sigma_r^{(1)} = \sigma_\theta^{(1)} &= \int_{T_c}^T \frac{12K_1(t)G_2(t)}{3K_1(t) + 4G_2(t)} [\alpha_2(t) - \alpha_1(t)] dt - \\ &\quad - \frac{K_1(T)[3K_2(T) + 4G_2(T)]}{K_2(T)[3K_1(T) + 4G_2(T)]} (P - P_c) - P_c; \\ \sigma_r^{(2)} &= -P + \frac{C(T)}{\rho^3}; \quad \sigma_\theta^{(2)} = -P - \frac{C(T)}{2\rho^3}; \quad (2) \\ C(T) &= \int_{T_c}^T \frac{12K_1(t)G_2(t)}{3K_1(t) + 4G_2(t)} [\alpha_2(t) - \alpha_1(t)] dt - \\ &\quad - \frac{4G_2(T)[K_1(T) - K_2(T)]}{K_2(T)[3K_1(T) + 4G_2(T)]} (P - P_c);\end{aligned}$$

where  $K_1$ ,  $K_2$ ,  $G_1$ ,  $G_2$ ,  $\alpha_1$ ,  $\alpha_2$  are the bulk moduli, shear moduli and coefficients of thermal expansion of the inclusion material and diamond material respectively;  $T$ ,  $P$  — temperature and pressure, acting upon the system.

If the inclusion is captured in liquid state, these formulas are valid only for the description of stresses in the system at  $t > T_{cr}$ , where  $T_{cr}$  is the temperature of inclusion crystallization. In this case  $K_1$  is the reciprocal of the compressibility of the inclusion.

The calculation showed that the crystallization of metal-solvent inclusion would lead to stress relaxation and formation of the pore, which volume is about 3% of the volume of correspondent inclusion. Thus crystallization of the inclusion leads to the following stress state of the system:

$$\begin{aligned}\sigma_r^{(1)} = \sigma_\theta^{(1)} &= 0; \\ \sigma_r^{(2)} &= -P + \frac{P}{\rho^3}; \\ \sigma_\theta^{(2)} &= -P + \frac{P}{2\rho^3};\end{aligned} \quad (3)$$

The exact calculation of stresses in the system by means of obtained formulas is not possible because the precise values of

coefficients of thermal expansion and elastic moduli are not known for the whole investigated T-P-region. But it is possible to estimate by means of these formulas the regularities of stress dependence from P-T-parameters of synthesis, type and thermo-mechanical properties of inclusions. For example let us estimate the stresses in the system "nickel inclusion-diamond matrix" at the stages of temperature lowering after the completion of synthesis (1), pressure decrease (2) and subsequent heating at the normal pressure (3). The following values of thermal expansion coefficients and elastic moduli were used in calculations:

$$\begin{aligned}\alpha_{Ni} &= (12.8 + 0.0094T) \cdot 10^{-6}, \text{ grad}^{-1}, \\ K_{Ni} &= 184 - 0.03T, \text{ GPa}; \\ \alpha_C &= (2.5 + 0.0025T) \cdot 10^{-6}, \text{ grad}^{-1}; \\ K_C &= 442 \text{ GPa}, G_C = 536 \text{ GPa}.\end{aligned} \quad (4)$$

The following synthesis parameters were chosen:

1.  $T_c = 1200^\circ\text{C}$ ,  $P_c = 4.5 \text{ GPa}$  (—),
2.  $T_c = 1300^\circ\text{C}$ ,  $P_c = 5.0 \text{ GPa}$  (....).

The results of stress calculations for inclusions, captured in liquid and solid state, are shown at Fig.1 and Fig.2 respectively.

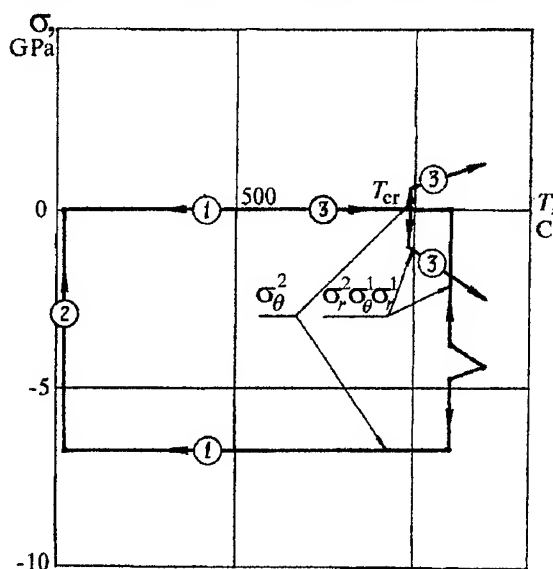


Fig 1. Stresses in diamond matrix (2) and inclusion (1), captured in liquid state.

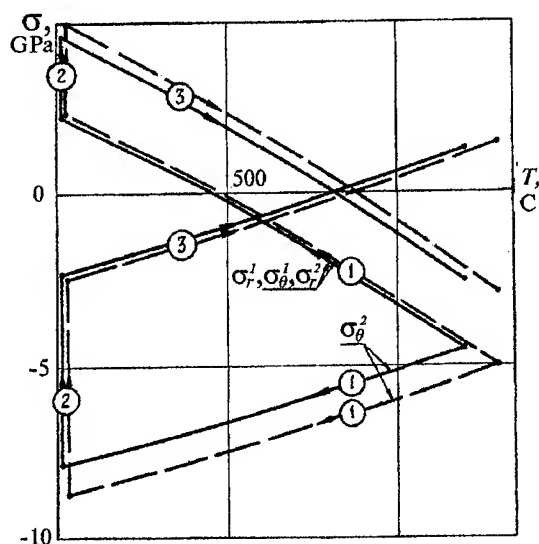


Fig 2. Stresses in diamond matrix (2) and inclusion (1), captured in solid state.

As follows from Fig.1, there are no stresses in diamond matrix and inclusion, captured in liquid state.

Compressive radial and tensile tangential stresses in diamond matrix appear only after heating the crystal at normal pressure up to the inclusion melting temperature  $T_{cr}$ . If the inclusion is captured in solid state, the significant tensile radial and compressive tangential stresses remains in diamond matrix at normal P-T-parameters. The following heating at normal pressure leads to the decrease of those stresses up to zero at temperature 800...900°C. The subsequent heating will cause the rise of stresses of reciprocal sign. So the calculation results are in good agreement with the experimental results, obtained by the method of birefringence.

The formulas obtained were used also for calculation of stresses in high-pressure-sintered composites, containing diamond matrix and metal or carbide inclusions. It was shown, that the carbide inclusions, whose coefficients of thermal expansion are sufficiently close to diamond's one ( for instance SiC, WC ), may cause compressive tangential stresses in diamond matrix, thus leading to the strengthening of composite.

# COBALT AND MANGANESE AS IMPURITIES IN SYNTHETIC DIAMONDS

X.JIA<sup>1</sup>, H.KAGI<sup>1</sup>, W.LI<sup>1</sup>, M.WAKATSUKI<sup>1</sup>, S.HAYAKAWA<sup>2</sup> and Y.GOHSHI<sup>2</sup>

<sup>1</sup>*Institute of Materials Science, University of Tsukuba, Ibaraki 305, Japan*

<sup>2</sup>*Department of Applied Chemistry, Faculty of Engineering,  
University of Tokyo, Tokyo 113, Japan*

## ABSTRACT

X-ray fluorescence analysis using synchrotron radiation gave an evidence for Co and Mn to be incorporated as impurities dispersed in diamonds, which were prepared at high pressure and high temperature using metallic solvents of Co and a Mn-containing alloy. It was found that concentrations of Co in the {111} growth sector were clearly higher than that in the {100} or {311} growth sector. Solubility of Co in diamond seems less than that of Ni by about one order of magnitude. The growth sector-preference was not clearly found for Mn, for which the chemical state in diamond is unknown.

## Introduction

Single crystals of diamond are grown in metallic solvents, and it is important to know about impurities in them incorporated from the solvents, as a basic demand in using impurity-controlled crystals. Main elements used to compose the metallic solvent are Cr, Mn, Fe, Co and Ni. For eliminating nitrogen from diamond, Al, Ti and Zr are added to the solvent. Some of these elements are expected to be incorporated into the diamond lattice as well as being contained as inclusions. As for Ni it was believed to be an impurity dissolved in the lattice of diamond. Collins et al.[1] attributed some optical absorption centers to the dissolved Ni and first reported the distribution of the absorption centers in the {111} growth sector. EPR (electron paramagnetic resonance) studies by Isoya et al.[2,3] proved that Ni atoms can be dissolved at the substitutional or the interstitial sites in synthetic diamonds. Our previous studies, based on the X-ray fluorescence method using synchrotron radiation[4,5], gave a direct evidence for distribution of the dissolved Ni in the {111} growth sector, and determined reliable values of its concentration.

In our recent studies, Co and Mn were detected by the same method[6], and more detailed studies have been continued.

## Experimental Procedures

Two single crystals, O and R, were grown by the temperature gradient method. The Sample O was grown in an alloy of Ni<sub>70</sub>Mn<sub>25</sub>Co<sub>5</sub> at 5.5 GPa and 1200°C for 20 hours, and the sample R, in pure Co at 5.5 GPa and 1300°C for 20 hours. Then, the crystals were cut parallel to a {110} plane, and formed into wafers of about 200  $\mu$ m in thickness.

The growth sector boundaries in the wafer were observed using a differential interference microscope. Brightness distribution of cathodoluminescence was also utilized to distinct the boundaries.

The metal impurities were detected by the method of X-ray fluorescence, using synchrotron radiation[5]. The synchrotron radiation beam was monochromatized at 9 keV, concentrated with an ellipsoidal mirror, and then limited to a size of 100  $\mu$ m  $\times$  100  $\mu$ m.

Two dimensional abundance distribution of the impurities in the sample was observed and their concentrations were determined.

## Results and Discussion

### Cobalt

Figures 1 and 2 show the growth sectors of the both samples. They also show the positions on which the concentration was evaluated. The concentration of the concerned impurities are summarized in Tables 1 and 2.

The two dimensional mapping of the Co

abundance over the whole sample was very similar to that of Ni. That is, Co is incorporated preferentially in the {111} growth sector, as Ni is. This behavior of Co is clearly seen in Table 1, and these results are quite consistent with our preliminary results[6]. A value, 5.66 ppm, for the position 3 in the Table 1, may be mixed with some contribution from the adjacent {111} sector, because of the large beam size. The sector preference of the Co distribution is also shown in Table 2 (Sample O), though less remarkable than in Table 1. This is because of the very low concentration of Co, near the statistical limit for meaningful determination of the concentration.

Based on the similar behavior of distribution shown by Ni and Co, it is considered that Co is dissolved in the diamond lattice at the same site(s) as occupied by Ni. Hayakawa et al.[5] reported X-ray Absorption Near-Edge Structure (XANES) spectrum for dissolved Ni, and discuss the feature of the spectrum as suggesting the dissolved Ni occupying the tetrahedral site in the diamond lattice. According to the feature of the spectrum for incorporated Co, quite similar to that for Ni, Co is expected to occupy the same site as Ni does.

EPR measurement was tried on another diamond grown in pure Co, but no signal was detected to be attributed to Co at all.

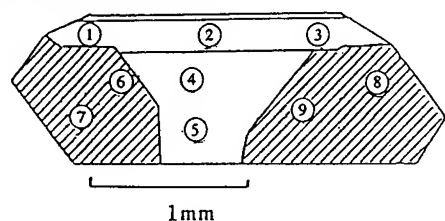


Fig.1 Points of concentration determination for Co in sample R.

Table 1 Concentrations of Co determined for sample R (grown in 99.9% Co)

point	growth sector	Co(ppm)
1	{311}	1.44
2	{311}	0
3	{311}	5.66
4	{100}	0
5	{100}	0.78
6	{111}	12.6
7	{111}	18.3
8	{111}	5.33
9	{111}	13.5

Cobalt is dissolved also in the {100} and the {311} sectors, though at a low level of around 1 ppm. The same behavior of Ni is shown in Table 2,

though Ni could be detected neither in the {100}, nor in the {311} sector when the crystal was grown in a different solvents ( $\text{Fe}_{55}\text{Ni}_{29}\text{Co}_{16}$ ).

The maximum value of the concentration of Co determined in the sample R, which was grown with pure Co, was around 20 ppm. While, the maximum concentration of more than 100 ppm has been evaluated for Ni in diamonds grown in other solvents including pure Ni. Thus, the concentration level of dissolved Co seems to be smaller than that of Ni by about one order of magnitude.

### Manganese

Concentrations of Mn are small in the sample O, but they are obviously higher than the limit of detection ( $< 0.05$  ppm), as shown in Table 2. There is an exceptionally high value of 86.3 ppm at the position 14. The reason is not known at present. There may be supposed a possibility of existence of very small inclusions, though they have not been observed with a usual optical microscope.

Manganese showed a distribution behavior having some domain-preference in the two dimensional mapping figure, but it does not seem to be related to the growth sector. This fact can also be understood in Table 2, in which rather high concentrations often appear in the {100} sectors, in contrast to the case of Ni or Co. Besides, higher concentrations of Mn were detected at positions near the seed, if comparison was made within the central growth sector of {100}. Thus, it can be considered large growth rate in the initial growth stage[7] would result in more impurities incorporated.

The chemical state of Mn incorporated in diamond can not be understood at all, at present. XANES spectra were measured for Mn incorporated in diamond, together with those for inclusions in diamond, for the solvent alloy and for a few compounds of Mn. Possibly, the detected Mn will be in a state that is different from usual inclusions of the metallic solvent. There is also an expectation that Mn exists as very small particles, of a separated phase, dispersed in diamond. Results of examination on this problem will be reported in the future.

In our very recent study, Cr could also be detected, too, though its concentration was further small compared to that of Co. Iron can

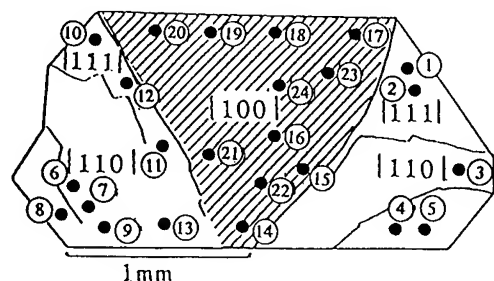


Fig.2 Points of Concentration Determination for Ni, Co and Mn in sample O.

Table 2 Concentrations of Ni, Mn and Co determined for sample O (grown in Ni<sub>70</sub>Mn<sub>25</sub>Co<sub>5</sub>-allory)

Point	Growth sector	Ni(ppm)	Mn(ppm)	Co(ppm)
1	{111}	31.8	1.22	0.63
2	{111}	19.2	0	0.32
3	{100}	1.39	0.26	0
4	{111}	8.91	0.26	0.04
5	{111}	12.9	0.92	0.33
6	{311}	1.08	1.52	0
7	{100}	1.09	0.83	0.13
8	{311}	1.14	1.08	0
9	{311}	0.81	1.31	0
10	{111}	18.6	1.08	0.39
11	{111} + {100}	15.2	16.1	0.40
12	{111}	30.0	2.59	0.50
13	#	496	337	22.0
14	{100}	2.23	86.8	0
15	{100}	1.99	7.00	0.18
16	{100}	2.71	5.89	0.04
17	{100}	0.21	0.28	0.18
18	{100}	0.18	0.29	0.19
19	{100}	0.25	0	0
20	{100}	0.26	0.10	0
21	{100}	1.11	2.86	0.17
22	{100}	1.78	6.15	0.19
23	{100}	0.27	0.22	0.23
24	{100}*	1.25	2.51	0.13

\*: near the boundary #: on an inclusion

occasionally be detected, but its concentration is very low, about 1ppm or smaller. A possibility remains that the detected Fe is due to some contamination from the environment.

## Conclusions

(1) Direct evidence is given for incorporation of

Co and Mn in diamond at concentrations of around 10 or 20 ppm. Other elements to compose the solvent, Cr and Fe, may be dissolved or dispersed in diamond, but their concentrations are likely below 1 ppm.

(2) The distribution behavior of Co and XANES spectrum are quite similar to those of Ni, and Co is most possibly dissolved in diamond to occupy the same site as that of Ni.

(3) Features of Mn in diamond are different from those of Ni and Co, suggesting its chemical state also different.

## Acknowledgment

The authors are grateful to Ogura Jewel Industry Co., for kind help in cutting and polishing samples. The experiments using synchrotron radiation were performed as the subjects, 92G247 and 94G307, in Photon Factory of The Institute for Research in High Energy Physics. This study was supported by Grant-in Aid for a Priority Area Research (03204003, 04204002) and also by an encouragement of Young Scientists (04780060) from the Ministry of Education, Science and Culture of Japan.

## References

- [1] A. T. Collins, H. Kanda and R. C. Bowens: *Phi. Mag.* **B61**(1990)797.
- [2] J. Isoya, H. Kanda, J. R. Noris, J. Tang and M. K. Bowman: *Phys. Rev.*, **B41**(1990)3905
- [3] J. Isoya, H. Kand and Y. Uchida: *Phys. Rev.*, **B42**(1990)9843
- [4] M. Wakatsuki, S. Hayakawa, S. Aoki, Y. Gohshi and A. Iida: *New Diamond Science and Technology* (Proc. 2nd ICNDST, Washington, 1990)(1991)143
- [5] S. Hayakawa, F. Nakamura, Y. Gohshi, M. Wakatsuki and H. Kagi: *Proc. 3rd IUMRS Int. Conf. on Advanced Materials*, Tokyo, 1993 (1994)1559
- [6] X. Jia, H. Kagi, S. Hayakawa, M. Wakatsuki and Y. Gohshi: *Proc. 4th ICNDST, Kobe*, 1993 (1994)525
- [7] W. Li, et al: *J. Crst. Growth*(to be published)



# THE EFFECT OF ISOTOPIC COMPOSITION ON DIAMOND THERMAL CONDUCTIVITY

A. WITEK

*High Pressure Research Centre, Polish Academy of Sciences, Sokolowska St. 29/37, 01-142  
Warsaw, Poland*

A.P. PODOBA and S.V. SHMEGERA

*V.N. Bakul Institute for Superhard Materials of the Ukrainian National Academy of Sciences,  
Avtozavodskaya St.2 254074, Kiev, Ukraine*

Experimental data were analysed in the framework of Debye's model using Klemens -Callaway's expression for the thermal conductivity. The C-13 isotope effect on the diamond thermal conductivity was considered with allowance made for the earlier-added assumption that the presence of isotopic impurity, apart from the direct resistive effects, results in the activation of the normal phonon scattering processes. As a result, the relaxation time of normal phonon scattering processes turns out to depend on the isotopic concentration. In this case, a good agreement for the theory and experiment is observed.

## 1 Introduction

The effect of isotopic composition on thermal conductivity of diamond single and polycrystalline produced by the thermal gradient method has been theoretically analysed. The analysis was based on the Klemens - Callaway model<sup>1</sup> with regard to the mechanism of isotopic impurity effect on the diamond lattice thermal conductivity suggested by the authors<sup>2</sup>. The mechanism is built upon the assumption that an isotope impurity present in the lattice activates normal scattering processes resulting in the energy redistribution between long wave (passive) and short -wave phonons which are capable to contribute into resistive processes.

## 2 Theoretical results

Qualitatively, the mechanism of normal processes activation by isotopic impurities reduces to the following. The phonon resistive scattering on isotopes results in the formation of long wave phonons that increase the probability of normal scattering processes, which are known to occur with the involvement of both long-wave phonons and those with a shorter wavelength.

The temperature and frequency dependencies in expressions for the relaxation time of the basic resistive processes (U-processes, scattering on isotopes and grain boundaries) were assumed to be in the form given in<sup>3</sup>.

Taking into account both the process activation by isotopic impurity and the dominating contribution of phonons with cross-polarization into the heat

transfer, the equation for the N-process relaxation time  $\tau_N$  was used in the form

$$\tau_N^{-1} = A \sqrt{c(1-c)} T^3 \omega$$

where A is constant, c is the isotope concentration, T is the temperature,  $\omega$  is the phonon frequency. The entering of the concentrational dependence into the expression for the relaxation time shows the initiating role of isotopic impurity relative to normal processes.

When calculated the phonon boundary scattering contribution into a heat resistance, the real structure of diamond polycrystallines, that is responsible for the efficient thermal conductivity, was taken into account.

Temperature dependencies of thermal conductivity of diamond single and polycrystallines of various grit sizes have been constructed for different concentrations of isotopic impurities. The limiting values of the isotope concentration, in which the isotopic impurity exert the predominant effect of the thermal conductivity value are defined for different temperatures ranges.

According the Callaway expression for the thermal conductivity has the form:

$$\lambda = \lambda_1 + \lambda_2$$

### 3 Diamond single crystals

Fig 1 shows the results of calculation of room temperature diamond thermal conductivity as a function of an isotopic impurity content.

$$\lambda_1 = \frac{k}{2\pi^3 v} \left( \frac{k}{\hbar} \right)^3 \int_0^{\theta/T} \frac{dx}{\tau_R^{-1} + \tau_N^{-1} [\exp(x) - 1]^2} x^4 \exp(x)$$

$$\lambda_2 = \frac{k}{2\pi^3 v} \left( \frac{k}{\hbar} \right)^3 \left[ \int_0^{\theta/T} \frac{\tau_N^{-1}}{\tau_R^{-1} + \tau_N^{-1} (\exp(x) - 1)^2} x^4 \exp(x) dx \right]^2$$

$$x \left[ \int_0^{\theta/T} \frac{\tau_N^{-1} \tau_R^{-1}}{\tau_R^{-1} + \tau_N^{-1} (\exp(x) - 1)^2} x^4 \exp(x) dx \right]^{-1}$$

Where  $x = \hbar\omega/2\pi kT$ . The  $v$  denotes average phonons velocity,  $\tau_R$  is the relaxation time the of resistive processes,  $\tau_N$  is the relaxation time of the normal processes. In the lattice containing an isotopic impurity only, three types of resistive processes are possible: umklapp processes, isotope scattering and scattering on the grain boundaries. In this case the expression for  $\tau_R$  can be presented in the form<sup>3</sup>

$$\tau_R^{-1} = A \exp \left( -\frac{\Theta}{bT} \right) T^m \omega^n + c(1-c) \frac{V_0}{\pi v^3} \left( \frac{\Delta M}{M_{12}} \right)^2 \omega^4 + \frac{v}{1.12(d_1 d_2)^{1/2}},$$

where  $V_0$  is the volume per one atom,  $\Delta M$  is the isotope mass deficiency,  $d_1$  and  $d_2$  characterises of a crystal.

Concentration dependence of  $N$  processes relaxation time represents an attempt to account for the initiating role of isotopic impurity with respect to  $N$  processes. From known experimental data, the following values of  $A, B, b, m$  and  $n$  constants (for  $a=1850$  K,  $v=1.22 \times 10^4$  m/s) has been determined, in which the most agreement with experiment is observed:

$$A=3.6 \times 10^{-23} \text{ s/K}^2; B=4.4 \times 10^{-11} \text{ K}^{-3}; b=8.36; m=n=2.$$

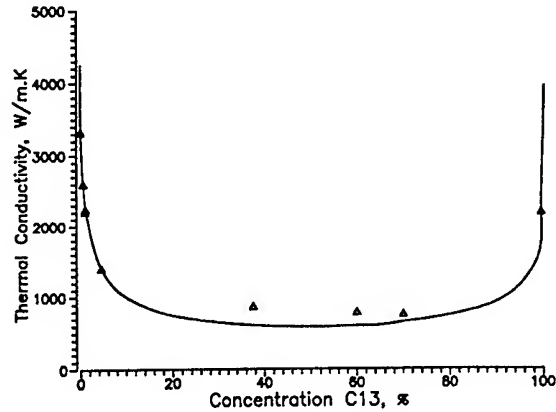


Figure 1 The room temperature thermal conductivity of the synthetic diamond single crystals vs. isotope content

Phonon boundary scattering effect for crystalites with the different isotope C-13 concentration is shown on the Fig 2. Starting from the 300  $\mu\text{m}$  grit size the decreasing of the thermal conductivity is observed.

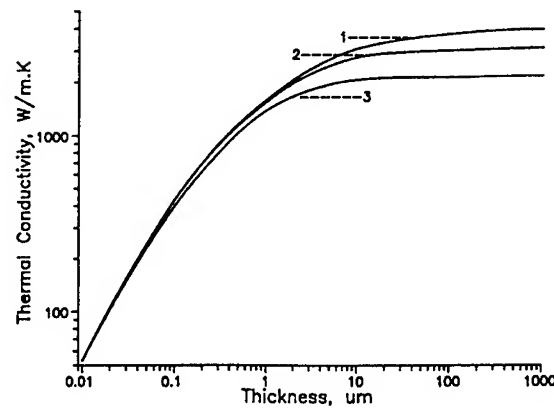


Figure 2 Thermal conductivity of the diamond crystals, 1, 2 and 3 correspond to C-13 concentration equal to 0%, 0.07% and 1% respectively

On the Fig. 3 we compare the Onn's data<sup>4</sup> for the thermal conductivity temperature dependence measured for the single crystals of diamond with different isotope content with our theoretical curves.

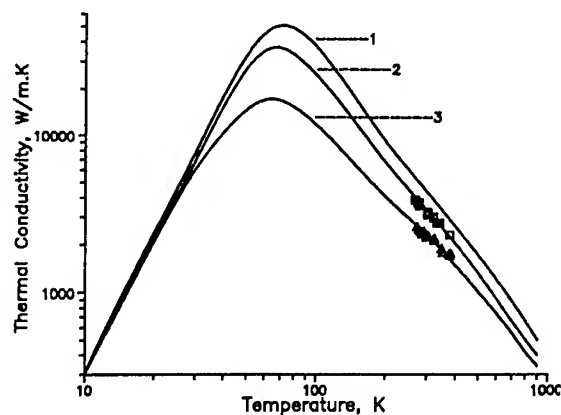


Figure 3 Theoretical dependence and experimental data of thermal conductivity vs. temperature for diamond single crystals. curves 1, 2 and 3 denote the  $^{13}\text{C}$  isotope concentration equal to 0, 0.07% and 1.1 % respectively. Experimental data came from<sup>4</sup>

The agreement with our theory and experimental data available for the single crystals of diamond is apparent.

#### 4 Diamond films

On the basis of our theory we were able to predict the temperature dependence of the thermal conductivity of isotopically pure diamond films. Aforementioned dependencies are shown on the Fig. 4.

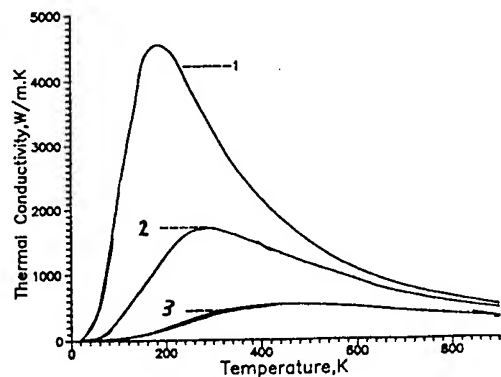


Figure 4 Thermal conductivity of the isotopically pure diamond films for a different grid size ; 1 - 10  $\mu\text{m}$ , 2 - 1  $\mu\text{m}$  and 3 - 0.1  $\mu\text{m}$

Its worth to mention that for the diamond films the grit size is crucial for the thermal conductivity absolute value even for the isotopically pure samples.

#### References

- 1 J. Callaway, *Phys.Rev.* **113** 1046 (1959)
- 2 T.D. Ositinskaya, A.P. Podoba and S.V. Smegera *Diamond and Related Mat.* **2** 1500 (1993)
- 3 R. Berman, *Thermal Conduction of Solids*, (Oxford University Press, Oxford 1976)
- 4 D.G. Onn, A.Witek, Y.Z.Qiu, T.R. Anthony and W.F. Banholzer, *Phys.Rev. Lett.* **68** 2806 (1992)

# HIGH PRESSURE AND FLUORESCENCE LIFETIME OF R LINE IN $\text{MgO}:\text{Cr}^{3+}$

B.R.JOVANIĆ, B.RADENKOVIĆ\* AND LJ.D.ZEKOVIĆ#  
*Institute of Physics, Center of Experimental Physics, (E-11), P.O.Box 68,  
Pregrevica 118, 11080 Zemun, Yugoslavia*

(\*) *Dept. of Simulation, FON, P.O.Box 770, 11000 Belgrade, Yugoslavia*  
(#) *Faculty of Physics, Univ. of Belgrade, P.O.Box 368, 11000 Belgrade, Yugoslavia*

## ABSTRACT

The fluorescence lifetime  $\tau$  of R line,  ${}^2\text{E} \rightarrow {}^4\text{A}_2$  transition, in  $\text{MgO}:\text{Cr}^{3+}$  has been measured under hydrostatic high-pressure condition (up to 120 kbar). The increase of pressure causes the increase of lifetime  $\tau$ . Dependence of  $\tau$  upon pressure can be expressed by exponential regression  $\tau = -19.699 + 21.728 \exp(P/154.237)$ .

## Introduction

The optical (position, width, refractive index) and physical (inter ionic distance, bonding and compressibility) properties of  $\text{MgO}$  crystal doped by  $\text{Cr}^{3+}$  ions upon high pressure have been the subject of a large amount of research [1;2;3;4;5]. But, the effect of high pressure on R line lifetime  $\tau$ ,  ${}^2\text{E} \rightarrow {}^4\text{A}_2$  transition when  $\text{Cr}^{3+}$  ions are in cubic sites [6], has not been experimentally investigated, yet. Here we report the spectroscopic measurement of lifetime  $\tau$  of  ${}^2\text{E} \rightarrow {}^4\text{A}_2$  transition in  $\text{MgO}$  doped by  $\text{Cr}^{3+}$ .

## Experimental methods

We reported the results of  $\text{MgO}:\text{Cr}^{3+}$  crystal (0.05% wt  $\text{Cr}^{3+}$ ) in hydrostatic experimental conditions. The pressure was generated in a diamond anvil cell of the NBS type with 1/3 carat stones. The crystal chip a  $\approx 60 \mu\text{m}$  -diam were put in an  $250 \mu\text{m}$  hole of preindented stainless steel gasket, together with a methanol - ethanol (4:1) mixture that served as hydrostatic medium. The pressure was determined by the red-shift of the R line,  $d\lambda/dP = 0.350 \text{ \AA/kbar}$  [1]. The position of R line was obtained by using double optical monochromator with  $0.2 \text{ nm}$  spectral resolution and a photon counter with multiscaler. The samples were excited by the chopped beam of He/Ne laser at  $632.8 \text{ nm}$  with IF filter ( $632 \text{ nm} \pm 2 \text{ nm}$ ) in front of the laser. Our optical system consisted of several optical ports, allowing the focusing laser beam to about  $300 \mu\text{m}$ . The decay

curves have been measured at the maximum ( for given pressure) of the R line , using well known method for lifetime measurement [7]. Illumination lasted about 1ms, and the total measuring time (for one scan) varied from 20ms to 120ms. The data collected by the multiscaler after 10000 excitation pulse were transferred to PC in order to obtain decay curve, lifetime values and standard deviation.

## Results and discussion

The R,  ${}^2\text{E} \rightarrow {}^4\text{A}_2$  transition, line decay curves for all cases are as in ruby, nonexponential. The decay curves, obtained for atmospheric pressure (1 bar) and 123 kbar, are shown on fig. 1. All other curves, obtained for any pressure in the range of 1 bar to 123 kbar, lay between the presented curves on fig. 1.

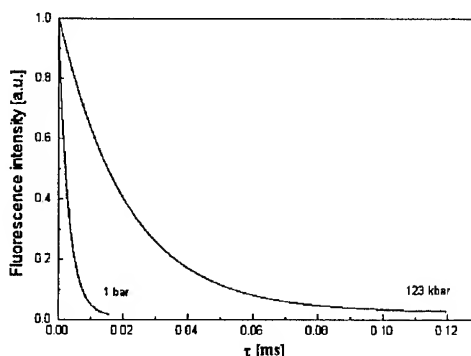


Fig. 1. Decay curves for 1 bar and 123 kbar

The dependence  $\tau$  for R line upon pressure P, is shown on fig 2.

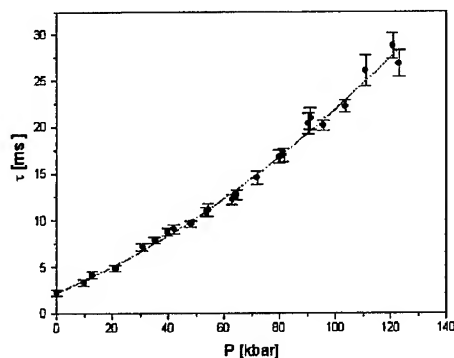


Fig. 2. Dependence of lifetime  $\tau$  for R line upon pressure

From fig. 2. one can see that increasing pressure causes an enormous increase of lifetime. So at atmospheric pressure (1 bar) the lifetime is 2.2 ms and about 28 ms at 123 kbar. The dependence of lifetime  $\tau$  for R line upon pressure, shown on fig. 2. can be expressed by exponential regression:

$$\tau = -19.699 + 21.728 \exp(P/154.237) \text{ [ms]}$$

The obtained standard deviations for lifetime are usual for lifetime measurements upon high pressure [8,9]. Goodness of fit is 0.992.

The high pressure experiments show that position of R lines, in  $\text{MgO:Cr}^{3+}$  crystals, strong depend upon applied pressure [1]. High pressure causes the significant change of refractive index  $n$  of MgO crystals [2]. Also, theoretically great effect of high pressure on oscillator strength  $f$  for R line was predicted [11]. So, knowing the connection between the lifetime  $\tau$  for R line in  $\text{MgO:Cr}^{3+}$

crystals [10], the position of R line, oscillator strength  $f$  and  $n$  it can be expected that the high pressure can causes change of  $\tau$ .

### Conclusion

The high pressure, in the range (0-123kbar), has the great effect on R lifetime  $\tau$ ,  ${}^2\text{E} \rightarrow {}^4\text{A}_2$  transition, in  $\text{MgO:Cr}^{3+}$  crystal. The lifetime  $\tau$  at 123 kbar is about twelve times greater than at zero pressure. The change of lifetime  $\tau$  upon pressure is exponential..

### Acknowledgement

The authors are grateful to Professor G.F.Imbusch, from the University College Galway - Ireland, who sent us the considered crystal. The authors are also grateful to the MSTs for financial support.

### References

1. D.Ma et all, *Phys.Lett.*, **121** (1987) 97.
2. K.Vedam and E.D.D.Schmidt, *Phys.Rev.*, **146** (1966) 548.
3. E.A.P.Albuene and H.G.Drickamer, *J.Chem.Phys.*, **43** (1965) 1381.
4. M.O.Henry et all, *Phys.Rev.B.*, **13** (1976) 1893.
5. M.S.T.Bukowinski, *Geophys.Res.*, **85** (1980) 285.
6. S.Sugano et all, *Phys.Rev.*, **120** (1960), 2045 .
7. D.I.Klick et all, *Phys.Rev.B*, **16** (1974)4599.
8. J.H.Eggert et all, *Phys.Rev.B*, **40** (1989), 5733.
9. Y.S.Sorensen, *J.Appl.Phys.* **60** (1986), 2985.
10. G.F.Imbusch, *Phys.Rev*, **153** (1967), 326.
11. B.R.Jovanic et all., ICL'93, Conecticat, USA, 9-13 August, 1993, Th4-82Q.

# MIXING OF ELECTRONIC STATES OF $\text{KZnF}_3:\text{Cr}^{3+}$

V. Lemos, P.T.C. Freire[\*]

Instituto de Física - UNICAMP Campinas, São Paulo, 13083-970, Brazil

O. Pilla

Università degli Studi di Trento, 38050, Povo, Trento, Italy

Luminescence measurements were performed on  $\text{KZnF}_3:\text{Cr}^{3+}$  at low temperature and high pressures. The pressure allows the tuning of crystal field including the crossing region from low- to high-field regime in this material. Close to the crossing region, the sharp lines in the spectra are observed to shift and broaden. Also the trigonal emission consists of broadband and sharp lines appearing simultaneously. These effects are interpreted as evidences of the mixing of electronic states.

Several solid-state wide band tunable lasers developed in the past few years stimulated recent basic research [1],[2]. The laser suitability of single crystals doped with Transition Metal Ions (TMI) is widely recognized [3]. Among them, the system  $\text{KZnF}_3:\text{Cr}^{3+}$  is attractive due to its excellent optical properties: this is the only TMI laser material for which the emission can be made to occur in the red portion of the visible spectrum by application of small amounts of pressure [1]. Therefore it is fundamental that a complete understanding of emission properties of this material is achieved.

Sharp lines appear in the emission of  $\text{KZnF}_3:\text{Cr}^{3+}$  in the pressure range of high-crystal-field. The identification of these lines was made by using energy diagrams, as shown in Fig. 1 [4]. The lines with non-zero slope are representative of  ${}^4\text{T}_2 \rightarrow {}^4\text{A}_2$  transition energy and those parallel to the pressure axes correspond to  ${}^2\text{E} \rightarrow {}^4\text{A}_2$  transitions. In the diagram, the states  ${}^4\text{T}_2$  and  ${}^2\text{E}$  cross at  $P_C = 6.2$  GPa,  $P_\square = 6.5$  GPa and  $P_\Delta = 7.7$  GPa, where the symbols C,  $\square$  and  $\Delta$  are for cubic, tetragonal and trigonal centers, respectively. The crossover points define the transition region from low- to high-crystal-field regimes. Included in the upper left side of the figure are energy-level diagrams for the crystal in the low-crystal-field regime. The counterpart diagram for high-crystal-field is found at the bottom right side of the figure.

The diagrams serve to show the allowed transitions through electric-dipole process (straight vertical lines) and magnetic-dipole process (dashed dotted lines). If the electronic states are well separated the interpretation of line spectra in terms of isolated  ${}^2\text{E}$  and  ${}^4\text{T}_2$  states is meaningful. When the states are close enough in energy they may interact and the luminescence spectra reflect a superposition of the properties of these states.

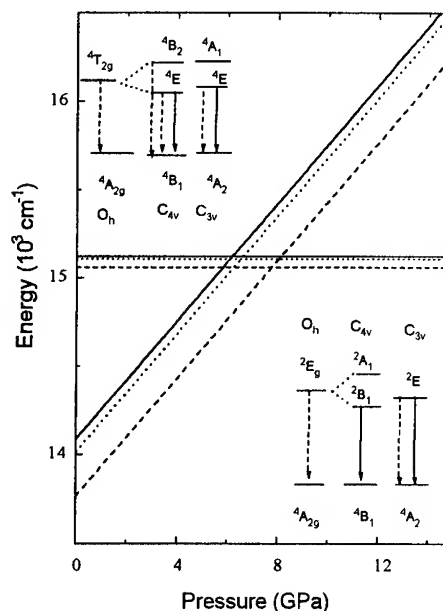


Fig.1. Dependence of emission energies with pressure, for cubic (solid lines), tetragonal (dotted lines) and trigonal (dashed lines) symmetries. Energy diagrams are for low- and high-crystal-field respectively.

The concurrence of mixing of states through spin-orbit coupling apart from thermal population effects, adds complexity to the problem. We notice that the close proximity of the states  ${}^2E$  and  ${}^4T_2$  produces broadening and changes in position. In Fig. 2 spectra at two sets of pressure and temperature values are presented. The cubic  ${}^2E_g$  line is degenerate at the lowest temperature value  $T = 25$  K (and  $P = 8.5$  GPa) in contrast with the breakdown of degeneracy occurring at  $T = 54$  K (and  $P = 11.0$  GPa). The spectra represented in Fig. 2 gave the results for the energies and linewidths also listed in Table 1. It is possible to see in that Table that the positions of the lines  $\square$  and  $\Delta$  are considerably changed with respect to their 11.0 GPa values. This is completely unexpected based on our simplified model giving zero slope for the  ${}^2E_g \rightarrow {}^4A_{2g}$  transition energies with pressure. It was also observed that those lines shift towards higher energy on lowering the temperature from 65 K to 25 K (not shown here). This is surprising in the light of the behavior of electronic levels which have negligible displacements with temperature below 90 K in high-crystal-field  $3d^3$  systems.

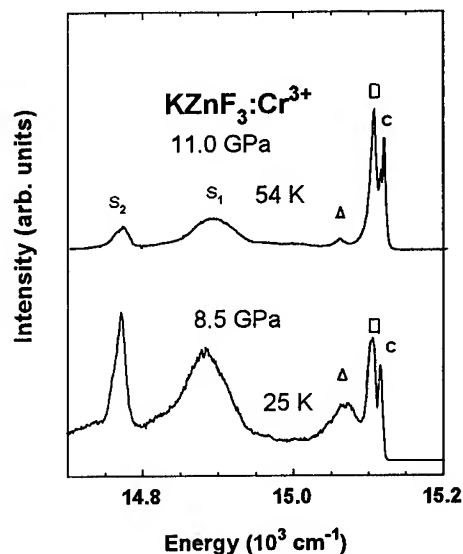


Fig. 2. High resolution luminescence spectra taken away from and close to the crossing region from low- to high-crystal-field.

Severe broadenings are observed to occur for all  ${}^2E_g$  lines at 8.5 GPa as compared with their linewidths in the higher pressure spectrum. Non hydrostaticity conditions should not be attempted to justify these broadenings because linewidths are larger at the lower pressure value. Also, populational effects should be discarded because the lines are broader at  $T = 25$  K than at higher temperature and higher pressure conditions. These effects are probably a result of the mixing of electronic states. The mixing of such states has been considered previously through a configurational-coordinate model in the harmonic approximation to describe the vibrational states of small  ${}^4T_2$ - ${}^2E_g$  energy separation,  $\Delta$ , in  $3d^3$ -ion systems [5]. The calculated zero-vibrational states energy plots show marked variations with temperature in the case of very small  $\Delta$ . This calculation also shows that broadening of R lines with temperature should be larger in smaller  $\Delta$  systems. These findings indicate that the anomalous spectral properties of  $KZnF_3:Cr^{3+}$  at  $P = 8.5$  GPa described above should be attributed to the mixing of states effect. The degree of mixing should be described by an analogous model. The specific case of this material is complicated by the need to consider the wavefunctions of cubic and distorted centers. For the sake of completeness we add that the relative intensities of  ${}^2E_g$ -lines was observed to vary according to the fact that population of the upper levels diminish on lowering the temperature, for both pressure values 8.5 GPa and 11.0 GPa. The most striking evidence of this mixture, however is obtained isolating the trigonally distorted centers. It is known that the trigonal emission lifetime is  $\sim 300 \mu s$  whereas the emissions from cubic and tetragonal centers have a long lifetime ( $\sim 4$  ms). The selection was performed by time resolved spectroscopy and the results are given in Fig. 3. The spectra were taken with  $\lambda_{ex} = 632.8$  nm to favor distorted center emission. In that figure, curve (a) corresponds to the total emission. The frequency span, from  $13.5 \times 10^3 \text{ cm}^{-1}$  to  $15.5 \times 10^3 \text{ cm}^{-1}$ . In this wide range the resolution employed did not allow to separate the peaks arising from cubic centers from the tetragonal ones.

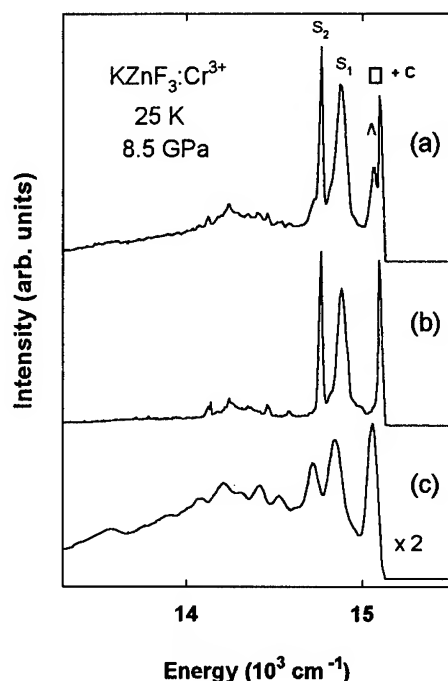


Fig. 3. Time resolved spectra for (a) total emission, (b) slow component ( $\tau \sim 2$  ms) and (c) difference between spectra (a) and (b) giving the fast component of emission.

The peak labeled  $\square + C$  in Fig. 3 represents the unresolved components. The intermediate curve (b) is the spectrum of slow electronic transitions ( $\tau \sim 2$  ms). It contains contributions from tetragonal and cubic site symmetries, but rules out any component of trigonal centers. It is noticeable in (b) the disappearing of the peak labeled  $\Delta$  in (a) and of the broad-band emission centered at about  $14300 \text{ cm}^{-1}$ . Curve (c) is the difference between (a) and (b). Being the fast emission, it selects the pure trigonally distorted contribution from the others. It contains the ZPL, the highest energy line, and two phonon bands at the lower energy side, corresponding to  $S_1$  and  $S_2$  of the total emission, respectively. Also present is a broadband which is due to a multiphonon sideband of the ZPL. The presence of both the broadband multiphonon and sharp line emission with comparable intensities is a clear evidence of the mixing of states effect. In fact, the trigonal crossover point,  $P_\Delta$ , is the closest to the pressure analysed here, 8.5 GPa, and the trigonal lines the most

Table I. Position and linewidth of sharp lines.

symbol	$\omega(\text{cm}^{-1})$ 11.0 GPa	$\Gamma(\text{cm}^{-1})$ 54 K	$\omega(\text{cm}^{-1})$ 8.5 GPa	$\Gamma(\text{cm}^{-1})$ 25 K
C	15117	3	15118	5
*	15112	5		
$\square$	15103	7	15106	12
$\Delta$	15057	16	15073	42

affected accordingly (see Table 1).

Summarizing, high resolution luminescence measurements were performed in an interesting system with several distorted site symmetries. Broadenings and line displacements observed close to the crossing from low- to high-field region were attributed to the mixing of states effect. Time resolved spectroscopy results reinforce this interpretation.

## Acknowledgements

Financial support from Fundação de Amparo à Pesquisa do Estado de São Paulo (FAPESP), Conselho Nacional de Desenvolvimento Científico e Tecnológico (CNPq), Fundo de Apoio ao Ensino e à Pesquisa (FAEP/ UNICAMP) and Consiglio Nazionale delle Ricerche (CNR) is greatly acknowledged.

## References

- [\*] On leave from Universidade Federal do Ceará, 60455-760, Fortaleza, Ceará, Brazil.
- [1] P.T.C. Freire, O. Pilla, V. Lemos, *Phys. Rev. B* **49**, 9232 (1994).
- [2] J.F. Donegan, G.P. Morgan, T.J. Glynn and G. Walker, *J. Modern Optics* **37**, 769 (1990).
- [3] U. Dürr, U. Brauch, W. Knierin and C. Schiller, *Tunable Solid State Lasers*, edited by P. Hammerling, A.B. Bugdor and A. Pinto (Springer-Verlag, Berlin) 1985.
- [4] O. Pilla, P.T.C. Freire and V. Lemos, *Phys. Rev. B* **52**, to appear.
- [5] C.J. Donnelly, S.M. Healy, T.J. Glynn, G.F. Imbusch and G.P. Morgan, *J. Lumin.* **42**, 119 (1988).



# STUDIES ON LOCAL DISTORTIONS AROUND $\text{Sm}^{2+}$ in $\text{MFCI}$ HOST LATTICE BY HIGH PRESSURE FLUORESCENCE

Y. R. Shen and W. B. Holzapfel

*Fachbereich Physik, Universität-GH-Paderborn, D-33095 Paderborn, Germany*

## ABSTRACT

The fluorescence spectra from the  $^5D_J \rightarrow ^7F_J$  transitions of  $\text{Sm}^{2+}$  in  $\text{MFCI}$  ( $M = \text{Ba}, \text{Sr}, \text{and Ca}$ ) were measured at 20 K and under pressure up to 8 GPa. The crystal-field energy levels of the  $^7F_J$  and  $^5D_J$  multiplets are determined from the observed fluorescence spectra. The conventional one-electron crystal-field model is used to derive the crystal-field parameters  $B_q^k$  and their variations under pressure. Within the superposition model, the intrinsic crystal-field parameters  $\bar{B}_4$  and  $\bar{B}_6$  and their distance dependences are derived in this pressure range and they are then used to study quantitatively the local distortions around  $\text{Sm}^{2+}$  in these hosts.

## Introduction

When impurity ions are substitutionally incorporated in host crystals, the usual problem of local distortions can not be avoided due to a mismatch in size between the impurity and substituted host ions. Many experimental and theoretical studies were devoted to this subject. Since the crystal-field (CF) interaction for lanthanide ions are successfully described by the superposition model (SM), this model provides a particularly useful tool to determine the local structure around the lanthanide ions in host crystals.

Ternary  $\text{PbFCl}$ -type compounds  $\text{MFX}$  ( $X = \text{Cl}, \text{Br}, \text{and I}$ ) are suitable host crystals for divalent impurity ions. A previous attempt was made to study the local distortions around  $\text{Mn}^{2+}$  and  $\text{Eu}^{2+}$  in  $\text{SrFCl}$  using EPR measurements [1]. In the present work, the high-pressure fluorescence technique is used to study the local distortions around  $\text{Sm}^{2+}$  in different  $\text{MFCI}$  hosts within the SM.

## Experimental results

The present samples contained 0.1 mol %  $\text{Sm}^{2+}$ . The fluorescence measurements were performed at 20 K and pressures up to 8

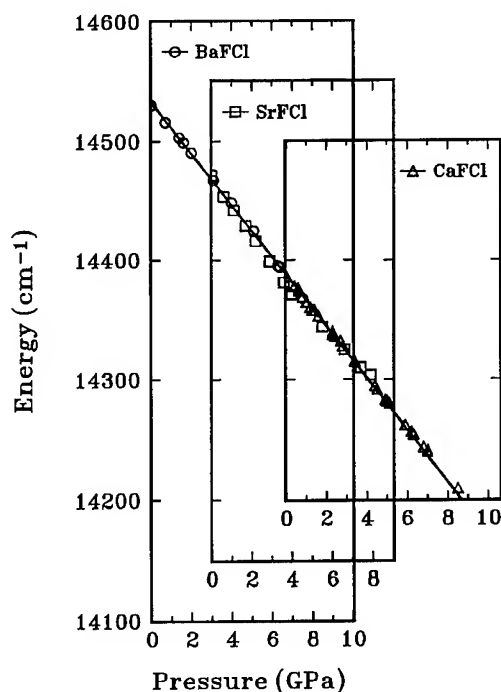


Fig. 1: Variation of the  $^5D_0$  multiplets for  $\text{Sm}^{2+}:\text{MFCI}$  under pressure. The data for  $\text{Sm}^{2+}:\text{SrFCl}$  and for  $\text{Sm}^{2+}:\text{CaFCl}$  are shifted with respect to  $\text{Sm}^{2+}:\text{BaFCl}$  by pressures of 3 GPa and 6.7 GPa, respectively.

GPa with the gasketed diamond-anvil cell (DAC) technique and the fluorescence measurement setup described in details elsewhere [2]. Methanol-ethanol-water mixture (16:3:1) was used as pressure-transmitting medium for  $\text{Sm}^{2+}:\text{BaFCl}$  and  $\text{Sm}^{2+}:\text{BaFCl}$ . Spectroscopic poly-chlorotrifluoroethylene-oil was used for  $\text{Sm}^{2+}:\text{CaFCl}$  due to the hygroscopic nature of this material.

Many groups of fluorescence lines in the spectral range of  $11500\text{ cm}^{-1}$  to  $18000\text{ cm}^{-1}$  were observed and attributed to the different  $^5D_J \rightarrow ^7F_J$  transitions. The fluorescence patterns of  $\text{Sm}^{2+}$  in these three hosts are very similar, however, with significant red-shifts of all the lines in the host series from  $\text{BaFCl}$  to  $\text{CaFCl}$ . As an example, the red-shifts and the pressure-induced shifts of  $^5D_0$  for  $\text{Sm}^{2+}:\text{MFCl}$  are shown in Fig. 1, where the data for  $\text{Sm}^{2+}:\text{SrFCl}$  and  $\text{Sm}^{2+}:\text{CaFCl}$  are shifted with respect to  $\text{Sm}^{2+}:\text{BaFCl}$  by pressures of 3 GPa and 6.7 GPa, respectively. Finally, the variation of the CF energy levels for  $^7F_J$  and  $^5D_J$  are determined from the observed high-pressure fluorescence spectra.

## Discussion

Since  $\text{Sm}^{2+}$  ions in  $\text{MFCl}$  hosts substitute  $M$ -cations with a  $C_{4v}$  site symmetry, the one-electron CF potential around  $\text{Sm}^{2+}$  is reduced to only five CF parameters, namely  $B_0^2$ ,  $B_0^4$ ,  $B_4^4$ ,  $B_0^6$ , and  $B_4^6$ . The CF analysis for the present systems uses least squares fitting to derive these five CF parameters and their variations under pressure. The results for the CF parameters show a very systematical variation in these three  $\text{MFCl}$  hosts.

It is well-known that the superposition model directly gives a relationship between CF interactions and local structures around lanthanide ions. Within this SM, the CF parameters are expressed as sums of contributions from the individual ligands  $L$ :

$$B_q^k = \sum_L \bar{B}_k(R_L) K_{kq}(\Theta_L, \Phi_L), \quad (1)$$

where  $L$  sums over all the next-nearest ligand ions with the spherical coordinates  $(R_L, \Theta_L, \Phi_L)$  around the central lanthanide ion. The coordination factors  $K_{kq}(\Theta_L, \Phi_L)$  are well-known angular functions of the ligand ions, and the  $\bar{B}_k(R_L)$ ,

usually referred to as intrinsic (i.e. geometry-independent) CF parameters, absorb all the physical contributions from the ligands. These  $\bar{B}_k(R_L)$  depend only on the ligand type and on the interionic distance  $R_L$  between the lanthanide ion and the ligand ion  $L$  in the coordination polyhedron. The intrinsic CF parameters are usually written as power-law expressions:  $\bar{B}_k(R) = \bar{B}_k(R_0)(R_0/R)^{t_k}$ , where  $R_0$  is a conveniently selected reference distance. In this sense, possible systematics for  $\bar{B}_k(R_0)$  and  $t_k$  should allow to make reasonable predictions on the CF interactions for the given lanthanide ion with the same ligands in different hosts.

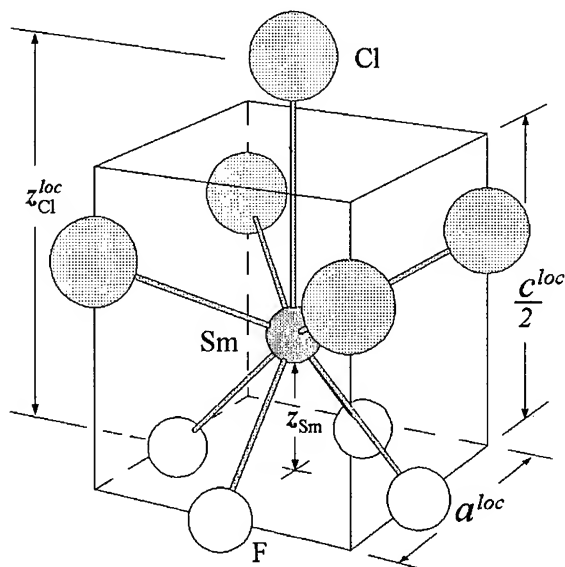


Fig. 2: Local unit cell. Four local structural parameters are defined as two local cell parameters ( $a^{\text{loc}}$  and  $c^{\text{loc}}$ ) and two local position parameters ( $z_{\text{Sm}}$  and  $z_{\text{Cl}}^{\text{loc}}$ ).

In the  $\text{MFCl}$  host crystals, the local coordination polyhedron around each  $\text{Sm}^{2+}$  ion consists of nine ligand ions, as shown in Fig. 2, whereby four F and four Cl ions are equivalent by symmetry and one extra Cl ion labeled as  $\text{Cl}'$  is located on the fourfold symmetry axis. The corresponding coordinates are denoted by  $(R_F, \Theta_F, \Phi_F)$ ,  $(R_{\text{Cl}}, \Theta_{\text{Cl}}, \Phi_{\text{Cl}})$ , and  $(R_{\text{Cl}'}, \Theta_{\text{Cl}'}, \Phi_{\text{Cl}'})$  with  $\Phi_F = (45^\circ, 135^\circ, 225^\circ, 315^\circ)$ ,  $\Phi_{\text{Cl}} = (0^\circ, 90^\circ, 180^\circ, 270^\circ)$ , and  $\Theta_{\text{Cl}'} = 0^\circ$ . These ligand coordinates

are calculated with the four local structural parameters as defined in Fig. 2.

For  $\text{Sm}^{2+}$  in  $\text{SrFCl}$  one can safely neglect the local distortions, since the ionic radii of  $\text{Sm}^{2+}$  and  $\text{Sr}^{2+}$  are almost identical and the structural parameters for  $\text{SmFCl}$  and  $\text{SrFCl}$  at ambient pressure as well as under pressure are also very similar. Therefore, the intrinsic parameters  $\bar{B}_k$  and the power-law parameters  $t_k$  for the  $\text{Sm}^{2+}\text{-F}^-$  and  $\text{Sm}^{2+}\text{-Cl}^-$  ion pairs are evaluated from the experimental CF parameters for  $\text{Sm}^{2+}\text{:SrFCl}$  with Eq. (1). The respective values for  $\bar{B}_k(R^0)$  and  $t_k$  are  $\bar{B}_4(R_{\text{Cl}}^0) = 124(14) \text{ cm}^{-1}$ ,  $t_4^{\text{Cl}} = 14(4)$ ,  $\bar{B}_6(R_{\text{Cl}}^0) = 152(16) \text{ cm}^{-1}$ ,  $t_6^{\text{Cl}} = 10(3)$ ,  $\bar{B}_4(R_{\text{F}}^0) = 245(25) \text{ cm}^{-1}$ ,  $t_4^{\text{F}} = 5.8(1.5)$ ,  $\bar{B}_6(R_{\text{F}}^0) = 172(18) \text{ cm}^{-1}$ , and  $t_6^{\text{F}} = 4.6(1.1)$ , where the reference distances  $R_{\text{Cl}}^0 = 311.4 \text{ pm}$  and  $R_{\text{F}}^0 = 249.6 \text{ pm}$  correspond to the values for  $\text{SrFCl}$  at ambient pressure.

According to the SM, the parameters  $\bar{B}_k$  and  $t_k$  for  $\text{Sm}^{2+}\text{-F}^-$  and  $\text{Sm}^{2+}\text{-Cl}^-$  ion pairs can be transferred directly to  $\text{Sm}^{2+}\text{:BaFCl}$  and  $\text{Sm}^{2+}\text{:CaFCl}$ . They are applied at first to  $\text{Sm}^{2+}\text{:BaFCl}$  and the local distortions around  $\text{Sm}^{2+}$  in  $\text{BaFCl}$  host are finally obtained with  $\Delta R_{\text{Cl}} = -7 \text{ pm}$ ,  $\Delta R_{\text{F}} = -6 \text{ pm}$ ,  $\Delta\theta_{\text{Cl}} = -1^\circ$ , and  $\Delta\theta_{\text{F}} = -1^\circ$ . Furthermore, it is observed that these local distortions are independent of pressure. These shorter distance distortions are expected, since the ionic radius for  $\text{Sm}^{2+}$  is much smaller than  $\text{Ba}^{2+}$ . The negative values for the angular distortions reflect a displacement of  $\text{Sm}^{2+}$  in  $\text{BaFCl}$  host towards the plane of the neighboring F ions, which is directly supported by EPR studies on  $\text{Mn}^{2+}$  and  $\text{Eu}^{2+}$  in  $\text{SrFCl}$  [1].

In the same way, the four local structural parameters  $a^{\text{loc}}$ ,  $c^{\text{loc}}$ ,  $z_{\text{Sm}}$ , and  $z_{\text{Cl}}^{\text{loc}}$  for  $\text{Sm}^{2+}$  in  $\text{CaFCl}$  are determined at each pressure with the following results: (i) The pressure dependences of the local cell parameters  $a^{\text{loc}}$  and  $c^{\text{loc}}$  are very similar to those of the host lattice parameters  $a$  and  $c$  [3]. The differences  $\Delta a = a^{\text{loc}} - a$  and  $\Delta c = c^{\text{loc}} - c$  are derived as  $12(2) \text{ pm}$  and  $-16(3) \text{ pm}$ , respectively. The opposite signs of  $\Delta a$  and  $\Delta c$  fit very well to the structural systematics of the  $\text{PbFCl}$ -type  $\text{MYX}$  compounds [3]. (ii) The  $\text{Sm}^{2+}$  position parameter in  $\text{CaFCl}$ ,  $z_{\text{Sm}} = 0.197(2)$  at ambient pressure, which is close to the value  $z_{\text{Ca}} = 0.196(2)$  for  $\text{CaFCl}$  at ambient conditions, increases slightly with a rate of  $9.2(8) \times 10^{-4} / \text{GPa}$ , and

(iii) the Cl positions around  $\text{Sm}^{2+}$  in  $\text{CaFCl}$  are given by  $z_{\text{Cl}}^{\text{loc}} = 0.658(2)$  at ambient pressure, which deviates only slightly from the Cl parameter  $z_{\text{Cl}} = 0.643(2)$  of the  $\text{CaFCl}$  host, and agrees well with the average value  $z_X = 0.647(14)$  for all the  $\text{MYX}$  compounds, where an almost constant value for  $z_X$  was noticed, in other words, a value independent of cation or anion sizes.

In both hosts,  $\text{CaFCl}$  and  $\text{BaFCl}$ , the local distances  $R_{\text{Cl}}$  and  $R_{\text{F}}$  change by about 11% of the difference in the ionic radii.

## Conclusion

The present results on  $\text{Sm}^{2+}\text{:MFCl}$  under pressure demonstrate, for the first time, that within the SM the local distortions around fluorescent lanthanide ions in different host lattices can be determined just by high pressure fluorescence studies. It is thus shown that the present method results in a valuable tool for the investigation of local distortions around optically active impurities.

1. D. Zevenhuijzen, J. A. van Winsum, and H. W. den Hartog, *J. Phys. C: Solid State Phys.* **9** (1976) 3113.
2. T. Gregorian, H. d'Amour-Sturm, and W. B. Holzapfel, *Phys. Rev. B* **39** (1989) 12497.
3. Y. R. Shen, et al., *J. Phys.: Condens. Matter* **6** (1994) 3197.

# LUMINESCENCE STUDIES ON $\text{Sm}^{2+}$ AND $\text{Eu}^{3+}$ IN DIFFERENT HOST MATERIALS UNDER PRESSURE – NEPHELAUXETIC EFFECTS

Y. R. Shen and W. B. Holzapfel

*Fachbereich Physik, Universität-GH-Paderborn, D-33095 Paderborn, Germany*

## ABSTRACT

Both  $\text{Sm}^{2+}$  and  $\text{Eu}^{3+}$  ions in different ternary compounds are used to investigate the reduction of the Coulomb and spin-orbit interactions of the  $4f$  electrons at ambient and high pressure. With the intermediate coupling scheme, the energy levels are simulated at first for both ions. The different distance dependences of the Slater parameter  $F_2$  and the spin-orbit coupling parameter  $\zeta_{4f}$  demonstrate then a breakdown of the common nephelauxetic series. When two microscopic covalency mechanisms, the central-field covalency and the symmetry-restricted covalency, are used together to describe the nephelauxetic effects on both ions, one can notice that the central-field covalency dominates in the case of the small  $\text{Eu}^{3+}$  ion, but the symmetry-restricted covalency is most dominant in the case of the larger  $\text{Sm}^{2+}$  ion.

## Introduction

When lanthanide ions are embedded into crystals, the reduction of the Slater and spin-orbit coupling parameters is commonly referred to as nephelauxetic effects. Empirical systematic considerations on contributions from different types of ligands to the reductions in the Slater parameters result in the so-called nephelauxetic series:

$$\text{free-ion} < \text{F}^- < \text{O}^{2-} < \text{Cl}^- < \text{Br}^- < \text{I}^- \approx \text{S}^{2-}.$$

Various models have been proposed to explain the nephelauxetic effects either by microscopic covalency or macroscopic dielectric mechanisms. However, the large number of experimental data for the chemically and pressure-induced nephelauxetic effects could not be explained reasonably within these models. Experimental data for  $\text{Sm}^{2+}$  and  $\text{Eu}^{3+}$  in different ternary host crystals at ambient pressure together with high-pressure results are used in the present study to derive a selfconsistent description for the nephelauxetic effects.

## Data

Experimental data on energy levels for the evaluation of the parameters  $F_k$  and  $\zeta_{4f}$  are

available for  $\text{Sm}^{2+}:\text{MFCl}$  ( $M = \text{Ba}, \text{Sr}, \text{and Ca}$ ) [1],  $\text{Eu}^{3+}:\text{LnOX}$  ( $\text{Ln} = \text{La}, \text{Gd}, \text{or Y}$  and  $X = \text{Cl}, \text{Br}, \text{or I}$ ) [2], and  $\text{Eu}^{3+}:\text{Ln}_2\text{O}_2\text{S}$  ( $\text{Ln} = \text{La}, \text{Gd}, \text{Y}, \text{and Lu}$ ) [3] at ambient pressure as well as for  $\text{Eu}^{3+}$  in  $\text{LaOCl}$  and  $\text{LaOBr}$  [4] at room temperature under pressures up to 13 GPa and for  $\text{Sm}^{2+}:\text{MFCl}$  at 20 K under pressures up to 8 GPa [1].

## Discussion

The hydrogenic approximation for the Coulomb interaction is used to derive the values of the parameters  $F_2$  and  $\zeta_{4f}$  for  $\text{Sm}^{2+}$  and  $\text{Eu}^{3+}$ . Remarkably good agreement between fitted and experimental energy levels with standard deviations  $\sigma$  around  $10 \text{ cm}^{-1}$  for  $\text{Sm}^{2+}$  and  $13.5 \text{ cm}^{-1}$  for  $\text{Eu}^{3+}$  is obtained in these cases.

To understand both the chemically and pressure-induced nephelauxetic effects on  $\text{Sm}^{2+}$  and  $\text{Eu}^{3+}$ , their distance dependences must be taken into account.

From the ternary  $\text{MFX}$ ,  $\text{LnOX}$ , and  $\text{Ln}_2\text{O}_2\text{S}$  host materials, both  $\text{MFX}$  and  $\text{LnOX}$  belong to a tetragonal  $\text{PbFCl}$ -type structure and  $\text{Ln}_2\text{O}_2\text{S}$  to a hexagonal structure.  $M$  or  $\text{Ln}$  cations in  $\text{PbFCl}$  are coordinated by nine ligands, four F or O anions at  $R_1$ , four X anions at  $R_2$ , and an extra X

anion located at  $R_3$  on the crystallographic axis  $c$ . In the hexagonal structure of  $Ln_2O_2S$ ,  $Ln$  cations are surrounded by three S anions at  $R_1$ , three O anions at  $R_2$ , and an extra O anion at  $R_3$ . An average interionic distance for the coordination polyhedra around  $Sm^{2+}$  and  $Eu^{3+}$  is defined with the coordination numbers  $n_i$  as  $\bar{R} = \sum n_i R_i / \sum n_i$ .

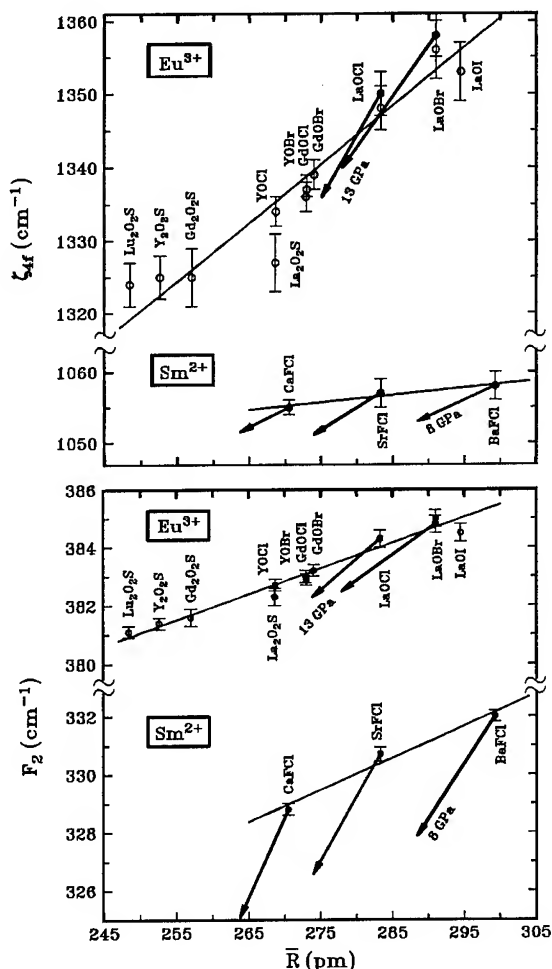


Fig. 1: Variations of the Slater parameter  $F_2$  and the spin-orbit parameter  $\zeta_{4f}$  (cm<sup>-1</sup>) for  $Sm^{2+}$  and  $Eu^{3+}$  in different host crystals as a function of  $\bar{R}$  (pm). Arrows with the closed circles denote the variations under pressure.

The dependence of the parameters  $F_2$  and  $\zeta_{4f}$  on  $\bar{R}$  is represented in Fig. 1, which shows that  $F_2$  and  $\zeta_{4f}$  decrease almost linearly with decreasing interionic distances. However, the pressure-induced decrease in  $F_2$  and  $\zeta_{4f}$  shows significant

deviations from the host-induced shifts. To a large extent, these deviations are accounted for by local distortions around the lanthanide ions in the different host crystals due to the different ionic size of the impurity ions with respect to the host lattice cations.

Figure 1 shows, however, very clearly that the decrease in both  $F_2$  and  $\zeta_{4f}$  for  $Eu^{3+}$  in the host series LaOI-LaOBr-LaOCl, GdOBr-GdOCl, and YOBr-YOCl is reversed with respect to the nephelauxetic series. Furthermore, the nephelauxetic series breaks down in the comparison of  $Eu^{3+}$ : $Ln_2O_2S$  with  $Eu^{3+}$ :LaOI, because the situation for  $S^{2-}$  and  $I^-$  should be similar in magnitude according to this series. For example, the La-O distances are approximately equal in the cases of  $La_2O_2S$  and LaOI crystals, so that  $O^{2-}$  ligands should contribute the same amount to the reduction of  $F_2$  and  $\zeta_{4f}$  in both cases. Thus, the surprisingly large difference in  $F_2$  and  $\zeta_{4f}$  between  $Eu^{3+}$ : $La_2O_2S$  and  $Eu^{3+}$ :LaOI must result from the difference of the  $S^{2-}$  and  $I^-$  ligands.

From the experimental data given in Fig. 1, one finds that the chemical shifts for  $Eu^{3+}$  from LaOI to  $Lu_2O_2S$  and for  $Sm^{2+}$  from BaFCl to CaFCl amount to -1.04% and -0.96% for  $F_2$ , and to -2.70% and -0.28% for  $\zeta_{4f}$ , respectively. The pressure-induced shifts for  $Sm^{2+}$  and  $Eu^{3+}$  show the same trend.

The microscopic covalency mechanism is used here to explain the chemical and pressure-induced shifts in  $F_2$  and  $\zeta_{4f}$  for  $Sm^{2+}$  and  $Eu^{3+}$  ions. Within this mechanism, the reductions of Slater and spin-orbit coupling parameters are ascribed to the 4f-electron cloud expansion of lanthanide ions in crystals. This expansion is described in terms of two different models, central-field covalency (CFC) and symmetry-restricted covalency (SRC). The CFC model relates such an expansion to an isotropic penetration of ligand electrons into the 4f orbitals. In other words, this penetration screens the effective nuclear charge  $Z_{eff}$  of the lanthanide ion and results in  $F_k \sim Z_{eff}$  and  $\zeta_{4f} \sim Z_{eff}^3$ .

On the other hand, the SRC model relates such an expansion to a symmetry-dependent covalency admixture of 4f orbitals with ligand orbitals. In a first approximation, the Slater and spin-orbit coupling parameters are then expressed within

the SRC by  $F_k = \mathcal{N}^4 F_k^0$  and  $\zeta_{4f} = \mathcal{N}^2 \zeta_{4f}^0$ , where the  $\mathcal{N}$ 's represent renormalization constants and  $F_2^0$  and  $\zeta_{4f}^0$  correspond to the values of the free ion.

Usually, either one or the other model has been used to describe the nephelauxetic effects of lanthanide ions. However, they may not also act simultaneously in the present cases of  $\text{Sm}^{2+}$  and  $\text{Eu}^{3+}$ . A suitable combination results then in  $\Delta Z_{\text{eff}}/Z_{\text{eff}} = -0.87\%$  and  $\Delta \mathcal{N}/\mathcal{N} = -0.04\%$  for  $\text{Eu}^{3+}$  in different hosts, and in the case of  $\text{Eu}^{3+}:\text{LaOCl}$  and  $\text{Eu}^{3+}:\text{LaOBr}$  under pressures up to 13 GPa,  $\Delta Z_{\text{eff}}/Z_{\text{eff}} = -0.36\%$  and  $\Delta \mathcal{N}/\mathcal{N} = -0.05\%$ . These results indicate that the contribution from the CFC to  $F_2$  and  $\zeta_{4f}$  dominates in the case of  $\text{Eu}^{3+}$ . In the case of  $\text{Sm}^{2+}$  in three MFCl hosts, the chemical shifts are modelled by  $\Delta Z_{\text{eff}}/Z_{\text{eff}} = 0.08\%$  and  $\Delta \mathcal{N}/\mathcal{N} = -0.28\%$  and the pressure-induced shifts for a pressure range of 8 GPa in these three hosts result just in the same values, where the small positive value for  $\Delta Z_{\text{eff}}/Z_{\text{eff}}$  seems not to be significant within the given uncertainty of this analysis. This shows an overwhelming dominance of the SRC in the case of  $\text{Sm}^{2+}$ .

## Conclusion

In summary, the present study on  $\text{Sm}^{2+}$  and  $\text{Eu}^{3+}$  ions in different host materials leads to the following results: (i) The nephelauxetic series breaks down in ternary compounds, at least in the cases of  $\text{Sm}^{2+}$  and  $\text{Eu}^{3+}$ . (ii) For small, trivalent lanthanide ions, like  $\text{Eu}^{3+}$ , the CFC or the "central-charge screening" is dominant, whereas the SRC or the "ligand hybridization" is the dominant mechanism in larger, divalent lanthanide ions like  $\text{Sm}^{2+}$ .

1. Y. R. Shen and W. B. Holzapfel, Phys. Rev. B **51** (1995) 15752; Y. R. Shen, Ph.D. Thesis, Universität-GH-Paderborn, 1994.
2. J. Hölsä and P. Porscher, J. Chem. Phys. **75** (1981) 2108 and **76** (1982) 2790.
3. O. J. Sovers and T. Yoshioka, J. Chem. Phys. **51** (1969) 5330.
4. Y. B. Chi, et al, Physica B **139/140** (1986) 555 and High Pressure Res. **3** (1990) 150.

## **VII(C) Semiconductors**

### **VII(C.1) Bulk Materials**

# THE USE OF HIGH PRESSURES IN THE INVESTIGATION OF THE ELECTRONIC PROPERTIES OF SEMICONDUCTORS

WILLIAM PAUL

*Physics Department, Harvard University  
Cambridge, Massachusetts 02138, USA*

An historical review will be given of the earliest investigations of the effect of high pressures on the transport properties of semiconductors, and of the development of techniques permitting the repetition at high pressures of most of the experiments giving fundamental information. The background of the much-used Empirical Rule governing the shift with pressure of the principal conduction band extrema in the Si family will be given, and the use of the Rule to help determine band structures and elucidate phenomena examined.

## Introduction

At our 1993 meeting, my group discussed measurements at high hydrostatic pressures on the Si family of semiconductors, which were used to obtain new information about the band structures and properties of the atmospheric pressure material [1]. Central to the discussion was an Empirical Rule [2] governing the pressure coefficients of the energy gaps between the valence band (VB) maximum energy and the energies of the three lowest conduction band (CB) minima of  $\Gamma$  (000),  $L$  (111) and  $X$  (100) symmetry: independent of the family member studied, the pressure coefficient of the direct energy gap at  $\Gamma$  falls in the range 10–15 meV/kbar, that of the indirect gap at  $L$  near 5 meV/kbar, and that of the indirect gap at  $X$  between -1 and -2 meV/kbar (see Figure 1). Our research report was updated at a special conference in 1994 [3]. In this paper I shall try to set this work in perspective in a more historical review outlining the changing role of high pressures in semiconductor research.

## Change in the Role of High Pressures

Revisiting the establishment of the Empirical Rule immediately reveals several changes in approach and technique. Before 1950 the pressure measurements were not part of systematic research on a single material. When Bridgman established a new technique, he evidently felt obliged to explore a wide variety of substances, an approach absolutely appropriate to his time. But, by 1952, it was also appropriate to examine the many experiments one could do to gain a detailed understanding of a limited class of substances. It then

made sense to choose a class like the Si family about which there was great scientific interest and technological application. A diversity of experiments, representing a different philosophical approach, was needed to fully understand all of the individual parameters affected by pressure, and to permit extrapolation to atmospheric pressure, in order to gain information not otherwise attainable about the band structure, and about the dependent physical processes. The necessary experiments required the development of experimental techniques permitting the repetition at high pressures of almost all of the experiments giving fundamental information at atmospheric pressure [4]. A simple catalog of some of these experiments will illustrate the point: (1) extrinsic and intrinsic conductivity, at different temperatures; (2) Magnetotransport at different temperatures; (3) static and high frequency dielectric constant; (4) refractive index; (5) drift mobilities of electrons and holes; (6) ultrasonic wave velocity; (7) indirect and direct transition optical absorption spectra; (8) photoconductivity spectra; (9) ionization energies of hydrogenic and deep impurities; (10) hot electron and transferred electron effects; (11) tunnel diode characteristics; (12) Faraday rotation; (13) ultraviolet reflectivity spectra; and (14) Seebeck coefficients. Among the new types of apparatus were (1) the development of thin, flexible stainless steel tubing to separate the final high pressure vessel from the pressure-generating equipment, (2) the development of BeCu and stainless steel vessels for magnetic experiments, and (3) the use of sapphire, germanium, silicon and Irtran optical windows.

The approach in the present era is somewhat modified, and the dominant technique is differ-



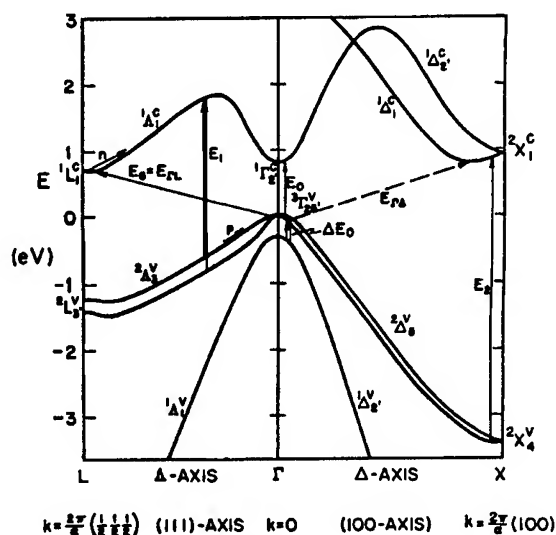


Figure 1: Electronic energy band structure of Ge.

ent. Examination of recent conferences shows that most experiments are optical ones done in diamond anvil cells. By contrast, when I started high-pressure work in 1952, I knew of no published work on the optical properties of semiconductors at high pressures, and there were no diamond anvil cells. Historically, electrical, magnetic, optical and mechanical properties have all been used to establish the overall picture of how semiconductors change with pressure. Today, accepting the common restriction on the range of useable techniques in the diamond anvil cell, it is possible to do only optical experiments and to draw conclusions regarding atmospheric pressure band structures and physical processes, precisely because the effect of pressure on the other (non-optical) parameters is reasonably well established.

### Early Experiments on Ge

I shall begin by giving a historical account, although it is easier to understand the results by inverting the order of presentation, and deducing the pressure effect on properties from the known effect on band structure. Figure 2 shows measurements of the resistivity of intrinsic and extrinsic Ge at several temperatures [5]. It was straightforward to deduce that, for the sample remaining intrinsic at 349 K and all pressures, the resistiv-

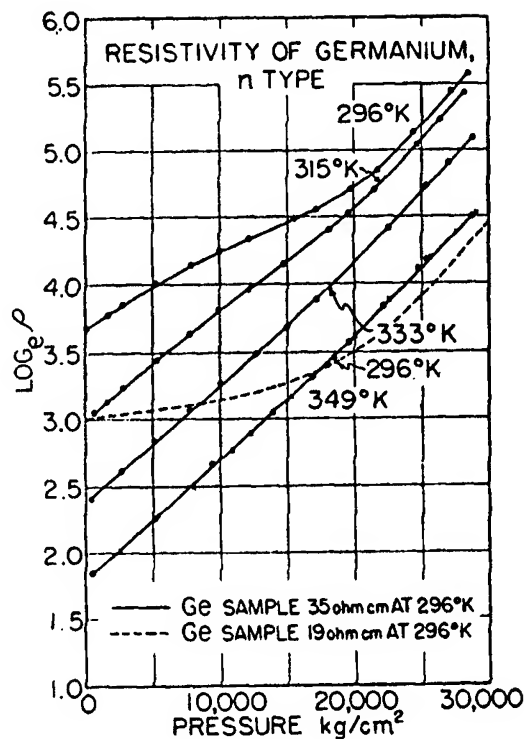


Figure 2: Resistivity of Ge versus pressure at several temperatures.

ity increase was primarily caused by a decrease in the intrinsic carrier density resulting from the known increase of the energy gap. But, observe that the increase above 20 kbar is about the same for the intrinsic and extrinsic samples. Note also that Bridgman found in quasi-hydrostatic experiments to 100 kbar that the *extrinsic* resistivity passed through a maximum near 50 kbar.

We now know that the increase in resistivity in *all* extrinsic *n*-type Ge is caused by electron transfer from the lowest-lying CB (111) minima to the higher-lying (100) minima, produced by an increase of the gap between the VB maximum and the (111) minima, and a decrease of that to the (100) minima. We also now know that the maximum in the resistivity is caused by the existence of (111) to (100) interband scattering, which is greatest when the (111) and (100) minima are nearly degenerate. Thus the behavior of the resistivity for all the *extrinsic n*-type samples reflects that of an effective mobility.

This was not clear in 1952. There were so many unknowns that many "explanations" easily dismissed today had to be considered. Among the unknowns were the location in  $k$ -space of the VB and CB extrema, the magnitude of the effective masses, the existence of higher energy CB or VB extrema, and the effect of pressure on gaps, masses, impurity ionization energies, dielectric constants, phonon spectra and carrier mobilities. This long list explains why no semiconductor system has been examined in the detail of the Si family. Brooks and I sought to explain the large increase in resistivity of *extrinsic* Ge above 15 kbar in either a decrease in carrier density caused by an increase in impurity ionization energy or in a decrease of the electron mobility. The first possibility was easily discounted. However, the postulated strong change of the electron mobility above 15 kbar implied that, for an *intrinsic* sample, there would be both a rapid decrease in carrier density and a decrease in carrier mobility, yet the resultant effect was measured to be the same as for an extrinsic sample.

To account for this behavior, it was necessary to suppose that at the pressure where the mobility change begins there is a reduction in the rate of increase in band gap. In our paper we wrote, "Such a change is not too unlikely if it is assumed, as seems probable, that the change in mobility is associated with a change of the point in  $k$ -space at which the minimum energy in the conduction band comes." This is, as far as I know, the first mention in the semiconductor literature of the possible importance of higher-lying CB minima.

The next step was to do something entirely new: to attempt to explain in detail the resistivity-pressure relation, by establishing the pressure dependence of all the relevant parameters. This involved (1) examining the effect of pressure on the hydrogenic impurity ionization energy of  $E_H m^*/K^2$ , or alternatively on the effective mass  $m^*$  and the dielectric constant  $K$ ; (2) examining the effect of pressure by direct measurement of the mobilities of electrons and holes, or by the effect on parameters such as  $m^*$ ,  $K$  and elastic constants determining them; (3) establishing a theory of interband carrier transfer from the lower band to a higher one of unknown energy, effective mass and pressure coefficient, and establishing a theory of interband scattering processes. This program was carried out, as I shall briefly describe.

### Subsequent Tests of the Two-CB Model

The effect of pressure on hydrogenic ionization energies was tested by measurement of the resistivity of  $n$ - and  $p$ -type *silicon* at low temperatures [6]. The pressure coefficient was small, as expected, but fitted experimental determinations of the effect of pressure on the dielectric constant and plausible estimates of the change in effective mass.

A classic experiment of the 1950's era was the determination of the drift mobility of Ge by Haynes and Shockley. In their experiment, minority carriers were injected into a bar at a point contact, drifted down the bar by an applied field, and detected at a down-stream point by the modification of the back-bias impedance at the point. Smith [7] used welded contacts to repeat the experiment on  $p$ -type Ge to 30 kbar, and reproduced exactly the inverse of the resistivity versus pressure plot for an extrinsic  $n$ -type sample shown in Figure 2. This completely validates the model of a decreasing mobility in  $n$ -type Ge, which is an average over two conduction bands.

The interband transfer is too complex to discuss here. Suffice to say that contributions from many sources validated the two-band hypothesis and established its parameters within acceptable limits [4]. However, the symmetry of the transferred electrons has never been satisfactorily established by a direct experiment, although Howard [8] attempted to do so in a study of magnetoconductance to 20 kbar. He had insufficient sensitivity at his limiting pressure in a BeCu vessel to identify the higher minima. Perhaps, using better modern material and a low-Si-content GeSi alloy to lower the energy of the higher minima, magnetoresistance or piezoresistance experiments would confirm the symmetry.

### Band Structures of Si and Ge

The symmetries of the CB extrema of Ge ((111)) and Si ((100)) were established in 1954 and 1955 respectively. Before this, however, pressure experiments had established that the CB symmetries had to be different. Measurements of the intrinsic resistivity of Si under pressure [9] determined that the resistivity *decreased*, corresponding to a *decrease* in fundamental gap at a rate of -1.5 meV/kbar, in contrast to the established *increase* for Ge of 5 meV/kbar. This result was later sup-

ported by measurements of the displacement under pressure of the optical absorption edge. At about the same time, experiments on Ge-Si alloys [10] showed a discontinuous break in the variation of the optical energy gap with composition, interpreted as a changeover in the symmetry of the lowest CB minima from (111) to (100) at about 15 at % Si content. Extrapolation of the high Si content variation to zero Si content suggested (100) minima in Ge about 0.2 eV above the (111) minima. The negative pressure coefficient of the gap in Si and the required negative coefficient of the postulated higher energy minima in the model for Ge provided a coherent picture, and the first significant contribution to the notion that minima of the same symmetry have very similar pressure coefficients. The subsequent demonstration of a negative coefficient for the Ge optical gap at very high pressures [11] clinched the overall model in a very satisfactory way.

Measurements of intrinsic resistivity versus pressure were used to establish an increase of the indirect Ge energy gap at 5 meV/kbar. Optical measurements of the effect of pressure on the indirect gap were often misinterpreted, however, to give different values. An approximate form for the absorption coefficient suitable for our present purpose is

$$\alpha = a(h\nu - E_g)^2 / (E_{g0} - E_g)^2, \quad (1)$$

where  $E_g$  is the indirect band gap,  $E_{g0}$  the direct band gap at  $\Gamma$ , and  $a$  a constant. The quantity  $(E_{g0} - E_g)^2$  is expected to increase very rapidly from its atmospheric pressure value of  $(0.15 \text{ eV})^2$  (see the effect of pressure on  $E_{g0}$  below), which leads to a distinct change in shape of the absorption edge. Thus, simple isoabsorption plots do not give the shift in the indirect gap with pressure, but larger coefficients in the 8 meV/kbar range. By applying the requisite corrections to  $(E_{g0} - E_g)(P)$ , Paul and Warschauer [12] were able to rationalize, albeit with low precision, a coefficient of 5 meV/kbar for the Ge indirect gap, and also a changeover to a coefficient of -1.5 meV/kbar as GeSi alloys changed from Ge to Si.

By 1955 it was known that the direct band gap of Ge at  $\Gamma$  was only 0.15 eV larger than the indirect gap at room temperature. Early pressure measurements to 1 kbar to energies up to 0.80 eV, which were actually smaller than the accepted gap value (from magnetoabsorption) of 0.805 eV, gave

a coefficient of about 12 meV/kbar. Cardona [13] remeasured the direct edge to 7 kbar, using thin samples, to photon energies of 1.25 eV, and found a coefficient of  $13 \pm 1$  meV/kbar. Later, Melz [14] used a modulated reflectivity measurement to obtain 14.2 meV/kbar.

We note that there is a large difference between these values for the gap at  $\Gamma$  (10–15 meV/kbar) and those for the gaps at  $L$  (5 meV/kbar) and  $X$  (-1.5 meV/kbar). In the next section, we shall compare the value for  $\Gamma$  with similar determinations for the 3–5 compounds.

## The Empirical Rule

### *The 3–5 Compounds Under Pressure*

The change with pressure of the (direct) gap in InSb was reported as early as 1955 by Long [15] and by Keyes [15] who found coefficients of 14.2 and 15.5 meV/kbar respectively. Before long it became apparent that the same three CB extrema at  $\Gamma$ ,  $L$  and  $X$  were important in all of the 3–5 compounds, that their relative energies at atmospheric pressure varied systematically with composition, and that their pressure coefficients invariably fell into the same categories. The details of these studies are described in Reference 2.

The Empirical Rule enunciated earlier became accepted fact. Unanticipated theoretically, it was to become the instrument both of clarifying band structures and physical phenomena. It is also useful in amplifying the traditional role of pressure experiments in checking band calculational techniques. The foundation for the Rule must ultimately rest on a basic similarity in the properties of electrons of a given symmetry in the different members of the Si family; that similarity may be argued very plausibly on the basis of an empirical pseudopotential approach to the evaluation of band structures. Discussion of this may be found in the several reviews cited (especially Martinez) which also refer to the original theoretical papers.

### Use of the Empirical Rule in Establishment of Band Structures

As an example I shall discuss only GaP [16]. Figure 3 is constructed at least in part from high pressure measurements. First, the fundamental gap is

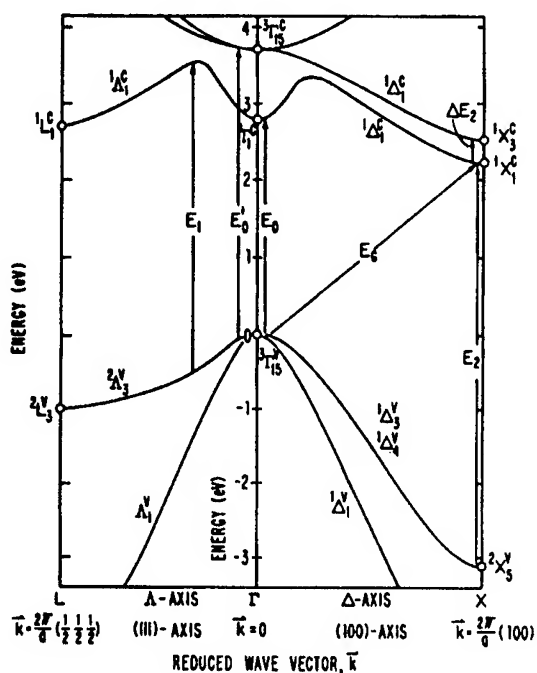


Figure 3: Electronic energy band structure of GaP.

between an  $X$  conduction band state and a  $\Gamma_{15}$  valence band state. The first demonstration that this was appropriate came from the fact that the pressure coefficient of the smallest gap in this material was negative.

Second, the lowest conduction band state at the center of the zone is 2.8 eV above the VB maximum, or 0.6 eV above the state lying in the (100) direction. Again, the first quantitatively correct estimate of the energy of this state was made as a result of reflectivity measurements which showed structure at this energy which displaced to higher energies precisely at the rate expected from the empirical rule for the  $\Gamma_1$  state.

Third, absorption measurements had suggested that the direct gap was about 2.6 eV, that is, that there was a separation of 0.4 eV between the  $\Gamma_1$  state and that forming the lowest conduction band state. This deduction was made on the basis of the observation of a bump in the infrared absorption near 0.4 eV, which was attributed to the electron transfer from the lowest minimum into the  $\Gamma_1$  state. Investigation of the displacement of this bump pressure was decisive. For, if we accept the empirical rule that under pressure

the  $\Gamma_1$  and the  $X_1$  states will separate at a net rate of about  $14 \times 10^{-6}$  eV/bar, then we can test the correctness of the assigned reason for the optical absorption by measuring the shift of the absorption bump under pressure. The result is that the observed displacement is more than an order of magnitude smaller than that predicted on the basis of the supposed identification. This measurement was used first to eliminate the original explanation of the bump, second to invalidate the identification of the energy of the  $\Gamma_1$  minimum and third to suggest that the transition was between the lowest  $X$  minimum and another one at the same  $k$ -vector just directly above it ( $\Delta E_2$ ).

These demonstrations were clean and conclusive, and represented a unique contribution of high pressures to semiconductor research. There were similar contributions in many of the other 3-5 compounds [4]. Perhaps, however, the most spectacular of this use of pressure was the determination of the inverted band structure of  $\alpha$ -Sn [17]. This was a true discovery, stemming directly from pressure studies, and unanticipated by other experiment or by theory.

### Use of the Empirical Rule to Help Establish Physical Phenomena

As an example I shall discuss the Gunn effect [18]. This effect is due to the existence in some semiconductors of a range of electric fields in which the electron drift velocity decreases with increasing field, an instability which has been exploited in devices. Here we are concerned only with the conditions of band structure responsible for it. Although, in principle, several mechanisms are possible, Hutson *et al.* [18] were able to identify that responsible in GaAs. They showed that the threshold field for the Gunn effect decreased with increasing pressure. This fit with a model that electric field heats electrons in the lowest  $\Gamma_1$  minimum to energies higher than the bottom of subsidiary minima and causes transfer of the electrons to these minima. Since the mobility in the higher minima is lower than in  $\Gamma_1$ , the average mobility and drift velocity of electrons decrease with increasing applied field. The threshold field clearly depends on the separation in energy between  $\Gamma_1$  and the higher minima, and thus the reduced threshold is just what one would expect of either the  $L$  or  $X$  minima. In fact, the quantitative

data identify the  $X$  minima as those operating at high pressures. The Gunn effect disappears when the  $\Gamma$  and  $X$  extrema are nearly equal in energy since the carriers are shared even at zero field.

There have also been studies of the Gunn effect in  $n$ -InSb [19] where the band structure situation is quite different. The energy gap is smaller than the distance from the  $\Gamma_1$  CB edge to the bottom of the next set of minima. As a result, an electron requires less energy to impact-ionize another electron from the valence band to the conduction band than to transfer into a higher-lying minimum. Two interesting results occur. First, high pressure produces in InSb a favorable band structure for Gunn effect, by increasing the fundamental gap and decreasing the energetic distance from  $\Gamma_1$  to higher minima. Second, it is found that Gunn effect occurs right down to atmospheric pressure, where the gap is much smaller than the separation between conduction bands. This occurs because the cross-section for impact ionization is too small to prevent carrier heating into the higher minima at strong fields. High pressure proved a superb vehicle to observe these phenomena.

### More Recent Experiments and the Future

Much of the recent work was reviewed in my 1994 paper [3] and will not be repeated here. It is, however, clear that more can be done on the properties of deep impurity levels, and of quantum wells, heterostructures and band offsets in the Si family of materials. Other families, particularly the Se-Te one and that constituted by the NaCl-structure of Pb  $X$ , Sn  $X$ , Ge  $X$ , where  $X = [S, Se, Te]$  (which is possibly linked to the slightly distorted structures of As, Sb and Bi) deserve fuller examination. An even more recent investigation, which I expect to continue, has been the study of the effect of pressure on the optical properties of nanocrystals, such as Si or Ge implanted in SiO<sub>2</sub>, or "porous" Si. On the technique side, it would be advantageous if the use of electrical feedthroughs in DAC's were more widespread.

### References

1. W. Paul, J.H. Burnett and H.M. Cheong, in *Proceedings of the XIV International Conference on High Pressure Science and Technology*, Colorado Springs, CO (1993) (American Institute of Physics, New York, 1994) 545.
2. W. Paul, *J. Appl. Phys.* **32** (1961) 2082.
3. *J. Phys. Chem. Solids* **56**(3/4), eds. P.Y. Yu, W. Paul and B.A. Weinstein (Pergamon, 1995).
4. For example: W. Paul and H. Brooks, in *Progress in Semiconductors* **7** (Heywood and Co., London, 1963) 135; W. Paul in *The Optical Properties of Solids*, ed. J. Tauc (Academic, New York, 1966) 257; R. Zallen and W. Paul, *Phys. Rev.* **134** (1964) A 1628; **155** (1967) 703; W. Paul, in *Propriétés Physiques des Solides sous Pression* (C.N.R.S., Paris, 1970) No. 188, p. 199; G. Martinez, in *Handbook on Semiconductors*, Vol. 2, ed. M. Balkanski (North-Holland, 1980) 181.
5. W. Paul and H. Brooks, *Phys. Rev.* **94** (1954) 1128.
6. M.G. Holland and W. Paul, *Phys. Rev.* **128** (1962) 30,43.
7. A.C. Smith, Thesis, Harvard University, 1958. See Ref. 4.
8. W.E. Howard, Thesis, Harvard University, 1961.
9. W. Paul and G.L. Pearson, *Phys. Rev.* **98** (1955) 1755.
10. E.R. Johnson and S.M. Christian, *Phys. Rev.* **95** (1954) 560; F. Herman, *Phys. Rev.* **95** (1954) 847.
11. T.E. Slykhouse and H.G. Drickamer, *J. Phys. Chem. Solids* **7** (1958) 210.
12. W. Paul and D.M. Warschauer, *J. Phys. Chem. Solids* **5** (1958) 89; **6** (1958) 6.
13. M. Cardona and W. Paul, *J. Phys. Chem. Solids* **17** (1960) 138.
14. P.J. Melz and I.B. Ortenburger, *Phys. Rev.* **B3** (1971) 3257.
15. D. Long, *Phys. Rev.* **99** (1955) 388; R.W. Keyes, *Phys. Rev.* **99** (1955) 490.
16. R. Zallen and W. Paul, first Reference 4.
17. S.H. Groves and W. Paul, *Phys. Rev. Lett.* **11** (1963) 194.
18. A.R. Hutson, A. Jayaraman, A.G. Chynoweth, A.S. Coriell and W.L. Feldman, *Phys. Rev. Lett.* **14** (1965) 639.
19. S. Porowski, W. Paul, J.C. McGroddy, M.I. Nathan and J.E. Smith, Jr., *Solid State Comm.* **7** (1969) 905.

1. W. Paul, J.H. Burnett and H.M. Cheong, in *Proceedings of the XIV International Conference on High Pressure Science and Technology*, Colorado Springs, CO (1993) (American Institute of

## IS LIGHT COMING OUT OF SILICON IN POROUS SILICON ?

J. ZEMAN, M. ZIGONE, G.L.J.A. RIKKEN AND G. MARTINEZ

*Grenoble High Magnetic Field Laboratory, Max-Planck Institut für Festkörperforschung and  
Centre National de la Recherche Scientifique  
BP 166, 38042 Grenoble Cedex 9, France*

Recent high pressure measurements performed on different kinds of oxydized porous silicon (PS) samples are reviewed. They involve a luminescence and Raman scattering investigation under hydrostatic pressure up to 22 GPa. The results show that the luminescence efficiency is not much affected as long as the PS sample has not been pressurized beyond about 17 GPa though at that pressure it has already been transformed into the metallic  $\beta$ -Sn phase. The persistence of the luminescence is also observed on samples recovered at 1 bar in the BC8 phase. In addition the existence of a Raman structure specific of PS samples appearing after the phase transformation is demonstrated for the first time. The analysis of all the data leads to conclude that the PS luminescence is very likely related to surface complexes possibly involving Si-Si bonds.

### Introduction

Very soon after the discovery of the strong visible photoluminescence (PL) in anodically etched porous silicon, a large number of experimental and theoretical investigations have been performed in order to determine the mechanisms of this luminescence [see for instance Ref. 1]. Two different kinds of mechanisms have been invoked either those originally proposed by L.T. Canham [2] involving confinement effects in nanosize silicon particles or those, of extrinsic nature, related to surface defects [3] or complexes [4]. There is not yet a definitive proof in favour of any of these possibilities especially because there exists a large variety of samples without reproducible properties. Many attempts to vary the PS surface properties gave indeed a strong variation of the luminescence efficiency without proving its origin. There is an alternative way to look at the problem which is to change the bulk properties of the silicon.

This can be achieved by the application of the hydrostatic pressure which transforms silicon first from the diamond (Td) phase to the  $\beta$ -Sn (metallic) phase at around 12-13 GPa, then from the  $\beta$ -Sn phase to the Sh (metallic) phase at around 16 GPa and on releasing pressure from the  $\beta$ -Sn phase to the BC8 phase which remains metastable at 1 bar. The existence of this phase is therefore a proof that at least one phase transformation has been performed [5]. Luminescence experiments performed as a function of pressure [6] showed indeed the persistence of the intense PL through the different phases as long as a critical upper pressure was not exceeding about 17 GPa. In order to follow the

nature of the phase it was necessary to characterize it and systematic Raman scattering measurements were performed to try to correlate the properties of the luminescence with the phase of the bulk matter. This is possible since Td,  $\beta$ -Sn and BC8 phases are Raman active with characteristic Raman signatures

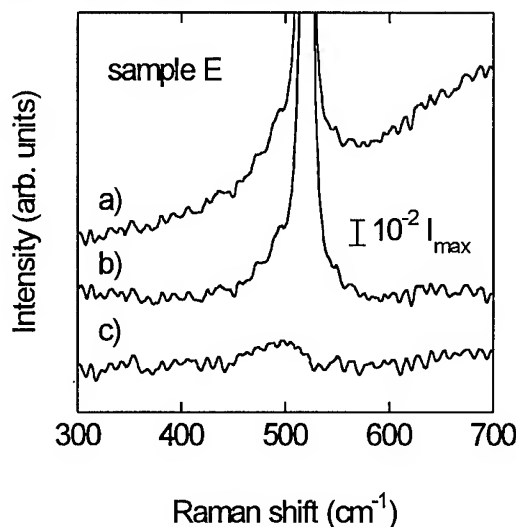


Fig. 1 : Comparison of the Raman line shape of PS and bulk silicon in the diamond Td phase. The spectrum a) corresponds to the PS Raman line of sample E ; the spectrum b) is obtained from a) after correction for the luminescence; the lower spectrum c) is the result obtained after subtracting out the bulk silicon Raman line shifted by  $0.7 \text{ cm}^{-1}$  towards lower energies.

[7, 8]. In addition to these features a specific Raman band of the PS samples is observed on samples structurally transformed. All these results are reviewed and strongly suggest that the PS

luminescence is very likely not originating from the bulk part of the samples.

### Samples and experimental procedure

In the present context the nature of samples is important to specify: five different types of PS samples have been used including supported films of PS obtained from 10  $\Omega\text{cm}$  p-type Si (samples A, B, E), a free standing PS film originating from the same bulk Si (sample C) and a supported film of PS made from a 15  $\Omega\text{cm}$  n-type Si substrate (sample D). All samples are oxydized. The porosity of all samples is in the range of 80 % with a thickness of the porous layer ranging around 10 and 15  $\mu\text{m}$ . Some of the original wafers have been checked by scanning tunnelling microscopy revealing particles with sizes larger than 15 to 20 nm, but systematic and independent Raman line shape analysis have been performed in order to check and quantify these aspects. Such results are shown in Fig. 1 where the Raman spectrum of the PS sample (a) is first corrected from the luminescence (b). Then a Raman spectrum obtained in the same conditions on the substrate, normalized and shifted of about  $0.7\text{ cm}^{-1}$  towards lower energies, is subtracted out from spectrum (b) which results in spectrum (c). There are different ways to analyse such a size dependent shift of the Raman mode [9, 10] but they all converge to insure that the sizes of particles should be larger than 10 nm leaving at most  $10^{-2}$  to  $5 \times 10^{-3}$  the total volume of the sample unidentified. The luminescence and Raman experiments have been performed with either green or blue lines of an  $\text{Ar}^+$  laser, keeping the incident power lower than 0.5 mW focused to a spot of about 30  $\mu\text{m}$ , in order to minimize «aging effects». The high pressure experiments were performed in a diamond anvil cell with different pressurizing media such as the standard methanol-ethanol mixture or the Xe gas. None of these different experimental conditions gave significant differences in the experimental results.

### Results and discussion

The PS luminescence spectrum is composed of a broad band with characteristic features easily discussed in terms of moments [6]. The first moment (mean energy) varies in a non monotonic way as a function of the pressure: the energy first increases

(Fig. 2) and then decreases beyond around 3 to 5 GPa at a rate of -25 to -35 meV/GPa.. This luminescence is observed together with the Raman Td mode of silicon up to about 12 GPa where this mode disappears. At higher pressures the luminescence is still observed though the Raman Td mode has disappeared. On releasing pressure, the variation of the luminescence is reversible though the Raman Td mode is no longer observed (full symbols in Fig. 2). Within the statistical error observed for these samples, we notice that there is no discontinuity at the expected Td  $\rightarrow$   $\beta$ -Sn phase transition or  $\beta$ -Sn  $\rightarrow$  BC8 phase transition. The variation of the width of the luminescence band (second moment) does not show any discontinuity as well [6]. The intensity of the PL is also not very affected as long as the higher pressure  $P_u$  applied to the sample has not exceeded about 17 GPa. In Fig. 3 one compares luminescence spectra *measured at 1 bar* after pressure runs up to  $P_u$ . Note that the two middle spectra ( $P_u = 9.3\text{ GPa}$  and  $P_u = 14\text{ GPa}$ ) are not very different in intensity whereas for the lower spectrum ( $P_u = 20\text{ GPa}$ ) the intensity has collapsed. One can also note that for spectra of PS samples in the BC8 phase the mean energy has slightly shifted to lower energy as compared to that of PS samples in the Td phase. This collapse of the intensity, first noticed by Ryan et al [11] is depicted clearly in Fig. 4. The black labels represent data where the Raman Td line is not observed.

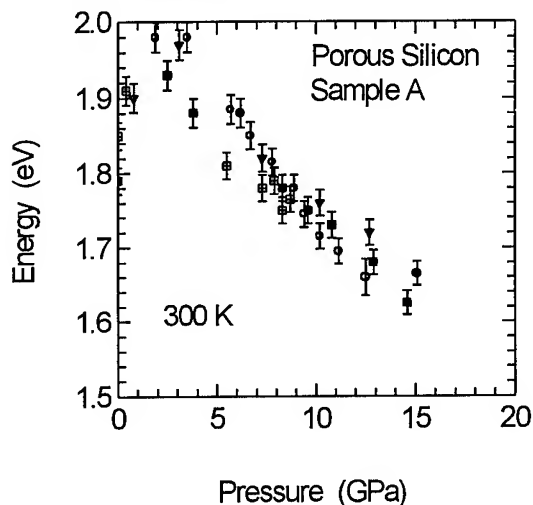


Fig. 2 - Variation of the first moment of the luminescence band as a function of pressure for a supported film of porous silicon. Open symbols correspond to spectra where the Raman line of the diamond phase is observed.

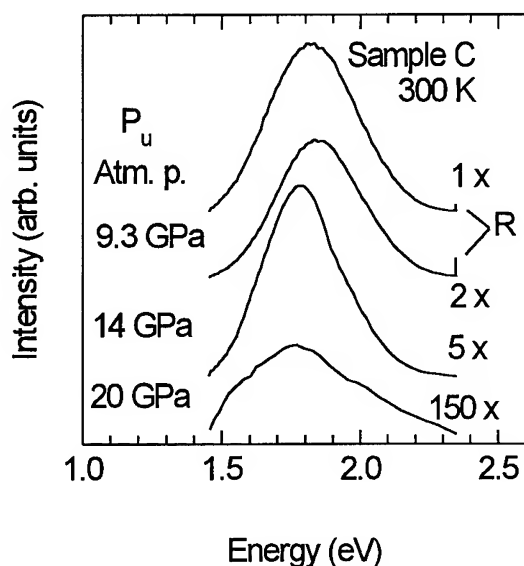


Fig. 3 - Luminescence spectra, recorded at atmospheric pressure, of free standing porous silicon samples submitted to the upper pressure  $P_u$ . The diamonds Td Raman lines (labelled R) are seen in the two upper spectra.

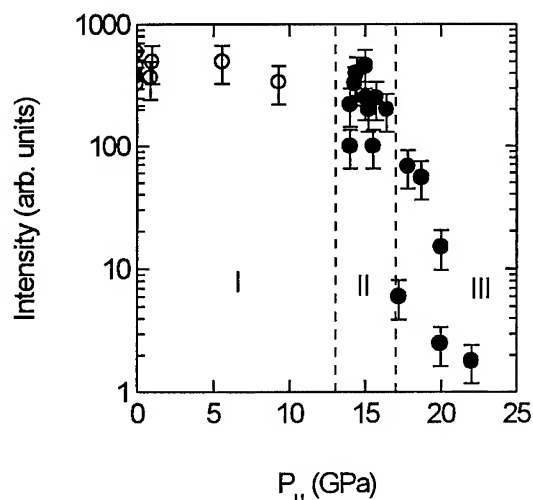


Fig. 4 - Relative intensity (measured at 1 bar) of the PS luminescence of samples pressurized to the upper pressure  $P_u$ . The data are for all samples A to E and the full symbols correspond to spectra where the Td Raman line was not detected.

This figure shows that there are three different ranges of pressures : domain I (<12-13 GPa) where the diamond phase is preserved, domain II an intermediate range between 13 and 17 GPa where the phase has changed but the main PL characteristics

are preserved and domain III an upper range of pressure where the system has undergone an irreversible transformation seriously degrading the luminescence properties of the system.

The Raman response of the sample is also very interesting to follow. Fig. 5 shows the evolution of the spectra along the pressure cycle. On increasing pressure the single Raman mode of the diamond is followed up to about 13 GPa and then disappears. At 15 GPa the spectrum shows the  $\beta$ -Sn mode at around  $420 \text{ cm}^{-1}$  and a broad band BR (dotted area). This broad band dominates at lower pressures (10.1 GPa) against the  $\beta$ -Sn signature at around  $385 \text{ cm}^{-1}$ . It persists at 7.5 GPa in the BC8 phase though its intensity has decreased. It is still observed at 1 bar. It is easy to show that this broad band is characteristic of the PS samples because it is not seen on the back side (bulk) of sample A which has been transformed [12]. Its relative strength as compared to that of the BC8 spectrum seems to be independent of the upper pressure  $P_u$  reached by the sample. In particular the Raman intensity of the band is roughly the same for strength as compared to that of the BC8 spectrum and seems to be independent of  $P_u$ . In particular the Raman intensity of the band is roughly the same

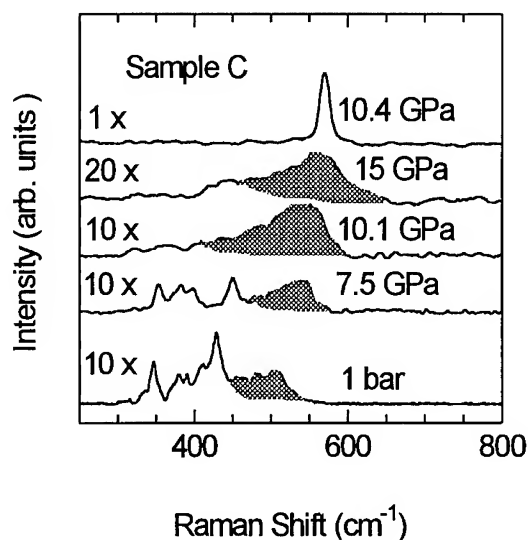


Fig. 5 - Raman spectra recorded at different pressures on the free standing PS sample. The shadowed area shows the BR band characteristic of the PS samples. In all spectra a baseline correction is applied in order to subtract the luminescence contribution.



for samples subjected to 15 or 22 GPa [12] though the luminescence intensity is quite different. All Raman data are resumed in Fig. 6. The evolution of the BR band (full dots) is compared to that of the diamond Raman line (continuous line) and to the Raman signatures of  $\beta$ -Sn and BC8 phases [7, 8]. Note that the BR band is observed for pressures higher than 17 GPa when the TO  $\beta$ -Sn Raman mode has disappeared because one is very likely entering the domain of the sh phase which has no Raman response. One can also notice that the evolution of that band follows quite closely that of the Td Raman mode at least below 13 GPa. All these results clearly show that there exists a medium distinct from pure silicon in porous silicon samples. This medium is luminescent enough to emit light whereas the substrate (Si nanocrystals) is in a metallic state ( $\beta$ -Sn and domain II of Fig. 4). This medium is then very likely located at the surface of the nanocrystallites. The pressure variation of the BR band leads to think that it partly involves Si-Si bonds, in accordance with results obtained from EXAFS measurements [13]. This is not very surprising since whatever is the nature of the luminescent medium,

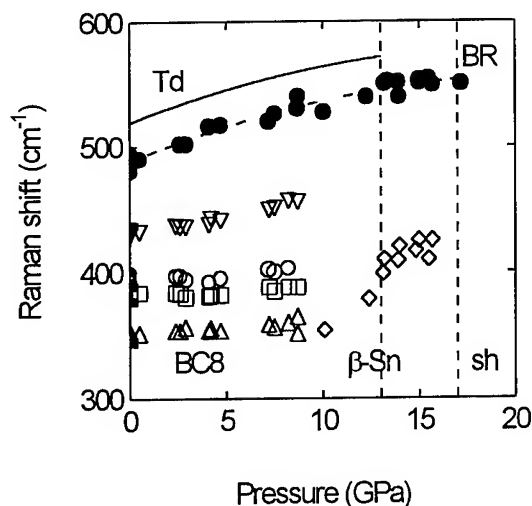


Fig. 6 - Variations of Raman features as a function of pressure; full circles: BR band ; open diamonds: mode of the  $\beta$ -Sn phase ; empty triangles, circles and squares: modes of BC8 phase. The vertical lines indicate the pressure values of the phase transitions when pressure increases. The full line characterizes the variation of the Td Raman line as observed when pressure increases, whereas the dashed line corresponds to the best fit of the experimental data of the BR band.

one expects the complex to grow at the surface of silicon. However the collapse of the PL intensity (domain III) without affecting much that of the BR band leads to think that the dipoles emitting light are involving bonds distinct from those active in the Raman band. It is, at present, difficult to explain the abrupt decrease of the PL intensity at 17 GPa. It could be due to the collapse of the PS skeleton at the second phase transition ( $\beta$ -Sn  $\rightarrow$  sh) or simply to an irreversible transition of the emitting medium.

Whatever is the answer to that question it cannot influence one of the interesting results deduced from data obtained in domain II. After the first phase transition the PS luminescence still exists with small variations of the intensity and of the mean energy which could be easily accounted for by the large volume change ( $\Delta V/V \simeq 30\%$ ) at the phase transition. How complete is the phase transition at that level can be evaluated from the Raman data at better than 99 %. Recent X-ray measurements [14] show indeed that it is better than 99.9 %. So the assumption that the PL observed after the first phase transition could be due to nanosize particles not yet transformed has to be rejected. We are then lead to conclude that the origin of the PS luminescence is very likely related to surface complexes which remain to be identified.

### Conclusion

In conclusion, the investigation of the luminescence and Raman properties of different kinds of PS samples as a function of hydrostatic pressure over a range covering different phases of silicon shows that the PS luminescence can preserve its efficiency though the sample has been structurally transformed. On those transformed samples, a specific Raman band is observed and seems to involve Si-Si bonds. All these properties strongly favor the assumption that the mechanism responsible for the strong luminescence of oxydized PS samples implies very likely surface related complexes.

### Acknowledgments:

The Grenoble High Magnetic Field Laboratory is Laboratoire associé à l' Université Joseph Fourier de Grenoble. One of us (J.Z.) acknowledges the partial support provided by the grant ESPRIT/PECO 7839.

## References

1. *Mater. Res. soc. Symp. Proc.*, **256** (1992) ; **283** (1993) ; **298** (1993)
2. L. T. Canham, *Appl. Phys. Lett.*, **57** (1990) 1046
3. T. P. Pearsall, J. C. Adams, J. E. Wu, B. Z. Noshov, C. Aw, and J. C. Patton, *J. Appl. Phys.*, **71** (1992) 4470
4. M. S. Brandt, H. D. Fuchs, M. Stutzmann, J. Weber and M. Cardona, *Solid State Commun.*, **81** (1992) 307; H. D. Fuchs, M. Stutzmann, M. S. Brandt, M. Rosenbauer, J. Weber, A. Breitschwerdt, P. Deak and M. Cardona, *Phys. Rev. B*, **48** (1993) 8172
5. J. Z. Hu and I. L. Spain, *Solid State Commun.*, **51** (1984) 263; H. Olijnyk, S. K. Sileka and W. B. Holzapfel, *Phys. Lett.*, **103A** (1984) 137
6. J. Zeman, M. Zigone, G. Martinez and G. L. J. A. Rikken, *Europhys. Lett.*, **26** (1994) 625 and *Thin Solid Films*, **255** (1995) 35
7. H. Olijnyk, *Phys. Rev. Lett.*, **68** (1992) 2232
8. M. Hanfland and K. Syassen, *Proceedings of the 12th AIRAPT and 27th EHPRG conference*, University of Paderborn 1989, (Edited by W. B. Holzapfel and P. G. Johannsen), p 242, Gordon and Breach Science Publishers (1989)
9. A. K. Sood, K. Jayaram and D. V. S. Muttu, *J. Appl. Phys.*, **72** (1992) 4963
10. Z. Sui et al, *Appl. Phys. Lett.*, **60** (1992) 2086
11. J. M. Ryan, P. R. Wamsley and K. L. Bray, *Appl. Phys. Lett.*, **63** (1993) 2260
12. J. Zeman, M. Zigone, G. L. J. A. Rikken and G. Martinez, *Solid State Commun.* (under press)
13. S. C. Bayliss et al, *Solid State Commun.*, **91** (1994) 371
14. J. Zeman, M. Zigone, G. L. J. A. Rikken, G. Martinez, D. Häusermann and M. Hanfland (to be published).

## STRUCTURAL AND OPTICAL PROPERTIES OF GaN SINGLE CRYSTALS

T.SUSKI, P. PERLIN, H. TEISSEYRE, M. LESZCZYNSKI  
I. GRZEGORY, J. JUN, M. BOCKOWSKI, S. POROWSKI

*High Pressure Research Center, Polish Academy of Sciences, ul. Sokolowska 29/37, 01 142 Warsaw,  
Poland*

### ABSTRACT

Bulk crystals of gallium nitride can be obtained by use of the high-pressure high-temperature method of crystal growth (Grzegory et al.). The samples have usually a very high crystallographic quality and may serve for evaluating the basic properties of this material. In this paper we present results of optical investigation performed at hydrostatic pressure up to 32 GPa. The following problems will be discussed: i) an origin of n-type conductivity in undoped GaN crystal and ii) a mechanism of the radiative recombination leading to the yellow luminescence observed in majority of GaN crystal.

### Introduction

GaN and its allied compounds, AlGa<sub>N</sub> and InGa<sub>N</sub>, exhibit electrical and optical properties that are well suited for applications to green/blue/ultraviolet emitters and detectors, and high temperature electronics. Most of the research is done on the epitaxial layers grown by molecular beam epitaxy (MBE) or metal-organic chemical vapor deposition (MOCVD) on sapphire or silicon carbide. Unfortunately, these substrates have a large lattice mismatch (of about 16% and 3.4% respectively) relaxed by a creation of the misfit dislocations of a very high density. The presence of dislocations, which act as non-radiative recombination centers, is the main obstacle in constructing blue-light emitting lasers. This is why there is an urgent need for bulk crystals of GaN which could be used as substrates in homoepitaxial growth.

Such bulk crystals cannot be grown from a stoichiometric melt because the melting point (about 2800 K) is much higher than the decomposition temperature (about 1300 K at 1 bar). An application of vapour phase growth is not of much help because the growth-rate below 1300 K is rather low. Another possibility is the growth from gallium solution saturated

with nitrogen at temperatures 1600-1900 K and pressures 1-2 GPa. This method is successfully used in our center (Ref. 1). In the presented paper we will show what kind of crystal defects is present in these high-pressure grown GaN bulk crystals.

In the first part we will show the main crystallographic features examined by using high-resolution X-ray diffractometry. This technique is especially useful for detecting extended defects (e.g. dislocations). In the second part we will report on the results of investigations on optical properties of GaN induced likely by the presence of native point defects. These experiments were performed at high pressure and are good examples how high-pressure helps in solving problems in semiconductor physics. In particular, we will prove the existence of a donor state resonant with the conduction band and we will shed light on the initial and final states of the radiative recombination leading the parasitic effect, so called "yellow" luminescence.

### Crystallographic properties

The samples were grown at pressures 1-2 GPa and temperatures 1500-1900 K. At every

experiment a large number (20-50) of crystals is grown, of size 0.1-10 mm. At present, we have not succeeded in finding a relation between growth conditions and crystal quality. Instead, the density of extended defects depends on the crystal size. In Fig.1 we show the typical X-ray rocking curves for crystals of different size. For a comparison we also inserted results for epitaxial layers grown on sapphire and SiC. From these figures, as well as from similar measurements for other Bragg reflections (Ref. 2) we could draw the following conclusions:

a) the GaN bulk samples of size up to 1 mm (about 0.1 mm thick) are nearly perfect. The dislocation density in these small crystals is smaller than  $10^6 \text{ cm}^{-2}$ . This finding has been confirmed by the transmission electron microscopy (Ref. 3).

b) Bigger crystals (up to about 2 mm) have the dislocation density of  $10^6$ - $10^7 \text{ cm}^{-2}$ . Some of the crystals possess unrelaxed strain. The maximum observed strain was about 0.1% for  $1 \times 0.5 \times 0.1 \text{ mm}^3$  crystal. The origin of this strain is not clear yet. It can be either caused by non-homogenous stoichiometry (including gallium inclusions) or growth stimulated by the presence of extended defects (for example, screw dislocations).

c) The crystals of lateral dimensions of 2-10 mm are mosaic. Excluding the low-angle boundaries of 1-3 arc min, the crystallites possess a similar dislocation density as smaller samples. Majority of the big crystals are not strained. This finding suggests that the low-angle boundaries are formed by relaxation of the strain at the early stage of the growth.

d) The epitaxial layer on silicon carbide possesses a very high crystallographic perfection taking into account the 3.4 % lattice mismatch between GaN and SiC. Such a mismatch is relaxed by misfit dislocations spaced by 50-100 Å of the interface region. From our diffractometric measurements the density of dislocations is estimated as  $10^8$ - $10^9 \text{ cm}^{-2}$  what indicates that the density of threading dislocations is rather small.

e) The epitaxial layer grown on sapphire is of much worse crystallographic quality. For 16% mismatch between GaN and sapphire the average distance between misfit dislocations is 10-25 Å. The density of threading dislocations is estimated as about  $10^{12} \text{ cm}^{-2}$ . For this layer also a small (0.04%) thermal strain is present. This strain is caused by a higher thermal expansion coefficient for sapphire than for GaN (Ref. 4).

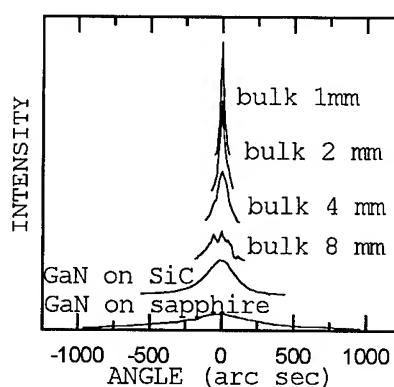


Fig.1 X-ray diffraction rocking curves of 00.4  $\text{CuK}\alpha_1$  reflection from GaN samples.

### Pressure induced freeze-out of electrons

The bulk GaN crystals possess a high concentration of free electrons ( $2\text{-}8 \cdot 10^{19} \text{ cm}^{-3}$ ). These concentrations have been measured by the Hall method, the blue-shift of the absorption edge (Burnstein-Moss effect) and by infrared reflectivity (Ref. 5).

The origin of the free electrons had been supposed to be either nitrogen vacancies or impurities (oxygen, carbon). Recently, P. Boguslawski et al. (Ref. 6) calculated by use of the first principle method that the level of the nitrogen vacancy is resonant with the conduction-band (800 meV above the conduction-band). The position of such a deep level is not significantly changed by high hydrostatic pressure, whereas the conduction-band minimum shifts up by about 40 meV/GPa. Therefore, at pressure of about 20 GPa the nitrogen-vacancy-level should enter the energy

gap. This results in a decrease of the free-electron concentration as they are captured by this level

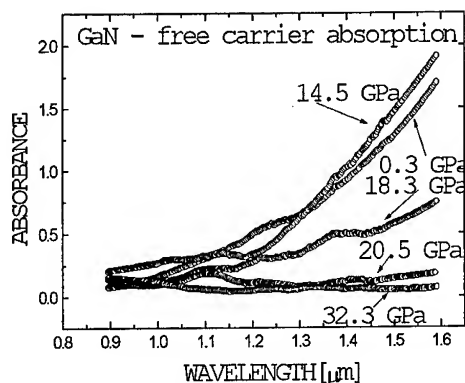


Fig.2 The pressure dependence of the absorption up to 33 GPa. For pressures lower than 20 GPa the absorption is practically constant. The absorption decrease starts at 20 GPa.

We performed a number of experiments (Ref. 7) verifying this expectation. First, we observed a decay of the infrared (IR) absorption at pressures higher than about 20 GPa (Fig. 2). At this spectral region we expect only an absorption due to the free electrons and phonons. The latter factor should not change substantially with pressure. Therefore, the observed IR absorption decay we may relate to a decrease of the free-carrier concentration.

Then, we performed Raman scattering measurements. Figure 3 shows the difference between the spectra taken at relatively low pressure and at 32.2 GPa. It can be seen, that the latter spectrum contains additional peaks. Especially significant is the presence of  $L_5$  mode which was suppressed at lower pressure by the high free-electron concentration (phonon-plasmon interaction).

### Yellow luminescence

The luminescence spectra for most of the GaN samples (bulk and epitaxial layers) contain, apart the band-edge luminescence peaks, broad band of the yellow luminescence. This parasitic effect exists in various kind of

epitaxial samples and is also observed in our bulk crystals. The origin of this peak is still not clear.

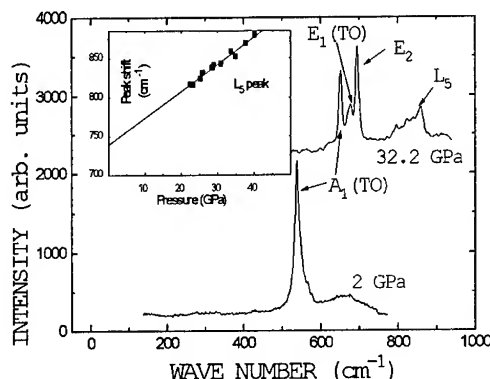


Fig.3 Comparison of two Raman spectra of bulk GaN obtain at low (2 GPa) pressure and at very high (32.2 GPa) pressure.

The yellow luminescence peak has broad and symmetrical shape and is centered at about 2.2 - 2.3 eV (at ambient pressure). In Fig. 4 we present the pressure dependence of the yellow luminescence up to about 26 GPa. The pressure coefficient of this luminescence is  $30(+/-2)$  meV/GPa and is similar to the pressure changes of the energy gap ( $dE_g/dp=40$  meV/GPa). This similarity in pressure coefficients suggests that the initial state of this transition is the conduction band (or shallow donor) and the final one should be a deep level.

Recently Glaser et al (Ref. 8) presented the result of optically detected magnetic resonance (ODMR) which indicate that a double donor state is involved in the transition responsible for the yellow luminescence. Glaser assigned that double donor level as an initial state of the considered recombination. Our high-pressure data indicates that it could be a final state. Possible candidate could be a nitrogen antisite which is a deep double donor. From the first principle calculations (Ref. 9) we know that nitrogen antisite state is in the energy gap about 700 meV above the maximum of the valence band and the pressure coefficient of this state is about 10 meV/GPa lower than  $dE_g/dp$ . These

two theoretical results agree well with our experimental observations.

However, since for GaN crystals are grown at Ga - rich conditions, nitrogen atoms could hardly form both vacancy and antisite defects therefore, it is suggestive to look for other possible defects (maybe complexes including nitrogen antisite) whose properties match to our experimental data.

Above about 20 GPa the peak position does not change any more with pressure. This observation is consistent with the previously discussed fact that at this pressure the level of the nitrogen vacancy enters the energy gap. In this situation the transition is between two deep centers whose energy levels do not change strongly with pressure.

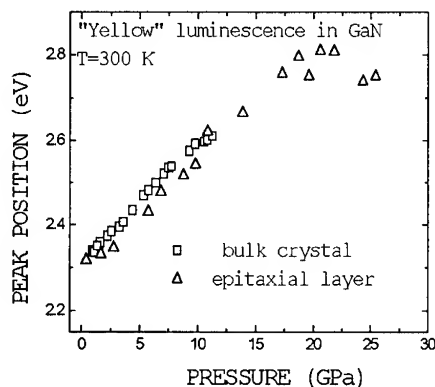


Fig. 4 The pressure dependence of the "yellow" luminescence.

## Conclusions

Small (up to 1 mm) gallium nitride crystals grown at high hydrostatic pressure, apart of high concentration of the conducting electrons and related point defects, possess a very low concentration of dislocations. This concentration is lower by a few orders of magnitude from that found in the epitaxial layers grown on the mismatched substrates. The freeze-out of electrons from the conduction band for pressure above 20 GPa is due to an emergence of a conduction band resonance into the forbidden gap. We believe that this

resonance represents a donor level caused by a nitrogen vacancy. Though less likely, Ga interstitial can be also considered as responsible for the formation of the found resonance level.

The significant blue-shift of the yellow luminescence band with pressure followed by the saturation of this variation (above ~20 GPa), strongly suggest that this effect is related to the electron transition between shallow donor (or a band state) and a deep-gap state of a donor or acceptor character.

## Acknowledgements

The work was supported by the grant of Polish Committee for Scientific Research (KBN) 288/P4/94/06

## References

- [1] S.Porowski, I. Grzegory and J. Jun. 1989 *High Pressure Chemical Synthesis* ed J. Jurczak and B. Baranowski (Amsterdam: Elsevier) p 21.
- [2] M.Leszczynski, I. Grzegory, M.Bockowski, J.Jun, S. Porowski, J.Jasinski, J.Baranowski *Acta.Phys.Polon.* (to be published)
- [3] Z. Liliental-Weber private communication
- [4] M.Leszczynski, T.Suski, H.Teisseyre P.Perlin, I. Grzegory, J.Jun and S. Porowski *J.Appl.Phys.* **76** 4909, (1994)
- [5] H.Teisseyre, P.Perlin, T.Suski, I.Grzegory, J.Jun, A. Pietraszko, T.D. Moustakas, *J.Appl.Phys.* **76**, 2429 (1994)
- [6] P. Boguslawski, E.Briggs and J. Bernholc *Phys.Rev.* **B51**, 17255 (1995).
- [7] P.Perlin, T.Suski, H. Teisseyre, M. Leszczynski, I. Grzegory, J.Jun, S. Porowski, P. Boguslawski, J. Bernholc, J.C. Chervin, A.Polian, and T.D. Moustakas *Phys.Rev.Lett* **75**, 296 (1995).
- [8] E.R. Glaser, T.A. Kennedy, K.Dover-spike, L.B. Rowland, D.K. Gaskill, J.A Freitas, M. Asif Khan, D.T. Olson, J.N. Kuznia, D.K. Wickenden, *Phys.Rev.* **B51**, 13362 (1995).
- [9] I. Gorczyca, N.E. Christensen, A.Svane *Acta.Phys.Polon.* (to be published)

# CARRIER-INDUCED STRAIN IN SILICON NANOCRYSTALS

XUE-SHU ZHAO, PETER D. PERSANS AND JOHN SCHROEDER

Department of Physics, Rensselaer Polytechnic Institute  
Troy, N.Y. 12180, U.S.A.

New experimental results on Raman scattering and photoluminescence from porous silicon under high pressure are reported. We observe anomalous pressure dependence of the PL peak energy and pressure-dependent splitting of the Raman modes. We propose that the strong luminescence in porous silicon results from strained silicon quantum dots.

## I. INTRODUCTION

In this paper, we present detailed pressure-dependent Raman scattering, photoluminescence (PL) studies on  $p^+$  and  $p^-$  porous silicon. The experimental results demonstrate that the behavior of the optical properties of porous silicon are the same as those of small silicon particles. We propose that the strong luminescence of porous silicon indeed comes from the strained silicon quantum dots residing in etched silicon. A strained silicon nanoparticle is a special Jahn-Teller system induced by sixfold degenerate electron levels, namely extended states rather than localized states. Thus the constraint of crystal momentum conservation in optical transitions is totally relaxed in small silicon particles. Raman scattering and the PL of small silicon particles are thus typical multi-phonon assisted electronic transition processes. All observed anomalous properties of porous silicon can be explained by a strained quantum dot model.

## II. EXPERIMENT

Porous silicon  $p^+$  and  $p^-$  samples were prepared by etching of  $p^+$  and  $p^-$  single crystal silicon wafers (0.01  $\Omega\text{cm}$  for  $p^+$ , 5-10  $\Omega\text{cm}$  for  $p^-$  wafer) in solutions of 20%  $\text{HF}/\text{H}_2\text{O}$ . The anodization was done with current density of about 150  $\text{mA}/\text{cm}^2$  for two hours. Both samples were prepared under the same conditions. The brown powder was collected from the top layer of the porous silicon wafer and mixed into a uniform colloid in ethyl alcohol. The colloidal absorption spectra were used to estimate the energy gap between occupied and unoccupied states for both samples. The absorption behavior of the colloid sample made from  $p^+$  porous silicon is quite similar to that of  $p^+$  silicon particles and can be well fitted with  $\alpha=A(h\nu-E_g)^2$ . The energy gap thus is found 1.98 eV for  $p^+$  porous silicon. For the  $p^-$  colloid sample, the absorption

curve can be fitted with indirect absorption relation  $\alpha=A(h\nu-E_g)^{3/2}$ . The energy gap for  $p^-$  porous silicon thus measured is about 2.05 eV. The same colloid samples were loaded in a diamond anvil cell to measure Raman scattering and PL spectra under high pressure at room temperature.

$p^+$  silicon particles were made from the same characteristic  $p^+$  silicon wafer. The x-ray and electron diffraction patterns of these small silicon particles show that the small silicon particles have the same crystal structure as that of bulk silicon. The typical size of silicon particles measured by TEM is about  $4\text{nm}\pm0.1\text{nm}$ . The energy gap (1.58 eV) between occupied and unoccupied states was obtained from absorption spectra of  $p^+$  silicon particle colloid. The silicon particle colloids were dried on stainless steel substrates for Raman scattering and PL spectra measurements at room temperature. The 488nm line of an  $\text{Ar}^+$  laser was used as the excitation source. The pressure was measured in the Diamond Anvil cell by the Ruby Fluorescence method.

## III. RESULTS

Fig. 1 shows ( $p^+$ ) the PL spectra of porous Si at several pressures. The PL peak energy at one bar for  $p^+$  porous Si are 1.74 eV. The Stokes shift between absorption and the PL is thus 0.24 eV for  $p^+$  porous silicon. In Fig. 2 we show the pressure dependence of the PL peak energy for both  $p^+$  and  $p^-$  samples. For  $p^+$  ( $p^-$ ) sample the PL peak energy shifts to higher energy with increasing pressure at the rate of 6.2 (6.5) meV / kbar up to a pressure of about 26 (17) kbar. At higher pressure the peak energy decreases with pressure at the rate of -4.1 and -2.8 meV / kbar for  $p^-$  and  $p^+$  sample respectively. The pressure coefficient of the band gap for bulk silicon is -1.4 meV / kbar over the entire pressure range<sup>[1]</sup>.

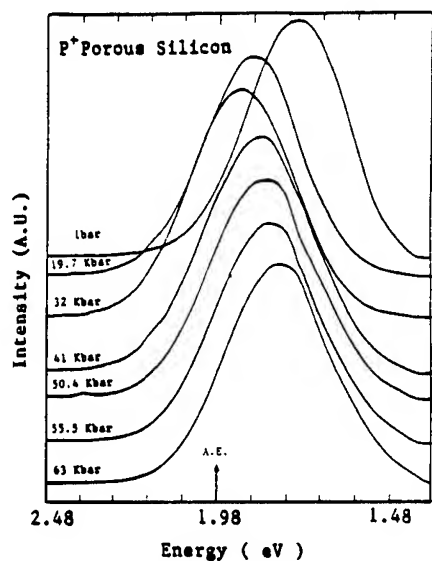


Fig. 1 Photoluminescence spectra of  $p^+$  porous silicon at different pressure at room temperature. The arrow shows the absorption edge at atmospheric pressure.

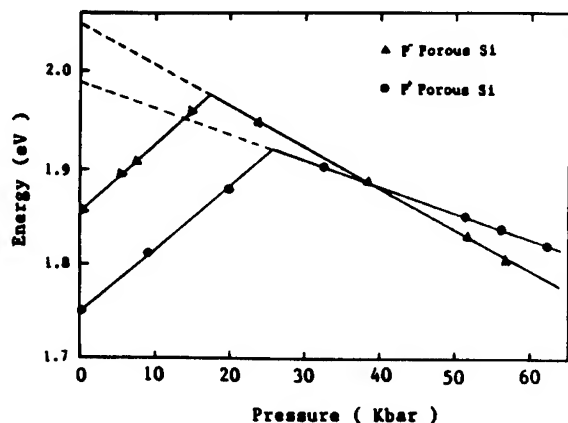


Fig. 2 The PL peak energy plotted against hydrostatic pressure ( $\Delta$   $p^-$  porous Si;  $\circ$   $p^+$  porous Si). The absorption edge 2.05 eV and 1.98 eV for  $p^-$  and  $p^+$  sample are obtained by extrapolating the negative part of the pressure coefficient to one bar.

Fig. 3 shows Raman spectra of a  $p^+$  porous Si sample for several pressures. At atmospheric pressure we observe two peaks for each sample. We assign these peaks as the T and L peaks at 515 and 490  $\text{cm}^{-1}$  respectively<sup>[2]</sup>. The T peak and L peak are downshifted from normal triplet at  $k=0$  by 5  $\text{cm}^{-1}$  and 30  $\text{cm}^{-1}$  respectively. As pressure is increased the L peak shifts to higher energy at the rate of  $+0.75 \pm 0.05 \text{ cm}^{-1} / \text{kbar}$  and

the T peak shifts at  $+0.60 \pm 0.05 \text{ cm}^{-1} / \text{kbar}$ . The pressure coefficient for bulk silicon is  $+0.52 \text{ cm}^{-1} / \text{kbar}^2$ .

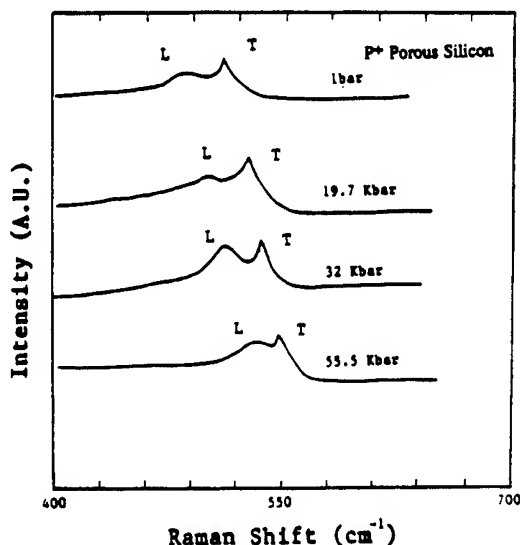


Fig. 3 The Raman scattering spectra at several pressures for  $p^+$  porous silicon.

#### IV. DISCUSSION

Studies of the pressure dependence of the band edge and luminescence peaks in porous and nanocrystalline silicon address the basic nature of the band edge states, electron-lattice coupling, and strain effects. Anomalous behavior has been observed in our measurements in which the photoluminescence peak energy first increases with pressure, up to 25-30 kbar at the rate of +4 to +9 meV/kbar and then decreases at the rate of -2 to -4 meV/kbar at higher pressures. This behavior is reversible in pressure<sup>[3]</sup>. We propose that free carriers induce strain in Si nanoparticles which is responsible for these effects. Free carriers in Si bulk materials can remarkably decrease the elastic constants for the shear strain that splits the symmetry degeneracy of the valleys<sup>[4]</sup>.

Quantum confinement greatly increases the free energy density in a nanocrystal. The increase of kinetic energy of electrons due to quantum confinement breaks down the crystalline symmetry when the nanocrystals have degenerate lowest excited states. Based on our study on Si<sup>[3]</sup>, we have proposed that strain induced by excited free carriers is a common feature of confined systems. If this effect is large enough then carrier-induced strain may explain many of the unusual properties of porous silicon.

Crystalline Si has indirect band structure. The



lowest minima of the conduction band of silicon are located on the <100> direction at a k value at 85% of the maximum value in those directions. There are six equivalent valleys in the bulk. When a nanocrystal is smaller than the free exciton diameter (~10 nm in Si), the quantum confinement effect increases the carrier kinetic energy and transforms the equivalent conduction band valleys into degenerate levels as long as the crystal geometry is cubic. In addition, the original zone center valence band degeneracy splits into heavy and light hole levels.

The key to the importance of excited free carriers in the stability of nanocrystals is the fact that a single excitation in a semiconductor particle of diameter  $\approx 2$  nm corresponds to an increase of  $10^{20}$  eV/cm<sup>3</sup> in the free energy density. The increase of free energy in a nanoparticle will lead to a lattice relaxation. The stress caused by increasing the energy  $\Delta E$  in a particle with volume  $V$  is:  $\Delta P^2 = 2\Delta E / KV$

where  $K = -(dV/dP)/V$  is the compressibility, ( $K = 1.02 \times 10^{-6}$  bar<sup>-1</sup> for bulk Si). Suppose a nanocrystal with volume  $V$  absorbs one photon with energy 2.5 eV. We further assume that on the average the excited carriers release 1 eV energy to produce lattice strain and 1.5 eV to emission of light. We have shown that a 2.5 nm particle which absorbs one photon may have a stress equivalent to 2 GPa of hydrostatic pressure, leading to photon shifts of 11 and 4.4 cm<sup>-1</sup> for  $\Gamma$  and TA(X) modes respectively<sup>[5]</sup>.

This simple strain model above gives the order of magnitude for hydrostatic strain. Of course one would expect excited carriers to produce uniaxial strain as well, which results from degenerate excited states. We note that small particle shape alone will lead to splitting of some degeneracies even in the absence of any other anisotropy. These effects must also be taken into account in any model for optical and phonon properties of nanoparticles. If we assume that the relaxational energy for the lower four levels results from electron-phonon coupling, we can estimate the order of magnitude for the splitting of the six-fold degenerate conduction band edge in silicon due to the presence of a free electron in that band. Neglecting the strain effect on the heavy hole, the uniaxial stress in the <100> direction should be<sup>[5]</sup>

$$P = \frac{3S\hbar\omega}{\epsilon_u (S_{11} - S_{12})}$$

where  $S$  is the electron-phonon coupling strength,  $\hbar\omega/2\pi$  is the optical phonon energy,  $\epsilon_u$  is the shear deformation potential (8.3 eV for Si) and  $(S_{11} - S_{12})$  is the elastic compliance constant ( $9.75 \times 10^{-3}$  GPa<sup>-1</sup>). Shear strain of

this magnitude will influence basic optical properties of any indirect gap semiconductor. Aside from energy shifts, optical cross sections, and carrier lifetimes will be altered.

A positive strain along the <100> direction in Si will thus split the six-fold conduction band states into two groups. Two levels will move up by  $2\Delta E$ , while the other four levels move down by  $\Delta E$  with respect to the weighted average of the six levels. The hydrostatic part of the dilatation strain will move the weight of the levels up at the rate of 15 meV/GPa<sup>[6,7]</sup>.

The results shown in Figures 2 and 3, namely the apparent Stokes shift of the PL peak and change in the pressure coefficient suggests that the particles are strained by excited carriers and the splitting in the vibrational modes suggests a low pressure distortion which decreases as pressures increases. These results seem to be qualitatively consistent with the above discussion.

## V. SUMMARY AND CONCLUSION

Based on the investigation of Raman and PL spectra for porous silicon and small particles, we demonstrate that porous silicon and small silicon particle have the same optical properties which are dominated by strain induced by extended electron states. All anomalous optical properties observed from porous silicon can be explained by the strained quantum dot model. In this model, crystal momentum conservation required in optical transition is totally relaxed due to strain induced by excited free carriers. So the PL and Raman scattering in a small silicon particle are typical multiphonon assisted electron transition processes.

## ACKNOWLEDGEMENT

This work was partially supported by the NSF under Grant NSF DMR-9104086.

## REFERENCES

1. W. Paul and D. M. Warshauer, *Solids under Pressure*, (McGraw-Hill, NY 1963), p. 222.
2. C.J. Buchenauer, F. Cerdeira and M. Cardona, in *Light Scattering in Solids*, ed. Balkanski, (1971), p. 280.
3. X.S. Zhao, P.D. Persans, J. Schroeder, and Y.J. Wu, *MRS Symp. Proc.* **283** (1993), 127.
4. R. W. Keyes, in *Solid State Physics* **20**, (1967), p. 37.
5. X.S. Zhao, Y.R. Ge, J. Schroeder, and P.D. Persans, *Appl. Phys. Lett.* **65** (1994), 2033.
6. M.F. Li, X.S. Zhao, Z.Q. Gu, J.X. Chen, Y.J. Li and J.Q. Wang, *Phys. Rev. B* **43** (1991), 14040.
7. V.J. Tekippe, H.R. Chandrasekhar, P. Fisher, and A.K. Ramdar, *Phys. Rev. B* **6** (1972), 2348.

# RESONANT RAMAN SCATTERING AND PHOTOLUMINESCENCE IN II-VI SEMICONDUCTOR NANOCRYSTALS: ENHANCED HIGH PRESSURE PHASE STABILITY

JOHN SCHROEDER, MARKUS R. SILVESTRI, LIH-WEN HWANG AND PETER D. PERSANS

Department of Physics, Rensselaer Polytechnic Institute  
Troy, N.Y. 12180, U.S.A.

We report pressure dependent optical studies for different sized  $\text{CdS}_x\text{Se}_{1-x}$  nanocrystals embedded in a glass matrix. The increased phase stability of wurtzite to rock salt structure is reversible and size dependent. Different possible sources such as strain from defects, semiconductor to glass matrix thermal expansion mismatch, increase in the electronic energy due to confinement, and surface tension which may cause this effect are discussed. Results indicate that surface tension is the major contribution and a simple model is used that produces estimates of the size distribution and difference of the surface tensions in the two phases.

## I. INTRODUCTION

Many studies have found changes in the thermodynamic properties of II-VI semiconductor nanocrystals such as reduction of the melting temperature<sup>[1,2]</sup> or an increase in the structural phase transition pressure point<sup>[3-9]</sup>. This is a novel phenomenon: The stability of nanocrystals can be controlled by an external parameter such as the size. Tolbert *et al.*<sup>[3,4]</sup> conducted a series of studies on nearly monodisperse CdSe nanocrystals in a colloidal suspension and confirmed a size dependence which was attributed to surface tension. However, similar size dependent studies have not been performed on nanocrystals embedded in a solid glass matrix, which is a composite that has promising potential for technical applications<sup>[10]</sup>. The diffusion grown nanocrystals in a glass matrix pose in many ways a different problem with respect to phase stability. Strains, a broad size distribution, and a low concentration of the nanocrystals complicate the picture.

It is the goal of this paper to examine these effects in more detail. A model is used that can account for the observed enhanced phase stability of the nanocrystals. This model, which we had developed previously, is based on the difference of the surface tension in both phases<sup>[11]</sup>.

## II. EXPERIMENT

As samples we used Schott filters RG630 and OG570. These filters are composite materials based on borosilicate glass containing  $\text{Cd}_x\text{Se}_{1-x}$  crystallites. Their compositions were determined through the relative shift between the S-like and Se-like peak positions in the

Raman spectra<sup>[9]</sup> and their sizes by TEM<sup>[12]</sup> or by x-ray diffraction through the Debye-Scherrer broadening. The composition of RG630 and samples grown from its melt<sup>[12]</sup> is  $\text{CdS}_{0.44}\text{Se}_{0.56}$  and their sizes are given in the legend of Fig. 3.

For the pressure measurements the samples were polished down to about 40 - 80  $\mu\text{m}$  thickness and then loaded into a diamond anvil pressure cell, which is described in detail elsewhere<sup>[7]</sup>. A 4:1 methanol-ethanol mixture served as a pressure medium. The pressures were measured with the standard ruby fluorescence technique. The shape of the ruby lines and their spacing did not alter indicating that hydrostatic pressure was well maintained throughout all our experiments.

All optical experiments were carried out at 135° scattering geometry at room temperature unless otherwise noted. This setup has the advantage of higher collection efficiency and better signal to noise ratio compared to the 180° backward scattering geometry.

## III. RESULTS AND DISCUSSION

Typical photoluminescence spectra of C6 grown from the melt of RG630 is shown in Fig. 1. The strong band edge luminescence peaks in the energy range of 2.0 - 2.2 eV are clearly visible at pressures far beyond the bulk structural phase transition pressure point (~ 30 kbar at room temperature). In CdS the high pressure rock salt phase has an indirect band gap of about 1.5 eV and a similar reduction is also expected for CdSe; thus, the band edge luminescence at high pressure clearly indicate that nanocrystals remain in the low pressure wurtzite structure.

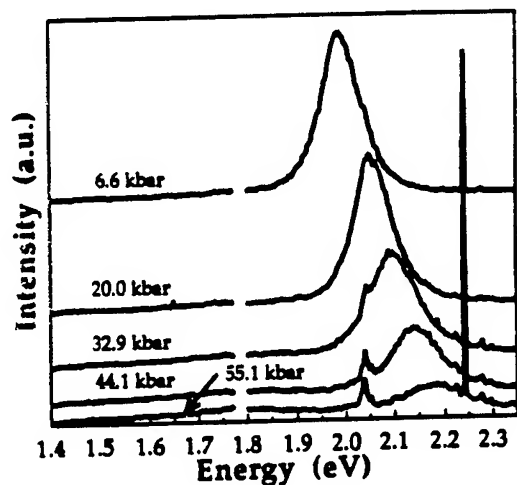


Fig. 1 Typical photoluminescence spectra of sample C6 at different pressures at room temperature. The spike around 2.25 eV is due to the diamond anvil and the emerging peak at around 2.05 eV is from the pressure transmitting medium. Note the emergence of a broad deep level defect at high pressures.

This experimental observation is further supported by the Raman spectra: Raman lines typical for the wurtzite structure persist up to the same high pressures. However, for quantitative estimates, the Raman lines are difficult to interpret since they are also subject to resonance effects<sup>[13]</sup>. Also, at high pressures, broad featureless peaks of a deep level defect are visible. At room temperature they are not easy to make out nevertheless are present and are more distinct at liquid nitrogen temperature.

In Fig. 2 the energy positions of the band edge and deep level defect peaks for C6 are plotted as a function of pressure. The different energy shift of the deep level defect with respect to the band edge indicates that the defect is situated closer to the conduction band edge than the valence band edge.

The filled symbols in Fig. 2 represent measurements returning from high pressure. There is no hysteresis or shifts in position from the initial atmospheric pressure point. Neither was any significant hysteresis or shifts in the Raman spectra detected in contrast to 30 nm crystallites<sup>[14]</sup> and bulk material<sup>[15]</sup>. When bulk material is cycled through a phase transition, it breaks up into many small crystallites which in turn cause local strains; hence the changes. Venkateswaren *et al.*<sup>[16]</sup> observed that bulk GaAs and AlAs films break up into 6.5 and 17.5 nm sized crystallites with corresponding shifts in the Raman spectra

after cycling through a high pressure phase. Assuming that similar critical sizes exist for our composites, the results here indicate that the crystallites apparently do not break up into smaller pieces.

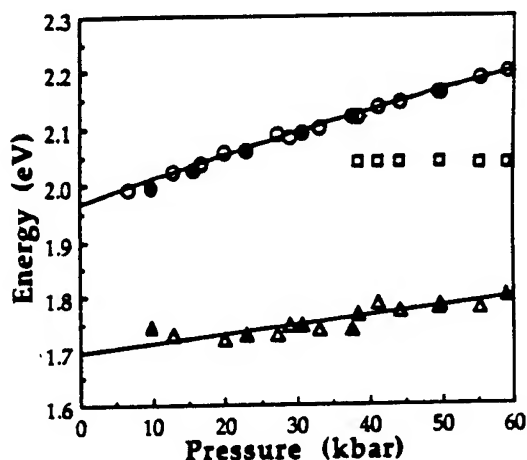


Fig. 2 Pressure dependence of the energy position of the band edge and defect luminescence peaks of C6.  $\square$  are the peaks from the pressure medium. open  $\Delta$  represent increasing pressure and filled  $\Delta$  represent decreasing pressure.

The relative intensities of the band edge luminescence for nanocrystals of four different average sizes are given in Fig. 3. In order to compare the different samples, the intensities were normalized to the average intensity of measurements that were taken below the bulk phase transition pressure point. Increased phase stability with decreasing size is observable. A number of effects may account for this phenomenon. The most important are: effects from the glass matrix, strains, from defects, changes in the electronic energy due to confinement, and surface tension.

We have shown previously<sup>[11]</sup> that effects from the glass matrix, strains from defects, and changes in the electronic energy due to confinement contribute energetically too little to the total free energy of the nanocrystallites to be responsible for the pressure enhanced phase stability. Surface tension however may certainly be the mechanism that brings about the enhanced high pressure phase stability in the nanocrystallites. If the surface tension in the rock salt phase is larger than in the wurtzite phase, the Gibbs free energy will not be minimum, due to its additional energy term, and this energy must be overcome in the phase transition.

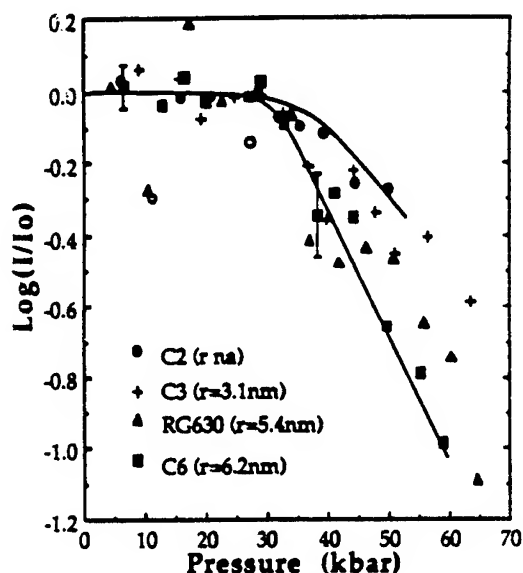


Fig. 3 Phase stability for different average sized nanocrystals. The luminescence intensities were normalized to the average intensities below 30 kbar. Open figures were considered as outliers. The lines are only guides for the eye to appreciate the change in phase stability.

The result is a shift in the phase transition pressure to higher values. In a solid the temperature dependence of the surface tension is very small, consequently the surface tension is nearly equal to the surface energy. Higher surface tension in the rock salt phase is expected since the rock salt structure has a higher coordination number than wurtzite structure. A surface atom in the rock salt phase has on the average more bonds, meaning that it will have a greater inward attraction or potential energy. Such a model has been constructed<sup>[11]</sup> and it does give a qualitative explanation to the observed pressure enhanced phase stability of nanocrystallites.

#### IV. SUMMARY AND CONCLUSION

From photoluminescence and Raman spectra measurements we found that the structural phase transition induced by pressure in nanocrystalline systems is quite different from bulk material. The phase transition in bulk is sharp<sup>[15]</sup> but for nanocrystals it is broad and occurs at higher pressures. A size study of the phase stability was conducted and a correlation between size and increase in phase stability was definitely established.

Of the several possible "sources" causing this effect glass matrix, defects, confinement, and surface

tension, it was found that three of them are unlikely. For the remaining possible cause, surface tension was shown to be the responsible mechanism.

#### ACKNOWLEDGEMENTS

The authors gratefully acknowledge NSF support under DMR-88-01002 and the DARPA OSP-17816-5079.

#### REFERENCES

1. A.N. Goldstein, C.M. Echer, and A.P. Alivisatos, *Science*, **256**, (1992), p. 1425
2. P. Buffat and J.P. Borel, *Phys. Rev. A*, **13**, (1976), p. 2287.
3. S.H. Tolbert and A.P. Alivisatos, *Science*, **265**, (1994), p. 373.
4. S.H. Tolbert, A.B. Herhold, C.S. Johnson, and A.P. Alivisatos, *Phys. Rev. Lett.*, **73**, (1994), p. 3266.
5. A.P. Alivisatos, T.D. Harris, L.E. Brus, and A. Jayaraman, *J. Chem. Phys.*, **89**, (1988), p. 5979.
6. M. Haase and A.P. Alivisatos, *J. Phys. Chem.*, **96**, (1992), p. 6756.
7. X.S. Zhao, J. Schroeder, P.D. Persans, and T.G. Bilodeau, *Phys. Rev B*, **43**, (1991), p. 12580.
8. X.S. Zhao, J. Schroeder, M.R. Silvestri, T.G. Bilodeau, and P.D. Persans, in *Clusters and Cluster Assembled Materials*, ed. R.S. Averback, J. Bernholc, and D.L. Nelson, MRS Symposia Proceedings No. 206, (Materials Research Society, 1991), p. 151.
9. J. Schroeder et al., in *Chemical Processes in Inorganic Materials: Metal and Semiconductor Clusters and Colloids*, ed. P.D. Persans, J.S. Bradley, R.R. Chianelli and G. Schmid, MRS Symposia Proceedings No. 272, (Materials Research Society, 1990), p. 251.
10. N.M. Lawandy and R.L. MacDonald, *J. Opt. Soc. Am. B*, **8**, (1991), p. 1307.
11. M.R. Silvestri and J. Schroeder, *J. of Phys: Condensed Matter*, **7**, (1995).
12. G. Mei, S. Carpenter, L.E. Felton, and P.D. Persans, *J. Opt. Soc. Am. B*, **9**, (1992), p. 1394.
13. M.R. Silvestri and J. Schroeder, *Phys. Rev. B*, **50**, (1995), p. 15108.
14. B.F. Variano, N.E. Schlotter, D.M. Hwang, and C.J. Sandroff, *J. Chem. Phys.*, **88**, (1988), p. 2848.
15. X.S. Zhao, J. Schroeder, T.G. Bilodeau, and L.G. Hwa, *Phys. Rev. B*, **40**, (1989), p. 1257.
16. U.D. Venkateswaren, L.J. Cui, and B.A. Weinstein, *Phys. Rev. B*, **45**, (1992), p. 9237.

# ELECTRICAL CONDUCTIVITY AND THERMO-EMF OF THE HIGH PRESSURE PHASE OF CdX AND ZnX (X= O, S, Se, Te)

A.N.Babushkin, O.A.Ignatchenko

Department of Physics, Urals State University, Ekaterinburg,  
620083, Russia

## ABSTRACT

Electrical conductivity and thermo-EMF pressure dependencies (10 - 50 GPa) of a wide group of  $A_2B_6$  semiconductors have been studied in the diamond anvil cell with the anvils of the "rounded cone-plane" (Verechagin-Yakovlev) type at 77 - 400 K. Some general regularities of electron property changes of compounds studied, the conditions for the electric conductivity and thermo-EMF baric hysteresis (CdSe, CdTe, ZnTe) and the irreversible changes of properties after pressure treatment (CdS, ZnO, ZnS, ZnSe) are discussed.

## Introduction

In the wide temperature and pressure range physical property's cadmium and zinc chalcogenides are well known. At pressures higher than 10 GPa in this one exists structure transitions that accompanied by an electron structure transformations: sudden resistivity change, colour alteration, changes thermoEMF sign. In CdS, ZnO, ZnS, ZnSe after pressure treatment irreversible changes of physical properties take place. In this article we analyse the results of experimental investigation's cadmium and zinc chalcogenides resistivity and thermoEMF at wide pressures (15 - 50 GPa) and temperatures (77 - 400 K) ranges.

## Experimental procedure

High pressures have been generated in the diamond anvil cell (DAC) with anvils the "rounded cone-plane" (Verechagin-Yakovlev) type made of synthetic carbonado-type diamonds [1]. These diamonds are good conductors, permitting us to measure the resistance temperature and pressure dependencies and the thermal electromotive force (TEMF) of the sample placed between the anvils in the DAC using the anvil as the electrical contacts to the sample. The DAC resistivity without the sample is several ohms in magnitude and increases slightly in the temperature range 4.2-400 K. Thus, if we study the kinetic properties of samples whose resistivity is greater than the resistivity of the DAC without a sample, the anvils will not significantly influence on the dependencies under study.

Control measurements of the TEMF have been made on Cu and Si samples. The results are in good agreement with the data obtained in [2].

The estimation of pressure magnitude in our DAC is not easy since the pressure obtained depends on the elastic properties of the compressed layer and anvils as

well the anvil geometry. The procedure for estimation of the pressure magnitude reached in a DAC of Verechagin-Yakovlev-type has been described in our previous works [3,4].

The elastic layer thickness value used in the pressure estimations has been measured with an interference microscope. The radius of the conic anvil curvature (1.0-1.3 mm in the different anvils) has been measured with a micrometer microscope. The different thicknesses of the samples measured at the position of anvil contact after the pressure treatment are 2 - 15  $\mu\text{m}$ .

## Results and discussion

**CdO.** CdO alone from cadmium and zinc chalcogenides at normal pressures crystallise in NaCl-type structure (see table). Electrical resistivity in pressure range 20 - 50 GPa decrease monotonously by one order of magnitude and in temperature range 77 - 400 K has an activation nature. TEMF gradually decreases with pressure increase. This results show that in study temperature and pressure ranges crystal and electron structure radical changes absent.

**CdS.** At pressures about 29 GPa the electron structure changes take place. It is manifested through the nonmonotonicity of baric dependence of the electron activation energy and is the cause of the resistivity maximum [6,7]. After pressure treatment sample has irreversible changed its colour and resistivity. Transition to the metal like state (with positive temperature resistivity coefficient (TRC)) not been found.

**CdSe.** Above 250 K resistivity's temperature dependencies have a positive TRC in pressure range 25 - 50 GPa. The high pressure phase is rather a degenerate semiconductor (semimetal) with low charge carrier density (see table) [8]. The transition to phase with positive TRC (at room temperature) is revealed a baric hysteresis of the resistivity and thermoEMF.

Table

Charge carrier characteristics (type, chemical potential  $\xi$ , charge density  $n$ ) and resistivity at appropriate pressures (room temperatures) for materials under investigations. Thermoelectric power data use for estimate  $\xi$  and  $n$  in state with positive temperature resistivity coefficient. Materials with irreversible transitions asters marked.

Material (structure type)	Carrier type	$\xi$ eV	$n$ $10^{18} \text{ m}^{-3}$	$\rho$ Ohm*cm	Anion-cation distance, nm
ZnS* (sphalerite)	n	0.15 (50 GPa)	0.026 (50 GPa)	~ 1 (22 GPa) ~ 0.1 (50 GPa)	0.235
ZnSe* (sphalerite)	n (P<33 GPa) p (P>33 GPa)	1 (50 GPa)	0.45 (50 GPa)	~ 10 (22 GPa) ~ 1 (50 GPa)	0.245
ZnTe (sphalerite)	p (P<30 GPa) n (P>30 GPa)	1.46 (50 GPa)	0.81 (50 GPa)	~ 0.1 (50 GPa)	0.263
CdTe (sphalerite)	p (P<30 GPa) n (P>30 GPa)	3.65 (50 GPa)	3.2 (50 GPa)	~ 0.01 (50 GPa)	0.280
ZnO* (wurtzite)	p (P<40 GPa) n (P>40 GPa)	7-10 (P>40 GPa)	10 (P>40 GPa)	300 (22 GPa) 100 (50 GPa)	0.211
CdS* (wurtzite)	n	-	-	~ 10000 (22 GPa) ~ 100 (50 GPa)	0.252
CdSe (wurtzite)	n	0.09 (22 GPa) 0.36 (50 GPa)	0.01 (22 GPa) 0.1 (50 GPa)	~ 10 (22 GPa) 0.6 (50 GPa)	0.262
CdO (NaCl)	n	-	-	50 (22 GPa) 3 (50 GPa)	0.230

**ZnO.** Conductivity determined by activation mechanism at low temperatures. After temperature increase to a certain critical point (near 250 K) the positive TRC occurs. At 35 - 40 GPa the baric dependence of resistivity and activation energy have a minimum. The studies of the influence of pressure cycling on ZnO electrophysical properties have provide the probability of the structural transition to the high pressure phase at pressures below 20 GPa.

**ZnS.** The experimental results demonstrate that the transition at about 16 GPa at room temperature occurs from a state with the low conductivity to the high conducting phase with positive TRC [9-11]. This phase is more likely to be a degenerate semiconductor (semimetal) with the low conduction electron density (see table). At the low temperatures (below 200 K) conductivity has activation nature in the all pressure range under investigation. The singularities of the resistance, thermoEMF and activation energy at pressures 41-47 GPa associate with a modification of the electron spectrum. After pressure treatment sample has the colour and resistivity irreversible changes.

**ZnSe.** The conductivity between 22-35 GPa is of activation nature and the predicted "dielectric (semiconductor) - metal" transition at 12 - 13 GPa is

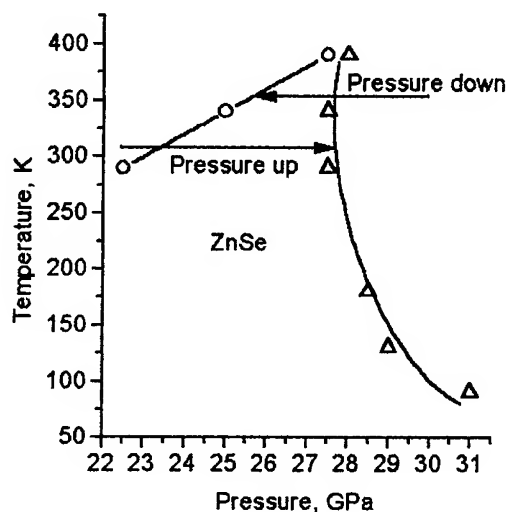
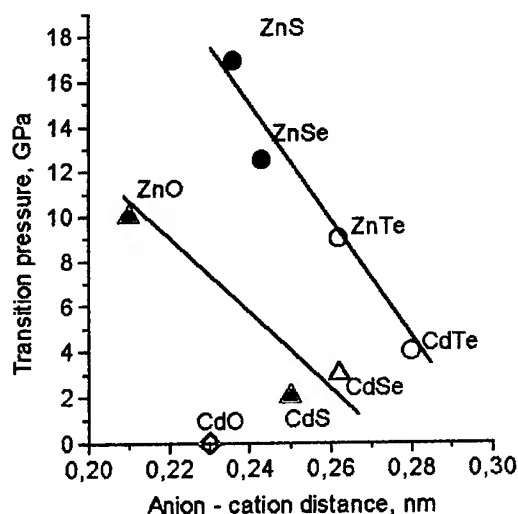


Fig.1. ZnSe P-T diagram for transition to state with positive TRC.

not found [12,13]. The overlap of the valent and conduction bands can be expected at about 35 GPa. We fixed the resistivity and TEMF baric hysteresis after ZnSe pressure cycling at temperatures higher 300 K (fig.1). At temperatures below 300 K after pressure treatment sample has the colour and resistivity irreversible changes.

**CdTe and ZnTe.** The predicted presence of the state with positive TRC at 20 - 30 GPa [14, 15] between 77 - 370 K has been validated [16]. The further temperature increase involves the change of conductivity from the metal-like to the activation type. At 30 - 50 GPa ZnTe has the activation conductivity, but CdTe has conductivity with positive TRC (see table). The resistivity baric hysteresis have been fixed after pressure cycling.

In the table the information about materials under investigations — chemical potential  $\xi$ , charge carrier density  $n$  (both in the state with positive TRC), charge carrier type and resistivity is summarized. All (exclude  $\rho$ ) data have been estimated from TEMF at appropriate pressures.



We see, that the transition reversibility (after pressure treatment) is connect with the initially structure (sphalerite or wurtzite) and anion—cation distance (at normal pressures) (fig.2). After pressure treatment the reversible transitions detected if the cation—anion distance at normal pressures higher then 0.26 nm. In other cases after high pressure treatment irreversible electrical characteristics and colour changes take place.

Fig.2. Correlation's between the anion-cation distance (at normal pressure) in CdX and ZnX (X = O, S, Se, Te) and the transition pressure to the state with NaCl-type structure. Initially phase is sphalerite (circle) or wurtzite (triangle). Open symbol - the reversible transition, solid symbol - the irreversible transition. CdO at normal pressure has NaCl-type structure.

## References

1. L.F. Verechagin, E.N. Yakovlev, G.N. Stepanov et al., *JETP Lett.*, **16** (1972) 169.
2. V.V. Stchennikov, *Raspilavy*, **2** (1988) 33.
3. A.N. Babushkin, *High Pressure Res.*, **6** (1992) 349.
4. A.N. Babushkin, G.I. Pilipenko and F.F. Gavrilov, *J. Phys.: Condens. Matter*, **5** (1993) 8659.
5. A.P. Makushkin, *Sov. J. Friction and Wear* **6** (1984) 823.
6. G.A. Samara and A.A. Giardini, *Phys. Rev.* **140** (1965) 388.
7. A.N. Babushkin, G.V. Babushkina, L.Ya. Kobelev et al., *Izv. Akad. Nauk SSSR Neorg. Mater* **27** (1991) 1147.
8. O.A. Ignatchenko and A.N. Babushkin, *Phys. Solid State* **35** (1993) 2231.
9. S. Minomura, G.A. Samara and H.G. Drickamer, *J. Appl. Phys* **33** (1962) 3196.
10. S. Block, G.J. Piermarini, R.G. Munro and E. Fuller, *Physica A (Utrecht)* **156** (1989) 341.
11. A.N. Babushkin, *Sov. Phys. Solid State* **34** (1992) 875.
12. G.A. Samara and H.G. Drickamer, *J. Phys. Chem. Sol.* **23** (1962) 457.
13. O.A. Ignatchenko and A.N. Babushkin, *Phys. Solid State* **35** (1993) 3313.
14. Jing Zhu Hu, *Solid State Commun.* **63** (1987) 471.
15. A. San-Miguel, A. Polian, J.P. Itie et al., *Phys. Rev.* **48** (1993) 8683.
16. O.A. Ignatchenko and A.N. Babushkin, *Phys. Solid State* **36** (1994) 3596.

# HIGH PRESSURE STUDY OF IMPURITY STATES IN CUBIC GaN AND AlN CRYSTALS

I. GORCZYCA

*High Pressure Research Center PAN, Sokolowska 29, 01-142 Warsaw, Poland*

A. SVANE, N.E. CHRISTENSEN

*Institute of Physics, Aarhus University, DK-8000 Aarhus C, Denmark*

We performed self-consistent calculations of the electronic structure for impurities in cubic GaN and AlN for different values of hydrostatic pressure. We used the Green-function matrix technique based on the linear muffin-tin orbital method in the atomic-spheres approximation. Nitrogen antisite and substitutional acceptor impurities - Zn, Mg, Cd in different charge states are investigated. Resulting positions of the impurity levels at atmospheric pressure are compared with the results of some experiments and pseudopotential calculations. Pressure dependences of the impurity levels are studied in comparison with experimental data.

## 1 Introduction

Little is known about point defects and their properties in semiconducting nitrides. Such states may increase the density of point charges with a consequent decreasing of mobility. Deep levels might trap electrons or holes, leading to enhanced non-radiative recombination rates and luminescence degradation. Also autocompensation, involving the interaction between dopant atoms and doping-generated point defects, can limited the range of applications. It is also important very important for applications to find schemes for doping the material both  $n$  and  $p$  type.

In this paper we concentrate on some point defects as Nitrogen antisite, Zn, Mg, and Cd, in the most important representatives of nitrides - GaN and AlN. We examine effects of applying hydrostatic pressure. Changes of the impurity levels with pressure for some defects are compared with other theoretical and experimental results.

Both, GaN and AlN can crystalized in two phases, the cubic and wurtzite phase. We focus here on the cubic one believing that there is no substantial difference in impurity level positions between these two phases and conclusions arising from the present calculations can be applied to wurtzite phase as well.

This work is a continuation of the previous one on points defects in cubic GaN<sup>1</sup>, where some native defects (vacancies and antisites) and Zn, C, Ge dopants were analysed shortly.

## 2 Method

The 'first-principles' linear muffin tin orbital (LMTO) Greens function method<sup>2</sup> is used to perform our calculations. This method is based on the local-density approximation (LDA)<sup>3</sup> to density-functional theory (DFT), by which exchange and correlation effects are accounted for by a simple local potential. In LDA approximation the fundamental gaps of semiconductors generally are computed 50-100% too small. This is overcome in our case by rigidly shifting the conduction bands upwards (the 'scissors operator').

The valence electronic structure of the impurity atom is obtained from the solid Greens function  $G$ , which is found by solving the Dyson equation:  $G = G^0 + G^0 \Delta V$  where  $G^0$  is the Green's function of the pure crystal host and  $\Delta V$  the perturbation due to the impurity<sup>2</sup>. In the LMTO method the host Greens function is calculated from the band structure of the pure crystal with the atomic sphere approximation (ASA), i.e., the crystal volume is approximated by slightly overlapping atom centered spheres, inside which the potential is taken spherically symmetric. Additional 'empty' spheres are introduced centered on the tetrahedral interstitial sites<sup>4</sup>. In this work we choose all spheres to have the same size determined by the experimental host lattice constant. In the calculations we have used the 'standard' basis set which includes partial waves of  $s$ ,  $p$ , and  $d$  character on each atomic and interstitial site to give a total of 36 LMTO orbitals per unit cell. The



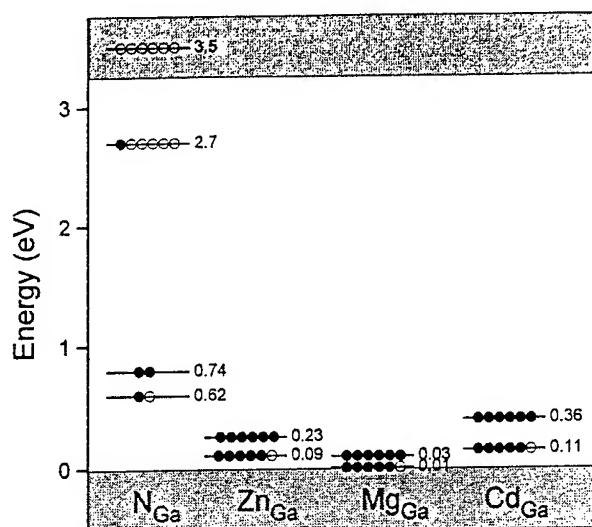


Figure 1: Impurity level positions in GaN

unperturbed Greens function is calculated with the tetrahedron method using 95 k points in the irreducible edge of the Brillouin zone. The impurities considered are all ideal substitutional ones, i.e., no relaxation of the neighboring atoms is allowed for.

### 3 Positions of the defect levels

#### 3.1 GaN

At first we will discuss the positions of the defect levels in GaN. The main energy gap in zinc-blende-structure GaN, calculated by us<sup>5</sup> is 3.25eV. Our results for nitrogen antisite,  $N_{Ga}$ , and for substitutional acceptors:  $Zn_{Ga}$ ,  $Mg_{Ga}$ , and  $Cd_{Ga}$  are shown in Figure 1, where the positions of defects levels in neutral and charged states are indicated.

In the neutral charge state  $N_{Ga}$  introduces a doubly occupied singlet at 0.74eV above the v.b. maximum and an empty doublet at 3.5eV (0.25eV above the conduction band minimum). These values can be compared with the results of the pseudopotential calculations<sup>6</sup>. As it is shown in Fig.1, the charged state occupied only by one electron is lying somewhat lower - at 0.62eV and corresponding doublet at 2.7eV.

One of the most interesting dopant in GaN is Zn - not effective as an acceptor but crucial for the blue luminescence. There are some experimental

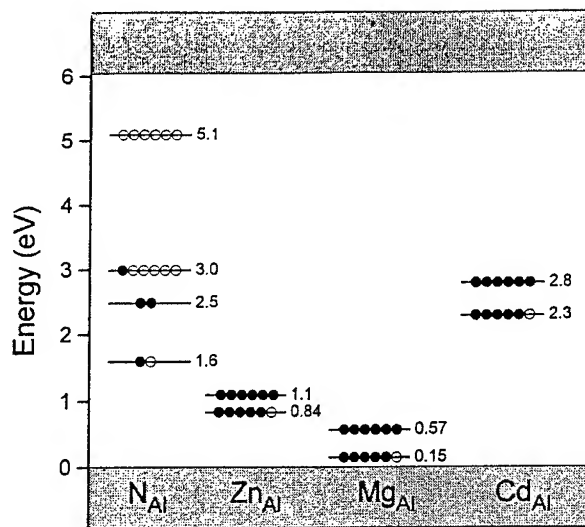


Figure 2: Impurity level positions in AlN

evidences that Zn introduces several deep states in GaN<sup>7</sup>. The Zn on Ga site ( $Zn_{Ga}$ ) forms a shallow acceptor state - our result is 0.23eV for charged and 0.09eV for the neutral state, in a good agreement with the experimental data (0.34eV<sup>8,9</sup>).

We have also calculated the level positions for two other acceptors: Cd and Mg on the Ga site. In both cases we have got the shallow acceptor levels - Cd-neutral state is situated 0.11eV and Mg-neutral state only 0.01eV above the maximum of the valence band. Charged states are lying slightly above.

#### 3.2 AlN

There are similar tendencies in the defect levels positions in GaN and AlN, but the absolute values are different mainly due to the different values of the energy gaps. The main energy gap of AlN in the zinc-blende structure as calculated by us<sup>5</sup> is equal 6.1eV, being almost twice bigger than for AlN.

The results for nitrogen antisite,  $N_{Al}$ , and for substitutional acceptors:  $Zn_{Al}$ ,  $Mg_{Al}$ , and  $Cd_{Al}$  are shown in Figure 2, where the positions of defects levels in neutral and charged states are indicated.

Analogically to GaN -  $N_{Al}$  in the neutral charge state introduces a doubly occupied singlet at 2.5eV above the valence band maximum - closer

to the middle of the energy gap comparing with GaN, and an empty doublet at 5.1eV - also in the energy gap (in the GaN case it is resonant with the conduction band). Generally, sequence of states is the same, but relative positions are not.

Considering the substitutional acceptors:

-  $Mg_{Al}$  forms the shallowest acceptor state, our result is 0.57eV for charged and 0.15eV for the neutral state.

-  $Zn_{Al}$  states are lying slightly above, at 1.1eV and 0.84eV, respectively.

-  $Cd_{Al}$  forms the deepest acceptor state, close to the middle of the band gap, at 2.3eV and 2.8eV for neutral and charged state, respectively.

#### 4 High pressure behaviour

The pressure behaviour was studied for two different types of states: 1) deep donor-like state - N-antisite, 2) shallow acceptors - Zn, Mg, and Cd.

For each of the case we have calculated the energy positions of defect levels at the pressure values: 5, 10, 20 and 24 GPa.

##### 4.1 GaN

The pressure coefficient of the main energy gap calculated by us is 38meV/GPa<sup>5</sup>.

As results from our calculations the deep donor-like level coming from  $N_{Ga}$  is shifted up with respect to the valence band edge with the pressure coefficient 6meV/GPa (32meV/GPa down with respect to the conduction band).

In the case of the shallow acceptors we found that the defect states does not shift with pressure with respect to the valence band ( $Mg_{Ga}$ ) or are shifted slightly  $Zn_{Ga}$  - about 1meV/GPa and  $Cd_{Ga}$  - 9meV/GPa.

We can see from the above, that the pressure coefficient values are proportional to the values of the corresponding level positions.

##### 4.2 AlN

The pressure coefficient of the main energy gap calculated by us is 42 meV/GPa<sup>5</sup>.

Higher values of the level positions in AlN results in higher values of the corresponding pressure coefficients.

Going from the higher to lower positions of the states we have: for  $N_{Al}$  - 26meV/GPa (neutral

charge state), for  $Cd_{Al}$  - 17meV/GPa, for  $Zn_{Al}$  - 7meV/GPa, and for  $Mg_{Al}$  - 1.5meV/GPa.

Concluding, high pressure behaviour of the defect states, both in GaN and in AlN, depends on the position of the state in the band gap and it seems that it does not depend on the type of state (donor, acceptor).

#### References

1. I. Gorczyca, A. Svane, and N.E. Christensen, *Acta Phys. Polon.* **9**, 175 (1995).
2. O. Gunnarson, O. Jepsen, and O.K. Andersen, *Phys. Rev. B* **27**, 7144 (1983).
3. R.O. Jones and O. Gunnarson, *Rev. Mod. Phys.* **61**, 681 (1989).
4. D. Gltzel, B. Segall, and O.K. Andersen, *Solid State Commun.* **9**, 175 (1971).
5. N.E. Christensen and I. Gorczyca, *Phys. Rev. B* **50**, 4397 (1994).
6. P. Boguslawski, to be published.
7. B. Monemar, *Phys. Rev. B* **10**, 676 (1974).
8. R. Dingle and M. Heger, *Solid State Commun.* **9**, 175 (1971).
9. T.L. Tansley and R.J. Egan, *Mat. Res. Soc.* **242**, 395 (1992).

# EFFECT OF PRESSURE ON DIRECT OPTICAL TRANSITIONS IN InSe FROM PHOTOREFLECTANCE SPECTROSCOPY

C. Ulrich<sup>1</sup>, A. R. Goñi<sup>1</sup>, K. Syassen<sup>1</sup>, O. Jepsen<sup>1</sup>, A. Cantarero<sup>2</sup>, and V. Muñoz<sup>2</sup>

<sup>1</sup>*Max-Planck-Institut für Festkörperforschung, 70569 Stuttgart, Germany*

<sup>2</sup>*Universidad de Valencia, 46100 Burjassot, Spain*

We report photoreflectance (PR) measurements on  $\gamma$ -InSe in the spectral range from 1.1 to 3 eV at room temperature and pressures up to 8 GPa. Up to four well resolved structures are observed in the PR spectra corresponding to direct interband transitions in InSe. The energy of the lowest optical transition exhibits a strong nonlinear dependence on pressure. For the assignment of the observed transitions LMTO band structure calculations within the local density approximation were performed. The nonlinear behavior of the lowest transition energy is well reproduced by the LMTO calculations.

## 1 Introduction

Indium selenide is a layered semiconductor characterized by a strong anisotropy in chemical bonding. The layers consist of In-In dumbbells oriented perpendicular to the layers and sandwiched between Se sheets. The In-In and In-Se bonds within the layers are of the covalent type, whereas bonding between the layers is much weaker. Four possible layer stacking sequences give rise to the four polytypes  $\beta$ ,  $\epsilon$ ,  $\gamma$  and  $\delta$ . Bridgeman growth InSe crystals are usually of the  $\gamma$ -polytype with a rhombohedral (trigonal) crystal structure (space group  $R\bar{3}m$ ).<sup>1,2</sup> As a consequence of the pronounced anisotropy in bonding the crystal axes compressibilities parallel and perpendicular to the layers differ significantly.<sup>3</sup> This, for instance, leads to strong nonlinearities in the pressure dependence of physical properties.<sup>4</sup>

In this work we have studied the pressure dependence of the direct optical transitions of  $\gamma$ -InSe using photoreflectance (PR) spectroscopy. The motivation was to investigate the pressure dependence of interband excitations above the fundamental gap energy (1.23 eV at zero pressure). A second aspect of this work is to assign the observed optical excitations to interband transitions and to get a better understanding of the strong nonlinear shift of the fundamental band gap. For this purpose we have performed tight-binding LMTO calculations.

## 2 Experimental

The InSe samples were grown by the Bridgeman method and uniformly doped ( $n \simeq 10^{17} \text{ cm}^{-3}$ )

by neutron transmutation of  $^{115}\text{In}$  in  $^{116}\text{Sn}$ .<sup>5</sup> The doping enhances the build-in electric field resulting in a larger PR signal. For high pressure experiments the samples were cleaved perpendicular to the (001) direction (thickness  $17 \mu\text{m}$ ) and then cut into pieces of about  $100 \times 100 \mu\text{m}^2$  in size. Pressure was applied using a gasketed diamond-anvil cell with a 4:1 methanol-ethanol mixture as pressure transmitting medium. All measurements were carried out at room temperature.

The PR setup used here is similar to that described in the literature.<sup>6,7</sup> The variable-wavelength probe beam of constant photon flux and the photomodulation source (He-Cd laser, 325 nm line) were focused onto the same spot of the sample ( $50 \mu\text{m}$  diameter). The reflected probe light was detected by a Si diode. A double lock-in technique was used, where the probe and laser beam are chopped at different frequencies and where the PR signal is measured at the sum frequency.

## 3 Results and Discussion

Figure 1 shows a PR spectrum of InSe at ambient pressure. The arrows indicate the transition energies obtained from lineshape fits using Aspiners third derivative functional form.<sup>8</sup> There are four clearly resolved features labelled A (1.228(5) eV),  $E'_1$  (2.430(8) eV), C (2.513(20) eV), and  $E_1$  (2.764(15) eV).

Transition energies as a function of pressure are given in Fig. 2. The lowest energy transition exhibits a pronounced nonlinear pressure behavior. With increasing pressure its energy decreases first, reaches a minimum at about 0.5 GPa

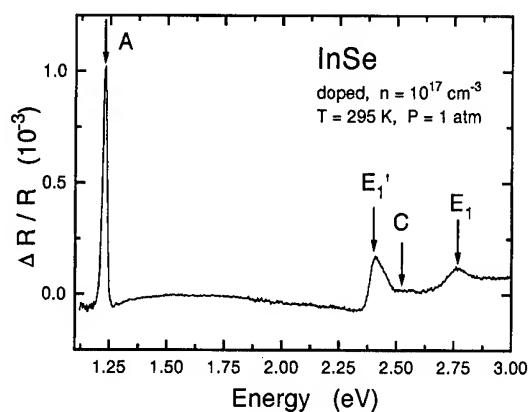


Figure 1: Photoreflectance spectrum of  $\gamma$ -InSe measured at room temperature and ambient pressure. The arrows correspond to the transition energies obtained from line-shape fits.

and then increases strongly at higher pressures (average rate above 2 GPa is 55(5) meV/GPa). This behavior is in good agreement with previous absorption studies.<sup>4,9</sup> In contrast, the energies of the higher-lying transitions increase almost linearly with pressure (e.g., by 28(3) meV/GPa for the  $E_1'$  transition).

To assign the observed optical transitions to interband excitations we have performed self-consistent tight-binding LMTO-ASA calculations in the local density approximation (LDA)<sup>10,11</sup> for the  $\gamma$ -polytype. The calculations are scalar relativistic, thus the spin-orbit coupling is not taken into account. The zero pressure lattice parameters ( $a = 4.001$  Å and  $c = 25.13$  Å) and interatomic distances were taken from x-ray data.<sup>2,3</sup>

Figure 3 shows the calculated band structure of  $\gamma$ -InSe. In contrast to the  $\beta$  modification<sup>12</sup> the lowest direct transition is located at the Z point of the rhombohedral Brillouin zone (zone boundary in direction perpendicular to the layers). This is consistent with results from pseudopotential calculations for  $\gamma$ -InSe.<sup>13</sup> Feature A in the PR spectra corresponds to the fundamental gap transition. Features  $E_1'$  and  $E_1$  are assigned to direct optical transitions between the second and third uppermost valence bands (VB) and the conduction band (CB) minimum. Transition C possibly arises from the splitting of the degenerate second and third uppermost VBs due to spin-orbit coupling.<sup>13</sup> The gap energies calculated here are about 0.6 eV

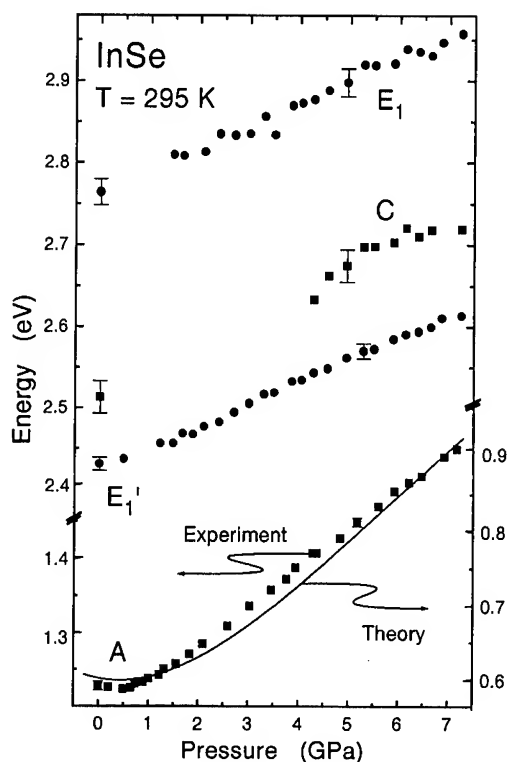


Figure 2: Pressure dependence of the measured transition energies (symbols) in  $\gamma$ -InSe. The solid line represents the results of LMTO calculations.

smaller than the experimental ones, which reflects the characteristic effect of the LDA methods to underestimate the energies of the CB states.

For LMTO calculations at reduced volume we assumed that the layers are compressed isotropically, with compression given by the change in  $a$ -axis. The stronger change in the length of the  $c$ -axis<sup>3</sup> is mainly due to the decrease of the interlayer separation. The change in length of the In-In bond was assumed to be that of InS.<sup>14</sup> In the atomic spheres approximation (ASA), additional "empty spheres"<sup>15</sup> are introduced. Under pressure calculations were done always with the same number of spheres. The overlap between spheres stayed nearly constant.

The solid curve in Fig. 2 represents the result of the LMTO calculations for the lowest band gap of  $\gamma$ -InSe under pressure. (shifted up by 0.64 eV in order to facilitate comparison with experimental data). In spite of the LDA error in the absolute value of the gap energy, the experimental and cal-

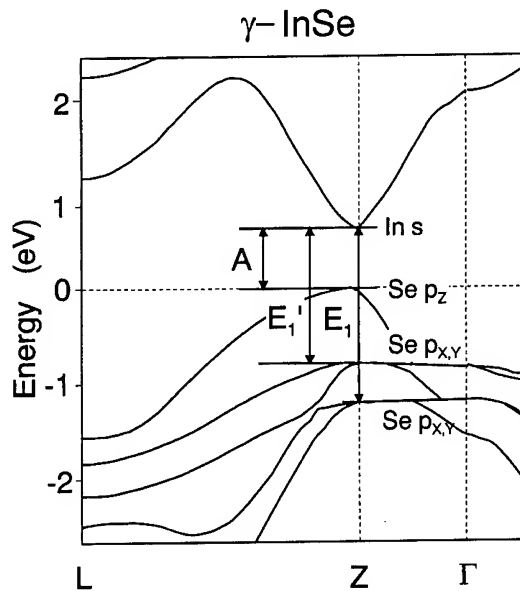


Figure 3: Band structure of  $\gamma$ -InSe obtained from LMTO-calculations (spin-orbit splitting is omitted).

culated pressure dependencies agree quite well for the lowest gap.

The nonlinear pressure dependence of the lowest optical gap can be explained as follows: The CB minimum at the Z-point is mainly formed by antibonding In  $s$  states. The crystal field splits the selenium  $4p$  levels such that the main contribution to the uppermost VB arises from antibonding Se  $p_z$  states. The interlayer interaction is mediated by the Se  $p_z$ -orbitals. With increasing pressure both the CB minimum (In  $s$ ) and the top of the VB (Se  $p_z$ ) rise in energy. At low pressures the decrease of the interlayer separation dominates the compression of the crystal, and therefore the top of the VB rises more rapidly in energy than the CB minimum, resulting in a decrease of the fundamental band gap under pressure. At higher pressures compression becomes more isotropic. Now the energy increase of the CB edge with pressure overcomes that of the VB maximum, and the band gap increases with pressure. The initial VB states for the higher-lying transitions are mainly of Se  $p_x$  and  $p_y$  character. These states are less sensitive to the initial decrease of the interlayer separation, and therefore the related interband transitions show no pronounced nonlinearities.

In conclusion, we have determined the pressure dependence of four direct optical transitions of  $\gamma$ -InSe by photoreflectance measurements at room temperature for pressures up to 7.3 GPa. The energy of the lowest band gap of InSe shows a pronounced nonlinear pressure dependence with a minimum at 0.5 GPa. This behavior is interpreted in terms of tight-binding LMTO band structure calculations as due to the anisotropy of intralayer and interlayer bonding and the particular Se  $p_z$  and In  $s$  antibonding character of the valence and conduction band edges, respectively.

#### 4 References

1. A. Likforman, D. Carre, J. E. Bachet, and B. Bachet, *Acta Crystallogr. Sect. B* **31**, 1252 (1975).
2. J. Rigault, A. Rimskey, and A. Kuhn, *Acta Cryst. B* **36**, 916 (1980).
3. U. Schwarz, A. R. Goñi, K. Syassen, A. Cantarero, and A. Chevy, *High Press. Res.* **8**, 396 (1991).
4. A. R. Goñi, A. Cantarero, U. Schwarz, K. Syassen, and A. Chevy, *Phys. Rev. B* **45**, 4221 (1992).
5. B. Mari, A. Segura, and A. Chevy, *Appl. Surface Science* **50**, 415 (1991).
6. J. L. Shay, *Phys. Rev. B* **2**, 803 (1970).
7. O. J. Glembocki, and B. V. Shanabrook, *Semiconductors and Semimetals* vol. **36**, 221 (1992).
8. D. E. Aspnes, *Surface Sci.* **37**, 418 (1973).
9. N. Kuroda, O. Ueno, and Y. Nishina, *J. Phys. Soc. Japan* **55**, 581 (1986).
10. O. K. Andersen, *Phys. Rev. B* **12**, 3060 (1975).
11. TB-LMTO-ASA program of G. Krier, O. Jepsen, A. Burkhardt, and O. K. Andersen.
12. M. Piacentini, E. Doni, R. Girlanda, V. Grasso, and A. Balzarotti, *Nuovo Cimento* **B54**, 269 (1979).
13. P. Gomes da Costa, R. G. Dandrea, R. F. Wallis, and M. Balkanski, *Phys. Rev. B* **48**, 14135 (1993).
14. U. Schwarz, H. Hillebrecht, and K. Syassen, *Z. Kristallogr.* **210**, 494 (1995).
15. D. Glözel, B. Segall, and O. K. Andersen, *Solid State Commun.* **36**, 403 (1980).

# THE U-PARAMETER AND OPTICAL PROPERTIES UNDER PRESSURE ON AgGaS<sub>2</sub>

Y.MORI<sup>a</sup>, K.TAKARABE<sup>a</sup>, Y.KANDA<sup>a</sup>, S.MINOMURA<sup>a</sup>, E.NIWA<sup>b</sup> and K.MASUMOTO<sup>c</sup>

<sup>a</sup>Department of Physics, Okayama University of Science, Ridai, Okayama 700, Japan

<sup>b</sup>Res. Inst. Electr. Mag. Mater., 2-1-1 Yagiyama-minami Taihakuku, Sendai 982, Japan

<sup>c</sup>Ishinomaki Senshu University, 1 Shin-mito, Minami-sakai, Ishinomaki 986, Japan

## ABSTRACT

The tetragonal distortion ( $c/a$ ) and anion displacement ( $u$ -parameter) of AgGaS<sub>2</sub> were studied under high pressure by using the Rietveld refinement (RIETAN-94). The ratio  $c/a$  decreased with increasing pressure, but the  $u$ -parameter remained to be constant within the experimental error of  $\pm 2\%$ . The bond compressibilities of Ag-S and Ga-S bonds were almost same.

## Introduction

Ternary chalcopyrite ABX<sub>2</sub> is slightly deformed from an ideal zinc-blende(ZB) structure due to unequal two bond lengths  $R_{AX} \neq R_{BX}$ . Its crystal structure is characterized with the tetragonal distortion ( $\eta=c/a \neq 2$ ) for two principal  $a$ - and  $c$ -axis and the parameter  $u$ . The  $u$ -parameter describes the anion(X) displacement in the  $c$ -plane along the  $a$ -axis and is related with the inequality of two bonds:

$$u = \frac{1}{4} + \frac{R_{AX}^2 - R_{BX}^2}{a^2}.$$

Silver gallium disulfides (AgGaS<sub>2</sub>) investigated in this experiment are largely deformed ( $\eta=1.79, u=0.29$ ) in ternary chalcopyrites at an atmospheric pressure.

According to Keating model calculation of phonon for AgGaS<sub>2</sub>, the ratio of stretching force constant  $\alpha(\text{Ag-S})/\alpha(\text{Ga-S})$  is estimated to be 0.38[1], which suggests that the Ag-S bond is much weaker than the Ga-S bond. We report the result of X-ray diffraction measurement and atomic position under high pressure before the first phase transition( $\sim 4\text{GPa}$ )[2].

## Experimental

AgGaS<sub>2</sub> crystal were grown by a Bridgeman method. A gasketed diamond-anvil cell techniques was used with a 4:1 mixture of

ethanol and methanol as a pressure transmitting medium. Pressure was determined by a ruby fluorescence technique. Powder X-ray diffraction pattern under high pressure were recorded up to 23 GPa on a two-dimensional imaging plate (IP) using synchrotron radiation source at the Photon Factory National Laboratory (PF) in Japan. The obtained diffraction patterns were analyzed by using the Rietveld refinement (RIETAN-94[3]).

## Results and Discussion

### Lattice constants under pressure

The observed and calculated powder X-ray diffraction profile for AgGaS<sub>2</sub> at 4.14GPa is

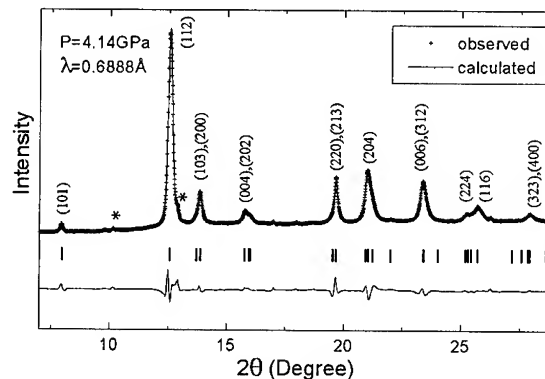


Fig. 1. X-ray powder diffraction pattern (+) of AgGaS<sub>2</sub> at 4.14GPa with the calculated curve(line) by Rietveld refinement.

shown in Fig.1. The R-factors for the refinement are smaller than 4% in all experimental runs. In the case of Fig.1, the R-factors  $R_{wp}$ ,  $R_e$  and  $R_F$  are 3.81%, 1.49% and 0.31%, respectively. The higher pressure phase appears at the angle of about 10 and 13 degree (\*) at this pressure. The lattices  $a$  and  $c$  and the volume were decreased by 1%, 2.5% and 4% at 4 GPa, respectively. Thus, the tetragonal distortion ( $\eta=c/a$ ) decreased by 2% at 4 GPa, or more distorted under pressure[4]. According to fitting of the compression curve up to 4 GPa with Birch's equation, the bulk modulus  $B_0$  of  $\text{AgGaS}_2$  is evaluated to be 62 GPa. It is smaller than that of the binary analog of  $\text{Zn}_{0.5}\text{Cd}_{0.5}\text{S}$  (70 GPa).

#### The atomic position

Figure 2 shows the pressure dependence of the  $u$ -parameter. It shows that the  $u$ -parameter remains unchanged within the experimental error of  $\pm 2\%$ . The change of two bonds (Ag-S and Ga-S) under pressure are shown in Fig.3 with the both calculated compression curves for bonds under the constant  $u$ -parameter. It is seen that both compressibilities are almost same, though the large difference exists in the stretching force constants between both bonds.

The values of three angles at ambient pressure are  $\text{Ag-S-Ga}=106.0^\circ$ ,  $\text{S-Ga-S}=108.7^\circ$  and  $\text{Ag-S-Ga}_{(2)}=114.7^\circ$ , respectively. Their pressure dependences up to 4 GPa are shown in Fig.4 with the calculated line upon the constant  $u$ -parameter. Three angles have the same absolute compressibility within the experimental error.

If the tetragonal distortion and the  $u$ -parameter are the same as the ambient pressure values, those angles are constant under pressure. The  $u$ -parameter is constant from Fig.2, thus the change in the bond angles is due to the decrease of  $\eta$  under pressure.

*The correlation between the distortions and optical properties.*

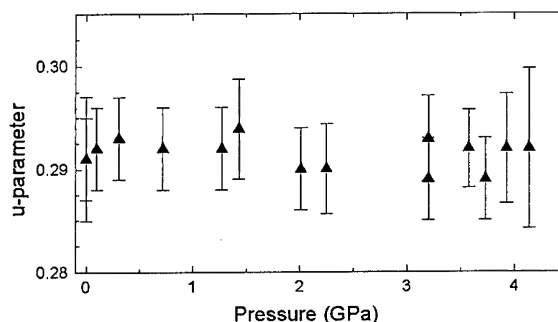


Fig. 2. Pressure dependence of the  $u$ -parameter for  $\text{AgGaS}_2$  evaluated by two experimental runs. The  $u$ -parameter remains unchanged within the error by  $\pm 2\%$ .

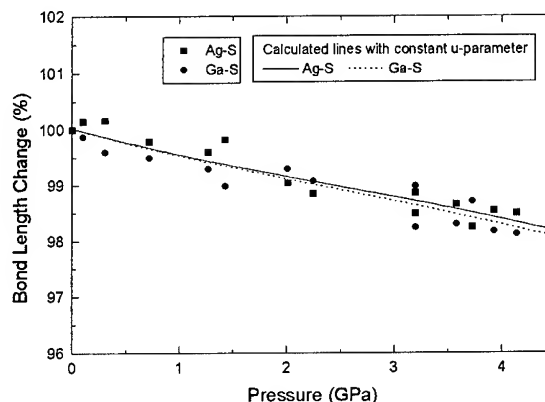


Fig. 3. Pressure dependence of the compressibilities of Ag-S and Ga-S bonds with calculated lines upon the constant  $u$ -parameter under pressure.

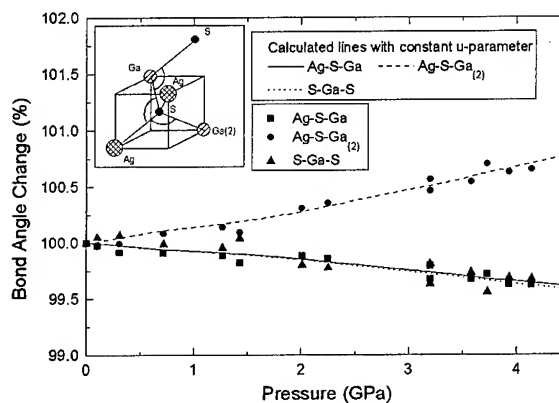


Fig. 4. Pressure dependence of the bond angles with calculated upon the constant  $u$ -parameter under pressure.

Both of a  $p$ - $d$  hybridization between  $d$ -orbital (noble atom) and  $p$  orbital (chalcogen atom) and a crystal-field splitting determine a fine-electronic structure near the top of the valence band in chalcopyrite. The reflection studies on  $\text{AgGaS}_2$  under pressure shows that the splitting at the valence-band top decreases with increasing pressure[4]. The above X-ray study shows that the tetragonal distortion decreases and the Ag-S bond length decreases with increasing pressure. Accordingly, the crystal-field splitting at the top of valence band and the  $p$ - $d$  hybridization increase under pressure. These results are a key to consider the electronic structure of the chalcopyrite under pressure.

#### References

- [1] W.H.Koschel *et. al.*, *phys. Stat. sol.*, (b) 72 (1975) 729.
- [2] A.Werner *et. al.*, *Phys. Rev.*, B23 (1981) 3836.
- [3] F.Izumi "The Rietveld Method", ed. by R.A.Young, Oxford Univ. Press, (1993), Chap. 13; Y. -I. Kim and F.Izumi, *J. Ceram. Soc. Jpn.*, 102(1994)401.
- [4] K.Takarabe *et. al.*, Proc. 14th AIRAPT Conf. (in Colorado Springs, 1993).



# OBSERVATION OF RESONANT DEFECT STATES IN HEAVILY CARBON DOPED GaAs UNDER HYDROSTATIC PRESSURE

UMA D. VENKATESWARAN

Department of Physics, Oakland University, Rochester, MI 48309 USA.

J. BAK and R. SOORYAKUMAR

Department of Physics, The Ohio State University, Columbus, OH 43210 USA.

S. SUBRAMANIAN

Department of Electrical & Computer Eng., Oregon State University, Corvallis, OR 97331 USA.

A set of sharp lines is observed in low temperature photoluminescence (PL) from heavily carbon doped MBE grown GaAs epilayers (GaAs:C) at high pressures. The energy positions and pressure shifts of these transitions compare well with those of nitrogen trap bound excitons observed in n-type GaAs. We discuss an alternate possibility that these transitions might arise from near donor-acceptor pair recombinations involving deep donor states which are resonant in the conduction band at atmospheric pressure but emerge into the band gap at high pressures. We speculate that  $C_{Ga} - C_{As}$  pairs might be responsible for these sharp transitions in heavily doped GaAs:C samples.

Carbon is an unintentional background impurity in GaAs grown by molecular beam epitaxy (MBE). Heavily carbon doped GaAs (GaAs:C) is increasingly being used in modern devices such as heterojunction bipolar transistors. Thus, a study of carbon doping in GaAs is important for the understanding of both the fundamental aspects and device operation. In this paper, we present a study of the hydrostatic pressure dependence of low temperature photoluminescence (PL) from heavily doped GaAs:C.

Two samples of GaAs:C (labeled B and C) grown on semi-insulating GaAs substrate using MBE, with carrier concentration  $p = 3.5$  and  $8.5 \times 10^{19} \text{ cm}^{-3}$  and epilayer thickness of 1.0 and 0.75  $\mu\text{m}$  respectively, were used in this study. PL was excited with 488 nm laser line. At 20 K with low laser power densities ( $< 10 \text{ W/cm}^2$ ), a broad main peak due to near-band-edge excitonic emission and a high energy shoulder are observed. The high energy peak has been previously interpreted as indirect transitions from the conduction band (CB) minimum to the Fermi level[1,2] or as vertical transitions from CB to the light hole valence band[3,4]. We observe in both our samples B and C that: (a) the relative intensities of the PL peaks change significantly as the laser power increases between 10 and 2000  $\text{W/cm}^2$ ; and (b) the low energy peak is dominant at high excitation intensities. Preliminary analysis of this excitation power dependence supports vertical transitions for the origin of the high energy peak better than stress indirect transitions to the Fermi level. Uniaxial

measurements would help in deciding if light holes are involved in this transition.

Figure 1 displays the PL spectra of sample B recorded at 20 K for several pressures using a diamond anvil cell. The behavior in sample C is essentially the same. The sharp peak at  $\sim 1.52 \text{ eV}$  in the 1 bar spectrum, denoted as  $D_T(s)$  in Fig. 1, is due to the emission from the substrate and it serves as an internal reference. The broad main peak ( $D_T^0$ ) seen at  $\sim 1.46 \text{ eV}$  is identified as the band to band emission from the GaAs:C epilayer. Its energy position is consistent with the band gap narrowing expected for  $p = 3.5 \times 10^{19} \text{ cm}^{-3}$ . Around 3 GPa, a few sharp peaks riding on the low energy side of  $D_T^0$  are observed. Near the  $\Gamma$ -X CB cross-over pressure ( $\sim 4.2 \text{ GPa}$ ), a second broad peak ( $D_X$ ) is seen. For  $P \geq 4 \text{ GPa}$ , the sharp peaks are seen more clearly, superposed now on  $D_X$  since their pressure coefficients are about five times smaller than that of  $D_T^0$ .

The inset in Fig. 1 gives the plot of the energy positions of  $D_T^0$  and the strongest of the sharp peaks as a function of pressure.  $D_T^0$  and  $D_T(s)$  shift at  $\sim 0.102 \text{ eV/GPa}$ , which is typical of the  $\Gamma$ -CB in GaAs.[5,6] Although it is hard to locate accurately the peak position of  $D_X$  due to the superposition of several sharp peaks, a red shift of  $\sim -0.01 \text{ eV/GPa}$  can be deciphered. All sharp peaks have a blue shift of  $\sim 0.02 \text{ eV/GPa}$ .

The power dependence of the PL in sample B near the  $\Gamma$ -X CB cross-over pressure is shown in Fig. 2. At low excitation densities ( $\sim 10 \text{ W/cm}^2$ ),  $D_X$  is dominant indicating an efficient transfer of

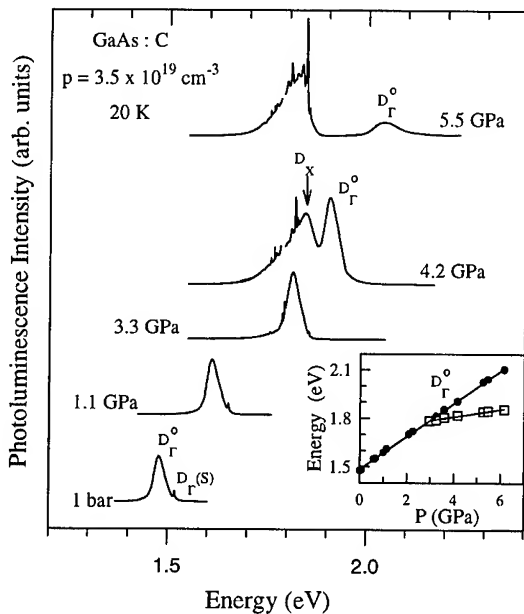


Fig. 1. PL spectra of sample B at 20 K for several pressures.  $D_r(s)$  denotes emission from the substrate and  $D_r^0$ ,  $D_x$ , and the sharp peaks are from GaAs:C epilayer. The pressure shifts of  $D_r^0$  and the most intense sharp transitions are shown in the inset.

electrons from  $\Gamma$ - to X-CB. As we pump more carriers into  $\Gamma$ -CB, there is a competition between vertical recombinations ( $D_r^0$ ) and scattering to X-CB which is evident from the changes in the relative intensities of  $D_x$  and  $D_r^0$  (see Fig. 2). Notice that the sharp peaks are stronger at high excitation powers. The intensity of  $D_r^0$  scales almost linearly with excitation power density whereas that of  $D_x$  exhibits a saturation at high laser powers. The observed pressure coefficient and laser power dependence of  $D_r^0$ ,  $D_x$ , and all the sharp transitions in GaAs:C samples studied here, are similar to those reported by Liu *et al.*, [7] for  $D_r$ ,  $D_x$ , and  $D^*$  states in lightly doped n-type GaAs.

The details of the sharp transitions seen in the PL spectra of GaAs:C are shown in Fig. 3 for pressures between 4 and 6 GPa. As many as eight sharp peaks riding over a broad  $D_x$ , all having a pressure shift of 0.02 eV/GPa can be identified in these spectra. It is possible that pairs labeled (1, 6), and (2, 7) are zero phonon lines and their respective LO replicas. We do not observe any significant shift in the energy positions of these sharp transitions when changing the excitation intensity by three orders of magnitude. Similar behavior was seen in

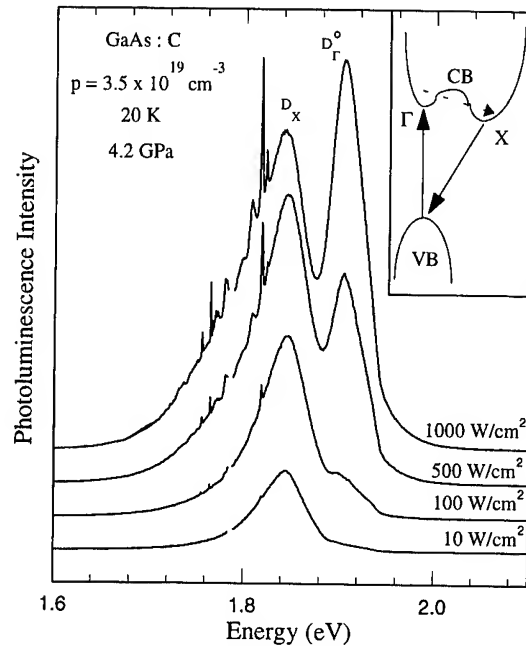


Fig. 2. PL spectra recorded with various excitation laser powers near the  $\Gamma$ -X CB cross-over pressure. Strong ruby R-lines are removed for clarity. Inset gives the schematics of the absorption, scattering, and recombination processes.

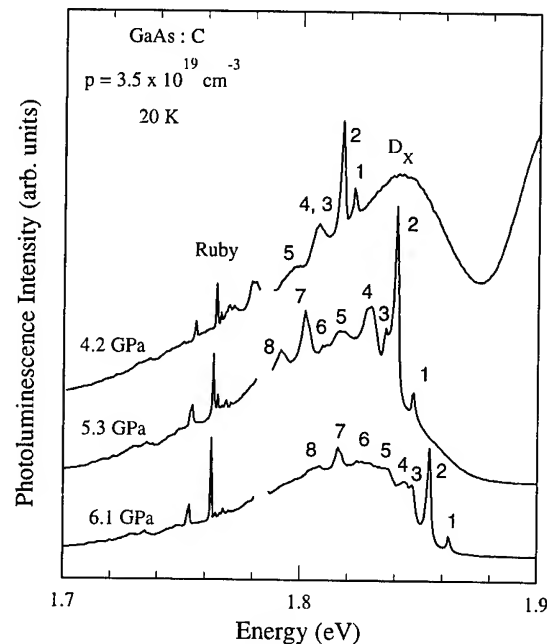


Fig. 3. Sharp PL peaks seen in GaAs:C after  $\Gamma$ -X CB cross-over. Discontinuities in the spectra are due to the removal of strong ruby R-lines.

cathodoluminescence for donor to acceptor transitions in p-type GaAs.[8]

The pressure shifts of the sharp transitions are close to those reported for a deep donor state  $D^*$ [7] or deep nitrogen trap bound excitons  $N_x$ [9, 10] in n-type GaAs. This indicates that the initial states involved in these transitions are deep donor states. The sharpness of these transitions suggest that their final states are not the broadened acceptor states in the valence band tail. Leroux *et al.*[10] observed a set of transitions similar to those shown in Fig. 3, in MBE grown Si-doped n-type GaAs under pressure and attributed them to  $N_x$  and its phonon replicas. Although contamination of nitrogen from BN crucibles is possible in MBE samples, it may be difficult to obtain nitrogen in the atomic form suitable for incorporation in GaAs. We consider an alternate possibility for these strong PL peaks *viz.*, the recombination of near donor-acceptor pairs (DAP).

Discrete DAP spectrum with a rich fine structure has been observed at atmospheric pressure in semiconductors such as GaP, CdS, and ZnS[11, 12]; but the DAP spectrum reported so far in GaAs is generally a broad band. The energy of a PL transition arising from a DAP separated by a distance  $r$  in a medium of dielectric constant  $\epsilon$  is:

$$E_{\text{DAP}} = E_g - E_D - E_A + q^2/\epsilon r, \quad (1)$$

where  $E_g$  is the band gap,  $E_D$  and  $E_A$  are the ionization energies of isolated donor and acceptor impurities respectively. Since  $r$  can take only a set of discrete values in the lattice, DAP transitions arising from near pairs give rise to sharp lines. In GaAs at atmospheric pressure,  $E_D$  ( $\sim 5$  meV) and  $E_A$  ( $\sim 30$  meV) are small and so the Coulomb term in Eq. 1 makes  $E_{\text{DAP}}$  for near pairs larger than  $E_g$ . DAP transitions would have to compete with the (direct) band to band transition. Since the density of states in the bands is very large, sharp line features would not be observed at 1 bar unless the DAP transitions are extremely efficient. On the other hand, for distant pairs,  $r$  is large and so the Coulomb term is small and changes more gradually. Hence,  $E_{\text{DAP}} < E_g$  and its values are quasi-continuous resulting in a broad spectrum as has been previously observed in GaAs.

With the application of pressure ( $P$ ), the deep donor states which are resonant in the CB at 1 bar pressure are pulled into the band gap. The existence of a deep donor state at  $\sim 100$ -150 meV above  $\Gamma$ -CB minimum at atmospheric pressure and its emergence into the band gap for  $P > 2.5$  GPa, have been well known in GaAs. The deepening of

the donor energy makes the value of  $E_{\text{DAP}}$  for near pairs  $\leq E_g$ . Furthermore, with the cross-over of  $\Gamma$  and X CBs at  $\sim 4.2$  GPa, the DAP transitions could compete more favorably against the indirect band to band emission.

Thus, it is possible to observe sharp transitions due to near DAP in GaAs under high pressures. Further experiments are clearly needed to unambiguously confirm the origin of these sharp lines observed in the PL spectra of GaAs:C.

The donor defects participating in the DAP transitions in our samples might be residual donor impurities (possibly Si) or substitutional carbon on Ga sites ( $C_{\text{Ga}}$ ). The latter is interesting because of the possibility of an amphoteric doping behavior for carbon in GaAs. Although n-type conduction has never been observed in GaAs:C, one cannot rule out the presence of compensating  $C_{\text{Ga}}$  donors in p-type GaAs:C. In particular, it is plausible that a significant concentration of  $C_{\text{Ga}} - C_{\text{As}}$  near pairs occurs in heavily doped GaAs:C samples. Though speculative at this point, it will be useful to further explore this possibility in future studies.

1. J. De-Sheng, Y. Makita, K. Ploog, and H. Queisser, *J. Appl. Phys.* **53** (1982) 999.
2. D. Olego and M. Cardona, *Phys. Rev.* **B22** (1988) 886.
3. B. Sernelius, *Phys. Rev.* **B33** (1986) 8582.
4. S. Kim, M-S. Kim, S-K. Min, and C. Lee, *J. Appl. Phys.* **74** (1993) 6128.
5. D.J. Wolford and J.A. Bradley, *Solid State Commun.* **53** (1985) 1069.
6. A.R. Goni, A. Contarero, K. Syassen, and M. Cardona, *Phys. Rev.* **B41** (1990) 10 111.
7. X. Liu, L. Samuelson, M. Pistol, M. Gerling, and S. Nilsson, *Phys. Rev.* **B42** (1990) 11791.
8. J.I. Pankove, *J. Phys. Soc. Japan* **21** Supplement (1966) 298.
9. D.J. Wolford, J.A. Bradley, K. Fry, and J. Thompson, *Proceedings of 17th International Conference on the Physics of Semiconductors*, edited by J.D. Chadi and W. A. Harrison (Springer, New York, 1984) p. 627.
10. M. Leroux, G. Neu, and C. Verie, *Solid State Commun.* **58** (1986) 289.
11. See for a review, P.J. Dean in *Progress in Solid State Chemistry*, edited by J.O. McCaldin and G. Somarjai (Pergamon, 1973) Vol. 8.
12. D.G. Thomas, M. Gershezon, and F.A. Trumbore, *Phys. Rev.* **133** (1964) A269.

# SHALLOW AND DEEP STATES OF GROUP VI DONORS IN GaAs and $\text{Al}_x\text{Ga}_{1-x}\text{As}$ AT HIGH PRESSURES.

J.E. DMOCHOWSKI, M.A. SADLO, R.S. JAKIELA,  
*Institute of Physics, Polish Academy of Sciences*  
 02-668 Warszawa, Al. Lotnikow 32/46, POLAND.

R.A. STRADLING,  
*Blackett Laboratory, Imperial College of Science, Technology and Medicine,*  
*Prince Consort Road, London SW7 2BZ, UK.*

A.D. PRINS, J.L. SLY, and D.J. DUNSTAN,  
*Physics Department, University of Surrey, Guildford, GU2 5XH, UK.*

K.E. SINGER  
*The University of Manchester Institute of Science and Technology,*  
*Sackville Street, PO Box 88, Manchester, M60 1QD, UK.*

Photoluminescence under high pressure in a Dunstan-type diamond-anvil cell is used to investigate the  $\Gamma$ -shallow-deep  $A_1$  transition for the Se donor in moderately doped ( $n = 1.7 \cdot 10^{18} \text{ cm}^{-3}$ )  $\text{Al}_x\text{Ga}_{1-x}\text{As}:\text{Se}$  ( $x=0.19 \pm 0.03$ ) grown by MBE. A photoluminescence line due to the deep Se donor to shallow acceptor transition is observed above the shallow-deep transition at 18 kbar, in the 18-23 kbar pressure range. Its energy is independent of pressure and is  $1.825 \pm 0.005 \text{ eV}$ . The results are compared with an analogous experiment with the Te donor in bulk GaAs ( $n=10^{18} \text{ cm}^{-3}$ ) and previous observations on Se and S donors in GaAs. The change in critical pressure for the shallow-deep transition from 30 kbar for GaAs:Se to 18 kbar for  $\text{Al}_{0.19}\text{Ga}_{0.81}\text{As}:\text{Se}$  is well understood in terms of the similar effects of pressure and of alloying with Al on the GaAs band structure. In contrast to the other donors the Te state which emerges into the gap of GaAs on applying pressure is predominantly effective mass-like with X character.

It has been demonstrated that donor impurities can form generally three different types of states: shallow effective mass states, deep DX-type states with a strongly relaxed lattice configuration and weakly relaxed deep localised states of  $A_1$  symmetry [1,2]. Different experimental techniques are sensitive to different donor states and several experiments are necessary to obtain a full picture of a specific donor impurity in a particular host. We have already studied different substitutional donors (Si, Se, S, Ge, Sn, ) in one host, GaAs, using high pressure photoluminescence [2-6]. A pressure induced shallow ( $\Gamma$ )-deep ( $A_1$ ) transition was reported for all these species.

In this communication we report similar studies of the Te donor in GaAs and of the Se donor in  $\text{Al}_x\text{Ga}_{1-x}\text{As}$ . Alloying GaAs with AlAs and applying pressure lead to similar changes in the band structure of GaAs.

The epi-layer of Se doped  $\text{Al}_x\text{Ga}_{1-x}\text{As}$  ( $x=0.19 \pm 0.03$ ) was grown by MBE. The sample no.1964 consists of a GaAs semiinsulating (SI) substrate, GaAs buffer layer,  $0.5 \mu\text{m}$  undoped  $\text{Al}_x\text{Ga}_{1-x}\text{As}$  buffer layer,  $1 \mu\text{m}$  Se-doped  $\text{Al}_x\text{Ga}_{1-x}\text{As}$

and  $10 \text{ nm}$  undoped GaAs cap layer. The 300K Hall concentration of the sample is  $n_{300} = 1.7 \cdot 10^{18} \text{ cm}^{-3}$ .

A Dunstan-type diamond anvil cell technique and luminescence set-up was used for the low-temperature experiments [5,6]. The band edge shift of the GaAs substrate observed in transmission was used as a pressure sensor as described in refs. 5, 6.

Photoluminescence spectra of the sample (Fig.1,3) at low pressures consist of three main peaks. Two of these can be assigned to  $\text{Al}_x\text{Ga}_{1-x}\text{As}$ : the high energy peak to a conduction band-shallow acceptor ( $eA_{\text{AlGaAs}}$ ) transition, the broad luminescence at low energy ( $Y_{\text{AlGaAs}}$ ) is similar to the  $1.2 \text{ eV}$  band in n-type doped GaAs assigned to a donor impurity-gallium vacancy complex [8]. The third peak can be assigned to near-band-edge luminescence from the GaAs cap (most likely shallow donor-shallow acceptor transitions) since its energy position and pressure dependence follow those of the GaAs-substrate. This line at pressures in the 24-35 kbar range is obscured by the very strong  $N_x$  GaAs nitrogen-bound exciton luminescence of the cap layer characteristic of MBE-grown GaAs [3-5].

Up to 18 kbar the energy positions of all three features follow the GaAs band-edge. Above a critical pressure of 18 kbar the energy positions of

both  $\text{Al}_x\text{Ga}_{1-x}\text{As}$  related lines do not follow the GaAs line but become pressure independent in the 18-23 kbar range (within experimental error). The

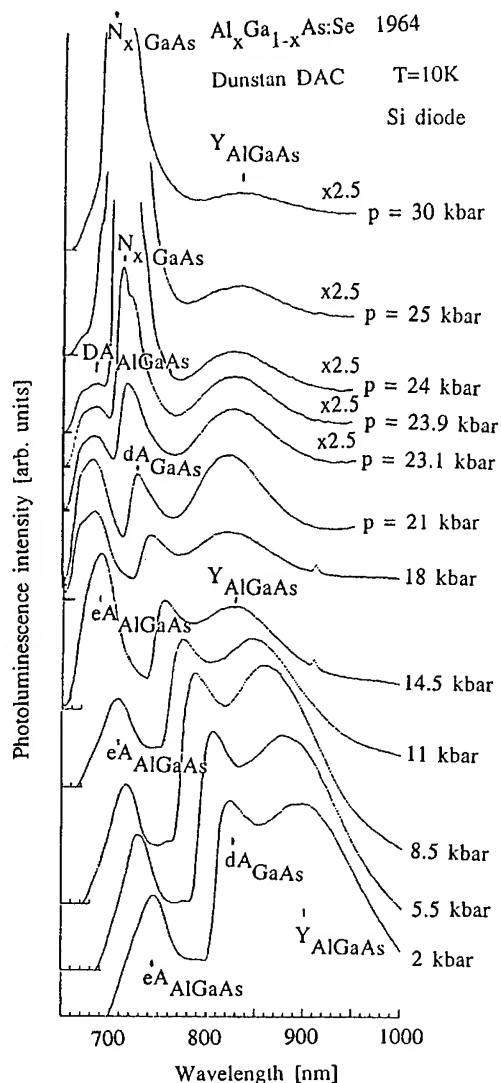


Fig.1. Low temperature (10K) photoluminescence spectra of the Se-doped  $\text{Al}_x\text{Ga}_{1-x}\text{As}$  ( $x=0.19$ ) layer at different pressures.

effect is analogous to that observed with Se-doped GaAs and S-doped GaAs [5,7] above 30 kbar. The saturated energy position of the line,  $1.825 \pm 0.005$  eV, is also very similar to that observed in the 30-40 kbar range in Se-doped GaAs,  $1.815 \pm 0.005$  eV. We assign this effect to Fermi-level pinning to the deep Se donor state of  $A_1$  character. Consequently the high energy line is depicted as a deep donor shallow acceptor line ( $\text{DA}_{\text{AlGaAs}}$ ). The  $\text{DA}_{\text{AlGaAs}}$  line loses

intensity with increasing pressure and the very strong excitonic  $\text{N}_x\text{GaAs}$  luminescence of the GaAs

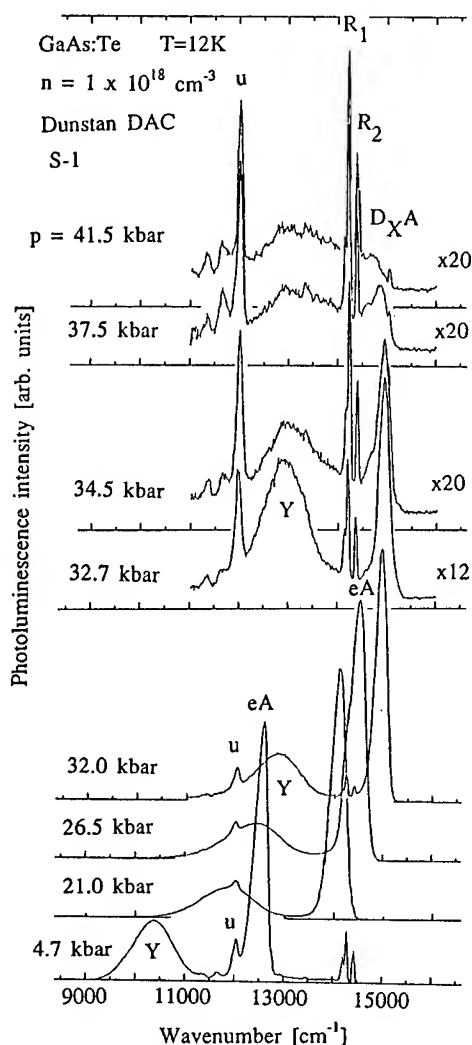


Fig.2. Low temperature (12K) photoluminescence spectra of GaAs:Te (eA,  $\text{D}_X\text{A}$ , Y) at different pressures. Ruby ( $R_1$  and  $R_2$ ) and unknown background luminescence (u) are marked.

cap layer emerges. Consequently the position of  $\text{DA}_{\text{AlGaAs}}$  could not be determined above 24 kbar.

Unlike S and Se, the shallow ( $\Gamma$ ) donor character is observed for Te doped bulk GaAs sample ( $n=10^{18} \text{ cm}^{-3}$ ) (Fig.2) with band-to-acceptor (eA) luminescence up to energy of 1.86 eV i.e. 33 kbar pressure, followed by the X-like pressure coefficient of the donor-acceptor line ( $\text{D}_X\text{A}$ ) at

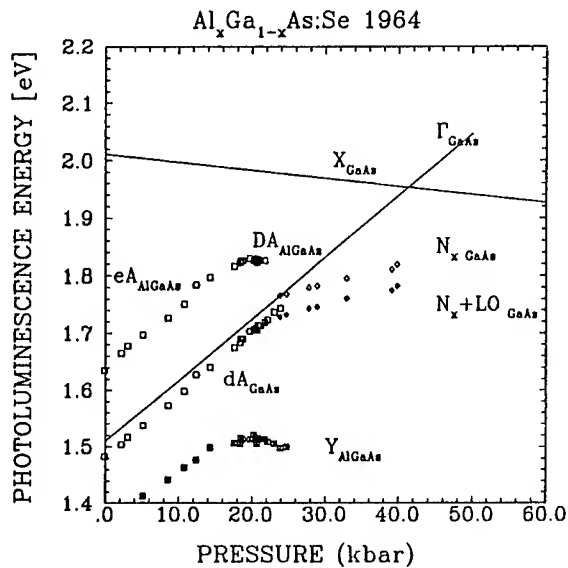


Fig.3 Pressure dependence of different spectroscopic features for the sample with Se-doped  $\text{Al}_x\text{Ga}_{1-x}\text{As}$  ( $x=0.19$ ) layer.

higher pressures (Fig. 2,4), confirming another report on GaAs:Te under pressure [8]. Thus, the evidence is that the Te state that emerges into the gap of GaAs on applying pressure is predominantly effective-mass-like with X character and with a binding energy of  $\sim 90$  meV.

The relative energy positions of the deep  $A_1$ -like states for different donor species and the change in critical pressure for the shallow-deep transition from 30 kbar for GaAs:Se to 18 kbar for  $\text{Al}_x\text{Ga}_{1-x}\text{As}$ :Se can be well understood in terms of the similar effects of pressure and of alloying with Al on the GaAs band structure. Theoretically pressure and alloying with Al are expected to have

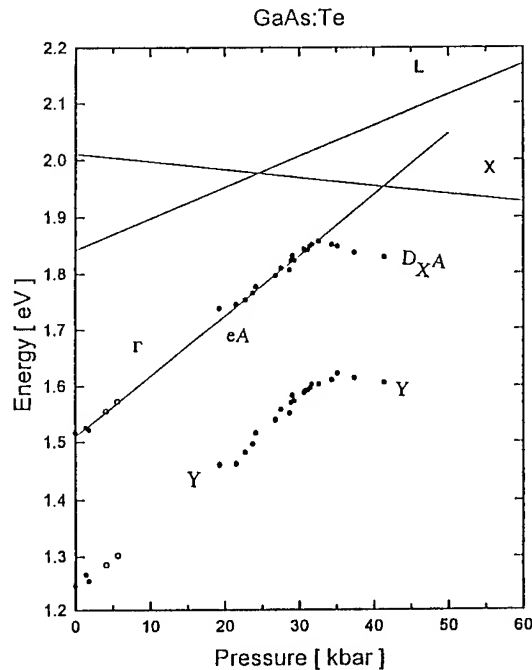


Fig.4. Pressure dependence of different spectroscopic features for the GaAs:Te sample.

a similar effect of moving the  $\Gamma$ -conduction band upwards in energy (in relation to the valence band) while the deep  $A_1$  donor states have much weaker pressure (and alloying) dependence [9].

We can conclude that at high pressures, in the 18-23 kbar range, a deep state of Se donor exists in  $\text{Al}_x\text{Ga}_{1-x}\text{As}$  ( $x=0.19\pm 0.03$ ) which has the properties expected for the deep  $A_1$ -type state of substitutional impurity.

This work is supported by KBN grant No.2 P302 109 04 in Poland, SERC in UK and EC mobility Grant CIPA3510PL927857 and RS-PAS exchange scheme for visits of J.E. Dmochowski in UK.

## References

1. Z.Wasilewski, R.A.Stradling, *Semicond. Sci. Technol.*, **1** (1986) 264
2. J.E.Dmochowski, Z.Wasilewski, R.A. Stradling, *Mater. Sci. Forum* **65-66** (1990) 449
3. J.E.Dmochowski, R.A.Stradling, P.D.Wang, S.N.Holmes, M.Li, B.D.McCombe, B.Weinstein, *Semicond. Sci. Technol.*, **6** (1991) 476
4. J.E.Dmochowski, R.A.Stradling, *Japan. J.Appl. Phys.*, **32 Suppl.32-1** (1993) 227

5. J.E.Dmochowski, R.A.Stradling, D.J.Dunstan, A.D.Prins, A.R.Adams, K.E.Singer, T.Fujisawa, H.Kukimoto, *Mater.Sci.Forum*, **143-147**(1994)1075.
6. J.E.Dmochowski, R.A.Stradling, J.Sly, D.J. Dunstan, A.D.Prins, A.R.Adams, *Acta Physica Polonica A* **87** (1995) 457
7. M.Kobayashi, T.Yokoyama, S.Narita, *Jap.J. Appl. Phys* **22** (1983) L612.
8. M.Zigone, P.Seguy, H.Roux-Buisson, G.Martinez, *Mater. Sci. Forum*, **38-41**(1989) 1097
9. E.Yamaguchi, *J.Phys.Soc.Japan*, **56** (1987) 2835

# ELECTRON EMISSIONS FROM Si-DX AND Te-DX UNDER PRESSURE

K.Takarabe, N.Shirase, and S.Minomura

*Okayama University of Science, Ridai, Okayama 700, Japan*

## ABSTRACT

We report the effect of pressure on electron emission rate of Si- and Te-DX center up to 2 GPa. There appears no pressure effect in Si-DX but the change of pressure coefficient in Te-DX with the band crossing. The implication of this difference is considered.

## Introduction

Capture and emission of electron into and out of DX centers occur only by surmounting potential barriers. It naturally accounts for persistent photoconductivity(PPC), most distinguished nature of DX centers(1). The potential barrier is determined by the adiabatic potential curves of three charge states of donor:-1, 0, and +1(2,3). According to the recent elaborate calculation for the potential barrier of Si-DX in GaAs:Si based upon Chadi-Chang's model, the thermal emission barrier is identified to be the energy difference between the negatively charged DX state and the so-called transition state rather than the crossing point with other charge states. The calculated pressure coefficient of the thermal emission is very small in the direct bandgap(4). Unfortunately, there is no calculation in the indirect bandgap and also no calculation for Te-DX in the both bandgaps.

We will report pressure effects on electron emission spectra on Si and Te-DX centers.

## Experiments

Schottky diodes were prepared by evaporating gold onto  $\text{Al}_x\text{Ga}_{1-x}\text{As}$  ( $x=0.3(\text{Si}), 0.35(\text{Te})$ ) layers doped with Si or Te to  $10^{18}$  or  $10^{17}\text{cm}^{-3}$ , respectively, grown on (001)GaAs substrate by MBE. Isothermal capacitance transients,  $C(t)$ , after a filling pulse, were measured by transient capacitance recorder DA-1500(Horiba Ltd.). The stored transient capacitance was numerically processed to yield the signal  $S(t) = td\Delta C^2/dt$  called an ICTS signal(5).

The ICTS signal  $S(t)$  for multiple electron emis-

sion rates is equal to:

$$S(t) = \frac{q\epsilon_r\epsilon_0 A^2}{2(V_d - V_b)} \sum_{i=1}^{i=n} N_T^i (-e_n^i t) \exp(-e_n^i t) \quad (1),$$

where  $i$  denotes the  $i$ th component,  $q$  is electronic charge,  $\epsilon_r$  and  $\epsilon_0$  are the dielectric constants of material and vacuum, respectively,  $A$  is the diode area,  $V_d$  the diffusion voltage,  $V_b$  the bias voltage, and  $N_T$  and  $e_n$  the concentration of the filled trap(the electron occupancy of the center) and the emission rate(relaxation time  $\tau_n=e_n^{-1}$ ) for the center, respectively. The ICTS signal  $S(t)$  has the maximum magnitude at  $t = \tau = e_n^{-1}$  and the magnitude is proportional to electron occupancy of the center. We used a piston-cylinder pressure apparatus and a mixture of normal- and iso-penthanes as pressure medium. The sample was compressed at room temperature in every cycle of the experiment before cooling down. The Schottky diode was biased at -3 V and an electron injection pulse of 2.9 V peak-to-peak amplitude was applied. These conditions were maintained throughout the experiment.

## Result and Discussion

ICTS experiment monitors the entire time decay of occupancy of DX center at each temperature after releasing a filling pulse. We refer to Morgan's discussion for the emission kinetics of DX center(6). According to Morgan(6), the emission rate is given by

$$e_n = 1/\tau = AT^\nu P_b \quad (2),$$

where  $A$  is a constant, the exponent  $\nu$  is assumed to be two. The probability  $P_b$  is the electron occupancy of the barrier state. The probability factor

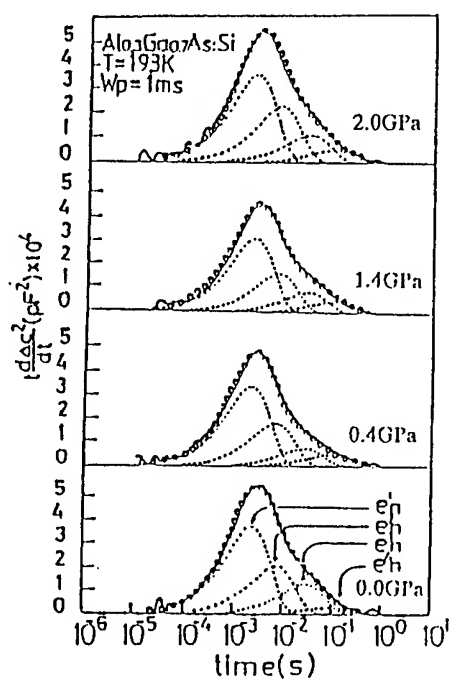


Fig1 A set of ICTS signals under various pressures at 193K. Each signal is well fitted to four components. There is no pressure effect on the electron emission process.

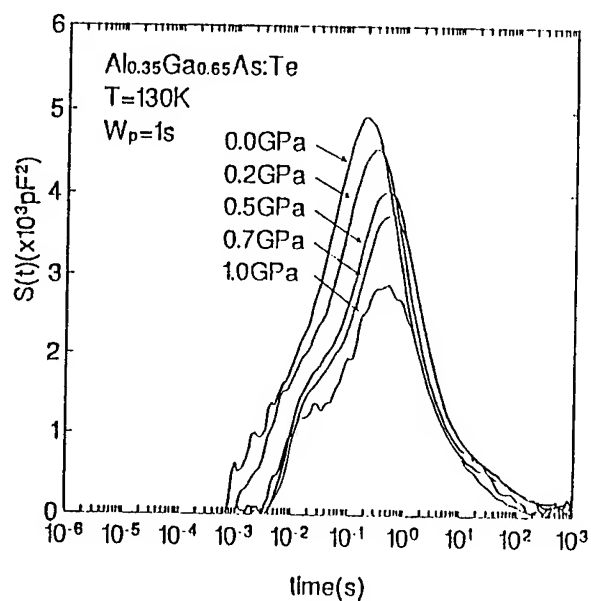


Fig.2 Pressure dependence of the ICTS signals of Te-DX. It moves to longer relaxation time (slower emission rate) at initial pressures and then to shorter relaxation time (faster emission rate). The turn over is clear and its pressure is a little bit larger than the expected IX crossover pressure 0.6 GPa of this sample.



$P_b$  is written as

$$P_b = g_b \exp\left(\frac{-E_B}{kT}\right) \bigg/ \sum_{i=1}^{i=n} g_i \exp\left(\frac{-E_i}{kT}\right) \quad (3),$$

normalized by a sum over all DX states  $j$  with free energy  $E_j$  and degeneracy  $g_j$ . Moragan did not take into account the negative-U character in the above equation. The negative-U character may change the probability  $P_b$  if it is properly taken into account.

A typical set of ICTS signals of Si-DX under pressure is shown in Fig. 1. The emission rate is decomposed into four components. There appears no change in the emission signal itself. This result indicates that the barrier height from the Si-DX ground state to the transition state is insensitive to pressure; therefore, these two states have the same pressure coefficient. The barrier potential consists of three contributions: electronic, phonon, and electron-phonon interaction energies. It is improbable to consider that no pressure change of the barrier potential is due to the cancellation of pressure effects among the above-mentioned three contributions. According to the chemical bonding analysis for these two states(4), the Si-DX ground state in GaAs:Si has the  $sp^{2.4}$  hybridized orbital but the barrier(transition) state does the  $sp^{2.0}$  hybridized orbital. The pressure up to 2 GPa changes the electronic band structure of this sample from the direct to the indirect bandgap, and also reduces the interatomic distance by about 1 %. It is well established by high-pressure studies that the electronic wavefunction at each symmetry point in Brillouin zone(BZ) has a different pressure coefficient. The transition and ground states wavefunctions could be derived by the linear combination of various wavefunction from each BZ points. It is not still clear the physics why these two different chemical bondings have the same pressure coefficient.

Figure 2 shows the result of Te-DX. It is seen that the emission rate moves to the longer relaxation time at initial pressure and then the turn over occurs. The turn over pressure is about 0.7 GPa which slightly exceeds a critical value 0.6 GPa of the  $\Gamma$ X band crossing of this sample( $x=0.35$ ). Unfortunately, the data is still lack after the band

crossing, but the turn over is clear. The pressure coefficients is about  $16 \pm 4$  and  $-10$  meV/GPa before and after the crossing, respectively. The similar result was reported by Li et al.(7) and also the positive pressure coefficient of  $6.5 \pm 1$  meV/GPa was reported for  $\text{Al}_{0.2}\text{Ga}_{0.3}\text{As:Te}$  up to 1.2 GPa, namely in the direct bandgap, by using the thermally stimulated Hall effect(8). Further investigations are need to solve this disagreement on the reported pressure coefficients for Te-DX. We can say, however, that Te-DX has the positive pressure coefficient except for the accurate value in the direct bandgap from the three separate experiments and the negative pressure coefficients in the indirect bandgap from the separate experiments. This difference in the pressure dependence of Te-DX requires a different scenario for the potential barrier from Si-DX.

### Summary

The emission barrier of Si-DX is insensitive to the change from the direct to the indirect bandgap. On the other hand, that of Te-DX changes its sign of the pressure coefficient accompanied with the change from the direct to the indirect bandgap. This indicates that the single physical scenario for the potential barrier for DX state is not satisfactory to explain each pressure dependence of DX centers.

### References

1. D.V.Lang and R.A.Logan, Phys.Rev.Lett., **39**(1977)635.
2. D.J.Chadi and K.J.Chang, Phys.Rev.B, **39**(1989)10063.
3. J.Dabrowski and M.Scheffler, Mat.Sci.Forum, **83-87**(1992)735.
4. M.Saito, A.Oshiyama, and O.Sugino, Phys.Rev.B,**47**(1993)13205.
- 5.H.Ohkushi,Jpn.J.Appl.Phys.,**19**(1980)L335.
- 6.T.N.Morgan,J.Electron.Mater.,**20**(1991)63.
- 7.M.F.Li,W.Shan,P.Y.Yu,W.L.Hansen, E.R.Weber, and E.Bauser,Mat.Sci.Forum, **38-41**(1989)1103.
- 8.R.Piotrkowski,E.Litwin-Staszewska,T.Suski, L.Konczewicz, and J.L.Robert, Jpn.J.Appl.Phys. Suppl.**32-1**(1993)252.

## **VII(C.2) Heterostructures**

# HIGH PRESSURE STUDIES OF RESONANT TUNNELING IN SEMICONDUCTOR HETEROSTRUCTURES

P C KLIPSTEIN

*Dept. of Physics, University of Oxford, Clarendon Laboratory, Parks Road, Oxford, OX1 3PU, U.K.*

## ABSTRACT

Some recent high pressure investigations are reviewed for intraband and interband resonant tunneling in GaAs/AlAs and InAs/GaSb heterostructures respectively. The results provide a new insight into the X-states and a new probe of small differences between *normal* and *inverted* interface roughness in GaAs/AlAs. For InAs/GaSb, high pressure provides one of the most powerful tools with which to determine differences both in the band overlap and in the resonant conduction mechanisms for the InSb- and GaAs-like interfaces.

## 1. Introduction

When Esaki and Tsu first proposed the idea of a semiconductor superlattice in 1970, the new physics of such structures was discussed directly in terms of the resonant tunneling of electrons in the material [1]. Studies of resonant tunneling, even in devices containing only a few layers, can thus provide essential insight into the physics of more complex heterostructure materials.

In a typical resonant tunneling structure, an external voltage controls the energy difference of quasi-bound or resonant states which are in different regions of the sample but whose wavefunctions overlap, giving rise to a current with a non-linear dependence on voltage which frequently exhibits negative differential resistance (NDR). It is often the case that several competing processes may contribute to the current so that the application of an external perturbation, such as a variation in temperature, pressure or magnetic field, can be necessary to obtain a full understanding of the tunneling mechanism. Of these, pressure plays a particularly significant role because not only can it influence the extent of the wavefunction envelope, by changing the values of basic parameters such as effective masses, but it can also change the energy separation of different states and even give access to states which are inaccessible at ambient pressure.

In this paper two examples of recent pressure dependent studies at Oxford will be described: *intraband* resonant tunneling in GaAs/AlAs and

*interband* resonant tunneling in InAs/GaSb. In GaAs/AlAs double barrier structures (DBS's), resonant tunneling has been widely studied at ambient pressure by many research groups, when electrons with  $\Gamma$  symmetry in the doped GaAs emitter layer tunnel through quasi-bound states confined by the two AlAs barriers. However, when pressure is applied several new effects are observed which have received far less attention but which are useful to understand the lesser investigated X symmetry states and their interaction with the  $\Gamma$  states. This is the subject of section 2 below. The second system, described in section 3, involves n-InAs/p-GaSb heterojunctions, in which the GaSb valence band overlaps the InAs conduction band. Since InAs and GaSb share no common cation or anion, ideal heterojunctions may be grown either with a "heavy" InSb-like or a "light" GaAs-like interface [2-4]. High pressure can be used to reveal differences due to the interface type, both in the ambient pressure band overlap and in the interband tunneling mechanism.

## 2. GaAs/AlAs

The conduction band profile for a DBS at ambient pressure is compared in fig. 1(a) with that at a pressure of about 16 kbar in fig. 1(b). At ambient pressure a clear resonance can be observed in structures with thin barriers due to the usual tunneling of  $\Gamma$ -like electrons as depicted in fig. 1(a). However, this resonance is suppressed by

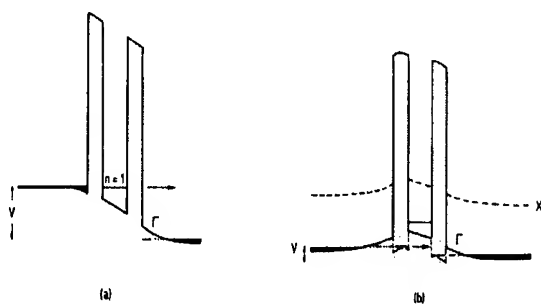


**Figure 1.** The conduction band profile for a biased DBS at a) 1 bar and b) 16 kbar

transfer into evanescent transverse  $X$ -states in the emitter AlAs barrier, which becomes dominant either when the barrier thickness is greater than  $50\text{\AA}$  [5], or when pressure reduces the energy separation between the  $\Gamma$ -like electrons in the emitter and the  $X_i$  barrier states [6].

Fig. 2 shows how the  $\Gamma$ -like resonance is suppressed with pressure in a DBS in which  $30\text{\AA}$  AlAs layers surround a  $40\text{\AA}$  layer of GaAs. The resonance has virtually vanished at 9.5 kbar. Note that the resonance appears to strengthen at 12 kbar but weakens again by 16 kbar [6]. At approximately the same pressure as the resonance appears to strengthen, a new family of resonances appears at much lower bias. These strengthen up to about 14 kbar, before the lowest bias resonance starts to weaken at higher pressure and at the same time to shift up in bias [6]. Their temperature dependence at 14.5 kbar is shown in fig. 3. They are due to the tunneling, depicted in fig. 1(b), of  $X$ -like electrons which occupy the AlAs barriers at high pressure [7]. Since the  $X_i$  states have a lower effective mass in the growth direction than the  $X_1$  states, the electrons all occupy the lowest confined longitudinal state  $X_{i1}(1)$  at low temperature, while at higher temperatures they may be thermally excited into the lowest transverse state,  $X_{i1}(1)$  [6,8]. Thus a resonance which vanishes at  $\sim 4\text{K}$  must have  $X_{i1}(1)$  as its initial state whereas a resonance which retains its strength must originate from  $X_{i1}(1)$ . In ref. 6 we have attributed the four resonances of fig. 3 in order of ascending bias to the processes  $X_{i1}(1) \rightarrow X_{i1}(1)$ ,  $X_{i1}(1) \rightarrow X_{i1}(1) + \text{LO}$ ,  $X_{i1}(1) \rightarrow X_{i1}(1) + P_1$  and  $X_{i1}(1) \rightarrow X_{i1}(1) + 2P_2$ , where LO,  $P_1$  and  $P_2$

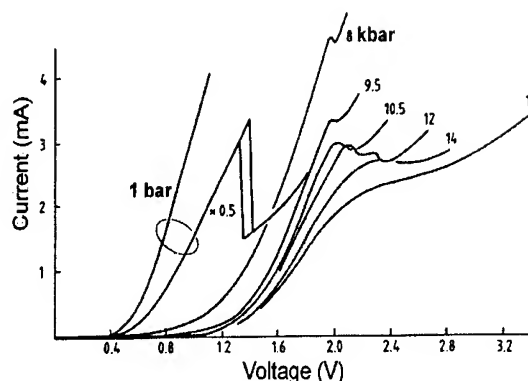


**Figure 2.** Pressure dependence of the  $\Gamma$ -like resonance (forward bias) at 77K for a  $30\text{\AA}$  AlAs /  $40\text{\AA}$  GaAs DBS

are different types of phonon. Resonances involving  $X_{i1}(1)$  as the initial state may be understood in terms of phonon scattering to the  $X_{i1}(1)$  state in the collector AlAs layer which has an evanescent part of its wavefunction extending into the emitter AlAs layer. A rough estimate for the probability of this process may be obtained from the product of the phonon scattering efficiency to a virtual  $X_{i1}(1)$  state in the emitter AlAs, the lifetime of the virtual state and the quantum beat frequency for  $X_{i1}(1)$  states separated by a similar GaAs barrier.

Surprisingly, the  $\Gamma$ -like resonance at 12 kbar in fig. 2 is suppressed at helium temperatures in contrast to its behaviour at ambient pressure, and so must have  $X_{i1}(1)$  as its initial state. It is

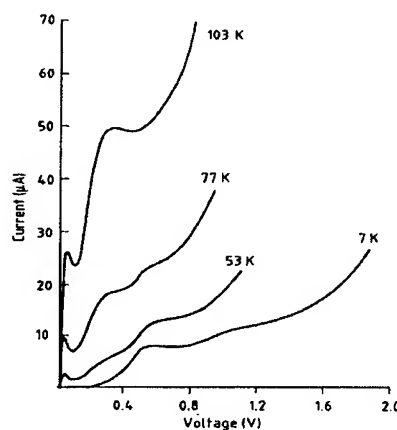


**Figure 3.** Temperature dependence of the lowest bias  $X$ -like resonances (forward bias) for the sample of fig. 2 at 14.5 kbar

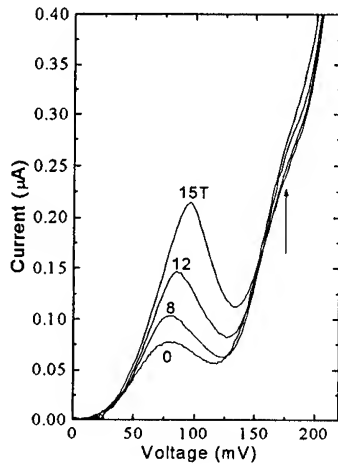


**Figure 4.** The first X-resonance (reverse bias) at 4.2K and 8.3 kbar for a 60Å AlAs/40Å GaAs DBS as a function of magnetic field in the [110] direction

tentatively attributed in ref. 6 to the process  $X_t(1) \rightarrow \Gamma_1 + P_1$ .

Because the process  $X_t(1) \rightarrow X_t(1)$  does not conserve wave-vector parallel to the interface it shows particularly interesting behaviour, including a large difference in strength between forward and reverse bias. In ref. 9 we have shown that the peak current in reverse bias (electrons travelling from the substrate to the top of the mesa) is larger than in forward bias, with a ratio of magnitudes of as much as 6:1 in structures which have closely similar AlAs layer widths and which exhibit a  $\Gamma$ -like resonance with negligible dependence on bias direction. We explain the bias asymmetry of the X resonance in terms of differences in roughness at the normal and inverted interfaces, since the roughness is thought to provide the required in-plane wave-vector. Further evidence that the form of this high pressure resonance is indeed controlled by the efficiency with which electrons may gain in-plane wave-vector can be seen in fig. 4, where the resonance at 8.3 kbar for a structure with 60Å AlAs layers surrounding a 40Å layer of GaAs is plotted as a function of an in-plane magnetic field. In this structure  $X_t(1)$  lies below  $X_i(1)$  due to a strain induced inversion of the ordering of these sub-bands for AlAs thicknesses above about 50Å, so the resonance first appears at a slightly lower pressure

and is not suppressed at 4.2K [8]. Fig. 5 shows that the first high pressure resonance is very sensitive to the in-plane magnetic field whereas the next resonance, in which a phonon provides the required change of in-plane wave-vector and whose position is indicated by an arrow, is not. This is true for fields oriented in both the [100] and [110] directions, whereas the field has negligible effect when oriented along the [001] growth direction. It may be explained by the in-plane momentum which the field can provide only when it is oriented parallel to the layers [10], and is discussed in detail elsewhere [11].

### 3. InAs/GaSb

The resonant conduction in n-InAs/p-GaSb heterojunctions ( $n \approx 4 \times 10^{16} \text{ cm}^{-3}$  and  $p \approx 1 \times 10^{16} \text{ cm}^{-3}$ ) with both GaAs-like and InSb-like interfaces has been studied in 10  $\mu\text{m}$  diameter mesa diodes as

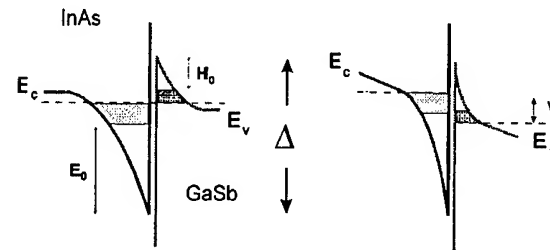


**Figure 5.** Band alignment close to the interface of a n-InAs/p-GaSb diode at a) zero bias and b) when a forward bias,  $V$ , is applied

a function of temperature, pressure and magnetic field [12,13]. Fig. 5 shows the crossed band alignment in the vicinity of the interface (a) at zero bias and (b) when a small forward bias is applied (n-InAs negative with respect to p-GaSb). At zero bias electron transfer due to the band overlap,  $\Delta$ , results in the formation of a two dimensional electron gas (2DEG) in the InAs adjacent to a two dimensional hole gas (2DHG) in the GaSb. Applying a small forward bias increases the confinement energies,  $E_0$  and  $H_0$ , of the lowest electron and hole sub-bands. Full electron states and empty hole states begin to overlap and conduction through the interface can take place. When the lowest energy electron sub-band is made to rise above the lowest hole energy sub-band the

current is expected to fall, giving rise to NDR...a 2D analogue of Esaki's original tunnel diode [14]. NDR observed at room temperature and 77K is shown in fig. 6 for devices with (a) GaAs-like and (b) InSb-like interfaces. There are striking differences in behaviour for the two interface types, not only in the bias of the NDR feature but also in the temperature dependence. If this is due only to the difference in the band overlaps [15], the bias for the GaAs-like interface should be lower than that for InSb-like because as shown below,  $\Delta_{\text{GaAs}} < \Delta_{\text{InSb}}$ . Since it is not the case, a different resonant conduction mechanism appears to operate for the two interface types. This is confirmed in fig. 7 by measurements of the forward bias characteristic as a function of pressure up to 21 kbar. Pressure increases the band gaps of InAs and GaSb so that the band overlap,  $\Delta$ , goes to zero at 16 kbar for an InSb-like interface and at 13 kbar for GaAs-like, as discussed below. The NDR for the InSb-like interface appears to vanish at the pressure at which

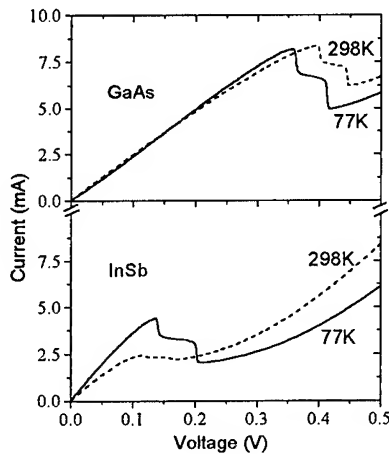


Figure 6.  $I$ - $V$  in forward bias at 298K and 77K for the diode of fig. 5 with a) GaAs and b) InSb interface

the bands uncross. However, the NDR for the GaAs-like interface persists after the bands have uncrossed, showing clearly and for the first time that a new resonant conduction process is involved for this interface. Measurements in magnetic fields up to 40T also support such a conclusion. These results are reported in detail elsewhere[13].

The relative sizes of  $\Delta_{\text{GaAs}}$  and  $\Delta_{\text{InSb}}$  used above

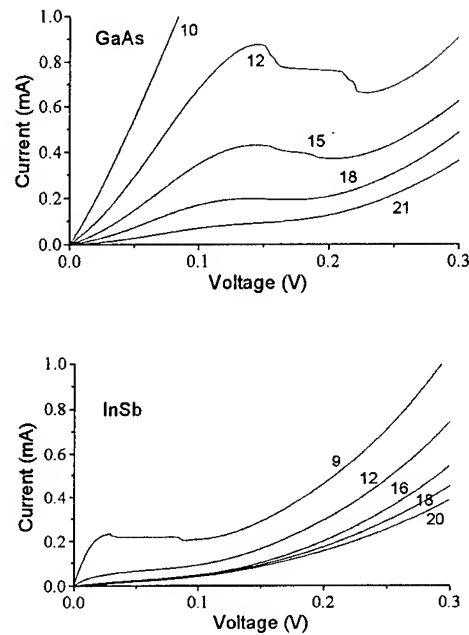


Figure 7. Pressure dependence of NDR at 77K close to  $P_T$ , for a) GaAs-like and b) InSb-like interfaces. Pressures are indicated by each curve in kbar

can be deduced from measurements at a fixed reverse bias ( $-0.1V$ ) of the current due to Zener-like conduction as a function of pressure as shown in fig. 8. Since the current depends principally on the overlap of full bulk GaSb valence states with empty bulk InAs conduction states, it should be proportional to a universal function of the band overlap. In fig. 8 the curve of  $I$  vs.  $P$  for the device with the GaAs-like interface lies almost exactly on top of that for the InSb-like interface if it is first shifted up by  $\sim 3$  kbar. This shows that  $\Delta$  has a

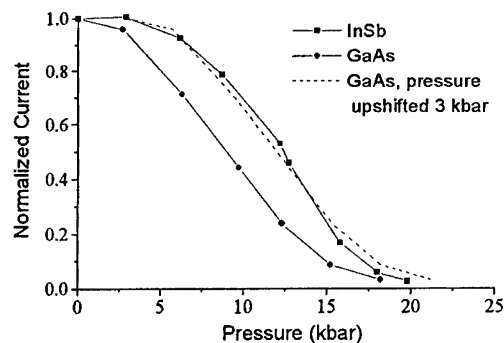


Figure 8. Pressure dependence of normalised current at 77K and  $-0.1V$  bias, for each interface type

very similar pressure variation for both interface types and that  $P_T^{\text{InSb}} - P_T^{\text{GaAs}} \approx 3$  kbar, where  $P_T$  is the threshold pressure at which  $\Delta \rightarrow 0$ . Parallel transport measurements as a function of pressure on superlattices grown in the same reactor show that the overlap decreases at the rate of about  $-9.5$  meV kbar $^{-1}$  for both interface types, and that  $\Delta_{\text{InSb}} \approx 155$  meV and  $\Delta_{\text{GaAs}} \approx 125$  meV [16]. Comparing these results with fig. 8 shows that  $P_T$  is the pressure close to which the Zener like current appears to exhibit a point of inflection.

#### 4. Conclusions

The foregoing examples of resonant tunneling in GaAs/AlAs and InAs/GaSb demonstrate how high pressure can be an essential tool with which to investigate important new physical phenomena. In GaAs/AlAs high pressure provides access to the X-states. These exhibit new types of process including tunneling from an initial longitudinal state to a final transverse state. The X-states also offer an extremely sensitive probe of small differences in roughness at the normal and inverted interfaces which appear invisible to the ambient pressure  $\Gamma$ -like resonance. In InAs/GaSb, high pressure has been used to deduce that the band overlap for a GaAs-like interface is smaller than for an InSb-like interface. The different interface types give rise to very different NDR features at ambient pressure with very different temperature dependences. For an InSb-like interface, NDR vanishes at pressures above  $P_T$ , the pressure at which the bands uncross. However, for a GaAs-like interface, the persistence of NDR above  $P_T$  provides the first clear evidence for a new resonant conduction mechanism.

*Acknowledgements* - Special acknowledgement is made of the contributions to this work of many research students and other collaborators, in particular D G Austing, U M Khan Cheema, J M Smith, S G Lyapin, M E Eremets, N J Mason, G W Smith, R Grey, and G Hill. This work was supported by the Engineering and Physical Sciences Research Council of the U.K. and the Human Capital and Mobility programme of the European Community, contract no. CHRXCT930321.

#### References

1. L Esaki and R Tsu, *IBM. J. Res. Dev.* (1970) 61
2. A Fasolino, E Molinari and J C Maan, *Superlattices and Microstructures*, **3** (1987) 117
3. S G Lyapin, P C Klipstein, N J Mason and P J Walker, *Phys. Rev. Lett.* **74**, 3285 (1995)
4. S G Lyapin, P C Klipstein, N J Mason and P J Walker, *Sup. and Microst.* **15**, 499 (1994)
5. E E Mendez, E Calleja and W I Wang, *Appl. Phys. Lett.* **53** (1988) 977
6. D G Austing, P C Klipstein, A W Higgs, H J Hutchinson, G W Smith, J S Roberts and G Hill, *Phys. Rev. B* **47** (1993) 1419
7. D G Austing, P C Klipstein, J S Roberts and G Hill, *J Appl. Phys.* **74** (1993) 7340
8. D G Austing, P C Klipstein, J S Roberts, C B Button and G Hill, *Phys. Rev. B* **48** (1993) 11905
9. J M Smith, P C Klipstein, D G Austing, R Grey and G Hill, *J. Phys. Chem. Sol.* **56** (1995) 475
10. G Goldoni and A Fasolino, *Phys. Rev. B* **48** (1993) 4948
11. J M Smith, P C Klipstein, R Grey and G Hill, *to be published*.
12. P C Klipstein et al., *Proceedings of Int. Conf. on Semiconductor Heteroepitaxy, Montpellier 4-7 July 1995*, edited by B Gil (World Scientific, 1996): in press.
13. U M Khan-Cheema, P C Klipstein, N J Mason, G Hill and P J Walker, *to be published*
14. L Esaki in *Solid State Physics in Electronics and Telecommunications*, (Academic Press, New York, 1960), p 518
15. Y Foulon and C Priester, *Phys. Rev. B* **45** (1992) 6529; L A Hemstreet, C Y Fong and J S Nelson, *J. Vac. Sci. Technol. B* **11** (1993) 1693; R G Dandrea, C B Duke and A Zunger, *J. Vac. Sci. Technol. B* **10** (1992) 1744
16. M S Daly, D M Symons, M Lakrimi, R J Nicholas, N J Mason and P J Walker, *Proc. Int. Conf. on EP2DS, Nottingham 7-11 August 1995* (1996): in press

# HIGH PRESSURE STUDY OF ELECTRON-ELECTRON INTERACTIONS IN DOUBLE-LAYER 2D ELECTRON GASES

A.R. GOÑI, S. ERNST, K. SYASSEN, and K. EBERL

*Max-Planck-Institut für Festkörperforschung, Heisenbergstr. 1, 70569 Stuttgart, Germany*

We report inelastic light scattering measurements of elementary excitations of 2D electron gases in modulation-doped double quantum well (DQW) structures. The 2D electron density  $n$  is continuously tuned by applying hydrostatic pressure. Inelastic light scattering yields detailed information on collective as well as single-particle intersubband excitations from which the Hartree and exchange terms of the Coulomb interaction are obtained as a function of carrier density. The effects of interlayer correlations in DQW's manifest themselves in the energies of the excitations. In an asymmetric DQW structure the metal-nonmetal transition, which has been observed for a single-layer electron gas at  $n \approx 2 \times 10^{10} \text{ cm}^{-2}$ , is suppressed due to the enhancement of screening effects in the interacting bilayer system. For a symmetric DQW the strong interlayer correlations, which give rise to the symmetric-antisymmetric subband splittings, are responsible for the abrupt drop in the strength of the Hartree interaction at relatively high electron densities.

## 1 Introduction

Double-layer electron gases produced in modulation-doped double quantum wells (DQW) exhibit a variety of new phenomena associated with interlayer electronic correlations.<sup>1,2</sup> For example, these interactions are responsible for the appearance of new fractional quantum Hall states in strong magnetic fields<sup>3</sup> and for the suppression of spin-density excitations at zero field and high electron densities.<sup>4</sup> Also, the transport properties of double-layer systems appear to be influenced by coulombic interlayer friction.<sup>5</sup>

Electron-electron interactions manifest themselves in the spectrum of elementary excitations of the 2D electron gas, which can be probed by resonant inelastic light scattering.<sup>6</sup> Figure 1 shows an example of light scattering spectra of 2D intersubband excitations measured in a single quantum well (SQW) sample. The interacting electron gas sustains collective charge-density excitations (CDE), which correspond to in-phase fluctuations of the electron density, and spin-density excitations (SDE), in which the number of electrons with spin-up or spin-down components is spatially modulated. The CDE appears as a sharp peak in spectra measured with parallel polarization of the incident and scattered beams, whereas in depolarized spectra the SDE is active. In addition, single-particle (SPE) or electron-hole pair excitations are observed as a broad feature at the subband spacing in spectra of both polarizations.<sup>7</sup>

The observed energy shifts of 2D collective excitations relative to the SPE are a measure of

the strength of Coulomb interactions. Within the local-density approximation the energies of the collective modes associated with transitions between an occupied subband  $i$  with 2D density  $n_i$  and an empty one  $j$  are expressed for long wavelengths as:<sup>8</sup>

$$\omega_{SDE}^2 = E_{ij}^2 - 2n_i E_{ij} \beta_{ij} \quad (1)$$

$$\omega_{CDE}^2 = E_{ij}^2 + 2n_i E_{ij} (\alpha_{ij}/\epsilon - \beta_{ij}) \quad (2)$$

where  $E_{ij}$  is the intersubband spacing energy. The so-called *excitonic* shift  $\beta_{ij}$  of the collective SDE

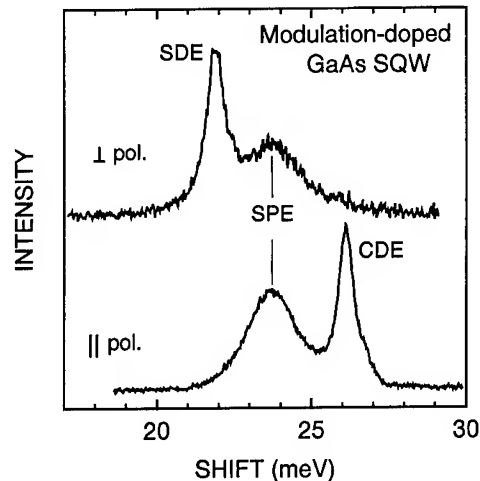


Figure 1: An example of inelastic light scattering spectra by elementary excitations of a SQW measured with parallel and crossed polarizations at 0.75 GPa.



to lower energies with respect to the SPE is due to exchange-correlations vertex corrections. The missing exchange interaction of the excited electron in the upper subband leads to an exciton-like binding to the hole left behind in the lower subband. The CDE is shifted upwards from the SDE due to the Hartree interaction or *depolarization* shift  $\alpha_{ij}$ . This shift is associated with the macroscopic electric field of the charge density fluctuations. The screening of the Coulomb interaction is taken into account by the factor  $\tilde{\epsilon}$ , which is the phonon contribution to the dielectric function of the polar lattice.

The energy of the elementary excitations as well as the many-body effects strongly depend on the 2D electron density. Electronic correlations become increasingly important at low carrier densities leading to new physical behaviors of the dilute electron gas, which exhibits a variety of quantum phases as a function of temperature, density and magnetic field.<sup>9,10,11</sup> DQW's are of particular interest because the coupling between layers introduces an additional degree of freedom. New phenomena arising from electron-electron interactions are anticipated to occur in bilayer systems due to correlations between particles in different quantum wells. For example, at low electron densities and zero magnetic field an intersubband spin-density excitonic instability has been predicted to occur in DQW's induced by enhanced exchange vertex corrections.<sup>12</sup> It has also been suggested that Wigner crystallization is favored for double-layer electron systems because of interlayer correlations.<sup>13</sup>

In a recent paper we have demonstrated that the 2D electron density can be tuned in modulation-doped GaAs SQW structures by applying hydrostatic pressure.<sup>14</sup> The pressure-induced reduction of the free carrier density by more than two orders of magnitude makes accessible the very dilute regime for studies of many-body behaviors of the electron gas by optical spectroscopies.

Here we are concerned with the elementary excitations of 2D electron gases in modulation-doped GaAs DQW structures at very low electron densities achieved by applying pressure. Using inelastic light scattering we have measured the excitation energies from which the Hartree and exchange terms of the Coulomb interaction are obtained as a function of carrier density. For this study

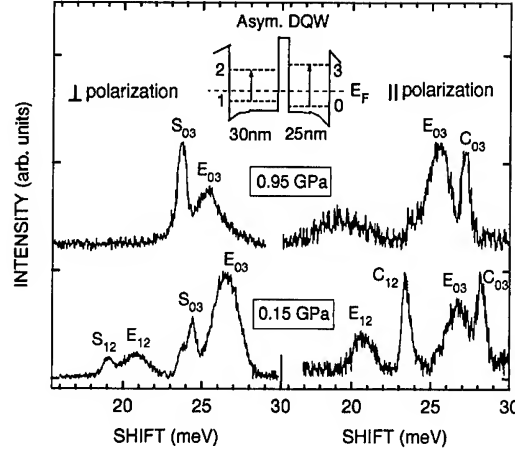


Figure 2: Depolarized ( $\perp$ ) and polarized ( $\parallel$ ) light scattering spectra of intersubband excitations of the asymmetric DQW for different pressures. The peaks labelled as  $S_{12}$ ,  $E_{12}$ ,  $C_{12}$  and  $S_{03}$ ,  $E_{03}$ ,  $C_{03}$  are assigned to spin-density (SDE), single-particle (SPE), and charge-density excitations (CDE) between the 1,2-subbands and the 0,3-subbands of the DQW, respectively, as indicated in the inset.

we have chosen an asymmetric and a symmetric DQW structure for which the relative importance of intra- and interlayer correlations is very different. In the very dilute regime we have observed for the asymmetric DQW enhanced exchange-correlation effects revealed by many-body couplings of collective and single-particle intersubband excitations. We have also obtained evidence for stronger screening effects in DQW's due to interlayer correlations which become important at low densities. These correlations play a fundamental role in a symmetric DQW, in which the quenching of macroscopic depolarization fields associated with intersubband charge-density excitations is induced by decreasing the 2D density.

## 2 Experimental

The modulation-doped GaAs/AlGaAs DQW structures were grown by MBE. The asymmetric DQW sample consists of a 300 Å and a 250 Å GaAs well separated by 50 Å of  $\text{Al}_{0.33}\text{Ga}_{0.67}\text{As}$ . In the symmetric DQW both GaAs wells are 250 Å wide and the separating AlGaAs barrier is only 35 Å thick. Further details of

the growth sequence are given elsewhere.<sup>14,15</sup> The Si doping is incorporated into the two outer AlGaAs barriers resulting in a total electron density of  $7.9(2) \times 10^{11} \text{ cm}^{-2}$  and  $7.7(2) \times 10^{11} \text{ cm}^{-2}$  for the asymmetric and symmetric DQW, respectively.

For high pressure experiments the samples were mechanically thinned to a total thickness of 35  $\mu\text{m}$ . Condensed helium was used as the pressure-transmitting medium to ensure hydrostatic conditions at low temperatures. Pressure was always changed at room temperature. Photoluminescence (PL) and light scattering spectra were excited with tunable Ti:sapphire and dye lasers and recorded using optical multichannel detection. PL measurements were performed with different power densities ranging from 2  $\text{mW/cm}^2$  to 5  $\text{W/cm}^2$ . Light scattering spectra were measured in backscattering geometry in resonance with excitonic transitions to higher excited states of the DQW.

### 3 Results and discussion

#### 3.1 The asymmetric DQW sample

The main motivation for studying a DQW system was to investigate the influence of a second highly polarizable layer of electrons on the many-body behavior of a dilute 2D electron gas. In an asymmetric DQW the wavefunctions of the discrete levels are confined to one of the wells. The energy splitting between the two lowest states is thus controlled by the difference in well width. At ambient pressure there are two occupied subbands as shown schematically in the inset to Fig. 2. In this particular structure with the 300  $\text{\AA}$  wide well closer to the sample surface, the self-consistent confining potential is such that the lowest state is confined to the thinner well.

For all the QW structures studied so far we find that the effect of increasing pressure is a continuous reduction of the 2D electron density  $n$ . This results from the different dependence on pressure of the conduction band edge, the surface states that pin the Fermi level, and the Si donor levels.<sup>14,15</sup> For a SQW sample<sup>14</sup> and the symmetric DQW discussed below, the dependence of  $n$  on pressure has been determined from a quantitative analysis of the PL lineshapes. For the asymmetric DQW sample it is not possible to determine reliable values for the 2D densities due to the spectral

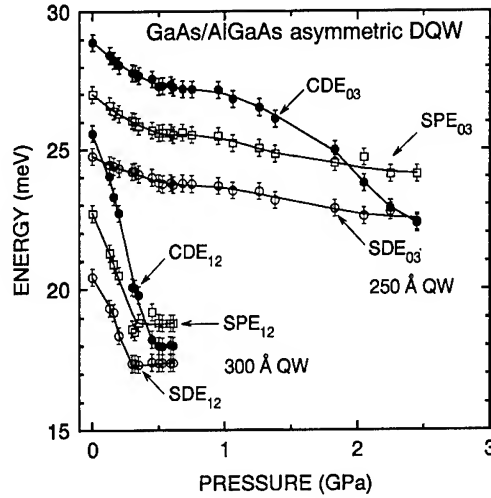


Figure 3: Dependence on pressure of the excitation energies in the asymmetric DQW. Lines are a guide to the eye.

superposition of the PL emission arising from optical transitions between different electron and hole states of the DQW. Nevertheless, the observed decrease of the total PL bandwidth with pressure clearly indicates the reduction of the carrier density. From the combined PL and light scattering data we infer that with increasing pressure the overall electron density is reduced in such a way that the 300  $\text{\AA}$  wide well is depleted first.<sup>15</sup>

The intersubband excitations studied here by inelastic light scattering are associated with electronic transitions between different confined states of the DQW as indicated by arrows in the inset to Fig. 2. Representative polarized and depolarized spectra are shown in Fig. 2 for two pressures. At low pressures we clearly distinguish two sets of excitations consisting of a broad SPE peak and sharp collective CDE and SDE features at higher and lower energy, respectively. Peaks labelled as  $S_{12}$ ,  $E_{12}$  and  $C_{12}$  correspond to intersubband excitations of the 300  $\text{\AA}$  wide well. This well is the first one to be depopulated with pressure, as indicated by the disappearance of the related features at about 0.7 GPa. The structures denoted with  $S_{03}$ ,  $E_{03}$  and  $C_{03}$  are assigned to excitations of the thinner well.

In Fig. 3 we summarize the pressure dependence of the energies of the excitations for the asymmetric DQW. The overall decrease of the ex-

citation energies with increasing pressure is a direct consequence of the pressure-induced reduction of the electron density. An interesting result concerns the crossings between the SPE's and the collective CDE's, which occur at about 0.5 GPa and 2.0 GPa for the 300 Å and 250 Å well, respectively. Such a behavior of 2D intersubband excitations has been predicted to occur at low densities.<sup>10</sup> The crossing is an indication that at these densities excitonic vertex corrections in the 2D electron gas overcome the Hartree interaction.

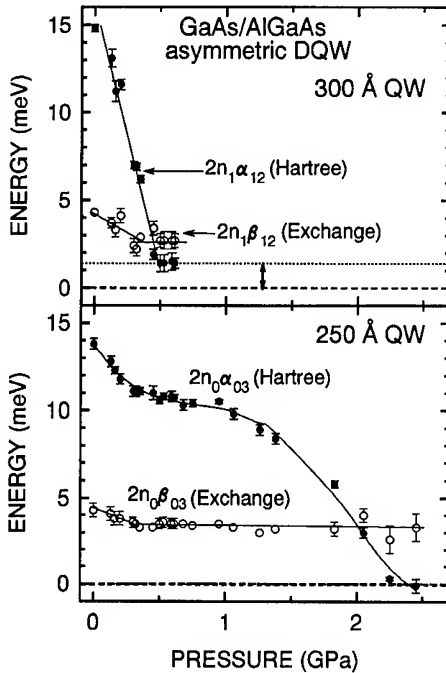


Figure 4: Dependence on pressure of the parameters  $\alpha_{ij}$  and  $\beta_{ij}$  which represent the Hartree and exchange Coulomb interactions, respectively. Lines are a guide to the eye.

Using Eq. (1) and (2) we obtain from the measured energies of the excitations the pressure dependence of the direct and exchange terms of the Coulomb interaction. The parameters  $\alpha_{ij}$  and  $\beta_{ij}$ , which account for the Hartree and exchange Coulomb interaction, respectively, are plotted in Fig. 4 as a function of pressure for both sets of intersubband transitions. A striking result is that the metal-nonmetal transition of the 2D electron gas revealed by the collapse of the Hartree term

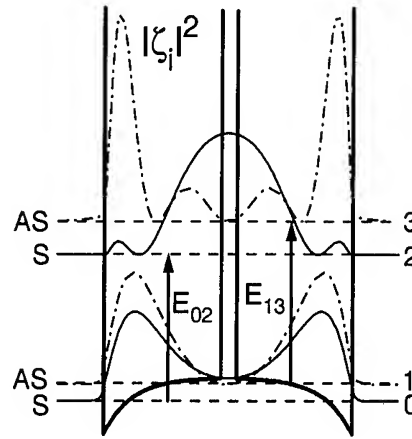


Figure 5: Confining potential of the symmetric DQW structure, energy level scheme and electronic charge densities given by the square modulus of the self-consistent envelope functions  $\zeta_i(z)$ .

(i.e. the parameter  $\alpha_{ij}$ ) at low densities<sup>14</sup> takes place only for the 250 Å wide well. For very low densities in the 300 Å well the parameter  $\alpha_{12}$  remains constant but finite. We interpret this behavior as a direct evidence for enhanced screening effects in the bilayer system. By comparing with the 250 Å SQW sample<sup>14</sup> we infer that although the density  $n_1$  of the wider well falls below the critical value determined for the single layer, the disorder potential produced by remote ionized donors is still effectively screened by the second layer of electrons due to interlayer correlations. This prevents the collapse of the macroscopic depolarization shift  $\alpha_{12}$ .

### 3.2 The symmetric DQW sample

The interlayer correlations discussed in the previous section are expected to be the largest in the case of a symmetric DQW. Degenerate states confined to different layers mix with each other forming symmetric (S) or antisymmetric (AS) linear combinations. Coupling between these levels opens up the symmetric-antisymmetric gap  $\Delta_{SAS}$  which is larger for higher excited states. Figure 5 schematically shows the electronic density along the growth direction  $z$  for the first four subbands of the symmetric DQW given by the square modulus of the corresponding envelope wavefunctions  $\zeta_i(z)$ . The subband indices are again chosen to

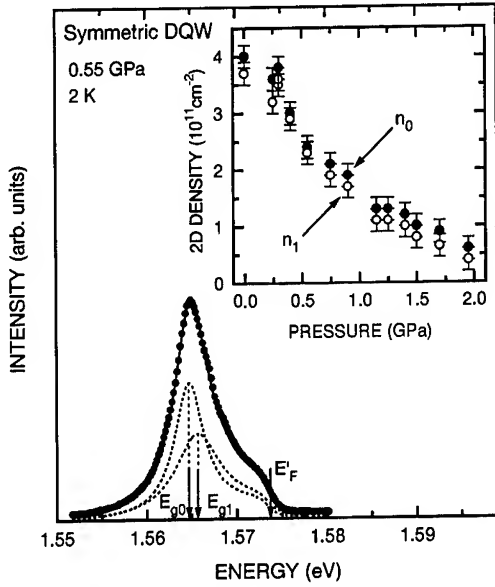


Figure 6: PL spectrum of the symmetric DQW at 0.55 GPa. Solid and dashed curves represent the results of lineshape fits. The inset shows the variation of the 2D electron densities in the DQW as a function of pressure.

increase with energy. For the S states the electronic charge density is more concentrated in the center region of the DQW compared with the AS states; the difference becoming more pronounced with increasing subband index.

For the symmetric DQW we were able to obtain the 2D densities  $n_0$  and  $n_1$  of the two occupied subbands from lineshape fits to the PL data. Figure 6 shows a typical PL spectrum of the symmetric DQW measured at 0.55 GPa with low power densities in order to minimize the hot luminescence from higher excited states. The solid curve represents the result of fitting the model function.<sup>14,15</sup> It consists of two terms (dashed lines) corresponding to the PL emission from each occupied conduction subband. The onset for radiative recombination corresponds to the bandgap  $E_g$ , whereas the PL bandwidth is given by  $E_F' = E_F(1 + m_e/m_h)$ , where  $E_F$  is the Fermi energy and the factor containing the electron and hole effective masses accounts for the different band parabolicities. In this case a quantitative analysis of the PL data is possible because the bandgap energy difference  $E_{g1} - E_{g0}$  has been experimentally determined by light scattering, as

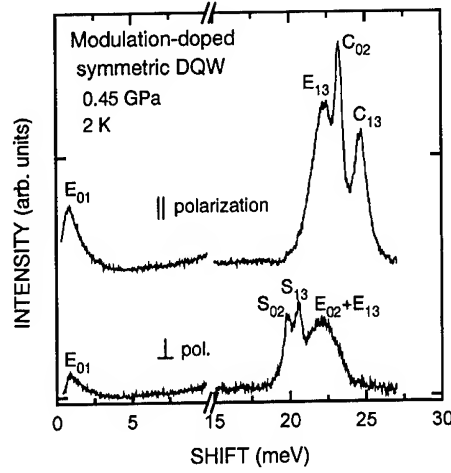


Figure 7: Polarized and depolarized light scattering spectra of the symmetric DQW at 0.45 GPa. The assignment of the peaks to charge-density ( $C_{ij}$ ), spin-density ( $S_{ij}$ ) and single-particle excitations ( $E_{ij}$ ) is indicated.

discussed below. The results for the 2D electron densities as a function of pressure are displayed in the inset to Fig. 6. A very similar pressure dependence of the carrier density has been previously obtained for a 250 Å SQW sample.<sup>14</sup> In contrast to the case of the asymmetric DQW, here the two densities are reduced with pressure by the same amount, in such a way, that the inversion symmetry of the structure is essentially retained in the whole pressure range of the experiment.

Figure 7 shows inelastic light scattering spectra of the symmetric DQW for both polarizations at 0.45 GPa. A rich structure is apparent at around 22 meV corresponding to intersubband excitations associated with electronic transitions between symmetric or antisymmetric states (see Fig. 5), as allowed by symmetry. At very low energies ( $\approx 1$  meV) a well defined peak is observed for both polarizations. We interpret this feature as the SPE between the two lowest subbands of the DQW with energy  $E_{01}$ , i.e. it appears at the gap energy  $\Delta_{SAS}$ . Such an excitation together with the collective ones have been previously observed for a similar modulation-doped DQW by Decca et al.<sup>4</sup> Although this transition is forbidden by symmetry it might be activated by interface roughness. With increasing pressure the excitations at

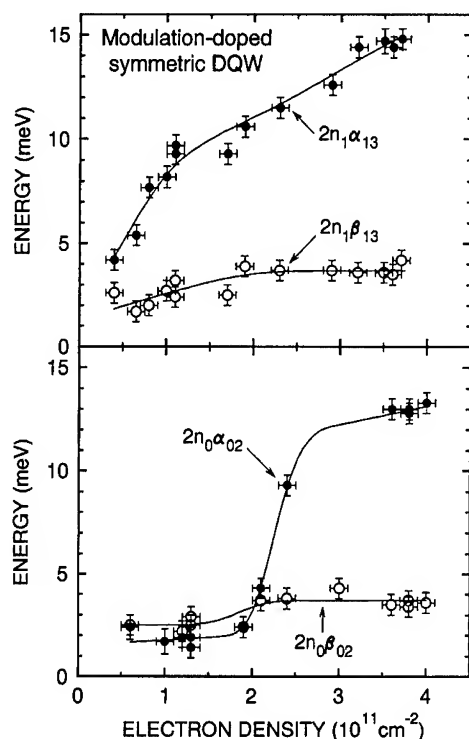


Figure 8: Dependence on electron density of the depolarization ( $\alpha_{ij}$ ) and excitonic ( $\beta_{ij}$ ) shifts for the symmetric DQW. Lines are a guide to the eye.

higher energy exhibit a redshift according to the reduction of the electron density, but they are observable in the entire pressure range up to 2 GPa. The position of the low energy peak, on the contrary, is fairly independent on pressure. This behavior is consistent with the fact that the Fermi energy is always larger than the  $\Delta_{SAS}$  splitting and that the two lowest subbands remain occupied with electrons.<sup>4,12</sup>

From the differences in the excitation energies we obtain the depolarization and excitonic shifts which are plotted in Fig. 8 as a function of electron density. Absolute values and the almost linear dependence at intermediate densities  $5 \times 10^{10} < n < 5 \times 10^{11} \text{ cm}^{-2}$  compare well with the results obtained for a 250 Å SQW.<sup>14</sup> The depolarization shift  $\alpha_{02}$  is an exception showing a pronounced decrease in its magnitude at a relatively high electron density of  $2.5 \times 10^{11} \text{ cm}^{-2}$ . Such behavior is a unique characteristic of symmetric DQW's and it cannot be ascribed to the same many-body cou-

pling which causes the crossing between SPE and CDE at much lower densities in other QW structures. The quantity  $\alpha_{02}$  is a measure of the effects of the depolarization field created by coherent addition of the dipole moments associated with transitions between both *symmetric* states. From the electronic charge densities of Fig. 5 it can be seen that the promotion of an electron to the excited S subband, leaving a hole in the lower one, induces two electric dipoles pointing in opposite directions roughly 280 Å apart (approximately the distance between the quantum well centers). The mean particle separation within each well, which is given by twice the Wigner-Seitz radius  $r_s$ , increases with decreasing electron density. For  $n_0 = 2.2 \times 10^{11} \text{ cm}^{-2}$  the interparticle distance  $2r_{s,0} = 250$  Å is of the same order of the dipoles separation, thus leading to a mutual cancellation of the dipole electric fields for other electrons in the wells. This explains the abrupt decrease of  $\alpha_{02}$  at high densities. A similar effect occurs for  $\alpha_{13}$  but at much lower densities because the induced dipoles are further apart for intersubband transitions between the antisymmetric states.

#### 4 Summary

In summary, we have studied electron gases in modulation-doped semiconductor DQW structures, whose electron density has been tuned by applying hydrostatic pressure. Using inelastic light scattering we have measured the elementary excitations of the 2D electron gas, from which we determine the Hartree and exchange terms of the Coulomb interaction. Here we show that the crossing between SPE and collective CDE in the dilute regime due to enhanced exchange vertex corrections is a general characteristic of intersubband excitations of the 2D electron gas, which is observed in SQW as well as in DQW structures. The metal-nonmetal transition observed at very low densities for a single layer electron gas, which is driven by the disorder potential of remote impurities, is inhibited for one of the layers of an asymmetric DQW due to a more efficient screening in the correlated bilayer system. In a symmetric DQW prominent interlayer electronic correlations are at the origin of the large reduction of the depolarization shifts observed at high electron densities  $n > 1 \times 10^{10} \text{ cm}^{-2}$  for intersubband excitations between symmetric states. In this way,

we have provided new and clear evidence for the striking effects of electron-electron interactions in bilayer electron gases.

### Acknowledgments

We thank M. Hauser, W. Dieterich, U. Oelke, and U. Engelhardt for expert technical assistance and H. Wendel for the preparation of samples.

### References

1. T. Ando, A.B. Fowler and F. Stern, *Rev. Mod. Phys.* **54**, 457 (1982).
2. *Proc. of the 9<sup>th</sup> International Conference on Electronic Properties of 2-Dimensional Systems (EP2DS)*, Nara, Japan, 1991 [*Surf. Sci.* **263** (1992)]; *Proc. of the 10<sup>th</sup> EP2DS*, Newport, USA, 1993 (in press).
3. Y.W. Suen, L.W. Engel, M.B. Santos, M. Shayegan and D.C. Tsui, *Phys. Rev. Lett.* **68**, 1379 (1992); J.P. Eisenstein, G.S. Boebinger, L.N. Pfeiffer, K.W. West and Song He, *ibid.* **68**, 1383 (1992).
4. R. Decca, A. Pinczuk, S. Das Sarma, B.S. Dennis, L.N. Pfeiffer and K.W. West, *Phys. Rev. Lett.* **72**, 1506 (1994).
5. T.J. Gramila, J.P. Eisenstein, A.H. MacDonald, L.N. Pfeiffer and K.W. West, *Phys. Rev. B* **47**, 12957 (1993), and references therein.
6. A. Pinczuk and G. Abstreiter, in *Light Scattering in Solids V*, ed. M. Cardona and G. Güntherodt (Springer, Berlin, 1989), and references therein.
7. A. Pinczuk, S. Schmitt-Rink, G. Danan, J.P. Valladares, L.N. Pfeiffer and K.W. West, *Phys. Rev. Lett.* **63**, 1633 (1989); D. Gammon, B.V. Shanabrook, J.C. Ryan, D.S. Katzer and M.J. Yang, *Phys. Rev. Lett.* **68**, 1884 (1992).
8. S.L. Chuang, M.S.C. Luo, S. Schmitt-Rink and A. Pinczuk, *Phys. Rev. B* **46**, 1897 (1992); T. Ando, *J. Phys. Soc. Jpn.* **51**, 3893 (1982); A.C. Tselis and J.J. Quinn, *Phys. Rev. B* **29**, 3318 (1984); L. Wendler and V.G. Grigoryan, *Solid State Commun.* **71**, 527 (1989); D.A. Dahl and L.J. Sham, *Phys. Rev. B* **16**, 651 (1977).
9. R. Price, P.M. Platzman and S. He, *Phys. Rev. Lett.* **70**, 339 (1993); B. Tanatar and D. Ceperly, *Phys. Rev. B* **39**, 5005 (1989); D.C. Glatli, G. Deville, V. Duburcq, F.I.B. Williams, E. Paris, B. Etienne and E.Y. Andrei, *Surf. Sci.* **229**, 344 (1990).
10. S. Das Sarma and I.K. Marmorkos, *Phys. Rev. B* **47**, 16343 (1993); I.K. Marmorkos and S. Das Sarma, *ibid.* **48**, 1544 (1993).
11. S.T. Chui and B. Tanatar, *Phys. Rev. Lett.* **74**, 458 (1995).
12. S. Das Sarma and P.I. Tamborenea, *Phys. Rev. Lett.* **73**, 1971 (1994); P.I. Tamborenea and S. Das Sarma, *Phys. Rev. B* **49**, 16821 (1994).
13. L. Swierkowski and D. Neilson, *Phys. Rev. Lett.* **67**, 240 (1991); D. Neilson, L. Swierkowski, A. Sjölander and J. Szymański, *Phys. Rev. B* **44**, 6291 (1991).
14. S. Ernst, A.R. Goñi, K. Syassen and K. Eberl, *Phys. Rev. Lett.* **72**, 4029 (1994).
15. A.R. Goñi, S. Ernst, K. Syassen and K. Eberl, *J. Phys. Chem. Solids* **56**, 367 (1995).

# **QUANTUM HALL EFFECT IN Be-DOPED GaAs/AlGaAs HETEROSTRUCTURE UNDER UNIAXIAL COMPRESSION**

O.P.Hansen<sup>a)</sup>, W.Kraak<sup>b)</sup>, N.Minina<sup>c)</sup>, J.S.Olsen<sup>a)</sup>, A.Savin<sup>c)</sup>, B.Saffian<sup>b)</sup>

<sup>a)</sup> Niels Bohr Institute, Oersted Laboratory, DK-2100 Copenhagen, Denmark

<sup>b)</sup> Institute of Solid State Physics, Humboldt University, D-10115 Berlin, Germany

<sup>c)</sup> Physics Department, Moscow State University, 119899 Moscow, Russia

Quantum Hall effect and quantum oscillations of magnetoresistance in a 2D hole gas on p-GaAs/Al<sub>0.5</sub>Ga<sub>0.5</sub>As (001) heterostructure interface indicate that under uniaxial compression in [110] direction a redistribution of carriers between two spin-split uppermost heavy hole subbands takes place while the total concentration density remains almost unchanged. A reduction of spin-splitting under uniaxial stress is suggested.

Owing to 4 fold degeneracy of GaAs valence band, a two-dimensional (2D) hole gas on GaAs/AlGaAs heterostructure interface reveals extremely complicated energy spectra of heavy hole and light hole subbands [1,2,3], that dramatically change under uniaxial stress [4]. Although uniaxial stress is acknowledged to be a powerful tool for investigation of electronic properties of 3D and 2D systems, only optical measurements of 2D hole gas in semiconductor heterostructures were performed under uniaxial compression and, to the best of our knowledge, no information of magnetotransport experiments in this field exists in the literature.

We have investigated quantum Hall (QH) effect in magnetic field up to 10T in a 2D hole gas at a Be-doped GaAs/Al<sub>0.5</sub>Ga<sub>0.5</sub>As heterostructure (100) interface under in-plane uniaxial compression in [110] direction up to  $\sigma=2.8$ kbar. At T=1.6K several numbers of rather well resolved QH plateaus have been detected both at  $\sigma=0$  and  $\sigma=2.8$ kbar (Fig.1). The QH plateau numbers  $\nu$  (filling factors) plotted versus the inverse magnetic field  $B_V^{(*)}$  permit to calculate the slope of  $S=\nu/(1/B_V)$  that determines the total 2D hole concentration density  $N_S=\nu B_V/(h/e)=S/(h/e)$ . At zero pressure  $S=40.2$ T and  $N_S=9.7 \cdot 10^{11} \text{cm}^{-2}$ . The last magnitude is in a fair agreement with the value  $1/eR_{\text{Hall}}=9.72 \cdot 10^{11} \text{cm}^{-2}$  obtained from the Hall measurements in a weak field.

\* More precisely  $B_V$  can be determined from the position of the corresponding  $\partial \rho_{xy} / \partial B$  minima.

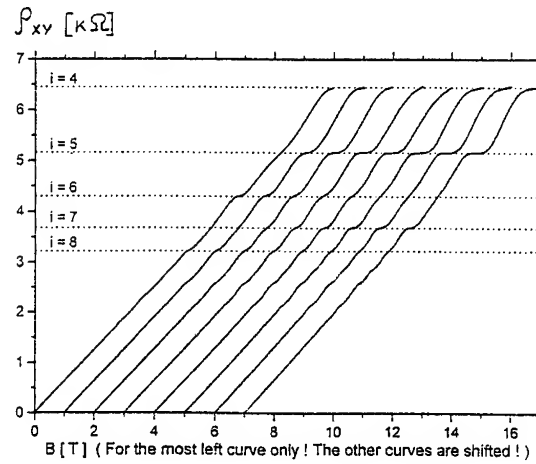


Fig.1. Hall resistivity as a function of the magnetic field for different uniaxial stress from left to right at 0; 0.51; 0.97; 1.4; 1.8; 2.35; 2.53; 2.81kbar. The curves are shifted with a mutual distance of 1T. The QH plateau numbers are denoted.

Under the uniaxial compression up to 2.8kbar the total concentration exhibits only a slight 4% decrease. At the same time the resistance  $\rho_{xx}(0)$  of the 2D hole system reveals about 1.5 times decrease, and there occurs a strong change in the QHE plateau picture. Some plateaus that were not resolved at  $\sigma=0$  become more pronounced under the pressure and quite the reverse - those ones that were well detectable at  $\sigma=0$  almost disappear (Fig.1). In low magnetic field a positive magnetoresistance is observed and  $\rho_{xx}(B)$

dependence decreases when the pressure is applied.

According to the ref. [1,2,3], in the 2D hole gas of the similar heterostructure there exists below the Fermi level only the uppermost heavy hole subband that is spin-split into two different so-called "spin-subbands" because of the lack of inversion symmetry in the asymmetrical triangular quantum well. The effective mass in the more populated spin-subband was found to be almost two times more heavy than in the less populated subband [2]. It should be noted that in a square (symmetric) quantum well only one effective mass was detected and the uppermost heavy hole subband remains doubly degenerated [3].

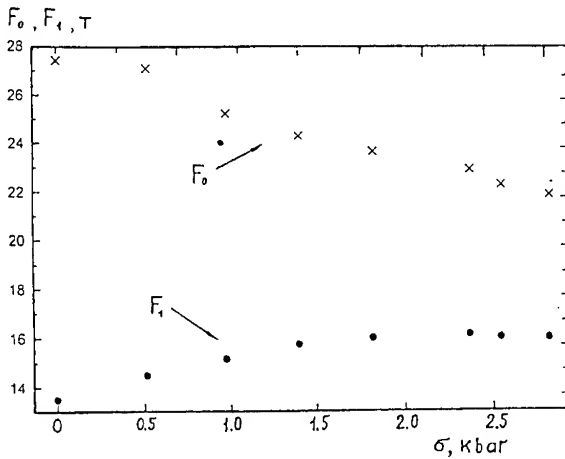


Fig.2. Pressure dependence of the two SdH oscillation frequencies from Fourier-transform in magnetic fields  $B=1-4$  T at 1.6 K.

The change which we observe in the QH plateaus width under stress becomes understandable if results of Shubnikov-de Haas (SdH) measurements are taken into consideration. SdH data indicate two frequencies in magnetoresistance oscillations: decreasing  $F_0$  and increasing  $F_1$  in dependence on applied stress  $\sigma$  (Fig.2). Assuming them to belong to two different spin-subbands with indexes  $i=0$  and  $i=1$ , we can find the corresponding concentration densities  $n_i$  from relation:  $F_i = n_i \cdot h/e$ . In the more populated spin-subband "0" carrier

concentration  $n_0 = 6.56 \cdot 10^{11} \text{ cm}^{-2}$  at  $\sigma=0$  decreases under compression to  $n_0 = 5.38 \cdot 10^{11} \text{ cm}^{-2}$  at  $\sigma=2.8$  kbar, while in the spin-subband "1" it increases from  $n_1 = 3.28 \cdot 10^{11} \text{ cm}^{-2}$  at  $\sigma=0$  to  $n_1 = 3.94 \cdot 10^{11} \text{ cm}^{-2}$  at  $\sigma=2.8$  kbar. One can see that the total concentration  $N_s = n_0 + n_1$  reveals only 5% decrease in a good agreement with the value obtained from the Hall measurements. It implies the redistribution of carriers under compression going mainly between subband "0" and "1".

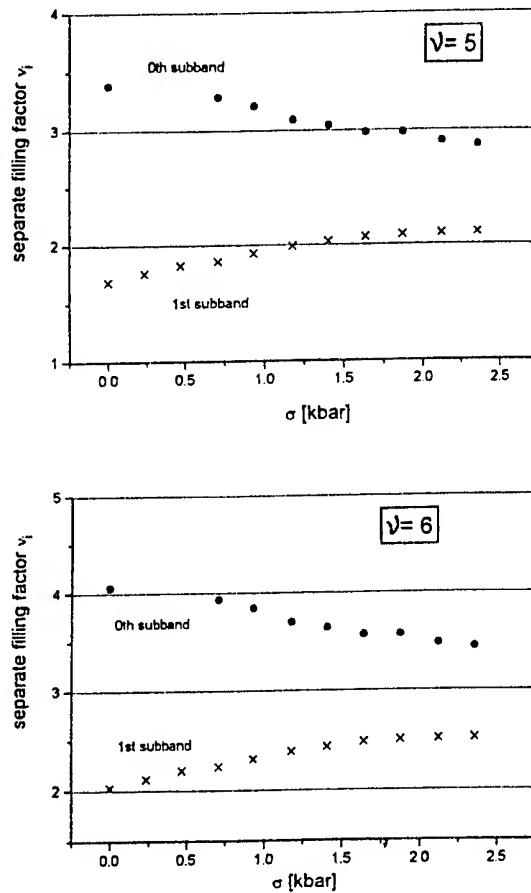


Fig.3. Separate subband filling factors as a function of applied uniaxial stress for total filling factors  $\nu=5$  and  $\nu=6$ .

As far as the Landau level degeneracy in a magnetic field  $B_v$ , corresponding to the QH plateau  $\nu$ , is  $B_v/(h/e)$ , the separate filling factors  $\nu_i$



for the both spin-subbands can be calculated from the relation  $\nu_i = \nu \cdot n_i / N_s$  ( $i=0,1$ ), where the total filling factor  $\nu = \nu_0 + \nu_1$ . Values of  $\nu_i$  versus the stress  $\sigma$  for the two spin-subbands "0" and "1" are shown on Fig.3 for  $\nu=5$  and  $\nu=6$ ; the analogous pictures take place for  $\nu=4$  and  $\nu=7$ . Now we can conclude that QH plateaus are well resolved in the case when the corresponding separate filling factors are nearly integer and are smeared if  $\nu_i$  are not integer. The observed change in the QH plateaus resolution under stress (Fig.1) may occur only if we really have at least two different independent sets of Landau levels that shift relative to each other when the pressure is applied.

Strong drop of  $\rho_{xx}(0)$  under stress in 2D hole system with almost constant carrier concentration means increase of mobility and together with the observed decrease of  $\rho_{xx}(B)$  in low magnetic fields implies reduction of the difference between effective masses in "0" and "1" spin-subbands. As far as the carrier redistribution in favor of less populated subband "1" has been detected, we can assume that strong non-parabolic  $E(k_{||})$  dispersion curves for the both spin subbands become closer to each other in  $k$ -space. It means that the uniaxial stress reduces the spin-splitting in the uppermost heavy hole subband under investigation.

Quantitative evaluation of this reduction is possible if effective masses in "0" and "1" subbands as well as their dependence on applied stress are determined. At present the preliminary results on the temperature dependence of SdH amplitude indicate that at  $B=0$  the effective mass  $m_1^*$  in the spin subband "1" reveals about 30% increase under compression  $\sigma \approx 2.8$  kbar.

This work has been supported by NATO Likage Grant 931579 and by grants 11-1080-1, 11-1124-1 and 9401081 from the Danish Research Council. C.B. Sorensen is acknowledged for the sample growth and contact preparation.

1. U.Ekenberg, M.Altarelli. *Phys. Rev. B* **32** (1982) 3712.
2. H.L.Stormer, Z. Schlesinger, A.Chang, D.S.Tsui, A.C.Gossard, W.Wiegmann, *Phys.Rev. Lett.* **51** (1983) 126.
3. J.P.Eisenstein, H.L.Stormer, V.Narayanamurti, A.C.Gossard, W.Wiegmann. *Phys. Rev. Lett.* **53** (1984) 2579.
4. B.Gil, P.Lefebvre, H.Mathieu, G.Platero, Altarelli, T.Fukunaga, H.Nakashima. *Phys. Rev. B* **38** (1988) 1215.

# ABSORPTION OF ZnSe/ZnSSe AND ZnCdSe/ZnSe SUPERLATTICES UNDER HIGH HYDROSTATIC PRESSURE

E. GRIEBL and G.F. SCHÖTZ, W. KERNER, CH. BIRZER, T. REISINGER, B. HAHN and W. GEBHARDT

*Inst. für Festkörperphysik, Universität Regensburg, 93040 Regensburg, Germany*

We present measurements of two pseudomorphic superlattices, ZnSe/ZnS<sub>0.24</sub>Se<sub>0.76</sub> and Zn<sub>0.82</sub>Cd<sub>0.18</sub>Se/ZnSe, under high hydrostatic pressure applied by a diamond anvil cell (DAC). Excitonic transitions as 1s-heavy hole, 1s-light hole and in ZnSe/ZnSSe also 2s-heavy hole between the first mini-bands are visible. Transition energies are well understood by calculations of the band structure near  $\Gamma$  which take strain effects into account. Calculations for the ZnSe/ZnS<sub>0.24</sub>Se<sub>0.76</sub>-superlattice suggest to a type-II to type-I transition. Experimental evidence for this gives an increase of the 1s-2s-energy distance, which is caused by an increase of the electron confinement.

## 1 Samples and experimental setup

The presented structures were grown on (001)-GaAs-substrates. A 20x ZnSe/ZnS<sub>0.24</sub>Se<sub>0.76</sub>-superlattice (SL) with 10nm well and barrier thickness on a 770nm ZnS<sub>0.13</sub>Se<sub>0.87</sub> buffer layer was grown by MOCVD, a 20x Zn<sub>0.82</sub>Cd<sub>0.18</sub>Se/ZnSe-SL,  $d_w=1.4$ nm,  $d_b=3.3$ nm on a 600nm ZnSe-Buffer was prepared by MBE. The substrate was selectively etched off by a mixture of 82% NaOH and 18% H<sub>2</sub>O<sub>2</sub> (30%) solution. For high pressure measurements we used a gasketed Syassen-Holzappel-type DAC with liquid helium as pressure transmitting medium and ruby fluorescence for pressure calibration.

## 2 Optical transition energies: simple calculations

### 2.1 Strain of heterostructures

First of all the hydrostatic and biaxial strain ( $\epsilon_{hyd}$ ,  $\epsilon_{bi}$ ) of the superlattice was calculated as a function of the applied hydrostatic pressure  $P$ . In order to derive  $\epsilon_{hyd}$  from  $P$  we used the Murnaghan-equation<sup>13</sup>

$$\epsilon_{hyd} = \left(1 + \frac{B'_0}{B_0} P\right)^{-\frac{1}{3B'_0}} - 1 \quad (1)$$

The bulk module  $B_0$  and its pressure derivative  $B'_0$  for binary compounds is given in table 1. At ternary compounds we used a linear interpolation.

The lattice constant  $a_{hyd}$  under pure hydrostatic pressure is given by  $a_{hyd} = a_0 \cdot (1 + \epsilon_{hyd})$ . An averaged lattice constant  $\bar{a} = \sum_i a_{hyd}^i d^i$  was taken to determine the biaxial strain of each layer  $i$  with thickness  $d^i$ :

$$\epsilon_{bi}^i = \frac{\bar{a} - a_{hyd}^i}{a_{hyd}^i} \quad (2)$$

If samples are etched off the substrate,  $\bar{a}$  is close to the lattice constant of the buffer layer.

Under the present experimental conditions an additional biaxial strain in the (001)-plane was observed due to freezing of the helium in the DAC. This was taken into account in the calculations.

### 2.2 Strain effects on the band structure

Strain effects on the energies of valence- and conduction band (vb, cb) at the  $\Gamma$ -point were calculated by F. Pollak<sup>14</sup>. The energy shift under hydrostatic and biaxial strain within the 001-plane is given for the conduction band and the heavy hole- and light hole- (hh, lh) component of the valence band:

$$\begin{aligned} E_{cb} &= E_0 + \delta E_{cb} \\ E_{vb}^{hh} &= \delta E_{vb} + \delta E_s \\ E_{vb}^{lh} &= \delta E_{vb} - \frac{1}{2}(\Delta_0 - \delta E_s) \\ &\quad + \frac{1}{2}\sqrt{\Delta_0^2 + 2\Delta_0\delta E_s + 9\delta E_s^2} \end{aligned} \quad (3)$$

with the abbreviations:

$$\begin{aligned} \delta E_{cb/vb} &= a_{c/v} \left( 3\epsilon_{hyd} + \left( 2 - \frac{2C_{12}}{C_{11}} \right) \epsilon_{bi} \right) \\ \delta E_s &= -b \left( 1 + \frac{2C_{12}}{C_{11}} \right) \epsilon_{bi} \end{aligned}$$

where  $E_0$  is the fundamental gap energy,  $\Delta_0$  the split off energy.  $a_v$ ,  $a_c$  and  $b$  are the hydrostatic valence band-, conduction band- and the biaxial-deformation potential. At ternary compounds linear interpolations of binary parameters were used again; bowing of  $E_0$  and  $\Delta_0$  was taken into account. Bowing parameters:

Table 1: material parameters of cubic crystals (<sup>†</sup>: derived from ZnSe; <sup>‡</sup>: calculated; \*: at 2K)

	ZnSe	ZnS	CdSe
$a_0$ [Å]*	5.6596 <sup>18</sup>	5.4041 <sup>15</sup>	6.0672
$C_{11}$ [GPa]	85.9 <sup>10</sup>	106.7 <sup>5</sup>	66.7 <sup>21</sup>
$C_{12}$ [GPa]	50.6 <sup>10</sup>	66.6 <sup>5</sup>	46.3 <sup>21</sup>
$E_0$ [eV]*	2.8234 <sup>1</sup>	3.837 <sup>1</sup>	1.757 <sup>1</sup>
$\Delta_0$ [meV]*	432 <sup>1</sup>	68 <sup>1</sup>	410 <sup>1</sup>
$a$ [eV]	-4.9 <sup>1</sup>	-5.0 <sup>19</sup>	-2.7 <sup>1</sup>
$b$ [eV]	-1.14 <sup>1</sup>	-0.75 <sup>3</sup>	-0.65 <sup>†</sup>
$a_v$ [eV]	-1.0 <sup>17</sup>	-1.8 <sup>17</sup>	-0.6 <sup>†</sup>
$m_c/m$	0.145 <sup>12</sup>	0.221 <sup>12</sup>	0.12 <sup>†7</sup>
$\gamma_1$	2.45 <sup>6</sup>	3.4 <sup>9</sup>	3.33 <sup>†7</sup>
$\gamma_2$	0.61 <sup>6</sup>	1.3 <sup>9</sup>	1.11 <sup>†7</sup>
$B_0$ [GPa]	62.4 <sup>10</sup>	75.0 <sup>19</sup>	53 <sup>21</sup>
$B'_0$	4.77 <sup>10</sup>	4.0 <sup>19</sup>	4.77 <sup>†</sup>

$$-\text{ZnSSe}: b_{E_0} = 0.51^1, b_{\Delta_0} = -0.22^1$$

$$-\text{ZnCdSe}: b_{E_0} = 0.35^1, b_{\Delta_0} = 0^1$$

However, the elastic moduli  $C_{11}$  and  $C_{12}$  show a weak pressure dependence which is known for ZnSe to be  $\frac{\partial C_{11}}{\partial P} = 4.44^{10}$  and  $\frac{\partial C_{12}}{\partial P} = 4.93^{10}$ .  $b$  of ZnSe is also dependent on  $P$ :  $\frac{\partial b}{\partial P} = -0.17 \frac{\text{eV}}{\text{GPa}}$ <sup>16</sup>. These values are used for all compositions.

In order to derive the absolute band structure the band offsets of ZnSe/ZnS<sub>x</sub>Se<sub>1-x</sub> and Zn<sub>x</sub>Cd<sub>1-x</sub>Se/ZnSe must be known. From the observed transitions  $n_{cb}=1 \rightarrow n_{vb}=1$  it is not possible to obtain bandoffsets. Therefore we used results of photoreflection measurements on single quantum wells, which yield  $\Delta E_c(\text{ZnSe/ZnSSe}) = -6 \text{ meV}$  and  $\Delta E_c(\text{ZnCdSe/ZnSe}) = 140 \text{ meV}$ <sup>8</sup>. The valence band offset of ZnSe/ZnSSe is negative, but too small to confine electrons in the ZnSe-well.

### 2.3 Bound states, minibands

Bound energy states  $E_n$  in uncoupled type-I single quantum wells are well known<sup>20</sup>. For superlattices these states are broadened to "minibands". If coupling of vb and cb is neglected, the miniband energies  $E_n$  are given by the solutions of the dispersion relation<sup>20</sup>:

$$\left| -\frac{1}{2} \left( \tilde{\xi} - \frac{1}{\tilde{\xi}} \right) \sin(k_w L_w) \sinh(\kappa_b L_b) + \cos(k_w L_w) \cosh(\kappa_b L_b) \right| \leq 1 \quad (4)$$

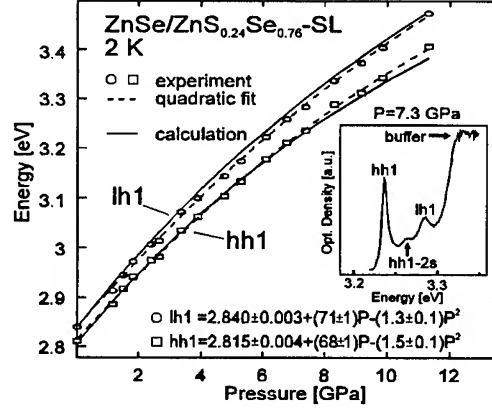


Figure 1: Experimental and calculated pressure dependence of the hh1- and lh1-absorption of the 20x ZnSe/ZnS<sub>0.24</sub>Se<sub>0.76</sub>-SL

with zero energy at the bottom of the well and  $L_w, L_b$ : well-, barrier-thickness;  $\tilde{\xi} = \frac{k_w}{\kappa_b} \times \frac{m_{eff,b}}{m_{eff,w}}$ ;  $k_{w,n} = \sqrt{\frac{2m_{eff,w}E_n}{\hbar^2}}$ ,  $\kappa_{b,n} = \sqrt{\frac{2m_{eff,b}(\Delta E_{cb/vb} - E_n)}{\hbar^2}}$ .  $\Delta E_{cb/vb}$  is the band offset of cb or vb,  $m_{eff,b/w}$  are the effective masses  $m_{cb}, m_{hh/lh} = \frac{m_c}{\gamma_1 \mp 2\gamma_2}$ . At the ZnSe/ZnSSe type-II-superlattice (negative valence band offset at low pressures) a transition from the conduction band of the barrier to confined hole states was supposed.

Electronic transitions have excitonic character. An increase of the excitonic binding energy  $R$  under pressure is caused by a change of the confinement, the effective masses and the dielectric constant  $\epsilon_{stat}$ . In this work we used an analytical model by H. Mathieu et al<sup>11</sup>. Change of carrier masses and of  $\epsilon_{stat}$  was taken into account<sup>2</sup>.

## 3 Experimental results and discussion

### 3.1 ZnSe/ZnS<sub>0.24</sub>Se<sub>0.76</sub>-SL

The averaged sulfur concentration and lattice constant of this SL is approximately the same as that of the buffer layer. Therefore the structure shows no relaxation effects although the layers are 10nm thick. A quadratic fit of the measured pressure dependence of the hh1- and lh1-absorption energies is given in figure 1. This agrees well with the theoretical transition energies mentioned above. The results of the calculations suggest to a transition from type-II to type-I structure at 2.4GPa (see fig 2). This is evidenced experimentally by an in-

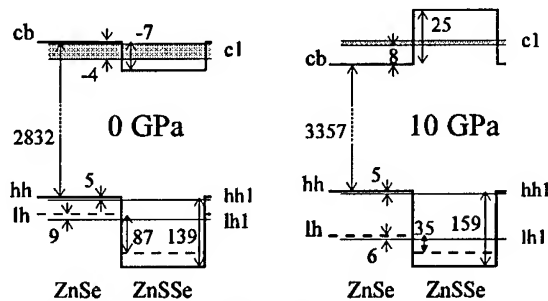


Figure 2: ZnSe/ZnSe<sub>0.24</sub>Se<sub>0.76</sub>-SL: calculated band structure at P=0 GPa and P=10 GPa (energies given in meV)

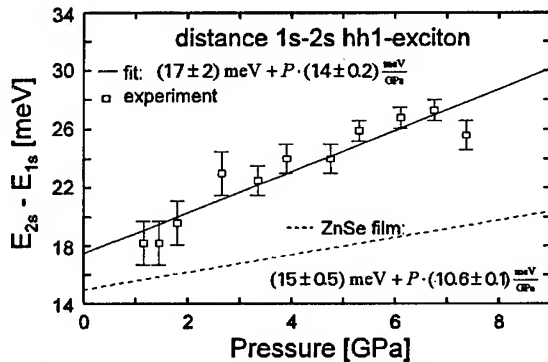


Figure 3: ZnSe/ZnSe<sub>0.24</sub>Se<sub>0.76</sub>-SL: 1s-2s distance of hh1

crease of the distance of the hh1-1s and hh1-2s absorption, which is considerably stronger than in pure ZnSe<sup>2</sup> and caused by an increase of the electron confinement (see fig. 3)

### 3.2 Zn<sub>0.82</sub>Cd<sub>0.18</sub>Se/ZnSe-SL

This superlattice is grown on a ZnSe buffer, which leads to a strong compression of the ZnCdSe wells. Their thickness was always kept below the critical thickness to avoid plastic relaxation. Figure 4 shows the measured and calculated pressure shift of transitions  $n_{cb}=1 \rightarrow n_{vb}=1$ . The theoretical calculations fit well to the experimental data, but note, that some parameters of cubic CdSe were not available and had to be extrapolated (see tab. 1) The FWHM of the absorption bands increase with pressure in both investigated systems, however this was especially strong in the ZnCdSe/ZnSe-SL. As at the ZnSe/ZnSSe-SL a phase transition (zincblende  $\rightarrow$  rocksalt structure) took place at 13.5 GPa.

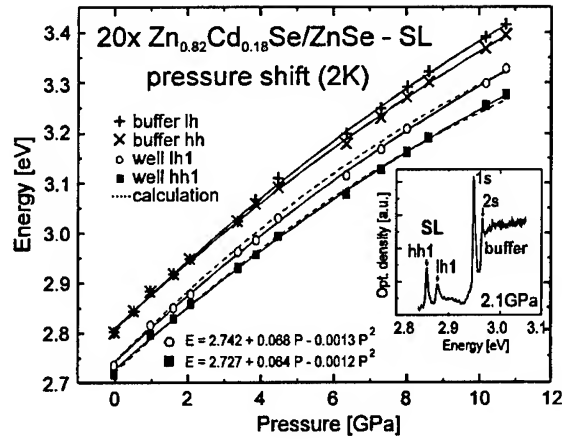


Figure 4: Experimental and calculated pressure dependence of the hh1- and lh1-absorption of the 20x Zn<sub>0.82</sub>Cd<sub>0.18</sub>Se/ZnSe-SL and quadratic fit of experiment

### Acknowledgments

This work was supported by the Deutsche Forschungsgemeinschaft (DFG).

### References

1. G.F. Schötz, Thesis (Roderer, Regensburg 1995).
2. E. Griehl et al, *Act. Phys. Pol.*, accepted (1995)
3. A. Blacha et al, *Phys. Stat. Sol. b* **126**, 11 (1984)
4. A.R. Göni et al, *Phys. Rev. B* **41**, 10111 (1990)
5. R.B. Hall, J.D. Meakin, *Thin Solid Films* **63**, 203 (1979)
6. H.W. Hölscher et al, *Phys. Rev. B* **31**, 2379 (1985)
7. Y. D. Kim et al, *Phys. Rev. B* **49**, 7262 (1994)
8. S. Lankes et al, *Phys. Stat. Sol.*, accepted (1995).
9. P. Lawaetz, *Phys. Rev. B* **4**, 3460 (1971)
10. B.H. Lee, *J. Appl. Phys.* **41**, 2988 (1970)
11. H. Mathieu et al, *Phys. Rev. B* **46**, 4092 (1992)
12. N. Miura, Y. Imanaka, *II-VI-Compounds and semimagnetic semicond.; Material Sc. Forum* **182-184** (Trans Tech Publications, Swiss 1994).
13. F.D. Murnaghan, *Proc. Nat. Acad. Sci.* **30**, 244 (1944).
14. F.H. Pollak in *Semicond. and Semimetals* **32**, ed.: T.P. Pearsall (Academic Press, New York 1992).
15. R.R. Reeber, *Phys. Stat. Sol.(a)* **32**, 321 (1975)
16. B. Rockwell et al, *Phys. Rev. B* **44**, 11307 (1991)
17. G.F. Schötz et al, *J. Phys. Cond. Mat.* **7**, 795 (1995)
18. B. Seagull, D.T.F. Marple in *Physics and Chemistry of II-VI Compounds* eds.: M. Aven, J.S. Prener (North Holland, Amsterdam 1967).
19. S. Ves et al, *Phys. Rev. B* **42**, 9113 (1990)
20. C. Weissbuch in *Semicond. and Semimetals* **24** ed.: R. Dingle (Academic Press, New York 1987).
21. D.M. Young et al, *Phys. Rev. B* **49**, 7424 (1994)

# PHOTOREFLECTANCE SPECTROSCOPY OF GaAs/Al<sub>x</sub>Ga<sub>1-x</sub>As SQW STRUCTURES UNDER PRESSURE

C. ULRICH, A.R. GOÑI, K. EBERL, and K. SYASSEN

*Max-Planck-Institut für Festkörperforschung, Heisenbergstr. 1, D-70569 Stuttgart, Germany.*

We have measured room temperature photorefectance spectra of a modulation-doped GaAs/Al<sub>0.3</sub>Ga<sub>0.7</sub>As single quantum well structure at hydrostatic pressures up to 9.5 GPa. Transitions between confined electron and hole states of the quantum well with subband index up to 6 are observed. The optical transition energies increase sublinearly with pressure. The renormalization of transition energies is observed to vanish near 1.5 GPa due to the depletion of carriers in the well. Above 1.5 GPa, the linear pressure coefficients decrease with increasing subband index. Based on a *k*·*p* calculation within the envelope-function approximation this behavior is in part attributed to the increase in effective masses and related changes in confinement energies

## 1 Introduction

Modulation-doped single quantum well (SQW) structures are particularly suitable for studying the behavior of 2D electron gases. Recently it was demonstrated that external pressure allows to continuously tune the 2D electron density in a given SQW sample with simultaneous access for optical investigations.<sup>1</sup> We report here a study of the electronic structure of doped and undoped GaAs/Al<sub>0.3</sub>Ga<sub>0.7</sub>As SQW samples using photorelectance (PR) spectroscopy. The primary motivation was to investigate optical transitions involving higher-lying SQW subbands over a wide pressure range ( $P \leq 10$  GPa), with particular emphasis on the pressure dependence of band renormalization and confinement effects. Compared to photoluminescence (PL) spectroscopy, which provides information on the lowest-energy SQW transition only, PR spectroscopy has the advantage to resolve direct optical transitions to higher-lying excited states even at room temperature.

## 2 Experimental

The SQW structures were grown by molecular beam epitaxy. The growth sequence starts with a 0.3  $\mu\text{m}$  GaAs layer and 100 periods of a buffer superlattice with alternating 30 Å Al<sub>x</sub>Ga<sub>1-x</sub>As ( $x = 0.3$ ) and 100 Å GaAs. Then follows the 245 Å thick GaAs quantum-well, a 650 Å AlGaAs top barrier and a 100 Å GaAs cap layer. In the modulation-doped sample Si doping was incorporated into the top barrier. Hydrostatic pressures were applied using a gasketed diamond anvil cell.

The PR setup used here was similar to

that described in the literature.<sup>2,3</sup> The variable-wavelength probe beam of constant photon flux and the photomodulation source (Kr ion laser, 406.7 nm line) were focused onto the same spot on the sample (50  $\mu\text{m}$  diameter). The reflected probe light was detected by a Si diode or a photomultiplier. In order to suppress the detection of the strong sample luminescence and laser stray light, both beams were chopped at different frequencies, and the PR signal was detected at the sum frequency using lock-in techniques.

## 3 Results and Discussion

Figure 1(a) shows a PR spectrum of the undoped SQW sample at ambient pressure. Sharp features originating from transitions involving different SQW subbands and from bulk GaAs and AlGaAs are clearly resolved. The assignment has been performed by comparing the PR spectra with theoretical calculations of confined subband energy levels using the transfer-matrix method within the envelope-function approximation.<sup>4</sup> Arrows in Fig. 1(a) indicate calculated transition energies for heavy (H) and light (L) hole initial states. Note that only SQW transitions with the same subband index  $n$  are allowed. Furthermore, the ratio of the intensities between the light ( $L_{nn}$ ) and heavy hole ( $H_{nn}$ ) transitions is roughly given by the 1:3 ratio of the effective masses.<sup>3</sup> Therefore, up to six  $H_{nn}$  transitions are clearly seen, while only the first light hole transition can be determined unambiguously.

Experimental values for optical transition energies are obtained from lineshape fits to the PR spectra using the third derivative functional

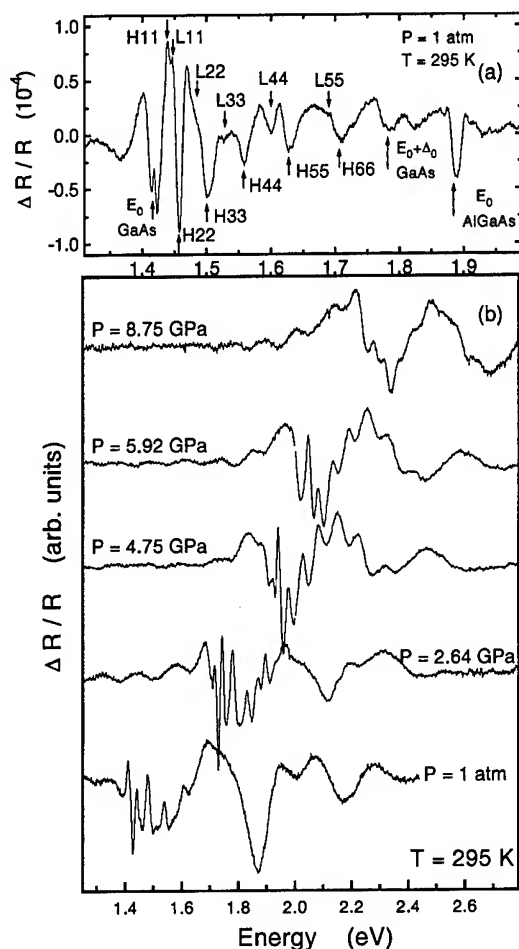


Figure 1: (a) Photoreflectance spectra of the undoped GaAs/Al<sub>0.3</sub>Ga<sub>0.7</sub>As SQW sample at ambient pressure (T=300K). The arrows indicate calculated transition energies between SQW hole and electron states with the same subband index. (b) PR spectra of the doped SQW sample at different pressures.

form given by Aspnes.<sup>5</sup> At ambient pressure the SQW transition energies of the doped sample are about 18 meV below those of the undoped sample. This is attributed to the bandgap renormalization effect for the doped GaAs well. Another difference between doped and undoped samples is that the built-in electric field gradient between SQW and surface results in a more efficient separation of laser-excited electron-hole pairs, which leads to more pronounced PR signals compared to undoped samples.

For the remainder of the paper we focus on

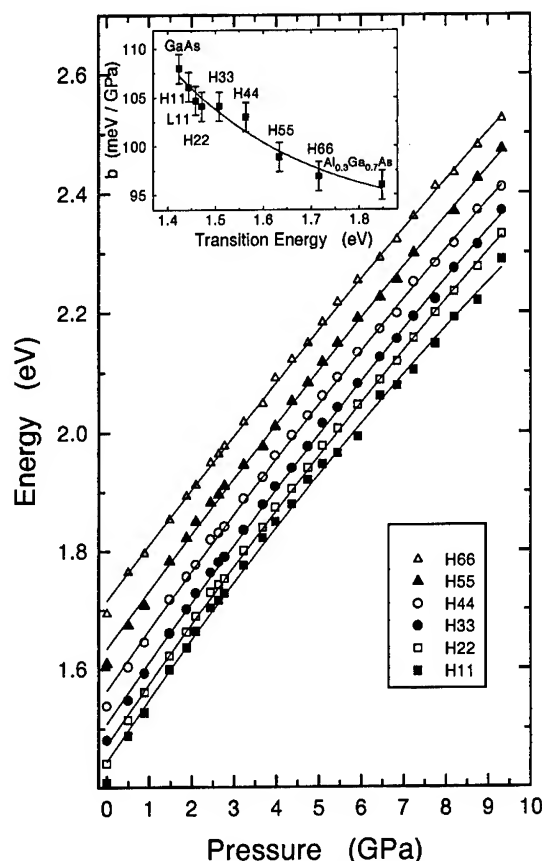


Figure 2: Heavy hole transition energies between quantum well states of the doped SQW as function of pressure. The lines represent results of least squares fits to the data above 1.5 GPa. The inset shows the linear pressure coefficients as a function of the subband transition energy. The line in the inset is a guide to the eye.

results obtained for heavy hole transitions in the doped sample under pressure. Figure 1(b) shows PR spectra measured at various pressures up to 9.5 GPa. Sharp features due to SQW transitions and broad structures originating from bulk GaAs and AlGaAs shift to higher energy with increasing pressure. Results for heavy hole excitation energies are summarized in Fig. 2, where the solid lines represent fitted second order polynomials. Only data above 1.5 GPa were used in the fitting procedures because of the pressure dependence of renormalization effects in the low pressure regime (see below). We find that the linear pressure coefficients show a systematic decrease with increa-

sing subband index (e.g. 106 meV/GPa for  $H_{11}$ , 97 meV/GPa for  $H_{66}$ ). A similar tendency was previously observed for undoped multi-quantum-well samples measured up to 5.6 GPa.<sup>7,8</sup> We note that PL studies also revealed a systematic decrease of the linear pressure coefficient with decreasing well width  $L_z$ .<sup>9</sup>

The observed differences in the linear pressure coefficients are small. Furthermore, linear and nonlinear pressure coefficients of band gap energies obtained by least-squares fits are usually strongly correlated. Therefore, we need to take a closer look at the experimental SQW data. Figure 3 shows the difference  $\Delta H_{nn}$  of heavy hole transition energies for the doped SQW sample relative to the experimental band gap energy of bulk GaAs under pressure.<sup>10</sup> The initial positive slope, which is quite pronounced for the lower-energy transitions, is consistent with results of recent PL and Raman studies of the same SQW system.<sup>1</sup> In these experiments it was demonstrated that the carrier density in the SQW decreases rapidly when applying hydrostatic pressure. Thus, the gap renormalization is reduced under pressure, and the above-mentioned energy differences for corresponding transitions in doped and undoped SQW sample indeed vanish at about 1.5 GPa.

Above 2 GPa, the  $\Delta H_{nn}$  values show an overall negative slope. For the *low-energy* transitions, this effect can be attributed to pressure-dependent changes in the electric field gradient across the SQW arising from charge redistribution between donor and surface states. On the other hand, *higher-lying* transitions should be insensitive to electric field gradients. For these transitions, we attribute the decrease of  $\Delta H_{nn}$  with pressure to changes in effective masses and the related changes in confinement energies.

The latter interpretation is consistent with results of subband structure calculations within the envelope function approximation. In this calculation we included the change of the SQW depth due to the different pressure dependence of the band gaps of the barrier and well materials. The relative valence band offset ( $Q_V = 0.3$ ) was assumed to be constant, in accordance with other theoretical calculations.<sup>11,12,13</sup> In terms of  $\mathbf{k} \cdot \mathbf{p}$  theory, the electron and light hole masses are proportional to the energy gap.<sup>14</sup> Changes in heavy hole mass and well width with pressure can be neglected. With these assumptions we, for instance, find that the

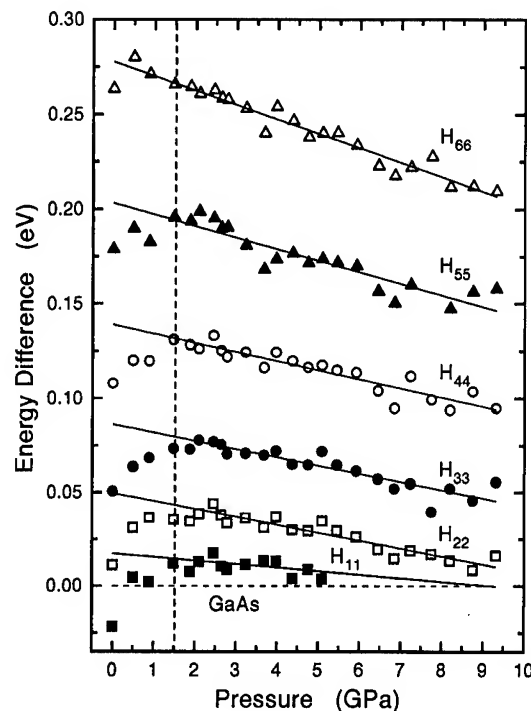


Figure 3: Difference between heavy hole transition energies of the doped SQW and the band gap energy of bulk GaAs under pressure. The lines represent results of least squares fits to data above 2 GPa.

calculated energy difference  $\Delta H_{nn}$  for the  $n = 6$  transition decreases by 70 meV in 10 GPa. This is in good agreement with the corresponding experimental data shown in Fig. 3.

Finally, for all pressures additional features are observed in the PR spectra *below* the lowest direct gap of GaAs (see Fig. 1(b)). Similar structures have been seen earlier<sup>7</sup> in PR spectra of multi-quantum-well samples at pressures above the  $\Gamma$ - $X$  crossover of GaAs (4.2 GPa). They were attributed to indirect optical transitions between the  $\Gamma$ - $X$  and  $\Gamma$ - $L$  points of the Brillouin zone. In our case careful analysis shows that these features are due to multiple internal reflections between the SQW and the GaAs substrate. Thus, indirect transitions are not observed in the PR spectra.

In conclusion, we have determined the energies of six heavy-hole subband transitions of a modulation-doped GaAs/ $\text{Al}_{0.3}\text{Ga}_{0.7}\text{As}$  single quantum well over a wide pressure range ( $P \leq 9.5$  GPa) using photoreflectance spectroscopy.

Gap renormalization effects originating from a reduction of carrier density in the well are clearly observed for pressures below 1.5 GPa. This is in accordance with previous PL and Raman measurements.<sup>1</sup> Above 1.5 GPa, the linear pressure coefficients of direct optical transitions show an overall tendency to decrease with increasing subband index. This effect can in part be attributed to pressure-induced changes in confinement energies. Theoretical calculations of electronic subband structure within the envelope-function approximation fully support this interpretation. Low-lying transitions, however, appear to be also affected by changes under pressure of the electric field gradient across the well.

## References

1. S. Ernst, A.R. Goñi, K. Syassen, and K. Eberl, *Phys. Rev. Lett.* **72**, 4029 (1994).
2. J.L. Shay, *Phys. Rev. B* **2**, 803 (1970).
3. O.J. Glembocki, *Proc. SPIE* **1286**, 2 (1990); O.J. Glembocki, and B.V. Shanabrook, *Semiconductors and Semimetals* **36**, 221 (1992).
4. A.R. Goñi, K. Syassen, Y. Zhang, K. Ploog, A. Cantarero, and A. Cros, *Phys. Rev. B* **45**, 6809 (1992).
5. D.E. Aspnes, *Surf. Sci.* **37**, 418 (1973).
6. S. Adachi, *J. Appl. Phys.* **58**, R1 (1985).
7. A. Kangarlu, H.R. Chandrasekhar, M. Chandrasekhar, Y.M. Kapoor, F.A. Chambers, B.A. Vojak, and J.M. Meese, *Phys. Rev. B* **38**, 9790 (1988); M. Chandrasekhar, H.R. Chandrasekhar, A. Kangarlu, and U. Venkateswaran, *Superlattices and Microstructures* **4**, 107 (1988).
8. H.R. Chandrasekhar and M. Chandrasekhar, *Proc. SPIE* **1286**, 207 (1990).
9. U. Venkateswaran, M. Chandrasekhar, H.R. Chandrasekhar, B.A. Vojak, F.A. Chambers, and J.M. Meese, *Phys. Rev. B* **33**, 8416 (1986).
10. A.R. Goñi, A. Cantarero, K. Syassen, and M. Cardona, *Phys. Rev. B* **41**, 10111 (1990).
11. C.G. Van de Walle and R.M. Martin, *Phys. Rev. B* **35**, 8154 (1987).
12. P. Lefebvre, B. Gil, and H. Mathieu, *Phys. Rev. B* **35**, 5630 (1987).
13. D.Z.-Y. Ting and Yia-Chung Chang, *Phys. Rev. B* **36**, 4359 (1987).
14. M. Cardona, in *Atomic Structure and Properties of Solids*, edited by E. Burstein (Academic, New York, 1972).



## PRESSURE TUNING OF SEMICONDUCTOR LASER DIODES

P. STĘPIŃSKI\*, Y. TYAGUR, T.P. SOSIN\*, W. TRZECIAKOWSKI,

*High Pressure Research Center "Unipress", Polish Academy of Sciences,  
01-142 Warszawa, Sokołowska 29, Poland*

*\* also at the Institute of Physics, Warsaw University of Technology, 00-662 Warszawa, Poland*

Room-temperature emission of GaAs/AlGaAs, InGaP/InGaAlP, and InGaAsP/InP laser diodes has been studied as a function of hydrostatic pressure in an optical clamp cell up to 20 kbar. The diodes were commercial single-mode devices by Sharp, Sanyo, Sony and Siemens. The emission wavelength shifted towards the blue similarly to the bandgap of the constituent materials. The tuning range was limited by the  $\Gamma$ -X crossover in the active layer and by the increase of the threshold current with pressure. In the low threshold-current InGaAsP/InP laser the tuning range was over 200 nm. The pressure tuning seems promising for spectroscopic applications and for the analysis of transmission and dispersion in optical fibers.

### Introduction

Semiconductor lasers have been studied under pressure by many groups (see e.g. [1-3]). Due to the rapid progress in epitaxial growth technology the quality of the lasers is improving and the spectral range is broadened. Since low-current, single-mode cw devices are now commercially available, we decided to study the possibility of their tuning by pressure. A special optical cell was designed in Unipress so that 2 GPa pressures can be routinely achieved. With such a limit the pressure tuning should yield a much broader wavelength range than tuning with temperature or with external resonator. This should be interesting for spectroscopy where the laser emission energy has to match some narrow atomic or molecular transitions. Another possible application of tunable diodes could be the measurement of dispersion in optical fibers.

Let us first discuss qualitatively the effect of pressure on the laser diodes. Both in AlGaAs and in InGaAlP we can expect  $\Gamma$ -X crossover under pressure. At room temperature the radiative recombination will be reduced a few kbar before the crossover pressure. In the case of InGaAsP lasers we do not expect the  $\Gamma$ -X crossover in the 2 GPa range. The lasing can be negatively affected by another pressure effect; the increase of the refraction index of the liquid surrounding the laser. This will reduce the amount of light in the resonant cavity and may increase the threshold current. If we use the Clausius-Mossotti law to relate the changes of the refractive index  $n$  to the changes of the density of the

liquid [4,5] we obtain an increase from  $n=1.35$  to  $n=1.81$  at about 12 kbar. This effect should occur for all materials we studied. Finally, the denser liquid under pressure can reduce the heat dissipation and raise the effective temperature of the diode. This effect has been studied for AlGaAs lasers [6] and it should be eliminated by pulsed current supply. It should be more important for lasers with high threshold current. Therefore we will first present our results for the InGaAsP/InP diode where the threshold current is low and we do not expect the  $\Gamma$ -X crossover.

### Experimental

The optical cell was made of maraging steel with an insert. It had a sapphire window and the electrical feedthrough in the piston. We used commercial lasers 5.6 mm in diameter. The window of the laser package was cut off and a small spherical lens (2 mm in diameter) was placed in front of the diode (inside the cell) to collimate the laser beam. Gasoline was used as a pressure-transmitting medium. The current was supplied by the Melles Griot driver 06 DLD 201 which also measured the signal from the built-in photodiode. The spectrum was analyzed by the Spex 500M monochromator with PbS photoresistor (for 1300 nm lasers) or with GaAs photomultiplier (for 780 and 670 nm lasers) as a detector. The pressure in the cell was calibrated with the InSb gauge [7].

### InGaAsP/InP diode

The 1.3 mm diode (Siemens SFH4410) had a low threshold current (14 mA), and nice single-mode spectrum. It had a built-in Si collimating lens. The threshold current showed only about 50% increase in the whole 2 GPa range and the spectrum shifted more than 170 meV (200 nm) as shown in Fig.1. The shift of the emission line was linear in pressure with the coefficient 87 meV/GPa. This is not far from the value 80 meV/GPa obtained in [3] given the large scatter of points in [3].

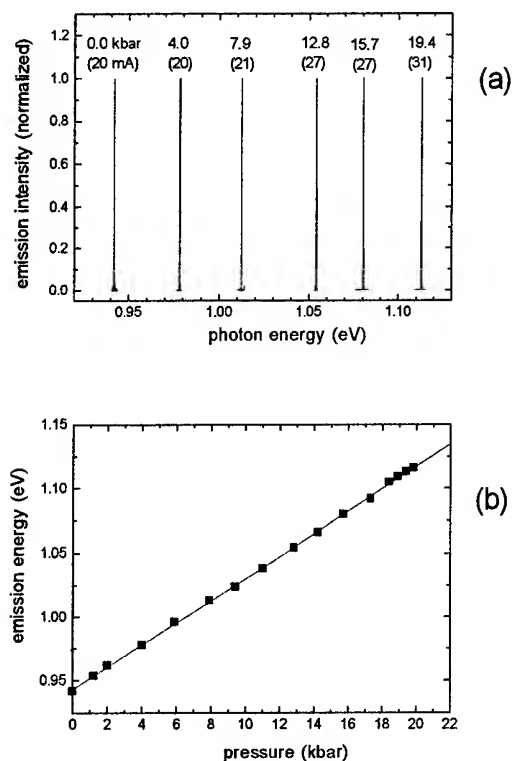


Fig.1 Pressure shift of the emission spectrum of the InGaAsP/InP diode (a) and the pressure dependence of the emission energy (b). The currents supplied to the laser are given in brackets.

The relatively small changes in the threshold current indicate that the increase of the refractive index of the pressure-transmitting medium has a moderate effect on the emission efficiency. Nice single-mode operation and the stability of the threshold current make this laser a good candidate for an accurate pressure gauge [8]. Pulsed operation should reduce the heating effects so it should be recommended for metrological applications.

### GaAs/AlGaAs diodes

We studied the 780 nm diodes by Sharp (LT022) and by Sanyo (DL2140). The threshold current was around 46 mA at ambient pressure and it increased up to 80 mA at 1.1 GPa. Therefore the single-mode operation could only be achieved up to 1.2 GPa (Fig.2) and the tuning range was about 120 meV (55 nm). Similar increase of the threshold current with pressure was observed in [6] and in the considered spectral range it turned out to be mainly due to heating at cw operation and only partly due to the proximity of the  $\Gamma$ -X crossover in layers with high AlAs content. The emission energy shifted quadratically with pressure ( $\Delta E = 120 \text{ p} - 22 \text{ p}^2$  where p is in GPa, energy in meV). The quadratic coefficient is much higher than what we observed in PL experiments on quantum wells [9] (the PL results are represented by the dashed line in Fig.2b). Again this is due to heating; the increase of the gap

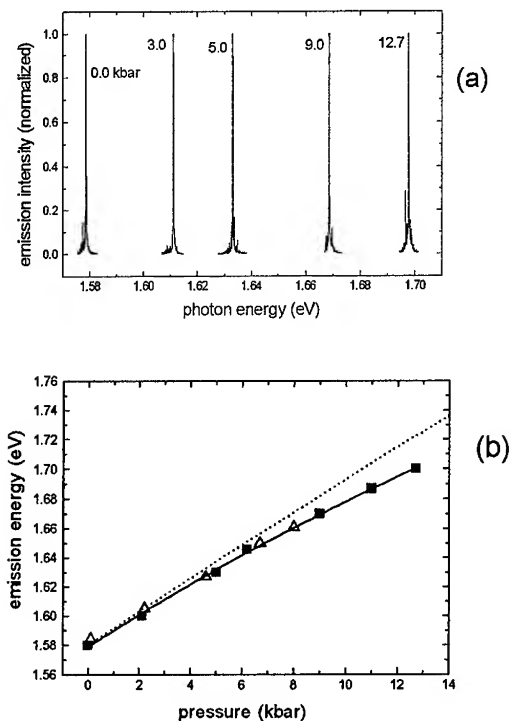


Fig.2 Pressure shift of the emission spectrum of the Sharp LT022 GaAs/AlGaAs diode (a) and the pressure dependence of the emission energy for Sharp LT022 (squares) and for Sanyo DL2140 (triangles).

with pressure is partly compensated by its decrease with increasing temperature (higher current required for single-mode operation).

### InGaP/InGaAlP diodes

The red-emitting (670 nm) laser by Sony (SLD1121) and the similar laser by Toshiba (TOLD 9211M) showed the fast increase of the threshold current with pressure (Fig.3). This limited the pressure range to 1 GPa and the tuning range to 84 meV (30 nm). Again we attribute this to the worse heat dissipation under pressure and to the pressure-induced  $\Gamma$ -X crossing. The emission energy shifted linearly with the pressure coefficient of 84.8 meV/GPa.

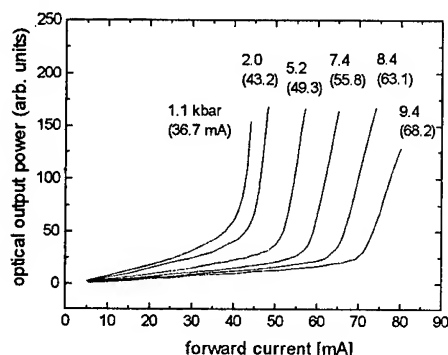


Fig.3 Optical power vs current for the InGaP/InGaAlP diode at different pressures indicated above each curve. The numbers in brackets are the threshold currents.

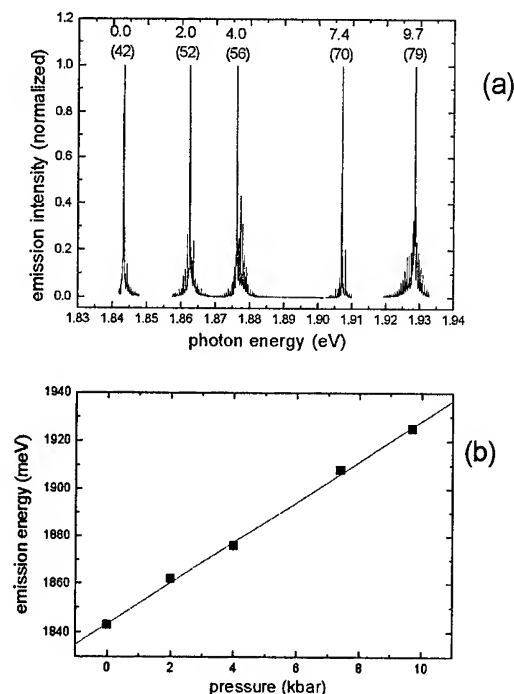


Fig.4 Pressure shift of the emission spectrum of the Sony SLD1121 InGaP/InGaAlP diode (a) and the pressure dependence of the emission energy (b).

### Summary

We found that commercial laser diodes with low threshold currents can be tuned with pressure over a wide spectral region. The tuning range is much higher for InP based lasers than for GaAs based lasers because of the  $\Gamma$ -X crossover in AlGaAs. Good heat sinking is very important in case of cw operation. We plan to use our pressure tuning in the spectroscopy of molecules where the laser diodes have already proved to be superior to gas lasers [10] due to their better power stability and narrower lines achievable (with external resonators).

### References

1. S.W. Kirchoefer, N. Holonyak, K. Hess, K. Meehan, D.A. Gulino, H.G. Drickamer, J.J. Coleman, and P.D. Dapkus, *Journal of Applied Physics* **53**, 6037 (1982)
2. K.C. Heasman, A.R. Adams, P.D. Greene, and G.D. Hensall, *Electronics Letters* **23**, 493 (1987)
3. D. Patel, C. Menoni, H. Temkin, C. Tome, R.A. Logan, D. Coblenz, *J.Appl.Phys.* **74**, 737 (1993)
4. K. Vedam and P. Limsuwan, *J.Chem.Phys.* **69**, 4762 (1978)
5. M. Gauthier, A. Polian, J.M. Besson, *Phys.Rev.B* **40**, 3837 (1987)
6. J.E. Epler, R.W. Kaliski, N. Holonyak, M.J. Peanasky, G.A. Herrmannsfeldt, H.G. Drickamer, R.D. Burnham, and R.L. Thornton, *J.Appl.Phys.* **57**, 1495 (1985)
7. M. Kończykowski, M.Baj, E. Szafarkiewicz, L. Kończewicz, and S. Porowski, "High Pressure and Low-Temperature Physics", eds. C.V. Chu and J.A. Woolam, (Plenum, New York 1978) p.523
8. T.P. Sosin, W. Trzeciakowski, P. Stępiński, and M. Hopkinson, this conference
9. P. Perlin, W. Trzeciakowski, E. Litwin-Staszewska, J. Muszalski, and M. Micovic, *Semiconductor Science and Technology* **9**, 2239 (1994)
10. C.E. Wieman, *Review of Scientific Instruments* **62**, 1 (1991)

## SPATIAL CORRELATIONS OF DONOR-CHARGES IN $\delta$ -DOPED AlGaAs/InGaAs/GaAs STRUCTURES

E. Litwin-Staszewska<sup>1</sup>, T. Suski<sup>1</sup>, P. Wiśniewski<sup>1</sup>,  
F. Kobbi<sup>2</sup>, S. Contreras<sup>2</sup>, J.L. Robert<sup>2</sup> and V. Mosser<sup>3</sup>

<sup>1</sup>Unipress, Polish Academy of Sciences, 01-142 Warszawa, POLAND

<sup>2</sup>GES, Universite Montpellier II, Place E. Bataillon, 34095, Cedex 05, FRANCE

<sup>3</sup>Schlumberger Industries Recherche, 92-542 Montrouge, France

### ABSTRACT

We have studied properties of  $\delta$ -doped layer of pseudomorphic Si:Al<sub>0.32</sub>Ga<sub>0.68</sub>As / In<sub>0.15</sub>Ga<sub>0.85</sub>As / GaAs structures. Transport experiments have been performed on four samples with various spacer thicknesses. Hydrostatic pressure up to 14 kbar has been used to obtain nonequilibrium occupation of the DX<sup>-</sup> states. We have studied nonrandom distribution of charges among the impurity sites of Si-remote-donors. The most important result of this work consists in the clear demonstration of mobility enhancement (up to 25%) due to the spatial correlations of remote impurity charges. Moreover, changes in the correlation degree caused by the variation of the ratio  $d^+/DX^-$  can explain a maximum on  $\mu$  versus two-dimensional electron gas density ( $n_{2D}$ ) observed in the studied pseudomorphic samples. The latter phenomenon has been erroneously ascribed previously to alloy scattering effect.

### Introduction

It has been proposed recently that electrons localized by donors in GaAs and AlGaAs can be distributed in a spatially correlated manner (see e.g. [1] and references therein). In samples doped above the Mott critical concentration (silicon donor concentration about  $10^{18}\text{cm}^{-3}$ ) the shallow donor state does not exist. Ionized donor represents a substitutional impurity with a positive charge,  $d^+$ . The donor can trap two electrons and becomes negatively charged ( $DX^-$ ). These two possible charge states of the Si-center can be presented by the transition  $d^+ + 2e^- \rightarrow DX^-$  [2].  $DX^-$  center has a metastable character consisting in thermally activated barriers for electron emission and capture (relevant at temperatures below about 100 K). It turns out, that empty donor centers  $d^+$  and occupied  $DX^-$  ones (coexisting in the system) form dipole-like objects: close  $d^+-DX^-$  pairs. As a result spatial correlations among donor charges appear and fluctuations of the potential (originating from the nonhomogeneous distribution of the donors), are significantly reduced.

Enhancement of the two-dimensional electron gas (2 DEG) mobility,  $\mu$ , due to the correlations has been studied theoretically and experimentally in modulation and  $\delta$ -doped heterostructures GaAs/AlGaAs [3-6]. The authors observed that depending on the manner in which electrons are

distributed among Si-donors, different values of  $\mu$  are achieved for the same 2 DEG density,  $n_{2D}$ .

The purpose of this work is to evidence the existence of spatial correlation of donor charges in  $\delta$ -doped AlGaAs / GaInAs / GaAs structures. This can explain the variation of  $\mu$  vs  $n_{2D}$  in this pseudomorphic heterostructure.

### Experiment

We investigated four Si- $\delta$ -doped Al<sub>x</sub>Ga<sub>1-x</sub>As / Ga<sub>1-y</sub>In<sub>y</sub>As / GaAs structures grown by molecular beam epitaxy. The Al and In mole fractions were  $x=0.3$  and  $y=0.15$  respectively. The quantum well of 13 nm thickness was separated from the  $\delta$ -doping plane by a spacer equal to 4 nm for samples 1 and 3, to 6 nm for sample 2, and to 2 nm for sample 4. The effective doping density of the AlGaAs barrier was  $N_d=1.7 \cdot 10^{12}\text{cm}^{-2}$  (Sample 1) and  $N_d=2.5 \cdot 10^{12}\text{cm}^{-2}$  (samples 2, 3, 4). The samples were patterned in a Hall-bar geometry with six AuGeNi contacts. Conductivity and Hall effect measurements were performed at 77 K at ambient pressure. Hydrostatic pressure of helium gas up to 14 kbar was used as a tool to obtain nonequilibrium occupancy of DX centers by means of the high pressure freezeout (HPFO) procedure [5]. It consists of i) applying pressure at room temperature (resulting in the enhanced occupation of DX centers

which are in thermal equilibrium with the 2 DEG at this temperature), ii) cooling the sample at the constant pressure and iii) releasing the pressure at 77 K. The whole procedure results in a persistent lowering of  $n_{2D}$  and this value decreases with increasing freezeout pressure. Such pressure-induced capture of electrons onto DX centers favours high values of mobility corresponding to a given  $n_{2D}$ . This is because electrons populate likely  $d^+$  centers located close to other  $d^+$  centers [5]. As a result, high degree of correlations in the donor system can be achieved. Open points in Fig. 1 correspond to the variation of  $\mu$  with decreasing  $n_{2D}$  induced by HPFO procedure. The observed increase of  $\mu$  before reaching a maximum results from a significant reduction of the scattering caused by the creation of close dipoles  $d^+-DX^-$ . When almost all  $d^+-d^+$  pairs are replaced by  $d^+-DX^-$  dipoles then the changes of scattering potential fluctuations caused by the further increase of DX center are smaller. In this case we can observe a typical for 2D structure decrease of mobility with decreasing  $n_{2D}$  [8].

A reduction of the correlation degree may be obtained by the thermal ionization of DX centers. In our experiments we prepared the samples by HPFO procedure (a reservoir of metastable electrons captured on DX-centers) and we annealed them at temperatures above 100-120 K (characteristic temperature for emission from DX-centers). At every annealing cycle the temperature was increased from 77 K, at which all measurements of  $\mu$  vs  $n_{2D}$  were performed. Higher annealing temperature causes more effective emission of electrons to the 2 DEG channel due to emptying of DX centers as they tend to their thermal equilibrium.

The electron emission induced by annealing cycles occurs from randomly chosen  $DX^-$  centers and therefore leads to the destruction of correlations in the distribution of charges among the remote-donor sites [5].

Solid symbols in Fig. 1 show changes of  $\mu$  as  $n_{2D}$  is increased by annealing procedure. The different behavior of  $\mu$  (observed for the samples 2, 3 and 4) in comparison with that related to HPFO is due to a decrease in the degree of correlations among remote-donor charges (RDC). For sample 1 the value of  $\mu$  was measured for only one 2DEG concentration (one point in Fig.1). The concentra-

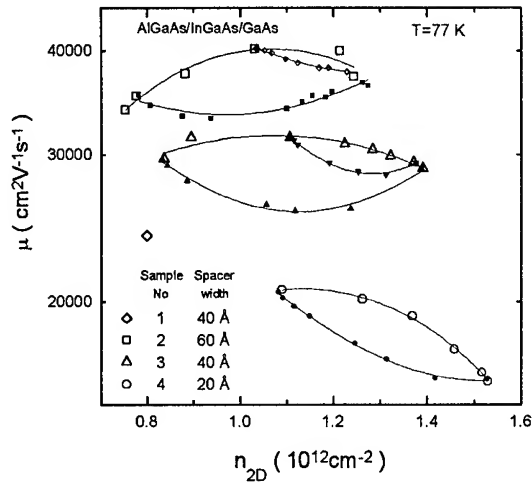


Fig. 1. Hall mobility  $\mu$  vs carrier concentration  $n_{2D}$  for different samples (measured at 77 K and  $p=1$  bar). Open symbols represent the path achieved by HPFO procedure performed at different freezeout pressures (capture). The branches with solid symbols correspond to the path produced by the sample subsequent annealing (emission).

tion  $n_{2D}$  in sample 1 ( $N_s = 1.7 \cdot 10^{12} \text{ cm}^{-2}$ ) does not depend on pressure and this suggests that Fermi level is lower than DX state energy and all Si donors are ionised. For  $n_{2D} = 0.8 \cdot 10^{12} \text{ cm}^{-2}$  the mobility for the sample 1 is 25% lower than for the sample 3 with the same spacer width (40 Å). For the sample 3 with higher Si donor concentration ( $N_s = 2.5 \cdot 10^{12} \text{ cm}^{-2}$ ) one could expect a lower mobility but the existence of spatial correlations of RDC significantly reduces electron scattering. Thus, we can conclude that the increase of electron mobility caused by RDC correlations is at least 25%.

## Conclusions

In conclusion, we have demonstrated that depending on the method which is used to populate the metastable donor states of Si-remote impurities, different values of mobility can be obtained for the same 2DEG density in the same pseudomorphic heterostructure. This experimental finding is explained by the concept of the correlation in the spatial distribution of the remote dopant charges: positively and negatively charged states of Si-donors. This factor should be taken into account together with an alloy scattering or a cluster scattering [10] as mechanisms determining the

mobility maximum in AlGaAs/GaInAs/GaAs structures.

All these mechanisms can explain the mobility behavior versus the electron density in the InGaAs channel during the capture. However, only the correlation concept accounts for the different dependencies of  $\mu$  vs  $n_{2D}$  for electron capture and emission.

E.L.-S., T.S., and P.W. acknowledge the partial financial support of KBN (Poland) grant No.3 P407 028 07.

### References

- [1] J. Kossut, Z. Wilamowski, T. Dietl and K. Świątek, in Proc. 20th Int. Conf. on the Physics of Semiconductors, ed. E.M. Anastassakis and J.D. Joannopoulos, World Scientific, Singapore 1990, p. 613.
- [2] D.J. Chadi and K.J. Chang, Phys. Rev. Lett. **61**, 873 (1988).
- [3] A.L. Efros, F.G. Pikus, and G.G. Samsonidze, Phys. Rev B**41**, 8295 (1990).
- [4] Coleridge, Phys. Rev. B**44**, 3793 (1991).
- [5] T. Suski, P. Wiśniewski, I. Gorczyca, L.H. Dmowski, R. Piotrzkowski, P. Sobkowicz, J. Smoliner, E. Gornik, G. Bohm, and G. Weimann, Solid-St. Electron., **37**, 677 (1994), Phys. Rev. B**50**, 2723 (1994).
- [6] E. Buks, M. Heiblum and H. Shtrikman, Phys. Rev. B**49**, 14790 (1994), Semicond. Sci. Technol., **9**, 2031 (1994).
- [7] E. Litwin-Staszewska, T. Suski, C. Skierbiszewski, F. Kobbi, J.L. Robert, and V. Mosser, J. Appl. Phys. **77**, 405 (1995).
- [8] W. Walukiewicz, H.E. Ruda, J. Lagowski and H.C. Gatos, Phys. Rev. B**30**, 4571 (1984).
- [9] L. Kończewicz, E. Litwin-Staszewska, A. Masłowska, R. Piotrzkowski, J.L. Robert and J.P. Andre, Phys. Status Solidi **b157**, 593 (1990).
- [10] H. Ohno, J.K. Luo, K. Matsuzaki, and H. Hasegawa, Appl. Phys. Lett. **54**, 36 (1989).

# STUDY OF CLASSICAL AND QUANTUM SCATTERING TIMES IN PSEUDOMORPHIC AlGaAs/InGaAs/GaAs HETEROSTRUCTURES BY MEANS OF PRESSURE

\*L.H. DMOWSKI, #A. ZDUNIAK, \*E. LITWIN-STASZEWSKA, #S. CONTRERAS,  
#W. KNAP, #J.L. ROBERT and #V. MOSSER

#Groupe d'Etude des Semiconducteurs, Universite Montpellier II, 34-095 Montpellier, France

\*High Pressure Research Center, Polish Academie of Sciences, 01-142 Warsaw, Poland

&Institute of Experimental Physics, Warsaw University, 02-658 Warsaw, Poland

#E.T.L. Schlumberger, 92-542 Montrouge, France

Classical (transport) and quantum (single particle) scattering times have been measured and analysed as a function of density of two-dimensional electron gas (2dEG) in pseudomorphic AlGaAs/InGaAs/GaAs heterojunction structures. Hydrostatic pressure was used as an efficient tool for tuning down the 2dEG density and infra-red light emission diode (LED) light pulses for tuning it up again. Based on this analysis we conclude about spatial correlation of charges on remote donors and about contribution to the scattering from a small-angle scattering by remote donors in the barrier as well as large or moderate-angle scattering mechanisms in the 2dEG layer.

## Introduction

It has been well established that scattering times measured via either mobility ("classical" or "transport" scattering time) or from Shubnikov de Haas oscillation envelope ("quantum" or "single particle" lifetime) and in particular the comparison of the both scattering times have become a very useful tool for directly selecting the dominant scattering mechanisms among competing effects in two dimensional electron gas (2dEG) systems [1,2,3]. Classical (transport) scattering time,  $\tau_c$ , is derived from transport expressions assuming relaxation time approximation. The Drude mobility is related directly to this scattering time by:  $\mu = e\tau_c/m^*$  where  $m^*$  is electron effective mass. Quantum scattering time (or single particle lifetime)  $\tau_q$ , is related to the half-width  $\Gamma$  of the collision broadened Landau level through:  $\Gamma = \hbar/2\tau_q$ . Both (classical and quantum) scattering times are not equal due to the presence of an extra  $(1-\cos\Theta)$  weighting factor in the expression for  $\tau_c$  (where  $\Theta$  denotes the scattering angle). Therefore  $\tau_c$  is insensitive to small-angle scattering while  $\tau_q$  is sensitive to all scattering events. Thus in systems where the scattering is mostly small angle, the transport to quantum scattering time ratio can be large;  $\tau_c/\tau_q > 1$ . In contrast in systems with isotropic scattering  $\tau_c/\tau_q \approx 1$ . We measured  $\tau_c$  and  $\tau_q$  as a function of electron channel density and the way in which each value of the density was achieved -

spontaneous population of DX donors when pressure was applied or random ionization of defects by infra-red light pulses. From a selection of pseudomorphic  $\text{Al}_{0.32}\text{Ga}_{0.68}\text{As}/\text{In}_{0.15}\text{Ga}_{0.85}\text{As}/\text{GaAs}$   $\delta$ -doped heterostructures with different spacers thickness, different doping densities and different depletion charges we chose a sample with nominal sheet electron concentration  $n_s = 1.35 \times 10^{12} \text{cm}^{-2}$  for which in the whole range of tuning - from 0.92 to  $1.77 \times 10^{12} \text{cm}^{-2}$  we observed excellent agreement of concentration values obtained from classical Hall effect, and Shubnikov de Haas oscillation period. Thus we could conclude that we dealt with one channel - one subband conduction process in the whole range of electron concentrations and mobilities under study.

## Experiment

The sample studied was pseudomorphic  $\text{Al}_{0.32}\text{Ga}_{0.68}\text{As}/\text{In}_{0.15}\text{Ga}_{0.85}\text{As}/\text{GaAs}$  quantum well grown by the molecular beam epitaxy technique. The 2dEG was formed in the 13 nm thick InGaAs layer (this thickness is below the critical value above which the strain is relieved by creation of dislocations [4]). The sample was  $\delta$ -doped with  $N_D = 2.5 \times 10^{12} \text{cm}^{-2}$  doping density and 4 nm spacer thickness. Si  $\delta$ -layer was followed by 50 nm undoped AlGaAs and 10 nm doped GaAs cap layer. The sample was mounted inside the Cu-Be high pressure chamber connected to a helium gas compressor with a flexible capillary tube.

In order to lower persistently the 2dEG density at atmospheric pressure (below its nominal dark value) we used high pressure freezeout (HPFO) procedure. This procedure consists in applying pressure at room temperature (resulting in an increased occupation of DX centres), subsequently cooling the sample at constant pressure and finally releasing the pressure at 77K. The whole procedure results in persistent lowering of  $n_s$  value which decreases with increasing freezeout pressure. We could realise such a procedure due to the metastability of occupation of DX donors at low temperatures and due to the possibility of release the pressure at low temperature in our helium gas pressure system. Thus we could tune the 2dEG channel density still keeping constant parameters corresponding to atmospheric pressure (electron effective mass, strain etc. which usually change with pressure).

To increase the 2dEG concentration at low temperature we used persistent photo conductivity effect. For this purpose we mounted inside the pressure chamber an infra-red LED at a distance of about 14 mm from the sample. This geometry illuminated the entire sample uniformly and thus avoided creating inhomogeneities in the sample during pulsed illumination.

The 2dEG concentration in our sample was tuned in the range between  $0.92 \times 10^{12} \text{ cm}^{-2}$  and  $1.77 \times 10^{12} \text{ cm}^{-2}$  by three sets of measurements: (i) sample cooled (in dark) at atmospheric pressure and then illuminated step by step, starting from  $n_s = 1.35 \times 10^{12} \text{ cm}^{-2}$ , (ii) sample cooled at  $p=5.05$  kbar with subsequent releasing of pressure (HPFO-procedure) and then illuminated step by step, starting from  $n_s = 1.2 \times 10^{12} \text{ cm}^{-2}$ , (iii) sample cooled at  $p=8.85$  kbar with subsequent releasing of pressure and then illuminated step by step, starting from  $n_s = 0.92 \times 10^{12} \text{ cm}^{-2}$ .

## Results and discussion

Figure 1(a) shows classical scattering time,  $\tau_c$ , as a function of sheet electron density  $n_s$  for our three sets of measurements. The classical scattering time values were deduced from mobilities (determined from the zero-field resistivities with carrier densities obtained from the periodicity of Shubnikov de Haas oscillations) taking into account the evolution of electron effective mass  $m^*$  with electron density  $n_s$ .

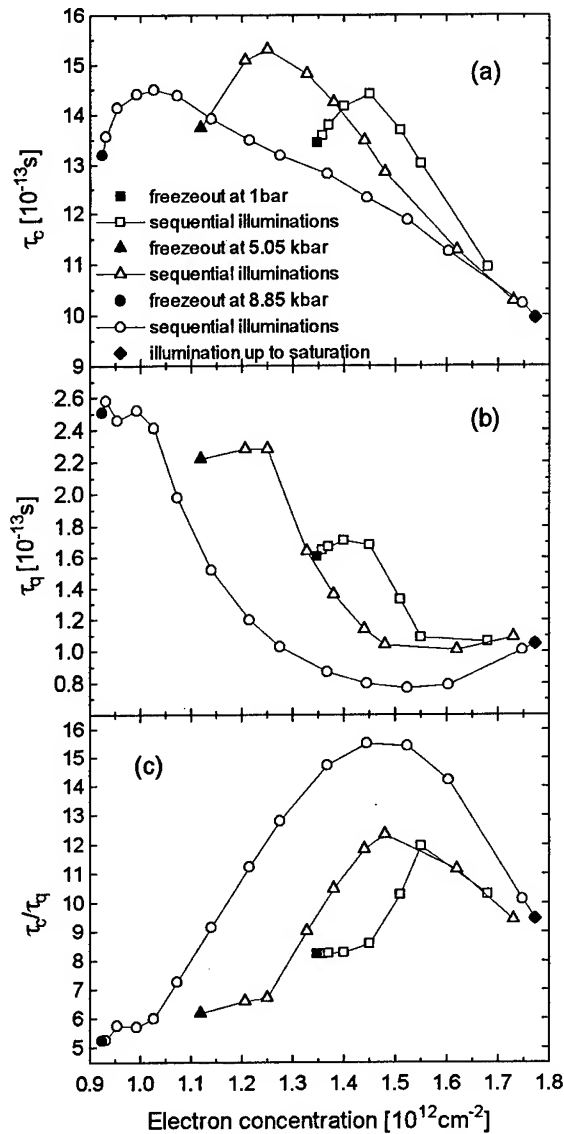


Fig.1 Classical scattering time  $\tau_c$ , (a), quantum scattering time  $\tau_q$ , (b), and scattering to quantum time ratio  $\tau_c/\tau_q$ , (c) as a function of sheet electron concentration  $n_s$ .

Figure 1(b) shows corresponding quantum lifetime  $\tau_q$ . The quantum lifetime was deduced from Dingle plots made according to the procedure given in Ref.[3]. Figure 1(c) shows the ratio  $\tau_c/\tau_q$  which, as we have mentioned, is very sensitive to a change of contribution of various scattering mechanisms. As we can see in Figs.1(a) and (b),  $\tau_c$  and  $\tau_q$  increase slightly when we start to illuminate the sample after



HPFO procedure, then they reach a maximum and finally they decrease with further step by step illuminations. The decrease is more pronounced for  $\tau_q$  than for  $\tau_c$ . Moreover, for the same value of the sheet electron concentration  $n_s$  we could produce different values of  $\tau_q$  or  $\tau_c$  depending on the way in which this value was achieved. These facts confirm the existence of correlation of charges on remote impurities in the Si  $\delta$ -doped sheet in the AlGaAs layer. When Si-DX centres are being populated by electrons (while pressure is applied and (or) temperature is decreased (but still above some critical temperature  $T_c$ ), the charges on the DX centres can be arranged in such a way that minimizes the Coulomb interactions between the charges, thus reducing the efficiency of scattering. Random persistent photoionization of the occupied DX centres at low temperatures spoils the correlation between the charges and causes an increase of scattering efficiency which results in the decrease of  $\tau_c$  and  $\tau_q$ .

Now let us return to the increase of  $\tau_c$  and  $\tau_q$  at the beginning of each step by step illumination procedure. This increase is associated with the initial increase in the sheet electron density of about  $\Delta n_s = 10^{11} \text{ cm}^{-2}$ . As we can see in Fig.3 the ratio  $\tau_c/\tau_q$  remains almost unchanged during this initial increase of electron concentration in contrast with subsequent strong increase of  $\tau_c/\tau_q$  corresponding to the process which we have identified as a destruction of correlated arrangement of charges on remote DX donors. It means that the initial increase  $\Delta n_s$  originates from different photoionisation process and is connected with large or moderate angle scattering mechanism to which both scattering times are equally sensitive. If we will take into account that the emission energy of infrared LED used in the experiment ( $h\nu = 1.43 \text{ eV}$ ) exceeds the energy gap of  $\text{Ga}_{0.85}\text{In}_{0.15}\text{As}$  strained layer ( $E_G = 1.35 \text{ eV}$ ) we can conclude that the initial increase of the sheet electron concentration is due to generation of electron - hole pairs in the GaInAs layer. Electrons and holes are separated by the depletion electric field with electrons going to 2dEG channel and holes neutralizing negatively ionized background acceptors in the GaInAs depletion layer (some of the holes may also be trapped at deep levels in the GaAs substrate). Thus the initial increase of sheet concentration  $\Delta n_s$  which does not

influence the  $\tau_c/\tau_q$  ratio is approximately equal to the total depletion charge density  $n_a$  in the structure and can be used as a method for estimation of  $n_a$ .

## Conclusions

We have studied classical and quantum scattering times as a function of 2dEG density, tuned by means of hydrostatic pressure and persistent photoconductivity effects, in the same sample in the range of  $0.92$  to  $1.77 \times 10^{12} \text{ cm}^{-2}$  under one-channel one-subband conduction conditions. For a given  $n_s$ , classical and quantum scattering times have different values depending on the way in which  $n_s$  was achieved. Different values of the scattering time can arise due to: (i) various persistent photo ionization processes leading to the increase of 2dEG density; photoionization of remote DX donors in the AlGaAs barrier leaving behind charged centres and electron-hole pairs generation neutralizing charged acceptors in the GaInAs depletion layer, (ii). various spatial arrangement of scattering charges on remote DX donors which can be either optimally ordered during the capture process to minimize the energy of Coulomb interaction between them, or can be destroyed by random persistent photoionization events at low temperatures.

L.H.D. and E.L.S. acknowledge a partial financial support of KBN (Poland) grant No.3 P407 028 07.

## References

1. J. P. Harrang, R. J. Higgins, R. K. Goodall, P. R. Jay, M. Laviro and P. Delescluse, *Phys.Rev. B* **32** (1985) 8126.
2. K. P. Martin, R. J. Higgins, J. J. L. Rascol, H. M. Yoo and J. R. Arthur, *Surf. Sci.* **196** (1988) 332.
3. P. T. Coleridge, *Phys.Rev. B* **44** (1991) 3793.
4. J. J. Harris, M. Brugmans, P. Dawson, J. P. Gowers, C. M. Hellon, J. Hewlet, P. F. Roberts, K. Woodbridge and S. Auzout, *Semicond. Sci. Technol.* **5** (1990) 669.

# HIGH TEMPERATURE ELECTRICAL PROPERTIES OF Si-PLANAR DOPED GaAs-AlAs SUPERLATTICES UNDER HYDROSTATIC PRESSURE

F. BOSC, J. SICART and J.L. ROBERT

*Groupe d'Etudes des Semiconducteurs, URA 357*

*Université Montpellier II, 34095 - Montpellier-Cédex 5, France*

## ABSTRACT

We have investigated the electrical properties of GaAs-AlAs short period superlattices at temperatures above the room temperature and under hydrostatic pressure. The samples were doped selectively with silicon to generate different DX deep levels. We have found that a multilevel conduction model must be applied to interpret the experimental results. This model accounts for the interdiffusion of silicon in the samples.

## Introduction

During the last decade, both the electronic properties and the diffusion of species in III-V semiconducting compounds have been the subject of extensive research. It has been demonstrated that n-type doping in alloys as like as GaAs, AlAs, (GaAl)As leads to peculiar properties due to the presence of large lattice relaxation states hereafter denoted as DX states [1]. Otherwise, the use of very clean growth techniques such as MBE or OMCVD allows to realize very sharp interfaces and in-situ doping in III-V microstructures. They provided heterostructures such as multiple quantum wells (MQW) and short period superlattices (SPS) taking advantage in modulation of both band structure and doping density. We have previously studied GaAs-AlAs SPSs selectively doped with silicon [2]. Due to the modulation of the band profile (alternate GaAs well and AlAs barrier sequence), we were able to make the DX states in GaAs or in AlAs resonant (i.e. in the conduction miniband) or in the gap of the superlattice.

Because of the Ga/Al spatial separation in superlattices, we separated spatially the DX state in GaAs (so-called DX<sub>0</sub> level) from the DX state in AlAs (denoted as DX<sub>3</sub> level). In order to eliminate the mixing of several DX levels in SPSs, we introduced the dopant selectively in the GaAs layers or in the AlAs layers. However we have demonstrated that this doping modulation is controlled by the silicon segregation in the post grown layer even in the case of planar doping. To evidence this dopant segregation, we have

performed a Hall effect spectroscopy of the DX states under high hydrostatic pressures [3] since it is well known that the energy of the  $\Gamma$ , X, L minima is in relationship with the applied pressure (e.g. around 10 meV/Kbar for the E $_{\Gamma}$  minimum). Consequently, the energy of the DX levels may cross over the energy of the  $\Gamma$  conduction miniband by increasing the pressure so that the DX state pass from a resonant level into a non-resonant level. When the level lies in the gap of the superlattice, a strong capture of the electrons from the conduction miniband onto the DX state arises.

In this paper, we have investigated the SPSs under pressure in the high temperature conduction regime (i.e. above the room temperature). We find that the Hall effect model previously proposed to interpret the persistent photoconductivity (PPC) and the pressure induced carrier freeze out (PIFO) in the low temperature conduction regime needs to be applied to account for the experimental results in the high temperature range.

## Experiment

All the samples were grown by molecular beam epitaxy at 550°C except sample HA09 grown at 650°C. They were formed from 135 periods of GaAs-AlAs deposited on a AlGaAs thick layer and separated from the substrate by a GaAs buffer layer. The nominal period was 37 Å (28.5 Å of GaAs and 8.5 Å of AlAs). The growth was halted during the silicon introduction in sample HB11 (planar doping in the GaAs layers) and in sample HC01 (planar doping in the AlAs layers) while sample HA09 was

doped uniformly both in GaAs and in AlAs. The sample HC03 was planar doped at the interface, the Si plane being deposited only on the AlAs layers. Hall effect measurements were performed between the room temperature and 450K. The hydrostatic pressure was supplied by a Unipress helium gas compressor. Figure 1 shows the carrier concentration vs temperature. It decreased when temperature increased indicating that electrical conduction cannot be interpreted by a simple model. Note that the planar doped samples were doped at the same silicon concentration. However, they did not show the same carrier concentration at high temperature since the donor state introduced in each sample was different. Consequently, shallower the level in the gap, higher the free carrier concentration in the sample is.

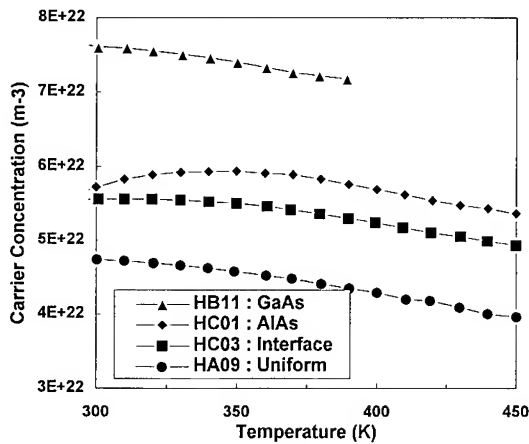


Fig. 1 : Carrier concentration vs temperature. Solid lines are guides for eyes.

Figure 2 shows the carrier concentration in the samples at room temperature vs applied pressure. All samples had both their carrier concentration and their mobility decreasing when increasing pressure. This experimental fact corresponds to the electron capture onto the DX levels and a transition from a high mobility  $\Gamma$  miniband conduction to a low mobility X miniband conduction. Larger the DX<sub>3</sub> concentration in the sample (e.g. sample HC01), more pronounced is the decrease since that level lies around 120 meV below the DX<sub>0</sub> level in GaAs. It is worth noticing that the sample HC03 behaved similarly to the sample HA09 because of the Si out-

diffusion from the interface both into AlAs and GaAs.

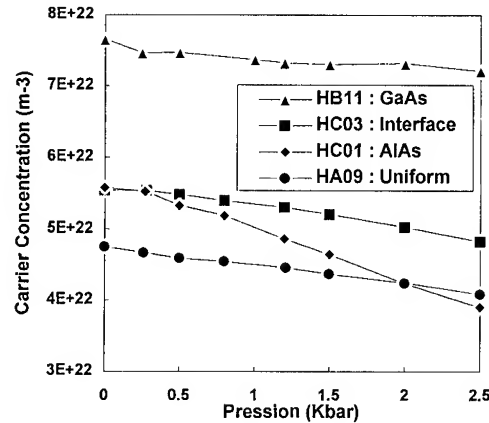


Fig.2 : Carrier concentration vs pressure at room temperature. Solid lines are guides for eyes.

This experimental result is a striking proof of the Si interdiffusion in the adjacent layers. The two samples differed only by their Si doping concentration, the uniformly doped sample HA09 being less doped. Figure 3 shows the Arrhenius plot of the Hall carrier concentration at two pressures from 77K up to 450K in sample HA09 whereas Figure 4 shows the Hall carrier concentration in the high temperature conduction regime in the same sample at various pressures.

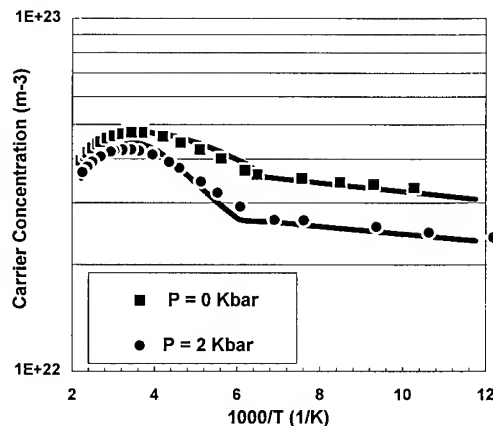


Fig. 3 : Carrier concentration vs 1000/T in sample HA09 at two pressures. Solid lines correspond to the modelling.

Figure 3 shows the thermal activation of the DX states at temperatures higher than the low temperature carrier freeze out. At temperatures above the room temperature, the carrier concentration saturates and then decreases as shown in Fig. 4. This anomalous decrease at high temperatures corresponds in fact to the thermally induced transfer of electrons from the high mobility  $\Gamma$  miniband to the low mobility X miniband resulting in a apparent Hall carrier concentration decreasing when increasing temperature.

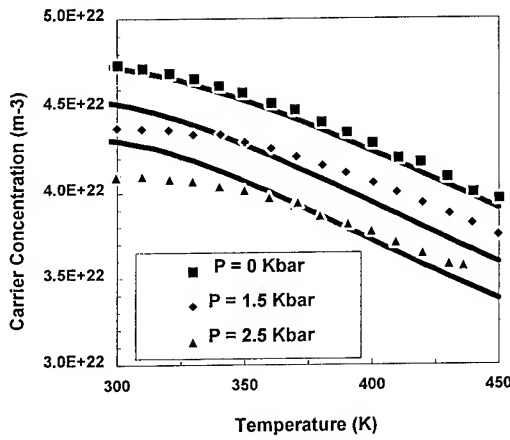


Fig. 4 : Carrier concentration vs temperature in sample HA09 at high temperatures and various pressures. Solid lines correspond to the modelling.

### Interpretation of Hall data under pressure

To interpret our Hall data in planar doped samples, we probed first a one DX level double donor model [4]. We took the energies 270 meV and 140 meV found previously for the corresponding  $DX_0$  and  $DX_3$  states [3]. The reference in energy is the  $\Gamma$  band in the GaAs wells. To match to the Hall data in the sample HA09 uniformly doped in both layers, we took into account the two  $DX_0$  and  $DX_3$  levels and applied a previously developed two donor model [2]. Introducing the silicon concentration as the maximum donor concentration and assuming the existence of a silicon shallow single donor level and a compensator level ( $N_a$ ), we were unable to fit to the data in the four samples. On the contrary, the fit is properly made when assuming segregation of

silicon in the adjacent layers in planar doped samples. Indeed, the apparent thermal activation energy of the Hall carrier concentration depend strongly on the single DX level or two DX level assumption.

When assuming the existence of different deep DX levels and taking into account the two band electron statistics, we used the following expressions for the total carrier concentration:

$$n = \sum_i N_{di} \frac{1 - \exp\left[-2 \frac{(E_{DXi} - E_f)}{kT}\right]}{1 - \exp\left[-\frac{(E_{DS} - E_f)}{kT}\right] + \exp\left[-2 \frac{(E_{DXi} - E_f)}{kT}\right]} - N_a$$

$$\text{and } n(P, T) = n_{\Gamma}(P, T) + n_X(P, T)$$

where  $n_{\Gamma}$  and  $n_X$  denote the free carrier density in the  $\Gamma$  and X conduction miniband respectively.

The energies of the  $\Gamma$  and X conduction minima in GaAs and AlAs are functions of temperature (in Kelvins) and pressure (in Kbars) and expressed as :

$$E(T, P) = E_0 - aT^2/(T+204) + bP$$

where values of the energies and coefficients of temperature (a) and pressure (b) are given below according to the literature.

	$E_{0\Gamma} / E_{0X}$ (eV)	$a_{\Gamma} / a_X$ ( $10^{-4}$ )	$b_{\Gamma} / b_X$ meV/Kbar
GaAs	1.52/1.98	5.4/4.6	11.5/-0.8
AlAs	3.13/2.23	5/4.6	10.2/-0.8

Due to the short period in our samples, we have found that Si out-diffusion is larger in sample HC01 (around 40%) than in sample HB11 (around 5%) according to the respective thicknesses (28.5 Å of GaAs and only 8.5 Å of AlAs).

Figures 3 and 4 show the conduction model applied on sample HA09 at various pressures. It is worth mentioning that the best fit is made introducing a non negligible concentration of an intermediate state at 180 meV (around 14 %) since that sample was uniformly doped (existence of  $DX_1$  and  $DX_2$  states at the interface). The model accounts for the thermal activation of a shallow donor level at low

temperatures and for the thermal activation of the deep donor levels at temperatures above the temperature of the metastable regime. It accounts also for the maximum of the carrier concentration near room temperature and for its decrease at high temperatures due to the thermal redistribution of electrons in the  $\Gamma$  and X conduction minibands.

### Conclusion

We have studied short period superlattices planar doped with silicon in the high temperature conduction regime at various pressures. To interpret the experimental results we had to use a two DX donor model taking into account segregation of the dopant in the adjacent layer during epitaxy. To match to the Hall data, we took the ionization energies of the silicon DX center determined

previously in the low temperature conduction regime. Consequently, this conduction model accounts properly for the electrical behaviour of selectively doped short period superlattices under pressure in a wide temperature range.

### References

- [1] P.M. Mooney, *J. Appl. Phys.*, **67**, R1 (1990) and references therein.
- [2] P. Sellitto, P. Jeanjean, J. Sicart, J.L. Robert and R. Planel, *J. Appl. Phys* **74** (1993) 7166.
- [3] J. L. Robert, P. Sellitto, A. Gougam, J. Sicart and R. Planel, *J. Phys. Chem. Solids* **56** (1995) 615 or P. Sellitto, J. Sicart, J.L. Robert and R. Planel, *Phys. Rev. B* **51** (1995) 16778.
- [4] T. N. Theis, P. M. Mooney and B. D. Parker, *J. Electron. Mater.* **20** (1991) 35.

## EFFECT OF "MEMORY" IN P-TYPE GaAs/AlGaAs HETEROSTRUCTURE PIEZORESISTIVITY

O.P. Hansen\*, V. Kravchenko\*\*, N.Ya. Minina\*\*, J.S. Olsen\*, A. Savin\*\*

\* *Niels Bohr Institute, Oersted Laboratory, DK-2100 Copenhagen, Denmark*

\*\* *Physics Faculty, Moscow State University, 119899 Moscow, Russia*

Electrical resistance of 2D hole gas in a Be-doped GaAs/AlGaAs heterostructure has been investigated under uniaxial compression in [110] direction up to 2.2 kbar over the temperature interval 4.2-200K. Specific "memory" of the previous loading and unloading processes has been observed in the piezoresistance of the samples under investigation.

We have studied the electrical resistance of a 2D hole gas at a Be-doped GaAs/Al<sub>0.5</sub>Ga<sub>0.5</sub>As heterojunction under in plane uniaxial compression up to  $\sigma=2.2$  kbar over the temperature interval 4.2-200K. To the best of our knowledge there has been no study of kinetic characteristics of the 2D carriers under these conditions, except for those preliminary to the present one [1].

The samples were obtained by cleavage along [110] direction from the same MBE grown wafer that consisted of a (100) GaAs substrate followed by 1  $\mu\text{m}$  of undoped GaAs buffer layer, 70Å of Al<sub>0.5</sub>Ga<sub>0.5</sub>As undoped spacer, 500Å of Al<sub>0.5</sub>Ga<sub>0.5</sub>As active layer doped with Be up to  $1 \times 10^{18} \text{cm}^{-3}$ . The structure was covered with 50Å GaAs cap doped with Be to  $2 \times 10^{18} \text{cm}^{-3}$ . The samples had dimension (3x0.8x0.625) mm<sup>3</sup> and were contacted by standard Au:Zn or Au:Mg diffusion in two different configurations. One of these had just four parallel stripes evaporated directly on the sample. On the other one a Hall bar mesa was first made and afterwards contact pads were evaporated. The contacts exhibit ohmic behavior. Uniaxial compression of the samples was produced in [110] direction by technique developed in ref [1].

The Hall density of 2D-holes in the quantum well at the heterostructure interface was  $N_s=9.7 \times 10^{11} \text{cm}^{-2}$  in uncompressed state at 4.2K and revealed only a slight decrease  $\sim 3\%$  at  $\sigma \sim 2.2$  kbar. The resistance of 2D hole system, quite the reverse, exhibited 1.5-2 times decrease under compression. (fig.1) Specific memory of the previous loading and unloading processes has been

observed in piezoresistivity of the samples under investigation.

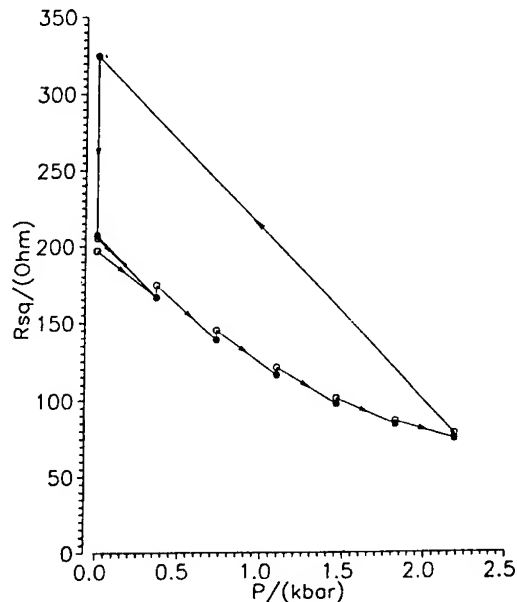


Fig.1 Resistivity of the samples in dependence on stress at 4.2K with thermocycling up to 200K (see the text).

This effect is connected with the long time relaxation of electrical resistance phenomenon in p-GaAs/Al<sub>0.5</sub>Ga<sub>0.5</sub>As 2D hole system caused by uniaxial stress that was detected for the first time in ref.[2]. It reveals in overshoot and slow increase (under loading) or decrease (after unloading) of the resistance to its stable state which may be reached by heating of the sample up to 200K and slow cooling to the temperature of experiment (fig1). On Fig 1 black circles correspond to the resistance

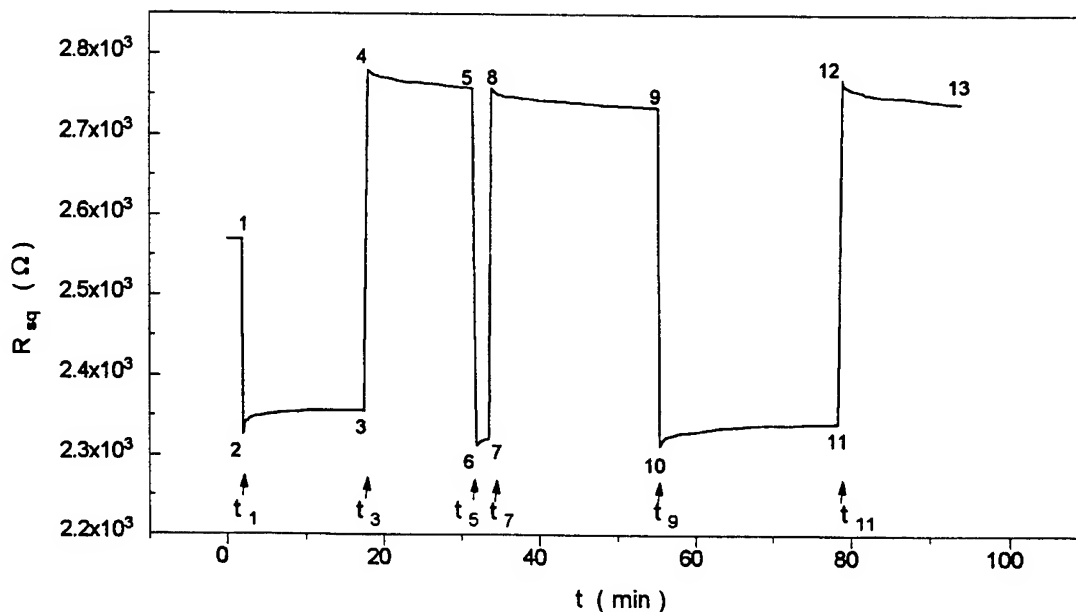


Fig.2 Time dependence of the resistivity in the course of loading and unloading of the sample at  $T=77\text{K}$ . At the moments  $t_1, t_5, t_9$  uniaxial pressure  $\sigma=0.83$  kbar is applied; at the moments  $t_3, t_7, t_{11}$  pressure is removed.

of the 2D hole gas after 20 minutes from the moment when the stress was applied (removed). Empty circles were taken after heating of the samples up to 200K and cooling back to 4.2K. Arrows show the sequence of the experimental points.

The relaxation process in the unloaded state "remembers" the previous disturbance (loading) if it is interrupted by the new one of the same level (fig 2). The initial resistance  $R_0$  on Fig 2 corresponds to the point 1 and can be reached in unloaded state by heating of the sample up to 200K and slow cooling down to the temperature of experiment ( $T=77\text{K}$ ). Intervals between points 2-3; 6-7; 10-11 show the relaxation processes in loaded state and intervals 4-5; 8-9; 12-13 reveal relaxation in unloaded state. The effect of "memory" is demonstrated by the points 4-5-8-9. Point 12 is taken after rather long relaxation time ( $\sim 30$  min) in loaded state (interval 10-11), that is "memorized" by the system of carriers, so that the line 12-13 is not the prolongation of the line 4-5-8-9.

Effect of memory is characteristic for long time relaxation processes, that mostly are considered to be due to the presence of energetic barriers of different kinds. The "barrier model" for long time relaxation effects was developed for not homogeneous semiconductors [3] and seems to be fairly valid for artificially constructed heterostructure. But there exists a significant difference: in our case the relaxation processes and strong decrease of 2D hole resistivity appear on the background of almost unchanged carrier concentration while in the course of penetration through a barrier carrier concentration varies.

According to calculations and optical measurements, the energetic spectrum of 2D holes is extremely complicated and dramatically changes under uniaxial stress [4]. In ref [5] for the similar p-GaAs/ $\text{Al}_{0.5}\text{Ga}_{0.5}\text{As}$  heterostructure it was shown that in the QW even at  $\sigma=0$  there exist two spin-split uppermost heavy hole subbands. Our measurements\* of Quantum Hall effect and Shubnikov-de Haas oscillations in the samples of

the present study, subjected to uniaxial stress, reveal only  $(4\pm 1)\%$  decrease of the total 2D hole concentration in the QW. At the same time a significant redistribution of the carriers between the two spin-split subbands with different effective masses takes place. The small change of the 2D hole concentration leads to the conclusion that the observed effect of memory as well as the relaxation effects in resistivity are due to some electronic processes inside the QW and are not connected with recombination of 2D holes and electrons on charged impurities (Be) outside the barrier.

If we restrict the consideration to the electronic system we can suppose that the long time relaxation processes in resistivity under uniaxial stress may have their origin in the redistribution of carriers between the two spin-split subbands and that these spin-flip processes have low probability. But long characteristic time of the observed relaxation process, that is almost "frozen" at 4.2K, does not exclude the possibility that this process is caused by transitions in the lattice subsystem. For example, it could be configuration change in the system of impurities and (or) defects on heterostructure interface. Large magnitude of atomic masses and low temperature can make this change extremely slow and enlarge the characteristic time of the relaxation process to macroscopic range.

For more definite conclusion additional experiments and calculations are to be performed.

This work has been supported by NATO Linkage Grant 931579 and by grants 11-1080-1, 11-1124-1 and 9401081 from the Danish Research Council. The authors are grateful to S.Beneslavsky for helpful discussions.

1. V.N.Kravchenko, N.Ya.Minina, A.Savin, J.S.Olsen, O.P.Hansen *JETP Lett.* **61** (1995) 424.
2. N.B.Brandt, V.S.Egorov, M.Yu.Lavrenyuk, N.Ya.Minina, A.M.Savin *Sov. Phys. JETP* **62** (1985) 1303.
3. M.K.Sheinkman, A.Ya.Shik, *Sov.Phys.Semicond.* **10** (1976) 128.
4. B.Gil, P.Lefebvre, H.Mathieu, G.Platero, M.Altarelli, T.Fukunaga, H.Nakashima, *Phys. Rev. B* **38** (1988) 1215.
5. H.L.Stormer, Z.Schlesinger, A.Chang, D.C.Tsui, A.C.Gossard, W.Wiegman, *Phys.Rev.Lett.* **51** (1983) 126.



# POTENTIAL BARRIER AT A GRAIN BOUNDARY IN p-Hg<sub>1-x</sub>Cd<sub>x</sub>Te (x=0.23) UNDER UNIAXIAL COMPRESSION

Butko N.B.\*, Kraak W.\*\*\*, Minina N.Ya.\*, Savin A.\*

\* Physics Department, Moscow State University, 119899 Moscow, Russia.

\*\* Institute of Solid State Physics, Humboldt University, D-10115 Berlin, Germany.

The potential barrier at a grain boundary in p-Hg<sub>1-x</sub>Cd<sub>x</sub>Te (x=0.23) was determined from the temperature dependence of grain boundary resistance at temperatures, when thermionic emission over the barrier dominates. The barrier magnitude is  $\Phi_B = 207 \text{ meV}$  at  $T = (100-160) \text{ K}$  and increases under uniaxial compression up to  $\sigma = 1.5 \text{ kbar}$  with the rate  $\Delta\Phi_B/\Delta\sigma = 44 \text{ meV/kbar}$ . Increase of the positively charged defects at the grain boundary interface is suggested to be responsible for the observed effect.

Two dimensional (2D) inversion layers of charge carriers at grain boundaries (GB) of semiconductor bicrystals, e.g. in p-InSb, p-Hg<sub>1-x</sub>Mn<sub>x</sub>Te, p-Hg<sub>1-x</sub>Cd<sub>x</sub>Te, arise naturally in the course of crystal growth and, in contrast to heterostructures created artificially at semiconductor interfaces, are in the interior of the sample. The current flow across the GB meets a potential barrier that equals the distance between the quantum well (QW) bottom and the top of the valence band in the bulk (Fig.1a). The electrical properties of polycrystalline semiconductors are frequently dominated by these electrostatic potential barriers which surround the GB. The magnitude of the potential barrier may be significant. So in the vicinity of the GB in p-InSb the pronounced potential barrier  $\Phi_B \sim 200 \text{ meV}$  at  $T = 150 \text{ K}$  was detected [1]. Investigations under pressure are of great interest and expected to clear the problem of charged states on a GB interface.

The potential barrier at a GB in p-Hg<sub>1-x</sub>Cd<sub>x</sub>Te (x=0.23) bicrystals with carrier concentration  $p = N_A - N_D = 10^{15} \text{ cm}^{-3}$  has been investigated under uniaxial compression up to  $\sigma = 1.5 \text{ kbar}$  in perpendicular to the GB direction.

For the measurement of the barrier height  $\Phi_B$  we used the method described in ref.[1]. The current flow across the grain boundary can be determined by various mechanisms. Generally, thermionic emission over the barrier dominates at higher temperatures; at lower temperatures tunneling through the boundary barrier occurs. The current flow  $j$  over the barrier in the region of thermionic emission is given by [1,2]:

$$j = A^* T^2 \exp(-(\Phi_B + \xi)/kT) \cdot [1 - \exp(-eU/kT)], \quad (1)$$
 where  $k$  is the Boltzmann constant,  $A^* = 4\pi m^* k^2/h^3$  is an effective Richardson constant,

$\xi = E_{FL} - E_V = kT \ln(N_V/N_A)$  and  $m^*$  is the valence band effective mass. In general case one can suppose that the barrier height  $\Phi_B$  is a function of the applied voltage  $U$ . Our measurements were carried out in the Ohmic region of the current-

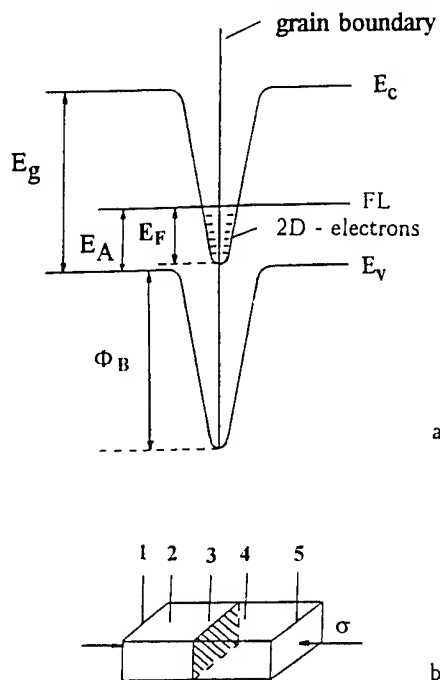


Fig.1 a) Band structure model for a grain boundary in p-Hg<sub>1-x</sub>Cd<sub>x</sub>Te;  $E_c$ ,  $E_v$  are the conduction and the valence band respectively; FL is the Fermi level;  $E_F$  is the Fermi energy,  $E_g$  is the energy gap,  $E_A$  - activation energy of the acceptor level in the bulk material;  $\Phi_B$  is the magnitude of the potential barrier;

b) Sample geometry and the arrangement of the contacts: 2, 3, 4 - potential, 1, 5 - current. GB is dashed.

voltage characteristic at low voltages  $U = 0.1-0.2\text{mV}$ , when  $eU \ll kT$ . In this case the magnitude of the barrier  $\Phi_B = \text{const}$  and it follows from (1):

$$j = A^* T \exp[-(\Phi_B + \xi)/kT] eU/k. \quad (2)$$

The temperature dependence of the boundary resistance is given by

$$R_{GB} = [k/(FA^*eT)] \cdot \exp[(\Phi_B + \xi)/kT], \quad (3)$$

where  $F$  is the area of the grain boundary interface. According to (3) the barrier height can be evaluated from the slope of the dependence  $\ln(R_{GB}T) = f(1/T)$ .

The samples with dimensions  $0.7 \times 0.7 \times 3\text{mm}$  were subjected to uniaxial compression by the method of ref.[3]. The direction of stress  $\sigma$  is perpendicular to the grain boundary and makes angles  $\sim 30^\circ$  with  $[100]$ ,  $51^\circ$  with  $[111]$ , and  $14^\circ$  with  $[100]$  crystallographic directions. The arrangement of the current 1, 5 and the potential 2, 3, 4 contacts is shown in Fig.1b. The special configuration of the potential electrodes permits to separate the GB resistance from the resistance of the bulk material. In order to exclude geometrical factors, the distance  $l_{2,3} = l_{3,4}$  and the pure boundary resistance  $R_{GB} = R_{3,4} - R_{2,3}$ , where  $R_{3,4}$  is the resistance of

the bicrystal with the GB, and  $R_{2,3}$  is the resistance of the bulk material.

Fig.2 shows typical examples of the temperature dependence of the resistance for p-Hg<sub>1-x</sub>Cd<sub>x</sub>Te bicrystals  $R_{3,4}$  (curve 1) and the related bulk materials  $R_{2,3}$  (curve 2); the temperature dependence of the GB resistance  $R_{GB}$  is represented on the inset. Three characteristic regions (I-III) are evident from this plot. In region I of the intrinsic conductivity (temperature interval 180–270K) no difference between  $R_{3,4}$  and  $R_{2,3}$  was found. In this region the barrier can not influence the conductivity due to thermoactivation process over the barrier. From the slope of  $\ln R_{2,3}(1/T)$  the energy gap in the bulk can be evaluated. In region II ( $T=100-180\text{K}$ ) the current flow in the bicrystals is determined by thermionic emission over the potential barrier at the GB. The bicrystal resistivity (curve 1) rapidly increases with the temperature decrease in this region. In region III ( $T < 100\text{K}$ ) tunneling of carriers through the barrier and surface conductivity may determine the current transport in the bicrystal. At low temperature ( $T \sim 77\text{K}$ ) the electrical resistivity of the bicrystals under investigation is about 1.5–2 times larger than the electrical resistivity of the bulk material.

The potential barrier in the vicinity of the GB was estimated from the temperature dependence of the resistance  $R_{GB}$  in the temperature range from 100K to 180K, and the expression (3) for the current flow over the barrier in the region of thermionic emission was used for the calculations. For the samples under investigation the potential barrier  $\Phi_B$  occurs to be 207meV at  $T=100-180\text{K}$  and its magnitude increases under uniaxial compression with the rate  $\Delta\Phi_B/\Delta\sigma = 44\text{ meV/kbar}$  (Fig.3). This result implies that the QW, that confines the 2D electrons on the GB, becomes more deep when pressure is applied. It corresponds to increase of 2D carrier concentration obtained previously from Shubnikov - de Haas (SdH) effect under uniaxial compression [4], but is opposite to the effect observed under hydrostatic pressure [5]. According to the ref.[5,6], the decrease of 2D electron concentration under hydrostatic pressure is caused by the increase of the energy gap  $E_g$  in the bulk part of the sample that leads to a negative shift of the bottom of the QW with respect to the

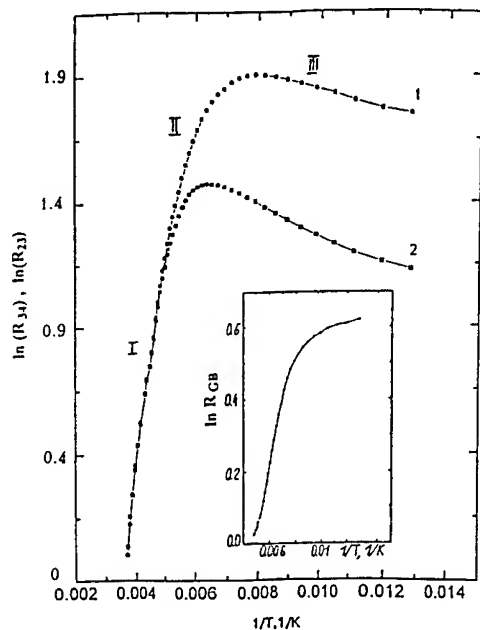


Fig.2 Temperature dependence of the resistance for p-Hg<sub>1-x</sub>Cd<sub>x</sub>Te bicrystals  $R_{3,4}$  (curve 1) and the related bulk materials  $R_{2,3}$  (curve 2); on the inset the temperature dependence of the GB resistance  $R_{GB}$  at  $\sigma=0$  is represented.

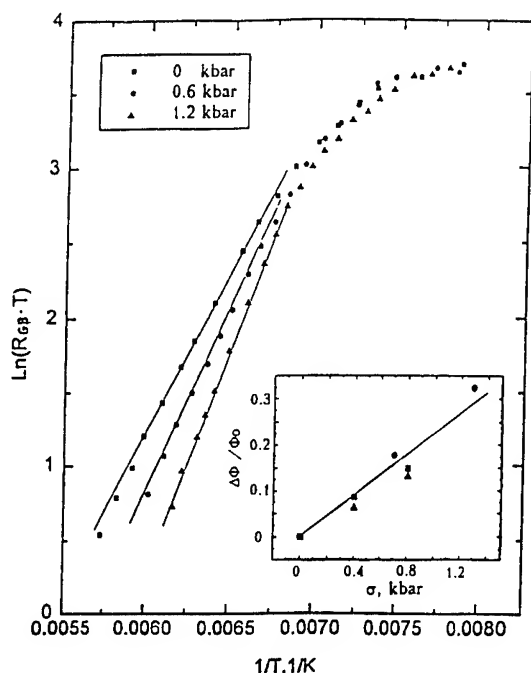


Fig.3 Temperature dependence of the GB resistance  $R_{GB}$  at different  $\sigma$ . On the inset - relative increase of the potential barrier under uniaxial compression.  $\bullet, \blacksquare, \blacktriangle$  - data for the three different samples.

Fermi level approximately at the same rate.

The independent estimation of the potential barrier magnitude  $\Phi_B = E_F - E_A + E_g$  (Fig.1a) and its dependence on uniaxial strain may be carried out on the base of ShH data [4], that were obtained for the similar  $p\text{-Hg}_{1-x}\text{Cd}_x\text{Te}$  samples with GBs. In ref. [4] the strain dependence of  $E_F, E_i$  for each of the energetic  $i$ -subbands in QW on the GB as well as energy gap  $E_g(0)=82\text{meV}$ ;  $\Delta E_g/\Delta\sigma=5\text{meV/kbar}$  and activation energy  $E_A(0)=3.5\text{meV}$ ;  $\Delta E_A/\Delta\sigma = -1.6\text{meV/kbar}$  in the bulk were determined. In the assumption of a symmetrical triangular potential well  $V(z)=e\epsilon|z|$ , where  $\epsilon$  is the electrical field strength in a GB vicinity, the subband levels  $E_i$  are given by the well known formula [7]:

$$E_i = [(h\epsilon e)^2/2m]^{1/3} \cdot [(3\pi/8) \cdot (2i+1)]^{2/3}, \quad (4)$$

$i = 0, 1, 2, \dots$

The system of equations (4) permits to calculate the Fermi energy  $E_F$  of 2D electrons, counted from the bottom of the QW,  $E_F(0)=112\pm 1\text{meV}$  as well as strain dependence  $\Delta E_F/\Delta\sigma=34\pm 1\text{meV/kbar}$ . The obtained values of  $\Phi_B(0)=190\pm 4\text{meV}$  and

$\Delta\Phi_B/\Delta\sigma=41\pm 1\text{meV/kbar}$  are in a good agreement with the result of the present study.

The calculations on the base of data of ref.[4] show also that the electrical field in the GB vicinity is  $\epsilon(0)=(1.9\pm 0.3)\cdot 10^6\text{V/m}$  and reveals two times increase under uniaxial compression  $\sigma\sim 1.5\text{kbar}$ . It implies the increase of positively charged states on the GB, that are usually ascribed to dangling bonds or segregated impurities at the GB. The density of positively charged segregates at the GB we consider to be constant in the course of compression. Moreover, the potential barrier in the similar  $p\text{-InSb}$  bicrystals was found to be almost independent on the impurity concentration in the bulk part if  $N_A-N_D\leq 10^{16}\text{cm}^{-3}$  [1]. Therefore we suggest that the observed increase of the potential barrier at the GB under uniaxial compression is mainly caused by increasing density of positively charged defects (dangling bonds) that form the net of line dislocations on the GB interface. We can suppose this because uniaxial stress should definitely increase (or decrease) the bicrystal lattice mismatch on the grain boundary interface. Under uniform compression there is no reason for dangling bonds increase and the decrease of the QW depth is mostly connected with the energy structure of the bulk (widening of the energy gap  $E_g$ ).

Acknowledgments - The authors are grateful to S.Beneslavski and O.P.Hansen for helpful discussions. This work was partly supported by the Deutsche Forschungsgemeinschaft.

1. R. Herrmann, W. Kraak, G. Nachtwei, *Phys. Stat. Sol. (b)* **128** (1985) 337.
2. G.E. Pike, C.H. Seager, *J. Appl. Phys.* **50** (1979) 3414.
3. N.B. Brandt, V.S. Egorov, M.Yu. Lavrenyuk, N.Ya. Minina, A.M. Savin, *Sov. Phys. JETP* **62** (1985) 1303.
4. N.B. Butko, W. Kraak, S. Krause, N.Ya. Minina, A.M. Savin, *JETP Lett.* **59** (1994) 790.
5. W. Kraak, J. Kaldash, P. Gille, Th. Schurig, R. Herrmann, *Superlattices and Microstructures* **9** (1991) 471.
6. R. Herrmann, W. Kraak, G. Nachtwei, Th. Schurig, *Phys. Stat. Sol. (b)* **135** (1986) 423.
7. G. Paasch, T. Fiedler, M. Kolar, I. Bartos, *Phys. Stat. Sol. (b)* **118** (1983) 641.

## **VII(D) Superconductors**

# PRESSURE-INDUCED OXYGEN ORDERING EFFECTS IN HIGH- $T_c$ SUPERCONDUCTORS

J.S. SCHILLING, A. K. KLEHE and C. LOONEY

*Physics Department, Washington University, C.B. 1105, St. Louis, MO 63130, U.S.A.*

Oxygen defects in the superconducting oxides are known to exhibit considerable mobility at room temperature. In some systems this high mobility leads to local oxygen ordering effects when hydrostatic pressure is applied at ambient temperature and results in anomalously large changes in  $T_c$ . Recent experiments on  $Tl_2Ba_2CuO_{8+\delta}$  reveal the existence of two distinct oxygen ordering processes which become activated for temperatures above 60 K and 150 K, respectively. Evidence is discussed for the existence of oxygen ordering processes in  $YBa_2Cu_3O_{7-\delta}$  which may be responsible for the phenomena of both transient and persistent photo-induced superconductivity.

One of the more promising strategies for furthering our understanding of the superconducting state in the high- $T_c$  oxides is to search for systematics in the variation of the transition temperature  $T_c$  with parameters such as the concentration  $n$  of charge carriers per  $CuO_2$ -plane or the applied pressure  $P$ .<sup>1,2</sup> Unfortunately, the true dependence of  $T_c$  on  $n$  or  $P$  valid for an ideal isostructural system is sometimes masked by atomic rearrangements or structural phase transitions, some of which occur in the oxygen sublattice.<sup>1</sup> In spite of these difficulties, systematic experimentation has revealed that the true dependence of  $T_c$  on  $n$  or  $P$  is remarkably simple. For hole-doped oxide superconductors,  $T_c$  appears to be a parabolic function of  $n$ ,<sup>3</sup>

$$T_c \simeq T_c^{\max} [1 - 82.6(n - 0.16)^2], \quad (1)$$

as seen in Figure 1. The hole-carrier content  $n$  in the oxides can be enhanced in one of three ways: cation substitution, as in  $La_{2-x}Sr_xCuO_4$ ,<sup>4</sup> an increase in oxygen content,<sup>5</sup> or the application of high pressure.<sup>6</sup>

Murayama et al.<sup>6</sup> find in high-pressure Hall-effect studies on oxide superconductors that typically  $d \ln n / dP \approx +10 \text{ \% / GPa}$ . This observed increase in  $n$  under pressure would lead to the expectation from Eq.1 that  $dT_c/dP > 0$  for underdoped ( $n < n_{\text{opt}}$ ),  $dT_c/dP = 0$  for optimally doped ( $n = n_{\text{opt}}$ ), and  $dT_c/dP < 0$  for overdoped ( $n > n_{\text{opt}}$ ) samples. Unfortunately, as indicated in Fig.1, this simple charge-transfer model does not agree well with experiment. For optimally doped ideal samples, where no pressure-induced phase transitions are known to occur, it is typically found that  $dT_c/dP \approx +1$  to  $+3 \text{ K/GPa}$ ,<sup>1,7,8,9,10</sup> implying that  $T_c$  must depend on further variables

than  $n$ . As indicated in Fig.1, underdoped samples tend to have more positive values of  $dT_c/dP$  and

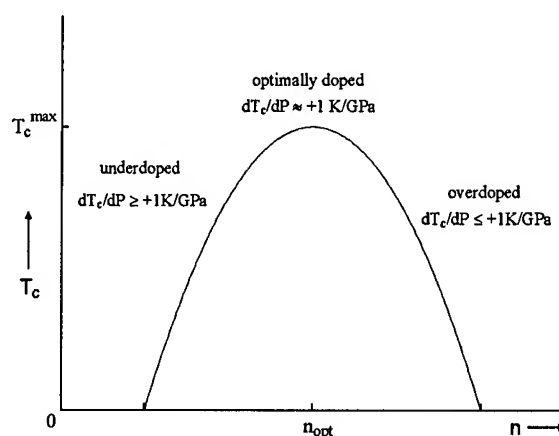


Figure 1: Dependence of  $T_c$  on hole-carrier content  $n$  according to Eq.1. Representative experimental values of  $dT_c/dP$  for underdoped, optimally doped and overdoped oxides are given from Ref.10.  $T_c = T_c^{\max}$  when  $n = n_{\text{opt}}$ .

overdoped samples more negative values. These observations for cation substituted  $YBa_2Cu_3O_{7-\delta}$  (Y-123) prompted Neumeier and Zimmermann<sup>7</sup> to propose that there are two primary contributions to the total pressure derivative,  $dT_c/dP$ , one reflecting the increase of  $n$  with pressure and another "intrinsic" contribution arising from all other sources at constant  $n$ , namely

$$\frac{dT_c}{dP} = \left(\frac{dT_c}{dn}\right)\left(\frac{dn}{dP}\right) + \left(\frac{dT_c}{dP}\right)^{\text{int}}. \quad (2)$$

Since  $dT_c/dn = 0$  for an optimally doped sample, Eq.2 implies that  $(dT_c/dP)^{\text{int}} = dT_c/dP \simeq +1$  to  $+3 \text{ K/GPa}$ . Using known or estimated values of

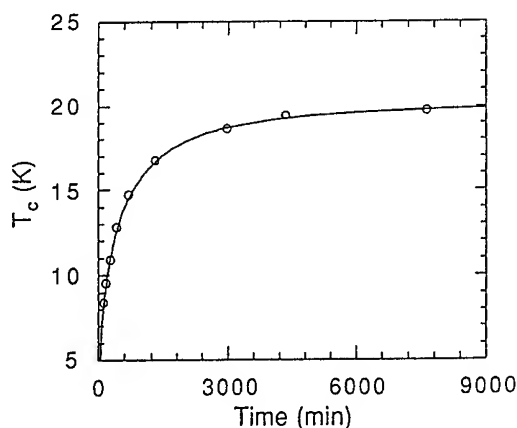


Figure 2:  $T_c$  as function of annealing time  $t$  at room temperature for a quenched sample of  $\text{YBa}_2\text{Cu}_3\text{O}_{6.41}$  (Ref.15).

the bulk modulus  $B$ ,<sup>11</sup> Klehe et al.<sup>12,13</sup> have obtained the following values of the exponent  $\alpha$  in  $T_c \propto V^{-\alpha}$  for the intrinsic dependence of  $T_c$  on sample volume  $V$  at constant  $n$ :  $\text{HgBa}_2\text{CuO}_{4+\delta}$  ( $-1.22 \pm 0.05$ ),  $\text{HgBa}_2\text{CaCu}_2\text{O}_{6+\delta}$  ( $-1.19 \pm 0.06$ ),  $\text{HgBa}_2\text{Ca}_2\text{Cu}_3\text{O}_{8+\delta}$  ( $-1.20 \pm 0.05$ ),  $\text{YBa}_2\text{Cu}_3\text{O}_{7-\delta}$  ( $-1.25 \pm 0.06$ ),  $\text{Tl}_2\text{Ba}_2\text{CuO}_{6+\delta}$  ( $-1.35 \pm 0.4$ ),  $\text{Tl}_2\text{Ba}_2\text{CaCu}_2\text{O}_{8+\delta}$  ( $-0.9 \pm 0.2$ ),  $\text{Tl}_2\text{Ba}_2\text{Ca}_2\text{Cu}_3\text{O}_{10+\delta}$  ( $-1.16 \pm 0.3$ ),  $(\text{Bi}_{1.8}\text{Pb}_{0.4})\text{Sr}_{1.85}\text{Ca}_{2.05}\text{Cu}_3\text{O}_{10+\delta}$  ( $-1.36$ ),  $\text{Bi}_2\text{Sr}_2\text{CaCu}_2\text{O}_{8+\delta}$  ( $-1.04 \pm 0.15$ ). This simple approximate result that  $T_c \propto V^{-1.2}$  must be accounted for by any theory claiming to describe the superconducting state in the oxides.

As stated above, the true dependence of  $T_c$  on a given parameter can be masked by concomitant structural changes. In this paper we could like to summarize the existing evidence that in some, and perhaps many, high- $T_c$  oxides the application of pressure causes a redistribution within the oxygen sublattice which can lead to changes in both  $n$  and  $T_c$ .

In the high- $T_c$  superconductors it is well known that oxygen defects possess a sizeable mobility, even at room temperature (RT).<sup>14</sup> As seen in Fig.2, oxygen vacancy ordering in underdoped Y-123 leads to an increase in  $T_c$  by  $\sim 20\text{K}$  if the sample is annealed at RT for sufficient time following a quench to 77K from high temperature.<sup>15</sup> This enhancement in  $T_c$  is believed to arise from local oxygen ordering in the CuO-chains which leads to an increase in the number of  $\text{Cu}^{1+}$  relative to

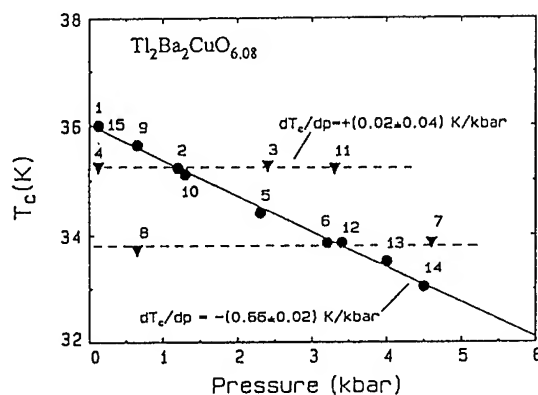


Figure 3:  $T_c$  versus pressure for  $\text{Tl}_2\text{Ba}_2\text{CuO}_{6.08}$  from Ref.17. Regarding oxygen content, see caption for Fig.4. Numbers give order of measurement. Points give data for pressure change at room temperature. Triangles give data for pressure change at low temperature (50K).

$\text{Cu}^{2+}$  in these chains, thereby increasing the hole-carrier density  $n$  in the superconducting  $\text{CuO}_2$ -planes.<sup>16</sup> From the data in Fig.2, an activation energy  $E_A \approx 1\text{eV}$  can be estimated,<sup>15,16</sup> in excellent agreement with tracer diffusion experiments.<sup>14</sup>

Following these studies on the influence of thermal history on oxygen defect ordering, Sieburger and Schilling<sup>17</sup> found that the application of hydrostatic pressure can also influence the degree of oxygen defect ordering. They studied the pressure dependence of  $T_c$  for polycrystalline  $\text{Tl}_2\text{Ba}_2\text{CuO}_{6+\delta}$  (Tl-2201) using a He-gas pressure system (Unipress, Warsaw) which allows precise pressure changes over a wide temperature range. As seen in Fig.3, if the pressure is applied or released at RT,  $T_c$  changes reversibly with pressure at the rate  $(dT_c/dP)_{RT} \simeq -6.6\text{ K/GPa}$ . If, however, the pressure is varied at low temperatures (LT) near 50K, no change in  $T_c$  occurs. The pressure derivative  $dT_c/dP$  thus depends in both magnitude and sign on the temperature at which the pressure is changed! Further studies on Tl-2201 revealed that  $(dT_c/dP)_{RT}$  is a strong function of the oxygen content, as seen in Fig.4. For  $\delta = 0$  or 0.11, the two pressure derivatives  $(dT_c/dP)_{RT}$  and  $(dT_c/dP)_{LT}$  are seen to assume the same values.

That these anomalous results are not due to the polycrystallinity of the samples is shown by very recent studies<sup>18</sup> on a Tl-2201 single crystal (Figs.5 and 6) where the sharp superconducting transition in the ac-susceptibility is seen to shift

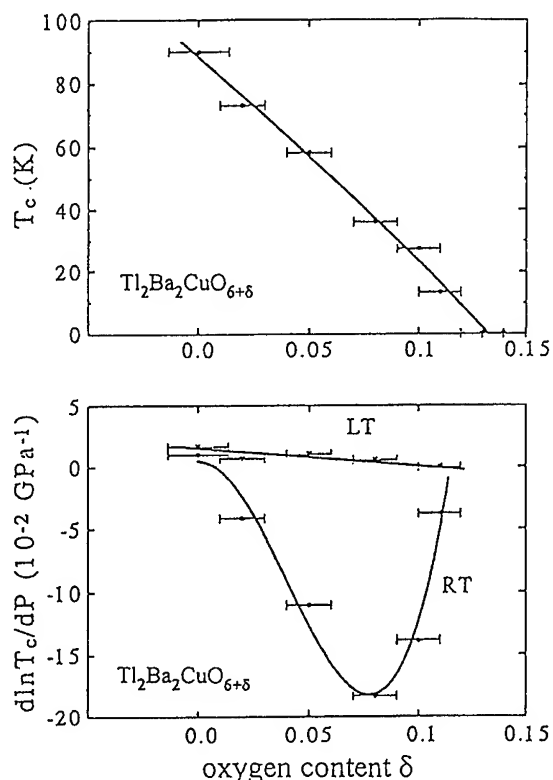


Figure 4: Dependence of  $T_c$  (upper) and the relative pressure dependence  $d\ln T_c/dP$  (lower) on oxygen content  $\delta$  in  $\text{Ti}_2\text{Ba}_2\text{CuO}_{6+\delta}$  for pressure change at both low (LT) and ambient (RT) temperature. Figure is adapted from Ref.17 by setting  $\delta = 0$  for an optimally doped sample, as reported in Ref.25.

rapidly to lower temperatures if the pressure is applied at RT, but to *decrease* slightly further if the pressure is released at LT (55K). Our interpretation of these results has been<sup>17</sup> that the application of pressure at RT results in the usual moderate changes in  $T_c$  for an ideal isostructural sample, as described above, *plus* an anomalous decrease in  $T_c$  due to pressure-induced oxygen ordering. This ordering results in a significant additional increase in  $n$  which leads to an enhanced decrease in  $T_c$  for overdoped samples (see Fig.4). On the other hand, if the pressure is changed at LT ( $\sim 50\text{K}$ ), the oxygen is frozen in place and thus is unable to order when pressure is applied. This scenario has received strong support from neutron diffraction studies on Tl-2201 in a He-gas system where the lattice parameters are found to depend markedly

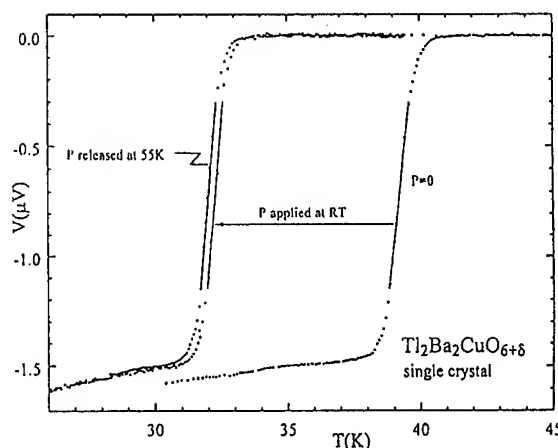


Figure 5: ac susceptibility signal versus temperature for a Tl-2201 single crystal showing the transition to superconductivity at different pressures.  $H_{ac} = 0.15 \text{ Oe}$  (Ref.18).

on the T-P history.<sup>19</sup>

Returning to Fig.6, following the release of pressure at LT (55K), the Tl-2201 crystal was annealed at progressively higher temperatures  $T_{\text{anneal}}$ , normally for 1 hour (h), before cooling down to determine  $T_c$ . This relaxation is seen in more detail in Fig.7. At selected temperatures additional annealing was carried out for the total times given in the figure. The essential (and unexpected) result here is that the relaxation takes place in two separate temperature regimes, a LT regime  $60\text{K} \leq T_{\text{anneal}} \leq 105\text{K}$  and a HT regime  $170\text{K} \leq T_{\text{anneal}} \leq 270\text{K}$ , with a plateau inbetween. This clearly points to the existence of two distinct relaxation processes within the oxygen sublattice. This two-step relaxation phenomenon was first observed by Klehe et al.<sup>13,18,20</sup> on a polycrystalline Tl-2201 sample with  $T_c(0) \simeq 23\text{K}$ . From these studies we estimate that for the LT relaxation processes, the activation energy is  $E_A \simeq 0.25\text{eV}$ , whereas for the HT processes,  $E_A \simeq 0.72\text{eV}$ . A complete exposition of these results is given in a separate publication.<sup>18</sup>

The crystal structure of Tl-2201 is shown in Fig.8. The superconducting  $\text{CuO}_2$  layer is situated between two  $\text{Tl}_2\text{O}_2$  double layers which act as charge reservoirs. Varying the oxygen content in  $\text{Ti}_2\text{Ba}_2\text{CuO}_{6+\delta}$  changes the amount  $\delta$  of interstitial oxygen within the  $\text{Tl}_2\text{O}_2$  double layer. Since the anomalous effects in  $dT_c/dP$  appear to disappear for  $\delta \simeq 0$  or  $0.11$ , as seen in Fig.4, it would seem likely that it is the interstitial oxygen O(4)

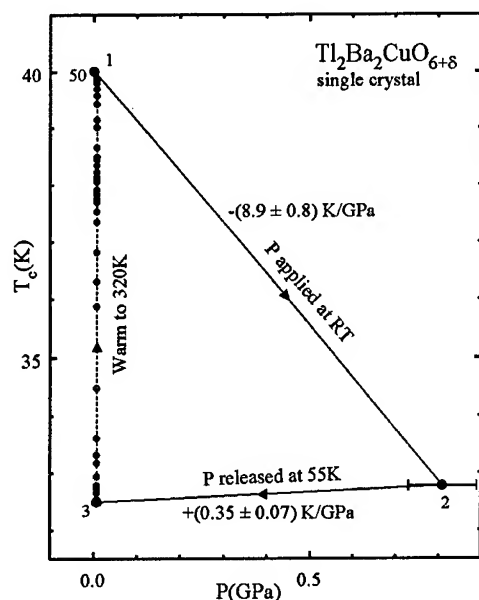


Figure 6: Dependence of  $T_c$  on pressure for a Tl-2201 crystal, from Ref.18. Data points and arrows give order of measurement.

which is ordering rather than the oxygen O(3) in the  $\text{Tl}_2\text{O}_2$  planes. The concentration  $\delta \approx 0.11$  corresponds to one interstitial oxygen per nine unit cells in a plane. This may be a particularly stable configuration which inhibits pressure-induced interstitial oxygen ordering. However, in Fig.4 it is seen that for  $\delta = 0$  the sample is optimally doped and  $T_c$  takes on its maximum value ( $\sim 92\text{K}$ ). From Fig.1 we see that in this case an increase in  $n$ , even if anomalously large, would to first order cause no change in  $T_c$ , so that any effects of oxygen ordering on  $n$  would be expected to have little or no influence on  $T_c$ . In fact, parallel Hall-effect studies<sup>13,18,21</sup> have shown that it is the change in  $n$  through oxygen ordering which primarily affects  $T_c$ . In addition, as we discuss below, for samples with high transition temperatures,  $T_c \gtrsim 90\text{K}$ , a sizeable, if not dominant, portion of the oxygen ordering may no longer be frozen in at temperatures comparable with  $T_c$ . It is thus not yet clear whether the interstitial O(4) or the planar O(3) oxygen are primarily responsible for the ordering effects observed. A discussion of the mechanism by which oxygen ordering affects  $n$  in Tl-2201 as well as a model for short-range oxygen ordering effects involving the planar O(3) oxygen in the

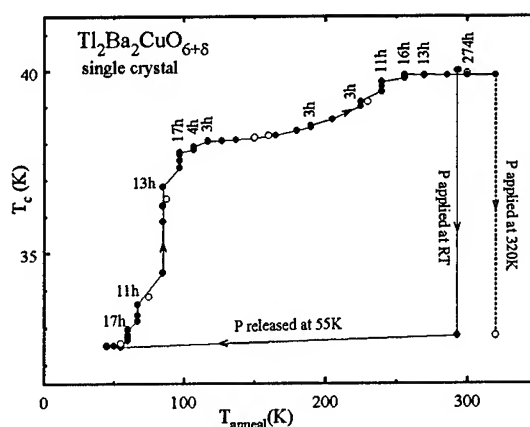


Figure 7: Data from Fig.6 replotted as  $T_c$  versus annealing temperature, from Ref.18. Two data series are shown: first ( $\bullet$ ), second ( $\circ$ ).

$\text{Tl}_2\text{O}_2$  double layer has been given by A.-K. Klehe at this conference.<sup>22</sup>

Since the HT relaxation mode in Tl-2201 involves activation energies  $E_A \approx 0.72\text{eV}$  near those obtained in tracer diffusion experiments ( $E_A \approx 1\text{eV}$ ) on other high- $T_c$  oxides, it would seem likely that the HT processes involve the migration of O(3) or O(4) oxygen from one unit cell to another. On the other hand, the very low value  $E_A \approx 0.25\text{eV}$  for the LT relaxation modes would speak for ordering processes whereby the oxygen ions never leave the unit cell but rather shift from one equivalent site to another *within* the unit cell (see Fig.8).<sup>13,22</sup>

The phenomena of pressure-induced oxygen ordering is not restricted to the single system Tl-2201, but has also been found to occur in superoxygenated  $\text{La}_2\text{CuO}_{4+\delta}$ ,<sup>23</sup> in oxygen depleted Y-123,<sup>24</sup> and most recently in  $\text{Tl}_2\text{Sr}_2(\text{Tl}_{0.8}\text{Ca}_{0.2})\text{Cu}_2\text{O}_{6.86}$ .<sup>18</sup> Other than for Tl-2201, it has not yet been determined in which temperature regime the oxygen ordering processes are activated when pressure is applied.

We would like to emphasize that oxygen ordering phenomena, whether activated by annealing temperature-quenched samples or by applying high pressure, may occur to some extent in many, if not all, superconducting oxides. This does not, however, necessarily imply that this oxygen redistribution will lead to a measurable change in  $n$  or  $T_c$ . For  $n$  or  $T_c$  to change it is neces-



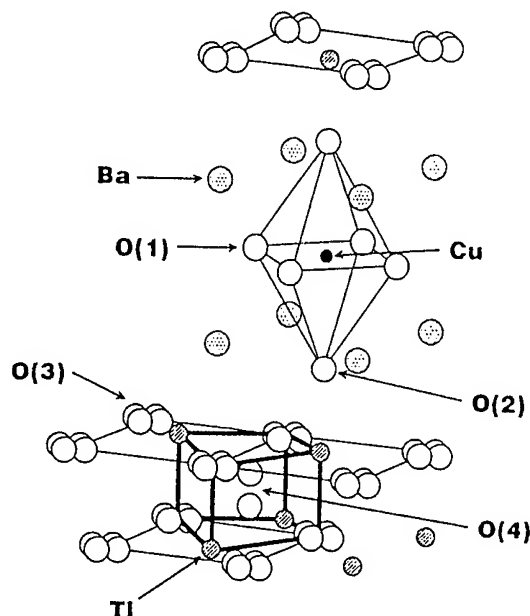


Figure 8: Crystal structure of Tl-2201 from Ref.25. Each oxygen O(3) in the  $\text{Ti}_2\text{O}_2$ -double layer has four equivalent positions. Each interstitial oxygen O(4) within the double layer has two equivalent positions.

sary both that an ambivalent cation, like thallium ( $\text{Tl}^{1+}$  or  $\text{Tl}^{3+}$ ) or copper ( $\text{Cu}^{1+}$  or  $\text{Cu}^{3+}$  in the chains of Y-123), be present in the charge reservoir *and* that the local oxygen ordering be capable of switching the nearby cation from one valence state to another.<sup>22</sup> This may be the reason why  $(dT_c/dP)_{LT} \simeq (dT_c/dP)_{RT}$  in Bi-2212: local oxygen ordering is not capable, for energetic reasons, of switching bismuth between  $\text{Bi}^{3+}$  and  $\text{Bi}^{5+}$ .<sup>9</sup> What does the cation valence have to do with the hole-carrier density  $n$  in the  $\text{CuO}_2$ -planes? As the O(3) or O(4) oxygen in Tl-2201 order when pressure is applied at RT, some Tl-ions will switch from a  $\text{Tl}^{3+}$  to a  $\text{Tl}^{1+}$  valence state, thus tying up two additional electrons which must come from the  $\text{CuO}_2$ -plane, i.e. an increase in the density of holes.<sup>13,22</sup>

Another reason that oxygen ordering effects have been observed in relatively few high- $T_c$  oxides may be that for many systems the values of  $T_c$  are simply so high that most of the ordering has been annealed out at temperatures *below*  $T_c$ . Indeed, in Tl-2212 ( $T_c^{\text{max}} \simeq 115\text{K}$ ) and Tl-2223 ( $T_c^{\text{max}} \simeq 125\text{K}$ ) the values of  $T_c$  lie well above the

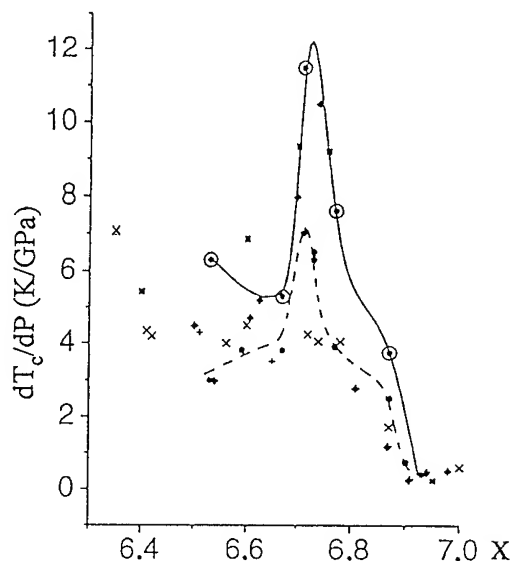


Figure 9: Pressure derivative of  $T_c$  for  $\text{YBa}_2\text{Cu}_3\text{O}_x$  as function of oxygen content  $x$  from Ref.24. Solid line through data when pressure applied at RT, dashed line when pressure applied at 90K.

entire temperature region  $60\text{K} \leq T_{\text{anneal}} \leq 105\text{K}$  where the LT relaxation in Tl-2201 is observed. In the Hg-based superconductors the stability of the  $\text{Hg}^{2+}$  valence state may account for the apparent lack of pressure-induced oxygen ordering effects.<sup>22</sup>

Recent internal friction measurements on Tl-2201 give some evidence for a LT relaxation peak, but further studies are needed.<sup>26</sup> LT relaxation peaks have been observed at  $E_A \approx 0.28\text{eV}$  for Bi-2212 and at  $E_A \approx 0.08, 0.12$ , and  $0.18\text{eV}$  for Y-123.<sup>27</sup> In addition, we find what we believe to be evidence for both HT and LT relaxation effects in the extensive high-pressure data on underoxygenated Y-123 recently published by Fietz et al.,<sup>24</sup> and shown in Fig.9. In their detailed study of  $T_c(P)$  over a wide range of oxygen concentrations, the value of  $(dT_c/dP)_{RT}$  is found to be strongly peaked at the very large value  $+12\text{ K/GPa}$  for the oxygen content  $\text{O}_{6.7}$ . It is interesting to note that the pressure derivative  $(dT_c/dP)_{90\text{K}}$ , where the pressure is changed at 90K instead of RT, is diminished for all oxygen concentrations, but is *still peaked* at  $\text{O}_{6.7}$ . We believe that the existence of this residual peak provides clear evidence that pressure-induced oxygen relaxation phenom-

ena occur in Y-123 at temperatures below 90 K, in analogy with our findings for Tl-2201. In fact, we would like to suggest that the existence of both LT and HT relaxation modes in Y-123 may provide the key to understanding the phenomena of both transient and persistent photo-induced superconductivity in this compound.<sup>28</sup> In particular, relaxation processes with activation energies at or below 0.1 eV could result in nanosecond relaxation times at 90 K.

The above results on Tl- and Y-based systems indicate that, on both fundamental and applied levels, oxygen ordering effects may play an important role in the superconductivity of many high- $T_c$  oxides. Further experiments are currently being carried out to enhance our understanding of these interesting phenomena.

This research is supported by the National Science Foundation under grant DMR 95-09885.

## References

1. J.S. Schilling and S. Klotz in: *Physical Properties of High Temperature Superconductors*, ed. D.M. Ginsberg (World Scientific, Singapore, 1992) p. 59.
2. H. Takahashi and N. Môri in: *Studies of High Temperature Superconductors, Vol. 16/17*, ed. A.V. Narlikar (Nova Science Publishers, Inc., N.Y., 1995).
3. M.R. Presland, J.L. Tallon, R.G. Buckley, R.S. Liu, and N.D. Flower, *Physica C* **176** (1991) 95.
4. J.B. Torrance, Y. Tokura, A.I. Nazzari, A. Bezing, T.C. Huang, and S.S.P. Parkin, *Phys. Rev. Lett.* **61**, (1988) 1127.
5. R.J. Cava, B. Batlogg, K.M. Rabe, E.A. Rietman, P.K. Gallagher, L.W. Rupp, Jr., *Physica C* **156** (1988) 523.
6. C. Murayama, Y. Iye, T. Enomoto, N. Môri, Y. Yamada, T. Matsumoto, Y. Kubo, Y. Shimakawa, and T. Manako, *Physica C* **183** (1991) 277.
7. J.J. Neumeier and H.A. Zimmermann, *Phys. Rev. B* **47** (1993) 8385.
8. J.E. Schirber, E.L. Venturini, B. Morosin, D.C. Ginley, *Physica C* **162-164** (1989) 745.
9. R. Sieburger, P. Müller and J.S. Schilling, *Physica C* **181** (1991) 335.
10. A.-K. Klehe, A.K. Gangopadhyay, J. Diederichs, and J.S. Schilling, *Physica C* **213** (1993) 266.
11. A. Cornelius, J.S. Schilling, *Physica C* **218** (1993) 369; A. Cornelius, S. Klotz, J.S. Schilling, *Physica C* **197** (1992) 209.
12. A.-K. Klehe, J.S. Schilling, J.L. Wagner, and D.G. Hinks, *Physica C* **223** (1994) 313.
13. A.-K. Klehe, Ph.D. Thesis (Washington University, 1995).
14. J.L. Routbort, S.J. Rothman, *J. Appl. Phys.* **76** (1994) 5615.
15. J.D. Jorgensen, Shiyong Pei, P. Lightfoot, Hao Shi, A.P. Paulikas, and B.W. Veal, *Physica C* **167** (1990) 571.
16. B.W. Veal, A.P. Paulikas, Hoydoo You, Hao Shi, Y. Fang, and J.W. Downey, *Phys. Rev. B* **42** (1990) 6305.
17. R. Sieburger and J.S. Schilling, *Physica C* **173** (1991) 403.
18. A.-K. Klehe, C. Looney, J.S. Schilling, H. Takahashi, N. Môri, Y. Shimakawa, Y. Kubo, T. Manako, S. Doyle, A.M. Hermann (submitted to *Physica C*).
19. H. Takahashi, J.D. Jorgensen, B.A. Hunter, R.L. Hitterman, Shiyong Pei, F. Izumi, Y. Shimakawa, Y. Kubo, T. Manako, *Physica C* **191** (1992) 248.
20. A.-K. Klehe, C. Looney, J.S. Schilling, N. Môri, Y. Shimakawa, Y. Kubo, T. Manako, *Bull. Amer. Phys. Soc.* **40** (1995) 743.
21. H. Takahashi, A.-K. Klehe, C. Looney, J.S. Schilling, N. Môri, Y. Shimakawa, Y. Kubo, T. Manako, *Physica C* **217** (1993) 163.
22. A.-K. Klehe and J.S. Schilling (contributed paper, this conference).
23. J.E. Schirber, W.R. Bayless, R.C. Chou, D.C. Johnston, P.C. Canfield, Z. Fisk, *Phys. Rev. B* **48** (1993) 6506.
24. W.H. Fietz, J. Metzger, T. Weber, K. Grube, H.A. Ludwig, *AIP Conf. Proc.* **309** (1993) 703.
25. Y. Shimakawa, Y. Kubo, T. Manako, H. Igarashi, F. Izumi, H. Asano, *Phys. Rev. B* **42** (1990) 10165.
26. M. Gazda, Technical University of Gdansk, Poland (private communication).
27. M. Weller, *Mater. Sci. Forum* **119-121**, (1991) 667.
28. E. Osquiguil, M. Maenhoudt, B. Wuyts, Y. Bruynseraede, D. Lederman, I.K. Schuller, *Phys. Rev. B* **49** (1994) 3675, and references therein.

# A MODEL FOR SHORT-RANGE OXYGEN-ORDERING EFFECTS IN HIGH- $T_c$ SUPERCONDUCTORS

A. K. KLEHE and J.S. SCHILLING

*Physics Department, Washington University, C.B. 1105, St. Louis, MO 63130, U.S.A.*

The carrier concentration of a high- $T_c$  superconductor can be strongly influenced by oxygen-ordering processes in the sample. It was demonstrated that in  $\text{Tl}_2\text{Ba}_2\text{CuO}_{6+\delta}$  (Tl-2201) these oxygen-ordering effects have activation energies as low as  $\sim 0.2$  eV, indicating a fast process involving local ordering. A model will be introduced which describes the effect of short-range oxygen-ordering processes on the carrier-concentration in Tl-2201 and which can predict which other high- $T_c$  superconductors should also show similar effects.

## 1 Introduction

The superconducting transition temperature,  $T_c$ , of a high- $T_c$  superconductor depends in a very sensitive way on the carrier concentration of the sample. Recent experiments demonstrate that in some high- $T_c$  oxides this carrier concentration changes not only with the oxygen concentration, but also with the degree of oxygen-ordering.<sup>1</sup> Measurements on Tl-2201 have shown that oxygen-ordering effects can occur at temperatures as low as 60K.<sup>1</sup> The estimated activation energies of  $0.2\text{eV} \leq E_A \leq 0.3\text{eV}$  are much lower than those observed for the long-range diffusion of oxygen ( $\sim 1\text{eV}$ ),<sup>2</sup> thus making it likely that these oxygen-ordering processes are of a local character. Relaxation processes with similar or lower activation energies have been detected in internal friction measurements in Y-123,<sup>3</sup> Bi-2212,<sup>3</sup> and Tl-2201,<sup>4</sup> indicating a common mechanism for low energy relaxation in high- $T_c$  superconductors. The origin of this activation process is still under discussion; however, a dependence of these activation processes on the oxygen concentration of the investigated samples has been observed.<sup>3</sup>

Using the example of tetragonal Tl-2201, a model for low energy relaxation processes is developed and later generalized to other high- $T_c$  superconductors. This model is based on the idea that the amount of charge localized in the charge reservoir layer, here the  $\text{Tl}_2\text{O}_2$  double-layer, must be compensated by the charge in the conducting  $\text{CuO}_2$  layer to achieve overall neutrality in the structure. The localized charge in the  $\text{Tl}_2\text{O}_2$  layer, however, is influenced strongly by the degree of oxygen-ordering in this layer.

## 2 Model

Like other high- $T_c$  superconductors, Tl-2201 has a layered structure where the overall in-plane dimensions are primarily determined by the  $\text{CuO}$ -bonds in the  $\text{CuO}_2$  plane. To achieve favorable bond lengths to the Tl in its plane, the oxygen in the  $\text{Tl}_2\text{O}_2$  layer has to occupy an off-centered, four-fold degenerate position, binding each oxygen to its neighboring in-plane Tl by two short and two long bonds. XAFS studies on a tetragonal sample found bond-lengths of  $2.31\text{\AA}$  and  $3.20\text{\AA}$ , respectively.<sup>5</sup> Based on bond-valence-sum calculations,<sup>6</sup> the long bonds in the  $\text{Tl}_2\text{O}_2$  layer can be neglected, so the Tl can be considered to be only bound to the oxygen it has short bonds with.

Each oxygen ion is assumed to have a valence of 2-. Tl ions exist in two stable oxidation states  $\text{Tl}^{1+}$  and  $\text{Tl}^{3+}$ , with  $\text{Tl}^{1+}$  generally being energetically more favorable. On the average each Tl-ion in the structure is bound to two oxygens in the plane (neglecting the long bonds). This means that locally a Tl ion can be bound to either zero or up to four oxygens in the plane, as can be seen in Fig.1. Bond-valence-sum calculations estimate a valence of 2+ for thallium with no in-plane oxygen bonds. One can conclude that these Tl-ions are in an oxidation state of  $\text{Tl}^{1+}$ , whereas Tl-ions with one or more in-plane bonds experience a stronger redox potential and are assumed to be in the oxidation state of  $\text{Tl}^{3+}$ . In agreement with this model XAFS measurements found the average valence of Tl in Tl-2201 to be less than 3+.<sup>5</sup>

Each  $\text{Tl}^{1+}$  binds two electrons at the  $\text{Tl}^{1+}$  site, which has to create holes somewhere else in the structure. It is assumed that these holes are created in the conducting  $\text{CuO}_2$  planes. Changing

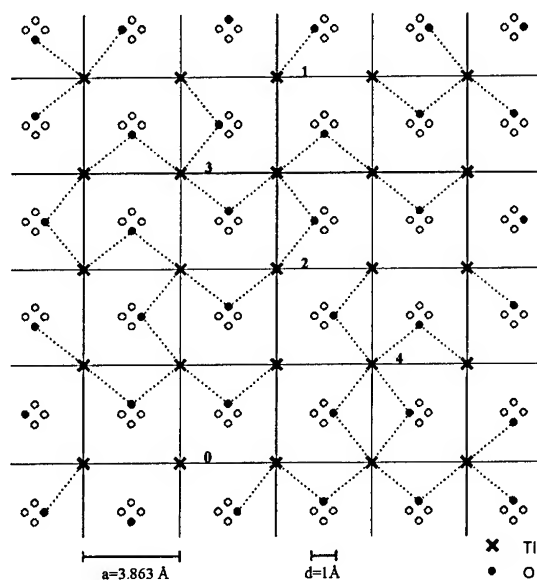


Figure 1: A schematic drawing of one layer of the  $\text{Tl}_2\text{O}_2$  double-layer in Tl-2201. The four crystallographically equivalent oxygen sites in the plane are shown as empty circles, of which one is occupied (filled circles). The oxygen ions are relatively disordered. Only the short in-plane Tl-O bonds are shown. "a" is the in-plane lattice parameter and "d"  $\simeq 1\text{\AA}$  is the maximum distance an oxygen has to move in its local ordering process.

the distribution of Fig.1 to the more ordered one in Fig.2 increases the number of  $\text{Tl}^{1+}$  and thus the number of holes in the  $\text{CuO}_2$  planes. In this model the number of holes created depends strongly on the local distribution of oxygen around the Tl-sites. Each oxygen needs to move less than  $\sim 1\text{\AA}$  to affect the hole concentration of the sample. The infinite number of possible configurations in the surrounding of a relaxing oxygen is expected to result in a broad distribution of activation energies involved in the relaxation process.

According to neutron diffraction studies,<sup>7</sup> the additional oxygen  $\delta$  in Tl-2201 occupies an interstitial position between the two layers of the  $\text{Tl}_2\text{O}_2$  double-layer. Fig.3 shows a possible distribution of in-plane oxygen around an interstitial site. Due to the coulomb repulsion between the interstitial oxygen and the nearest oxygen in the  $\text{TlO}$ -layer, the latter ones are expected to occupy oxygen sites away from the interstitial site. The oxygen around an interstitial site can no longer order freely to change the hole concentration of the sample. Thus, one would expect less low-temperature

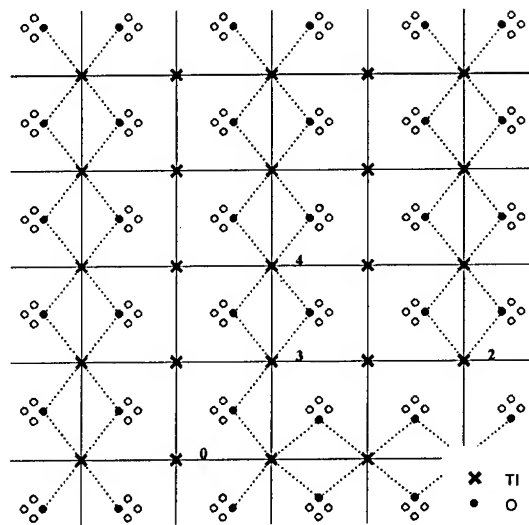


Figure 2: Proposed local arrangement of the oxygen ordered state in the  $\text{TlO}$  layer. Each Tl-ion with no in-plane bonds is assumed to be  $\text{Tl}^{1+}$ ; two electrons are frozen out at the  $\text{Tl}^{1+}$  site, thus increasing the hole concentration of the sample.

relaxation the more interstitial oxygen there is in the sample. This is in agreement with the observation that samples with high interstitial oxygen concentrations and a low  $T_c$  show relatively weak relaxation effects. However, also in samples with little or no interstitial oxygen, only small relaxation effects are observed both structurally and in  $T_c$ . This would indicate that the interstitial oxygen itself may order locally in disagreement with the above model. However, samples of Tl-2201 with no interstitial oxygen have a higher  $T_c$  than the observed starting temperature for relaxation and partial relaxation might already have occurred before  $T_c$  is measured. On the other hand, Y-123<sup>8</sup>, which has no interstitial oxygen appears to also exhibit fast oxygen ordering processes.

### 3 Comparison with Experiment and Generalization

Assuming a random binomial distribution of oxygen bonds in the  $\text{Tl}_2\text{O}_2$ -layer and no interstitial oxygen, our model predicts 0.25 holes/unit-cell, which is in excellent agreement with the hole carrier concentration from Hall effect measurements at 120K for a Tl-2201 sample with  $T_c \sim 92\text{K}$  and no interstitial oxygen.<sup>9</sup> Due to oxygen ordering the

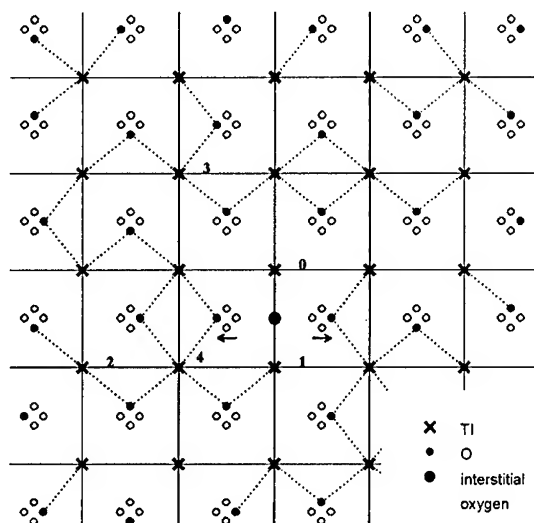


Figure 3: A schematic drawing of the interstitial oxygen position between the two TiO-layers. Due to coulomb repulsion, the in-plane oxygens seek a position away from the interstitial site and thus can no longer order freely.

hole concentration in the sample is expected to increase up to 2 holes/unit-cell and thus to decrease the  $T_c$  of the sample to 0K. This potentially large increase of the hole concentration due to oxygen ordering might explain the observed strong negative pressure dependence of  $T_c$  for a pressure change at RT.<sup>11</sup>

Fig.2 partially resembles the ordered ortho II phase of Y-123. The main difference is that in Y-123 the diffusion of oxygen between unit cells is necessary to achieve this phase<sup>10</sup> whereas in Tl-2201 only local ordering processes within a unit cell are required. The proposed "chain" ordering in Tl-2201 might happen on too local a scale to be detectable as a structural distortion by x-ray or neutron diffraction. XAFS and NMR measurements during a relaxation process could be used to examine the proposed changes in local ordering.

Low energy relaxation processes have also been detected in other high- $T_c$  superconductors by internal friction measurements. According to the above model, there are two requirements for a high- $T_c$  superconductors to show low energy relaxation effects in  $T_c$ : (1) the cation in the charge reservoir layer should have more than one easily accessible valence state, and (2) the local ordering of oxygen can trigger a change in its valence state. Thus, the above model cannot explain the low en-

ergy relaxation of  $T_c$  in  $\text{La}_2\text{CuO}_{4+\delta}$ . However, the above conditions are fulfilled for all Tl-compounds as well as for Y-123, where local oxygen-ordering processes can account for the anomalous oxygen dependence of the low-temperature pressure dependence.<sup>8</sup> No oxygen-ordering processes are expected in Bi- or Hg-compounds due to the dominant stability of one valence state in these cations which, in case of Hg, is determined to be 2+ by the out-of-plane oxygen-bonds. To test this prediction, underdoped samples of  $\text{HgBa}_2\text{CuO}_{4+\delta}$  should be examined for relaxation effects in  $T_c$ .

### Acknowledgments

A.-K. Klehe thanks the Physics Department at Oxford University for their financial support to visit this conference. This research is supported by the National Science Foundation under grant DMR 95-09885.

### References

1. J.S. Schilling, A.-K. Klehe, C.W. Looney (invited paper, this conference).
2. J.L. Routbort, S.J. Rothman, J. Appl. Phys. **76** (1994) 5615.
3. M. Weller, H. Jaeger, N. Rüffer, G. Kaiser, K. Schulze, Proc. ICMC May 1990.
4. M. Gazda (privat communication)
5. G.G. Li, J. Mustre de Leon, S.D. Conradson, M.V. Lovato, M.A. Subramanian, Phys. Rev. B **50** (1994) 3356.
6. I.D. Brown, in "Structure and Bonding in Crystals" (Acad. Press, N. Y., 1981).
7. Y. Shimakawa, Y. Kubo, T. Manako, T. Satoh, S.Iijima, T. Ichihashi, H. Igarashi, Physica C **157** (1989) 279.
8. W.H. Fietz, J. Metzger, T. Weber, K. Grube, H.A. Ludwig, AIP Conf. Proc. (USA), p. 703-706 (1994).
9. Y. Kubo, Y. Shimakawa, T. Manako, H. Igarashi, Phys. Rev. B **43** (1991) 7875.
10. B.W. Veal, A.P. Paulikas, Hoydoo You, Hao Shi, Y. Fang, J.W. Downey, Phys. Rev. B **42** (1990) 6305.
11. R. Sieburger and J.S. Schilling, Physica C **173** (1991) 403.

# T<sub>c</sub>(P) FROM MAGNETIC SUSCEPTIBILITY MEASUREMENTS IN HIGH TEMPERATURE SUPERCONDUCTORS: YBa<sub>2</sub>Cu<sub>3</sub>O<sub>7-x</sub> AND HgBa<sub>2</sub>Ca<sub>2</sub>Cu<sub>3</sub>O<sub>8+x</sub>

V. V. Struzhkin\*, Yu. A. Timofeev <sup>†</sup>, R. T. Downs, R. J. Hemley, H. K. Mao  
*Geophysical Laboratory and Center for High-Pressure Research,  
 Carnegie Institution of Washington, 5251 Broad Branch Rd., N.W., Washington, DC 20005-1305*

## ABSTRACT

We have measured the pressure dependence of the critical temperature of the superconducting transition in YBa<sub>2</sub>Cu<sub>3</sub>O<sub>7-x</sub> and HgBa<sub>2</sub>Ca<sub>2</sub>Cu<sub>3</sub>O<sub>8+x</sub> using a highly sensitive diamagnetic susceptibility technique. Samples were investigated with quasihydrostatic (NaCl) and hydrostatic (He) pressure media. Our results for HgBa<sub>2</sub>Ca<sub>2</sub>Cu<sub>3</sub>O<sub>8+x</sub> are consistent with previous measurements by resistive techniques under quasihydrostatic conditions. The results for YBa<sub>2</sub>Cu<sub>3</sub>O<sub>7-x</sub> are much more sensitive to sample variability than to the pressure medium used. We observed the well-known rapid increase in T<sub>c</sub> with increasing pressure for underdoped samples, with T<sub>c</sub> reaching its maximum 98 K at 12 GPa. For overdoped samples, T<sub>c</sub> has a maximum value about 92 K at 4 GPa. We fit our data for YBa<sub>2</sub>Cu<sub>3</sub>O<sub>7-x</sub> using a phenomenological inverse parabolic dependence of T<sub>c</sub> on hole concentration in CuO<sub>2</sub> planes and compare our high pressure results with previous low-pressure data.

## Introduction

The pressure dependence of T<sub>c</sub> in YBa<sub>2</sub>Cu<sub>3</sub>O<sub>7-x</sub> has been measured many times using different techniques [1-6]. An approach proposed by Almasan et al. [2] and Neumeier and Zimmerman [3] incorporates essential features required to explain the available low-pressure experimental data. This approach is based on the phenomenological inverse parabolic dependence of T<sub>c</sub> on carrier concentration, n, [7]

$$T_c/T_c^{\max} = 1 - A(n - n_{\text{opt}})^2. \quad (1)$$

Here T<sub>c</sub><sup>max</sup> is the critical temperature reached at optimum doping, n<sub>opt</sub>. Carrier concentration is referred to a single CuO<sub>2</sub> unit in CuO<sub>2</sub> planes, and A is a universal constant. Tallon et al. [8] found recently that A=82.6 and n<sub>opt</sub>≈0.16 holes/CuO<sub>2</sub> for YBa<sub>2</sub>Cu<sub>3</sub>O<sub>7-x</sub>. It was proposed in Refs. [2,9] that n = n(0) + (dn/dP)P, where dn/dP accounts for the charge transfer from CuO chains to CuO<sub>2</sub> planes, A=16.9 [2] or A=27.7 [9], n<sub>opt</sub>≈0.25 and

$$T_c^{\max}(P) = T_c^{\max}(0) + (dT_c^{\max}/dP) P \quad (2)$$

The motivation for the present work was (i) to examine the application of the low-pressure charge transfer model [2,3,9] at higher pressures, and (ii) to determine the value of the intrinsic pressure

derivative, dT<sub>c</sub><sup>max</sup>/dP, for YBa<sub>2</sub>Cu<sub>3</sub>O<sub>7-x</sub> and to compare it with data for the HgBa<sub>2</sub>Ca<sub>2</sub>Cu<sub>3</sub>O<sub>8+x</sub>.

## Experiment

We have used a new versatile magnetic susceptibility technique proposed by Timofeev [10] to measure the superconducting transition temperature in diamond anvil cells. The information on the YBa<sub>2</sub>Cu<sub>3</sub>O<sub>7-x</sub> samples is summarized in Tables 1 and 2. We estimate x=0 for our best untwinned sample C (T<sub>c</sub>(0) = 89.7 K). We use the c-axis dependence on oxygen deficiency, x, from Refs. [11] to determine x in the samples A and B. Pressure was measured in situ using ruby pressure scale [12].

Table 1. Unit cell parameters from single crystal X-ray diffraction for YBa<sub>2</sub>Cu<sub>3</sub>O<sub>7-x</sub> samples.

Sample	a, Å	b, Å	c, Å
A	3.823(1)	3.886(1)	11.705(1)
B	3.8186(6)	3.8861(9)	11.6960(9)
C	3.818(1)	3.887(1)	11.689(1)

Table 2. T<sub>c</sub>(onset) versus estimated oxygen deficiency, and sample dimensions for YBa<sub>2</sub>Cu<sub>3</sub>O<sub>7-x</sub> samples.

Sample	T <sub>c</sub> , K	x	dimensions
A	93	0.11(2)	80x80x13 μ
B	92	0.04(2)	50x30x13 μ
C	89.7	0.00(2)	40x40x7 μ

The samples of HgBa<sub>2</sub>Ca<sub>2</sub>Cu<sub>3</sub>O<sub>8+x</sub> used in this study were optimally doped polycrystalline samples

[13]. Pressures were determined at room temperature for  $\text{HgBa}_2\text{Ca}_2\text{Cu}_3\text{O}_{8+x}$  and were corrected to low temperatures using previous in situ  $P(T)$  measurements. This introduces an error about 1-2 GPa in pressure determination.

## Results

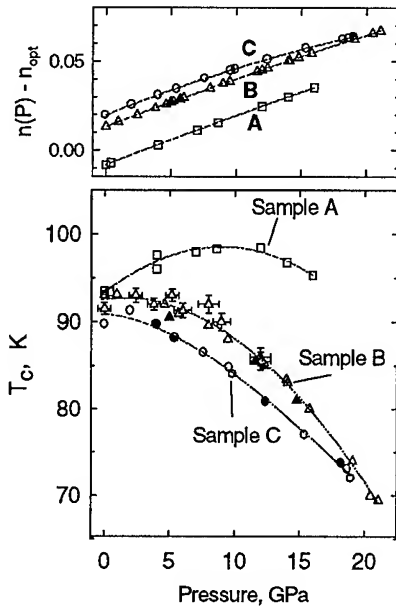


Fig.1.  $T_c$  versus pressure for several  $\text{YBa}_2\text{Cu}_3\text{O}_{7-x}$  samples. Sample A - NaCl medium (squares), sample B - He medium (triangles), NaCl medium (triangles with error bars), sample C - He medium (circles). Open symbols correspond to compression, and full symbols to decompression. The pressure dependence of the hole concentration is also shown (see text).

The pressure dependence of  $T_c$  for  $\text{YBa}_2\text{Cu}_3\text{O}_{7-x}$  samples is shown in Fig. 1.  $T_c(P)$  apparently follows an inverse parabolic dependence, and we can apply Eqs.(1,2) to calculate the pressure dependence of  $T_c^{\max}$  in linear approximation (see Eq.(2)). We use the charge transfer term in the form

$$n(P) = n_0 + (dn/dP)P + (d^2n/dP^2)P^2, \quad (3)$$

where  $n_0 = n(0) - n_{\text{opt}}$ . We obtain

$$T_c(P) = (T_c^{\max}(0) + (dT_c^{\max}/dP)P)(1 - 82.6 n^2(P)) \quad (4)$$

We have included pressure derivatives up to second order into the charge transfer term (Eq.(3)) because a linear approximation was not sufficient to fit all three data sets. The resulting parameters obtained from fitting Eq.(4) to the experimental data are summarized in Table 3. The fits and the calculated pressure dependence of the hole concentration  $n(P)$  for all three samples are shown in Fig. 1.

Table 3. Parameters are determined by fitting Eq. (4) to experimental data in Fig. 1. The values  $T_c^{\max}(0) = 93.89(10)$  K and  $dT_c^{\max}/dP = 0.77(5)$  K/GPa were constrained to be equal for all three samples and were determined from the fit.

Sample	$n_0$ , holes/ $\text{CuO}_2$	$dn/dP \times 10^3$ , holes/ $\text{CuO}_2$ 1/GPa	$d^2n/dP^2 \times 10^5$ , holes/ $\text{CuO}_2$ 1/GPa <sup>2</sup>
A	-0.008(3)	2.8(6)	-0.6(30)
B	0.013(2)	2.8(2)	-1.2(7)
C	0.020(2)	3.0(2)	-3.4(9)

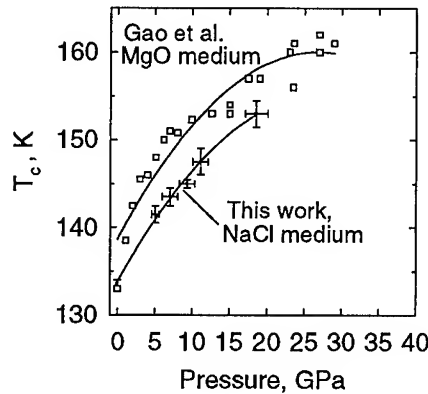


Fig.2.  $T_c$  versus pressure for  $\text{HgBa}_2\text{Ca}_2\text{Cu}_3\text{O}_{8+x}$  samples.

We have also measured  $T_c(P)$  in optimally doped  $\text{HgBa}_2\text{Ca}_2\text{Cu}_3\text{O}_{8+x}$  samples in a NaCl medium. The results are shown in Fig. 2. There is an offset of about 6-7 K between previous resistivity data [13] and our measurements at  $P > 0$ . We attribute this offset to the procedure of  $T_c$  determination used by Gao et al. [13]. They determined  $T_c$  as the onset of the drop in resistivity. However,  $T_c$  could have been overestimated due to contributions from inter-

grain boundaries. Grain boundaries are stressed more than the rest of the sample volume and could have higher  $T_c$  values. Our data at room pressure agree with the data of Gao et al. ( $T_c=134$  K). It is evident from Fig. 2, that the offset between resistivity and susceptibility data is rapidly increasing at low pressures. This supports our hypothesis concerning the contribution from grain boundaries to resistivity onset of  $T_c$ . We obtain  $(dT_c/dP)_{P=0} = 1.4$  K/GPa.

### Discussion

There is a striking difference in  $T_c(P)$  behavior between  $\text{HgBa}_2\text{Ca}_2\text{Cu}_3\text{O}_{8+x}$  and  $\text{YBa}_2\text{Cu}_3\text{O}_{7-x}$  samples.  $T_c(P)$  in  $\text{YBa}_2\text{Cu}_3\text{O}_{7-x}$  is governed mainly by the charge transfer term  $dn/dP$  and decreases rapidly with pressure for nearly optimally doped samples, because the samples become heavily overdoped with increasing pressure. For  $\text{HgBa}_2\text{Ca}_2\text{Cu}_3\text{O}_{8+x}$ , we probably have the case, where the contribution from charge transfer is small and the intrinsic  $dT_c^{\text{max}}/dP$  dominates the pressure dependence of  $T_c$  [13,14]. If this indeed is the case, Hg-based superconductors are the best candidates to study the pressure effect on intrinsic properties of high- $T_c$  superconductors. Further pressure studies of underdoped and overdoped Hg-based superconductors would be very helpful in providing information on the charge transfer contribution to  $T_c(P)$ . If this contribution is appreciable at 30-40 GPa,  $T_c$  values even higher than 164 K [13] can be reached for properly doped samples.  $dT_c^{\text{max}}/dP$  is not known yet for  $\text{HgBa}_2\text{Ca}_2\text{Cu}_3\text{O}_{8+x}$ , but it should not be less than our measured  $(dT_c/dP)_{P=0} = 1.4$  K/GPa for optimally doped samples. This value is even higher than  $dT_c^{\text{max}}/dP$  for  $\text{YBa}_2\text{Cu}_3\text{O}_{7-x}$ .

Comparing our data for sample C with Fig. 3 in Refs. [9], which predicts  $T_c=80.5$  K at  $P=25$  GPa for  $\text{YBa}_2\text{Cu}_3\text{O}_7$ , we immediately come to the conclusion that the parameters used by Almasan et al. [2] and Gupta and Gupta [9] fail to reproduce the high-pressure data. However, our charge transfer term  $dn/dP=3.0 \times 10^{-3}$  (holes/ $\text{CuO}_2$ )  $\text{GPa}^{-1}$  at  $x=0$  is the same as that given by Almasan et al. [2]. This value is close to the results from theoretical calculations and to estimates from bond-valence-sum analyses (for further references see [9]). Almasan et al. [2] fit their data to the charge transfer term  $dn/dP$  given by bond-valence-

sum analysis. However, they underestimated the parameter A (Eq.(1)), which results in failure to describe the high-pressure behavior determined here.

### Acknowledgments

This work was supported by the NSF and the Carnegie Institution of Washington.

### References

- \* On leave from the Institute for High Pressure Physics, Russian Academy of Sciences, 142092 Troitsk, Moscow district.
- ◊ Permanent address: Institute for High Pressure Physics, Russian Academy of Sciences, 142092 Troitsk, Moscow district.
1. J. S. Schilling and S. Klotz, in *Physical Properties of High Temperature Superconductors*, edited by D. M. Ginsberg (World-Scientific, Singapore, 1992), p.59.
2. C. C. Almasan, S. H. Han, B. W. Lee, L. M. Paulius, M. B. Maple, B. W. Veal, J. W. Downey, A. P. Paulikas, Z. Fisk, J. E. Schirber, *Phys. Rev. Lett.* **69** (1992) 680.
3. J. J. Neumeier, H. A. Zimmerman, *Phys. Rev. B* **47** (1993) 8385.
4. W. H. Fietz, J. Metzger, T. Weber, K. Grube, H. A. Ludwig, in *High Pressure Science and Technology - 1993*, edited by S. C. Schmidt, et al. (AIP Conf. Proc., 1994), p.703.
5. S. Klotz, W. Reith, J. S. Schilling, *Physica C* **172** (1991) 423.
6. S. W. Tozer, J. L. Koston, E. M. McCarton III, *Phys. Rev. B* **47** (1993) 8089.
7. M. R. Presland et al., *Physica C* **179** (1991) 95.
8. J. L. Tallon, C. Bernard, H. Shaked, R. L. Hitterman, J. D. Jorgensen, *Phys. Rev. B* **51** (1995) 12911.
9. R. P. Gupta, M. Gupta, *Phys. Rev. B* **51** (1995) 11760.
10. Yu. A. Timofeev, *Pribory i Tekhnika Eksperimenta* (in Russian) **5** (1992) 190.
11. R. J. Cava et al., *Physica C* **165** (1990) 419.
12. I. F. Silvera and R. J. Wijngaarden, *Rev. Sci. Instrum.* **56** (1985) 121.
13. L. Gao et al., *Phys. Rev. B* **50** (1994) 4260.
14. D. J. Singh, W. E. Pickett, *Physica C* **233** (1994) 231.



# On the dependence of the critical temperature on pressure in the bipolaron model of high $T_c$ superconductors

Giuseppe G.N. Angilella, Renato Pucci, Fabio Siringo

*Dipartimento di Fisica dell'Università di Catania and G.N.S.M. Unità di Catania  
57, Corso Italia, I-95129 Catania, Italy*

The dependence of the critical temperature  $T_c$  on the hole concentration  $n$  and on the pressure  $p$  for the high  $T_c$  superconductors  $\text{YBa}_2\text{Cu}_3\text{O}_{6+x}$  and  $\text{La}_{2-x}\text{Sr}_x\text{CuO}_4$  has been studied in the framework of the bipolaronic model of the high  $T_c$  superconductivity. Our results, in comparison with the available experimental data, suggest the presence of an intermediate or even strong coupling between  $\mathbf{r}$  space pairs. The capability of the model to reproduce the experimental data for  $T_c$  as a function of  $n$  at a given pressure in those compounds allows as well to fit the general trend of the experimental estimate of their  $\partial \log T_c / \partial \log V$  vs  $T_c$ .

One of the most remarkable universal behaviour of most families of the high  $T_c$  cuprate superconductors is a non-trivial dependence of  $T_c/T_{c,\text{max}}$  vs  $n$ , the hole content per unit  $\text{CuO}_2$ .<sup>1</sup> In particular, the critical temperature of basic compounds such as  $\text{YBa}_2\text{Cu}_3\text{O}_{6+x}$  and  $\text{La}_{2-x}\text{Sr}_x\text{CuO}_4$  is seen to vary strongly with the doping  $x$ , reaching a well pronounced maximum for low values of the hole content  $n$  and then decreasing to zero for  $n \lesssim 0.5$ .<sup>2,3</sup>

In this short contribution, we aim to show how this characteristic behaviour, together with the typical ranges in the critical temperature, may be easily reproduced within the framework of bipolaronic superconductivity.<sup>4</sup>

Following a suggestion by Wijngaarden *et al.*,<sup>5</sup> we eventually use these results to fit the general trends of the known experimental data for  $\partial \log T_c / \partial \log V$  vs  $T_c$  in  $\text{YBa}_2\text{Cu}_3\text{O}_{6+x}$  and  $\text{La}_{2-x}\text{Sr}_x\text{CuO}_4$  under pressures up to  $\sim 50$  GPa.<sup>6</sup>

When a strong interaction is taken into account between the electrons in a lattice and its harmonic excitations, it is convenient to assume a particular description of the nature and of the dynamics of the charge carriers. In the language of Landau quasiparticles, each electron should be pictured as surrounded by a cloud of phonons in the lattice, a polaron, which renormalizes its band width  $2D$  and its effective mass. Nonetheless, these new carriers are still able to tunnel between neighbour sites, though with a far reduced hopping integral. They interact with each other and at low temperature they may even couple into spinless pairs (bipolarons), thus showing bosonic behaviour, which may further condense into a super-

fluid. Due to the narrowing of the half bandwidth:

$$w = De^{-g^2}, \quad (1)$$

where  $g^2$  is the phonon equilibrium distribution, this mechanism may account for the high  $T_c$  superconductivity.<sup>4</sup>

The average over the phononic equilibrium state yields a renormalized polaron Hamiltonian, which in the mean-field approximation may be written as:

$$H_p = \sum_{\mathbf{k},s} \varepsilon_{\mathbf{k}} c_{\mathbf{k},s}^\dagger c_{\mathbf{k},s} + \sum_{\mathbf{k}} [\Delta_{\mathbf{k}} c_{\mathbf{k},\uparrow}^\dagger c_{-\mathbf{k},\downarrow}^\dagger + \text{H.C.}],$$

where  $c_{\mathbf{k},s}^\dagger$  creates a polaron with wave-vector  $\mathbf{k}$ , spin  $s = \uparrow, \downarrow$ , and renormalized energy  $\varepsilon_{\mathbf{k}}$ , measured relative to the Fermi energy  $\mu$ . The singlet energy gap:

$$\Delta_{\mathbf{k}} = \sum_{\mathbf{q}} v_{\mathbf{q}} \langle c_{-\mathbf{k}-\mathbf{q},\downarrow}^\dagger c_{\mathbf{k}+\mathbf{q},\uparrow}^\dagger \rangle \quad (2)$$

takes into account, in the mean-field approximation, of the interaction  $v_{\mathbf{q}}$  close to the Fermi surface. At a finite temperature  $T$ , standard BCS techniques lead to a non-linear, self-consistent equation for the gap Eq. (2), which may be written as:

$$\begin{aligned} \Delta(\varepsilon) &= - \int d\varepsilon' N(\varepsilon) v(\varepsilon, \varepsilon') \frac{\Delta(\varepsilon')}{2E(\varepsilon')} \tanh \frac{\beta E(\varepsilon')}{2} \\ E(\varepsilon) &= \sqrt{\varepsilon^2 + \Delta^2(\varepsilon)}, \end{aligned} \quad (3)$$

where  $\beta = 1/k_B T$  and the integration is restricted to the polaronic band,  $-w \leq \varepsilon \leq w$ . A polaronic density of states

$$N(\varepsilon) = \frac{1}{N} \sum_{\mathbf{k}} \delta(\varepsilon - \varepsilon_{\mathbf{k}})$$

has been introduced, together with the identification  $\Delta(\varepsilon) \equiv \Delta_{\mathbf{k}}$  if  $\varepsilon_{\mathbf{k}} = \varepsilon$ . Assuming a narrow polaronic bandwidth  $2w$ , the density of states may be said constant,  $N \approx 1/2w$ , and a linear relationship between the number  $n$  of carriers in the band and the Fermi energy  $\mu$  results:

$$\frac{n}{2} = \int_{-w}^{\mu} d\varepsilon N(\varepsilon) \approx \frac{\mu + w}{2w}. \quad (4)$$

We choose the band dispersion relation to be a tight-binding one, allowing for nearest-neighbours hopping only,  $\varepsilon_{\mathbf{k}} = -w \cos \mathbf{k} \cdot \mathbf{a}$ , where  $\mathbf{a}$  denotes the vector displacement between a couple of nearest-neighbours. In a recent work we studied how the competition between an on-site and an inter-site, nearest-neighbours interaction is able to reproduce a wide range of behaviours.<sup>7</sup> Taking into account only for such interactions, one may easily show that:

$$v(\varepsilon, \varepsilon') = v_0 - zv_1 \frac{\varepsilon \varepsilon'}{w^2} \quad (5)$$

$$\Delta(\varepsilon) = \Delta_0 - \Delta_1 \frac{\varepsilon}{w}, \quad (6)$$

being  $v_{0,1}$  the on-site, inter-site interaction strengths and  $z$  the number of nearest-neighbours. The gap parameters  $\Delta_{0,1}$  are self-consistently derived using Eq. (3) at a given temperature  $T$ . In the limit  $T \rightarrow T_c$ ,  $\Delta_{0,1}$  are expected to vanish, which allows to linearize Eq. (3). The condition for the existence of a nontrivial solution to the equations for the gap parameters can be worked out to yield the following approximate form for the critical temperature in the limit of weak or intermediate coupling:<sup>8</sup>

$$k_B T_c \simeq 1.14w \sqrt{n(2-n)} \exp \left( \frac{2w}{v_0 + zv_1(n-1)^2} \right), \quad (7)$$

where use of Eq. (4) has been made.

Eq. (7) has been used to fit the experimental data<sup>2,3</sup> known for  $\text{YBa}_2\text{Cu}_3\text{O}_{6+x}$  and  $\text{La}_{2-x}\text{Sr}_x\text{CuO}_4$ . Standard best-fit routines allow us to estimate  $w$ ,  $v_0$  and  $zv_1$ . Fig. 1 reports our results. In each case, a correct order of magnitude for  $T_{c,\text{max}}$  can be achieved, together with the experimental trend, often pointed out as a distinctive and universal feature of high  $T_c$  superconductors.<sup>1</sup>

In order to allow a comparison with the known experimental data, we use Eq. (7) to obtain  $\partial \log T_c / \partial \log V$  as a function of  $T_c$ . Following a

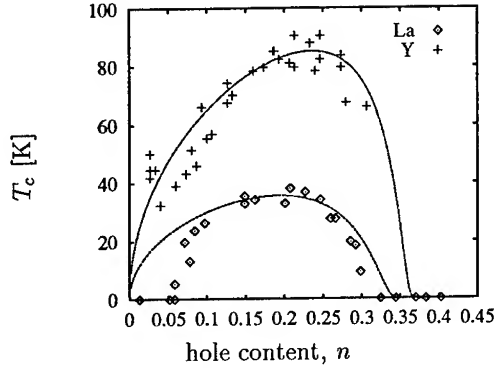


Figure 1: Experimental data for the critical temperature  $T_c$  vs the hole content  $n$  per unit  $\text{CuO}_2$  in  $\text{La}_{2-x}\text{Sr}_x\text{CuO}_4$  (diamonds<sup>3</sup>) and in  $\text{YBa}_2\text{Cu}_3\text{O}_{6+x}$  (crosses<sup>2</sup>) together with our fit curves, Eq. (7).

suggestion by Wijngaarden *et al.*,<sup>5</sup> the main dependence of  $T_c$  on pressure and thus on the volume  $V$  should be provided by its dependence on the hole content,  $n$ , which is experimentally seen to be linear,<sup>5</sup> with:

$$\frac{\partial \log n}{\partial \log V} = S. \quad (8)$$

Besides, we assume that the only parameters figuring in Eq. (7) which actually depend on  $V$  are the effective half-bandwidth  $w$  and the inter-site coupling  $zv_1$ . In particular, we may neglect the dependence on the volume of the renormalization factor  $\exp(-g^2)$  for the effective half-bandwidth, Eq. (1), and relate  $\partial \log w / \partial \log V$  to  $\partial \log J / \partial \log a$ , being  $J$  the overlap integral between nearest neighbours as a function of the in-plane lattice spacing  $a$ , in the LCAO approximation. Using the known structure parameters for  $\text{La}_{2-x}\text{Sr}_x\text{CuO}_4$ <sup>11</sup> and assuming the overlap of a  $2p_x^5$  atomic orbital centered on an in-plane O and a  $3d_{x^2-y^2}^{10}$  one centered at the nearest Cu,<sup>12</sup> one eventually finds:

$$\frac{\partial \log w}{\partial \log V} = \frac{1}{3} \frac{\partial \log J}{\partial \log a} = 0.064. \quad (9)$$

Due to its coulombic origin, it is then natural to assume, for the inter-site coupling,  $v_1 \approx V^{-1/3}$ , so that:

$$\frac{\partial \log(zv_1)}{\partial \log V} = -\frac{1}{3}. \quad (10)$$

Using Eq. (7) and assuming Eqs. (9) through (8), one may straightforwardly derive an analyt-

ical expression for  $\partial \log T_c / \partial \log V$ . Pressure effect measurements for the Hall resistance  $R_H$  allow to estimate  $S \approx -30$  for YBCO, whereas we assume  $S \approx -100$  for LSCO, in order to fit the data of Fig. 2, which is slightly larger than the value  $S \approx -12$ ,<sup>9</sup> desumable from the pressure and doping dependence of the upper critical field  $H_{c2}$ .<sup>10</sup> Using the fit values for the parameters at normal pressure, we are eventually able to reproduce the general trend of the known data for  $\partial \log T_c / \partial \log V$  vs  $T_c$  in those materials<sup>6</sup> (Fig. 2).

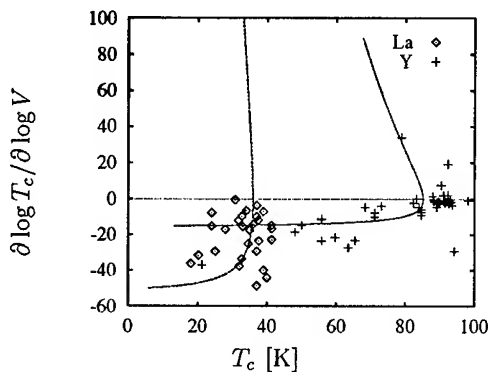


Figure 2: Experimental data for  $\partial \log T_c / \partial \log V$  vs the critical temperature  $T_c$  in YBCO (crosses) and LSCO (diamonds) compounds.<sup>6,13</sup> The fit lines have been obtained according to the text.

A similar trend had been reported in a work by Brizhik *et al.*,<sup>13</sup> where use was made of a bisoliton model of the superconductivity. However, the present contribution greatly differentiates from Ref. 13, not only because a bipolaron model is here employed, instead of the bisoliton one, but also because the gap function is here derived rigorously in the framework of a mean-field approach.<sup>4</sup>

The present results are in agreement with the work of March, Pucci and Egorov,<sup>14</sup> where evidences were presented for the existence of doubly-charged bosons above  $T_c$  in underdoped  $\text{YBa}_2\text{Cu}_4\text{O}_8$ . However, since we believe that the trend of  $T_c$  vs  $p$  is mainly determined by the dependence of  $T_c$  on  $n$ , we also believe that any theory, which correctly reproduces the experimental data of  $T_c$  as a function of  $n$ , would be able to give the correct trend of  $T_c$  as a function of  $p$ . In this sense, our results are not able to discriminate between different theories, but strongly point to the need of  $r$  space doubly-charged bosons to explain high  $T_c$  superconductivity.

Of course, no indication is given in this context on the nature of these couples. For instance, recently Egorov and March<sup>15</sup> have argued that these bosons could be  $r$  space biholons.

## References

1. H. Zhang, H. Sato, *Phys. Rev. Lett.*, **70**, 11 (1993) 1697.
2. Y. Tokura, J.B. Torrance, T.C. Huang, A.I. Nazzari, *Phys. Rev. B*, **38**, 10 (1988) 7156.
3. J.B. Torrance, Y. Tokura, A.I. Nazzari, A. Beziinge, T.C. Huang, S.S.P. Parkin, *Phys. Rev. Lett.*, **61**, 9 (1988) 1127.
4. See, e.g., A.S. Alexandrov, N.F. Mott, *Rep. Prog. Phys.*, **57** (1994) 1197, for a review.
5. R.J. Wijngaarden *et al.*, *High Press. Res.*, **10** (1992) 479.
6. R.J. Wijngaarden *et al.*, in *Molecular systems under high pressure*, p. 157, ed. by R. Pucci and G. Piccitto (Elsevier Science, 1991).
7. F. Siringo, G.G.N. Angilella and R. Pucci, submitted to *Phys. Rev. B* (1995).
8. No conceptual objection arises as to extend Eq. (7) beyond the intermediate coupling regime. Numerical work is in progress, which employs the present formalism. Analogous results have been already presented by G. Iadonisi *et al.*, *Phys. Lett. A*, **196** (1995) 359.
9. R.J. Wijngaarden *et al.*, NATO ASI Series, vol. **B286**, p. 399 (Plenum Press, 1991), and private communication.
10. It should be however mentioned that C. Murayama *et al.*, *Physica C*, **183** (1991) 277, observed a remarkably lower pressure effect for  $R_H$  in LSCO than in YBCO, thus suggesting  $dn/dp \approx 0$  for the former compound, whereas  $dn/dp > 0$  for the latter.
11. L.F. Mattheiss, *Phys. Rev. Lett.*, **58**, 10 (1987) 1028. See also R.J. Cava *et al.*, *Phys. Rev. B*, **35**, 13 (1987) 6716.
12. D.I. Khomskii, *Physica B*, **171** (1991) 44.
13. L. Brizhik, A. La Magna, R. Pucci, F. Siringo, *High Press. Res.*, **11** (1994) 375.
14. N.H. March, R. Pucci, and S.A. Egorov, *Phys. Chem. Liquids*, **28** (1994) 141.
15. S.A. Egorov and N.H. March, preprint (1995). Courtesy of N.H.M.

# PECULIARITIES OF CRYSTAL LATTICE DYNAMICS FOR HT<sub>c</sub>SC CERAMICS YBa<sub>2</sub>Cu<sub>3</sub>O<sub>7-δ</sub> OBTAINED UNDER HIGH PRESSURE

A.D.SHEVCHENKO

*Institute of Metal Physics Ukrainien AS, 36 Vernadsky pr., Kiev-252142, Ukraine*

Experimental investigations of specific heat  $C_V$  dependencies in the temperature range 5 - 270 K have been carried out on the HT<sub>c</sub>SC-ceramics YBa<sub>2</sub>Cu<sub>3</sub>O<sub>7-δ</sub> samples with  $T_c = 92$  K obtained by sintering under high (up to 4 GPa) pressure conditions. The Debye temperature, the specific electron heat, the value of density of electron states on the Fermi level and the anharmonicity parameter have been calculated from the analysis of  $C_V(T)$  dependencies in the low- and high temperature expansions.

## 1. Introduction

At present time one of the fundamental tasks of solid state physics as applied to HT<sub>c</sub>SC materials is an investigation of the outer effect influences on electron properties and lattice dynamics of such materials in normal state as far as, it is well known, the characteristics of electron and phonon spectra are determined the peculiarities of superconductivity.

The present work is devoted to experimental investigations of the specific heat  $C_V$  temperature dependencies on the HT<sub>c</sub>SC ceramics samples obtained by sintering under high pressure conditions with an aim to study the peculiarities of electron properties and crystal lattice dynamics of the materials.

## 2. Experimental results and discussion

The measurements were performed on the samples prepared according to the sintering technology of 1-2-3 compound YBa<sub>2</sub>Cu<sub>3</sub>O<sub>7-δ</sub> powder under high pressure conditions (up to 4 GPa) using high pressure solid chambers of "toroid" and "lens" type and Hydraulic press of 600 and 2000 tones stress. While thermobaric processing the oxygen loss was eliminated by using a special technological methods allowing to provide airtightness of the high pressure chamber, in it 1-2-3 compound powder was<sup>1</sup>. Microstructure and composition of obtained samples were investigated with the help electron scanning microscope of "Camscan" firm. X-ray structural analysis of the samples showed that they have the structure 1-2-3 type. The

temperature control of superconducting transition  $T_c$  was performed by magnetic method on magnetization temperature dependence measurement  $M$ . The value  $M$  was measured by the magnetometer with the vibrating sample. While performing the investigation of  $C_V$  on the samples, the value  $T_c$  was equal to 92 K. At the temperature below  $T_c$  the samples diamagnetic response was 100 %. Measuring of  $C_V$  was performed in the temperature range 5 - 270 K with relative error of 0,5 % on the low-temperature calorimeter. At  $T_c = 92$  K the dependence  $C_V$  has a jump. The analysis of  $C_V$  in the low-temperature resolution showed that in the low-temperature region the dependence  $C_V(T)$  is well approximating by the polynom of the next view:

$$C_V = C_e + C_f = \gamma_1 T + 234RT^3/\theta_1^3,$$

where  $C_e$  is the electron contribution into specific heat;  $C_f$  is to phonon contribution into specific heat;  $\theta_1$  is Debye temperature;  $\gamma_1$  is specific electron heat coefficient renormalized owing to interaction of electrons and phonons and equal to

$$\gamma_1 = \gamma_h(1 + \lambda) = 2/3(\pi K_B)^2 N(E_F),$$

$$(1 + \lambda) = 2/3(\pi K_B)^2 \tilde{N}(E_F),$$

where  $\lambda$  is the electron-phonon interaction constant;  $\gamma_h$  is high temperature coefficient of specific electron heat;  $K_B$  - is Boltzman constant;  $N(E_F)$  is the value of electron density of electron states on Fermi level. The results of the

investigation of  $C_V/T$  versus  $T^2$  are given in figure 1.

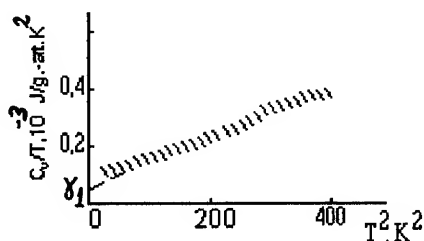


Figure 1: Temperature dependence of the  $C_V/T$  vs  $T^2$  for  $\text{YBa}_2\text{Cu}_3\text{O}_{7-\delta}$  samples obtained under high pressure.

The values  $\gamma_1$  and  $\theta_1$  calculated from the dependence  $C_V/T$  from  $T^2$  with using the expression for  $C_V(T)$ , as it turned out, are equal to:

$$\gamma_1 = 2,14 \cdot 10^3 \text{ J/g.at.K}^2, \theta_1 = 351 \text{ K}.$$

Taking into consideration the connection between  $\gamma_1$  and  $N(E_F)$  ( $\gamma_1 = 2/3 \cdot (\pi \cdot K_B)^2 \cdot N(E_F)$ ) the value  $\tilde{N}(E_F) = 0,84 \text{ st/eV.at.O}$  was determined. The graphic analysis of the dependence  $C_V(T)$  in high - temperature expansion gives the possibility to calculate the Debye temperature  $\theta_h$  and the anharmonicity parameter  $A$  which characterizes mean temperature shift of the phonon modes caused by crystal lattice anharmonicity vibrations. Taking into account anharmonicity of vibrations the dependence  $C_V(T)$  in the high-temperature expansion may be presented in the form:

$$C_V - 3R/T = -3R\theta_h^2/20T^3 + (-A + \gamma_h).$$

The results of the investigation of  $C_V - 3R/T$  versus  $T^{-3}$  are given in figure 2.

From the dependence  $C_V - 3R/T = f(T^{-3})$  using the expression for  $C_V$  in high-temperature expansion, the value  $\theta_h = 448 \text{ K}$  was determined. The difference  $\theta_h$  from  $\theta_1$  associates with the temperature changing of the phonon spectrum frequencies. Extrapolation of liner dependence  $C_V - 3R/T$  from  $T^{-3}$  into the infinite temperature

region gives the cutting off on the axis of coordinate which corresponds to the negative member:

$$B = -A + \gamma_h = -2,0 \cdot 10^{-3} \text{ J/g.at.K}^2.$$

Presence of additional negative member of big value in the specific heat points at strong anharmonicity of crystal lattice vibrations of  $\text{HTcSC } \text{YBa}_2\text{Cu}_3\text{O}_{7-\delta}$  obtained under high pressure conditions.

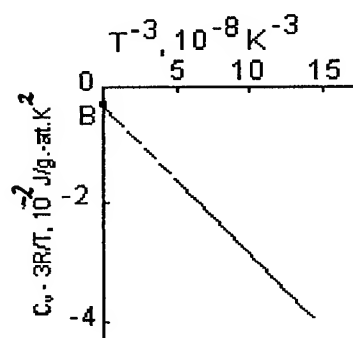


Figure 2: Temperature dependence of the  $C_V - 3R/T$  vs  $T^{-3}$  for  $\text{YBa}_2\text{Cu}_3\text{O}_{7-\delta}$  samples obtained under high pressure.

### 3. Conclusions

On the basis of performed investigations of specific heat  $C_V$  the following results were obtained: the Debye temperature, the electron specific heat coefficient, the value of electron state density on the Fermi level and anharmonicity parameters were calculated.

### Reference

1. V.V.Hemoshkalenko and A.D. Shevchenko, *Cryogenics. 32 ICMC Supplement*, (1992) 361

## STRONTIUM -BASED MERCURY CUPRATES WITH PEROVSKITE-LIKE STRUCTURE.

E.P.KHLYBOV<sup>1,2</sup>, G.M.KUZMICHEVA<sup>3</sup>, V.N.KOCHETKOV<sup>2</sup>,  
T.PALEWSKI<sup>1</sup>, J.WARCHULSKA<sup>1</sup>, I.N.AFANAS'IEVA<sup>3</sup>.

1. - International Laboratory of high Magnetic Fields and Low Temperatures, 53-529 Wroclaw, Gajowicka 95, Poland.

2 - Institute for High Pressure Physics Russian Academy Sciences, 142092 Troitsk, Moscow Reg., Russia.

3 - Moscow State Academy for Fine Chemical Technology, 117926, Moscow, Vernadski prospect 96, Russia.

### ABSTRACT.

Condition of synthesis, structure and temperature of superconducting transitions of strontium-based mercury cuprates  $\text{HgSr}_2(\text{Ln,Ce})_{k-1}\text{Cu}_k\text{O}_{2k+2+x}$  with  $k=1,2$  are presented. The dependence between lattice parameters of  $\text{HgSr}_2(\text{Ln,Ce})_{k-1}\text{Cu}_k\text{O}_{2k+2+x}$  and content of Ce in phases is revealed. An anomaly of resistivity was observed around 200 K for some of investigated samples. In some cases the presence of heteropolytype  $\text{Hg}_2\text{Sr}_4(\text{Ln,Ce})_3\text{Cu}_5\text{O}_y$  is found.

### Introduction.

It is well known that barium-based mercury cuprates have the highest value of a critical temperature  $T_c = 133$  K [1].

In searching for new high temperature superconductors (HTSC) we have investigated a number of phases with perovskite-like structure. Among them there were cuprates with general formulae  $\text{HgSr}_2(\text{Ln,Ce})_{k-1}\text{Cu}_k\text{O}_{2k+2+x}$  [2]. The difficulty of obtaining the "strontium" phases in comparison with "barium" ones is due to a higher polarizability of the "barium" ion that promotes the change of the Ba-O distance in the wide limits and facilitates the formation of perovskite-like structure. In the homologous series  $\text{MA}_2\text{Ca}_{k-1}\text{Cu}_k\text{O}_{2k+2+x}$  ( $M = \text{Tl}$  or  $\text{Hg}$ ;  $A = \text{Sr}$  or  $\text{Ba}$ ) a partial displacement in thallium or mercury position, and a partial or complete substitution by the rare earth elements favourably influence the structure stability due to the effect of interconnection of polyhedra. The change in the crystal structure influences on the value of critical temperature. The oxygen content in mercury cuprates is very important as with its increase the transition of  $\text{HgO}_2$  dump-bells polyhedron to  $\text{HgO}_6$  distorted octahedron is observed. Such a distorted octahedron is an element of crystal structure of many superconducting mercury cuprates. On the basis of this consideration and the model of crystallochemical construction [3], compositions  $\text{HgSr}_2(\text{Ln,Ce,Ca})_m\text{Cu}_p\text{O}_y$  for synthesis of strontium-based mercury cuprates were selected.

### Experimental.

The samples were obtained by the high pressure - high temperature technique in the "thoroid" pressure cell. Stoichiometric mixture of  $\text{HgO}$  and of a precursor obtained from the thermal decomposition of mixtures of oxides or carbonates of  $\text{Ln}$ ,  $\text{Ca}$ ,  $\text{Sr}$ ,  $\text{Cu}$  were used starting materials.

High pressure synthesis was performed at temperatures 750-950°C during 5-30 minutes at pressures 4-7 GPa. The samples (3-5 mm in diameter, 3-5 mm in height) were insulated from graphite heater by coats of hexagonal boron nitride and foils of molybdenum tungsten or gold. The diffraction analyses (qualitative and quantitative ones) were performed with the "Geigerflex" diffractometer with  $\text{Cu-K}\alpha$ -radiation using a curved graphite monochromator. For some of the samples additional X-ray diffractograms were obtained at 100, 200, 240 and 295K by means of Stoe and DHN powder diffraction system. The qualitative X-ray analyses were performed by comparing X-ray data for obtained phases with isostructural ones. The electric resistivity measurements were performed by the standard four probe dc and ac methods.

### Results and discussion.

As it follows from X-ray data most of obtained samples are multiphase containing mercury-based perovskite-like cuprates and admixed phases  $\text{CeO}_2$ ,  $\text{CuO}$  and solid solutions with  $\text{La}_2\text{CuO}_4$ ,  $\text{Nd}_2\text{CuO}_4$  type structures and  $\text{CaCuO}_2$ ,  $\text{Sr}_2\text{CuO}_3$ . Phases belonging homological

series  $\text{HgSr}_2(\text{Ln,Ce})_{k-1}\text{Cu}_k\text{O}_{2k+2+x}$  are obtained with  $k = 1$  (1201 structure) for  $\text{Ln}=\text{La}$  ( $r^{\text{VIII}}_{\text{La}}=1.16\text{\AA}$ ), with  $k=2$  (1212 structure) for  $\text{Ln}=\text{La,Pr,Nd,Sm,Eu,Gd,Dy, Ho,Y}$  ( $r^{\text{VIII}}_{\text{Ln}}=1.16 - 1.02\text{\AA}$ , and with  $k = 3$  (1223 structure) for  $\text{La}$  ( $r^{\text{VIII}}_{\text{Ln}}$  - radius of  $\text{Ln}$  and  $\text{Y}$  for co-ordination number of eight in Shannon system. The increasing of the synthesis temperature  $T_a$  and increasing of  $\text{Ln}$  radius leads to formation 1223 structure. Phase with 1201 type structure was obtained only for  $r^{\text{VIII}}_{\text{Ln}}=1.12-1.16\text{\AA}$ . X-ray analysis some samples obtained from mixtures with starting content  $\text{HgSr}_2(\text{Ln,Ce})\text{Cu}_2\text{O}_y$  ( $\text{Ln} = \text{Pr,Nd,Sm}$ ) revealed a system of reflection belonging to the phase with sublattice parameters  $a_0 = 3.85\text{\AA}$  and  $c_0 = 14.1\text{\AA}$ . For this phase two contents may be proposed -  $\text{Hg}_2\text{Sr}_2(\text{Ln,Ce})\text{Cu}_2\text{O}_x$  (2212-structure) and  $\text{Hg}_2\text{Sr}_4(\text{Ln,Ce})_3\text{Cu}_5\text{O}_y$  (2435-structure). The phase with 2212-structure (S.G.  $I/4mmm$ ) has two main peaks 110 and 105 (as analogous phases  $\text{Bi}_2\text{Sr}_2\text{CaCu}_2\text{O}_8$  and  $\text{Tl}_2\text{Ba}_2\text{CaCu}_2\text{O}_8$ ) with double layers  $\text{Hg}_2\text{O}_2$ . Phase with 2435 is the heteropolytype containing superposing of two structures - 1212 and 1223 with single layers  $\text{HgO}$  (S.G.  $P4/mmm$  with main reflections 110 and 106). As it follows from X-ray data and calculations the phase with 2435-structure is very probable in our case. Analogous phase in the  $\text{Hg-Ba-Ca-Cu-O}$  system was revealed by electron microscopy method [4].

It ought to be noted that in many cases the electric resistivity measurements revealed an anomaly of resistivity around 230 K for samples with different composition (see Fig.).

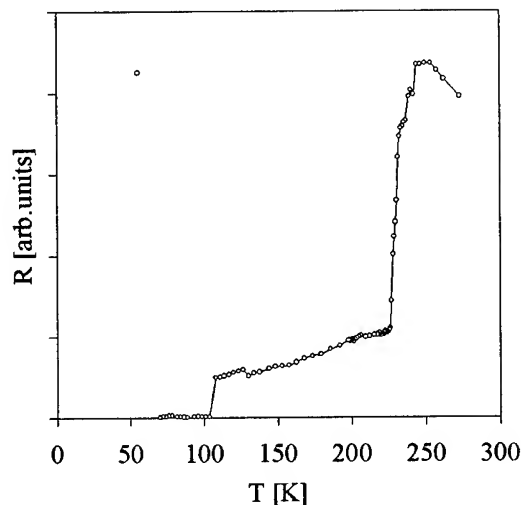


Fig. Temperature dependence of resistivity for  $\text{HgSr}_2(\text{Sm}_{1/3}\text{Ce}_{2/3})\text{Cu}_2\text{O}_{6+x}$  sintered at 40 kBar,  $800^\circ\text{C}$  for 15 min.

It is interesting to note that the melting point of mercury is equal to 234 K (very close to this anomaly). The low temperature X-ray analyses do not confirm the presence of the metallic mercury in the sample and any changes in the diffractograms. Sharp drops of resistivity at the barium content phases  $\text{HgBa}_2\text{Ca}_2\text{Cu}_3\text{O}_{8+x}$  and  $\text{HgBa}_2\text{Ca}_4\text{Cu}_5\text{O}_{12+x}$  were observed by other authors [5]. They supposed that this effect may result from superconducting inclusions (filamentary superconductivity). It is not excluded that in the class of mercury cuprates one can probably find new superconductors with value of  $T_c$  higher than those known to date.

#### References.

1. S.N.Putlin, E.V.Antipov, O.Grimaissen and M.Maresio, *Nature* 36 (1993) 226.
2. G.M.Kuzmicheva, E.P.Khlybov, V.N.Kochetkov, J. Warchulska and I.N.Afanas'ieva, *Cryst.Res.Technol.* 30 (1995) 451.
3. N.E.Alekseevskii, A.V.Mitin, G.M.Kuzmicheva, T.N.Tarasova, E.P.Khlybov and V.V.Evdokimova, *Superconductivity: Physics, Chemistry, Technology* 2 (1989) 60.
4. M.Cantoni, A.Schilling, H.-U.Nissen and H.R.Ott, *Physica C* 215 (1993) 11.
5. J.-L.Tholence, B.Souletle, J.-J.Laborde and M.Maresio *Phys.Lett.* 184A (1994) 215.

# SUPERCONDUCTIVITY AND MAGNETISM IN $\text{Gd}_{1+x}\text{Ba}_{2-x}\text{Cu}_3\text{O}_{7-y}$ SYSTEM. INFLUENCE OF PRESSURE AND Gd, OCCUPYING Ba- SITE.

V.N. NAROZHNYI<sup>1,2\*</sup>, V.I. NIZHANKOVSKI<sup>2</sup>, E.P. KHLYBOV<sup>1,2</sup>, A.V. GUSEV<sup>3</sup>,  
G.G. DEVYATYKH<sup>3</sup>, A.V. KABANOV<sup>3</sup>, Z. BUKOWSKI<sup>4</sup>

<sup>1</sup>*Institute for High Pressure Physics, Russian Acad. of Science, Troitsk, Moscow Region, 142092, Russia*

<sup>2</sup>*International Lab. High Magnetic Fields and Low Temperatures, Gajowicka 95, Wroclaw 53-529, Poland*

<sup>3</sup>*Institute of Chemistry, Russian Academy of Science, Tropinina 49, Nizhnii Novgorod, 603600, Russia*

<sup>4</sup>*Institute for Low Temperature and Structure Research Polish Acad. of Science., Wroclaw, 50-950, Poland*

The influence of high hydrostatic pressure and Gd substitution on Ba-site on magnetic and superconducting properties of  $\text{GdBa}_2\text{Cu}_3\text{O}_{7-y}$  compound have been investigated. AFM-transition of Gd-123 shifts to higher temperatures with increase of pressure,  $\partial T_N/\partial P$  is  $+7 \cdot 10^{-6}$  K/bar. The estimation of  $|\partial \ln T_N / \partial \ln V|$  gives  $\approx 5$ , indicating on the importance of superexchange interaction in AFM-ordering. Gd substitution on Ba site increases  $\text{Gd}^{3+}$  concentration, at the same time it leads to the effect of "chemical" pressure. The results of Gd substitution on the Ba-site are discussed in connection with hydrostatic pressure data.

## Introduction

Remarkable feature of  $\text{REBa}_2\text{Cu}_3\text{O}_{7-y}$  (RE-123; RE - rare earth) compounds is the possibility to observe the coexistence of superconductivity and long range AFM-ordering of RE ions. RE atoms form layered structure with RE interplane distance being approximately three times higher then intralayer one. The nature of magnetic ordering in such highly anisotropic compounds has attracted a great attention. We have investigated the influence of high hydrostatic pressure and Gd substitution on Ba-site, positioned between adjacent Gd-layers, on magnetic and superconducting properties of  $\text{GdBa}_2\text{Cu}_3\text{O}_{7-y}$  compound. Gd substitution on Ba position increases the concentration of magnetic ions in this system, at the same time it leads to the effect of "chemical" pressure due to the smaller ionic radius value of  $\text{Gd}^{3+}$  in comparison with  $\text{Ba}^{2+}$ . Hydrostatic pressure data and the results of Gd substitution on the Ba-site are discussed accompanying each other.

## Results and discussion

The value of AFM-ordering temperature

$T_N$  was determined by heat capacitance measurement. The influence of hydrostatic pressure up to 7.3 kbar on the heat capacitance of Gd-123 compounds was measured using small high pressure cell. Sharp  $\lambda$ -type anomaly

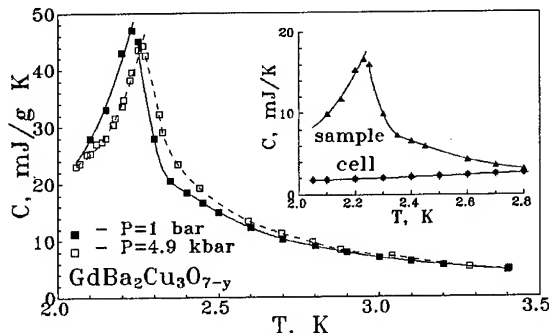


Fig.1. Specific heat vs. temperature for  $\text{GdBa}_2\text{Cu}_3\text{O}_{7-y}$  at  $P=1$  bar and 4.9 kbar. On the inset: absolute values of sample ( $m=0.355$ g) and cell ( $m=52$ g) heat capacitance.

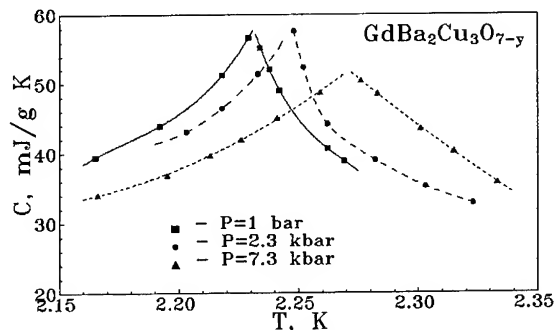


Fig.2. Specific heat vs. temperature for  $\text{GdBa}_2\text{Cu}_3\text{O}_{7-y}$  near  $T_N$  at various pressures.

\*Corresponding author. E-mail: hpp@adonis.iasnet.com;  
Tel: (7-095) 334 08 08; Fax: (7-095) 334 00 12.



was clearly seen nearby  $T_N \approx 2.23$  K both at normal and high pressures, see Fig. 1, 2. Sample contribution to heat capacitance near  $T_N$  was about an order of magnitude higher then contribution of the cell. The value of  $\partial T_N / \partial P$  is  $+7 \cdot 10^{-6}$  K/bar, see Fig. 3. (Shift of the  $\lambda$ -anomaly to the higher temperatures under pressure for Gd-123 was observed for the first time by our group [1]).

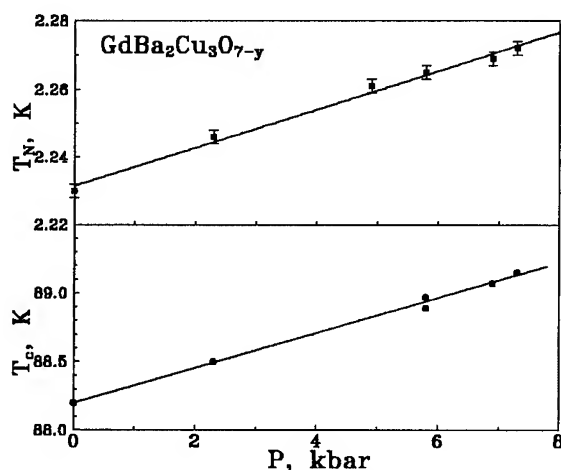


Fig. 3. Neel temperature (up) and critical temperature (down) vs. pressure for  $\text{GdBa}_2\text{Cu}_3\text{O}_{7-y}$  sample.

The estimation of  $|\partial \ln T_N / \partial \ln V| = |\kappa^{-1} \partial \ln T_N / \partial P|$  value using compressibility  $\kappa = 0.65 \cdot 10^{-6} \text{ bar}^{-1}$  [2] gives  $\approx 5$ . In case of magnetic dipole-dipole interaction the value of  $|\partial \ln T_N / \partial \ln V|$  derivative should be close to 1, because in that case  $T_N \sim \mu_{\text{eff}}^2 / r^3 \sim \mu_{\text{eff}}^2 / V$ . The obtained result means that some other kind interaction, probably superexchange-type, gives an important contribution in AFM-ordering of Gd-123 compound. The RKKY-type interaction can not play a significant role in  $\text{Gd}^{3+}$  AFM-ordering in Gd-123 system because  $T_N$  values are very close for fully oxidized superconducting compound ( $y \approx 0$ ) and for oxygen reduced insulating one ( $y \approx 1$ ), [3].

Very recently the essential role of superexchange-type interaction in AFM-ordering was pointed out using high pressure results for Nd-123 compound [4]. At the same time the dipole-dipole interaction seems to be

the dominant mechanism for Dy-123 compound [4]. So, the type of interaction leading to AFM-ordering in RE-123 systems may not be the same for different rare earth ions  $\text{RE}^{3+}$ .

Superconducting transition of Gd-123 shifts to the higher temperatures under pressure applying, see Fig. 3. The value of  $\partial T_c / \partial P$  is  $+1.2 \cdot 10^{-4}$  K/bar, being in agreement with previously published data. (The value of  $T_c$  was determined at the middle of inductively measured superconducting transition).

Substitution of Gd on Ba site also increases the  $T_N$  value, the  $\lambda$ -anomaly for the  $\text{Gd}_{1+x}\text{Ba}_{2-x}\text{Cu}_3\text{O}_{7-y}$  being surprisingly narrow in spite of random Gd atoms distribution on Ba-plane, see Fig. 4. (Solid solutions of  $\text{Gd}(\text{Ba}_{2-x}\text{Gd}_x)\text{Cu}_3\text{O}_{7-y}$  were synthesized by a citrate pyrolysis method. The oxygen contents determined by iodometric titration are 6.93, 6.96 and 7.03 for  $x=0$ ; 0.1

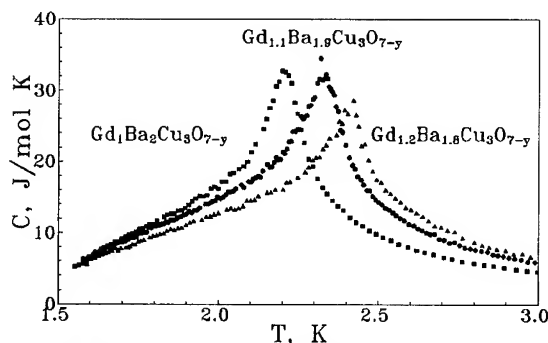


Fig. 4. Specific heat vs. temperature for three samples of  $\text{Gd}_{1+x}\text{Ba}_{2-x}\text{Cu}_3\text{O}_{7-y}$  system.

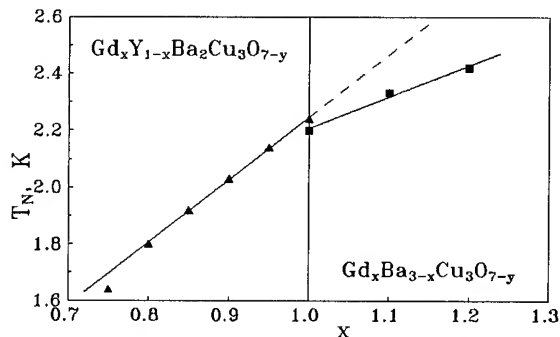


Fig. 5. Neel temperature vs. Gd-concentration  $x$  for  $\text{Gd}_x\text{Y}_{1-x}\text{Ba}_2\text{Cu}_3\text{O}_{7-y}$  [5] (left) and  $\text{Gd}_{1+x}\text{Ba}_{2-x}\text{Cu}_3\text{O}_{7-y}$ , represented as  $\text{Gd}_x\text{Ba}_{3-x}\text{Cu}_3\text{O}_{7-y}$ , (right).

and 0.2 respectively). The observed  $\partial T_N/\partial x$  value (1.2 K) is approximately two times lower than for Gd substitution for Y-site,  $Y_{1-x}Gd_xBa_2Cu_3O_{7-y}$ , [5], see Fig.5. This fact may be probably connected with two Ba-planes in Gd-123 unit cell where the additional Gd could take place instead of the only one Y-plane position in  $Y_{1-x}Gd_xBa_2Cu_3O_{7-y}$  system.

Gd substitution on Ba-site decreases the value of  $T_c$  and leads to gradual transformation of the temperature dependence of resistance from "metallic" to "semiconducting"-like near superconducting transition, see Fig.6.

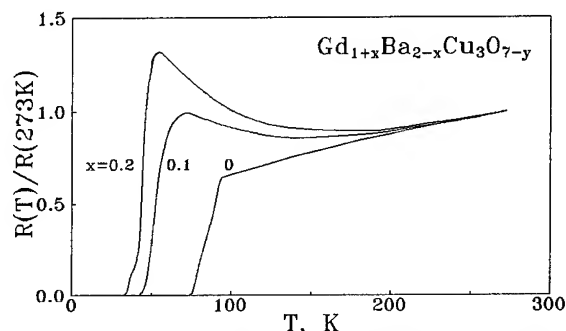


Fig.6. Normalized resistance vs. temperature for three  $Gd_{1+x}Ba_{2-x}Cu_3O_7$  samples.

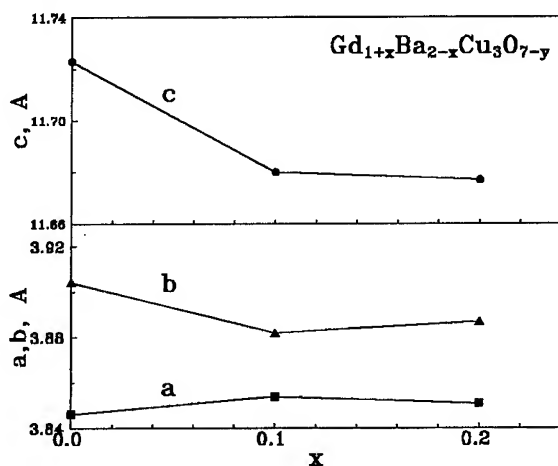


Fig.7. Crystal structure parameters vs. Gd concentration for  $Gd_{1+x}Ba_{2-x}Cu_3O_7$  system.

Gd substitution on Ba-site leads to the contraction of the unit cell due to the smaller ionic radius value of  $Gd^{3+}$  in comparison with  $Ba^{2+}$ , see Fig. 7. "Chemical" pressure effect on

$T_N$  could be estimated using the obtained value of  $\partial T_N/\partial P$  for Gd-123 compound and the value of compressibility  $\kappa$  from [2]. For  $x=0.2$  the evaluation of "chemical" pressure effect gives shift of  $T_N$  on approximately 0.05K, that is five times lower than it has been experimentally found, see Fig.5. So "chemical" pressure effect can not explain the observed  $\partial T_N/\partial x$  value for  $Gd_{1+x}Ba_{2-x}Cu_3O_7$  system.

It is of interest to note that for  $Pr_{1+x}Ba_{2-x}Cu_3O_{7-y}$  system Pr substitution on Ba-site decreases  $T_N$  value [6].

## Conclusion

The pressure induced increase of  $Gd^{3+}$  AFM-ordering temperature  $T_N$  has been found for the  $GdBa_2Cu_3O_{7-y}$  high- $T_c$  compound using specific heat measurements under high pressure. The essential role of superexchange-type interaction between  $Gd^{3+}$  ions is pointed out taking into account the relatively large value of  $|\partial \ln T_N / \partial \ln V| \approx 5$ . The observed increase of  $T_N$  for the Gd substitution on the Ba-site in  $Gd_{1+x}Ba_{2-x}Cu_3O_{7-y}$  system can not be described by the effect of "chemical" pressure.

## References

- [1] N.E. Alekseevskii, A.V. Gusev, G.G. Devyatikh *et al.*, *JETP Lett.* **48** (1988) 585.
- [2] J. Ecker, W.H. Fietz, M.R. Dietrich *et al.*, *Physica C* **153-155** (1988) 954.
- [3] G. Hilscher, T. Holibar, G. Schaudy *et al.*, *Physica C* **224** (1994) 330.
- [4] P. Allespach, B.P. Lee, D.A. Gajewski *et al.*, *Z. Phys. B* **96** (1995) 455.
- [5] F. Nakamura, T. Fukuda, Y. Ochiai *et al.*, *Physica C* **153-155** (1988) 178.
- [6] S.K. Malik, S.M. Pattalwar, C.M. Tomy *et al.*, *Phys. Rev. B* **46** (1992) 524.

## **VII(E) Fullerenes**

# FULLERENES UNDER PRESSURE: STRUCTURE, ORDER, AND DISORDER

B. SUNDQVIST, O. ANDERSSON, A. LUNDIN\*, P-A. PERSSON\*, AND A. SOLDATOV

*Department of Experimental Physics, Umeå University, S-90187 Umeå, Sweden*

## ABSTRACT

The weak intermolecular interactions in solid  $C_{60}$  and other fullerenes make crystal structures and other properties very sensitive to applied pressure. We review below recent results on the properties and phases of fullerenes under pressure, concentrating on the low- $p$  range up to about 1 GPa. Subjects discussed include compression and transport studies, orientational and rotational disorder, the glassy crystal transition, and pressure-induced polymerization.

## Introduction

The weakness of intermolecular interactions in solid fullerenes implies that even small changes in external environment may give significant changes in the translational, orientational, or rotational structure of the material, and thus also in other physical properties. We give here a brief overview of recent studies of the structures, phases, and other properties of fullerenes under high pressure,  $p$ , concentrating on the region below about 1.5 GPa since other invited papers in this volume discuss the higher pressure ranges. Space being limited we focus on areas where recent rapid advances have been made. After a brief overview of the pressure-temperature ( $p$ - $T$ ) phase diagram of  $C_{60}$ , describing the general structural evolution with  $T$  and  $p$ , we discuss the structure and properties of pressure polymerized  $C_{60}$ , in particular material treated at "low"  $p$  and  $T$  near 1.1 GPa and 550 K. In following sections we discuss data for the bulk modulus of  $C_{60}$ , the orientational structure of the simple cubic phase and its effects on material properties, and the effects of non-equilibrium orientational structures on the glassy crystal transition. Finally, we review very briefly some recent high- $p$  studies of  $C_{70}$  and of modified fullerenes such as  $C_{61}H_2$ .

## Structure and phases of $C_{60}$

Fig. 1 shows the reasonably well known low- $p$ , low- $T$  phase diagram of  $C_{60}$ , based on refs. (1-6). The high- $T$  structure is face centered cubic (fcc) with free molecular rotation, but below  $T_c$  ( $= 260$  K

at  $p = 0$ ) rotation stops and a simple cubic (sc) phase with a variable degree of orientational order forms. The boundary between these phases has been well investigated (1-3). On cooling below 90 K all molecular reorientation is stopped and a glassy crystal or orientational glass is formed (7). The glass transition line has also been well mapped up to 0.8 GPa (4,5). In the sc phase the molecules have two possible orientational states, the hexagon (H) and pentagon (P) oriented states. The energy balance will shift with pressure, and at high  $p$  most molecules will reorient into the H state (8) which dominates completely above a critical pressure (4,9) shown as a dashed line in Fig. 1. Finally, at high  $p$  ( $> 1$  GPa) and  $T$  (near 500 K) increasing intermolecular interactions lead to the formation of

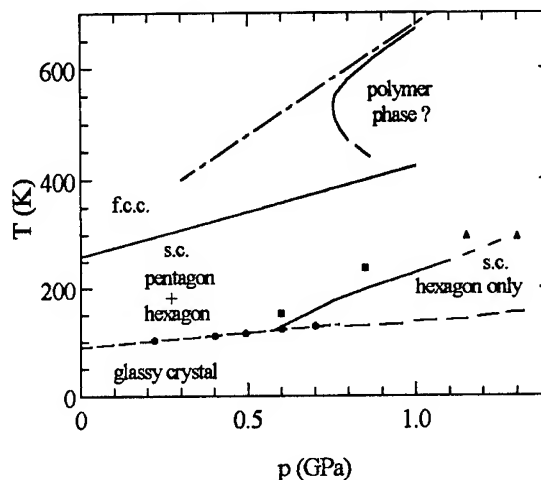


Fig. 1. Low- $p$  part of the phase diagram for  $C_{60}$ , adapted from ref. (9).

\* Present address: Dept. of Applied Physics and Electronics, Umeå University

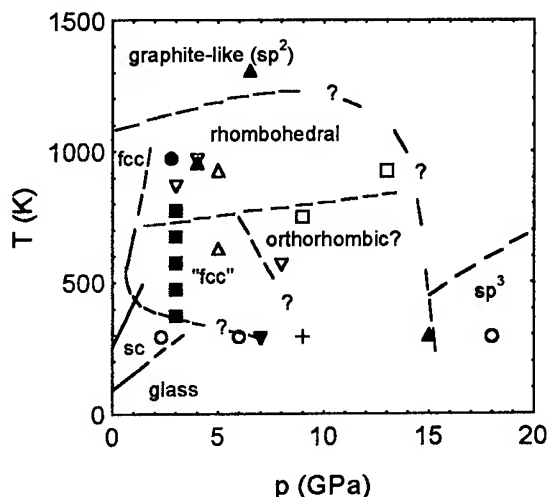


Fig. 2. p-T phase diagram of C<sub>60</sub>. Symbols denote approximate p-T coordinates for structural and other studies in Refs. 10 (+), 11 (▼), 12 (Δ), 13 (○), 14 (▲), 15 (▽), 16 (●), 17 (■), and 18 (□). Full curves show known phase boundaries while areas where different structures are found are arbitrarily separated by dashed curves.

an insoluble polymeric phase (6) with intermolecular bonds much stronger than in normal C<sub>60</sub>. This phase will be discussed further below.

The polymeric phase is only one of a number of such phases, as shown in the rather speculative high p - high T phase diagram in Fig. 2. The phase boundaries shown in Fig. 1 are shown as full lines and curves, while dashed ones are extrapolations and/or speculations. Several groups have carried out structural and spectroscopic studies over large areas in the p-T plane. While there is no detailed agreement between the results and the exact structures and other properties of the various phases are not yet known, there seems to exist at least three different "polymer" phases: A "distorted fcc" phase (6,13,15,17) at low p and T, probably identical to that appearing in Fig. 1, a very hard rhombohedral phase (13-18) at T > 700 K, and a high-p orthorhombic phase (15,18). All these show very little long range order since polymerization probably occurs in random directions, and the structures assigned are still preliminary. We have plotted in Fig. 2 selected p and T coordinates where structural results have been reported (13-18), and we have drawn dashed lines to separate different groups of results. The lines should not be taken as phase boundaries since those are still unknown, and since other structures have been reported and results do

not always agree between different groups further phases may exist.

At 295 K we have plotted some points near 2.5, 6, 10, and 15 GPa, where anomalies are observed (10,11,13). The 2.5 GPa anomaly (13,20) agrees well with the extrapolated glass transition line (5,9) but could also be connected with the P→H reorientation. Slow polymerization is observed at 4 - 7 GPa (11), possibly into the "distorted fcc" low-p phase, and structural anomalies are also observed at 6 - 10 GPa (10,13,21). The structure above is unknown but might be either the "distorted fcc" or the orthorhombic phase. Above 15 - 25 GPa extremely hard, transparent sp<sup>3</sup> amorphous carbon or diamond phases are formed (13,14,22).

Above T > 1000 K, finally, C<sub>60</sub> collapses into graphite-like, often amorphous sp<sup>2</sup> phases at all pressures (14,23).

#### Properties of low-p polymerized C<sub>60</sub>

As shown in Figs. 1 and 2, the lowest p and T conditions necessary for polymerization are about 550 K and 1.1 GPa (6). Material treated under such conditions has recently been extensively studied by us and others by widely different methods (24). At 293 K the treated material has a lattice parameter 1.1 - 1.6% smaller than that of normal C<sub>60</sub> and is completely insoluble in organic liquids. Specific heat measurements show a large increase in the effective low-T Debye temperature and the thermal expansivity is smaller than for normal C<sub>60</sub> at all T < 300 K. No rotational transition is observed, and Raman data show a large number of new peaks probably resulting from distortion of the molecules, plus peak shifts characteristic for polymerized C<sub>60</sub>. The material reverts to normal C<sub>60</sub> on heating to 500 - 600 K. These data are consistent with new, strong intermolecular bonds. In spite of this, the NMR spectrum shows one single broad line at the same position as for pristine C<sub>60</sub>, indicating that no covalent bonds have been formed between molecules. This contrasts sharply with other polymeric phases treated at higher p and T, which are known to be very much harder (13,16) and for which NMR measurements show strong evidence for the formation of covalent bonds (12). However, our results agree well with a recent model suggested by Kozlov and Yakushi (17), in which distorted C<sub>60</sub> molecules are held together by π-type bonds (24).

### Compressibility of $C_{60}$

One of the most important properties of a solid is its bulk modulus  $B$ . The compression properties of solids are determined by intermolecular potentials, and compression studies thus form a benchmark against which theoretical calculations can be tested. Many such studies have been carried out on  $C_{60}$  in the range from 150 K (19,25) to 700 K (6), and the volume  $V$  has been measured vs  $p$  by x-ray diffraction (XRD) in diamond anvil cells (10,21,26,27 and others), neutron scattering in a gas environment (28) and piston displacement in piston-cylinder vessels (6,25). Selected results below 1.4 GPa are compared in Fig. 3. Our own data (25) are represented by the solid curve since the scatter in the data is smaller than the width of the line. All studies except that of Duclos et al. (10) give very similar results for  $V$  vs  $p$  in this range, and also for  $B$  in the sc phase ( $> 0.3$  GPa). However, there are still some open questions: First, no standard equation of state describes  $V$  vs  $p$  well at all  $p$  (27), and compression properties above about 5 GPa seem to be very sensitive to non-hydrostatic  $p$ . This might be due to formation of polymer phases (11). Second, in the fcc phase x-ray (27) and neutron (28) studies as well as simple theory (29) give zero- $p$  bulk moduli near 12 GPa, almost twice the value 6.8 GPa given by the piston displacement method (25). Such a disagreement is surprising since all

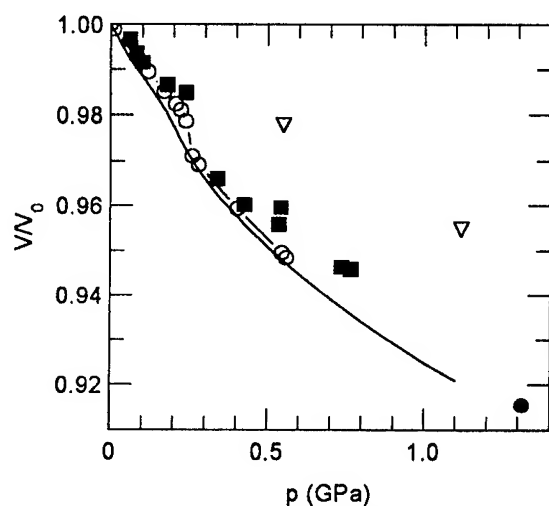


Fig. 3. Volume vs.  $p$  for  $C_{60}$  near 295 K from several sources: Full curve ref. (25) (piston-cylinder), ( $\nabla$ ) ref. (10), ( $\bullet$ ) ref. (26), ( $\blacksquare$ ) ref. (27) (all XRD), and ( $\circ$ ) ref. (28) (neutron diffraction).

methods give similar results near the phase transformation to sc. Fig. 3 shows that the difference is probably not due to the method of analysis. Since the measurements are repeatable, pressure amorphization can probably also be ruled out, and the most likely explanation is that the measured  $B$  is very sensitive to non-hydrostatic stress in the fcc phase. However, why this is so has not yet been explained.

### Orientational order and disorder in the sc phase

As mentioned above there are two possible orientational states in  $C_{60}$  in the orientationally ordered sc phase. David and Ibberson (19) showed that the energy balance shifts with  $p$ . Since the hexagon (H) state has a smaller molecular volume than the pentagon (P) state that is stable at normal  $p$ , the H state becomes more favourable under pressure. This idea was used by Sundqvist et al. (4,9) to explain anomalies in the bulk modulus  $B$  and the thermal conductivity  $\kappa$ , within the sc phase as well as at  $T_c$  and at the glassy crystal transition temperature  $T_g$ .

It is well known that at  $p=0$  there is a continuous  $P \rightarrow H$  reorientation with increasing  $T$  because of thermal excitation over an energy threshold. Since the volume of the H oriented structure is smaller, this leads to an anomalously small thermal expansion between  $T_g$  and  $T_c$  (7). In analogy with this, the  $P \rightarrow H$  reorientation with pressure gives an extra volume decrease with increasing  $p$ , and thus a small value for  $B$  (9).

Extrapolating the measured  $P/H$  ratio (19) linearly with  $p$ , Sundqvist et al. (4) hypothesized the existence of a fully H oriented state above some critical pressure. Anomalies in  $B$  and  $\kappa$  were indeed found (4,5,9) near the transition pressures calculated in this simple model, and recent Raman results (8) proved the existence of a high- $p$ , H oriented phase. However, the fraction of P oriented molecules is given by  $f(T) = [1 + \exp(-\Delta/kT)]^{-1}$ , where  $\Delta$  is an energy parameter, so neither a "pure H" nor a "pure P" phase exists above 0 K since an exponential tail in  $f(T)$  remains at low  $T$ . We expect a similar continuous change with  $p$  and no sharply defined phase boundary should thus exist. However, due to an inflexion point  $f(T)$  varies approximately linearly with  $T$  (or  $p$ ) over a large range between  $f = 0.7$  and  $>0.95$ , then bends over sharply. This should show up as an anomaly in any property

sensitive to the orientational structure, and these anomalies would define a virtual "phase line". For simplicity, Sundqvist et al. (4,9) assumed the fraction of P oriented molecules to vary linearly with  $p$  as observed (19) below 0.3 GPa, but there is no physical model behind this. The observed linearity translates into an almost linear variation of  $\Delta$  on  $p$  (19), and an alternative approach is to extrapolate  $\Delta$  linearly and use  $f(T)$  to calculate a phase line, using some suitable semi-arbitrary criterium such as 97% H oriented molecules. However, the intermolecular interaction in  $C_{60}$  is of the van der Waals type, modified by electrostatic forces, and we have no reason to assume that  $\Delta$  should vary linearly over any appreciable range in  $p$ . Further experimental data are thus needed to characterize fully the orientational structure of  $C_{60}$  above 1 GPa.

#### Non-equilibrium orientational structures near $T_g$

As found by Sundqvist et al. (4) and investigated in detail through thermal conductivity measurements by Andersson et al. (5,9,30) a non-equilibrium mixture of orientational phases can be frozen in by simply cooling  $C_{60}$  slowly at constant pressure, then changing  $p$  in the glassy crystal phase below the glass transition line. On reheating, the material will then still contain a P/H orientational ratio equal to that at  $T_g$  at the original cooling pressure, and on approaching  $T_g$  the molecules will reorient so as to approach the equilibrium ratio characteristic of the new pressure. The difference in relaxation behaviour between the equilibrium and non-equilibrium cases is large. We show in Fig. 4 data for the thermal conductivity  $\kappa$  as a function of  $T$  between 50 and 170 K and at 0.1 to 0.25 GPa, for three different cases. In all experiments  $\kappa$  was measured while increasing  $T$ . The data obtained at 0.1 GPa shows the typical "equilibrium" behaviour for samples cooled and heated at the same  $p$ , where  $T_g$  shows up as a sharp change in  $d\kappa/dT$  (5,9,30). The other data sets are obtained for the non-equilibrium cases: The 0.25 GPa data were taken for a sample cooled at higher  $p$  (0.5 GPa) and those at 0.2 for one cooled at lower  $p$  (0.1 GPa), freezing in a surplus of H and P oriented molecules, respectively. Since different orientations give different volumes the relaxation now occurs at a  $T$  different from that in the equilibrium situation, such that the effective  $T_g$  will be lower if we have a fraction of P oriented

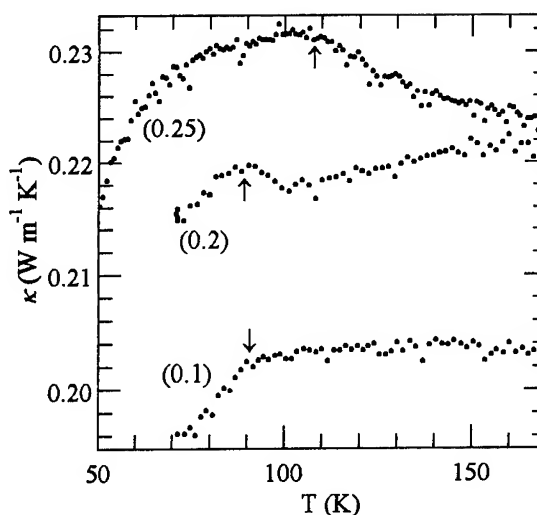


Fig. 4. Thermal conductivity vs.  $T$  at the pressures (in GPa) indicated, for equilibrium and non-equilibrium orientational structures. Arrows indicate  $T_g$  (see text).

molecules higher than the equilibrium one. Wolk et al. (8) cooled their samples at low  $p$  and thus found a slope  $dT_g/dp$  lower than the "equilibrium" slope  $62 \text{ K GPa}^{-1}$  given by Andersson et al. (5).

#### High pressure properties of $C_{70}$ and $C_{61}H_2$

The production of  $C_{60}$  yields as a by-product small amounts of  $C_{70}$ . Due to difficulties in purifying the material less is known about  $C_{70}$  than about  $C_{60}$  under pressure. The high- $T$  structure is fcc with free molecular rotation (31). On decreasing  $T$  the rotation turns into uniaxial near 350 K, then stops completely near 280 K. Models suggest that uniaxially rotating molecules could line up in parallel, giving a rhombohedral (rh) lattice, while non-rotating molecules may form an orientationally ordered low- $T$  monoclinic (mc) phase. Although these phases have been observed by several authors, the fcc phase is often metastable to low  $T$  and many other phases have also been observed.

Kawamura et al. (32) investigated the high- $T$  phase diagram of  $C_{70}$  using XRD and mapped the fcc-rh transformation phase line above 400 K. Surprisingly, even at 293 K a fcc-to-rh transition is found under pressure (33), probably due to the presence of metastable fcc phase. A recent thermal conductivity study (34) mapped the phase line for complete rotational arrest, in theory corresponding to the rh-mc transition, and proposed a  $p$ - $T$  phase

diagram in agreement with the work discussed above and with a recent compression study (35).

Finally, fullerenes can be modified by adding small sidegroups. Although many of these are known the only one studied at high  $p$  is deuterated  $C_{61}H_2$ , the compressibility of which has been measured between 175 and 350 K (36). At  $p = 0$  the structural behaviour is very similar to that of  $C_{60}$ , except that  $T_g$  (37) and  $T_c$  (38) are shifted upwards. The high- $p$  data (36) show unexplained anomalies above 280 K which can not be correlated with  $T_c$ , and no clear sign of  $T_g$  is found under pressure. The magnitude of  $B$  agrees reasonably well with data for  $C_{60}$  if extrapolated to the larger lattice parameter of  $C_{61}H_2$ , indicating that the main intermolecular interaction is still between the "bellies" of the molecules and not with the sidegroups.

#### Acknowledgements:

This work was financially supported by the Swedish Research Councils for Natural Sciences (NFR) and Engineering Sciences (TFR).

#### References

- G.A. Samara et al., *Phys. Rev. Lett.* **67** (1991) 3136.
- G. Kriza et al., *J. Physique I* **1** (1991) 1361.
- G.A. Samara et al., *Phys. Rev. B* **47** (1993) 4756.
- B. Sundqvist et al., *Solid State Commun.* **93** (1995) 109.
- O. Andersson, A. Soldatov and B. Sundqvist, *Phys. Lett A* (1995, in press).
- I.O. Bashkin et al., *J. Phys.: Condens. Matter* **6** (1994) 7491.
- C. Meingast and F. Gugenberger, *Mod. Phys. Lett. B* **7** (1993) 1703.
- J.A. Wolk, P.J. Horoyski and M.L.W. Thewalt, *Phys. Rev. Lett.* **74** (1995) 3483.
- B. Sundqvist et al., in *Recent Advances in the Physics and Chemistry of Fullerenes*, vol. 2, ed. K.M. Kadish and R.S. Ruoff (in press).
- S.J. Duclos et al., *Nature* **351** (1991) 380.
- H. Yamawaki et al., *J. Phys. Chem.* **97** (1993) 11161.
- Y. Iwasa et al., *Science* **264** (1994) 1570.
- V. Blank et al., *Phys. Lett. A* **188** (1994) 281.
- M. Núñez-Regueiro et al., in *Recent Advances in the Physics and Chemistry of Fullerenes and Related Materials*, ed. K.M. Kadish and R.S. Ruoff (ECS, Pennington 1994) p. 519.
- M. Núñez-Regueiro et al., *Phys. Rev. Lett.* **74** (1995) 278.
- M.E. Kozlov et al., *Appl. Phys. Lett.* **66** (1995) 1199.
- M.E. Kozlov and K. Yakushi, *J. Phys.: Condens. Matter* **7** (1995) L209.
- V.D. Blank, B.A. Kulnitskiy and Ye.V. Tatyannin, *Phys. Lett. A* **204** (1995) 151.
- W.I.F. David and R.M. Ibberson, *J. Phys.: Condens. Matter* **5** (1993) 7923.
- A.P. Jephcoat et al., *Europhys. Lett.* **25** (1994) 429; K.P. Meletov et al., *Chem. Phys. Lett.* **236** (1995) 265.
- G. Oszlanyi et al., *Solid State Commun.* **84** (1992) 1081; J.H. Nguyen, M.B. Kruger and R. Jeanloz, *Solid State Commun.* **88** (1993) 719.
- M. Núñez-Regueiro and P. Monceau, *Nature* **355** (1992) 237; C.S. Yoo and W.J. Nellis, *Chem. Phys. Lett* **198** (1992) 379; C.S. Yoo et al., *Appl. Phys. Lett.* **61** (1992) 273.
- C.S. Sundar et al., *Solid State Commun.* **84** (1992) 823.
- P.-A. Persson et al. (these Proceedings).
- A. Lundin and B. Sundqvist, *Europhys. Lett.* **27** (1994) 463.
- J.E. Fischer et al., *Science* **252** (1991) 1288.
- H.A. Ludwig et al., *Z. Phys. B* **96** (1994) 179.
- J.E. Schirber et al., *Phys. Rev. B* **51** (1995) 12014.
- L.A. Girifalco (private communication).
- O. Andersson, A. Soldatov and B. Sundqvist, in *Sci. and Technol. of Fullerene Materials*, ed. P. Bernier et al. (MRS 1995), p. 549.
- G.B.M. Vaughan et al., *Chem. Phys.* **178** (1993) 599.
- H. Kawamura et al., *J. Phys. Chem. Solids* **54** (1993) 1675.
- C. Christides et al., *Europhys. Lett.* **22** (1993) 611.
- A. Soldatov and B. Sundqvist, in *Recent Adv. in the Phys. and Chem. of Fullerenes*, vol. 2, ed. K.M. Kadish and R.S. Ruoff (in press).
- A. Lundin, A. Soldatov, and B. Sundqvist, *Europhys. Lett.* **30** (1995) 469.
- A. Lundin et al. (to be published).
- C. Meingast et al. (to be published).
- A.N. Lommen et al., *Phys. Rev. B* **49** (1994) 12572.



# FULLERENES TRANSITION TO DIAMOND UNDER HIGH PRESSURE AND HIGH TEMPERATURE

YANZHANG MA and GUANGTIAN ZOU

*State Key Laboratory for Superhard Materials  
Jilin University, Changchun 130023, P.R. China*

C<sub>60</sub>, fullerenes and the remainder of carbon soot after fullerenes being extracted have been adopted as carbon sources in the attempt to synthesize diamond under high pressure and high temperature, with the existence of a NiMnCo catalyst. Fullerenes have been converted to diamond crystals at about 5 GPa and 1700 K as well as RCS. Transformation from pure C<sub>60</sub> to diamond has not been found under the same condition. The electric resistance of fullerenes has been found decrease several orders of magnitude at high pressure in an in situ measurement. The high temperature processed and the high temperature and high pressure processed fullerenes has been measured by Raman spectra and X-ray diffraction, and several phase transitions have been found. A mechanism for fullerenes transition to diamond has been proposed.

## Introduction

In 1990, Kratschmer et al.<sup>1</sup> successfully isolated macroscopic quantity of C<sub>60</sub> and C<sub>70</sub> from carbon soot. This fascinating new form of carbon soon began to draw much attention of high pressure research. Many works have been undertaken on the study of their properties at high pressure and several phase transitions have been observed. Duclos et al.<sup>2</sup> measured the room-temperature pressure-volume equation of state of C<sub>60</sub> fullerite to 20 GPa. Fischer et al.<sup>3</sup> studied the compressibility of C<sub>60</sub> by XRD at hydrostatic pressure of 1.2 GPa, and found a higher volume compressibility of C<sub>60</sub>. Moshary and Snoko et al.<sup>4,5</sup> found the collapse of solid C<sub>60</sub> to a new phase of carbon at about 20 GPa. Regueiro et al.<sup>6</sup> measured the electric resistivity of C<sub>60</sub>, and also found an insulating state at 15-20 GPa. Yoo et al.<sup>7</sup> studied the phase transformation of carbon fullerenes at high shock pressure. The effects of high pressure on Raman and IR spectra were also studied<sup>8-11</sup>.

Because the valence bonds in fullerenes' molecules contain *sp*<sup>3</sup>-hybridized state and one of their characteristic carbon bonding angle 108° approaches to that 109° of diamond, it has been expected easier for the conversion of fullerenes to diamond. Ruoff et al.<sup>12</sup> even speculated that compressed fullerite might be harder than diamond. However, early works did not found the transition of fullerenes to diamond at high pressures even upto 36 GPa. In 1992, Regueiro et al.<sup>13</sup> reported an irreversible pressure-induced transformation of fullerite to diamond crystals under nonhydrostatic

pressures of 20±5 GPa, but other attempts failed to repeat their experiment. We believe that it is difficult to convert fullerenes to diamond only by means of high pressure process. Considering that most of the previous works were accomplished in diamond-anvil cells at room temperature without using a catalyst, we employed a cubic high-pressure apparatus and adopted a metal alloy as catalyst, and successfully converted fullerenes to diamond at about 5 GPa and 1700 K<sup>14</sup>. Meanwhile Bocquillon et al.<sup>15</sup> also successfully synthesized diamond from fullerenes at 6.7 GPa and temperatures of 1200-1850°C, using several different catalysts.

In this paper we present the comparison experimental results of fullerenes with pure C<sub>60</sub>, and the remainder of carbon soot after fullerenes being extracted (RCS) as starting materials for diamond synthesis, the study of the properties of fullerenes at high pressure and high temperature and the discussion about the mechanism for the transformation of fullerenes to diamond.

## Experimental

In the preparation of the carbon samples, the electric arc method was adopted to produce carbon soot. The soot was undertaken a benzene extraction process in a Soxhlet extractor. The soluble extract was dried and adopted as the sample of fullerenes. Continue the extraction for long enough time, dried the insoluble remainder and used it as carbon sample of RCS. The Pure C<sub>60</sub> sample was obtained from the chromatographic separation of the extracted fullerenes. Each sample was compacted into a

drilled hole of a catalyst flake between two others as a combined unit. Such a unit with fullerenes and a unit with  $C_{60}$  (or RCS) were respectively placed at the symmetric position of the cylinder sample chamber of a cubic body of pyrophyllite to study their distinction under high pressure and high temperature. The high pressure and high temperature experiments were carried out in a 6×600 ton cubic high pressure apparatus with an electric current heating device. The pressure was calibrated by the phase transition points of Bi(I-II), Tl and Ba, and the temperature was measured by the 6%PtRh~30% PtRh thermo-couple. The processed pressures were 5, 4.7 and 4.5 GPa with the temperatures 920, 1320, 1520 and 1700 K, respectively. The processed time was 8 minutes. These processed samples were quenched down to the ambient pressure and temperature and undertaken Raman spectra measurements. A T6400 Raman system was used in the measurements with the 514.5 nm radiation from a Spectra Physics Argon ion laser for excitation at an out put of 20 mW.

In the studies of the effects of high temperature on the electric resistance of fullerenes, we implanted two pieces of conducting wire (Pt/Rh) along the opposite direction on the wall of a cylinder hole of pyrophyllite, compacted the powder of fullerenes into the hole and sealed it with the mixture of powder pyrophyllite and liquid sodium silicate. This sealed body was heated in an electric resistance furnace and an in situ measurement of its resistance was undertaken with a Keithley 105 A digital multimeter. We also heated fullerenes samples sealed in pyrophyllite to several selected temperatures from 670 to 970 K for 30 minutes, cooled them down with the furnace and undertook Raman and X-ray diffraction spectra measurements.

## Results and discussion

Diamond crystals have been found in the samples of fullerenes and RCS at about 1700 K and 5 GPa, which were tested by Raman Spectra as Ref. 14. However the nuclear ratio of fullerenes are much lower than that of RCS. While the temperatures lower than 1520 K diamond crystals disappear. Under lower pressures of 4.5 and 4.7 GPa and different temperatures no diamond can be found. No diamond has been found in all the processed  $C_{60}$  samples under these conditions. It seems that 5 GPa

and 1520 K are the lowest conditions for the transition of fullerenes to diamond.

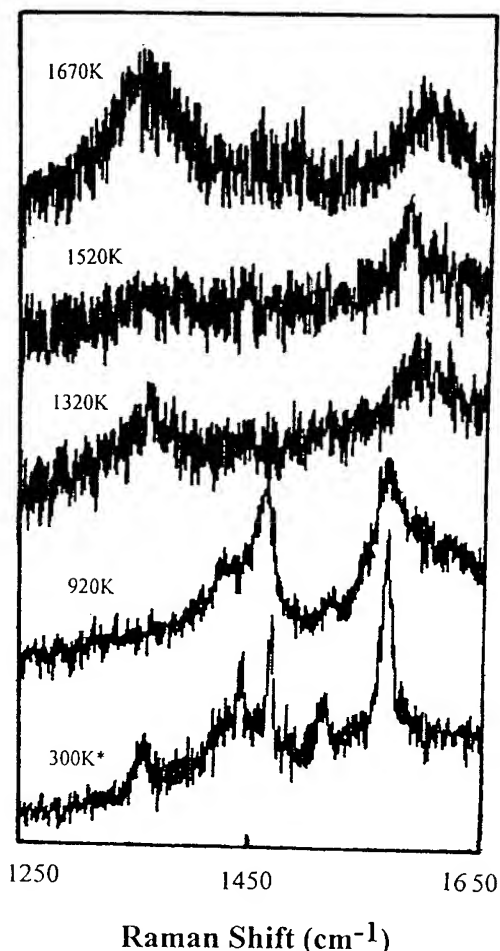


Fig.1 Raman spectra of fullerenes under 5 GPa and different temperatures (\* Spectra at ambient pressure)

From the Raman spectra it is observed that the Raman peak at  $1468\text{ cm}^{-1}$  of  $C_{60}$  in fullerenes shifts to  $1461\text{ cm}^{-1}$  under 5 GPa and 920 K. This result is similar to that of Iwasa et al.<sup>16</sup>. It is caused by the formation of valance bonds between fullerene molecules, i.e., the so called cross-linking process<sup>17</sup>. Under the pressure of 5 GPa and temperatures higher than 1320 K, this peak disappears and two broad bands exist at  $1360$  and  $1580\text{ cm}^{-1}$  instead. At 1670 K, the broad band at  $1580\text{ cm}^{-1}$  shift to  $1600\text{ cm}^{-1}$  (Fig.1). Similar spectra of fullerenes are also observed at lower pressure (4.5 and 4.7 GPa) and temperatures higher than 1320 K. It is believed that fullerenes transform into amorphous carbon at

temperatures higher than 1320 K. Further discussion can be found behind.

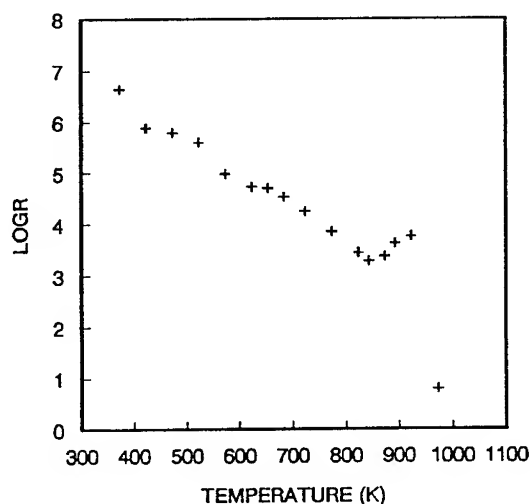


Fig.2 Resistance of fullerenes change with high temperatures

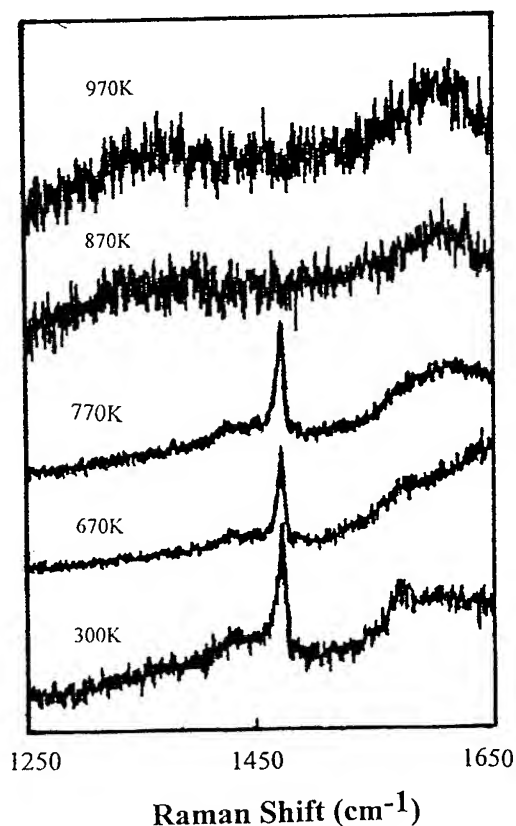


Fig. 3 Raman spectra of the high temperature processed fullerenes

Fig. 2 shows the experimental result of the electric resistance measurement of fullerenes at high temperatures. It is found that the resistance of fullerenes decreases dramatically with the increase of temperature until it reaches  $6 \Omega$  at 970 K. This result is similar to that of Sunda et al.<sup>18</sup>. The resistance increases at 870 K may be caused by the phase transition of pyrophyllite. Details could be found elsewhere. In our previous research, we had ever filled fullerenes in the chamber between two flakes of the catalyst and found the similar phenomenon. When the samples were pressurized and a certain electric voltage was applied, the indicator of the electric current meter almost stand at 0 point at the beginning. Then it moved up continuously until reaching a certain point. It is believed that at ambient and high pressure the electric resistance of fullerenes decreases with the increase of temperature.

Fig.3 shows the Raman spectra of high temperature processed fullerenes. When the processed temperature lower than 770 K the Raman peak of  $C_{60}$  at  $1468 \text{ cm}^{-1}$  remains unchanged. At 870 and 970 K, it disappears and there exist two broad bands at  $1367$  and  $1600 \text{ cm}^{-1}$  instead. X-ray diffraction analyses indicate that the diffraction background increases at 670 K, and it increases with the increase of temperature. At 970 K, all peaks disappear and only a broad band at  $2\theta = 22$  degrees exists (Fig. 4). From these experiment results we believe that fullerenes transform to an amorphous state at 970 K and ambient pressure.

Although we believe that fullerenes transform into amorphous carbon under high temperature at both ambient and high pressures, the transition mechanisms are distinction. At ambient pressure, fullerenes' molecules sublime at high temperature, i.e., the molecules are in a gaseous state. The outside supplied thermal energy mainly causes the high speed motion of the molecules. These moving molecules collide each other in the limited space. When the supplied energy is higher enough, the molecular structure of fullerenes could be destroyed by the collision and transform to an amorphous carbon. In this case there don't exist the conditions for the formation of valence bonds between fullerenes molecules.

Previous experiments indicated that the high pressure of 5 GPa could not affect the molecular structure of fullerenes. Therefore, it is believed that the main effects of high pressure on fullerenes in our

experiments are to limit the motion of the fullerenes' molecules in a certain scope and decrease the inter-molecular distance. Therefore the molecules are in a solid state at high pressure and high temperature instead of a gaseous one. In such restricted molecules, the thermal energy is mainly concentrated on the thermal vibration of the atoms on fullerenes' molecules. The vibration of these atoms becomes heavier when the temperature increases, which causes the atoms on two different molecules closer and forms valence bonds at appropriate conditions of high pressure and high temperature. This is the so called cross-linking state of fullerenes<sup>16,17</sup>.

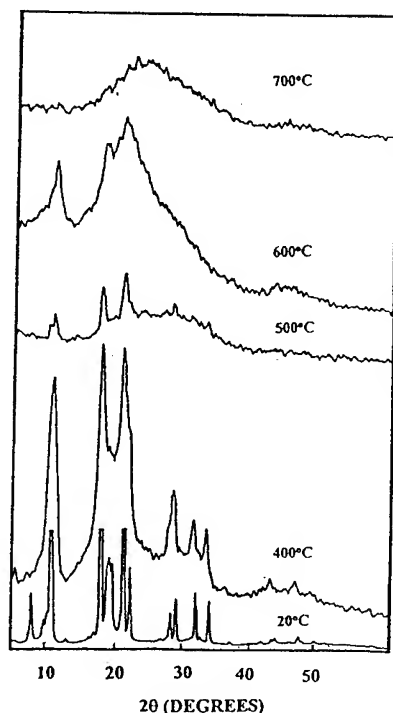


Fig.4. X-ray diffraction spectra of high temperature processed fullerenes

However, this cross-linking state is not the final one in our high pressure and high temperature experiment. With further increase of the processed temperature, the thermal vibration becomes much heavier. When the vibration energy is higher than the bond energy of fullerenes' molecules, the fullerenes' molecular structure becomes fragmented, and forms an amorphous carbon. Such situation takes place at temperatures higher than 1320 K in our experiments. It is proposed that after the

fragmentation process, the pentagon and hexagon radicals remain in the fragments.

At 5 GPa and 1700 K, the conditions for the conversion of fullerenes to diamond, the metal catalyst in the high pressure chamber is in a molten state, which provides a liquid environment for the phase transition, chemical reaction and crystal growth. The carbon radicals dissolve in the molten metal solvent and form a carbon-metal solution. The high pressure decreases the inter-atom distance of the hexagonal radicals, and the high temperature causes their severe vertical vibration along its parallel direction to the plane, which together with the absorbing action of the metal catalyst atoms at the even numbered atoms in the plane causes the hexagonal plain folded, i.e., the even numbered atoms move above the original plane and the odd numbered atoms move below. The hexagonal radical therefore transforms to a diamond radical. With the generation of a diamond radical, there form dangling bonds. They bind with the metal atoms, and hence a metal-carbide (C-M) radical forms. However this process is reversible and there is a transformation equilibrium among hexagonal, diamond and C-M radicals. Because of the stronger affinity between carbon atoms, carbon atoms in a C-M radical tend to absorb other carbon atoms in place of the metal ones. When a C-M radical reacts with another one, one of the metal atoms should be replaced by a carbon atom on the other radical and forms a micro particle. It is believed that a carbon atom bind with four other carbon atoms does not dissolve in the molten metal liquid because of its strong valence bonds. Therefore the replacing process is irreversible. In fact, this replacing process may also take place between particles. The process continues and the micro particle grows up. It seems that the metal catalyst acts as a carrier of carbon radicals. When the particle becomes bigger than the critical size, it forms a nuclear of diamond and participates from the liquid. Other radicals and particles of diamond continue the replacement in the surface of the nuclear and a diamond crystal grows up continuously. Meanwhile, with the participation of diamond crystals, the concentration of C-M radical decreases in the solution. New hexagonal radicals continually dissolve in the molten liquid and repeating the above processes.

It should be noticed that we have proposed both hexagonal and pentagon radicals remain in the fragment of fullerenes. A pentagon radical, however,

as a ring with 5 carbon atoms, and therefore unable to undergo the folding process. It needs more energy to form a ring or line with even number atoms before it transforms to a diamond radical. Therefore pentagon is harder to be transformed to diamond than hexagon. There are 12 pentagons in a  $C_{60}$  molecule. Each carbon atom is linked by a pentagon ring. In the fragmentation of  $C_{60}$ , it may create more (up to 12) pentagon radicals than other fullerenes. Because the provided energy in our experiments is not enough for such a transition, it is hardly to transform  $C_{60}$  into diamond.

### Conclusion

It is indicated that the action formulas of high temperature on fullerenes are different. At ambient pressure, it causes the motion of fullerenes' molecules in gaseous state which will collide each other and destroy themselves into an amorphous state. At high pressure, it makes the atoms vibrate severely on the fullerenes' molecules, which causes the molecules cross-link at apparently lower temperature and their fragmentation at higher temperature. Under the diamond synthesizing conditions, the hexagonal radicals dissolve in the molten metal catalyst. With the heavy vibration and the absorption of the metal atoms, they fold to diamond radicals. Through a carbon-metal replacing process these diamond radicals grow up and participate from the molten metal liquid after they become bigger than critical size. The carbon-metal replacement continues on the surface of the participated diamond nucleus and forms diamond crystals. It is hard to transform a pentagon radical into a diamond radical. The functions of the metal alloy are to provide environment for the diamond formation, absorb even numbered atoms and preserve the transition of hexagonal radical to diamond radical, and carry diamond radicals in the nucleation and growing up processes.

### Acknowledgment

This work is supported by the National Science

Foundation of China.

### References

1. W. Kratschmer, L.D. Lamb, K. Fostiropoulos, and D.R. Huffman, *Nature* **347**, 354(1990)
2. S. J. Duclos, K. Brister, R.C. Haddon, A.R. Kortan, and F.A. Thiel, *Nature* **351**, 380(1991)
3. J.E. Fischer, P.A. Heiney, A.R. McGhie, W. J. Romanow, A.M. Denenstein, J.P. McCauley, Jr, A.B. Smith III, *Science* **252**, 1288(1991)
4. F. Moshary, N.H. Cen, I.F. Silvera, C.A. Brown, H.C. Dorn, M.S. De Vries, and D.S. Bethune, *Phys. Rev. Lett.* **69**, 466 (1992)
5. D.W. Snoke, Y.S. Raptis, and K. Syassen, *Phys. Rev B* **45(24)** 14419(1992)
6. M.N. Regueiro, P. Monceau, A. Rassat, P. Bernier and A. Zahab, *Nature* **354**, 289 (1991).
7. C. S. Yoo and W. J. Nellis, *Science* **254**, 1489 (1991)
8. Y. Huang, D. F. R. Gilson, and I. S. Butler, *J. Phys. Chem.* **95**, 5723 (1991)
9. D. D. Klug, J. A. Howard, and D. A. Wilkinson, *Chem. Phys. Lett.* **188**, 168 (1992)
10. S. Tolbert, P. Alivisatos, H. Lorenzana, M. Kruger and R. Jeanloz, *Chem. Phys. Letters* **188**, 163 (1991)
11. Y.S. Raptis, D.W. Snoke, K. Syassen, S. Roth, P. Bernier, and A. Zahab, *Proc. 24th Annual Sci. Meeting of European High Pressure (Thessaloniki, Oct 24-26, 1991)*
12. R.S. Ruoff and A.L. Ruoff, *Nature (London)* **350**, 663 (1991)
13. M.N. Regueiro, P. Monceau, and J.L. Hodeau, *Nature* **355**, 237 (1992)
14. Y.Z. Ma, G.T. Zou, H.B. Yang, and J.F. Meng, *Appl. Phys. Lett.* **65(7)**, 822 (1994)
15. G. Bocquillon, C. Bogicevic, C. Fabre, and Rassat *J. Phys. Chem.* **97** 12924 (1993)
16. Y. Iwasa, T. Arima, and R.M. Fleming, et al. *Science* **264** 1570(1994)
17. J.E. Fischer *Science* **264** 1548(1994)
18. C.S. Sundar, A. Bharathi, Y. Hariharan, V. S. Sastry, and T.S. Radhakrishnan *Solid. State Comm.* **84(8)** 823(1992)

# EXPERIMENTAL STUDY OF THE HARDNESS AND ELECTRIC CONDUCTIVITY OF SUPERHARD BULK SAMPLES CREATED FROM SOLID C<sub>60</sub> UNDER PRESSURE UP TO 13 GPa AND TEMPERATURE UP TO 1830K

V.D.BIANK, S.G.BUGA, G.A.DUBITSKIY, M.YU.POPOV, N.R.SEREBRYANAYA

"Superhard materials" scientific and technical research center, 142092, Troitsk, Moscow reg., Russia

## ABSTRACT

Physical properties of the wide range of new metastable carbon structures recently synthesized from C<sub>60</sub> fullerite are investigated experimentally. Their hardness, strength and firmness in oxidizers found to be close to diamond. At least one of new phases is harder than diamond. Energy gap and resistivity of semiconductor phases are determined. Metal-type conductivity is revealed in some amorphous samples.

## Introduction

Physical properties of the new fullerite metastable phases obtained by us and described in [1,2] attract great interest due to predicted anomalous stiffness of C<sub>60</sub> molecule and opportunity of the formation of covalent bonds between the molecule cages in the high-pressure phases of this substance [3,4]. Until now only soft metastable phases of C<sub>60</sub> fullerite were obtained in macroscopic quantities under pressure up to 5 GPa and high temperature [5,6]. Using of special high-pressure (up to 13 GPa) and high-temperature (up to 1830 K) technique allowed us synthesize a row of superhard (harder of cubic BN) and even ultrahard (harder of diamond) bulk samples of stable under ambient conditions carbon phases with the different crystal and amorphous structures [2]. Great quantities of the new materials let us carry out experimental study of their properties. In this paper some results of the mechanical and electric tests of the synthesized materials are described.

## Samples

The dimensions of the samples synthesized from pristine pure f.c.c. C<sub>60</sub> were up to 4 mm in diameter and 4 mm in height. The experiments were performed on the tungsten carbide anvil chambers - shear chamber with the Bridgman-type anvils [7] and "toroid" type chamber [8] under nonhydrostatic pressure conditions.

X-ray study of the crystal structure of samples obtained revealed that the majority of them are not homogeneous and their powder diffraction patterns contain broad bands as well as the thin lines, attributed to the cubic and hexagonal structures with different

parameters [2]. On the fig.1 presented is the P-T map of the synthesized samples (point symbols) and P-T-regions of the most homogeneous quenched states.

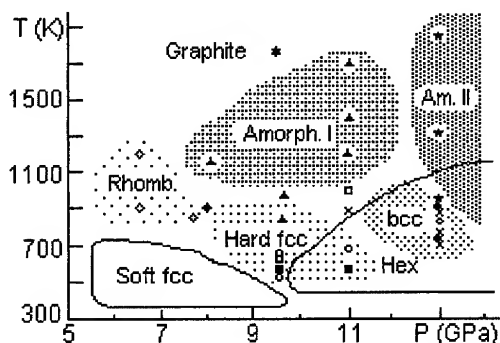


Fig.1. P-T-regions of synthesis of the different most homogeneous C<sub>60</sub> fullerite states. Circular, triangle and the other symbols mark the experimental points and denote different structure types. The notations *Amorph.I*; *Am.II*; *Hex* specify amorphous I, amorphous II and hexagonal structure types of the samples.

There were no indications of the strongest diamond line at 2.06 Å *d*-spacing, in our samples. These data and particular specific weights of the samples (Table 1 adopted from [2]), as well as Raman data [2] prove that they don't contain diamonds and their components can't be related to any already known carbon polymorphs. More detailed data about the conditions of the phase transitions of C<sub>60</sub>, and structure of the phases are given in [2].

## Hardness

All the samples exhibit anomalous hardness - they easily scratch tungsten carbide alloy,

Table 1. The number of the sample  $No$ , hardness  $H$  by the Moos scale, the cubic parameter  $a$  or the name of the structure, the measured specific weight  $\rho_{exp}$  (in  $g/cm^3$ ), the energy gap  $E_g$ , and the resistivity  $r$  of  $C_{60}$  after the heat treatment at temperature  $T$  under pressure  $P$  (symbol "s.c." means semiconductor type conductivity; "SD"-shear deformation; "-"no data).

$No$	$P(GPa)$	$T(K)$	$H$	$a(A)$	$\rho_{exp}$	$E_g(eV)$	$r(Ohm \cdot cm)$
1	8	1200	>9.5	aI	2.05	metal	0.03
2	9.5	620	>9.5	13.3	2.01	s.c.	-
3	9.5	650	>9.5	12.98	2.10	s.c.	-
5	9.5	700	$\approx 10$	12.6+hex	2.25	0.015	1÷10
6	9.5	520+SD	$\approx 10$	hex+aI	2.8	s.c.	-
7	9.5	750	$\approx 10$	aI	2.65	0.35	1÷10
8	9.5	800	$\approx 10$	aI	2.9	metal	0.03
9	9.5	900	$\approx 10$	hex+aI	2.95	0.3	1÷10
10	11	820	>9.5	13.4+bcc	-	s.c.	-
11	11	1400	$\approx 10$	aI	2.25	metal	0.02
12	13	900	>10	12.4+bcc+aII	2.95	s.c.	-
13	13	1270	>10	12.4+bcc+aII	3.3	0.2	$10^5$
14	13	1830	>10	aII	3.3	s.c.	> $10^5$

sapphire and even cubic BN (until now only diamond was known to be harder of it). The ordinary methods of measurement of hardness by indentation of diamond tip (Knoop method) could not be used, because diamond tip didn't produce traces on the polished surface of the hard bulk samples. Attempts to use the modified atomic-force microscope applied for the measurement of hardness by the tiny diamond thorn got failure too. By means of shear experiment in the diamond anvil cell we got the evidence that hardness of the samples obtained may exceed those of diamond. When the part of the hard sample No 5 (Table 1) was used as the specimen in the shear cell we produced traces of plastic deformation on the working surface of the diamond anvil under average pressure in the cell 2-3 GPa. That means, that at least one of the structural components of the sample is harder than plane diamond (100).

Direct proof that hardness of new fullerite material by the Moos scale exceeds hardness of diamond was obtained by mechanical cutting of the plane (111) of natural diamond with the sharp edge of the sample No.12. The most hard diamonds surface was scratched without high-pressure technique, we just took the sample by hand and move it on the diamond surface with the force of 1-3 kg. The area of the contact was  $10^{-4} cm^2$  approximately. Thus the average value of pressure at the contact point was 1-3 GPa. So, this simple but convincing test of the hardness shows that we need to expand the

range of the Moos scale beyond the magnitude of 10 attributed to diamond. We gave more attention to the methods of measurement of hardness and to results in work [2].

### Specific weights

Specific weights of the samples were calculated after measurements of their volumes (by weighting in a distilled water) and weights. The obtained values of densities cover wide range from 2,05 to 3,3  $g/cm^3$ .

### Firmness

The strength of new materials and its temperature dependence is the other important physical and technological properties. Tests of strength of hard fullerite grains were done by standard method using the grains of the following sizes: 400/315  $\mu$  and 500/400  $\mu$ . Strength of the grains of new fullerenes is higher of the strength of synthetic diamond "ballas" type grains and corresponds to the range of the values characteristic to the grains of "carbonado"-type synthetic diamond. After the annealing of the grains in a vacuum  $5 \times 10^{-5}$  Torr during half of an hour under 1200K their firmness reduced approximately on 25% what is a really good technical parameter.

Chemical firmness of the samples was tested by boiling in a mixture of HCl and HNO<sub>3</sub> acids during 2 hours. No changes of mass of the

samples were observed, i.e. the obtained materials are highly chemically inertial.

### Conductivity and energy gap

Last columns of the table presents the values of resistivity and of energy gap  $E_g$  of the samples calculated from the temperature dependence data of resistance at the range 177-370K. Two curves are shown on the Fig.2 for example.

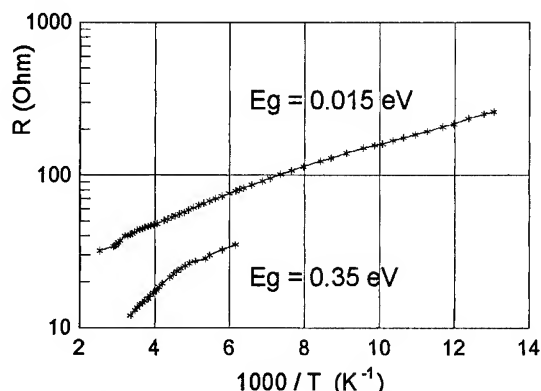


Fig.2. Resistance of the samples No. 5 and 7 depending on reciprocal temperature.

The resistance of the samples with high conductivity was measured by 4-wires method with the use silver paste or gallium contacts. Resistance of the low conductive samples was measured with silver paste contacts under low (few Volts) voltage. Metal type conductivity or more precisely - semimetal type like it is in graphite, was registered by low resistivity and very weak dependence of it on temperature. The resistance of these samples was increased monotonically on 2-5% under cooling from 300 to 100 K, but heating to the starting value caused farther growth of the resistivity on few percents more. Perhaps not perfect quality of the gallium contacts was the reason of some experimental error. But this error does not alternate the conclusion about the graphite-like type of conductivity. This is a very interesting result, that the amorphous I samples with the specific weights 2.05, 2.25 and 2.9 g/cm<sup>3</sup> have metal type conductivity, but sample No. 7 with the similar by X-ray data structure and 2.65 g/cm<sup>3</sup> specific weight is a typical semiconductor as well as the other crystal and amorphous II studied phases. We suppose that this peculiarity may be caused by a particular short-range order of this specific amorphous I state. One more sample - namely sample No.5, is distinctive by

its very narrow energy gap. The value 0.015 eV probably presents the characteristic property of the most dense f.c.c. structure.

All the samples look black, glancing, but thin plates cleaved from the most dense samples are slightly transparent and their color is yellow-brown, very similar to the color of the transparent phase, obtained in the Shear DAC [1].

### Conclusion

The results presented here supplement our previous research at room temperature[1] and confirm theoretical predictions of [3,4] about the anomalous stiffness of fullerite with the covalent bonds between C<sub>60</sub> molecules. To determine the value of the hardness of ultrahard fullerites new experimental methods of measurements should be designed.

Although an opportunity of the semiconductor-metal transition in C<sub>60</sub> fullerite was discussed earlier (see [9] for example) we confirmed this transition experimentally for the first time. The combination of good semiconductor or semimetal properties, extreme hardness and firmness will be useful for the future application of the new family of carbon materials.

### References

1. V. D.Blank, S.G. Buga, M.Yu.Popov et al, *Phys.Lett.A* **188** (1994) 281.
2. V.D.Blank, S.G. Buga, N.R.Serebryanaya et al, *Phys.Lett.A* **205** (1995) 208
3. R.S.Ruoff, A.L.Ruoff, *Nature* **350** (1991)663.
4. Y.Wang, D.Tomanek and G.F. Bertsch, *Phys.Rev.* **44** (1991) 6562.
5. Y.Iwasa, T.Arima, R.M.Fleming et al., *Science*, **264** (1994) 1570.
6. I.O. Bashkin, V.I.Rashchupkin, A.F. Gurov et al., *J.Phys. Condens. Matter* **6** (1994) 7491.
7. V.V.Aksenonkov, V.D.Blank et al., *Fizika Metallov i Metallovedenie (in Russian)* **57** (1993) 394.
8. N.N.Kuzin, A.A.Semerchan and N.N.Skasyrskaya, *Doklady Akademii Nayk USSR (in Russian)* **286** (1986) 1391.
9. M. Nunez-Regueiro, P.Monceau, A.Rassat, P.Bernier and A.Zahab. *Letters to Nature*. **354** (1991) 289.



## THE STRUCTURAL PECULIARITIES OF C<sub>60</sub> AFTER HIGH PRESSURE AND TEMPERATURE TREATMENT

V.D.BLANK, B.A.KULNITSKIY

*Institute of Spectroscopy, Russian Academy of Sciences  
Troitsk, Moscow region, 142092, Russia*

YE.V.TATYANIN

*Institute of High Pressure Physics, Russian Academy of Sciences  
Troitsk, Moscow region, 142092, Russia*

### ABSTRACT

The present study is concerned with X-ray and Transmission Electron Microscopy investigations of C<sub>60</sub>-samples after nonhydrostatic compression up to 13 GPa and heating up to 1050K. The X-ray powder diffraction data resulted in appearance of amorphous and new crystalline states. The shifted diffusion peak position when high pressure applied increases corresponds to changing of d-value from 0.335 nm to 0.314 nm. These diffractive patterns could be correlated with chains of equally oriented molecules. By TEM analysis the new fcc-structure ( $a=1.29\pm0.01$  nm) and the distorted fcc-lattice with rhombohedral structure ( $a=1.30\pm0.01$  nm,  $\alpha=87^\circ$ ) were identified. The growth of pressure and temperature gave rise to the structure near the cubic lattice with parameter  $a=1.17$  nm.

The significant interest over fundamental properties of C<sub>60</sub>-fullerite has been generated since its discovery. Among the interesting peculiarities of this material after high pressure treatment there are the mechanical properties comparable to natural diamond [1,2]. Phase transition in C<sub>60</sub> under pressure have been studied by many investigators. Two polymorphous transformations have been discovered under pressure up to 5 GPa and at temperature 1100K [3]. Three structural transitions in solid C<sub>60</sub> after nonhydrostatic compression up to 40 GPa and shear deformation were observed in [2]. At the same time it was shown in [4] that high pressure treatment up to 20 GPa at the temperature 300K leads to break-up of C<sub>60</sub>-molecules and appearance of diamond structure. The present work was undertaken to study C<sub>60</sub>-samples after nonhydrostatic compression at pressure about 13 GPa and temperature up to 1050K. The purity of initial samples (not less than 99% of C<sub>60</sub>) has been controlled by the different scanning calorimetry method. X-ray phase analysis was carried out by HZG-4A-diffractometer, CuK $\alpha$ -radiation. Transmission

electron microscopy (TEM) and electron diffraction techniques have been employed in the present investigation to study the details of the phase transformations. TEM images were obtained from a JEM-100C instrument. According to TEM-data the thermobaric treatment resulted in appearance of amorphous and new crystalline states in solid C<sub>60</sub>. The more interesting changes were revealed after 650K heating. It should be noted that as a rule two haloes at  $4.5\text{nm}^{-1}$  and  $8.3\text{nm}^{-1}$  are always presented on diffraction pattern (DP). These haloes are the same as the ones in amorphous carbon. Except the above noted haloes diffusion ring is exhibited near to (002) reflection, the most intensive reflection of the graphite structure. The following heating of samples up to 1250K in vacuum did not change this DP. Thus, the new structure state of carbon remains by the high temperature heating which destroys the C<sub>60</sub> molecules as it was shown earlier [3]. The more accurate definition of the diffusion ring position was carried out by using of Cu-standard (Cu was precipitated on substrate at the high-temperature heating). It was shown that this value is equal to  $0.336\pm$

0.005nm. For all the samples treated by high pressure up to 95 GPa corresponded diffusion peak was observed in room temperature X-ray powder diffraction. The position of this diffusion ring was found to be  $0.333 \pm 0.001$ nm. We found the displacement of this broadened peak position to the greater  $\theta$ -angles when the pressure applied increased up to 13 GPa in temperature range from 750K to 1050K. The shifted peak position corresponds to changing of d-value from 0.335nm to 0.314nm. It is known that  $d_{002}$  of different kinds of graphite structures can vary from 0.339nm to 0.345nm. The observed shifting can be explained by the appearance of aggregates of linear-polymerized molecules of  $C_{60}$ . We consider three possible orientations between two molecules: side to side, pentagon to pentagon and hexagon to hexagon. The spacings between these elements in  $C_{60}$  molecule are to be calculated as:

0.668nm ( $d_{002}=0.334$ nm) for the two-fold axis,

0.636nm ( $d_{002}=0.318$ nm) for the five-fold axis and

0.620nm ( $d_{002}=0.310$ nm) for the three-fold axis.

The appearance of the chains of equally oriented molecules can be correlated with DP observed.

It was established that beside amorphous state  $C_{60}$ -specimens contain the crystal structures. The sequence of face-centered-cubic phases has been found by X-ray powder diffraction data for the specimens treated by 13 GPa in the temperature range from 800K to 1050K. The lattice parameter decreased from 1.417nm to 1.30nm when the applied high pressure increased. The fragments of the crystal structure have been observed by TEM after pressing up to 9.5 GPa and heating up to 750K. The growth of pressure to 13 GPa gave rise to the appearance of structure close to the cubic with parameter  $a=1.17$ nm. Some electron DP from these fragments were analogous to ones of initial fcc-structure. On the other hand the

evident change of lattice parameter has been observed. For more accurate definition of the arising crystal structure the different sections of the reciprocal lattice were examined by specimen tilting around the chosen crystallographic directions. The obtained DP and their changes during the tilting have been found to correspond to the fcc-structure. The lattice parameter of new fcc phase was defined to be as  $1.29 \pm 0.01$ nm by using the Au-standard (Fig 1).

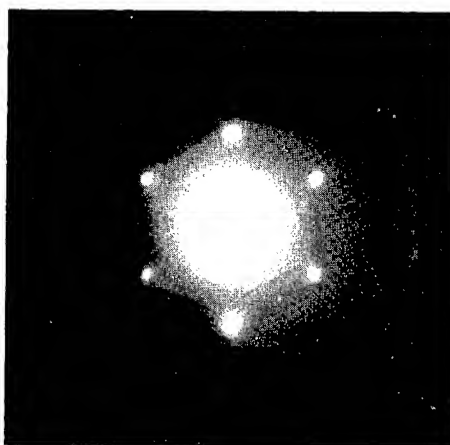


Fig.1. The joint diffraction pattern from the new crystalline structure and the Au- film.

In parallel with the fcc-structure we observed the distorted fcc-lattice. Sometimes it was possible to explain this distortion of fcc-structure by the appearance of rhombohedral structure with lattice parameter:  $a=1.30 \pm 0.01$ nm and  $\alpha=87^\circ$ . However not all the experimental DP with distortion could be described on the base of this approach. It is possible to explain the distortion appearance by the different contents of admixtures of oxygen and nitrogen or P-T conditions in the volume of sample. In the present study the new crystalline structure of  $C_{60}$  was found to be very stable by the heating up to 1100K in the vacuum with the heating rate about 70 degree/min. The further increase of temperature led to break-up of the crystal structure. This destruction in the electron DP corresponded to the appearance of the diffusion ring in the (002)-reflection area of the graphite

structures. The analogous diffusion ring has been never observed by the thermal destruction of the initial fcc-structure in our "in situ" experiments with the heating. In the last case the crystal structure degradation, concerned with the collapse of  $C_{60}$ -molecules, began by the appearance of diffuse rings in the region of the base reflections of the initial fcc-phase. The further heating led to disappearance of these reflections and appearance of two haloes of the amorphous carbon.

#### Conclusion:

The several new metastable phases of  $C_{60}$  were found after the thermobaric treatment upon the nonhydrostatic loading. First, three new crystal structures:

- 1) fcc-structure with  $a=1.29 \pm 0.01 \text{ nm}$ ;
- 2) rhombohedral structure:  $a=1.30 \pm 0.01 \text{ nm}$ ,  $\alpha=87^\circ$ .
- 3) structure with crystal lattice near cubic with parameter  $a=1.17 \text{ nm}$ .

Secondly, the production of X-ray-amorphous carbon structures based on linear -polymerized  $C_{60}$ -molecules corresponded axes 2, 5 and 3-fold with the diffuse reflection  $d=0.335\text{-}0.314 \text{ nm}$ . The formation of this structure is conducive to the strong strengthening. It is possible that the

polymerization of  $C_{60}$ -molecules under pressure above 5 GPa conditions takes place through the formation  $sp^3$ -bond between carbon-atoms. It is confirmed by the very high hardness of this new phases, which scratch easily the cubic BN and the natural diamond.

#### References:

1. V.Blank, M.Popov, S.Buga, V.Davydov, V.N.Denisov, A.N.Ivlev, B.N.Mavrin, V.Agafonov, R.Ceolin, H.Szwarc, A.Rassat, *Phys.Lett., A* **188**(1994), 281.
2. V.Blank, S.Buga, M.Popov, V.Davydov, B.Kulnitskiy, Ye.Tatyanin, V.Agafonov, R.Ceolin, H.Szwarc, A.Rassat, C.Fabre, *Mol. Mat.*, **4** (1994), 149.
3. Y.Iwasa, T.Arima, R.M.Fleming, T.Siegrist, O.Zhou, R.C.Haddon, L.J.Rothberg, K.B.Lyons, H.L.Carter Jr., A.F.Hebard, R.Tycko, G.Dabbagh, J.J.Krajewski, G.A.Thomas, T.Yagi, *Science*, **264** (1994), 1570.
4. M.Nunez-Regueiro, P.Monceau, J.L.Hodeau, *Nature*, **355** (1992), 237.
5. B.Sundqvist, O.Andersson, A.Lundin, A., Soldatov, Proc.XXX EHPRG, Brno, (1994), 109.

## RAMAN STUDY OF ULTRA- AND SUPERHARD PHASES OF C<sub>60</sub>

V.D.BLANK , S.G.BUGA , G.A. DUBITSKY

Scientific and technical Center "Superhard materials", Troitsk, Moscow Region, 142092  
Russia

V.N.DENISOV, A.N.IVLEV , B.N.MAVRIN , M.YU.POPOV

Institute of Spectroscopy of the Russian Academy of Sciences, Troitsk, Moscow Region,  
142092 Russia

### ABSTRACT

*Investigations of Raman spectra were carried out for fullerite after heat treatment up to 1830 K at 9.5 and 13 GPa nonhydrostatic pressure of bulk samples. Ultrahard forms of carbon have been obtained from C<sub>60</sub> at T = 570-1830 K. The hardness of the materials exceeded that of diamond. The Raman measurement has shown that the fullerene molecules C<sub>60</sub> remained in ultrahard state, but a gradual increase of disorder occurred to form a random network of linked molecules at high temperatures.*

Our earlier experimental study of solid C<sub>60</sub> in Shear Diamond Anvil Cell (SDAC) up to 40 GPa at room temperature [1,2], has shown, that due to the great shear deformations a transformation of fullerite into an ultrahard state was activated under pressure higher than 18 GPa.

In the present study bulk fullerite samples were obtained in tungsten carbide anvil chambers. We used a shear chamber with Bridgman-type anvils with 3 mm working surfaces and a "toroid" type chamber which enabled us to obtain the samples up to 4x4x3 mm<sup>3</sup> dimensions. Pure fullerite (C<sub>60</sub> - 99.98%, C<sub>60</sub>O - 0%, C<sub>70</sub> - 0%) was used.

The Raman spectra of fullerites after a treatment at 520 K and 9.5 GPa pressure has all features of that of the initial fullerite, only the frequencies of most bands were somewhat decreased and bands were broadened. Except bands of the initial fullerite, one can see also a 960 cm<sup>-1</sup> additional band. In principle, a weak maximum in the density of vibrational states (DVS) was observed in this region earlier [3]. Since other more intense maxima of DVS weren't seen, we don't think that the 960 cm<sup>-1</sup> band represents DVS.

A broadening and a low-frequency shift of the Raman bands at 520 K may be due to a formation of strong bonds between neighbouring molecules with a formation of cross-linked fullerenes ("polymerization" [2,4]) at high pressure when intermolecular distances

become comparable with intramolecular lengths of C-C bonds. The carbon atoms in the initial fullerite have only sp<sup>2</sup>-bonds. At polymerization sp<sup>2</sup>-bonds of the carbon atoms that form strong bonds with atoms of neighbouring molecules may be transformed into sp<sup>3</sup>-bonds [5]. In accordance with the simulation results [6] a low-frequency band shift may be interpreted as a consequence of the appearance of sp<sup>3</sup>-bonds that are formed in the polymerization process.

An additional band at 960 cm<sup>-1</sup> is located in a region which is characteristic for the four-membered carbon ring stretch [7]. If polymerization of the fullerene molecules may be imagined as 2+2 cycloaddition with a formation of four-membered carbon rings between molecules [5], then one can assign the additional band to a spectroscopic display of polymerization of the fullerene molecules. This assumption is consistent with the observation of the additional bands in the region at 950 cm<sup>-1</sup> in the Raman spectra of chain-polymerized fullerene molecules in RbC<sub>60</sub> [8].

A further broadening of the fullerite bands occurs with a temperature increase. The observation of these bands at 520, 570 and 620 K may give evidence to the existence of the fullerene molecules at least up to 620 K. However, a gradual change of relative band intensities occurs. At 620 K the peak intensity of the breathing mode of pentagons at ~1450 cm<sup>-1</sup> and the graphitelike mode at ~1550 cm<sup>-1</sup> are almost the same, although the intensity of the

graphitelike mode in the initial fullerite was smaller by a factor of five. The Raman bands of the initial fullerite at 1100, 1250, 1424 and 1468  $\text{cm}^{-1}$  and the 960  $\text{cm}^{-1}$  additional band are smeared and form one broad band at  $T > 600$  K. The band intensity at 273  $\text{cm}^{-1}$  decreases and with bands at 430 and 495  $\text{cm}^{-1}$  also originate one broad band at  $T > 600$  K.

It should be noted that fullerites after heating up to 520 - 620 K at the 9.5 GPa pressure showed the destruction threshold to be low enough under the laser radiation. For example, the focused exciting beam ( $F = 70$  mm) at the grazing incidence with power more than 3 - 5 mW transformed readily samples into a-C. At  $T > 620$  K the samples showed the high stability to laser radiation.

At the further increase of temperature (670 - 870 K) the Raman spectra contained only two visible bands: very broad low-frequency band at 200-800  $\text{cm}^{-1}$  and more intense asymmetrical band at 1550  $\text{cm}^{-1}$ . These spectra were similar to those that were obtained for state V of fullerite [2]. This enabled us to suppose a relationship of these structures. The low-frequency band at 200 - 800  $\text{cm}^{-1}$  showed some features in place of bands of the initial fullerite. Therefore, on the one hand, one can talk about the existence of the fullerene molecules also under this conditions, but, on the other hand, the smearing of the Raman bands gives evidence that the fullerene molecules in fullerites at 9.5 GPa and heating  $T > 620$  K probably aren't the characteristic structural elements because in this case molecules are covalently bonded to form a continuous three-dimensional random network. Therefore the Raman spectra become similar to those of the highly disordered carbon structures containing both  $\text{sp}^2$ - and  $\text{sp}^3$ -bonds.

Above 770 K a low-frequency shoulder of the 1550  $\text{cm}^{-1}$  band became intense that gave rise to an appearance of a doublet in the Raman spectra. One can suppose for this highly disordered fullerites that the Raman spectra should contain not only the Raman-active bands of the  $\text{C}_{60}$  molecule, but also the maxima of DVS and, in particular, the broad intense maximum near 1400  $\text{cm}^{-1}$ . Therefore the low-frequency shoulder of the 1550  $\text{cm}^{-1}$  band at 670 - 770 K and the appearance of a band near 1400  $\text{cm}^{-1}$  at  $T > 770$  K possibly represents DVS.

At 1770 K the Raman spectrum was close to that of microcrystalline graphite with sizes of grains about 50 Å [9]. Hence, the graphitization

of fullerite at the 9.5 GPa pressure occurred at  $T > 1300$  K.

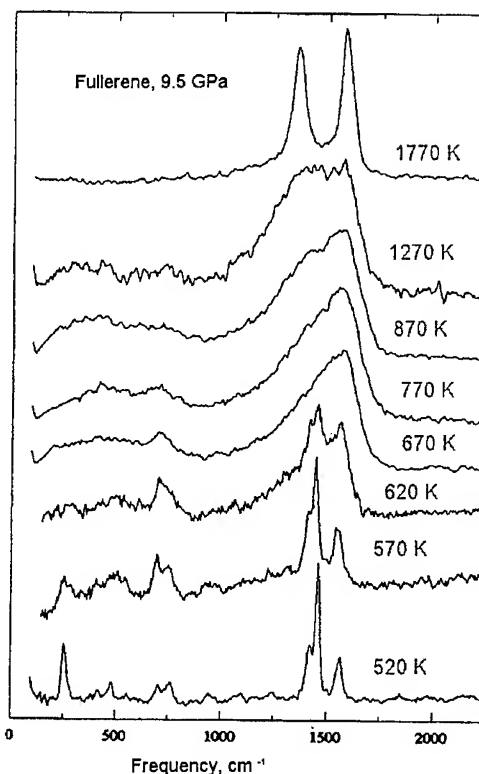


Fig.1. The Raman spectra of the fullerite after a heat treatment at the different temperatures under the 9.5 GPa pressure.

Let us discuss the temperature behaviour of the Raman bandwidths on the assumption that fullerite has the same structural phase in the temperature region 520 - 770 K. More definitive conclusions could be made only for the bandwidth of the graphitelike mode. The bandwidth of this mode increases with temperature at  $T < 700$  K from 37  $\text{cm}^{-1}$  to 135  $\text{cm}^{-1}$ . At the further increase of  $T$  the Raman bandwidth decreased slightly. It should be noted that the temperature increase of this band correlates with the growth of the angle width of the diffracted maxima in the X-ray spectra. We assign this broadening to an increase of the degree of the molecule linkage in fullerite. Assuming that a linkage is a random process, it follows from the general thermodynamic considerations that the concentration of defects in fullerite due to a linkage of molecules may be expressed by a simple Arrhenius law:

$$C = C_0 \exp(-V_0/RT), \quad (1)$$

where  $C_0$  is the concentration of defects at very high temperature,  $V_0$  is the activation energy of defects and  $R$  is gas constant. In this case the problem of the determination of the temperature dependence of the Raman bandwidth is similar to that of the reorientational motion of molecules. Then the temperature dependence of the Raman bandwidth may be represented as [10]

$$g = g_0 \exp(-V_0/RT), \quad (2)$$

where  $g_0$  is the measured Raman bandwidth. Eq.(2) enables one to find  $V_0$ , if we shall construct the temperature dependence of the measured bandwidths in the Arrhenius coordinates  $\ln(1/g) - 1/T$  at  $T < 700$  K. We can say only about the approximated estimation of this energy ((24 + 4) kJ/mol or  $\sim 0.24$  eV). We note that approximately such a gain of energy by dimerization of the fullerene molecules was found from the LDA analysis [11].

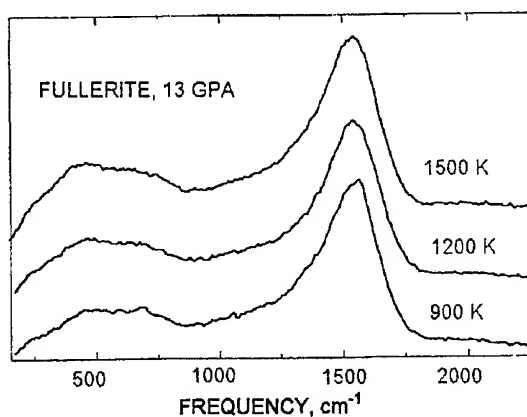


Fig.2. The Raman spectra of the fullerite after a heat treatment at the different temperatures under the 13 GPa pressure.

The heat treatment of fullerite at 13 GPa gave rise to a molecule linkage also, moreover the stability range of the random network of linked molecules in fullerite has essentially expanded. From Fig. 2 it is seen that the Raman spectra change slightly from 900 to 1500 K and these spectra are similar to those of fullerite after the heat treatment at 770 K under  $p = 9.5$  GPa.

From the Raman spectra we have found that a gradual linkage of the fullerene molecules occurs if fullerite is heated at high pressure. In the Raman spectra additional bands at  $960 \text{ cm}^{-1}$  appeared that may be assigned to breathing vibrations of four-membered rings of carbon atoms connecting neighbouring molecules. Probably fullerite becomes superhard at  $T > 620$

K due to the formation of  $sp^3$ -bonds between molecules. The activation energy of the formation of polymerized bonds ( $sp^3$ -bonds) is estimated as  $(24 + 4) \text{ kJ/mol}$ . Although the fullerene molecules exist up to 1270 K, however, at  $T > 620$  K they very likely aren't the characteristic structural elements of material because of the formation of a random network of the linked fullerene molecules.

## References

1. V.Blank, S.Buga, M.Popov et al. CNRS - INFO 275 (1993)9;  
V.Blank, S.Buga, M. Popov et al. *Mol. Mat.* 4 (1994) 149;  
V.Blank, S.Buga, M.Popov et al. *Zhurnal Tekhnicheskoi Fiziki (in Russian)* 8 (1994) 153.
2. V.Blank, M.Popov, S.Buga, V.Davydov, V.Denisov, A.Ivlev, B.Mavrin, V.Agafonov, R.Ceolin, Szwarc and A.Rassat, *Phys.Lett.* A188 (1994) 281.
3. R.L.Cappelletti, J.R.D.Copley, W.A.Kamitakahara F.Li, J.S.Lannin and D.Ramage, *Phys.Rev.Lett.* 66 (1991) 3261
4. H.Yamawaki, M.Yoshida, Y.Kakudate, S.Usaba, H.Yokoi, S.Fujiwara, K.Aoki, R.Ruoff, R.Malhotra and D.Lorents, *J.Phys.Chem.* 97 (1993) 11161.
5. A.M.Rao, P.Zhou, K.A.Wang, G.T.Hager, J.M.Holden, Y.Wang, W.T.Lee, X.-X.Bi, P.C.Ecklund, D.S.Cornett, M.A.Duncan and I.J.Amster, *Science* 259 (1993) 955.
6. D.Beeman, J.Silverman, R.Lynds and M.R.Anderson, *Phys.Rev.* B30 (1984) 870.
7. F.A.Miller, R.J. Capwell, R.C.Lord, D.E.Rea, *Spectrochim. Acta* A28 (1972) 603.
8. M.C.Martin, D.Koller, A.Rosenberg, C.Kandziora and L.Mihaly, *Phys.Rev.* B51 (1995) 3210.
9. P.Lespade, R.Al-Jishi and M.S.Dresselhaus, *Carbon* 20 (1982) 427.
10. M.M.Suschinskii. *Raman spectra of Molecules and crystals*(Nauka, Moscow, 1969)
11. M.R.Pederson and A.A.Quong, *Phys.Rev.Lett.* 74 (1995) 2319.

## PHYSICAL PROPERTIES OF PRESSURE POLYMERIZED C<sub>60</sub>

P-A. PERSSON<sup>1,2</sup>, U. EDLUND<sup>3</sup>, Å. FRANSSON<sup>2</sup>, A. INABA<sup>4</sup>, P. JACOBSSON<sup>1</sup>,  
D. JOHNELS<sup>3</sup>, C. MEINGAST<sup>5</sup>, A. SOLDATOV<sup>1</sup>, AND B. SUNDQVIST<sup>1</sup>

<sup>1</sup>*Department of Experimental Physics, Umeå University, S-90187 Umeå, Sweden*

<sup>2</sup>*Department of Applied Physics and Electronics, Umeå University, S-90187 Umeå, Sweden*

<sup>3</sup>*Department of Organic Chemistry, Umeå University, S-90187 Umeå, Sweden*

<sup>4</sup>*Department of Chemistry, Faculty of Science, Osaka University, Toyonaka, Osaka 560, Japan*

<sup>5</sup>*Forschungszentrum Karlsruhe, INFP, PO 3640, D-76021 Karlsruhe, Germany*

### ABSTRACT

The properties of C<sub>60</sub> have been studied after treatment at high temperature and high pressure (1.1 GPa and 565 K for 2 h). The treated material is insoluble in organic solvents. We present results obtained in NMR and Raman studies and measured data for the specific heat and the thermal expansion. Our results show clearly that there are no covalent intermolecular bonds and no molecular rotation, but suggest that the molecules are slightly deformed and held together by weak  $\pi$ -type bonds.

### Introduction

A number of recent studies have indicated that C<sub>60</sub> can be polymerized by radiation (1) or the application of high pressure  $p$  and high temperature  $T$  (2-4). Thermal treatment of alkali metal, A, doped AC<sub>60</sub> gives either a polymer (5) or a dimer (6), and even superconducting A<sub>3</sub>C<sub>60</sub> can be polymerized under pressure (7). Although "normal" pure C<sub>60</sub> can be dissolved in a number of organic liquids the polymerized forms are insoluble, indicating that the molecules are held together by forces stronger than the van der Waals-type interactions of the original material. We have recently treated C<sub>60</sub> under the conditions given by Bashkin et al. (3,4), and made extensive studies of the properties of the resulting material. We report here experimental data for the specific heat capacity  $c_p$  and the thermal expansivity  $\alpha$ , as well as the results of NMR and Raman studies. Although the treated material is insoluble in organic liquids we find no trace of covalent bonds between the individual molecules.

### High pressure treatment

The C<sub>60</sub> specimens were placed in thin-walled stainless steel cylinders and treated at high  $T$  and  $p$  in a 45 mm piston-and-cylinder device equipped with internal heating. The sample containers were surrounded by NaCl powder acting as a semihydrostatic pressure medium. Various  $p$ - $T$  conditions

were tested in the range indicated by Bashkin et al. (3,4). The most homogeneous material was obtained using  $T \approx 565$  K at a pressure of 1.1 GPa for about 2 h. After treatment, the specimens were cooled to room temperature before decreasing the pressure. The resulting material was insoluble in both toluene and the significantly better solvent 1,2-dichlorobenzene. When shorter reaction times were used, some unreacted material was usually present as indicated by a slight coloration on immersion in 1,2-dichlorobenzene (but not toluene). X-ray studies of the treated material gave results in very good agreement with those of Bashkin et al. (4) and indicated a lattice volume reduction of 3.4 - 5.0 % at 295 K compared to normal C<sub>60</sub>. However, the measured density after treatment was 1.683 g cm<sup>-3</sup>, only about 1 % higher than for pristine C<sub>60</sub>, possibly indicating a small amount of pressure amorphization as often observed for C<sub>60</sub>.

### Thermal properties

The specific heat capacity was measured both in Umeå using differential scanning calorimetry (DSC) and in Osaka using adiabatic calorimetry with intermittent heating. The DSC results shown in Fig. 1 show no rotational transition at 260 K in the pressure treated material, and we conclude that the molecules no longer rotate. On heating a large peak is observed above 500 K, and in subsequent runs on the same sample we obtain data typical for

pristine  $C_{60}$  verifying that the material reverts to "normal"  $C_{60}$  on heating. Low-T data obtained by adiabatic calorimetry are shown in Fig. 2. The upper trace shows data for pristine  $C_{60}$  while the lower trace is for high pressure treated material.  $c_p$  differs little between the two states except at very low temperatures and near 250 K. The low-T results can be fitted to a model with a Debye term, corresponding to interatomic vibrations, plus one or more Einstein peaks corresponding to intramolecular ones. The fitted Debye temperatures are 41 K for pristine  $C_{60}$  and 54 K for the pressure treated material, showing that the intermolecular bonds are much stronger in the latter.

The linear thermal expansivity  $\alpha$  was measured vs T in Karlsruhe on a sample which unfortunately contained a small fraction of unreacted  $C_{60}$ . As shown in Fig. 3, these measurements showed no trace of any glassy crystal transition near 90 K, although the unreacted fraction gave rise to a small anomaly near 250 K. For the pressure treated material  $\alpha$  was also significantly smaller than for pristine  $C_{60}$ , again suggesting that the intermolecular bonds have changed their character.

### NMR and Raman data

NMR has previously been used to study  $RbC_{60}$  (8) and pure  $C_{60}$  (2), both pressure polymerized at significantly higher p and T than used here. In both cases the single narrow line at 144 ppm typical for pristine  $C_{60}$  broadened significantly and moved towards smaller shifts, about 125 ppm (2) and 110 ppm (8), respectively. In addition, in both cases new peaks appeared indicating the existence of several inequivalent carbon sites and thus the presence of covalent intermolecular bonds.

For our specimens, on the other hand, magic angle spinning  $^{13}C$  NMR at 100.48 MHz and both 11.9 T and 2.3 T showed a single, broad line, probably a badly resolved multiplet, still centered on the value 144 ppm typical for pristine  $C_{60}$ . No trace was found of any other signals, such as the 55 ppm signals indicating covalent bonding found in Ref. (8). Since the broadening of the 144 ppm line is also much less than that observed for other  $C_{60}$ -based polymers we conclude that treatment under the conditions used here does *not* result in the formation of covalent intermolecular bonds in  $C_{60}$ .

The material was also characterized by Raman scattering, using a near IR (1064 nm) Nd-YAG

laser as a light source to avoid photopolymerization (1) or photoinduced oxidation of the specimens. We show in Fig. 4 a Raman spectrum of pressure treated  $C_{60}$ . In comparison with data for pristine material there is a large number of additional

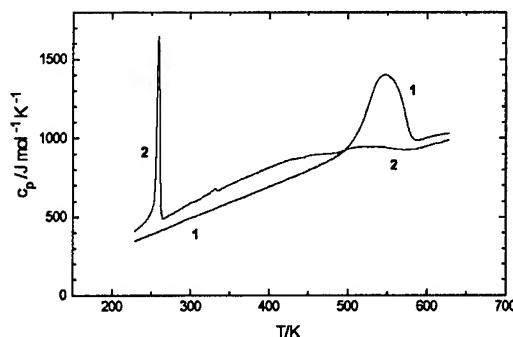


Fig. 1. Specific heat of pressure treated  $C_{60}$ . 1: first heating, 2: second run.

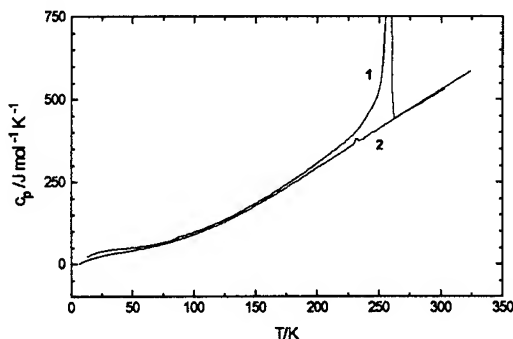


Fig. 2. Specific heat vs T. Curve 1: pristine  $C_{60}$ , curve 2: pressure treated  $C_{60}$ .

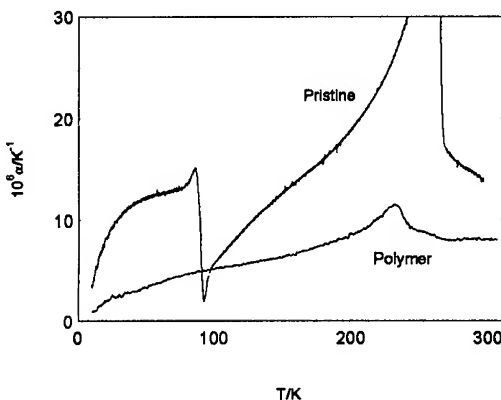


Fig. 3. Linear thermal expansivity  $\alpha$  of  $C_{60}$ . Upper curve: pristine  $C_{60}$ , lower curve: pressure treated material.



peaks, indicating that the symmetry has been broken by distortion of the molecule or strong intermolecular interactions. In particular, two new peaks appearing in the low frequency region indicate the presence of new bonds between adjacent molecules, stronger than the normal (van der Waals type) interactions in pristine  $C_{60}$ .

Fig. 5 shows on an enlarged scale the region near the well known  $1469\text{ cm}^{-1}$  pentagonal pinch mode, which shifts to  $1458\text{ cm}^{-1}$  on photopolymerization and also during pressure treatment. In addition, an intermediate peak often appears at

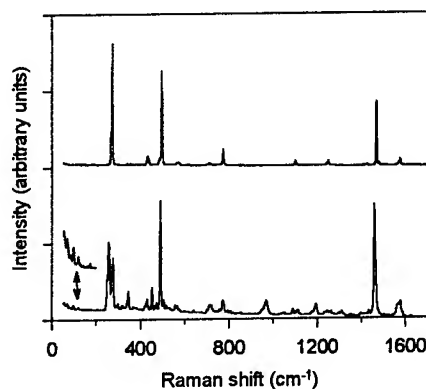


Fig. 4. Raman spectra of  $C_{60}$ . Upper spectrum: Pristine  $C_{60}$ , lower spectrum: pressure treated  $C_{60}$ .

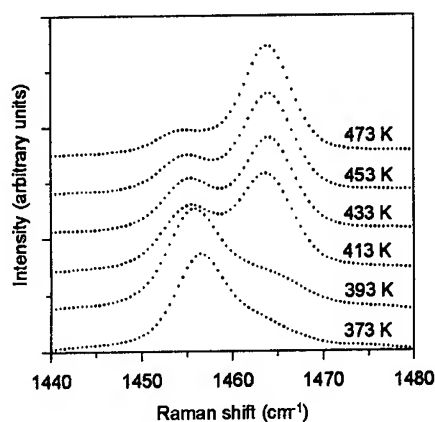


Fig. 5. Raman spectra near the pentagonal pinch mode for pressure treated  $C_{60}$  at the temperatures indicated. Note that all peaks move towards smaller Raman shifts as  $T$  increases.

$1463\text{ cm}^{-1}$  in our material. The spectra shown were measured while gradually increasing the temperature of the material in small steps. The "polymer" peaks gradually disappear with increasing  $T$  and between 500 and 600 K, depending on initial treatment conditions, the specimen reverts to normal  $C_{60}$  as also observed in the DSC study of  $c_p$ .

## Conclusions

Our NMR results clearly show that there are no covalent bonds between the molecules in nominally "polymerized"  $C_{60}$ , treated under the comparatively gentle conditions used here. This material is the simplest modification in a series of polymerized  $C_{60}$  phases (2-4,9-11) obtainable at high pressures, and material treated under more severe conditions clearly show evidence for covalent bonding (2). However, our Raman data indicate a significant amount of molecular distortion and the results for  $c_p$  and  $\alpha$  indicate a stronger intermolecular interaction than in pristine  $C_{60}$ . All these results seem to agree with the recent model of Kozlov and Yakushi (9) in which molecules are assumed to be packed densely enough to be slightly deformed by nearest-neighbour interactions and probably held together by weak graphite-like  $\pi$  bond interactions between slightly flattened areas of neighbouring molecules.

## References

1. A.M. Rao et al., *Science* **259** (1993) 955.
2. Y. Iwasa et al., *Science* **264** (1994) 1570.
3. I.O. Bashkin et al., *Pis'ma Zh. Eksp. Teor. Fiz.* **59** (1994) 258; *JETP Lett.* **59** (1994) 279.
4. I.O. Bashkin et al., *J. Phys.: Condens. Matter* **6** (1994) 7491.
5. P.W. Stephens et al., *Nature* **370** (1994) 636.
6. Q. Zhu, D.E. Cox and J.E. Fischer, *Phys. Rev. B* **51** (1995) 3966.
7. Q. Zhu, *Phys. Rev. B* **52** (1995) R723.
8. T. Kälber, G. Zimmer and M. Mehring, *Z. Phys. B* **97** (1995) 1.
9. M.E. Kozlov and K. Yakushi, *J. Phys.: Condens. Matter* **7** (1995) L209.
10. M. Núñez-Regueiro et al., *Phys. Rev. Lett.* **74** (1995) 278.
11. V.D. Blank, B.A. Kulnitskiy and Ye.V. Tatyagin, *Phys. Lett. A* **204** (1995) 151.

## C<sub>60</sub>-POLYMORPHOUS TRANSFORMATIONS AT 300 - 1800 K UP TO 13 GPa

N.R. SEREBRYANAYA, V.D. BLANK, G.A. DUBITSKIY, S.G. BUGA, V.V. AKSENENKOV,  
M.YU. POPOV

*Institute of Spectroscopy of RAS, 142092 Troitsk, Moscow region, Russia*

### ABSTRACT

Superhard and ultrahard phases have been obtained by quenching C<sub>60</sub> from  $P > 8$  GPa and  $T > 673$  K with a special pressure-transmitting medium in a "toroid"-chamber. It was found two types of structure for hard material: 1) fcc- and bcc-crystalline structures and 2) disordered (amorphous like) structures.

### Introduction

Earlier [1] it was shown that a superhard state of C<sub>60</sub> fullerite, comparable with natural diamond, was observed by shear deformation apparatus (SDAC) at high pressure up to 37 GPa and besides it was shown that the C<sub>60</sub>-molecule was not destroyed. The size of these samples was: the diameter 100  $\mu$ m, height 20  $\mu$ m. The shear deformation effects on the kinetics of high pressure phase transitions should be noted; the hysteresis of the transition is decreasing. It was known that the enhancement of temperature is decreasing the hysteresis also. Our preliminary study of the effect of heating up to 250° C on the phase transformations in solid C<sub>60</sub> in SDAC revealed, that creation of an ultrahard state of C<sub>60</sub> starts under much lower value of pressure than 18 GPa (room temperature [1]) - namely at 12 GPa.

Considering the superhard state of C<sub>60</sub> obtained at room temperature under shear deformation and non-hydrostatic conditions, in this report we have a goal to obtain bulk superhard samples using high temperature and to study crystal structures of this samples.

### Experimental

The bulk samples were obtained under non-hydrostatic conditions using the "toroid"-type of chamber [2]. Non-hydrostatic pressure conditions and thus great values of deformation were obtained by a special choice of the pressure-transmitting medium in the chamber. Experiments were carried out in the 6.5-13 GPa pressure interval and the temperature interval: 300-1800 K.

We have used a X-ray powder diffraction method with photoregistration of diffraction pattern, CuK $\alpha$  and CoK $\alpha$ -radiation and a stan-

dard Debye camera with 114 mm. For better accuracy of measurements we have used also X-ray diffractometer HZG-4a.

### Results and discussion

We used the original fullerite C<sub>60</sub> with cubical parameter  $a=14.17$  Å. The (200) reflex is absent. Having soft phases at pressures  $< 9$  GPa, we used higher pressure for obtaining more dense and hard phases. There are several series of samples: at  $P=6.5$  GPa, 8 GPa, 11 GPa and 13 GPa and different temperatures - from 300 K to 1800 K. The results for the samples are shown on Figure 1. Samples for X-ray study are taken from different parts of bulk quenched samples because of the heterogeneity effect.

Samples, quenched from  $T < 650$  K, crystallize in fcc-structure. At this temperature interval the (200)-reflex is appearing and it is getting stronger with increasing synthesis temperature. It is necessary to note that two phases with cubic parameters 12.6 Å and 13.6 Å (Fig.1) have the same structures as the phases, obtained in other conditions earlier [3-5]. The rhombohedral phase, reported in [3,4] was found at  $P < 8$  GPa and at temperatures up to 1100 K. Our cubic phases, quenched from  $P > 8$  GPa, are not returning to original pristine at heating up to 1300 K.

We have found an inverse dependence of the cubic parameter  $a$  on temperature and a decrease of the unit-cell volume at increasing synthesis temperature. It is observed an increase of the intensity ratio  $I_{(200)}/I_{(111)}$  in accordance with the alternation of the form factor from a reduction of the unit-cell parameter [5].

Fig.1 shows a bend at  $T > 570$  K, after which the volume is sharply decreasing. This bend is a border between soft and hard phases. The borderline crystal structure has an unit-cell para-

meter  $a=13.6\text{\AA}$ . The diffraction lines are getting more broad and diffusive and their quantity are decreasing with increasing temperature. According to diffraction patterns cubic structure remains up to 700 K at 9.5 GPa and 1000 K at 13 GPa. Therefore we suppose that the  $C_{60}$  molecules do not collapse at these temperatures and the intermolecular C-C distances are decreased from 2.97 Å (300 K) to 1.86 Å.

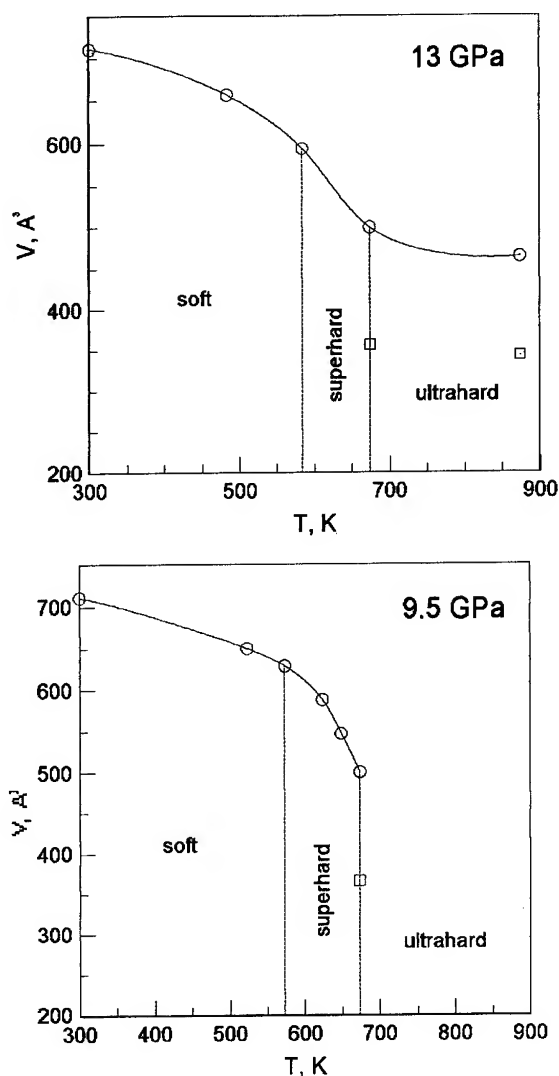


Fig.1. The temperature dependence of the unit-cell volume of  $C_{60}$ -samples quenched from different temperatures at 9.5 GPa and 13 GPa. Circles are measured data,  $\square$  - bcc-phase.

The samples, obtained above 800 K (9.5 GPa) and 1000 K (13 GPa) have a totally disorga-

nized crystal structure. Broad diffusive maximas are observed at the pattern. This diffraction picture can be conceived as disordered hexagonal layers, because the strongest maximum is close to (002)-graphite. There are no (hkl) reflexes in this diffraction pattern. Parameters of a hexagonal layer structure:  $a=2.38 - 2.42\text{\AA}$ ,  $c=6.5 - 6.2\text{\AA}$ , are much less than for turbostratic graphite. The broad line (002) is decreasing with a temperature enhancement, it has a value about 3.13 Å at 1300 K. Probably, fullerite molecules are stopping the rotation, "freezing" into orientationally disordered state. The superhardness of high-temperature samples is likely to be associated with the original value of 3-fold (6.19 Å) and 5-fold (6.46 Å) diameters of  $C_{60}$ -molecule into the formation of a hexagonal parameter  $c$  or the interlayer distances. Diffraction patterns of samples, obtained at 1770 K, have corresponded to the structure of turbostratic graphite.

At  $T > 800\text{ K}$  new diffraction lines with interplanar spacings 4.15 Å, 3.74 Å, 3.36 Å and some others were found. The cubic structure is totally disordered in these samples. These lines are getting strongest in samples, obtained by using the shear high pressure chamber with tungsten carbide anvils at 9.5 GPa and 523 K. The diffraction picture is close to cubic with  $a=11.75\text{\AA}$ , and the best indexing is in a hexagonal system with unit-cell parameters:  $a=11.44\text{\AA}$ ,  $c=8.33\text{\AA}$ ,  $Z=3$ . The crystal structure will be published elsewhere.

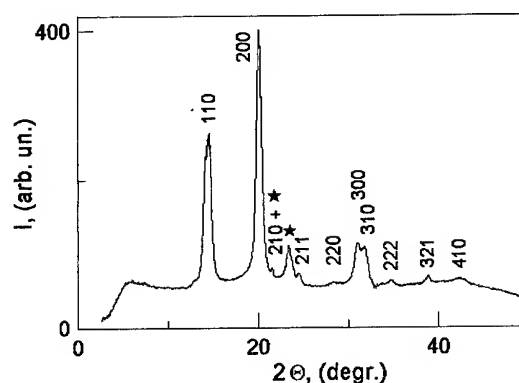


Fig 2. The diffraction pattern of bcc-structure at 13 GPa and 673 K ( $\text{CuK}\alpha$ -radiation). \* - hexagonal phase.

At 13 GPa and the temperature interval 800-1850 K (Fig.1) it was found that the enhance-

ment of pressure is favourable for a retention of the fcc-structure up to a more high temperature (1000 K). At temperatures above 673 K the diffraction pattern is different, the strongest lines are (200), (220) but (111) is disappearing. The new diffraction picture has been indexed in a bcc-type of structure (Fig.2). This structure type for the densest phase of  $C_{60}$  was theoretically proposed earlier [6]. The cubic diffraction patterns are getting broad and diffusive at increasing temperature. The disordered structure is formed at  $T > 1300\text{K}$ . The strongest halo is located in the 2.1 Å region of interplanar spacings, while at 9.5 GPa there was a strongest halo in the 3.1-3.3 Å region. It is a region of diamond strongest line 2.06 Å, but the halo is displaced to smaller angles of  $\Theta$ .

The peculiarities of our superhard and ultrahard samples are the strongest halos at 3.1 Å (superhard) and 2.1 Å (ultrahard) and the detection of fcc-phases and the densest crystalline phase with bcc-structure.

## References

1. V.D. Blank, M. Popov, S. Buga et al., *Phys. Lett. A* **188** (1994) 281.
2. N. Kuzin, A.A.Semerchan, N.N.Skassyrskaya et al., *Doklady Akademii Nauk USSR (in Russian)* **286** (1986) 1391.
3. Y. Iwasa, T. Arima, R.M. Fleming et al., *Science* **264** (1994) 1570.
4. M. Nunez-Regueiro, L. Maques, J-L. Hodeau et al., *Phys. Rev. Lett.* **74** (1995) 278.
5. S.J. Duclos, K. Brister, R. Haddon et al., *Nature* **351** (1991) 380.
6. M. O'Keeffe, *Nature* **352** (1991) 674.

## **VII(F) Metals and Intermetallics**

# ELECTRONIC PROPERTIES OF SOLIDS UNDER PRESSURE

N. E. CHRISTENSEN

*Institute of Physics and Astronomy, University of Aarhus, DK-8000 Aarhus C, Denmark*

First-principles density-functional calculations are used to predict structural and vibrational properties of solids under pressure. As examples we discuss various phases of tin, in particular the bct structure that is stable between 100 and 500 kbar. Elastic properties of Mo are calculated for pressures up to  $\sim 15$  Mbar and used in model calculations of the pressure strengthened yield stress. In this way we show why pressures of several megabars may be achieved in diamond anvil cells with Mo gaskets. Finally we discuss the structures of III-V nitrides as well as phonon frequencies in crystals under pressure.

## 1 Introduction

The present paper presents examples of theoretical studies of structural, electronic and vibrational properties of solids under pressure. The numerical results are obtained by means of first-principles total energies derived within the density-functional theory. In most cases, the one-electron equation is solved by means of the Linear Muffin Tin Orbital (LMTO) method<sup>1,2</sup>. We discuss results obtained for metals (tin, molybdenum, and tungsten) as well as semiconductors (III-V nitrides). Tin is chosen because it is an elemental metal that nevertheless has interesting structural properties. For example, it exhibits, at ambient pressure, the well-known transition from 'white tin' ( $\beta$ -Sn) to 'gray tin' ( $\alpha$ -Sn) upon cooling below  $13^\circ\text{C}$ .

The  $\alpha$ -form has an equilibrium volume which is 20% larger than that of  $\beta$ -Sn, and the transition is thus often rather damaging ('tin plague'). At very high pressures the stable structure of Sn appears to be the bcc, but  $\beta$ -Sn does not transform directly to this structure as pressure is increased. In the range 95-400 kbar Sn prefers a body-centered tetragonal (bct) structure with a large  $c/a$  ratio. This may seem puzzling but we shall see that a simple explanation is obtained from the band structure alone.

Whereas the calculations predict the high-pressure phase of Sn in bcc, we find to our surprise that this is not the case for Mo and W. They indeed assume, from 0 up to  $\sim 6$  Mbar, the bcc structure, but our results suggest that above 6 Mbar the bcc cannot be stable for these metals. We calculate structural energies and elastic properties up to very high pressures ( $> 11$  Mbar). One purpose of this is to demonstrate how 'pressure strengthening' increases the yield strength<sup>3</sup>.

The results show why a static pressure of several megabars can be reached in a diamond anvil cell using a Mo gasket although its yield strength at zero pressure is only 0.04 Mb.

The structures of bulk semiconductors have been studied extensively experimentally as well as by theoretical means. Here, as examples, we shall discuss recent results for III-V nitrides (AlN, GaN, InN, BN) because they have interesting possible applications in optoelectronic devices. We present calculations of optical spectra, phonon frequencies and structural parameters as functions of applied pressure. Predictions of pressure coefficients of impurity levels by means of Greens function calculations are presented in a separate contribution<sup>4</sup> to this conference.

## 2 Tin

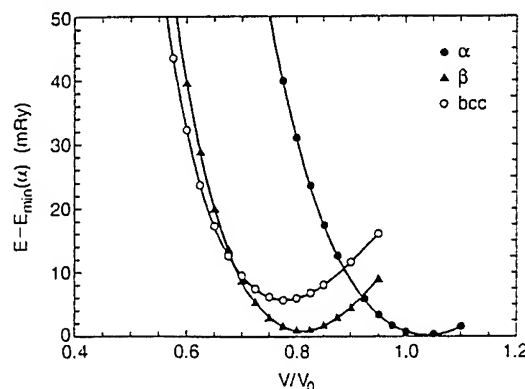


Figure 1: Total energies (per atom) as functions of volume (per atom) calculated by means of the full-potential LMTO method for  $\alpha$ -,  $\beta$ -, and bcc-Sn.  $V_0$  is the observed equilibrium volume for  $\alpha$ -Sn.

Figure 1 shows the total energies as calculated<sup>5</sup> by means of the full-potential (FP) LMTO method

for tin in three structures, bcc, diamond type ( $\alpha$ ) and  $\beta$ -Sn. The  $\alpha$ -Sn has the lowest minimum energy, but only a very small external pressure is needed to cause the transition to the  $\beta$  form.

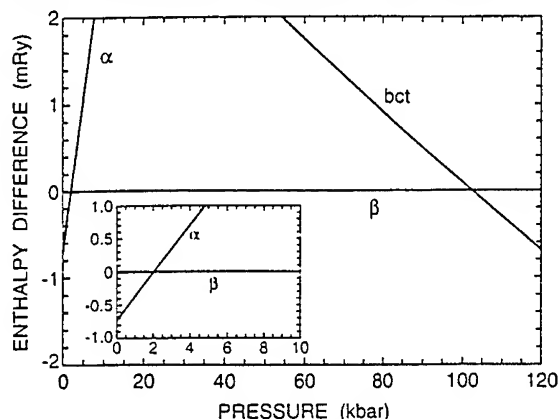


Figure 2: Enthalpies for  $\alpha$ -,  $\beta$ -, bct-Sn (bcc) vs (theoretical) pressure. The  $\beta$  phase is taken as a reference. The insert shows the regime close to  $P = 0$  on an expanded scale.

This is more clearly seen in Fig. 2 where the theoretical enthalpies of  $\alpha$ -Sn,  $\beta$ -Sn and bct Sn are shown as functions of pressure. The same figure also shows that  $\beta$ -Sn transforms to the bct structure close to 100 kbar. This agrees well with experiments<sup>6</sup>. The experiment further demonstrated that the bct structure is stable up to  $\sim 500$  kbar. Above this pressure Sn should assume the bcc structure. The existence of the bct structure with a large  $c/a$  ratio ( $\sim 0.90$ ) seemed surprising and we have tried to understand this peculiarity.

First we notice (see Fig. 3) that the full density functional calculation of total energies clearly predicts the stability of the bct structure with  $c/a \sim 0.91$  in the pressure range mentioned, and also that a first-order transition to the bcc phase occurs at high pressure. Thus, the numbers come out right, but "what is the physics?" - Why does tin not transform directly into the bcc structure? The explanation is simple. The stability of the bct phase is caused by a particular feature of the band-structure; i.e., it can be understood from the one-electron energies alone. Figures 4 and 5 show the band structure of Sn in the bcc and bct structures, respectively. The bcc state labeled  $H_{15}$  at the  $Z$ -point ( $H$  in bcc) is a triply degenerate  $p$ -state located just below the Fermi level in bcc-Sn. A tetragonal strain along (001) (bcc  $\rightarrow$  bct transformation) splits this level into the doubly degene-

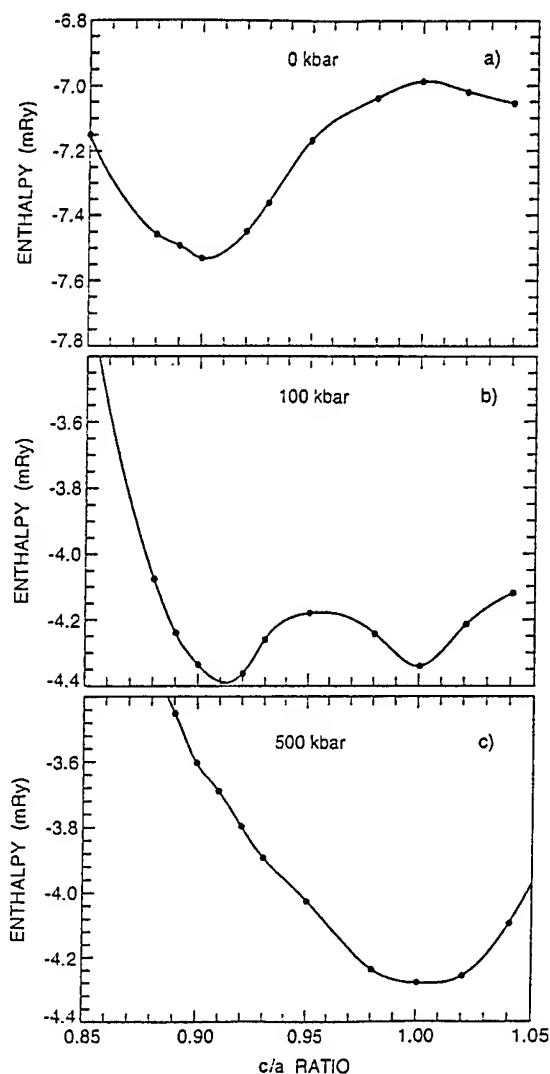


Figure 3: BCT-Sn. Enthalpy vs. axial ratio,  $c/a$ , at various pressures,  $P$ . (a)  $P = 0$ ; (b) 100 kbar; (c) 500 kbar

rate ( $p_x, p_y$ ) and the  $p_z$  state. The latter moves above  $E_F$  by  $\Delta E(z) \equiv E_z^{bct} - E_F^{bct}$ , and is therefore empty in the bct case (Fig. 5). The splitting also causes the center of gravity of the level to move by:

$$\Delta E_{xyz}^{av} = (2E_{xy}^{bct} + E_z^{bct} - 3E_{xy}^{bcc}) / 3, \quad (1)$$

and the Fermi level is slightly shifted ( $\Delta E_F$ ). Thus, in a crude model where we only consider the change in the  $H_{15}$  state, we could estimate the bct-bcc total energy difference from where  $n$

### 3 Molybdenum and Tungsten

$$\begin{aligned}\Delta E &= E(bct) - E(bcc) \\ &= n(3\Delta E_{xyz}^{au} - (E_z^{bct} - E_F^{bct}) + \Delta E_F/2)\end{aligned}\quad (2)$$

is the number of electrons that are shifted above  $E_F$  with  $E_z^{bct}$  and subsequently relaxed to the Fermi surface.

The various contributions to  $\Delta E$  in Eq.(2) are shown as functions of  $c/a$  in Figs. 6a and b for a 'low' and a 'high' pressure, respectively<sup>8</sup>. It follows that the stability of the bct structure, as well as the numerical value of  $c/a$ , including, in fact, its volume dependence, are given by this simple model. Also, the almost volume-independent  $\Delta E(z)$  function ensures that, as long as Sn is in the bct structure, its  $c/a$  ratio cannot exceed  $\approx 0.95$ . Thus, upon transition to bcc, a finite jump in  $c/a$  must occur. The transition is of first order.

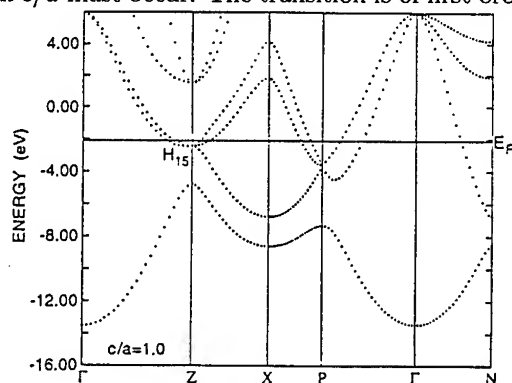


Figure 4: Band structure of tin in the bct structure with  $c/a = 1.0$ , i.e. the cubic (bcc) structure. The point Z is in this case the H point of the bcc zone.

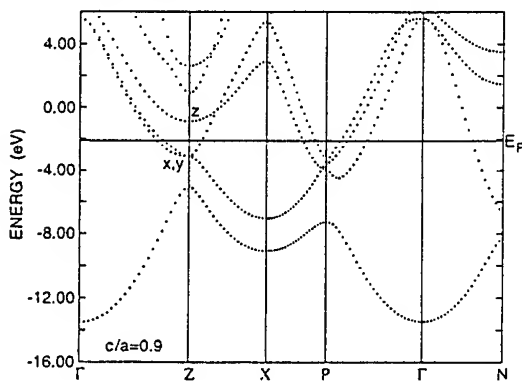


Figure 5: As Fig. 4, but for  $c/a = 0.90$ .  $H_{15}$  has been split into (x, y) (below  $E_F$ ) and z (above  $E_F$ ).

Total energies were calculated for Mo and W for up to 60% volume compression for bcc, fcc, hcp, dhcp and  $\omega$ -type structures. From these results, and the calculated pressures, we derived structural enthalpy differences, as functions of pressure, and Fig. 7 shows the results for W. It follows that for W the bcc structure cannot be stable above  $\sim 6$  Mbar. Similar conclusions apply to Mo. The  $\omega$  phase may be viewed as an  $L(\frac{2}{3}, \frac{2}{3}, \frac{2}{3})$  phonon-mode distortion with two lattice planes in the hexagonal representation of bcc being collapsed.

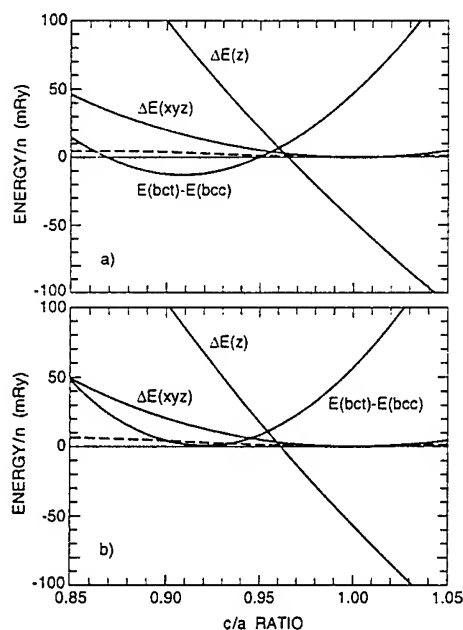


Figure 6: Structural bct-bcc energy difference,  $E(bct) - E(bcc)$ , as functions of the axial  $c/a$  ratio, per electron transferred due to the tetragonal splitting of  $H_{15}$ . The individual contributions are defined in the text; the dashed line is  $\Delta E_F$ ,  $\Delta E(z)$  the energy of the  $p_z$  level at Z minus the Fermi energy, and  $\Delta E(xyz)$  is the strain-induced shift in the center-of-gravity of the  $p_x, p_y$  and  $p_z$  levels at Z (multiplied by 3). (a) refers to the "low pressure", whereas, b is for the "high pressure".

Calling the displacement of the relevant planes  $d$ , we can continuously change the structure from bcc to  $\omega$ . The energy variation is shown in Fig. 8 for  $V = 0.40 \times V_0$ ,  $V_0$  being the equilibrium volume. Clearly the  $\omega$ -phase has a higher energy.

In Figs. 9a and b we show the calculated elastic shear constants for Mo (bcc). The trigonal constant,  $C_{44}$ , hardens when pressure is applied,



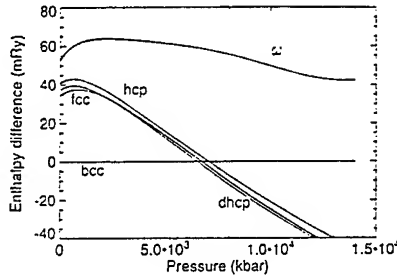


Figure 7: Calculated enthalpy of tungsten relative to bcc-W.

whereas the tetragonal shear constant starts to decrease at extreme pressures. This is, however, after the structural phase transition. The fcc results, down to  $V/V_0 = 0.40$ , do not exhibit a similar softening.

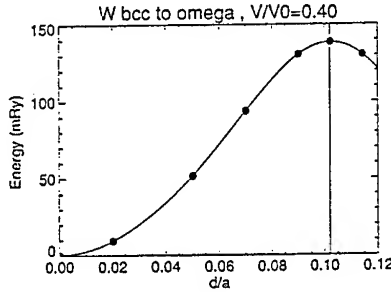


Figure 8: Compressed tungsten. Bcc  $\rightarrow$   $\omega$  (bcc for  $d = 0$ ) transformation in  $L(\frac{2}{3}, \frac{2}{3}, \frac{2}{3})$  mode.

These results are then used<sup>9</sup> with the variational method of Hashin and Shtrikman<sup>10</sup> to compute the shear modulus  $G(P)$  and the Poisson ratio,  $\nu(P)$ , of polycrystalline Mo. These are then further used to calculate the pressure dependent yield stress according to<sup>1</sup>

$$\sigma_0(P) = \sigma_0(0) [G(P)(1 - \nu(0)) / G(0)(1 - \nu(P))] . \quad (3)$$

At  $P = 6$  Mb we find  $\sigma_0(P)/\sigma_0(0) \simeq 4.53$ , i.e., the yield stress has been increased substantially.

With a gasket thickness  $h$  separating the diamond faces (assumed parallel), the pressure gradient in the cell is given<sup>12</sup> by

$$\frac{dP}{dr} = -\frac{\sigma_0(P)}{h} . \quad (4)$$

This can be integrated numerically, and with an

assumed maximum pressure of 6 Mb, we find (choosing  $\sigma_0(0) = 0.04$  Mb) that  $h = 2.6 \mu\text{m}$ . It is thus shown that a Mo gasket of this final thickness can support  $\sim 6$  Mb as a result of pressure strengthening.

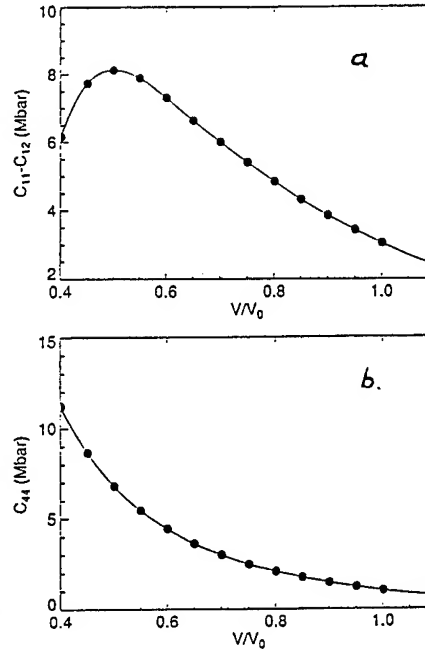


Figure 9: Calculated elastic constants of Mo versus volume.

#### 4 III-V Nitrides

The nitride semiconductors, AlN, GaN, InN, and BN were studied<sup>13,14,15</sup>. Several structures were examined, and among these the rocksalt structure appears to be the high-pressure phase in all four cases. The wurtzite structure has internal parameters,  $u$  ( $c$ -axis bond-length parameter) and  $c/a$ , that depend on pressure. In the theoretical study they must therefore be optimized at each volume<sup>14</sup>. The ideal wurtzite structure corresponds to all bond lengths being equal, and for  $c/a = \sqrt{8/3}$  this yields  $u = 3/8$ . For AlN, however, we find<sup>14</sup> the equilibrium values (at  $P = 0$ )  $c/a = 1.596$  and  $u = 0.3820$ . The experimental<sup>16</sup> values are 1.501 and 0.3821, respectively. Since the direct gaps depend on these structural parameters<sup>14</sup>, their optimization is also important for calculation of the difference between the gaps in the cubic (zinc-blende) and hexagonal phases.

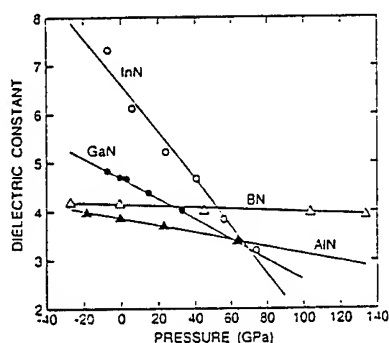


Figure 10: Pressure dependence of  $\epsilon(0)$  for the III-V nitrides in the wurtzite structure.

The compounds AlN and GaN have very similar bond lengths and ionicities, and it was therefore somewhat surprising to us,<sup>15</sup> that the wurtzite-rocksalt transition pressures, 51.8 GPa for GaN and 16.6 GPa for AlN, differ by a factor of three. Analysis of partial pressures showed<sup>15</sup> that the Ga-3d states in GaN are responsible for the much higher transition pressure in that compound.

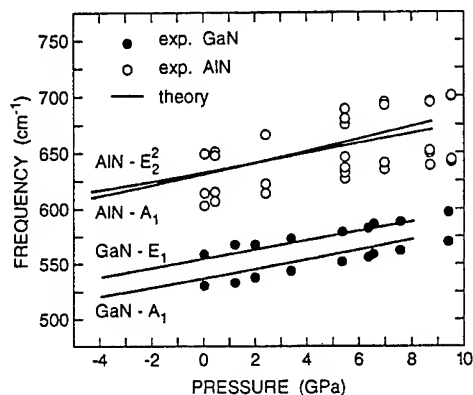


Figure 11: Optical zone-center phonon frequencies for the wurtzite structure (high-frequency modes) as functions of hydrostatic pressure. Calculated values (solid lines) are compared with experimental data (open and filled circles) obtained by Perlin *et al.* [(Ref. 18), AlN (Ref. 19)]

The optical properties of the nitrides under pressure are discussed in<sup>15</sup>. These calculations also yield the pressure dependence of the dielectric constant (Fig.10). As a final example of calculated pressure effects in solids we<sup>17</sup> consider optical zone-center phonon modes in GaN and AlN zincblende as well as wurtzite structures. The calculation of the TO-phonon frequencies in the cubic structure is simple, whereas the mode decoupling requires the calculation of a dynamical ma-

trix in the case of wurtzite structures. Here we just present some of the results (Fig.11). It is seen that the frequencies as well as their pressure dependence agree well with experiments.<sup>18,19</sup>

## References

1. O. K. Andersen, Phys. Rev. B12, 3060 (1975)
2. M. Methfessel, Phys. Rev. B38, 1537 (1988)
3. K. S. Chan, T. L. Huang, T. A. Grzybowski, T. J. Whetten, and A. L. Ruoff, J. Appl. Phys. 53, 6607 (1982).
4. I. Gorczyca, A. Svane, and N. E. Christensen, p. xxx of these proceedings.
5. N. E. Christensen and M. Methfessel, Phys. Rev. B48, 5797 (1993)
6. H. Olijnyk and W. B. Holzapfel, J. Physique (Paris) Colloq. 45, Suppl. 11, C8-153 (1984)
7. N. E. Christensen, Solid State Commun. 85, 151 (1993)
8. In fact the model has been slightly refined by taking into account that a small pocket of states move along with  $E_z^{bct}$  (see<sup>7</sup>).
9. N. E. Christensen, A. L. Ruoff, and C. O. Rodriguez, Phys. Rev. B (1995 in print).
10. Z. Hashin and S. Shtrikman, J. Mech. Phys. Solids 10, 343 (1962)
11. J. O. Chua and A. L. Ruoff, J. Appl. Phys. 46, 4659 (1975)
12. A. L. Ruoff, H. Xia and Q. Xia, Rev. Sci. Instrum. 63, 4342 (1992)
13. P. Perlin, I. Gorczyca, N. E. Christensen, T. Suski, H. Teisseyre, and I. Grzegory, Phys. Rev. B45, 13307(1992)
14. N. E. Christensen and I. Gorczyca, Phys. Rev. B47, 4307 (1993)
15. N. E. Christensen and I. Gorczyca, Phys. Rev. B50, 4397 (1994)
16. H. Schulz and K. Thiemann, Solid State Commun. 23, 815 (1977)
17. I. Gorczyca, N. E. Christensen, E. L. Peltzer y Blancá, and C. O. Rodriguez, Phys. Rev. B51, 11936 (1995)
18. P. Perlin, C. Jamberthie-Cavillon, J. P. Itie, A. San Miguel, I. Grzegory, and A. Polian, Phys. Rev. B45, 83 (1992)
19. P. Perlin, A. Polian, and T. Suski, Phys. Rev. B47, 2874 (1993)

# PRESSURE DERIVATIVE OF BULK MODULUS OF METALS FROM A UNIFORM INTERSTITIAL ELECTRON GAS MODEL

N. Suresh, Satish C. Gupta and S.K. Sikka

*High Pressure Physics Division, Bhabha Atomic Research Centre, Bombay 400 085, India.*

A relation for the pressure derivative of the bulk modulus ( $K'_0$ ) of the metallic solids has been derived employing the interstitial electron gas model. It is shown that it simulates well the trends in the experimental values of  $K'_0$  for elements.

## 1 Introduction

Current *ab initio* band structure methods, based on the density functional theories coupled with local density approximation provide capabilities not only for accurate computations of the equation of state, phonon frequencies and other ground state properties of materials,<sup>1,2</sup> but also for calculations of the small Gibbs energy differences between different crystal structures for phase stability analysis.<sup>3</sup> However, for understanding the trends in the physical properties, it is highly desirable to develop simple models involving only a few parameters. Several workers have related the so-called electron gas model to the bulk modulus and elastic constants of metals. Moruzzi, Janak and Williams<sup>4</sup> calculated the bulk modulus up to 4-d transition metals and found that it is a function of the electron density in the interstitial region (the region outside the muffin-tin sphere). Recently, Rose and Shore<sup>5,6</sup> have shown that the cohesive energies and the elastic constants of metals also primarily depend on this electron density. In the present paper, we have extended this interstitial electron gas model for the pressure derivative of the bulk modulus.

## 2 Formalism

Many different analytical forms of equation of state (EOS) of solids have been developed by various workers. Most of these forms involve two parameters, bulk modulus  $K_0$  and its pressure derivative  $K'_0$  at zero pressure; in fact these parameters are generally determined by fitting the experimental isotherm to one of the forms. Among these, the empirical EOS suggested by Holzapfel<sup>7</sup> appears to be attractive, as at extreme compressions it approaches the correct Fermi gas limit. In the zeroth order approximation, it has the follow-

ing form,

$$P = P_{FG0} x^{-5} (1 - x) \exp[-cx]$$

where  $P_{FG0} = a_{FG}(Z/V_0)^{5/3}$ ,  $x = (V/V_0)^{1/3}$ , and  $V$  and  $V_0$  are volume per atom at pressure  $P$  and at 0.1 MPa respectively.  $c = \ln(P_{FG0}/3K_0)$  with  $a_{FG} = 2.3366 \times 10^{-2} \text{ GPa}(nm)^5$ , and  $Z$  is the atomic number.

$K'_0$  is related to  $K_0$  through the Fermi gas pressure  $P_{FG0}$  as

$$K'_0 = 3 + \frac{3}{2} \ln(P_{FG0}/3K_0) \quad (1)$$

In the framework of the uniform interstitial electron gas model, the bulk modulus of a metallic solids  $K_0$  scales as  $r_s^{-5}$ , provided the electron density parameter  $r_s$  is determined from the electron density in the interstitial region.<sup>4</sup> In terms of the bonding valence  $Z_B$ , defined as the product of this interstitial electron density and the volume per atom at ambient conditions, the  $K_0$  has the following dependence,

$$K_0 \sim G(Z_B/V_0)^5$$

Invoking this dependence in Eq.1, we obtain

$$K'_0 = A + B \ln(Z/Z_B) \quad (2)$$

where  $A$  and  $B$  are constants not dependent on the nature of a given material.

## 3 Comparison With Experimental Data

In figure 1, we plot the experimental values of  $K'_0$  against  $\ln(Z/Z_B)$  for 26 elements for which data are available. The values of  $K'_0$  and  $Z_B$  used for the plot are listed in Table 1. The  $K'_0$  values are mainly taken from the compilations by Steinberg<sup>9</sup> and by Clark<sup>10</sup>, and are based on the ultrasonic

Table 1: Experimental values of pressure derivative of bulk modulus<sup>9,10</sup> and calculated values of bonding valence.<sup>5</sup>

Element	Atomic number	Bonding valence	$K'_0$ experimental
Li	3	1.09	3.52
Be	4	1.99	4.60
Mg	12	2.08	3.90
Al	13	2.76	4.85
			3.95
			5.19
K	19	1.21	3.96
			4.07
V	23	3.45	4.26
Cr	24	3.53	4.89
Fe	26	3.32	5.29
			5.30
			6.0
Co	27	3.09	4.26
Ni	28	2.83	5.26
Cu	29	2.57	5.48
			3.91
			5.59
Zn	30	2.40	6.40
Nb	41	4.14	4.06
Mo	42	4.42	4.50
			4.70
Rh	45	3.67	4.50
Pd	46	3.15	5.42
Ag	47	2.70	6.12
			5.87
Cd	48	2.48	6.48
In	49	2.51	6.00
Ta	73	4.51	3.79
W	74	4.79	4.33
			4.50
Ir	77	4.36	4.83
Pt	78	3.90	5.18
Au	79	3.26	6.29
			5.90
Tl	81	2.38	5.70
Pb	82	2.35	5.53
			5.45

measurements and shock wave data. It may be noted that the reported values of  $K'_0$  for the same element display a lot of scatter and may depend on whether these are measured from single crystals or polycrystalline materials. The values of the bonding valence used here are obtained from the work of Rose and Shore,<sup>5</sup> who computed these using the average interstitial electron densities determined from the detailed density functional calculations of Moruzzi et al.<sup>4</sup> and those of Segalas et al.<sup>8</sup>

Figure 1 clearly shows that, notwithstanding the large scatter in the experimental data, the measured values of  $K'_0$  are well simulated by relation 2. Thus, this equation provides a simple relationship between the pressure derivative of the bulk modulus and bonding valence. This has an important implication for the EOS of metals. Now, both its determining parameters  $K_0$  and  $K'_0$  are a function of a single fundamental property.

#### References

1. S.K. Sikka, B.K. Godwal and R. Chidambaram, in *High Pressure Shock Compression of Solids*, ed. L. Davison and M. Shahinpoor (Springer Verlag - under publication).
2. B.K. Godwal, S.K. Sikka and R. Chidambaram, *Phys. Rep.* **102**, 121 (1983).
3. Satish C. Gupta, Jyoti M. Daswani, S.K. Sikka and R. Chidambaram, *Current Science* **65**, 399 (1993).
4. V.L. Moruzzi, J.F. Janak and A.R. Williams in *Calculated Electronic Properties of Metals*, (Pregamon, New York, 1978).
5. J.H. Rose and H.B. Shore, *Phys. Rev. B* **49**, 11588 (1994).
6. J.H. Rose and H.B. Shore, *Phys. Rev. B* **43**, 11605 (1991).
7. W.B. Holzapfel, *Europhys. Lett.* **16**, 67 (1991).
8. M. Sigalas, D.A. Papaconstantopolous and N.C. Bacalis, *Phys. Rev. B* **45**, 5777 (1992).
9. D.J. Steinberg, *J. Phys. Chem. Solids* **43**, 1173 (1982).
10. *Handbook of Physical Constants*, ed. Sydney P. Clark Jr., (The Geological society of America, New York, 1966, p124).

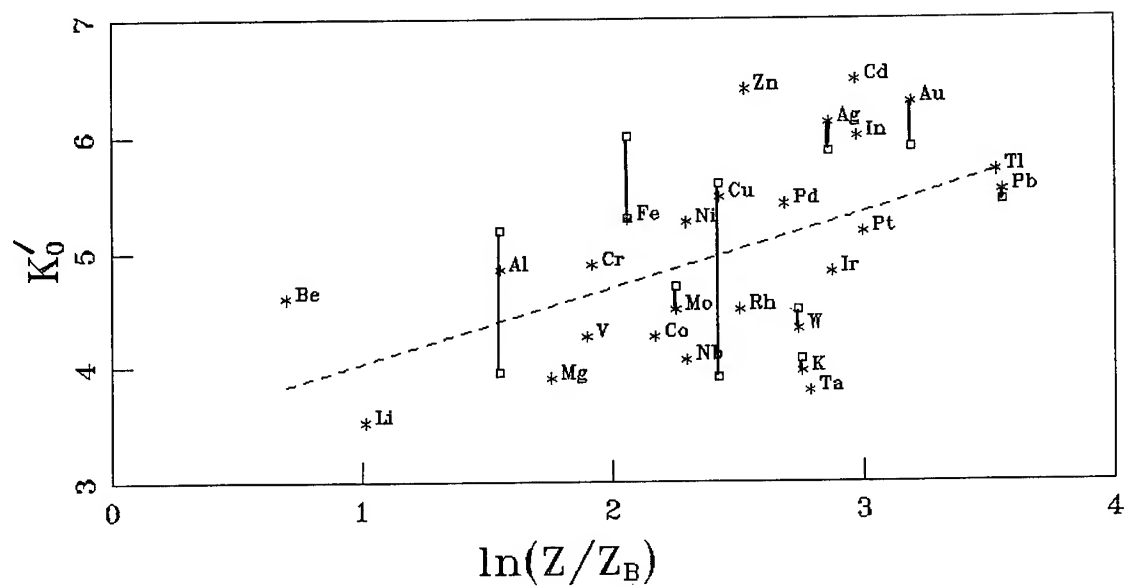


Figure 1: Measured pressure derivative of bulk modulus versus  $\ln(Z/Z_B)$ . Vertical lines display the range in the measured values for some elements. The dotted line indicates the best fit for the measured values.

## COMPRESSIBILITY AND MAGNETOVOLUME EFFECTS IN NOVEL R-Fe INTERMETALLICS

J. Kamarád, Z. Arnold, K.V. Kamenev\*, M.R. Ibarra<sup>§</sup>

*Institute of Physics, AV CR, Cukrovarnická 10, 162 00 Praha 6, Czech Republic*

*<sup>§</sup>Dpto. Física de la Materia Condensada-ICMA, Facultad de Ciencias, Universidad de Zaragoza-CSIC,  
50009 Zaragoza, Spain*

### ABSTRACT

To get better insight into the large magnetovolume effects in the novel Fe-rich rare earth intermetallics  $R(\text{FeTi})_{12}$ ,  $R_3(\text{FeTi})_{29}$  and  $R_2\text{Fe}_{17}$ , we have recently studied the pressure dependence of the Curie temperature  $T_C$ , the compressibility and the thermal expansion of these intermetallics in the pressure range up to 1.4 GPa. The observed pronounced pressure shift of  $T_C$  verified the high volume sensitivity of the strongest Fe-Fe exchange interaction, which is uniform ( $dT_C/d\ln V \sim 3100$  K) for all the studied intermetallics. The anomalous Invar-like temperature behaviour of the thermal expansion and the compressibility of these intermetallics has been observed nearby  $T_C$ .

### Introduction

The Fe-rich rare earth (R) intermetallic compounds belong to a family of materials with high magnetic moments per formula unit and with pronounced magnetic anisotropy. These properties are outstanding for permanent magnet applications. The complex magnetic behaviour of these intermetallic compounds is a consequence of the interplay of both the localized and the itinerant magnetic moments on R and Fe atoms, respectively.

The  $R(\text{FeTi})_{12}$ ,  $R_3(\text{FeTi})_{29}$  and  $R_2\text{Fe}_{17}$  compounds crystallise in the tetragonal (phase 1-12), monoclinic (phase 3-29), rhombohedral or hexagonal (phase 2-17 with light or heavy R, resp.) crystal structures [1, 2]. The Curie temperatures  $T_C$  of these intermetallics (as a critical temperature of the ferromagnetic ordering) are given by the strongest Fe-Fe exchange interaction and lie in the temperature range from 300 to 550 K. As a result of a competition of the magnetic anisotropies of the Fe- and R- sublattices, the spin reorientation transitions at the temperature  $T_{SR}$  (accompanied by a change of the easy magnetization direction) was detected in some intermetallics. The crystal electric field (CEF) and the exchange interactions are considered to be responsible for that magnetic behaviour.

Recently, an anomalous Invar-like behaviour of the thermal expansion of these intermetallics

has been observed under the normal pressure at temperatures near  $T_C$  [3]. The rather low  $T_C$  of the compounds was increased by introducing of interstitial atoms [4] and actually this has stimulated the pressure studies presented below. In spite of the volume changes evoked by the interstitial atoms, the effect of high pressure is not accompanied by extra electronic changes and thus the pressure experiments are very effective tools of the basic and the applied investigation of these compounds.

### Experimental

The polycrystalline samples of the  $\text{Nd}(\text{FeTi})_{12}$ ,  $R_3(\text{FeTi})_{29}$  ( $R = \text{Ce, Pr, Nd, Gd and Tb}$ ) and  $R_2\text{Fe}_{17}$  ( $R = \text{Y, Nd and Er}$ ) were prepared in an argon-arc furnace. They were annealed at 1370 K under argon atmosphere then water quenched and tested by X-ray diffraction analysis to confirm the presence of the noticed phases.

The pressure dependence of the Curie temperature  $T_C$  of the intermetallics was studied in the maraging steel pressure apparatus which consists of two parts. A pressure generator was connected by a water-cooled pressure capillary with a pressure cell placed in a furnace. The generator with the Manganin pressure sensor was kept at room temperature. The silicon oil has been used as a pressure transmitting medium at temperatures up to 600 K.

The initial susceptibility method was used for detection of the magnetic transition from the ferromagnetic to the paramagnetic state at the temperature  $T_C$  and for detection of the spin reorientation transition at  $T_{SR}$  under pressure. The direct measurements of the linear thermal expansion and of the compressibility of the studied intermetallics have been performed under the hydrostatic pressure up to 1.4 GPa using the foil micro-strain gages (Micro-Measurements Inc.). The details of the temperature and pressure calibration of the micro-strain gages are described within another contribution in this Conference [5].

### Results & Discussion

The temperature dependence of the initial susceptibility of the intermetallic  $Nd_3(FeTi)_{29}$  compound under different hydrostatic pressures is shown in Fig.1.

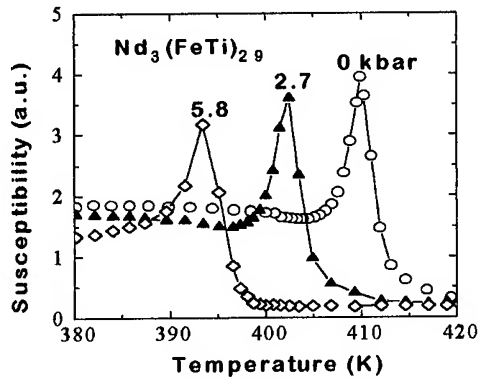


Fig.1: The initial susceptibility of  $Nd_3(FeTi)_{29}$  under pressure,  $T_C$  was determined as an inflexion point of the decreasing part of the  $\chi(T)$  curve.

The pronounced pressure decrease of  $T_C$  was indicated in all the studied intermetallics [6,7] and the observed values of  $T_C$  and  $dT_C / dp$  are collected in Tab.1. A dependence of the parameter  $dT_C / dp$  on  $T_C$  (see Fig.2) can be well described by the known Wohlfarth's relation

$$dT_C / dp = - A / T_C \quad (1)$$

where  $A$  is a constant.

Tab.1: The experimental values of  $T_C$ ,  $dT_C / dp$  and isothermal compressibility  $\kappa$  of the studied intermetallics.

	$T_C$ [K]	$dT_C / dp$ [K/GPa]	$\kappa$ [ $10^{-2}$ GPa $^{-1}$ ]
$Nd(FeTi)_{12}$	555	-26	0.87
$Ce_3(FeTi)_{29}$	319	-38	1.25
$Pr_3(FeTi)_{29}$	389	-31	0.99
$Nd_3(FeTi)_{29}$	412	-29	0.95
$Gd_3(FeTi)_{29}$	523	-27	-
$Tb_3(FeTi)_{29}$	455	-26	-
$Nd_2Fe_{17}$	330	-36	1.16
$Er_2Fe_{17}$	299	-43	-
$Y_2Fe_{17}$	310	-39	-

Using our experimental data, we obtain the value  $A = 12.5 \pm 1.5 \times 10^3 \text{ K}^2 \text{ GPa}^{-1}$  for all the studied intermetallics. Relation (1) was derived originally for the very weak itinerant ferromagnets. Similarly to the case of the amorphous Fe-rich alloys with the Invar-like magnetic behaviour [8], we have verified more general validity of the relation (1).

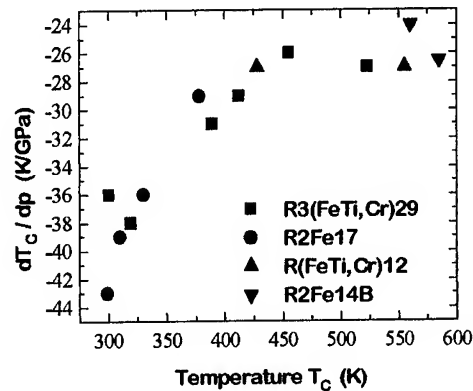


Fig.2:  $dT_C / dp$  vs  $T_C$  plot.

The curves of the thermal expansion of the intermetallics measured under different pressures were used to determine the thermal expansion

coefficient  $\alpha(T)$  and the compressibility  $\kappa(T)$  of the intermetallics. The observed temperature dependencies of both magnitudes exhibit the pronounced  $\lambda$ -shaped anomaly in the vicinity of  $T_C$ , (see Fig.3). The negative value of  $\alpha(T)$  near  $T_C$  belongs to the known set of the Invar characteristics. The anomalous behaviour of the compressibility, i.e. the pronounced softening of the crystal lattice within the transition from ferro- to paramagnetic state, was firstly observed in the FeNi Invar alloy [9] and can be classified as the new Invar characteristic.

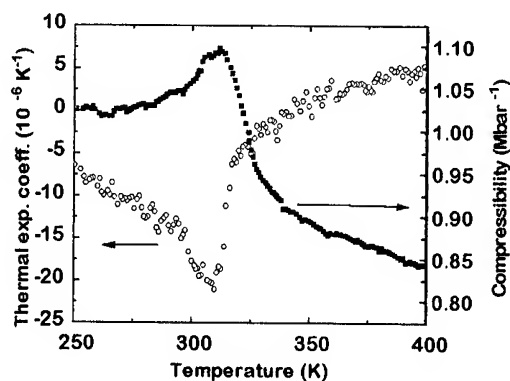


Fig.3: The thermal expansion coefficient  $\alpha(T)$  and the compressibility  $\kappa(T)$  of the intermetallic  $\text{Ce}_3(\text{FeTi})_{29}$  compound at the vicinity of  $T_C=319$  K.

Using the values of  $dT_C/dp$  and  $\kappa(293\text{K})$ , i.e. the value of the compressibility of the studied intermetallics (see Tab.1) measured in the ferromagnetic state, we have obtained a constant value of  $dT_C/d\ln V \sim 3100$  K (see Tab.1). This result is very surprising with respect to the different crystal structures of the intermetallics. We can conclude, that the volume dependence of the strongest Fe-Fe exchange interaction is not only extremely sensitive to the molar volume but also uniform for all the studied intermetallics. It supports the theoretical models considering the volume instability of the magnetic moments as a source of the high sensitivity of the magnetic properties to volume changes [10-11].

The study of  $T_{SR}$  under pressure confirmed that the effect of pressure on magnetic anisotropy of the iron-based intermetallics is very complex but

it can be described within a single ion model of the crystal electric field (CEF) interaction, where the second order CEF parameters exhibit an extreme sensitivity to the interatomic distances [12]. On the other hand, the intersublattice R-Fe exchange interaction seems to be practically pressure independent.

## References

1. C. D. Fuerst, F. E. Pinkerton, J. E. Herbst, *J. Magn. Magn. Mater.* **129** (1994) L115.
2. Y. Hu, W. B. Yelon, *Solid State Commun.* **91** (1994) 223.
3. L. Morellon, P. A. Algarabel, B. Garcia-Landa, M. R. Ibarra, F. Albertini, A. Palouzi, L. Paretti, *Proceedings of the 8th International Symposium on Magnetic Anisotropy and Coercitivity in Rare Earth Transition Metal Alloys*, (Birmingham, 1994).
4. D. H. Ryan, J. M. Cadogan, A. Margarian, J.B. Dunlop, *Proc. of 6-th Joint MMM-Intermag Conf.*, (Albuquerque, 1994).
5. J. Kamarád, K. V. Kamenev, Z. Arnold - in this Proc.
6. Z. Arnold, J. Kamarád, L. Morellon, P. A. Algarabel, M. R. Ibarra, *Solid State Commun.* **92** (1994) 807.
7. Z. Arnold, J. Kamarád, L. Morellon, P. A. Algarabel, M. R. Ibarra, C. D. Fuerst, *J. Appl. Phys.* - in press.
8. J. Kamarád, Z. Arnold, *Physica* **139-140 B** (1986) 382.
9. G. Oomi, N. Mori, *J. Magn. Magn. Mater.* **10** (1979) 170.
10. V. L. Moruzzi, *Physica* **161 B** (1989) 99.
11. E. F. Wassermann, *J. Magn. Magn. Mater.* **100** (1991) 346.
12. M. R. Ibarra, Z. Arnold, P. A. Algarabel, L. Morellon, J. Kamarád, *J. Phys. Condens. Mater.* **4** (1992) 9271.

\* on the leave from the Donetsk Physico-Technical Institute of the Ukrainian Academy of Sciences



# INFLUENCE OF HIGH PRESSURE HYDROGENATION ON ELECTRICAL RESISTANCE, MAGNETORESISTANCE AND MAGNETIC SUSCEPTIBILITY OF DISORDERED Ni-Mn ALLOYS

D. K. Schwarz, I. Dugandžić, S. M. Filipek\* and H. J. Bauer

*Sektion Physik, Ludwig-Maximilians-Universität München, Fed. Rep. Germany*

*\*Institute of Physical Chemistry, Polish Academy of Sciences, Warsaw, Poland*

## ABSTRACT

The cancelling of the matrix ferromagnetism of disordered Ni-Mn alloys (with Mn contents below 20at%) during its transformation in the hydride state by exposition in high pressure of gaseous hydrogen also leads to a large lowering of the temperature coefficient of the electrical resistance. From the known resistance anomalies of the disordered Ni-Mn alloys near 20 K and 50 K (explained by two possible orientations of the magnetic moments of the Mn atoms) the interstitial hydrogenation moreover totally removes the anomaly near 50 K, while the anomaly near 20 K remains, what excludes a significant influence of the hydrogen on the spin glass character in this range of Ni-Mn alloys. - Concerning the behaviour of the longitudinal magnetoresistance of these alloys at low temperature the introduction of interstitial hydrogen in the alloy matrix exhibits similar consequences - corresponding to the resistance behaviour - as an increase of the content of (substitutional) Mn atoms in the hydrogen-free alloy. - Measurements of the reversible magnetic susceptibility show that the hydrogenation of an alloy with e. g. 13.7 at% Mn delivers a magnetic hysteresis loop behaviour which changes drastically in the dependence on the magnetic field applied. This is comparable to observations on  $\text{Cu}_{0.86}\text{Mn}_{0.14}$ , interpreted as caused by local cluster effects.

The interstitial hydrogenation of nickel based alloys up to a non-ferromagnetic hydride state also leads to significant changes of the transport properties as shown e. g. at Ni-Cu alloys [1] or Ni-Mn and Ni-Cr alloys [2, 3].

Continuing the previous investigations [2] concerning the temperature dependence of electrical resistance of disordered Ni-Mn alloys the matrix ferromagnetism of which is neutralized electrochemically by interstitial hydrogen [4] we here treat the same range of Ni-Mn alloys (with manganese contents between 4.7 and 19.8 at.%) however transformed in the hydride state by exposition in high pressure gaseous hydrogen [5].

In [2] it was shown that known anomalies in the temperature dependence of the electrical resistance  $R(T)$  near  $T_1=20$  K and  $T_2=50$  K found by Beilin et al. [6, 7] and regarded as resulting from an interaction between the magnetic moments of the Mn atoms and the matrix magnetization withstand the electrochemical interstitial hydrogenation in spite of the cancelling of the ferromagnetism [4] connected with a distinct lowering of  $R(T)$ , see Fig. 1 (In the interest of a better recognizability of the anomalies we present the results by the

temperature dependence of the temperature coefficient of electrical resistance  $dR/dT$ ). This observations can probably be a sign that a small Ni-area around each impurity has not yet been magnetically neutralized because the hydrogen could not enter the closest neighborhood of the impurity [2].

In the present paper we report about the application of high pressure hydrogenation of these disordered Ni-Mn alloys in gaseous hydrogen of about 1 GPa with the result that the above-mentioned resistance anomaly near  $T_2$  disappears, Fig 1. Obviously the hydrogen activity which is higher by orders of magnitude in comparison with the electrochemical hydrogenation (correspondingly an application of pressure of about 0.6 GPa of gaseous hydrogen [10]) forces the hydrogen to enter also the closest neighborhood of the impurity and so to cancel the magnetic moments of the surrounding Ni-area.

Moreover the remaining shape of the  $dR/dT(T)$  curves (without the anomaly near  $T_2$ ) of the Ni-Mn alloys hydrogenated under high pressure condition also after desorption of the hydrogen suggests that the hydrogen has resolved the cluster

arrangement of the atoms around the 'impurity' atom. - The resistance anomaly near  $T_1$  of this alloy range however largely withstands also a high pressure hydrogenation at 1 GPa, accordingly also the spin glass character below  $T_1$  suggested in [2] by evaluation of resistance measurements remains.

The different withstands of the anomalies against hydrogenation, such as the preservation of the anomaly near  $T_1$  but the desintegration of the anomaly near  $T_2$  support the suggestions [6, 7] that up to  $T_1$   $\text{Mn}(\downarrow)\text{Mn}(\downarrow)$ -clusters and up to  $T_2$   $\text{Ni}(\downarrow)\text{Mn}(\downarrow)$ -clusters (oriented antiparallel to the matrix magnetization) exist insofar as the hydrogen preferentially cancels the magnetic moments of the clustered Ni atoms.

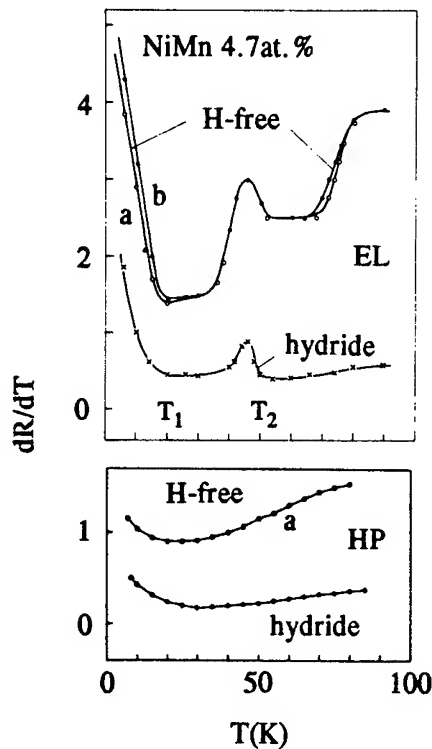


Fig. 1. Example of the influence of hydrogenation on the temperature dependence of the temperature coefficient  $dR/dT$  ( $\Omega/K$ ) of a disordered Ni-Mn alloy. The graph above (EL) refer to electrochemical [2], the graph below (HP) to high pressure hydrogenation of the alloy (a after desorption, b before hydrogenation).  $T_1$ ,  $T_2$ : temperatures whereby the respective clusters producing the anomalies get destroyed.

Further we could confirm the tendency (found in [2] by analysis of the impurity resistance) that interstitial hydrogen has the same consequences on the resistance behaviour of the Ni-Mn alloys as an increase of the content of (substitutional) Mn atoms in the hydrogen-free alloy also by including a magnetic criterion, given by the behaviour of the longitudinal magnetoresistance at 4.2 K, Fig. 2.

The negative magnetoresistance (MR) of the H-free Ni-Mn alloys (regarded as associated with a decrease of the probability for s-d scattering [11]) increases with increasing manganese content. The

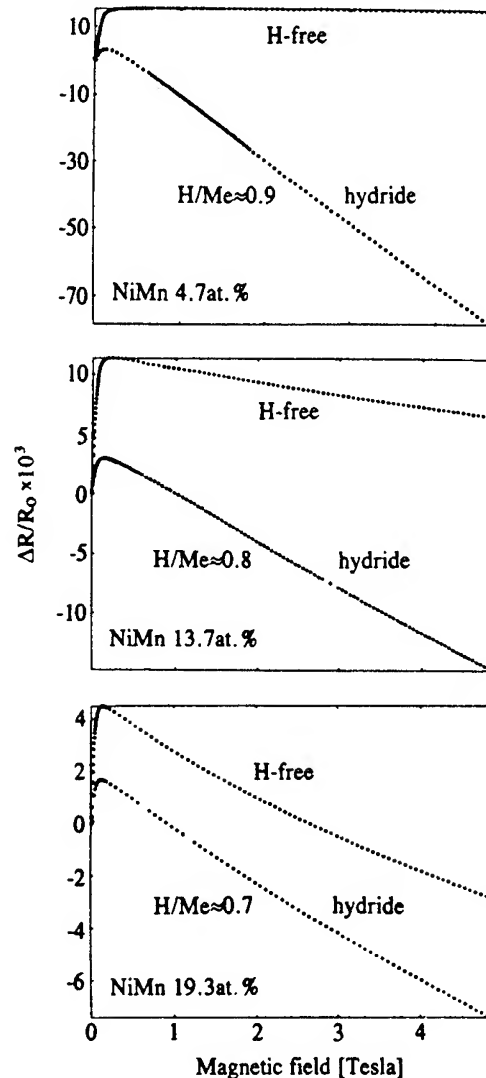


Fig. 2. Longitudinal magnetoresistance of disordered Ni-Mn alloys and their hydrides at 4.2 K. The hydrides are formed under hydrogen pressure of 1 GPa with the hydrogen contents H/Me [5] noted in the graphs.

hydrogenation magnifies this behaviour for each alloy. However, the fact that the absorbed H-amount increases with decreasing Mn content finally leads to a maximal increase of the negative MR for the alloy with the smallest Mn content (4.7 at%). The steep rise of the MR of the H-free samples at low fields due to ferromagnetic behaviour gets strongly reduced by the hydrogenation. The remaining part could be related to the manganese.

In view of the apparent spin glass character of this Ni-Mn alloy range [2] the behaviour of the reversible magnetic susceptibility and the corresponding magnetic hysteresis loop of high

pressure hydrogenated Ni-Mn13.7at% in dependence of the maximal applied magnetic field is presented in Fig. 3. The graph shows a drastic irreversible increase of the height of the hysteresis loop by transition from a low magnetic field of about 0.2 Tesla to a high one of nearly 5 Tesla: thus also after returning again to the low field the increased shape of the hysteresis remains the same. This appearance is comparable to observations on  $\text{Cu}_{0.86}\text{Mn}_{0.14}$ , interpreted as caused by local cluster effects [12].

The last examples point out that interstitial hydrogenation cancelling the ferromagnetism of the host matrix of an alloy can reveal correlations which otherwise remain hidden. Generally the presented findings may show that the rôle of hydrogen as alloy partner or as metal physical sound in connection also with the alternative hydrogenation of the metals by the electrochemical method or by application of high pressure make us expect further valuable informations.

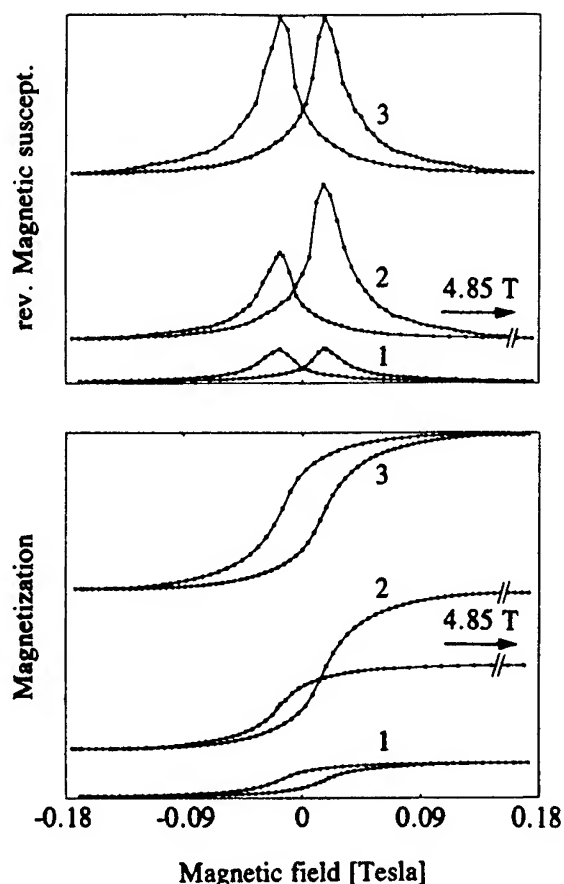


Fig. 3. Reversible magnetic susceptibility and magnetization of a Ni-Mn13.7 at% hydride at 4.2 K in dependence of the maximal applied magnetic field. Sequence: 1 low field, 2 high field, 3 low field.

#### REFERENCES

1. H. U. Daniel and H. J. Bauer, *J. Magn. Mater.* **6**, 303 (1977).
2. I. Czusda and H. J. Bauer, in P. Jena and C. B. Satterwaite (Eds.), 'Electronic Structure and Properties of Hydrogen in Metals', Plenum, New York, 1983, p. 653.
3. D. K. Schwarz and H. J. Bauer, *J. Less Common Metals* **103**, 375 (1984).
4. H. J. Schenk and H. J. Bauer, *Z. Phys. Chem. N. F.* **115**, 213 (1979).
5. M. Krukowski, B. Baranowski, *J. Less-Common Metals* **49**, 385 (1976).
6. V. M. Beilin, I. L. Rogelberg and V. A. Cherenkov, *Sov. J. Low Temp. Phys.* **4**, 11 (1978).
7. V. M. Beilin, T. I. Zeynalov, I. L. Rogelberg and V. A. Cherenkov, *Phys. Met. Metall.* Vol. **46**, 5, 163, (1979).
8. H. J. Schenk, H. J. Bauer and B. Baranowski, *Phys. Stat. Sol. (a)* **52**, 195, (1979).
9. H. J. Schenk, H. J. Bauer and B. Baranowski: in 'High Pressure Science and Technology' ed. by B. Vodar and Ph. Marteau, Pergamon Press, Oxford and New York 1979, Vol 1, p. 444.
10. B. Baranowski, *Ber. Bunsenges. Phys. Chem.* **76**, 714 (1972).
11. N. H. Mott, *Proc. Roy. Soc. A* **153**, 699 (1936).
12. U. Schulze, G. Felton and Ch. Schwink, *J. Magn. Mater.* **15-18**, 205-206 (1980).

# Hyperfine magnetic fields at $^{119}\text{Sn}$ nuclei and Curie temperature in Heusler alloy $\text{Ni}_2\text{MnSn}$ under High pressure.

A.G. Gavriluk<sup>1</sup>, G.N. Stepanov<sup>1</sup>, V.A. Sidorov<sup>1</sup> and S.M. Irkaev<sup>2</sup>

<sup>1</sup>*Institute for High Pressure Physics, Russian Academy of Science, Troitsk, Moscow Region, 142092, Russia*

<sup>2</sup>*Institute for Analytic Instruments, Russian Academy of Science, 198103, S.-Petersburg, Russia*

## ABSTRACT

The pressure dependence of the "hyperfine magnetic field"  $H_{\text{hpf}}$  at the nuclei of the diamagnetic atoms  $^{119}\text{Sn}$  was investigated in Heusler alloy  $\text{Ni}_2\text{MnSn}$  using Mössbauer absorption spectroscopy with pressures up to 10.8 GPa at room temperature. Hyperfine fields were measured at pressure increase and at pressure decrease as well. In the range of the experimental errors the dependencies of  $H_{\text{hpf}}^{\text{Sn}}$  at increase and decrease of pressure are the same. The dependence can be fitted by linear function  $H_{\text{hpf}}^{\text{Sn}}(P)/H_{\text{hpf}}^{\text{Sn}}(0)=1+k_H \cdot P$  with the coefficient  $k_H=-0.095 \pm 0.015 \text{ GPa}^{-1}$ , where  $H_{\text{hpf}}^{\text{Sn}}(0)=4.60 \pm 0.12 \text{ T}$ . Diamond anvil cells (DAC) were used for the high pressure generation. The Curie temperature ( $T_C$ ) have been measured up to 9 GPa in "toroid" high pressure device using thermal ac-susceptibility measurements. The dependence is linear with the coefficient  $dT_C/dP=7.44 \text{ K/GPa}$  ( $T_C(0)=341.3 \text{ K}$ ). To study compressibility of the sample the pressure dependence of the volume have been measured by means of the resistive strain gauges at hydrostatic pressure up to 9 GPa. The equation  $(V-V_0)/V_0=-a \cdot P+b \cdot P^2$  have been fitted to the experimental data with the coefficients  $a=8.64 \cdot 10^{-3} \text{ GPa}^{-1}$ ,  $b=1.13 \cdot 10^{-4} \text{ GPa}^{-2}$ . The drop of the  $H_{\text{hpf}}^{\text{Sn}}$  in pressure range 0-10.8 GPa can be explained on the basis of empirical theory developed by Delyagin et al [1].

## I. INTRODUCTION

The purpose of the investigation described in this paper was to study the  $H_{\text{hpf}}^{\text{Sn}}$  dependencies on the interatomic distances in Heusler alloy  $\text{Ni}_2\text{MnSn}$  and to compare experimental observations with the empirical model developed by Delyagin et al [1]. The statement of the investigations of hyperfine interactions at Sn nuclei in Heusler alloys under pressure and general introduction see in Ref. [2].

## II. EXPERIMENTS

The  $H_{\text{hpf}}^{\text{Sn}}$  was investigated in Heusler alloy  $\text{Ni}_2\text{MnSn}$  at room temperature with the help of the Mössbauer absorption spectroscopy of the nuclei  $^{119}\text{Sn}$  at atmospheric pressure and under high pressure up to 10.8 GPa. The lattice parameters of the sample were  $a=b=c=6.052 \text{ \AA}$ ,  $\alpha=\beta=\gamma=90^\circ$  [4]. Curie temperature was  $T_C \sim 340 \text{ K}$  [4,5].

Any enhancement of an amount of Mn or disordering of the crystal lattice result to lowering magnetization and  $T_C$  [10]. To be sure that at high nonhydrostatic pressure there was no disordering, the measurements have been carried out at pressure decrease.

The typical Mössbauer spectra for  $\text{Ni}_2\text{MnSn}$  at normal conditions are shown on the figure 1. These spectra have been measured for different parts of the same sample. From these data one can conclude that the sample is not homogeneous. These spectra could be fitted by three subspectra (example on the Fig. 2(a)): (1) subspectrum with the large magnetic splitting - ordered  $\text{Ni}_2\text{MnSn}$  ferromagnetic phase (FP) that have eight Ni atoms in the first nearest-neighbor (1nn) Ni sites and six

Mn atoms in the second nearest-neighbor (2nn) Mn sites; (2) subspectrum with the lower magnetic splitting - magnetic

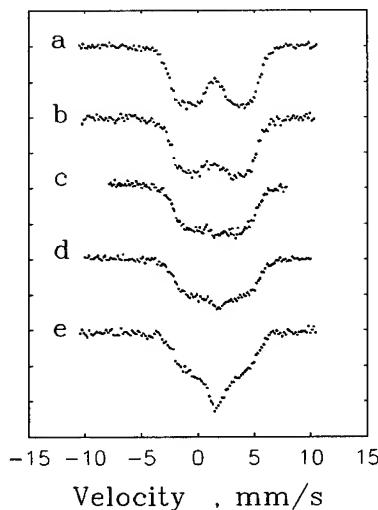


FIG.1. Mössbauer spectra of different parts of  $\text{Ni}_2\text{MnSn}$  sample at normal conditions.

phase (LMP) with partly disordered Mn-Sn sublattice; (3) nonmagnetic broad singlet - nonmagnetic phase (NP) with strongly disordered and (or) inhomogeneous compound of  $\text{Ni}_2\text{MnSn}$ . Nevertheless the x-ray patterns, Curie temperatures and maximal hyperfine magnetic fields at  $^{119}\text{Sn}$  for these parts are the same. The relative

areas of the subspectra with the larger magnetic hyperfine field are 61%, 51%, 41%, 43% and 34% for (a), (b), (c), (d) and (e) respectively. The  $H_{\text{Sn}}^{\text{hpf}}$  is changed from 45.5 kOe to 47.3 kOe (spectra on Fig. 1(c) and Fig. 1(a) respectively). From this consideration we can conclude that the ordered  $\text{Ni}_2\text{MnSn}$  phase is present even in the mostly inhomogeneous sample (Fig. 1(e)).

It was the sample (b) (Fig. 1(b)) that have been studied at high pressure Mössbauer experiment.

Figures 2(a), 2(b) show Mössbauer spectra obtained in this study at  $P=0$  and at 10.8 GPa, respectively. Our fits assume two sextets at high pressure, and two sextets and one singlet at atmospheric pressure. At high pressure relative area of LMP and NP phases enhance. We think that in the Heusler alloy the disorder transitions can take place under nonhydrostatic pressure or during various mechanical treatments [10], and this enhancement is the result of these transitions.

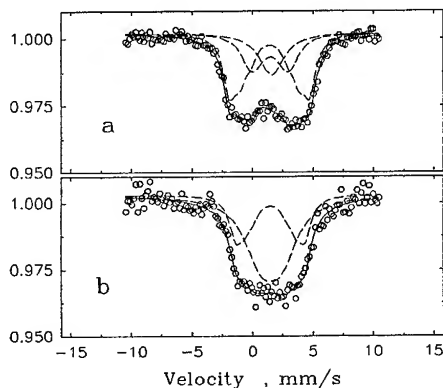


FIG. 2. Mössbauer spectra of  $^{119}\text{Sn}$  in  $\text{Ni}_2\text{MnSn}$  at room temperature (295K): (a)  $P=0$ , (b)  $P=10.8$  GPa. O: experiment, solid lines: fitted curves, dashed lines: fitted subspectra.

Figure 3 shows the pressure dependence of  $H_{\text{Sn}}^{\text{hpf}}$  corresponding to the larger hyperfine field (open circles: experiment at pressure increase; filled circles: experiment at pressure decrease; solid line: linear fit to the experimental points). The fit gives  $H_{\text{Sn}}^{\text{hpf}}(P)/H_{\text{Sn}}^{\text{hpf}}(0)=1+k_H P$  with the coefficient  $k_H=-0.095\pm0.015$  GPa $^{-1}$  where  $H_{\text{Sn}}^{\text{hpf}}(0)=4.6\pm0.12$  T.

Changes of both  $T_C$  and  $H_{\text{Sn}}^{\text{hpf}}(0\text{K})$  under pressure influence the measured value of  $H_{\text{Sn}}^{\text{hpf}}(295\text{K})$ . Therefore measurements of  $T_C$  at high pressure are important for understanding the  $H_{\text{Sn}}^{\text{hpf}}$  behavior. Kaneko *et al* [5] have measured pressure dependence of  $T_C$  for  $\text{Ni}_2\text{MnSn}$  at hydrostatic pressure up to 0.55 GPa.

The measured value of linear growth was  $(T_C)^{-1}$ .  $dT_C/dP=1.6\cdot10^{-2}$  GPa $^{-1}$  [5].

At present study have been measured pressure dependence of  $T_C$  for  $\text{Ni}_2\text{MnSn}$ . Experimental procedure have been based on the measurements of the initial ac-susceptibility [6].

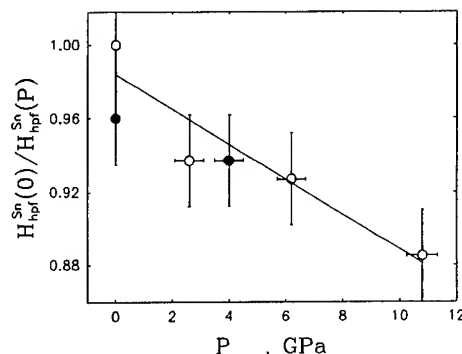


FIG. 3. The dependence on the pressure of  $H_{\text{Sn}}^{\text{hpf}}$ . Symbol O: our experimental points at pressure increase; ●: our experimental points at pressure decrease; solid line - linear fitting to experimental data.

This experimental data have been fitted by the linear function  $T_C(P)=T_C(0)+K_{T_C}\cdot P$ ; where  $K_{T_C}=7.44$  K/GPa,  $T_C(0)=341.3$  K (see fig. 4).

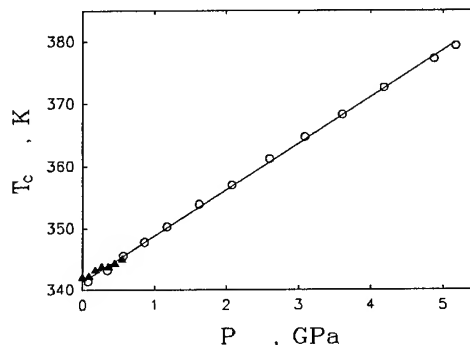


FIG. 4. Pressure dependence of  $T_C$  for  $\text{Ni}_2\text{MnSn}$ : Y: our experimental points; ▲: experimental points from Ref. [5]; solid line - linear fitting to experimental data.

V-P relationship for  $\text{Ni}_2\text{MnSn}$  have been measured by means of the resistive strain gauge [7]. This experimental data have been fitted to the one of the standard form of the state equation of solids:  $(V-V_0)/V_0=a\cdot P+b\cdot P^2$ , where parameters  $a=8.64\cdot10^{-3}$  GPa $^{-1}$ ,  $b=1.13\cdot10^{-4}$  GPa $^{-2}$  have been found.

### III. DISCUSSION

To calculate extrapolated pressure dependence of  $H_{\text{Sn}}^{\text{hpf}}(0\text{K})$  one can use pressure dependencies of  $T_C$  and of  $H_{\text{Sn}}^{\text{hpf}}(295\text{K})$ , and some suggestion on the shape of the temperature dependence of  $H_{\text{Sn}}^{\text{hpf}}$  at any pressures. Using experimental values for atmospheric pressure of  $H_{\text{Sn}}^{\text{hpf}}$ : 45 kOe (present work and Ref. [3]), 87 kOe [3], 97 kOe [3,9] for  $T=295\text{K}$ ,  $T=77\text{K}$  and  $T=0\text{K}$  respectively one can construct curve of  $H_{\text{Sn}}^{\text{hpf}}(T)$  (solid line on the Fig.5). Using fitting

procedure the parameters of this curve have been calculated. Then let us suppose that a function  $h(t)$ , where  $h = H_{\text{hpf}}^{\text{Sn}}(T)/H_{\text{hpf}}^{\text{Sn}}(0)$  and  $t = T/T_C$ , is independent on the pressure. Function  $h(t)$  for  $\text{Ni}_2\text{MnSn}$  is shown on the pasted picture of the figure 5. At this assumption and taking into account dependence  $H_{\text{hpf}}^{\text{Sn}}(P)$  at room temperature and dependence  $T_C(P)$  one can draw curves  $H_{\text{hpf}}^{\text{Sn}}(T)$  for different pressures. At such suggestions these curves have been constructed (example for  $P=10$  GPa is shown on the Fig.5 - dotted line), and extrapolated pressure dependence of  $H_{\text{hpf}}^{\text{Sn}}(0\text{K})$  have been computed. Figure 6 shows fitted experimental curve  $H_{\text{hpf}}^{\text{Sn}}(P)$  for room temperature - solid line, extrapolated pressure dependence  $H_{\text{hpf}}^{\text{Sn}}(P)$  for  $T=0\text{K}$  - dotted line.

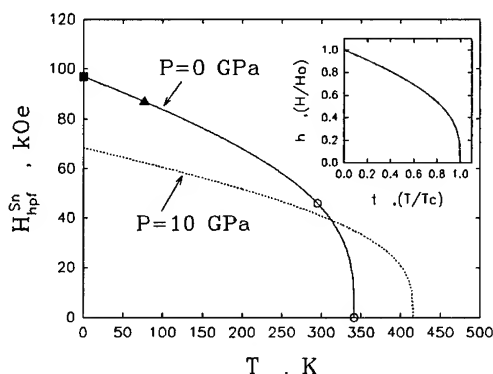


FIG. 5. Experimental data: ■: from nmr by Shinohara [9]; ▲: from Mössbauer by Leiper *et al* [3]; ○: our experimental data. Computations: solid line - fitting to experimental data; dotted line - extrapolation using  $H_{\text{hpf}}^{\text{Sn}}(P)$  for room temperature and  $T_C(P)$ . On the pasted figure the dependence  $h = H_{\text{hpf}}^{\text{Sn}}(T)/H_{\text{hpf}}^{\text{Sn}}(0)$  on  $t = T/T_C$  that have been assumed independent on the pressure.

Using Delyagin's empirical model [1] one can write the dependence of  $H_{\text{hpf}}^{\text{Sn}}$  on distance from Sn atom to  $1nn$ ,  $r_1$ , and on distance from Sn atom to  $2nn$ ,  $r_2$ :

$$H_{\text{hpf}}^{\text{Sn}} = M_1(r_1)p(r_1) + M_2(r_2)p(r_2) + C \cdot \mu, \quad (1)$$

To calculate  $H_{\text{hpf}}^{\text{Sn}}(P)$  we assume: 1)  $M_1$ ,  $M_2$  and  $C \cdot \mu_B$  are approximately constant at all pressures, 2) the largest contribution to the  $H_{\text{hpf}}^{\text{Sn}}$  decrease is due to the  $p(r)$  variation. We suppose that  $M_1=5.23$  (to fit  $H_{\text{hpf}}^{\text{Sn}}(0\text{K})$  we assume that there is localized magnetic moment  $\sim 0.65 \mu_B$  on Ni atom),  $M_2=24$  and  $C \cdot \mu=20$  [1]. Thus we can write [1]:

$$H_{\text{hpf}}^{\text{Sn}}(P) = 5.23 p[r_1(P)] + 24 p[r_2(P)] + 20. \quad (2)$$

where  $M_1(r_1)$  and  $M_2(r_2)$  - sum of the magnetic moments of atoms in  $1nn$  and  $2nn$ , respectively (in  $\mu_B$  units),  $p(r)$  - empirical Delyagin function for the radial dependence of the partial contributions to the hyperfine field (in  $T/\mu_B$  units),  $C \cdot \mu_B$  - contribution to  $H_{\text{hpf}}$  proportional to the average atomic moment of the

material  $\mu$ . Function  $p(r)$  has been constructed as a best fit to the experimental data for b.c.c. and f.c.c. magnetic compounds [1].

For estimating the interatomic distances with pressure, we have used the equation  $(V-V_0)/V_0 = -a \cdot P + b \cdot P^2$  and parameters for Heusler alloy  $\text{Ni}_2\text{MnSn}$  measured at present work. The dashed curve on figure 6 was calculated from Eq. 2.

The results seem to verify the Delyagin model to describe the dependence  $H_{\text{hpf}}^{\text{Sn}}$  up to 10.8 GPa [1].

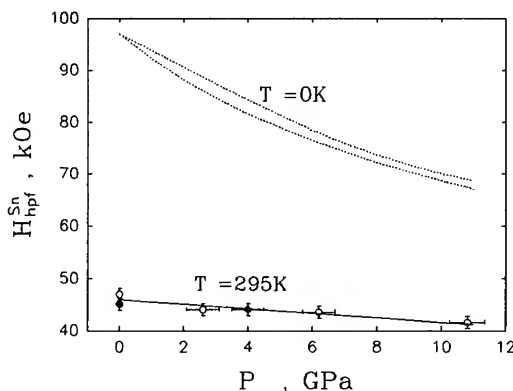


FIG. 6. Fitted experimental curve  $H_{\text{hpf}}^{\text{Sn}}(P)$  for room temperature - solid line, extrapolated pressure dependence  $H_{\text{hpf}}^{\text{Sn}}(P)$  for  $T=0\text{K}$  - dotted line. Theoretical curve from Delyagin *et al* [1] - dashed curve.

## REFERENCES

1. N.N. Delyagin, V.I. Krylov, V.I. Nesterov, JETP **79**(8), 1050(1980).
2. G.N. Stepanov, A.G. Gavriluk, O.B. Tsiok and S.M. Irkaev, "Mössbauer Study of High Pressure Influence on Hyperfine Fields at Tin and Compressibility Measurements in  $\text{Co}_2\text{MnSn}$  up to 12 GPa", *this issue* (AIRAPT&IHPRG 95 Conference).
3. W. Leiper, D.J. Geldart, P.J. Pothier, Phys. Rev. B **3**, 1837(1971).
4. C.C.M. Campbell, J. Phys. F: Metal Phys. **5**, 1931(1975).
5. T. Kaneko, H. Yoshida, S. Abe, K. Kamigaki, J. Appl. Phys. **52**(3), 2046(1981).
6. V.A. Sidorov, L.G. Khvostantsev, Jour. of Mag. and Mag. Mat. **129**, 356(1992).
7. O.B. Tsiok, V.V. Bredikhin, V.V. Sidorov, L.G. Khvostantsev, High Pres. Res. **10**, 523(1992).
8. L.G. Khvostantsev, L.F. Vereshchagin, A.P. Novikov, High Temp.-High Press. **9**(6), 637(1977).
9. T. Shinohara, J. Phys. Soc. Japan **28**, 313(1970).
10. R.M. Bozorth, *Ferromagnetism*, D. Van Nostrand Co., Inc., London (1951).

# Mössbauer Study of High Pressure Influence on Hyperfine Fields at Tin and Compressibility Measurements in $\text{Co}_2\text{MnSn}$ up to 12 GPa

G.N. Stepanov<sup>1</sup>, A.G. Gavriluk<sup>1</sup>, O.B. Tsiok<sup>1</sup> and S.M. Irkaev<sup>2</sup>

<sup>1</sup>*Institute for High Pressure Physics, Russian Academy of Science, Troitsk, Moscow Region, 142092, Russia*

<sup>2</sup>*Institute for Analytic Instruments, Russian Academy of Science, 198103, S.-Petersburg, Russia*

## ABSTRACT

The dependence on the pressure of the "hyperfine magnetic field"  $H_{\text{hpf}}^{\text{Sn}}$  at the nuclei of the diamagnetic atoms  $^{119}\text{Sn}$  was investigated in Heusler alloy  $\text{Co}_2\text{MnSn}$  using Mössbauer absorption spectroscopy under pressure up to 12 GPa at room temperature. Hyperfine fields were measured at pressure rising and at pressure falling as well. In the range of the experimental errors direct and inverse pressure dependence of  $H_{\text{hpf}}^{\text{Sn}}$  are the same. The dependence can be fitted by linear function  $H_{\text{hpf}}^{\text{Sn}}(P)/H_{\text{hpf}}^{\text{Sn}}(0)=1+k_H P$  with the coefficient  $k_H=-0.020\pm0.001 \text{ GPa}^{-1}$ , where  $H_{\text{hpf}}^{\text{Sn}}(0)=10.5\pm0.3 \text{ T}$ . Diamond anvil cell (DAC) was used for the high pressure generation. To study isothermal compressibility of the sample the pressure dependence of the volume have been measured by means of the resistive strain gauges at hydrostatic pressure up to 9 GPa in "toroid" high pressure camera. The equation  $(V-V_0)/V_0=-aP+bP^2$  have been fitted to the experimental data with the coefficients  $a=7.52\cdot10^{-3} \text{ GPa}^{-1}$ ,  $b=1.16\cdot10^{-4} \text{ GPa}^{-2}$ . The drop of the  $H_{\text{hpf}}^{\text{Sn}}$  in pressure range 0-12 GPa can be explained on the basis of empirical theory developed by Delyagin *et al.* [3].

## I. INTRODUCTION

Heusler alloys are ternary intermetallic compounds of stoichiometric composition  $X_2YZ$  [1,2]. The structure is cubic  $L2_1$  with  $X$  ions at the cube corners and  $Y$  and  $Z$  ions occupying alternate body centers of successive cubes. Crystal structure is shown on the figure 1. Alloys with  $Y=\text{Mn}$  and  $Z=\text{Sn}$  are magnetically ordered. In these alloys the large magnetic moment  $\sim 4\mu_B$  is localized on the  $\text{Mn}$  ion. In the Heusler alloy  $\text{Co}_2\text{MnSn}$  there is also a magnetic moment  $\sim 0.7\mu_B$  on  $\text{Co}$  ion [3].

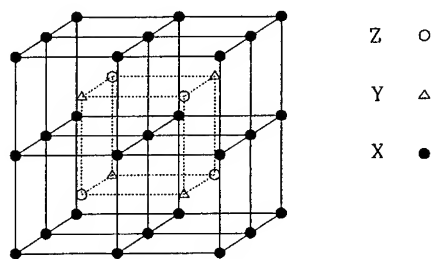


FIG.1. Heusler alloy structure.

The Mössbauer study of Heusler alloys is of interest as it yields information concerning the electronic structure and magnetic properties of concentrated magnetic alloys. The electronic shells of the diamagnetic ions  $\text{Sn}$  are compensated in the absence of a magnetic environment. Therefore hyperfine magnetic fields at the

nuclei of the diamagnetic ions  $H_{\text{hpf}}^{\text{Sn}}$  in crystal with cubic symmetry as a whole arise as a result of Fermi contact interactions with polarized  $s$  - shells of  $\text{Sn}$  that are induced by the polarized conductivity electrons and by the paramagnetic  $\text{Mn}$  ions. There are some alternative microscopic models of  $H_{\text{hpf}}^{\text{Sn}}$  nature in Heusler alloy [4,5,6]. All of these models contain parameters not determinable from the experiment, and therefore it is difficult to compare theoretical results with the experimental measurements.

Delyagin *et al* [3] interpret the  $H_{\text{hpf}}^{\text{Sn}}$  on the basis of the empirical function for the radial dependence of the partial contributions to the hyperfine field,  $p(r)$ , derived by a combined analysis of the data for 16 metallic ferromagnetic matrices. The fact that the broad range of data can be interpreted by means of a single function  $p(r)$  confirms the weak dependence of the partial contributions on the structure and composition of the alloys.

The purpose of the investigation described in this paper was to study the  $H_{\text{hpf}}^{\text{Sn}}$  dependencies on the interatomic distances and to compare experimental observations with the empirical model developed by Delyagin *et al* [3].

## II. EXPERIMENT

The  $H_{\text{hpf}}^{\text{Sn}}$  was investigated in Heusler alloy  $\text{Co}_2\text{MnSn}$  at room temperature with the help of the Mössbauer absorption spectroscopy of the nuclei  $^{119}\text{Sn}$  under high pressure up to 12 GPa.

The pressure  $P$  was generated in the diamond-anvil cell (DAC) device [8]. The technique for the determination of the pressure exerted on the sample

gasket also served as the collimator of the  $\gamma$ -radiation. Typical counting times at pressure were  $\sim 240$  h. The pressure remained constant in the range of experimental errors. The difference in the pressure measured at the various parts of the sample was less than 10%. The Mössbauer spectra were treated using a computer-fitting program based on the Kundig model [9].

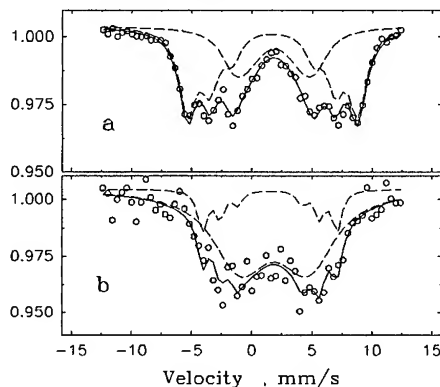


FIG. 2. Mössbauer spectra of  $^{119}\text{Sn}$  in  $\text{Co}_2\text{MnSn}$  at room temperature: (a)  $P=0$ , (b)  $P=10$  GPa.  $\circ$ : experiment; solid lines - fitted curves, dashed lines - fitted subspectra.

The method of volume measurements under high pressure, was described in details in [12]. High pressure was generated with the use of "toroid" device [13]. Methanol- ethanol (4:1) was used as a pressure transmitting medium. Changes in linear dimensions of the sample under pressure was measured with the use of a miniature single wire resistive strain gauge of original design.

The lattice parameters of the sample were  $a=b=c=5.98\text{Å}$ ,  $\alpha=\beta=\gamma=90^\circ$  [3]. Curie temperature was  $T_C \sim 800\text{ K}$  [7].

In the Heusler alloys may take place disorder transitions at various mechanical treatments or at treatment with nonehydrostatic pressure. Any enhancement of an amount of  $\text{Mn}$  or disordering of the crystal lattice result to lowering magnetization and  $T_C$  [10]. To be sure that at high pressure there was no disorder, some points have been measured at pressure decrease.

### III. RESULTS AND DISCUSSION

Figures 2 (a) and 2(b) show the examples of the Mössbauer spectra obtained in this study at  $P=0$  and at 10 GPa respectively. The spectra consist of more than one sextet that reflects imperfection of the alloy and the distinction in the local environments of Sn. Most of the Sn atoms are in perfect local environment and have eight Co atoms in the first nearest-neighbor ( $1nn$ ) Co sites and six Mn atoms in the second nearest-neighbor ( $2nn$ ) Mn

sites. The maximum split of the spectrum and accordingly the maximum of  $H_{\text{hpf}}^{\text{Sn}}$  is assigned to this case. The sextets corresponding to smaller  $H_{\text{hpf}}^{\text{Sn}}$  are the result of the Sn local environment distortions. We computed Mössbauer spectra assuming the existence of two sextets. The main goal of the computation was to determine maximal field with the relative error no more 0.05.

Figure 3 shows the pressure dependence of  $H_{\text{hpf}}^{\text{Sn}}$  corresponding to perfect local environment (halo circles - experiment at pressure rising, filling boxes - experiment at pressure falling, solid line - fitting to experimental points). Experimental points have been fitted by linear function  $H_{\text{hpf}}^{\text{Sn}}(P)/H_{\text{hpf}}^{\text{Sn}}(0)=1+k_H \cdot P$  with the coefficient  $k_H=-0.020 \pm 0.001\text{ GPa}^{-1}$  where  $H_{\text{hpf}}^{\text{Sn}}(0)=10.5 \pm 0.3\text{ T}$ .

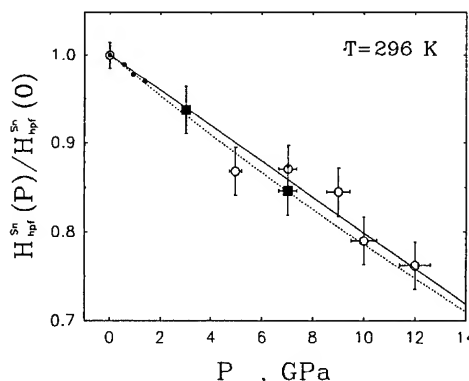


FIG. 3. The dependence on the pressure of  $H_{\text{hpf}}^{\text{Sn}}$ .  $\circ$ : experimental points at pressure increase;  $\blacksquare$ : experimental points at pressure decrease;  $\bullet$ : experimental points from Ref.[11]; solid line: fitting to experimental data; dotted line: theoretical curve using Delyagin's model.

To demonstrate the absence of the irreversible "order-disorder" transition some points were measured at the decrease of pressure. In the case of disordering at the Mn-Sn sublattice the value of  $H_{\text{hpf}}^{\text{Sn}}$  will be dramatically changed [10]. The dependence at the decrease of pressure demonstrates absence of irreversible "order-disorder" transition.

Nikolayev *et al* [11] have measured the pressure dependence of the hyperfine fields at  $^{119}\text{Sn}$  nuclei in tin sites in  $\text{Co}_2\text{MnSn}$  up to 1.4 GPa at room temperature (filled circles on figure 3). Their coefficient is  $(1/H(0)) \cdot (dH(P)/dP) = -0.022\text{ GPa}^{-1}$ . The experimental results have been discussed from the viewpoint of alternative models of the mechanisms of appearance of magnetic fields at nuclei of nonmagnetic ions in ferromagnetic matrices [3,4].

Changes of both  $T_C$  and  $H_{\text{hpf}}^{\text{Sn}}(0\text{K})$  under pressure influence the measured value of  $H_{\text{hpf}}^{\text{Sn}}(296\text{K})$ . However, because of the large value of the Curie



temperature ( $T_C \sim 800K$ ), we can neglect any contribution from a  $T_C$  change. Moreover the position of  $Co_2MnSn$  near the maximum on Castellitz's empirical curve [7] is an additional reason to ignore the influence on  $H_{Sn}^{hypf}$  of a  $T_C$  variation; that is, this variation must be small. We can also assume the value of  $H_{Sn}^{hypf}(296K)$  is close to that of  $H_{Sn}^{hypf}(0K)$  and will simply use  $H_{Sn}^{hypf}$ .

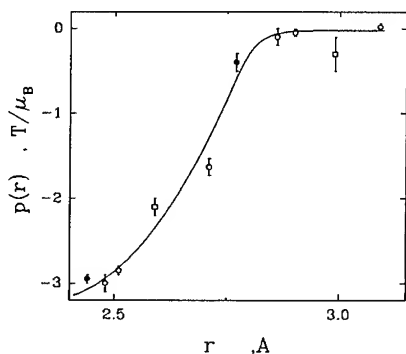


FIG.4. Empirical Delyagin's curve of the function for the radial dependence of the partial contributions to the hyperfine field,  $p(r)$ . Solid line - theoretical curve  $p(r)$ ; O: experimental points for b.c.c. compounds; ●: experimental points for f.c.c. compounds; □: experimental points for  $Co_2MnSn$ .

Using Delyagin's empirical model [3] one can write the dependence of  $H_{Sn}^{hypf}$  on distance from Sn atom to  $1nn$ ,  $r_1$ , and on distance from Sn atom to  $2nn$ ,  $r_2$ :

$$H_{hypf}^{Sn} = M_1(r_1)p(r_1) + M_2(r_2)p(r_2) + C \cdot \mu, \quad (1)$$

## REFERENCES

1. D.J.W.Geldart, C.C.M.Campbell, P.J.Pothier, W.Leiper, *Canad. J. Phys.* **50**, 206(1971).
2. W.Leiper, D.J.Geldart, P.J.Pothier, *Phys. Rev. B.* **3**(5), 1837(1971).
3. N.N. Delyagin, V.I.Krylov, V.I.Nesterov, *JETP* **79**, 8(9), 1050(1980).
4. B.Caroli, A.Blendin, *J. Phys. Chem. Solids.* **27**, 503(1966).
5. M.B.Stearns, *J. Appl. Phys.* **50**(3), 2060(1979).
6. J.R.Reitz, M.B.Stearns, *J. Appl. Phys.* **50**(3), 2066(1979).
7. T.Kaneko, H.Yoshida, S.Abe, K.Kamigaki, *J. Appl. Phys.* **52**(3), 2046(1981).
8. A.Jayaraman, *Rev. Mod. Phys.* **55**, 65(1983).
9. W.Kundig, *Nucl. Instr. Methods* **48**, 219(1967).
10. Richard M. Bozorth, in *Ferromagnetism*, D. Van Nostrand Company, Toronto- New York - London, 1951.
11. I.N.Nikolayev, V.P.Potapov, V.P.Marin, *JETP* **67**(9), 1190(1974).
12. O.B. Tsiok, V.V. Bredikhin, V.A. Sidorov, L.G. Khvostantsev, *High Press. Res.* **10**, 523(1992).
13. L.G. Khvostantsev, L.F. Vereshchagin, A.P.Novikov, *High Temp.-High Press.* **9**(6), 637(1977).

where  $M_1(r_1)$  and  $M_2(r_2)$  - sum of the magnetic moments of atoms in  $1nn$  and  $2nn$ , respectively (in  $\mu_B$  units),  $p(r)$  - empirical Delyagin function for the radial dependence of the partial contributions to the hyperfine field (in  $T/\mu_B$  units),  $C\mu$  - contribution to  $H_{Sn}^{hypf}$  proportional to the average atomic moment of the material  $\mu$ . Function  $p(r)$  is shown on the figure 4 (solid line). This curve has been constructed as a best fit to the experimental data for b.c.c. and f.c.c. magnetic compounds. Points on figure 4 are experimental values of  $p(r)$  for interatomic distances from Sn to  $1nn$  and  $2nn$  [3].

To explain the variation of  $H_{Sn}^{hypf}$  with pressure we can take into account the decrease of the interatomic distances. To calculate  $H_{Sn}^{hypf}(P)$  we assume: 1)  $M_1$ ,  $M_2$  and  $C\mu$  are approximately constant at all pressures, 2) the largest contribution to the  $H_{Sn}^{hypf}$  decrease is due to the  $p(r)$  variation. Thus we can write [3].

$$H_{hypf}^{Sn}(P) = 6p[r_1(P)] + 21.5p[r_2(P)] + 20 \cdot 1.27. \quad (2)$$

For estimating the interatomic distances with pressure, the compressibility of the sample have been measured up to 9 GPa. The equation  $(V-V_0)/V_0 = -a \cdot P + b \cdot P^2$  have been fitted to the experimental data with the coefficients  $a=7.52 \cdot 10^{-3} \text{ GPa}^{-1}$ ,  $b=1.16 \cdot 10^{-4} \text{ GPa}^{-2}$ .

The dotted curve on figure 3 was calculated from Eq.2.

The results seem to verify the Delyagin model to describe the dependence  $H_{Sn}^{hypf}$  up to 102 GPa [3].

# PRESSURE DEPENDENCE OF THE DEBYE TEMPERATURE IN ALUMINIUM, COPPER AND BRASS AT HIGH PRESSURE UP TO 6 GPa

K. SUIITO, T. SASAKURA, J. HAMA, H. FUJISAWA<sup>A</sup>

*Faculty of Engineering Science, Osaka University, Toyonaka, Osaka 560, Japan*

<sup>A</sup>*Earthquake Research Institute, University of Tokyo, Tokyo 113, Japan*

## ABSTRACT

The pressure dependence of the Debye temperature in aluminum, copper and brass were studied under quasi-hydrostatic pressure up to 6 GPa by measuring the ultrasonic wave velocities. The longitudinal and shear wave velocities were measured up to 6 GPa and at room temperature, using a split-sphere type high-pressure apparatus. The Debye temperatures ( $\theta_{D0}$ ) at atmospheric pressure and their pressure derivatives ( $d\theta_{D0}/dP$ ) are  $\theta_{D0}=387$ (K),  $d\theta_{D0}/dP=12.2$  (K/GPa) for aluminum,  $\theta_{D0}=316$ (K),  $d\theta_{D0}/dP=3.2$ (K/GPa) for copper, and  $\theta_{D0}=288$ (K),  $d\theta_{D0}/dP=3.8$ (K/GPa) for brass. The result for aluminum is compared with that of x-ray determination of the Debye temperature by Matsumuro et al.

## Introduction

The Debye temperature in a solid at high pressure provide important physical understanding of many solid-state problems. However, only a few study has been reported. Matsumuro et al.[1] determined the Debye temperature in aluminum at high pressure up to 6 GPa from the integrated intensity ratio at different temperature by using high-energy synchrotron radiation.

In the present study the pressure dependence of the Debye temperatures in aluminum, copper and brass have been obtained by measuring the ultrasonic wave velocities at room temperature. Using the pressure dependence of the Debye temperature, the melting curve of aluminum at high pressure was calculated by the Lindemann equation[2].

## Experimental method

High-pressure experiments have been carried out in a uniaxial split-sphere type apparatus. The sample were prepared in the form of cylinder with a diameter of 3.0 mm and a length of 3.5 mm. Teflon capsule with silicon grease was employed as a pressure medium to provide pseudo hydrostatic conditions. Pressure was calibrated up to 6 GPa against oil pressure by using the calibration curve obtained from resistance change of Black P(1.6GPa, 4.5GPa),

Bi(2.5GPa, 2.7GPa), Tl(3.6GPa) and Yb(4.0GPa). The errors in pressure measurement were estimated to be less than 1%.

Ultrasonic wave velocities were measured by the pulse-echo-overlap method. The precision in the measurement of ultrasonic wave velocities was estimated to be less than 0.1%. The experimental details have been described elsewhere[3].

The specimen used in the present study were polycrystalline substances of aluminum(99.6wt%), copper(99.97wt%) and Brass(Cu:56.7wt%, Zn: 39.2wt%).

## Results and Discussion

The pressure dependence of the longitudinal and transverse wave velocities in aluminum(Au), copper(Cu) and brass(CuZn) at room temperature are shown in Fig.1. In the case of elastically isotropic medium, the Debye temperature is expressed as the following;

$$\theta_D = \hbar / k (9\rho N / 4\pi MV)^{1/3} (1/V_L^3 + 2/V_T^3)^{-1/3} \quad (1)$$

$\hbar$ : Planck's constant,  $k$ : Boltzmann's constant,  $\rho$ : density,  $N$ : Avogadro's number,  $M$ : the mean atomic weight,  $V_L$ : longitudinal wave velocity,  $V_T$ : transverse wave velocity,

Using the results in Fig.1 and the equation (1), the pressure dependence of the Debye temperature in Al, Cu and CuZn at room tem-

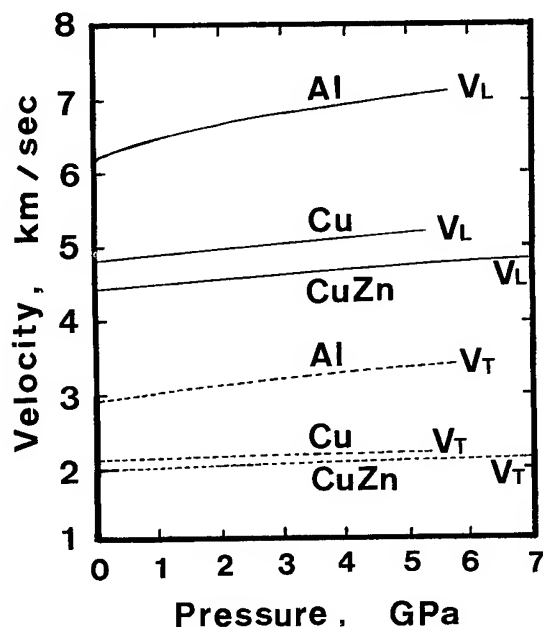


Fig.1 Pressure dependence of longitudinal ( $V_L$ ) transverse ( $V_T$ ) wave velocities for Al, Cu and CuZn.

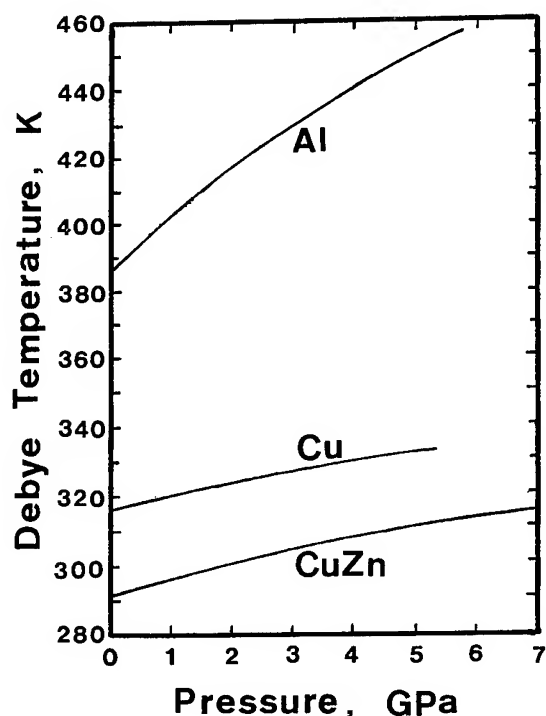


Fig.2 Pressure dependence of the Debye temperature for Al, Cu and CuZn.

perature have been obtained. The results are shown in Fig.2. The pressure dependence of the Debye temperature in Al is larger than those in Cu and CuZn. The Debye temperature ( $\theta_{D0}$ ) at atmospheric pressure and their pressure derivatives ( $d\theta_{D0}/dP$ ) are  $\theta_{D0}=387(4)$  K,  $d\theta_{D0}/dP=12.2$  (K/GPa) for aluminum,  $\theta_{D0}=316(4)$  K,  $d\theta_{D0}/dP=3.2$  (K/GPa) for copper, and  $\theta_{D0}=288(4)$  K,  $d\theta_{D0}/dP=3.8$  (K/GPa) for brass.

In Fig.3, the present results are compared with that of x-ray determination of the Debye temperature by Matsumuro et al.[1]. The results determined from the elastic constants obtained at a pressure of up to 1 GPa by the ultrasonic method [5] are also shown. Our result agree with that of Matsumuro et al. The gradients of pressure dependence for three results are similar. The Debye temperatures at atmospheric pressure are 425K(Lazarus), 387(4) K(the present study) and 367(30)K(Matsumuro et al.)

The Debye temperature can be related with many solid-state problems. Lindemann showed the Debye temperature  $\theta^M$  is related to the melting point  $T_m$ , atomic mass  $M$ , and atomic volume  $V$ , of a substance, according to the following expression[2]:

$$\theta^M = K(T_m/M)^{1/2} (1/V)^{1/3} \quad (2)$$

$K$  is a constant approximately equal to 30.

From the obtained pressure dependence of the Debye temperature and the equation (2), the melting curve at high pressure was calculated for aluminum. The result is shown in Fig.4 with the experimental results by Jayaraman et

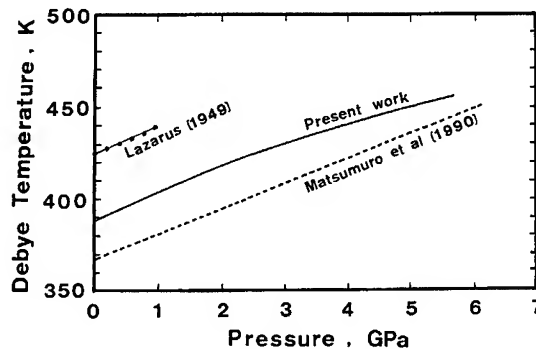


Fig.3 Comparison of our result for Al with the other results of Matsumuro et al. [1] and Lazarus[5].

al.[6] and Lees and Williamson[7]. The present result agree approximately with the experimental ones.

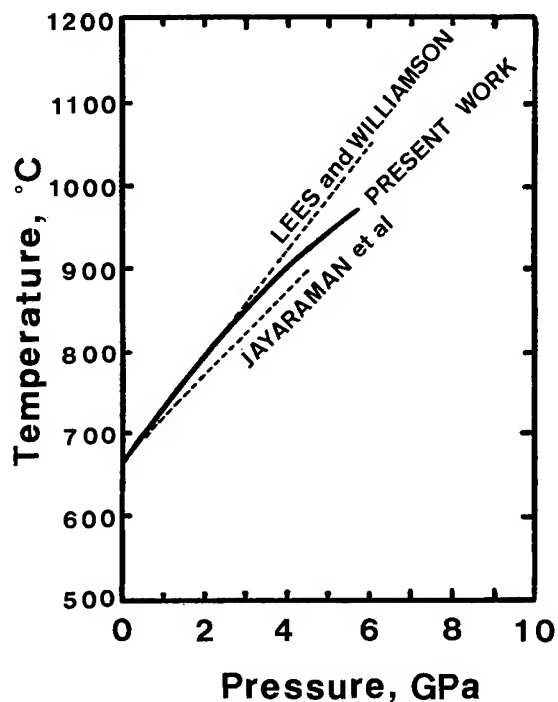


Fig.4 Calculated melting curve of Al with the experimental results of Jayaraman et al.[5] and Lee and Williamson [6].

## References

- [1] A. Matsumuro et al., *J. Appl. Phys.* **68** (1990) 2719.
- [2] K. A. Gschneider, *Solid State Physics*, Vol **16** (1964) 275.
- [3] K. Suito et al., *High pressure research; Application to Earth and Planetary Sciences*, (Tokyo/Washington D.C., TERAPUB/AGU, 1992) p217
- [4] O. L. Anderson and R. C. Liebermann, *Physical Acoustics* (Academic Press, 1968), Vol 4-B, p329.
- [5] D. Lazarus, *Phys. Rev.* **75** (1949) 545.
- [6] A. Jayaraman et al., *J. Phys. Chem. Solids* **24** (1963) 7.
- [7] J. Lees and B. H. J. Williamson, *Nature*, **208** (1965) 278

# HIGH - PRESSURE X RAY STUDY OF ZN

TAKEMURA Kenichi

*National Institute for Research in Inorganic Materials,  
Namiki 1-1, Tsukuba, Ibaraki 305 Japan*

Angle-dispersive powder x ray diffraction experiments have been carried out on Zn under pressures of up to 126 GPa at room temperature. Zn remains stable in the hcp structure over the pressure range investigated. The  $c/a$  axial ratio continuously decreases with pressure. The volume-dependence of the  $c/a$  axial ratio changes the slope at  $V/V_0 = 0.893$  ( $P = 9.1$  GPa), where the  $c/a$  ratio becomes exactly  $\sqrt{3}$ . The anomaly is most likely related to the electronic topological transition (ETT) recently found with the Mössbauer spectroscopy. On the other hand, the special value ( $\sqrt{3}$ ) of the axial ratio at the anomaly is difficult to be explained simply by the ETT.

## Introduction

Zinc has an unusually large  $c/a$  axial ratio ( $c/a=1.856$ ) for a hcp metal. Most hcp metals have the values  $c/a=1.58-1.64$ , close to the "ideal" value of 1.633. The origin of the distortion of Zn from the ideal hcp has been discussed in terms of the density of states at the Fermi energy [1] or the contribution of the  $d$  bands to the bonding [2]. Pressure affects the bonding anisotropy, which manifests itself most sensitively in the axial ratio.

The change in the axial ratio of Zn with pressure may have an anomaly. It was first reported by Lynch and Drickamer around 7 GPa [3]. Schulte, Nikolaenko, and Holzapfel, on the other hand, have found no anomaly in their x ray diffraction study on Zn up to 32 GPa [4]. The existence of the anomaly in the axial ratio of Zn is thus controversial. Meenakshi *et al.* have calculated the change in the axial ratio of Zn under pressure with the use of the linear-muffin-tin orbital (LMTO) method [5]. They noticed that the volume dependence of the axial ratio changes slope around the relative volume of 0.92.

Very recently, Potzel *et al.* have detected an anomaly in the Mössbauer spectra of Zn at  $\sim 6.6$  GPa and 4.2 K [6]. Based on the scalar-relativistic linear augmented plane wave calculation, they conclude that the anomaly is related to the topological change of the Fermi surface or an

electronic topological transition (ETT). In the present study, we report on the precise powder x ray diffraction experiments on Zn under pressures of up to 126 GPa at room temperature. Part of the present work has been reported elsewhere [7].

## Experiment

Angle-dispersive powder x ray diffraction experiments have been carried out at the Photon Factory, National Laboratory for High Energy Physics (KEK). Diffraction patterns were obtained with the use of a diamond anvil cell, synchrotron radiation, and an imaging plate. The x ray was monochromatized either to 18.00 keV or 32.57 keV. Fine powder of Zn (99 % purity) with an average particle size of 4  $\mu\text{m}$  was enclosed in the gasket hole together with ruby powder as a pressure marker, and methanol-ethanol-water mixture as a pressure transmitting medium. The pressure was determined on the basis of the ruby scale [8].

## Results and discussion

Figure 1 shows the powder x ray diffraction patterns of Zn under high pressure. Zn remains stable in the hcp structure up to the highest pressure of 126 GPa. Figure 2 shows the volume dependence of the  $c/a$  axial ratio. The  $c/a$  ratio

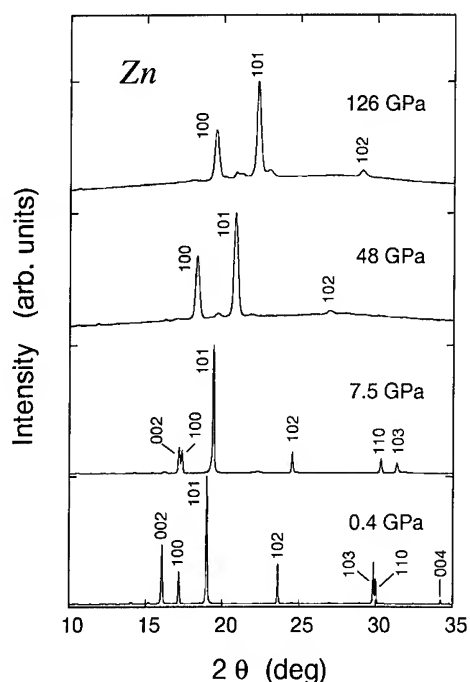


Fig. 1 Powder x ray diffraction patterns of Zn under high pressure. Weak unindexed peaks are of ZnO formed on the surface of Zn powder.

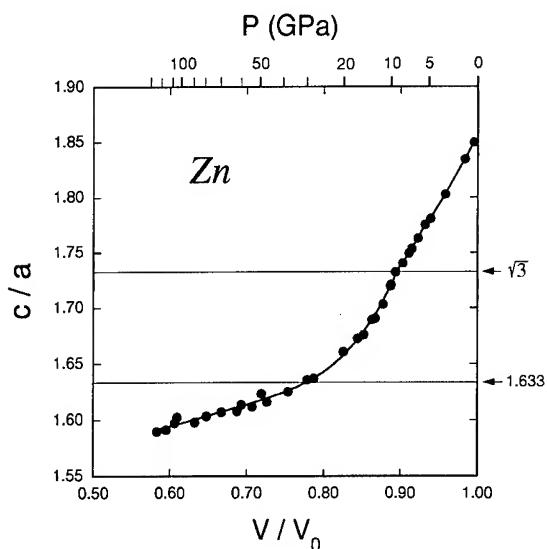


Fig. 2 The change in the  $c/a$  axial ratio of Zn as a function of the relative volume.

continuously decreases with pressure from 1.856 at atmospheric pressure to 1.59 at 126 GPa. One may expect that the axial ratio of hcp metals approaches the ideal value of 1.633 under pressure, since a close-packed structure should be more favored at high pressures. This seems to be true for Zn in the low-pressure region. However, taking the ideal value around 30 GPa, the axial ratio of Zn further decreases at higher pressures. This clearly shows that the packing of hard spheres fails to explain the bonding properties of hcp metals.

In Fig. 2 one notices that the volume-dependence of the  $c/a$  axial ratio changes the slope when the  $c/a$  ratio becomes exactly  $\sqrt{3}$ . On the other hand, there is no anomaly when the axial ratio passes through the ideal value of 1.633. Figure 3 shows the plot of the axial ratio around the anomaly. The present data are in reasonable agreement with the previous measurement by Schulte, Nikolaenko, and Holzapfel [4], but have better precision. The change in the axial ratio is also in good agreement with the LMTO calculation [5]. The location of the anomaly

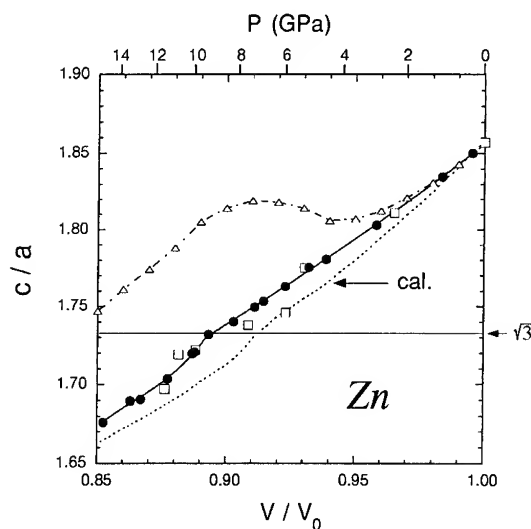


Fig. 3 The change in the  $c/a$  axial ratio around the anomaly. The solid circles are from the present experiments. The open triangles and the open squares are from Refs. 3 and 4, respectively. The dotted curve is the result of the LMTO calculation (Ref. 5).

is  $V/V_0 = 0.8932 \pm 0.0005$ ,  $P = 9.1 \pm 0.1$  GPa and  $c/a = 1.7320 \pm 0.0008$ .

Potzel *et al.* have detected an anomaly in the Mössbauer spectra of Zn at  $\sim 6.6$  GPa and 4.2 K [6]. We can estimate the axial ratio for this anomaly to be  $1.73 \pm 0.01$ , based on the axial ratio at atmospheric pressure and low temperature (1.828), and on the assumption that the volume dependence of the axial ratio at low temperature is similar to the present result at room temperature. Within the experimental errors the axial ratio for the anomaly in the Mössbauer spectra coincides with  $\sqrt{3}$ . We thus infer that the ETT takes place at  $c/a = \sqrt{3}$ . On the other hand, since the ETT is caused by the interplay between the Brillouin zone and the Fermi surface, there is no reason why the ETT takes place at such a special value ( $\sqrt{3}$ ) of the axial ratio.

In this respect we notice that a number of diffraction peaks overlap when  $c/a = \sqrt{3}$ . In other words, the reciprocal lattice vectors of the hcp lattice degenerate at  $c/a = \sqrt{3}$ . The point  $c/a = \sqrt{3}$  should be a singular point for the hcp structure, where the bonding character and the lattice dynamics may drastically change. Consequently the hcp structures above and below  $c/a = \sqrt{3}$  should be different from one another. The anomaly in the Mössbauer spectra could also be explained by this structural singularity of the hcp lattice.

Cd has also a large axial ratio  $c/a = 1.886$  at atmospheric pressure. Our preliminary x ray diffraction experiments on Cd under high pressure have revealed that the volume dependence of the axial ratio also changes the slope at  $c/a = \sqrt{3}$  [9]. This suggests that the anomaly at  $c/a = \sqrt{3}$  is a rather common feature for the hcp structure. Further theoretical investigations on this subject are encouraged.

Figure 4 shows the pressure-volume relationship of Zn up to 126 GPa. By fitting the data with the Birch-Murnaghan equation of state, we obtained the bulk modulus and its pressure derivative as  $B_0 = 66(2)$  GPa and  $B_0' = 4.6(1)$ , respectively.

## Acknowledgments

The author would like to thank Drs. N. Hamaya and

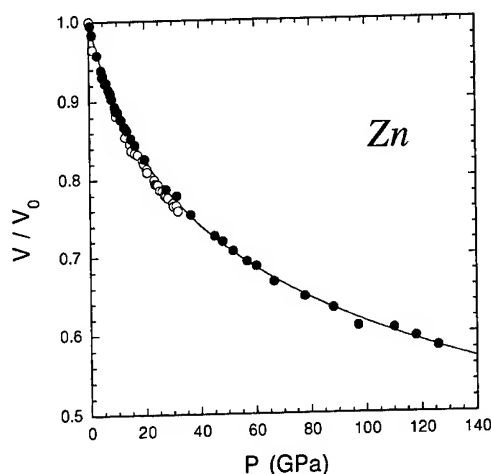


Fig. 4 The pressure-volume relationship of Zn. The solid and the open circles indicate the present result and the previous data (Ref. 4), respectively.

H. Fujihisa for their help in the experiment. He wishes to thank Dr. S.M. Sharma for informing him with the Zn problem. Part of the present work has been done under the proposal No. 93G105 and 95G138 of the Photon Factory.

## References

- [1] D. Singh and D.A. Papaconstantopoulos, Phys. Rev. **B42**, 8885 (1990).
- [2] J.A. Moriarty, Phys. Rev. **B10**, 3075 (1974).
- [3] R.W. Lynch and H.G. Drickamer, J. Phys. Chem. Solids **26**, 63 (1965).
- [4] O. Schulte, A. Nikolaenko, and W.B. Holzapfel, High Press. Res. **6**, 169 (1991).
- [5] S. Meenakshi, V. Vijayakumar, B.K. Godwal, and S.K. Sikka, Phys. Rev. **B46**, 14359 (1992).
- [6] W. Potzel, M. Steiner, H. Karzel, W. Schiessl, M. Köfferlein, G.M. Kalvius, and P. Blaha, Phys. Rev. Lett. **74**, 1139 (1995).
- [7] Takemura Kenichi, Phys. Rev. Lett. **75**, 1807 (1995).
- [8] H.K. Mao, P.M. Bell, J. W. Shaner, and D.J. Steinberg, J. Appl. Phys. **49**, 3276 (1978).
- [9] Takemura Kenichi, (unpublished).

## **VII(G) Magnetic- and Heavy-Fermion Compounds**



# PRESSURE-INDUCED INSTABILITY OF HEAVY FERMION STATE IN Ce COMPOUNDS

GENDO OOMI and TOMOKO KAGAYAMA

Department of Physics, Faculty of General Education, Kumamoto University, 2-40-1 Kurokami,  
Kumamoto 860, Japan

## ABSTRACT

Electrical resistances of three heavy fermion (HF) compounds, CeInCu<sub>2</sub>, CeAl<sub>3</sub> and CePtSi<sub>2</sub>, have been measured under high pressure. X-ray diffraction study was also carried out under high pressure at room temperature. It is found that the HF states having low Kondo temperature  $T_K$  are collapsed by an application of pressure without any volume anomalies and the pressure-induced new phase may be described as an intermediate valence state having high  $T_K$ . The Grüneisen parameter  $\Gamma$  is estimated using the present results to show that  $\Gamma$  decreases with increasing pressure accompanied by the crossover in the electronic state.

## Introduction

Electronic and magnetic properties of heavy fermion (HF) systems containing lanthanide or actinide elements have been investigated extensively because these compounds give a lot of useful information for studying the role of strong electron correlations in metals. The HF compounds are characterized by an extremely large coefficients  $\gamma$  of  $T$ -linear term in the specific heat, a large value of the coefficient of  $T^2$ -term in the electrical resistivity  $\rho(T)$  at low temperature, a  $\log T$  term in the  $\rho(T)$  at high temperature and so forth[1].

It is well known that the hybridization between  $4f$  electron and conduction band,  $V_{sf}$  plays an important role in determining the electronic state of Kondo compounds including HF substances. The electronic states of these systems are usually described by a characteristic temperature  $T_K$ , which is called "Kondo temperature" and depends on the magnitude of  $V_{sf}$  as  $T_K \propto \exp[-e_f/V_{sf}^2 N(0)]$ , where  $e_f$  is the distance between  $4f$  level and Fermi surface and  $N(0)$  is the density of state at Fermi level. The HF compounds generally have low  $T_K$  but the intermediate valence state (IVS) compounds show high  $T_K$  as much as several hundreds degree Kelvin because of large hybridization[2]. Since the value of  $V_{sf}$  is affected strongly by a change in volume or pressure, the HF state or Kondo state is expected to show a crossover in the electronic states through a large change in  $T_K$  by an application of pressure[3].

In the present paper we summarize the recent

experimental results for the Ce-compounds at high pressure. The results are explained on the basis of recent theoretical works and briefly analyzed by using volume dependent Grüneisen parameters.

## Results of high pressure study of typical heavy fermion compounds

In this section we present a brief survey of high pressure experiment of three HF compounds CeInCu<sub>2</sub>, CeAl<sub>3</sub> and CePtSi<sub>2</sub>.

CeInCu<sub>2</sub> is a cubic Heusler-type HF compound having  $\gamma$ -value of 1.2 J/mol·K<sup>2</sup> at 1 K and shows antiferromagnetic ordering below 0.8 K[4, 5].  $T_K$  is estimated to be nearly 4 K.

Figure 1 shows the pressure dependence of the electrical resistivity  $\rho$ [3].  $\rho$  increases linearly below 2 GPa showing a maximum around 3.8 GPa and then begins to decrease by further compression.

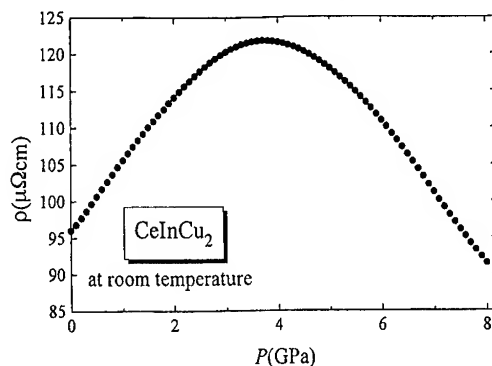


Fig. 1 Electrical resistivity  $\rho$  of CeInCu<sub>2</sub> at room temperature as a function of pressure.

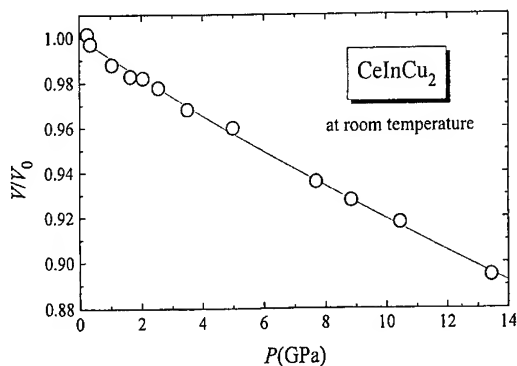


Fig. 2 Pressure dependence of volume  $V/V_0$  at room temperature.

Such behavior against pressure was observed in the other HF compounds[6]. The maximum in the  $R$ - $P$  curve is due to Kondo effect as will be mentioned later.

Figure 2 shows the relative change in volume  $V/V_0$  at room temperature, where  $V$  and  $V_0$  are the volumes at high and ambient pressure, respectively[7]. The volume of CeInCu<sub>2</sub> decreases smoothly up to 8 GPa without any anomaly. Particularly there is no discontinuity in the value of  $V/V_0$  around 4 GPa. This fact indicates that the electronic transition or the crossover in the electronic state occurs without volume anomaly and crystal structure change.

Figure 3 shows the  $\rho(T)$  curve of CeInCu<sub>2</sub> below room temperature up to 8 GPa[3]. At ambient pressure  $\rho$  increases gradually with decreasing temperature, reaches a maximum around 27 K and then decreases by further cooling. The temperature of resistivity-maximum  $T_{\max}$  is found to increase with increasing pressure and the maximum in the  $\rho(T)$  curves tends to become less clear at high pressure. Similar observations in the  $\rho(T)$  curve have been reported for other HF compounds[6].

The change in the overall behavior in the  $\rho(T)$  curves in Fig. 3 implies a pressure-induced crossover from HF state to IVS state, which has been emphasized by many authors[8, 9]. This consideration is also consistent with the theoretical predictions, which will be mentioned later.

In order to examine the pressure dependence of  $T_{\max}$  above 4 GPa we observed  $R(T)$  above room

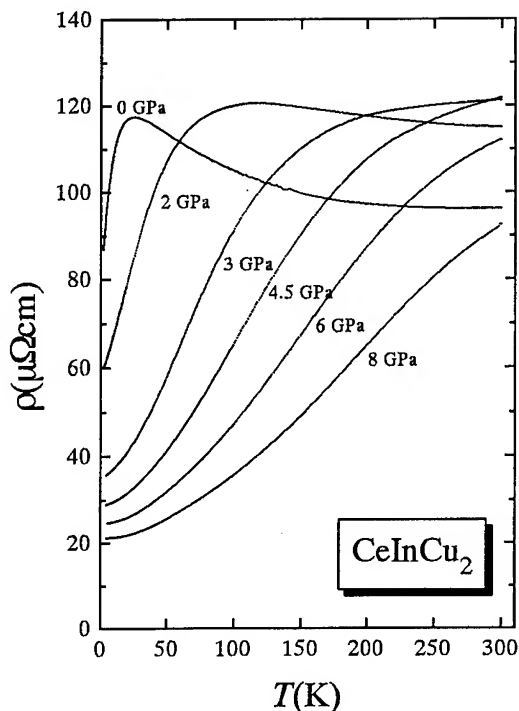


Fig. 3 Electrical resistivity  $\rho(T)$  of CeInCu<sub>2</sub> below room temperature at various pressures.

temperature. The results are shown in Fig.4[10]. The  $R(T)$  curve is found to have a broad peak because of Kondo effect.  $T_{\max}$  is indicated by an arrow in Fig. 4.

$T_{\max}$  is summarized in Fig. 5 as a function of pressure. Since  $T_{\max}$  is considered to be proportional to  $T_K$ [11], the present result indicates that  $T_K$  is enhanced by applying pressure, i.e., the

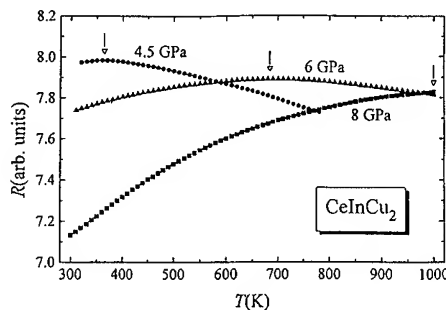


Fig. 4 Electrical resistivity  $\rho(T)$  of CeInCu<sub>2</sub> above room temperature at various pressure.

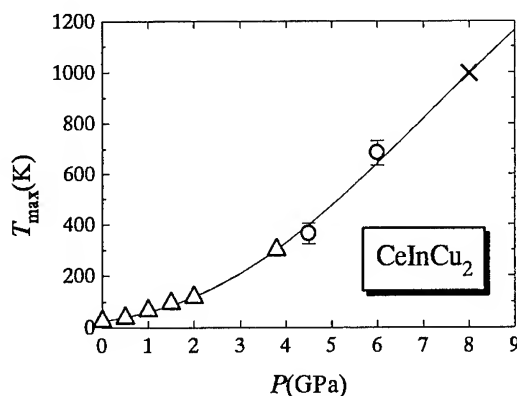


Fig. 5 Pressure dependence of  $T_{\max}$  of  $\text{CeInCu}_2$ .

HF state having low  $T_K$  changes into IVS with high  $T_K$  at high pressure. It is shown that the Grüneisen parameter  $\Gamma$  at ambient pressure is 84 but it decreases at 8 GPa to about a half[10].

$\text{CeAl}_3$  is well known as a prototypical HF compound having huge  $\gamma$ -value of  $1.5 \text{ J/mol}\cdot\text{K}^2$ [12]. Although several high pressure works have been reported until now[13, 14], there are no systematic

studies at high pressure up to 10 GPa.

Temperature dependent electrical resistivity  $\rho(T)$  is illustrated at various pressure in Fig. 6[15, 16]. At ambient pressure the  $\rho(T)$  curve shows typical HF behavior having a maximum centered around  $T_{\max}=34 \text{ K}$ . As pressure increases,  $T_{\max}$  increases, the maximum becomes broader and then there is no peak in the  $\rho(T)$  curve above 6 GPa below 300 K.  $\rho(T)$  at 8 GPa is found to be similar to that of  $\text{LaAl}_3$  which has no  $4f$  electrons. This fact indicates that the nature of localized  $4f$  electrons at ambient pressure disappears at high pressure around 8 GPa, *i.e.*, the system shows a pressure-induced crossover from HF state with low  $T_K$  to IVS with high  $T_K$ .

Figure 7 shows the pressure dependence of lattice constants  $a/a_0$  and  $c/c_0$  up to 16 GPa at room temperature, where  $a_0$  and  $c_0$  are the lattice constants at ambient pressure. The relative change of volume  $V/V_0$  is also shown in the figure. The electrical resistance of  $\text{CeAl}_3$  has a maximum near 4 GPa at room temperature[16]. There is no anomaly in the compression curve in Fig. 7 around

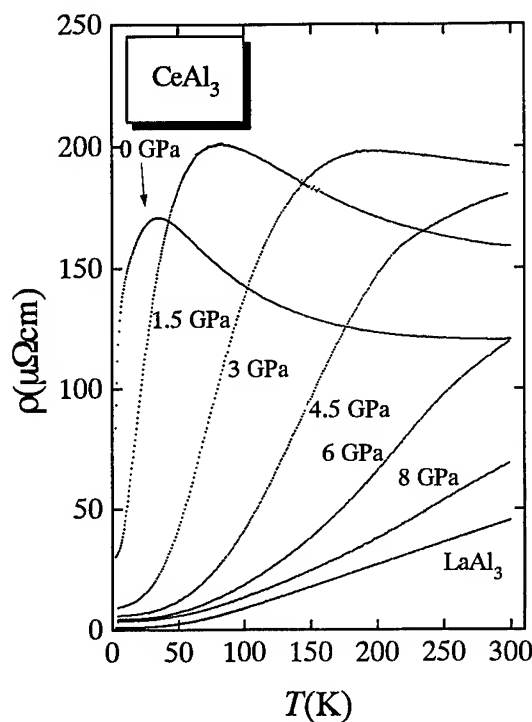


Fig. 6 Electrical resistivity  $\rho(T)$  of  $\text{CeAl}_3$  at high pressure.

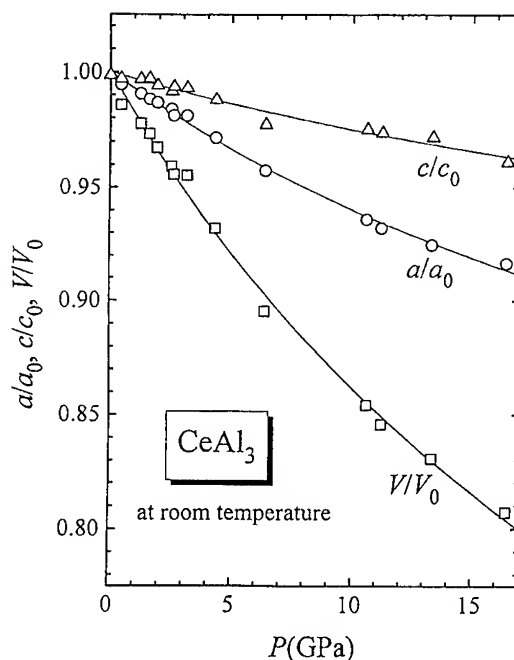


Fig. 7 Pressure dependence of lattice constants,  $a/a_0$  and  $c/c_0$  and volume  $V/V_0$  of  $\text{CeAl}_3$  at room temperature.

4 GPa. This fact also indicates that the pressure-induced crossover in  $\text{CeAl}_3$  occurs without any volume anomaly, which is the same as  $\text{CeInCu}_2$ .

$\text{CePtSi}_2$  is a magnetically ordered Kondo compound ( $T_N=1.5$  K) with a large value of  $C/T$  of about  $1.5 \text{ J/mol}\cdot\text{K}^2$  at 1.5 K[18, 19].  $T_K$  of  $\text{CePtSi}_2$  was estimated to be about 3 K. Fig. 8 shows the  $\rho(T)$  curves of  $\text{CePtSi}_2$  at high pressure up to 8 GPa and  $\text{LaPtSi}_2$  at ambient pressure[20]. A drastic change is seen in  $\rho(T)$ . At ambient pressure  $\rho(T)$  shows a typical temperature dependence of HF compound:  $\rho(T)$  increases with decreasing temperature until it shows two maxima at 28.5 K ( $=T_2$ ) and 5.4 K ( $=T_1$ ), which is due to the effect of crystalline electric field.  $\rho(T)$  of  $\text{LaPtSi}_2$  shows a smooth change against temperature, behavior as that of normal metal. This result indicates that the anomalous temperature dependence of  $\text{CePtSi}_2$  originates from the unstable  $4f$  electrons of Ce.

By applying pressure, the two maxima at  $T_1$  and  $T_2$  in the  $\rho(T)$  curve are found to merge into one maximum ( $T_{\text{max}}$ ).  $T_{\text{max}}$  also increases with

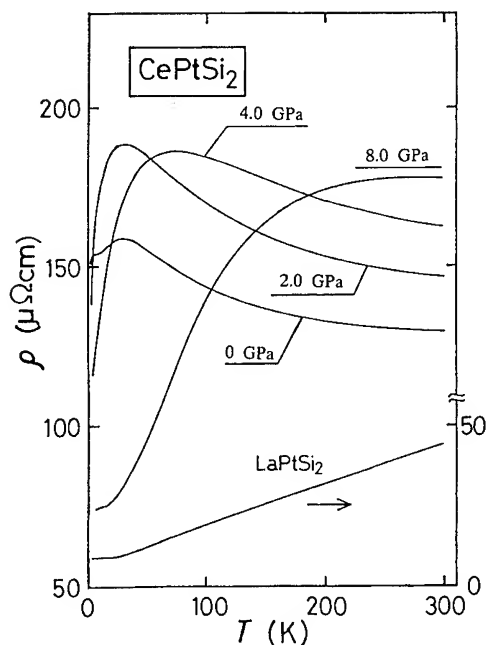


Fig. 8 Electrical resistivity  $\rho(T)$  of  $\text{CePtSi}_2$  and  $\text{LaPtSi}_2$  at various pressure.

increasing pressure but the maximum becomes broader than that at ambient pressure. It seems to be difficult to define  $T_{\text{max}}$  in the  $\rho(T)$  curve at 8 GPa.  $T^2$ -dependence in the resistivity was found above 4 GPa and the coefficient decreased with increasing pressure[20]. Similar behavior in the  $\rho(T)$  curve at high pressure has been observed in  $\text{CeCu}_2\text{Si}_2$ [8], which is interpreted as a pressure-induced crossover from the HF state (low  $T_K$ ) to the IVS (high  $T_K$ ).

Figure 9 shows  $T_1$ ,  $T_2$  and  $T_{\text{max}}$  as a function of pressure.  $T_{\text{max}}$  increases with pressure and its pressure coefficient is larger than  $\partial T_1/\partial P$  and  $\partial T_2/\partial P$ . It is difficult to determine at what pressure  $T_1$  and  $T_2$  merge into  $T_{\text{max}}$ .

## Discussion and conclusion

The pseudobinary system  $\text{Ce}(\text{In}_{1-x}\text{Sn}_x)_3$  is well known to show a crossover from HF ( $x=0$ ) to IVS ( $x=1$ ) at ambient pressure[21]. The  $\rho(T)$  at  $x=0$  ( $\text{CeIn}_3$ ) shows a well-defined maximum around 50 K. The maximum becomes less prominent with increasing  $x$ . At  $x=1$  ( $\text{CeSn}_3$ ),  $\rho(T)$  increases only monotonously with temperature ( $T<300$  K) showing that the compound is in IVS. Taking these facts into consideration, the change in the overall behavior in the  $\rho(T)$  of HF compounds at high pressure

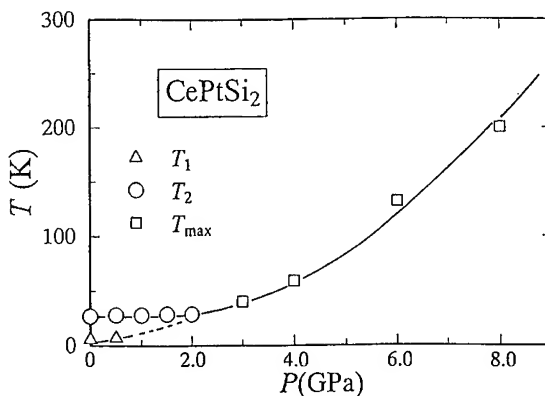


Fig. 9  $T$ - $P$  phase diagram of  $\text{CePtSi}_2$ .

observed in the preceding section implies a crossover from HF at low pressure (low  $T_K$ ) to IVS at high pressure (high  $T_K$ ). The maximum of the  $R$ - $P$  curve in Fig. 1 is due to a shift of  $T_{\max}$  to higher temperatures by applying pressure:  $T_{\max}$  may be around 300 K at 3.8 GPa for CeInCu<sub>2</sub> and 4 GPa for CeAl<sub>3</sub>. Ohkawa proposed a phase diagram of HF systems on the basis of periodic Anderson model[22]. According to that, a crossover from HF state to IVS takes place when the number of  $f$  electrons,  $n_f$ , changes from  $n_f \approx 1$  to  $n_f < 1$ . A decrease in  $n_f$  indicates an increase in  $T_K$  because  $T_K$  is roughly proportional to  $(1-n_f)/n_f$ . In the present case IVS is induced by pressure since the  $f$  electrons may be delocalized at high pressure to increase  $T_K$ . Thus the results in the present work are explained as a crossover from the HF state to the IVS induced by pressure.

Finally we discuss the present results by using volume dependent Grüneisen parameter  $\Gamma$  for Kondo temperature  $T_K$ [10].  $\Gamma$  of HF compounds has been reported to be extremely large, particularly at low temperature[23]. Assuming that  $T_K$  is proportional to  $T_{\max}$ [11],  $\Gamma$  is defined as  $\Gamma = -\partial \ln T_K / \partial \ln V = -\partial \ln T_{\max} / \partial \ln V$ . By using the present results, we can estimate the values of  $\Gamma$  as a function of volume. It was revealed [10, 24] that  $\Gamma$  decreases with increasing pressure. It is well known that the values of  $\Gamma$  of IVS compounds are smaller than those of HF ones[2]. Thus the result obtained here supports that the HF compound shows a crossover from HF state to IVS by applying pressure.

To conclude, we observe pressure-induced crossover in the electronic states of HF compounds by the electrical resistances at high pressure. The Grüneisen parameter  $\Gamma$  of HF compounds is found to decrease with pressure indicating the crossover.

#### Acknowledgement

The authors would like to express their sincere thanks to Profs. N.Möri, Y.Önuki, T.Komatsubara and Dr. J.D.Thompson for their generous cooperation and useful comments.

#### References

- [1] G.R.Stewart, Rev.Mod.Phys. **56**(1984)755.
- [2] G.Oomi and N.Möri, J.Alloys and Compounds **207&208**(1994)278.
- [3] T.Kagayama, G.Oomi, H.Takahashi, N.Möri, Y.Önuki and T.Komatsubara, Phys.Rev.B **44**(1991)7690.
- [4] Y.Önuki, T.Yamazaki, A.Kobori, T.Omi, T.Komatsubara, S.Takayanagi, H.Kato and N.Wada, J.Phys.Soc.Jpn. **56**(1987)4251.
- [5] R.Lahiouel, J.Pierre, E.Siaud, R.M.Galera, M.J.Besnus, J.P.Kappler and A.P.Murani, Z.Phys.B **67**(1987)185.
- [6] T.Kagayama and G.Oomi, Jpn.J.Appl.Phys. **32**(1993)318.
- [7] T.Kagayama, K.Suenaga, G.Oomi, Y.Önuki and T.Komatsubara, J.Magn.Magn.Mater. **90&91**(1990)451.
- [8] B.Bellarbi, A.Benoit, D.Jaccard and J.M.Mignot, Phys.Rev.B **30**(1984)1182.
- [9] G.Oomi, T.Kagayama, H.Takahashi, N.Möri, Y.Önuki and T.Komatsubara, J.Alloys&Compounds **192**(1993)236.
- [10] T.Kagayama, G.Oomi, E.Ito, Y.Önuki and T.Komatsubara, J.Phys.Soc.Jpn. **63**(1994)3927.
- [11] A.Yoshimori and H.Kasai, J.Magn.&Magn.Mater. **31-34**(1983)475.
- [12] K.Andres, J.E.Graebner and H.R.Ott, Phys.Rev.Lett. **35**(1975)1779.
- [13] A.Percheron, J.C.Achard, O.Gorochov, B.Cornut, D.Jérôme and B.Coqblin, Solid State Commun. **12**(1973)1289.
- [14] G.E.Brodale, R.A.Fisher, N.E.Phillips and J.Flouquet, Phys.Rev.Lett. **56**(1986)390.
- [15] T.Kagayama, T.Ishii and G.Oomi, J.Alloys&Compounds **207&208**(1994)263.
- [16] T.Kagayama *et al.*, (to be published).
- [17] T.Kagayama and G.Oomi, J.Magn.&Magn.Mater. **140-144**(1995)1227.
- [18] W.H.Lee, K.S.Kwan, P.Klavins and R.N.Shelton, Phys.Rev.B **42**(1990)6542.
- [19] C.Geibel, C.Kömmere, B.Seidel, C.D.Bredl, A.Grauel and F.Steglich, J.Magn.&Magn.Mater. **108**(1992)207.
- [20] G.Oomi, T.Kagayama, Y.Uwatoko, H.Takahashi and N.Möri, J.Alloys&Compounds **207&208**(1994)278.
- [21] R.A.Elenbaas, C.J.Schinkel and C.J.M.Deudekom, J.Magn.&Magn.Mater. **15-18**(1980)979.
- [22] F.J.Ohkawa, J.Magn.&Magn.Mater. **52**(1985)217.
- [23] A.de Visser, A.Lacerda, P.Haen, J.Flouquet, F.E.Kayzel and J.J.M.Franse, Phys.Rev.B **39**(1989)11301.
- [24] T.Kagayama, Thesis (1994, Kumamoto Univ.)

## PRESSURE STUDIES OF ELECTRONIC INSTABILITIES IN HEAVY-FERMION COMPOUNDS

A. DE VISSER, K. BAKKER, N.H. VAN DIJK AND J.J.M. FRANSE

*Van der Waals-Zeeman Institute, University of Amsterdam,  
Valckenierstraat 65, 1018 XE Amsterdam, The Netherlands*

### ABSTRACT

Strongly correlated electron systems may display a number of electronic instabilities, which are generally referred to as small-moment magnetism, large-moment magnetism, pseudo-metamagnetism and unconventional superconductivity. High-pressure experiments present a powerful tool to study these phenomena. We illustrate this by reviewing recent high-pressure studies on the exemplary system  $\text{U(Pt,Pd)}_3$ .

### Introduction

In the study of the basic electronic properties of intermetallic compounds a number of cerium and uranium compounds takes a special place, because they exhibit extraordinary hybridization phenomena [1]. In these materials, at elevated temperatures the magnetic and electronic properties of the 4f (Ce) or 5f (U) electrons show a localized behaviour, whereas at low temperatures ( $T \sim 10$  K) a crossover to an itinerant electron nature is observed. This delocalization is attributed to the hybridization of the f-electron wave functions with the p- or d-electron wave functions at the ligand atoms.

At the center of the research efforts are compounds where the hybridization leads to anomalously strong electronic interactions at low temperatures, giving rise to a description in terms of the Fermi-liquid model, with an enhanced quasiparticle mass exceeding the free electron mass by a factor of  $\sim 100$ . These materials are termed strongly correlated electron systems or heavy-fermion compounds. The characteristic energies of the interactions that build up the heavy-fermion state can be tuned to a large extent and, consequently, a wide range of phenomena is observed: the Kondo (lattice) effect, the Ruderman-Kittel-Kasuya-Yosida (RKKY) interaction, (weak) long-range magnetic order, pseudo-metamagnetism and unconventional (non-singlet) superconductivity. In the past years many studies have been conducted to investigate the electronic instability of the Fermi-liquid, thereby focusing on: i) the competition between the Kondo and RKKY interactions and the proximity of the

magnetic instability, ii) the occurrence of unconventional superconductivity and its interplay with antiferromagnetic order, and, more recently, iii) non-Fermi-liquid effects. Archetypal compounds which served to investigate these phenomena are prime compounds like  $\text{CeAl}_3$ ,  $\text{CeCu}_2\text{Si}_2$ ,  $\text{CeCu}_6$ ,  $\text{CeRu}_2\text{Si}_2$ ,  $\text{UPt}_3$ ,  $\text{URu}_2\text{Si}_2$ ,  $\text{UPd}_2\text{Al}_3$  and pseudobinaries or pseudoternaries based upon these.

In this paper, we choose to address the issue of the electronic instability by considering the exemplary pseudobinary heavy-fermion system  $\text{U(Pt,Pd)}_3$ , which features most of the aforementioned phenomena [2,3]. During the past decade, the electronic and magnetic properties of the  $\text{U(Pt,Pd)}_3$  system have been characterized experimentally, on high-quality single crystals, to a large extent, by a variety of techniques, which include the application of high pressures and strong magnetic fields. Special attention will be given to the effect of uniaxial pressure on the unconventional superconducting state, as well as to high-pressure experiments in very strong magnetic fields (25 T) which were carried out in order to investigate the suppression of the heavy-fermion state.

### Electronic Instabilities in the $\text{U(Pt,Pd)}_3$ System

The formation of a strongly correlated electron liquid in  $\text{UPt}_3$  below  $T^* \approx 20$  K is inferred from the thermal, magnetic and transport properties [2,4], which show the well-known heavy-fermion characteristics: a large coefficient of the linear term in the electronic specific heat,  $c(T) = \gamma T$  with

$\gamma = 420 \text{ mJ/molK}^2$ , a concurrent enhanced Pauli susceptibility,  $\chi$  (for  $T \rightarrow 0 \text{ K}$ ), and a Fermi-liquid  $\rho(T) = AT^2$  regime ( $T < 1.5 \text{ K}$ ) in the electrical resistivity, with a coefficient  $A$  enhanced two orders of magnitude over that of a standard metal. Magnetoresistance measurements [2] provide evidence that antiferromagnetic spin-fluctuation phenomena play an important role below a temperature  $T^* \sim 20 \text{ K}$ , which is further supported by the observation of a pronounced maximum in  $\chi(T)$  at  $T_{\text{max}} = 18 \text{ K}$  ( $\cong T^*$ ) [5]. However, alloying experiments, i.e. progressive replacement of U or Pt by other elements, and specific-heat studies in very strong magnetic fields (up to 24.5 T), show that competing electronic interactions (RKKY and Kondo interactions) build up the heavy-electron state.

The correlated electron liquid in  $\text{UPt}_3$  shows three remarkable instabilities: i) *pseudo-metamagnetism* at  $B^* \approx 21 \text{ T}$  (for  $T < T^*$ ) [5], which is interpreted as a strong suppression of the inter-site antiferromagnetic correlations by the applied magnetic field, ii) weak antiferromagnetic order with a Néel temperature  $T_N = 5 \text{ K}$ , which is often referred to as *small-moment antiferromagnetism* because of the extremely small ordered moment ( $|\mu| = 0.02 \mu_B/\text{U-atom}$ ) [6], and iii) *unconventional superconductivity* with two consecutive superconducting transitions in zero field at  $T_c^+ = 0.49 \text{ K}$  and  $T_c^- = 0.44 \text{ K}$  [7], and a non-trivial superconducting phase diagram, which delineates three superconducting phases exhibiting different order parameters, in the field-temperature ( $B$ - $T$ ) plane [8]. In the following three sections we will examine these electronic instabilities in more detail, thereby concentrating on the high-pressure work.

### *Pseudo-metamagnetism*

The pseudo-metamagnetic transition in  $\text{UPt}_3$  occurs at liquid helium temperatures ( $T < T^*$ ) in a very strong magnetic field  $B^* \approx 21 \text{ T}$  directed in the hexagonal plane (because of the hexagonal structure the electronic and magnetic properties are strongly anisotropic, with the hexagonal plane as the easy plane for magnetization). The transition shows up as a pronounced increase (of approximately  $0.6 \mu_B/\text{U-atom}$ ) in the magnetization [5] and as a sharp maximum in the magnetoresistance [2]. Taking into account the various thermal, magnetic, transport

and alloying studies performed on  $\text{UPt}_3$ , the 21 T anomaly is most likely connected to a strong reduction of the inter-site antiferromagnetic correlations. Specific-heat experiments in strong magnetic fields [9] have shown that fields much larger than  $B^*$  are required in order to suppress the heavy-fermion state. In a magnetic field the  $\gamma$ -value increases and passes through a pronounced maximum at  $B^*$ , where the field-induced quasi-particle mass enhancement amounts to 1.4 times the zero-field value. For fields  $B > B^*$ , the  $\gamma$ -value starts to drop, but at the maximum field applied so far (24.5 T) the  $\gamma$ -value is still larger than in zero field. This indicates that correlated electron phenomena, probably of the on-site Kondo-type, persist in very strong magnetic fields.

An important issue in modelling heavy-fermion systems is the equivalency of the thermal and magnetic energy scales [10]. In the case of  $\text{UPt}_3$  one indeed finds  $k_B T^* \approx \mu_B B^*$ . An appropriate test to check the close relation between  $T^*$  and  $B^*$  further is by the so-called *one-parameter scaling law*, which expresses that the thermal and magnetic properties can be scaled by a single volume dependent energy parameter, i.e. the relevant free energy term can be written as  $F = F(T/T^*(V), B/B^*(V))$ . Consequently, the thermal,  $\Gamma_T = -\partial \ln T^* / \partial \ln V$ , and magnetic,  $\Gamma_B = -\partial \ln B^* / \partial \ln V$ , Grüneisen parameters are equal:  $\Gamma_T = \Gamma_B$ . In the case of  $\text{UPt}_3$ ,  $\Gamma_T$  amounts to 60 [11], i.e. roughly two orders of magnitude larger than for ordinary metals, which indicates that the heavy-electron state is extremely sensitive to volume (and shape) effects. In order to verify the scaling law we have determined  $\Gamma_B$  directly in a high-field high-pressure experiment [12]. This was achieved by measuring the longitudinal magnetoresistance of a single-crystalline  $\text{UPt}_3$  sample in fields ( $B \parallel I \parallel a$ ) up to 28 T under hydrostatic pressures up to 5 kbar. The results are shown in fig.1. Upon the application of pressure, the maximum in the magnetoresistance shifts rapidly towards higher fields. The pressure variation of  $B^*$  is plotted in fig.2, from which it follows that  $dB^*/dp$  is constant over the pressure range 0-5 kbar and amounts to 0.60 T/kbar. Hence, the magnetic Grüneisen parameter  $\Gamma_B$  equals 59. The thermal Grüneisen parameter  $\Gamma_T$  of  $\text{UPt}_3$  has been determined in several ways. From the combination of thermal-expansion and specific-heat data a value of 71 results [11]. Pressure experiments (see Ref.12 and references therein)

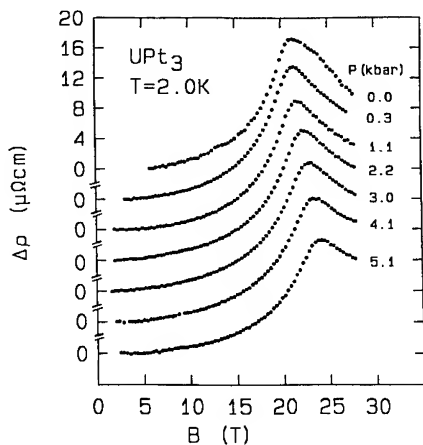


Figure 1. High-field magnetoresistance of  $\text{UPt}_3$  ( $B \parallel I \parallel a$ ) at  $T = 2.0$  K under hydrostatic pressures up to 5.1 kbar [12].

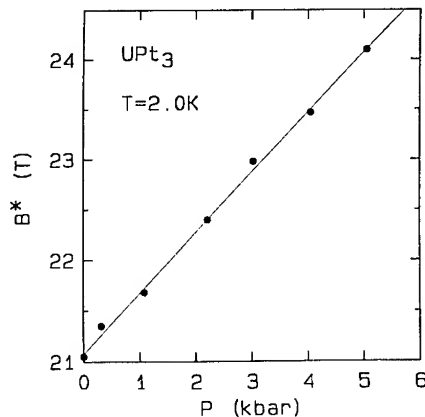


Figure 2. Pressure variation of the pseudo-metamagnetic threshold field  $B^*$  of  $\text{UPt}_3$  at  $T = 2.0$  K.  $B^*$  increases at a constant rate of 0.60 T/kbar [12].

yield values of 52 (from the pressure dependence of the coefficient of the  $T^2$ -term in the resistivity, where  $A \propto 1/(T^*)^2$ ), 58 (from the pressure-induced shift of  $T_{\text{max}} \propto T^*$  in the susceptibility) and 55 (from specific-heat experiments under pressure, where  $\gamma \propto 1/T^*$ ). Hence, we conclude  $\Gamma_T \approx \Gamma_B$ .

The one-parameter scaling law is not easily reconciled with the notion that competing electronic interactions, namely the Kondo-screening and the RKKY exchange build-up the heavy quasiparticle states, as this invokes two energy scales. The scaling via  $B^*$  suggest that inter-site fluctuations set the characteristic energy scale. However, the intricate processes of f-electron screening and f-electron exchange likely imply that the on-site and

inter-site interactions are intimately connected.

### Antiferromagnetism

The origin of the weak antiferromagnetic order observed in  $\text{UPt}_3$  at  $T_N = 5$  K with an extremely small ordered moment  $|\mu|$  of  $0.02 \pm 0.01 \mu_B/\text{U-atom}$  [6] is still subject of lively debates. Unfortunately, a detailed study is thwarted by the fact that the standard techniques for measuring thermal, magnetic and transport properties are not able to resolve the magnetic moment. Hitherto, the small-moment magnetism has only been detected by sensitive neutron-diffraction and  $\mu\text{SR}$  techniques.

However, large magnetic moments can be induced when Pt is replaced by iso-electronic Pd. Detailed studies of the thermal, magnetic and transport properties [2] of a series of  $\text{U(Pt,Pd)}_3$  compounds demonstrated that antiferromagnetic order of the spin-density wave type occurs in a limited concentration range of 1-10 at% Pd. Neutron-diffraction experiments on a 5 at% Pd sample revealed that the ordered moment is substantial,  $|\mu| = 0.6 \pm 0.2 \mu_B/\text{U-atom}$  [13], and, therefore, the order is referred to as *large-moment antiferromagnetism*. At present it is not clear whether the small and large-moment antiferromagnetism in the  $\text{U(Pt,Pd)}_3$  series are connected. Interestingly, the neutron-diffraction experiments on pure  $\text{UPt}_3$  ( $T_N = 5$  K) and on the 5 at% Pd compound ( $T_N = 5.8$  K) show that the small and large-moment antiferromagnetism have the same magnetic ordering vector ( $q = [1/2, 0, 0]$ ). However, the variation of  $T_N$  with Pd concentration, as determined from the thermal and transport properties, suggests that below  $\sim 1$  at% Pd and above  $\sim 10$  at% Pd large-moment antiferromagnetism is absent, which implies that both types of antiferromagnetism are not connected and possibly arise from different parts of the Fermi surface.

The approach of the magnetic instability in heavy-fermion systems induced by alloying is normally explained by the increase in volume (i.e. a negative chemical pressure). The volume increase weakens the hybridization and results in a reduction of the exchange coupling constant  $J$ , i.e. an increase of local f-electron character. As  $T_{\text{RKKY}} \propto N(E_F)J^2$  and  $T_K \propto e^{-1/|J|N(E_F)}$  (where  $N(E_F)$  is the density of states at the Fermi surface), the RKKY interaction dominates the Kondo interaction below a critical



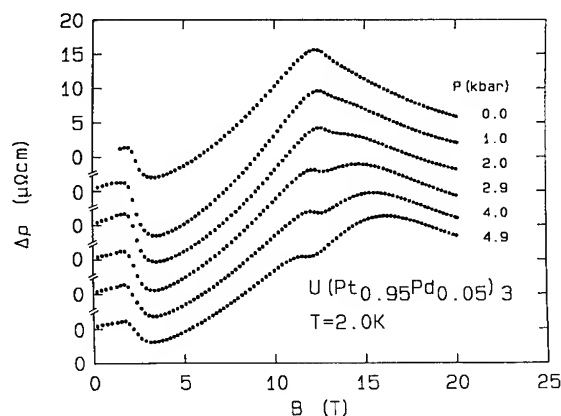


Figure 3. High-field magnetoresistance of  $U(Pt_{0.95}Pd_{0.05})_3$  ( $B \parallel I \parallel a$ ) at  $T = 2.0$  K under hydrostatic pressures up to 4.9 kbar as indicated [14].

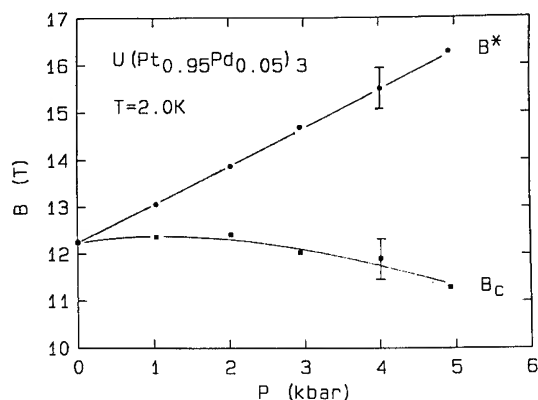


Figure 4. Pressure variation of the pseudo-metamagnetic threshold field ( $B^*$ ) and the antiferromagnetic phase boundary ( $B_c$ ) of  $U(Pt_{0.95}Pd_{0.05})_3$  at  $T = 2.0$  K [14].

value  $J < J_c$ , and antiferromagnetic order might occur. This behaviour has been delineated by the well-known Doniach phase diagram (see e.g. Ref.10). In the case of the  $U(Pt,Pd)_3$  system, however, the appearance of the large-moment magnetism is far more complex, as it cannot be explained by the volume effect. In contrary, as Pd is smaller than Pt, the volume decreases by alloying. The tendency of the f moments to localize, is therefore most likely related to a subtle decrease in the c/a ratio of the hexagonal structure on alloying by Pd, which effects the strongly anisotropic hybridization. Pressure experiments [13] up to 5 kbar on the 5 at% Pd compound show that the Néel temperature drops at a rate  $dT_N/dp = -0.3$  K/kbar, which is in line with the c/a ratio

increasing because of the anisotropic compressibility.

By substituting Pt by Pd, the pseudo-metamagnetic transition field  $B^*$  decreases gradually, which indicates that the inter-site fluctuations weaken, while for 10 at% Pd the pseudo-metamagnetic transition and the large-moment magnetism are no longer observed [2]. It is interesting to note that the size of the ordered moment for the optimal Pd content (5 at%) for long-range antiferromagnetic order is roughly equal to the increase of the moment at the pseudo-metamagnetic transition field  $B^*$  for pure  $UPt_3$  ( $0.6 \mu_B/U\text{-atom}$ ), which suggests a close relation between both types of moments. In order to elucidate this, high-field high-pressure magnetoresistance experiments [14] have been performed on a single-crystalline sample of  $U(Pt_{0.95}Pd_{0.05})_3$  for  $B \parallel I \parallel a$ . For this compound the antiferromagnetic phase boundary ( $T \rightarrow 0$  K) occurs at  $B_c = 13$  T ( $B \parallel a$ ), which shows up as a pronounced maximum in the magnetoresistance. The magnetoresistance under pressure is shown in fig.3. The anomalous behaviour at low fields ( $B < 5$  T) is related to the field effect on the magnetic domains. The most important result, inferred from fig.3, is that the antiferromagnetic phase boundary and the pseudo-metamagnetic transition are separated under pressure, but merge at zero pressure. The pressure variations of  $B_c$  and  $B^*$  are plotted in fig.4.  $B^*$  increases at a constant rate of 0.81 T/kbar, while the suppression of  $B_c$  takes place non-monotonously, so that  $B_c = 11.3$  T at 4.9 kbar. This indicates that the electronic state of pure  $UPt_3$  is restored, were the experiments to be performed at much higher pressures. These results show that when the antiferromagnetism becomes weaker ( $B_c$  drops), the pseudo-metamagnetism becomes stronger ( $B^*$  increases). For a more detailed analysis of this problem high-field high-pressure magnetization experiments are highly desirable. These could quantify the variation of the fluctuating and localized moments under pressure.

#### Unconventional Superconductivity

The occurrence of superconductivity in the strongly correlated electron liquid of  $UPt_3$  is highly remarkable, the more because the alloying studies with Pd indisputably reveal the proximity of a magnetic instability. Therefore, it has been

suggested that electron-electron interactions mediate superconductivity, instead of the conventional electron-phonon interaction. This point is however, not easily accessible by experiments, and conclusive evidence for it is lacking, although hydrostatic pressure experiments [15] have revealed a correlation between  $T_c$  and the spin-fluctuation temperature ( $T^*$ ). As far as the superconducting order parameter is concerned, the electronic activation energy studied by techniques like specific heat [7] or sound attenuation [16], yields a temperature dependence which can be expressed as a power law in  $T$ , which provides strong evidence for an unconventional ( $L \neq 0$ ) Cooper state and a superconducting gap function with reduced symmetry. Recently, research has been directed towards more solid evidence for unconventional superconductivity in  $UPt_3$ , namely the observation of a second superconducting transition that takes place at  $T_c^- = 0.44$  K, i.e.  $\sim 50$  mK below the normal-superconducting transition at  $T_c^+ = 0.49$  K [7]. In an external magnetic field a complex superconducting phase diagram is found with three distinct phases that meet at a tetracritical point (see fig.5) [8,17]. Currently, much theoretical effort is put in a phenomenological interpretation of the phase diagram using the Ginzburg-Landau (GL) formalism for second order phase transitions, where the free energy near  $T_c$  is expanded in terms of a *vector* superconducting order parameter (see Ref.18 for a review). In the most extensively studied GL model, a two-dimensional vector superconducting order parameter couples to a symmetry breaking field (SBF), which lifts the degeneracy of  $T_c$  and causes the double transition in zero magnetic field (E-model). Plausible candidates for the SBF are the small-moment antiferromagnetism found below  $T_N = 5$  K and the structural modulation which was recently detected by transmission electron microscopy [19]. An alternative GL scenario makes use of two nearly degenerate one dimensional order parameters (AB model) [18]. Clearly, the identification of the order parameters in the different superconducting phases is still not settled, although the number of possible order parameters is limited more and more, by taking into account the following experimental observations: i) the (anisotropic) power laws in the thermal properties measured below  $T_c$ , ii) the anisotropy of the phase diagram with respect to the direction of the magnetic field, iii) the unusual behaviour of the

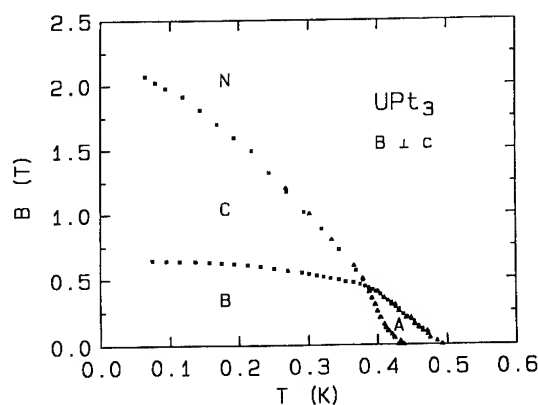


Figure 5. Superconducting phase diagram of  $UPt_3$  for  $B \perp c$ , determined from magnetostriction (■) and thermal expansion (●) data (after Ref.17).

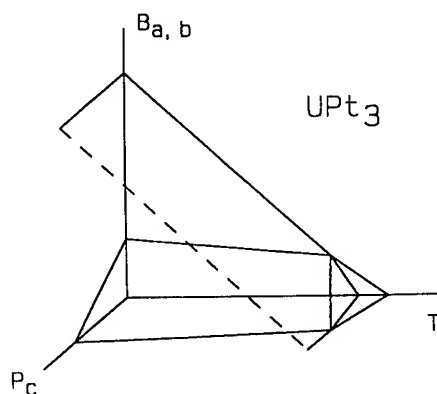


Figure 6. Schematic variation of the superconducting phases of  $UPt_3$  for a stress along the hexagonal axis and a magnetic field in the basal plane (after Ref.17). The low-field phases (A and B) disappear at moderate pressures (2-3 kbar in zero field).

surface critical field  $H_{c3}$  [20], and iv) the superconducting phase diagram as function of pressure.

Regarding the superconducting phase diagram under pressure, a number of experimental studies has been performed hitherto. Measurements of the specific heat under hydrostatic pressure [21] showed that the transitions at  $T_c^+$  and  $T_c^-$  merge at a pressure of approximately 3.7 kbar. Subsequent specific-heat measurements using uniaxial pressure [22] showed that the pressure effects are strongly anisotropic with the dominant effect for a stress along the hexagonal axis (c-axis). The uniaxial

pressure dependence of the full phase diagram in the  $B$ - $T$  plane could be derived indirectly from a combination of specific-heat and thermal expansion data in field using Ehrenfest relations [17,23]. From these experiments it could be inferred that both the so-called A and B phase disappear for a moderate stress of 2-3 kbar along the  $c$ -axis (in zero field). The schematic phase diagram for a magnetic field in the hexagonal plane ( $B_{a,b}$ - $T$ - $p_c$  parameter space) is shown in fig.6. For a stress in the basal plane the effects are at least one order of magnitude smaller. More recently, the phase diagram was mapped out directly by measuring the sound velocity under uniaxial stress along the  $c$ -axis [24]. The phase diagram as shown in fig.6 favours the AB-model over the E-model within the GL-formalisms. On the other hand, neutron-scattering experiments under pressure [25], which were conducted to investigate the role of the antiferromagnetic moment as symmetry breaking field, showed the moment to vanish at a critical pressure  $p_c \approx 4$  kbar, just as the splitting  $\Delta T_c = T_c^+ - T_c^-$ . Moreover,  $\Delta T_c$  was found to vary proportionally to the size of the antiferromagnetic moment squared  $m^2(T_c^+)$ , independent of pressure, in accordance with the E-model [18]. However, in these experiments  $T_N$  did not change with pressure, which casts some doubts on the interpretation of the data.

### Concluding Remarks

The pseudobinary  $\text{U(Pt,Pd)}_3$  series presents undoubtedly one of the best characterized heavy-fermion systems. It also features most of the electronic instabilities that are intrinsic to the heavy-electron state: small-moment and large-moment antiferromagnetism, pseudo-metamagnetism and unconventional superconductivity. In order to investigate the suppression of the heavy-fermion state, high-pressure techniques must be combined with high-magnetic field techniques, while uniaxial pressure studies are essential for examining the unconventional superconducting state. We trust that the experiments reviewed here illustrate the richness of heavy-fermion physics. The interrelation of these phenomena, as hinted by the pressure experiments, should present a challenge for further theoretical studies.

### References

1. See e.g.: N. Grewe and F. Steglich, in *Handbook of Physics and Chemistry of Rare Earth*, Vol. 14, ed. K.A. Gschneidner, Jr., and L. Eyring (Elsevier Science Publishers, 1991), p.343.
2. A. de Visser, A. Menovsky and J.J.M. Franse, *Physica* **147B** (1987) 81.
3. A. de Visser and J.J.M. Franse, *J. Magn. Magn. Mat.* **100** (1994) 204.
4. A. de Visser, in *Transport and Thermal Properties of f-Electron Systems*, ed. G. Oomi, H. Fujii and T. Fujita (Plenum Press, 1993), p.203.
5. P.H. Frings, J.J.M. Franse, F.R. de Boer and A. Menovsky, *J. Magn. Magn. Mat.* **31-34** (1983) 240.
6. G. Aeppli, E. Bucher, C. Broholm, J.K. Kjems, J. Baumann and J. Hufnagl, *Phys. Rev. Lett.* **60** (1985) 615.
7. R.A. Fisher, S. Kim, B.F. Woodfield, N.E. Phillips, L. Taillefer, K. Hasselbach, J. Flouquet, A.L. Giorgi and J.L. Smith, *Phys. Rev. Lett.* **62** (1989) 1411.
8. G. Bruls, D. Weber, B. Wolf, P. Thalmeier, B. Lüthi, A. de Visser and A. Menovsky, *Phys. Rev. Lett.* **65** (1990) 2294.
9. H.P. van der Meulen, Z. Tarnawski, A. de Visser, J.J.M. Franse, J.A.A.J. Perenboom, D. Althof and H. van Kempen, *Phys. Rev.* **B41** (1990) 9352.
10. See e.g.: J.D. Thompson and J.M. Lawrence, *Handbook on the Physics and Chemistry of Rare Earth*, Vol 19, ed. K.A. Gschneidner, Jr., L. Eyring, G.H. Lander and G.R. Choppin (Elsevier Science Publishers, 1994), p.383.
11. A. de Visser, J.J.M. Franse and J. Flouquet, *Physica* **B161** (1989) 324.
12. K. Bakker, A. de Visser, A.A. Menovsky and J.J.M. Franse, *Phys. Rev.* **B46** (1992) 544.
13. J.J.M. Franse, K. Kadowaki, A. Menovsky, M. van Sprang and A. de Visser, *J. Appl. Phys.* **61** (1987) 3380.
14. K. Bakker, A. de Visser, A.A. Menovsky and J.J.M. Franse, *Physica* **B186-188** (1993) 687.
15. J.O. Willis, J.D. Thompson, Z. Fisk, A. de Visser, J.J.M. Franse and A. Menovsky, *Phys. Rev.* **B31** (1985) 1654.
16. B.S. Shivaram, Y.H. Jeong, T.F. Rosenbaum and D.G. Hinks, *Phys. Rev. Lett.* **56** (1986) 1078.
17. N.H. van Dijk, A. de Visser, J.J.M. Franse, S. Holtmeier, L. Taillefer and J. Flouquet, *Phys. Rev.* **B48** (1993) 1299.
18. J.A. Sauls, *Adv. Phys.* **43** (1994) 113.
19. P.A. Midgley, S.M. Hayden, L. Taillefer, B. Bogenberger and H. von Löhneysen, *Phys. Rev. Lett.* **70** (1993) 678.
20. N. Keller, J.L. Tholence and J. Flouquet, preprint.
21. T. Trappmann, H. von Löhneysen and L. Taillefer, *Phys. Rev.* **B43** (1991) 13714.
22. D.S. Jin, S.A. Carter, B. Ellman, T.F. Rosenbaum and D.G. Hinks, *Phys. Rev. Lett.* **68** (1992) 1597.
23. N.H. van Dijk, A. de Visser, J.J.M. Franse and L. Taillefer, *J. Low Temp. Phys.* **93** (1993) 101.
24. M. Boukhny, G.L. Bullock, B.S. Shivaram and D.G. Hinks, *Phys. Rev. Lett.* **73** (1994) 1707.
25. S.M. Hayden, L. Taillefer, C. Vettier and J. Flouquet, *Phys. Rev. Lett.* **46** (1992) 8675.

## HIGH PRESSURE STUDY OF CeTX COMPOUNDS

T.ISHII, G.OOMI, Y.UWATOKO<sup>a</sup>, T.TAKABATAKE<sup>b</sup> and S.K.MALIK<sup>c</sup>

*Department of Physics, Faculty of General Education, Kumamoto University,  
Kumamoto 860, Japan*

*<sup>a</sup>Department of Physics, Faculty of Science, Saitama University  
Urawa, Saitama 338, Japan*

*<sup>b</sup>Faculty of Integrated Arts and Science, Hiroshima University,  
Higashi-Hiroshima, Hiroshima 734, Japan*

*<sup>c</sup>Tata Institute of Fundamental Research, Homi Bhabha Road, Coraba,  
Bombay 400 005, India*

### ABSTRACT

Electrical resistivity of CeRhSb and CePtGa has been measured under hydrostatic pressure up to 2.3 GPa. In an antiferromagnetic Kondo compound CePtGa with  $T_N=3.5$  K,  $T_N$  decreases with increasing pressure and disappears above 1 GPa. On the other hand, in a mixed valent Kondo insulator CeRhSb, the hybridization gap is enhanced by applying pressure.

### Introduction

Recently a wide variety of electronic and magnetic properties of Ce-based ternary compounds has attracted a lot of interest of many investigators [1]. These properties are mainly dominated by the magnitude of hybridization between localized 4f electrons and conduction band. On this point of view, pressure is a good probe to study electronic structure of this system because we can control the hybridization strength by applying pressure.

In this paper, we concentrate our attention on two compounds, CePtGa and CeRhSb. Both compounds crystallize in the orthorhombic TiNiSi-type structure, but CePtGa is a concentrated Kondo compound with antiferromagnetic ordering below  $T_N=3.5$  K [2]. On the other hand, CeRhSb is a mixed valent compound having a gap which grows with decreasing temperature [3].

In order to get the information about the relation between hybridization effect and the electronic structure in these compounds, we made an attempt to measure the electrical resistivity  $\rho(T)$  of CePtGa and CeRhSb under hydrostatic pressure

up to 2.3 GPa.

### Experimental procedure

Polycrystalline samples of CeRhSb and CePtGa were prepared by arc melting in a purified argon atmosphere. Hydrostatic pressure up to 2.3 GPa was generated by using a Cu-Be piston-cylinder device and a 1:1 mixture of Fluorinert, FC 70 and 77 as a pressure transmitting medium. The pressure was kept constant by means of controlling the load within  $\pm 1\%$  throughout the measurement. Electrical resistivity was measured in temperature range from 2 K to 300 K by a standard dc four-probe technique.

### Results and Discussion

Figure 1 shows magnetic contribution to  $\rho(T)$  of CePtGa,  $\rho_{\text{mag}}(T)$ , at various pressures.  $\rho_{\text{mag}}(T)$  was estimated in a conventional way by subtracting the resistivity of LaPtGa. At ambient pressure,  $\rho_{\text{mag}}(T)$  of CePtGa exhibits a peak at  $T=3.4$  K corresponding to antiferromagnetic ordering [2]. Above 3.4 K,  $\rho_{\text{mag}}(T)$  shows  $\log T$  dependence in two temperature range,  $7 \text{ K} < T < 15 \text{ K}$

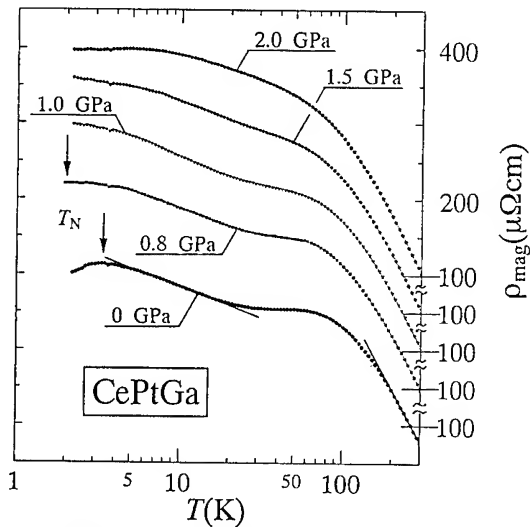


Figure 1: Magnetic contribution to electrical resistivity  $\rho_{\text{mag}}(T)$  of CePtGa as a function of temperature under various pressures. Néel temperature  $T_N$  is shown by arrows.

and  $250 \text{ K} < T < 300 \text{ K}$ . This is a typical behavior of Kondo compounds having non-cubic crystal structure by crystal field splitting such as  $\text{CeCu}_2\text{Si}_2$  [4].  $\rho_{\text{mag}}(T)$  increases with increasing pressure as a whole and turns to smooth temperature dependence at 2 GPa. Similar change is observed in  $\text{CePtSi}_2$  [5]. Two Kondo peaks due to crystalline field splitting are merged at high pressure. The peak due to antiferromagnetic ordering shifts to lower temperature and above 0.8 GPa, it is not observed down to 2 K. This variation against pressure reflects the competition between Kondo effect and RKKY interactions. According to Doniach [6], if hybridization strength is large enough, Kondo effect would dominate over RKKY interaction, and then the magnetism may be suppressed. Since Kondo effect favors non-magnetic ground state, CePtGa loses the magnetic ordering at high pressures.

Néel temperature  $T_N$  is plotted as a function of pressure in Fig. 2.  $T_N$  is defined as the temperature where  $\rho(T)$  curve exhibits a peak

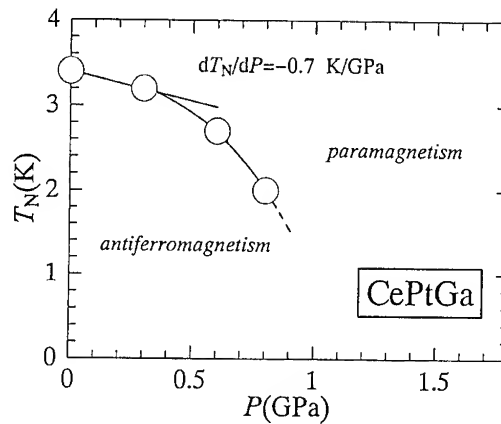


Figure 2 Néel temperature  $T_N$  of CePtGa as a function of pressure. The solid curve is a guide to eye.

(shown by arrows).  $T_N$  decreases with increasing pressure having an initial rate of  $dT_N/dP = -0.7 \text{ K/GPa}$ . By a simple extrapolation,  $T_N$  seems to disappear around 1.2 GPa. Hence above 1.2 GPa, CePtGa may be a nonmagnetic Kondo compound. We note that at 2 GPa  $\rho_{\text{mag}}(T)$  exhibits a new maximum around 6 K, which may correspond to Kondo temperature.

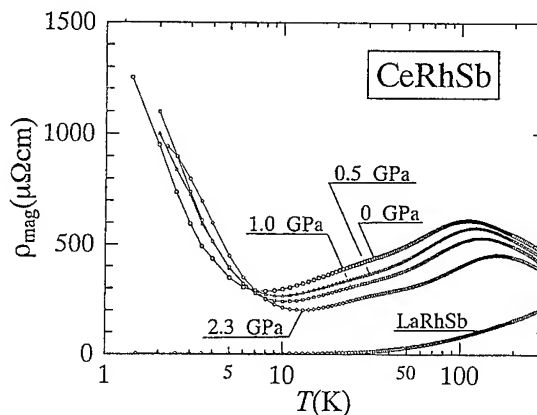


Figure 3  $\rho_{\text{mag}}(T)$  of CeRhSb as a function of temperature under various pressures.

Figure 3 presents  $\rho_{\text{mag}}(T)$  of CeRhSb under various pressures in logarithmic scale of  $T$ . At ambient pressure,  $\rho_{\text{mag}}(T)$  exhibits a broad maximum centered around  $T_{\text{max}} = 120 \text{ K}$  and decreases with decreasing temperature due to

development of coherent Kondo state. At lower temperatures, rapid increase in  $\rho_{\text{mag}}(T)$  is observed, which is due to a gap opening in the narrow band of heavy quasiparticles. Both characteristic temperatures,  $T_{\text{max}}$  and  $T_{\text{min}}$  where  $\rho_{\text{mag}}(T)$  shows a broad maximum and a minimum respectively, increase by applying pressure. The result indicates that both coherency and hybridization gap in CeRhSb are enhanced at high pressure. However,  $\rho_{\text{mag}}(T)$  at 2.3 GPa seems to saturate below 4.2 K. According to electrical resistivity measurement under higher pressure, the gap turns to decrease above 3 GPa [7]. Therefore, this saturation reflects an instability of the gap under high pressure.

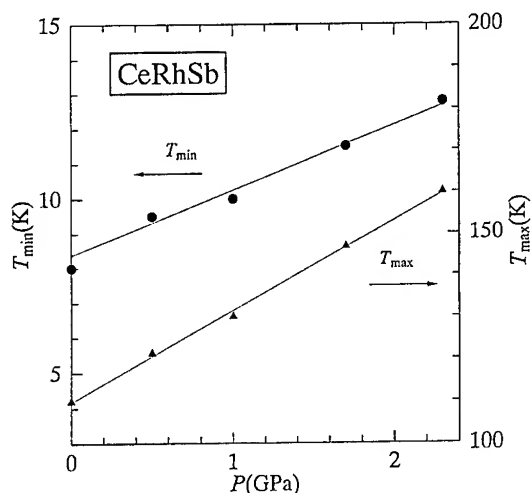


Figure 4: Pressure dependence of characteristic temperature  $T_{\text{max}}$  and  $T_{\text{min}}$ .

Figure 4 shows pressure dependence of  $T_{\text{max}}$  and  $T_{\text{min}}$ . Both  $T_{\text{max}}$  and  $T_{\text{min}}$  increase with increasing pressure having a rate of  $dT_{\text{max}}/dP=21.8$  K/GPa and  $dT_{\text{min}}/dP=1.9$  K/GPa respectively. This suggests that the origin of the gap is closely related with coherency.

In conclusion, we have reported the electrical resistivity of CePtGa and CeRhSb under hydrostatic pressure. For CePtGa,  $T_N$  decreases with increasing pressure having an initial rate of  $dT_N/dP=-0.7$  K/GPa and disappears above 1.2 GPa. For CeRhSb, two characteristic temperatures  $T_{\text{max}}$  and  $T_{\text{min}}$  increase with increasing pressure having a rate of  $dT_{\text{max}}/dP=21.8$  K/GPa and  $dT_{\text{min}}/dP=1.9$  K/GPa, respectively. The results indicate that the hybridization gap is enhanced with coherency by applying pressure.

### References

1. See, for example, S. K. Malik and D. T. Adroja in *Transport and Thermal Properties of f-Electron Systems*, ed. G. Oomi, H. Fujii and T. Fujita, (Plenum, 1993) p. 55.
2. J. Sakurai, Y. Yamaguchi, S. Nishigori, T. Suzuki and T. Fujita, *J. Magn. Magn. Matter.* **90&91**(1990) 422.
3. S. K. Malik and D. T. Adroja, *Phys. Rev. B* **43** (1991) 6277.
4. B. Bellarbi, A. Benoit, D. Jaccard and J. M. Mignot, *Phys. Rev. B* **30**(1984) 1182.
5. G. Oomi, T. Kagayama, Y. Uwatoko, H. Takahashi and N. Mori, *J. Alloys Comp.* **207&208**(1994) 278.
6. S. Doniach, in *Valence Instabilities and Related Narrow-Band Phenomena*, ed. R. D. Parks (Plenum, 1977) p. 169.
7. Y. Uwatoko *et al.*, to be published.

## PRESSURE-INDUCED VALENCE CHANGES IN $\text{Yb}_4\text{As}_3$

N. MÔRI, H. TAKAHASHI, Y. OKUNUKI, S. NAKAI<sup>1</sup>, T. KASHIWAKURA<sup>1</sup>,  
A. KAMATA<sup>1</sup>, H. TEDUKA<sup>1</sup>, Y. KOZUKA<sup>1</sup>, Y. YOKOHAMA<sup>1</sup>, Y. HAGA<sup>2</sup>,  
A. OCHIAI<sup>3</sup>, T. SUZUKI<sup>4</sup> and M. NOMURA<sup>5</sup>

*Institute for Solid State Physics, The University of Tokyo, Roppongi, Minato-ku, Tokyo 106, Japan*

<sup>1</sup>*Faculty of Engineering, Utsunomiya University, 2753 Ishii, Utsunomiya 321, Japan*

<sup>2</sup>*Japan Atomic Energy Research Institute, Tokai, Ibaraki 319-11, Japan*

<sup>3</sup>*The Oarai Branch, Institute for Material Research, Tohoku University, Oarai, Ibaraki 311-13, Japan*

<sup>4</sup>*Department of Physics, Faculty of Science, Tohoku University, Sendai 980, Japan*

<sup>5</sup>*National Laboratory for High Energy, Photon Factory, Tsukuba, Ibaraki 305, Japan*

### ABSTRACT

The increase of the trivalent component in  $\text{Yb}_4\text{As}_3$  has been clearly observed with increasing pressure. This behavior corresponds well to the decrease in the phase transition temperature associated with an order-disorder transition due to the atomic arrangement between  $\text{Yb}^{3+}$  and  $\text{Yb}^{2+}$ . The spectrum at atmospheric pressure, however, shows no change in valency above and below the transition temperature. These results indicate that the order-disorder phase transition is affected strongly by the trivalent component and that the anomalous transport properties are caused by the change in the band structure associated to this phase transition.

### Introduction

$\text{Yb}_4\text{As}_3$  shows the structural phase transition at around 300 K. It shows the cubic anti- $\text{Th}_3\text{P}_4$  structure and a small trigonal distortion above and below the transition temperature, respectively. This material is a mixed valence compound with the ratio of  $\text{Yb}^{2+}$  and  $\text{Yb}^{3+}$  being 3:1. It is thought that  $\text{Yb}_4\text{As}_3$  is in the thermal valence fluctuating state above the phase transition temperature and in the charge ordered state below it. Its large  $\gamma$ -value of specific heat ( $\gamma \sim 200 \text{ mJ/molK}^2$ ) and large  $T^2$ -coefficient of the resistivity at low temperature specify  $\text{Yb}_4\text{As}_3$  as one of the heavy Fermion compounds<sup>(1)</sup>.

An unusual feature of this compound is

that the heavy Fermion properties arise even though the density of charge carriers is extremely low. Recent experiment on the temperature dependence of the resistivity and of the Hall coefficient under pressure revealed that the carrier number changes drastically with temperature and pressure<sup>(2)</sup>.

In order to investigate the relation between the anomalous transport phenomena and the pressure-induced valence changes in  $\text{Yb}_4\text{As}_3$ , an x-ray absorption spectroscopy was applied using diamond anvil cells in synchrotron radiation and the electrical resistivity was measured up to 8 GPa using a cubic anvil apparatus.

## Experimental

We used good qualified single crystalline samples of  $\text{Yb}_4\text{As}_3$  which were prepared by Ochiai et al.<sup>(1)</sup> The temperature dependence of the resistivity was measured using a four-terminal method under high pressure up to 8GPa. The pressure was generated in a cubic anvil apparatus with a 1:1 mixture of Fluorinert FC-70 and FC-77 as a pressure transmitting medium. In order to achieve hydrostatic conditions, the measurements were carried out at fixed pressure with variable temperature between 4.2-320K, the applied pressure changed at room temperature after each low temperature run. The pressure was calibrated using the superconducting transition temperature of Pb at low temperature.

The x-ray absorption measurements were performed at room temperature in transmitting geometry on powdered sample at the EXAFS beamline of KEK Photon Factory using a Si(111) monochromator providing a energy resolution of about  $\sim 2$  eV at Yb  $L_{\text{III}}$ -thresholds at 8.9eV. The pressure was generated using a diamond anvil cells, where the sample was contained in the hole in a metal gasket.

## Results and Discussion

Figure 1 shows the temperature dependent resistivity of  $\text{Yb}_4\text{As}_3$  at various pressures. The resistivity decreases rapidly with increasing pressure. The phase transition temperature decreases strongly with pressure. It disappears at a pressure near 9GPa. Above the phase transition temperature, the resistivity increases with a T-linear relationship. Below the transition temperature, however, the resistivity exhibits unusual behavior. A broad peak observed at around 170K at 2.5GPa is shifted toward lower temperature with increasing pressure. The resistivity shows  $T^2$  dependence below 50 K. The temperature coefficient is reduced rapidly with increasing pressure. The residual resistivity also decreases rapidly with pressure. The initial pressure derivative of the residual resistivity is about -50%/GPa which is almost the same value as that of the Hall coefficient<sup>(2)</sup>.

$L_{\text{III}}$ -edge absorption spectra at room temperature for  $\text{Yb}_4\text{As}_3$  at different pressures are shown in Fig.2 together with the spectra of  $\text{Yb}_2\text{O}_3$  at 0GPa as a reference of  $\text{Yb}^{3+}$ . The intensity of the  $\text{Yb}^{3+}$  component is seen to increase largely with

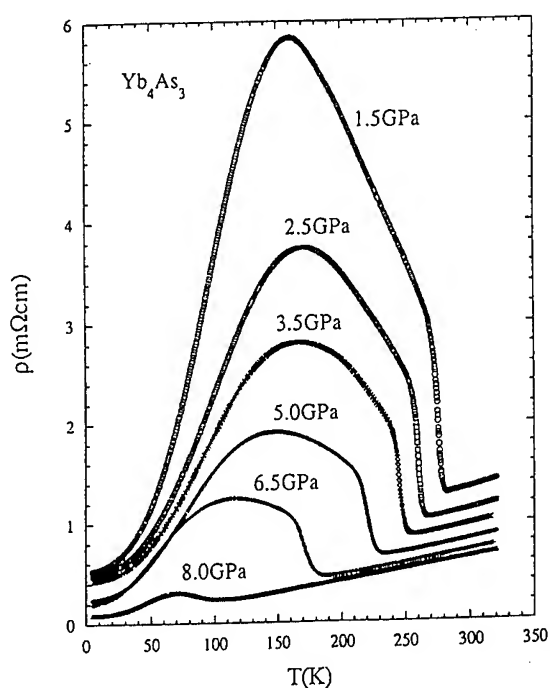


Figure 1. Resistivity vs temperature at various pressures.

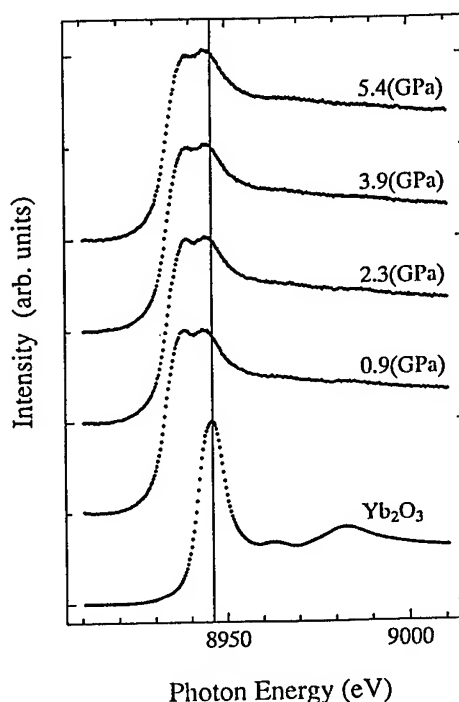


Figure 2.  $L_{\text{III}}$ -edge absorption spectra.



pressure. The change of the intensity ratio as a function of pressure is shown in Fig.3. This result clearly indicates that the  $\text{Yb}^{3+}$  is stabilized under high pressure in  $\text{Yb}_4\text{As}_3$  as similar as in other Yb compounds<sup>(3)</sup>. It is noted, however, that at ambient pressure we could not find any change in the spectra below and above the phase transition temperature.

From the measurements of electrical resistivity, especially the large suppression of the residual resistivity induced by pressure the low temperature transport property is shown to be explained well if one assumes one carrier model as proposed before<sup>(2)</sup>. In case of one carrier model, the pressure derivative of residual resistivity is given by

$$d\ln\rho_0/dP = d\ln m^*/dP - d\ln n/dP - d\ln\tau/dP$$

where  $m^*$  is the effective mass,  $n$  the number of carrier and  $\tau$  the relaxation time. Taking into account that the impurity concentration does not change under pressure and the Fermi velocity is inversely proportional to the effective mass,

$$d\ln\rho_0/dP \sim -d\ln n/dP.$$

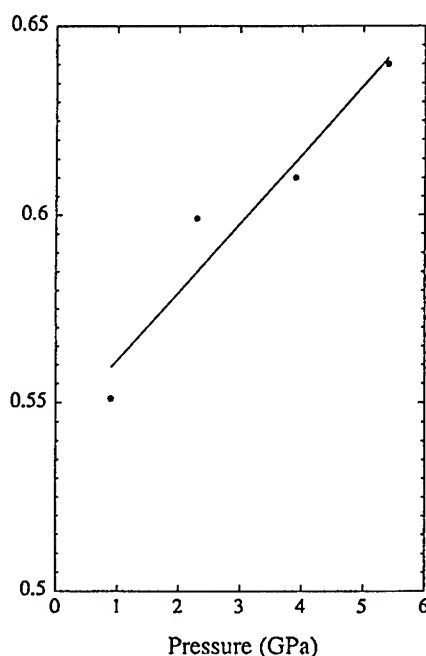


Figure 3. Intensity ratio as a function of pressure.

This result agrees well with our experimental data<sup>(2)</sup>. To explain the anomalous transport behavior, more realistic two-band model is applied by Kasuya<sup>(4)</sup>.

On the other hand, from the  $L_{III}$ -edge absorption spectra the large suppression of the phase transition temperature seems to correlate to the increase in the trivalent component. Furthermore, the anomalous transport behavior observed below the phase transition is caused not by the change in valency, but by change in the band structure associated to this phase transition. These experimental results may be explained by a model proposed by Fulde et al.<sup>(5)</sup> which is based on a band Jahn-Teller effect of correlated electron system. It is worth noticing, however, that the pressure dependence of the  $T^2$ -coefficient of the resistivity contrasts with other Yb based heavy Fermion compounds, in which the sign of the pressure derivatives of the coefficient tends to be positive<sup>(6)</sup>.

To make clear the electronic structure in this compound, the determination of the Fermi surface under pressure is required.

#### Acknowledgments

The authors like to thank Professor T.Kasuya for fruitful discussions. This work was supported by a Priority-Areas Grant from Ministry of Education, Science and Culture.

#### References

1. A.Ochiai, T.Suzuki and T.Kasuya, *J. Phys. Soc. Jpn.* 59 (1990) 4124.
2. Y.Okunuki, N.Mori, A.Ochiai, Y.Haga, and T.Suzuki, *J. Phys. Soc. Jpn.* 64 (1995) 533.
3. G.Schmiester, G.Wortmann, H.Winzen, K.Syassen and E.Kaldis, *High Pressure Research* 3 (1990) 186.
4. T.Kasuya, *J. Phys. Soc. Jpn.* 63 (1994) 2481.
5. P.Fulde, B.Schmidt and P.Thalmeier, *preprint*

## **VII(H) Other Solids**

# MÖSSBAUER AND XPS STUDIES ON $\text{Sr}_{1-x}\text{Eu}_x\text{TiO}_{3+y}$ SYNTHESIZED BY HIGH PRESSURE AND TEMPERATURE

LI LIPING<sup>a</sup>, WEI QUAN<sup>b</sup>, SU WENHUI<sup>a,c,d</sup>

<sup>a</sup>(Department of Physics, Jilin University, Changchun 130023)

<sup>b</sup>(The Center of Measurement and Analysis, Jilin University, Changchun 130023)

<sup>c</sup>(Center for Condensed Matter and Radiation Physics, CCAST(World Lab.) P.O.Box 8730, Beijing 100080)

<sup>d</sup>(International Centre for Materials Physics, Academia Sinica, Shenyang 110015)

## ABSTRACT

The high pressure and temperature method was used to synthesize the compound of  $\text{Sr}_{1-x}\text{Eu}_x\text{TiO}_{3+y}$  ( $x=0.0-0.5$ ). The analysis of XRD shows that the sample is cubic structure. The results of XPS and Mossbauer spectra indicate that there is a mixing valence Eu(II) and Eu(III) in the compound. With  $x$  increasing, Eu(II)/Eu(III) increases. The charge of  $(\text{TiO}_{3+y})^{n-}$  calculated from the ratio of Eu(II) to Eu(III) is about 2.1, 2.15 and 2.2 for  $x=0.3, 0.4, 0.5$  respectively.

## Introduction

We have known that the stable valence of metal element Ti is +4 in compound. It is very difficult to obtain single phase of  $\text{ATiO}_3$  (A=alkali earth metals) which are doped with rare earth ions by solid state reaction method. So, to obtain such compounds as  $\text{A}_{1-x}\text{R}_x\text{TiO}_{3+y}$  (A=alkali earth ions, R=rare earth ions), some special methods are necessary[1, 2]. In this paper, the high pressure and temperature method was used to synthesize the compound  $\text{Sr}_{1-x}\text{Eu}_x\text{TiO}_{3+y}$ . To obtain information about the change of valence of Eu, XPS and Mossbauer spectra are measured.

## Experiment

The raw materials of  $\text{SrCO}_3$ ,  $\text{Eu}_2\text{O}_3$  and  $\text{TiO}_2$  used in experiment were weighed according to stoichiometric relation of  $\text{Sr}_{1-x}\text{Eu}_x\text{TiO}_{3+y}$ . The well ground mixture was pressed into 6mm cylinder under a pressure of 0.5GPa, then put into high-pressure chamber, following by loading pressure to 2.7GPa. The temperature was then increased gradually to 1000°C. After being kept at high temperature and pressure for 30min, the specimen was quenched to room temperature under high pressure, and finally the pressure was released. The high pressure chamber used here is the same as that described in reference[3]. The sample was examined at room temperature on a Rigaku 12KW Copper rotating anode X-ray diffractometer with a graphite monochromator attachment. The XPS for powder sample was measured on an ESCALAB MKII X-ray photoelectron spectrometer. See reference[4] for experimental conditions. The  $^{151}\text{Eu}$  Mossbauer spectrum at room temperature was recorded by means of an Oxford MS-500 constant acceleration spectrometer. The velocity was calibrated with an  $\alpha\text{-Fe}$  foil. The radiation source was  $^{151}\text{Eu}/\text{SmF}_3$ . The thickness of the absorber

used in the measurement was about 10~15mg  $\text{Eu}/\text{cm}^2$ .

## Results and discussion

XRD shows that the pattern of  $\text{Sr}_{1-x}\text{Eu}_x\text{TiO}_{3+y}$  ( $x=0.0-0.5$ ) synthesized by high pressure and high temperature is similar to that of  $\text{SrTiO}_3$ . It indicates that this compound belongs to cubic perovskite structure. Lattice parameters are give in Table 1. As  $x$  increases,  $a$  and  $V$  parameters do not change. Because the ionic radius of  $\text{Eu}^{3+}$  is smaller than that of  $\text{Sr}^{2+}$ , Eu ion must be in mixed valence state.

The Mossbauer spectra of sample for  $x=0.4$  and  $0.5$  are shown in Fig.1. It is evident that Eu is in two states. The peak observed around 0 mm/s is attributed to the Eu(III), and that between -13 and -10 mm/s to Eu(II). The difference in isomer shift between Eu(II) and Eu(III) is about 9 mm/s. This can be explained by the larger shielding effect of  $4f^7$  electrons on the s-orbital for  $\text{Eu}^{2+}$ , whereas  $\text{Eu}^{3+}$  ion has a  $4f^6$  configuration. From Fig.1, it can be seen that  $^{151}\text{Eu}$  Mossbauer spectra of samples exhibit a slightly asymmetric broad single line. The half-width is very broad as compared with that of the natural single line. This means the presence of unresolved quadrupole interaction. So, we fit the spectra by using twelve transition lines. Mossbauer parameters obtained by fitting are given in Table1. When  $x$  increases from 0.3 to 0.4, IS is same within the error range. But for  $x=0.5$ , the IS value of Eu(II) increases about 2mm/s. As known, isomer shift is a measure of the electron density at the nucleus, which is affected by the valence, electronic state and coordination number of the element, as well as the electronegativity of neighboring ligands. For our samples, the change of IS may be ascribed to the distribution of Sr and Eu ions at  $x=0.5$ , which results in the change of coordination state. Using the ratio of absorption line, the content of Eu(II) or Eu(III) can be calculated. With  $x$  increasing, the values of Eu(II)/Eu(III)

decreases. From the datum of Eu(II)/Eu(III) and considering electronic neutrality of compound, we can obtain that the charges carried out by  $(\text{TiO}_{3+y})^n$  are 2.1, 2.15 and 2.2 for  $x=0.3, 0.4$  and  $0.5$ , respectively, which is more than that carried out by  $(\text{TiO}_3)^n$  in compound  $\text{SrTiO}_3$ .

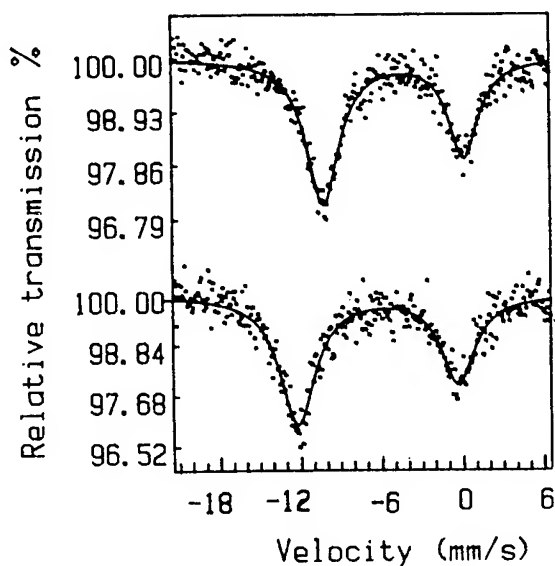


Fig.1.  $^{151}\text{Eu}$  Mossbauer spectra for  $x=0.4$  (bottom) and  $0.5$  (top).

The energy shift due to the quadrupole interaction is given by the following equation

$$E_q = \frac{e^2 q Q}{4I(2I-1)} [3m_I^2 - I(I+1)] (1 + \eta^2/3)$$

Where  $eQ$  is the nuclear quadrupole moment,  $eq$  is the principal of electric field gradient (EFG),  $I$  is the nuclear spin and  $\eta$  is asymmetric parameters. The result obtained by fitting shows that the quadrupole interaction is negative. For rare earth element, there can be three

contributions to  $q$ : the first-order  $4f$  contribution, the lattice contribution and the second-order  $4f$  contribution.

$$q = q_{4f}^{(1)} + q_L + q_{4f}^{(2)}$$

For  $\text{Eu}^{3+}$  with ground state of  $^7F_0$ , the main contribution is the latter two, and for  $\text{Eu}^{2+}$ , as its ground state is  $^3S_{7/2}$ , only lattice contribution is appreciable. The lattice contribution is negative, so we can conclude that, for our sample, the contribution to EFG from the lattice is larger than the second-order  $4f$  contribution. Considering that the second-order  $4f$  contribution is weakly temperature dependent, the  $^{151}\text{Eu}$  Mossbauer spectrum at 90K was recorded for  $x=0.4$ . We found that  $eQV_{zz}$  has a small change for  $\text{Eu(III)}$ , which indicates that second-order  $4f$  contribution is not zero.

The compound  $\text{EuTiO}_3$  possesses the ideal perovskite structure and its unit cell is symmetrical about axis. However, when Eu ions are doped, Sr and Eu ions may distribute asymmetrically. Thus, the symmetry about axis is deformed. It also shows this conclusion that the background of XRD pattern is becoming larger. Therefore, by fitting  $\eta$  is not zero, which is completely different from the case that the compound  $\text{EuTiO}_3$  presents symmetry about axis.

The binding energy measured by XPS is listed in Table 1. After comparing the value of  $\text{Sr}_{3p}$  (269.2eV) with that of  $\text{SrTiO}_3$  (268.6eV), we found that  $\text{Sr}_{3p}$  level shifts to high binding energy. This result is consistent with that of Mossbauer spectrum. The charges of  $(\text{TiO}_{3+y})^n$  increase with  $x$  increasing, which results in that the amount of negative charge around Sr ion increases. So, the attraction of oxygen anion to the outer electrons of Sr ion is becoming stronger, which increases the net nuclear charge and enhances the attraction of the nuclear to the electrons of  $\text{Sr}_{3p}$ . As a result, the binding energy of  $\text{Sr}_{3p}$  increases. In addition, the peak of  $\text{Ti}_{2p}$  near lower binding energy exhibits asymmetric apparently. It indicates that a part of  $\text{Ti}^{4+}$  ions may be transformed to low valence.

Table 1. Lattice Parameter, Mossbauer parameters and binding energy of XPS

x	Lattice parameters		Mossbauer parameters				Binding Energy (eV)			
	$a \times 10^3 (\text{nm})$	$V \times 10^3 (\text{nm}^3)$	IS (mm/s)*	$eQV_{zz}$ (mm/s)	$\eta$	Eu(II)/Eu(III)	O1s	Eu3d <sub>5/2</sub>	Ti2p <sub>3/2</sub>	Sr3p <sub>3/2</sub>
0.0	3.905	59.57					531.0		458.3	268.6
0.1	3.906	59.57					531.3	1134.6 1125.0	458.5	268.8
0.2	3.902	59.39					531.6	1135.4 1125.7	458.5	268.9
0.3	3.905	59.58	-12.9(0.3) -0.36(0.03)	-7.5(0.5) -6.4(0.2)	0.96 0.97	1.70	531.5	1134.9 1125.9	458.7	269.1
0.4	3.903	59.48	-12.9(0.3) -0.42(0.03)	-5.7(0.5) -6.1(0.2)	0.98 0.98	1.57	531.4	1134.7 1125.2	458.6	269.2
0.5	3.909	59.73	-10.9(0.3) 0.12(0.03)	-6.2(0.5) -6.9(0.2)	0.93 0.89	1.40	531.1	1135.0 1125.0	458.5	269.2

\*The value of IS refers to  $\text{Eu}_2\text{O}_3$ .

## Conclusion

(1) In the single phase compound of  $\text{Sr}_{1-x}\text{Eu}_x\text{TiO}_{3+y}$  synthesized by high pressure and high temperature, Eu and Ti ions are both in mixed valence state. The presence of low valence of Eu and Ti shows the reduction role of high pressure and high temperature.

(2) The IS of  $^{151}\text{Eu}$  Mossbauer spectra becoming large at  $x=0.5$  suggests that electronic state has a distinct change.

(3) The value of  $\text{Eu(II)}/\text{Eu(III)}$  decreases with  $x$  increasing indicates that more  $\text{Eu}^{3+}$  ions doped into the lattice, which results in the change of A-site( including Sr and Eu ions) and  $(\text{TiO}_{3+y})^{-n}$  increasing.

(4) Quadrupole interaction is negative. So the lattice contribution is larger than 4f contribution, which is

consistent with the results observed in many other perovskite and related oxides[5, 6].

## References

1. Lichtenber, D. Widmer and Reller A. *Z. Phys. B* **82** (1991) 211.
2. M. Kauzlarich, *NIST Spec. Publ.* **804** (1991) 217.
3. Liu Hongjian and Su Wenhui., *Chin. J. High Pressure Phys.* **4** (1990) 284
4. Li Liping, Wen Quan, Su Wenhui, *Chem. J. Chin. Universities* **13** (1992) 217.
5. Chien, C. L., Sleight A. W., *Phys. Rev. B*, **18**(1978) 2031.
6. Jin M. Z., Liu X. W., *Solid State Commun.*, **76** (1991) 985.

# HIGH PRESSURE RESISTIVITY STUDIES ON Cu-Ge-Te GLASSES

K.RAMESH, S.ASOKAN<sup>†</sup>, K.S.SANGUNNI and E.S.R.GOPAL\*

Department of Physics

<sup>†</sup> Instrumentation and Services Unit

Indian Institute of Science

Bangalore 560012, India.

(\* also at National Physical Laboratory, New Delhi, India)

## ABSTRACT

The electrical resistivity and conductivity activation energy of Cu-Ge-Te glasses decrease continuously with pressure, with the samples undergoing metallization around 5 GPa. At high temperatures, though there is no change in trend in the high pressure resistivity behaviour, the metallization occurs at lower pressures. The composition dependence of activation energy for electrical conduction at different pressures is found to exhibit an anomaly at 5 atom % Cu, which is explained on the basis of Rigidity Percolation.

## Introduction

In the group of Ge-Te based ternary glasses, Cu-Ge-Te has been taken up for investigations only recently (1). In this system, the glass formation is centered around 20 atom % of Ge (13 - 23) and bulk glasses can be obtained by progressively replacing Te by Cu up to 10 atom % (2). The addition of Cu is found to increase density, micro-hardness and glass transition temperature of Ge-Te glasses indicating that there is a substantial strengthening of the glass structure (1). Consequently, the addition of Cu can alter many structure related high pressure phenomena such as crystallization, metallization, etc. of Ge-Te glasses. In the present work, efforts have been made to understand the high pressure electrical resistivity behaviour and its dependence on composition of  $\text{Cu}_x\text{Ge}_{15}\text{Te}_{85-x}$  glasses.

## Experimental

$\text{Cu}_x\text{Ge}_{15}\text{Te}_{85-x}$  glasses ( $2 < x < 10$ ) have been prepared by melt quenching method. Electrical resistivity measurements at high pressures have been undertaken in a Bridgman anvil set up, using pyrophyllite as the gasket material and steatite as the quasi-

hydrostatic pressure transmitting medium (3). High pressure Low temperature electrical resistivity studies have been conducted in a Fugii-Nagano type high pressure system (4). A heater is used around the anvil for high temperature studies.

## Results and Discussion

Figure 1 shows the pressure dependence of

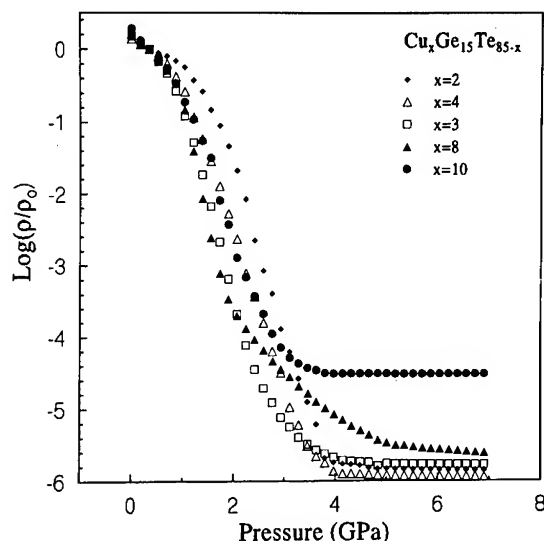


Figure:1 The variation of normalized resistivity with pressure for  $\text{Cu}_x\text{Ge}_{15}\text{Te}_{85-x}$  glasses.

electrical resistivity of  $\text{Cu}_x\text{Ge}_{15}\text{Te}_{85-x}$  glasses at ambient temperature. It shows that the resistivities of these samples decrease continuously with pressure. The resistivities fall by six orders of magnitude at around 4 GPa pressure, suggesting the metallization of the glasses at high pressures.

High pressure-low temperature investigations indicate that at lower pressures (below 4 GPa), the electrical conduction in Cu-Ge-Te glasses is thermally activated with single activation energy in the temperature range of investigation (300-77K). The activation energy, estimated from  $\log(\text{conductivity})$  versus  $1000/T$  curves, is found to continuously decrease with pressure becoming zero around 4 GPa. Figure 2 shows the pressure dependence of activation energy for a representative Cu-Ge-Te sample, which confirms the continuous metallization at higher pressures.

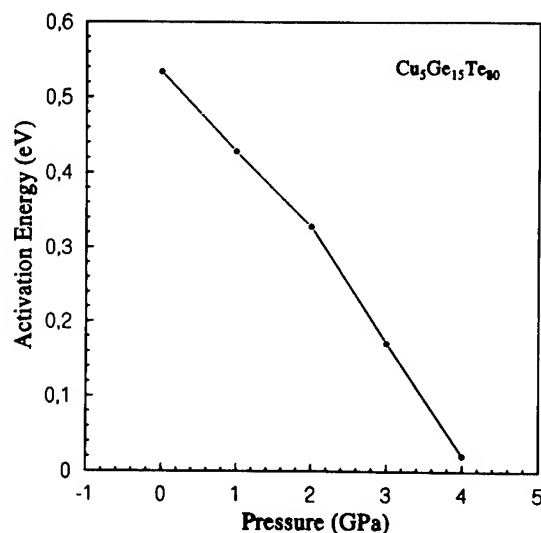


Figure 2: Pressure dependence of conductivity activation energy of  $\text{Cu}_5\text{Ge}_{15}\text{Te}_{80}$  sample.

It is interesting to note here that the addition of Cu changes the sharp, discontinuous metallization in Ge-Te glasses (5) to a continuous transformation. The most interesting outcome of the present investigations is

the composition dependence of conductivity activation energy at different pressures (figure 3). The addition of a metallic dopant such as copper should result in a reduction in the resistivity, activation energy, etc. of Ge-Te glasses. However, it is observed that the variation of activation energy with composition of  $\text{Cu}_x\text{Ge}_{15}\text{Te}_{85-x}$  exhibits a maximum at  $x = 5$ . In chalcogenide network glasses, germanium is normally four fold coordinated and Te two fold coordinated. It has been proposed by Liu and Taylor(6) that Cu in Cu-As-Ch (Ch=Chalcogen) glasses is four

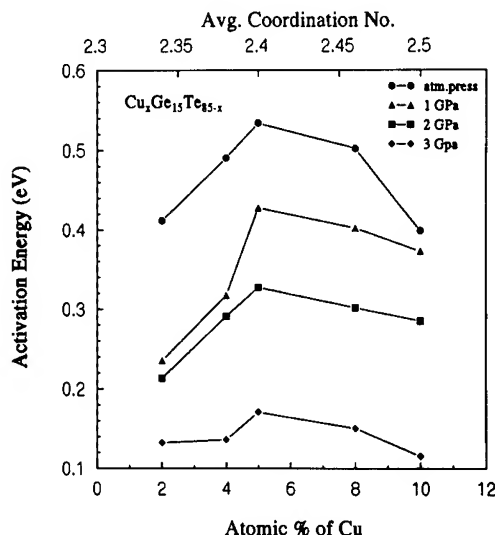


Figure 3: The variation of conductivity activation of  $\text{Cu}_x\text{Ge}_{15}\text{Te}_{85-x}$  with composition.

fold coordinated. This conjecture is also supported by structural studies (7,8). Assuming that Cu is four fold coordinated in Cu-Ge-Te system, the average coordination ( $Z_{av}$ ) for  $\text{Cu}_5\text{Ge}_{15}\text{Te}_{80}$  glass can be calculated to be 2.4. Theoretical investigations based on the constraints theory predict that there is a critical average coordination ( $Z_c = 2.4$ ) in chalcogenide network glasses (known as rigidity percolation threshold) at which there is a transformation in the structural rigidity of the material (9,10). Unusual variations are observed in the physical properties at the

percolation threshold.

Present high pressure investigations on Cu-Ge-Te glasses reveal an anomaly in the conductivity activation energy at the composition corresponding to  $Z_{av} = 2.4$ .

High pressure-high temperature investigations (at 50° C and 100° C ) reveal that at high temperatures though there is no change in trend in the high pressure resistivity behaviour, the metallization occurs at lower pressures (Figure 4).

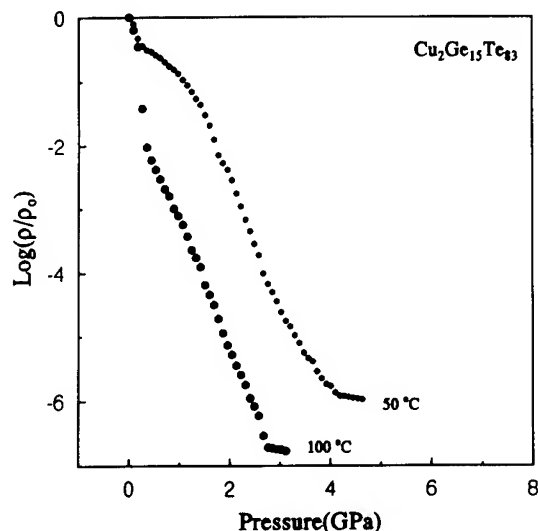


Figure 4: Pressure dependence of electrical resistivity of  $\text{Cu}_2\text{Ge}_{15}\text{Te}_{83}$  at 50° C and 100° C.

## References

5. S.Asokan, G.Parthasarathy and E.S.R.Gopal, *Philos. Mag.*, **57** (1988) 49.
6. J.Z.Liu and P.C.Taylor, *J.Non-Cryst.Solids*, **114** (1989) 25.
7. S.Hunter, A.Bienenstock and T.M.Hayes, in *The Structure of Non-cryst. Materials*, ed.P.H.Gaskell, (Taylor and Francis, 1977) p.73.
8. D.Gomez-Vela, L.Esquivias and C.Prieto, *Phys.Rev.* **B48** (1993) 10110.
9. J.C.Phillips, *Phys. Rev.*, **B31** (1985) 8157.
10. J.C.Phillips and M.F.Thorpe, *Solid State Commun.*, **53** (1985) 699.

1. R.A.Ligero, M.Casa-Ruiz, M.P. Trujillo, A.Orozco and Jimenez Garay, *R.,Phys.chem. Glasses*, **35** (1994) 115.
2. Z.U.Borisova, *Glassy semiconductors* (Plenum, 1981) p.436.
3. A.K.Bandyopadhyay, A.V.Nalini, E.S.R.Gopal and S.V.Subramanyam, *Rev. Sci. Instrum.*, **51** (1980) 136.
4. G.Fugii and Nagano, H., *Cryogenics*, 1971, **11**, 142.



## REFRACTIVE INDEX OF SOLID ARGON UP TO 45 GPa AT 298 K

N. RAMBERT, B. SITAUD and Th. THEVENIN

*Commissariat à l'Energie Atomique, Centre d'Etudes de Bruyères-le-Châtel,  
BP 12, F-91680 Bruyères-le-Châtel, France*

A new optical method for the measurement of refractive indices of a sample in a diamond anvil cell (DAC) is presented. It uses both interferometric and imaging techniques and has been developed to increase the pressure range of refractive index studies. Up to now, interferometric measurements under high pressure by themselves required a DAC with a large numerical aperture and a thick gasket cavity, thus limiting the maximum reachable pressure to the 20 GPa range. We studied the refractive index of solid argon at room temperature up to 45 GPa. The results are in agreement with literature data obtained at lower pressures. Standard deviation is less than  $\pm 2\%$  of nominal index value. The best fit of data in the range 5 GPa - 45 GPa is represented by  $n = 1.3803 + 7.4548 \times 10^{-3} P$  where  $P$  is expressed in GPa. Experimental details and theoretical assumptions that we made are discussed. Moreover, information on the metallic gasket behavior at high pressure is obtained from geometrical considerations.

### Introduction

The refractive index measurements by interferometric methods are very common and give generally precise results. Diamond anvil cells (DAC) with their diamond culets can be considered as the resonant cavity of a Fabry-Perot interferometer, and thus seem to be well adapted to this kind of measurements. Nevertheless, a single interference technique just allows the evaluation of the optical thickness. In order to determine the refractive index of a material in a DAC, the high pressure cavity thickness must be known from another mean.

To overcome this difficulty, several methods could be considered. Among them, two interferometric set-ups using respectively monochromatic and white light are simultaneously used as it has been developed by Le Toullec et al. (1). This method leads to precise values of the refractive index but needs a large optical aperture of the DAC and a thick gasket, thus limiting the investigated pressure range. Another technique that was proposed by Johannsen (2) consists in placing side by side in the DAC cavity two samples including one with a well-known refractive index, and in measuring for each of them their optical thickness. As the geometrical thickness is identical for both samples, the refractive index of the second one may be evaluated. However, this method does require to know with a good accuracy the refractive index of an inert, transparent, solid and soft sample.

The method of the present work is based on

white interferometric measurements associated with a geometrical study of the high pressure cavity, and on two assumptions : *i)* the number of moles of sample in the cavity remains constant during all the experiment ; *ii)* the cavity shape is considered to be the same along its thickness whatever the pressure may be. Both hypothesis do not seem unrealistic since the pressure in a DAC stays constant over a long period of time and the thickness is always very small with regard to other dimensions. We performed measurements of the refractive index of solid argon up to 45 GPa at room temperature and compared with literature data (3). Moreover, from geometrical considerations, the gasket behavior under pressure is quantitatively approached and discussed in respect to theoretical calculations (4).

### Experimental technique

Our experiments were performed in a pressure cell developed in the laboratory (5). The numerical aperture of the cell is equal to 0.28. The high pressure cavity consisted in a 160  $\mu\text{m}$  of diameter hole drilled by electroerosion in a T301 stainless-steel gasket and was loaded with pressurized argon and a small spherical ruby. The pressure was measured using the non-linear ruby fluorescence scale used in hydrostatic conditions (6).

The refractive index of argon at a given pressure is deduced from the volume of the experimental cavity (surface  $\times$  thickness) which is first calculated from the equation of state of argon (7) fitted to a Murnaghan's law ( $B_0 = 10.67$  GPa

and  $B_0' = 4.05$ ).

From the above assumptions, the refractive index  $n$  is :

$$n = \frac{E \times S}{\frac{P_o \times S_o \times L_o \times V_{mol}(P)}{22.689 \times PV_{mol}(P_o)} + V_r \times \left(1 - \frac{P_o \times V_{mol}(P)}{22.689 \times PV_{mol}(P_o)}\right)}$$

where  $V_r$ ,  $L_o$ ,  $S_o$ ,  $S$ ,  $PV_{mol}$ ,  $V_{mol}$ ,  $E$  are respectively, the volume of spherical ruby inside the cavity, the geometrical thickness and the surface of cavity at loading pressure  $P_o$ , the surface of cavity at pressure  $P$ , the pressure times the molar volume expressed in Amagat at  $P_o$ , the molar volume of sample at  $P$  and the optical thickness. The pressure times volume of argon was estimated from (8).

To determine the surface of the cavity, a CCD camera fixed on a microscope is used. This set-up provides images with a magnification of 700 which are analyzed by a computer. In order to increase experimental precision, the DAC is always placed in the same position under the microscope which is illuminated by transmission with a stabilized monochromatic light (the focus is adjusted on ruby). The surface value is calculated from averaging three measurements. One should add that the difference between two consecutive measurements is less than 0.05% (at a given pressure).

The two culets of diamond anvils and the intermediate medium (loaded sample) form the resonant cavity of a Fabry-Perot interferometer. Such an interferometer that is illuminated with a source of wavelength  $\lambda$  gives a fringe pattern equivalent to the one obtained with a multitude of sources of the same wavelength with optical paths successively shifted by  $2nL$ ,  $n$  being the refractive index of the medium inside the interferometer and  $L$  its thickness. Thus, this fringe pattern is directly related to  $nL/\lambda$ . For an incident intensity  $I_o$ , the reflected intensity going into the spectrometer  $I_r$  is given by :

$$I_r = I_o \times \left[ 1 - \left[ 1 + m \sin^2 \left( 4\pi \times \frac{n \times L}{\lambda} \right) \right]^{-1} \right] \quad (2)$$

where  $m$  is a constant factor depending on the interferometer.

The experimental set-up is shown in fig. 1.

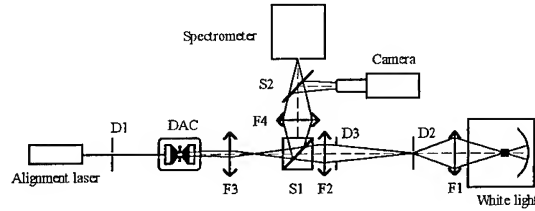


Figure 1 : Optical set-up.  $F_1$ ,  $F_2$ ,  $F_3$  and  $F_4$  are lenses.  $D_1$ ,  $D_2$  and  $D_3$  are diaphragms.  $D_2$  ( $\phi = 50 \mu\text{m}$ ) is considered to be the real illumination source.  $S_1$  and  $S_2$  are respectively a separating cube and a beamsplitter.

Each experimental measurement is done as follows :

i) the white light interference pattern is collected. These interferences are obtained by illuminating the DAC cavity with a  $50 \mu\text{m}$  diameter white spot of a stabilized Xe-lamp. Around 60 interference fringes were recorded for each spectrum in the wavelength range 500-950 nm.

ii) a diamond anvil like those of the DAC is used instead of the DAC to act as a mirror and the white-light spectrum as a function of wavelength through all the optical components is recorded.

iii) finally,  $I_r/I_o$  is calculated vs wavenumbers (fig. 2).

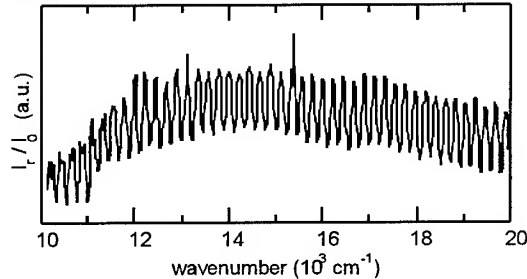


Figure 2 : Fringe pattern obtained at 41.6 GPa. The reduced intensity is plotted against wavenumbers.

A finite Fourier transform of the last plot leads to the optical thickness of the cavity (fig. 3).

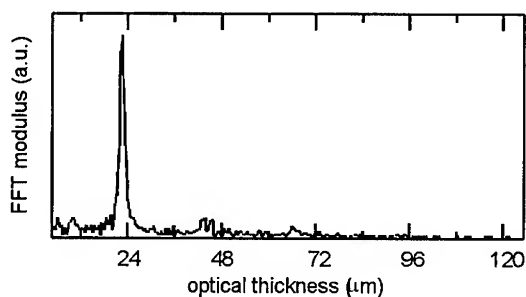


Figure 3 : FFT of the fringe pattern shown in fig. 2. The sharp peak around 24  $\mu\text{m}$  is assigned to the optical thickness of the cavity at 41.6 GPa.

## Results and discussion

During the experiments, no significant dispersion of refractive index with wavelength was appeared over the investigated pressure range. The experimental results are plotted in fig. 4 with values of refractive index of argon in the liquid (9,10) and solid (3) states. Inside the common pressure range, a good agreement with literature data (3) is found. Standard deviations of  $2 \times 10^{-2}$  up to 26 GPa and of  $3 \times 10^{-2}$  beyond are measured, corresponding to less than  $\pm 2\%$  of nominal index value. For pressure greater than 5 GPa, the refractive index is well represented by the linear form  $n = 1.3803 + 7.4548 \times 10^{-3} P$  with  $P$  in GPa.

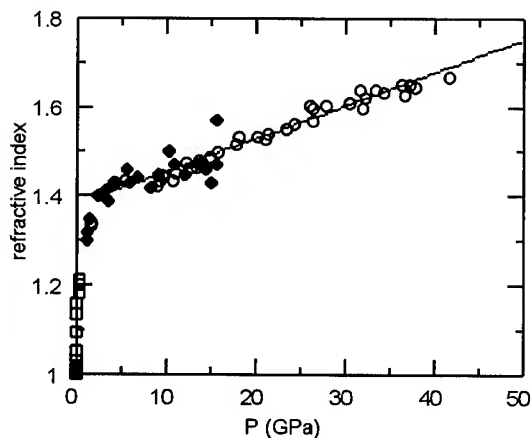


Figure 4 : Refractive index of argon vs pressure. Open circles, present data; solid line, linear fit; open squares, ref. (10); solid diamonds, ref. (3).

Through the whole experiment, since we record the thickness of the high pressure cavity, we have been able to observe the thick and thin regimes of the metallic gasket during upstroke predicted in ref. (4). Moreover, the phase transition from fcc to hcp which occurs around 26 GPa is evidenced.

Notwithstanding the present measurement accuracy is less than the one obtained in ref. (1), we show that the present technique may be used on a large pressure range. Here, the limiting factor is the gasket thickness and not the geometrical aperture of the DAC. Using rhenium gasket instead of stainless-steel should increase the maximal reachable pressure.

## Acknowledgements

We would like to thank Lionel Vialatte for helping us in preparing the experiments and Jean-Louis Truffier for fruitful discussions.

## References

1. R. Le Toullec, P. Loubeyre and J.P. Pinceaux, *Phys. Rev.* **B 40** (1989) 2368.
2. P.G. Johannsen, *Meas. Sci. Technol.* **4** (1993) 237.
3. M. Grimsditch, R. Le Toullec, A. Polian and M. Gauthier, *J. Appl. Phys.* **60** (10) (1986) 3479.
4. D. J. Dunstan, *Rev. Sci. Instrum.* **60** (12) (1989) 3789.
5. N. Dahan, R. Couty, A. Lefèvre, A. Berthault, J. Boutroux and J. Péré, *French Patent* n° 9005814 (1990).
6. H.K. Mao, J. Xu and P.M. Bell *J. Geophys. Res.* **91**(B5) (1986) 4673.
7. M. Ross, H.K. Mao, P.M. Bell and J.A. Xu *J. Chem. Phys.* **85** (1986) 1028.
8. A. Michels, R.J. Lunbeck and G.J. Wolkers *Appl. Sci. Res.* **A2** (1951) 345.
9. A. Michels and A. Botzen *Physica* **15** (1949) 769.
10. M. Lallemand and D. Vidal *J. Chem. Phys.* **66** (1976) 4776.

## **VII(I) Liquids and Gases**

## ABSORPTION COEFFICIENT IN LIQUID IODINE UNDER HIGH PRESSURE

U. Buontempo.

Dip. di Fisica, Universita' di L'Aquila, Via Vetoio, Coppito, I-67010, L'Aquila, Italy

P. Postorino

Dip. Fisica, Universita' di Roma "La Sapienza" Piazzale Aldo Moro 2, I-00185, Roma, Italy

M. Nardone

Dip. di fisica, Universita' di Roma III, Via Segre 2, I-00146, Roma, Italy

### ABSTRACT

Near infrared absorption spectra of liquid and solid iodine along the melting curve up to 1.52 GPa and 683 K are reported. In the liquid phase the spectra are dominated by exponential tails of the "Urbach" type with strongly temperature dependent slopes and amplitudes. The relation between this spectral feature with the conductivity jump recently observed in liquid iodine around 3 GPa is discussed.

### Introduction

In the last years metal-nonmetal transitions have been theoretically predicted and experimentally observed in many molecular systems [1]. In particular the metallization of solid  $I_2$  has been extensively studied. Both theory and experiment support the idea that the approach towards metallic behavior, which starts around 16 GPa, is associated to a reduction of the energy gap as the pressure, and hence the density, is increased [2,3].

Rather recently a transition to a high conductivity regime has been observed experimentally in liquid iodine around 3 GPa [4]. This transition appears to be peculiar of the liquid state since below the melting curve, in the solid region, no anomaly in the conductivity has been observed. The last finding and the rather large difference in the pressure and density at which the metallic transition occurs in the two phases as well as the abrupt nature of the change in the conductivity in the liquid, indicate that for the latter the mechanism underlying the onset of metallic behavior can be quite different than in the solid.

In order to understand the origin of the metallization in liquid phase we have undertaken an extended study of the electronic absorption spectra of iodine along the melting curve. In this paper we present the spectra of the low frequency

tails of the absorption band, on both sides of the melting curve, up to a temperature of 683 K and a pressure of 1.52 GPa. From the analysis of the spectra and from their pressure dependence some insight of the microscopic origin of the metallization transition can be obtained.

### Experimental

The absorption spectra have been collected by a rapid scanning Bomem interferometer. The sample, commercial doubly resublimated  $I_2$ , has been handled under inert atmosphere. The low pressure absorption spectrum has been obtained using a heatable, variable thickness cell described elsewhere [5]. The high pressure absorption spectra have been obtained using a commercial membrane diamond anvil cell heated under vacuum. The resistance to corrosion of the metallic gasket (tantalum and molybdenum), which rapidly decreases as the temperature raises, has limited the maximum temperature to 650 K. The sample thickness, measured by the interference generated by the inner diamond surfaces, ranged from 20 to 80  $\mu\text{m}$ . Due to the high absorbance of iodine, these relatively large thickness values were the limiting factor for the frequency range explored in both liquid and solid phases under pressure (namely 4000-10000  $\text{cm}^{-1}$ ). Further details of the high pressure apparatus and measurements are reported in ref. 6.

## Results and Discussion

A comparison between absorption coefficients for almost coexisting liquid and solid iodine at two different temperatures and pressures is reported in fig. 1. It is evident that extended and well defined exponential tails appear on melting. It is well known that in disordered (both amorphous and liquid) semiconductors the absorption spectrum shows a relevant exponential tail on the low frequency side of the band edge. This feature, usually referred to as "Urbach tail" is due to the appearance within the energy gap, of localised states related to molecular disorder [7].

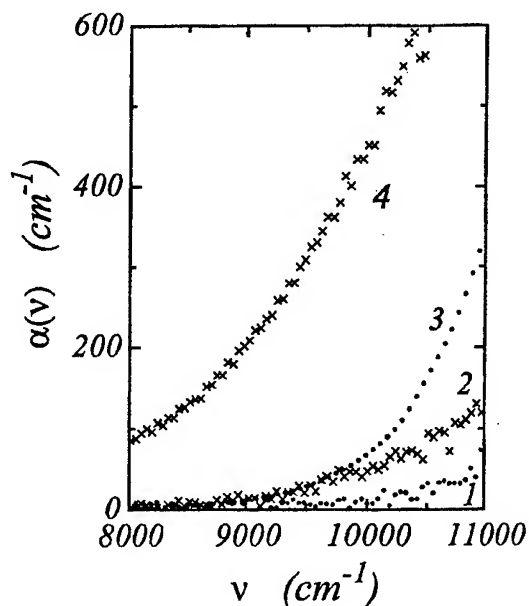


FIG. 1. Absorption spectra of solid (1 and 2) and liquid (3 and 4)  $I_2$  in two coexisting states. Spectra 1 and 3 are close to the triple point, while 2 and 4 are taken at  $P=1$  GPa.

The behavior of the band tails in liquid iodine, as we climb up along the melting curve, is shown in fig. 2. For absorption coefficient values lower than  $400 \text{ cm}^{-1}$  we have fitted the empirical expression  $\alpha(v) = A \exp(\Gamma v)$  to the spectra obtaining the parameter values reported in Tab. 1.

When Urbach tails are relevant, the absorption spectra do not show a well defined band origin. In order to obtain some value for the energy gap we can however make use of a widespread criterion following which an empirical energy gap ( $E_{e.e.g.}$ )

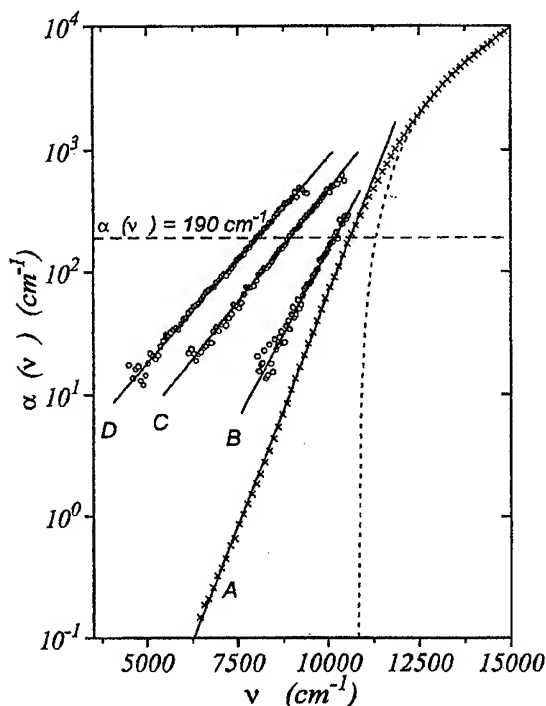


FIG. 2. Logarithmic plot of the absorption spectra of liquid  $I_2$  at thermodynamic conditions reported in Tab. 1. The solid lines are the best exponential fits obtained using the parameters reported in the table. The dotted line is the best fit of the band edge assuming a quadratic density of states. The intercepts between absorption spectra and the horizontal dashed line give the values  $E_{e.e.g.}$ .

can be defined as the energy value for which the absorption coefficient reaches a given value  $\alpha_g$ . Following reference [2] we have chosen  $\alpha_g = 190 \text{ cm}^{-1}$ . The values for the  $E_{e.e.g.}$  determined using this criterion are also reported in Tab. 1. It is evident that as we climb up the melting curve the  $E_{e.e.g.}$  is rapidly decreasing. Depending on whether a quadratic or linear extrapolation is adopted, the pressure at which  $E_{e.e.g.}$  vanishes

TABLE 1. Thermodynamic conditions of the experimental absorption spectra of liquid  $I_2$  and parameters of exponential fit. In the last column values of the empirical energy gap as defined in the text, are reported.

	P (GPa)	T (K)	A ( $\text{cm}^{-1}$ )	$\Gamma \times 10^3$ (cm)	$E_{e.e.g.}$ ( $\text{cm}^{-1}$ )
A	0.00	413	$1.7 \times 10^{-6}$	1.74	10600
B	0.13	428	$4.4 \times 10^{-4}$	1.27	10100
C	1.09	619	$1.0 \times 10^{-1}$	0.85	8940
D	1.52	683	$3.6 \times 10^{-1}$	0.78	8030

ranges from 4.4 GPa to 6.7 GPa i.e. not too far from the metallization pressure in the liquid [4].

It is anyway not trivial that a reduction of the e.e.g. is driven by a shift of the band edge  $E_g$ . The value of  $E_g$  can be obtained by fitting band models to the absorption spectra beyond the exponential tail region. Assuming a quadratic joint density of states we have fitted the experimental data of the  $P=0$  sample obtaining  $E_g=10800\text{ cm}^{-1}$  which is close to the  $E_{e.e.g}$  (see tab. 1).

Due to the limited frequency range up to now explored for high pressure liquid samples, we cannot use this procedure to obtain values for  $E_g$  along the melting curve. We have reason to believe however that at high pressure the values of  $E_g$  may differ substantially from those of  $E_{e.e.g}$  [6].

## Conclusions

Our measurements clearly show that extended exponential tails appear in the absorption spectra of iodine upon melting. The zero frequency extrapolation of these tails increases by several orders of magnitude moving along the melting curve. This indicates that the band gap is definitely filling up. Although we are not yet able to determine unambiguously whether this is due to a closure of the gap or to an increase of localised states within the gap, there are indications that the latter is more probably the case [6,8]. Even under this circumstance the observed increase in the band tails intensity could be related to the observed conductivity jump. Indeed also the localised states could contribute significantly to the conduction process if their number increases above some percolation threshold.

## Acknowledgements

We are grateful to Prof. F. P. Ricci for stimulating our interest in the properties of liquid iodine. We wish to thank also Mr. C. Piacenti and Mr. A. Salvati for their skillful technical assistance.

## References

[1] See for instance "*Molecular Systems under High Pressure*", R. Pucci and G. Piccitto editors,

North Holland, (Amsterdam), (1991)

[2] B. M. Riggelman and H. G. Drickamer, J. Chem. Phys. **38**, (1963) 2721.

[3] G. Piccitto and R. Pucci, to be published in High Pressure Research.

[4] V. V. Brazhkin, S. V. Popova, R. N. Voloshin and A. G. Umnov, High Pres. Res., **06**, (1992), 363

[5] E. Degiorgi, P. Postorino and M. Nardone, Meas. Sci. Technol., **6**, (1995), 929

[6] U. Buontempo, E. Degiorgi, P. Postorino and M. Nardone, Phys. Rev B, **51**, (1995), to be published.

[7] N. F. Mott and E. A. Davis, "*Electronic Processes in Non-Crystalline Materials*", Clarendon Press, Oxford, (1979).

[8] U. Buontempo, P. Postorino and M. Nardone, J. non Cryst. Sol., to be published.

# CHARACTERIZATION OF THERMODYNAMIC PROPERTIES OF AQUEOUS SALINE SOLUTIONS AT HIGH PRESSURES. A NEW APPROACH USING ULTRASOUND VELOCITY DATA

S. YE, H. CARRIER and P. XANS

*Laboratoire Haute Pression, C.U.R.S, Université de Pau  
Av. de l'Université, 64000 PAU, France*

## ABSTRACT

A new approach, using the ultrasonic velocity in electrolyte solution, has been successfully tested in order to determine the pressure dependence of Pitzer parameters.

## Introduction

The thermodynamic properties of saline solutions have above all been studied at low pressures, and in this domain the effects of pressure are often slight or negligible. However, little research has been devoted to the description of these properties at high pressures, i.e. up to 1000 bar, a domain which is of interest in geochemistry and geophysics.

The Pitzer model was developed to characterize the thermodynamic properties of aqueous solutions of electrolytes. It has been widely used for a number of systems at high concentrations. The effect of pressure is not generally taken into account; and yet in order to model new applications, such as phase equilibria of water-salt-hydrocarbon systems at high pressures and temperatures, the pressure parameter is essential.

By means of measurements of ultrasonic velocity (a property which can be easily measured) we determined the variation of Pitzer coefficients as a function of pressure, for NaCl solutions, for which the parameters are known. Once this feasibility study had been carried out, the same approach was applied to other solutions.

Close agreement between calculated and experimental values support the validity of this new approach.

In this communication we will present only the first part of this work and the results of the parameter fitting will be published elsewhere.

## Calculation of Ultrasonic Velocity Using Pitzer's Model

### Pitzer's Model

The detail of the Pitzer's model has been described in a lot of paper (1, 2) and so only the expression used in our calculation procedure is presented here.

The parametric equation used by Pitzer for the excess Gibbs energy of a binary electrolyte solution containing  $n_w$  kg of solvent is

$$\frac{G^{ex}}{n_w RT} = -A_\phi \left( \frac{4I}{b} \right) \ln(1 + b I^{1/2}) + 2 \nu_M \nu_X [m^2 B_{MX} + m^3 \nu_M \nu_X C_{MX}] \quad (1)$$

with

$$B_{MX} = \beta_{MX}^{(0)} + 2\beta_{MX}^{(1)} [1 - (1 + \alpha I^{1/2}) \exp(-\alpha I^{1/2})] / \alpha I^{1/2} \quad (2)$$

$$C_{MX} = C_{MX}^\phi / 2 |Z_M Z_X|^{1/2} \quad (3)$$

For each electrolyte MX, containing  $\nu_M$  and  $\nu_X$  ions of charge  $z_M$  and  $z_X$ , there are three specific parameters,  $\beta^{(0)}$ ,  $\beta^{(1)}$  and  $C^\phi$ .  $I$  is the ionic strength,  $I = \frac{1}{2} \sum_i m_i z_i^2$  and  $A_\phi$  is the Debye -

Hückel slope for the osmotic coefficient,

$$A_\phi = \frac{1}{3} \left( \frac{2\pi N_A d_w}{1000} \right)^{1/2} \left( \frac{e^2}{DkT} \right)^{3/2} \quad (4)$$



where  $d_w$  is the density and  $D$  the dielectric constant of pure water,  $e$  and  $N_A$  stands for the electronic charge and Avogadro's number, respectively.

The specific parameters,  $\beta^{(0)}$ ,  $\beta^{(1)}$  and  $C^\phi$ , are functions of temperature and pressure. In the case of NaCl, Pitzer has given the following expressions:

$$\begin{aligned} \beta^{(0)} = & z_{17}/T + z_{18} + z_{19}P + z_{20}P^2 + z_{21}P^3 + z_{22}\ln T \\ & + (z_{23} + z_{24}P + z_{25}P^2 + z_{26}P^3)T \\ & + (z_{27} + z_{28}P + z_{29}P^2)T^2 \\ & + (z_{30} + z_{31}P + z_{32}P^2 + z_{33}P^3)/(T-227) \\ & + (z_{34} + z_{35}P + z_{36}P^2 + z_{37}P^3)/(680-T) \end{aligned} \quad (5)$$

$$\beta^{(1)} = z_{38}/T + z_{39} + z_{40}T + z_{41}/(T-227) \quad (6)$$

$$\begin{aligned} C^\phi = & z_{42}/T + z_{43} + z_{44}P + z_{45}\ln T \\ & + (z_{46} + z_{47}P)T + (z_{48} + z_{49}P)T^2 \\ & + (z_{50} + z_{51}P)/(T-227) + (z_{52} + z_{53}P)/(680-T) \end{aligned} \quad (7)$$

#### Thermodynamic Properties

The relation between the apparent molal property  $^\phi X_B$  and the corresponding extensive property  $X$  for the solute component  $B$  of a solution is given by

$$^\phi X_B = \frac{X - n_S \bar{X}_S^0}{n_B} \quad (8)$$

where  $n_S$  and  $n_B$  are the numbers of moles of the components present,  $X$  is the value of the extensive property for the total quantity of solution ( $n_S + n_B$  mol), and  $\bar{X}_S^0$  is the molal extensive for the solvent at the same temperature and pressure.

The apparent molal heat capacity is related to the apparent molal enthalpy by

$$^\phi C_p = \bar{C}_{p,2}^0 + \left( \frac{\partial^\phi L}{\partial T} \right)_p \quad (9)$$

where  $\bar{C}_{p,2}^0$  is the partial molal heat capacity of the solute at infinite dilution and the apparent molal enthalpy  $^\phi L$  is defined by

$$^\phi L = L/n_B \quad (10)$$

where  $L$  is the excess enthalpy and is related to the excess Gibbs energy of the solution by the equation

$$L = G^{ex} - T \left( \frac{\partial G^{ex}}{\partial T} \right)_p = -T^2 \left( \frac{\partial G^{ex}/T}{\partial T} \right)_p \quad (11)$$

Combination of above equations yields

$$\begin{aligned} ^\phi C_p = & \bar{C}_{p,2}^0 + \nu |z_M z_X| A_J \ln(1 + b I^{1/2}) / 2b \\ & - 2 \nu_M \nu_X R T^2 [m B_{MX}^I + m^2 (\nu_M z_M) C_{MX}^I] \end{aligned} \quad (12)$$

$$\begin{aligned} B_{MX}^I = & \left( \frac{\partial^2 B_{MX}}{\partial T^2} \right)_p + \frac{2}{T} \left( \frac{\partial B_{MX}}{\partial T} \right)_p \\ = & \beta_{MX}^{(0)I} + 2 \beta_{MX}^{(1)I} \left[ 1 - (1 + \alpha I^{1/2}) e^{-\alpha I^{1/2}} \right] / \alpha^2 I \end{aligned} \quad (13)$$

with

$$\beta_{MX}^{(i)I} = \left[ \partial^2 \beta_{MX}^{(i)} / \partial T^2 \right]_p + 2 \left[ \partial \beta_{MX}^{(i)} / \partial T \right]_p / T \quad (14)$$

for  $i=0,1$

$$C_{MX}^I = \left[ \partial^2 C_{MX} / \partial T^2 \right]_p + 2 \left[ \partial C_{MX} / \partial T \right]_p / T \quad (15)$$

and  $A_J$  is the Debye Hückel slope for the heat capacity as defined by

$$A_J / R = [\partial(A_H/R) / \partial T]_p \quad (16)$$

with

$$A_H = -6 A_\phi R T \left[ 1 + T \left( \frac{\partial \ln D}{\partial T} \right)_p + \frac{T \alpha_w}{3} \right] \quad (17)$$

where  $\alpha_w$  is the coefficient of expansion.

In the case of volume, in the same way, we have:

$$\begin{aligned} ^\phi V = & \bar{V}_2^0 + \nu |z_M z_X| (A_V / 2b) \ln(1 + b I^{1/2}) \\ & + 2 \nu_M \nu_X R T [m B_{MX}^V + m^2 (\nu_M z_M) C_{MX}^V] \end{aligned} \quad (18)$$

where

$$\begin{aligned} B_{MX}^V = & \left( \frac{\partial B_{MX}}{\partial P} \right)_T \\ = & \beta_{MX}^{(0)V} + 2 \beta_{MX}^{(1)V} \left[ 1 - (1 + \alpha I^{1/2}) e^{-\alpha I^{1/2}} \right] / \alpha^2 I \end{aligned} \quad (19)$$

with

$$\beta_{MX}^{(i)V} = \left[ \partial \beta_{MX}^{(i)} / \partial P \right]_T \quad (20)$$

$i = 0, 1$

$$C_{MX}^V = \left[ \partial C_{MX} / \partial P \right]_T \quad (21)$$

and

$$A_V = 2 A_\phi RT \left[ 3 \left( \frac{\partial \ln D}{\partial P} \right)_T + \left( \frac{\partial \ln V_w}{\partial P} \right)_T \right] \quad (22)$$

### Ultrasound Velocity

The ultrasonic velocity is related to other thermodynamic properties as follows :

$$\begin{aligned} U^2 &= 1 / \rho \beta_s \\ &= 1 / \rho \left( \beta_T - \frac{\alpha^2 VT}{C_p} \right) \end{aligned} \quad (23)$$

where  $\rho$  is the density and  $\beta_s$  is the adiabatic compressibility.

$\rho$ ,  $V$  and  $C_p$  has been calculated directly using Pitzer's model,  $\beta_T$  and  $\alpha$  are calculated numerically. In the case of NaCl, Pitzer has provided the values of standard molal properties of  $V$  and  $C_p$ . In the other cases, the Helgeson's equation of state will be used.

### Results and Conclusion

This approach has been tested for NaCl aqueous solution at three temperature up to 400 bar and 1 molality. The mean deviation is about 1.3 %.

The close agreement between the results generated by the proposed procedure and experimental values (3) give considerable support to this new approach. This new approach must be useful in the prediction of the thermodynamic behavior of aqueous species at high pressure. The results of the parameter fitting for several electrolytes will be published elsewhere.

### Reference

1. K.S. Pitzer and J.C. Peiper, *J. Phys. Chem. Ref. Data*, **13** (1984) p. 1-102.
2. D.J. Bradley and K.S. Pitzer, *J. Phys. Chem.* **83** (1979) p. 1599-1603.
3. C.T. Chen, L.S. Chen and F. J. Millero, *J. Acoust. Soc. Am.*, **63** (1978) p. 1795-1800.

## MEASUREMENT AND PREDICTION OF ULTRASOUND VELOCITY UNDER HIGH PRESSURE IN A CONDENSATE GAS

J.L. DARIDON , B. LAGOURETTE , P. LABES , H. SAINT-GUIRONS

*Laboratoire Haute Pression, Université de Pau et des Pays de l'Adour*

*Avenue de l'Université, 64000 PAU (France)*

### ABSTRACT

This work deals with ultrasound velocimetry investigation of a condensate gas up to a pressure of 70MPa and for various temperatures. Comparisons between these ultrasound velocity data and the values predicted by several equations of state which are widely used in the petroleum industry are also reported and discussed.

### Introduction

Dealing with certain problems encountered in the oil industry (e.g. predicting the behaviour of reservoirs during petroleum production or of crude fluids during the production stages) requires the combined use of experimental information specific to the fluids and of values predicted by thermodynamic models. As reservoir fluids can exist in different states, improvement of oil and gas recovery depends significantly on their characterization at reservoir pressure-temperature conditions and during depletion. Depending on the origin of the reservoir and the nature of the fluids involved (dry gas, wet gas, condensate gas, under-saturated oil, critical fluids, ...) the pressure domains related to depletion may differ substantially from one case to another. But as a general rule the intervals concerned are always extensive with respect to pressure, and in some cases may be close to or even exceed the 100 MPa mark.

The objective of this study is the characterization by ultrasonic velocimetry of a liquid-phase condensate gas at different temperatures and pressures. It should be recalled that simulating fluid behaviour necessitates models of the fluid state and in particular the most practical of such methods, equations of state associated with mixing rules, involving parameters which must be set according to carefully selected thermophysical data for the mixtures. Ultrasound velocity, which may be assimilated with a thermodynamic property, can

serve as a reference property for use in developing models. However, it is another of the capabilities of ultrasound velocity which is of major interest to us in this paper: ultrasound velocity is used as a discriminatory property in order to identify which of a number of existing models has the most accurate predictive capacities with respect to condensate gas. Moreover, comparative analyses of this type make it possible to follow step by step the numerical predictions as a function of pressure and to determine the thresholds beyond which the validity of the models can be called into doubt.

### Sample and experimental technique

In the composition of the natural fluid considered, the methane represents less than two thirds of the compounds in molar proportion and the medium-heavy components occupy a significant place. There is also a C<sub>11</sub>+ fraction grouping into one single pseudo-component all the components with at least 11 carbon atoms. The relatively high proportion of this heavy fraction, for a gaseous system in bottomhole conditions, with respect to the other compounds is one of the compositional characteristics of condensate gases. It will be recalled that for this category of fluids the bottomhole isotherm cuts the phase envelope dew curve. The result is that depletion leads to a two-phase production at the separator and condensate deposition

at the bottom of the reservoir, a phenomenon known as retrograde condensation.

The experimental apparatus used to measure the ultrasound velocity is a pulse transmission apparatus (nominal frequency 2 MHz) and measurement of the transmission time through the sample is effected by direct chronometry, according to the protocol previously described by Daridon (1). The accuracy obtained for ultrasound velocity is estimated at 0.2% over the entire range of pressure-temperature domains investigated.

## Results

This condensate gas accepts the phase envelope reproduced in figure 1 ; the bottomhole conditions are 45.5 MPa for pressure and 405 K for temperature, and thus depletion leads inevitably to precipitation of condensate within the reservoir itself. Exploiting such a fluid therefore requires particular attention as a result of the high energy and commercial value of the condensate.

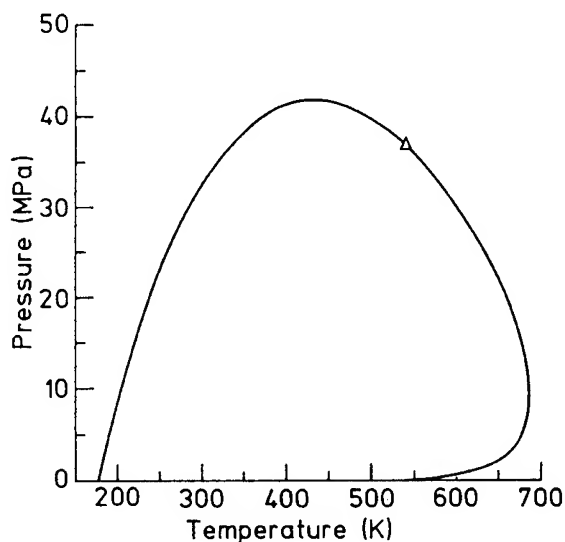


Fig.1 : Phase envelope of the condensate gas.

It is for this reason that the fluid was studied by ultrasound velocity measurement between 273.15 K and 373.15 K within the pressure interval 40.0 - 70.0 MPa, in other words in a P-T domain in which the sample is in a single phase state. The

ultrasound velocity values are plotted on Figure 2 which represents the bundle of isothermal curves  $U = f(P)$ . The shape of the curves is consistent with the classical behaviour of ultrasound velocity in a liquid single-phase domain, illustrated by the pressure coefficients  $(\partial U / \partial P)_T$  and temperature coefficients  $(\partial U / \partial T)_P$  respectively  $>0$  and  $<0$ . It will be observed that the velocity values shown are low, closer to those of a gas than to those of a liquid.

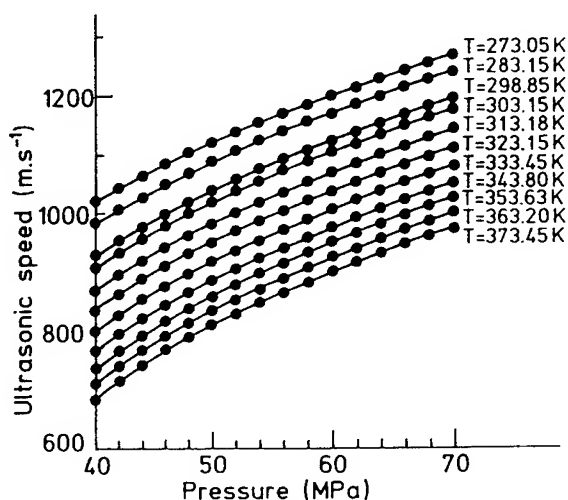


Fig.2: Isotherm curves characterizing variations of ultrasound velocity versus pressure.

## Comparative numerical studies

The experimental conditions of ultrasound velocity determination are sufficiently distant from the system's critical point for ultrasound velocity and speed of sound to be assimilated. The speed of sound  $U$  is expressed in terms of the isothermal compressibility  $\beta_T$ , of the thermal expansion coefficient  $\alpha$ , of the density  $\rho$ , of the molar volume  $V$  and the molar heat at constant pressure  $C_P$ , in the form :

$$U^2 = 1/\rho \left[ \beta_T - (\alpha^2 VT) / C_P \right] \quad (1)$$

As all these properties can be determined on the basis of equations of state representative of the fluid state, we used the experimental data for  $U$  in the condensate gas in order to compare the predictive

performances of several equations regularly used in petroleum engineering. It should be indicated that calculation of the term  $C_p$ , defined by :

$$C_p(P, T) = C_p^*(T) + \int_{\infty}^V T \left( \frac{\partial^2 p}{\partial T^2} \right)_V dV - T \frac{(\partial p / \partial T)_V^2}{(\partial p / \partial V)_T} - R \quad (2)$$

assumes prior adoption of a representation of the ideal contribution  $C_p^*(T)$ ; the representation selected in this work was that of Aly and Lee :

$$C_p^*(T) = C_1 + C_2 \left[ (C_3/T) / \text{sh}(C_3/T) \right]^2 + C_4 \left[ (C_5/T) / \text{ch}(C_5/T) \right]^2 \quad (3)$$

The equations of state tested in the comparative tests are those proposed by Soave-Redlich-Kwong (hereafter referred to as SRK), Peng-Robinson (PR), of Peng-Robinson corrected by the volumetric translation proposed by Rauzy-Peneloux (PR-RP), Simonet-Behar-Rauzy-Jullian (SBRJ) and Lee-Kesler (LK). As the system studied, the condensate gas, is a mixture of several components, use of equations of state necessitates the adoption of mixing rules, and so the numerical tests carried out can identify the most effective combinations of equations of state and mixing rules. Mixing rules on the critical properties of the components were used. They were the rules devised by Pedersen et al. (no. 1), Spencer-Danner (no. 2), Hankinson-Thomson (no. 3), Teja (no. 4), Lee-Kesler (no. 5) and Plocker-Knapp-Prauznitz (no. 6). For equations of state other than the Lee-Kessler model, the usual mixing rules combining the intrinsic parameters of the models were also tested. The corresponding results are grouped together in the column "internal". All the details concerning these equations of state and mixing rules can be found in the references Yé et al, (2,3).

In the following table we present the AAD (%) determined between the experimental ultrasound velocitys and the values generated by the different equation of state — mixing rule combinations.

Whereas in the case of purely gaseous samples the external mixing rules lead to more or less equivalent deviations, the above table shows that the deviations differ significantly from one mixing rule

to another in the case of this condensate gas. This result reflects the non negligible pseudo-critical pressure differences  $P_{\text{mix}}$  and temperature differences  $T_{\text{c mix}}$  of the complex mixture generated by the various rules used to estimate them. It appears that the choice of a combining rule for the critical properties may have a large impact, despite the formulations of the rules which may be sometimes very similar.

EOS	Mixing rules						
	1	2	3	4	5	6	Internal
SRK	7.5	40.0	18.9	19.0	12.7	17.2	2.2
PR	2.0	51.8	13.3	13.4	6.3	11.3	9.7
PR-RP	7.2	65.1	6.8	6.9	2.1	4.7	1.8
SBRJ	22.8	90.4	6.6	6.4	15.4	9.0	9.8
LK	16.4	71.4	2.7	2.6	10.6	4.8	-

Examination of the table also shows the existence for each equation of state of one or two preferential combinations for which the absolute average deviation is acceptable. The thermodynamic models which emerge particularly from this study are the Lee-Kessler correlation associated with either rules 3 or 4 and the equation of state PR-RP combined with its own internal mixing laws. We should indicate that the predictions of these two models are acceptable throughout the whole range of pressures studied, a performance which should give rise to applications in the case of hyperbaric-type fluids, i.e. natural fluids whose conditions of existence in the reservoirs correspond to very high pressures (of the order of 100 MPa or even greater).

## References

1. J.L. Daridon, *Acustica* **80** (1994) 416.
2. S. Yé, B. Lagourette, J. Alliez, H. Saint-Guirons, P. Xans and F. Montel, *Fluid Phase Equilibria* **74** (1992) 157.
3. S. Yé, B. Lagourette, J. Alliez, H. Saint-Guirons, P. Xans and F. Montel, *Fluid Phase Equilibria* **74** (1992) 177.

# COMPUTER SIMULATIONS OF THE RAMAN Q-BRANCH IN FLUID NITROGEN

J.P.J. Michels, M.I.M. Scheerboom and J.A. Schouten  
Van der Waals-Zeeman Institute, University of Amsterdam, Valckenierstraat 65,  
1018 XE Amsterdam, The Netherlands

## ABSTRACT

We performed dynamical computer simulation on a model system for fluid nitrogen in order to investigate the vibrational motions at room temperature, at pressures up to the melting line. The results can be compared with experimental data of Raman spectroscopy, available in the literature. In contrast with earlier attempts by others, realistic results have now been obtained for the line width. These results do not depend on any ad hoc adjustment of parameters, but are based on the inter- and intramolecular potentials, obtained from other sources. Moreover, the molecular dynamical simulations reveal a detailed insight in the relaxation of the vibrational motions, including the individual contributions of the underlying mechanisms.

## Introduction

In recent years the study of the vibrational spectrum of simple fluids has been extended to high pressures. Raman and infrared spectroscopy is used to probe the interaction of a molecule with the local environment and to study the dynamics of fluids. Meanwhile the dephasing time, the change in vibrational frequency and the line shape of nitrogen has been measured up to the melting line at room temperature.[1-5] Various investigators have tried to calculate the line width and the shift, but quantitative agreement appears hard to obtain. Levesque et.al. have carried out a computer simulation of liquid N<sub>2</sub> at the boiling point.[6] They investigated the distinct contributions to the dephasing. An important conclusion was that the cross terms are essential and that one can not treat the contributions separately. A numerical investigation of the density dependence of the dephasing time has been made by Chesnoy and Weis.[7] Their results are mainly qualitative.

## Method

Dynamical simulations have been performed on a model system for N<sub>2</sub> to calculate the line width at room temperature and pressures up to  $\approx 2.16$  GPa. The system consisted of 256 rigid rotors with site-site interactions; the sites coincided with the constituent atoms. The intermolecular potential was defined corresponding the potential given by Etters et.al.[8], but without the quadrupole terms. Moreover it was assumed that vibrations do not influence the intermolecular interactions. It has been shown that

vibron-vibron transfer is small, therefore, this was not taken into account.

The simulations have been performed throughout a simulated time of 60 ps for each run. The change in vibrational frequency has been calculated from the momentary forces acting on the sites e.g. the atoms. In the first approach, three mechanisms that influence the vibration frequency, have been considered.

- 1) External forces which change the bond length, called below the 'first order effect'
- 2) The non-uniformity of the external forces, called the 'second order effect'
- 3) The vibration-rotation coupling.

The changes in vibration frequency are, in first order, proportional to resp.: the axial force exerted on the molecule, the derivative of that force to the bond length and the rotational frequency squared. The proportionality constants have been calculated from the intramolecular potential, given by Herzberg [9] and Lavorel et al.[5]

The total shift for each particle has been calculated by adding the three terms to the value of the vibration frequency of an isolated non-rotating molecule. [6]

Three topics of interest have been surveyed:

- 1) the mean value for the vibration frequency  $\langle\omega_{\text{vib}}\rangle$
- 2) the width of the distribution of the momentary individual values of  $\omega_{\text{vib}}$ :

$$\Delta = \{ \langle\omega_{\text{vib}}^2\rangle - \langle\omega_{\text{vib}}\rangle^2 \}^{1/2} \quad (1)$$

- 3) the time correlation function:

$$\Omega(t) = \frac{\langle\omega_{\text{vib}}(0)\omega_{\text{vib}}(t)\rangle - \langle\omega_{\text{vib}}(0)\rangle^2}{\Delta^2} \quad (2)$$

from which the correlation time  $\tau_c$  was calculated by:

$$\tau_c = \int_0^\infty \Omega(t) dt \quad (3)$$

Kubo[10] has shown that under the condition  $\Delta \tau_c \ll 1$  the line shape is Lorentzian and the line width, defined as the 'full width at half maximum' (FWHM) can be calculated with  $\text{FWHM} = 2 \Delta^2 \tau_c$ .

## Results

All simulations concern fluid  $N_2$  at 296 K only. Firstly  $\Delta \tau_c$  was determined as a function of pressure. It turned out that its value is about 0.08 at 0.2 GPa, goes through a minimum of 0.045 at 0.65 GPa and increases again to 0.07 at 2.65 GPa. The conclusion is that within this pressure range, the above expression can be used for the calculation of the line width. The results are displayed in fig.1 by the open circles.

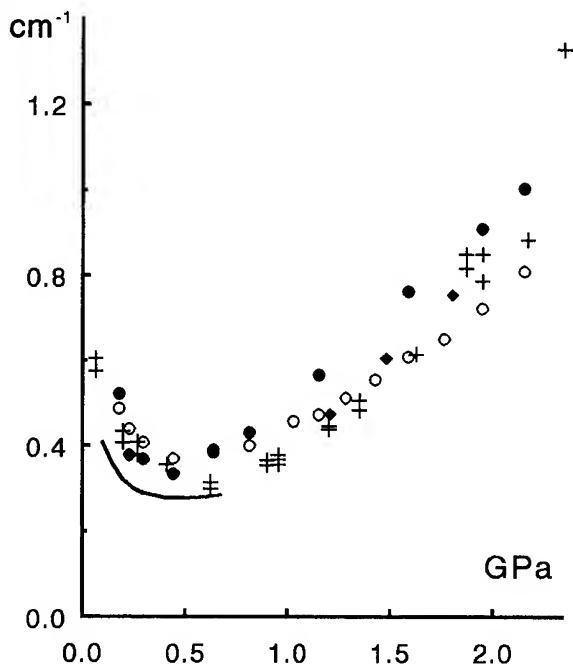


fig.1. The FWHM as a function of the pressure. a) from Raman spectroscopy: Lavorel et.al.[3]:line; Scheerboom and Schouten[4]: diamonds. b) from  $T_2$  measurements: Kroon et.al.[1,2]: crosses. c) from simulations: circles and dots.

In this figure a comparison is made with experimental data from Raman spectroscopy by

Lavorel et.al.[3] and by Scheerboom and Schouten.[5] Moreover, results from the vibrational decay time  $T_2$  have been shown. The line width is related to  $T_2$  by  $\text{FWHM} = (\pi c T_2)^{-1}$ . As can be seen, the simulation results for the line width are in rather good correspondence with the experimental values. In particular, the minimum at about 5 GPa is reproduced by the calculations. A remarkable observation is that the increase above this pressure is not only due to an increase in  $\Delta$  but in  $\tau_c$  as well. fig. 2 displays the pressure dependence of  $\tau_c$ .

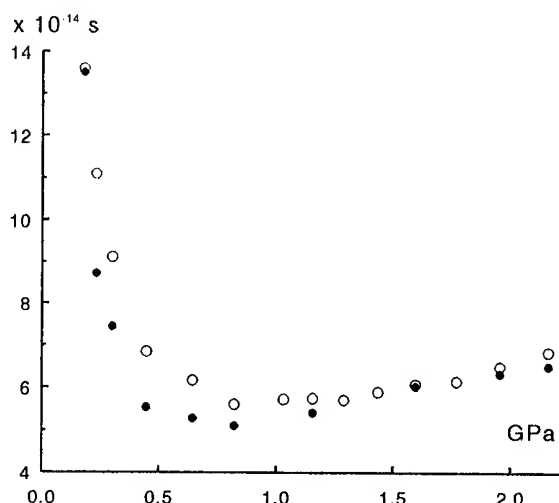


fig.2. The relaxation time  $\tau_c$  as a function of the pressure.

It is evident from (2) that the value of  $\tau_c$  depends on the behaviour of the time correlation function of the frequency. The relaxation of this function depends in our model on the three mechanisms mentioned above. An example of the behaviour for each of the constituent parts is given in fig 3, concerning the system at 1.1 GPa. Omitting any of these three mechanisms changes the behaviour of the correlation function drastically. The resulting function shows a rapid decrease at short times and a slowly decaying long time tail. With increasing pressure, the initial decay becomes even more rapid, while the tail becomes more pronounced. The latter effect surpasses the first at high pressures, giving rise to an increase of  $\tau_c$ . Another matter of interest is the value for  $\langle \omega_{\text{vib}} \rangle$ . It turns out that this value increases monotonously with the pressure. The first order and the second order effect are positive, while the value for the second order effect amounts to about 19 % of the first order effect throughout the whole pressure

region; the vibration-rotation is obviously constant at constant temperature.

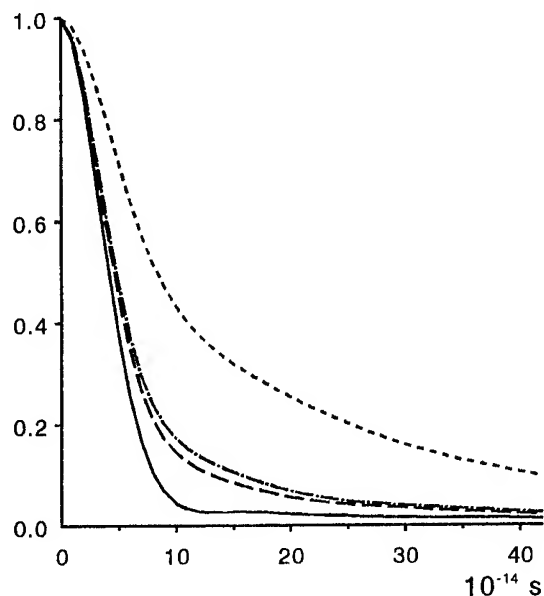


fig.3. Decay of the autocorrelation of  $\omega_{\text{vib}}$  at 1.1 GPa. Dashed line: only by the vibration-rotation coupling; dash-dot: by the 'first order' and dashed: by the second order effect only. Solid line: the complete autocorrelation function  $\Omega(t)$

In fig. 4 a comparison is made between  $\langle\omega_{\text{vib}}\rangle$  and the experimental shift: an evident discrepancy is seen.

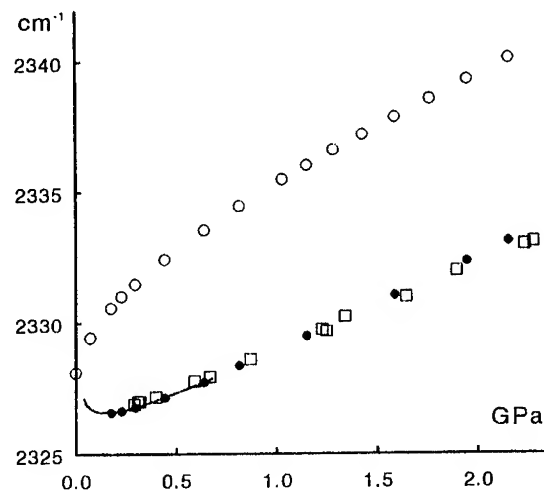


fig.4. The Raman shift as a function of the pressure. Lavorel et.al[3]: line; Scheerboom and Schouten[4]: squares. Simulations: circles and dots.

A serious simplification in our model is the assumption that the intermolecular potential is the

same for excited molecules as for molecules in the ground state. It is known for instance, that the polarizability increases at excitation, but it is hard to quantize this effect (often called the attractive contribution) and to include it in the simulation model. Therefore, we determined the change in potential energy at excitation directly from the difference in frequency, i.e. the energy gap, between the simulated  $\langle\omega_{\text{vib}}\rangle$  and the experimental data of the shift. For this purpose we introduced an additional intermolecular site-site potential function  $\Delta\phi$  which describes the pressure dependence of this energy gap. A suitable functional form turned out to be the Lennard-Jones 12-6 potential with:

$$\epsilon/k_B = 0.30 \text{ K}; \quad \sigma = 2.95 \times 10^{-10} \text{ m.} \quad (4)$$

We emphasise that no acceptable fit can be obtained with a  $r^{-6}$  term only but that it is absolutely necessary to incorporate a repulsive part. This energy jump  $\Delta\phi$  results in a frequency jump  $\Delta\omega = \Delta\phi/2\pi c$ . The quality of the fit can be seen from in fig 4 (dots). A logical step is now to include  $\Delta\omega$  as a fourth contribution in the calculations of  $\langle\omega_{\text{vib}}\rangle$  and repeat the simulations for the line width. In figs 1 and 2 the new results have been displayed by dots. Note that  $\Delta\phi$  is negligible for the dynamics of the system: the potential minimum of the site-site interaction  $\phi(r)$  amounts to 40 K and equals zero at  $3.3 \times 10^{-10} \text{ m}$ .

## References

1. R. Kroon, M. Baggen and A. Lagendijk, *J. Chem. Phys.* **91** (1989) 74.
2. R. Kroon, *thesis*, University of Amsterdam (1993)
3. B. Lavorel, B. Oksengorn, D. Fabre, R. Saint-Loup and H. Berger, *Mol. Phys.* **75** (1992) 397
4. M. I. M. Scheerboom and J. A. Schouten, *Phys. Rev. E* **51** (1995) R2747.
5. B. Lavorel, R. Chaux, R. Saint-Loup and H. Berger, *Opt. Commun.* **62** (1987) 25.
6. D. Levesque, J.J. Weis and D. W. Oxtoby, *J. Chem. Phys.* **72** (1980) 2744.
7. J. Chesnoy, D. Levesque and J. J. Weis, *J. Chem. Phys.* **84** (1986) 5378.
8. R. D. Etters, V. Chandrasekharan, E. Uzan and K. Kobashi, *Phys. Rev. B* **33** (1986) 8615.
9. G. Herzberg, in *Infrared and Raman Spectra of Polyatomic Molecules*, (Van Nostrand, 1966)
10. R. Kubo, in *Fluctuation, Relaxation and Resonance in Magnetic Systems*, ed. by D. ter Haar Oliver & Boyd Ltd. Edinburgh, (1962).



## **VIII Chemistry and Physics of Organic Materials**

# THE EFFECTS OF PRESSURE AND OF RADIATION ON THE PHOSPHORESCENCE OF A SERIES OF NITRILES, ALDEHYDES AND KETONES DISSOLVED IN SOLID POLYMERS

H. G. Drickamer, Z. A. Dreger and J. M. Lang

School of Chemical Sciences and the Frederick Seitz Materials Research Laboratory, University of Illinois  
Urbana, IL 61801, USA

## ABSTRACT

At room temperature pressure induces strong phosphorescence in a series of nitriles, aldehydes and ketones dissolved in a solid polymer. Phosphorescence, apparently from a chemically modified molecule is introduced by radiation. Both the pressure induced (PIP) and radiation induced (LIP) phosphorescence are characterized in terms of a kinetic model based on the relative characters and pressure induced perturbations of  $n\pi^*$  and  $\pi\pi^*$  and singlet and triplet states.

## Introduction

Two years ago we observed a pressure induced phosphorescence at room temperature in 4, 4'-dimethylaminobenzonitrile (DMABN)<sup>(1)</sup> dissolved in polymers. A little later we observed in the same molecule a radiation induced phosphorescence whose characteristics were pressure dependent.<sup>(2)</sup> Since

DMABN is the paradigm of a class of molecules which fluoresce from two different excited states of different geometry, (TICT molecules) it was reasonable to associate these emissions with processes involving the two geometries. Since then we have observed these effects in a variety of aldehydes and ketones as shown in Fig 1.<sup>(3)</sup> Note that both pressure induced and radiation induced phosphorescence occur in benzophenone (BP) and benzaldehyde (BA) although neither of these molecules can exhibit TICT behavior and, in fact, neither exhibits any fluorescence emission. Most of the measurements have involved polyethylmethacrylate (PEMA) as a medium, but qualitatively similar results are obtained in polyvinylchloride (PVCL). Both the pressure and radiation effects can be induced either by the 325nm line of a He-Cd laser or by the 365nm line of an Hg arc lamp if the molecules absorb in an appropriate region. In this brief presentation we present a few typical examples which illustrate the general behavior and outline the similarities and differences between BP and BA and the molecules which contain dialkylamino (charge donating) groups.

## Results

Figure 2 exhibits the pressure induced phosphorescence in dimethylaminobenzaldehyde (DMABA). These are typical for the TICT molecules studied. Note that, in addition to the very large growth of the phosphorescence by a factor of  $\sim 200$ , there is a significant increase in intensity of the fluorescence peak located at  $\sim 5000\text{ cm}^{-1}$  higher in energy. Fig 3 shows comparable data for benzophenone (BP). The results, although quantitatively quite different, are qualitatively similar. In BA the phosphorescence first appears at  $\sim 20\text{ kbar}$  and increases by a factor of  $\sim 7$  by  $90\text{ kbar}$ .

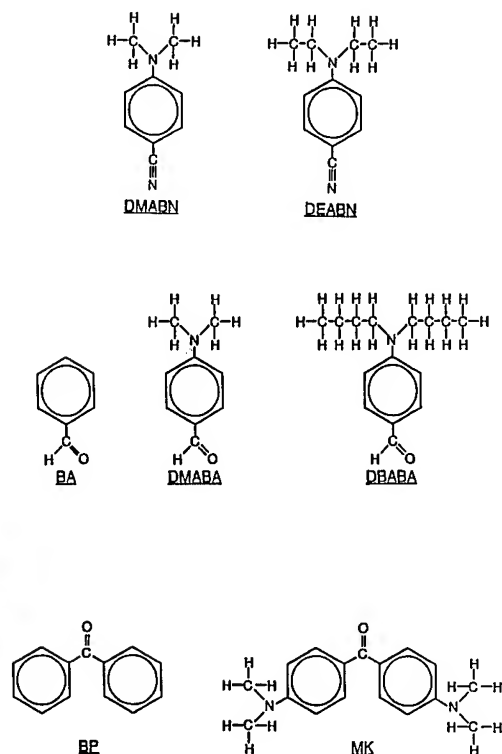


Fig 1 Structure of molecules studied

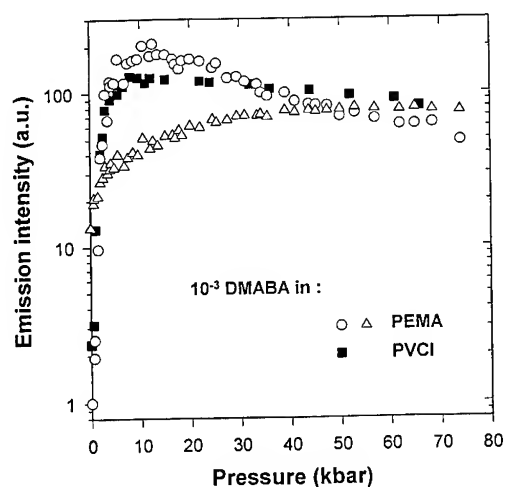


Fig 2 Pressure induced luminescence for DMABA: in PEMA; 0 - phosphorescence;  $\Delta$  - fluorescence - in PVCI;  $\blacksquare$  - phosphorescence

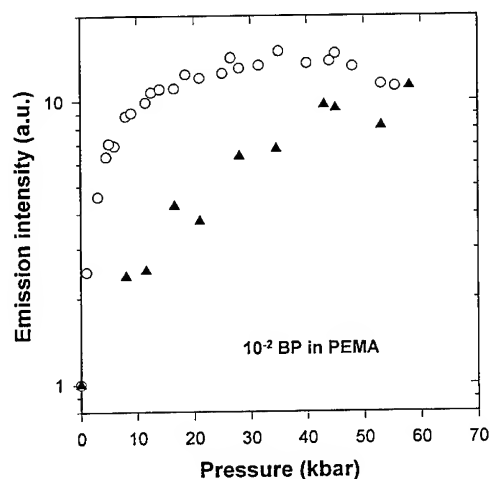


Fig 3 Pressure induced phosphorescence in BP - 0 excited by 325 nm laser;  $\blacktriangle$  excited by 365 nm mercury arc

The radiation effect for DMABA is shown as a function of pressure in Fig 4. Note, there is an initiation period where there is only fluorescence at 480 nm. This is especially clear at 0 kbar. It increases with decreasing concentration approximately as  $C^{-1/2}$ . The corresponding results for BP appear in Fig 5.

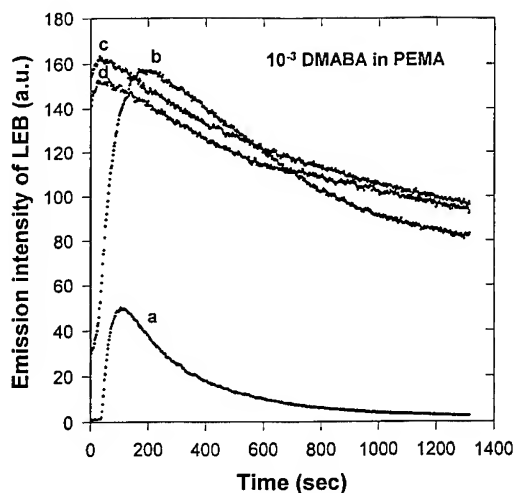


Fig 4 Radiation induced phosphorescence in DMABA - a = 0 kbar; b = 2 kbar; c = 11 kbar; d = 20 kbar

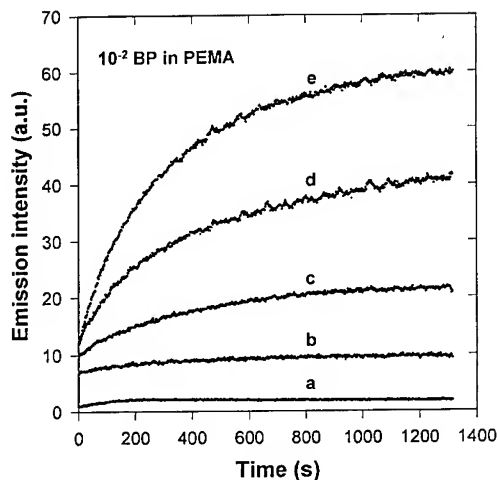


Fig 5 Radiation induced phosphorescence in BP - a = 0 kbar; b = 5 kbar; c = 13 kbar; d = 30 kbar; e = 48 kbar

Although the pressure induced phosphorescence (PIP) and the radiation induced phosphorescence (LIP) occur at almost the same energy, the LIP is evidently from a photochemically modified molecule. Fig 6 shows, for DMABN, the relaxation of this molecule back to the original ground state. At intervals of 30

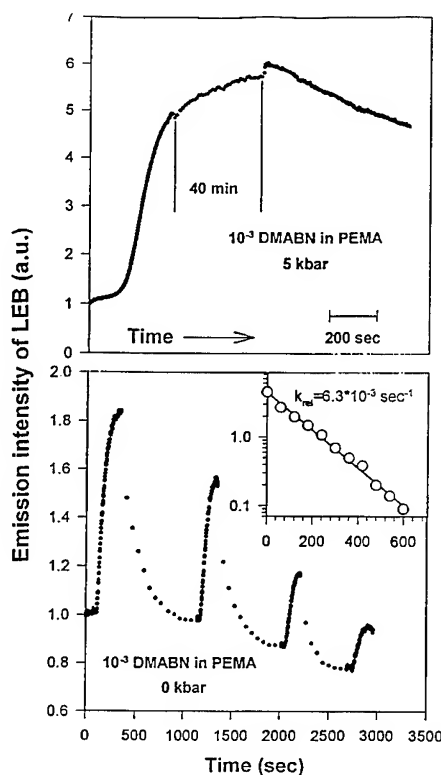


Fig 6 Relaxation by reversion of radiation induced phosphorescence for DMABN at 0 kbar and 5 kbar

seconds to 10 minutes the sample was excited for two seconds. At one atmosphere the relaxation to the original structure took  $\sim 15$  minutes. At five kilobars in five hours there was only a 25 - 30% reversion of the sample.

The "pure" pressure effect (PIP) is separated from the effect of radiation by loading a cell at some pressure and measuring the emission intensity at wavelengths corresponding to the LEB and HEB for two seconds each. Then a new load is made and the procedure repeated at each different pressure, so that each point represents a non-radiated sample.

It should be noted that in liquid solution at one atmosphere these molecules tend to abstract a hydrogen from the medium and form radicals which give a number of metastable products generally not well defined.<sup>(4)</sup> These products are non-luminescent.

It is useful to summarize the factors that these molecules have in common as well as any

differences. All of them contain oxygen or nitrogen which supplies a nonbonding orbital. Thus, in addition to the usual bonding - antibonding ( $\pi\pi^*$ ) excitations there exist  $n\pi^*$  excitations. For BP, and apparently for the other molecules, a number of analyses indicate that the lowest triplet is primarily  $T(n\pi^*)$  with  $T(\pi\pi^*)$  sufficiently close that there is some mixing even at one atmosphere.<sup>(5)</sup> For BP the lowest singlet is  $S(n\pi^*)$ . There is evidence for DMABA, DBABA and MK that the lowest singlet is  $S(\pi\pi^*)$ . In addition those molecules with electron donor groups can have charge transfer excitations which may be mixed with the  $\pi\pi^*$  excitations. These various molecular states have different characteristics, including response to compression.  $\pi\pi^*$  emissions are much more intense than  $n\pi^*$ , frequently by several orders of magnitude<sup>(6)</sup>. On the other hand  $T(n\pi^*)$  states are much more photochemically reactive than  $T(\pi\pi^*)$ <sup>(4)</sup>. It is more difficult to give a general characterization to charge transfer states.  $S \rightarrow T$  crossing is much less rapid between states of the same character (ie  $\pi\pi^* \rightarrow \pi\pi^*$  or  $n\pi^* \rightarrow n\pi^*$ ) than is intersystem crossing involving a change of character.  $\pi\pi^*$  excitations shift to lower energy with pressure much more strongly than  $n\pi^*$  excitations. Also  $\pi\pi^*$  excitations involving singlets show larger red shifts with pressure than those involving triplets.<sup>(6)</sup> These factors can be used to describe a large number of the observations noted above. Using the model of Fig 7, one can describe the PIP and the major features of the LIP. One obtains:

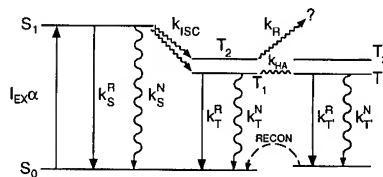


Fig 7 Generalized: kinetic scheme

$$I_F = \left[ \frac{\alpha I_{EX}}{1 + \frac{k_S^N + k_{ISC}}{k_S^R}} \right] \quad (1)$$

$$I_P = \alpha I_{EX} \left[ \frac{1}{1 + \frac{k_T^N + k_R + k_{HA}}{k_T^R}} \right] \left[ \frac{1}{1 + \frac{k_S^R + k_S^N}{k_{ISC}}} \right] \quad (2)$$

where  $k_S^R$ ,  $k_S^N$ ,  $k_T^R$ ,  $k_T^N$  are the radiative and non-radiative decay rates for the singlet and triplet states;  $k_{ISC}$  is the rate of  $S \rightarrow T$  intersystem crossing,  $k_{HA}$  is the rate of hydrogen abstraction and  $k_R$  is the rate of an irreversible reaction apparently induced by radiation only in molecules with electron donor side groups.

### Pressure induced Phosphorescence (PIP)

The results in Fig 2 are typical of the materials with dialkylamino sidegroups. There is a very steep rise in the intensity of the phosphorescence in the first ten kbar or so. As the  $\pi\pi^*$  transition is stabilized by pressure  $k_R^T$  rapidly increases since  $T(\pi\pi^*)$  can have several orders of magnitude higher emission intensity (than  $T(n\pi^*)$ ). At the same time  $k_{HA}$  decreases as  $T(\pi\pi^*)$  is much less reactive than  $T(n\pi^*)$ .

The shift of the fluorescence emission peak with pressure is the same as the  $\pi\pi^*$  absorption, so  $S_1$  is  $S(\pi\pi^*)$ . Initially  $k_{ISC}$  is large as  $T_1$  is largely  $T(n\pi^*)$ , but with pressure  $k_{ISC}$  decreases as  $T_1$  assumes more  $\pi\pi^*$  character. It can be shown that this change accounts for (a) the amount and shape of the increase in fluorescence intensity with pressure and (b) the decrease in phosphorescence intensity beyond 10-15 kbar.

For BP (and BA) the situation is somewhat different as  $S_1$  has  $n\pi^*$  character.  $k_{ISC}$  is sufficiently large at all pressures so that, combined with weak emission for  $S(n\pi^*)$ , no fluorescence is observed at any pressure. The increase in phosphorescence intensity by a factor of 12-15 in 50 kbar, is due to the increase in  $k_T^R$  and the decrease in  $k_{HA}$  due to increased  $\pi\pi^*$  character of the lowest triplet.

### Light Induced Phosphorescence (LIP)

The light induced phosphorescence is a more complex phenomenon. LIP occurs both in the dialkylamino substituted molecules and in BP and BA

but with rather different characteristics. In neither case have we been able to establish the exact chemical structure of the emitting entity, but it must be either the radical formed by hydrogen abstraction or a closely related molecule as it emits at the same energy as the original molecule. If it is excited directly it must absorb at the same energy also. If it is excited by triplet-triplet energy transfer it must be very close to an unmodified molecule as T-T energy transfer is very short range.

In Fig 4 we show results for DMABA; qualitatively similar behavior is observed in DBABA, DMNBN and MK. After an induction period which shortens with increasing concentration (or pressure) there is a sharp increase in emission intensity occurring after only one to two minutes of irradiation.

Since only a modest amount of emitting molecule can have formed, the lowest triplet must be an efficient emitter and therefore is of  $\pi\pi^*$  character at all pressures. As pressure increases the amount of radiation induced phosphorescence decreases and disappears by 10-20 kbar depending on the molecule. As indicated above,  $k_{ISC}$  and  $k_{HA}$  decrease rapidly as the original triplet assumes more  $\pi\pi^*$  character so less of the modified molecule is formed. At all pressures, after sufficient radiation time, there is a radiation induced decrease in the pressure created phosphorescence. This process is irreversible and is relatively independent of pressure and concentration. It is not observed in BP or BA so it must be a reaction induced by the electron donor character of the side groups.

As seen in Fig 6, the effect in BP is quite different. At one atmosphere the radiation induced phosphorescence is very weak, but it increases with pressure to ~ 50 kbar and then levels or decreases slightly at higher pressures. Evidently the emitting product from BP has a lowest triplet of  $n\pi^*$  character at one atmosphere with a  $T(\pi\pi^*)$  not much above. With increasing pressure the  $\pi\pi^*$  character of the lowest triplet increases significantly and thus the emission intensity increases until, above 50 kbar the decrease in  $k_{HA}$  counteracts this effect. The behavior of BA is very similar. The pressure effect is well described by the model, as well as major features of the radiation effect. Undetermined factors include the nature of the molecule involved in the radiation induced phosphorescence and its mode of excitation, as well as the nature of the radiationless products

produced by light in molecules with electron donor substituents.

There remain unsolved aspects, but it is clear that the two new phenomena uncovered in this investigation are of general occurrence. Since essentially all the molecules involved in light-emitting polymers, electrooptical polymers and molecular electronic devices contain non-bonding orbitals, a thorough understanding of the effects of radiation, pressure, etc. on the electronic behavior of such molecules is essential to establish the long range possibilities and limitations of these devices.

#### Acknowledgment

The authors wish to express their sincere gratitude to the Materials Science Division of the Department of Energy for the support of this work under Contract DEFG02-91R45439.

#### References

- (1) J. M. Lang, Z. A. Dreger and H. G. Drickamer, *J. Phys Chem* **98** (1994) 11308.
- (2) Z. A. Dreger, J. M. Lang and H. G. Drickamer, *Chem. Phys Lett.* **232** (1995) 351.
- (3) Z. A. Dreger, J. M. Lang and H. G. Drickamer *J. Phys. Chem.* (submitted).
- (4) C. Brauchle, D. M. Burland and G. C. Bjorkland, *J. Phys. Chem.* **85** (1981) 123 (and references therein).
- (5) M. Lipson, P. McGarry, I. Kuptyug, H. Staab, N. Turro and D. Doetschman, *J. Phys. Chem.* **98** (1994) 7504 (and references therein).
- (6) H. G. Drickamer in *Photochemistry and Photophysics Vol. I*, J. R. Rabeked CRC Press 1989, p. 137 (and references therein).

# RECENT ADVANCES IN HIGH PRESSURE ORGANIC SYNTHESIS: HIGH PRESSURE-MEDIATED MACROCYCLIZATION PROCESSES

J. JURCZAK,<sup>a,b</sup> K. CHMURSKI,<sup>b</sup> D.T. GRYKO,<sup>b</sup> P. LIPKOWSKI,<sup>b</sup> R. OSTASZEWSKI,<sup>b</sup> P. SAŁAŃSKI<sup>b</sup>

<sup>a</sup> Department of Chemistry, Warsaw University, Pasteura 1, 02-093 Warsaw, Poland

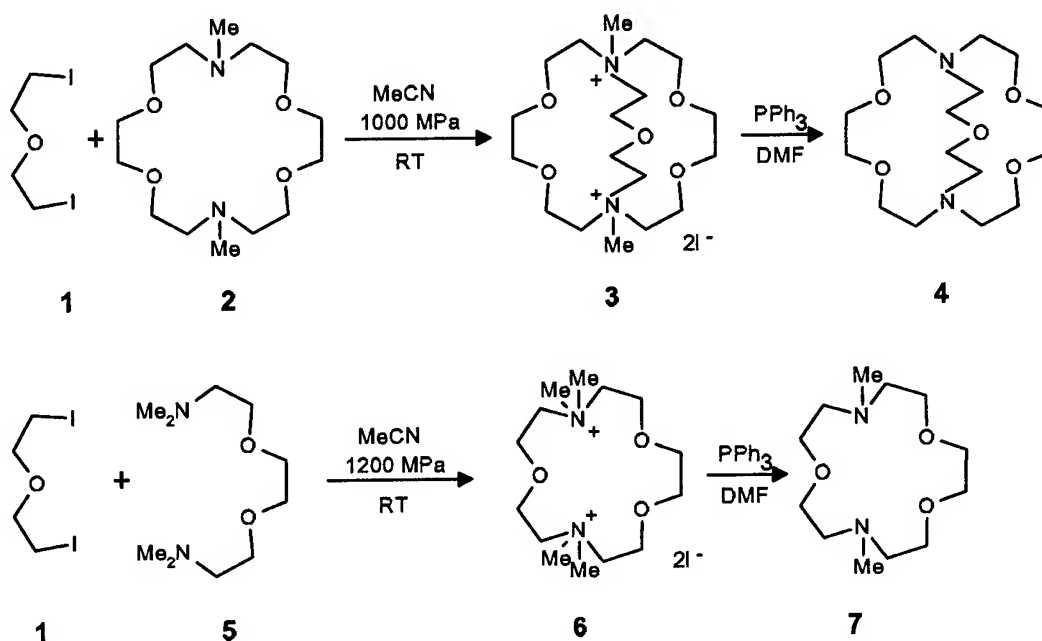
<sup>b</sup> Institute of Organic Chemistry of the Polish Academy of Sciences, Kasprzaka 44/52, 01-224 Warsaw, Poland

The effect of pressure on the rate and direction of macrocyclization reactions in solutions is presented in order to illustrate the present status and prospects of high-pressure techniques in the organic synthesis.

Assumption that the double-quaternization reaction between N,N'-dimethyl diazacoronands and  $\alpha,\omega$ -diiodo ether would be accelerated by pressure, was a basis of our first method of the synthesis of cryptands.<sup>1</sup> The formation of charged products from neutral substrates usually results in increased solvation. Thus, when the charge develops along the reaction coordinate, the reaction volume is often large and negative.<sup>2</sup> Historically the first high-pressure double

quaternization was performed between diiodo-derivative **1** and N,N'-dimethyl diazacoronand **2** (Scheme 1).<sup>3</sup>

For preparative performance, an equimolar mixture of compounds **1** and **2** (ca. 0.08M solution in acetonitrile) was exposed to a 1000 MPa pressure for 20 hours. During the reaction the bis-quaternary salt **3** precipitated quantitatively. The methyl groups of the salt **3** was removed by treatment with triphenyl-

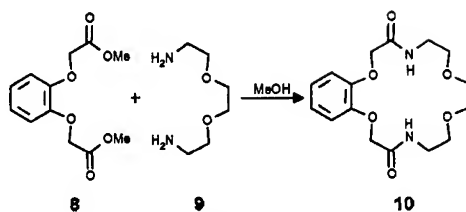


Scheme 1

phosphine in boiling dimethyl formamide, this affording the desired cryptand **4** in a very good (85%) yield.

It was expected that a open chain tertiary  $\alpha,\omega$ -diamine would react under high-pressure conditions with an appropriate  $\alpha,\omega$ -diiodo compound to form a cyclic bis-quaternary salt. Indeed, when the amine **5** reacted with diiododerivative **1** under 1200 MPa pressure, it afforded the desired crystalline bis-quaternary salt **6** in a quantitative yield. Subsequent demethylation yielded N,N'-dimethyl diaza-coronand **7**, as shown in Scheme 1.<sup>4</sup>

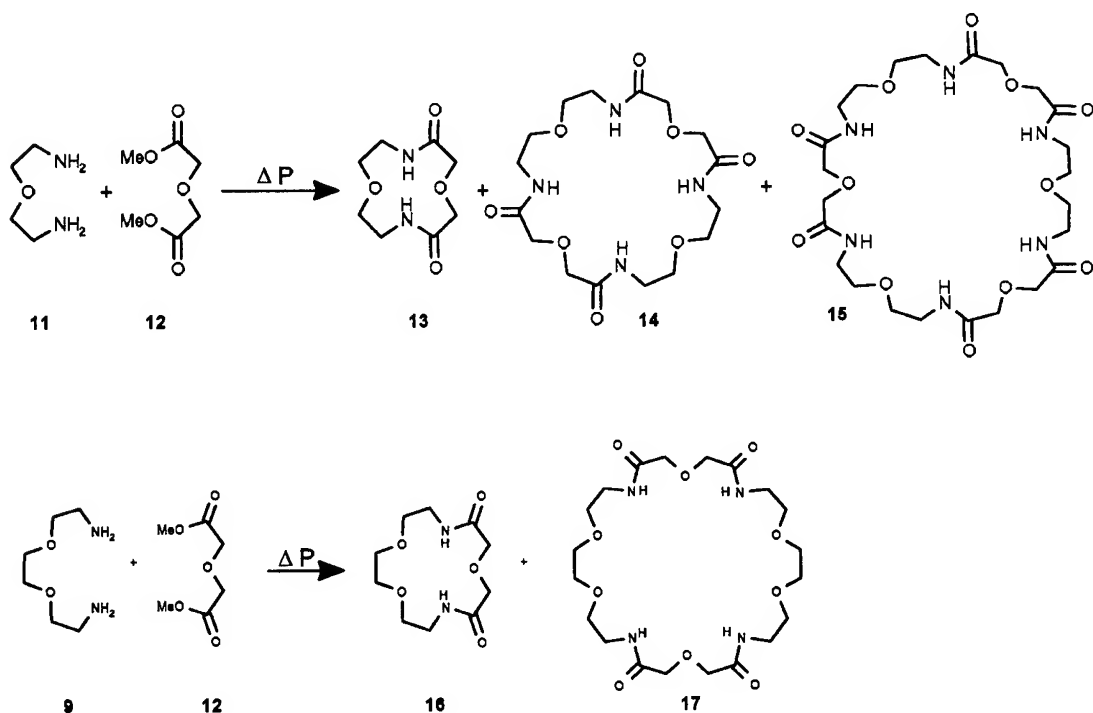
The macrocyclization process based on acylation of primary amines under high-dilution conditions was introduced by Lehn *et al.*<sup>5</sup> This method was then developed by us using the reaction between dimethyl esters of type **8** and primary diamines **9** in methanol as solvent, as shown in Scheme 2.<sup>6</sup>



Scheme 2

The reaction was carried out at room temperature under atmospheric pressure for several days. Application of the high-pressure conditions (800 - 1500 MPa) caused shortening of time required for completion of the reaction.

In the reaction of terminal diamine **11** with dimethyl ester **12** carried out in methanol under ambient conditions, macrocyclic azacoronands **13**, **14**, and **15** are formed in a ratio 50:50:1. Application of high-pressure conditions to this reaction led to formation of products **13** and **14** in a ratio 3:2, respectively. (Scheme 3).<sup>7</sup>



Scheme 3

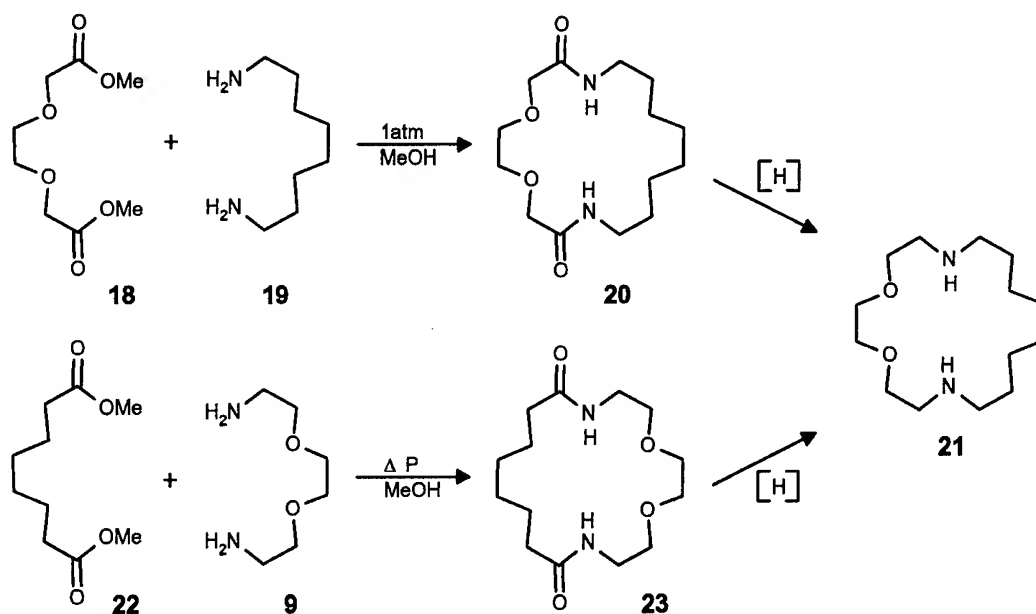


In the case when compound **11** was replaced by longer diamine **9**, two azacoronands **16** and **17** are formed in a ratio 5:1, respectively. Under high-pressure conditions this ratio changed to 5:2. In the case when compound **12** was replaced by longer ester, only the respective diazacoronands are formed.

The reaction between diester **18** and 1,8-diamino octane **19** furnished, under ambient conditions (methanol as solvent, RT, 7 days, reagent concentrations 0.1M/L) the diamide **20** in a 30% yield (Scheme 4).<sup>8</sup>

diazacoronand **21**.

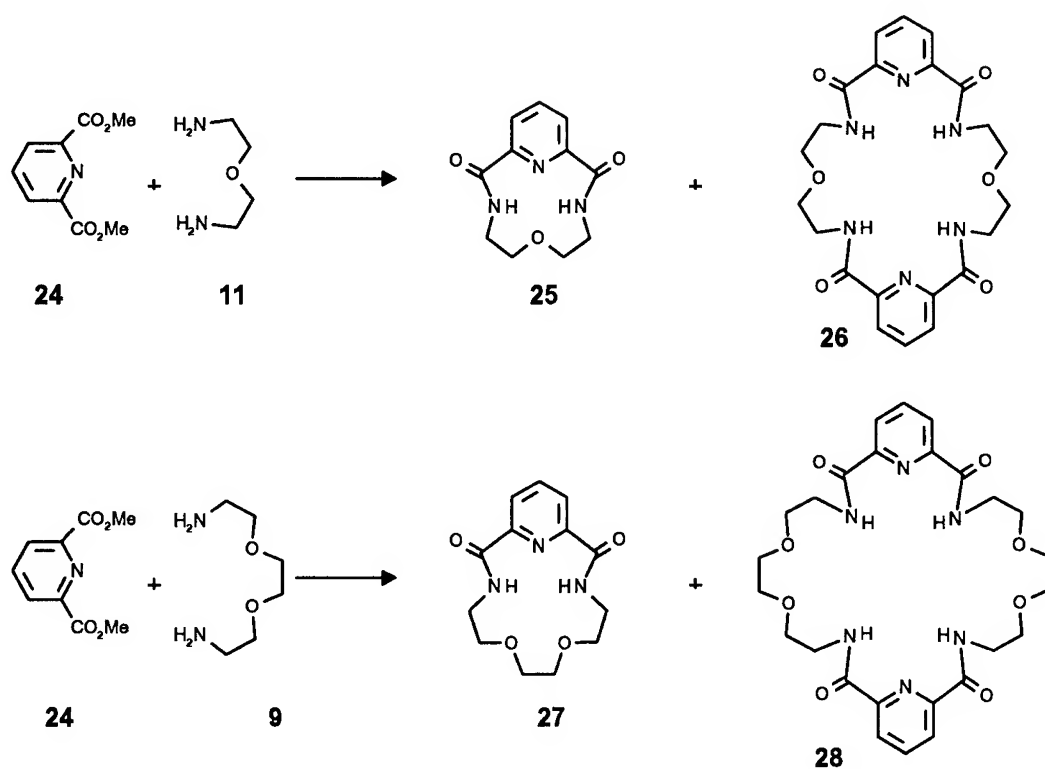
Very interesting examples of the synthesis of artificial molecular receptors are given in Scheme 5.<sup>9</sup> The reaction of diester **24** with diamine **11**, carried out under ambient conditions, afforded the dimeric azacoronand **26** in a 21% yield; the expected monomeric azacoronand **25** was not formed. When the high-pressure conditions (1200 MPa) were used for this reaction, the yield of the dimer **26** slightly increased (24%), whereas the monomer **25** was also not formed (Scheme 5).



Scheme 4

The reaction of diester **22** with diamine **9** failed, however, under ambient conditions. In this case we successfully applied high-pressure conditions (800 MPa, methanol as solvent, RT, 48 h, reagent concentrations 0.1 M/L) affording the diamide **23** in a 25% yield. Reduction of both diamides **20** and **23** led to the same

In the case of reaction between diester **24** and diamine **9**, carried out under ambient conditions, led to a mixture of azacoronands **27** and **28** in a ratio 13:1, respectively, with a very high overall yield (89%). Application of the high-pressure conditions (1200 MPa) changed the ratio of compounds **27** and **28** as 29:1, respectively.



Scheme 5

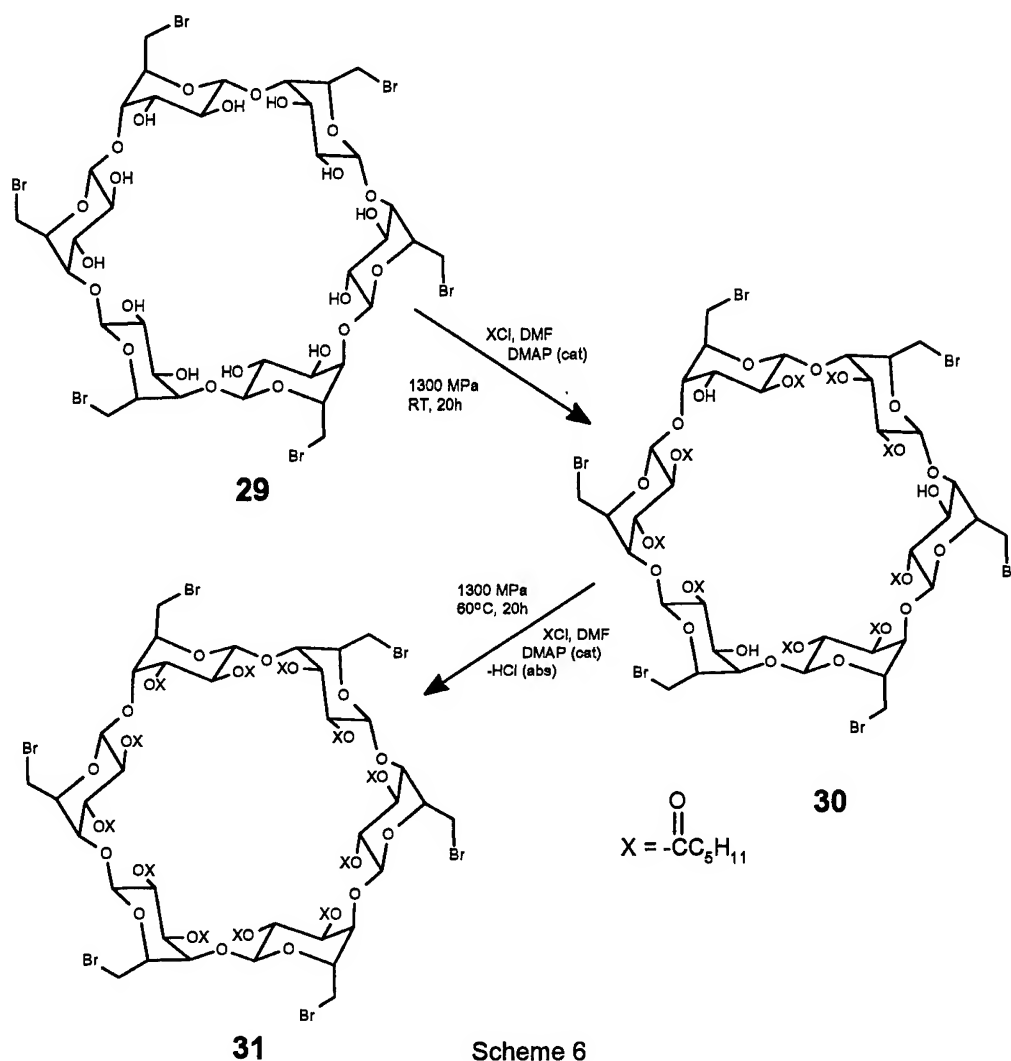
Apart from above presented double amidation procedures, the high-pressure technique seemed to be useful for preparation of other supramolecular systems via an acylation reaction. The interesting example of such approach consists of high-pressure mediated O-acylation of sterically hindered secondary hydroxy groups in cyclodextrins as shown in Scheme 6.

The 6-bromo  $\beta$ -cyclodextrin derivative **29** was treated with hexanoyl chloride under 1300 MPa pressure at room temperature to afford a mixture of partially acylated products including compound **30**. Subsequent acylation of this mixture under the same pressure, but at elevated (60 °C) temperature in the presence of an acid

scavenger, afforded the desired fully acylated product **31**.<sup>10</sup>

The above-presented high-pressure methods seem to be important contribution to modern synthetic chemistry. The essential points are that the high-pressure reactions offer very good yield and purity of products. Secondly, the easy and mild work-up of these reactions greatly extends the scope of the potential applications for the preparation of much more elaborated, polyfunctional structures including chiral compounds.

Summing up, it can be stated that the high-pressure approach adds to the versatility of the synthesis of supramolecular systems with, moreover, its marked simplification.



## References

- 1 J.Jurczak and M.Pietraszkiewicz, *Top. Curr. Chem.* **130**, 183 (1985).
- 2 J.Jurczak and M.Pietraszkiewicz in *High Pressure Chemical Synthesis*, eds J.Jurczak and B.Baranowski (Elsevier, Amsterdam, 1989).
- 3 M.Pietraszkiewicz, P.Salanski, R.Ostaszewski, and J.Jurczak, *Heterocycles* **24**, 1203 (1986).
- 4 J.Jurczak, R.Ostaszewski, P.Salanski, and T.Stankiewicz, *Tetrahedron* **49**, 1471 (1993).
- 5 B.Dietrich, J.M.Lehn, and J.P.Sauvage, *Tetrahedron Lett.* 2885 (1969).
- 6 J.Jurczak, S.Kasprzyk, P.Salanski, and T.Stankiewicz, *High Press. Res.* **11**, 139 (1992).
- 7 J.Jurczak, T.Stankiewicz, P.Salanski, S.Kasprzyk, and P.Lipkowski, *Tetrahedron* **49**, 1478 (1993).
- 8 J.Jurczak, S.Kasprzyk, P.Salanski, and T.Stankiewicz, *J.Chem.Soc., Chem. Commun.* 956 (1991).
- 9 J.Jurczak and D.T.Gryko, unpublished.
- 10 K.Chmurski and J.Jurczak, unpublished.

# HIGH PRESSURE HYDROTHERMAL COMBUSTION

E.U. FRANCK

Institut für Physikalische Chemie, Universität Karlsruhe  
Kaiserstr. 12, D-76128 Karlsruhe, Germany

G. WIEGAND<sup>1</sup>

Institut für Technische Chemie — Chemisch-Physikalische Verfahren  
Forschungszentrum Karlsruhe GmbH, Technik und Umwelt,  
Postfach 3640, D-76021 Karlsruhe, Germany

## ABSTRACT

*Hydrothermal Combustion* describes oxidation processes in aqueous fluids at temperatures somewhat below or above the critical temperature of water ( $T_c = 647.1$  K) and at high densities. Dense supercritical water is an excellent mixture partner for nonpolar compounds which participate in combustion processes. Recently, chemical reactions in supercritical fluids are being studied extensively. Supercritical water as a solvent permits controlled oxidation of organic compounds with oxygen or air. Of special interest is the hydrothermal high pressure oxidation of hazardous wastes. Effective flow reactors have been designed. The combustion in dense supercritical water can be performed as flame reaction. Continuously burning flames have been produced at 400 and 500°C up to pressures of 200 MPa. With OH—radical spectra the high pressure flame temperatures were determined. Flame front calculations could be extended to 300 MPa and higher.

## Introduction

*Hydrothermal Combustion* means oxidation processes in dense aqueous environments. The term *hydrothermal* — widely used in the geosciences — is not very strictly defined. For the present purpose it is used for fluid phases near and above the critical density of water. The critical data of pure water are  $T_c=647.1$  K,  $p_c=22.1$  MPa and  $\rho_c=0.32$  g/cm<sup>3</sup>. To establish such conditions, high pressure must be applied. The supercritical high pressure water as a reaction medium has a number of advantages: Pressures to 100 MPa and much higher can easily be transmitted to the chemically interacting species and the relevant thermophysical properties of water can be changed within wide ranges. The static dielectric constant near the critical point is about 8, but with increasing density, values of 10 to 25 can easily be reached between 400 and 500°C (Fig. 1)

<sup>1</sup>Present address: ETH Zürich, Institut für Mineralogie, Arbeitsgruppe Geochemie, CH-8092 Zürich, Switzerland.

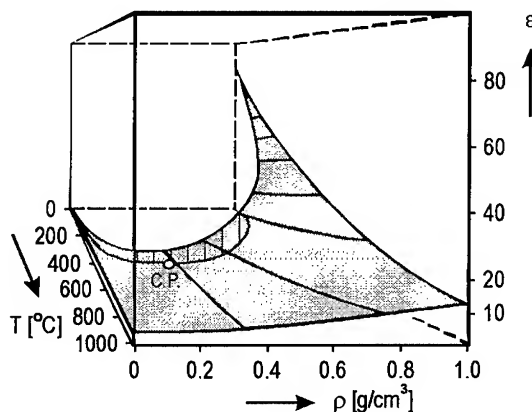


Fig. 1: Static dielectric constant of water as a function of temperature and density. C.P.: Critical point.

[1, 2, 3]. This is enough to dissolve many electrolytes and to form hydrated ions. The water viscosity at these supercritical temperatures and at densities between the critical and twice the critical value is of the order of one tenth of the liquid viscosity [4, 5, 6]. Accordingly, the diffusion coefficients are inversely higher and diffusion controlled chemical reactions are fast even at high

density. Correspondingly, the thermal conductivity is high [5, 7] and reactions can be rapidly quenched.

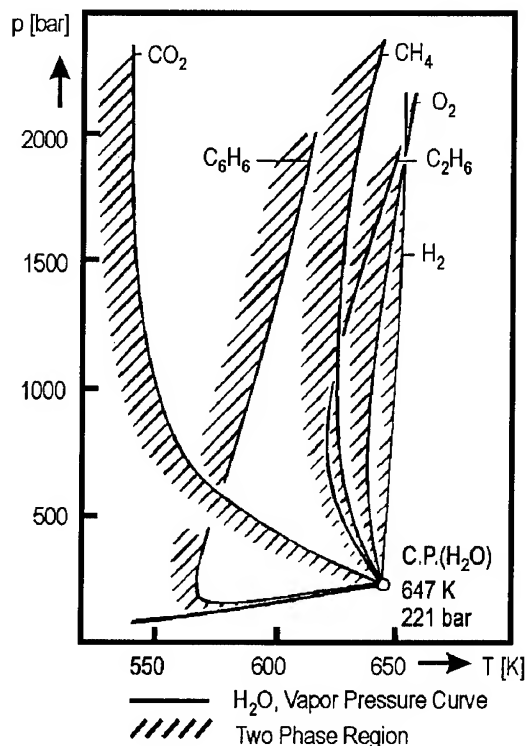


Fig. 2: Critical curves of binary systems for  $\text{H}_2\text{O}$  and nonpolar partners.

The ionic product of liquid water at room temperature is about  $10^{-14} \text{ mol}^{-2} \text{ l}^{-2}$ . At constant density of  $1 \text{ g/cm}^3$  (ca. 900 MPa), this value increases to  $10^{-8} \text{ mol}^{-2} \text{ l}^{-2}$  at  $500^\circ\text{C}$  [5, 8, 9]. Accordingly, hydrolysis reactions are greatly favoured.

Another special characteristic of dense supercritical water is its miscibility with many other substances of unpolar molecular particles. This is remarkable, because the water molecules are highly polar (dipole moment of 1.8 Debye) and associate strongly via hydrogen bonds in the liquid at lower temperatures.— In the three-dimensional temperature, pressure, composition diagram the binary fluid systems have a critical curve. If the two partners are similar in size or polarity, like two alkanes, the critical curve ex-

tends uninterrupted between the critical points of the two pure substances in such a  $T, p, x$ -diagram. If the two partners are dissimilar, the critical curve is interrupted, which is often the case with the present aqueous systems. An upper branch begins at the critical point of the higher boiling partner (here often water) and proceeds to higher pressures and temperatures with or without passing through a temperature minimum. These critical curves are envelopes to the heterogeneous two phase region in the  $T, p, x$ -diagram. Knowledge of particular critical curves is desirable to plan high pressure hydrothermal combustion in homogeneous phases. Fig. 2 gives a number of projections on the  $T, p$ -plane of critical curves relevant for combustion. To the left of these curves is the two phase region. A number of such binary aqueous systems have been investigated experimentally [2]. A number of ternary aqueous systems have also been investigated [10]. These systems have a critical surface in the four-dimensional  $T, p, x_1, x_2$ -space.

With a suitable equation of state (EOS) such binary and ternary systems can be calculated and the phase equilibrium surfaces, the critical curves, and the supercritical mixture volumes can be predicted [10]. These calculations can be extended to pressures of 200 MPa or more. For practical purposes quite often pressures to 50 MPa may suffice. In order to fully exploit the variation from gas-like to liquid-like properties at supercritical conditions, pressures to 200 MPa or higher are desirable. An ACS monography gives an older survey of EOS application [11]. Jurszak and Baranowski have described high pressure chemical reactions in general [12]. Progress in high pressure hydrothermal reaction for waste disposal is described elsewhere [13]. Some recent developments of very high pressure combustion are discussed in the present contribution.

## Experimental

Several types of high pressure hydrothermal chemical reactors for different purposes have been described. If it is the main purpose to dispose of organic toxic wastes by hydrothermal oxidation, long, heated tube reactors can be applied, different types of which are described in the literature. Within a high pressure steel chamber

supercritical water, organic waste or other fuel, and air or pure oxygen are mixed, for example at 500°C and 30 MPa. Subsequently, the fluid mixture enters and passes the flow reactor of several millimeters internal diameter and up to several meters length with high flow rate. The tube reactor is within a thermal bath. A series of thermocouples on the outside of the reactor permits to observe approximately the progress of the reaction (for example [14]).

Another possibility is to use a thick-wall vertical reactor of 30 to 40 cm in length and 100 cm<sup>3</sup> internal volume, which can either be charged at room temperature and heated subsequently until complete mixing of the components can be expected or it can be charged at high temperature with previously heated and pressurized components [15]. The superalloy corrosion resistive autoclave is thermostated for example at 500°C and small samples can be taken at different heights while in operation, or the whole contents can be discharged and analyzed after different periods of operation.

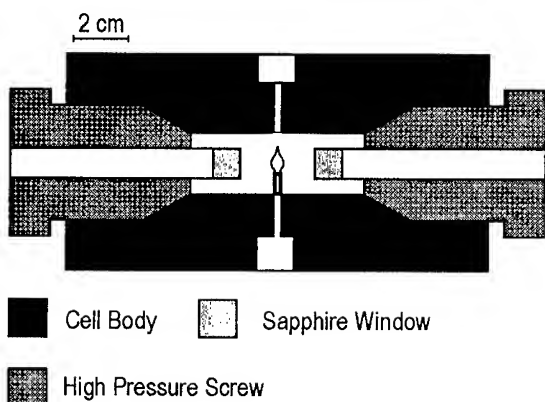


Fig. 3: High pressure optical cell.

A different type of reaction vessel has been used for flame generation and flame maintainance in the oxidation environment. A schematic diagram of such a reactor is shown in Fig. 3 [16, 17]. It is a horizontally mounted thick-wall high pressure vessel of about 30 cm<sup>3</sup> internal volume. The desired amount of water and fuel gas, for example, can be introduced to create a homogeneous supercritical mixture. The thin nozzle in

the center permits introduction of oxygen and the production of a vertical flame. Two axial sapphire windows permit observation of mixing processes and flames. Microscope and video camera serve to record the flames. Recently, the group of Trepp, ETH Zürich, Switzerland, have been able to create a flame even in a flowing high pressure system, which may permit interesting future applications [18].

To study ignition and flame front propagation in supercritical aqueous systems cylindric vessels are not well suited. A spherical autoclave with 34 mm inner diameter has been used [19]. It consists of two half spheres pressed together and sealed with a stainless steel double delta ring and a 100 ton hydraulic press. Forced ignition could be performed with heated wires in the center. Ignition could also be started by slowly heating up the mixture together with the autoclave from outside.

## Results

In the present work, the vertical autoclave was mainly used to study the methane oxidation in the hydrothermal environment in dependence of temperature, pressure, and composition from 380 to 440°C and from 30 to 100 MPa at flameless conditions [15]. The results could be compared with the tube reactor data from other groups [20, 21, 22]. With a methane mole fraction  $x=0.3$  and pressures of 100 MPa, 390°C could be obtained as lowest ignition temperature. Among several others the partial oxidation of methane to methanol could be studied. Higher pressure always increases the methanol selectivity [23]. Hydrothermolysis of methane, ethane, and methanol were also studied using the horizontal window cell with nozzle. The introduction of about 3 mm<sup>3</sup> per second of oxygen into the homogeneous supercritical 70–30 water–methane mixture produced steadily burning diffusion flames at pressures from 30 to 200 MPa. The flames are very bright. At the highest applied pressures of 100 to 200 MPa the spontaneous ignition appeared at about 390°C. At atmospheric pressure, dry stoichiometric methane–oxygen mixtures ignite spontaneously between 500 and 600°C. High pressure considerably reduces the ignition temperature in spite of the quenching ability

of the surrounding pressurised water [16]. The height of the flame at constant flow rate increases with pressure, which is in agreement with the Burke-Schumann rule and is caused by a decreasing effective diffusion coefficient. Fig. 4 shows a photograph of a 3 mm high flame, burning in a 70–30 supercritical water-methane fluid at 500°C and 100 MPa. A number of experiments

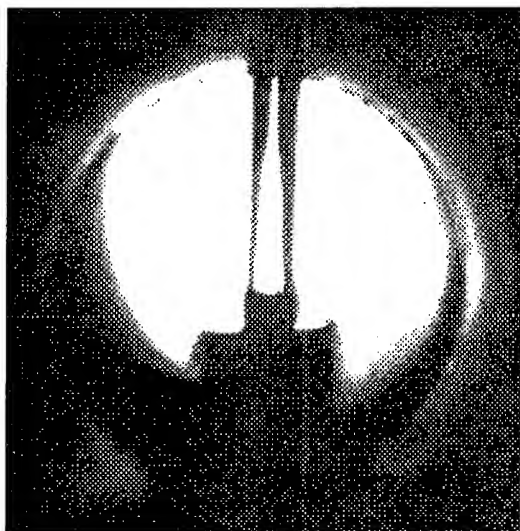


Fig. 4: Hydrothermal flame. Environment: 100 MPa, 440°C, 70 mol% H<sub>2</sub>O, 30 mol% CH<sub>4</sub>. Oxygen influx through nozzle: 3 mm<sup>3</sup>/sec.

has been made with helium and argon instead of water as the flame surrounding fluid. The differences in appearance are moderate. The physical interaction of H<sub>2</sub>O, He and Ar with the reacting partners seems to be not too different. Flame experiments have also been made with hydrogen, ethane, hexane, and toluene as fuels. With fuel molecules larger than ethane, soot formation may occur and obscures the vision. It is also possible to produce similar flames with pressurized supercritical water and oxygen and inject methane. A similar but somewhat pale looking flame could be made by injecting hydrogen into pure oxygen at 100 MPa. The experiment requires carefulness.

## Discussion

Combination of results from flow reactors [20, 21] and batchwise experiments [15, 22] permits de-

termination of the energies of activation for hydrothermal methane oxidation in the wide region from 400 to 700°C. The results are values between 132 and 143 kJ mol<sup>-1</sup>. The global rate constant for the decrease of methane concentration, assuming first order kinetics, for pressures between 30 and 100 MPa at 380°C was found to be  $(1.5 \pm 0.1) \cdot 10^{-4} \text{ sec}^{-1}$  with little pressure dependence.

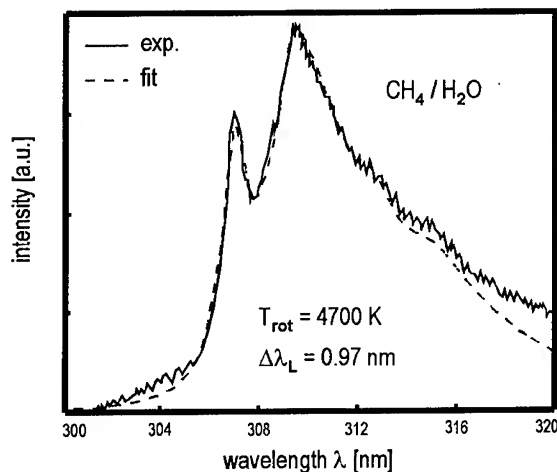


Fig. 5: OH emission spectrum (experimental: solid curve; fitted: dashed curve) of a flame in a supercritical 70–30 H<sub>2</sub>O–CH<sub>4</sub> mixture at 97 MPa and 500°C. Assumed Lorentz-line half-width  $\Delta\lambda_L = 0.97 \text{ nm}$ . Rotational fit temperature  $T_{\text{rot}} = 4700 \text{ K}$ . Vibrational  $v' = 0 \rightarrow v'' = 0$  transition

The main part of the present investigation was concerned with high pressure flames. Obviously, the flame temperatures are of special interest. Gases of polyatomic molecules can be excited with several molecular degrees of freedom. If the Maxwell-Boltzmann distribution functions are satisfied separately, translational, rotational, vibrational, and electronic temperatures can be defined. If the gaseous system has time enough, a single temperature of the system is defined. After a thorough discussion, the *OH rotational temperature* was preferred. The rotational fine structure of the vibrational O–O transition of the electronic A<sup>2</sup>Σ–X<sup>2</sup>Π transition of OH radicals was used [17, 24]. The corresponding emission spectrum of OH radicals is located between 300 and 320 nm. A special FORTRAN program, originally developed to analyse flame emissions from solid combustion [25] was converted to fit

the emission spectra. Several parameters have to be adjusted: The rotational temperature, the Lorentz half-width  $\Delta\lambda_L$  for the individual rotational lines, the apparatus constant, and the high pressure wavelength shift between experimental and theoretical spectra. The procedure is described in detail elsewhere [17]. Fig. 5 gives an example for a flame in a supercritical 70–30 water–methane mixture at 97 MPa and 500°C. The agreement between experiment and fit is satisfactory. The resulting rotational temperature 4700 K is very high. It is conceivable that equilibrium between rotation and the other ways of excitation is not established in the flame.

Obviously, direct measurements of flame temperatures with thermocouples could not be made because of very high temperatures and the small flame size (ca. 3 mm). So called adiabatic temperatures, using the balance of heat liberated by the reactions and the heat needed to warm up the gas mixture to final temperature were approximately calculated for the present flames. The results are mostly lower than the values from the OH spectra. Line reversal experiments with sodium lines were tried in vain, because even very small additions of sodium components etched the sapphire windows.

For comparison with experiments, calculations of high pressure one-dimensional counterflow diffusion flames up to 300 and even 1000 MPa were made, however [26]. A suitable equation of state and reasonable high pressure transport equations have been used. It turned out that at pressures of 100 MPa and higher the reaction zones become very flat. In a qualitative way, the positive pressure dependence of the experimental flame temperatures agree with those at the one-dimensional counterflow diffusion flame. Above 100 MPa, the pressure dependence becomes small or even negative. At 300 and 1000 MPa, the calculated flame temperatures have considerably decreased, so that a high pressure quenching of the flames can be foreseen, which is not unexpected considering the low compressibility and high thermal conductivity of such a very highly pressurised fluid.

## Outlook

Some further developments of practical or scientific character can be foreseen or suggested: The supercritical waste disposal with its possibility to release harmless aqueous product solutions [27] can be technically further developed. Combination with supercritical flames in a fluid flow environment as achieved at the ETH Zürich would give further useful results. The possibility of performing oxidation and other chemical reactions in a dense supercritical aqueous environment containing high concentrations of inorganic electrolytes, for example NaOH [28], has not yet been explored. Inverse flames can be produced. At elevated, but subcritical temperatures dense water–gas suspensions might be used, by taking advantage of low interfacial tensions at high pressures and temperatures [29].— An extended version is intended for publication in the Polish Journal of Chemistry.

## References

- [1] M. Uematsu and E.U. Franck. *J. Phys. Chem. Ref. Data*, **9** (1980) 1291–1305.
- [2] E.U. Franck. *J. Chem. Thermodynamics*, **19** (1987) 225–242.
- [3] E.U. Franck, S. Rosenzweig and M. Christoforakos. *Ber. Bunsenges. Phys. Chem.*, **94** (1990) 199–203.
- [4] K.H. Dudziak and E.U. Franck. *Ber. Bunsenges. Phys. Chem.*, **70** (1966) 1120–1128.
- [5] L. Haar, J.S. Gallagher and G.S. Kell. *NBS/NRC Steam Tables: Thermodynamic and transport properties and computer programs for vapor and liquid states of water in SI units*. National Standard Reference Data System, (1984).
- [6] K. Tödheide. In: F. Franks(ed.), *Water, a comprehensive treatise*, number 1, page 463. Plenum Press, New York, 1972.
- [7] F.J. Dietz, J.J. de Groot and E.U. Franck. *Ber. Bunsenges. Phys. Chem.*, **85** (1981) 1005–1009.
- [8] W.L. Marshall and E.U. Franck. *J. Phys. Chem. Ref. Data*, **10** (1981) 295–304.
- [9] W. Holzappel and E.U. Franck. *Ber. Bunsenges. Phys. Chem.*, **70** (1966) 1105–1112.
- [10] M. Heilig and E.U. Franck. *Ber. Bunsenges. Phys. Chem.*, **94** (1990) 27–35.
- [11] K.C. Chao and R.L. Robinson. *Equation of State, Theories and Applications*, volume 300 of ACS Symposium Series. American Chemical Society, Washington, D.C., 1986.



- [12] J. Jurczak and B. Baranowski. High pressure chemical synthesis. Elsevier, Amsterdam, 1989.
- [13] WCM Forums. Proc. 1st Int. Workshop on Supercritical Water Oxidation, February 1995.
- [14] G. Wiegand, H.-J. Bleyl, H. Goldacker, G. Petrich and H. Schmieder. In: Proc. 1st Int. Workshop on Supercritical Water Oxidation, February 1995. WCM Forums.
- [15] T. Hirth and E.U. Franck. Ber. Bunsenges. Phys. Chem., **97** (1993) 1091-1098.
- [16] W. Schilling and E.U. Franck. Ber. Bunsenges. Phys. Chem., **92** (1988) 631-636.
- [17] G.M. Pohsner and E.U. Franck. Ber. Bunsenges. Phys. Chem., **98** (1994) 1082-1090.
- [18] H.L. LaRoche, M. Weber and Ch. Trepp. In: Proc. 1st Int. Workshop on Supercritical Water Oxidation, February 1995. WCM Forums.
- [19] J.U. Steinle and E.U. Franck. Ber. Bunsenges. Phys. Chem., **99** (1995) 66-73.
- [20] J.W. Tester, H.R. Holgate, F.J. Armellini, P.A. Webley, W.R. Killilea, G.T. Hong and H.E. Barner. In: D.W. Tedder and F.G. Pohland(eds.), Emerging technologies in hazardous waste managements III, ACS Symposium Series 518, Industrial and Engineering Chemistry Special Symposium, chapter 3, pages 35-76. October 1991.
- [21] E.F. Gloyna and L. Li. Waste Management, **13** (1993) 379-394.
- [22] M.A. Abraham and M.T. Klein. Ind. Eng. Chem. Prod. Res. Dev., **24** (1985) 300.
- [23] T. Hirth and E.U. Franck. Chem.-Ing.-Techn., **66** (1994) 1284-1287.
- [24] R.K. Crosley, D.R. amd Lengel. J. Quant. Spectrosc. Radiat. Transfer, **15** (1975) 579-591.
- [25] N. Eisenreich and W. Liehmann. Bericht 12/86, Fraunhofer-Institut für Treib- und Explosivstoffe (ICT, Karlsruhe-Pfinztal, Germany), (1986) .
- [26] A.M. Saur, F. Behrendt and E.U. Franck. Ber. Bunsenges. Phys. Chem., **97** (1993) 900-908.
- [27] M. Modell. In: H.M. Freeman(ed.), Standard Handbook of Hazardous Waste Treatment and Disposal, pages 8.153-8.168. McGraw Hill, New York, 1989.
- [28] S. Kerschbaum and E.U. Franck. Ber. Bunsenges. Phys. Chem., **99** (1995) 624-632.
- [29] G. Wiegand and E.U. Franck. Ber. Bunsenges. Phys. Chem., **98** (1994) 809-817.

# HIGH-PRESSURE KINETICS OF Z/E ISOMERIZATION AT HIGHLY VISCOUS CONDITIONS. FURTHER EVIDENCE FOR SOLVENT REARRANGEMENT PRIOR TO THE RATE-DETERMINING STEP

TSUTOMU ASANO, HIROYUKI FURUTA, and HITOSHI SUMI†

Department of Chemistry, Faculty of Engineering, Oita University, Oita 870-11, Japan and  
Institute of Materials Science, University of Tsukuba,† Tsukuba 305, Japan

## ABSTRACT

Effects of pressure on thermal Z/E isomerization of substituted *N*-benzylideneanilines (BA's) and azobenzenes (AB's) were studied in 2-methyl-2,4-pentandiol (MPD) and compared with the results in glycerol triacetate (GTA) reported earlier. Despite the large activation energies (50–73 kJ mol<sup>-1</sup>), pressure-induced retardations that cannot be rationalized in the framework of the transition state theory were observed. The results were analyzed on the basis of Sumi's two-dimensional reaction coordinate model which assumes solvent rearrangement prior to the rate-determining energy barrier crossing. The rate constants for this solvent rearrangement  $k_f$  were derived. The  $k_f$  values for BA's at the same solvent viscosity showed little temperature dependence both in GTA and MPD. On the other hand, they were clearly dependent on the temperature for AB's in MPD but not in GTA. From these results, it was concluded that solvent rearrangements for accommodating the transition state require an appreciable energy in the case of AB's in MPD.

## Introduction

Slow thermal reactions with a large activation energy ( $E_a \geq 20RT$ ) usually have a rate constant  $k_{TST}$  describable by the transition state theory (TST) because the activated complexes are equilibrated with the reactants throughout the reaction. However, in very fast reactions with low activation energies ( $E_a \leq 5RT$ ), TST is not valid any more because thermal fluctuations are not fast enough to maintain the equilibration. Under such conditions, the reaction is called "fluctuation-controlled" and it is retarded by an increase in the solvent viscosity  $\eta$ . A theory proposed by Kramers (1) predicts that the rate constant will be inversely proportional to  $\eta$ . As a result of extensive experimental works, however, it now became clear that rate constants are inversely proportional to the *fractional power* of  $\eta$  in most of the cases studied (eq 1). The meaning of

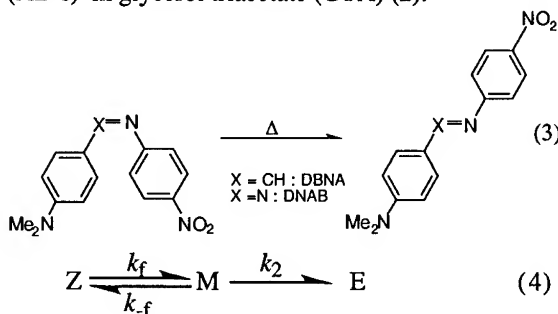
$$k_{obs} = B\eta^{-\beta} \quad 0 < \beta < 1 \quad (1)$$

this deviation from the theoretical prediction remains as a fundamental problem in the field of chemical kinetics. In order to analyze the situation, it is highly desirable to measure the deviations of the observed rate constant from the one expected by the TST. Reactions with low activation energies are not suited for this purpose because TST has been already invalidated in usual solvents.

It has been known for many years that viscosity of liquids  $\eta$  increases exponentially with increasing pressure (eq 2). If a reaction is run under high

$$\eta = \eta_0 e^{\alpha P} \quad \eta_0: \eta \text{ at } 0.1 \text{ MPa} \quad (2)$$

pressure in a liquid with large  $\eta_0$  and  $\alpha$ , it would be possible to put the reaction under the state of fluctuation-control even if the activation energy is as high as  $20RT$ . TST is valid undoubtedly in such slow reactions at low viscosities (namely at low pressures) and it has been demonstrated repeatedly that the TST-expected kinetic effects of pressure can be described as a continuous function of pressure virtually in every type of reactions. Therefore, we would be able to observe a continuous shift from TST-valid to TST-invalid region by increasing pressure and  $k_{TST}$  in the latter region will be estimated by extrapolations. This expectation was met in the study of thermal Z/E isomerization (eq 3) of *N*-benzylideneanilines (BA's) and azobenzenes (AB's) in glycerol triacetate (GTA) (2).



The results were analyzed by assuming a two-step mechanism of eq 4 which is based on the two-dimensional reaction coordinate model proposed by

Sumi (3). The first step in this mechanism describes rearrangement of solvent molecules by thermal fluctuations and it is retarded by an increase in  $\eta$ . The energy barrier crossing to the product takes place in the second step and this is effected by rapid atomic movements which is not influenced by a change in  $\eta$ . In the steady state in eq 4, the rate constant should be given by

$$k_{\text{obs}} = 1/(k_{\text{TST}}^{-1} + k_f^{-1}) \quad (5)$$

with  $k_{\text{TST}} = k_2 k_f / k_f$ . We can derive  $k_f$  values by fitting  $k_{\text{obs}}$  and  $k_{\text{TST}}$  to eq 5. It was shown that the values thus obtained obeyed eq 1 as expected for a fluctuation-controlled rate process. In the present paper, the results obtained in 2-methyl-2,4-pentanediol (MPD) will be presented and compared with the ones in GTA.

## Results and Discussion

Figure 1 shows the observed rate constants for the isomerization of N-[4-(dimethylamino)benzylidene]-4-nitroaniline (DBNA). Similar results were obtained with other BA's. The isomerization proceeds *via* the transition state 1 by nitrogen-atom inversion. Since the polarity of 1 is expected to be

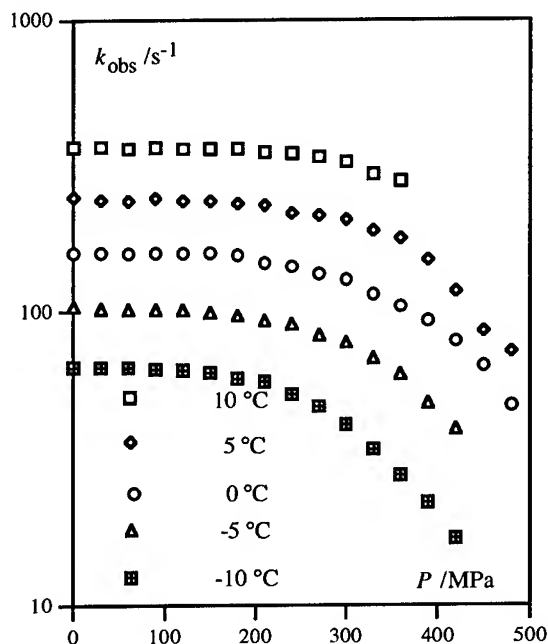
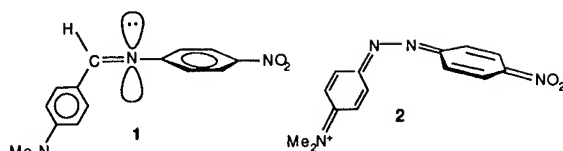


Figure 1. Pressure effects on Z/E isomerization of DBNA in MPD at various temperatures



more or less the same with that of the Z-isomer, small pressure effects at lower pressures are reasonable. By linearly extrapolating the results at low pressures,  $k_{\text{TST}}$  values at higher pressures were estimated and used in the calculations of  $k_f$  according to eq 5. The  $k_f$  values thus obtained are plotted against solvent viscosity in Figure 2. As can be

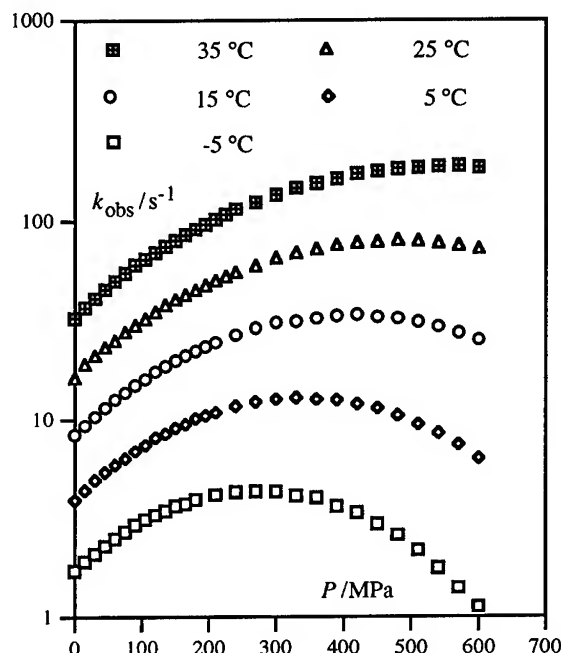


Figure 2. Plots of fluctuation-limited rate constant against solvent viscosity for Z/E isomerization of DBNA in MPD

seen clearly, the rate constant was almost independent of temperature compared at the same viscosity. The results in GTA (2) showed the same tendency. The  $k_f$  values at the same viscosity were similar in GTA and MPD indicating that the hydroxyl groups in MPD had little effect on the rate of solvent rearrangement. The fact that the isoviscosity  $k_f$  is independent of temperature shows that the apparent temperature dependence mostly comes from that of the solvent viscosity and little chemical transformations are required in order to rearrange solvent molecules to accommodate the transition state.

In the isomerization of 4-(dimethylamino)-4'-nitroazobenzene (DNAB), the nitrogen-nitrogen  $\pi$  bond is cleaved heterolytically and rotation around the remaining  $\sigma$  bond results in the *E*-isomer. The transition state 2 is highly dipolar and solvent molecules are electrostricted around it (4, 5). The reaction is characterized by a large negative activation volume. The accelerations at lower pressures in Figure 3 show that TST is valid up to

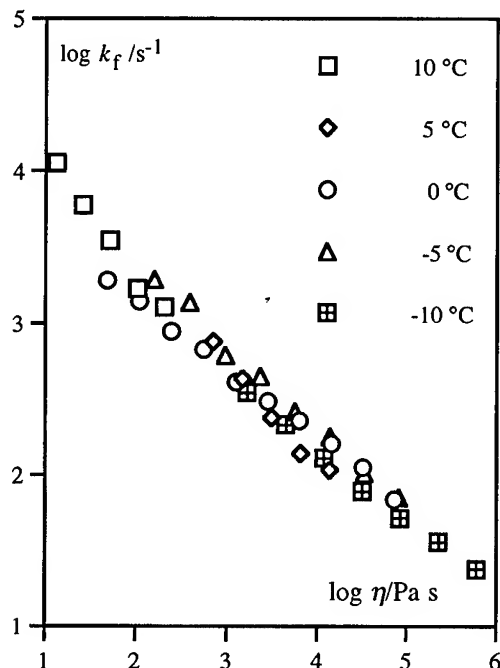


Figure 3. Pressure effects on Z/E isomerization of DNAB in MPD at various temperatures

$\alpha$ . 200 MPa in MPD. Despite the different mechanism, pressure-induced retardations as observed for DBNA can be seen clearly in the Figure. The results in GTA were qualitatively the same. High pressure  $k_{\text{TST}}$  values were estimated by fitting  $k_{\text{obs}}$  at low pressures to an empirical nonlinear function of pressure. The fluctuation-limited rate constants obtained are plotted against  $\eta$  in Figure 4. Contrary to the results with DBNA, the isoviscosity  $k_f$  was clearly dependent on the temperature. This means that the solvent rearrangements involve chemical transformations and require an appreciable activation energy. Since such temperature dependence was observed neither for AB's in GTA nor for BA's in both of the solvents (6), a polarity increase in the activation

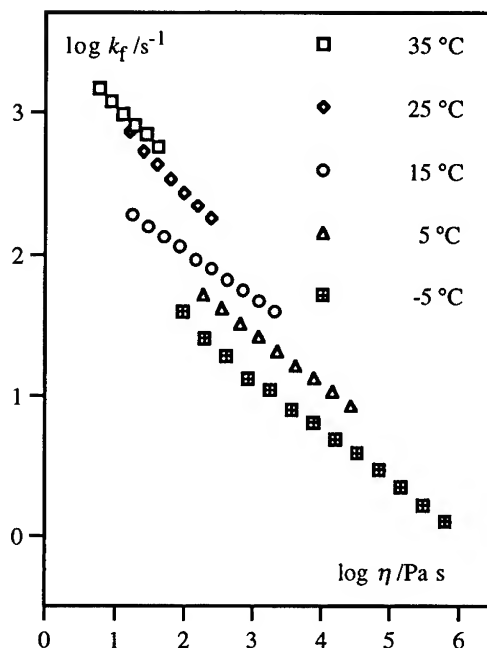


Figure 4. Plots of fluctuation-limited rate constant against solvent viscosity for Z/E isomerization of DNAB in MPD

step as well as the existence of the hydroxyl group in the solvent are likely to be related to this energy increase. Probably, solvent molecules hydrogen bonded to the dimethylamino group have to be desolvated in order to form a suitable solvent arrangement and this desolvation might induce a polarity increase and partial structural changes in the reactant as well.

#### Acknowledgment

Financial support from the Nishida Research Fund for Fundamental Organic Chemistry is greatly appreciated.

#### References

1. H. Kramers, *Physica*, **7**, 284 (1940).
2. T. Asano, H. Furuta, and H. Sumi, *J. Am. Chem. Soc.*, **116**, 5545 (1994).
3. H. Sumi, *J. Phys. Chem.*, **95**, 3334 (1991).
4. T. Asano and T. Okada, *J. Org. Chem.*, **51**, 4454 (1986).
5. D.-M. Shin and D. G. Whitten, *J. Am. Chem. Soc.*, **110**, 5206 (1988).
6. One case of similar temperature dependence was reported for a BA in GTA (2).

# HIGH PRESSURE STUDIES OF DYNAMIC SOLVENT EFFECTS ON THE INTRAMOLECULAR CHARGE TRANSFER (ICT) IN THE EXCITED STATE

KIMIHIKO HARA, DMITRY S. BULGAREVICH AND NORITSUGU KOMETANI

*Department of Chemistry, Faculty of Science,  
Kyoto University, Sakyo-ku, Kyoto 606-01, Japan*

## ABSTRACT

The formation of the intramolecular charge-transfer (ICT) state in the excited state for 4-(N,N-dimethylamino)triphenyl phosphine (DMATP) and 4,4'-diaminodiphenyl sulphone (DAPS) has been investigated by using steady-state and picosecond time-resolved fluorescence spectra at high pressures. The shift of the reaction path depending on the solvent viscosity was observed. This is caused by the strong viscosity dependence of the solvent relaxation time.

## Introduction

Charge transfer (or electron transfer) is among the important elementary rate process in chemistry and biochemistry [1]. The mechanism of the charge transfer in the excited state is often described by the coupling of intramolecular twisting motion with solvent dynamics. The molecules designated "twisted intramolecular charge transfer (TICT)" compounds [2] typically exhibit dual fluorescence in polar solvents. The mechanism responsible for the TICT-state formation has been supposed to involve intramolecular twisting process in the  $S_1$  excited state. Contrary to the early expectation [2], no simple correlation between the TICT-state formation rate and the solvent shear viscosity has been reported for DMABN in different polar solvents [3].

By using high-pressure method, we have investigated the influence of solvent viscosity on various barrier crossing processes involving large amplitude twisting conformational changes due to bulky aromatic groups [4]. In particular, the observation of a weak viscosity dependence on the barrier crossing rate has been discussed. The use of high-pressure is a favorable method for studying the dynamic solvent effects, because it enables us to change the solvent viscosity for a *single* solvent greatly and continuously without serious modification of solvent-shell structure. According to the solvent change

method, which is ordinarily used for changing solvent viscosity, the small viscosity dependence on the ICT reaction is likely to be hidden by the comparatively large shift of activation barrier.

This work is a high-pressure investigation of the effect of solvent dynamics on the ICT-state formation rate in the excited state for DMATP and DAPS in alcohol solvents.

The high-pressure optical cell and emission equipment for steady-state fluorescence spectra have been described previously [4,5]. Picosecond time-resolved fluorescence spectra at high pressures were measured by time-correlated single-photon counting (TCSPC) method. The detailed experimental arrangement of the laser system was also reported previously [6]. The second or third harmonic radiation of a mode-locked Ti:sapphire laser was used as the excitation light source.

## Absorption and Fluorescence Spectra

The fluorescence spectra of DMATP and DAPS in polar solvents such as alcohols consist of two bands. One is the emission from the locally excited (LE) state and the other is from the ICT state. The half-width of the absorption band is about twice as large as that of the LE fluorescence band. This indicates that the ground-state potential well is broader than the LE-state potential well.

The absorption spectrum in polar solvent has a tail in the lower energy region. In

addition, the fluorescence spectrum is dependent on the excitation wavelength ( $\lambda_{ex}$ ). The excitation at the longer wavelength causes the relative increase in the intensity of the CT band, as compared with the excitation at shorter wavelength. These results lead to a conclusion that the absorption spectrum in polar solvents consists of an overlap of both transitions;  $S_0 \rightarrow LE$  and  $S_0 \rightarrow CT$ .

### Viscosity Effect on the Fluorescence Yield

The yield of the long wavelength CT band decreases relatively with increasing pressure. This behavior is similar to what occurs when the temperature is decreased. The pressure shift of the CT band is fairly small, as compared with those of other reported TICT bands for various molecules. Fig. 1 shows the fluorescence yield ratio of the CT state to the LE state ( $\Phi_{CT}/\Phi_{LE}$ ) of DMATP in compressed linear alcohols as a function of solvent shear viscosity ( $\eta$ ). The logarithm of ( $\Phi_{CT}/\Phi_{LE}$ ) decreases linearly with  $\ln \eta$ . The slope ( $\alpha$ ) decreases with increasing the chain length of alcohols. The  $\alpha$  value approaches each limiting value;  $\alpha=0.31$  for DMATP and  $\alpha=0.2$  for DAPS.

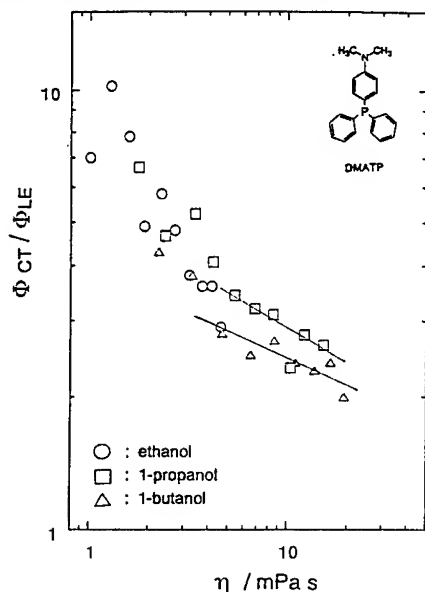


Fig. 1 Plot of  $\Phi_{CT}/\Phi_{LE}$  as a function of  $\eta$ .

The reaction barrier is quite small (2.2 kJ/mol for DMATP), as compared with the activation energy of solvent viscous flow.

### Rate of ICT-State Formation

For the fluorescence response curves which were excited at the absorption maxima and monitored at the LE emission maxima, fits with double exponential functions do not reproduce the experimental results [6]. This means that the simple two state model of LE and CT states is inapplicable.

To obtain the dynamics of the population decay of the LE state, the fluorescence response decay curves were fitted to the multiple exponential function:

$$I(t, \lambda) = \int [\sum A_i \exp(t - \tau_i / \tau_i) G(\tau) d\tau] \quad (1)$$

$A$  and  $\tau_i$  are the amplitudes and time constants for the component of a multiexponential fit.  $G(\tau)$  is the instrumental response function. For DMATP and DAPS in alcohols the decay curves of the LE state are mostly fitted by triple exponential functions.

Average lifetime  $\tau_a$  can be determined by

$$\tau_a = \sum \tau_i A_i \quad (2)$$

where  $\tau_a$  is related to the survival probability  $Q(t)$ , i. e.,  $\tau_a = \int Q(t) dt$ , which measures the time dependence of the population of the reacting state. When the decay rate from the LE state to the ground state is sufficiently

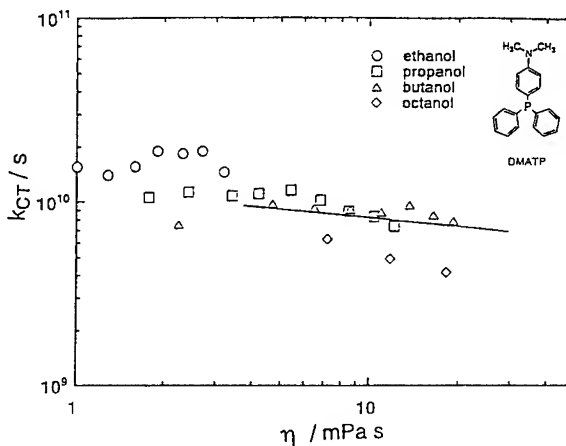


Fig. 2 Plot of  $k_{CT}$  as a function of  $\eta$ .

slow as is the present case,  $\tau_a$  is correlated to the inverse of the average rate of the CT formation ( $k_{CT}$ ), namely

$$k_{CT} = (\tau_a)^{-1} \quad (3)$$

Fig. 2 shows the plot of  $\ln k_{CT}$  against  $\ln \eta$  for DMATP in butanol. The slope (0.30) is in excellent agreement with the result of yield ratio.

### Summary

The viscosity dependence of the ICT in DMATP and DAPS in alcohols in the  $S_1$  excited state can be explained by the free energy surface, shown schematically in Fig. 3. In low viscosity regime where the solvent relaxation is fast enough to keep up with the reactive motion, the reaction proceeds along the completely relaxed path (I). Conversely, in high viscosity regime where the solvent motion is frozen, the reaction starts from the Franck-Condon state (F) along a nonrelaxed path (II). The shift of reaction path toward the nonrelaxed path (II) occurs with increasing pressure. This could be called as a "pressure tuning" effect of the solvent viscosity on ICT reactions. It should be noted that the present shift of the reaction path is caused by the stronger viscosity dependence on the solvent relaxation time. The longitudinal dielectric

relaxation time of solvents ( $\tau_L$ ) is used as a measure of solvent dipole relaxation time. This has been described by  $\tau_L(\eta) \propto \eta^\beta$  with the exponent  $\beta \geq 1$  [7].

### References

1. M. D. Newton and N. Sutin, *Ann. Rev. Phys. Chem.* **35** (1984) 437; R. A. Marcus and N. Sutin, *Biochem. Biophys. Acta* **811** (1985) 265.
2. Z. A. Grabowski, R. Rotkiewicz, A. Siemiarczuk, D. J. Cowley and W. Baumann, *Nouv. J. Chim.* **3** (1979) 443; W. Rettig, *Angew. Chem. Int. Ed. Engl.* **25** (1986) 971; E. Lippert, W. Rettig, V. Bonacis-Koutecky, F. Heisel and J. A. Miehe, *Adv. Chem. Phys.* **68** (1987) 1; W. Rettig, *Modern Models of Bonding and Delocalization*, ed. by J. F. Liebman and A. Greeberg (VCH Publishers, 1988), ch. 5, p. 229.
3. J. M. Hicks, M. T. Vandersall, E. V. Sitzmann and K. B. Eisenthal, *Chem. Phys. Lett.* **135** (1987) 413; J. M. Hicks, M. T. Vandersall, Z. Babarogic and K. B. Eisenthal, *Chem. Phys. Lett.* **115** (1985) 18; J. D. Simon and S.-G. Su, *J. Phys. Chem.* **94** (1990) 3656.
4. K. Hara, T. Arase and J. Osugi, *J. Am. Chem. Soc.* **106** (1984) 1968; K. Hara and H. Yano, *J. Phys. Chem.* **90** (1988) 4265; *J. Am. Chem. Soc.* **110** (1988) 1911; K. Hara and S. Akimoto, *J. Phys. Chem.* **95** (1991) 5811; *High Press. Res.* **11** (1992) 55; K. Hara, *High Pressure Liquids and Solutions* ed. by Y. Taniguchi, M. Senoo and K. Hara (Elsevier Applied Science, (1994), p. 67.
5. K. Hara and I. Morishima, *Rev. Sci. Instrum.* **59** (1988) 2397.
6. K. Hara, N. Kometani and O. Kajimoto, *Chem. Phys. Lett.* **225** (1995) 381.
7. H. Mandel, D. G. Frood, M. A. Saleh, B. K. Morgan and S. Walker, *Chem. Phys.* **134** (1989) 441; E. W. Castner, B. Bagchi, M. Maroncelli, S. P. Webb, A. J. Ruggiero and G. R. Fleming, *Ber. Bunsenges. Phys. Chem.* **92** (1988) 363.

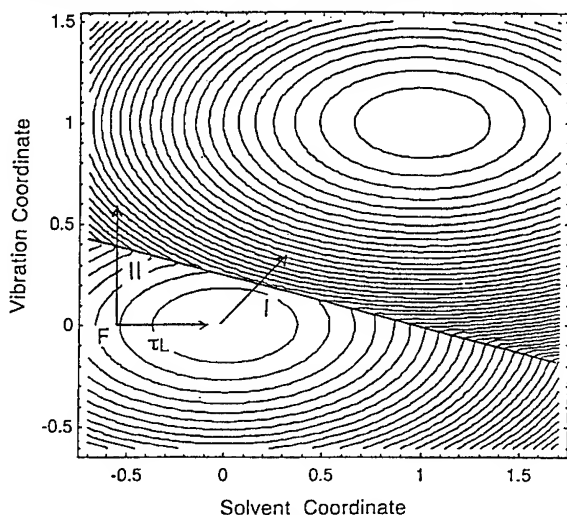


Fig. 3 Free energy surface of ICT reaction in the excited state.

# PRESSURE STUDIES IN TWO-DIMENSIONAL ORGANIC SUPERCONDUCTORS

YURI V. SUSHKO

Fundamental Research Laboratories, NEC Corporation, 34 Miyukigaoka, Tsukuba, Ibaraki 305, Japan,  
Institute for Semiconductor Physics, National Academy of Sciences, Kiev 252650, Ukraine

## ABSTRACT

The anomalous sensitivity of the organic superconductors to rather weak elevated pressures is illustrated by the pressure-temperature phase diagram of organic superconductor  $\kappa$ -(BEDT-TTF)<sub>2</sub>Cu[N(CN)<sub>2</sub>]Cl. Hydrostatic pressure studies of this salt and related compounds reveal the new aspect of interplay between magnetism and superconductivity in 2-dimensional organic crystal.

## INTRODUCTION

Typically, molecular crystals are insulators or at best semiconductors. Organic conductors and superconductors (for a review of recent developments see Ref. [1, 2]) represent a relatively small number of the intermolecular compounds, known as charge transfer complexes and organic salts, which are stabilized by partial electron transfer between constituent molecules. To provide the optimal overlap between  $\pi$ -molecular orbitals, the molecules in constructing organic conductors are arranged in linear chains or planar layers. As a result, the electronic properties are highly anisotropic (i.e. the conductivity along the chain is several orders of magnitude greater than in any other direction) and such a materials are quasi-one-dimensional (q-1-d) or quasi-two-dimensional (q-2-d) conductors.

However, the metallic-like conduction of the organic salts at about room temperature does not lead automatically to superconductivity (SC) or even to a highly conducting metallic state at low temperatures. The principal difficulty arises because the quasi-one-dimensionality has a strong tendency to drive Fermi surface instability, which results in an insulator ground state. SC in a class of organic solids has been first discovered in the family of Bechgaard salts (TMTSF)<sub>2</sub>X due to application of pressures exceeding  $P_{crit} \sim 6-9$  kbar [3]. The indispensable role of high pressure in stabilizing of a metallic state and inducing of SC in these q-1-d materials is attributed to the increase in the transverse transfer energies

resulting in the suppression of Fermi surface nesting [1, 2].

It is not surprising therefore, that the next generation of organic conductors, q-2-d compounds based on the electron-donor molecule ET or BEDT-TTF (bis-ethylendithia-tetrathiafulvalene) that are packed into planar layers, not chains, have yielded a number of ambient pressure metals and superconductors - due to layered structure the effects of low dimensionality in these materials are strongly reduced comparing to the (TMTSF)<sub>2</sub>X salts. Nevertheless, the anomalous pressure sensitivity of the electron properties appeared to be intrinsic to the salts of this new generation and remains the subject of keen interest since the time of discovery of a more than five-fold increase of  $T_c$  under pressure in a first ambient pressure (BEDT-TTF) superconductor, salt  $\beta$ -(BEDT-TTF)<sub>2</sub>I<sub>3</sub> [4]. Since the framework of current presentation provides no scope for a comprehensive analysis of the subject, we present here a brief survey of the most recent experiments illuminating the unique role played by pressure in modern organic superconductors.

## PRESSURE DEPENDENCE OF $T_c$ : $\kappa$ -(BEDT-TTF)<sub>2</sub>Cu[N(CN)<sub>2</sub>]Cl<sub>1-x</sub>Br<sub>x</sub>

An enormously rapid decrease of  $T_c$  under pressure is a kind of a hallmark of organic superconductors. The pressure derivative of  $T_c$  varies in a range from -2 K/GPa for (TMTSF)<sub>2</sub>PF<sub>6</sub> and related q-1-d salts [1-3] to -14 K/GPa for  $\beta$ -(BEDT-TTF)<sub>2</sub>I<sub>3</sub> and other  $\beta$ -



type (BEDT-TTF) superconductors [4, 5].  $dT_c/dP$  reaches an even higher value of -30 K/GPa for  $\kappa$ -type salts, such as  $\kappa$ -(BEDT-TTF)<sub>2</sub>Cu(NCS)<sub>2</sub> [6] and series  $\kappa$ -(BEDT-TTF)<sub>2</sub>Cu[N(CN)<sub>2</sub>]Cl<sub>1-x</sub>Br<sub>x</sub> [7]. This enormous pressure sensitivity of  $T_c$  is displayed by Figure 1 where the results of static magnetization studies under He-gas pressure for four members of the latter series are shown. As even more intriguing feature of the data of Fig. 1, we note the huge positive slope  $dT_c/dP = +60$  K/GPa, that compounds with a minimum content of Br ( $x < 0.2$ ) exhibit in the low pressure region  $P < 270$  bar before reaching maximum  $T_c$  of 13 K. To throw more light on this spectacular behavior we shall address a very rich and complex pressure hierarchy of different phases, both of metallic and non-metallic origin, that are inherent to the structure of pure Cl-salt,  $\kappa$ -(BEDT-TTF)<sub>2</sub>Cu[N(CN)<sub>2</sub>]Cl.

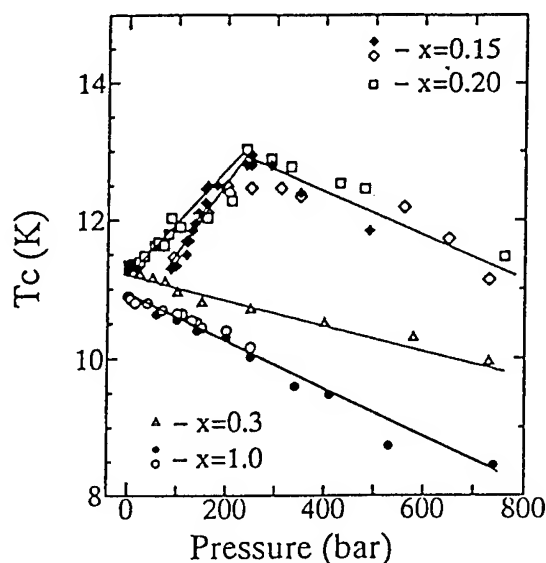


FIG. 1. Pressure dependence of  $T_c$  (diamagnetic onset) for isostructural series  $\kappa$ -(BEDT-TTF)<sub>2</sub>Cu[N(CN)<sub>2</sub>]Cl<sub>1-x</sub>Br<sub>x</sub> [7]. Lines are guides for eyes.

#### PRESSURE-TEMPERATURE PHASE DIAGRAM: $\kappa$ -(BEDT-TTF)<sub>2</sub>Cu[N(CN)<sub>2</sub>]Cl

The superconductor with the highest among organic crystals  $T_c$  (13 K at  $P=300$  bar),  $\kappa$ -(BEDT-TTF)<sub>2</sub>Cu[N(CN)<sub>2</sub>]Cl has been discovered by Williams *et al.* [8] simultaneously with other "high-

$T_c$ " salt, an isostructural Br analog that possesses  $T_c=11.6$  K at ambient pressure. Interestingly however, it was reported that in spite of having the same crystal structure, the Cl-salt exhibits a non-metallic ground state at ambient pressure.

The relationship between the non-metallic state and the SC in  $\kappa$ -(BEDT-TTF)<sub>2</sub>Cu[N(CN)<sub>2</sub>]Cl has attracted a keen interest when a direct transformation from a semiconductor-like behaviour to a SC state has been observed under modest pressure  $P > 80$  bar [9, 10]. The interest to this point has been raised even more due to discovery of the magnetic, presumably weak ferromagnetic, origin of the ambient pressure non-metallic state [11]. The detailed study of pressure and temperature dependencies of resistivity by use of a He-gas pressure system has revealed a very complex pressure-temperature phase diagram of the salt [12]. As shown in Fig. 2, it is enriched by the presence of

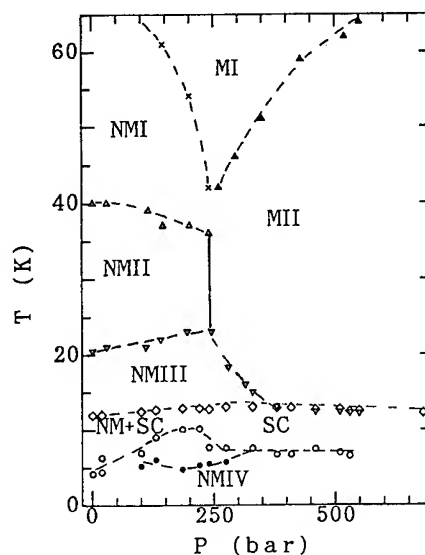


FIG. 2. T-P phase diagram of  $\kappa$ -(BEDT-TTF)<sub>2</sub>Cu[N(CN)<sub>2</sub>]Cl [12]. Boundary lines derived from the singularities of  $R(T)$  and  $R(P)$  experimental curves. M, NM, SC stand for metallic, non-metallic and superconducting phases, respectively. NM+SC indicates the low-pressure region of coexistence (presumably non-homogeneous) of two phases. Broken lines are guides for eyes.

a number of different phases- metallic, non-metallic, and superconducting. The magnetically ordered state

associated with reported by Welp et al [11] steep increase in magnetization below  $T_F=22$  K at ambient pressure has been identified in transport properties as the non-metallic phase NMIII that originates from the pronounced upturn of resistivity on cooling across  $T_F$ . The novel for organic solids effect of reentrant superconductivity is a striking characteristics of the low-temperature region of phase diagram. As it was first observed by resistivity measurements [12] and later confirmed by static magnetization experiments under He-gas pressure [13], the superconducting state first appears upon cooling at the upper critical temperature,  $T_{C1}$  but disappears on further slow cooling ( $<0.1$ K/min.) at the lower critical temperature,  $T_{C2}$ . It is more surprising to note that the resistive state NMIV that emerged below  $T_{C2}$  is evidently distinct from the metallic normal state MII existing above  $T_{C1}$  since the former one possesses several order of magnitude higher resistivity.

In the absence of an external magnetic field, the reentrant transition disappears by application of pressure of about 550 bar. However, the application of a magnetic field of about several Tesla normal to conducting layers induces the  $T_{C2}$  transition to a resistive ground state even in the high pressure region [14]. The another observed magnetic field effect, namely the irreversible enhancement of resistivity of NMIV phase due to the slow cycling of the magnetic field [14, 15] rules out the explanation of the phenomenon in terms of magnetoresistance for single particles. Instead, the cooperative electron transition of the magnetic origin has been argued to take place.

Strong competition between SC and magnetism with the effect of reentrant superconductivity have been reported previously in the ternary rare earth compounds, e.g. in  $\text{ErRh}_4\text{B}_4$  [16], where the electrons which undergo magnetic order are distinct from those which are superconducting: the 4f-electrons of the rare earth are responsible for magnetism, while 4d-electrons in Rh work for the SC.

For the organic material the situation is quite novel and unique. The present salt contains no rare earth, no magnetic atoms at all. This means that

only  $\pi$ -electrons in organic cation layer must be taken into account when consider both the conduction and localized magnetism and therefore, the magnetism and SC are not separated although they may stem from separate portions of the Fermi surface. This may indicate the presence of a non-trivial relationship between magnetism and SC for this system. Still lacking the data of direct mapping of spin structure of the material, the type of magnetic ordering and nature of its close relationship with superconductivity in layered compound  $\kappa\text{-(BEDT-TTF)}_2\text{Cu[N(CN)}_2\text{]Cl}$  remain not yet understood. Neutron diffraction studies, both at ambient and elevated pressures, may shade light on this problem.

## REFERENCES

1. D. Jerome and H. J. Schulz, *Adv. Phys.* **31** (1982) 299.
2. T. Ishiguro and K. Yamaji, *Organic Superconductors*, (Springer-Verlag, 1990).
3. D. Jerome *et al.*, *J. Phys. Lett. (Paris)* **41** (1980) L95
4. V. N. Laukhin *et al.*, *JETP Lett.* **41** (1985) 81.
5. K. Murata *et al.*, *J. Phys. Soc. Jpn.* **54** (1985) 1236; H. Veith *et al.*, *Solid State Commun.* **56** (1985) 1015; J. E. Schirber *et al.*, *Phys. Rev. B* **33** (1986) 1987.
6. J. E. Schirber *et al.*, *Physica C* **152** (1988) 157.
7. Yu. V. Sushko *et al.*, *Solid State Commun.* **87** (1993) 589.
8. J. M. Williams *et al.*, *Inorg. Chem.* **29** (1990) 3272; J. E. Schirber *et al.*, *Phys. Rev. B* **44** (1991) 4666.
9. Yu. V. Sushko *et al.*, *J. Phys. II (France)* **1** (1991) 1015; *Physica C* **185-189** (1991) 2683.
10. Yu. V. Sushko and K. Andres, *Phys. Rev. B* **47** (1993) 330.
11. U. Welp *et al.*, *Phys. Rev. Lett.* **69** (1992) 840.
12. Yu. V. Sushko *et al.*, *Solid State Commun.* **87** (1993) 997.
13. H. Posselt *et al.*, *Phys. Rev. B* **49** (1994) 15849; *Solid State Commun.* **92** (1994) 613.
14. Yu. V. Sushko *et al.*, *J. Phys. Soc. Jpn.* **62** (1993) 3372.
15. Yu. V. Sushko *et al.*, *Synth. Metals* **70** (1995) 907.
16. See, for example, *Superconductivity in Ternary Compounds*, ed. M. B. Maple and Ø. Fisher, (Springer-Verlag, 1982).

## PRESSURE DEPENDENCE OF PRIMARY CHARGE SEPARATION IN A PHOTOSYNTHETIC REACTION CENTER

H.-C. Chang, R. Jankowiak, N. R. S. Reddy, and G. J. Small  
*Ames Laboratory-USDOE and Department of Chemistry*  
Iowa State University, Ames, IA 50011, USA

### ABSTRACT

Effect of high pressure on the primary charge separation kinetics of the PS II RC has been investigated using spectral hole burning. The results show that the 4.2 K lifetime of P680\*, the primary donor state, lengthens from 2.0 ps at 0.1 MPa to 7.0 ps at 267 MPa. This effect is plastic (irreversible) in nature in contrast with the elastic effects of pressure on the low temperature  $Q_y$ -absorption and non-line narrowed hole spectra of P680. The electron-phonon coupling shows only a weak dependence on pressure. Nonadiabatic rate expressions, which take into account the distribution of energy gap values, are used to estimate the linear pressure shift of the acceptor state energy for both the superexchange and two-step mechanisms for primary charge separation. For both mechanisms shifts in the vicinity of  $1\text{ cm}^{-1}/\text{MPa}$  are required to explain the data.

### Introduction

The problem of primary charge separation in photosynthetic reaction centers (RC) remains as one of long-standing and much current interest [1-6]. Primary charge separation in the D1-D2-cyt  $b_{559}$  RC of photosystem II has received increased attention [7,8] since its isolation in 1987 by Nanba and Satoh [9]. Both ultrafast and spectral hole burning spectroscopies have been extensively applied to the study of the bacterial and the PS II RC.

Recently, we initiated a program to study the effects of pressure on the excited electronic state structure and transport dynamics of photosynthetic protein complexes. Windsor and coworkers [10,11] had already demonstrated that pressures of  $\sim 350\text{ MPa}$  have a significant effect on the kinetics of secondary charge separation in the RC of *Rb. sphaeroides* and *Rps. viridis*. These works and those on the  $Q_y$ -absorption spectra of the *Rps. viridis* [12] and *Rb. sphaeroides* [13,14] RC and of the FMO antenna complex of *Chlorobium tepidum* [15] have clearly demonstrated that the linear pressure shifts (to the red) of  $Q_y$ -states can be large ( $\sim 0.5\text{ cm}^{-1}/\text{MPa}$  for P870 and P960 of *Rb. sphaeroides* and *Rps. viridis*). In addition, the pressure shifts for different  $Q_y$ -states of a given complex are generally not the same. This is important since one can alter the energy gap(s) associated with energy and electron transfer. Finally, pressure may affect other parameters important to transfer such as the

reorganization energy, the electronic coupling and the structural heterogeneity which leads, for example, to a distribution of values for donor-acceptor energy gaps. Fortunately, spectral hole burning can be used to examine the pressure dependencies of these quantities.

Despite similarities with bacterial RCs in pigment composition, the low temperature (4.2 K)  $Q_y$ -region absorption spectrum of the PS II RC consists of only two bands (at 681 and 670 nm). This spectral congestion in the PS II RC absorption spectra has made the understanding of excited state electronic structure and primary charge separation kinetics more difficult. Both the special pair, P680 and the active pheophytin molecule contribute to the 680 nm band [17]. Fortunately, spectral hole burning can isolate P680\* and the Pheo  $a$   $Q_y$ -state. The latter gives rise to persistent nonphotochemical hole burning while P680\* does not [17]. Hole burning studies of many different preparations have shown that the P680\* lifetime (at 4.2 K) is about 2 ps [16-19].

In this paper we present some of our results of high pressure-hole burning studies of the primary charge separation kinetics of the PS II RC. Full report of these studies will appear elsewhere [16].

### Experimental

Both hole burning and high pressure experimental setups have been described in detail in Ref. 16. Briefly, high pressures (up to 1.5 GPa) were generated by a three-stage compressor (model U11, Unipress-

equipment Division, Polish Academy of Sciences, Warsaw, Poland). The high pressure cell located in the sample chamber of a liquid helium cryostat contains the sample under study and is connected to the compressor by a flexible capillary tube. Helium gas is used as the pressure transmitting medium. Absorption and hole burned spectra were recorded with a Bruker HR120 Fourier transform spectrometer. Typically, the spectrometer was used at a resolution of  $4\text{ cm}^{-1}$  except for high resolution scans of the zero phonon holes where a resolution of  $0.2\text{ cm}^{-1}$  was used. A Coherent CR699-21 ring dye laser (linewidth =  $0.07\text{ cm}^{-1}$ ), pumped by a 6 W Coherent Innova argon ion laser, was used for hole burning.

Samples of the D1-D2-cyt  $b_{359}$  RC complex from spinach leaves were generously provided by M. Seibert and R. Picorel.

## Results and Discussion

Using the  $Q_y$ -absorption spectra (at 77 K) of the PS II RC (data not shown) obtained at various pressures, we estimate the linear pressure shift rates for the 680 and 670 nm bands to be  $-0.08$  and  $-0.04\text{ cm}^{-1}/\text{MPa}$ , respectively. Linear shift rates for P680 and pheophytin, both absorbing at 680 nm can be separated by employing triplet bottleneck hole burning and nonphotochemical hole burning, respectively. These values (at  $T = 77\text{ K}$ ) are  $-0.09\text{ cm}^{-1}/\text{MPa}$  for P680 and  $-0.04\text{ cm}^{-1}/\text{MPa}$  for pheophytin [16].

Transient hole profiles obtained at 4.2 K under non-line-narrowing conditions ( $\lambda_b = 665\text{ nm}$ ) are shown in Fig. 1 for pressures of 0.1 MPa (a) and 267 MPa (b). The transient hole near 680 nm is dominated by P680 although there is a small contribution from the 684 nm linker Chl  $a$  [18], dashed arrow in spectrum a. From the data in the inset the linear pressure shift at  $T = 4.2\text{ K}$  of the 680 nm hole is  $-0.07\text{ cm}^{-1}/\text{MPa}$ . There is also a significant pressure broadening effect [see Ref. 16]. The broad and relatively weak ( $\sim \times 10$ ) hole near 668 nm is the upper dimer component of the special pair [18,19]. By analogy with the special pair of the bacterial RC, the upper and lower components can be referred to as  $P_+$  and  $P_-$  (P680\*) [18,19]. The hole spectra obtained at pressures of 0.1, 141, and 267 MPa indicate that the linear pressure shift for  $P_+$  is the same as that for  $P_-$  within experimental uncertainty,  $\pm 0.01\text{ cm}^{-1}/\text{MPa}$ .

We point out that the 4.2 K linear pressure shifts for  $P_+$  and  $P_-$  of the PS II RC are both  $-0.07\text{ cm}^{-1}/\text{MPa}$  while those for *Rps. viridis* are  $-0.42$  and  $-0.15\text{ cm}^{-1}/\text{MPa}$  [16],

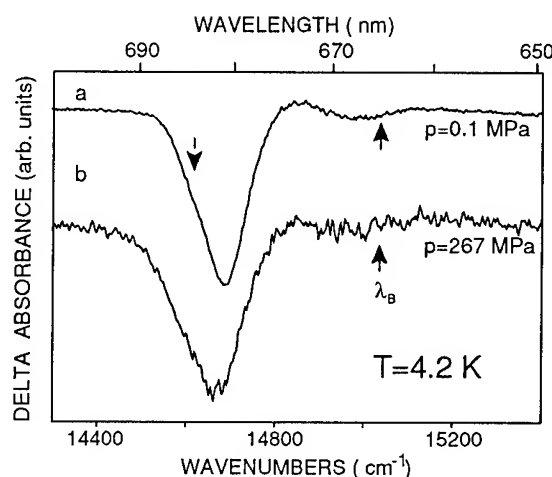


Fig. 1. Transient triplet bottleneck hole spectra of PS II RC obtained under non-line-narrowing conditions with  $\lambda_b = 665\text{ nm}$  at  $T = 4.2\text{ K}$  and  $p = 0.1\text{ MPa}$  (curve a) and  $p = 267\text{ MPa}$  (curve b). Burn intensity at the sample  $\sim 200\text{ mW}/\text{cm}^2$ .

respectively. The unequal shifts for  $P_+$  and  $P_-$  of *Rps. viridis* can be qualitatively understood in terms of the simple dimer exciton model when the dispersion shift (D) of the dimer is pressure dependent or in terms of the differing contributions of the internal charge transfer states of the special pair to  $P_+$  and  $P_-$  [20]. For the special pair of *Rps. viridis*, the Mg ... Mg and interplanar separation distance is 7.0 and 3.3 Å, respectively [21]. The smallness of the linear pressure shifts for  $P_+$  and  $P_-$  of the PS II RC provides additional evidence for the interaction between the monomers of the special pair being weak [18,19]. The small special pair splitting of  $\sim 300\text{ cm}^{-1}$  for the PS II RC (the splitting for the *Rps. viridis* RC is  $1900\text{ cm}^{-1}$  at 4.2 K [22] was used to estimate a Mg ... Mg distance of  $\sim 11\text{ Å}$  [19]. Why the linear pressure shifts for the 670 nm absorption band and the 681 nm  $Q_y$  band of the active Pheo  $a$  are so small is an interesting question but one that need await an X-ray structure of the PS II RC.

The pressure dependence of the primary charge separation kinetics was determined using line narrowed triplet bottleneck hole burning. Two of the hole burned spectra obtained at 0.1 MPa and 267 MPa are shown in Figure 2. Spectrum a, obtained at 0.1 MPa, shows the ZPH at the burn laser frequency and the associated phonon side band structure. The ZPH width of  $5.2 \pm 0.3\text{ cm}^{-1}$  yields a P680\* lifetime of  $1.9 \pm 0.2\text{ ps}$ . Upon increasing the pressure to 267 MPa, the ZPH width decreases to  $1.5\text{ cm}^{-1}$  (P680\* lifetime 7.0 ps) showing that primary charge separation is

retarded at higher pressures. To the best of our knowledge, our data are the first to show that pressure can have a significant effect on primary charge separation. Interestingly, when the pressure is decreased from 267 MPa to 0.1 MPa the ZPH width does *not* recover to its virgin sample value ( $5.2 \text{ cm}^{-1}$ ). That we continue to burn narrow ZPH at high pressures, together with the fact that the transient hole also broadens with pressure, shows that the aforementioned broadening of P680 band is due to increase in inhomogeneous broadening.

The elastic nature of the low temperature absorption spectrum and non-line narrowed P680 hole spectrum upon pressure cycling suggest that dark charge transfer states are important in understanding the pressure

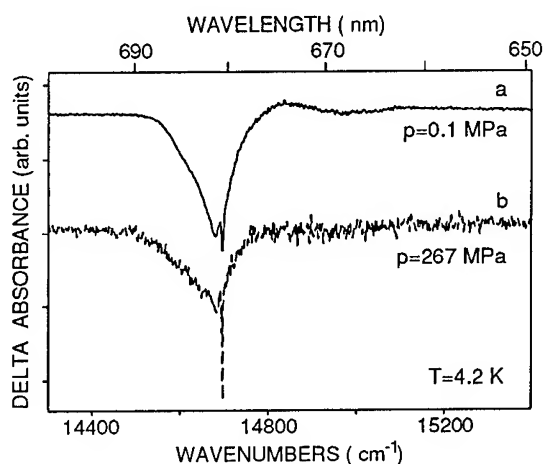


Fig. 2. Line-narrowed transient triplet bottleneck hole spectra (4.2 K) obtained at two different pressures:  $p = 0.1 \text{ MPa}$  (a) and  $p = 267 \text{ MPa}$  (b), respectively;  $\lambda_b = 680.4 \text{ nm}$ . The ZPH widths are  $5.2 \text{ cm}^{-1}$  at  $p = 0.1 \text{ MPa}$  and  $1.5 \text{ cm}^{-1}$  at  $p = 267 \text{ MPa}$ . Burn intensity at the sample  $\sim 100 \text{ mW/cm}^2$ .

effects on primary charge separation. Combined with the weak pressure dependence of the electron-phonon coupling the just mentioned elastic behavior rules out the energy of P680\* and the electronic coupling  $V$  as sources for the plastic pressure dependence of the primary charge separation (for details see Ref. 16).

A theory of hole profiles in the low temperature limit valid for arbitrarily strong electron-phonon coupling has been recently generalized for arbitrary temperature and used to accurately account for the temperature and burn frequency dependence of P680 hole spectra at 1 atm [16]. Use of this theory to simulate the absorption and non-line narrowed hole burned spectra at elevated pressures, including those shown in Figures 1 and 2,

yields the following information: the mean protein phonon frequency,  $\omega_m$  ( $\approx 20 \text{ cm}^{-1}$ ) and the associated Huang-Rhys factor,  $S$  ( $\approx 1.9$ ) are independent of pressure. The change in the intensity of the ZPH can be well accounted for by a decrease in the homogeneous width of the zero phonon line for the P680\*-P680 transition. This, however, does not explain the broadening of the structure accompanying the ZPH. Simulations that include an increase in the inhomogeneous broadening,  $\Gamma_{inh}$ , with pressure ( $d\Gamma_{inh}/dp = 0.16 \text{ cm}^{-1}/\text{MPa}$ ) account well the high pressure spectra (see Ref. 16).

Small *et al* [23] have developed a theory for non-adiabatic electron-transfer and obtained the following expression for the electron transfer rate. Denoting the donor state, P680\* by D and the acceptor state, P\*Chl<sup>-</sup> (two-step model) or P\*Pheo<sup>-</sup> (superexchange model) by A, the rate expression for the superexchange model is

$$\langle k_{DA} \rangle = 2\pi V^2 (2FC_{loc}) \{ 2\pi [\Gamma^2 + \Sigma(T)^2] \}^{-1/2} \exp \{ -(\Omega_0 - \omega_{loc} - S\omega_m)^2 / 2[\Gamma^2 + \Sigma(T)^2] \}$$

where  $\Omega_0$  is the mean donor-acceptor energy gap,  $V$  is the electronic coupling matrix element,  $\Sigma(T)$  is the homogeneous width of the nuclear factor associated with the Golden rule and  $\Gamma^2$  is the variance in  $\Omega$  values [23].  $\Sigma(T)^2 = \tilde{S}(\sigma^2 + \omega_m^2)$  where  $2\sigma$  is the width of the one-phonon profile and  $\tilde{S}(T) = S \text{ctnh}(\hbar\omega_m/2kT)$ .  $\omega_{loc}$  is the frequency of a localized intramolecular Chl/PhEO mode with a Franck-Condon factor  $FC_{loc}$ . For calculations  $\omega_{loc}$  was set to  $710 \text{ cm}^{-1}$  and  $FC_{loc}$  was taken to be 0.2 [16]. In the case of a two-step model  $\omega_{loc}$  is set to zero and  $FC_{loc} = 1$  since no modes other than the phonon modes are considered. The values of  $\sigma = 13.8$  and  $\omega_m = 20 \text{ cm}^{-1}$  were obtained from hole burning results. The room temperature free energy gap between P680\* and P680\*Pheo<sup>-</sup> has been reported to be  $890 \text{ cm}^{-1}$  [24]. For uncorrelated distributions of donor and acceptor levels, we obtain  $2.35\Gamma \approx (\Gamma_{inh,D}^2 + \Gamma_{inh,A}^2)^{1/2}$ . The value of  $\Gamma$  was set to either 100 or  $200 \text{ cm}^{-1}$  [16]. The latter value is due to recent reports that  $\Gamma_{inh}$  for charge separated states could be significantly larger than  $100 \text{ cm}^{-1}$  [25].

The pressure dependence of primary charge separation kinetics can be modeled as due to structural changes (irreversible) affecting the acceptor state. These structural changes affect both the inhomogeneous broadening and energy of the acceptor state. We present results only for the case  $\Omega_0$  (two-step),  $\Omega_0 - \omega_{loc}$  (superexchange) =  $S\omega_m$  at 0.1 MPa. For the two step model, assuming that the  $\Gamma_{inh,A}$

increases by a factor of 1.5 for pressure increase from 0.1 MPa to 267 MPa, calculations [16] show that  $\Omega_0$  increases by 259 and 427  $\text{cm}^{-1}$  for  $\Gamma(0.1 \text{ MPa}) = 100$  and 200  $\text{cm}^{-1}$ , respectively. For the superexchange model the corresponding increases are 231 and 410  $\text{cm}^{-1}$ , respectively. Thus, explanation of the pressure dependence of  $\langle k_{\text{DA}} \rangle$  (reduction in ZPH width) requires a pressure shift of the acceptor (A) state energy of about 1  $\text{cm}^{-1}/\text{MPa}$  in magnitude. For pressures  $\leq 400$  MPa, Rollinson *et al* [26] report the linear pressure shift rates (at room temperature) for intramolecular charge transfer states of several compounds to be in the vicinity of 1  $\text{cm}^{-1}/\text{MPa}$ . Thus, the pressure shift value suggested by our calculations does not appear to be unreasonable.

### Acknowledgments

Research at the Ames Laboratory was supported by the Division of Chemical Sciences, Office of Basic Energy Sciences, U.S. Department of Energy. Ames Laboratory is operated for USDOE by Iowa State University under contract W-7405-Eng-82.

### References

1. R. M. Pearlstein, in *Photosynthesis: Energy Conversion by Plants and Bacteria*, ed. Govindjee (Academic, NY, 1982), pp 293-330.
2. R. van Grondelle, *Biochim. Biophys. Acta* **811** (1985), 147-195.
3. R. S. Knox, in *Encyclopedia of Plant Physiology*, Vol. 19 ed. L. A. Staehelin and C. J. Arntzen (Springer-Verlag, Berlin, 1986), p. 86.
4. N. R. S. Reddy, P. A. Lyle and G. J. Small, *Photosyn. Res.* **311** (1992) 167-194.
5. W. W. Parson, in *Chlorophylls*, ed. H. Scheer, (CRC Press, Boca Raton, 1991), pp 1153-1180.
6. R. A. Friesner and Y. Won, *Biochim. Biophys. Acta* **977**, (1989) 99-122.
7. M. Seibert, in *The Photosynthetic Reaction Center*, Vol I; (ed. J. Deisenhofer and J. R. Norris, (Academic Press, NY, 1993), pp. 319-356.
8. G. Renger, in *Topics in Photosynthesis*, Vol. 11, ed. J. Barber, (Elsevier, 1992), pp. 45.
9. O. Nanba and K. Satoh, *Proc. Natl. Acad. Sci. USA*, **84** (1987) 109-112.
10. N. L. Redline and M. W. Windsor, *Chem. Phys. Lett.*, **186** (1991) 204-209.
11. N. L. Redline and M. W. Windsor, *Chem. Phys. Lett.* **198** (1992) 334-340.
12. N. R. S. Reddy and G. J. Small, *Advances in Photosynthesis* (in press).
13. R. K. Clayton and D. DeVault, *Photochem. Photobiol.* **15** (1972) 165-175.
14. A. Freiberg, A. Ellervee, P. Kukk, A. Laisaar, M., Tars, and K. Timpmann, *Chem. Phys. Lett.* **214** (1993) 10-16.
15. N. R. S. Reddy, R. Jankowiak and G. J. Small, *J. Phys. Chem.* (accepted).
16. H.-C. Chang, R. Jankowiak, N. R. S. Reddy and G. J. Small, *Chem. Phys.* (in press).
17. R. Jankowiak, D. Tang, G. J. Small and M. Seibert, *J. Phys. Chem.* **93** (1989) 1649-1654.
18. H.-C. Chang, R. Jankowiak, N. R. S. Reddy, C. F. Yocum, R. Picorel, M. Seibert and G. J. Small, *J. Phys. Chem.* **98** (1994) 7725-7735.
19. S. L. S. Kwa, C. Eijkelhoff, R. van Grondelle and J. P. Dekker, *J. Phys. Chem.* **98** (1994) 7702.
20. M. A. Thompson and J. Fajer, *J. Phys. Chem.* **96** (1992) 2933.
21. J. Deisenhofer, O. Epp, K. Miki, R. Huber and H. Michel, *Nature* **318** (1985) 618-624.
22. N. R. S. Reddy, S. V. Kolaczowski and G. J. Small, *Science* **260** (1993) 68.
23. G. J. Small, J. M. Hayes and R. J. Silbey, *J. Phys. Chem.* **96** (1992) 7499-7501.
24. P. J. Booth, B. Crystall, I. Ahmad, J. Barber, G. Porter and D. R. Klug, *Biochemistry* **30**, (1991) 7573-7586.
25. M. Bixon, J. Jortner and M. E. Michel-Beyerle, *Chem. Phys.* (1995) (in press).
26. A. M. Rollinson and H. G. Drickamer, *J. Chem. Phys.* **73** (1980) 5981-5996.

# CONFORMATIONAL CHANGES OF POLY(3-ALKYLTHIOPHENE)S WITH PRESSURE

P. BARTA, T. KANIOWSKI, W. LUŻNY, S. NIZIOL,

*Faculty of Physics and Nuclear Techniques, University of Mining and Metallurgy, al. Mickiewicza 30,  
30-059 Cracow, Poland*

J. SANETRA,

*Institute of Physics, Technical University of Cracow, Podchorążych 1, 30-084 Cracow, Poland*

M. ZAGÓRSKA

*Department of Chemistry, Technical University of Warsaw, Noakowskiego 3, 00-664 Warsaw, Poland*

## ABSTRACT

The thermochromic effect (simply, the change in colour with temperature measured in 300-450 K range), as observed for poly(3-alkylthiophene)s is closely related to the evolution of conformation of polymer backbone. This is due to strong electron-phonon coupling in such system as conjugated polymers. Thus, it is expected that external, hydrostatic pressure can also modify the conformation (higher pressure, more planar backbone) of the polymer thereby inducing change in electronic band structure. Our experimental setup consists of SPECOL UV-VIS spectrometer, compressor CGA 10 and UNIPRESS optical pressure cell. Measurements were performed for pressure up to 0.6 GPa at room temperature. The observed decrease of optical energy gap is about 0.2 eV for all polymers subjected to the measurements. That is interrelated to the results of temperature dependence of electrical conductivity measured at different pressure.

## Introduction

One of the major properties of classical polymers that apparently distinguishes them from metals is their high electrical resistance. During the past two decades, however, a new class of conjugated, organic polymers capable of conduct electrical current in a doped state has been developed. Only when MacDiarmid, Heeger and associates [1] reported their work on electrical conductivity arising in polyacetylene, the field of highly conducting polymers became a fashionable research subject.

□Polyalkylthiophenes-PATs, as a relatively wide class of conjugated polymers, are of great interest mainly because of their stability, processability and applicational properties [2]. However, the substitution of thiophene ring which, in principle, gives such extra-ordinary processability also results in decreasing of effective conjugation length. This is primarily due to increased repulsive interactions, in the case of head-to-head configuration between the substituent and the  $sp^2$  lone pair on sulphur, which forces the backbone out of co-planarity. Here, we report results of investigations of the evolution of molecular and electronic structure and additionally, the electrical properties of polyalkylthiophenes as a function of the high external, hydrostatic pressure. The evolution of electronic, optical and electrical

properties of well known PATs as a function of external pressure was reported previously by several authors [3,4] for either pristine or doped (oxidized) sample. In the present paper the optical absorption spectroscopy results are reported and compared for three different polyalkylthiophene systems (see Fig. 1): (1) well known, poly(3-alkylthiophene) system-P3AT, (2) its regio-regular analogue, that is, poly(4,4'-dialkyl-2,2'-bithiophene)-PDABT and finally, (3) thiophene copolymer: poly(2,2'-bithiophene-4,4'-dialkyl-2,2'-bithiophene)

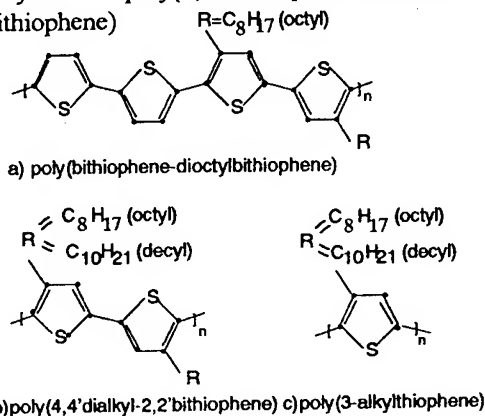


Fig. 1 Different polyalkylthiophene system

## Experimental

The exact procedure for the polymerisation of poly(3-decylthiophene)s were reported by Kluszewicz-Bajer and co-workers [5]. The

polymerisation of poly(4,4'-didecyl-2,2'-bithiophene) has been reported in details by Zagórska *et al.* [6]. Doping was carried out by placing a sample in solution of dried, anhydrous  $\text{FeCl}_3$  in acetonitrile (0.1 M). The doping level was determined from mass-uptake and was verified by elemental analysis for selected samples. Detailed description of the experimental techniques used can be found elsewhere [7].

The absorption spectra of the polyalkylthiophene system subjected to the reported studies were measured by means of a di-beam spectrophotometer SPECORD-Carl Zeiss Jena. The thin film on substrate were mounted into a pressure chamber. The hydrostatic pressure was obtained from a gas-helium compressor IFP012 UNIPRESS (Poland). The equipment allows to carry out the measurements in pressure up to 1.5 GPa. The exact value of the pressure applied was measured by means of a DC-bridge with a manganite coil as a sensing resistance. The D.C. conduction measurements under pressure were carried out using the two-point method applied directly in the pressure cell.

## Results and discussion

Typical pressure dependent photo-absorption spectra are presented in Fig. 2. The same wavelength dependent behaviour was observed both for poly(4,4'-didecyl-2,2'-bithiophene) and poly(bithiophene-4,4'-dioctyl-2,2'-bithiophene) samples. The presence of the true isosbetic point around 2.4 eV indicates that an equilibrium between two phases of the polymer film is present. Optical gap decreases with increasing pressure and, simultaneously, the intensity of the maximum of absorption decreases with pressure. The latter effect is presumably due to pressure induced decreasing of the total thickness of the polymer.

The decreasing of the value of the optical gap can be rationalised as the effect of decreasing of the torsion angle between adjacent thiophene rings. It has been already reported [8] that under normal, external conditions pure "head to head", "tail to tail" coupled polyalkylthiophene chain is strongly distorted in the meaning of the lack of planarity of the polymer backbone. Increasing of the external, hydrostatic pressure leads the polymer system to the new thermodynamic state of equilibrium, where

the increasing of the planarity is more likely. Additionally the measurements of the temperature dependence conductivity with pressure as a parameter for PDDBT were carried out. During the

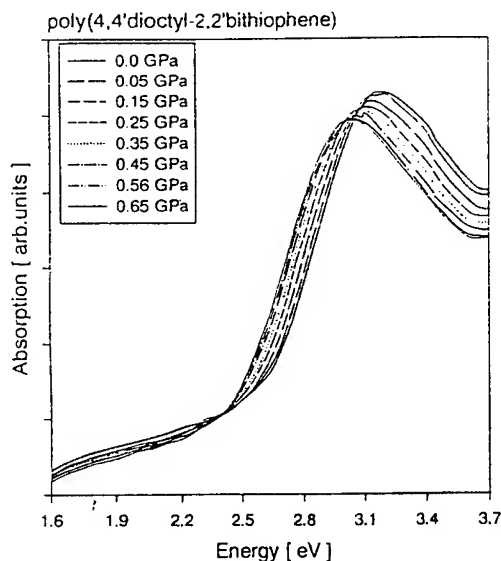


Fig.2 Pressure dependent photo-absorption spectra of PDOBT

temperature increasing of 80 K (100 K-180 K) the magnitude of conductivity increases over one order. The pressure increase induces the increase of conductivity of sample, whereas the temperature dependence of conductivity is the same.

We tried to fit the variable range hopping model to the experimental data. In the 3D VRH model the pressure-dependent conductivity is given by [4]:

$$\sigma = \sigma_0 \exp \left[ - \left( \frac{T_0}{T} \right)^{1/4} (1 - c_0 P) \right] \quad (1)$$

where  $c_0 = (\epsilon_0 + K_0)/4$  and  $\epsilon_0$  is the zero pressure compressibility of the energy gap and  $K_0$  the zero pressure bulk compressibility. Conductivity data were fitted to eq.(1) for two free parameters:  $\sigma_0$  and  $B = T_0^{1/4}(1 - c_0 P)$ .

Values of  $c_0$  was obtained from fitted parameters for samples with different doping levels. For  $y=0.15$  is  $c_0 = 4.6 \cdot 10^{-10} \text{ m}^2/\text{N}$  and for  $y=0.22$   $c_0 = 2.3 \cdot 10^{-10} \text{ m}^2/\text{N}$ . Compressibility decreases when doping level increases, and this fact can be rationalized as the effect of dopant species insertion between the polymer backbones. Comparing  $c_0$  with value  $\epsilon_0$  obtained from optical



absorption data ( $2 \cdot 10^{-10} \text{ m}^2/\text{N}$ ) we can assume that bulk compressibility more influences pressure-dependence conductivity, because of morphological structure of polymer. So pressure influences intrachain rather than interchain conductivity.

The third polymeric system subjected to our measurements, i.e., poly(3-decylthiophene), however, represents apparently different pressure-dependent behaviour, as it is shown in Fig. 3. First, three clear shoulders exist around 2.0 eV, 2.2 eV on the low-energy side of the main peak (at atmospheric pressure). These peaks gradually lose

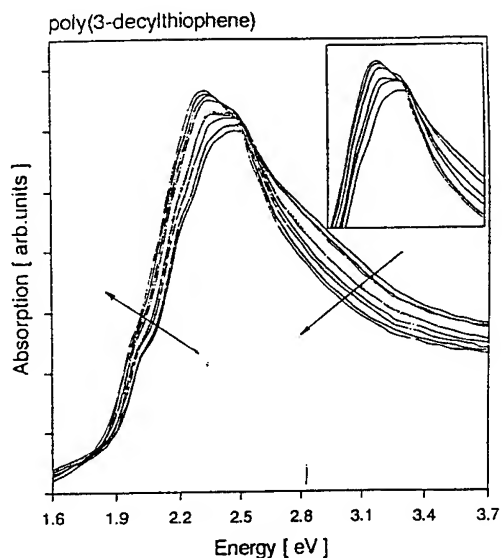


Fig. 3 Pressure dependent photo-absorption spectra of P3DT

their intensity with increasing pressure and appear to shift in energy position (the shift is towards lower energy value). On contrary, the shoulder highest in energy gradually develops and eventually becomes the main absorption peak, as it is presented in details in the inset of Fig.3. Second, higher external, hydrostatic pressure leads to higher absorption intensity. This phenomenon is completely opposite to that one observed for previously mentioned polythiophene systems and is consistent with previously reported results for poly(3-dodecylthiophene) [3].

The presence of equally spaced side peaks on low energy side ( $\Delta E = 0.194$ ) of photoabsorption spectrum of poly(3-alkylthiophene)s was reported by several authors [9,3]. These shoulders are reported only for highly crystalline samples and

their presence does not depend directly upon the presence of long alkyl chains. As it was shown by Fichou *et al* [10], the clearly distinguishable shoulders can be observed also for thiophene oligomers. In case of real polymeric system the presence of long side chains enhances the crystallinity of the sample-so called "zipper" effect [11], thereby resulting in presence of the shoulders on the absorption edge of polythiophene derivatives is usually associated with the hypothesis of coupling of the fundamental  $\pi-\pi^*$  electronic transition with vibrational levels of the excited state [9,10]. Combining this results with the observed increase in the total absorption intensity together with decreasing of partial intensities of the shoulders described above a following conclusion can be drawn: the pressure induced changes in the polymer backbone structure (and, since strong electron-phonon coupling, changes in electronic band structure) pronounce one of vibrational transitions and decrease transition moments of other transitions.

This work was supported by KBN grant No.3P40505707

## References

1. C.K.Chiang, C.R.Fincher, Y.W.Park, A.J.Heeger, H.Shirakawa, E.J.Louis, S.C.Gau, A.G.MacDiarmid *Phys. Rev. Lett.*, **39** 1098 (1977)
2. M.Berggren, G.Gustafsson, O.Inganas, M.R.Andersson, T.Hjertberg, O.Wennerstrom, *J.Appl. Phys.*, **76**(11), 7530 (1994) and references herein
3. K.Yoshino, K.Nakao, M.Onoda, R.Sugimoto, *Sol. St. Comm.*, **68**(6), pp. 513-516 (1988)
4. H.Isotalo, M.Ahlskog, H.Stubb, *Synth. Met.*, **48**, 131 (1992),
5. I.Kluszewicz-Bajer, I.Pawlicka, J.Plenkiewicz, A. Proń, *Synth. Met.*, **30**, 61 (1989)
6. M.Zagórska and B.Krische, *Polymer*, **31**, 1379 (1990)
7. P.Barta, S.Nizioł, M.Zagórska, A.Proń, Z.Trybula, *Phys. Rev. B*, **48**(1), 243 (1993)
8. P.Barta, P.Dannetun, S.Stafstrom, M.Zagórska, A.Proń, *J. Chem. Phys.*, **100**(2), 1731 (1994)
9. M.Sundberg, O.Inganas, S.Stafstrom, G.Gustafsson, B.Sjogren, *Sol. St. Comm.*, **71**(6), pp435-439(1989)
10. D.Fishou, G.Horowitz, B.Xu, F.Gamier, *Synth. Met.*, **48**, pp. 167-179 (1992)
11. M. J.Winokur, D.Spiegel, Y.Kim, S.Hotta, A.J. Heeger, *Synth. Met.*, **28**, C419 (1989)

**VISCOSITY AS A FUNCTION OF PRESSURE  
AND TEMPERATURE OF THREE CONTRASTED BINARIES :  
A REPRESENTATION WITH A SELF-REFERENCING METHOD**

A. ET-TAHIR , C. BONED , B. LAGOURETTE , J. ALLIEZ

*Laboratoire Haute Pression, Centre Universitaire de Recherche Scientifique  
Avenue de l'Université, 64000 PAU (France)*

**ABSTRACT**

The dynamic viscosity values (268 values) of the binaries toluene + tétraméthylpentadécane, toluene + méthyl-naphtalène, toluene + heptaméthyl-nonane (measured for  $25 \leq T \leq 90^\circ\text{C}$  and  $P \leq 100 \text{ MPa}$  and for several values of molar fraction  $x$  for toluene) are discussed in the framework of a self-referencing model developed in our laboratory. The absolute average deviation (6.9%) obtained is satisfactory. Moreover when coupled with mixing rules (Grunberg-Nissan equation) without adjustable parameters it was able to account satisfactorily for the variations  $\eta(P,T,x)$  of the mixtures on the simple basis of knowledge of the viscosity of the components of the binary considered, at  $25^\circ\text{C}$  and at  $0.1 \text{ MPa}$ . For all the binaries an absolute average deviation of 9.5% was observed.

**Introduction**

In the petroleum industries there is an increasingly pressing need for an effective tool for estimating various properties as a function of temperature, pressure and the proportions of the substances which make up the mixture. This article focuses on the dynamic viscosity  $\eta$  and on its representation at high pressures. Real fluids in oil reservoirs are complex fluids with a large number of components whose properties can be very different. Therefore we have used our experimental determination (1,2) concerning three strongly contrasted binaries (i.e. systems for which the viscosities of the pure components are very different for each  $P,T$  set). The systems are : toluene + tétraméthylpentadécane, toluene + méthyl-naphtalène, toluene + heptaméthyl-nonane. They have been studied for various values of the molar fraction  $x$  in toluene at  $T = 25, 40, 60, 80, 90^\circ\text{C}$  and  $P = 0.1, 20, 40, 60, 80, 100 \text{ MPa}$  and we have 268 experimental values for these three binaries ( $x \neq 0$  and  $x \neq 1$ ). The values were obtained with a falling body viscometer with relative uncertainty on viscosity estimated at 2%. The data has been used to make a critical analysis of a self-referencing model previously developed in our laboratory (3). The article focuses on a new development of this model

which simplifies significantly its use : now it is possible to estimate  $\eta$  at high  $P$  and  $T$  for binaries, knowing only viscosities of the two pure components at  $25^\circ\text{C}$  and  $0.1 \text{ MPa}$ .

**The self-referencing method**

In a previous study carried out at the laboratory (3) a method was presented whereby  $\eta(P,T)$  of a fluid in the liquid state could be calculated from its viscosity at  $P_0 = 0.1 \text{ MPa}$  and at a reference temperature  $T_0$  (generally ambient temperature). As the coefficients used in the method are fixed independently of the nature of the system studied, this gives a character of generality to the model. The approach is derived from earlier work by Kashiwagi and Makita (4). They represented  $\eta$  at  $T$  as a function of  $P$  simply on the basis of measurement at  $P_0 = 0.1 \text{ MPa}$  and at the temperature  $T$  considered. This assumes that this particular value contains within itself information specific to the fluid studied. They proposed the formulation :

$$\ln \left[ \frac{\eta(P,T)}{\eta(0.1,T)} \right] = E \ln \left[ \frac{D+P}{D+0.1} \right] \quad (P \text{ in MPa})$$

in which  $E$  and  $D$  are constants to be adjusted. This relationship requires measurement of  $\eta$  at

$P_0 = 0.1\text{MPa}$  and but the determination of  $E$  and  $D$  implies prior knowledge of  $\eta(0.1, T)$  for several values of  $T$ . In this sense it is not predictive except in so far as it allows interpolation between two values of  $P$ . In order to remedy this disadvantage we proposed [3] to adopt the form :

$$\eta(0.1, T) = \eta(0.1, T_0) \exp \left[ \alpha \left( \frac{1}{T} - \frac{1}{T_0} \right) \right]$$

$\alpha = gy_0^2 + hy_0 + i$  with  $y_0 = \ln \eta(0.1, T_0)$ ,  
 $E = ay^2 + by + c$ ,  $D + 0.1 = dy^2 + ey + f$  with  
 $y = \ln \eta(0.1, T)$ . This formulation has the advantage that it only requires one experimental determination at  $0.1\text{MPa}$  and temperature  $T_0$ . It is for that reason that this method can be referred to as a self-referencing model. It is not essential to choose ambient temperature as  $T_0$ . The method does not involve molar mass, nor any other physical properties or critical parameters. It can be applied without restriction indifferently to pure substances, to synthetic mixtures or to chemically very rich systems such as petroleum cuts for which we originally developed it. The coefficients  $a \dots i$  were determined (3) by numerical analysis on an adjustment base consisting of linear alkanes and alkylbenzenes. On the basis of knowledge of the set of coefficients  $a \dots i$  the method can be used directly without further adjustment. For this reason it may be considered that it is general and predictive. On this subject it is appropriate to recall a recent paper (5) on heavy oils and bitumens, in which a similar idea is developed.

### Results obtained for the binaries

In order to assess and compare the performance of the model, we defined the following quantities :

$$\text{Dev}(i) = (1 - \eta_{\text{cal}}/\eta_{\text{exp}}) ; \text{DM} = \text{MAX}(|\text{Dev}(i)|)$$

$$\text{AAD} = \frac{1}{\text{Nb}} \sum_{i=1}^{\text{Nb}} |\text{Dev}(i)| \geq 0 ; \text{Bias} = \frac{1}{\text{Nb}} \sum_{i=1}^{\text{Nb}} \text{Dev}(i)$$

in which  $\text{Nb}$  is the number of experimental points,  $\eta_{\text{exp}}$  the measured viscosity value and  $\eta_{\text{cal}}$  the value calculated using the model. The model can be applied without modification to binaries. All one

needs to know is the viscosity at  $0.1\text{MPa}$  and the reference temperature  $T_0$  for the desired volume fraction  $x$ . The model was successfully tested in this way on petroleum cuts (3). In all cases we took  $T_0 = 25^\circ\text{C}$  as the reference temperature. The overall result on all 268 experimental sets (from which the reference points are of course excluded) show that  $\text{AAD} = 6.9\%$ ,  $\text{Bias} = -3.3\%$  and  $\text{DM} = 22.8\%$ , which is a very satisfactory result. It is the use of the reference measurement which is important because it is this measurement which provides the information on the system studied, which is then a factor involved in the terms  $y$  and  $y_0$  of the equations.

### Association of the self-referencing method and mixing rules

The objective of the mixing rules is to account for the viscosity of the mixture from knowledge of the viscosities of the pure substances, their molar fractions, with, where appropriate, specific interaction parameters. In particular we used the following classical formulations which have proved effective in different cases :

$$\eta^{1/3} = x \eta_1^{1/3} + (1-x) \eta_2^{1/3} \quad (\text{equ.1})$$

$$\ln \eta = x \ln \eta_1 + (1-x) \ln \eta_2 \quad (\text{equ.2})$$

Equation 1 had been postulated previously by Kendall and Monroe (6) and equation 2 by Grunberg and Nissan (7). As they involve no adjustable parameters they are said to be characteristic of an "ideal" behaviour though this is probably an inaccurate term. In fact, for a mixture of spherical compounds of similar size and properties, the relationship of Katti and Chaudhri (8) which has a more physical basis, has been justified theoretically, and it may be thought more representative of an ideal behaviour. It is expressed in the form :

$$\ln(\eta V) = x \ln(\eta_1 V_1) + (1-x) \ln(\eta_2 V_2) \quad (\text{equ.3})$$

in which  $V, V_1, V_2$  are molar volumes. The results obtained are :  $\text{AAD} = 9.7\%$ ,  $\text{DM} = 48.0\%$  and  $\text{Bias} = -7.1\%$  for equation 1 ;  $7.7\%$ ,  $24.7\%$  and  $5.0\%$  for equation 2 ;  $13.1\%$ ,  $36.3\%$  and  $11.8\%$  for equation 3.  $\text{AAD}$ ,  $\text{DM}$  and  $\text{Bias}$  values for  $P, T$

sets associated with  $x = 0$  and  $x = 1$  (pure substances) have of course been omitted. One should note the good results provided by the ideal Grunberg and Nissan relationship (equation 2). These results, for asymmetrical and contrasted binaries, may by analogy give rise to applications in the case of systems for which it is required to simulate at least the order of magnitude of the dynamic viscosity from those of the pure substances. Let us observe at this stage that all these relationships, generally tested at atmospheric pressure, prove just as successful at high pressures: the introduction of the pressure parameter did not lead to a deterioration in their respective performances.

The principal drawback of mixing rules, lies in the fact that the viscosities of the pure substances have to be known for each P,T set. We saw above that the self-referencing method could yield very acceptable results. We therefore associated the self-referencing model applied to pure substances (to generate their viscosities versus P and T) with mixing rules (to generate the viscosity of each binary as a function of the respective proportions of each component). Implementation of this procedure requires only knowledge of the viscosity of each of the pure components at 0.1MPa and at the reference temperature  $T_0$  to simulate the behaviour of each binary. For our verifications we chose  $T_0 = 25^\circ\text{C}$ . The results are : AAD = 16.0%, DM = 59.4% and Bias = -15.6% for equation 1 ; 9.5% , 41.8% , and -4.2% for equation 2 ; 13.6% , 40.0% and 3.2% for equation 3. A loss of accuracy will be noted, but this is not very large considering the disproportion of information required. For example with the ideal rule of Grunberg and Nissan the deviations observed are AAD = 9.5%, DM = 41.8% and Bias = -4.2% instead of 7.7%, 24.7% and 5%. Naturally, direct application of the self-referencing method to the three binaries provides a better representation (6.9%, 22.8% and -3.3%). However it does require knowledge of the viscosity at 0.1MPa and at  $T_0$  for each value of  $x$ .

## Conclusion

It can therefore be seen that if one wants to generate viscosity values of a binary using a minimum amount of data, in such a way as to appraise its behaviour under pressure, without implementing specific experimental procedures, the combined use of the self-referencing method and the ideal rules of Grunberg-Nissan or Katti-Chaudhri (i.e. without adjustable parameter) provides a reasonable response, at least for binaries whose viscosity is a monotonic function of the molar fraction  $x$ , in other words often binaries with non-polar components and relatively low levels of interaction and self-association. From a practical point of view, the usefulness of developing excessively sophisticated models, which are therefore complex and difficult to implement, and which one encounters with increasing frequency, is not immediately apparent. They do not generally lead to an easier description of the phenomenon.

## References

1. A. Et-Tahir, *Thèse de Doctorat de l'Université de Pau et des Pays de l'Adour*, (1993).
2. A. Et-Tahir, C. Boned, B. Lagourette and P. Xans, *International Journal of Thermophysics*, (in press 1995).
3. M. Kanti, H. Zhou, S. Yé, C. Boned, B. Lagourette, H. Saint-Guirons, P. Xans and F. Montel, *J. Physical Chemistry* **93** (1989) 3860.
4. H. Kashiwagi and T. Makita, *International Journal of Thermophysics* **3** (1982) 289.
5. V.R. Puttagunta, A. Miadonye, S.B. Dyer and S.S. Huang, *AOSTRA - Journal of Research*. **7** (1991) 251.
6. J. Kendall and K.P. Monroe, *J. of the American Chemical Society* **39** (1917) 1802.
7. L. Grunberg and A.H. Nissan, *Nature* **164** n°4175 (1949) 799.
8. P.K. Katti and M.M. Chaudhri, *J. of Chemical and Engineering Data* **9** (1964) 442.

# LIGHT SCATTERING OF LINOLENIC ACID AND TRIOLEIN LIQUIDS UNDER HIGH PRESSURE

R. M. SIEGOCZYŃSKI, R. WIŚNIEWSKI and W. EJCHART  
*Institute of Physics, Warsaw University of Technology (WUT),  
ul. Koszykowa 75, 00-662 Warszawa, Poland*

## ABSTRACT

Liquid castor oil, oleic and linoleic acids (at temperature  $T = 20^{\circ}\text{C}$ ) exhibit a strong scattering of light in the case when pressures above 0.36, 0.21, and 0.20 GPa are applied, respectively. The transmitted and scattered light of linolenic acid and triolein have been viewed at angles near  $\Theta = 0^{\circ}$  to the direction of propagation of the incident beam at pressures up to 0.9 GPa. Present experimental results show that liquids of linolenic acid (one of components of castor oil) and triolein (whose molecular structure is similar to one of castor oil) also exhibit the phenomenon of the scattering of light similar to castor oil, oleic and linoleic acid. In conclusion we can say that the important role in all observed behaviours seems to be played by the unsaturated double bond  $\text{C} = \text{C}$  existing in all molecules of investigated liquids and the double bonds  $\text{C} = \text{O}$  existing in molecules of castor oil.

KEY WORDS: Light scattering, oleic, linoleic and linolenic acid, triolein, castor oil.

## Experimental

### Introduction

It is known that castor oil, oleic acid and linoleic one exhibit a strong scattering in the case when pressures above 0.36, 0.21 and 0.20 GPa are applied, respectively [1-3]. Now, we have found the liquids, linolenic acid (one of components of castor oil) and triolein (whose molecular structure is similar to the molecular structure of castor oil), which exhibit the similar scattering of light to that of castor oil, oleic and linoleic acid.

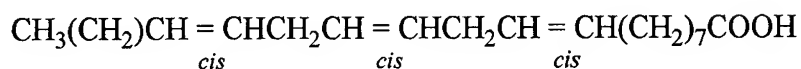
For the application of pressure above about 0.38 GPa for linolenic acid and 0.40 GPa for triolein a strong increase of the scattered light intensity (by a factor  $10^2 - 10^3$ ) compared with molecular light scattering before the application of pressure and the strong decrease of the transmitted light some seconds after an application of pressure in the case of linolenic acid and some minutes in the case of triolein have been observed. This effect is reversible for triolein and partly reversible for linolenic acid.

Commercially available and chemically pure linolenic acid and triolein were used in these experiments. In order to prevent degradation, the samples were stored in the dark and cool until ready to use.

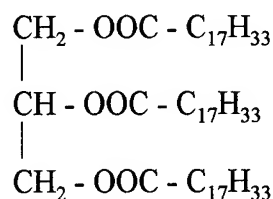
The optical high pressure apparatus designed and constructed in our laboratory was used for pressures up to 1 GPa [1].

The transmitted light was viewed at angles near  $\Theta = 0^{\circ}$  and the scattered light was viewed at angles near  $\Theta = 90^{\circ}$  to the direction of propagation of the incident beam of light from pink diode. The incident wavelength  $\lambda$  ( $= \lambda_0/n$ ,  $n$  - refractive index of liquid,  $\lambda_{\text{max}} = 0.75 \text{ nm}$ ) far from the UV absorption region of linolenic acid and triolein was chosen so as to avoid the bulk molecular absorption.

Two methods of applied pressure "the slow case" and "the rapid one" were used in these study, too [1]. The temperature was controlled by a system thermostated with a copper-constantan thermocouple and controlled (microprocessor system) to an accuracy of  $\pm 0.1^{\circ}$ .



linolenic acid



triolein

## Results and Discussion

The earlier studies [1-4] show that the most important role in all phase transitions of this type seems to be played by double bond  $\text{C}=\text{C}$  existing in all molecules of investigated liquids. Therefore for further studies we have chosen linolenic acid - liquid with molecules containing three double bounds and triolein which molecular structure is

the most similar to structure of castor oil molecules.

The time dependencies of the intensity of the transmitted light  $I_{tr} (\Theta = 0^\circ)$  and the time dependence of applied pressure in the case of linolenic acid are shown in Figure 1 and in the case of triolein are shown in Figure 2.

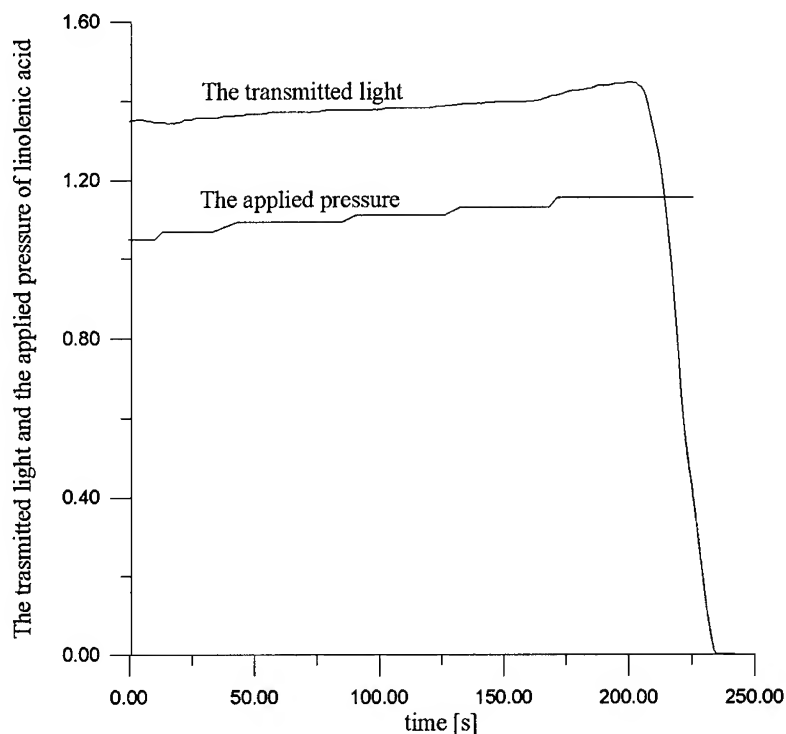


Figure 1. The time dependencies of the intensity of the transmitted light and applied pressure for linolenic acid sample (*in arbitrary units*).

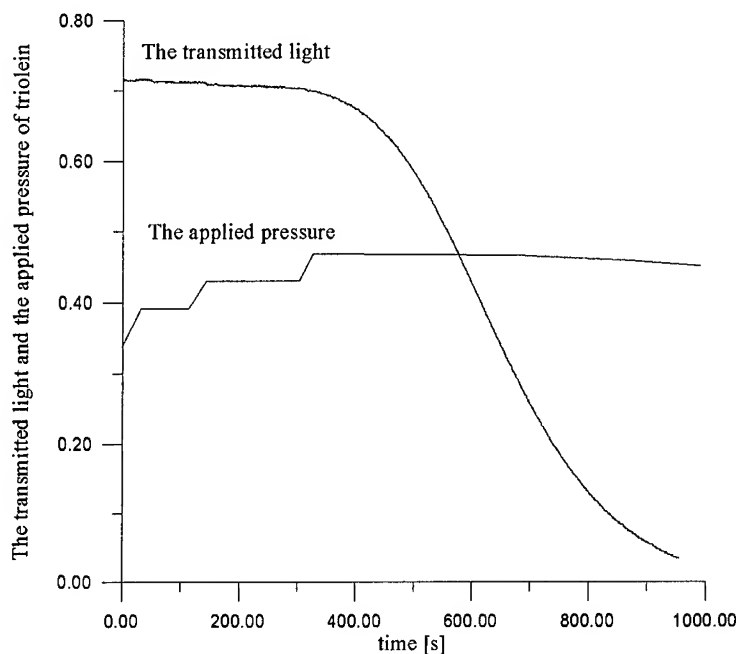


Figure 2. The time dependencies of the intensity of the transmitted light and applied pressure for triolein sample (in arbitrary units).

One can see that there are threshold pressures (0.38, 0.40 GPa) above that the strong decrease of the intensity of the transmitted light is observed in these two cases similar to all earlier investigated cases [1-4]. The analyses of all curves in the case of the slow application of pressure and the returning to the original state show the phenomenon of the optical hysteresis for linolenic acid and triolein, too [3].

The transition time of triolein is much longer than in the cases of oleic, linoleic and linolenic acids and much shorter than in the case of castor oil. It is not surprised because molecules of triolein contain three chains with double bond

C=C what gives the steric obstacles to move of molecules. The double bounds C=O existing in molecules of castor oil are additional steric obstacles.

Generally we have seen that the observed optical behaviour of linolenic acid and triolein are similar to that of oleic, linoleic acid and castor oil liquids. Therefore we have evidence that the most important role in the above observed behaviours seems to be played by the unsaturated double bond (hybridisation  $sp^3$ ) C=C in *cis* configuration for all kinds of molecules in all examined liquids and the double bounds C=O existing in molecules of castor oil.

## References

1. R. M. Siegoczyński, J. Jędrzejewski and R. Wiśniewski, *High Pres. Res.* **1** (1989) 225.
2. R. M. Siegoczyński, *High Pres. Res.* **13** (1994) 89..
3. R. M. Siegoczyński et al., *High Pres. Res.* **13** (1994) 93..
4. R. M. Siegoczyński et al. *High Pressure in Material Science and Geoscience*, Brno, 1994 p.101.

# THE RELATIVE PERMITTIVITY AND DIELECTRIC LOSS OF BIS (2 - ETHYLHEXYL) SEBACATE UNDER PRESSURE UP TO 1.5 GPa AT ROOM TEMPERATURE

Wiśniewski R., Buchner T.<sup>\*</sup>, Jaroszewicz A.<sup>\*</sup>, Kuciński T.<sup>\*</sup>

*Institute of Physics, Warsaw University of Technology,  
Koszykowa 75 00-662 Warsaw, Poland*

*<sup>\*</sup> Student of Technical Physics and Applied Mathematics at WUT*

## ABSTRACT

The relative permittivity and dielectric loss, measured by  $\tan \delta$  of bis (2-ethylhexyl) sebacate (further referred to as BDS) at pressure up to 1.5 GPa were measured. Hysteresis of the electric permittivity above 0.6 MPa was observed. The molecule dipole moment of BDS was also analysed on the base of Kirkwood-Fröhlich formula. Some evidence suggests that BDS undergoes phase transition above 600MPa at room temperature. The solidification curve at p,T variables for pressure up to 1.5 GPa is presented.

## Introduction

Bis (2-ethylhexyl) sebacate -  $C_{26}H_{50}O_4$  is an alkyl ester built in reaction of sebacic acid and two diethylhexyl alcohol molecules. It is a polar liquid, appearing in both cis and trans configurations. It is commonly used as a lubricant and pressure transmitting medium. Its viscous behaviour was carefully examined so it can also be used as a calibrating fluid for secondary type viscometers. It is also useful as working fluid in controlled clearance high pressure tester (up to 1GPa).

## Materials and methods

The simple piston-cylinder high pressure apparatus and method of measurement of dielectric properties of the investigated liquid, used by authors, are described in [2]. As the investigated material, commercially available, chemically pure BDS was used.

## Results

### *Pressure dependence of electrical permittivity below 1GPa*

Below 1GPa BDS reacts to changes of pressure in two different ways.

Below 0.6 GPa changes of electrical permittivity are positive and proper for polar liquids. The changes of relative permittivity and dielectric loss,

(which at the beginning decreased, then practically did not change up to 1GPa - see Fig. 2) were fully reversible ( see Fig. 1, curve a ).

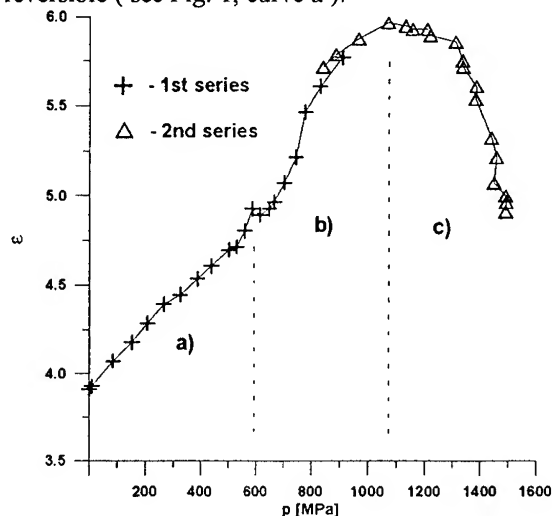


Figure 1. Relative permittivity of BDS as function of pressure up to 1.5 GPa, at constant  $T=293$  K. Two data series are shown: up to 1GPa and from 0.8 GPa to 1.5 GPa, denoted by crosses and triangles, respectively. The whole plot can be divided into three curves - a, b and c (see text).

Above 0.6 GPa hysteresis of electrical permittivity was observed ( not shown in Fig. 1).

It is interesting, that other investigations show no irreversible changes of volume in this region. [2] Curve c) in Fig. 1 depicts pressure dependence of relative permittivity at pressure up to 1.5 GPa - in solidification region.



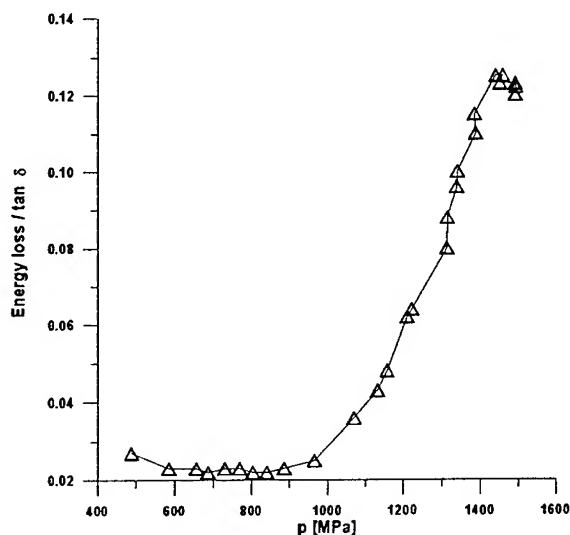


Figure 2. Dielectric loss of BDS as function of pressure up to 1.5 GPa, at constant  $T=293$  K.

#### Pressure dependence of effective molecule dipole moment

For further analysis of obtained results on basis of the Kirkwood-Fröhlich formula it was necessary to find an equation determining pressure dependence of refractive index. After W.G. Scaife [3] it has been assumed that refractive index of BDS depends on density like the permittivity of n-alkanes, described by following equation:

$$\frac{n^2 - 1}{(n^2 + 2)\rho} = a_n + b_n \rho \quad (1)$$

Here  $\rho$  denotes density,  $n$  denotes refractive index, and  $a_n, b_n$  are some coefficients, that should be estimated experimentally. After [3] it has also been assumed, that relative magnitudes of the coefficients are  $b_n \approx -0.1a_n$ .

With use of known values of density and refractive index in room temperature, under atmospherical pressure, values of  $a_n$  and  $b_n$  coefficients were easily computed. Then it was possible to obtain the equation for refractive index as function of density.

Using evaluation, developed by Wisniewski *et al* in [1], describing density as function of pressure:

$$\rho(p) = 912.666 + 0.44p + 0.0004p^2 + 2.07 \cdot 10^{-7} p^3 \quad (2)$$

finally we obtained the formula for pressure

dependence of refractive index. For pressure of range 0-900 MPa, refractive index increases within 7.4% of the initial value 1.4499.

The Kirkwood - Fröhlich formula, developed by Kirkwood (1939) and modified by Fröhlich (1949), describes the dependence of dipolar moment on refractive index for polar liquids:

$$\frac{9(\epsilon_0 - n^2)(2\epsilon_0 + n^2)}{\epsilon_0(n^2 + 2)^2 \rho} \cdot \frac{MkT}{4\pi N_A} = g\mu^2 \quad (3)$$

In this  $\epsilon_0$  is the equilibrium low frequency value of dielectric constant,  $n$  is the refractive index,  $N_A$  - the Avogadro's number,  $M$  - the molecular weight of BDS,  $k$  - the Boltzmann's constant,  $T$  is the temperature,  $\rho$  is the density,  $\mu$  is the dipole moment and  $g$  is the Kirkwood's "correlation factor". Using results of calculations of pressure dependence of refractive index in that formula, finally, we obtained pressure dependence curve of the  $g\mu^2$  factor, as shown in Fig. 3.

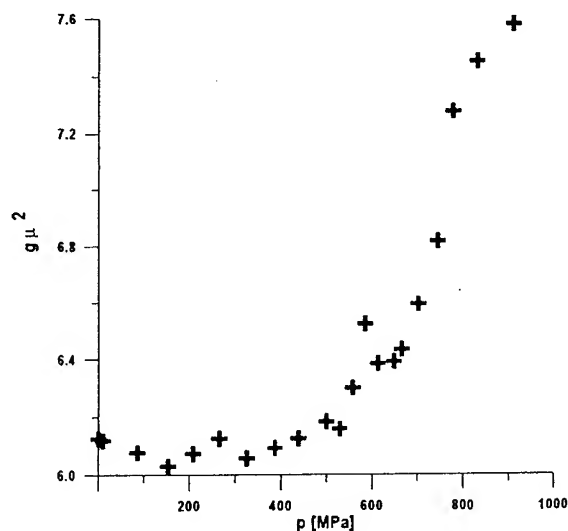


Figure 3. Pressure dependence of the  $g\mu^2$  factor, up to 1 GPa.

According to our data linear decrease of the  $g\mu^2$  factor, observed by W.G. Scaife in [3] up to ca 350 MPa is evident up to 200 MPa, where the factor falls by about 2%, as shown in Fig.3. Although above 400 MPa the step-by-step increase, that becomes significant above 700 MPa, can be observed.

The dipole moment of BDS may vary from 3.5 D

to 1.5 D depending on configuration of alkyl groups (cis or trans) [4].<sup>1)</sup> Assuming after Scaife [3] that  $g$  is unity, our calculations gave the result  $\mu = 2.45$  D at temperature  $T = 20^\circ\text{C}$  and for low pressures (below 180 MPa), with accuracy 2%.

When pressure rises to 900 MPa,  $g\mu^2$  also rises up. Due to assumption that  $g$  is unity, it can be interpreted as significant rise of the molecule dipole moment to 2.76 D. It suggests that configuration of molecules has changed from trans to cis. Although if we have assumed that dipole moment doesn't vary much as the function of pressure, it could also be interpreted as rise of the  $g$  factor, that describes intermolecular associations. That rise can be effect of grouping of molecules before a phase transition.

#### Phase diagram construction

Part of our data was also used to construct the phase diagram for pressure range 0-1.5 GPa. Phase diagram was constructed according to the algorithm used in [2], that will be presented in short: position of the starting point of the phase transition on the pressure axis was found out as the point of intersection of two lines of linear regression of the curve of dielectric constant as the function of temperature. It gave the value 1180 MPa at  $293^\circ\text{K}$ . Central point of the phase transition (centre of an intermediate state) was given by the maximum of energy loss tangent (1450 MPa according to Fig.2). The next central point was given by similar analysis for data acquired at  $298^\circ\text{K}$  (with the result of 1493 MPa). The final result - phase diagram of BDS for pressure range 0-1.5 GPa is shown in figure 4. Part of data used to construct phase diagram was used by courtesy of authors of [2].

#### Conclusions

Decrease of the  $g\mu^2$  factor, as observed by W.G. Scaife [3], takes place under relatively low hydrostatic pressure. Assuming, that  $\mu$  is constant in low pressure region, small decrease of correlation factor is possible. For pressure exceeding 600 MPa, when the investigated liquid is, as we presume, in "near to phase transition" conditions, the molecular

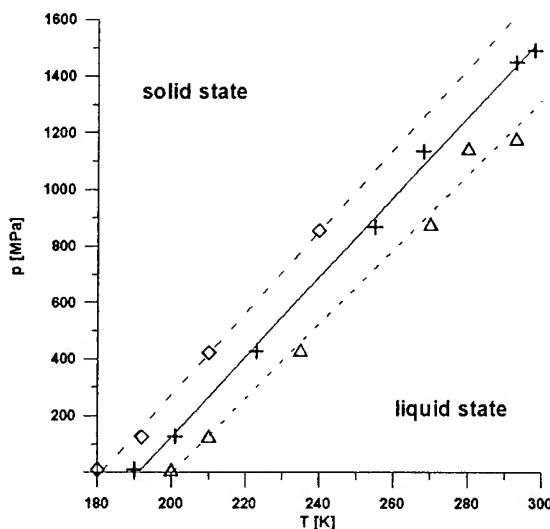


Figure 4. Phase transition in BDS in  $p, T$  variables. Central curve of phase transition is indicated by solid line with crosses, boundary curves - by dashed lines with triangles and squares.

correlating process is more probable than change of molecular dipole moment or change of the molecule state from trans to cis. Presence of threshold pressure, above which the hysteresis of relative permittivity was observed can be interpreted as result of "freezing" of some irreversible effects, due to large viscosity of investigated liquid, that takes place in presolidification conditions.

#### Acknowledgements

The authors wish to thank authors of [2] for the permission to use part of their data.

Main part of that work was done during Physics Laboratory III at Faculty of Technical Physics and Applied Mathematics WUT.

#### References

- [1] R. Wisniewski, P. Komorowski, P. Machowski "State equation of BDS for pressure range (0-1) GPa and room temperature." This Conference.
- [2] R. Wisniewski, P. Machowski, P. Komorowski "Phase diagram of BDS.", *High Temperatures - High Pressure*, in press.
- [3] W.G. Scaife *High Temperatures - High Pressure*, 1970, vol 2, p. 453-460.
- [4] M. Davies *Some Electrical and Optical Aspects of Molecular Behaviour* (Pergamon Press, London 1965)

1)  $1\text{D} = 3.336 \cdot 10^{-30} \text{ C} \cdot \text{m}$

# STATE EQUATION OF BIS (2-ETHYLHEXYL) SEBACATE FOR PRESSURE RANGE 0-1 GPa AT ROOM TEMPERATURE

R. WIŚNIEWSKI, P. KOMOROWSKI<sup>(\*)</sup> AND P. MACHOWSKI<sup>(\*)</sup>

*Institute of Physics, Warsaw University of Technology, ul. Koszykowa 75, 00-662 Warszawa, Poland*

*(\*) Student of the Technical Physics and Applied Mathematics of WUT*

## ABSTRACT

The state equation of one of the most common pressure transmitting medium-bis (2-ethylhexyl) sebacate - in form of PVT data is given. The investigations were conducted in pressure domain up to 1 GPa and at room temperature. Compressibility and density data are graphically presented. Virial form of state equation for 10 sets of the pressure range is discussed. The density, in its polynomial form, versus pressure for the whole pressure range is also presented.

## Introduction

Bis (2-ethylhexyl) sebacate is a  $C_{26}H_{50}O_4$  compound with molecular weight  $M=426$  and density  $\rho=912.666$  kg/m<sup>3</sup> at room temperature and 0,1 MPa. It is commonly used as lubricant and pressure transmitting liquid, especially in high pressure standards controlled-clearance piston gauges. Recently elastic light scattering experiments performed on bis (2-ethylhexyl) sebacate reveal unexpected high pressure behaviour i.e. strong increase of the transparent light intensity within the pressure range of 400-500 MPa [1]. This fact suggests that either the fluctuations are suppressed by diminishing of preference for molecules to associate with the raise of pressure or in opposite the fluctuations attain large dimensions comparable with length of light wave used in experiment and at low angle light scattering plays an important role. The first interpretation would indicate the improvement of bis (2-ethylhexyl) sebacate pressure transmitting properties under high pressure conditions. The aim of this work was to verify the above mentioned hypothesis on the base of compressibility measurements. We have used Kamerling-Onnes equation of state to describe the change of volume as a function of pressure. According to this equation the  $p(V)$  dependence can be presented as

$$pV = nRT \{1 + nB/V + n^2C/V^2 + \dots\} \quad (1)$$

where virial expansion coefficients (B, C,...) are functions of temperature. The second virial coefficient B is responsible for nonideality of the liquid. If B is negative then the molecules prefer to

associate and thus to increase the intensity of the scattered light [2]. Since the previous experimental results show that this property can changes with pressure, we assume that virial coefficients in equation (1) are dependent not only on temperature but also on pressure.

## Experimental system and results

The simple piston -cylinder high pressure apparatus with piston displacement gauge has been used (more details see paper [4]). High pressure vessel had inside diameter 17 mm and volume capacity 29.0 cm<sup>3</sup>. So, we have conducted the measurements using 29 cm<sup>3</sup> sample of bis (2-ethylhexyl) sebacate. Pressure changes of investigated liquid were determined mainly by piston displacement measurements but corrections connected with deformations of pressure vessel, piston, leads-through plug and so on had to be taken into account. According to the density and molecular weight values given in the the introduction, our sample had a mass  $m = 26,47$  g which made a number of moles equal to  $n = 0,06213$ .

We have obtained PVT data in the pressure range 0 - 920 MPa, at room temperature for 81 measurement points equally spaced. For illustration of obtained data, volume, relative change of volume and density of investigated liquid as a function of pressure are given in figures 1, 2 and 3, respectively.

Compressibility measurements did not show any long time relaxation effects under constant pressure up to 920 MPa, even after 170 hours of

observation. Such effects were noticed in the case of castor oil [3], [4]. The results of regression analysis show that density of bis (2-ethylhexyl) sebacate can be evaluated using the following function:

$$\rho(p) = 912,666 + 0,444144p - 0,000428p^2 + 2,073283 \cdot 10^{-7} p^3 \quad (2)$$

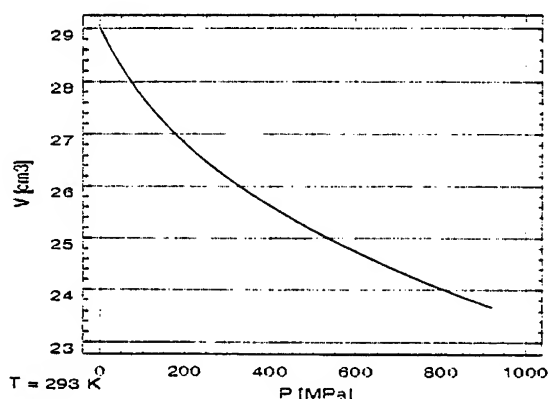


Fig. 1. Volume as the function of pressure for 29 cm<sup>3</sup> sample of bis (2-ethylhexyl) sebacate.

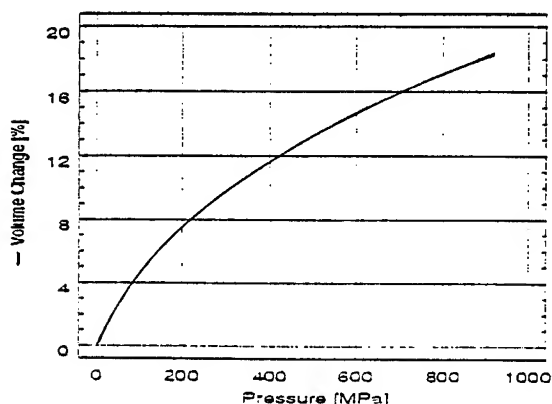


Fig.2. Relative change of volume as a function of pressure.

The squared correlation coefficient between the experimental data and the fitted model equals to  $r=0,9999$ . Standard errors of the coefficients of equation (2) are  $0,002724$ ,  $9,149091 \cdot 10^{-6}$  and

$7,331655 \cdot 10^{-9}$  respectively. Thus function (2) provides an excellent reflection of experimental data. Pressure in this equation is expressed in MPa and density is in kg/m<sup>3</sup>.

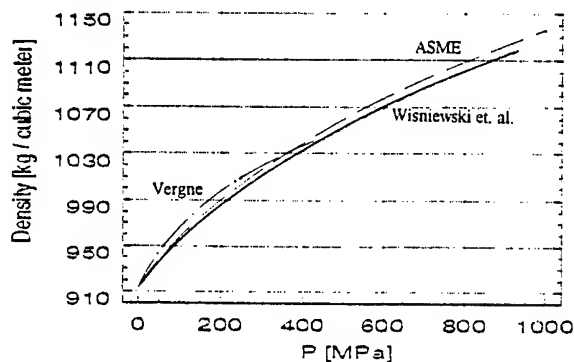


Fig. 3. Density as the function of pressure, continuous line-authors data, dashed line-derived from ASME data [5], points line-data from Vergne et. al. [6]

### Virial form of state equation

Since we have assumed that virials coefficient depend on the temperature and as well as on the pressure, we divided the obtained data into ten intervals covering the range of about 80 MPa each. Then we carried out regression analysis for each of the subsets separately. Data sets were constructed as follows:

number of set	pressure range [MPa]
1	0 - 68,987
2	79,361 - 151,460
3	161,834 - 232,377
4	243,270 - 315,888
5	329,374 - 425,334
6	441,413 - 537,892
7	548,784 - 631,258
8	647,860 - 726,180
9	740,184 - 822,658
10	832,513 - 919,655

The pressure and volume in each set were expressed in pascals and in cubic meters respectively before fitting. The next table shows regression analysis results for equation (1) only

for B and C virial coefficients because the other that follows are supposed equal to zero. Consecutive entries represent: numbers of the data sets, fitted virials coefficients, standard errors and squared correlation coefficient. We can see here that B is always negative, but its absolute value of B increased with pressure.

set	B	C	$S_B$	$S_C$	R - SQ
1	-0,170320	0,000079	0,001918	$8,7992 \cdot 10^{-7}$	0,9997
2	-0,200737	0,000093	0,001886	$8,3625 \cdot 10^{-7}$	1,0000
3	-0,225931	0,000104	0,001752	$7,5688 \cdot 10^{-7}$	1,0000
4	-0,241706	0,000111	0,002651	$1,1217 \cdot 10^{-6}$	1,0000
5	-0,280472	0,000127	0,002444	$1,0122 \cdot 10^{-6}$	1,0000
6	-0,284682	0,000129	0,003900	$1,5814 \cdot 10^{-6}$	1,0000
7	-0,297446	0,000134	0,002210	$8,8071 \cdot 10^{-7}$	1,0000
8	-0,303680	0,000136	0,003736	$1,4674 \cdot 10^{-6}$	1,0000
9	-0,323472	0,000144	0,005472	$2,1215 \cdot 10^{-6}$	1,0000
10	-0,300995	0,001744	0,001744	$6,6772 \cdot 10^{-7}$	1,0000

## Conclusions

It is obvious that the present discussion about properties of bis (2-ethylhexyl) sebacate - viscous, large molecule liquid, basing on Kamerling-Onnes equation - has only large approximate character. According to the classical interpretation of virial coefficients, the value of B coefficient is connected with two particle interactions. Then it is negative and increase its absolute value with pressure it means that the preference for molecules to associate is stronger and this effect increase with increasing pressure. The coefficient C, representing three molecules interactions, has only a tendency to increase and has positive values. Such tendency would not result in the increased intensity of transparent light. The intensity of scattered light would be raised instead. The main problem in our analysis is to determine what type of associations contribute to the inner structure of the compound. If, for example three-molecule associations are more significant than two-molecules ones, than we should take into account further coefficients in virial equation (1).

Obtained data for second fitting, which took also the coefficient D into account gave not successful interpretation. Finally a small angle light scattering on large dimension associate of investigated liquid in previously mentioned phenomenon was observed.

Our results concerning pressure dependence of density are in accordance to ASME data [5] and differ to data presented in [6].

## Acknowledgment

The authors thanks Dr GF. Molinar for his fruitful discussion and cooperation.

## References

1. R. Wiśniewski, GF. Molinar and R. Siegoczyński, *High Pressure in Material Science and Geoscience*, Proceedings of the XXXII Annual Meeting of the EHPRG (Brno, Czech Republic, 1994), p.93
2. B. R. Ware, *Optical Technics in Biological Research*, ed. D. L. Rousseau, Academic press Inc., (1984), p.5
3. R. Siegoczyński, J. Jedrzejewski and R. Wiśniewski, *High Pressure Research*, Vol. 1, (1989), p 225
4. R. Wisniewski et. al., *High Pressure Research*, Vol. 11, (1994), p. 385
5. ASME Report, *Viscosity and density of over 40 Lubricating Fluids...*, (Published by ASME, New York, 1953)
6. Vergne P., *High temp.-High Press.*, (1990), 22, p. 613-621

# THE SPONTANEOUS HIGH PRESSURE GENERATION AND STABILITY OF HYDROCARBONS: THE GENERATION OF *n*-ALKANES, BENZENE, TOLUENE & XYLENE AT MULTI-KILOBAR PRESSURES.

J. F. Kenney

INSTITUTE OF EARTH PHYSICS, Russian Academy of Sciences, Moscow, C.I.S.  
GAS RESOURCES CORPORATION, 3730 Kirby suite 1200, Houston, TX 77098, U.S.A.

Central to any analysis of chemical stability are the relative chemical Affinities which determine the direction of development of a system in accordance with the second law of thermodynamics<sup>1</sup> as expressed by De Donder's inequality<sup>2,3</sup>,  $dQ' = Ad\xi \geq 0$  in which  $\xi$  represents the variable of extent, and for which the Affinity of an  $n$ -component, multiphase system of  $p$  phases involving  $r$  chemical reactions is given by

$$A = - \sum_{\rho=1}^r \sum_{\alpha=1}^p \sum_{i=1}^n v_i^{\alpha,\rho} \mu_i^{\alpha,\rho}(p, T, \{n_j\}). \quad (1)$$

The chemical Affinities of these restricted but representative hydrogen-carbon (H-C) systems have been calculated from first principles using the formalism of the Simplified Perturbed Hard Chain Theory<sup>4</sup> (SPHCT). The SPHCT provides a specific analytical function for the Helmholtz free energy from which the pressure of the system obtains as a sum of three contributions,

$$p^{\text{SPHCT}} = - \left( \frac{\partial F}{\partial V} \right)_{T, \{n_j\}} \quad (2)$$

$$= p^{\text{IG}} + p^{\text{hc}} + p^{\text{vdw}}$$

where, for a pure material,

$$p^{\text{IG}} = \frac{nRT}{V}, \quad (3)$$

$$p^{\text{hc}} = \frac{nRT}{V} c \frac{2\eta(2-\eta)}{(1-\eta)^3}, \quad (4)$$

$$p^{\text{vdw}} = - \frac{nRT}{V} c Z_m \frac{1}{(1 + \tau / \eta Y)}. \quad (5)$$

In equations (3), (4), and (5),  $R$  is the universal gas constant;  $\tau$  is a geometric close-packing factor equal to 0.7405. The parameter  $c$  is the Prigogine  $c$ -factor which accounts for the volume of phase space occupied by the set of molecular vibrations and rotations which may be treated similarly as translational degrees of freedom. The contribution to the pressure from the short-range hard-core potential,  $p^{\text{hc}}$ , obtains from the monte carlo analysis by Alder and Wainwright<sup>5</sup> as further developed by Carnahan and Starling<sup>6</sup>, for which  $\eta$  is the "free-volume" parameter. The contribution to the pressure from the long-range van der Waals potential,  $p^{\text{vdw}}$ , obtains from a mean-field calculation carried out employing the Bethe-Peierls-Prigogine "lattice-gas" model, for which  $Z_m$  represents the number of "near-neighbor" molecular interactions, equal to 18<sup>7</sup>. The three constants,  $c$ ,  $\eta$ , and  $Y$ , are determined by the critical state variables,  $p_c$ ,  $T_c$ , and  $V_c$ . It is emphasized that the SPHCT partition function and the equation of state generated by it obtain from first principles statistical mechanics arguments. The SPHCT does not at all invoke fitted parameters<sup>8</sup> and is therefore valid for use in general regimes of temperature and density. Similarly, the SPHCT generates

explicit expressions for the chemical potentials as the sum of three components,

$$\begin{aligned}\mu_i^{\text{SPHCT}} &= \left( \frac{\partial F}{\partial n_i} \right)_{V,T,\{n_j\}} \\ &= \mu_i^{\text{LG}} + \mu_i^{\text{hc}} + \mu_i^{\text{vdW}}\end{aligned}\quad (6)$$

in which

$$\begin{aligned}\mu^{\text{LG}} &= RT(\ln n - \ln V + \ln \lambda^3) \\ &\quad + RT \ln N_A\end{aligned}\quad (7)$$

$$\begin{aligned}\mu^{\text{hc}} &= RT \left[ c \frac{\eta(4-3\eta)}{(1-\eta)^2} \right] \\ &\quad + RT \left[ c \frac{2\eta(2-\eta)}{(1-\eta)^3} \right],\end{aligned}\quad (8)$$

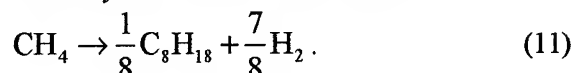
$$\begin{aligned}\mu^{\text{vdW}} &= -RT [cZ_m \ln(1 + \eta Y / \tau)] \\ &\quad - RT \left[ cZ_m \frac{1}{(1 + \tau / \eta Y)} \right].\end{aligned}\quad (9)$$

The analogous expressions for mixtures have the same form as (3)-(6) and (7)-(9) in which the constants,  $c$ ,  $\eta$ , and  $Y$ , are calculated as averages or combinations of those for the pure components according to specific mixing rules. Here have been used the mixing rule by Kim<sup>9</sup> for the van der Waals terms and of Kenney for the hard-core terms which involve a two-fluid model for which each binary correction term has the form,

$$\begin{aligned}(\delta\mu_{\alpha\beta}^{\text{hc}})_{\alpha} &= RT \cdot c_{\alpha} \left[ \frac{(\eta_{\alpha\beta}^{\text{eff}})_{\beta} (4 - 3(\eta_{\alpha\beta}^{\text{eff}})_{\beta})}{(1 - (\eta_{\alpha\beta}^{\text{eff}})_{\beta})^2} \right] + \\ &\quad + \frac{n_{\beta}}{n_{\alpha}} RT \cdot c_{\alpha} \left[ \frac{2(\eta_{\alpha\beta}^{\text{eff}})_{\alpha} (2 - (\eta_{\alpha\beta}^{\text{eff}})_{\alpha})}{(1 - (\eta_{\alpha\beta}^{\text{eff}})_{\alpha})^3} \right]\end{aligned}\quad (10).$$

The Gibbs potentials and the resulting chemical Affinities of the methane  $\leftrightarrow$  (hydrocarbon) system have been

evaluated for normal alkanes, butane (n-C<sub>4</sub>H<sub>10</sub>), hexane (n-C<sub>6</sub>H<sub>14</sub>), octane (n-C<sub>8</sub>H<sub>18</sub>), decane (n-C<sub>10</sub>H<sub>22</sub>), and the cyclic compounds benzene (C<sub>6</sub>H<sub>6</sub>), toluene (methylbenzene, C<sub>7</sub>H<sub>8</sub>), and p-xylene (p-dimethylbenzene, p-C<sub>8</sub>H<sub>10</sub>) at pressures ranging from 1-80,000 bar and at supercritical temperatures, 800-1,200°K, corresponding to geological regimes characterized by the respective pressures. The values of the constants,  $c$ ,  $\eta$ , and  $Y$ , used were from van Pelt et al.<sup>10</sup> and the reference values of the pure component chemical potentials from standard reference tables kcal<sup>11,12</sup>. Because methane is the sole hydrocarbon specie which is thermodynamically stable at low pressures, the chemical Affinities of each of the heavier species has been calculated in comparison with methane. At normal temperatures and pressures, the evolution of methane will dominate and effectively exhaust the H-C system of its elemental components. Accordingly, the chemical Affinity calculated for the thermodynamic stability of, for example, the methane  $\leftrightarrow$  n-octane system is that for the reaction



The results of the analysis are shown graphically for the temperature 800°K in Fig. 1. These results demonstrate clearly that all hydrocarbon molecules are chemically and thermodynamically unstable relative to methane at pressures less than approximately 9 kbar for the lightest, butane, and 30 kbar for the heaviest, decane, and that benzene, toluene and xylene are similarly unstable relative to methane at pressures less than approximately 35 kbar. It is seen clearly in that figure that, at a pressure of approximately 28,000 atm, both the sign of the Affinity changes from negative to positive and the Gibbs potential for the mixture of (1/8)n-octane+(7/8)hydrogen cross that of methane. At pressures above 30,000 atm, the chemical Affinity continues to increase sharply and the

relative Gibbs potentials diverge. The latter property assures that the evolution of the system proceeds continuously above 30,000 atm to evolve more n-octane at the expense of methane, and similarly for the evolution of the other hydrocarbons

These results establish the following:

1.) All hydrocarbon molecules other than methane are high pressure polymorphs of the H-C system.

2.) With the exception of methane, heavier hydrocarbon molecules of higher chemical potentials will not be generated spontaneously in the low pressure regime of methane synthesis.

3.) Contrary to experience of refinery operations conducted at low pressures, heavier alkanes, alkenes, cyclic and aromatic compounds are *not* unstable and do *not* necessarily decompose at elevated temperatures. Contrarily, at elevated pressures, methane transforms into the heavier alkanes, alkenes, cyclic and aromatic compounds, which transformation processes are enhanced by elevated temperatures.

These results are consistent with those developed previously by Chekaliuk, Stefanik, Kenney, and others using, for example, the Law of Corresponding States<sup>13</sup>.

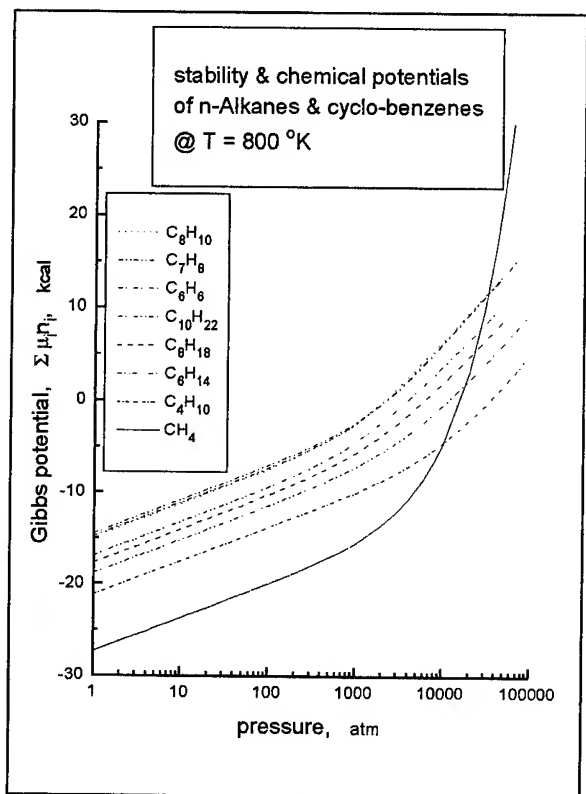


Fig. 1 Chemical Affinities of methane; of n-C<sub>4</sub> - n-C<sub>10</sub>; and of benzene, toluene & p-xylene.

<sup>1</sup> R. J. E. Clausius, *Ann. Phys.*, **125**, (1865), 353.

<sup>2</sup> Th. De Donder and P. Van Rysselberghe, *The Thermodynamic Theory of Affinity*, (1936), Stanford, 1208 pp.

<sup>3</sup> I. Prigogine and R. Defay, *Chemical Thermodynamics*, (1954), Longmans, London, 545 pp.

<sup>4</sup> S. Beret and J. M. Prausnitz, *Macromolecules*, **8**, (1975), 878-882.

<sup>5</sup> B. J. Alder and T. E. Wainwright, *J. Chem. Phys.*, **27**, (1957), 1208

<sup>6</sup> N. F. Carnahan and K. E. Starling, *J. Chem. Phys.*, **53**, (1970), 600-603.

<sup>7</sup> R. J. Lee and K. C. Chao, *Mol. Phys.*, **61**, (1987), 1431-1442.

<sup>8</sup> As, for examples, the Redlich-Kwong or Soave equations of state.

<sup>9</sup> C-H. Kim, P. Vimalchand, P. Donohue and S. I. Sandler, *AIChE. J.*, **32**, (1986), 1726-1734.

<sup>10</sup> A. van Pelt, C.J. Peters and J. de Swaan Arons, *Fluid Phase Equilibria*, **74**, (1992), 67-83.

<sup>11</sup> *Selected values of chemical thermodynamic properties*, Bureau of Standards, Washington, (1947-1952).

<sup>12</sup> *Selected properties of hydrocarbons*, A.P.I. Project 41, Bureau of Standards, Washington, (1946-1952).

<sup>13</sup> E. B. Chekaliuk, *The Thermodynamic Basis for the Theory of the Abiotic Genesis of Petroleum*, (1971), Nauka, Moscow, pp 257, [in Russian].



# HYDROGENATED AMORPHOUS CARBON FROM COMPRESSION OF ACETYLENE AND POLYACETYLENE

M. BERNASCONI, M. PARRINELLO

*Max-Planck-Institut für Festkörperforschung, Stuttgart, 70569, Germany*

G.L. CHIAROTTI, P. FOCHER and E. TOSATTI

*International School for Advanced Studies, Via Beirut 4, I-34014 Trieste, Italy*

We have simulated by constant pressure *ab-initio* molecular dynamics the transformation under pressure of crystalline acetylene and polyacetylene into a-C:H. Both molecular crystals undergo a gradual saturation of carbon-carbon bonds under pressure, ending up at  $\sim 50$  GPa with a-C:H containing up to  $\sim 80$  %  $sp^3$  carbons. The  $sp \rightarrow sp^2 \rightarrow sp^3$  conversion is irreversible and the final a-C:H samples are wide gap insulators in agreement with experimental findings.

Hydrogenated amorphous carbon (a-C:H) films are important as coating materials since they offer a unique combination of high hardness, chemical inertness and optical transparency<sup>1</sup>. Much work has been done on the preparation of a-C:H by using rf and dc plasma deposition, ion beam and sputtering technique<sup>2</sup>. An alternative route to produce a-C:H is the direct compression to the GPa range of unsaturated hydrocarbons in the solid phase. This unconventional way for producing a-C:H is likely to lead to novel properties and eventually to a viable alternative to the a-C:H synthesis, provided that the pressure needed is low enough.

In this paper we report, based on *ab initio* constant pressure molecular dynamics simulations<sup>3</sup>, examples of such irreversible transformations, namely the generation of tetrahedrally connected a-C:H via compression of crystalline acetylene and polyacetylene. In both cases, in the pressure generated a-C:H  $\sim 80$  % of carbon atoms are four-fold coordinated ( $sp^3$  atoms) and the atomic H concentration is 50 %. Experimental evidences of a structural change in polyacetylene at 300 K and 20 GPa come from optical and vibrational measurements<sup>4</sup>. On the other hand crystalline acetylene is known to polymerize at 3.5 GPa and 300 K<sup>5</sup>. At higher pressure the polymeric sample obtained from compression of acetylene undergoes another structural transformation which opens the electronic band gap<sup>5</sup>. The present simulation characterizes the struc-

ture of the transformed materials and provides insights into the transformation path.

We first reproduced the polymerization reaction of acetylene under pressure. We started a simulation with 16  $C_2H_2$  molecules in the *Cmca* structure<sup>5</sup>, and increased pressure initially as high as 9 GPa at 400 K, observing only a gradual rotation of the  $C_2H_2$  molecules (fig. 1a). However, after the pressure was increased to 25 GPa the  $C_2H_2$  molecules reacted forming polyacetylene chains in a mixture of *trans* and *cis* forms (figs. 1b-1c). By doubling the size of the simulation cell (32  $C_2H_2$ ) the polymerization reaction still took place at 25 GPa. However, the polymeric chains in the large sample are more disordered than in the single plane in fig. 1c. By further increasing the pressure a gradual conversion of  $sp^2$  into  $sp^3$  bonds took place ending up at 65 GPa with a-C:H containing 85 % of  $sp^3$  carbon sites. We then released the pressure back to  $P=0$ . The  $sp^3$  bonds content decreased only slightly (72 %). The  $sp \rightarrow sp^2$ , and the  $sp^2 \rightarrow sp^3$  conversions are irreversible. A snapshot of a-C:H sample at  $P=0$  obtained from compression of acetylene (16  $C_2H_2$ ) is reported in fig. 2a.

In order to study in details the mechanism of chain interlinks formation we performed another simulation starting from crystalline *trans*-polyacetylene (32 or 64 (CH) groups) in the  $P2_1/n$  geometry<sup>6</sup> shown in fig. 3a. After equilibration at 300 K and at  $P=0$  the sample was compressed up to 30 GPa with a rate

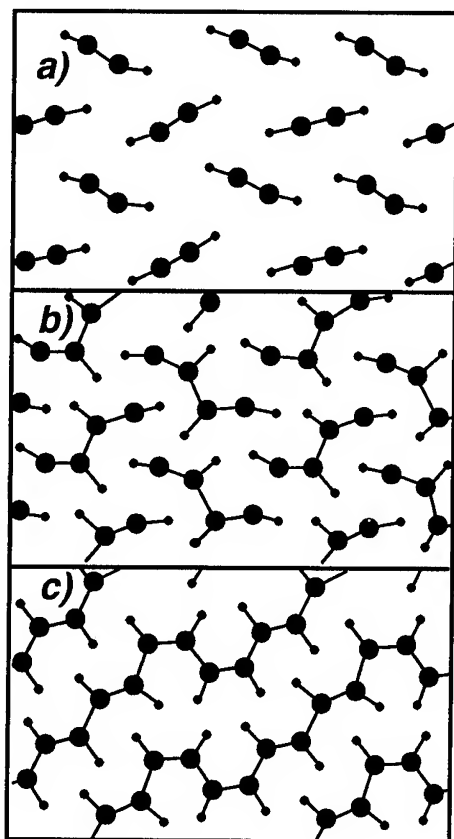


Figure 1: Snapshots of a single (001) plane of the original  $Cmca$  structure of acetylene during the simulation at 400 K. a) 9 GPa. b) intermediate configuration at 25 GPa c) final configuration at 25 GPa. The simulation cell contains 4  $C_2H_2$  molecules per (001) plane. In the other (001) planes similar polymeric chains are present but with some interlinks between different planes.

$\sim 45$  GPa/psec. Under pressure the setting angle  $\phi$  and the  $b/a$  ratio in fig. 3a rapidly decrease from  $\phi = 55^\circ$  and  $b/a = 1.73$  down to  $\phi \sim 0$  and  $b/a \sim 1.2$  at 20 GPa (fig. 3b). At  $\sim 30$  GPa the adjacent chains, now all parallel, start to interlink following the paths depicted in fig. 3c-d. By bending the CH bond, still keeping the carbon backbone in the original planes of the chains, one promotes  $sp^2 \rightarrow sp^3$  hybridization change and the formation of interlinks as in fig. 3c. Occasionally a "kink" appears on the polyacetylene chain, as in the central chain in fig. 3d, therefore allowing simultaneous interlink with the lower and upper adjacent chains.

In order to speed up the transformation we

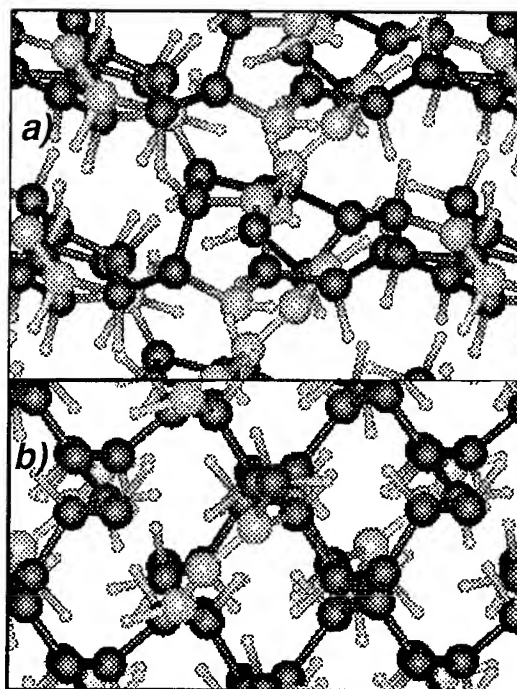


Figure 2: Snapshot of the transformed samples at 0 K  $P=0$ . a) a-C:H from compression of crystalline acetylene. b) a-C:H from compression of crystalline polyacetylene. Small spheres depict hydrogens. Large dark and light spheres depict respectively 4-fold and 3-fold coordinated carbons.

then increased simultaneously temperature and pressure to 400 K and 50 GPa. Finally at 50 GPa 80 % of carbon atoms were 4-fold coordinated. The final configuration recovered at 0 K and  $P=0$  is reported in fig. 2b.

In both a-C:H samples in fig. 2 some carbons are deprotonated (6 % in fig. 2a and 15 % in fig. 2b), the protons being transferred to form neighboring  $CH_2$   $sp^3$  groups.  $CH_2$  groups are found experimentally in a-C:H generated by radio-frequency plasma deposition from hydrocarbons vapor<sup>7</sup>. The sample generated from crystalline polyacetylene (although mainly  $sp^3$ ) is highly anisotropic. The transformation paths in figs. 3c-d keep the uniaxial symmetry of original polyacetylene. As a consequence the elastic constant for a-C:H in fig. 2b are highly anisotropic,  $C_{||}/C_{\perp} \sim 1.8$ , where  $C_{||}$  and  $C_{\perp}$  are the elastic constants in the direction parallel and perpendicular to the chains respectively. Furthermore the CH and  $CH_2$  bonds always lie

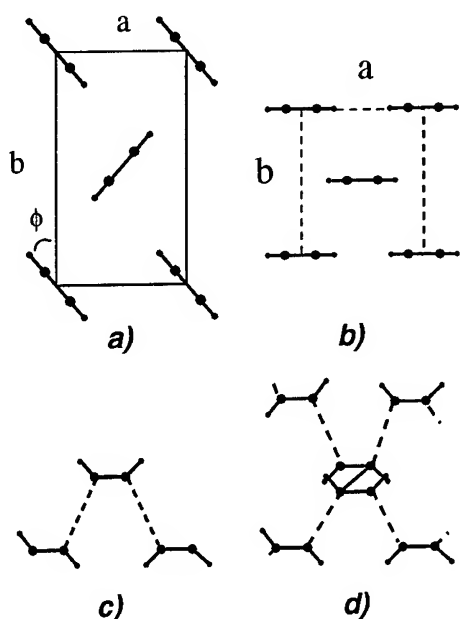


Figure 3: Schematic paths for the chain interlink as observed in the simulated compression of crystalline polyacetylene. a) View of *trans*-polyacetylene at normal condition on a plane perpendicular to the chains axis. b) same as a) at high pressure. c) Path for the chain interlink which keeps the original backbone of the chain flat. d) alternative path with the appearance of a "kink" in the central chain and the simultaneous interlink with upper and lower adjacent chains.

in a plane perpendicular to the original chains axis. Thus we expect anisotropies in the IR and Raman spectra in the region of CH and CH<sub>2</sub> modes. By contrast the polymeric chains generated from compression of acetylene are not all aligned along a unique axis. Therefore the a-C:H obtained from acetylene is more isotropic, and the simple transformation paths in fig. 3 do not apply in this latter case.

The structural changes obviously induce profound modifications in the electronic properties. The electronic band gap obtained from the  $\Gamma$  point only in the a-C:H sample from compression of acetylene is 5 eV. The electronic band gap of a-C:H obtained from polyacetylene is 5.2 eV as well, provided we consider as defect states in the gap some  $p_z$ -like states localized in the  $sp^2$  regions. Therefore the two samples of a-C:H, although differing largely in the microstructure, are both wide band gap insulators in agreement with experimental findings<sup>4,5</sup>.

1. J. Angus and C.C. Hayman, *Science* **241**, 913 (1988).
2. *Diamond and Diamond-like Films and Coatings*, edited by J. C. Angus, R. E. Clausing, L. L. Horton, and P. Koidl (Plenum, New York, 1991).
3. P. Focher *et al*, *Europhys. Lett.* **36**, 345 (1994); M. Bernasconi *et al*, *J. Phys. Chem. Solids*, **56**, 501 (1995); S. Scandolo *et al*, *Phys. Rev. Lett.*, **74**, 4015 (1995).
4. A. Brillante, M. Hanfland, K. Syassen, and J. Hocker, *Physica* **139&140 B**, 533 (1986).
5. K. Aoki *et al*, *J. Chem. Phys.* **89**, 529 (1988); K. Aoki *et al*, *Solid State Comm.* **64**, 1329 (1987); K. Aoki *et al*, *Synthetic Metals*, **28**, D91 (1989).
6. Q. Zhu, J.E. Fischer, R. Zuzok, and S. Roth, *Solid State Comm.*, **83**, 179 (1992).
7. B. Dischler, A. Bubenzer, and P. Koidl, *Solid State Comm.*, **48**, 105 (1983).

## X-RAY DIFFRACTION STUDY OF SOLID ACETYLENE UNDER PRESSURE

M. SAKASHITA, H. YAMAWAKI, and K. AOKI

*National Institute of Materials and Chemical Research*

*1-1, Higashi, Tsukuba, Ibaraki 305 JAPAN*

### ABSTRACT

Powder x-ray diffraction patterns of crystalline acetylene have been obtained at high pressure and room temperature. Lattice parameters and intermolecular distances in the orthorhombic structure were calculated for the pressure range from 1.2 to 3.1 GPa using the observed x-ray data. The nearest-neighbor C-C distance between adjacent molecules was estimated to be 3.2 Å at 3.5 GPa, whereby polymerization started. This intermolecular distance was about 2 times larger than the length of C-C single bond, suggesting that large orientational and translational motions of molecules would be needed for the reaction.

### Introduction

Acetylene with a carbon-carbon triple bond is a prototype of simple molecules showing solid-state polymerization under pressure. Infrared measurement has revealed that acetylene undergoes phase transitions from a liquid to a cubic phase at 0.7 GPa and to an orthorhombic phase at 1.0 GPa. On further compression to 3 - 4 GPa, acetylene molecules react with each other to form polymers containing *trans*- and *cis*- C=C bonds, and saturated C-C bonds (1-3). Besides the structural data about the reaction product, those of the molecular phase of acetylene are of great use for investigation of the mechanism of the pressure-induced polymerization.

We have performed high-pressure x-ray diffraction experiment of acetylene with a diamond anvil cell (DAC) at room temperature. Structural data obtained by x-ray diffraction will provide an insight into the polymerization mechanism.

### Experimental

A wedge-driven diamond anvil cell was used for high-pressure x-ray diffraction measurement. We used a commercially obtained acetylene gas after purification by removing acetone and water. Purified gas was condensed in DAC which was cooled with liquid nitrogen in advance. Small crystals initially trapped in a hole of a metal gasket tend to gather to

form large domain during warming of DAC to room temperature. We put fine powder of amorphous boron into the gasket hole with solidified acetylene to prevent crystal growth and consequently to obtain good powder diffraction patterns. X-ray diffraction measurement was carried out using a rotating anode x-ray generator and an imaging plate detector at room temperature. The x-ray generator was operated at a low power of typically 2.4 kW (40 kV / 60 mA) to avoid radiation-induced polymerization. The pressure was determined from positions of ruby fluorescence peaks based on the ruby scale (4).

### Results and Discussion

For the orthorhombic phase, powder x-ray diffraction patterns were obtained for a pressure region from 1.2 GPa, just above the cubic-orthorhombic transition pressure, to 3.1 GPa. The quality of powder patterns were significantly improved by mixing the specimen with amorphous boron but not sufficient for intensity analysis. Diffraction rings recorded as a two-dimensional image were integrated along rings and converted to a conventional one-dimensional diffraction profile as shown in Figure 1. Five strong peaks observed in the low diffraction angle region were assigned to (111), (200), (020), (002), and (211) reflections in the order of increasing angle based on the orthorhombic unit cell and used for calculation of

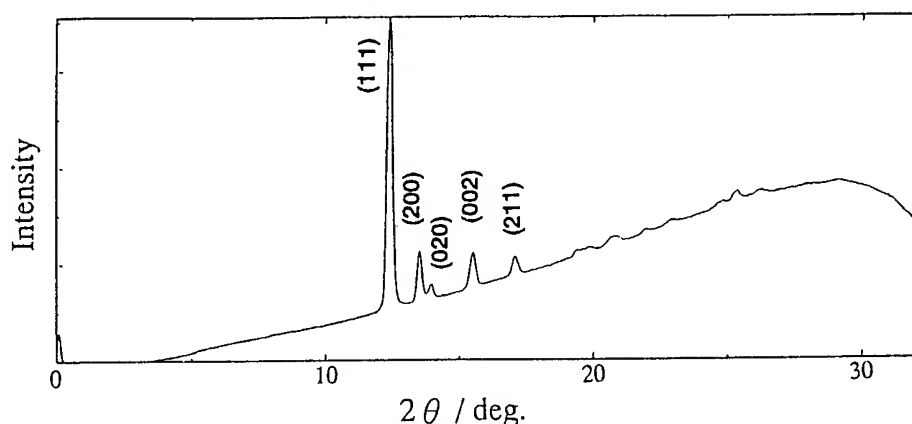


Fig.1 X-ray diffraction profile of orthorhombic acetylene measured at 1.4 GPa and at room temperature.

lattice parameters. Reliable peak-fitting results were not obtained for the other weak peaks observed in the high angle. Unit cell dimension of orthorhombic phase at 1.2 GPa, for instance, were calculated to be  $a=6.082$ ,  $b=5.883$ , and  $c=5.333$  Å in good agreement with the previous preliminary data obtained by single-crystal diffraction (5). Thus addition of amorphous

boron was shown to give no influence on the compression.

Pressure variation of the lattice constants of orthorhombic cell is plotted in Figure 2. For the cubic phase existing in a very narrow pressure range between 1.0 and 1.2 GPa, only one x-ray datum was obtained. The length of the orthorhombic  $c$  edge contracts by 8.1 % with increase in pressure from 1.2 to 3.1 GPa, while the  $a$  and  $b$  edges show small contractions of 3.4 and 2.3%, respectively. The large contraction of  $c$  edge indicates that the plane of molecules parallel to the crystallographic  $ab$  plane becomes closer rapidly with increasing pressure (see an insertion of Figure 3). The axis ratio  $a/b$  decreases toward a unity, indicating a gradual change in the  $ab$  base plane from a rectangle to square.

The nearest-neighbor C-C distance between the adjacent molecules locating along the diagonal axis in the  $bc$  plane is given by

$$r_{nn} = [(r_{c\equiv c} \sin \theta)^2 + (r_{c\equiv c} \cos \theta - b/2)^2 + (c/2)^2]^{1/2},$$

where  $r_{c\equiv c}$  is the triple bonding distance of acetylene and  $\theta$  the angle between molecular axis and the  $b$  axis. In the present calculation,  $r_{nn}$  and  $\theta$  were fixed to 1.18 Å and 39.5 degrees, respectively (6). The intermolecular distances thus calculated are plotted as a function of pressure in Figure 3, giving the distance of 3.2 Å at the reaction pressure. This value is about 2 times larger than the C-C single bond length, suggesting that large orientational and

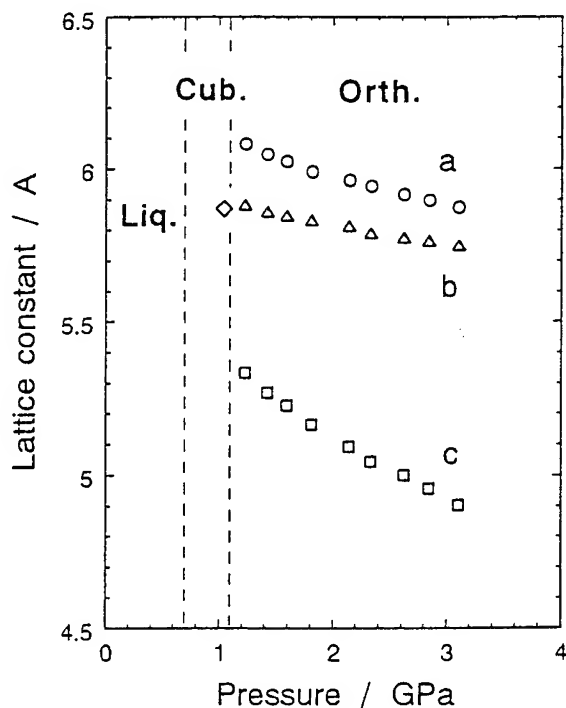


Fig.2 Variation of lattice constants with pressure measured for the cubic and orthorhombic phases of acetylene.

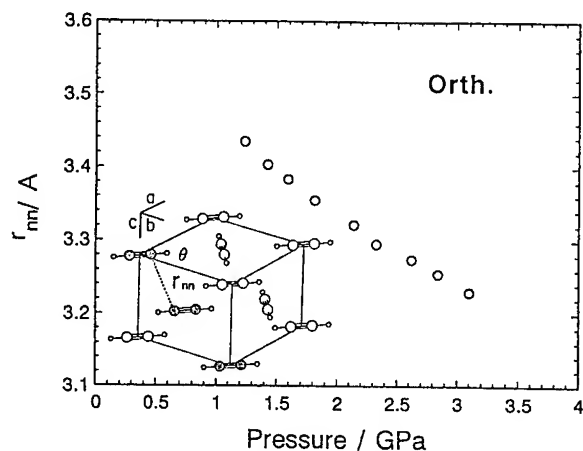


Fig.3 Variation of the nearest - neighbor C-C distance with pressure calculated for the orthorhombic structure of acetylene.

translational motions of molecules are needed for reaction. The molecular arrangement in the orthorhombic structure may be destroyed in the vicinity of the reaction points, and therefore selective reaction paths is no longer expected. This is consistent with Raman and infrared measurements which showed presence of rather short conjugated polymers in the recovered reaction product.

## References

1. K. Aoki, Y. Kakudate, S. Usuba, M. Yoshida, K. Tanaka, and S. Fujiwara, *J. Chem. Phys.*, **88** (1988) 4565.
2. K. Aoki, S. Usuba, M. Yoshida, Y. Kakudate, K. Tanaka, and S. Fujiwara, *J. Chem. Phys.*, **89** (1988) 529.
3. M. Sakashita, H. Yamawaki, and K. Aoki, under preparation.
4. G. J. Piermarini, S. Block, J. D. Barnett, and R. A. Forman, *J. Appl. Phys.*, **56** (1985) 115.
5. K. Aoki, Y. Kakudate, M. Yoshida, S. Usuba, K. Tanaka, and S. Fujiwara, *Synth. Met.*, **28** (1989) D91.
6. H. K. Koski and E. Sandor, *Acta. Crystallogr.*, Sect. **B31**, (1975) 350.

## **IX Biology and Food Processing**

## HIGH PRESSURE EFFECTS ON STRUCTURE AND FUNCTION OF NUCLEIC ACIDS

Andrzej Krzyżaniak<sup>1</sup>, Piotr Salański<sup>2</sup>, Janusz Jurczak<sup>2,3</sup> and Jan Barciszewski<sup>1</sup>

<sup>1</sup>*Institute of Bioorganic Chemistry, Polish Academy of Sciences, Noskowskiego 12, 61-704 Poznań, Poland,*

<sup>2</sup>*Institute of Organic Chemistry Polish Academy of Sciences, Kasprzaka 44 01-224 Warszawa, Poland*

<sup>3</sup>*Department of Chemistry, Warsaw University, Pasteura 1, 02-093 Warszawa, Poland*

### ABSTRACT

We found that high pressure (6 kbar) can change the DNA conformation from its B to Z form in low salt buffer. Under the conditions at which B-Z DNA transition easily occurs, RNA acquires a conformation only slightly different from original A-RNA. However, exposure of two different oligoribonucleotides r(CGCGCGCGCGCG) or r(AUAUAUAUAUAU) to high pressure (6 kbar) in the presence of 5M NaCl, induces conformation change of the both oligoribonucleotide duplexes from their A to Z-RNA forms. Complementary oligoribonucleotides with r(AAUUAACCGGCC)\*r(GGCCGGUUAUU) sequence do not change conformation to Z-RNA. The structure of native ribonucleic acids as tRNA and 5S rRNA undergo small conformational changes at high pressure. At the same time, at high pressure conditions (6 kbar) phenylalanine specific tRNA can be aminoacylated (charged) specifically with aminoacids, in absence of the specific aminoacyl tRNA synthetases and ATP. We found that the esterification reaction at high pressure, similarly to the enzymatic one, takes place at the 3'-end of the tRNA molecules. It seems plausible that a conformation of tRNA induced by the aminoacyl tRNA synthetase during enzymatic aminoacylation and that one induced at high pressure are very similar or identical. We think that the "unique" tertiary structure of tRNA creates an active centre which could itself catalyses an ester bond formation. Furthermore, one can suggest that a structure of the aminoacid stem of tRNA could determine specificity of specific tRNA with aminoacid. Phe-tRNA<sup>Phe</sup> obtained at the high pressure was as good substrate as that one obtained enzymatically for *in vitro* polyphenylalanine synthesis in the presence of poly U.

### Introduction

Hydrostatic pressure is an emerging physical parameter in biological studies and biotechnology. It is efficient to perturbate equilibrium and rate processes and useful in structural biology, aimed at establishing relationships between structure and function of biological macromolecules. It is known that pressure dependence of reaction velocity is due entirely to the activation volume of the reaction, assuming that the reacting molecule is not subject to denaturation by the increased pressure [1].

Having this in mind we applied high pressure to investigate structural changes of nucleic acids. There are three main different conformations of nucleic acids: A, B and Z. The most prevailing conformation for DNA is B, present in solution under normal conditions [2]. The three various conformations differ one from another significantly. In the B conformation about 10 base pairs are present in one complete turn of the helix and two grooves - deep, called major groove and a shallow one, called minor. In the A conformation there are 12 base pairs in one helical turn, therefore whole molecule structure is more compact and the both grooves are similar in depth. The left handed Z conformation has been found

for DNA with alternating purines and pyrimidines sequences [3]. Because in the Z conformation the purine residues exist in *syn* conformation, the phosphate backbone forms a zig-zag shape and helix is left handed [3]. DNA in the Z conformation has only one deep groove.

RNA occurs mainly in A conformation as a consequence of the presence of 2'-OH group on the ribose residues. This group interacts with O2 or N3 of the same residue through water molecule [4]. A crystal structure of Z form of RNA is not known up to now, however there are some evidences from NMR and CD measurements that such structure exists [5,6]. There are many factors influencing structural changes of nucleic acids: high salt and alcohol concentration, high temperature etc. Here we will show high pressure effect on structure and function of nucleic acids.

### Effect of high pressure on the conformation of DNA

One of the best methods for analysis of conformational changes of nucleic acids in solution is circular dichroism (CD) spectroscopy [3]. B-DNA to Z-DNA conformational change can be traced with negative Cotton effect at 295 nm.



Poly (dGdC) effected by high pressure of 6 kbar for 19 hours undergoes conformational change from B to Z [7]. The effect obtained is identical to the one which is caused by salt or alcohol at high concentration [8,9]. It should be added that this effect is completely reversible after 5 hours at atmospheric pressure at room temperature. At 10 kbar, however, there is almost no change what can be explained by unusual water structure. At this conditions water forms ice VI, which is considerably different from the ice formed at atmospheric pressure [10]. If it is so it restricts, of course changes of conformation of DNA. Fig. 1 shows schematically B to Z-DNA conformational change.

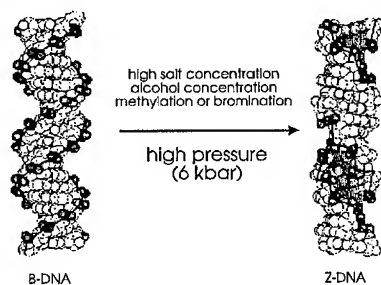


Fig. 1. Schematic drawing of conformational change from B-DNA to Z-DNA in different conditions.

### Effect of high pressure on RNA

RNA exists in A conformation due to the presence of 2'-OH group [4]. Z-RNA occurs in solution containing 2.85M  $\text{MgCl}_2$  or 6M  $\text{NaClO}_4$  at 42°C. To study pressure effects on RNA, we used two oligoribonucleotides  $\text{r(GC)}_6$  and  $\text{r(AU)}_6$ . After 18 hours treatment at 6 kbar the CD spectra were measured. Firstly, maximum of the CD spectra was shifted to higher wavelengths. Secondly, a new CD peak appeared in the spectra beyond 300 nm. It suggests light scattering and/or aggregation of the oligoribonucleotide. Similar effects can be noticed for  $\text{r(AU)}_6$  [11]. The spectra of both oligoribonucleotides after high pressure treatment resemble very much those for  $\text{r(GC)}_3$  obtained in the presence of 5M NaCl [6] or poly  $\text{r(GC)}$  in 6M  $\text{NaClO}_4$  at normal temperature [5]. Clearly high pressure alone does not induce A-Z RNA transition of the oligoribonucleotide duplexes. Next we checked combined effect of

high salt concentration and high pressure on oligonucleotide conformation. Exposure of  $\text{r(CG)}_6$  to high pressure of 6 kbar in the presence of 5M NaCl shows a positive Cotton effect at about 295 nm in the CD spectrum. The absence of a CD band above 300 nm means that RNA aggregation does not occur. Effect observed at 295 nm for  $\text{r(AU)}_6$  is similar although less pronounced [11]. A similar spectrum has been previously ascribed to the Z RNA form [5,6]. On the Fig.2 three CD spectra of  $\text{(CG)}_6$ , poly  $\text{(GC)}$  and  $\text{(CG)}_3$  are shown. All of them are similar and characterize Z-RNA form.

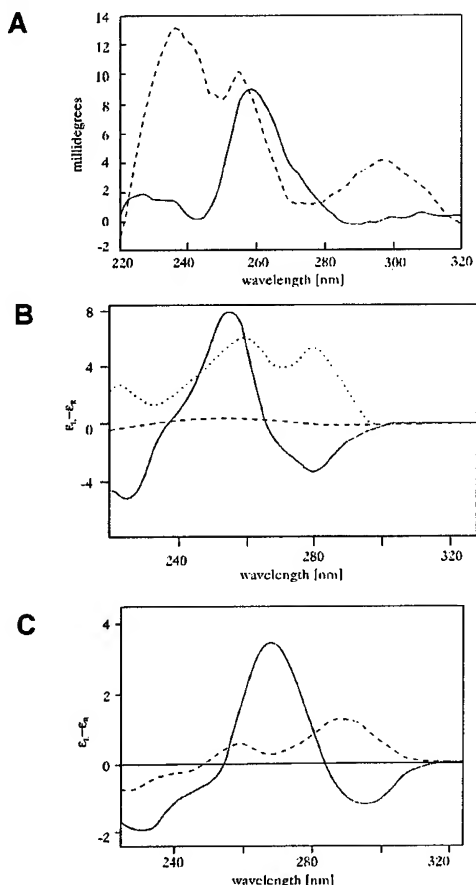


Fig. 2. Comparison of CD spectra of different oligoribonucleotides. A. Circular dichroism spectra of the  $\text{r(GC)}_6$  at atmospheric pressure (solid line) and at the 6 kbar and 5 M NaCl (dashed line) [11]. B: CD spectra of poly  $\text{rGC}$  in 6M  $\text{NaClO}_4$ , 22°C (solid line) and in 6M  $\text{NaClO}_4$  45°C (dotted line) [5] and C: CD spectra of  $\text{r(GC)}_3$  in 0.05 phosphate with 0 (solid line) and 2.85 M  $\text{MgCl}_2$  (dashed line) [6].

To learn more about contribution of RNA and DNA strands to overall structure of nucleic acid, we treated heteroduplexes RNA-DNA of alternating purine-pyrimidine sequences with high pressure but conformational change to the Z form was not observed neither under high pressure alone nor at high pressure and high salt applied together [12]. From CD spectrum it seems that heteroduplex does not exactly A nor B form. When high pressure together with 5M sodium chloride is applied, small hyperchromic Cotton effect at ca. 265 nm is visible suggesting occurrence of A conformation. This is in good agreement with an earlier observations, that at lower humidity samples of heteroduplexes tend toward canonical A-RNA structure [13].

#### Rationale for the conformational changes of nucleic acids

It has been suggested that the main factor responsible for conformational changes of nucleic acids is their hydration [2]. It is well known that the B form is the most hydrated form for DNA and the left handed Z form is the least hydrated one [2]. In B form each phosphate in the sugar-phosphate backbone is hydrated separately whereas in A and Z forms, water makes bridges between neighbouring phosphates. The 2'-OH group of RNA and water molecules are involved in formation of hydrogen bond network which stabilizes the overall molecule structure. Therefore, removing water of RNA by high pressure is more difficult. From other studies it is known that only the first layer of water which is close to nucleic acid molecule, is responsible for conformational changes [14]. It seems that high pressure can change not only molar volume of nucleic acid, but also, a molar volume of solvent. Recently on the basis of theoretical calculations, a new model of water structure has been proposed [15]. Water molecules can exist probably in tetrameric and octameric forms. In cubic (octameric) form water molecules occupy a volume  $16.6 \text{ cm}^3/\text{mol}$  of  $\text{H}_2\text{O}$ , but in tetrameric form the value is  $17.9 \text{ cm}^3/\text{mol}$  of  $\text{H}_2\text{O}$  [15]. Volume difference between these two forms is ca. 8% in contrast to 20% which has been observed

for water pressed with 1 kbar at  $25^\circ\text{C}$  [14]. It is generally accepted that pressure causes lowering of water volume due to shortening of the H-bonds [16]. We therefore suggest that pressure induce lower molecular volume by change of a tetrameric to an octameric form of water, which long chain located in the groove of Z-DNA interacts with the phosphate groups. The other factor which play an important role in conformational changes of oligonucleotide is its nucleotide sequence. The B to Z or A to Z conformational changes are possible only when alternating purine-pyrimidine sequence is present. In DNA:RNA heteroduplex, however there is no conformational change even when correct sequence is present. It can be due to different hydration of the both DNA and RNA strands and therefore water would not be able to stabilize a new conformation.

#### Aminoacylation of tRNA at high pressure

It was found that phenylalanine charges nonenzymatically *E.coli* tRNA<sup>Phe</sup> at high pressure in the absence of aminoacyl-tRNA

##### tRNA<sup>Phe</sup> from *E.coli*

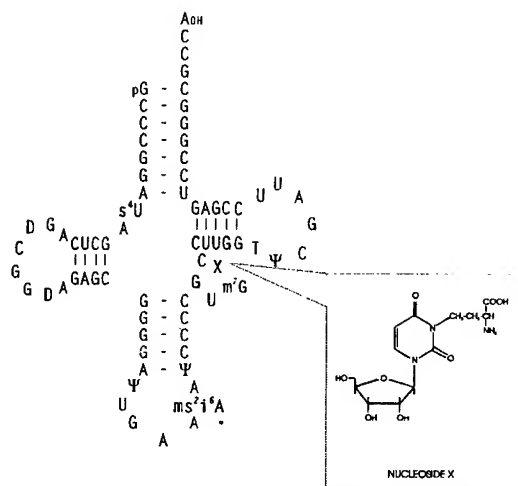


Fig. 3. Secondary structure of tRNA<sup>Phe</sup> from *E.coli* and the structure of nucleoside X.

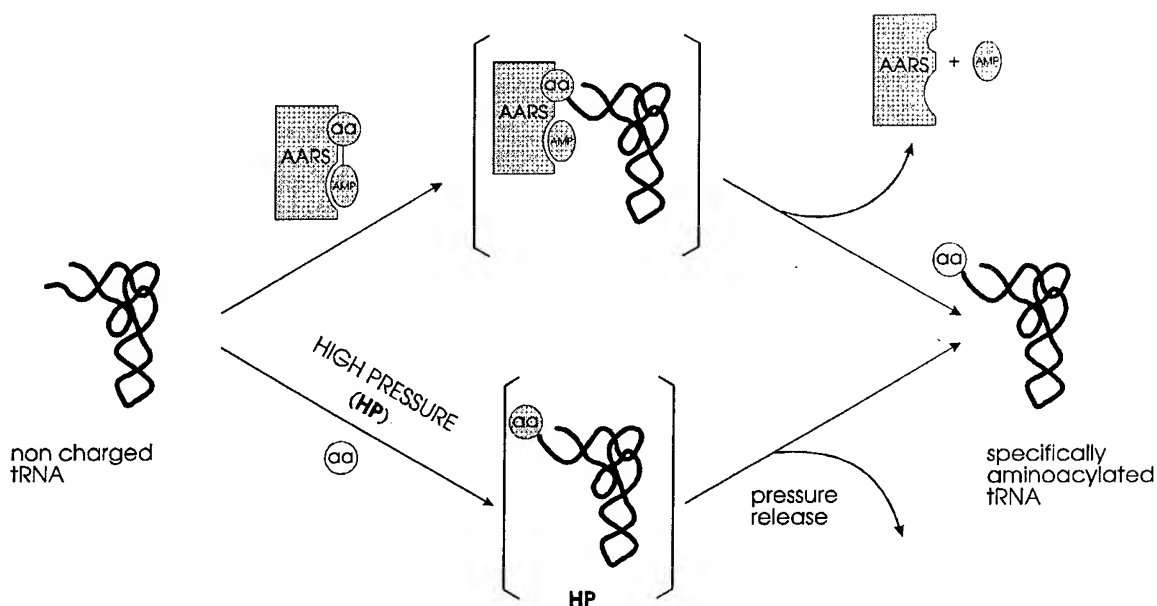


Fig. 4. A scheme of the aminoacylation reaction carried out enzymatically (top) and at high pressure (bottom). Final product of these two reactions is the same. Putative intermediate conformation in the enzymatic coupling and the one generated by high pressure are similar or identical.

synthetase and ATP. Yield of this reaction is about 10% of an enzymatic aminoacylation [17].

In tRNA<sup>Phe</sup> from *E.coli* there are at least two possible targets for reaction with amino acids: 3' hydroxyl group of terminal adenosine (acyl bond) and nucleoside X (3 amino-3 carboxypropyl uridine) in position 47 of tRNA molecule (amide bond) (Fig. 3). Both sites are able to react with an amino acid.

To prove that tRNA aminoacylation takes place on the terminal adenosine, a hydrolysis reaction in mild alkaline conditions (pH 8.2) was carried out. Curves of spontaneous hydrolysis of the aminoacyl bond of [<sup>14</sup>C] Phe-tRNA<sup>Phe</sup> obtained enzymatically and at high pressure are almost identical [17]. If putative amide bond is formed it would be resistant to alkaline hydrolysis. HPLC analysis of non digested and ribonuclease A hydrolyzed [<sup>14</sup>C] Phe-tRNA<sup>Phe</sup> was carried out to find correct site of tRNA aminoacylation. After digestion a new peak appeared which was analysed on a TLC plate what allowed us to conclude that phenylalanine is bound to terminal adenosine [18].

To prove specificity of this reaction we made two different experiments. First tRNA<sup>Phe</sup> from *E.coli* was aminoacylated with [<sup>14</sup>C]-phenylalanine in the presence of increasing amount of cold serine. There was no inhibition of aminoacylation level [17]. In the second experiment tRNA<sup>Met</sup> from yellow lupin was aminoacylated with methionine and separately with serine. tRNA<sup>Met</sup> is not significantly charged with serine [17]. From these experiments one can conclude that specificity is encoded in the tRNA structure itself.

To find out whether the product of aminoacylation reaction is biologically active two different reactions were carried out. In the first Phe-tRNA<sup>Phe</sup> was bound to poly U programmed ribosomes and in the second synthesis of polyphenylalanine was performed. Kinetics in both reactions for high pressure and enzymatically charged tRNAs is very similar if not identical [18]. The data clearly show that product of the high pressure aminoacylation reaction is biologically active.

CD spectrum of tRNA<sup>Phe</sup> treated under high pressure reveals small changes in comparison with spectrum recorded at the atmospheric pressure

[17]. It means that high pressure induces some conformational changes. It is already known that conformations of free and aminoacylated tRNA are different [19]. Based on this finding and having the same product we can assume that conformation adopted at high pressure and induced by the enzyme are the same. Scheme of the enzymatic and high pressure reaction is shown on the Fig 4.

### Acknowledgements

This work was supported by the grant from the Committee for Scientific Research.

### References

1. P. Douzou, (1992) in *High Pressure and Biotechnology*, eds. C.Balny, R.Hayashi, K.Heremans and P.Masson. Colloque INSERM/John Libbey Eurotext Ltd. vol. 224, 3
2. W. Saenger, W. N. Hunter and O. Kennard, (1986) *Nature*, **324**, 385
3. A. Rich, A. Nordheim and A. H. -J. Wang, (1984) *Annu.Rev.Biochem.*, **53**, 791
4. E. Westhof (1988) *Annu. Rev .Biophys. Biophys. Chem.*, **17**, 125
5. K. Hall, P. Cruz, I. Tinoco Jr., T. M. Jovin and J. H. van de Sande (1984) *Nature*, **311**, 584
6. R. W. Adamiak, A. Gałat and B. Skalski, (1985) *Biochim. et Biophys. Acta*, **825**, 345
7. A. Krzyżaniak, P. Salański, J. Jurczak, and J. Barciszewski, (1991) *FEBS Lett.*, **279**, 1
8. F. M. Pohl and T. M. Jovin (1972) *J.Mol.Biol.*, **67**, 375
9. M. J. Behe, G. Felsenfeld, S. C. Szu, and E. Charney (1985) *Biopolymers*, **24**, 289
10. K. Heremans (1992) in *High Pressure and Biotechnology*, eds. C.Balny, R.Hayashi, K.Heremans and P.Masson. Colloque INSERM/John Libbey Eurotext Ltd. vol. 224
11. A. Krzyżaniak, J. P. Fürste, R. Bald, P. Salański, J. Jurczak, V. A. Erdmann and J. Barciszewski, (1994) *Int.J.Biol.Macromol.*, **16**, 159
12. A. Krzyżaniak, J. P. Fürste, V. A. Erdmann, P. Salański, J. Jurczak and J. Barciszewski (submitted for publication)
13. S. -H. Chou, P. Flynn and B. Reid (1989) *Biochemistry*, **28**, 2435
14. T. V. Chalikian, A. P. Sarvazyan, E. Plum and K. J. Breslauer (1994) *Biochemistry*, **33**, 2394
15. S. W. Benson and E. D. Siebert (1992) *J.Am.Chem.Soc.*, **114**, 4269
16. D. B. Kitchen, L. H. Reed and R. M. Levy., (1992) *Biochemistry*, **31**, 10083
17. A. Krzyżaniak, P. Salański, J. Jurczak and J. Barciszewski (1994) *Int.J.Biol.Macromol.*, **16**, 153
18. A. Krzyżaniak, P. Salański, J. Jurczak and J. Barciszewski (submitted for publication)
19. M., Haruki, R. Matsumoto, M. Hara-Yokoyama, T. Miyazawa, and S. Yokoyama, (1990) *FEBS Lett.*, **263**, 361

# NMR STUDIES OF PRESSURE-INDUCED REVERSIBLE UNFOLDING OF PROTEINS

JIRI JONAS

Beckman Institute for Advanced Science and Technology, University of Illinois, 405 N. Mathews,  
Urbana, Illinois 61801, USA

## ABSTRACT

This overview of recent high resolution NMR studies of pressure-induced reversible unfolding of proteins performed in our laboratory focuses on several fundamental problems: the cooperativity of the unfolding process; structural differences in cold, pressure and heat denatured states; pressure-temperature phase diagrams of proteins. The specific protein systems studied include ribonuclease A and lysozyme.

### Introduction

Most studies dealing with protein denaturation have been carried out at atmospheric pressure using various physicochemical perturbations, such as temperature, pH, or denaturants, as experimental variables. Compared to varying temperature, which produces simultaneous changes in both volume and thermal energy, the use of pressure to study protein solutions perturbs the environment of the protein in a continuous, controlled way by changing only intermolecular distances. In addition, by taking advantage of the phase behavior of water high pressure can substantially lower the freezing point of an aqueous protein solution. Therefore, by applying high pressure one can investigate in detail not only pressure-denatured proteins, but also cold-denatured proteins in aqueous solution (1).

In this contribution I illustrate the advantages of using high pressure, high resolution  $^1\text{H}$  NMR techniques (2) to study the reversible pressure, cold, and heat denaturation of ribonuclease A (RNase A) (3). This work is a continuation of our systematic studies of pressure induced unfolding of proteins (4-7) and has the following specific objectives: to investigate the pressure unfolding of RNase A; to characterize the structure of the pressure denatured protein; to compare the unfolded structures of RNase A produced by cold, heat and pressure denaturation.

RNase A is a single-domain protein, a pancreatic enzyme which catalyses the cleavage of single-stranded RNA. This protein consists of 124 amino acid residues with a molecular mass of 13.7 kDa. It has traditionally served as a model for protein folding because it is small, stable and has a well-known native structure. The  $\epsilon\text{l}$  protons of the four RNase A histidine residues are well-resolved

from other protons in the  $^1\text{H}$  NMR spectrum of the native protein in  $\text{D}_2\text{O}$ ; they have been used in this work to monitor the structural changes of four distinct segments in the molecule during cold, heat and pressure denaturation processes.

In addition, the performance of the new high resolution NMR probe (8) permitting experiments up to 9 kbar will be illustrated on the study pressure induced denaturation of lysozyme. This specific set of experiments is a continuation of our earlier study (4) of lysozyme using maximum pressure of 5 kbar.

### Experimental

The experimental procedures are discussed in detail elsewhere (2,3).

### Results and Discussion

The  $\epsilon\text{l}$  proton peaks of the four histidine residues are well resolved from other proton peaks in the 1D  $^1\text{H}$  spectrum of the native RNase A in  $\text{D}_2\text{O}$ . They have been assigned and used to probe the folding and unfolding processes of the protein. Figure 1 shows the behavior of the proton spectrum in the histidine region during pressure unfolding at  $\text{pH}^* 2.0$ ,  $10^\circ\text{C}$ . With increasing pressure, the intensity of the native histidine peaks decreases. At about 4 kbar, all native histidine resonances disappear, indicating that the protein is pressure denatured. As pressure increases, two denatured resonances of the histidine residues, D and D', are observed. The chemical shift of resonance D is very similar to the composite resonance observed in the thermally denatured state and in the urea or guanidine hydrochloride denatured states of the protein. The interesting feature in the pressure unfolding process is that besides the composite

denatured histidine resonance D, another denatured histidine resonance, D', appears as the pressure increases.

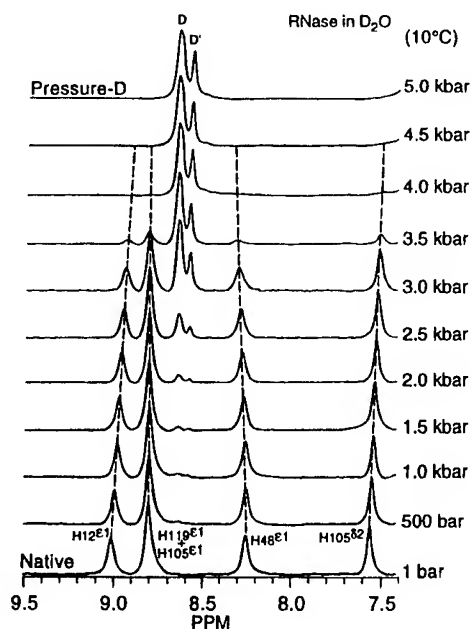


Fig. 1 The histidine region of the  $^1\text{H}$  NMR spectra of RNase A in  $\text{D}_2\text{O}$  at various pressures (10°C,  $\text{pH}^* 2.0$ ). The standard in the insets is sodium 3-(trimethylsilyl)tetrauteriopropionate.

This resonance was not observed either in the thermal denatured state or in the urea or guanidine hydrochloride denatured states. In the completely pressure denatured state, the intensity ratio of D to D' is three to one, suggesting that D' comes from one of the four histidine residues. In order to assign the D' resonance, a magnetization transfer NMR experiment was performed. It was found that the intensity of resonance D' decreased when the native histidine 12 peak was selectively irradiated. The result of the magnetization transfer test indicates that resonance D' comes from the histidine 12, and that resonance D comes from histidines 48, 105 and 119.

It is difficult to attain the completely cold denatured state of proteins in aqueous solutions by decreasing the temperature below the freezing point of 0°C at ambient pressure. However, taking advantage of the pressure phase behavior of water, one can lower the temperature of aqueous solutions well below 0°C. At 3 kbar the RNase A solution, can be cooled to -25°C without freezing. It should be noted here that the protein solution in the high salt buffer freezes well below the freezing point

given in the phase diagram of water at 3 kbar (-15°C). The phase behavior of water allows us to obtain the completely cold denatured state of RNase A with the assistance of pressure. In Figure 2, we demonstrate the behavior of the proton spectrum of the histidine region of RNase A undergoing cold denaturation at 3 kbar and  $\text{pH}^* 2.0$ . The protein becomes cold denatured at -22°C. In the cold denatured state, one finds in addition to the composite resonance D, another resonance D', which likely has the same origin as D' in the pressure denatured state. This is not surprising because the protein is subjected both to a high pressure of 3 kbar and to low temperature. The linewidth broadening of resonances D and D' is due to slower motions at low temperatures.

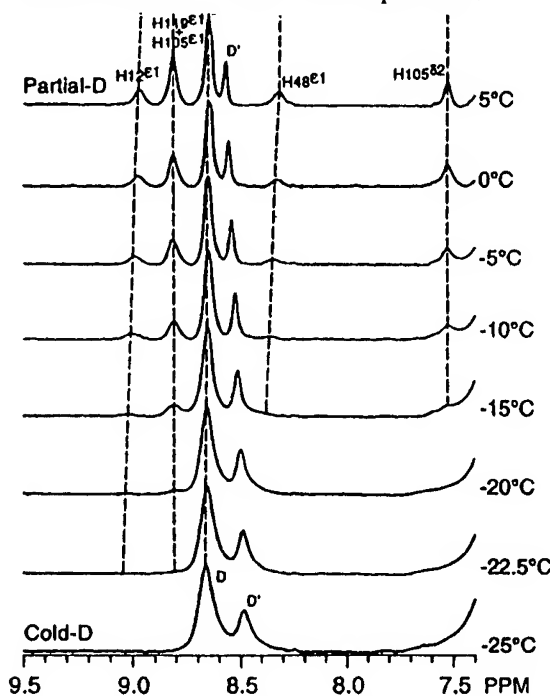


Fig. 2 Cold denaturation of RNase A. The histidine region of the  $^1\text{H}$  NMR spectra of RNase A in  $\text{D}_2\text{O}$  at various temperatures (3 kbar,  $\text{pH}^* 2.0$ ).

The experimental data obtained allowed us to construct a pressure-temperature phase diagram of RNase which is shown in Fig. 3.

Above the curve the protein is in the denatured state. It can be seen that the cold and heat denaturation temperatures change with pressure, and that below 2 kbar the heat denaturation temperature is not sensitive to pressure. The cold denaturation temperature data below 3 kbar are not

available because the aqueous protein solution freezes before it can be completely cold denatured.

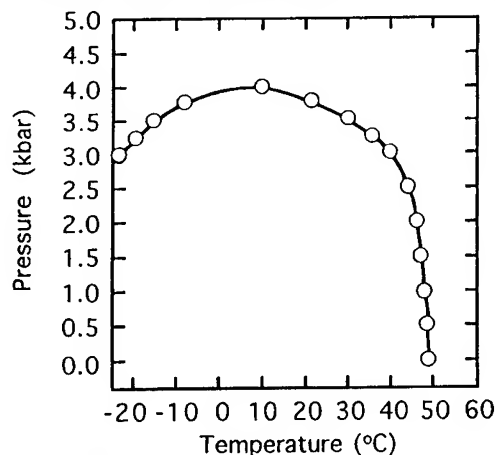


Fig. 3 Phase diagram of RNase A at pH 2.0.

In addition, hydrogen exchange experiments were performed to confirm the presence of partially folded structures in the pressure denatured state. Stable hydrogen-bonded structures protecting the backbone amide hydrogens from solvent exchange were observed in the pressure denatured state. These experimental results suggest that the pressure denatured RNase A displays the characteristics of a molten globule. The cold, heat and pressure denaturation experiments on the complex of RNase A with the inhibitor 3'-UMP showed that the RNase A-inhibitor complex is more stable in comparison to RNase without the inhibitor.

In our earlier NMR study (4) of pressure-induced reversible unfolding of hen egg white lysozymes the NMR probe (2) limited us to maximum pressures of 5 kbar. In order to achieve 100% denaturation under the experimental conditions used we needed to achieve pressures up to 9 kbar. Therefore, we built a new high resolution NMR probe (8) which allows us to reach 9 kbar with very high resolution (for 8 mm sample at 300 MHz the linewidth is better than 1 Hz). Details of the construction and performance features of this NMR probe will be given elsewhere (8). In this overview we only discuss in detail the pressure denaturation curve for lysozyme at 37.5°C and pH-2.2. Work is in progress to answer the question of whether the denaturation of lysozyme is a two-state process.

The most promising future technical developments in this relatively young field will

include the use of advanced two-dimensional and three-dimensional NMR techniques in high-pressure NMR studies of proteins and model membranes, as well as the development of high pressure, high-resolution NMR probes for high-field experiments. Clearly, the use of pressure as an experimental variable combined with the high information content of advanced NMR techniques provides a unique approach, particularly in studies of the protein-unfolding problem. The finding that pressure denaturation is less drastic than temperature and/or chemical denaturation may facilitate the detection, stabilization, and characterization of various partially folded intermediates.

#### Acknowledgments

The work discussed in this review was supported in part by the National Institutes of Health grants PHS 1 R01 GM42452 and PHS 5 R01 HL16059, and by the National Science Foundation grant NSF CHE 90-17649.

#### References

1. J. Jonas and A. Jonas, *Annu. Revs. Biophys. Biomol. Structure* **23** (1994) 287.
2. J. Jonas, X. Peng, P. Koziol, C. Reiner and D. M. Campbell, *J. Magn. Reson.* **102B** (1993) 299.
3. J. Zhang, X. Peng, A. Jonas, and J. Jonas, *Biochem.*, **34**, (1995) 8631.
4. S. D. Samarasinghe, D. M. Campbell, A. Jonas and J. Jonas, *Biochem.* **31** (1992) 7773.
5. X. Peng, J. Jonas, and J. Silva, *Proc. Natl. Acad. Sci. USA* **90** (1993) 1776.
6. C. A. Royer, A. P. Hinck, S. N. Loh, K. E. Prehoda, X. Peng, J. Jonas, and J. L. Markley, *Biochem.* **32** (1993) 5222.
7. X. Peng, J. Jonas, and J. Silva, *Biochem.* **33** (1994) 8323.
8. L. Ballard, C. Reiner, and J. Jonas, Manuscript in preparation.

## HIGH PRESSURE FT-IR STUDIES ON HEMOPROTEINS

LÁSZLÓ SMELLER<sup>1</sup>, KOEN GOOSSENS<sup>2</sup>, KAREL HEREMANS<sup>2</sup>

<sup>1</sup>Institute of Biophysics, Semmelweis Medical University, Puskin u. 9. PF 263, H-1444 Budapest, Hungary

<sup>2</sup> Department of Chemistry, Katholieke Universiteit Leuven, Celestijnenlaan 200 D, B-3001 Leuven, Belgium

### ABSTRACT

Five different kind of myoglobins (from sperm whale, horse skeletal muscle, horse heart muscle, dog skeletal muscle and apomyoglobin from horse heart) and three different mixtures of horseradish peroxidase isoenzymes were studied by high pressure Fourier-transform infrared spectroscopy. Denaturation of myoglobins were observed in the 6-7 kbar range except for the apomyoglobin, which denatures at very low pressure of 1.3 kbar. All the horseradish peroxidases were found to be more stable against the pressure denaturation, they denature in the range of 7-10 kbar.

### Introduction

Hemoproteins play a very important role in the basic life processes, like in the O<sub>2</sub> transport and storage (hemoglobin and myoglobin), electron transfer (cytochromes) and catalysis of the oxidation of H<sub>2</sub>O<sub>2</sub> (peroxidases). This is why their structure and function are in the focus of the biophysical and biochemical researches and have been studied by series of methods (1-9).

Whereas the powerful methods of the modern biochemistry make it possible to create and investigate different site-directed mutation of proteins, the study of some natural mutants can also give important information about these proteins.

We studied two group of hemoproteins: myoglobin from different source (sperm whale, horse skeletal muscle, horse heart muscle, dog skeletal muscle and apomyoglobin from horse heart) and three different composition of horseradish peroxidase isoenzymes.

### Materials and Methods

Myoglobins were purchased from Sigma. Two horseradish peroxidase (RZ=1 and RZ=3 was produced by Reanal (Hungary)\*. The RZ=2 was a generous gift of prof. F. Kálmán (Debrecen, Hungary). All proteins were obtained in lyophilized form and were used without further purification.

High pressure was created by a diamond anvil cell (DAC). The pressure range used was 0-15 kbar, which is enough to denature the protein in the case of all investigated samples. The ruby fluorescence was used to measure the pressure (10).

The proteins were dissolved in Tris-DCl buffer pD 7.5 at a concentration of 50 mg/ml. The solutions were left overnight (at room temperature) to facilitate H/D exchange.

Infrared spectra were obtained with a Bruker IFS66 FT-IR spectrometer equipped with broad band MCT detector. Infrared light was focussed on the sample by a NaCl lens (11). 350 interferograms with a resolution of 2 cm<sup>-1</sup> were coadded in order to increase signal to noise ratio.

The amide I' band in the 1600-1700 cm<sup>-1</sup> region of the infrared spectra was used to detect the secondary structure of the protein. The spectra were processed by the program developed in our laboratory (12). Fourier self deconvolution and fitting of Gaussian profiles of the resolution enhanced spectra enabled us to characterize the elastic and conformational changes caused by the pressure (13)

### Results and discussion

Fig. 1 shows the maximum position of the amide I' band of myoglobins versus pressure. All the compared myoglobin molecules were denatured in the range of 5-7 kbar with the exception of the apomyoglobin. The fact that the apomyoglobin

\* RZ =  $A_{403}/A_{280}$ , where  $A_x$  is the absorbance at wavelength x nm.



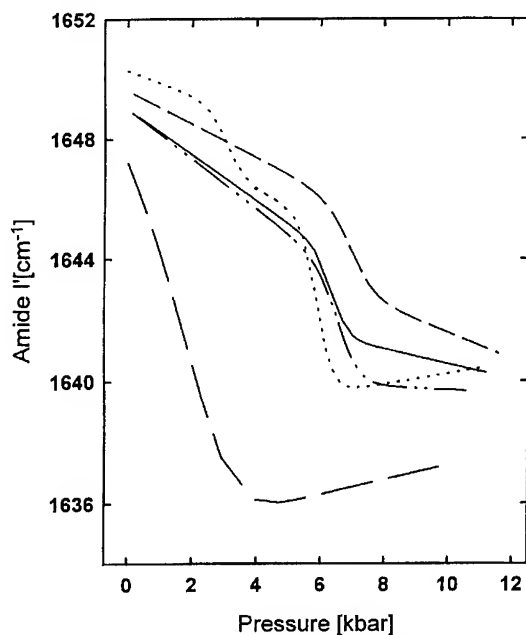


Fig. 1. The maximum positions of the amide I' band of myoglobins from different source: — sperm whale skeletal muscle, — · — horse heart muscle, — · — horse skeletal muscle, · · · dog skeletal muscle, — — — apomyoglobin from horse skeletal muscle.

denatures at quite low pressure confirms that the protein cannot form stable enough structure without its prosthetic group. Slight differences in the denaturation pressure and in the volume changes during the denaturation can be observed among the wild type proteins which are from different source. In the case of dog skeletal muscle myoglobin there is a partial unfolding at 3 kbar pressure.

The closer look to the infrared spectra by deconvolution and curve fitting shows that the individual spectral lines get broadened when the pressure is increasing. At the denaturation pressure, the whole spectrum becomes broad and looks featureless. These changes are partially reversible. Appearance of side bands of the amide I' band after releasing the pressure shows increased intermolecular interactions. Small shift of the component bands were also observed. These can be attributed to the increased H/D exchange at higher pressures.

While myoglobin is a very widely studied protein, relatively less is known about the second object of our investigation. Horseradish peroxidase (HRP) is

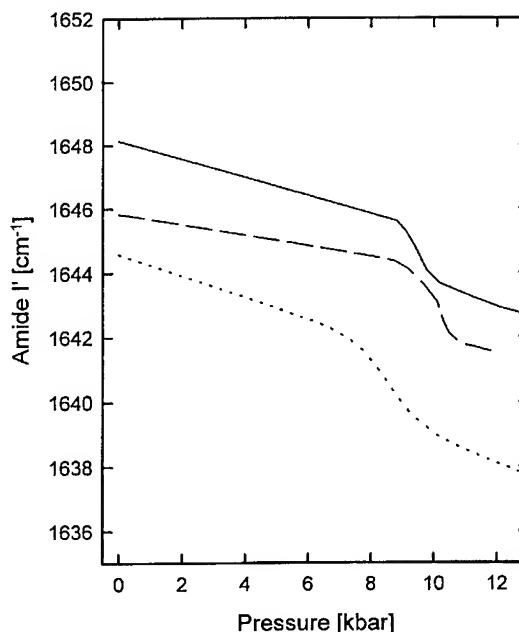


Fig. 2. The maximum positions of the amide I' band of horseradish peroxidases. · · · RZ=1, — — RZ=2, — RZ=3.

particularly suitable for physical investigation, because the porphyrin is located in a relatively narrow hem pocket where its position is well defined (14). This is not valid for all heme proteins, e.g. in myoglobin there are two possible orientations of the heme. There is another reason for the investigation of the HRP, namely its high stability even at higher temperatures. The question appears naturally whether the high stability against temperature is accompanied with an increased stability against the pressure.

Almost nothing is known about the pressure effect on the HRP. Only one article was published in the literature (15), where the visible absorption spectrum of several hemoprotein molecules (among them HRP) was measured as a function of the pressure.

Our method enables to follow the protein conformation in function of pressure. We studied the HRP in three kind of isoenzyme composition. The isoenzyme mixtures are characterized by the so called RZ value, which is the ratio of the UV-VIS

absorption peak heights of porphyrin and aromatic side chains of the protein.

Figure 2 shows the maximum of the amide I' band versus pressure for the three investigated HRP samples.

Our measurements show a relatively high unfolding pressure in case of all of the studied HRP's. The denaturation pressure is in the range of 7-10 kbar. In some cases one can observe slight conformational changes at lower pressure. There are small differences in the volume changes associated with the denaturation process.

Comparison of the myoglobins with horseradish peroxidases shows a correlation between the stabilities against the temperature and pressure denaturation.

#### Acknowledgment

The authors thank prof. F. Kálmán (Debrecen, Hungary) for one of the horseradish peroxidase. LS thanks the Hungarian Acad. Sci. and the Belgian Natl. Found for Sci.

#### References

1. H. Frauenfelder, N.A. Alberding, A. Anasari, D. Braunstein, B.R. Cowen, M.K. Hong, I.E.T. Iben, J.B. Johnson, S. Luck, M.C. Marden, J.R. Mourant, P. Ormos, L. Reinisch, R. Scholl, A. Schulte, E. Shyamsunder, L.B. Sorensen, P.J. Steinbach, A. Xie, R.D. Young, and K.T. Yue, *J. Phys. Chem.* **94** (1990) 1024.
2. J. C. Kendrew, H. C. Watson, B. E. Strandberg, R. E. Dickerson, D. C. Phillips and V. C. Shore, *Nature* **190** (1961) 666.
3. K. Heremans and M. Bormans, *Physica* **139&140B** (1986) 870.
4. R. Lange, I. Heiber-Langer, C. Bonfils, I. Fabre, M. Negishi and C. Balny, *Biophys. J.* **66** (1994) 89.
5. A. Zipp and W. Kauzmann, *Biochemistry* **21** (1973) 4217.
6. A.D. Kaposi and J. M. Vanderkooi, *Proc. Natl. Acad. Sci. USA* **89** (1992) 11371.
7. V. Le Tilly, O. Sire, B. Alpert and P.T.T. Wong, *Eur J. Biochem* **205** (1992) 1061.
8. B. Defaye and D. A. Ledward, *J. Food Sci.* **60** (1995) 262.
9. L. Herényi, J. Fidy, J. Gafert and J. Friedrich, *Biophys. J.* **69** (1995) 577.
10. J. D. Barnett, S. Block and G. J. Piermarini *Rev. Sci. Instrum.* **44** (1973) 1.
11. P.T.T. Wong, *Can. J. Chem.* **69** (1991) 1699.
12. L. Smeller, K. Goossens and K. Heremans, *Appl. Spectrosc.* **49** (1995) (in press).
13. L. Smeller, K. Goossens and K. Heremans, *Vibr. Spectrosc.* **8** (1995) 199.
14. J. Fidy, J. M. Vanderkooi, J. Zollfrank and J. Friedrich, *Biophys. J.* **63** (1992) 1605.
15. G. B. Ogunmola, A. Zipp, F. Chen and W. Kauzmann, *Proc. Natl. Acad. Sci. USA* **74** (1977) 1.

# THE HIGH PRESSURE EFFECTS ON THE SECONDARY STRUCTURE OF BOVINE PANCREATIC TRYPSIN INHIBITOR STUDIED BY FT-IR SPECTROSCOPY

NAOHIRO TAKEDA, MINORU KATO, AND YOSHIHIRO TANIGUCHI\*  
*Department of Chemistry, Faculty of Science and Engineering, Ritsumeikan University, 1916 Noji-cho, Kusatsu, Shiga 525, Japan*

## ABSTRACT

Fourier transform infrared (FT-IR) spectroscopy combined with a resolution enhancement technique has been used to characterize pressure-induced structural changes in bovine pancreatic trypsin inhibitor (BPTI) in D<sub>2</sub>O solution at 25°C. According to the observed changes in the amide I' band, the polypeptide backbone of BPTI is slightly rearranged by application of high pressure, and is not fully unfolded even at 1000 MPa. The pressure-induced structural rearrangements are completely reversible. Pressure effects on the individual secondary structure elements of BPTI are not uniform. The unfolding of BPTI induced by application of high pressure is not confirmed by FT-IR spectroscopy as well as by molecular dynamics simulation.

## Introduction

For globular proteins, structural characterization of not only native but also nonnative (partially folded and denatured) states is essential for understanding the mechanisms of folding/unfolding and the principles of structure stabilization. The reversible denaturation of globular proteins induced by pressure have been studied by means of UV-visible, fluorescence, FT-IR, and NMR spectra. The molecular dynamics simulation study<sup>1,2</sup> of BPTI has observed no evidence of the pressure-induced unfolding of the molecule even at 1000 MPa where the pressure-induced denaturation of proteins is usually complete. The average root mean square deviations of the backbone atoms of BPTI between the high pressure simulated and X-ray crystal structure might suggest the pressure-induced minor changes in the polypeptide backbone. In contrast, FT-IR spectroscopic study<sup>3,4</sup> has revealed that pressure-denatured ribonuclease A does not have any residual secondary structure elements. The detailed structural features upon the pressure-induced denaturation of proteins are still uncertain.

In this paper, we have used FT-IR spectroscopy combined with a resolution enhancement technique to probe the pressure-induced conformational changes in BPTI. This technique provides a sensitive diagnostic tool for monitoring the nature of changes in the conformation of the protein backbone in aqueous solution. We examine whether BPTI is actually unfolded by application of high pressure. The structural features of BPTI at high pressure are additionally

characterized by the behavior of hydrogen-deuterium exchange of the backbone amide protons.

## Experimental

Bovine pancreatic trypsin inhibitor (type I-P), Sigma Chemical Co., was used without further purification. Sample solution was prepared by dissolving BPTI in 0.05 M Tris-DCI D<sub>2</sub>O buffer, pD 7.0. The protein concentration was 50 mg/ml. The pD was read directly from a pH meter, and no adjustments were made for isotope effects. All exchangeable backbone amide protons in BPTI were deuterated by means of cooling rapidly in an ice/water bath after incubating the solution at 85 °C for 12 minutes.

The sample solutions were placed together with a small amount of powdered  $\alpha$ -quartz in a 1.0 mm diameter hole of a 0.05 mm thick stainless-steel (SUS 304) gasket mounted on a diamond anvil cell. The  $\alpha$ -quartz was used as an internal pressure calibrant. Infrared spectra were recorded at 25 °C using a Perkin-Elmer 1725X Fourier transform infrared spectrometer equipped with a liquid-nitrogen cooled MCT detector. The temperature was controlled by a circulating water jacket within 0.3°C. The infrared beam was condensed by a zinc selenide lens system onto the sample in the diamond anvil cell. For each spectrum, 1000 interferograms were co-added and Fourier transformed to give a spectral resolution of 2 cm<sup>-1</sup>. Thirty minutes was allowed to equilibrate the sample solution at the chosen pressure prior to each infrared measurement which itself

takes 16 minutes. The average increasing or decreasing pressure rate was about 150 MPa/h. In order to eliminate spectral contributions from atmospheric water vapor, the spectrometer and sample chamber were continuously purged with dry air.

## Results and Discussion

**Pressure-Induced Changes in the Secondary Structure of BPTI.** The changes in the amide I' band shown in Figure 1 directly indicate the pressure-induced changes in the secondary structure of BPTI, because hydrogen-deuterium exchange of the backbone amide protons has been already completed. As pressure is increased up to 550 MPa, little frequency shift is observed in all of the four amide I' component bands. An increase in pressure induces the appearance of an amide I' component band centered around 1630  $\text{cm}^{-1}$ . Relative intensity at high pressure is the ratio to the band intensity at 0.1 MPa. Pressure dependence of the relative intensity on the five amide I' component bands at 1630, 1638, 1654, 1669, and 1682  $\text{cm}^{-1}$  are different from one another below 600 MPa as shown in Figure 2. BPTI dissolved in  $\text{D}_2\text{O}$  buffer is reversibly precipitated above about 600 MPa under the present experimental conditions. The precipitation phenomenon was found with the naked eye. Such additional bands as are characteristically found upon the aggregation of many other thermally-denatured proteins are not observed in the amide I' band at all. Only the band at 1654  $\text{cm}^{-1}$  is shifted to 3  $\text{cm}^{-1}$  lower frequency, while the frequency shifts in the other bands are less than 1  $\text{cm}^{-1}$ . It is surprising that the secondary structure in pressure-precipitated BPTI is not fully disrupted even above 1000 MPa, judging from the amide I' band contour shown in Figure 1 at 1120 MPa. The band at 1612  $\text{cm}^{-1}$  primarily arising from side-chain absorption of the tyrosine residues splits into the two bands at 1610 and 1612  $\text{cm}^{-1}$  at 550 MPa, adding the band at 1614  $\text{cm}^{-1}$  with further increasing pressure. This result may suggest the change in micro environment of the tyrosine residues. All of the observed changes in the amide I' region above 780 MPa may be correlated with the pressure-induced precipitation.

**Pressure Effects on the Hydrogen-Deuterium Exchange of BPTI.** Figure 3 shows the second-derivative infrared spectra of partially deuterated BPTI in the amide I/I' region upon increasing pressure. Band intensity is defined in the same manner as completely deuterated BPTI. The most striking behavior with

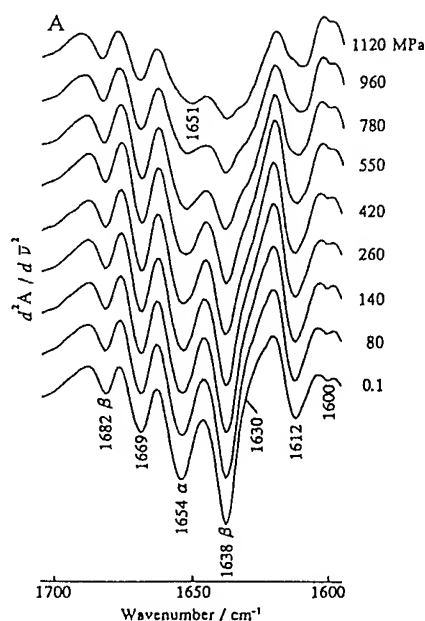


Figure 1: Second-derivative infrared spectra in the amide I' region of completely deuterated BPTI up to 1120 MPa at 25 °C.

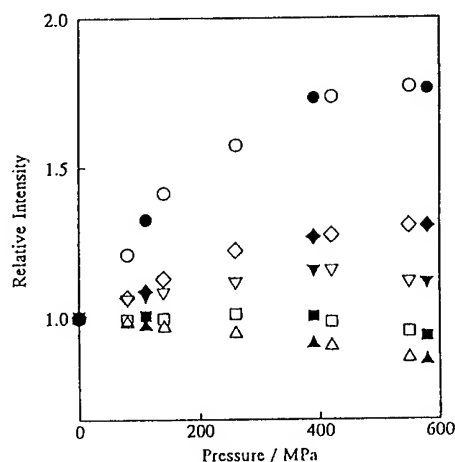


Figure 2: Pressure dependence of the relative intensity on the amide I' component bands at 1630 (O, ●), 1638 (Δ, ▲), 1654 (□, ■), 1669 (▽, ▼), and 1682  $\text{cm}^{-1}$  (◇, ◆) for completely deuterated BPTI shown in figure 1. Open symbols refer to the process of pressure increase, and closed symbols refer to the process of pressure decrease.

increasing pressure is that the bands at 1642 and 1688  $\text{cm}^{-1}$  are not shifted to lower frequency, and are decreased in their intensities. This result suggests that the protected backbone amide protons involved in the  $\beta$ -sheet stable at high pressure can not be exchanged with solvent deuterons, while the others in the  $\beta$ -sheet rearranged by application of high pressure can be exchanged. Indeed, the bands at 1641 and 1685  $\text{cm}^{-1}$  after pressure is released are observed between the bands at 1642 and 1688  $\text{cm}^{-1}$  of partially deuterated BPTI and the bands at 1638 and 1682  $\text{cm}^{-1}$  of completely deuterated BPTI, respectively. It is considered that hydrogen-deuterium exchange of the peptide segments in the  $\alpha$ -helix proceeds without any pressure-induced unfolding as a result of the low frequency shift of the band around 1656  $\text{cm}^{-1}$  over the relatively low pressure range, at least below 460 MPa, where the relative band intensity at 1654  $\text{cm}^{-1}$  is little changed. The band at 1653  $\text{cm}^{-1}$  after pressure is released indicates that the exchange is completed by application of high pressure. The

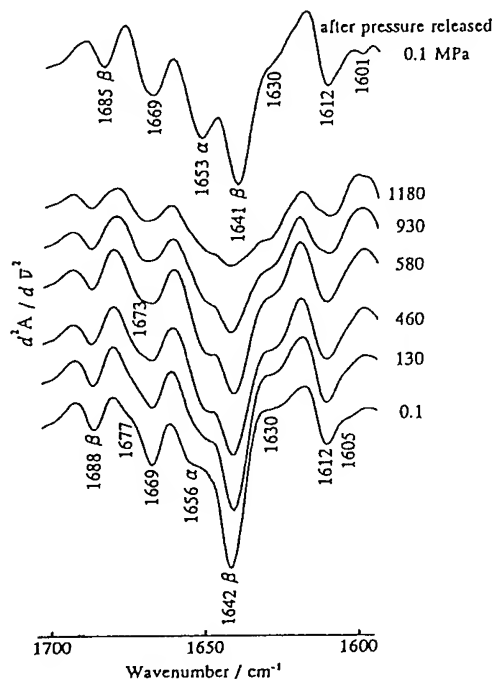


Figure 3: Second-derivative infrared spectra in the amide I/I' region of partially deuterated BPTI up to 1180 MPa at 25 °C.

gradual changes in the bands between 1660 and 1680  $\text{cm}^{-1}$  are observed with increasing pressure. The band

around 1669  $\text{cm}^{-1}$  after pressure is released is more asymmetric than that of completely deuterated BPTI, which suggests incomplete hydrogen-deuterium exchange. There seems likely to be the pressure resistible region in the turn and/or  $3_{10}$ -helix. Frequency shifts in the bands at 1630, 1642, 1669, and 1688  $\text{cm}^{-1}$  are not observed in the pressure range where BPTI is not precipitated. Pressure dependence of relative intensity on these four bands are shown in Figure 4. It is possible that the pressure-induced precipitation above 600 MPa hinders the rest of the exchangeable backbone amide protons involved in BPTI from being exchanged with solvent deuterons.

In conclusion, the present results imply that the pressure-induced structural rearrangements of BPTI, with individual differences in the secondary structure elements, are minor in aqueous solution. The unfolding of BPTI is not confirmed by FT-IR spectroscopy as well as by molecular dynamics simulation.

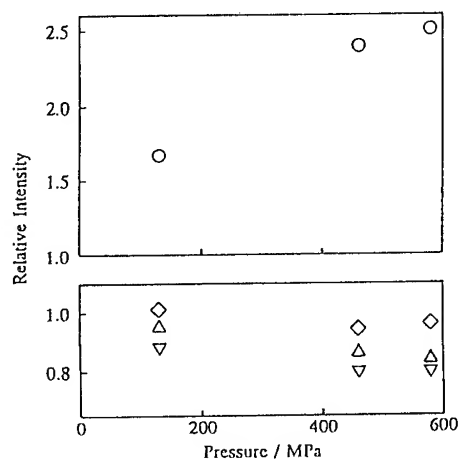


Figure 4: Pressure dependence of the relative intensity on the amide I/I' component bands at 1630 (○), 1642 (△), 1669 (▽), and 1688  $\text{cm}^{-1}$  (◇) for partially deuterated BPTI showing figure 3.

## References

1. R. M. Brunne, W. F. van Gunsteren, *FEBS Lett.* **323** (1993) 215.
2. D. B. Kitchen, L. H. Reed, and R. M. Levy, *Biochemistry* **31** (1992) 10083.
3. N. Takeda, M. Kato, and Y. Taniguchi, *Biochemistry* **34** (1995) 5980.
4. N. Takeda, M. Kato, and Y. Taniguchi, *Biospectroscopy* **1** (1995) *in press*.

# GENE EXPRESSION OF ASPARTATE $\beta$ -D-SEMIALDEHYDE DEHYDROGENASE AT ELEVATED HYDROSTATIC PRESSURE IN DEEP-SEA BAROPHILIC AND BAROTOLERANT BACTERIA

CHIAKI KATO, MARIA SMORAWINSKA, KOKI HORIKOSHI

*The DEEPSTAR group, Japan Marine Science and Technology Center,  
2-15 Natsushima-cho, Yokosuka, 237, Japan*

Aspartate  $\beta$ -D-semialdehyde dehydrogenase genes (*asd*) were cloned and sequenced from the deep-sea barophilic bacterium, strain DB6705, and the barotolerant bacterium, strain DSS12. The determined *asd* sequences of both strains were very similar, and the similarity of the deduced amino acids sequences was 96.2%. The mRNA 5' ends from both strains were localized at the same points by primer extension analysis, and two transcriptional starting points which were just 1 base difference were detected. 1st transcript from the nucleotide 792 was minor transcript, and 2nd transcript from the nucleotide 793 was major transcript in the barophilic strain DB6705, however 1st transcript was major, and 2nd was minor in the barotolerant strain DSS12. We observed that 2nd transcript was clearly regulated by elevated hydrostatic pressure in both strains. In *E. coli*, three *asd* transcripts were detected up to 30 MPa, but at 50 MPa, these were almost undetectable.

## 1. Introduction

The deep-sea environment is a unique habitat characterized by extremely high pressure and low temperature. Microorganisms living there have adapted to such extreme environment. To investigate the mechanisms of adaptation to high pressure in the deep-sea, we isolated several barophilic and barotolerant bacteria from deep-sea mud samples (1). The isolated strains are gram negative, and belong to the Proteobacterium  $\gamma$ -subgroup, based on phylogenetic analysis of 16S rDNA sequences. The ability of these bacteria to grow at high hydrostatic pressure indicates that they are probably specifically adapted to the deep-sea environment. Therefore, some gene expression systems of these bacteria may be regulated by high pressure. Investigation of the gene expression systems under high pressure is important to understand how deep-sea bacteria grow in their natural environment.

Filament formation in 1 atmosphere adapted bacteria, *E. coli*, grown at increased hydrostatic pressure was reported (2, 3). We observed the filament formation when barophilic bacteria were grown at low hydrostatic pressure, however no pressure effect was identified on cell sharps in barotolerant bacteria. Thus, it is possible that high pressure affects the cell division and may influence composition of bacterial cell wall. Aspartate  $\beta$ -D-semialdehyde dehydrogenase (ASD) is a key enzyme in the biosynthetic pathway of lysine, threonine, methionine, diaminopimelic acid (DAP), and isoleucine. DAP is an essential component present in the peptidoglycan in all gram negative and some gram positive bacteria (4). Therefore, the gene expression of ASD in deep-sea barophilic and barotolerant bacteria, and in *E. coli*, may be influence

by hydrostatic pressure.

To analyze the *asd* gene expression under high pressure, we cloned *asd* genes from the barophilic bacterium, strain DB6705, and barotolerant bacterium, strain, DSS12. We determined the nucleotide sequence of the cloned fragments, and discussed the phylogenetic relations of the ASD amino acids sequences. We detected two transcriptional starting points of the *asd* genes from both the barophilic and barotolerant strains, and showed that the gene expression of the 2nd transcript was clearly controlled by pressure in both strains. And finally, we also detected the transcripts of *asd* gene in *E. coli* by primer extension analysis, and compared the *asd* gene expression systems between the deep-sea bacteria and *E. coli*.

## 2. Materials and Methods

### 2.1 Bacterial strains, plasmids and recombinant DNA techniques and the cloning procedure

The barophilic bacterium, strain DB6705, isolated from the Japan trench (depth; 6356m), and the barotolerant bacterium, strain DSS12, isolated from the Ryukyu trench (depth; 5110m) were used as the DNA donor of *asd* genes (1). *E. coli* strain  $\chi$ 6097 ( $\Delta$ *asd*; 5) was used for cloning of the genes. The phage plasmids, pUC119, and the host strain, *E. coli* strain JM109 were used for cloning and DNA sequencing study (6). Recombinant DNA work was carried out as described by Sambrook et al. (7). The cloned DNA was sequenced using an automated DNA sequencer, model 373A (Perkin Elmer/Applied Biosystems), by the dideoxy terminator procedure (8), as described in the manual. The GENETYX-MAC program (Software Co.) was used to analyze DNA

sequences. Chromosomal DNAs from the barophilic bacterium, strain DB6705, and the barotolerant bacterium, strain DSS12, were extracted by the method of Saito and Miura (9). Chromosomal DNAs were digested with *Hind*III, and ligated into the vector pUC119 digested with the same restriction endonuclease. The ligated DNAs were introduced into *E. coli* strain  $\chi$ 6097, and transformants were selected on LB agar medium without DAP, containing ampicillin (50  $\mu$ g/ml), grown for over night at 37°C. Growing colonies (*asd*<sup>+</sup>) on the plates were obtained and the recombinant plasmids, named pMSDB1 and pMSDS1 containing *asd* from the strain DB6705 and the strain DSS12, respectively, were isolated from the *asd*<sup>+</sup> transformants.

## 2.2 RNA preparation and the procedure of genetic analysis

RNA preparation from the barophilic strain, DB6705, and barotolerant strain, DSS12, were carried out as described previously (10). Total RNA from *E. coli* strain JM109 (*asd*<sup>+</sup>) was prepared as described by Ausubel et al. (11). The transcriptional start point was determined by primer extension analysis with the biotinylated oligonucleotides, 5'-AATGGTTTGACC CACTGCGCCCGATGCACC-3' for strain DB6705, 5'-CATGGTTTGACCCACTGCGCCCGATGCACC-3' for strain DSS12, and 5'-GAACGGAGCCGACC AACCGCGCCAGCCGA-3' for *E. coli*, synthesized on an Applied Biosystems Model 392 DNA/RNA Synthesizer. The sequence of these primers are complementary to the nucleotides 858 to 887 of DB6705 *asd*, the nucleotides 858 to 887 of DSS12

*asd*, and the nucleotides 259 to 288 of *E. coli asd* according to the sequence reported by Haziza et al. (12). The transcripts of these strains at several pressures were detected using chemiluminescent as described previously (10). To see how high pressure regulated the RNA transcripts from the *asd* genes, the effect of increasing pressure on the abundance of the mRNA transcript was also examined using total RNA from these strains grown at several pressures at the same time as the primer extension study.

## 3. Results

### 3.1 Sequencing of *asd* genes from the barophilic bacterium, strain DB6705, and barotolerant bacterium, strain DSS12

The *asd* genes of the barophilic bacterium, strain DB6705, and the barotolerant bacterium, strain, DSS12, were cloned as 2.0 kb *Hind*III fragment in the plasmid, pMSDB1, and 1.9 kb *Hind*III fragment in the plasmid, pMSDS1, from the *asd*<sup>+</sup> *E. coli*  $\chi$ 6097 transformants, respectively. DNA sequences of these fragments were determined (deposited in the DDBJ, EMBL, and GenBank nucleotide sequence data bases as the accession numbers, D49539 from strain DB6705, and D49540 from strain DSS12) and amino acids sequences of the ASDs, which were consist of 338 amino acids for both strains, were deduced. Both of the DNA sequences are very similar, and the similarity of the deduced amino acids sequence of both ASDs was 96.2%.

### 3.2 Analysis of transcription by primer extension

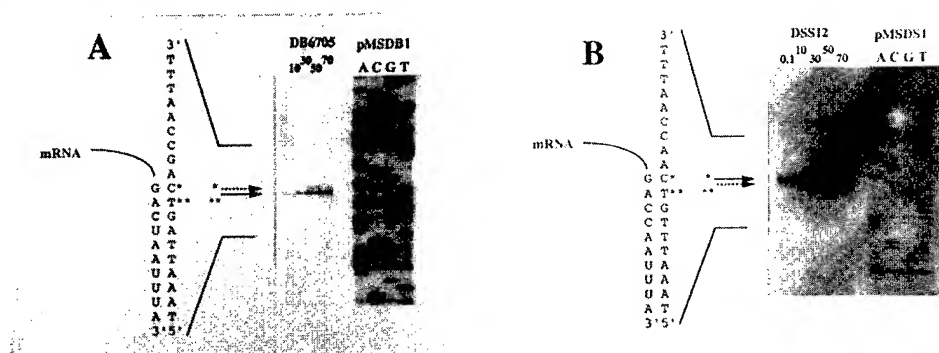


Fig. 1. Primer extension analysis to determine the transcriptional start point for the *asd* genes in the barophilic bacterium, strain DB6705, (A) and barotolerant bacterium, strain DSS12, (B) and level of mRNA derived from the promoter in response to elevated pressure. The DNA sequence ladders of the DB6705 *asd* gene (from pMSDB1) and the DSS12 *asd* gene (from pMSDS1) were obtained by the method of Sanger et al. (8), employing the same primers. The nucleotide sequence corresponding to the ladder is written on the left. The transcriptional start points are indicated by arrows and asterisks, and the 5' end of the mRNA is also shown. Lined arrows show the major transcript, and dotted arrow show the minor transcript. Asterisks "\*" and "\*\*\*" show the transcript #1 and #2, respectively as described in the text. Lanes: 0.1, RNA from the strain DSS12 (B) grown at 0.1 MPa, 10, at 10 MPa, 30, at 30 MPa, 50, at 50 MPa, and 70, at 70 MPa.

The 5' ends of the mRNA were identified as nucleotide 792 and 793 in the strain DB6705, and the strain DSS12, as indicated by "\*" and "\*\*\*" in Fig 1. We defined 1st transcription from the nucleotide 792 (\*) as transcript #1, and 2nd transcription from the nucleotide 793 (\*\*) as transcript #2. In the barophilic strain, DB6705, transcript #1 was minor, and transcript #2 was major, however, in the barotolerant strain, DSS12, transcript #1 was major and transcript #2 was minor. In both strains, transcript #2 was clearly enhanced at elevated hydrostatic pressures, so high pressure affected the gene expression of the transcript #2 of the both *asds*. However, the transcript #1 may not be affected by pressure.

The transcripts of the *E. coli asd* gene were also analyzed by primer extension at elevated hydrostatic pressures (Fig. 2). Three different sizes of transcripts were found as defined the transcripts #1, #2, and #3 in Fig. 2. Interestingly, the transcripts #1 and #2 were decreasing at high pressure, however the transcript #3 was increasing up to 30 MPa like as the transcript #2 of the deep-sea bacteria's *asd*. But at 50 MPa, *asd* transcripts were almost undetectable, this might mean very little ASD enzyme was synthesized in the bacterial cell, so this may be one of the cause of filament formation and growth inhibition at high pressure in *E. coli*.

#### 4. Discussion

We have cloned *asd* genes from the deep-sea adapted barophilic bacterium, strain DB6705, and the barotolerant bacterium, strain DSS12, and determined their nucleotide sequences. The gene expression of the *asds* was analyzed by primer extension, and the results suggested that the gene expression of one of the transcript (#2) was regulated by elevated hydrostatic pressure in both the barophilic strain and the barotolerant strain (Fig. 1). In both strains, the transcriptional starting points were at the same location, and the putative -10 [TAAATT] and -35 [TAAACA] sequences of the promoter region which were different from the *E. coli* consensus sequence (13) were present in both strains. The nucleotide sequences around the *asd* promoter regions of both strains were very similar, thus, the cause of difference in *asd* transcription of both strains may depend on differences in transcription factors between barophilic bacteria and barotolerant bacteria. These results suggested that the gene expression systems of barophilic bacteria might express the function under the high pressure, and those of barotolerant bacteria might express it under any pressures. This may be one of answer why barophiles can not grow at atmospheric pressure, and barotolerants can grow at

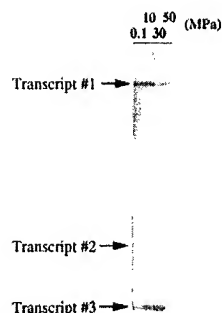


Fig. 2. Primer extension analysis of the *E. coli asd* gene. Lined arrows show the transcripts #1, #2, and #3. Lanes: 0.1, RNA from the *E. coli* JM109 grown at 0.1 MPa, 10, at 10 MPa, 30, at 30 MPa, and 50, at 50 MPa.

any pressures. It is very interesting that 1 atmosphere adapted *E. coli* expresses several *asd* transcripts which respond to high pressure, so that two of them are pressure sensitive and one of them is pressure dependent up to 30 MPa (Fig. 2). We have reported that some *E. coli* gene expressions are influenced by high hydrostatic pressure (14, 15), and the *asd* expression of *E. coli* may be similar. This suggests that it is possible that *E. coli* conserves the function of high pressure adapted microorganisms in the mechanisms of gene expression. The results of gene expressions of bacterial *asds* suggest that the morphological changes under high pressure conditions correspond the bacterial growth abilities, therefore *asd* gene expression controlled by pressure in deep-sea adapted bacteria is one of the important mechanisms to survive at deep-sea environment.

#### References

1. C. Kato *et al*, *Biodiv. Conserv.* **4**, 1 (1995).
2. C.E. Zobel and A.B. Cobet, *J. Bacteriol.* **87**, 710 (1963).
3. K. Tamura *et al*, *FEMS Microbiol. Lett.* **99**, 321 (1992).
4. K.H. Schleifer and O. Kandler, *Bacteriol. Rev.* **36**, 407 (1972).
5. J.E. Galan *et al*, *Gene* **94**, 29 (1990).
6. C. Yanisch-Perron *et al*, *Gene* **33**, 103 (1985).
7. J. Sambrook *et al*, in *Molecular Cloning: a laboratory manual*, 2nd ed. (Cold Spring Harbor Laboratory, New York, 1989).
8. F. Sanger *et al*, *Proc. Natl. Acad. Sci. USA* **74**, 5463 (1977).
9. H. Saito and K. Miura, *Biochim. Biophys. Acta* **72**, 619 (1963).
10. C. Kato *et al*, *J. Bar. Biotechnol.* **2**, 125 (1995).
11. F.M. Ausubel *et al*, in *Short protocols in molecular biology*, 2nd ed. (John Wiley & Sons, New York, 1992).
12. C. Haziza *et al*, *EMBO J.* **1**, 379 (1982).
13. D.W. Cowing *et al*, *Proc. Natl. Acad. Sci. USA* **82**, 2679 (1985).
14. C. Kato *et al*, *FEMS Microbiol. Lett.* **122**, 91 (1994).
15. T. Sato *et al*, *J. Mar. Biotechnol.* in press.



## PRESSURE EFFECTS ON PROTEIN STRUCTURE-FUNCTION

Claude BALNY and Reinhard LANGE  
*INSERM U 128, BP 5051, 34033 MONTPELLIER Cedex 1, France*

High hydrostatic pressure induces changes in protein conformation, solvation and enzyme activities via reversible and non-reversible effects on the intra- and inter-molecular interactions (noncovalent bonds). To have access to these structural modifications, spectroscopic investigations are required. Recent improvements in resolution are second and fourth order derivative spectroscopies in the ultraviolet region of proteins. A complementary approach can be to record the protein activities under pressure, in order to probe the thermodynamics of the interconversion of successive intermediates in an enzyme reaction pathway. When, in addition to the pressure parameter, a second variable, the temperature, is considered, it is thereby possible to obtain the complete set of the activation parameters  $\Delta G^\ddagger$ ,  $\Delta S^\ddagger$ ,  $\Delta H^\ddagger$  and  $\Delta V^\ddagger$ .

### Introduction

Since some years, the studies of high pressure effects on living systems have gained importance. There are at least four main reasons for the introduction of pressure as a variable acting on biological systems : deep-sea world, physico-chemical approaches, biotechnological applications and the study of proteins from extremophiles bacteria. The effects of pressure on proteins, nucleoproteins and membranes have been recently reviewed, including the applications point of view (1-4).

### Methods

Most biophysical techniques for protein structure investigation may be used at high pressure. The classical setup for high pressure measurements comprises high pressure generation, pressure control and detection systems. UV-visible and fluorescence spectroscopy, NMR, infrared, Raman, Fourier transform infrared and light scattering spectroscopy have been adapted to high pressure. New techniques have also been introduced recently such as gel electrophoresis which permit to follow pressure-induced changes in subunit interactions and ligand binding (5). In the field of enzymology, the use of rapid mixing methods is a real improvement which permits to have access to elementary steps of reactions. Some years ago, in this laboratory, we have developed the stopped-flow method operating up to 200 MPa, in a temperature range + 40 to - 40 ° C, (dead time of about 5 ms) with a detection either in absorbancy or in fluorescence mode (6).

Derivative spectroscopy adapted to high pressure (up to 500 MPa) is a new tool for analyzing the effects of pressure on the denaturation of proteins. The UV-spectrum is dominated by the overlapping absorbance bands of the aromatic amino acids (phe, tyr or tryp), and of visible chromophores like heme groups.

High hydrostatic pressure induces changes in protein conformation, solvation and enzyme activities via reversible and non-reversible effects on the intra- and inter-molecular interactions (noncovalent bonds). To have access to these structural modifications, spectroscopic investigations are required, including heavy techniques such as NMR or FTIR which are limited to certain types of proteins, or UV spectroscopy which is a relatively accessible technique. Improvements in spectroscopic resolution are second and fourth order derivative spectroscopies in the ultraviolet region of proteins which are used to study the polarity of the microenvironment of the aromatic amino acid residues. Indeed, the polarity of the medium affects the amplitude, the position and the shape of the fourth order derivative spectral bands. Hereby it is possible to evaluate the pressure induced conformation modifications (7).

### Results

The behaviour of proteins under high pressure is governed by Le Chatelier's principle : application of pressure shifts an equilibrium towards the state that occupies a smaller volume.

Non-covalent molecular interactions are affected by pressure : solvation of charged groups is accompanied by volume reduction (phenomenon called electrostriction), formation of coulombic interactions is accompanied by positive changes in volume, formation of hydrophobic interaction is characterized by positive values of changes in volume. Charge-transfer interactions and stacking of aromatic rings show small negative volume variation and hydrogen bonds are almost pressure-insensitive. The direct consequences are that coulombic interactions are not favoured by pressure and hydrophobic interactions are destabilized by pressure. Therefore, pressure affects protein structure, at the secondary, tertiary and quaternary levels, generating protein denaturation, a field very well documented (4).

Solvation is also involved in high pressure studies. As pointed-out thirty years ago by C. Tanford, the physico-chemical properties of enzymes depend largely on the direct or indirect role of water in various noncovalent interactions including solvation of ionic groups and dipoles, hydrogen bonding and hydrophobic interactions. An approach to elucidate the role of water in protein structure and function is to investigate reactions in hydrated organic solvents and to perturb the systems under study using physico-chemical parameters such as temperature and pressure. For many years we have developed the use of water miscible organic solvent, first for cryo-enzymology purposes to do experiments in the fluid state below zero degrees, second as a tool to perturb reaction pathways and thus to obtain mechanistic information. More recently, we have combined solvent, temperature and pressure perturbation in a new technology : cryo-baro-enzymology. Indeed, as pointed out by Low and Somero, one can gain information by perturbing the system, i.e., by varying the physico-chemical properties of the medium (solvent, salt, pH, etc.) (8).

Pressure modifies also the rate of enzyme-catalysed reactions via changes in the structure of an enzyme or changes in reaction mechanism. Depending on the reaction under study, a reaction rate can be accelerated or decelerated by increasing pressure (the sign of the activation volume term  $\Delta V^\ddagger$  can be negative or positive)(9-10).

In this laboratory, we develop this enzymology in extreme conditions, recording the protein activities under pressure, in order to probe the

thermodynamics of the interconversion of successive intermediates in an enzyme reaction pathway.

Furthermore, when the enzyme reaction is explored as a function of both pressure and temperature, we can determine the complete set of the activation parameters  $\Delta G^\ddagger$ ,  $\Delta S^\ddagger$ ,  $\Delta H^\ddagger$  and  $\Delta V^\ddagger$  (10-13).

A classical example experimented in this laboratory deals with the hydroxylamine oxidase reaction (HAO) from *Nitrosomonas europaea* (10). The first step of this reaction is the reduction of the enzyme by its substrate - hydroxylamine - which proceeds in two phases. Changing the solvent from water to 40 % ethylene glycol enabled to experiment the system in fluid media below 0 ° C. For the first phase, between - 15 ° C and room temperature, the activation volume of the reaction increased with increasing temperature. The Arrhenius plot had a downward inflection at about 0 ° C. At atmospheric pressure, this inflection was weak. At high pressure (800 MPa), the break was strongly pronounced with an inversion of the sign of the activation enthalpy term :  $\Delta H^\ddagger = - 18$  and  $+ 58$  kJ/mol in the temperature ranges 20 to 3 ° C and 3 to - 15 ° C, respectively. This has been interpreted as a physical modification of the orientation of the hemes of the protein as a function of the temperature, the application of high pressure, magnifying the phenomena.

As above-mentioned, in complement to kinetic approaches, structural information can be achieved using fourth order derivative spectroscopy where, comparatively to classical UV spectroscopy, a better resolution is obtained by transforming the spectra into derivatives. Fourth order derivative spectroscopy has the advantage that a maximum in the original spectra corresponds to a maximum of the derivative spectrum. Usually, the derivatives are computed by shifting a spectrum for a given wavelength difference and its subsequent subtraction from the original spectrum. This method is suitable to analyse solvent and pressure effects and offers a simple way to determine the polarity in the vicinity of the aromatic amino acids. The development of this method is in progress in the laboratory and is actually applied to the study of pressure induced protein structural changes. As a matter of fact, the observation of pressure-induced changes of enzyme activity and spectral properties leads frequently to the question of how to interpret these features in structural terms. The fourth order derivative spectroscopy might be

able to answer this question because we have verified that the method is free of eventual conceptual artifacts. So, we can use it safely at high pressure. Moreover, this method appears as a suitable tool to evaluate changes of the dielectric constant in the vicinity of the aromatic amino acids in proteins which undergo pressure induced structural changes.

In collaboration with Dr. J. Frank (Delft University, The Netherlands), different proteins are studied by this method : adrenodoxin (a small iron-sulfur protein which serves as an electron donor for cytochrome P450<sub>scc</sub>), ribonuclease A and methanol dehydrogenase (a tetrameric protein).

These approaches which include general thermodynamic considerations and specific technologies have two consequences : they permit to discuss results in terms of changes in protein conformation and they permit, when the pressure is applied, to magnify phenomena, which are only slightly detectable at atmospheric pressure. On the other hand, if many biochemists regard high pressure as a physical parameter mainly of theoretical interest and of a rather limited value in experimental biochemistry, actual results from this laboratory and from many other groups show that pressure is a powerful tool for the study of proteins and modulation of enzymatic activity.

### Use of high pressure in bioscience

In addition to the studies of the pressure effects on protein structure-function, we must point out the possibility to apply pressure in specific biotechnological areas, mainly for food processing. The use of high pressure instead of high temperature in food processing leads to an improved preservation of food taste, flavour and color. This is based on the stability of the covalent structures of proteins (and related components), in contrast with their relative instability towards increased temperatures.

At present, several commercial food products using the high pressure technique are on the market in Japan, and research and development in this field are in progress in Europe (1, 3).

### Acknowledgements

We thank Drs J. Frank, A.B. Hooper, P. Masson, V. Mozhaev, Mme Bec and Mr J-L. Saldana for help and discussion.

### References

1. C. Balny, R. Hayashi, K. Heremans and P. Masson, P. (Eds) *High Pressure and Biotechnology*, vol.224, (J. Libbey Eurotext, London, Montrouge, 1992).
2. C. Balny, P. Masson and F. Travers, *High Pres. Research.*, **2** (1989) 1-28.
3. V. Mozhaev, K. Heremans, J. Frank, P. Masson and C. Balny, *TIBTECH*, **12**, (1994) 493-501.
4. V. Mozhaev, K. Heremans, J. Frank, P. Masson and C. Balny, *Proteins : Structure, Function and Genetics* (1995) in press.
5. P. Masson in *High Pressure Chemistry and Physics*, ed. N. S. Isaacs (Oxford University Press, 1995) in press.
6. C. Balny, J-L. Saldana and N. Dahan, *Anal. Biochem.*, **163** (1987) 309-315.
7. R. Lange, N. Bec, V. Mozhaev and J. Frank, *Biophys. J.*, submitted.
8. P.S. Low and G.N. Somero, *Proc. Natl. Acad. Sci. USA*, **75** (1975) 3305-3018.
9. C. Balny, F. Travers, T. Barman and P. Douzou, *Eur. Biophys. J.*, **14** (1987) 375-383.
10. C. Balny and A.B. Hooper, *Eur. J. Biochem.*, **176** (1988) 273-279.
11. I. Heiber-Langer, A.B. Hooper and C. Balny, *Biophys. Chem.* **43** (1992) 265-277
12. R. Lange, I. Heiber-Langer, C. Bonfils, I. Fabre, M. Negishi and C. Balny, *Biophys. J.*, **66** (1994) 89-98.
13. C. Balny, *High Pres. Research.* **12** (1994) 187-191.

# EFFECT OF HYDROSTATIC PRESSURE ON THE YEAST VACUOLES

FUMIYOSHI ABE AND KOKI HORIKOSHI

*The DEEPSTAR Group, Japan Marine Science and Technology Center,  
2-15 Natsushima-cho, Yokosuka 237, Japan*

## ABSTRACT

The yeast vacuole is an acidic compartment involved in cellular ion homeostasis and degradation of proteins. Hydrostatic pressure of 40 MPa reduced the vacuolar pH by 0.2 pH units in *Saccharomyces cerevisiae* ATCC 60782, defined using 6-carboxyfluorescein (6-CF). Vacuolar uptake of the weak base quinacrine was increased by hydrostatic pressure, suggesting that accumulation of the dye was induced by the increased pH gradient across the vacuolar membrane. Meanwhile, hydrostatic pressure inhibited proton extrusion from the cells, which might cause cytoplasmic acidification. In order to maintain the cytoplasmic pH, it is possible that the yeast vacuole serves as a proton sequesterant under high pressure conditions.

## Introduction

It has been reported that hydrostatic pressure has a large effect on the biological functions and viability of living organisms (1, 2, 3). However, little is known about the physiological and biochemical bases of the cellular responses to hydrostatic pressure. In the budding yeast *Saccharomyces cerevisiae*, high hydrostatic pressure above 100MPa induces cytoplasmic petite mutation (4), and tetraploid or homozygous diploid forms (5). However, few data have been reported on biological effects at moderate or nonlethal hydrostatic pressure. The yeast vacuoles contain a large amount of hydrolytic enzymes, and plays an important role in protein degradation and the storage of amino acids, carbohydrates, polyphosphates and ions (6, 7). The vacuole is an acidic organelle, preserving the low pH through the function of vacuolar  $H^+$ -ATPase (V- $H^+$ -ATPase) on its membrane. (8, 9). Acidification of vacuoles is principal for the activity of vacuolar enzymes, protein transport, and cytosolic ion homeostasis (7, 10, 11). In this study, we describe the effect of hydrostatic pressure on vacuolar acidification and a vacuolar function under high pressure condition.

## Materials and Methods

### *Yeast strains and culture conditions*

The yeast strain used in this study was *Saccharomyces cerevisiae* ATCC 60782. Cells were grown at 24°C in YPD broth (2% w/v bacto-peptone, 1% w/v yeast extract, 2% w/v glucose) in 100ml Erlenmeyer flasks on an orbital shaker at 150rpm.

### *Application of hydrostatic pressure*

Cells from the logarithmic phase of growth ( $2 \times 10^7$

cells  $ml^{-1}$ ) were placed in plastic tubes. After sealing with parafilm, the tubes were put into titanium pressure vessels (Rigo-sha, Tokyo) and were subjected to hydrostatic pressure. The required hydrostatic pressure was reached within 1min. To obtain samples, the pressure was released for a few seconds.

### *Vacuole labeling with fluorescent dyes*

6-CFDA and quinacrine were used to label yeast vacuoles in YPD containing 50mM citric acid (pH 3.0), and YPD containing 50mM  $Na_2HPO_4$  (pH7.6), respectively (12, 13). The final concentration of 6-CFDA was 10 $\mu$ M, and that of quinacrine was 1mM. Cells from the logarithmic phase of growth ( $2 \times 10^7$  cells  $ml^{-1}$ ) were harvested by centrifugation (5000rpm, 20sec.), resuspended in the medium, and incubated with each dye for 1h at atmospheric or high hydrostatic pressure. The labeled cells were immediately cooled on an ice, collected by centrifugation, and washed three times in MHG buffer (50mM MES, 50mM HEPES, 50mM KCl, 50mM NaCl, 110mM glucose, pH6.0).

### *Fluorescence analysis*

The labeled cells were analyzed using a CAF-110 fluorometer (Jasco, Tokyo). Vacuolar pH was determined as described by Preston et al. (12) Fluorescence emissions of 540nm were measured when cells were excited at 458nm and 488nm. The fluorescence ratio (emission with 488nm excitation / emission with 458nm excitation) of the 6-CF-labeled cells was calculated and checked against calibration curves. *In vitro* calibration curves of 6-CF fluorescence were determined with 0.25mM 6-CF in MHI buffer (50mM MES, 50mM HEPES, 50mM KCl, 50mM NaCl, 0.2M ammonium acetate, 10mM  $NaN_3$ , 10mM 2-deoxyglucose, 50mM carbonylcyanide m-chlorophenylhydrazone) at

specified pHs. *In vivo* calibration curves were determined by equilibrating vacuolar pH of labeled cells to that of external pH in MHI buffer at specified pHs (12). Quinacrine-labeled cells ( $10^8$  cells  $\text{ml}^{-1}$  in MHG buffer, pH6.0) were excited at 450nm (10nm band-width), and the emitted fluorescence of 540nm was measured (arbitrary units).

#### Measurement of changes in proton extrusion

Proton extrusion by the cells was determined by measuring the external pH. Logarithmic phase cells were washed three times in distilled water, resuspended in 2% (w/v) glucose at  $6 \times 10^7$  cells  $\text{ml}^{-1}$ , and placed in sterile tubes. Immediately after sealing the tubes, the cells were subjected to hydrostatic pressure for 1h. External pH was measured using  $\Phi 50$  pH meter (Beckman).

### Results and Discussion

#### Vacuolar acidification under high pressure conditions

Cells were incubated with 6-CFDA for 1h at each pressure. 6-CF was localized in vacuoles at both atmospheric and high pressure (data not shown). At atmospheric pressure, the vacuolar pH was 6.32. The value was similar to a previous report (12). High pressure treatment for 1h reduced vacuolar pH (Fig. 1). The vacuolar pH values of the cells incubated at 20MPa, 40MPa and 60MPa fell to 6.24, 6.12 and

6.14, respectively. Similar results were obtained with other industrial yeast strains. While, no considerable change was observed in viability of the cells incubated for 1h at each pressure (data not shown).

#### Quinacrine accumulation under high pressure condition

The weak base quinacrine accumulates in acidic compartments, depending on the pH gradient across the membrane (13, 14). We analyzed the effect of high pressure on vacuolar uptake of quinacrine. At atmospheric pressure, fluorescence emissions of quinacrine-labeled cells ( $10^8$  cells  $\text{ml}^{-1}$  in MHG buffer, pH6.0) were 104.1(arbitrary units). Fig. 2 shows the vacuolar fluorescence of the cells after application of hydrostatic pressure. Accumulation of quinacrine was greatly increased by hydrostatic pressure 40 to 60MPa. Increased accumulation of quinacrine strongly confirmed the pressure-induced acidification of the yeast vacuoles.

#### Activities of plasma membrane $H^+$ -ATPase under high pressure conditions

At atmospheric pressure, cells reduced the external pH from 5.55 to around 4.0, within 1h in the presence of 2% (w/v) glucose. Increases in hydrostatic pressure severely repressed the proton extrusion (Fig. 3), suggesting that the plasma

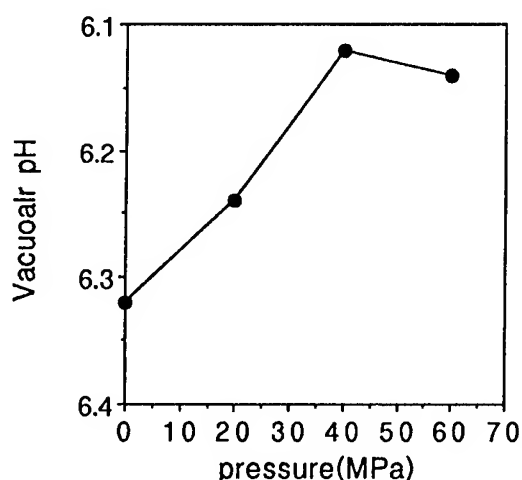


Fig.1 Vacuolar pH under several pressure conditions. Cells were incubated with 6-CFDA at atmospheric pressure or high pressure, and analyzed by a fluorometer.

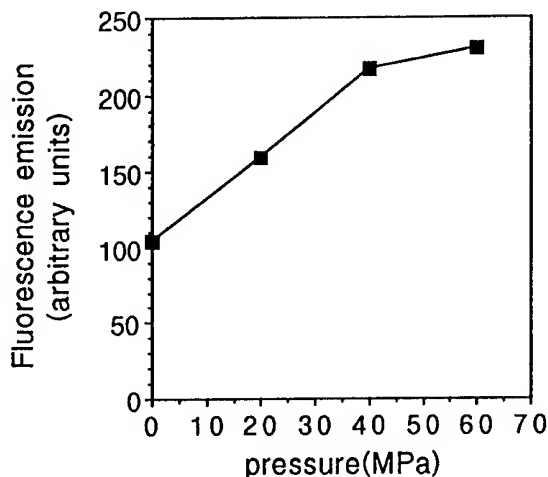


Fig.2 Vacuolar accumulation of quinacrine under several pressure conditions. Cells were incubated with quinacrine at atmospheric pressure or high pressure, and fluorescence emission of 540nm with 450nm excitation was measured (arbitrary units).

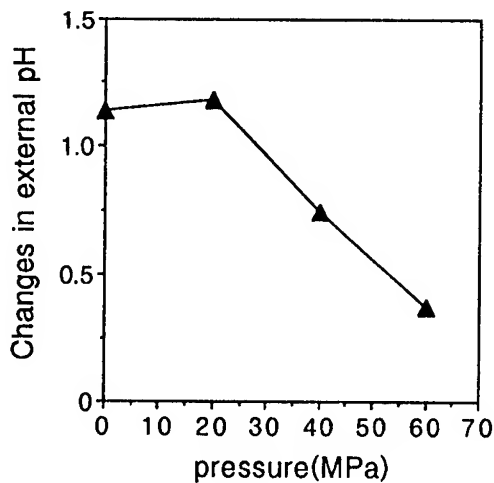


Fig. 3 Changes in external pH under several pressure conditions. Cells were incubated in 2% glucose at atmospheric pressure or high pressure. External pH was determined by a pH meter.

membrane  $H^+$ -ATPase may be inactivated. Subsequently, this may cause the cytoplasmic acidification of cells incubated in an acidic medium such as YPD. Acidification of cytoplasm is a critical condition in many enzyme activities and cell viability. In order to maintain the cytoplasmic pH, it is possible that the vacuoles served as a proton sequestrant when high hydrostatic pressure was applied. It is still unknown whether there is a unique pressure-sensing factor or a specific mechanism involved in the pressure-induced acidification, however, V- $H^+$ -ATPase could play an important role in the regulation.

## References

1. Zimmerman, A.M. and Marsland, D. (1964) Cell division: effects of pressure on the mitotic mechanism of marine eggs (*Arbacia punctulata*) *Exp. Cell Res.* **35**, 293-302.
2. Landau, J. V. (1970) Hydrostatic pressure on the biosynthesis of macromolecules. In *High Pressure Effects on Cellular Processes* (ed. A.M. Zimmerman), pp.45-70. New York and London: Academic Press.
3. Zimmerman, A.M. (1971) High pressure studies in cell biology. *Int. Rev. Cytol.* **30**, 1-47.
4. Rosin, M.P. and Zimmerman, A.M. (1977) The induction of cytoplasmic petite mutants of *Saccharomyces cerevisiae* by hydrostatic pressure. *J. Cell Sci.* **26**, 373-385.
5. Hamada, K., Nakatomi, Y. and Shimada, S. (1992) Direct induction of tetraploids or homozygous diploids in the industrial yeast *Saccharomyces cerevisiae* by hydrostatic pressure. *Curr. Genet.* **22**, 371-376.
6. Sato, T., Ohsumi, Y., Anraku, Y. (1984) Substrate specificities of active transport systems for amino acids in vacuolar-membrane vesicles of *Saccharomyces cerevisiae*. *J. Biol. Chem.* **259**, 11505-11508.
7. Kitamoto, K., Yoshizawa, K., Ohsumi, Y. and Anraku, Y. (1988). Mutants of *Saccharomyces cerevisiae* with defective vacuolar function. *J. Bacteriol.* **170**, 2687-2691.
8. Kakinuma, Y., Ohsumi, Y. and Anraku, Y. (1981) Properties of  $H^+$ -translocating adenosine triphosphatase in vacuolar membranes of *Saccharomyces cerevisiae*. *J. Biol. Chem.* **256**, 10859-10863.
9. Uchida, E., Ohsumi, Y., Anraku, Y. (1985) Purification and properties of proton-translocating magnesium ATPase from vacuolar membranes of *Saccharomyces cerevisiae*. *J. Biol. Chem.* **260**, 1090-1095.
10. Latterich, M. and Watson, M.D. (1991) Isolation and characterization of osmosensitive vacuolar mutants of *Saccharomyces cerevisiae*. *Mol. Microbiol.* **5**, 2417-2426.
11. Klionsky, D.J., Nelson, H. and Nelson, N. (1992) Compartment acidification is required for efficient sorting of proteins to the vacuole in *Saccharomyces cerevisiae*. *J. Biol. Chem.* **267**, 3416-3422.
12. Preston, R.A., Murphy, R.F. and Jones, E.W. (1989) Assay of vacuolar pH in yeast and identification of acidification-defective mutants. *Proc. Natl. Acad. Sci. USA* **86**, 7027-7031.
13. Weisman, L.S., Bacallao, R. and Wickner, W. (1987) Multiple methods of visualizing the yeast vacuole permit evaluation of its morphology and inheritance during the cell cycle. *J. Cell Biol.* **105**, 1539-1547.
14. Banta, L.M., Robinson, J.S., Klionsky, D.J. and Emr, S.D. (1988) Organelle assembly in yeast: Characterization of yeast mutants defective in vacuolar biogenesis and protein sorting. *J. Cell Biol.* **107**, 1369-1383.

## HIGH PRESSURE STUDIES OF EXCITONICALLY COUPLED PHOTOSYNTHETIC ANTENNA COMPLEXES

N. R. S. Reddy, H.-M. Wu, R. Jankowiak, and G. J. Small  
Ames Laboratory-USDOE and Department of Chemistry  
Iowa State University, Ames, IA 50011, U.S.A.

### ABSTRACT

Pressure dependence of the B800 and B850 bands has been measured for the LH II antenna complex of *Rb. sphaeroides*. A possible explanation for the pressure independence of the B800→B850 energy transfer rate is provided.

### Introduction

Excitation energy transfer and primary charge separation in photosynthetic units are problems of long-standing interest [1-9]. In recent years there has been a burgeoning of activity because of the increasing availability of X-ray structures for protein complexes. Both ultrafast and spectral hole burning spectroscopies have been extensively applied to the study of the bacterial RC and the PS II RC as well as several antenna complexes. In this paper we present the results of our high pressure studies on energy transfer in the LH II antenna complex (NF57 mutant devoid of RC and LH I) of *Rb. sphaeroides*.

We have reported recently on the effects of pressure on the excited electronic state structure and transport dynamics in *Rps. viridis* [10] and PS II reaction centers [11] as well as the FMO antenna complex of *Chlorobium tepidum* [12]. Pressure dependence of the secondary charge separation kinetics in the RC of *Rps. viridis* and *Rb. sphaeroides* has also been reported [13-15]. These results show that the linear pressure shifts for the various  $Q_y$ -states can be large and are generally not the same. This is important since one can alter the energy gap(s) associated with energy and electron transfer.

Recent structural data [16] for the LH II complex from *Rb. acidophila* show that within a structural subunit the B850 BChl *a* are closely spaced with strong excitonic interactions between BChls. The B850 and B800 BChl on the other hand are farther apart (21 Å). These data thus confirm the results of earlier hole burning studies that the B850 BChl *a* are strongly exciton coupled [17,18] and that their coupling with B800 BChl *a* is weak. Narrow ( $4.5 \pm 0.5$  cm<sup>-1</sup>) zero phonon holes (ZPH) burned into the B800 band established the B800→B850 energy transfer time to be  $2.4 \pm 0.2$  ps at 4.2 K [17,19]. Hole burning has also established [17] that the 750 cm<sup>-1</sup> BChl *a* vibrations promote the B800 to B850

Förster type energy transfer. The low temperature (4.2 K) homogeneous width of 220 cm<sup>-1</sup> for the B850 band further explains the weak temperature dependence of the B800→B850 energy transfer [17]. Novel non-photochemical action spectroscopy has been used to identify the weakly absorbing B870 and B896 states [18]. These states have been identified as the lowest excitonic levels of the B850 and B875 bands. These states had further been implicated [20,21] as "shuttle" states for energy transfer from B850 to B875 and from B875 to P870, respectively. Recent X-ray structure data does *not* identify any 'special' BChls among the 18 (B850) BChls supporting the interpretation of B870 and B896 states based on exciton bands. Hole burning at high pressures has shown that the B800→B850 energy transfer rate remains unchanged for pressures of up to 680 MPa even though the energy gap is increased by 190 cm<sup>-1</sup>.

### Experimental

Detail reports on the high pressure and hole burning setups have been published [11]. Briefly, high pressures were generated using a three stage compressor (model U11, Unipressequipment Division, Polish Academy of Sciences, Poland) using helium gas as the pressure transmitting medium. Absorption spectra were obtained using a Bruker 120 HR Fourier Transform Spectrometer. A Ti:sapphire ring laser (Coherent CR 899-21) was used for hole burning.

### Results and Discussion

The pressure dependence of low temperature (85 K)  $Q_y$ -absorption spectra of the LH II antenna complex is shown in Figure 1. Both the B800 and B850 bands shift to the red as the pressure is increased from 0.1 MPa to 770 MPa. Similar data were obtained at 4.2 K. The linear pressure shift rates (4.2 K) for the two bands are -0.10 and -0.28 cm<sup>-1</sup>/MPa, respectively. Owing to the difference

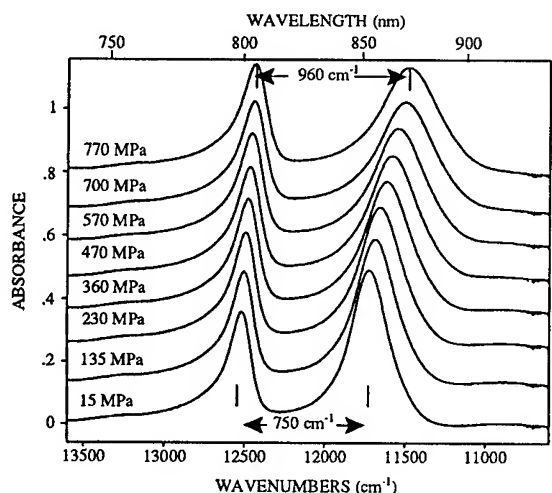


Fig. 1. Absorption spectra (at 85 K) of the B800-B850 antenna complex of *Rb. sphaeroides* at various high pressures. The separation of the B800 and B850 bands increases from 750  $\text{cm}^{-1}$  at 0.1 MPa to 960  $\text{cm}^{-1}$  at 770 MPa. The 750  $\text{cm}^{-1}$  vibrational mode, promoting the Förster type energy transfer between B800 and B850 at ambient pressure is replaced by the 920  $\text{cm}^{-1}$  vibrational modes at high pressures. The pressure shift rates for the B800 and B850 bands are  $-0.084 \text{ cm}^{-1}/\text{MPa}$  and  $-0.28 \text{ cm}^{-1}$ , respectively.

in shift rates the separation between the B800 and B850 bands increases from 750  $\text{cm}^{-1}$  to 960  $\text{cm}^{-1}$  at 770 MPa. We examine later on what, if any, effect this increase in the donor-acceptor energy gap has on the B800→B850 electronic energy transfer.

Reddy *et al* [17] have established that the widths of the narrow ZPHs burned in the B800 band are determined by the B800→B850 energy transfer time, i.e., the observed ZPH width (at 0.1 MPa) of  $5.5 \pm 0.3 \text{ cm}^{-1}$  reflects the B800\* lifetime  $1.9 \pm 0.1 \text{ ps}$ . The B800 bandwidth of 170  $\text{cm}^{-1}$  is then due to inhomogeneous broadening. The burn wavelength independence [17] (except for  $\lambda_b > 858 \text{ nm}$ ) of the broad hole in the B850 band and the accompanying vibronic hole structure in B800 region establish that the B850 band is predominantly homogeneously broadened. The large homogeneous width is a consequence of exciton level structure and ultrafast interexciton level scattering [17]. These studies also identified the dominant intramolecular modes (at 750  $\text{cm}^{-1}$  and  $\sim 920 \text{ cm}^{-1}$ ) promoting the B800→B850 Förster energy transport [17]. With increasing pressure while the width of B800 band is, within experimental error, constant, the B850 band broadens at a rate of  $0.2 \text{ cm}^{-1}/\text{MPa}$ . The integrated intensity however, does not change either with pressure or pressure cycling.

To study the pressure effects on energy transfer dynamics, low temperature (4.2 K) hole burned

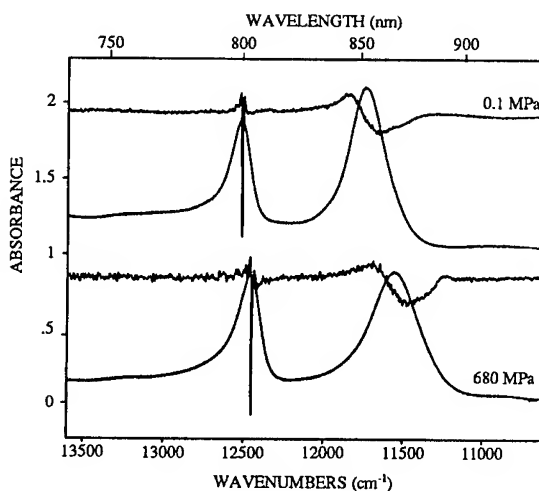


Fig. 2. Low temperature (4.2 K) hole burned spectra obtained by burning in the B800 band show efficient energy transfer to the B850 band both at ambient (top) and high (bottom) pressures ( $p=680 \text{ MPa}$ ). The ZPH width of 5.5  $\text{cm}^{-1}$  at ambient pressure is essentially unchanged at 680 MPa.

spectra were obtained at various pressures by burning in the B800 band. Figure 2 shows one such spectrum obtained at a pressure of 680 MPa. An ambient pressure hole burned spectrum is also shown. High resolution scans show that the ZPH width ( $5.3 \pm 0.3 \text{ cm}^{-1}$ ) at 680 MPa differs very little from that at ambient pressure ( $5.5 \pm 0.3 \text{ cm}^{-1}$ ) obtained from the same sample. These hole widths translate to B800\* lifetimes of 2.0 and  $1.9 \pm 0.1 \text{ ps}$  respectively. This result would at first sight appear to be very surprising since the applied pressure increases the separation between the B800 and B850 bands by 190  $\text{cm}^{-1}$ . For a theoretical explanation of this result we refer to the expression for average rate constant for energy transfer. Small *et al* [23] have developed a theory for nonadiabatic electron-transfer and obtained the following expression for the electron transfer rate. (D = donor state, B800\*, and A = acceptor state, B850)

$$\langle k_{DA} \rangle = 2\pi n^4 V^2 (1 - e^{-\tilde{S}}) (2FC_{loc}) \{ 2\pi [\Gamma^2 + \Sigma(T)^2] \}^{-1/2} \exp \{ -[(\Omega_0 - \omega_{loc}) - \tilde{S}\omega_m]^2 / 2[\Gamma^2 + \Sigma(T)^2] \}$$

where  $\Omega_0$  is the mean donor-acceptor energy gap,  $V$  is the electronic coupling matrix element,  $\Sigma(T)$  is the homogeneous width of the nuclear factor associated with the Golden rule and  $\Gamma^2$  is the variance in  $\Omega$  values [23].  $\Sigma(T)^2 = \tilde{S}(\sigma^2 + \omega_m^2) + (\Gamma_{hom}/2)^2$  where  $2\sigma$  is the width of the one-phonon profile,  $\tilde{S}(T) = \tilde{S} \text{ctnh}(\hbar\omega_m/2kT)$  and  $\Gamma_{hom}$  is the homogeneous width associated with the donor and acceptor states.  $\omega_{loc}$  is the frequency of a localized intramolecular BChl *a*



mode with a Franck-Condon factor of  $FC_{loc}$ . Hole burning provides experimental values for all parameters (except  $V$ ) required in the above calculation. Using available structural information, the value of the electronic coupling matrix element has been estimated to be  $-160 \text{ cm}^{-1}$ . For calculations  $\omega_{loc}$  was set to  $750 \text{ cm}^{-1}$  and  $FC_{loc}$  was taken to be 0.05. For uncorrelated distributions of donor and acceptor energy levels, we obtain  $2.35\Gamma \approx (\Gamma_{inh,D}^2 + \Gamma_{inh,A}^2)^{1/2}$ . Since  $\Gamma_{inh,B800} = 170 \text{ cm}^{-1}$  and  $\Gamma_{inh,B850} = 60 \text{ cm}^{-1}$ , we obtain  $\Gamma = 77 \text{ cm}^{-1}$ . The value of  $\Omega_0$  is equal to the separation of the B800 and B850 absorption bands. For burn wavelengths greater than 858 nm narrow ZPHs could be burnt in the B850 band. From the position and shape of the phonon side band holes associated with these narrow ZPH, the values of  $\sigma=13.8$  and  $\omega_m=20 \text{ cm}^{-1}$  were estimated. From the width of the broad B850 hole obtained for various burn wavelengths, the homogeneous width of the B850 band is established to be at least  $220 \text{ cm}^{-1}$ . Before considering that equation however, we describe an important result obtained in our studies on pressure dependence of the energy transfer dynamics in the FMO complex from *Chlorobium tepidum* [12]. The  $Q_y$ -absorption spectra for this complex has three prominent peaks at 804, 814 and 825 nm. The linear pressure shift rates (data not shown) for these bands are  $-0.08$ ,  $-0.11$  and  $-0.11 \text{ cm}^{-1}/\text{MPa}$  respectively. The 814 and 825 nm bands are predominantly contributed to by BChls 6 and 7 (numbering scheme of Fenna *et al* [24]). That the shift rates for these two bands are identical can be understood if one assumes that the coupling ( $V$ ) between BChls 6 and 7 is pressure independent. The shift of the bands is then mainly due to lowering of the diagonal energies of the individual BChls. Returning to the LH II complex, given the weak pressure dependence of electronic coupling matrix element,  $V$ , and  $\Gamma$  and  $\Sigma(T)$ , we note (based on the rate equation) that the energy transfer rate is dependent on the overlap provided by an active intramolecular mode(s) (further details in ref. 22). The  $750 \text{ cm}^{-1}$  mode has been identified as the dominant mode for energy transfer at ambient pressure. Pressure independence of  $B800 \rightarrow B850$  energy transfer rate now follows from the expression for  $\langle k_{DA} \rangle$  when it is realized that at high pressures the  $920 \text{ cm}^{-1}$  modes, instead of the  $750 \text{ cm}^{-1}$  mode, become active in the energy transfer. Note also that the Franck-Condon factor for the  $920 \text{ cm}^{-1}$  modes is the same as for the  $750 \text{ cm}^{-1}$  mode. The average rate constant calculated using the experimental data is

$(1.6 \text{ ps})^{-1}$  and  $(1.2 \text{ ps})^{-1}$  at 4.2 K and 300 K, respectively. These values are in reasonable agreement with experiment,  $(2.4 \text{ ps})^{-1}$  and  $(0.7 \text{ ps})^{-1}$ .

Currently, there exists no theory for the effects of pressure on the absorption and hole burned spectra of excitonically coupled pigment molecules. The experimental and theoretical study on the pressure dependence of the ZPH of isolated (non-interacting) chromophores in polymer films by Sesselman *et al* [25], led Laird and Skinner to develop a microscopic theory [26] which has been applied with considerable success to isolated chromophores in proteins [27-29]. The theory assumes that the positions of host molecules relative to the pigment molecule are uncorrelated, the host medium is homogeneous and isotropic and local compressibilities can be replaced by the bulk compressibility. For systems which would appear to conform to these restrictions, the agreement between the  $\kappa$ -values determined by pressure dependent hole burning and the bulk values has been good. A key equation which is obtained from the Laird and Skinner theory is

$$\Delta\nu(v,\Delta p) = n\kappa 3^{-1}(v-v_v)\Delta p$$

where  $v_v$  is the vacuum frequency,  $(v-v_v)$  the solvent shift at ambient pressure and  $n$  is the power of the attractive solute-solvent pair-wise potential ( $\alpha R^{-n}$ ) which is assumed to dominate the repulsive interaction for pressures which are not too high. Using a BChl *a* vacuum frequency of  $13340 \text{ cm}^{-1}$  and  $\kappa=0.19/\text{GPa}$  [30], the above equation predicts that pressure shift rates of B800 and B850 differ at most by a factor of 2. But experimental values differ by almost a factor of three. Similarly, the observed shift rates for P960 and B1015 bands are the same even though they both are BChl *b* complexes absorbing at different wavelengths. In view of the above stated assumptions, it would thus seem unjustifiable to apply the theory to complexes with excitonically coupled pigment molecules.

We now compare the pressure broadening of B850 band with that of P960 band. While the B850 broadens with pressure at the rate of  $0.2 \text{ cm}^{-1}/\text{MPa}$ , the width of P960 band, within experimental error, remains unchanged. We propose that this difference is due to the differences in structural arrangement of BChl *a* in the two systems. The eighteen B850 BChl *a* within a structural subunit [16] are arranged as dimers with a ninefold symmetry. The Mg...Mg distance of  $8.7 \text{ \AA}$  within a dimer is comparable to the BChl *b* separation ( $7 \text{ \AA}$ ) of the P960 special pair [31]. However, while the B850 dimers are still closely spaced ( $9.7 \text{ \AA}$ ) and strongly interacting, the P960

special pair dimers are not. In the case of P960 special pair BChls the two dimer components are widely separated ( $\sim 1900 \text{ cm}^{-1}$ ). Any change in BChl interaction due to pressure would only result in a change in the dimer component separation. A decrease in the B850 inter/intra dimer separation on the other hand would result in an increase in the homogeneous bandwidth. That the B850 band broadening is due to an increase in homogeneous width has been proved by burn wavelength dependence of hole spectra at high pressure. This increase in the homogeneous band width explains the B850 broadening with pressure.

To summarize, the pressure dependence of the B800 and B850 bands as well as the B800 $\rightarrow$ B850 energy transfer rate have been measured in *Rb. sphaeroides* LH II antenna complex. A possible explanation for the pressure independence of the energy transfer rate is provided.

#### Acknowledgements

This work was supported by the Division of Chemical Sciences, U.S. Department of Energy. Ames Laboratory is operated for USDOE by Iowa State University under contract W-7405-Eng-82. The LH II antenna complex was provided by R. Picorel.

#### References

- Geacintov, N.E. and Breton, J. (1987) in *Critical Reviews in Plant Science*; (Congor, B.V. ed.) CRC Press, Boca Raton, p. 1.
- Pearlstein, R.M. (1982) in *Photosynthesis: Energy Conversion by Plants and Bacteria*; (Govindjee ed.) Academic, New York, p 293.
- van Grondelle, R. (1985) *Biochim. Biophys. Acta* 811, 147.
- Knox, R.S. (1986) in *Encyclopedia of Plant Physiology*; (Staehelin, L.A. and Arntzen, L.A. eds.), Springer-Verlag, Berlin.
- Reddy, N.R.S., Lyle, P.A. and Small, G.J. (1992) *Photosyn. Res.* 311, 167.
- Feher, G., Allen, J.P., Okamura, M.Y. and Rees, D.C. (1989) *Nature* 339, 111.
- Parson W.W. (1991) in *Chlorophylls*; (Scheer, H. ed.) CRC Press, Boca Raton, p. 1153.
- Kirmaier, C. and Holten, D. (1993) in *The Photosynthetic Reaction Center*, Vol. II; (Deisenhofer, J. and Norris, J.R. eds.) Academic Press, New York, p 49.
- Friesner, R.A. and Won, Y. (1989) *Biochim. Biophys. Acta* 977, 99.
- Reddy, N.R.S. and Small, G.J. (1995) *Advances in Photosynthesis* (in press).
- Chang, H.-C., Jankowiak, R., Reddy, N.R.S. and Small, G.J. (1995) *Chem. Phys.* 197, 307.
- Reddy, N. R. S., Jankowiak, R. and Small, G.J. (in press) *J. Phys. Chem.*
- Redline, N.L. and Windsor, M.W. (1991) *Chem. Phys. Lett.* 186, 204.
- Redline, N.L. and Windsor, M.W. (1992) *Chem. Phys. Lett.* 198, 334.
- Hoganson, C.W., Windsor, M.W., Farkas, D.I. and Parson, W.W. (1987) *Biochim. Biophys. Acta* 892, 275.
- McDermott, G., Prince, S.M., Freer, A.A., Hawthornthwaite-Lawless, A.M., Papiz, M.Z., Cogdell, R.J. and Isaacs, N.W. (1995) *Nature*, 374, 517.
- Reddy, N.R.S., Small, G.J., Seibert, M. and Picorel, R. (1991) *Chem. Phys. Lett.* 181, 391.
- Reddy, N.R.S., Seibert, M., Picorel, R., and Small, G.J. (1992) *J. Phys. Chem.* 86, 6458.
- van der Laan, H., Schmidt, Th., Visschers, R.W., Visscher, K.J., van Grondelle, R. and Völker, S. (1990) *Chem. Phys. Lett.* 170, 231.
- Bolt, J. and Sauer, K. (1979) 546, 54.
- Borisov, A.Y., Gadonas, R.A., Danielius, R. V., Piskarskas, A.S. and Razjivin, A.P. (1982) *FEBS Letts.* 138, 25.
- Reddy, N. R. S., Wu, H.-M., Jankowiak, R. and Small, G.J. (manuscript in preparation).
- Small, G.J., Hayes, J.M. and Silbey, R.J. (1992) *J. Phys. Chem.* 96, 7499.
- Fenna, R.E., Matthews, B.W. (1975) *Nature*, 258, 573.
- Sesselmann, Th., Richter, W., Haarer, D. and Morawitz, H. (1987) *Phys. Rev. B*, 14, 7601.
- Laird, B.B. and Skinner, J.L. (1989) *J. Chem. Phys.*, 90, 3274.
- Freidrich, J., Gafert, J., Zollfrank, J., Vanderkooi, J.M. and Fidy, J. (1994) *Proc. Natl. Acad. Sci.* 91, 1029.
- Zollfrank, J., Freidrich, J. and Parak, F. (1992) *Biophys. J.* 61, 716.
- Zollfrank, J., Freidrich, J., Fidy, J. and Vanderkooi, J.M. (1991) *J. Chem. Phys.* 94, 8600.
- Tars, M., Ellervee, A., Kuk, P., Saarnak, A. and Freiberg, A. (1995) *Lith. J. Phys.* 34, 320.
- Deisenhofer, J., Epp, O., Miki, K., Huber, R. and Michel, H. (1985) *Nature*, 318, 618.

# EFFECT OF DYNAMIC HIGH PRESSURE ON FISH BACTERIA: A CASE STUDY

K.D. Joshi, G. Jyoti, Satish C Gupta, S.K. Sikka, R. Chidambaram

*High Pressure Physics Division, Bhabha Atomic Research Centre, Bombay 400 085, India.*

A.S. Kamat, V. Venugopal, Paul Thomas and P.C. Kesavan

*Food Technology Division, Bhabha Atomic Research Centre, Bombay 400 085, India*

We have examined the effect of dynamic high pressure on the load of spoilage as well as pathogenic bacteria in 'Indian Mackerel', a popular fish item available in Bombay. The 63 mm bore gas-gun was used to impart dynamic pressures of about 4 - 7 kbars lasting for a time period of around  $4\mu s$  in the fish samples. The temperature of the specimen in compressed state was estimated to be  $15^\circ - 25^\circ C$  above ambient. Five experiments have been conducted: two on fresh fish samples, two on spoiled fish samples having  $\sim 10^{11}/gm$  bacterial load and one on the sample inoculated with *Salmonella typhimurium*, a pathogenic bacterium. On shock loading, the bacterial load reduction in the fresh fish samples was found to be 1 - 2 log cycle whereas the reduction in the spoiled fish was observed to be 3 - 4 log cycles. On the other hand, 1 - 2 log cycle reduction of *Salmonella* was observed in the inoculated fish sample. These experiments show that the short duration, high pressure shock treatment could be used as a novel method in reducing microbial contamination of fishery products.

## 1 Introduction

Application of high pressure is an emerging technology for food preservation. The fact that high pressure can kill microorganisms in milk and meat was discovered as early as in 1899<sup>1</sup>. Since then, although a large body of experimental data has been accumulated on the effect of pressure on the biological systems, a systematic study concerning the use of pressure for food preservation and processing has been carried out only during past few years. Pressure treatment of a few kbar range for about half an hour is observed to cause denaturation of proteins, gelatinization of starch and inactivation of microorganisms without degrading the nutritional value of food and without much affecting its taste and flavour<sup>2,3</sup>. The pressure technique is of special interest for the food items whose nutritional and sensory characteristics are sensitive to thermal processing<sup>4</sup>.

Although there have been many studies on the use of hydrostatic pressure for food processing, the utilization of dynamic pressure loading (shock waves) for food items has not been investigated so far. Shock waves are known to accelerate the kinetics of phase transitions in condensed matter. A phase transition that takes place in about a few hours under hydrostatic pressure gets completed within a few microseconds upon dynamic compression<sup>5</sup>. It is, therefore, interesting to examine the application of a microsecond duration

pulse on bacteria in the biological systems.

In the present study, we have investigated the effect of dynamic high pressure on the load of spoilage as well as pathogenic bacteria in 'Indian Mackerel', a popular fish item available in Bombay. We find that the short duration, shock pressure treatment is quite effective in reducing the microbial load for food preservation.

## 2 Experimental

'Indian Mackerel' fish has been chosen as the experimental specimen as several aspects on the radiation preservation of this item have been studied in detail at our laboratory<sup>6</sup>. Experiments have been performed on fresh fish (bacterial load  $\sim 10^4 cfu/gm$ ) as well as spoiled fish samples having large bacterial load and also fresh fish samples inoculated with pathogenic bacteria. Gas gun instrument which can accelerate projectiles to predetermined velocities in a well controlled manner has been used for dynamic compression of the samples<sup>7</sup>. The analysis of spoilage flora and *Salmonella* in the untreated and pressure treated samples has been carried out using the standard bacteriological methods.

### 2.1 Sample Preparation

The fresh samples were prepared from the belly portion of the fish. In order to get the inocu-

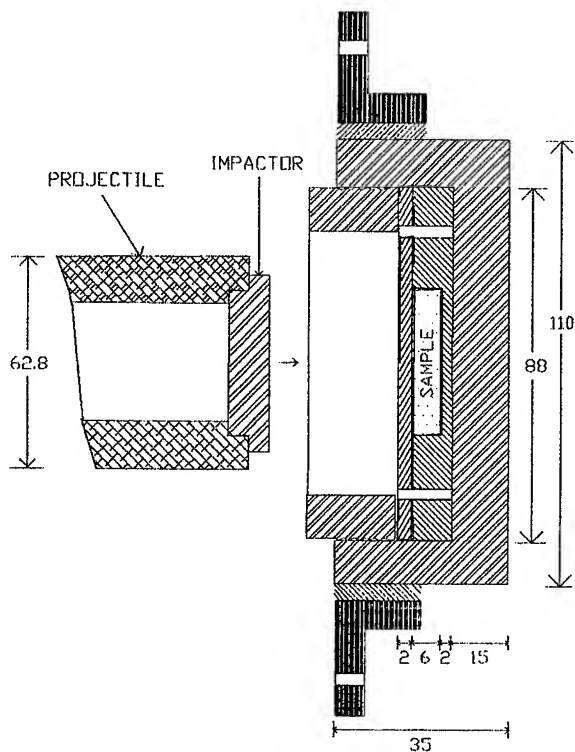


Figure 1: Schematics of the target assembly (not to scale). All dimensions are in mm.

lum of spoilage flora, the fish was allowed to spoil at ambient temperature ( $24^{\circ}$  -  $25^{\circ}\text{C}$ ) for one day. The spoiled fish (10 gm) was homogenised in sterile saline (90 ml) in a Sorwal Omnimixer cup. The homogenate was used as a source of spoilage flora. For inoculating with spoilage or pathogenic bacteria, a piece of fresh fish (flesh with skin) was completely submerged aseptically in spoiled fish homogenate or cell suspensions of *Salmonella typhimurium* in sterile phosphate buffer (pH 7.2, 0.1M). The strain of *Salmonella typhimurium* used was isolated from chicken meat and also well studied in our laboratory<sup>8</sup>. After half an hour at  $0^{\circ}\text{C}$  the sample was removed, drained and used in the experiment.

## 2.2 Dynamic Pressure Treatment

The sample holder consists of SS304 plate of thickness 8 mm and diameter 86 mm. On one face of it, a groove of depth 6 mm and diameter 45 mm was made. These dimensions were chosen to optimize the sample size required for biological anal-

ysis and experimental limitations put by the gas gun. The sample was kept in this groove under aseptic condition and covered with a 2 mm thick SS304 plate. The two plates were held together by four SS screws. Before placing the sample, both the holder and the cover plates were sterilised. After placing the sample, the whole assembly was kept in a shock recovery fixture<sup>9</sup> as shown in figure 1 and locked by the locking plug. This was finally fixed onto a target ring that was mounted at the muzzle end of the gun in the target chamber so that the sample was aligned parallel to the impactor. Shock compression of the samples was achieved by using the 63 mm bore gas gun<sup>7</sup>. The samples were shock loaded by impact of a flyer plate attached to the nose of the projectile, which was accelerated to the velocity of  $0.21\text{mm}/\mu\text{s}$  by suitably selecting the breech pressure. In each experiment the projectile velocity was measured before the impact. Using the measured projectile velocity coupled with the Hugoniot of fish, approximated with that of water, the pressure in the sample was estimated to be 4 - 7 kbar, lasting for about  $4\mu\text{s}$ . The temperature of the specimen in compressed state was calculated to be  $15^{\circ}$  -  $25^{\circ}\text{C}$  above ambient.

## 2.3 Bacteriological Analysis

Viable cell counts in untreated and shock pressurized samples were determined by standard bacteriological methods. The fish sample (10g) was aseptically homogenized in 90 ml sterile saline in a Sorwal Omnimixer. The homogenate was serially diluted and appropriate dilutions were poured into petri plates. Colony forming units were determined using plate count agar (PCA) (Difco). The plates were incubated at  $37^{\circ}\text{C}$  for 48 hours before the colonies were counted. In order to isolate the number of *Salmonella* from the fish Bismuth Sulphite Agar (BSA) (Difco) was used.

## 3 Results and Discussions

Five experiments have been conducted: two on fresh fish samples, two on spoiled fish samples and one on the sample inoculated with the *Salmonella*. The results of the bacteriological analysis before and after the shock pressure treatment are given in Table 1. Upon shock loading the bacterial load reduction in the fresh fish sample was found

Table 1: Experimental results on the reduction of bacteria in fish on shock pressure treatment.

Experiment #	Sample	Initial Counts (cfu/gm)	Final counts (cfu/gm)	Log cycle reduction
1	fresh	$5.1 \times 10^4$	$5.3 \times 10^2$	2
2	fresh	$1.8 \times 10^4$	$6.3 \times 10^3$	~ 1
3	spoiled	$2.8 \times 10^{11}$	$2.7 \times 10^7$	4
4	spoiled	$1.1 \times 10^{11}$	$8.6 \times 10^7$	3 - 4
5	inoculated (Salmonella)	$5.4 \times 10^8$	$9.3 \times 10^6$	1 - 2

to be 1- 2 log cycles whereas the reduction in the spoiled fish was observed to be 3 - 4 log cycles. On the other hand 1 - 2 log cycles reduction of Salmonella was observed in the inoculated fish samples. These experiments clearly demonstrate that the microsecond duration shock pressure treatment is quite sufficient to reduce the level of spoilage bacteria as well as Salmonella in fish.

The higher extent of bacterial load reduction in spoiled fish on shock pressure treatment could be attributed to higher sensitivity of predominating gram negative flora in the fish. In fresh fish, since the proportion of gram negative organisms is less, decrease in bacterial load by pressure treatment was also less (1 - 2 log cycles). The results are in agreement with the observation of Hoover et al<sup>10</sup> on the effect of high pressure on microorganisms.

Thus shock pressure treatment is beneficial for significant elimination of spoilage causing and pathogenic microorganism in fish. Apart from high pressure, radiation treatment is also known to improve the quality of fishery products by elimination of spoilage microorganisms<sup>6</sup> and pathogens<sup>8</sup>. The present technique in combination with ionising radiation might have potential to control food-borne hazards arising from radiation resistant pathogens like *Clostridium* spores. Further work is in progress to make use of high pressure treatment in combination with gamma irradiation for enhancement of shelf life as well as microbial safety of fishery products.

## References

1. B.H. Hite, W. Va., *Agric. Exp. Stn. Bull.*, **58**, 15 (1899)
2. R. Hayashi, *High press. Res.*, **7**, 15 (1991)
3. N.K. Rastogi, R. Subramanian and K.S.M.S. Raghavarao, *Indian Food Ind.* **51**, 30 (1994)
4. J.C. Cheftel, *IAA MARS*, **141** (1991)
5. G.E. Duvall and R.A. Graham, *Rev. of Mod. Phys* **49**, 523 (1977)
6. V. Venugopal and P.M. Nair, *J. Fishery Tech.*, **29**, 114 (1992)
7. S.C. Gupta, R.G. Agarwal, J.S. Gyanchandani, S. Roy, N. Suresh, S.K. Sikka, A. Kakodkar and R. Chidambaram in *Shock Compression of Condensed Matter, 1991*, ed. S.C. Schmidt, R.D. Dick, J.W. Forbes and D.G. Tasker (Elsevier, Amsterdam, 1992), 839
8. A.S. Kamat, M.D. Alur, D.P. Nerkar, P.M. Nair, *J. Food Safety*, **12**, 59 (1991)
9. N. Suresh, G. Jyoti, Satish C. Gupta, S.K. Sikka, Sangeeta and S.C. Sabharwal *J. Appl. Phys.*, **76**, 1530 (1994)
10. D.G. Hoover, C. Metrick, A.M. Papineau, D.F. Farkas, D. Knorr, *Food Tech.*, **43**, 99 (1989)

## EMPLOYMENT OF HIGH PRESSURE FOR KEEPING BIOLOGICAL MATERIALS

V.L.Serebrennikov\* and Yu.A.Kudenko\*\*

\* *The Building Engineering Institute of Krasnoyarsk,  
Krasnoyarsk 660041, Russia*

\*\* *Institute of Biophysics, Krasnoyarsk 660036, Russia*

The principal difficulty of freezing process of cellular structures is that cells are destroyed by osmotic shock and an increasing ice's volume. In this connection one suggests two methods of a conservation of biological materials:

- a) the conservation of biological materials at low temperature and high pressure in a liquid state (LTHP);
- b) the method of aqueous gel vitrification (AGV).

The apparatus have been designed for the conservation of biological materials at low temperature: an autonomous high pressure chamber, a device for regulating pressure and one for a rapid drop of pressure.

### Introduction

It is known there is a problem of freezing objects for keeping them at low temperatures. A principal difficulty of the freezing process of cellular structures is that the volume of water increases by 8% and the cells are destroyed. Another problem is that a concentration of ions grows on during the crystallization process and it causes an osmotic shock.

There is a number of methods with an employment of cryoprotectors making possible to freeze and to unfreeze the cellular structures. However, an output of living cells comes to 25...30% and it does not allow to keep multicellular structures alive (tissues,organs). In this connection we suggested two methods of conservation of biological materials.

#### 1. The method of the conservation of biological materials at low temperature and high pressure in a liquid state (LTHP)

In 1984 we have got an author certificate of USSR on a method of keeping blood in a liquid state at the temperatures -4...-6°C an

400...600 atm pressures [1]. In this method we have used that a water-ice phase transition temperature is displaced down by an increasing pressure. On cooling the blood the pressure is raised in such a way as not cross the phase transition line. As a result the blood has an equilibrium liquid state at the temperature below zero centigrade. In these conditions metabolic processes slow down into the cells that allows to preserve almost all components of a living blood for a month.

In the Institute of Biophysics of Krasnoyarsk one carries out investigations of animal organs (liver, kidney) which are preserved by the described method [2-4]. We have designed an autonomous high pressure chamber (Fig.1) in which necessary pressure is automatically supported with decreasing temperature [5]. The chamber has a heat insulation shell (1) opened from side of a metallic top (2). A water (3) is a medium transmitting pressure on a specimen (4). On cooling the chamber below 0°C the water is crystallizing on inside of a top (5). Therefore a water's pressure is increasing and it is reaching a value corresponding to the temperature of the water-ice phase transition. Thus the pressure on the specimen can be regulated by changing water's temperature.

The autonomous high pressure chamber has a safety-valve (6) coupled to an elastic capacity (7) filled with an unsolid fluid (8) at the temperatures below  $0^{\circ}\text{C}$ : an alcohol and a glycerin. If the water were into this elastic capacity, it would crystallize into a hole of the valve on decreasing pressure and the safety-valve would be put out of action.

This autonomous chamber may be used for keeping food in home refrigerators.

Another device allows to regulate the pressure into a closed volume with a precession up to a few atmospheres [6]. This device (Fig.2) contains a heat chamber (1) linked by a pipeline (2) with a working chamber (3) in which necessary value of hydrostatic pressure is supported. When the pressure is altering the temperature of medium (4) is altering into the heat chamber by a heater (5) connected with a regulating electronic device (6) and a pressure gauge (7) so that heat expansion of medium is restoring the necessary pressure.

## 2. The method and technique of aqueous gel vitrification (AGV)

It is known a volume of vitreous ice nearly equals to a volume of water and a liquid inside a living cell is an aqueous gel. In this respect we have carried out a number of investigations and have discovered that aqueous solutions of substances forming gels can be transferred in vitreous solid state [7].

For this purpose the solution was put into a high pressure chamber, then it was compressed and was cooled down to  $-20^{\circ}\text{C}$  under the pressure of 2000 atmospheres. Under these conditions the aqueous solution is in a liquid state. Then the pressure was reduced during the time of 1 msec. Simultaneously with decreasing the pressure the specimen was moved to a zone of liquid nitrogen temperature.

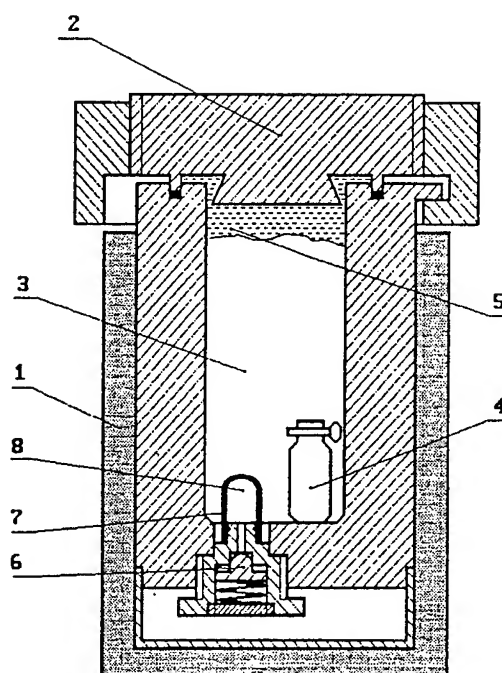


Figure 1: The autonomous high pressure chamber for keeping biological materials.

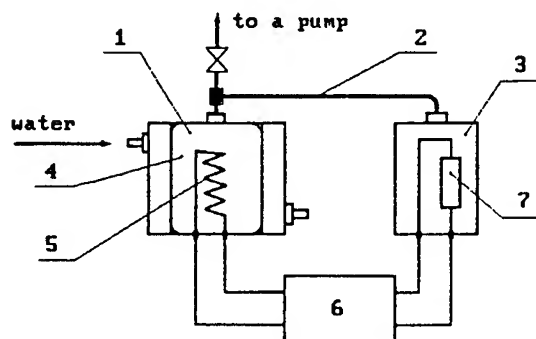


Figure 2: The device for regulating pressure into a closed volume.

A device for a rapid drop of the pressure (fig.3), described in [8], contains a chamber (1) with a rotating mechanism (2) placed in a steel body (3) with a heat-insulation (4). A bath (5) filled a liquid nitrogen (6) is situated at the bottom of the steel body.

The cylinder (7) of the rotating mechanism has a flange with three shaped cuts. The flange (8) of the chamber has three ledges.

Soon after necessary values of the pressure and temperature were fixed, the cylinder of the rotating mechanism was turned and a plug (9) with the specimen (10) dropped into the liquid nitrogen.

The obtained specimens have been studied by X-ray diffractometer DRON-4 from  $-190^{\circ}\text{C}$  to  $+5.5^{\circ}\text{C}$  under atmospheric pressure. We have prepared vitreous specimens of the aqueous solutions with following compositions:

- 1) 5...10% of a glucose and 2...4% of a gelatine;
- 2) 5...10% of a glucose and 2% of an agar;
- 3) 0.1...1% of a polivinil alcohol (PVA);
- 4) 0.1...1% of a poliacylamide (PAA).

The first two solutions are physiological solutions which can be poured in the blood. The last two solutions are used for a conservation of biological objects without subsequent washing off. We have tried to use the obtained results for freezing the blood.

We have added 8% of the glucose and 4% of the gelatine to a rabbit's blood. This solution frozen by method of AGV is an X-ray vitreous ice.

It is known a pure vitreous ice is crystallizing on the temperature increasing. We have carried out calorimetric measurements of a heating-melting process of the specified vitreous gel solutions. These measurements have shown that a crystallizing temperature of these aqueous solutions is equal to  $-10^{\circ}\text{C}$ .

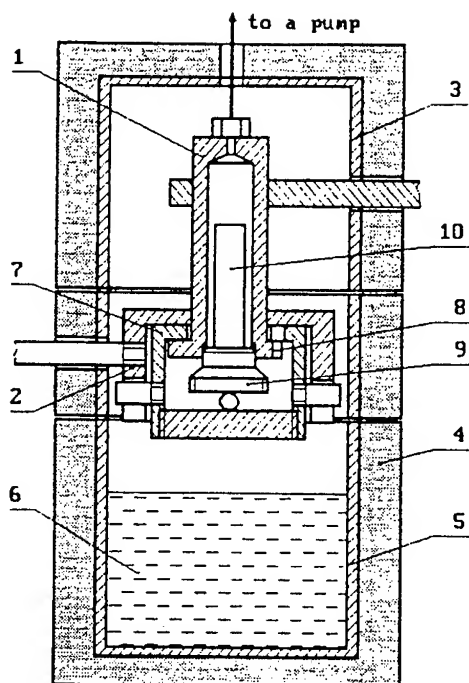


Figure 3: The device for a rapid drop of the pressure.

It is necessary to emphasize that the indicated initial parameters  $-20^{\circ}\text{C}$  and 2000 atm are not optimum for freezing the biological materials. Our last investigations showed that the working pressure could be reduced at any rate to 1000 atm.

The described method of the virification can be applied for preparing vitreous substances possessing phase P-T diagrams of these as the water's diagram.

### Conclusions

1. The method of LTHP allows to preserve the biological materials for limited time, since metabolic processes in the cells go with some rate that is conditioned by a molecular diffusion in the liquid solution at the high pressure and the temperature below  $0^{\circ}\text{C}$ .



2. The method of AGV allows to decrease concentrations of the cryoprotectors, or to escape the employment of them at freezing the cellular structures. The keeping time of the biological materials is practically unlimited at the liquid nitrogen temperature.

### References

1. Yu. A. Kudenko, I. I. Gitelzon, A. G. Zve-gintzev, R. A. Pavlenko and V.L.Serebren-nikov, Author's certificate No.1124974, USSR, A61K 35/14, Bull. No.43 (1984), p.19.
2. И. И. Гительзон, Ю. А. Куденко и Р. А. Павленко, Сочетанное действие на клетки крови гипербарии и отрицательных температур, Доклады АН СССР, 291 (1986), с.476.
3. И. И. Гительзон, Р. А. Павленко и Ю. А. Куденко, Исследование возможности хранения клеток крови охлажденной ниже 0°C в условиях высокого давления, Гематология и трансфузиология, N 10 (1986), с.15.
4. Ю. А. Куденко и Р. А. Павленко, Исследование действия высокого давления и температуры на биологические объекты, Кробиология, N 3 (1986), с.39.
5. V. L. Serebrennikov and Yu. A. Kudenko, An application for invention rights No. 94009064, Russia, priority March 14, 1994.
6. V. L. Serebrennikov, V. P. Ranshikov and V. A. Kapustin, Author's certificate No. 696426, USSR, G05D 23/12, Bull. No.41 (1979).
7. Yu. A. Kudenko and V. L. Serebennikov, An application for invention rights No. 5009542, USSR, priority eptember 20, 1991.
8. V. L. Serebrennikov and Yu. A. Kudenko, An application for invention rights No.5009842, USSR, priority September 20, 1991.

# HIGH PRESSURE TECHNIQUE FOR STERILIZATION OF MANDARIN ORANGE JUICE

TOMOHIRO YAMAMOTO

*Yamamoto Suiatu Kogyosho, Co., Ltd, Shomoto Toyonaka City, Osaka, Japan*

YASUSHI IFUKU

*Wakayama Nokyo Food Industry Co., Ltd, Hikata, Shinhamu  
Kainan City Wakayama, Japan*

## Abstract

We have developed a new high-pressure processing machine which can produce mandarin juice of 4ton per hour under 400MPa. The object of pressurizing is sterilization of microbes, and maintaining a natural fresh condition of juice just after harvest through all seasons. This technique has never obtained before by conventional heat pasteurization based on the food sanitation law in Japan, and was the first attempt from it's object to a practical machine.

## 1. Introduction

About 10 years have passed since high-pressure technology for food processing was proposed by Dr.Hayashi<sup>1)</sup> in Japan. Since then, fruit jams, juices and cut fruits have been commercialized, and a liquor, ham, others have been tried.<sup>1)</sup> Sterilization is the object for jams & juices, and the objects of others are various. "High-Pressure-Juice" packed with a fresh taste, flavor and natural conditions of many nutrients, has never been before in commercial pasteurization method.

We report these results for sterilization of a mandarin juice, and the development for a practical new machine for juice processing.

## 2. Demand for pressurizing of mandarin juice

Recently, due to free import move of Japan, the domestic fruit makers and the processors are compelled to improve the quality and the processing technology for juices in order to be more competitive to the imported.

As shown in Table 1,<sup>2)</sup> Wakayama mandarin

Table 1 Analysis of MMS in citrus Juices

Concentration of Methylmethionine sulfonium (MMS)	
Fruits	Content of MMS
Lemon	1.8 $\mu$ M
Grapefruit	4.0
Valencia orange	5.8
Moro orange	6.0
Nova mandarin	11.2
Wilking mandarin	12.1
Hamlin orange	13.0
Wakayama mandarin	21.0
Pixie mandarin	29.0

contains much methylmethionine sulfonium (MMS).

MMS easily turns into dimethyl sulfide (DMS) which has an unfavorable flavor, caused by the chemical change on heat-pasteurizations.<sup>3)</sup>

There have been many attempts to control DMS flavor<sup>4)</sup> in the past, but none was applied to practical use. The chemical change would be avoided by using this non-thermal process.

Against the above-mentioned background, we have newly introduced a high-pressure sterilization technique for juice processing.

## 3. High-pressure technique for juice process

It has been well known that high pressure is effective for inactivation of microbes for decades. But no commercial application for food processing has ever been made until this time. High-pressure (H-P) techniques have been adopted mainly to non living materials in industrial use. Our development of this project is shown in Fig.1.

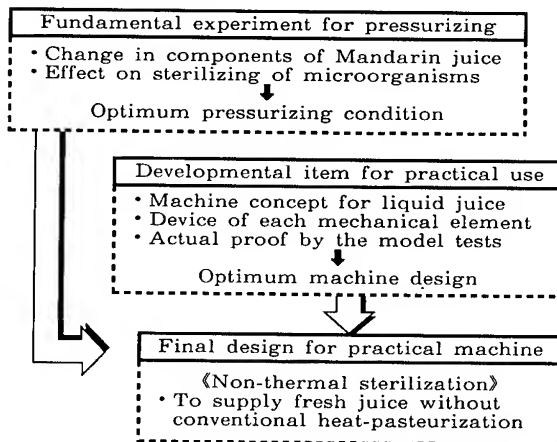


Fig.1 The development of this project

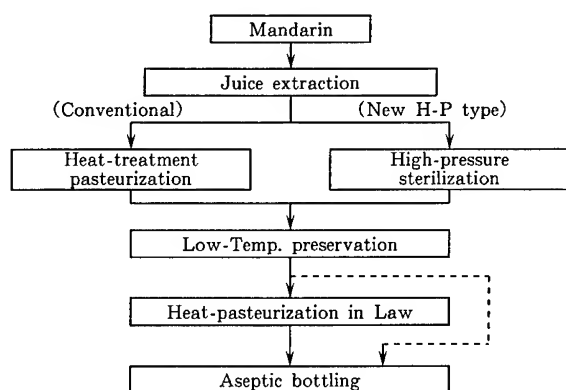


Fig.2 Manufacturing flow of "H-P juice"

Usually, mandarin juice goes through two heat-pasteurizations as in Fig.2. The first heating is for a long time preservation all the year round and the second is for the last bottling based on the present Japanese law. In high-pressure flow, we are adopting the process reducing one half of the heat cycles in law, in future we intend to take the non-thermal process as the last target, as shown by the dotted line in Fig.2.

#### 4. Experiment for optimum pressurizing

High-pressure test was made using a lab-scale equipment. Sample juices incubated with various microbes, are heat-sealed in polyethylene bags, and then are placed in pressure capsule with water pressure medium. As shown in Fig.3, it was found that both molds and yeasts were killed under 300MPa and 47°C during 5 minutes, and *Bacillus* having strong resistance to pressurizing was also inactivated by elevating temperature. And no appreciable changes were observed in such important juice factors

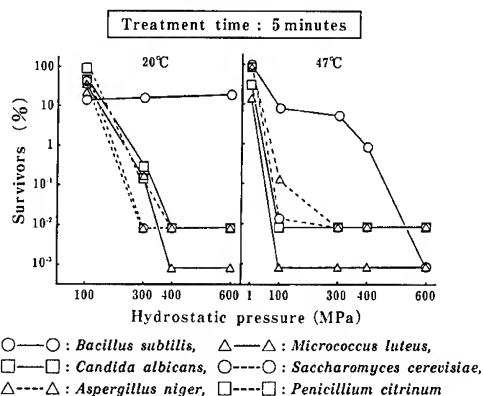
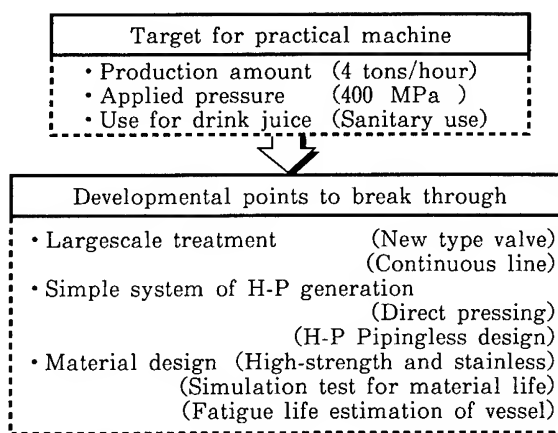
Fig. 3 Effect of hydrostatic pressure on survivors of microbes in mandarin juice<sup>5)</sup>

Fig.4 Target points for a practical machine

as concentrations of various nutrients and volatile elements.

#### 5. Points of development for practice

Based on the above experimentals<sup>5)</sup>, we realized our targets as follows.

There have been many high-pressure equipments as CIP or HIP for practical uses for many years. But, industrial applications up to 400MPa have been very rare. Indeed, there have been large scale treatments. But there have been few applicable techniques to our purpose.

As lab-equipment, higher pressures have been applied, but they are too different in size and using frequency to suit this high-pressure machine. Our developmental points to actualize this new concept different from the others so far, are shown in Fig.4.

#### 6. A new design concept for practical use

It is our original sealing mechanism that has enabled this development, as shown in Fig. 5. This device was developed for a hydrostatic pipe testing machine to steel tube in oil line industry, and is still now operating in main pipe makers almost over the world.

As in Fig.5, this seal mechanism consists of a flexible-rubber ring and separate buck-up metal segments mounted in the ring. This ring is compressed to seal the gap by pre-sealing pressure, while it releases the gap easy to open by decompressing.

Based on this experience, we developed new valve having two functional roles, sealing & valving, without scrubbing in the operation.

The valve is batch-type, but a continuous line is possible using plural valves.

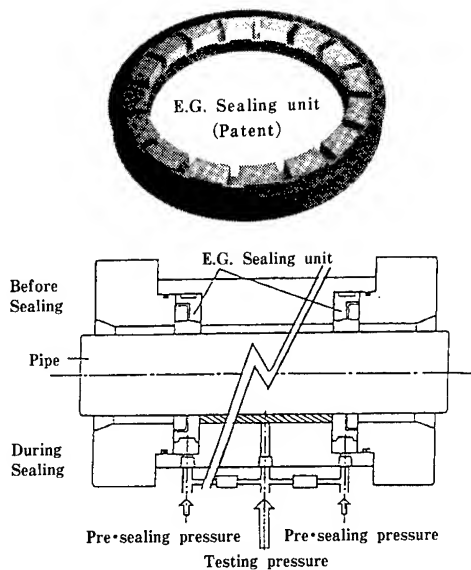


Fig.5 Original model for a new valve

In the new design of Fig.6, direct pressure, primary oil pressure (G), is applied to move the pressure vessel (E) up and down. The raw juice sucked from tank (A) goes into sterilization room (B) via new valve (I), is treated by a fixed pressurizing condition, and is sent to tank (C) via the valve again.

As shown in Fig.6, we have realized a new design with no high-pressure-piping, without contamination with the primary oil. To liquid juices, a specific caution is necessary for sanitation and cleanliness. We used noted 17-4 PH high-tensile stainless steel modified by Mo. to get the same corrosion resistance as SUS304 and the balanced toughness & strengths throughout inner surfaces of the high-pressure line.

To obtain high quality steel for this pressure vessel, ESR (Electro-Slug-Remelting) was adopted, and forging was improved to get optimum properties in the inner surfaces in the tangential direction, where the highest

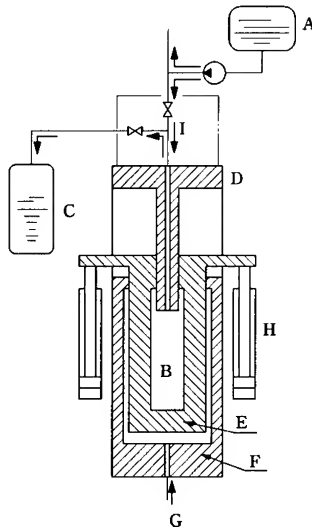


Fig.6 Concept design

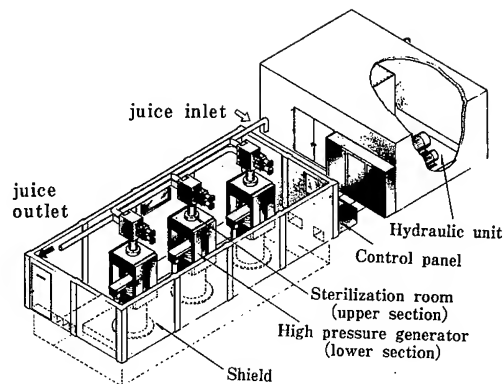


Fig.7 Image design of the H-P equipment for juice processing "HYDRO-PASTEUR"

stress by pressurizing works.

And, this concept design is founded on our simulation model affirming the long life operation, based on fatigue design under-ruled now in High-Pressure Institute of Japan.

The image design of practical H-P machine is shown in Fig.7. The total line has three pressurizing units, each as in Fig.6, which means one continuous treating equipment.

The specification of this equipment is as follows;

- ① Working pressure 400MPa
- ② Processing capacity 4.0 tons/h
- ③ Electric power 220kw
- ④ Machine weight 75tons

It is a eternal dream for juice processors to get fresh one for a long time after harvest except any loss of the natural quality of fruits. If our high-pressure processing technique to match the dream could get more attention in these fields, we will feel much rewarded.

## Reference

1. The joint meeting with the 1st. European Seminar on High Pressure & Biotechnology and 5th. Symposium on High Pressure & Food Science. Sept., (1992), Montpellier, France.
2. M. Shimoda, et al, Nihon Nougakagaku Kaishi 58, 1217 (1984).
3. M. Shimoda, et al, *ibid*, 55, 319 (1981).
4. Y. Osajima, et al, *ibid*, 59, 501 (1985).
5. Y. Takahashi, Y. Ifuku, International Journal of Food and Technology, 28, 95 (1993).

# THE EFFECT OF HIGH HYDROSTATIC PRESSURE ON VEGETATIVE BACTERIA AND SPORES OF ASPERGILLUS FLAVUS AND BACILLUS CEREUS

M. FONBERG-BROCZEK<sup>1,2</sup>, B. WINDYGA<sup>2</sup>, H. ŚCIEŻYŃSKA<sup>2</sup>, K. GÓRECKA<sup>2</sup>,  
A. GROCHOWSKA<sup>2</sup>, B. NAPIÓRKOWSKA<sup>2</sup>, K. KARŁOWSKI<sup>2</sup>, J. ARABAS<sup>1</sup>,  
J. JURCZAK<sup>3</sup>, S. PODLASIN<sup>1</sup>, S. POROWSKI<sup>1</sup>, P. SZAŁAŃSKI<sup>3</sup>, J. SZCZEPEK<sup>1</sup>

1. High Pressure Research Center of Polish Academy of Sciences  
ul. Sokołowska 29/37, 01-142 Warszawa, Poland
2. National Institute of Hygiene, Dept. of Food Research,  
ul. Chocimska 24, 00-791 Warszawa, Poland
3. Institute of Organic Chemistry of Polish Academy of Sciences,  
ul. Kasprzaka 24, 00-224 Warszawa, Poland

## ABSTRACT

The effects of hydrostatic pressure of cultures of Gram-positive and Gram-negative bacteria, conidia of *Aspergillus flavus* and spores of *Bacillus cereus* were investigated. Significant differences between Gram-positive and Gram-negative bacteria were observed. Combined high pressure treatment up to 800 MPa and temperature 50°C is needed to kill whole spores of *Bacillus cereus*. For inactivation of conidia of *Aspergillus flavus* suffices 400 MPa, 20°C and 10 minutes.

## Introduction

Development of high pressure in food industry may result in longer shelf-life, better health quality and organic value of food products. Ultra High hydrostatic Pressure (UHP) can inactivate microorganisms and their spores (1).

The mechanism of killing microorganisms with Ultra High Pressure (UHP) is thought to be based on the destruction of the membrane and wall of the cell. The destruction is caused by changes of the cell volume and by the denaturation of proteins (2).

## Experimental

The effects of hydrostatic pressure on cultures of Gram-positive bacteria, *Staphylococcus aureus* and Gram-negative bacteria: *Salmonella*, *Escherichia coli*, *Proteus mirabilis* were investigated. Initial counts were  $10^6$  cells/ml for *Staphylococcus aureus* and *Proteus mirabilis* and  $10^7$  cells/ml for the other bacteria in saline solution. For spores of *Bacillus cereus* and *Aspergillus flavus* initial counts were  $10^4$ - $10^5$  cells/ml. Cultures of bacteria were treated at hydrostatic pressure ranged 100 MPa

to 1000 MPa for 5, 10 and 15 minutes at 10°C, 20°C and 50°C. Spores were treated at hydrostatic pressure from 200 to 1000 MPa for 10 minutes at 10°C, 20°C or 50° C for *Bacillus cereus* and from 100 to 1000 MPa for 10 minutes at 10°C or 20° C for *Aspergillus flavus*.

The results of inactivation achieved after 10 minutes treatment were used to compare the response of the various microorganisms to pressure.

The experiments were carried out in piston-cylinder-type high pressure vessels with maximum pressure of 1500 MPa and volumes of 30 - 50 cc, developed in the High Pressure Research Center. Distilled water was used as pressure transmitting

medium. The samples were closed in Teflon or polypropylene ampoules. Working temperature were stabilized by the heating/cooling jacket mounted to the vessel.

### Results

Inactivation of microorganisms (tab. 1) was found to be directly correlated to the level of high hydrostatic pressure but significant differences between Gram-positive and Gram-negative microorganisms were observed. Pressure of 500 MPa in 10 min. reduced population of Gram-negative bacteria: *Salmonella*, *Escherichia coli*, *Proteus mirabilis* of 6-7 log.

Table 1

PRESSURE INACTIVATION OF MICROORGANISMS IN PHOSPHATE BUFFERED SALINE [ $10^6$ - $10^7$  CFU/ML]

Microorganism	Pressure	Temp. deg.C	Time min.
Mould <i>Aspergillus flavus</i>	400	20	10
Gram (-) <i>Salmonella</i> <i>Escherichia coli</i> <i>Proteus mirabilis</i>	500	20	10
Gram (+) <i>Staphylococcus aureus</i>	800	20	10
Gram (+) <i>Staphylococcus aureus</i>	600	10	10
Spores <i>Bacillus cereus</i>	800	50	10

Population of  $10^6$  cells/ml of Gram-positive bacteria - *Staphylococcus aureus* was inactivated at 800 MPa in temperature of 20° C and at 600 MPa in temperature 10°C.

Spores of *Bacillus cereus* were very resistant. A combined treatment - 800 MPa and 50°C, 10 min., kills whole *Bac. cereus* spores -  $10^6$  /ml. For inactivation of conidia of *Aspergillus flavus* suffices 400 MPa, 20°C, 10 min. Inactivation is slowest at room temperature, high and low temperatures give better results.

### Conclusions

High hydrostatic pressure can be used to inactivate microorganisms including vegetative pathogens. Investigation of microorganisms was found to be directly correlated to the level of high hydrostatic pressure, but significant differences between Gram-positive and Gram-negative bacteria were observed.

For investigation of conidia of *Aspergillus flavus* suffices 400 MPa, 20°C, but combined treatment of 800 MPa and temperature of 50°C, 10 minutes is needed to kill whole *Bacillus cereus* population.

### References

1. Gould G.W.: in: *High pressure processing of foods* 1995, 20  
Ed: Ledward D.A., Johnson D.E.,  
Earnshaw R.G., Hasting A.P.M.,  
Nottingham University Press  
1995
2. Knorr D. *Food Technology*,  
1993, 47, 156 - 161

### Acknowledgements

Research sponsored by Committee of  
Scientific Research, Poland  
Grant Nr 5 S307 005. 05 1993/1996

## FTIR STUDIES ON FOOD COMPONENTS IN DIAMOND ANVIL CELL

LÁSZLÓ SMELLER<sup>1</sup>, KOEN GOOSSENS<sup>2</sup>, PETER RUBENS<sup>2</sup> and KAREL HEREMANS<sup>2</sup>

<sup>1</sup>Institute of Biophysics, Semmelweis Medical University, Budapest, H-1444 Hungary

<sup>2</sup>Katholieke Universiteit Leuven, Department of Chemistry Celestijnenlaan 200 D, B-3001 Leuven, Belgium

### ABSTRACT

Pressure effects on the transformation of food components can be studied, *in-situ*, in the diamond anvil cell with Fourier-Transform InfraRed (FT-IR) spectroscopy. The differences that are found in the infrared spectra of pressure- and temperature-induced gels of proteins point to stronger *inter*-molecular interactions in the temperature-induced in contrast to the pressure-induced gels.

### Introduction

At the beginning of this century, Bridgman observed that the white of an egg is coagulated after a pressure treatment for 30 min at 700 MPa. The appearance of the pressure-induced coagulum was hereby quite different from the coagulum induced by temperature. In addition the original publication states that it "seems to be such that the ease of (the pressure-induced) coagulation increases at low temperatures, contrary to what one might expect".

It is now clear that these observations are the consequence of the unique behaviour of proteins. The phase diagram for the conditions under which the native and the denatured conformation occur reflects the differences between the native and the denatured state of the protein. (1-3) The study of the effects of pressure on proteins has received considerable attention in recent years because of an increasing interest of the food industry for the high pressure treatment of food materials as a possible alternative for temperature treatment (4-6)

Pressure effects on the transformation of food components can be studied, *in-situ*, in the diamond anvil cell with Fourier-Transform InfraRed (FT-IR) spectroscopy. The so called amide I' infrared bands of the proteins in the sample are used to characterise their conformation. Resolution enhancement is used to extract the maximum extent of information out of the spectra. Gel formation can simultaneously be followed from the changes in turbidity.

There is excellent agreement with the results obtained with pressure sampling procedures. The technique is useful as a tool for a rapid screening of pressure or temperature-induced phenomena in proteins, polysaccharides, bacterial cells and spores.

One of the important findings with this technique is the observation of substantial differences in the infrared spectra of pressure- and temperature-induced gel formation of proteins. The results point to stronger *inter*-molecular interactions in the temperature-induced in contrast to the pressure-induced gels. We have made this observation on many proteins but have studied it in detail for  $\beta$ -lactoglobulin, a protein from milk and lipoxygenase an enzyme from soybean.

The protection of proteins against heat denaturation by polyols (such as sugars and sorbitol) is also observed for the denaturation by pressure (7). This suggests that the water activity is an important factor in pressure-induced protein denaturation. The differences that are found in the infrared spectra of pressure- and temperature-induced gels of proteins point to stronger *inter*-molecular interactions in the temperature-induced in contrast to the pressure-induced gels. Combined pressure and temperature measurements were also used to understand the denaturation processes. While the temperature denaturation is always irreversible, in some cases partial refolding of the protein was observed after the release of the pressure.



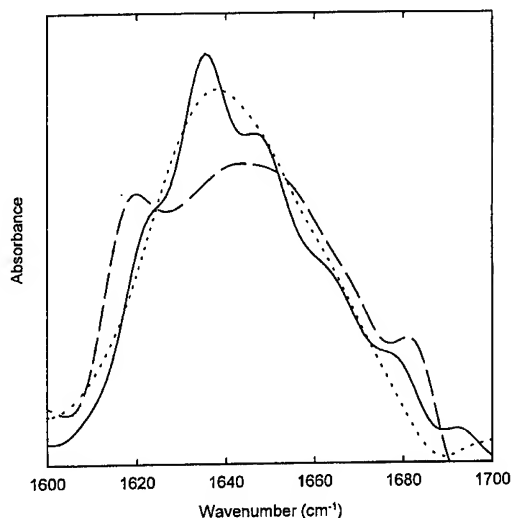


Fig 1. Deconvoluted spectra of the temperature and pressure denatured  $\beta$ -lactoglobulin. Solid line: ambient condition. Dashed line temperature denatured protein. Dotted line pressure denatured protein.

## Materials and Methods

Lipoxigenase from soybeans was kindly prepared by Dr J. Frank, Delft University of Technology. The  $\beta$ -lactoglobulin protein isolate (Besnier-Bridel, France) was obtained from Dr. J. C. Cheftel, University of Montpellier II. his sample contains about 90% native  $\beta$ -lactoglobulin.

The proteins were dissolved in Tris-HCl buffer pH 7.5 at a concentration of 150 mg/ml. The solutions were left overnight (at room temperature) to facilitate H/D exchange. High pressure was created by a diamond anvil cell (DAC). The fluorescence of a small ruby chip in the DAC was used to measure the pressure (8). In some cases the pressure was obtained from the shift of the sulfate stretching mode of  $\text{BaSO}_4$  (9). Temperature measurements were performed in a Specac liquid cell with CaF windows. The rate of the temperature increase was about 10 °C/hour.

Infrared spectra were obtained with a Bruker IFS66 FT-IR spectrometer equipped with broad band liquid nitrogen cooled MCT detector. Infrared light was focussed on the sample by a NaCl lens (10). 350 interferograms with a resolution of

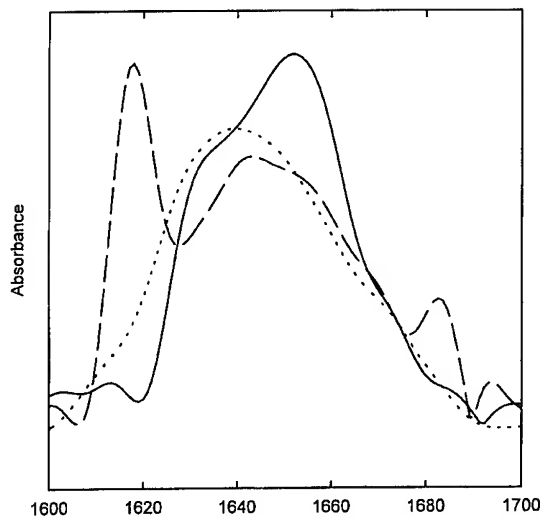


Fig 2. Deconvoluted spectra of the temperature and pressure denatured lipoxigenase. Solid line: ambient condition. Dashed line temperature denatured protein. Dotted line pressure denatured protein.

2  $\text{cm}^{-1}$  were coadded in order to increase signal to noise ratio.

The amide I band in the 1600-1700  $\text{cm}^{-1}$  region of the infrared spectra was used to detect the secondary structure of the protein. The spectra were processed by the program developed in our laboratory (11). Fourier self deconvolution and fitting of Gaussian profiles of the resolution enhanced spectra enabled us to characterize the elastic and conformational changes caused by the pressure (12)

## Results and discussion

Figure 1. shows the superposition of the deconvoluted spectrum of the temperature and pressure denatured  $\beta$ -lactoglobulin isolate. Pressure denaturation was observed above 2 kbar and temperature denaturation above 75 °C.

The same information for lipoxigenase is shown on Figure 2. In this case the pressure needed for denaturation was 6 kbar and the temperature for that was 70 °C. Resolution enhancement was used in both case to emphasise the structure of the spectral band.

Our results show that the infrared technique explores aspects of the behaviour of proteins under

extreme conditions that cannot be detected by other methods demonstrating the sensitivity of FTIR to detect pressure-induced phenomena in proteins.

Our results make it also possible to correlate the macroscopic appearance, the microscopic structure and the molecular conformation of pressure treated food components. The process of gel formation is the macroscopic consequence of the denaturation on the molecular level of proteins or other biomacromolecules such as polysaccharides. The native structure (in the case of an enzyme the active conformation) is transformed by denaturation. This denatured state forms a gel or a precipitate according to the chemical and physical circumstances. In many cases, the process is much more complex.

A comparison of the results obtained with infrared spectroscopy with those obtained from rheological techniques, reveals some interesting correlations. The storage modulus  $G'$  and the loss modulus  $G''$  are higher for the temperature-induced gels than for the pressure-induced gels. Scanning electron microscopy shows that the temperature-gels have a higher number of links. Creep and stress relaxation on the other hand are higher for the pressure-gels. The porosity of these gels is higher. Taken together these results suggest stronger interactions in the temperature-gels in contrast to the weaker interactions of the pressure-gels (13-14). This correlates rather well with the presence of intermolecular hydrogen bonding in the temperature-gels as is observed in the infrared spectra. No such interactions have been observed in pressure-gels. A detailed analysis of the changes in conformation suggests that this may be due to the difference in the degree of unfolding.

A more detailed correlation is now possible between the macroscopic appearance, the microscopic structure and the molecular conformation of pressure treated food components.

The use of pressure as an alternative to temperature treatment, has brought about the need for fundamental studies on the pressure-temperature behavior of macromolecular food constituents. The mechanisms of protein gelation and the sol-gel

behaviour of polysaccharides is far from being understood. The correlation between the results of spectroscopic techniques with those from rheology is a fruitful area of research.

### Acknowledgement

Part of the work is supported by the Commission of the European Union, contract No. AIR1-CT92-0296

### References

1. K. Suzuki, *Rev. Phys. Chem. Japan* **29** (1960) 91.
2. S.A. Hawley, *Biochemistry* **10** (1971) 2436.
3. O. Heinisch, E. Kowalski, K. Goossens, J. Frank, K. Heremans, H. Ludwig and B. Tauscher, *Zeitschrift für Lebensmittel-Untersuchung und -Forschung* (1995 in press).
4. C. Balny, R. Hayashi, K. Heremans and P. Masson, P. (Eds.) *High Pressure and Biotechnology*, (John Libbey Eurotext Ltd, Montrouge, 1992)
5. V. V. Mozahev, K. Heremans, J. Frank, P. Masson and C. Balny, *Trends in Biotechnology* **12** (1994) 493.
6. B. Tauscher, *Zeitschrift für Lebensmittel-Untersuchung und -Forschung* **200** (1995) 3.
7. K. Heremans, K. Goossens and L. Smeller, in *Molecular Biophysics and Enzymology*, ed. J. L. Markley, C. Royer and D. Northrup (Oxford University Press, 1995 in press)
8. J. D. Barnett, S. Block and G. J. Piermarini *Rev. Sci. Instrum.* **44** (1973) 1.
9. P.T.T. Wong and D. J. Moffat, *Appl. Spectrosc.* **43** (1989) 1297.
10. P.T.T. Wong, *Can. J. Chem.* **69** (1991) 1699.
11. L. Smeller, K. Goossens and K. Heremans, *Appl. Spectrosc.* **49** (1995) (in press).
12. L. Smeller, K. Goossens and K. Heremans, *Vibr. Spectrosc.* **8** (1995) 199.
13. J. Van Camp and A. Huyghebaert, *Lebensm. Wiss. u. Techn.* **28** (1995) 111.
14. J. Van Camp, and A. Huyghebaert, *Food Chem.* (1995, in press)

# INFLUENCE OF HIGH PRESSURE ON CHANGES OF CHEESE CHARACTERISTICS

**PIOTR KOŁAKOWSKI, ARNOLD REPS, ANDRZEJ BABUCHOWSKI, LIDIA ŻMUJDZIAN, <sup>1</sup>STEFAN PODLASIN, <sup>1</sup>SYLWESTER POROWSKI**

Olsztyn University of Agriculture and Technology, Institute of Food Biotechnology, Heweliusza Str. 1, 10-957 Olsztyn, Poland

<sup>1</sup>High Pressure Research Center (UNIPRESS) Polish Academy of Sciences, Sokołowska Str. 29, 01-142 Warsaw, Poland

## ABSTRACT

Gouda and Camembert cheeses at different ripening stages were treated with high pressures up to 1200 MPa in order to determine of their influence on microorganisms inactivation and cheese proteolysis. Independent of ripeness of cheeses, significant reduction of microorganisms count in cheeses was observed at pressures above 400 MPa. Extent of microorganisms inactivation was more dependent on applied pressure than its duration. Use of pulsating pressure additionally increased inactivation of microorganisms. In all cases, the inactivation of microorganisms was irreversible. No significant influence of the applied high pressures was found on Gouda cheese protein degradation. On the other hand, in Camembert cheese, the most intense proteolysis was observed in cheeses treated with pressure 50-70 MPa as compared to the control ones. This was confirmed by analysis of proteolytic activity of Camembert cheese enzymes. Higher level of proteolysis in Camembert cheese resulting from applied high pressures did not adversely influenced its quality.

## Introduction

High pressure technology offers the food industry a numerous opportunity to develop novel foods of high nutritional and sensory quality, novel texture and increased shelf life (1, 2, 3). Key effects of high pressure as related to food system encompass inactivation of microorganisms (4), modification of biopolymers including enzyme activation and inactivation, protein denaturation, gelatinization of starch or susceptibility to enzymatic action (5). Since high pressure acts on food by affecting mostly noncovalent bonds it doesn't cause changed natural flavour, colour, vitamins and taste of foods (1).

Yokoyama et al. (6) showed that high pressures could be useful to control enzymatic proteolysis of cheddar cheese.

The aim of this research was to determine an influence of high pressure on:

- total bacterial count in Gouda and Camembert cheeses at different ripening stages,
- degree of proteolysis of Gouda and Camembert cheeses,
- activity of enzymes present in Gouda and Camembert cheeses.

## Methods

An influence of high pressure on total bacterial count and degree of proteolysis of Gouda and Camembert cheeses was investigated. The pressurized cheeses were at different stages of ripening: two and six weeks old Gouda cheese and five, ten and fourteen days old Camembert cheese.

Samples of cheeses were packed in experimentally selected, high pressure resistant plastic foils and then pressurized in hydraulic pressure generators from UNIPRESSEQUIPMENT in High Pressure Research Center of Polish Academy of Sciences in Warsaw.

Microorganisms count was determined in cheeses, treated with pressure ranging from 0 to 1200 MPa and lasting for 10, 15, 20 and 240 minutes, immediately after processing and after subsequent storage at 5°C for 12 weeks. An influence of applied cyclic pressure with cycles lasting five and ten minutes on total bacterial count in cheese was also investigated. Viability of microorganisms was based on total microbial count and determined according to Polish Standard PN-93A-86034/04.

Extent of proteolysis in cheeses pressurized in a range from 0 to 500 MPa for 20, 240 and 1200

minutes was evaluated acc. to the following determinations:

- pH
- nitrogen soluble at pH 4.6
- non-protein nitrogen
- peptide nitrogen
- amino acid nitrogen.

Proteolytic activity and enzymes content in proteinaceous extracts from pressurized cheeses were determined acc. to modified Anson method, and lipolytic activity acc. to diffusion method of Lawrence.

An organoleptic assessment of the pressurized cheeses was made by expert panel.

## Results and Discussion

### *Influence of high pressures on viability of microorganisms in cheese*

There was a significant influence of a pressure on number of microorganisms present in cheese. With increased pressure viability of microorganisms decreased. In cheese pressurized at 800 MPa for 15 minutes microorganisms count decreased by order of magnitude from 4 to 6 (Fig. 1).

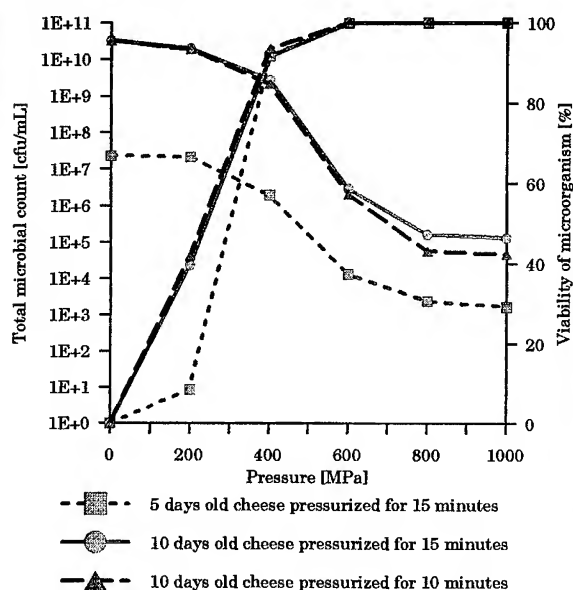


FIGURE 1. Influence of applied pressure on micro-organism count in Camembert cheese

For instance, in milk at room temperature pressurized at 680 MPa for 10 minutes total microbial count decreased from  $10^7$  cfu/cm<sup>3</sup> to  $10^1$ - $10^2$  cfu/cm<sup>3</sup> (7).

Viability of microorganisms depended also on type and ripeness of cheese hence in the same treatment conditions higher reduction of microorganisms was observed in 10 days old Camembert cheese (99.9938%) than in 6 weeks old Gouda cheese (99.8581%).

Susceptibility of microorganisms to high pressure is influenced also by type of microorganisms and medium composition. Styles et al. (8) found that inactivation of *Listeria monocytogenes* strain Scott A was much faster in buffer than in milk.

Independent of type and ripeness of cheeses, significant reduction of microorganisms was observed at pressures above 400 MPa.

It was found that for inactivation of microorganisms applied pressure is more important factor than its time, eg. in 10 days old Camembert cheese pressurized at 200 MPa for 10, 15 and 240 minutes microorganisms reduction was 39.6875%, 41.9753% and 71.7143% respectively. On the other hand applied pressure 400 MPa during 10 minutes caused 93.5802% inactivation of microorganisms.

TABLE 1. Influence of pulsating pressure on microorganisms count in two weeks old Gouda cheese

Pres- sure  [ MPa ]	Total bacterial count [ cfu/g ]		Reduction of microorganisms count [ % ]	
	Pressurization time [ min ]			
	15	3 × 5	15	3 × 5
0	3,90 × 10 <sup>10</sup>	3,90 × 10 <sup>10</sup>	0	0
200	2,35 × 10 <sup>10</sup>	1,80 × 10 <sup>8</sup>	39,1192	99,5385
400	4,20 × 10 <sup>8</sup>	1,14 × 10 <sup>8</sup>	97,8000	99,7077
600	4,00 × 10 <sup>6</sup>	7,50 × 10 <sup>5</sup>	99,9896	99,9981
800	4,40 × 10 <sup>5</sup>	2,51 × 10 <sup>5</sup>	99,9989	99,9994
1000	3,00 × 10 <sup>5</sup>	1,25 × 10 <sup>5</sup>	99,9992	99,9997

In spite of significant reduction of microorganisms in the investigated cheeses even at pressure 1200 MPa no complete sterilization of cheeses was obtained.

Taking into account that generation of high pressures creates technical and economic problems in order to avoid these obstacles and to maintain a high inactivation rate of microorganisms a pulsating pressure was applied. It was found that pulsating pressure increased inactivation of microorganisms in cheese. In 2 weeks old Gouda cheese treated with 200 MPa pulsating (3x5 minutes) and constant pressure for 15 minutes viability of microorganisms was  $1.8 \times 10^8$  cfu/g and  $2.35 \times 10^{10}$  cfu/g respectively. At higher pressure applied effect of pressure pulsation was less pronounced (Tab.1).

In the pressurized Gouda cheese stored at 5°C for 12 weeks there were observed similar trends concerning the viability of microorganisms as in the control one. The above presented results indicate for permanent inactivation of microorganisms under applied high pressures.

#### *Influence of high pressures on cheese proteolysis*

For Camembert cheese there was significant influence of high pressure on proteolysis. The extent of protein degradation depended on applied pressure and cheese ripeness. For 10 days old Camembert cheese the highest degree of proteolysis was observed when pressure of 50 MPa

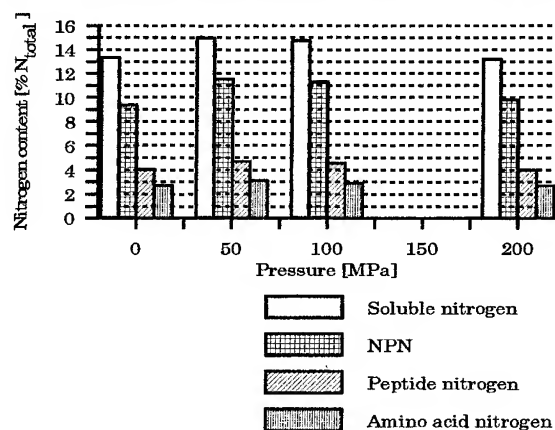


FIGURE 2. Influence of 4 hours pressurisation on content of individual forms of nitrogen in ten days old Camembert cheese

was applied for 4 hours. This resulted in 32.4% increase in soluble nitrogen content, 27.8% increase in NPN, 40.2% and 31.5% increase in peptide and amino acid nitrogen content, respectively as compared to data from control cheese. Smaller increase in the investigated nitrogen forms content was observed in 10 days old Camembert cheese pressurized at 100 MPa for 4 hours and no changes as compared to the control one was observed in the same Camembert cheese pressurized at 200 MPa for 4 hours (Fig.2).

For 5 days old Camembert cheese the influence of pressure on extent of proteolysis was similar to that one in 10 days old cheese. The highest degree of proteolysis was found at pressure 50 MPa applied for 4 hours but the percentage differences were smaller than these ones in 10 days old cheese (Fig.3).

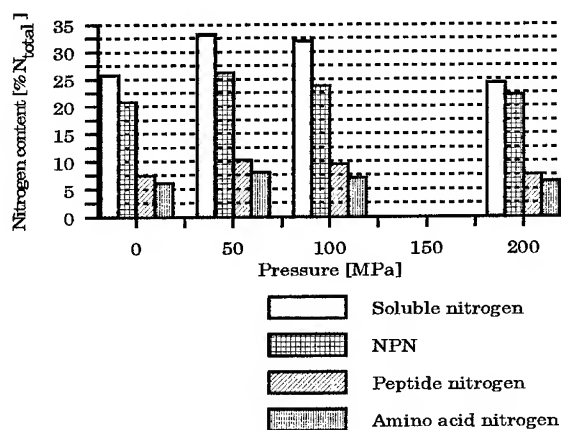


FIGURE 3. Influence of 4 hours pressurisation on content of individual forms of nitrogen in five days old Camembert cheese

In case of Gouda cheese, there was not any significant influence of pressure on protein degradation within applied pressure and time despite a substantial increase in pH of cheese mass in some samples compared to these treated with pressure 250 and 500 MPa. Increase the treatment time to 60 hours at pressure 50 MPa did not cause significant differences in proteolysis as compared to that one in control cheese.

Proteolytic activity of enzymes extract from Camembert cheese depended heavily on applied pressure but lipolytic activity was only little affected (Tab.2).

TABLE 2. Activity of proteolytic and lipolytic enzymes in cheese treated with high pressure

Type of cheese	Age	Pressure [ MPa ]	Time [ min ]	Activity	
				proteolytic in $\mu\text{M}$ of released tyrosine/min/cm <sup>3</sup> of extract	lipolytic in mm <sup>3</sup> of liquified zone
Camembert	5	0	0	16,14	28,45
		50	240	28,25	30,75
		100	240	25,56	25,92
		200	240	22,87	23,24
	10	0	0	21,52	39,55
		50	240	29,59	37,23
		100	240	26,90	38,43
		200	240	24,21	41,73
	14	0	0	19,24	102,56
		70	240	45,46	94,46
		500	20	3,50	130,62
Gouda	42	0	0	45,73	21,28
		70	240	45,73	20,45
		500	20	40,35	29,50

Extent of proteolysis in the pressurized cheeses was confirmed by analysis of proteolytic enzymes activity in cheese. The highest proteases activity in 5 and 10 days old Camembert cheese was observed when pressure 50 MPa was applied. At pressures 100 and 200 MPa activity decreased but it was still higher than that in the control cheeses.

In Gouda cheese, independent of applied pressures, the proteolytic and lipolytic activities remained on similar level.

The applied pressure influenced rheological properties of the investigated cheese. Evaluation of the cheeses by an expert panel indicated that pressurized Gouda cheese was more elastic than the control one. In 5 days old Camembert cheese pressurized at 200 MPa for 4 hours slight whey syneresis was observed.

According to the panel of experts, Gouda cheese, in the investigated range of applied

pressures, had higher organoleptic properties than the control one traditionally ripened.

Higher proteolysis in the pressurized Camembert cheese did not adversely affected its quality.

## Conclusions

1. Significant reduction in microorganisms count in the investigated cheese, independent of their type and ripeness, was found at pressure above 400 MPa.
2. Inactivation of microorganisms was more influenced by applied pressure than its duration.
3. Uses of pulsating pressure increased inactivation of microorganisms.
4. Applied pressure caused irreversible inactivation of microorganisms.
5. There was not any significant influence of applied pressures on protein degradation in Gouda cheese.
6. Intensity of protein degradation under pressure in the investigated cheeses was confirmed by analysis of proteolytic activity of cheese enzymes.
7. Higher degree of proteolysis in Camembert cheese resulting from high pressures applied did not influence negatively of its quality.

## References

1. Effects of high pressures on foods, European Symposium, 1995. Montpellier, France.
2. B. Mertens, *Int. Food Manufacturing* 44 (1993) 100.
3. P. Kołakowski, A. Reps & A. Babuchowski, *Przem. Spoż.* 48 (1994) 108.
4. D.G. Hoover, C. Metrick, A.M. Papineau, D.F. Farkas & D. Knorr, *Food Technol.* 43 (1989) 99.
5. B. Taucher, *Z. Lebensm. Unters. Forsch.* 200 (1995) 3.
6. H. Yokoyama, N. Sawamura & N. Motobaya-shi, *USA Patent US005 180 596A* (1993).
7. B.H. Hite, *West Virginia Agric. Exp. Station Morgantown Bull.* 58 (1889) 15.
8. M.F. Styles, D.G. Hoover & D.F. Farks, *J. Food Sci.* (1991) 1404.

## EFFECT OF DYNAMIC HIGH PRESSURE ON MODEL BACTERIAL CULTURES

M. RADOMSKI<sup>1)</sup>, M. FONBERG-BROCZEK<sup>2,3)</sup>, H.ŚCIEŻYŃSKA<sup>3)</sup>, B. WINDYGA<sup>3)</sup>

<sup>1)</sup> *Institute of Mechanics and Design, Warsaw University of Technology,  
ul. Narbutta 85, PL-02-524 Warsaw, Poland*

<sup>2)</sup> *High Pressure Research Centre, Polish Academy of Sciences,  
ul. Sokołowska 29/37, PL-01-142 Warsaw, Poland*

<sup>3)</sup> *National Institute of Hygiene,  
ul. Chocimska 24, PL-00-791 Warsaw, Poland*

### ABSTRACT

The objective of the task was to verify the possibilities of application of dynamic, short duration high isostatic pressure for the technology of high pressure food treatment. The experiments have been carried out on model bacterial cultures, in the pressure range up to 500MPa.

### Objective, Subject and Scope of Research

The objective of the task was to verify the possibilities of application of dynamic, short duration high isostatic pressure for the technology of high pressure food treatment. Short time of the pressing operation (within the range of tenths of a second) is essential for introducing this operation to the process line of packing of the final product. This solution could lead to the elimination of big and therefore expensive machines for isostatic pressing. These machines could be substituted by automatic process lines equipped with units for isostatic pressing operations. This would contribute to the spreading of the idea of high pressure food processing.

The experiments have been carried out on model bacterial cultures of: *Salmonella* ( $10^5$  and  $10^3$  cells per ml), *Saccharomyces cerevisiae* ( $10^4$  and  $10^3$  cells per ml), *Staphylococcus aureus* ( $10^4$  cells per ml), *Candida albicans* ( $1,7 \cdot 10^6$  cells per ml). The experiments have been carried out in the pressure range up to 500MPa. The pressure media was water at ambient temperature.

### Test Stand

Figures 1 and 2 show the diagrams of the laboratory stand and the pressure chamber.

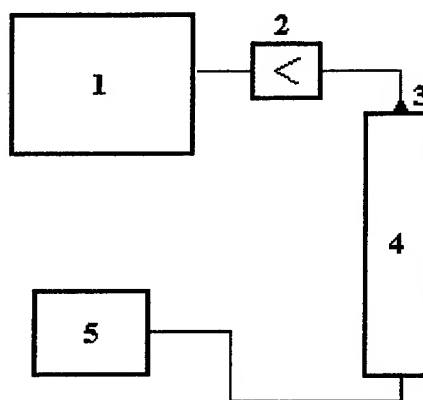


Fig. 1. The diagram of the laboratory stand.

- 1 - data acquisition and processing system,
- 2 - charge amplifier,
- 3 - pressure transducer,
- 4 - pressure chamber,
- 5 - ignition generator.

The propellant's chemical decomposition reaction has been used to generate the pressure

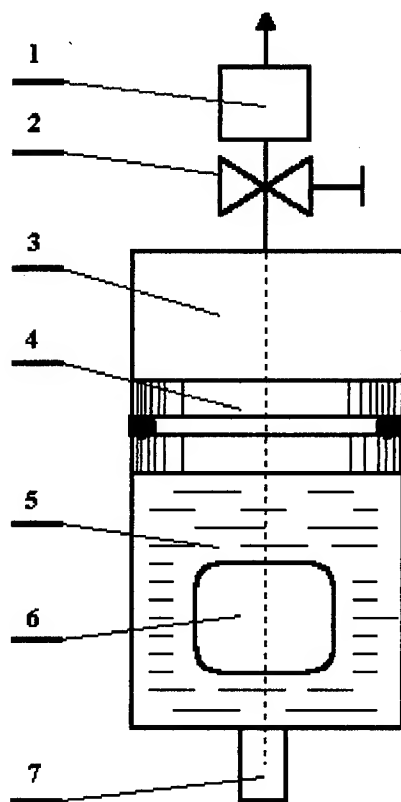


Fig.2. Pressure chamber diagram

- 1 - throttling element,
- 2 - stop valve,
- 3 - gas chamber,
- 4 - piston,
- 5 - water chamber,
- 6 - test sample,
- 7 - pressure transducer.

in the test stand. High pressure and high temperature gases are the products of such reaction. This reaction proceeds in the gas chamber of the pressure chamber. The shape of a pressure curve is programmed by choosing the combination of ballistic properties of the propellant, propellant's mass and the throttling element. Pressure force of the gases affecting the piston produces hydrostatic pressure in the water chamber area of the pressure chamber. The test sample is located in the water chamber area. This design of the pressure chamber ensures the

isolation of the test sample from the direct contact with the gases.

The pressure is measured using a piezoelectric transducer model 6201B by KISTLER. The electric signal from the transducer after being transformed and amplified by the charge amplifier is registered in a digital form by a data acquisition and processing system. This system is PC based and equipped with a specialised A/D transducer card model DAS-58 by KEITHLEY. Data acquisition and processing system is capable to register one million of pressure values at a frequency of 1 MHz. The test stand enabled to achieve the pressure profiles as shown on the Figures 3 and 4.

#### Experiment Results and Conclusions

During the experiments the bacterial load reduction was found to be lower than 1 log. Therefore pressure in a range of 400 to 500 MPa applied for less than 10 ms was found to be insufficient to pasteurise food products. It can be assumed that high viscosity of the intercellular fluid enabled the survival of the micro-organisms. It seems advisable to continue the experiments for a range of higher pressures, namely from 500 to 1500 MPa. Such experiments should lead to the development of a rheological model of intercellular fluid. This would be a step towards the closer identification of the mechanism of destruction of micro-organisms under high hydrostatic pressure.

#### Acknowledgements

Research sponsored by Committee of Scientific Research, Poland, Grant No 5S 307 005 1993/1994.



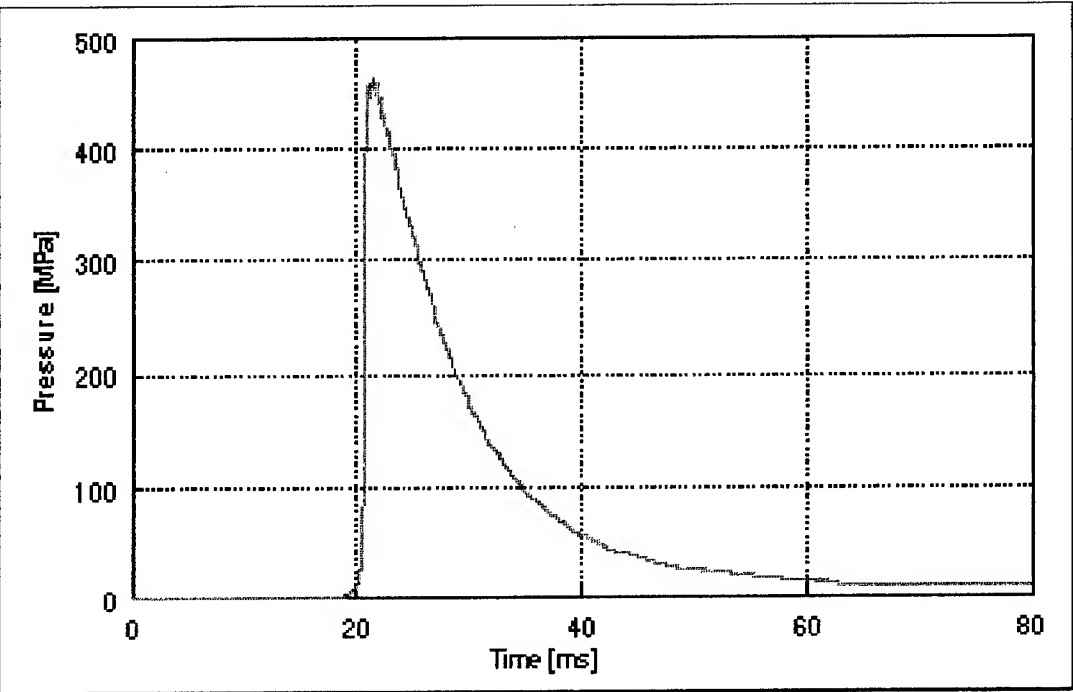


Fig. 3. Example pressure profile as time function.

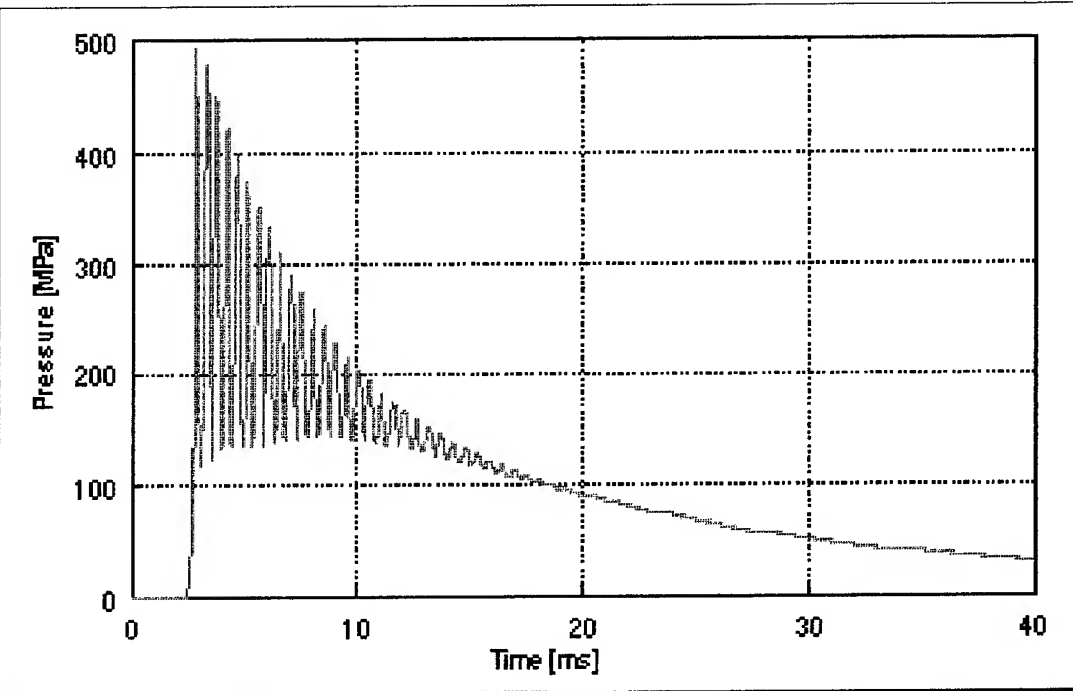


Fig. 4. Example pressure profile as time function.

## **X Geophysical and Planetary Sciences**

# MAGNETIC PARAMETERS OF ROCKS UNDER STRESS CONDITIONS OF THE KTB MAIN DRILL AND INVESTIGATION OF ANISOTROPY CARRIERS

A. KAPIČKA, E. PETROVSKÝ

Geophysical Institute Acad. Sci., Boční II/1401, 141 31 Prague 4, Czech Republic

J. POHL

Geophysical Institute, University of München, Theresienstrasse 41a, 80333 München, Germany

## ABSTRACT

Pressure-induced changes in magnetic anisotropy parameters were studied on a set of samples from the upper part of the main KTB borehole. The study is aimed at quantification of stress stability of magnetic anisotropy associated with major lithological units embedded in different depths. On the basis of stress field data, obtained *in situ* from the borehole, laboratory modelling of magnetic anisotropy was carried out under stresses corresponding to actual borehole conditions. Dominant carriers of magnetic anisotropy were determined and reasons for stress instability of samples containing either magnetite or different phases of pyrrhotite are discussed.

## Introduction

The subject matter of the paper includes modelling of magnetic anisotropy under actual pressure conditions of the KTB main drill (4000 - 8201m) and investigations of carriers of anisotropy of magnetic susceptibility (AMS). Laboratory pressure modelling contributes to the general knowledge on the actual vertical profile of magnetic parameters and their anisotropy throughout the depth range. Our measurements are closely connected with the results of depth variations of the stress fields within the borehole [1,2]. The output to be achieved is to determine the coefficients of stress sensitivity corresponding to the principal lithospheric units along the whole depth profile and to discuss the physical background of the zones exhibiting low stress stability of magnetic anisotropy.

## Results and discussion

Firstly, magnetic parameters under atmospheric pressure were examined for all the samples from depths of 4000 - 8201 m. Secondly, samples from depths down to 6245 m were studied from the point

of view of the stress stability of magnetic anisotropy parameters.

Mean magnetic susceptibility of the samples studied varies from  $0.3 - 3.1 \times 10^{-3}$  SI, consistent increase being observed in deeper layers ( $h > 6000$  m). The highest susceptibility values ( $1.1 - 3.1 \times 10^{-3}$  SI) were expressed by metabasic rocks from the depths of 6150 - 6245 m and 6355 - 6666 m. These samples also exhibited high values of natural remanent magnetization (NRM). Contrary to the majority of samples with low degree of anisotropy ( $P = 1.03 - 1.20$ ), metabasic rock samples are characterized by high values of  $P$ , varying from 1.24 to 2.15. Completely different behaviour was observed in samples from layers between 6149 and 6666 m, where rocks of high susceptibility and anisotropy values alternate with layers with low values of the susceptibility parameters. Temperature dependence of magnetic susceptibility and magnetization proved that pyrrhotite is the main magnetic carrier. In most cases, monoclinic phase was identified, at depths of 6243 and 6400 - 6540 m the hexagonal phase was found as well. Magnetite as the dominant magnetic mineral was identified in depths from 4400 to 4800 m and in the deepest layers at about 8000 m.

In order to evaluate the stress stability of the KTB samples, depth profiles of changes in magnetic parameters induced by directional pressure were studied. Special non-magnetic chamber was constructed in the Geophysical Institute in Prague for pressure studies of the anisotropy of magnetic susceptibility under uniaxial pressures up to 60 MPa [3]. Coefficients of stress sensitivity  $\beta_{\text{par}}$  and  $\beta_{\text{per}}$  were used to quantify the stress sensitivity of individual samples

$$\beta_{\text{par}} = \frac{\kappa_0 - \kappa_{\text{par}}}{\kappa_0 \sigma}; \quad \beta_{\text{per}} = \frac{\kappa_{\text{per}} - \kappa_0}{\kappa_0 \sigma},$$

where  $\kappa_0$  denotes initial magnetic susceptibility and  $\sigma$  is stress.

Magnitude of these parameters is inversely proportional to the stability of magnetic anisotropy in inhomogeneous stress fields.

Metabasic rocks from the depth of 4686 m appear to be the most unstable with a 9% pressure-induced change in the anisotropy degree  $P$  with respect to the original value. Increased instability was also found in samples from the depths below 5500 m. These regions are characterised by high values of the coefficients  $\beta$ . While in the former case magnetite appears to be the main reason for the instability [4], rock samples from the deeper layers

contain prevalingly pyrrhotite. Their pressure instability is most probably related to the pressure instability of mean susceptibility, which increased significantly (both reversibly and irreversibly) with increasing pressure. This effect is reflected in the change of the sign of the  $\beta_{\text{par}}$  coefficient (Fig. 1). Several special measurements were carried out in order to elucidate this behaviour (e.g. measurements of high field anisotropy and temperature dependence of susceptibility). Our results suggest that antiferromagnetic (hexagonal) pyrrhotite, present in these layers, shows a metastable behaviour and might turn to the ferrimagnetic phase upon the action of high stress fields. This conclusion is in agreement with the results of recent measurements of the magnetic field within the KTB borehole [5] which revealed anomalous increase of the magnetic field in the lower part of the borehole down to 6000 m.

#### Acknowledgements

This study was supported by the Granting Agency of the Czech Republic through a grant No205/93/0414.

#### References

1. A. Zang, H. Berckhemer and K. E. Wolter, Interfering the in situ state of stress from relief microcracking in drill cores. *KTB Report 90-8*, (NLB Hannover 1990) F1.
2. H. Berckhemer and M. Lienert, *Working report for DFG Project Be 299/68/199* (1993)
3. A. Kapička, Anisotropy of magnetic susceptibility in a weak magnetic field induced by stress. *Phys. Earth Planet. Int.* **51** (1988) 349.
4. A. Kapička, E. Petrovský and J. Pohl, Modelling magnetic anisotropy of samples from KTB-1 pilot hole under pressure. *Geologica Carpathica* **43** (1992) 173.
5. F. Fieberg and F. Khunke, The increase in the total magnetic field in the KTB pilot and main drillhole. *Scientific Drilling* **4** (1994) 139.

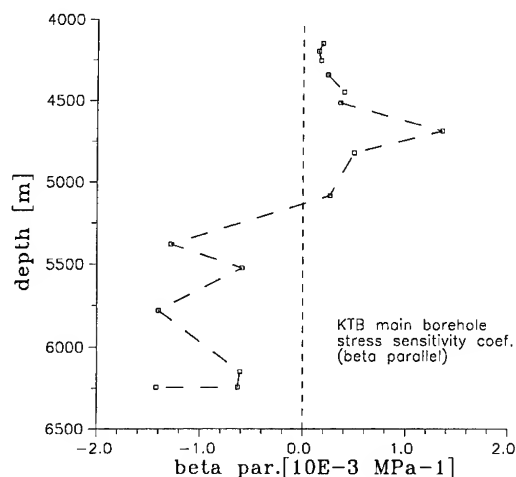


Fig. 1. Stress sensitivity coefficient parallel to the stress direction ( $\beta_{\text{par}}$ ) of samples from the KTB main borehole in dependence of the sample's burial depth.

# PERMANENT CHANGES IN DEFORMATIONS AND STRENGTHS OF ROCKS DUE TO HYDROSTATIC PRESSURE

JERZY GUSTKIEWICZ

*Strata Mechanics Research Institute of the Polish Academy of Sciences  
ul. Reymonta 27, 30-059 Kraków, Poland*

## ABSTRACT

Several series of cylindrical rock specimens were compressed with hydrostatic pressure reaching values up to 1200 MPa. Those series were then examined in a classical way with the use of a Karman type device, as the result, the relationships between the deviatoric stress and the specimen strains were determined. This was followed by the determination of the strength limit, treated as a function of the confining pressure. The results were related to the those obtained for the series of specimens which had not been compressed before the experiment. In addition to this, microscopic examinations of the rocks were conducted both before and after the hydrostatic compression. The values under investigation showed changes caused by plastic deformations, crack growth and calcite-aragonite transition as the results of hydrostatic compression.

## Introduction

The study of the properties and behavior of rocks is conducted either by observation in nature or by laboratory experiments. The latter aim at reconstructions the conditions to which a rock is exposed in nature and which are vital for the determination of its properties.

For the Laboratory of Rock Deformation of Strata Mechanics Research Institute at the High Pressure Research Center, devices have been constructed for examination of mechanical properties of rocks in a triaxial state of stress. They are:

- apparatus GTA-10, which can be used for investigating deformations and failure of cylindrical specimens axially loaded with both constant pressure, so called confining pressure, exerted on the specimen and the pore pressure of the sorbing or not fluid, or without it. Both pressures can be determined independently at any level reaching 400 MPa.

- apparatus GCA-30 which makes it possible to compress a specimen in liquids or gases with the pressure up to 1500 MPa.

The article describes permanent changes of certain properties of selected kinds of sedimentary rocks, resulting from the history they undergo because of their exposure to short-duration (of the order of minutes) hydrostatic pressure at the ambient temperature.

## 1. Volumetric rock strains as a result of growing hydrostatic pressure

Elastic strain of a rock is caused by relatively low pressure. Rock, however, is a nonhomogeneous and, usually, porous medium. In such a medium hydrostatic pressure can induce deviatoric stresses. They can reach values that exceed the limits of elasticity or of the strength of rock constituents, causing brittle fractures or plastic deformations. Consequently, that leads to permanent rock strains.

The value of hydrostatic pressure at which noticeable permanent strains appear is called consolidation pressure. For many rocks it is a value at which the relation between the growing hydrostatic pressure and the volumetric strain of the rock ceases to be rectilinear. Frequently, the initial part of such a relation is not rectilinear and its convexity is turned downwards. This particular shape results from the existence of rock cracks, which under the influence of growing pressure get closed, usually reversibly.

Fig.1 shows examples of the description presented above. It refers to a Permian sandstone from the Vosges Mts. Two characteristic pressures in the first loading cycle can be seen: cracks closing pressure  $p_0$  and consolidation pressure  $p_c$ . The upper rounded part of the curve suggests the appearance of viscous strains, apart from plastic deformations. In the second cycle the fracture closing pressure increases, which suggests the growth of cracks in the preceding cycle. The hysteresis loop is now of

the elastic type.

A gaize from Louny near Prague is an example of rock where under hydrostatic pressure plastic deformations of significant size can be found. It is a carbonate-silicious sedimentary rock from the Cretaceous period. It contains grains of calcite and quartz as well as those of silica formed as chalcedony and opal. The content of calcite is about 45%. The porosity of the rock ranges from 26% to 37%.

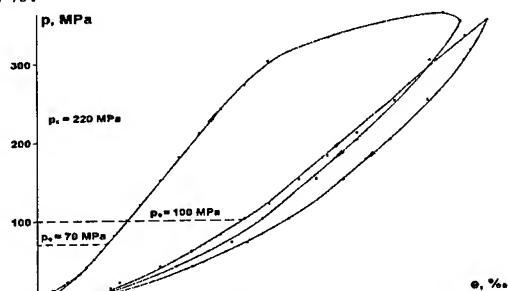


Fig.1 Hydrostatic pressure vs. volumetric strain; Vosges sandstone

The relation between the pressure and volumetric strain for this rock is presented in Fig.2A. The curve marked  $q = 0$  was obtained, just as in the case of Fig.1, for a specimen enclosed in a rubber jacket, which served as a protection against the penetration of the pressure liquid (kerosene in this case) into the pores of the specimen. The relation  $p = q$  was obtained for a specimen without a jacket, saturated with the pressure liquid in vacuum before the experiment.

Due to the changes of pressure and temperature, new structural modifications of minerals may sometimes appear. For instance, compression of calcite produces aragonite.

The compression of the gaize saturated with kerosene in vacuum at the pressure level 500-600 MPa indicates a dependence between pressure and volumetric strain suggesting calcite-aragonite transition, which can be seen in Fig.2B.

Series of gaize specimens were compressed in rubber jackets, with pressures of values 300, 350, 500, 600, 800 and 1000 MPa. The results of microscopic observation of the percentage of calcite crystals containing twins, varying according to the exerted pressure, as performed by Gustkiewicz et al. (1989) and by Sass-Gustkiewicz and Smoleńska (1989) are summed up in Fig.3. The rapid jump in

the shape of the curve for the pressure of about 500 MPa corresponds to the jump in Fig.2B. Moreover, microscopic examination showed collapse of pores and formation of micro-cracks.

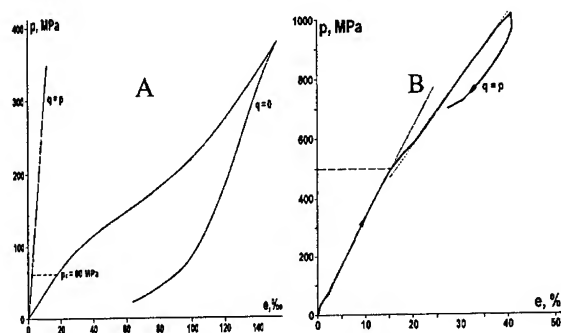


Fig.2 Hydrostatic pressure vs. volumetric strain,  $q=0$  pore pressure equals atmospheric pressure,  $q=p$  pore pressure equals confining pressure; Louny gaize

The Lower-Carboniferous limestone from Czatkowice near Cracow is a rock characterized by high content of calcium carbonate. It contains about 97% of calcite. The remaining 3% include magnesium carbonate, a little silica and other trace constituents. Its porosity is low, below 1%. Specimens of this limestone were compressed with the pressure reaching 1400 MPa, in the atmosphere of nitrogen in the way that produces the pore pressure equal to the pressure outside the specimen.

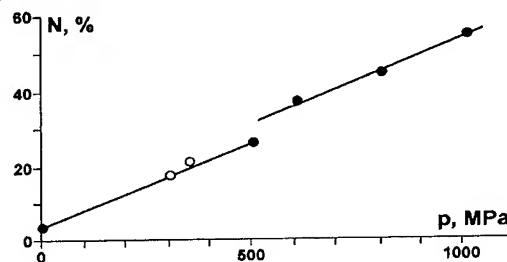


Fig.3 Percent of twinned calcite crystals vs. hydrostatic pressure; Louny gaize  
● after Sass-Gustkiewicz and Smoleńska (1989)  
○ after Gustkiewicz et al. (1989)

According to the curves in Fig.4A, the calcite-aragonite transition appears as a reversible process. On the other hand, Fig.4B suggests that the transition does not always take place although the experiment was repeated in the same way.

A microscopic study of a rock compressed with the pressure up to 600 MPa and 1200 MPa did not

show any changes in comparison with the non-compressed material. The lack of traces of changes in the limestone in the microscopic picture may be connected with the reversibility of the transition.

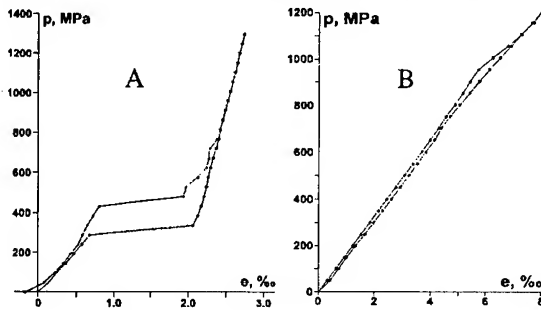


Fig.4 Hydrostatic pressure vs. volumetric strain, pore pressure equals confining pressure; Czatkowice limestone

Minimal porosity and the content of calcite reaching almost 100% probably prevented the limestone from the appearance of permanent deformations.

## 2. Permanent changes of rock strength and deformability as a result of hydrostatic pressure.

In order to estimate the influence of hydrostatic pressure upon the changes of properties at least two series of specimens were examined. The first one was examined without any mechanical action on the specimens. The specimens of the second series were hydrostatically compressed with identical pressure called primary pressure.

Fig.5 is an example of the results obtained for two series of fine-grained Carboniferous sandstone from the hard coal mine Centrum, Upper Silesia. The figure shows the strength limit expressed by differential stress as a function of the confining pressure. The lower curve was obtained for the specimens which had not been originally compressed, the upper curve refers to the specimens after the initial compression, that is before the experiment in GTA-10, with the pressure of 350 MPa. Above 180 MPa the lower curve indicates a quicker growth of strength than below this pressure. It is the consolidation pressure  $p_c$ , above which there appear permanent strains, causing material hardening under hydrostatic pressure.

As in the case of the sandstone, three series of the gaize were examined. Two series of specimens were compressed with the primary pressure 600 MPa and 1000 MPa respectively. Fig.6 shows

differential strength as a function of the confining pressure of those two series in relation to the series of specimens which had not been previously

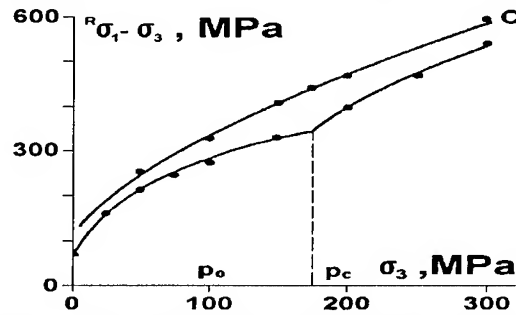


Fig.5 Differential strength vs. confining pressure; Centrum sandstone

compressed. There is a distinct growth of strength and the vanishing of singularity which occurs for the consolidation pressure. The growth of the strength with the primary pressure corresponds to the increase in the number of calcite grains with twins in Fig.3.

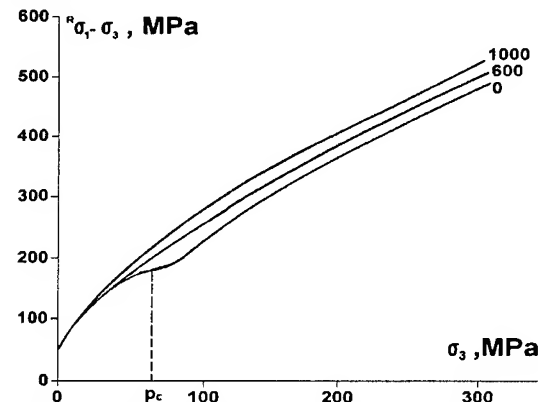


Fig.6 Differential strength vs. confining pressure; Louny gaize

In comparison with Fig.6, Fig.7 presents strain failure as a function of confining pressure. The point of inflection at the curve marked with the coordinate  $p_T$  determines the pressure of transition between brittle fracture and ductile flow of the rock. The evidence for such determination of the transition pressure for many different rocks was supplied by Gustkiewicz (1985). Above  $p_T$ , a significant strain growth can be observed. The curves in Fig.7 show that the increase of the primary pressure is accompanied by a decrease in the rock deformability and an increase of the transition pressure.

This pressure is presented in Fig.8 as function of the primary pressure. The jump at the level of about 500 MPa corresponds to the changes in Figure 2B and 3.

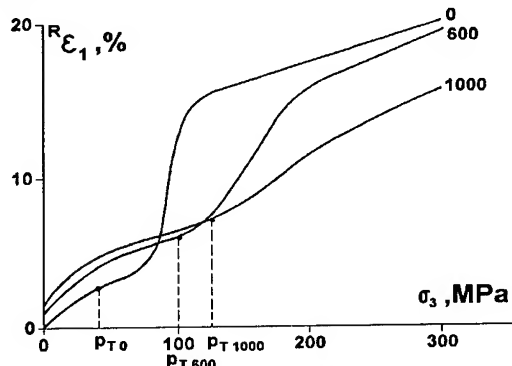


Fig.7 Longitudinal and transverse strain at failure vs. confining pressure; Louny gneiss

The last example concerns the results of the examination of the Czatkowice limestone. Although the study of its compressibility suggests the appearance of calcite-aragonite transition (Fig.4A).

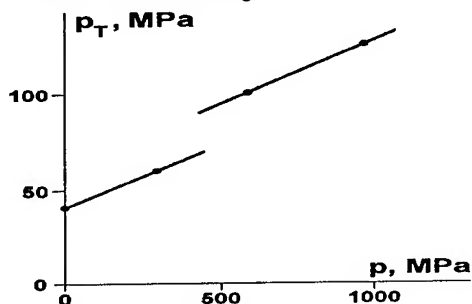


Fig.8 Transition pressure from brittle fracture to ductile flow vs. primary hydrostatic pressure; Louny gneiss

The series of non-compressed specimens and of those compressed with pressure to 600 MPa and 1200 MPa produce results which in the case of the strength limit treated as a function the confining pressure oscillate around the same curve (Fig.9). Numerous examinations of the compressibility of this rock, both in a jacket and without it, did not indicate (within the range of the pressures applied) either the consolidation pressure or the presence of cracks. Therefore the gain in strength which can be seen in Fig.9 (approximate to 300 MPa) is caused neither by plastic deformations nor by the closing of cracks or blocking the slipping on them. It may be a result of the calcite-aragonite transition and, consequently, of the increase of rock density.

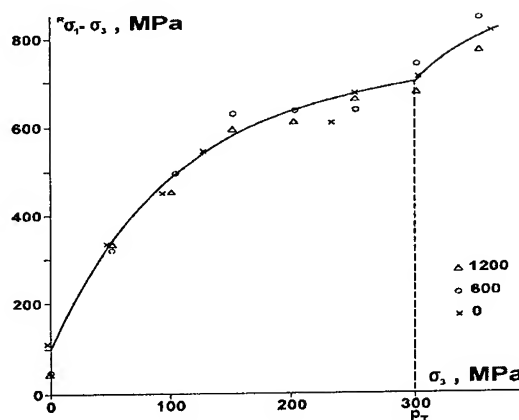


Fig.9 Differential strength vs. confining pressure; Czatkowice limestone

Similarly, the curves representing the relationships between the strain failure and the confining pressure for each series seem to be identical.

### Conclusions

The hydrostatic pressure, homogenous on the surface of a rock element, can induce deviatoric stresses leading to brittle fractures and/or plastic flow of rock components. These two phenomena, acting in the opposite senses, produced as a result strain hardening of the rocks. It seems that the weakening can be also possible in certain rocks.

Finally a sufficiently high pressure can cause permanent or reversible phase transitions. Even reversible changes can lead to permanent deformations and changes of the rock properties.

### References

1. J. Gustkiewicz, Transition of rocks from the brittle to the ductile state: strain at failure as a function of confining pressure, *Acta Geoph. Pol.* 33; (1985) p. 169-181
2. J. Gustkiewicz, K. Mochnacka, Y. Orengo, Modifications permanentes d'une roche par pression hydrostatique in: *Rock at Great Depth*, Maury & Fourmaintrax (eds) (Balkema, 1989) p. 131-139
3. M. Sass-Gustkiewicz, A. Smoleńska, Study of permanent mineralogical and petrographical changes of rocks due to pressure. Unpublished rapport in Polish (1989)



# PLANETARY PHASE EQUILIBRIA AND CONSTITUTION OF THE TERRESTRIAL PLANETS

O.L.KUSKOV

*Vernadsky Institute of Geochemistry and Analytical Chemistry, Russian Academy of Sciences, 117975 Moscow, Russia*

## ABSTRACT

The present research has been devoted towards the investigation of the physico-chemical principles which govern the chemical composition and mineral structure of a planet and should serve as a basis for creating the physico-chemical theory of the constitution of the terrestrial planets. A major objective of the paper is to use a strictly thermodynamic approach for modelling of planetary phase equilibria and for construction of self-consistent petrological-geophysical models of the Earth's, Martian and lunar interiors.

### Thermodynamic approach

Phase transformations in the mineral systems at high pressure provide an excellent qualitative explanation of the principal features of mineral structure of a planet. The most interesting petrologic system is CaO-FeO-MgO-Al<sub>2</sub>O<sub>3</sub>-SiO<sub>2</sub> which provides over 98% of the actual mantle composition. We have examined whether the phase transformations in this system including solid solutions are capable of providing a quantitative explanation of the physical property distribution and the magnitudes of the changes in the velocities associated with the seismic discontinuities in the planetary mantles. The method of calculation of phase diagrams, elastic properties and density for an equilibrium phase assemblage and internally consistent thermodynamic approach which relate thermochemical and thermophysical properties of minerals and convert them to petrological and seismic models has been described [1-3]. For computation of phase equilibria, the method of minimization of the total Gibbs free energy and the potential method for the construction of the equations of state, written in the Mie-Gruneisen form as well as optimization programs for assessment of thermodynamic constants and activity-composition relations for solid solutions were

used. On the basis of THERMOSEISM database including data on thermophysical properties, we calculated phase diagrams of the mineral systems and the velocity and density profiles in the Earth's and lunar mantle, compared them with available seismic models, retrieved a composition for a depth interval of a stratified planet and specified the mineral nature of the mantle discontinuities.

### Chemical composition and structure of the planetary interiors

#### *The Earth.*

On the basis of a mathematical model of the fractional condensation of elements and compounds from a cooling nebula of solar composition the condensation product has been obtained, which presumably could be considered as corresponding to the average chemical composition of the terrestrial planets [4]. This equilibrium mineral assemblage was designated as solar chondrite. The composition of the solar chondrite assemblage is in agreement with the major petrological models of the Earth's upper mantle, and its seismic properties are in agreement with the global seismological models (PREM, ACY-400). It has been found that the 400 km seismic discontinuity

may be interpreted as the phase transformation in olivine. The seismic discontinuity at the depths of about 650 km may be interpreted in terms of dissociation of spinel into perovskite + magnesiowüstite. Kuskov and Panferov [2] have discussed the difficulties of explaining the 650 km discontinuity and velocity distribution in the transition zone and lower mantle on the basis of isochemical phase transformations and concluded that 650 km discontinuity should represent a chemical boundary.

#### *The Moon*

For petrological-geophysical purposes, it is important to retrieve the most accurate composition of the lunar mantle on the basis of the similarities between calculated velocities and velocities based on seismic observations. It is possible to distinguish two approaches. The first one consists in calculating seismic velocities along a chosen selenotherm starting from a proposed bulk composition. Since a composition of the lunar mantle is uncertain, it will take a great variety of input compositions. The second approach involves computation of seismically admissible bulk compositions from the given seismic data [5], so that these compositional models were in agreement with the mean density and moment-of-inertia constraints.

The final determination of chemical composition of the mantle shells and radius of the core depends on a measure of how well the calculated velocity and density profiles for the zoned Moon can satisfy the observed geophysical data (seismic velocities, moment of inertia and mass of the Moon).

**Upper mantle.** A number of compositional models satisfy the seismic velocities at depths of the upper mantle and moment of inertia of the Moon. These models show that phase changes from plagioclase-spinel-pyroxenite field to quartz-pyroxenite field taking place at depths of 130-180 km are not able to explain the nature of the 270 km discontinuity. The changes in the calculated

velocities across the phase transition are 0.02-0.04 km/s for  $V_s$  and 0.04-0.06 km/s for  $V_p$ . The calculated velocity profiles at depths of the upper mantle agree with seismic profiles within the limits of uncertainties in both thermodynamic and seismic data. The comparison of the most probable seismic profiles [5] and previous seismic results with those from thermodynamic modelling shows their practical compatibility. This is a reason to believe that the entire upper mantle depth interval 58-270 km is chemically uniform and may be composed of pyroxenite containing 0.5-9 mol.% of free silica.

**Middle mantle.** As noted earlier [3], an olivine-bearing pyroxenite model had the best fit to the middle mantle seismic velocities and satisfied the moment of inertia as well as the mean density and lower mantle density constraints. These results show that there is no reason for density inversion in the Moon. The preferred solutions for the chemical composition of the middle mantle have 50-53 %  $\text{SiO}_2$  and 14-18% FeO indicating that the middle mantle is more iron-rich than the upper mantle. Such an enrichment in FeO may be responsible for the low-velocity zone at depths of 270-500 km. The derived composition is similar to that for the source region of Apollo 11 basalts [6].

**Lower mantle.** It follows from our modelling that an increase in the  $\text{Al}_2\text{O}_3$  content up to 6-9 wt. % produces the calculated seismic properties which are close to those estimated from seismic observations. Two additional data such as the lunar bulk density and moment of inertia value show that the calculated densities for the Ol-Opx-Cpx-Gar assemblage do not contradict the requirement for density increase with depth. The temperature distribution in the lower mantle is always below solidus.

**Core.** The seismic constraints, combined with mass and moment of inertia calculations, suggest the presence of a core: 310 km in radius for the  $\gamma$ -Fe(Ni)-core and 480 km for the FeS-core.

**Composition of the silicate Moon.** The upper mantle of the Moon is enriched in  $\text{SiO}_2$

(54-57%) and depleted by FeO (7-9%) relative to the middle mantle (50-53% SiO<sub>2</sub>, 14-18% FeO), whereas the middle mantle is enriched in SiO<sub>2</sub> and FeO in comparison with the lower mantle (41-48 % SiO<sub>2</sub>, 6-10% FeO). We conclude from this attempt to translate the seismic model into the petrological models and vice versa that the

upper and middle mantle consist essentially of pyroxenite. The 58-500 km depth interval is important for magma genesis and for the interpretation of the crust composition. The Al-Ca-rich model composition (6-9% Al<sub>2</sub>O<sub>3</sub>, 5-7% CaO) gives the best fit to the lower mantle seismic properties

Table. Chemical composition of the silicate portion of the Moon

	Crust	Mantle			Entire mantle	Crust+ mantle
		upper	middle	lower		
SiO <sub>2</sub>	45.5	56.0	52.5	44.0	50.3	49.9
MgO	7.0	30.5	24.5	32.0	29.4	27.5
FeO	6.5	8.0	17.5	9.5	11.2	10.8
Al <sub>2</sub> O <sub>3</sub>	25.0	3.0	3.0	8.5	5.2	6.9
CaO	16.0	2.5	2.5	6.0	3.9	4.9

### *Mars.*

Thermodynamic and seismological models for the Martian mantle are constructed. It is shown that there is no sharp seismic discontinuity between the upper mantle and transition zone. It has been found that a composition of the Martian olivine is very similar to the olivine composition in the meteorite Chassigny.

### References

1. O.L. Kuskov, Pure Appl. Chem. 59: (1987) 73.
2. O.L. Kuskov O.L. and A.B.Panferov, Phys. Chem. Minerals 17 (1991) 642.
3. O.L. Kuskov, Phys. Earth Planet. Inter. 90 (1995) 55.
4. O.L.Kuskov, Yu.I.Sidorov and A.I.Shapkin, Geokhimiya, 8/9 (1994) 1140.
5. Y.Nakamura, J. Geophys.Res. 88 (1983): 677.
6. A.E.Ringwood and E.Essene E., Proc. Apollo 11 Lunar Sci. Conf. 1 (1970) 769.

# CRYSTALLIZATION OF "SHUNGITE" AT HIGH PRESSURE AND HIGH TEMPERATURE

K.SUITO, H.SHINN and S.OHBAYASHI  
*Faculty of Engineering Science, Osaka University,  
Toyonaka, Osaka 560, Japan.*

## ABSTRACT

Shungite has been the subject of intensive investigation for over a century. It occurs in a metamorphosed carbon-rich Precambrian rock in Russia. It is an amorphous carbon. Crystallization of shungite was studied at pressure up to 14 GPa and at temperature up to 1800 °C by using a split-sphere type high pressure apparatus. Graphitization of shungite was observed at 4~8 GPa and at temperature above 1200 °C. Diamond formation from shungite was observed at pressure higher than 10.5 GPa.

## Introduction

Shungites are highly carbonaceous, highly metamorphosed Precambrian rocks at Karelia in Russia. The study of shungite was commenced more than 100 year ago. Nevertheless, many aspects of their composition and genesis still remain unclear. Recently, Buseck et al.[1] reported that both  $C_{60}$  and  $C_{70}$  fullerenes were found in shungite. In their paper, they reviewed the some opinions about the origin of shungite. Shungite is a natural amorphous carbon and consists of masses containing up to 99% carbon.

G. Khavari-Khorasani and D. Murchison [2] studied the x-ray diffraction investigation of shungite and showed that even when carbonized at 2900 °C, there was no suggestion of graphitization of shungite. In the present study, the behavior of shungite at high pressure and high temperature has been studied.

## Experimental method

Experiments were carried out by a uniaxial split-sphere type apparatus in the pressure range from 4 GPa to 14 GPa and the temperature range from 1000 °C to 1800 °C. Figure 1 (a) and (b) shows an assemblage of an octahedral sample cell made of pyrophyllite. At pressure higher than 10 GPa, a direct heating method as shown in Fig 1. (b) is used. The specimen of

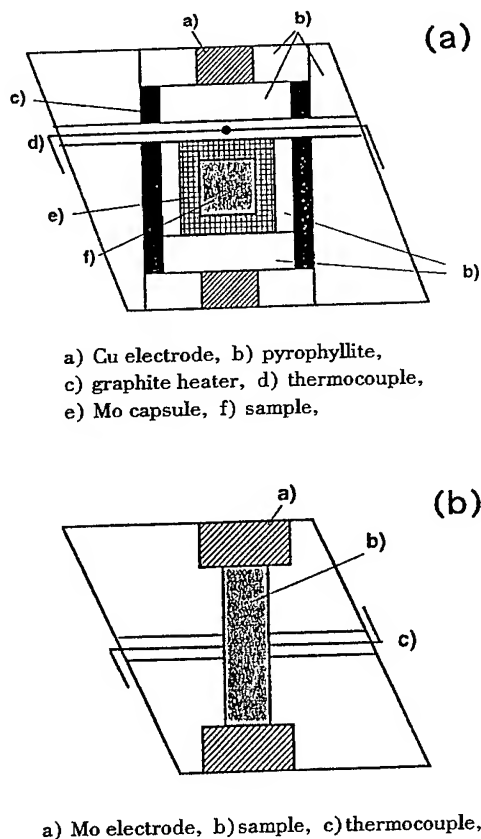


Fig.1 Cross section of an octahedral cell assembly  
(a) cell for graphitization of shungite,  
(b) cell for direct heating

shungite was given by Geological Museum of Institute of Geology and Geophysics, Siberian Branch of the Russian Academy of Sciences at Novosibirsk. The properties of shungite were not clear. It seemed to be "bright type" described in the paper of G. Khavari-Khorasani and D. G. Murchison, judging from the glassy cleavage flakes.

## Results and Discussion

### Graphitization of shungite

The samples were pressurized at 4, 6 and 8 GPa. At each pressure, temperature was increased up to 1000°C, 1200°C, 1500°C and 1500°C. After duration of high temperature for 10 min, the sample was rapidly cooled to room temperature. The pressure was then released to retrieve the sample. All the retrieved sample were examined by x-ray diffraction. In Fig. 2 the typical example of x-ray patterns at 8 GPa is shown. On increasing temperature, the peak (002) shifts to higher angle of  $2\theta$ , and the broad peak (the halo showing an amorphous state) changes to sharper ones at higher temperature. The (10) band splits into the peak (100) and (101) at temperature higher than 1200 °C. From the present experiment, it has been found that

graphitization of shungite occurs at pressure higher than 4GPa and above 1200 °C.

### Diamond formation

At pressure higher than 10 GPa, experiments of direct heating were carried out. Above 10.5 GPa, diamond formation was observed. Figure 3 shows x-ray diffraction pattern obtained at 13.5 GPa and about 1500 °C. The crystallized diamond of several  $\mu\text{m}$  are colorless and translucent under the optical microscope.

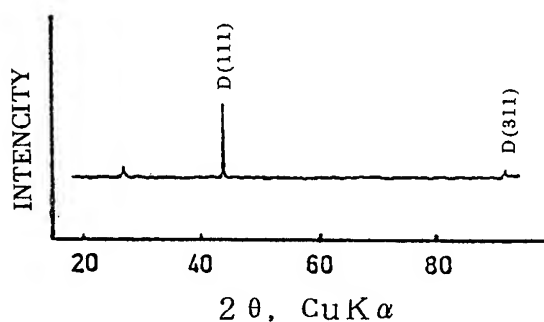


Fig.3 X-ray diffraction patterns of shungite obtained at 13.5 GPa and 1500 °C

## References

- [1] P. R. Buseck et al., *Science* **257** (1992) 215.
- [2] G. Khavari-Khorasani and D. G. Murchison, *Chem. Geol.* **26** (1979) 165.

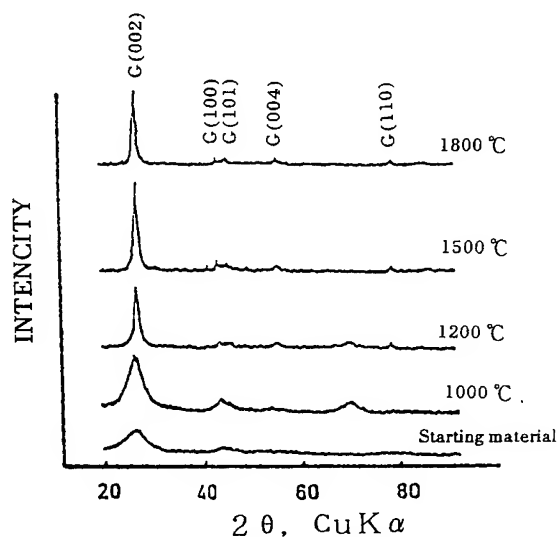


Fig.2 X-ray diffraction patterns of shungite obtained 8 GPa

## PROPERTIES OF MgO-SiO<sub>2</sub> PHASES: LATTICE AND MOLECULAR DYNAMICS STUDY

ANATOLY B. BELONOSHKO and LEONID S. DUBROVINSKY

*Theoretical Geochemistry Program, Institute of Earth Sciences, Uppsala University,  
Box 555, S-752 36 Uppsala, Sweden*

### ABSTRACT

We have developed a transferable interatomic potential to describe interaction in minerals of MgO-SiO<sub>2</sub> composition. This potential was used to study thermoelastic properties of minerals of that composition and melting of periclase, MgSiO<sub>3</sub>-perovskite, and stishovite. Calculated and experimental structural and thermoelastic properties are in reasonable agreement wherever comparison is possible. The calculated melting curves (using two-phase molecular dynamics simulation) are in good agreement with the melting curves calculated earlier utilizing other models of interatomic potentials (1-3) and with experimental data (4,5) except periclase melting curve (6). The analysis shows that the experimental periclase melting temperatures are likely too low due to thermal stress (7).

### Introduction

Compositional models of the Earth based on cosmic abundancies of elements suggest that most of the Earth's mantle consists of minerals of MgO-SiO<sub>2</sub> composition. Experimental studies of these minerals and their melts face significant difficulties under extreme pressure (P) and/or temperature (T) of the mantle (up to 1.4 Mbar and 6000 K). Molecular (MD) and lattice dynamics (LD) methods have proven to be reliable tools for studying material properties. These methods rely on a description of interatomic interaction. To be more reliable, such a description should allow us to reproduce reliably measured properties using as few adjustable parameters as possible. Clearly, the existence of a variety of phases in the MgO-SiO<sub>2</sub> system requires such a description of interatomic interaction, i. e. interaction potential (IP), which should be transferable from phase to phase.

The existing transferable IP's are either not precise enough or it is not clear how they will work under high PT. We describe here the transferable IP which is capable to reproduce properties of more than a dozen phases including melts (e. g., properties of silica phases at room conditions are better reproduced with our IP than with any other). The application of the IP to calculation of melting curves using two-phase MD simulation is presented further. A comparison with experimental data on melting of mantle minerals is

provided and reasons for discrepancies are discussed.

### Methods and results

As a basis for our transferable IP we have chosen our IP (8) for silica, which was obtained by fitting experimentally obtained properties of  $\alpha$ -quartz at ambient conditions to those calculated by LD method. Then, we calculated optimum parameters for Mg (fitting structure, bulk modulus, thermal expansion and heat capacity at constant volume of MgO at room TP) fixing short-range IP parameters for O and changing effective charge and short-range parameters for Mg in MgO. For  $n\text{MgO} \cdot m\text{SiO}_2$  compounds the effective charges of atoms are determined from following equations

$$\begin{aligned} n \cdot q_{\text{Mg}} + m \cdot q_{\text{Si}} + (n + 2m) \cdot q_{\text{O}} &= 0 \\ n \cdot q_{\text{Mg}} + m \cdot q_{\text{Si}} &= Q_{\text{Mg}} \cdot n + Q_{\text{Si}} \cdot m \\ q_{\text{Mg}} &= -q_{\text{O}} \end{aligned} \quad (1)$$

( $q$  is effective charge in  $n\text{MgO} \cdot m\text{SiO}_2$  compounds,  $Q$  is effective charge in MgO and SiO<sub>2</sub>).

Thus, atomic interactions in minerals of MgO-SiO<sub>2</sub> composition are described by the potential

$$U_{ij} = q_i q_j / R_{ij} + \epsilon_{ij} f(\rho_i + \rho_j) \exp[(r_i + r_j - R_{ij}) / (\rho_i + \rho_j)] + \sqrt[6]{(1 - \epsilon_{ij}) D_{ij} [\exp(-2\alpha_{ij}(R_{ij} - R_{ij0})) - 2\exp(-\alpha_{ij}(R_{ij} - R_{ij0}))] + C_{ij} / R_{ij}^6} \quad (2)$$

where  $i$  and  $j$  - atomic indexes (Mg, Si, O),  $q$  - effective charge (calculated according to equation 1),  $\rho$  and  $r$  - parameters of Gilbert-like repulsive potential,  $f$  - units constant (1 kcal/mole),  $D$ ,  $\alpha$  and  $R_0$  - parameters of Morse potential,  $C$  - van der

Waals constant, and  $\epsilon_{ij}$  is bond ionicity, ( $q_i q_j / z_i z_j$ ,  $z$  - formal charge). IP parameters are listed in Table 1.

The parameters were fitted using lattice dynamics method. Cross-check by MD simulation shows good consistency at ambient conditions.

Table 1. Interaction potential parameters for MgO-SiO<sub>2</sub>.

Atom	$z$	$Q^{***}, e$	$\rho_i, \text{\AA}$	$r_i, \text{\AA}$	$D_i^*, \text{ kcal/mole}$	$\alpha_i^*, \text{\AA}^{-1}$	$R_{i0}^*, \text{\AA}$	$C_i^*, 10^3 \text{ kcal}^{1/2} \text{ nm}^3/\text{mole}$
Mg**	2.0	1.280	0.09567	1.11780	9.489	1.0708	1.40022	0.000
Si**	4.0	2.202	0.22333	1.37107	24.970	1.3540	1.23732	0.000
O	-2.0		0.18307	2.17600	4.911	0.5492	0.58978	3.576

\*  $D_{ij} = D_i + D_j$ ,  $\alpha_{ij} = \alpha_i + \alpha_j$ ,  $R_{ij0} = R_{i0} + R_{j0}$ ,  $C_{ij} = C_i C_j$ ; \*\*  $D_{\text{SiSi}} = 0$ ,  $D_{\text{MgSi}} = 0$ ,  $D_{\text{MgMg}} = 0$ ; \*\*\* see Eq. (1)

This IP provides perfect description of MgO and SiO<sub>2</sub> phases (7,8). Properties of other phases are reproduced not so good, but still in very reasonable agreement with experiment (e. g.  $V_0$  is usually within 3% error). Extended MD simulations were done in order to create equations of state of major mantle minerals and their melts (7).

To determine PT range of melts stability calculation of melting curves of MgO, SiO<sub>2</sub>, and MgSiO<sub>3</sub> were done using two-phase MD simulations. The main idea of two-phase simulation is to place pre-simulated melt and solid in one computational box and in course of the simulation to observe which phase will grow. By repeating such procedure at different  $P$  and  $T$ , it is possible to determine the melting conditions by bracketing (for details see (2,3,8)). The calculated melting curves are shown in Fig. 1. According to these curves, the temperature of eutectic melting in binary system MgSiO<sub>3</sub>-MgO at the pressure of the core-mantle boundary (1.36 Mbar) is about 5000 K. According to our analysis of temperature at CMB (7), partial melting is possible, producing melt of approximately olivine composition. The simulated data provides us with equation of state and composition of the material presumably produced

in course of thermal plume generation at the CMB. The melting curves are in good agreement with experimental data (4,5), except for the melting curve of periclase. This curve was measured up to 300 kbar and the measured melting temperature ( $T_m$ ) was about 4000 K (6). As one can see (Fig. 1), it amounts to about 1000 K difference between theory and experiment.

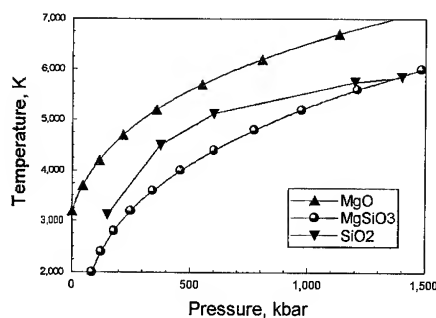


Fig. 1. Melting curves of periclase (MgO), perovskite (MgSiO<sub>3</sub>), and stishovite (SiO<sub>2</sub>), obtained by 2-phase MD simulations.

The MD simulated MgO melting curve is consistent with other theoretical predictions. Analyzing particulars of the experimental technique, one of the factors was found to be responsible for the reason of the discrepancy, namely, enormous thermal gradient (up to  $10^6$  K/cm). Such gradient not only makes difficult to precisely measure  $T_m$ , but also creates thermal stress. Thermodynamic analysis of non-hydrostatically stressed solid in equilibrium with melt (hydrostatic by definition) shows that  $T_m$  can be decreased by a few hundred degrees (7). The difference between  $T_m$  under hydrostatic and non-hydrostatic conditions rapidly increases with  $T$ , for temperature gradient across the sample also increases. MD simulations were done to get a microscopic picture of the impact of thermal stress on the stability of periclase. A slab consisting of 2048 Mg and O atoms was placed in the computational box so that XY surfaces were free. It was subjected to equal stress in X and Y directions. At the same time, the size in Z direction was fixed. The simulations were done at 3000 K which is below simulated  $T_m$  at 0 pressure.

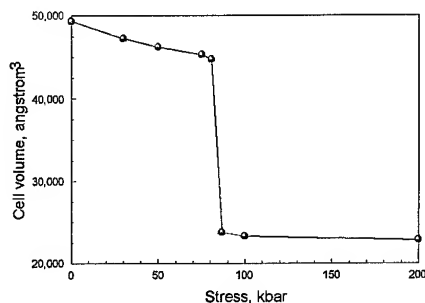


Fig. 2. Dependence of the computational cell volume at 3000 K on the stress applied on sides of the slab. The dots indicate MD simulated points.

Below the stress of about 80 kbar, the slab can sustain the stress. At stresses above that value, the atoms begin to advance into the initially empty half of the computational cell. Simultaneously, X and Y sizes of the cell change. The process develops until the cell is completely filled with atoms and pressures in X, Y, and Z directions become equal

(Fig. 2). The analysis of the structure shows that it changes from B1 to that of liquid. The magnitude of the stress can be achieved in experiment due to thermal gradient. Therefore, we conclude that the measured  $T_m$  are too low due to thermal stress. Of course, similar effects are certainly present in other experiments. However, the real magnitude of the effect should be evaluated in each particular case.

## Conclusions

The transferable IP allows us to reliably describe properties of the phases of MgO-SiO<sub>2</sub> composition in the PT range of the mantle. Moreover, it allows to resolve controversy between theory and experiment on a quantitative level. In combination with the MD method it makes the IP a valuable mean for predicting properties of mantle minerals (7), calculating phase equilibria, and for finding experimental pitfalls (6,7,9). The phenomenon of stress-induced melting is potentially capable of solving the existing controversy between shock-wave measurements of iron melting and those using diamond anvil cell with laser heating.

## Acknowledgments

The research was supported by the Swedish Natural Sciences Research Council Grant. No. G-Gu 06901-301.

## References

1. A.B. Belonoshko, *Geochim. Cosmochim. Acta* **58** (1994) 1557.
2. A.B. Belonoshko, *Geochim. Cosmochim. Acta* **58** (1994) 4039.
3. A.B. Belonoshko and L.S. Dubrovinsky, *Amer. Miner.* (1995), in press.
4. G. Shen, *Melting of minerals under the Earth's lower mantle conditions*. Ph. D. thesis. (Uppsala University, Sweden, 1994).
5. A. Zerr and R. Boehler, *Science* **262** (1993) 553.
6. A. Zerr and R. Boehler, *Nature* **371** (1994) 506.
7. A.B. Belonoshko and L.S. Dubrovinsky, *Geochim. Cosmochim. Acta* (1995a,b,c), submitted.
8. A.B. Belonoshko and L.S. Dubrovinsky, *Geochim. Cosmochim. Acta* **59** (1995) 1883.
9. K. J. Kingma, R. E. Cohen, R. J. Hemley, and H. K. Mao, *Nature* **374** (1995) 243.



## NEW HIGH PRESSURE SILICA PHASES OBTAINED BY COMPUTER SIMULATION

L. S. Dubrovinsky, A. B. Belonoshko, N. A. Dubrovinsky, S. K. Saxena  
Theoretical Geochemistry, Institute of Earth Sciences, Uppsala University,  
Norbyvägen 18 B, Uppsala, Sweden

### ABSTRACT

Numerous studies have suggested the existence of a post-stishovite phase. However, none of the theoretical studies discovered a phase which could be more stable than stishovite at high pressures, except for the possibility of transition to  $\text{CaCl}_2$  structure (1), which is likely to be a second order transition. Quasiharmonic lattice dynamic (QLD) and molecular dynamics (MD) studies with recently developed interatomic potentials (2,3) were used for simulation of phase diagram of silica up to 150 GPa. The possibility of a new silica phase with  $Pnc2$  structure was found. This phase is more stable than stishovite at pressures above approximately 90-120 GPa at a wide range of temperature. Hence, silica with this structure should be considered as a phase which can stably exist at lower mantle pressures and temperatures. Our analysis of simulated X-ray diffraction patterns of various hypothetical post-stishovite phases shows that this new phase should always be considered in the treatment of high-pressure experiments involving silica.

It is shown that stishovite might undergo stress-induced phase transition to  $\text{CaCl}_2$ -type structure at pressures significantly lower than under hydrostatic conditions. The pressure of transition under deviatoric stress of about 1.5 GPa is approximately 40 GPa. This provides an alternative explanation of the Kingma et al. (1995) data.

Silica is one of the most studied materials. It attracts special attention in Earth sciences. Crystalline  $\text{SiO}_2$  is known to stably exist in the form of cristobalite, quartz, tridymite, coesite, and stishovite. Various experimental and theoretical studies have suggested the possible existence of another, so called "post-stishovite" phase. Possible post-stishovite phases can be separated into two groups. Crystal chemical analogues of  $\text{AX}_2$ -type oxides such as  $\alpha\text{-PbO}_2$ -, fluorite ( $\text{CaF}_2$ )-, cottunite ( $\alpha\text{-PbCl}_2$ )-like phases and baddeleyite ( $\text{ZrO}_2$ )-like phase observed experimentally belongs to the first group, and the phases proposed for explaining the results of high-pressure experiments on  $\text{SiO}_2$  ( $\alpha\text{-PbO}_2$ ,  $\text{Fe}_2\text{N}$ , disordered nyceline  $\text{NiAs}$ , and  $\text{CaCl}_2$  structures) to the second. However, the reliability of the interpretations of experimental data is questionable (4,5). Despite all attempts, none of the possible post-stishovite phases with energy lower than that of stishovite was simulated at pressures up to 150 GPa, except for the transition to  $\text{CaCl}_2$ -like structure.

The purpose of this work is to investigate all the suggested post-stishovite phases on a systematic basis using molecular dynamic (MD) and quasiharmonic lattice dynamic (QLD) simulations with our new (2) and previously developed (3) interatomic potentials, starting from various reasonable post-stishovite structural types: fluorite,  $\alpha\text{-PbO}_2$ , modified  $\alpha\text{-PbO}_2$  (4) (with space

group  $I2/a$ ),  $\alpha\text{-PbCl}_2$ , and baddeleyite  $\text{ZrO}_2$  structural types.

For the MD calculations we have used the Parrinello-Rahman modification of MD method, calculating coulombic interaction with the Ewald technique (2). The calculations were done using the parallel version of program Moldy (kindly provided by K. Refson).

Gibbs free energy at given P,T was simulated using the following equation (6,7):

$$G_{P,T} = \frac{1}{2} \sum_{l,m} \phi_{lm} + kT \sum_i^M \left( \frac{\hbar \omega_i}{2kT} + \ln \left( 1 - \exp \left( -\frac{\hbar \omega_i}{2kT} \right) \right) \right) + PV$$

where  $\phi_{lm}$  is pair potential of interatomic interaction,  $k$  Boltzmann constant,  $\hbar$  Plank constant,  $M$  total number of phonon frequencies,  $\omega_i$  frequency,  $V$  molar volume.

For every given vector of reciprocal lattice  $\vec{q}$  within the first Brillouin zone, a set of frequencies  $\omega_i$  is obtained as a result of solution of corresponding determinantal equation

$$\left| D(\vec{q}) - I \omega^2(\vec{q}) \right| = 0$$

where  $D(\vec{q})$  is dynamic matrix (6),  $I$  is identity matrix.

Frequencies were calculated on a three-dimensional mesh of 64 points within the first

Brillouin zone. Parker and Price (1989) showed that for temperatures above 50 K thermodynamic properties converge rapidly with the size of the mesh and for the range of materials there is only small difference in magnitude of the thermodynamic properties for a mesh containing more than eight distinct points. Raman active frequencies were calculated at  $q=0$  (7).

We used non-gradient Powell method (8) to minimize the Gibbs energy with respect to structural parameters.

We obtained the following results starting from all the above described structural types considered to be reasonable high-pressure modifications of  $\text{SiO}_2$ :

(1) The quasi-harmonic lattice dynamic (QLD) allows to reproduce the known part of silica diagram in good agreement with experimental data (Fig. 1).

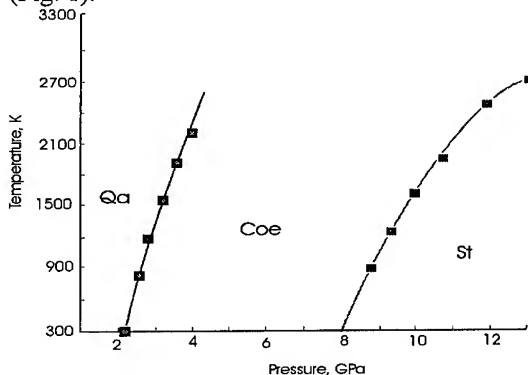


Fig. 1. Phase relations of some silica phases up to 15 GPa calculated by QLD (symbols - calculated points, lines - experimental data (9,10)).

(2) Fluorite-,  $\alpha$ - $\text{PbO}_2$ , modified  $\alpha$ - $\text{PbO}_2$  (4) (with space group  $I2/a$ ), and  $\alpha$ - $\text{PbCl}_2$ -like phases of  $\text{SiO}_2$  are unstable with respect to stishovite up to pressures 150 GPa and temperature up to 2500 K. The phase closest to stishovite in stability is modified  $\alpha$ - $\text{PbO}_2$  (4) (with space group  $I2/a$ ). Their energies according to MD at 300 K and 150 GPa are -4352 and -4332 kJ/mole, respectively. This result is in perfect agreement with that obtained by Tse et al. (4).

(3) At pressures higher than 80 GPa and temperature 300 K according to QLD (100 GPa according to MD), orthorhombic distortion of stishovite unit cell gradually increases, what may

be interpreted as a transition from stishovite to  $\text{CaCl}_2$ -like structure. The value of distortion increases smoothly with pressure. This possible phase transition "stishovite -  $\text{CaCl}_2$ -like modification of  $\text{SiO}_2$ " is probably of the second order.

We calculated pressure dependence of Raman frequencies under hydrostatic and non-hydrostatic conditions. Experimental results (1) can be reproduced up to pressure about 40 GPa. Agreement with the experiment above that pressure can be achieved by assuming presence of a non-hydrostatic stress about 1.5 GPa at 43 GPa and 2.5 GPa at 60 GPa with close agreement with estimation of possible non-hydrostatic stress in DAC (11). Calculated Raman frequencies are shown in Fig. 2.

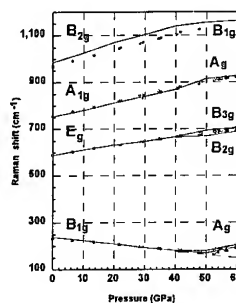


Fig. 2. Pressure dependence of calculated (lines) Raman frequencies of stishovite compared to experimental (spheres) data (1). Raman frequencies at pressures above 40 GPa were calculated assuming deformed stishovite ( $\text{CaCl}_2$ ) structure under stress. The value of stress varied from 1.5 to 2.5 GPa at pressures from 40 to 60 GPa. The appearance of higher frequency branch of  $B_{1g} \rightarrow A_g$  mode was calculated assuming the same stress causing  $c/a$  deformation of stishovite structure. Pressure dependence of  $B_{1g} \rightarrow A_g$  without stress is shown by dashed line.

The good agreement between experimental data (1) and calculated values suggests that the experiment was conducted in the presence of deviatoric stress.

(4) Starting from baddeleyite structure, the structure with  $Pnc2$  space group was obtained (Fig. 3). This structure (which we term SBAD) can be considered as an intermediate between  $\alpha$ - $\text{PbO}_2$  ( $Pbcn$ ) and baddeleyite ( $P2_1/c$ ). Indeed, octahedra of this structure are gradually distorted

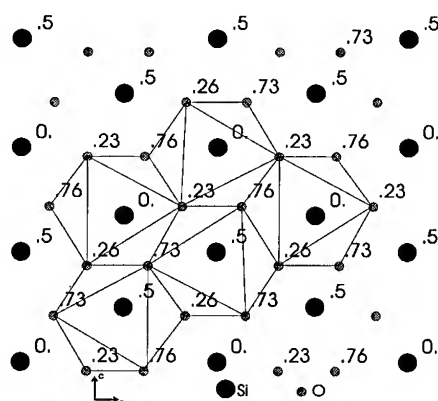


Fig. 3. Projection along  $b$ -axis of the new  $\text{SiO}_2$  structure (space group  $C_{2v}^6 - Pnc2$ ) simulated with QLD at 100 GPa and 300 K [ $a=4.2275$  Å,  $b=3.8900$  Å,  $c=4.7225$  Å,  $Z=4$ , Si(1) (0., 0., 0.145), Si(2) (0.5, 0., 0.8271), O(1) (0.8322, 0.2636, 0.3680), O(2) (0.6672, 0.7586, 0.1050)]. The numbers indicate positions of atoms along vertical axis.

and transformed to seven-apex polyhedra (characteristic of baddeleyite) during pressure decrease to 10 GPa. At pressures higher than 70 GPa, the density of SBAD becomes greater than that of stishovite and at 150 GPa and 300 K the difference amounts to 0.8%, at 150 GPa and 2000 K - 1.6% according to QLD. The SBAD structure becomes more stable than stishovite (or rather  $\text{CaCl}_2$ -like silica) at pressure above 90 GPa according to QLD (Fig. 4) and 120 GPa according to MD.

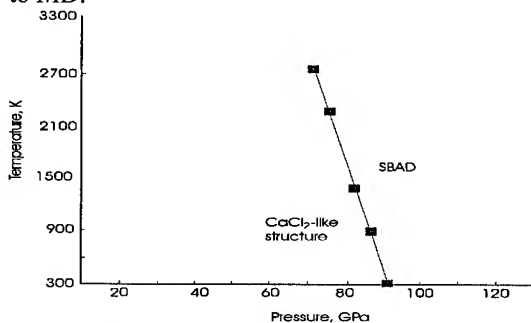


Fig. 4. Phase relations of  $\text{CaCl}_2$ -like and SBAD phases calculated by QLD.

The transition to SBAD structure has weak dependence on temperature up to 3000 K (Fig. 4). Therefore, we conclude that the SBAD phase is the candidate structure to represent silica phase in the Earth's lower mantle.

(4) Table 1 presents X-ray diffraction patterns of some  $\text{SiO}_2$  phases obtained in this study at 100 GPa and 300 K.

Table 1. Calculated X-ray patterns ( $\text{MoK}\alpha_1$  radiation) of different crystal structures of  $\text{SiO}_2$  obtained by QLD simulations at 100 GPa and 300 K.

Stishovite		$\text{CaCl}_2$		$\alpha\text{-PbO}_2$		SBAD	
d, Å	I, %	d, Å	I, %	d, Å	I, %	d, Å	I, %
				3.8260	59		
				2.9560	57	3.0025	49
2.7595	100	2.7591	100	2.8226	49		
				2.4137	62	2.4479	100
						2.3612	4
2.1446	29	2.1401	18	2.0905	8	2.1137	5
		2.1349	12	2.0340	16	2.0615	6
				1.9888	17		
1.8795	44	1.8747	44	1.8345	54	1.8573	27
1.7453	16	1.7493	5	1.7959	100	1.8215	51
		1.7407	11	1.7068	21	1.7284	15
						1.5749	4
						1.5013	4
1.4433	72	1.4434	41	1.4409	12	1.4592	18
				1.4382	6	1.4313	33
1.3797	22	1.4386	33	1.4113	46	1.4147	54
		1.3795	24	1.3935	88		
				1.3600	10		
				1.3095	4	1.2737	17
		1.2775	14	1.2753	2		
1.2835	14			1.2606	8	1.2504	2
1.2341	8	1.2380	10	1.2300	4	1.2204	3
				1.2198	4		
		1.2299	2			1.2101	27
		1.2139	16	1.1958	42		

The shift or even splitting of reflections with respect to the stishovite pattern can be interpreted as transformation of stishovite to any post-stishovite  $\text{SiO}_2$  phase (Table 1), including the  $\text{CaCl}_2$ -like modification (12). It was (4) also noted that the four observed diffraction peaks and attributed to  $\text{CaCl}_2$ -structure (12), are in common with the ideal and modified  $\alpha\text{-PbO}_2$  structures. These reflections can also belong to new discovered SBAD phase.

1. K. J. Kingma, R. E. Cohen, R. J. Hemley, and H. K. Mao, *Nature* **374** (1995) 243.
2. A. B. Belonoshko and L. S. Dubrovinsky, *Geochim. Cosmochim. Acta* **59** (1995) 1883.
3. S. Tsuneyuki, Y. Matsui, H. Aoki, and M. Tsukado, *Nature* **339** (1989) 209.
4. J. S. Tse, D. D. Klug, and Y. L. Page, *Phys. Rev. Letters* **69** (1992) 3647.
5. D. J. Lacks and R. G. Gordon, *J. Geophys. Res.* **98** (1993) 22147.
6. M. Born and K. Huang, *Dynamical theory of crystal lattices* (Clarendon Press, Oxford, 1954).
7. S. C. Parker and G. D. Price, *Adv. Solid-State Chem.* **1** (1989) 295.
8. W. H. Press, B. P. Flannery, S. A. Teukolsky, and W.T.Vetterling, *Numerical recipes*. (Cambridge University Press, 1992).
9. P. W. Mirwald and H.-J. Massone, *J. Geophys. Res.* **85** (1980) 6983.
10. V. Swamy, S. K. Saxena, B. Sudman, and J. Zhang, *J. Geophys. Res.* **99** (1994) 11787.
11. Y. Meng, D. J. Weidner and Y. Fei, *Geophys. Res. Lett.* **20** (1993) 1147.
12. Y. Tsuchida and T. Yagi, *Nature* **340** (1989) 217-220.

# PHASE AND GLASS TRANSITIONS IN CRUDE OILS AND THEIR FRACTIONS AT HIGH PRESSURE

Vladimir Kutcherov<sup>1,2</sup>, Russell Ross<sup>1</sup>, and Alexei Chernoutsan<sup>1,2</sup>

<sup>1</sup>Department of Experimental Physics, Umeå University, S-901 87 Umeå, Sweden

<sup>2</sup>State Academy of Oil and Gas, Moscow 117917, Russia

## ABSTRACT

Phase and glass transitions in crude oils and their fractions were detected at high pressures (up to 2 GPa) and different temperatures, both in isobaric and isothermal measurements, using transient hot-wire method and DSC. Glass transition point is found to be independent on wax, asphaltene and pitches content. Its position changes on boiling out different components of light fraction, showing strong dependence on boiling temperature.

Information on the phase and glass transitions in complex oil systems at different pressures and temperatures is of great value to the oil industry. At the same time, these results are interesting from the point of view of the physics of disordered multicomponent matter, oils being complex liquid mixtures with a colloidal structure.

The characteristics of phase and glass transitions strongly depend on the chemical content of oil system. One can expect the specific role of different components in the formation of these transitions. For example, *petroleum wax* (or simply *wax*) can easily form crystal clusters and precipitate from solution. On the other hand, low content of *light fraction* should lead to an increase of viscosity, which is of great importance for the onset of the glass transition. In order to understand more clearly the influence of chemical composition on transitions in oil systems one should investigate not only crude oils, but also their different fractions.

The investigation of viscous oils without wax [1,2] revealed the presence of glass transition which occurs as at decreasing temperature so at increasing pressure. Heavy fractions of such oils are even more viscous and they demonstrate the same transition but at higher temperature (lower pressure).

In this paper we present the results of our investigation of multiple transitions in Kumkolsk

crude oil which has a considerably lower value of viscosity, which is due to the higher content of

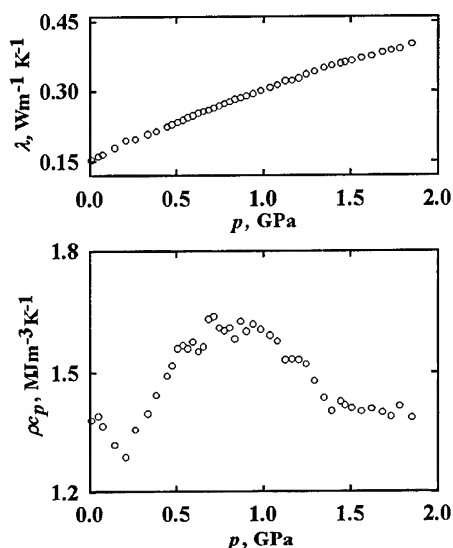


Fig.1. Pressure dependence of  $\lambda$  and  $\rho c_p$  for Kumkolsk crude oil at 250 K

light fraction. Three fractions of this oil and four model oil systems have been investigated also. The first fraction (heavy 1) was obtained by removing light fraction (the boiling temperature less than 250°C) from crude oil. Removing further asphaltenes and pitches from this

sample, we obtained the second fraction (heavy 2) — heavy fraction without asphaltenes and pitches. Finally, the removal of petroleum wax from second fraction provided the third fraction (heavy 3) — heavy fraction without asphaltenes, pitches and petroleum wax.

The experiments were carried out in the temperature range 200–350 K at pressure up to 2 GPa. Using the transient hot-wire method, we measured thermal conductivity and heat capacity per unit volume. We also measured the specific heat capacity at atmospheric pressure using a differential scanning calorimeter.

We have detected the presence of two consequent phase transitions for crude oil and its fractions. These transitions could be detected

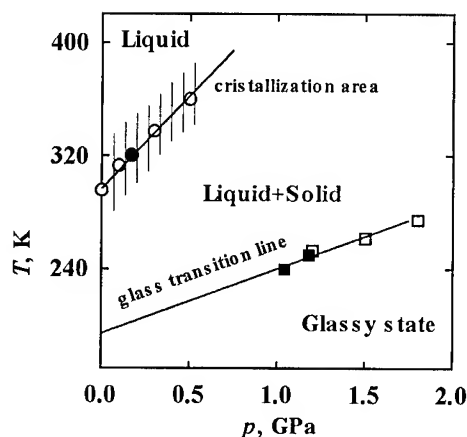


Fig. 2.  $T$ - $p$  diagram for Kumkolsk crude oil. Filled points - isotherms, empty - isobars.

both in isobaric and isothermal measurements. Typical experimental curves for hot wire measurements are presented in Fig. 1. We have interpreted the first transition as wide-range crystallisation and the second one as glass transition.

The whole data were used to draw the phase diagrams for crude oil (Fig. 2) and its fractions. We would like to underline the important

feature of these plots: each transition line is formed both by isobaric and isothermal data.

The glass transition temperature was found to have the same value for all three fractions. This fact is in agreement with qualitative

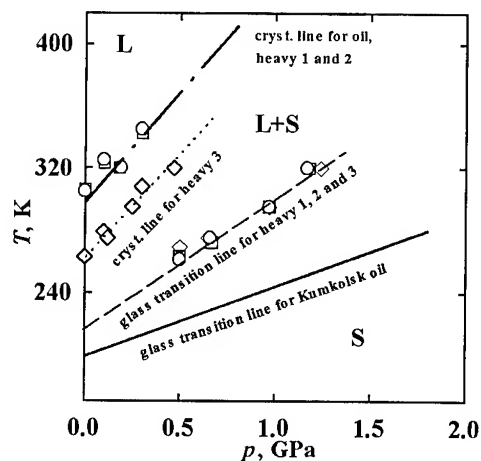


Fig. 3.  $T$ - $p$  diagram for heavy fractions of Kumkolsk oil (heavy 1 - circles, heavy 2 - squares, heavy 3 - diamonds).

observations of different authors [3-6] that glass transition should not depend on wax content. However, this suggestion was not of really quantitative character, because these authors were comparing glass transition temperatures of different oils with similar content and properties. In present investigation this property of glass transition is verified by changing wax and asphaltene content of the same oil, with the same hydrocarbon solvent matrix. Our results show that oil matrix does not change on extracting wax or asphaltenes and pitches.

The properties of matrix, however, are directly influenced by boiling out different components of the light fraction (distillation process). This is demonstrated first by the noticeable shift of glass transition line on boiling out of light fraction component at 250 K (Fig. 3). The further increase of boiling temperature, corresponding to boiling out new components of

light fraction leads to corresponding change of glass transition temperature (Fig. 4). We found the direct correlation between the value of glass transition temperature and sample viscosity at room temperature.

We would like to note on the interesting properties of crystallisation line (the point of the onset of crystallisation) of different fraction. The position of this line is influenced mainly by extracting petroleum wax (heavy 3) but not by the removal of light fraction or asphaltenes and

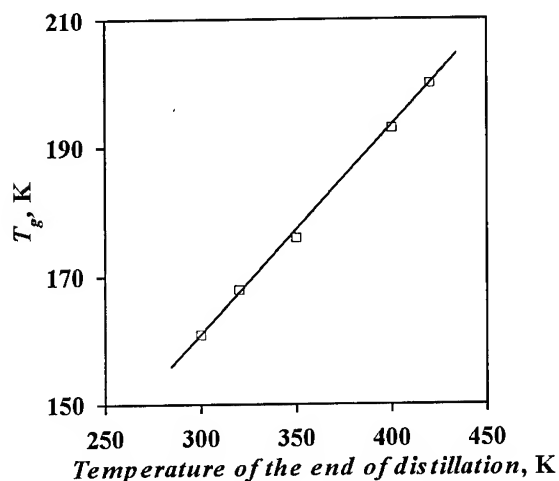


Fig.4. Correlation between glass transition temperature and distillation end temperature.

pitch.

These conclusions were tested on several model oil systems.

The present results are a continue of an experimental series concerned with the investigation of a behaviour of complex oil systems in a wide temperature and pressure range.

## References

1. V.Kutcherov, G.Bäckström, M.Anisimov and A.Chernoutsan, *Int. J. Thermophys.* 14: 91 (1993).
2. V.Kutcherov, A.Lundin, R.G.Ross, M.Anisimov and A.Chernoutsan, *Int. J. Thermophys.* 15: 165 (1994).
3. F.Nöel, *Thermochim. Acta* 4: 377 (1972).
4. P.Claudy, J.-M.Létoffé, B.Chagué, J.Orrit, *Fuel* 67: 58 (1988).
5. H.P.Rønningsen, B.Bjørndal, A.B.Hansen, W.B.Pedersen, *Energy Fuels* 5: 895 (1991).
6. A.B.Hansen, E.Larsen, W.B.Pedersen, A.B.Nielsen, *Energy Fuels* 5: 914 (1991).

## Acknowledgements

Authors are grateful to Prof. G. Bäckström and Prof. M.A.Anisimov for helpful discussions. One of authors (A.Ch.) acknowledges the support International Science Foundation (ISF grant M4G000).

## **XI Shock Waves**

**XI(A) Material Treatment Using Shock Waves, Explosives**



# THE ROLE OF DYNAMIC SHOCK COMPACTION IN THE DEVELOPMENT OF DENSE, SINTERED CERAMIC MICROSTRUCTURES

JOHN FREIM<sup>a</sup>, J. MCKITTRICK<sup>a</sup> and W.J. NELLIS<sup>b</sup>

<sup>a</sup> Dept. of Applied Mechanics and Engineering Sciences and Materials Science Program  
University of California at San Diego, San Diego, CA 92093

<sup>b</sup> Institute of Geophysics and Planetary Physics and H Division,  
Lawrence Livermore National Laboratory, Livermore, CA 94550

## ABSTRACT

The densification and sintering behavior of dynamically shock compacted alumina-zirconia powder has been studied. The results indicated that the physical properties of the specimens were strongly dependent on the size of the powder from which the compacts were fabricated. The shock compacted specimens fabricated from coarse powders exhibited the highest as-compacted densities although the shock compacted specimens fabricated from fine powders exhibited higher sintered densities. These results were compared to conventionally processed specimens. The data indicated that the shock compaction process significantly enhanced the sintered densities of specimens fabricated with the coarser particle size distributions, with the enhancement diminishing as the particle size was reduced. For specimens fabricated with the finer particle size distributions, equal to or less than 5  $\mu\text{m}$ , the densities of the shock compacted specimens and the pressed specimens were comparable.

## Introduction

Nanocrystalline ceramic composites are of interest due to the novel physical properties which they exhibit. The synthesis of composites containing fine grain sizes is of particular interest in zirconia-toughened-alumina (ZTA) composites since the tetragonal zirconia ( $t\text{-ZrO}_2$ ) polymorph is stable only in sub-micron crystallites [1]. The metastable  $t\text{-ZrO}_2$  grains will transform to the monoclinic zirconia ( $m\text{-ZrO}_2$ ) polymorph upon application of a tensile stress. The stresses which accompany this transformation absorb fracture energy and subject the surface of a crack to compressive tractions resulting in a substantial toughening enhancement [2].

Grain growth which occurs during sintering can often result in crystallite dimensions which are too large to be stable as  $t\text{-ZrO}_2$  and the crystallites will transform to the undesired  $m\text{-ZrO}_2$  phase upon cooling from peak sintering temperatures. Thus, it is of interest to develop techniques which facilitate the sintering of the material to high densities without significant grain growth.

Rapid solidification was used to synthesize the starting material which contained nanocrystalline

$t\text{-ZrO}_2$ . Unfortunately, we have determined that conventional cold pressing (to densities averaging 50% of theoretical) and sintering (to densities averaging 80% of theoretical) are inadequate process routes [3].

Dynamic shock compaction (DSC) is a novel process alternative which has the potential to produce the dense, fine grained specimens which can facilitate the achievement of high sintered densities. The DSC process produces pressures ranging from 1-100 GPa on a microsecond time scale. The extreme conditions which accompany the shock process can be used to produce physical properties which are difficult to achieve using conventional processing routes. Considering ceramic materials, the novel processes which can be produced include high bulk densities [4] and high defect densities [5]. It has been shown [6] that green (pre-sintered) bodies which possess high densities will attain high sintered densities through the use of relatively short sintering cycles. In addition, the introduction of shock induced defects in the material has been shown [7] to enhance diffusivity rates in the material. Our goal is to identify and optimize the

DSC process parameters with the goal of attaining crack-free, dense as-compacted specimens which can be sintered to high final densities.

### Experimental Procedure

The rapidly solidified material was prepared using procedures which have been described elsewhere [8]. The material was milled and classified using microsieving and sedimentation techniques in order to allow for the investigation of a wide range of particle sizes distributions on the densification behavior of the powder. The average particle size of the powders, which contained the smaller nanocrystalline grains, are shown in Table 1. The shock compacted specimens are identified by a three digit number preceded a D while the conventionally processed specimens are identified as C1-C4.

Table 1

#### Pre-sintered densities of the specimens

<u>ID/ Avg. Size</u>	<u>Shock Pressure</u>	<u>Green Density</u>
D465/100 nm	10.5 GPa	66%
D466/4.0 $\mu\text{m}$	10.5 GPa	72%
D324/ 5.3 $\mu\text{m}$	7.4 GPa	77%
D426/ 6.0 $\mu\text{m}$	8.2 GPa	73%
D425/ 6.3 $\mu\text{m}$	8.6 GPa	74%
D424/ 15 $\mu\text{m}$	7.7 GPa	76%
D423/ 29 $\mu\text{m}$	7.9 GPa	78%
D422/ 30 $\mu\text{m}$	9.1 GPa	78%
C1/100 nm	Filter Pressed	45%
C2/ 6.0 $\mu\text{m}$	Cold Pressed	52%
C3/ 15 $\mu\text{m}$	Cold Pressed	54%
C4/ 30 $\mu\text{m}$	Cold Pressed	56%

Dynamic shock compaction was performed on specimens containing ~0.2 g of powder, which was loaded into stainless steel shock capsules. The dimensions of the specimens were 10 mm in diameter and ~1 mm thick. The experimental procedure has been described elsewhere [9]. The specimens were then subjected to pressures ranging from 7.4-10.5 GPa by impacting the shock capsule with a 3 mm thick aluminum projectile traveling at ~1 km/s. The compacted specimens were recovered and the densities of the discs were measured using the Archimedes principle. For comparison,

conventionally processed specimens were fabricated. Specimens C2-C4 were cold pressed while specimen C1 was filter pressed from a colloiddally processed slurry.

The specimens were then sintered at a peak temperature of 1650°C for 2 hours with the exception of the filter pressed specimen C1 which was sintered at 1600°C with no hold and specimen D324 which was sintered at 1650°C for 15 min. These sintering cycles produced a microstructure which generally retained the t-ZrO<sub>2</sub> crystallites. The densities of the sintered samples were measured, and then mounted in epoxy and polished through 1  $\mu\text{m}$  for SEM analysis.

### Results and Discussion

Each of the shock compacted specimens was recovered structurally intact with the exception of specimen D465, which was cracked. The pre-sintered densities of the specimens are provided in Table 1. The table is arranged according to particle size, from low to high.

Table 2

#### Density of the specimens after sintering at 1650°C

<u>ID/Avg. Size</u>	<u>Shock Pressure</u>	<u>Sintered Density</u>
D465/100 nm	10.5 GPa	Cracked
D466/4.0 $\mu\text{m}$	10.5 GPa	87%
D324/ 5.3 $\mu\text{m}$	7.4 GPa	95%
D426/ 6.0 $\mu\text{m}$	8.2 GPa	86%
D425/ 6.3 $\mu\text{m}$	8.6 GPa	83%
D424/ 15 $\mu\text{m}$	7.7 GPa	82%
D423/ 29 $\mu\text{m}$	7.9 GPa	76%
D422/ 30 $\mu\text{m}$	9.1 GPa	75%
C1/ 100 nm	Filter Pressed	95%
C2/ 6.0 $\mu\text{m}$	Cold Pressed	85%
C3/ 15 $\mu\text{m}$	Cold Pressed	64%
C4/ 30 $\mu\text{m}$	Cold Pressed	58%

The results indicated that DSC process significantly enhanced the green densities of the material in relation to their conventionally processed counterparts. The DSC densities followed a trend in which the compacts which were fabricated with larger powders exhibited higher densities. This is presumed to be a result of an enhanced particle

packing which is characteristic of coarser powder fractions [10]. The densities of the DSC compacts were significantly less than theoretical however. It is believed that the net effect of the shock compaction process was to produce a highly efficient particle packing configuration with plastic deformation acting to a lesser extent at these pressures [11].

The sintered densities of the specimens are provided in Table 2. This data indicated that, in contrast to the green densities, specimens fabricated with smaller particle size distributions generally exhibited higher sintered densities. This result is consistent with models governing the sintering behavior of ceramic powders which predict a strong inverse relationship between particle size and densification kinetics [12].

Fig. 1. Sintered Densities of the Shock Compacted (DSC) and Cold Pressed Specimens

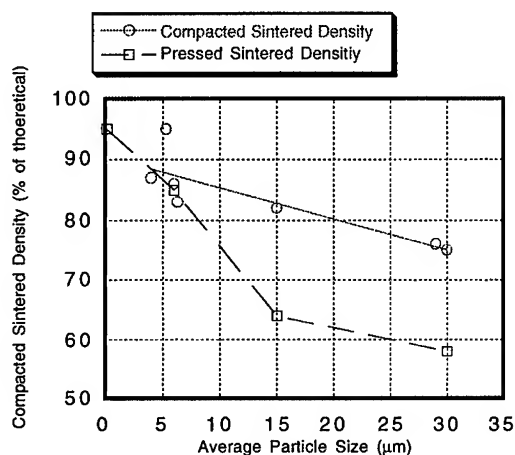


Fig. 1 shows the sintered densities of the shock compacted and pressed specimens as a function of their average particle sizes. The data indicated that the DSC process significantly enhanced the sintered densities of specimens fabricated with the coarser particle size distributions, with a convergence of the two curves at a particle size of  $\sim 5 \mu\text{m}$ . For specimens fabricated with the finer particle size distributions, equal to or less than  $5 \mu\text{m}$ , the

densities of the DSC specimens and the pressed specimens were comparable.

### Conclusions

We believe that further enhancements in the density of the sintered specimens is predicated on fabricating a green microstructure which contains a fine, homogeneous pore size distribution. Smaller pores as associated with shorter diffusion distances which enhance the kinetics of sintering. Smaller pores also possess concave surface curvatures which are thermodynamically favorable toward pore closure [13]. Process techniques which should help accomplish this goal include colloidal processing (filter pressing or centrifugal casting) and the incorporation of bimodal powder size distributions.

### References

1. R.C. Garvie, *J. Mater. Sci.* **20** (1985) 3499.
2. P.F. Becher and W.H. Warwick, *J. Am. Ceram. Soc.* **77** (1994) 2689.
3. J. Freim, J. McKittrick, W.J. Nellis and J. Katz, accepted *J. Mater. Res.* (1995).
4. R.A. Pruemmer and G. Ziegler, *Powder Metall. Int.* **9** (1977) 11.
5. E.K. Beauchamp, M.J. Carr and R.A. Graham, *J. Am. Ceram. Soc.* **68** (1985) 696.
6. A. Roosen and H.K. Bowen, *J. Am. Ceram. Soc.* **71** 970 (1988).
7. O.R. Bergmann and J.A. Barrington, *J. Am. Ceram. Soc.* **49** (1966) 503.
8. J. McKittrick, B. Tunaboylu and J. Katz, *J. Mater. Sci.* **29** (1994) 2119.
9. B. Tunaboylu, J. McKittrick, W.J. Nellis, and S.R. Nutt, *J. Am. Ceram. Soc.* **77** (1994) 1605.
10. S. Taruta, K. Kitajima, N. Takusagawa, K. Okada, and N. Otsuka, *J. Ceram. Soc. Japan, Int. Ed.* **101** (1993) 570.
11. J. Freim, J. McKittrick and W.J. Nellis, submitted to *EXPLOMET 95 Conference Proceedings*, El Paso, TX, Aug. 7-10, 1995.
12. R.L. Coble, *J. Appl. Phys.* **32** (1961) 787.
13. F.F. Lange, *J. de Phys. Colloq. C1* **47** (1986) 205.

# DIFFERENTIATION OF TRANSITION PATHWAY - DIAMOND TRANSITION AND GRAPHITIZATION - UNDER SHOCK COMPRESSION

HISAKO HIRAI and KEN-ICHI KONDO

Research Laboratory of Engineering Materials, Tokyo Institute of Technology  
4259 Nagatsuta, Midori-ku, Yokohama 226, Japan

## ABSTRACT

Differentiation of shock-induced transition pathways from graphite materials - i.e., diamond transition and graphitization - was examined under standardized experimental conditions and using starting materials with wholly identical material parameter such as crystallite size and crystallinity. Products and changes characterized by transmission electron microscopy were plotted in a tentative pressure-temperature-material diagram. The diamond transition was affected predominantly by the material parameter. The differentiation of pathways fit a concept of alternative metastable behavior; graphitization was more favored kinetically than diamond transition under the shock conditions examined.

## Introduction

Shock-induced transition from graphite to diamond depends strongly on kinetics and has parameters that can be divided into two groups: external parameters (the experimental conditions) and internal parameters (the characteristics of the starting material; crystallite size, crystallinity and so on). The actual transition mechanism has not yet been defined and remains controversial because these parameters are complicated (1-5). The conventional powder method employed in shock experiments results reverse transition caused by high residual temperature during post-shock, and a complicated temperature distribution was introduced into the sample because of heterogeneous pore distribution. It therefore was difficult to determine the conditions under which transition occurred. Besides, characterization of the starting materials was either insufficient or absent in previous studies.

Recently, we developed a quenching technique that standardizes shock conditions in order to distinguish material parameters from experimental ones (6,7). In the present work, three graphite materials with totally identical material parameters were shock-compressed at the standardized conditions. Based on detailed characterization of the recovered samples by TEM, a tentative Pressure-Temperature-Material diagram was constructed. Predominant parameters affecting the diamond transition are discussed in

relation to differentiation of the diamond transition from the progress of graphitization.

## Experimental

The quenching method involved sandwiching crushed sample chips less than 5  $\mu\text{m}$  in size between silver heat-sink disks. The shock temperatures of the samples, therefore, were the same as the heat-sink temperature, assuming that a specimen chip less than 5  $\mu\text{m}$  thick would reach thermal equilibrium in the heat-sink disks during the rise-up and maintaining times (8). For the higher-temperature experiment, a powder method was used, which involved filling the capsule with the powdered samples alone. In such a way, the standardized conditions,  $\sim 55$  GPa (750 K),  $\sim 55$  GPa (1200 K),  $\sim 55$  GPa (3500 K), and 80 to 90 GPa (1400 to 1600 K), were generated (Table 1). The sample assembly was subjected to the impact of a tungsten flyer accelerated by a powder gun. The shock duration was  $\sim 0.3$   $\mu\text{s}$  at peak pressure, and estimated cooling rates were  $10^6$  to  $10^{10}$  K/s (8,9).

Three graphite materials, a glassy carbon (GC-20S, Tokai Carbon Co. Ltd), a carbon black (so-called channel black) (SEAST-6, Tokai Carbon Co. Ltd.), and a natural graphite (from Sri Lanka) were selected as the starting materials, because these materials represented the fully homogeneous microtexture; that is, they all possessed equal crystallite size and crystallinity throughout. The characteristics and properties of these materials were described elsewhere

Table 1 Experimental Conditions and Products Identified

Run no.	starting material	specimen-assembly type	capsule-heat-sink	peak pressure (GPa)	peak temp. (K)	products/changes
1	glassy carbon	chip-A	SUS-Cu	55	750	grtz
2	glassy carbon	chip-A	SUS-Ag	56	1200	dia, grtz
3	glassy carbon*	chip-A	SUS-Ag	55	1200	dia, grtz
4	glassy carbon	chip-A	W- Ag	91	1600	dia, grtz
5	glassy carbon	powder-B	SUS-Ag	59	3500	dia, grtz, re-gr
6	carbon black	chip-A	SUS-Cu	55	750	mgr
7	carbon black	chip-A	SUS-Ag	57	1200	grtz, mgr
8	carbon black	chip-A	W- Ag	81	1400	grtz, mgr
9	carbon black	powder-B	SUS-Ag	56	3500	dia, grtz, tgr, re-gr
10	natural graphite	chip-A	SUS-Cu	56	750	mgr, uc
11	natural graphite	chip-A	SUS-Ag	62	1200	mgr, uc
12	natural graphite	chip-A	W- Ag	82	1400	mgr
13	natural graphite	powder-B	SUS-Ag	50	3500	dia, mgr, tgr, re-gr

A: the quenching method, B: the powder method, dia: diamond, grtz: further graphitization, mgr: mechanical deformation, tgr: thermal deformation, re-gr: reverse transition to graphite, uc: unchanged, \* glassy carbon heat-treated at 1000 K

(6). The crystallite sizes of the three materials were 1 to 2 nm, 2 to 10 nm, and 1 to 2  $\mu\text{m}$ , respectively. The degrees of disorder of the graphite structures, characterized by  $I_D/I_G$  in Raman spectroscopy (10), were  $\sim 1.5$ ,  $\sim 1.0$ , and  $\sim 0$ , respectively. The glassy carbon therefore ranked lowest in both crystallite size and crystallinity. The parameters then improved, in order, from glassy carbon through carbon black to natural graphite.

## Results

The transition ratio of diamond and the degree of graphitization varied with the different material and experimental parameters (Table 1). The features of diamond transition and graphitization for each material were mentioned previously (7). All results observed are summarized in terms of pressure, temperature, and material-parameter axes to form a hypothetical "P-T-Material diagram" in Fig.1. This diagram represents the behavior of the graphite (carbon) materials under dynamic shock compression over  $\sim 0.3 \mu\text{s}$ . As seen along the material axis, the degrees of change decreased as crystallite size increased, in the following manner: At 750 K ( $\sim 55$  GPa), graphitization ( $\sim 1$  nm, glassy carbon) - mechanical deformation ( $< 10$  nm, carbon black) - mechanical deformation and no change ( $\sim 1 \mu\text{m}$ , natural graphite). At 1200 K (50 to 60 GPa), diamond transition and graphitization ( $\sim 1$  nm) - graphitization and mechanical deformation ( $< 10$  nm) - mechanical

deformation and no change ( $\sim 1 \mu\text{m}$ ). At 1400 to 1600 K (80 to 90 GPa), diamond transition and graphitization ( $\sim 1$  nm) - graphitization and mechanical deformation ( $< 10$  nm) - mechanical deformation only ( $1 \mu\text{m}$ ). At 3500 K (50 to 60 GPa), the diamond transition occurred for all three materials, and thermal deformation occurred only for the latter two materials.

## Discussion

Comparing the modes of change reveals that the diamond transition was affected primarily by the material parameters of the starting graphite materials: The smaller the crystallite size or the lower the crystallinity, the more easily the diamond transition occurred. The smaller crystallite size and lower crystallinity of the starting material elevated its own initial energy state, mainly because of surface energy and strain energy. The relative magnitude of the activation-energy barrier to diamond thus seemed to be reduced, and consequently the diamond transition was achieved more easily. And, pressure thus was ineffective and temperature fairly effective in regard to the diamond transition. The strong temperature dependence is in agreement with the theory that the rate of reaction is proportional to  $\exp(-\Delta G_a/RT)$ , suggesting a diffusion-controlled process.

The different transition pathways observed can be explained by a combination of the Ostwald Step Rule(11) with a concept of alternative metastable behavior, as illustrated schematically in Fig.2. The

graphite materials have different crystallite sizes and crystallinity, so that their initial energy states are elevated depending on their material parameters, forming several steps (heavy solid line in Fig.2). Each step involves a relatively small deviation of activation-energy ( $\Delta E_g$ ) because of structural similarity. The three light solid curves in Fig.2 show the changes in free energy involving transitions from the individual initial states of the three graphite materials to diamond. In any of the three curves, the change from the initial state to diamond is opposed by a high activation-energy barrier ( $\Delta E_d$ ). These activation-energy barriers are much higher than  $\Delta E_g$ , but the magnitudes of  $\Delta E_d$  decrease with increasing initial energy state. Only the glassy carbon therefore was able to achieve the transition to diamond. As shown in Fig.2, changes via the sequence of steps, i.e., the progress of graphitization in this case, might be more favorable kinetically. Graphitization thus predominated over the diamond transition for the glassy carbon and carbon black. For the natural graphite, with an initial state nearly equal to that of ideal graphite, further graphitization was impossible, but the pathway to diamond transition was opposed to the highest barrier.

The activation energy for such transitions normally is supplied by thermal fluctuations (12). The main reason for the higher transition ratio at 3500 K was the extra localized thermal energy provided easily, in addition to a higher bulk temperature, by the heterogeneous temperature distribution resulting from

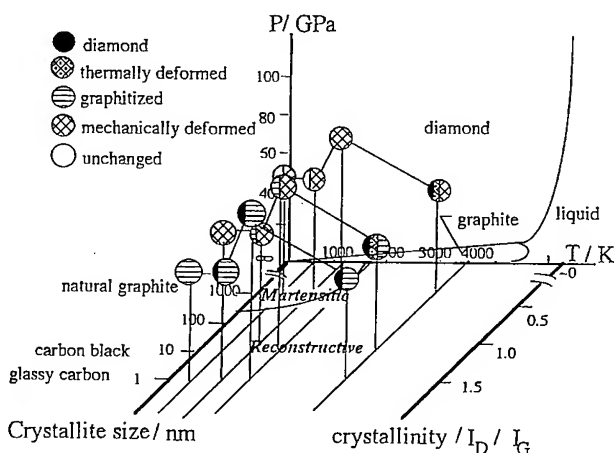


Fig. 1 A tentative P-T-Material diagram. An equilibrium phase diagram derived (11) is inserted at infinite crystallite size.

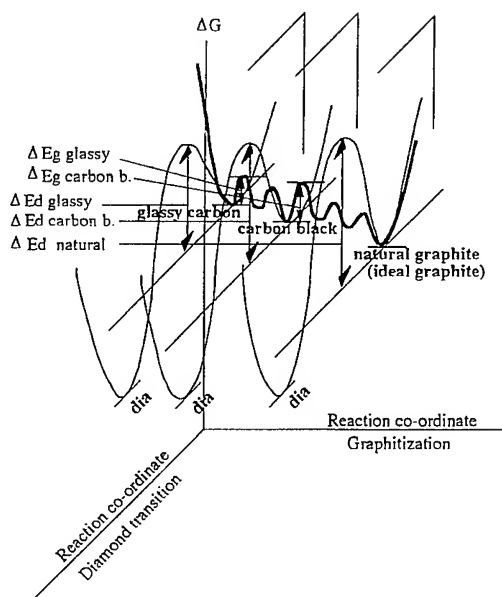


Fig.2 Schematic illustration of the activation energies in terms of two reaction coordinates, graphitization and diamond transition.

the powder method. This extra thermal energy is indispensable for achieving the diamond transition, especially under shock compression, in which the transition occurs within a fraction of a microsecond or less.

## References

1. P.S. DeCalri and J.C. Jamieson, *Science*, **133**, 1821 (1961).
2. D.J. Erskine and W.J. Nellis, *Nature*, **349**, 317 (1991).
3. L.F. Trueb, *J. Appl. Phys.*, **42**, 503 (1971).
4. D.G. Morris, *J. Appl. Phys.*, **51**, 2059 (1980).
5. Kleiman, et al., *J. Appl. Phys.*, **56**, 1440 (1984).
6. H. Hirai, T. Ohwada, and K. Kondo, *J. Mater. Res.*, **10**, 175 (1995).
7. H. Hirai, S. Kukino, T. Ohwada, and K. Kondo, *J. Am. Ceram. Soc.*, **78**, (1995).
8. H. Hirai, K. Kondo, N. Yoshizawa, and M. Shiraishi, *Appl. Phys. Lett.*, **64**, 1797 (1994).
9. H. Hirai and K. Kondo, *Science*, **253**, 772 (1991).
10. D.S. Knight and W.B. White, *J. Mater. Sci.*, **4**, 385 (1989).
11. F.P. Bundy, *Physica A*, **156**, 169 (1989).
12. A. Putnis and J.D.C. McConnell, in "Principles of Mineral Behaviour" (Blackwell, Oxford, 1980), p.140.

## COMPACTION OF ULTRADISPERSE DIAMONDS BY WEAK SHOCK LOADING

E.E. LIN, V.A. MEDVEDKIN, and S.A. NOVIKOV

Russian Federal Nuclear Center,  
All-Russian Scientific Research Institute of Experimental Physics,  
607200, Arzamas-16 Nizhni Novgorod Region, Russia

### ABSTRACT

Diamond micropowder production technique based on dynamic compacting of ultradisperse diamonds powder in weak shock wave has been developed. The crystalline properties of micropowder particles are in keeping with the data for natural polycrystalline diamonds.

Up to date shock induced synthesis of ultradisperse diamonds (UDD) under solid explosives (SE) detonation has been investigated in detail both theoretically and experimentally (see, for example, [1-6]). It has been stated that sizes of the great bulk of UDD particles of cubic modification do not depend on SE charge sizes and are  $a = 2 - 20$  nm (see [4]). The mean size of UDD is equal to  $\langle a \rangle = 4 - 6$  nm. Stochastic model [5] of crystalline clusters aggregation in shock wave (SW) in condensed matters permits to estimate the characteristic time scale of UDD formation when phonon excitations of their crystalline lattice occur immediately in the course of aggregation from small nuclei, namely, from the products of benzene rings destruction within SW. Such estimation shows that the formation time of UDD particles having the size  $\langle a \rangle = 4$  nm is approximately equal to 2 ns. It can be concluded that a great bulk of UDD particles have been generated within the SW front in condensed explosives and organic materials. By this reason the sizes of UDD do not depend on explosive charge sizes. Experimental data, presented in [6], confirm directly the existence of above mentioned phonon excitations by means of observation of UDD nonequilibrium luminescence in the course of explosion process.

At the same time, diamond powder, consisting of polycrystalline particles with the sizes  $a \geq 1$   $\mu\text{m}$ , is acceptable material for abrasive tools [7]. In this light it is of interest to investigate a behaviour of closed system of UDD particles under dynamic loading. Compaction of UDD in shock wave, generated by massive piston, have been studied by experiment in [8, 9]. It has been found that mean size of diamond particles increases

by several orders on UDD powder shock loading with amplitude  $P \sim 10$  GPa and duration  $\tau \sim 10$   $\mu\text{s}$ . Apparently, this effect results from phonon excitation of diamond clusters in "weak" SW, corresponding to the lower boundary of diamond stability field on carbon phase diagram. When loading duration is much greater than characteristic time  $T$  of oscillatory interaction between clusters ( $\tau \gg T$ ) the number  $N$  of interaction acts is great:  $N \sim \tau/T \gg 1$ . Therefore, bonding of crystalline skeletons of clusters and formation of more large particles from UDD is greatly probable. The characteristic time of UDD oscillatory interaction can be estimated as  $T \sim 2\langle a \rangle/c_0 \approx 1$  picosecond. Here  $c_0 = 13.42$  km/s is effective sonic speed in diamond (see, for example, [10]). So the number of interaction acts is equal to  $N \sim 10^7$ . Such amount of "attempts" is quite enough for bonding of a great number of clusters and for dynamic compaction of UDD.

In the present work compaction of UDD in SW, generated by massive piston, have been studied at greater length. Shock loading of ampoules with UDD powder has been carried out with the help of steel pistons with diameter  $D = 29.3$  mm and with altitude  $L = 50$  mm, accelerated to velocities  $V = 340$  m/s, 550 m/s and 800 m/s. Piston acceleration to given velocity has been provided with the help of ballistic equipment of explosive type. The ampoule construction and material permit to retain the diamond powder in the course of shock experiment.

Analytical estimations and numerical calculations show that the pressure impulse of the amplitude  $P \approx 7 - 16$  GPa and the duration  $\tau \sim 10$   $\mu\text{s}$  has been created within the

sample of UDD powder during shock loading. The pressure was determined using impedance mismatch procedure, based on equation of state of UDD powder, which has been written in standard Me-Grueneisen form.

After shock loading the samples of diamond powder have been tested with the help of methods of analytical chemistry, X-raying, electronic and optical microscopy, and also of metallography. Shock produced diamond powder consists of polycrystalline particles with the lattice of cubic modification having interplate distances  $d_{111} = 0.2059$  nm,  $d_{220} = 0.1260$  nm, and  $d_{311} = 0.1072$  nm. The measured  $d$ -values are in exact keeping with the lattice spacings of the starting UDD. The mean crystalline density of particles is equal to  $3.2$  g/cm<sup>3</sup>. The particle sizes lie in a region  $a \approx 0.5 - 600$   $\mu$ m. First-handly after extraction of the samples from the ampoules and after breacing up of these samples we have recorded two modes of powder with the characteristic sizes  $\langle a \rangle_1 \sim 10^1$   $\mu$ m for the first mode, and  $\langle a \rangle_2 \sim 10^2$   $\mu$ m for the second one. Histogram of the first mode of shock produced powder can be approximated with the help of logarithmic-normal distribution, indicating to cluster-cluster interaction of UDD in weak SW (see [8]). Histogram of the second mode can be described by normal distribution, indicating to diffusive mechanism of growth of more large particles (see [9]).

These modes of diamond powder can be separated. As a result of special processings we can obtain diamond micropowders with the mean particle sizes  $\langle a \rangle \approx 1.5 - 10$   $\mu$ m, chemical purity amounting up to 99.5 %, yield constituting 70-90 % of initial UDD powder mass. Crystalline properties of these micropowders are in keeping with the data for natural polycrystalline diamonds. Elaborated technique enables the production of white grains as well as transparent crystals with sizes from 50 to 600  $\mu$ m and mean microhardness  $H \approx 30 - 40$  GPa.

The authors wish to thank their colleagues I.F. Kazakova, V.G. Kuropatkin, L.M. Sinitsina, V.I. Sukharenko, B.P. Tikhomirov, and N.A. Jukina for the assistance in carrying out of the investigations.

Russian Fund of Fundamental Investigations has provided implementation of this work with financial support (Project code 93-01-16504).

## REFERENCES

1. M.S. Shaw, and J.D. Jonson, J. Appl. Phys., 5 (1987) 2080.
2. V.M. Titov, V.F. Anisichkin, and I.Yu. Malkov, The Physics of Combustion and Explosion, 3 (1989) 117.
3. K.V. Volkov, V.V. Danilenko, and V.I. Elin, Ibidem, 3, (1989) 123.
4. B.A. Vyskubenko, V.V. Danilenko, E.E. Lin, V.A. Mazanov, T.V. Serova, V.I. Sukharenko, A.P. Tolochko, Ibidem, 2 (1992) 108.
5. E.E. Lin, Khimicheskaya Fizika, 3 (1993) 299.
6. B.A. Vyskubenko, E.E. Lin, A.V. Sirenko, The Physics of Combustion and Explosion, 1 (1993) 134.
7. Abrasive Materials. U.S. DEPARTMENT OF THE INTERIOR. Bruce Babbitt Secretary. BUREAU OF MINES. August 1993.
8. E.E. Lin, V.A. Medvedkin, and S.A. Novikov, Khimicheskaya Fizika, 1 (1995) 59.
9. E.E. Lin, S.A. Novikov, V.G. Kuropatkin, V.A. Medvedkin, V.I. Sukharenko, The Physics of Combustion and Explosion, 5 (1995) 110.
10. I.S. Grigoriev, and E.Z. Meilikhova (editors), The Physical Values. Reference Book, (Moscow, Energoatomizdat, 1991).



# BAUSHINGER EFFECT IN STEEL UNDER DYNAMIC LOADING

V.A. PUSHKOV, P.A. TSOI, S.A. NOVIKOV

Russian Federal Nuclear center VNIIEF Arzamas-16, Russia

This work is devoted to development of technique for investigation of Baushinger dynamic effect in structure materials using scheme of symmetric small-cycle loading of sample.

Until recently there have been no data available in the literature on Baushinger dynamic effect in materials. This paper is devoted to development of technique for investigation of Baushinger dynamic effect in structure materials using scheme of symmetric small-cycle loading of sample, which has been first suggested by K. Ogawa [1].

The proposed technique employs Hopkinson gauge bars and dynamic loading of sample with help of explosion. Loading bar is a three-step one and is produced so that the subsequent waves of compression and extension are formed, when the primary extension wave is reflected from bar step boundaries. The primary extension wave is formed during collision of tubular striker accelerated by energy of explosion with small ledge of three-step bar. The striker and bar steps are of the same lengths and materials, so the compression and extension waves follow each other without pauses and distortion in turn causing extension-compression-extension and etc. Thus the sample between three-step loading bar and one-step support bar is subjected to small-cycle loading for one experiment.

Stress  $\sigma(t)$  and deformation  $\varepsilon(t)$  of sample are determined using relationships of stress elastic wave theory by Kolsky method.

$$\sigma = \frac{EA_1}{A} \varepsilon_i(t) \quad \varepsilon = \frac{2C}{l} \int_0^t [\varepsilon_i(t) - \varepsilon_i(t-\tau)] dt \quad (1),$$

where  $A$ ,  $l$  - cross-section area and sample length;  $E$ ,  $C$  - modulus of elasticity and acoustic velocity in the bars;  $\varepsilon_i(t)$ ,  $\varepsilon_r(t)$  - strains of the bars under loading pulses, which fall down on sample and pass it. (Strain gauges measure them).  $\tau$  - time of stress wave run through sample;  $A_1$  - area of support bar cross-section.

Strain rate  $\dot{\varepsilon}$  is estimated by strain law  $\varepsilon = \varepsilon(t)$ . Using formulas (1) it is possible to plot extension-compression  $\sigma$ - $\varepsilon$  diagram, which defines the measure of Baushinger

effect:  $\delta = |\sigma_{-0.1}| / \sigma_{+T}$ , where  $\sigma_{+T} = \sigma_{+T}(\varepsilon_p)$ , see Figure 1.

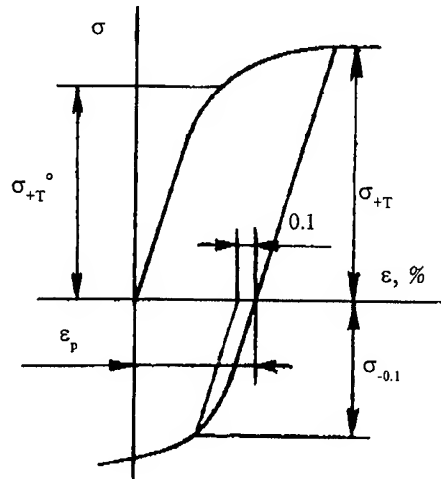


FIGURE 1. Baushinger effect during extension-compression.

In the experiment in both phases of extension and compression the strain rate  $\dot{\varepsilon}_p$  in plastic parts of the diagram remains approximately similar and in each phase the strain rate is constant ( $\dot{\varepsilon}_p = \text{const}$ ). To meet the first condition has happened to be a great difficulty for the researchers that to a considerable extent has affected the absence of experiments studying Baushinger dynamic effect.

Explosive test device which is based on this scheme of small-cycle loading of sample is depicted in Fig.2. The device allows  $\dot{\varepsilon}$  and  $\dot{\varepsilon}_p$  variation changing striker velocity as well as its length and lengths of three-step bar parts.

The technique suggested is elaborated in the explosive experiments.

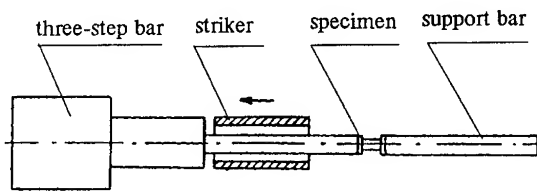


FIGURE 2. Scheme of explosive test device.

Fig. 3 shows the dynamic cyclic diagram of extension-compression  $\sigma$ - $\epsilon$  for steel St.3 as illustration, which has been obtained at average strain rate in plastic parts of the diagram  $\dot{\epsilon}_p = 680 \text{ s}^{-1}$  (here at extension phase  $\dot{\epsilon}_p = 560 \text{ s}^{-1}$ , at compression phase  $\dot{\epsilon}_p = 800 \text{ s}^{-1}$ ). It has been shown that  $\epsilon_p = 0.96\%$ ,  $\sigma_{+T} = 584 \text{ MPa}$ ,  $\sigma_{-0.1} = -318 \text{ MPa}$ ,  $\delta = 0.54$ ,  $\alpha_o = 1.65$ . Here  $\alpha_o = (\sigma_{+T} - \sigma_{-0.1}) / \sigma_T^0$  (see Fig.1) is defined on the base of generalized Masing principle.

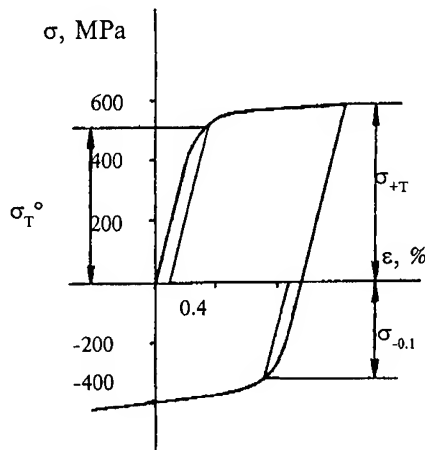


FIGURE 3. Dynamic diagram of extension-compression for steel St.3.

## REFERENCE

1. Ogawa K. Impact-tension compression test by using a split-Hopkinson bar. *Exper.mech.*, 1984, vol.24, N2, pp.81-86.

# SPALL BEHAVIOR AND DAMAGE EVOLUTION IN TANTALUM

A. K. ZUREK, W. R. THISSELL, AND D. L. TONKS

*Los Alamos National Laboratory*

*Los Alamos, NM 87545, USA*

We conducted a number of plate impact experiments using an 80-mm launcher to study dynamic void initiation, linkup, and spall in tantalum. The tests ranged in shock pressure so that the transition from void initiation, incipient spall, and full spall could be studied. Wave profiles were measured using a velocity interferometry system (VISAR), and targets were recovered using "soft" recovery techniques. We utilized scanning electron microscopy (SEM), metallographic cross-sections, and plateau etching to obtain quantitative information concerning damage evolution in tantalum under spall conditions. The data (wave profiles and micrographs) are analyzed in terms of a new theory and model of dynamic damage cluster growth. We have developed a model of ductile damage based on void coalescence of initially nucleated voids that leads to clusters of voids. The biggest cluster has time to grow much more rapidly than smaller cluster at low strain rates, resulting in sample failure. Large clusters cannot grow any faster than smaller clusters at high strain rates so the sample breaks when enough clusters grow independently to form a fracture surface by random accumulation.

## Material and Experiment Description

In this study we used commercially-pure (triple-electron-beam, arc melted) unalloyed tantalum plate with the measured composition (in at. %) of carbon-6 ppm, nitrogen-24 ppm, oxygen-56 ppm, hydrogen- <1 ppm, iron-19 ppm, nickel-25 ppm, chromium-9 ppm, tungsten-41 ppm, niobium-26 ppm and balance tantalum. The tantalum plate was in an annealed condition and had an equiaxed grain structure of 68  $\mu\text{m}$  grain size [1]. We performed the uniaxial strain spall tests utilizing an 80-mm single-stage launcher and recovery techniques as previously described [2]. Tantalum samples were spalled at 9.5 and 17 GPa pulse pressure and 1  $\mu\text{s}$  pulse duration under symmetric impact conditions. Recovered spalled samples were analyzed using optical and scanning electron microscopes.

Previous recovery and non-recovery spall tests reported a 5.2 GPa spall strength for 6 GPa shock amplitude, 7.3 GPa spall strength for 9.5 GPa shock amplitude, and 3.0 to 4.5 GPa spall strength for 15 GPa shock amplitude [1, 3, 4]. These compare favorably with our results.

## Results and Discussion

We were particularly interested in the dynamic void initiation, void linkup and fracture by spall. Therefore, we have chosen

the applied pulse pressure to either fully spall the sample or to introduce the spall surface but not to allow the surfaces to fully separate creating so called incipient spall. A typical VISAR spall trace is presented in Figure 1.

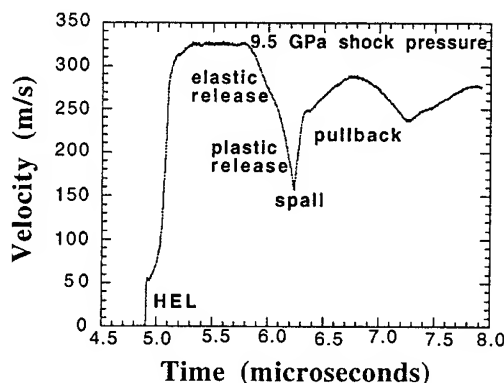


Figure 1. VISAR spall trace of tantalum spalled at 9.5 GPa.

The spall test at 9.5 GPa pulse pressure produced an incipient spall fracture. The cross section of the recovered spall sample showed distinctive cracks running across the entire diameter of the sample with multiple branched and interlocking cracks extending into the sample away from the principal fracture surface. The two halves of the spall sample did not separate from each other, regardless of the fact that the pulse pressure

exceeded the expected spall strength of this material. Figure 2 shows the optical micrograph of the cross section of the tantalum sample spalled at 9.5 GPa shock pressure. We have sectioned off part of the spalled sample to allow it to separate the spall surfaces. Figure 3 shows the typical ductile dimple fracture surface characteristic for metals in Group V<sub>A</sub>. Multiple impurities on the fracture surface are present, and most likely they are responsible for the void initiation.

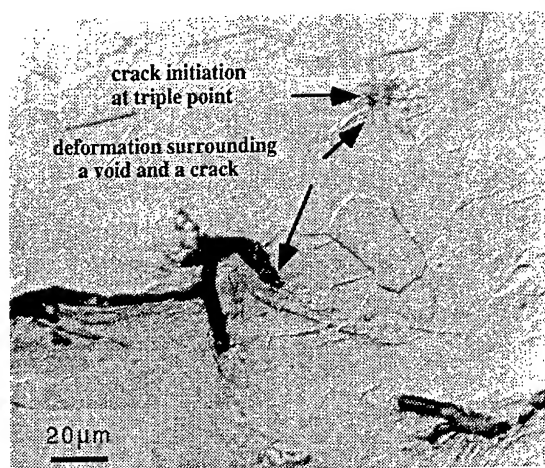


Figure 2. Cross section of tantalum sample spalled at 9.5 GPa showing void initiation at the point of intersection of several grains and propagating cracks with deformation surrounding a void and a crack (optical micrograph).

The spall was complete and two halves of the spalled sample fully separated to reveal fracture surface under increased loading pulse pressure (17 GPa). Scanning electron microscopy pictures of the fractured surfaces showed a mixture of ductile dimple and cleavage fracture (Figure 4).

This change in the fracture morphology can be induced by significant deformation twinning which will initiate cleavage [1]. The etched cross section, orthogonal to the spall fracture surface, reveals a significant density of deformation twins and only a few twins in the sample spalled at the lower pulse pressure (compare Figure 2 with Figure 5).

The sample tested at the higher pulse amplitude did not show crack branching, unlike the sample tested at the lower pulse amplitude. This observation, and the change in mode fracture from ductile to a mixture of ductile and cleavage fracture explains an observed decrease in spall strength with

increased applied pulse amplitude in this material [1,3,4].

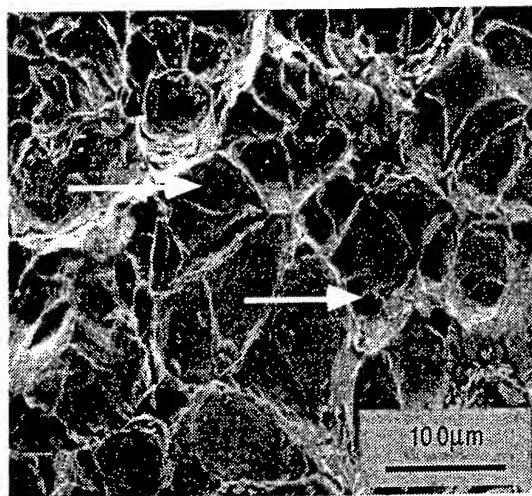


Figure 3. Spall fracture surface of tantalum spalled at 9.5 GPa. Arrows point to the particles which most likely initiated dimples on a ductile fracture surface.

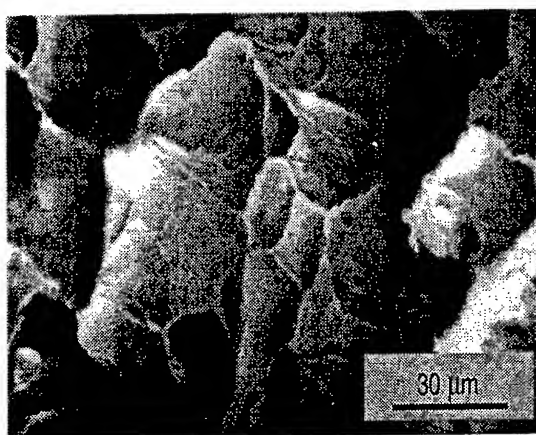


Figure 4. Fracture surface of tantalum spalled at 17 GPa shock pressure. The micrograph shows a mixture of cleavage fracture and ductile dimples present on the fracture surface.

Cleavage fracture is associated with the ductile-to-brittle transition in this material especially under severe loading rates or low temperatures [1, 5]. High hydrostatic tensile stress develops at the spall plane. The ductile-to-brittle transition is pushed to higher temperatures with increases in applied stress. The fracture stress therefore increases because, to a first approximation, it is linearly proportional to the applied stress. The combination of this effect and a significant amount of deformation twinning triggers cleavage fracture.

It would be interesting to investigate the susceptibility of different fracture modes to the impurity levels, since these could impinge the dislocation motion and influence dislocation storage and twin interaction in this material.

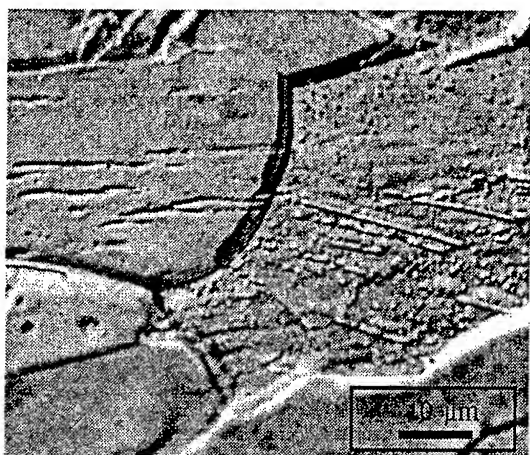


Figure 5. Deformation twins present on the cross section of the tantalum sample spalled at 17 GPa shock pressure.

A theoretical program is underway to model the damage evolution observed in materials such as tantalum. The model includes damage induced by shear stress as well as damage caused by volumetric tension. Spallation is included in the model as a special case and strain induced damage is also treated. Void nucleation and growth are taken into account, and give rise to strain rate effects through elastic release wave propagation between damage centers (voids). The underlying physics of the model is the nucleation, growth, and coalescence of voids in a plastically flowing solid. The model is intended for hydrocode based computer simulation. The details of the model are published elsewhere [6].

## Conclusions

We studied damage evolution in tantalum under the spall conditions for impact stresses of 9.5 and 17 GPa. The lower shock pressure amplitude (9.5 GPa) formed an incipient spall with ductile fracture characteristics and cracks in a primary spall plane which extend over a few of grains in the direction of wave propagation. Spall was complete and we observed a mixed (ductile and cleavage) fracture mode at the higher shock pressure. Cross sections of the spall surfaces revealed twinning for the higher

pressure spall case and only a few twins in the lower pressure case. A theoretical program is underway to model the damage evolution observed in tantalum.

## Acknowledgments

We are pleased to acknowledge support from the US Joint DoD/DOE Munitions Technology Development Program and the US DOE. Carl Trujillo is thanked for performing the spall tests. Rob Hixon and Max Winkler are greatly appreciated for assistance and tutelage in setting up and operating the VISAR apparatus. Sheri Bingert is thanked for annealing the samples. Mike Lopez is appreciated for help in optical microscopy.

## References

1. G. T. Gray III, "Shock-Loading response of advanced materials," Proc. of AIP Conference on *High-Pressure Science and Technology*, eds. S. C. Schmidt, J. W. Shaner, G. A. Samara and M. Ross, American Institute of Physics, 1994.
2. A. K. Zurek, P. S. Follansbee, and J. Hack, *Met. Trans.*, 21 (1990) 431-439.
3. J. N. Johnson, R. S. Hixson, D.L. Tonks, and A. K. Zurek, "Rate-Dependent Spallation Properties of Tantalum" in 1995 APS Topical Conference on the *Shock Compression of Condensed Matter*, 13-18 August, 1995, Seattle, WA.
4. G. T. Gray III and A. D. Rollett, "The high-strain-rate and spallation response of tantalum, Ta-10W, and T-111," in *High Strain Rate Behavior of Refractory Metals and Alloys*, eds.: R. Asfahani, E. Chen, and A. Crowson, The Minerals, Metals and Materials Society, 1992, pp 303-315.
5. R. W. Armstrong, J. H. Bechtold, and R. T. Begley, "Mechanisms of alloy strengthening in refractory metals," in *Refractory Metals and Alloys* eds.: R. Asfahani, E. Chen, and A. Crowson, The Minerals, Metals and Materials Society, 1992.
6. D. L. Tonks, A. K. Zurek, and W. R. Thissell, "Ductile Damage Modeling Based on Void Coalescence and Percolation Theories", Proceedings of EXPLOMET'95, The International Conference, El Paso, TX, August 1995.

# CAVITATION EROSION AS A PROCESS OF FATIGUE SPALLATION

S. BURAVOVA

*Institute of Structural Macrokinetics Russian Academy of Sciences, 142432, Chernogolovka,  
Moscow district, Russia.*

## ABSTRACT

Surface erosion is considered from the position of wave mechanics, taking into account solid compression. Damage is spallation by its nature and is due to the interference of rarefaction waves which accompany a compression impulse. The cavitation action is regarded as a result of loading of spherical shock waves, generated from the cavitation zone. During repeated shock loading the damage is accumulated while channel crack appears. The dynamic fatigue is distinguished from quasi-static case by the damage location in the zone of rarefaction waves interference. Cavitation erosion is accompanied by three types of spalling damage: channel cracks, a system of circular longitudinal cracks and transverse cracks, which generated near the zone of impulse loading. Face spallation is a principal cause of the intensive material loss during cavitation erosion.

## Introduction

Damage of many objects such as screw propellers, submerged ship wings is caused by cavitation. Extensive studies of the erosion problem (1,2) have not resulted in understanding of damage processes in the surface layer. It is supposed that shallow depression is formed during surface loading of cumulative streams, generated by collision of nonsymmetrical cavitation bubbles. Observation of pits at the bottom of the depression is believed to confirm the stream mechanism (1). Deep valleys are formed during the action of collective shock wave, generated by simultaneous collision of many cavitation bubbles. Pressure in such shock waves is estimated to be as large as 1000 MPa.

Works (3,4) suggested the spallation mechanism of erosion. The mechanism is based on the analysis of surface damage under impulsive loading, such as the plate impact (5), the detonation spraying (6), the laser irradiation impact (7) and public information. Spallation damage results from interference or focusing of rarefaction waves, accompanying a compression impulse. Focusing of rarefaction waves leads to longitudinal cracks. A system of circular cracks is formed around the channel cracks as a result of repeated loading of the zone of shock loading. The removal of debris from the zone of multiple longitudinal spallation results in valleys on the target. The interference of rarefaction waves occurring on valley walls and faces causes face

spallation leading to erosion material losses. The conditions for which the approach developed in Refs. (3,4) is valid involve higher compression amplitude, than one would normally consider to be "cavitational".

The objective of this paper is to show that the spallation erosion mechanism properly describes the features of erosion damage at low impact loading which takes place during cavitation action.

## The initial state of cavitation erosion

The cavitation action is regarded as a result of loading of spherical shock waves, generated from cavitation zone. A high pressure area forms during shock loading. The velocity of the boundary of the contact zone varies from infinity at the initial moment of impact to the sound speed in liquid  $c_1$ , where the cavitation phenomena occur. The reflected shock wave in liquid is always "attached" to the boundary. When the velocity of the contact boundary becomes equal to the sound speed in target  $c_0$ , the shock wave in solid separates from the boundary and the resultant rarefaction waves, spread into the high pressure areas. At this moment the maximum distance of shock wave from the solid surface is

$$x_0/r_0 = k [k/(k^2 - 1) - 1/(k^2 - 1)^{1/2}] \quad (1)$$

Here  $r_0$  is radius of the contact zone in moment of separation of shock waves and  $k = c_0/c_1$ .

Impulsive loading of a solid is accompanied by two simultaneous processes: hardening and damage of the surface layer. The passage of a compression impulse through the material causes the structural changes, and, as a consequence, hardening of the material. The impulse intensity at the cavitation action is less than the Hugoniot limit of elasticity  $P_H$ , because the surface layer hardening occurs through deformation accumulation upon repeated loading. The dynamic fatigue is distinguished from quasi-state case by the damage location in the zone of rarefaction waves interference. The thickness of the hardened layer  $x = x_0 + x_1$ . For cavitation action it is typical, that the hardened layer appears only after the critical number of loading cycles is exceeded and small parameter  $\sigma$  becomes equal  $\sigma_H$ . The layer thickness at this moment is  $x_{II} = (1 + 0.5\sigma_H)/\sqrt{\sigma_H}$ . When the small parameter  $\sigma$  exceeds  $\sigma_H$  the equation for  $x$  takes the form characteristic of the spallation mechanism of erosion (3,4):

$$x_{II}[x_{II} + (2\sqrt{\sigma_H - \sqrt{\sigma_N}})/(1 - 0.5\sigma_N - \sigma_H + 2\sqrt{\sigma_H\sigma_N})] = 2 \quad (2)$$

where  $\sigma$  is a small parameter,

$$\sigma_H = 0.5(n+1)P_H/\rho_0 c_0^2,$$

$\sigma_N = 0.5(n+1)P_0(1+\xi N)/\rho_0 c_0^2$ ,  $n$  is the isentropic coefficient,  $P_0$  is initial pressure in the target,  $N$  is the number of loading cycles,  $\xi$  is the elastic-plastic hysteresis. The Table illustrates the dependence of the hardened layer thickness on the number of loading cycles  $N$ .

Table. Characteristics of the target surface layer after the cavitation action.

$\sigma_N$	0.02	0.03	0.04	0.05	0.06	0.07	0.08	0.09	0.1
$N$	600	1400	2200	3000	3800	4600	5400	6200	7000
$X$		6.360	6.390	6.410	6.440	6.470	6.500	6.530	6.560
$L_0$					0	0.610	0.880	1.120	1.330

It should be noted that no elastic-plastic hysteresis is known for the cavitation action. In the present calculation, demonstrating a principal feasibility of description of cavitation erosion by wave mechanics techniques, the following values were taken:  $\sigma_0 = 0.0125$ ,  $\sigma_H = 0.03$ ,  $k = c_0/c_1 = 4$ ,  $\xi = 0.001$ ,  $\sigma^* = 0.06$ .

In the hardened layer the interference of the rarefaction waves results in the formation of longitudinal channel zone with tensile strength under the contact zone. The channel spall is a non-one-dimensional spallation phenomena, which has

not yet been investigated. Mathematical techniques for the rigorous calculation of spherical wave focusing are still underdeveloped. In our calculation it was assumed, that the negative pressure in the rarefaction interference zone was equal to the initial pressure  $P_0$ .

In this work, the failure is supposed to take place in the zone of the rarefaction wave interaction, if the tensile strain exceeds the critical value equal to the dynamic spallation strength  $P^*$ .

The depth of the longitudinal channel spallation  $L_0$  can be evaluated by realization of the failure criterion at the end of the crack:

$$L_0 = \tan \cos^{-1} [P^*/P_0 (1 + \xi N)] \quad (3)$$

The table shows the dependence of the channel spall depth on the number of loading cycles. Each shock intensity is associated with the critical number of cycles, which it exceeded gives rise to the formation of a longitudinal channel crack under the contact zone. Subsequent loading leads to the crack deepening.

#### Dynamics of development of damage region

The formation of the longitudinal channel crack changes the character of the subsequent loading. The channel crack acts as an inner free surface, and, consequently, as a source of new rarefaction waves. As a result, a circular crack is formed in half way between the neighboring sources of rarefaction waves. Its penetration depth decreases by a factor of two,  $L_1 = 1/2 L_0$ . The circular crack in turn gives rise to new sources of

rarefaction and hence further circular cracks at positions given by:

$$L_i = 1/2 L_{i-1} = (1/2)^i L_0.$$

Fragmentation of material from the zone of circular spallation forms a surface valley. Multiple longitudinal spallation is the main mechanism forming surface topography with characteristic alternation of hills and valleys.

Repeated shock loading on the bottom of deep valleys is accompanied by formation of transverse cracks. When the valley side slope  $\varphi_0$  becomes less than

$\tan^{-1}[1-0.25(n+1)P_0/\rho_0 c_0^2] / \sqrt{0.5(n+1)P_0/\rho_0 c_0^2}$  a compression impulse arising on the valley bottom during the cavitation action is capable of passing through the side wall into the hill. The ejection of the impulse on the target face results in the formation of a transverse zone of high tensile stress. The valley wall and the target surface face are sources of rarefaction waves. The transverse cracks are formed in regime of dynamic fatigue. Calculations (3,4) show, that the transverse section slope to the target surface is close to  $50^\circ$  for a wide range of cavitation intensity. The spallation plate width is an order of magnitude greater than its thickness. The erosion products are plate-shaped. The main material loss occurs in the immediate vicinity of the valleys.

The fatigue spallation mechanism of cavitation erosion is based on the physical laws of a compressible solid. Wave mechanics makes it possible to determine the causes of damage and to explain the fundamental experimental facts, such as the valley formation, the appearance of longitudinal and transverse cracks, the small size of debris during incubation stage of erosion wear and the formation of great flaking during steady state stage.

The fatigue spallation mechanism of cavitation erosion is a particular case of the common spallation mechanism of impulsive damage of solid.

#### Acknowledgements

The author is grateful to her colleagues A.F.Belikova, A.A.Goncharov, Yu.N.Kiselev, Yu.P.Fedko and E.A.Mironov for help in the experiments and discussion.

#### References

1. C.M.Preece, In: *Erosion*, ed. C.M.Preece, Acad. Press, New York, 1979, p. 269
2. E. P. Georgievskaya, *Kavitatsionnaya eroziya grebnyh vintov*, Sudostroenie, Leningrad, 1978
3. S.Buravova, *Wear*, 157, (1992), p. 353
4. S.Buravova, *Zhurnal Technicheskoi Fiziki*, 62, N 8, (1992), p.58
5. G.A.Adadurov, A.Belikova and S.Buravova, *Fizika Goreniya i Vzryva*, 4, (1992), p.95
6. A.F. Belikova, S.N. Buravova, et al., *Poverkhnost*, 10, (1989), p. 134
7. A.F.Belikova, S.N.Buravova et al., *Fizika i Khimiya Obrabotki Materialov*, 4, (1989), p 100



# NONLOCAL EFFECTS IN THE HIGH STRAIN-RATE PROCESSES IN SOLIDS

T.A.Khantuleva, Yu.I.Mescheryakov

*Institute of the Mechanical Engineering Problems, Russian  
Science Academy, Bolshoj, 61, Saint Petersburg, 199178, RUSSIA*

A new nonlocal hydrodynamical approach to description of the structural media is developed. According to this approach the nonlocal and spin properties of medium are closely correlated. The concrete kind and scale of the medium structure resulted from the strain process are defined by the initial and boundary conditions in a nonunique way due to the branching of solutions to the nonlinear problem. The solution obtained is used then to explain experimental results on the shock-induced shear bands and vortex structures in metals.

## Introduction

In series of experimental investigations in the shock loading of some materials, the unusual regions of strain localization have been discovered by Mescheryakov et al. (1992). These regions have a round cell and/or chain of cells form, which is believed to have a rotational/vortical origin. Similar to the shear bands, the latter are in the wave propagation direction crossing grain boundaries without deviation. Their nucleation is thought to be localized in the mixing layers on the boundaries of microflows moving with different velocities in the direction of a wave propagation as result of the structure and velocity inhomogeneity of the shock compression of solids. In shock compressed solids the rotational cell diameter has been ascertained to be proportional to the difference in accelerations of adjacent microflows between which the rotational motion of a medium initiated.

All inhomogeneities arising during the dynamic straining may be related to the so-called mesoscopical scale level (0.1–10  $\mu\text{m}$ ) which occupies an intermediate position between atom-dislocation level and macrolevel.

## Self-consistent nonlocal hydrodynamical approach

At present there is no satisfactory theory to describe the mesoscopical effects. Therefore, one needs an approach which is macroscopic

and could take into account the processes of the re-arrangements of the inner structure of solid during dynamical straining.

The greater the inhomogeneity of a medium, the greater the internal structure effects are. Then one can say that the greater the parameter  $\varepsilon = \lambda/L$  ( $\lambda$  – the scale of the medium internal structure,  $L = \frac{a}{|\text{grad } a|}$ ,  $a$  is a macroscopical variable), the higher the nonequilibrium of a system is. On the nonequilibrium conditions the macroscopical balance equations are not entirely localized. They imply nonlocal in space and time constitutive relationships between macroscopical gradients  $G$  and dissipative fluxes  $P$ :

$$P(\vec{r}, t) = \int_V d\vec{r}' \int_0^t dt' \mathcal{L}(\vec{r}, \vec{r}', t, t'; \varepsilon, \tau) \cdot G(\vec{r}', t') + P_0(\vec{r}, t), \quad (1)$$

where the weight factors  $\mathcal{L}$  represent relaxation transport kernels depending on the space coordinates  $\vec{r}$ ,  $\vec{r}'$  in the volume  $V$ , the time coordinates  $t$ ,  $0 \leq t' \leq t$ , and the scale parameters  $\varepsilon$ ,  $\tau$ . Similar to the relative space scale  $\varepsilon$ , the parameter  $\tau$  is the relative time scale. These relationships had been derived from the first principles in the nonequilibrium statistical mechanics by Zubarev et al. (1972). In the general case  $\mathcal{L}$  are defined by unknown functionals of the hydrodynamical variables.

A new trend of the nonlocal hydrodynamics developed by one of the authors of the paper

Khantuleva et al. (1982, 1994) is a construction of self-consistent models of the relaxation transport kernels. Herewith, the boundary effects connected with the interaction of an open system with its surroundings, can be involved as an additional element of modeling.

According to the self-consistent approach the model relaxation parameters are related to any integral properties of a system either through integral relationships, or by imposing additional boundary conditions. These additional relationships make the formulation of the boundary problem self-consistent.

### Mathematical basis of the proposed nonlocal approach

Recently new results in the theory of nonlinear operator sets had been obtained and applied in mechanics of the resonance systems by Vavilov et al. (1993). Recall that the case  $\varepsilon \sim 1$  just corresponds to the resonance situation where the external field scale almost coincides with the internal structure one. Moreover, one can show that the boundary-value problem for the nonlocal equations in the self-consistent formulation can be reduced to the special type nonlinear operator set

$$u = F(u, \xi), \Phi_j(u, \xi) = 0, j = 1, \dots, n \quad (2)$$

with respect to unknown element  $u \in \mathbf{E}$  in Banach space and involved  $n$  model parameters  $\xi \in \mathbf{R}^n$ ;  $F$  is nonlinear operator:  $\mathbf{E} \times \mathbf{R}^n \rightarrow \mathbf{E}$ ;  $\Phi_j$  are nonlinear functionals.

In this formulation it is possible to solve the boundary-value problems correctly, to find the solvability conditions as a set of nonlinear inequalities with respect to the input parameters of a problem, and to analyze the branching processes in a region  $\varepsilon \sim 1$ .

### Nonlocal effects in the nonstationary shear flow of structure medium

Unlike the well-known Rayleigh problem for structureless media one can formulate the nonlocal extension of the problem for the structure media.

$$\frac{\partial u}{\partial t} = \nu \frac{\partial^2 u(y, t)}{\partial y^2} + N_\varepsilon(y, t; \alpha, \gamma), \quad (3)$$

where the nonlocal term

$$N_\varepsilon(y, t; \alpha, \gamma) \equiv \nu \frac{\partial}{\partial y} \left[ (1 + \alpha) \cdot \int_0^\infty \frac{dy'}{\varepsilon} e^{-\frac{\gamma}{2}(y'-y-\gamma)^2} \frac{\partial u}{\partial y'} - \frac{\partial u}{\partial y} \right] \quad (4)$$

involves an effective Gaussian model of the shear relaxation transport kernel with the model parameters  $\alpha, \gamma$  to be defined through the given values of the plate acceleration  $\dot{U}$  and the friction on the plate  $P_W$ . Here and above  $\nu$  is kinematic viscosity of a liquid.

If the scale parameter  $\varepsilon \rightarrow 0$ ,  $\dot{U} \rightarrow 0$ ,  $P_W \rightarrow P_W^0$ , then  $\alpha, \gamma \rightarrow 0$ ,  $u \rightarrow u^0$ , where  $u^0$  is the solution to the parabolic equation (3) with  $N_\varepsilon = 0$  on the initial and boundary conditions

$$u^0(y, t = 0) = 0, u^0(y = 0, t > 0) = U_0, \quad (5)$$

$$u^0(y \rightarrow \infty, t > 0) \rightarrow 0,$$

We shall seek a solution to Eqs.(3)-(4) on conditions (5), where  $U_\varepsilon(t) \rightarrow U_0 = \text{const}$ ,  $t \rightarrow \infty$ ,  $\varepsilon \rightarrow 0$ , is taken instead of  $U_0$ , in a form  $u = u^0 + \varphi$ ,  $\varphi(0, t) = \varphi(\infty, t) = 0 \quad \forall t > 0$ . In order to reduce the problem to the operator form (2) we have to take the Green function for the parabolic Eq.(3) with a source  $N_\varepsilon$

$$\varphi(y, t) = \nu \int_0^t \int_0^\infty \frac{N_\varepsilon(\xi, \theta; \varphi(\xi, \theta); \alpha, \gamma)}{2\sqrt{t\nu(t-\theta)}} \cdot e^{-\frac{(y-\xi)^2}{4\nu(t-\theta)}} d\xi d\theta. \quad (6)$$

As the Green function is of the  $\delta$ -type we can obtain an approximate solution when  $\nu \ll 1$ :

$$\varphi(y, t) = \nu \int_0^t N_\varepsilon(y, \theta; \varphi(y, \theta); \alpha(\theta), \gamma(\theta)) d\theta \quad (7)$$

In order to define the model parameters  $\alpha(t), \gamma(t)$  as functions of time we have two relationships

$$\Phi_\varepsilon^1(\varphi; \alpha, \gamma) \equiv \nu(1 + \alpha) \cdot \int_0^\infty \left[ \frac{\partial}{\partial y} e^{-\frac{\gamma}{2}(y'-y-\gamma)^2} \right]_{y=0} \cdot \frac{\partial(u^0 + \varphi)}{\partial y'} - \dot{U}(t) = 0; \quad (8)$$

$$\Phi_\varepsilon^2(\varphi; \alpha, \gamma) \equiv \nu(1 + \alpha) \cdot \int_0^\infty \frac{dy'}{\varepsilon} e^{-\frac{\gamma}{2}(y'-y-\gamma)^2} \frac{\partial(u^0 + \varphi)}{\partial y'} - P_W(t) = 0. \quad (9)$$

where the dependencies  $\dot{U}(t)$ ,  $P_W(t)$  are given by the experimental data. In the formulation (7)–(9) the extended Rayleigh problem entirely corresponds to the operator formulation (2). Due to the nonlinear character of the set (7)–(9) it can have more than one solution.

Further we can linearize the Eqs.(7)–(9) near the solution  $u^0$  using the asymptotics of the model kernels at  $\varepsilon \rightarrow 0$ . In this case the formulation (7)–(9) becomes more simple and the asymptotical values of the model parameters are unique:

$$\varphi(y, t) = \nu \int_0^t dt \left\{ \alpha(t) \frac{\partial^2 u^0}{\partial y^2} + \gamma(t) \frac{\partial^3 u^0}{\partial y^3} \right\}; \quad (10)$$

$$\gamma(t) = \frac{\dot{U}}{U_0} \sqrt{\nu t^3}; \quad (11)$$

$$\alpha(t) = \frac{P_W^0(t) - P^0(0, t)}{P^0(0, t)}.$$

Herewith, the shift parameter of the kernel  $\gamma(t)$  has sense of the thickness of a near-boundary layer which related to the structure effects and can be much thinner than the classical Prandtl layer.

## Discussion

1) In scope of the proposed approach the internal structure effects manifest themselves as the nonlocal ones which emerge only at finite accelerations of a plate  $\dot{U}(t) \neq 0$ .

2) The nonlocal effects in movements with accelerations cause the medium polarization along a direction normal to the plate (a direction of the greatest gradients). It is found that the shift parameter  $\gamma \neq 0$  in the momentum relaxation transport kernel is directly proportional to the plate acceleration  $\dot{U}(t)$ :  $\gamma(t) \sim \dot{U}(t)$  (Eqs.(11)). A medium becomes anisotropic due to an asymmetry of the viscous stress tensor.

3) The medium anisotropy may follow from the emergence of turning moments of the medium structure elements. Accordingly to results of the paper by Aero (1981) the turning moments appear in a medium composed of finite size elements under the influence of nonuniform stresses. Herewith, it is the acceleration  $\dot{U}(t) = 0$  is responsible for the rotations of structure

elements generated by the nonlocal correlations among microscopical elements of a lower scale level.

4) After the critical moment  $t^*$  when the acceleration changes a sign the two type nonclassical solutions can appear: vortical formations or rotations ( $\gamma \neq 0$ ), and shear with a slip ( $\gamma = 0$ ).

5) The space distributions of the values  $\dot{U}$ ,  $\Delta$ ,  $\varepsilon$  over a material has stochastic character. Hence, the conditions on which all nonclassical solutions emerge, are also of probability kind. It has been experimentally confirmed by the results of Mescheryakov et al. (1992).

## Summary

In scope of the developed self-consistent non-local hydrodynamical theory of nonequilibrium transport processes first, we succeeded in determining an explicit relationships between the nonequilibrium effects as the nonlocality ones followed the internal structure of a medium and accelerations at a nonstationary movement of structure media. At high space inhomogeneities of macroscopic fields the accelerations cause the emergence of nonclassical solutions to the problem of a viscous shear. These solutions correspond to the probable formation of new space structures in materials during high strain-rate processes.

## References

- Mescheryakov YI, Atroshenko SA (1992) Int. J. Solids Structures. 29, 22: 2761–2778
- Zubarev DN, Tischenko SV (1972) Physica 59, 2: 285–304
- Khantuleva TA, Philippov BV (1984) Boundary Problems of the Nonlocal Hydrodynamics. Leningrad State Univ., USSR
- Khantuleva TA, Vavilov SA (1994) In Book of Abstr. of the 19th Int. Symp. on RGD, Oxford Univ., England
- Vavilov SA, Yuhnevich SV (1993) Nonlinear Vibration Problems. 25: 475–482
- Aero EL (1981) Fluid Mechanics. Soviet Research. 4.

## STRUCTURAL AND PHASE TRANSITIONS OF ZIRCONIUM AND ITS ALLOYS WITH NIOBIUM IN SPHERICAL STRESS WAVES

E.A.Kozlov, B.V.Litvinov, E.V.Abakshin, G.V.Kovalenko  
*Russian Federal Nuclear Center - Research Institute of Technical Physics*  
*P.O. Box 245, 456770, Snezhinsk (Chelyabinsk-70),*  
*Chelyabinsk region, Russia*

V.K.Orlov, V.M.Teplinskaya, S.S.Kislyakov, A.A.Kruglov  
*Academician A.A.Bochvara Research Institute of Inorganic Materials,*  
*Box A-39, 123060, Moscow, Russia*

A.V.Dobromyslov, N.I.Taluts, N.V.Kazantseva, G.G.Taluts  
*Institute of Metal Physics, Ural Branch of Russian Academy of Sciences,*  
*18 S.Kovalevskaya str., GSP-170, 620219, Ekaterinburg, Russia*

### ABSTRACT

The phase and structural states of two zirconium balls, as well as two samples made of its alloys with 1—2,5 % by mass niobium, were loaded by spherically converging shock waves of various intensity and were studied layer-by-layer. The trajectories (in T-P coordinates) of the states of Lagrangian particles positioned at various radii were calculated for various loading conditions. A comparison of the phase and structural states with calculated data allowed us to explain changes in these states by the occurrence of the  $\alpha \rightarrow \omega \rightarrow \beta \rightarrow L$  transformations and plastic deformations which take place during the action of pulsed loading.

### Introduction

The study of the effect of spherical stress waves on the structure, mechanical properties, and phase state of metals and alloys is of great interest nowadays because this method of pulsed loading allows one to obtain extremely high pressures and temperatures in rather large volumes of material and to preserve specimens unbroken after such loading [1-4]. Phase transformations and high-rate plastic deformation can occur in the material during the propagation of shock and isentropic waves. In the case of converging shock waves, the peak values of pressure and temperature, as well as their changes with time [5,6], substantially depend upon the position of the area studied at the ball radius. Moreover, it should be kept in mind that the residual temperatures, retained after unloading of a specimen, can produce a certain effect of the phase and structural states of the material. All these factors make interpretation of the data on microstructure examination difficult. However, in the case of a properly selected subject of experimentation and its

adequate initial treatment, we can follow the phase and structural changes occurring during the impact action of converging shock waves reasonably well. Zirconium is one of the best suited subjects for this investigation. The aim of this investigation was to study microstructure and phase state of recovered spherical specimens shock-wave loaded in the region of  $\alpha-\omega-\beta-L$  (liquid) transformations.

### Experiment

Material for the study was obtained by vacuum remelting of iodide zirconium. Two unalloyed zirconium balls 24 mm in radii were put into special vacuum shells of stainless steel. The shell thickness was 11 and 8 mm on balls 1 and 2, respectively. Loading was performed by spherical converging detonation waves. The external radius of the explosive was 40 mm. The experiments were performed [1,2,6-8] with various compositions and thicknesses of the explosive, as well as with or without a heavy case. Specimens 3 and 4 - balls 35 mm in radii made of alloys Zr-1% Nb and Zr-2.5% Nb -

also underwent loading by spherical converging detonation wave. X-ray diffraction analysis, optical and transmission electron microscopy, as well as microhardness measurements along the radius, were used to study the structure, phase composition and mechanical properties of the recovered samples.

## Results

The recovered samples have the shape of a thick-wall spherical shell with central cavities of various sizes appeared in the process of loading of the initially full spheres by spherically converging shock waves. The average volume deformations of the recovered samples were different. Local deformation was changed over a wide range along the radius.

In the initial state, zirconium has a single-phase structure of the hexagonal  $\alpha$  phase. By evidence of X-ray diffraction, shocked specimens 1,3 and 4 have a two-phase structure composed of the  $\alpha$  and  $\omega$  phases. The amount of the  $\omega$  phase is largest in the layers near the external surface of the specimens and decreases until it completely disappears when the center of the balls is approached. Growth of retained  $\omega$ -phase quantity was noted under analogous loading conditions in specimen 3 and 4 where the niobium content in the initial material was increasing. Shock-loaded specimen 2 has an  $\alpha$  single-phase structure.

Optical microscopy with a polarized light shows [7,8] that the initial microstructure of zirconium consists of irregular  $\alpha$  phase grains containing numerous twins in several twinning systems. The average grain size is 500-600  $\mu\text{m}$ .

The microstructure of the shock-loaded specimens [7,8] strongly depends both on the loading conditions and on the layer depth. In specimen 1, the effect of the spherical shock wave leads to structure refinement due to the appearance of a great amount of deformation twins, as well as of twins caused by the  $\alpha$ - $\omega$  and  $\omega$ - $\beta$  phase transformations. The most coarse structure is observed in the layers near the loaded surface of the specimens 1,3 and 4. The twins in these layers are characterized by the greatest thickness and extension. As the depth of the layer position increases, twins become finer and their distribution becomes more ordered. In the layers near the cavity of these specimens, the twin density becomes high to such an extent that, in

some cases, regular geometric patterns in the form of characteristic ornaments are present.

A more pronounced microstructure changes occur in specimen 2. The deformation twins, as well as the twins caused by the  $\alpha$ - $\omega$  and  $\omega$ - $\beta$  transformations, are present only in the subsurface and medium-depth layers. The microstructure of these layers is similar to that observed in specimen 1. The microstructure of deeper layers is characterized by a high density of the twins and by uniformity of their distribution. In the layers near the cavity of the specimen the transition from twinned microstructure to an ultrafine-grained microstructure with a micron-scale grain size occurs. A sharp increase in grain size is observed with further approaching the cavity. The grain size in these layers ranges from 40  $\mu\text{m}$  - 100  $\mu\text{m}$  in the immediate neighbourhood of the cavity.

Electron-microscopic examination shows that, in the initial state, zirconium has a rather uniform structure. Because the  $\alpha$  phase grains are very coarse, only their internal structure containing some polygonal walls or microtwins can be examined by this method. After shock-wave loading, the  $\omega$  phase is revealed only in the subsurface layers of specimens 1,3 and 4. This phase appeared as plates alternating with the plates of the  $\alpha$  phase [8]. Both phases contain a number of dislocations. In some places, the dislocation density is so high that quantitative estimations are very difficult. In addition to dislocations, microtwins are present in the subsurface layers of balls. However, the microtwin density is low. As the layer depth increases, the  $\omega$  phase amount decreases and the number of microtwins substantially increases. The dislocation distribution becomes nonuniform. Areas with a cellular structure are present, together with areas with high dislocation density. Nonuniformity of the dislocation distribution further increases in the layers adjacent to the cavity. These layers contain areas with a polygonized structure and areas with a very low dislocation density. Only separated fragments of microtwins are retained in these layers.

In the structure of specimen 2 subjected to more intense loading  $\omega$  phase is not observed. In the subsurface layers, the  $\alpha$  phase has a strongly fragmented and nonuniform structure. Together with areas with a cellular structure, areas with a uniform as well as a nonuniform distribution of dislocations, are present. Microtwins are found

relatively rarely. As the layer depth increases, the amount of microtwins substantially increases whereas the dislocation density decreases. Recrystallized grains begin to appear together with polygonized grains and twins. A sharp change in structure occurs in the layers adjacent to the cavity: the amount of dislocation decreases, microtwins completely disappear, and boundaries of the  $\alpha$ -phase grains become perfect. Areas with very fine grains 0.1–0.3  $\mu\text{m}$  in size are observed in all recovered specimens. Such areas are present inside adiabatic shear bands.

### Discussion of the results

The conditions of loading with spherical stress waves were selected so that the flow parameters  $P(R,t)$  and  $T(R,t)$  realized in balls 1 and 2 of unalloyed zirconium were overlapped in some region along the radius. This allowed us to adequately study the entire field of the  $\alpha \rightarrow \omega \rightarrow \beta \rightarrow L$  phase transformations by a layer-by-layer analysis of the structure of only two shock-loaded and recovered balls.

The peak pressure at the surfaces of all balls exceeds the pressure required for the  $\alpha \rightarrow \omega$  transformation. Therefore, the  $\omega$  phase forms in the entire volume of the balls upon the propagation of a loading pulse. Under unloading, two versions [8] are possible for the position of trajectory in (P,T) coordinates. In the layers whose state trajectories intersect the temperature axis above 450–550°C, the  $\omega$  phase disappears during subsequent cooling because it is unstable at these temperatures in the absence of pressure. If the isentropic curve of the particle intersects the temperature axis below 450°C, the  $\omega$  phase in the corresponding layer remains in metastable state. In specimen 1, this occurs in the external layers with radii  $R$  ranging from 10–24 mm [5,8]. In specimen 2, no  $\omega$  phase is detected in the final structure because trajectories of the states of all layers intersect the temperature axis above 450°C [8].

In the absence of pressure the  $\beta$  phase is unstable. Therefore, we should look for evidence of  $\omega \rightarrow \beta$  transformations in the special features of final structure of the  $\alpha$  phase. According to [8], for the particles with radii  $R$  ranging from 7–10 mm (sample 2), the trajectories in (P,T) coordinates completely fall in the  $\beta$  phase field and intersect the temperature axis above the

temperature  $T_{pt} = 863^\circ\text{C}$  of the polymorphous transformation in zirconium at atmospheric pressure. For the particle at  $R=15$  mm, the trajectory of states intersects the temperature axis below  $T_{pt}$ . Due to the difference in these trajectories, the formation of the final structure in the corresponding layers proceeds in different ways. It is well known that the highest recrystallization rate corresponds to the  $\beta$ -phase field. This reflected by the  $\alpha$  phase grain size. In the layers for which the trajectories in the (P,T) coordinates intersect the temperature axis in the  $\alpha$  phase field, the grain size of the final structure is very small because recrystallization in the  $\alpha$  phase proceeds much slower than in the  $\beta$  phase.

### Conclusion

Analysis of radial changes in the phase state and special structural features of zirconium balls as well as two samples made of its alloys with 1–2.5% by mass niobium and loaded by spherical converging waves of various intensity allowed us to associate the observed features with the occurrence of  $\alpha \rightarrow \omega \rightarrow \beta \rightarrow L$  phase transformations and plastic deformation directly during shock-wave processes.

### References

1. E. A. Kozlov, *High Pressure Research*, **10** (1992) 541.
2. E.A. Kozlov, in *Shock Compression of Condensed Matter 1991*, ed. S.C. Schmidt et al. (Elsevier Science Publishers B.V., 1992), p.169.
3. E.A. Kozlov, *J.Phys. (Paris)* **1** (1991) C3-675.
4. E.A.Kozlov, B.V.Litvinov, and I.G.Kabin, in *Shock Compression of Condensed Matter 1991*, ed. S.C.Schmidt et al. (Elsevier Science Publishers B.V., 1992), p. 535.
5. E.A.Kozlov, G.V.Kovalenko, V.F. Kuropatnenko, and G.N.Sapozhnikova, *Bull. Am. Phys. Soc.*, **36** (1991) 1831.
6. E.A.Kozlov and A.V.Zhukov, in *High Pressure Science and Technology*, ed. S.C.Schmidt, J.W.Shaner, G.A.Samara, M.Ross, (AIP, New York, 1994), p. 977.
7. E. A. Kozlov, B. V. Litvinov, V. K. Orlov, V.M. Teplinskaya, and Z.P. Nikolaeva, in *Zababakhin's Scientific Readings*, ed. E.N. Avrorin (Kyshtym, RUSSIA, 1992), p. 173.
8. E.A.Kozlov, A.V.Dobromyslov, and N.I.Taluts, *Phys. Met. & Metallog.*, **79** (1995) 662.

# THE BEHAVIOUR OF $\alpha$ -QUARTZ UNDER HIGH DYNAMIC AND STATIC PRESSURES: NEW RESULTS AND VIEWS

YU. N. ZHUGIN

*Russian Federal Nuclear Center—All-Russian Research Institute of Technical Physics,  
P.O. Box 245, Snezhinsk, Chelyabinsk region, 456770, Russia.*

## ABSTRACT

The short review of the results concerning the modern experimental and theoretical investigations into the behaviour of quartz under high dynamic and static pressures as well as the analysis and the comparison of these results are given.

## Introduction

By 1990 the views have been settled with respect to the absence of the unstationary bifurcation of the shock-wave front in quartz in the whole phase mixture region beginning from 12-14 GPa and having an abnormal spread (more than 20 GPa) in stress amplitude between the origin and the completion of the quartz transformation into stishovite (1-10). Many researchers believed also that quartz has no shear strength behind the shock-wave front under stresses exceeding the dynamic limit of elasticity. For the sake of discussion simplification we shall hold the same point of view, i.e. the terms "pressure" and "stress" will be identified in the given work. The possible reason for the bifurcation absence has been considered in work (4) on the phenomenological level. The attempts of theoretical generalizations have been undertaken in works (6-10). However, since 1980 principally different results (11-24) began to appear and new views essentially differed from the known ones have been formed.

## Results of dynamic experiments

By applying the technique of the manganin gauges with a high time resolution the study into the dynamics of propagation of shock waves with initially right-angled profile and different amplitude has been performed on the samples of monolithic quartz rocks up to ~ 10 mm in thickness and with the content of  $\text{SiO}_2$  no less than 96% (11,12). It has been established that after passage of the distance equal to ~ 10 mm by the wave its profile remains to be right-angled if the pressure value behind the front does not exceed the threshold value equal to 23 GPa. In the range from 23 to 35 GPa the kinetic phenomena (Fig. 1: a-e, g) similar to the processes developing in substances with typical phase transitions (25,26) at the early stage in the formation of an unstationary system of two shock

waves have been registered in the structure of the shock wave propagating with lower velocity after the powerful (~ 6 GPa) elastic precursor. The second wave became noticeable in quartz rocks experiments with the aluminium impactor velocity  $W = 3.79$  km/s (Fig. 1: f, h), in monocrystal quartz (Z-cut) — with  $W = 3.56$  km/s (Fig. 1: i). The first shock wave amplitude amounts to  $23 \pm 1$  GPa. The existence of critical transition stress for quartzite have been verified in laboratory experiments (20) by means of the laser interferometer technique.

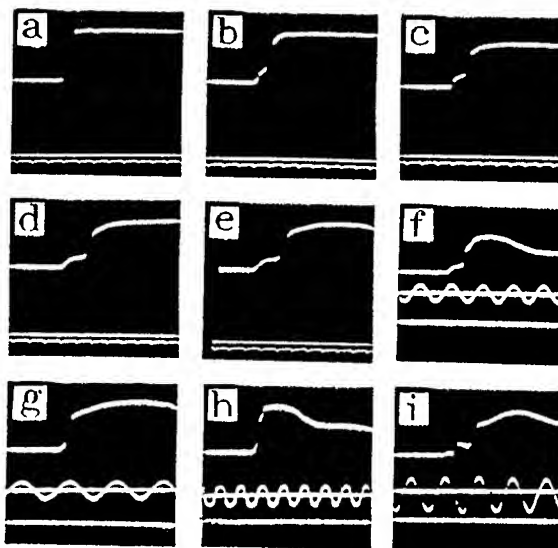


Figure 1. Oscillograms of manganin transducer experiments with quartz rocks of two deposits and monocrystalline quartz. Quartzite — a,b,c,d,e : distance covered by a shock wave  $L = 0.5, 4, 6, 8, 11$  mm, respectively, period of time marks  $T = 0.1$   $\mu\text{s}$ , aluminium impactor velocity  $W = 3.56$  mm/ $\mu\text{s}$ ; f:  $L = 11$  mm,  $T = 0.4$   $\mu\text{s}$ ,  $W = 3.79$  mm/ $\mu\text{s}$ . Quartzite-sandstone — g, h :  $L = 11$  mm,  $T = 0.4$   $\mu\text{s}$ ,  $W = 3.56$  and  $3.79$  mm/ $\mu\text{s}$ , respectively. Monocrystalline quartz (Z-cut) — i :  $L = 10.5$  mm,  $T = 0.4$   $\mu\text{s}$ ,  $W = 3.56$  mm/ $\mu\text{s}$ .

The authors (11,12) believed that the more confident observation of the shock wave front bifurcation effect in quartz rocks can be possible in experiments with the samples whose thickness essentially exceeds 10 mm. This supposition was substantiated by the large-scale experiment realized under conditions of the powerful underground explosion (24) in quartzite.

In work (19) shock compressibility for the mixtures of dispersive polycrystalline  $\alpha$ -quartz with paraffin and fluoroplastic has been investigated in detail for the range of pressures from 5 to 50 GPa. In the additive approximation (27) the curves of the dynamic compression for quartz being a part of the mixture composition have been determined. Two bends have been revealed on the curves of pressure (P) versus specific volume (V) (Fig. 2). The first bends – under pressures equal to 20.5 and 21.5 GPa, the second bends corresponding to the beginnings of the steep branches of the dynamic compression curves – under

pressures equal to 26.3 and 30.1 GPa. The position of the dynamic compression curve for quartz in P-V – plane has been estimated for the case (not yet experimentally realized) of the agreement of the dynamic rigidities for the mixture components.

The results (11,12) have been compared in work (16) with data and views (31-33) of the geologists who studied the dependence of the residual properties of the recovery quartz (index of refraction, density) on the amplitude of a single shock loading in laboratory experiments. The identification of the glass mass concentration with the stishovite content behind the shock wave front (33) made it possible to calculate (16,19,21,23) the hypothetical shock adiabat of quartz (curve 6 in Fig. 2) in the additive approximation (27) according to the data (31,32). It is interesting that the position of the hypothetical Hugoniot practically coincides with that of a single compression of quartz that has been estimated in work (19) on the basis of the mixture data. The shape of both curves in P-V – coordinates is qualitatively in agreement with the results of the registration (11,12,23) at the early stage of the shock wave front bifurcation in the monolithic  $\alpha$ -quartz in the range from 23 to 35 GPa.

### Results of static experiments

In work (13) the results of X-ray diffraction investigations into the  $\alpha$ -quartz behaviour at room temperature and under the conditions of quasi-hydrostatic loading of powders by pressures up to 40 GPa are set forth. Transformation into stishovite has not been revealed in this case. The obtained experimental data and thermodynamic analyses have shown that under  $P \approx 30$  GPa almost all the quartz evolved into the amorphous form of silica with its density close to the density of stishovite. The noticeable transformation into this high-density amorphous form begins with  $P = 20 - 25$  GPa. The more sensitive investigations, performed with monocrystals (14), have evidenced that the gradual amorphization induced by pressure begins from the pressure level approximately equal to 12.5 GPa that coincides practically with the beginning of the phase mixture region in the shock-wave experiments. On the basis of their results and thermodynamic analysis the authors (13) has suggested that the high – density amorphous phase but not stishovite is also formed directly from quartz under the shock loading of quartz by pressures more than 30 GPa.

The more detailed investigations are given in work (17). The simultaneous changes in X-ray and Raman

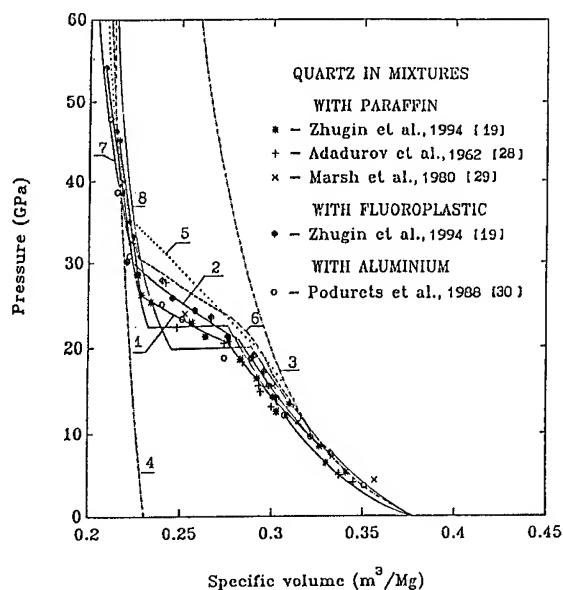


Figure 2. Observed and calculated P-V – curves for  $\alpha$ -quartz. Experimental curves of dynamic compression for quartz in mixtures with paraffin and fluoroplastic, respectively – 1, 2: Zhugin et al. (19). Calculated Hugoniot of metastable quartz – 3 (23) and quartz completely transformed to stishovite – 4 (19). Smoothed – out experimental Hugoniot – 5: Wackerle (1); Fowles (2); Ahrens and Rosenberg (3), Lyzenga and Ahrens (8). Hypothetical Hugoniot calculated by the experimental dependencies of residual properties for quartz on pressure of a single shock loading – 6 (16). Molecular – dynamics simulation – 7: Tse and Klug (15) and 8: Somayazulu et al. (18).



spectra have been interpreted by the authors (17) as the evidence of a new phase transition of the first kind in  $\alpha$ -quartz under pressure equal to 21 GPa. The further increase in pressure leads to the fact that the new crystalline phase became amorphous. The investigation of samples undergone the action of pressures in the range from 21 and 30 GPa shows that the new phase transformation is reversible to a great extent, but the conserved samples are heterogeneous and contain the different quantities of the amorphous and crystalline components depending on the applied pressure. The authors (17) do not exclude possibilities for the partial amorphization of the new phase when pressure is removed. The samples, obtained after their loading by pressures equal to 30 GPa and the higher ones, are completely amorphous.

### Results of molecular - dynamics calculations

In the works (15,18) the behaviour of quartz under high pressure and room temperature has been studied by the molecular-dynamics method. In work (18) the calculations have been also performed for increased temperatures. In the above mentioned works carried out by two groups of the researchers the structural changes with increasing in pressure have been followed, the curves of the quartz compression under room temperature in  $(P-V/V_0)$  - coordinates have been determined. The obtained results are close although the potentials of interaction among atoms and the approaches to the determination of the transformation pressure have noticeably differed. It has been shown that the jump-wise decrease in volume by 15 per cent has taken place in  $\alpha$ -quartz under pressure in the range from 20 to 23 GPa. The high-pressure phase is disordered, i.e. it is amorphous.

As opposed to works (15,18) the authors of the work (22) consider that the resulting phase does not represent a special amorphous state but it is a complex crystalline structure. In their opinion the real amorphization is beyond the possibilities of simple molecular-dynamics calculations.

### Analysis and comparison of results. Conclusions

The hypothetical shock adiabat has been determined in works (16,19) on the basis of views (32,33) supported by the known experimental data on the shock-wave properties of quartz (1-3,8) and on the basis of the results of the laboratory recovery experiments (31,32) with the conservation of quartz samples undergone a single shock loading. The hypothetical shock adiabat has practically coincided

with the curve of a single shock compression of quartz which has been estimated in work (19) on the basis of the results of the shock-wave experiments with mixtures of quartz with paraffin and fluoroplastic. Both curves in  $P-V$  - coordinates under  $P \sim 23-35$  GPa are located below the wave ray corresponding to the critical pressure equal to 23 GPa that leads to the shock-wave front bifurcation (12,20,23,24) in this range of pressures.

When comparing the results of shock-wave and static experiments the attention is paid to the proximity of the pressure values corresponding to the beginning of the more sharp increase in dynamic compression (20-23 GPa) and to the beginning of the more marked static amorphization (20-25 GPa). The availability of these characteristic pressure levels can be associated with the quartz transformation (in the range from  $\sim 12$  to 30 GPa) into the high-density amorphous form with the appreciable disturbance of monotony in the phase concentration increase with pressure growth under pressure equal to 20-25 GPa.

When comparing the dynamic  $P-V$  - curve with the results of the molecular-dynamics computations the impression is produced by the practical coincidence of the experimentally determined critical pressure equal to 20-23 GPa with pressure under which the jump-wise decrease in volume by  $\sim 15$  per cent is observed. In the molecular-dynamics calculations there is no pressure level equal to 30 GPa which is typical for dynamics. This fact can be explained by the absence of the mechanisms hampering the transformation development in molecular-dynamics calculations and by the availability of the kinetic factors in dynamics.

Thus, by analyzing and comparing the presented results it is shown that the recent results of the static experiments and the molecular-dynamics calculations correlate well with the modern results of the dynamic experiments and confirm the new views based on the latter with respect to the shock-wave front instability in quartz in the pressure range from 23 to 35 GPa and the formation of the unstationary system of two shock waves with the phase precursor amplitude equal to 23 GPa.

### References

1. J. Wackerle, *J. Appl. Phys.* 33, 2 (1962) 922.
2. R. Fowles, *J. Geophys. Res.* 72, 22 (1967) 5729.
3. T. J. Ahrens, J. T. Rosenberg, in *Shock Metamorphism of Natural Materials* (Baltimore: Mono Book Corp., 1968), p. 59.

4. M. A. Podurets, R. F. Trunin, *Dokl. Akad. Nauk SSSR* 195, 4 (1970) 811.
5. D. E. Grady, W. J. Murri, G. R. Fowles, *J. Geophys. Res.* 79, 2 (1974) 332.
6. D. E. Grady, *J. Geophys. Res.* 85, B2 (1980) 913.
7. A. I. Voropinov, M. A. Podurets, *Zh. Prikl. Mekh. Tekhn. Fiz.* 6 (1980) 70.
8. G. A. Lyzenga, T. J. Ahrens, *J. Geophys. Res.* 88, 33 (1983) 2431.
9. H. Tan, T. J. Ahrens, *J. Appl. Phys.* 67, 1 (1990) 217.
10. J. W. Swegle, *J. Appl. Phys.* 68, 4 (1990) 1563.
11. Yu. N. Zhugin, K. K. Krupnikov, *Investigation of Some Peculiarities of Quartzite Behaviour in Shock Waves. RFNC-VNIITF Report G88519*, (Chelyabinsk-70, 1980).
12. Yu. N. Zhugin, K. K. Krupnikov, in *Problems of nonlinear acoustics. Proc. of XI - th Int. (IUPAP-IUTAM) symp. on nonlin. acoust.* (Novosibirsk: Acad. Sci. USSR, Sib. Branch, 1987), part II, p. 196.
13. R. J. Hemley, A. P. Jephcoat, H. K. Mao, L. C. Ming, M. H. Manghnani, *Nature* 334, 6177 (1988) 52.
14. R. M. Hazen, L. W. Finger, R. J. Hemley, H. K. Mao, *Solid State Commun.* 72, 5 (1989) 507.
15. J. S. Tse, D. D. Klug, *Phys. Rev. Lett.* 67, 25 (1991) 3559.
16. Yu. N. Zhugin, *Abstr. of papers for "Geolog. systems synergetics" workshop* (Irkutsk: Inst. of the Earth's crust, RAS., Sib. Branch, 1992), p. 100.
17. K. J. Kingma, R. J. Hemley, H. K. Mao, D. R. Veblen, *Phys. Rev. Lett.* 70, 25 (1993) 3927.
18. M. S. Somayazulu, S. M. Sharma, N. Garg, S. L. Chaplot, S. K. Sikka, *J. Phys.: Condens. Matter* 5, 35 (1993) 6345, UK.
19. Yu. N. Zhugin, K. K. Krupnikov, N. A. Ovechkin, E. V. Abakshin, M. M. Gorshkov, V. T. Zaikin, V. M. Slobodenyukov, *RAN. Fiz. Zemli* 10 (1994) 16.
20. D. E. Grady, Yu. N. Zhugin, *Bull. Amer. Phys. Soc.*, ser. 2, 39, 1 (1994) 410.
21. Yu. N. Zhugin, in *Abstract Volume Limoges 1994, Third Int. Workshop, Shock Wave Behavior of Solids in Nature and Experiments* (Limoges, France, September 18-21, 1994), p. 73.
22. N. Binggeli, J. R. Chelikowsky, R. M. Wentzcovitch, *Phys. Rev. B. Condens. Matter* 49, 3-th ser., 4 (1994-I) 9336.
23. Yu. N. Zhugin, *Khim. Fizika* 14, 1 (1995) 69.
24. V. G. Vildanov, M. M. Gorshkov, V. M. Slobodenyukov, P. N. Senichev, *Khim. Fizika* 14, 2-3 (1995) 122.
25. Ya. B. Zeldovich, Yu. P. Raizer, *Physics of Shock Waves and High-Temperature Hydrodynamic Phenomena*. (Moscow, Nauka, 1966), p. 584.
26. G. E. Duvall, R. A. Graham, *Rev. Modern Phys.* 49, 3 (1977) 523.
27. Yu. F. Alekseev, L. V. Altshuler, V. P. Krupnikova, *Zh. Prikl. Mekh. Tekhn. Fiz.* 4 (1971) 152.
28. G. A. Adadurov, A. N. Dremin, S. V. Pershin, et al., *Zh. Prikl. Mekh. Tekhn. Fiz.* 4 (1962) 81.
29. *LASL Shock Hugoniot Data*, ed. S. P. Marsh (Berkeley: Univ. of Calif. Press, 1980), p. 499.
30. M. A. Podurets, G. V. Simakov, R. F. Trunin, *Izv. Akad. Nauk SSSR, Fiz. Zemli* 4 (1988) 28.
31. F. Hörz, in *Shock Metamorphism of Natural Materials* (Baltimore: Mono Book Corp., 1968), p. 243.
32. D. Stöffler, *Fortsch. Min.* 51 (1974) 256.
33. E. P. Gurov, D. P. Demenko, E. P. Gurova, *Dokl. Akad. Nauk SSSR* 280, 4 (1985) 983.

## COMPARISON OF THE EFFECTS OF LOADING ALUMINA IN SHOCK AND DETONATION WAVES

R. TRĘBIŃSKI, E. WŁODARCZYK, S. CUDZIŁO, A. MARANDA, J. NOWACZEWSKI, W. TRZCIŃSKI  
*Department of Armament and Aviation Technology, Military University of Technology, ul. Kaliskiego 2  
Warsaw 01-489, Poland*

### ABSTRACT

This work is a preliminary study of the effects of the detonative loading of  $\gamma$  alumina. Charges of mixtures of explosives and  $\gamma$  alumina were detonated in an explosion chamber. Estimated values of the detonation pressures varied within the range from 5 to 20 GPa. Solids remaining of explosions were extracted from the chamber and some minor impurities were removed by a chemical treatment. The phase composition analysis was accomplished by the use of the X-ray method. SEM images were used for the analysis of the changes of the topology of particles. For comparison, the characteristics of  $\gamma$  alumina loaded in a cylindrical container were determined.

### Introduction

Effects of loading ceramic powders in shock waves have been extensively investigated [1]-[6]. It was established that the shock loading introduces structural modifications and defect states highly activating the sintering. Effects responsible for enhanced activity of shocked powders are: point defects, dislocations, twinning, residual strains, particle comminution, reduction in crystallite size, structural phase changes and interparticle bonding.

All accessible data concerning the shock loading of ceramic powders concern the case of ceramic powders closed in metal containers and subjected to the action of an explosion or an impact. There are no data concerning the direct action of explosion on ceramic powders. This can be accomplished by a detonation of a mixture of an explosive and ceramic powders in a closed explosion-proof chamber ("detonative loading"). The detonative loading is used for producing fine diamond and  $\beta$ BN particles from carbonaceous materials and  $\alpha$ BN [7],[8]. Extensive investigations of the detonative synthesis of diamond and  $\beta$ BN have been carried out, but the effects of the detonative loading on other ceramic powders than carbonaceous materials and  $\alpha$ BN have remained unrecognised.

This work is a preliminary study of the effects of the detonative loading on  $\gamma$  alumina. We present results of investigations of changes of the morphology, size and phase composition of alumina particles which have undergone action of the detonation wave. For comparison, results obtained for alumina loaded by shock waves in closed cylindrical containers are also presented. Effects of the both types of dynamic loading are discussed on the basis of results of the mathematical modelling

of physical processes involved in the dynamic loading.

### Experiment

#### Loaded material

Commercially available, chemically pure  $\text{Al}_2\text{O}_3$  with mean particle size  $5\text{ }\mu\text{m}$  was used. The shape of the alumina particles is shown in Fig.1. The X-ray diffraction pattern (Fig.2) has wide, asymmetric peaks and elevated background. It proves that the crystalline structure is not well developed. Positions of peaks suggest that the structure of the initial material is  $\gamma$  alumina.



Fig.1. SEM image of the initial alumina.

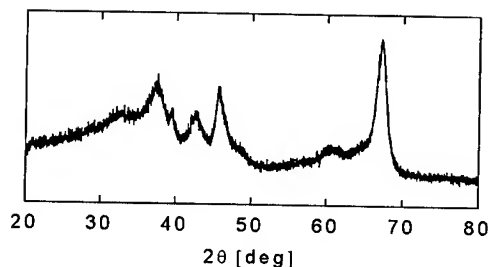


Fig.2. X-ray diffraction pattern of the initial alumina.

### Loading procedure

Plastic or pressed mixtures of explosives and alumina were detonated in an explosion chamber with a capacity of 0.15 m<sup>3</sup>. Estimated values of the detonation pressures varied within the range from 5 to 20 GPa. Solids remaining after explosion were extracted from the chamber and some minor impurities were removed by a chemical treatment.

The second loading procedure consists in the action of a convergent shock wave on alumina powder closed in a cylindrical container. The shock wave was generated by a detonation of an explosive charge surrounding the container. Two different explosives were used. Their detonation velocities were 3000 m/s and 6500 m/s.

### Effects of loading

The phase composition analysis was accomplished by the use of the X-ray method. SEM images were used for the analysis of the changes of the topology of particles.

At the modest loading level (5 to 10 GPa), significant changes of the topology of particles were discovered for powders loaded in the cylindrical containers - Fig.3. A large number of small scraps with rounded edges appeared. Larger particles also had rounded edges; however, their sizes approached the initial size.

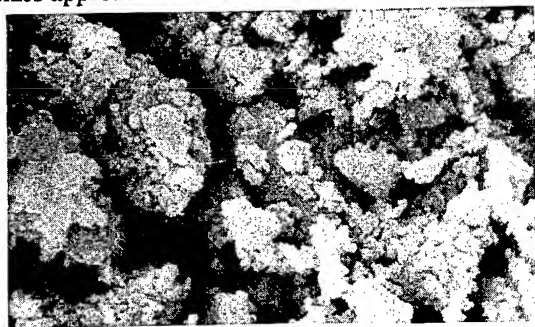


Fig.3. SEM image of alumina loaded in the cylindrical container at the modest level of loading.

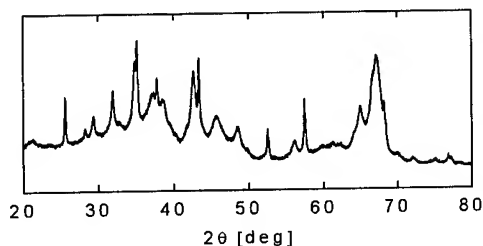


Fig.4. X-ray diffraction pattern of alumina loaded in the cylindrical container at the modest level of loading.

From the X-ray diffraction pattern (Fig.4) it can be deduced that a small amount of  $\alpha$  modification arose. Some evidence of the partial transformation into the  $\kappa$  phase was also obtained.

No changes in topology and phase composition were discovered for powders subjected to the modest detonative loading. This result shows that effects of shock loading described in the literature can be attributed to the complex deformation process during shock compacting of granular media rather than to the action of the hydrostatic pressure.

At the high level of loading (10 to 30 GPa) both methods caused the transformation of  $\gamma$  alumina into the  $\alpha$  modification - Fig.5. Differences in the X-ray patterns for  $\alpha$  Al<sub>2</sub>O<sub>3</sub> obtained in various conditions suggest that controlling the conditions may result in producing various defect states.

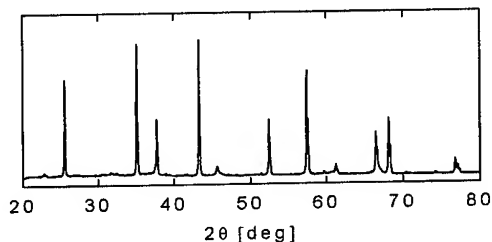


Fig.5. X-ray diffraction pattern of alumina loaded in the cylindrical container at the high level of loading.

Significant changes of the topology were discovered - Fig.6. Powders loaded in the cylindrical container were highly comminuted; however, large agglomerates of them were also seen. Very similar effects were discovered for powders obtained by detonative loading when plastic explosives were used.

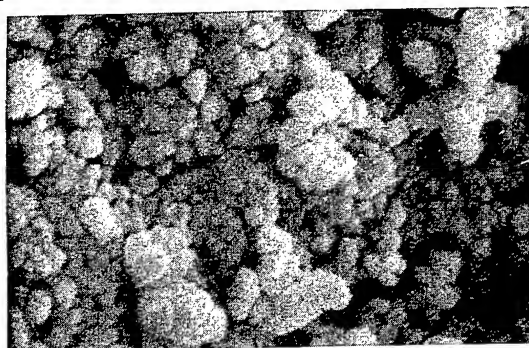


Fig.6. SEM image of alumina loaded in the cylindrical container at the high level of loading.

A different character of particle topology changes was discovered for  $\gamma$  alumina loaded during detonation of pressed charges - Fig.7. Spherical particles of the mean size of 5  $\mu\text{m}$  appeared. Agglomerates of those particles were also present.

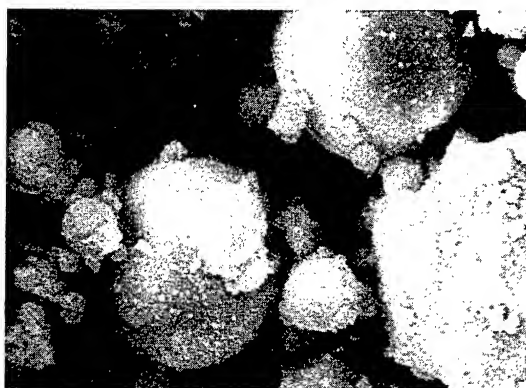


Fig.7. SEM image of alumina loaded by detonation at the high level of loading (pressed charges).

### Analysis

The pressure-temperature history of the loading material in the cylindrical container, as well as in the detonation process, was reconstructed on the basis of mathematical modelling. Pressure and temperature fields in shocked powder samples were calculated by a two-dimensional hydrodynamic code [9]. Evolution of the temperature field after unloading was determined by the modelling of temperature equilibration due to the heat conduction in a cylinder. For the detonative loading, the detonation parameters were calculated first by a thermochemical code. Then the process of expansion of a spherical cloud composed of gaseous detonation products and solid particles in a spherical chamber was modelled [10]. The temperature histories along paths of particles placed initially in various positions inside the cloud were determined.

The results of calculations showed that in the central parts of samples shocked in the cylindrical containers at the modest loading level, the temperature was higher than the  $\gamma$ - $\alpha$  transformation temperature for a time less than 100 ms. This explains a small degree of the transformation; for the high level of loading the temperature in the whole sample is high enough to cause the transformation.

During the expansion of detonation products, in the case of the decreased initial pressure of gas filling the chamber (applied for pressed charges),

the temperature of gases may reach several thousand of degrees K. Therefore the observed effects of the detonative loading in this case are caused by the action of the high temperature and ablation phenomena.

### Conclusions

1. Effects of comminution and changing of topology of alumina grains under detonative loading are much weaker than under action of shock wave propagating in a porous sample at comparable level of loading.
2. A modest shock loading of  $\gamma$  alumina causes a distinct change of the topology of grains and partial transformation into the  $\kappa$  phase.
3. Intensive loading in the cylindrical fixture causes transformation into the  $\alpha$  modification due to the high postshock temperature.
4. Observed effects of detonative loading are mainly caused by the thermal component of the loading. These effects can be enhanced by lowering the initial pressure in the blast chamber.

*The paper was prepared as a part of the project 7095499101 financed in the years 1991-1994 by the Scientific Research Committee.*

### References

1. J.Barrington, O.R.Bergman, US Patent 3367766, 16.06.1965.
2. J.Barrington, O.R.Bergman, *J.Am.Ceram.Soc.* **49** (1966) 502.
3. R.A.Graham, B.Morosin, E.L.Venturini, M.J.Carr, *Ann.Rev.Mater.Sci.* **16** (1986) 315.
4. T.Z.Blazynski, *Dynamically consolidated cpmposites: manufacture and properties* (Elsevier Applied Science, 1992).
5. N.N.Thadhani, *Progress in Materials Science* **37** (1993) 117.
6. R.A.Graham, N.N.Thadhani, in *Shock Waves in Material Science*, ed. A.B.Sawaoka, (Springer-Verlag, 1993) 35.
7. G.A.Adadurov, A.V.Ananin, T.V.Bavina et al, GB Patent 2090239, 9.07.1982.
8. R.Trębiński, W.Trzciński, E.Włodarczyk, *J.Tech.Phys.* **32** (1991) 219.
9. R.Trębiński, E.Włodarczyk, in *Proc. of HDP IV, Tours, France* (1995) 97.
10. R.Trębiński, W.Trzciński, E.Włodarczyk, *J.Tech.Phys.* **32** (1991) 199.

## PHYSICAL AND CHEMICAL TRANSFORMATIONS OF SERPENTINITE IN SPHERICAL STRESS WAVES

E.A.Kozlov, Yu.N.Zhugin, B.V.Litvinov, V.N.Kozlovsky, E.V.Abakshin,  
*Russian Federal Nuclear Center - Research Institute of Technical Physics,  
P.O. Box 245, 456770, Snezhinsk (Chelyabinsk-70), Russia*

D.D.Badjukov,  
*V.I.Vernadsky Institute of Geochemistry and Analytical Chemistry,  
Russian Academy of Sciences,  
117975, Moscow, GSP-1, Kosygin st., 19*

L.A.Ivanova, F.A.Letnikov  
*Institute of Earth's Crust, Siberian Branch of Russian Academy of Sciences,  
644033, Irkutsk, 33, Lermontov st., 128*

V.N. Anfilogov, E.V. Belogub, V.A. Kotljarov  
*Institute of Mineralogy, Ural Branch of Russian Academy of Sciences,  
456301, Miass-1, Chelyabinsk Region*

### ABSTRACT

Explosive experiments are described and the new results in addition to [1-2] are presented for the investigation into the mineral composition of the serpentinite decomposition products in the spherical hermetic ampoules of conservation undergone the loading by converging waves of different intensity.

### Introduction

Minerals of the serpentine group are the basic components of the matrix for carbonaceous chondrites-meteorites. The peculiarities investigations in the process of the serpentinite dehydration, amorphization, dissociation into the more simple chemical compounds in the stress waves of different amplitudes and durations can give a new information relative to the Earth's hydrosphere formation, including the oceans.

The equilibrium phase diagrams of rocks and minerals, used for constructing the equation of state which takes into account physical and chemical transformations in matter under finite pressures and temperatures, are studied in static as well as in shock-wave experiments [2,3].

The bends on the serpentine Hugoniot adiabat at  $\sigma_{xx}=40$  — 55 GPa and  $\sigma_{xx}=125$  GPa have been discovered in [3]. These features indicate the occurrence of several physical and chemical transformations in mineral under loading. However, the nature of these transformations is not revealed in such experiments.

The aim of this work is to analyse the mineral composition of the serpentinite decomposition products obtained in the hermetically sealed spherical ampoules of conservation by varying the amplitude and duration of the load pulse.

### Investigated material

Prior to its loading the serpentinite is the massive average-grainy rock of greenish colour with black embedments. In addition to serpentine in the rock composition there are magnesite (up to 10 per cent), dolomite (3 per cent) and magnetite (2-3 per cent). Antigorite with the perfect structure prevails in the initial serpentinite structure. The presence of lizardite as the admixture to antigorite is also substantiated by the XRD, TEM and DTA-DTG investigations.

The chemical formula of the pure (ideal) serpentine (chrysotile) is  $Mg_3Si_2O_5(OH)_4$  and its water content is 13.0 per cent by mass. The theoretical density of serpentine is equal to  $\rho_{ok} = 2.55$  g/cm<sup>3</sup>. The average density of the material investigated by us is 2.71 g/cm<sup>3</sup> as a result of the

above mentioned contaminations in the natural serpentinite sample.

#### Samples and the conditions of their explosive loading

For performing investigations two samples in the form of a full sphere with 48 mm diameter and the control samples have been cut out of the serpentinite lump. Prior to loading, these balls have been subjected to welding in vacuum ( $10^{-6}$  mm Hg) in the double pressure-sealed jackets of stainless steel 12C18N10T with the external diameters equal to 64 and 70 mm. After that, the first sample has been subjected to loading by the detonation of the spherical layer of high explosive of the type TNT/RDX (3/7) with  $\rho_{\text{exp}} = 1.72$  g/cm<sup>3</sup>, detonation velocity  $D = 8.05$  km/s, and calorific value  $Q = 5.466$  KJ/g. The explosive layer thickness  $h_{\text{exp}}$  amounts to 8 mm. The detonation initiation was realized on the radius  $R_{\text{exp}} = 40$  mm. The scatter of the explosion products has been restrained in this experiment by the case of lead and steel. The second sample has been subjected to loading by the converging detonation of the thinner layer ( $h_{\text{exp}} = 5$  mm) of the less powerful explosive-plasticized PETN with  $\rho_{\text{exp}} = 1.51$  g/cm<sup>3</sup>,  $D = 7.800$  km/s, and  $Q = 5.120$  KJ/g.

#### Methods and techniques used for investigations of recovered samples

Gamma-scscopy of the hermetically sealed balls before and after their explosive loading has been realized by using the stationary installation on the basis of the source Co-60 with radioactivity up to 12 Ci. The microphotometry of the shadow photographs and the restoration of the radial density distribution in the material of the compressed samples have been performed according to the method [1] analogously to [1,2].

Research of spherical shock wave recovered samples was carried out by Optical Polarization Microscopy (OPM), Scanning Electron Microscopy (SEM), Transmission Electron Microscopy (TEM), X-Ray Diffractometry (XRD) and Differential - Thermo - Gravimetric analysis (DTA-DTG).

#### Results

The external view of the equatorial sections and the enlarged photographs of the central regions of the serpentinite samples 1 and 2

undergone the spherical shock-wave loading of different intensity are presented in [2] as well as the computational & experimental evaluations of the radial density distribution for the compressed and conserved samples.

Cavities 6 mm in diameter are formed in the central zone of the recovered samples 1 and 2 of the initially homogeneous full spheres of serpentinite in the process of its loading by spherically converging shock waves of different amplitudes and durations [1,2]. These cavities are concentrically surrounded by the spherical layers of the matter having different densities, colours and composition. Results of OPM, SEM, TEM and XRD - investigations have been published in [2]. In this work new results of the differential thermogravimetric analysis are presented.

The thermal analysis has been performed on the derivatograph 0-1500. Conditions for registration are the following: sensitivity of DTA-250, DTG-500, TG-100, 50; weighted sample - 200-150 mg, rate of heating  $-10^{\circ}$ /min, inert substance-annealed  $\text{Al}_2\text{O}_3$ . Heating up to  $1000^{\circ}\text{C}$  is carried out in air using platinum crucibles. The endothermal effect resulting from the dissociation of magnesite is observed on the DTA curves for all the samples in the temperature interval  $410-640^{\circ}\text{C}$ . As for all the carbonates, the endothermal effect has an asymmetrical form in the TG curve and is followed by the loss of weight associated with the liberation of  $\text{CO}_2$ . The initial temperature of the magnesite decomposition is the initial temperature of the weight loss of the investigated samples, and the final temperature is the initial temperature of the serpentine decomposition. The content of magnesite (according to the  $\text{CO}_2$  quantity) is very non-uniform and it varies within 5.8-20 per cent.

The thermal effects of serpentinite in DTA curves are presented in the temperature interval from  $600$  to  $800^{\circ}\text{C}$  by the intensive endothermal effect which is stipulated for all the serpentines by the destruction of the crystal lattice with the simultaneous removal of structural water and by the exothermic peak in the crystallization of the new phases out of the decomposition products.

According to the DTA curves for the initial samples  $S_1$  and  $S_2$ , the investigated serpentine has been determined as antigorite with the small admixture of lizardite that is substantiated by the bifurcation of the endothermal effect and the



availability of the exothermic peak under 820-825° in DTA. The first sample was successfully investigated [2] over all the distinguished zones 1.1—1.7. This has not been made in a full volume for the second sample. The derivatographic curves have been obtained only for some zones. The samples 2.1—2.5 were chosen according to the following radii: (22-24 mm), (16-22 mm), (11-16 mm), (6-11 mm) and (5-6 mm). The performed analysis results are given in Table.

Table

Thermogravimetric analysis results

1	2	3	4	5	6
control samples	S <sub>init</sub>	17		12.8	
sample 1	1.1	—	—	—	—
	1.2	2.5	14.7	—	—
	1.3	14.5	85.3	5	39.1
	1.4	17	100	9	70.3
	1.5	17	100	10	78.1
	1.6	16.5	97.1	10	78.1
	1.7	14.5	85.3	10	78.1
sample 2	2.1	12.7	74.7	8.78	68.6
	2.2	12.5	73.5	10	78.1
	2.3	15	88.3	10.6	82.8
	2.4	14.5	85.3	9.6	75
	2.5	12.9	75.9	10.1	78.9

Note:

- 1- Sample number; 2- Test number (zone);
- 3 - Total loss of volatile substances in per cent;
- 4 - Total loss of volatile substances in serpentinite (in per cent from the initial one);
- 5 - Loss of H<sub>2</sub>O in serpentinite in per cent;
- 6 - Loss of H<sub>2</sub>O in serpentinite (in per cent from the initial one).

Structural water in the serpentinite composition is separated out in two stages: the first - in the interval of 600-700° C simultaneously with the destruction of the mineral crystal lattice, the second - under 800-900° C (approximately 0.4 per cent in the minerals with the perfect structure). In our case we operate with the total loss of weight.

Thus, in the sample 1 the most "dried" zones are the zones 1.7 — 1.5 (near the cavity) characterized [2] by the complete transformation of serpentinite into forsterite, enstatite and periclase. The dehydration degree and the

serpentinite structural perfection from other zones are changed along the recovered sample radius. In the sample 2 loaded less intensively, the zone 2.3 located at  $11 \leq r \leq 16$  mm is absolutely "dried", since only in this region the complete decomposition of serpentinite into forsterite, enstatite, periclase and tridymite is noted [2]. The dehydration degree will apparently depend here on the structural perfection of serpentinite along the radius of the loaded sample.

### Conclusion

It is shown [2] that in the described experiments the basic decomposition products of the serpentinite  $Mg_3Si_2O_5(OH)_4$  are forsterite ( $Mg_2SiO_4$ ) and enstatite ( $MgSiO_3$ ) in addition to water whereas in the decomposition region there are only trace concentrations of SiO<sub>2</sub> and MgO. The change of the transformation zones location along the radius of the recovered samples, their quantity as well as the completeness of physical and chemical transformations proceeding in them were analyzed by varying the intensity of the shock-wave loading and the subsequent thermal post-shock effects. The extent of the volatiles loss and, in particular, the hydration extent of magnesium silicates in each of the revealed transformation zones has been estimated.

The arising of the small well-edged crystals of enstatite practically free of admixtures and formed in glass voids has been discovered [2] when glass has been simultaneously enriched by the admixtures of iron and titanium which are the admixtures of the initial natural serpentinite. In studies of the serpentinite sample undergone the high-intensive impulse loading, the secondary (after unloading) serpentization absence of the physical & chemical transformation products of the initial rock material has been revealed. The given circumstance is apparently associated with the dissociation of water into hydrogen and oxygen under pressures, temperatures and energy densities achieved in the process of loading.

### References

1. E.A.Kozlov, Y.N.Zhugin, B.V.Litvinov et al., *Russ.J.Chem. Phys.* **14** (1995) N1, 108-118.
2. E.A.Kozlov, L.A.Ivanova, E.V.Belogub et al., *Russ.J.Chem.Phys.* **14** (1995) N 2-3, 68-96.
3. J.A.Tuburczy, T.S.Duffy, T.J.Ahrens, M.A. Lange, *J.Geophys.Res.*, **96** (1991) 18011.



## FREEZE-OUT OF CARBON MONOXIDE IN CALORIMETRY TESTS

F. H. Ree, W. J. Pitz, M. van Thiel, and P. C. Souers  
Lawrence Livermore National Laboratory  
P.O. Box 808, Livermore, CA 94550, USA

### ABSTRACT

The amount of carbon monoxide recovered from calorimetry tests of high explosives is far larger than the amount predicted by equilibrium calculations. The present analysis shows that chemical reactions which produce  $\text{CH}_4$  are the most important ones to lead to equilibrium below 1000 K but are effectively blocked by a rapid cooling of the calorimetric bomb. Furthermore, the reaction  $\text{CO} + \text{H}_2\text{O} \rightleftharpoons \text{H}_2 + \text{CO}_2$ , which is the key reaction at  $T > 1000$  K slows down at lower temperatures. The observed overabundance of CO is a direct consequence of both factors.

Calorimetry tests [1] provide data on detonation products and the heat of formation of high explosives. This is important to the understanding of the physics and chemistry of detonation processes. There is extensive experimental literature on calorimetry data. Carbon monoxide recovered from calorimetry tests of high explosives has been found to be always larger than the amount predicted by equilibrium calculations.[2] Previous practices to circumvent this dilemma are to "freeze" equilibrium codes along the release path of the Chapman-Jouguet (CJ) adiabat of explosives at some temperature to match with experiment. However, the resulting CO concentration differs significantly from equilibrium predictions. The exact mechanism that is responsible for this so-called "freeze-out" has so far remained somewhat of mystery.

To find out the exact cause for the overabundance of CO, we employed a state-of-art kinetic code[3] to simulate a time evolution of detonation products in a calorimetric test. We used the results coupled with equilibrium predictions based on the CHEQ code[4] to find out those reactions which can lead to equilibrium but are blocked by their slow reaction rates.

We will choose PETN (nitro oxymethyl propanediol dinitrate,  $\text{C}_5\text{H}_8\text{N}_4\text{O}_{12}$ ) as an example and simplify the calorimetry

bomb employed by Ornellas[1] as shown below:

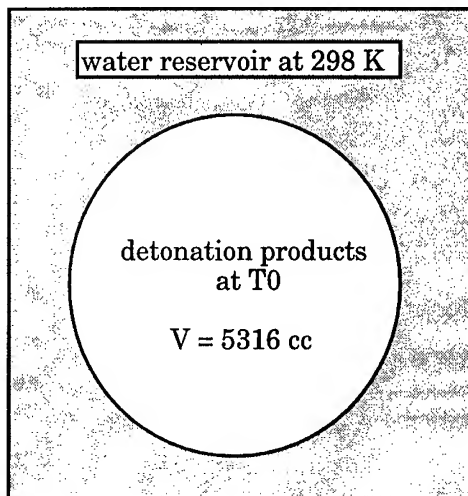


Fig. 1. Simplified geometry of calorimetry in [1].

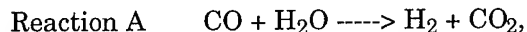
The volume  $V$  of the calorimetry bomb is large relative to the initial volume  $V_0$  of the explosive sample, i.e.,  $V/V_0 = 370$ . Detonation of PETN produces an adiabatically expanding rarefaction wave from the Chapman-Jouguet point. When the PETN/gold capsule reaches the wall of the bomb, the entire volume is filled with detonation products with average density of  $0.0047 \text{ g/cm}^3$ . The CHEQ code predicts at this point to be at 791 K and 9.3 atm. After hitting the wall of the bomb, the detonation products gains the internal

energy by transfer from the translational energy of the gas and their temperature jumps from 789 K to 2078 K. It takes less than 1 ms to reach this point. Detonation products in mole per mole of PETN are 1.63CO, 3.37CO<sub>2</sub>, 3.63H<sub>2</sub>O, 2.00N<sub>2</sub>, 0.407H<sub>2</sub>, 0.32CH<sub>4</sub>. Other products (NH<sub>3</sub>, NO, N<sub>2</sub>O, NO<sub>2</sub>, N, O, graphite, and diamond) included in the calculations are zero or negligible.

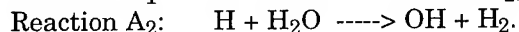
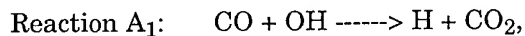
Our calculations with the HCT code[3] start from this point in time. The HCT code integrates the species conservation equations as a function of time. The gaseous mixture in the calorimetry bomb was treated as homogenous, so that no spatial variation in temperature, pressure and composition is considered. The chemical kinetic mechanism used included CO, CO<sub>2</sub>, H<sub>2</sub>O, N<sub>2</sub>, H<sub>2</sub>, CH<sub>4</sub>, O<sub>2</sub>, and 152 additional gaseous species and 1002 chemical reactions with rate constants expressed in an Arrhenius form. The present reaction mechanism neglects reactions leading to the solidification of carbon, as its coagulation rate is presently not well-known.

The calculations allow a convective heat transfer between detonation products within the calorimetry bomb and the water reservoir at temperature  $T_0$  with the total heat flow  $q$  given by  $q = h A (T - T_0)$ , where  $A$  is the surface area of the bomb and  $h$  is the convective heat transfer coefficient. The present calculation uses  $h = 30 \text{ watt/m}^2\text{K}$ . However, because of a turbulent nature of the expansion wave, the rate of convective cooling of the expanded detonation products is rather uncertain.

Figure 2 shows that CO slightly decreases during the first 4 seconds by the overall reaction,



which represents a pair of reactions,



The forward rate constant for Reaction A<sub>1</sub> has no kinetic barrier, while that for

Reaction A<sub>2</sub> is  $9.3 \times 10^8 T^{1.51} \exp(-18,580 \text{ cal/RT}) \text{ cm}^3/\text{mole}\cdot\text{sec}$  which will considerably slow down the reaction for temperatures below 1000 K.

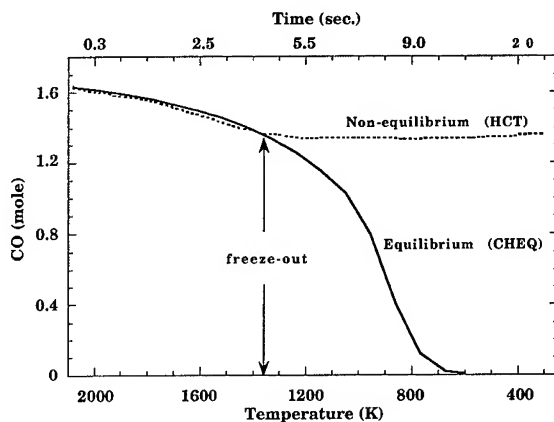
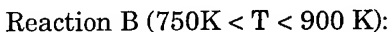
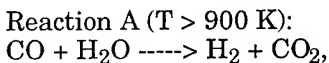
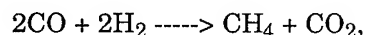


Fig. 2. Equilibrium and non-equilibrium CO concentration per mole of PETN.

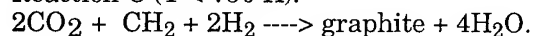
Figure 2 shows that the composition of CO remains nearly the same after 4 sec. The convective heat loss to the water reservoir causes a rapid cooling in temperature to 1350 K below which the rate constant for Reaction A becomes very small. At later time ( $> 4 \text{ sec.}$ ), the concentration of CO still changes but slowly and in very small amount ( $\approx 0.02 \text{ mole}$ ) until about 7 sec., or until the system cools down to about 1000 K. So, for all practical purposes, CO can be considered to be effectively frozen (i.e., quenched) below an "apparent" freeze-out temperature of 1350 K.

The equilibrium chemistry which takes place below the freeze-out temperature helps understand the nature of this phenomenon. If we assume that equilibrium is maintained throughout the isochoric cooling process, the composition of the detonation products traverses three separate temperature regions governing different equilibrium chemistry; i.e.,





Reaction C ( $T < 750 \text{ K}$ ):



Reaction A is the same reaction discussed earlier in connection with the HCT calculation. At  $750 \text{ K} < T < 900 \text{ K}$ , the equilibrium calculation predicts the formation of  $\text{CH}_4$ . The HCT calculation failed to produce  $\text{CH}_4$  in any observable quantity, suggesting that the equilibration time for Reaction B will be an astronomical time scale (!).

To form  $\text{CH}_4$  from CO requires the breaking of a double bond. This process requires reaction steps with very high activation energies (50 to 100 kcal/mole). Consequently, even though the formation of  $\text{CH}_4$  is favored thermodynamically, the reactants have insufficient energy to overcome the energy barriers to proceed to methane.

Figure 2 also shows a comparison of the CO concentration between the equilibrium (CHEQ) and non-equilibrium (HCT) calculations. Both data follow each other closely until temperature drops below the apparent freeze-out point (1350 K). Within this temperature regime, the kinetics (i.e., Reaction A) which can lead to an thermodynamic equilibrium state occurs very fast. Accordingly, the equilibrium assumption is valid here. However, deviations between the two grow rapidly below 1350 K. Reaction A slows down rapidly with temperature below 1350 K. This would have been less significant, had there been a kinetic pathway to Reaction B. Thus, we conclude that *the slowing-down of Reaction A and the absence of any realizable reaction path to create  $\text{CH}_4$  are the reason for the freeze-out phenomenon under consideration.*

In summary, the observed overabundance of CO is a direct consequence of a rapid cooling of the calorimetric bomb. The cooling effectively blocks all kinetic pathways leading to the formation of  $\text{CH}_4$ . Furthermore, reaction  $\text{CO} + \text{H}_2\text{O} \text{-----} \text{H}_2 + \text{CO}_2$  slows down considerably at temperatures below 1000 K. In view of several approximations

employed in this work, the result obtained here is in reasonable agreement with experimental data which indicate a freeze-out temperature of 1500 K to 1800 K and the CO concentration of 1.6 mole.

Finally, there is extensive experimental literature of calorimetry data on other high explosives. Their main constituents are C, H, N, and O atoms, as in the case of PETN. We expect that the same physics and chemistry will be responsible to cause the freeze-out of CO.

This work was done under the auspices of the US. Department of Energy at the Lawrence Livermore National Laboratory under Contract No. W-7405-Eng-48.

## References

1. D. L. Ornellas, *Calorimetric Determinations of the Heat and Products of Detonation for Explosives: October 1961 to April 1982*, Lawrence Livermore National Laboratory, Livermore, CA, UCRL-52821 (1982) and references quoted therein.
2. P. C. Souers and A. Nichols III, unpublished work.
3. C. M. Lund (revised by L. L. Chase), *HCT: A General Computer Program for Calculating Time-Dependent Phenomena Involving One-Dimensional Hydrodynamics, Transport, and Detailed Chemical Kinetics*, Lawrence Livermore National Laboratory, Livermore, CA, UCRL-52504 (1995).
4. F. H. Ree, *J. Chem. Phys.* **81** (1984) 1251.

## **XI(B)   Ultrahigh Dynamic Pressures, Equation of State**

## THE PRESSURE REGIME 10 - 750 MBAR: USE OF LASERS IN EOS MEASUREMENTS

R. CAUBLE, L. B. DA SILVA, B. A. HAMMEL, N. C. HOLMES,  
R. W. LEE, T. S. PERRY and D. W. PHILLION  
*University of California, Lawrence Livermore National Laboratory  
Livermore, CA 94550 USA*

### ABSTRACT

The use of intense lasers has long been proposed as a means to generate Mbar pressures in matter for the study of high energy density equations-of-state. This effort has been hampered by technology, mainly by the small spatial scales necessary to obtain the required high intensities and the inability to produce a uniform shock. Recently, the use of smoothed laser beams and indirect drive have led to the reliable production of uniform  $> 10$  Mbar shocks in solids over  $> 0.5$  mm surface. Direct laser irradiation can produce shock pressures up to  $\approx 30$  Mbar. Indirect irradiation using high-Z hohlraums can exceed 100 Mbar. Accelerated foils, where the driver is an indirect x-ray field produced by a kilojoule-class laser, have produced pressures of 750 Mbar. This opens the door to use high power lasers for EOS studies. It is predicted that a megajoule-class laser, such as NIF, will be able to produce energy densities an order of magnitude greater than these.

### Introduction

There is a great deal of uncertainty in equations-of-state for pressure regimes greater than a few Mbar, although there are many astrophysical and terrestrial problems involving this apparently extreme regime. In particular, one earthly example is the prediction of Gbar pressures in spherically compressed capsules typical of inertial confinement fusion targets.<sup>1</sup> In the limiting case of extremely high pressure, the EOS is described by a Thomas-Fermi model; however the regime of applicability and approach to this limit are not known, and, for metals, this model may not be valid for pressures under several Gbar.<sup>2</sup> Fig. 1 shows a plot of several EOS model principal Hugoniots for aluminum;<sup>3</sup> note the uncertainty in the Hugoniot for a metal long used as a standard in EOS measurements. The reason for this uncertainty is the limited amount of EOS data at pressures above  $\approx 3$ -4 Mbar because of the difficulty in producing high pressure conditions and simultaneously measuring relevant parameters. We consider here the use of high intensity lasers for achieving these conditions.

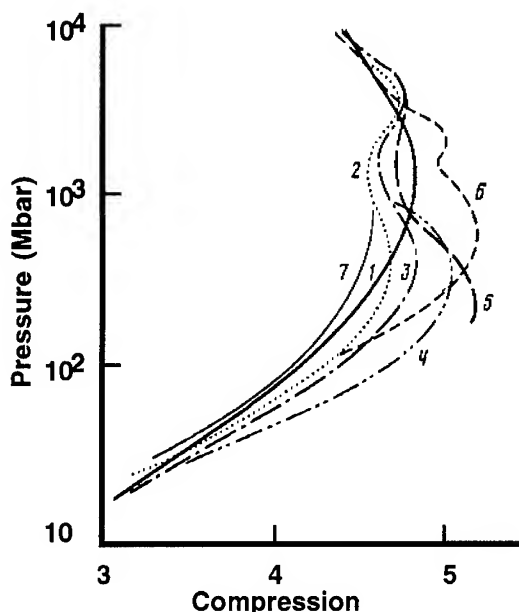


Figure 1. Plot taken from Ref. 3 showing aluminum Hugoniots predicted by seven currently-used EOS models. Note the considerable variation near one Gbar.

### Directly Driven High Pressure Shocks

It was recognized more than two decades ago that high intensity lasers would provide access to

multi-Mbar energy density regime. Dimensional arguments suggest that the pressure in a solid obtained by a laser driven shock can be estimated as<sup>4</sup>

$$P[\text{Mbar}] \approx 16 (I_{14} / \lambda_{\mu\text{m}})^{2/3},$$

where  $I_{14}$  is the laser intensity in units of  $10^{14}$  W/cm<sup>2</sup> and  $\lambda_{\mu\text{m}}$  is the laser wavelength in units of microns. Although this formula generally overestimates the pressure, it is readily seen that conventional lasers focused to high intensities can achieve multi-Mbar conditions. To be useful for EOS measurements, however, additional criteria must be met. It is desirable that the shock be planar, rather than in a convergent geometry, to make measurements and interpretation easier. The shock must be spatially uniform, steady on the timescale of the diagnostics and the initial material conditions accurately known (meaning that the material cannot be subject to preheat). Early attempts to use lasers as shock drivers for potential EOS experiments<sup>5</sup> met with the following problems: 1) the laser beam was not sufficiently smooth, thus structure in the beam drove unpredictable, highly modulated shocks into the material; 2) laser structure also produced hot spots which led to suprathermal electrons and high energy x rays which heated the material before shock arrival (preheat); and 3) high intensities required tight focusing and thus small laser spots ( $\approx 100 \mu\text{m}$ ) resulting in shocks that were not planar. Although pressures of 10 - 100 Mbar were detected,<sup>5,6</sup> all of the above difficulties compromised direct laser irradiation as an EOS tool.

The laser beam far field can be smoothed with the use of a random phase plate (RPP), dramatically reducing intensity structure and hot spots.<sup>7</sup> We have used a plate with hexagonal phase plate elements 3 mm in diameter producing a far field which is nearly an Airy pattern with a 1 mm zero-to-zero diameter and a characteristic speckle size of  $6 \mu\text{m}$ . Since such a sharply peaked spot would not provide the planar conditions needed in our experiment, steering

wedges were also used. The wedges steer different parts of the beam in the near field to different spots in the focal plane to produce a more flat-topped distribution. On the

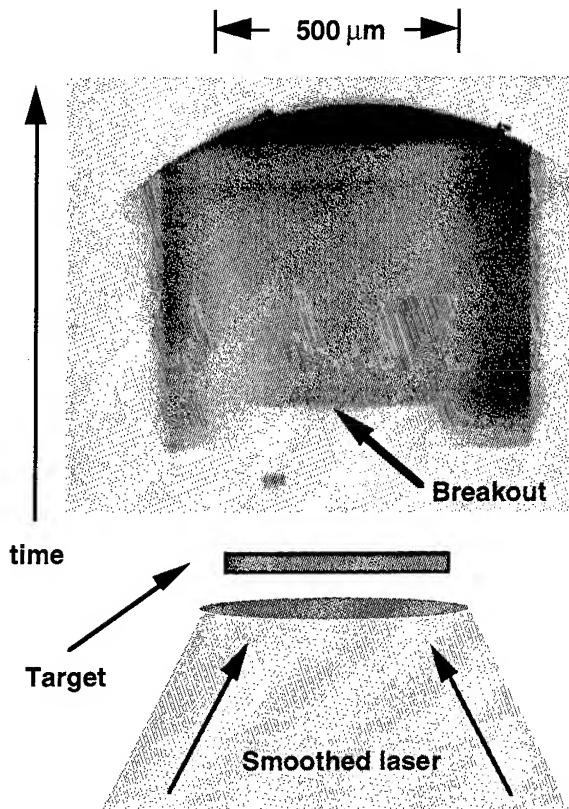


Fig. 2. Schematic of a directly driven laser shock breakout experiment and a streak image of breakout on the rear side.

Nova laser, intensities of  $3 \times 10^{14}$  W/cm<sup>2</sup> of  $0.53 \mu\text{m}$  light over 1 ns are possible with this arrangement. This intensity produces a shock of nearly 30 Mbar in aluminum. One mm is a sufficiently large spot so that a planar shock can be generated and observed. The use of the RPP and wedges reduces the probability of hot spot creation, but as a precaution we coated  $2 \mu\text{m}$  of plastic (CH) on the front of the sample in order to reduce the electron density in the ablation region. Preheat was further controlled by simply making the target material thick enough so that preheat and memory of the deposition region were lost by the time measurements were made.

Fig. 2 shows a streak of a shock breakout on the rear side of a 25  $\mu\text{m}$  thick aluminum disk; the image was made with a UV streak camera. Temporal variation of the breakout indicates that the shock is planar across the disk by less than  $1^\circ$ ; an extremely planar shock.<sup>8</sup>

### Indirectly Driven High Pressure Shocks

Using lasers, high pressure shocks can be created with excellent uniformity by converting the laser light to x rays by the use of a high-Z secondary target, such as a foil. The laser irradiates the foil which then emits x rays in a broad frequency band. Some energy is lost in the laser-to-x-ray-field conversion process so that drive intensity is sacrificed for drive uniformity. Much of the intensity can be recovered by irradiating the interior of a hohlraum instead of an open foil. Laser energy is deposited into a metallic cavity where it is absorbed and re-radiated; the resulting energy source has a broad-spectrum and is very uniform. Although much of the laser energy is lost to the walls of the hohlraum, the result is a radiation drive with near-black-body characteristics at effective temperatures of 100 - 300 eV.<sup>9</sup> The drive has been smoothed by interactions inside the hohlraum and is not at a single frequency, thus it is smoother than direct laser irradiation.<sup>10</sup> Shock pressures of more than 100 Mbar can be obtained with millimeter-scale cylindrical gold hohlraums irradiated by 25 kJ of 0.35  $\mu\text{m}$  light. Both direct drive and indirect drive can be used in impedance match EOS measurements: there is sufficient room to accommodate both the standard and the sample.

### Colliding Foil Experiments

Lasers can be used as drivers in a variation and miniaturization of the well known flyer plate technique.<sup>11</sup> In this method, the flyer, here a foil, stores energy from the driver over an acceleration time and delivers it rapidly as thermal energy in collision with another foil. In addition, the flyer acts as a preheat shield. This technique was

demonstrated using a laser in a directly driven arrangement to achieve pressures of more than 100 Mbar.<sup>12</sup>

However, directly driven foils have the same problems as discussed earlier with direct drive shocks. Recently, it was shown that even with a smoothed laser beam, micron-scale intensity fluctuations in the beam causes the foil, typically very thin, to break up on the scale of the fluctuations.<sup>13</sup> Thus the flyer foil becomes a set of streaming plasma jets.

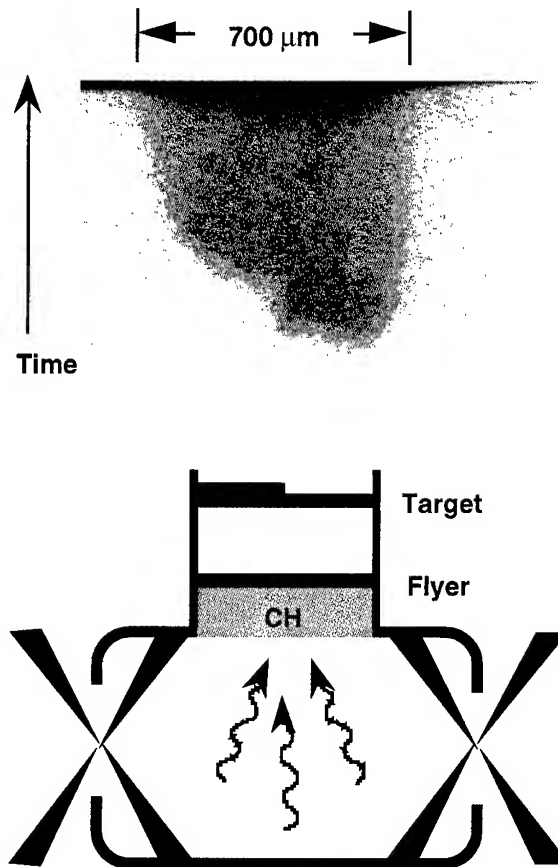


Fig. 3. Experimental schematic and a streak result of a hohlraum driven colliding foil experiment at Nova. The pressure inferred on the target was 750 Mbar.

A set of flyer foil experiments was conducted at Nova using a millimeter-scale gold hohlraum so that the flyer would be indirectly, rather than directly, accelerated.<sup>14</sup> The setup and a streak result are seen in Fig. 3. Shock uniformity was demonstrated by breakout measurements. The

hohlraum x-rays ablate a CH layer to which is attached a 3-mm-thick gold foil. This flyer foil accelerates through a void region and, near the end of the laser pulse and collides with a stepped stationary gold target foil.

The shock velocity was obtained by measuring the breakout on the two steps. The measured average shock velocity was  $70 \pm 6$  km/sec implying a density of  $90 \text{ g/cm}^3$  and a pressure of 0.75 Gbar in the target, which remains the highest planar pressure produced without the aid of a nuclear weapon. If the density of the flyer could be determined at impact, Hugoniot measurements could be made in this regime.<sup>14</sup>

#### Indirectly Driven Hugoniot Experiments on Polystyrene

Plastics are very different materials than aluminum or gold, but they are just as pervasive in ICF experiments as major constituents of spherical capsule targets. Since plastics, unlike metals, are largely transparent to high energy x rays, x rays can be used to backlight relatively thick samples of CH and provide information on the sample as a function of time. In particular, the

shock front in a sample of CH can be seen on a streak camera by simultaneously imaging the transmission of an x-ray backlighter through the shocked and unshocked material; the transmission through the denser, shocked CH is significantly less than through normal density CH (about 70% less for a compression of 4 in a 0.7 mm thick sample using a 7 keV backlighter energy). If, at the same time, motion of the material behind the shock can also be imaged, Hugoniot data can be directly obtained without having to compare to a standard.

An experimental arrangement which accomplishes this is depicted in Fig. 4. The material motion behind the shock is viewed as the difference in transmission of the backlighter through shocked, doped CH and shocked undoped CH; this is the interface shown in the figure. The drive is provided by a hole in the side of a gold hohlraum. Eight beams of Nova are used for the drive, saving two beams for the backlighter.<sup>15</sup>

Predicted shock pressure is controlled by varying the thickness of the doped CH layer. The regime from  $\approx 10$  Mbar to  $\approx 40$  Mbar has so far been explored. [Higher pressures have not yet been examined because the interface must be protected from preheat-causing x rays emanating from the hohlraum. Although the 2% bromine dopant in the first CH section serves as a preheat shield, predominant protection is provided by additional mass in a long first section. This means that the shock is decaying upon arrival at the interface. Measurements can be made with sufficient speed to obviate problems caused by the decaying shock.] The backlight beam was initiated near the time the shock arrived at the interface. It is necessary to view the shock as it passes through the interface as well as the interface as it picks up speed behind the shock front. This is because the shock speed and the interface speed will likely decay at different rates. Data from these experiments are still being analyzed. However, we expect there to be sufficiently clear results to be able to differentiate different EOS models.

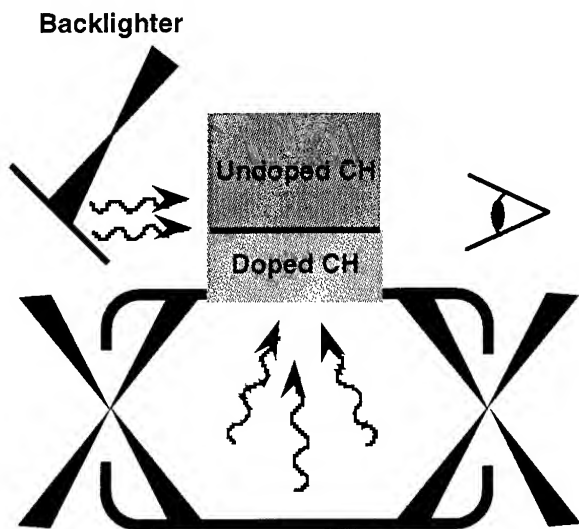


Fig. 4. Experimental setup for performing two parameter Hugoniot measurements on plastic. A streak camera records x-ray transmission showing shock and contact interface motion.



## Conclusions

Extremely planar shocks in the 10 - 30 Mbar regime by direct illumination of metals with highly smoothed beams. Indirect drive at high intensities can provide uniform shocks in the 100 Mbar regime. Indirectly driven colliding foils have demonstrated pressures near one Gbar. It is clearly possible to create extreme conditions in the laboratory and we have shown that it is possible to obtain relevant measurements under these conditions.

We can scale these results to a next-generation, megajoule-class laser, such as the National Ignition Facility planned for Livermore or the megajoule laser, planned for Bordeaux. Large-scale, hohlraum driven shocks will be possible with drive pressures near one Gbar. Pressures reached in a flyer foil experiment are predicted to be near 10 Gbar, an order of magnitude higher energy density than presently available in the laboratory.

## Acknowledgments

This work was performed under the auspices of the US Department of Energy under Contract No. W-7405-ENG-48.

## References

1. John D. Lindl, Robert L. McCrory, and E. Michael Campbell, *Physics Today* **45**, No.9, 32 (1992).
2. A. V. Bushman and V. E. Fortov, *Sov. Phys. Usp.* **26**, 465 (1984).
3. E. Avrorin *et al.*, *Sov. Physics JETP* **66**, 348 (1987).
4. Th. Löwer and R. Sigel, *Contrib. Plas. Phys.* **33**, 355 (1995).
5. L. R. Veaser and J. C. Solem, *Phys. Rev. Lett.* **40**, 1391 (1978); R. J. Trainor *et al.*, *Phys. Rev. Lett.* **42**, 1154 (1979); F. Cottet *et al.*, *Phys. Rev. Lett.* **52**, 1884 (1984).
6. N. C. Holmes *et al.*, in *Proceedings of 8th AIRAPT and 19th EHPRL Conference*, eds. C. M. Backman, T. Johannisson, and L. Thenér (Uppsala, 1981); F. Cottet, *App. Phys. Lett.* **47**, 678 (1985); J. D. Kilkenny, in *Laser Program Annual Report, 1986*, UCRL 50021-86 (1987), p. 3.
7. S. Skupsky *et al.*, *J. Appl. Phys.* **66**, 3456 (1989).
8. R. Cauble *et al.*, *ICF Quarterly Report* **3**, UCRL-LR-105821-93-3 (1993), p. 131.
9. S. Sakabe *et al.*, *Phys. Rev. A* **38**, 5756 (1988); G. D. Tsakiris and R. Sigel, *Phys. Rev. A* **38**, 5769 (1988); R. Sigel *et al.*, *Phys. Rev. A* **38**, 5779 (1988).
10. Th. Löwer *et al.*, *Phys. Rev. Lett.* **72** 3186 (1994).
11. L. V. Al'tshuler *et al.*, *Sov. Phys. JETP* **7**, 606 (1958).
12. S. P. Obenschain *et al.*, *Phys. Rev. Lett.* **50**, 44 (1983); R. Fabbro, *et al.*, *Laser Part. Beams* **4**, 413 (1986).
13. R. Cauble *et al.*, *Phys. Rev. Lett.* **74**, 3816 (1995).
14. R. Cauble, *et al.*, *Phys. Rev. Lett.* **70**, 2102 (1993).
15. B. A. Hammel, *et al.*, *Phys. Fluids B* **5**, 2259 (1993).

# PLASMA PHYSICS RESEARCH WITH SHOCK WAVES

ANDREW NG

*Physics Department, University of British Columbia,  
6224 Agricultural Road, Vancouver, B.C., V6T 1Z1, Canada*

## ABSTRACT

Shock waves driven by intense laser radiation have yielded a new avenue for plasma physics research in the interesting regime of strongly coupled plasmas. An overview is presented on several examples including the studies of plasma electrical conductivity, electron-ion coupling coefficient for thermal equilibration, and inner shell photoabsorption.

### I. Introduction

The advent of multi-megabar shock waves generated by laser-driven ablation in solids renders it possible to produce in the laboratory hot (few to tens of electron-Volts), dense (near to above solid densities) matter. This has led to the development of many experimental studies of the so-called strongly coupled plasmas (SCP) in which the Coulomb potential energy of the ions exceeds their thermal kinetic energy. Such strongly-interacting, many-body systems are of fundamental interest in plasma physics because the usual concept of charge screening and corresponding perturbative treatments can no longer provide a satisfactory theoretical description. They are also pertinent to research in other areas such as inertial confinement fusion, hypervelocity impact, and astrophysics.

In this paper, I will present a brief overview of laser-generated shock waves in solids for the production of strongly coupled plasmas and some sample studies on their properties including electrical conductivity, thermal equilibration, and inner-shell photoabsorption.

### II. Strongly coupled plasmas produced by laser-driven shock waves

The notion of strongly coupled plasmas is generally based on the concept of a One-Component Plasma which consists of a single species of ions immersed in a uniform background of neutralizing electrons. The effect of particle correlation is characterised by an ion-ion coupling constant defined as:

$\Gamma_{ii} = (Ze)^2 / R_0 k_B T$  where  $Z$  is the ion charge,  $e$  the electron charge,  $R_0$  the ion-sphere radius,  $k_B$  the Boltzmann constant and  $T$  the ion temperature. The plasma is said to be strongly coupled when  $\Gamma_{ii}$  exceeds unity, i.e., when the Coulomb energy of interaction among the ions exceeds their thermal kinetic energy. Since  $\Gamma_{ii}$  varies inversely proportional to the ion-sphere radius and the ion temperature, strongly coupled plasmas correspond to those with high densities but relatively low temperatures. This is precisely the regime that is readily attainable by intense shock waves in solids. As an example, Figure 1 shows the different regimes of aluminum over five decades of variations in temperature and density. Only relatively small portions of this temperature-density space are occupied by partially ionized plasmas (PIP), solid, or ideal plasmas (IP). The major portion bounded by the  $\Gamma_{ii}=1$  and  $\Gamma_{ii}=170$  contours is occupied by strongly coupled plasmas (SCP). Most interestingly, the range of in-between  $\Gamma_{ii}$  is traversed by the Hugoniot from 1 MBar to 10 GBar. Thus, it may be said that the physics of ultrahigh pressure shock waves is the physics of strongly coupled plasmas.

Although multi-GBar shock waves have only been demonstrated with nuclear explosions, shock

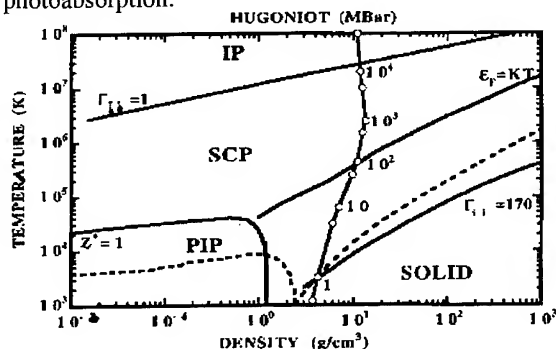


Figure 1: Phase diagram of aluminum.

pressures of nearly 1 Gbar [1] can be accessed using laser-produced shock waves via direct or indirect drives. Figure 2 shows a schematic of shock waves driven directly by laser deposition in a solid. Laser heating of the solid first produces a hot plasma which continues to absorb laser radiation by collisional (Inverse Bremsstrahlung) absorption. The resulting temperature gradient drives a heat flux into the solid causing ablation. As the ablated material expands into the surrounding vacuum producing a rocket-like exhaust, a strong shock is driven into the target by conservation of momentum. The process is similar for indirectly driven shock waves except that the laser radiation is first converted into x-rays which are deposited in the solid.

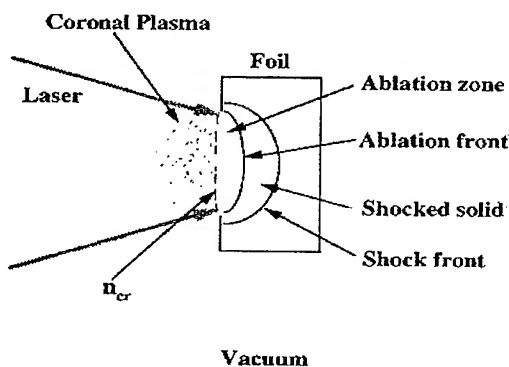


Figure 2: Schematic of laser-driven shock wave.

### III. Studies of plasma electrical conductivity I n shock release

The first example of using shock waves for the study of strongly coupled plasmas is the measurement of electrical conductivity in shock released states [2,3].

Transport properties such as electrical conductivity provide a critical test of our understanding of electron-ion collisions in a plasma. The Spitzer [4] and Braginski [5] formulae for conductivities are rigorously valid for fully ionized, non-degenerate plasmas. The electrical conductivity of a partially ionized, moderately coupled plasma has been computed by Rogers, DeWitt, and Boercker [6]. Their numerical results for argon and xenon showed much better agreement with observation than the Spitzer theory. The work of Sommerfeld and Frank on degenerate electrons was extended by Ziman [7] to

explain electron conductivity in liquid metal. The model also forms the basis of the Sesame tabulated data [8]. In 1984, a dense plasma model was described by Lee and More [9], in which transport coefficients were obtained from solutions of the Boltzmann equation in the relaxation time approximation and the effect of strong coupling was modelled using phenomenological cut-offs in the collisional mean-free-path and Coulomb logarithm. This became the stimulus for experimental tests in the regime of minimum conductivity predicted by the model.

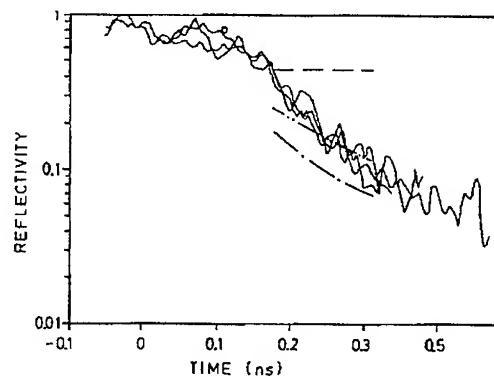


Figure 3: Reflectivity of a release wave in aluminum. Dashed line corresponds to calculations using the Sesame conductivity; dot-dashed and dot-dot-dashed lines are for Lee and More's dense plasma conductivity with minimum mean-free-path of ion sphere radius and diameter, respectively.

The methodology for measuring the electrical conductivity of a strongly coupled plasma was based on the reflectivity of the release wave at the free surface of a shocked solid. In the experiment, MBar shocks were produced by direct laser ablation of a foil target. The shock pressure was characterized from the shock speed derived from transit time measurements. The release of the shocked free surface was modelled using a 1-dimensional hydrodynamic code. The time-evolution in the reflectivity of the expanding plasma in the release wave was calculated [3] using WKB approximation [10] and Lee and More's dense plasma conductivity model. Figure 3 shows a comparison of theory and observation for the release of a nearly 4 MBar shock in aluminum. Temporal resolution of the reflectivity measurement using a 570 nm dye laser probe and a Hamamatsu C1370 streak camera was 10 ps. The conductivity model of Lee and More with the minimum electron mean-free-path limited to the ion

sphere radius or diameter appeared to show much better agreement than the Sesame tabular data. Similar agreement was found for measurements of shock release at about 7 MBar although significant discrepancies appeared for a 10 Mbar shock release [2]. Nonetheless, the study provided the first experimental test of conductivity models for strongly coupled plasmas.

#### IV. Thermal equilibration between electrons and ions in shock waves

Equilibration between electrons and ions is another basic process of fundamental importance in plasma physics. At the same time, the issue of thermal equilibration posts special significance in understanding shock wave physics. The general

treatment of a shock wave as a propagating discontinuity in pressure, density, and temperature considers only equilibrium states across the shock front, governed by the Rankin-Hugoniot relation of mass, momentum and energy conservation. However, it is also recognized that the transition from an unperturbed state to a shocked state occurs along a finite thermodynamic path influenced by various relaxation processes such as the thermal equilibration between the electrons and the ions. The existence of unequal electron and ion temperatures at the shock front not only complicates the theoretical treatment of shock waves but also impacts on the proper interpretation of pyrometric measurements of shock temperature.

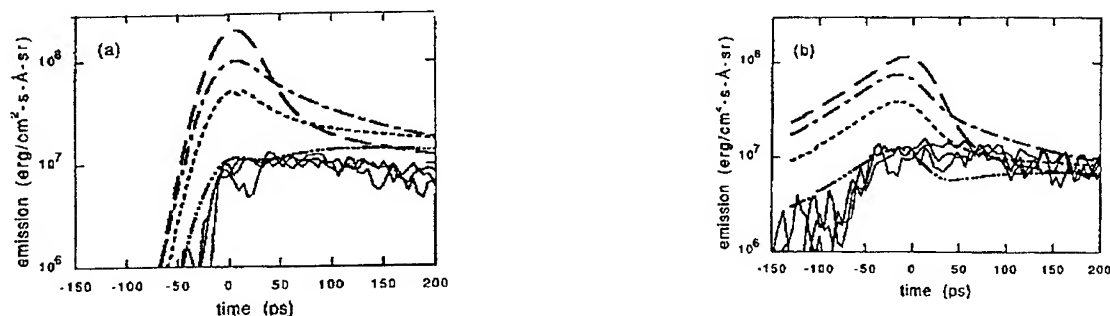


Figure 4: Intensity of emissions from a shock front in silicon. Dashed line corresponds to calculations using Spitzer Conductivity and the dot-dashed line using Lee and More's conductivity. The dotted and dot-dot-dashed lines are from non-equilibrium calculations with electron-ion coupling constants of  $10^{17}$  and  $10^{16}$  W/m<sup>3</sup>·K, respectively.

In this study [11,12], the approach is to produce a strongly coupled plasma in a shock compressed solid using laser-driven shock waves. The parameters of the plasma are derived from the observed shock speed together with a theoretical equation of state. The absolute intensity of optical emission from the shock front in-flight inside the solid is measured to yield a brightness temperature which is then compared with the theoretical Hugoniot temperature. The experiment is rendered viable using silicon. With a 1.2 eV bandgap, optical absorption in the unperturbed material is sufficiently low to allow the observation of the shock front inside the solid. Closure of the bandgap at about 120 KBar yields a

metallic state, which eliminates the need to treat kinetic effects associated with interband excitations. Examples of the observed shock emission intensities for a 6 MBar shock wave are shown in Figure 4. The lower absorption in cold silicon at the longer wavelength leads to earlier appearance of the shock emission.

Also shown in the figure are theoretical predictions assuming different conductivity models as well as different electron-ion equilibration rates. Details of the calculations have been described elsewhere [11,12]. The shock state represents a strongly coupled plasma where simple treatment of electron-ion interactions with Debye screening is not expected to be valid. Thus, it is not surprising that

single-temperature ( $T_e=T_i$ ) calculations using Spitzer conductivity show strong disagreements with data. However, substantial disagreement remains even when the dense plasma conductivity model of Lee and More is used. To assess the rate of energy equilibration between electrons and ions, we have used a simple relaxation-conduction model [11,12]. In the absence of theoretical calculations of the electron-ion energy exchange rate in strongly coupled plasmas, the corresponding coupling coefficient is left as an adjustable, constant parameter. The results presented in Figure 4 as well as similar measurements for shock waves of 3 and 5 MBar [11,12] suggested an electron-ion coupling coefficient of  $10^{16}$  W/m<sup>3</sup>K. This has yielded not only an experimental observation of non-equilibrium in a shock wave but also an assessment of the thermal equilibration process in strongly coupled plasmas.

#### V. K-shell photoabsorption in shock-compressed plasmas

While extensive shock wave research has been focused on the thermodynamic properties of high density matter, there exists few studies on the atomic properties such as the electronic structure, ionization state and ionization potential. Such atomic properties play a crucial role not only in plasma physics governing radiative opacities and transfer, but also in shock physics in the calculation of equation of state.

The first attempt to use the K-shell photoabsorption edge as a probe of the atomic properties of a dense plasma was reported by Bradley *et al.* [13] by observing the structure and position of the chlorine K-edge in radiatively heated and shock-compressed KCl embedded in a multi-layer target. Our approach [14] was to produce a dense aluminum plasma by a single laser-driven shock wave in a uniform target. The parameters of the plasma were derived from the measured shock speed coupled with an established equation of state. At pressures of several MBar in aluminum, the ionization state was limited to the valency of the simple metal and K-shell photoabsorption was a single-configuration transition.

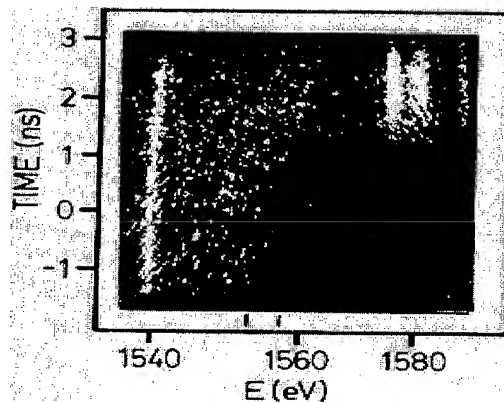


Figure 5: X-ray transmission spectrum through a shocked 25  $\mu$ m aluminum foil.

Details of the experiment have been described elsewhere [14,15]. Figure 5 shows the temporal history of the x-ray spectrum transmitted through a shock-compressed aluminum plasma during the 2.3 ns (FWHM) laser pulse which produces a peak shock pressure of 3.5 MBar and a corresponding maximum compression of 2.2. The unshifted position of the K-edge is at 1560 eV. Time zero corresponds to the time of peak laser intensity. A red-shift in the K-edge is clearly observed over a relatively long period before the shock wave reaches the target free surface (near time zero). The edge then shifts back towards its normal position at 1560 eV as the target is decompressed by shock release. The maximum red-shift observed is  $7 \pm 2$  eV. The variation of the shift in the K-edge as a function of compression is presented in Figure 6. Also shown in the comparison with the calculation from a Density Functional Theory model [16]. Neglecting 2-dimensional effects in the experiment, the prediction appears to be in good agreement with data.

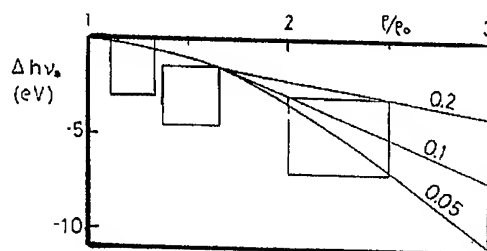


Figure 6: Shock-induced shift in aluminum K-edge as a function of compression.

## VI. Conclusions

The above examples illustrate some interesting applications of intense shock waves for plasma physics research. They are by no means exhaustive. As evident from Figure 1, ultrahigh pressure shock waves render ready access to an important regime of plasma physics, namely, the regime of strongly coupled plasmas.

On the other hand, it should be noted that the study of strongly coupled plasmas also impacts on the advance of shock wave research. For example, understanding of electrical conductivity leads to accurate modelling of thermal conductivity which is an important energy transport mechanism in shock waves. The issue of thermal equilibration between electrons and ions suggests the need for accurate two-temperature equation of state calculations. The atomic properties of dense plasmas will be crucial for the proper treatment of radiation transfer processes in the GBar regime.

## Acknowledgments

I am greatly indebted to the many important contributions of my colleagues, P. Celliers, G. Chiu, F. Cottet, L. Da Silva, A. Forsman, B.K. Godwal, P.A. Jaanimagi, Y.T. Lee, D.A. Liberman, R. M. More, D. Parfeniuk, M.C. Richardson, and G. Xu. This work is supported by the Natural Sciences and Engineering research Council of Canada.

## References

1. R. Cauble, D.W. Phillison, T.J. Hoover, N.C. Holmes, J.D. Kilkenny, and R.W. Lee, *Phys.Rev.Lett.* 70 (1993) 2102
2. A. Ng, D. Parfeniuk, P. Celliers, L. Da Silva, R.M. More, and Y.T. Lee, *Phys. Rev. Lett.* 57 (1986) 1595.
3. D. Parfeniuk, A. Ng, L. Da Silva, and P. Celliers, *Optics Commun.* 56 (1986) 425.
4. L. Spitzer and R. Harm, *Phys. Rev.* 89 (1953) 977.
5. S.I. Braginski, *Sov. Phys. JETP* 6 (1958) 358.
6. F.J. Rogers, H.E. DeWitt, and D.B. Boercker, *Phys. Lett.* 82A (1981) 331.
7. J.M. Ziman, *Philos. Mag.* 6 (1961) 1013.
8. Sesame Data Library, Los Alamos National Laboratory, Material Number 23713.
9. Y.T. Lee and R.M. More, *Phys. Fluids* 27 (1984)1273.
10. V.L. Ginsburg, *The propagation of electromagnetic waves in plasmas*, Chapter IV (Pergamon Press, Oxford, 1970).
11. P. Celliers, A. Ng, G. Xu, and A. Forsman, *Phys.Rev. Lett.* 68 (1992) 2305.
12. A. Ng, P. Celliers, G. Xu, and A. Forsman, to appear in *Phys. Rev. E* (1995).
13. D.K. Bradley, J. Kilkenny, S.J. Rose, and J.D. Hares, *Phys. Rev. Lett.* 59 (1987)2995.
14. L. Da Silva, A. Ng, B.K. Godwal, G. Chiu, F. Cottet, M.C. Richardson, P.A. Jaanimagi, and Y.T. Lee, *Phys. Rev. Lett.* 62 (1989) 1623.
15. B.K. Godwal, A. Ng, L. Da Silva, Y.T. Lee, and D.A. Liberman, *Phys. Rev.* A40 (1989) 4521.
16. F. Perrot and M.W.C. Dharma-wardana, *Phys.Rev Lett.* 71, (1993) 797.

# SHOCK WAVE MEASUREMENTS

NEIL C. HOLMES

*Lawrence Livermore National Laboratory, Livermore, CA 94550, USA*

Much of our knowledge of the properties of matter at high pressures, from the static ruby pressure scale to shock compression at Gbar pressures, rests ultimately on the use of shock waves. Simple conservation relations define the initial and final states, leading to absolute measurements. I will describe some methods for measuring the equation of state of materials under shock loading for a variety of methods of shock production, and also describe the basis for other optical methods used widely in shock physics.

## 1 Introduction

The ubiquitous use of shock waves in high pressure physics may be due to the fact that shock waves are easy to generate, but more importantly because the final state of the shocked material can be determined absolutely through measurement of the initial conditions and kinetic variables. The Rankine-Hugoniot relations express the conservation of momentum, mass, and energy:

$$P - P_0 = \rho_0 u_s u_p \quad (1)$$

$$\rho = \rho_0 \left(1 - \frac{u_p}{u_s}\right)^{-1} \quad (2)$$

$$E - E_0 = \frac{1}{2}(P + P_0)(V_0 - V) \quad (3)$$

where  $P, \rho, E$  refer to the final shock pressure, density, and internal energy;  $P_0, \rho_0 \equiv 1/V_0, E_0$  are the initial pressure, density, and energy, respectively. The propagation velocity of the shock is  $u_s$ , and the velocity of the material behind the shock, the mass velocity, is  $u_p$ . Measurement of  $\rho_0$ , and any two of the variables  $P, E, \rho, u_s, u_p$  determine the final shock state. In practice, it is easiest to determine  $u_s$  and  $u_p$ ; this paper describes methods for these measurements for a variety of typical shock environments.

We will describe temperature measurements, for we note that Eq. 3 only gives the change in total energy, and the partition function for its distribution among the internal and external degrees of freedom is unspecified. Temperature measurements have proven invaluable in studies of phase changes and deserve special treatment. A large body of work has also developed using a variety of electrical gauges embedded in, or adjacent to, the materials of interest. I've chosen not to discuss

these in this brief report, and refer the interested reader to other sources.<sup>1</sup> In fact, the scope of shock measurements is so broad that only a sketch of the field can be attempted here.

Before describing the measurement techniques, a brief description of shock generation methods is in order. These divide naturally into impact and ablation methods. In the impact method, a plate of material is made to impact onto another at high velocity, producing a shock wave. Both high explosive and gun techniques are in this class. In the ablation method, a sample of material is rapidly heated to a very high temperature. This causes the material to expand rapidly into the surrounding material, producing a shock wave. Lasers and nuclear explosions are examples of this method of shock generation. The ablation methods are capable of achieving the highest pressures, while impact experiments generally offer the greatest opportunity for high absolute accuracy. In this paper, I will limit my discussion to impact experiments, since the methods for ablatively driven experiments are more challenging to perform (and to describe!), and are still under development.

## 2 Measurements of $u_p$

When a shock passes from one material to another, the pressure and mass velocity are continuous across the interface. In the simplest impact experiment between identical materials, the mass velocity of the generated shock is just  $u_p = u_i/2$ , where  $u_i$  is the impactor velocity. So a precise measurement of the impactor velocity allows us to find  $u_p$  easily. This is usually accomplished using flash x-radiography<sup>2</sup>, lasers, or magnetic coils to find the time required for the projectile to traverse a known distance. This quantity can be measured

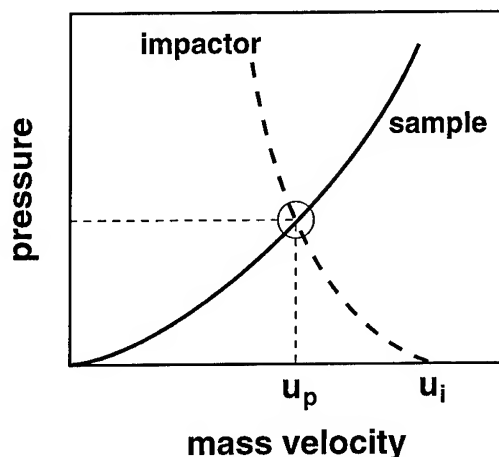


Figure 1: Finding the value of  $u_p$  for an impact of dissimilar materials using impedance-matching. The impactor velocity is  $u_i$ . The intersection the Hugoniot of the impactor and sample expresses continuity across the boundary of pressure and mass velocity for the point at  $(P, u_p)$ , denoted by the small circle.

to an absolute accuracy of  $\approx 0.1\%$ . In many high-explosive experiments, the free-flight distance is too small to permit these methods. In that case, spaced pins are used which protrude through the sample to measure the projectile velocity by contact. When the impact is between dissimilar materials, we must know the Hugoniot of the two materials. Since  $P$  and  $u_p$  are continuous across the interface, the Hugoniot of each material will intersect in the  $P$ - $u_p$  plane at a point which satisfies Eq. 1 for each material. This is depicted graphically in Fig. 1 by the intersection inside the small circle. Finally, if the sample has an unknown Hugoniot, a measurement of the shock velocity in the sample provides the necessary additional information to find  $u_p$ . In this case the intersection is between the known impactor Hugoniot and a line of slope  $\rho_0 u_s$  (in the sample). These methods are the basis for determination of the Hugoniot equation of state of solids and liquids.

The motion of the interface between two shocked materials may also carry important additional information. The elastic and plastic properties of the material behind the interface between a sample and transparent window can be studied by recording the velocity history (wave profile) of the interface as a shock traverses the assembly. Such records are used to determine elastic lim-

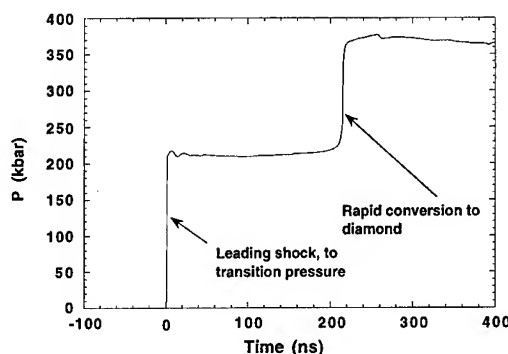


Figure 2: Wave profile for a shock in pyrolytic graphite. The shock is parallel to the  $c$ -axis. The step in the leading edge indicates the martensitic graphite-diamond phase transition.

its, phase transition behavior, the effects of release waves, and many other phenomena. Usually a form of laser interferometry is used, and the motion of the interface is determined by measuring the time-varying Doppler shift of a laser source.<sup>3</sup> For example, we show in Fig. 2 the wave profile of a shock generated in pyrolytic graphite.<sup>4</sup> The step in the leading edge indicates the graphite-diamond phase transition. Two such measurements carried out at different levels in a sample will yield the values of  $u_s$ ,  $u_p$ , and the wave profiles. This allows a solution to Eqs. 1-3 to determine the final state parameters.

### 3 Measuring Shock Velocity

Shock velocities are usually measured using electric or optical methods. As an example of the electrical method, we will describe the method developed by Mitchell,<sup>5</sup> since it is both intuitive and produces highly accurate results. In this method, shock arrival at two planes on the rear surface of a sample is detected by electrical shorting pins in contact with the sample. With most impact experiments, the shock can be made steady, so for an inter-plane distance and time of  $\Delta x$  and  $\Delta t$ , respectively,  $u_s = \Delta x / \Delta t$ . The value of  $\Delta x$  is usually found using some form of interferometric system to provide better than  $1 \mu\text{m}$  accuracy over mm dimensions. The pins are arranged in two circular arrays of six pins, with an additional pin on the center, as shown in Fig. 3. When a planar shock arrives with tilt angle  $\theta$  and with angular phase  $\phi$  relative to the array, it introduces a time



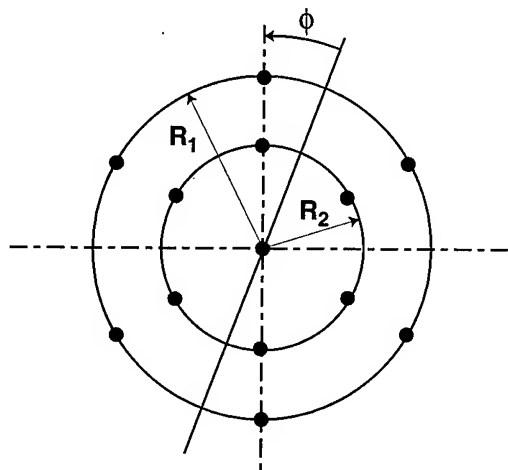


Figure 3: Layout of pin circles for shock velocity measurements. 13 pins are arranged in two circular arrays of radius  $R_1$  and  $R_2$  of six pins each and a centered pin. The two arrays are located on two stepped planes on the rear surface of the target, and the centered pin is on the same level as the outer pin circle. The shock arrives with phase  $\phi$ .

delay across the outer pin circle  $\tau = R_1 \sin \theta / u_s$ . The arrival times of the pins on the two circular arrays vary as  $\tau \cos(\pi n/3 + \phi)$  for the outer array, and  $\Delta t + (R_2/R_1)\tau \cos(\pi n/3 + \phi)$  for the inner array, where  $n = (1, 2, \dots, 6)$  refers to the pin locations on the arrays. Least-squares fitting is used to find the values of  $\tau$  and  $\phi$ . An attractive feature of this method is that each pair of opposed pins have the same average shock arrival time, which allows a simple check of the consistency of the data. The center pin is used to correct for the typically small parabolic distortions of the impactors in high-velocity gun experiments.<sup>6</sup> In practice, fast oscilloscopes with real-time sweep calibration or digitizers can be used to record shock arrival signals with an accuracy of  $\leq 0.5$  ns, leading to overall accuracies in shock velocity of typically 0.5 %.

In recent years, we have developed optical methods of performing the same kind of measurement using fast electronic streak cameras. The method is a hybrid between the technique initially developed for laser shock experiments<sup>7</sup> and the pin methods with corrections for tilt and distortion. In this method, we use light generated at or behind the shock front to detect shock arrival. Instead of circular arrays, we record the image of the shock arrival across a diameter of the sam-

ple. In the case of strong shocks or highly porous materials, the light emitted by the shocked sample is sufficient,<sup>8</sup> and in other cases an indicator fluid such as benzene or bromoform can be used in contact with the sample rear surface. At pressures above about 10 GPa, these hydrocarbons react and dissociate, have temperatures of  $\geq 2500$  K, and are efficient light sources. The streak camera used must have a real-time sweep calibration, which we have performed using mode-locked Ar<sup>+</sup> lasers. These methods have the advantage in that they allow very compact samples, no contact is needed with the sample, and that they are at least as accurate as pin methods.

#### 4 Temperature Measurements

As we noted above, Eq. 3 does not yield information about the temperature of the shocked material, yet temperature is an explicit variable in many models of material response at extreme conditions. The temperature of a shocked material is extremely sensitive to phase changes, chemical reactions, dissociation, ionization, and so on. It is of vital importance in understanding the state of the shocked material. For most shocked materials, the temperature is unknown, but significant progress has been made during the last decade. The short time scale of shock experiments, typically less than  $10^{-6}$  s, make electrical measurements impractical, so we employ optical methods. We assume that the emission is of grey-body character, and spectroscopic measurements usually confirm this. This means that measurements of the radiance of the shocked material at multiple wavelengths can be used to determine the temperature using the Planck formula:

$$I(\lambda) = \epsilon \frac{2\pi hc^2}{\lambda^5} \left( \exp \frac{hc}{\lambda k_B T} - 1 \right)^{-1}, \quad (4)$$

where  $I$  is the radiance,  $\epsilon$  is the emissivity,  $\lambda$  is the wavelength,  $T$  the (Kelvin) temperature,  $h$  is Planck's constant,  $c$  the velocity of light, and  $k_B$  is Boltzmann's constant. This is rather simple to perform in initially transparent materials, since the material ahead of the shock front does not interfere with the measurement, and the emission can be recorded in real time as the shock traverses the sample. While imaging systems have traditionally been used to collect and record the

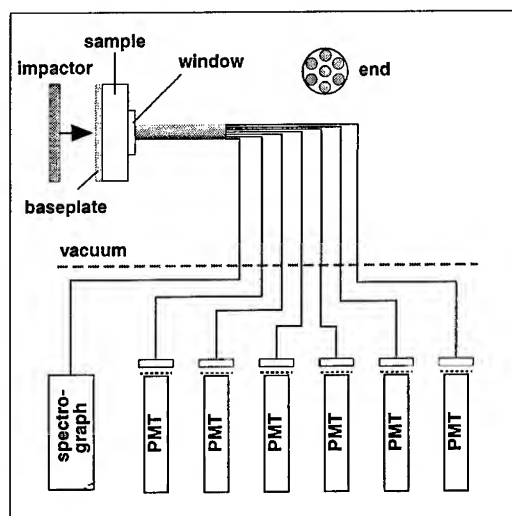


Figure 4: Optical pyrometer for shock experiments featuring fiber-optic coupling to an array of detectors.

shock emission, the use of fiber-optic methods developed by Holmes provide increased sensitivity, time-resolution, and eliminates geometric effects which can obscure the time dependence of the emission.<sup>9</sup> This is shown schematically in Fig. 4. When calibrated against a radiance standard, such as a tungsten (W) ribbon lamp, it is possible to determine the temperature and the emissivity of the shocked material. However, it is important to note that any variations of emissivity with wavelength at these extreme conditions have to be determined by other means. When one desires to determine the temperature of an opaque material, such as a metal, the situation is much more complicated. In this case, the temperature is measured at the interface between a window and the metal. Since the interaction of the shock with the window will generally alter the pressure and temperature, corrections must be included. Furthermore, heat conduction across the interface can introduce yet another uncertainty. Even so, this method has proven valuable to determine, for example, the melting temperature of Fe at Earth core conditions.<sup>10</sup>

### Acknowledgments

I am indebted to my colleagues at Livermore and elsewhere for teaching me about the methods and challenges of shock physics. In particular, spe-

cial thanks are due W. J. Nellis, A. C. Mitchell, and R. J. Trainor. This work was performed by Lawrence Livermore National Laboratory under the auspices of the U. S. Department of Energy under Contract No. W-7405-ENG-48.

### References

1. see, for example, D. Bernstein, C. Godfrey, A. Klein, and W. Shimin, *Behavior of Dense Media Under High Dynamic Pressures*, Gordon and Breach (New York, 1968); François Bauer, in *Shock Waves in Condensed Matter*, Y. M. Gupta, ed. Plenum (New York, 1986, p. 483 ff.
2. A. C. Mitchell and W. J. Nellis, *Rev. Sci. Instrum.* **52**, 347 (1981).
3. L. M. Barker and R. E. Hollenbach, *J. Appl. Phys.* **43**, 4669 (1972).
4. D. J. Erskine and W. J. Nellis, *Nature* **349**, 317 (1991).
5. A. C. Mitchell and W. J. Nellis, *J. Appl. Phys.* **52**, 3363 (1981).
6. A. C. Mitchell and W. J. Nellis, *Rev. Sci. Instrum.* **52**, 347 (1981).
7. L. Veaser and J. Solem, *Phys. Rev. Lett* **40**, 1391 (1978).
8. N. C. Holmes, *Rev. Sci. Instrum.* **62**, 1990 (1991).
9. N. C. Holmes, *Rev. Sci. Instrum.* **66**, 2615(1995).
10. C.S. Yoo, N.C. Holmes, M. Ross, D.J. Webb, and C. Pike, *Phys. Rev. Lett.* **70**, 3931(1993).

# WIDE-RANGE EQUATION OF STATE

N.N.KALITKIN

*Institute for Mathematical Modelling, Russian Academy of Sciences  
Miusskaya sq. 4-A, Moscow, 125047, RUSSIA*

## ABSTRACT

A wide-range equation of state (EOS) under extreme conditions TEPHYS is based on three models: 1) the model of ionization-chemical equilibrium with the microfield correction for nonideality at low densities; 2) the quantum-statistical model for highly compressed matter; 3) the quasi-band model for intermediate densities. This EOS has a good accuracy 1-2% above critical parameters; it is more precise in this region than the famous SESAME library.

### The problem of accuracy

Equations of state (EOS) have always been important in physics and technology. They are an essential part of hydrodynamic codes used for applied problems. Wide-range EOS (WREOS) are especially valuable.

Many attempts were undertaken to construct WREOS on a basis of the only theoretical model (for example, [1-3]). Of course statistic models gave poor accuracy up to 50% because they didn't account effects of shell structure. But till now shell models as [3] had an error up to 20-40% in some regions of temperatures and densities, though they described shell effects qualitatively.

That is why WREOS of good accuracy are usually constructed by the *shred cover* method, i.e. by using different models and interpolating them onto the boundaries of their application fields; some of them are based also on experimental data at modest pressures and temperatures. The well known examples are the WREOS libraries SESAME (Los-Alamos National Laboratory) [4] and VOLNA (*a wave*, Chelyabinsk-70) [5]. The first one contains at least 10 different models, 6-7 of them for an extreme conditions region (see Fig.1, where italic letters denote SESAME models and thin dashed lines are lines of sewing; thick solid lines correspond to phase transitions, thick dashed lines are the main Hugoniot and one of isentrops).

The library TEPHYS [6] is described below. It is based on three models in all: the ionization-chemical equilibrium with microfield nonideality,

the quantum-statistical model and the quasi-band interpolation (see Fig.1, where normal letters denote these models and thin solid lines are

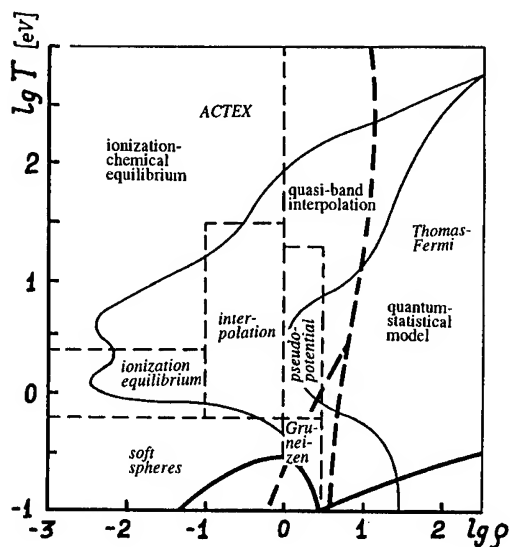


Fig.1. EOS for Al

boundaries of interpolation). Nevertheless these models are so precise that the accuracy of WREOS is 1-2% in overcritical region; this is essentially better than for any other library. Experimental data using improves this WREOS in undercritical region.

### Gas-plasma mixtures

Equations of ionization-chemical equilibrium (ICE) are well known. They may be easily

derived from a free energy  $F$  expression [7]. They contain the shift of ionization potentials

$$\Delta\varphi_{ik} = \left( \partial / \partial x_{ik} - \partial / \partial x_{i,k-1} - \partial / \partial x_e \right) \Delta F, \quad (1)$$

where  $\Delta F$  is a correction for nonideality, and  $x_{ik}$ ,  $x_e$  are concentrations of ions of  $i$ th kind with charge  $k$  and electrons respectively. Many different theoretical expressions  $\Delta F$  were proposed for weakly nonideal plasma. But it was shown [7] that they all are not adequate to experimental data for strongly coupled plasma.

A quite new approach was proposed [8]. A heat motion of charged particles in plasma gives birth to an electric microfield. Theoretical models for this microfield are known; they are improved in [8]. The microfield leads to a certain shift  $\Delta\varphi_{ik}$ . Then integration of differential equations (1) gives the value of  $\Delta F$  [8].

This *microfield nonideality model* (MFN) agrees with experiments even for strongly coupled plasma. It explains as thermodynamic so optical properties. For example, it gives numbers of electron levels occupation which agree with numbers of spectral lines observed in dense plasma. It describes not only thermal ionization, but also ionization by compression at low temperatures.

ICE with MFN model is applicable even for dense substances if temperature is large enough (Fig.1). It predicts shell effects in thermodynamics: oscillations of Hugoniot curves, etc. (Fig.2). These oscillations are sharp at low densities and smooth when density increases.

### Superdense substance

It is well described by the quantum-statistical model (QSM) [2], which is an improvement of the Thomas-Fermi model [1] by the quantum and exchange corrections. This model doesn't contain shell effects, but they are very small for enormous densities. The reason is that bands (or quasi-bands) of electron spectrum become so wide that neighbour bands conjoin and an electron spectrum becomes continuous [9].

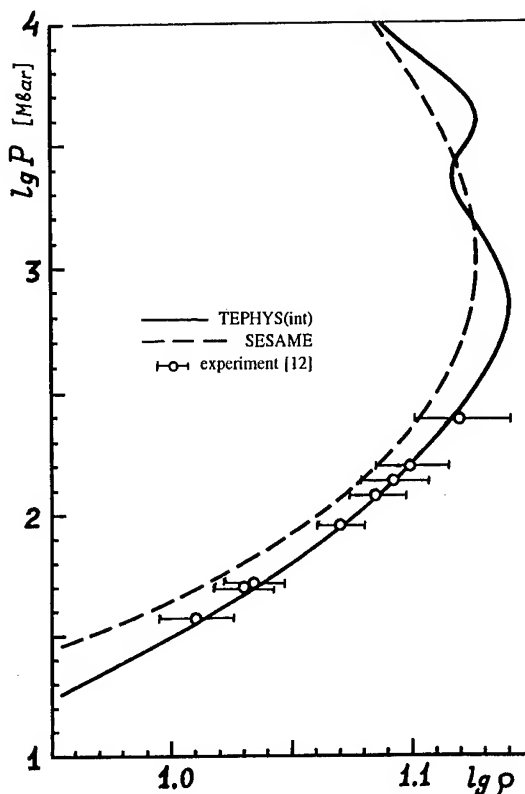


Fig.2. The main Hugoniot for Al

Heat motion of nuclei contributes significantly to thermodynamic functions. A model of *oscillating nuclei* (MON) was developed (see [9]), when outer electrons considered as free ones, and ionic cores oscillate near equilibrium points in the electric field of outer electrons. MON improved agreement with experiments for condensed matter.

### Quasi-band effects

They are essential at intermediate densities. Bands are specific forms of electron spectrum for crystals, when atoms have a strict order. But in dense medium at high temperatures atoms are in heat motion; that leads to quasi-bands instead of bands [9]. For low densities quasi-bands become narrow and turn into usual electron levels; then equation of state corresponds to the ICE. For

enormous densities quasi-bands conjoin to continuum, as described above.

A simple method of EOS calculation in this field is a quasi-band interpolation between ICE with MFN and QSM. Coefficients of this interpolation depend on a microfield shift of ionization potentials and a structure of atomic shells.

This interpolation joins the ICE and QSM and gives wide-range EOS.

### Fitting to experiments

These results may be improved using shock wave data from experiments with explosives [10,11], as it was done in [4,5]. For example, this gives such approximations for the main Hugoniot curves above the turning point but below the second oscillation:

$$D = c + b \cdot u + a \cdot u^2 \quad (2)$$

where coefficients for Fe and Cu are the next:

subst.	c km/s	b	a s/km	u km/s	accuracy
Fe	3.590	1.850	-0.0344	1÷9.474	0.8%
	6.688	1.196	$9.5 \cdot 10^{-5}$	9.474÷300	0.8%
Cu	3.926	1.502	-0.00845	0÷18.03	0.3%
	6.703	1.194	$9.3 \cdot 10^{-5}$	18.03÷330	0.3%

Results are seen from Fig.2,3. Experiments in underground nuclear explosions [12,13] were not used for fitting. A good agreement with them confirm that this wide-range EOS is precise and the most reliable in overcritical region.

### Acknowledgements

This work was supported by Russian Foundation of Fundamental Researches, grant ТЕФИС №93-01-00861.

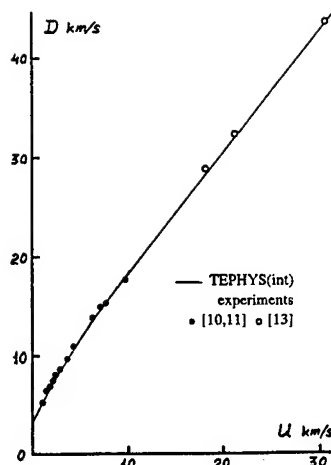


Fig.3. The main Hugoniot for Fe

### References

1. R.P.Feynman, N.Metropolis, E.Teller, *Phys. Rev.* **75** (1949) 1561.
2. N.N.Kalitkin, L.V.Kuzmina, *Sov. Plasma Phys.* **2** (1976) 858.
3. B.F.Rozsnyai, *Phys. Rev. A* **5** (1972) 1137.
4. R.M.More, J.F.Barnes, R.D.Cowan, *Bull. Am. Soc. II*, **21** (1976) 1153.
5. V.F.Kuropatenko, *Sov. Mathem. Modeling*, **4** (1992) №12, 112.
6. N.N.Kalitkin, *Sov. Metals* (1993) №3, 78.
7. I.O.Golosnoy, N.N.Kalitkin, V.S.Volokitin, *Sov. Izvestia Vuzov, Fizika* (1994) №11, 23.
8. *ibid*, (1995) №4, 11.
9. N.N.Kalitkin, *Sov. Mathem. Modeling* **1** (1989) №2, 64.
10. LASL shock Hugoniot data, *Univ. Calif. Press* (1979).
11. Properties of condensed substances at high pressures and temperatures, *Russ. Inst. Exp. Phys.* (1992).
12. E.N.Avrarin et al., *Sov. Phys. JETP* **93** (1987) 613.
13. R.F.Trunin, *Sov. Uspekhi Fiz. Nauk* **164** (1994) 1215.

# MICROFIELD MODELLING IN NONIDEAL MULTICOMPONENT PLASMAS

I.O. GOLOSNOY

*Institute for Mathematical Modelling, Miusskaya sq. 4-A,  
Moscow, 125047, Russia*

E-mail: golosnoy@imamod.msk.su

## ABSTRACT

The new model of ionic microfield in multicomponent plasma (MSHO) for the case of neutral test particle was constructed. The analytic approximation for microfield distribution (MAPEX) based on well-known model APEX was obtained. Merging these two models we obtain the wide-range microfield model. It is both extremely fast and very accurate and it is suitable for multiply computations of microfield distribution in calculating some properties of matter.

## Introduction

Many investigation of Equation of State and some other properties of matter at high pressure are made by dynamical methods. Intense shock waves, generated in that experiment, produce a dense matter at extremely high pressure. The conditions of that hot, high compressed plasmas are determined by spectra methods.

Ionic microfield distribution in dense plasmas has long been of interest in plasma spectroscopy and astrophysics since spectra line shapes are determined essentially by the influence of fluctuating plasma microfield which acts on plasmas particles. Recently some new methods based on microfield have been obtained for determination of transport properties of dense plasmas. Moreover, investigations fulfilled during the last few years indicate that the thermodynamic properties of plasmas (energy levels occupation, equation of state) depend on plasma microfield too. Therefore it is very important to know the ionic microfield distribution function in a wide range of densities and temperatures.

We are interested in probability density  $p(E)$  for microfield intensity  $E$  near a test particle with the charge  $Z_0$ .  $N$  ions and  $N_e$  electrons of plasma are immersed in a volume  $\Omega$  at a temperature  $T$ . We assume that ions moving in a uniform neutralizing background of electrons (so-called one component plasmas - OCP). Let us denote  $x_k = N_k/N$  for a concentration of ions with charges  $Z_k$  and  $x_e = N_e/N$  for an electronic concentration.

We can define the mean radius of ionic cell  $R$  and parameter of nonideality  $\Gamma$  from formulas:

$$(4\pi/3)NR^3 = \Omega, \quad \Gamma = e^2/(RT).$$

It is now customary to calculate  $p(E)$  by means of approximations of the corresponding generating functional  $Q(l)$ ,

$$p(E) = (2\pi/E) \int_0^\infty \sin(lE) Q(l) l \, dl, \quad (1)$$

where the Fourier transformation of  $p(E)$  is

$$Q(l) = \langle \exp(i\mathbf{l}\mathbf{E}) \rangle. \quad (2)$$

The angular brackets in (2) denote a canonical ensemble average over configurations weighted with a Boltzmann factor,  $\mathbf{E}$  denotes the electric field on the test particle due to any configuration.

For calculating the electric microfield distribution function  $p(E)$  at a charged ion a convenient model has been proposed (APEX, [1]). However, APEX is less accurate for microfield distribution at a neutral atom ( $Z_0=0$ ) in strongly coupled plasma ( $\Gamma>3$ ). Corrections to APEX for the case  $Z_0=0$  (APXC) were presented in [2] and the agreement of APXC with Monte-Carlo calculations for  $\Gamma<10$  is quite good. However, in [2] it is emphasised that APXC will not be very accurate for very large  $\Gamma>10$ . Moreover, APEX and APXC are rather complicated.

## Microfield model

A simple model for microfield distribution function at a neutral atom in strongly coupled plasma (MSHO) is presented in this paper. MSHO is the modification of simple harmonic oscillators model (SHO, [3]).

The SHO approximation is valid for the case  $Z_0 > 0$  when  $\Gamma > 10$ . Close collisions are neglected in SHO because the charged ion repels the field particles. But just these collisions form the "tail" of the microfield distribution at a neutral atom. That is why SHO is not valid for the case of  $Z_0 = 0$ .

Let us consider the case  $Z_0 = 0$ . Divide the matter by the cells. One ion is immersed into the each cell. We assume that ions execute the harmonic oscillations near their equilibrium. The neutral test particle  $Z_0$  is moving free from the matter. In the present model we assume that the electric field on the  $Z_0$  is the sum of two parts. The first part is the field of the centre ion. The second part is the mean field of other ions. This mean field is taken from the following assumptions:

1. It have to provide the harmonic oscillations of  $Z_k$  with the frequency from SHO model.

2. The sum of the mean field and the field of  $Z_k$  is zero at the boundary of the cell. That is why we approximate the mean field by the simple formula:

$$\mathbf{E}_m = -\mathbf{r} x_e e / R^3.$$

The cells of ions with different charges  $Z_k$  have the different sizes. The radius  $R_k$  for  $Z_k$  is taken from the electric neutral of the cell:

$$R_k = Z_k^{1/3} x_e^{-1/3} R. \quad (3)$$

So, the sum field in the cell is

$$\mathbf{E}_k = \left[ \frac{Z_k (\mathbf{b} - \mathbf{y})}{|\mathbf{b} - \mathbf{y}|^3} - x_e \mathbf{b} \right] \frac{e}{R^2}, \quad 0 \leq y, b \leq R_k / R. \quad (4)$$

The average (2) is calculated independently at each cell with taking into account the formulas (3), (4).

Consider the limiting cases. When  $\mathbf{b} \approx \mathbf{y}$ , than  $E \rightarrow \infty$  and  $l \rightarrow 0$ . The main part of microfield is produced by the nearest particle in this case. Then we can consider the relative motion of  $Z_0$  and  $Z_k$  and assume  $\mathbf{y} = 0$ . The result is:

$$Q(L) = 3 \sum_k x_k \int_0^{(Z_k/x_e)^{1/3}} db b^2 \frac{\sin\{L(Z_k/b^2 - bx_e)\}}{L(Z_k/b^2 - bx_e)}, \quad (5)$$

where  $L = le/R^2$ .

If  $E \ll e/R^2$  it means that  $L \gg 1$ . Then the main contribution to  $Q(L)$  is given by the region which near the boundary of the cell, because of in this

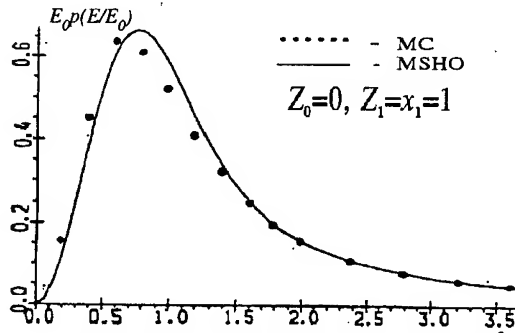


Fig.1.  $p(E)$  as a function of  $E$  for  $\Gamma = 10$ ,  $E_0 = e/R^2$ .

region  $E_k$  is near the zero. The probability to locate of the centre ion  $Z_k$  near the boundary of the cell is very small. So we can assume that  $y \ll b \approx R_k$ . That is why we expand the first part of (4) in a power series of  $y$ :

$$\frac{(\mathbf{b} - \mathbf{y})}{|\mathbf{b} - \mathbf{y}|^3} \approx \frac{(\mathbf{b})}{b^3} - \mathbf{y} \left\{ \frac{1}{b^3} - 3(\mathbf{b}) \frac{\mathbf{b}}{b^5} \right\}. \quad (6)$$

Substitution the formula (4) with expansion (6) into (2) and some manipulations for the limiting case  $L \gg 1$  result to the following expression:

$$Q(L) = 3 \sum_k x_k \int_0^{(Z_k/x_e)^{1/3}} \frac{\sin\{L(Z_k/b^2 - bx_e)\}}{L(Z_k/b^2 - bx_e)} \times \exp\left(-\frac{L^2 Z_k}{2x_e \Gamma b^6}\right) b^2 db. \quad (7)$$

The investigation of asymptotics for  $L \ll 1$  and

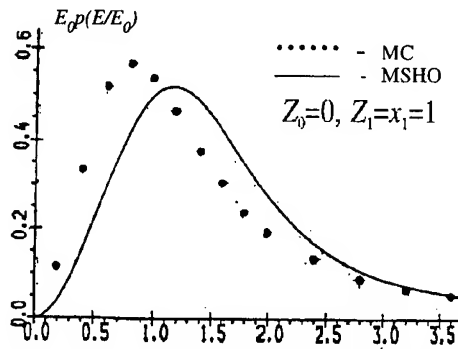


Fig.2.  $p(E)$  as a function of  $E$  for  $\Gamma = 3.9$ ,  $E_0 = e/R^2$ .

$L \gg 1$  of (5) and (7) allows to construct the simple approximation (MSHO) which connect the limiting cases:

$$Q(L) = 3 \sum_k x_k \exp \left[ -\frac{L^2 Z_k}{x_e \Gamma} \right] \times \\ \times \int_0^{(Z_k/x_e)^{1/3}} db b^2 \frac{\sin \{ L(Z_k/b^2 - bx_e) \}}{L(Z_k/b^2 - bx_e)}. \quad (8)$$

## Results and approximations

Comparison of  $p(E)$  and  $Q(l)$  calculations over MC [2,4] and MSHO a given in Fig.1,2. The approximation (8) gives good results in the case  $\Gamma=10$ . When  $\Gamma$  decreasing the accuracy of (8) is fell off (Fig.2 for  $\Gamma=3.9$ ). Thus MSHO is suitable for plasmas with  $\sum Z_k^2 x_k \Gamma > 10$  in the case  $Z_0=0$ . However, APEX is quite good for  $Z_0 > 0$ , all  $\Gamma$  and for  $Z_0=0$ ,  $\sum Z_k^2 x_k \Gamma < 10$ . Merging two models: MSHO and APEX, we obtain the wide-range microfield model for OCP plasmas. We propose a simple analytic approximation (MAPEX) for the Fourier transform of  $p(E)$  obtained from APEX.

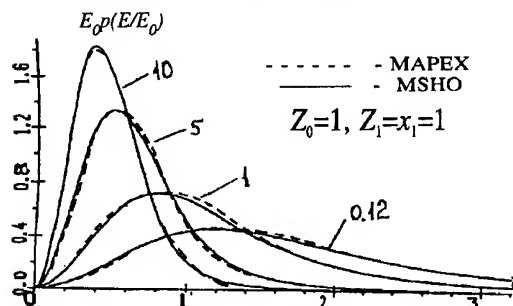


Fig.3. Same as Fig.1 for different  $\Gamma$ . The value of  $\Gamma$  is shown near the curves.

MAPEX can be applied to a multicomponent plasma with any degree of nonideality. It differs from the test MC calculations no more than the error of APEX method. Besides MAPEX requires thousand-fold less calculation time then APEX.

We approximate  $Q(l)$  by the following formula (MAPEX):

$$Q(L) = \exp \left[ -\sum_k x_k W_k(L) \right],$$

where  $W_k(L)$  depends on composition, density and temperature of the plasma and on the charge  $Z_0$  of the test particle:

$$W_k(L) = (Z_k L)^{3/2} \chi_k^{-1},$$

$$\chi_k = 0.5 \alpha (L Z_k)^{1/2} + \beta_k (1.2 + 0.8 \beta_k (1 + \beta_k^{1/2})^{-2}), \\ \alpha = 0.637 (3 \Gamma x_e)^{1/2} Z_s \arctg \left[ 2.418 (3 \Gamma)^{-1/2} (x_e^{1/2} Z_s)^{-1} \right], \\ \beta_k = \Gamma Z_k Z_0 (L Z_k)^{-1/2}, \quad Z_s = \left( \sum_k x_k Z_k^2 \right)^{1/2}.$$

The  $p(E)$  calculated by MAPEX and MC methods for various nonideality parameters  $\Gamma$  are compared in Fig.3. It can be seen that the MAPEX has an excellent accuracy.

The MSHO and MAPEX models have been used for calculating the opacity of Al [5]. One can see (Fig.4) that the models obtained drive to

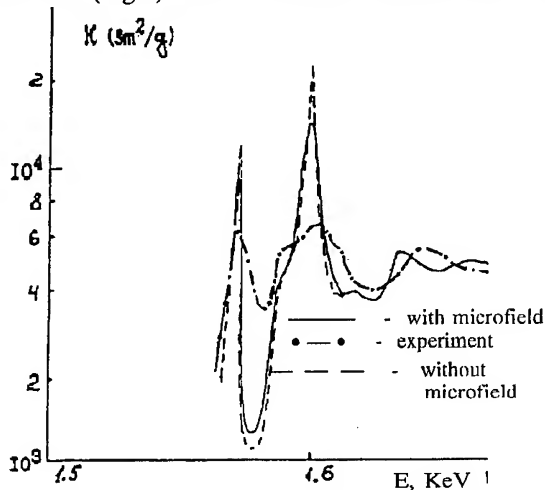


Fig.4. The opacity of Al at  $T=18$  eV,  $\rho=0.05$  g/cm<sup>3</sup>.

the better fitting to experiment [6].

## Acknowledgements

This work was supported by Russian Foundation of Fundamental Researches, Grant № 93-01-00861.

## References

1. C.A.Iglesias, J.L.Lebowitz, *Phys.Rev.A.* **30** (1984), 2001.
2. J.W.Duffy, D.B.Boercker, C.A.Iglesias, *Phys. Rev.A.*, **31** (1985), 1681.
3. A.D.Selidovkin, *Teplofizika visokih temperatur (USSR)*, **6** (1968), 10.
4. A.Alastuey, J.L.Lebowitz, D.Levesque, *Phys. Rev.A.*, **43** (1991), 2673.
5. O.B.Denisov, I.O.Golosnoy, N.Yu.Orlov. *Mathematical Modelling (Russia)*, **6** (1994), 3.
6. S.J.Davidson et al., *Appl.Phys.Lett.*, **52**, (1988), 847.



## MEASUREMENT OF NEAR-MBAR SHOCK FRONTS IN CRYSTALS BY X-RAY DIFFRACTION

N. C. WOOLSEY, A. ASFAW, R. W. LEE, J. S. WARK\* & R. CAUBLE

*University of California, Lawrence Livermore National Laboratory Livermore, CA 94550*

*\*Department of Physics, Clarendon Laboratory, University of Oxford Oxford OX1 3PU, UK*

### ABSTRACT

A highly uniform, near-Mbar shock can be created in a test material by laser-irradiating a secondary target to create a soft x-ray radiation source, which then drives the shock. If the test material is a crystal, the strain profile within the crystal can be dynamically examined by x-ray diffraction. The soft x-radiation source heats a thin layer of the crystal; ablation of this layer then produces the uniform shock. We discuss how x-ray diffraction can be used to give information on the strain profile within a shock-compressed solid. The x-ray diffraction technique is described and experimental data are compared to simulated diffraction records.

### Introduction

There are two main approaches to studying materials at high pressure. One method is to compress the solid isotropically, the other is to compress the solid rapidly in a shock wave. Static measurements are currently limited to pressures below 6 Mbar.<sup>1</sup> At these pressures a large array of diagnostic tools (mechanical, x-ray, optical, and electrical) have been applied to investigate the nature of the compressed state. X-ray diffraction has been used to determine the lattice structure and this has been related to the mechanical, electrical and optical properties of the solid. Using shock waves, pressures significantly higher than static pressures are obtainable. However, the difficulty in diagnosing the compressed state has become severe due to the dynamic nature of the experiment. Successful mechanical, optical and electrical studies of the compressed state have been made, this has driven the development of models based on constitutive relations and continuum mechanics.<sup>2</sup> Fundamental questions about which atomic mechanisms are important and their role in, for example, inelastic deformation, microscopic defects, phase changes still need to be addressed. This limited understanding is largely due to the lack of data.

Quintin Johnson and colleagues were the first to obtain x-ray diffraction images from shocked solids.<sup>3</sup> They demonstrated that a solid retains its crystalline

structure as it is rapidly compressed and later provided the first direct evidence of a shock induced phase transition through x-ray diffraction.<sup>4</sup>

Synchronizing an explosively driven shock with a pulsed, high brightness x-ray source is problematic and has hindered further development of the technique. Here we describe an experimental technique which eliminates the synchronization problem by utilizing a laser to create both the compression wave and the x-ray source.<sup>5</sup>

In the past we have directly irradiated single crystals with a laser to create an abrupt pressure pulse, and then probed the compressed solid with x-rays emitted from an independent plasma created by a second synchronized laser beam. High power lasers are prone to large non-uniformities in their beam profiles, which result in non-planar shocks. This problem is addressed in the current experiments by removing the laser from the shock generation process and instead using a soft x-ray source. X-rays from this near Planckian x-ray source volumetrically heat a thin layer of the crystal. Ablation of this heated layer launches a shock into the cold material. The experiment is depicted in Fig 1.

### The Experiment

Five beams of the Nova laser are focussed into a 1 mm diameter spot on a 2000 Å thick free standing

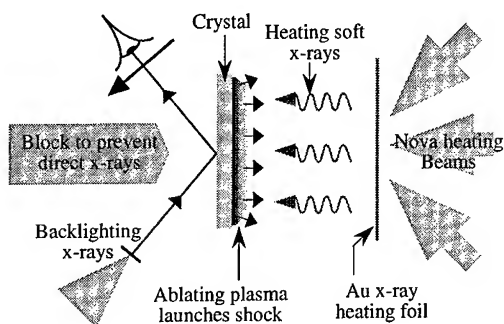


FIG. 1. Schematic illustration of the experiment.

gold foil. A 2 ns square laser pulse with up to 10 kJ of energy in the 3rd harmonic of Nd:glass ( $0.35\mu\text{m}$ ) is used to irradiate the foil. Approximately 10% of the laser energy is converted into soft x-rays.<sup>6</sup> X-rays from the rear of the gold foil volumetrically heat the front layer of a silicon (111) crystal.

Using the published spectral data<sup>6</sup> and cold mass absorption coefficients<sup>7</sup> we determine that 95% of the energy produced by the gold foil is absorbed within the first  $5\mu\text{m}$  of the silicon crystal. Temperatures of 15 eV are reached in the first  $2\mu\text{m}$  of the crystal generating pressures of order 0.5 Mbar.

The shock takes  $\sim 4$  ns to traverse a typical crystal thickness of  $40\mu\text{m}$ . When the shock is within 2 or 3 absorption depths of the rear surface an additional set of synchronized Nova beams are used to create a vanadium plasma that emits efficiently the helium-like resonance lines.<sup>8</sup> This line radiation is diffracted from the rear side of the crystal onto x-ray film and a temporally resolving x-ray streak camera.

### Experimental Data and Simulations

Example x-ray diffraction data from laser shocked silicon is shown in Fig 2. This data was taken using the VULCAN laser system at the Rutherford Appleton Laboratory, U.K.<sup>5</sup> Here a short,  $\sim 60$  ps Gaussian laser pulse was used to drive an approximately 100 kbar shock wave into the crystal.

This data should be compared to the simulated x-ray streak camera image in Fig 3. This simulation is intended to aid the interpretation of diffraction data such as Fig 2. The simulation consists of a hydrodynamics model<sup>9</sup> used to calculate the shock generating mechanism (x-ray heating, or in case of

Figs 2 & 3, laser heating) producing the shock and strain profiles in the solid. Once depth dependent strain profiles are calculated each timestep is post processed to give a diffraction profile as a function of time. The instrument response is then included to give a simulation of the experiment. The hydrodynamics model does not include material dependent physics other than a Mie-Gruneisen equation of state for silicon, and the diffraction code assumes a monochromatic x-ray source.

### Discussion

A reasonable degree of understanding of time-resolved x-ray diffraction from shocked compressed solids is indicated by the qualitative agreement between simulation, Fig 3, and the experimental data, Fig 2. Both the simulated and experimental data show diffraction simultaneously at the Bragg angle and at angles higher than Bragg angle. Here the Bragg angle is defined as the diffraction angle from the unperturbed solid. Diffraction at greater angles correspond to diffraction from a compressed lattice. As time evolves the diffraction profile at high angles rapidly shifts back towards the Bragg angle and decays to near zero compression 1 ns later. The backlighter has turned off in Fig 2 by this time. A few tens of picoseconds after the compression amplitude starts to decrease, we see that diffraction is now observed at angles lower than the Bragg angle. This indicates some part of the probed solid is in tension. As the compression decays the tensile strain increases until it plateaus at approximately 1 ns.

The diffracting x-ray beam and streak camera combination has a finite depth resolution within the crystal. In this case the probe depth normal to the diffracting surface is approximately  $11\mu\text{m}$ . At early times, *e.g.*,  $t = -0.4$  ns, the diffracting x-rays probe predominantly unperturbed crystal; beneath the crystal surface the compression wave is traveling towards the rear surface. Diffraction is principally from the unperturbed solid with a component shifted to higher angle strongly attenuated by photoelectric absorption. Diffraction at high angle gets brighter as the shock wave moves towards the rear surface as material ahead of the shock is reduced in thickness.

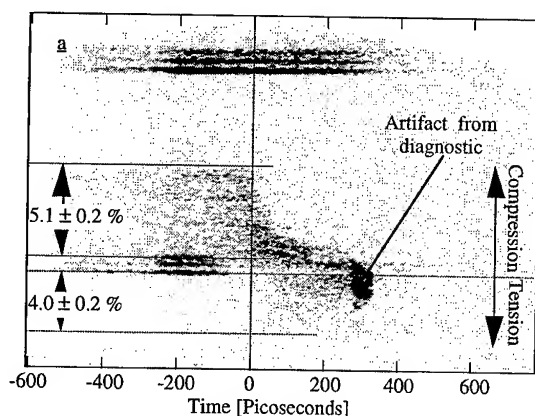


FIG 2. Diffraction record of laser shocked crystal of SiO (111). a incident radiation from a spectrometer.  $t=0$  is shock breakout.

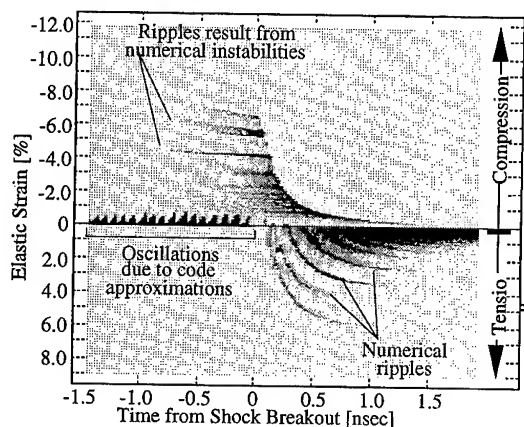


FIG 3. Simulation of Fig 2. Time  $t=0$  indicates shock breakout.

At shock breakout the entire volume being probed is strained, the unperturbed signal disappears; see  $t=0$ . Immediately following this a rarefaction wave forms and travels back into the solid. Tensile states are created as this rarefaction crosses a second rarefaction created at the front of the crystal as the pressure drive stops. Depth-dependent strain data is clearly demonstrated just after breakout as both tensile and compressive strains are observed.

Grady found the fracture strength of a brittle solid to be a function of strain-rate;<sup>10</sup> observed peak tensile strengths of solids may be lower than the ideal fracture strength of the solid due to the influence of material defects followed by spall.

In these experiments the strain rates are between  $10^8$  and  $10^{10} \text{ s}^{-1}$  and are several orders of magnitude higher than the strain rates reached by other techniques. The brittle fracture model of Grady<sup>11</sup>

indicates that the ideal strength of silicon should be reached at strain-rates above  $10^9 \text{ s}^{-1}$ . Analysis of Fig 2, where the strain rates are  $1 \times 10^9 \text{ s}^{-1}$ , indicates a peak tensile strain of 4.0% is reached. This implies a fracture strength of  $\sim 75 \text{ kbars}$  which is close to the strengths recorded from single crystal whiskers.<sup>12</sup>

## Conclusions

We have demonstrated x-ray diffraction can be used to investigate solids at high pressure in the transient environment of a shock wave. The measurement of the fracture strength of solids at ultra-high strain rates has been illustrated. A reasonable degree of understanding of the time-dependent diffraction patterns obtained has been achieved through the use of computer simulations. This has allowed us to assess the possibilities of the technique. With the development of a soft x-ray heating source to launch highly uniform shocks we plan to investigate shock fronts with a resolution previously unrealized.

## Acknowledgments

This work was performed under the auspices of the UK EPSRC and US DOE contract W-7405-ENG-48.

## References

1. A.L. Ruoff, H. Xia, Q. Xia, *Rev. Sci. Instrum.* **63**, 4342 (1992).
2. Graham, R.A. *Solids Under High-Pressure Shock Compression*. N Y, Springer-Verlag, (1993).
3. Q. Johnson *et al.*, *Nature* **231**, 310 (1971)
4. Q. Johnson *et al.* *Phys. Rev. Lett.* **29**, 1369 (1972)
5. J. S. Wark, *et al.*, *Phys. Rev.* **B35**, 9391 (1987); N. C. Woolsey, *D.Phil Thesis* (University of Oxford, 1994).
6. C. A. Back, *et al.* *JQSRT* **51**, 19 (1994); D. R. Kania, *et al.* *Phys. Rev.* **A46**, 7853 (1992).
7. B. L. Henke, *et al.*, *Atomic Data & Nuclear Data Tables* **27**, 1 (1982).
8. N.C Woolsey *et al.*, *Shock Compression of Condensed Matter*, Ed. S.C. Schmidt (1995).
9. J. P. Christiansen, *et al.*, *Comp. Phys. Comm.* **7**, 272 (1974).
10. D.E. Grady, J. Lipkin, *J. Geophys. Res. Lett.* **7**, 255 (1980).
11. D. E. Grady, *J. Mech. Solids* **36**, 353 (1988).
12. R. L. Eisner, *Acta Mett.* **3**, 414 (1955).

## QUASI-ISENTROPIC COMPRESSION OF LIQUID ARGON AT PRESSURE UP TO 500 GPa.

V. D. URLIN, M. A. MOCHALOV, O. L. MIKHAILOVA  
*RFNC-Institute of Experimental Physics, Arzamas-16, Russia*

### ABSTRACT

Density of argon has been measured upon isentropic compression in a shell accelerated by high explosives. The compressed argon pressure has been determined from its equation of state. It has been shown that in the density range up to  $7.5 \text{ g/cm}^3$  there are no anomalies in the argon compressibility.

Investigation of argon compressibility under very high pressures is interesting from the point of view of identifying structural phase transitions and also due to the lack of experimental data in this field. Work (1) shows no anomalies connected with a phase transition under quasi-isentropic compression of argon at 60 GPa up to the density of  $3.9 \text{ g/cm}^3$ . In xenon (2), under compression in a similar way at 200 GPa up to  $13 \text{ g/cm}^3$ , data have been obtained indicative of the phase transition from face-centered cubic (fcc) to hexagonal close-packed (hcp) structure which according to experiments on isothermal compression (3) occurs at  $8.37 \text{ g/cm}^3$ .

In the present work density of liquid argon in the pressure range from 90 to 500 GPa has been measured. In the experiment, using cylindrical explosive charge, the copper and tungsten casing with liquid argon inside it was accelerated towards the axis. Its trajectory was measured with the help of a gamma-graphic setup having short exposure time (4). The value of pressure was determined from gas-dynamic calculations using equation of state of materials contained in constructions and the equation of state for argon (5).

The equation of state for Ar describes solid and liquid phases of this material including the melting curve. It also takes into account thermal excitation of electrons. This equation of state describes practically all experimental data on the isotherm at 298 K (6) and shock compression (7) including the brightness temperature (5) of shock

wave front. Calculated isentropes, values of pressure and density at the boundary of the shell and argon are compared with the experiment in Fig. 1, there data on shock compression and the isotherm at 298 K are presented. The good coincidence of calculation and experiment on quasi-isentropic compression shows that in the pressure range up to 500 GPa and densities up to  $7.5 \text{ g/cm}^3$  in argon there is no anomalous increase in compressibility connected with the predicted in (8) transition from fcc to hcp structure under  $7.1 \text{ g/cm}^3$  and 230 GPa.

### References

1. L. A. Adamskaya, F. V. Grigoriev, V. D. Urlin et al, *Zh.Eksp.Ther.Fis.* **39** (1987) 647
2. V. D. Urlin, M. A. Mochalov, O. L. Mikhailova, *High Pressure Research* **8** (1992) 595
3. A. Jephcoat, H. Mao, L. Finger et al, *Phys. Rev. Lett.* **59** (1987) 2670
4. A. I. Pavlovski, T. D. Kuleshov, G. V. Sklizkov et al. *Dokl.Akad.Nauk SSSR* **160** (1965)68
5. F. V. Grigoriev, S. B. Kormer, V. D. Urlin et al, *Zh.Eksp.Ther.Fis.* **88** (1985) 1271
6. M. Ross, H. Mao, P. Bell, J. Xu, *J.Chem.Phys.* **85** (1986) 1028
7. M. Ross, W. Nellis, A. Mitchell, *Chem.Phys.Lett.* **68** (1979) 532
8. A. McMahan, *Phys.Rev.B* **33** (1986) 5344

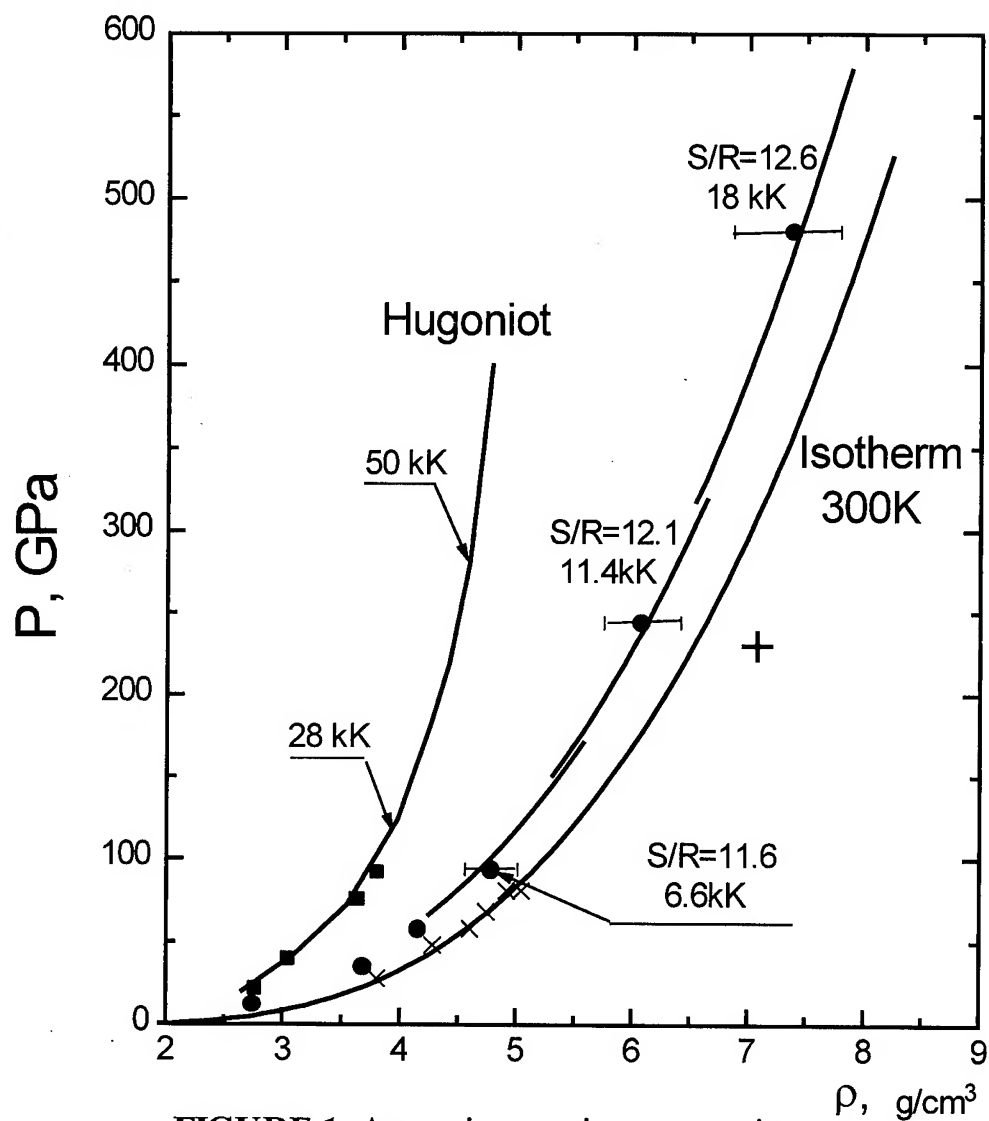


**FIGURE 1** Argon isentropic compression

Experiment:

(●) Isentrope of the present work

(x) Isotherm, M.Ross et al, J.Chem. Phys. (1987)

(■) Hugoniot, M.Ross et al, J.Chem. Phys. (1979)

Calculation:

(—) the present work

(+) fcc-hcp, McMahan A., Phys.Rev.B (1986)

## STRONG SHOCK WAVE EXCITATION BY Z-PINCH GENERATED SOFT X-RAYS.

M. LEBEDEV, K. DYABILIN, V. FORTOV, V. SMIRNOV,  
E. GRABOVSKIJ, K. DANILENKO, I. PERSIANTZEV,  
A. ZAKHAROV

*High Energy Density Research Center,  
Izhorskaya 13/19, Moscow, 127412, Russia*

### ABSTRACT

The behavior of matter under intensive soft x-radiation is considered. An impulse of x-radiation (about  $2 \cdot 10^{12}$  W/cm<sup>2</sup>) produced strong shock wave in the sample. The velocity of this shock wave was measured. A shock compression about 300 GPa in the lead target was achieved.

### Introduction

A fundamental problem in the use of concentrated fluxes of charged particles and laser light in the dynamic physics of high energy densities [1] is the substantial spatial nonuniformity of the power which is released. This nonuniformity disrupts the symmetry of the spherical compression of the fusion fuel [2] and hinders the excitation of plane shock waves in the experiments on the behavior of matter under extreme conditions. One of the most effective ways to solve this problem is to use x-ray emission from a plasma with an approximately thermal spectrum which arises when directed energy fluxes are applied to a target [3] or during the electrodynamics compression of cylindrical shells in a Z-pinch geometry [4]. Planar shock waves excited by this radiation, which are an extremely simple type of self-similar hydrodynamic flow [5], may be a more natural and rich source of experimental information on both the intensity of the incident x-radiation and of the thermophysical properties of matter under influence of this radiation with condensed targets.

Z-pinch plasmas produced in big installations by electrodynamic compression of cylindrical liners seem to be one of the most favorable candidates for the source of the such x-radiation.

This paper presents the measurements of the shock waves intensities generated by soft

x-radiation in Al, Sn, Fe and Pb targets. The scheme with the conversion of the laser to soft x-radiation, described in [6,7], is different from that used here: the soft x-radiation was induced by the dynamic compression and heating of the plasma in the cylindrical Z-pinch geometry in the ANGARA-5-1 installation [8,9]. As a result, the radiation pulse duration was about an order of magnitude more, with the power level being nearly the same as in [6,7].

### Experiment

The Z-pinch plasma radiates soft x-rays with a temperature on the order of 60-120 eV. The x-ray pulse duration was 30 ns FWHM [9]. This radiation was incident on a planar target positioned above the inner liner (at a distance 1 mm) [10]. The experimental set-up is shown in Fig. 1. The targets were made as step 16-32  $\mu$ m Al and 80-200  $\mu$ m Pb, or pure 180  $\mu$ m Pb, or stepped 16  $\mu$ m Sn and 180  $\mu$ m Pb plates being connected together. Such large thickness allowed the elimination of the thermal preheating of the target. The diameter of target was about 5 mm. The velocity of the shock wave was defined by the optical base method as the difference between the moments in the flashes of light emitted as the shock waves break out at the rear surface of a sample. The sample was imaged with the help of a  $f/10$  ( $f=1.5$  m) objective and

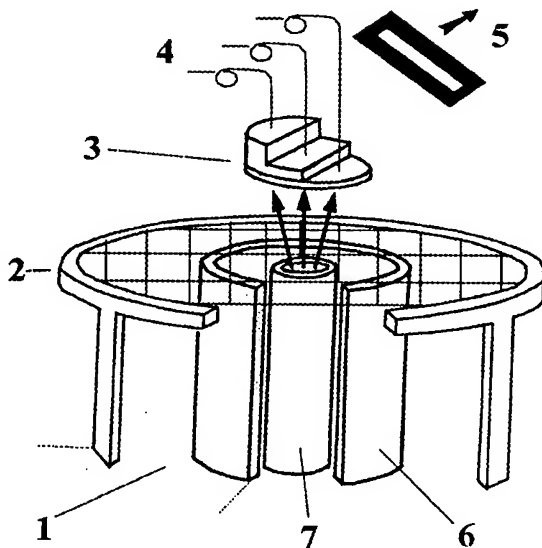


Fig.1 Experimental set-up: 1 - cathode; 2 - anode; 3 - step target; 4 - optical fibers; 5 - orientation of streak camera's slit; 6 - xenon annular (outer liner); 7 - inner liner (three arrow - soft x-radiation)

a  $f=3$  m objective with 2-fold magnification onto the photocathode of a SNFT-2 streak camera. Spatial resolution corresponds to 20 lp/mm in sample plane; temporal resolution less than 0.3 ns was provided. Optical fibers (quartz-polymer, length 80 m, 0.4 Db dumping, bandwidth 2 GGz) were also used, providing the high enough noise shielding from the experiment apparatus. The ends of a fibers (400  $\mu$ m in diameter) were butted directly against the free surfaces of the stepped sample. To eliminate the influence of the hard x-ray, which can induce the light inside the fibers, they were positioned inside the steel tube. Optical radiation from the fibers was detected by silicon photodiodes with a time resolution less than 1 ns. The time difference between the signal fronts was used, so temporal resolution of less than 1 ns in this fiber method was provided.

Typical streak camera records are shown in Fig. 2.

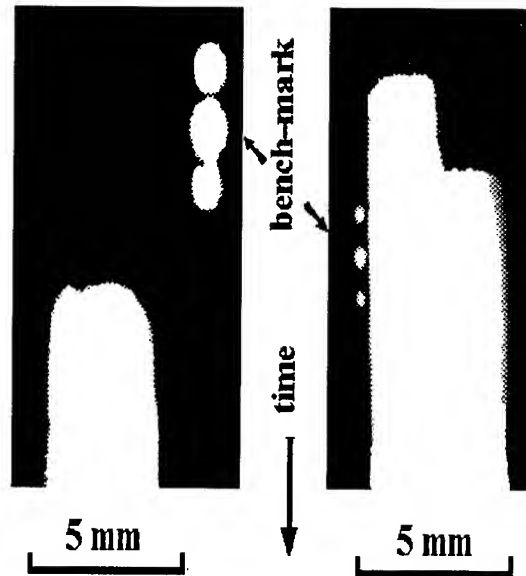


Fig.2 Streak camera records (positive) of shock break out from sample obtained in ANGARA-5-1 experiments: left - plane target: lead-180  $\mu$ m; right - stepped target: tin-16  $\mu$ m, lead-180  $\mu$ m. Between bench-marks - 13 ns

The averaged (over the target volume) shock wave velocity for Al plus Pb stepped target is  $(7.3 \pm 0.6) \cdot 10^3$  m/s for 80  $\mu$ m Pb thickness, and  $(4.6 \pm 0.3) \cdot 10^3$  m/s for 200  $\mu$ m. In accordance with the lead Hugoniot, this means that the shock compression pressures were 300 GPa and 90 GPa correspondingly [12]. In stepped tin plus lead target, a shock compression of lead (thickness 180  $\mu$ m) about 120 GPa was measured.

An important question was the spatial uniformity of the irradiated power. As shown in Fig. 2, the spatial uniformity of the shock front can be seen in streak photographs with plane and step samples. Let us define the uniformity as:

$$\xi = \frac{\Delta q}{q} \approx \frac{\Delta T}{T}$$

where  $q$  is radiative flux and  $T$  is time of shock front arriving at the free surface. Across the 4 mm diameter of shock sample we estimated the uniformity about 2 %.

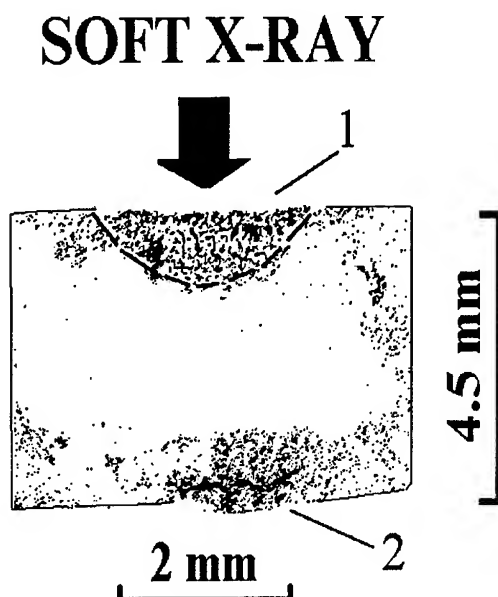


Fig. 3 Microphotography of a polished section of a pure iron target after intensive soft x-radiation interaction (power level  $0.5 \cdot 10^{12} \text{ W/cm}^2$ ): 1 - phase ( $\alpha - \epsilon$ ) transition region,  $P_h$  more than 13 GPa; 2 - split

In addition to the measurements of the shock-wave velocities, direct estimations of the size of the shock compression region were carried out. In these experiments, no internal liner was used. As it is known [11], in iron under the pressures of more than 13 GPa there exists a phase transition which can be visible on the metallic surface. Figure 3 shows such an image of the phase transition induced by the shock wave in our experiments. The pure iron target was positioned on the cathode, so the possible influence of the electron beams was excluded. One can see that in this experimental scheme, when only the external liner was compressed on itself, the typical radial radiative region size is about 2 mm. One should note that in a standard double-liner scheme, this size is to be somewhat more. But direct measurements in a standard scheme (double liners scheme) are impossible because of the target damage due to the strong radiative flux.

### Conclusion

The results presented above show that uniform intense shock waves can be generated by Z-pinch soft x-ray plasma radiation. The uniformity of shock wave is very high. At a flux power about some  $\text{TW/cm}^2$ , a shock pressure of some hundreds GPa was achieved.

### References

1. S. Anisimov, V. Fortov and A. Prohorov *Sov. Phys. Usp.* **27** (1984) 181.
2. J. J. Duderstadt, *Inertial Confinement Fusion* (New York, 1982).
3. D. L. Matthews et al., *J. Appl. Phys.* **54** (1983) 4260.
4. P. J. Turchi and W. L. Baker, *J. Appl. Phys.* **44** (1973) 4936.
5. Ya. B. Zel'dovich and Yu. P. Raizer, *Physics of Shock Waves and High Temperature Hydrodynamic Phenomena*, (Academic Press, New York, 1966).
6. T. Endo et al., *Phys. Rev. Lett.* **60** (1988) 1022.
7. Th. Lower and R. Sigel, in *Proc. 7th Int. Workshop of the Physics on Nonideal Plasma*, (Markgrafeneheide, 1993).
8. V. Smirnov et al., in *Proc. 8th Int. Conf. BEAMS-90*, (Novosibirsk, 1990).
9. V. Gasilov, S. Zakharov and V. Smirnov, *JETP Lett.* **53** (1991) 83.
10. E. Grabovskij et al., *JETP Lett.* **60** (1994) 3.
11. I. Rinehart and J. Pearson, *Behavior of Metals under Impulsive Loads*, (ASM, Cleveland, 1954).



## AUTHOR INDEX

Abakshin E.V.	950, 960	Bindal M.M.	346
Abe F.	875	Bini R.	375
Abgarowicz E.	247	Birzer Ch.	644
Adamczyk J.	264	Blank V.D.	325, 430, 707, 710, 713, 719
Afanas'ieva I.N.	690	Blinov V.M.	195
Akahama Y.	360	Bochechka A.A.	121
Akella J.	387	Bock W.J.	78
Aksenonkov V.V.	719	Bockowski M.	264, 596
Alekseev V.A.	552	Boehler R.	302, 357
Alliez J.	831	Bogatyeva G.P.	250, 328
Amaya K.	498	Boned C.	317, 831
Andersson O.	697	Bordet P.	438
Anfilogov V.N.	960	Borovikov H.F.	231
Angilella G.G.N.	685	Bosc F.	660
Aoki K.	241, 354, 849	Bozhko S.A.	127
Arabas J.	60, 892	Brauninger S.	435
Arnold Z.	51, 733	Brazhkin V.V.	285
Asadov S.K.	351	Brister K.E.	363
Asano T.	815	Buchner T.	837
Asbrink S.	414	Bucki J.J.	165
Asfaw A.	989	Buga S.G.	35, 665, 707, 713
Asokan S.	776	Bugaetz O.	211
Atouf A.	405	Bukowski Z.	692
Babuchowski A.	898	Bulgarevich D.S.	818
Babushkin A.N.	606	Buontempo U.	785
Bacmann M.	457	Buravova S.	944
Badjukov D.D.	960	Butko N.B.	667
Bak J.	618	Buzare J.Y.	411
Bakker K.	758	Canny B.	366
Bakon A.	247	Cantarero A.	612
Balny C.	872	Carrier H.	788
Baranowski B.	3, 524, 536	Cauble R.	969, 989
Baranowski J.M.	264	Chang H.-C.	824
Barciszewski J.	855	Chen N.H.	517
Barta P.	828	Chernoutsan A.	924
Batsanov S.S.	430	Chernysheva E.V.	399
Bauer H.J.	736	Chervin J.C.	366
Bazaliy G.A.	328	Chiarotti G.L.	846
Beh C.Y.	478	Chidambaram R.	882
Beigelzimer Ya.E.	141, 150, 162	Chmurski K.	804
Beke D.L.	173	Chong T.C.	420, 478
Belogub E.V.	960	Chopra R.	346
Belonoshko A.B.	918, 921	Christensen N.E.	609, 725
Beloshenko V.A.	153	Chvanski P.	275
Belousov I.S.	238	Contreras S.	654, 657
Belyavina N.N.	127	Couty R.	314
Bernasconi M.	846	Cudzilo S.	957
Bezhenar N.P.	127	Czarnota-Kubaszewska I.	41
Bhaumik S.K.	115		

Da Silva L.B.	969	Frasunyak V.M.	493
Danilenko K.	994	Freim J.	931
Danilenko V.	211	Freire P.T.C.	573
Daridon J.L.	317, 791	Frommeyer G.	198
Datchi F.	54	Fruchart D.	457
Deguchi K.	475	Fruchart R.	460
Demazeau G.	255, 249, 275, 278	Fujisawa H.	745
Denisov V.N.	713	Fukunaga O.	228
Derevskov A.Yu.	48	Funamori N.	183, 381
Desgreniers S.	130, 363	Furuta H.	815
Devyatykh G.G.	692	Gasanly N.M.	427
van Dijk N.H.	758	Gauthier M.	336, 372
Divakar C.	115	Gavaleshko N.P.	493
Dmitriev D.R.	399	Gavriliuk A.G.	208, 739, 742
Dmochowski J.E.	621	Gebhardt W.	644
Dmowski L.H.	657	Gerasimovich A.V.	29
Dobrikov A.A.	192, 195	Gerward L.	549
Dobromyslov A.V.	124, 393, 950	Ghandehari K.	441, 539
Dolgikh G.V.	393	Gierlotka S.	211
Domareva A.S.	192, 195	Gladkovskii S.V.	162
Downs R.T.	682	Gohshi Y.	565
Dreger Z.A.	799	Golosnoy I.O.	986
Drickamer H.G.	799	Goncharov A.	427, 533
Dubitskiy G.A.	707, 719	Goncharova V.A.	396, 399
Dubitsky G.A.	325, 713	Goni A.R.	423, 612, 634, 647
Dubrovinsky L.S.	918, 921	Gonnet V.	255
Dubrovinsky N.A.	921	Gontar A.G.	559
Dugandzic I.	736	Gonzalez J.	445
Dumez M.C.	102	Gonzalez Penedo A.	438
Dunstan D.J.	621	Gonzalez-Jimenez F.	445
Duraj R.	463	Goossens K.	863, 895
Dyabilin K.	994	Gopal E.S.R.	346, 776
Eberl K.	634, 647	Gorczyca I.	609
Edlund U.	716	Gorecka K.	892
Efros B.M.	141, 152, 159, 162	Grabovskij E.	994
Eggert J.H.	533	Greene R.G.	441
Ejchart W.	834	Griebel E.	644
Ekimov E.A.	231	Grigoriev N.M.	29
Elf F.	343	Grima P.	445
Endo S.	32, 475, 498	Grin Yu.	435
Ernst S.	634	Grishkov V.N.	399
Et-Tahir A.	831	Grochowska A.	892
Faupel F.	178	Gromnitskaya E.L.	285
Filipek S.M.	736	Gryaznov V.G.	208
Filonenko V.P.	107, 110, 208	Gryko D.T.	804
Flower E.C.	135	Grzegory I.	14, 264, 596
Focher P.	846	Guillot M.	460
Fonberg-Broczek M.	892, 902	Gupta S.C.	730, 882
Fortov V.	994	Gusev A.V.	692
Fournes L.	269	Gustkiewicz J.	909
Franck E.U.	809	Gvyazdovskaya V.L.	328
Franse J.J.M.	758	Haga Y.	767
Fransson A.	716	Hagino T.	487

Hahn B.	644	Jia X.P.	219, 565
Haines J.	405	Jodl H.J.	375
Hama J.	745	Johnels D.	716
Hammel B.A.	969	Jonas J.	860
Hanfland M.	360, 366, 372	Jones S.	432
Hansen O.P.	641, 664	Joshi K.D.	882
Hara K.	818	Jovanic B.R.	571
Hausermann M.	372	Jun J.	264, 469, 596
Hausermann D.	360, 366	Jung A.	496
Hayakawa S.	565	Jung D.Y.	269
Hearne G.R.	454	Jurczak J.	804, 855, 892
Heesemann A.	178	Jyoti G.	882
Hemley R.J.	505, 533, 682	Kabanov A.V.	692
Heremans K.	863, 895	Kagayama T.	487, 753
Hinze E.	198	Kagi H.	258, 565
Hirai H.	934	Kalitkin N.N.	983
Holmes N.C.	521, 969, 979	Kamarad J.	51, 733
Holzappel W.B.	69, 384, 576, 579	Kamat A.S.	882
Honda M.	32	Kamata A.	767
Honig J.M.	454	Kamenev K.V.	51, 351, 733
Hopkinson M.	75	Kamenev V.I.	351
Hori H.	32	Kanda Y.	615
Horikoshi K.	869, 875	Kang Y.-S.	99
Hotta E.	466	Kaniowski T.	457, 828
Hozumi S.	189	Kapieka A.	907
Hu Z.P.	417, 420, 478	Karlowski K.	892
Hwang L.-W.	603	Kashiwakura T.	767
Ibarra M.R.	733	Kato C.	869
Idesman A.V.	144	Kato M.	866
Ifuku Y.	889	Katrusiak A.	472
Ignatchenko O.A.	606	Katsura K.	258
Ikegaya A.	99	Kawamura H.	360
Il'nitskaya G.D.	328	Kazantseva N.V.	950
Imada S.	32	Kenney J.F.	843
Inaba A.	716	Kerner W.	644
Ingalls R.	289, 432	Kesavan P.C.	882
Irkaev S.M.	739, 742	Khantuleva T.A.	947
Ishii T.	764	Khlybov E.P.	690, 692
Isnard O.	457	Kikegawa T.	408
Itie J.P.	372, 438, 445	Kindo K.	32
Ivakhnenko S.A.	238	Kislyakov S.S.	950
Ivakhnenko S.M.	244	Kitazawa H.	451
Ivanov A.N.	369	Klehe A.K.	673, 679
Ivanova L.A.	960	Klimin S.A.	231
Ivdenko V.A.	430	Klipstein P.C.	629
Ivlev A.N.	713	Klug D.D.	530
Jacobsson P.	716	Knap W.	657
Jakiela R.S.	621	Kobayashi Y.	475
Jaman P.M.	115	Kobbi F.	654
Jankowiak R.	824, 878	Kochetkov V.N.	690
Jaroszewicz A.	837	Kocks U.F.	138
Jemielniak R.	45	Kodama T.	222
Jepsen O.	612	Kolesnikov A.I.	369

Kolakowski P.	898	Li T.	441
Kometani N.	818	Li W.	219, 222, 565
Komorowski P.	840	Li Z.S.	99
Konakova I.	159	Lin E.E.	937
Kondo K-I	934	Lin F.	272
Konstantinova T.E.	118	Lipkowski P.	804
Kooi M.E.	305	Litvinov B.V.	950, 960
Korablev S.F.	121	Litwin-Staszewska E.	654, 657
Kornilov A.V.	63	Liu W.N.	272
Kotljarov V.A.	960	Liu X.Y.	272
Koto K.	475	Loginova O.B.	244
Kovalenko G.V.	950	Lojkowski W.	186, 189
Kozlov E.A.	950, 960	Loladze L.V.	159, 162
Kozlov G.V.	153	Looney C.	673
Kozlovsky V.N.	960	Lotkov A.I.	399
Kozlowski M.S.	165	Loubeyre P.	54
Kozuka Y.	767	Lucznik B.	264
Kraak W.	641, 667	Lundin A.	697
Kravchenko V.	664	Luo H.	441
Kremer R.	423	Lyafer E.I.	118
Kruglov A.A.	950	Lyapin A.G.	285
Krukowski S.	264	Luzny W.	828
Krupski M.	411	Ma Y.Z.	702
Krzyzaniak A.	855	Machowski P.	840
Kucinski T.	837	Maciejowska S.	247
Kudrenko Yu.A.	885	Maghenzani R.	90
Kulik O.G.	308	Magiera A.	90
Kulnitskiy B.A.	710	Malik S.K.	764
Kuok M.H.	417, 420, 478	Mao H.-K.	505, 533, 682
Kusaba K.	408	Maranda A.	957
Kuskov O.L.	913	Margolin L.G.	135
Kutcherov V.	924	Marin-Ayral R.M.	102
Kuzenkov S.	211	Markiv V.Ya	127
Kuzmicheva G.M.	690	Martem'yanov A.N.	393
Labes P.	791	Martinez G.	591
Lafon F.	275	Masuda Y.	258
Lagarec K.	130	Masumoto K.	615
Lagourette B.	791, 831	Matsui Y.	241
Lang J.M.	799	Matsumoto T.	451
Lange R.	872	Matsushita A.	451
Lapshin V.P.	399	Maudlin P.J.	138
Largeteau A.	269, 275	Mavrin B.N.	713
Lazos-Martinez R.J.	84	Maydanyuk A.P.	225
Lebedev M.	994	Mazin I.I.	533
Lee R.W.	969, 989	Mazur A.	165
Leger J.M.	405	McKittrick J.	931
Lemos V.	573	Medvedkin V.A.	937
Leshchuk A.A.	225	Meingast C.	716
Leszczynski M.	231, 596	Mescheryakov Yu.I.	947
Letnikov F.A.	960	Metcalf P.A.	454
LeToullec R.	54	Michels J.P.J.	794
Levitas V.I.	147	Mikhailova O.L.	992
Li L.P.	773	Minamino Y.	189

Minina N.Ya.	641, 664, 667	Osotov V.I.	493
Minomura S.	615, 624	Ostaszewski R.	804
Miraglia S.	457	Ostrovskaya L.Yu.	244
Miroshnichenko S.V.	38	Otto J.W.	198
Mitchell A.C.	521	Palewski T.	690
Miyamoto S.	32	Palosz B.	211, 231
Miyamoto Y.	99	Parrinello M.	846
Mochalov M.A.	992	Pasternak M.P.	454
Mohan M.	115, 390	Paul W.	585
Molinar G.F.	81, 90	Pere J.	314
Molodov D.A.	186	Perevertailo V.M.	244
Montigaud H.	255	Perlin P.	596
Morawski P.	411	Perry T.S.	969
Mori Y.	615	Persans P.D.	600, 603
Mori N.	466, 767	Persiantzev I.	994
Moriguchi H.	99	Persson P.-A.	697, 716
Mosser V.	654, 657	Petrovsky E.	907
Moya E.	445	Petrusha I.	333
Mukherjee S.	25	Petrusha I.A.	121, 562
Munoz V.	612	Peun T.	198
Nagata S.	487	Peytavin Y.	275
Nagorny P.A.	328	Phillion D.W.	969
Nakai S.	767	Pina E.	84
Napiorkowska B.	892	Pitz W.J.	963
Nardone M.	785	Pilla O.	573
Narozhnyj V.N.	692	Plotyanskaya S.A.	325
Naslain R.	278	Podlasin S.	892, 898
Natkaniec I.	369	Podoba A.P.	568
Nayar R.K.	346	Pohl J.	907
Nellis W.J.	521, 931	Polian A.	372, 438, 445
Nevstruyev G.F.	328	Polotnyak S.B.	144
Ng A.	974	Poon H.	25
Niedbalska A.	247	Popov M.Yu.	707, 713, 719
Niwa E.	615	Popova S.V.	285
Nizhankovskii V.I.	692	Porowski S.	264, 596, 892, 898
Niziol S.	457, 460, 828	Postorino P.	785
Nomura M.	767	Prins A.D.	621
Nomura T.	99	Pruzan Ph.	366
Novikov N.V.	29, 225, 250	Pucci R.	685
Novikov S.A.	937, 939	Pudalov V.M.	63
Nowaczewski J.	957	Pushkov V.A.	939
Obyden S.K.	231	Qin L.	417
Ochiai A.	466, 767	Quetel C.	275
Ohashi N.	228	Radenkovic R.	571
Ohbayashi S.	916	Radhika Rao M.V.	481
Ohtani T.	183	Radomski M.	902
Okuda M.	258	Ramasesha S.K.	481
Okunuki Y.	767	Rambert N.	54, 779
Oleinik N.A.	328	Ramesh K.	776
Olsen J.S.	549, 641, 664	Ratzke K.	178
Ono F.	32	Reddy N.R.S.	824, 878
Oomi G.	487, 706, 753	Ree F.H.	963
Orlov V.K.	950	Reichmann H.J.	357

Reig P.	278	Shen Y.R.	576, 579
Reisinger T.	644	Shen Z.X.	417, 420, 478
Reps A.	898	Shevchenko A.D.	688
Rewaj T.	411	Shimizu K.	498
Riedel M.R.	35	Shimomura O.	360, 408
Rikken G.L.J.A.	591	Shinn H.	916
Robert J.L.	654, 657, 660	Shirase N.	624
Roitsin A.B.	250	Shishkova N.V.	159, 162
Romodanov V.A.	552	Shmegeera S.V.	568
Ross M.	521	Shulhzenko A.A.	121
Ross R.	924	Shulzhenko A.A.	261
Rostocki A.J.	87	Shvedov L.K.	144
Rozenberg G.Kh.	454	Shvindlerman L.S.	186
Rubens P.	895	Sicart J.	660
Ruddle Ch.	387	Sidorov V.A.	739
Ruoff A.L.	25, 441, 511, 539	Siegoczynski R.M.	834
Rylov S.V.	552	Sienkiewicz A.	57
Ryzhkov Yu.F.	552	Sikka S.K.	730, 882
Sadlo M.A.	621	Silvera I.F.	517
Saffian B.	641	Silvestri M.R.	603
Sahota M.S.	138	Singer K.E.	621
Saidi Z.	371	Singh A.K.	115, 390, 481
Saint-Guirons H.	791	Singh B.P.	346
Sakashita M.	354, 849	Singhal S.K.	346
Sakurai Y.	487	Siringo F.	685
Salvi P.R.	375	Sitaud B.	54, 314, 779
Salacinski R.	247	Slobodina V.G.	153
Salanski P.	804, 855, 892	Sly J.	621
San Miguel A.	438, 445	Small G.J.	824, 878
Sanchez J.P.	269	Smehknov A.A.	261
Sanetra J.	828	Smekhnov A.	211
Sangunni K.S.	776	Smekhnov A.A.	244
Saparin G.V.	231	Smeller L.	863, 895
Sasakura T.	745	Smirnov L.S.	369
Savin A.	641, 664, 667	Smirnov V.A.	48
Savin V.I.	552	Smirnov V.	994
Saxena S.K.	921	Smith G.S.	387
Scheerboom M.I.M.	527, 794	Smorawsinska M.	869
Schilling J.S.	673, 679	Sokolov A.N.	261
Schotz G.F.	644	Soldatov A.	697, 716
Schouten J.A.	305, 527, 794	Solozhenko V.L.	255, 338, 343
Schroeder J.	600, 603	Sooryakumar R.	618
Schulte O.	405	Sosin T.P.	75, 651
Schwarz D.K.	736	Soubeyroux J.L.	457
Schwarz U.	427, 435	Souers P.C.	963
Sciezynska H.	892, 902	Spuskanyuk A.V.	141, 150
Scuratnik Ya.B.	552	Stalgorowa O.V.	285
Serebrennikov V.L.	885	Steenstrup S.	549
Serebryanaya N.R.	430, 707, 719	Stepanov G.N.	208, 739, 742
Serghiou G.	357	Sterer E.	517
Sharupin B.	333	Stepinski P.	75, 651
Shchennikov V.V.	48, 490, 493	Stradling R.A.	621
Shen A.H.	35	Stroka A.	536

Strunnikov V.M.	552	Timofeev Yu.A.	682
Struzhkin V.V.	682	Tinoco T.	445
Su W.H.	203, 272, 773	Tkach V.N.	559
Subramanian S.	618	Tkacz M.	543
Sugano T.	228	Todris B.M.	351
Suharevskii B.Ya	292	Tonks D.L.	941
Sui Yu	203	Tosatti E.	846
Suito K.	745, 916	Trankovskaya L.D.	156
Sukhoparov V.A.	63	Trebinski R.	957
Sumi H.	815	Truffier J.L.	314
Sundberg M.	108	Trzcinski W.	957
Sundquist B.	697, 716	Trzeciakowski W.	75, 651
Suresh N.	730	Tse J.S.	530
Sushko Yu.V.	821	Tsiok O.B.	285, 742
Suski T.	596, 654	Tsoi P.A.	939
Suzuki T.	466, 767	Tsuchida I.	258
Svane A.	609	Tsurumi T.	228
Svirid A.	333	Turkevich V.Z.	308, 311
Syassen K.	423, 427, 435, 612, 634, 647	Tyagur Yu.	469, 651
Synkov S.G.	156	Uchida T.	183, 381
Synkov V.G.	38, 156	Uliivi L.	375
Syono Y.	408	Ulrich C.	612, 647
Szafranski A.W.	546	Umarji A.M.	481
Szczepek J.	57, 892	Urbanovich V.S.	110
Szymanski A.	247	Urlin V.D.	992
Szytula A.	463	Usha Devi S.	115
Takabatake T.	764	Uwatoko Y.	764
Takahashi H.	466, 767	Vaills Y.	411
Takanabe R.	235	Varyukhin V.N.	141, 153, 195
Takarabe K.	615, 624	Vasiliev V.I.	552
Takeda N.	806	Vassiliou J.K.	198
Takemura K.	241, 748	Venkateswaran U.D.	618
Takeuchi T.	32	Venugopal V.	882
Taluts G.G.	950	Verderber R.R.	135
Taluts N.I.	124, 950	Ves S.	423
Tan Y.T.	420	de Visser A.	758
Tang J.	451	Voronin G.A.	562
Tang S.H.	417, 420, 478	Wachter P.	496
Tanguy B.	255	Wakatsuki M.	219, 222, 235, 258, 565
Taniguchi Y.	866	Wang F.	289, 432
Tanihata K.	99	Wang X.B.	417, 420
Tatyanin Ye.V.	710	Wang Y.	235
Tchurbaev R.V.	124	Warchulska J.	690
Tedenac J.C.	104	Wark J.S.	989
Teduka H.	767	Waskowska A.	414
Teisseyre H.	596	Wei Q.	773
Teplinskaya V.M.	950	Weir S.T.	387, 521
Terentyev S.A.	238	Wiegand G.	809
Thevenin Th.	54, 314, 779	Will G.	343, 346
van Thiel M.	963	Windyga B.	892, 902
Thissell W.R.	941	Winzenick M.	384
Thomas P.	882	Wisniewski P.	654

Wisniewski R.	87, 90, 834, 837, 840	Yusa H.	241
Witczak P.	45	Zach R.	457, 460
Witczak Z.	45, 164, 396	Zackiewicz A.	78
Witek A.	264, 568	Zagorska M.	828
Wlodarczyk E.	957	Zakharov A.	994
Wolanin E.	366	Zanevsky O.A.	238
Wolinski T.R.	78	Zavadskii E.A.	292, 351
Woolsey N.C.	989	Zduniak A.	657
Wright S.I.	138	Zekovic Lj.D.	571
Wroblewski .M.	264	Zeman J.	591
Wu H.M.	878	Zhao X.D.	272
Wyrzykowski J.	189	Zhao X.-S.	600
Xans P.	317, 788	Zheng F.L.	203
Xu D.P.	203	Zhou T.	423
Yagi T.	183, 381	Zhugin Yu.N.	953, 960
Yamamoto T.	889	Zibrov I.P.	107, 110
Yamane T.	297	Zigone M.	591
Yamawaki H.	241, 354, 849	Zou G.T.	702
Ye S.	788	Zurek A.K.	941
Yokohama Y.	767	Zwolinski J.	60
Yoshida I.	487	Zmujdzian L.	898